Maxillofacial Cone Beam Computed Tomography

Principles, Techniques and Clinical Applications

William C. Scarfe
Christos Angelopoulos
Editors

Springer

Maxillofacial Cone Beam Computed Tomography

William C. Scarfe
Christos Angelopoulos
Editors

Maxillofacial Cone Beam Computed Tomography

Principles, Techniques and Clinical Applications

Springer

Editors
William C. Scarfe
Division of Radiology and Imaging Science
Department of Surgical/Hospital Dentistry
University of Louisville School of Dentistry
Louisville, KY
USA

Christos Angelopoulos
Aristotle University of Thessaloniki
Thessaloniki
Greece

Columbia University
College of Dental Medicine
New York City, NY
USA

ISBN 978-3-319-62059-6 ISBN 978-3-319-62061-9 (eBook)
https://doi.org/10.1007/978-3-319-62061-9

Library of Congress Control Number: 2017960175

Printed on acid-free paper

This Springer imprint is published by Springer Nature
The registered company is Springer International Publishing AG
The registered company address is: Gewerbestrasse 11, 6330 Cham, Switzerland

Foreword

“Cone Beam” refers to the divergence of the X-ray beam following its origin at the anode of the X-ray tube. This being the case, dentists have employed “Cone Beam Technology,” since 1896, just a few weeks following the discovery of the X-ray on November 8, 1895. The images produced with this technology, until relatively recently, have only been two-dimensional (2-D): intraoral bitewings and periapical images of the teeth, and extra-oral projections of the jaws and head. To be pedantically correct, only round collimation leads to a conical beam; rectangular collimators result in a pyramidal beam in these circumstances, but the essence of a divergent beam is held in common.

Commercial Cone Beam Computed Tomography (CBCT) was initially designed in the early 1980s for three-dimensional (3-D) angiography, pairing a C-arm to a circular image intensifier and did actually use a “Cone Beam.” The hundreds of individual images that are integrated to provide a 3-D dataset are similar to their individual 2-D predecessors. The development of maxillofacial CBCT awaited the development of inexpensive but powerful computers, appropriate algorithms and software, resilient X-ray tubes that could fire hundreds of times in a matter of a fraction of a minute, and detectors that could acquire those images rapidly without afterglow from the prior frame. It was the year 2000 before the first CBCT system was cleared by the Food and Drug Administration - Center for Devices and Radiological Health (FDA-CDRH) for sale and use in the United States. In less than two decades, many different maxillofacial CBCT units have become available with few manufacturers of dental X-ray equipment yet to become involved in this market. CBCT is now a valued and validated adjunct to dental and dental specialty practice throughout the world.

This book represents the first comprehensive treatment of maxillofacial CBCT. It is not merely an atlas of normal anatomy or of pathological processes. The book is designed for advanced general dentistry and for all of the clinical dental specialties, both as a reference for existing practitioners and also as a standard text for residents in advanced dentistry and the dental specialties. Drs. Scarfe and Angelopoulos have brought together top clinicians, researchers, and engineers from around the world to compile this work. It provides timely insight and vision into the basics of CBCT physics, engineering, radiation safety, quality assurance, image selection, parameter selection, image creation, image and volume post-processing, clinical usage, interpretation of anatomy, artifact and pathological processes, and of reporting findings.

Allan G. Farman, B.D.S., Ph.D., D.Sc., M.B.A.
Emeritus Professor, The University of Louisville School of Dentistry
Louisville, KY, USA

Independent Consultant in Maxillofacial Imaging Science
Chicago, IL, USA

Contents

About the Editors

Professor Scarfe graduated from the University of Adelaide School of Dentistry in 1982 and was awarded Fellowship in the Royal Australasian College of Dental Surgeons in 1986. He graduated from the University of Texas Health Science Center at San Antonio with a Certificate in Dental Diagnostic Science and Master's in Oral and Maxillofacial Radiology and has been on the faculty at the University of Louisville School of Dentistry since 1993. Dr. Scarfe is a Diplomate of the American Board of Oral and Maxillofacial Radiology and a registered specialist in Oral and Maxillofacial Radiology in the Commonwealth of Kentucky. He is Past Treasurer and currently President-elect of the *American Academy of Oral and Maxillofacial Radiology*, immediate past editor of the Radiology Section of *Oral Surgery, Oral Medicine, Oral Pathology, and Oral Radiology*, and Past-Vice President and Past North American Regional Director of the *International Association of Dento-Maxillofacial Radiology*. He is Fellow of the International Team for Implantology (ITI). He is a reviewer for over 30 journals including the *Journal of the Canadian Dental Association, Journal of Dento-Maxillo-Facial Radiology*, the *American Journal of Orthodontics and Dentofacial Orthopedics*, and *The Angle Orthodontist*. Dr. Scarfe has published extensively on cone beam computed tomography (CBCT) including recent consensus statements on general and specific use guidelines and discipline-specific applications of CBCT. He presents internationally as well as nationally and is active in research on the clinical applications of CBCT imaging.

Dr. Angelopoulos is a graduate of the Aristotle University, School of Dentistry, Thessaloniki, Greece. His postdoctoral training includes a 2-year internship in Oral Surgery (Aristotle University) and a 1-year GPR program (Truman Medical Center, Kansas City). In addition, he has completed a 3-year Oral and Maxillofacial Radiology residency program at the University of Missouri-Kansas City, School of Dentistry, and he was awarded the M.S. degree in Oral Biology. Dr. Angelopoulos is a diplomate of the American Board of Oral and Maxillofacial Radiology and a fellow of the International College of Oral Implantologists. He has held university appointments at the University of Missouri-Kansas City, School of Dentistry (assistant professor 08/02–02/07) and at Columbia University, College of Dental Medicine (associate professor and director of Oral and Maxillofacial Radiology 03/07–12/10). Currently, he is an associate professor at the Aristotle University of Thessaloniki, Greece, and an adjunct professor of Oral and Maxillofacial Radiology at Columbia University. Dr. Angelopoulos is the past president of the American Academy of Oral and Maxillofacial Radiology (AAOMR) and has served as the Executive Director of this organization for the last 4 years. He has served in several leadership positions and committees at the AAOMR as well as IADMFR (International Association of Dento-Maxillofacial Radiology). Last, he is a past Associate Editor of OOOO (the official journal of the AAOMR). He has published over 40 scientific papers and has spoken in several conventions and CE courses, nationally as well as internationally, on a variety of radiology topics. Moreover, he is a frequent speaker for the ADA annual conventions.

Contributors

Chapter 2

William C. Scarfe, B.D.S., F.R.A.C.D.S., M.S. Division of Radiology and Imaging Science, Department of Surgical/Hospital Dentistry, University of Louisville School of Dentistry, Louisville, KY, USA

Allan G. Farman, B.D.S., Ph.D., D.Sc., M.B.A. Emeritus Professor, The University of Louisville School of Dentistry, Louisville, KY, USA

Independent Consultant in Maxillofacial Imaging Science, Chicago, IL, USA

Roberto Molteni, Ph.D. Skanray Europe srl, San Lazzaro di Savena, Bologna, Italy

Christos Angelopoulos, D.D.S., M.S. Aristotle University of Thessaloniki, Thessaloniki, Greece

Columbia University, College of Dental Medicine, New York City, NY, USA

Chapter 3

Christos Angelopoulos, D.D.S., M.S. Aristotle University of Thessaloniki, Thessaloniki, Greece

Columbia University, College of Dental Medicine, New York City, NY, USA

Ruben Pauwels, Ph.D. Department of Radiology, Faculty of Dentistry, Chulalongkorn University, Bangkok, Thailand

OMFS-IMPATH Unit, Department of Imaging and Pathology, Oral Imaging Center, Biomedical Sciences Group, KU Leuven, Leuven, Belgium

Allan G. Farman, B.D.S., Ph.D., D.Sc., M.B.A. Emeritus Professor, The University of Louisville School of Dentistry, Louisville, KY, USA

Independent Consultant in Maxillofacial Imaging Science, Chicago, IL, USA

Chapter 4

Christos Angelopoulos, D.D.S., M.S. Aristotle University of Thessaloniki, Thessaloniki, Greece

Columbia University, College of Dental Medicine, New York City, NY, USA

Emmanuel Mazinis, D.D.S., M.S., Ph.D. Private Practice, Veria, Greece

Otávio Umetsubo Tomovale—Centro de Diagnóstico por Imagem, São José dos Campos, SP, Brazil

Zhimin Li, D.D.S., Ph.D. Department of Oral Radiology, Jilin University School and Hospital of Stomatology, Chang Chun, Jilin Province, China

Wael Aboelmaaty, B.D.S., M.S., Ph.D. Faculty of Dentistry, Department of Oral Medicine and Periodontology, Mansoura University, Mansoura, Egypt

Allan G. Farman, B.D.S., Ph.D., D.Sc., M.B.A. Emeritus Professor, The University of Louisville School of Dentistry, Louisville, KY, USA

Independent Consultant in Maxillofacial Imaging Science, Chicago, IL, USA

Chapter 5

Roberto Molteni, Ph.D. Skanray Europe srl, San Lazzaro di Savena, Bologna, Italy

Pierluigi Mozzo, Ph.D. Pixirad Imaging Counters srl, Verona, Italy

University of Verona, Verona, Italy

Ruben Pauwels, Ph.D. Department of Radiology, Faculty of Dentistry, Chulalongkorn University, Bangkok, Thailand

OMFS-IMPATH Unit, Department of Imaging and Pathology, Oral Imaging Center, Biomedical Sciences Group, KU Leuven, Leuven, Belgium

Allan G. Farman, B.D.S., Ph.D., D.Sc., M.B.A. Emeritus Professor, The University of Louisville School of Dentistry, Louisville, KY, USA

Independent Consultant in Maxillofacial Imaging Science, Chicago, IL, USA

Predrag Sukovic, Ph.D. Xoran Technologies, Ann Arbor, MI, USA

Jack Fisher Artistic Smiles Orthodontics, Cordova, TN, USA

Chapter 7

William C. Scarfe, B.D.S., F.R.A.C.D.S., M.S. Division of Radiology and Imaging Science, Department of Surgical/Hospital Dentistry, University of Louisville School of Dentistry Louisville, Louisville, KY, USA

Chapter 10

Bruno Azevedo, D.D.S., M.S. Division of Radiology and Imaging Science, Department of Surgical/Hospital Dentistry, University of Louisville, School of Dentistry, Louisville, KY, USA

Chapter 11

Bruno Azevedo, D.D.S., M.S. Division of Radiology and Imaging Science, Department of Surgical/Hospital Dentistry, University of Louisville, School of Dentistry, Louisville, KY, USA

Chapter 14

Thomas E. Underhill, D.D.S., M.S., M.D. Private Practice, Richmond, VA, USA

Chapter 15

Allan Abuabara, D.D.S. Oral and Maxillofacial Radiologist, Joinville Municipal Authority, Joinville, SC, Brazil

Jason Chan, D.D.S. 604 Dental, Vancouver, BC, Canada

Kenneth Chow, D.D.S. OMS Group, Vancouver, BC, Canada

David Gane, D.D.S. LED Medical Diagnostics, Inc., Burnaby, BC, Canada

Alexandre Khaireallah, B.D.S. Department of Oral and Maxillofacial Imaging, Faculty of Dentistry, The Lebanese University, Beirut, Lebanon

Leif Kullman, D.D.S., Ph.D. Department of Diagnostic Sciences, Faculty of Dentistry, Kuwait University, Kuwait City, Kuwait

George Kushner, D.M.D., M.D. Department of Surgical/Hospital Dentistry, University of Louisville School of Dentistry, Louisville, KY, USA

Thomas Li, B.D.S. Oral and Maxillofacial Radiology, Hong Kong, People's Republic of China

Ekaterini Nikopoulou-Karayianni, D.D.S., Ph.D. National and Kapodistrian University of Athens, Athens, Greece

Emmanuel Mazinis, D.D.Es., Ph.D. Private practice, Veria, Greece

Michael Matwychuk, D.D.S. Okanagen Endodontic Specialists, Kelowna, BC, Canada

Raman Sumanth, B.D.S. Melaka Manipal Medical College, Manipal University, Manipal, Malaysia

Raphael Trentin, D.D.S. Odontoradio Centro de Diagnostico, Chapecó, SC, Brazil

Kostas Tsiklakis, D.D.S., M.S., Ph.D. Department of Oral Diagnosis and Radiology, National and Kapodistrian University of Athens, Athens, Greece

Douglas W. Wallace, D.D.S., M.S. Affiliates in Oral and Maxillofacial Surgery, Fairfield, OH, USA

Lewei Zhang, B.D.S., Ph.D., F.R.C.D.(C) Department of Oral Biological and Medical Sciences, Faculty of Dentistry, University of British Columbia, Vancouver, BC, Canada

Chapter 16

Marcelo Augusto Oliveira de Sales, D.D.S., M.S., Ph.D. Department of Clinical and Social Dentistry, Universidade Federal da Paraíba, João Pessoa, Paraíba, Brazil

Chapter 17

Marcelo Augusto Oliveira de Sales, D.D.S., M.S., Ph.D. Department of Clinical and Social Dentistry, Federal University of Paraiba, João Pessoa, PB, Brazil

Jack Fisher, D.D.S. Artistic Smiles Orthodontics, Cordova, TN, USA

Bruno Azevedo, D.M.D., M.S. Division of Radiology and Imaging Science, Department of Surgical/Hospital Dentistry, University of Louisville School of Dentistry, Louisville, KY, USA

Chapter 18

Christos Angelopoulos, D.D.S., M.S. Aristotle University of Thessaloniki, Thessaloniki, Greece

Columbia University, College of Dental Medicine, New York City, NY, USA

Joe Mayes, D.D.S., M.S.D. Lubbock, TX, USA

Anatomage, San Jose, CA, USA

Dolphin Imaging and Management Solutions, Chatsworth, CA, USA

Alan G. Hannam Department of Oral Health Sciences, Faculty of Dentistry, University of British Columbia, Vancouver, BC, Canada

G.E.J. Langenbach Department of Oral Health Sciences, Faculty of Dentistry, University of British Columbia, Vancouver, BC, Canada

Chapter 19

Christos Angelopoulos, D.D.S., M.S. Aristotle University of Thessaloniki, Thessaloniki, Greece

College of Dental Medicine, Columbia University, New York City, NY, USA

Lewis Jones, D.M.D., M.D. Department of Surgical/Hospital Dentistry, University of Louisville School of Dentistry, Louisville, KY, USA

Chapter 20

Paulo Henrique Couto Souza, D.D.S., Ph.D., M.S. Dental School, Pontifical Catholic University of Paraná, Curitiba, Brazil

Daniel van Steenberghe, M.D., D.D.S., Ph.D., Dr., H.C. Katholieke Universiteit Leuven, Leuven, Belgium

Marc Quirynen, D.D.S., Ph.D. Periodontology and Oral Microbiology, Department of Oral Health Sciences, Katholieke Universiteit Leuven, Leuven, Belgium

Marjolein Vercruyssen, D.D.S., Ph.D., M.S. Periodontology and Oral Microbiology, Department of Oral Health Sciences, Katholieke Universiteit Leuven, Leuven, Belgium

Private Periodontal Practice, Hoogstraten, Belgium

Nele Van Assche, D.D.S., Ph.D., M.S. Periodontology and Oral Microbiology, Department of Oral Health Sciences, Katholieke Universiteit Leuven, Leuven, Belgium

Private Periodontal Practice, Geel, Belgium

Scott D. Ganz, D.M.D. Maxillofacial Prosthetics and Implant Dentistry, Fort Lee, NJ, USA

Bruno Azevedo, D.M.D., M.S. Division of Radiology and Imaging Science, Department of Surgical/Hospital Dentistry, University of Louisville School of Dentistry, Louisville, KN, USA

Thomas Fortin, D.D.S., Ph.D. Department of Oral Surgery, Dental University of Lyon, Lyon, France

Luc Vrielinck, M.D., D.D.S. Department Oral and Maxillofacial Surgery, Ziekenhuis Oost-Limburg, Genk, Belgium

Chapter 21

Michael M. Bornstein, Prof. Dr. med. dent. Oral and Maxillofacial Radiology, Applied Oral Sciences, Faculty of Dentistry, The University of Hong Kong, Prince Philip Dental Hospital, Hong Kong SAR, China

Bruno C. Azevedo, D.D.S., M.S. Division of Radiology and Imaging Science, Department of Surgical/Hospital Dentistry, University of Louisville School of Dentistry, Louisville, KN, USA

Chapter 22

Scott K. Hetz, D.M.D. Advanced Endodontic Associates, Washington, DC, USA

William Nudera, D.D.S., M.S. Specialized Endodontic Solutions, Bloomingdale, IL, USA

David Landwehr, D.D.S., M.S. Capital Endodontics, Madison, WI, USA

Michael J. Ribera, D.M.D. Advanced Endodontic Associates, Washington, DC, USA

Christos Angelopoulos, D.D.S., M.Sc. Aristotle University of Thessaloniki, Thessaloniki, Greece

College of Dental Medicine, Columbia University, New York, NY, USA

Chapter 23

José Ribamar Azevedo Instituto Odonto Radiológico de Brasília, Brazilia, Brazil

Instrumentarium Dental, Tuusula, Finland

Air Techniques, Inc., Melville, NY, USA

Telesystems Co. Ltd, Osaka, Japan

Chapter 24

Bruno Azevedo, D.D.S., M.S. Division of Radiology and Imaging Science, Department of Surgical/Hospital Dentistry, School of Dentistry, University of Louisville, Louisville, KY, USA

Kazuya Honda, D.D.S., Ph.D. Department of Radiology, Nihon University School of Dentistry, Tokyo, Japan

Ryan Lee, D.D.S., M.S. Cor Imaging, Honolulu, HI, USA

Emmanuel Mazinis, D.D.S., Ph.D. Private practice, Veria, Greece

Juliana R.V. Mussi, D.D.S. Clínica Volte A Sorrir, Tupã, São Paulo, Brazil

Marcelo Augusto Oliveira de Sales, D.D.S., M.S., Ph.D. Department of Clinical and Social Dentistry, Federal University of Paraiba, João Pessoa, PB, Brazil

Chapter 28

Glenn T. Clark, D.D.S., M.S. Orofacial Pain and Oral Medicine Ctr., Division of Periodontology, Diagnostic Sciences and Dental Hygiene, Herman Ostrow School of Dentistry of the University of Southern California, Los Angeles, CA, USA

Allan G. Farman, B.D.S., Ph.D., D.Sc., M.B.A. Emeritus Professor, The University of Louisville School of Dentistry, Louisville, KY, USA

Independent Consultant on Maxillofacial Imaging Science, Chicago, IL, USA

Bruce S. Haskell, D.M.D., Ph.D. Department of Surgical/Hospital Dentistry, University of Louisville School of Dentistry, Louisville, KY, USA

William E. Harrell Jr, D.M.D. Harrell Orthodontics, Alexander City, AL, USA

Chapter 29

Marcelo Augusto Oliveira de Sales, D.D.S., M.S., Ph.D. Department of Clinical and Social Dentistry, Federal University of Paraiba, João Pessoa, PB, Brazil

Bruno Azevedo, D.D.S., M.S. Division of Radiology and Imaging Science, Department of Surgical/Hospital Dentistry, University of Louisville School of Dentistry, Louisville, KY, USA

Chapter 30

Bruno Azevedo, D.M.D., M.S. Division of Radiology and Imaging Science, Department of Surgical/Hospital Dentistry, School of Dentistry, University of Louisville, Louisville, KY, USA

Jack Fisher, D.D.S. Artistic Smiles Orthodontics, Cordova, TN, USA

Part I

Fundamentals of CBCT

1 Historical Perspectives on CBCT

Allan G. Farman and William C. Scarfe

Contents

A.G. Farman, BDS, PhD, EdS, MBA, DSc (✉)
Emeritus Professor, The University of Louisville School of Dentistry, Louisville, KY, USA

Independent Consultant in Maxillofacial Imaging Science, Chicago, IL, USA
e-mail: allanfarman@aol.com

W.C. Scarfe, B.D.S., F.R.A.C.D.S., M.S.
Division of Radiology and Imaging Sciences, Department of Surgical/Hospital Dentistry, The University of Louisville School of Dentistry, Louisville, KY, USA
e-mail: wcscar01@louisville.edu

1.1 Introduction

There can be no denying that Cone Beam Computerized Tomography (CBCT) is an in-office diagnostic imaging technology that has taken maxillofacial imaging by storm (Farman 2006; Farman and Scarfe 2006; Farman et al. 2005, 2007a, b; Hayakawa et al. 2005; Kursağlu et al. 2005; Scarfe et al. 2006; Scarfe and Farman 2007) and the most significant advance in extra-oral dental imaging since the introduction of rotational panoramic radiography.

With CBCT, imaging is accomplished using a rotating gantry to which an X-ray source and detector are fixed. A divergent pyramidal- or cone-shaped source of ionizing radiation is directed through the middle of the area of interest onto an area X-ray detector on the opposite side. The X-ray source and detector rotate around a fixed fulcrum within the region of interest (ROI). During the exposure sequence hundreds of sequential planar projection images are acquired of the field of view (FOV) in an arc generally of at least 180°. In this single rotation, CBCT provides precise, essentially immediate and accurate three-dimensional (3D) radiographic image volumes. As CBCT exposure incorporates the entire FOV, only one rotational sequence of the gantry is necessary to acquire enough data for image reconstruction. The significant advancements and applications provided by this technology do not compete with standard digital radiographic

W.C. Scarfe, C. Angelopoulos (eds.), *Maxillofacial Cone Beam Computed Tomography*,
https://doi.org/10.1007/978-3-319-62061-9_1

applications. Rather, CBCT is a complementary modality for specific applications (Scarfe et al. 2006; Scarfe and Farman 2007; Farman et al. 2007a, b; Karellas et al. 2008).

1.2 Development of Maxillofacial CBCT Systems

It is sometimes thought mistakenly that CBCT is specific to dentistry and originated for maxillofacial imaging alone. Nothing can be further from the truth. While the principles of tomosynthesis providing the theoretical basis of the integration of multiple planar images had been described as early as 1934 (Ziedses des Plantes 1973; Webber and Horton 1997), four technological developments converged to facilitate construction of affordable CBCT units small enough to be used in the dental office for maxillofacial imaging (Fig. 1.1):

- Introduction of X-ray detectors capable of rapid acquisition of multiple basis images. The demands on any X-ray detector in clinical CBCT are hard to fulfill. The detector must be able to record X-ray photons, read off and send the signal to the computer, and be ready for the next acquisition many hundreds of times within a single rotation. As rotation is usually performed within times equivalent or less to panoramic radiography (5–20 s), this necessitates frame rate image acquisition times of milliseconds. Manufacturers that make area X-ray image sensors suitable for CBCT include Hamamatsu Photonics K.K (Hamamatsu City, Japan), Varian Medical Systems (Salt Lake City Utah, USA), and Samsung (Seoul, South Korea).
- The development of suitably resilient X-ray generators (Scarfe and Farman 2007). The X-ray generators used in maxillofacial CBCT machines are far simpler than those in multi-detector computed tomography (MDCT),

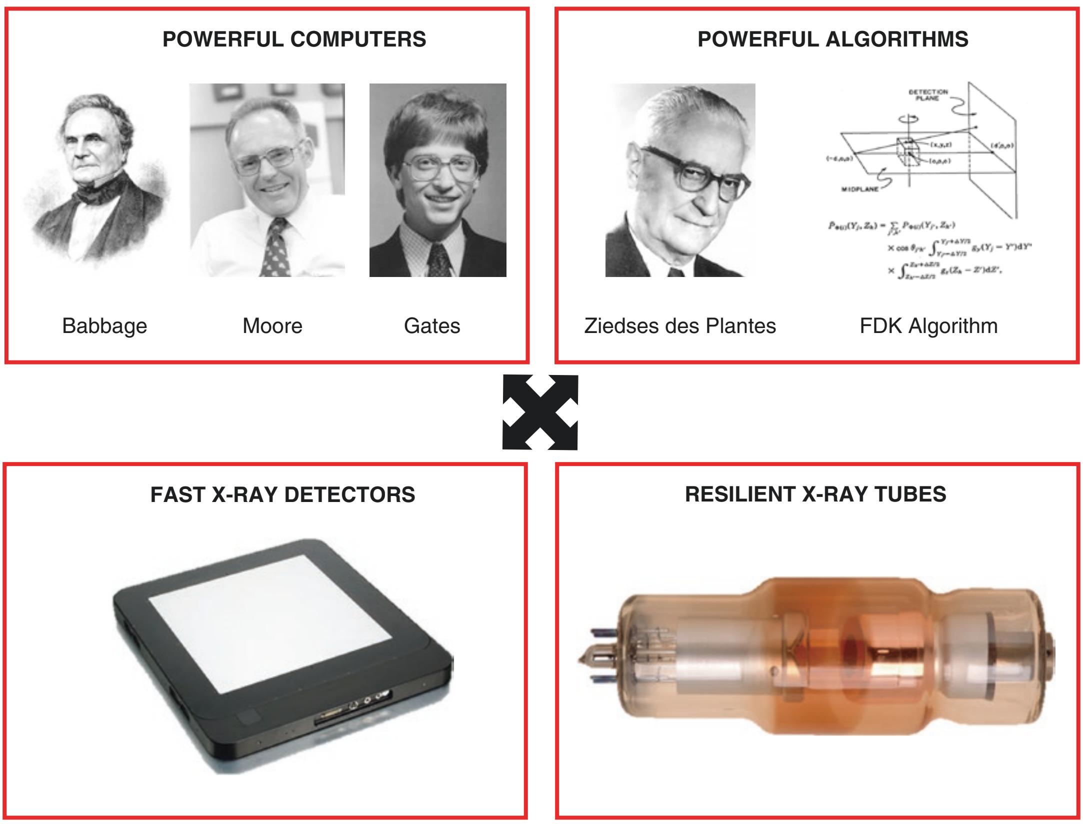

Fig. 1.1 Schematic representation of the four technological developments which converged in the late 1990s to facilitate the construction of affordable in-office maxillofacial CBCT

with an operating voltage between 80 kVp and 120 kVp. The majority of the units operate toward the lower end of this range which does not differ substantially from operating parameters in panoramic radiographic machines. Although the focal spot size is no different than MDCT (0.5–0.8 mm nominally), unlike MDCT the anode is stationary in most systems, with one or two exceptions. The tube current is generally much lower than MDCT which reduces power of the generator as well as the production of heat. Finally, in most CBCT systems, X-ray generation is pulsed to coincide with the detector activation. Pulsed X-ray beam generation is preferable as it markedly reduces total scan time and therefore heat production with a less radiation dosage to the patient. However, the relatively low power used in this type of X-ray generator provides limitations in image quality. Manufacturers that make area X-ray tube heads with high heat capacity suitable for CBCT include Toshiba (Toshiba Electron Tubes and Devices Co., Ltd., Tochigi, Japan), Varian Medical Systems (Salt Lake City Utah, USA), and Samsung (Seoul, South Korea).

- The evolution of suitable image acquisition and integration algorithms (Feldkamp et al. 1984; Grangeat 1991; Wischmann et al. 2002). To reconstruct 3D objects from cone beam projections is a fairly recent accomplishment. In MDCT individual axial slices of the object are sequentially reconstructed using a well-known mathematical technique (filtered back projection) and subsequently assembled to construct the volume. However, with 2D X-ray area detectors and cone-beam geometry, a 3D volume must be reconstructed from 2D projection data. This is referred to as cone beam reconstruction. The first and the most popular approximate reconstruction scheme for cone-beam projections acquired along a circular trajectory is the FDK (Feldkamp-Davis-Kress) algorithm (Feldkamp et al. 1984). This algorithm, used by most research groups and commercial vendors for cone-beam CT with 2D detectors, employs a convolution-back projection method.
- The availability of computers powerful enough to process the enormous amount of acquired image data (Aziz et al. 2008). While Charles Babbage, along with Ada Lovelace, is best remembered for originating the concept of a programmable computer, it is only because of the introduction of the micro-chip based computer by Gordon Moore and the Windows operating system by Bill Gates that in the late 1990s small, low cost computers capable of computational complexity enabled clinical systems to be manufactured for use in the dental office.

1.2.1 Computed Tomography

In 1972, Hounsfield revolutionized diagnostic medicine with the invention of the Computed Tomography (CT) scanner, which gained him the honors of British Knighthood and, with Cormack, the Nobel Prize in Medicine in 1979 (Hounsfield 1980; Cormack 1980). The independent discoveries of Hounsfield and Cormack showed that it was feasible to reconstruct a cross-sectional slice of an object, experimental animal, and eventually a human with fairly high accuracy, making it possible to visually inspect a person's anatomy without the need for invasive surgery. In the following years, CT acquisition has subsequently been refined to incorporate a helical or spiral synchronous motion, fan-shaped beam and multiple detector acquisition (MDCT) enabling fast scan times and providing high quality images which can be integrated to produce a volumetric dataset. While CT has been available for many years, its applications in dentistry has always been limited because of equipment cost, access, and radiation dose considerations.

1.2.2 Cone Beam Acquisition

Cone beam acquisition uses a beam geometry providing multiple transmission images that are integrated directly forming volumetric information (Sukovic 2003). This provides an alternate method of image production allowing more rapid acquisition of data for a region of interest (ROI) using a less expensive radiation detector than conventional CT. One of the earliest 3D volumetric scanners was the Dynamic Spatial Reconstructor (DSR), conceived as early as 1975

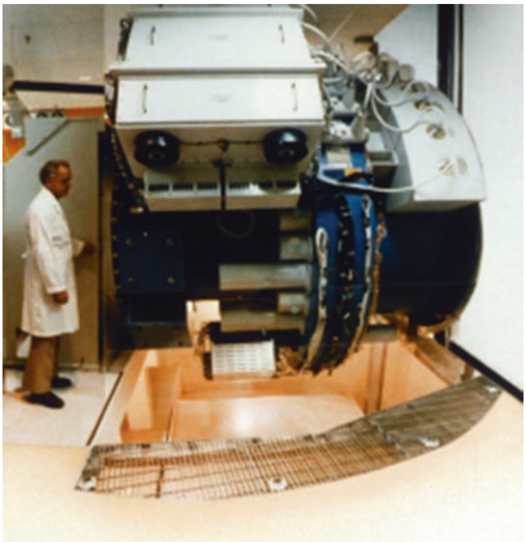

Fig. 1.2 Dynamic Spatial Reconstructor (DSR). The physical machine comprises: 14 rotating 2D cameras with 240 scan lines each receive photons of 14 opposing X-ray point sources at a frequency of 1/60 s. The system was very large, having a gantry measuring 4.57 m in diameter and 6.24 m in length. The device weighed more than 15,200 kg. (Image courtesy, Mayo Clinic, Rochester, Minnesota, USA)

by the Biodynamics Research Unit and finally installed in the Medical Sciences Building on the Mayo Clinic Rochester campus in 1978 (Fig. 1.2) (Robb et al. 1980; Robb 1982).

At the time the DSR was developed, 3D reconstruction was still in its infancy and no true 3D reconstruction algorithm was available. In need of pioneering results, the DSR was forced to employ a standard 2D reconstruction algorithm, originally designed to reconstruct cross-sectional slices from fan-beam projection data. In an approach termed the "stack-of-fans" method, the DSR simply treated each axial row of projection data as coming from a rotating virtual 2D fan-beam source, located in the same plane. The DSR was used as a noninvasive diagnostic device to detect lung cancer and heart disease in their early stages.

CBCT prototypes based upon C-arms were demonstrated as early as 1983. Several CBCT systems have been developed specifically for angiography (Saint-Felix et al. 1994; Rougée et al. 1994; Fahrig et al. 1997; Kawata et al. 1996; Schueler et al. 1997; Ning et al. 2000). CBCT systems have also been introduced for radiation therapy planning (Cho et al. 1995; Petit et al. 2008; Li et al. 2008) and mammography (Chen and Ning 2002; Marchant et al. 2008; Karellas et al. 2008).

1.2.3 CBCT Technology Transfer for Maxillofacial Applications

While CT was conceived in the mid-1970s, its application in dentistry was not immediate because of cost, size, and dose considerations. The technology transfer of CBCT to imaging of the maxillofacial region heralded a major advance both in data acquisition and in image reconstruction. The unprecedented interest in CBCT from all fields of dentistry is because it has facilitated the transition of radiographic imaging in dental diagnosis from 2D to 3D and expanded its role to image guidance of operative and surgical procedures.

1.2.3.1 Early Maxillofacial CBCT Units

As early as the early 1990 studies were under way in multiple places on adaptation of existing robotic platforms and investigation of image sensors for maxillofacial CBCT but mostly kept as trade secrets or under confidentiality agreements at that time.

A patent application for the first commercially successful maxillofacial CBCT was made in Italy in 1995 with Attilio Tacconi and Piero Mozzo as coinventors and the system was designed and produced by QR, Inc. of Verona, now a Cefla company (Molteni personal communication). The system was reported at SIRM Milano in June 1996, ECR Vienna in March 1997, and CARS/CMI Paris June 1999 (Farman et al. 2007a, b) and first described in the literature in 1998 (Mozzo et al. 1998). Prototypes were tested by Polizzi (Verona, Italy, 1996), Novarad (Venice, Italy, March 27 1997), Bianchi (Torino, Italy, April 8, 1997), Ortega (Madrid, Spain, May 16, 1997), and Jacobs (Maerburg, Germany, September 5, 1997) (Molteni, personal communication). FDA clearance for sale in the USA was granted on March 8, 2001, with the first installation being at the University of Loma Linda, California (April 2001). The NewTom DVT 9000 (Maxiscan in Italy only, branded by Esaote) was the first generation (1997–2004) followed by the NewTom 3G from 2004 onwards and the NewTom VG from 2007 onwards. All NewTom versions prior to the VG had the patient supine. The VG has the patient positioned standing vertically.

In the late 1990s prototypes were also being developed in Japan including the Ortho-CT (Arai et al. 1999) and Dental 3D-CT (Nakagawa et al. 2002) based on a multifunctional maxillofacial tomography unit (Scanora, Soredex, Helsinki, Finland) and PSR 9000 (Asahi Roentgen, Kyoto Japan), respectively. In 2000, the Ortho-CT technology was transferred to J. Morita Co. Ltd. through the Nihon University Business Incubation Center (Hashimoto et al. 2003). The original version of this was called the 3DX multi-image micro-CT (3DX) and subsequently became known commercially as the Accuitomo.

US FDA (United States Food and Drug Administration) clearances for the J. Morita Manufacturing Corporation's 3D Accuitomo were obtained on March 6, 2003, for the Imaging Sciences International (ISI) i-CAT on October 2, 2003, and for the Hitachi CB MercuRay on October 20, 2003. All three of these systems had the patient seated with the head vertical (Farman et al. 2007a, b). Subsequent generations of the Accuitomo and i-CAT are still in production as of the writing of this chapter however, production of the MercuRay has been suspended.

The original Accuitomo (J. Morita Manufacturing Corp., Kyoto, Japan) model initially had a 4 cm FOV that has subsequently been expanded to more than four times that size. J. Morita also released a hybrid CBCT, cephalometric and panoramic unit, the Veraviewepocs-3D at the International Dental Show in Cologne, Germany, in 2007, and this was subsequently FDA cleared for sale in the USA (Farman et al. 2007a, b, 2008).

The ISI i-CAT is a product that was initiated at the Engineering School, The University of Michigan, Ann Arbor, USA, and was advanced as part of the doctoral program for a bright young student, Predrag Sukovic (Fig. 1.3), from Belgrade, Serbia. In prototype, this system was termed the DentoCAT (Sukovic 2003) (Fig. 1.4). Drs. Sharon L. Brooks and Allan G. Farman acted as dental consultants for the Small Business Innovation grants awarded to Predrag Sukovic by the National Institutes of Health to develop this CBCT system. Many of the component parts used to construct the prototype were donated by Eric Stetzel, who at the time was owner of Panoramic Corporation, Fort Wayne, Indiana. Subsequently Panoramic Corporation was purchased by Young Dental Corporation, and a decision was made for Panoramic Corporation not to enter the CBCT market at that time. ISI (Hatfield, Pennsylvania USA) stepped in and within a remarkably short time of approximately 6 months from entering a licensing arrangement helped design an ergonomically efficient unit, received FDA clearance, and had the first commercial units rolling off the production line. They subsequently took a major position in the market for CBCT units worldwide.

Hitachi engineer, Rika Baba, had a major role in helping develop the Hitachi MercuRay (Hitachi

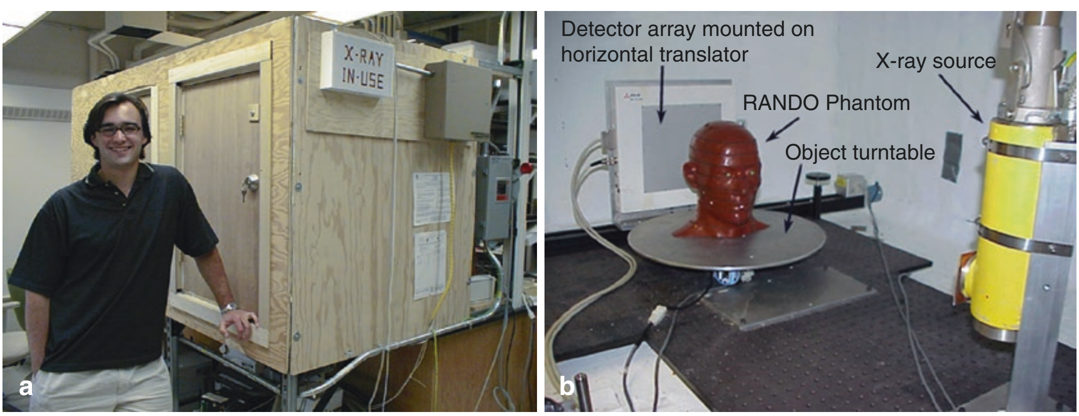

Fig. 1.3 Predrag Sukovic (**a**) in his laboratory with the initial experimental configuration of CBCT (**b**)

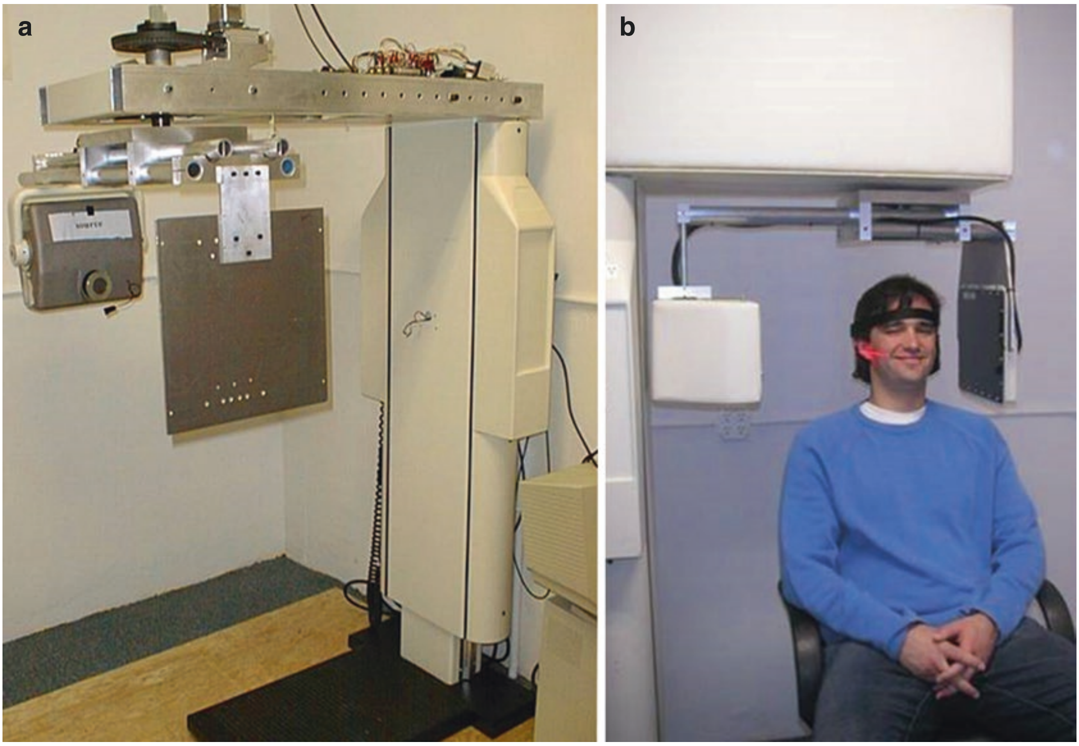

Fig. 1.4 The DentoCAT prototype (**a**) and inventor Predrag Sukovic (**b**). This was later to become the i-CAT (Imaging Sciences International. Hatfield, Pennsylvania USA)

Medico Technology, Chiba, Japan) (Seo et al. 2002; Yamamoto et al. 2003), and subsequently in extending the range of Hitachi CBCT products for anatomical sites other than the maxillofacial region. The MercuRay is a relatively large and heavy unit that in Japan has been replaced by the smaller Hitachi CB Throne and was withdrawn from the American market (Yajima et al. 2006; Farman et al. 2008).

1.2.3.2 Current Status

Early devices were unimodal, capable of CBCT image acquisition only and performed scanning with the patient either supine or seated. These units were specifically designed on a robotic platform capable of achieving a 360° or greater rotation arc for X-ray generator/detector geometry. Since 2007, more and more manufacturers have produced hybrid, multimodal systems based on existing dental panoramic machine structural platforms. Numerous systems are currently commercially available at the time this chapter was written providing a wide range of choices for the purchaser of CBCT systems (Table 1.1).

For practitioners, the choice has expanded enormously to over 50 models ranging from a full maxillofacial FOV to a hybrid unit panoramic unit with or without 2D digital cephalometric capabilities. Many units now offer a range of FOVs with small FOVs capable of providing fine details related to the structure, location, and status of specific teeth. The smaller the CBCT FOV, generally the lower the cost of the system, so the hybrid approach might be considered economical. Nevertheless, a large FOV is required if one wishes to include the whole maxillofacial region in the scan.

1.3 Thoughts on the Future

CBCT has a longer history than most readers might have known; however, history is a continuum and the future will see research to better delineate the selection criteria of CBCT for use

Table 1.1 Selected CBCT imaging systems

Unit	Model(s)	Manufacturer/distributor
Accuitomo	3D Accuitomo—XYZ Slice View Tomograph[a], FPD[a], 3D Accuitomo 170, Veraviewepocs 3D R100, Veraviewepoc 3D F40	J. Morita MFG Corp., Kyoto, Japan
Acteon	X-Mind Trium	Acteon North America, Mt Laurel, New Jersey, USA
Asahi Roentgen	Auge Solio, Aliloth, Alphard 3030 (PSR 9000 N), Alphard 2520	Asahi Roentgen Ind. Co. Ltd. Kyoto, Japan
Belmont	Bel-Cat, Bel-Cat PA, Bel-Cat CM	Takara Belmont Corporation, Somerset, New Jersey, USA
Carestream	CS 81003D, CS 9000, CS 9300, CS9500[a]	Carestream Dental, Atlanta, Georgia, USA
CRANEX	3Dx, 3D, and 3D for Endo, Scanora 3D	SOREDEX, Tuusula, Finland
Galileos	Comfort[a], Compact[a], ComfortPLUS, Orthophos XG 3D, Orthophos SL 3D	Sirona Dental Inc., Charlotte, North Carolina, USA
Gendex	GXCB-500[a], GXCB-500HD, GXPD-800, GXPD-700 with 3D CBCT	Gendex Dental Systems, Hatfield, Pennsylvania, USA
Hitachi	CB MercuRay[a]/CB Throne[a]	Hitachi Medical Systems, Tokyo, Japan
i-CAT	Classic[a], Next Generation (Model 17–19, Platinum), i-CAT FLX, i-CAT FLX MV	Imaging Sciences International, Hatfield, Pennsylvania, USA
I-MAX	I-MAX Touch 3D	Owandy Corporation, Paris, France
KaVo	3D eXam, 3D eXam+	KaVo Dental Corp., Biberach, Germany
Newtom	3G[a], VG[a], 5G, VGi, VGi Fex Giano	QR, Inc. Verona, Italy (a Cefla company)
OP 300	OP 300, OP 300 Maxio 3D	Instrumentarium Corporation, Milwaukee, Wisconsin USA
Biolase	DaVinci Imaging D3D	Biolase Irvine, California USA
Panoramic Corp.	Encompass Eagle 3D	Panoramic Corporation, Fort Wayne, Indiana USA
PreXion (Fine Cube)	PreXion3D Elite, PreXion 3D Eclipse	Yoshida Dental Mfg. Co. Ltd., Tokyo, Japan/ Distributed by TeraRecon Inc., San Mateo, California USA
Promax	3D, 3Ds, 3D Plus, 3D Mid, 3D Max	Planmeca OY, Helsinki, Finland
Ray	RayScan 3D Alpha	LED Dental, Atlanta, Georgia, USA
MyRay	SkyView 3D Panoramic imager[a], Hyperion X5, Hyperion X9	My-Ray Dental Imaging, Imola, Italy
Suni	3D, 3D HD	Suni Medical Imaging, Inc. San Jose, California, USA
VaTech	Picasso Series (Trio/Pro/Master)[a], PaX-i3D, PaX-Flex 3D, PaX-Uni 3D, PaX-Duo 3D, Pax-Zenith 3D, PaX-Reve 3D	Vatech, Giheung-gu, Korea

[a]No longer manufactured/unavailable

in dentistry based upon clinical evidence of impact on treatment outcomes. Further, there will be a surge in development of 3D analyses and refinements in multimodality fusion of images with CBCT datasets. In Chap. 2 potential technologic advancements are presented. While CBCT robotic platforms are now mature, there is the possibility of refinement of approximate cone beam algorithms. While the FDK algorithm (Feldkamp et al. 1984) can be easily implemented with currently available hardware and is a good reconstruction for images at the center or "mid-plane" of the cone-beam, it nevertheless provides an approximation that causes some unavoidable distortion in the noncentral transverse planes, as well as resolution degradation in the longitudinal direction. In order to address this deficiency, several other approaches have been proposed using different algorithms (Wischmann et al. 2002) and cone-beam geometries (e.g., dual orthogonal circles, helical orbit, orthogonal circle-and-line), and will no doubt be implemented into future CBCT designs. As computer data-crunching power continues to increase at ever-lower costs, the use of iterative techniques for image processing is moving from the laboratory to clinical used for MDCT and for research into CBCT applications.

References

Arai Y, Tammisalo E, Iwai K, Hashimoto K, Shinoda K (1999) Development of a compact computed tomographic apparatus for dental use. Dentomaxillofac Radiol 28:245–248

Aziz O, Lo B, Pansiot J, Atallah L, Yang GZ, Darzi A (2008) From computers to ubiquitous computing by 2010: health care. Philos Trans A Math Phys Eng Sci 366(1881):3805–3811

Chen B, Ning R (2002) Cone-beam volume CT breast imaging: feasibility study. Med Phys 29:755–770

Cho PS, Johnson RH, Griffin TW (1995) Cone-beam CT for radiotherapy applications. Phys Med Biol 40:1863–1883

Cormack AM (1980) Early two-dimensional reconstruction (CT scanning) and recent topics stemming from it. Nobel lecture, December 8, 1979. J Comput Assist Tomogr 4:658–664

Fahrig R, Fox AJ, Lownie S, Holdsworth DW (1997) Use of a C-arm system to generate true three-dimensional computed rotational angiograms: preliminary in vitro and in vivo results. AJNR Am J Neuroradiol 18:1507–1514

Farman AG (2006) Image-guidance: the present future of dental care. Pract Proced Aesthet Dent 18:342–344

Farman AG, Scarfe WC (2006) Development of imaging selection criteria and procedures should precede cephalometric assessment with cone-beam computed tomography. Am J Orthod Dentofac Orthop 130:257–265

Farman AG, Scarfe WC, Hilgers MJ, Bida O, Moshiri M, Sukovic P (2005) Dentomaxillofacial cone-beam CT for orthodontic assessment. Int Congress Ser 1281:1187–1190

Farman AG, Levato CM, Scarfe WC (2007a) 3D X-ray: an update. Inside Dent 3:70–74

Farman AG, Levato CM, Scarfe WC (2007b) A primer on cone beam computed tomography. Inside Dent 3:90–92

Farman AG, Levato CM, Scarfe WC, Mah J (2008) Education in the round: multidimensional imaging in dentistry. Inside Dent 4:39–41

Feldkamp LA, Davis LC, Kress JW (1984) Practical cone-beam algorithm. J Opt Soc Am A 1:612–619

Grangeat P (1991) Mathematical framework of cone beam 3D reconstruction via the first derivate of the radon transform. In: Herman GT, Luis AK AK, Natterer F (eds) Mathematical methods in tomography. Springer, Berlin, pp 66–97

Hashimoto K, Arai Y, Iwai K, Araki M, Kawashima S, Terakado M (2003) A comparison of a new limited cone beam computed tomography machine for dental use with a multidetector row helical CT machine. Oral Surg Oral Med Oral Pathol Oral Radiol Endod 95:371–377

Hayakawa Y, Sano T, Sukovic P, Scarfe WC, Farman AG (2005) Cone beam computed tomography—a paradigm shift for clinical dentistry. Nippon Dent Rev 65:125–132

Hounsfield GN (1980) Nobel lecture, 8 December 1979. Computed medical imaging. J Radiol 61:459–468

Karellas A, Lo JY, Orton CG (2008) Point/Counterpoint. Cone beam x-ray CT will be superior to digital x-ray tomosynthesis in imaging the breast and delineating cancer. Med Phys 35:409–411

Kawata Y, Niki N, Kumazaki T (1996) Measurement of blood vessel characteristics for disease detection based on cone beam CT images. IEEE Trans Med Imaging 43:3348–3354

Kursağlu P, Sukovic P, Scarfe WC, Farman AG (2005) Dental Volumetrik Bilgisayarli Tomograti [Dental volumetric computed tomography]. Akademik Dental Dişhekimliği Dergisi 26:30–36

Li H, Zhu XR, Zhang L, Dong L, Tung S, Ahamad A, Chao KS, Morrison WH, Rosenthal DI, Schwartz DL, Mohan R, Garden AS (2008) Comparison of 2D radiographic images and 3D cone beam computed tomography for positioning head-and-neck radiotherapy patients. Int J Radiat Oncol Biol Phys 71:916–925

Marchant TE, Amer AM, Moore CJ (2008) Measurement of inter and intra fraction organ motion in radiotherapy using cone beam CT projection images. Phys Med Biol 53:1087–1098

Molteni R. Personal communication

Mozzo P, Procacci C, Tacconi A, Martini PT, Andreis IA (1998) A new volumetric CT machine for dental imaging based on the cone-beam technique: preliminary results. Eur Radiol 8:1558–1564

Nakagawa Y, Kobayashi K, Ishii H, Mishima A, Ishii H, Asada K, Ishibashi K (2002) Preoperative application of limited cone beam computerized tomography as an assessment tool before minor oral surgery. Int J Oral Maxillofac Surg 31:322–326

Ning R, Chen B, Yu R, Conover D, Tang X, Ning Y (2000) Flat panel detector-based cone-beam volume CT angiography imaging: system evaluation. IEEE Trans Med Imaging 19:949–963

Petit SF, van Elmpt WJ, Nijsten SM, Lambin P, Dekker AL (2008) Calibration of megavoltage cone-beam CT for radiotherapy dose calculations: correction of cupping artifacts and conversion of CT numbers to electron density. Med Phys 35:849–865

Robb RA (1982) Dynamic spatial reconstruction: an x-ray video fluoroscopic CT scanner for dynamic volume imaging of moving organs. IEEE Trans Med Imaging 1:22–23

Robb RA, Lent AH, Gilbert BK, Chu A (1980) The dynamic spatial reconstructor: a computed tomography system for high-speed simultaneous scanning of multiple cross sections of the heart. J Med Syst 4:253–288

Rougée A, Picard C, Saint-Félix D, Trousset Y, Moll T, Amiel M (1994) Three-dimensional coronary arteriography. Int J Card Imaging 10:67–70

Saint-Felix D, Trousset Y, Picard C, Ponchut C, Roméas R, Rougée A (1994) In vivo evaluation of a new system for 3D computerized angiography. Phys Med Biol 39:583–595

Scarfe WC, Farman AG (2007) Cone beam computed tomography: a paradigm shift for clinical dentistry. Aust Dent Pract 1:102–110

Scarfe WC, Farman AG, Sukovic P (2006) Clinical applications of cone-beam computed tomography in dental practice. J Can Dent Assoc 72:75–80

Schueler BA, Sen A, Hsiung HH, Latchaw RE, Hu X (1997) Three-dimensional vascular reconstruction with a clinical X-ray angiography system. Acad Radiol 4:693–699

Seo K, Yamamoto K, Ueno K, Tanaka K, Matsuoka M, Okabe K et al. (2002) Development of dento-maxillofacial cone beam X-ray CT system model CB MercuRay. In: Kazunori M, editor. MEDIX (Hitachi Medical Corp). 37:40–5

Sukovic P (2003) Cone beam computed tomography in maxillofacial imaging. Orthod Craniofacial Res 6(Suppl 1):31–36

Webber RL, Horton RA (1997) Tuned-aperture computed tomography: theory and application in dental radiology. In: Farman AG, Ruprecht A, Gibbs SJ, Scarfe WC (eds) Advances in maxillofacial imaging. Elsevier, Amsterdam, pp 359–366

Wischmann H-A, Luijendijk HA, Meulenbrugge HJ, Overdick M, Schmidt R, Kiani K (2002) Correction of amplifier nonlinearity, offset, gain, temporal artifacts, and defects for flat-panel digital imaging devices. In: Antonuk LE, Yaffe MJ (eds) Medical imaging 2002: physics of medical imaging—proceedings of SPIE volume 4682. San Diego, CA, SPIE, pp 427–437

Yajima A, Otonari-Yamamoto M, Sano T, Hayakawa Y, Otonari T, Tanabe K, Wakoh M, Mizuta S, Yonezu H, Nakagawa K, Yajima Y (2006) Cone-beam CT (CB Throne) applied to dentomaxillofacial region. Bull Tokyo Dent Coll 47:133–141

Yamamoto K, Ueno K, Seo K, Shinohara D (2003) Development of dento-maxillofacial cone beam X-ray computed tomography system. Orthod Craniofacial Res 6(Suppl 1):160–162

Ziedses des Plantes B (1973) Selected works of Ziesdes des Plantes. Excerpta Medica, Amsterdam, pp 137–140

What Is CBCT and How Does It Work?

2

Ruben Pauwels

Contents

R. Pauwels, Ph.D.
Department of Radiology, Faculty of Dentistry, Chulalongkorn University, Bangkok, Thailand

OMFS-IMPATH, Department of Imaging & Pathology, Biomedical Sciences Group, KU Leuven, Leuven, Belgium
e-mail: ruben.pauwels@kuleuven.be, pauwelsruben@hotmail.com

2.1 Introduction

In this chapter, the technical principles of cone beam computed tomography (CBCT) are described. Maxillofacial CBCT imaging is perhaps the most significant advance in dental imaging since rotational panoramic radiography. At the time of writing, there are more than 50 CBCT models available for clinical use worldwide (Nemtoi et al. 2013). Although there are several similarities between these models, they can differ considerably in terms of imaging hardware, exposure parameters and image reconstruction and processing.

2.2 Stages of CBCT Imaging

The production of CBCT images occurs in two stages, each with sequential phases: *image acquisition*, comprising X-ray exposure and detection, and *image reconstruction* (Fig. 2.1).

2.2.1 Image Acquisition

2.2.1.1 X-ray Source

CBCT scanners use a conventional X-ray source, consisting of a vacuum tube (Fig. 2.2) containing a cathode and anode. A filament at the cathode is heated by a large current, leading to the release of

W.C. Scarfe, C. Angelopoulos (eds.), *Maxillofacial Cone Beam Computed Tomography*,
https://doi.org/10.1007/978-3-319-62061-9_2

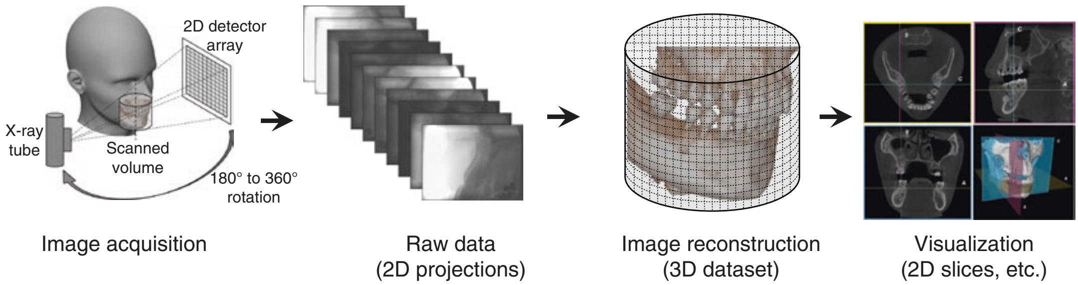

Fig. 2.1 Schematic diagram showing the stages of CBCT image production. During a 180°–360° rotation of the X-ray tube and detector, multiple planar *basis projections* (raw data) are acquired. The raw data is then reconstructed into a volumetric dataset (primary reconstruction), which is subsequently reformatted as sequential, contiguous orthogonal slices (secondary reconstruction). The data may be further reformatted (e.g., volume rendering, curved reformatting, maximum intensity projection). Partially adapted from Pauwels et al. (2015a) under the British Institute of Radiology's License to Publish

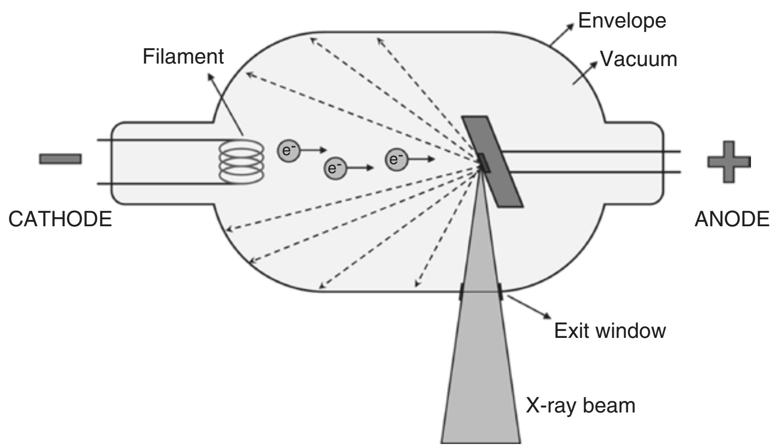

Fig. 2.2 Schematic diagram of the components of an X-ray tube. Electrons are released from the filament at the cathode and accelerated to the focal spot (*dark grey*) within the anode due to a high tube voltage. After electrons hit the anode material at the focal spot, part of the energy is released as X-rays. Figure reproduced from Pauwels et al. (2015a) under the British Institute of Radiology's License to Publish

electrons through a process known as *thermionic emission*. These electrons are accelerated across a small gap to a small area of the anode (i.e., focal spot), composed of a high-density material such as tungsten. The degree of acceleration is determined by the potential difference between the cathode and the anode, created by a high tube voltage. Collision between the accelerated electrons emitted from the cathode and orbital electrons in the anode reduces the kinetic energy of the former electrons, and energy is released through the law of conservation of energy. While most of this energy is lost as heat, a small amount is released as electromagnetic radiation in the X-ray spectrum through a process called *Bremsstrahlung* (literally (German) "braking radiation"). In addition, X-rays at specific energy levels (*characteristic X-rays*) are produced when inner-shell electrons are ejected in the anode material, after which outer-shell electrons lose energy in the form of specific X-ray emission as they occupy an inner shell. X-rays generated in an X-ray tube exhibit a wide range (spectrum) of energies, with the maximum energy determined by the tube voltage (kV) (Fig. 2.3).

X-rays generated at the focal spot diverge in all directions. Those X-rays not directed towards the detector are blocked before exiting the tube.

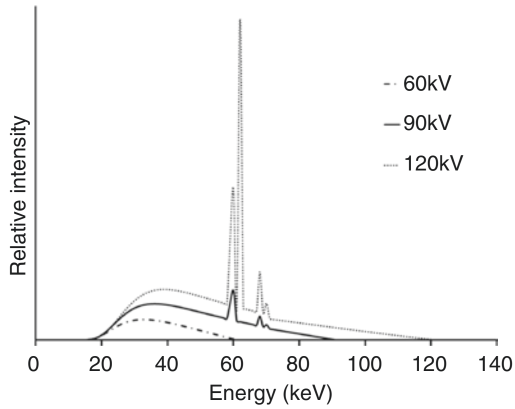

Fig. 2.3 Graph of relative intensity versus energy (X-ray spectra) for three representative tube voltages. Filtration is 2.5 mm aluminum in all cases. An increased kV results in an increased mean (shift to the *right*) and maximum (*x-axis intercept*) X-ray energy as well as an increased total intensity (*area under the curve*). Characteristic X-ray peaks are shown at fixed energy levels (i.e., for tungsten anodes: at approx. 58 keV, 53 keV, 67 keV, and 69 keV). Spectral curves were plotted using data from Birch and Marshall (1979). Figure reproduced from Pauwels et al. (2015a) under the British Institute of Radiology's License to Publish

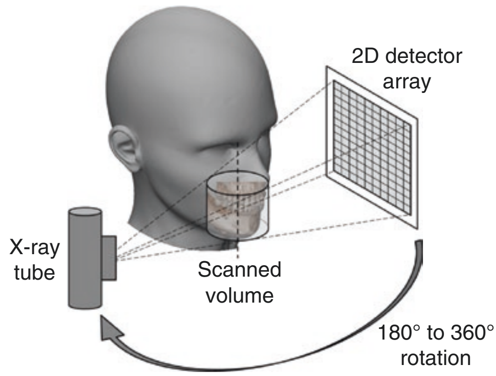

Fig. 2.4 Schematic representation of dental and maxillofacial CBCT geometry demonstrating a cylindrical scanned volume acquisition centered with the FOV size and position determined by the region of interest. Figure reproduced from Pauwels et al. (2015a) under the British Institute of Radiology's License to Publish

This is achieved by shielding surrounding the X-ray tube (tube housing) as well as high-density X-ray blockers called *collimators,* precisely restricting the aperture. Most CBCT models use rectangular collimation, resulting in a pyramid-shaped beam. Circular collimation, resulting in an actual "cone" beam, is mainly used on earlier units to correspond with the circular shape of image intensifier detectors.

2.2.1.2 Projection Geometry

In CBCT, image acquisition is performed through a single partial (≥180°) or full (360°) rotational scan of an X-ray source and a reciprocating 2D flat detector array. The axis of rotation of this configuration is centered at a certain region of interest (ROI) within the patient's head (Fig. 2.4). Throughout the rotation, a divergent pyramidal- or cone-shaped beam of X-rays is directed towards the detector on the opposite side, with the field of view (FOV) being determined by the physical collimation applied. During the rotation, many sequential 2D projection images (typically a few hundred) are acquired, each covering the FOV from a slightly different horizontal angle. These image projections constitute the raw data and are individually referred to as *basis, frame, projection, or raw images*. Because X-ray beam projections incorporate the entire FOV, only one rotational sequence (or, at the very least, half a rotation) of the gantry is necessary. The beam geometry in CBCT differs from that of multi-detector CT (MDCT), which uses a fan-shaped X-ray beam with a simultaneous translation of the patient table (gantry) and rotation of the X-ray source and detector, resulting in a helical trajectory (Fig. 2.5).

In the most basic CBCT configuration, the central ray of the X-ray beam from the generator is directed through the middle of the FOV and the transmitted, non-attenuated radiation for this central ray is projected perpendicular to the middle of the area image receptor on the opposite side. In maxillofacial CBCT noncentral rays are incident on the detector at a non-perpendicular angle. In MDCT (Fig. 2.5) the detectors are configured along an arc, assuring that the X-ray beams are incident to each detector at 90°. While divergent projection angles in CBCT can be accounted for during image reconstruction, image quality is typically optimal at the center of the FOV.

Modified Geometric Configurations

Several modified geometric configurations have been incorporated into various CBCT devices.

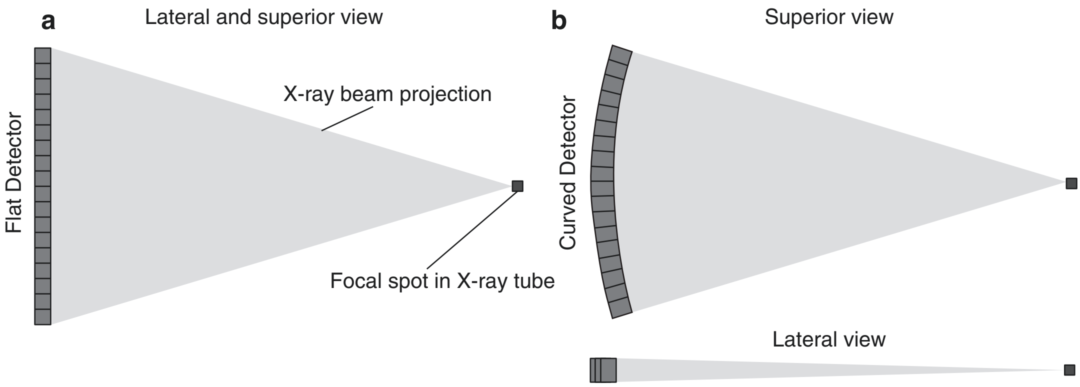

Fig. 2.5 Schematic demonstrating the difference between cone beam (**a**) versus "fan beam" (**b**) projection geometry used in CBCT and MDCT units, respectively. In CBCT, the beam is collimated as a *cone or pyramid*, and a 2D detector array is used to capture the raw data; thus, a single rotation suffices to reconstruct the FOV. In MDCT, a *fan-shaped* beam is used in concordance with an arc of detectors, resulting in the FOV being captured as a sequence of axial slices. Current MDCT units use several rows of detectors such that the X-ray beam is no longer fan-shaped but pyramid-shaped, with the divergence of the beam determined by the width and number of detector rows

Fig. 2.6 Schematic (*lower* diagrams) and actual representative datasets (*upper* images) demonstrating *horizontal* (**a**) and *vertically* (**b**) stitched CBCT FOVs from separate sequential scans

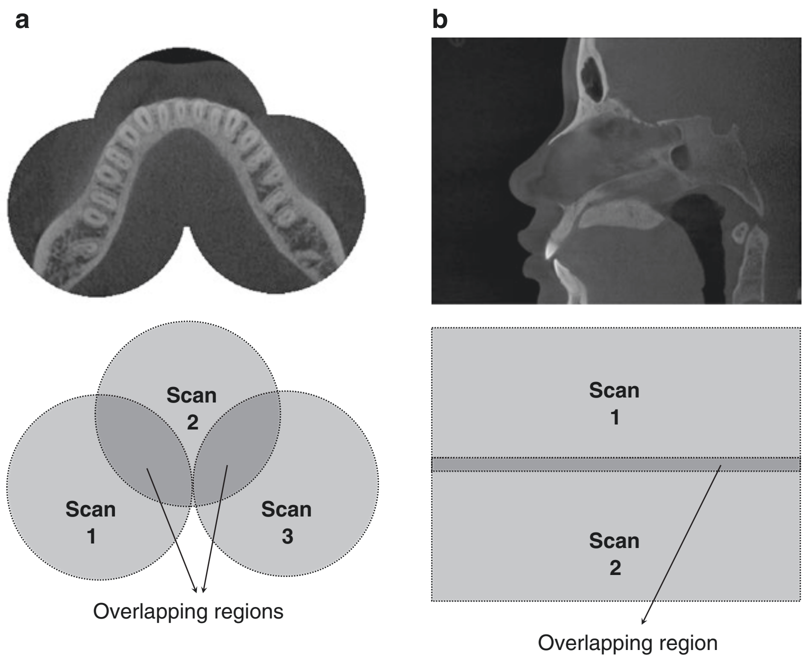

Volumetric Stitching

One method involves obtaining data from two or more separate scans, superimposing partially overlapping CBCT data volumes through a process called *image registration* (or mosaicing) and fusing the adjacent image volumes (*stitching* or *blending*) to create a larger volumetric dataset either in the horizontal or in the vertical dimension (Fig. 2.6). This process is usually performed automatically by the CBCT software. The disadvantage of stitching overlapped regions is that such overlapped regions are exposed twice (i.e., over-scanned), resulting in doubling the radiation dose to such regions.

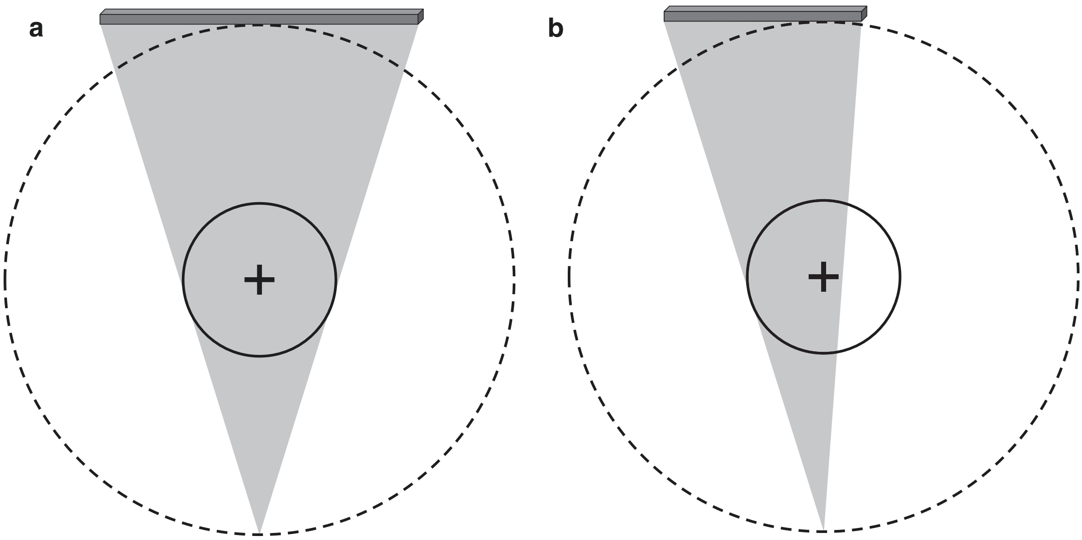

Fig. 2.7 Schematic representing conventional (**a**) and off-axis (**b**) CBCT exposure geometry in the *axial plane*. The *inner* (*solid*) *circle* denotes the FOV; the *outer* (*hashed*) *circle* shows the trajectory of the X-ray tube and detector. In the conventional geometric arrangement (**a**), the central ray of the X-ray beam from the focal source is directed through the middle of the object (+) to the center of the detector. In the off-axis geometry (**b**), only part of the FOV (at least 50%) is covered at any given exposure. An off-axis geometry allows for the use of a smaller detector for a given FOV size

Horizontal Off-Axis Geometry

A second method involves positioning of the X-ray tube and detector eccentrically to the rotational center of the FOV (isocenter) to provide an off-axis geometry (Fig. 2.7). In this configuration, the detector is offset to an asymmetrically collimated beam. As a result, only a portion of the FOV is scanned for a full 360° rotation, whereas other portions of the FOV are scanned for angles between 180° and 360° (Figs. 2.8 and 2.9).

Vertical Off-Axis Geometry

A third modified geometric configuration involves alteration of the X-ray beam projection angle in the vertical dimension (cranio-caudal plane) (Fig. 2.10). The normal cross section of X-ray beam in the vertical dimension is an isosceles triangle; thus, X-rays hit the detector perpendicularly in the central axial plane (i.e., the cranio-caudal mid-point of the FOV). Image quality is highest in this plane and slightly decreases towards the upper and lower borders of the FOV (i.e., with increasing beam divergence). If the main region of interest is expected not be in the central axial plane (e.g., a maxillofacial scan, with the main region of interest being the dentoalveolar area), optimal image quality in that region can be achieved using a scalene triangular beam shape.

2.2.1.3 Image Detector

CBCT units use either an image intensifier (II) or one of several types of flat panel detectors (FPD) as the image detector (Fig. 2.11).

- **II based systems.** Using this technology, the attenuated X-ray beam is converted into electrons. These electrons are then amplified before being reconverted into photons, which are recorded using a charge-coupled device (CCD). Currently, few CBCT units incorporate II detectors. These systems tend to be relatively large and most frequently result in circular basis image areas (spherical volumes) rather than rectangular ones (cylindrical volumes). Furthermore, they are prone to geometric distortion and have a relatively narrow dynamic range (i.e., difference between the highest and lowest detectable signal).
- **Indirect FPD systems.** An indirect system consists of two components: a scintillator

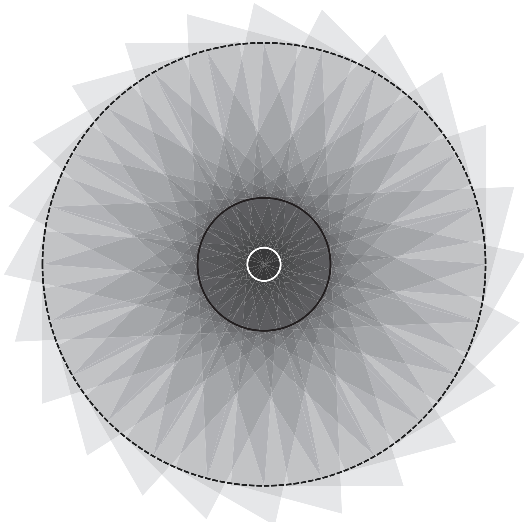

Fig. 2.8 Schematic representing the radiation coverage distribution within a rotational arc (*outer circle*) using the off-axis geometry shown in Fig. 2.7 with 24 projections. The *outer* (*hashed*) *circle* represents the trajectory of X-ray tube and detector. The *inner* (*solid*) *circle* represents the FOV. *Darker grey shades* correspond to an increased coverage. The central region of the FOV (*white circle*) is scanned through 360°. Other areas of the FOV are scanned at rotation arcs varying from 180° to 360°. The *outer edge* of the FOV (*dashed circle*) is scanned for 180°

medium which converts X-ray radiation into visible light and a photon detector which converts light into an electrical signal, which can then be digitized (Fig. 2.11). The scintillator used in CBCT is typically cesium iodide (CsI). Below the scintillator layer, FPDs comprise a thin film photodiode/transistor matrix in a 2D pixel array. Read-out of the electrical signal is done using complementary metal oxide semiconductors (CMOS) or amorphous silicon (a-Si) thin film transistors (TFT). Quality factors such as detector size, pixel size, electronic noise, sensitivity, and read-out speed depend on the technology and technical specifications of the detector.

- **Direct FPD systems.** Direct X-ray conversion detection systems (e.g., photon counting) are being developed for CBCT and have been used experimentally. FPD systems currently comprise an amorphous selenium (a-Se), cadmium telluride (CdTe), or cadmium zinc telluride (CdZnTe) photoconductor, which converts X-ray photons into an electrical charge, directly connected to a TFT or CMOS

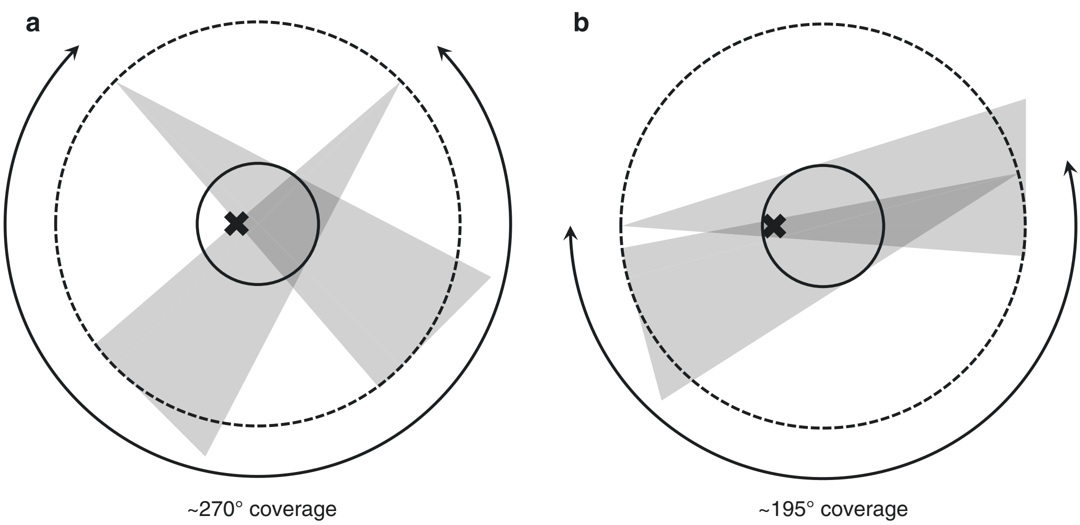

Fig. 2.9 Schematic showing the dependence of FOV coverage on location for off-axis X-ray beam projections. The trajectory of X-ray tube and detector (*hashed circle*) and FOV (*solid circle*) are shown for the off-axis geometry shown in Fig. 2.7. The start- and end-angles of the X-ray beam for which a location within the FOV (*black cross*) is covered, rounded to 15° (24-projection geometry) is shown, for a point close to the *center* of the FOV (**a**) and a point close to the *edge* (**b**). Points closer to the center of the FOV are covered using a wider rotation arc than points closer to the edge of the FOV, resulting in improved image quality closer to the center

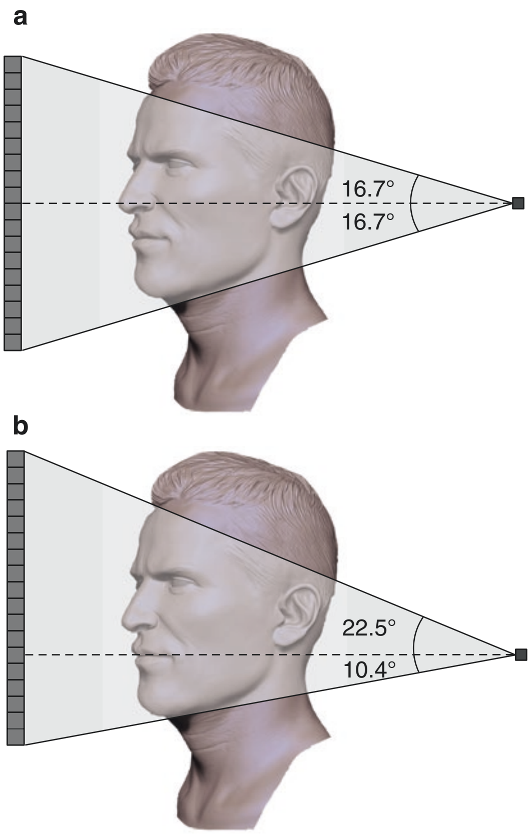

Fig. 2.10 The normal cranio-caudal geometric configuration of the X-ray beam projection (**a**) is an *isosceles triangle*, with the *central plane* of the beam (*hashed line*), at which image quality is optimal, projected perpendicular to the detector and coinciding with the center of the FOV. The use of a *scalene triangular* beam X-ray projection geometry (**b**) shifts the central plane coincides with the center of the FOV. Image quality will be highest in this plane to the area of highest diagnostic interest, usually the dentoalveolar region. (Adapted from Molteni (2013); 3D head model image courtesy of Rodrigue Pralier)

panel (Fig. 2.11). Images from direct detector systems are inherently less unsharp than those from indirect detector systems, as the latter involves a conversion to visible light, which is laterally spread between detector elements.

For each projection image during acquisition, the detector receives incident X-ray photons, collects a charge proportionally to the X-ray intensity at a given point, and sends a signal to the computer. As rotation is usually performed within times equivalent to panoramic radiography (typically 15 –20 s, although scan times below 10 s or above 30 s are possible), each of the hundreds of projection images is acquired and transmitted within milliseconds. The speed with which a detector performs this acquisition is called the *frame rate*. The limited frame rate of FPD detectors used in CBCT, as well as the potential afterglow effect if consecutive projections are acquired with a too short lag period, limits the minimal exposure time needed in CBCT.

FPD have limitations in their performance including linearity of response to the radiation spectrum, lack of uniformity of response throughout the area of the detector, and possible nonfunctioning pixels (see also Sect. 2.2.2.1). To overcome this, units with FPDs should be recalibrated periodically.

An important property of X-ray detectors is their *pixel size* (i.e., the physical size of individual detector elements), which is a principal determinant of resolution and therefore detail of CBCT images. The theoretical spatial resolution in CBCT is dependent on the nominal pixel size of the detector array, but is reduced to some extent by other factors in the imaging chain (e.g., focal spot size, voxel size of the reconstructed image). On the other hand, detectors with smaller pixels capture less X-ray photons per detector element, resulting in increased image noise. This can be compensated for in two ways. First of all, detector elements can be binned (e.g., grouped together and considered as one element), for example, in a 2 × 2 configuration; while this reduces image noise, spatial resolution will be reduced as well. Alternatively, the tube output (and thus the patient dose) can be increased to achieve an adequate signal-to-noise ratio.

2.2.2 Image Reconstruction

In CBCT, each projection image consists of a pixel matrix with a 12- to 16-bit value (proportionate to the detected X-ray intensity) assigned to each pixel. This data is then reconstructed into a 3D volumetric dataset composed of cubical volume elements (voxels) by a sequence of software algorithms. Subsequently, orthogonal (i.e.,

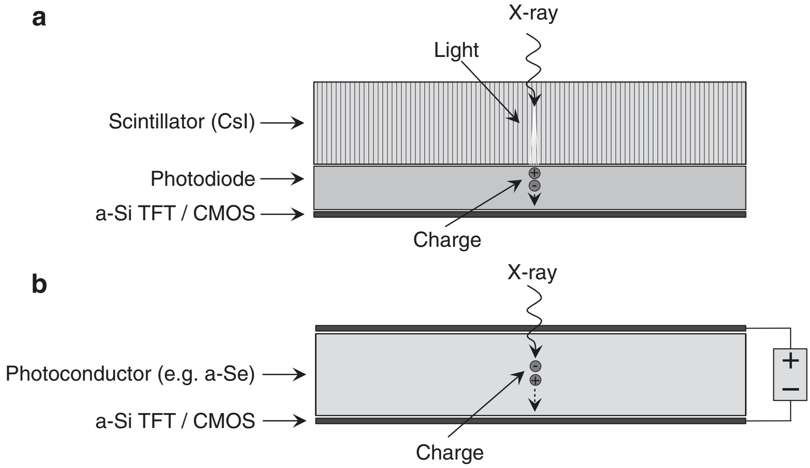

Fig. 2.11 Schematic representation of indirect (**a**) and direct (**b**) FPD systems. (Adapted from Seibert (2006), reproduced under the Creative Commons Attribution Noncommercial License)

perpendicular images in all three planes) sectioning of the volumetric dataset is provided, and additional visualizations can be created.

Reconstruction is computationally complex, so, to facilitate workflow, data is often acquired by one computer (acquisition computer) and transferred via Ethernet connection to a second computer (workstation) for processing. Reconstruction times vary depending on the acquisition parameters (voxel size, FOV, number of projections), hardware (processing speed, data throughput from acquisition to workstation computer) and software (pre- and post-processing, reconstruction algorithm) used. Reconstruction should be accomplished in an acceptable time (usually less than 5 min) to complement patient workflow. The reconstruction process consists of numerous steps.

2.2.2.1 Pre-processing

Due to spatially varying physical properties of the detector elements, as well as variations in the X-ray sensitivity of the scintillator layer, raw images from CBCT detectors have spatial variations referred to as dark image *offset* and *pixel gain* variation. The dark image offset (i.e., the detector output signal without any X-ray exposure), and its spatial variations are mainly caused by dark current of the photodiodes. Pixel gain variations are caused both by varying sensitivity of the detector elements and by deviations of the local conversion efficiency of the scintillator or direct conversion material due to, for example, slight variation in thickness or density. In addition to these spatial variations, detectors exhibit inherent pixel imperfections or defects. To compensate for these inhomogeneities, raw images require systematic offset and gain calibration as well as a *correction of defective pixels* (Fig. 2.12). Subsequently, temporal artifact correction can be applied by estimating and then subtracting the *afterglow* signal from prior projection images. This sequence of calibration steps is referred to as *detector pre-processing*.

2.2.2.2 Reconstruction

The most widely used reconstruction algorithm in CBCT is the Feldkamp (FDK) algorithm, which is a modified *filtered backprojection* (FBP) method (Feldkamp et al. 1984). Using backprojection, the total X-ray attenuation measured at a detector pixel is equally distributed to all voxels in the FOV which are traversed by the X-rays reaching that particular pixel. A simple representation of backprojection is shown in Figs. 2.13, 2.14, 2.15, 2.16, and 2.17.

Figure 2.13 shows 1D projections of a 2D image using parallel projection lines. After backprojecting, the detected attenuation value along every point of the projection line, backprojections from different projection angles can be averaged (Fig. 2.14). When a larger number of projection angles are combined, the reconstruction represents the original object more accurately

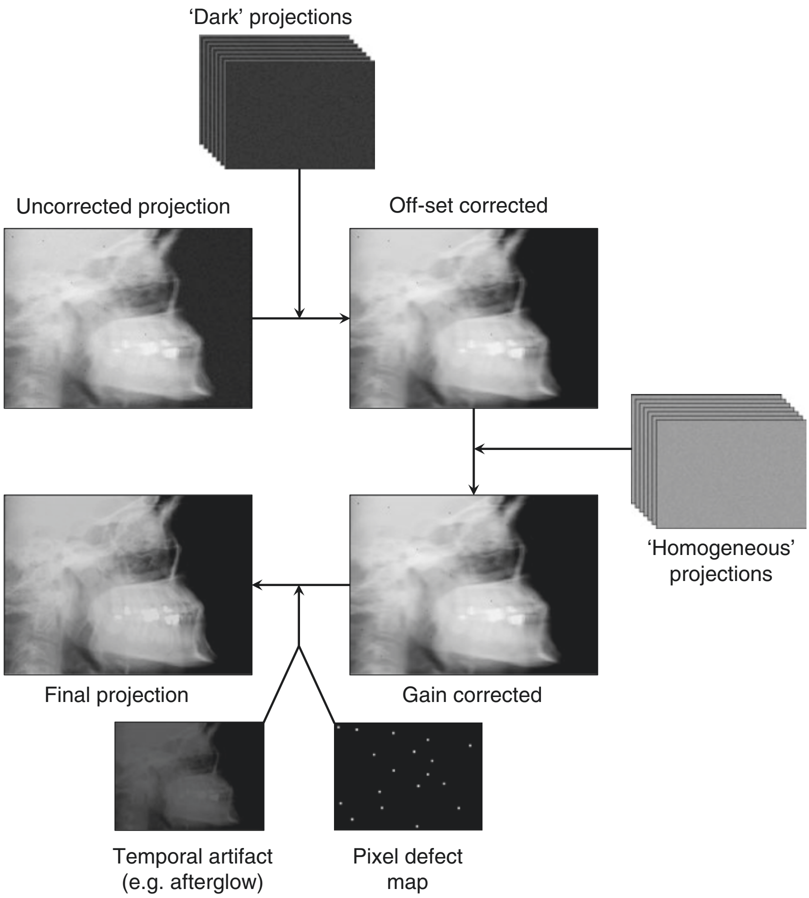

Fig. 2.12 Schematic diagram illustrating CBCT preprocessing steps. Initially, offset correction is performed by pixel-wise subtraction of an individual offset value computed by averaging over a series of *dark* images (acquired without any X-ray exposure). Next, linear gain calibration is performed, consisting of dividing each pixel by its individual gain factor. Gain factors are obtained by averaging a sequence of homogeneous exposures, which have their own sequence of *dark* images, without any object between the X-ray source and detector. Finally, defect interpolation is performed. Each pixel that shows unusual behavior, either in the gain image or in the average *dark* sequence, is marked in a defect map. The *grey* values of pixels classified as defective in this way are computed by interpolation. For flat panel detectors, there is usually an additional procedure to correct for temporal artifacts. These arise in flat detectors because both the scintillator and the read-out panel at the detector exhibit residual signals (i.e., afterglow).

(Fig. 2.15). Nonetheless, the backprojected image is a blurred representation of the original. To compensate for this, the projections can be filtered to enhance the edges (Fig. 2.16). Different filters with varying levels of sharpness/smoothness can be used (Fig. 2.17) (Pauwels et al. 2015a).

An alternative reconstruction method is *iterative reconstruction*. This is a general name for an algorithm which undergoes several repetitions (i.e., iterations) before the final reconstructed image is produced. Typically, iterative reconstruction is done by forward projecting an initial estimate (which can be a conventional FBP reconstruction, a crude model of the expected anatomy or a blank image) and comparing the result with the actual projection data. The estimate is then corrected accordingly, a new forward projection is generated and the process is repeated for a set number of iterations or until a predetermined level of agreement is found (Fig. 2.18). In MDCT, iterative reconstruction has been introduced in clinical practice by all manufacturers, generally resulting in substantial noise reduction (and as a result, a potential mAs reduction) compared with FBP reconstruction without sacrificing spatial resolution. Also, more advanced iterative reconstruction techniques (e.g., metal artifact reduction, noise suppression) have been proposed (Beister et al. 2012). Despite its versatility, the main disadvantage of iterative reconstruction is the large amount of computation involved, which increases proportionally with the number of iterations. Therefore, in CBCT, iterative reconstruction is still largely absent in clinical practice, but is expected to become more common in the near future.

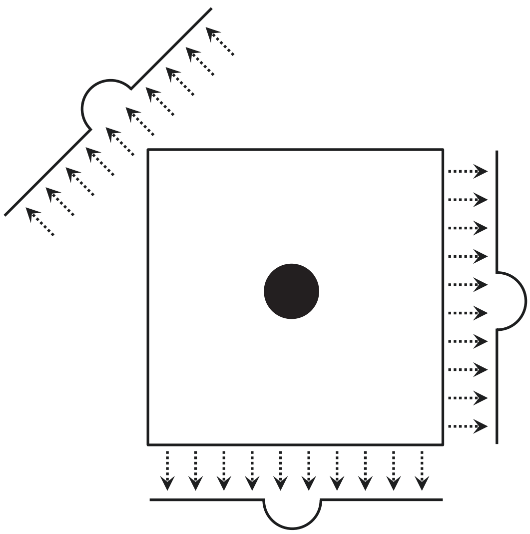

Fig. 2.13 Forward X-ray projection of a circular object using parallel projection lines

2.2.3 Grey Values vs. Hounsfield Units

CBCT images are reconstructed as a 3D stack of *voxels*, in which each voxel is assigned a *grey value* (i.e., a whole number) according to its estimated X-ray attenuation. A lower grey value corresponds to a lower attenuation, with the lowest grey values corresponding to air. Typically, grey values are distributed along a 12-bit scale, implying that 4096 possible grey values can be assigned. Extended bit depths along nominal scales up to 16 bit (with the actual bit depth typically at 13–14 bit) are used as well, although it is somewhat questionable whether image quality (esp. contrast) is improved as a result.

In MDCT, grey values can be calibrated along the *Hounsfield scale*, allowing for quantitative evaluation of attenuation. The Hounsfield scale is determined using the attenuation of air and water as calibration points, with air corresponding to

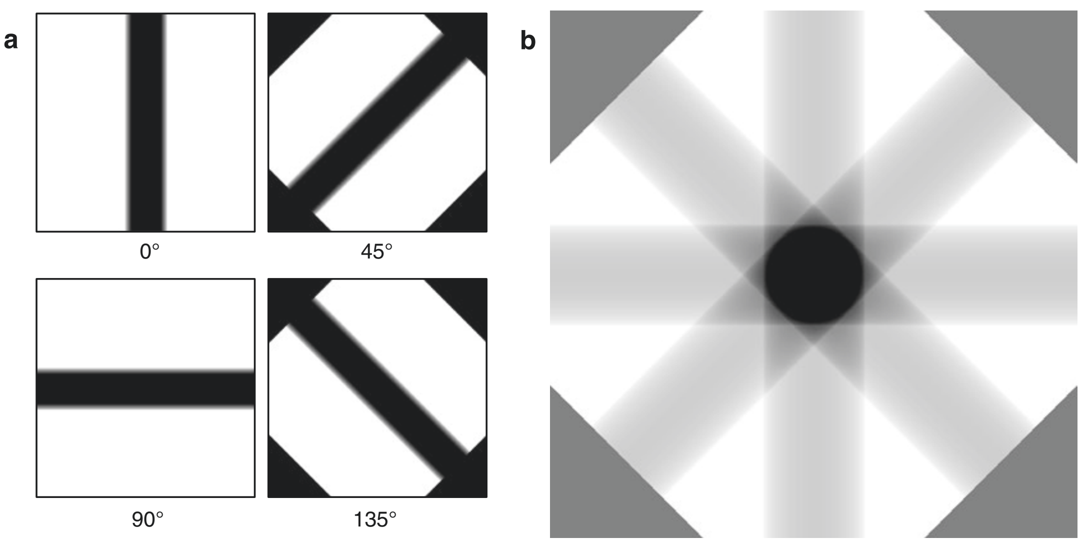

Fig. 2.14 Backprojection of the object in Fig. 2.13 from four projection angles (**a**) providing an average of the four backprojections (**b**)

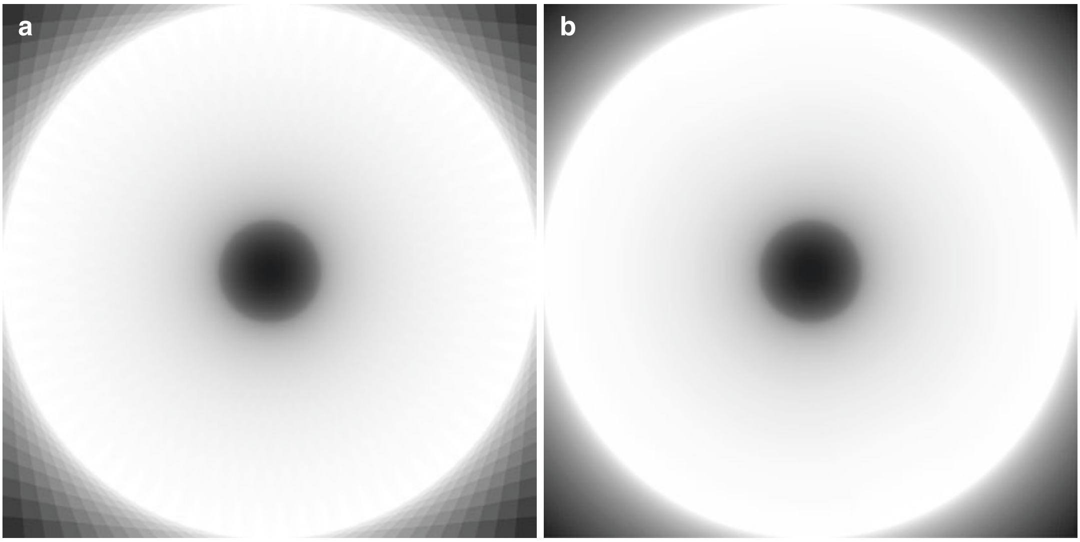

Fig. 2.15 Average of 36 (**a**) and 180 (**b**) backprojections of the object in Fig. 2.13

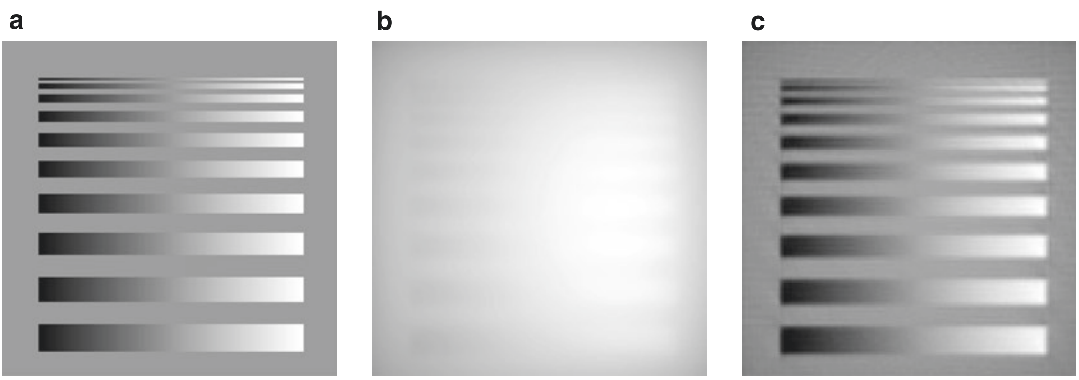

Fig. 2.16 Line pattern original image (**b**), unfiltered backprojection (**b**), and filtered backprojection (**c**)

−1000 Hounsfield units (HU) and water to 0 HU. HU calibration has several potential applications, including the discrimination of solid- and liquid-filled growths, and the estimation of bone mineral density (BMD). In CBCT, however, the use of HU is severely limited by several inherent issues regarding grey value stability. Some of the most notable issues are:

- **High amount of detected X-ray scatter.** Although uniformly distributed scatter (as well as other sources of noise) does not affect overall grey value stability, scatter can be non-uniform leading to image shading.
- **Beam hardening.** Beam hardening is the increase in mean energy of an X-ray beam passing through tissue. When not properly compensated for, it can lead to darkening in regions where the beam was "harder." As CBCT units typically operate at a lower kV than MDCT (and thus contain a higher proportion of low-energy X-rays), beam hardening is more pronounced.
- **Effect of tissues outside FOV.** The use of horizontal collimation results in the "local tomography" effect, in which asymmetrically distributed tissue is found outside the FOV. This tissue leads to varying degrees of

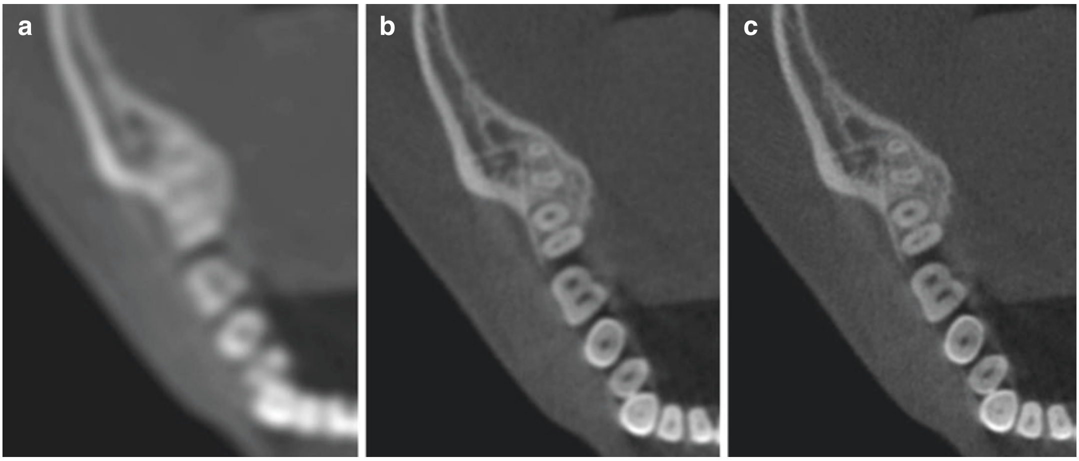

Fig. 2.17 Axial CBCT images showing the effect of different cutoff frequencies (expressed as a fraction of the Nyquist frequency) using cosine reconstruction filters (**a**) 0.2 cutoff; (**b**) 0.6 cutoff; (**c**) 1.0 cutoff. A larger cutoff frequency during filtration increases both spatial resolution and noise. (Figure reproduced from Pauwels et al. (2015a) under the British Institute of Radiology's License to Publish

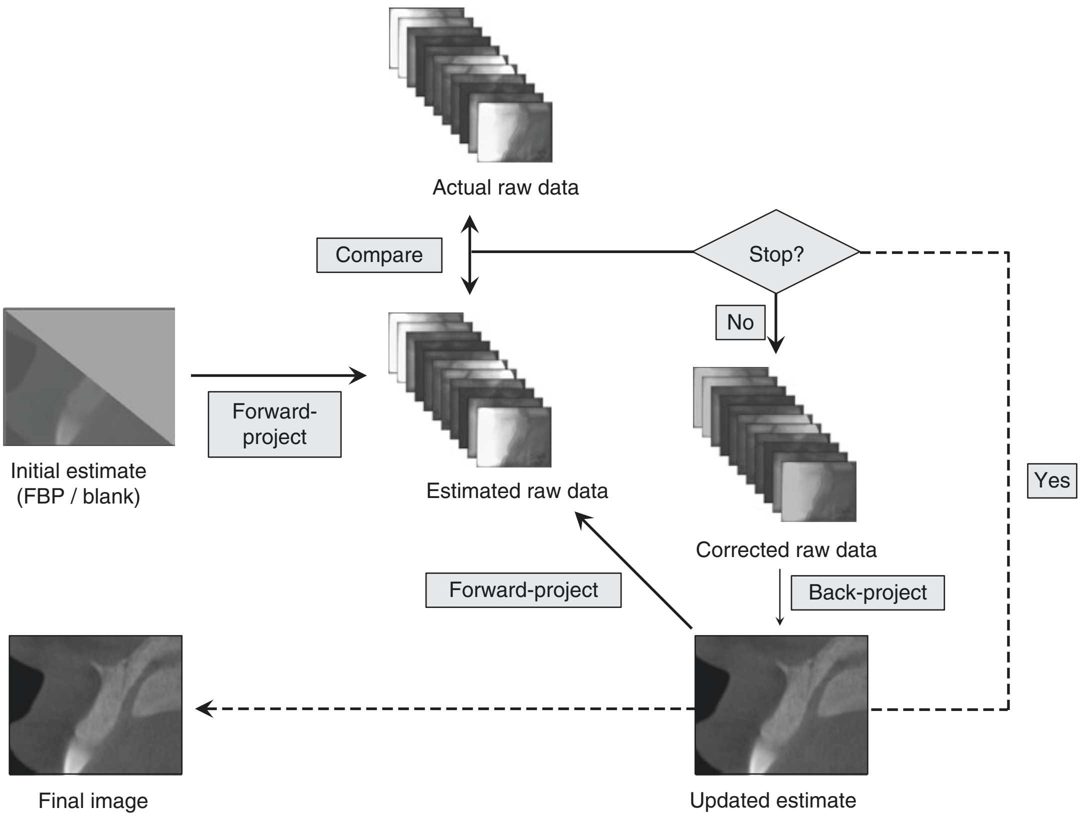

Fig. 2.18 Schematic representation of iterative reconstruction approach in CT. An initial image estimate (which can be a blank image or an FBP reconstruction) is forward-projected, and the estimated raw data is compared with the actual raw data acquired by the CT scanner. The estimated raw data is then corrected and backprojected to obtain a new image estimate. This process is repeated until sufficient agreement between the estimated and actual raw data is found, or until a fixed number of iterations has been made

added attenuation for projections acquired at different angles, and can lead to a grey value gradient (typically an anteroposterior shading for dental scans).

- **Metal artifacts.** Although metal artifacts are not exclusive to CBCT, they commonly occur in dental scans due to the large amount of metallic restorations found in the patients' dentition. Metal artifacts are manifested as dark and bright streaks and areas, close to or radiating from the metal object. The appearance and severity of metal artifacts depend on the number, size, shape, and relative locations of the metals. Because of the CBCT imaging geometry, they are mainly found in the axial plane, with a slight divergence along the z-axis depending on the X-ray beam angle.

In general, the use of grey values as HU (or in any quantitative way) should be avoided in CBCT, although it may have some limited use in controlled circumstances. A detailed description of grey value stability issues in CBCT can be found in the reviews by Pauwels et al. (2015b) and Molteni (2013). More information regarding grey value uniformity and artifacts can be found in Sect. 2.5.1.

2.3 Comparison to Multi-Detector Computed Tomography (MDCT)

The principal difference in volumetric data acquisition between CBCT and MDCT is that the latter uses a fan-shaped X-ray beam (Fig. 2.5) in a helical progression acquiring individual image slices of the FOV, which are then stacked to obtain a 3D representation. Each slice requires a separate rotation and separate 2D reconstruction. However, modern MDCT scanners use a large number of detector rows in order to increase the number of slices acquired simultaneously. Therefore, MDCT has become somewhat more akin to CBCT in terms of beam geometry, with newer models providing an increasingly divergent X-ray beam. However, there are still essential differences between the two technologies (Table 2.1). As a result, patient dose and image quality can differ considerably between CBCT and MDCT.

Patient dose from MDCT is generally higher than that of a corresponding CBCT scan (Loubele et al. 2009), as CBCT is usually associated with a lower tube output (kV, mAs) and a horizontally collimated FOV. However, low-dose MDCT protocols for implant planning, with doses overlapping with the high end of the dose range of CBCT, have been proposed (Loubele et al. 2005). As a result of recent technological innovations in MDCT, such as noise reduction through iterative reconstruction, it can be expected that scans of the hard tissues of the dentomaxillofacial region can be acquired at a very low dose using current-generation MDCTs. However, as MDCT is scarcely used in dentistry nowadays, dedicated low-dose protocols for dental applications and accompanying dose reports are lacking. In terms of image quality, as discussed in Sect. 2.5.1, CBCT images are characterized by a high spatial resolution owing to the use of small detector pixels and correspondingly small image voxels. However, contrast resolution is limited by the detector's dynamic range, and a relatively high proportion of scattered radiation at the detector, among other factors. X-ray scatter, along with the small detector pixels and image voxels and the low tube output, also results in a high image noise compared with MDCT.

While CBCT imaging is considered to be superior for visualization of small details with high anatomical contrast, it cannot be used for applications in which soft tissue discrimination is needed (e.g., characterization of tumors or cysts). In these circumstances, MDCT or magnetic resonance imaging with or without contrast is indicated. In terms of artifacts, while CBCT and MDCT are generally prone to the same types of artifacts, motion artifacts can be more pronounced in CBCT (especially when long scanning times are used). Furthermore, CBCT images can have poor uniformity of grey values due to the use of horizontal collimation and the subsequent presence of tissue outside of the FOV (see Sect. 2.5.1.4). As for metal artifacts, there are little or no reasons for differences in terms of artifact severity between CBCT or MDCT images as

Table 2.1 General similarities and differences at each stage of imaging between MDCT and CBCT

Stage	Similarities	Differences
X-ray beam shape	• Pyramid-shaped beam (albeit with different relative dimensions)	• Full coverage in MDCT in terms of beam diameter; diameter of beam is collimated to as small as 4 cm in CBCT • Beam divergence in CBCT at upper and lower borders of the FOV is typically larger than that of MDCT, even when many detector rows are used • Beam in MDCT can be narrow if few detector rows are used
Detector	• Typically, indirect X-ray detection (using scintillator, or xenon gas ionization chamber for some MDCT units)	• Different scintillator material used, typically cesium iodide in CBCT and gadolinium oxysulfide in MDCT. As a result, detector sensitivity, efficiency, dynamic range, and speed differs
	• Detector elements can be binned to increase signal-to-noise ratio (at the cost of spatial resolution)	• Image intensifier detectors used in older CBCT models • Flat detector used in CBCT, detector arc (with perpendicular X-ray detection throughout the FOV) used in MDCT • Size of detector elements can vary between central and peripheral slices in MDCT; detector pixels are uniform in size in CBCT • The use of a flat detector in CBCT, along with a generally short patient-detector distance, increases the proportion of detected X-ray scatter. Physical collimation between detector rows in MDCT can lead to additional scatter reduction along the z-direction
Technique factors	• kVp, mA, field of view settings determine image quality and patient radiation dose	• Certain technique factors differ: MDCT involves selection of pitch, acquired slice thickness, and pixel size, whereas CBCT involves selection of rotation arc, voxel size, and number of projection images • Automatic exposure control is ubiquitous in MDCT but largely absent in CBCT • CBCT typically operates at a lower mAs (although low-dose MDCT protocols can reach similar mAs levels) • Dual energy imaging possible in MDCT, but not yet implemented in CBCT
Patient preparation	• For some CBCT models, patients is supine as in MDCT	• Patient is standing or seated for most CBCT units
Patient protection	• Lead torso shield • Thyroid shield is desirable, especially for maxillary scans. For lower jaw or maxillofacial scans, potential metal artifacts should be considered	• Extra care should be taken in MDCT with automatic exposure control, as the use of shielding in the primary beam may lead to a severe increase in tube output
Exposure	• Patient informed to keep still	• Scan time varies from 5 s to greater than 30 s in CBCT whereas modern MDCT scanners allow for sub-second scans; thus, motion artifacts are more likely to occur in CBCT • Patient is stationary in CBCT (with the exception of dual acquisition in which the chair may move between scans). In MDCT, the table moves continuously during exposure
Image viewing	• Image must be reconstructed before viewing (30 s–>10 min)	• Secondary, multi-planar and other reformatted images are of almost equal resolution in CBCT because of isotropic voxels. In MDCT, coronal and sagittal slices can have poorer resolution than axial images (depending on slice thickness and pitch)
	• Images are conventionally reconstructed using a type of filtered backprojection • Basic image processing possible, e.g., contrast, brightness, zoom, filtering	• Advanced reconstruction techniques (e.g., iterative reconstruction, noise reduction, metal artifact reduction) common in MDCT but not yet in CBCT

a result of fundamental differences between the imaging techniques. Different appearances of metal artifacts between CBCT and MDCT can be attributed to scanner and reconstruction factors (e.g., beam energy, calibration of the grey value histogram, beam hardening correction, and other metal artifact suppression techniques).

2.4 Unit Configurations

In 2013, it was determined that 47 CBCT models from 20 manufacturers were used in Europe (Nemtoi et al. 2013). At the time of writing, over 50 models are found worldwide. There are a few pronounced differences in terms of configuration between these systems. They can be distinguished based on patient orientation during image acquisition, whether they are hybrid systems with panoramic (and cephalometric) functionality, and on the available FOV options.

2.4.1 Patient Orientation

Most CBCT units operate with the patient in a *standing or sitting* position. Standing/seating units are typically compact (i.e., small physical footprint), allowing them to be placed in private dental clinics or other environments where little space is available. Few CBCT models are available where the patient is scanned in the supine position, as in MDCT. Furthermore, different head restraint mechanisms are used, as patient motion may limit spatial resolution. Combinations of head rests, chin rests or bite blocks, straps and lateral fixation are currently used.

2.4.2 Functionality

CBCT systems can be stand-alone or hybrid systems. Hybrid or multi-modal systems combine digital panoramic and/or cephalometric radiogra-

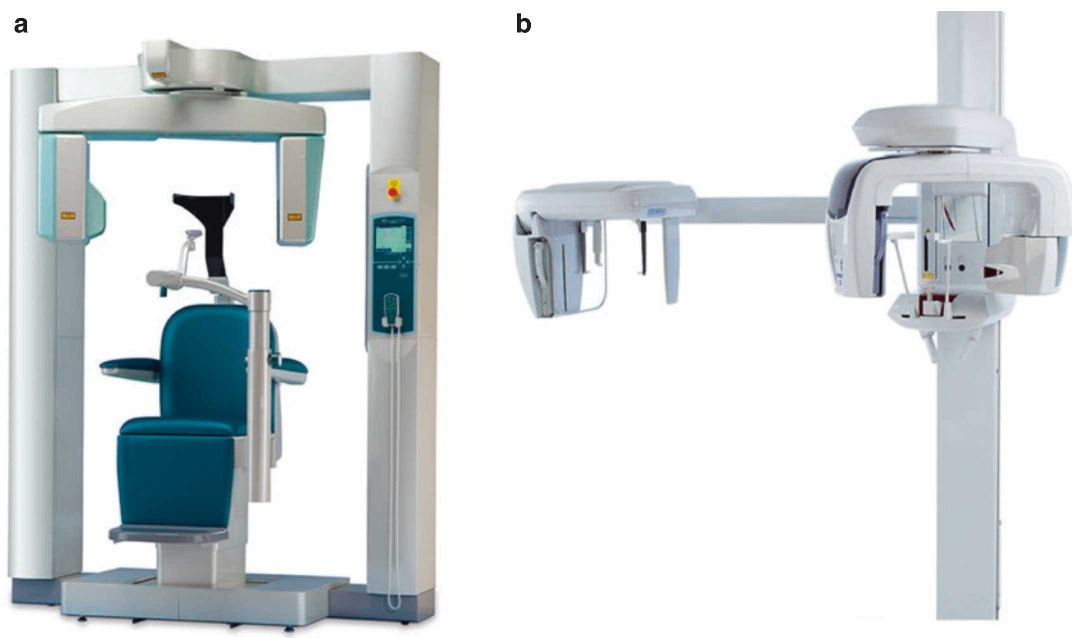

Fig. 2.19 Examples of stand-alone (**a**) 3D Accuitomo 170, (J. Morita, Osaka, Japan) and all-in-one hybrid unit configurations with CBCT, panoramic and cephalometric imaging (**b**) Veraviewepocs 3D R100, (J. Morita, Osaka, Japan). Images courtesy of J. Morita, Osaka, Japan

phy with CBCT in a single equipment (Fig. 2.19). The use of hybrid systems can be cost- and space-efficient.

2.4.3 Volume Acquisition

CBCT units can be assigned into four broad categories based on the vertical and horizontal dimensions of the FOV (Fig. 2.20):

- **Large (Maxillofacial).** Covers most of the craniofacial skeleton, at least from below the hard tissue of the chin to the nasion. Usually greater than 15 cm in any dimension.
- **Dentoalveolar (both jaws)**. Usually 8 cm or more in diameter and height.
- **Single jaw/dual TMJ.** Can cover a single full jaw (excl. ramus for mandibular scans) or both temporomandibular joints. Wide in diameter ($\geq$ 10 cm, or $\geq$ 14 cm if used for TMJs) but small in height (4–6 cm).
- **Small (localized)**. As small as 3 cm in any dimension, covering localized regions such as 2–4 teeth and surrounding alveolus or a single temporomandibular joint.

As discussed in Chap. 7, the FOV size is one of the primary determinants of radiation dose; thus, proper selection of the FOV according to the diagnostic task is paramount. This also implies that the purchase of a CBCT machine should take its intended use (and the minimal and maximal FOV size required to cover this intended use) into account.

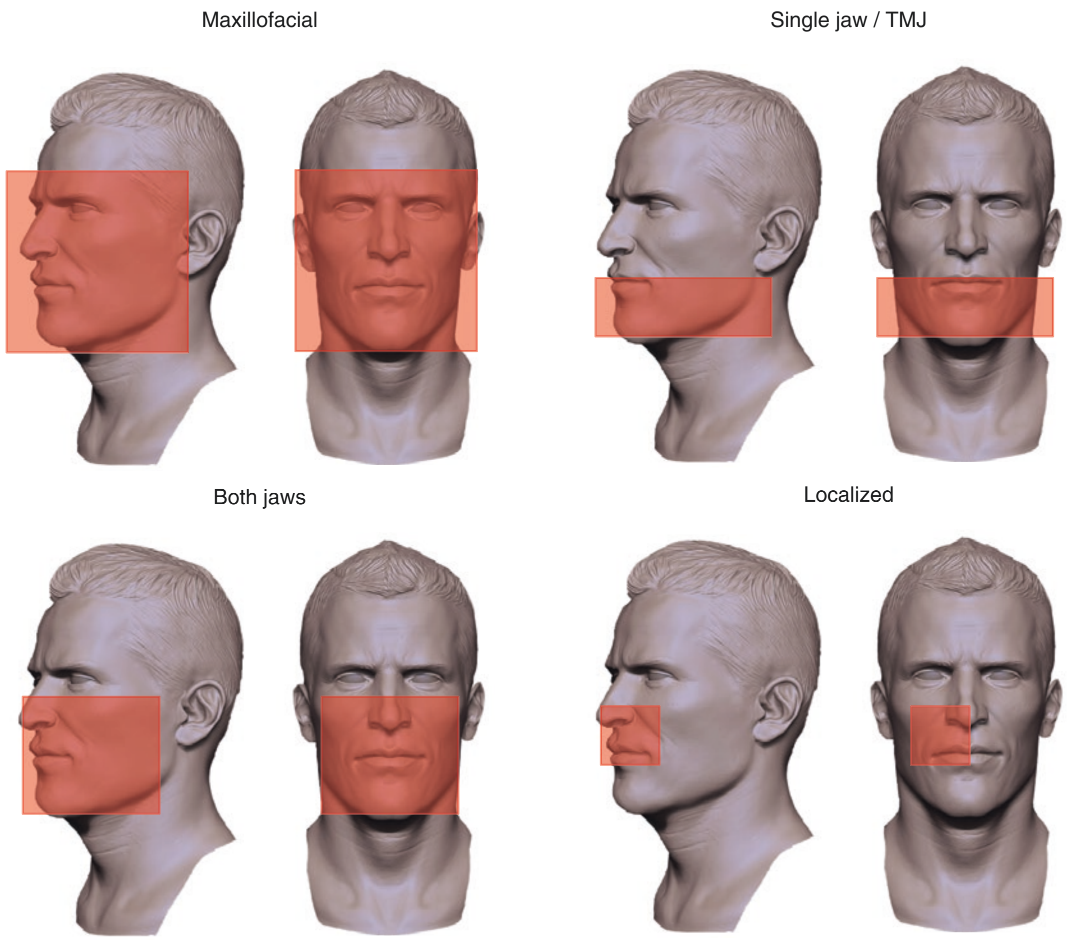

Fig. 2.20 Examples of four broad categories of FOV sizes used in dental and maxillofacial CBCT. 3D head model images courtesy of Rodrigue Pralier

2.5 Technical Parameters

While CBCT units are relatively simple to operate, they exhibit wide differences in technical parameters available to the operator. CBCT users must be able to choose an appropriate imaging protocol (i.e., a selection of specific technical parameters) for each patient to *optimize image quality and minimize radiation dose* for a specific imaging task. Therefore, practitioners and operators using CBCT must have theoretical knowledge and a practical understanding of the effects of available technical parameters on image quality and radiation dose. Readers are referred to Chaps. 5 and 7 for more details regarding radiation dose and radiation protection.

2.5.1 Image Quality

Image quality can be described using four fundamental parameters: *spatial resolution, contrast resolution, noise, and artifacts* (Fig. 2.21). Additionally, *geometric accuracy/distortion* can

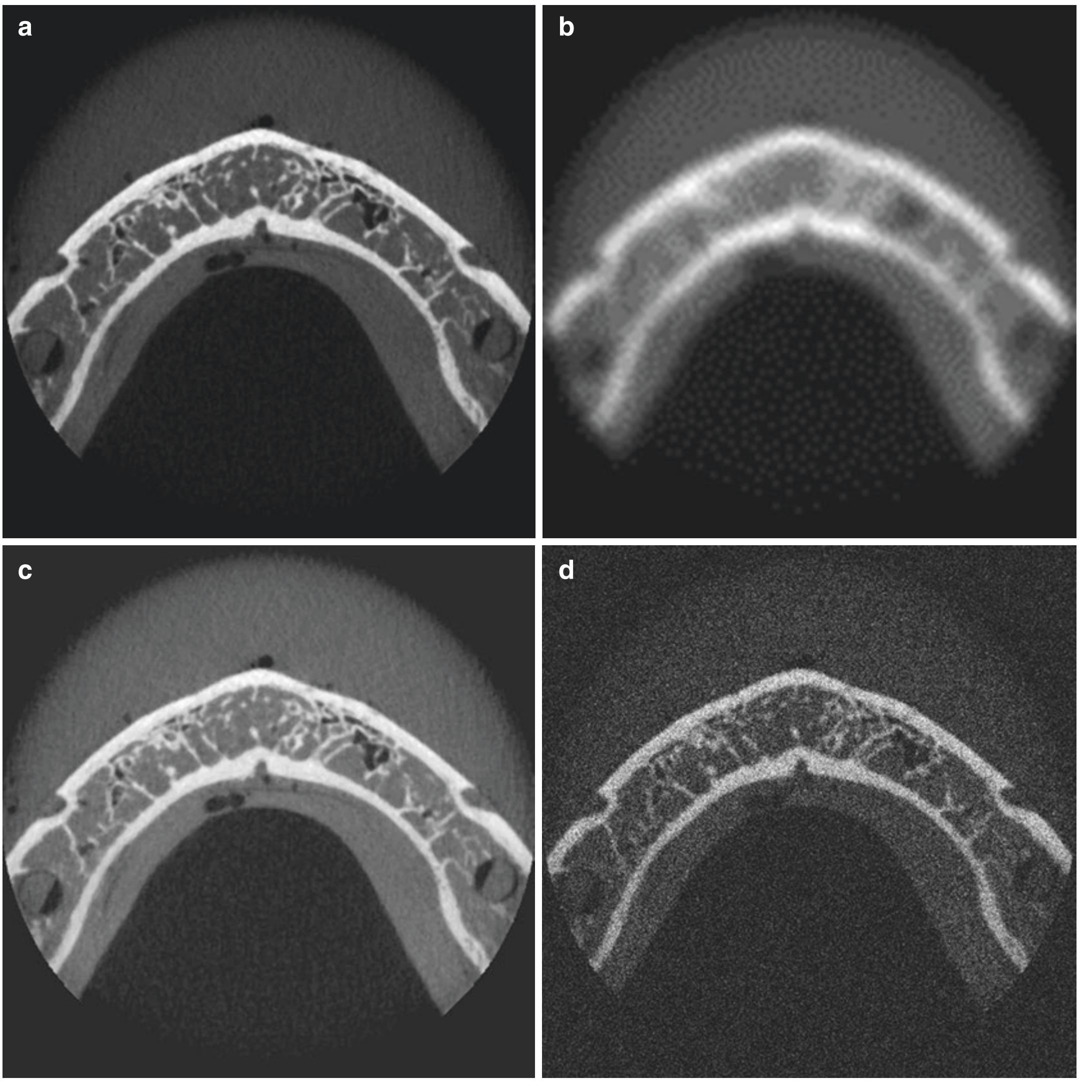

Fig. 2.21 Representative axial CBCT images demonstrating visual differences observed with changes in spatial resolution, contrast resolution and noise. Original image (**a**) can be compared to a smoothed image (**b**), showing reduced spatial resolution (as well as reduced noise), and image with reduced contrast resolution (**c**), and one with artificial noise added (**d**)

be considered as another image quality metric for medical images which involve distance calibration, including CBCT. This section will provide a brief overview of these image quality parameters; information on their assessment during quality control is presented in Chap. 6.

2.5.1.1 Spatial Resolution

Spatial resolution (or sharpness) is the ability to distinguish small details in the image, and can be expressed, for example, as the ability to discriminate two small-sized structures. The spatial resolution of CBCT images is related to, but not exclusively determined by, the *voxel size* (Fig. 2.22). CBCT units nominally provide isotropic (i.e., cubical) voxels, implying that spatial resolution should be approximately the same in all three orthogonal dimensions. The voxel size is thus expressed as the length of any side of the voxel. It should be noted that CBCT images are often displayed using a certain "slice thickness." The use of a slice thickness larger than the voxel size effectively leads to cuboidal voxels, and reduces noise at the cost of a lower spatial resolution in the dimension perpendicular to the slice.

Voxel sizes range between CBCT units and exposure protocols, and are found between 0.07 and 0.6 mm. The small voxel size in CBCT, along with other factors affecting spatial resolution, facilitates its application in dentistry for those tasks requiring high detail, such as the evaluation of root and periapical pathology, ankylosis, root resorption, and impaction.

Apart from the voxel size, spatial resolution of CBCT systems strongly depends on the detector's nominal pixel size and fill factor, although other factors can affect the maximum achievable resolution (e.g., beam projection geometry, X-ray scatter, detector and patient motion, focal spot size, number of basis images, and reconstruction algorithm).

For larger FOV sizes, the reconstructed voxel size cannot be as small as for small FOVs due to computational limitations. However, it is theoretically possible to re-reconstruct all or a part of a large FOV at a smaller voxel size, allowing for an increased spatial resolution. Several manufacturers have implemented this function.

2.5.1.2 Contrast Resolution

Contrast resolution in X-ray imaging can be defined as the ability to discriminate objects of different density (or, specifically, attenuation).

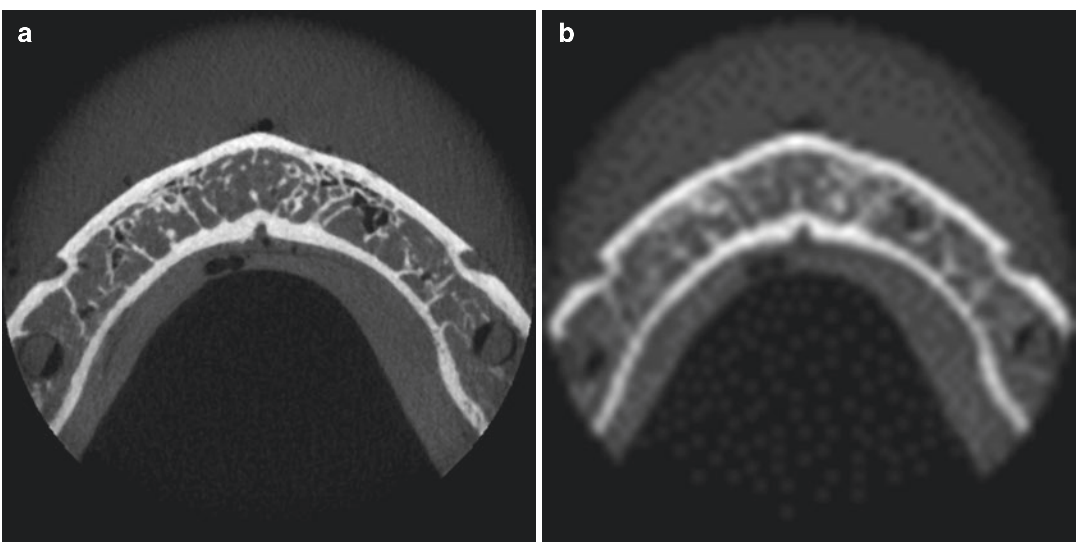

Fig. 2.22 Visual comparison of an original axial CBCT image at a 0.125 mm × 0.125 mm × 0.125 mm voxel size (**a**) and a resampled image at a 1 mm × 1 mm × 0.125 mm voxel size (**b**). The increased voxel size reduces both spatial resolution and noise

Whereas spatial resolution of CBCT is generally considered high compared to MDCT, contrast resolution is limited by numerous factors. The inherent geometric configuration of CBCT results in a high amount of detected scatter radiation. The two main reasons for this are the relatively short object-detector distance and the use of 2D detector panels with no collimation at the detector level. This is a significant factor in reducing the contrast of any CBCT system. In addition, the inherent efficiency, as well as the stability and linearity of the response, is lower for currently used CBCT detectors than for MDCT detectors. For these reasons, as well as the relatively low tube output (i.e., kV and mAs) used in CBCT, CBCT images cannot reveal subtle differences between soft tissues, such as between fluids and solid tumors, and are primarily applied for the visualization of tissues with high anatomical contrast.

2.5.1.3 Noise

Image noise in radiography can be defined as the variability (e.g., standard deviation) of grey values in a homogenous object or tissue. There are various sources of noise in CBCT. As it involves relatively low exposure levels, the random nature of X-ray interactions results in an inhomogeneous signal at the detector (i.e., quantum noise). X-ray scatter, especially when randomly distributed, further adds to the noise of the incoming signal. The detector itself causes electronic noise during signal transmission. Furthermore, filtering during image reconstruction can either suppress or enhance noise (balancing it with spatial resolution).

2.5.1.4 Artifacts

Artifacts in radiography are appearances in the image that do not correspond to the physical reality. While metal artifacts are often most commonly encountered in CBCT, there are various other sources of artifacts.

Metal artifacts are the result of exuberant absorption of X-rays by the metal, and the inability of the reconstruction algorithm to cope with this, leading to dark and bright regions and streaks in the vicinity of the metal. Metal artifacts can severely affect the visibility of structures in the vicinity of, or in-between, metal objects. Therefore, metal objects should be removed prior to scanning if possible (e.g., removable prosthesis). The adjustment of exposure parameters such as kV and mAs has little effect on metal artifacts, and the effect on radiation dose is disproportionate (Pauwels et al. 2013). In addition, current metal artifact reduction techniques in CBCT do not consistently lead to an improvement in diagnostic image quality (Bechara et al. 2012; Bezerra et al. 2015; Kamburoğlu et al. 2013; Parsa et al. 2014). Since metal artifacts manifest primarily in the axial plane because of the X-ray beam geometry, the patient's head can be tilted in some cases to avoid interference of metal artifacts with a certain region of interest.

A relatively common type of artifact in CBCT is due to *patient motion*. The fact that the patient is in a sitting or standing position for most units, along with the relatively long scan time (usually 15–20 s), can result in slight or more severe motion blurring. While slight movements (e.g., swallowing, regular breathing) does not lead to considerable image degradation, excessive movement can lead to severe distortion, possibly requiring retakes (Nardi et al. 2016; Spin-Neto et al. 2013) (Fig. 2.23).

Furthermore, the (lack of) stability of grey values of identical tissues throughout the FOV (i.e., uniformity) can be considered as an image artifact, although it does not necessarily affect the perceived spatial or contrast resolution. Various types of uniformity issues are present in CBCT (Fig. 2.24). Anteroposterior shading can occur for small or noncentrally positioned FOVs in particular, due to the effect of tissues outside the FOV (Siltanen et al. 2003). Central-to-peripheral grey value gradients, known as *cupping and doming* (or '*capping*') artifacts, also commonly occur in CBCT due to the effect and overcorrection, respectively, of beam hardening.

Furthermore, ring artifacts can occur due to improper detector calibration, as any detector pixel giving a consistently overestimated or

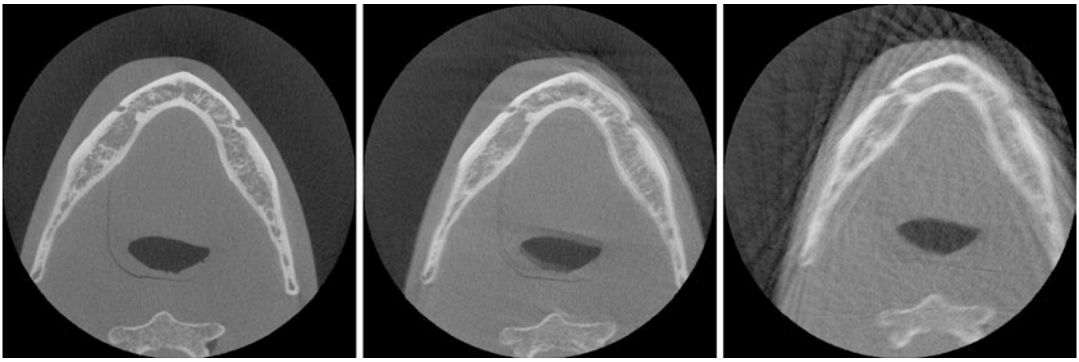

Fig. 2.23 Axial slices of CBCT scans of an anthropomorphic phantom, illustrating the effect of motion during CBCT acquisition. *left*: stationary phantom. *middle*: moderate motion. *right*: severe motion

underestimated read-out value will manifest itself as a circle on the reconstructed image.

2.5.1.5 Geometric Accuracy

The geometric accuracy of CBCT can be expressed as the accuracy of linear, area, and volume measurements. It is affected by the spatial resolution of the image, the accuracy of geometric calibration, and the presence of geometric distortion.

- **Spatial resolution—partial volume averaging.** The accuracy of a measurement partially relies on the ability to identify the boundaries of the measured structure. Images with poor resolution suffer from an effect known as partial volume averaging, in which the edges between different tissues are not properly represented (Fig. 2.25). This can lead to deviations in manual or automatic measurements.
- **Geometric calibration.** As CBCT images are calibrated for absolute distance measurements, it is essential that the voxel size correctly represents the actual physical size. Over- or underestimation of the voxel size can lead to consistent measurement deviations.
- **Geometric distortion.** Image intensifier-based CBCT units were prone to geometric distortion such as the pincushion effect. Flat panel CBCTs are less susceptible to geometric distortion, although it may still occur, e.g., due to deviations in tube/detector rotation from a perfect circular trajectory (and improper compensation thereof).

2.5.2 Exposure Parameters

Several exposure parameters determine the energy and quantity of the X-ray beam as well as the quality of the projection image. Some of the factors, such as focal spot size, source-object distance, object-detector distance, beam filtration, and beam frequency, are equipment-dependent and cannot be altered by the operator. Others, such as milliamperage (mA), exposure time (s), and kilovoltage (kV), can be operator-controlled within a certain range, depending on the CBCT model.

2.5.2.1 Equipment-Dependent Factors

- **Focal Spot Size.** The focal spot is the area at the anode which is hit by the electron beam, leading to the production of X-rays. The focal spot determines the penumbra or geometric unsharpness of the projection images, seeing that the reconstruction algorithm assumes that all X-rays originate from an infinitely small point source. Smaller focal spot sizes result in a smaller penumbra and theoretically sharper images (Fig. 2.26). Most CBCT units have a nominal focal spot of 0.5 mm, although smaller focal spots are used by some models. When using a smaller focal spot, care has to

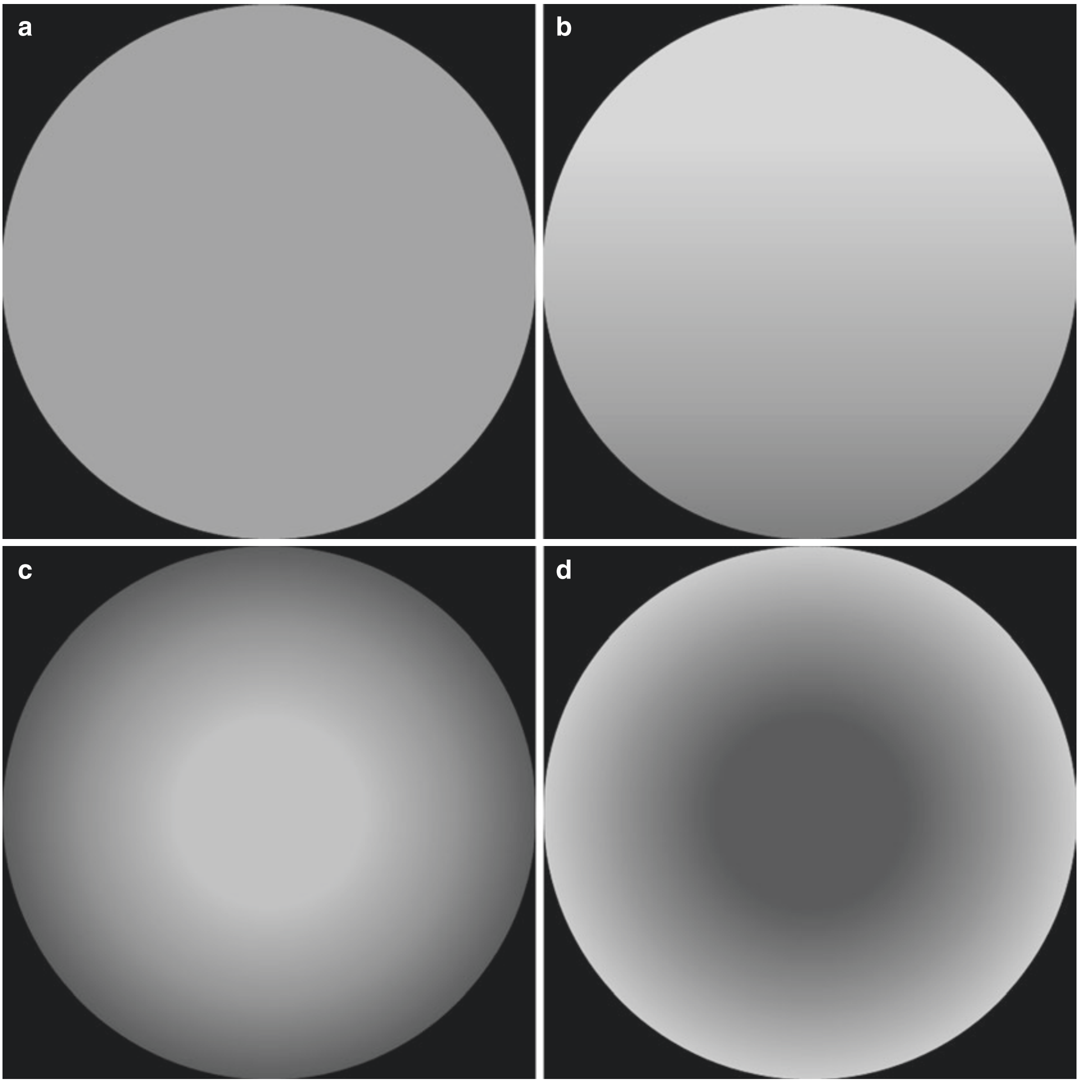

Fig. 2.24 Simulated images representing axial CBCT slices of a homogeneous object of water-equivalent (or similar) density demonstrating grey value uniformity issues encountered within the FOV for CBCT. Perfect uniformity (**a**) demonstrates homogeneous grey values throughout the image as compared with images showing anteroposterior shading (**b**), capping/doming artifact (**c**), and cupping artifact (**d**)

be taken to avoid overheating and damaging of the anode (e.g., by reducing the kV or mAs or increasing the cool-down time between consecutive exposures).

- **Source-Object Distance (SOD) and Object-Detector distance (ODD).** A shorter SOD increases the penumbra (Fig. 2.26) and results in a higher local skin exposure at the entrance point of the beam. However, a shorter SOD increases geometric magnification of the projection image. A longer SOD and/or shorter ODD decreases the penumbra and allows for the use of smaller detectors (Fig. 2.26); however, the proportion of detected X-ray scatter, which deteriorates image quality, increases at a shorter ODD. For very short ODDs, there is a higher risk of the patient's shoulder interfering with the rotational motion, especially that of the detector. This can be negated by the manufacturer by slightly tilting the detector or

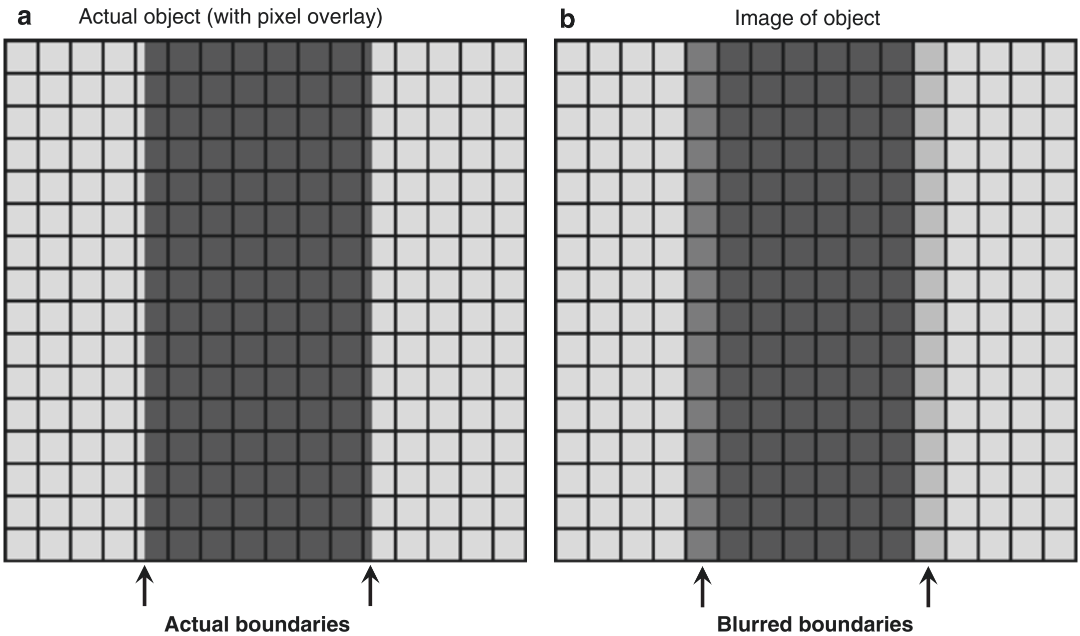

Fig. 2.25 Two-dimensional schematic representation demonstrating partial volume averaging. If an image pixel matrix is layered over an object (**a**) it is possible that the boundary between the object and the pixel matrix does not coincide. When this occurs, the grey value in the pixel containing the boundary will represent the volume-averaged attenuation of the materials comprising it, resulting in a blurring of the boundary in the image of the object (**b**). In actual radiographic images, blurring is further enhanced due to other factors (e.g., focal spot size, motion blur)

by the operator by performing a collision check (rotating the C-arm without exposure) before image acquisition.

- **Beam Filtration.** Before exiting the tube, X-ray beams are filtered by both the tube housing and a thin sheet of metal (e.g., aluminum, copper). This is done to remove the low-energy X-ray photons from the beam, as they are more susceptible for photoelectric absorption than high-energy X-rays. Low-energy photons are not of use for diagnostic imaging, as they are very likely to be absorbed in the patient (contributing to the radiation dose, but not contributing to image formation). Furthermore, the patient also acts as a filter, which can lead to beam hardening artifacts in CBCT, especially in the presence of high-density material (see Sect. 2.5.1.4). Increased filtration at the X-ray tube "pre-hardens" the beam (i.e., increases its mean energy), leading to greater dose efficiency and reduced beam hardening artifacts, but also reduces the total beam intensity. Therefore, there is a limit as to how much the beam can be filtered while still being able to reach a sufficient detector signal at an acceptable tube load. The minimum beam filtration is determined by international standards; the actual beam filtration can vary between CBCT models. While flat filters result in uniform beam filtration, other filter shapes (e.g., bowtie) can be used to reduce beam uniformity issues such as the heel effect.
- **X-ray Frequency.** Technically, the simplest method of acquiring images in a single rotational scan is to use a constant beam of radiation and to allow the X-ray detector to sample the attenuated beam during its trajectory. Alternatively, the X-ray beam may be pulsed to coincide with the detector activation or sampling. The latter approach results in a reduced overall exposure time and, as a result, a lower patient radiation exposure. It also reduces the impact of detector afterglow such that the number of frames acquired per second can, to some

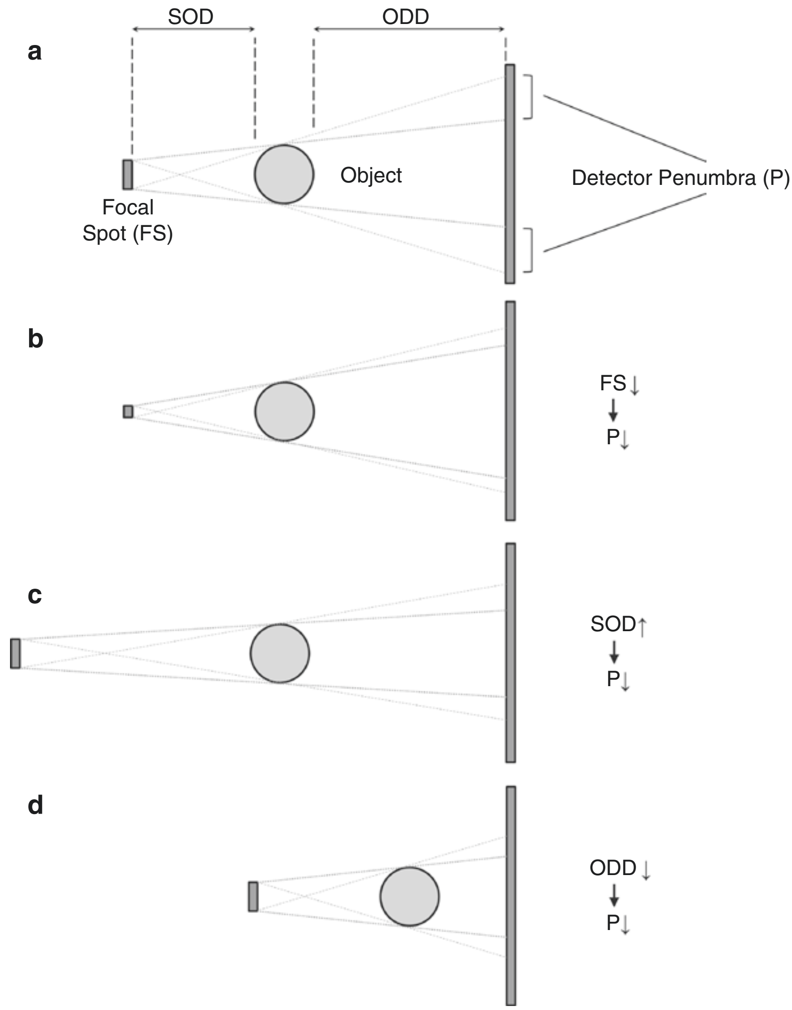

Fig. 2.26 Schematic representation of the effect of focal spot (FS) size, source-object distance (SOD) and object-detector distance (ODD) on image penumbra (**a**). A smaller focal spot size (**b**), larger SOD (**c**) and smaller ODD (**d**) all decrease the penumbra width, which increases image sharpness. (Figure reproduced from Pauwels et al. (2015a) under the British Institute of Radiology's License to Publish)

extent, be increased, which leads to faster rotation times and potentially reduced motion artifacts. In addition, pulsed systems result in substantially reduced tube load; therefore, less cool-down time is necessary between patients. On the other hand, the use of continuous exposure can result in a more homogenous tube output throughout the time in which a projection is acquired. The use of pulsed exposure requires recurrent on and off switching of the tube voltage, which coincides with a certain build-up and shut-down period in which tube voltage is between 0 and the peak kV. If the projection windows (partly) cover these two lag periods, image quality can be affected. In dental CBCT, pulsed exposures are used by most models; thus, the exposure time is often much lower than the scan time. The frequency and duration of pulsing, however, varies between CBCT units. The effect of pulsed exposure on dose efficiency (i.e., radiation dose vs. image quality) has not yet been definitively addressed.

2.5.2.2 Operator-Dependent Factors

The available ranges of exposure factors in CBCT greatly depend on the manufacturer. Whereas some manufacturers allow for a limited selection of exposure protocols, others allow for manual adjustment of exposure settings within a certain range. While the former is a more user-friendly approach, the latter allows for increased patient-specific dose optimization, providing that the user understands the effects of each parameter on image quality and radiation dose. It is essential to select exposure settings or protocols yielding the lowest possible dose for a given patient according to the *ALARA* (As Low As Reasonably Achievable) principle.

- **Milliamperage (mA).** The mA determines the number of X-rays exiting the tube per unit time. The mA required for a diagnostically acceptable image is coupled with the kV and exposure time; thus, CBCT units have shown wide ranges in terms of mA. The radiation dose increases proportionately with the mA at a 1:1 ratio. In terms of image quality, a higher mA results in an increased detector signal which reduces image noise (Fig. 2.27). In clinical practice, mA should be varied with

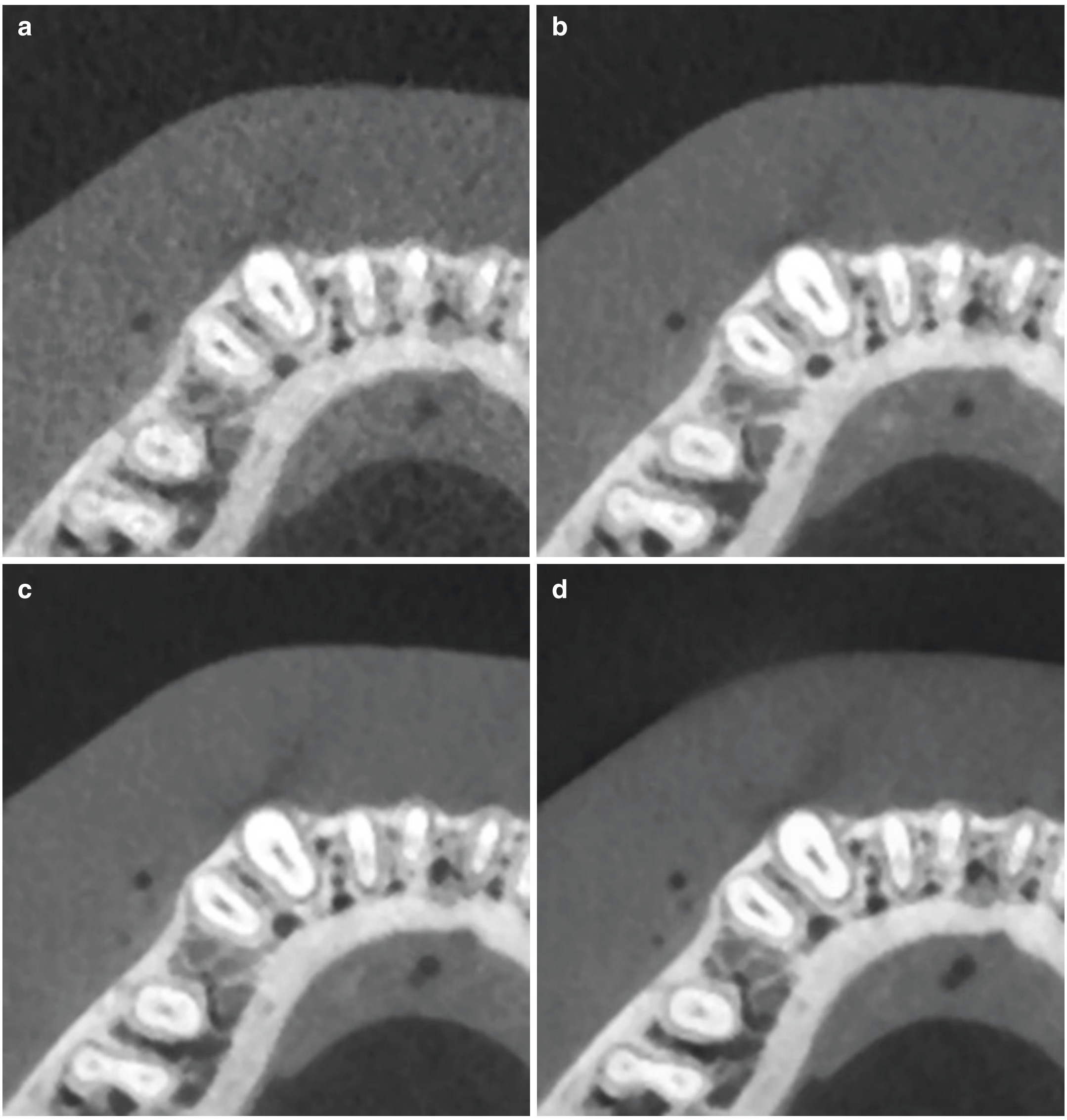

Fig. 2.27 Cropped (*right*) axial images of the right anterior mandible of an anthropomorphic phantom scanned at 1 mA (**a**), 3 mA (**b**), 5 mA (**c**), and 7 mA (**d**) exposure (3D Accuitomo 170, J. Morita, Kyoto, Japan) operating at 90 kV, and 17.5 s exposure time. At lower exposure levels, there is a clear effect of mA on noise, depicted as graininess. The effect diminishes at higher exposure levels

patient size, with smaller patients (e.g., children) requiring a lower mA to reach the same image quality as larger patients (Pauwels et al. 2017). Furthermore, the mA (or other exposure parameters) can be adjusted to the diagnostic task, with certain clinical indications (e.g., implant planning) requiring a lower image quality level than others (e.g., endodontic evaluation).

- **Kilovoltage (kV).** Adjustment of kV has a more complicated effect on radiation dose than that of mA. An increase in kV leads to a greater number of X-rays per unit time, but also increases the mean and maximum energy of these X-rays. The relationship between kV and dose is approximately quadratic within the diagnostic energy range. An increase in voltage from 60 to 90 kV can triple the radiation dose if all other exposure parameters remain the same (Pauwels et al. 2014). In terms of image quality, a higher kV reduces image noise and beam hardening, but affects contrast as well through an interplay between X-ray scatter (Compton and Rayleigh scatter, both of which are kV-dependent) and beam penetration (which increases with the kV) (Fig. 2.28). Most CBCT units operate at or below 90 kV, whereas a few can operate at higher kVs, up to 120 kV. In general, low-kV units operate at a higher mA. This lack of standardization indicates that the most dose-efficient combination of kV and mA in CBCT imaging has not yet been determined.

2.5.3 Projection Images

The number of projections acquired during a CBCT scan is determined by the frame rate (number of projections acquired per second), the extent of the rotation arc (180°–360°), and the speed of the rotation.

- **Exposure time (s)**. In CBCT, whether or not pulsed exposure is used, the exposure time is proportionate to the number of acquired projections. Typically, a few discrete options in terms of exposure time are available. Units using pulsed exposure have a lower exposure time for a given number of projections than those with continuous exposure.
- **Frame Rate.** Higher frame rates allow for shorter scan time, which can lead to images with less artifacts and better image quality. High frame rates require detectors with pixels sensitive enough to reach an adequate signal-to-noise ratio during a short time frame.

In CBCT, the number of projections typically ranges between 150 and 1000. While the use of too few projections results in aliasing artifacts due to undersampling (Fig. 2.29), this is not seen during normal CBCT use. An increased number of projections provides more information to reconstruct the image, resulting in a decreased image noise (Fig. 2.30). An increased number of projections would therefore allow the image to be reconstructed at a smaller voxel size while keeping

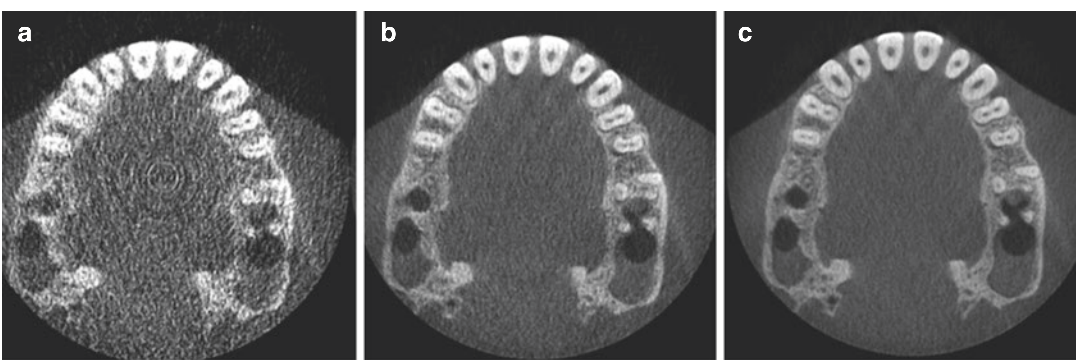

Fig. 2.28 Axial images of a plastic encased skull at (**a**) 60 kv, (**b**) 75 kV and (**c**) 90 kV acquired on a 3D Accuitomo 170 (J. Morita, Kyoto, Japan) operating at 5 mA, and 17.5 s exposure time, showing the effect of increasing kilovoltage on image quality, such as noise (Courtesy of William C. Scarfe)

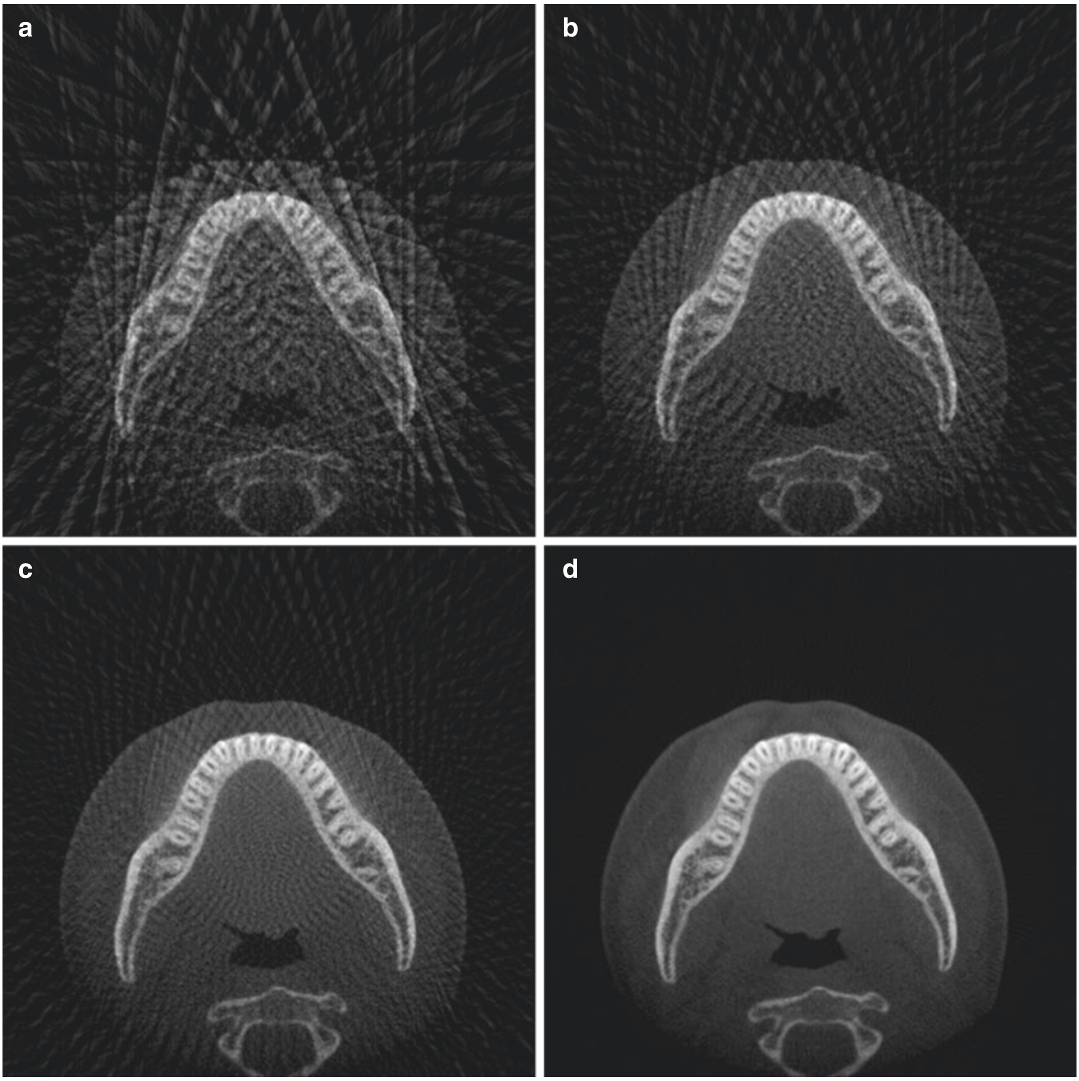

Fig. 2.29 Simulated FBP reconstruction of an axial slice using (**a**) 18 (**a**), 36 (**b**), 60 (**c**), and 180 projections (**d**). As the number of frames increases so does the exposure time and therefore radiation dose to the patient

noise at a reasonable level, effectively increasing spatial resolution. Therefore, the choice between a low or high number of projections (i.e., a short or long exposure time) is often coupled with larger or smaller voxel sizes, respectively; thus, imaging protocols with relatively short and long exposure times are often referred to as low- and high-resolution protocols. The user should adapt the number of projections to the patient, mainly depending on the spatial resolution required by the clinical indication at hand. It should be taken into account that a larger number of projections coincides with a longer scan time, a proportionately higher patient dose, an increased lag time between patients to allow for cooling of the generator tube and a longer reconstruction time. In addition, patient motion can be more severe, leading to potential image blurring and artifacts.

2.5.4 Rotation Angle

As one can imagine from Fig. 2.13, projections from opposing angles are redundant, as the backprojection would be identical (although this is not entirely the case when a divergent beam does not

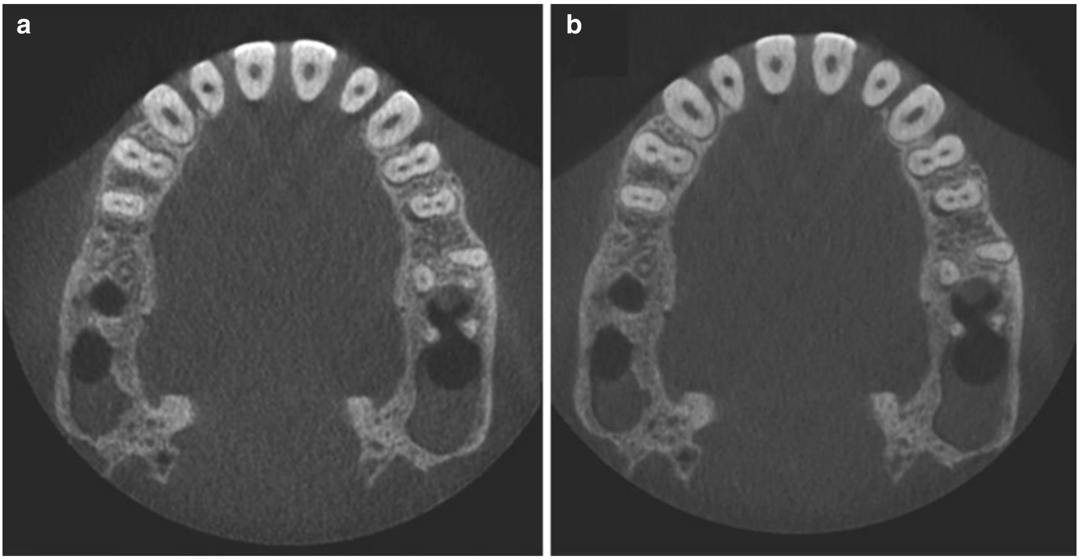

Fig. 2.30 Axial CBCT images of a plastic encased skull (3D Accuitomo 170, J. Morita, Kyoto, Japan) acquired at 5 mA and 512 (**a**) and 1024 (**b**) projection images, showing the effect of increasing number of basis projections on noise. (Courtesy of William C. Scarfe)

fully cover the diameter of the scanned object; see Sect. 2.2.1.2). While many CBCT units acquire projections over a rotation arc of 360°, a shorter rotation would theoretically suffice. As with any change in exposure time, the use of a shorter rotation arc decreases patient dose and potentially reduces motion blurring at the cost of an increased image noise (Fig. 2.31). In some cases, the use of a partial rotation is done for practical reasons, as it allows the unit to be more compact (e.g., hybrid CBCT-panoramic systems). Certain units allow the user to choose between a full or partial rotation.

2.5.5 Field of View

The dimensions of the FOV, or scan volume, are primarily dependent on the detector size and the beam projection geometry (e.g., source-object and object-detector distance). The shape of the scan volume can be either cylindrical (pyramid-shaped X-ray beam) or spherical (cone-shaped X-ray beam). As discussed in Chap. 7, collimation of the primary X-ray beam can considerably reduce patient radiation dose and is an essential technique for dose optimization. The FOV should be minimized according to the region of interest corresponding to the diagnostic task.

Reduction in the FOV usually can be accomplished mechanically or, in some instances, electronically. Currently, most CBCT units use adjustable metallic shields acting as primary collimation at the radiation source. Electronic collimation involves elimination (i.e., cropping) of projection data in order to reduce the reconstructed image to the area of interest. Both techniques reduce the computational time during reconstruction, but only physical collimation results in reduced patient dose collimation should be strongly discouraged.

Effects of FOV size on image quality can be seen in some cases. Larger FOVs increase the amount of scatter per detector area, reducing image quality (Pauwels et al. 2016). In addition, larger FOVs coincide with a higher beam divergence at the edge of the FOV, which results in image quality deterioration. On the other hand, a FOV with a larger diameter reduces the “local tomography” effect, which is the effect of tissue outside the FOV (which is only partially exposed) on grey value uniformity (Siltanen et al. 2003).

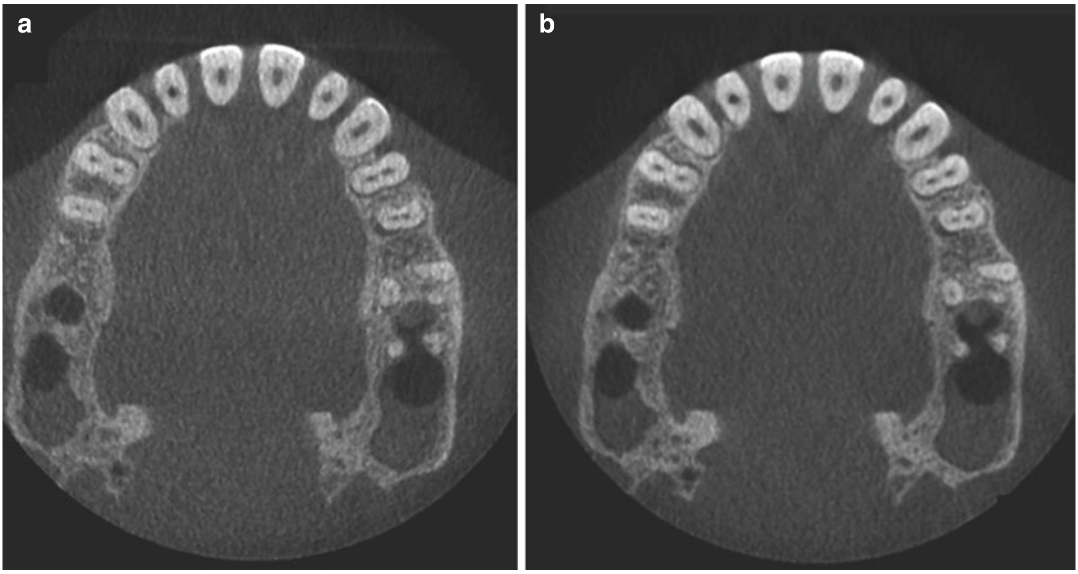

Fig. 2.31 Axial and cross-sectional CBCT images of a plastic encased skull (3D Accuitomo 170, J. Morita, Kyoto, Japan) acquired at 90 kV, 5 mA, and 180° (**a**) and 360° (**b**) rotational angle, showing the effect of rotation angle on noise

2.6 Future Technical Developments

Several technical developments in terms of CBCT image acquisition and reconstruction can be expected in the near future. Most of these are already applied in MDCT imaging pre-clinically or clinically.

The use of dual energy imaging in MDCT has led to dramatic improvements in terms of tissue characterization, in some cases avoiding the need for contrast media. Typically, this involves an overlapping image acquisition using 2 kV settings (either by the same X-ray generator, or separate sources) (Karçaaltıncaba and Aktas 2011). Dual energy imaging allows for a greater contrast resolution, although it is not yet clear if it would be cost-efficient for dental and maxillofacial CBCT.

A technique which has been implemented in MDCT imaging for several years is the use of automatic exposure control (AEC). Various levels and methods of AEC exist; the main principle is the adjustment of tube output (typically the mA) according to the size and density distribution of the object under investigation (Alibek et al. 2011). While a slice-by-slice AEC is obviously not feasible in CBCT, seeing that the entire volume is acquired in one rotation, the application of AEC could still lead to considerable dose reduction. First of all, it would enable a constant image quality between patients of different sizes, without the need for manual adjustment of exposure parameters. Secondly, AEC could be applied during an image acquisition, seeing that the detector signal varies considerably between lateral projection angles and A-P or P-A angles. If the tube output could automatically be adjusted throughout the scan depending on the amount and density of the traversed tissue (i.e., using real-time feedback of the acquired projections), the dose for each projection would be minimized.

Several innovations at the level of the detector are also currently under investigation, or expected in the near future. General improvements to FPDs (e.g., sensitivity, frame rate, uniformity, electronic noise) could lead to considerable improvements in terms of dose efficiency. On the other hand, CBCT could evolve towards the use of photon counting or energy-resolving detectors, which could lead to an improvement in terms of image quality, especially when coupled with dedicated reconstruction techniques.

It can be expected that image reconstruction algorithms will evolve from the currently used FDK technique to iterative reconstruction. Iterative reconstruction techniques, which are a class of reconstruction techniques involving multiple rounds ("iterations") of image reconstruction (see Fig. 2.18), have resulted in noise and artifact reduction in clinical MDCT imaging (Korn et al. 2012), and are expected to become more widely used in CBCT.

A more challenging innovation is the use of X-ray phase-contrast (Pfeiffer et al. 2008). Currently, X-ray imaging is based on attenuation. However, X-rays also exhibit a phase shift while passing through matter, which is currently ignored because it cannot be detected using conventional X-ray sensors. The use of phase-contrast would lead to a much improved contrast in the soft tissue density range. While phase-contrast imaging is in a relatively early stage, 2D and 3D imaging modalities based on phase-contrast could change the paradigm of X-ray imaging at some point.

Acknowledgments 3D head model images in Figs. 2.10, 2.17, and 2.20 are courtesy of Rodrigue Pralier. Figures 2.1, 2.2, 2.3, 2.4, 2.1, and 2.25 are partially adapted from Pauwels et al. (2015a) under the British Institute of Radiology's License to Publish. Images used in Fig. 2.19 are courtesy of J. Morita, Osaka, Japan.

References

Alibek S, Brand M, Suess C, Wuest W, Uder M, Greess H (2011) Dose reduction in pediatric computed tomography with automated exposure control. Acad Radiol 18:690–693

Bechara BB, Moore WS, McMahan CA, Noujeim M (2012) Metal artefact reduction with cone beam CT: an in vitro study. Dentomaxillofac Radiol 41:248–253

Beister M, Kolditz D, Kalender WA (2012) Iterative reconstruction methods in X-ray CT. Phys Med 28:94–108

Bezerra IS, Neves FS, Vasconcelos TV, Ambrosano GM, Freitas DQ (2015) Influence of the artefact reduction algorithm of Picasso Trio CBCT system on the diagnosis of vertical root fractures in teeth with metal posts. Dentomaxillofac Radiol 44:20140428

Birch R, Marshall M (1979) Computation of bremsstrahlung X-ray spectra and comparison with spectra measured with a Ge(Li) detector. Phys Med Biol 24:505–517

Feldkamp LA, Davis LC, Kress JW (1984) Practical cone-beam algorithm. J Opt Soc Am A 1:612–619

Kamburoğlu K, Kolsuz E, Murat S, Eren H, Yüksel S, Paksoy CS (2013) Assessment of buccal marginal alveolar peri-implant and periodontal defects using a cone beam CT system with and without the application of metal artefact reduction mode. Dentomaxillofac Radiol 42:20130176

Karçaaltıncaba M, Aktas A (2011) Dual-energy CT revisited with multidetector CT: review of principles and clinical applications. Diagn Interv Radiol 17:181–194

Korn A, Fenchel M, Bender B, Danz S, Hauser TK, Ketelsen D, Flohr T, Claussen CD, Heuschmid M, Ernemann U, Brodoefel H (2012) Iterative reconstruction in head CT: image quality of routine and low-dose protocols in comparison with standard filtered back-projection. AJNR Am J Neuroradiol 33:218–224

Loubele M, Jacobs R, Maes F, Schutyser F, Debaveye D, Bogaerts R, Coudyzer W, Vandermeulen D, van Cleynenbreugel J, Marchal G, Suetens P (2005) Radiation dose vs. image quality for low-dose CT protocols of the head for maxillofacial surgery and oral implant planning. Radiat Prot Dosim 117:211–216

Loubele M, Bogaerts R, Van Dijck E, Pauwels R, Vanheusden S, Suetens P, Marchal G, Sanderink G, Jacobs R (2009) Comparison between effective radiation dose of CBCT and MSCT scanners for dentomaxillofacial applications. Eur J Radiol 71:461–468

Molteni R (2013) Prospects and challenges of rendering tissue density in Hounsfield units for cone beam computed tomography. Oral Surg Oral Med Oral Pathol Oral Radiol 116:105–119

Nardi C, Molteni R, Lorini C, Taliani GG, Matteuzzi B, Mazzoni E, Colagrande S (2016) Motion artefacts in cone beam CT: an in vitro study about the effects on the images. Br J Radiol 89:20150687

Nemtoi A, Czink C, Haba D, Gahleitner A (2013) Cone beam CT: a current overview of devices. Dentomaxillofac Radiol 42:20120443

Pauwels R, Stamatakis H, Bosmans H, Bogaerts R, Jacobs R, Horner K, Tsiklakis K, SEDENTEXCT Project Consortium (2013) Quantification of metal artifacts on cone beam computed tomography images. Clin Oral Implants Res 24(Suppl A100):94–99

Pauwels R, Silkosessak O, Jacobs R, Bogaerts R, Bosmans H, Panmekiate S (2014) A pragmatic approach to determine the optimal kVp in cone beam CT: balancing contrast-to-noise ratio and radiation dose. Dentomaxillofac Radiol 43:20140059

Pauwels R, Araki K, Siewerdsen JH, Thongvigitmanee SS (2015a) Technical aspects of dental CBCT: state of the art. Dentomaxillofac Radiol 44:20140224

Pauwels R, Jacobs R, Bogaerts R, Bosmans H, Panmekiate S (2016) Reduction of scatter-induced image noise in cone beam computed tomography: effect of field of view size and position. Oral Surg Oral Med Oral Pathol Oral Radiol 121:188–195

Pauwels R, Jacobs R, Bogaerts R, Bosmans H, Panmekiate S (2017) Determination of sizespecific exposure settings in dental cone-beam CT. Eur Radiol 27:279–285

Pfeiffer F, David C, Bunk O, Donath T, Bech M, Le Duc G, Bravin A, Cloetens P (2008) Region-of-interest tomography for grating-based X-ray differential phase-contrast imaging. Phys Rev Lett 101:168101

Parsa A, Ibrahim N, Hassan B, Syriopoulos K, van der Stelt P (2014) Assessment of metal artefact reduction around dental titanium implants in cone beam CT. Dentomaxillofac Radiol 43:20140019

Seibert JA (2006) Flat-panel detectors: how much better are they? Pediatr Radiol 36:173–181

Siltanen S, Kolehmainen V, Järvenpää S, Kaipio JP, Koistinen P, Lassas M, Pirttilä J, Somersalo E (2003) Statistical inversion for medical x-ray tomography with few radiographs: I. General theory. Phys Med Biol 48:1437–1463

Spin-Neto R, Mudrak J, Matzen LH, Christensen J, Gotfredsen E, Wenzel A (2013) Cone beam CT image artefacts related to head motion simulated by a robot skull: visual characteristics and impact on image quality. Dentomaxillofac Radiol 42:32310645

Image Processing and Visualization Techniques

3

William C. Scarfe, Roberto Molteni, and Pierluigi Mozzo

Contents

W.C. Scarfe, B.D.S., F.R.A.C.D.S., M.S. (✉)
Division of Radiology and Imaging Science, Department of Surgical/Hospital Dentistry, University of Louisville School of Dentistry, Louisville, KY, USA
e-mail: William.Scarfe@louisville.edu

R. Molteni, Ph.D.
Skanray Europe srl, San Lazzaro di Savena, Bologna, Italy
e-mail: robertodocmolteni@yahoo.com

P. Mozzo, Ph.D.
Pixirad Imaging Counters srl, Verona, Italy

University of Verona, Verona, Italy
e-mail: pierluigi.mozzo@gmail.com

3.1 Introduction

The technical elements for optimal imaging in CBCT comprise a sequence of discrete but interrelated processes, referred to as the *imaging chain*. These include:

- A source of X-radiation.
- The object to be imaged (in CBCT, a Volume Of Interest (VOI) within the craniofacial skeleton).
- A device capable of detecting the remnant radiation after attenuation by the object.
- A mechanism to archive the resultant image.
- A method to retrieve and display the image.

In analog radiography, the imaging chain is reduced to three elements as the radiographic film serves as the image detector, the media for both display and image archiving. This tri-functionality has blurred conceptual and technical differences within and between these elements that become important with the use of digital imaging systems.

In digital radiography, digital sensors are used only to detect photons and generate the digital image, which is then stored on a separate digital medium. In addition, display of the image requires a separate presentation medium, usually a computer monitor. In projection radiography, the direct outcome of the process using either analog or digi-

W.C. Scarfe, C. Angelopoulos (eds.), *Maxillofacial Cone Beam Computed Tomography*,
https://doi.org/10.1007/978-3-319-62061-9_3

tal media is a single or limited sequence of planar two-dimensional (2-D) images of a solid three-dimensional (3-D) object. This paradigm has changed with CBCT, where the outcome of the process is not directly a 2-D image.

3.2 Image Display

There are four independent operations involved in image display for CBCT (Udupa 1999):

- **Reconstruction.** The primary data from CBCT are images that undergo reconstruction to generate a 3D volumetric dataset. Often primary images are preprocessed before reconstruction.
- **Visualization.** The images from CBCT reconstruction are optimized to facilitate visual display by various rendition techniques in both 2- and 3-D.
- **Post-processing**. In this operation, an observer interacts with the image to alter the representation of features within the image dataset. This involves specific image enhancement techniques.
- **Analysis.** The assessment of various image characteristics is performed to provide quantitative information from the dataset (See Chap. 5).

3.2.1 Understanding CBCT Data

3.2.1.1 Reconstruction of the Volumetric Dataset

The primary images captured during a CBCT scan consist of a sequence of 2D projection images, referred to as *projection data*, *raw data*, *basis projections,* or *basis frames*. In clinical practice, projection data are viewed only as an aid for patient positioning or to assist in calibration of the instrument. Projection data is immediately reconstructed into a volumetric dataset. While this is the real output of CBCT imaging, it is never used as a display format.

Once acquired, the projection data is mathematically processed to create the volumetric dataset. This reconstruction process is previously described (*see* Chap. 2). There may be between 100 to over 1000 individual projection frames, each with up to over half a million pixels with 12- to 16-bits of data assigned to each pixel. The reconstruction of the data is therefore computationally complex. To expedite handling, two computers may be used; data is acquired by an acquisition computer and transferred to a workstation computer for reconstruction, visualization, post-processing, and analysis. Reconstruction times vary depending on the acquisition parameters (e.g., voxel size, field of view (FOV), number of projections), hardware (processing speed, data throughput from acquisition to workstation computer) and software (reconstruction algorithms) used. Reconstruction should be accomplished in an acceptable time (less than a few minutes) to facilitate patient flow.

3.2.1.2 Voxel Properties

A volumetric dataset is the three-dimensional equivalent of a two-dimensional image. It is a contiguous collection of cuboidal data points within a field of view, with two properties: a 3-D location (a spatial coordinate) and an intensity value (associated with the radiographic density at that coordinate). Each discrete spatial unit in the volumetric data, or *points cloud,* is called a *voxel (volumetric element).* This is the 3-D equivalent of the *pixel* (picture element) of a 2-D image.

While the spatial location of the voxel is invariant after reconstruction, the intensity value depends on the ability of the system to detect subtle contrast differences (contrast resolution). Local contrast resolution in CBCT is ultimately limited by the system's bit-depth. Several factors interact to determine bit-depth, with the signal-to-noise ratio being the most notable. Bit-depth corresponds to the number of shades of gray available to record the attenuation. Several factors determine the practical bit-depth of a CBCT system including:

- **Acquisition Bit-Depth.** CBCT units use detectors capable of recording grayscale differences of at last 12-bit (2^{12} or 4096 shades of gray) and, recently, 14-bit (2^{14} or 16,384 shade).

However, 16-bit (2^{12} or 64,524 shades) or 8-bit (2^8 or 256 shades) are used for subsequent file handling and processing because of operational and file storage format requirements. Acquisition bit-depth is dependent on the detector signal grayscale. While a CBCT detector always acquires a continuous (analog) signal, it is invariably digitized. *Digitalization range* (how many discrete units the analog signal is digitized) is CBCT unit dependent and determined by the manufacturer. It is a balance between the recorded information and the inherent noise of the detector.

- **Photometric Interpretation.** The data in each voxel is associated with the radiographic density of the spatial coordinate to which it corresponds. If a voxel corresponds to a point of extremely high radiodensity (e.g., a metallic restoration), it will have nearly no signal. Similarly, if a voxel corresponds to a point of extremely low radiodensity (e.g., air), it will have signal at the top of the available signal range. For visualization, the intensity level of each voxel is set to correspond to a specific signal level (gray shade) in a two-dimensional array of pixels on a monitor display. Images are displayed in reverse grayscale (negative), a convention called *reverse photometric interpretation* such that no radiodensity is represented as black (full signal range) and maximum radiodensity as white (no signal). *Direct photometric interpretation* (positive image grayscale or "black-on-white") is an option to enhance visualization in certain applications.
- **Monitor Limitations and Adjustments.** The most direct way to display each original discrete voxel intensity is to represent it on a monitor with a specific display pixel gray value. This is visually represented by a graphical 2-D plot—a *look-up table* (LUT)—that translates original gray intensity levels into display pixel values. Often this is combined with a representation of the number of pixels having a specific gray intensity level—a histogram. The mathematical relationship between original and displayed gray values is a *transfer function*. The most common relationship between is linear, however enhancements are often necessary to accommodate the psychometric response of the human eye (*see later*) and the inherent transfer function of the display monitor. The DICOM file format standard incorporates calibration instructions for DICOM-conformant monitors to provide a consistent response. Pre-processing is often performed to provide better visualization by transforming the LUT, for instance with a gamma curve (Fig. 3.1).
- All image displays used in CBCT are relatively low cost, liquid crystal display (LCD) personal computer (PC) color monitors with a display capacity limited to only 8-bit (2^8 or 256) shades of gray. Therefore, higher bit CBCT acquired images are invariably converted to 8-bit for display by truncating data to their eight *Most Significant Bits* (Fig. 3.2).
- Another graphical representation comparing available signal data to displayed data is the *histogram*, a plot that associates the signal content of each pixel with the total number of pixels with that signal value in the image. Processing an original 16-bit to an 8-bit image (Fig. 3.3) eliminates the highest gray levels (black) and results in very dark images with little visual contrast. To optimize the display, linear stretching is performed to register the histogram of the displayed image so that the highest bin with significant data is made to correspond to the maximum value of the scale. The slope of the transfer function corresponds to contrast and offset corresponds to brightness (*see later*).

3.3 Visualization

Visualization describes the software driven methods and techniques that provide clinically useful and diagnostically optimal information from the volumetric dataset. Functionally, computer-based methods either enhance the visual presentation of an image or provide an alternate display of the dataset. Visualization applications are often task specific and complementary.

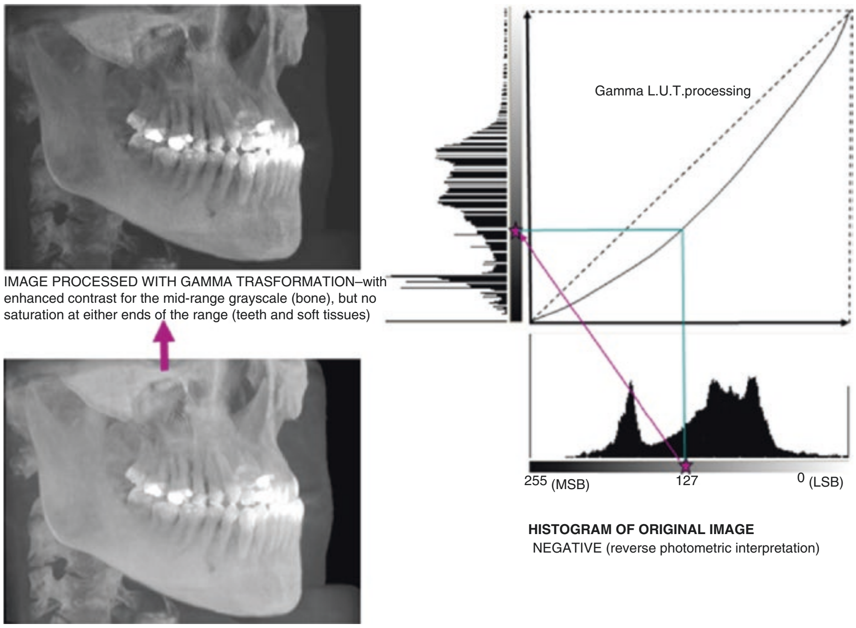

Fig. 3.1 The same image before (*lower left*) and after (*upper left*) application of a gamma-transform. On the *right* is a LUT plot with each axis showing the original histogram (*x*-axis) and after (*y*-axis) gamma transform. The linear (*dashed line*) and gamma (*solid curved lines*) show the transfer function. Note that while the areas at the extreme ends of the scale (*white* (0) and *black* (256)) are unaltered, the distribution of the gray levels now improves the contrast visibility of certain details in the gamma processed image (*upper left*)

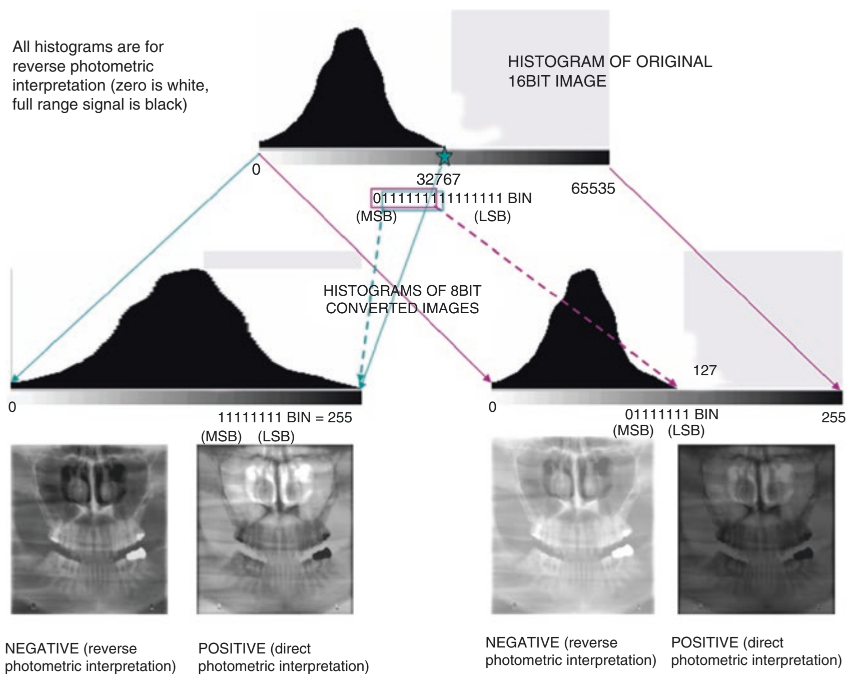

Fig. 3.2 Schematic demonstrating truncation of 16-bit to 8-bit Most Significant Bits image. The histogram of a 16-bit image (*top center*) shows a range of gray values (0–32,767) representing *white* to the *middle gray* region. Truncation of the image to its 8 Most Significant Bits is achieved by one of two methods: The first takes the first 8 bits of the uppermost value and displays it on an 8-bit scale (*middle right*)—this may result in a low-contrast image (*lower right*). The second method involves fitting the scale such that this uppermost value is now *black* (255) (*middle right*). In this case, an image with optimal density and contrast is obtained (*lower right*)

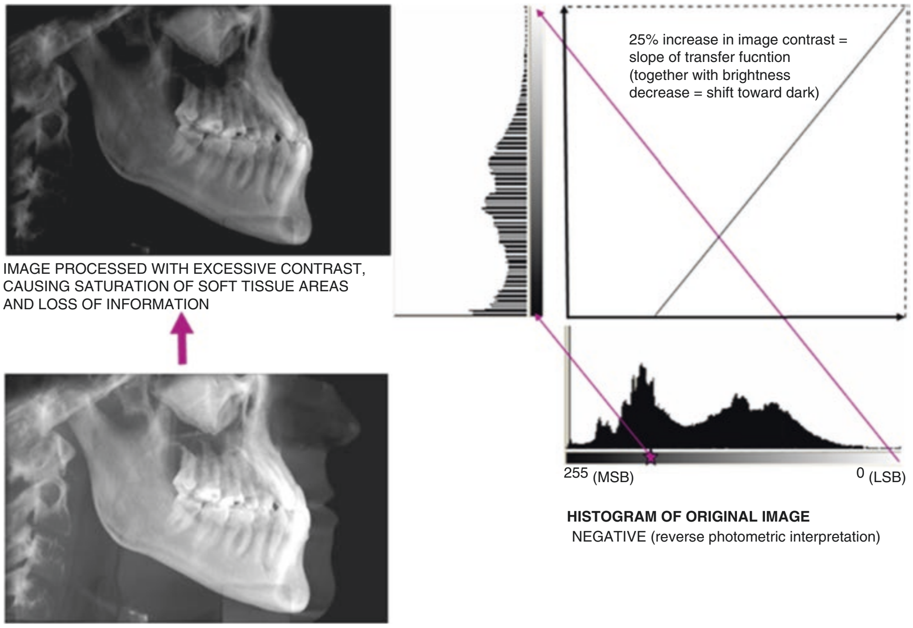

Fig. 3.3 A hypothetical grayscale histogram (*lower right*) of an unprocessed 16-bit radiographic image (*lower left*). Typically, the highest used bin in the histogram may be significantly below the maximum value. Clearance from the top-of-range value (*darkest shades*) is necessary to prevent the risk of saturation. In the processed image (*upper left*) there is no clearance between the *top end* of the grayscale shown in the histogram. Therefore, some of the low-density areas (soft tissues) are saturated and blend into the air

3.3.1 Two-Dimensional Techniques

The default display of imaging software for CBCT volumetric data is as a panel of three correlational, thin sectional images in each orthogonal plane (axial, sagittal, and coronal). Visual perception and subsequent interpretation of the CBCT volumetric dataset is not dependent on these images alone and requires reformatting to provide various renderings.

3.3.1.1 Orthogonal Sectional Display

Secondary reconstruction of the volumetric dataset often provides, by default, a presentation of four images: an overall volumetric rendering and three images each representing an orthogonal plane within the midpoint of the volume (Fig. 3.4).

Navigation through CBCT datasets begins with a review of multiple sectional single images in at least two orthogonal planes. This can be performed as a conventional montage, where sections are displayed in sequence side by side (Fig. 3.5) or by scrolling through a stack of contiguous images dynamically, providing a “pseudo-cine” movie as sections are visualized rapidly. Coronal and axial images remain the most valuable tools for preliminary diagnostic assessment.

3.3.1.2 Multi-Planar Reformatting (MPR)

MPR enables volumetric data sectioning to provide non-orthogonal or oblique images and has become a common approach to represent a dental and maxillofacial CBCT volumetric dataset. Reformatting occurs through the volumetric dataset along an arbitrary axis that is tilted from either the *x*- or *y*-plane (Fig. 3.6). CBCT isotropic volumetric acquisition allows for creation of MPR views in any plane at the same spatial resolution as the original voxel size. Therefore, positioning of the head in CBCT equipment becomes less critical.

By aligning the long axis of the imaging plane with a specific anatomic structure, MPR can be

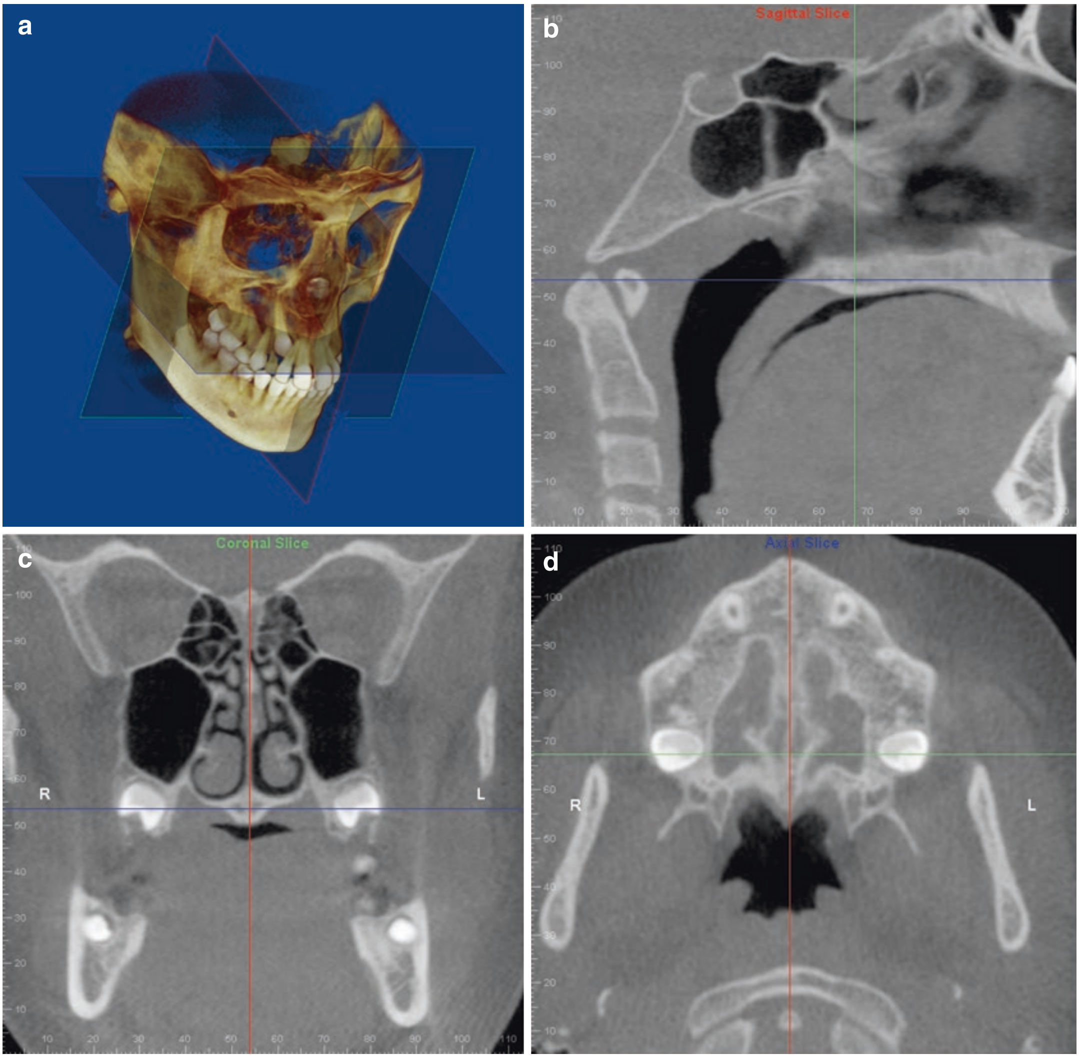

Fig. 3.4 Screen shot of standard imaging software window showing a typical default display of CBCT dataset—an overall volumetric rendering (**a**), and sagittal (**b**), coronal (**c**), and axial (**d**) orthogonal images. The axial image is a *horizontal* section in the *x*-axis representing width; the sagittal image is a *vertical* section in the *y*-axis representing anteroposterior depth; and the coronal image is a vertical section in the *z*-axis representing superior-inferior height. The thickness of each plane is set at a default but can be adjusted by the operator

useful to visualize anatomic features. The orientation of this MPR plane is operator derived and can be curved, linear, or serial (i.e., multiple) transplanar. These techniques create trans-axial 2D images by transecting a set or "stack" of axial images (Fig. 3.7).

Curved Planar Reformation

This mode is useful in displaying anatomic structures that are nonlinear. The most common application of curved MPR is demonstration of the mandibular and maxillary dental arches, providing a familiar panorama-like thin-slice image (Fig. 3.8) corresponding to the special narrow-beam rotational scanography that is commonly known as dental panoramic radiography. This technique may also be applied to view the temporomandibular joints, the orbits, cervical vertebrae, hyoid bone, or maxillary sinuses (Fig. 3.9). Because CBCT data is isotropic,

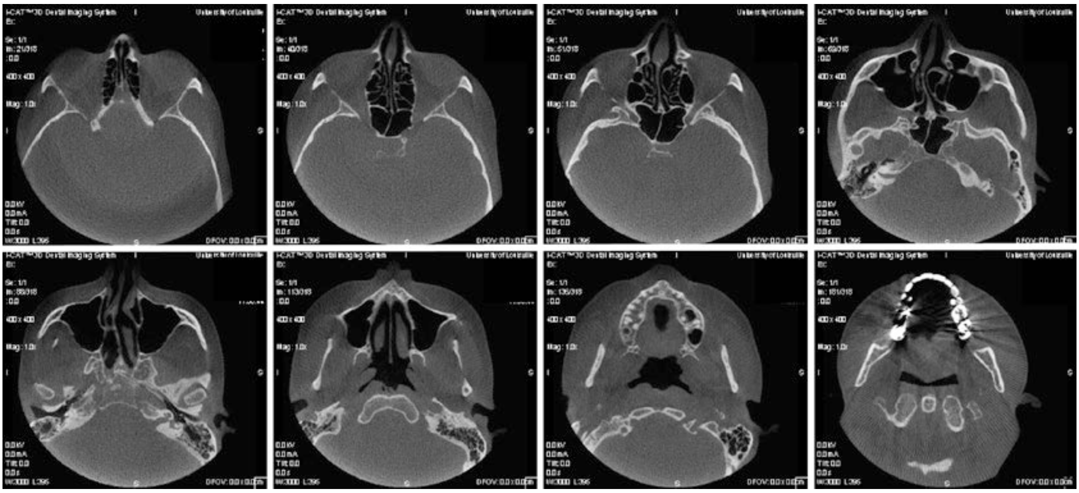

Fig. 3.5 A 4 × 2 (columns × rows) format display of a series of contiguous axial images at a default slice thickness (e.g., 0.4 mm slice thickness). Interslice distance is usually set to be the same as the slice thickness to provide a contiguous display. Slice and interslice thickness as well as display matrix format are all adjustable

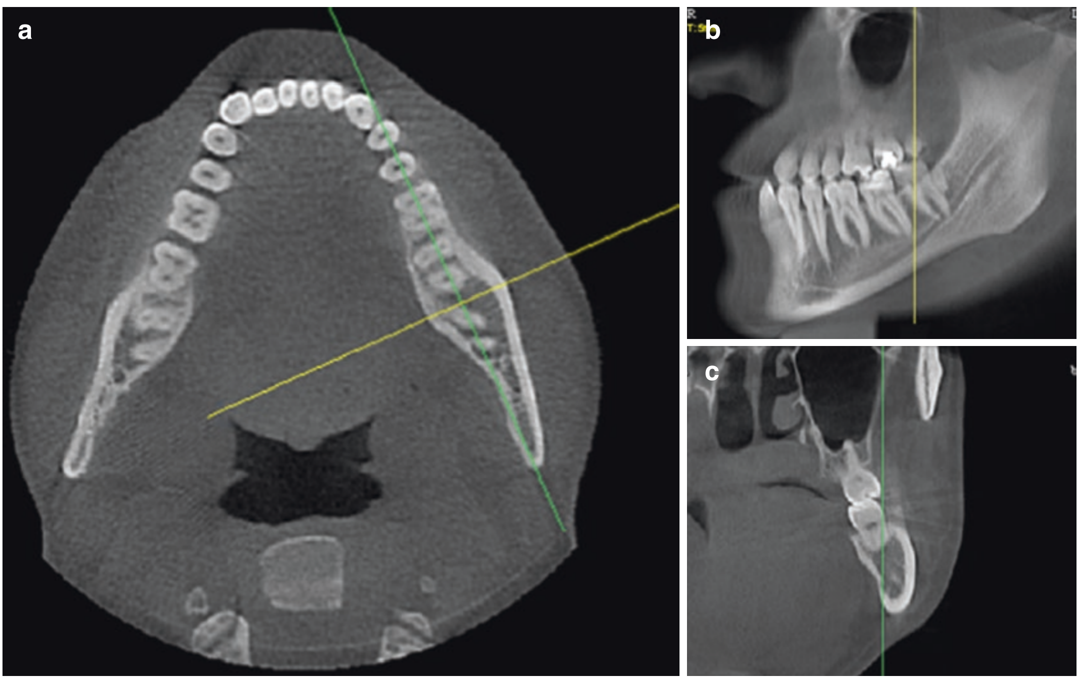

Fig. 3.6 Axial (**a**) orthogonal CBCT image with MPR images parasagittally (**b**) and trans-axially (**c**) corresponding to the long axis of the body of the mandible and bucco-lingual cross-sectional projection, respectively

reconstructed images are undistorted with linear and angular measurements having minimal error.

For the gnathic structures, an axial image is used to identify the curve of the jaw(s). For scans including both dental arches, two curves are often created reflecting differences in shape between the mandible and maxilla. For a dentate arch, the most appropriate axial image is usually approximately 5–10 mm below the junction between the teeth and alveolar ridge. For an edentulous arch,

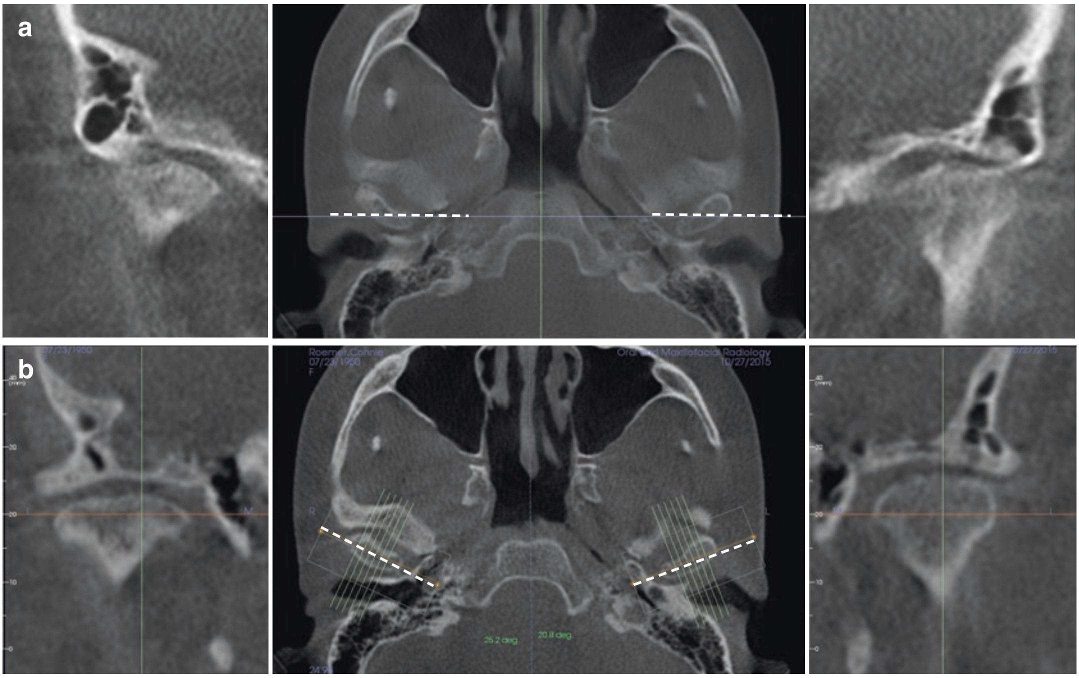

Fig. 3.7 Axial image (**a**) showing image section (*dashed lines*) of TMJ articulations showing orthogonal coronal images of right and left mandibular condyles. Axial image (**b**) showing image section along long axis of the mandibular condyle (*dashed lines*) showing linear MPR paracoronal images of the right and left mandibular condyles. Orthogonal coronal images demonstrate parallax representation whereas linear MPR images show true anatomic presentation

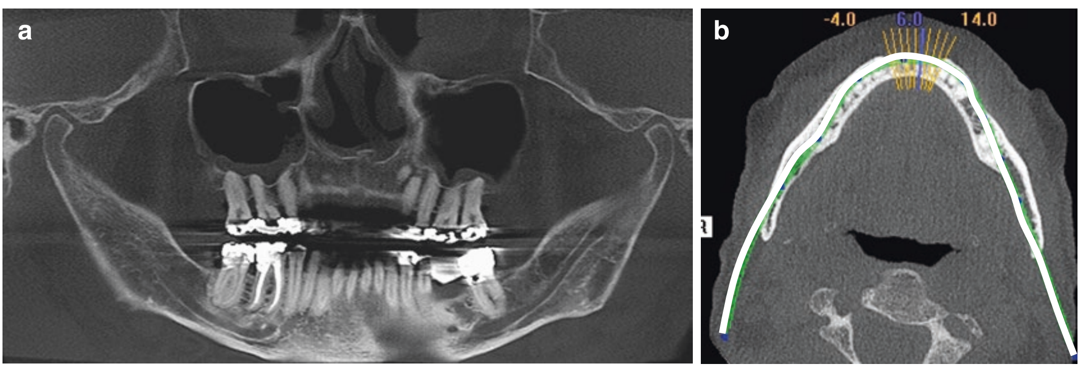

Fig. 3.8 Dental panoramic-like image (**a**) demonstrating some maxillary and mandibular structures reconstructed from a 2 mm thick oblique curved MPR plane following the dental arch on axial slice (**b**). Numerous structures (e.g., maxillary anterior teeth, zygomatic arches) are not displayed because they are outside the thin MPR plane

this is 5–10 mm below the alveolar crest. At a default image thickness (usually 1 mm), this provides the best compromise between providing an approximation of the shape of the jaw, pertinent regional anatomy (e.g., inferior alveolar canal), and position of the teeth (Fig. 3.10).

The technique to provide a curved planar MPR display is simple. Most software applications provide an option to “trace” the outline of a structure on the axial image by sequential location of points. A cursor is used to indicate a number of points (nodes) along the position of

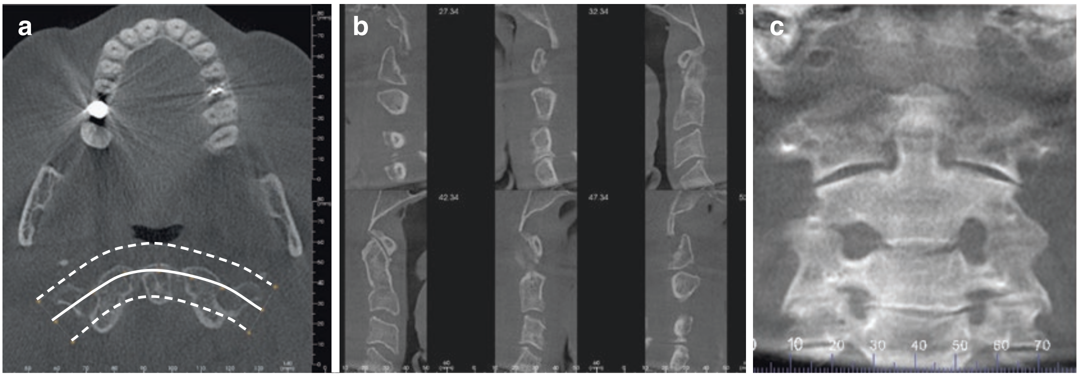

Fig. 3.9 Axial image at the level of the second cervical vertebrae (C2) (**a**) showing the use of a curved oblique MPR through the transverse arches to provide trans-axial (**b**) and expanded, curved coronal projection of the upper cervical vertebrae (**c**)

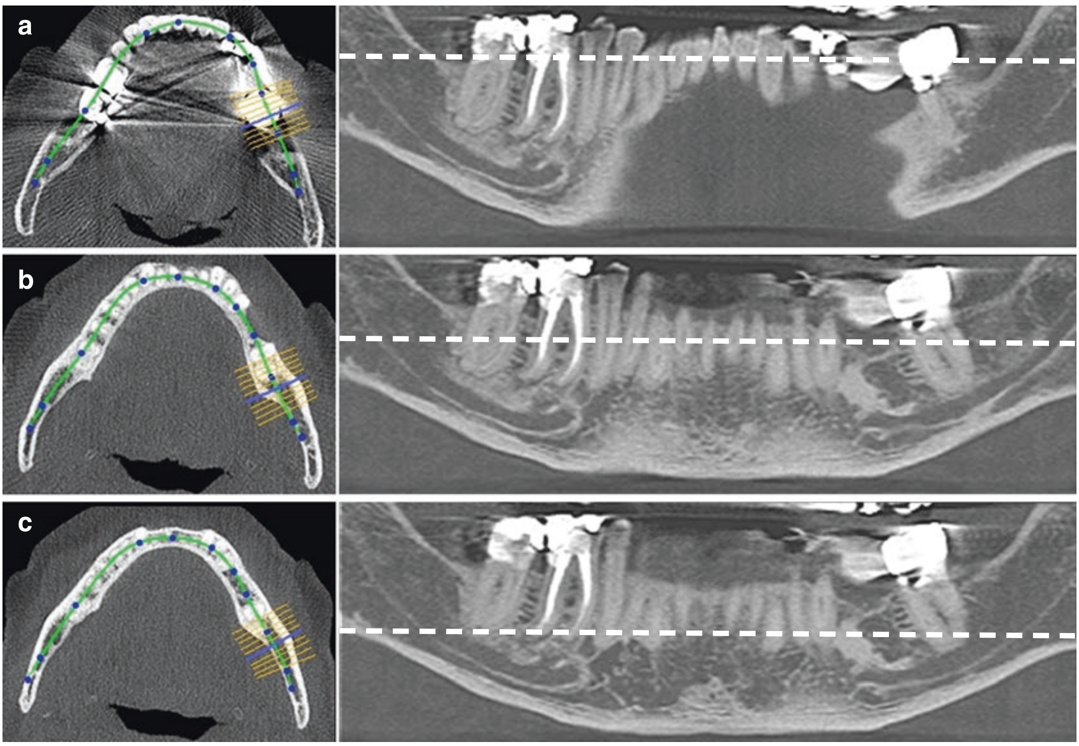

Fig. 3.10 Axial CBCT and corresponding thin section MPR panoramic images constructed at progressively axial lower levels. Axial image at level of crowns (**a**) provides poor panoramic image because transverse slice does not include alveolar and basilar bone. Axial image at level of mid-root (**b**) 10 mm inferior to alveolar crest) provides a good panoramic image because transverse slices include the alveolar and basilar bone, the inferior alveolar canal and mental foramen with reasonable inclusion of the teeth. Axial image at level of root apices (**c**) provides reasonable panoramic image of alveolar and basilar bone, inferior alveolar canal and mental foramen but poor representation of the dentition, especially anteriorly

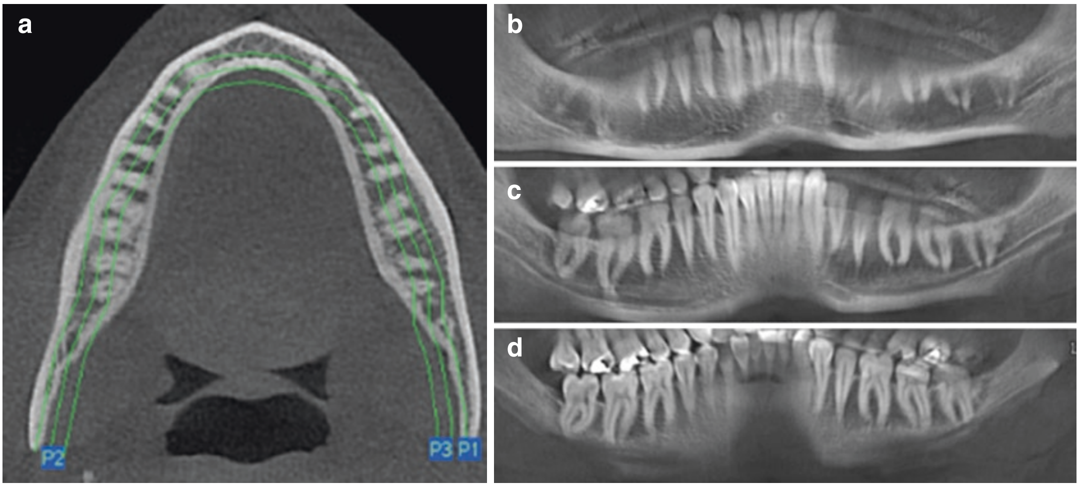

Fig. 3.11 Axial image (**a**) with a central curved designated plane aligned along the long axis of the imaging plane of the dental arch provides sequential and contiguous panoramic MPR images buccally (**b**), central (**c**), and lingually (**d**)

the structure that are then connected by the software program to form a smooth curved line that is superimposed on the axial image. This line indicates the curved planar trans-axial MPR. Because the thickness of the resultant panoramic MPR may not adequately demonstrate all structures in this plane, software programs allow for increased thickness of the panoramic MPR, or alternately may provide several other panoramic sections parallel and both buccal and lingual to the central MPR (Fig. 3.11). Predefined curves conforming to average jaw shapes (Welander et al. 1989) may be implemented by default, with further manual adjustment by the operator. Some software programs provide automatic identification of the dental arch on the axial section to produce a panoramic MPR, but the effect of beam hardening artifact by dental restorations often interferes with the efficacy of these algorithms.

Oblique Planar Reformation

This mode is particularly useful for evaluating three specific structures in the maxillofacial complex as certain features may not be readily apparent on perpendicular images. These include the temporomandibular articulation (Fig. 3.12), the inferior alveolar canal in relation to impacted third molars (Fig. 3.13), and the middle and internal ear within the temporal bone (Fig. 3.14). Often the selection of this MPR provides bilateral images generated to compare relative anatomy.

Most dental imaging software provides a function enabling cursor selection of the location of two points connected by a linear plane and superimposed on the axial image. This line indicates the location where the oblique planar trans-axial section will be reformatted. This line is duplicated to an approximate position on the opposite side of the axial image. Because the thickness of the resultant oblique MPR may not adequately demonstrate all structures in this plane, several other oblique sections parallel to the created MPR may be generated. Alternately, the thickness of the single section may be possible to provide for increased thickness of the oblique MPR.

Serial Cross-Sectional Reformations

This technique produces a series of sequential cross-sectional images perpendicular to the oblique or curved planar reformation (Fig. 3.15). These images are also called *transaxial sections*. Images are usually stacked, contiguous thin slices (e.g., 1 mm thick at 1 mm intervals) with no loss of information. This sequence is useful in the assessment of specific morphologic features such as alveolar bone height and width for implant site assessment (Fig. 3.16), the inferior alveolar canal in relation to impacted mandibular molars (Fig. 3.17), condylar surface and shape in the

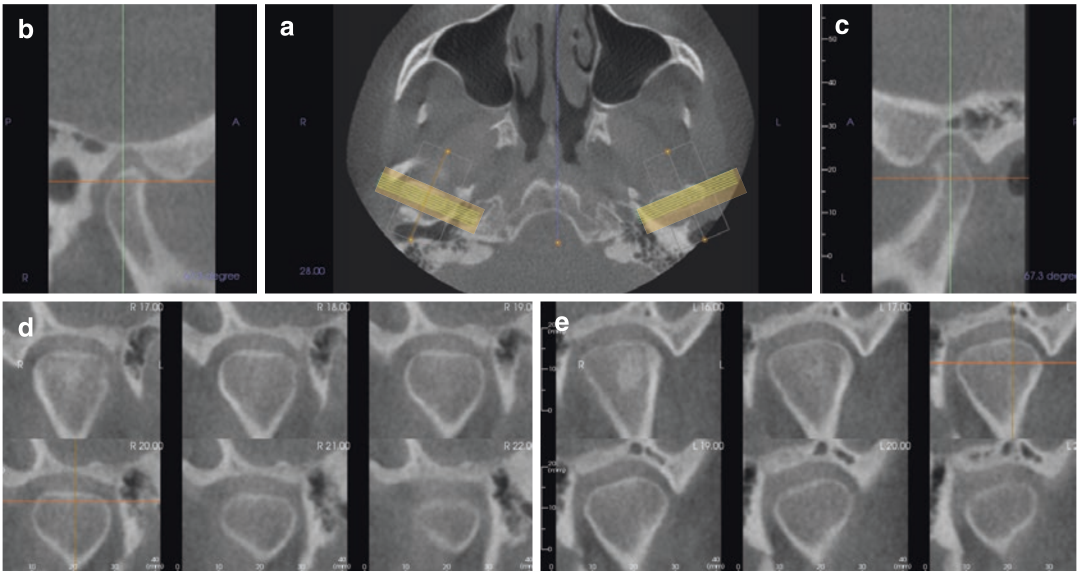

Fig. 3.12 *Right* (**b**) and *left* (**c**) 6 mm thick ray sum parasagittal images of the temporomandibular articulation generated from bilateral linear oblique MPR constructed through the lateral and medial poles of the mandibular condyle using an axial image (**a**) as a reference. Thin (1 mm thickness) contiguous (1 mm slice interval) paracoronal MPR sections of the *right* (**d**) and *left* (**e**) TMJ show higher detail of the intramedullary space and cortical outline

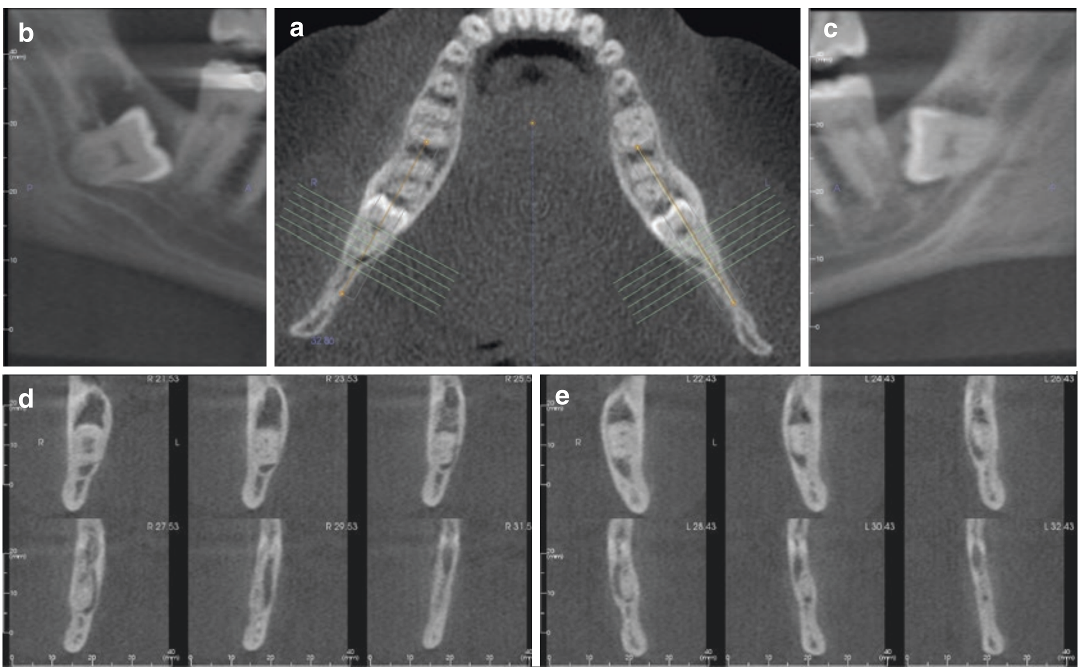

Fig. 3.13 *Right* (**b**) and *left* (**c**) 6 mm thick ray sum parasagittal images of bilateral bony impacted mandibular third molars generated from bilateral linear oblique MPR lines constructed through the long axis of the respective impacted teeth using an axial image (**a**) as a reference. Thin (1 mm thickness) contiguous (2 mm slice interval) MPR sections of the *right* (**d**) and *left* (**e**) third molars. For displaying impacted third molars, the axial image should be located at the apices of the third molars, ideally demonstrating the course of the inferior alveolar canal (IAC). The oblique MPR line is drawn along the IAC or long axis of the teeth to include at least one tooth crown length (approx. 20 mm) anteriorly and far enough posteriorly to include the anterior border of the ascending ramus

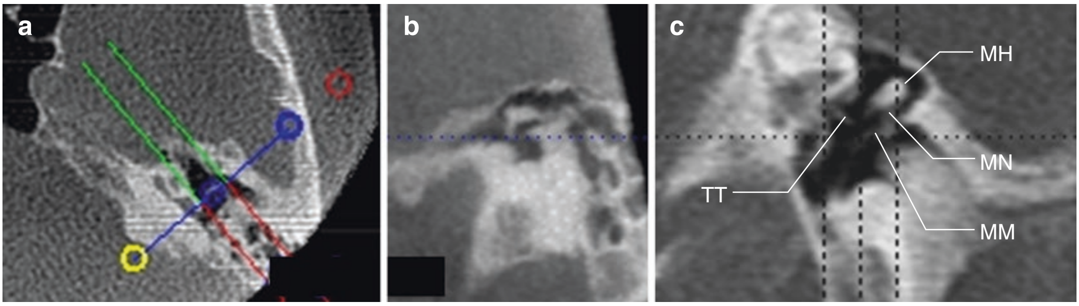

Fig. 3.14 Orthogonal axial CBCT reference image (**a**) shows the reconstruction plane (*blue line*) angled posteriorly and medially optimally depicting the structures of the internal ear. Paracoronal oblique planar MPR CBCT image (**b**) parallel to the long axis of the petrous bone (Stenvers projections) is useful for obtaining short-axis views of the cochlea, vestibular aqueduct, facial nerve canal, round window, and incudomallear joint. Parasagittal "double oblique" MPR images in the plane parallel to the short axis of the petrous pyramid (Poschl projections) (**c**) are useful to optimally depict the superior semicircular canal and the long axis of the cochlea including the mallar head (MH), manubrium (MM), and neck (MN) and the tensor tympani (TT) tendon (Cody 2002)

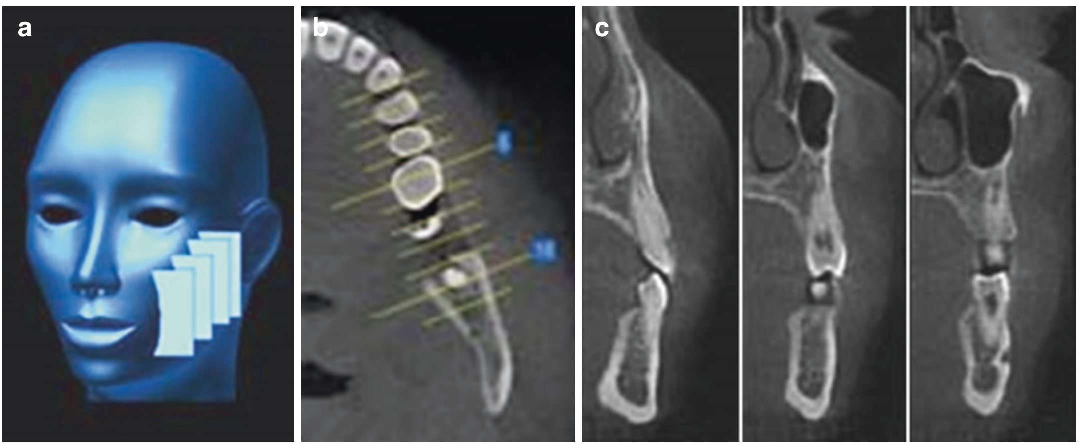

Fig. 3.15 Schematic (**a**) depicting multiple stacked contiguous trans-axial sections generated perpendicular to a linear or curved oblique MPR identified on an axial image (**b**). The resultant cross-sectional/transaxial images (**c**) are stacked and demonstrate features relative to pertinent anatomic structure, in this case the right dentition

symptomatic TMJ or evaluation of pathological conditions affecting the jaws (Fig. 3.18).

The matrix dimensions of cross-sectional images may be adjusted to include a greater region of interest. This includes increasing the height to make the region of interest taller or increasing the length of the slice to make each slice wider. While the default thickness of the cross-sectional images is often interpolated to standard 1 mm and 2 mm cross-sectional formats, some software programs allow trans-axial imaging at either the native voxel resolution, or multiple increments thereof.

3.3.2 Volumetric Techniques

There are essentially two approaches that can be applied to volumetric CBCT datasets to visualize 3D data two dimensionally providing *Volumetric* or *Voxel Vision*—variable thickness viewing and volumetric rendering. In both, a volumetric dataset is represented by a two-dimensional rendering by inclusion of adjacent voxels using a projection technique (Fig. 3.19). The term "3D image" is often used: however, this is a misnomer as the image itself is not three-dimensional. Holograms and stereoscopic visualization are examples of true 3D images.

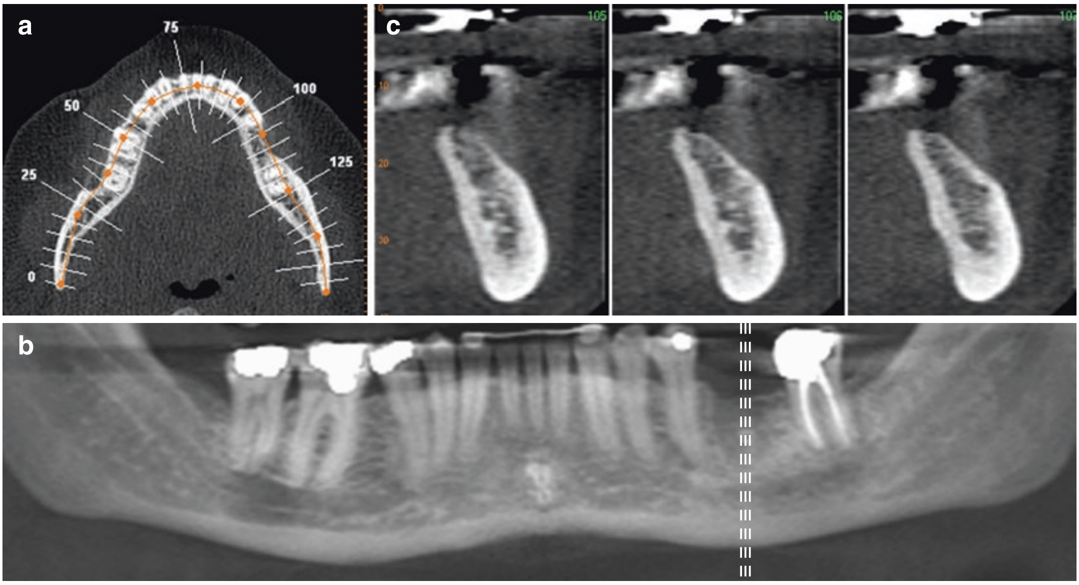

Fig. 3.16 Axial CBCT image (**a**) with curved oblique plane along the entire dental arch produces a simulated panoramic image (**b**). Serial trans-planar images (**c**) provide a series of thin (e.g., 1 mm) stacked sequential cross-sectional images orthogonal to the curved planar reformation (**c**—*dashed white lines*) in the *left* edentulous region are useful in the assessment of specific morphologic features such as alveolar bone height and width as well as the location of the inferior alveolar canal for implant site assessment

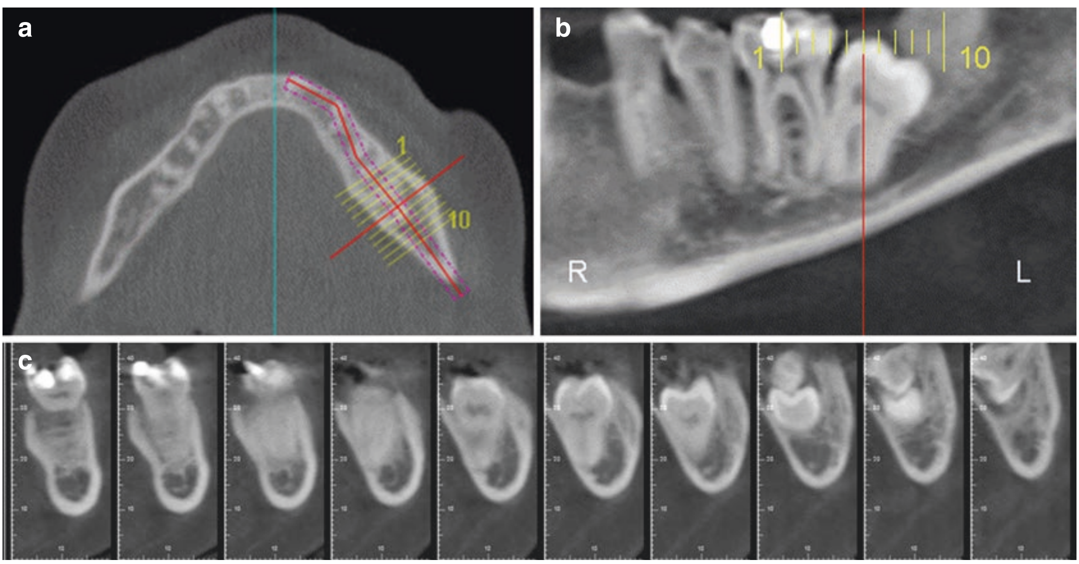

Fig. 3.17 Axial CBCT image (**a**) with a limited curved oblique plane along the left dental arch in the region of an distoangular impacted second molar produces a thin section (5 mm) regional panoramic image (**b**). Serial trans-planar images (**c**) of the posterior mandible used to evaluate the location of the inferior alveolar canal (IAC) in relation to impacted and unerupted third molars. In this example, the IAC traverses obliquely immediately adjacent and below the second molar to lie lingual and deep to the third molar

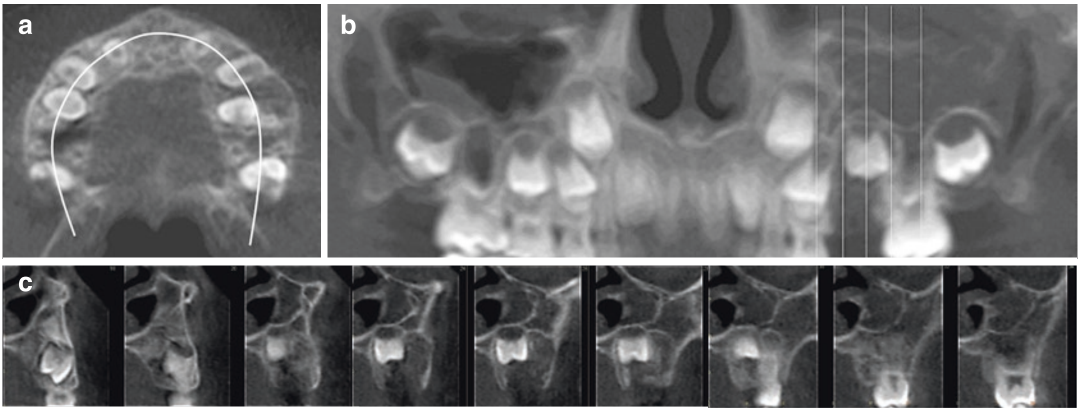

Fig. 3.18 Axial CBCT image (**a**) with a curved oblique plane along the entire dental arch in a young patient with delayed eruption of the left second premolar produces a medium section (10 mm) panoramic image (**b**). Serial transplanar images (**c**) of the left maxilla mandible can be used to evaluate the hypodensity immediately buccal and inferior to the tooth follicle (histologically diagnose as an odontogenic myxoma) and involvement of adjacent teeth and the maxillary sinus

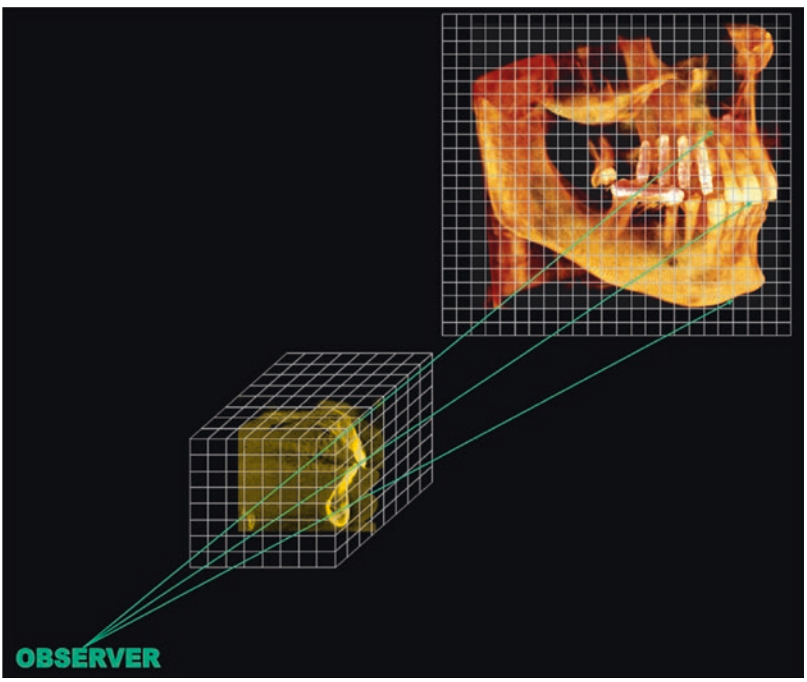

Fig. 3.19 Imaginary rays originating from the observer point are projected through the voxels of volume dataset to render a volumetric representation of the object on a display surface by projection. The rays can be either parallel or diverging. Each display pixel is assigned a gray level or a color in relation to the densitometry of the voxels crossed by the corresponding ray. The projection sequence can be either image or object-guided. Image guided projections are developed when the rays are traced from the observer viewpoint to the pixel on the screen. Object guided projections occur when each of the elements of the object dataset is projected onto the display. Changing the positions of the virtual observer viewpoint and of the display with respect to the object, projections, or renderings with different angulations are possible

3.3.2.1 Variable Thickness Viewing

Any multi-planar image can be "thickened" by increasing the number of adjacent voxels included in the display. This creates a rendered image that represents a specific volume of the patient. The addition of intensity values of adjacent voxels throughout a particular section slice by increasing the section thickness creates a "slab" of the section. Slabs are usually either "thin" (approximately 5–10 mm) or "thick" (>20 mm).

Although CBCT datasets are acquired at submillimeter voxel size resolution, it is not always necessary to view images at a section thickness equaling the voxel size. Usually images are viewed at section thicknesses comparable to conventional CT protocols. For example, coronal slice thickness for sinus examinations may be from 2 to 5 mm. The visual effect of combining multiple image thicknesses to view them as "slabs" is to improve noise and coplanar effects (Fig. 3.20). This method results in images of superior quality compared to images acquired at an equivalent thickness. The number of images averaged is generally variable, and this combination can be smoothly scrolled through the entire sequence of thin images affording rapid visualization of the entire sequence of thin images. Another advantage of this approach is that if the images are routinely interpreted in the "slab" mode and if something suspicious is detected, the thinner original images can easily be examined.

Thick slabs simulate conventional projections and provide information on structural relationships. They are especially useful in providing reference images from which cross-sectional images at higher resolution are determined. The intensity values between adjacent voxels in thick slab renderings account for a form of volumetric rendering known as *direct volume rendering*, more fully described in the next section.

3.3.2.2 Volumetric Rendering

Volume rendering refers to methods that allow the visualization of volumetric data by selective display of voxels as a 2D projection. These methods are classified as direct volume rendering (DVR) and indirect volume rendering (IVR) (Fig. 3.21). The actual rendering process consists of three basic steps: projection of the volumetric dataset, hidden part removal, and shading (Udupa 1999). Each technique has advantages and limitations when used in clinical practice. Clinicians should understand when and how to apply each technique and understand the limitations of both.

Indirect Volume Rendering (IVR)

IVR, also known as surface rendering, is a volumetric rendering modality that provides a representation of the surfaces of the object within the dataset. A number of techniques are used in medical imaging; however, the most common is shaded surface display (SSD).

Shaded Surface Display (SSD)

SSD is a projection technique incorporating a ray-casting method whereby the only voxel portrayed corresponds to a specific threshold density value or narrow range of values, usually that

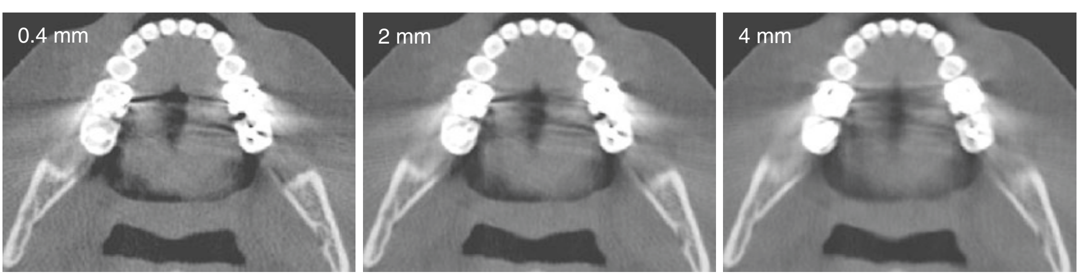

Fig. 3.20 Sequence of axial images with increasing section thickness (0.4 mm (*top*), 2 mm (*center*), and 4 mm (*lower*)). As image thickness increases, the noise of the image (evidenced by the degree of speckled appearance in the buccal soft tissue) as well as the effect of beam hardening artifacts on local structures decreases

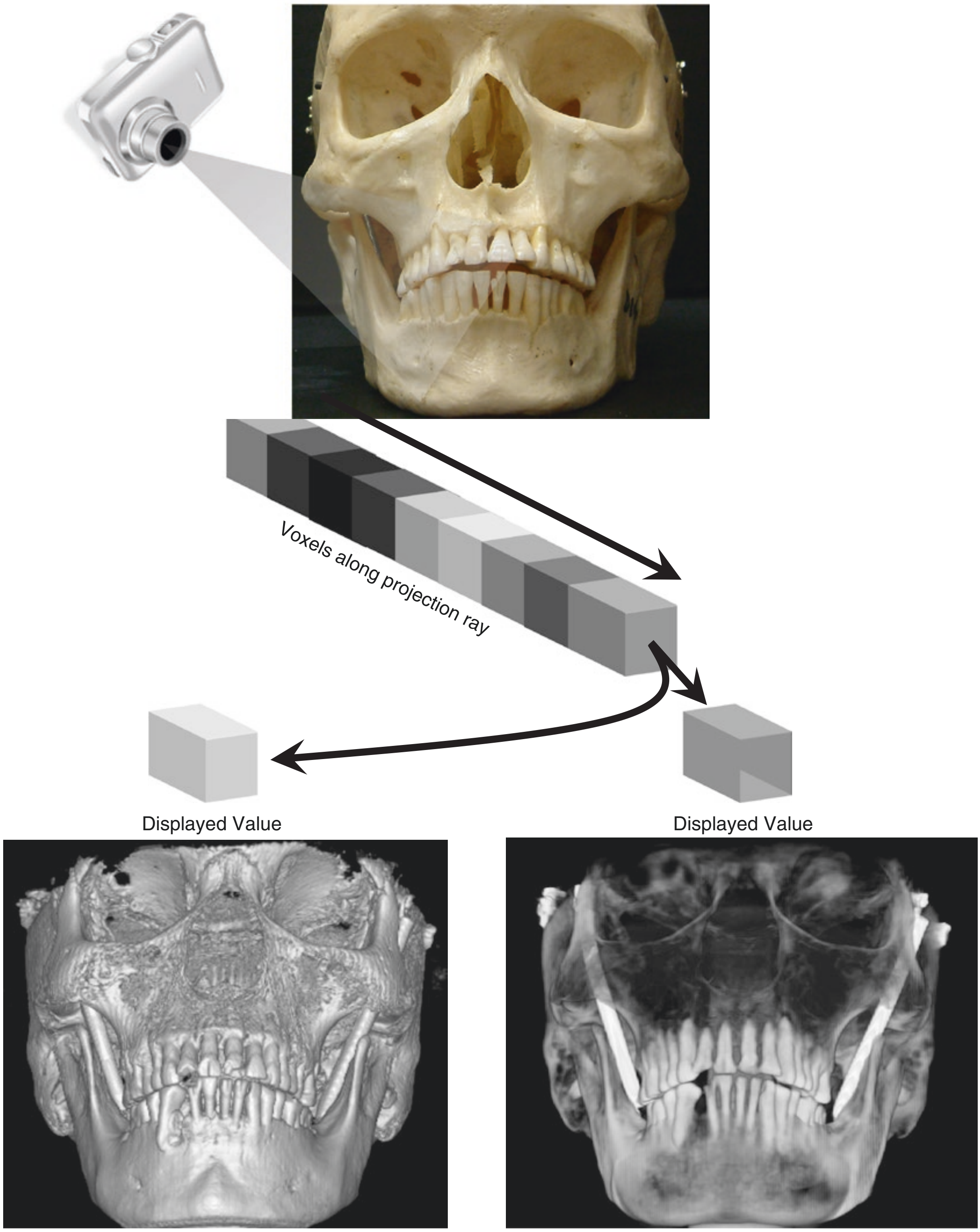

Fig. 3.21 Indirect volumetric rendering (IVR) methods such as shaded surface display (SSD) (*lower left*) and direct volume rendering (DVR) (*lower right*) both involve the transmission and attenuation of X-rays from a point source and the production of voxels along multiple projection paths. The SSD is generated from considerations of the voxel of the highest intensity and a threshold of intensity whereas DVR is generated by considerations of the number and intensity values of all voxels along the projection path as well as attributes such as transparency and color

of cortical bone. To display the surface, a mesh representation is used comprising a large number of interconnected polygons (usually triangles), that approximate the actual surface. The quality of the rendering depends upon the number of polygons used.

Placement of the triangles (or polygons) to represent the surface (isocontouring, isosurfacing, or surface extraction) requires either thresholding or gradient techniques. In thresholding, a voxel of a given type of tissue is either included or excluded based on the reconstructed radiographic density. For instance, in a dataset composed of bone and soft tissue, it is possible to assign "bone" the set of voxels whose gray intensity value exceeds 200. The gradient technique is based upon the rate of variation in radiographic density among adjacent voxels. High gradients identify a surface separating adjacent tissues. Basing upon these concepts, various algorithms have been developed to build the mathematical description of the surface, including the cuberille technique (Chen et al. 1985; Cline et al. 1988), the dividing cube algorithm (Cline et al. 1988), and, the most popular, the marching cube algorithm (Lorensen and Cline 1987; Cline et al. 1988).

The shading step in surface rendering consists of assigning a gray level (or color) to each projected triangle, which is directly proportional to the amount of light reflected from the surface toward the observer. In this way, a pseudo 3D visual effect is rendered.

This technique is very fast and effective in providing 3D visualization because it uses only a small part of the complete dataset to generate the rendering. However, the method is problematic for the visualization of small details, and sometimes introduces artifacts in the reconstructed images.

Clinical Maxillofacial Applications

SSD, in combination with two-dimensional images, is useful for the assessment of trauma and for surgical planning in maxillofacial surgery. However, SSD rendering discards more than 90% of the available data other than that defining the surface features. While SSD is capable of demonstrating gross interrelationships of osseous structures, it fails to display lesions or defects below the cortical surface. The binary nature of surface rendering often limits the flexibility of the data and may subject it to undesirable artifacts such as the stair-step artifact. This leads to difficulties in identification and evaluation of smaller structures such as the inferior alveolar canal (Solar et al. 2001) and segmentation of cortical structures with finer detail. Volume rendering should be considered complementary to SSD for most, if not all, maxillofacial applications as it allows visualization of various interfaces and tissues rather than just one, permitting an appreciation of the spatial relationships between multiple structures.

The availability and use of programs offering volumetric rendering applications in maxillofacial imaging have increased substantially with advances in computer hardware. Perception in volume rendering is best if multiple colors are applied to enhance discrimination between structures. While color schemes can be applied to resemble anatomic structures, they are applied arbitrarily and do not represent the true optical color of the tissues. The assignment of color should be applied to accentuate differences between tissues and is task specific.

IVR has particular clinical application in localizing a specific feature or providing information on the effect of a condition in numerous areas.

- **Trauma.** The purpose of imaging in trauma is to define the number and degree of fractures and qualitatively assess the displacement of segments to provide guidance for therapy. The radiologic evaluation of facial fractures by cross-sectional and MPR alone is often difficult due to the complex anatomy and the fact that most fracture patterns do not conform to imaging planes. 3D visualization facilitates evaluation of CT data in patients with facial trauma by displaying the spatial relationship of the different anatomical and pathological structures and displaying the effects of trauma holistically. Volumetric rendering is beneficial for radiological diagnosis, presentation, and surgical planning (Mankovich et al. 1994;

Reuben et al. 2005). Both SSD and VR have advantages and disadvantages when used for clinical imaging. SSD post-processing is optimal for visualization of thin bones, sutures, and fractures (Udupa 1999). However VR is the preferred reconstruction method by some authors (Kuszyk et al. 1996; Benateau et al. 2002). 3D visualization augments fracture detection compared to axial and MPR imaging and is particularly useful for localization of complex facial fractures (Fig. 3.22) (Fox et al. 1995) and mandibular condyle fractures (Costa et al. 2003)

- **Temporomandibular Joint Disorders.** Three-dimensional images of the condyle and surrounding structures facilitate analysis and diagnosis of bone morphology, joint space and dynamic function, critical keys to providing appropriate treatment outcomes in patients with TMJ signs and symptoms. While surface changes are difficult to discern, 3D imaging, in conjunction with 2D MPR, is well suited to demonstrating severe and often complex morphologic changes of the condyle and temporal articulation associated with degenerative joint disease, prior trauma or fractures (Fig. 3.23) or ankylosis (Fig. 3.24) (Ciccarelli et al. 1998). Developmental TMJ anomalies and their effects on occlusion are clearly demonstrated, as are structural impediments to mandibular opening (Figs. 3.25 and 3.26).
- **Dental anomalies.** The inherent submillimeter resolution of CBCT data ensures accurate representation of the teeth and their surrounding structures. Volumetric techniques provide images to assist in the localization of impacted teeth particularly third molars and maxillary canines and the location of supernumerary and ectopically positioned teeth especially in patients presenting with syndromic or congenital conditions.
- **Dentomaxillofacial deformities**. Large FOV imaging of patients with craniofacial anomalies can be analyzed using additional software such that precise measurements of the skull and facial bones can be performed (Fig. 3.27)
- **Orthodontic Analysis.** Imaging is the most common method used by orthodontists to evaluate and measure the size and quantify the relationships of the craniofacial structures to each other. Lateral and, in some cases, frontal skull projection images taken using a cephalostat and at a fixed geometric arrangement are commonly used to provide quantitative measurements. However, their use has limited validity in describing the 3D relationships of craniofacial structures because of inherent projection (internal and external orientation error, geometric and association error) and landmark identification error. Volumetric-based cephalometry based on the Cartesian analysis of volume renderings has been proposed and methods described by numerous authors (Fig. 3.28) (Swennen et al. 2004; Park et al. 2006; Kwon et al. 2006).
- Such CBCT-based cephalometric techniques provide clinicians with a powerful craniofacial measurement tool; however, clinical implementation has been limited in that the procedure takes longer to perform, the cost of software is expensive, and there is a greater radiation exposure for patients.
- **Postoperative evaluation.** For patients that have had trauma or orthognathic surgery, vol-

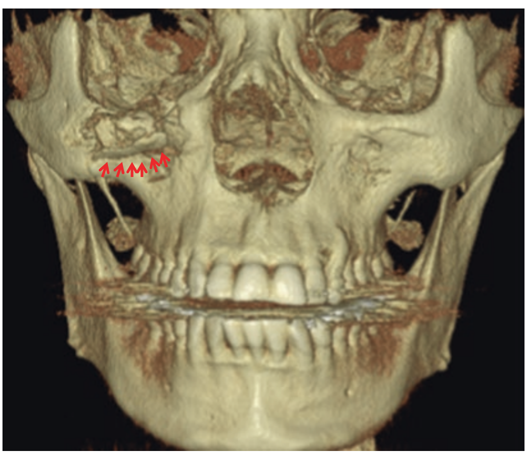

Fig. 3.22 Frontal surface display rendering demonstrating a complex, comminuted fracture of the right inferior orbital rim which is involving the right infra-orbital foramen. 3D reconstructions are excellent in providing a full view of a fracture and in conceptualizing possible spatial displacements of the fragmented parts

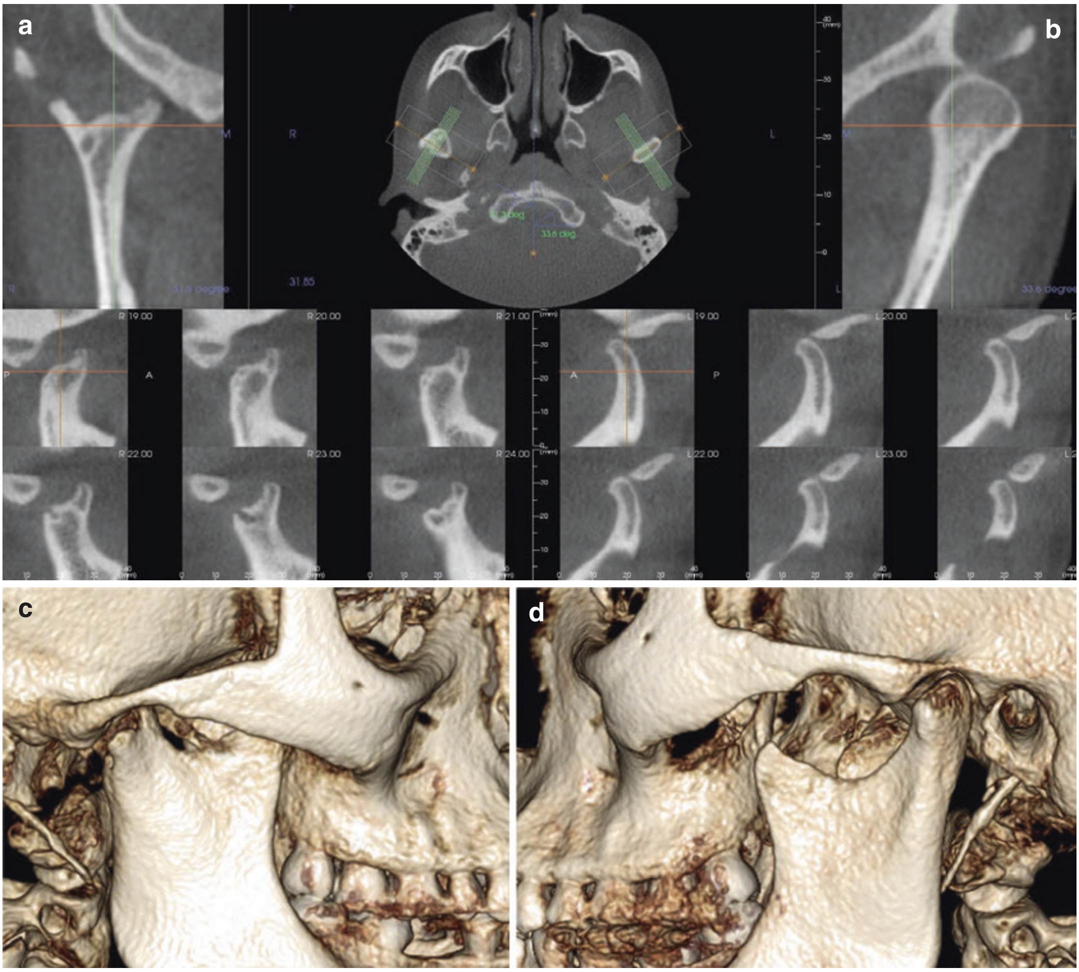

Fig. 3.23 Thin slice coronal and sagittal MPR imaging of the *right* (**a**) and *left* (**b**) TMJ articulations of a patient with a substantial facial asymmetry demonstrating severe developmental morphologic changes in the right mandibular condyle attributed to previous unrecognized/untreated fracture. *Right* (**c**) and *left* (**d**) lateral volumetric renderings clearly demonstrate the morphological changes in the right condyle

umetric imaging can provide visualization of the final position of the bony elements of the maxillofacial region and prove useful in the assessment of the results of surgery (Fig. 3.29).

- **Soft Tissue Calcifications.** Numerous calcifications can occur in the head and neck region. Radiographic characterization and location of these can help distinguishing benign (e.g., tonsiloliths, lymph nodes, salivary gland stones) from potentially significant vascular calcifications (e.g., external or internal carotid artery calcifications) or veins (e.g., phleboliths). Volumetric imaging can assist in correlating hard tissue structures to soft tissue interfaces to assist in diagnosis (Fig. 3.30).
- **Pathology.** CBCT is capable of demonstrating the location, size, shape extent and full involvement of osseous pathology in the upper or lower jaws. In addition, volumetric imaging defines the extent of osteolytic involvement noted on initial 2DCT images in oral metastasis, allowing better localization and visualization of the anatomical regions involved. Together with MPR, volumetric imaging is a useful adjunct for the management of maxillofacial benign tumors involving bone and

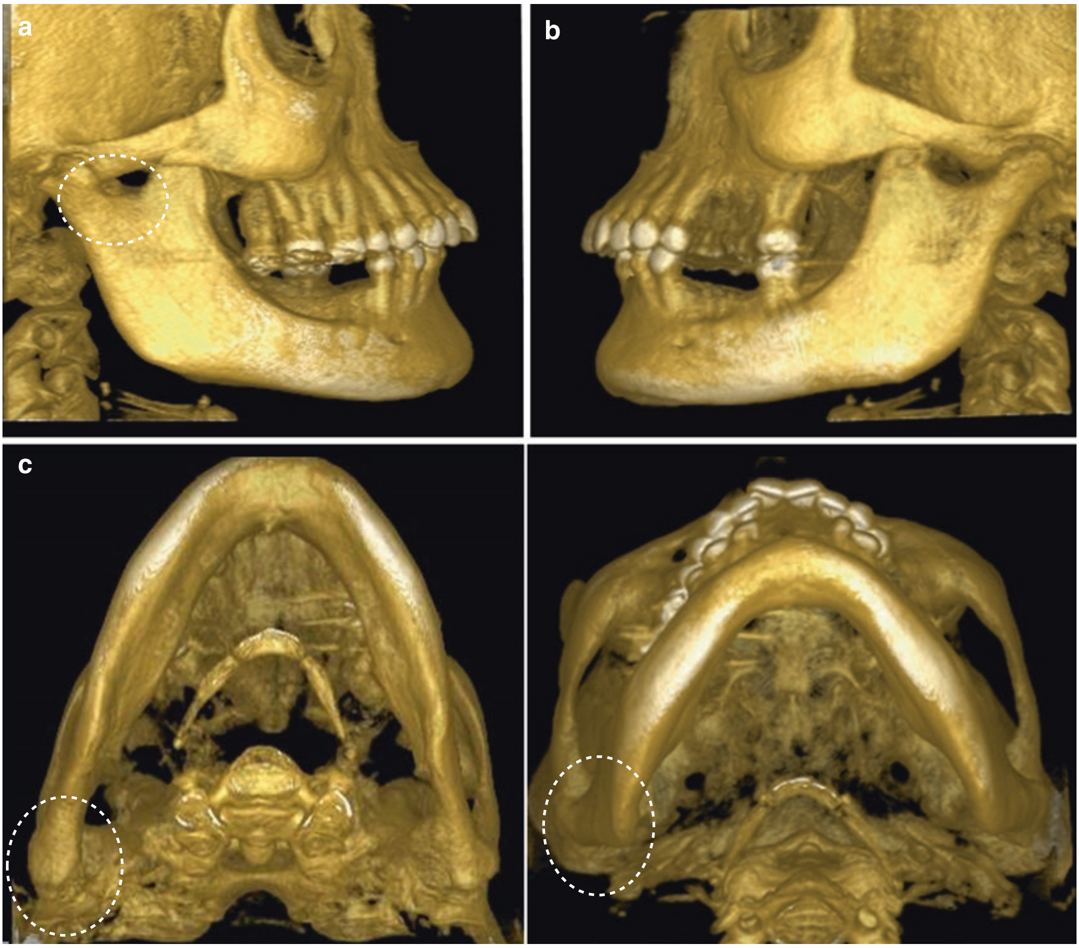

Fig. 3.24 *Right* (**a**) and *left* (**b**) lateral and SMV (**c**) volumetric renderings demonstrating a deformity on the *right side* consistent with fusion (ankylosis) of the condyle to the skull on a patient presenting with progressive limited opening of the mandible

provides accurate and reliable volumetric measurements for follow-up.

- **Conditions affecting the temporal bone**. Volumetric rendered images can depict microanatomic structures, such as the osseous spiral lamina and hamulus, and evaluate various conditions of the temporal bone, including congenital malformations, vascular anomalies, inflammatory or neoplastic conditions, and trauma (Fatterpekar et al. 2006).

Direct Volume Rendering (DVR)

In DVR, the whole dataset is projected onto the virtual display without explicitly extracting geometric surfaces from the data. DVR techniques are computationally more difficult than IVR, because for each projection the whole dataset must be processed. Therefore, in practice, a low-resolution projection is implemented with a coarse sampling pitch, and, once the desired projection geometry is established, the full-resolution projection is implemented. Various rendering modalities are available, but all share the basic ray-casting algorithm. With ray casting, a scene is rendered by projecting an imaginary ray through each row of the selected dataset according to the projection selected and evaluating the scalar intensity values encountered in the volume

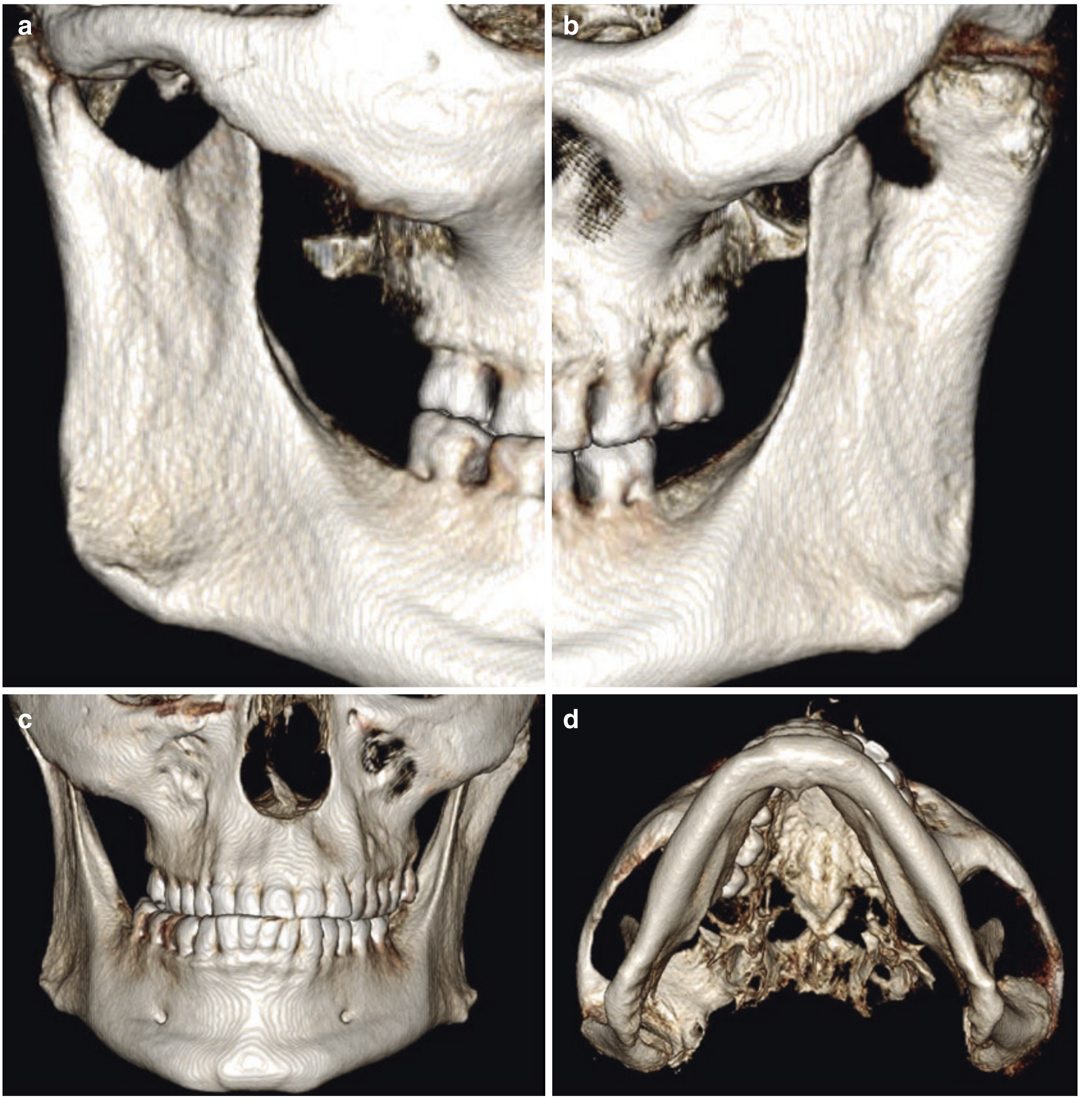

Fig. 3.25 *Right* (**a**) and *left* (**b**) lateral volumetric images showing substantial enlargement of the left condylar head (subsequently diagnosed as an osteochondroma) (*arrows*) of a patient who presented with a changing bite. Frontal (**c**) and SMV (**d**) volumetric rendering showing a significant midline shift

using a specific function. The projection could be orthogonal to the data or tilted/rotated by some angle; it can be also orthogonal or perspective with reference to the point of view. Various rendering modes can be applied, each resulting in a volumetric rendering with a particular visual appearance:

- **Ray Sum.** The values are simply summed (or averaged), simulating the effect of a radiography taken along the current viewing direction (Fig. 3.31).
- **Maximum Intensity Projection (MIP).** Only the largest value is considered (Fig. 3.31).
- **Full volume.** All the values along the ray are processed and combined according to one of the "blending" models.
- **Iso-surface**. This is a special case of the previous mode which provides a rendering effect similar to SSD.

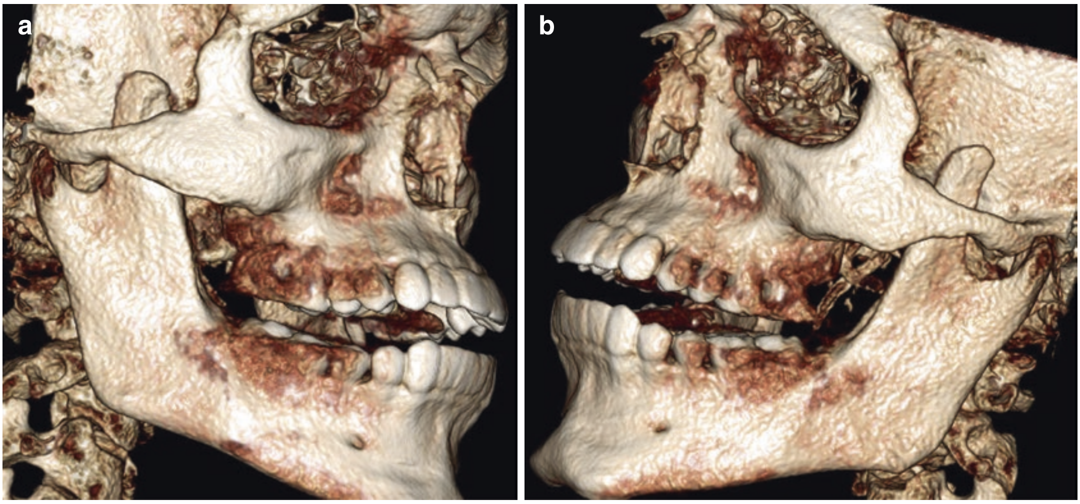

Fig. 3.26 *Right* (**a**) and *left* (**b**) lateral oblique volumetric renderings of the mandible of a patient with progressing limited opening of the mandible demonstrating bilateral coronoid hyperplasia

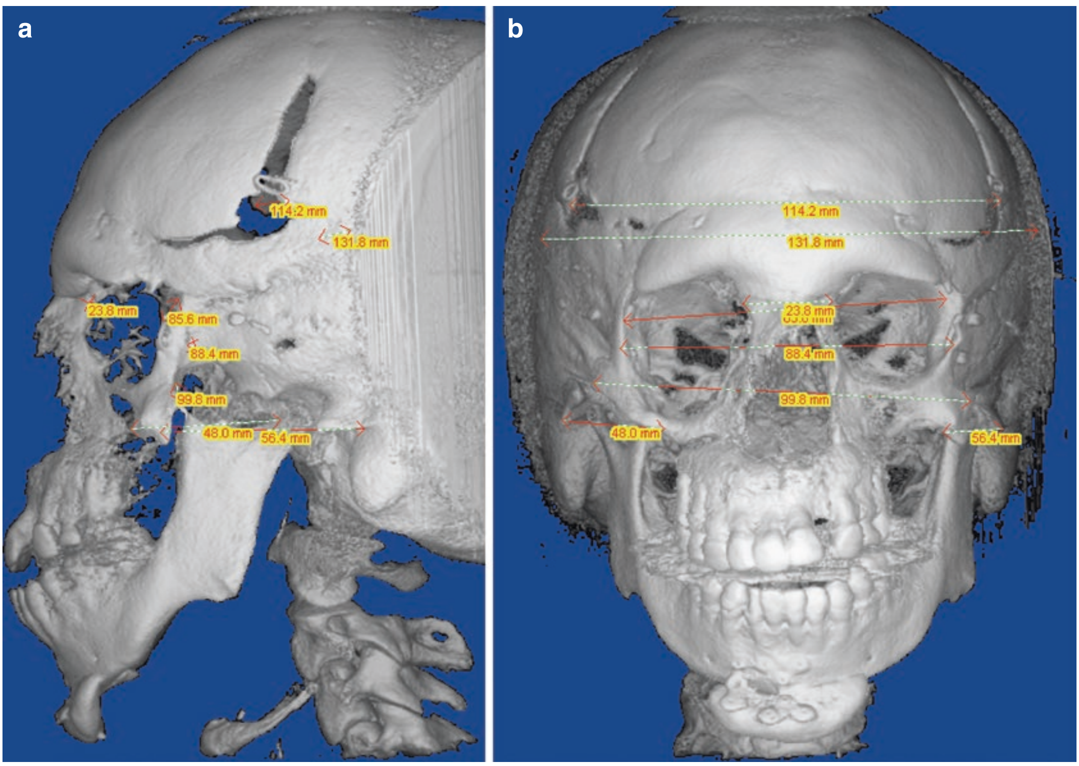

Fig. 3.27 Left lateral (**a**) and frontal (**b**) shaded surface display of a young patient with partially repaired craniofacial deformity (Crouzon's syndrome). Quantitative measurements of head (cranial vault), eyes (orbits), and cheek (zygoma) can be performed and compared to normal age-related values such that further surgical procedures can be planned accurately

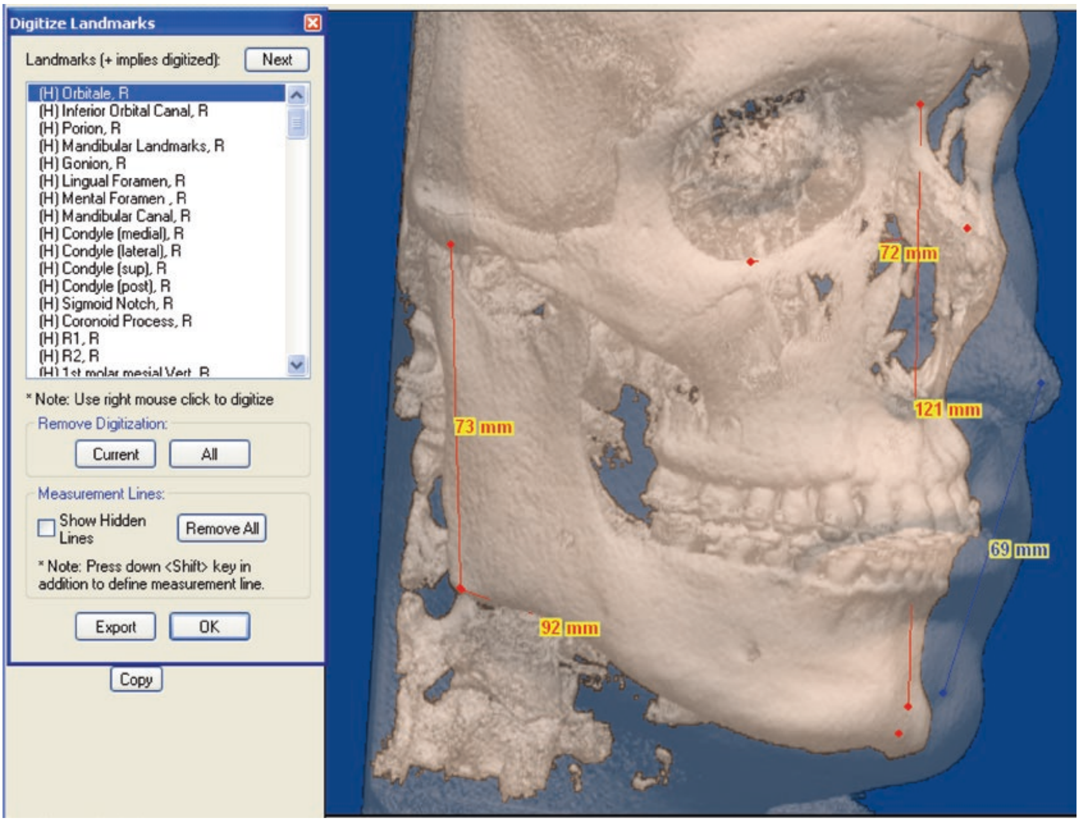

Fig. 3.28 Volumetric cephalometry performed on right lateral volumetric rendered image providing hard (*red dot*) and soft (*blue dot*) landmark identification and respective linear measurements in three dimensions (*red* and *blue lines*)

MinIP (Minimum Intensity Projection) (Fig. 3.31) may also be employed, but rarely in CBCT imaging.

Ray Sum Rendering

If the intensity values of each voxel along each projection ray are treated as relative transparency values and accumulated, then the resultant scene is a rendition of the accumulation of voxel gray values. This mode, referred to as *ray sum*, generates scenes that simulate projection radiographs. This method can be employed to develop 2D renderings either from limited area "thick" (>30 mm) slabs in the axial plane to produce simulated occlusal images (e.g., mandibular thickness) (Fig. 3.32), in a curved MPR to produce simulated panoramic images (Fig. 3.33) or from full thickness (130–150 mm) datasets. The latter are most useful in producing lateral and frontal (or PA) cephalometric images (Fig. 3.34). Unlike conventional radiographs, these composite value ray sum images are without magnification and are undistorted. However, this technique uses the entire volumetric dataset and interpretation suffers from the problems of "anatomic noise"—the superimposition of multiple structures.

Maximum Value (Maximum Intensity Projection)

The maximum intensity projection (MIP) was one of the first volume visualization techniques and remains widely used because of the simplicity of application of the algorithm. MIP is a volume rendering technique that evaluates each voxel value along an imaginary projection ray from the observer's eyes within a particular volume of interest and then represents only the highest value as the display value (Cody 2002; Calhoun et al. 1999). Depending on the quality requirements of the resulting image, different

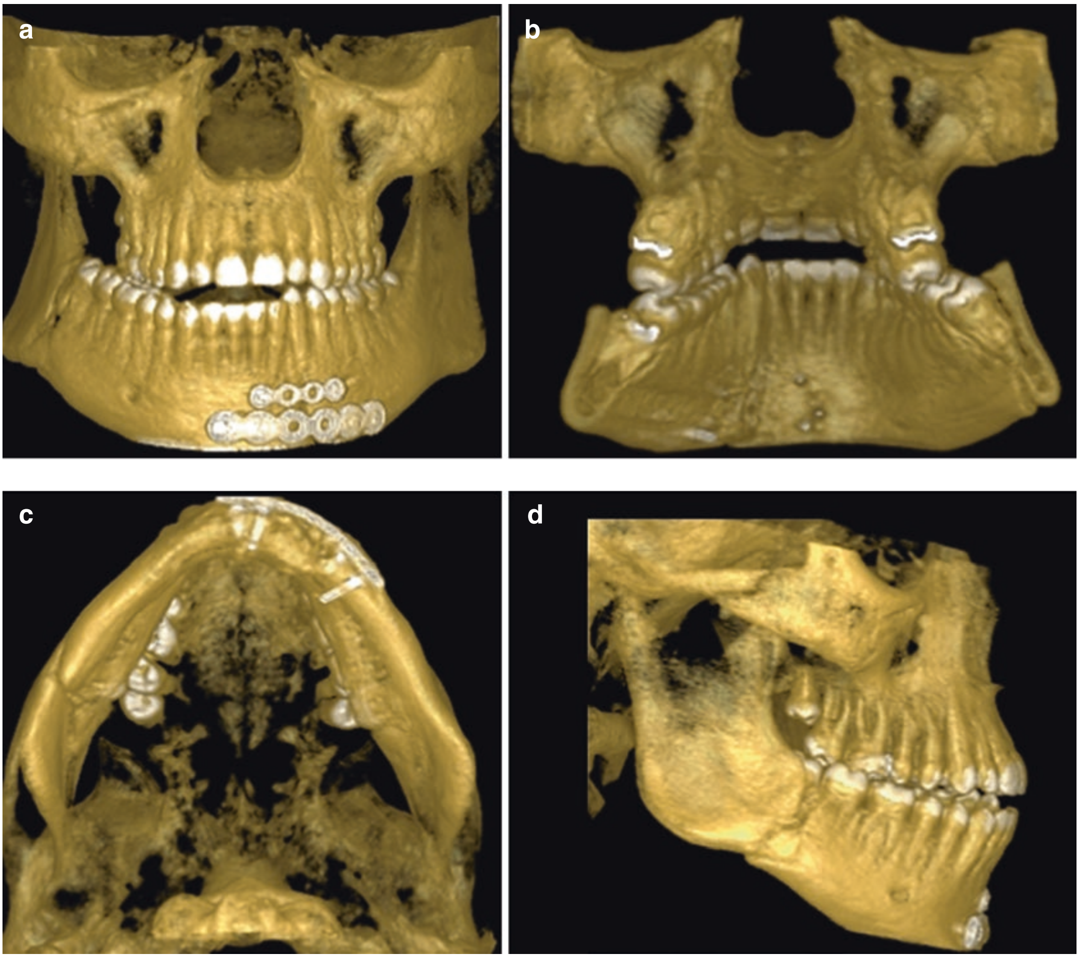

Fig. 3.29 Frontal (**a**), lingual (**b**), SMV (**c**), and right lateral (**d**) volumetric renderings of a patient referred for evaluation of the success of surgical plating of an anterior mandibular fracture. The images demonstrate integrity of the surgical plates and fracture elements however reveal a previously undiagnosed mildly displaced fracture of the right mandibular body, inadvertently overlooked in the original evaluation

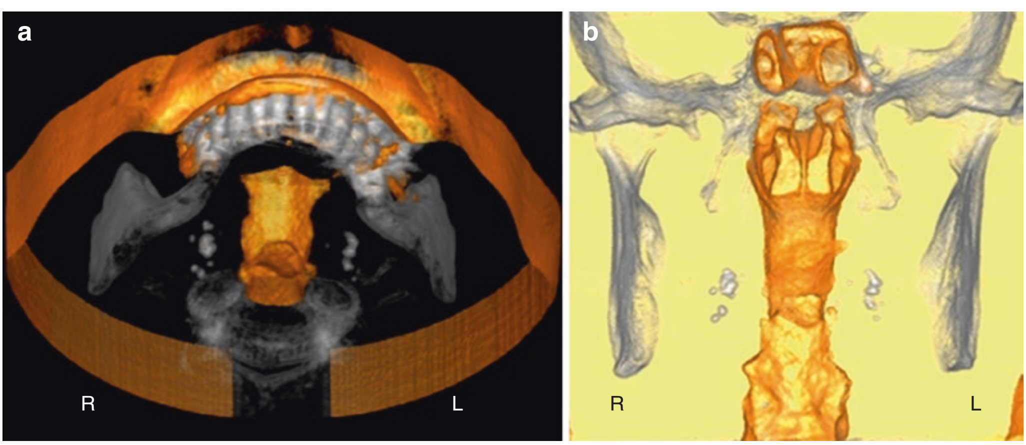

Fig. 3.30 Thin section composite volumetric rendering showing hollow modeled airway space or skin surface (*orange*) from an axial inferior oblique (**a**) or coronal perspective (**b**) showing a series of small concrescences in the parapharyngeal soft tissues adjacent the oropharyngeal airway, consistent with bilateral tonsiloliths (*R* right, *L* left)

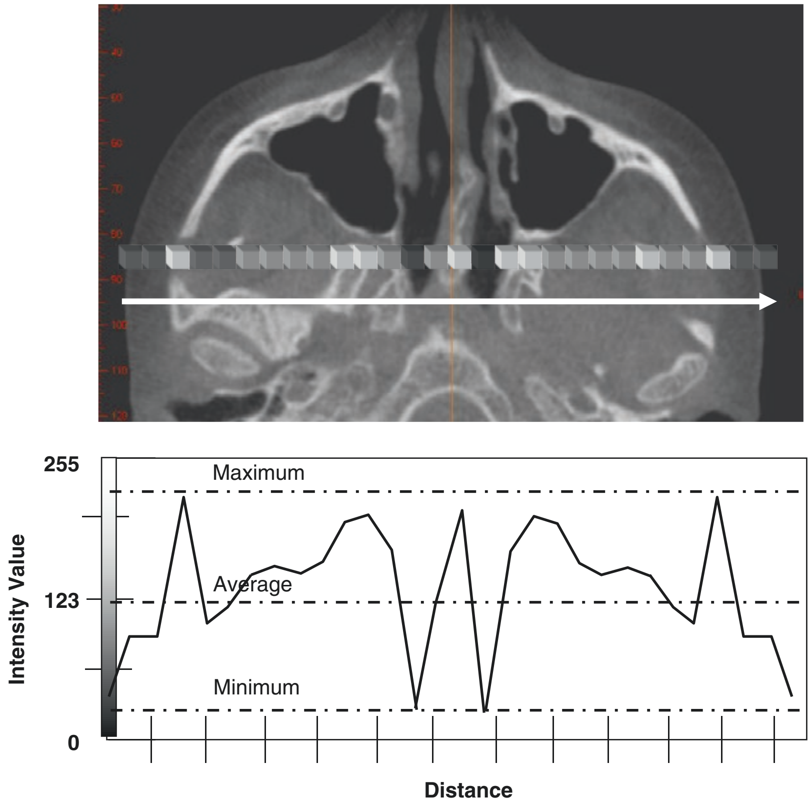

Fig. 3.31 The axial image (*top*) demonstrates the representative voxels along an imaginary projection line (*arrow*). The *lower graph* plots the intensity values (*grayscale*) with distance, from *left* to *right*, through the axial image along the imaginary line. The voxels along this line can be represented as image order rendering by applying various functions to sample the plot. A resultant projection scene could represent only the maximum, average or, minimum intensity values along the projection ray casting

mathematical strategies for finding the maximum value along a ray can be used (Zuiderveld et al. 1994; Sakas et al. 1995; Cai and Sakas 1998). Voxel intensities below an arbitrary threshold are eliminated (Fig. 3.35).

If the dataset includes bone surrounded by soft tissues, the maximum intensity projection renders only values have the highest intensity—bone—ignoring the soft tissue values. This technique can be adopted with windowed thresholds, so as to involve only those voxels whose radiodensity is inside the window itself.

The principal benefit of this method is to provide an operator-independent, "pseudo" 3D renderings representative of the volumetric dataset. MIP images usually contain 10% or less of the original data and are rapidly reconstructed because only data with the highest value are used. MIP is particularly useful in representing the bony surface morphology of the maxillofacial region. In addition, MIP is extremely useful for evaluating and locating high "contrast," high attenuating substances. In medical imaging, this is particularly important to visualize contrast filled structures such as vessels. In maxillofacial imaging, it is often better than surface rendered 3D images to evaluate the location of third molars (Fig. 3.36) or applied to evaluate the presence of a foreign body material or calcification in soft tissue structures.

The main limitation of MIP images is that they have a limited ability to represent anatomical spatial interrelations. This is because it does not contain shading information or visual clues for perception depth. Therefore, MIPs have a tendency to misrepresent positions because the projection technique does not take spatial location into account—only the maximal or (most attenuated) value is displayed. Therefore, some structures may be obscured which may lead to suboptimal interpretation. This concept is particularly important to appreciate when viewing full thickness MIP images in the orthogonal projections. In such situations, it is advisable to employ

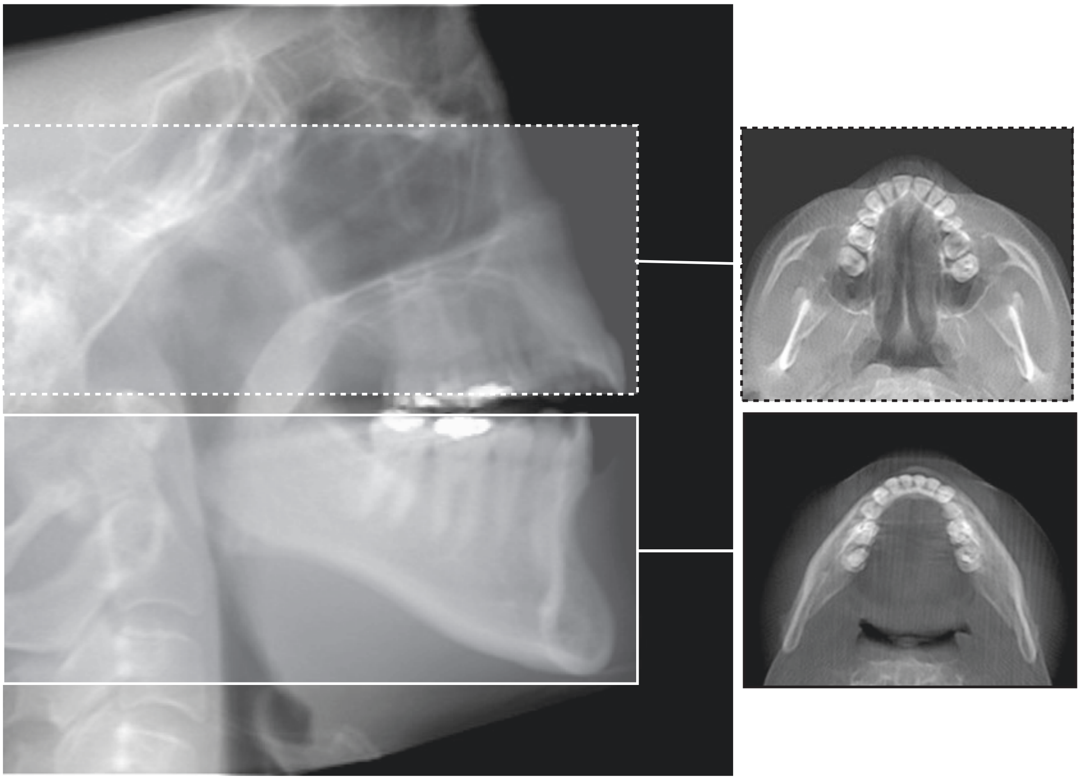

Fig. 3.32 A simulated maxillary (*upper right*) and mandibular (*lower right*) true or vertex occlusal image can be generated from creating a "thick" (40 mm) slab centered at the apices of the teeth in each arch extending 20 mm superiorly to include the crowns of the teeth and 20 mm inferiorly to incorporate part of the basilar bone

volume rendered projection techniques in conjunction with MPR projections to assist in the interpretation process (Fig. 3.37).

One technique to overcome this inherent limitation is to minimize the thickness and/or volume of the MIP image. This is called *Limited Volume MIP*. Limiting the volume under consideration can improve pixel selection and enhance the accuracy of maximum intensity pixel projection. The ability to create an image based on regions of anatomy for inclusion or exclusion in the MIP is widely available and commonly employed. Isolating individual structures under evaluation, (e.g., bilateral structures of the maxilla) improves the accuracy of rendering and reduces overlap with adjacent structures (Fig. 3.38). Another approach is to animate the projection while viewing or to modulate the data values by their depth to achieve a kind of depth shading (Heidrich et al. 1995).

Overlapping, limited volume (OLIVE) MIP rendering can overcome many of the limitations of full-volume and regionally circumscribed MIP. These studies, also known as sliding thin-slab MIPs (Napel et al. 1993) are essentially a hybrid between multi-planar reformation and MIP. To obtain this MIP, a thin-slab MPR is selected from which an MIP image is reconstructed. This slab is moved through the volume, with the slab movement distance smaller than the slab thickness, and at each step an MIP is created. Applications of this technique include implant site and TMJ assessment.

Maxillofacial Applications of MIP

In medical imaging, MIP algorithms are used to depict volumetric vascular datasets acquired with both computed tomography (Napel et al. 1992, 1993; van Ooijen et al. 2003; Prokop et al. 1997).

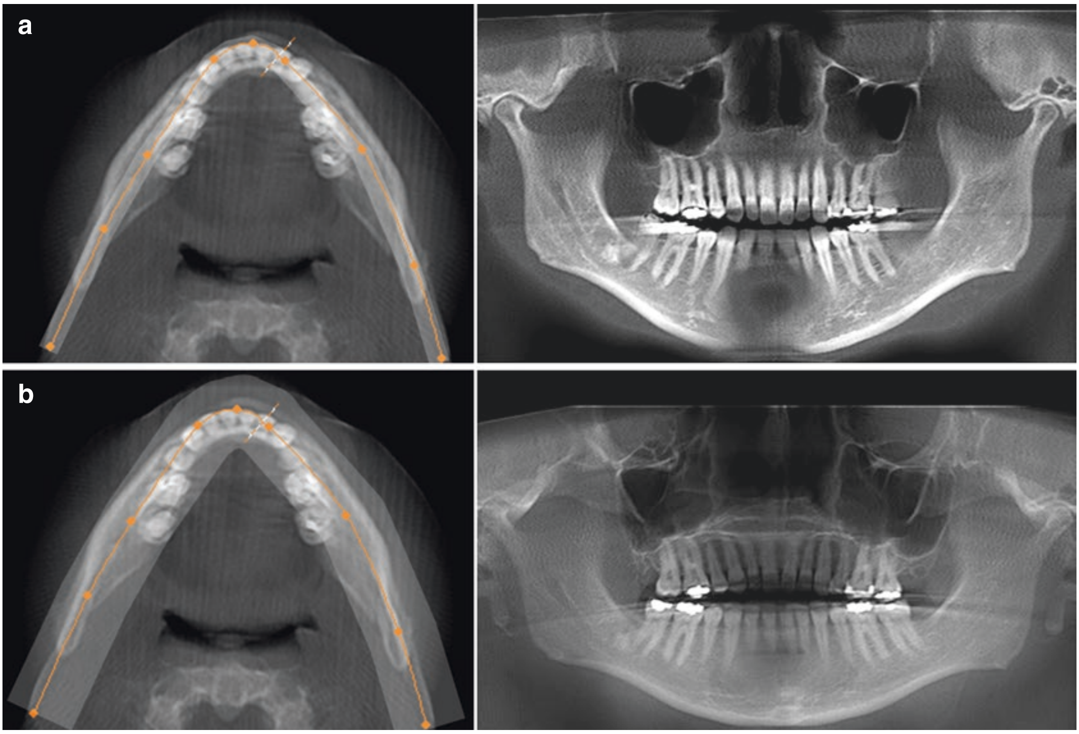

Fig. 3.33 A simulated panoramic image can be generated from a curved oblique MPR that follow the contour of the dental arches. A simulated occlusal radiograph provides an axial reference to identify the location of the nodes used to identify the MPR plane. A thin slab (10 mm) thickness of the MPR provides a sharply defined reformatted panoramic image (**a**) however, the limited thickness creates numerous areas with loss of information (e.g., maxillary left tuberosity, mandibular anterior symphyseal region). In addition, there are notable metallic artifacts associated with the restorations in the teeth A thick slab (40 mm) thickness of the MPR provides a reconstructed panoramic image that represents all areas (**b**)

In maxillofacial CBCT imaging MIP images have great utility in many clinical situations.

- **Impacted teeth.** Successful surgical planning of impacted teeth depends on accurate localization, an understanding of orientation, depth, and angulation, and appreciation of proximity and relationship to other anatomic structures. MIP is of great value in the assessment of impacted teeth, providing the clinician with the ability to generate multiple 3D image projections at various angles with inherent image transparency (Fig. 3.39).
- **Implant imaging.** For implant site assessment, the most common display format includes a thin slice axial and panoramic oblique planar reference images, as well as cross-sectional serial trans-planar images. While most information is from cross-sectional images, panoramic and axial views are used to identify and locate important reference structures. In our experience, we often supplement the standard display formats with 10 mm thick OLIVE MIP images in the axial view to provide better visualization of the occlusal topography of the crowns of the teeth and alveolar crest and in the panoramic view to localize the position of the mental foramen in relation to the dentition (Fig. 3.40).
- **TMJ Evaluation.** Narrow interval, overlapping, sub-volume MIP slabs offer a valuable tomographic assessment augmenting evaluation of TMJ condylar orientation and shape (Fig. 3.41). Limiting the volume in MIP

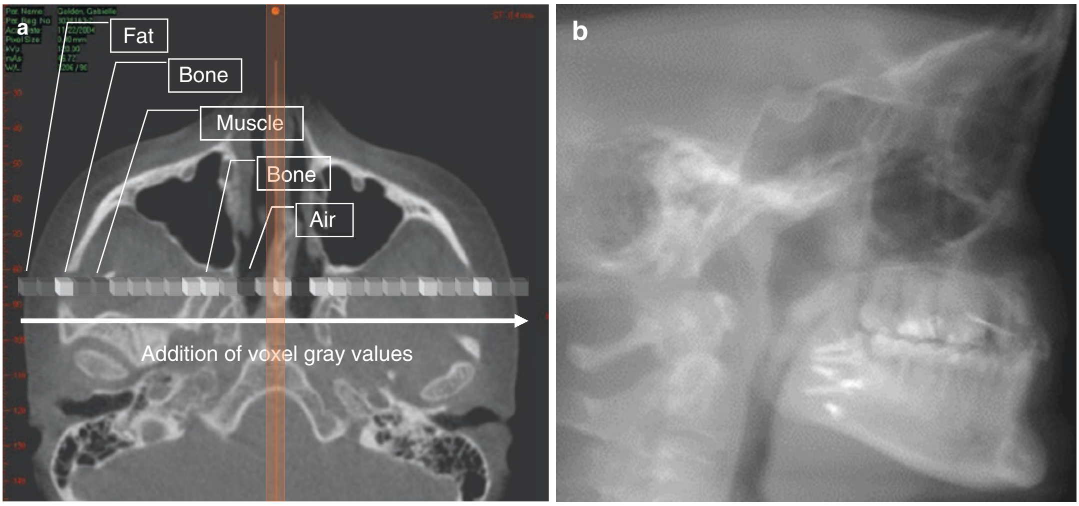

Fig. 3.34 Schematic demonstrating the generation of a composite ray sum "simulated" lateral cephalometric image. An axial projection (**a**) is used as the reference image. A section slice is identified (*orange*) corresponding to the midsagittal plane and the thickness of this increased to include both *left* and *right sides* of the volumetric dataset. As the thickness of the "slab" increases, adjacent voxels representing elements such as air, bone, and soft tissues are included. The resultant image generated provides a simulated lateral cephalometric (**b**)

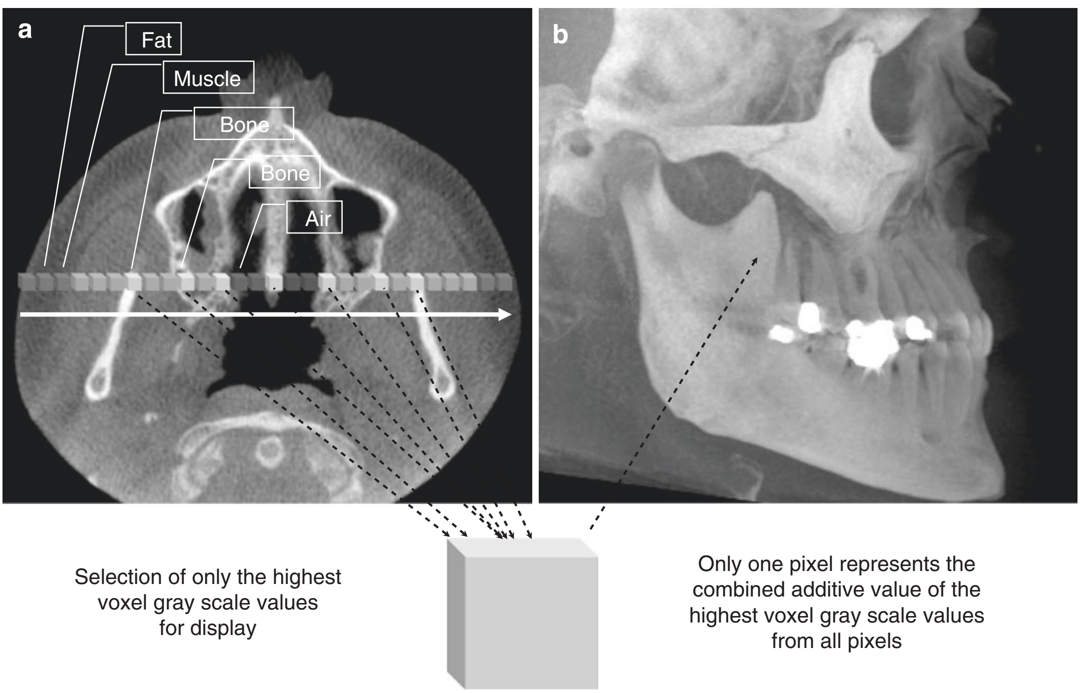

Fig. 3.35 Schematic demonstrating the maximum intensity projection (MIP) technique. This method produces an image by evaluating each voxel value along an imaginary projection ray from the observer's eyes within the dataset and then representing only the highest value as the display value. In this example, an axial projection (**a**) is the reference image. A projection ray is cast (*orange*) throughout the entire volumetric dataset along which individual voxels are identified, each with varying grayscale intensity corresponding to various tissue densities such as fat, muscle, air and bone. The MIP algorithm selects only those values along the projection ray that have the highest values (corresponding usually to bone) and represents this as only one pixel on the resultant image (**b**)

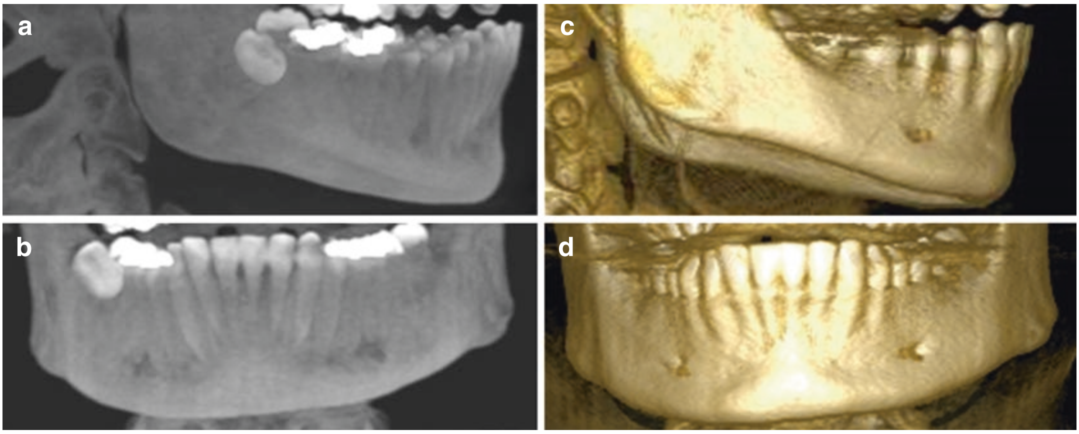

Fig. 3.36 Comparison of lateral (**a**) and frontal (**b**) MIP rendered images and lateral (**c**) and frontal (**d**) volumetric surface rendered images. Unlike the surface renderings, which display the surface features of the volumetric dataset, MIP images inherently demonstrate all highly attenuating structures, irrespective of whether these are on the surface or not. MIP images present with a characteristic "opaque glass" appearance, allowing features within the bone to be visualized. In this example, the location and depth of the mesioangular impacted third molar in the mandibular right is more clearly demonstrated using MIPs than 3D surface renderings

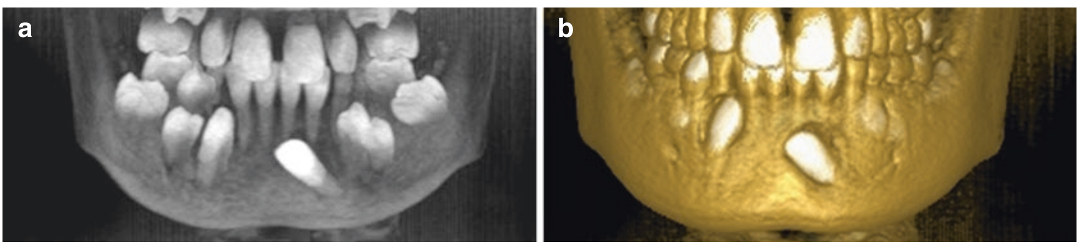

Fig. 3.37 MIP images have limitations in illustrating relative position and location because structures with higher value voxels lying behind a lower valued voxel appear to be in front of it. In this example of a patient with multiple mandibular impactions, the MIP image (**a**) demonstrates the relative angulation of the unerupted and impacted mandibular left canine but provides no information on its relative bucco-lingual position. The 3D surface rendering (**b**) however clearly demonstrates the buccal position of the crown

reconstruction improves the integrity of MIP, limits overlap from adjacent bony structures, and provides greater visualization of thinly corticated structures.

- **Fractures.** MIP images demonstrate disruption and discontinuity of osseous structures well. Heiland et al. (2004) first described an example of the use of maxillofacial MIP images for visualization of a mandibular fracture. Simple display protocols using limited volume MIPs in the region of interest in three planes enable visualization of the extent, direction, and degree of displacement of most fractures (Fig. 3.42).
- **Soft tissue hyperdensities.** Hyperdensities within soft tissue have high voxel grayscale intensity values compared to adjacent soft tissue voxels and appear as bright spots on MIP images. MIP provides valuable information on the distribution and location of soft tissue vascular, glandular and cerebral calcifications including tonsiloliths, salivary gland stones, calcified lymph nodes, and carotid artery calcifications (Fig. 3.43).
- **Craniofacial Anomalies.** Medina (2000) first described the application of MIP images in conventional CT images for the assessment of craniofacial anomalies. Araki et al.

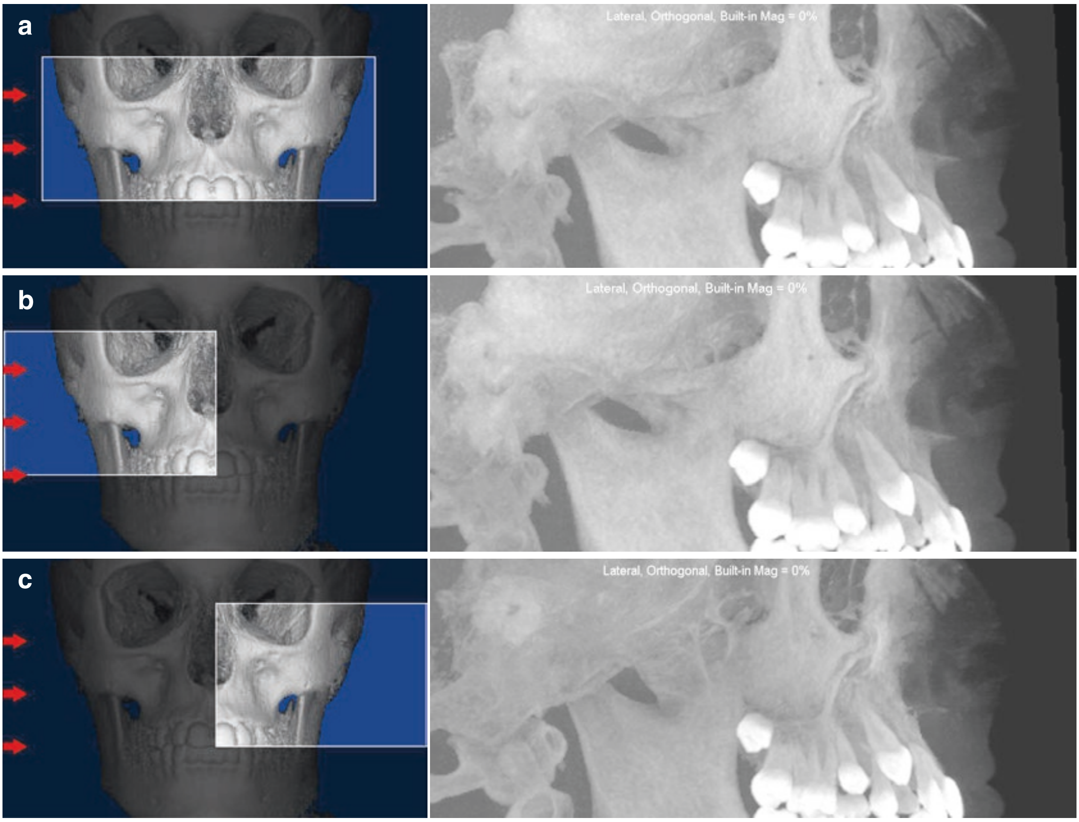

Fig. 3.38 Schematic demonstrating limited volume MIP of a patient with bilateral, impacted and unerupted maxillary canines. A lateral MIP (**a**) using the entire volume of the maxilla (**a**—insert) provides a composite image representing both sides. Generation of a *right* (**b**) and *left* (**c**) limited volume MIP indicates remarkable symmetry in the position of the impacted canines and in the eruption sequence of the remaining unerupted teeth

(2004) demonstrated the application of this technique for cleft palate and lip applications. A standardized imaging display protocol provides a full assessment of the deficiencies in sutural closure and bone formation associated with craniosynostosis (Fig. 3.44).

- **Surgical follow-up.** Visualization of metallic structures using CBCT imaging, particularly with thin section orthogonal views, is problematic because of scatter artifact. This is especially noticeable in images of patients who present for postoperative assessment with extensive maxillofacial reconstruction. 3D volumetric surface renderings are subject to difficulties in segmentation also because of artifact scatter. In these patients, MIP imaging provides a simple method to visualize surgical plates, determine fracture segment stability, and evaluate displacement (Fig. 3.45).
- **Cervical Spine.** The cervical spine is a structural feature often included in CBCT scans of the maxillofacial region, particularly with larger field of view protocols. Congenital anomalies of the cervical spine have been associated with osteogenesis imperfecta and other craniofacial anomalies including Crouzon (Anderson et al. 1997a) and Pfeiffer's (Anderson et al. 1997b) syndromes, hemifacial microsomia (Figueroa and Friede 1985), and Goldenhar's syndrome (Gosain et al. 1994). Cervical anomalies present as a failure of formation, failure of segmentation, or combinations of both. Initial evaluations of the cervical spine with conventional plain film

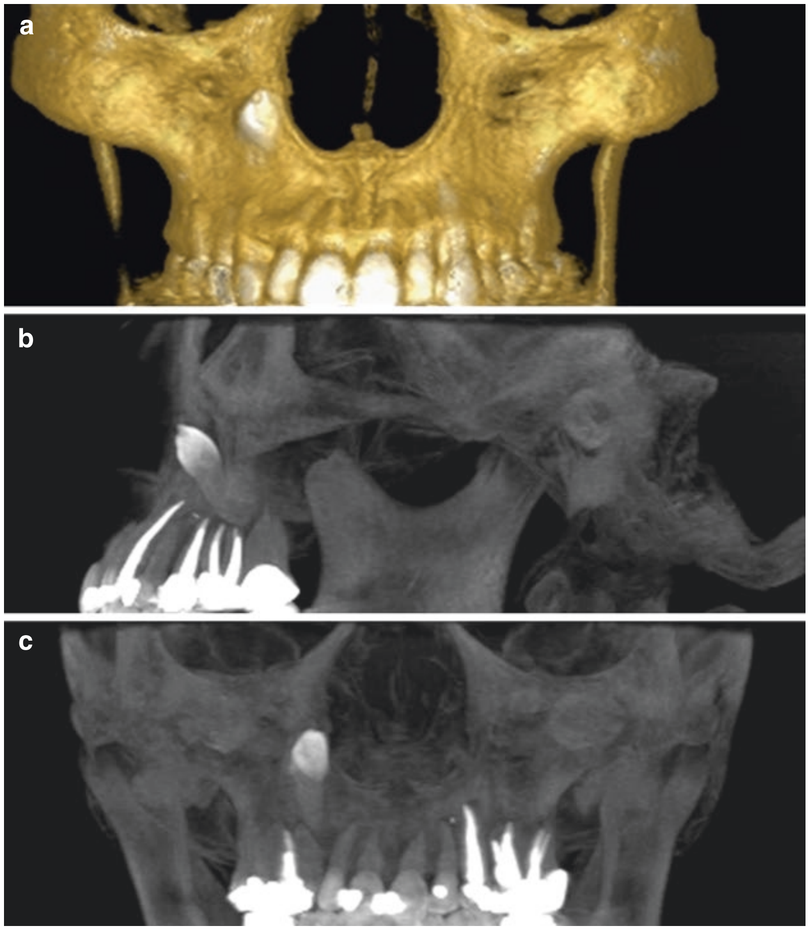

Fig. 3.39 Volumetric shaded surface volume rendering (**a**) of a patient with an impacted maxillary right canine provides little information for surgical planning apart from indicating that the crown is erupting at the lateral border of the right lateral nasal fossa. Full thickness lateral (**b**) and frontal (**c**) MIP images clearly demonstrate the tooth is inverted and vertically embedded and the root is straight

radiography includes anteroposterior, an open-mouth odontoid and lateral neutral, flexion, and extension projections (Brinker et al. 1997). MIP at these modified projections can demonstrate the extent and nature of cervical anomaly (Fig. 3.46).

- **Orthodontic analysis.** MIP images assist in establishing the location of topographic landmarks as they clearly demonstrate the surface features of the maxillofacial complex. Orthodontic tracings using a combination of ray sum and MIP images are particularly useful. The ray sum image provides a simulated lateral cephalometric view of the maxillofacial region and, being transparent, provides identification of midsagittal features such as Sella and posterior nasal spine (PNS) (Fig. 3.47). Ray sum images suffer the same limitations as conventional images in that they provide limited identification of surface features. In comparison, MIP images more clearly allow identification of landmarks associated with curved surfaces (e.g., Orbitale, zygomatic arch), sutures (Nasion), orifices (e.g., Porion), and thinner structures (e.g., Point A and anterior nasal spine). The use of supplemental images can potentially increase the reliability and accuracy of measurements obtained from cephalometric analysis.

The MIP is a simple, easily applied 3D visualization tool for CBCT datasets to be used as an adjunct, not as a replacement, to thorough and systematic evaluation of the constructed CBCT images.

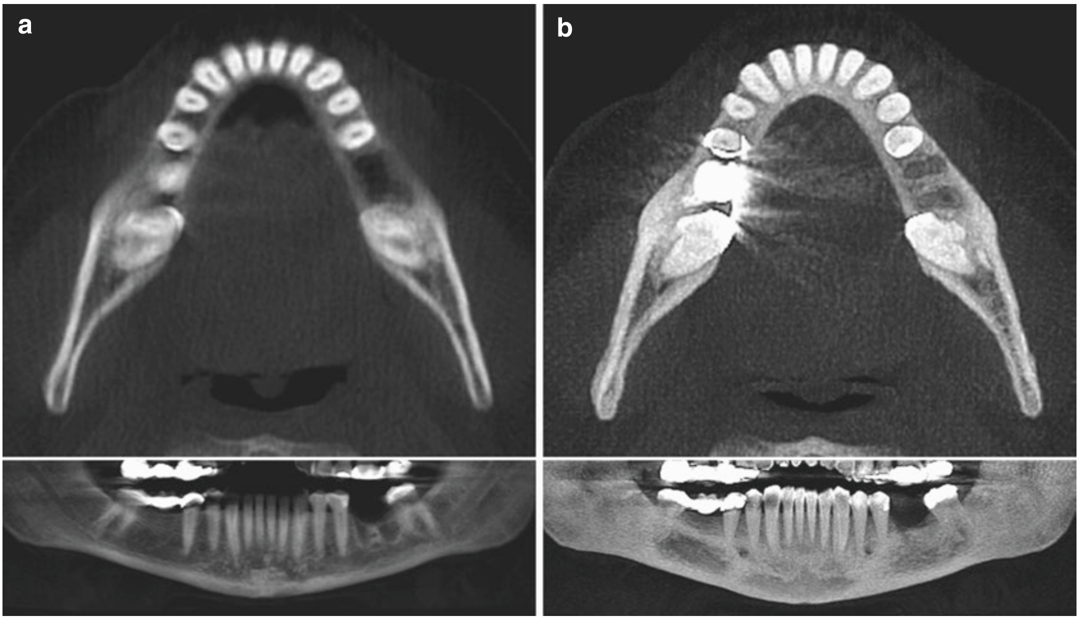

Fig. 3.40 Ten millimeter ray sum axial and panoramic MPR images (**a**) are useful in that they provide an indication of the maximum available bucco-lingual width (axial view) and information of the orientation of the cross-sectional slices with respect to the occlusal and mandibular planes as well as the alveolar crest (panoramic view). Additional 10 mm OLIVE MIP axial and MPR panoramic images (**b**) provide better visualization of the occlusal topography of the crowns of the teeth and alveolar crest (note the residual extraction defects) (axial view) and the position of the mental foramen in relation to the dentition (panoramic view)

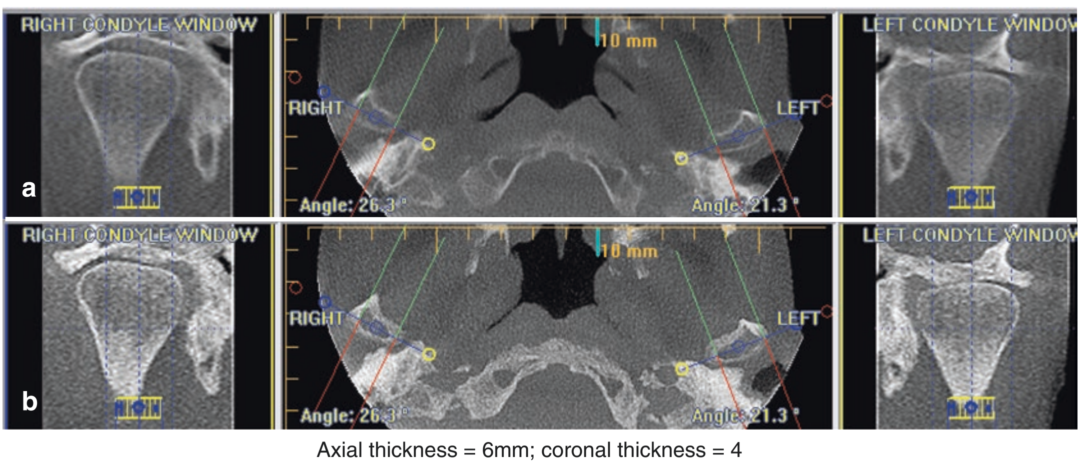

Fig. 3.41 Comparison of ray sum (**a**) and MIP (**b**) *left* and *right* 4 mm thick para-coronal corrected (labeled "right and left condyle window") and 6 mm thick axial (*center*) images of the temporomandibular joints. MIP images more clearly demonstrate the integrity and relationship of the cortical bone of the mandibular condyles and shape of the glenoid fossa as well as illustrate the long axis orientation of the condyles on the axial images than the ray sum images

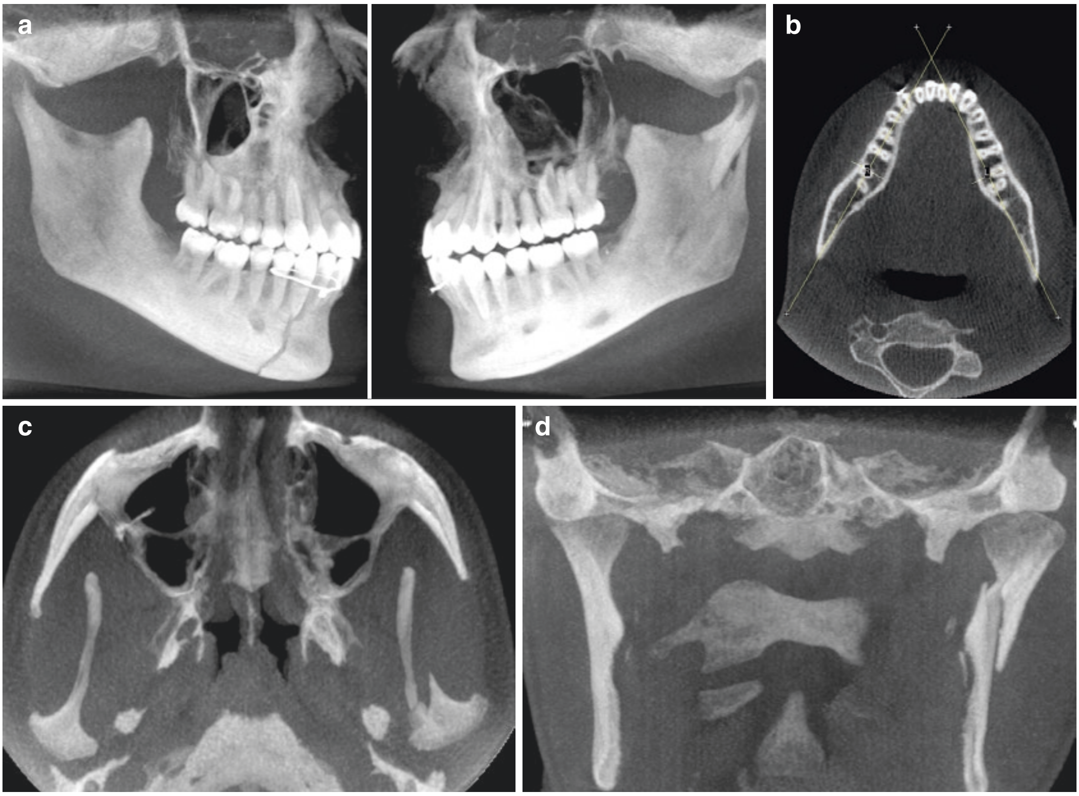

Fig. 3.42 MIP image display protocol incorporating bilateral linear oblique 10 mm thick MIP MPR images (**a**) created from the axial image (**b**), and axial (**c**) and coronal (**d**) 10 mm thick MIP orthogonal images. This MIP image sequence clearly demonstrates a simple slightly displaced fracture of the right parasymphyseal region and comminuted and displaced left sub-condylar neck fracture

Full-Volume Rendering

Texture mapping uses an optical model to map data values with optical properties such as coloring and transparency to visualize simultaneously different tissues or structures. This technique comprises three steps:

- **Voxel classifications.** This process aims to discover and emphasize interesting structures embedded in the data, while de-emphasizing or completely culling away occluding structures that are currently of no interest, in order to produce a volumetric rendering of diagnostic value. This can be performed by identification and subsequent inclusion, selective omission or de-emphasis of various intensity ranges within the image (intensity windowing) or by means of the so-called "transfer function." Figures 3.48 and 3.49 show examples of intensity window setting. Inclusion or exclusion of various intensities prior to rendering may substantially influence the resultant image. The use of preset gray value ranges for volume renderings relies on the consistency of these values between scans; therefore, an offset correction or manual manipulation of the ranges may be required to optimize the rendering.
- Correction for inherent variations between different scans requires a calibration of window level of a specific homogeneous tissue to a fiducial level, usually a large homogeneous

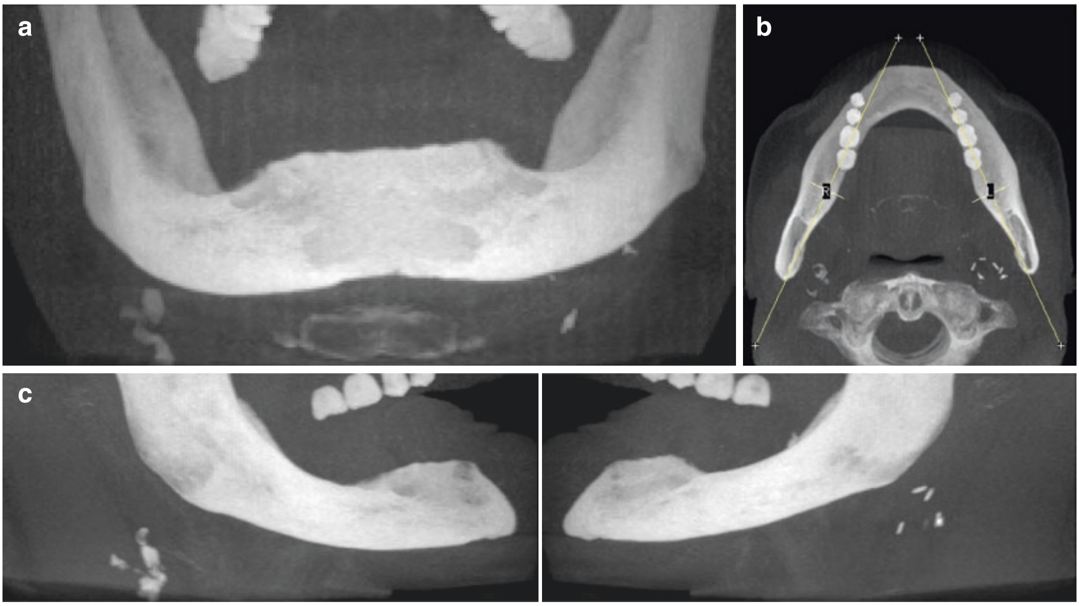

Fig. 3.43 Frontal full thickness MIP of the mandible of an edentulous patient with bilateral lateral neck hyperdensities, immediately inferior to the angle of the mandible (**a**) Axial MIP (**b**) shows location of linear left and right MPR MIP reconstructions (**c**) identifying artery clips consistent with a carotid endarterectomy on the *right* and substantial hyperattenuation consistent with calcified carotid artery atheroma at the level of the bifurcation on the *left*

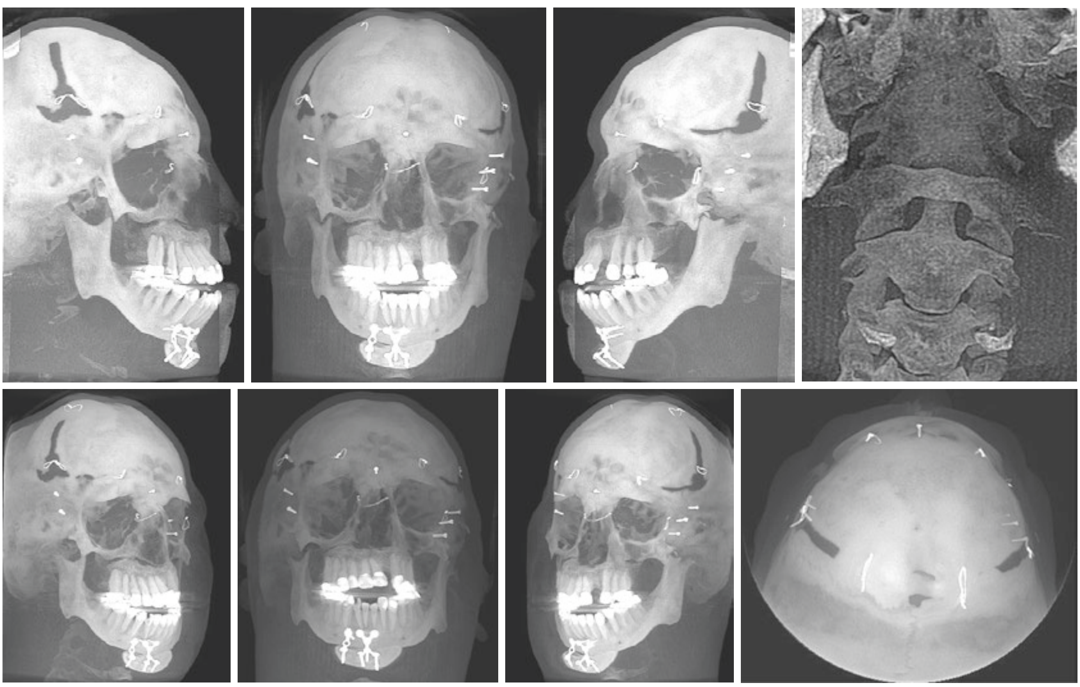

Fig. 3.44 A standard eight projection MIP series comprising 100 mm thick right and left lateral and lateral oblique images, frontal and frontal oblique, occipital and cervical images provides a convenient method to visualize the complex relationships of the maxillofacial bones, especially useful for the assessment of craniofacial anomalies

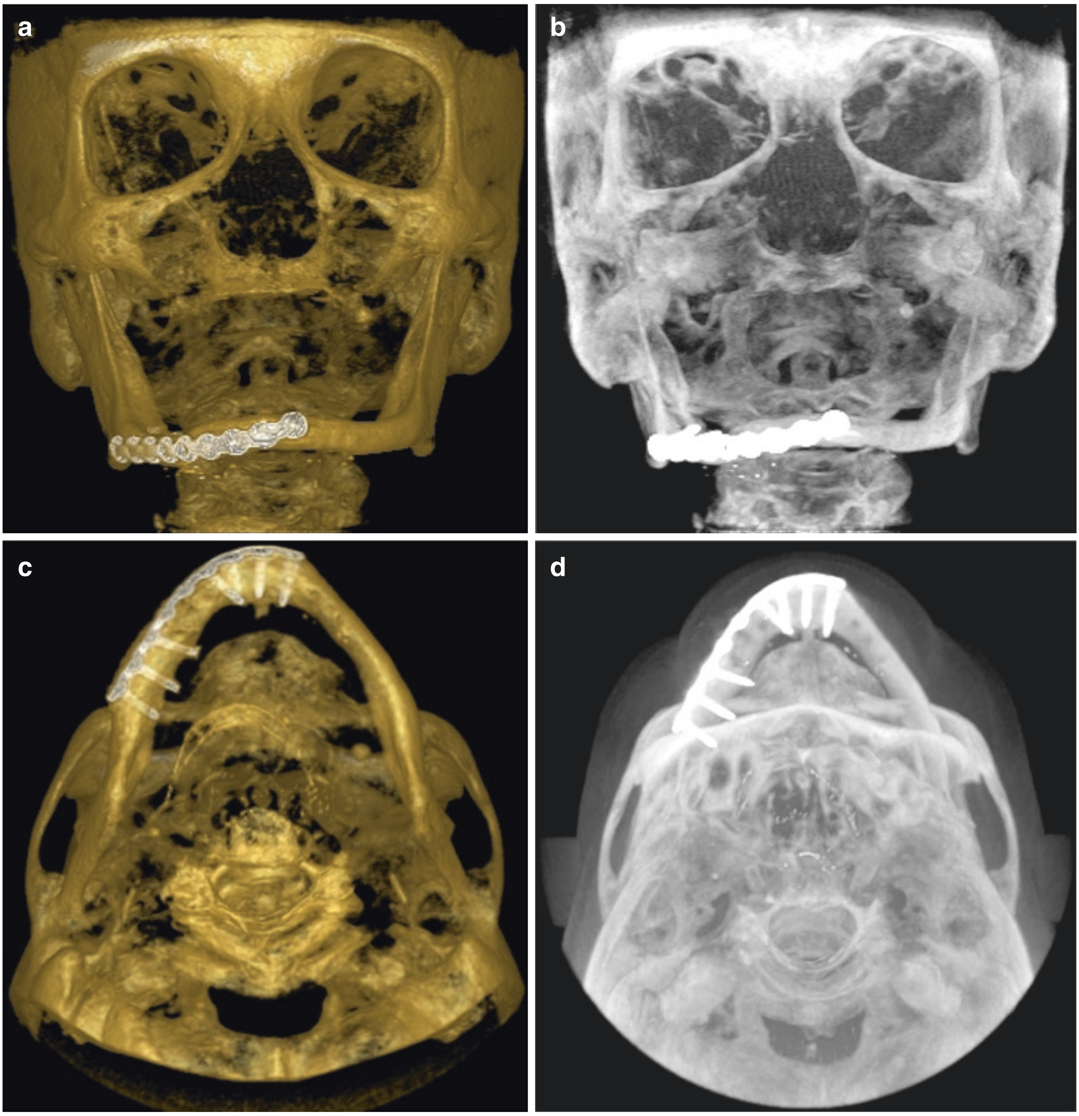

Fig. 3.45 Comparison of frontal volumetric surface (**a**) and MIP (**b**) and SMV volumetric (**c**) and MIP (**d**) images for a patient reconstructed with tibia graft material stabilized with surgical plates after pathologic fracture associated with mandibular atrophy

structure, such as the tongue. Ideally the soft tissue should have a mean voxel intensity of approximately +50. If the value varies from this, then an offset calculation should be performed and the resultant offset used to calibrate the mean voxel intensity value to be +50. Not only does the offset have a visible effect on the brightness and contrast of the axial images, it significantly influences the visual characteristics of the resultant 3D rendering (Fig. 3.48). Offset is usually applied on most dental software by use of a sliding scale and observers adjust the image qualitatively to provide a visually optimal image. However, interpretation related to the presence or absence of bone in many cases must be made

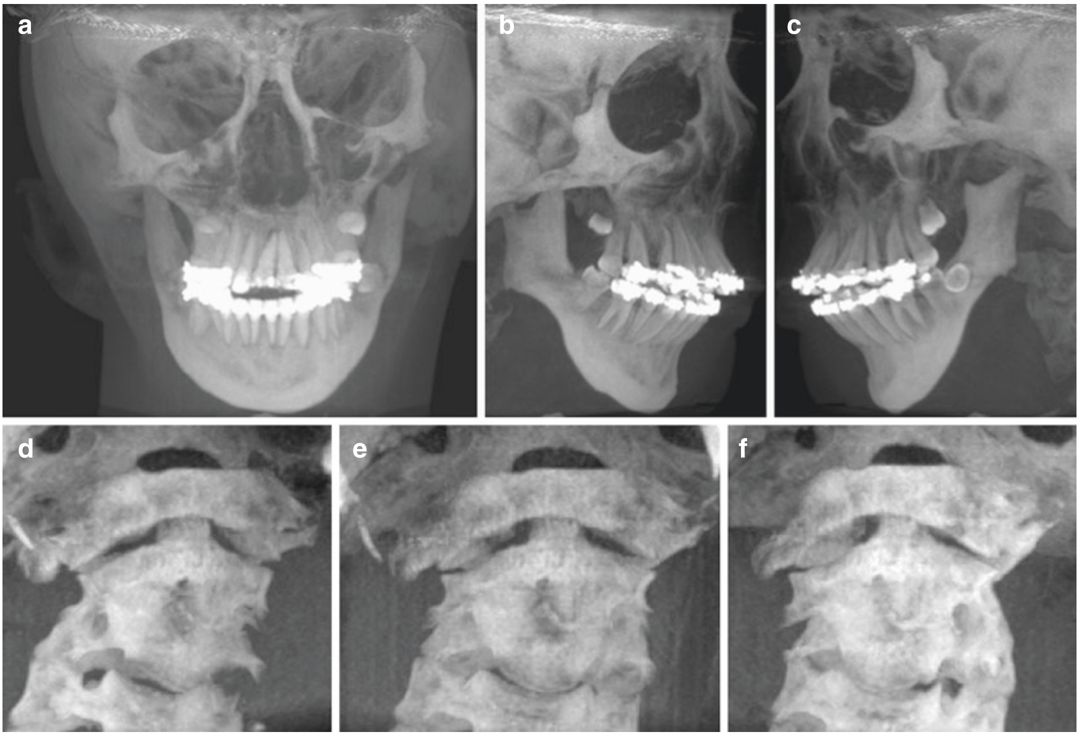

Fig. 3.46 Standard full field of view MIP images comprising frontal (**a**), right lateral (**b**) and left lateral (**c**) projections demonstrate the maxillofacial facial features associated with this patient with Goldenhar's syndrome. In addition, limited volume (50 mm thickness) right 45° oblique (**d**), coronal (**e**) and left 45° oblique (**f**) MIP projections clearly demonstrate compensatory cervical spine scoliosis with marked deviation to the right and anteriorly with fusion of the anterior vertebral bodies of C2 and C3

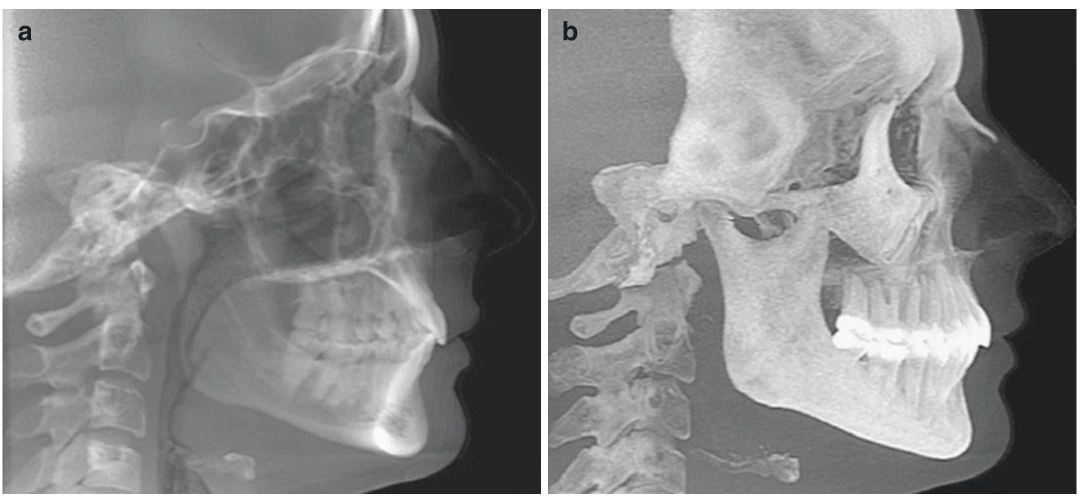

Fig. 3.47 Comparison of simulated lateral cephalometric ray sum (**a**) and MIP (**b**) images. Note the clarity with which notoriously difficult topographic landmarks on conventional ray sum images (e.g., ANS, porion, orbitale, nasion) are easily identified on the MIP images

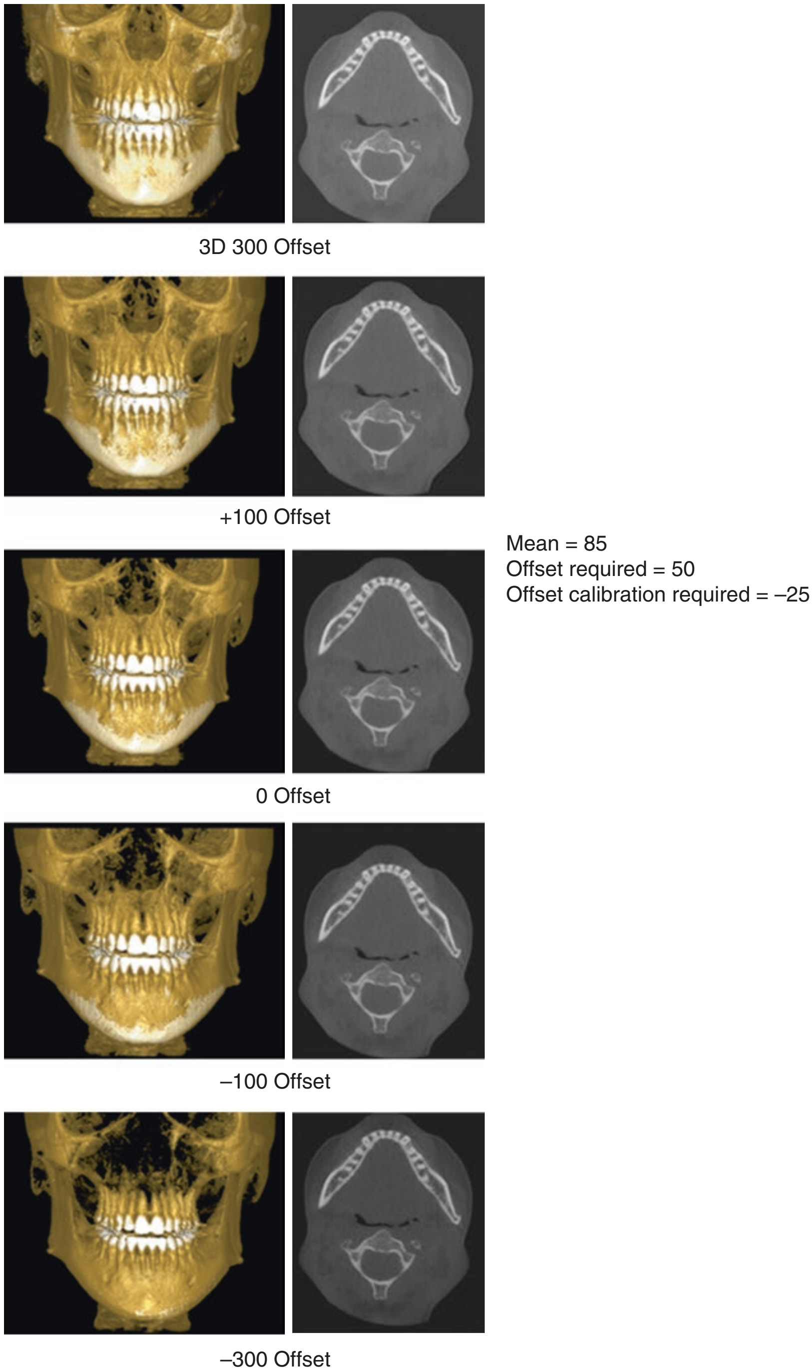

Fig. 3.48 Sequence of volumetric renderings (*left*) and axial images (*right*) showing the effect of addition or subtraction correction of a fixed intensity value (offset) relative to a tongue soft tissue value of +50. The *middle row* shows the original axial (*right*) and 3D volumetric rendered image (*left*) based on voxel intensity range presets. The mean voxel intensity for the soft tissue of the tongue is +85; therefore, an offset of −25 is required to calibrate the image such that the soft tissue is +50. The rows *above* and *below* the *central row* graphically represent the visual effects of over (*upper rows*) and under (*lower rows*) offset calibration

on the understanding that offset correction has a global effect on the image (Fig. 3.49).

- With transfer function, each voxel within the dataset has an assigned value according to three parameters:
- *Color Mapping.* A color scheme or mapping is usually applied to a specific intensity range so that particular tissue element can have a distinct color coding or color label, applied according to color Look-Up-Tables (LUT). Presets are generally applied based on the visual characteristics of the tissue to be represented. For example, bone is white, muscle is red, and fat is beige. In this way, multiple segmentations can be applied to visualize various anatomic structures. The simplest method is to assign all voxels in the bone range of grayscale intensities a white or yellow color. However, a gradient of color can be applied such that the lower intensity values within this range have one color and the upper value voxels have another color. This is called *gradient color mapping*. This application and considerations of relative thickness can provide a more realistic volumetric rendering (Fig. 3.50).
- *Opacity.* This refers to the degree of transparency of each voxel within a designated range of voxel grayscale intensities by assigning opacity values ranging from 0% (completely transparent) to 100% (completely opaque). Greater values provide structures with similar appearance to SSD, whereas lower values provide see-through transparency (Fig. 3.51). As a general rule, for volumetric rendering comprising multiple elements (i.e., more than one range of voxel intensities) the opacity of the deepest structure is the lowest. By convention, specific levels of opacity are applied to each tissue with bone being opaque, muscle being semitransparent, and fat being mostly transparent.
- *Brightness.* This parameter affects every color value in the image by assigning a percentage value of brightness to every pixel. The selection of this value is mostly subjective (Fig. 3.52); however, as a general rule, soft tissue brightness is the same or slightly lower than bone which is lower than dental hard tissue. The starting point is most often the brightness of the bone that provides the most detail.

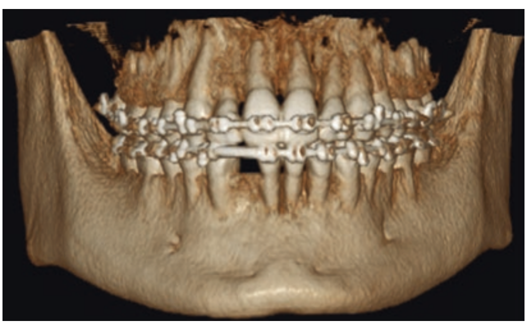

Fig. 3.49 In this texture mapped DVR offset correction has been applied to remove bone voxel intensities associated with thin cortical plates in the maxilla to reveal the roots of the maxillary teeth and demonstrate tooth root alignment. However, an untoward effect of this is that other elements of cortical bone are also removed (e.g., cortical bone associated with the buccal surfaces of the mandibular teeth) and could be misinterpreted as fenestration

Specific tissues and structures are rarely represented by a discontinuous intensity value range; moreover, they form a Gaussian distribution of intensities around a peak range, which theoretically represents 100% of the tissue type. Therefore, unlike SSD or MIP, voxels in volumetric renderings are not represented in the image with an all-or-nothing distribution. Often they will have overlapping intensity ranges between selected voxel intensity ranges. This effect tends to complement the resultant image by filling in deficiencies.

In clinical practice, volumetric rendering involves a complex interaction of color and opacity and brightness; therefore, it is important to choose colors and opacity carefully in order to obtain a proper result. The most important is color. Color tables are useful to assist in the application of different color mapping to the rendered image. Depending on the specific application, the utilization of one color table may prove superior to another.

- **Voxel-based projection.** This is the process of creating a 2D image from the classified 3D

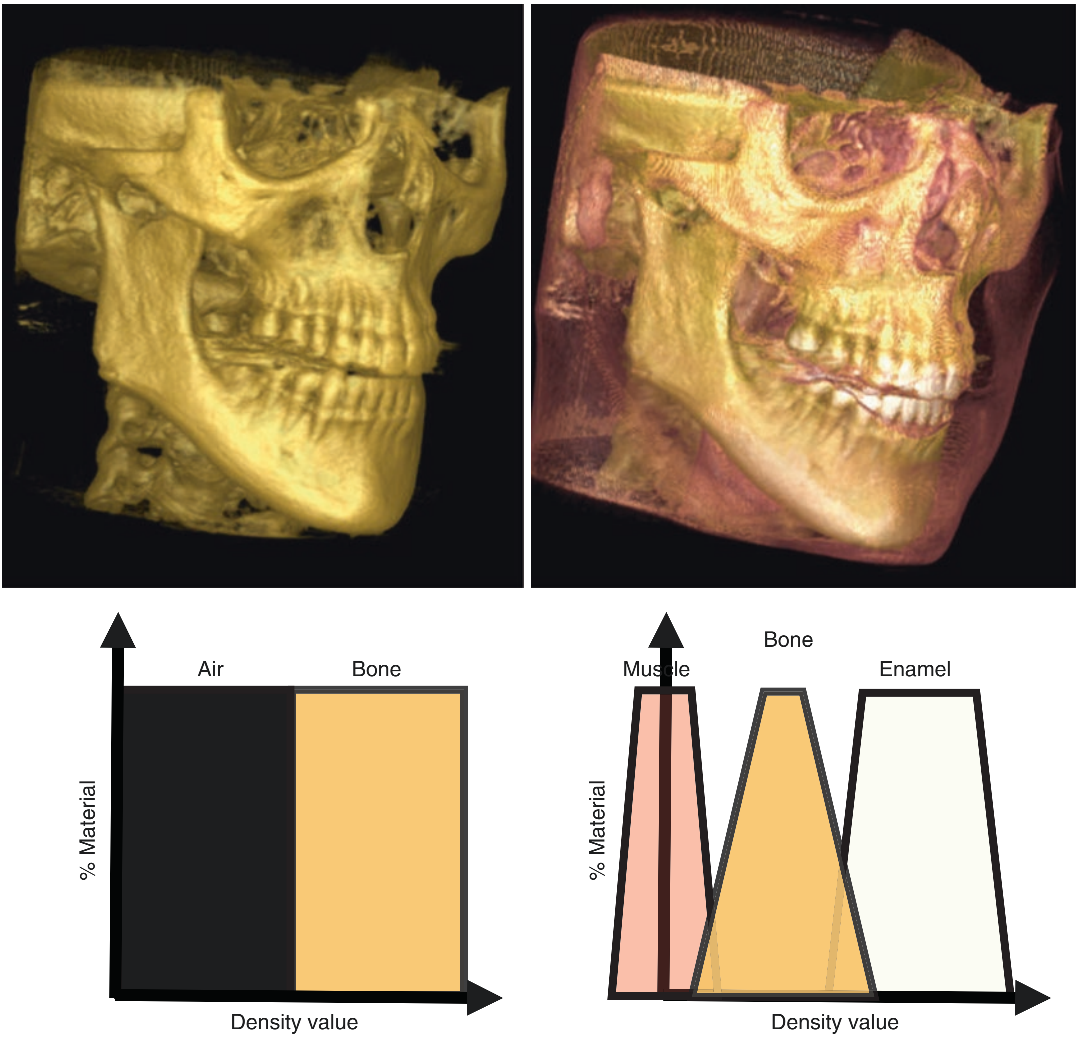

Fig. 3.50 The *upper left* volumetric rendering shows the use of color as an iso-density to discriminate between air and bone. The corresponding graph (*lower right*) shows the threshold for bone is a fixed value of density. In addition, all of the bone (material %) is shown as one color whose intensity is above this range. The *upper right* volumetric rendering shows representation of three anatomic structures (air, soft tissue, and bone) within the dataset demonstrated using three colors). The corresponding graph (*lower right*) shows there is overlap in representation of the structures and a range in the relative intensity presented determined by the thickness and demonstrated by the amount of color present in particular region. This provides for a transition between elements within the volume

volumetric data. The result can be achieved using an object-order (forward mapping scheme where the volume is mapped onto the image plane) or an image-order (backward scheme where rays are cast from each pixel in the image plane through the volume data). The process has a high computational complexity; therefore, many acceleration techniques have been developed which benefit from the performance of modern GPU (Graphics Processing Unit) in graphics rendering. Particularly the texture mapping capability of such hardware devices allows to obtain a true interactive volume rendering also with very large volume datasets.

- **Shading.** Shading or illumination refers to a well-known technique used in conventional computer graphics to greatly enhance the

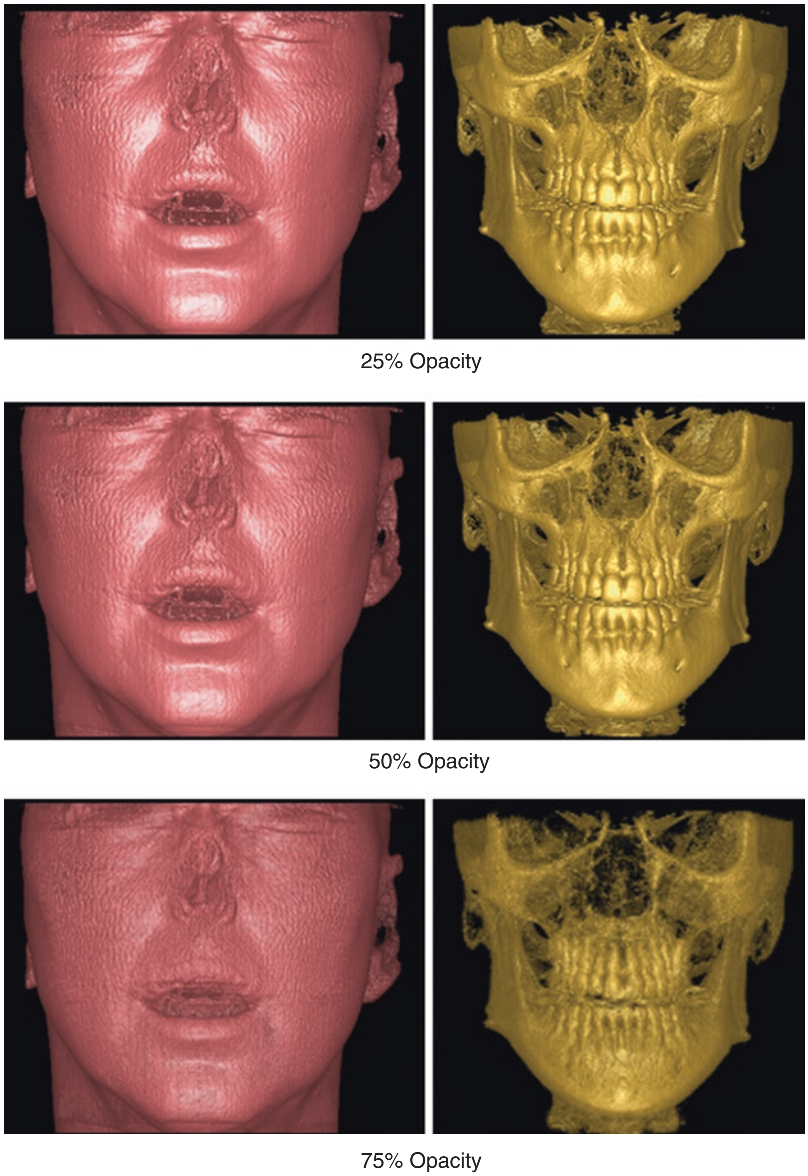

Fig. 3.51 The *left* images represent soft tissue voxel intensity range (−400 to 0) displayed with a *red/pink* color whereas the *right* images represent bone voxel intensity range (400–1400) displayed with a *gold* color. As the opacity level (transparency) increases, the more soft tissue and bone voxels are suppressed

appearance of a geometric object that is being rendered (Fig. 3.53). Shading tries to model effects like shadows, light scattering, and absorption in the real world when light falls on an object. Shading in volumetric rendering is technically and computationally complicated; however, the technique is based on lights setting to illuminate the scene and on calculation of the gradient of intensity values for the purpose of estimating the amount of light reflected from volumetric surfaces toward the eye (point of view).

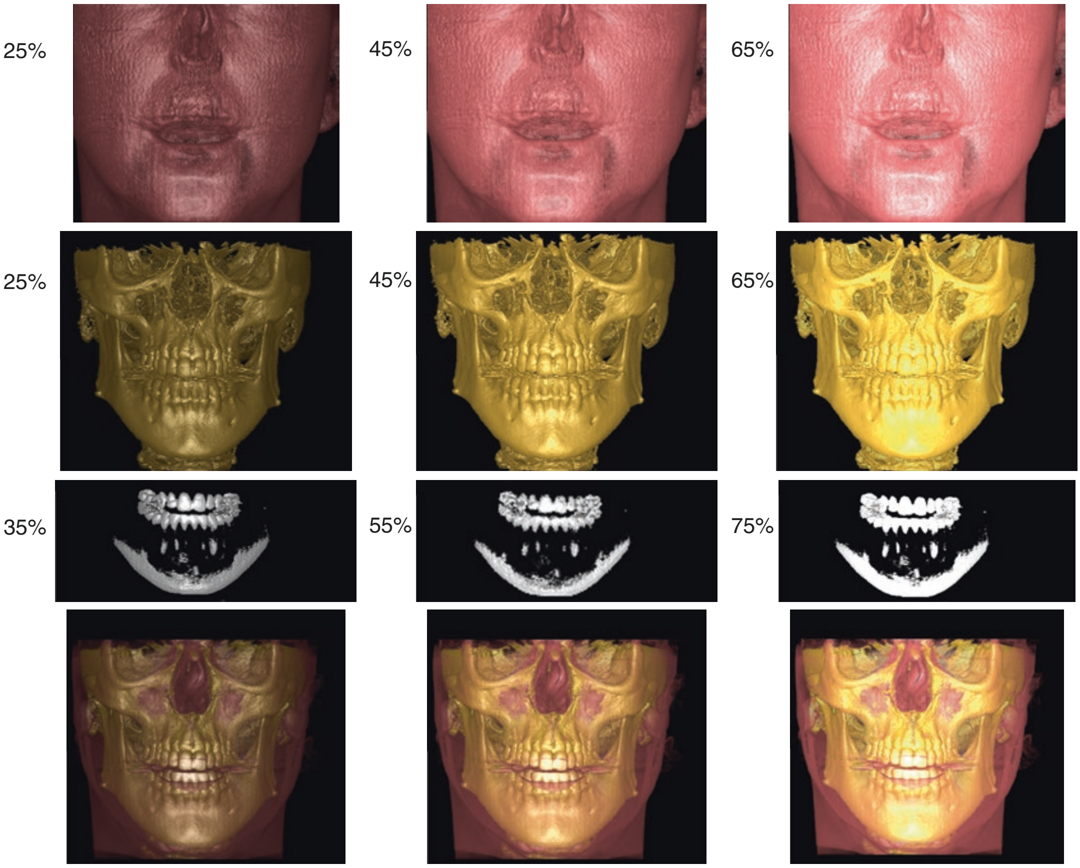

Fig. 3.52 Three individual elements are often used to form a composite 3D volumetric rendering—soft tissue (*first row*), bone (*second row*) and dental structures (*third row*). Using a standard intensity range and opacity (soft tissue; voxel intensity range (−700 to 0) opacity (80%); bone; voxel intensity range (400–1400) opacity (25%) and: dental structures; voxel intensity range (1600–3000) opacity (1%)) initial empirical brightness adjustment of the bone voxel intensities indicated that a 45% level in brightness produced a bone image demonstrating the most detail (*second row*, *middle* image). As the brightness of the soft tissue image should be approximately the same or less as the bone image and the brightness of the dental structures should be slightly higher than the bone images, the selection of brightness for these elements were empirically derived (45% and 55%, respectively). The addition of elements at these brightness values is shown at the *bottom* of the *middle* column. Bone, soft tissue, dental structure and resultant 3D volumetric images at a 20% higher (*right* column) and 20% lower (*left* column) are shown for comparison

Iso-Surface Rendering

Iso-surface rendering is a special case of the general full-volume rendering, where a quick transition from 0 to 1 of the opacity transfer function at some threshold density value allows to obtain an effect similar to surface rendering (Fig. 3.54). Iso-surface rendering is more suitable for medical images, because the parameters of rendering can be interactively changed allowing to obtain significant diagnostic images.

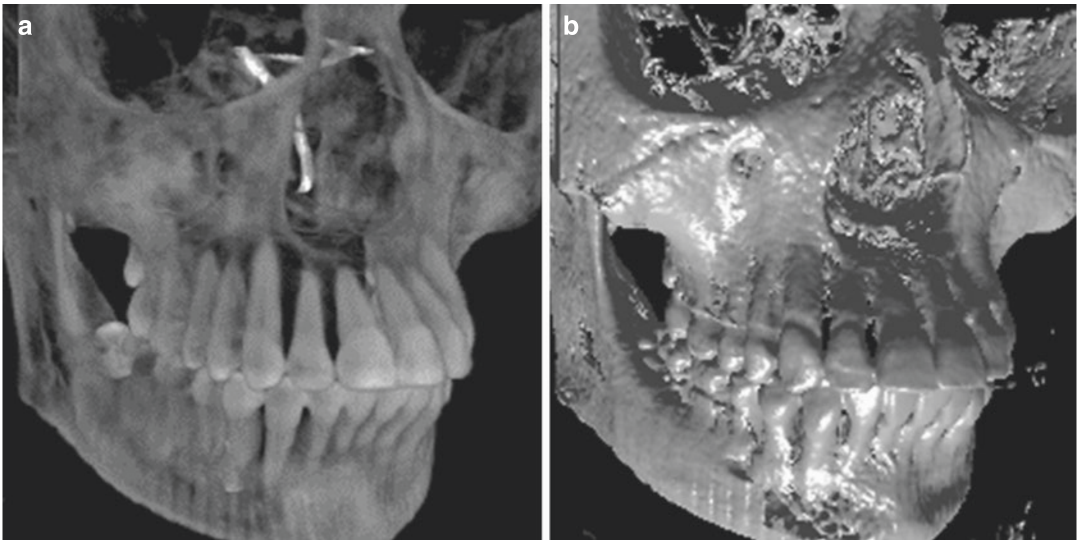

Fig. 3.53 Comparison between nonshaded (**a**) and shaded (**b**) volume rendering

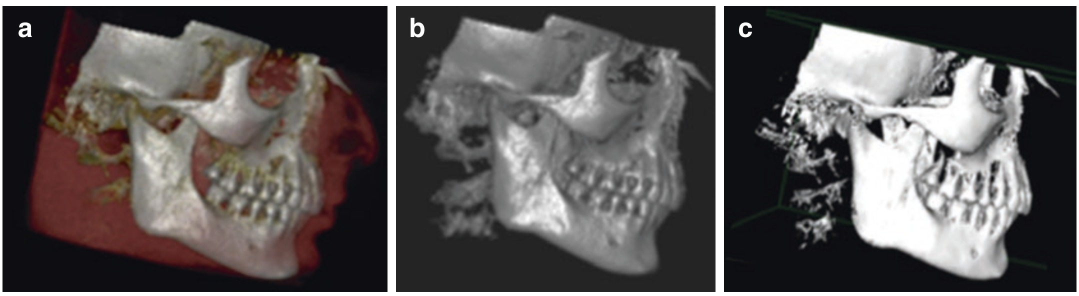

Fig. 3.54 Full-volume DVR (**a**), iso-surface DVR (**b**), and SSD (**c**) rendering of the same patient volumetric CBCT data

3.4 Post-Processing

3.4.1 Image Enhancement

Image enhancement is the process of applying various techniques to alter the appearance of the image to make diagnostic features easier to interpret. This can be performed simply to bring out detail or contrast that is obscured or to highlight certain features of interest in an image. It is perhaps the most easily applied image processing technique.

The appropriate use of numerous image enhancements available with imaging software used to improve image display may not be well understood by many clinicians. As digital image display is now becoming the de facto interpretive mode, clinicians must become familiar with these techniques and incorporate them into specific display protocols.

In the area of computer graphics, image enhancements are mathematical functions on pixels within a digital image. In this arena, enhancements can be classified according to their mode of operation; they either act on the location of the pixel or modifying the intensity value of the pixel either individually (spatial domain) or

Table 3.1 Classification of image enhancement techniques based on how they act on pixels individually (spatial) or as a group (frequency)

Spatial domain		Frequency domain
Point processing	Nearest neighbor operations	Global operations
Gray level (LUT) transformations	Smoothing	Smoothing (Low pass)
Histogram processing	Median filter	Sharpening (High pass)
	Sharpening	Unsharp masking

as a group (frequency domain). Image enhancement in both the spatial and frequency domain encompasses numerous techniques (Table 3.1). Image enhancements are performed on the original acquired intensity value of each pixel to change the displayed image. Most CBCT images require some form of enhancement to optimize their appearance on the computer display.

3.4.1.1 Enhancement Methods

In principle, the various shades of gray that make up the display are determined by the density of a structure and the amount of X-ray energy that passes through it. This phenomenon is referred to as attenuation. In conventional CT imaging, the relative amount of radiation attenuated by each voxel element is represented by the CT number, defined as the difference in attenuation of the contents of the voxel relative to water.

$$\text{CT number} = \left[\mu_{\text{structure}} - \mu_{\text{water}}\right] F,$$

where: $\mu_{\text{structure}}$ = attenuation of the structure,
μ_{water} = attenuation of water, and
F = a scaling factor used to define the scale of numbers over the range of values encountered in the body.

This scale is commonly referred to as the Hounsfield scale and expressed in Hounsfield Units (HU). In the Hounsfield scale, water is given a value of zero and air a value of −1000. The numeric value of the scale is dependent on the recording and display capabilities of the CT scanner. For example, a CT with a 12-bit detector is capable of recording grayscale differences of 2^{12} (4096 shades of gray). This corresponds to a CT number scale from −1000 for air (e.g., the oropharynx) to +3095 for the densest object that can be measured by the scanner (e.g., compact bone). However while a 12-bit device is able to measure tissue attenuation within a range of 4096 CT numbers, the human eye is not capable of distinguishing this range of pixel intensities. Nor are most monitors used in dentistry capable of displaying more than 256 levels of gray. Therefore, the available grayscale must be mapped onto the portion of the Hounsfield scale that is to be displayed. This mapping is performed by adjusting two parameters, the window level and window width. The window level specifies the CT number for centering the grayscale whereas the window width defines the range of CT numbers over which the grayscale is to extend.

While it is inappropriate to refer to pixel intensities as HU in CBCT imaging (see Chap. 2), the concept of adjusting window level and window width as they relate to pixel intensity display is still applicable (See Chap. 5 for specific clinical procedures). A signal range of 12- (4096) to 16-bits (65,536) can be recorded by CBCT systems. High or low exposure ranges can also be recorded. However, display of the full range of data presents the information with very poor contrast. Therefore, it is necessary to determine the grayscale values of interest for the acquired signal data.

There are three mathematical ways of representing the relationship between the original intensity grayscale value of CBCT data within an image and that displayed on computer monitor pixels. Clinically, enhancements are used to optimize image brightness and contrast, filter the image to reduce noise (graininess) or sharpen the edges.

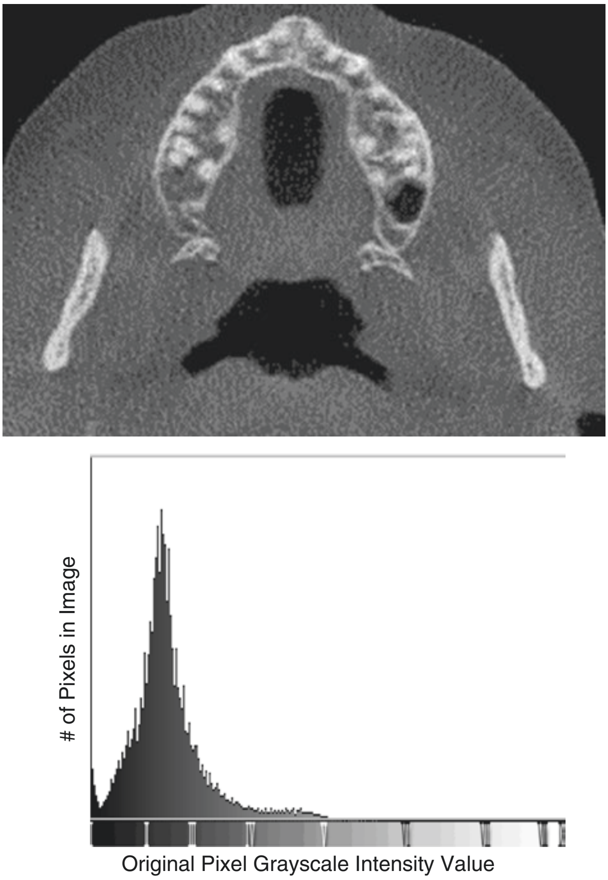

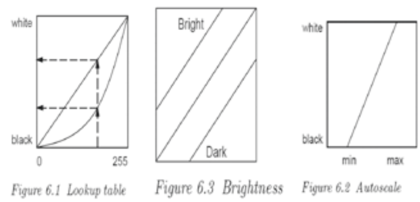

Fig. 3.55 Axial sction at the level of the maxillary arch showing corresponding histogram. In this example, most of the pixels are *dark* and therefore distributed unevenly (shifted to the *left*) across the full range of available pixel intensity values (0–255 for an 8-bit image)

- **Look-Up Table (LUT)** The most direct way to represent an image is a graphical 2D plot visually comparing the original gray density levels (*x*-axis) to display pixel values (*y*-axis). This graph is called a look-up table (LUT) and the nature of the plot between the two referred to as a *transfer function* or *grayscale rendition*. The LUT allows for the simplest manipulation of the brightness or darkness of the image.
- **Histogram.** A useful method of characterizinf a displayed image is by associating the pixel intensity value of each pixel with the total number of pixels with that value in the image. The resultant plot is called a *histogram* and is therefore a graphical representation of the distribution of signal values of the entire image (Fig. 3.55).
- **2D Matrix.** Another method of representing mathematical operations on an image is to

consider the image to be comprised of a series of matrices consisting of neighboring pixel intensities. As each grayscale value in the pixel matrix is determined by a numeric intensity value, the matrix comprises a matrix of numbers. As such, local operations are performed on neighboring pixels that process the image. In most cases, the grid of operations or *convolutions* layered on the image, called a *kernel* or *mask*, is rectangular or square and defines the specific mathematical functions to be applied to the values of the pixels. (Fig. 3.56).

3.4.1.2 Image Filters

Filters are secondary image enhancement tools used to improve image quality and diagnostic interpretability. The most common filtering operations are smoothing and sharpening. They act on an image matrix kernel through the application of various convolutions (Fig. 3.57).

- **Smoothing.** Smoothing filters remove random inhomogeneities that provide the speckled appearance of the image. Most often, such random inhomogeneities are originated by noise, including in particular quantum radiographic noise. In maxillofacial imaging, this filter is most advantageous with thin sections, where image noise results in a "salt and pepper" appearance within the image (Fig. 3.58).

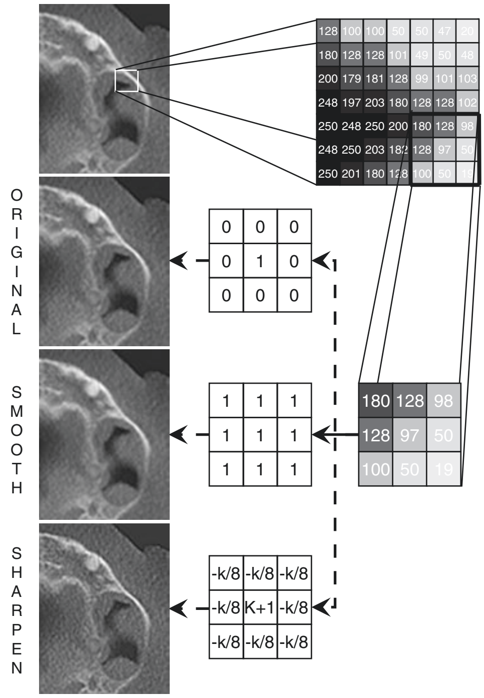

Fig. 3.57 Schematic comparing the effect on an original cropped CBCT axial image of the left maxilla (*left*) with the application of smooth and sharpen convolution filters. A magnification of a region of interest (*white square*) provides a matrix of individual pixels with specific gray level intensities, represented numerically (*white* numbers). If the 3 × 3 matrix in the *lower right hand corner* of the ROI matrix is separated, then the mechanism of the convolution filters can be demonstrated. When this image is convolved with a 3 × 3 kernel comprising a one surrounded by 8 zeros, the image remains unchanged. However, application of a matrix of 1 s (simple smoothing filter) or a matrix of derivatives (edge enhancement filter) provides differing effects on images

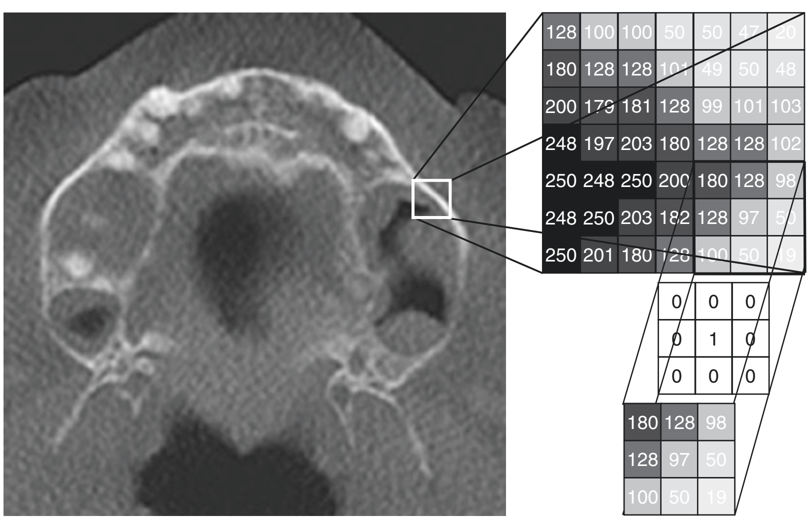

Fig. 3.56 Cropped axial CBCT image (*left*) with a region of interest (*white square*). Highly magnified ROI (*upper right*) provides a matrix of individual pixels with specific gray level intensities represented numerically (*white* numbers). If the 3 × 3 matrix (*lower right*) of the ROI matrix is considered then a 3 × 3 kernel can be applied to this region to provide a modified image. If the kernel values are 1, as in this case, then no changes to the image occur

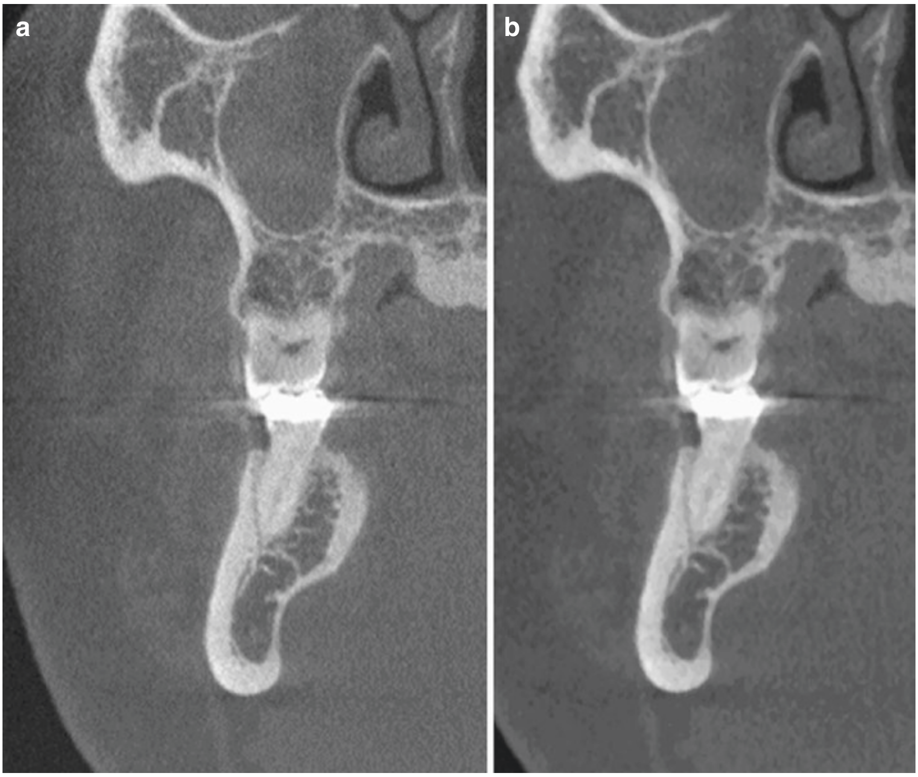

Fig. 3.58 Original (**a**) and enhanced (**b**) coronal images of the right maxilla and mandible demonstrating the effect of applying a median filter at an acquired (0.25 mm) thickness. Smoothing filters decrease "salt and pepper" inhomogeneities but degrade image quality by adding blur and reducing image sharpness

The major disadvantage of this operation is the production of considerable blurring and loss of image quality. Filters can be either multiplicative or rank-order based.

- **Sharpening**. Sharpening filters either enhance the detection of edges or emphasize existing edges of objects and adjust the contrast and the shade characteristics of the image. While most operate in the spatial domain (unsharp masking, Sorbel (3 × 3 matrix) or Laplacian (5 × 5 matrix)) by the application of kernels, others can be applied in the frequency domain (Fast Fourier Transform). Most are applied to images that have good contrast (an appropriate level of darkness and lightness) but blurry edges (Fig. 3.59). Edge enhancement filters increase image noise to an even greater extent than sharpening filters.

3.4.2 Image Manipulations

Images manipulations involve geometric transformations that address issues related to 2D or 3D image spatial deformation or reformation. Transformations map each pixel or voxel coordinate within a 2D image or 3D dataset, respectively, and then relocates each pixel or voxel coordinate to a new location within the parameters of the transformed image or volume. There are two common geometric transformations.

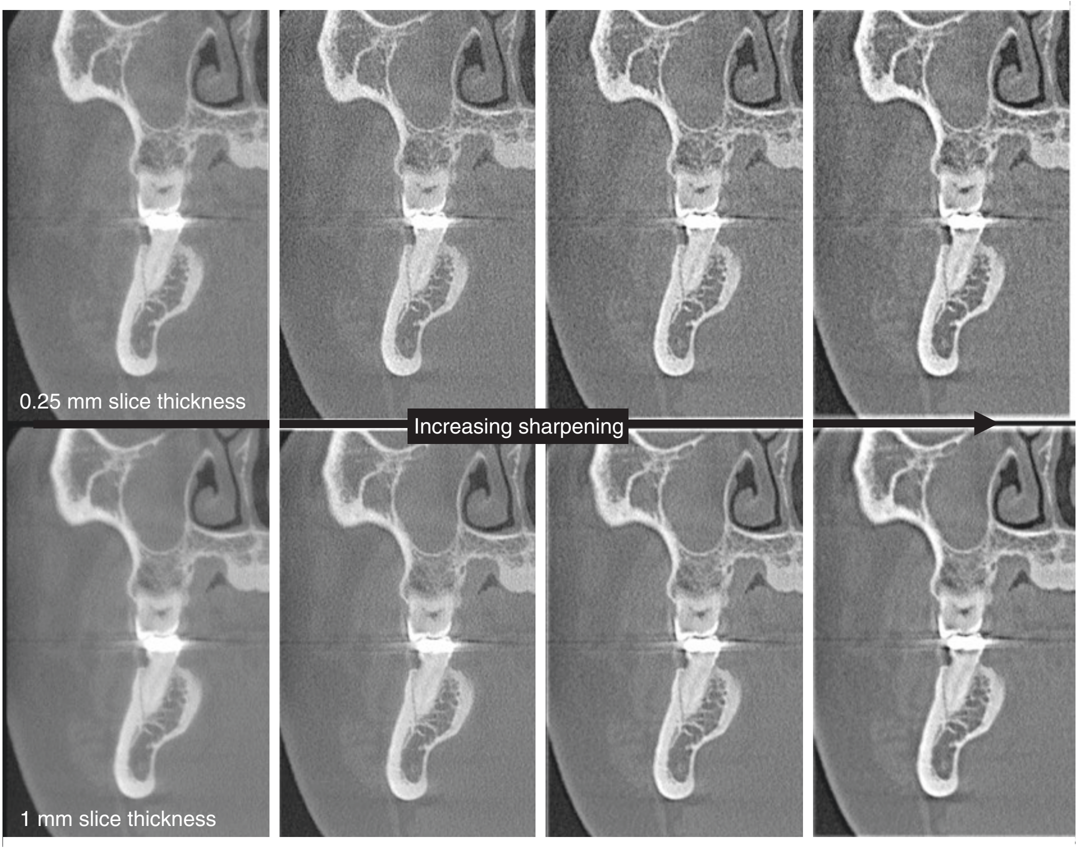

Fig. 3.59 Schematic of the effect of applying increasing Laplacian sharpening filter to coronal images at two thicknesses—acquired (0.25 mm) and viewed (1 mm). Sharpening filters increase identification of intramedullary trabeculae and cortical boundaries (e.g., walls of the maxillary sinus) but increases noise and image beam hardening artifact associated with metallic restorations. Thin image slices (*top row*) require less edge enhancement than thick image sections

- **Spatial reorientation.** This involves rotation of the volumetric dataset in three orthogonal dimensions to coincide with specific topographic reference planes so that sectional images present bilateral anatomic structures accurately without parallax misrepresentation (Fig. 3.60).
- **Magnification (Zoom).** When CBCT images are represented on a display monitor at an image matrix/display matrix ratio of 1:1, they may be too small for adequate visual interpretation in which case CBCT images are displayed on monitors as magnified images. Excessively zoomed images have a blocky appearance (pixilation), reflecting the larger size of each effective pixel (Fig. 3.61). Although the application of a smoothing filter can reduce this pixelation effect, a more visually pleasing result can be generated using spatial interpolation techniques (Fig. 3.62).

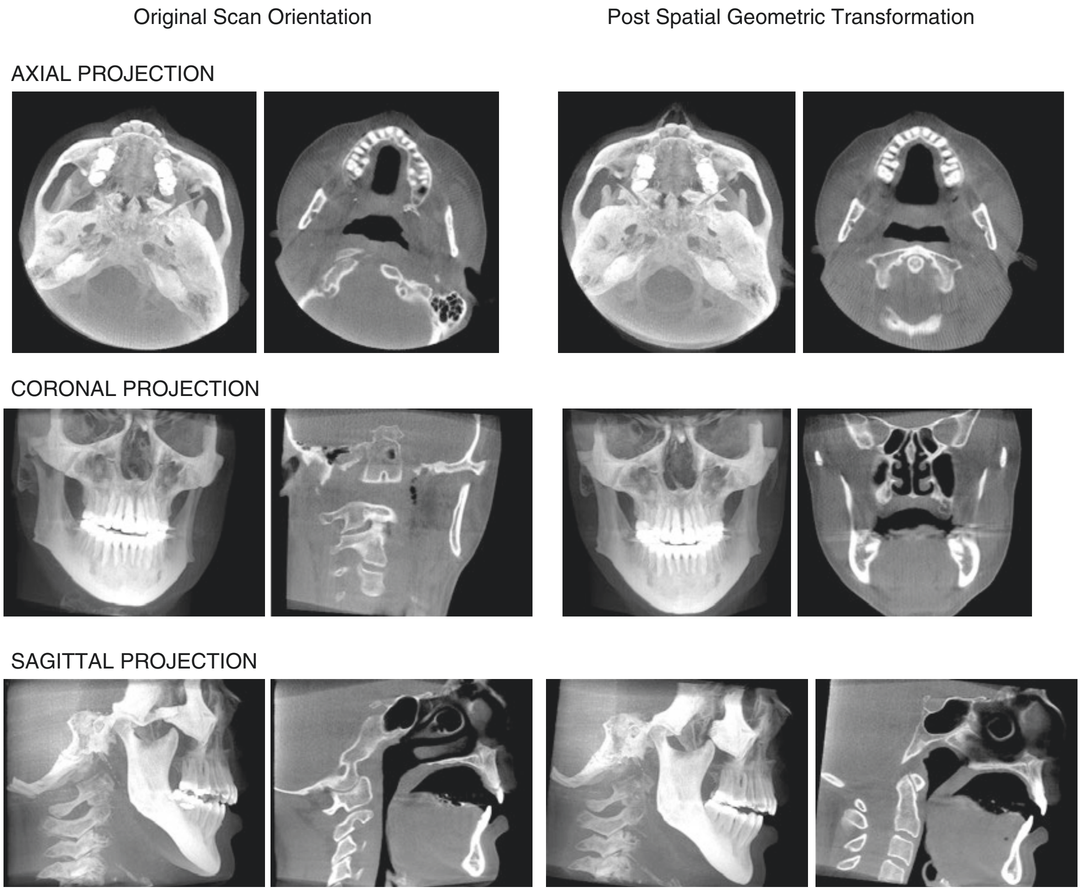

Fig. 3.60 The original CBCT volumetric data was obtained with the patient incorrectly positioned in the CBCT machine. The orientation of the patient's head is demonstrated by MIP reformatting. Mid volumetric orthogonal thin slice sections of the original dataset demonstrate marked asymmetric anatomic differences in all three orthogonal planes. Reorientation of the volumetric dataset with the palatal plane parallel to the floor (sagittal projection), interorbital line parallel to the floor (coronal projection) and mid-palatal suture perpendicular to the posterior of the dataset (axial projection) provides orthogonal sections with minimal asymmetric differences

Fig. 3.61 Example of the effect of magnified axial (*top row*), reformatted cropped panoramic (*middle row*) and cross-sectional image before (*left column*) and after (*right column*) spatial interpretation with resulting reduction in pixilation

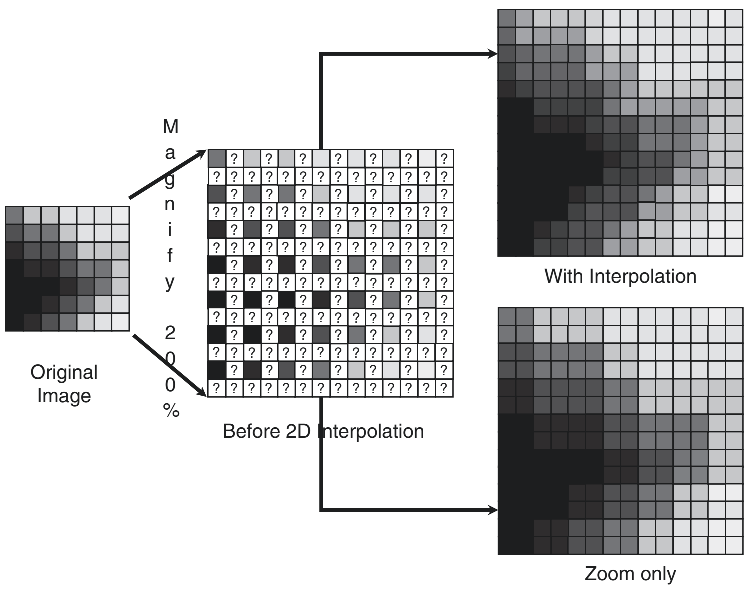

Fig. 3.62 An original image, represented by a matrix of known pixel intensities can be magnified (in this example by 200%) by one of two methods. First the overall dimensions of the matrix are increased by the magnification factor. This resultant larger matrix has pixels of unknown intensity (shown as "?") in both *x*- and *y*-dimensions. Most simplistically the pixels to the right, below and diagonally are allocated the intensity value of the pixel from which it was derived. This method results in a magnified image (*lower right*). However, because of the magnification, the visual display effect of pixelation is prominent. Alternately, the unknown intensity values are estimated as being the arithmetic mean of adjacent pixels (*upper right*). This produces an image that is more visually pleasing

References

Anderson PJ, Hall CE, Evans RD, Hayward RD, Harkness WJ, Jones BM (1997a) Cervical spine anomalies in Crouzon syndrome. Spine 22:402–405

Anderson PJ, Hall CE, Evans RD, Hayward RD, Harkness WJ, Jones BM (1997b) Cervical spine anomalies in Pfeiffer's syndrome. J Craniofac Surg 7:275–279

Araki K, Maki K, Seki K, Sakamaki K, Harata Y, Sakaino R, Okano T, Seo K (2004) Characteristics of a newly developed dentomaxillofacial X-ray cone beam CT scanner (CB MercuRayTM): system configuration and physical properties. Dentomaxillofac Radiol 33:51–59

Benateau H, Chevallier E, Hamon M, Edy E, Keswani R, Labbe D et al (2002) The three-dimensional spiral scanner and volume rendering technique: importance in craniofacial traumatology and reconstructive surgery. Rev Stomatol Chir Maxillofac 103:233–238

Brinker MR, Weeden SH, Whitecloud TS 3rd (1997) Congenital anomalies of the cervical spine. In: Frymoyer JW (ed) The adult spine: principles and practice. Lippincott-Raven, Philadelphia, pp 1205–1222

Cai W, Sakas G (1998) Maximum intensity projection using splatting in sheared object space. In: Proceedings EUROGRAPHICS '98, pp C113–C124

Calhoun PS, Kuszyk BS, Heath DG, Carley JC, Fishman EK (1999) Three-dimensional volume rendering of spiral CT data: theory and method. Radiographics 19:745–764

Chen LS, Herman GT, Reynolds RA, Udupa JK (1985) Surface shading in the cuberille environment. IEEE Comput Graph Appl 5:33–43

Ciccarelli R, Di Salle F, Guidi G, Lavorgna G, Sagliocco R, Rotondo A, Smaltino F (1998) Three-dimensional imaging with computerized tomography. Etiologic considerations and methods for studying temporomandibular joints. Radiol Med (Torino) 95:417–423. (In Italian)

Cline HE, Lorensen WE, Ludke S, Crawford CR, Teeter BC (1988) Two algorithms for the three-dimensional reconstruction of tomograms. Med Phys 15:320–327

Cody DD (2002) AAPM/RSNA physics tutorial for residents: topics in CT. Image processing in CT. Radiographics 22:1255–1268

Costa E, Silva AP, Antunes JL, Cavalcanti MG (2003) Interpretation of mandibular condyle fractures using 2D- and 3D-computed tomography. Braz Dent J 14:203–208

Fatterpekar GM, Doshi AH, Dugar M, Delman BN, Naidich TP, Som PM (2006) Role of 3D CT in the evaluation of the temporal bone. Radiographics 26(Suppl 1):S117–S132

Figueroa AA, Friede H (1985) Craniovertebral malformations in hemifacial microsomia. J Craniofac Genet Dev Biol Suppl 1:167–178

Fox LA, Vannier MW, West OC, Wilson AJ, Baran GA, Pilgram TK (1995) Diagnostic performance of CT, MPR and 3DCT imaging in maxillofacial trauma. Comput Med Imaging Graph 19:385–395

Gosain AK, McCarthy JG, Pinto RS (1994) Cervicovertebral anomalies and basilar impression in Goldenhar syndrome. Plast Reconstr Surg 93:498–506

Heidrich W, McCool M, Stevens J (1995) Interactive maximum projection volume rendering. IEEE Proceedings Visualization '95, pp 11–18

Heiland M, Schmelzle R, Hebecker A, Schulze D (2004) Intraoperative 3D imaging of the facial skeleton using the SIREMOBIL IsoC3D. Dentomaxillofac Radiol 33:130–132

Kuszyk BS, Heath DG, Bliss DF, Fishman EK (1996) Skeletal 3-D CT: advantages of volume rendering over surface rendering. Skelet Radiol 25:207–214

Kwon TG, Park HS, Ryoo HM, Lee SH (2006) A comparison of craniofacial morphology in patients with and without facial asymmetry—a three-dimensional analysis with computed tomography. Int J Oral Maxillofac Surg 35:43–48

Lorensen WE, Cline HE (1987) Marching cubes: a high resolution 3D surface construction algorithm. Comput Graph 21:163–169

Mankovich NJ, Samson D, Pratt W, Lew D, Beumer J 3rd (1994) Surgical planning using three-dimensional imaging and computer modeling. Otolaryngol Clin N Am 27:875–889

Medina LS (2000) Three-dimensional CT maximum intensity projections of the calvaria: a new approach for diagnosis of craniosynostosis and fractures. AJNR Am J Neuroradiol 21:1951–1954

Napel S, Marks MP, Rubin GD et al (1992) CT angiography with spiral CT and maximum intensity projection. Radiology 185:607–610

Napel S, Rubin GD, Jeffrey RB Jr (1993) STS-MIP: a new reconstruction technique for CT of the chest. J Comput Assist Tomogr 17:832–838

van Ooijen PM, Ho KY, Dorgelo J, Oudkerk M (2003) Coronary artery imaging with multidetector CT: visualization issues. Radiographics 23:e16

Park SH, Yu HS, Kim KD, Lee KJ, Baik HS (2006) A proposal for a new analysis of craniofacial morphology by 3-dimensional computed tomography. Am J Orthod Dentofac Orthop 129:600.e23–600.e34

Prokop M, Shin HO, Schanz A, Schaefer-Prokop CM (1997) Use of maximum intensity projections in CT angiography: a basic review. Radiographics 17:433–451

Reuben AD, Watt-Smith SR, Dobson D, Golding SJ (2005) A comparative study of evaluation of radiographs, CT and 3D reformatted CT in facial trauma: what is the role of 3D? Br J Radiol 78:198–201

Sakas G, Grimm M, Savopoulos A (1995) Optimized maximum intensity projection. In: Proceedings of 5th EUROGRAPHICS Workshop on Rendering Techniques, Dublin, Ireland pp 55–63

Solar P, Gahleitner A, Bednar A, Rodinger S, Watzek G (2001) Detection of the mandibular canal via shaded surface display and multiplanar reconstruction of CT data. J Oral Rehabil 28:243–256

Swennen GRJ, Barth EL, Schutyser F, De Groeve P, Lemaitre A (2004) Three-dimensional (3-D) cephalometry, the basics for virtual planning. J Cranio Maxillofac Surg 32(Suppl 1):135

Udupa JK (1999) Three-dimensional visualization and analysis methodologies: a current perspective. Radiographics 19:783–806

Welander U, Nummikoski P, Tronje G, McDavid WD, Legrell PE, Langlais RP (1989) Standard forms of dentition and mandible for applications in rotational panoramic radiography. Dentomaxillofac Radiol 18:60–67

Zuiderveld KJ, Koning AHJ, Viergever MA (1994) Techniques for speeding up high-quality perspective maximum intensity projection. Pattern Recogn Lett 15:507–517

Image Quality

4

Ralf Schulze, William C. Scarfe, Roberto Molteni, and Pierluigi Mozzo

Contents

R. Schulze (✉)
Poliklinik für Zahnärztliche Chirurgie, Universitätsmedizin der Johannes Gutenberg-Universität Mainz, Mainz, Germany
e-mail: rschulze@uni-mainz.de

W.C. Scarfe, B.D.S., F.R.A.C.D.S., M.S.
Division of Radiology and Imaging Science, Department of Surgical/Hospital Dentistry, University of Louisville School of Dentistry, Louisville, KY, USA
e-mail: William.scarfe@louisville.edu

R. Molteni, Ph.D.
Skanray Europe srl, San Lazzaro di Savena, Bologna, Italy
e-mail: robertodocmolteni@yahoo.com

P. Mozzo, Ph.D.
Pixirad Imaging Counters srl, Verona, Italy

University of Verona, Verona, Italy
e-mail: pierluigi.mozzo@gmail.com

4.1 Introduction

Defining image quality and comparing differences between CBCT systems is inherently problematic. Image quality has two components, one being subjective and the other objective. The interaction between technical (objective) parameters and subjective quality as determined by the observer is complex image and still not well understood (Doi 2006). In maxillofacial radiology, subjective image quality is usually obtained from averaging multiple observer ratings of perceived clarity in visibility of specific anatomic structures, such as the periodontal ligament space or trabecular pattern in the mandible (Hashimoto et al. 2003, 2006). Objective assessment of image quality is based on quantitative measurements of particular patterns in a test object or quality assurance (QA) phantom. These include CT number correlation, contrast resolution, image homogeneity and uniformity, point spread or modulation transfer function, noise and artifacts. Because the use of acceptable quality assurance phantoms has only recently become available for CBCT, few

W.C. Scarfe, C. Angelopoulos (eds.), *Maxillofacial Cone Beam Computed Tomography*,
https://doi.org/10.1007/978-3-319-62061-9_4

authors have directly compared image quality of analogous objects imaged on different systems (Loubele et al. 2008; Suomalainen et al. 2009; Pauwels et al. 2011). In effect, the image quality of a volumetric radiographic imaging system, such as CBCT, determines how accurately that system spatially reproduces the object and represents the three-dimensional attenuation distribution in an imaging volume (Kalender 2005).

Spatial and contrast resolution, image noise and artifacts are the main objective determinants of image quality. Several technical variables have an effect on each of these determinants.

4.2 Resolution

There are two types of image resolution which effect image quality equally: spatial resolution, a measure of determining the proximity (and size) of details able to be recorded separately or, in other words, the ability of an image to distinguish structures that lie close to each other, and contrast resolution, a measure of distinguishing between tissues with minor differences in attenuation and to display them with different grey levels.

4.2.1 Acquired/Reconstructed Spatial Resolution

CBCT units provide voxel resolutions that are isotropic—equal in all three orthogonal dimensions. CBCT imaging produces images with submillimeter voxel resolution ranging, according to the various manufacturers' technical specifications, from 0.4 mm to as low as 0.076 mm. Subsequent secondary orthogonal (axial, coronal, and sagittal) and multi-planar reformatted images achieve a level of "nominal" spatial resolution that is accurate enough for most measurements in maxillofacial applications, especially where precision is important such as the assessment of root canal configuration. Generally clinical tasks requiring high spatial resolution should be performed at a voxel resolution of 0.2 mm or less. Despite the high "nominal" voxel resolution of modern CBCT systems, the actual effective spatial resolution of the CBCT is always lower than the nominal. This is due to different technical factors and inevitable (small) patient motion during exposure (Brüllmann and Schulze 2015).

Spatial resolution of CBCT systems is primarily a function of detector pixel pitch; however, factors such as beam projection geometry, patient X-ray scatter, detector motion blur, X-ray generator focal spot size, number of basis images, and reconstruction algorithm all contribute to the final maximum achievable resolution (Brüllmann and Schulze 2015; Chen et al. 2008). Most manufacturers provide options for varying resolution of CBCT data. However, detectors cannot, per se, be altered to change the number of pixels within the area matrix that capture X-ray photons. For a given projection geometry and FOV there is a geometrical maximum nominal spatial resolution (i.e., a minimum voxel size) in which most of the machines reconstruct their data. A higher level of detail than that acquired by the detector is useless as the latter determines the maximum information content contained in the image (Fig. 4.1). Although lowering nominal spatial resolution (i.e., voxel size) is always possible, it does not make sense reducing it beyond the threshold where detector pixel size and volume voxel size match. In some CBCT units, resolution can be increased by altering projection geometry, reducing the object-to-focal spot distance.

Electronic pixel binning is often used as an image pre-processing treatment which may have an effect in the resulting image quality. Pixel binning is the process of combining charge from adjacent pixels from the detector during readout. The two primary benefits of binning are improved contrast due to an improved signal-to-noise ratio and the ability to increase frame rate, albeit at the expense of reduced spatial resolution. While higher resolution may be considered desirable for many tasks in dentistry, it should be used judiciously for procedures demanding accuracy to the level of the detail of approximately the periodontal ligament space (i.e., approximately 0.2 mm or less). Images taken at high resolution often have reduced brightness and contrast, increased noise, and require increased reconstruction time. While increased image resolution in some CBCT units does not affect changes in exposure parameters, some manufacturers incorporate reduced-dose exposure protocols for low-resolution settings (Qu et al. 2010).

As CBCT data is inherently volumetric, it is possible, once the image is acquired, to provide

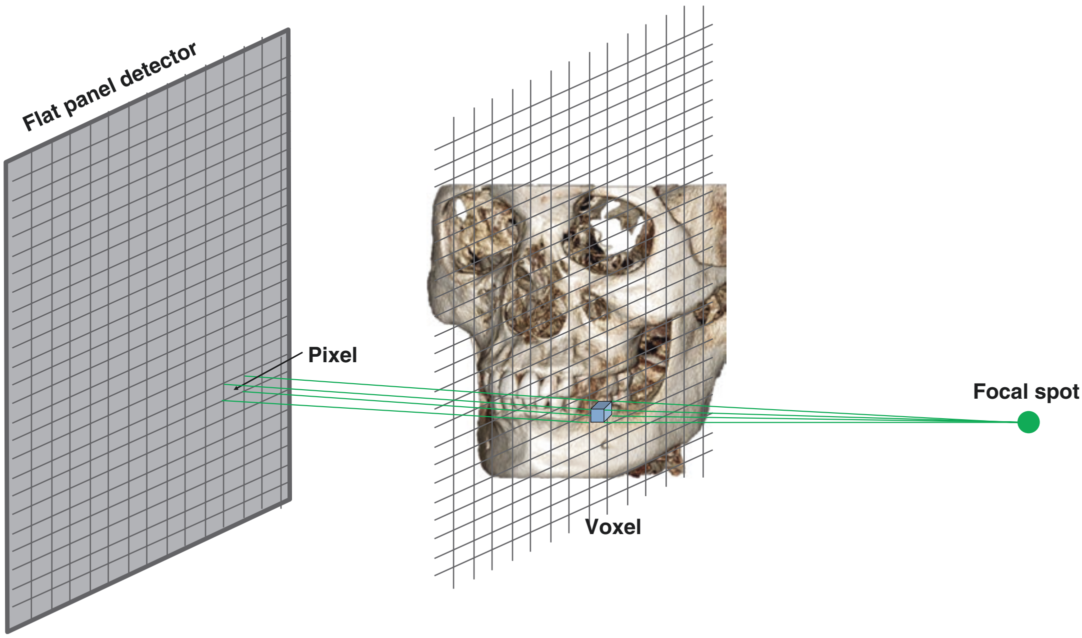

Fig. 4.1 Schematic showing the relationship between pixel size on the detector and resulting voxel size in the reconstructed 3D volume. For illustration purposes, only one exemplary voxel is shown. Note that reducing voxel size is meaningless, since no more information comes from the fixed detector pixel size

multi-planar images at "resolutions" actually higher than that at which is acquired. This is referred to as reconstructed resolution. As with other forms of digital radiography, care should be taken to distinguish between acquired nominal resolution based on specified pixel or voxel values and the actual acquired resolution achieved due to the various constraints within the total imaging chain and reconstructed resolution. For clinical applications spatial resolution for CBCT generally ranges between 1 Lp/mm and somewhat above 2 Lp/mm (Brüllmann and Schulze 2015). In addition, it is important to realize that these values are all derived from steady (non-moving) phantoms (Fig. 4.2). One line-pair requires at least two voxels to be depicted: one bright voxel displaying the "gap" between two adjacent lead lines in the phantom plus one voxel displaying the lead-line itself. A spatial resolution of 2 Lp/mm means that two such pairs are displayed per millimeter. Two pairs of two voxels mean four voxels per millimeter, i.e., a size of ¼ mm = 0.25 mm. Considering the presence of additional patient motion, a true (available) spatial resolution between 0.3 and 0.5 mm is realistic (Brüllmann and Schulze 2015).

4.2.2 Contrast Resolution

Numerous factors limit the contrast resolution of CBCT. The inherent geometric configuration of CBCT image acquisition produces considerable patient scatter radiation. This is a significant factor in reducing the contrast of any CBCT system. Since the detector covers an area, many more scattered X-rays hit the detector than in fan-beam CT where the detector consists of a line of pixels and thus is inherently collimated. For this reason, along with the limited mA of current maxillofacial CBCT systems, images lack adequate greyscale sensitivity to discern subtle differences between soft tissues, such as between fluids and solid tumors, though are excellent for demonstrating air to soft tissue boundaries.

Greyscale intensity values measured on CBCT images do not directly represent Hounsfield units (HU): HU are quantities that represent the density of the different body tissues as reflected by the attenuation of X-rays through those tissues. In fact, they express the relative density of body tissues according to a calibrated grey-level scale, based on normalized HU values for air (−1000 HU) and water (0 HU)

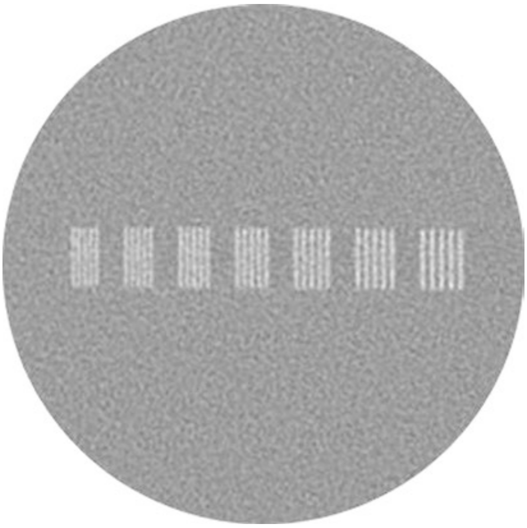

Fig. 4.2 CBCT image of a typical line-pair-phantom used to visually assess spatial resolution of the system. From *right* to *left* the *lines* become thinner and are closer to one another. This system is capable of resolving the required 1 LP/mm (*left* group)

(Bryant et al. 2008; Nackaerts et al. 2011). Medical CT devices are regularly re-calibrated to this scale thus providing more reproducible greyscale values in regard to HU. Therefore, in most cases, CBCT data reproduce tissue density as a grey scale in a relative fashion, intrinsic to a particular device. Absolute grey values as HU as obtained from medical CT are not provided with sufficient accuracy by current maxillofacial CBCT devices. While these conditions limit the application of maxillofacial CBCT imaging for the assessment of density of various osseous structures, several techniques and devices are currently being investigated to suppress these effects or derive HU from grey density levels in dental CBCT (Lagravere et al. 2008; Mah et al. 2010; Molteni 2013).

4.3 Noise

Image noise refers to the local nonuniform density differences in a radiographic image and may affect diagnostic efficiency. In other words, noise includes all those greyscale inhomogeneities in a CBCT image, or any radiographic image for that matter, which are not attributed to tissue differences or the effects of developing disease that have a detriment effect on image quality. Generally, the main goal in an imaging system is to increase the signal (i.e., the image producing measurements) as much as possible over the inevitable amount of noise. In other words, a high signal-to-noise ratio is aimed for. Noise represents itself in attenuation (grey) values in the projection images inconsistent, and consequently also in the reconstructed volume (Fig. 4.3). The cone beam projection acquisition geometry results in a large volume being irradiated with every basis image projection. As a result, a large portion of the photons engage in interactions by way of attenuation. Most of these occur by Compton scattering producing scattered radiation.

Most of the scattered radiation is produced omni-directionally and recorded by pixels on the cone beam area detector (Fig. 4.4), which does not reflect the actual attenuation of the object within a specific path of the X-ray beam. This additional recorded X-ray irradiation accounts for a large proportion of the overall noise-content of the image. Because of the use of an area detector, much of this additional non-information-bearing irradiation is recorded and contributes to image degradation or noise. The scatter-to-primary ratios are about 0.01 for single-ray CT and 0.05–0.15 for fan-beam and spiral CT, and may be as large as 0.4–2.0 in CBCT (Siewerdsen and Jaffray 2001).

Noise can be generated from anywhere along the imaging chain; however, the principal sources include:

- **Photon count noise.** The total number of photons recorded on the detector pixels for a given CBCT system also determines the degree of noise within the system. A high number of photons per pixel increases the signal-to-noise ratio and vice versa. Maxillofacial CBCT systems use mAs settings (to which the cumulated photon fluence is linearly proportional) approximately 1/10th than what generally used with MDCT; therefore, lower signal-to-noise ratios are usually obtained compared to MDCT.

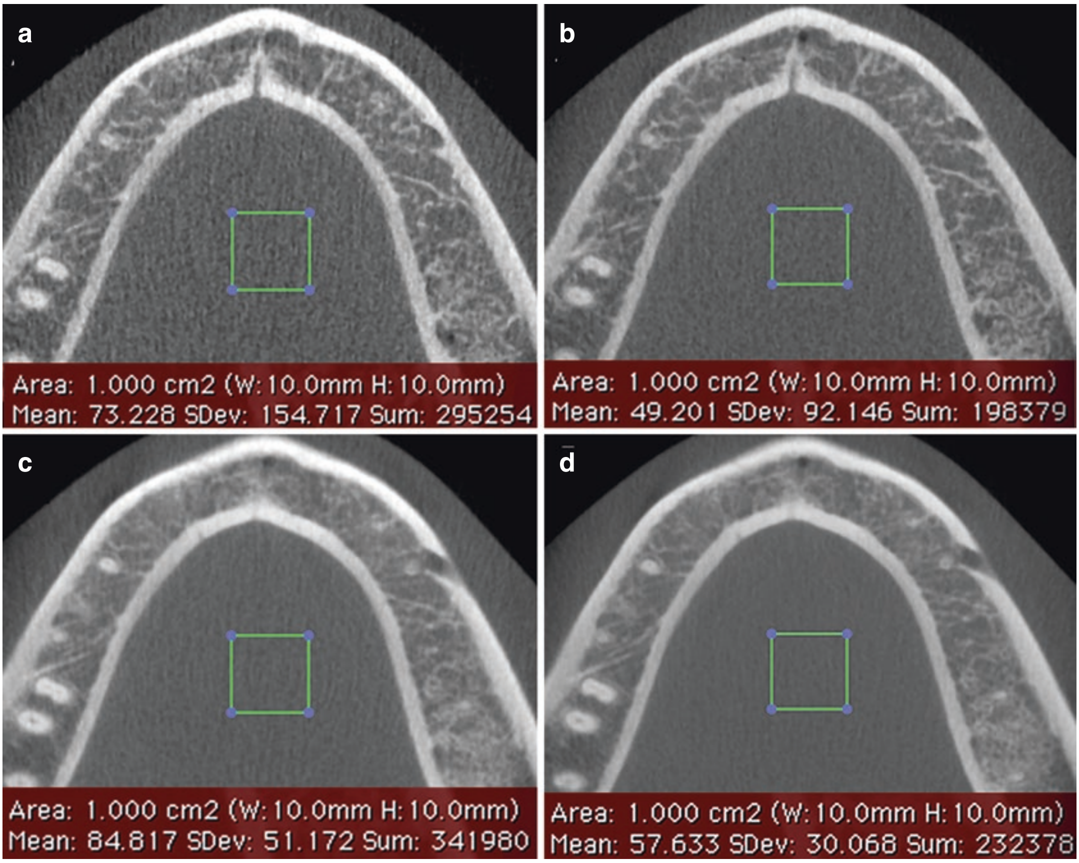

Fig. 4.3 Axial images with default resolution thickness (0.16 mm) images of a plastic encased skull performed on a Morita Accuitomo 170 (5 mA, 512 basis images) at a reduced 75 kVp (**a**) and at 90 kVp exposure (**b**). The mean pixel intensity of a 100 pixel × 100 pixel region of interest of uniform density in the same region provides higher noise (pixel inhomogeneity) as represented by the measured standard deviation (SDev). Images (**c**) and (**d**) were acquired under identical exposure conditions as images (**a**) and (**b**), respectively, except that the displayed thickness is 1 mm

- **Electrical noise.** Solid-state detectors are imperfect and gradually accumulate charge over a period of inactivity. This can dilute the received signal when acquisition occurs, presenting as noise. Background signal generated without any interaction with radiation is termed dark-current and manifests itself as a “fixed pattern noise” from the detector. However, this can be estimated and is normally subtracted from the image to largely remove it, in a manner transparent to the user.

All the rest being the same, the signal-to-noise ratio achieved is greatly affected by the reconstruction algorithm and filters used, and by the size of the voxel.

4.4 Artifacts

A general definition for artifacts in CT images is: “… any discrepancy between the reconstructed value in the image and the true attenuation coefficients of the object” (Hsieh 2002).

This definition is very broad in scope. A more practical definition is any error in an image that is unrelated to the subject being studied. In contrast to random noise effects, artifacts occur in more or less identical patterns when an image is repeated

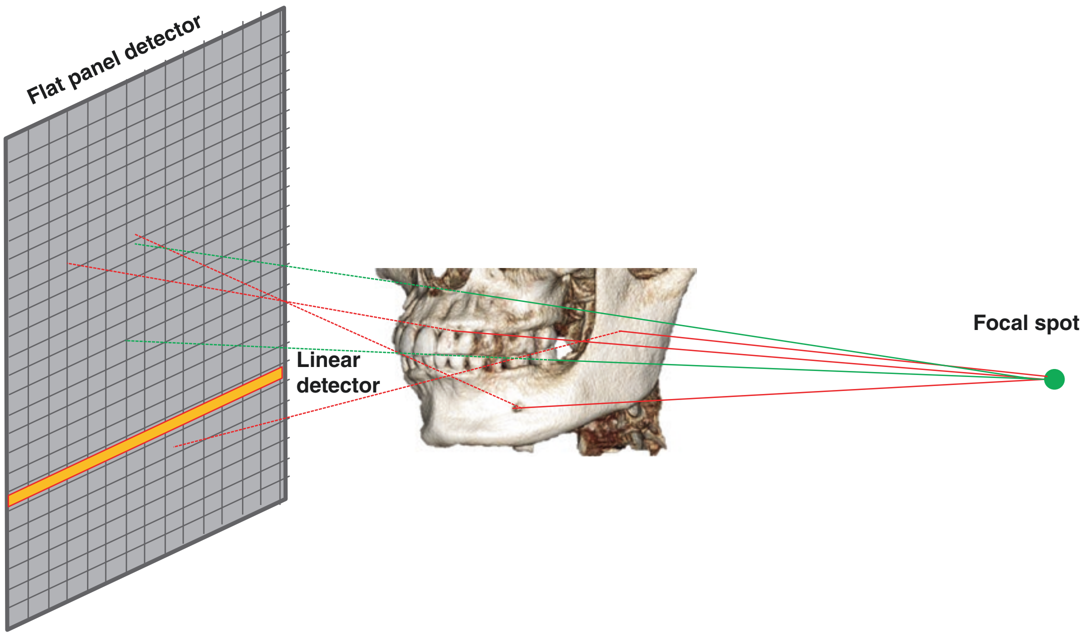

Fig. 4.4 A large flat panel area detector (*large grey rectangle* on the *left*) has a much higher probability that scattered photons (*red lines*) impact on it than a line-detector (narrow orange rectangle with red periphery). This effect accounts for a large proportion of additional noise in CBCT when compared to classic fan-beam CT

under the same conditions. Artifacts are induced by discrepancies between the actual physical conditions of the measuring setup (i.e., the CBCT scanner's technical composition plus the composition, position, and behavior of the object under investigation) and the simplified mathematical assumptions used for 3D reconstruction (Schulze et al. 2011). Artifacts are inherently present in all CBCT images; hence, knowledge about their presence and their appearance is essential for every user.

There are numerous sources of artifacts, many of which are related to inaccuracies of the device itself (i.e., geometry-related artifacts). Others are caused by incorrect (yet often unavoidable because no better method is available) assumptions made in the reconstruction process. These include artifacts caused by limited projection angles, a finite number of available projection images, or local tomography issues. A fundamental drawback of the state-of-the-art acquisition geometry used by current CBCT machines lies in image acquisition from a circular orbit around the head of the patient. Unfortunately, a circular orbit results in mathematically insufficient data sampling since this geometry violates the so-called "Tuy-condition" (Tuy 1983). Hence an exact reconstruction (in a mathematical sense) can only be obtained in the central plane of the reconstruction. Due to this violation, the further the reconstructed region is away from the central plane, the more erroneous the reconstruction is. Thus, when evaluating a CBCT image it is important to realize that the image is a computed "estimation" of the real situation and not reality itself.

Artifacts can be classified based on either their appearance in the image or according to where they occur in the imaging chain. In the first category, four types of artifacts are usually considered (Hsieh 2002): streaks, shadings, rings/bands, and miscellaneous (Table 4.1). In the second category, artifacts can be due to image acquisition (e.g., beam hardening producing scatter streaks and dark bands), patient-related artifacts (e.g., patient motion leading to unsharpness), the scanner itself (e.g., ring artifacts), or the beam projection geometry (e.g., image errors in the periphery).

Table 4.1 Classification of CT artifacts according to appearance

Appearance of artifact	Definition	Possible causes
Streaks	Intense straight lines (dark or bright) across the image	Aliasing, partial volume, motion, metal, beam hardening, noise, mechanical failure
Shadings	Dark or bright areas, particularly near objects of high contrast	Partial volume, beam hardening, scatter radiation, incomplete projections
Rings/bands	Rings (full or arcs) or bands superimposed on the image	Calibration error, crude interpolation in the reconstruction, offset projection
Miscellaneous	Cupping, densitometric inaccuracy	Beam hardening, scatter radiation, reconstruction algorithm

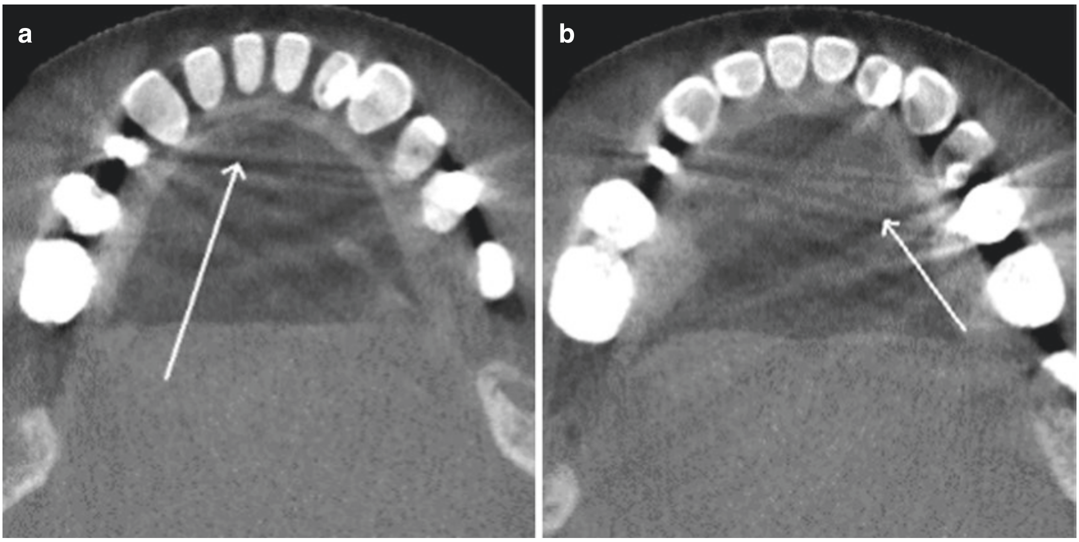

Fig. 4.5 Axial CBCT images at the level of the cemento-enamel junction (**a**) and inter-proximal coronal contact area (**b**) showing dark streaks (*arrows*) in the direction of projection/backprojection, typical of artifact due to scatter

4.4.1 X-ray Beam Related

Numerous artifacts are produced in association with the interaction of the X-ray beam with high-density materials (HDM) often present in the jaws such as composite resin, titanium, and dental alloys.

4.4.1.1 Scatter

When X-ray photons are diffracted from their original path after Compton interaction with HDM, they add to the primary intensity of the X-ray beam and produce dark linear streaks in reconstructed images (Fig. 4.5). Scatter is more prominent in larger array detector systems, such as CBCT (Kalender and Kyriakou 2007) (Fig. 4.4), reduces overall soft tissue contrast, and affects the density values of all voxels in the region of interest.

4.4.1.2 Beam Hardening

Beam hardening is caused since real-world X-ray beams are poly-energetic (i.e., are composed by a mixture of photons having different energies), and the average energy of the beam increases (the beam "hardens") as it crosses the object (i.e., the patient), due to selective absorption of the less energetic components. In other words, the patient or parts thereof act as a filter that mainly absorbs the lower-energetic X-rays so that the beam impacting onto the detector has a relatively higher energy when compared to the emitted

X-ray beam. As the reconstruction process neglects this phenomena, the energy in the reconstruction is incorrectly distributed within the reconstructed object image. Particularly HDMs, such as metal, produce strong beam hardening artifacts. It is very important to note, however, that also bone or dental tissue (enamel, dentin) produce substantial beam hardening. This phenomenon causes two simultaneous artifacts that deteriorate regional image quality significantly and may affect diagnosis:

- **Cupping.** Cupping can be considered as special sub-form of beam hardening originating from cylindrical objects. As the human body, and the skull as well, have a cylindrical cross section, these artifacts are clinically relevant. When X-rays pass through an object, those rays passing through the center of it undergo stronger beam hardening than those passing through the periphery. This occurs because there is simply more absorbing material in the path of the beam and hence relatively more rays of lower energy are being absorbed, i.e., the error is larger in the rays projected through the center. This effect results in a relatively higher energy reaching the detector in the center area (Fig. 4.6). This effect is especially noticeable with cylindrical objects, which are therefore often used to demonstrate it. In the reconstruction this relatively too high energy is being backprojected and thus causes relatively lower density values (darker shades of grey) in the center in comparison to the periphery.
- **Streaks and dark bands.** Dark shading radiates from and between HDM (Fig. 4.7). It is caused by the discrepancy (due to beam hardening) among the projection of X-rays that cross only one of the objects, and those that cross both objects. Streak artifacts present as linear hyperdensities radiating from the metallic object that may extend the entire width of the field, affecting even the visualization of areas on the opposite side. Associated with these are beam hardening artifacts which appear as dark voids adjacent to high-density structures and may mimic disease (Draenert et al. 2007). Examples include dark zones around endodontic filling material of root canal systems which imitate voids and linear

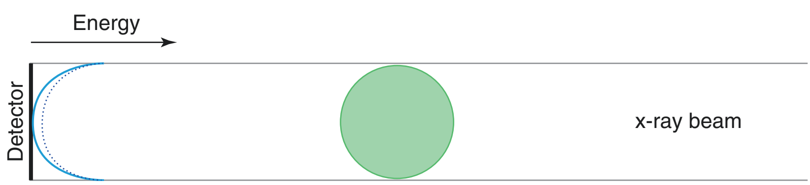

Fig. 4.6 Cupping artifacts originate from the relatively higher energy spectrum (*dotted blue line*) recorded on the detector when a polychromatic X-ray beam passes through cylindrical objects as in CT. The correct energy spectrum should follow the continuous *blue line*

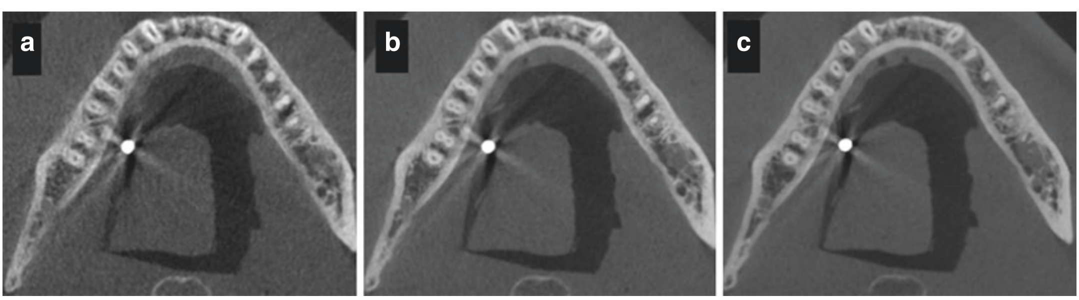

Fig. 4.7 Axial images of a phantom taken on a Morita Accuitomo 170 (5 mA, 512 basis images) showing the differences in HDM artifact production at 60 kV (**a**), 75 kV (**b**), and 95 kV (**c**)

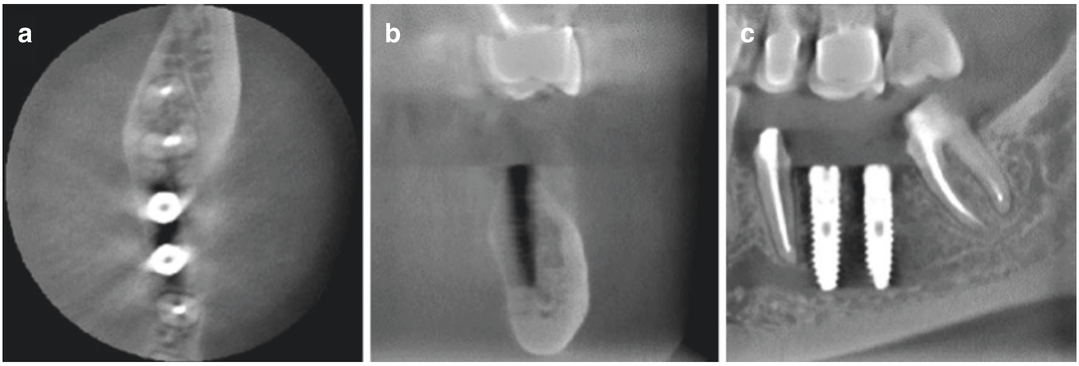

Fig. 4.8 Axial (**a**), cross-sectional (**b**), and sagittal (**c**) CBCT images showing beam hardening artifacts between titanium implants. This effect can be misinterpreted as absence of the inter-implant alveolar bone. The effect is particularly striking in the cross-sectional image (**b**) where the shape of the implant is depicted as *dark* (hypodense) "ghost shadow" even though in this area regular bone is present

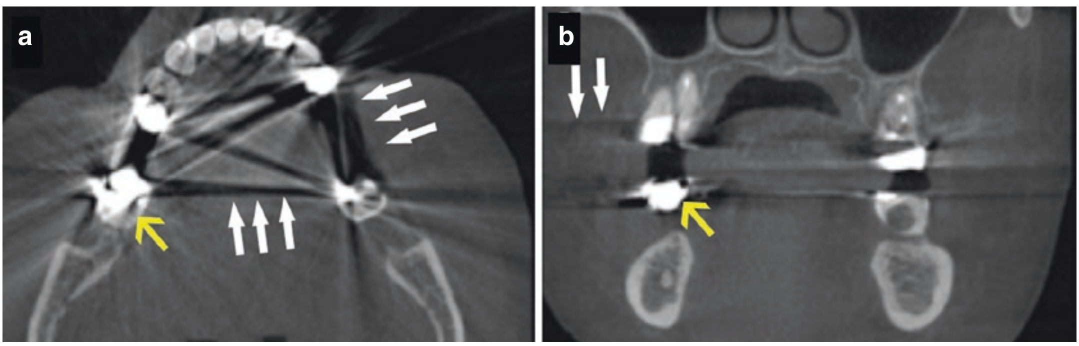

Fig. 4.9 Axial (**a**) and coronal (**b**) images showing intense beam hardening effects (cupping artifacts—*yellow arrows*) and streaks and dark bands (*white arrows*) caused by metal crowns

low density bands around dental implants that may mimic lack of osseointegration (Fig. 4.8). It is important to realize that those artifacts always appear along the projection/backprojection lines, i.e., the direction in which the X-rays traversed the object (the reverse of which is the direction of backprojection in the reconstruction process) (Schulze et al. 2010).

- Compared to CT, these artifacts (Figs. 4.7, 4.8, and 4.9) may be more pronounced on CBCT images when these systems use lower mean kV. In clinical practice, it is advisable to reduce the FOV to avoid scanning regions susceptible to beam hardening (e.g., metallic restorations, dental implants) (Schulze et al. 2011). This can be achieved by collimation, modification of patient positioning, or separation of the dental arches. There are also specific image processing techniques which do not compute the reconstruction in only one step as the well-known Feldkamp-Algorithm (FDK) (Feldkamp et al. 1984). Rather, they iteratively step-by-step arrive at a "best-fit" solution in the sense of an optimization algorithm. Often such algorithms are termed "algebraic reconstruction algorithms" (ART). More appropriately, the general term for this class of algorithms is iterative reconstruction algorithms. In dental CBCT, iterative algorithms have, thus far, only been implemented rarely (e.g., Scanora 3D, SOREDEX, Helsinki, Finland; X-Mind Trium, Acteon North America, Mt Laurel, New Jersey, USA). These algorithms are very flexible, they can better deal with image noise and potentially also can reduce metal, and motion-related artifacts (Fig. 4.10) (Geyer et al. 2015). In

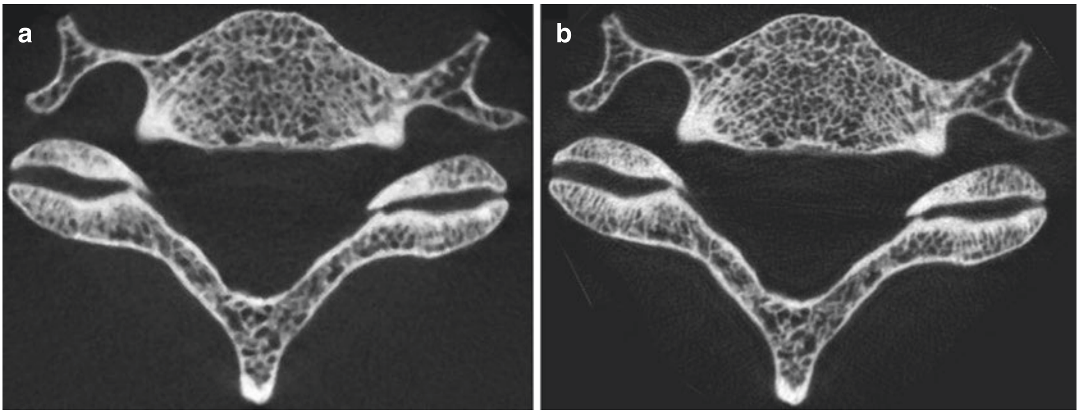

Fig. 4.10 Axial image of the cervical vertebrae reconstructed using the Feldkamp reconstruction (**a**) versus iterative reconstruction (**b**) (ART: 50 iterations). Clearly visible is the high level of detail in the ART reconstruction (**b**)

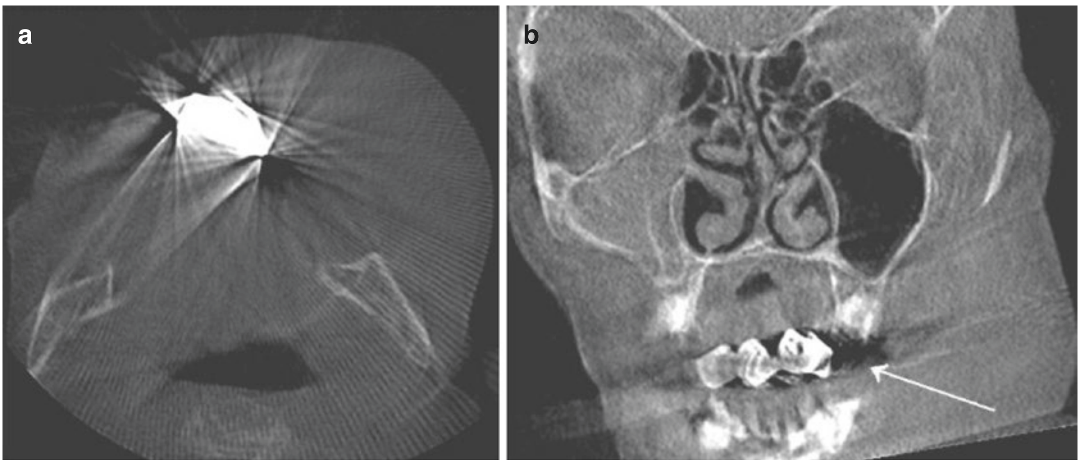

Fig. 4.11 Axial (**a**) and coronal (**b**) CBCT images showing typical extinction artifacts surrounding the image of the gold restorations in the direction of the beam (*arrow*)

addition, they require fewer projection images and therefore may allow for a lower acquisition dose. However, they are computationally demanding and require increased reconstruction times (Mueller 1998).

4.4.1.3 Extinction

Extinction artifacts, also known as missing value artifacts, occur in regions where a HDM completely absorbs the X-ray beam (e.g., gold) to a level such that there is little photon fluence recorded and the area appears as dark voids (Fig. 4.11). This is prominent in regions where there are adjacent HDM and there is crossover of the X-ray projection beam (e.g., adjacent titanium implants, dental restorations).

4.4.1.4 Exponential Edge Gradient Effect

This effect occurs whenever long, sharp edges of high contrast are encountered. This occurs commonly in maxillofacial imaging such as at the borders of metallic crowns or implants. It is caused by the interaction of several factors effective in CT or CBCT imaging: (1) the exponential nature of the radiation attenuation (Beer–Lambert law), (2) averaging of the measured intensity over a finite beam width (and finite focal spot width), and (3) presence of high-density objects with straight edges (Joseph and Spital 1981). It is closely related to the mathematics used for the reconstruction, which assumes zero beam width (Schulze et al. 2011).

The most common effect is streaks emerging from single straight edges in the direction of the projection (Fig. 4.12).

4.4.2 Patient-Related Artifacts

One of the most frequent artifacts in CBCT imaging results from patient motion. Patient motion during the CBCT gantry rotation can cause misregistration of data, and most visibly appear as a “double contour” (Figs. 4.13, 4.14, and 4.15). Patient motion changes the acquisition geometry, which is essential for reconstruction yet unfortunately not known to the machine. Patient motion can be minimized by use of a head restraint and by using as short as scan time as possible. The higher the acquisition resolution of the volumetric dataset and the longer the scan time, the more likely motion artifacts are to appear.

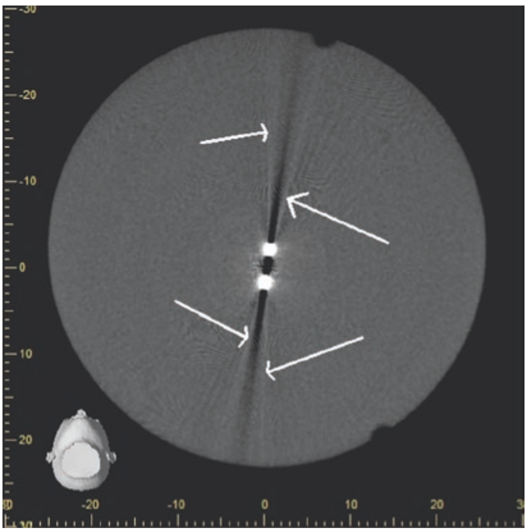

Fig. 4.12 Axial image of a high-density metallic object submerged in water showing an exponential edge gradient effect presenting as thin lines tangent to high-contrast edges

Subtler motion artifacts presenting as image unsharpness and loss of resolution may also originate. Motion blur is a well-known artifact that, in the case of MDC, led to the development of ultrafast acquisition times below 1 s (Kalender 2006). It is noteworthy that identical geometry artifacts often result from inaccuracies in the motion of components of the system (the X-ray-generator-detector unit). The effect of such reduced spatial resolution, which is not obviously recognizable by the observer, may be crucial to fine diagnostic tasks such as accurate measurements or identification of anatomical structures of significance (e.g., mandibular canal, alveolar crest, floor the maxillary sinus). This is important when considering the effective (true) spatial resolution the image offers (Brüllmann and Schulze 2015). Scanner-related geometry issues are commonly reduced by the use of dampening systems. Repeated use of CBCT equipment over time may result in slight configuration changes and components may need to be periodically re-aligned.

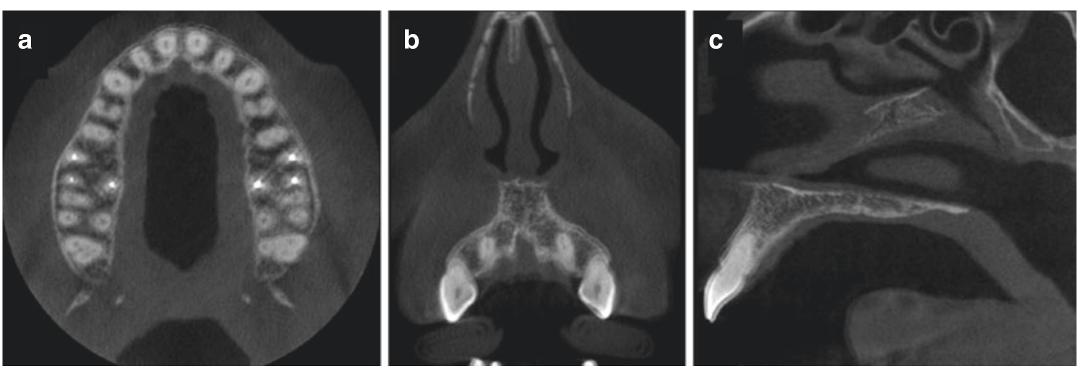

Fig. 4.13 Axial (**a**), coronal (**b**), and sagittal (**c**) images acquired on a Prexion 3D unit (90 kVp, 4 mA, 512 basis image, FOV 8 cm × 8 cm and voxel size 0.15 mm) showing double contour of cortical bone and dental crowns. It is typical artifact caused by patient slight movement (Images courtesy, Dr. Otávio Umetsubo)

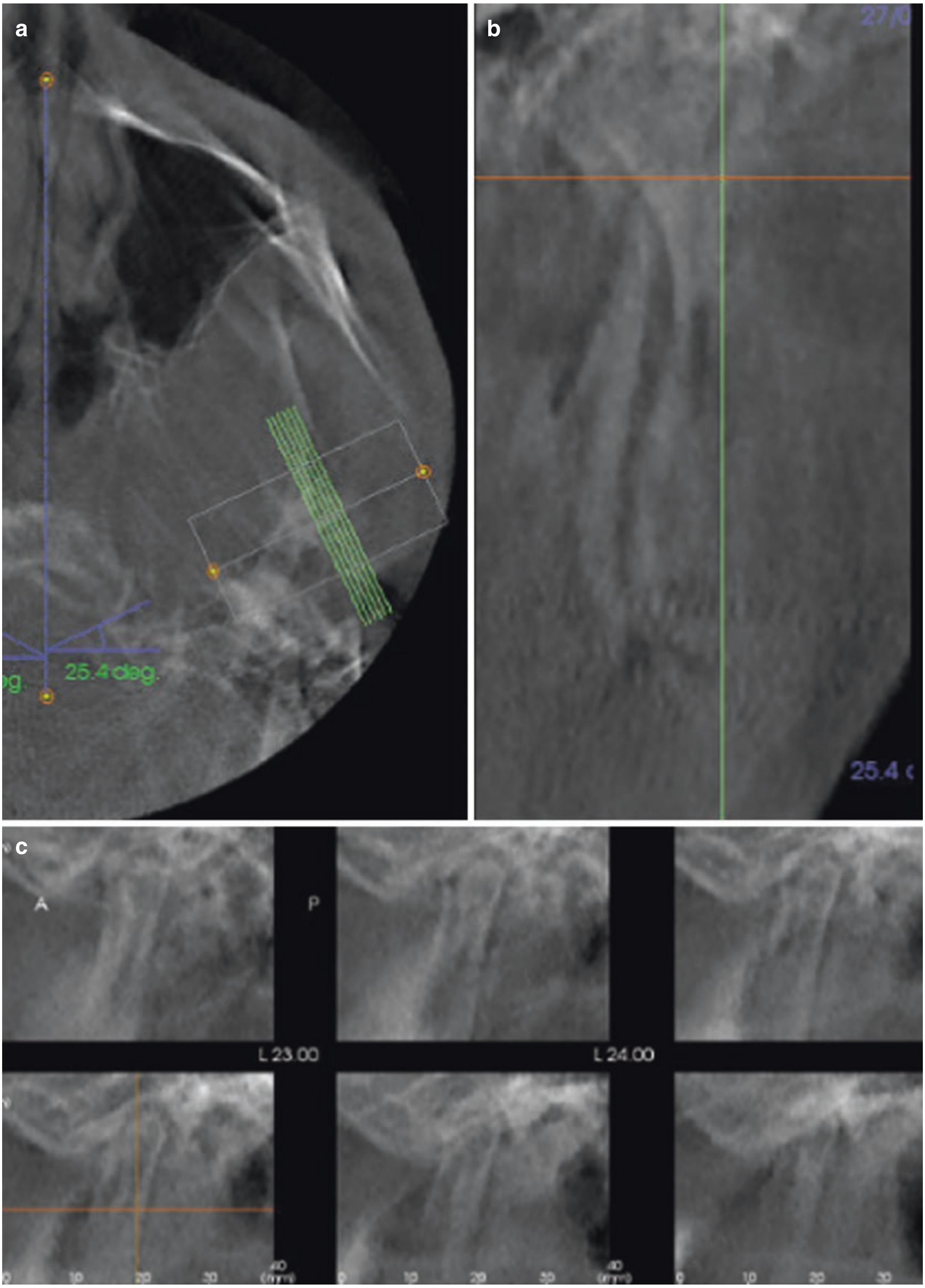

Fig. 4.14 Axial (**a**), coronal (**b**), and serial cross-sectional para-sagittal (**c**) images of the left temporomandibular articulation showing generalized double contouring of cortical bone in the left condylar neck and head

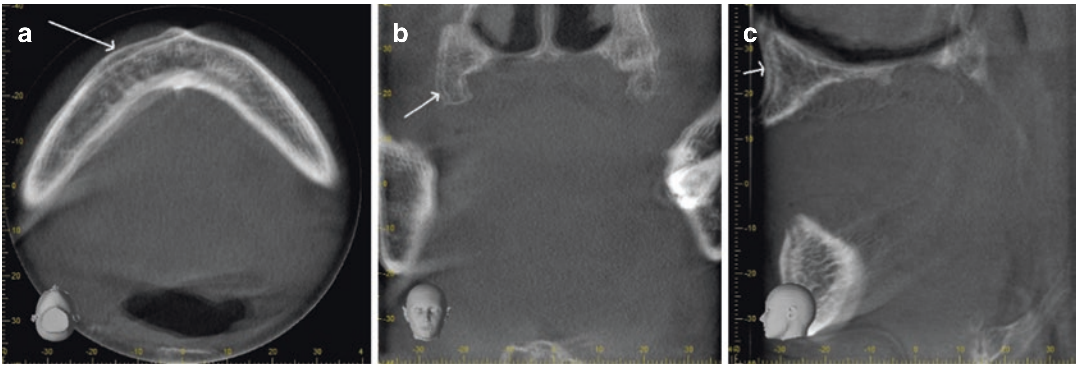

Fig. 4.15 Axial (**a**), coronal (**b**), and sagittal (**c**) CBCT images showing apparent double contours (*arrows*) indicating patient motion during the scan. Clearly discernible double contours like this are indicative for a one-step motion at a certain moment of the scan

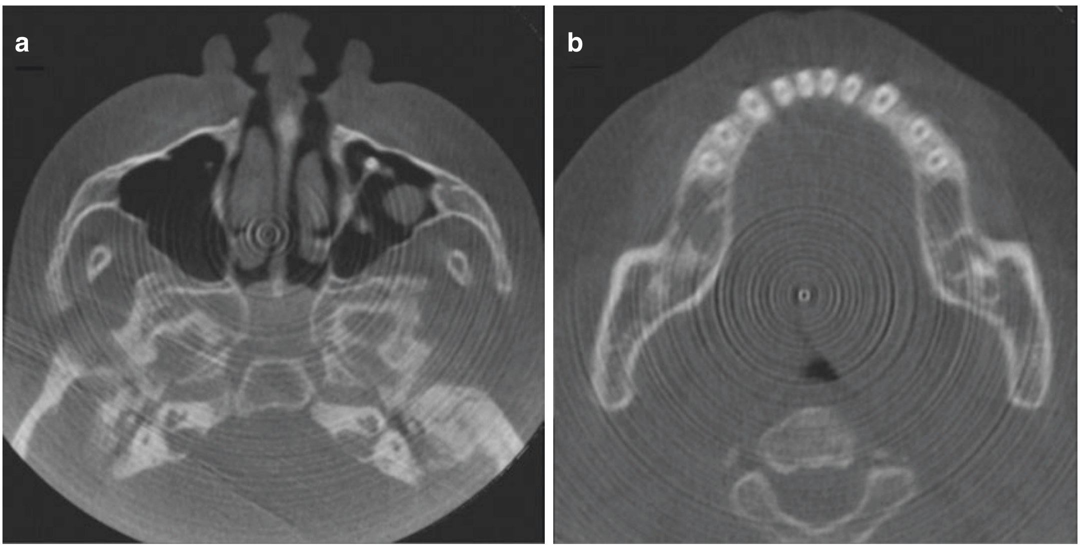

Fig. 4.16 Maxillary (**a**) and mandibular (**b**) axial CBCT images (120 kV, 5 mA, 360 basis images, FOV 8 cm × 16 cm, voxel 0.25 mm) showing concentric hypodense and hyperdense *circles* indicative of scanner-related artifacts

4.4.3 Scanner-Related Artifacts

Typically, scanner-related artifacts present as circular or concentric dark rings in the axial plane centered about the location of the axis of rotation (Fig. 4.16). They result from poor calibration or imperfections in scanner detector, such as blemishes or debris on the entrance surface. Recalibration of the machine often resolves the problem. Discrete sampling of an inherently continuous object may also contribute to this type of artifact.

The beam projection geometry of CBCT and subsequent image reconstruction methods produce numerous cone beam-related artifacts.

4.4.3.1 Partial Volume Effect

This is a feature of both fan-beam CT and CBCT imaging. This artifact is also a direct effect of sampling the object in discrete entities, i.e., the voxels. In theory, a voxel represents the density of a point in three-dimensional space. However, since a voxel has finite (relatively large) dimensions, densities from smaller structures are invari-

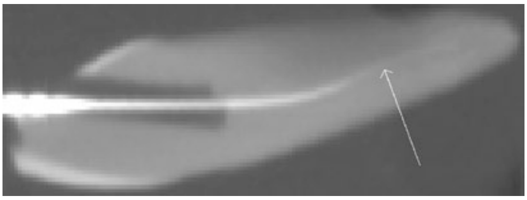

Fig. 4.17 Magnified CBCT reconstruction of a tooth with a small-sized endodontic file. Since the thin file lower third (*arrow*) only partially fills the voxel, the true attenuation is largely underestimated, i.e., the resulting grey value is too low (*dark*)

ably averaged. More precisely, the logarithm of the measured integral intensity (derived from the well-known Beer–Lambert law) is not proportional to the integral in attenuation within the patient volume sampled by the detector (Glover and Pelc 1980). Nonrepresentative grey values are generated when all of the densities within an individual voxel are averaged to produce a single attenuation coefficient (Chakeres 1984).

Nonlinear partial volume effects occur when the selected voxel resolution of the scan is greater than the spatial or contrast resolution of the object to be imaged. In this case, the pixel is not representative of the tissue or boundary however becomes a weighted average of the different density values. To understand this common artifact, it is helpful to recall that the grey value in a voxel is an average over all grey values of those pixels that contribute to the voxel in the reconstruction process. It was shown that the computed density underestimates the true one, i.e., the grey value will be overly dark (Glover and Pelc 1980) (Fig. 4.17). This may result in some loss of fine diagnostic detail. Selection of the smallest acquisition voxel can reduce the presence of these effects yet unfortunately increases noise and the blur due to patient motion.

4.4.3.2 Sampling Artifacts

In CBCT, as well as CT, an inherently continuous object necessarily has to be sampled in discrete small units—the volume elements (voxels). This procedure induces artifacts which are termed aliasing. Aliasing occurs when the sampling rate is too small for the details being imaged. It can occur when too few basis projections are provided for the reconstruction. Aliasing is a phenomenon caused by the manner by which the CBCT projections are sampled by the digital image capture system. The Tuy-condition, with its effect on data sampling, is one reason for artifacts (Tuy 1983). In addition, according to the Nyquist–Shannon Theorem, in order to achieve an information-lossless sampling of any information-carrying signal (including an image) the sampling frequency—in case of a spatial signal, i.e., an image, the number of sampled data per unit length, e.g., the DPI or "Dots Per Inch"—must be at least twice larger than the maximum frequency component in the signal. In case of an image, the latter is inverse-proportional to the size of the smallest detail present in the image of the object. If this condition is not satisfied, the reconstruction of the reduced data sample leads to misregistration and sharp edges and noisier images due to aliasing, where fine line striation patterns (moiré patterns), appear in the image (Fig. 4.19).

4.4.3.3 Cone Beam Effect

Sampling errors in the sense of moiré patterns also occur due to the conical beam shape. This is sometimes also termed *cone beam effect*. It is caused by the cone-shape of the beam in CBCT. The upper and lower voxels in the volume are traversed by fewer "rays" than those in the center of the grid. This results in a reduction of recorded information the further the voxels are away from the central slice of voxels (Fig. 4.18). If not well interpolated, this may cause stripe patterns (moiré patterns) in addition to greater noise in the upper and lower periphery of the reconstructed image. This effect can be minimized by the manufacturers using more advanced reconstruction algorithms than the common FDK. Clinically it can be reduced by positioning the region of interest adjacent to the horizontal plane of the X-ray beam and collimation of the beam to an appropriate FOV.

Aliasing effects often may not degrade the image severely; however, when resolution of fine detail is important, under-sampling artifacts need to be avoided as far as possible, such as by maintaining the number of basis projection images. Also, the regular stripe patterns (Fig. 4.19) may,

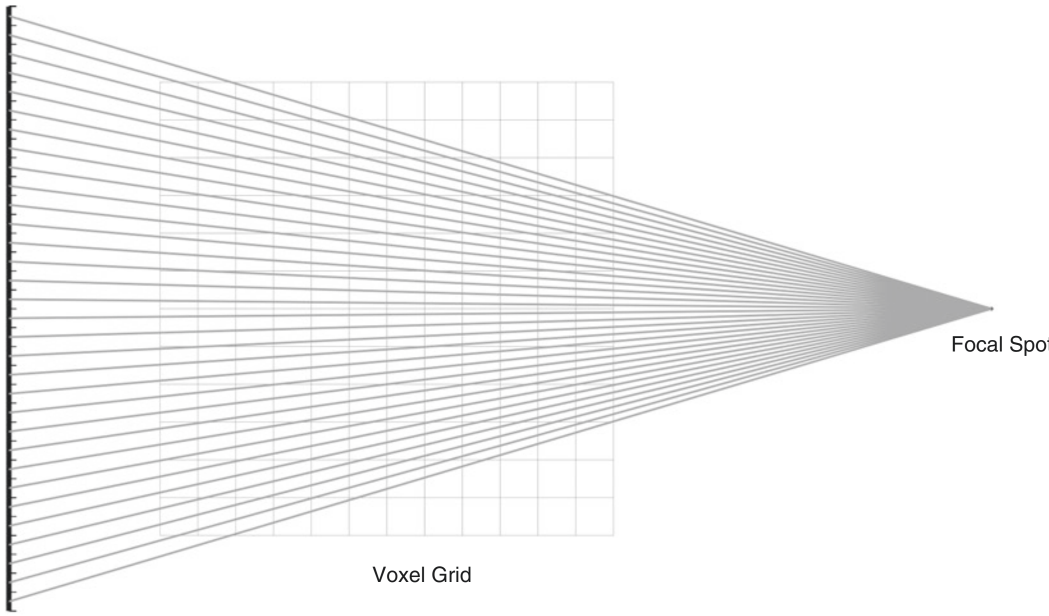

Fig. 4.18 Due to the divergence of the X-ray beam associated with the cone-shape-geometry in CBCT, voxels in the upper and lower periphery of the volume (defined by the voxel grid) receive fewer "rays" than those in the center of the volume. This effect also produces aliasing (moiré) patterns

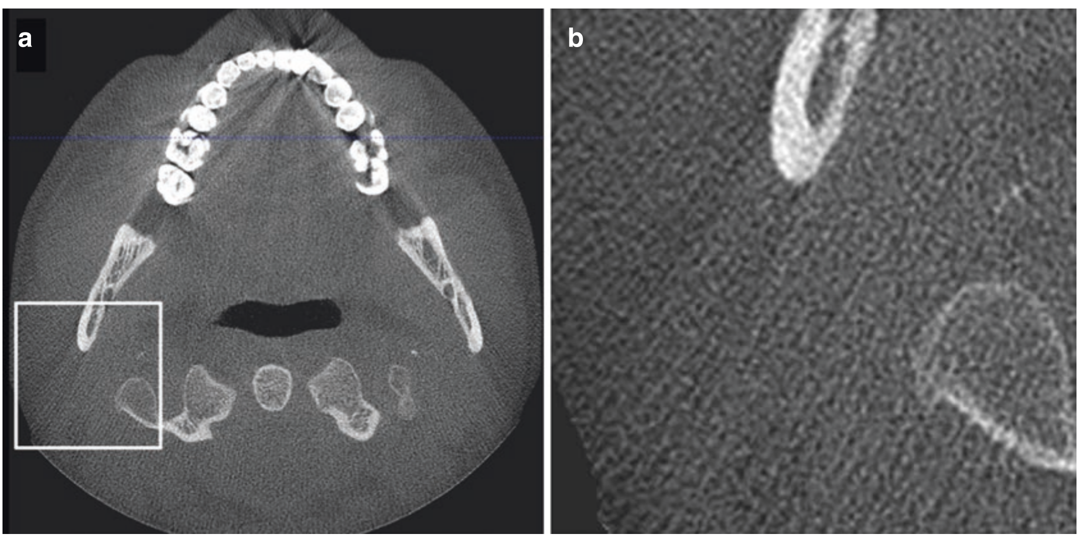

Fig. 4.19 Axial (**a**) and magnified, cropped insert (**b**) demonstrating typical moiré patterns due to insufficient sampling rates in the periphery of a CBCT image. Note the thin hyperdense lines diverging radially into the periphery in the magnified (**b**) image representing the highlighted region in the *left* scan

in certain cases, be misinterpreted as anatomic or pathologic structures. To reduce aliasing, manufacturers of CBCT systems need to improve the sampling, by increasing the number of data sampled out of each projection, and by increasing the total number and rate of projections. However, the latter is limited due to concerns of increased radiation exposure. Enhanced reconstruction methods, such as iterative reconstructions, can also reduce such artifacts. In addition, more sophisticated interpolation algorithms can smooth out the aliasing streaks. Simple post-processing algorithms that just “beautify” the image, for example, by averaging, are not adequate since this does not enhance the information content and gives an incorrect impression of a high-quality image.

4.4.3.4 Local Tomography

This artifact is commonly also referred to as truncated view artifact. In small FOV imaging of a ROI located within a larger object (e.g., FOV of 6 cm × 6 cm diameter within the maxillofacial region), artifacts occur by additional attenuation from the adjacent tissue outside the FOV that cannot be avoided. The attenuation caused by such tissues contributes to the overall attenuation measured on the detector. Consequently, attenuation values higher than those within the ROI are back-projected into the FOV during reconstruction. Artifacts appear in the reconstructed volume because structures that lie adjacent and outside the FOV are only irradiated over small angular distances, yet are still incorporated in the backprojection algorithm (Fig. 4.20).

4.4.3.5 Offset Projection

To reduce manufacturing costs yet construct a CBCT unit with a relatively large FOV, companies use detectors of smaller size and an X-ray generator/detector system gantry offset to the center of rotation (Fig. 4.21). Depending on the actual geometry, this results in a limited angle of projections for either the entire object or parts within it. In this projection geometry, peripheral parts of the object are reconstructed from a smaller number of projections (over 180°) while for central areas the full number of projections over 360° is available for reconstruction. Typical circular artifacts result at the interface between these zones. The abrupt transition between the two zones may show on images as border ring-like artifacts (Fig. 4.22). These artifacts are commonly corrected later by means of image post-processing methods incorporated within the system by the manufacturer.

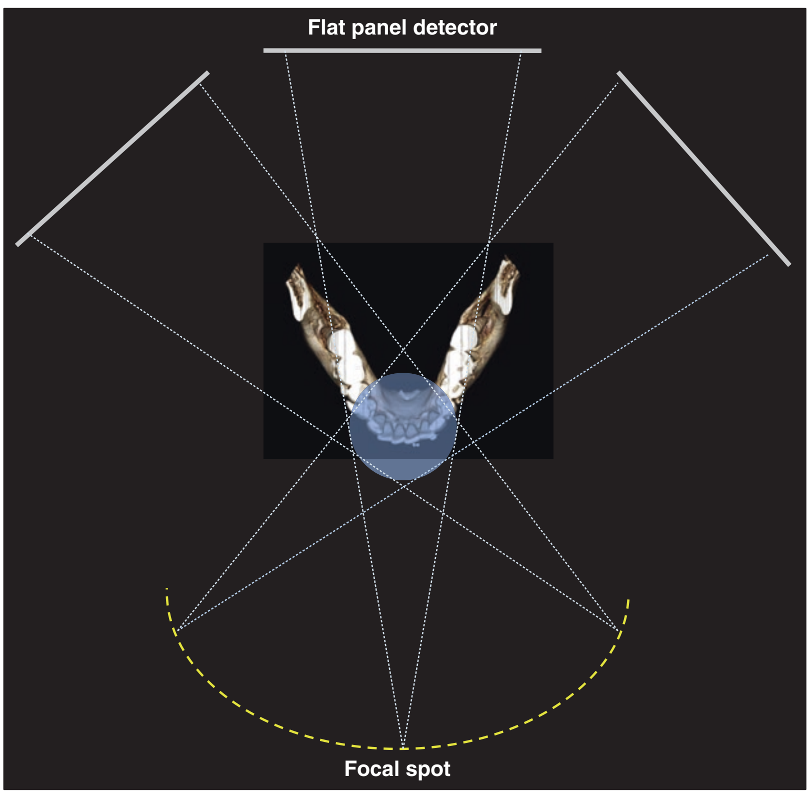

Fig. 4.20 Schematic diagram showing the origin of local tomography artifact. If the FOV (*blue circle* centered in the anterior mandible) is small and is a part of, or located within, the object (in this case the entire mandible), tissue outside the FOV (the right and left posterior mandible) contribute to the total attenuation for some of the projection images. Since only the FOV is reconstructed, the additional contribution from tissue outside the FOV remains unknown, and the distribution of the attenuation values (*grey* values) from these projections will be incorrect

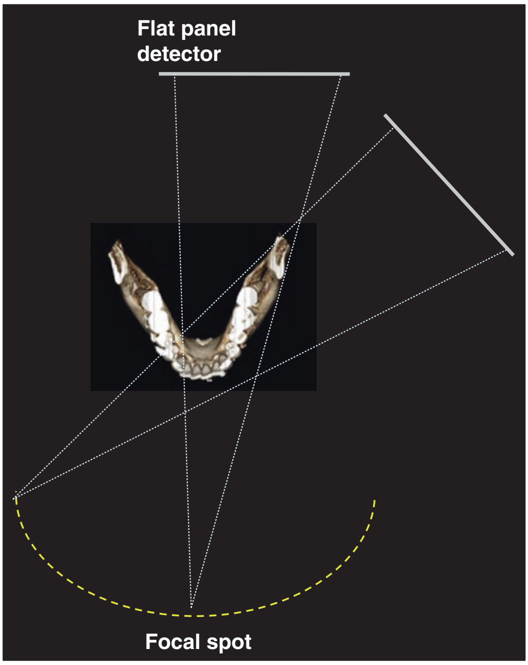

Fig. 4.21 Representative geometry for an offset-projection for two arbitrary positions. The circular motion between these positions is indicated by the dashed path (*yellow*). Since the detector is smaller than the object under study (in this case, the entire mandible), only a part of it is imaged in each projection. This means that the reconstruction only has a relatively small number of projections available for each part of the object, yielding typical artifacts

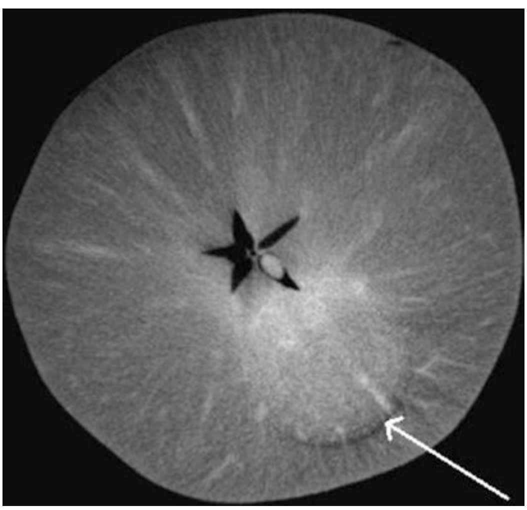

Fig. 4.22 Axial iterative reconstruction of an CBCT volumetric dataset of an apple without correction of typical offset projection artifact (*arrow*)

4.4.4 Clinical Perspective on Artifacts

This chapter has illustrated a wide variety of image artifacts exhibited by CBCT acquisition. Many present as stripes in the direction of projection/backprojection and can therefore be distinguished from anatomy or pathological features. In particular, extinction and beam hardening artifacts from HDM can be easily misinterpreted as "missing bone," fracture lines, or dental caries since they occur in the alveolar bone between implants or the coronal portions of teeth respectively. Coronal enamel itself may act as a HDM and produce noticeably beam hardening image artifacts that might be incorrectly interpreted as inter-proximal dental caries. Moiré patterns present as periodic line patterns and may, under certain circumstances, also mimic anatomic structure or pathologic lesions. Inevitably, a variety of artifacts will be present in each CBCT image. Therefore, clinicians must be aware of the characteristic imaging presentation of different artifacts and be knowledgeable of their cause. Whenever possible, positioning of high-density structures or sharp edges appropriately so that the resulting artifacts are distributed over regions outside the main focus of interest in the image is an imaging strategy that can be helpful. Manufacturers are urged to provide software capable of post-processing routines able to smooth out typical, yet often unavoidable, sampling artifacts. Artifact-suppressing algorithms are being developed, many of which use very promising approaches. Artifact reduction should be directed towards discerning anatomy and pathology from artifact. Simple "beautification" of the image by post-processing in the sense that artifact-regions are simply adapted in their grey level to the surrounding areas is not at all helpful. Users should always be aware that both CT and CBCT images provide a technically acquired interpolation or "best-guess" representations of reality, obtained from (mathematical) assumptions that are simplified in comparison to the underlying physical process. Understanding the limitation of CBCT image production, recognizing the imaging appearance of artifacts and understanding their cause and prevention can assist the practitioner in avoiding interpretive pitfalls.

References

Brüllmann D, Schulze RK (2015) Spatial resolution in CBCT machines for dental/maxillofacial applications-what do we know today? Dentomaxillofac Radiol 44:20140204

Bryant JA, Drage NA, Richmond S (2008) Study of the scan uniformity from an i-CAT cone beam computed tomography dental imaging system. Dentomaxillofac Radiol 37:365–374

Chakeres DW (1984) Clinical significance of partial volume averaging of the temporal bone. Am J Neuroradiol 5:297–302

Chen L, Shaw CC, Altunbas MC, Lai CJ, Liu X (2008) Spatial resolution properties in cone beam CT: a simulation study. Med Phys 35:724–734

Doi K (2006) Diagnostic imaging over the last 50 years: research and development in medical imaging science and technology. Phys Med Biol 51:R5–R27

Draenert FG, Coppenrath E, Herzog P et al (2007) Beam hardening artifacts occur in dental implant scans with the NewTom come beam CT but not with the dental 4-row multidetector CT. Dentomaxillofac Radiol 36:198–203

Feldkamp LA, Davis LC, Kress JW (1984) Practical cone-beam algorithm. J Opt Soc Am A 1:612–619

Geyer LL, Schoepf J, Meinel FG, Nance JW, Bastarrika G, Leipsic JA, Paul NS, Rengo M, Laghi A, De Cecco CN (2015) State of the art: iterative CT reconstruction techniques. Radiology 276:339–357

Glover GH, Pelc NJ (1980) Nonlinear partial volume artifacts in x-ray computed tomography. Med Phys 7:238–248

Hashimoto K, Arai Y, Iwai K et al (2003) A comparison of a new limited cone beam computed tomography machine for dental use with a multi-detector row helical CT machine. Oral Surg Oral Med Oral Pathol Oral Radiol Endod 95:371–377

Hashimoto K, Katsumata S, Araki M et al (2006) Comparison of image performance between cone beam computed tomography for dental use and four-row multi-detector helical CT. J Oral Sci 48:27–34

Hsieh J (2002) Computed tomography: principles, design, artifacts, and recent advances. SPIE Optical Engineering Press, Bellingham, WA

Joseph PM, Spital RD (1981) The exponential edge-gradient effect in x-ray computed tomography. Phys Med Biol 26:473–487

Kalender WA (2005) Computed tomography. Fundamentals, system technology, image quality, applications, 2nd edn. Puplicis Corporate Publishing, Erlangen

Kalender W (2006) X-ray computed tomography. Phys Med Biol 51:R29–R43

Kalender WA, Kyriakou Y (2007) Flat-detector computed tomography (FD-CT). Eur Radiol 17:2767–2779

Lagravere MO, Carey J, Ben-Zvi M, Packota GV, Major PW (2008) Effect of object location on the density measurement and Hounsfield conversion in a NewTom 3G cone beam computed tomography unit. Dentomaxillofac Radiol 37:305–308

Loubele M, Maes F, Jacobs R, van Steenberghe D, White SC, Suetens P (2008) Comparative study of image quality for MSCT and CBCT scanners for dentomaxillofacial radiology applications. Radiat Prot Dosim 129:222–226

Mah P, Reeves TE, McDavid WD (2010) Deriving Hounsfield units using grey levels in cone beam computed tomography. Dentomaxillofac Radiol 39:323–335

Molteni R (2013) Prospects and challenges of rendering tissue density in Hounsfield units for cone beam computed tomography. Oral Surg Oral Med Oral Pathol Oral Radiol 116:105–119

Mueller K (1998) Fast and accurate three-dimensional reconstruction from cone-beam projection data using algebraic methods. Ph.D. thesis, Ohio State University, Columbus

Nackaerts O, Maes F, Yan H, Couto Souza P, Pauwels R, Jacobs R (2011) Analysis of intensity variability in multislice and cone beam computed tomography. Clin Oral Implants Res 22:873–879

Pauwels R, Stamatakis H, Manousaridis G, Walker A, Michielsen K, Bosmans H, Bogaerts R, Jacobs R, Horner K, Tsiklakis K (2011) Development and applicability of a quality control phantom for dental cone-beam CT. J Appl Clin Med Phys 12:3478

Qu XM, Li G, Ludlow JB, Zhang ZY, Ma XC (2010) Effective radiation dose of ProMax 3D cone-beam computerized tomography scanner with different dental protocols. Oral Surg Oral Med Oral Pathol Oral Radiol Endod 110:770–776

Schulze RK, Berndt D, d'Hoedt B (2010) On cone-beam computed tomography artifacts induced by titanium implants. Clin Oral Implants Res 21:100–107

Schulze R, Heil U, Gross D, Bruellmann DD, Dranischnikow E, Schwanecke U, Schoemer E (2011) Artefacts in CBCT: a review. Dentomaxillofac Radiol 40:265–273

Siewerdsen JH, Jaffray JH (2001) Cone-beam computed tomography with a flat-panel imager: magnitude and effects of x-ray scatter. Med Phys 28:220–231

Suomalainen A, Kiljunen T, Käser Y, Peltola J, Kortesniemi M (2009) Dosimetry and image quality of four dental cone beam computed tomography scanners compared with multislice computed tomography scanners. Dentomaxillofac Radiol 38:367–378

Tuy K (1983) An inversion formula for cone-beam reconstruction. SIAM J Appl Math 43:546–552

Part II

CBCT in Daily Clinical Practice

CBCT Use in Daily Practice

5

William C. Scarfe and Christos Angelopoulos

Contents

W.C. Scarfe, B.D.S., F.R.A.C.D.S., M.S. (✉)
Division of Radiology and Imaging Science, Department of Surgical/Hospital Dentistry, University of Louisville School of Dentistry, Louisville, KY, USA
e-mail: william.scarfe@louisville.edu

C. Angelopoulos, D.D.S., M.S.
Aristotle University of Thessaloniki, Thessaloniki, Greece

Columbia University, College of Dental Medicine, New York City, NY, USA
e-mail: angelopoulosc@gmail.com

5.1 CBCT Operation

The operation and ease of use of maxillofacial CBCT equipment is technically simple and similar, in many respects, to dental panoramic radiography (DPR). In fact, since 2007, many DPR platforms are configured to provide additional CBCT functionality, sharing the same mechanical assembly and X-ray generator. This has led to some regulatory ambiguities regarding the categorization of dental and maxillofacial CBCT units as either dental or medical devices, and credentialing issues for facilities and personnel who operate this equipment. Operator requirements differ markedly between countries. For example, in many jurisdictions in the United States, maxillofacial CBCT devices are operated by dental auxiliaries with nominal radiographic qualifications, whereas in some European countries they can only be operated by dentists with special training.

W.C. Scarfe, C. Angelopoulos (eds.), *Maxillofacial Cone Beam Computed Tomography*,
https://doi.org/10.1007/978-3-319-62061-9_5

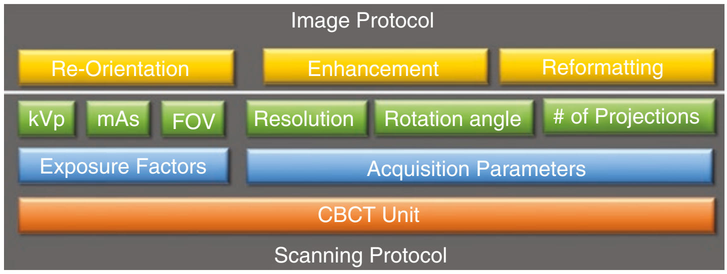

Fig. 5.1 Schematic diagram showing the relationship of the two aspects of CBCT operation and elements to be considered within each technical competency

While there are similarities between DPR and CBCT, a number of differences in acquisition and technique exist which distinguish the latter as a maxillofacial imaging modality that demands a higher level of technical competency and expertise. The operation of CBCT devices should be considered in two sequential and distinct phases (Fig. 5.1):

- **Scanning Protocol.** The choice of specific technical parameters to optimize image quality and minimize exposure for a specific imaging task is called the *imaging acquisition* or *scan protoco*l. Perhaps the greatest distinction between DPR and CBCT imaging lies in the fact that CBCT provides the operator with the choice of many more technique variables (Table 5.1). Practitioners and operators using CBCT must have a thorough understanding of the available operational exposure and acquisition parameters and the effects of these parameters on image quality and radiation safety (Carter et al. 2008).

- **Image Protocol.** Once acquired, it is necessary to interact with volumetric CBCT data to optimize image display on the monitor. The principle components of this are to reorient the data, enhance the data, and then to reformat the data so that the clinician can explore, analyze, and interpret the volume (See Sect. 5.2).

5.1.1 Scan Protocol

5.1.1.1 Exposure Factors

Four exposure parameters determine the quality and quantity of the X-ray beam. Two of the factors, focal spot size and beam frequency, are equipment dependent and fixed whereas the other two, milliamperes (mA) and kilovoltage (kV), may be variable and are operator controlled.

Equipment Dependent

The following factors should be considered when purchasing a CBCT unit and while are not specifically adjusted clinically, do introduce potential limitations on image quality and patient radiation dose optimization:

- **Focal spot size.** Focal spot size is one parameter that determines the penumbra or geometric unsharpness of CBCT image formation. CBCT units with smaller focal spot sizes theoretically produce less penumbra and consequently sharper images. Most CBCT units have a nominal focal spot of 0.5 mm; however, some are lower at 0.3 mm with the lowest at 0.15 mm. Lower focal spot size has two disadvantages.
  - The maximum field of view (FOV) of the CBCT unit may be limited because of increased projection divergence at the peripheral of the X-ray beam.
  - Low mAs must be used or otherwise a longer duty cycle is necessary, especially with greater numbers of basis images, so as to not overheat the generator.
- **X-ray Generator Frequency.** In most CBCT units, X-ray generation is pulsed to coincide with the detector activation. Pulsed X-ray beam generation is preferable to continuous exposure as it markedly reduces total *exposure* scan time with less radiation dose to the patient. In addition, there is diminished heat production at the anode and reduces the impact of detector afterglow. However, the relatively low power used in this type of X-ray generator provides some limitations in image

Table 5.1 Comparison of the similarities and differences between the operation and techniques of DPR and maxillofacial CBCT devices

Technique stage	Similarities	Differences
Set technique factors	• Made before exposure; kVp and mA settings determine image quality and patient radiation dose	• CBCT offers additional choices influencing image quality and patient radiation dose including FOV, arc trajectory, resolution and, number of projection images
	• Exposure factors are adjusted according to head size	• Scan factors for CBCT should be adjusted to be diagnostic task as well as size specific
Prepare patient	• Patient standing or seated, head stabilized, position critical to resultant image	• Patient may also be standing, seated or, in some units, supine
	• Anterior bite block always used to stabilize and localize head position	• Instead of bite block, head position may be stabilized by chin rest, head restraint or occlusal bite plane
		• Panoramic head position critical to minimizing image projection errors
Protect patient	• Lead torso shield used	• Additional thyroid shield is desirable for CBCT only, especially for maxillary scans if possible.
Expose	• Patient informed to keep still during exposure	• Motion artifacts affecting the entire image are more likely to occur with longer scan times.
		• Sensor image calibration may be required periodically
View image	• Basic image processing possible (if using digital panoramic radiography), e.g., contrast, brightness, zoom, filtering	• Image must be reconstructed before viewing (30s–10 min), unlike panoramic images that are viewed immediately after scan
		• Secondary orthogonal images must be reformatted;
		• Data is interactive (contrast, brightness, image mode);
		• Resultant data can be reoriented to compensate for head position.
		• CBCT data allows for advanced reformatting (e.g., curvilinear) and 3D visualization (e.g., maximum intensity projection, volume rendering) (see Chap. 3)

FOV field of view, *CBCT* cone beam computed tomography, *s* seconds, *min* minutes

quality. Continuous exposure units produce X-ray spectra with a higher peak kV and capable of faster acquisition of a greater number of basis frames with theoretically less image noise.

Operator Controlled

CBCT manufacturers approach setting exposure factors in one of three ways.

- **Fixed.** Operators are offered a selection of predetermined or "fixed" exposure setting combinations (e.g., PreXion, PreXion Co., Ltd, Tokyo, Japan; GALILEOS, Sirona AG, Bensheim, Germany; Newtom5g/VGi, QR, Inc. (a Cefla Company), Milano, Italy).
- **Variable.** Operators can manually adjust kV and/or mA settings. Operators who use CBCT units with operator adjustable exposure settings should be aware that these parameters affect both image quality (See Chap. 2) and have patient radiation dose consequences. Careful selection is required to fulfill the ALARA (As Low As Reasonably Achievable) principle. Manufactures may incorporate "preset" exposure settings for different sized individuals (Fig. 5.2) or specific imaging scan protocols (Fig. 5.3).
- **Automatic Exposure Control.** Automatic exposure control (AEC) is a dose reduction strategy used in most MDCT devices to optimize patient doses. AEC attempts to adjust and customize (i.e., modulate) tube current (mA) specifically for each patient according to the radiation intensity detected by using a short pre-examination (scout) exposure

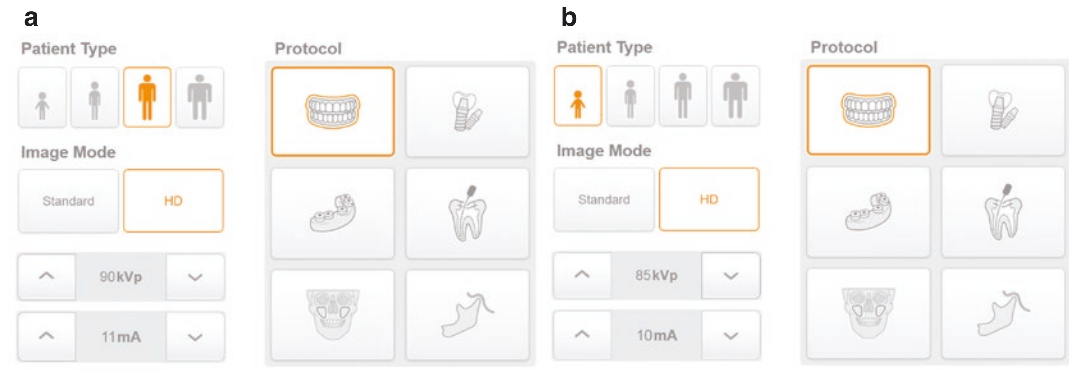

Fig. 5.2 Screen shot of exposure panel for a CBCT device (RayScan Alpha, LED Medical Diagnostics Inc., Vancouver, British Columbia, Canada) that adjusts exposure settings for different sized individuals. Exposure settings for a high definition scan (HD) of the dentition, (highlighted occluding teeth icon) for an "average" sized individual (**a**) (90 kVp and 11 mA) is higher than that for a child (**b**) (85 kVp and 10 mA)

Fig. 5.3 Screen shot of exposure panel for a CBCT device (Accuitomo 170, J. Morita, Kyoto, Japan) that has default exposure settings based on number of basis projection images. Manufacturer default exposure settings for a 360° standard (Std), 80 mm × 80 mm scan (HD) (**a**) (90 kVp and 5 mA), is identical to that of a 360° standard (Std) with a smaller FOV (40 mm × 80 mm) (**b**). Exposure settings for a 360° 80 mm × 80 mm scan with a greater number of basis projection images (HiFi) (**c**) requires an increased mA setting (7 mA)

(NewTom-FP; Quantitative Radiology s.r.l., Cefla Group, Verona, Italy) or using a exposure modulation during the rotation (SafeBeam™ technology, NewTom VGI evo/NewTom GiANO, Quantitative Radiology s.r.l., Cefla Group, Verona, Italy) (Pauwels et al. 2014a, b; Pauwels et al. 2015a, b, c). It is expected that widespread implementation of AEC in CBCT will avoid the need for manual adaptation of exposure parameters based on patient size (Pauwels et al. 2012).

Effects of Exposure Setting Adjustments

Manufacturer recommended default exposure settings should be adjusted with caution as each parameter has effects on the image quality and patient radiation exposure (Goulston et al. 2016). Any exposure setting adjustment should be directed towards reducing exposures to levels as low as diagnostically acceptable (ALADA principle), particularly for children (White et al. 2014).

- **mA.** The range of mA settings in available CBCT devices is extensive with most operating at less than 12 mA while some operate as high as 20 mA. mA may be adjustable on some units with higher levels producing darker images with less noisy image. However, patient effective dose increases proportionately, almost in a 1:1 ratio.
- **kV.** Most CBCT units operate in the range less than 90 kV, whereas a few can operate at higher kV, up to 120 kV. The effect of kVp on dose and image quality is more intricate owing to a combination of several energy-dependent

X-ray interactions (See Chap. 2). Higher kV units theoretically produce images with a higher contrast-to-noise ratio, particularly at lower exposures because of increased photon count and a decreased absorption ratio (Pauwels et al. 2014a, b). Adjustment of kV has an even greater effect on dose than does mA, with each decrease in 10 kV approximately halving dose if all other parameters remain the same (Pauwels et al. 2014a, b). In general, low kV units operate at higher mA.

The effect of changing one or both exposure factors on image quality and dose is not straightforward and should be balanced, ensuring that an adequate image quality is achieved at the lowest possible dose level. Currently (2017) there is still a low level of evidence on the effect of adjusting exposure settings (Goulston et al. 2016). Exposure setting adjustments may be considered in the following situations:

- **Patient size.** In clinical practice, mA changes are preferable to kVp changes to compensate for differences in patient size as the increase in noise for a given dose reduction is smaller for mA adjustments. Smaller patients (e.g., children) can be exposed using a lower (20–30% less) mA and produce images of acceptable diagnostic quality as for larger patients (Pauwels et al. 2015c, 2017).
- **Diagnostic task.** For specific diagnostic tasks requiring reduced image quality, mA can be reduced without reducing diagnostic efficacy (Pauwels et al. 2015c). Significant dose reductions can be achieved by reducing tube current by up to 50% without substantial loss of diagnostic quality for relatively low-resolution tasks such as assessment of the paranasal sinuses (Güldner et al. 2013), presurgical implant planning (Sur et al. 2010; Dawood et al. 2012; Panmekiate et al. 2012; Bohner et al. 2017), or orthodontic diagnosis (Kwong et al. 2008). However, for diagnostic tasks requiring images with optimal image quality, mA can be increased. For example, dental periapical diagnosis involving visualizing the periodontal ligament space and subtle changes in bone trabeculation may benefit from moderate increases in mA producing images with reduced noise.
- Similarly, a higher kVp may be considered in patients with high-density objects, such as teeth with root canal fillings (Chindasombatjareon et al. 2011; Vasconcelos et al. 2015; Helvacioglu-Yigit et al. 2016) or dental implants (Panjnoush et al. 2016; Vasconcelos et al. 2017), as beam hardening artifacts from these materials may be reduced. Conversely, lower kVp settings may also be considered for low discriminating diagnostic tasks such as orthodontics (Kwong et al. 2008).

5.1.1.2 Acquisition Parameters

Scan Time

The number of images comprising the projection data throughout the scan is determined by the frame rate (number of images acquired per second), the completeness of the trajectory arc, and the speed of the rotation. CBCT units may be configured to have a fixed or variable number of projection basis images comprising a single scan. This is usually referred to as *scan time*. Within the cost limitations of solid-state detectors used in CBCT construction and the need for short scanning time in a clinical setting, the number of images available for construction ranges from 150 to over 1000.

Increasing scan time provides more information to reconstruct the image and has multiple beneficial effects on the image including greater contrast resolution, improved signal-to-noise ratio producing “smoother” images, and reduces metallic artifacts (Fig. 5.4). This is usually associated with a longer duty cycle between patients to allow for cooling of the generator tube and a longer primary reconstruction time. For a given CBCT unit, a greater number of projections increases the amount of radiation a patient receives linearly—a scan comprising 1000 basis images delivers 2× the radiation dose to the patient than a scan reconstructed from 500 basis images. In accordance with the ALARA principle, the number of basis images should be optimized to produce an image of diagnostic quality considering the diagnostic task. Increasing scan time may be considered for patients with high-density objects within

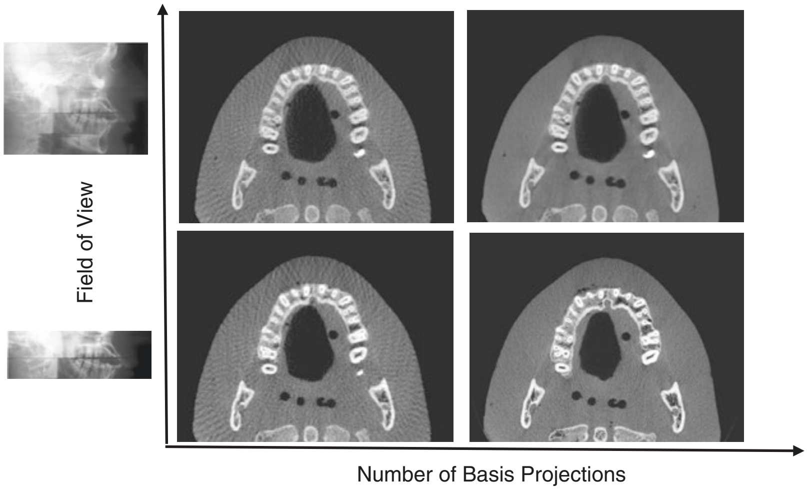

Fig. 5.4 Schematic plot of the effect of reduction in the field of view (FOV) and increasing the number of basis projection images (BPI) on improving the quality (noise and contrast resolution) of a representative axial image of the maxilla at the level of the nasopalatine canal. Four scans were performed on a Alderson-Rando® phantom (The Phantom Laboratory, Salem, NY) providing four volumes: limited FOV, Low number of BPI (*lower left*); limited FOV, high number of BPI (*lower right*); full FOV, low number of BPI, (*upper left*); and full FOV, high number of BPI. Optimal image quality is provided by reducing FOV and increasing the number of BPI (*lower right*)

the FOV, such as dental implants (Nardi et al. 2015), as artifacts from these materials may be reduced. However, this improvement in image quality may be negated by the possibility of motion artifacts (Nardi et al. 2015) and the introduction of inconsistencies in gray density measurements (Parsa et al. 2013).

Relationship Between Scan, Exposure, and Reconstruction Time

Most CBCT units acquire all projection images in a single rotation. The actual period in which the gantry revolves around the patient's head, or *scan time*, ranges from ~5 s to, at most, 40 s (Nemtoi et al. 2013). The total time that the X-ray generator is producing x-radiation for pulsed CBCT units, *exposure time*, is less than the actual scan time. This ranges from 2 s to approximately 12 s, with a maximum of up to 34 s.

Ideally, scan time should be comparable to panoramic radiography so that artifacts associated with subject movement are minimized. However, motion artifacts are common, reportedly ranging from 21 to 42% of CBCT examinations (Spin-Neto et al. 2015; Nardi et al. 2015). Correction algorithms to adjust for small patient movements and reduce the effects of motion artifacts have been proposed (Schulze et al. 2015) and advertised (Planmeca CALM™; Planmeca OY, Helsinki Finland) but as of 2017, not yet implemented. Different types of movements induce different artifacts, in different parts of the anatomy (Nardi et al. 2016). Artifacts can be described as smearing, double contour (Fig. 5.5), cancellous bone fading resulting from loss of trabeculae visibility and general unsharpness (Fig. 5.6). In general, movement of short duration may lead to double contours (bilateral or monolateral depending upon the angle of the scan at which they occur), whereas gradual movements result in blurring. The plane in which the artifact is most pronounced corresponds with the direction in which the movement occurs.

Reconstruction time is the time taken by the workstation computer for dataset reconstruction and varies depending on FOV, the number of basis images acquired, resolution and reconstruction algorithm and ranges from less than 30 s to over 5 min. The application of secondary reconstruction methods, such as iterative reconstruction for streak artifact reduction, can run considerably more than 5 min (Dong et al. 2013).

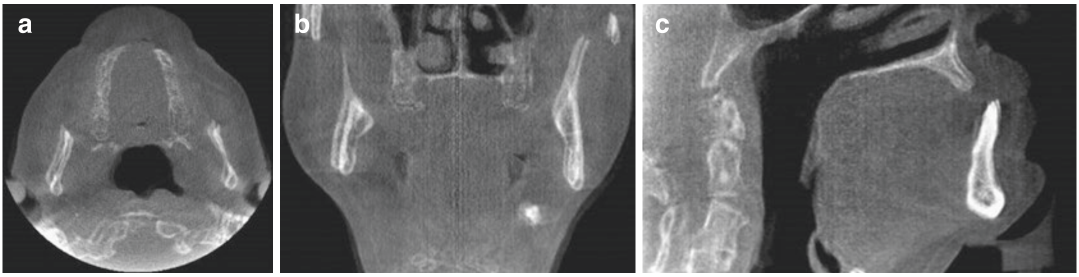

Fig. 5.5 Axial (**a**), coronal (**b**), and sagittal (**c**) CBCT images showing double contours indicating patient motion during the scan. Clearly discernible double contours like this are indicative of an artifact resulting from sudden patient moment during the scan (Images courtesy, Predrag Sukovic)

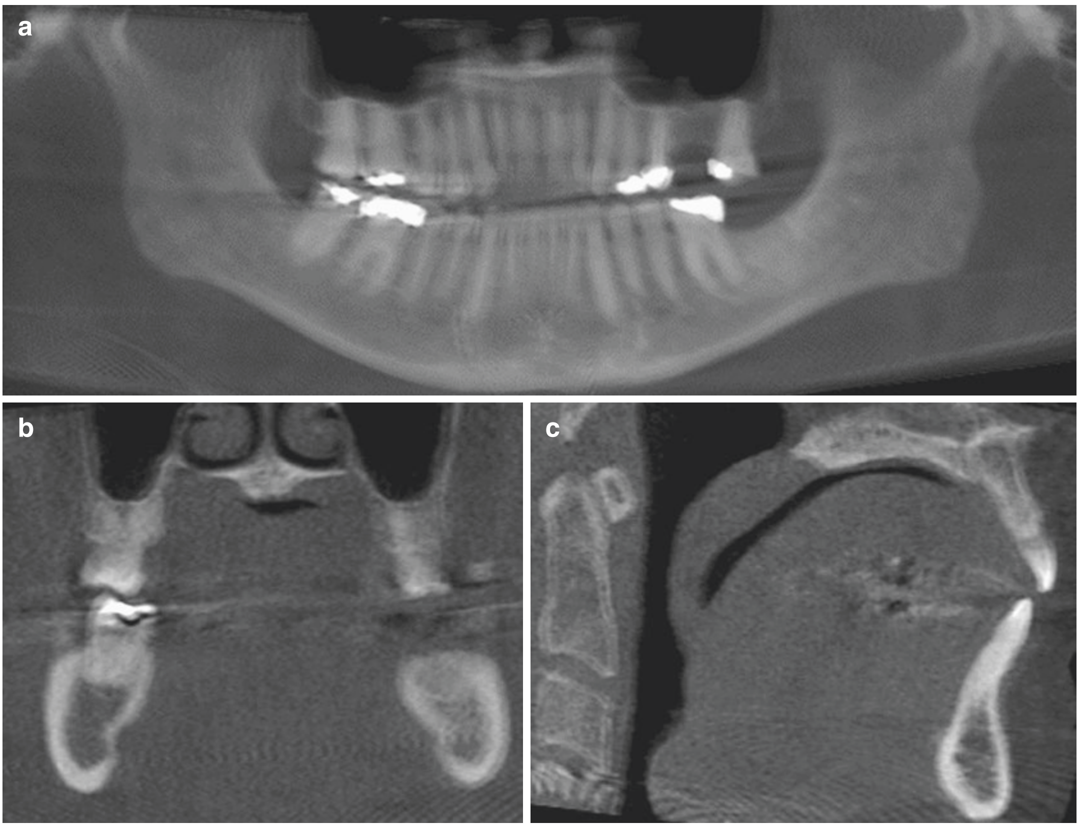

Fig. 5.6 Reformatted panoramic (**a**), coronal (**b**), and sagittal (**c**) CBCT images showing generalized unsharpness indicating continuous patient motion during the scan

Rotation Angle

Most reconstruction algorithms (e.g., FDK algorithm) require that projection data is acquired from a complete circular trajectory of 360°. This rotational angle is also called the scan arc or orbital angle. However, it is possible to reduce the rotation angle of the CBCT gantry and still reconstruct a volumetric dataset. This approach potentially reduces the scan time and allows the robotic arm of a panoramic platform to provide the gantry motion for CBCT imaging. Images produced by this method may have greater noise and suffer from reconstruction interpolation artifacts (Fig. 5.7). CBCT systems may therefore

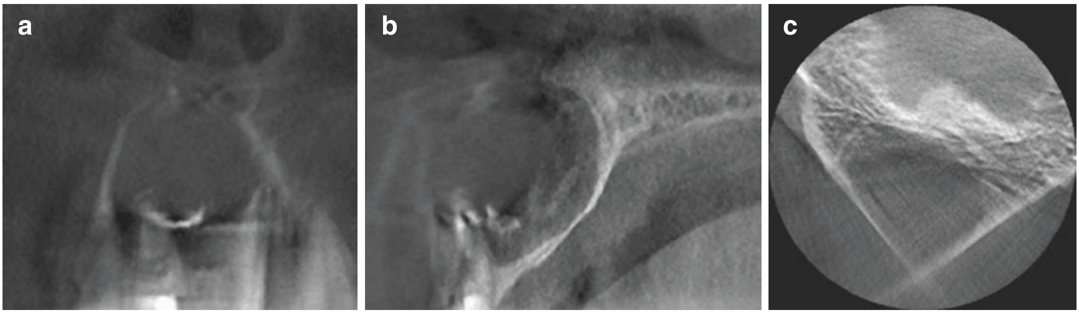

Fig. 5.7 Coronal (**a**), sagittal (**b**), and axial (**c**) images of a patient with a large nasopalatine canal cyst associated with the maxillary incisors. The scan was performed with a half-arch rotational angle scan (180°) and clearly demonstrates interpolation artifacts resulting in loss of detail of the extent and presence or degree of cortication of the buccal bony expansion

have three rotational angle configurations: (1) Fixed full (360°) trajectory, (2) Full but variable, usually with two trajectory settings, or (3) Fixed partial (Table 5.2).

For most diagnostic tasks, CBCT should be performed using the greatest scan arc available. In those units that provide reduction of rotation angle, degradation in image quality (Al-Okshi et al. 2017) may be offset by considerations of a proportionate reduction in patient radiation dose (Pauwels et al. 2014b). Reduction of trajectory arc is not recommended for the assessment of periodontal structures (Al-Okshi et al. 2017) and introduces inconsistency in grayscale density values (Parsa et al. 2013) however, may be considered for periapical diagnosis and implant planning (Lofthag-Hansen et al. 2011).

Field-of-View (FOV)

The volume of tissue of the patient's head irradiated during exposure is referred to as the FOV or scan volume. The dimension of the FOV is primarily dependent on the detector size and shape, beam projection geometry, and beam collimation. The shape of the scan volume is determined by the sensor technology and acquisition method.

Spherical FOVs are characteristic of image intensifier detectors. Most flat panel detector (FPD) systems produce a cylindrical FOV with a height and circular diameter. A few devices limit the FOV to the jaw shape, restricting the region of interest (ROI) to the dental structures. The CS 9000 3D (Carestream, Atlanta, Georgia, USA) stitches three cylindrical FOVs from consecutive exposures in the horizontal axis enough to cover a single jaw. An alternate method to cover the shape of the jaws is provided by the Accuitomo R100 (J. Morita Corporation, Kyoto, Japan) (Fig. 5.8). This maxillofacial CBCT device is the only unit which produces a convex triangular shape from a complex motion of the gantry during exposure, referred to as 3D Reuleaux Full Arch (patent pending; J. Morita Corporation, Kyoto, Japan).

Collimation of the primary X-ray beam limits x-radiation exposure only to the region of interest (ROI). Effective dose ranges for field of views (FOVs) with height ≤ 5 cm between 9.7 and 197.0 μSv, for FOVs of heights 5.1–10.0 cm between 3.9 and 674.0 μSv, and for FOVs >10 cm between 8.8 and 1073.0 μSv (Al-Okshi et al. 2015). An optimal FOV should be selected for each patient based on diagnostic task and the region of interest (ROI).

Reduction in the FOV usually can be accomplished mechanically or, in some instances, electronically. Mechanical reduction in the dimensions of the X-ray beam can be achieved by either pre-irradiation (reducing primary radiation dimensions) or post-irradiation (reducing the dimensions of the transmitted radiation, before it is detected) collimation. Currently most CBCT units use adjustable metallic shields as primary collimation at the radiation source. Electronic collimation involves elimination of data recorded on the detector peripheral to the area of interest. In this case there is no physical reduction in irradiation of the ROI by physical means. Both techniques reduce the amount of data for

Table 5.2 Rotational arcs of various CBCT Units (Based on data from Nemtoi et al. (2013) and current manufacturer websites)

Rotation arc	Manufacturer	Model	Rotational angle
Fixed full	Acteon Group[a]	WhiteFox, X-Mind Trium	360
	Takara Belmont Corporation[b]	Bel-Cat	360
	Carestream Dental[c]	CS 9500, CS 9300, CS 9300 Select	360
	Gendex USA/Imaging Sciences International[d]	Gendex GXCB-500, i-CAT NG (3D eXam)	360
	Genoray[e]	Papaya 3D plus/Volux 21C (China), Papaya 3D/Volux 21 (China)	360
	PaloDex Group[f]/KaVo Dental Corp.[g]	Orthoceph OC200 D VT, Scanora 3D, Cranex 3D	360
	PointNix Co., Ltd.[h]	Point 3D Combi 500	360
	Quantitative Radiology s.r.l.,[i]	NewTom 5G, NewTom Vgi, NewTom $Vgi_{evo,}$ NewTom GiANO, NewTom Go	360
	Vatech[j]	PaX-Duo3D, PaX-Reve3D, PaX-Zenith3D	360
	Yoshida Dental Mfg. Co. Ltd.[k]	PreXion 3D Excelsior Pro	360
Full variable	Asahi Roentgen Ind. Co. Ltd.[l]	AUGE ZIO CM, AUGE X ZIO CM, AUGE ZIO maxim, AUGE X ZIO maxim, Alioth CM	360/180
	J. Morita Mfg. Corporation[l]	3D Accuitomo 170, 3D Accuitomo 80	360/180
	Imaging Sciences International[d]/ KaVo[g]	i-CAT FLX, i-CAT FLX V series/KaVo 3D eXam + V series/KaVo ORTHOPANTOMOGRAPH OP 3D Vision	360/180
		i-CAT CLassic	360/72
	MyRay[m]	SkyView	360/190
	Planmeca Oy[n]	Promax 3D Mid, Promax 3D Plus	360/200
		Promax 3D Max	360/210
	Vatech[j]	Pax-Flex3D	360/240
		PaX-Uni3D (EU)/Suni 3D (USA)	360/220
	Yoshida Dental Mfg. Co. Ltd.[k]	PreXion 3D Elite	360/217
Fixed partial	J. Morita Mfg. Corporation[l]	Veraviewepocs 3De	180
	Carestream Dental[c]	CS 9000 3D	180
	Owandy[o]	I-Max Touch 3D	200
	Planmeca Oy[n]	Promax 3Ds, Promax 3D Classic	200
	Dentsply Sirona Imaging[p]	Orthophos SL 3D, Orthophos XG 3D	200
		GALILEOS Compact, GALILEOS Comfort	204

EU European Union, *USA* United States of America, *NG* next generation, *LFOV* limited field of view, *SFOV* standard field of view
[a]Milan Italy
[b]Somerset, New Jersey USA
[c]Atlanta, Georgia, USA
[d] Hatfield, Pennsylvania, USA
[e]Gyeonggi-do, Korea
[f]Tuusula Finland
[g]Biberach, Germany
[h]Seoul, Korea
[i]Cefla Group, Verona, Italy
[j]Giheung-gu, Korea
[k]Tokyo, Japan
[l]Kyoto, Japan
[m]Imola, Italy
[n]Helsinki, Finland
[o]Croissy-Beaubourg, France
[p]Bensheim, Germany

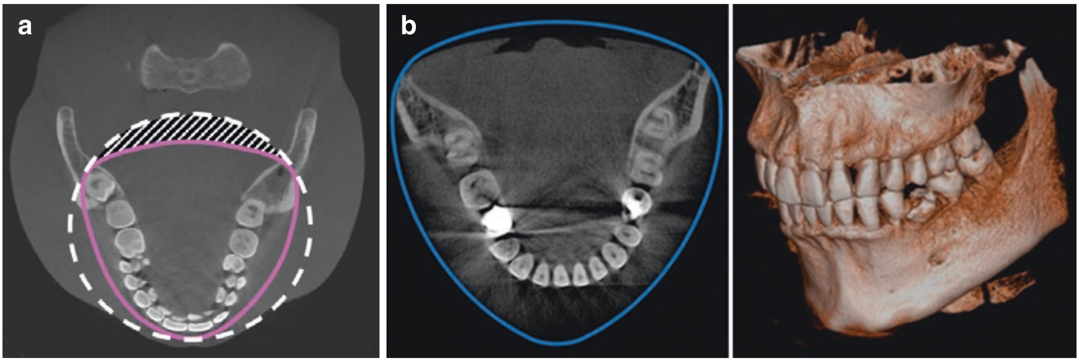

Fig. 5.8 Axial CBCT image showing the lower jaw with a cylindrical (*dashed line*) and 3D Reuleaux Full Arch (patent pending; J. Morita Corp., Kyoto, Japan) (*solid line*) FOV shapes superimposed (**a**) showing the difference in coverage and therefore reduction in dose achieved by conforming the FOV to the shape of the dental arch. Actual axial image shape and resultant volumetric acquisition achieved (**b**)

computational purposes and reduce reconstruction time; however, only pre-irradiation physical collimation results in reduced patient radiation exposure.

Effects of FOV size on image quality can be seen in some circumstances (Fig. 5.4). Larger FOVs increase the amount of scatter per detector area, reducing image quality (Lofthag-Hansen et al. 2011). In addition, larger FOVs coincide with a higher beam divergence at the edge of the FOV, which results in image quality deterioration. On the other hand, a FOV with a larger diameter reduces the "local tomography" effect of tissue outside the FOV (which is only partially exposed) on gray value uniformity. While an FOV height of 4–6 cm may be adequate for a mandibular scan, an FOV height of 8 cm or even up to 10 cm may be advisable for the maxilla if sinus augmentation procedures are anticipated to adequately demonstrate the ostiomeatal complex.

Resolution

- **Contrast Resolution**. The contrast resolution (ability to detect subtle differences in attenuation by differences in gray-level intensity) is device dependent and is influenced by several interacting acquisition variables (see Chap. 2). Maxillofacial CBCT images lack adequate grayscale sensitivity to discern subtle differences between soft tissues, such as between fluids and solid tumors, though are excellent for demonstrating air to soft tissue boundaries. Grayscale intensity values from CBCT images do not directly represent Hounsfield units (HU), the relative density of body tissues according to a calibrated gray-level scale, based on normalized-HU values for air (−1000 HU), water (0 HU), and dense bone (+1000 HU) (Bryant et al. 2008; Nackaerts et al. 2011; Molteni 2013). Several techniques and devices are currently being investigated to compensate for the deficiencies of CBCT acquisition such that derive gray density levels more accurately correlate with HU (Lagravere et al. 2006, 2008; Mah et al. 2010; Molteni 2013).
- **Spatial Resolution**. The spatial resolution of maxillofacial CBCT systems is primarily a function of detector nominal pixel size and fill factor; however, many interrelated factors contribute to the final maximum achievable resolution (see Chap. 2). Most manufacturers provide options for varying resolution of CBCT data. However, the number of pixels within the area matrix of a sensor that capture x-rays is fixed. For a given projection geometry and FOV, the acquired dataset is always acquired at the highest, default resolution. In some CBCT units, resolution can be increased by altering projection geometry, reducing the object to focal spot distance. More often, electronic pixel binning is used to provide reconstructed images with voxel resolution less than that acquired. Pixel binning is the process of combining charge from adjacent electronic

"wells" from the detector during readout. The two primary benefits of binning are improved contrast due to an improved signal-to-noise ratio and the ability to increase frame rate, albeit at the expense of reduced spatial resolution.

- Higher resolution may be considered desirable for many tasks in dentistry demanding accuracy to the level of the detail of approximately the periodontal ligament space (i.e., approximately 0.2 mm or less) (Fig. 5.9). Images taken at high resolution often have reduced brightness and contrast, increased noise (when displayed in thin slice thickness), and require increased reconstruction time. While increased image resolution in some maxillofacial CBCT units does not affect changes in exposure parameters, some manufacturers incorporate reduced-dose exposure protocols for low-resolution settings.

As CBCT data is inherently volumetric, it is possible to resample the dataset to provide images with higher resolutions than originally reconstructed. This is known as *reconstructed resolution*. Previous iCAT models (Classic and Next-Generation (17/19), Imaging Sciences International, Hatfield, PA, USA) and the current 3D Accuitomo 170 (J. Morita Corp., Kyoto, Japan) allow for reconstructed resolution. The 3D Accuitomo 170 "zoom reconstruction" feature is unique in that for large FOV acquisitions, often displayed at low resolutions to reduce reconstruction time and file size, a small region of interest within the original scan can be identified and a small FOV with an 80 μm voxel resolution can be reconstructed from the original data (Fig. 5.10). As with other forms of digital radiography, acquired nominal resolution based on specified physical pixel or voxel values should be distinguished from the actual acquired resolution achieved due to the various constraints within the total imaging chain and reconstructed resolution.

Calibration

Maxillofacial CBCT acquisition and image reconstruction result from a balance and coordination of an invariant and reproducible rotational geometric relationship between the X-ray generator and image sensor and the fidelity of the image sensor (Wischmann et al. 2002). Any disruption or disturbance in this geometric relationship, degradation of the image sensor, or variabilities in the preprocessing reconstruction algorithm will produce any number of scanner-related artifacts (See Chap. 2) (Schulze et al. 2011; Pauwels et al. 2015a).

Optimal image quality should incorporate a quality assurance (QA) plan including periodic calibration of both geometric and electronic components (see Chap. 7) (Vassileva and Stoyanov 2010; Health Protection Agency 2010). Tube- or detector-related geometric mismatch (Fig. 5.11) or preprocessing algorithmic incongruities (Fig. 5.12) may produce variations in signal intensities resulting in obvious or subtle disruptions in anatomic structures. Geometric artifacts are of particular importance in CBCT systems that use X-ray beam projection and sensor offset or data stitching techniques to increase the region of interest with a smaller sensor (See Chap. 2). Local artifacts in the digital sensor induce (usually circular) artifacts in the reconstructed slices (Fig. 5.13). The geometric accuracy of the CBCT unit should be regularly checked by use of a specific QA device. Calibration requires the absence of any object between the X-ray source and sensor, otherwise "ghost shadows" of the object will be present in subsequent images (Fig. 5.14).

5.2 Generic Steps to Optimize Volumetric Data Display

Most dental imaging software programs present CBCT data on the monitor with a default display. This is commonly as a series of three panes demonstrating secondary planar reconstructed images in one of each of three orthogonal planes (axial, sagittal, and coronal) at a defaulted thickness with a fourth pane demonstrating a volumetric image (Fig. 5.15). Each panel of the display software presents one of a series of contiguous images in that plane. Each image is interrelational such that the location of the image in the sequence within the volume can be identified in each of the other two planes.

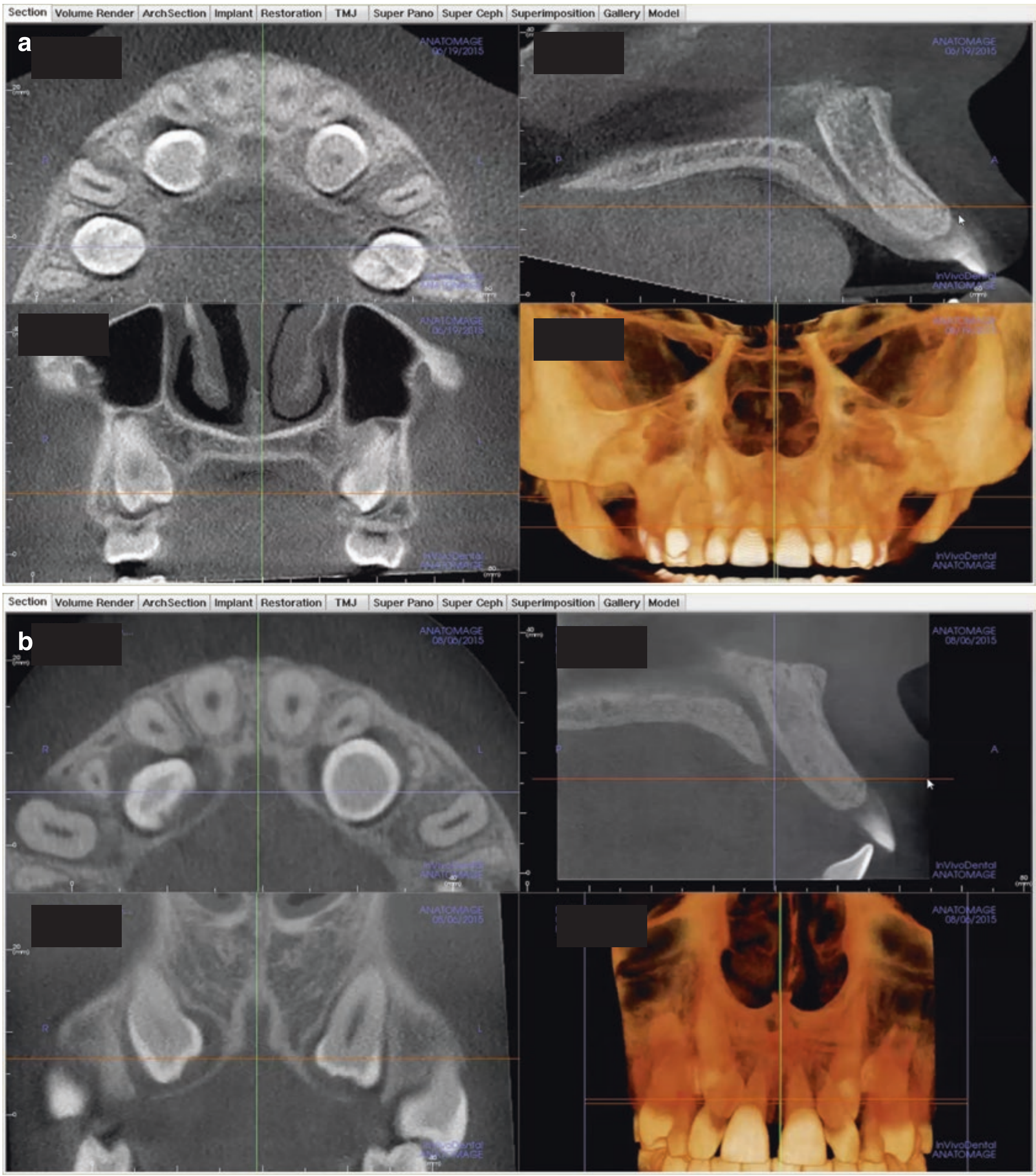

Fig. 5.9 Default display of a dental imaging software (InVivo, Anatomage, San Jose, California USA) showing orthogonal projections and volumetric rendering of two CBCT examinations—one performed at 0.4 mm (**a**) and a second at 0.08 mm voxel resolution (**b**)—for an individual with bilateral impacted and unerupted maxillary canines. Orthogonal images at the higher resolution (**b**) more clearly show the periodontal ligament space and subtle root resorption associated with the adjacent lateral incisors

CBCT data should be considered as a volume to be explored from which selective images are extracted. Consequently volumetric data is reformatted depending on the diagnostic task for which the acquisition was performed. As a rule of thumb for formatting, thin images provide structure detail whereas thick images provide structural relationships.

Technically four generic steps provide an efficient and consistent systematic and

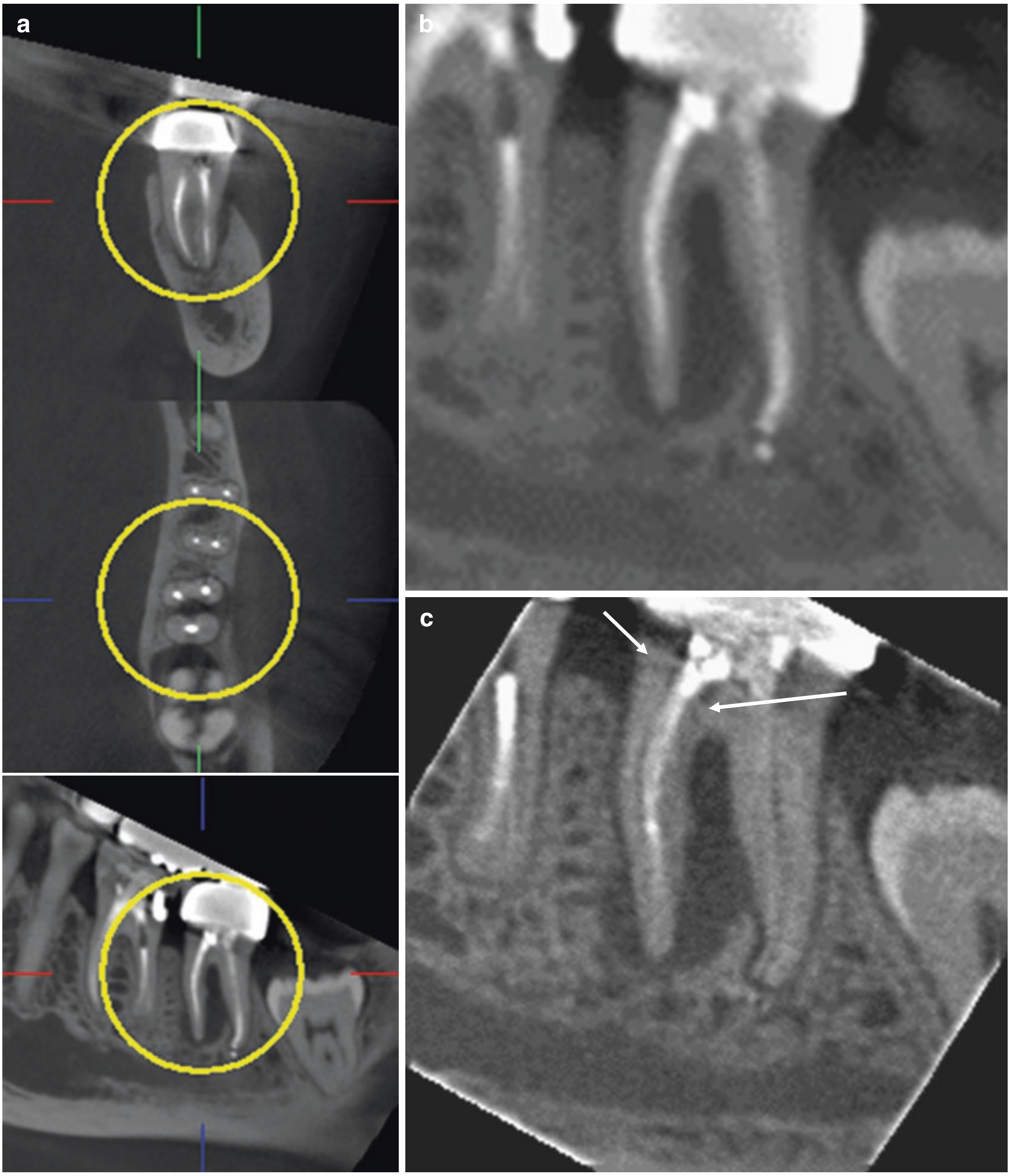

Fig. 5.10 Cross-sectional, axial, and parasagittal maxillofacial CBCT orthogonal images (3D Accuitomo 170, J. Morita Corp., Kyoto, Japan) (**a**) of a mandibular left root canal filled second molar for a patient who presents with local pain and suspicion of a fractured tooth. A cropped, magnified sagittal image at the standard resolution (0.25 mm voxel size) (**b**) shows an apical hypodensity and associated furcation bone loss. Reconstructed resolution or "zoom reconstruction" was applied to a limited spherical region within the FOV of the original volumetric dataset (*yellow circle*—**a**). Comparable sagittal image of the reconstructed volume (**c**) at a higher 0.08 mm voxel resolution demonstrates a root fracture through the cervical portion of the mesial root extending into the furcation (*arrows*) accounting for the failure of the root canal treatment

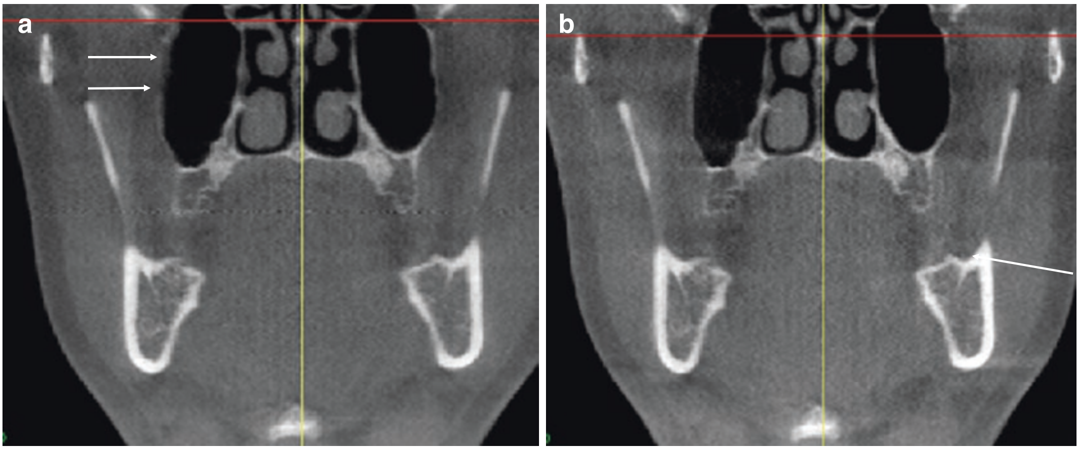

Fig. 5.11 Coronal CBCT image before (**a**) and after (**b**) geometric calibration showing subtle but noticeable regional cortical unsharpness in the supero-lateral wall of the maxillary sinus. This could be mistakenly be considered as a discontinuity in the wall with subsequent diagnostic implications (Images courtesy, Predrag Sukovic)

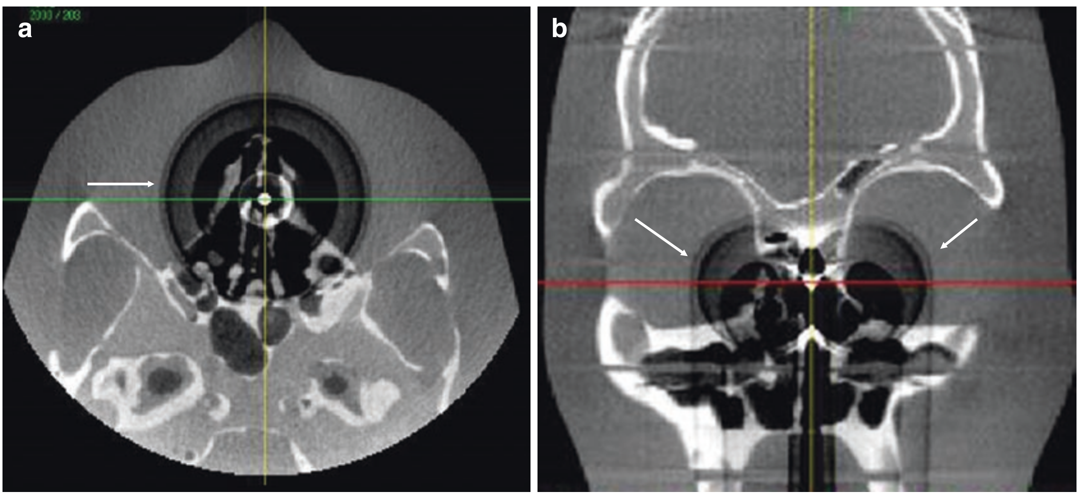

Fig. 5.12 Axial (**a**) and coronal (**b**) CBCT images demonstrating a semicircular and circular hypodense ring artifact. This artifact is indicative of bad linear gain in the preprocessing of the sensor primary data. Calibration of the sensor will remove this diagnostically unacceptable artifact (Images courtesy, Predrag Sukovic)

methodological approach to optimize CBCT image display prior to image interpretation. This approach is not equally applicable to all dental software, but serves as a guide to improve the visibility of anatomic structures.

5.2.1 Reorient the Data

The first step in optimizing display of the volumetric dataset is to ensure that the orthogonal projections provide an adequate representation of the imaged object. This requires that the orthogonal planes are perpendicular to the area of interest. This geometric transformation is important in various clinical scenarios including minimizing parallax error in the measurement of alveolar bone height (Fig. 5.16), detection of the inferior alveolar canal and its relationship to the roots of the third molar (Fig. 5.17), and assessment of craniofacial anomalies (Fig. 5.18).

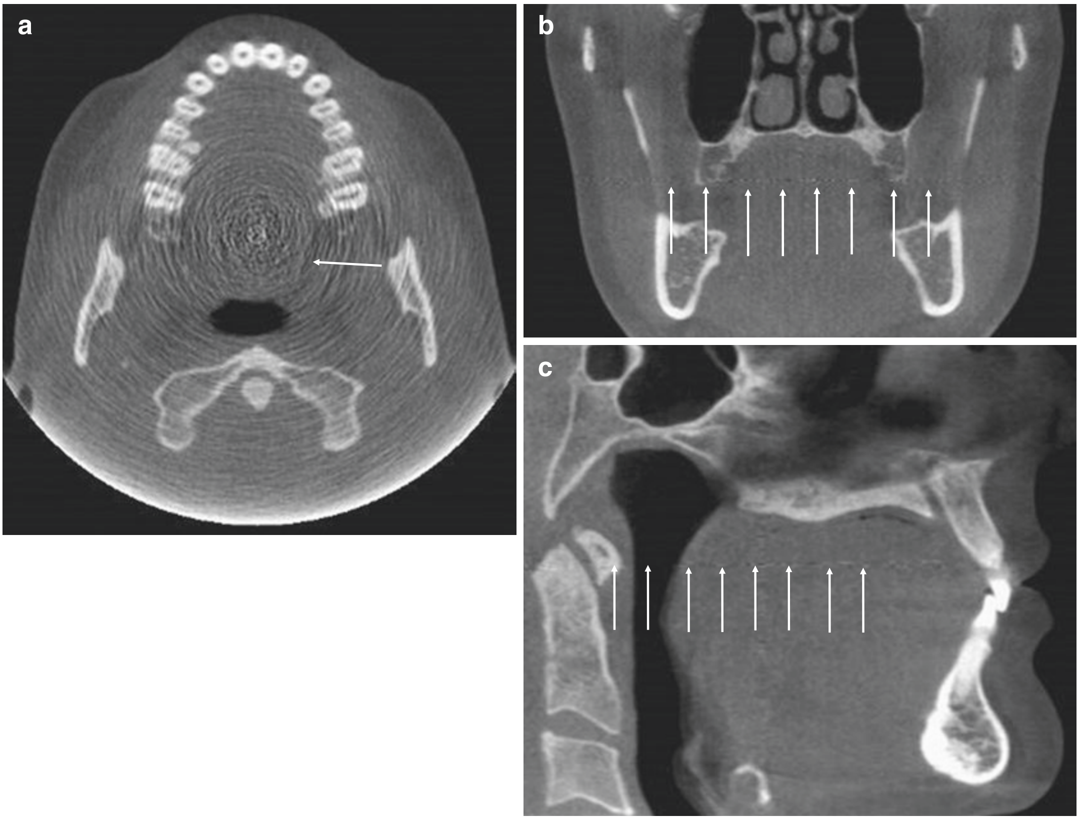

Fig. 5.13 Axial (**a**) CBCT image demonstrating radial hypo- and hyperdense artifacts with the epicenter being the center of rotation. Coronal (**b**), and midsagittal (**c**) images show the localized horizontal linearity of the artifact indicative of a bad detector row (Images courtesy, Predrag Sukovic)

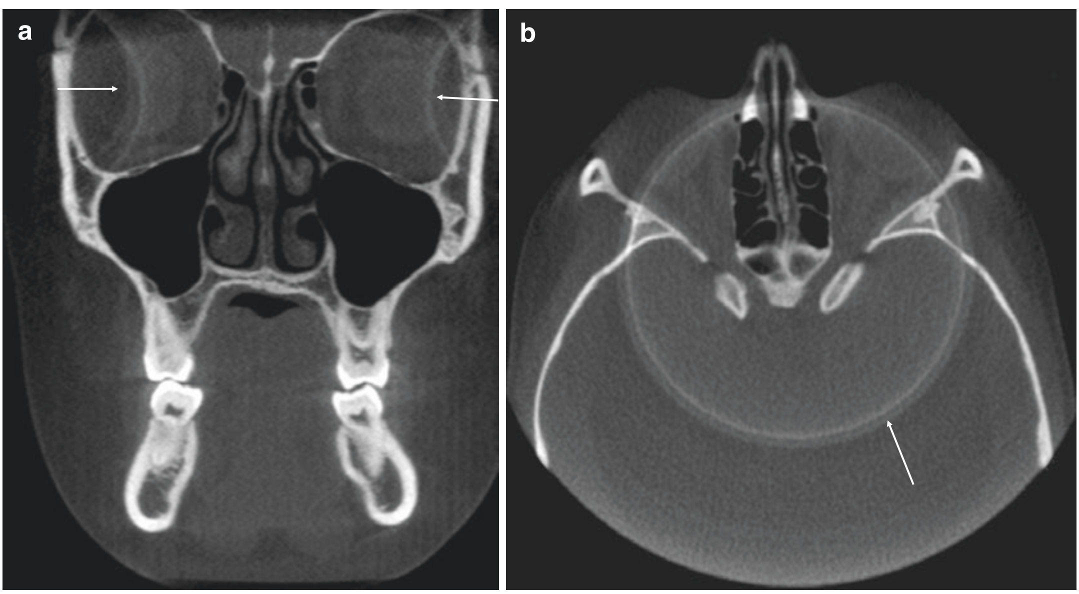

Fig. 5.14 Coronal (**a**) and axial (**b**) CBCT images demonstrating a semicircular and circular hyperdense ring artifact. Prior calibration of the CBCT unit was performed with the lateral plastic head restraint with circular head supports in position resulting in “ghosting” of this structure in subsequent images

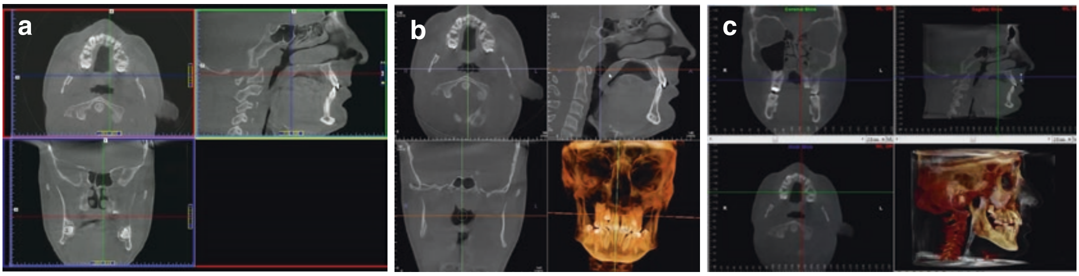

Fig. 5.15 Representative screen shots of the default display of three dental software programs using the same volumetric dataset: iCATVision (Imaging Science International, Hatfield, Pennsylvania, USA) (**a**); In Vivo (Anatomage, San Jose, California, USA) (**b**); and Dolphin Imaging (Dolphin Imaging and Management Solutions, Chatsworth, California, USA (**c**)

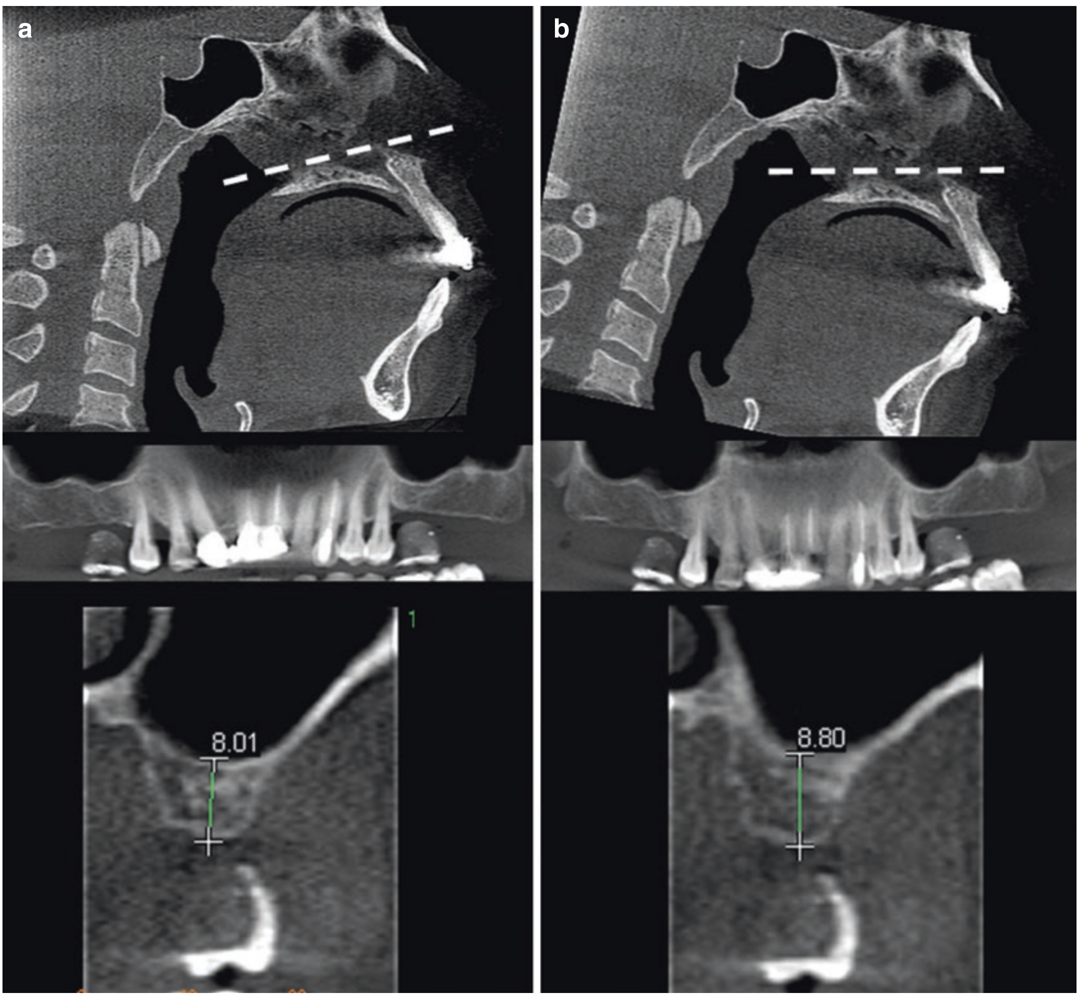

Fig. 5.16 Series (from *top* to *bottom*) of midsagittal, reconstructed panoramic and cross-sectional image of the maxillary left first molar region showing original display (**a**) and after spatial geometric transformation (tilting) of the volumetric dataset in the sagittal plane (**b**) to provide alignment of the palatal plane with the axial plane (approx. 15°). Measured values in comparative trans-axial cross sections of geometrically transformed dataset (*lower images*) are greater by approximately 0.8 mm or 10%

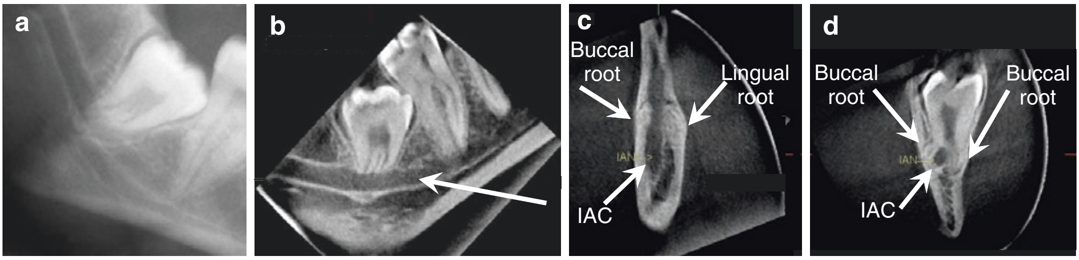

Fig. 5.17 Conventional cropped panoramic image (**a**) and parasagittal (**b**), cross-sectional (**c**, **d**) limited FOV CBCT images show reorientation of volumetric dataset to provide orthogonal images perpendicular to the inferior alveolar canal (IAC). The panoramic image shows the mesio-angular complete bony impaction of the right third molar and superimposition of the IAC over the apices of the roots of this tooth. The angle of the IAC to either the occlusal and mandibular plane is approx. 80° therefore standard trans-axial cross-sectional imaging will not provide accurate representation of the relationship of the IAC to the roots of this molar because of projection parallax. Optimal image display is achieved by rotating the volume such that the sagittal plane (**b**) is parallel to the long axis of the mandible and the axial plane is parallel to the occlusal plane of the impacted molar. This spatial geometric transformation ensures that resultant trans-axial images (**c**, **d**) clearly demonstrate the route of the IAC between both buccal and lingual roots and curvature of the roots around the IAC

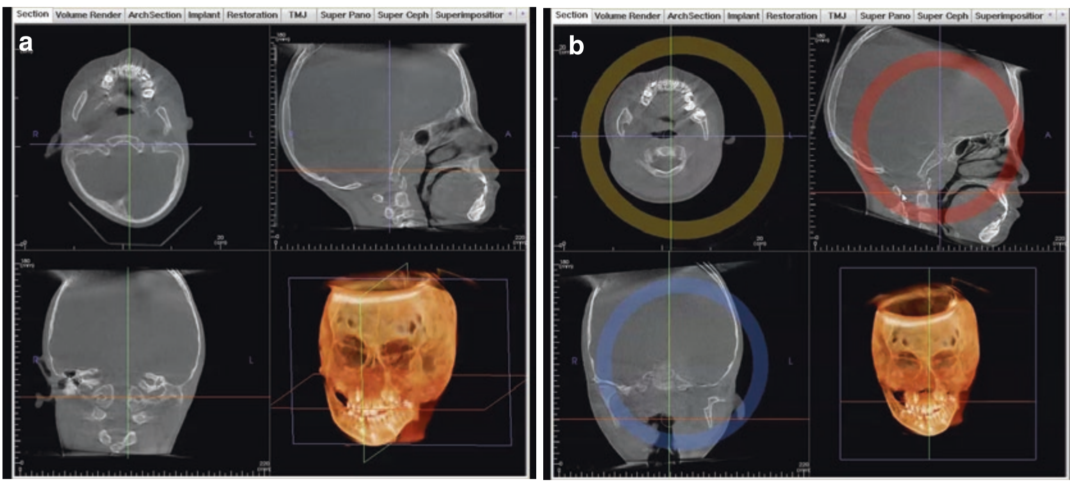

Fig. 5.18 Default window comprising four panes (axial, sagittal, coronal, and volumetric) of a child with a severe craniofacial deformity showing original display (**a**) and after spatial geometric transformation of the volumetric dataset (**b**) to provide alignment of the Frankfurt Horizontal (sagittal), midsagittal plane (coronal), and intercondylar plane (axial). In the software shown, the colored circles superimposed in the orthogonal images assist to rotate the planes

Before proceeding in correcting, exploring, and reformatting volumetric data, it is important to apply a spatial geometric transformation to align the orthogonal planes to a standard orientation. As CBCT volumetric datasets are isotropic, dental imaging software may provide one of two methods to achieve this:

- **Reorient the volume.** The entire volume can be reorientated such that the patient's anatomic features are realigned to specific orthogonal reference planes (e.g., InVivo, Anatomage, San Jose, California USA; NNT 6.0, QR Verona, Verona, Italy and: Dolphin Imaging, Dolphin Imaging and Management Solutions, Chatsworth, California, USA) (Figs. 5.19 and 5.20).
- **Reorient the orthogonal planes.** Alternately, the volumetric dataset remains visually invariant and the orthogonal planes are

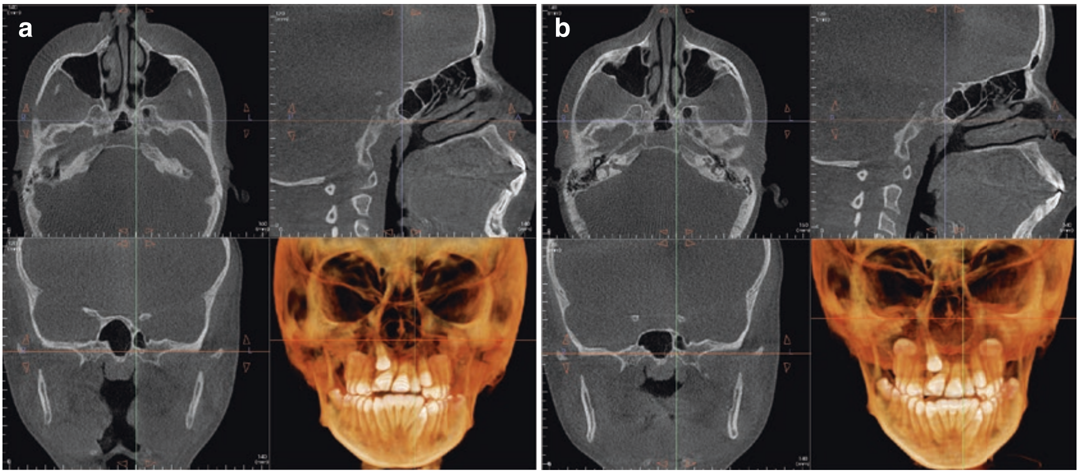

Fig. 5.19 Example of default dental software display (InVivo, Anatomage, San Jose, California, USA) before (**a**) and after (**b**) adjustment of axial, sagittal, and coronal planes. In this software the orientation of the volume, as shown by the volumetric rendering (*lower right*) is reoriented using *arrows* (*open red*) associated with the respective panes to more accurately represent the entire maxillofacial region

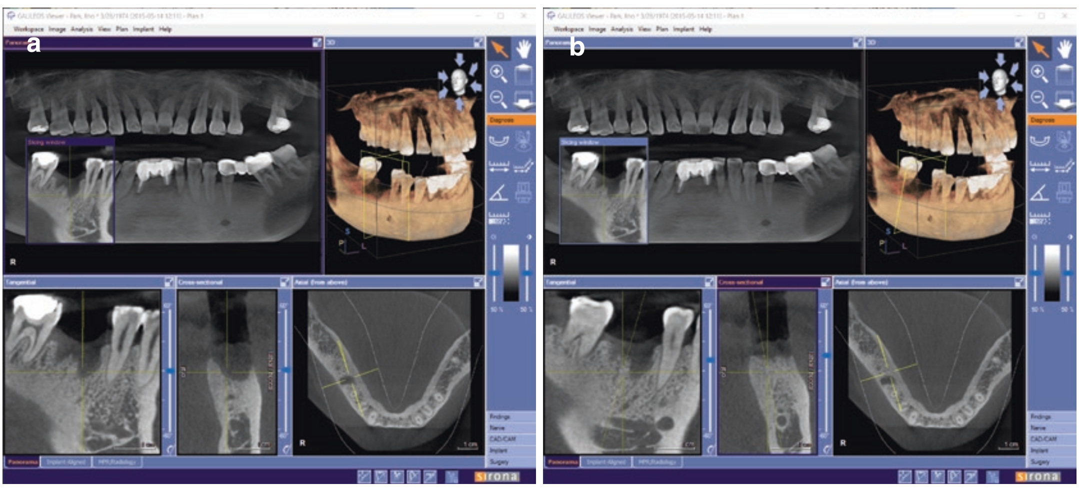

Fig. 5.20 Example of default dental software display (Galaxis, Dentsply Sirona Imaging, Bensheim, Germany) before (**a**) and after (**b**) adjustment of parasagittal (called tangential) and coronal (called cross-sectional) planes. In this software the orientation of the volume, as shown by the volumetric rendering (upper right), remains the same and the coronal (cross-sectional) and parasagittal (tangential) planes are adjusted using sliders to adjust the respective panes to more accurately represent the available edentulous area in the right mandibular molar region

adjusted (e.g., Galaxis/Sidexis 4, Dentsply Sirona Imaging, Bensheim, Germany; OnDemand3D, CyberMed, Seoul, Korea; NNT 6.0, QR Verona, Verona, Italy; and Kodak Dental Imaging Software 3D module [KDIS], Carestream, Atlanta, Georgia, USA) (Figs. 5.20, 5.21, 5.22 and 5.23).

Many planes on interrelational orthogonal displays may be used for reference.

- **Sagittal Planes.** The following planes can be used to adjust the vertical (y–z) axis:
  – *Inferior alveolar canal (IACP) plane.* Parasagittal plane transecting the length of

a
b

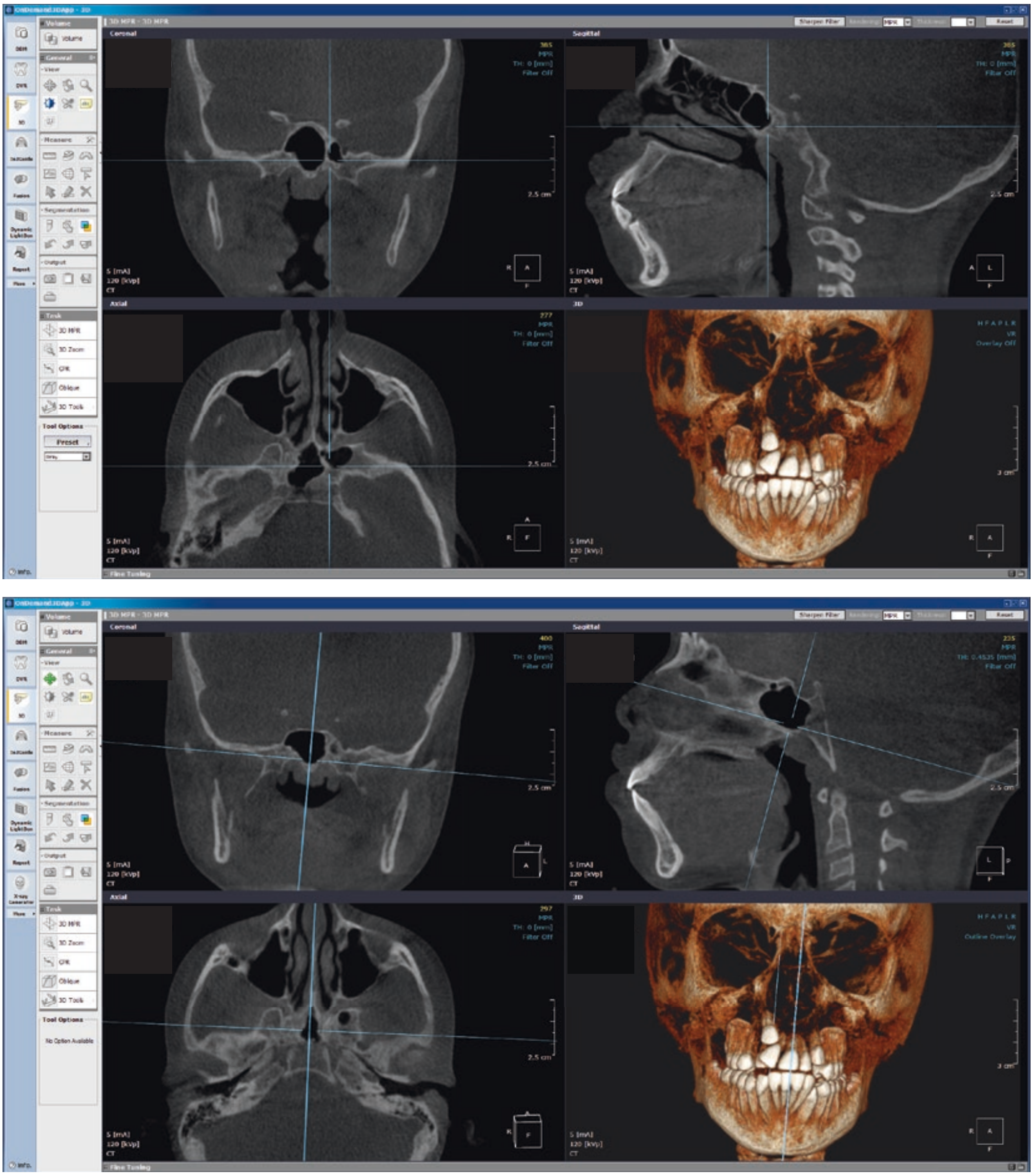

Fig. 5.21 Example of default dental software display (OnDemand3D, CyberMed, Seoul, Korea) before (**a**) and after (**b**) adjustment of axial, sagittal, and coronal planes. In this software the orientation of the volume, as shown by the volumetric rendering (*lower right*), remains the same and the orthogonal planes are adjusted using the superimposed multipurpose cross-hairs (*blue lines*) associated with the respective panes to symmetrically reorient the planes to the entire maxillofacial region

the IAC in the region of the mandibular third molar. Used in third molar assessments (Fig. 5.24)

– *Midsagittal plane (MSP).* Plane transecting the middle of the hard palate, anterior nasal spine, crista galli, and the middle of the occipital basilar bone. Used in orthodontic assessments (Fig. 5.25).
– *Long axis of the tooth (LATs).* Parasagittal plane transecting the long axis of the tooth

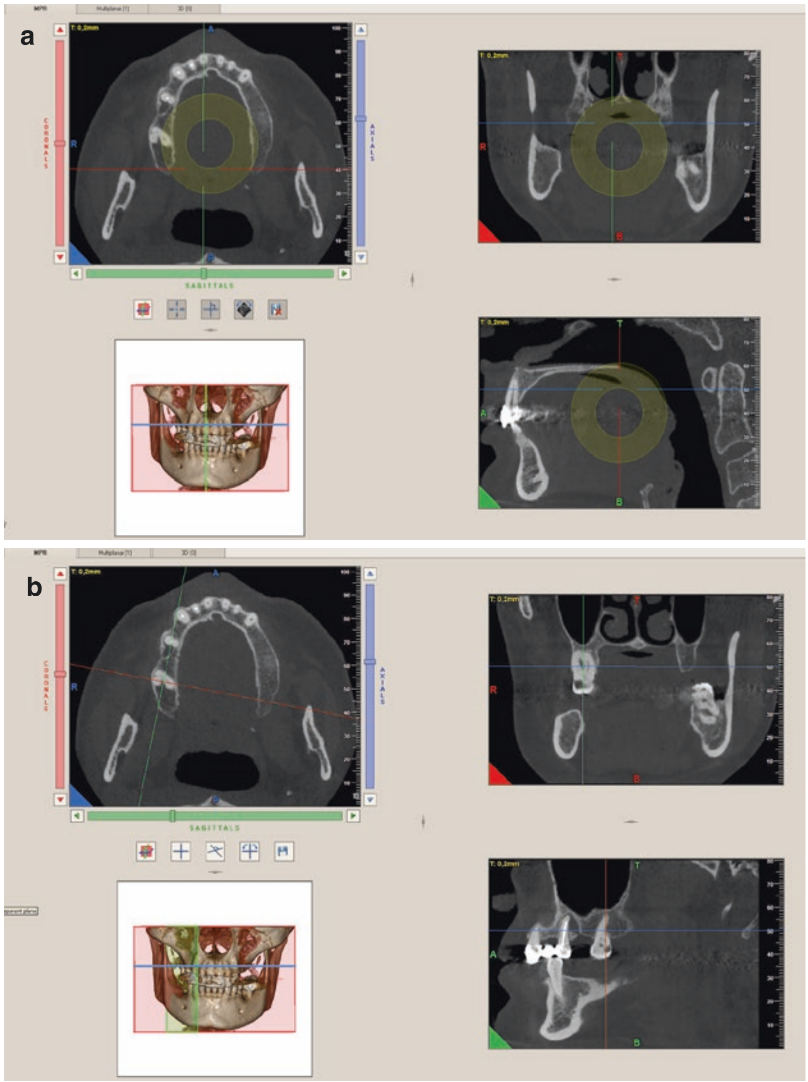

Fig. 5.22 Example of default software display (NNT 6.0, QR Verona, Verona, Italy) showing (**a**) the axis reorientation screen enabling the user to rotate the imaging volume with respect to the three orthogonal planes. An alternate screen (**b**) shows a different function of the NNT software that permits the reconstruction of multiple oblique non-orthogonal planes based on the diagnostic need. In this example, an oblique section of the maxillary right posterior region is identified by orienting the green line on the upper left pane and a parasagittal image reconstructed (*lower right pane*)

(middle of the occlusal surface/incisal edge and apical terminus of the root of the tooth) (Fig. 5.26).

- **Axial Planes.** The following planes can be used to adjust the horizontal (x–z) axis:
  - *Frankfort Horizontal (FH).* The imaginary plane transecting the most superior extent of the external auditory meatus and the most inferior portion of the orbital rim bilaterally. Used in orthodontic assessments (Fig. 5.27).
  - *Intercondylar plane (ICPa).* Imaginary axial plane transecting the medial or lateral poles of the mandibular condyles and parallel to FH. Used in TMJ assessment (Fig. 5.28).
  - *Occlusal plane (OP).* Imaginary plane transecting and parallel to the occlusal surfaces of the crowns of the teeth equally bilaterally (Fig. 5.29).
  - *Palatal plane (PP).* Imaginary plane transecting and parallel to the hard palatal (Fig. 5.30).
  - *Long axis of the tooth (LATa).* Axial plane transecting the long axis of the tooth (middle of the occlusal surface/incisal edge and apical terminus of the root of the tooth) (Fig. 5.25).

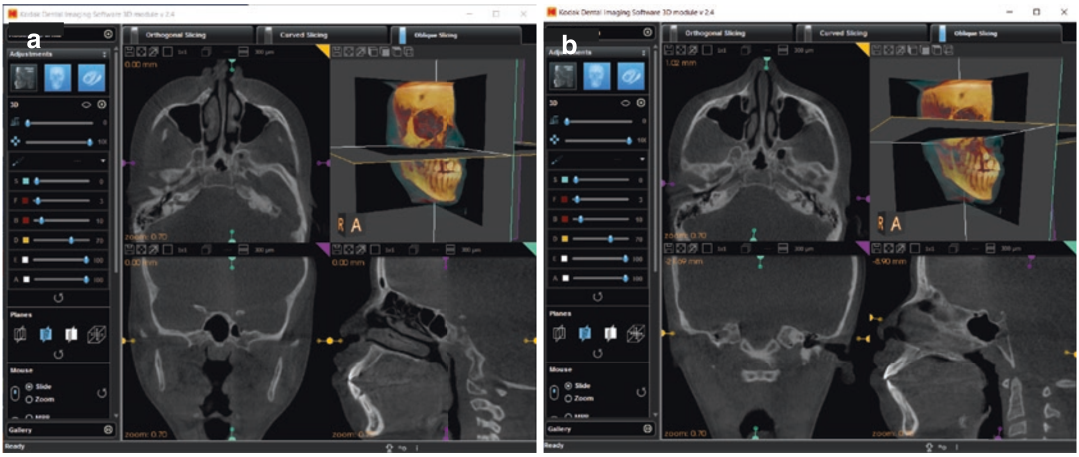

Fig. 5.23 Example of default dental software display (KDIS 3D module, Carestream, Atlanta, Georgia, USA) before (**a**) and after (**b**) adjustment of axial (*orange*), sagittal (*turquoise*), and coronal (*purple*) planes. In this software the orientation of the volume, as shown by the volumetric rendering (*upper right*), remains the same visually and the orthogonal planes are adjusted using the superimposed cross-hairs (*orange*, *purple,* and *green lines*) associated with the respective orthogonal images to symmetrically reorient the planes to the entire maxillofacial region

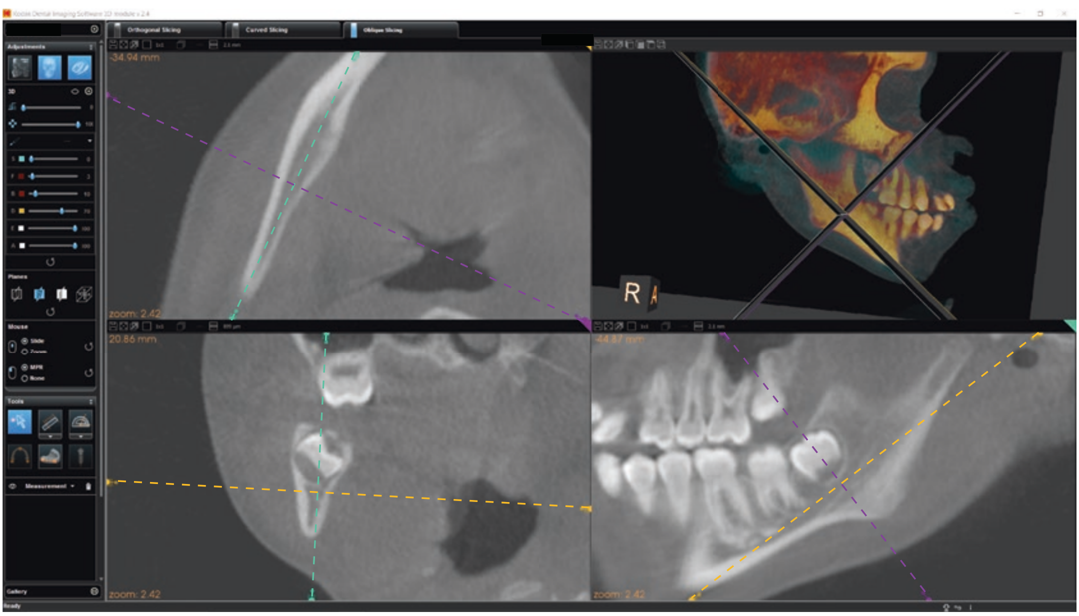

Fig. 5.24 Example of default dental software display (KDIS 3D module, Carestream, Atlanta Georgia, USA) showing the adjustment of the sagittal, coronal, and axial planes relative to the inferior alveolar canal plane (IACP, *orange*) and resultant orthogonal images

- **Coronal Planes**. The following planes can be used to adjust the vertical (*y*–*x*) axis:
  - *Interorbital plane (IOP).* An imaginary coronal plane transecting the most anterior-inferior portion of the orbital rim bilaterally and perpendicular to FH (Fig. 5.31).
  - *Infraorbital foraminae plane (IOFP).* The imaginary plane transecting the infraorbital foramina bilaterally and perpendicular to FH (Fig. 5.32).
  - *Intercondylar plane (ICPc).* Imaginary coronal plane transecting the medial or lateral poles of the mandibular condyles. Used in TMJ assessment (Fig. 5.28).
  - *Inter-porionic axis (IPAc).* Imaginary coronal plane transecting the most superior

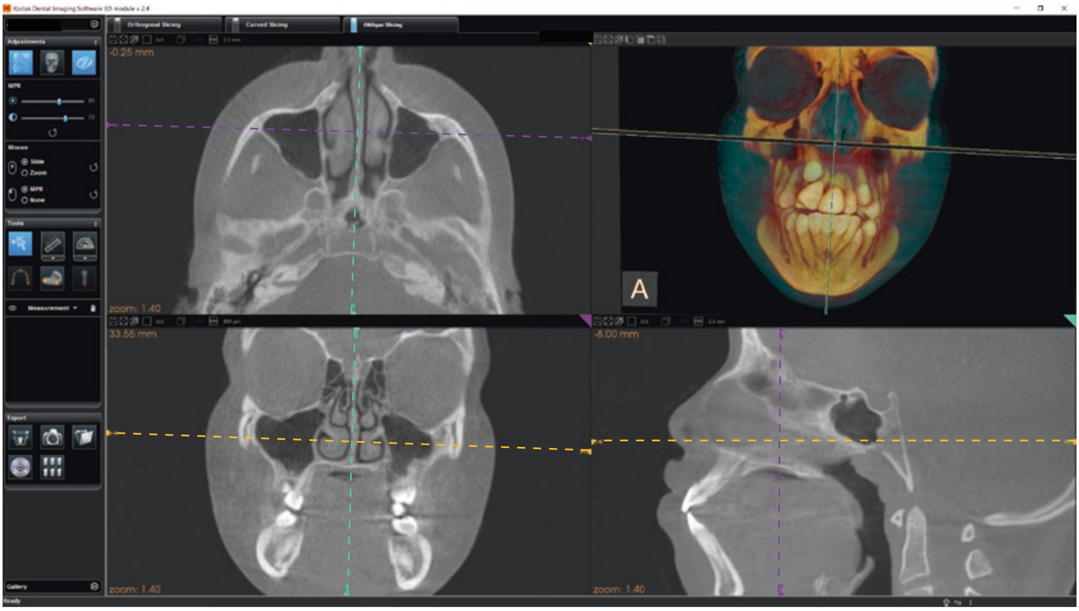

Fig. 5.25 Example of default dental software display (KDIS 3D module, Carestream, Atlanta Georgia, USA) showing the adjustment of the sagittal, coronal, and axial planes relative to the midsagittal plane (MSP, *turquoise*) and resultant orthogonal images

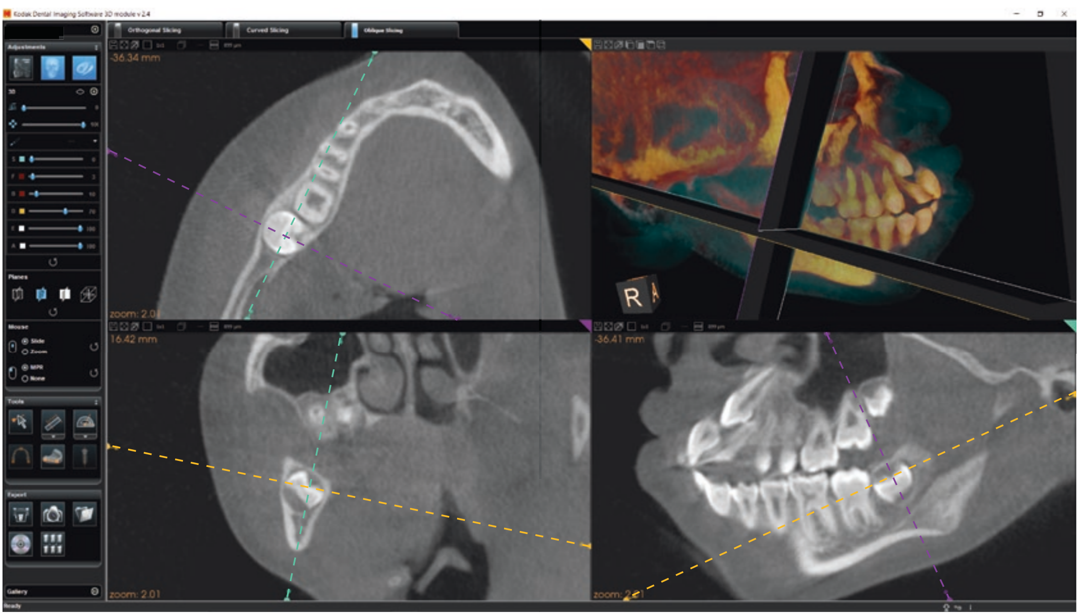

Fig. 5.26 Example of default dental software display (KDIS 3D module, Carestream, Atlanta Georgia, USA) showing the adjustment of the sagittal, coronal, and axial (*orange*) planes relative to the long axis of the tooth (LATs, *turquoise*; LATc, *purple*; LATa, *orange*) and resultant orthogonal images

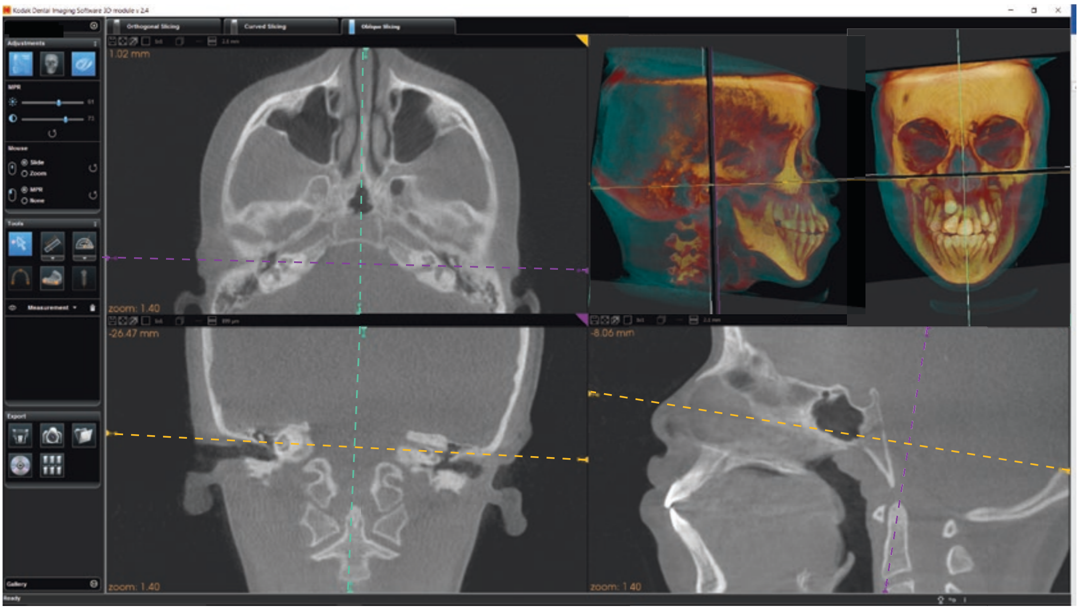

Fig. 5.27 Example of default dental software display (KDIS 3D module, Carestream, Atlanta Georgia, USA) showing the adjustment of the sagittal, coronal, and axial (*orange*) planes relative to Frankfort Horizontal (FH, *orange*) and resultant orthogonal images

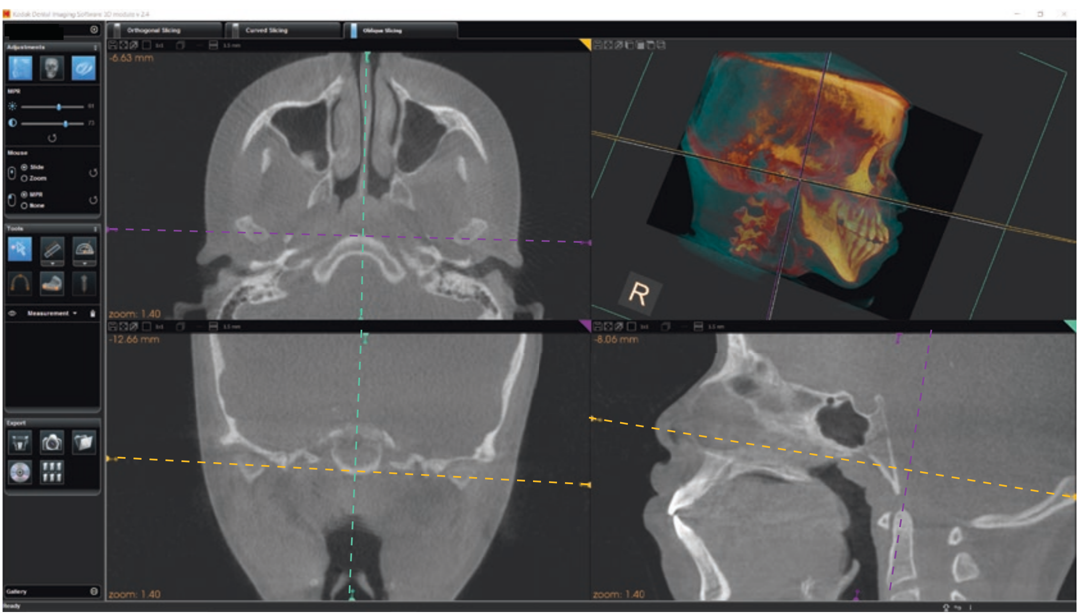

Fig. 5.28 Example of default dental software display (KDIS 3D module, Carestream, Atlanta Georgia, USA) showing the adjustment of the sagittal, coronal, and axial (*orange*) planes relative to the axial and coronal intercondylar plane (ICPa, *orange*; ICPc, *purple*) and resultant orthogonal images

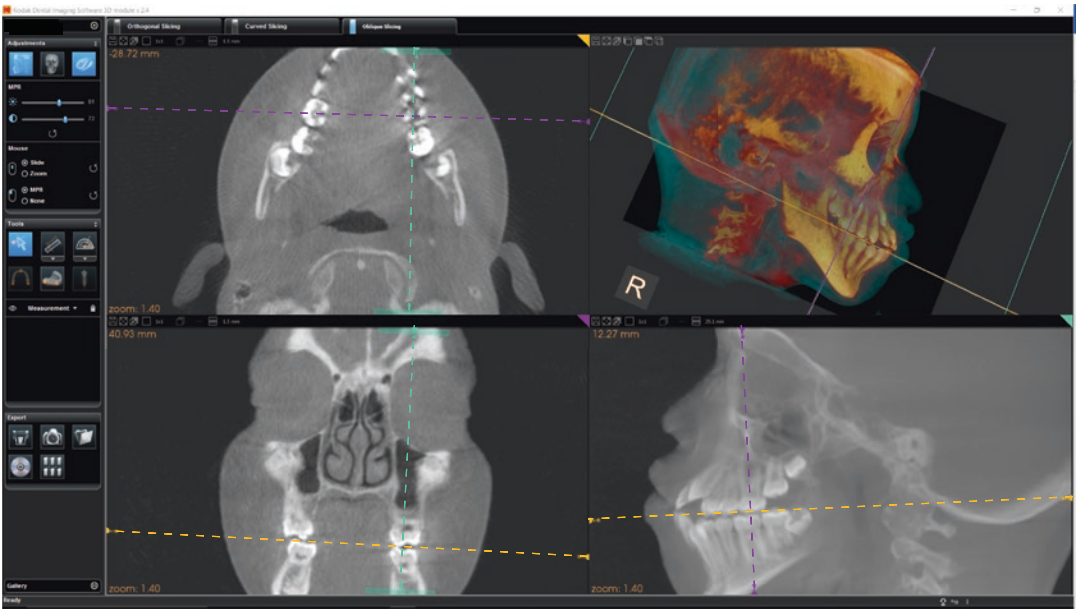

Fig. 5.29 Example of default dental software display (KDIS 3D module, Carestream, Atlanta Georgia, USA) showing the adjustment of the sagittal, coronal, and axial (*orange*) planes relative to the occlusal plane (OP, *orange*) and resultant orthogonal images

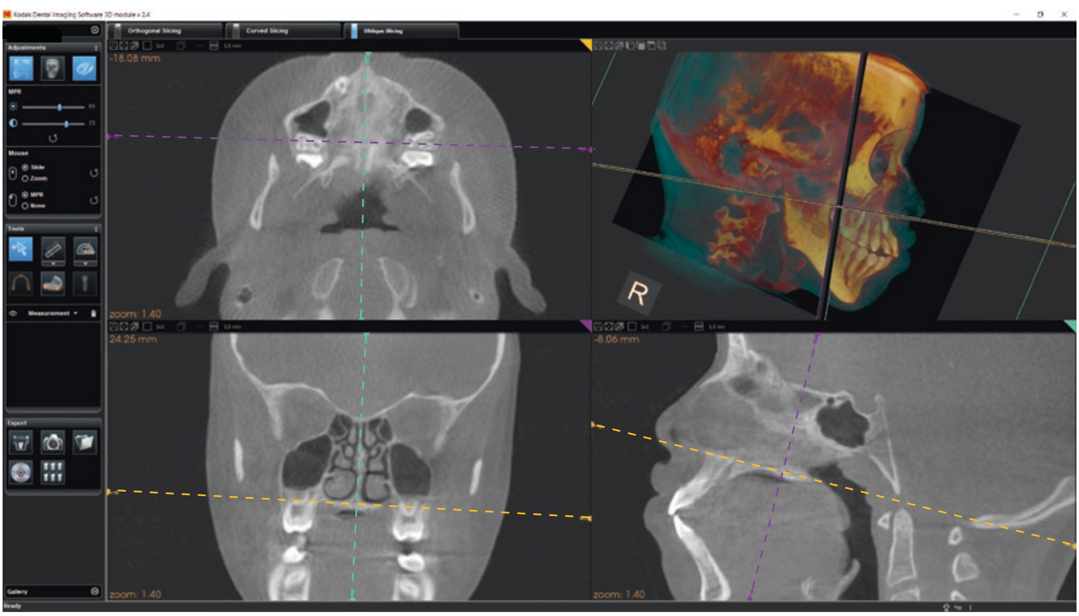

Fig. 5.30 Example of default dental software display (KDIS 3D module, Carestream, Atlanta Georgia, USA) showing the adjustment of the sagittal, coronal, and axial (*orange*) planes relative to the palatal plane (PP, *orange*) and resultant orthogonal images

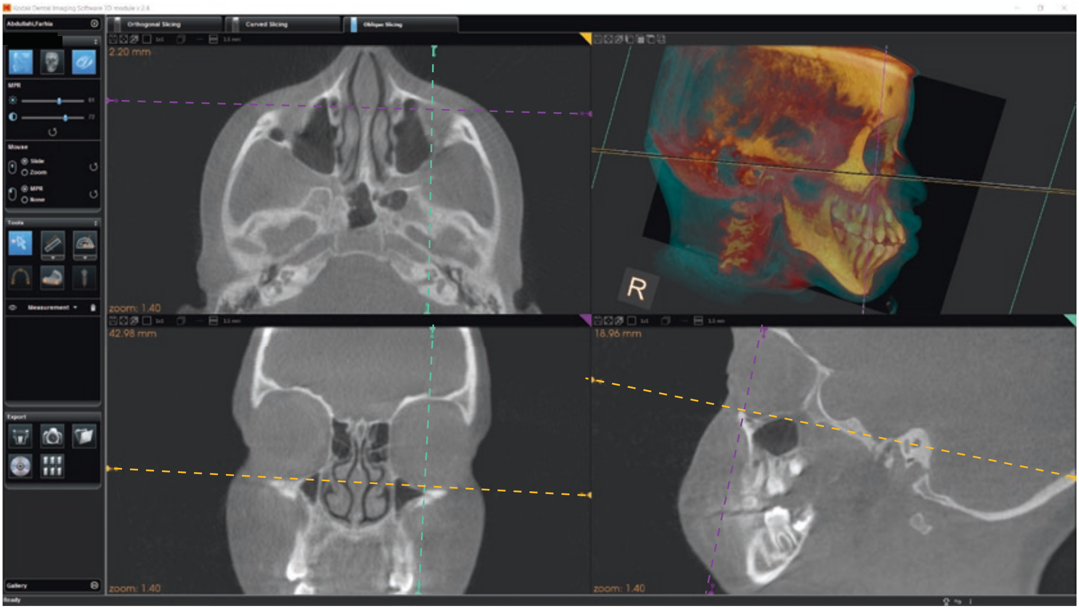

Fig. 5.31 Example of default dental software display (KDIS 3D module, Carestream, Atlanta, Georgia, USA) showing the adjustment of the sagittal, coronal, and axial planes relative to the interorbital plane (IOP, *purple*) and resultant orthogonal images

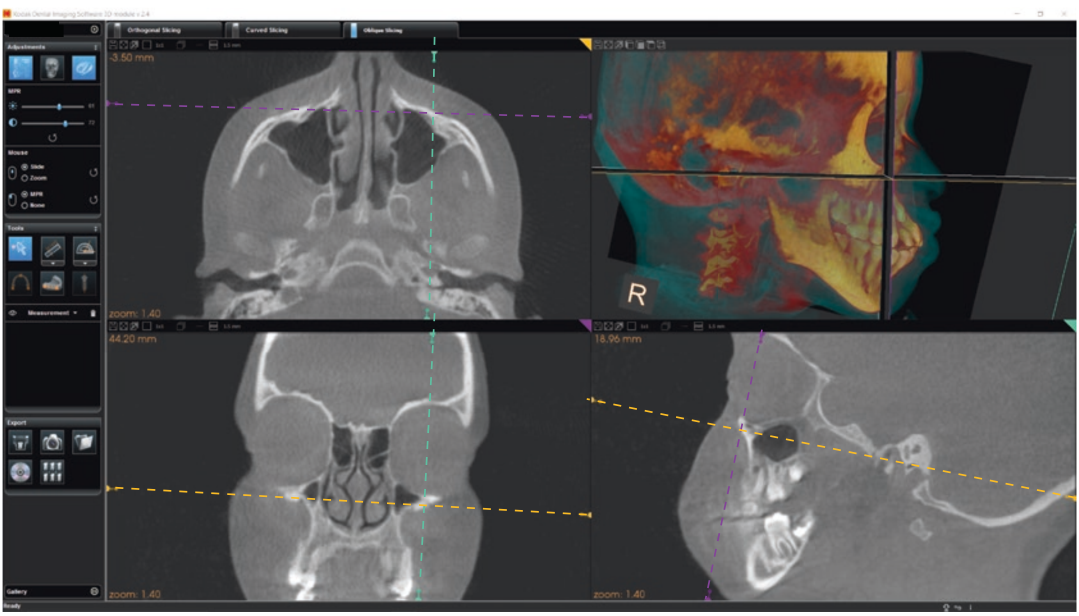

Fig. 5.32 Example of default dental software display (KDIS 3D module, Carestream, Atlanta, Georgia, USA) showing the adjustment of the sagittal, coronal, and axial planes relative to the infraorbital foraminae plane (IOFP, *purple*) and resultant orthogonal images

aspect of the external auditory meati (EAM) bilaterally and perpendicular to FH (Fig. 5.33).

– *Long axis of the tooth (LATc)*. Paracoronal plane transecting the long axis of the tooth (middle of the occlusal surface/incisal edge and apical terminus of the root of the tooth) (Fig. 5.26).

For full volume scans, reorientation usually conforms to cephalometric reference planes (Table 5.3) (Figs. 5.34 and 5.35) whereas for limited volume scans and certain MPR reformations, the specific region of interest should be reoriented to regional reference planes (Tables 5.4, 5.5, 5.6, 5.7, 5.8 and 5.9) (Figs. 5.36, 5.37, 5.38, 5.39, 5.40, 5.41 and 5.42).

5.2.2 Correct the Data

While there is substantial preprocessing of CBCT data, the default display of images on the monitor immediately after acquisition may not be optimized for the visualization of important structures. Displayed images often need to be manually

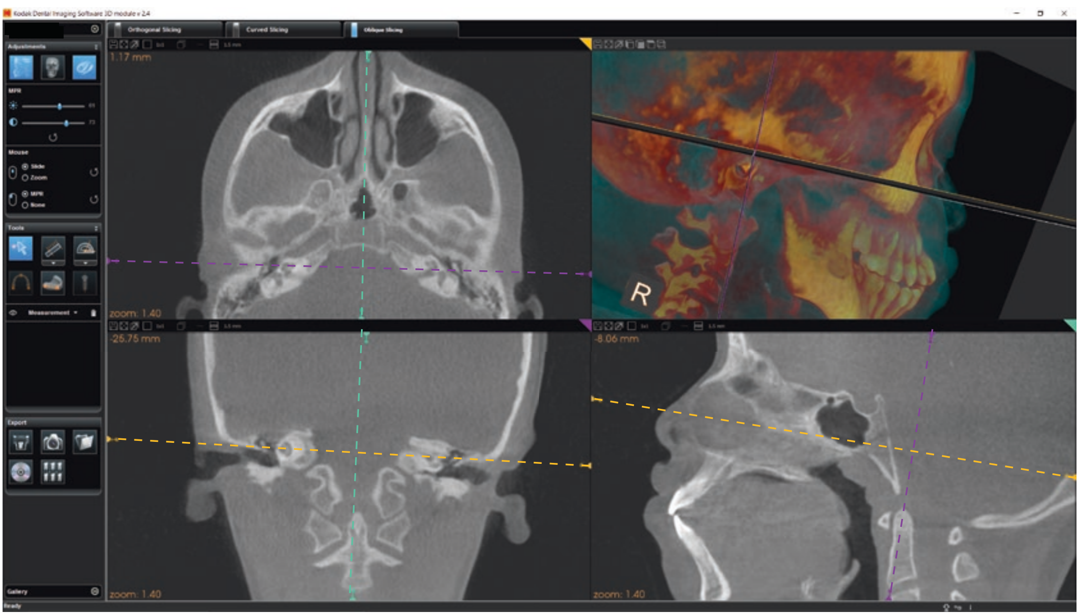

Fig. 5.33 Example of default dental software display (KDIS 3D module, Carestream, Atlanta, Georgia, USA) showing the adjustment of the sagittal, coronal, and axial (*orange*) planes relative to the Inter-porionic axis (IPA, *purple*) and resultant orthogonal images

Table 5.3 Reference planes used to reorient full FOV CBCT volumetric datasets (craniofacial deformities, cephalometric analysis, and asymmetry) (Figs. 5.34 and 5.35)

	Reference planes		
Rationale	Axial	Sagittal	Coronal
To minimize asymmetry by establishing a standard cephalometric position and enable comparison of skeletal elements	Coincide with FH	Coincide with the MSP	Coincide with IIOFP and IOP anteriorly and IPAc posteriorly

CBCT cone beam computed tomography, *FOV* field of view, *FH* Frankfort Horizontal, *MSP* midsagittal plane, *IOP* interorbital plane, *IIOFP* inter infraorbital foraminae plane, *IPAc* inter-porionic axis in the coronal plane

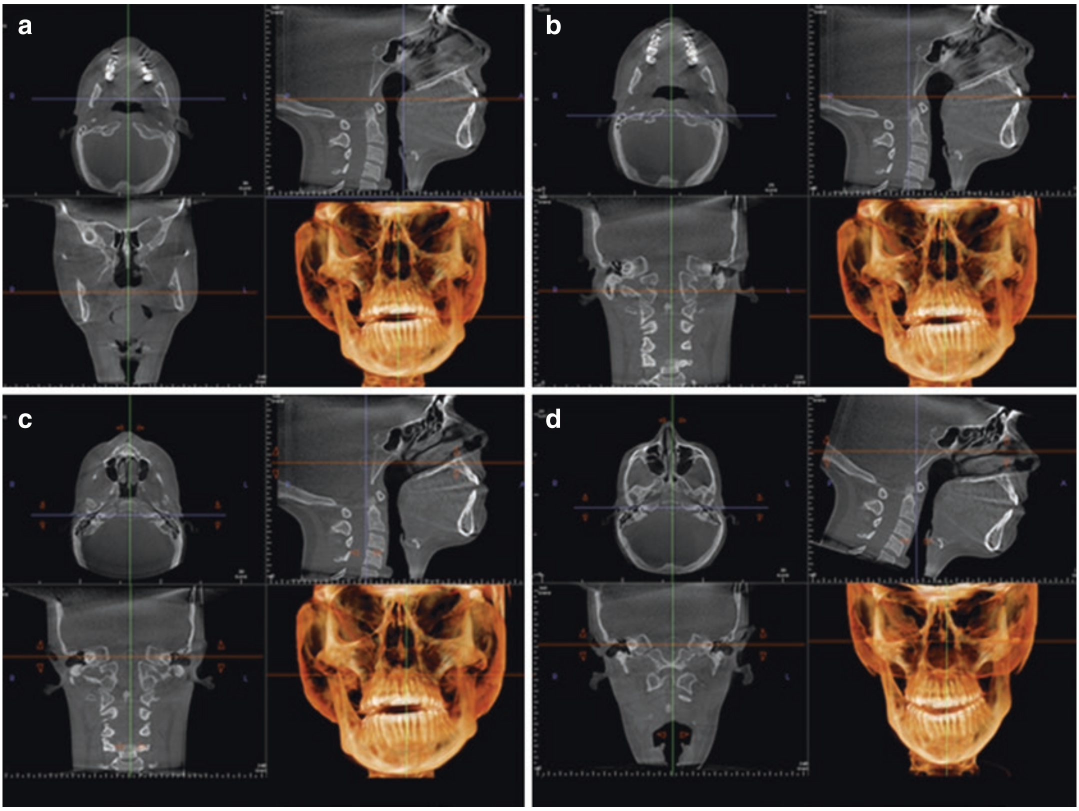

Fig. 5.34 Comparison of orthogonal and volumetric rendering panes at default acquisition (**a**) and after reorientation for a patient presenting with mandibular asymmetry (**d**). Reorientation of the volumetric dataset was achieved such that the axial plane was parallel to FH, sagittal plane coincided with the midsagittal plane and the coronal plane with the inter external auditory meati plane. This was achieved by translating the coronal (**b**) and axial planes to coincide with the external auditory meati bilaterally, rotating the axial and coronal planes to achieve symmetry (**c**) and then rotating the sagittal plane around the pivot through the external auditory meati such that the axial plane also bisected the infraorbital rim bilaterally (**d**)

corrected by the use of various postprocessing enhancement techniques to make diagnostic features easier to interpret (See Chap. 3). The aims of image enhancement in the clinical setting form the sequential image protocol for the application of these processes (Table 5.10) (Figs. 5.43, 5.44, 5.45, 5.46, 5.47, 5.48, 5.49, 5.50, 5.51, 5.52, 5.53, 5.54, and 5.55).

5.2.2.1 Interpolation

Interpolation is a geometric transformation process that compensates for the mismatch between the size of the voxels acquired and inherent corresponding pixel magnification of the 2-D image representation on the display monitor (See Chap. 2). Interpolation mitigates against the visual effect of "block" artifact effects, particularly evident along curved surfaces, and represent the native pixelation derived from voxel acquisition. This process may be applied either within a preprocessing "preference" file or available as an option image enhancement feature.

5.2.2.2 Adjust Contrast and Brightness

Contrast and brightness are the principal methods for improving overall CBCT image visibility. Contrast, also referred to as the *window width* (W), is adjusted to displaying only part of the available full gray value range. For a 12-bit image, the available gray value range is 4096. However, for optimal display of bone and adjacent soft tissue on CBCT images, display of all

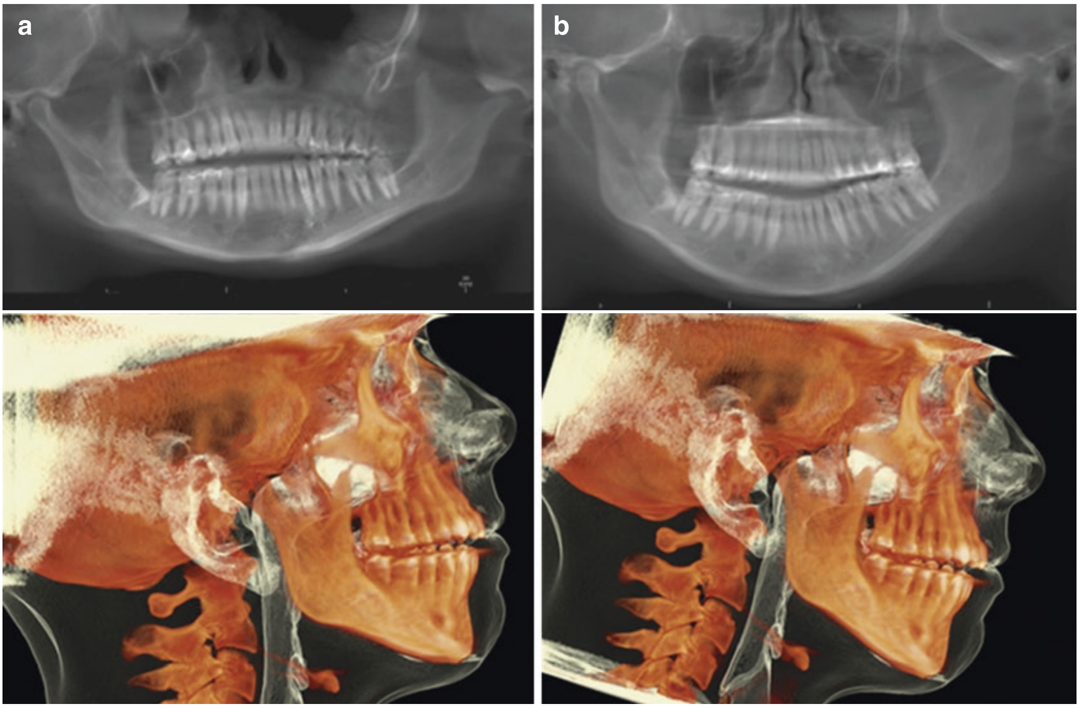

Fig. 5.35 Comparison of reformatted panoramic (*upper*) and right lateral volumetric images (*lower*) at default acquisition (**a**) and after reorientation for the same patient as in Fig. 5.34 (**b**). Notice that the images in (**b**) more clearly identify a minor left ramal and severe left condylar hypoplasia as the origin of the asymmetry

Table 5.4 Reference planes used to reorient limited FOV CBCT volumetric datasets of both the maxilla and mandible (Fig. 5.36)

	Reference planes		
Rationale	Axial	Sagittal	Coronal
To minimize asymmetry and enable comparison of interarch relationships (e.g., occlusion, interincisal angle, alveolar ridge)	Coincide with either OP or PP	Coincide with MSP	Perpendicular to the OP

CBCT cone beam computed tomography, *FOV* field of view, *OP* occlusal plane, *PP* palatal plane, *MSP* midsagittal plane

Table 5.5 Reference planes used to reorient limited FOV CBCT volumetric datasets of the TMJ (Fig. 5.37)

	Reference planes		
Rationale	Axial	Sagittal	Coronal
To minimize asymmetry and enable comparison of condylar morphology. To allow establishment of condylar axis using linear MPR	Coincide with ICPa or FH	Coincide with MSP and perpendicular to ICPc or FH	Coincide with ICPc or IPAc or perpendicular to FH or ICPa

CBCT cone beam computed tomography, *FOV* field of view, *FH* Frankfort horizontal, *MSP* midsagittal plane, *IPAc* inter-porionic axis in the coronal plane, *ICPc* intercondylar plane in the coronal axis, *ICPa* intercondylar plane in the axial axis

Table 5.6 Reference planes used to reorient limited FOV CBCT volumetric datasets of the maxilla (maxillary sinus) (Fig. 5.38)

Rationale	Reference planes		
	Axial	Sagittal	Coronal
To minimize asymmetry and allow comparison of maxillary sinus morphology	Coincide with PP	Perpendicular to PP	Perpendicular to PP

CBCT cone beam computed tomography, *FOV* field of view, *PP* palatal plane

Table 5.7 Reference planes used to reorient limited FOV CBCT volumetric datasets of the maxillary alveolus (implants) (Fig. 5.39)

Rationale	Reference planes		
	Axial	Sagittal	Coronal
To minimize asymmetry and allow assessment of the alveolar ridge via trans-axial XS	Coincide with OP of dentition on radiographic template, alveolar crest (partially dentate) or alveolar ridge (edentulous)	Coincide with MSP and perpendicular to OP	Perpendicular to OP

CBCT cone beam computed tomography, *FOV* field of view, *OP* occlusal plane, *MSP* midsagittal plane

Table 5.8 Reference planes used to reorient limited FOV CBCT volumetric datasets of the mandibular alveolus (implants) (Fig. 5.40)

Rationale	Reference planes		
	Axial	Sagittal	Coronal
To minimize asymmetry and allow assessment of the alveolar ridge via trans-axial XS	Coincide with OP of dentition on radiographic template, alveolar crest (partially dentate) or alveolar ridge (edentulous)	Coincide with MSP and perpendicular to OP	Coincide with IOP or IIOFP or perpendicular to OP

FOV field of view, *IOP* interorbital line, *IIOFP* inter infraorbital foraminae line, *OP* occlusal plane, *MSP* midsagittal plane

Table 5.9 Reference planes used to reorient limited FOV CBCT volumetric datasets of the impacted teeth (including maxillary canines and mandibular third molars) (Figs. 5.16, 5.41, and 5.42)

Rationale	Reference planes		
	Axial	Sagittal	Coronal
To reorient the volumetric dataset such that orthogonal planes are perpendicular to the tooth or adjacent vital structure	Coincide with vital structure (e.g., IAC) for third molars; coincide with LATa for other impacted teeth	Coincide with vital structure (e.g., IAC) for third molars and LATs for other impacted teeth	Coincide with vital structure (e.g., IAC) for third molars and LATc other impacted teeth

CBCT cone beam computed tomography, *FOV* field of view, *IAC* inferior alveolar canal, *LATa* long axis of tooth in the axial plane, *LATc* long axis of tooth in the coronal plane, *LATs* long axis of the tooth in the sagittal plane

4096 gray values is not necessary and actually produces a washed out or overall light image. Adjustment of W to 1000 indicates that 1000 gray values are considered for display, with the lowest gray value (and all values below it) being displayed as black and the highest (and all above it) as white. Brightness, also referred to as the *window level* (L), determines the central gray value within the window width. For example, a W/L of 1000/0 implies that gray values between −500 and +500 are considered for display, with all other values showing as black (−500) or white (+500) (Fig. 5.43) (Pauwels et al. 2015a).

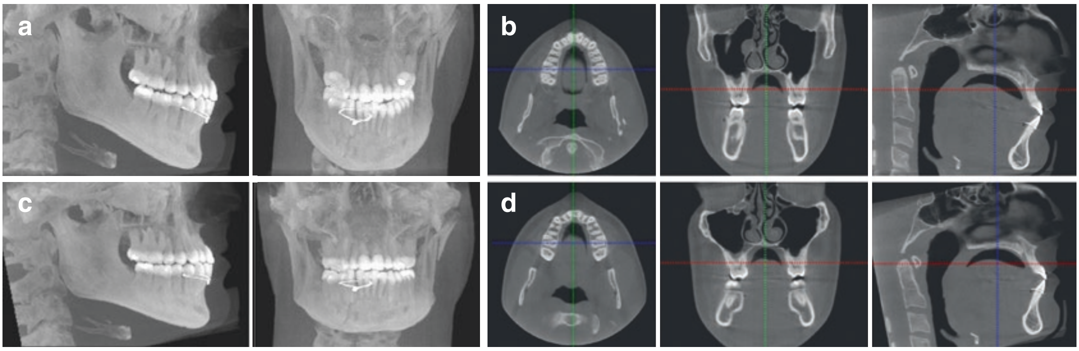

Fig. 5.36 Comparison of right lateral and frontal maximum intensity projections and orthogonal images (from *left* to *right*, axial, coronal and sagittal) at default acquisition (**a**, **b**) and corresponding projections after reorientation (**c**, **d**). Notice that the reoriented images (**c**, **d**) more clearly identify relationships between the dentition including inter-digitation, posterior cross-bite (*right*) and interincisal edge-to-edge occlusion

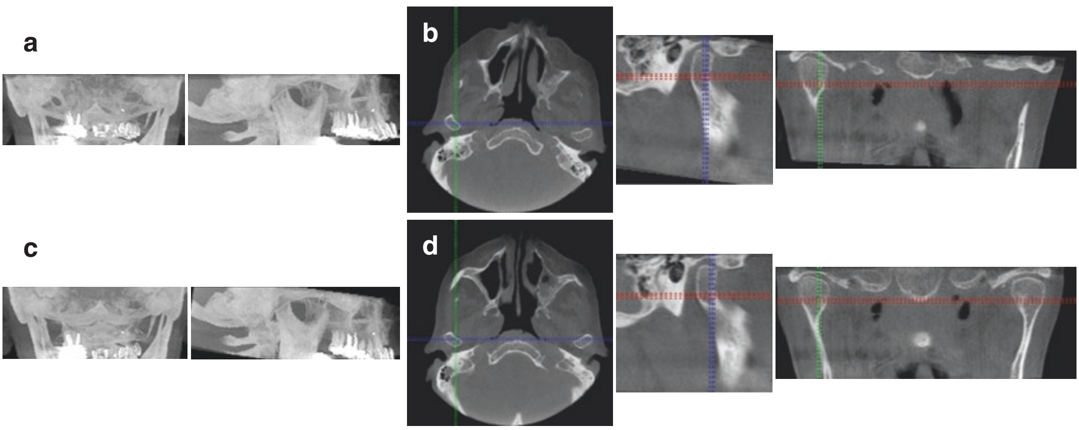

Fig. 5.37 Comparison of frontal and right lateral maximum intensity projections and orthogonal images (from *left* to *right*, axial, parasagittal, and coronal) at default acquisition (**a**, **b**) and corresponding projections after reorientation (**c**, **d**). The orthogonal images were reoriented such that the axial plane was parallel to FH, the sagittal plane parallel to the MSP and the coronal plane parallel to the IPA. Notice that the reoriented images (**c**, **d**) more clearly characterize the similarity in morphology between the left and right sides and concentricity of the mandibular condyle within the fossa

Dental imaging software often provide sliding bars with brightness and contrast options or allow direct alteration on the image using the mouse cursor where brightness and contrast adjustments are the vertical and horizontal motions on the display. Often preset levels are available, some of which designate color to particular grayscale intensities. Because CBCT provides excellent spatial resolution of high contrast material, initial display, at least of orthogonal slices at native resolution, should be adjusted to provide high contrast between bone and soft tissue. Unlike conventional CT imaging, where Hounsfield Units correlate well with attenuation and the optimal window width/level settings for bone, called the bone window, is approximately 300/2000, the absolute values for pixel intensity for CBCT is highly equipment dependent. Therefore, it is necessary to develop a bone display protocol specific for each CBCT equipment used. This should be based on manufacturers' preset intensity value recommendations and a

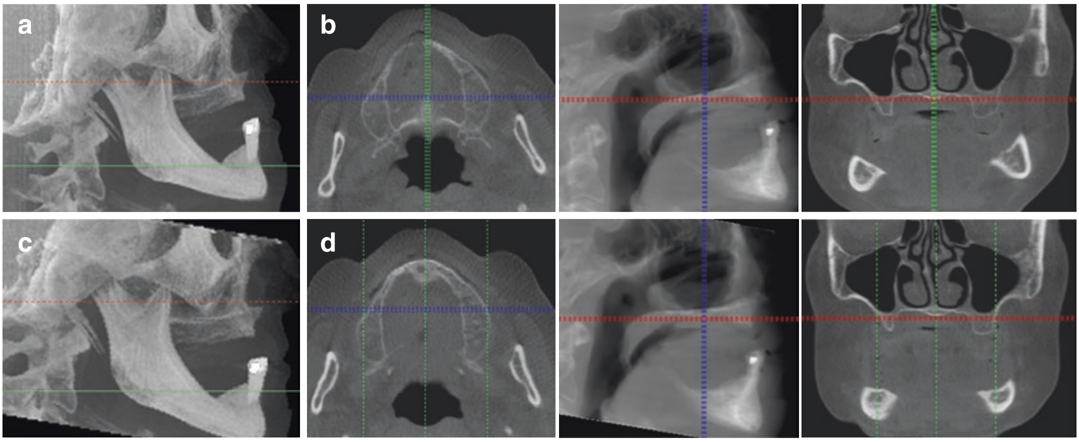

Fig. 5.38 Comparison of right lateral maximum intensity projection and 5 mm thick orthogonal images (from *left* to *right*, axial, sagittal, and coronal) at default acquisition (**a**, **b**) and corresponding projections after reorientation (**c**, **d**). The orthogonal images were reoriented such that the axial plane was parallel to PP, the sagittal plane parallel to the MSP and the coronal plane parallel to the IPA. Notice that the reoriented images (**c**, **d**) more clearly characterize the differences in size and shape between the left and right maxillary sinuses and depth of the palate

consistent, clinically efficient methodology to adjust the brightness and contrast to reliably optimize image display.

- **Qualitative.** Adjustment of brightness and contrast can be performed empirically based on the visual appearance on the image and image thickness.
- Increasing image sectional thickness increases the relative proportion of the voxels that are low or minimally attenuating (Fig. 5.44). Therefore, in principle, as section thickness increases, the window level for optimal display should also be reduced. In addition, because there is less signal variation in highly attenuating structures such as bone, the window width should also be reduced with increasing section thickness.
- The purpose of window and leveling for thin section thicknesses (less than 5 mm) is to provide local detail of fine structures such as thin cortical bone and trabeculae and maximize intensity differences between dental structures such as enamel and dentin and minimize beam hardening artifacts. Adjustment of both brightness and contrast is performed using tissues within the image as an internal calibration according to the following guidelines (Fig. 5.45).
  - There should be a clear distinction at the dento-enamel-junction (DEJ).
  - There should be clear identification of the soft tissue within the maxillary sinus.
  - Thin cortical bone should show little or no “bleed” of either highly attenuating (bone) or poorly attenuating (air) structures.

The best section to view while performing these adjustments is therefore a cross section of the maxillary or mandibular bone demonstrating trabeculae. Too high a level setting results in loss of thin structures while too low a level setting results in apparent fusion of structures (e.g., root and cortical bone). The window width should be adjusted to provide contrast between the attenuating structures of interest; this is usually the dentition and the bone, or the bone and soft tissue (e.g., maxillary sinus). Too high a width setting results in loss of contrast between thin cortical bone and surrounding soft tissues appearing as a “washed out appearance” while too low a window setting results in accentuation of beam hardening artifacts (e.g., extension of metallic artifacts from restorations).

- The purpose of window and leveling for greater thicknesses (more than 5 mm) is to

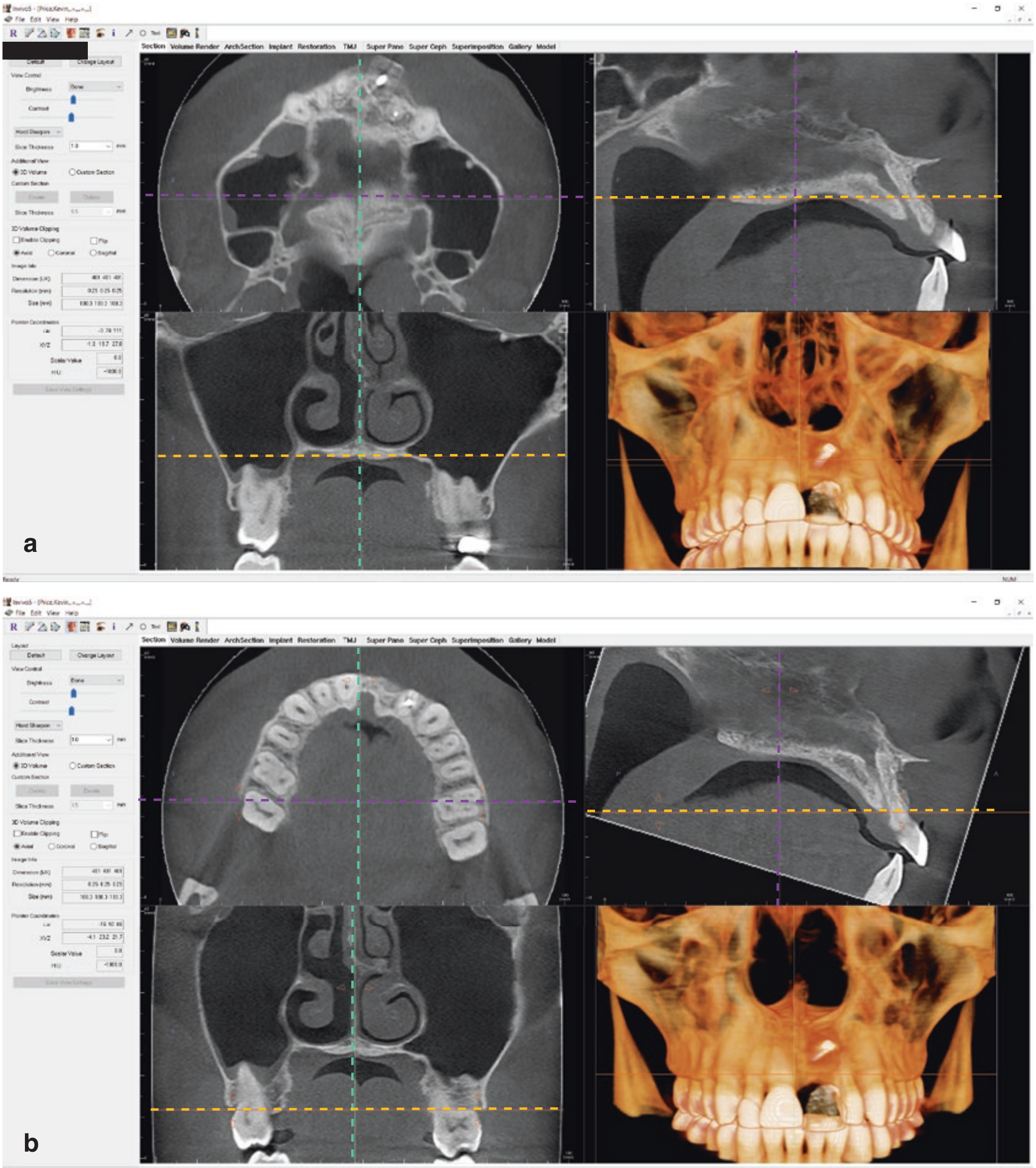

Fig. 5.39 Comparison of orthogonal and volumetric rendering panes at default acquisition (**a**) and after reorientation for a partially dentate patient presenting with a missing left maxillary incisor and subsequent labial mini-implant retained bone graft (**b**). Reorientation of the volumetric dataset was achieved such that the axial plane (*orange*) was parallel to OP and incorporating the outline of the missing tooth on the radiographic template, the sagittal plane (*turquoise*) coincided with the MSP and the coronal plane (*purple*) perpendicular to the OP

demonstrate the relationship between maxillofacial structures such as the dentition and the supporting bone. Specific adjustments of images should be made according to the relative amount of tissue present. Usually both the window level and the width will be reduced compared with thin section images. For the most common medium section

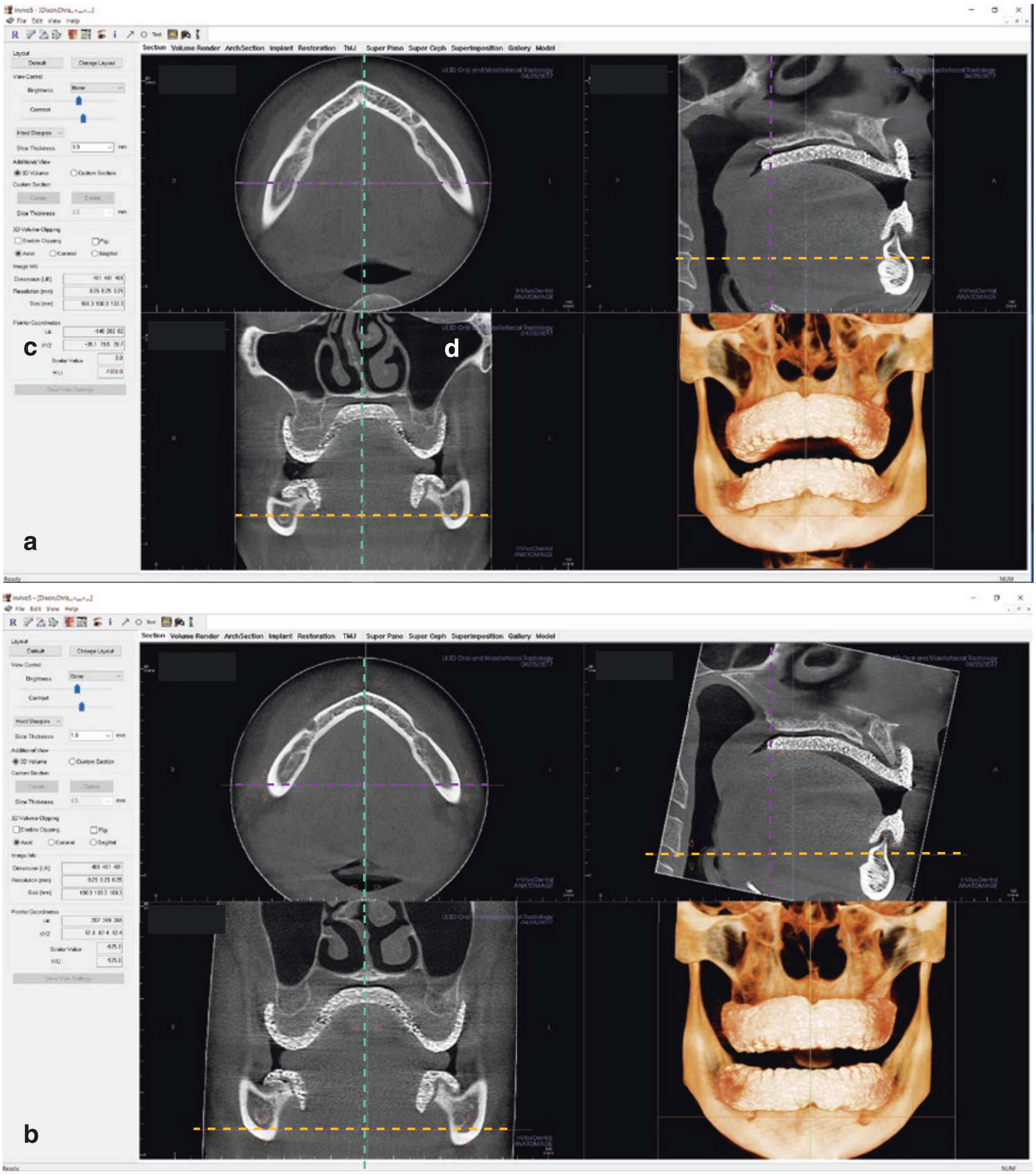

Fig. 5.40 Comparison of orthogonal and volumetric rendering panes at default acquisition (**a**) and after (**b**) reorientation for the mandible for a completely edentulous patient. Reorientation of the volumetric dataset was achieved such that the axial plane (*orange*) was parallel to the OP as determined by the position of the teeth on the mandibular radiographic template, the sagittal plane (*turquoise*) coincided with the MSP and the coronal plane (*purple*) perpendicular to the OP

thickness image, the curved oblique simulated panoramic image, the level should be adjusted to enable visualization of the fine structures of the lower border of the orbit and ethmoid sinuses without burning these structures out whereas the width should then be adjusted to a value that optimizes distinction between the most highly attenuating

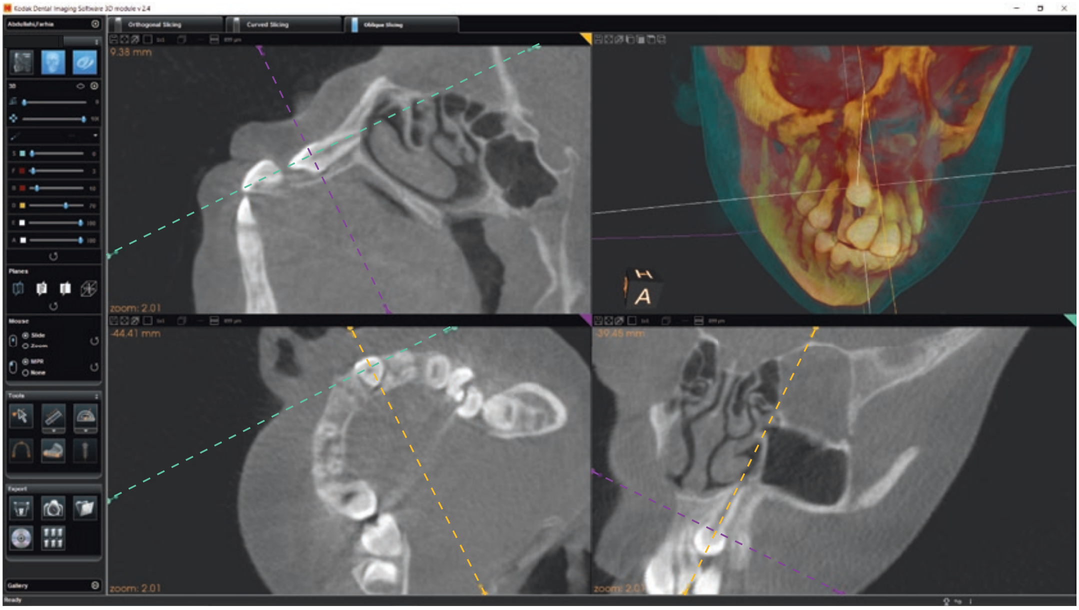

Fig. 5.41 Example of default dental software display (KDIS 3D module, Carestream, Atlanta, Georgia, USA) showing the adjustment of the sagittal, coronal, and axial (*orange*) planes relative to the long axis of the maxillary canine (LATs, *turquoise*; LATc, *purple*; LATa, *orange*) and resultant orthogonal images

structures in the maxillofacial region (enamel and dentin). For thicker ray sum sections, such as simulated cephalometric projections, brightness and contrast adjustments must be adjusted accordingly (Fig. 5.46).

- **Semiquantitative.** Some dental software programs allow adjustment of brightness and contrast by providing interactive LUT and histogram controls. Adjustment of these controls considering the histogram of the available voxels of the image according to specific protocols is the most reliable and consistent method of optimizing the display of CBCT data. However, semiquantitative adjustment requires a fundamental understanding of the effects of LUT operations in relation to the available range of gray intensity values (histogram).
  - **Linear LUT operations.** The brightness of the image is adjusted by changing the position of the linear relationship whereas the contrast is adjusted by changing the angle of the slope. Changing the slope of the LUT may also change the number of gray levels displayed and effectively produces a threshold at either end of the grayscale histogram. Optimal contrast and brightness on any image is obtained by adjusting the linear LUT to correspond to the available histogram (Figs. 5.47, 5.48, and 5.49). Appropriate selection of the level should be approximately midway between the lowest and highest available pixel intensities whereas the width should be reduced to include the range of values available. The areas beyond the range are therefore masked from display and in the case of high pixel intensities, may prevent bright light from adversely effecting visual adaptation (Fig. 5.49).

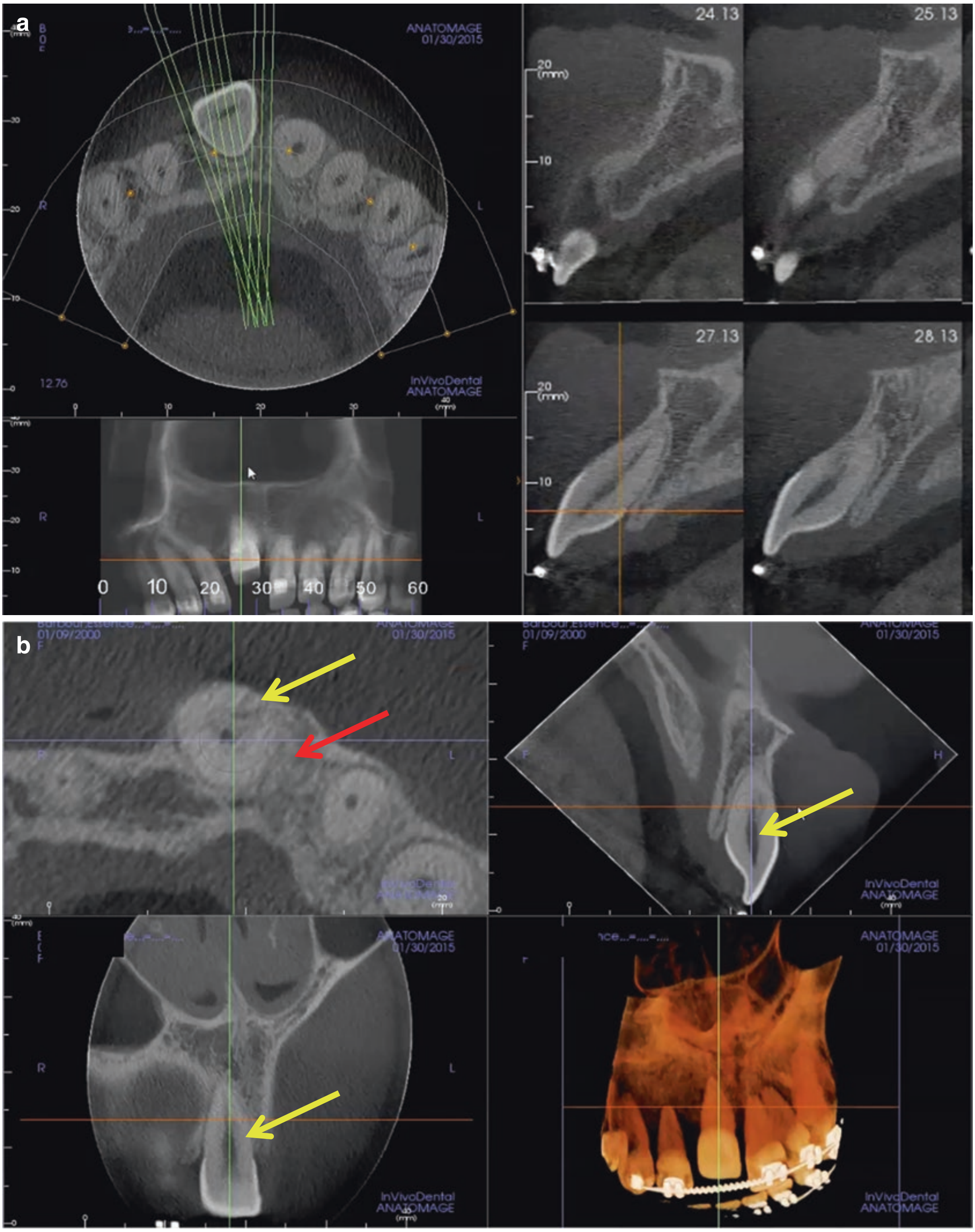

Fig. 5.42 Example of the importance of adjusting all orthogonal planes to the long axis of the tooth. Dental imaging software display (InVivo, Anatomage, San Jose, California, USA) showing reconstructed panoramic, reference axial and cross-sectional images of an unerupted and labially positioned maxillary right central incisor (**a**). Reorientation of the volume such that the orthogonal images coincide with the long axis of the tooth (**b**) clearly demonstrates both external resorption (*yellow arrow*) and bony ankyloses (*red arrow*) not observable on the panoramic cross sections because of parallax projection error

– **Nonlinear Operations.** Typically, high contrast images are visually more appealing than low contrast. However, a drawback of linear contrast enhancement is that it leads to saturation at both the low and high end of the intensity range. This is avoided by employing nonlinear contrast adjustments. The most standard approach is *gamma correction*, where the LUT takes the form of a sigmoid (Fig. 5.50) and there is no saturation at the low or high end. Gamma correction is widely used because it yields reasonable results. One disadvantage is that gray values are mapped asymmetrically with respect to midlevel gray. This could be of concern if there is an uneven representation within the image of either high or low level pixel values. Other nonlinear applications include logarithmic and exponential mapping techniques.

Table 5.10 Summary of systematic image enhancement protocol and rationale for CBCT Data

Image enhancement stage	Rationale
Apply interpolation transformations	Reduces block “pixelation” artifacts
Adjust brightness levels and contrast range	Display and maximize differences in important pixel intensities
Sharpen edges	Accentuate the differences between structural groups of pixels
Reduce noise	Eliminate unwanted pixels

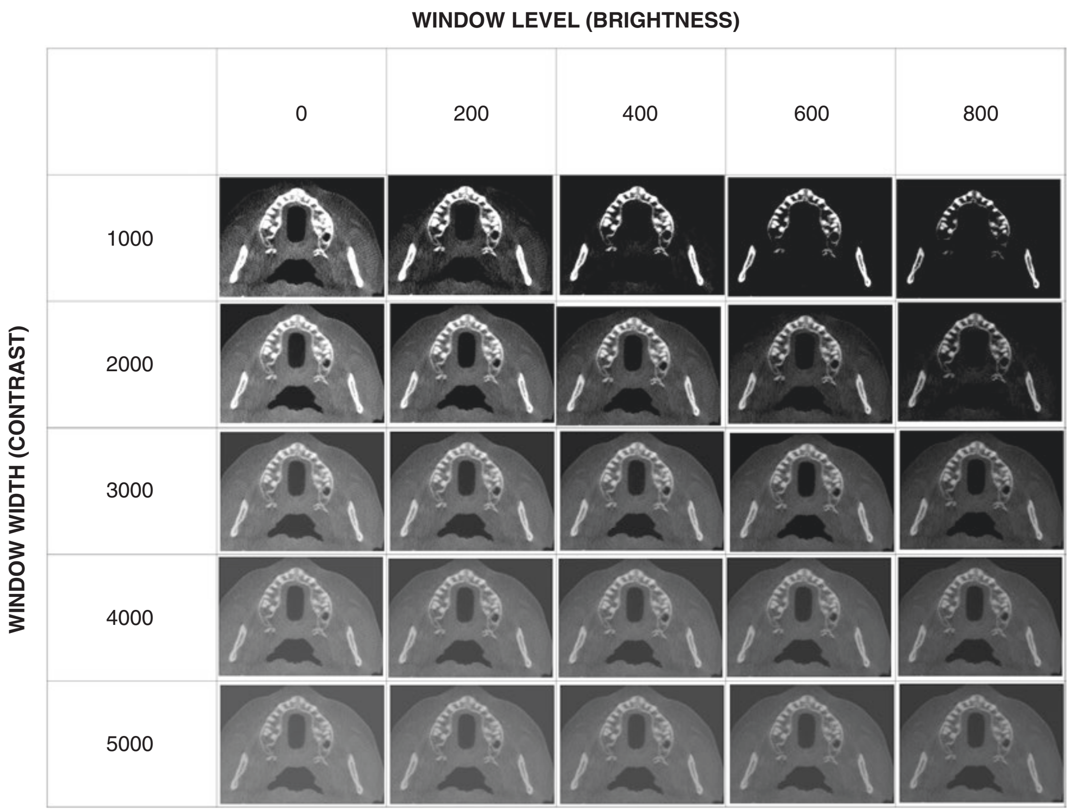

Fig. 5.43 Schematic matrix demonstrating the visual effect of brightness (window level or L) and contrast (window width or W) on a representative thin section 12-bit CBCT axial image. Over 4096 gray values are potentially captured and available for display. Displaying them all with a wide window width (*bottom row*) or only showing a limited window width (*top row*) produces images that are washed out or overall too dark, respectively, lacking distinction between structures. Setting the window level (columns) too low (0) or too high (800) compared to the window width produces images that are too bright or too dark overall. Optimal visual display requires a balance between W/L

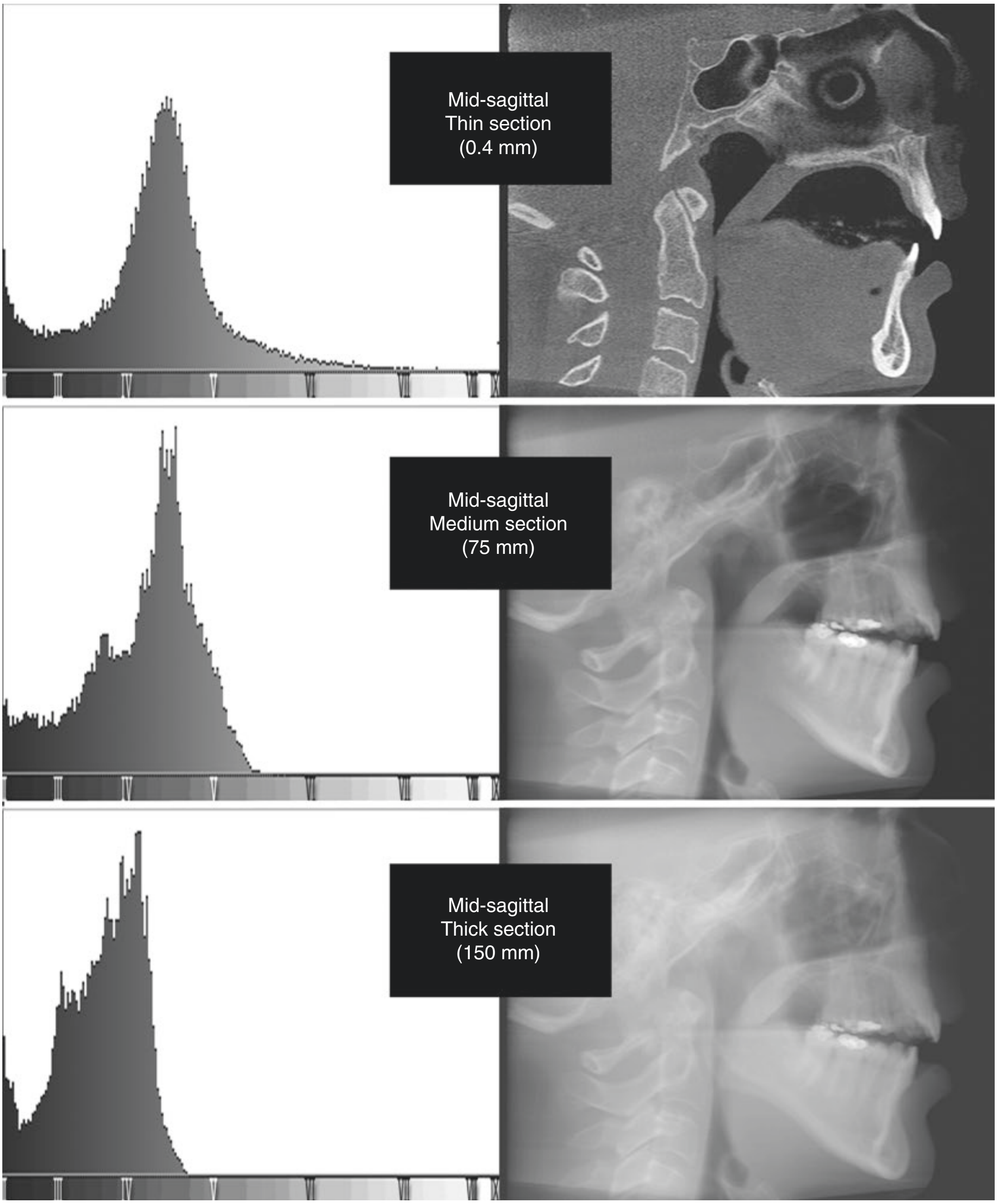

Fig. 5.44 This diagram demonstrates the effect of increasing sectional thickness on the pixel spectrum. As the midsagittal orthogonal layer is increased from the native 0.4 mm display (*upper right*), to a medium sectional thickness (75 mm) to a full section thickness (150 mm) there is a noticeable shift in the spectrum of component voxel intensities to darker values—the resultant image becomes appreciably darker overall. Therefore, to optimize the display of the images created in the medium and full thickness sections, it would be necessary to reduce the window level to coincide with the available pixel intensities

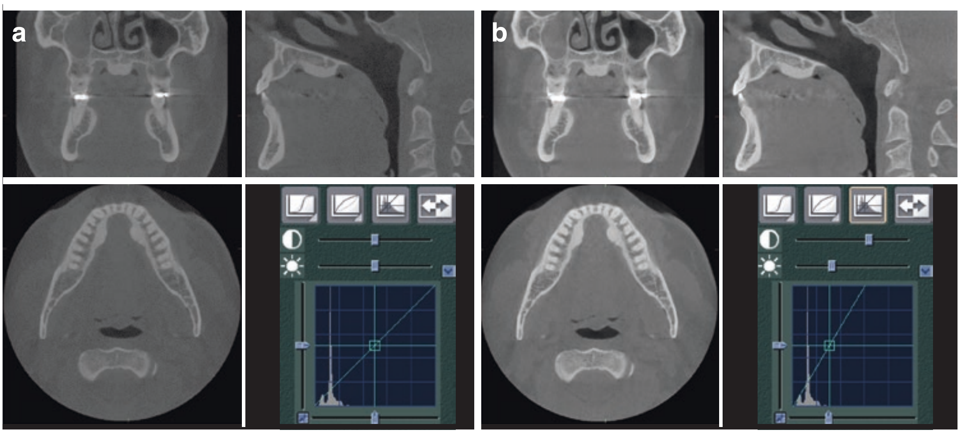

Fig. 5.45 Unenhanced orthogonal 1 mm thick images with corresponding contrast and brightness slider adjustments showing corresponding histogram and LUT graphs (**a**). Enhanced images after empirical adjustment of contrast and brightness using the slider controls (**b**). The corresponding LUT indicates that the slope of the linear transfer function is now much steeper and while the origin is the same, the upper limit corresponds more to the upper limit of the *gray shades* available observed on the histogram

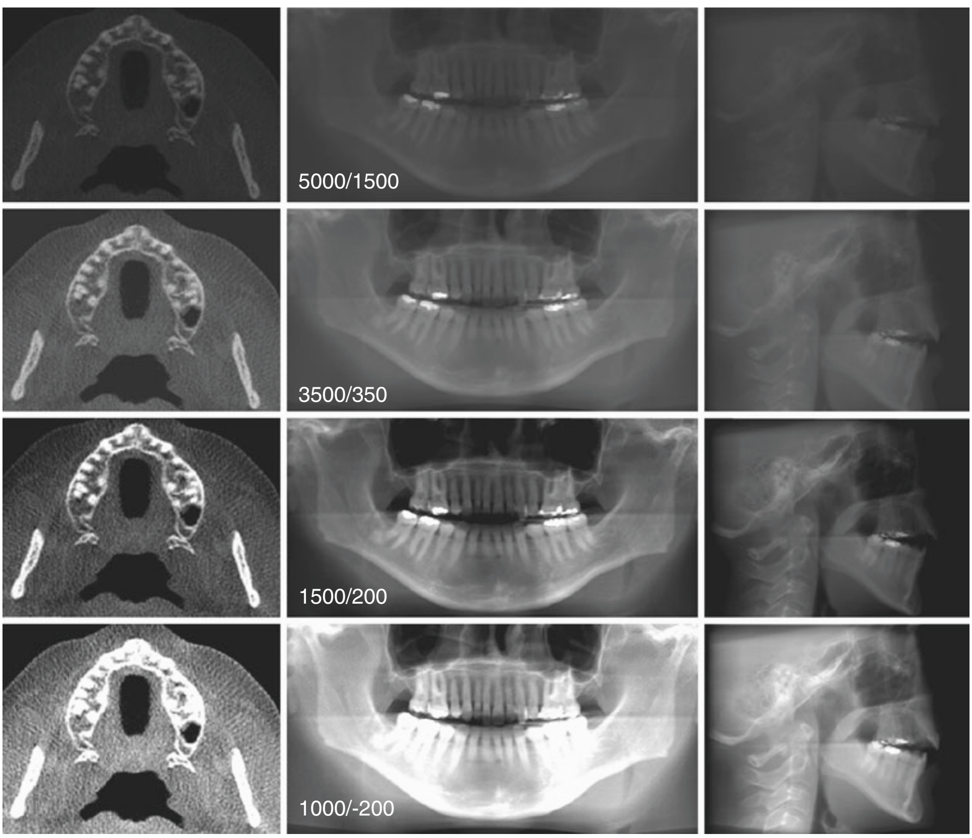

Fig. 5.46 Schematic matrix demonstrating the visual effect of brightness (window level or L) and contrast (window width or W) on a representative thin section 12-bit axial image (*left column*), 30 mm thick reformatted panoramic image (*middle column*) and 160 mm full thickness lateral cephalometric projection. The optimal settings for the axial image are 3500/350, 1500/200 for the reformatted panoramic image and, 1000/−200 for the lateral cephalometric. As a general trend for thicker images, both W and L should be reduced

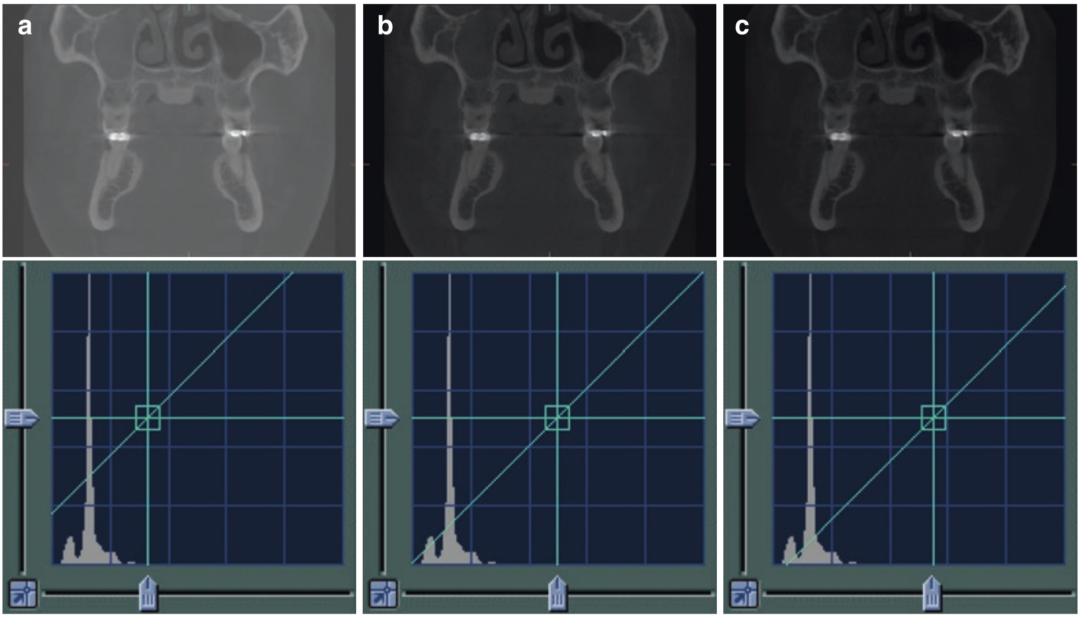

Fig. 5.47 Schematic demonstrating the visual effect on a thin section coronal image (*top row*) of a brightness LUT adjustment superimposed over a histogram of the same image. The histogram of the original image has a predominance of dark gray intensity values. A complete linear representation of all available pixels (**b**) provides an overall *dark* image (*top center*). Shifting the linear transfer function to the left (**a**) increases the overall brightness of the displayed *gray* (*top left*), whereas shifting the transfer function to the right (**c**) decreases the overall brightness of the image (*upper right*)

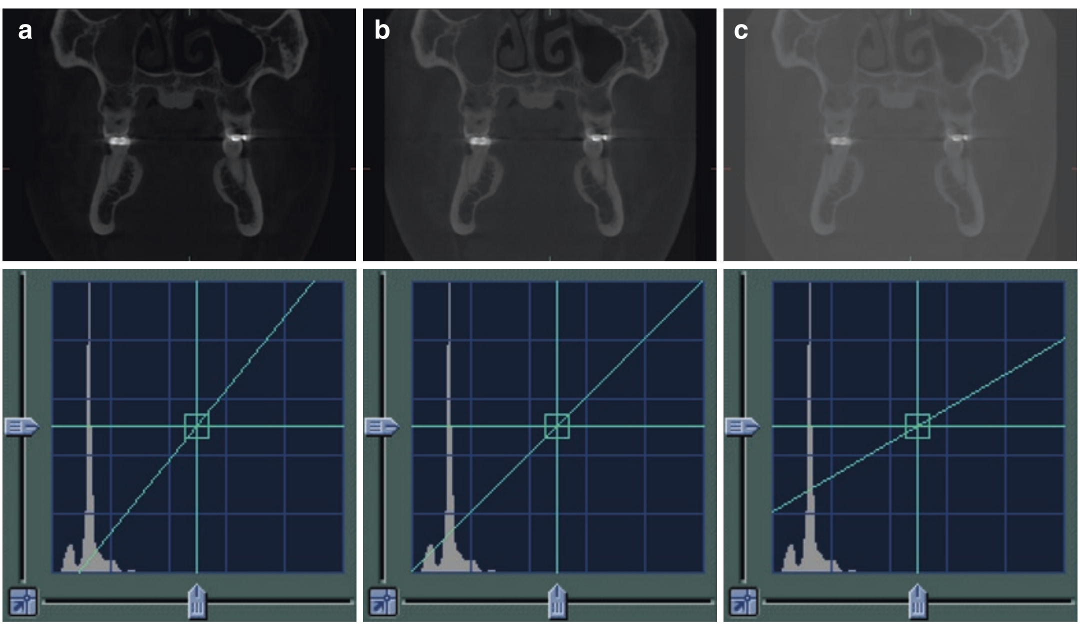

Fig. 5.48 Schematic demonstrating the visual effect on a thin section coronal image (*top row*) of a contrast LUT adjustment superimposed over a histogram of the same image. The histogram of the original image has a predominance of dark gray intensity values. A complete linear representation of all available pixels (**b**) provides an overall dark image (*top center*). Increasing the slope of the linear transfer function to the left (**a**) increases the overall contrast of the displayed gray intensity values (*top left*), whereas decreasing the slope (**c**) decreases the overall contrast of the image (*upper right*)

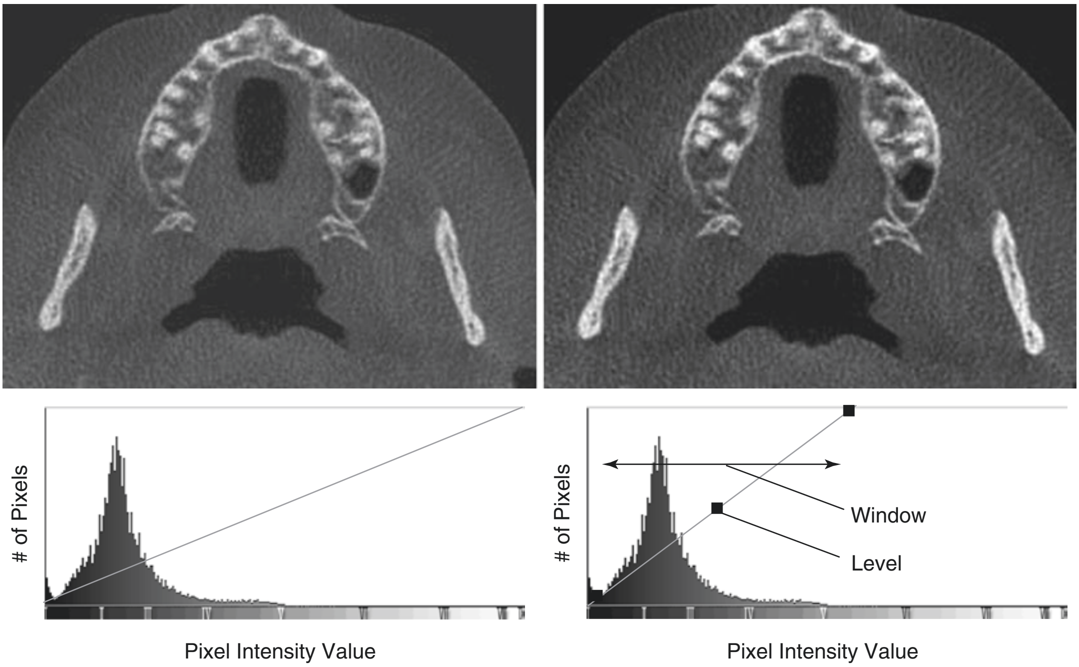

Fig. 5.49 Schematic demonstrating the visual effect on a thin section axial image (*top row*) of a LUT adjustment superimposed over a histogram of the same image. The histogram of the original image is shifted to the left with a predominance of dark gray intensity values. A complete and linear representation of all available pixels provides an unreadable image (*top left*). Reducing the range (window) of displayed gray intensities to correspond with the range of available gray intensities by moving the top of the linear graph to the left increases the slope of the LUT (W) and changes the position of the slope increasing both contrast and brightness, respectively, and provides a diagnostically acceptable image

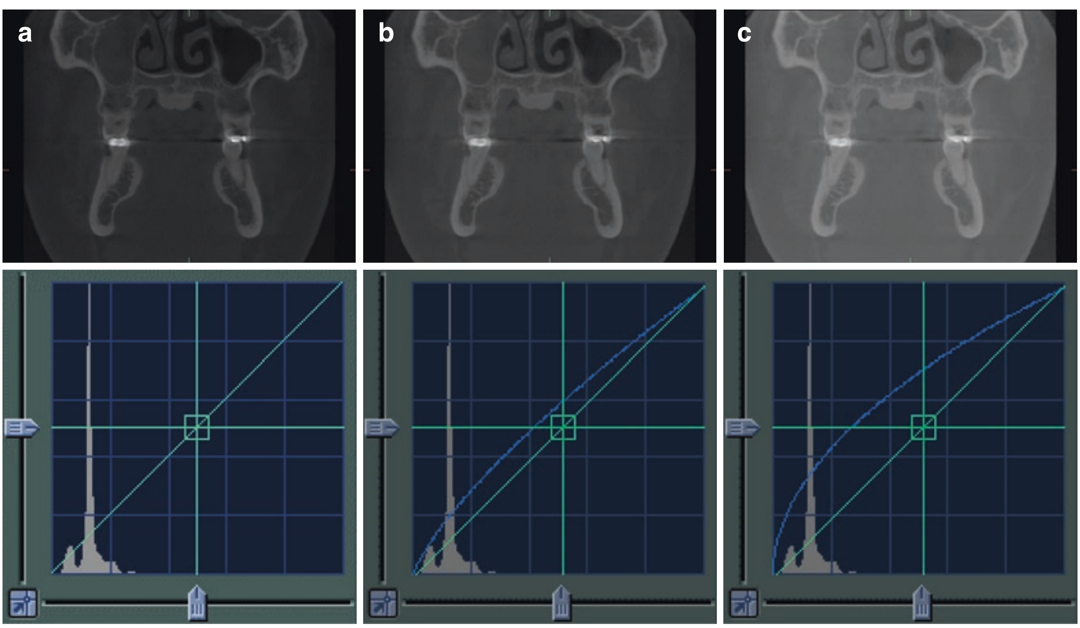

Fig. 5.50 Effect of nonlinear 1.33 (**b**) and 2.0 (**c**) "gamma" contrast and brightness enhancements on an unenhanced image (**a**). The nonlinear gamma transfer function (*blue*) shows high contrast and at the low pixel values and low contrast at high pixel values. In this example because the pixel intensity distribution has predominantly dark pixel values (the histogram is shifted to the left) the effect of gamma is less effective

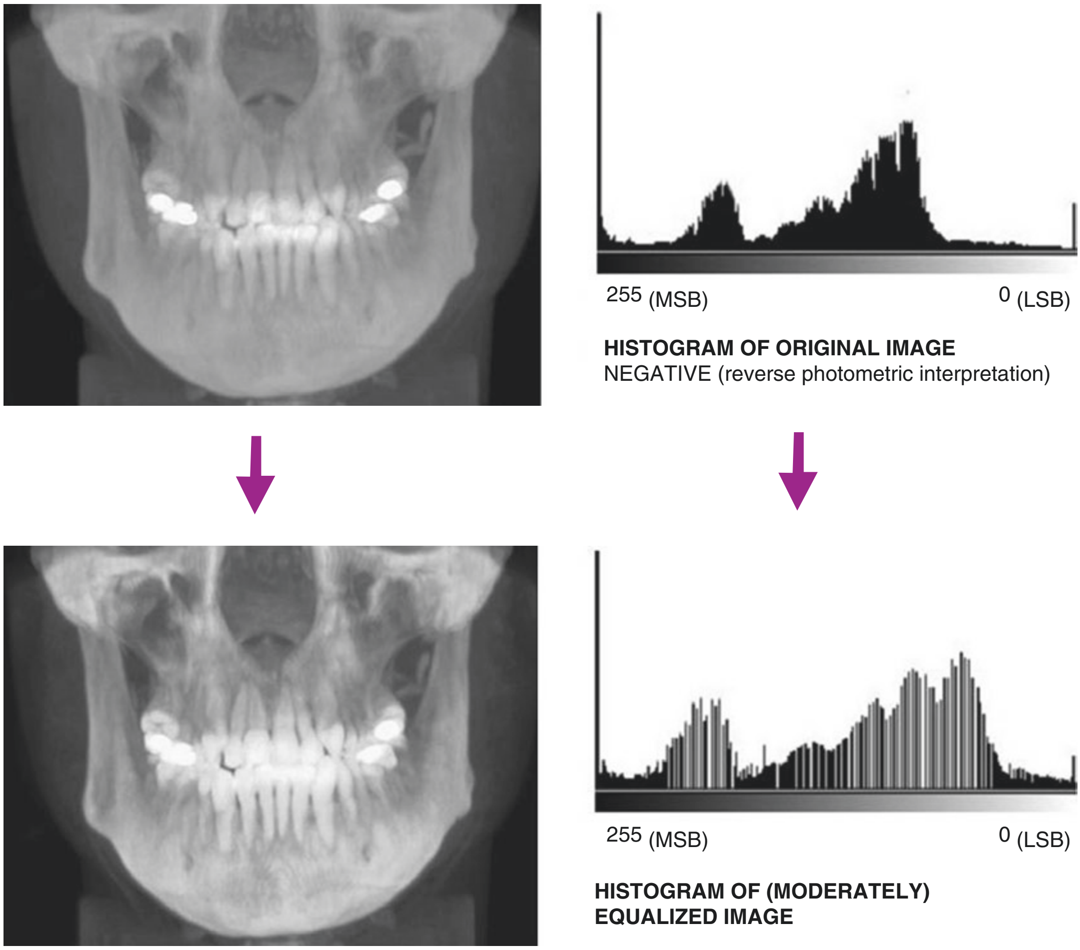

Fig. 5.51 MIP full thickness frontal original image (*top left*) and corresponding histogram (*upper right*) shows a bimodal distribution of gray intensity values with few pixels in the white region (*right side* of the histogram). Modified image (*lower left*) after the available gray intensities are stretched more evenly over the grayscale range. Contrast is improved, but some information is lost at the extremes of the range

- **Histogram Equalization.** Ideally, for a bell-shaped distribution of gray intensity values in an image histogram, optimal presentation should be such that most of the pixels should be represented at the mid-gray (128) level with the low and high pixel values falling on either side. It is possible that an image can be transformed so that the distribution of intensity values is equally represented in the image. This process is called *histogram equalization*. It has an effect similar to contrast adjustment but distributes the available pixel intensities (or bins) equally over the displayed range (Fig. 5.51).
- Full image equalization resulting into a truly flat histogram—where every bin is associated to the exact same number of pixels—most usually results into harshly contrasted and noisy images of little appeal and diagnostic value. Therefore, partial image equalization is commonly used with radiographic images, whereas the histogram resulting after the application of this transformation is intermediate between the original (unprocessed) histogram and a fully equalized histogram.
- Histogram equalization, whether full or partial, also implies the stretching of the original histogram, where the first and the last useful bins of the original histogram correspond to the first and the last level of the grayscale, respectively.

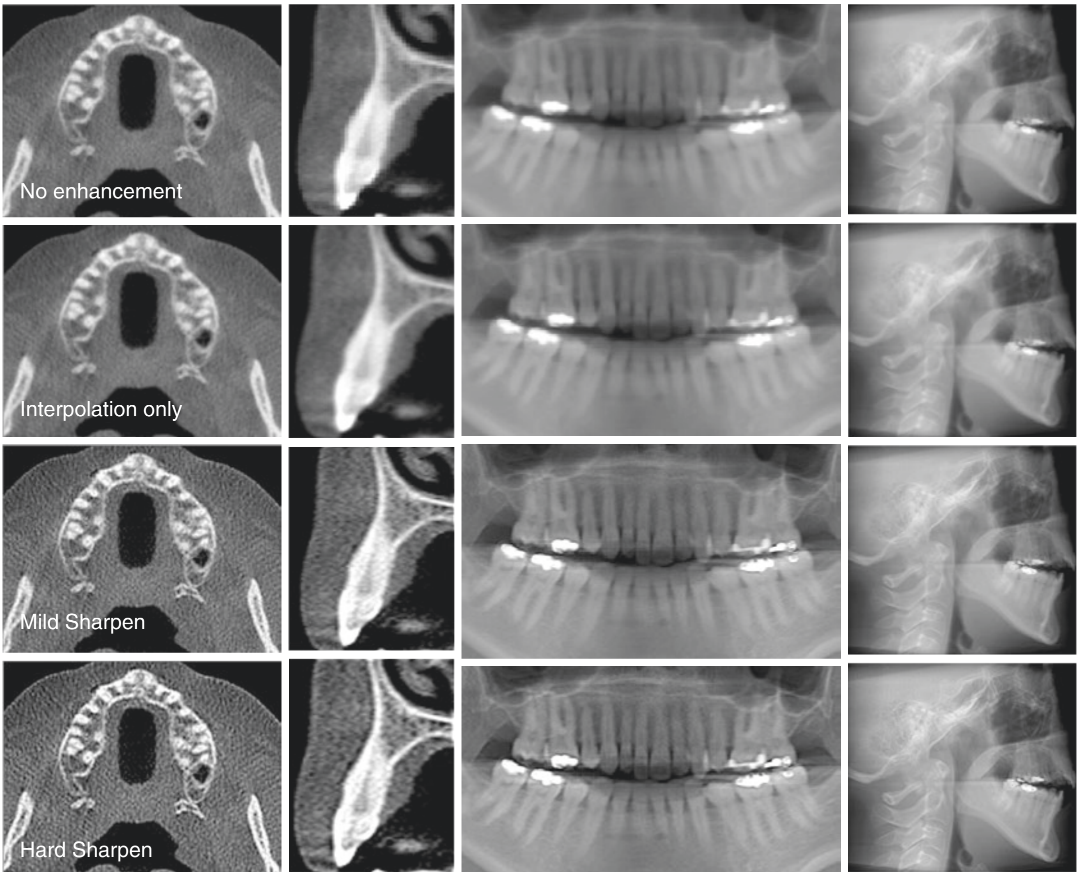

Fig. 5.52 Schematic chart of the effects of various image enhancements (*rows*) and 0.4 mm thick axial (*first column*), 1 mm thick cross-sectional (*second column*), 30 mm thick MPR ray sum panoramic (*third column*) and 160 mm thick lateral cephalometric ray sum projection. As a general trend, (1) more robust image enhancements are necessary with greater sectional thickness to improve image readability, and (2) robust image enhancements applied to thin sections degrade image readability by introducing excessive noise

5.2.2.3 Sharpen the Edges

To improve the differentiation of, and detail related to, bony structures it is necessary to sharpen of the definition of edges. This can be achieved by applying edge detection enhancement algorithms (See Chap. 3). The selection of an appropriate edge enhancement algorithm depends on the nature of the image itself (CBCT system) and the thickness of the image section thickness (Fig. 5.52). Combining histogram enhancement and sharpening filters in succession is the most efficient method of improving image quality for most clinical scenarios (Fig. 5.53).

5.2.2.4 Reduce Noise

With CBCT imaging (like with any other radiographic technique) there are two apparently competing priorities to improve image quality: sharpening edges while limiting noise. The effect of noise on the image can be reduced by applying a smoothing enhancement algorithm (See Chap. 3). However, this will compete with edge enhancement algorithms. Therefore a method is required that will reduce noise and maintain sharpness. Increasing image section thickness from the submillimeter to millimeter range minimizes the effect of noise on the resulting image and still produces diagnostically acceptable images (Fig. 5.54).

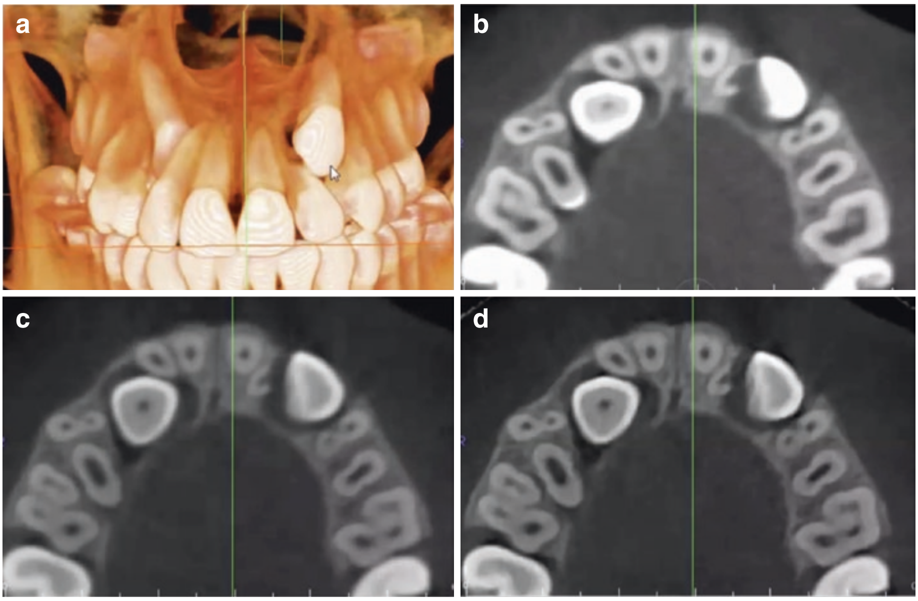

Fig. 5.53 Volumetric rendering (**a**) showing bilateral impacted and unerupted maxillary canines and axial images at default (**b**), after histogram adjustment (**c**) and after histogram adjustment and mild sharpening algorithm (**d**). Image contrast and detail (e.g., midline suture, surface resorption of adjacent roots of teeth) is discernably improved

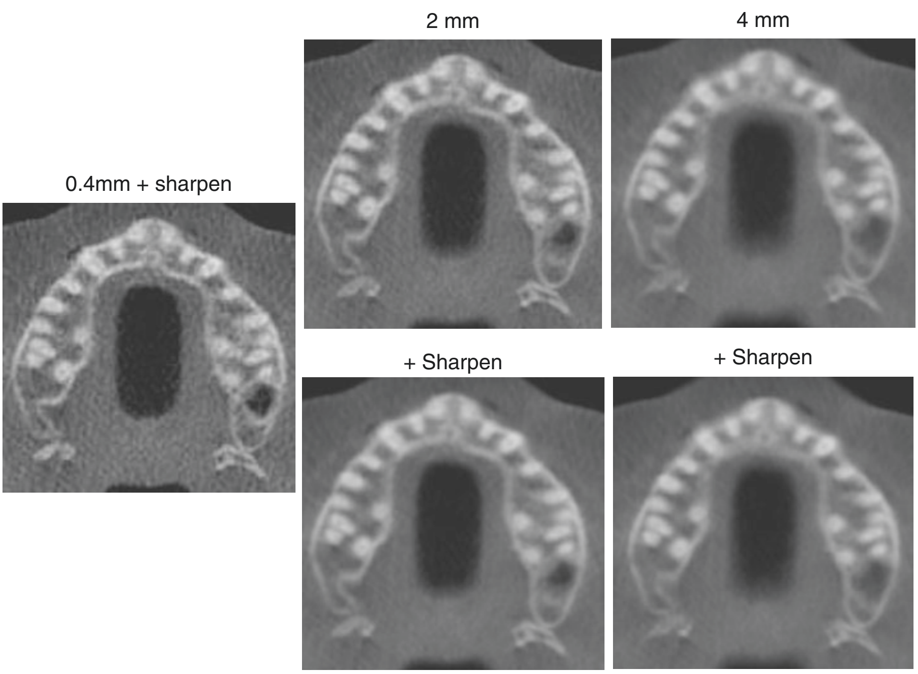

Fig. 5.54 This graphic pictorially demonstrates the effect of increasing section thickness and mild sharpening on the noise of an axial slice. The original axial image at the default resolution (0.4 mm) has had a mild sharpening filter applied. Increasing the section thickness to 2 mm alone provides a comparable image with substantially reduced noise. Adding a mild sharpened filter to this 2 mm thick image provides the optimal image. Increasing the axial image thickness to 4 mm reduces noise but is associated with the loss of edge contrast, particular in those areas that have pronounced curvature (e.g., anterior palatal cortical bone). The addition of a mild sharpening algorithm at this thickness does not improve image quality

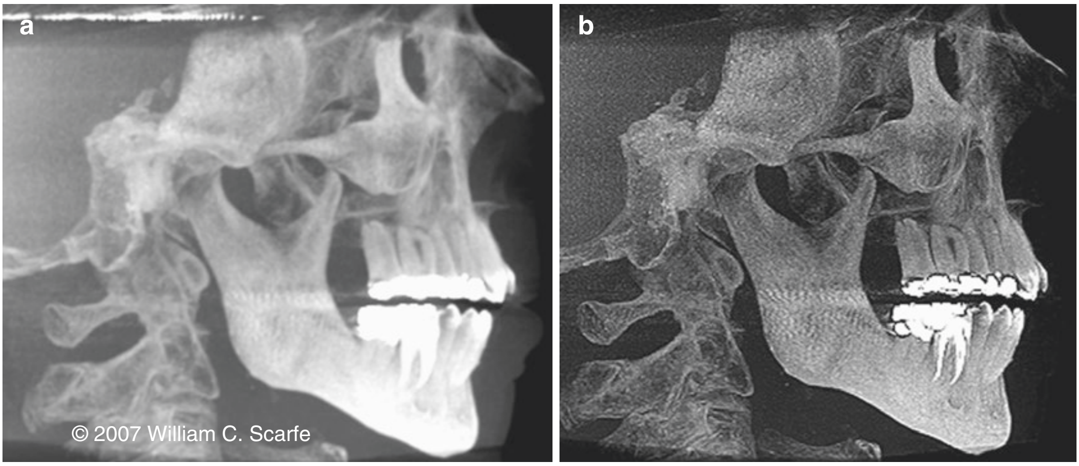

Fig. 5.55 High intensity grayscale artifacts, created due to scatter radiation or the cone beam effect can present as noise on MIP images. In this instance, the original full thickness MIP image (**a**) demonstrates unwanted noise at the level of the amalgam restorations and at the upper edge whereas image (**b**) has had a stray pixel correction applied. Note that while this reduces the effects mentioned, the resultant image is somewhat darker and grainier

In addition, the maximum intesnsity projection (MIP) algorithm can be applied. MIP algorithms determine the threshold for inclusion by considering the full range of intensities in the imaging volume, including quality signal and (interfering) noise. As all information is rendered at the same level of intensity, residual noise can become as conspicuous as anatomy. Some MIP programs provide options to optimize the performance of MIP rendering directed towards identifying noncontributing voxels and selectively eliminating them from the rendering process (Fig. 5.55).

5.2.3 Explore the Data

All maxillofacial CBCT software is screen based, providing a graphic-user-interface within a separate screen or *window* for navigation and display of image data. Each window may be subdivided into two or a series of separate compartments referred to as *frames, panels,* or *panes* (consistent with the windows analogy). The default window may allow selection or customization of the layout of the panes of that window.

All CBCT software, be it either proprietary acquisition and display original equipment manufacturer (OEM) or commercial third party display programs are capable of multiple functions. These functions can be accessed either by a series of labels or tabs identifiable within the application window or as options under specific menus on the menu bar.

The most common default presentation mode of most CBCT software and comprises three or sometimes four separate panels allowing viewing of the X–Y, Z–Y, and Z–X sections orthogonal sections (i.e., axial, coronal, and sagittal) and custom sections or a 3D to be viewed either simultaneously or individually.

Navigation refers to the process of reviewing each orthogonal series dynamically by scrolling through the consecutive image "stack" in a "cine" or "paging" mode. This can be performed either with mouse controls or by using a separate slider bar. Scrolling should be performed cranio-caudally (i.e., from "head-to-toe") and then in reverse, slowing down in areas of greater complexity (e.g., temporomandibular joint articulations, ostiomeatal complex). This scrolling process should be performed in at least two planes (e.g., coronal and axial). Viewing orthogonal projections at this stage is recommended as an overall survey for disease and to establish any presence of asymmetry.

The total number of times one should scroll through the data in each orthogonal plane is determined by a systems approach to interpretation. The maxillofacial skeleton can be considered as two interlacing components: the gnathic and the extragnathic. As one scrolls through the volume, particular attention should be paid towards the anatomy, anomalies, and pathology that presents within each structural element within that component (Table 5.11) (Figs. 5.56, 5.57, 5.58, 5.59, 5.60, 5.61, 5.62, and 5.63). Hence, with a large volume, exploring the volume may consist of multiple scrolling navigations in at least two orthogonal planes. The purpose of this is to identify incidental conditions that may influence diagnosis, treatment or have medical significance.

5.2.4 Reformat the Data

5.2.4.1 The Radiographic Toolbox

Table 5.12 summarizes various options available in the "radiographic toolbox" to reformat CBCT data providing optimal visualization and specific clinical applications for each tool (for details, see Chap. 5).

5.2.4.2 Task Specific Image Display

CBCT image display is specific to the diagnostic task as not all data reformats are necessary to adequately illustrate each clinical scenario. The set of image tools used for each diagnostic scenario is known as an image display protocol. Recognizing that facilities have different CBCT units and dental imaging software available, Tables 5.13, 5.14, 5.15, 5.16, and 5.17 provide the rationale for and guidance on image display protocols we have found useful for some clinical indications based on our experience since 2004. Detail on additional image display protocols are provided in specific chapters. For whatever diagnostic task, imaging display protocols should be based on specific rationale.

Table 5.11 Navigation checklist of elements within the two components of the maxillofacial skeleton

Components	Structural element	Region	Specific features
Gnathic	Maxilla	Dentition/Alveolus	Supernumerary teeth, intramedullary calcifications, retained root fragments
	Mandible	Dentition/Alveolus	As above
		TMJ	Intra-articular calcifications (Fig. 5.56), condylar and glenoid fossa morphology
	Soft tissues	Facial	Dermal calcifications (Fig. 5.57), localized soft tissue swellings
		Intraoral	Ductal or parenchymal salivary gland calcifications
Extragnathic	Airway	Nasal cavity	Nasal septal deviation, conchae bullosa, meatal obstructions, evidence of surgical intervention (Fig. 5.58)
		Maxillary sinus	Developmental anomalies (Fig. 5.59), partial or full opacification, ostiomeatal obstruction, intraluminal calcifications
		Upper airway	Soft tissue-based airway narrowing (e.g., adenoids, tonsils) (Fig. 5.60), calcifications
	Orbit		Physiologic calcifications, evidence of previous trauma (e.g., uncorrected orbital floor or ethmoidal blow-out fracture)
	Cervical spine		C1 and C2 anomalies, degenerative joint disease, secondary airway narrowing (Fig. 5.61)
	Cranial	Pituitary fossa	Cardiovascular calcifications (calcified internal carotid artery atheroma) (Fig. 5.62)
		Base of skull	Cardiovascular calcifications (calcified basilar artery atheroma)
		Vault	Physiologic (e.g., pineal, choroid plexus) and asymmetric pathologic calcifications (e.g., meningioma)
	Neck soft tissues		Calcified external carotid artery atheroma, physiologic calcifications (e.g., thyroid and trititeous cartilages) (Fig. 5.63)

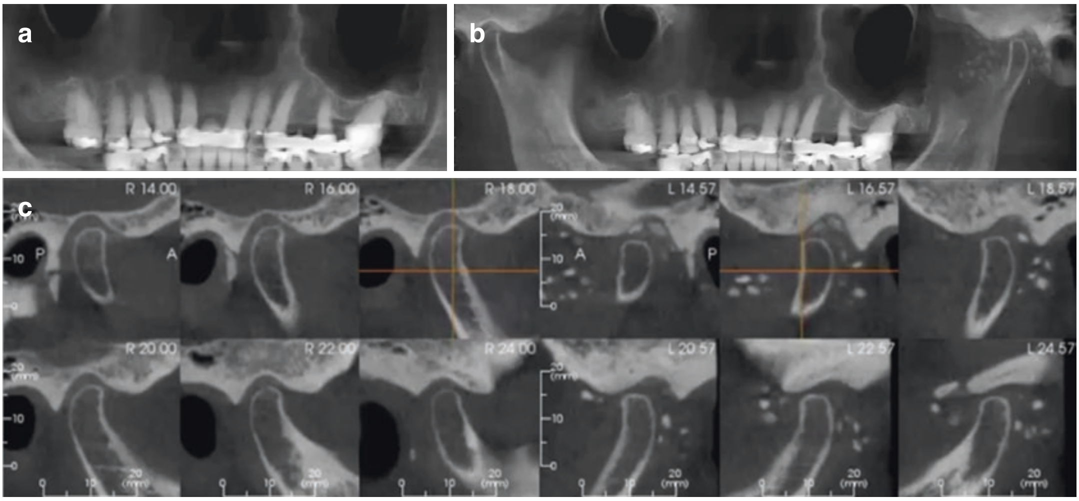

Fig. 5.56 Original reformatted panoramic image (**a**) for a patient presenting for implant site assessment in the maxillary right central incisor. Extension of the panoramic reconstruction spline to include both TMJ articulations (**b**) and subsequent para-sagittal multisectional images of the right (*right*) and left (*left*) mandibular condyle and glenoid fossa (**c**) reveal multiple intra-articular "joint mice" in the left TMJ suggestive of synovial chondromatosis. This incidental finding has substantial ramifications regarding the left joint position and therefore occlusal stability as well as the possibility of surgery

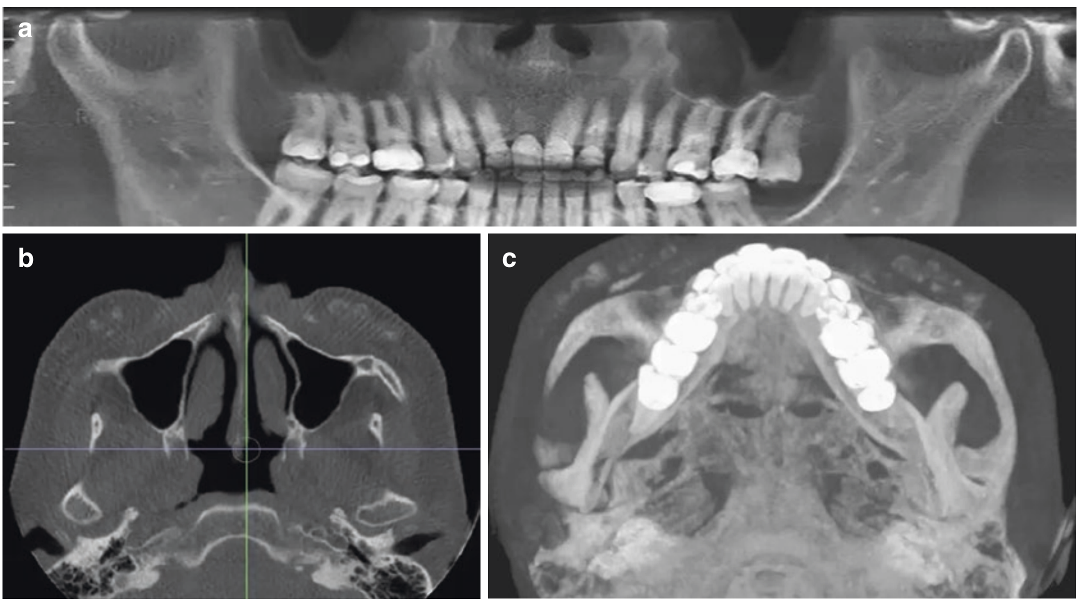

Fig. 5.57 Original reformatted panoramic image (**a**) for a patient presenting for implant site assessment in the maxillary right central incisor. Subsequent exploration of the entire volume including axial images (**b**) reveals multiple subdermal soft tissue globular calcifications in the checks bilaterally. This incidental finding was confirmed using a SMV maximum intensity volumetric rendering (**c**) and is consistent with facial aesthetic dermal filler, most likely calcium hydroxide. This finding has no consequence to the proposed treatment

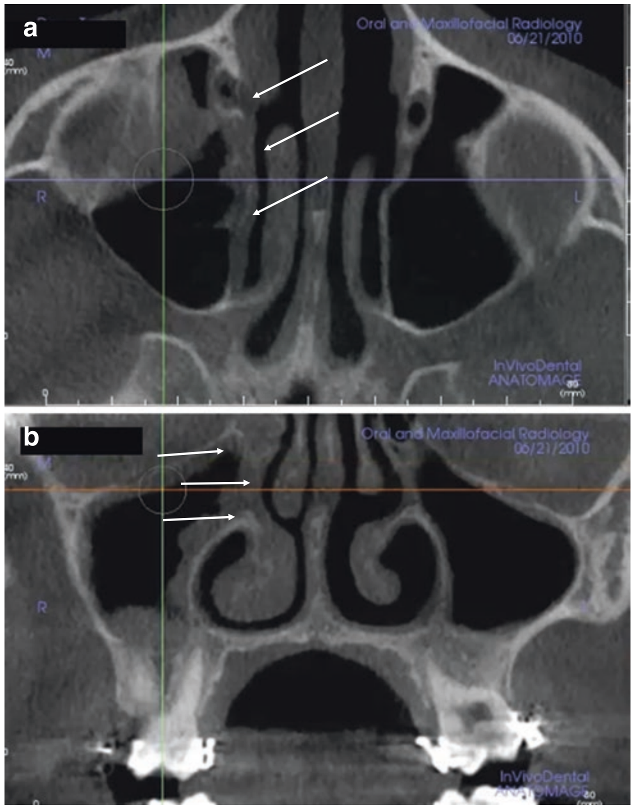

Fig. 5.58 Axial (**a**) and coronal (**b**) CBCT images demonstrating a large defect in the right superior lateral wall of the nasal cavity. Follow-up questioning revealed a patient history of chronic nasal discharge, maxillary sinus pain and recent fiber optic endoscopic sinus surgery (FESS)

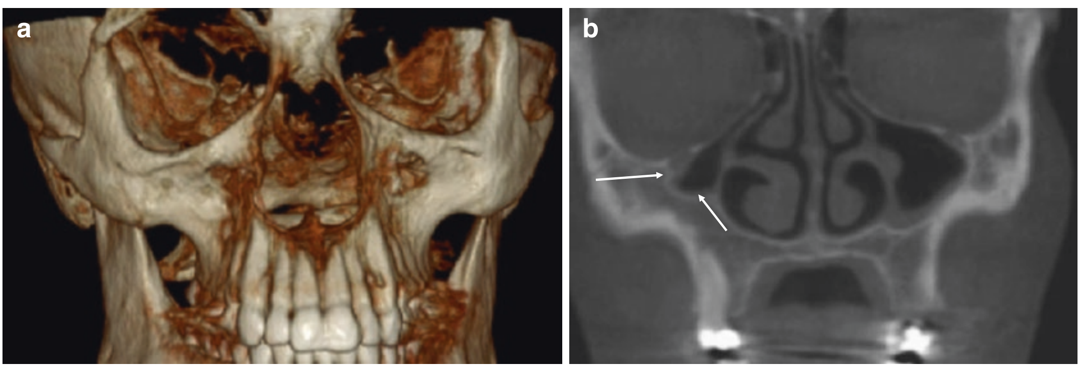

Fig. 5.59 Frontal volumetric rendering (**a**) and coronal image (**b**) showing maxillary transverse deficiency and bilateral posterior cross-bite with lack of development of the right maxillary sinus with compensatory growth of the alveolus and lateral extension of the wall of the nasal cavity. These findings are indicative of right maxillary hypoplasia and have potential significance if orthognathic surgery is anticipated because of the excessive thickness of the maxilla

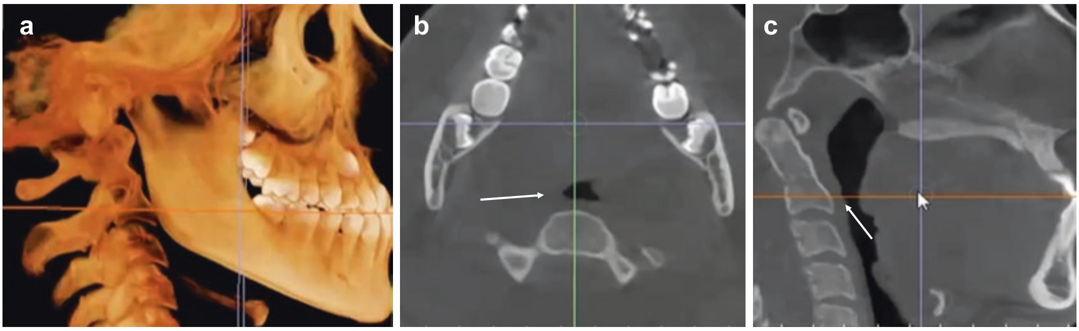

Fig. 5.60 Lateral volumetric rendering (**a**) of a patient with a skeletal Class III malocclusion and bilaterally impacted maxillary canines. Subsequent exploration of the axial (**b**) and coronal (**c**) orthogonal images reveals marked narrowing of the oropharyngeal airway space in the retropalatal region. While it was anticipated that orthognathic surgery involving a Le Forte I osteotomy would alleviate this relative obstruction, the imaging findings prompted a more thorough intraoral investigation that found enlarged tonsils contributing to the airway narrowing

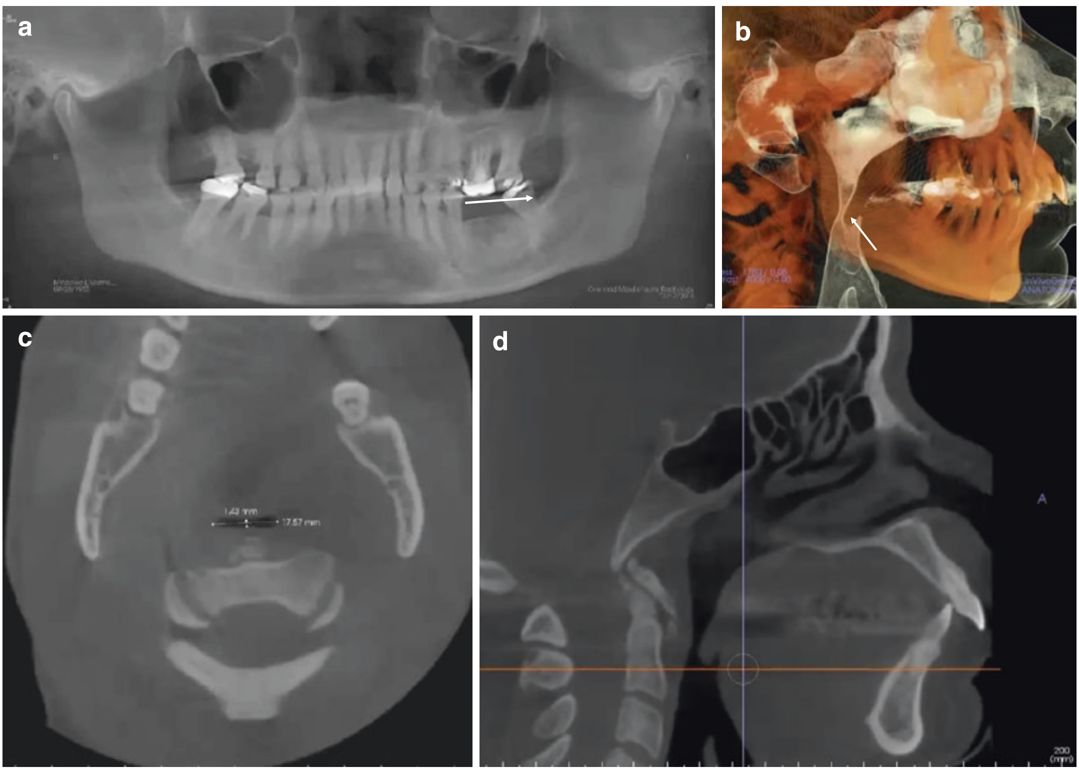

Fig. 5.61 Reformatted panoramic (**a**) and lateral volumetric rendering (**b**) of a patient with a skeletal Class II malocclusion and a history of moderate obstructive sleep apnea referred for imaging prior to orthognathic surgery. Subsequent exploration of the axial (**c**) and sagittal (**d**) orthogonal images reveal significant upper airway narrowing in the retropalatal region. Further examination of the images indicates that there is substantial osteophyte formation in the prevertebral space contributing to the airway obstruction (Image courtesy, Jack Fisher)

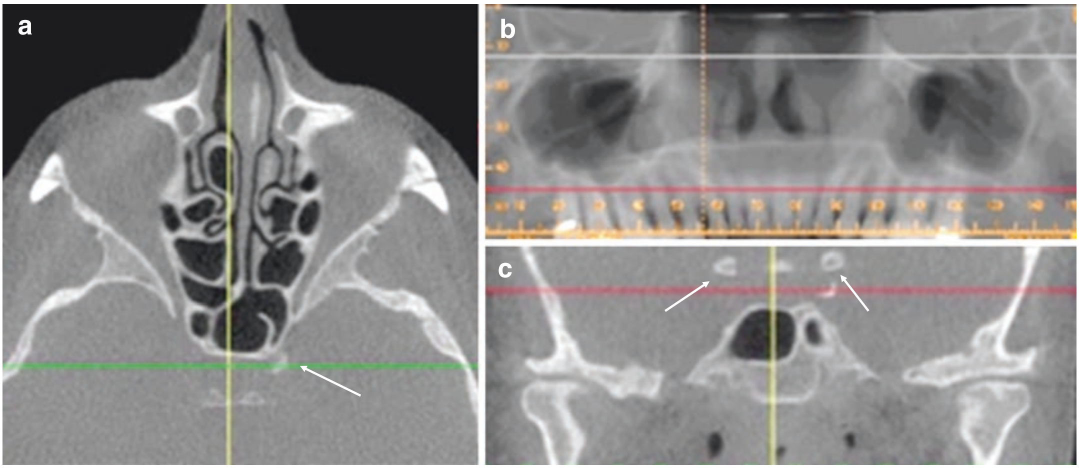

Fig. 5.62 Axial (**a**), reformatted panoramic (**b**), and coronal (**c**) images of a symptomatic patient referred for assessment of the periapical status of the maxillary posterior teeth. Subsequent exploration of the axial (**a**) and coronal (**c**) orthogonal images at the level of the pituitary fossa reveals bilateral hyperdense tubular calcified structures immediately laterally indicative of calcified internal carotid artery atheroma. In the absence of a patient history, this is a risk factor for cardiovascular disease

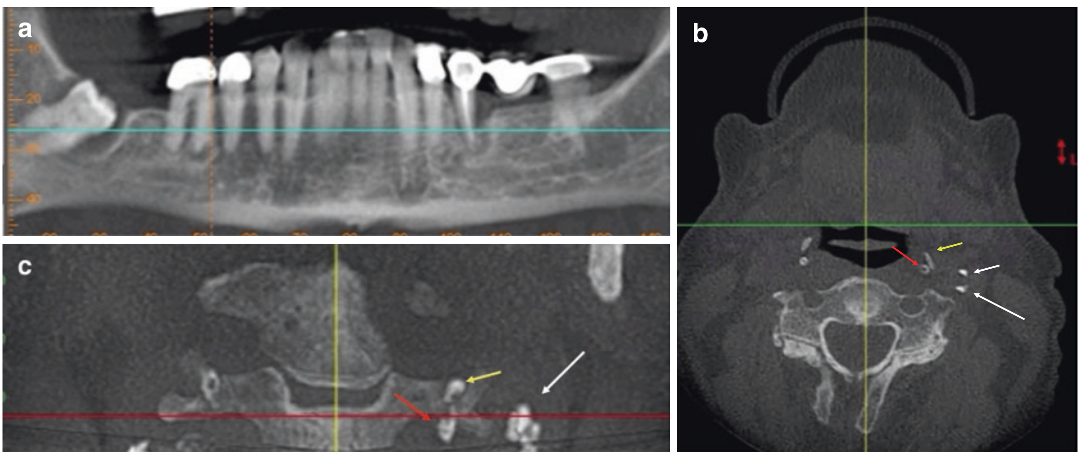

Fig. 5.63 Reformatted panoramic (**a**) demonstrating an impacted and unerupted mandibular right third molar with a pericoronal unilocular well defined hypodensity. Subsequent exploration of the axial (**b**) and coronal (**c**) images reveals a left curvilinear globular calcification (*white arrow*) anterior to the lateral tubercle of C3 and lateral to both the triticeous cartilage (*red arrow*) and greater horn of the right hyoid (*yellow arrow*) consistent with calcified internal carotid artery atheroma

Table 5.12 Summary of the radiographic reformatting options for CBCT data and their most useful clinical applications

Technique	Category	Type	Example: Most common	Example: Others
2-D	Orthogonal		Pathology, airway	Benign cysts and tumors, airway assessment
	MPR	Curved planar	Panoramic of the jaws	TMJ, the orbits, cervical vertebrae, hyoid bone or maxillary sinuses
		Linear oblique	TMJ	The inferior alveolar canal in relation to impacted third molars middle and internal ear within the temporal bone
		Serial transplanar	Cross-sectional images of the jaws	IAC in relation to impacted mandibular molars
				TMJ condylar surface and shape evaluation of pathology
Volumetric	IVR	SSD	"Solid" representation of orthodontic skeletal malocclusion	Trauma, TMJ, dental anomalies, dentomaxillofacial deformities, postoperative evaluation, soft tissue calcifications, pathology
	DVR	Ray sum	Simulated panoramic image	Simulated cephalometric image
		MIP	High contrast surface cephalometric image	Soft tissue calcifications, impacted teeth, TMJ, fractures, surgical follow-up
		Full volume texture mapping	Simultaneous representation of hard and soft tissue	Trauma, TMJ, dental anomalies, dentomaxillofacial deformities, postoperative evaluation, soft tissue calcifications, pathology
		Iso-surface rendering	Hollow modeling for airway assessment	As above

2-D two dimensional, *3-D* three dimensional, *MPR* multiplanar reformatting, *IAC* inferior alveolar canal, *IVR* indirect volume rendering, *DVR* direct volume rendering, *SSD* shaded surface display, *MIP* maximum intensity projection, *TMJ* temporomandibular joint

Table 5.13 Rationale and suggested CBCT image display protocols for a specific diagnostic task (impacted teeth) (Fig. 5.64)

Rationale	Orthogonal	MPR	Volumetric	Other
Determine tooth anatomy/ position		Pan	TMR	Cine
		XS		
Identify adjacent dental effects (e.g., resorption, ankylosis)	Orthogonal projections corrected to LAT			
Highlight surgical anatomic considerations		MIP		IAC tracing
		SSD		

MPR multiplanar reformatting, *SSD* shaded surface display, *MIP* maximum intensity projection, *Cine* dynamic volume rendering (a.k.a. movie), *TMR* texture mapped volumetric rendering, *LAT* long axis of the tooth, *Pano* reformatted "simulated: panoramic, *XS* cross-sectional images, *IAC* inferior alveolar canal

Table 5.14 Rationale and suggested CBCT image display protocols for a specific diagnostic task (Temporomandibular Joint) (Figs. 5.65, 5.66, and 5.67)

Rational	Orthogonal	MPR	Volumetric	Other
Determine TMJ morphology	Axial	Pan	TMR	
		Paracoronal and parasagittal linear oblique—closed		
Identify dental and craniofacial relationships		XS	MIP	Cine
			SSD	
Assess condylar position with jaw motion		Paracoronal and parasagittal linear oblique—open		Superimposition

MPR multiplanar reformatting, *SSD* shaded surface display, *MIP* maximum intensity projection, *Cine* dynamic volume rendering (a.k.a. movie), *TMR* texture mapped volumetric rendering, *Pano* reformatted "simulated" panoramic, *XS* cross-sectional images

Table 5.15 Rationale and suggested CBCT image display protocol for a specific diagnostic task (asymmetry) (Figs. 5.68, 5.69, 5.70, and 5.71)

Rational	Orthogonal	MPR	Volumetric	Other
Craniofacial relationships			MIP	Cine
			RS	
			TMR	
Intra-arch dental status	Axial and coronal	Pan	SSD	
		XS	RS	
Interarch dental relationship	Axial and coronal	Pan	MIP	
TMJ protocol	As in Table 5.3			
Follow-up				Superimposition

MPR multiplanar reformatting, *SSD* shaded surface display, *MIP* maximum intensity projection, *Cine* dynamic volume rendering (a.k.a. movie), *RS* ray-sum, *TMR* texture mapped volumetric rendering, *Pano* reformatted “simulated: panoramic, *XS* cross-sectional images

Table 5.16 Rationale and suggested CBCT image display protocol for a specific diagnostic task (upper airway) (Figs. 5.72, 5.73, 5.74, and 5.75)

Rationale	Orthogonal	MPR	Volumetric	Other
Airway morphology	Axial, midsagittal and coronal		ISR	Cine
			TMR	
Airway analysis	Axial, midsagittal and coronal		ISR	
Relationship to craniofacial structures (e.g., hyoid, palate, mandible)		MIP	TMR	
			RS	
Predictive or treatment effects				Superimposition

MPR multiplanar reformatting, *ISR* iso-surface rendering, *SSD* shaded surface display, *MIP* maximum intensity projection, *Cine* dynamic volume rendering (a.k.a. movie), *RS* ray-sum, *TMR* texture mapped volumetric rendering, *Pano* reformatted “simulated: panoramic, *XS* cross-sectional images

Table 5.17 Rationale and suggested CBCT image display protocol for specific diagnostic task (pathology) (Figs. 5.76, 5.77, and 5.78)

Rationale	Orthogonal	MPR	Volumetric	Other
Lesion features (e.g., location, margins, size, shape, borders, internal structure)	Axial, sagittal and coronal	Pano XS	TMR	Cine
Effect and relationship to adjacent structures	As above		MIP	
			TMR	
Surgical considerations	As above		TMR	IAC tracing
			RS	

MPR multiplanar reformatting, *ISR* iso-surface rendering, *SSD* shaded surface display, *MIP* maximum intensity projection, *Cine* dynamic volume rendering (a.k.a. movie), *RS* ray-sum, *TMR* texture mapped volumetric rendering, *Pano* reformatted “simulated: panoramic, *XS* cross-sectional images, *IAC* inferior alveolar canal

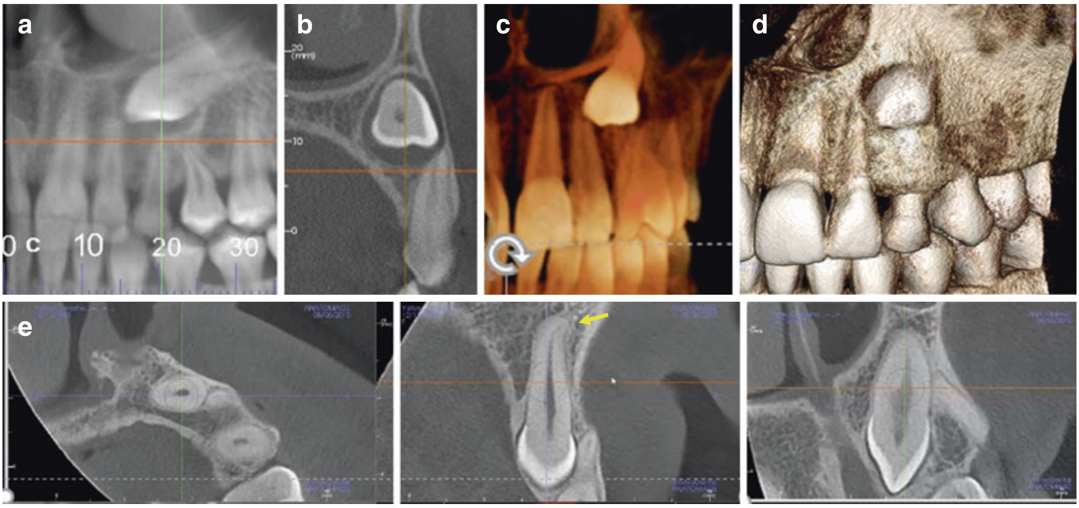

Fig. 5.64 Representative task specific display for an impacted tooth (maxillary canine) consisting of reconstructed simulated panoramic (**a**), cross-sectional images (XS) (**b**), texture mapped rendering (**c**), shaded surface display (SSD) (**d**) and orthogonal (axial, coronal, and sagittal) projections corrected to the long axis of the impacted tooth. Note that the only image that clearly identifies an apical dilaceration (*yellow arrow*) potentially inhibiting orthodontic retraction of this impacted maxillary canine is the sagittal image aligned to the long axis of the tooth (**e**). In addition, while the SSD shows that the crown of the tooth perforates the buccal cortical plate, the XS and orthogonal projections clearly demonstrate an intact labial cortical bone

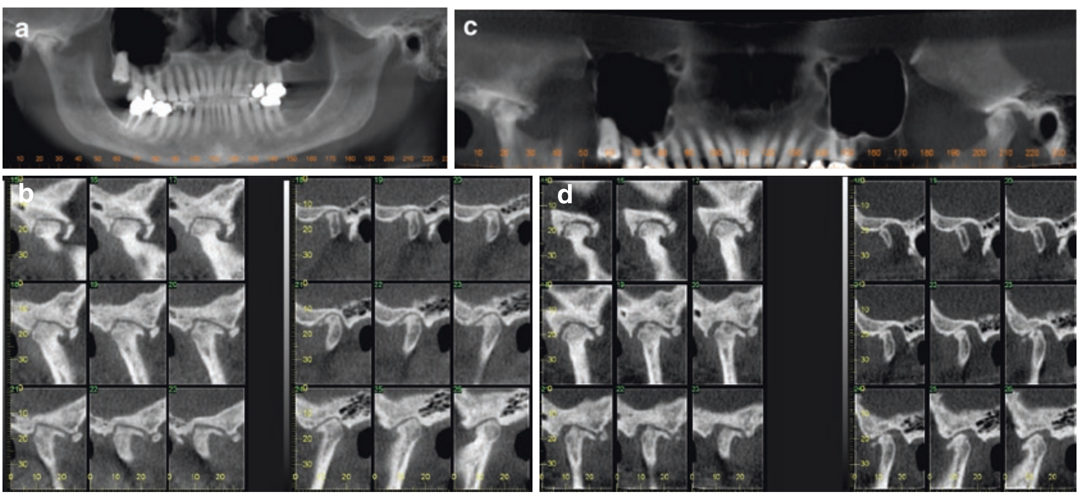

Fig. 5.65 Representative task specific display for the TMJ consisting of reconstructed simulated panoramic (*upper*) and left and right parasagittal cross-sectional images (*lower*) in both closed (**a**, **b**) and open (**c**, **d**) jaw position

5.3 Image Analysis

The purpose of image analysis is to provide quantitative evaluation of morphologic features and interrelationships of various objects and structures within the volumetric dataset. The most common metrics are linear, area and volumetric measurements and grayscale intensity values together with numerous image feature identification aides.

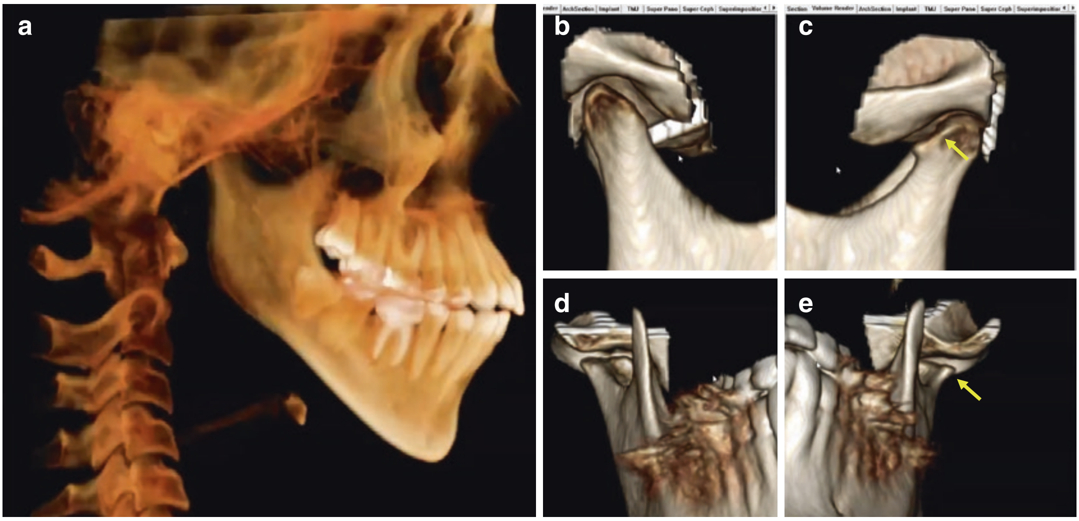

Fig. 5.66 Comparison of full texture volumetric rendering (**a**) and shaded surface display (SSD) (lateral, **b** and **c**; frontal inferior oblique, **d** and **e**) for a young adult with high mandibular plane angle, shortened ramus and anterior open bite. Subtle flattening of the lateral pole of both condyles (more severe on the *left—yellow arrow*) is visually demonstrated by the SSD renderings

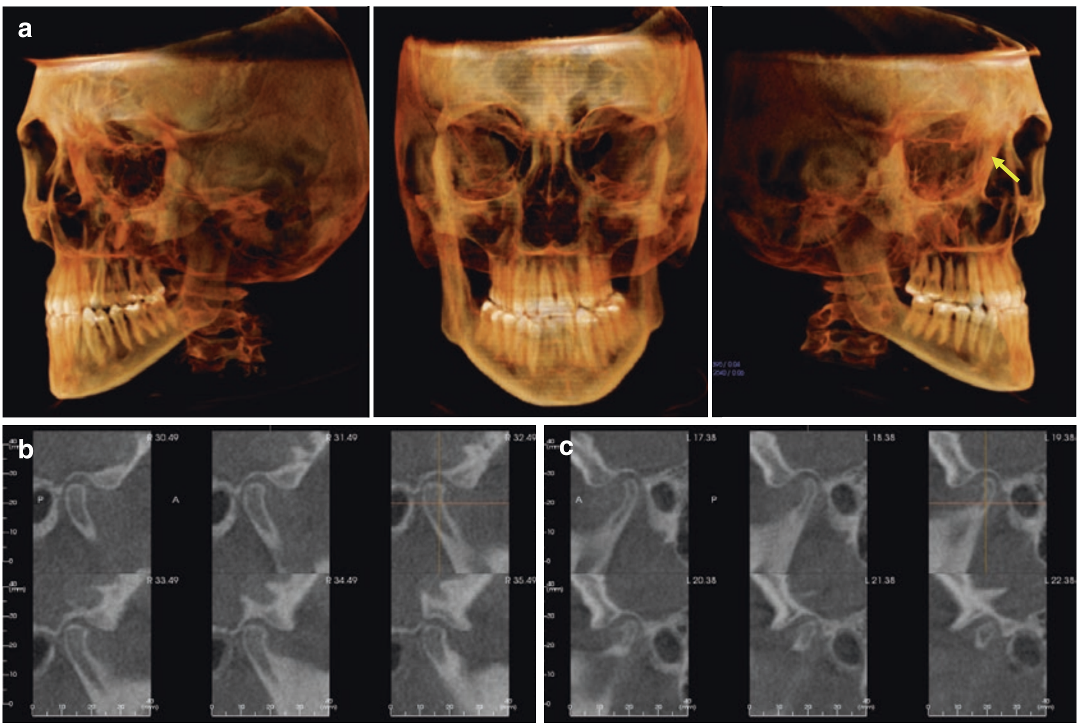

Fig. 5.67 Left oblique, frontal and right oblique full texture volumetric rendering (TVR) (**a**) and serial parasagittal images of the *right* (**b**) and *left* (**c**) TMJ articulations for a young man with a skeletal and dental Class III malocclusion with anterior and posterior cross-bites. The left parasagittal images (**c**) demonstrate a relatively hypoplastic mandibular condyle and substantial osteophyte formation; however, the maxillary transverse discrepancy (more severe on the *left*) is only demonstrated by the TVR images

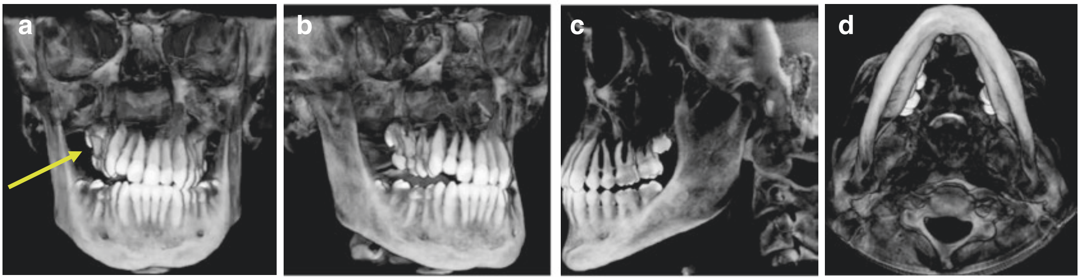

Fig. 5.68 Sequential maximum intensity projection (MIP) frontal (**a**), right lateral oblique (**b**), left half lateral (**c**), and submentovertex (**d**) key frames in a cine format (i.e., movie) demonstrating maxillary asymmetry due to right maxillary alveolar dental hypoplasia (*yellow arrow*) and effects on craniofacial relationships

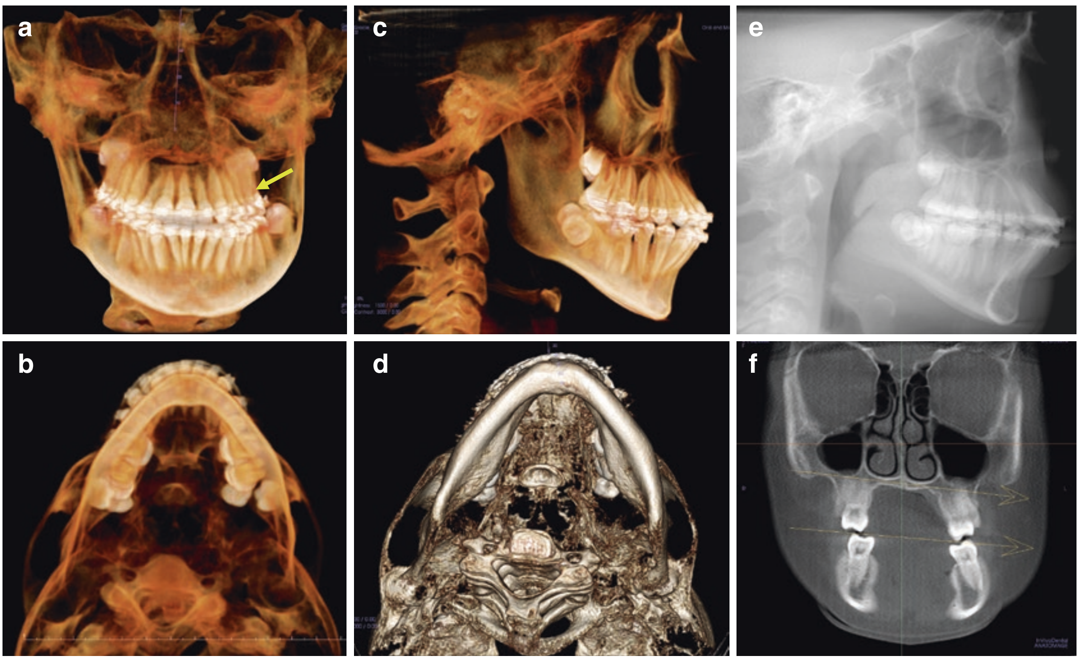

Fig. 5.69 Frontal (**a**), submentovertex (**b**) (SMV) and right lateral (**c**) texture mapped volumetric rendering and corresponding shaded surface display SMV (**d**) pictorially shows craniofacial relationships including a maxillary unilateral cross-bite due to left maxillary hypoplasia and concomitant anterior open bite with bi-maxillary protrusion. The right lateral ray sum image (**e**) is used to provide a cephalometric analysis whereas the coronal orthogonal image (**f**) shows interarch dental relationships including asymmetry of the palatal plane and occlusal cant

5.3.1 Dimensional Accuracy

In CBCT, volumetric reconstructions are usually performed such that voxels are isotropic—dimensionally the same in all directions resulting in a cubic voxel. Ideally, the dimension of the reconstructed voxel side may correspond to the dimension of the pixel side in the image detector. This condition results into optimization of the relation between information content (i.e., maximum spatial resolution) and size of the volumetric dataset. However, it is not unusual that the reconstructed voxel side is larger than the original pixel side in the detector, and sometime that the longitudinal dimension of the voxel (= the “slice thickness”) is different (and usually larger) than the voxel

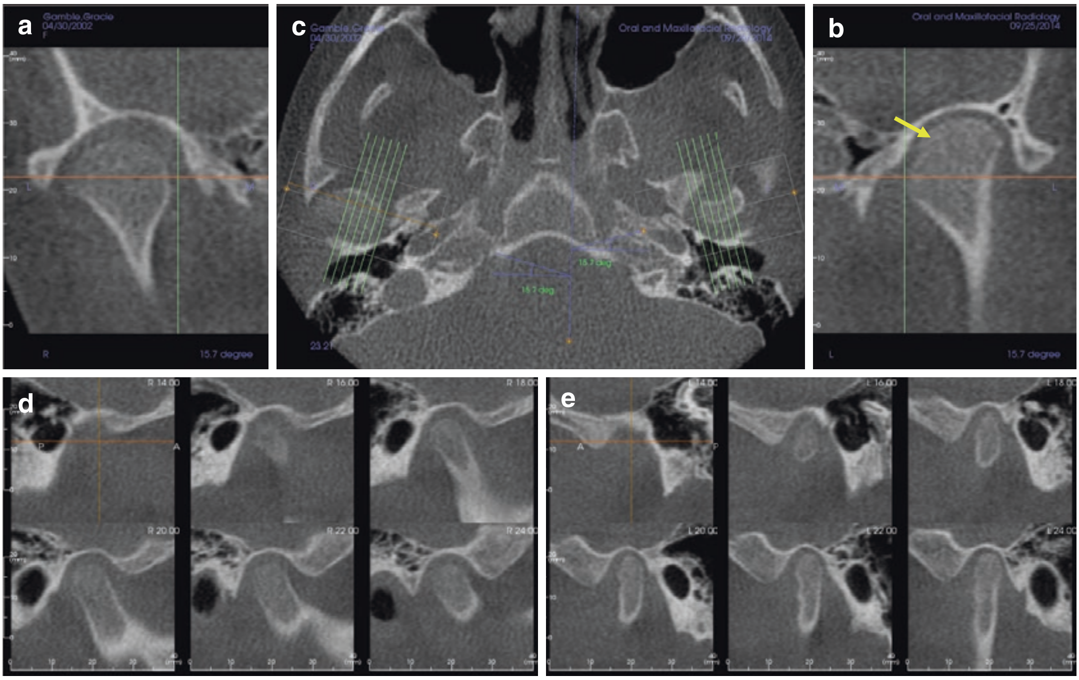

Fig. 5.70 TMJ imaging protocol of the same individual in Fig. 5.69 consisting of *right* (**a**) and *left* (**c**) paracoronal, reference axial (**b**) and *right* (**d**) and *left* (**e**) parasagittal images demonstrating concomitant left mandibular condylar hyperplasia. Task specific imaging protocols including the TMJ display form an integral component in the assessment of asymmetry

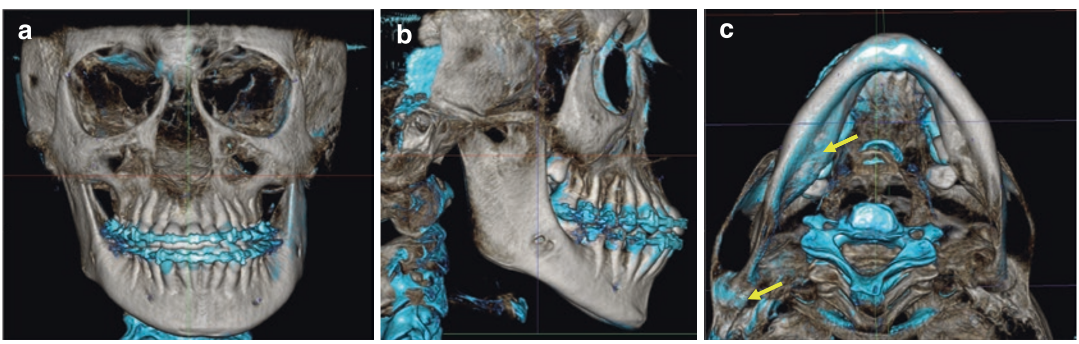

Fig. 5.71 Shaded surface display frontal (**a**), right lateral (**b**) and SMV (**c**) superimposition of the same individual in Figs. 5.69 and 5.70 showing a 6-month discrepancy (*blue*) after fixed orthodontic appliance therapy. Little change is noted except in the position of the crowns of the right dentition and right mandibular condyle (*yellow arrows*)

dimensions on the axial "slices." This is because: (1) the dataset at full spatial resolution often results in image rendition being noisier than desirable, and (2) to provide a method (slice thickness) of adjusting resolution—and consequently controlling noise—familiar to the user of conventional CT systems. Note that volumetric reconstruction may produce voxels with sides smaller than the pixels in the image detector ("oversampling"). However, this results in very

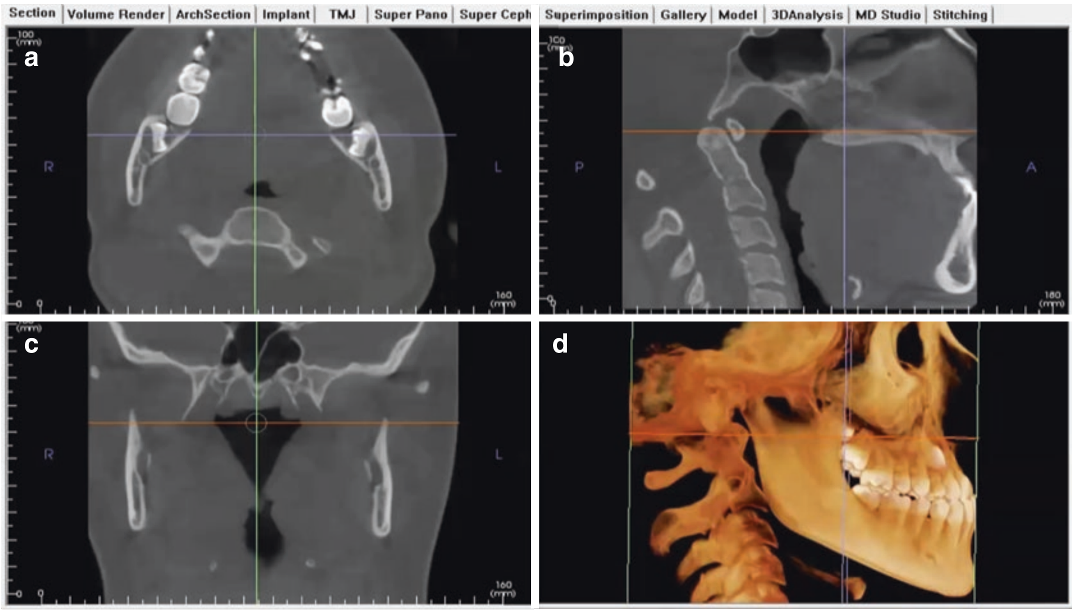

Fig. 5.72 Axial (**a**), midsagittal (**b**), and coronal (**c**) orthogonal images and a right lateral textured mapped volumetric rendering (**d**) of an individual demonstrating a Class III skeletal and dental malocclusion and concomitant marked reduction in the retropalatal airway

large and noisy volumetric datasets without better actual resolution or information content.

No matter what the voxel dimensions are or whether they are isometric or not, the rendition of a CBCT reconstructed volumetric dataset can theoretically be achieved with near-perfect geometrical accuracy. This is because the software locates the geometrical characterization of the voxel within the dataset. However, numerous acquisition parameters may influence dimensional accuracy of the volumetric dataset. Inadequate calibration of the geometrical parameters in reconstruction program may lead to inaccuracies.

Of particular note, image intensifier detectors, unlike flat panel detectors, inherently suffer from minor geometric distortions. Therefore, image intensifier-based CBCT systems need to preprocess the raw images prior to volumetric primary reconstruction in order to eliminate or reduce such geometric distortions. This is accomplished by acquiring raw datasets of a calibration test phantom of precisely known geometrical characterization; a software algorithm automatically computes the geometrical transformations that—frame by frame—must be applied to the acquired raw images in order to display the test phantom undistorted; such transformation is then automatically applied to all subsequently acquired datasets. However, geometric distortions in image intensifiers are affected by the local magnetic field (including, to some extent, the Earth's magnetic field) and may change over the time. Geometrical calibration may need to be repeated frequently, and there is no absolute guarantee that the geometrical distortions have been completely compensated at a given time. This could affect the resolution, or image sharpness. However, spatial measurement accuracy of the reconstructed volumetric datasets is not significantly affected.

Numerous authors reporting measurements obtained from axial, MPR, or 3D reconstructed images of CBCT images for various clinical applications indicate a sub-millimeter accuracy consistent within ±2× the voxel resolution of the system investigated.

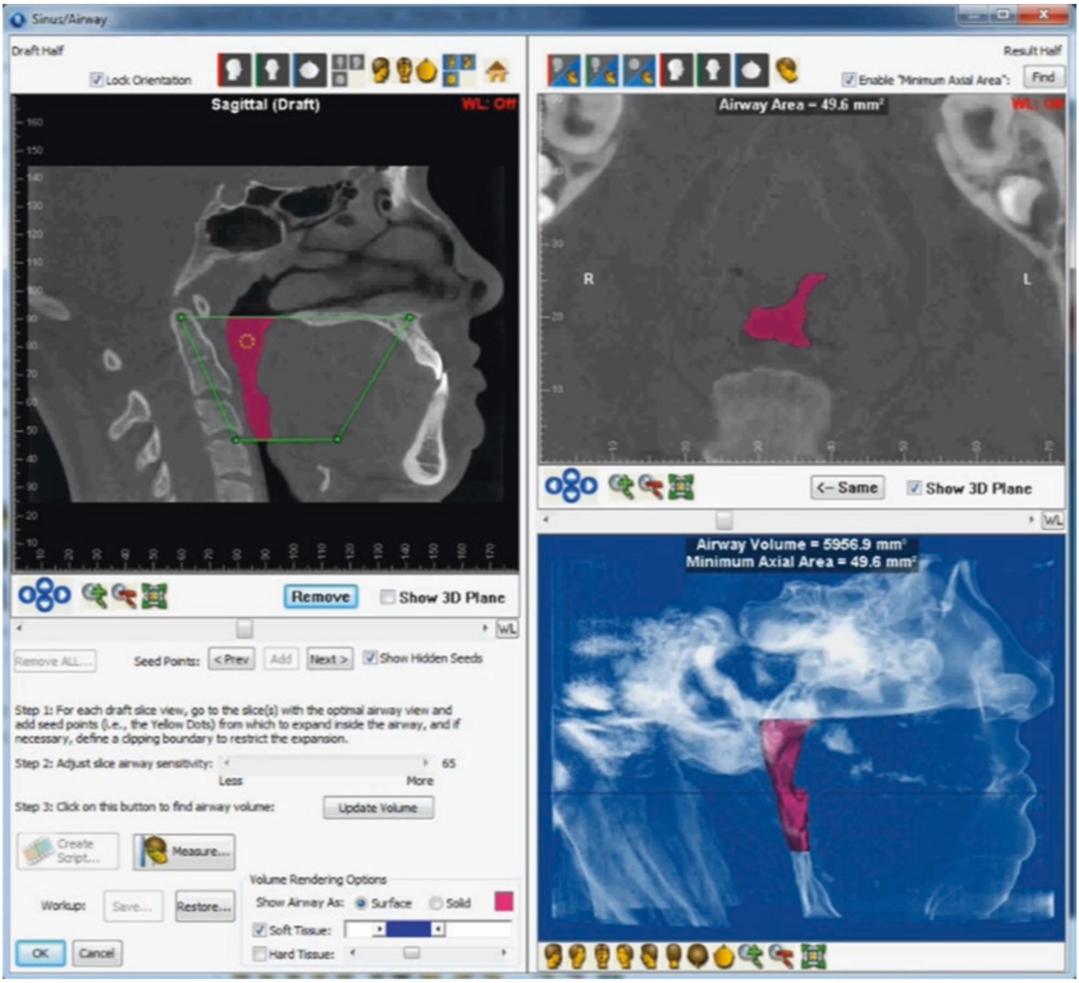

Fig. 5.73 Screen capture of airway analysis module of dental imaging software (Dolphin Imaging, Dolphin Imaging and Management Solutions, Chatsworth, California, USA) of the same patient in Fig. 5.72 with reference midsagittal orthogonal plane (*upper left*) showing the upper and lower boundaries for the analysis. The axial image (*upper right*) shows the level of the airway with the minimal cross-sectional area (49.6 mm^2) and the iso-surface rendering of the airway and the face (*lower right*) shows a volumetric solid rendering based on a limited range of values

5.3.2 Contrast Accuracy in CBCT

Multi-detector CT has been used for the assessment of intramedullary bone quality using region of interest Hounsfield units (HUs) as an index of bone density. For the jaws, Misch characterizes quality into four levels based on HU range (D1 bone, >1250 HU; D2 bone, 750–1250 HU; D3 bone, 375–750 HU; D4 bone, <375 HU) (Misch 2008). However, there are differences between cone beam and conventional CT imaging that make the conversion of gray intensity values recorded in CBCT to HU problematic (Molteni 2013; Pauwels et al. 2015b). These include differences in acquisition geometry producing substantial scatter, imaging detector inefficiencies, the presence of inherent artifacts (e.g., projection data discontinuity-related (Katsumata et al. 2007)) and introduced high-density (e.g., metallic) artifact effects, as well as the limitations of current reconstruction algorithms software.

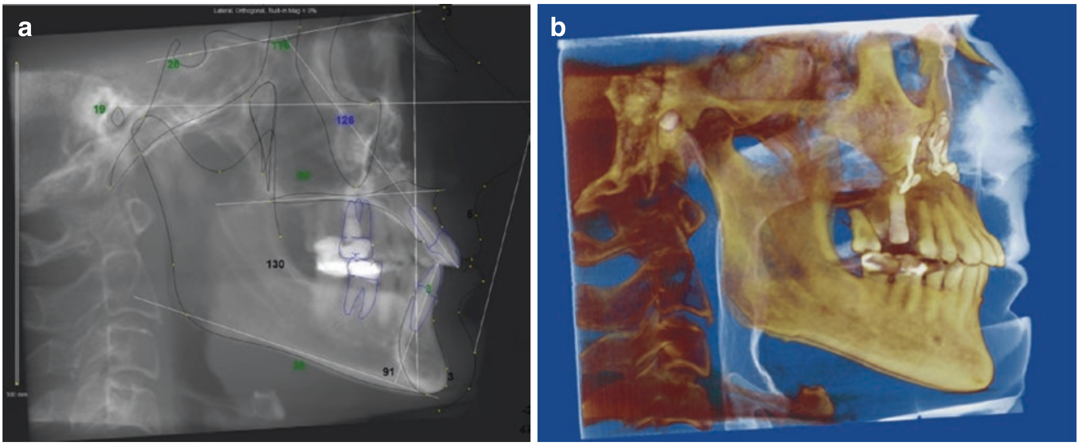

Fig. 5.74 Right lateral ray sum (**a**) with superimposed cephalometric analysis and corresponding composite texture mapped and iso-surface volumetric rendering (**b**) demonstrate the relationship of the airway to the craniofacial structures

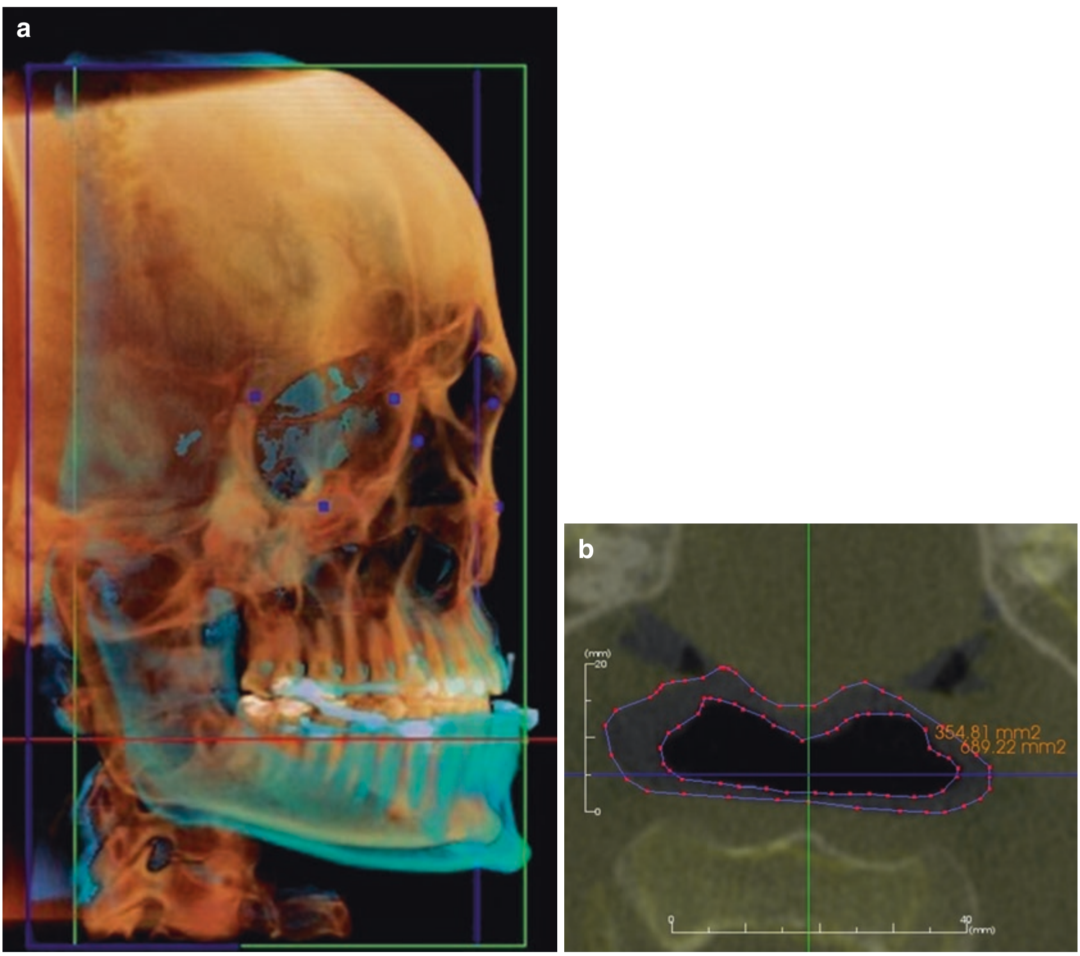

Fig. 5.75 Right lateral oblique projection of a texture mapped volumetric rendering superimposition before and after (*turquoise*) insertion of a mandibular advancement device (**a**) to assess the possible therapeutic change in airway. Superimposition of the axial images at the level of the minimal cross-sectional area before and after (*turquoise*) insertion of a mandibular advancement device (**b**) clearly demonstrates an almost 200% increase in airway surface area

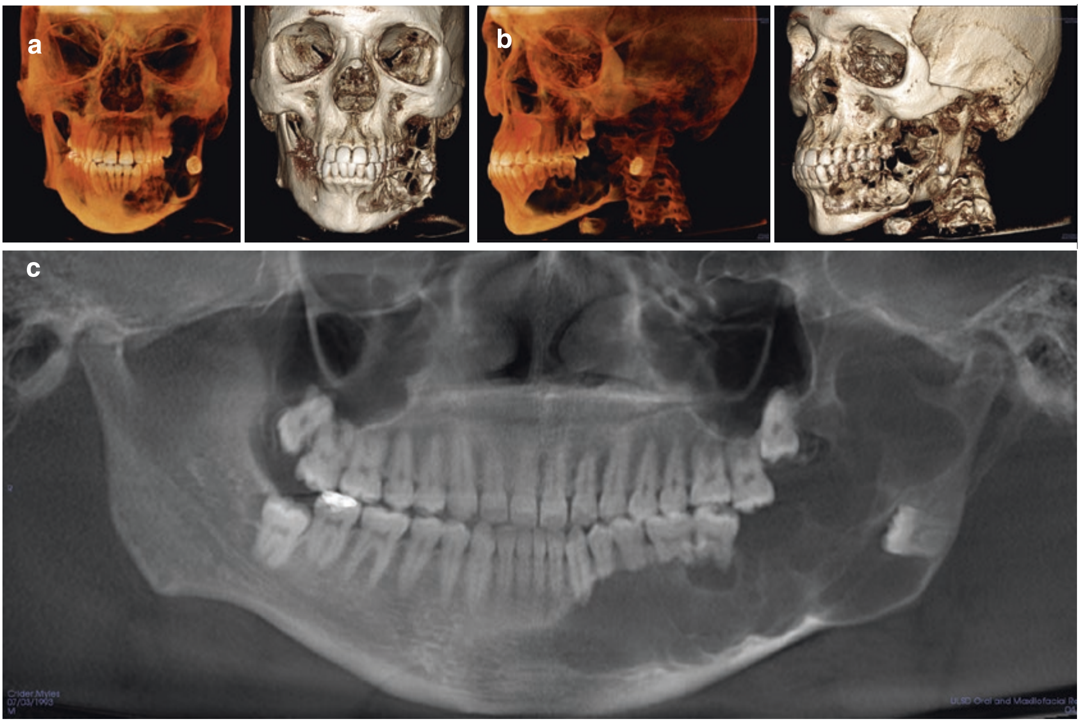

Fig. 5.76 Frontal (**a**) and right lateral oblique (**b**) volumetric and shaded surface renderings and a reformatted panoramic image (**c**) showing lesional features and the effect and relationship of a left mandibular multilocular hypodensity (histologically confirmed as an ameloblastoma)

The resultant interaction of these effects means that identical tissues may present apparently different grayscale intensity values depending upon their position and relation with other tissues in the irradiated field (Fig. 5.79) (Katsumata et al. 2007; Pauwels et al. 2015b). While some authors have reported a level of inter equipment reliability (Aranyarachkul et al. 2005; Lagravere et al. 2006; Kim et al. 2014), currently the Hounsfield scale index from CBCT machines should be recognized as being subject to significant variability and avoided. In fact, some commercially available CBCT systems do not provide readouts in HU. Continuing research into density corrections via calibration using software compensation are necessary before the clinical significance of quantitative bone density measurements from these devices can be established. In addition, recent investigators have shifted bone quality assessment from a density-based analysis to a structural evaluation of the bone.

5.3.3 Feature Identification Aids

Various graphic user interface (GUI) choices are available to accentuate, highlight, or identify specific anatomic features or relationships on CBCT images, some of which are proprietary or patented.

5.3.3.1 Inferior Alveolar Canal Tracing

Tracing the path of the inferior alveolar canal (IAC) for the purpose of better recognizing its spatial relationship to the roots of teeth or course within the intramedullary mandibular bone is one of the most popular and common feature identification aids available in the majority of commercial software for dental imaging. The method always consists of identifying the position—in three dimensions—of a sufficient number of nodal points within the inferior alveolar canal, from its origin at the mandibular foramen, to the mental foramen and, in some cases, the terminal

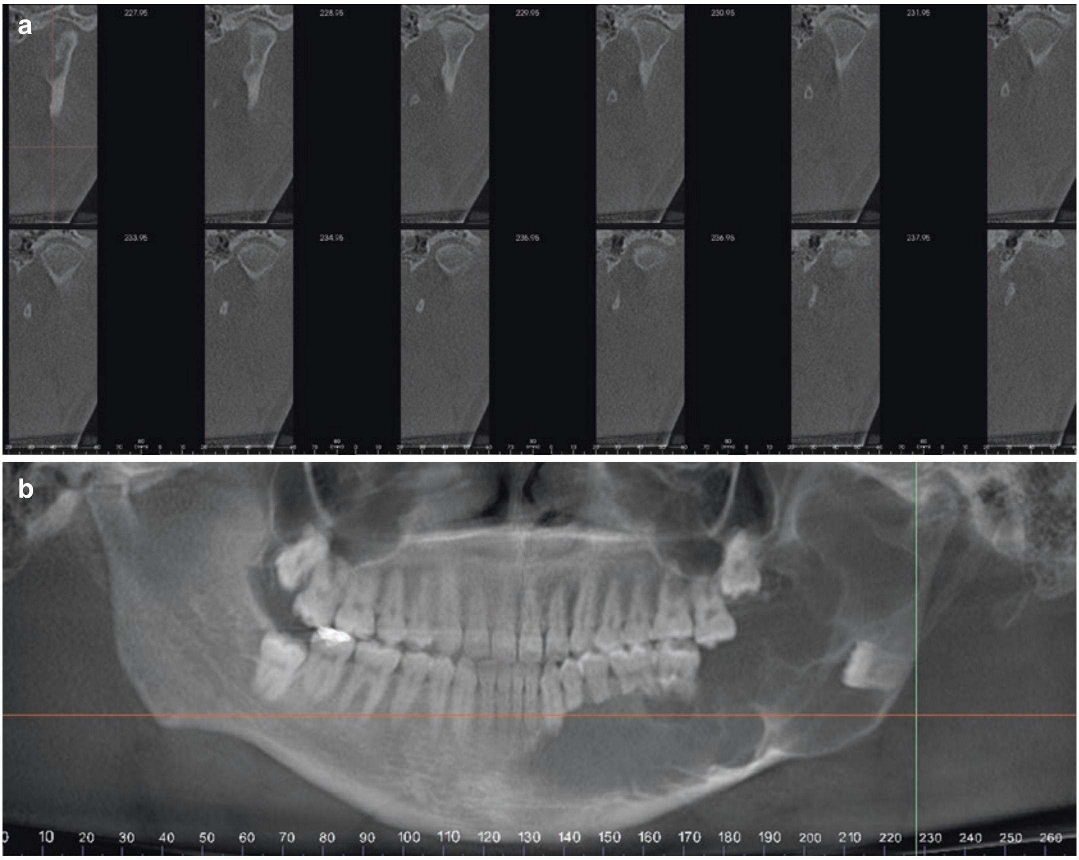

Fig. 5.77 Serial cross-sectional (**a**) and reference reformatted panoramic image (**b**) of the same individual as in Fig. 5.76 showing the extent of the lesion in the region of the left mandibular condyle. Because of the extension of the lesion and involvement of the condyle, the surgical resection included this structure

intramedullary branch, the incisive canal. Nodal points are connected automatically by a line in bright and contrasting color to highlight the path of the IAC. The thickness of the line is adjustable by the operator. The line is visible in all 2D images and volumetric renderings (Fig. 5.80). Nodal points may be identified and marked by the operator on a thin section MPR panoramic image projection. Alternately, the position of the IAC may be identified and marked from (thin) transversal slices of the mandible.

5.3.3.2 Volume Measurement

The representation of luminal space represented on CBCT by volumetric segmentation techniques currently has applications in two areas within dentistry.

- *Upper Airway Assessment.* The evaluation of the characteristics of the upper airway involves segmentation of the airway space. Segmentation is achieved either manually or semiautomatically. The manual approach requires that segmentation is performed slice by slice by an operator and then all slices combined to form a 3D volume. Semiautomatic segmentation of the airway is more commonly available in dental software. It requires (1) identification of the upper and lower limits of the segmentation (boundaries) and (2) identification of the airway space by cursor driven placement of a “seed” point. The seed point identifies the gray value intensity threshold interval or range of values to be used for segmentation. Current dental

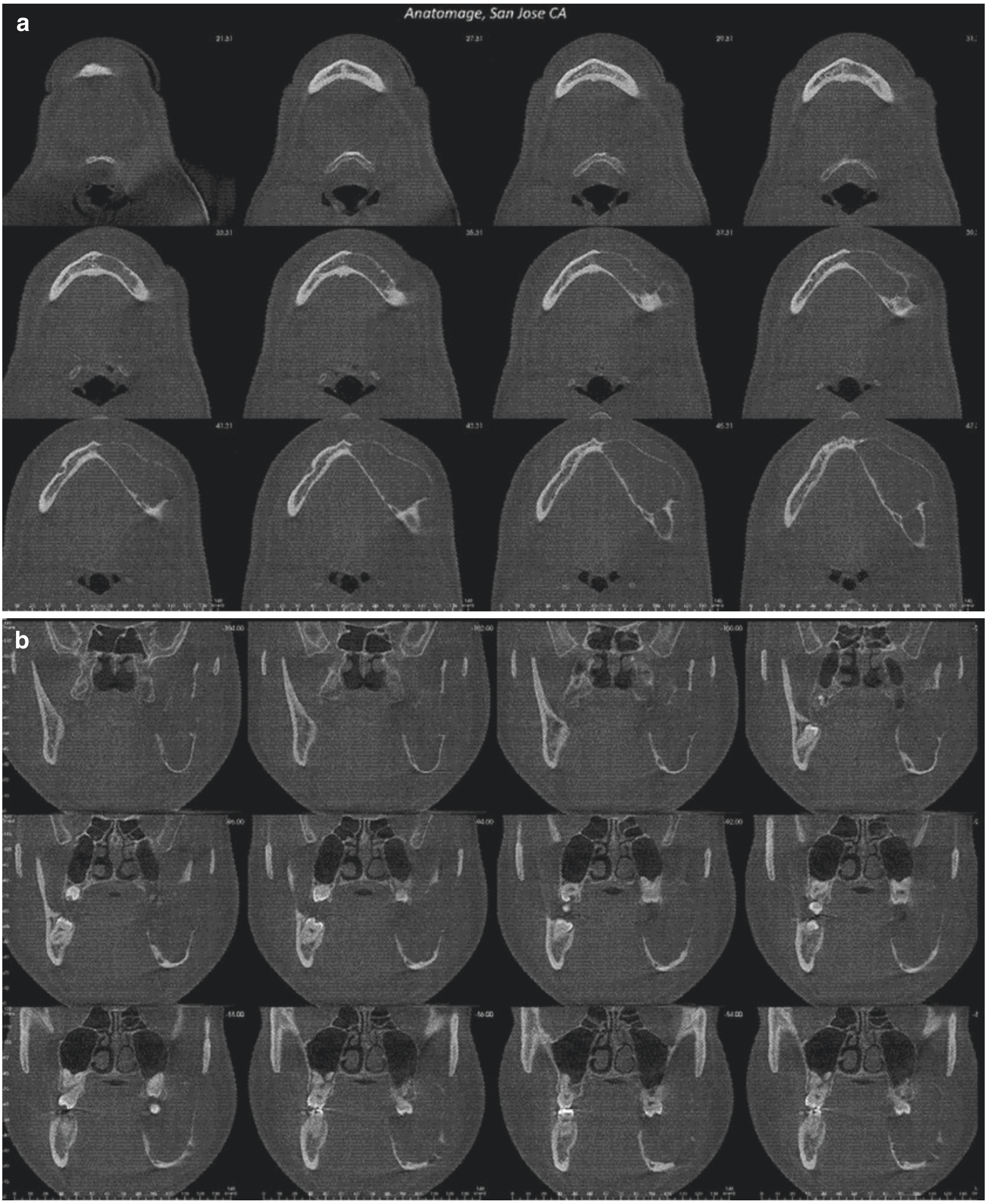

Fig. 5.78 Serial axial (**a**) and coronal (**b**) images of the same individual as in Fig. 5.76 establishing the anterior extent of the left mandibular lesion and demonstrating lesional borders, expansion and internal structures

software is reliable in calculating volume with interactive thresholding software (Fig. 5.81) having less than 2% error and fixed threshold software (Fig. 5.82) having 6.4–11.7% error (Weissheimer et al. 2012). Once an airway has been segmented into a volume, other dimensions such as volume and minimal cross-sectional area and minimal transverse and AP distances can be measured.

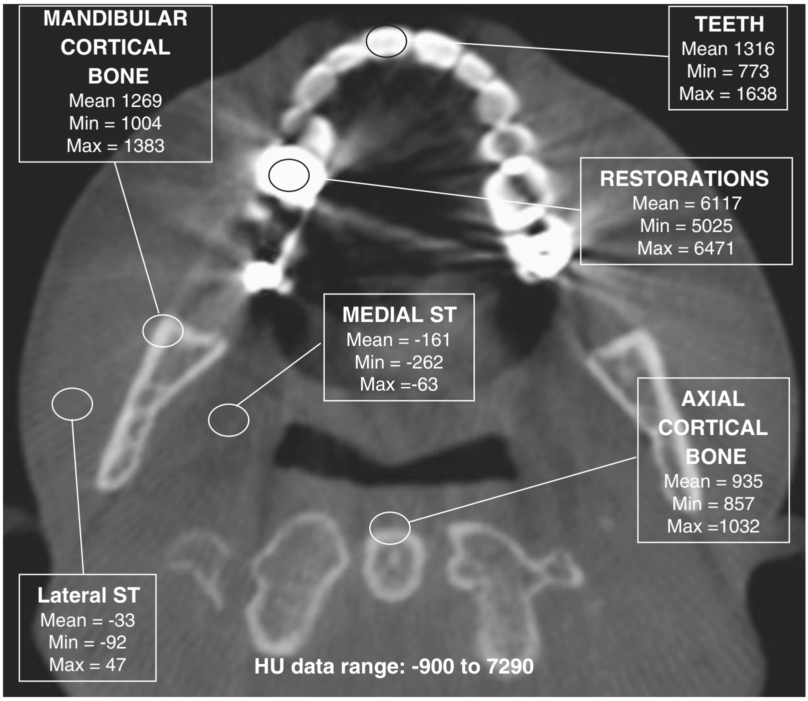

Fig. 5.79 Representative axial image providing standard area mean, minimum (Min) and maximum (Max) gray intensity values for multiple regions of interest (*white* and *black circles*). While many areas should provide similar intensity values (e.g., lateral soft tissue (ST) = medial ST; axial cortical bone = mandibular cortical bone), the measured values vary greatly

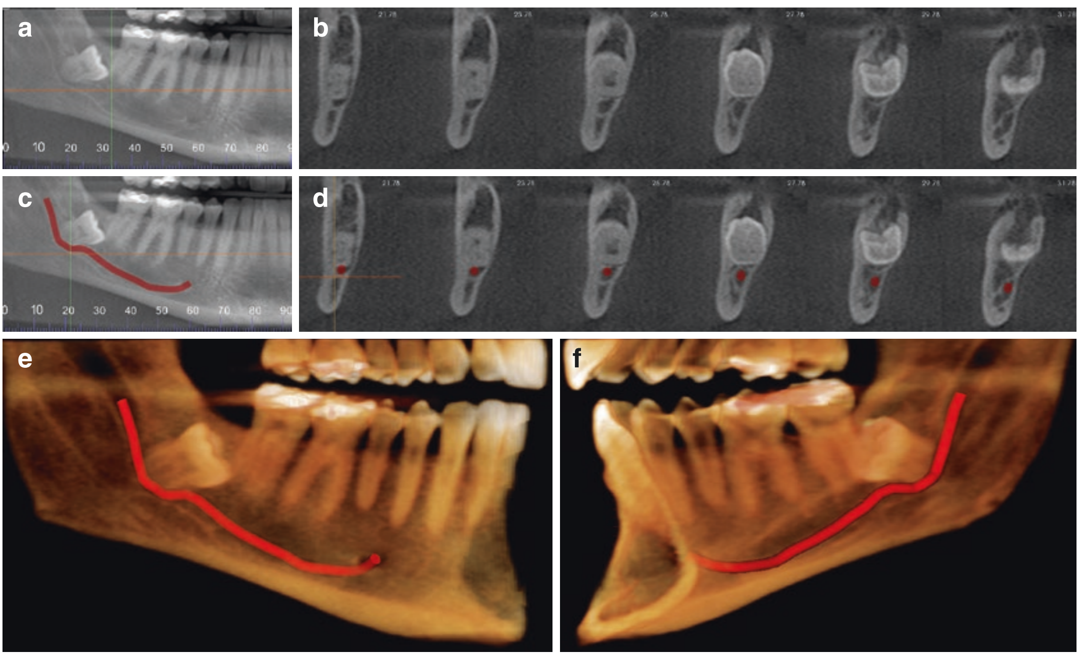

Fig. 5.80 Right mandibular cropped panoramic MPR (**a**) with corresponding 1 mm thick cross-sectional images (**b**) through the apical third of the root. Identical panoramic (**c**) and cross-sectional images (**d**) with the inferior alveolar canal (IAC) traced and highlighted (*red*). Volumetric facial (**e**) and lingual (**f**) renderings with the IAC identified

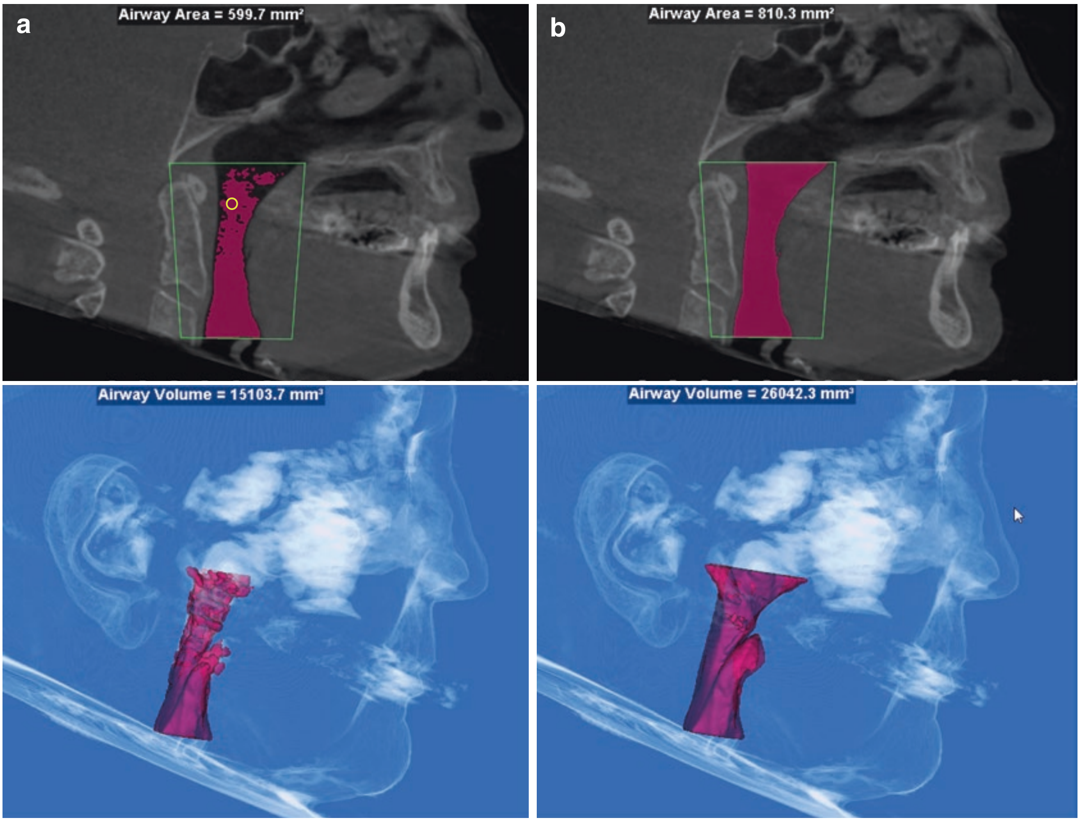

Fig. 5.81 Example of interactive thresholding software demonstrating midsagittal CBCT image (*upper*) with variably defined boundaries (*green lines*) with corresponding hollow model (*lower*) volumetric images. Significant differences in calculation of total airway volume and minimal airway cross-sectional dimension occur based on adjust of the sensitivity of seed point (*yellow dashed circle*) from a default value (**a**—25) to a value manually adjusted to include the entire airway periphery (**b**—50)

- *Maxillary Sinus Graft Volume Assessment.* The required graft volume for maxillary sinus floor augmentation can be calculated using a similar technique to upper airway segmentation or specific additive, free-form simulations. Calculation of the augmentation size may be helpful in determining the surgical approach or to quantitatively monitor postoperative volumetric bone changes.

5.3.3.3 Virtual Reality

In addition to static volume rendering, dynamic volume rendering functions are able to develop interactive images using various techniques.

- *Movie.* Using pre-defined or customized scripts identifying specific projection perspectives, a pre-scripted movie can be captured providing a specific sequence of renderings (Fig. 5.83).
- *Perspective volume rendering* (*immersive rendering*). This type of volumetric representation assumes a viewpoint at a finite distance, usually from within a lumen, and simulates a “fly through.” This technique can be applied to any space or lumen, with the most common being evaluation of the pharyngeal airway and osteomeatal complex (Fig. 5.84). Perspective volume rendering may be of benefit in planning sinus endoscopic procedures in that they demonstrate relationships between anatomic structures.
- *Cine Imaging (4D).* Real-time acquisition of the maxillofacial dynamic actions (e.g., swallowing, mandibular movement) is currently

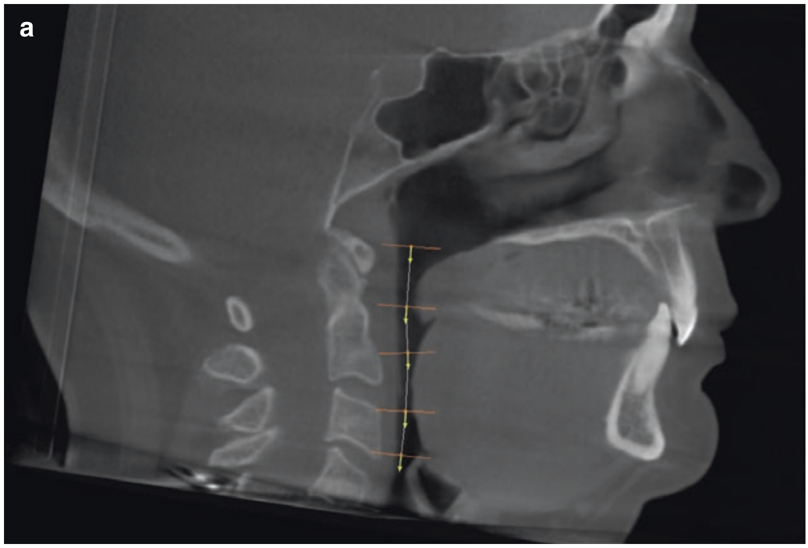

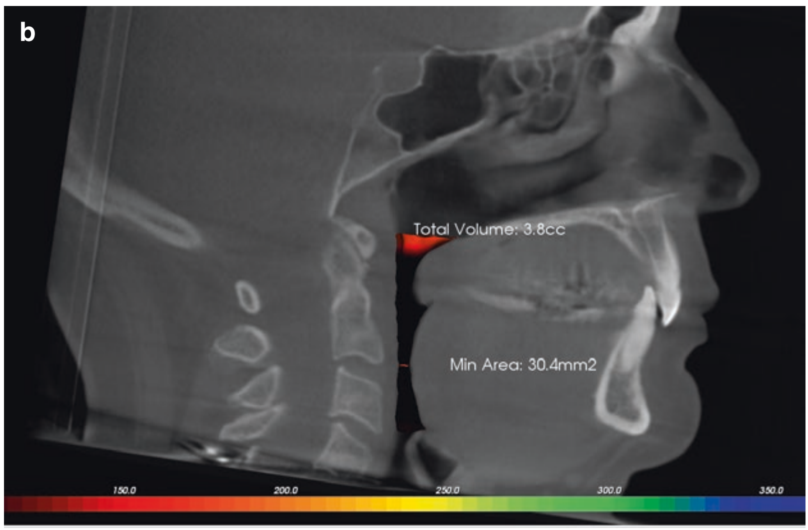

Fig. 5.82 Example of fixed threshold software showing midsagittal CBCT image with multiple airway seed points and linear boundaries (**a**) for upper airway assessment with a software using fixed threshold segmentation providing total volume and minimal cross-sectional area (**b**). Minimal airway cross-sectional dimensions are color-coded with *red* and *black* indicating values less than an arbitrary 150 mm^2

limited. Two approaches are possible. One approach requires multiple low dose acquisition of the same object at specific phases motion and generation of intermediate images to create a movie of a particular action. A second method uses the fluoroscopic potential of the flat panel display for continuous acquisition (Fig. 5.85).

- *Anatomic real-time image fusion.* A promising alternate to cine imaging is a software-based approach merging CBCT data with dynamic inputs such as electronic jaw motion tracking (Terajima et al. 2008; Hanssen et al. 2015) or ultrasound data from TMJ imaging to provide an anatomically precise yet real-dynamic rendering of jaw movement. This technique requires only one CBCT exposure with other positions (e.g., maximum opening, excursions, centric relation, centric occlusion) derived via correlation with electronic measurements.

5.4 Documentation

Cone beam imaging comprises the technical component of patient exposure (radiographic component) and a professional duty of a practi-

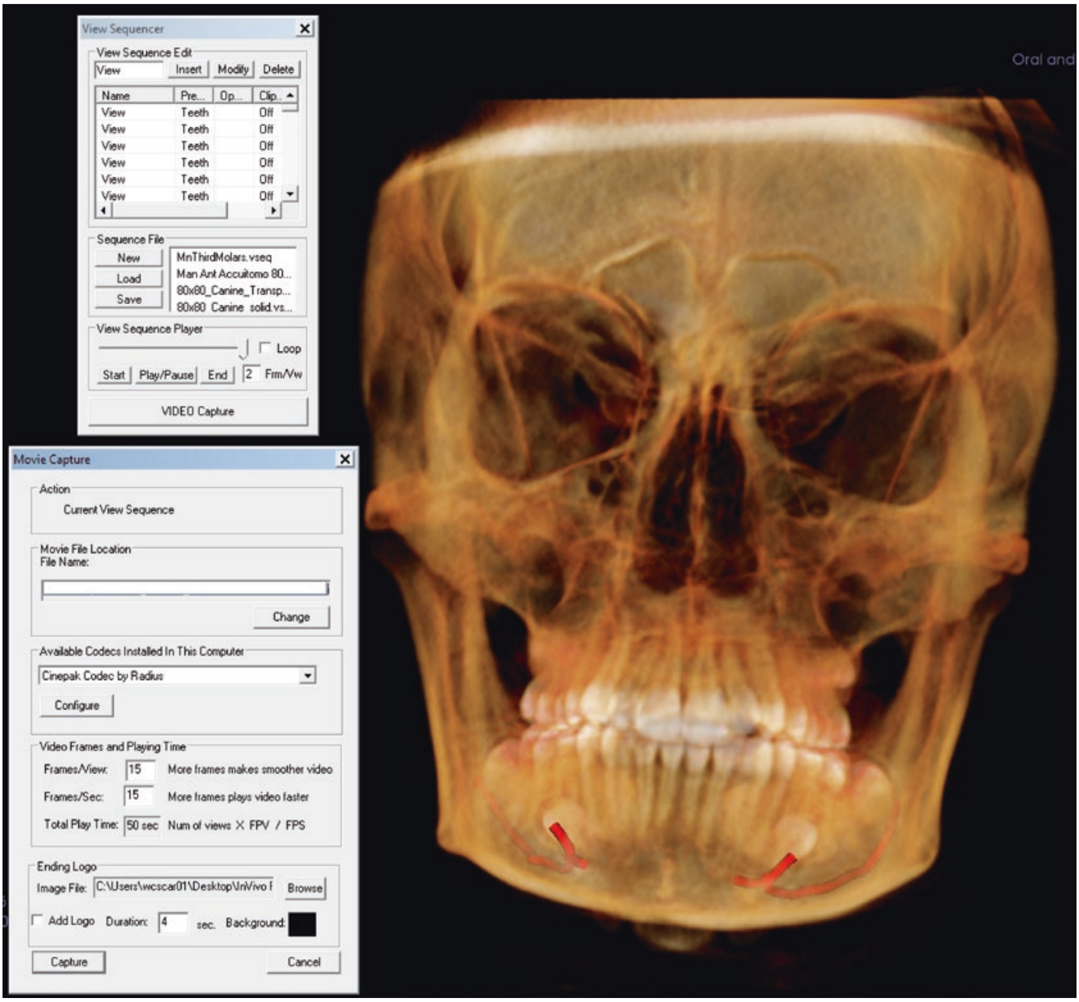

Fig. 5.83 Cropped screen shot of typical movie capture function in dental imaging software (InVivo 5.3, Anatomage, San Jose California, USA). In this example, activation of the movie capture icon launches a panel (*top left*) requesting location of previous script or allows creation of a new script by sequential capture of specific projections. A "video capture command" then launches a second panel (*lower left*) that provides the operator with choices relating to type of movie format to be generated, particular CODEC to be used and frames per second

tioner who operates a CBCT unit or requests a specific CBCT study to provide information on the imaging findings based on examination of the entire image dataset (radiologic component). In some jurisdictions, this is also legally mandatory either for reimbursement of the costs of the procedure from a third party health insurance payer or to maintain professional medical liability protection. An opinion expressed by some individuals has been that the user is not responsible for the radiologic findings beyond those needed for a specific task (e.g., implant treatment planning). Professional bodies in both the United States (Carter et al. 2008) and Europe (Horner et al. 2009) vigorously oppose this position.

Documentation of a CBCT procedure by the inclusion of an interpretive report is an essential element of CBCT imaging and should form part of a patient's record (Carter et al. 2008). Patient diagnosis may often be complex and management may involve numerous practitioners. An interpretation report serves as the optimal method of communication of interpretation findings for CBCT. The mechanics of reporting include the

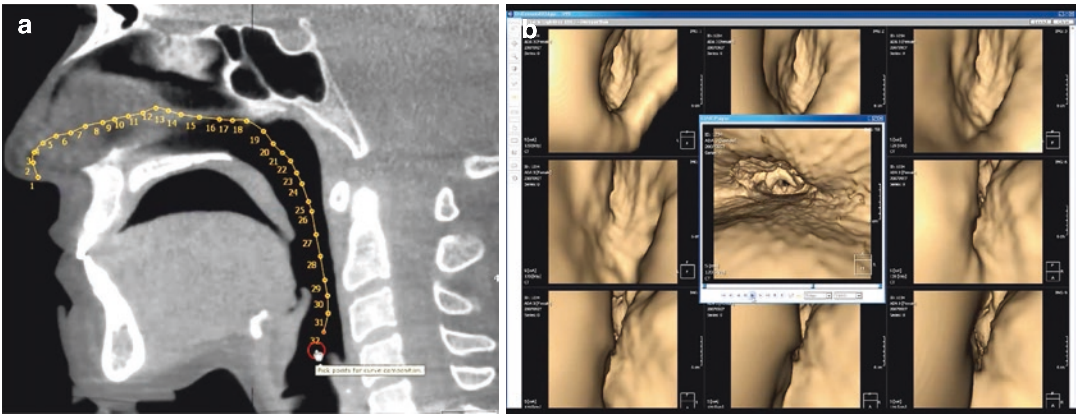

Fig. 5.84 Example of immersive rendering creating a "fly though" virtual naso-pharyngoscopy of the upper airway space (OnDemand3D, CyberMed Inc., Seoul, Korea). Midsagittal screen capture (**a**) shows placement of nodes and pathway along the naso-pharyngeal airway space to be used as specific viewpoints. Individual shaded surface hollow rendered images at each viewpoint (**b**) along the pathway are combined to generate a movie from the perspective of being in the airway cavities

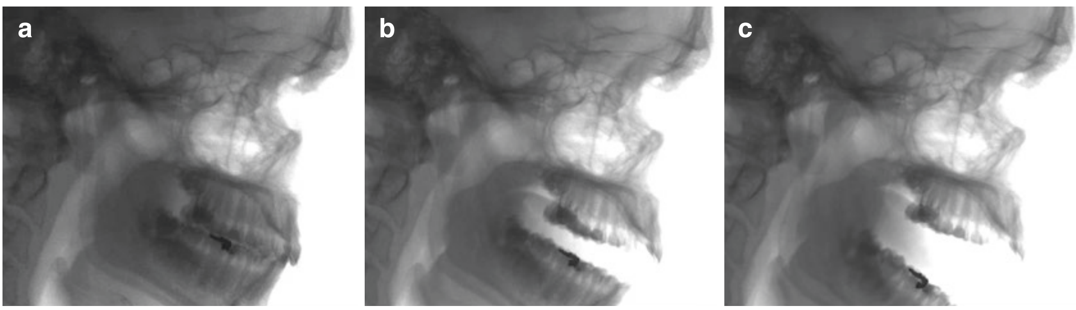

Fig. 5.85 Closed (**a**), partially open (**b**), and fully open (**c**) fluoroscopic images of a patient as part of a cinematic sequence. Note the relationship of the mandibular condyles, airway changes and tongue position (CineX, NewTom VGi evo, Quantitative Radiology s.r.l., Cefla Group, Verona, Italy)

development of a series of images formatted to display the condition/region appropriately (image report) and a cognitive interpretation of the significance of the imaging findings (interpretation report).

5.4.1 Interpretation Reports

It is imperative that all images within the volumetric dataset be reviewed systematically not only for the purpose for which the scan was ordered and performed but also to rule out synchronous disease. Competency in interpretation of both anatomic and pathologic findings on CBCT images varies depending principally on practitioner experience and the FOV of the scan. Qualified specialist oral and maxillofacial radiologists may be able to assist diagnostically when practitioners are unwilling to accept the responsibility to review the entire exposed tissue volume.

Currently, there is no consensus among professional dental organizations on the specific requirements for CBCT reporting. However, maxillofacial CBCT credentialing authorities in the United States (Intersocietal Accreditation Commission 2012) and professional medical radiology organi-

Table 5.18 Essential components of a CBCT interpretation report

Heading		Details
Patient Information	Patient ID	Patient name, unique identifier code, date of birth or age
	Prescriber details	Referring practitioner's name and contact details, rationale for the procedure,
	Study indication	Rationale for the study, patient clinical presentation, working (preliminary) diagnosis.
Scan information	Scan ID	Succession number, date of procedure, date the report was generated, the location of the facility, the equipment used,
	Procedure details	Scan protocol parameters used and images provided.
		Problems encountered during the procedure (e.g., patient motion)
	Patient exposure	Scan protocol specific patient radiation exposure details, such as DAP or CITI, may be reported
Findings	General	Reference to the gnathic (dental status including specific missing teeth, restorative status, root canal filled teeth, periapical lesions, general marginal alveolar bone status and status of edentulous regions) and extragnathic (TMJ, paranasal sinuses, naso-pharyngeal airway, soft tissue of the neck, intracranial calcifications) structures.
	Specific	Specific findings should provide observations addressing the rationale for the procedure
	Incidental	Significant incidental findings should be described.
Impression	Definitive or a differential diagnosis	Related to the rationale for the imaging examination or for serendipitous findings.
	Correlation	Correlation to patient presentation addressing pertinent clinical issues
	Comparison	To previous imaging studies, if available
	Recommendations	Suggestions for follow-up or additional diagnostic or clinical studies, as appropriate, to clarify, confirm or exclude the diagnosis.
Authorization	Signature	Separate region for manual/electronic signature and date

ID identification

zations (American College of Radiology 2005; European Society of Radiology 2011) provide guidelines for the reporting of CBCT and MSCT images, respectively. Within these frameworks, the essential components of a CBCT radiologic report can be outlined (Table 5.18).

- **Patient Information.** This section should include pertinent information to identify the patient and provide possible relevant demographic data.
- **Scan Information.** This section provides the when, where, why, and how for the CBCT procedure. This would include succession number, date the scan was performed, date the report was generated, the location of the facility, the equipment used, scan parameters, the referring practitioner's name, rationale for the procedure, and images provided. In addition information should be provided on any problems encountered during the procedure (e.g., patient motion)
- **Radiographic Findings.** This section should be subdivided into general imaging findings, specific findings pertinent to the imaging rationale and incidental findings. General imaging findings should include reference to the dentoalveolar status whereas specific findings should use precise anatomic, pathologic, and radiologic terminology to accurately describe features regarding the region of interest. In the maxilla, the paranasal sinuses should be examined with particular reference to the characteristics of any opacification, if present. Incidental findings should comment on significant conditions observed in non-

gnathic structures including the cranial cavity (e.g., physiologic and pathologic calcifications), the base of the skull including the auditory apparatus, the naso- and oropharyngeal airway spaces, the cervical spine, and the soft tissues of the neck.

- **Radiologic Impression.** Either a definitive or a differential diagnosis should be provided, whichever is appropriate. In this section, the radiologic findings should be correlated to patient presentation and address or answer any pertinent clinical issues raised in the request for the imaging examination. If available, findings should be compared to previous examinations or reports. Finally, recommendations for follow-up or additional diagnostic or clinical studies should be suggested, as appropriate, to clarify, confirm, or exclude the diagnosis.

5.5 Practical Dose Reduction Strategies for Maxillofacial CBCT

Chapter 7 deals with the issues of the measurement of radiation dose and risk assessment. The use of any radiographic technique demands that each patient exposure be justified clinically (justification) and that principles and procedures are applied that minimize patient radiation exposure while optimizing maximal diagnostic benefit (optimization). The extension of this principle, referred to as the "as low as reasonably achievable" (ALARA), to CBCT imaging is supported by the American Dental Association (American Dental Association Council on Scientific Affairs 2012) and the countries of the European Union (European Commission 2012).

The radiation dose in maxillofacial CBCT has been extensively reported in the literature using a variety of models, dose quantities, and measurement methodologies. Reported adult effective doses for protocols ranged from 46 to 1073 µSv for extended fields of view (FOVs), 9–548 µSv for large FOVs, 4–421 µSv for medium FOVs, and 5–297 µSv for small FOVs (Ludlow et al. 2015). The results from these studies indicate that there is a wide range in patient dose for maxillofacial CBCT. This reflects the range of available maxillofacial CBCT device configurations (beam filtration, receptor technology, resolution) and parameters used in clinical practice such as FOV, exposure (kVp and ma), and acquisition (e.g., rotational arc, number of basis images) settings. As a comparison, and in order of decreasing magnitude, doses for digital panoramic radiography range from 14 to 38 µSv, for cephalometric radiography are 5.1–5.6 µSv, and for a four image bitewing radiographic series are approximately 5 µSv (Ludlow and Ivanovic 2008; Ludlow et al. 2015). Therefore, while CBCT doses are higher than those of intraoral and cephalometric radiography, the low end of the CBCT dose range overlaps with the range found in panoramic radiography, while the high end of the range overlaps that of CT.

A wide dose range implies a great potential for optimization. The following specific "best practice" recommendations are provided, grouped according to clinical workflow.

5.5.1 Establish Clinical Necessity

General (Carter et al. 2008; American Dental Association Council on Scientific Affairs 2012; Haute Autorité de Santé. 2009; Horner et al. 2009; Advies van de Hoge Gezondheidsraad nr. 8705. 2011. Noffke et al. 2011. European Commission 2012. Arbeitsgemeinschaft der Wissenschaftlichen Medizinischen Fachgesellschaften (AWMF) 2013) and discipline specific (Tyndall et al. 2012; American Academy of Oral and Maxillofacial Radiology 2013; Special Committee to Revise the Joint AAE/AAOMR Position Statement on use of CBCT in Endodontics 2015; Isaacson et al. 2008; Academy of Osseointegration 2010; Diangelis et al. 2012; Harris et al. 2012; Husain et al. 2012; Walter et al. 2011; American Association of Endodontists 2013; Counihan et al. 2013; Faculty of General Dental Practice (UK) 2013; Ngiam et al. 2013; Horner et al. 2015) guidelines have been published providing dental practitioners with best practices for the most appropriate use of maxillofacial CBCT in dentistry. These guidelines are detailed in specific chapters in this book. CBCT imaging is currrently considered a supplemental radiographic modality to conventional intraoral and extraoral radiographic imaging in dentistry.

The significant clinical efficacy of CBCT in specific diagnostic, simulation, and treatment scenarios is now well established by numerous authorities (above) and illustrated through this textbook. As an imaging modality, CBCT possesses high image detail, ease of use, data interactivity including multiplanar imaging capabilities surpasses multi-detector computed tomography (MDCT) in many clinical applications.

Undoubtedly, diagnostic applications are the mainstay for CBCT use in which it provides a greater diagnostic efficacy for many tasks compared to other imaging modalities in dentistry (Angelopoulos et al. 2008; Suomalainen et al. 2010). Shweel et al. (2013) found the diagnostic accuracy of CBCT to be comparable to MDCT for the assessment of odontogenic tumors and cysts and more accurate in linear measurements and feature detection (e.g., tooth displacement and cortical plate osseous defects) than MDCT. They concluded that CBCT is

> "… an optimal radiological modality for preoperative radiological assessment of odontogenic tumors and cysts".

On the other hand, poor soft tissue contrast limits the diagnostic utility of CBCT in assessing pathological entities that tend to show spread, like malignancies of the jaws. Though CBCT is adequate in characterizing hard tissue details such as the destruction osseous boundaries and patterns that may raise suspicion for an aggressive entity (erosion, permeative borders, "moth"-eaten appearance, etc.), it is inadequate at demonstrating spread into the surrounding soft tissues or lymph nodal involvement. This may also be true for some benign but locally aggressive tumors such as ameloblastoma and odontogenic myxoma which may show local soft tissue spread. In such cases, MDCT with contrast enhancement or magnetic resonance imaging (MRI) or a combination of both is the recommended imaging strategy (McDonald 2011; Meyer et al. 2011).

Similarly, CBCT is not indicated for the assessment of soft tissue pathologies of the maxillofacial region. CBCT soft tissue contrast is poor and, as a result, a soft tissue mass may not be identified unless:

- It is large enough to cause displacement and distortion of anatomical contours of the surrounding tissues (e.g., a parapharyngeal soft tissue mass altering the shape of the airway).
- It is aggressive enough to invade and erode adjacent osseous boundaries.
- It is associated with central or peripheral necrosis that produces calcified material (like a sialolith or a vascular calcification due to atheromatosis).

In such cases, magnetic resonance imaging (MRI), MDCT with contrast enhancement or diagnostic ultrasound (if the region under investigation is accessible) or combinations thereof are the most appropriate imaging modalities.

Given these considerations, CBCT is not indicated for the primary assessment of malignancy in the jaws, for staging of malignant tumors of the maxillofacial region or to distinguish soft tissue pathology, apart from determining presence or absence of soft tissue in the paranasal sinuses. In this situation, MRI and MDCT with contrast enhancement are the imaging methods of choice. In fact, MRI has been reported more accurate for the assessment of bony invasion of oral and oropharyngeal cancer (van den Brekel et al. 1998; Bolzoni et al. 2004).

5.5.2 Use Patient and Personnel Protection

For operators of CBCT devices, additional shielding and personnel radiation dosimetry (radiation dose monitor badges) are desirable, but not considered necessary by all authorities. Isodose curves at 1 m from CBCT units are reported to range from 2 to 40 μGy per scan (Holroyd and Walker 2010) compared with intraoral and panoramic radiography scatter doses of less than 1 μGy per exposure at 1 m (Sutton and Williams 2000).

Recent authors have reported that the use of a lead torso apron does not reduce patient absorbed doses or effective dose in panoramic (Rottke et al. 2013) or CBCT (Rottke et al. 2016) procedures. However, the use of a thyroid collar reduces total effective dose ranging from 9.8 to 22.7% for panoramic radiography (Han et al. 2013) and from 18 to 40.1% for CBCT imaging (Qu et al. 2012a, b). The use of thyroid collar in panoramic imaging is not advisable as it interferes with the projection geometry and introduces substantial artifacts.

5.5.3 Adjust Device Settings Appropriately

Device specific exposure settings and scan parameter *image acquisition protocols* should be developed for specific diagnostic tasks using the following guidelines:

5.5.3.1 Adjust Exposure Settings

- *Adjust exposure settings for children.* For the same exposure settings, children absorb more dose than adults and are thus at greater radiation risk (Brenner et al. 2001; Theodorakou et al. 2012). Therefore, it is highly recommended that exposure settings are reduced for a child or smaller patient to minimize radiation exposure.
- *Reduce mA.* Lowering exposure mA in CBCT devices results in a proportional decrease in patient dose. Although noise increases, clinical image quality may often remain acceptable for moderate or even large reductions in mA compared to the manufacturer's recommended setting (Pauwels et al. 2015a). The level of mA reduction achievable with appreciable reduction in image quality is equipment specific (Goulston et al. 2016). Pauwels et al. (2017) proposes a possible reduction in mAs (using a fixed 90 kVp exposure), ranging from 7 to 50%, based on exponential relation between head size and mAs. Reductions in mAs are more dose-efficient than kVp reductions.
- *Increase kVp.* Increasing the tube voltage may result in a decrease in skin and effective dose but an increase in scatter due to a proportionally higher percentage of Compton interactions. This is undesirable as may reduce image quality associated with image noise. However higher tube voltage may be clinically desirable, particularly in the assessment of bone associated with dental implants, as it reduces the beam hardening effect (Ludlow 2011).

5.5.3.2 Adjust Scanning Parameters

- *Reduce the number of projection images*. For a specific CBCT device, selection of a lower scan time results in less acquisition projection images and a proportional decrease in patient radiation exposure (Ludlow and Walker 2013). However, images reformatted from volumetric datasets reconstructed with reduced projection images generally have lower spatial resolution, reduced contrast and increased noise.
- *Consider Reducing Scan Trajectory Arc.* Some CBCT devices allow partial trajectory arc perform rotations (180°) instead of a full rotation (360°). This modality offers a 50% dose reductions to the patient and may be suitable for less demanding diagnostic tasks.
- *Collimate the FOV of the X-ray beam to the region of interest (ROI).* Patient dose is markedly reduced with collimation of the FOV. While the range of doses for various CBCT devices for specific FOVs is wide, median effective doses for FOV in the range of 5.1–10.0 cm are reduced 38% compared to >10 cm and for FOV < 5 cm are reduced 59% compared to FOVs with a height range of 5.1–10.0 cm (Al-Okshi et al. 2015). Similar FOVs including the lower jaw result in higher effective dose than those of the upper jaw because the salivary gland and thyroid tissues receive greater exposure (Lofthag-Hansen et al. 2011).

While reducing CBCT exposure and device parameters may result in dose reduction to the patient, there is often a concomitant decrease in image quality. Exposure parameters should be adjusted according to a specific clinical diagnostic task.

Diagnostic tasks requiring high spatial and contrast detail and reduced noise (e.g., periapical diagnosis, assessment of possible ankyloses of impacted teeth, external and internal root resorption, assessment of peri-implant bone loss, horizontal and vertical root fractures) (Lofthag-Hansen et al. 2011; Pinheiro et al. 2015; Salineiro et al. 2015) usually require higher exposures, the highest number of acquisition frames, a complete arc trajectory, the smallest voxel size, and a reduced FOV. Settings for less demanding clinical diagnostic tasks (e.g., bone volume assessment associated with dental implant planning, follow-up or progress orthodontic imaging, open mouth TMJ imaging) should be adjusted to minimize patient dose (Lofthag-Hansen et al. 2011). CBCT imaging of regions with higher density, such as the mandible, may require higher exposure parameters compared to the maxilla (Lofthag-Hansen et al. 2011). Optimization of CBCT exposure parameters to provide acceptable diagnostic images can result in a dose savings of up to 50% (Hidalgo Rivas et al. 2015; Pauwels et al. 2017).

5.5.4 Institute a Quality Assurance Program

Chapter 8 provides extensive information on the principles, techniques, and clinical protocols associated with quality assurance (QA) to ensure consistency in acceptable diagnostic image quality while reducing radiation exposure to the patient as low as reasonably achievable.

Most procedures and tests are performed by a radiation physicist at various times throughout the lifespan of the device. The regulations governing the necessity, periodicity, and extent of radiation physicist involvement vary greatly depending on country and even regional jurisdiction. Radiation physicists use dosimeters and image quality test devices to determine the physical requirements of the facility where the CBCT unit is located, test equipment performance when the equipment is first installed (acceptance and commissioning tests) and then periodically (routine tests) and establish radiation dose and image quality baseline information.

On a day-to-day basis, the operator of the unit is responsible for QA monitoring and should be able to identify and act on situations where image quality is obviously affected. CBCT images must be deemed qualitatively diagnostically clinically acceptable and this is usually done by comparison with high quality standard reference images. Recalibration of the sensor may be necessary and operators should be comfortable in performing this procedure.

An often overlooked but vital component of the clinical workflow is the display. Image quality is only as good as the monitor on which it is displayed. A suitable test pattern, such as an AAPM TG18 or SMPTE image, should be displayed routinely to examine monitor spatial and contrast resolution. Some dental software provides access to this test pattern (Fig. 5.86).

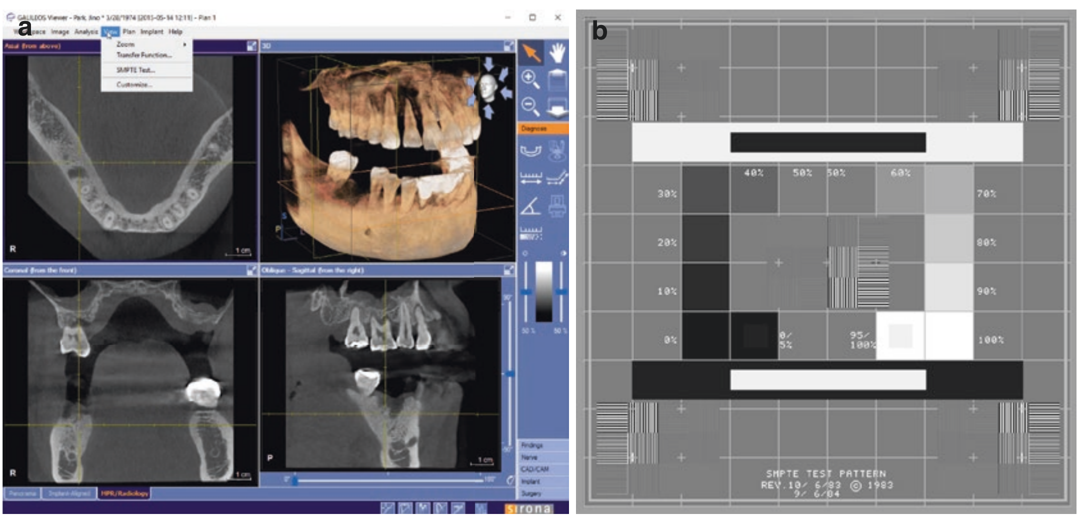

Fig. 5.86 Interface of Galaxis viewer software (Galaxis/Sidexis 4, Dentsply Sirona Imaging, Bensheim, Germany,) showing selection (**a**) and subsequent display (**b**) of SMPTE test pattern

References

Academy of Osseointegration (2010) 2010 guidelines of the Academy of Osseointegration for the provision of dental implants and associated patient care. Int J Oral Maxillofac Implants 25:620–627

Advies van de Hoge Gezondheidsraad nr. 8705 (2011) Dentale cone beam computed tomography. Hoge Gezondheidsraad, Brussel. www.health.belgium.be/internet2Prd/groups/public/@public/@shc/documents/ie2divers/19068321_en.pdf. Accessed 21 Dec 2016

Al-Okshi A, Lindh C, Salé H, Gunnarsson M, Rohlin M (2015) Effective dose of cone beam CT (CBCT) of the facial skeleton: a systematic review. Br J Radiol 88(1045):20140658

Al-Okshi A, Theodorakou C, Lindh C (2017) Dose optimization for assessment of periodontal structures in cone beam CT examinations. Dentomaxillofac Radiol 46(3):20160311

American Academy of Oral and Maxillofacial Radiology (2013) Clinical recommendations regarding use of cone beam computed tomography in orthodontics [corrected]. Position statement by the American Academy of Oral and Maxillofacial Radiology. Oral Surg Oral Med Oral Pathol Oral Radiol 116:238–257

American Association of Endodontists (2013) Recommended guidelines of the AAE for the treatment of traumatic dental injuries (revised 2013). http://www.aae.org/guidelines/

American College of Radiology (2005) ACR practice guideline for communication of diagnostic imaging findings. In: Practice Guidelines and Technical Standards 2005. American College of Radiology. Reston, VA. 2005. www.acr.org. Accessed 22 Dec 2012

American Dental Association Council on Scientific Affairs (2012) The use of cone-beam tomography in dentistry. An advisory statement from the American Dental Association Council on Scientific Affairs. J Am Dent Assoc 143:899–902

Angelopoulos C, Thomas SL, Hechler S, Parissis N, Hlavacek M (2008) Comparison between digital panoramic radiography and cone-beam computed tomography for the identification of the mandibular canal as part of presurgical dental implant assessment. J Oral Maxillofac Surg 66:2130–2135

Aranyarachkul P, Caruso J, Gantes B, Schulz E, Riggs M, Dus I, Yamada JM, Crigger M (2005) Bone density assessments of dental implant sites: 2. Quantitative cone-beam computerized tomography. Int J Oral Maxillofac Implants 20:416–424

Arbeitsgemeinschaft der Wissenschaftlichen Medizinischen Fachgesellschaften (AWMF) (2013) s2k-Leitlinie Dentale digitale Volumentomographie Version Nr. 9 vom 5 August 2013. AWMF-Register-Nummer:083–05. Dusseldorf: AWMF. http://www.awmf.org/uploads/tx_szleitlinien/083-005l_S2k_Dentale_Volumentomographie_2013-10.pdf. Accessed 21 Dec 2016

Bohner LO, Tortamano P, Marotti J (2017) Accuracy of linear measurements around dental implants by means of cone beam computed tomography with different exposure parameters. Dentomaxillofac Radiol:20160377. doi:10.1259/dmfr.20160377

Bolzoni A, Cappiello J, Piazza C, Peretti G, Maroldi R, Farina D, Nicolai P (2004) Diagnostic accuracy of magnetic resonance imaging in the assessment of mandibular involvement in oral-oropharyngeal squamous cell carcinoma: a prospective study. Arch Otolaryngol Head Neck Surg 130:837–843

Brenner D, Elliston C, Hall E, Berdon W (2001) Estimated risks of radiation-induced fatal cancer from pediatric CT. AJR Am J Roentgenol 176:289–296

Bryant JA, Drage NA, Richmond S (2008) Study of the scan uniformity from an i-CAT cone beam computed tomography dental imaging system. Dentomaxillofac Radiol 37:365–374

Carter L, Farman AG, Geist J, Scarfe WC, Angelopoulos C, Nair MK, Hildebolt CF, Tyndall D, Shrout M, American Academy of Oral and Maxillofacial Radiology (2008) American academy of oral and maxillofacial radiology executive opinion statement on performing and interpreting diagnostic cone beam computed tomography. Oral Surg Oral Med Oral Pathol Oral Radiol Endod 106:561–562

Chindasombatjareon J, Kakimoto N, Murakami S, Maeda Y, Furukawa S (2011) Quantitative analysis of metallic arte-facts caused by dental metals: comparison of cone-beamand multi-detector row CT scanners. Oral Radiol 27:114–120

Counihan K, Al-Awadhi EA, Butler J (2013) Guidelines for the assessment of the impacted maxillary canine. Dent Update 40(770–2):775–777

Dawood A, Brown J, Sauret-Jackson V, Purkayastha S (2012) Optimization of cone beam CT exposure for pre-surgical evaluation of the implant site. Dentomaxillofac Radiol 41:70–74

Diangelis AJ, Andreasen JO, Ebeleseder KA, Kenny DJ, Trope M, Sigurdsson A et al (2012) International Association of Dental Traumatology guidelines for the management of traumatic dental injuries: 1. Fractures and luxations of permanent teeth. Dent Traumatol 28:2–12

Dong J, Hayakawa Y, Kannenberg S, Kober C (2013) Metal-induced streak artifact reduction using iterative reconstruction algorithms in x-ray computed tomography image of the dentoalveolar region. Oral Surg Oral Med Oral Pathol Oral Radiol 115:e63–e73

European Commission. Radiation protection 172 (2012). Evidence based guidelines on cone beam CT for dental and maxillofacial radiology. Office for Official Publications of the European Communities, Luxembourg. http://ec.europa.eu/energy/nuclear/radiation_protection/doc/publication/172.pdf. Accessed 19 Dec 2016.

European Society of Radiology (ESR) (2011) Good practice for radiological reporting. Guidelines from the European Society of Radiology. Insights Imaging 2:93–96

Faculty of General Dental Practice (UK) (2013) In: Horner K, Eaton KA (eds) Selection criteria for dental radiography, 3rd edn. Faculty of General Dental Practice (UK) Royal College of Surgeons of Surgeons of England, London

Goulston R, Davies J, Horner K, Murphy F (2016) Dose optimization by altering the operating potential and tube current exposure time product in dental cone beam CT: a systematic review. Dentomaxillofac Radiol 45:20150254

Güldner C, Ningo A, Voigt J, Diogo I, Heinrichs J, Weber R et al (2013) Potential of dosage reduction in cone-beam-computed tomography (CBCT) for radiological diagnostics of the paranasal sinuses. Eur Arch Otorhinolaryngol 270:1307–1315

Han GS, Cheng JG, Li G, Ma XC (2013) Shielding effect of thyroid collar for digital panoramic radiography. Dentomaxillofac Radiol 42:20130265

Hanssen N, Ruge S, Kordass B (2015) SICAT function: anatomical real-dynamic articulation by merging cone beam computed tomography and jaw motion tracking data. Int J Comput Dent 17:65–74

Harris D, Horner K, Grondahl K, Jacobs R, Helmrot E, Benic GI et al (2012) E.A.O. Guidelines for the use of diagnostic imaging in implant dentistry 2011. A consensus workshop organized by the European Association for Osseointegration at the Medical University of Warsaw. Clin Oral Implants Res 23:1243–1253

Haute Autorité de Santé (2009) Tomographie Volumique a Faisceau Coniqué de la Face (Cone Beam Computerized Tomography). Rapport d'evaluation Technologique. Service évaluation des actes professionnels. Saint-Denis La Plainé: Haute Autorité de Santé. http://www.has-sante.fr/portail/upload/docs/application/pdf/2009-12/rapport_cone-beam_version_finale_2009-12-28_17-27-28_610.pdf. Accessed 21 Dec 2016

Health Protection Agency (2010) Guidance on the safe use of dental cone beam CT (Computed Tomography) equipment. HPA-CRCE-010. Health Protection Agency, Chilton

Helvacioglu-Yigit D, Demirturk Kocasarac H, Bechara B, Noujeim M (2016) Evaluation and reduction of artifacts generated by 4 different root-end filling materials by using multiple cone-beam computed tomography imaging settings. J Endod 42:307–314

Hidalgo Rivas JA, Horner K, Thiruvenkatachari B, Davies J, Theodorakou C (2015) Development of a low-dose protocol for cone beam CT examinations of the anterior maxilla in children. Br J Radiol 88(1054):20150559

Holroyd JR, Walker A (2010) HPA-RPD-065. Recommendations for the design of X-ray facilities and quality assurance of dental Cone Beam CT (Computed Tomography) systems. Health Protection Agency, Chilton

Horner K, Islam M, Flygare L, Tsiklakis K, Whaites E (2009) Basic principles for use of dental cone beam computed tomography: consensus guidelines of the European Academy of Dental and Maxillofacial Radiology. Dentomaxillofac Radiol 38:187–195

Horner K, O'Malley L, Taylor K, Glenny AM (2015) Guidelines for clinical use of CBCT: a review. Dentomaxillofac Radiol 44:20140225

Husain J, Burden D, McSherry P, Morris D, Allen M, Clinical Standards Committee of the Faculty of Dental Surgery RCoSoE (2012) National clinical guidelines for management of the palatally ectopic maxillary canine. Br Dent J 213:171–176

Intersocietal Accreditation Commission (2012) Section 5: 2B Section 5: Examination Interpretation. In: The IAC Dental CT Standards for Dental/Maxillofacial Computed Tomography (CT) Practice Accreditation Using Cone Beam Technology, p 20

Isaacson KG, Thom AR, Horner K, Whaites E (2008) Guidelines for the use of radiographs in clinical orthodontics, 3rd edn. British Orthodontic Society, London

Katsumata A, Hirukawa A, Okumura S, Naitoh M, Fujishita M, Ariji E, Langlais RP (2007) Effects of image artifacts on gray-value density in limited-volume cone-beam computerized tomography. Oral Surg Oral Med Oral Pathol Oral Radiol Endod 104:829–836

Kim DS, Rashsuren O, Kim EK (2014) Conversion coefficients for the estimation of effective dose in cone-beam CT. Imaging Sci Dent 44:21–29

Kwong JC, Palomo JM, Landers MA, Figueroa A, Hans MG (2008) Image quality produced by different cone-beam computed tomography settings. Am J Orthod Dentofac Orthop 133:317–327

Lagravere MO, Fang Y, Carey J, Toogood RW, Packota GV, Major PW (2006) Density conversion factor determined using a cone-beam computed tomography unit NewTom QR-DVT 9000. Dentomaxillofac Radiol 35:407–409

Lagravere MO, Carey J, Ben-Zvi M, Packota GV, Major PW (2008) Effect of object location on the density measurement and Hounsfield conversion in a NewTom 3G cone beam computed tomography unit. Dentomaxillofac Radiol 37:305–308

Lofthag-Hansen S, Thilander-Klang A, Gröndahl K (2011) Evaluation of subjective image quality in relation to diagnostic task for cone beam computed tomography with different fields of view. Eur J Radiol 80:483–488

Ludlow JB (2011) A manufacturer's role in reducing the dose of cone beam computed tomography examinations: effect of beam filtration. Dentomaxillofac Radiol 40:115–122

Ludlow JB, Ivanovic M (2008) Comparative dosimetry of dental CBCT devices and 64-slice CT for oral and maxillofacial radiology. Oral Surg Oral Med Oral Pathol Oral Radiol Endod 106:106–114

Ludlow JB, Walker C (2013) Assessment of phantom dosimetry and image quality of i-CAT FLX cone-beam computed tomography. Am J Orthod Dentofac Orthop 144:802–817

Ludlow JB, Timothy R, Walker C, Hunter R, Benavides E, Samuelson DB, Scheske MJ (2015) Effective dose of dental CBCT-a meta analysis of published data and additional data for nine CBCT units. Dentomaxillofac Radiol 44:20140197

Mah P, Reeves TE, McDavid WD (2010) Deriving Hounsfield units using grey levels in cone beam computed tomography. Dentomaxillofac Radiol 39:323–335

McDonald D (2011) Oral and maxillofacial radiology: a diagnostic approach. Willey-Blackwell, Chichester

Meyer KA, Bancroft LW, Dietrich TJ, Kransdorf MJ, Peterson JJ (2011) Imaging characteristics of benign, malignant, and infectious jaw lesions: a pictorial review. AJR Am J Roentgenol 197:23–32

Misch CE (2008) Density of bone: effects on surgical approach and healing. In: Misch CE (ed) Contemporary implant dentistry. Mosby, Elsevier, Toronto, pp 645–667

Molteni R (2013) Prospects and challenges of rendering tissue density in Hounsfield units for cone beam computed tomography. Oral Surg Oral Med Oral Pathol Oral Radiol 116:105–119

Nackaerts O, Maes F, Yan H, Couto Souza P, Pauwels R, Jacobs R (2011) Analysis of intensity variability in multislice and cone beam computed tomography. Clin Oral Implants Res 22:873-9

Nardi C, Borri C, Regini F, Calistri L, Castellani A, Lorini C, Colagrande S (2015) Metal and motion artifacts by cone beam computed tomography (CBCT) in dental and maxillofacial study. Radiol Med 120:618–626

Nardi C, Molteni R, Lorini C, Taliani GG, Matteuzzi B, Mazzoni E, Colagrande S (2016) Motion artefacts in cone beam CT: an in vitro study about the effects on the images. Br J Radiol 89(1058):20150687

Nemtoi A, Czink C, Haba D, Gahleitner A (2013) Cone beam CT: a current overview of devices. Dentomaxillofac Radiol 42(8):20120443

Ngiam J, Balasubramaniam R, Darendeliler MA, Cheng AT, Waters K, Sullivan CE (2013) Clinical guidelines for oral appliance therapy in the treatment of snoring and obstructive sleep apnoea. Aust Dent J 58:408–419

Noffke CE, Farman AG, Nel S, Nzima N (2011) Guidelines for the safe use of dental and max-illofacial CBCT: a review with recommendations for South Africa. SADJ 66(262):264–266

Panjnoush M, Kheirandish Y, Kashani PM, Fakhar HB, Younesi F, Mallahi M (2016) Effect of exposure parameters on metal artifacts in cone beam computed tomography. J Dent (Tehran) 13:143–150

Panmekiate S, Apinhasmit W, Petersson A (2012) Effect of electric potential and current on mandibular linear measurements in cone beam CT. Dentomaxillofac Radiol 41:578–582

Parsa A, Ibrahim N, Hassan B, Motroni A, van der Stelt P, Wismeijer D (2013) Influence of cone beam CT scanning parameters on grey value measurements at an implant site. Dentomaxillofac Radiol 42(3):79884780

Pauwels R, Jacobs R, Bosmans H, Schulze R (2012) Future prospects for dental cone beam CT imaging. Imaging Med 4:551–563

Pauwels R, Silkosessak O, Jacobs R, Bogaerts R, Bosmans H, Panmekiate S (2014a) A pragmatic approach to determine the optimal kVp in cone beam CT: balancing contrast-to-noise ratio and radiation dose. Dentomaxillofac Radiol 43(5):20140059

Pauwels R, Zhang G, Theodorakou C, Walker A, Bosmans H, Jacobs R, Bogaerts R, Horner K, SEDENTEXCT Project Consortium (2014b) Effective radiation dose and eye lens dose in dental cone beam CT: effect of field of view and angle of rotation. Br J Radiol 87(1042):20130654

Pauwels R, Araki K, Siewerdsen JH, Thongvigitmanee SS (2015a) Technical aspects of dental CBCT: state of the art. Dentomaxillofac Radiol 44:20140224

Pauwels R, Jacobs R, Singer SR, Mupparapu M (2015b) CBCT-based bone quality assessment: are Hounsfield units applicable? Dentomaxillofac Radiol 44:20140238

Pauwels R, Seynaeve L, Henriques JC, de Oliveira-Santos C, Souza PC, Westphalen FH, Rubira-Bullen IR, Ribeiro-Rotta RF, Rockenbach MI, Haiter-Neto F, Pittayapat P, Bosmans H, Bogaerts R, Jacobs R (2015c) Optimization of dental CBCT exposures through mAs reduction. Dentomaxillofac Radiol 44:20150108

Pauwels R, Jacobs R, Bogaerts R, Bosmans H, Panmekiate S (2017) Determination of size-specific exposure settings in dental cone-beam CT. Eur Radiol 27:279–285

Pinheiro LR, Scarfe WC, Augusto de Oliveira Sales M, Gaia BF, Cortes AR, Cavalcanti MG (2015) Effect of Cone-Beam computed tomography field of view and acquisition frame on the detection of chemically simulated peri-implant bone loss in vitro. J Periodontol 86:1159–1165

Qu XM, Li G, Sanderink GC, Zhang ZY, Ma XC (2012a) Dose reduction of cone beam CT scanning for the entire oral and maxillofacial regions with thyroid collars. Dentomaxillofac Radiol 41(5):373–378

Qu X, Li G, Zhang Z, Ma X (2012b) Thyroid shields for radiation dose reduction during cone beam computed tomography scanning for different oral and maxillofacial regions. Eur J Radiol 81:e376–e380

Rottke D, Grossekettler L, Sawada K, Poxleitner P, Schulze D (2013) Influence of lead apron shielding on absorbed doses from panoramic radiography. Dentomaxillofac Radiol 42:20130302

Rottke D, Andersson J, Ejima KI, Sawada K, Schulze D (2016) Influence of lead apron shielding on absorbed doses from cone-beam computed tomography. Radiat Prot Dosim 175(1):110–117

Salineiro FC, Pinheiro LR, dos Santos JO, Cavalcanti MG (2015) Detection of horizontal root fracture using four different protocols of cone-beam computed tomography. Braz Oral Res 29. doi:10.1590/1807-3107BOR-2015.vol29.0067

Schulze R, Heil U, Gross U, Bruellmann D, Dranischnikow E, Schwanecke U, Schoemer E (2011) Artefacts in CBCT: a review. Dentomaxillofac Radiol 40:265–273

Schulze RK, Michel M, Schwanecke U (2015) Automated detection of patient movement during a CBCT scan based on the projection data. Oral Surg Oral Med Oral Pathol Oral Radiol 119:468–472

Shweel M, Amer MI, El-shamanhory AF (2013) A comparative study of cone-beam CT and multidetector CT in the preoperative assessment of odontogenic cysts and tumors. Egypt J Radiol Nucl Med 44:23–32

Special Committee to Revise the Joint AAE/AAOMR Position Statement on use of CBCT in Endodontics (2015) AAE and AAOMR joint position statement: use of cone beam computed tomography in endodontics 2015 update. Oral Surg Oral Med Oral Pathol Oral Radiol Endod 120:508–512

Spin-Neto R, Matzen LH, Schropp L, Gotfredsen E, Wenzel A (2015) Factors affecting patient movement and re-exposure in cone beam computed tomography examination. Oral Surg Oral Med Oral Pathol Oral Radiol 119:572–578

Suomalainen A, Ventä I, Mattila M, Turtola L, Vehmas T, Peltola JS (2010) Reliability of CBCT and other radiographic methods in preoperative evaluation of lower third molars. Oral Surg Oral Med Oral Pathol Oral Radiol Endod 109:276–284

Sur J, Seki K, Koizumi H, Nakajima K, Okano T (2010) Effects of tube current on cone-beam computerized tomography image quality for presurgical implant planning in vitro. Oral Surg Oral Med Oral Pathol Oral Radiol Endod 110:e29–e33

Sutton DG, Williams JR (2000) Radiation shielding for diagnostic X-rays: report of a Joint BIR/IPEM Working Party. British Institute of Radiology, London, p 78

Terajima M, Endo M, Aoki Y, Yuuda K, Hayasaki H, Goto TK, Tokumori K, Nakasima A (2008) Four-dimensional analysis of stomatognathic function. Am J Orthod Dentofac Orthop 134:276–287

Theodorakou C, Walker A, Horner K, Pauwels R, Bogaerts R, Jacobs R, SEDENTEXCT Project Consortium (2012) Estimation of paediatric organ and effective doses from dental cone beam CT using anthropomorphic phantoms. Br J Radiol 85:153–160

Tyndall DA, Price JB, Tetradis S, Ganz SD, Hildebolt C, Scarfe WC, American Academy of Oral and Maxillofacial Radiology (2012) Position statement of the American Academy of Oral and Maxillofacial Radiology on selection criteria for the use of radiology in dental im-plantology with emphasis on cone beam computed tomography. Oral Surg Oral Med Oral Pathol Oral Radiol 113:817–826

van den Brekel MW, Runne RW, Smeele LE, Tiwari RM, Snow GB, Castelijns JA (1998) Assessment of tumour invasion into the mandible: the value of different imaging technique. Eur Radiol 8:1552–1557

Vasconcelos KF, Nicolielo LF, Nascimento MC, Haiter-Neto F, Bóscolo FN, Van Dessel J, EzEldeen M, Lambrichts I, Jacobs R (2015) Artefact expression associated with several cone-beam computed tomographic machines when imaging root filled teeth. Int Endod J 48:994–1000

Vasconcelos TV, Bechara BB, McMahan CA, Freitas DQ, Noujeim M (2017) Evaluation of artifacts generated by zirconium implants in cone-beam computed tomography images. Oral Surg Oral Med Oral Pathol Oral Radiol 123:265–272

Vassileva J, Stoyanov D (2010) Quality control and patient dosimetry in dental cone beam CT. Radiat Prot Dosim 139(1–3):310–312

Walter C, Weiger R, Zitzmann NU (2011) Periodontal surgery in furcation-involved maxillary molars revisited–an introduction of guidelines for comprehensive treatment. Clin Oral Investig 15:9–20

Weissheimer A, Menezes LM, Sameshima GT, Enciso R, Pham J, Grauer D (2012) Imaging software accuracy for 3-dimensional analysis of the upper airway. Am J Orthod Dentofac Orthop 142:801–813

White SC, Scarfe WC, Schulze RK, Lurie AG, Douglass JM, Farman AG et al (2014) The image gently in dentistry campaign: promotion of responsible use of maxillofacial radiology in dentistry for children. Oral Surg Oral Med Oral Pathol Oral Radiol 118:257–261

Wischmann H-A, Luijendijk HA, Meulenbrugge HJ, Overdick M, Schmidt R, Kiani K (2002) Correction of amplifier nonlinearity, offset, gain, temporal artifacts, and defects for flat-panel digital imaging devices. In: Antonuk LE, Yaffe MJ (eds) Medical imaging 2002: Physics of Medical Imaging-Proceedings of SPIE Volume 4682. San Diego, SPIE, pp 427–437

Ethical and Medicolegal Issues Related to CBCT

6

Bernard Friedland and William C. Scarfe

Contents

B. Friedland, B.Ch.D., M.Sc., J.D. (✉)
Department of Oral Medicine Infection and Immunity, Harvard School of Dental Medicine, Boston, MA, USA
e-mail: bernard_friedland@hsdm.harvard.edu

W.C. Scarfe, B.D.S., F.R.A.C.D.S., M.S.
Division of Radiology and Imaging Science, Department of Surgical/Hospital Dentistry, University of Louisville School of Dentistry, Louisville, KY, USA
e-mail: william.scarfe@louisville.edu

6.1 Introduction

Practitioners frequently consider the term *standard of care* to be a medicolegal mandate directing them how they should practice. However, the primary purpose of the *standard of care* is not medicolegal in nature, but rather is indispensable to the everyday practice of the dental profession. It is simply another way of prompting the clinician to consider the following:

> What is an appropriate course of action (diagnostic test, management, treatment or therapy) under the clinical circumstances?

Thus, medicolegal issues do not stand apart from and are not in addition to good practice, but are subsumed within it.

6.1.1 Clinical Case Scenario

An actual clinical case illustrates how good clinical practice and the *standard of care* are nothing more than two sides of the same coin.

W.C. Scarfe, C. Angelopoulos (eds.), *Maxillofacial Cone Beam Computed Tomography*,
https://doi.org/10.1007/978-3-319-62061-9_6

A patient who presented to his dentist complaining of a "toothache" in the mandibular right quadrant. A clinical examination revealed all teeth in this quadrant tested vital to pulp testing and no other tooth-related issue (e.g., periodontal disease) was evident. The examination was extended to the teeth in the ipsilateral posterior maxilla and no dental abnormalities were detected. A periapical image was acquired and nothing was apparent (Fig. 6.1). The practitioner e-mailed the periapical image to an oral and maxillofacial radiologist (OMFR) for a second opinion. The OMFR confirmed that there was no obvious radiographic cause of the patient's pain. A CBCT scan was performed by the dentist in their office, which also did not reveal anything obvious. The practitioner subsequently e-mailed the DICOM files to the OMFR. The CBCT scan was interpreted by the OMFR the next morning noting the presence of bilateral lobular mandibular tori. In addition, the OMFR suggested that perhaps the patient may have traumatized the overlying tightly bound soft tissue and that the cause for the pain was due to subsequent mucosal infection. Furthermore, the OMFR suggested that the dentist recall the patient immediately and examine the patient's lingual soft tissues. When the patient presented at noon on the second day, he complained that the pain had worsened and that his neck on the right side "does not feel right." A closer clinical examination revealed an ulcer on the mucosa overlying part of the torus on the right hand side, as well as a sinus tract that could be traced (Fig. 6.1). The presence of the ulcer, together with patient's description of the discomfort in his neck, were suggestive of an infection that had already spread to the right submandibular space. The patient was immediately placed on appropriate antibiotic therapy and recovered uneventfully.

In this situation, without the ability to rapidly communicate and commence treatment, the patient would likely have presented at an emergency room over the course of the weekend.

In this scenario, as in all patient encounters, there are many implied intellectual and technical competencies embedded within the clinical workflow. However, it is possible to reword clinical competencies in "legalese." In this specific situation, one necessary skill involves understanding the nature and format of CBCT data and the safe transfer of the data via the internet. The competency could be redrafted legally to read:

> The standard of care requires of a dentist using CBCT to be familiar with DICOM images and how to transfer them electronically

If presented with this phrase, many practitioners would likely respond by complaining that this was simply another medicolegal mandate imposed upon them. However, the previous case illustrates, in a practical way, that without this knowledge on the part of the dentist, communication would have been slowed when rapid communication was a sine qua non (essential) for a successful outcome.

Good clinical practice almost always satisfies a medicolegal standard. It is in this spirit and through this prism that practitioners should view medicolegal issues.

6.1.2 Standards Define Ethical and Medicolegal Issues Related to CBCT

To comprehend the application of good clinical practice as applied to CBCT imaging, one must consider the concept of "standards" in regard to at least five "stakeholders":

1. Those for whom imaging is performed—Patients.
2. Those who perform the imaging—Providers.
3. Those who make, market, sell, and service the equipment—The Dental Industry.
4. Those involved in developing, monitoring and enforcing regulations associated with imaging—Members of the health sciences

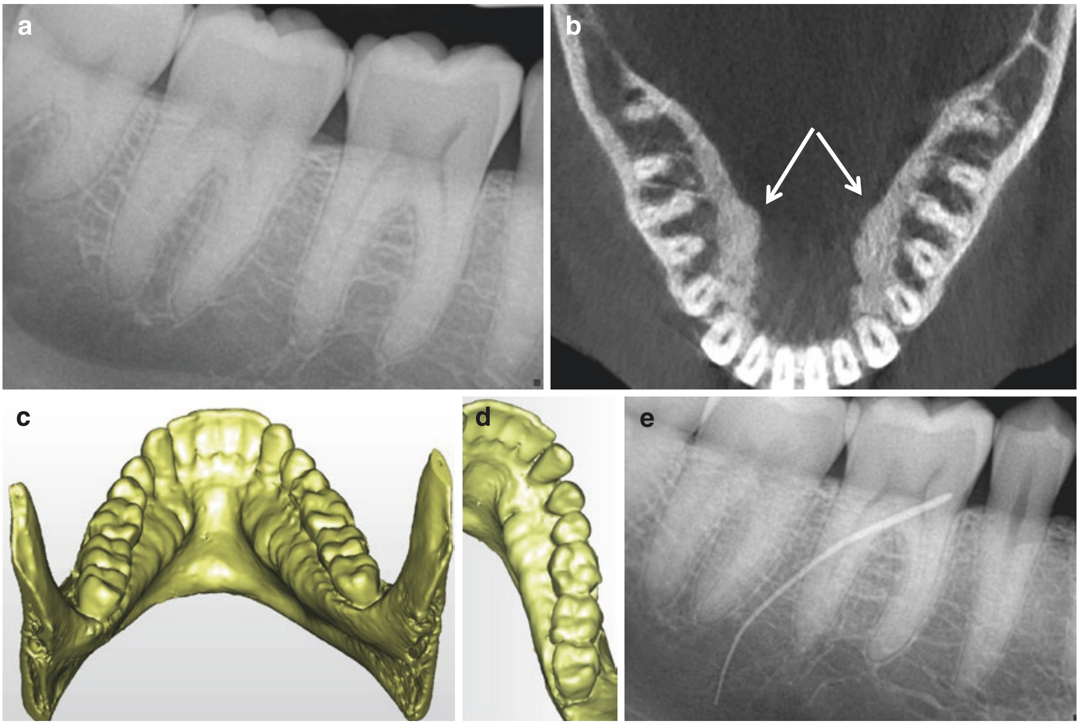

Fig. 6.1 Intraoral periapical image of the right posterior molars (**a**), and corresponding CBCT axial image (**b**) and surface volumetric renderings (**c**, **d**) of the mandible of a patient who presented to his dentist complaining of a "toothache" in the mandibular right quadrant. CBCT images demonstrate bilateral mandibular tori. Subsequent intraoral periapical image (**e**) shows gutta percha point inserted into fistulous tract

professions, health physicists, State and Federal regulators, the judicial system and malpractice carriers.

5. Those who pay for the imaging—Public, patient or patient guardian and third party payers.

Therefore, the concept of *standard* may well mean different things to different *stakeholders*. It is also quite likely that some stakeholders may be confused by discussions of "standards" by other stakeholders with whom they have less familiarity. In the broadest sense, standards may be considered in ethical, moral, and medicolegal context.

6.2 The Patient

When patients are informed of the availability of CBCT to examine their specific condition, they often look towards their dentist/provider determine whether the image will be useful before consenting to have it performed. Is it needed? Is it worth it? Is there any harm from it?

The practice of dentistry exposes practitioners at each patient encounter to an ethical obligation of beneficence—will the image *"serve the patient's best interests"?* Some may equate this with applying state-of-the-art diagnostic options for each patient. Professional opinion, however, involves judgment. One of the elements that make dentists professionals is the ability to balance the need for diagnostic information with the current scientific and technical reality of a particular modality to provide it whilst considering the costs and risks, both economic and actual. Practitioners are obliged ethically and morally to measure the benefit of the procedure versus the potential risk. Dentists may also owe legal duties that overlap with ethical considerations to some degree.

6.2.1 Assuring Diagnostic Efficacy

For more than a decade numerous authors, including the authors of this chapter, have expounded the diagnostic benefits of CBCT for specific applications. Most practitioners are able to provide patients with information regarding use of CBCT imaging from a technology assessment position—"It provides me with a 3D image of X, Y or Z." However, a fundamental distinction exists between determining the overall benefits of CBCT imaging and relating it to specific patient outcomes. This is because, unlike other areas of dentistry such as surgery, there is a chain of events that separates the accuracy of the diagnosis from patient treatment outcome. In other words, should a CBCT image be taken in cases where a conventional panoramic view is diagnostically sufficient?

Fryback and Thornbury (1991) formalized a hierarchical framework for the links in this chain for diagnostic radiology. While CBCT is often able to separate abnormal from normal anatomy (level 1) and provides images capable of accurate diagnoses (level 2), assessments above these levels, resulting in changes to working diagnosis (level 3) and therapy (level 4) are not able to be readily determined by OMR studies alone (Hollingworth 2005; Hollingworth and Jarvik 2007). However, unlike many other disciplines, it is difficult to provide a patient with a data-based response that addresses specific questions such as "… is it useful?"

Emerging articles describing the clinical efficacy of CBCT imaging for specific patient clinical presentations (Walter et al. 2009; Haney et al. 2010; Katheria et al. 2010) certainly assist clinicians in presenting information to patients and quantifying the intrinsic value of diagnostic information provided by CBCT imaging. However, there continues to be a dearth of level 3 and 4 research in the published literature.

6.2.2 Balancing the Possible Benefits vs. the Potential Risks

The increasing use of computed tomography (CT) in medicine has been acknowledged, particularly in pediatric diagnosis and adult screening (Brenner and Hall 2007). This trend is most likely mirrored in Dentistry by the utilization of CBCT. The primary risk of CBCT imaging for the patient is related to radiation-induced carcinogenesis. The risk for children is much greater than for adults from a given exposure because they are inherently more radiosensitive and have more remaining years of life during which a radiation-induced cancer could develop. There seems to be complacency demonstrated by some equating CBCT examinations in the same light as other dental radiologic procedures for single procedures, especially for children. However, radiation doses from specific CBCT units vary enormously with some rivaling medical multislice CT. The concern of numerous professional dental organizations[1] from increasing utilization of CBCT imaging in the pediatric setting is so great as to join the Image Gently™ in Dentistry Campaign (2016) (White et al. 2014; Scarfe 2014). Member organizations make six pledges on behalf of its members to raise awareness of the special considerations required in pediatric dental radiology, four of which are applicable to CBC. These pledges are based on the concepts of justification on the use and reduction of radiographic exposure in accordance with the principle of As Low As Diagnostically Acceptable (ALADA):

- All dental imaging, including CBCT
  - Select x-rays for individual's needs, not merely as a routine
  - Child-size the exposure time
  - Use cone-beam CT only when necessary
  - Always use thyroid collars
- Intraoral dental imaging only
  - Collimate the beam to the area of interest—Use rectangular collimation
  - Use the fastest image receptor possible: E- or F-speed film or digital sensors

[1]American Dental Association; American Academy of Oral and Maxillofacial Radiology; American Association of Oral and Maxillofacial Surgeons; American Association of Endodontists; American Academy of Oral and Maxillofacial Pathology; American Academy of Pediatric Dentistry; American Academy of Periodontology; American Dental Education Association; Canadian Association of Oral and Maxillofacial Radiology; and the European Academy of DentoMaxilloFacial Radiology.

6.3 The Provider

This group of stakeholders involves those who legally prescribe (dental practitioners), perform (practitioners, certified radiographers, qualified dental auxiliaries, imaging facilities), and interpret (practitioners, specialists, and oral and maxillofacial radiologists) CBCT images. All stakeholders in this group are accountable, either directly or vicariously, to various considerations in CBCT imaging.

6.3.1 Clinical Use Guidelines

The designation of dentists as professionals implies that they are able to exercise judgment in regard to all aspects of CBCT imaging by applying moral, ethical, and legal standards within a business environment. The interests of the latter, expediency and profit, should always be subservient to the former. CBCT technology applies ionizing radiation to produce a volumetric dataset. While this can be reconstructed to produce virtual surface, volumetric and subsequent physical models that may negate optical (e.g., photographic) or chemical impressions, dental practitioners who perform CBCT examinations have a moral and ethical responsibility to minimize radiation dose to individual patients, to staff, and to society as a whole. Based on this overriding responsibility, all providers should be familiar with documents providing professional guidance on the appropriate use of CBCT imaging to improve quality of patient care (Table 6.1). Horner et al. (2015) identified 26 publications as of 2015, 11 of which were specifically written to give guidelines on the clinical use of CBCT and contained sections on selection criteria. The remaining 15 included guidelines relating to various aspects of CBCT. These documents are derived either from group expert opinion or by consensus of a panel within an agency or organization.

6.3.2 Practitioner Education

Practitioners have a moral obligation to maintain and improve their professional skills through lifelong learning; this applies equally to clinical skills as well as to the adoption of new technologies. The educational standard is, therefore, that professionals become familiar with not only the technical and operational aspects of CBCT but understand the scientific validity and health risks of its use. This can be a daunting task at a time when information and evidence-based consensus is still evolving. Even after a decade of use, the majority of dental schools do not include instruction in higher level use of this technology for undergraduate/predoctoral students in the United States, the United Kingdom, and Australia (Parashar et al. 2012). This ethical standard has been translated into a legal requirement in a number of countries including Australia, the United Kingdom, Greece, Denmark, and Germany. However, in the United States most jurisdictions do not require formal training on the use of CBCT imaging before operation in clinical practice. There is an enormous need and desire from practitioners for education on all aspects of CBCT imaging including the appropriate use of the modality, technical parameters associated with scanning, practitioner and patient responsibilities, documentation, quality assurance, interpretation of resulting images, and dose considerations. The European Academy of DentoMaxilloFacial Radiology (EADMFR) has made recommendations for minimal educational standards of dentists in Europe who intend to be involved in any aspect of CBCT imaging (Brown et al. 2012). The EADMFR describe two levels of education—Level 1, for *Prescriber* dentists (those who refer for a CBCT examination and reviews the images, including the report) and Level 2, for *Practitioners* (*Prescriber* dentists who also report on CBCT imaging) (Table 6.2).

6.3.3 Image Interpretation

Inherent to the process of CBCT imaging is interpretation of the resulting images. This is an ethical responsibility of the individual who prescribes the imaging and either implied or specifically described legal requirement when

Table 6.1 Selected published guidelines for the use of maxillofacial CBCT

Author	Year	Organization	Application	Discipline/Specialty
Isaacson et al.	2008	BOS	Clinical	Orthodontics
AO	2010	AO	Clinical	Implant dentistry
Diangelis et al.	2012	IADT	Clinical	Dental trauma
Tyndall et al.	2012	AAOMR	Clinical	Implant
Benevides et al.	2012	ICOI	Clinical	Implant
Evans et al.	2012	FDSRCS	Clinical	Endodontics (surgical)
Harris et al.	2012	EAO	Clinical	Dental implants
Husain et al.	2012	FDSRCS	Clinical	Orthodontics (impacted canine)
AAOMR	2013	AAOMR	Clinical	Orthodontics
AAE	2013	AAE	Clinical	Dental trauma
FGDP	2013	FGDP	Clinical	Clinical and technical
Dula et al.	2014	SGDMFR	Clinical	Oral and maxillofacial surgery, temporomandibular joint dysfunctions and disorders, and orthodontics
ESE	2014	ESE	Clinical	Endodontics
Dula et al.	2015	SGDMFR	Clinical	Endodontics, periodontology, reconstructive dentistry and pediatric dentistry
AAE/AAOMR	2015	AAE/AAMOR	Clinical	Endodontics
Carter et al.	2008	AAOMR	General	Clinical and Technical
Haute Autorit'e de Sant'e	2009	FNAH	General	Clinical and technical
Horner et al.	2009	EADMFR	General	Clinical and technical
Horner et al.	2009	EADMFR	General	Clinical and technical
HPA	2010a, b	HPA (UK)	General	Technical
Superior Health Council (Advies van de Hoge Gezondheidsraad17)	2011	Federal Public Service (Belgium)	General	Clinical and technical
Noffke et al.	2011	SADA	General	Clinical and technical
EC	2012	EC	General	Clinical and technical
ADA Council on Scientific Affairs	2012	ADA	General	Clinical and technical
AWMF	2013	AWMF	General	Clinical and technical

AAOMR American Academy of Oral and Maxillofacial Radiology, *AAE* American Association of Endodontists, *AO* Academy of Osseointegration, *BOS* British Orthodontic Society, *EADMFR* European Academy of Dental and Maxillofacial Radiology, *EAO* European Association for Osseointegration, *EC* European Commission, *ESE* European Society of Endodontology, *FDSRCS* Faculty of Dental Surgery Royal College of Surgeons (England), *FGDP* Faculty of General Dental Practice (UK), *FNAH* French National Authority for Health, *HPA (UK)* Health Protection Agency, Centre for Radiation, Chemical and Environmental Hazards UK, *IADT* International Association of Dental Traumatology, *ICOI* International Congress of Oral Implantologists, *SGDMFR* Swiss Society of Dentomaxillofacial Radiology

using American Medical Association Current Procedural Terminology (CPT) or American Dental Association Council Dental Procedures and Nomenclature (CDT) codes. In the United States, the AAOMR (Carter et al. 2008) has underlined the necessity of interpretation as a practice standard when performing CBCT imaging:

> The practitioner who operates a CBCT unit, or requests a CBCT study, must examine the entire image dataset.

Furthermore, the AAOMR (Carter et al. 2008) state:

> Qualified specialist OMFRs may be able to assist diagnostically when practitioners are unwilling to accept the responsibility to review the whole exposed tissue volume.

Table 6.2 Education levels and area of competency for CBCT training (after Brown et al. 2012)

	Areas of competence	
Domain	Level 1	Level 2
Knowledge and understanding	• Concept of the imaging "chain" and the difference between two dimensional and 3D imaging	Level 1 plus
	• Fundamental concepts of radiology including how X-rays interact with matter, biological effects of radiation, background radiation and its origin, principles of image detectors and their influence on image quality	• Knowledge of the factors controlling X-ray quantity, quality and geometry and its influence on image quality, construction and function of CBCT equipment
	• Selection criteria for intraoral and panoramic radiography and its influence on radiation protection	• Principles of CBCT radiographical techniques
	• Knowledge of national and local CBCT regulations	• Principles of reformatting image
	• Importance of gaining new knowledge by following scientific developments and improvements in diagnostic imaging and technology	• Data
		• CBCT selection criteria
		• Knowledge of principles of diagnostics and how diagnostic radiology relates to other diagnostic methods
		• Preparation of a structured report
Skills and ability	• Correct use of CBCT equipment	Level 1 plus
	• Understand and implement CBCT regulations	• Recognize malfunctioning of CBCT devices
	• Support staff development in the use of CBCT	• Perform a quality control program
	• Analyze normal anatomical structures of the teeth, jaws and facial skeleton	• Use software and other measures for radiation protection
	• Recognize disease of the teeth and their supporting structures	• Differentiate between normal and diseased findings of the teeth, jaws and the facial skeleton
	• Search/identify adequate scientific literature	• Create a report
		• Critically review adequate scientific literature
Judgment and stance	• Strives for ALARA	Level 1 plus
	• Development of competence in OMFR	• Responsible for staff development
		• Identify when to refer for second opinion

ALARA as low as reasonably achievable, *OMFR* oral and maxillofacial radiology

This opinion has been supported by many in the literature (Jerrold 2007; Kuftinec 2007; Friedland 2010).

6.3.4 Qualifications for Owning and Operating a CBCT Unit

In the United States, most states permit any licensed dentist to purchase a CBCT machine, without the need for training beyond that of dental school. In most countries throughout Europe, CBCT is generally available to all dentists.

In some jurisdictions of the United States additional requirements are imposed before a dentist may purchase and operate a CBCT machine. Until recently, the State of Michigan had a detailed list of requirements (Michigan Department of Community Services 2006). On the other hand, in some American states such as California even non-dentists may own and operate CBCT units (California Health and Safety Code §§ 106955–107111). These states grant limited X-ray permits to individuals who have taken an approved course and passed an examination. Such permit holders typically operate so-called X-ray laboratories. They provide only technical services and images made in such facilities are not necessarily read by a radiologist, although some may make arrangements for radiologists to read and report on cases. Currently no state in the US requires practitioners to obtain advanced training in CBCT. Professional organizations, such as the American Dental Association, sponsor Level I, II, and III certification courses in conjunction with the American Academy of Oral and Maxillofacial Radiology (AAMOR 2016).

In Ontario, Canada, a dentist must undertake training to even prescribe a CT scan, let alone own a scanner (Royal College of Dental Surgeons of Ontario 2016). In Western Australia, extremely limiting requirements exist in that only those who are registered as a dental practitioner with the Australian Health Practitioner Regulation Agency (AHPRA) and have a Masters' Degree in Oral and/or Maxillofacial Radiology obtained at the University of Queensland or the University of Adelaide can own and operate CBCT equipment (Government of Western Australia Radiological Council 2016; Zhang et al. 2016).

In Europe, while many countries have varying regional requirements, member states of the European Union must ensure that any individual involved in radiological imaging has adequate and appropriate theoretical and practical training to undertake and, where appropriate, interpret a radiological examination, as well as relevant competence in radiation protection (European Council 1997). Furthermore, specific training curriculum content is prescribed (European Commission 2012; Brown et al. 2012) (Table 6.2) which a number of countries, such as Germany (Durchführung der Röntgenverordnung (RöV) 2005) have adopted. In this instance, training courses and vocational training programs must be accredited by a responsible authority.

It should be noted that CBCT operating legislation may be derived from various sources; In Michigan, it is the Michigan Department of Community Health, in Ontario, Canada, it is the Royal College of Dental Surgeons of Ontario, the Ontario dental board, and in Western Australia, it is the Radiological Council of the Government of Western Australia. With such variation in the nature and scope of authorities, dental practitioners should therefore check with all relevant authorities in their particular location before purchasing a CBCT machine.

6.3.5 Technical Aspects of CBCT Imaging

6.3.5.1 CBCT Acquisition

Field of View

The field of view (FOV) refers to the physical size of the area that is exposed in an image. Many dentists today own a CBCT machine and acquire their own images. Unfortunately, relatively few of them have formal training in interpreting the images. Since a practitioner is responsible for reading the entire image volume, and not just the reason for which the scan was taken (Friedland 2009; Turpin 2007), practitioners who obtain their own images and who do not routinely have the resulting scans read by a radiologist often elect to keep the FOV as small as possible in an attempt to limit liability. This is not good practice—the FOV should be dictated by the clinical needs of the patient and not by medicolegal considerations. Addressing CBCT examinations done for endodontic purposes, the American Association of Endodontists and the American Academy of Oral and Maxillofacial Radiology address this very issue of using a too small FOV (AAE/AAOMR 2015):

> The limited volume CBCT imaging in endodontics is advantageous, but by irradiating only one site or area, projections acquired may not contain the entire region of interest.

While it is true that a larger field of view makes it more challenging to interpret an image and thus increases potential liability, the solution is not to expose a smaller area than clinical needs require, but rather to have the scan interpreted by a radiologist.

Exposure Parameters

All exposure parameters (kVp, mA, time of exposure) should be appropriate for the patient and the purpose for which the scan is being taken. However, often the most problematic parameter in practice is resolution.

While there are technical definitions of resolution—line pairs/mm or the number of bits per pixel value—it simply refers to the ability of an imaging modality to differentiate two objects. The smaller the object, the greater the resolution that is needed to visualize it. Since patient dose usually increases with increasing resolution, a scan at too high a resolution may expose a patient to unnecessary radiation. A scan at too low a resolution may be inadequate for the purpose for which it was taken. For example, a scan done at 0.3 mm nominal voxel size will almost always be inadequate for an endodontic diagnosis, which typically requires a very high resolution scan. Thus, when presented with a scan of too low a resolution for the purpose for which it was taken, the practitioner or radiologist should not attempt to read more into it than is possible. For example, one may not be able to say from such a scan whether a second canal is present or absent in the mesio-buccal root of a maxillary molar (the so-called MB2). If MB2 is seen, one can report that it is present, but if it cannot be identified one cannot exclude the possibility of it being present. Instead, one ought to recommend another scan taken at the appropriate resolution.

Exposure parameters are most likely problematic in multi-specialty group practices where the same scanner is used by practitioners in different specialties for different purposes—a periodontist may take a large FOV scan at a low resolution to plan an implant surgery following which an endodontist takes a scan to rule out an MB2 without changing the resolution. A scan taken at too low a resolution may be as good as not taking a scan when one was indicated and could lead to potential liability. It is therefore highly recommended that in multi-specialty group practices dentists are especially vigilant about checking exposure parameters and develop task specific image acquistion protocols.

6.3.5.2 The DICOM File and Image Transfer

An understanding of the basic “element” or “unit” of a CBCT electronic information, the DICOM (Digital Imaging and Communications in Medicine) file format and compliance guidelines for communication is essential to prevent potential legal breaches of confidentiality of personal health information (PHI).

DICOM is the universal, non-proprietary, electronic digital image format and file structure standard for handling, storing, printing, and transmitting digital information in medical imaging. A DICOM file can include not only images but also the related information that distinguishes one image from another (e.g., pertinent details of the performed procedure, interpretation text, or the format settings for printing).

All CBCT units should be capable of exporting data in DICOM format, either as single or multiple files, compressed or uncompressed. DICOM files are the fundamental unit by which all radiologists communicate with one another independent of operating platform. Dental practitioners should know how to export them either to a CD, server or transmit them electronically. Although it cannot be stated with certainty that it is below the standard of care today for a practitioner not to understand the above, it is the authors’ opinion that this is such fundamental knowledge that a jury in a malpractice case is highly likely to consider it to be essential knowledge for anyone who owns or operates a CBCT machine. The inability to do so is akin to not knowing how to identify and forward a patient’s medical record.

Hard Copy Distribution

Most practitioners who operate a CBCT unit are likely familiar exporting digital data to a CD. Such CDs typically include an AUTORUN.INF file. When loaded into a recipient’s personal computer, the instructions contained within this file are automatically launch the viewer software. The problem using CDs to transfer information from one practitioner to another is that they frequently contain the information only in a proprietary format and do not contain the non-proprietary

DICOM files. This means that the recipient is able to view the study only in the proprietary viewing software on the autorun CD.

Just as dental practitioners have preferred patterns and techniques in clinical practice, radiologists have preferred application software with which to view and manipulate CBCT data. If the CD contains only the proprietary format, radiologists are precluded from viewing it in their preferred application and/or manipulating the image to optimize the image for a specific purpose. To avoid this problem, practitioners forwarding CDs should ensure that it includes a folder with the non-proprietary, uncompressed DICOM files. If the manufacturer does use DICOM files natively for the viewer software, it is advisable that when CDs are used to transfer digital data for example, if a patient is changing dentists and asks for a copy of his record, then practitioners should export DICOM files on a separate CD. There is an additional reason to include the DICOM files. In the event a radiologist wishes to consult with a colleague, then if the data is not available as DICOM, a duplicate CD has to be mailed or requested, thereby delaying the diagnosis. The availability of DICOM facilitates electronic transfer.

Unless specifically requested otherwise, all case digital data should be sent in the non-proprietary, uncompressed DICOM format.

Electronic Data Interchange

A component of electronic data interchange (EDI) involves transmission of DICOM data via the internet. Several countries including the United States and Canada, as well as organizations such as the European Union (EU) have developed similar, but slightly different, approaches to protecting PHI.

- **European Union.** Two main legal instruments regulate data protection: the Data Protection Directive 1995/46/EC (Section 2.1) and the e-Privacy Directive 2002/58/EC (Section 2.2). Chapter 11 of the former regulation has implications for the regulation of health data whereas the latter is more specific and is aimed at ensuring the protection of personal data in the field of telecommunications including electronic transmission of PHI.
- **Canada.** The Personal Information Protection and Electronic Documents Act (PIPEDA) is an Act that set parameters for the administration of personal data by businesses and extends to EMR (electronic medical records).
- **United States.** A number of federal regulatory statutes have been introduced to ensure protection for individually identifiable health data. That have broadened consideration and, to most, have complicated compliance. These include The Health Insurance Portability and Accountability Act of 1996 (HIPAA), Public Law 104–191 (initial compliance date April 14, 2003), the HIPAA Security Rule (initial compliance date April 20, 2005), the Health Information Technology for Economic and Clinical Health (HITECH) Act (initial compliance date February 22, 2010), and, most recently, the 2013 Privacy and Security Omnibus Final Rule (initial compliance date January 17, 2013). The Privacy and Security Rules provide more specific directives and technical precautions for dental practices to ensure “reasonable safeguards” regarding electronic patient information that are received, maintained, or transmitted. The HITECH Breach Notification Rule amends parts of the Privacy and Security Rules and requires dental practices, on certain occasions, to notify individuals, federal agencies, and even the media if a breach of unsecured PHI occurs. Finally, The HIPAA Omnibus Rule, apart from other functions, extends all previous requirements to include covered dental practices business associates (BA) (e.g., billing service, document transmission, or digital data storage company) and their contractors (Scarfe 2014). These regulations effectively codify the ethical responsibility to maintain patient confidentiality.

The International Organization for Standards and the International Electrotechnical Commission has established ISO 27001, an internationally recognized management standard to organize and control an Information Security Management System (ISMS). ISO 27001 address approximately 95% of the requirements of

HIPAA. ISO 27001 is supported by specific control objectives and definitions defined in ISO 27002 which details best practices for information security that includes the following considerations:

- **Confidentiality.** Protocols to ensure that information is accessible only to those who need to use it.
- **Integrity.** Procedures to safeguard the accuracy of information and the methods used to process it.
- **Availability.** Practice and procedures ensuring that authorized users have prompt access to the information when they need it.

While not specific to CBCT DICOM data, dental practitioners must understand specific technical matters related to the transmission of images in compliance with specific regulations.

Guidelines for CBCT DICOM Distribution via the Internet

Cases sent out on CD by mail are considered to be in compliance with the ethical responsibility to maintain patient confidentiality. However, E-mail has become the de facto Internet-based electronic communication portal for the exchange of various types of dental electronic health record (d-EHR) data. This includes provider-to-provider (e.g., transferring patient records, professional consultations as previous described), patient-to-provider (e.g., appointments, inquiries), and provider-to-third party (e.g., office to laboratory, office to health insurance plans) interactions (Scarfe 2014). Although health care providers treating the same patient may share health information such as CBCT DICOM data via e-mail for treatment purposes without patient authorization, reasonable safeguards should be in place when doing so to protect information from inappropriate or unauthorized use or disclosure in violation of regulatory statutes. Many of these have been specifically defined by HIPAA (Table 6.3).

Encryption is the process by which the message and any associated attachments of the e-mail are encoded by the sender and decoded by the recipient. Two protocols for e-mail encryption of radiographic images are possible: S/MIME (Secure/Multipurpose Internet Mail Extensions) and PGP (Pretty Good Privacy). S/MIME incorporates the

Table 6.3 Examples of safeguards ensuring confidentiality, integrity, and availability of electronic transmission of CBCT DICOM data via e-mail

	E-mail characteristics			
Local computer	Content	Addressees	Encryption	Data transfer protocols
Antivirus software	Inform recipients that the information contained therein is private and confidential	Recipient address should always be verified before sending e-PHI	Use of S/MIME or PGP	Use third party IES
Firewall protection	Inform recipients that e-mails should not be forwarded or shared with those who are not privileged to receive it.	Do not use Outlook, Gmail, Yahoo, and Hotmail directly		Alternately use direct d-EHR-based systems
Restricted password-based access	Inform recipients that if they have received the e-mail in error, they should notify the sender immediately.			Do not use Drop Box, OneDrive or Google Drive
	The subject line should never include any aspect of e-PHI			

EHR electronic health record, *e-PHI* electronic public health information (e.g., patient's name, date of birth, social security number, or chart number), *IES* information exchange service, *PGP* Pretty Good Privacy, *S/MIME* Secure/Multipurpose Internet Mail Extensions use of certificates of authority located on corresponding computers to authorize transmission and receipt of e-mails. Many e-mail clients use this type of encryption; however, the process involves acceptance of the rules for use by the recipient and establishment of yet another password hierarchy, which needs to be recovered with every e-mail. To add greater complexity to this situation, the sender is usually the individual who determines the passcode and the passcode cannot be sent in the subject line or body of the test that is to be encoded. Passcodes can be sent separately or the individual receiving the e-mail can be contacted by telephone. This encryption usually costs money to purchase. PGP encryption creates encryption keys with each e-mail (Scarfe 2014).

Although there are HIPAA compliant e-mail services, E-mailing entities like Outlook, Gmail, Yahoo, and Hotmail are not encrypted and therefore do not comply with minimal d-HER requirements of e-mail communication systems. In addition, image attachments to these messages are often compressed, usually in the form of lossy compression, particularly if they are large. This reduces image file size but also reduces image quality. The practitioner has a responsibility to ensure the integrity of d-EHR including CBCT DICOM data whether uploaded to a server, sent by e-mail or using a service. Guidelines for implementing secure electronic transmission of digital radiographs and photographs have been published by the American Dental Association (2011a, b, c).

The simplest approach for e-mail communication and distribution of dental radiographic images is to use a secure information exchange service (IES) acting as an intermediary providing temporary or permanent (cloud-based) archiving and transmission portal functions for unlimited clients (e-mail recipients). Examples of IES include ShareFile (Citrix ShareFile, Raleigh, NC), Accellion (Accellion, Palo Alto, CA), and CipherPost Pro (AppRiver, Gulf Breeze, FL). Some IESs are specifically developed for dental practices, such as eDossea (eDossea, Ankeny, IA) and Brightsquid Secure-Mail (Brightsquid Dental Ltd., Calgary, Alberta), or have dental applications (FastVaults [MEA\NEA, Norcross, GA]) or plug-ins for specific e-mail clients (e.g., ShareFile plug-in for Microsoft Outlook). In the United States, some states, with the assistance of federal stimulus funding, have developed HIPAA-compliant communication solutions at their regional level. Online transfer storage areas such as Dropbox [Dropbox, Inc., San Francisco, CA] or OneDrive [Microsoft Corp., Redmond, WA]) do not provide the privacy and security compliances necessary when dealing with electronic transactions involving patient information (Scarfe 2014).

An alternate approach has been directed toward establishing direct EHR-based systems providing compliant e-mail communications from within the patient image and management software. In the United States, The Direct Secure Messaging (Direct) protocol was established by the Office of the National Coordinator for Health Information Technology as the HIPAA-compliant national standard format and structure of EHR-based e-mail systems comprising both encryption and sender and recipient validation components. Vendors are now required to integrate Direct into the EHR. Direct has multiple data cross-platform communication functions in addition to e-mail, facilitating clinical interoperability and transitions in care from provider to provider. It is designed to provide a central portal for patient care enabling avenues for the transmission of documents including images without compression, "corridor consults," and multi-provider forums (Scarfe 2014).

6.3.5.3 Radiologic Interpretation

Implicit within the performance of medical CT imaging is the development of a radiologic interpretation or "report." In medical imaging, one entity is usually responsible for scanning the patient and generating the images (e.g., hospital radiology department) whereas a second (e.g., radiologist) is responsible for the radiologic report.

Most in-office dental and maxillofacial CBCT units are owned and operated by a non-radiologist who assumes the role of prescriber, radiographer, and radiologist. Dental practitioners who take their own scans or who use the services of facilities that perform them and do not include a report should be concerned about possible liability for reading the scan (Friedland 2010; Friedland and Miles 2014). The dentist is responsible not only for interpretation of the scan as it pertains to their area of expertise (e.g., the teeth and alveolus) or the particular reason for which the image was taken, but also for reading all of the anatomy imaged within the FOV. This standard, at least in the United States, is clearly underlined by numerous Professional guideline statements (Carter et al. 2008; American Dental Association Council on Scientific Affairs 2012). However, dentists who take their own scans are not required to read the scans themselves if they are uncomfortable or do not feel competent to do so. In these circumstances, the practitioner would be expected to refer the patient to a practitioner who is competent. Unless they have completed a formal training program incorporating oral and maxillofacial radiology, most dentists do not have the expertise to interpret CT scans and are therefore obliged to refer the reading of the images to an oral and maxillofacial or medical radiologist.

6.3.5.4 Teleradiology

Teledentistry is a combination of telecommunications and dentistry involving the exchange of clinical information and images over remote distances for dental consultation and treatment planning. Teledentistry can take a number of forms, including (American Dental Association 2015; American Dental Association House of Delegates 2015):

- **Live video.** Two-way interaction between a patient and dentist using audiovisual technology.
- **Store and forward.** Transmission of recorded health information (e.g., radiographic images, photos, video, digital impressions, or photomicrographs) through a secure electronic communications system to a practitioner who uses the information to evaluate the patient's condition or render a service outside of a real-time or live interaction.
- **Remote patient monitoring**. Personal health and medical information is collected from an individual in one location then transmitted electronically to a provider in a different location for use in care.
- **Mobile health.** Health care and public health practice and education supported by mobile communication devices such as cell phones, tablet computers, or personal digital assistants.

Specific to *store and forward*, Teleradiology consists of two components:

1. The transmission of radiographic images beyond the immediate vicinity of image acquisition, for the purpose of image interpretations by a referring practitioner to a receiving practitioner. This involves an understanding of the technical nature of the image data (DICOM) and electronic data transmission (see later).
2. The performance and subsequent transmission of radiologic interpretations by the receiving practitioner to the requesting clinician.

Dental and maxillofacial teleradiology in dentistry is an "asynchronous" modality (American Dental Association 2015) in that it involves:

> … transmission of recorded health information… to a practitioner, who uses the information to evaluate a patient's condition or render a service outside of a real-time or live interaction.

Furthermore, the ADA (American Dental Association 2015) states:

> Any dentist delivering services using teledentistry technologies will be licensed in the state where the patient receives services, or be providing these services as otherwise authorized by that state's dental board.

Recently the AAOMR Executive Committee recommend interpreting this specification in view of ADA Technical Report No. 1060 (Yang et al. 2011a, b), which proposes the concept of the *virtual patient* (AAOMR 2016). A *virtual patient* is that element(s) of the dental record this is:

> … transmitted to the receiving practitioner, who is held accountable by the appropriate laws and professional licensure of the state of the receiving practitioner.

In essence, the AAOMR (2016) supports the concept of radiologic interpretations, of CBCT images in particular, being performed in areas other than that where the scan was acquired by a licensed practitioner.

> The receiving practitioner, who provides the official diagnostic interpretation of images transmitted for consultation by the referring provider, should maintain appropriate licensure in the receiving state (Yang et al. 2011a, b; Yang et al. 2016).

While few technological hurdles exist to the electronic transfer of CBCT data for the purposes of radiologic interpretation, licensing laws may not have kept pace with the changes in technology (Magenau 1997) and professional sentiment. In countries with a national dental license, or at least a de facto national license, licensing laws do not present any impediment to the reading of scans by a radiologist situated anywhere in the country. However, in countries like the United States, Canada, and others that have state-by-state or province-by-province licensing, a dentist must have a valid license in that jurisdiction in order to practice in that state or province. Typically (New York State Department of Public Health 2009):

> It is the location of the patient that defines where the care has been delivered and the jurisdiction of applicable regulations.

Such laws currently present a significant obstacle to the implementation of the concept of the *virtual patient* and restrict reading of scans to those who are licensed in specific jurisdictions where the patient resides.

6.3.6 The Ethical Pitfalls of Self-Referral for CBCT Imaging

Although there is no study concerning dentists, the literature is clear that when non-radiologist physicians own and operate their own X-ray units and self-refer, their utilization is substantially higher than among physicians who refer their patients to others for radiologic procedures. (Hillman et al. 1990; Levin and Rao 2004; Gazelle et al. 2007). There is no reason to believe that dentists behave differently than their medical counterparts. Thus, a major potential ethical pitfall for dentists who own a CBCT machine or who have an interest in a facility that operates a CBCT machine is overutilization of the modality, to their patients' financial and dose exposure detriment.

Indeed, the United States government is so concerned about the temptations of self-referral that laws have been passed to make certain referrals illegal. The so-called *Stark Laws* (42 C.F.R. §411.350 through §411.389) and the federal anti-kickback statute (42U.S.C. §1320a-7b) only pertain to clinicians who accept government payments such as Medicare and Medicaid. In addition to federal laws, many states have passed similar legislation, often referred to as "mini" laws (e.g., mini-Stark laws). Clinicians should be sure to check on any state laws that may apply to them. Dentists may also find themselves subject to federal and state laws if they co-own a CBCT unit with a physician or have an interest in a radiology facility in which a physician also holds an interest.

There are a few ways in which a dentist can mitigate the financial temptation to over utilize CBCT. One way is to not charge for a scan. Another strategy is to democratize the cost over all patients by slightly increasing fees for each case, but to not have a specific charge for a scan. For example, an endodontist could estimate the percentage of scans he will take and slightly increase the fee for the endodontic therapy for all patients to cover the cost of the scans, and then not charge a fee for a specific scan. There are some ethical arguments that can be made against such an approach, but overall the authors feel that this is an ethically acceptable way to address the problem. Finally, a dentist could not refer to a facility in which he or she has a financial stake.

A second ethical pitfall is to miscode a diagnosis in order to obtain insurance coverage for a patient. While insurance coverage, both dental and medical, varies by insurance company, many patients' plans do not cover CBCT scans done for dental purposes (Pakchoian et al. 2015). Thus, while miscoding is not unique to CBCT scans, the temptation to do so is greater than for other dental procedures that are fully or partially covered. One example of such abuse is to miscode CBCT scans that were taken for implant planning purposes as a bone density study. The remedy for this is of course to simply practice and to code in an ethical manner.

6.4 The Dental Industry

The dental industry pioneered and commercially introduced dental and maxillofacial CBCT imaging to the dental profession and continues to facilitate much of the technically based research and development within this field. Dental manufacturers and distributors have a unique relationship with the dental profession—for the most part the value of establishing and maintaining relationships with their clients is understood as most will likely remain so for 20–30 years. Corporate viability is dependent on strong long-term relationships. Therefore, it is in the best interests of the dental trades to expand and consolidate this base. Commercial vendors of CBCT units must assure that such units satisfy certain minimal mandated operational performance standards associated with equipment capable of ionizing radiation at the national (e.g., In the United States, the FFDCA; In Europe, Council Directive 93/42/EC (1993) and Council Directive 2007/47/EC (2007)) and local level. Other standards include regarding safety issues related to construction (International Electrotechnical Commission—IEC 86B, including subcommittee 46) and manufacture (with Section 510(k) of FFDCA). There are also UL (Underwriters Laboratories), CE (European Community for all Electrical and Electronic equipment), and IEEE (Institute of Electrical and Electronics Engineers) specifications for certain components. In addition, Industry has entered into collaborative partnerships with the dental profession to ensure imaging standards for interoperability including establishment of a universal file format and standards for image display and e-mail transport through DICOM (Digital Image and Communications in Medicine) Standards Committee activities and IHE (Integrating the Healthcare Enterprise).

There is a vested commercial interest in the Dental Trades seeing judicious and appropriate use of their products on many levels including marketing leverage, establishment of after sales maintenance contracts, reduced after sales support activity and word of mouth referral.

6.5 The Legal System

There are two components of the legal system that offer minimal compliance guidelines, which some refer to as standards. These are equipment regulations (administered through regional and national statutes) and private civil actions based on professional negligence (malpractice-tort actions in court).

6.5.1 Equipment Safety Documentation

Operating and performing CBCT imaging in dental practice involves compliance with regulations related to the installation and operation of X-ray generating equipment. As described previously, national regulations are usually concerned with essential elements of equipment manufacture and the monitoring of radiation output periodically (Federal Food, Drug and Cosmetic Act (FFDCA) 2017; Council Directive 93/42/EC 1993; Council Directive 2007/47/EC 2007). Although not currently required, it is conceivable that standards in this domain may evolve to include demonstration of image quality assurance as a method of minimizing radiation dose and optimizing image quality. This certainly seems to be the direction a number of other countries are taking in response to the increased use of CBCT (HPA 2010a, b). Such quality control would most likely involve the use of a quality phantom as a method of demonstrating compliance with an imaging standard and periodic assurance of exposure compliance.

State regulations involve statutes that relate to two activities at the local level. The first pertains to the licensing and monitoring of CBCT equipment to ensure compliance with Federal radiation output regulations. The second involves regulation of those operating CBCT units. CBCT units are either registered as a dental or, in some jurisdictions, medical X-ray generator. Certification requirements vary according to equipment designation. This may necessitate specific training for CBCT licensing of “dental” radiographers, as is currently the case in at least two states in Australia (New South Wales and Queensland) and a number of other countries including Germany, Greece and Denmark. Furthermore, agencies in some regions, influenced by concerns from various stakeholders, may rigorously apply (e.g., Certificate of Need approving purchase and installation of CBCT equipment) or enact legislation to further regulate CBCT operation.

6.5.2 Professional Negligence

The standard of care is one of the most important legal constructs of professional liability in dental care. However, there is still confusion amongst many as to how it relates to the provision of care in general dental practice. The standard of care applicable to dentists in professional tort cases is defined by state law and derived from numerous elements including state statutes, licensing Board regulations, case law, ethical codes of professional organizations, and professional and community consensus (Scarfe 2011). While regional laws differ slightly, most jurisdictions define the standard of care as that which a reasonably skilled, educated and experienced dentist would do in similar circumstances. If the dentist is a specialist, some states recognize a "national" standard of care in terms of what a reasonable or ordinary "specialist" would do, because most dental specialty residencies require consistent education and testing standards in core specialty areas. It is a term that derives from the legal process in which the patient will have the burden of proving the four elements of a tort claim (Graskemper 2004) including what the standard of care requires, that the dentist violated this standard and that the violation caused an injury. In CBCT imaging this would most likely consist of a failure to identify, diagnose, and document a condition that lead to an absence or delay in treatment for which damages can be quantified. More importantly, the plaintiff will hire an "expert" to establish a breach of the standard of care. Any time lawyers and paid experts get involved in defining "standards," some unpredictable results are likely. This is even more true and problematic when there is a lack of consensus within the dental community on many of the issues discussed here, and also whether the same high standard of care required of a dental radiologist will be applied to other dentists who are allowed to take and interpret the same image, but with a different knowledge, skill, and training base. Various interpretations of the concept have been proposed as it relates to dentistry (Graskemper 2004) and, more specifically, CBCT imaging (Curley and Hatcher 2009; Curley and Hatcher 2010; Zinman et al. 2010; Friedland and Miles 2014).

6.5.3 Professional Liability Insurance

Dental professional liability insurance, commonly referred to as malpractice insurance, is available to practitioners to protect themselves from the financial costs associated with investigating and defending legal claims where there is an adverse patient outcome. Malpractice insurance covers bodily injury as well as liability for personal injury such as mental anguish. Insurance carriers do not set the standard of care, but they may set the requirements for coverage that may in turn diverge from the standard of care, or it may influence it. There are many unsettled questions that can only be resolved on a case-by-case basis as to what the standard of care may require.

As practitioners may perform CT imaging services in a variety of circumstances, there are three potential categories of risk associated with the practitioners' role in CBCT imaging (Holmes 2007):

1. **Radiologist.** As it is assumed that practitioners who perform CBCT in their office have both technical and interpretive competencies to do so. In this situation, failure to diagnose CBCT images arises as a potential liability issue (Bowlin 2010). Liability can arise from a failure to interpret the CBCT data or have it interpreted by a radiologist.
2. **Radiographer.** Some practitioners offer local dentists access to their CBCT units on an ad hoc basis for a modest per patient fee. In this situation, practitioners act as radiographers however consideration must be given as regards who will interpret images for patients specifically referred by other providers for CBCT images.

3. **Imaging facility.** Some practitioners establish a separate imaging facility independent of their practices.

Insurance carriers may require practitioners to disclose if they are performing CBCT imaging in their offices and offer specific side contracts, called *contract riders*, that specify the conditions under which this can be performed. Oral and maxillofacial radiologists may also be offered contract riders that include liability provisions for out-of-state teleradiology services, consulting services and for continuing education courses.

6.6 The Payer

There are four potential payment sources to providers for CBCT services: the patient, a third party—either private or government based, a combination of patient/third party payer, or the public through taxation.

Reimbursement for imaging procedures when third party payers are involved is geared towards reduction of their financial liability. These societies operate in a cost-conscious environment and are concerned with cost containment—reducing the general cost of health care and minimizing financial risk. The standard used here is cost effectiveness analysis (CEA), an objective technique used to assess whether a new or more effective test or treatment is worth the additional cost. Such analysis is highly complex and relies on considerations of not only the cost associated with correct diagnosis using the new modality, but costs involved with failure to diagnose by not using the test. Currently there are few studies on the economic impact of CBCT imaging for specific dental conditions (Petersen et al. 2014; Petersen et al. 2015).

Third party payers, those with whom patients contract to assist in the payment of health services, are understandably concerned about utilization rates and costs. Some contend that specific marketing efforts directed towards practitioners, especially those touting the use of CBCT imaging as a method of increasing practice revenues or improving workflow efficiency, may serve to increase these concerns and actually be counterproductive at efforts directed towards acceptance for payment of CBCT services. Commercial responses at this stage have been varied and range from specific non-inclusion clauses, financial limitations on payment or gatekeeper mechanisms such as “pre-certification” or payment related to specific disease entities.

In some countries accreditation of CBCT imaging facilities is either currently required or proposed as a prerequisite for reimbursement by point-of-care imaging sites (i.e., in-office scanners) by private insurance or government entities. In the United States, dental and maxillofacial CBCT accreditation is performed by the Intersocietal Accreditation Commission (IAC). IAC has developed a separate division, IAC-Dental CT, with accreditation standards specific for office-based oral and maxillofacial CBCT use in dentistry (Scarfe 2013). IAC Dental CT provides a method for dental practices to document their commitment to quality through compliance with nationally accepted minimal standards considered essential for high quality diagnostic imaging including:

1. Radiation safety through dose optimization and shielding verification.
2. Image and equipment quality assurance.
3. Comprehensive radiologic reporting.

The IAC Standards for Dental/Maxillofacial Computed Tomography (CT) Practice Accreditation using cone beam technology are available at http://www.intersocietal.org/dental/standards/IAC_DentalCT_Standards.pdf. The Standards detail the training and continuing education required for all staff members involved in the performance and interpretation of CT. Documentation of policies and procedures, such as radiation safety and patient identification are closely evaluated. Quality assurance measures including acceptance testing, quality control tests with results and phantom images, an annual physicist survey, preventative maintenance reports and radiation shielding verification, CT protocols, and technical and interpretive quality assessment policies are each considered important elements to the provision of quality patient care (Scarfe 2013).

6.7 Summary

There are many ethical and medicolegal standards to be considered with the performance of dental and maxillofacial CBCT imaging. However, the standard to which the dental profession is held, both by the public and within our own, transcends legal (standard-of-care) and technical (gold standard) definitions. The professional standard for CBCT is appropriate care—to choose CBCT imaging for each patient "wisely" based on selection criteria derived from the best available evidence. In this expanding era of CBCT imaging, the rush to apply technology to specific clinical scenarios should be balanced with diligent discovery and patience.

Acknowledgments Sections of this chapter are based on previously published works by Dr. Bernard Friedland (2010), Drs. Bernard Friedland and Dale Miles (2014), and Dr. William C. Scarfe (2011, 2013, 2015).

References

Academy of Osseointegration (2010) 2010 guidelines of the Academy of Osseointegration for the provision of dental implants and associated patient care. Int J Oral Maxillofac Implants 25:620–627

Advies van de Hoge Gezondheidsraad nr. 8705 (2011) Dentale cone beam computed tomography. Hoge Gezondheidsraad, Brussels. www.health.belgium.be/internet2Prd/groups/public/@public/@shc/documents/ie2divers/19068321_en.pdf. Accessed 1 Aug 2016

American Academy of Oral and Maxillofacial Radiology (2013) Clinical recommendations regarding use of cone beam computed tomography in orthodontics. [corrected]. Position statement by the American Academy of Oral and Maxillofacial Radiology. Oral Surge Oral Med Oral Pathol Oral Radiol 116:238–257

American Academy of Oral and Maxillofacial Radiology (AAOMR) (2016). Basic CBCT level 1 course. http://www.aaomr.org/?page=CBCTcourse. Accessed 24 June 2016

American Association of Endodontists (2013) Recommended guidelines of the AAE for the treatment of traumatic dental injuries (revised 2013). http://www.aae.org/guidelines/

American Dental Association (2011a) ADA Technical Report No. 1048 for Attachment of DICOM Datasets Using Email in Dentistry. http://ebusiness.ada.org/productcatalog/554/Informatics/ADA-Technical-Report-No-1048-for-Attachment-of-DICOM-Dataset/ADA1048-2011D. Accessed 4 Aug 2016

American Dental Association (2011b) ADA Technical Report No. 1048 for Attachment of DICOM Datasets Using Email in Dentistry. Available at : http://ebusiness.ada.org/productcat-alog/554/Informatics/ADA-Technical-Report-No-1048-for-Attachment-of-DICOM-Dataset/ADA1048-2011D. Accessed August 4, 2016

American Dental Association (2011c) ADA Technical Report No. 1023 for DICOM Requirements for Dentistry. http://ebusiness.ada.org/productcatalog/1058/Informatics/ADA-Technical-Report-No-1023-for-Implementation-Requirements/ADA1023. Accessed 4 Aug 2016

American Dental Association (2015) Comprehensive statement on Teledentistry. American Dental Association House of Delegates, ratified, November, 2015

American Dental Association Council on Scientific Affairs (2012) The use of cone-beam computed tomography in dentistry: an advisory statement from the American Dental Association Council on Scientific Affairs. J Am Dent Assoc 43:899–902

American Dental Association House of Delegates (2015) Resolution 45H-2015, Comprehensive ADA Policy Statement on Teledentistry. http://www.ada.org/en/publications/ada-news/2015-archive/december/house-passes-guidelines-on-teledentistry. Accessed 4 Aug 2016

Arbeitsgemeinschaft der Wissenschaftlichen Medizinischen Fachgesellschaften (AWMF) (2013) s2k-Leitlinie Dentale digitale Volumentomographie Version Nr. 9 vom 5 August 2013. AWMF-Register-Nummer: 083–05. AWMF, D¨usseldorf. http://www.awmf.org/uploads/tx_szleitlinien/083-005l_S2k_Dentale_Volumentomographie_2013-10.pdf

Benavides E, Rios HF, Ganz SD, An CH, Resnik R, Reardon GT, Feldman SJ, Mah JK, Hatcher D, Kim MJ, Sohn DS, Palti A, Perel ML, Judy KW, Misch CE, Wang HL (2012) Use of cone beam computed tomography in implant dentistry: the International Congress of Oral Implantologists consensus report. Implant Dent 21:78–86

Bowlin J (2010) Cone beam technology: legal caveats. Bull Am Assoc Orthodontists 28:24–25

Brenner DJ, Hall EJ (2007) Computed tomography—an increasing source of radiation exposure. N Engl J Med 357:2277–2284

Brown J, Jacobs R, Levring Jäghagen E, Lindh C, Baksi G, Schulze D, Schulze R, European Academy of DentoMaxilloFacial Radiology (2012) Basic training requirements for the use of dental CBCT by dentists: a position paper prepared by the European Academy of DentoMaxilloFacial Radiology. Dentomaxillofac Radiol 43:20130291

Carter L, Farman AG, Geist J, Scarfe WC, Angelopoulos C, Nair MK, American Academy of Oral and Maxillofacial Radiology et al (2008) Executive statement on performing and interpret-

ing diagnostic cone beam computed tomography. Oral Surg Oral Med Oral Pathol Oral Radiol Endod 106:561–562
Council Directive 93/42/EC of 14 June 1993 (1993) concerning medical devices. OJ L 169,12.7.1993, p. 1
Council Directive 2007/47/EC of the European Parliament and of the Council of 5 September 2007 (2007) amending Council Directive 90/385/EEC on the approximation of the laws of the Member States relating to active implantable medical devices, Council Directive 93/42/ECC concerning medical devices and Directive 98/8/EC concerning the placing of biocidal products on the market, OJ L247, 21.9.2007, p.21–55
Curley A, Hatcher DC (2009) Cone beam CT—anatomic assessment and legal issues: the new standards of care. J Calif Dent Assoc 37:653–662
Curley A, Hatcher DC (2010) Cone beam CT—anatomic assessment and legal issues: the new standards of care. Todays FDA 22:52–55, 57–9, 61–3
Diangelis AJ, Andreasen JO, Ebeleseder KA, Kenny DJ, Trope M, Sigurdsson A et al (2012) International Association of Dental Traumatology guidelines for the management of traumatic dental injuries: 1. Fractures and luxations of permanent teeth. Dent Traumatol 28:2–12
Dula K, Bornstein MM, Buser D, Dagassan-Berndt D, Ettlin DA, Filippi A, Gabioud F, Katsaros C, Krastl G, Lambrecht JT, Lauber R, Luebbers HT, Pazera P, Türp JC, SADMFR (2014) SADMFR guidelines for the use of cone-beam computed tomography/digital volume tomography. Swiss Dent J 124:1169–1183
Dula K, Benic GI, Bornstein M, Dagassan-Berndt D, Filippi A, Hicklin S, Kissling-Jeger F, Luebbers HT, Sculean A, Sequeira-Byron P, Walter C, Zehnder M (2015) SADMFR guidelines for the use of cone-beam computed tomography/digital volume tomography. Swiss Dent J 125:945–953
Durchführung der Röntgenverordnung (RöV) (2005) Fachkunde und Kenntnisse im Strahlenschutz bei dem Betrieb von Röntgeneinrichtungen in der Medizin oder Zahnmedizin [Specialist skills and knowledge in radiological protection when operating X-ray units for dental or general medical use]. https://www.bfs.de/SharedDocs/Downloads/BfS/DE/rsh/3-bmub/3_92_1112.pdf?__blob=publicationFile&v=1. Accessed 24 June 2016
European Commission (2012) Radiation protection 172. Evidence based guidelines on cone beam CT for dental and maxillofacial radiology. Office for Official Publications of the European Communities, Luxembourg. http://ec.europa.eu/energy/nuclear/radiation_protection/doc/publication/172.pdf. Accessed 1 Aug 2016
European Council (1997) Council Directive 97/43/EURATOM of 30 June 1997 on health protection of individuals against the dangers of ionizing radiation in relation to medical exposure, and repealing directive 84/466/EURATOM. EC, Luxembourg. http://ec.europa.eu/energy/nuclear/radioprotection/doc/legislation/9743_en.pdf. Accessed 24 June 2016
European Society of Endodontology, Patel S, Durack C, Abella F, Roig M, Shemesh H, Lambrechts P et al (2014) European Society of Endodontology position statement: the use of CBCT in endodontics. Int Endod J 47:502–504
Evans G, Bishop K, Renton T (2012) Guidelines for surgical endodontics version 2. http://www.rcseng.ac.uk/fds/publications-clinical-guidelines/clinical_guidelines/documents/surgical_endodontics_2012.pdf.
Faculty of General Dental Practice (UK) (2013) In: Horner K, Eaton KA (eds) Selection criteria for dental radiography, 3rd edn. Faculty of General Dental Practice (UK) Royal College of Surgeons of Surgeons of England, London
Federal Food, Drug and Cosmetic Act (FFDCA) (2017) Chapter V, Subchapter C—Electronic product radiation control; Title 21 Code of Federal Regulations (Subchapter J, Radiological health) Parts 1020.30 21 (1938) (revised April, 2017)
Friedland B (2009) Medicolegal issues related to cone beam CT. Semin Orthod 15:77–84
Friedland B (2010) Conebeam computed tomography: legal considerations. Alpha Omegan 103:57–61
Friedland B, Miles DA (2014) Liabilities and risks of using cone beam computed tomography. Dent Clin N Am 58:671–685
Fryback DG, Thornbury JR (1991) The efficacy of diagnostic imaging. Med Decis Mak 11:88–94
Gazelle GS, Halpern EF, Ryan HS, Tramontano AC (2007) Utilization of diagnostic medical imaging: comparison of radiologist referral versus same-specialty referral. Radiology 245:517–522
Government of Western Australia Radiological Council (2016) http://www.radiologicalcouncil.wa.gov.au/Pages/FAQ/Dentists.html
Graskemper JP (2004) The standard of care in dentistry: where did it come from? How has it evolved? J Am Dent Assoc 135:1449–1455
Haney E, Gansky SA, Lee JS, Johnson E, Maki K, Miller AJ, Huang JC (2010) Comparative analysis of traditional radiographs and cone-beam computed tomography volumetric images in the diagnosis and treatment planning of maxillary impacted canines. Am J Orthod Dentofac Orthop 137:590–597
Harris D, Horner K, Grondahl K, Jacobs R, Helmrot E, Benic GI et al (2012) E.A.O. guidelines for the use of diagnostic imaging in implant dentistry 2011. A consensus workshop organized by the European Association for Osseointegration at the Medical University of Warsaw. Clin Oral Implants Res 23:1243–1253
Haute Autorité de Santé (2009) Tomographie Volumique a Faisceau Conique de la Face (Cone Beam Computerized Tomography). Rapport d'évaluation Technologique. Service évaluation des actes professionnels. Haute Autorité de Santé, Saint-Denis La Plaine. http://www.has-sante.fr/portail/upload/docs/application/pdf/2009-12/rapport_cone-beam_version_finale_2009-12-28_17-27-28_610.pdf. Accessed 1 Aug 2016

Health Protection Agency (HPA) Working Party on Dental Cone Beam CT Equipment (2010a) Guidance on safe use of dental cone beam CT (Computed Tomography) equipment. HPA Centre for Radiation, Chemical and Environmental Hazards, Oxfordshire. pp 1–56, ISBN 978-0-85951-681-5. www.hpa.org.uk/web/HPAwebFile/HPAweb_C/1287143862981. Accessed 1 Aug 2016

Health Protection Agency (HPA) Working Party on Dental Cone Beam CT Equipment (2010b) Guidance on safe use of dental cone beam CT (computed tomography) equipment. HPA Centre for Radiation, Chemical and Environmental Hazards, Oxfordshire. http://www.hpa.org.uk/web/HPAwebFile/HPAweb_C/1287143862981. Accessed 3 Aug 2016

Hillman BJ, Joseph CA, Mabry MR, Sunshine JH, Kennedy SD, Noether M (1990) Frequency and costs of diagnostic imaging in office practice—a comparison of self-referring and radiologist-referring physicians. N Engl J Med 323:1604–1608

Hollingworth W (2005) Radiology cost and outcomes studies: standard practice and emerging methods. AJR Am J Roentgenol 185:833–839

Hollingworth W, Jarvik JG (2007) Technology assessment in radiology: putting the evidence in evidence-based radiology. Radiology 244:31–38

Holmes SM (2007) iCAT Scanning in the Oral Surgery Office. OMS National Insurance Company Newsletter, Rosemont, 2:181

Horner K, Islam M, Flygare L, Tsiklakis K, Whaites E (2009) Basic principles for use of dental cone beam computed tomography: consensus guidelines of the European Academy of Dental and Maxillofacial Radiology. Dentomaxillofac Radiol 38:187–195

Horner K, O'Malley L, Taylor K, Glenny AM (2015) Guidelines for clinical use of CBCT: a review. Dentomaxillofac Radiol 44:20140225

Husain J, Burden D, McSherry P, Morris D, Allen M, Clinical Standards Committee of the Faculty of Dental Surgery RCoSoE (2012) National clinical guidelines for management of the palatally ectopic maxillary canine. Br Dent J 213:171–176

Isaacson KG, Thom AR, Horner K, Whaites E (2008) Guidelines for the use of radiographs in clinical orthodontics, 3rd edn. British Orthodontic Society, London

Jerrold L (2007) Litigation, legislation, and ethics. Liability regarding computerized axial tomography scans. Am J Orthod Dentofac Orthop 132:122–124

Katheria BC, Kau CH, Tate R, Chen JW, English J, Bouquot J (2010) Effectiveness of impacted and supernumerary tooth diagnosis from traditional radiography versus cone beam computed tomography. Pediatr Dent 32:304–309

Kuftinec M (2007) Liability regarding computerized axial tomography scans. Am J Orthod Dentofac Orthop 132:569

Levin DC, Rao VM (2004) Turf wars in radiology: the overutilization of imaging resulting from self-referral. J Am Coll Radiol 1:169–172

Magenau JL (1997) Digital diagnosis: liability concerns and state licensing issues are inhibiting the progress of telemedicine. Commun Law 19:25–43

Michigan Department of Community Services (2006) Michigan Department of Community Healthcon-212, Certificate of Need Review Standards for CT Scanner Services. http://www.michigan.gov/documents/mdch/CON-212_CON_Rev_Stds_CT_Scanners_12-27-06_181839_7.pdf. Accessed 24 June 2016

New York State Department of Health Special Committee on Telemedicine (2009) Statements on telemedicine Board for Professional Medical Conduct, New York Department of Health. Revised: January 2009. http://www.health.ny.gov/professionals/doctors/conduct/telemedicine.htm. Accessed 9 Aug 2016

Noffke CE, Farman AG, Nel S, Nzima N (2011) Guidelines for the safe use of dental and maxillofacial CBCT: a review with recommendations for South Africa. SADJ 66(262):264–266

Pakchoian AJ, Dagdeviren D, Kilham J, Mahdian M, Lurie A, Tadinada A (2015) Oral and maxillofacial radiologists: career trends and specialty board certification status. J Dent Educ 79:493–498

Parashar V, Whaites E, Monsour P, Chaudhry J, Geist JR (2012) Cone beam computed tomography in dental education: a survey of US, UK, and Australian dental schools. J Dent Educ 76:1443–1447

Petersen LB, Olsen KR, Christensen J, Wenzel A (2014) Image and surgery-related costs comparing cone beam CT and panoramic imaging before removal of impacted mandibular third molars. Dentomaxillofac Radiol 43(6):20140001

Petersen LB, Olsen KR, Matzen LH, Vaeth M, Wenzel A (2015) Economic and health implications of routine CBCT examination before surgical removal of the mandibular third molar in the Danish population. Dentomaxillofac Radiol 44(6):20140406

Royal College of Dental Surgeons of Ontario (2016) Dental CT scanner—general information. http://rcdsoupgrade.staging.moveable.ca/Assets/DOCUMENTS/Forms/Dental_CT_Scanners/RCDSO_Dental_CT_Scanner_Information_sheet.pdf. Accessed 24 June 2016

Scarfe WC (2011) "All that glitters is not gold": standards for cone-beam computerized tomographic imaging. Oral Surg Oral Med Oral Pathol Oral Radiol Endod 111:402–408

Scarfe WC (2013) Accreditation of advanced imaging facilities for dentistry—assuring minimal standards for high quality diagnostic imaging. Oral Surg Oral Med Oral Pathol Oral Radiol 116:267–269

Scarfe WC (2014) Image gently. Responsible use of X-rays in dentistry for children is aim of new education and awareness initiative. J N J Dent Assoc 85:32

Scarfe WC (2015) Data, data everywhere but not a byte to share…? Oral Surg Oral Med Oral Pathol Oral Radiol 119:370–373

Special Committee to Revise the Joint AAE/AAOMR Position Statement on use of CBCT in Endodontics (2015) AAE and AAOMR joint position statement: use of cone beam computed tomography in Endodontics 2015 update. Oral Surg Oral Med Oral Pathol Oral Radiol 120:508–512

The Image Gently™ in Dentistry Campaign (2016) http://www.imagegently.org/Roles-What-can-I-do/Parent/Dentist. Accessed 1 Aug 2016

Turpin DL (2007) Befriend your oral and maxillofacial radiologist. Am J Orthod Dentofac Orthop 131:697

Tyndall DA, Price JB, Tetradis S, Ganz SD, Hildebolt C, Scarfe WC, American Academy of Oral and Maxillofacial Radiology (2012) Position statement of the American Academy of Oral and Maxillofacial Radiology on selection criteria for the use of radiology in dental implantology with emphasis on cone beam computed tomography. Oral Surg Oral Med Oral Pathol Oral Radiol 113:817–826

Walter C, Kaner D, Berndt DC, Weiger R, Zitzmann NU (2009) Three-dimensional imaging as a pre-operative tool in decision making for furcation surgery. J Clin Periodontol 36:250–257

White SC, Scarfe WC, Schulze RK, Lurie AG, Douglass JM, Farman AG, Law CS, Levin MD, Sauer RA, Valachovic RW, Zeller GG, Goske MJ (2014) The image gently in dentistry campaign: promotion of responsible use of maxillofacial radiology in dentistry for children. Oral Surg Oral Med Oral Pathol Oral Radiol 118:257–261

Yang Jie, Tamimi D, Farman AG, Benjamin S, Cordell KG, Zeller GG (2011a) The secure exchange and utilization of digital images in dentistry. American Dental Association Technical Report no. 1060

Yang J, Tamimi D, Farman AG, Benjamin S, Cordell KG, Zeller GG: American Dental Association (2011b) ADA Technical Report No. 1060 for the Secure Exchange and Utilization of Digital Images in Dentistry. http://ebusiness.ada.org/productcatalog/552/Informatics/ADA-Technical-Report-No-1060-The-Secure-Exchange-and-Utiliza/ADA1060-2011D. Accessed 4 Aug 2016

Yang J, Angelopoulos C, Mallya S, Liang H, Deahl T, Ganguly R, Ramesh A, Parashar V, Williamson G, Cederberg R, American Academy of Oral and Maxillofacial Radiology Executive Committee (2016) American Academy of Oral and Maxillofacial Radiology Executive opinion statement on Teleradiology. Oral Surg Oral Med Oral Pathol Oral Radiol 122(4):509–510

Zhang A, Critchley S, Monsour PA (2016) Comparative adoption of cone beam computed tomography and panoramic radiography machines across Australia. Aust Dent J 61(4):489–496. doi:10.1111/adj.12417

Zinman EJ, White SC, Tetradis S (2010) Legal considerations in the use of cone beam computer tomography imaging. J Calif Dent Assoc 38:49–56

CBCT Quality Assurance

7

Ruben Pauwels

Contents

R. Pauwels, Ph.D.
Department of Radiology, Faculty of Dentistry, Chulalongkorn University, Bangkok, Thailand

OMFS-IMPATH, Department of Imaging & Pathology, Biomedical Sciences Group, KU Leuven, Leuven, Belgium
e-mail: pauwelsruben@hotmail.com

7.1 Introduction

Quality Assurance (QA) is an essential aspect of medical imaging, ensuring that X-ray imaging modalities provide adequate diagnostic information at exposures that are as low as reasonably/diagnostically acceptable (ALARA/ALADA), minimizing the potential radiation risk to the patient. In diagnostic radiology, risks are a result of the stochastic effects of radiation. Other patient safety aspects associated with the operation of CBCT units, such as potential injury caused by mechanical movement, should also be considered. QA also involves a consideration of the risks and protection of operators of CBCT equipment as well as the general public.

A QA program consists of various safety- and performance-related aspects. In CBCT, it typically comprises considerations at various stages of use of the equipment, an acceptance of the level of radiation risk of the operator, and establishment of standard operational procedures such as:

- Acceptance testing: a check of performance before clinical use, using pass/fail acceptability criteria
- Commissioning testing: the acquisition of baseline values for image quality and radiation dose, for comparison with future tests
- Periodic testing (and maintenance) of performance throughout the use of the unit.

W.C. Scarfe, C. Angelopoulos (eds.), *Maxillofacial Cone Beam Computed Tomography*,
https://doi.org/10.1007/978-3-319-62061-9_7

- Establishment of exposure parameters for specific patient types, referred to as imaging protocols.
- Estimation of radiation dose to patients, workers, and public.
- Baseline and periodic training of workers.
- Adherence to policies and procedures.

This chapter will focus on general aspects of QA and briefly describe available European (SEDENTEXCT) (European Commission 2012) and United States (IAC-CT) (IAC 2012) guidelines. Readers are referred to regional or national authorities on dental CBCT for specific compliance recommendations (if available) and procedures.

7.2 CBCT as a Dental or Medical Device

There has been some debate regarding the classification of CBCT as either a dental or medical device. In some countries and states in the United States, this classification can depend on factors such as the kV range of the unit. For example, in the United States, the FDA (U.S. Food and Drug Administration) regulates manufacturers of dental CBCT devices through the Electronic Product Radiation Control (EPRC) and medical device provisions of the Federal Food, Drug, and Cosmetic Act. Dental CBCT systems are classified under 21 CFR 892.1750 as CT systems. In terms of QA, this classification could lead to more stringent (i.e., similar to multi-detector CT (MDCT)) or lenient (i.e., similar to dental radiographic equipment) QA requirements. However, specific (national or regional) QA requirements for dental CBCT are becoming more prevalent from regulatory bodies as well as government and third party (e.g., insurance) payers as the use of this modality within dental imaging steadily increases. Particularly, dose- and image-related aspects of CBCT warrant the same considerations as those of MDCT. On the other hand, not all performance metrics used in MDCT are valid for CBCT.

7.3 Elements of a QA Program

7.3.1 Quality Control (QC)

Quality control (QC) deals with the performance of the equipment after installation. It follows a regular timetable, comprising testing at the time of installation (*commissioning tests*), providing baseline comparative metrics (*acceptance tests*), and routine (*periodic*) tests. Usually, a medical physics expert is involved in performing QC procedures.

Acceptance tests are performed at installation of the equipment to ensure that their initial performance is at an acceptable level for clinical practice by comparing it to national or international standards. In addition, commissioning tests provide baseline values for image quality and radiation dose which can be compared with those of future periodic tests to evaluate whether the equipment has degraded over time.

Routine tests can involve the use of different testing timetables. Depending on the nature of the tests and the potential implications of a failed test, they should be performed daily, monthly, annually, etc.

QC tests can be categorized as follows (ICRP 2015):

- Safety system tests (e.g., emergency stop button, warning lights).
- X-ray tube performance (e.g., accordance between measured and nominal kV, mA, exposure time).
- Image quality tests (i.e., spatial resolution, contrast resolution, noise, artifacts, geometric accuracy).
- Image display tests (e.g., software processing during visualization, monitor performance).
- Dosimetry.

It is important that these tests are performed in a consistent way throughout the lifetime of the equipment, ideally involving the same measurement tools (e.g., dosimeters, test objects). In addition, testing should follow national or international standards, when available.

7.3.1.1 Safety System Tests

There are a few general safety systems associated with CBCT units. The operator and, in some cases, the patient should have access to an emergency stop button if any serious issue (e.g., excessive patient motion, no incoming raw data due to electronic problems) occurs during the exposure. Alternatively, if the unit requires an exposure button to be pressed for the full duration of the scan (dead-man switch), the release of this button can be considered as an emergency stop. Another safety system is that, when the tube is emitting X-rays, an audible signal and a warning light should indicate that an exposure is being made. Also, the unit should properly handle mechanical obstruction, by discontinuing the scan if the tube or detector hits the patient or any other object.

7.3.1.2 X-ray Tube Performance

It is essential that the X-ray tube operates repeatedly within acceptable parameters. The following should be evaluated during periodic QC testing:

- **Linearity and reproducibility of tube output.** Measurements can be performed with any type of dosimeter (Fig. 7.1) at a fixed point in the X-ray beam (e.g., at the detector or at the center of rotation). Repeated measurements at varying (linearity) and fixed (reproducibility) mAs levels should be performed.
- **Accuracy and reproducibility of tube voltage (kV).** If the unit allows for kV variation, measurements at different kV values should be performed.

During commissioning, and if the X-ray tube has been replaced or underwent extensive repair or modification, the following tests should be performed:

- **Total filtration.** This can be achieved through estimation of the half-value layer using conventional, direct or indirect, methods.
- **Tube housing leakage**. Leakage of X-rays (i.e., inadequate attenuation of X-rays by the tube housing).

Fig. 7.1 Example of a solid state sensor dosimeter (RaySafe Solo DENT, Unfors RaySafe AB Billdal, Sweden) allowing for the measurement of kVp, dose, dose rate, pulses, and time with options such as direct HVL measurements and waveform display. This unit is specific for CBCT, panoramic, and intraoral X-ray units

In addition, the field of view (FOV) dimensions and beam alignment with the detector should at least be verified during commission and if extensive modifications have been made. Finally, the accuracy of the laser alignment system and the scout view for FOV placement should be assessed.

7.3.1.3 Technical Image Quality Evaluation in CBCT

The different fundamental image quality parameters (a.k.a. technical image quality, as opposed to clinical image quality which is a more abstract, multi-factorial concept) have been described in Chap. 2. The quantitative assessment of technical image quality on CBCT requires the use of specialized test objects (i.e., *phantoms*). While image quality measurements in CBCT are very similar to those in CT, specific phantoms for CBCT have been developed such as the SEDENTEXCT IQ phantom (Leeds Test Objects, Boroughbridge, United Kingdom) (Fig. 7.2) and the QRM ConeBeam phantom (QRM, Moehrendorf, Germany) (Fig. 7.3). Many manufacturers provide proprietary QA phantoms (Fig. 7.4).

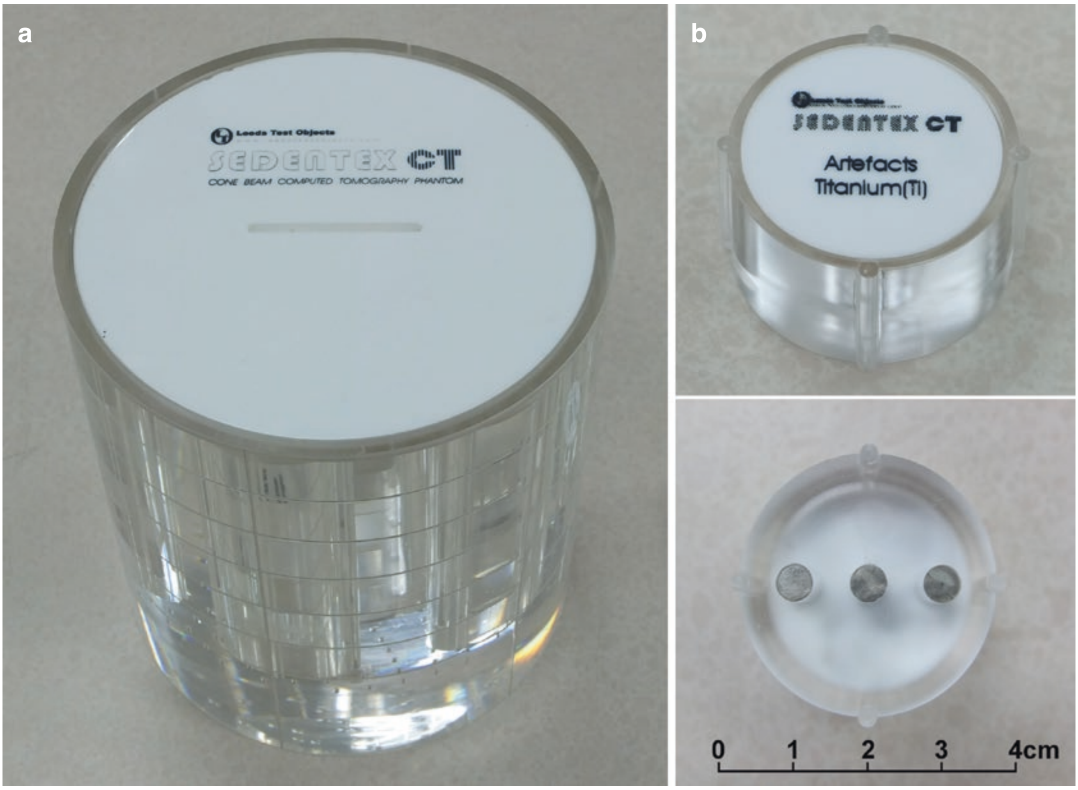

Fig. 7.2 The SEDENTEXCT IQ Cone Beam CT Dental Phantom (Leeds Test Objects, Boroughbridge, United Kingdom) (**a**) is a polymethyl-methacrylate (PMMA) cylinder with a 16 cm diameter with recesses to house test inserts. Within the body of the cylinder are features to test noise and uniformity by providing uniform PMMA in the lower section of the phantom. Geometric accuracy can be measured using an array of 2.0 mm diameter, 3.0 mm deep air gaps uniformly pitched through one slice of the cylinder. Test inserts are included to calculate multiple spatial resolution metrics (line spread function (LSF), point spread function (PSF), and line pairs/mm), contrast resolution, pixel intensity, and metal artifacts (**b**) Reproduced from Pauwels et al. (2013a) with permission from Springer

Spatial Resolution

Spatial resolution, or sharpness, can be measured in various ways. A common metric used for the evaluation of spatial resolution is the *modulation transfer function* (MTF), which evaluates the change in contrast at increasingly higher spatial frequencies (Fig. 7.5). It can be interpreted as the ability to discriminate objects of increasingly smaller size. While the MTF is a continuous curve, parameters such as the MTF_{50} and MTF_{10} can be used to express the frequency (in cycles or line pairs per millimeter) at which the contrast drops to 50% and 10% of the maximum, respectively. Practically, the MTF can be estimated using a line pair pattern (which also allows for visual evaluation of spatial resolution), a high-density thin wire or an edge (which can be used to calculate metrics such as point spread function or edge spread function, from which MTF can be derived) (Fig. 7.6).

Contrast and Noise

Contrast refers to the ability to discriminate (large) objects of different composition and density in the image, whereas noise is the random or structured variability of grey values (i.e., graininess) within a homogeneous material. CBCT is useful for imaging of high-contrast structures (bone, teeth, air) but poor in terms of low-contrast detectability (e.g., structures containing water or similar densities within soft tissue). Image noise in CBCT images is generally high due to the use of small image voxels (with correspondingly small detector pixels), the relatively low exposure levels (mAs and kV), and the high amount of detected scatter, among other reasons.

Contrast and noise can be evaluated concomitantly using the contrast-to-noise ratio (CNR).

Fig. 7.3 The QRM ConeBeam phantom (QRM, Moehrendorf, Germany) comprises seven sections providing metrics for contrast resolution, spatial resolution including line pairs/mm and modulation transfer function, noise and scaling

The CNR between two given materials can be expressed as:

$$\mathrm{CNR} = \frac{\mathrm{MGV}_1 - \mathrm{MGV}_2}{\sqrt{\mathrm{SD}_1^2 + \mathrm{SD}_2^2}} \tag{7.1}$$

with MGV denoting the *mean grey value* and SD being the *standard deviation* of grey values for different materials, depicted with subscripts 1 and 2. Figure 7.7 illustrates a CNR measurement. CNR typically increases with increasing mAs and kV (Fig. 7.8), but can be affected by detector performance as well; large variations in CNR found during periodic QC should therefore be further investigated to determine their cause.

The evaluation of contrast and spatial resolution can be combined through the analysis of contrast-detail patterns, in which objects of decreasing contrast and/or size are detected either visually or automatically (Fig. 7.9). Figure 7.10 shows a contrast-detail analysis of a CBCT image.

Contrast levels for CBCT are inherently lower than those in MDCT. Specifically, low-contrast objects (representing different tissues in the soft tissue range, e.g., fat, muscle, and water) are not expected to be detectable on CBCT. High-contrast objects, on the other hand, are expected to be visible even if such objects are small.

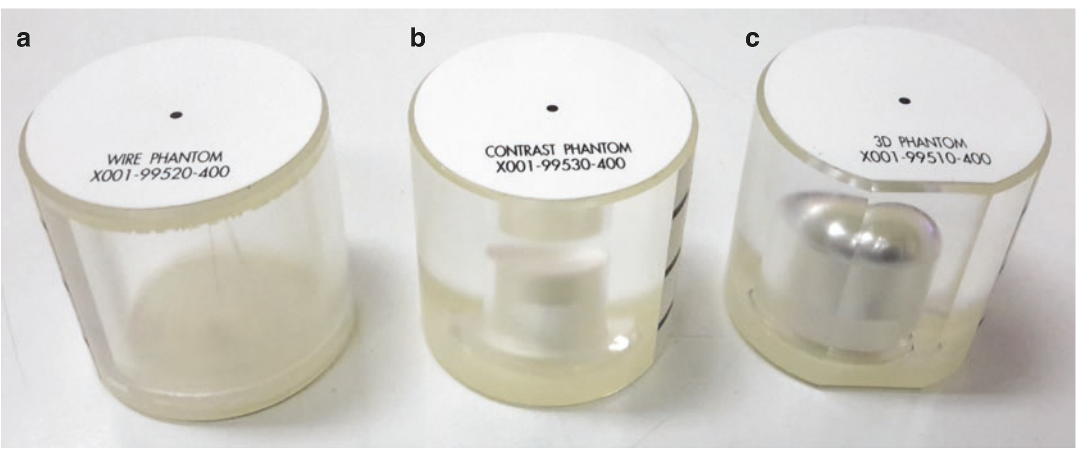

Fig. 7.4 Series of three separate phantoms for QA of 3D Accuitomo CBCT systems (J. Morita Corp., Kyoto, Japan). The wire phantom (**a**) comprises a 100 µm tungsten wire and is placed inside the scanner at a central position and scanned perpendicular to the plane of interest. Resultant images are used to determine the line spread function (LSF) and modulation transfer function (MTF) curves calculated by computing the Fourier transformation. Additional phantoms are provided for analysis of contrast (**b**) and artifacts (**c**)

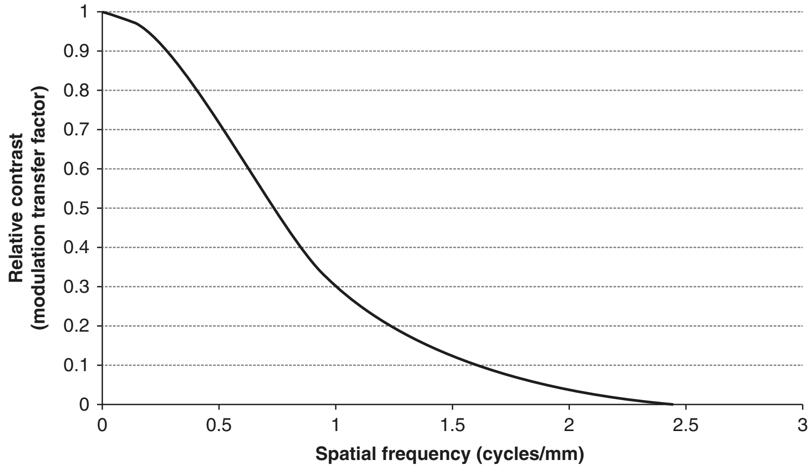

Fig. 7.5 Graph demonstrating spatial resolution as described by modulation transfer function (MTF). As the distance between objects become smaller, i.e., spatial frequency increases (x-axis), the relative contrast (y-axis) between them decreases

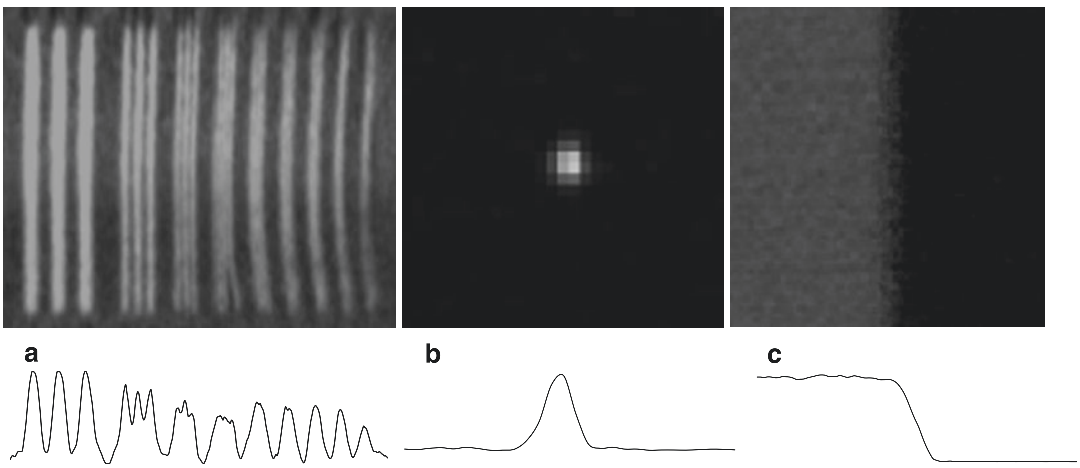

Fig. 7.6 Plot profile images depicting line pair pattern (**a**), steel wire in air (**b**) and PMMA-air edge methods to estimate spatial resolution in CBCT (through MTF and/or visual evaluation). The images show a decreased contrast at higher spatial frequencies for the line pair pattern (**a**) indicated by the difference in the minimum and maximum grey values within a given group of three lines, and a lateral spread of the boundary between the high- and low-density material for the steel wire (**b**) and PMMA-air edge (**c**)

Artifacts

In radiography, artifacts are defined as parts of the image which do not correspond to physical reality. There are many causes of artifacts in CBCT. A commonly seen type is *metal artifacts*, which occur when a metal object is in or near the FOV. Metal artifacts are the result of exuberant absorption of X-rays by the metal, and the inability of the reconstruction algorithm to cope with this, leading to dark and bright regions and streaks in the vicinity of the metal. While metal artifacts are unavoidable in a clinical situation unless the metal can be removed (e.g., prosthesis), their severity can be quantified during QC (Fig. 7.11), ensuring that they remain stable over time.

Other artifacts can be related to the equipment (e.g., excessive oscillation of the tube and/or detector, faulty detector pixels, improper calibration) or patient (i.e., motion); the former can be visually spotted during the evaluation of other image quality parameters in QC, the latter can only be evaluated during clinical image quality evaluation (*see* Sect. 7.3.3).

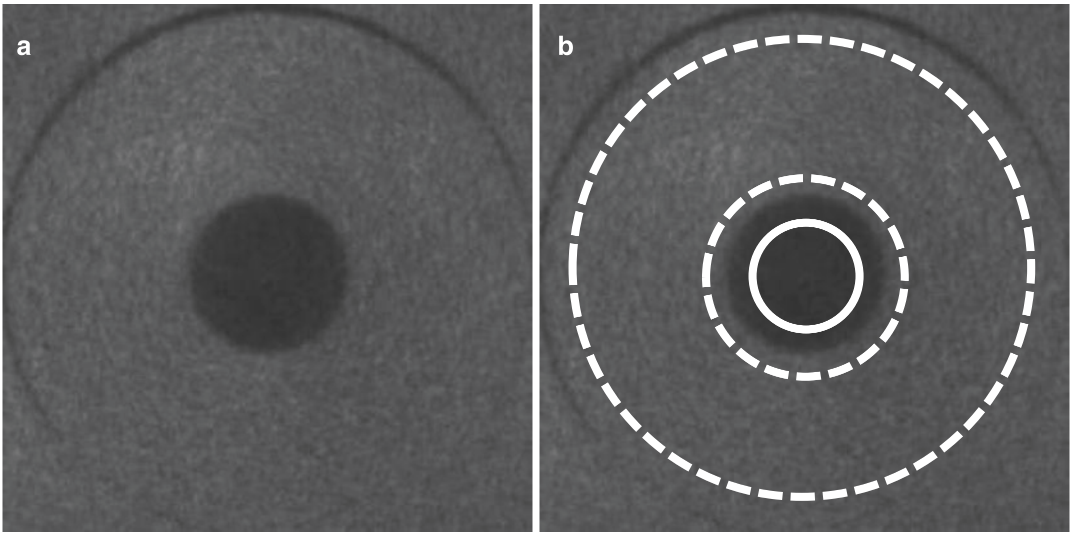

Fig. 7.7 Measurement of contrast-to-noise ratio (CNR) using the SEDENTEXCT IQ phantom. Axial CBCT image of an insert containing air (*dark central circle*) within a cylinder of polymethyl-methacrylate (PMMA) (**a**). The mean grey value (MGV) and standard deviation (SD) calculated for a region of interest containing air (*full circle*) and PMMA (in-between *hashed circles*) are used to calculate CNR (**b**)

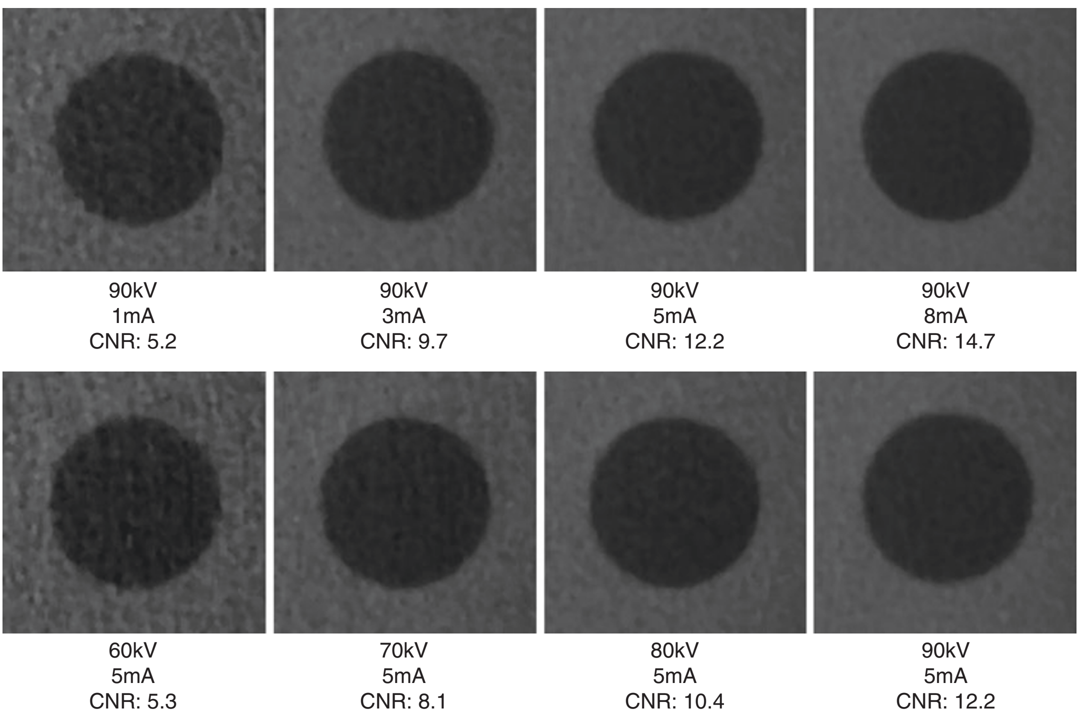

Fig. 7.8 Axial CBCT images cropped and magnified to show a central region of interest containing air (*dark circle*) and adjacent polymethyl-methacrylate (PMMA) (periphery). The effect of increasing mA (1–8 mA) at a fixed kilovoltage (90 kV) is pictorially shown by the *top row* of images. The *bottom row* of images shows the effect of increasing kV (60–90 kV) at a fixed milliamperage (5 mA). Calculations using the mean grey value (MGV) and standard deviation (SD) of the air and peripheral PMMA show that contrast-to-noise increases with increasing mA and kV. (Reproduced from Pauwels et al. (2014) under the British Institute of Radiology's License to Publish)

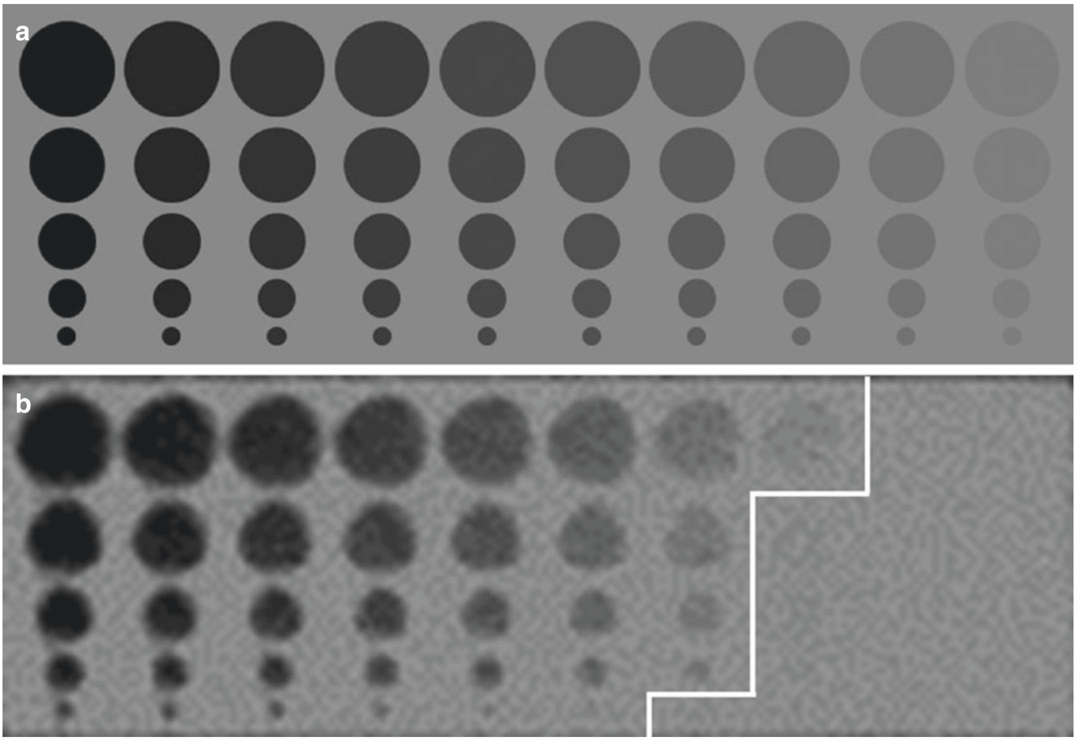

Fig. 7.9 Contrast-detail pattern (**a**) showing *circles* of decreasing contrast along the *horizontal* direction and of decreasing size in the *vertical* direction. Simulated image of the pattern (**b**). The *white line* distinguishes visible from invisible circles

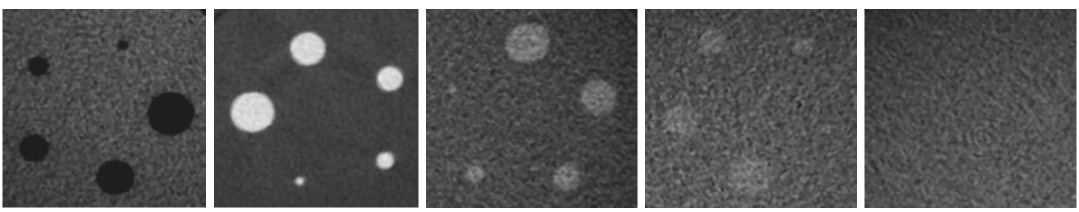

Fig. 7.10 CBCT images of contrast-detail patterns comprising a series of 1–5 mm diameter rods for five materials using the SEDENTEXCT IQ phantom with PMMA as background material. (*HA* hydroxyapatite, with the number indicating the concentration in mg/cm^3)

As mentioned in Chap. 2, a lack of *grey value uniformity* can also be considered as an artifact. Uniformity can be evaluated through scanning a homogeneous object and comparing grey values in different portions of the image (i.e., intra-scan uniformity) (Fig. 7.12). For small-diameter FOVs in particular, variability in grey values depending on FOV position (e.g., central in a phantom or closer to its edge) can also be evaluated (i.e., inter-scan uniformity) (Fig. 7.12).

Geometric Accuracy

The small size and isotropic (i.e., cubic) nature of voxels in CBCT result in high (sub-millimeter) geometric accuracy in all dimensions, providing that proper geometric calibration has been performed. CBCT units using an image intensifier as a detector are more prone to distortion compared to flat panel detectors, especially in the peripheral portion of the FOV. Nonetheless, high geometric accuracy is expected for several

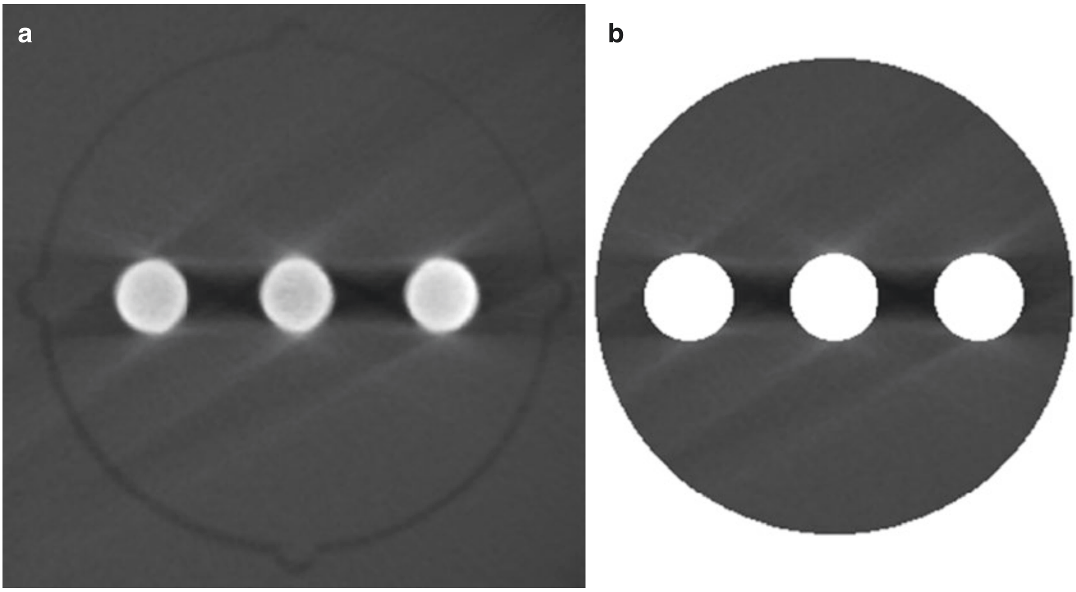

Fig. 7.11 CBCT scan of the metal artifact insert of the SEDENTEXCT IQ phantom, showing three titanium rods in PMMA (**a**). The standard deviation of grey values (SD) in a region including the PMMA but excluding the metal objects themselves represents the severity of the artifacts (**b**). (Reproduced from Pauwels et al. (2013b) with permission from John Wiley and Sons)

clinical applications (e.g., bone volume and root canal measurements).

Manual or automatic evaluation of geometric accuracy can be performed using any object or pattern with accurately known distances (Fig. 7.13). Ideally, assessment of geometric accuracy should be performed in each direction (i.e., anteroposterior, left-right, cranio-caudal) as deviations may not be isotropic. If performed manually, observer error resulting from identifying the start- and end-point of the measurement should be taken into account.

7.3.1.4 Image Display Tests

While basic image processing tools found in imaging software (i.e., zoom, window/level) partially negate the need for medical-grade flat panel displays, the performance of commercial off-the-shelf consumer-grade liquid crystal displays (LCDs) or any other type of display system should be periodically evaluated visually using test patterns (Fig. 7.14) and quantitatively using conventional display testing equipment such as luminance meters (Samei et al. 2005).

If the imaging software processes the images before display (e.g., filtering, slice thickness/interval), it should be assured that the native image quality is not degraded, and that settings are optimal for clinical viewing.

7.3.1.5 Dosimetry

Whereas radiation dose (typically in air) is measured during X-ray tube performance testing (see Sect 7.3.1.2), an estimation of patient dose using test objects (i.e., phantoms) is typically also performed during QC. Patient dose aspects and different dose metrics are covered in Chap. 8. The estimation of an "average" patient dose using test objects should be complemented with patient dose monitoring, as described in the following Sect. 7.3.2.

7.3.2 Patient Dose Monitoring

Dose measurements using test objects during QC should be complemented with the monitoring of patient dose during clinical use of the equipment, and comparison of patient dose with available

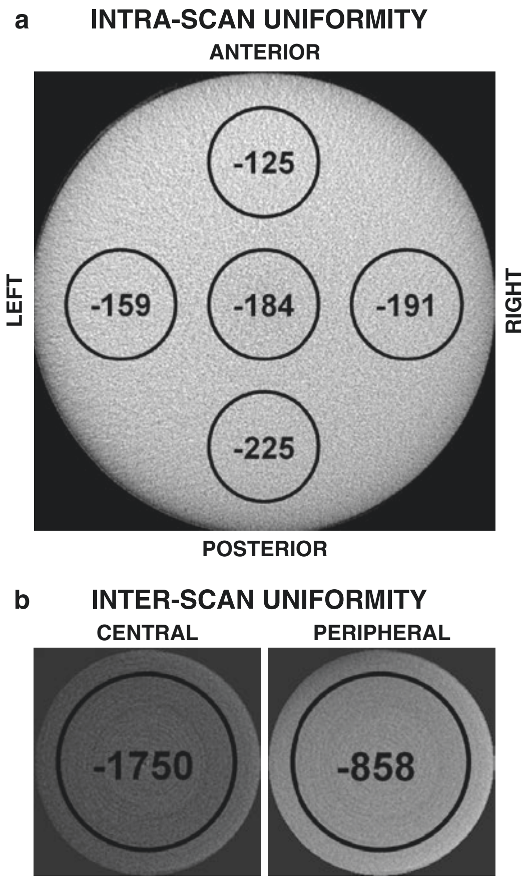

Fig. 7.12 Evaluation of intra- (**a**) and inter-scan (**b**) uniformity using the homogeneous PMMA section of the SEDENTEXCT IQ phantom. Each *black circle* shows the mean grey value inside it. Intra-scan uniformity (**a**) is calculated using differences in grey values between central and peripheral regions for a large-diameter (160 mm) CBCT scan. Inter-scan uniformity is determined by differences between central and peripheral field of view positions for a small-diameter (50 mm) CBCT scan. (Reproduced from Pauwels et al. (2015a) under the British Institute of Radiology's License to Publish)

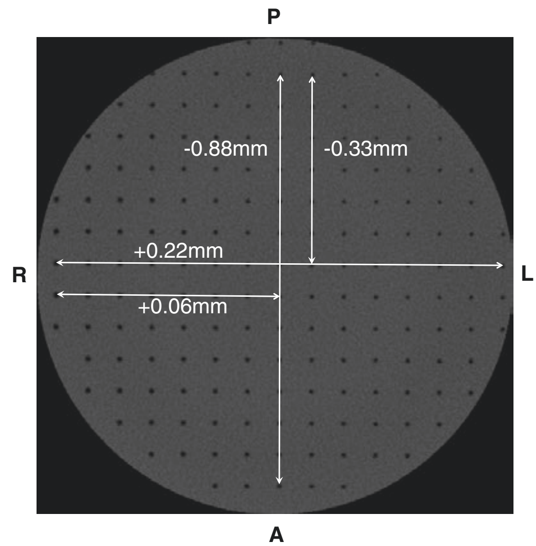

Fig. 7.13 Measurement of geometric accuracy using the SEDENTEXCT IQ phantom. A 1-cm grid pattern allows for center-to-edge and edge-to-edge measurements in all directions. In this example, measured distances show a slight underestimation of the true distance in the antero-posterior (A-P) direction and a very slight overestimation in the *right–left* (R–L) direction

standards. This is a direct implementation of the optimization principle of radiation protection, as it can be used to ensure that doses are as low as reasonably/diagnostically achievable (ALARA/ALADA).

Patient dose monitoring often relies on the display of dose estimates by the equipment. This allows for a straightforward collection of dose metrics for groups of patients. However, it should be assured that displayed dose estimates are accurate, and comparison with physical measurements should be performed periodically or whenever the equipment is modified.

Currently, there is a lack of standardization regarding the reporting of patient dose. The most common dose metrics used in CBCT are the *dose-area product* (DAP) and computed tomography dose index (CTDI), although alternative measurements have been proposed. The limitations of the CTDI measurement for wide-beam geometries have been extensively reported (see Chap. 8). Although the DAP is a measurement of tube output rather than patient dose, its inherent capability to take the wide range of beam sizes and shapes used in CBCT into account is of great relevance. Whereas a physical measurement of DAP in a rotating CBCT arm is somewhat impractical, a point measurement of the dose at a location where the beam area is known (i.e., at the isocenter or detector) allows for an estimation of the DAP.

7.3.2.1 Diagnostic Reference Levels

Comparing with standard dose levels usually involves the concept of diagnostic reference levels (DRL). DRLs are used in any type of X-ray

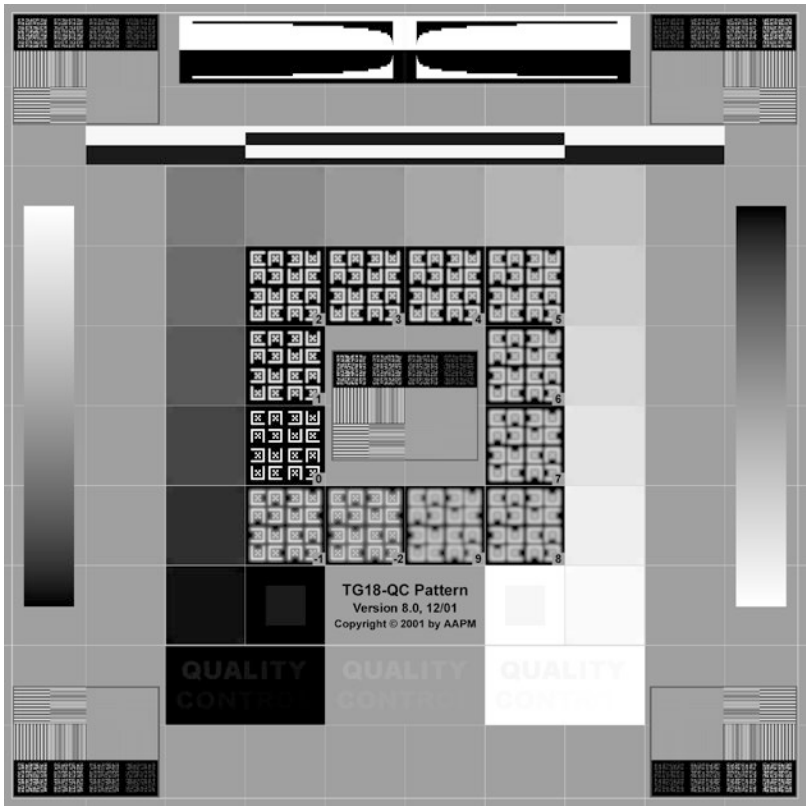

Fig. 7.14 AAPM TG18-QC multipurpose test pattern for evaluation of display monitors (Samei et al. 2005). The patterns should be maximized to fill the entire usable display area and examined from a viewing distance of 30 cm. This test pattern allows for visual assessment of general image display and artifacts, geometric distortion, luminance reflection, noise and glare and display resolution

imaging, and are based on dose audits in a defined region (e.g., a country or province). During these audits, patient dose is measured or estimated on all available equipment in that region, and a DRL is calculated as the *third quartile value*. In other words, a DRL is defined as the dose below which 75% of the equipment in a certain region operates (Fig. 7.15). Specific DRLs can be determined for different imaging protocols (e.g., for adults and children, or for clinical applications with different image quality criteria). Although DRLs have no legal value, equipment which is operating at a dose above its relevant DRL should be evaluated to ensure it is performing properly, and possible actions to reduce patient dose (including replacement of the equipment) should be considered. A proper implementation and follow-up of DRLs implies that their value changes over time (e.g., because of the optimization, repair or replacement of equipment operating above the DRL), and periodic reevaluation of DRLs is thus needed.

In CBCT, currently, there is still a lack of data on DRLs. The UK Health Protection Agency (HPA 2010) proposed an achievable dose based on an audit of 41 CBCT units regarding the dose used for the placement of an upper first molar implant of an adult patient. Using a DAP normalized to a beam area of 4 × 4 cm at isocenter, a third quartile value of 250 mGy cm^2 was derived from 52 DAP measurements. However, the normalization of the DAP nullifies the substantial effect of FOV size on patient dose. Actual DAP values ranged between approx. 80 and 2300 mGy cm^2, with a third quartile value of approximately 825 mGy cm^2 (values based on visual reading of the graph in the HPA document, rounded to 5 mGy cm^2). It can be expected that more data on DRLs for CBCT will become

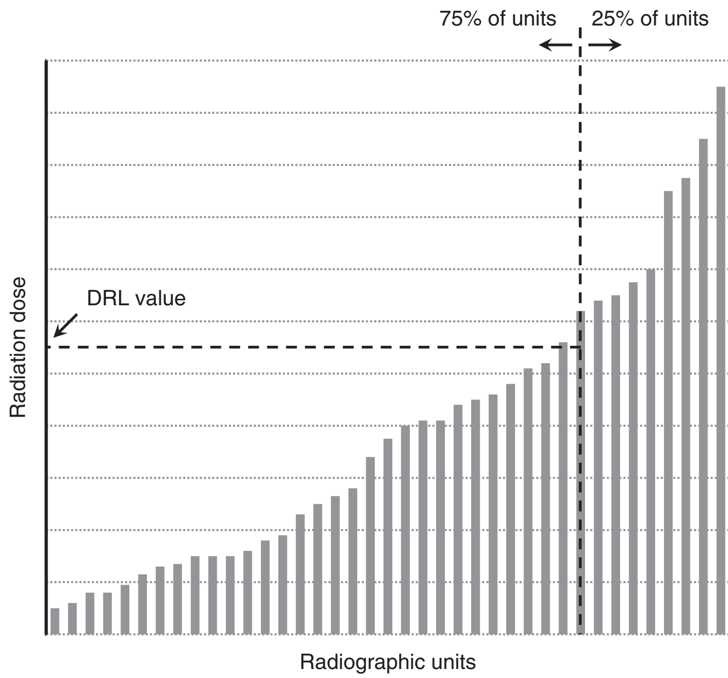

Fig. 7.15 Diagnostic reference levels (DRLs) are based on the third quartile value of standardized dose measurements on radiographic units within a defined region. Dose reduction strategies should be considered for the 25% of units operating above the DRL, implying that the value of the DRL is expected to vary (ideally, lower) over time.

available, allowing for proper monitoring of patient dose.

7.3.3 Clinical Image Quality Assessment

While technical image quality analysis is useful to objectively evaluate and follow up the performance of an equipment, there is no consistent relationship between quantitative parameters such as noise and the diagnostic suitability of an image (Pauwels et al. 2015b). Therefore, an assessment of clinical image quality is needed as well. Different approaches towards clinical image quality assessment are possible:

- **Reference images:** Clinical scans can be compared with a reference clinical, standardized image. Although this reference image is often determined to be of excellent quality, a more proper application of the optimization principle would be to use an image of adequate quality. Seeing that images of different CBCT models can appear very differently, scanner-specific reference images are required. In addition, application-specific reference images should be used, as image quality requirements can vary considerably for different clinical applications. Reference images can be provided by the manufacturer or acquired during acceptance testing using a diagnostic skull phantom.
- **Reject analysis:** This requires record keeping of all scans acquired during a given time period. An evaluation of rejected scans is made, including the reason for rejection (e.g., region of interest not included, poor image quality, excessive artifacts) and possible cause (e.g., operator error, patient movement, technical error). A target of the number of rejected image can be set; the UK HPA and EC guidelines both proposed that the number of unacceptable CBCT scans should be below 5%. If possible, corrective actions should then be taken to minimize the number of future rejects, such as:
    - A more thorough evaluation of removable metal objects before scanning
    - Improved FOV positioning procedures
    - Revision of exposure protocols

- **Clinical image quality criteria:** This involves the visual grading of anatomical features on an image, with specific criteria for acceptability. While such criteria have been established for CT, CBCT has very different image quality criteria requirements. Currently, there are no established criteria for CBCT at a national or international level.

7.4 Current QA Guidelines

7.4.1 European Commission (SEDENTEXCT)

In 2012, the European Commission published a report prepared by the SEDENTEXCT Project Consortium (EC 2012). Among other CBCT-related topics, the report covers QA aspects of CBCT. A set of 20 Basic Principles (BP) were determined, included general statements related to QA:

- **BP 11:** "A quality assurance program must be established and implemented for each CBCT facility, including equipment, techniques and quality control procedures."
- **BP 13:** "All new installations of CBCT equipment should undergo a critical examination and detailed acceptance tests before use to ensure that radiation protection for staff, members of the public and patient are optimal."
- **BP 14:** "CBCT equipment should undergo regular routine tests to ensure that radiation protection, for both practice/facility users and patients, has not significantly deteriorated."

Other BPs are related to specific QA aspects such as training and protection of workers.

A comprehensive QC manual was provided as an Appendix to the report, encompassing testing methodologies of the X-ray generator, dosimetry, technical image quality, and image display, along with suggested testing frequencies and action levels. It can be noted that these action levels were based on limited available data (including a lack of data on DRLs), and that evidence-based action/suspension levels should be determined.

7.4.2 Intersocietal Accreditation Commission (IAC)

In the United States (US), accreditation of CT imaging facilities is a voluntary process. There are three imaging accreditation bodies in the US recognized by the Centers for Medicare and Medicaid Services (CMS)—the federal government reimbursement authority for medical services: The American College of Radiology (ACR), the Intersocietal Accreditation Commission (IAC), and The Joint Commission (TJC), each of which have established standards for accreditation. IAC is the only organization that has developed a separate division, IAC-Dental CT, with accreditation standards accepted by CMS that are specific for office-based oral and maxillofacial CBCT use in dentistry. It is the only accrediting agency jointly sponsored by dental specialty organizations including The American Academy of Oral and Maxillofacial Surgeons (AAOMS) and the American Academy of Oral and Maxillofacial Radiology (AAOMR). As CBCT is considered an equivalent imaging modality to MDCT for CMS reimbursement in the United States, accreditation is also necessary for CBCT facilities. Several private insurance companies, such as United Healthcare, now also require facility accreditation for reimbursement. Several states including California and Minnesota have adopted policies requiring CT imaging accreditation in all practice settings.

The 2012 IAC Dental CT Standards for Dental/Maxillofacial Computed Tomography (CT) Practice Accreditation using Cone Beam Technology contains a number of QC requirements for CBCT testing (IAC 2012) including acceptance testing, quality control tests with results and phantom images, an annual physicist survey, preventative maintenance reports and radiation shielding verification, CT protocols and technical quality assessment policies. A few differences are apparent between the type and periodicity of tests in the EC and IAC documents (Table 7.1). Most notably, the IAC standards propose daily testing of the safety systems as well as image density, noise, and image artifacts. For these and other daily tests,

Table 7.1 Differences between European Commission (EC 2012) and Intersocietal Accreditation Commission (IAC 2012) regarding QC testing frequency

QC metric	EC (2012) frequency	IAC (2012) frequency
Safety systems	Critical examination at installation; no periodicity mentioned for further testing	Daily
Image density (i.e., CT number)	Monthly	Daily
Noise	Monthly	Daily
Image artifacts	Monthly	Daily

Differences in terms of "periodic vs. monthly" or "periodic vs. annual" were not included

the manufacturer is expected to provide an appropriate QC phantom.

Acknowledgments Image of RaySafe Solo DENT (Fig. 7.1) courtesy of Unfors RaySafe AB Billdal, Sweden. Image of the QRM ConeBeam phantom (Fig. 7.3) courtesy of QRM (Moehrendorf, Germany).

References

EC, European Commission (2012) Cone beam CT for dental and maxillofacial radiology: evidence based guidelines, radiation protection publication 172. European Commission, Luxembourg

HPA, Health Protection Agency (2010) Recommendations for the design of X-ray facilities and quality assurance of dental Cone Beam CT (Computed tomography) systems. HPA-RPD-065, by Holroyd JR and Walker A. Radiation Protection Division, Centre for Radiation, Chemical and Environmental Hazards, Health Protection Agency, Chilton

IAC, Intersocietal Accreditation Commission (2012) The IAC dental CT standards for dental/maxillofacial Computed Tomography (CT) practice accreditation using cone beam technology. Intersocietal Accreditation Commission, Ellicott City

ICRP, International Commission on Radiological Protection (2015) Radiological protection in Cone Beam Computed Tomography (CBCT). Ann ICRP 44:1–127

Pauwels R, Stamatakis H, Bosmans H, Bogaerts R, Jacobs R, Horner K, Tsiklakis K, SEDENTEXCT Project Consortium (2013) Quantification of metal artifacts on cone beam computed tomography images. Clin Oral Implants Res 24(Suppl A100):94–99

Pauwels R, Jacobs R, Bosmans H, Pittayapat P, Kosalagood P, Silkosessak O, et al. (2014a) Automated implant segmentation in cone-beam CT using edge detection and particle counting. Int J Comput Assist Radiol Surg 9:733–43

Pauwels R, Silkosessak O, Jacobs R, Bogaerts R, Bosmans H, Panmekiate S (2014b) A pragmatic approach to determine the optimal kVp in cone beam CT: balancing contrast-to-noise ratio and radiation dose. Dentomaxillofac Radiol 43:20140059

Pauwels R, Jacobs R, Singer SR, Mupparapu M (2015a) CBCT-based bone quality assessment: are Hounsfield units applicable? Dentomaxillofac Radiol 44:20140238

Pauwels R, Seynaeve L, Henriques JC, de Oliveira-Santos C, Souza PC, Westphalen FH, Rubira-Bullen IR, Ribeiro-Rotta RF, Rockenbach MI, Haiter-Neto F, Pittayapat P, Bosmans H, Bogaerts R, Jacobs R (2015b) Optimization of dental CBCT exposures through mAs reduction. Dentomaxillofac Radiol 20:20150108

Samei E, Badano A, Chakraborty D, Compton K, Cornelius C, Corrigan K, Flynn MJ, Hemminger B, Hangiandreou N, Johnson J, Moxley M, Pavlicek W, Roehrig H, Rutz L, Shepard J, Uzenoff R, Wang J, Willis C (2005) Assessment of display performance for medical imaging systems, report of the American Association of Physicists in Medicine (AAPM) Task Group 18, Medical Physics Publishing, Madison, AAPM On-Line Report No. 03

Radiation Dose, Risks, and Protection in CBCT

8

Ruben Pauwels and William C. Scarfe

Contents

R. Pauwels, Ph.D. (✉)
Department of Radiology, Faculty of Dentistry, Chulalongkorn University, Bangkok, Thailand

OMFS-IMPATH, Department of Imaging and Pathology, Biomedical Sciences Group, KU Leuven, Leuven, Belgium
e-mail: pauwelsruben@hotmail.com

W.C. Scarfe, B.D.S., F.R.A.C.D.S., M.S.
Division of Radiology and Imaging Science, Department of Surgical/Hospital Dentistry, University of Louisville School of Dentistry, Louisville, KY, USA
e-mail: William.scarfe@louisville.edu

8.1 Radiation Dose, Risk, and Protection Considerations

CBCT imaging uses *ionizing radiation*, a potential long-term carcinogen. The general public's awareness of the increased radiation dose and associated risks with CBCT was highlighted in 2010 with the publication of a front-page article in *The New York Times* (Bogdanich and McGinty 2010) and more recently in Consumer Reports Magazine (Consumer Reports Magazine 2015). Scientific reports have increased professional concerns over the potential association between radiation exposure and cancer and raised the use of ionizing radiation for diagnostic dental imag-

W.C. Scarfe, C. Angelopoulos (eds.), *Maxillofacial Cone Beam Computed Tomography*,
https://doi.org/10.1007/978-3-319-62061-9_8

ing as an important public health issue (Hujoel and Hollender 2005; Longstreth et al. 2004; Claus et al. 2012). While the results of these studies are controversial (White et al. 2013; Tetradis et al. 2012), the use of any radiographic imaging technique, including CBCT, demands that:

- Any healthcare worker prescribing and/or operating radiographic equipment is aware of the effects of ionizing radiation and knowledgeable of potential radiation risks for specific procedures.
- *Justification*. Each radiographic examination is justified clinically, based principally on the individual patient's presentation including considerations of the chief complaint, medical and dental history, and assessment of the physical status as determined with a thorough clinical examination and an evaluation of treatment goals.
- An appropriate imaging modality is chosen based on selection criteria.
- Optimization. Principles and evidence-based procedures are incorporated into clinical practice that minimize patient radiation exposure while optimizing maximal diagnostic benefit.
- Healthcare workers are aware of their legal responsibilities when operating CBCT equipment and interpreting images and comply with all government and third party payer regulations.

The extension of the principles of "justification" and "dose optimization" such that total exposure is "as low as reasonably/diagnostically achievable" (ALARA/ALADA) (NCRP 1990, 2003, 2017; ICRP 2007) to CBCT imaging is supported by the various national and international authoritative agencies. (American Dental Association Council on Scientific Affairs 2012; European Commission 2012).

8.2 Effects of Ionizing Radiation

The effects of ionizing radiation on living tissue can be categorized as:

- **Deterministic.** This effect, also called *tissue reactions*, refers to the direct death of populations of cells, which requires a high dose over a short period of time and usually only presents after a dose level has been reached (threshold) below which no clinical changes have been reported to occur. Examples include skin erythema, hair loss, cataract formation, infertility, and effects to the vascular, hematopoietic, and gastroenterological systems. Thresholds for deterministic effects are never reached in the dose range encountered in conventional oral and maxillofacial radiology. However, they can be seen in dental patients who undergo radiotherapy to the head and neck region for the treatment of cancer. One example of this is the presentation of radiation-induced oral mucositis.
- **Stochastic.** The second effect is irreversible alteration of the cell, usually from damage to cellular DNA resulting in cancer, leukemia, and genetic (i.e., heritable) effects. Unlike deterministic effects, stochastic effects can result from very low dose levels.

8.2.1 Stochastic Effects

8.2.1.1 The Linear-Non-Threshold Model

To predict the probability of stochastic effects with changes in radiation dose, various models describing the relationships between the two

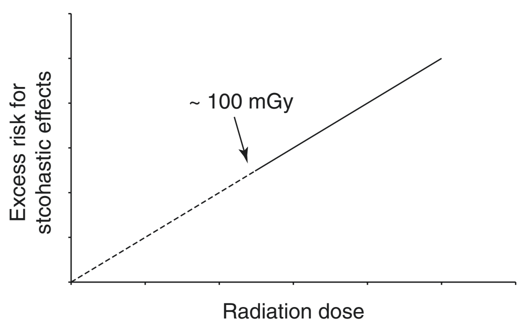

Fig. 8.1 Simplified representation of the linear-non-threshold model, which states that, at any radiation dose greater than 0, there is an excess risk for stochastic radiation-induced effects, with the probability of the effect (but not its severity) increasing with the dose. At doses above approximately 100 mGy or mSv (100,000 µSv), the validity of the LNT model has been demonstrated, but at lower doses and in the realm of dental diagnostic radiology, including CBCT, there is still uncertainty regarding the exact dose-effect relation

have been proposed. It is generally considered that cancer and genetic effects follow a random model, in which the probability of these effects increases directly proportionally to the radiation dose. Moreover, even the smallest radiation dose is believed to carry an additional risk for stochastic effects. This hypothesis is referred to as the *Linear-Non-Threshold (LNT) model* (Fig. 8.1). At doses above 100 mGy, the validity of this model has been demonstrated using epidemiological and experimental data (ICRP 2007), but at lower doses there is still a lot of uncertainty regarding the relation between radiation dose and probability of stochastic effects. Alternative models (e.g., linear-quadratic, supra-linear, hormesis) have been proposed but are not accepted as of yet (ICRP 2007). Furthermore, slighter modifications to the LNT model such as the use of a dose and dose-rate effectiveness factor (DDREF), the value of which has been under debate, have been proposed to take the lower biological effectiveness of low doses and dose rates into account (NRC 2006).

Despite its uncertainty, the LNT model is still almost universally accepted for accounting for stochastic effects at low doses, as it provides a conservative estimation of the radiation-induced risk. The LNT model implies that there is no safe limit or "safety zone" for radiation exposure in diagnostic CBCT imaging. Every exposure cumulatively increases the risk of cancer induction. Any statements regarding radiation risk and radiation protection in this chapter are based on the assumption that the LNT model applies.

8.2.1.2 Effect of Age and Gender on Stochastic Risk

Stochastic risks depend on various factors such as cell division rate, and often require a long time (several years) to present. The risk for stochastic effects is highly dependent on the age of the individual at time of exposure and, at younger ages, the gender of the individual. According to the BEIR VII model, the relative risk is highest at birth, and decreases considerably up to an adult age, after which a more gradual decrease is seen (NRC 2006). In addition, for all cancer combined, females are at a higher risk than males, especially at younger ages (Fig. 8.2).

The age-gender-risk relation is also organ-specific (Fig. 8.3), for example:

- Thyroid cancer incidence shows a more pronounced effect of age (with very small risks beyond the age of 40) and gender (with females being 4–5× more sensitive than males).
- Leukemia, while showing a similar age distribution as the total cancer risk, shows a 30–40% higher risk for males. Other organs for which risks are higher for males include colon and liver, while for bladder cancer risks are virtually equal between genders.
- Cancers which were designated as "other" in the BEIR VII report, which includes several organs of interest for dental radiography such

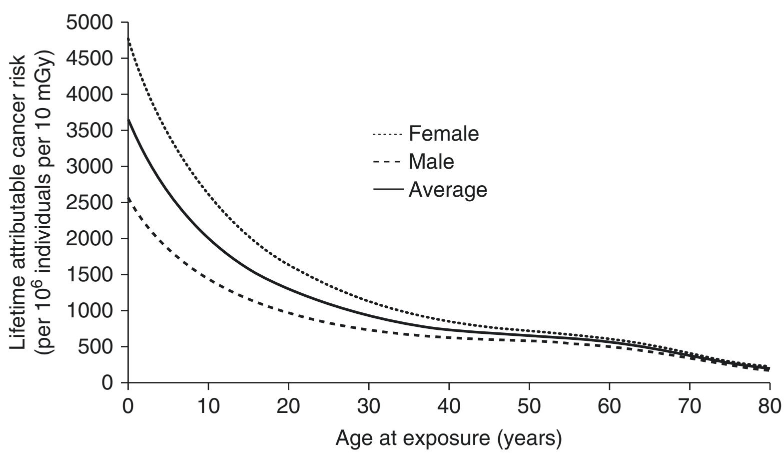

Fig. 8.2 Estimated lifetime attributable cancer risk from radiation, for all cancers, as a function of age at exposure, normalized to a dose of 10 mGy (Derived from the BEIR VII report (NRC 2006))

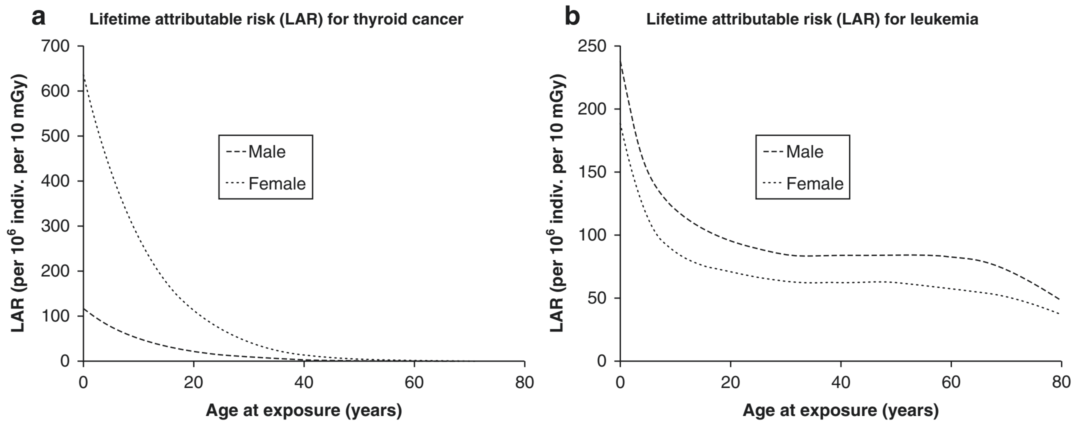

Fig. 8.3 Estimated lifetime attributable cancer risk from radiation, for thyroid cancer (**a**) and leukemia (**b**), as a function of age at exposure, normalized to a dose of 10 mGy (Derived from the BEIR VII report (NRC 2006))

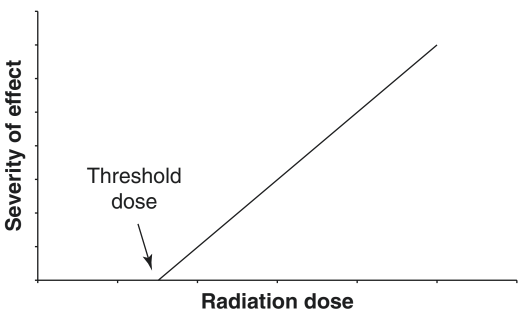

Fig. 8.4 Simplified representation of the dose-effect relation for deterministic effects

as salivary glands, brain, skin, and esophagus, show a similar age distribution to Fig. 8.2 but with only a slightly higher risk for females.

8.2.2 Deterministic Effects

Unlike stochastic effects, which are considered to be possible at even the lowest radiation dose, deterministic effects (or tissue reactions) are associated with a threshold dose (Fig. 8.4). As there are differences regarding individual sensitivity for tissue reactions, the threshold dose is defined as the dose level at which the incidence of tissue reaction is 1% (ICRP 2007); its value depends on the tissue and fractionation of the exposure. For a single exposure, the current threshold for cataract, depression of hematopoiesis and circulatory disease is 500 mGy. Deterministic effects are considered not to occur as a result of CBCT examinations since this threshold dose is much (>50×) higher than the maximum absorbed dose received in dental CBCT.

8.3 Radiation Dose

Different quantities and units are used to express radiation dose. When estimating patient dose, the following quantities are used, ranked from lowest to highest biological relevance: *absorbed dose, equivalent dose, and effective dose*. In addition, other dose quantities can be measured using test objects (e.g., computed tomography dose index, dose-area product) and converted to patient dose.

The term “kerma (K)” is often used instead of dose. Kerma (kinetic energy released per unit mass) is actually a unit of exposure, previously expressed in roentgens (R). K is expressed in the same units as absorbed dose and refers to the transferred energy from photons to electrons whereas dose refers to the deposited energy from secondary electrons to matter. While there is a difference between the two terms, this is negligible for diagnostic X-ray energies, implying that dose and kerma can be used interchangeably (Hendee and Ritenour 2002).

8.3.1 Dose Measurement Indices

Quantities used for patient dose estimation have been introduced by the International Commission on Radiological Protection (ICRP 1977, 2007).

Measurement values of radiation quantities are now reported in the International System of Units (SI units).

8.3.1.1 Absorbed Dose

The absorbed dose, D, is the most fundamental dose quantity, expressed as:

$$D = \frac{\mathrm{d}\bar{\varepsilon}}{\mathrm{d}m} \tag{8.1}$$

where $\mathrm{d}\bar{\varepsilon}$ is the mean energy imparted to matter of mass dm by ionizing radiation. The SI unit for absorbed dose is gray (Gy), equal to joule per kilogram (J kg^{-1}).

8.3.1.2 Equivalent Dose (Radiation Weighted Dose)

The equivalent dose, H_T, is the dose in a tissue or organ T given by:

$$H_T = \sum_R w_R D_{T,R} \tag{8.2}$$

where $D_{T,R}$ is the mean absorbed dose from radiation R in a tissue or organ T, and w_R is the radiation weighting factor. Since w_R is dimensionless, the SI unit for the equivalent dose is sievert (Sv), equal to J kg^{-1}.

For X-rays, the value of w_R is 1, implying that the numerical value of absorbed dose and equivalent dose is the same; only the unit changes.

8.3.1.3 Effective Dose

The effective dose, E, is the tissue-weighted sum of the equivalent doses in all specified tissues and organs of the body, given by the expression:

$$E = \sum_T w_T H_T \tag{8.3}$$

where H_T is the equivalent dose in a tissue or organ, T, and w_T is the tissue weighting factor. The SI unit for the effective dose is the same as for equivalent dose, sievert (Sv).

The tissue weighting factor is defined as the factor by which the equivalent dose in a tissue or organ T is weighted to represent the relative contribution of that tissue or organ to the total health detriment resulting from uniform irradiation of the body (ICRP 2007). It is weighted such that:

Table 8.1 ICRP 103 tissue weighting factors (ICRP 2007)

Tissue	w_T	Σw_T
Bone marrow (red), colon, lung, stomach, breast, remainder tissues[a]	0.12	0.72
Gonads	0.08	0.08
Bladder, esophagus, liver, thyroid	0.04	0.16
Bone surface, brain, salivary glands, skin	0.01	0.04
	Total	1.00

[a]Remainder tissues: Adrenals, extrathoracic (ET) region, gall bladder, heart, kidneys, lymphatic nodes, muscle, oral mucosa, pancreas, prostate (♂), small intestine, spleen, thymus, uterus/cervix (♀)

$$\sum_T w_T = 1 \tag{8.4}$$

Values for weighting factors are based on epidemiological (e.g., life span study of atomic bombing survivors) and experimental data, and are periodically reviewed by the ICRP. Table 8.1 lists the current weighting factors as per ICRP Publication 103 (ICRP 2007). For dental exposures, the following organs are of interest: red bone marrow, esophagus, thyroid, bone surface, brain, salivary glands, skin, and several remainder tissues (extrathoracic region, lymphatic nodes, muscle, oral mucosa). Organs in the thorax (lung, heart, thymus) or further down receive a negligible equivalent dose from dental exposures, and will thus have a negligible contribution to the effective dose.

While the effective dose is a widely used metric to express radiation-induced risk, it should be used with several caveats. While the weighting factors express the relative detriment of radiation imposed to each tissue, they are subject to considerable adjustment and rounding (Martin 2007). In addition, they do not take gender and age into account; for this reason, as well as other factors affecting individual radiation sensitivity, the effective dose and its associated cancer risk should never be applied to individuals, but used at a population level while taking its inherent limitations into account.

8.3.2 Other Dose Metrics

As mentioned in Chap. 6, quality control on CBCT involves the indirect estimation of patient dose through the measurement of a dose index, which can be converted to patient dose.

8.3.2.1 Computed Tomography Dose Index (CTDI)

The computed tomography dose index (CTDI) was the dose index of choice for CT for several years. Several types of CTDI have been defined. In practice, dose *D(z)* is measured in a cylindrical PMMA phantom using a 100-mm pencil ionization chamber, and CTDI_{100} for a CT device with *n* detector arrays of thickness (at isocenter) *T* was defined as:

$$CTDI_{100} = \frac{1}{nT}\int_{-50\,\mathrm{mm}}^{+50\,\mathrm{mm}} D(z)\,dz \qquad (8.5)$$

As the dose distribution may not be homogeneous throughout the phantom, measurements at the center and periphery of the phantom can be performed, and the weighted CTDI can be calculated as:

$$\mathrm{CTDI_w} = \frac{1}{3}\mathrm{CTDI}_{100}^{\mathrm{center}} + \frac{2}{3}\mathrm{CTDI}_{100}^{\mathrm{peri}} \qquad (8.6)$$

Furthermore, in helical CT, the pitch *p* (relative table movement per rotation) can be taken into account, in which case the dose index is referred to as $\mathrm{CTDI_{vol}}$:

$$\mathrm{CTDI_{vol}} = \frac{\mathrm{CTDI_w}}{p} \qquad (8.7)$$

The dose length product (DLP) can then be derived from the CTDI by multiplying it with the scan length *L*:

$$\mathrm{DLP} = \mathrm{CTDI_{vol}}\,L \qquad (8.8)$$

There are several issues regarding the use of CTDI in CBCT (Mori et al. 2005). Most importantly, because CBCT employs the use of a wide beam, the 100-mm pencil chamber is unable to capture all of the scattered radiation generated within the phantom (and, for very large fields of view (FOVs), part of the primary beam that extends beyond the pencil chamber as well). This issue is also applicable to multi-detector CT involving many detector rows (ICRU 2012). While the CTDI can still be estimated for CBCT using a combination of several measurements, this is impractical for QC testing.

Conversion factors (*k* factors) between CTDI, DLP, and effective dose have been determined for CT head scans. For head examinations they range, depending on age, from *k* = 0.0021 to *k* = 0.011 (AAPM 2008). As yet, no conversion factors for dental CBCT scans have been determined.

8.3.2.2 Dose-Area Product

The dose-area product (DAP), commonly used for planar radiographic modalities, has been proposed as a dose index for CBCT because of (1) its practicality in that it requires a single measurement per exposure setting with no phantom required and (2) inherent ability to cope with the wide variety of FOV sizes encountered in CBCT (EC 2012; HPA 2010). It can be measured directly using a DAP meter attached to the CBCT-arm, or indirectly by measuring the point dose at a location where the cross-sectional area of the beam is known (e.g., at the isocenter).

A major limitation is that DAP is a measurement of tube output rather than patient dose. Conversion factors between DAP and patient dose (taking FOV size, FOV position, and beam geometry into account) are not currently available.

8.3.2.3 Other Metrics

Alternative methods to evaluate dose in CBCT have been proposed. The SEDENTEXCT report defined two dose indices, both measured using a small-volume ion chamber in a cylindrical phantom (EC 2012). A first index measured the central and peripheral dose at the central axial plane (with the FOV positioned centrally), whereas the second index measured the dose along the diameter of the phantom (with the FOV positioned according to a dental scan). Both indices have shown consistent correlation with each other as well as the DAP.

The International Commission on Radiation Units and Measurements (ICRU) (ICRU 2012) proposed a dose index for CT which overcomes the limitations of the CTDI for modern scanners. For non-helical scans, it was proposed to measure the dose at the center of the beam for increasingly wide beams, plotting the measurements vs.

beam width and estimating the point at which the dose equilibrates (which was proposed to be at beam widths ≥470 mm). The practicality of such a measurement may be limited in dental and maxillofacial CBCT due to the limited subsets of beam width available on a typical unit.

The German standard DIN 6868-161 (DIN 2013) proposed a measurement at the detector (without the use of a phantom) which is corrected to estimate the dose at the isocenter.

While these different possible dose indices are expected to be interchangeable to some extent, a true standardization of CBCT dosimetry is called for, as it could lead to several improvements in dose management, including the determination of diagnostic reference levels.

8.4 Radiation Dose in CBCT

The radiation dose in CBCT has been extensively reported, using a variety of CBCT models, dose quantities, and measurement methodologies. A common conclusion from these studies is that there is a wide range in patient dose in CBCT, corresponding to the range of exposure parameters used in clinical practice. In terms of FOV size, as mentioned in Chap. 2, small (~2 teeth), intermediate (e.g., single or both jaws), and large (maxillofacial) FOVs are used in CBCT. In addition, tube voltage for clinical scans ranges between 70 and 120 kV, whereas mAs usually ranges between 20 and 150 mAs. As a result, while CBCT doses are higher than those of intraoral and cephalometric radiography, the low end of the CBCT dose range overlaps with the range found in panoramic radiography, while the high end of the range overlaps with that of CT (Ludlow and Ivanovic 2008; Ludlow et al. 2008; Gijbels et al. 2005b; Loubele et al. 2005). A wide dose range implies a great potential for optimization, and several dose-saving strategies have been proposed.

8.4.1 Effective Dose

Multiple studies on various CBCT models (Table 8.2) have demonstrated differences of an order of magnitude in effective dose (Fig. 8.5, 8.6, 8.7, and 8.8) (Tsiklakis et al. 2005; Ludlow et al. 2006; Coppenrath et al. 2008; Hirsch et al. 2008; Lofthag-Hansen et al. 2008; Ludlow and Ivanovic 2008; Palomo et al. 2008; Silva et al. 2008; Faccioli et al. 2009; Loubele et al. 2009; Okano et al. 2009; Roberts et al. 2009; Suomalainen et al. 2009; Carrafiello et al. 2010; Jadu et al. 2010; Qu et al. 2010; Vassileva and Stoyanov 2010; Librizzi et al. 2011; Ludlow 2011; Qu et al. 2011; Davies et al. 2012; Grunheid et al. 2012; Jeong et al. 2012; Okano et al. 2012; Pauwels et al. 2012a, b; Qu et al. 2012a, b; Sezgin et al. 2012; Theodorakou et al. 2012; Xu et al.

Table 8.2 Manufacturers and models of CBCT units with published data available on effective dose. Some units may no longer be manufactured

Manufacturer	Model(s)
Asahi Roentgen, Kyoto, Japan	Alphard VEGA; AZ3000 CT
Carestream Dental, Atlanta, Georgia, USA	CS 9000; CS 9300; CS 9500
NewTom, Cefla Dental Group, Imola, Italy	SkyView; NewTom 9000; NewTom 3G; NewTom VG; NewTom VGi
Hitachi, Tokyo, Japan	CB Mercuray
Imaging Sciences, Hatfield, Pennsylvania USA	i-CAT Classic; i-CAT FLX; i-CAT Next Generation
IMTEC, Ardmore, Oklahoma USA	Iluma; Ilumina; Iluma Elite
Instrumentarium, Helsinki, Finland	OP 300 Maxio
J. Morita Corp., Kyoto, Japan	3D Accuitomo; 3D Accuitomo FPD; 3D Accuitomo 170; Veraviewepocs 3D
KaVo Dental GmbH, Biberach, Germany	3D eXam; Pan eXam Plus
Planmeca Oy, Helsinki, Finland	ProMax 3D; ProMax 3D Mid
Sirona Dental Systems, Bensheim, Germany	Galileos; Galileos Comfort; Galileos Comfort Plus; Orthophos XG 3D
Soredex, Tuusula, Finland	SCANORA 3D
TeraRecon, Foster City, California USA	Prexion 3D
VATECH, Yongin, Korea	PaX-Uni3D; Pax-Zenith; DCT PRO; Picasso Trio; Master3 Ds; Implangraphy

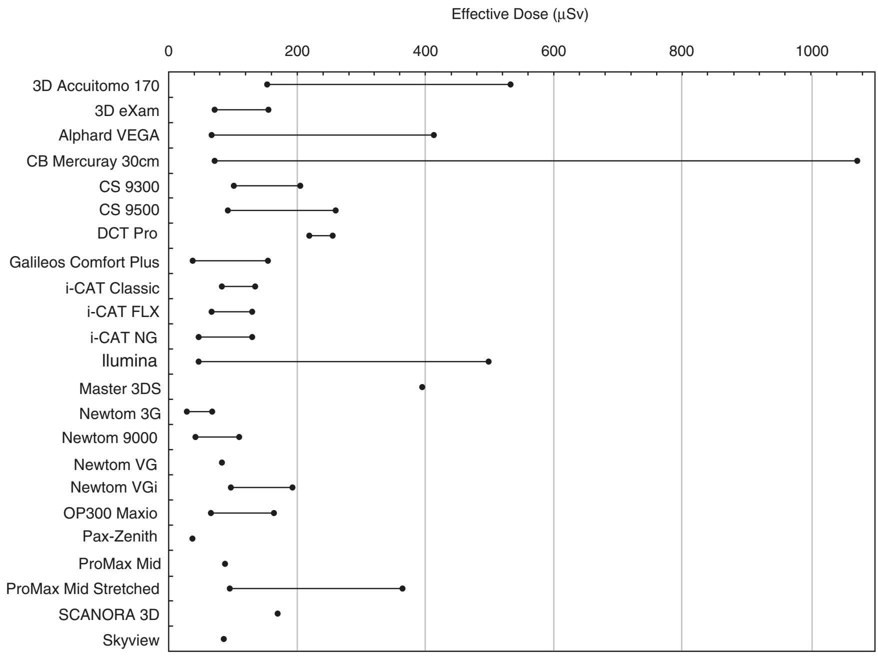

Fig. 8.5 Selected range (*horizontal bar*) and specific (*circle*) published data of effective doses (μSv) (ICRP 2007) for large-FOV CBCT units (>15 cm height) (Tsiklakis et al. 2005; Ludlow et al. 2006; Coppenrath et al. 2008; Palomo et al. 2008; Silva et al. 2008; Ludlow and Ivanovic 2008; Faccioli et al. 2009; Loubele et al. 2009; Roberts et al. 2009; Jadu et al. 2010; Vassileva and Stoyanov 2010; Librizzi et al. 2011; Ludlow 2011; Qu et al. 2011; Davies et al. 2012; Grunheid et al. 2012; Okano et al. 2012; Pauwels et al. 2012a; Qu et al. 2012a, b; Sezgin et al. 2012; Ludlow and Walker 2013; Morant et al. 2013; Rottke et al. 2013; Schilling and Geibel 2013; Kim et al. 2014; Koivisto et al. 2014; Ludlow et al. 2015; Feragalli et al. 2017) (*NG* Next Generation)

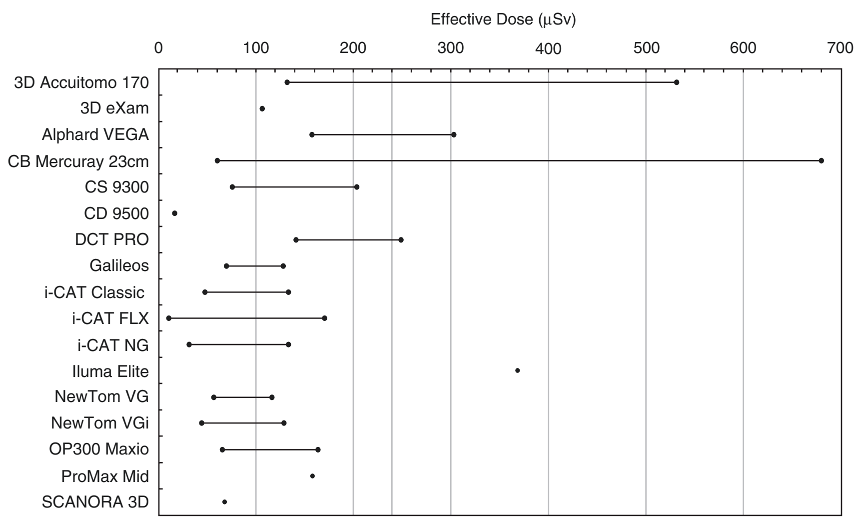

Fig. 8.6 Selected range (*horizontal bar*) and specific (*circle*) published data of effective doses (μSv) (ICRP 2007) for medium-FOV CBCT units (>10 cm to ≤15 cm height) (Ludlow et al. 2006; Ludlow and Ivanovic 2008; Palomo et al. 2008; Silva et al. 2008; Loubele et al. 2009; Roberts et al. 2009; Carrafiello et al. 2010; Jadu et al. 2010; Librizzi et al. 2011; Qu et al. 2011; Davies et al. 2012; Okano et al. 2012; Pauwels et al. 2012a; Qu et al. 2012a, b; Sezgin et al. 2012; Theodorakou et al. 2012; Xu et al. 2012; Ludlow and Walker 2013; Lukat et al. 2013; Morant et al. 2013; Rottke et al. 2013; Schilling and Geibel 2013; Deman et al. 2014; Kim et al. 2014; Koivisto et al. 2014; Pauwels et al. 2014c; Rampado et al. 2014; Ludlow et al. 2015) (*NG* Next Generation)

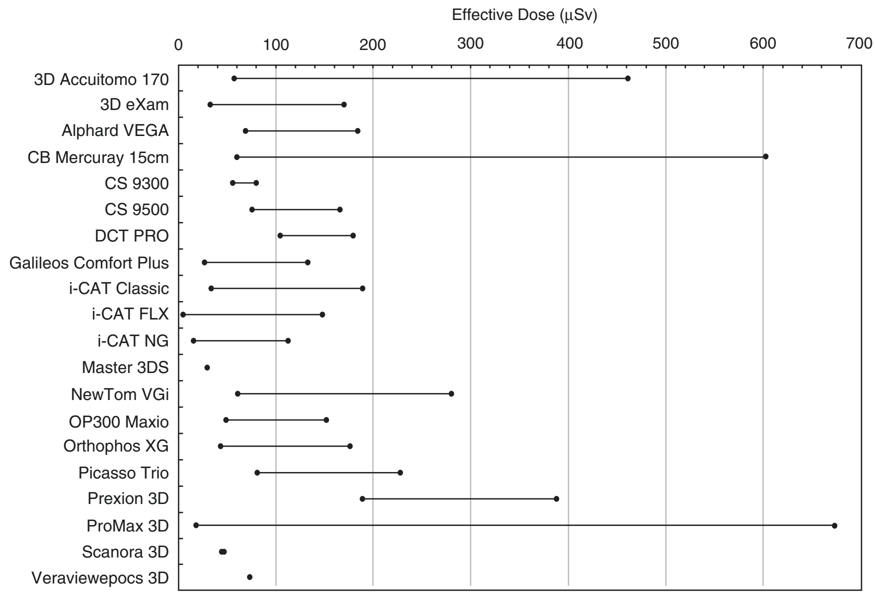

Fig. 8.7 Selected range (*horizontal bar*) and specific (*circle*) published data of effective doses (µSv) (ICRP 2007) for small-FOV (≤10 cm height, > 50 cm² beam area at isocenter) CBCT units (Ludlow and Ivanovic 2008; Palomo et al. 2008; Loubele et al. 2009; Okano et al. 2009; Roberts et al. 2009; Suomalainen et al. 2009; Jadu et al. 2010; Qu et al. 2010; Ludlow 2011; Davies et al. 2012; Grunheid et al. 2012; Pauwels et al. 2012a; Qu et al. 2012a, b; Sezgin et al. 2012; Theodorakou et al. 2012; Xu et al. 2012; Ludlow and Walker 2013; Morant et al. 2013; Rottke et al. 2013; Schilling and Geibel 2013; Deman et al. 2014; Kim et al. 2014; Pauwels et al. 2014c; Ludlow et al. 2015) (*NG* Next Generation)

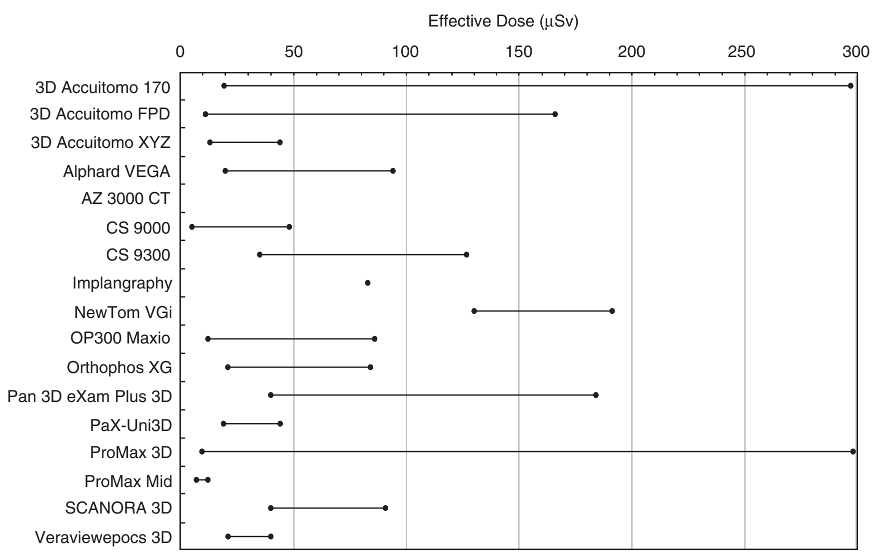

Fig. 8.8 Selected range (*horizontal bar*) and specific (*circle*) published data of effective doses (µSv) (ICRP 2007) for limited FOV (≤10 cm height, ≤50 cm² beam area at isocenter) CBCT units (Hirsch et al. 2008; Lofthag-Hansen et al. 2008; Loubele et al. 2009; Okano et al. 2009; Suomalainen et al. 2009; Jeong et al. 2012; Okano et al. 2012; Pauwels et al. 2012a; Qu et al. 2010, 2012a, b; Theodorakou et al. 2012; Xu et al. 2012; Al-Okshi et al. 2013; Ludlow and Walker 2013; Lukat et al. 2013; Rottke et al. 2013; Schilling and Geibel 2013; Deman et al. 2014; Kim et al. 2014; Koivisto et al. 2014; Pauwels et al. 2014c; Ludlow et al. 2015)

2012; Al-Okshi et al. 2013; Ludlow and Walker 2013; Lukat et al. 2013; Morant et al. 2013; Rottke et al. 2013; Schilling and Geibel 2013; Deman et al. 2014; Kim et al. 2014; Koivisto et al. 2014; Pauwels et al. 2014c; Rampado et al. 2014; Kadesjö et al. 2015; Ludlow et al. 2015; Feragalli et al. 2017).

Using anthropomorphic phantoms representing a reference adult male, Pauwels et al. (2012a) showed a 19-fold effective dose range on 14 CBCT models, whereas Ludlow and Ivanovic (2008) measured a 16-fold range for 8 models. Rottke et al. (2013) found a 23-fold dose range for 10 CBCT models, although they used the highest and lowest selectable exposure parameters rather than default clinical settings. In a meta-analysis, Ludlow et al. (2015) reported that adult effective doses for protocols ranged from 46 to 1073 μSv for large fields of view (FOVs) (Fig. 8.5), 9–560 μSv for medium FOVs (Fig. 8.6), and 5–652 μSv for small FOVs (Figs. 8.7 and 8.8). They reported pediatric effective doses ranged overall from 13–769 μSv for large or medium FOVs and 7–521 μSv for small FOVs. When grouping mean adult effective doses by FOV size, effective dose was 212 μSv (large), 177 μSv (medium), and 84 μSv (small). For pediatric effective doses, a mean effective dose of 175 μSv was reported for combined large and medium FOVs and 103 μSv for small FOVs.

8.4.2 Dose Distribution and Organ Doses

The calculation of effective dose is based on heavily rounded estimations of the relative detriment caused to specific organs and tissues by radiation. It is important to note that approximately 2/3rds of the weighted tissues that are included in the effective dose calculation are not found in the head and neck area and receive no significant doses from maxillofacial radiography. This is an important factor leading to the relatively low effective doses that are estimated for dental and maxillofacial radiographic examinations. Specific organ doses should be considered because of the large doses and variability reported for CBCT at specific radiosensitive sites such as the salivary glands (range, 130–13,900 μSv), brain (range, 23–8950 μSv), and thyroid (range, 1–6333 μSv) (Ludlow et al. 2015).

Unlike MDCT, CBCT has shown to have a complicated dose distribution due to the use of horizontal collimation (resulting in the FOV diameter generally being (much) smaller than the diameter of the head), off-axis beam geometries (see Chap. 2) and rotation arcs between 180° and 360°. As a result, whereas MDCT dose distributions are homogeneous (or, at least, concentrically from center to periphery of the body), CBCT doses can be localized. From experimental data, a few general considerations can be derived (Pauwels et al. 2012b):

- The dose is highest inside the FOV, regardless of its position (i.e., more centrally or peripherally in the head). Outside the FOV in the anteroposterior or left-right directions, dose gradually decreases with increasing distance to the FOV (as these areas are covered by the primary beam for only part of the rotation), with the dose gradient being higher for smaller FOV diameters (Fig. 8.9). In the craniocaudal direction, dose decreases sharply outside the FOV (as these areas only receive scattered radiation) (Fig. 8.10).
- For 180° rotations, the dose is highest at the “tube side” of the rotation, regardless of FOV size and position (Fig. 8.9).

The relatively sharp dose gradients found in CBCT, along with the fact that organs can be partially or not exposed by primary radiation, depending on the size and position of the FOV, results in organ dose variability of several orders of magnitude, as mentioned above (Ludlow and Ivanovic 2008; Pauwels et al. 2012a; Hirsch et al. 2008; Ludlow et al. 2006).

8.4.3 Cancer Risk

Despite its limitations and uncertainties, the LNT model applies to the estimation of cancer risk from CBCT and predicts that risk increases

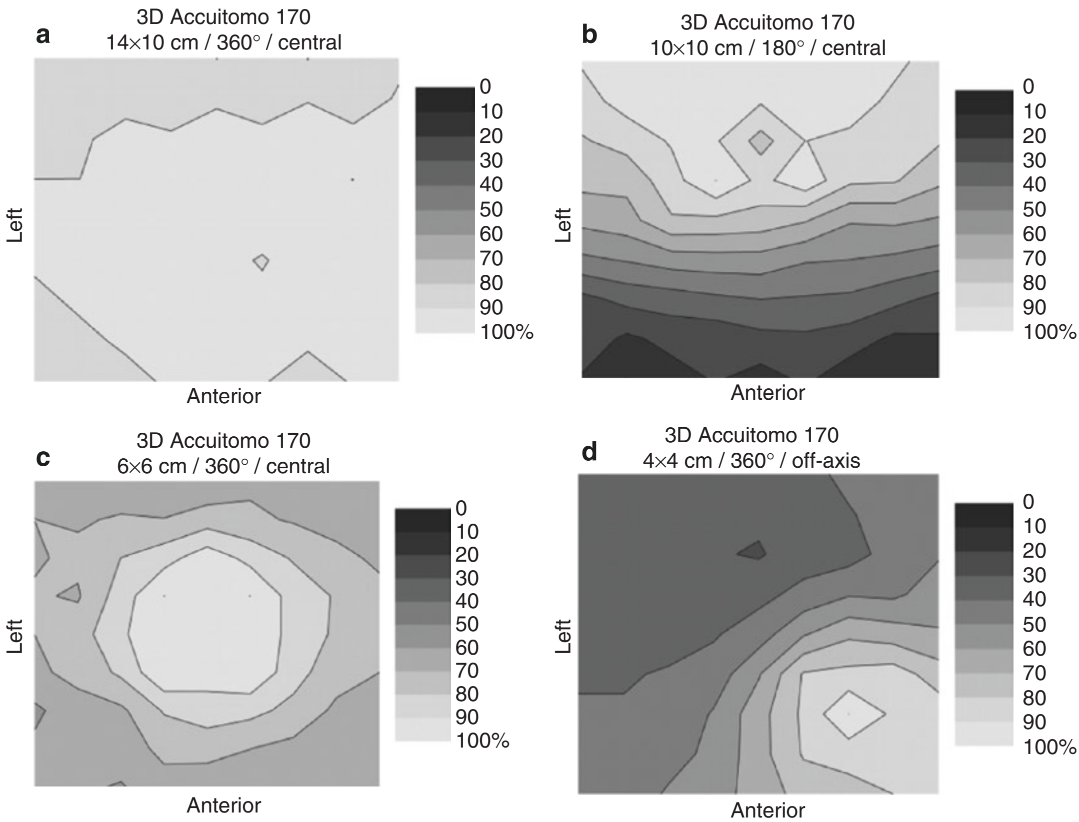

Fig. 8.9 Dose distribution in a PMMA phantom along the anteroposterior and left-right directions in CBCT. Brighter grey areas denote higher doses, normalized to the peak dose. A large-diameter FOV results in a homogenous dose distribution, with a slight decrease in dose outside the FOV (**a**). A 180° rotation results in a dose gradient with the highest dose found at the "tube side"; in this case, the tube rotated along the posterior side (**b**). A small-diameter FOV results in a concentric dose gradient, with the dose gradually decreasing with increasing distance to the FOV edge (**c**). "Off-axis" refers to the position of the FOV vs. the center of the phantom, not the shape of the beam (**d**) (Reproduced from Pauwels et al. (2012b) under the British Institute of Radiology's License to Publish)

linearly with dose. This risk can vary considerably between CBCT units and high- and low-dose exposure protocols. Furthermore, smaller patients (e.g., females and children) will receive a higher radiation dose at a given tube output (Theodorakou et al. 2012). Risk also varies with age and gender. Combining all factors, there can be a 35-fold difference between the highest and lowest risk for a particular patient sample (Pauwels et al. 2014a). The average risk for a CBCT scan can be almost 4× lower for patients over 60 years than for children younger than 12, with the risk for females 40%, on average, higher than for males (Pauwels et al. 2014a). Therefore, low-dose protocols should be used when scanning children in particular, adapting the tube output to the size of the patient.

8.4.3.1 Comparative Risk

Practitioners prescribing and performing CBCT must be knowledgeable of the radiation risk associated with the procedure and be able to communicate this risk effectively to their patients. Absolute effective dose values are meaningless to patients without context. Effective doses for CBCT can be compared to various other procedures and activities to provide an index of relative risk and include:

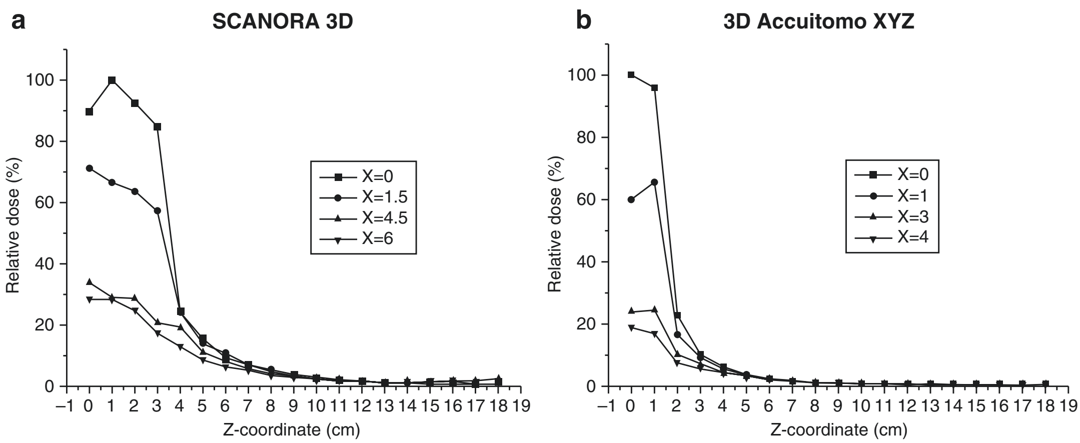

Fig. 8.10 Dose distribution for two CBCT units—the SCANORA 3D (**a**) and 3D Accuitomo XYZ (**b**) measured in a water phantom along the craniocaudal axis (i.e., z-axis). The relative dose, normalized to the peak dose was measured at various z-coordinates, with $z = 0$ cm corresponding to the central axial planes. For z-coordinates outside the FOV ($z > 3.75$ cm and $z > 1.75$ cm for the *left* and *right* graphs, respectively), dose decreases sharply. (Reproduced from Pauwels et al. (2012b) under the British Institute of Radiology's License to Publish)

- **Other imaging modalities.** To make risk understandable to patients, the effective dose of CBCT can be described in multiples of common dental radiographic procedures, most typically rotational panoramic radiography. The published effective dose for panoramic radiography ranges from 14.2 to 50 μSv (Ludlow et al. 2008; Gavala et al. 2009; Carrafiello et al. 2010; Grunheid et al. 2012). This implies that, depending on the panoramic radiography dose used for the comparison (e.g., equipment manufacturer and model, film vs. digital acquisition), the risk for CBCT can be reported either conservatively or liberally compared to panoramic radiography.
- The American College of Radiology (ACR) has categorized risk relative for specific imaging procedures and incorporated pediatric considerations of effective-dose estimates in their Relative Radiation Level (RRL) designations (Table 8.3) (American College of Radiology 2011).
- **Background equivalent radiation time.** Background exposures are most often based on an average annual full body natural radiation exposure of 3 mSv (3000 μSv per year) and expressed in days of background radiation.
- **Radiation detriment.** Radiation detriment is defined as the total harm to an exposed population and their descendants and could be calculated from effective dose (ICRP 1991). Detriment includes the weighted probabilities of fatal and nonfatal cancer, hereditary effects, and the relative length of life lost. The coefficient assigned to these combined effects is 7.3×10^{-2} Sv^{-1}. Because of great uncertainty

Table 8.3 Estimations of relative radiation level designations for children and adults for orthodontic imaging (with permission from ACR[a] 2011)

Relative radiation level	Effective dose estimate range (μSv)	
	Adult	Child
0	0	0
☢	<100	<30
☢☢	100–1000	30–300
☢☢☢	1000–10,000	300–3000
☢☢☢☢	10,000–30,000	3000–10,000

[a]Some of the information in this document was provided with permission from the American College of Radiology (ACR) and taken from the ACR Appropriateness Criteria. The ACR is not responsible for any deviations from original ACR Appropriateness Criteria content

on the form of the dose response below 0.1 Sv, the ICRP suggests that no specific judgment on low-dose risk of noncancer diseases is possible. Therefore, a risk coefficient of 5.5×10^{-2} Sv^{-1} based on cancer mortality risk alone can be used to calculate the expected incidence of radiation-induced cancers deaths per million scans for CBCT.

8.5 Optimization of Radiation Dose in CBCT

8.5.1 Technical Factors

8.5.1.1 Field of View Collimation

Arguably the most important dose reduction strategy in CBCT is the collimation of the X-ray beam, to ensure that the FOV is as small as possible. Considerable dose reductions can be achieved through beam collimation, with reductions in effective dose up to 82% being measured for a small FOV compared with a maxillofacial FOV at a constant kV and mAs (Fig. 8.11) (Pauwels et al. 2014c). Collimation can be achieved by reducing FOV height and width. While most CBCT units produce a cylindrical or spherical volume of interest, one manufacturer has developed panoramic/CBCT (Veraviewepocs 3D R100, J. Morita Corp., Kyoto, Japan) creating a 3D convex triangular shaped (Reuleaux) FOV providing optimal coverage to the shape of the jaw and dental arches reducing dose by approximately 10% (Fig. 8.12) (J. Morita Corp. 2015).

In addition, the FOV position can have a significant effect on organ doses and, thus, effective dose. In general, FOVs positioned more caudally (e.g., mandibular vs. maxillary scans) show an increased (up to 2×) effective dose, primarily due to an increased absorbed dose to the thyroid (Fig. 8.11). When possible, FOVs should thus be positioned as cranially as possible (although, ideally, FOVs should be collimated such as to not allow any leeway regarding cranial/caudal position).

In terms of image quality, while small FOVs increase the local tomography effect, leading to increased issues regarding grey value stability, large FOVs are prone to an increase in scattered radiation at the detector, resulting in image quality degradation.

While CBCT users usually have limited FOV options available, they should ensure that the

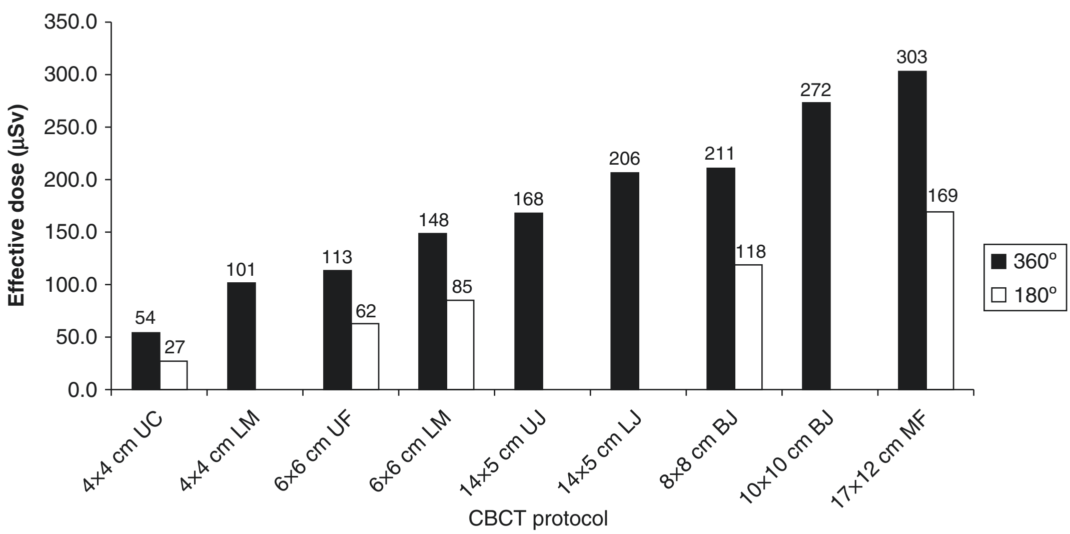

Fig. 8.11 Effective dose vs. field of view size and position, for the 3D Accuitomo 170 (J. Morita, Kyoto, Japan) at 90 kV, 87.5 mAs (360° rotation scan) and 45 mAs (180° rotation scan). Dose increases with increasing diameter and/or height of the FOV, and is higher for mandibular than maxillary scans. *BJ* both jaws, *CBCT* cone-beam computed tomography, *LJ* lower jaw, *LM* lower molar, *MF* maxillofacial, *UC* upper canine, *UF* upper frontal, *UJ* upper jaw. Reproduced from Pauwels et al. (2014c) under the British Institute of Radiology's License to Publish

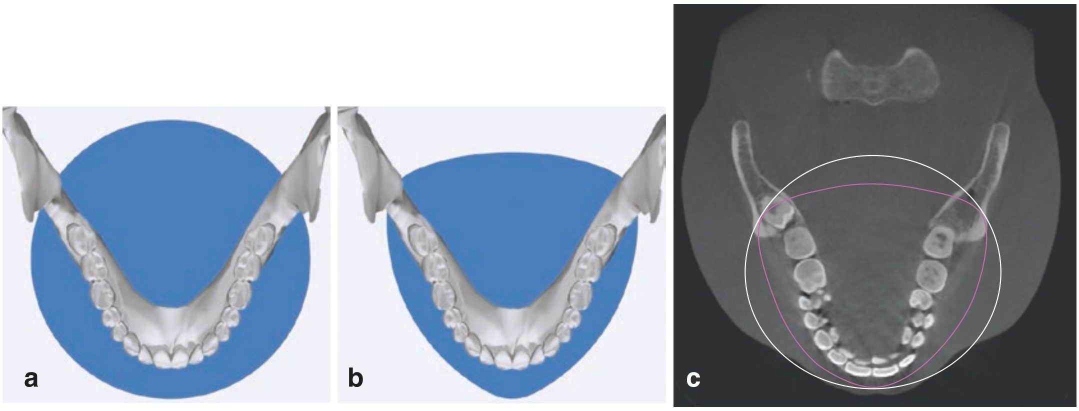

Fig. 8.12 Schematic showing superimposition of cylindrical FOV (**a**) and Reuleaux FOV (**b**) over mandibular jaw and dental arches. The difference in volume covered between the two types of FOV is shown as a white area in (**c**) (Image courtesy, J. Morita Corp., Kyoto, Japan)

smallest available option that covers the region of interest is selected for each patient. The acquisition of a low-dose scout image helps the user to collimate and position the FOV appropriately.

Exceptions occur when, as mentioned in Chap. 2, FOV size is linked to voxel size. For some CBCT units, larger FOVs are reconstructed at a larger voxel size for computational reasons as well as to limit data size. Furthermore, FOV can be linked to the mAs for these units, with smaller FOVs typically corresponding to a higher mAs; this is typically done to compensate for the higher noise when these FOVs are reconstructed at smaller voxel sizes. The user should thus be aware of the combined effect of FOV, mAs, and voxel size on image quality and radiation dose, and judiciously select the most appropriate option for a given patient.

8.5.1.2 Tube Voltage Selection and Beam Filtration

As shown in Chap. 2, the tube voltage (kV) has a multifold effect on radiation dose and image quality. A higher kV value leads to an increase in mean and maximum X-ray energy, as well as an increase in the X-ray flux. The probability of photoelectric absorption, Compton and Rayleigh scatter occurring varies with X-ray energy; in addition, the angular distribution of Compton scatter depends on X-ray energy.

It is important to consider both image quality and radiation dose when evaluating the effect of kV. While radiation dose increases with kV in a linear or quadratic fashion, image quality in CBCT is improved at a higher kV because of decreased noise. It can be expected that there is an optimal kV at which the ratio between image quality and radiation dose peaks, but this requires further investigation for dental CBCT imaging. Preliminary studies investigating contrast-to-noise ratio indicates that between 60 and 90 kV, the highest kV value was also the most dose-efficient (Pauwels et al. 2014b), independent of patient head size (Pauwels et al. 2016).

In practice, kV values are often fixed by manufacturers, and those allowing kV variation typically operate at relatively low kV levels (≤90 kV). If kV can be varied, users are advised to use the highest available kV option and reduce mAs instead, until more conclusive data is available.

The use of increased filtration to the X-ray beam has long been known to reduce patient exposure in dental radiography by preferential absorption of lower energy photons (Richards et al. 1970), effectively increasing beam energy (kV). The use of additional copper filtration has been reported to reduce patient dose from 43% (Ludlow 2011) to 57% (Ludlow and Ivanovic 2008) depending on amount of filtration used and unit. Novel nonuniform thickness and shapes of filtration such as bow-tie have been applied in maxillofacial CBCT imaging to produce uniform flux intensity and, in addition to reducing scatter, also reduce radiation dose at the periphery of the imaging FOV (Zhang et al. 2013).

8.5.1.3 Tube Current and Exposure Time Selection

The tube current (mA) and exposure time (s) are often combined as a product (mAs), as they largely have the same effect on radiation dose and image quality. The mAs is linearly proportionate to the radiation dose (e.g., a doubling in mAs results in a doubling of radiation dose). In terms of image quality, an increase in mAs results in a decreased image noise according to a hyperbolic relation (i.e., at low mAs levels, an increase in mAs results in a considerable decrease in noise; at high mAs levels, an increase in mAs only has a minor effect on noise).

The CBCT user is usually allowed to vary either tube current, exposure time, or both. They should judiciously choose the lowest possible mAs value at which image quality is expected to be acceptable. Due to the range in kV and hardware used in CBCT, minimally acceptable mAs values are highly dependent on the CBCT model under consideration.

An exception is when the mAs is linked to the FOV size and/or voxel size, as mentioned above. When this is the case, the user should judiciously select exposure protocols based on the size of the region of interest, and the desired image sharpness and noise, taking the combined effect of FOV size and mAs on image quality and radiation dose into account.

Automatic exposure control (AEC) is largely absent in current-generation CBCT units. It is expected that the implementation of advanced AEC methods, similar to those used in CT (Alibek et al. 2011), could lead to a consistent and standardized dose reduction for small-sized patients. In addition, AEC can be used not only to normalize exposures between patients of different size, but to vary the exposure during a scan as well. Depending on the FOV location and the position of tube and detector, detector signal will be low (e.g., A-P projections, lateral temporal bone projections) or high (e.g., lateral projections in the anterior region). Therefore, AEC could be used to take this variability in terms of tissue quantity and/or density for different projection angles into account.

8.5.2 Shielding

External X-ray blockers, usually containing lead, can be used to avoid exposure to certain organs. Popular shielding techniques used for patients as well as workers are lead aprons, thyroid collars, and leaded glasses. A few important remarks should be made regarding the use of shielding in CBCT:

- Shielding will almost exclusively absorb primary radiation (i.e., coming from the outside in). Scattered radiation from inside the patient will be blocked on the way out, but this will not lead to any dose reduction. An exception is when radiation is scattered from the anterior head in a caudal-posterior direction, exits the head below the chin and re-enters the body more caudally (e.g., at the level of the thyroid).
- If shielding is used in the primary beam area, it may lead to severe metal artifacts in the reconstructed image. If automatic exposure control is used, the use of shielding in the scanned region may dramatically increase the tube output.
- As mentioned above, deterministic effects to the lens of the eye only occur at doses several orders of magnitude above that of CBCT. The only actual benefit from leaded glasses is a small reduction of absorbed doses to other organs at the same level of the eyes (i.e., skin, bone, brain).

Several studies have investigated the use of thyroid shielding in CBCT (Goren et al. 2013; Hidalgo et al. 2015; Qu et al. 2012a, b; Tsiklakis et al. 2005). While considerable dose reductions have been reported, it is not always clear whether the thyroid collar partially blocked the primary beam (and, thus, led to artifacts in the reconstructed image). It can be concluded that thyroid collars, aprons, and leaded glasses can be used as long as the diagnostic region of interest is not at the same level as the shielding.

8.6 Protection of Workers and the Public

Protection of workers and public is covered by the principle of application of Dose Limits of the ICRP (2007), which states that:

"… the total dose to any individual from regulated sources in planned exposure situations other than medical exposure of patients should not exceed the appropriate limits specified by the Commission"

Dose limits to workers have been proposed by the ICRP, and are usually implemented in national and regional legislation unaltered. Current limits adhere to ICRP Publication 103 (ICRP 2007), except for the eye lens for which a lower dose limit for occupational exposure was proposed in 2012 (ICRP 2012) (Table 8.4).

The reduction of radiation dose to workers and public can be achieved by adhering to the following general principles:

- **Distance.** According to the inverse square law, the intensity of X-rays decreases proportionally to the square of the distance to the source. For example, a distance of 2 m reduces dose with a factor 4 compared with a distance of 1 m, and a distance of 3 m with a factor 9.
- **Shielding.** The use of shielding inside walls and windows can absorb a large amount of scattered and leaked radiation. High-density metals (typically lead and leaded glass) are often used, although an equivalent thickness of concrete or other materials can be considered, especially in low-dose environments. In special circumstances in which a worker or other individual (e.g., parent) is required to be in the room with the patient during the exposure, personal shielding such as lead aprons and collars should be used.
- **Time.** The time in which a worker is exposed should be limited as much as possible using rotation schedules. For example, if a clinic involves radiographic equipment with a high and low amount of scattered radiation, workers should be shifted between equipment rather than having the same worker operate in the high-scatter environment at all times.

Table 8.4 Dose limits for occupational and public exposure, according to ICRP Publication 103 (ICRP 2007) and ICRP's statement on tissue reactions (ICRP 2012)

Type of limit	Occupational	Public
Annual effective dose	20 mSv[b, c]	1 mSv[d]
Annual equivalent dose to:		
Eye lens	20 mSv[b]	15 mSv
Skin[a]	500 mSv	50 mSv
Hands and feet	500 mSv	–

[a]Averaged over 1 cm^2, regardless of the area exposed
[b]Averaged over 5 years, with no single year exceeding 50 mSv
[c]Additional restrictions apply for pregnant women
[d]Similar to the occupational dose, a higher annual dose could be allowed in a single year in special circumstances, providing that the average over 5 years does not exceed 1 mSv/year

In CBCT, depending on the unit, exposure of workers is in the range of 4 µSv/scan to 47 µSv/scan at 1 m (median: 7.4 µSv) (SEDENTEXCT 2010). In comparison, for intraoral and panoramic radiography, doses at 1 m of less than 1 µSv have been reported (Sutton and Williams 2000; Gijbels et al. 2005a). The SEDENTEXCT Guidelines on dental CBCT (EC 2012) state that:

> "… for worker protection from CBCT equipment, the guidelines detailed in Section 6 of the EC publication 'Radiation Protection 136. European Guidelines on Radiation Protection in Dental Radiology' (EC 2004) should be followed."

When installing a CBCT unit in a hospital and clinic, proper consideration should be given to the layout of the room and the need for shielding to protect workers and public. A qualified medical physicist is typically involved, on a case-by-case basis, to measure (or estimate) the dose in the vicinity of the unit, and to provide guidance on proper installation and shielding requirements. Table 8.5 contains the shielding requirements for CBCT equipment proposed by the SEDENTEXCT Guidelines (EC 2012).

Table 8.5 Shielding requirements (in terms of equivalent lead thickness) at 1 m for a dose constraint of 0.3 mSv per year, from the SEDENTEXCT Guidelines (EC 2012)

	Patients per week			
Dose per scan at 1 m (µSv)	5 (mm)	10 (mm)	25 (mm)	50 (mm)
4	0.5	0.5	1.0	1.0
8	0.5	0.5	1.0	1.5
12	0.5	1.0	1.0	1.5
16	0.5	1.0	1.5	1.5

Acknowledgments Images in Fig. 8.12 are used with permission of J. Morita Corp., Kyoto, Japan.

References

Alibek S, Brand M, Suess C, Wuest W, Uder M, Greess H (2011) Dose reduction in pediatric computed tomography with automated exposure control. Acad Radiol 18:690–693

Al-Okshi A, Nilsson M, Petersson A, Wiese M, Lindh C (2013) Using GafChromic film to estimate the effective dose from dental cone beam CT and panoramic radiography. Dentomaxillofac Radiol 42:20120343

American Association of Physicists in Medicine (AAPM) (2008) AAPM Report No. 96: the measurement, reporting, and management of radiation dose in CT. AAPM, College Park

American College of Radiology (2011) ACR appropriateness criteria®. Radiation dose assessment introduction. http://www.acr.org/~/media/ACR/Documents/AppCriteria/RRLInformation.pdf. Accessed 10 Oct 2015

American Dental Association Council on Scientific Affairs (2012) The use of cone-beam tomography in dentistry. An advisory statement from the American Dental Association Council on Scientific Affairs. J Am Dent Assoc 143:899–902

Bogdanich W, McGinty JC (2010) Radiation worries rise with 3-D dental images. The New York Times Nov 23; Sect. A

Carrafiello G, Dizonno M, Colli V, Strocchi S, Pozzi Taubert S, Leonardi A, Giorgianni A, Barresi M, Macchi A, Bracchi E, Conte L, Fugazzola C (2010) Comparative study of jaws with multislice computed tomography and cone-beam computed tomography. Radiol Med 115:600–611. [Italian]

Claus EB, Calvocoressi L, Bondy ML, Schildkraut JM, Wiemels JL, Wrensch M (2012) Dental x-rays and risk of meningioma. Cancer 118:4530–4537

Consumer Reports Magazine (2015) The surprising dangers of CT scans and X-rays. http://www.consumerreports.org/cro/magazine/2015/01/the-surprising-dangers-of-ct-sans-and-x-rays/index.htm. Accessed 9 Oct 2015

Coppenrath E, Draenert F, Lechel U, Veit R, Meindl T, Reiser M, Mueller-Lisse U (2008) Cross-sectional imaging in dentomaxillofacial diagnostics: dose comparison of dental MSCT and NewTom 9000 DVT. Rofo 180:396–401. [German]

Davies J, Johnson B, Drage NA (2012) Effective doses from cone beam CT investigation of the jaws. Dentomaxillofac Radiol 41:30–36

Deman P, Atwal P, Duzenli C, Thakur Y, Ford NL (2014) Dose measurements for dental cone-beam CT: a comparison with MSCT and panoramic imaging. Phys Med Biol 59:3201–3222

DIN, Deutsches Institut für Normung (2013) Image quality assurance in diagnostic X-ray departments—part 161: RöV acceptance testing of dental radiographic equipment for digital cone-beam computed tomography. Deutsches Institut für Normung, Berlin

EC, European Commission (2004) Radiation protection 136. European guidelines on radiation protection in dental radiology, Luxembourg, Office for Official Publications of the European Communities

EC, European Commission (2012) Radiation protection 172. Cone beam CT for dental and maxillofacial radiology. Evidence-based guidelines. Office for Official Publications of the European Communities, Luxembourg

Faccioli N, Barillari M, Guariglia S, Zivelonghi E, Rizzotti A, Cerini R, Mucelli RP (2009) Radiation dose saving through the use of cone-beam CT in hearing-impaired patients. Radiol Med 114:1308–1318

Feragalli B, Rampado O, Abate C, Macrì M, Festa F, Stromei F, Caputi S, Guglielmi G (2017) Cone beam computed tomography for dental and maxillofacial imaging: technique improvement and low-dose protocols. Radiol Med 122:581–588

Gavala S, Donta C, Tsiklakis K, Boziari A, Kamenopoulou V, Stamatakis HC (2009) Radiation dose reduction in direct digital panoramic radiography. Eur J Radiol 71:42–48

Gijbels F, Jacobs R, Debaveye D, Bogaerts R, Verlinden S, Sanderink G (2005a) Dosimetry of digital panoramic imaging. Part II: occupational exposure. Dentomaxillofac Radiol 34:150–153

Gijbels F, Jacobs R, Bogaerts R, Debaveye D, Verlinden S, Sanderink G (2005b) Dosimetry of digital panoramic imaging. Part I: patient exposure. Dentomaxillofac Radiol 34:145–149

Goren AD, Prins RD, Dauer LT, Quinn B, Al-Najjar A, Faber RD, Patchell G, Branets I, Colosi DC (2013) Effect of leaded glasses and thyroid shielding on cone beam CT radiation dose in an adult female phantom. Dentomaxillofac Radiol 42:20120260

Grunheid T, Kolbeck Schieck JR, Pliska BT, Ahmad M, Larson BE (2012) Dosimetry of a cone-beam computed tomography machine compared with a digital x-ray machine in orthodontic imaging. Am J Orthod Dentofacial Orthop 141:436–443

Hendee WR, Ritenour ER (2002) Medical imaging physics, 4th edn. Wiley-Liss, New York

Hidalgo A, Davies J, Horner K, Theodorakou C (2015) Effectiveness of thyroid gland shielding in dental CBCT using a paediatric anthropomorphic phantom. Dentomaxillofac Radiol 44:20140285

Hirsch E, Wolf U, Heinicke F, Silva MA (2008) Dosimetry of the cone beam computed tomography Veraviewepocs 3D compared with the 3D Accuitomo in different fields of view. Dentomaxillofac Radiol 37:268–273

HPA, Health Protection Agency (2010) Recommendations for the design of X-ray facilities and quality assurance of dental Cone beam CT (Computed tomography) systems. HPA-RPD-065. Health Protection Agency, Chilton

Hujoel P, Hollender LG (2005) More than 5 full-mouth radiographic series increases intracranial meningioma risk. J Evid Based Dent Pract 5:162–163

ICRP (International Commission on Radiological Protection) (1977) Recommendations of the ICRP. ICRP Publication 26. Ann ICRP 1:1–53
ICRP (International Commission on Radiological Protection) (1991) 1990 Recommendations of the International Commission on Radiological Protection: ICRP publication 60. Ann ICRP 21:1–201
ICRP (International Commission on Radiological Protection) (2007) The 2007 Recommendations of the International Commission on Radiological Protection. ICRP publication 103. Ann ICRP 37:1–332
ICRP (International Commission on Radiological Protection) (2012) ICRP statement on tissue reactions and early and late effects of radiation in normal tissues and organs—threshold doses for tissue reactions in a radiation protection context. ICRP publication 118. Ann ICRP 41:1–322
ICRU (International Commission on Radiation Units and Measurements) (2012) Radiation dose and image quality assessment in computed tomography. ICRU Report 87. J ICRU 12:1–149
J. Morita Corp (2015) Effective dose in 3D Veraviewepocs 3D R100. J. Morita Corp., Kyoto, Japan. http://207.38.115.52/dose_en/professional-detail-Vearviewepocs-3DR.php. Accessed 16 May 2016
Jadu F, Yaffe MJ, Lam EW (2010) A comparative study of the effective radiation doses from cone beam computed tomography and plain radiography for sialography. Dentomaxillofac Radiol 39:257–263
Jeong DK, Lee SC, Huh KH, Yi WJ, Heo MS, Lee SS, Choi SC (2012) Comparison of effective dose for imaging of mandible between multi-detector CT and cone-beam CT. Imaging Sci Dent 42:65–70
Kadesjö N, Benchimol D, Falahat B, Näsström K, Shi XQ (2015) Evaluation of the effective dose of cone beam CT and multislice CT for temporomandibular joint examinations at optimized exposure levels. Dentomaxillofac Radiol 44:20150041
Kim DS, Rashsuren O, Kim EK (2014) Conversion coefficients for the estimation of effective dose in cone-beam CT. Imaging Sci Dent 44:21–29
Koivisto J, Schulze D, Wolff J, Rottke D (2014) Effective dose assessment in the maxillofacial region using thermoluminescent (TLD) and metal oxide semiconductor field-effect transistor (MOSFET) dosemeters: a comparative study. Dentomaxillofac Radiol 43(8):20140202
Librizzi ZT, Tadinada AS, Valiyaparambil JV, Lurie AG, Mallya SM (2011) Cone-beam computed tomography to detect erosions of the temporomandibular joint: effect of field of view and voxel size on diagnostic efficacy and effective dose. Am J Orthod Dentofacial Orthop 140:e25–e30
Lofthag-Hansen S, Thilander-Klang A, Ekestubbe A, Helmrot E, Gröndahl K (2008) Calculating effective dose on a cone beam computed tomography device: 3D Accuitomo and 3D Accuitomo FPD. Dentomaxillofac Radiol 37:72–79
Longstreth WT Jr, Phillips LE, Drangsholt M, Koepsell TD, Custer BS, Gehrels JA, van Belle G (2004) Dental X-rays and the risk of intracranial meningioma: a population-based case-control study. Cancer 100:1026–1034
Loubele M, Jacobs R, Maes F, Schutyser F, Debaveye D, Bogaerts R, Coudyzer W, Vandermeulen D, van Cleynenbreugel J, Marchal G, Suetens P (2005) Radiation dose vs. image quality for low-dose CT protocols of the head for maxillofacial surgery and oral implant planning. Radiat Prot Dosimetry 117:211–216
Loubele M, Bogaerts R, Van Dijck E, Pauwels R, Vanheusden S, Suetens P et al (2009) Comparison between effective radiation dose of CBCT and MSCT scanners for dentomaxillofacial applications. Eur J Radiol 71:461–468
Ludlow JB (2011) A manufacturer's role in reducing the dose of cone beam computed tomography examinations: effect of beam filtration. Dentomaxillofac Radiol 40:115–122
Ludlow JB, Ivanovic M (2008) Comparative dosimetry of dental CBCT devices and 64-slice CT for oral and maxillofacial radiology. Oral Surg Oral Med Oral Pathol Oral Radiol Endod 96:930–938
Ludlow JB, Walker C (2013) Assessment of phantom dosimetry and image quality of i-CAT FLX cone-beam computed tomography. Am J Orthod Dentofacial Orthop 144:802–817
Ludlow JB, Davies-Ludlow LE, Brooks SL, Howerton WB (2006) Dosimetry of 3 CBCT devices for oral and maxillofacial radiology: CB Mercuray, NewTom 3G and i-CAT. Dentomaxillofac Radiol 35:219–226
Ludlow JB, Davies-Ludlow LE, White SC (2008) Patient risk related to common dental radiographic examinations: the impact of 2007 International Commission on Radiological Protection recommendations regarding dose calculation. J Am Dent Assoc 139:1237–1243
Ludlow JB, Timothy R, Walker C, Hunter R, Benavides E, Samuelson DB, Scheske MJ (2015) Effective dose of dental CBCT- a meta-analysis of published data and additional data for nine CBCT units. Dentomaxillofac Radiol 44:20140197
Lukat TD, Wong JC, Lam EW (2013) Small field of view cone beam CT temporomandibular joint imaging dosimetry. Dentomaxillofac Radiol 42:20130082
Martin CJ (2007) Effective dose: how should it be applied to medical exposures? Br J Radiol 80:639–647
Morant JJ, Salvado M, Hernandez-Giron I, Casanovas R, Ortega R, Calzado A (2013) Dosimetry of a cone beam CT device for oral and maxillofacial radiology using Monte Carlo techniques and ICRP adult reference computational phantoms. Dentomaxillofac Radiol 42:92555893
Mori S, Endo M, Nishizawa K, Tsunoo T, Aoyama T, Fujiwara H, Murase K (2005) Enlarged longitudinal dose profiles in cone-beam CT and the need for modified dosimetry. Med Phys 32:1061–1069
NCRP (National Council on Radiation Protection and Measurements) (1990) Implementation of the principle of As Low As Reasonably Achievable (ALARA) for medical and dental personnel (Report No. 107). NCRP Publication, Bethesda

NCRP (National Council on Radiation Protection and Measurements) (2003) Radiation protection in dentistry (Report No. 145). NRCP Publications, Bethesda

NCRP (National Council on Radiation Protection and Measurements) (2017) Radiation protection in dentistry and oral and maxillofacial imaging (Report No. 177). NRCP Publications, Bethesda [In Press]

NRC (National Research Council of the National Academies) (2006) Health risks from exposure to low levels of ionizing radiation: BEIR VII—phase 2. The National Academies Press, Washington, DC

Okano T, Harata Y, Sugihara Y, Sakaino R, Tsuchida R, Iwai K et al (2009) Absorbed and effective doses from cone beam volumetric imaging for implant planning. Dentomaxillofac Radiol 38:79–85

Okano T, Matsuo A, Gotoh K, Yokoi M, Hirukawa A, Okumura S et al (2012) Comparison of absorbed and effective dose from two dental cone beam computed tomography scanners. Nihon Hoshasen Gijutsu Gakkai Zasshi 68:216–25 [Japanese]

Palomo JM, Rao PS, Hans MG (2008) Influence of CBCT exposure conditions on radiation dose. Oral Surg Oral Med Oral Pathol Oral Radiol Endod 105:773–782

Pauwels R, Beinsberger J, Collaert B, Theodorakou C, Rogers J, Walker A, Cockmartin L, Bosmans H, Jacobs R, Bogaerts R, Horner K, SEDENTEXCT Project Consortium (2012a) Effective dose range for dental cone beam computed tomography scanners. Eur J Radiol 81:267–271

Pauwels R, Theodorakou C, Walker A, Bosmans H, Jacobs R, Horner K, Bogaerts R, SEDENTEXCT Project Consortium (2012b) Dose distribution for dental cone beam CT and its implication for defining a dose index. Dentomaxillofac Radiol 41:583–593

Pauwels R, Cockmartin L, Ivanauskaitė D, Urbonienė A, Gavala S, Donta C, Tsiklakis K, Jacobs R, Bosmans H, Bogaerts R, Horner K, SEDENTEXCT Project Consortium (2014a) Estimating cancer risk from dental cone-beam CT exposures based on skin dosimetry. Phys Med Biol 59:3877–3891

Pauwels R, Silkosessak O, Jacobs R, Bogaerts R, Bosmans H, Panmekiate S (2014b) A pragmatic approach to determine the optimal kVp in cone beam CT: balancing contrast-to-noise ratio and radiation dose. Dentomaxillofac Radiol 43:20140059

Pauwels R, Zhang G, Theodorakou C, Walker A, Bosmans H, Jacobs R, Bogaerts R, Horner K, SEDENTEXCT Project Consortium (2014c) Effective radiation dose and eye lens dose in dental cone beam CT: effect of field of view and angle of rotation. Br J Radiol 87:20130654

Pauwels R, Jacobs R, Bogaerts R, Bosmans H, Panmekiate S (2016) Determination of size-specific exposure settings in dental cone-beam CT. Eur Radiol 27(1):279–285

Qu XM, Li G, Ludlow JB, Zhang ZY, Ma XC (2010) Effective radiation dose of ProMax 3D cone-beam computerized tomography scanner with different dental protocols. Oral Surg Oral Med Oral Pathol Oral Radiol Endod 110:770–776

Qu XM, Li G, Zhang ZY, Ma XC (2011) Comparative dosimetry of dental cone-beam computed tomography and multi-slice computed tomography for oral and maxillofacial radiology. Chin J Stomatol:46, 595–599. [Chinese]

Qu XM, Li G, Sanderink GC, Zhang ZY, Ma XC (2012a) Dose reduction of cone beam CT scanning for the entire oral and maxillofacial regions with thyroid collars. Dentomaxillofac Radiol 41:373–378

Qu XM, Li G, Zhang Z, Ma X (2012b) Thyroid shields for radiation dose reduction during cone beam computed tomography scanning for different oral and maxillofacial regions. Eur J Radiol 81:e376–e380

Rampado O, Bianchi SD, Peruzzo Cornetto A, Rossetti V, Ropolo R (2014) Radiochromic films for dental CT dosimetry: a feasibility study. Phys Med 30:18–24

Richards AG, Barbor GL, Bader JD, Hale JD (1970) Samarium filters for dental radiography. Oral Surg Oral Med Oral Pathol 29:704–715

Roberts JA, Drage NA, Davies J, Thomas DW (2009) Effective dose from cone beam CT examinations in dentistry. Br J Radiol 82:35–40

Rottke D, Patzelt S, Poxleitner P, Schulze D (2013) Effective dose span of ten different cone beam CT devices. Dentomaxillofac Radiol 42:20120417

Schilling R, Geibel MA (2013) Assessment of the effective doses from two dental cone beam CT devices. Dentomaxillofac Radiol 42:20120273

SEDENTEXCT (2010) Deliverable 2.2: Completion of scatter dose measurements around CBCTs and recommendations for protective measures and positioning of CBCT units in dental offices. http://www.sedentexct.eu/system/files/SEDENTEXCT%20D2.2%20v1%20FINAL_0.pdf (checked on 18 Aug 2015)

Sezgin OS, Kayipmaz S, Yasar D, Yilmaz AB, Ozturk MH (2012) Comparative dosimetry of dental cone beam computed tomography, panoramic radiography, and multislice computed tomography. Oral Radiol 28:32–37

Silva MA, Wolf U, Heinicke F, Bumann A, Visser H, Hirsch E (2008) Cone-beam computed tomography for routine orthodontic treatment planning: a radiation dose evaluation. Am J Orthod Dentofacial Orthop 133:640.e1–640.e5

Suomalainen A, Kiljunen T, Käser Y, Peltola J, Kortesniemi M (2009) Dosimetry and image quality of four dental cone beam computed tomography scanners compared with multislice computed tomography scanners. Dentomaxillofac Radiol 38:367–378

Sutton DG, Williams JR (2000) Radiation shielding for diagnostic X-rays: report of a Joint BIR/IPEM Working Party. British Institute of Radiology, London

Tetradis S, White SC, Service SK (2012) Dental x-rays and risk of meningioma; the jury is still out. J Evid Based Dent Pract 12:174–177

Theodorakou C, Walker A, Horner K, Pauwels R, Bogaerts R, Jacobs R, SEDENTEXCT Project Consortium (2012) Estimation of paediatric organ and effective doses from dental cone beam CT using anthropomorphic phantoms. Br J Radiol 85:153–160

Tsiklakis K, Donta C, Gavala S, Karayianni K, Kamenopoulou V, Hourdakis CJ (2005) Dose reduction in maxillofacial imaging using low dose Cone beam CT. Eur J Radiol 56:413–417

Vassileva J, Stoyanov D (2010) Quality control and patient dosimetry in dental cone beam CT. Radiat Prot Dosimetry 139:310–312

White SC, Hildebolt CF, Lurie AG (2013) Dental x-rays and risk of meningioma. Cancer 119:464

Xu J, Reh DD, Carey JP, Mahesh M, Siewerdsen JH (2012) Technical assessment of a cone-beam CT scanner for otolaryngology imaging: image quality, dose, and technique protocols. Med Phys 39:4932–4942

Zhang G, Marshall N, Jacobs R, Liu Q, Bosmans H (2013) Bowtie filtration for dedicated cone beam CT of the head and neck: a simulation study. Br J Radiol 86(1028):20130002

Part III

Regional Maxillofacial Imaging

9 The Skull

William C. Scarfe and Christos Angelopoulos

Contents

W.C. Scarfe, B.D.S., F.R.A.C.D.S., M.S. (✉)
Division of Radiology and Imaging Science, Department of Surgical/Hospital Dentistry, University of Louisville School of Dentistry, Louisville, KY, USA
e-mail: william.scarfe@louisville.edu

C. Angelopoulos, D.D.S., M.S.
Aristotle University of Thessaloniki, Thessaloniki, Greece

Columbia University, College of Dental Medicine, New York City, NY, USA
e-mail: angelopoulosc@gmail.com

9.1 Overview of the Anatomy of the Skull

The skull comprises 22 individual bones, grouped into two functional elements.

- **The cranium** (**neurocranium).** The cranium encloses and protects the brain and comprises eight bones (Figs. 9.1 and 9.2).
  - *Occipital Bone.* A single occipital bone forms the posterior and inferior portion of the base of the cranium. It provides access of the spinal column to the brain stem and brain through the foramen magnum. It articulates inferiorly with the first cervical vertebrae, called C1 or the Atlas, via the atlanto-occipital articulation, the parietal bones bilaterally postero-superiorly via the lambdoid suture and the temporal bones antero-laterally.
  - *Temporal Bones.* The paired but separated (left and right) temporal bones form the lateral walls of the cranium, the lateral part of the base of the middle cranial fossa, and the external ear. The temporal bones consist of four anatomic regions including the squamous, mastoid, petrous, and tympanic. Structurally the temporal bone develops the glenoid fossa, which articulates with the condylar head of the mandible. The temporal bones also articulate with the occipital bone posteriorly (occipitomastoid

W.C. Scarfe, C. Angelopoulos (eds.), *Maxillofacial Cone Beam Computed Tomography*,
https://doi.org/10.1007/978-3-319-62061-9_9

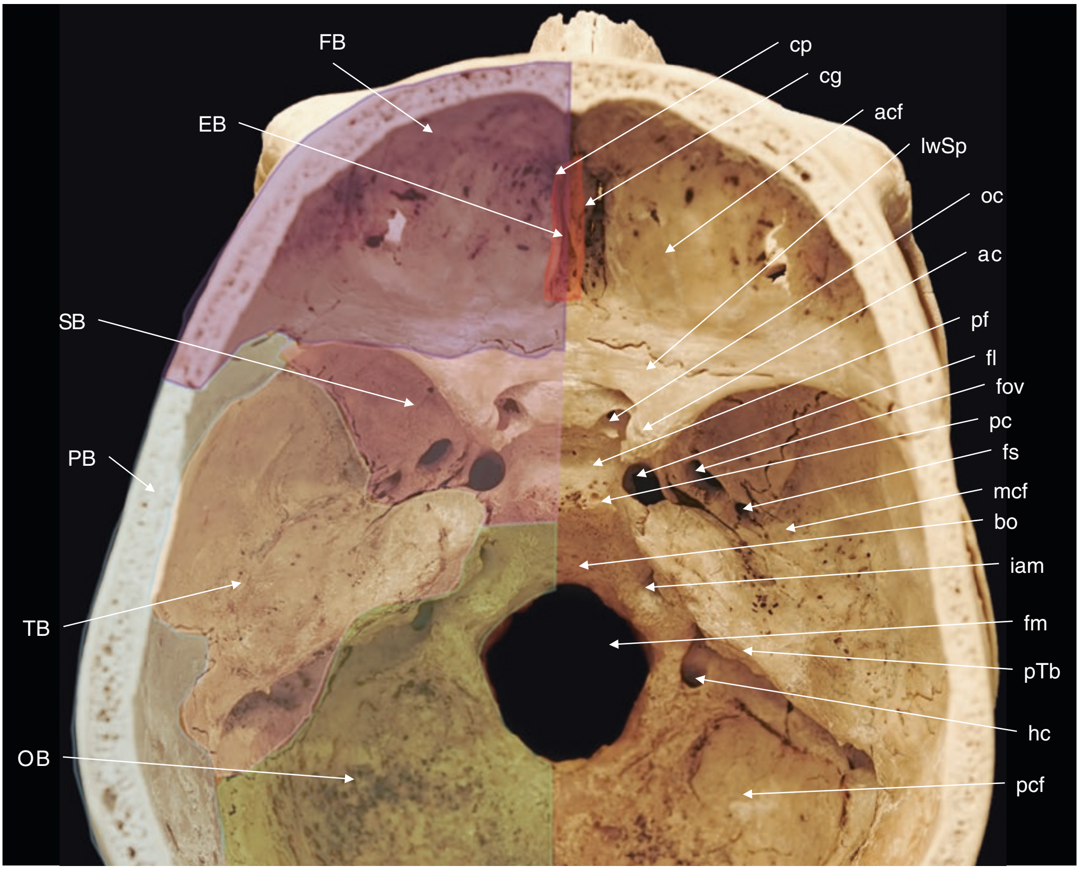

Fig. 9.1 Superior view of the cranial with component bones shaded and identified (*left*) and important anatomical features and foraminae identified (*right*) (*FB* frontal bone, *EB* ethmoid bone, *SB* sphenoid bone, *PB* parietal bone, *TB* temporal bone, *OB* occipital bone, *Cp* cribriform plate of the ethmoid, *cg* crista galli, *acf* anterior cranial fossa, *lwSp* lesser wing of the sphenoid bone, *oc* optic canal, *ac* anterior clinoid, *pf* pituitary fossa, *fl* foramen lacerum, *fov* foramen ovale, *pc* posterior clinoid, *fs* foramen spinosum, *mcf* middle cranial fossa, *bo*, basilar portion of the occipital bone, *iam* internal auditory meatus, *fm* foramen magnum, *pTb* petrous portion of the temporal bone, *hc* hypoglossal canal, *pcf* posterior cranial fossa)

suture), parietal bones laterally (squamosal suture), and anteriorly with the sphenoid bone centrally (sphenosquamosal suture) and zygomatic bone laterally (zygomatico-temporal suture)

– *Parietal Bones.* The paired (left and right) parietal bones form most of the superior and lateral portions of the cranium. They articulate at the vertex of the cranium via the sagittal suture, anteriorly with the frontal bone via the coronal suture, and posteriorly with the occipital bone via the lambdois suture.
– *Sphenoid Bone.* The sphenoid bone is the most central bone of the cranium and forms anterior portion of the cranial base and the posterior vertex of the orbit. It is the most morphologically variable bone of the cranium, being the “linchpin” of the cranial base, articulating in the anteriorly with the

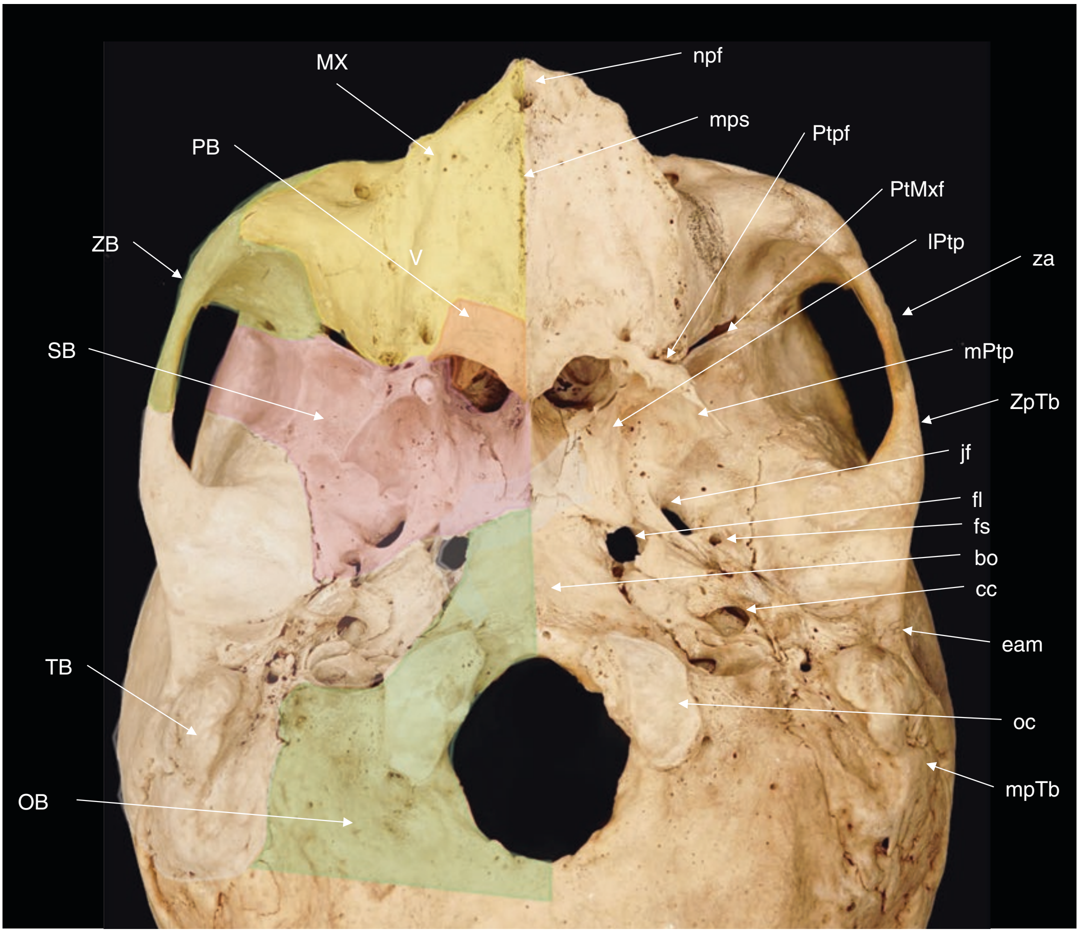

Fig. 9.2 Inferior view of the cranial with component bones shaded and identified (*left*) and important anatomical features and foraminae identified (*right*) (*MX* maxilla, *PB* palatine bone, *SB* sphenoid bone, *ZB* zygomatic bone, *TB* temporal bone, *OB* occipital bone, *Npf* nasopalatine fossa, *mps* median palatine suture, *Ptpf* pterygopalatine fossa, *ptMxf* pterygomaxillary fissure, *lPtp* lateral pterygoid plate, *za* zygomatic arch, *mPtp* medial pterygoid plate, *ZpTb* zygomatic process of the temporal bone, *jf* jugular foramen, *fl* foramen lacerum, *fs* foramen spinosum, *bo* basal portion of the occipital bone, *cc* carotid canal, *eam* external auditory meatus, *oc* occipital condyle, *mpTb* mastoid process of the temporal bone)

frontal, ethmoid and palatine bones centrally and laterally with the maxillary and zygomatic bones. Posteriorly the sphenoid bone articulates with the occipital bone centrally and temporal bone laterally.

– *Ethmoid Bone.* The ethmoid bone forms the medial portions of the orbit and roof of the nasal cavity, separating it from the cranial vault. From the superior view, the ethmoid bone articulates with the frontal bone laterally and sphenoid bone posteriorly, whereas from a frontal projection it articulates with the nasal bone anteriorly and maxilla inferiorly.
– *Frontal Bone.* The frontal bone is a single bone that forms the anterior part of the

cranial cavity including the forehead and supraciliary arches (brow). Superiorly the frontal bone acts as the base of the anterior cranial fossa and inferiorly comprises the uppermost extension of the orbit and nasal cavity.

- **Facial skeleton (viscerocranium).** The 14 facial bones makeup the lower portion of the orbit (Fig. 9.3) and upper and lower (Fig. 9.4) jaws. All the facial bones are paired, except for the mandible and the vomer in the midline of the nasal cavity.
  - *Mandible.* The mandible is the lower jaw and articulates with the glenoid fossa of the temporal bone via the mandibular condylar head. This forms the only freely moveable joint in the skull.
  - *Maxilla.* The left and right maxillae comprise the upper jaw and the key bone of the midface. They fuse in the midline and articulate with the palatine bones posteriorly, the nasal and lacrimal bones superiorly, and the zygomatic bones laterally. They contain the maxillary sinuses and form part of the nose, orbits, and roof of the mouth.
  - *Palatine bones.* The left and right palatine bones project posteriorly from the maxilla as a horizontal plate to form the posterior hard palate and provide extensions superiorly to form the posterior portion of the nasal cavity.

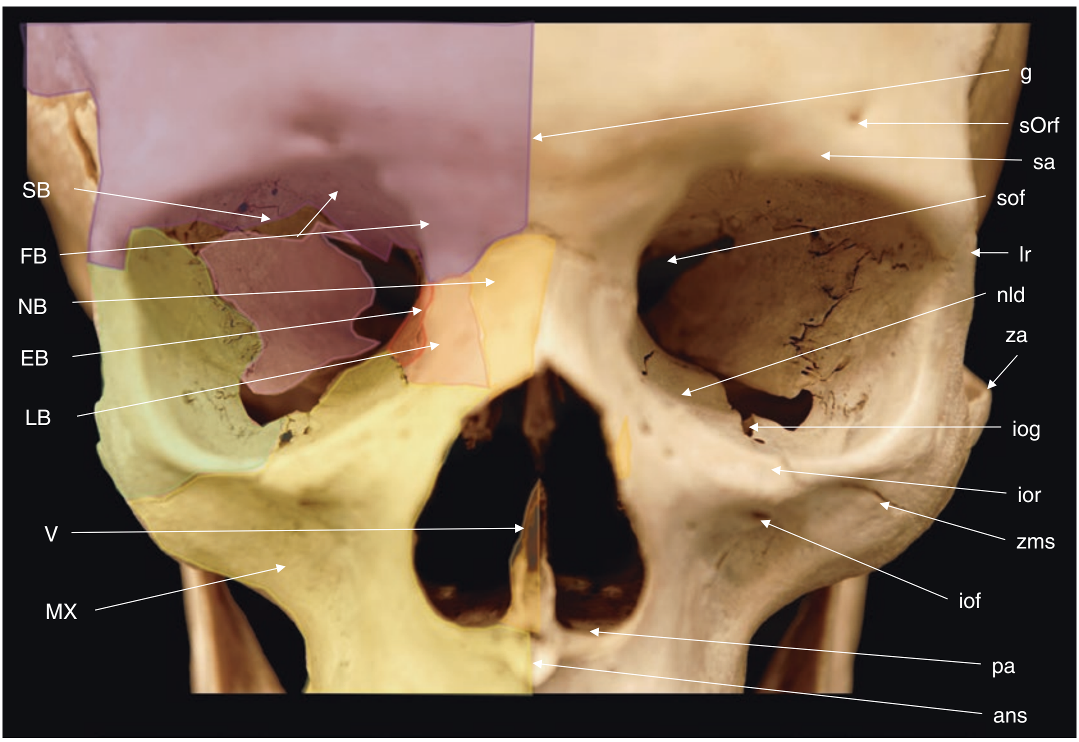

Fig. 9.3 Anterior view of the midface with component bones shaded and identified (*left*) and important anatomical features and foraminae identified (*right*) (*SB* sphenoid bone, *FB* frontal bone, *NB* nasal bone, *EB* ethmoid bone, *LB* lacrimal bone, *V* vomer, *MX* maxilla, *g* glabella, *sOrf* supra-orbital foramen, *sa* superciliary arch, *sof* superior orbital fissure, *lr* lateral rim of the orbit, *nld* nasolacrimal duct, *za* zygomatic arch, *iog* infra orbital groove/canal, *ior* infra orbital rim, *zms* zygomaticomaxillary suture, *iof* infraorbital foramen, *pa* pyriform aperture, *ans* anterior nasal spine)

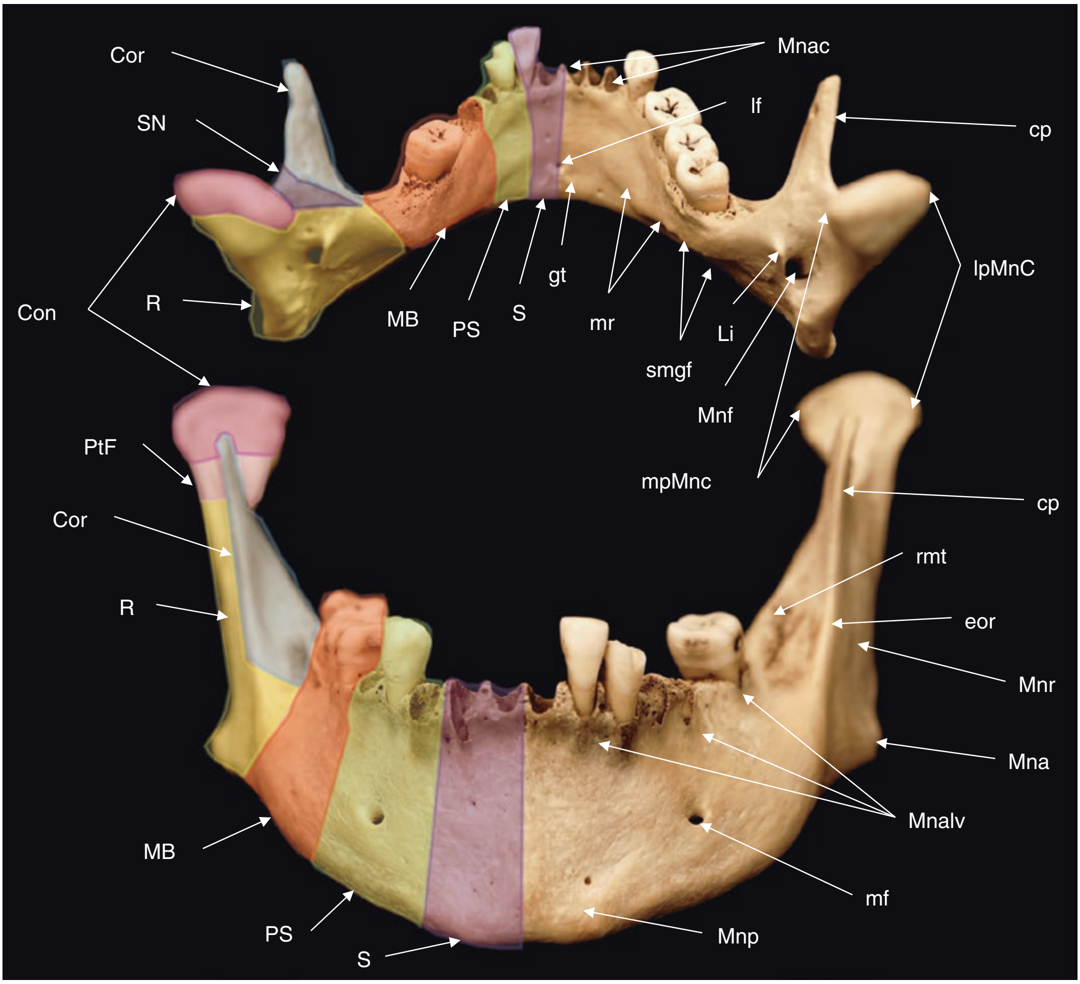

Fig. 9.4 Posterior (*upper*) and anterior (*lower*) view of the mandible with mandibular regions shaded and identified (*left*) and important anatomical features and foraminae identified (*right*) (*S* symphysis, *PS* parasymphysis, *MB* mandibular body, *R* ramus, *Cor* coronoid process, *PtF* pterygoid fovea, *Con* condyle, *SN* sigmoid notch, *Mnac* mandibular alveolar crest, *lf* lingual foramen, *cp* coronoid process, *lpMnc* lateral pole of the mandibular condyle, *mpMnc* medial pole of the mandibular condyle, *Mnf* mandibular foramen, *li* lingula, *smgf* submandibular gland fossa, *mr* mylohyoid ridge/internal oblique ridge, *gt* genial tubercles, *rmt* retromolar trigone, *eor* external oblique ridge, *Mnr* mandibular ramus, *Mna* angle of the mandibular body, *Mnalv* mandibular alveolus, *mf* mandibular foramen, *Mnp*, mandibular protuberance)

– *Zygomatic Bones.* The left and right zygomatic bones attach the maxilla to the frontal and temporal bones of the neurocranium. They also form the infero-lateral portions of the orbits.
– *Nasal bones.* The left and right nasal bones articulate with each other in the midline and comprise the superior portion of the bridge of the nose. They articulate with the lacrimal bones posteriorly and the maxilla inferiorly.
– *Lacrimal bones.* The left and right lacrimal bones articulate with the nasal bones anteriorly, the frontal bone superiorly, the ethmoid bone medially, and the maxilla

inferiorly to comprise part of the lateral portion of the medial wall of the orbit.

– *Inferior conchae.* These bones are most oftern referred to as the inferior turbinates when covered with nasal mucosa. They arise from the medial wall of the maxillary sinus and function physiologically to increase the surface area of the nasal cavity.
– *Vomer.* The vomer is a flat singular midline quadrilateral plate forming the posterior aspect of the nasal septum arising adjacent to the junction of the maxillae and articulating with the ethmoid bone anterosuperiorly, the palatine bone postero-superiorly, and sphenoid posteriorly.

9.2 Topographic Skull Anatomy

All of the bones of the skull in the adult, with the exception of the mandible, are connected by immobile, fibrous joints called sutures. These are named by location (sagittal and coronal), shape (e.g., lambdoid), or the bone surfaces (e.g., squamous).

Figures 9.5, 9.6, 9.7, and 9.8 depict the bones, sutures and important topographic features and foraminae of the cranium and facial skeleton as seen from the frontal (Fig. 9.5), lateral (Fig. 9.6), inferior (Fig. 9.7), and superior (Fig. 9.8) aspects.

9.3 Orthogonal Radiographic Anatomy

Orthogonal maxillofacial CBCT images of the skull in the axial, coronal, and sagittal planes often provide the practitioner with the first images displaying the volumetric dataset. Medical and oral and maxillofacial radiologists are familiar with correlating known skull osteology with orthogonal image presentation. The expansion of CBCT technology into general and specialist dental practice demands that dental professionals appreciate the complex bony interrelationships and anatomic features presented in these images. Since orthogonal

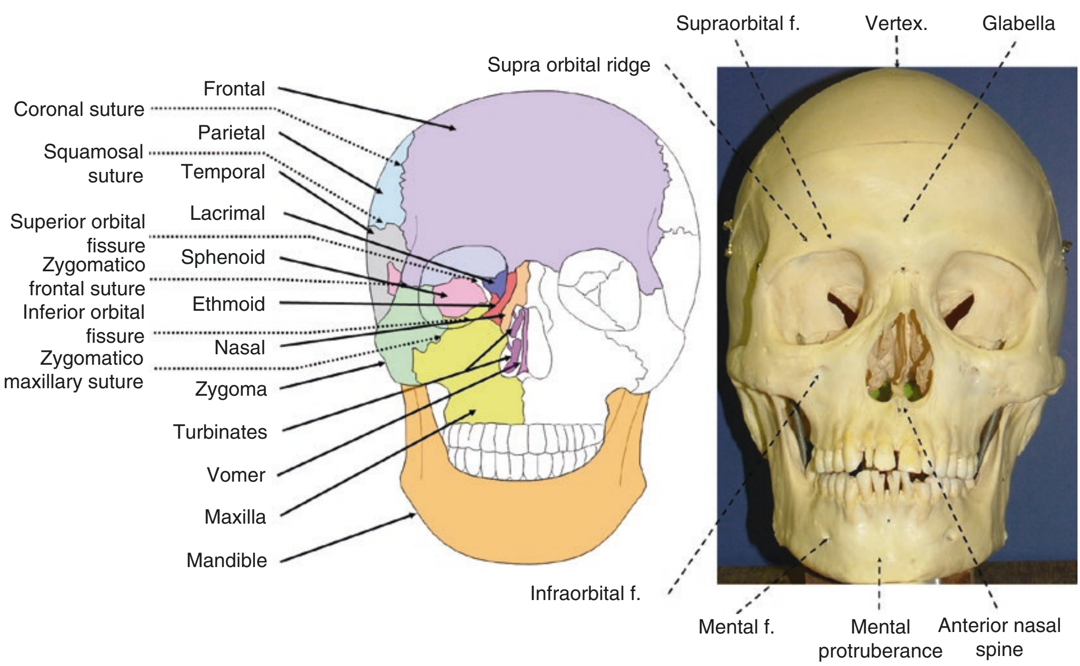

Fig. 9.5 Schematic (*left*) and actual (*right*) anterior posterior projection of the skull showing the component bones, sutures and important topographic features and foraminae of the cranium and facial skeleton

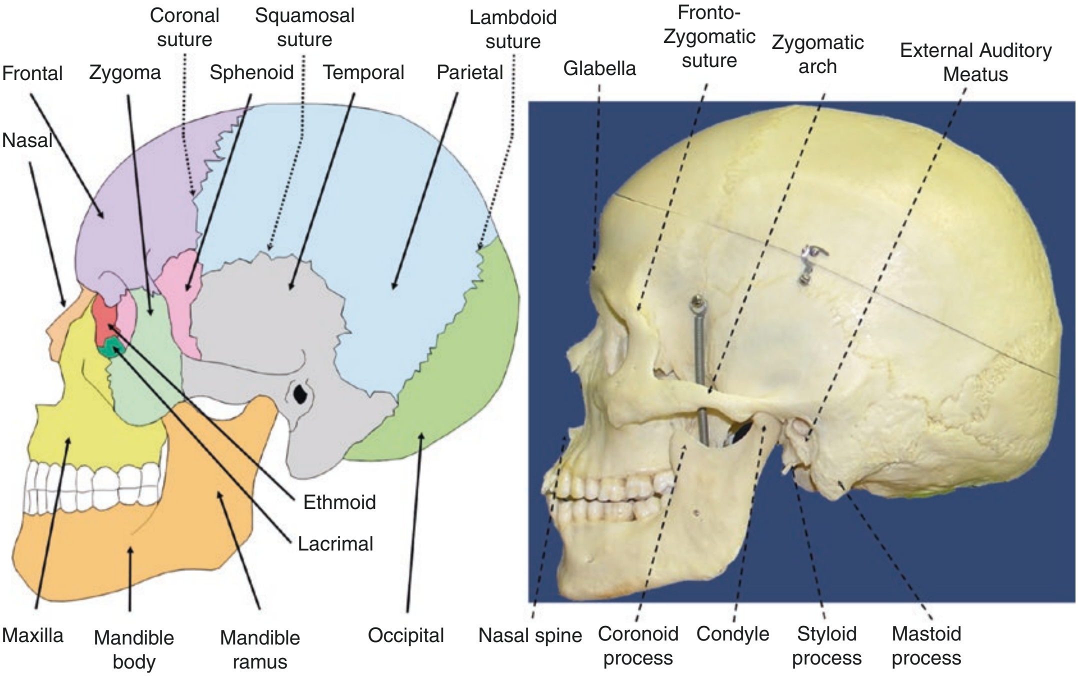

Fig. 9.6 Schematic (*left*) and actual (*right*) left lateral projection of the skull showing the component bones, sutures and important topographic features and foraminae of the cranium and facial skeleton

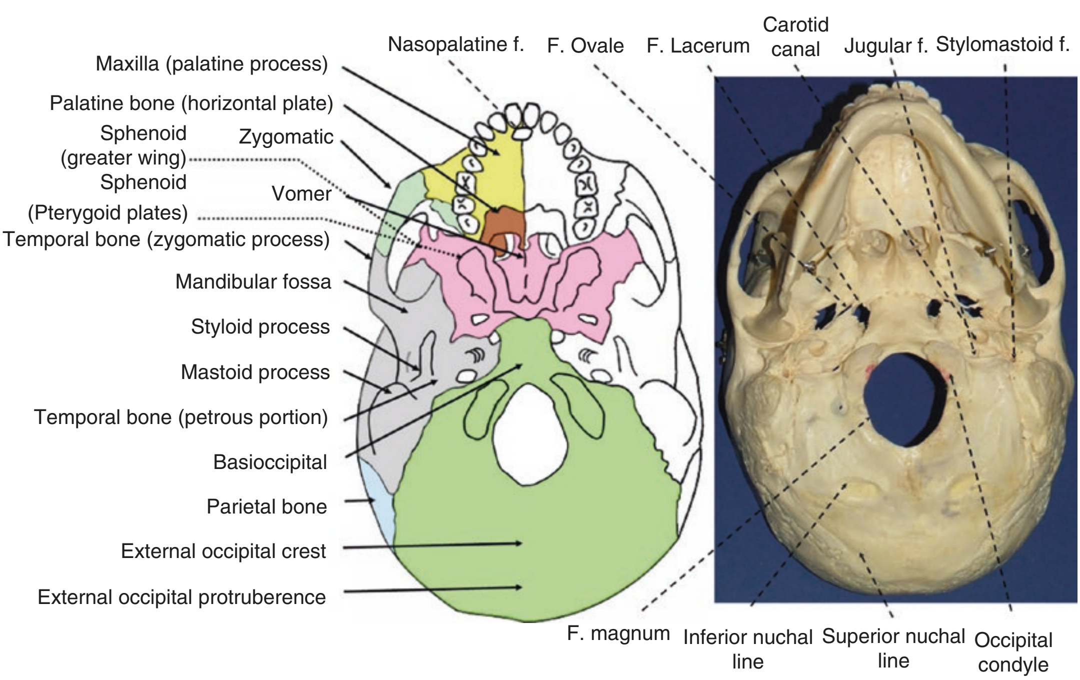

Fig. 9.7 Schematic (*left*) and actual (*right*) inferior projection of the skull showing the component bones, sutures and important topographic features and foraminae of the cranium and facial skeleton

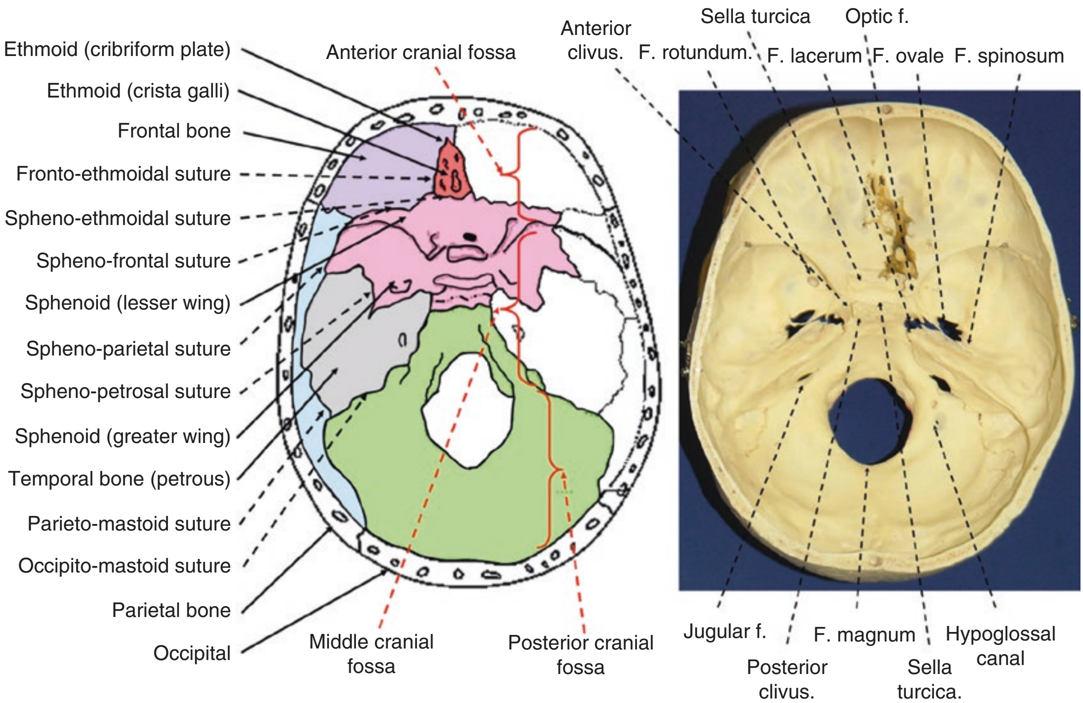

Fig. 9.8 Schematic (*left*) and actual (*right*) superior cranial projection of the skull showing the component bones, sutures and important topographic features and foraminae of the cranium and facial skeleton

sections demonstrate sub-millimeter resolution, the same anatomy is often shown on several consecutive "slices," with each section presenting the feature from a slightly different perspective. As practitioners navigate through each plane of the volume by scrolling sequential images, specific regions should be considered and anatomic features identified. Figures 9.9, 9.10, 9.11, 9.12, 9.13, 9.14, 9.15, 9.16, 9.17, 9.18, 9.19, 9.20, 9.21, 9.22, 9.23, 9.24, 9.25, 9.26, 9.27, 9.28, 9.29, 9.30, 9.31, 9.32, 9.33, 9.34, 9.35, 9.36, 9.37, and 9.38 show representative axial, coronal, and sagittal orthogonal images and identify the significant bones and structures in each plane within specific regions.

9.3.1 Axial

Images in the axial orthogonal plane demonstrate a continuum of anatomy extending from the supraorbital region of the frontal bone to the hyoid bone and vertebral bodies of the third cervical vertebrae.

9.3.1.1 Supra-Orbital

Axial images demonstrate the frontal, lateral, and posterior bony confines of the cranial vault, the frontal sinus, and cribriform plate of the ethmoid bone (Fig. 9.9).

9.3.1.2 Orbital

Images at various levels (Figs. 9.10, 9.11, and 9.12) caudally from the junction between the frontal and nasal bones—nasion—to the infraorbital rim show the increasing central prominence of the ethmoid bone anteriorly and sphenoid bone posteriorly as well as the temporal bones laterally.

9.3.1.3 Maxillary Sinus

Images at various levels (Figs. 9.13 and 9.14) caudally from the roof to the floor of the maxillary sinuses show the anterior prominence of the maxillary sinuses and zygomatic bones laterally, absence of the ethmoid bone, and increasing contribution of the temporal bones laterally compared with the sphenoid bone to the skull base. More

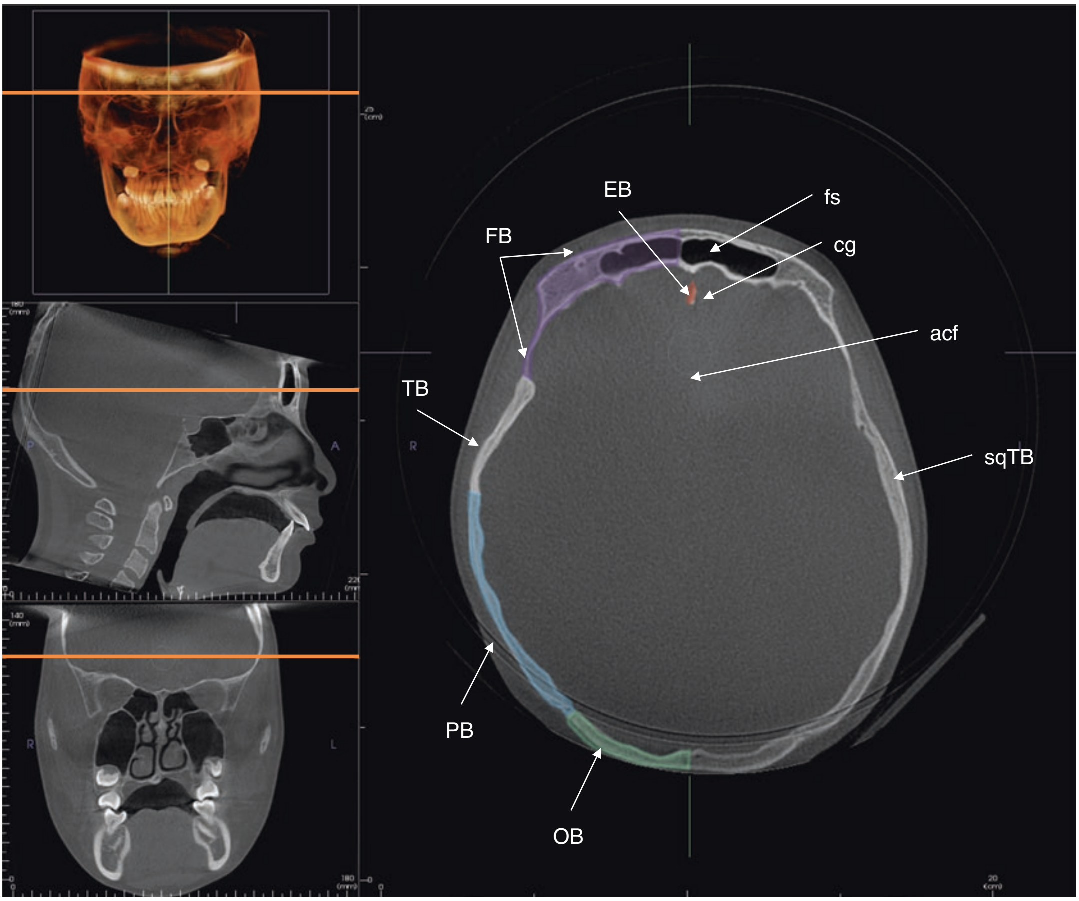

Fig. 9.9 Axial orthogonal CBCT image at the supra-orbital level (*right*) with frontal volumetric rendering (*upper left*), midsagittal (*middle left*), and coronal (*lower left*) reference images (*FB* frontal bone, *TB* temporal bone, *OB* occipital bone, *PB* parietal bone, *EB* ethmoid bone, *fs* frontal sinus, *CG* crista galli, *acf* anterior cranial fossa, *sqTB* squamous portion of the temporal bone)

inferior images introduce the basilar portion of the occipital bone and condylar head of the mandible.

9.3.1.4 Mandibular Ramus

Images at various levels (Figs. 9.15 and 9.16) caudally from the floor of the maxillary sinus and sigmoid notch to the lingula of the mandible show the anterior prominence of the maxillary dentition, oropharyngeal airway space, occipital condyles and first two cervical vertebrae centrally and ramus of the mandible laterally.

9.3.1.5 Mandibular Body

Topographically the mandible is a simple facial bone with numerous regions and easily identifiable anatomic features (Fig. 9.17). Images at various levels (Figs. 9.18, 9.19, and 9.20) caudally from the lingula of the ramus to the lower border of the mandible show the body of the ramus, oropharyngeal airway space, and the upper three cervical vertebrae.

9.3.2 Coronal

Images in the coronal orthogonal plane demonstrate facial and cranial anatomy extending from supraciliary arches of the frontal bone and mental protuberance of the mandibular symphysis to the occipital condyles of the occipital

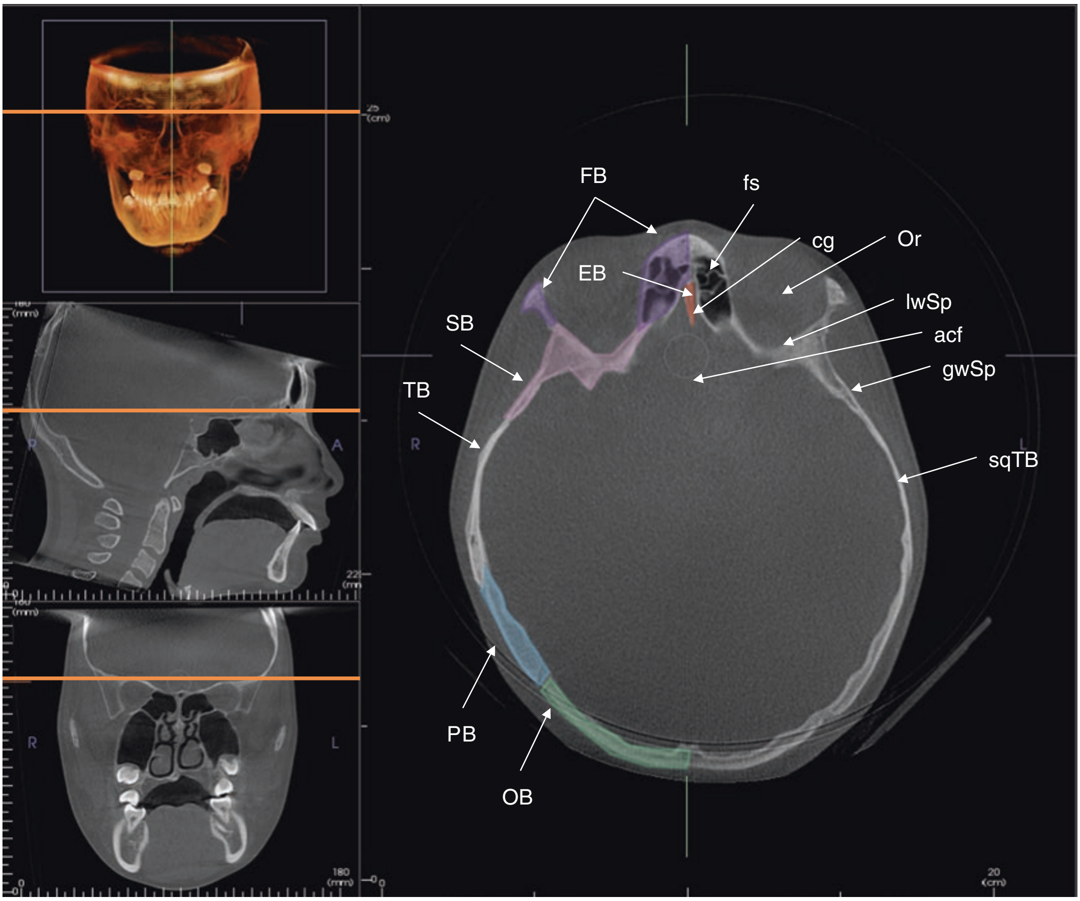

Fig. 9.10 Axial orthogonal CBCT image at the superior-orbital level (*right*) with frontal volumetric rendering (*upper left*), midsagittal (*middle left*), and coronal (*lower left*) reference images. (*FB* frontal bone, *EB* ethmoid bone, *SB* sphenoid bone, *TB* temporal bone, *PB* parietal bone, *OB* occipital bone, *fs* frontal sinus, *cg* crista galli, *Or* orbit, *lwSp* lesser wing of the sphenoid bone, *acf* anterior cranial fossa, *gwSp* greater wing of the sphenoid bone, *sqTB* squamous portion of the temporal bone)

bone and anterior processes of the cervical vertebrae.

9.3.2.1 Frontal Bone/Mental Protuberance to Infraorbital Rim

Images at various levels (Figs. 9.21, 9.22, and 9.23) dorsally from the glabella of the frontal bone or mental protuberance of the mandible to the lateral aspect of the orbit gradually depict, in order, the frontal sinus superiorly and nasal cavity centrally, the orbit and maxillary sinuses laterally and finally the ethmoid bone centrally and lateral orbital aspect of the zygomatic bone.

9.3.2.2 Lateral Orbital Rim/Ostiomeatal Complex

Images at various levels (Figs. 9.24, 9.25 and 9.26) dorsally from the infraorbital rim to the temporal process of the zygomatic bone show the anatomy of the ostimeatal complex, anterior cranial fossa and features of the premolar region of the maxilla and mandible including the mental foramen and hard palate.

9.3.2.3 Posterior Orbit to Posterior Choanae

Images at various levels (Figs. 9.27, 9.28, and 9.29) dorsal from the temporal process of the zygomatic

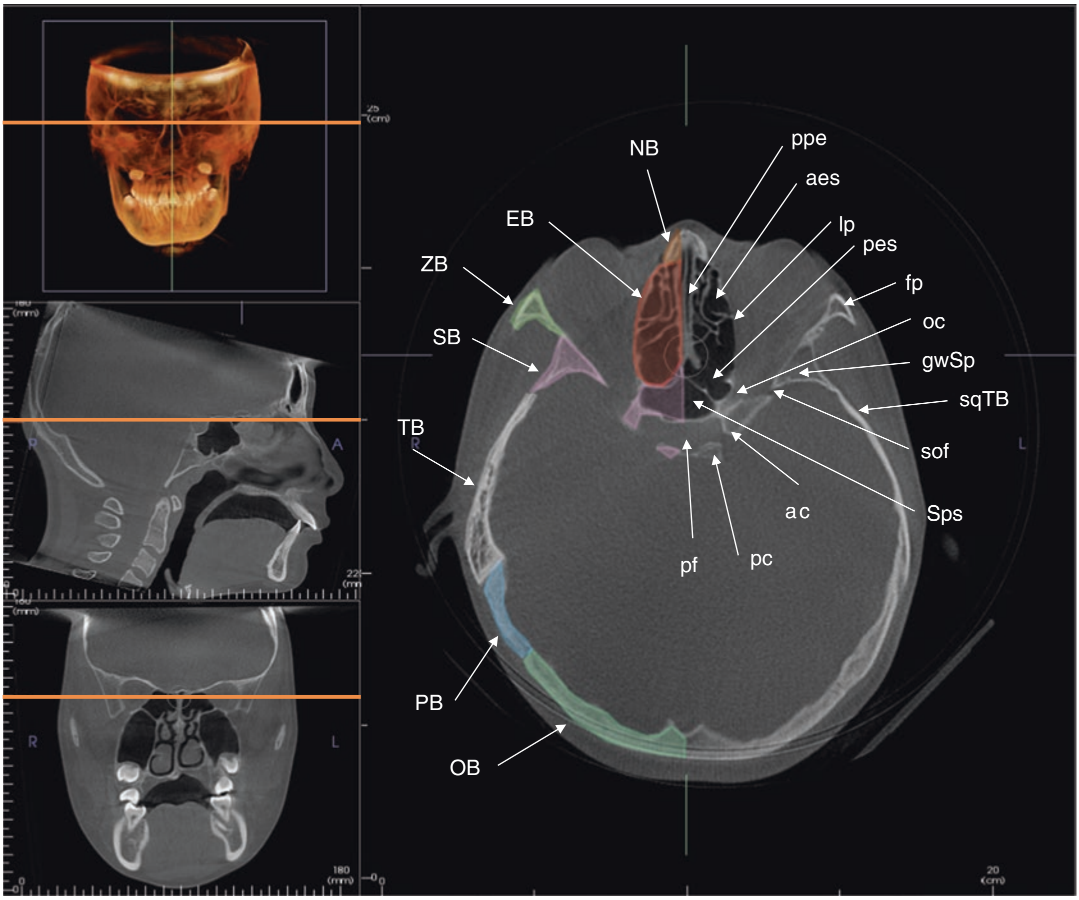

Fig. 9.11 Axial orthogonal CBCT image at the mid-orbital level (*right*) with frontal volumetric rendering (*upper left*), midsagittal (*middle left*), and coronal (*lower left*) reference images. (*NB* nasal bone, *EB* ethmoid bone, *ZB* Zygomatic bone, *SB* sphenoid bone, *TB* temporal bone, *PB* parietal bone, *OB* occipital bone, *ppe* perpendicular plate of the ethmoid, *aes* anterior ethmoid sinus, *lp* lamina papyracea, *pes* posterior ethmoid sinus, *fp* frontal process of the zygomatic bone, *oc* optic canal, *gwSp* greater wing of the sphenoid bone, *sqTb* squamous portion of the temporal bone, *sof* superior orbital fissure, *Sps* sphenoid sinus, *ac* anterior clinoid, *pc* posterior clinoid, *pf* pituitary fossa/dorsum sella/hypophyseal fossa)

bone to the posterior choanae show an increasing contribution to the floor of the cranial vault by the sphenoid bone, transition from the prominence of the maxilla to the pterygoid process and plates of the sphenoid bone, inclusion of the third molar region of the mandible and palatine bones of the hard palate.

9.3.2.4 Mandibular Ramus/Base of Skull

Images at various levels (Figs. 9.30) dorsal from the coronoid process to the ramus and condylar process of the mandible show variations in the contribution of the orbital, sphenoid, and temporal bones of the skull base and relationship of the mandibular condyle to the glenoid fossa of the temporal bone.

9.3.2.5 Base of Skull/Anterior Cervical Spine

At the level of the anterior processes of the cervical vertebrae (Fig. 9.31), dorsal to the ramus of the mandible, coronal images show the increasing contribution to the base of the skull by the temporal bones bilaterally and relationship of the

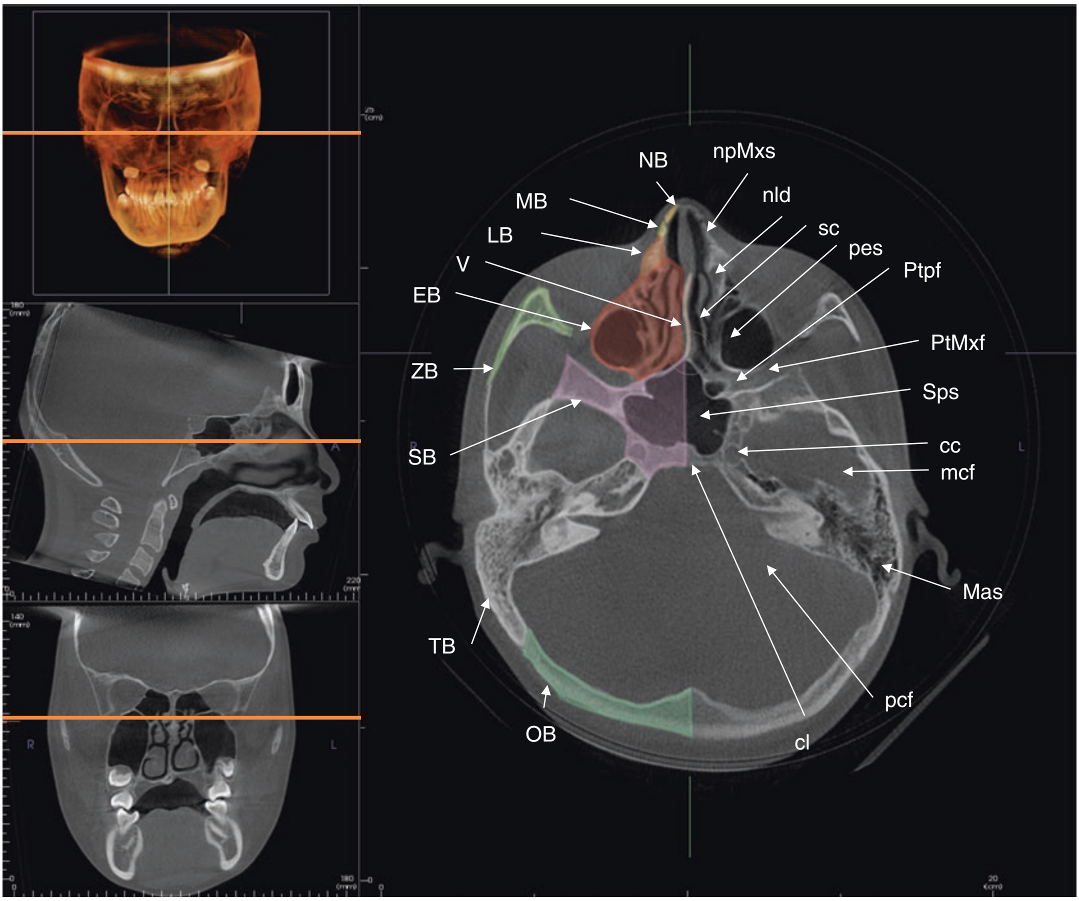

Fig. 9.12 Axial orthogonal CBCT image at the inferior orbital level (*right*) with frontal volumetric rendering (*upper left*), midsagittal (*middle left*), and coronal (*lower left*) reference images. (*NB* nasal bone, *MB* maxillary bone, *LB* lacrimal bone, *V* vomer, *EB* ethmoid bone, *ZB* Zygomatic bone, *SB* sphenoid bone, *TB* temporal bone, *OB* occipital bone, *mpMxs* nasal process of the maxillary bone, *nld* nasolacrimal duct, *sc* superior conchae, *pes* posterior ethmoid sinus, *Ptpf* pterygopalatine fossa, *PtMxf* pterygomaxillary fissure, *Sps* sphenoid sinus, *cc* carotid canal, *mcf* middle cranial fossa, *Mas* mastoid air cell, *pcf* posterior cranial fossa, *cl* clivus)

occipital bone to the anterior processes of the first and second cervical vertebrae.

9.3.3 Sagittal

Images in the sagittal orthogonal plane demonstrate a continuum of anatomy extending from the midline of the nasal cavity and cranial base laterally to the mastoid sinuses and glenoid fossa of the temporal bone and condylar head of the mandible.

9.3.3.1 Midsagittal

The image at this specific midline level (Figs. 9.32) shows all of the bones comprising the base of the skull/floor of the anterior, middle, and posterior cranial fossa, and midsagittal structures of the ethmoid, maxilla, and mandible as well as the upper cervical vertebrae.

9.3.3.2 Nasal Fossa

Images at various levels (Figs. 9.33, 9.34, and 9.35) lateral to the midline to the lateral wall of

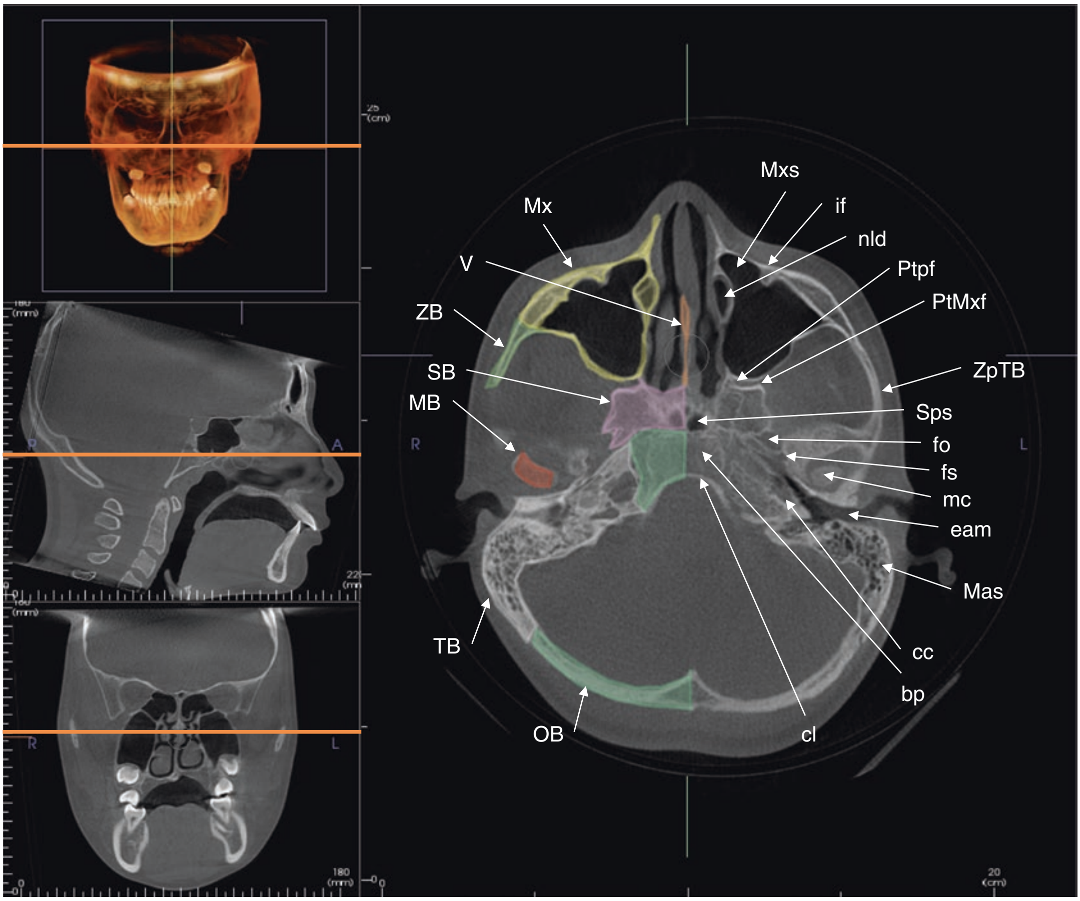

Fig. 9.13 Axial orthogonal CBCT image at the zygomatic arch level (*right*) with frontal volumetric rendering (*upper left*), midsagittal (*middle left*), and coronal (*lower left*) reference images. (*Mx* maxilla, *V* vomer, *ZB* Zygomatic bone, *SB* sphenoid bone, *MB* mandibular bone, *TB* temporal bone, *OB* occipital bone, *Mxs* maxillary sinus, *if* infraorbital foramen, *nld* nasolacrimal duct, *Ptpf* pterygopalatine fossa, *PtMxf* pterygomaxillary fissure, *ZpTB* zygomatic process of the temporal bone, *Sps* sphenoid sinus, *fo* foramen ovale, *fs* foramen spinosum, *Mc* mandibular condyle, *eam* external auditory meatus, *Mas* mastoid sinus, *cc* carotid canal, *bp* basilar portion of the occipital bone, *cl* clivus)

the nasal fossa/cavity show the relationship of the ethmoid and sphenoid sinuses and maxillary hard palate to the naso- and oropharyngeal airway space.

9.3.3.3 Maxillary Sinus

Images at various levels (Figs. 9.36 and 9.37) lateral to the medial wall of the maxillary sinus show the increasing prominence of the pterygoid plates of the sphenoid and appearance of the temporal bone.

9.3.3.4 Temporal Bone/Mandibular Condyle

Images in the region of the mandibular condyle and mastoid process of the temporal bone (Fig. 9.38) show the relationship of the condylar head of the mandible to the glenoid fossa of the temporal bone and floor of the middle cranial fossa.

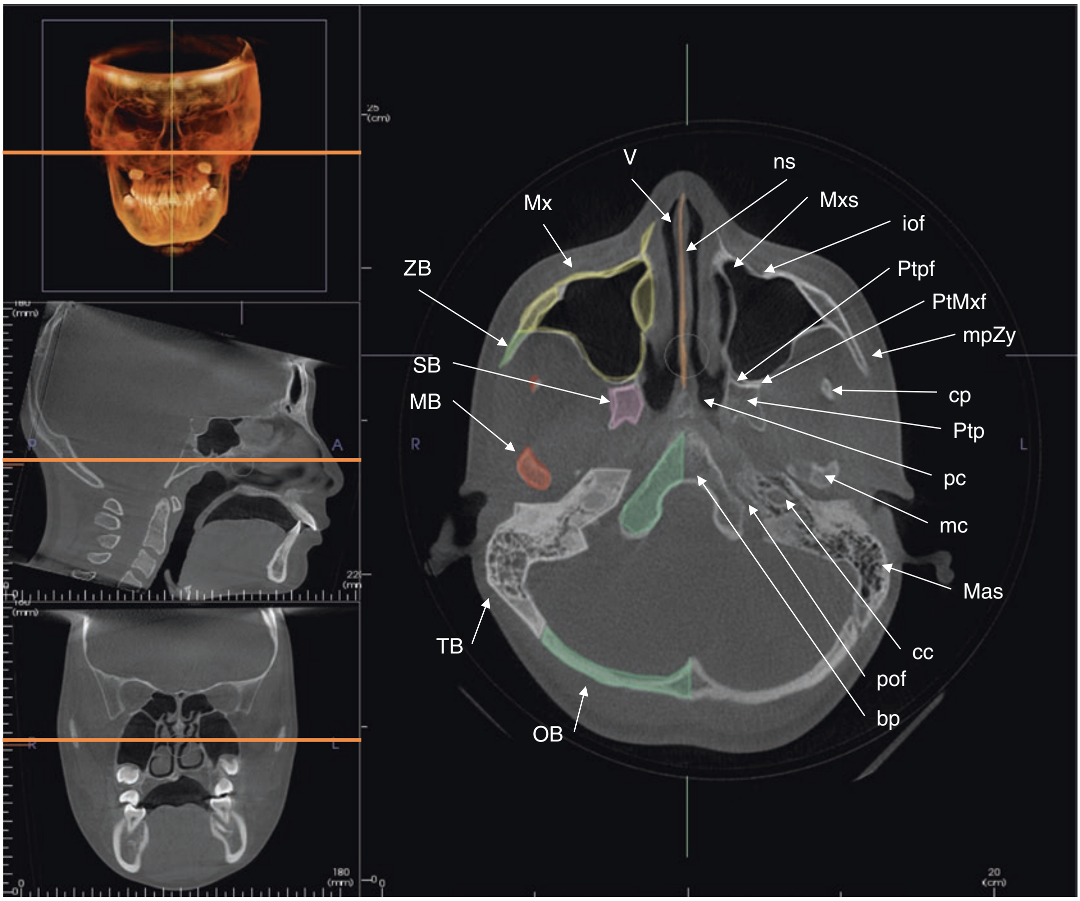

Fig. 9.14 Axial orthogonal CBCT image at the mid maxillary sinus level (*right*) with frontal volumetric rendering (*upper left*), midsagittal (*middle left*), and coronal (*lower left*) reference images. (*V* vomer, *Mx* maxilla, *ZB* zygomatic bone, *SB* sphenoid bone, *MB* mandibular bone, *TB* temporal bone, *OB* occipital bone, *ns* nasal septum, *Mxs* maxillary sinus, *iof* infraorbital foramen, *Ptpf* pterygopalatine fossa, *PtMxf* Pterygomaxillary fissure, *mpZy* maxillary process of the zygoma, *cp* coronoid process, *Ptp* pterygoid plates, *pc* posterior choanae, *Mc* mandibular condyle, *Mas* mastoid sinus, cc, carotid canal, pof, petro-occipital fissure, bp, basilar portion of the occipital bone)

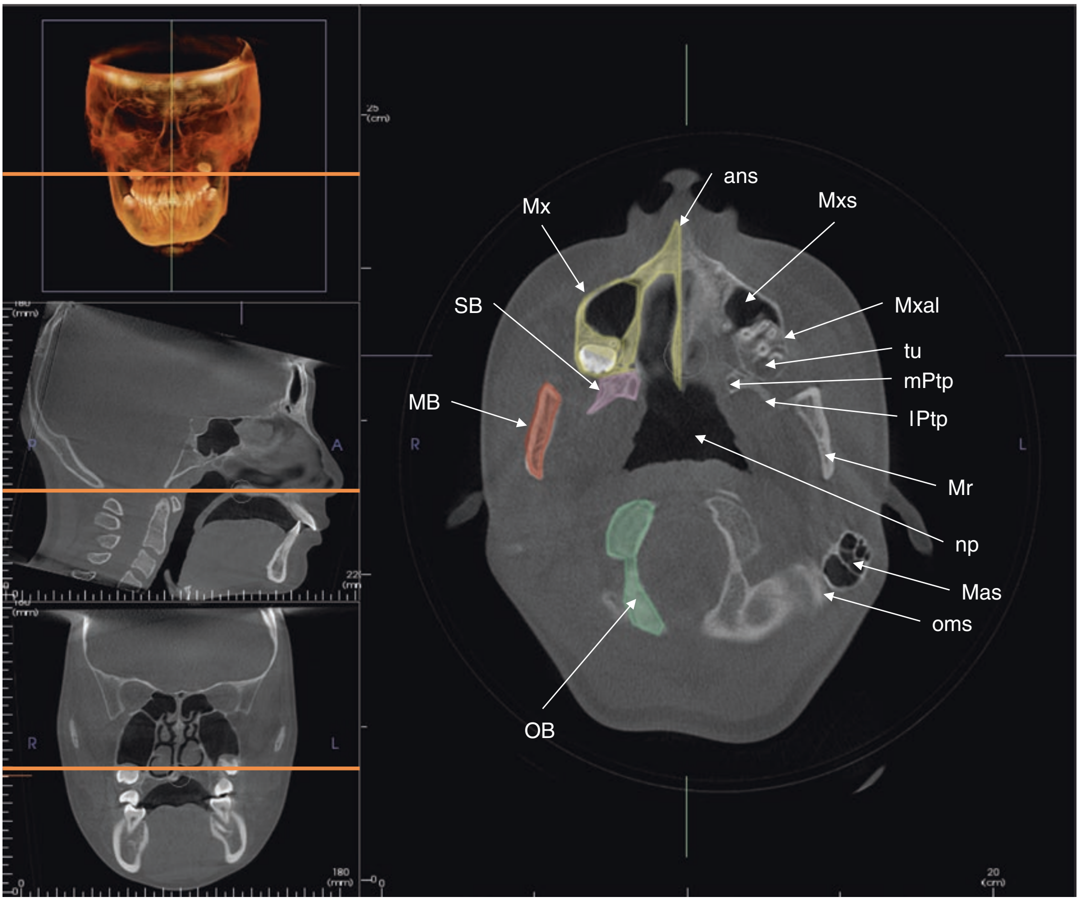

Fig. 9.15 Axial orthogonal CBCT image at the level of the superior portion of the maxillary alveolus (*right*) with frontal volumetric rendering (*upper left*), midsagittal (*middle left*), and coronal (*lower left*) reference images. (*Mx* maxilla, *SB* sphenoid bone, *MB* mandibular bone, *OB* occipital bone, *ans* anterior nasal spine, *Mxs* maxillary sinus, *Mxal* maxillary alveolus, *tu* tuberosity, *mPtp* medial pterygoid plates, *lPtp* lateral pterygoid plate, *Mr* mandibular ramus, *np* nasopharynx, *Mas* mastoid sinus, oms, occipitomastoid suture)

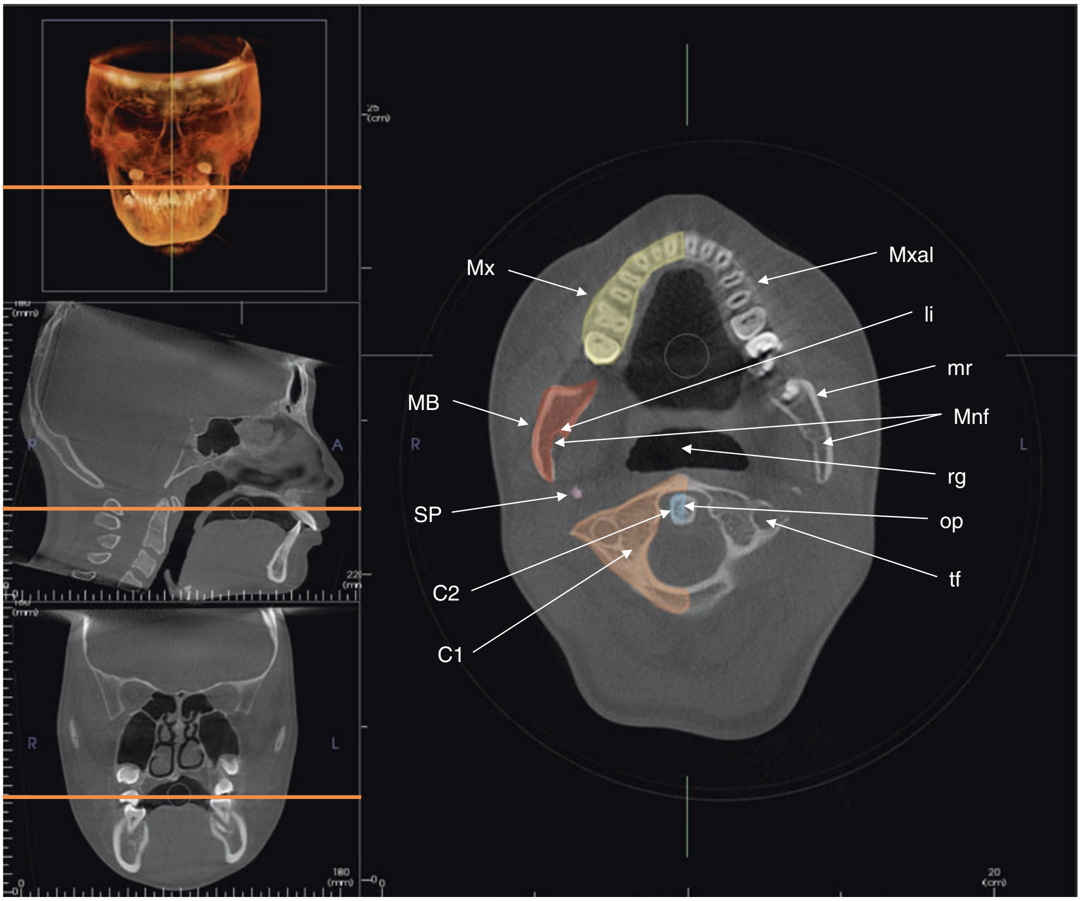

Fig. 9.16 Axial orthogonal CBCT image at the level of the mandibular foramen (*right*) with frontal volumetric rendering (*upper left*), midsagittal (*middle left*), and coronal (*lower left*) reference images. (*Mx* maxilla, *MB* mandibular bone, *SP* styloid process of the temporal bone, *C1* Atlas, first cervical vertebrae, *C2* Axis, second cervical vertebrae, *Mxal* alveolar process of the maxilla, *li* lingual, *mr* mandibular ramus, *Mnf* mandibular foramen, *rg* retroglossal portion of the oropharyngeal airway space, *op* odontoid process of C2, *tf* transverse foramen)

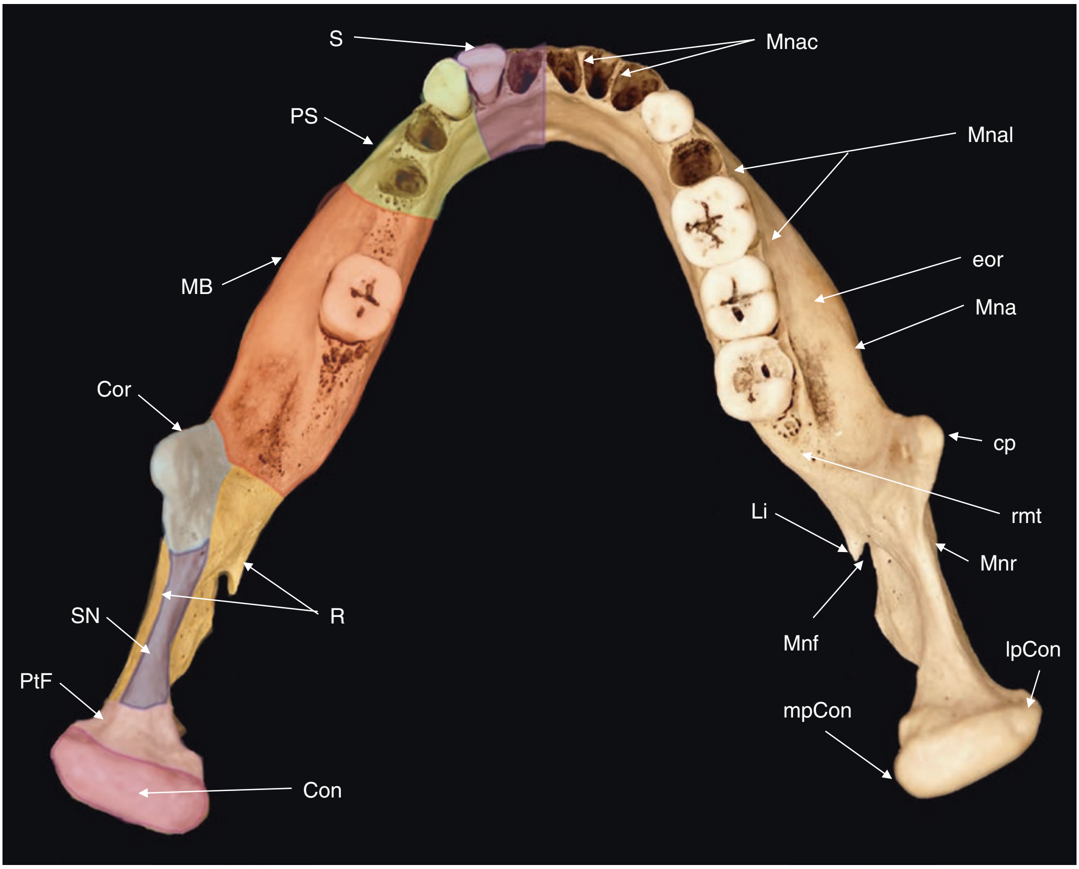

Fig. 9.17 Superior projection of the mandible showing anatomic regions (*left*) and specific anatomic landmarks (*right*) (*S* symphysis, *PS* parasymphysis, *MB* mandibular body, *Cor* coronoid, *R* ramus, *SN* sigmoid notch, *PtF* pterygoid fovea, *Con* condyle, *Mnac* mandibular alveolar crest, *Mnal* mandibular alveolus, *eor* external oblique ridge, *Mna* mandibular angle, *cp* coronoid process, *rmt* retromolar trigone, *Mnr* mandibular ramus, *Li* lingual, *Mnf* mandibular foramen, *mpCon* medial pole of the mandibular condyle, *lpCon* lateral pole of the mandibular condyle)

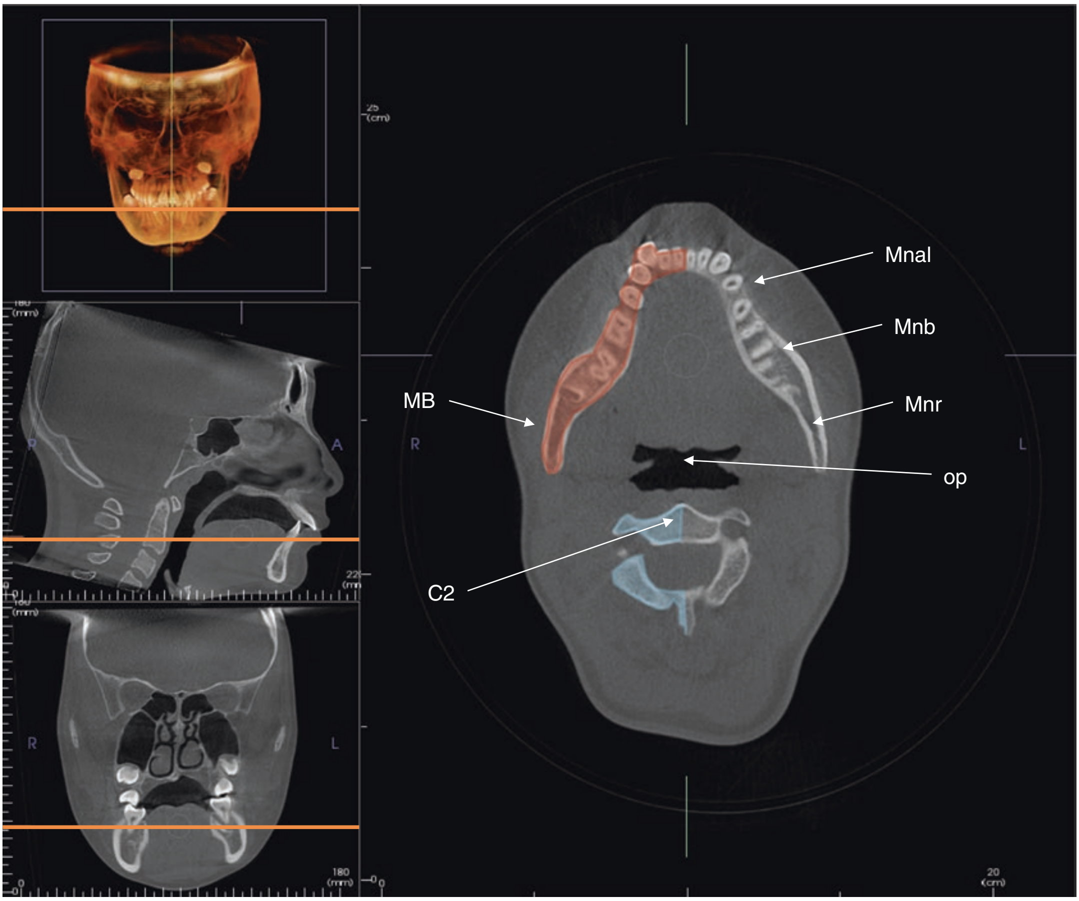

Fig. 9.18 Axial orthogonal CBCT image at the level of the alveolar process of the mandible (*right*) with frontal volumetric rendering (*upper left*), midsagittal (*middle left*), and coronal (*lower left*) reference images. (*MB* mandibular body, *C2* Axis, second cervical vertebrae, *Mnal* mandibular alveolus, *Mnb* mandibular body, *Mnr* mandibular ramus, *op* oropharyngeal airway space)

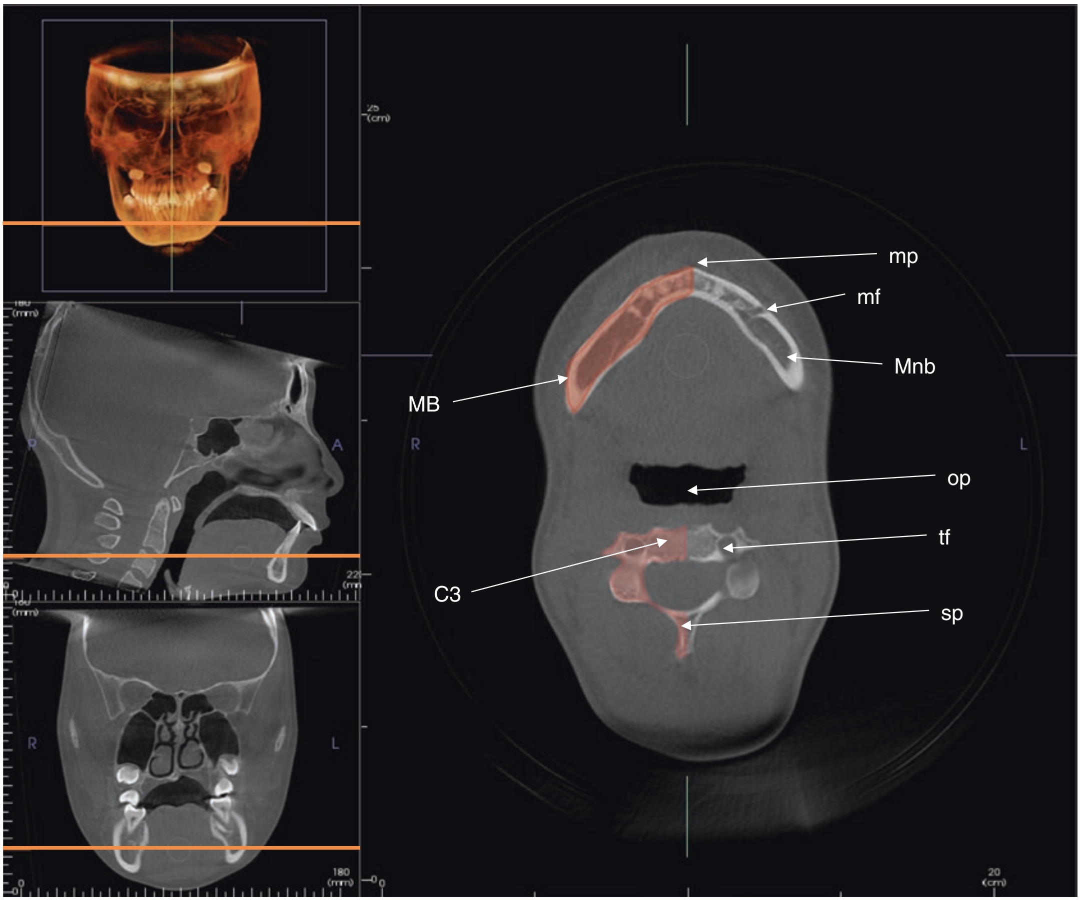

Fig. 9.19 Axial orthogonal CBCT image at the level of the mental foramen (*right*) with frontal volumetric rendering (*upper left*), midsagittal (*middle left*), and coronal (*lower left*) reference images. (*MB* mandibular body, *C3* third cervical vertebrae, *mp* mental protuberance, *mf* mental foramen, *Mnb* mandibular body, *op* oropharyngeal, *tf* transverse foramen of C3, *sp* spinous process of C3)

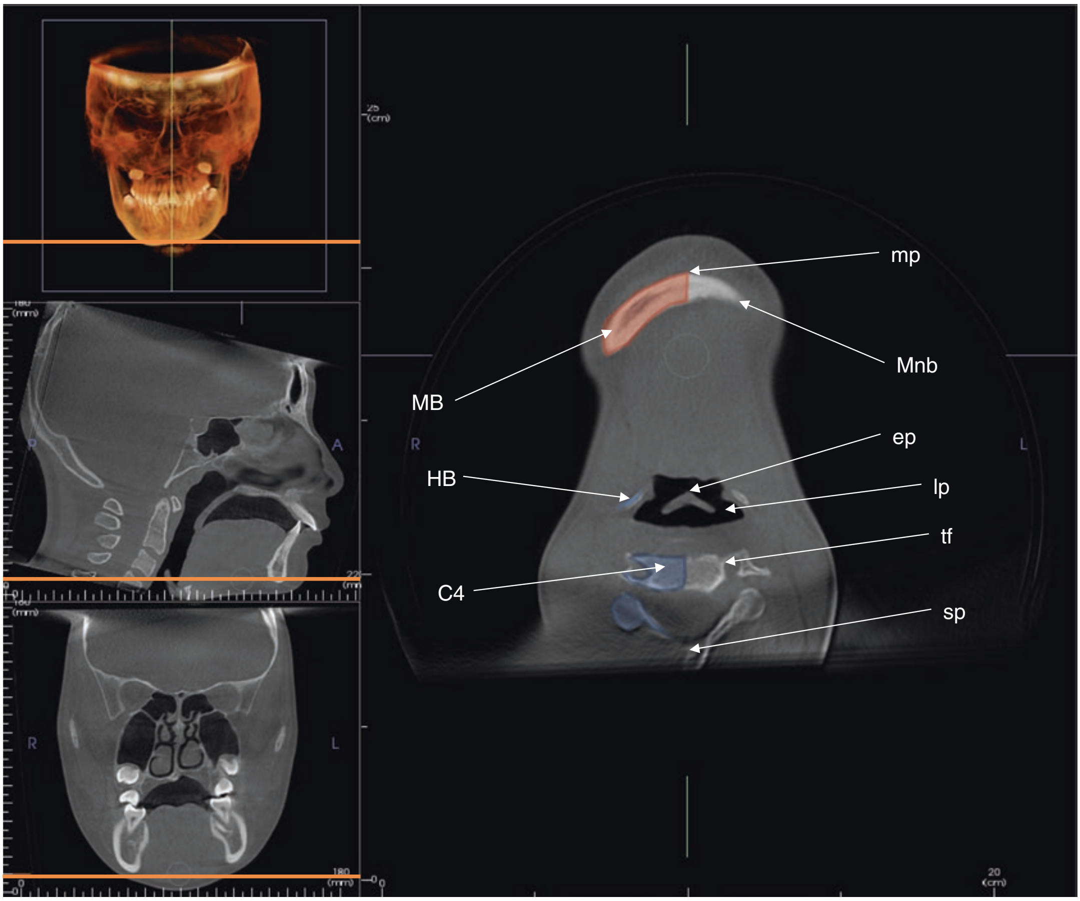

Fig. 9.20 Axial orthogonal CBCT image at the level of the lower border of the anterior mandibular symphysis (*right*) with frontal volumetric rendering (*upper left*), midsagittal (*middle left*), and coronal (*lower left*) reference images. (*MB* mandibular body, *HB* hyoid bone, *C4* fourth cervical vertebrae, *mp* mental protuberance, *Mnb* mandibular body, *ep* epiglottis, *lp* laryngopharynx, *tf* transverse foramen of C4, *sp* spinous process of C4)

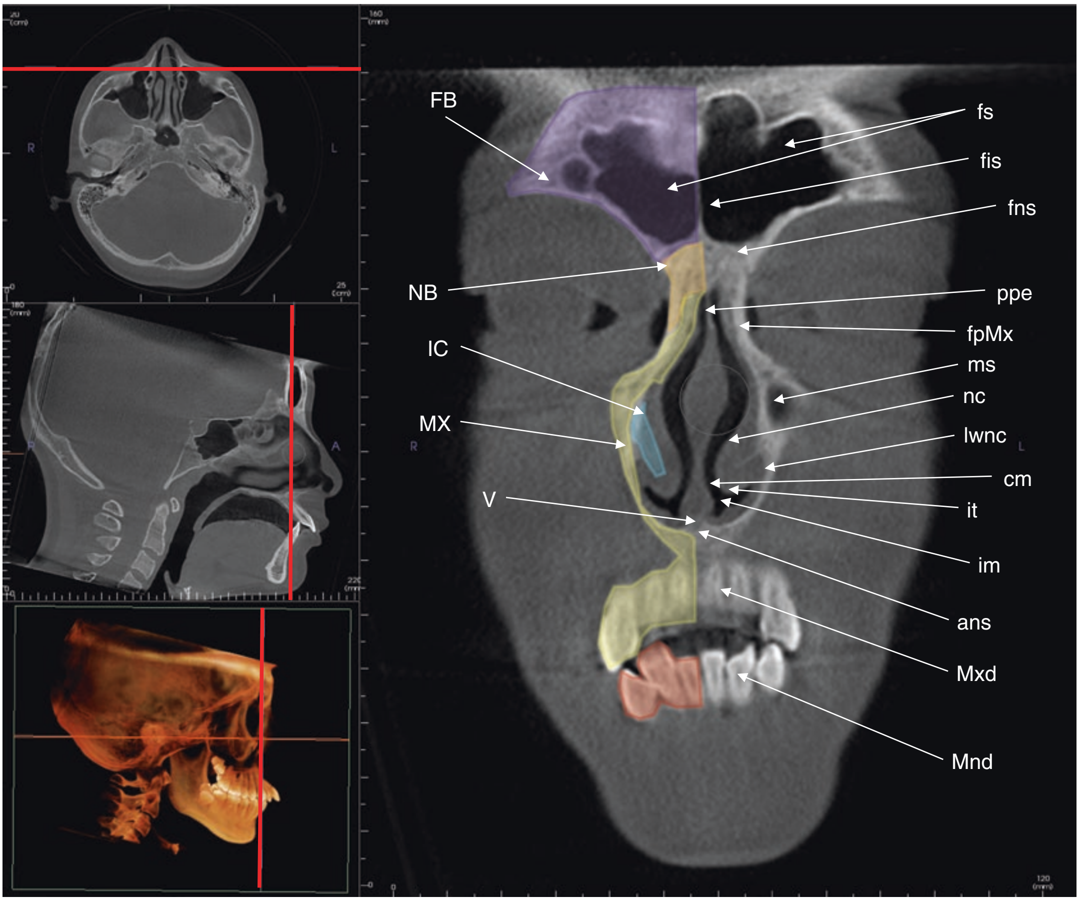

Fig. 9.21 Coronal orthogonal CBCT image at the level of the frontal sinus and anterior teeth (*right*) with axial (*upper right*), midsagittal (*middle left*), and right lateral volumetric rendering (*lower left*) reference images. (*FB* frontal bone, *NB* nasal bone, *IC* inferior conchae, *MX* maxilla, *V* vomer, *fs* frontal sinus, *fis* frontal intersinus septum, *fns* fronto-nasal suture, *ppe* perpendicular plate of the ethmoid bone, *fpMx* frontal process of the maxilla, *ms* maxillary sinus, *nc* nasal cavity/nasal fossa, *lwnc* lateral wall of the nasal cavity/fossa, *cm* common meatus, *it* inferior turbinate, *im* inferior meatus, *ans* anterior nasal spine, *Mxd* maxillary dentition [anterior incisors], *Mnd* mandibular dentition [anterior incisors])

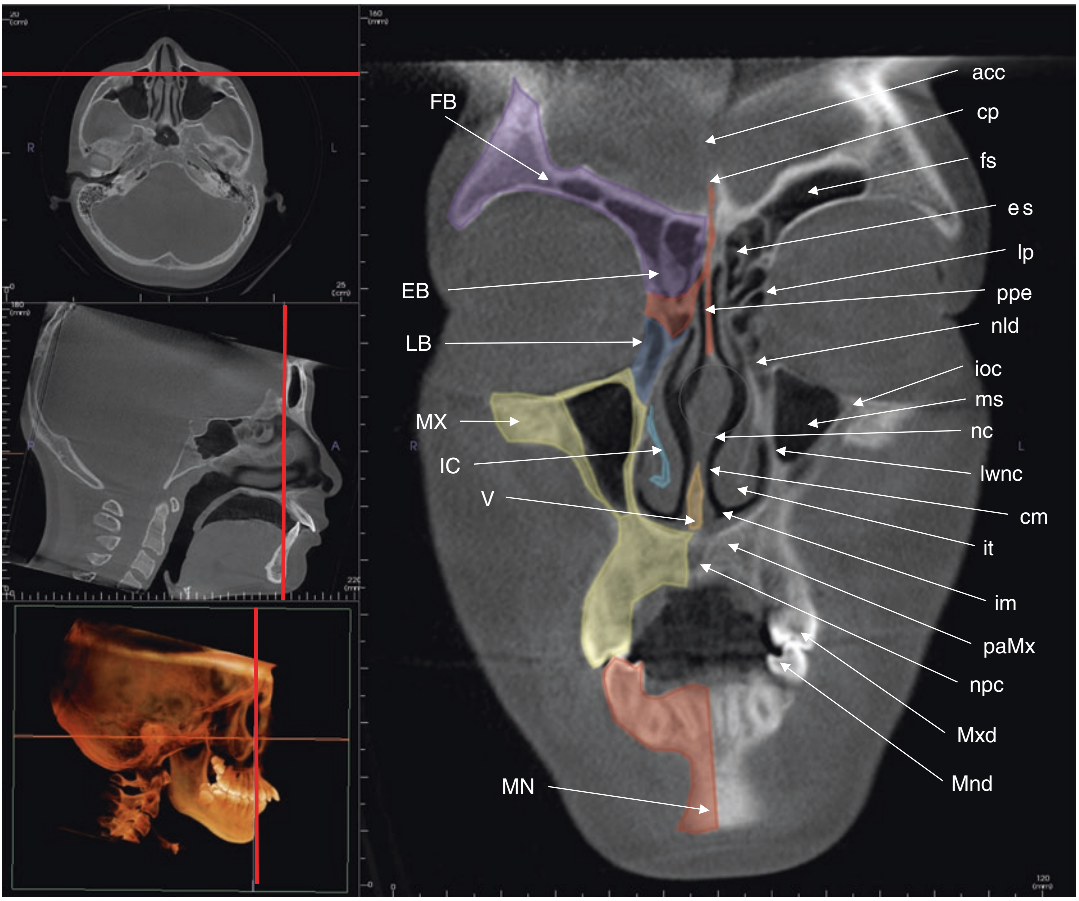

Fig. 9.22 Coronal orthogonal CBCT image at the level of the anterior maxillary sinus and premolar teeth (*right*) with axial (*upper right*), midsagittal (*middle left*), and right lateral volumetric rendering (*lower left*) reference images. (*FB* frontal bone, *EB* ethmoid bone, *LB* lacrimal bone, *MX* maxilla, *IC* inferior conchae, *V* vomer, *MN* mandible, *acc* anterior cranial cavity, *cp* cribriform plate of the ethmoid, *fs* frontal sinus, *es* ethmoid sinus, *lp* laminae papyracea, *ppe* perpendicular plate of the ethmoid bone, *nld* nasolacrimal duct, *ioc* infraorbital canal, *ms* maxillary sinus, *nc* nasal cavity/nasal fossa, *lwnc* lateral wall of the nasal cavity/fossa, *cm* common meatus, *it* inferior turbinate, *im* inferior meatus, *paMx* palatal alveolar process of the maxilla, *npc* nasopalatine/incisive canal, *Mxd* maxillary dentition [premolars], *Mnd* mandibular dentition [premolars])

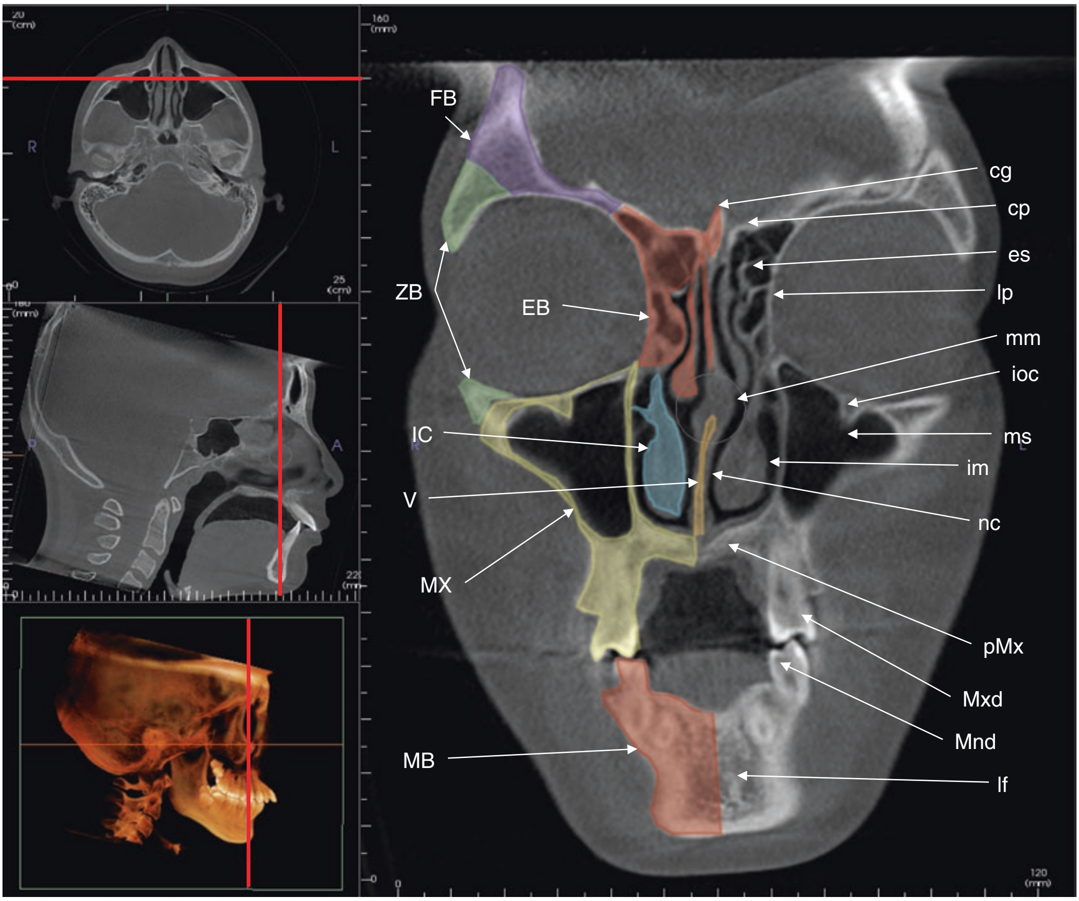

Fig. 9.23 Coronal orthogonal CBCT image at the level of the anterior orbital rim and zygomatic bone (*right*) with axial (*upper right*), midsagittal (*middle left*), and right lateral volumetric rendering (*lower left*) reference images. (*FB* frontal bone, *EB* ethmoid bone, *ZB* zygomatic bone, *MX* maxilla, *IC* inferior conchae, *V* vomer, *MB* mandible, *cg* crista galli, *cp* cribriform plate of the ethmoid, *es* ethmoid sinus, *lp* laminae papyracea, *mm* middle meatus, *ioc* infraorbital canal, *ms* maxillary sinus, *im* inferior meatus, *nc* nasal cavity/nasal fossa, *pMx* palatal alveolar process of the maxilla, *Mxd* maxillary dentition [premolars], *Mnd* mandibular dentition [premolars], *lf* lingual foramen)

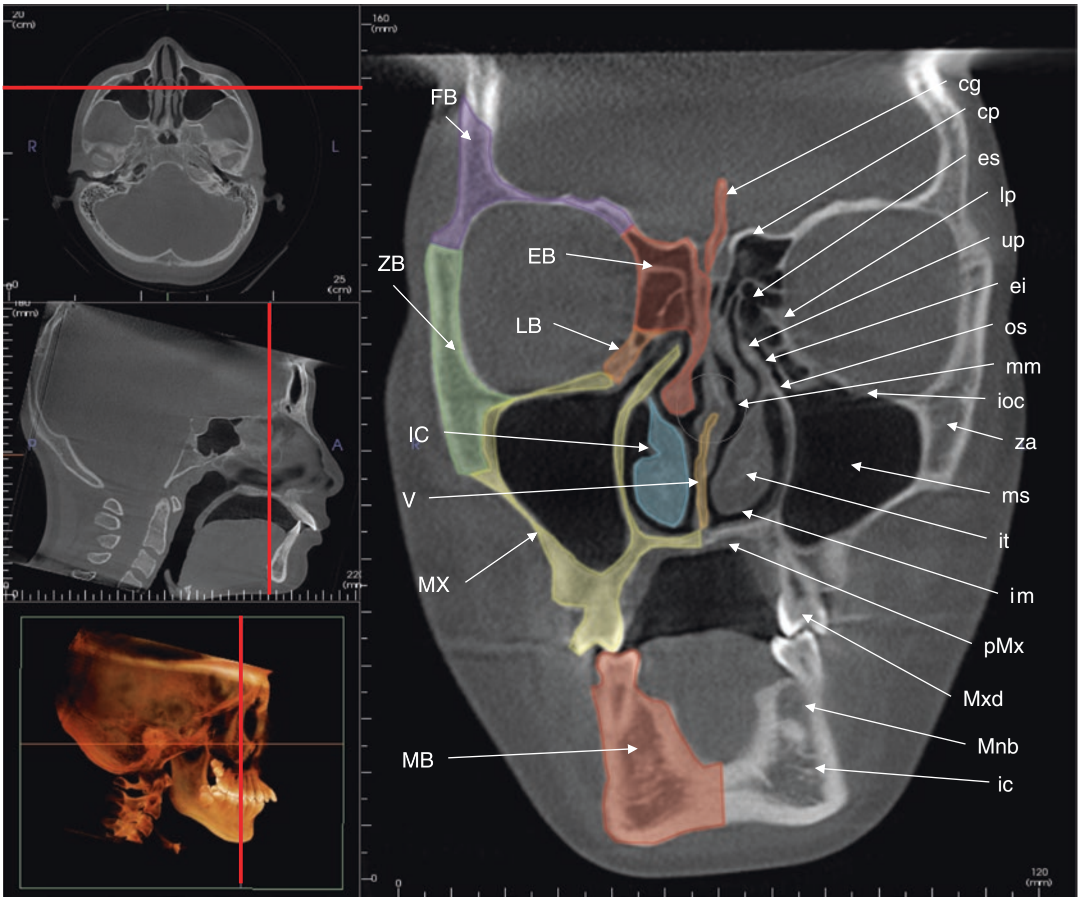

Fig. 9.24 Coronal orthogonal CBCT image at the level of the zygomatic arch and posterior teeth (*right*) with axial (*upper right*), midsagittal (*middle left*), and right lateral volumetric rendering (*lower left*) reference images. (*FB* frontal bone, *EB* ethmoid bone, *LB* lacrimal bone, *ZB* zygomatic bone, *IC* inferior conchae, *V* vomer, *MX* maxilla, *MB* mandible, *cg* crista galli, *cp* cribriform plate of the ethmoid, *es* ethmoid sinus, *lp* laminae papyracea, *up* uncinated process, *ei* ethmoid infundibulum, *os* ostia, *mm* middle meatus, *ioc* infraorbital canal, *za* zygomatic arch, *ms* maxillary sinus, *it* inferior turbinate, *im* inferior meatus, *pMx* palatal alveolar process of the maxilla, *Mxd* maxillary dentition [premolars], *Mnd* mandibular dentition [premolars], *ic* incisive canal)

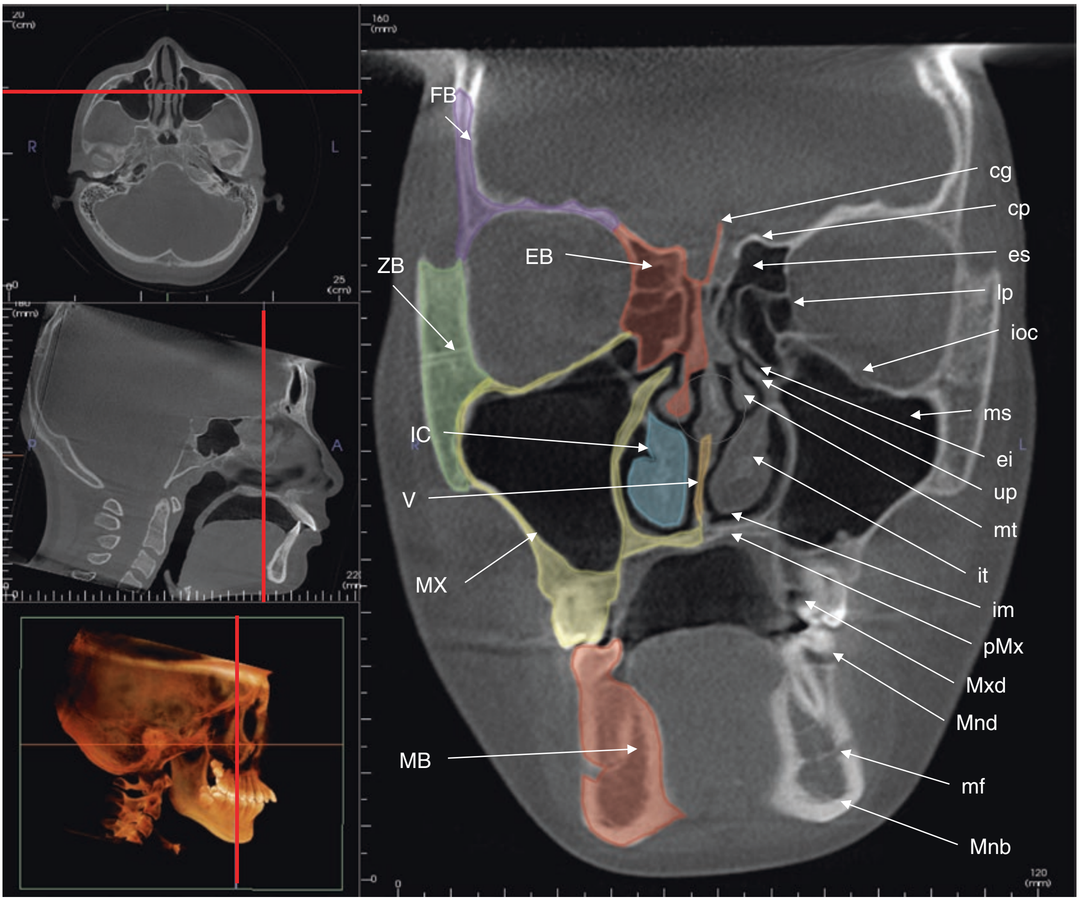

Fig. 9.25 Coronal orthogonal CBCT image at the level of the zygomatic arch and posterior teeth (*right*) with axial (*upper right*), midsagittal (*middle left*), and right lateral volumetric rendering (*lower left*) reference images. (*FB* frontal bone, *EB* ethmoid bone, *ZB* zygomatic bone, *IC* inferior conchae, *V* vomer, *MX* maxilla, *MB* mandible, *cg* crista galli, *cp* cribriform plate of the ethmoid, *es* ethmoid sinus, *lp* laminae papyracea, *ioc* infraorbital canal, *ms* maxillary sinus, *ei* ethmoid infundibulum, *up* uncinated process, *mt* middle turbinate, *it* inferior turbinate, *im* inferior meatus, *pMx* palatal alveolar process of the maxilla, *Mxd* maxillary dentition [premolars], *Mnd* mandibular dentition [premolars], *mf* mental foramen)

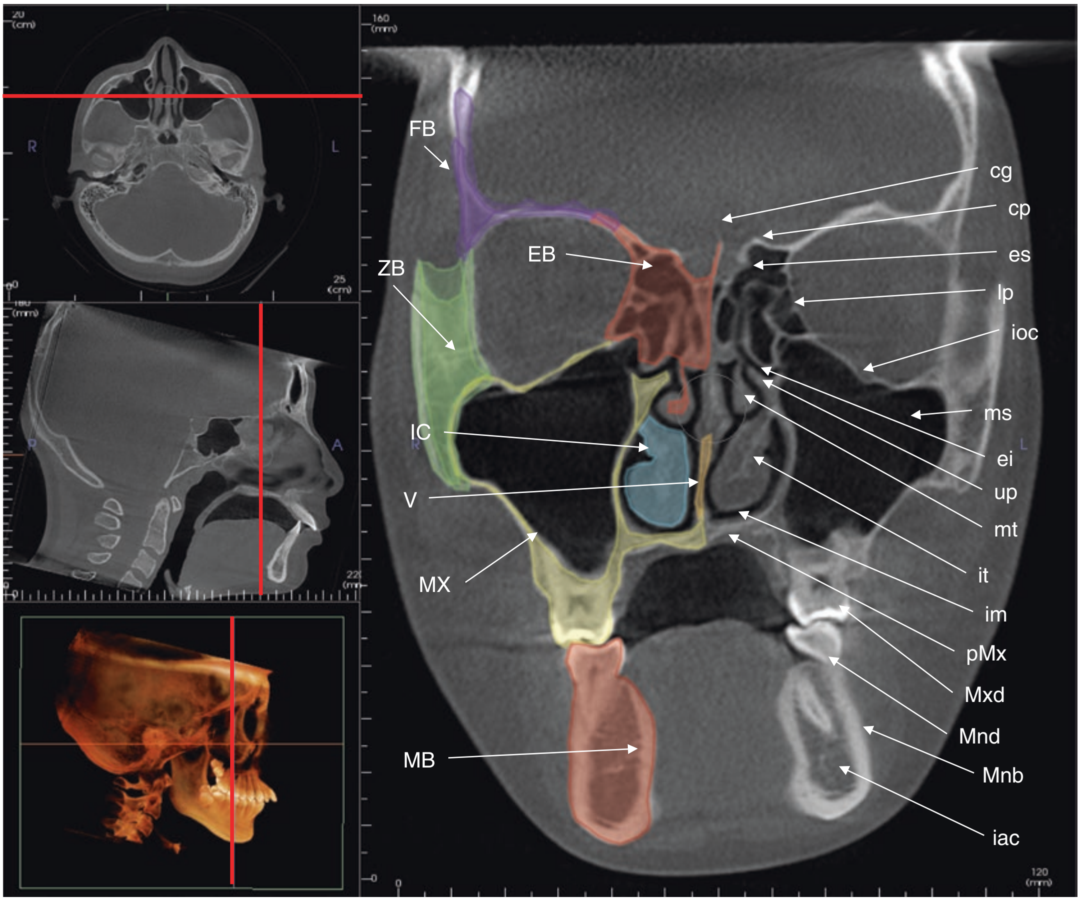

Fig. 9.26 Coronal orthogonal CBCT image at the level of the middle of the maxillary sinus (*right*) with axial (*upper right*), midsagittal (*middle left*), and right lateral volumetric rendering (*lower left*) reference images. (*FB* frontal bone, *EB* ethmoid bone, *ZB* zygomatic bone, *IC* inferior conchae, *V* vomer, *MX* maxilla, *MB* mandible, *cg* crista galli, *cp* cribriform plate of the ethmoid, *es* ethmoid sinus, *lp* laminae papyracea, *ioc* infraorbital canal, *ms* maxillary sinus, *ei* ethmoid infundibulum, *up* uncinated process, *mt* middle turbinate, *it* inferior turbinate, *im* inferior meatus, *pMx* palatal alveolar process of the maxilla, *Mxd* maxillary dentition [molars], *Mnd* mandibular dentition [molars], iac, inferior alveolar canal)

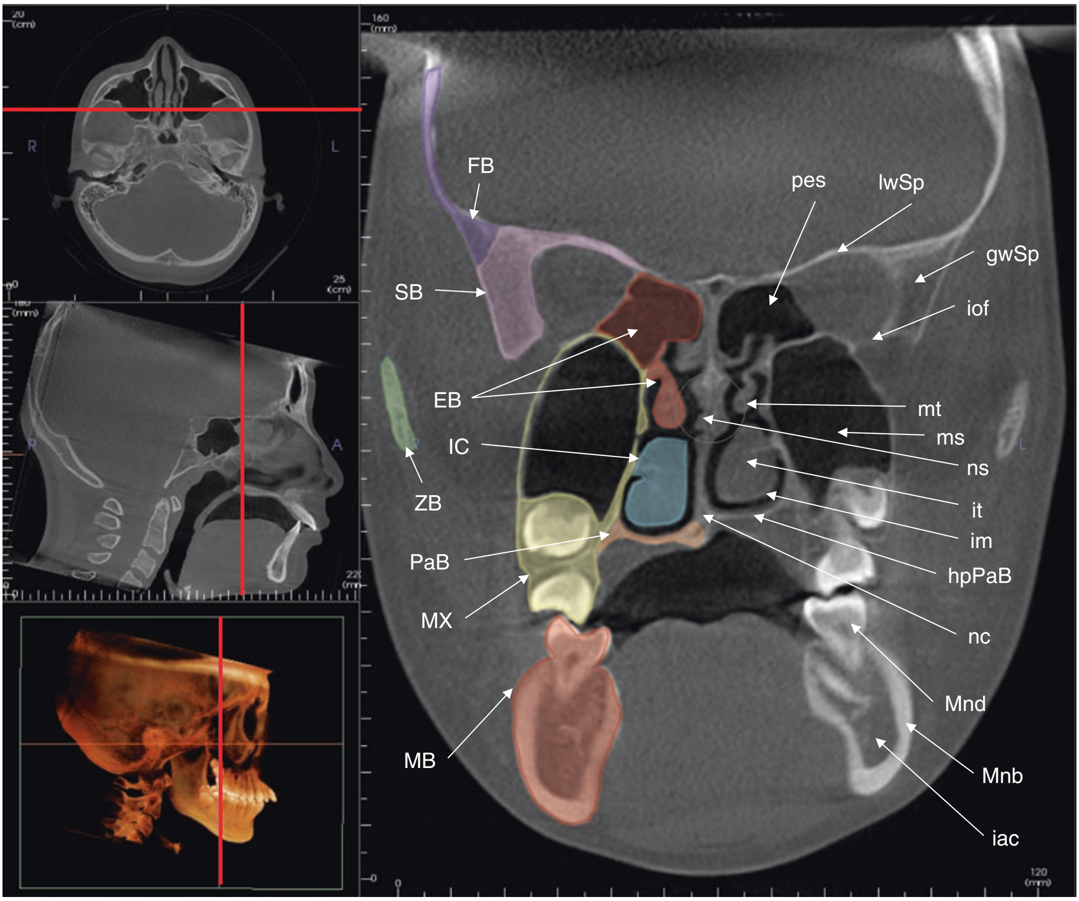

Fig. 9.27 Coronal orthogonal CBCT image at the level of the middle of the zygomatic arch and third molars (*right*) with axial (*upper right*), midsagittal (*middle left*), and right lateral volumetric rendering (*lower left*) reference images. (*FB* frontal bone, *SB* sphenoid bone, *EB* ethmoid bone, *IC* inferior conchae, *ZB* zygomatic bone, *PaB* palatine bone, *MX* maxilla, *MB* mandible, *pes* posterior ethmoid sinus, *lwSp* lesser wing of the sphenoid, *gwSp* greater wing of the sphenoid, *iof* inferior orbital fissure, *mt* middle turbinate, *ms* maxillary sinus, *ns* nasal septum, *it* inferior turbinate, *im* inferior meatus, *hpPaB* horizontal plate of the palatine bone, *nc* nasal crest of the palatine bone, *Mnd* mandibular dentition [molars], *Mnb* mandibular body, *iac* inferior alveolar canal)

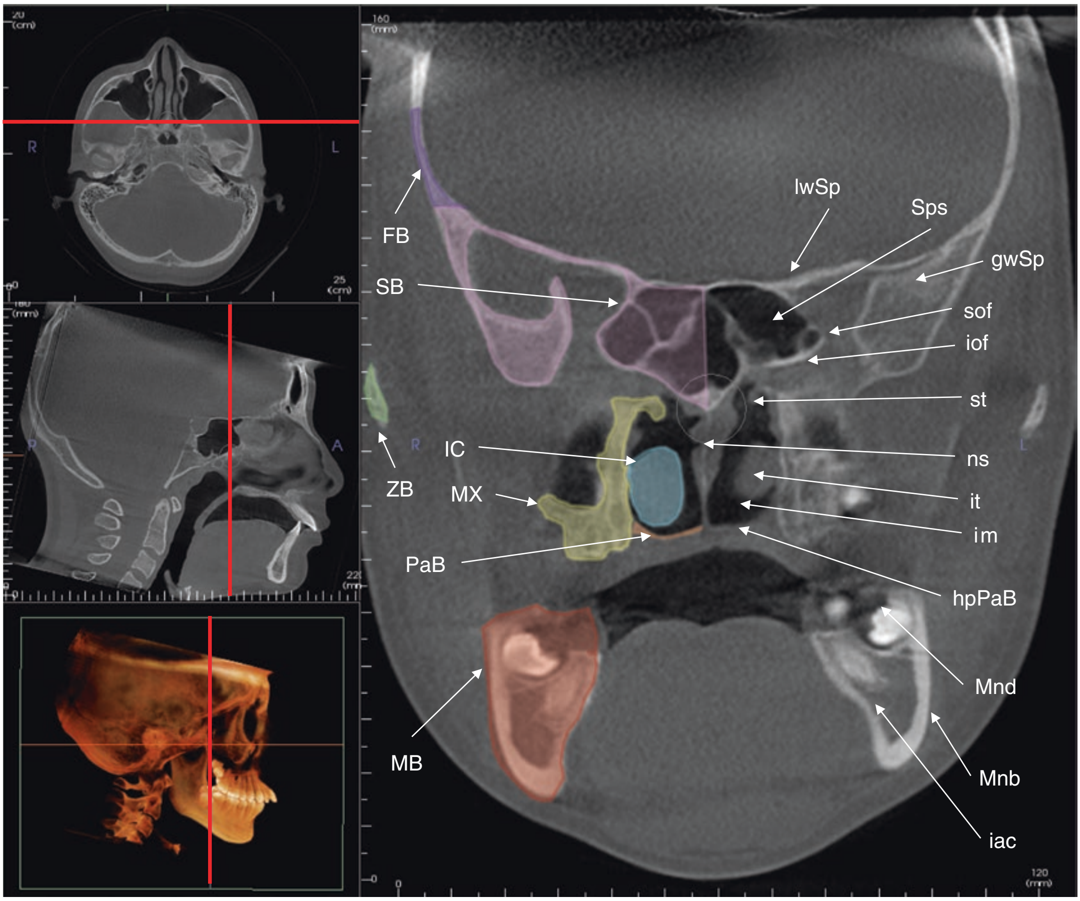

Fig. 9.28 Coronal orthogonal CBCT image at the level of the anterior sphenoid sinus, maxillary tuberosity and third molars (*right*) with axial (*upper right*), midsagittal (*middle left*), and right lateral volumetric rendering (*lower left*) reference images. (*FB* frontal bone, *SB* sphenoid bone, *ZB* zygomatic bone, *PaB* palatine bone, *IC* inferior conchae, *MX* maxilla, *MB* mandible, *lwSp* lesser wing of the sphenoid, *sps* sphenoid sinus, *gwSp* greater wing of the sphenoid, *sof* superior orbital fissure, *iof* inferior orbital fissure, *st* superior turbinate, *ns* nasal septum, *it* inferior turbinate, *im* inferior meatus, *hpPaB* horizontal plate of the palatine bone, *Mnd* mandibular dentition [third molars], *Mnb* mandibular body, iac, inferior alveolar canal)

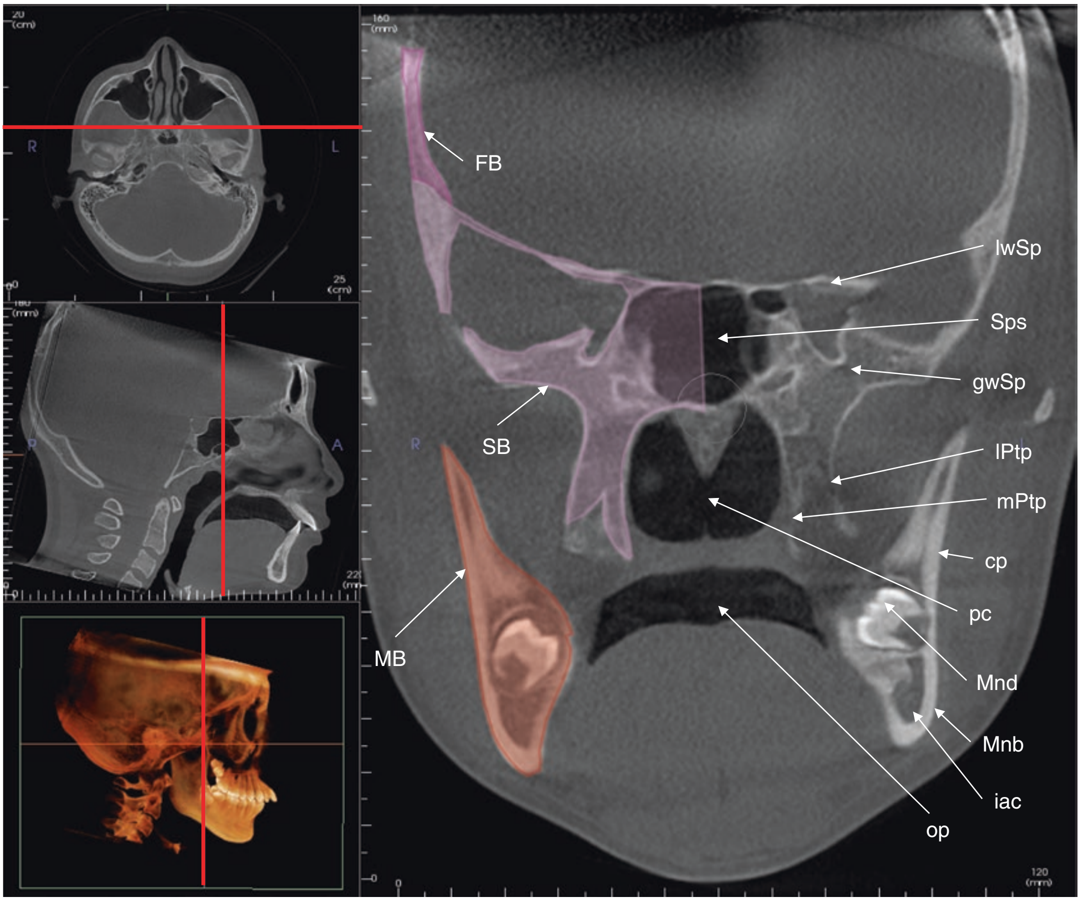

Fig. 9.29 Coronal orthogonal CBCT image at the level of the coronoid process and pterygoid plates (*right*) with axial (*upper right*), midsagittal (*middle left*), and right lateral volumetric rendering (*lower left*) reference images. (*FB* frontal bone, *SB* sphenoid bone, *MB* mandible, *lwSp* lesser wing of the sphenoid, *Sps* sphenoid sinus, *gwSp* greater wing of the sphenoid, *lPtp* lateral pterygoid plate, *mPtp* medial pterygoid plate, *cp* coronoid process, *pc* posterior choanae, *Mnd* mandibular dentition [third molars], *Mnb* mandibular body, *iac* inferior alveolar canal, *op* oropharyngeal airway space)

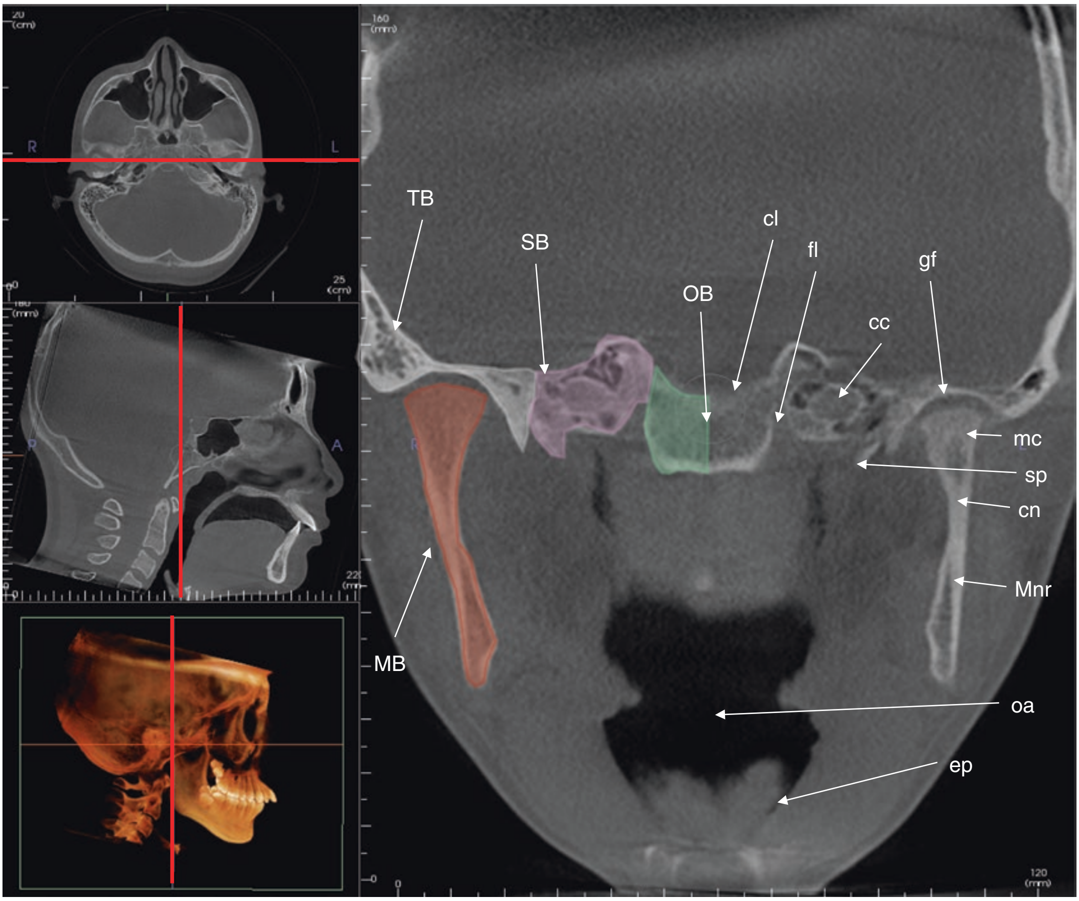

Fig. 9.30 Coronal orthogonal CBCT image at the level of the mandibular condyles (*right*) with axial (*upper right*), midsagittal (*middle left*), and right lateral volumetric rendering (*lower left*) reference images. (*TB* temporal bone, *SB* sphenoid bone, *OB* occipital bone, *MB* mandible, *cl* clivus, *fl* foramen lacerum, *cc* carotid canal, *gf* glenoid fossa, *mc* mandibular condyle, *sp* spinous process of the sphenoid bone, *cn* condylar neck, *Mnr* ramus of the mandible, *oa* oropharyngeal airway, *ep* epiglottis)

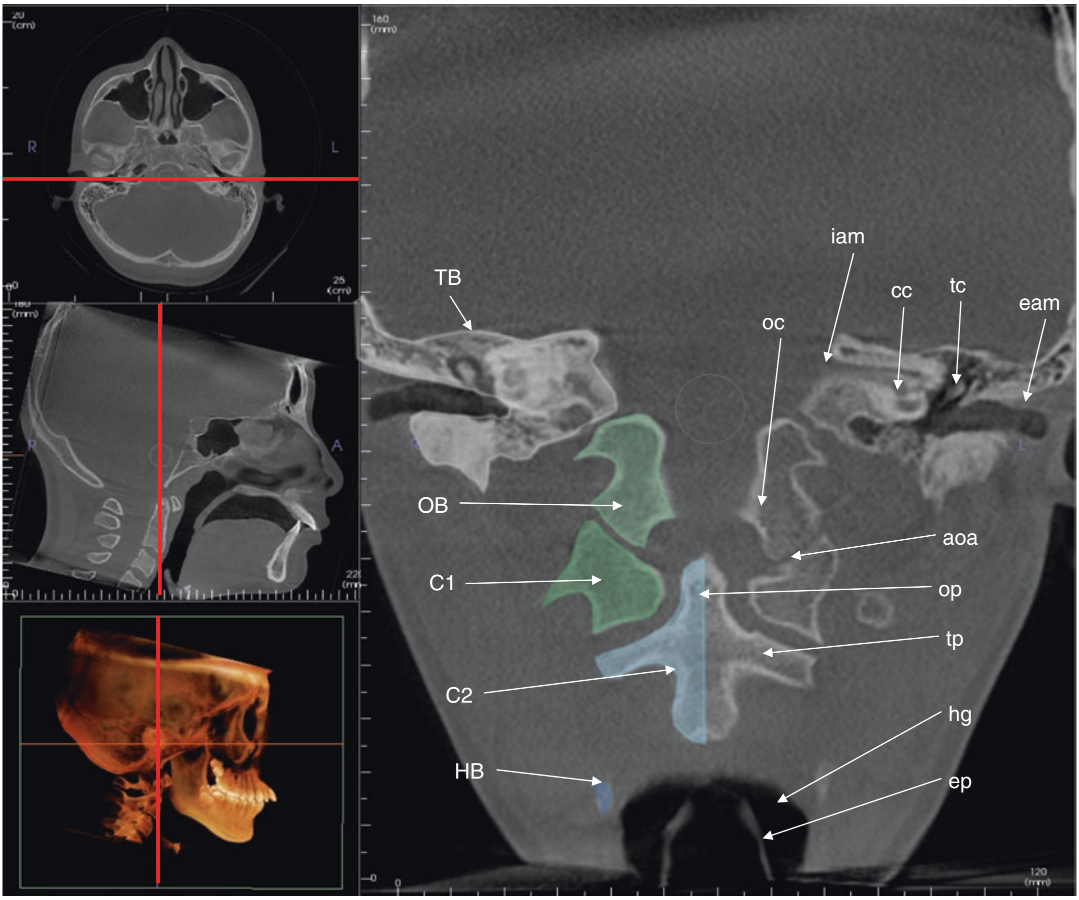

Fig. 9.31 Coronal orthogonal CBCT image at the level of the body of C1 and odontoid process of C2 (op) of the upper cervical spine (*right*) with axial (*upper right*), mid-sagittal (*middle left*), and right lateral volumetric rendering (*lower left*) reference images. (*TB* temporal bone, *OB* occipital bone, *C1* Atlas/first cervical vertebrae, *C2* Axis/second cervical vertebrae, *HB* hyoid bone, *oc* occipital condyle, *iam* internal auditory meatus, *cc* carotid canal, *tc* tympanic cavity, *eam* external auditory meatus, *ep* epiglottis, *aoa* atlanto-occipital articulation, *tp* transverse process of C2, *hg* hypoglossal airway space)

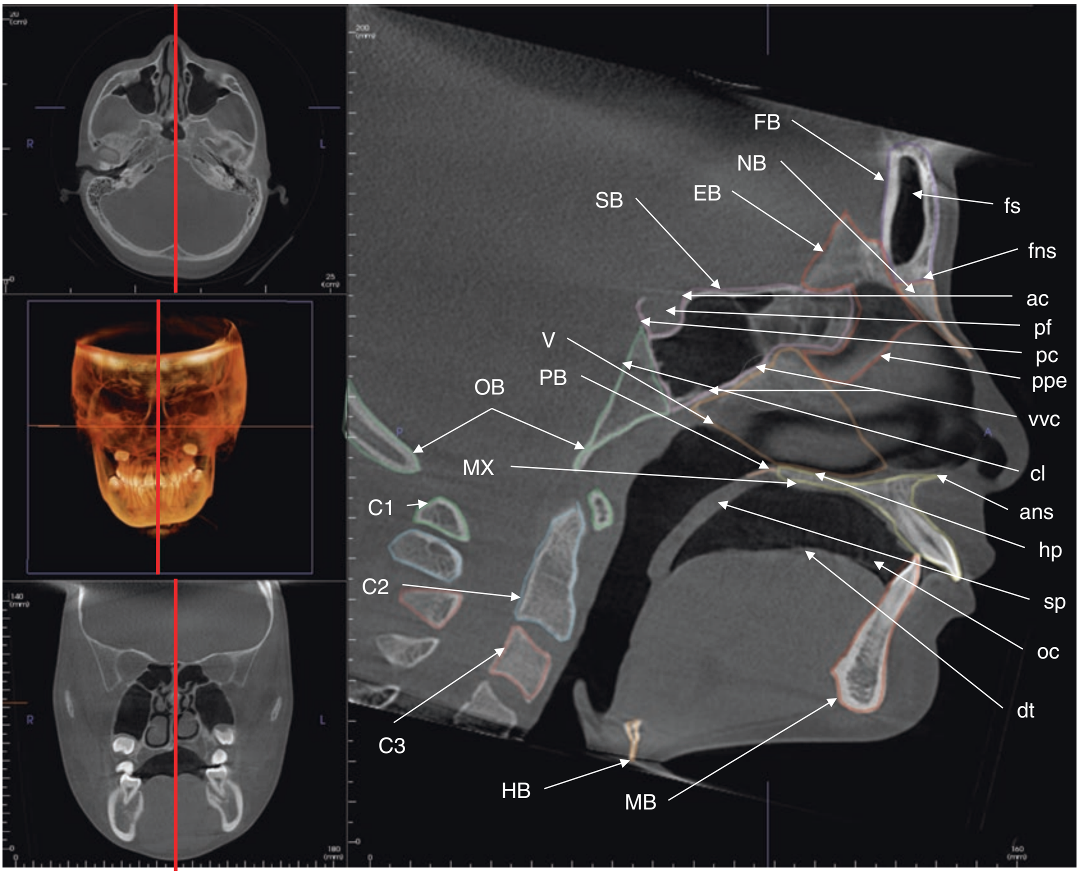

Fig. 9.32 Midsagittal orthogonal CBCT image (*right*) with axial (*upper left*), frontal volumetric rendering (*middle left*), and coronal (*lower left*) reference images. (*FB* frontal bone, *NB* nasal bone, *EB* ethmoid bone, *SB* sphenoid bone, *V* vomer, *PB* palatal bone, *OB* occipital bone, *MX* maxilla, *C1* Atlas/first cervical vertebrae, *C2* Axis/second cervical vertebrae, *C3* third cervical vertebrae, *HB* hyoid bone, *MB* mandible, *fs* frontal sinus, *fns* frontonasal suture, *ac* anterior clinoid, *pf* pituitary fossa, *pc* posterior clinoid, *ppe* perpendicular plate of the ethmoid bone, *vvc* vomerovaginal canal, *cl* clivus, *ans* anterior nasal spine, *hp* hard palate, *sp* soft palate, *oc* oral cavity, *dt* dorsum of the tongue)

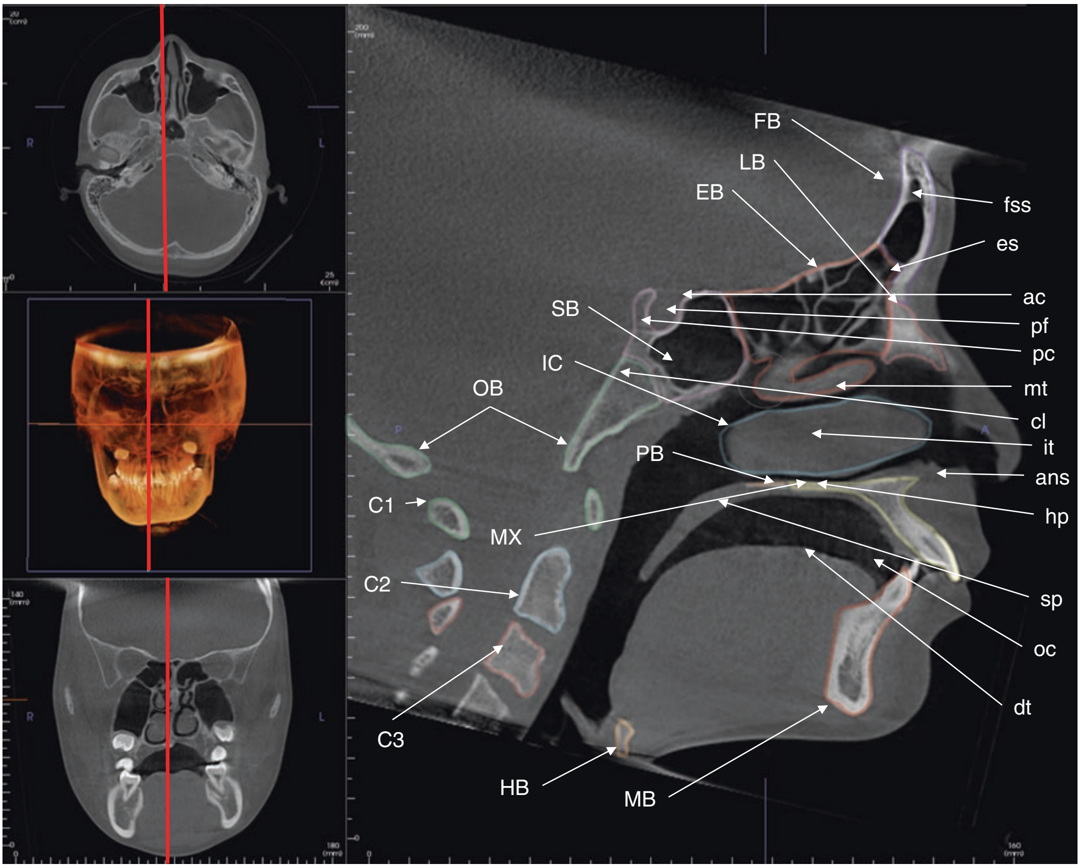

Fig. 9.33 Sagittal orthogonal CBCT image at the level of the middle of the right nasal aperture (*right*) with axial (*upper left*), frontal volumetric rendering (*middle left*), and coronal (*lower left*) reference images. (*FB* frontal bone, *LB* lacrimal bone, *EB* ethmoid bone, *SB* sphenoid bone, *IC* inferior conchae, *PB* palatal bone, *OB* occipital bone, *MX* maxilla, *C1* Atlas/first cervical vertebrae, *C2* Axis/second cervical vertebrae, *C3* third cervical vertebrae, *HB* hyoid bone, *MB* mandible, *fs* frontal sinus, *es* ethmoid sinus, *ac* anterior clinoid, *pf* pituitary fossa, *pc* posterior clinoid, *mt* middle turbinate, *cl* clivus, *it* inferior turbinate, *ans* anterior nasal spine, *hp* hard palate, *sp* soft palate, *oc* oral cavity, *dt* dorsum of the tongue)

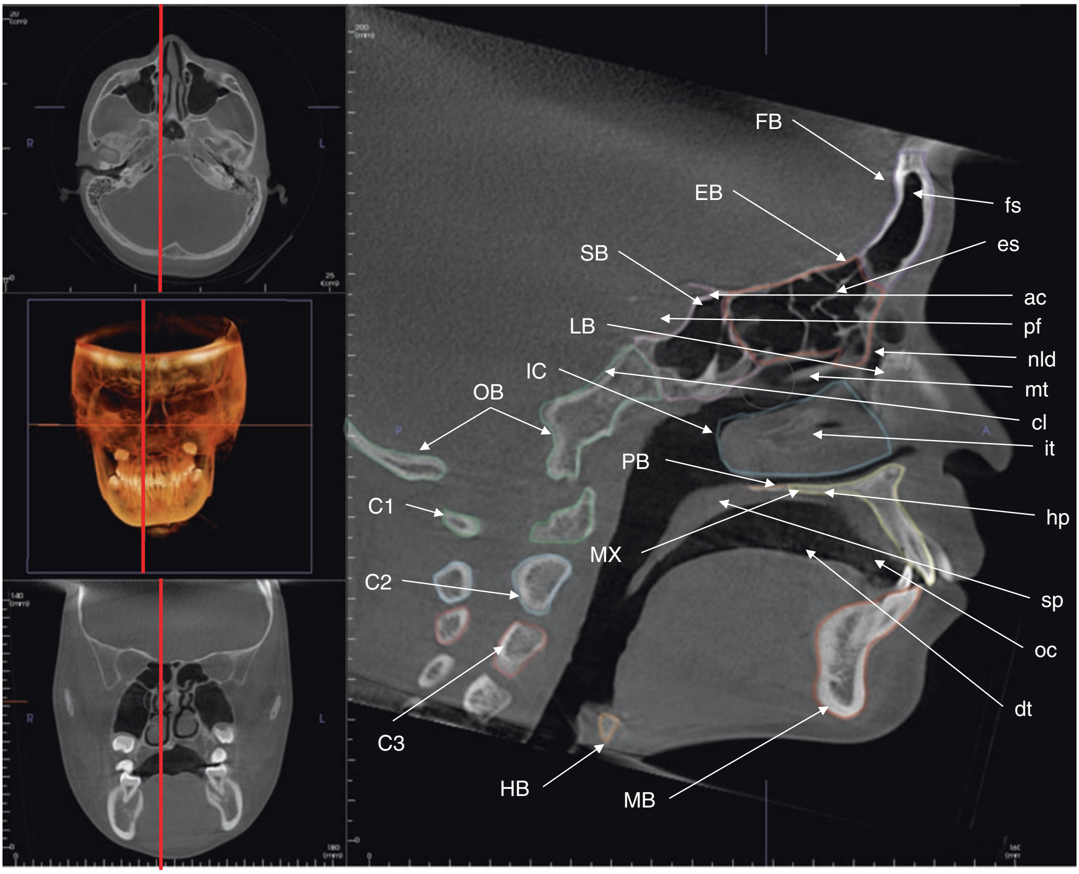

Fig. 9.34 Sagittal orthogonal CBCT image at the level of the nasolacrimal duct (nld) (*right*) with axial (*upper left*), frontal volumetric rendering (*middle left*), and coronal (*lower left*) reference images. (*FB* frontal bone, *EB* ethmoid bone, *SB* sphenoid bone, *LB* lacrimal bone, *IC* inferior conchae, *PB* palatal bone, *OB* occipital bone, *MX* maxilla, *C1* Atlas/first cervical vertebrae, *C2* Axis/second cervical vertebrae, *C3* third cervical vertebrae, *HB* hyoid bone, *MB* mandible, *fs* frontal sinus, *es* ethmoid sinus, *ac* anterior clinoid, *pf* pituitary fossa, *mt* middle turbinate, *cl* clivus, *it* inferior turbinate, *hp* hard palate, *sp* soft palate, *oc* oral cavity, *dt* dorsum of the tongue)

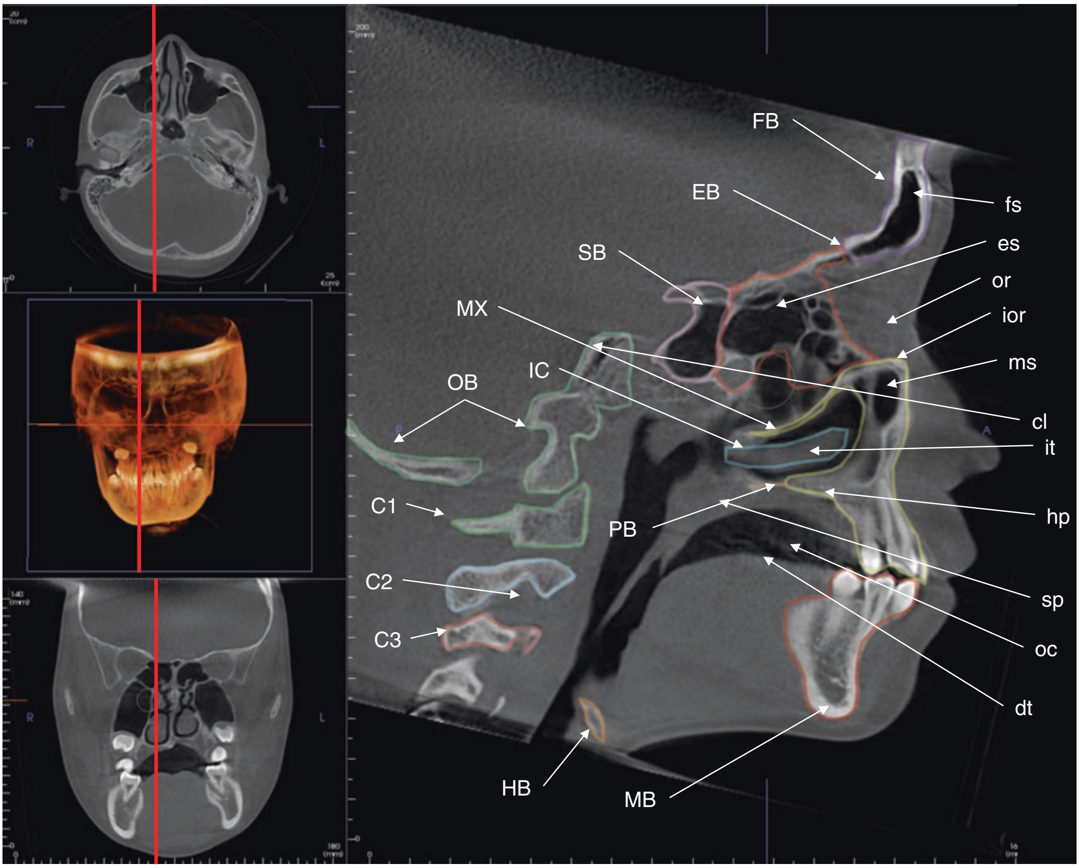

Fig. 9.35 Sagittal orthogonal CBCT image at the level of the medial wall of the right maxillary sinus (*right*) with axial (*upper left*), frontal volumetric rendering (*middle left*), and coronal (*lower left*) reference images. (*FB* frontal bone, *EB* ethmoid bone, *SB* sphenoid bone, *MX* maxilla, *IC* inferior conchae, *PB* palatal bone, *OB* occipital bone, *C1* Atlas/first cervical vertebrae, *C2* Axis/second cervical vertebrae, *C3* third cervical vertebrae, *HB* hyoid bone, *MB* mandible, *fs* frontal sinus, *es* ethmoid sinus, *or* orbit, *ior* intraorbital ridge, *ms* maxillary sinus, *cl* clivus, *it* inferior turbinate, *hp* hard palate, *sp* soft palate, *oc* oral cavity, *dt* dorsum of the tongue)

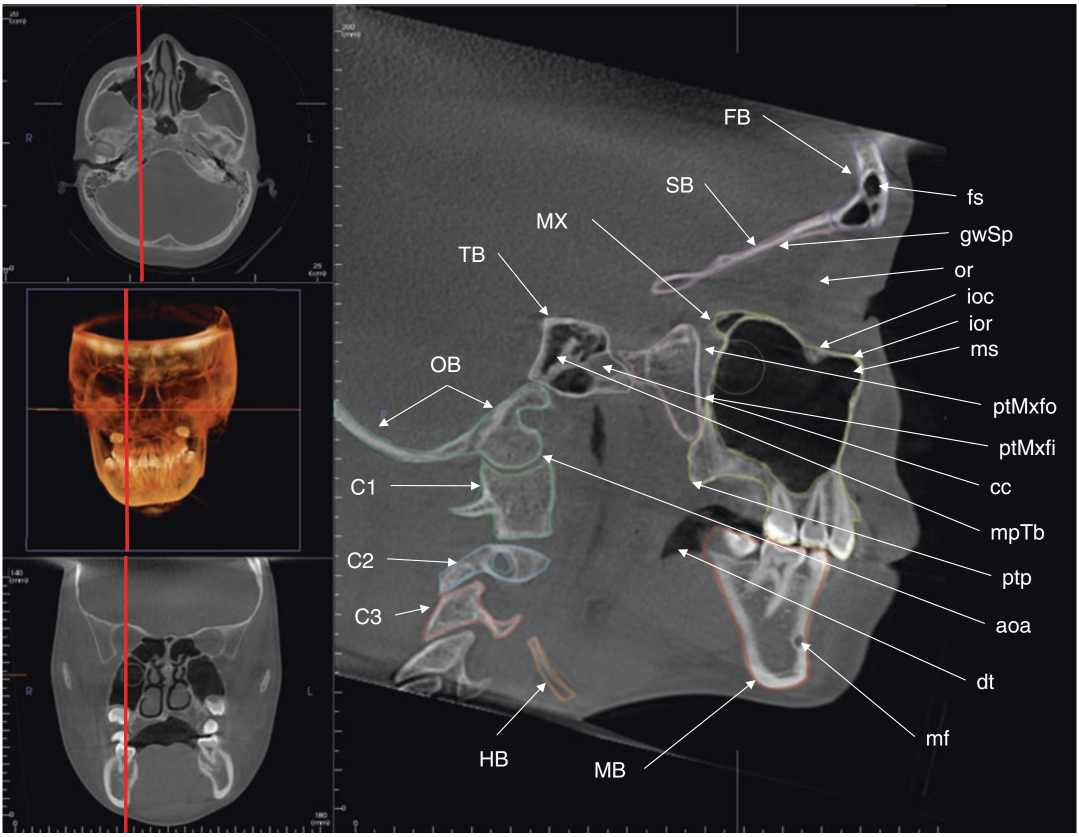

Fig. 9.36 Sagittal orthogonal CBCT image at the level of the medial wall of the right maxillary sinus (*right*) with axial (*upper left*), frontal volumetric rendering (*middle left*), and coronal (*lower left*) reference images. (*FB* frontal bone, *SB* sphenoid bone, *MX* maxilla, *TB* temporal bone, *OB* occipital bone, *C1* Atlas/first cervical vertebrae, *C2* Axis/second cervical vertebrae, *C3* third cervical vertebrae, *HB* hyoid bone, *MB* mandible, *fs* frontal sinus, *gwSp* greater wing of the sphenoid bone, *or* orbit, *ioc* infraorbital canal, *ior* intraorbital ridge, *ms* maxillary sinus, *ptMxfo* pterygomaxillary fossa, *ptMxfi* pterygomaxillary fissure, *cc* carotid canal, *mpTb* mastoid process of the temporal bone, *ptp* pterygoid plate of the sphenoid bone, *aoa* atlantooccipital articulation, *dt* dorsum of the tongue, *mf* mental foramen)

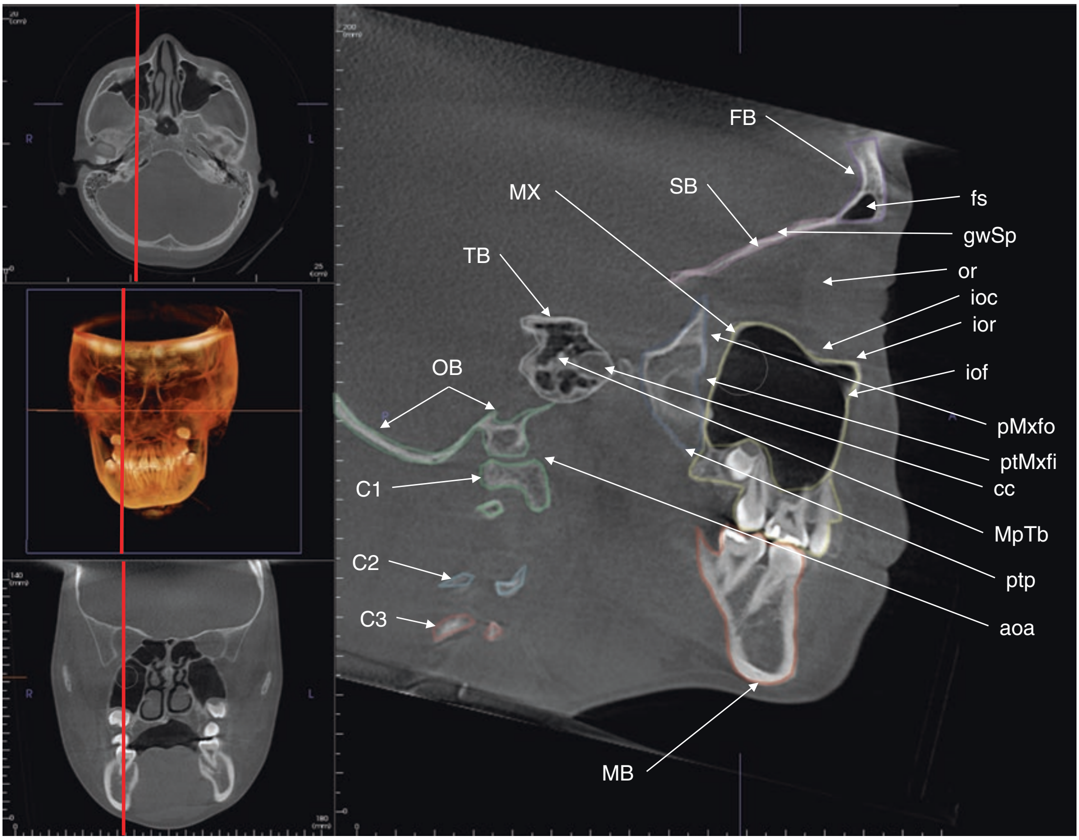

Fig. 9.37 Sagittal orthogonal CBCT image at the level of the right infraorbital foramen (*right*) with axial (*upper left*), frontal volumetric rendering (*middle left*), and coronal (*lower left*) reference images. (*FB* frontal bone, *SB* sphenoid bone, *MX* maxilla, *TB* temporal bone, *OB* occipital bone, *C1* Atlas/first cervical vertebrae, *C2* Axis/second cervical vertebrae, *C3* third cervical vertebrae, *MB* mandible, *fs* frontal sinus, *gwSp* greater wing of the sphenoid bone, *or* orbit, *ioc* infraorbital canal, *ior* intraorbital ridge, *iof* intraorbital foramen, *ptMxfo* pterygomaxillary fossa, *ptMxfi* pterygomaxillary fissure, *cc* carotid canal, *mpTb* mastoid process of the temporal bone, *ptp* pterygoid plate of the sphenoid bone, *aoa* atlantooccipital articulation)

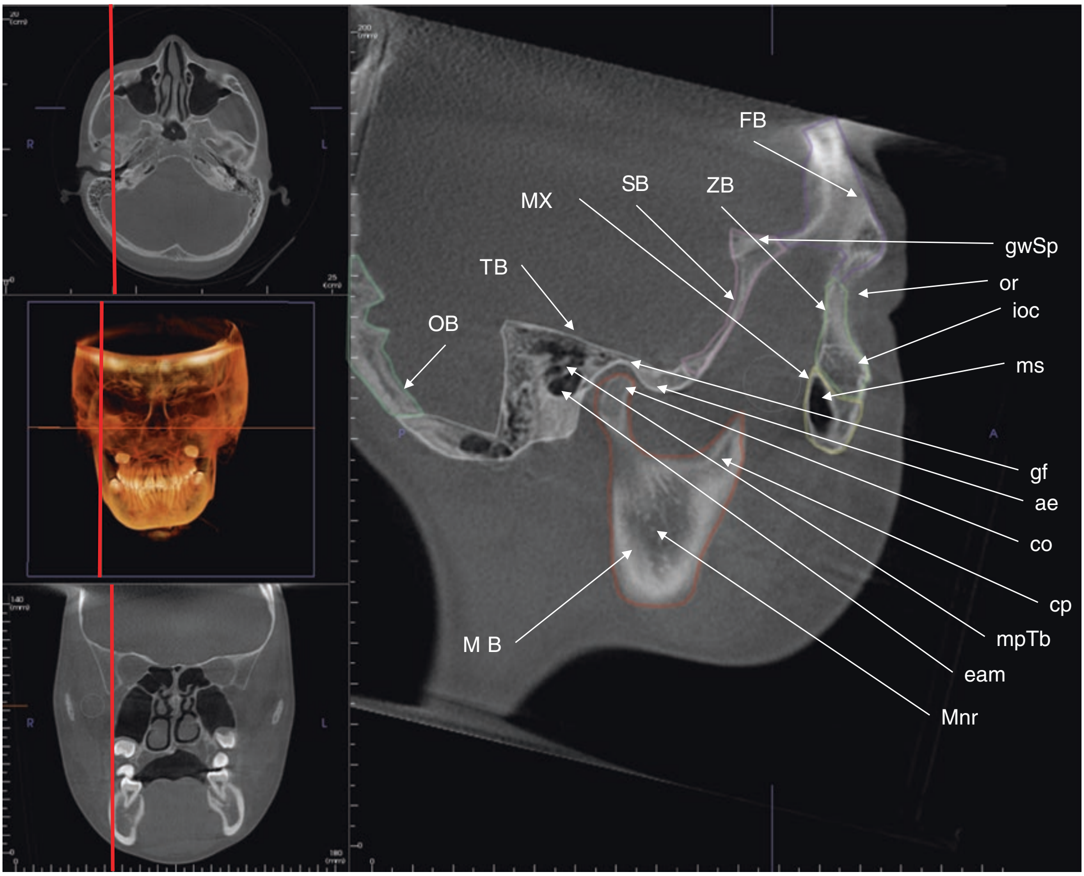

Fig. 9.38 Sagittal orthogonal CBCT image at the level of the right mandibular condyle (*right*) with axial (*upper left*), frontal volumetric rendering (*middle left*), and coronal (*lower left*) reference images. (*FB* frontal bone, *ZB* zygomatic bone, *SB* sphenoid bone, *MX* maxilla, *TB* temporal bone, *OB* occipital bone, *MB* mandible, *gwSp* greater wing of the sphenoid bone, *or* orbit, *ms* maxillary sinus, *gf* glenoid fossa, *ae* articular eminence, *co* condyle, *cp* coronoid process, *mpTb* mastoid process of the temporal bone, *eam* external auditory meatus, *Mnr* mandibular ramus)

The Jaws, Oral Cavity, and Nasopharynx

10

Christos Angelopoulos and William C. Scarfe

Contents

C. Angelopoulos, D.D.S., M.S. (✉)
Aristotle University of Thessaloniki, Thessaloniki, Greece

Columbia University, College of Dental Medicine, New York City, NY, USA
e-mail: angelopoulosc@gmail.com

W.C. Scarfe, B.D.S., F.R.A.C.D.S., M.S.
Division of Radiology and Imaging Science, Department of Surgical/Hospital Dentistry, University of Louisville School of Dentistry, Louisville, KY, USA
e-mail: william.scarfe@louisville.edu

10.1 Introduction

Maxillofacial cone beam computed tomographic (CBCT) images pose difficulties for many dental professionals because most are unfamiliar with developing and interpreting the image formats developed from the CBCT volume—they are like no other images previously available in the dental diagnostic imaging arsenal. This becomes even more challenging when evaluating tomographic images of the maxillofacial region due to the anatomical complexity of this area.

For years dental professionals have been trained in utilizing and interpreting traditional plain film dental imaging modalities, such as intraoral radiography, panoramic radiography, and cephalometric radiography, and are well aware of the advantages, indications, and contraindications for their use. Clinicians are also cognizant of the limitations of these images in that they are two-dimensional representations of three-dimensional structures, superimposing various osseous structures, and subject to geometric effects (image magnification and distortion) due to the projectional nature of traditional imaging. As described previously, CBCT acquisition is entirely different in that multiple projective frame data are reconstructed to provide a volumetric dataset. Unlike 2D projective imaging, primary reconstruction demonstrates the dataset as stacks of uniform and contiguous

W.C. Scarfe, C. Angelopoulos (eds.), *Maxillofacial Cone Beam Computed Tomography*,
https://doi.org/10.1007/978-3-319-62061-9_10

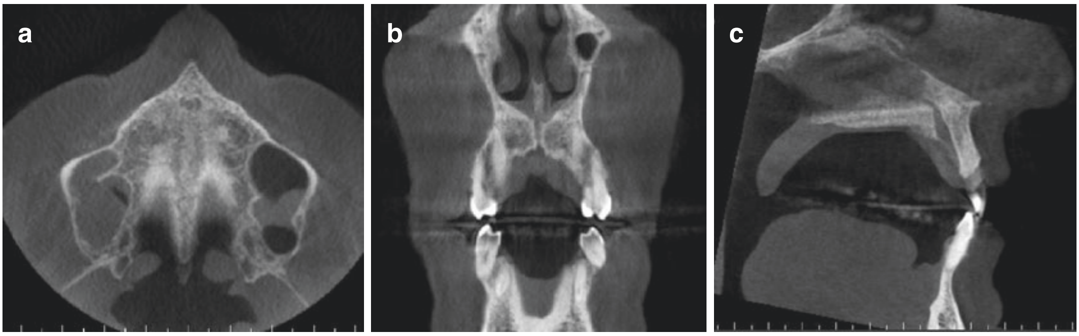

Fig. 10.1 Representative primary reconstruction of CBCT volumetric data as axial (**a**), coronal (**b**), and sagittal (**c**) orthogonal displays

sections in the three orthogonal planes (axial, coronal, and sagittal) (Fig. 10.1). Subsequently the volume can be sectioned and reconstructed in any possible plane, either linearly or obliquely providing a flat oblique or curved planar image, respectively (Scarfe et al. 2010). This property is known as *multiplanar imaging/reformatting* (MPR).

MPR is the capability to re-synthesize a multitude of images or sections with simple functions of data manipulation after a volume has been acquired. This function completely eliminates the superimposition of the anatomical structures or even pathology encountered with conventional imaging modalities, markedly increasing the diagnostic efficiency of CBCT (Angelopoulos 2008). MPR is most often used in combination with trans-axial imaging—multiple limited field of view (FOV) thin section contiguous slicing orthogonal to the MPR plane providing multiple cross sections. This additional display tool is perhaps the most useful in maxillofacial interpretation as it allows representation of features according to their anatomical orientation and eliminates the superimposition of adjacent structures with the control of MPR slice thickness. However, the application MPR may be challenging as it provides a sequence of multiple image sequences with unobscured detail and demands a higher level of professional competence than that necessary to interpret a single projective image. The diagnostic yield from orthogonal and MPR displays is dependent upon:

1. The knowledge, experience, and technical skill of the diagnostician in developing reconstructed images.
2. The correct application of the available MPR format.
3. Sound knowledge of the anatomy and interrelationships of elements within the region of interest.

In clinical practice, anatomical knowledge is perhaps the most demanding factor for successful interpretation since the maxillofacial skeleton is composed of numerous complex structures which form multidirectional spatial relationships with one another. Consequently, structural appearance will vary considerably in different tomographic planes (Angelopoulos 2014). Familiarity with the variable tomographic appearance of the maxillofacial structures and their spatial relationships is crucial in understanding the difference between diseased tissues and anatomical variants of the maxillofacial skeleton, disease origin and disease spread.

The goal of this chapter is to review maxillofacial anatomical structures and common variations which may be represented on CBCT images.

10.1.1 The Role of Reformatted Panoramic Imaging

Although review of orthogonal planar imaging (axial, coronal, and sagittal sections) is important for maxillofacial diagnosis, curved planar MPR reformatting with perpendicular trans-axial (cross-sectional) imaging of the maxilla and the mandible seems to be the most commonly used in maxillofacial CBCT applications. This is because MPR provides optimal imaging of the jaws as the curved plane conforms to the uniqueness of the jaw shape. Panoramic reformation is accompanied by creation of a series of sequential, cross-sectional images perpendicular to jaw which provide an "in depth assessment" of a certain region of the jaw. The combination of both formats negates the superimposition of anatomic structures inherent in 2D dental imaging. Moreover, it provides accurate representation of the alveolar ridge height and width that is crucial in specific treatment options especially in surgical procedures (Scarfe et al. 2006). Panoramic image creation is an integral part of most CBCT viewing software. It is mandatory that different panoramic reformats be generated for the maxilla and mandible when accurate measurements are required due to curvature differences of the two jaws (Figs. 10.2 and 10.3). In this way, parallax error will be minimized and measurements obtained of the residual alveolar ridge of edentulous areas the cross-sectional images for alveolar bone height and width will be the most accurate.

Cross-sectional imaging of the jaws provides information and details concerning:

- The shape, size, dimensions, and angulation of the edentulous alveolar ridge (Fig. 10.4). Although variations in the shape and size of the mandibular alveolar bone exist among dentate individuals, it is the residual alveolar ridge that undergoes the most changes with time due to resorption, after tooth extraction. Bone atrophy may alter the spatial relationship of the structures of concern and may add to the anatomical limitations in certain treatment options, especially in the placement of dental implants.

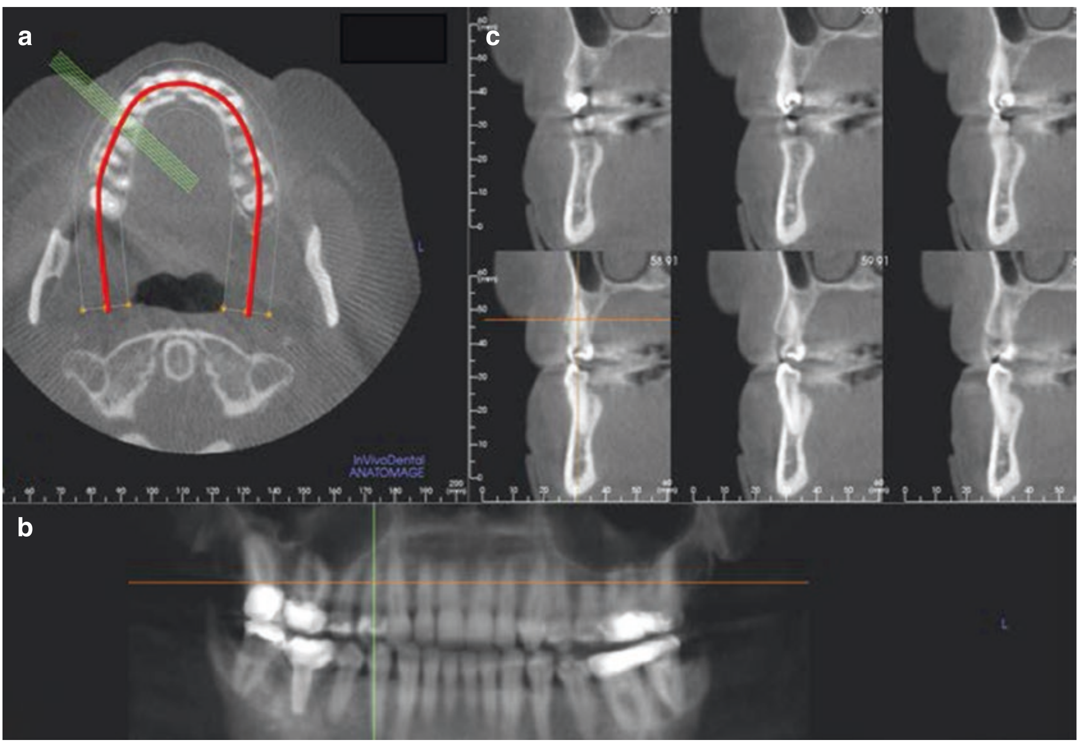

Fig. 10.2 The axial image (**a**) is used to create a "spline" at the mid-root level of the teeth along the arch shape of the maxilla from which a curved planar "panoramic" image (**b**) is reformatted. The *curvilinear line* (*red*) represents the center of the panoramic image. The *green lines*, perpendicular (or near perpendicular) to the *curvilinear line*, represent the reformatted cross sections (**c**) in the region of interest (maxillary right premolars). For accurate dimensions of the maxillary bone in cross section, the *green lines* (cross-sectional images) should be perpendicular to the maxillary bone

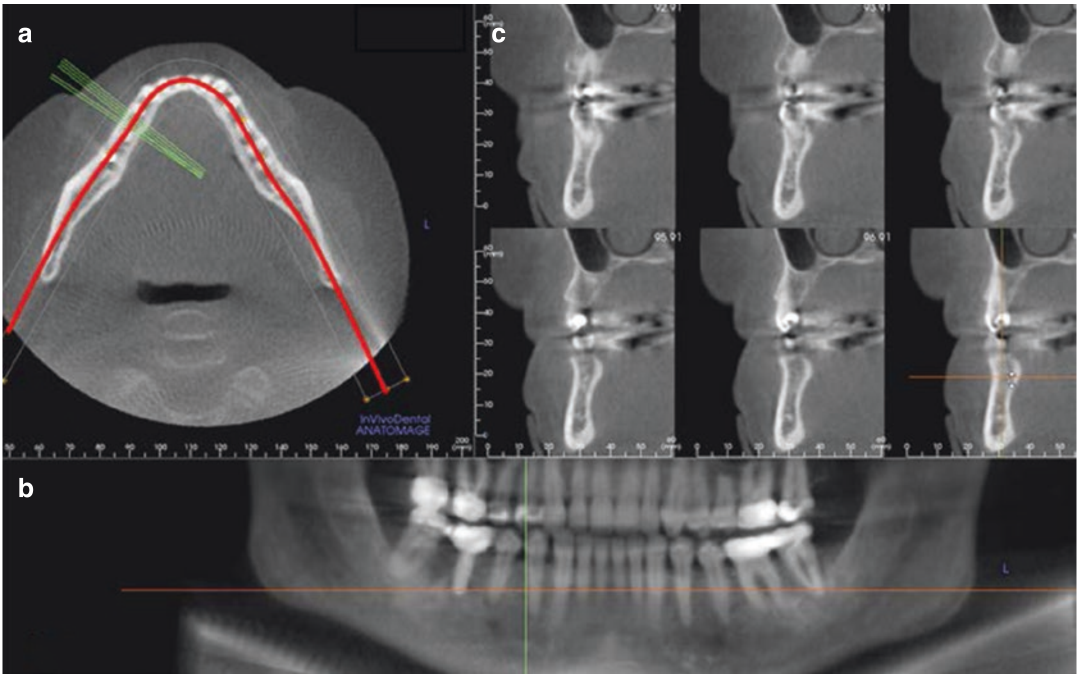

Fig. 10.3 Panoramic reformat of the same individual as Fig. 10.2 except that the "spline" is developed on an axial image (**a**) at the root apex level of the mandibular teeth along the arch shape of the mandible. Note that the reformatted panoramic image (**b**) and cross-sectional images (**c**) demonstrate the same anatomy in the right premolar region of the jaws somewhat differently

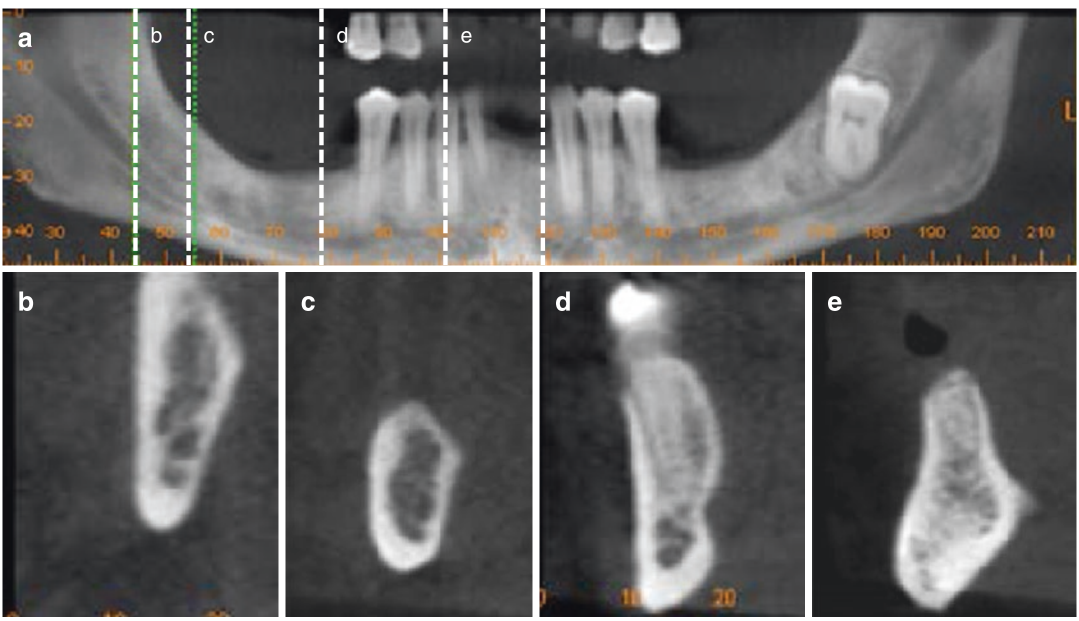

Fig. 10.4 Reference panoramic image (**a**) with a series of cross sections of the right mandible extending from the retromolar trigone (**b**) to the molar area (**c**) to the premolar area (**d**) and finally to the anterior mandible (**e**). The region from which each of the representative cross-sectional images is taken is shown by the *dotted white lines* on the panoramic image (**a**). Note the gradual changes in the shape and size of the mandibular bone from the posterior to anterior locations. Anatomical variation of the shape and size of the mandibular bone is very common

- The spatial relationship of the anatomical structures in the jaws that are routinely encountered in intraoral and panoramic images.
- The long axis of the alveolar bone and the related long axis of the teeth in the region which do not necessarily coincide (Fig. 10.5). This is an important information needed during dental implant treatment planning.

10.1.2 A Panoramic Approach to Regional CBCT Anatomy

For maxillofacial CBCT imaging, reformatted panoramic in combination with serial trans-axial (cross-sectional) images are the images of choice for the evaluation of the maxillary and mandibular dental arches including the dentition as well as the associated alveolar bone in edentulous regions. However, frequently, other reconstructions may be developed to assess the anatomic region from different perspectives including standard orthogonal multiplanar sections (axial, coronal, and sagittal), other region specific planar or curved planar MPR sections, and surface rendering reconstructions. For example, coronal sections provide a wider view of the maxillary and mandibular inter-arch relationships and more accurately demonstrate the spatial relationships of these structures.

Knowledge of the anatomic regions and specific topographic anatomy seen on reformatted panoramic images is essential to identify and describe the location of specific features or anomalies. However, differences between the

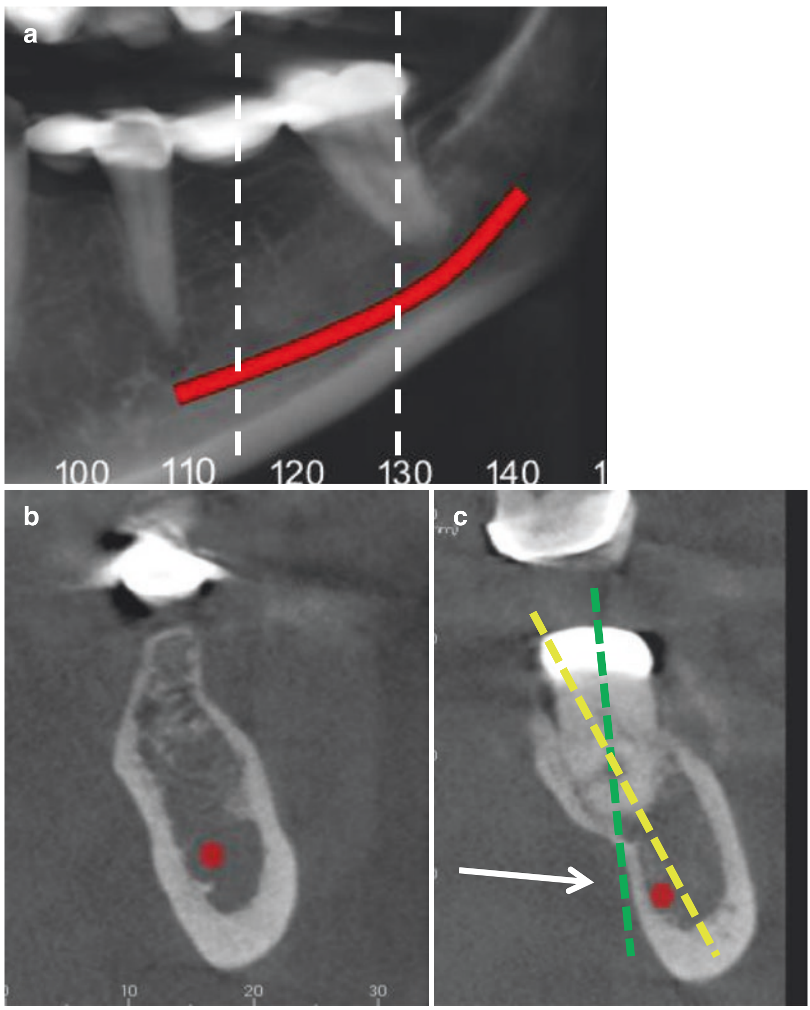

Fig. 10.5 Cropped panoramic image (**a**) and mandibular cross sections (**b**, **c**) in the molar region at the corresponding *dashed lines* in the panoramic image. The long axis of the mandibular bone (*yellow dashed line*) frequently does not correspond to the long axis of the teeth in the region (*green dashed line*). The faint low-density area indicated by the *white solid arrow* is the submandibular gland fossa (depression)

construction of reformatted panoramic images from CBCT data and production of conventional images from classical rotational panoramic radiography result in seemingly similar but, in many respects, different images (Table 10.1).

The process of creating a panoramic image also generates multiple trans-axial images perpendicular to the curved planar spline. Review of the volumetric data involving the jaws based on this reformation protocol is an essential radiologic skill for dental practitioners and involves a systematic approach and a detailed understanding of the anatomic features in each of six zones (Fig. 10.6). Three zones are in the midline and three zones are bilateral.

- **Zone 1**. Nasal fossa, nasopharynx (See Chap. 13), zygoma, maxilla, and maxillary sinuses (See Chap. 12).
- **Zone 2**. Temporomandibular joint (See Chap. 24) and temporal bone (See Chap. 14)
- **Zone 3**. Mandibular ramus, cervical vertebrae (See Chap. 11), oropharynx (See Chap. 13), and parapharyngeal soft tissues (See Chap. 11);
- **Zone 4.** Hyoid bone (See Chap. 11), lateral neck soft tissues (See Chap. 11), and oropharynx (See Chap. 13);
- **Zone 5.** Mandibular body.
- **Zone 6.** Maxillary and mandibular dental arches including the dentition and alveolus.

Table 10.1 Differences between reformatted panoramic images from CBCT data and conventional images from classical rotational panoramic radiography

	Panoramic image type		
Aspects	Reformatted	Conventional	Clinical significance
Construction	Layer position and width is most often user defined	Manufacturer defined, with limited modifications (e.g., “v” shaped, normal, broad arch shapes)	CBCT reformatted panoramic image is free from patient positioning errors and artifacts (e.g., “ghost” images)
			CBCT panoramic images can be constructed thin (5–10 mm) or thick (>25 mm) changing visibility of structures
	Custom curved layer to either the maxillary or mandibular dentition	Fixed, usually based on the average shape of the mandibular dentition	As the image layer corresponds to the position of the teeth, there is limited blur of teeth in the dental arch on reformatted panoramic images
	Projection is always perpendicular to the panoramic construction line (spline)	Projection is not perpendicular to the panoramic image layer	There is limited tooth overlap in reformatted panoramic images unlike conventional panoramic images that often show overlap of interproximal contacts, especially in the premolar region
Image layer	Uniform width	Variable width ranging from narrow (10 cm) in the anterior region to wider (25 mm) posteriorly	Anterior teeth, premaxilla and symphyseal region in CBCT reformatted panoramic image are usually in focus
	Structures outside the image layer are excluded from the image	Structures outside the image layer are also included in the image	Soft tissues and airway spaces (appearing as indistinct but characteristic radiopaque shadows superimposed over the osseous and dental structures—e.g., external nose and ear, tongue, airway spaces) and medial and lateral osseous structures (e.g., hyoid bone, zygomatic arch) may not be visualized on CBCT panoramic images
	Undistorted	Wide range of distortion of structures within the image layer not corresponding exactly to the center of the image layer	There is no magnification or distortion of structures, particularly teeth, on reformatted panoramic images

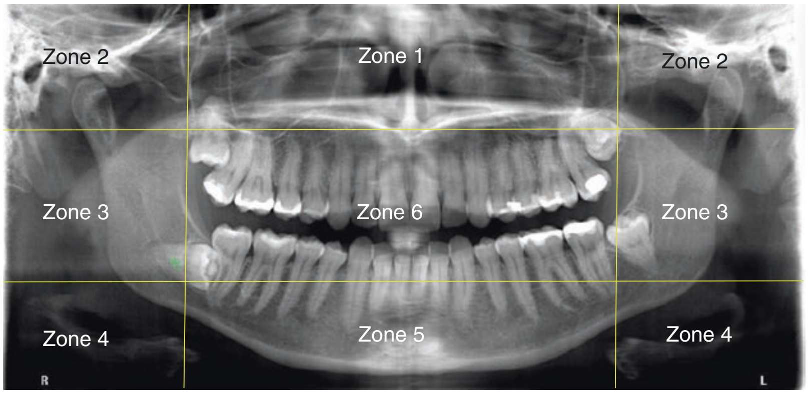

Fig. 10.6 Reformatted CBCT panoramic image demonstrating six regional zones for the assessment of cross-sectional images

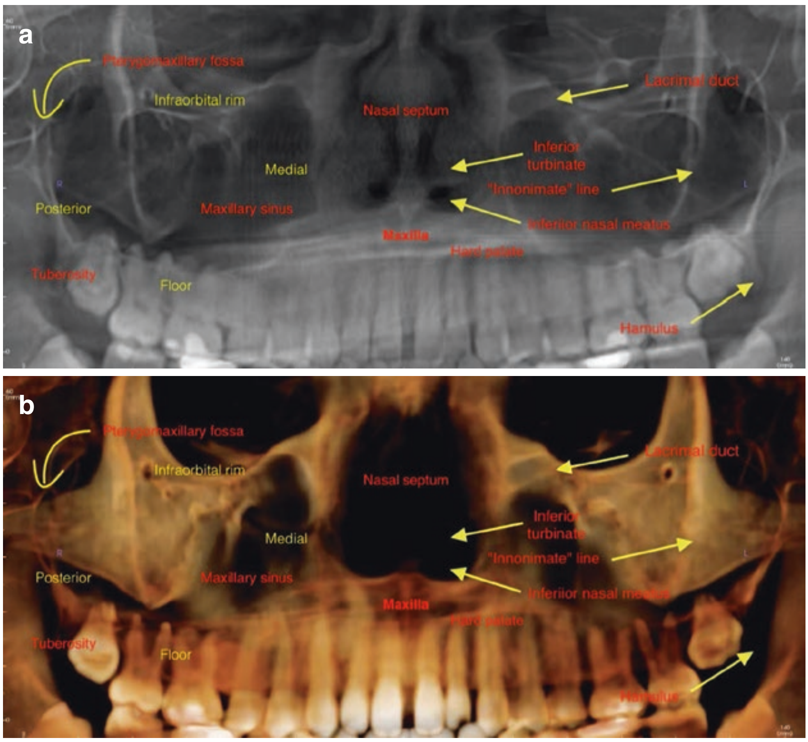

Fig. 10.7 Specific topographic features and anatomic landmarks seen on CBCT reformatted panoramic ray sum (**a**) and volumetric rendered (**b**) images for Zone 1

The utility of the reformatted panoramic image is that it provides a "dentition centric" representation of osseous anatomy of the maxillofacial region incorporating both the maxilla and mandible but also the including aspects of the nasal, sphenoid, zygomatic, and temporal bones (Figs. 10.7, 10.8, 10.9, 10.10, 10.11, and 10.12).

10.2 The Maxilla

The maxilla is an irregularly, pyramid-shaped, bone composed of two symmetrical components (hemi-maxillae) articulated together along the midline of the face with the medial palatine suture or inter-maxillary suture. The medial-superior aspect comprises the nasal

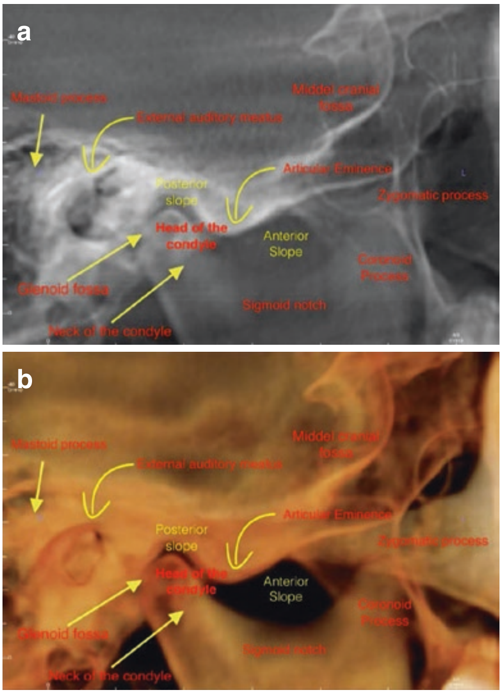

Fig. 10.8 Specific topographic features and anatomic landmarks seen on CBCT reformatted panoramic ray sum (**a**) and volumetric rendered (**b**) images for Zone 2

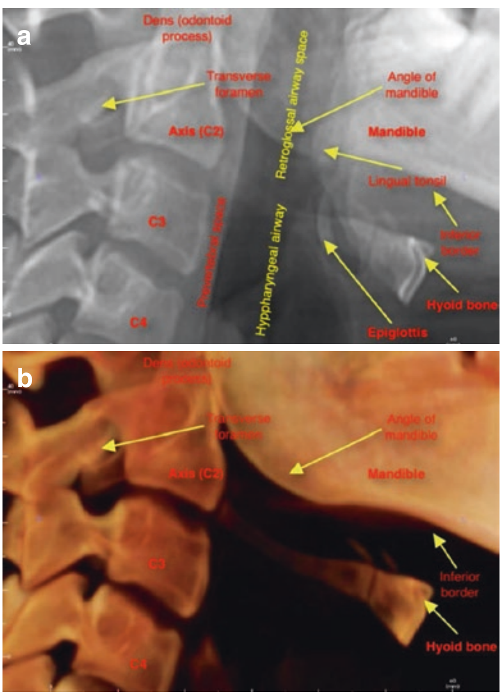

Fig. 10.10 Specific topographic features and anatomic landmarks seen on CBCT reformatted panoramic ray sum (**a**) and volumetric rendered (**b**) images for Zone 4

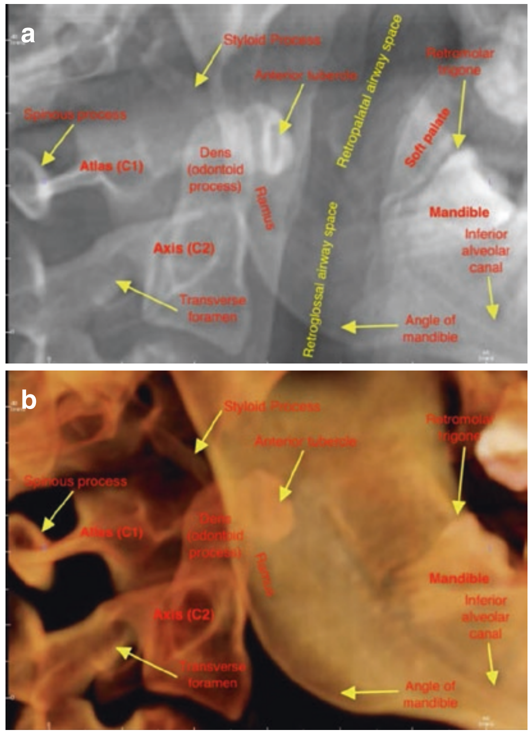

Fig. 10.9 Specific topographic features and anatomic landmarks seen on CBCT reformatted panoramic ray sum (**a**) and volumetric rendered (**b**) images for Zone 3

fossa, folded layers of cortical bone which contain large concavities and expand in all three dimensions, forming a large portion of the midfacial skeleton (Figs. 10.13 and 10.14). More laterally lies the largest component, the body of the maxilla, a "hollowed out" enclosure within which lies the maxillary sinus formed mostly by cortical bone lined by a thin layer of mucosa. The caudal (inferior) aspect of the maxillary bone is the alveolar process, an arch-shaped osseous projection and the palatine process (hard palate), a dome-shaped, concave layer of thick cortical bone which forms the roof of the oral cavity. The alveolar process is composed of cancellous bone lined by a varying thickness of cortical layer and houses the maxillary teeth in thin-walled cortical concavities, the tooth sockets.

Laterally the maxillary body has two zygomatic processes that articulate with the zygomatic bones on either side of the midface and superiorly two frontal processes that articulate

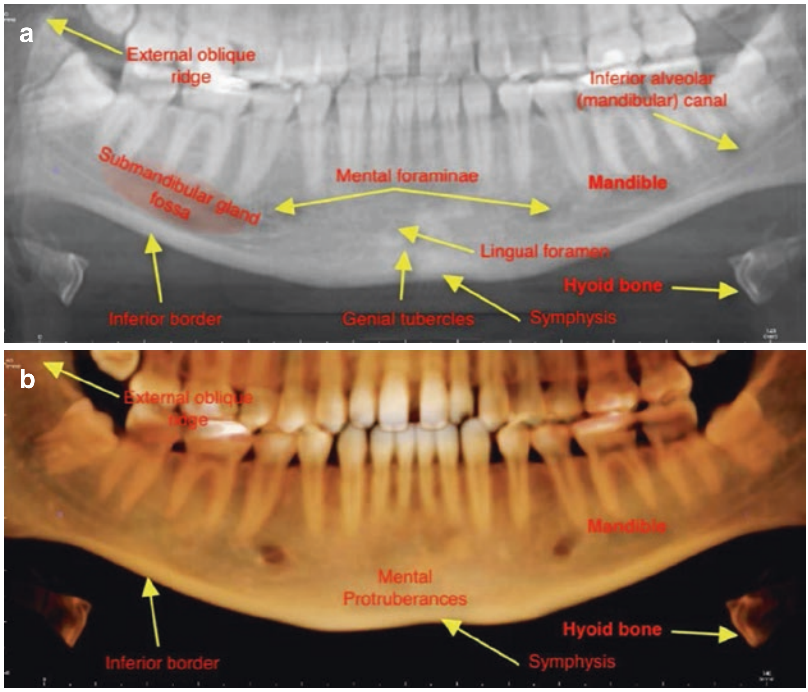

Fig. 10.11 Specific topographic features and anatomic landmarks seen on CBCT reformatted panoramic ray sum (**a**) and volumetric rendered (**b**) images for Zone 5

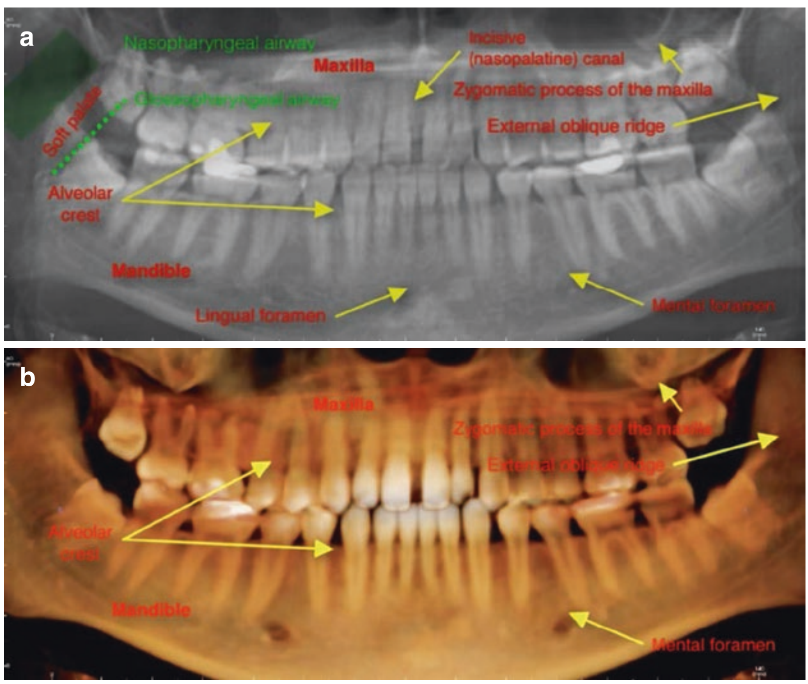

Fig. 10.12 Specific topographic features and anatomic landmarks seen on CBCT reformatted panoramic ray sum (**a**) and volumetric rendered (**b**) images for Zone 6

with the frontal bones and nasal bones. In addition, each hemi-maxilla presents a thick horizontal fold (inferior orbital rim) which extends dorsally forming a horizontal plate (orbital plate of the maxilla) contributing to the formation of the floor of each orbit.

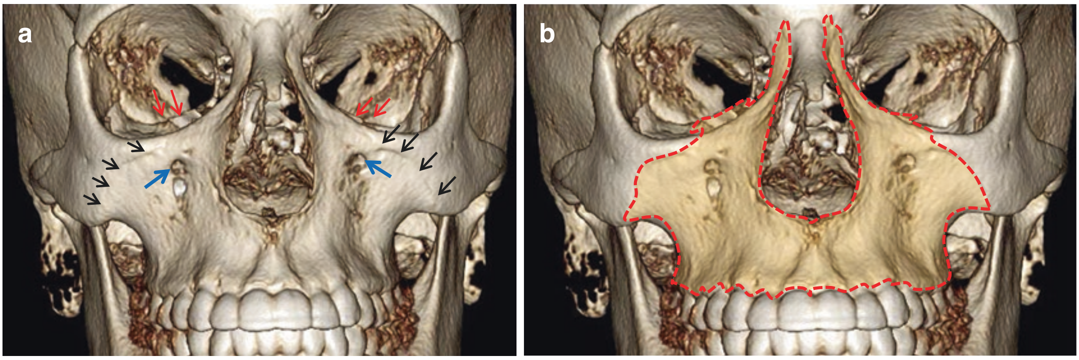

Fig. 10.13 Unmarked (**a**) and annotated (**b**) shaded surface frontal rendering of the midface (facial view) outlining the major components of the maxillary bone: The cephalad thin processes are the frontal processes of the maxilla; the lateral projections of the maxillary bone are the zygomatic processes (*black arrows*); maxillary orbital plates (*red arrows*). The alveolar process is the caudal end of the maxillary bone housing the maxillary teeth. The frontal surface openings are the infraorbital foramina (*blue arrows*)

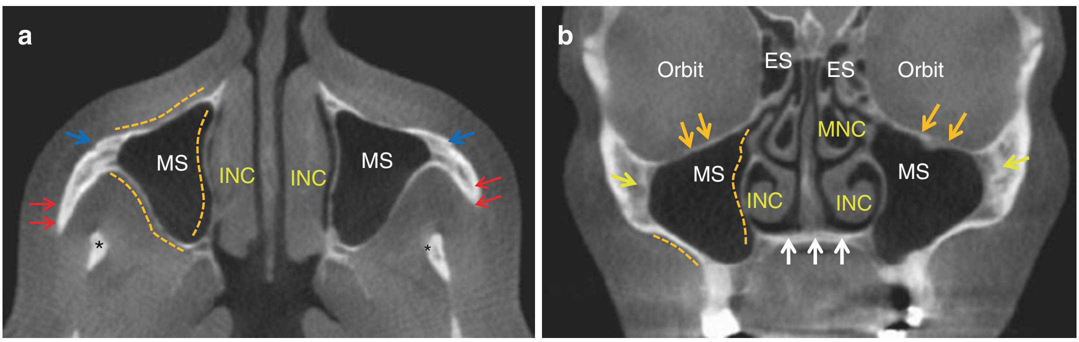

Fig. 10.14 Axial (**a**) and coronal (**b**) orthogonal image outlining the anterior, posterolateral and medial walls of the body of the maxilla (*orange dotted lines* in **a**) lateral and medial walls (**b**) floor of the orbit (*orange arrows* in **b**), zygomatic process of the maxilla (*yellow arrows* in **b**), hard palate (*white arrows* in **b**), zygomatic arch (*red arrows* in **a**), the maxillary sinus (MS), ethmoid sinus (ES), and coronoid process of the mandible (*black asterisk* in **a**)

10.2.1 The Infraorbital Foramen

The infraorbital foramen (IOF) (Figs. 10.15, 10.16, and 10.17) is an important anatomical landmark of the body of the maxillary bone. It is located on the facial aspect of the body of the maxilla approximately 5–6 mm below the inferior orbital rim and just cephalad to the canine fossa, a depression present above the canine, lateral to the ipsilateral nasal cavity. The IOF transmits the infraorbital nerve, a terminal branch of the maxillary nerve (V2), and respective blood vessels. The infraorbital nerve originates inside the pterygopalatine fossa, enters the infraorbital groove (a sulcus on the orbital plate of the maxilla), continues in the infraorbital canal, and exits to the face through the infraorbital foramen. The infraorbital nerve provides sensory innervation to anterior maxillary bone and soft tissue and anastomoses with terminal branches of the posterior superior alveolar nerves.

10.2.2 Posterior Superior Alveolar Canal

Two additional branches of the maxillary neurovascular bundle, the posterior superior alveolar (PSA) and middle superior alveolar (MSA), originate within the pterygopalatine fossa. Both branches travel within the lateral walls of the maxilla and are occasionally visible in either coronal or cross-sectional images of the maxilla

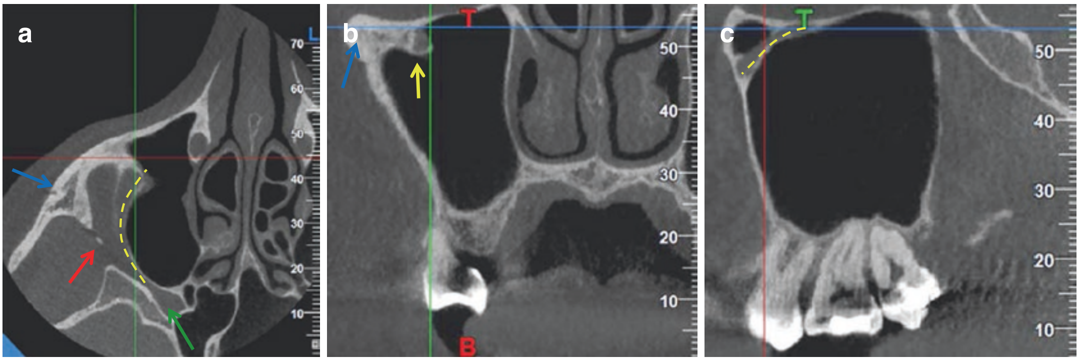

Fig. 10.15 Axial (**a**), coronal (**b**), and sagittal (**c**) orthogonal images depicting the course of the infraorbital nerve inside the orbital plate of the maxillary bone (*yellow dotted line*) from the pterygopalatine fossa (*green arrow*) to its exit point on the facial surface of the body of the maxilla as the infraorbital foramen (*yellow arrow*) (*blue arrow* zygomatic process, *red arrow* inferior orbital fissure)

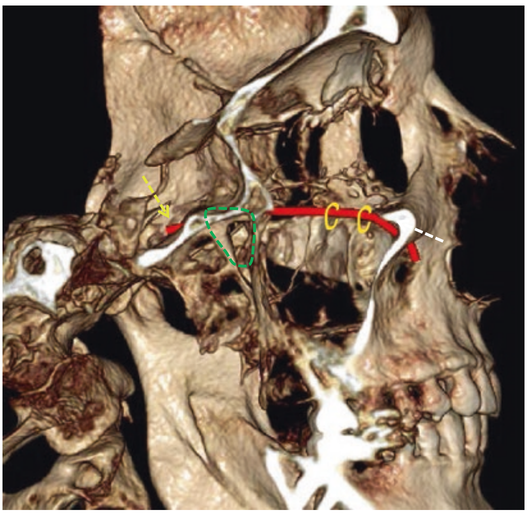

Fig. 10.16 Cropped lateral surface rendering of the midface illustrating the course of the maxillary nerve (V2) from the foramen rotundum (*yellow dashed arrow*) to the pterygopalatine fossa (*dashed green triangle*) where one of the branches, the infraorbital nerve traverses through the infraorbital groove (artistic representation with *orange rings*) to exit through the infraorbital foramen (*white dashed arrow*)

(Fig. 10.18). Both follow an almost horizontal course and appear as small linear hypo-densities at variable distances superior to the alveolar ridge in cross-sectional imaging (de Oliveira et al. 2017). Identification of both the PAS and MSA is important especially in sinus grafting procedures, where bleeding may occur from injury to the PAS artery. This osseous canal may not be visible when its diameter is less than the voxel resolution of the CBCT acquisition.

10.2.3 The Maxillary Alveolar Process

The alveolar process is a horseshoe-shaped, solid osseous inferior extension of the body of the maxilla. It comprises two main parts without obvious physical distinction between the two: the base and the alveolar ridge. The base is the supporting osseous tissue whereas the alveolar process is the tooth-bearing bone. The alveolar process houses the maxillary teeth, the roots of which are usually located within the cortical plates of the alveolar bone. The interproximal surface of the crowns of the teeth aligns in contact forming a continuous dental arch. Tooth position directs and distributes the occlusal forces of mastication to the base of the alveolar bone which is broader in comparison to the crest (Fig. 10.19). With tooth loss, the alveolar bone resorbs and atrophies due to loss of function.

Because the maxillary alveolar ridge is essentially “U” shaped, MPR panoramic reformat and multiple cross-sectional images (perpendicular to the alveolar arch) are the most appropriate images for evaluation (Figs. 10.20 and 10.21). Cross-sectional images of the anterior maxilla demonstrate the shape and size of the respective alveolar ridge around each existing tooth. The facial and palatal cortical plates are easily recognized and

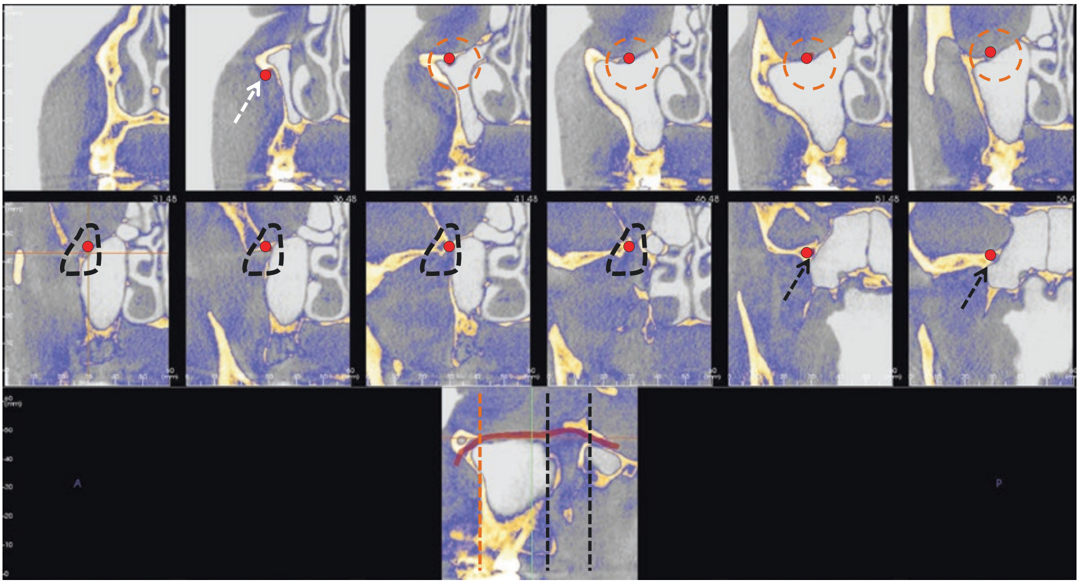

Fig. 10.17 A series of cross-sectional (filters applied) images (*above*) along a custom *curved line* (*below*) which follows the course of the maxillary nerve (V2) and its terminal branch, the infraorbital nerve from the foramen rotundum (*black dashed arrow*) to the pterygopalatine fossa (*black dashed triangle*) to the infraorbital groove (*brown dashed ring*) to its exit through the infraorbital foramen (*white dashed arrow*)

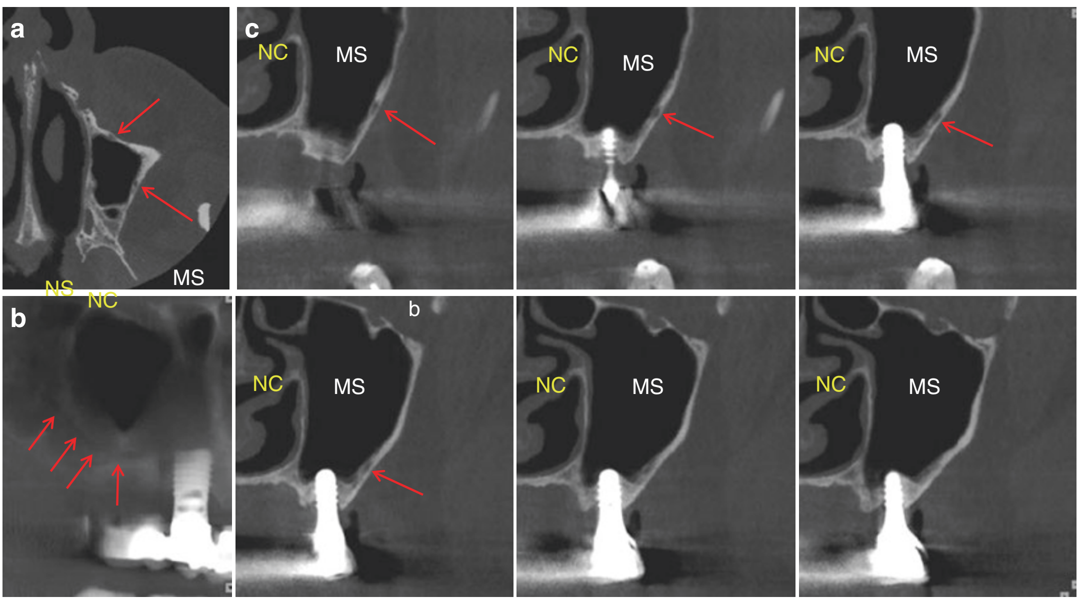

Fig. 10.18 Axial (**a**) and left posterior para-sagittal curved planar thick reformatted (**b**) and a series of cross-sectional images (**c**) show the course of the osseous canal for the PSA neurovascular bundle (*red arrows*) on the lateral wall of the maxillary sinus (MS) (*NC* nasal cavity, *NS* nasal septum)

their integrity and thickness can be assessed. Relevant anatomical limitations of the anterior maxilla are also clearly seen (e.g., the nasopalatine canal). The thickness of the cortical plates adjacent to the roots of the teeth vary and may range from 1 mm or more to imperceivible (Fig. 10.20). Compromised or eroded cortical

Fig. 10.19 Axial (**a**), coronal (**b**), orthogonal and thick panoramic reformatted (**c**) images of the maxillary alveolar process (*green dotted zone*) showing the existing maxillary teeth and neighboring anatomical structures (*green arrows* alveolar crest, *red arrows* buccal and palatal cortical plates, *white arrows* hard palate, *INC* inferior nasal concha, *MS* maxillary sinus, *NS* nasal septum)

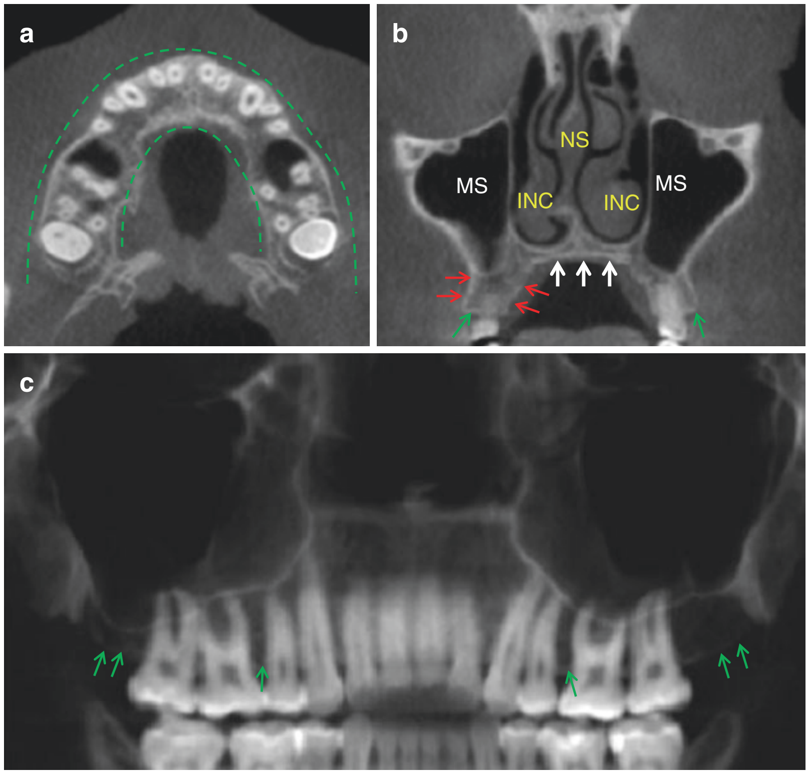

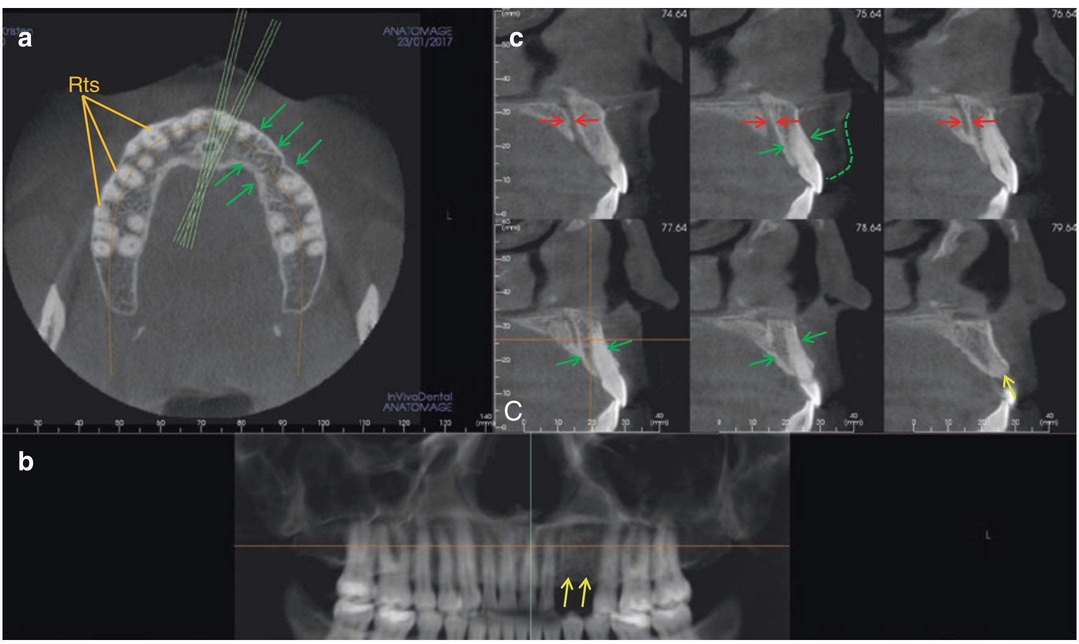

Fig. 10.20 Axial (**a**), thick panoramic reformatted (**b**) and sequential, trans-axial (cross-sectional) (**c**) images of the maxilla illustrating the maxillary alveolar process and regional anatomical structures of the left anterior maxilla (*green arrows* alveolar process, *yellow arrows* alveolar crest, *red arrows* nasopalatine canal, *Rt* roots of the maxillary teeth, *green dotted line* upper lip)

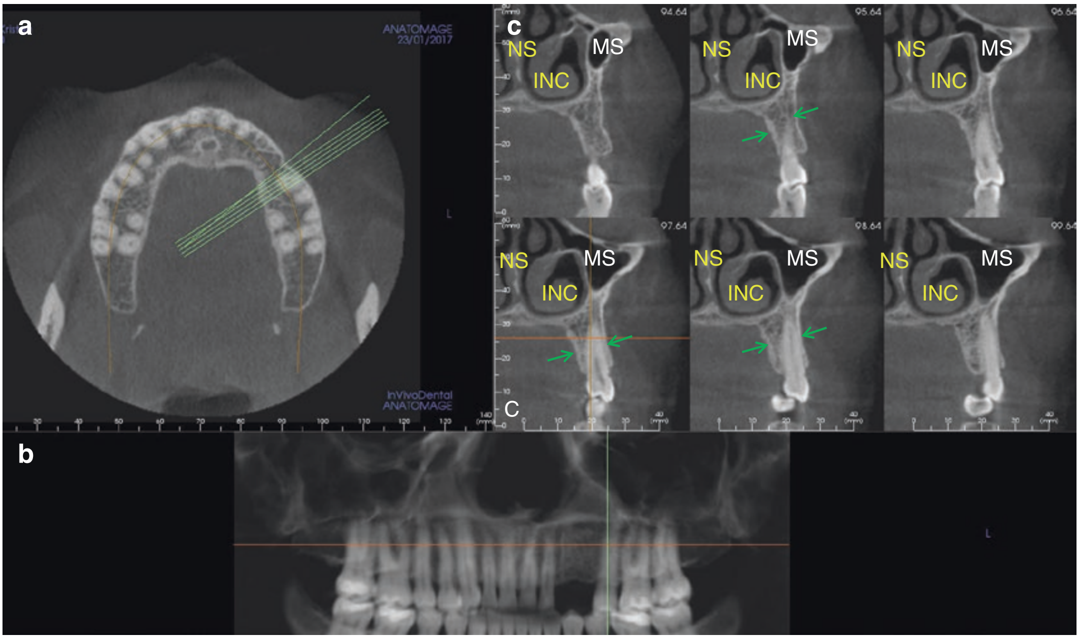

Fig. 10.21 Reference axial (**a**), thick panoramic reformatted (**b**), and sequential, trans-axial (cross-sectional) (**c**) images of the maxilla illustrating the maxillary alveolar process and regional anatomical structures of the left premolar maxilla (*green arrows* cortical plates of the alveolar process, *white arrows* hard palate, *NS* nasal septum, *INC* inferior nasal concha, *MS* maxillary sinus)

plates are often associated with apical pathology in adjacent teeth.

The assessment of the alveolar bone is crucial in edentulous as well as in dentate sites. In edentulous regions, the dimensions of the alveolar bone and its spatial relationship with the opposite alveolar ridge may be shown by sequential cross-sectional images. Moreover, nearby anatomical structures of importance such as the floor of the nasal cavity and floor of the maxillary sinus may be evaluated. Generally the alveolar bone is longer and thinner in the anterior maxilla to accommodate the comparable morphology of the roots of the anterior maxillary teeth.

Sequential cross-sectional images of the posterior maxillary region (Fig. 10.21) show that the alveolar bone gradually reduces in height and increases in width further posteriorly. Lateral portions of the ipsilateral nasal cavity and the entire maxillary sinus are visualized. The maxillary sinus initially appears narrow in the premolar region as this represents the anterior recess. Further posteriorly, the maxillary sinus becomes wider. The relationship of the roots of the premolar teeth to the maxillary sinus floor can be assessed which is important especially if there is developing apical pathology.

In posterior maxillary cross sections the molar teeth and their surrounding alveolar bone are seen (Fig. 10.22). The alveolar process becomes gradually thicker to accommodate the wider roots of the molars and decreases in height to accommodate the maxillary sinus. The thickness of the buccal and palatal cortical plates varies considerably from tooth to tooth. Variation in the root length and peculiarities in the floor of the maxillary sinus may result in an intimate relationship between the two and this should be determined in cases of developing pathology or possible surgical intervention. The maximum width of the maxillary sinus is displayed in this area and images in this region may demonstrate intrinsic or extrinsic sinus disease (see Chap. 30). Cross sections may also depict the PSA neurovascular bundle on the lateral wall of the maxillary sinus (Fig. 10.18).

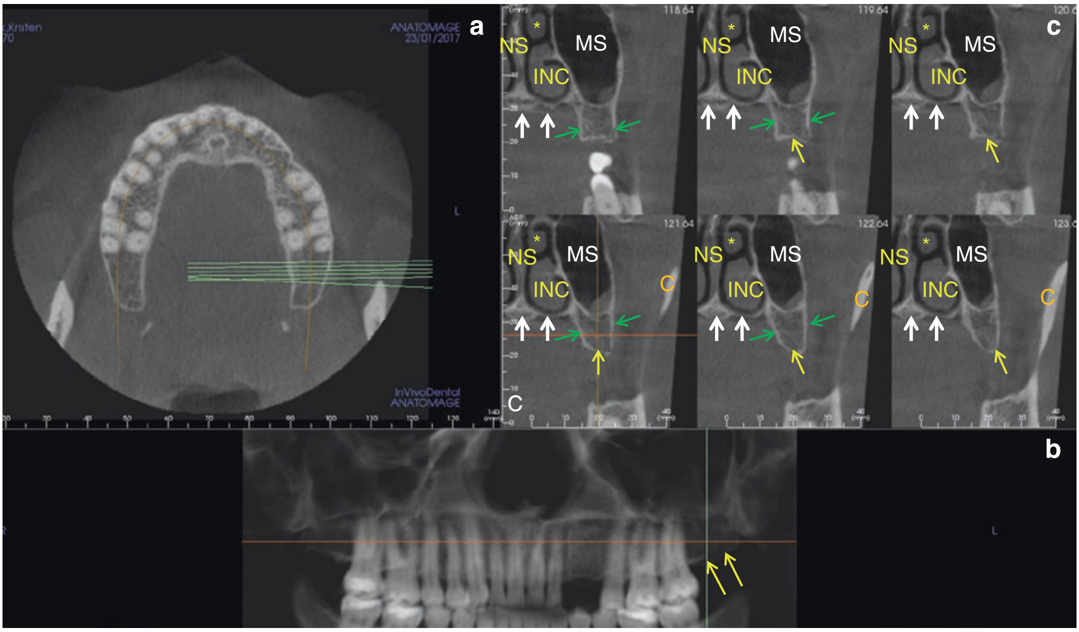

Fig. 10.22 Reference axial (**a**), thick panoramic reformatted (**b**), and sequential, trans-axial (cross-sectional) (**c**) images of the maxilla illustrating the maxillary alveolar process and regional anatomical structures of the left molar alveolar process and relevant neighboring anatomical structures (*green arrows* cortical plates of the alveolar process, *white arrows* hard palate, *NS* nasal septum, *INC* inferior nasal concha, *MS* maxillary sinus, *yellow arrows* alveolar crest, *C* coronoid process of mandible, *NS* nasal septum, *Asterisk* middle nasal concha)

The maxillary alveolar arch terminates at the maxillary tuberosity, a rounded osseous prominence distal to the last molar tooth (third molar). The tuberosity articulates with horizontal plate of the palatine bone and is adjacent to the vertical lateral pterygoid plate of the sphenoid bone. The pterygoid plates of the sphenoid bone may be visualized in the sequential cross sections in the posterior aspect of the maxillary arch if the panoramic spline is extended dorsally (Fig. 10.23). Pending on the height of the reconstructed cross sections, the pterygomaxillary fissure or a portion of it may be visualized (Fig. 10.24). This is a vertically oriented fissure between the posterior wall of the maxillary and the pterygoid process of the sphenoid bone. It connects the infratemporal fossa with the pterygopalatine fossa which serves as a passageway for the PSA neurovascular bundle (a branch of the maxillary nerve-V2) and terminal branches of the maxillary artery.

The alveolar process consists of intramedullary cancellous bone and a peripheral layer of compact, cortical bone, frequently called "the cortical plates." Cross-sectional images of the alveolar bone are best for the assessment of the fine details of bone composition and structure: The thickness of the cortical plates ranges from 1 to 3 mm depending on location, with the palatal cortical plate being thicker than the facial plate (Fig. 10.25). The cancellous bone pattern of the maxilla is usually a fine, delicate trabeculae with a random or occasionally horizontal orientation throughout the alveolar ridge; however, generalized hyperdensity (intrameduallary sclerosis) may also present (Fig. 10.26). Trabecular may be sparse in Type 4 bone or in patients with osteoporosis (White and Rudolph 1999; Monje et al. 2015).

10.2.4 The Hard Palate

The hard palate is an elevated, dome-shaped, high density structure that separates the oral cavity from the nasal cavity superiorly. It is formed by the junction of two bilateral horizontal plates. The anterior horizontal plate

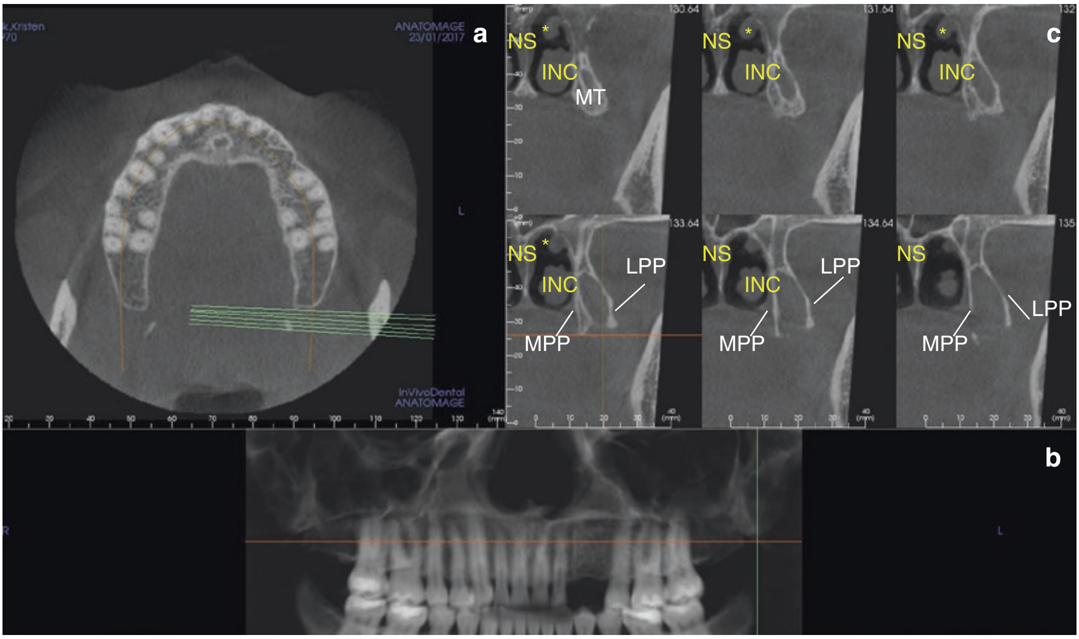

Fig. 10.23 Reference axial (**a**), thick panoramic reformatted (**b**), and sequential, trans-axial (cross-sectional) (**c**) images of the maxilla illustrating the maxillary alveolar process and regional anatomical structures of the left maxillary tuberosity (MT) region and relevant neighboring anatomical structures. (*LPP* lateral pterygoid plate, *MPP* medial pterygoid plate, *MT* maxillary tuberosity, *NS* nasal septum, *INC* Inferior nasal concha, *Asterisk* middle nasal concha)

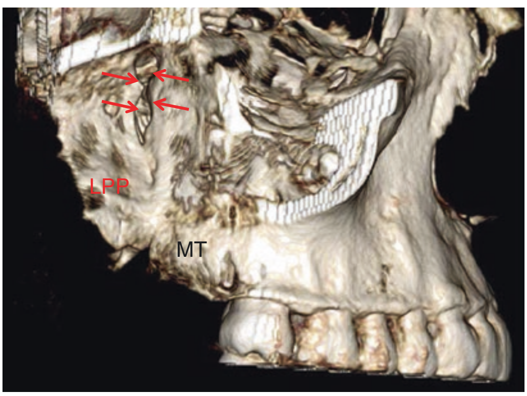

Fig. 10.24 Surface rendering of the right maxilla (lateral view with the zygomatic process segmented) for the assessment of the pterygomaxillary fissure (*red arrows*), the maxillary tuberosity (MT) and the lateral pterygoid process of the sphenoid bone (LPP)

extends medially from the maxillary alveolar process whereas the posterior horizontal plate is the separate palatine bone. The plates articulate in the midline as the medial palatine or the inter-maxillary suture (Fig. 10.27).

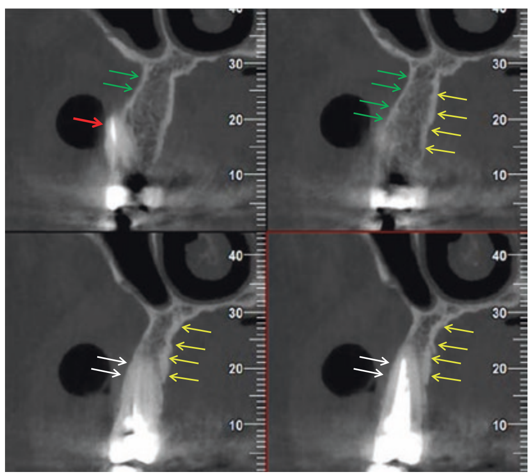

Fig. 10.25 A series of cross-sectional images of the maxillary right second premolar showing the bone architecture of the alveolar process. There is a clear delineation of the buccal (*green arrows*) and palatal (*yellow arrows*) cortical plates. The homogenous fine trabecular pattern of the cancellous bone is characteristic of the maxillary alveolus. Note the minimal buccal cortical coverage of the root of the root canal filled tooth (*white arrows*) and the fenestration of the mesio-buccal root of the adjacent first maxillary molar through the buccal alveolar plate

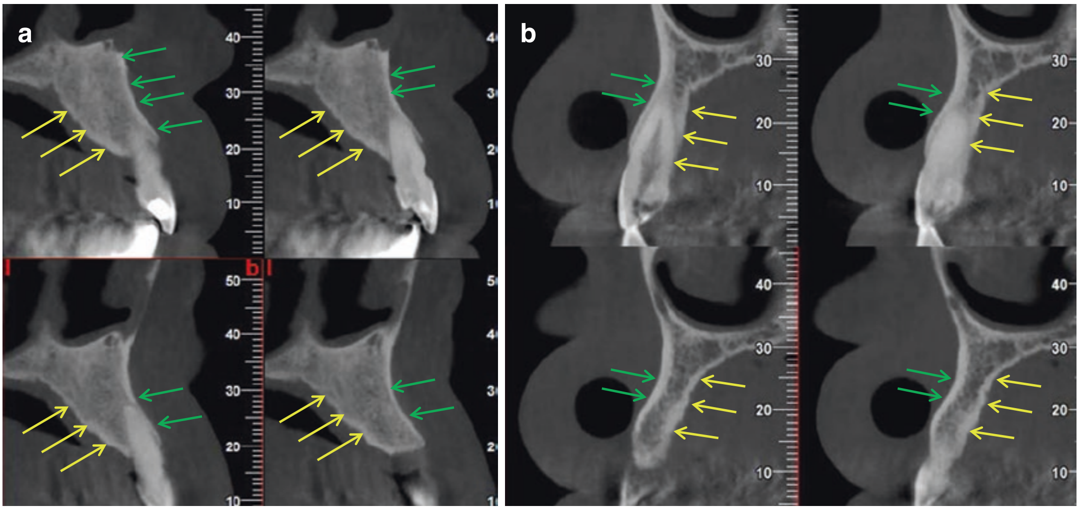

Fig. 10.26 Sequential cross-sectional images of the anterior maxilla in a patient with dense homogeneous trabeculation (**a**) and sparse fine trabecular pattern (**b**). The arrows show the buccal (*green arrows*) and palatal (*yellow arrows*) cortical plates in the respective alveolar processes

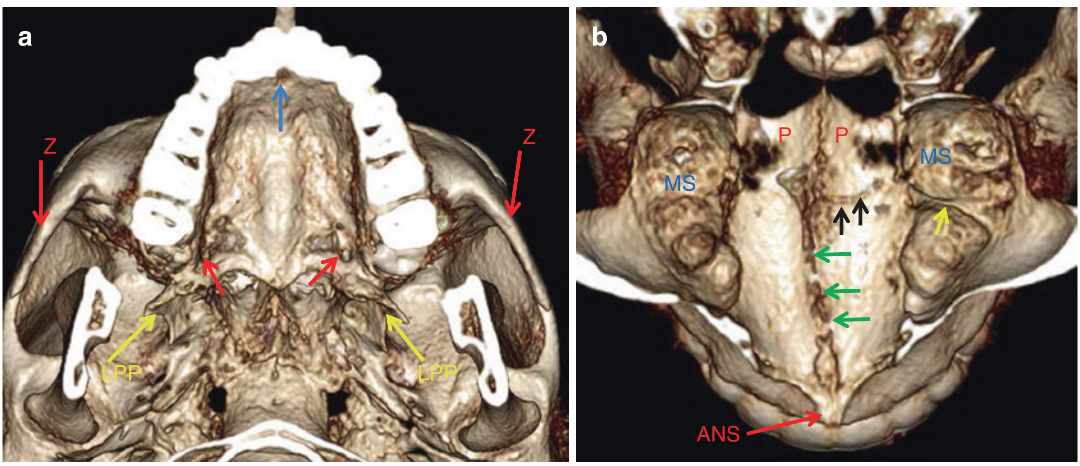

Fig. 10.27 Inferior (**a**) and superior (**b**) surface rendering projections of the hard palate and skull base (partially) showing the hard palate of the maxillary bone and relationship to the alveolar process (*LPP* lateral pterygoid plate, *Z* zygomatic arch, *MS* maxillary sinus floor, *P* palatine bone, *ANS* anterior nasal spine, *red arrow* greater palatine foramen, *blue arrow* incisive foramen, *green arrows* inter-maxillary suture, *black arrows* transverse palatine suture (junction of the maxillary bone and palatine bone), *yellow arrow* septum in maxillary sinus)

Important anatomical landmarks of the hard palate include the nasopalatine canal in the anterior hard palate and the greater and lesser palatine foramina in the posterior hard palate.

10.2.4.1 Nasopalatine Canal

The nasopalatine canal and its inferior opening, the incisive foramen are seen in the midline of the maxillary bone. The nasopalatine canal has its origin on the floor of the nasal cavity where it starts with two separate openings (Fig. 10.28), the superior foramina or foraminae of Scarpa. It continues in a caudal direction towards the palatal aspect of the maxillary bone and runs almost parallel to the labial cortical plate, as seen in the midline cross sections of the maxilla (Fernandez-Alonso et al. 2015). It terminates as the incisive foramen which is located just deep to the palatal papilla between the central incisors. The canal carries

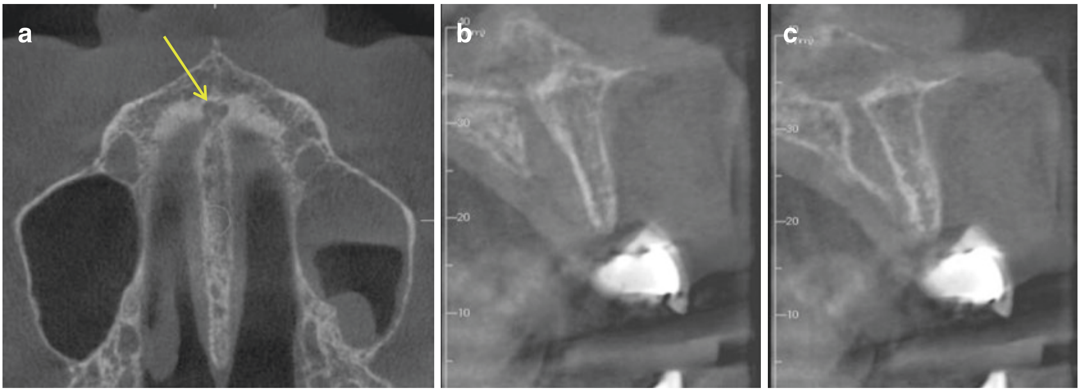

Fig. 10.28 Axial (**a**) and sequential cross-sectional images (**b**, **c**) of the nasopalatine canal. Two small foraminae are identified on the floor of the nasal cavity (*yellow arrow*) as the superior origin of the nasopalatine canal

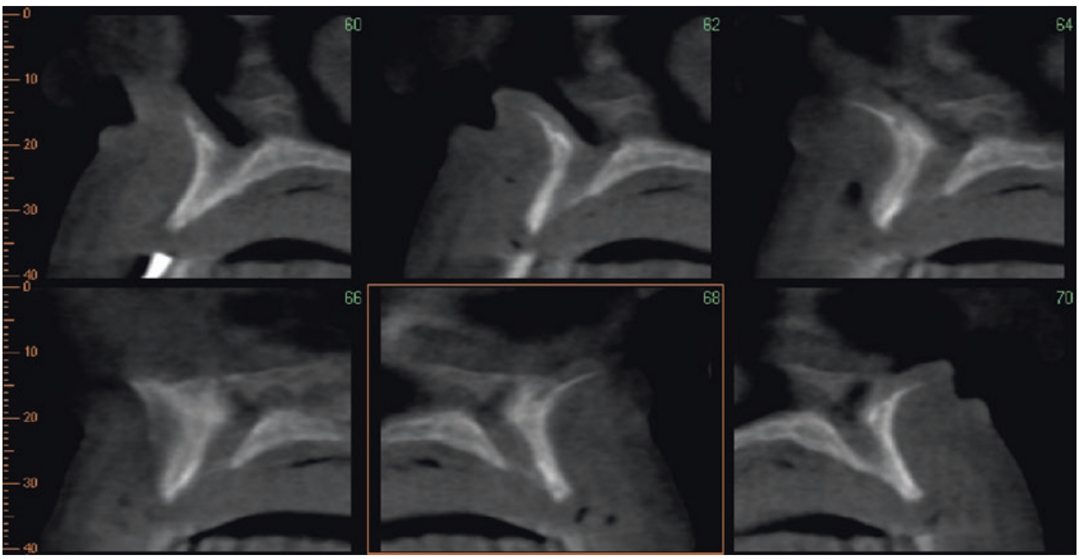

Fig. 10.29 Sequential cross-sectional images of an anterior edentulous maxilla depicting the nasopalatine canal. The canal appears to be considerably widened, reducing the width of the available residual alveolar ridge in the central incisor area

the nasopalatine nerve which supplies sensory innervation to the anterior hard palate. The diameter of the nasopalatine canal may vary, and due to its location, it may compromise the width of the maxillary alveolar bone close to the midline (Fig. 10.29).

10.2.4.2 Greater and Lesser Palatine Canals

The greater palatine foramen is located in the horizontal part of the palatine bone, on either side of the hard palate at the junction of the alveolus and opens medial to the second molar tooth, approximately 10 mm or less from the palatal alveolar crest (Figs. 10.30 and 10.31). It is the terminal end of the greater palatine canal, an osseous canal that connects the pterygopalatine fossa to the oral cavity. The canal contains the greater palatine nerve and respective blood vessels which exit the foramen and spread along the ipsilateral hard palate (Hafeez et al. 2015).

The lesser palatine foramen is located slightly posterior to the greater palatine one, is smaller in diameter, and contains the lesser palatine nerve and blood vessels (Fig. 10.30).

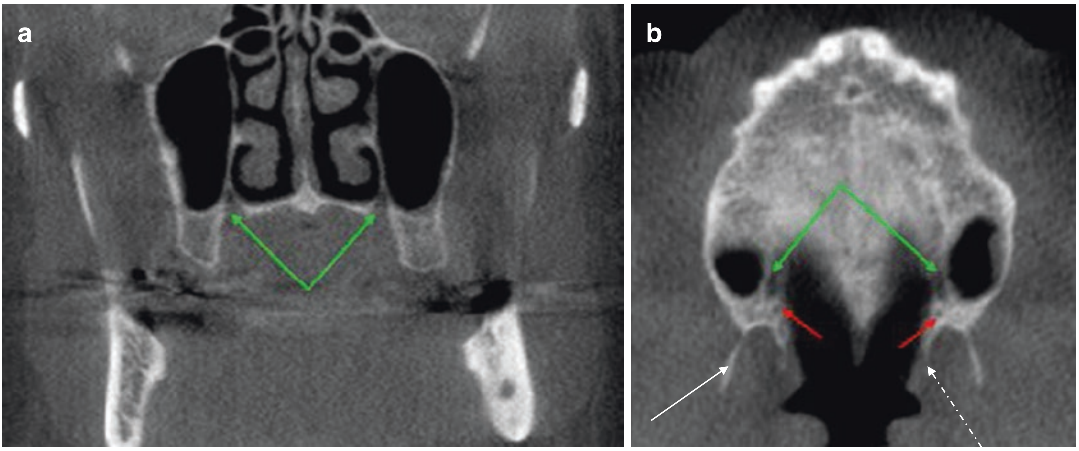

Fig. 10.30 Coronal (**a**) image through the posterior maxilla and axial image (**b**) at the level of the maxillary arch. The *green arrows* identify the greater palatine foramina at the junction of the hard palate and the palatal aspect of the alveolar ridges towards the posterior end of the maxillary arch. The *red arrows* show the lesser palatine foramina. The lateral (*solid white arrow*) and medial (*dashed white arrow*) pterygoid plates are also shown

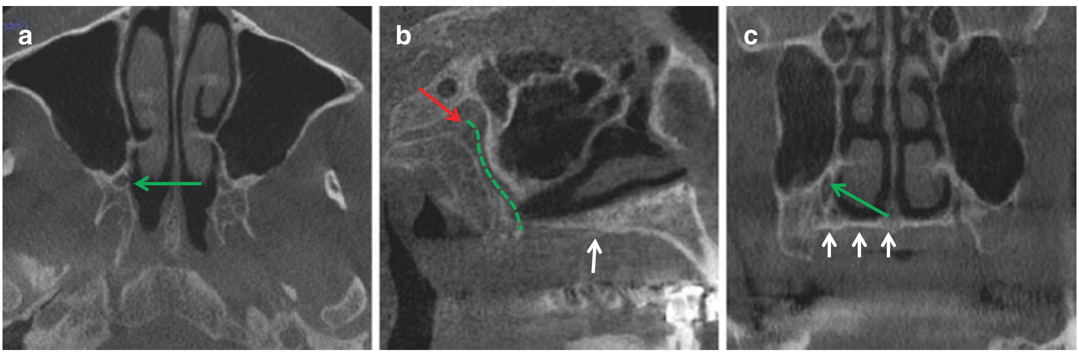

Fig. 10.31 Axial (**a**) corrected sagittal (**b**) and coronal (**c**) CBCT images of the hard palate tracking the course of the greater palatine canal (*green dashed line*) from the pterygopalatine fossa (*red arrow*) to the greater palatine foramen (*green arrow*) (*white arrows* hard palates)

10.3 The Mandible

The mandible is the largest bone of the facial skeleton and lies caudally (below), and articulates with, the maxilla. It forms the lower third of the face. It is "U" shaped bone with a thick outer layer of cortical bone. It is formed from the fusion of the two hemi-mandibles along a vertical line in the midline of the anterior mandibular symphysis. The mandible comprises the mandibular body and the posterior rami, two flattened, vertical projections that articulate with the temporal bone via the mandibular condyle. The mandibular alveolar process contains the teeth and lies integrated superiorly with the basal bone of the body of the mandible.

Each ramus ends in two individual osseous processes: the coronoid process (ventrally), a thin, triangular, and sharp process which serves for muscle attachment and the condylar process (dorsally), an ovoid structure which is articulated with the temporal bone to form the temporomandibular joint (TMJ) (Fig. 10.32).

10.3.1 Mandibular Body

The body of the mandible is composed of two indistinguishable parts: the tooth-bearing alveolar process and the base or basal bone of the mandible which serves as the tooth supporting part.

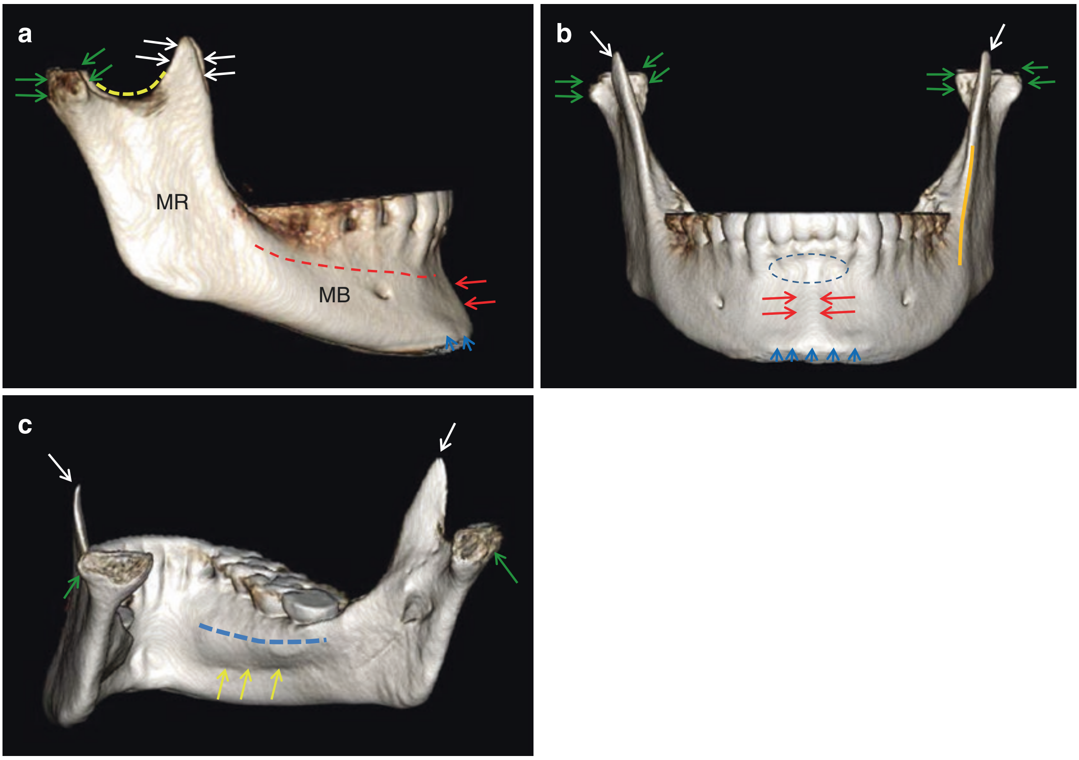

Fig. 10.32 Right lateral (**a**), frontal (**b**), and right lateral posterior (**c**) projections of a shaded surface rendering of the mandible showing anatomical landmarks and topographic features of the mandible (*MR* mandibular ramus, *MB* mandibular body, *green arrows* condylar process, *white arrows* coronoid process, *red arrows* mandibular symphysis, *yellow arrows* submandibular fossa, *blue arrows* mental ridge, *yellow dotted line* alveolar process, *orange line* external oblique ridge, *blue dotted line* internal oblique ridge, *dotted oval* mental fossa)

Severe atrophy may occur of the alveolar process with long-term edentulism leaving the residual basal bone.

A sequence of reformatted panoramic and serial trans-axial (cross-sectional) images are the most appropriate to assess the mandibular bone. These projections will demonstrate the composition of the mandibular bone, the spatial orientation of the alveolar ridge in relation to the opposing dentition and important anatomical structures in the region under examination.

The mandibular bone is surrounded by a thick cortex, thicker than that of the maxillary bone. While there is wide variation, the lingual cortex is often thicker than the labial. The thickest cortical bone is usually the inferior cortex whereas the thinnest cortical plates are in the anterior mandible.

The intramedullary cancellous bone of the mandible differs from that of the maxilla in that the trabeculae are more sparse, longer, sharper, and demonstrate a clear horizontal orientation (Figs. 10.33, 10.34, and 10.35). There is great variability in trabecular pattern related to numerous factors such as location, age, hormonal factors, and degree of edentulism.

10.3.1.1 Anterior Mandible

Sequential cross-sectional images of the anterior mandible demonstrate the orientation of the mandibular bone and anterior teeth in regard to the sagittal plane (Fig. 10.36). The mandibular bone shows a slight labial inclination in cross section that may be more prominent in some individuals. This may result in a prominent concavity, the mental fossa, which is bordered caudally by the mandibular symphysis, a vertical protuberance formed by the junction of the two hemi-mandibles along the midline. The mental

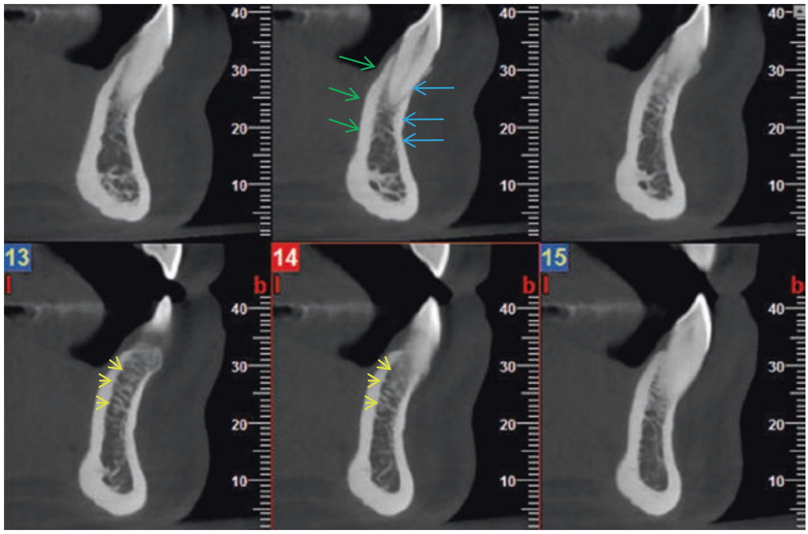

Fig. 10.33 Sequential 1 mm interval trans-axial images of the anterior mandible showing the labial (*blue arrows*) and lingual (*green arrows*) cortical plates as well as the trabecular pattern of the cancellous bone in the anterior mandible. Note the elongated, horizontally oriented trabeculae which become more sparse towards the base of the mandibular bone

ridge is a horizontal projection of the labial mandibular cortex which blends to the inferior cortex and forms the chin (Fig. 10.37). The mandibular bone is thinner superiorly towards the alveolar process and becomes considerably thicker and denser inferiorly.

In the edentulous anterior mandible, the alveolar bone varies considerably in height and width. Deviation between the long axis of the alveolar bone and that of the previous anterior teeth is not unusual. In addition, presence of labial and/or lingual undercuts may alter the shape of the alveolar bone dramatically and may render specific locations non-restorable with dental implants (Fig. 10.38).

Additional anatomical structures of importance visualized in the cross-sectional images of the anterior mandible include:

- **The genial tubercles**. The genial tubercle is a projection of the lingual mandibular cortex towards the inferior half of the mandibular bone. It is a high density area, frequently irregular in shape which serves as an attachment point for a number of muscles of the tongue as well as suprahyoid neck (Fig. 10.39).
- **Lingual foramen.** The lingual foramen (also reported as the median, middle, or central lingual foramen) is a vascular canal carrying the terminal branches of the sublingual artery located either on or in close proximity to the genial tubercles in the midline in up to 80% of individuals (Tepper et al. 2001). Smaller “inferior midline foramina” have also been reported, inferior to the genial tubercle(s) in up to 76% of individuals (Figs. 10.39 and 10.40) (Shiller and Wiswell 1954).
- **Accessory Lingual Foramina.** Lateral accessory lingual foramina have been detected between the regions of lateral incisors and the mandibular premolars, towards the inferior border of the mandible (Chapnick 1980) (Fig. 10.41).
- Some blood vessels associated with these accessory foramina may be of sufficient size to be implicated in severe hemorrhaging if injured during implant placement in the mandibular anterior region (Kalpidis and Setayesh 2004). Despite the fact that these vascular channels are identified fairly low on the lingual aspect of the mandibular bone (towards the inferior third of the mandibular bone height), their relative position in relationship to the crest of the alveolar bone may change if bone atrophy is present in the anterior mandible (Fig. 10.41). As a result they may pose as important anatomical limitations in implant surgery if considerable bone atrophy is noted.

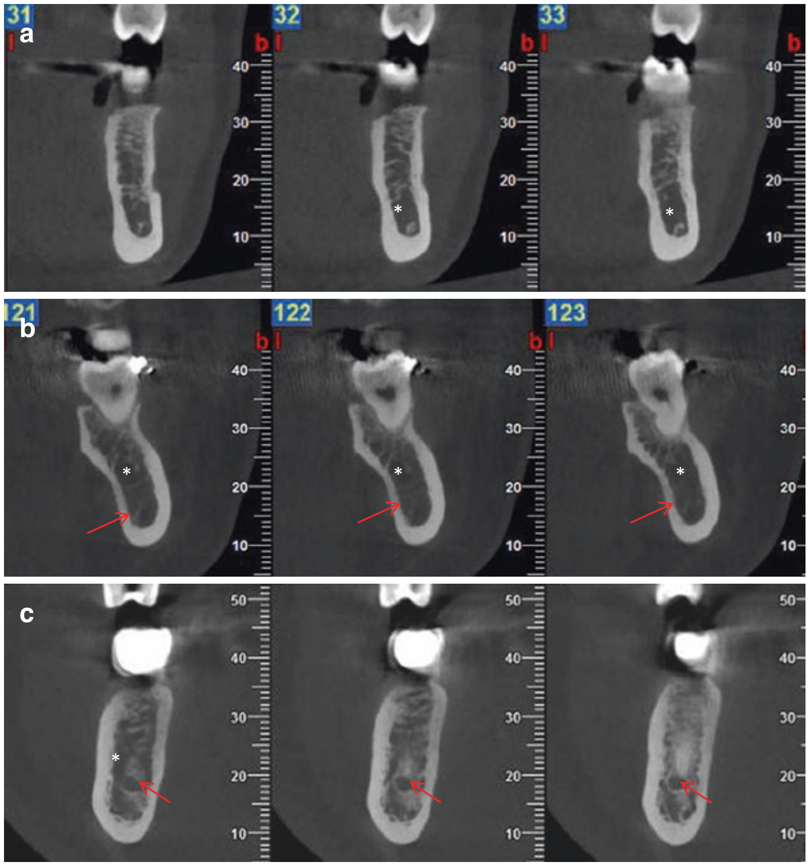

Fig. 10.34 Sequential, 1 mm interval, trans-axial images of the left posterior mandible at the level of the premolar and mental foramen (**a**) and molar (**b**) regions depicting gradual changes in the trabecular pattern. Note the long and narrow horizontal trabeculae which become more sparse within the basal bone and multiple voids (*Asterisk*). Trans-axial images of the same individual in the region of the right molar (**c**) showing a different trabecular pattern associated with the mandibular canal (*red arrows*)

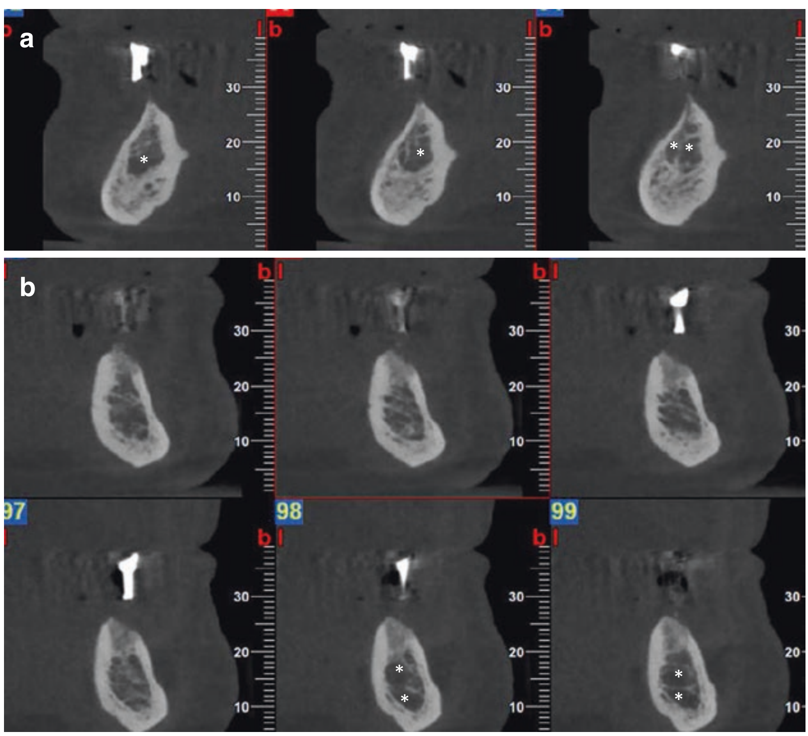

Fig. 10.35 Sequential trans-axial images of the right (**a**) and left anterior (**b**, **c**) edentulous mandible showing the variability in the trabecular pattern from site to site in the same individual. Note that the *horizontal* orientation of the trabeculae and sporadic presence of voids (*Asterisk*) in the mandibular bone

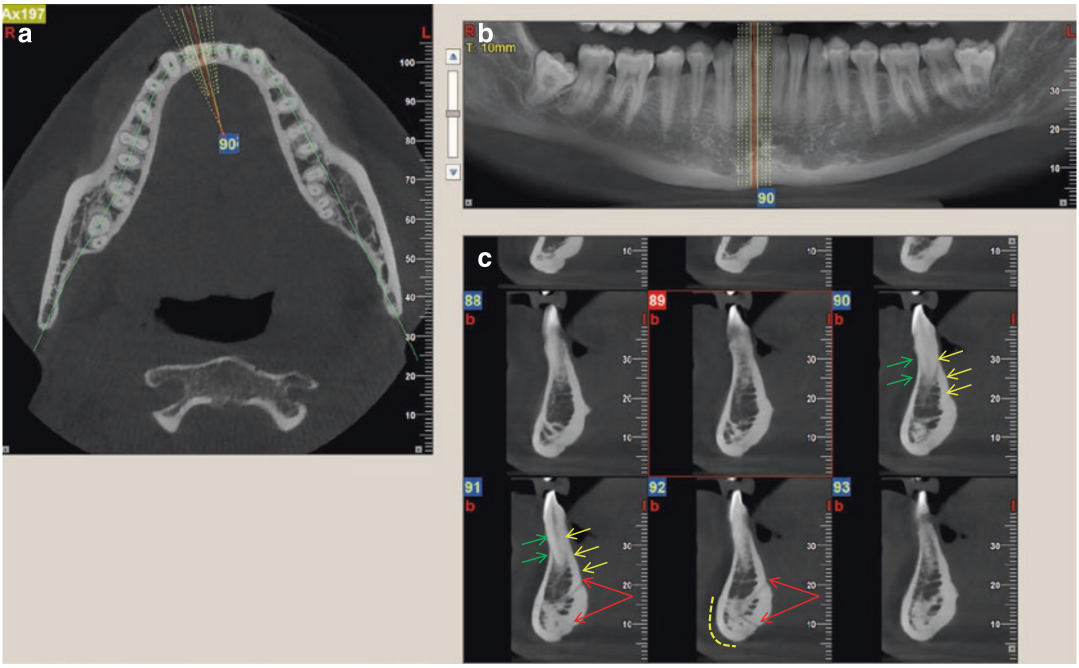

Fig. 10.36 Axial (**a**), reformatted panoramic (**b**), and serial cross-sectional (**c**) CBCT images of the mandible illustrating the mandibular alveolar process and relevant neighboring anatomical structures in the left anterior region. Cross-sectional images (**c**) are optimal in showing the alveolar bone height and width, labial (*green arrows*) and lingual (*yellow arrows*) cortices, the mental ridge (*yellow dotted line*) and the lingual foraminae (*red arrows*)

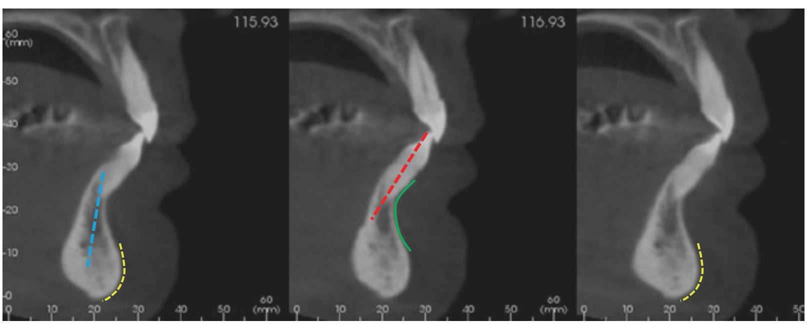

Fig. 10.37 Sequential 1 mm interval trans-axial images of the anterior mandible (central incisor region) demonstrating a marked labial inclination of the mandibular incisors (*red dotted line*) in relation to the more perpendicular orientation of the alveolar bone (*blue dotted line*). This discrepancy accentuates the anatomical concavity, mental fossa (*green curved line*) just below the alveolar crest (*yellow curved dotted line*, mental ridge)

10.3.1.2 Posterior Mandible

In posterior mandibular cross sections (Fig. 10.42, 10.43, and 10.44), the most important topographic anatomical structures include:

- **The external oblique ridge.** This is a fairly smooth ridge present on the buccal aspect of the mandibular bone (originating in the molar region) and extends posteriorly where it ends as the continuation of the anterior border of the mandibular ramus. This line serves as the linear bony attachment of the buccinator muscle) (Fig. 10.43 and 10.45).
- **The internal oblique ridge or mylohyoid line.** The mylohyoid muscle originates from the mylohyoid line (internal oblique ridge) and

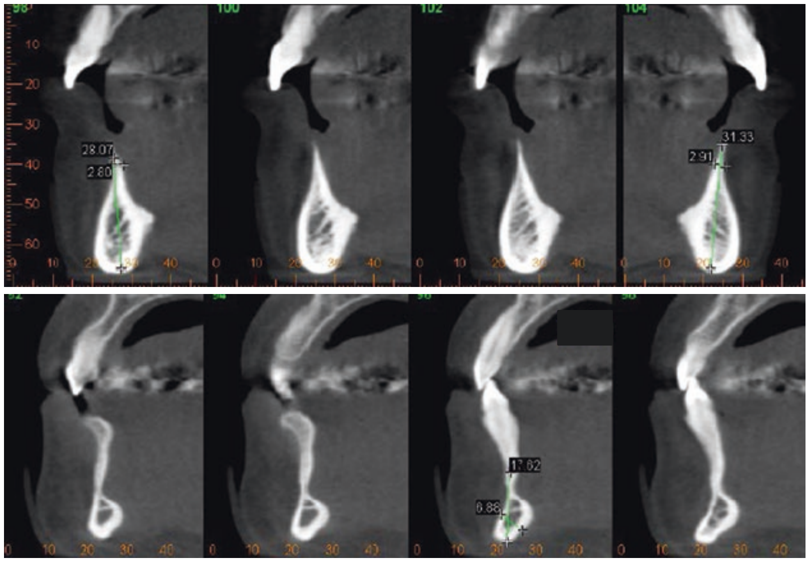

Fig. 10.38 Sequential trans-axial images at 1 mm intervals of the anterior edentulous mandibular region showing "knife-edged" appearance of the alveolar crest and severe horizontal atrophy of the alveolar bone resulting in thinning. Even the width of the tooth-bearing area is markedly reduced

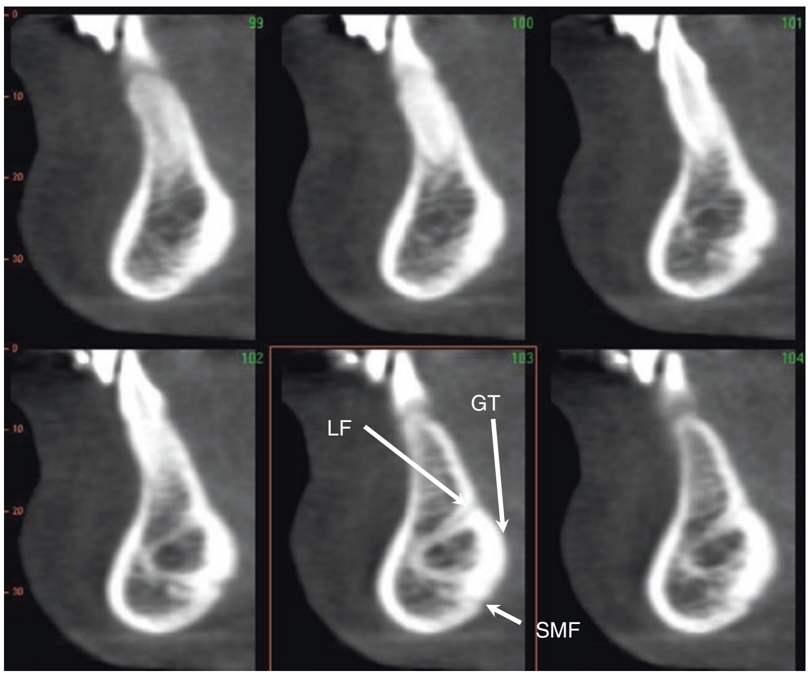

Fig. 10.39 Sequential 1 mm interval trans-axial images of the mandibular anterior midline demonstrating the genial tubercle (*GT*) and the lingual foramen (*LF*) or median lingual foramen. Additional midline foramina are not uncommon in the region. This includes the submental foramina (*SMF*) which contains an artery at the mid-symphysis and anastomoses with the incisive canal. These foramina/canals carry nutrient blood vessels, and may cause severe bleeding if they are perforated during implant surgery

continues in a downward direction towards the hyoid bone where it inserts (Fig. 10.42) This muscle is the biggest contributor to the formation of the floor of the mouth and its presence limits the detection of significant mandibular lingual undercuts. In addition, considerable variation exists as far as it determines the depth of the submandibular gland fossa.

- **The submandibular gland fossa (depression).** This is an anatomical concavity towards the lower half of the mandibular bone in the molar region which nests, partially, the submandibular salivary gland. This may pose an anatomical limitation in implant placement in the region due to the fact that important significant anatomical structures such as the lingual artery are located in the vicinity of the lingual mandibular cortex (Figs. 10.43 and 10.44). The mandibular canal is frequently seen as a well-defined, round or ovoid, small, low density area towards the inferior third of the alveolar bone.

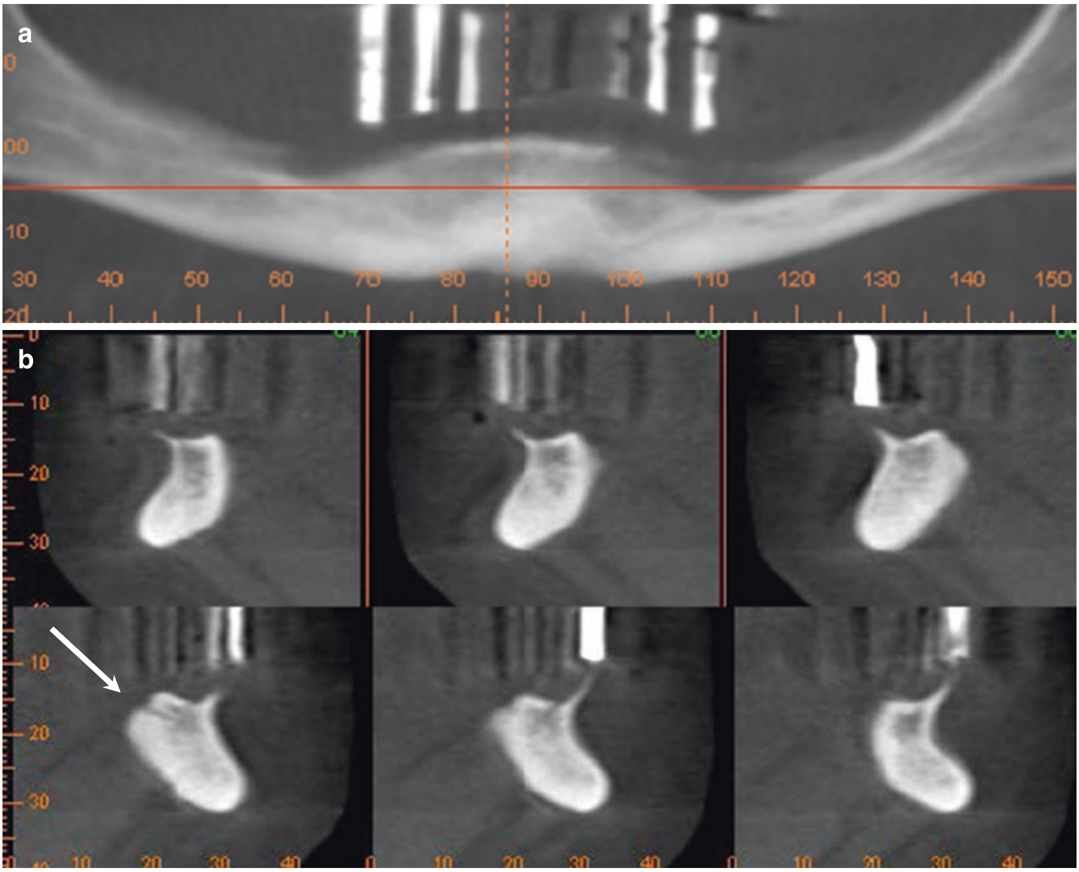

Fig. 10.40 Panoramic (**a**) and sequential trans-axial (**b**) images of the anterior region in a severely atrophic mandible. The cross-sectional images demonstrate an almost "knife-edged" crest and severe lingual inclination of the alveolar ridge. The lingual foramen (*arrow*) appears to be very close to the crest, in a site planned for implant placement (see opaque marker above the alveolar crest). The relative position of the lingual foramen has changed due to the severe atrophy

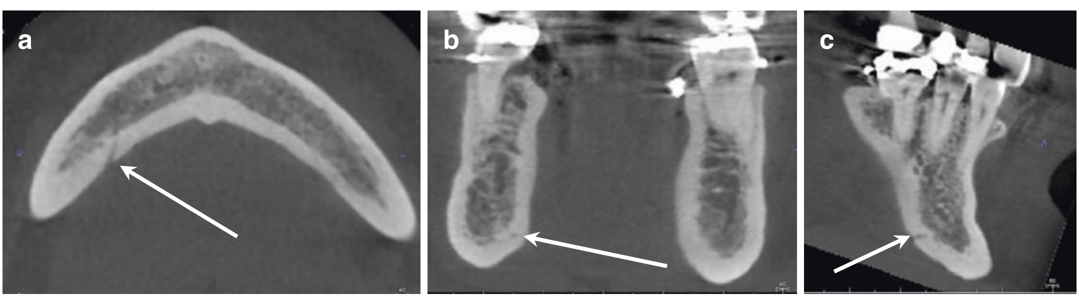

Fig. 10.41 Axial (**a**), coronal (**b**), and sagittal (**c**) CBCT images showing the location of sublingual foraminae (*arrow*) Accessory foramina, like the one demonstrated, have a reported incidence of approximately 65%

It is well known that the loss of teeth will result in a gradual atrophy of the alveolar bone in height and width (Fig. 10.44). As the edentulous bone becomes more atrophic, the relative position of crucial (for surgery) anatomical structures may become more important (Fig. 10.45). Moreover, the pattern of bone resorption (especially in the bucco-lingual aspect) in combination with the possible lingual undercuts mentioned earlier may alter considerably the angulation of

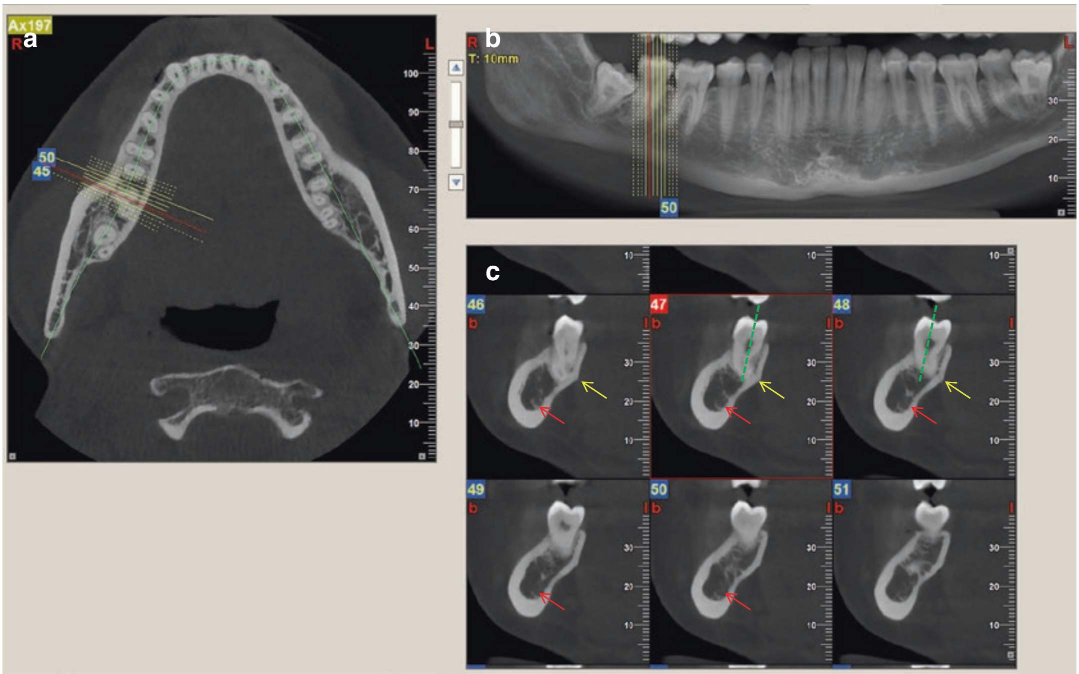

Fig. 10.42 Axial (**a**), reformatted panoramic (**b**), and serial cross-sectional (**c**) CBCT images of the right mandibular molar region illustrating the mandibular alveolar process and relevant neighboring anatomical structures. These images optimally depict the alveolar bone height and width, internal oblique ridge (*yellow arrows*) and the mandibular canal (*red arrows*). Note long axis of the molars (*green dotted line*) in comparison to that of the mandibular bone

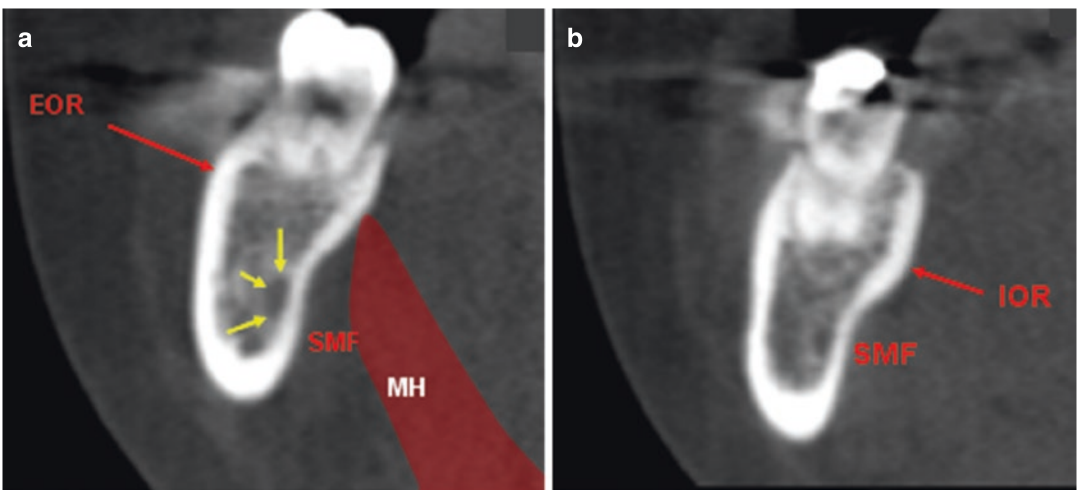

Fig. 10.43 Consecutive cross-sectional images (**a**, **b**) of the right posterior mandible. The superimposed schematic annotates the approximate origin of the mylohyoid muscle (*MH*) and submandibular gland fossa (*SMF*). The *arrows* show the right mandibular canal. Note that the soft tissue contrast of CBCT is inadequate to differentiate the musculature of the floor of the mouth (*EOR* external oblique ridge, *IOR* internal oblique ridge or mylohyoid line)

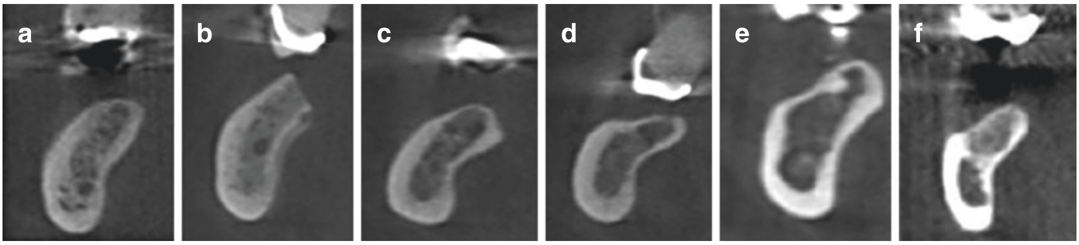

Fig. 10.44 Posterior right mandibular cross sections of the edentulous molar region from six different patients (**a**–**f**). Note the marked lingual undercuts in all cases (submandibular fossa). The tooth-bearing part of the mandibular bone rarely remains unchanged after tooth loss

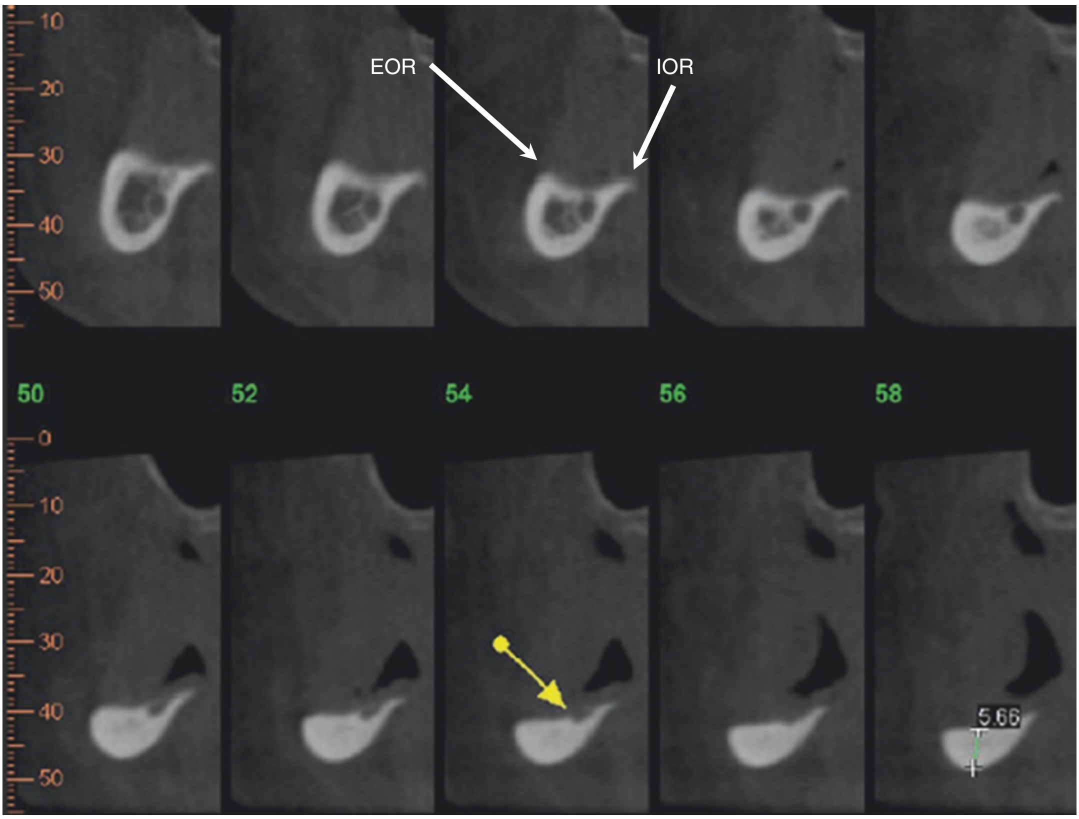

Fig. 10.45 Sequential trans-axial images at 1 mm intervals in a patient with long-term complete mandibular edentulousness showing severe atrophy of the edentulous alveolar bone in the right posterior mandible. The *yellow arrow* points out the right mental foramen which exits on the crest of the ridge. In fact no alveolar ridge is identified—the alveolar bone was at the level of the floor of the mouth. (*EOR* external oblique ridge, *IOR* internal oblique ridge)

the edentulous alveolar ridge which in turn may compromise future implant treatments.

Kottal et al. (2006) report that the angulation of the mandibular alveolar bone may deviate up to 30° from the favorable dental implant insertion path. Moreover, they found that the edentulous alveolar bone in the vast majority of the potential implant sites in their sample deviated from 10° to 30° from the preferred implant insertion path determined for optimal restoration and function.

The thickness of the cortical bone as well as the trabecular pattern of the cancellous bone are also shown in the mandibular cross sections. A number of investigators have attempted to associate this pattern to certain levels of "bone quality" (Angelopoulos and Aghaloo 2011).

Mandibular Canal

The mandibular (MC) or inferior alveolar (IAC) canal presents as a major anatomical limitation for the placement of implants in the posterior mandible. It contains the inferior alveolar nerve (IAN), artery, and vein. The MC is tube-like structure that runs the entire length of the body of the mandible, almost parallel to the inferior border and usually located within the lower third of the body. Its posterior opening on the lingual aspect of the ramus, the mandibular foramen, is the entry point of the IAN (Fig. 10.46).

The IAN is a branch of the mandibular nerve (V3) and provides sensory innervation to the mandibular bone, teeth, the lower lip, and partially the gingivae of the anterior teeth. In cross-sectional images, the canal is visualized as a well-defined, small, most often round, low density area which is frequently surrounded by a high density border. The presence of the high density outline is dependent upon the canal's cortication. As a result, the MC is not always well visualized (Fig. 10.47). Carter and Keen (1971) and Wuehrman and Manson-Hing (1981) agreed that the occurrence of "not visible" mandibular canals is related to the fact that the inferior alveolar bundle is not always surrounded by an ossified canal. Stella and Tharanon (1990) related the reliability and accuracy of diagnostic imaging to the visibility of the mandibular canal.

The intramedullary course of the MC may also vary. Although the MC is frequently identified closer to the lingual mandibular cortex, this should not be taken for granted. The development of teeth as well as pathological entities in the posterior mandible may displace the MC and affect the presence and extent of cortication (Fig. 10.48).

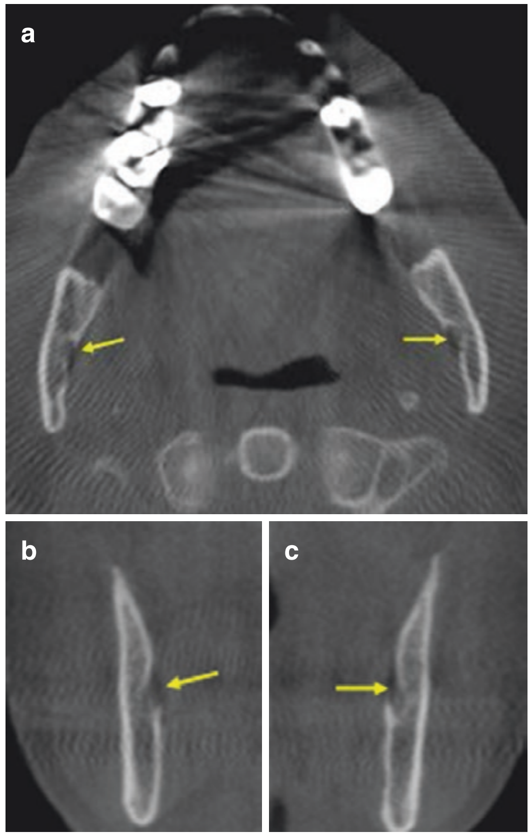

Fig. 10.46 Axial image (**a**) at the level of the mandibular rami and coronal cross-sectional images at the level of the *right* (**b**) and *left* (**c**) ascending rami. The *arrows* indicate the mandibular foramina, bilaterally, entry point of the IAN into the MC

Accessory branches of the IAN (other than its terminal branch) may sometimes emerge through the mandibular bone as smaller canals (Fig. 10.49).

Mental Foramen

The IAN perforates the buccal cortical plate of the mandible as the "mental nerve," through a small opening, the mental foramen. The mental foramen is located in the periapical region of the second premolar; however, there is considerable anatomic variability in location. It is best visualized in the cross-sectional images of the mandible (premolar region) as a variable in shape and size break in the continuity of the

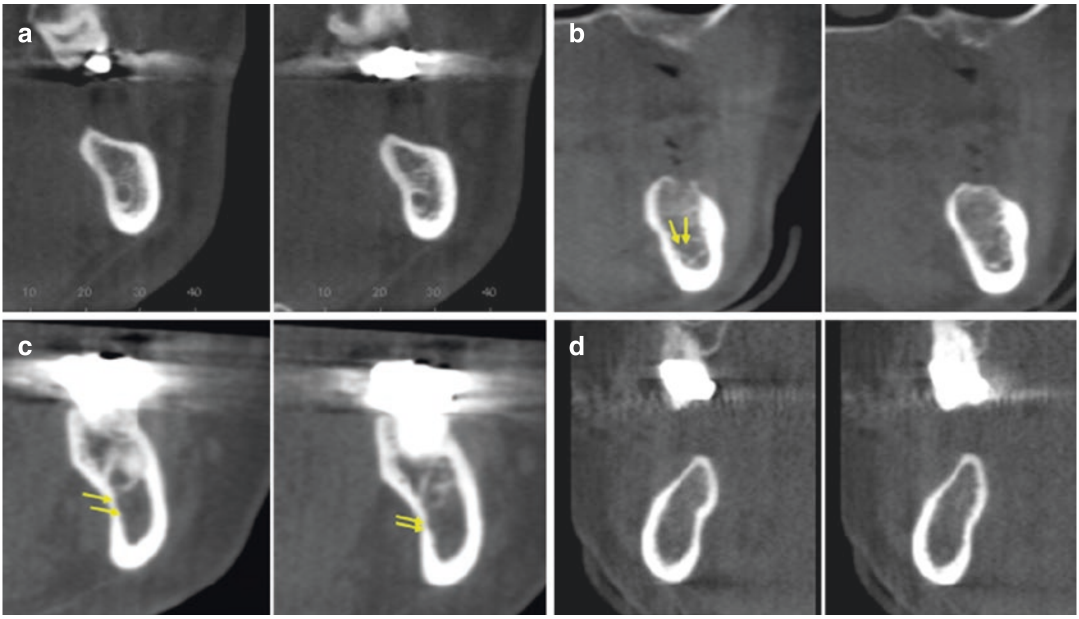

Fig. 10.47 The visualization of the mandibular canal is dependent upon the cortication of its borders. Adjacent sequential trans-axial images of corticated, easily visualized (**a**), partially corticated, well visualized (**b**), not corticated, poorly visualized (**c**) and not corticated non-visible (**d**) inferior alveolar canal. Note that the location of the inferior alveolar canal can be estimated when it grooves the internal margin of the lingual cortical plate—"niche sign" (**c**)

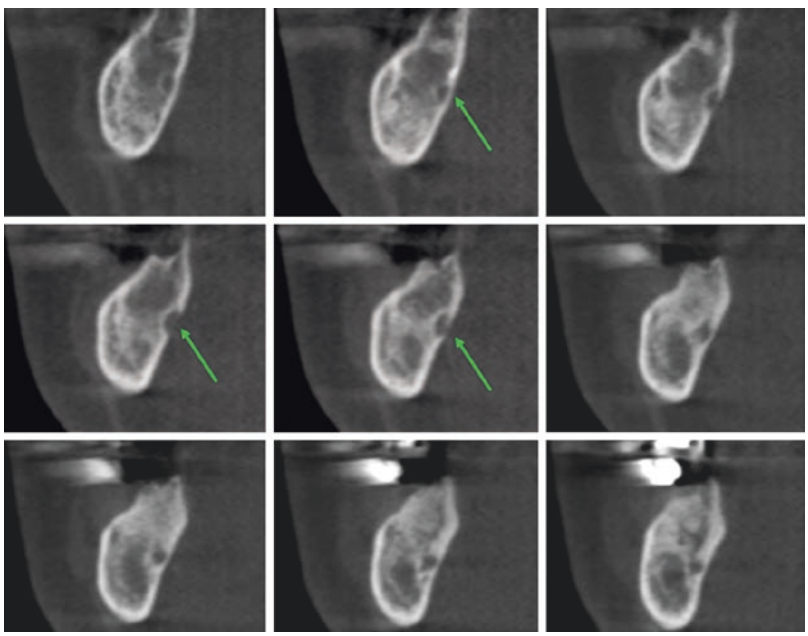

Fig. 10.48 Series of sequential 1 mm interval trans-axial sections showing the mandibular canal grooving and, in some areas, perforating the lingual cortex, exposed to the submandibular space

buccal cortex, in a small distance from the apices of the premolars (Fig. 10.50). The mental foramen represents a clear change of direction of a large part of the sensory fibers of the IAN which exit the mandibular canal. As a result, it may appear as a short tube-like structure, itself.

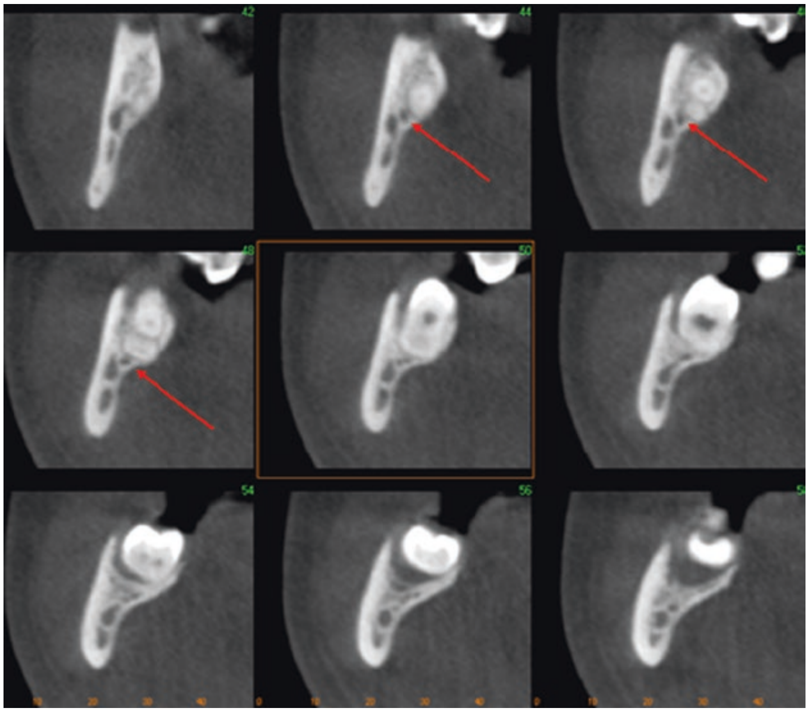

Fig. 10.49 Series of sequential 1 mm interval trans-axial sections showing the position of an impacted right mandibular third molar and its relationship to the inferior alveolar canal. Note the origin of a small accessory branch of the MC (*arrows*). Although the MC itself is located inferior and at some distance from the roots of the tooth, the accessory branch is in contact with the root

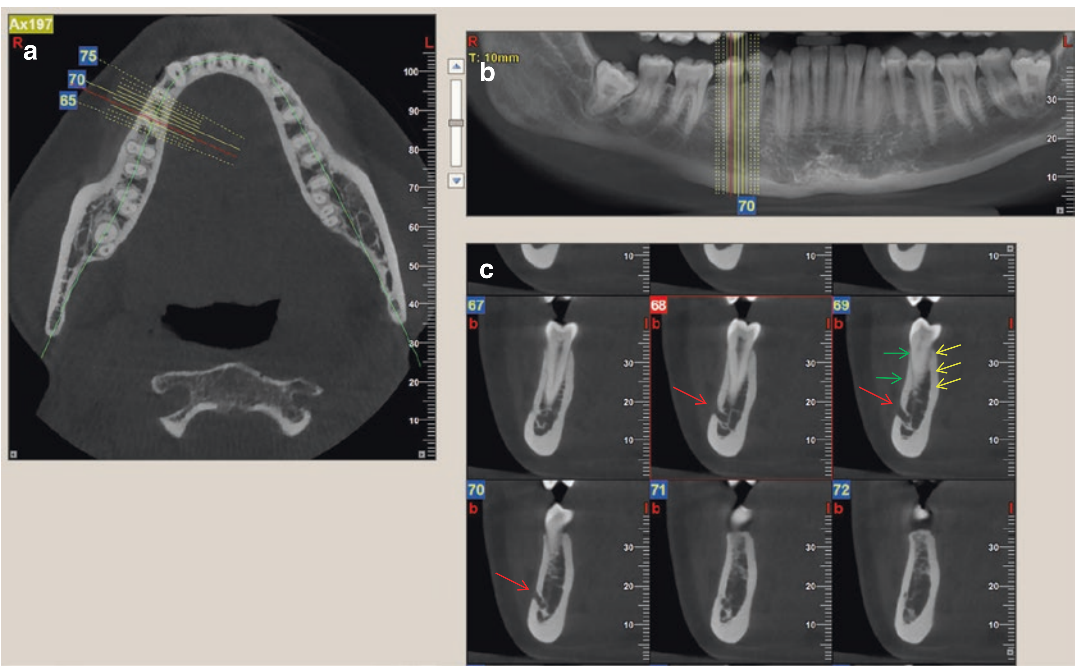

Fig. 10.50 Axial (**a**), reformatted panoramic (**b**), and serial cross-sectional (**c**) images of the premolar region of the mandible illustrating the mandibular alveolar process and relevant neighboring anatomical structures. These images depict alveolar bone height and width, buccal (*green arrows*) and lingual (*yellow arrows*) cortices and the mental foramen (*red arrows*). In this example, the mental foramen exits low through the inferior third of the buccal cortical plate

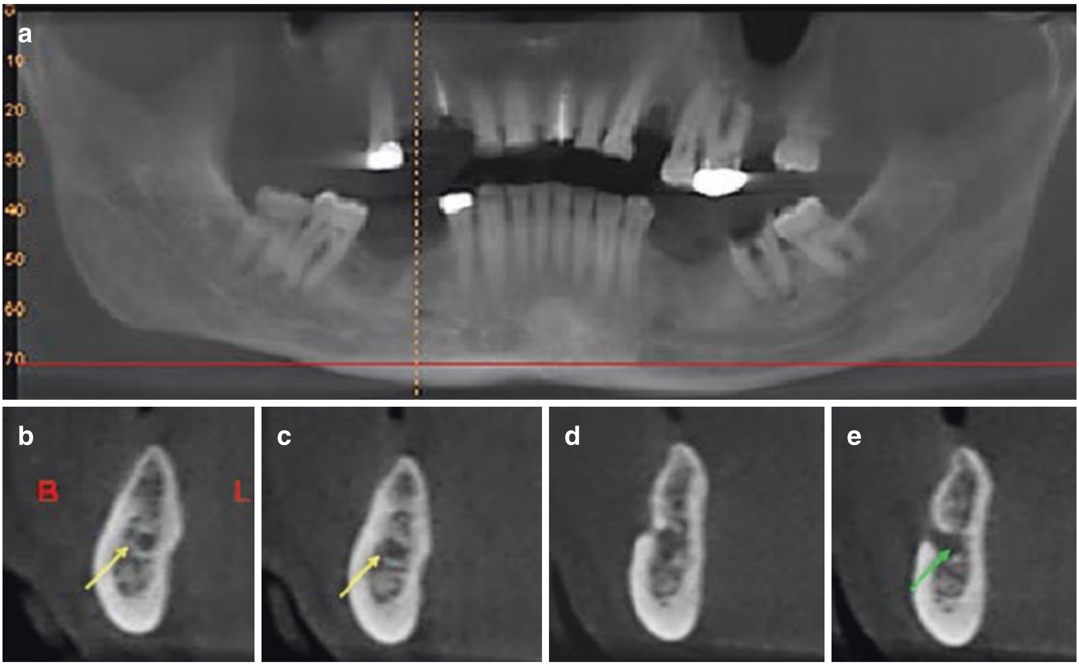

Fig. 10.51 Reformatted panoramic (**a**) and cross-sectional images (**b**–**e**) in the region mandibular of right premolars (*yellow dotted line* on panoramic image). The *yellow arrows* show the right mandibular canal and the *green arrow* shows the mental foramen as it exits high through the middle third of the buccal cortex of the mandible

The angle at which the mental foramen emerges through the buccal cortex as well as the level relative to the alveolar height is variable (Figs. 10.51 and 10.52).

After the mental branch exits through the mental foramen, the terminal branch of the IAN continues an intra-osseous course towards the midline of the mandible as the *incisive branch*, providing sensory innervation to the anterior mandibular teeth. A smaller diameter osseous canal may be seen anterior to the mental foramen (Fig. 10.53).

Proper knowledge and utilization of the tools available for image reformatting will assist in the identification of vital anatomical structures such as the MC when their location is unclearly visible. The use of consecutive thin sagittal sections of the posterior mandible (in the areas of interest) or consecutive panoramic sections may be of great assistance, if the MC is not visualized in the corresponding cross-sectional images. Abrahams and Levine (1990) introduced the concept of MC canal triangulation if the MC is not visible in some of the sections of interest. This concept includes proper use of the metric scales that often are provided on the borders of almost all types of sections. So, if the MC is visible in one image series (e.g., panoramic sections), the height of the superior border of the MC could be marked in the metric scale next to the panoramic sections; next this metric reading could be transferred to the corresponding scale in the cross-sectional images. In this way, a fairly accurate estimate of the mandibular bone height could be provided even if the MC is not visible in some of the sectional images. This concept is far more easily applicable to the CBCT images due to the interactivity that CBCT software offers (Fig. 10.54).

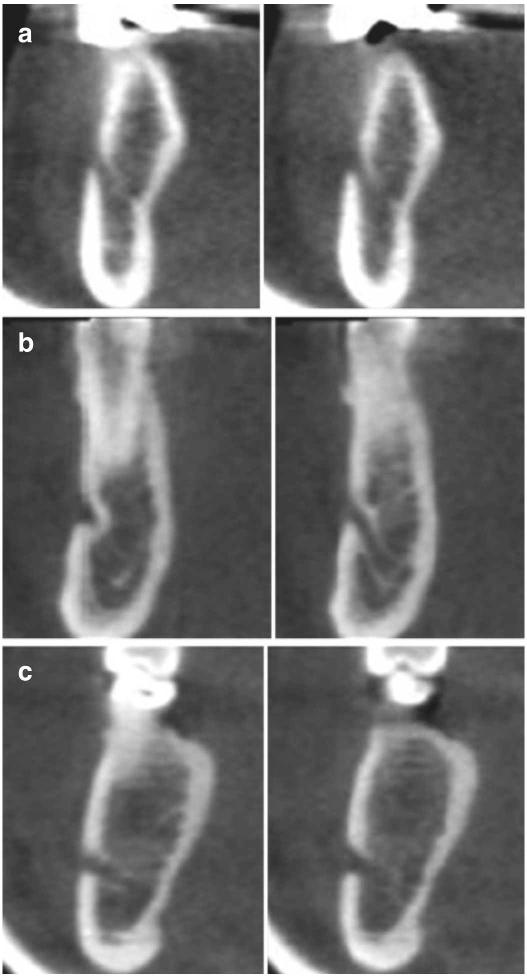

Fig. 10.52 Cross-sectional images in the area of mandibular premolars from three patients (**a**–**c**). There is considerable variation as far as the size and the opening angle of the mental foramen between different individuals ranging from very steep upwards angle of opening of the mental foramen (**a**, **b**) to an almost flat opening angle (**c**)

10.4 The Oral Cavity and Oropharynx

Because of their proximity and continuity, the oral cavity and oropharynx can be considered as a single anatomical unit.

The oral cavity/oropharynx is a semispherical common pathway which serves as the first component of the alimentary and respiratory tracts. It is bound by the lips and teeth (anterior), the teeth and cheeks (laterally), the tongue and the floor of the mouth (inferior), the hard and soft palate (superior), and the pharyngeal wall (posterior). It is almost entirely comprised of soft tissue elements and it is lined by mucosa. On CBCT imaging the surface outlines of these elements are often represented (Figs. 10.55, 10.56, and 10.57).

Shape alterations of the oropharynx may reflect developing pathology in its borders. Unfortunately the poor soft tissue contrast of CBCT is inadequate for soft tissue pathology diagnosis; however, due to the high contrast between air and the surrounding soft tissues, recognition of shape discrepancies or asymmetries in the upper airway may elevate suspicion for disease. For example, pathologic enlargement of superficial glandular tissues in the oral cavity (e.g., palatine, pharyngeal and lingual tonsils, and the tongue) may result in an alteration of the shape of the upper airway and may suggest pathology (Fig. 10.58). In addition, tissues that mineralize or produce calcified material as a result of pathology (e.g., sialoliths, or tonsilar calcifications) may be readily recognized with CBCT (Fig. 10.59).

10.5 The Nasopharynx

The nasopharynx is a short tube-like structure and the most superior section of the upper airway (Fig. 10.60). It is bounded by the soft palate caudally and the mucosal lining of the base of the sphenoid bone cranially. It extends posteriorly to the pharyngeal tonsils, adjacent the upper cervical spine, whereas anteriorly it extends to the posterior choanae (the posterior openings of the nasal cavity) and enters the nasal cavity. The lateral borders of the nasopharynx are formed by the pharyngotympanic or eustatian tube which connects the nasopharynx to the inner ear, the torus tubarius (the cartilaginous end of the eustachian tube), and the lateral pharyngeal recess (fossa of Rosenmuller) on either side.

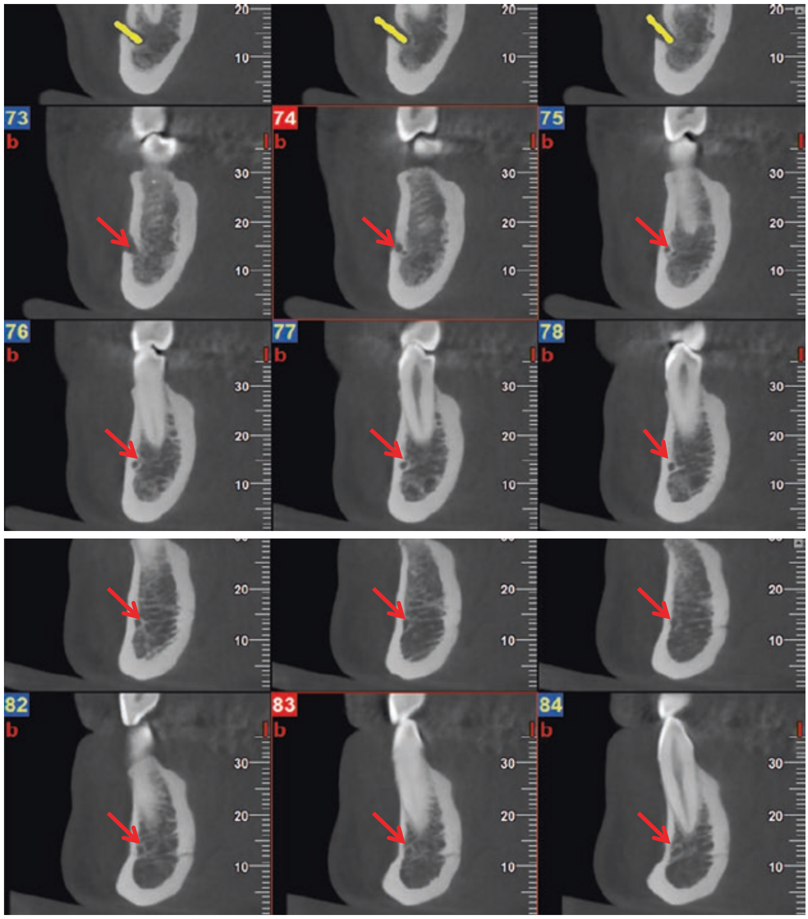

Fig. 10.53 Sequential 1 mm interval trans-axial images demonstrating a low density, round structure in the mandibular symphyseal region anterior to the mental foramen (*red arrows*) containing the incisive branch of the inferior alveolar neurovascular bundle

The eustachian tube originates from the nasopharynx as a collapsed narrow opening just posterior to the medial pterygoid plate and follows a lateral/superior course towards the auditory apparatus. Its posterior wall is the torus tubarius (or cushion of the tube); this is a finger-like projection which borders the lateral pharyngeal recess (fossa of Rosenmuller) from the eustachian tube. The fossa of Rosenmuller is of special significance since it is the most frequent site of nasopahryngeal carcinoma in older individuals, the most common nasopahryngeal malignancy.

The various soft tissue projections and recesses in the nasopharynx result in a characteristic "star" shape observed in axial sections (Fig. 10.60). Therefore, alterations in this shape may be associated with developing disease and require referral and further investigation (Fig. 10.61).

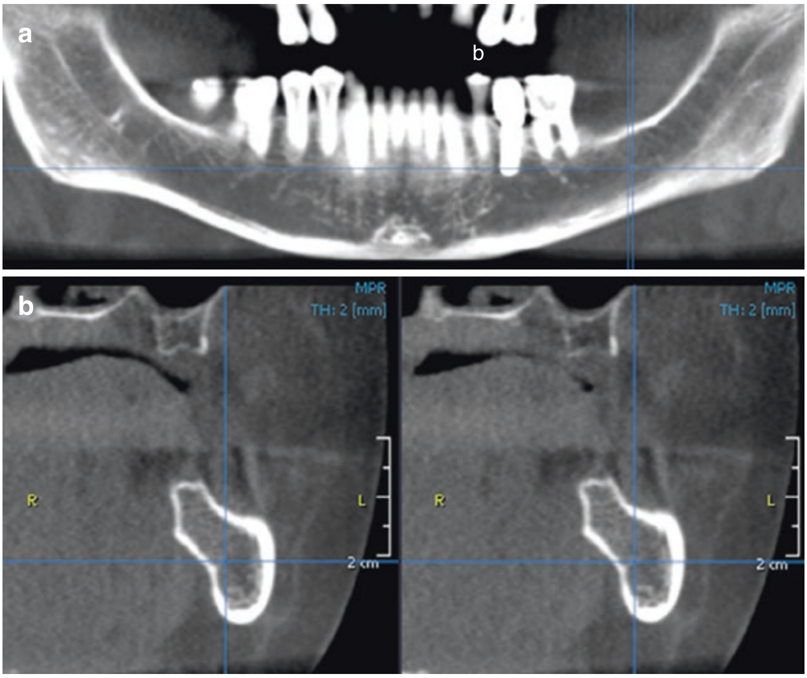

Fig. 10.54 Example of the use of triangulation to localize the inferior alveolar canal. Metric scales or reference lines displayed on various images can assist to "triangulate" the location of the MC. In this example the MC is fairly well visualized in the left mandibular edentulous area in the panoramic section (**a**). The two *vertical lines* represent the location of the two cross sections (**b**). The *horizontal blue* reference line corresponds to the axial mandibular section at this level which is at the same level in both panoramic and cross-sectional cuts. Consequently, if we move the *horizontal line* to coincide with the superior border of the MC, this will be transferred accordingly to the respective cross sections. The "cross-hair" point between the *horizontal* and *vertical* reference lines depicts the same anatomical location irrespective of the type of sectional images

Fig. 10.55 Coronal section through a posterior edentulous maxilla and mandible Note the severe atrophy of the maxillary alveolar bone bilaterally. The image shows the spatial relationships of the bony anatomic boundaries and soft tissue contents of the oral cavity including the nasal cavity (*NC*), oral cavity (*OC*), buccal soft tissues of the cheeks (*B*), maxillary sinus (*S*), tongue (*To*) and floor of mouth (*FM*). The red arrows show the hard palate and the green arrows indicate the patient's cheeks

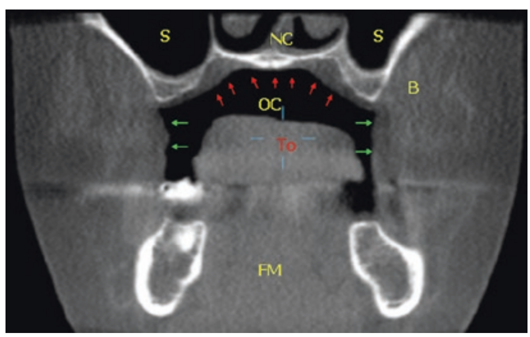

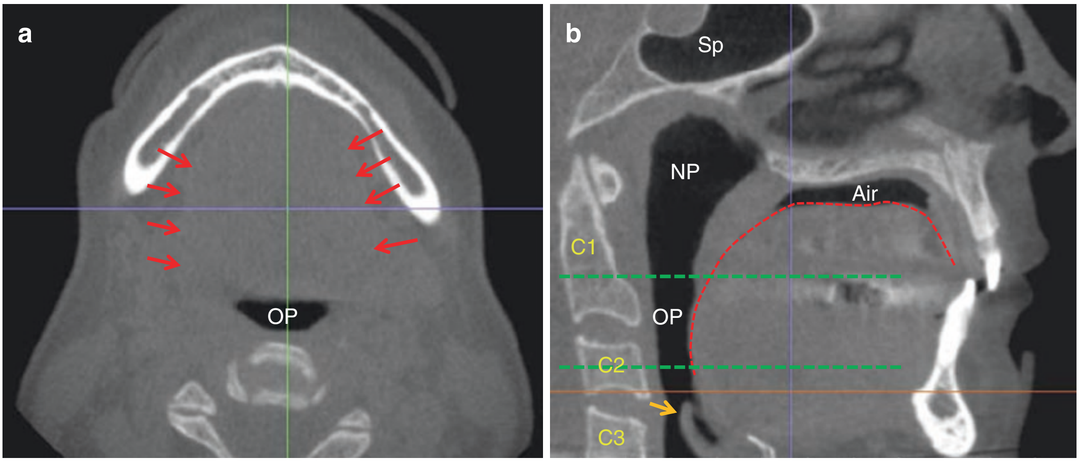

Fig. 10.56 Axial section at the level of the floor of the mouth (**a**) and midsagittal (**b**) section illustrating the lower borders of the oral cavity; tongue (*red arrows*) and the vertical relationship between the oropharynx (*OP*) and nasopharynx (*NP*). The *curved dotted red line* outlines the dorsum of tongue. (*orange arrow* epiglottis, *C1*, *C2*, *C3*, respective cervical vertebrae

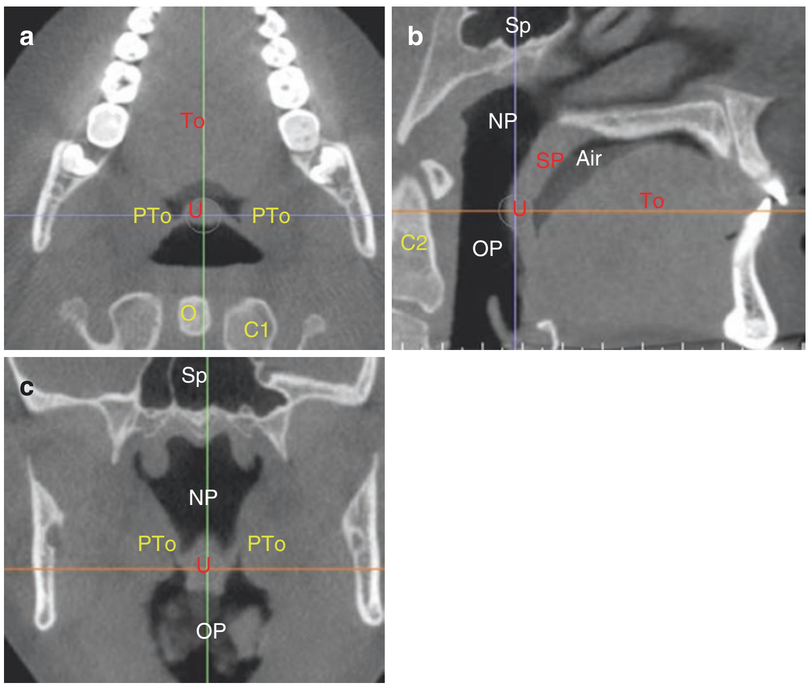

Fig. 10.57 Axial orthogonal section (**a**) at the level of the border between oropharynx/nasopharynx illustrating the lateral borders of the oral cavity/oropharynx. Midsagittal orthogonal section (**b**) showing the vertical relationship between the oropharynx (OP) and nasopharynx (NP) as well as the shape transition of these cavities. Coronal section through the upper airway (**c**) showing the lateral borders of the OP and NP and their shape changes in the coronal plane (*PTo* palatine tonsils, *To* tongue, *SP* soft palate, *U* uvula, *Sp* sphenoid sinus, *O* odontoid process of C2)

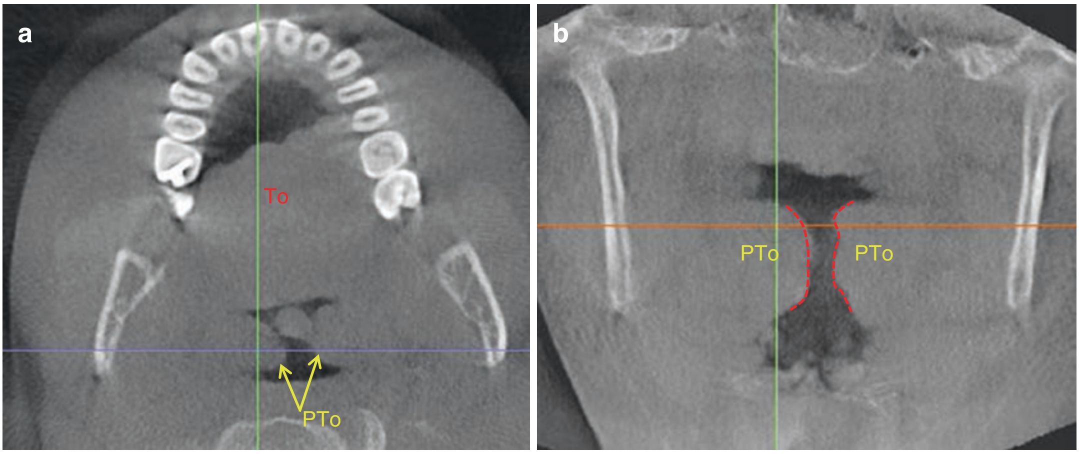

Fig. 10.58 Axial (**a**) CBCT image at the level of the maxillary teeth and coronal (**b**) CBCT image of the oropharynx showing severe narrowing of the airway by bilateral soft tissue masses, projecting into the lumen of the airway. The location and appearance of these masses is consistent with bilateral palatine tonsillar hypertrophy (*PTo* palatine tonsils, *To* tongue)

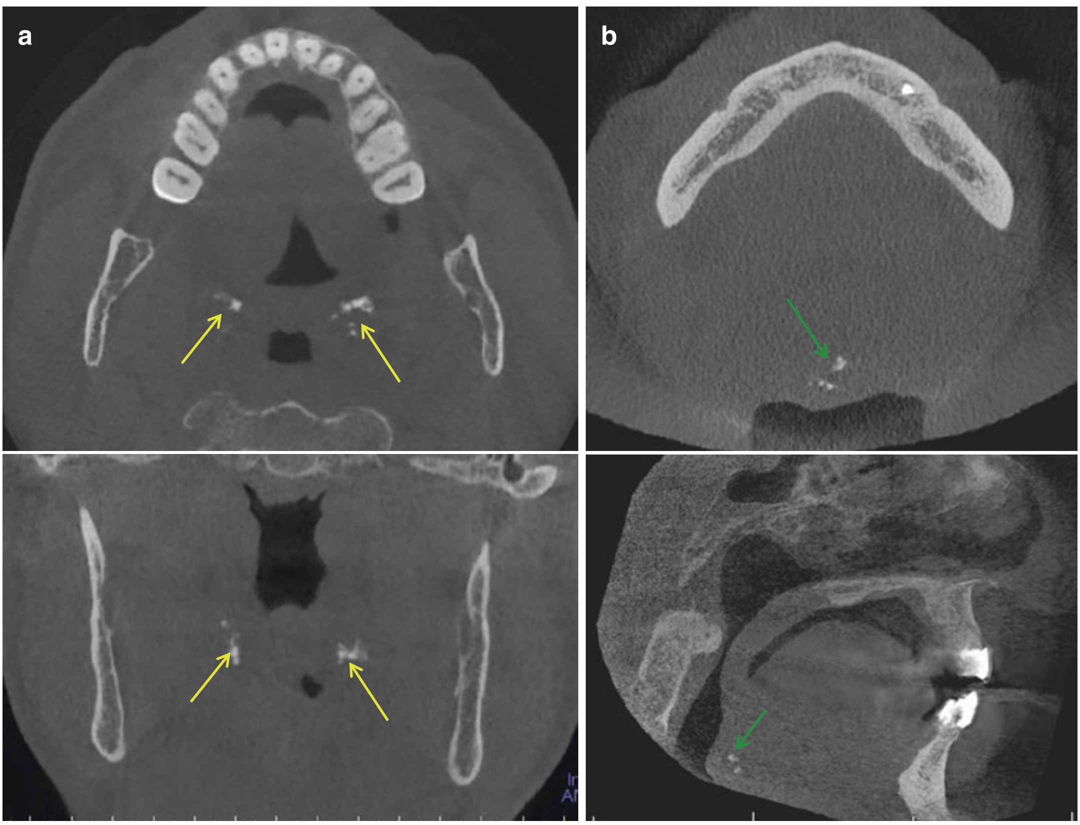

Fig. 10.59 Axial (*upper image*) and coronal (*lower image*) sections of the oropharynx of an individual (**a**) depicting lateral tonsilar calcifications in the palatine tonsils (*yellow arrows*) and axial (*upper image*) and midsagittal (*lower image*) sections of the oropharynx of a second individual (**b**) with calcifications in the lingual tonsils (*green arrows*). In both individuals the tonsillar tissue is not identified, however the presence and morphology of calcifications at these locations is highly suggestive of tonsilar mineralizations

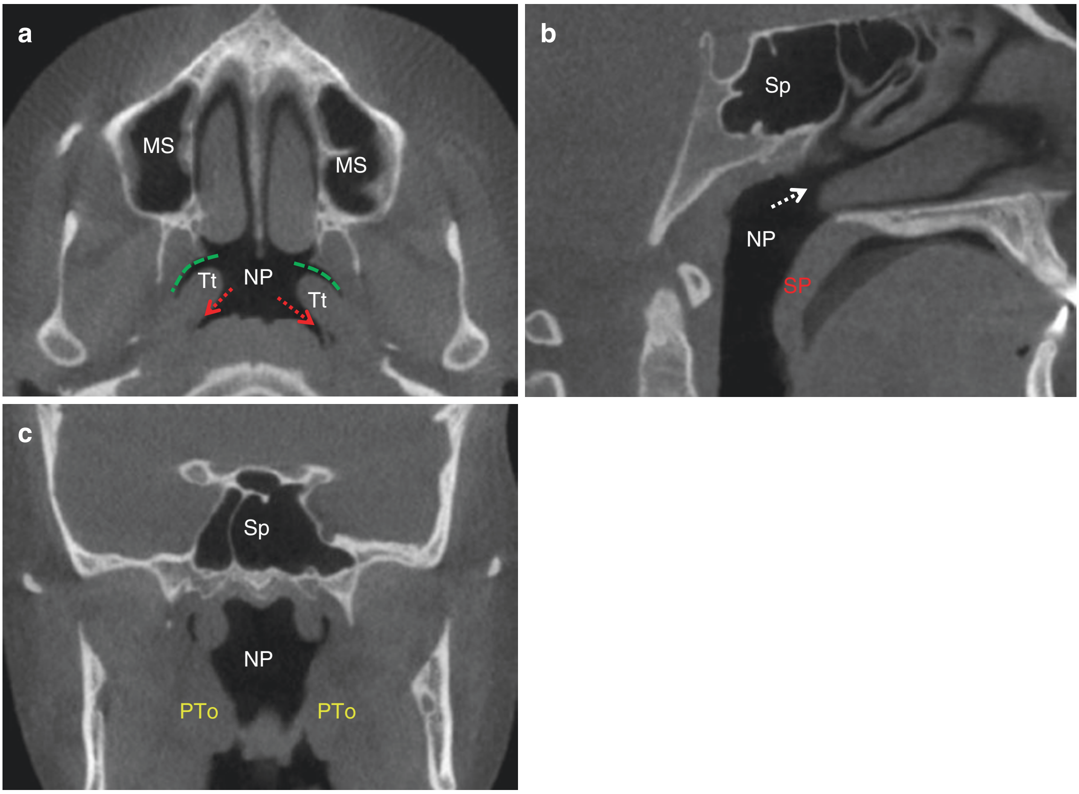

Fig. 10.60 Axial (**a**), midsagittal (**b**), and coronal (**c**) CBCT images of the nasopharynx (NP) demonstrating normal shape and size. (*green dotted line* the Eustachian tube, *Tt* the torus tubarius, *dashed red arrows* lateral pharyngeal recess or fossa of Rosenmuller, *MS* maxillary sinus; *Sp* sphenoid sinus, *PTo* palatine tonsils)

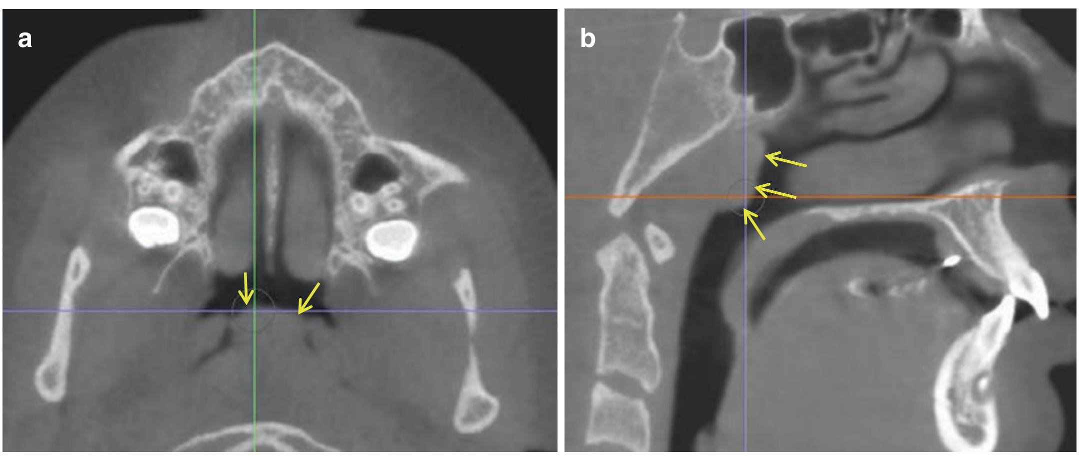

Fig. 10.61 Axial (**a**) and midsagittal (**b**) CBCT images of the nasopharynx showing a large soft tissue projection originating from the posterior wall of the nasopharynx, markedly narrowing the nasopahryngeal airway and altering its characteristic "star" shape. The imaging appearance is suggestive of posterior pharyngeal tonsilar hypertrophy (hypertrophic adenoids), however referral to an otolaryngologist should be considered based on clinical and medical history

Acknowledgments The concept of dividing the panoramic image into regions or zones for radiologic assessment is introduced courtesy of Dr. Bruno Azevedo.

References

Abrahams JJ, Levine B (1990) Expanded applications of DentaScan (multiplanar computer-ized tomography of the mandible and maxilla). Int J Periodontics Restorative Dent 10:464–471

Angelopoulos C (2008) Cone beam tomographic imaging anatomy of the maxillofacial region. Dent Clin N Am 52:731–752

Angelopoulos C (2014) Anatomy of the maxillofacial region in the three planes of section. Dent Clin N Am 58:497–521

Angelopoulos C, Aghaloo T (2011) Imaging technology in implant diagnosis. Dent Clin N Am 55:141–158

Carter RB, Keen EN (1971) The intramandibular course of the inferior alveolar nerve. J Anat 108(Pt 3):433–434

Chapnick L (1980) A foramen on the lingual of the mandible. J Can Dent Assoc 46:444–445

de Oliveira GJPL, Abdala MA, Nary-Filho H, Sakakura CE, Garcia VG, Leite FC (2017) Tomographic evaluation of prevalence, position, and diameter of the intraosseous branch of the posterior superior alveolar artery in fully edentulous individuals. J Craniofac Surg 28:279–283

Fernández-Alonso A, Suárez-Quintanilla JA, Rapado-González O, Suárez-Cunqueiro MM (2015) Morphometric differences of nasopalatine canal based on 3D classifications: descriptive analysis on CBCT. Surg Radiol Anat 37:825–833

Hafeez NS, Ganapathy S, Sondekoppam R, Johnson M, Merrifield P, Galil KA (2015) Anatomical variations of the greater palatine nerve in the greater palatine canal. J Can Dent Assoc 81:f14

Kalpidis CD, Setayesh RM (2004) Hemorrhaging associated with endosseous implant place-ment in the anterior mandible: a review of the literature. J Periodontol 75:631–645

Kottal S, Angelopoulos C, Parris V, Thomas S (2006) Classification of Edentulous Posterior Mandible by Means of Alveolar Ridge Angulation. Abstract book of the 10th European Congress of Dentomaxillofacial Radiology. p. 169 (Published abstract).

Wuehrman AH, Manson-Hing LR (1981) Dental Radiology, 5th ed. Mosby, St. Louis.

Monje A, González-García R, Monje F, Chan HL, Galindo-Moreno P, Suarez F, Wang HL (2015) Microarchitectural pattern of pristine maxillary bone. Int J Oral Maxillofac Implants 30:125–132

Scarfe WC, Farman AG, Sukovic P (2006) Clinical applications of cone-beam computed tomography in dental practice. J Can Dent Assoc 72(1):75–80

Scarfe WC, Farman AG, Levin MD, Gane D (2010) Essentials of maxillofacial cone beam computed tomography. Alpha Omegan 103:62–67

Shiller WR, Wiswell OB (1954) Lingual foramina of the mandible. Anat Rec 119:387–390

Stella JP, Tharanon W (1990) A precise radiographic method to determine the location of the inferior alveolar canal in the posterior edentulous mandible: implications for dental implants. Part 1: technique. Int J Oral Maxillofac Implants 5:15–22

Tepper G, Hofschneider UB, Gahleitner A, Ulm C (2001) Computed tomographic diagnosis and localization of bone canals in the mandibular interforaminal region for prevention of bleeding complications during implant surgery. Int J Oral Maxillofac Implants 16:68–172

White SC, Rudolph DJ (1999) Alterations of the trabecular pattern of the jaws in patients with osteoporosis. Oral Surg Oral Med Oral Pathol Oral Radiol Endod 88:628–635

Neck and Cervical Spine

11

Zhimin Li, Saulo L. Sousa Melo, Baijuan Gong, Kivanç Kamburoğlu, Christos Angelopoulos, and William C. Scarfe

Contents

11.1 Introduction

The neck is a cylindrical anatomical region composed of the cervical portion of the vertebral column and the respective spinal cord, muscles, blood

Z. Li, D.D.S., Ph.D.
Department of Oral Radiology, Jilin University, School and Hospital of Stomatology, Chang Chun, Jilin Province, China
e-mail: zhimin@jlu.edu.cn

S.L.S. Melo, D.D.S., M.S.D., Ph.D., M.S (✉)
Department of Oral Pathology, Radiology and Medicine, University of Iowa College of Dentistry, Iowa City, IA, USA
e-mail: saulo-sousamelo@uiowa.edu

B. Gong, D.D.S., Ph.D.
Department of Orthodontics, Jilin University, School and Hospital of Stomatology, Chang Chun, Jilin Province, China

K. Kamburoğlu, D.D.S., M.Sc., Ph.D.
Department of Oral and Maxillofacial Radiology, Faculty of Dentistry, Ankara University, Ankara, Turkey
e-mail: dtkivo@yahoo.com

C. Angelopoulos, D.D.S., M.S.
Aristotle University of Thessaloniki, Thessaloniki, Greece

Columbia University, College of Dental Medicine, New York City, NY, USA
e-mail: angelopoulosc@gmail.com

W.C. Scarfe, B.D.S., F.R.A.C.D.S., M.S.
Division of Radiology and Imaging Science, Department of Surgical/Hospital Dentistry, University of Louisville School of Dentistry, Louisville, KY, USA
e-mail: william.scarfe@louisville.edu

W.C. Scarfe, C. Angelopoulos (eds.), *Maxillofacial Cone Beam Computed Tomography*,
https://doi.org/10.1007/978-3-319-62061-9_11

vessels, nerves cartilages, and skin connecting the head to the torso. Its cephalad borders are the superior nuchal line of the cranium and the inferior border of the mandible and its caudal borders are the suprasternal notch and the clavicles.

Cone beam computed tomography (CBCT) examinations may be prescribed by specific dental specialists (orthodontists, oral surgeons, sleep apnea and temporomandibular joint specialists) to investigate the anatomical areas of the neck such as the upper airway (e.g., airway space, soft palate, tonsils, uvula), cervical spine, and adjacent soft tissues. Increasingly CBCT is being introduced as an initial in-office imaging modality of these structures by ear, nose and throat (ENT) surgeons or otolaryngologists. Hence, it is essential that the referring clinician who prescribes or performs CBCT imaging be familiar with the anatomy of the neck and common system based pathology and be aware of the presentation of possible incidental findings, especially in those occasions where this area is not the primary focus of the examination.

In most dental practices a maxillofacial CBCT machine will not image the entire neck because of the limited source to detector distance, a physical inability to translate the rotating gantry caudally below the level of the shoulders and the fact that most acquisition protocols now use a field of view (FOV) restricted to the dental region of interest (ROI). However, particularly when imaging the mandible, a portion of the neck (e.g., upper cervical spine, retroglossal airway, and upper peripheral soft tissues) may be included in the imaging volume. Most frequently, the caudal border of the imaging volume would be at the level of C4 to C5 vertebrae.

The goal of the chapter is to review of the anatomy of osseous and soft tissue elements of the neck, detail important clinical assessment techniques, and introduce the imaging features of common abnormalities and pathology such that the referring dental clinician may take an appropriate course of action.

11.1.1 Limitations of CBCT Assessment

Because of the necks morphologic simplicity, the best images to assess this region are sequential, orthogonal (axial, coronal, and sagittal) thin CBCT sections (Fig. 11.1). It is rather uncommon that such an extended portion of the neck be included in a CBCT scan; in most cases, a more limited portion of the neck is included which rarely exceeds C-4. All the elements of the neck (cervical spine, hyoid bone, airway, part of the thyroid cartilage complex, and relevant soft tissue) and their spatial orientation are visualized. Sometimes other multiplanar sections may be used, depending on need. Curved planar images best demonstrate the features the curved structures (e.g., the hyoid bone). For the gross assessment of large osseous structures, either surface renderings (3D) or maximum intensity projections (MIP) may be used.

CBCT is a diagnostic imaging tool predominantly for the evaluation of hard tissues. Because of high resolution, the maximum diagnostic efficacy of CBCT is achieved when used in the assessment of osseous changes or pathology. While inherent poor soft tissue contrast limits the contribution of CBCT in recognizing differences between soft tissue structures (e.g., fat as opposed to muscle), soft tissue anatomical boundaries can be identified. High inherent contrast can be useful in identifying an air/soft tissue interface such as upper airway shape alterations due to soft tissue or even pathological features such as inspissated secretions within the maxillary sinus.

11.2 The Cervical Spine

The cervical spine consists of the seven most cephalad vertebrae of the spinal column. The cervical vertebrae are located from the base of the skull to the first thoracic vertebra and identified as C1 (1st cervical vertebra) to C7 (7th cervical vertebra). Stacked vertically and viewed laterally, the cervical spine has a normal forward C-shape

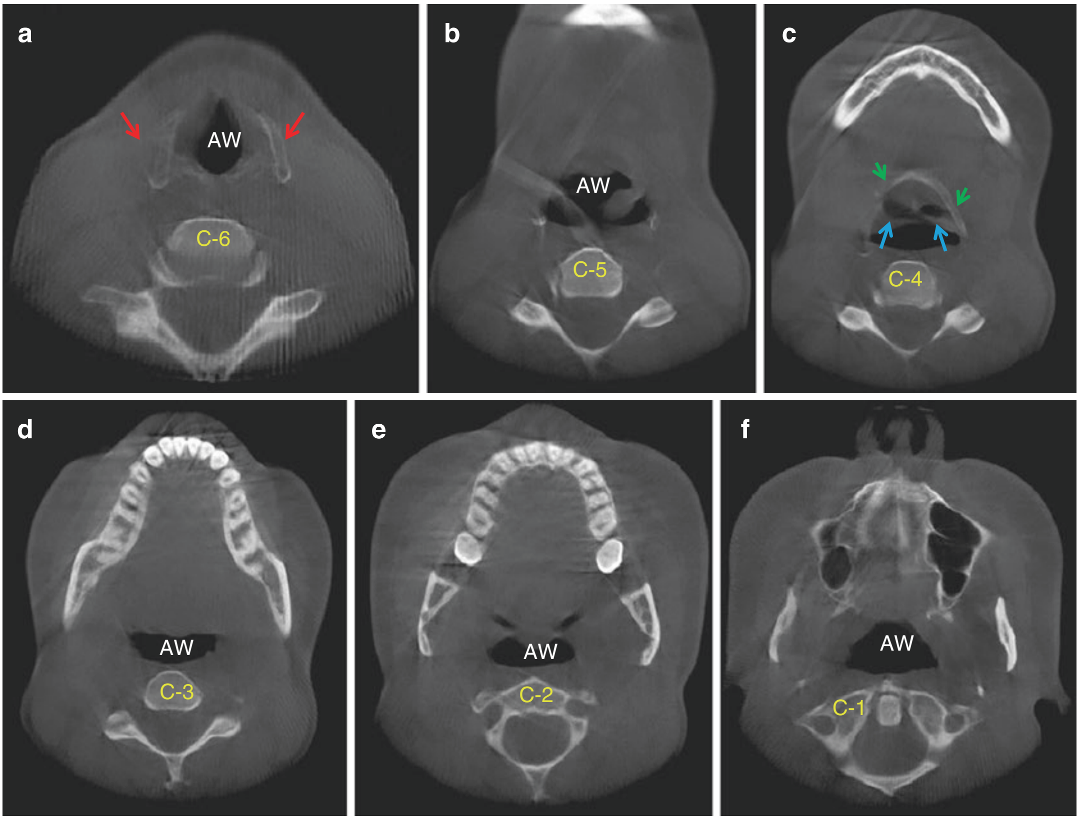

Fig. 11.1 Sequential series of CBCT axial sections of the neck (**a**–**f**) extending from the base of the spinal vertebrae (C6—**a**) to the uppermost spinal vertebrae (C1—**f**) depicting the shape changes in the gross contours of the neck and main osseous anatomical landmarks including the upper airway (AW), thyroid cartilage (*red arrows*), hyoid bone (*green arrows*), and epiglottis (*blue arrows*). Note the homogenous appearance of the soft tissues preventing the recognition of soft tissue structures such as fascial planes, soft tissue spaces, muscles, or glands

curvature, referred to as the *lordotic curve* (Fig. 11.2). They are held together by a number of ligaments and muscles which provided flexibility and enable a range of movements to the head and neck. Flattened, biconvex articular cartilaginous intervertebral disks are interposed between adjacent vertebrae. These act as cushions and contribute to the overall flexibility of the cervical spine.

The cervical vertebral column is best visualized in its entirety in sagittal and coronal images of the neck (Fig. 11.2). These sections, together with volumetric renderings (Fig. 11.3), depict possible shape alterations of the cervical spine as well as misalignment of the vertebrae. Coronal and axial orthogonal sections may assist in assessing the shape and size of the vertebral bodies and in evaluating the foramina.

11.2.1 Overview of Radiographic Anatomy

The general configuration of the cervical vertebrae consist of a body (ventrally), the transverse processes (bilaterally), and the spinous process (dorsally). These components form a “ring,” the central lumen of which is the *vertebral foramen*. Through the entire length of the vertebral column, consecutive vertebral foramina (in axial

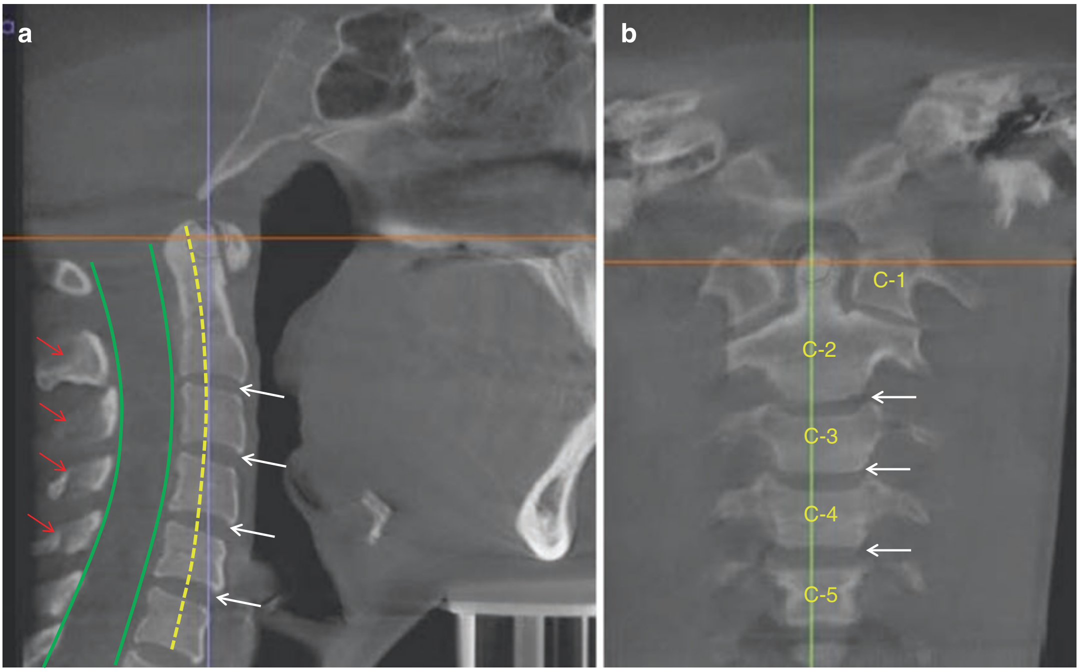

Fig. 11.2 Sagittal (**a**) and coronal (**b**) images of the cervical spine depicting vertebral bodies of C1 to C6. There is a slight curvature of the cervical spine (reversed C) (*dotted yellow line*). Note the "cupping" of the vertebral bodies toward their superior aspect, to accommodate the intervertebral disks; intervertebral disk space (*white arrows*), spinous processes (*red arrows*)

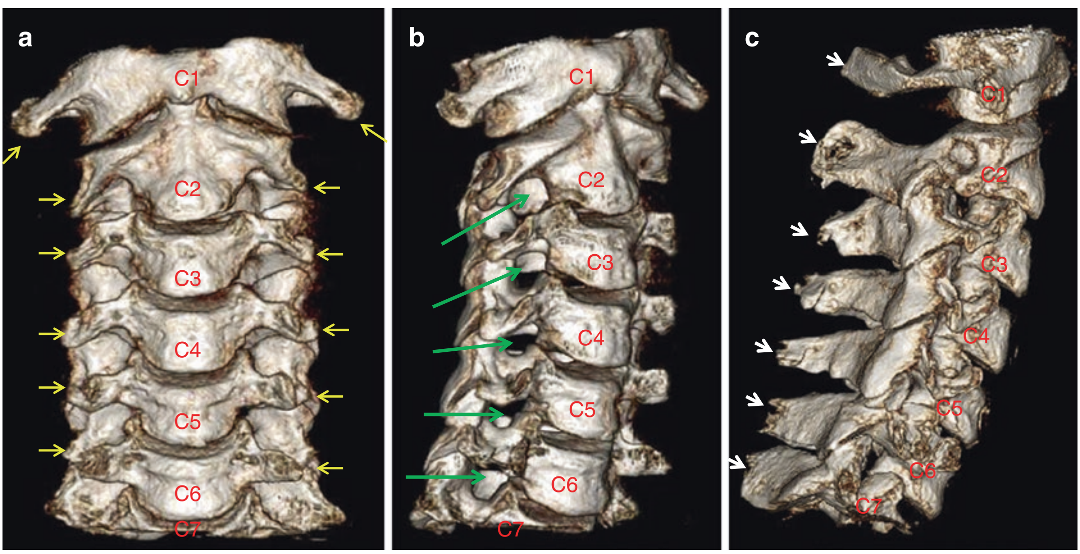

Fig. 11.3 Coronal (**a**), right lateral oblique (**b**), and right lateral (**c**) surface renderings of the cervical spine extending from C1 to C6 showing major anatomical landmarks of the cervical vertebrae including transverse processes (*yellow arrows*), spinous processes (*white arrows*), and intervertebral foramina for the passageway of the spinal nerves (*green arrows*)

projection) form the *spinal canal* (in sagittal and coronal projections), within which lies the spinal cord.

The vertebral body appears to be roughly square, surrounded by a thin cortical outline with homogenous intramedullary density in the sagittal image projections. Slight concavities of the superior and inferior articulating surfaces are common. Intervertebral articular disks are interposed between two proximal articular surfaces of adjacent vertebrae (Figs. 11.4, 11.5, and 11.6). The transverse processes of adjacent vertebrae form horizontal openings, the *intervertebral foramina*, for the passageway of the spinal nerves (Fig. 11.6). Furthermore, vertical foramina piercing the transverse processes (transverse foramina) of adjacent vertebrae form the vertebral canal for the passage of the vertebral artery and vein as well as sympathetic nerves.

The vertebrae of the entire vertebral column are primarily held together with two long ligaments: the anterior longitudinal ligament, which runs the ventral aspect of the vertebral bodies and the posterior longitudinal ligament, which lines the dorsal aspect of the vertebral bodies. These are not identifiable on CBCT images unless they develop dystrophic calcifications.

Numerous anatomic features distinguish the cervical vertebrae from those of the thoracic and lumbar spine:

- The cervical vertebrae are the smallest in the spine.
- They possess transverse foramen in the lateral process through which pass the vertebral artery and vein.
- They demonstrate bifid spinous processes in C2 through C6.
- Three of cervical vertebrae have unique anatomical features:
  – The 1st cervical vertebrae or *atlas* (C1).
  – The 2nd cervical vertebrae or *axis* (C2).
  – The 7th vertical vertebrae or *vertebra prominens* (C7).
- There is no intervertebral fibrocartilage disc between the skull and the *atlas*, nor between the *atlas* and the *axis* (Rosse and Rosse 1997).

11.2.2 The Atlas (C1)

The 1st cervical vertebra (C1) is termed the *atlas*. This name is derived from the fact that functionally it supports the skull, similar to the Greek

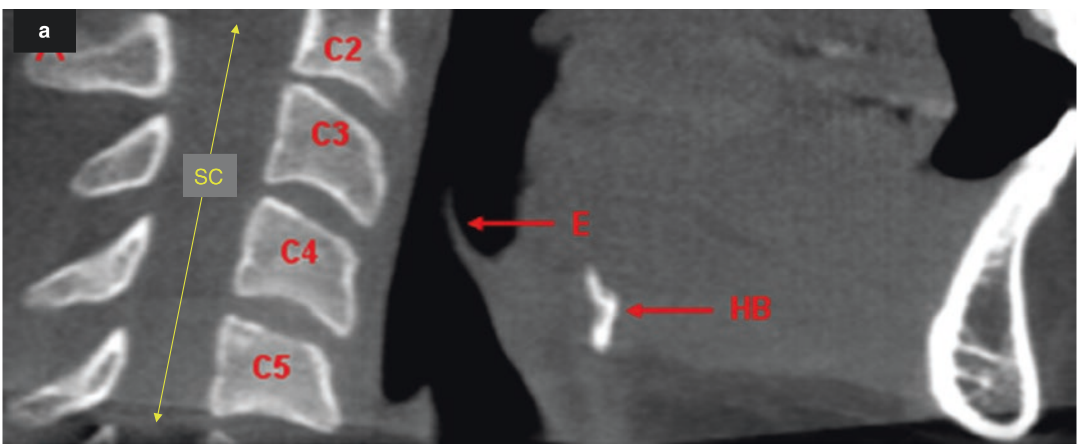

Fig. 11.4 Midsagittal CBCT image projection of the upper portion of the cervical spine demonstrating the general radiographic features of the cervical spine and anatomic shape and size of the vertebral bodies. The normal shape of each vertebral body is square, with cephalad and caudal concavities. Note the homogenous density of the cancellous bone in the vertebral bodies outlined by a thin continuous cortical outline. (*SC* spinal canal, *E* epiglottis, *HB* hyoid bone)

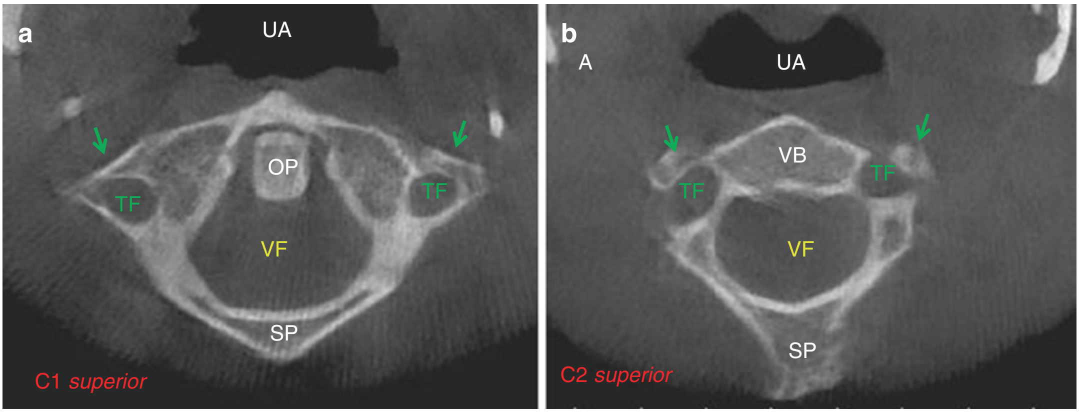

Fig. 11.5 Axial superior CBCT sections of C1 (**a**) and C2 (**b**) showing common radiographic anatomy of the respective vertebrae including vertebral foramen (VF), transverse foramen (TF), vertebral body (VB), spinous process (SP), transverse processes (*green arrows*), and relative relationship to the upper airway (UA). A separate circular feature is seen on the axial image of C1 (**a**) that appears to encroach on VF. This is a superior osseous extension from the VB of C2, the odontoid process (OP) or dens

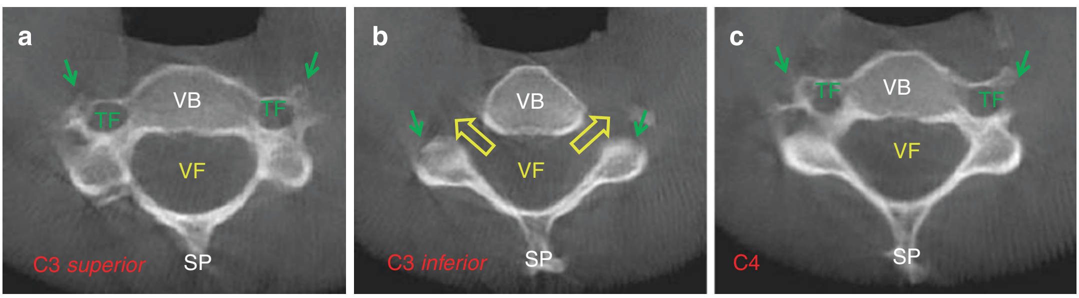

Fig. 11.6 Axial CBCT sections of C3 from both superior (**a**) and inferior (**b**) projections and a superior projection of C4 (**c**) showing common radiographic anatomy of the respective vertebrae including vertebral foramen (VF), transverse foramen (TF), vertebral body (VB), spinous process (SP), transverse processes (*green arrows*), intervertebral foramina (*yellow open arrows*), and relative relationship to the upper airway (UA)

mythological figure, *Atlas,* who supported the world. The *atlas* does not have a vertebral body or spinous process. It appears as a ring in shape and has an anterior arch, a posterior arch with two lateral masses and two transverse processes. The body of the atlas may fuse with that of the second cervical vertebra (C2). The lateral masses carry both the superior and inferior articular facets. The atlas comprises several anatomic features that can be identified in superior or inferior projections (Fig. 11.7).

- **Anterior Arch and Anterior Tubercle.** The anterior arch forms the front of the atlas. Its anterior surface is convex while the posterior surface is concave. The posterior surface of the anterior arch articulates with the odontoid process (dens) of the *axis* below. The anterior tubercle is the most prominent point of the anterior surface of anterior arch and serves as the attachment of the *Longus colli* muscles.
- **Posterior Arch and Posterior Tubercle.** The posterior arch forms the back of the atlas. The posterior tubercle is a rudimentary spinous process and the origination of the *recti capitis posteriores minores* muscle. Therefore, the atlas does not have a true spinous process.
- **Lateral masses.** The lateral masses form the side of the atlas. They are the largest and

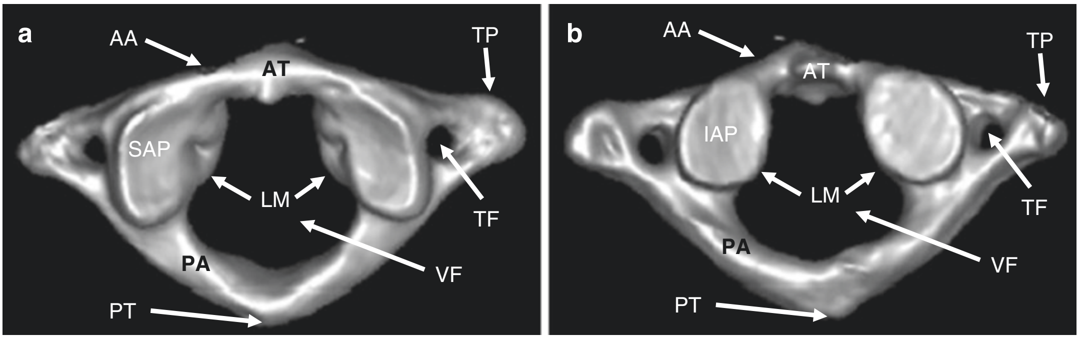

Fig. 11.7 Superior (**a**) and inferior (**b**) projection images of shaded surface volumetric rendering of the 1st cervical vertebrae (*atlas* or C1) (*AT* anterior tubercle, *AA* anterior arch, *IAP* inferior articular process, *TP* transverse process, *TF* transverse foramen, *VF* vertebral foramen, *PA* posterior arch, *PT* posterior tubercle, *SAP* superior articular process, *LM* lateral mass)

strongest parts of the atlas and support the weight of the skull.

- **Superior and Inferior Articular Process.** Two superior and two inferior articular processes project upward and downward from the lateral masses, respectively. The superior circular articular facets of atlas articulate with the occipital condyle of the skull and the inferior articular facets articulate with the second cervical vertebra below.
- **Transverse Process and Transverse Foramen.** The transverse processes extend laterally, anteriorly, and inferiorly from the lateral masses and provide surfaces for attachment of muscles that allow rotation of the skull. At their terminal ends, the anterior and posterior tubercles disappear and fuse into one mass to allow attachment of muscles. The base is perforated by a transverse foramen (*foramen transversarium*) allowing transmission of the vertebral artery and vein, which are directed inferiorly and anteriorly from above. Compared with other cervical vertebrae, the atlas is wider laterally due to the size of the large transverse processes.
- **Vertebral Foramen.** The vertebral foramen is a large opening in the center of the atlas. It is formed by the anterior and posterior arches and is much larger than the actual spinal cord diameter. Therefore, atlas displacement may occur without symptoms associated with compression of the spinal cord.

11.2.3 The Axis (C2)

The second cervical vertebra (C2) is commonly called the *axis*. It derives its name from the fact that it acts as a pivotal joint, allowing the atlas and consequently the head to rotate. It has a bony projection, the odontoid process, that protrudes superiorly from the upper surface of the body. The axis comprises several anatomic features that can be identified in superior or inferior projections (Fig. 11.8).

- **Odontoid process.** The odontoid process (dens or odontoid peg) projects superiorly through the anterior portion of the vertebra foramen of the atlas and articulates against the inner aspect of the anterior arch of the atlas behind the anterior tubercle.
- **Body.** The width of the anterior body extends anterior and inferiorly to overlap the superior and anterior position of the more caudal C3 vertebra below. The inferior surface is concave in the anterio-posterior dimension and convex in lateral dimension. A longitudinal ridge lies in the middle of the body.
- **Superior and inferior articular process.** Two (2) superior articular processes lie on each side of the junction of the body and pedicle. They are nearly circular in shape with a slight convexity, and directed supero-laterally. There is a very shallow superior vertebral notch behind each. The superior

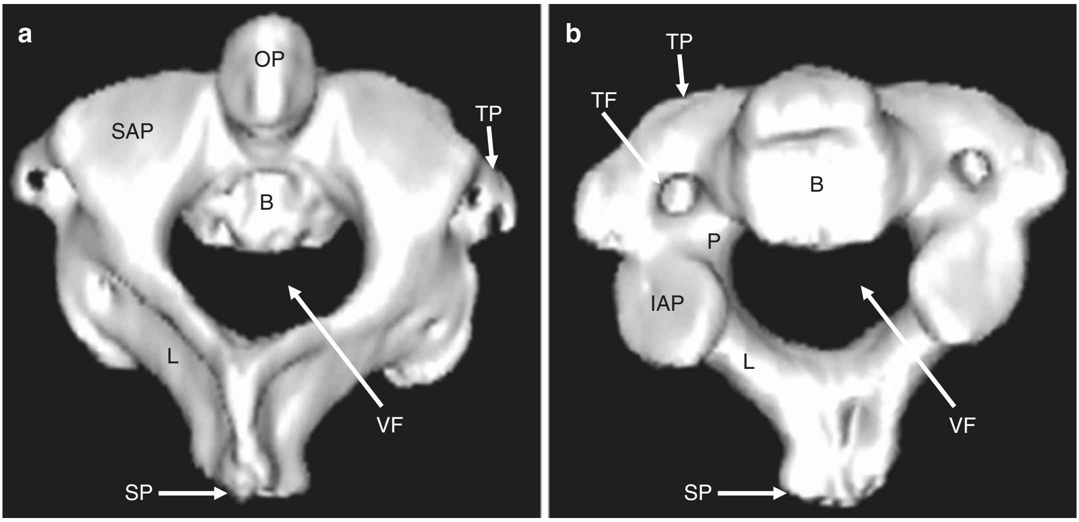

Fig. 11.8 Superior (**a**) and inferior (**b**) projection images of shaded surface volumetric rendering of the 2nd cervical vertebrae (*IAP* inferior articular process, *TP* transverse process, *TF* transverse foramen, *VF* vertebral foramen, *SAP* superior articular process, *L* lamina, *OP* odontoid process (dens), *B* body, *SP* spinous process, *P* pedicle)

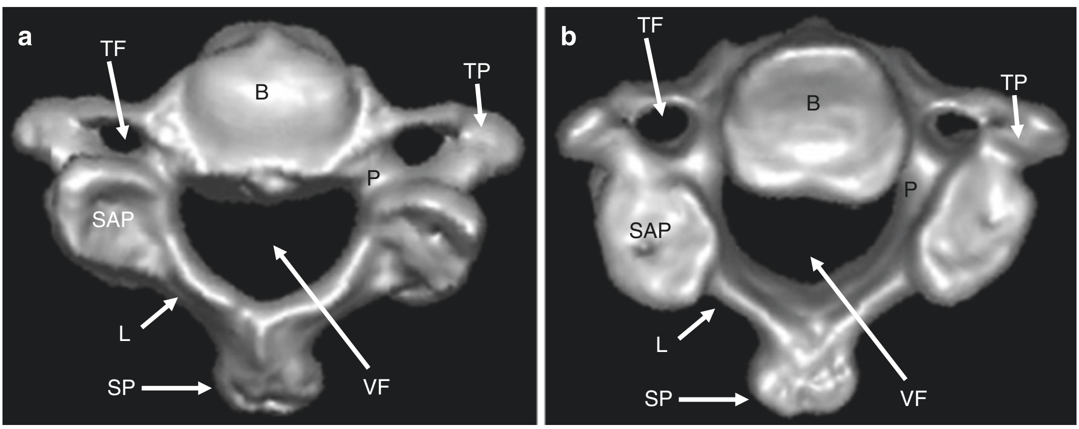

Fig. 11.9 Superior (**a**) and inferior (**b**) projection images of shaded surface volumetric rendering of the 3rd cervical vertebrae (C3). (*IAP* inferior articular process, *TP* transverse process, *TF* transverse foramen, *VF* vertebral foramen, *SAP* superior articular process, *L* lamina, *B* body, *SP* spinous process, *P* pedicle)

processes are directed posteriorly whereas the inferior processes face anterior C3 through C7. The vertebrae articulate with each other at the superior and inferior facets of articular process, separated by an intervertebral space.

- **Pedicle and lamina.** Two pedicles extend from the body to the transverse processes and two laminae extend from the transverse process to the spinous process, respectively. Together, they form the vertebra arch.
- **Transverse process and transverse foramen.** Two small transverse processes extend laterally from each side of the vertebra arch. Each has a supero-antero-laterally directed transverse foramen (foramen transversarium) and presents a non-bifid tuberculated extremity.
- **Spinous process.** The spinous process projects dorsally from the posterior junction of the two laminae and presents with a bifid tuberculated end.
- **Vertebral foramen.** The vertebral foramen is surrounded by the vertebral arch which is smaller than that of the *atlas* superiorly.

11.2.4 C3 to C6

These four cervical vertebrae are typical cervical vertebrae because they possess similar features to the other vertebrae in the spine, except for the presence of a transverse foramen. Each vertebra consists of two main parts, an anterior body and a posterior vertebral arch. The latter is composed of two pedicles and two laminae, carrying four articular processes, two transverse processes, and one spinous process. These vertebrae comprise several anatomic features that can be identified in superior or inferior projections (Fig. 11.9).

- **Body.** Cervical vertebral bodies are typically small and oval in shape. The maximum lateral dimension is greater than that from anteroposteriorly. Both upper and lower surfaces are slightly concave. The height of the anterior and posterior surface is equal and the anterior level is lower than the posterior, resulting in inferior border overlap of each vertebra inferiorly.
- **Pedicle.** Two pedicles are attached directly to the back of the vertebral body and form the anterior parts of the vertebral arch. There are two concave intervertebral notches on each side.
- **Laminae.** The laminae are composed of two bone plates that are connected with the pedicles and form the posterior part of the vertebral arch.
- **Transverse process.** There are two transverse processes extending from each side of vertebral arch. Each transverse process is short and has a bifid end with an anterior and a posterior tubercle. There is a groove along the upper surface through which passes the cervical spinal nerve. The length of transverse process increases from C3 to C7. The transverse processes also provides for attachment of muscles.
- **Transverse foramen.** The transverse foramen lies centrally in each transverse process of the cervical vertebrae and contains the vertebral artery and vein in C1 to C6.
- **Articular Process.** Two superior and two inferior articular processes extend from the junction of the pedicle and lamina, lateral to the vertebral foramen. The articular facets are oriented obliquely.
- **Spinous process.** The spinous processes of these cervical vertebrae are usually bifid and shorter than other vertebrae. They provide for attachment of muscles.
- **Vertebral foramen.** The alignment of the vertebral arches from stacked cervical vertebra form a large and triangular hollow cylinder called the vertebral foramen, containing the spinal cord.

11.2.5 Specific CBCT Projections

The normal CBCT radiographic appearance of the upper cervical vertebrae depends on axial (Figs. 11.10, 11.11, 11.12 and 11.13), coronal (Fig. 11.14), sagittal (Figs. 11.15 and 11.16), and volumetric (Figs. 11.17 and 11.18) imaging projections (Madden 2008; El-Khoury et al. 2007).

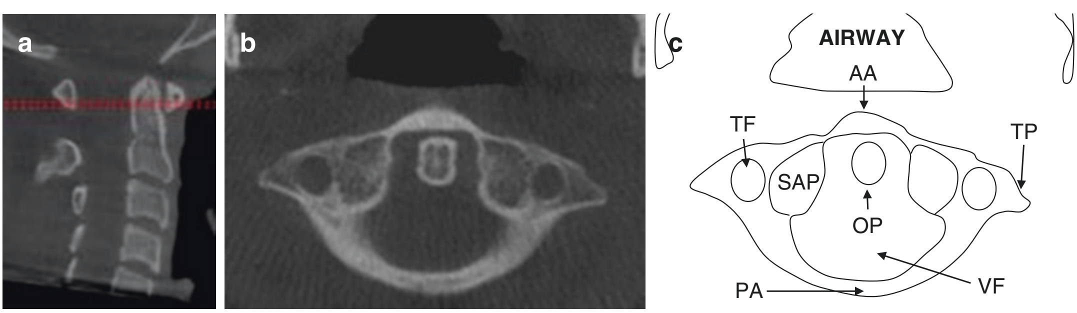

Fig. 11.10 Reference midsagittal (**a**) and axial CBCT images (**b**) with corresponding annotated axial schematic (**c**) at the level of the C1 arch showing the showing the normal anatomy (*AA* anterior arch, *OP* odontoid process, *TP* transverse process, *TF* transverse foramen, *SAP* superior articular surface, *VF* vertebral foramen, *PA* posterior arch)

Fig. 11.11 Reference midsagittal (**a**) and axial CBCT images (**b**) with corresponding annotated axial schematic (**c**) at the level of the body of C2 showing the normal anatomy (*B* body of the axis, *TP* transverse process, *P* pedicle, *VF* vertebral foramen, *L* lamina, *SP* spinous process)

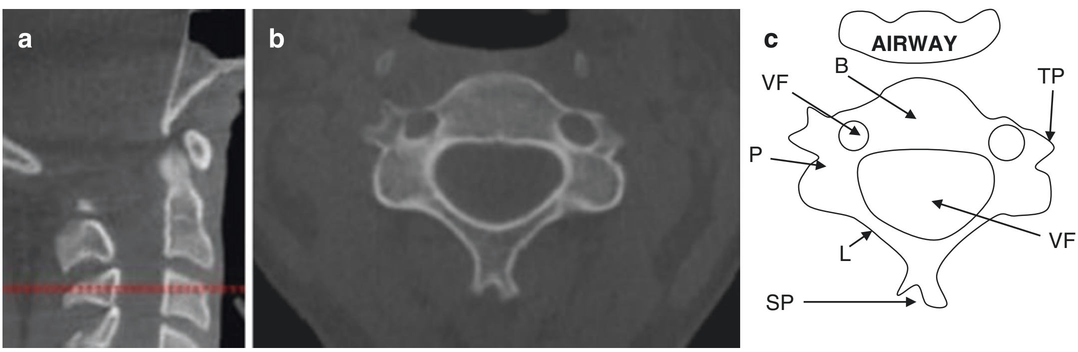

Fig. 11.12 Reference midsagittal (**a**) and axial CBCT images (**b**) with corresponding annotated axial schematic (**c**) at the level of the body of C3 showing the normal anatomy (*B* vertebral body of C3, *TP* transverse process, *TF* transverse foramen, *P* pedicle, *VF* vertebral foramen, *L* lamina, *SP* spinous process (bifid))

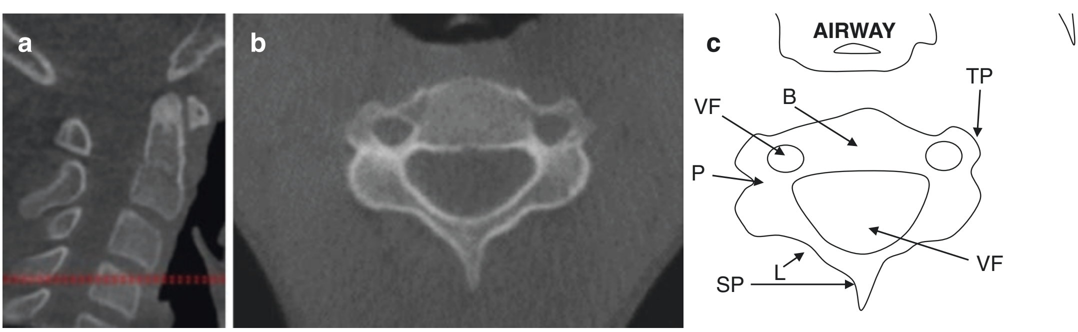

Fig. 11.13 Reference midsagittal (**a**) and axial CBCT images (**b**) with corresponding annotated axial schematic (**c**) at the level of the body of C4 showing the normal anatomy (**B** vertebral body of C4, *TP* transverse process, *TF* transverse foramen, *P* pedicle, *VF* vertebral foramen, *L* lamina, *SP* spinous process (bifid))

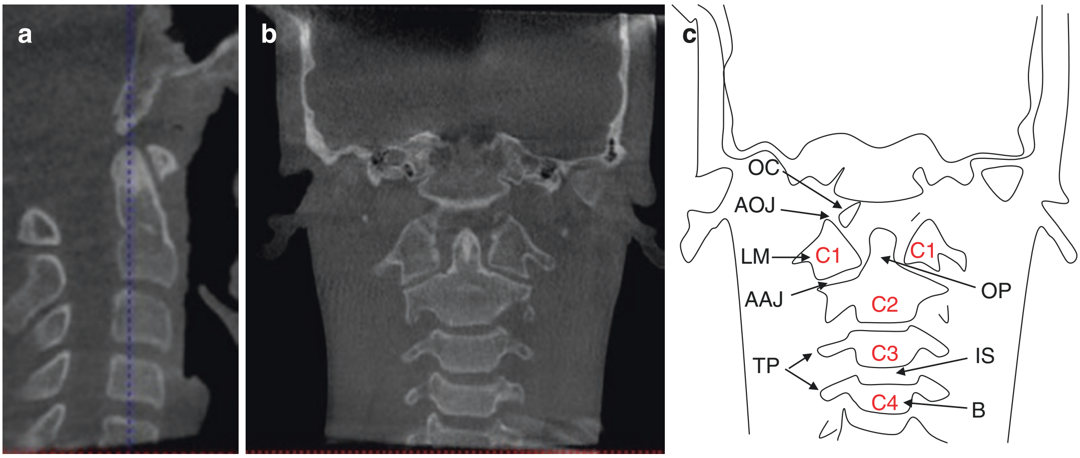

Fig. 11.14 Reference midsagittal (**a**) and coronal CBCT images (**b**) with corresponding annotated coronal schematic (**c**) through the anterior bodies of the upper cervical vertebrae showing the normal anatomy (*OC* occipital condyle, *AOJ* atlanto-occipital joint, *OP* odontoid process, *LM* lateral mass, *AAJ* atlanto-axial joint, *IS* intervertebral space, *TP* transverse process, *B* vertebral body)

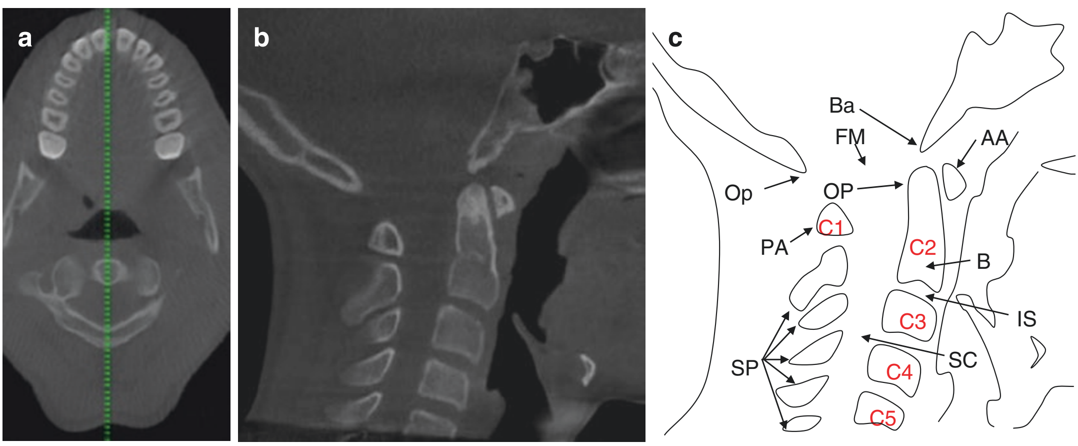

Fig. 11.15 Reference axial (**a**) and midsagittal CBCT images (**b**) with corresponding annotated midsagittal schematic (**c**) showing the normal anatomy of the upper cervical vertebrae (*Ba* basion, *AA* anterior arch of C1, *FM* foramen magnum, *Op* opisthion, *OP* odontoid process, *PA* posterior arch of C1, *B* vertebral body of C2 lateral mass, *SC* spinal cord, *SP* spinous processes, *IS* intervertebral space)

11.2.6 Neck and Cervical Spine Evaluation

Assessment of the cervical spine and adjacent soft tissue is an important phase in the evaluation of the patient who presents immediately after trauma, with chronic neck pain, with anomalies of the cervical spine (e.g., atlanto-occipital fusion, odontoid abnormalities), or with craniofacial abnormalities with associated anomalies of the skull base or cervical spine (e.g., cleft lip and cleft palate, Klippel-Feil syndrome, Down's syndrome). Most dental practitioners will not be involved in the management of these patients. However, maxillo-

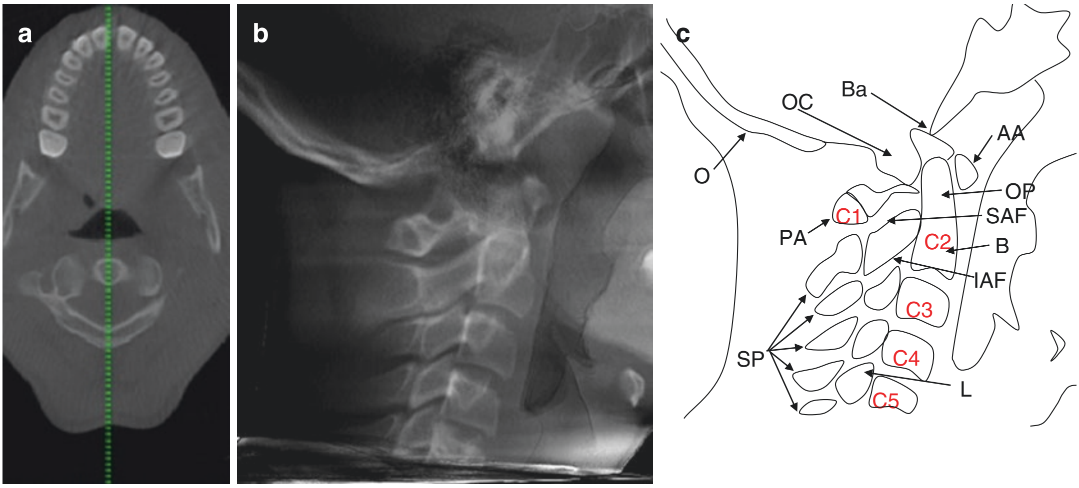

Fig. 11.16 Reference axial (**a**) and midsagittal thick (40 mm) CBCT images (**b**) with corresponding annotated midsagittal schematic (**c**) showing the normal anatomy of the upper cervical vertebrae (*Ba* basion, *AA* anterior arch of C1, *O* occiput, *OP* odontoid process, *PA* posterior arch of C1, *B* vertebral body of C2, *SAF* superior articulating facets, *IAF* inferior articulating facets, *L* lamina, *SP* spinous processes)

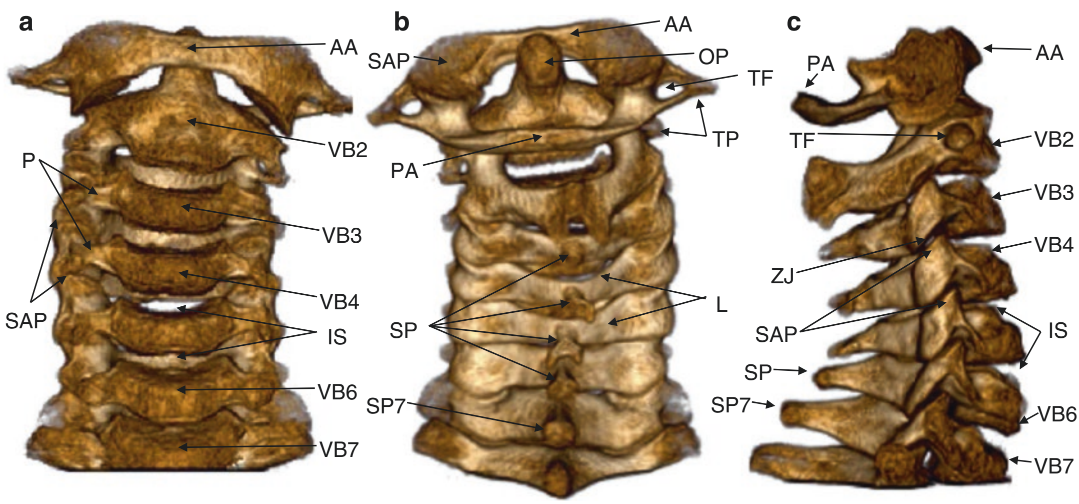

Fig. 11.17 Volumetric rendering of representative cervical vertebrae images of a 10-year-old girl generated from CBCT from the anterior (**a**), posterior (**b**), and right lateral (**c**) view. (*AA* anterior arch of C1 (atlas), *VB2* vertebral body of C2 (axis), *VB3* vertebral body of C3, *VB4* vertebral body of C4, *IS* intervertebral space, *VB6* vertebral body of C6, *VB7* vertebral body of C7, *P* pedicle, *SAP* superior articular process, *SAF* superior articular facet of *atlas*, *OP* odontoid process, *TP* transverse process, *TF* transverse foramen, *PA* posterior arch of C1, *L* laminae, *SP* spinous process, *SP7* spinous process of C7, *ZJ* zygapophyseal (facet) joint)

facial CBCT may subsequently be performed on these individuals for dental reasons and, in some instances (e.g., orthodontics, orthognathic surgery or reconstructive surgery, temporomandibular joint disorders), show the cervical spine and adjacent soft tissues. It is essential that practitioners using CBCT have some rudimentary knowledge on the radiographic characteristics of cervical alignment, the range of normal relationships between the cranium and cervical spine, interrelationships between the cervical vertebrae and normal prevertebral soft tissue.

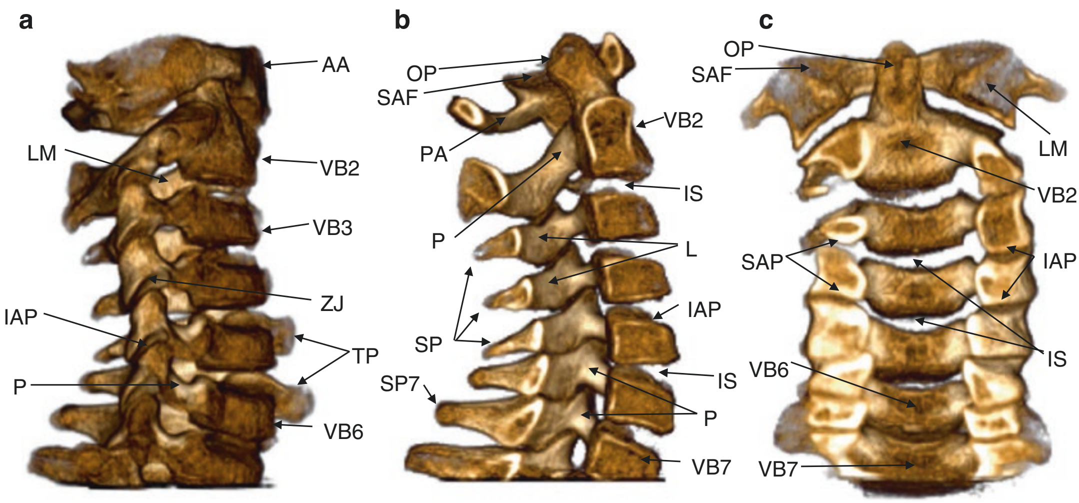

Fig. 11.18 Volumetric rendering of representative cervical vertebrae images of a 10-year-old girl generated from CBCT from the right lateral oblique (**a**), midsagittal (**b**), and mid-coronal (**c**). (*AA* Anterior arch of C1 (atlas), *VB2* vertebral body of C2 (axis), *VB3* vertebral body of C3, *ZJ* zygapophyseal (facet) joint, *TP* transverse process, *VB6* vertebral body of C6, *P* pedicle, *IAP* inferior articular process, *LM* lateral mass of *atlas*, *OP* odontoid process, *SAF* superior articular facet of the *atlas*, *PA* posterior arch of atlas, *SP* spinous process, *SP7* spinous process of C7, *IS* intervertebral space, *L* lamina, *IAP* inferior articular process, *VB7* vertebral body of C7, *SAP* superior articular process, *VB6* vertebral body of C6

11.2.6.1 Cervical Alignment

Four alignment reference lines (Fig. 11.19) are used to identify the cervical vertebral body displacement due to neck injury. Each should be a smooth, continuous curve in healthy individuals. The joint intervals between the vertebrae should be parallel and clearly visible.

- **Anterior spinal line**: The line connects the anterior margin of the atlas and anterior margins of other cervical vertebral bodies.
- **Posterior spinal line**: The line connects the posterior margins of the cervical vertebral bodies. It is the most sensitive line for the cervical spine injury assessment on lateral neck images.
- **Spinolaminar line**: The line connects the corticated line at the fusion of the laminae and spinous processes of cervical vertebrae.
- **Posterior spinous process line**: The line connects the posterior edges of the spinous processes.

11.2.6.2 Cranium to the Cervical Spine

The relationship between the base of the skull (occipital bone) and cervical spine is most often described by the relative position of the odontoid process to the foramen magnum (as defined on midsagittal images) (Table 11.1) (Fig. 11.20) and specific measurements of the cranio-cervical junction (Table 11.2) (Figs. 11.21, 11.22, 11.23, 11.24). In addition, various parameters describe the atlanto-axial relationship (Table 11.3) (Fig. 11.25).

11.2.6.3 Prevertebral Soft Tissue

The prevertebral soft tissue (PVST), also known as the *prevertebral fat stripe* or *prevertebral fat plane,* is the distance between the mid-anterior margin of cervical vertebral bodies to the closest point of the posterior wall of upper airway. This soft tissue linear area contains loose areolar tissue and lymph nodes in the retropharyngeal space and retro-esophageal space. An anterior displaced or widened fat stripe indicates underlying cervical disease, such as trauma or possibly adjacent neoplasms (Chen and Bohrer 1999; Franquet et al. 2002). Therefore, it is necessary to be knowledgeable of the normal limits of thickness of this tissue at various levels (Table 11.4) (Fig. 11.26).

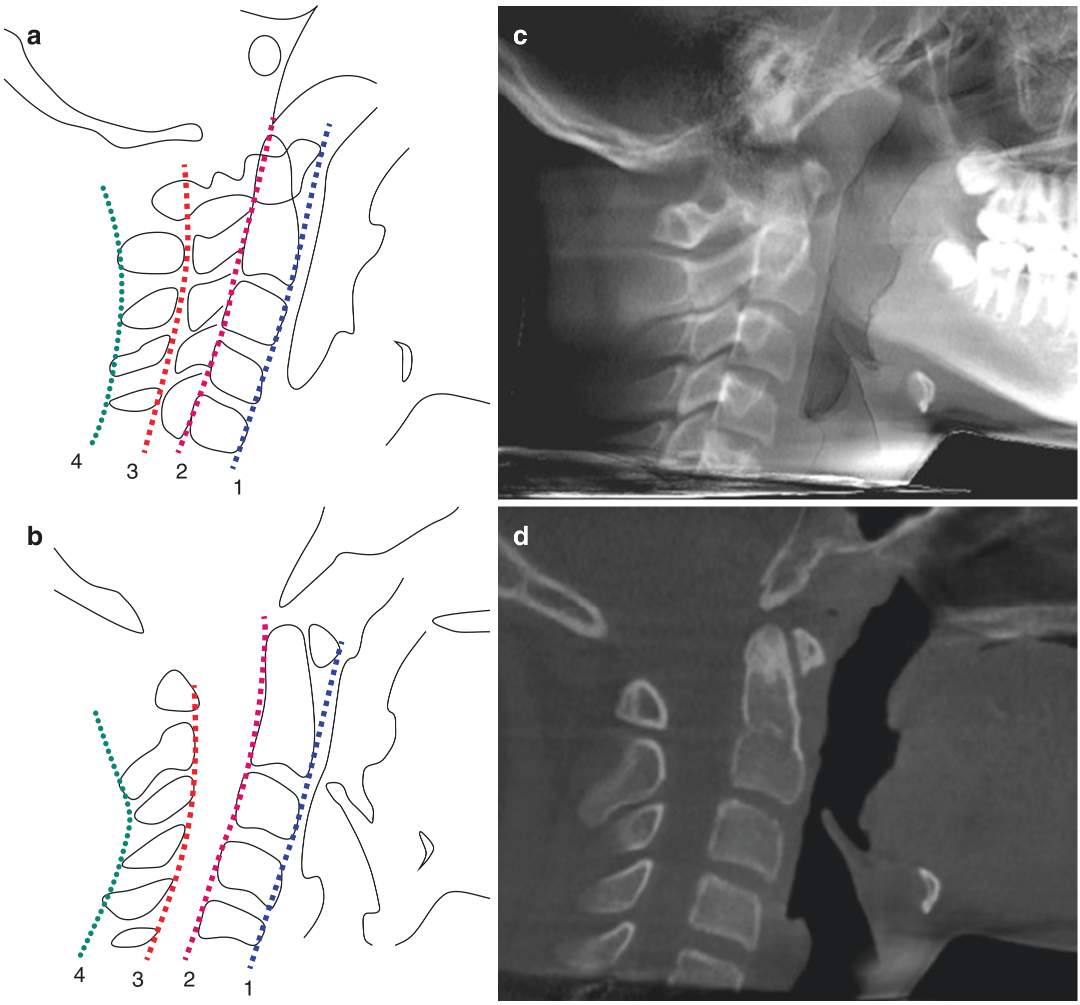

Fig. 11.19 Schematic (**a**, **b**) and corresponding lateral cephalometric (**c**), and midsagittal CBCT image (**d**) showing the cervical alignment lines the anterior spinal line (*1*), the posterior spinal line (*2*), the spinolaminar line (*3*), and the posterior spinous process line (*4*)

Table 11.1 Reference lines describing the relative position of the odontoid process to the foramen magnum (as defined on midsagittal images) and defining basilar invagination/impression

Line	Definition	Normal value
McGregor's line	Extends from the upper surface of the posterior point of hard palate to the base of occiput	Tip of dens should be ≤4.5 mm above this line
Chamberlain's line	The posterior end of the hard palate to the posterior margin of the foramen magnum	(1) tip of dens ≤3 mm above this line or (2) <1/2 depth of dens above this line
McRae's line	Extends from the anterior to the posterior margins of the foramen magnum	The apex of the odontoid process should not be above this line

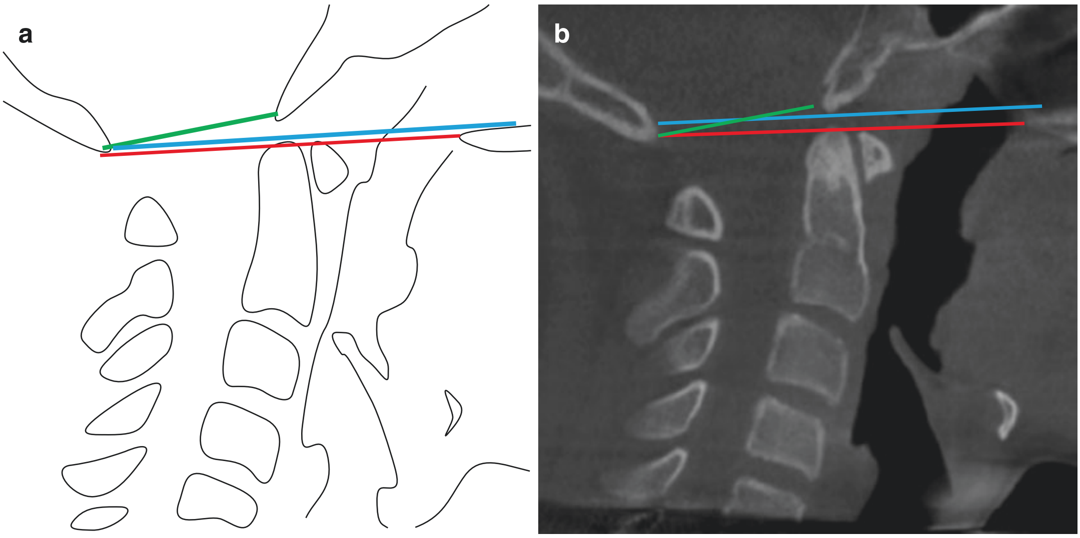

Fig. 11.20 Diagram (**a**) and corresponding mid-sagittal CBCT image (**b**) showing the lines for assessment of the position of the odontoid process of C2 relative to the foramen magnum (*Blue line* McGregor's line, *red line* Chamberlain's line, *green line* McRae's line)

Table 11.2 Measurements of the cranio-cervical junction

Parameter	Definition	Normal value
Atlanto-occipital condyle interval (Fig. 11.21)	Linear distance from the occipital condyles to the condylar surface of the atlas	≤5 mm
Harris lines (the BDI/BAI or the rule of twelve) (Fig. 11.22)	BAI: Perpendicular distance from basion (the anterior tip of the foramen magnum) to the line drawn along the posterior border of the body of the axial	≤12 mm, healthy
	BDI: Vertical distance from the basion to the apex of the odontoid process of C2	>12 mm indicates occipito-atlantal subluxation
Power's ratio (the ratio of BC to OA) (Fig. 11.23)	BC: Distance between basion to the posterior aspect of the spinolaminar line of the atlas	≤1, healthy
	OA: Distance between the tip of the foramen magnum to the anterior tubercle of the atlas	>1 suggests anterior occipito-atlantal subluxation
Wachenheim's line (Fig. 11.24)	The line drawn down the posterior aspect of the clivus to the odontoid process	This line should intersect or be tangential to the odontoid process. If this line is in front of or behind the odontoid process, anterior or posterior dissociation of cranio-cervical junction is suspected

11.2.7 Skeletal Maturation Assessment

There is a correlation between the development of cervical vertebrae and skeletal maturation during childhood and adolescence. Cervical vertebra maturation (CVM) is proposed as a predictor of skeletal maturation to determine the phase of pubertal growth in orthodontic treatment by using a lateral cephalometric image rather than performing a hand-wrist analysis. The segmentation of individual vertebrae from CBCT is also feasible (Shi et al. 2007).

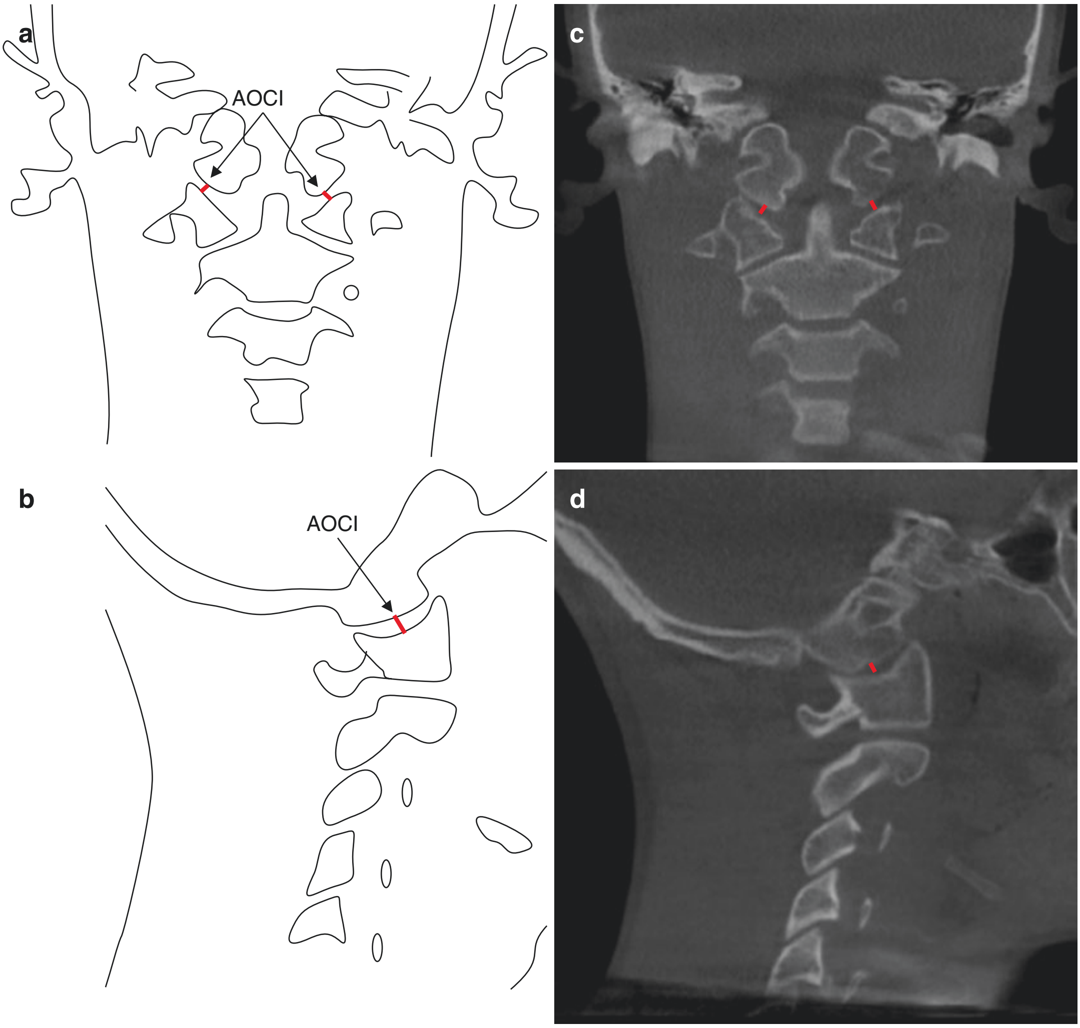

Fig. 11.21 Coronal (**a**) and lateral sagittal (**b**) schematic diagrams and corresponding coronal (**c**) and lateral sagittal (**d**) CBCT images showing the construction of the atlanto-occipital condyle interval (AOCI)

Table 11.3 Parameters defining the atlanto-axial relationship

Line/measurement	Definition	Normal value
The atlanto-dens interval (ADI) (Fig. 11.25)	The space between the odontoid process and the anterior portion of the ring of C1	Adults: ≤3 mm Children: ≤5 mm >values suggest instability
Para-odontoid space	Lateral aspect of odontoid process to the medial aspect of lateral mass	Bilateral symmetry

The cervical vertebra maturation (CVM) evaluation method proposed by O'Reilly and Yanniello (1988) comprises six stages according to the shape of cervical vertebrae on the lateral cephalometric image (Table 11.5) (Fig. 11.27).

Presently three predominant skeletal maturation assessment methods using cervical vertebrae have been established by Hassel and Farman (1995), Baccetti et al. (2002), and Seedat and Forsberg (2005).

The method proposed by Hassel and Farman (1995) (Table 11.6) refers to initiation, acceleration, transition, deceleration, maturation, and completion of pubertal growth as six CVM categories.

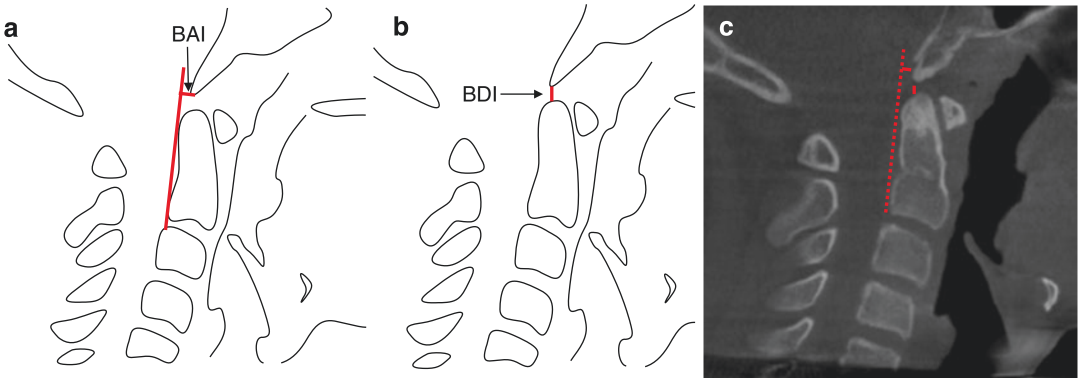

Fig. 11.22 Schematic diagrams (**a**, **b**) and corresponding midsagittal CBCT image (**c**) showing the construction of the Harris lines (BAI, basion-posterior axial line interval; BDI, basion-dental interval)

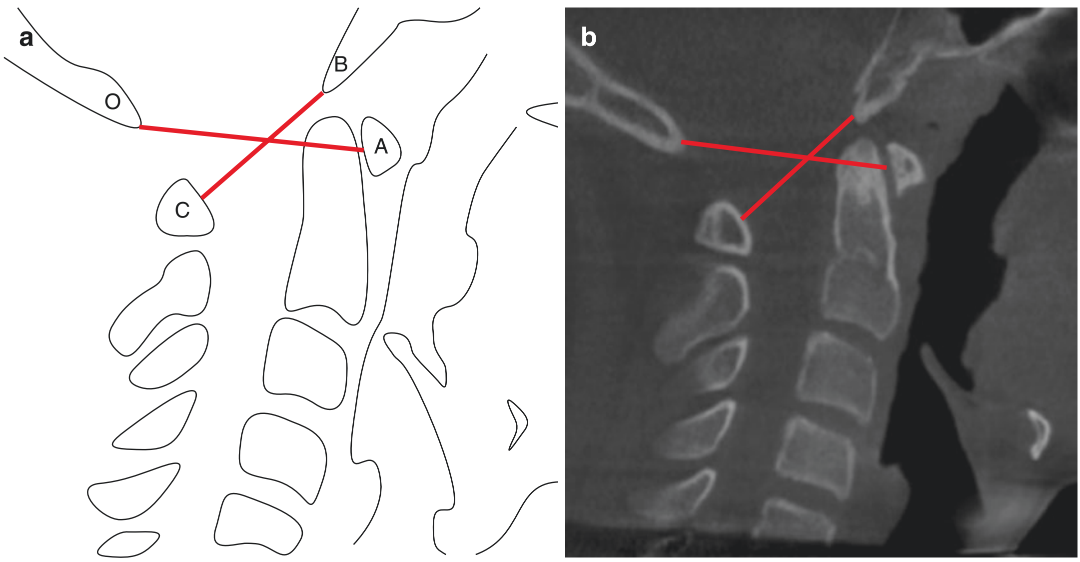

Fig. 11.23 Schematic diagram (**a**) and corresponding midsagittal CBCT image (**b**) showing the construction of the Power's ratio

Baccetti et al. (2002) use five CVM stages and Seedat and Forsberg (2005) use six stages but evaluate only the shape changes in C3, neglecting C2 and C4. Using all three methods, Jaqueira et al. (2010) found that while all can be used as predictor for skeletal maturation estimation, the Baccetti et al. (2002) method was most reliable followed by Hassel and Farman method (1995). They also reported that no method could be used as a sole predictor for skeletal maturation assessment.

11.2.8 Common Incidental Findings of the Cervical Spine

Moderate to large field of view maxillofacial CBCT imaging may invariably include the upper aspects of the cervical spine. Dental practitioners should understand normal developmental and ossification patterns if they image children and recognize the most common anomalies and pathologies of this region.

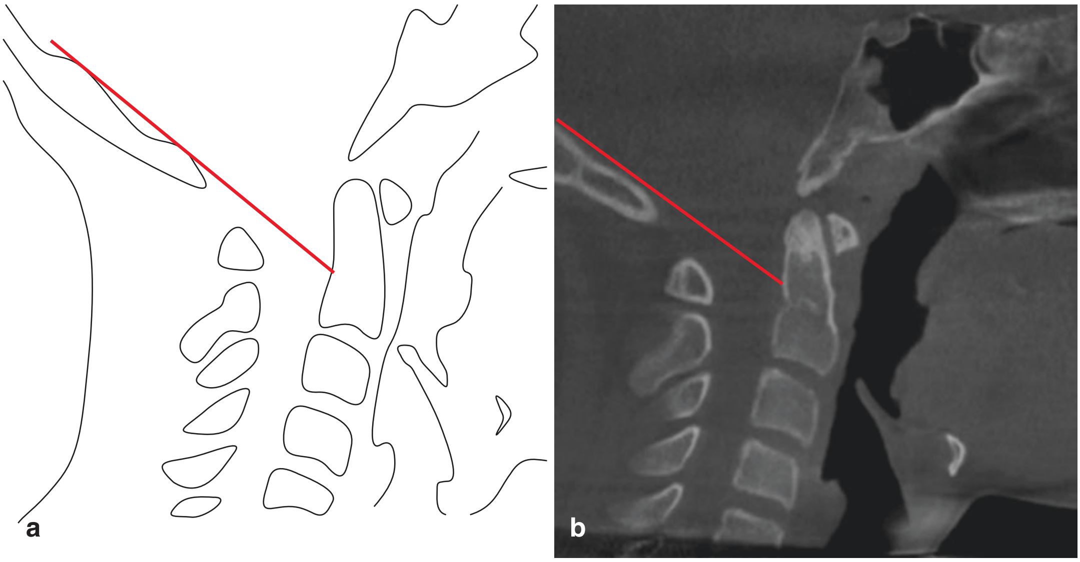

Fig. 11.24 Schematic diagram (**a**) and corresponding midsagittal CBCT image (**b**) showing the construction of Wachenheim's line

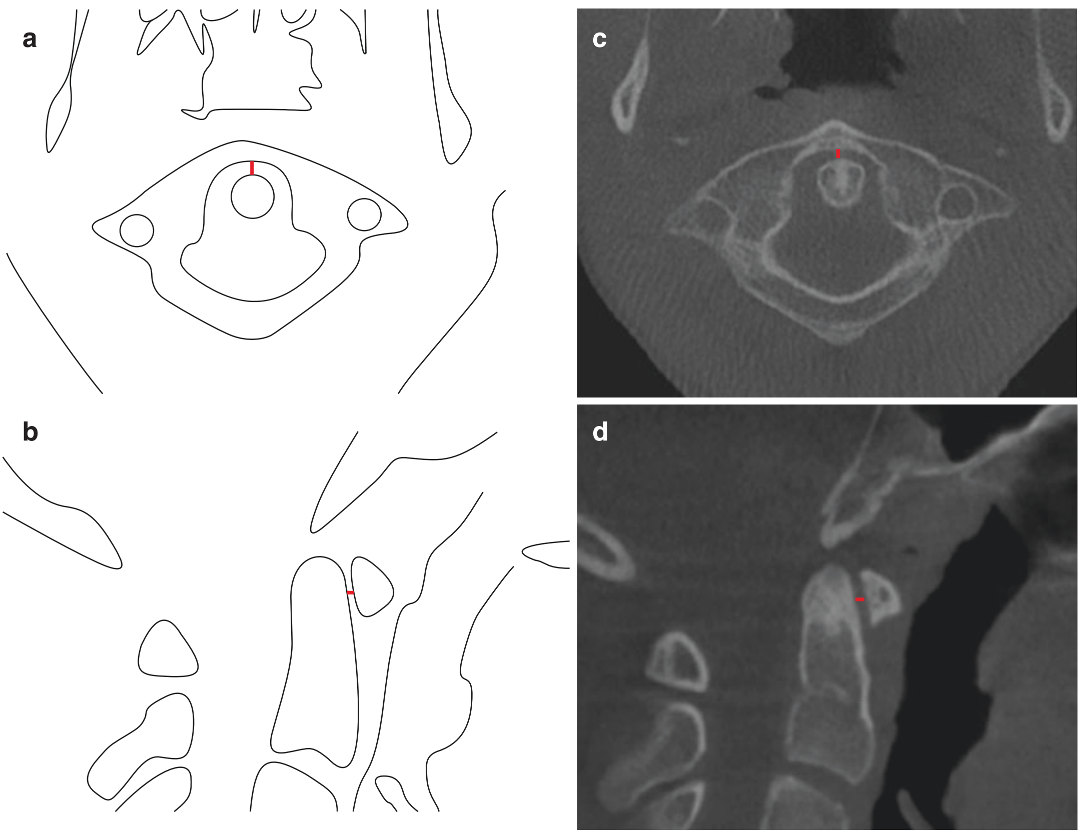

Fig. 11.25 Schematic axial (**a**) and midsagittal (**b**) diagrams and corresponding axial (**c**) and midsagittal (**d**) CBCT images showing the measurement of the atlanto-dens interval (ADI)

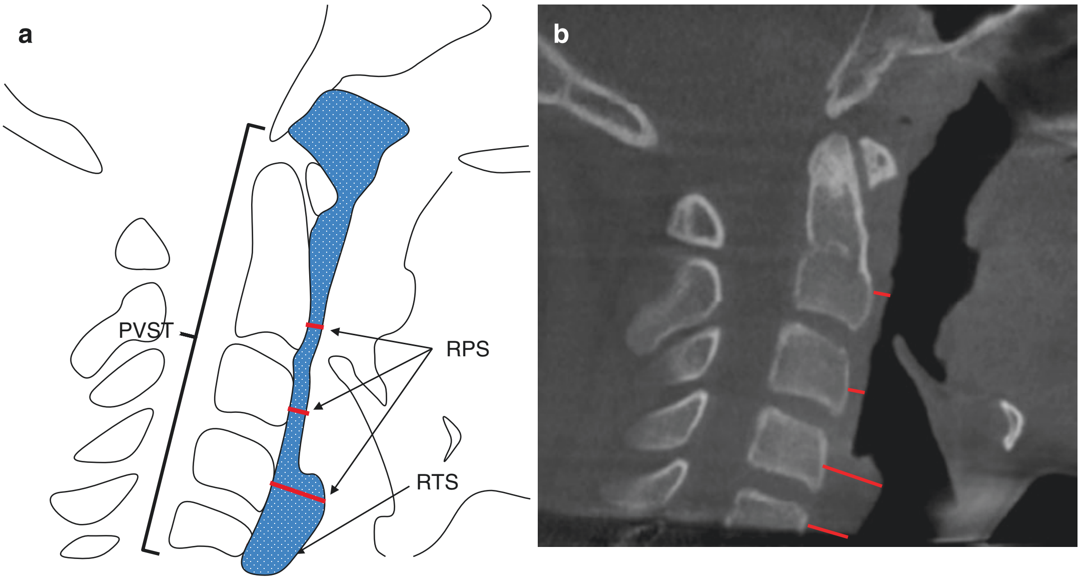

Fig. 11.26 Schematic (**a**) and corresponding midsagittal CBCT image (**b**) showing the measurement of the prevertebral soft tissue (PVST), retropharyngeal space (RPS) and retro-tracheal space (RTS)

Table 11.4 Normative values of the prevertebral soft tissue

Level	Definition	Normal value
Retropharyngeal space	C1	≤8.5 mm at C1
	C2	≤6 mm at C2
	C3 and C4	≤7 mm at C3 and C4
Retrotracheal space	C5 to C7	Adults: ≤22 mm at C6 and C7
		Children (<15 years): ≤14 mm or 1/3 to 2/3 vertebral body distance antero-posteriorly

11.2.8.1 Ossification Patterns

The atlas (C1) and axis (C2) are unique in their development and therefore familiarity with their growth patterns in children can avoid misinterpretation of normal epiphyses and anatomic variants.

C1 ossification patterns (Figs. 11.28a and 11.29) are variable (Junewick et al. 2011) as is the timing of synchondrosis fusion which differs between the posterior synchondrosis and neurocentral synchondroses (Fig. 11.28b) (Karwacki and Schneider 2012). For most individuals (60–70%) the anterior arch fuses with the neural arches by 7 years of age. For most individuals, the posterior arches fuse by 3 years of age. Nonfusion either before or after this age until 16 years may be mistaken for a fracture.

Table 11.5 The definitions of CVM stages (*after* O'Reilly and Yanniello)

Cervical vertebra stage	Definition
CVS 1	The inferior borders of the bodies of all cervical vertebrae are flat. The superior borders are tapered from posterior to anterior
CVS 2	A concavity develops in the inferior border of the second vertebra. The anterior vertical height of the bodies increases
CVS 3	A concavity develops in the inferior border of the third vertebra
CVS 4	A concavity develops in the inferior border of the fourth vertebra. Concavities in the lower borders of the fifth and of the sixth vertebrae are beginning to form. The bodies of all cervical vertebrae are rectangular in shape
CVS 5	Concavities are well defined in the lower borders of the bodies of all six cervical vertebrae. The bodies are nearly square in shape and the spaces between the bodies are reduced
CVS 6	All concavities have deepened. The bodies are now higher than they are wide

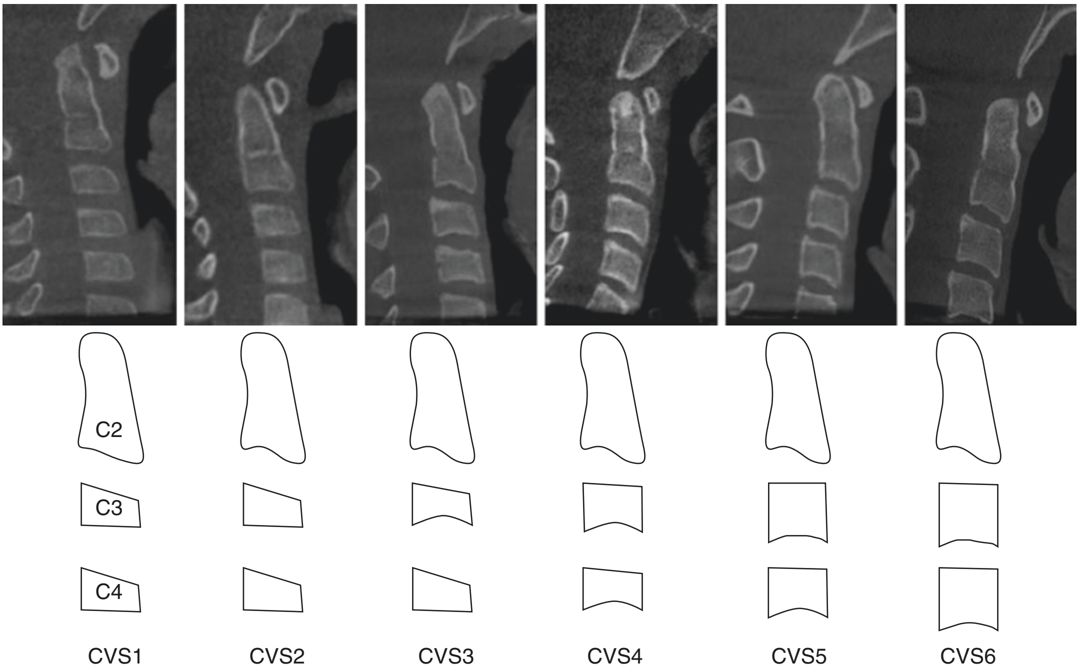

Fig. 11.27 CBCT radiographic examples of cervical vertebrae stages (CVS) and modified line drawing (O'Reilly and Yanniello 1988)

Table 11.6 The cervical vertebrae maturation indicators and hand wrist skeletal maturation index (SMI) (Fishman 1982) (*after* Hassel and Farman 1995)

Category	Maturation Indicators	(SMI) and % of adolescent growth
Initiation	C2, C3, and C4 inferior vertebral body borders are flat	This corresponded to a combination of SMI 1 and 2. At this stage, adolescent growth was just beginning and 80–100% of adolescent growth was expected
	Superior vertebral borders are tapered posterior to anterior	
Acceleration	Concavities developing in lower borders of C2 and C3	This corresponded to a combination of SMI 3 and 4. Growth acceleration was beginning at this stage, with 65–85% of adolescent growth expected
	Lower border of C4 vertebral body is flat	
	C3 and C4 are more rectangular in shape	
Transition	Distinct concavities in lower borders of C2 and C3	This corresponded to a combination of SMI 5 and 6. Adolescent growth was still accelerating at this stage toward peak height velocity, with 25–65% of adolescent growth expected
	C4 developing concavity in lower border of body	
	C3 and C4 are rectangular in shape	
Deceleration	Distinct concavities in lower borders of C2, C3, and C4	This corresponded to a combination of SMI 7 and 8. Adolescent growth began to decelerate dramatically at this stage, with 10–25% of adolescent growth expected
	C3 and C4 are nearly square in shape	
Maturation	Accentuated concavities of inferior vertebral body borders of C2, C3, and C4	This corresponded to a combination of SMI 9 and 10. Final maturation of the vertebrae took place during this stage, with 5–10% of adolescent growth expected
	C3 and C4 are square in shape	
Completion	Deep concavities are present for inferior vertebral body borders of C2, C3, and C4	This corresponded to SMI 11. Growth was considered to be complete at this stage. Little or no adolescent growth was expected
	C3 and C4 heights are greater than widths	

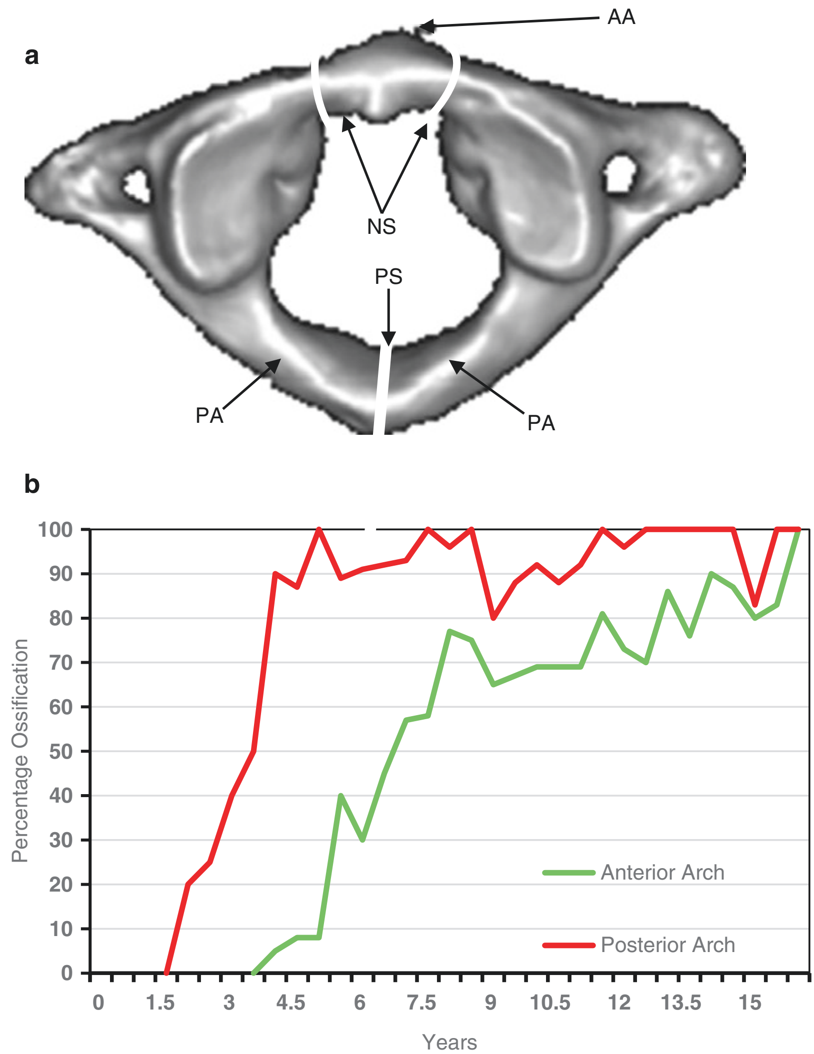

Fig. 11.28 Superior projection of shaded surface rendering demonstrating the three primary ossification centers and synchondroses of C1 These include two anterior neurocentral synchondroses (NS) with a single anterior arch (AA) and a posterior synchondrosis with two posterior arches (PA) (**a**). Ossification timetable (**b**) for the anterior (*green line*) and posterior (*red line*) synchondroses (Data from Karwacki and Schneider 2012)

C2 has a more complex developmental pattern, with four synchondroses and six ossification centers; however, by the age of 2–3 years all ossification centers except those associated with the odontoid process are fused. In the range of ages that are likely to be imaged using maxillofacial CBCT (greater than 4 years of age), four ossification centers may be visible, three of which are associated with the odontoid process (Figs. 11.29, 11.30 and 11.31).

11.2.8.2 Anomalies

Anomalies of the cervical spine can be either congenital or acquired, the latter usually as the result of trauma, postpartum. The majority of patients are asymptomatic or have only slight neurologic problems (Guille and Sherk 2002; Lustrin et al. 2003; Labrom 2007).

- **Aplasia or Hypoplasia of C1 or C2.** Aplasia or hypoplasia may occur at any portion of the atlas ring. It appears like a fracture line on CBCT images. Irregular margins of the lucent line involving the ring suggest fracture while a smooth sclerotic margin is usually indicative of a C1 ring anomaly.
- **Congenital anomalies of the odontoid peg (dens) of C2**. Congenital anomalies of the odontoid peg (dens) are considered rare but occur more frequently in patients with Down

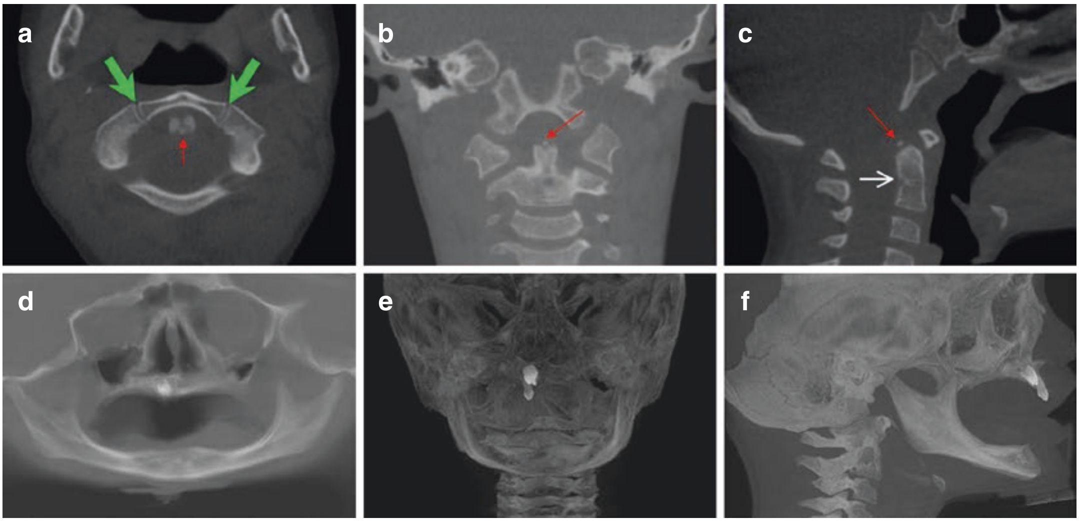

Fig. 11.29 Multiple images of a 5-year-old boy with ectodermal dysplasia including axial (**a**), coronal (**b**), midsagittal (**c**), ray sum panoramic (**d**), and maximum intensity frontal (**e**) and lateral (**f**) projections. The patient has only two unerupted teeth. Note the neurocentral synchondroses (*green arrows*) and anterior arch, apicodental synchondroses with os terminale calcification center (*red arrow*). Also note the hyperattenuated ossification spot corresponding with the subdental synchondrosis that should not be misinterpreted as a fracture

syndrome, Morquio syndrome, Klippel-Feil syndrome, and some skeletal dysplasias. They are classified into four types according to the lack of development of the cervical vertebrae and may result in atlanto-axial subluxation and neurologic symptoms (Arvin et al. 2010) (Fig. 11.32).

- **Occipito-atlantal fusion.** Occipito-atlantal fusion, or occipitalization of the atlas, is a result of partial or complete fusion of the atlas and the occiput. The anterior aspect is involved more commonly than the posterior part. This congenital spinal deformity is frequently seen in patients with achondroplasia, diastrophic dysplasia, spondyloepiphyseal dysplasia, Morquio syndrome, and Larsen syndrome (Popat et al. 2008).
- **C1/C2 (Atlantal-axial), C2/C3, and C3/C4 Fusion.** The fusion of two or more upper cervical vertebrae is often asymptomatic and not discovered until adolescence or young adulthood. Fusion may occur as a congenital anomaly or due to pathology (e.g., osteoarthritic degeneration, tuberculosis, juvenile rheumatoid arthritis, or previous trauma). Incidental presentation on CBCT imaging (Figs. 11.33, 11.34, 11.35 and 11.36) should prompt the clinician to develop a more detailed clinical history including signs and symptoms such as limitation in neck motion, peripheral nerve irritation such as pain, burning sensations and cramps or signs of nerve compression such as hypoesthesia/anesthesia or weakness. Referral to an appropriate medical physician should be considered based on presentation and medical history.

11.2.8.3 Osteoarthritis

The most common incidentally discovered pathology of the cervical vertebrae during CBCT examination is osteoarthritis (OA), also known as spondylosis deformans, degenerative joint disease (DJD), or degenerative arthritis. OA is commonly seen in older individuals and may be asymptomatic. OA is usually caused by the age-related degeneration of cartilage in the joint and may result in considerable loss of flexibility of the articulation and deformities of the affected articulation. Radiographically OA initially presents with both proliferative and degenerative features leading to vertebral shape alteration and reduction of intervertebral space. The principal radiographic

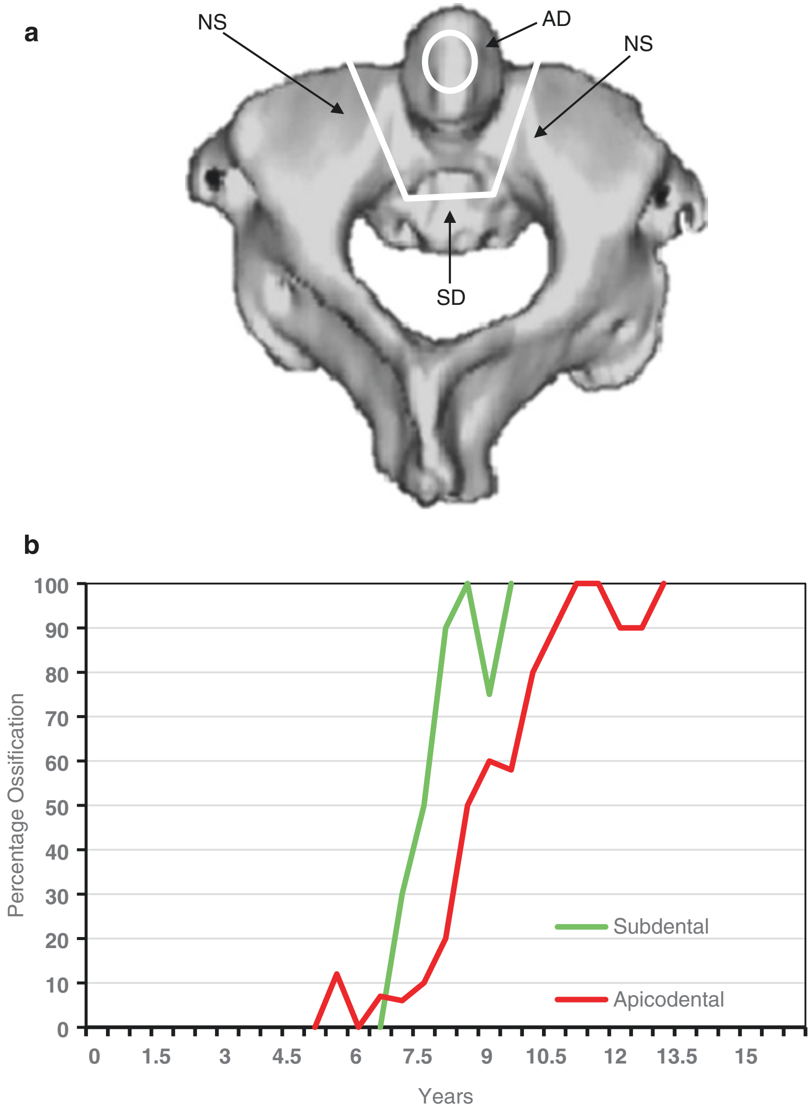

Fig. 11.30 Superior projection of the shaded surface display of C2 (**a**) showing the primary ossification centers and synchondroses in the young child associated with the odontoid process. The neurocentral synchondrosis (NS) and subdental (SD) synchondroses joining the neural arches to base of the odontoid process fuses between 3 and 6 years of age. The apicodental (AD) synchondrosis appears at the apex of the odontoid process (os terminale) as a secondary ossification center between 3 and 6 years of age, and is completely fused by 14 years of age (**a**). Ossification timetable (**b**) for the SD (*green line*) and AD (*red line*) synchondroses (Data from Karwacki and Schneider 2012)

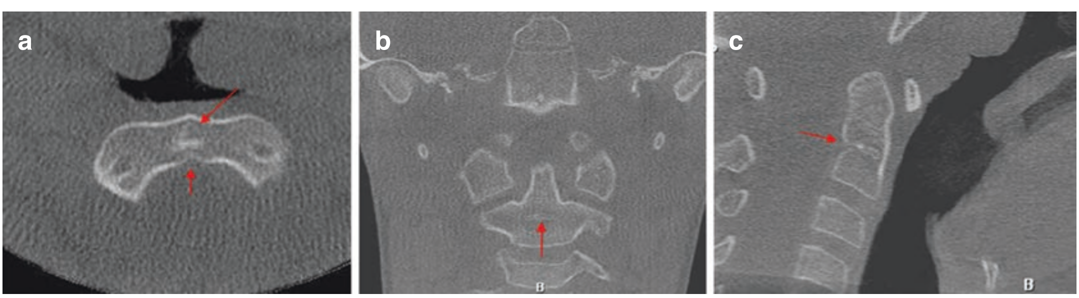

Fig. 11.31 Axial (**a**), coronal (**b**), and midsagittal (**c**) CBCT image of an 11-year-old girl with a central hyperattenuated ossification spot corresponding with the subdental synchondrosis clearly visible almost 3 years after complete ossification

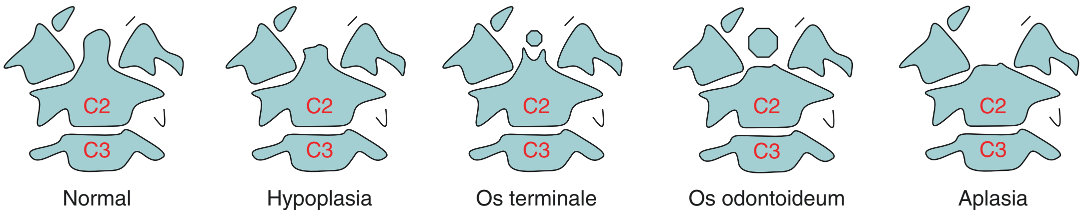

Fig. 11.32 Schematic diagram showing the classification of anomalies of the odontoid process

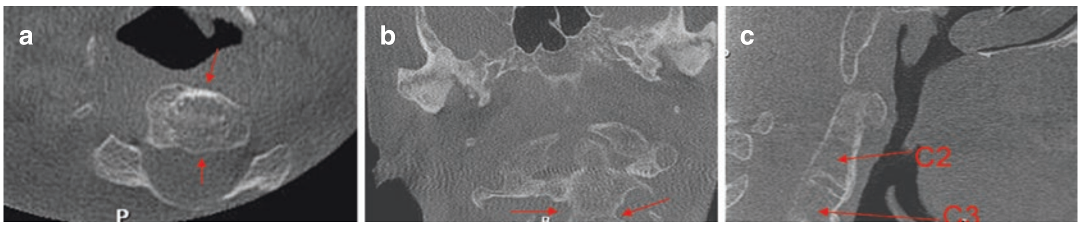

Fig. 11.33 Axial (**a**), coronal (**b**), and midsagittal (**c**) CBCT images of a 48-year-old man with an incidental finding of cervical osteoarthritis degeneration and vertebral fusion of C2 and C3

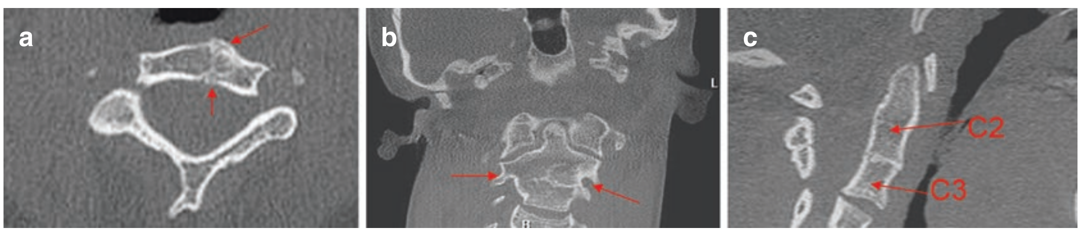

Fig. 11.34 Axial (**a**), coronal (**b**), and midsagittal (**c**) CBCT images of a 16-year-old girl with congenital complete fusion of C2 and C3

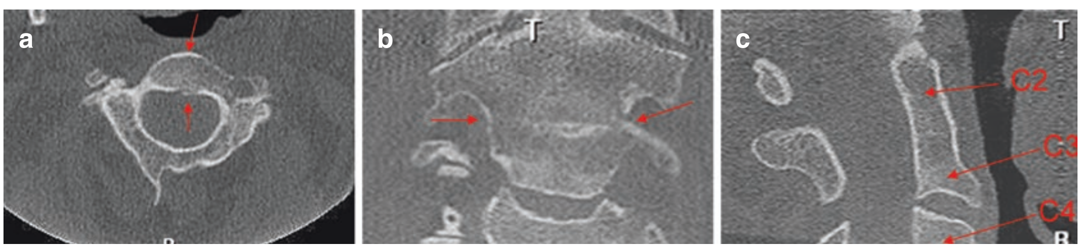

Fig. 11.35 Axial (**a**), coronal (**b**), and midsagittal (**c**) CBCT images of a 69-year-old woman with complete fusion of the vertebral bodies of C2 and C3

Fig. 11.36 Axial (**a**), coronal (**b**), and midsagittal (**c**) CBCT images of a 15-year-old girl with congenital partial fusion between the C3 and C4; the posterior vertebral bodies are fused but the anterior are open

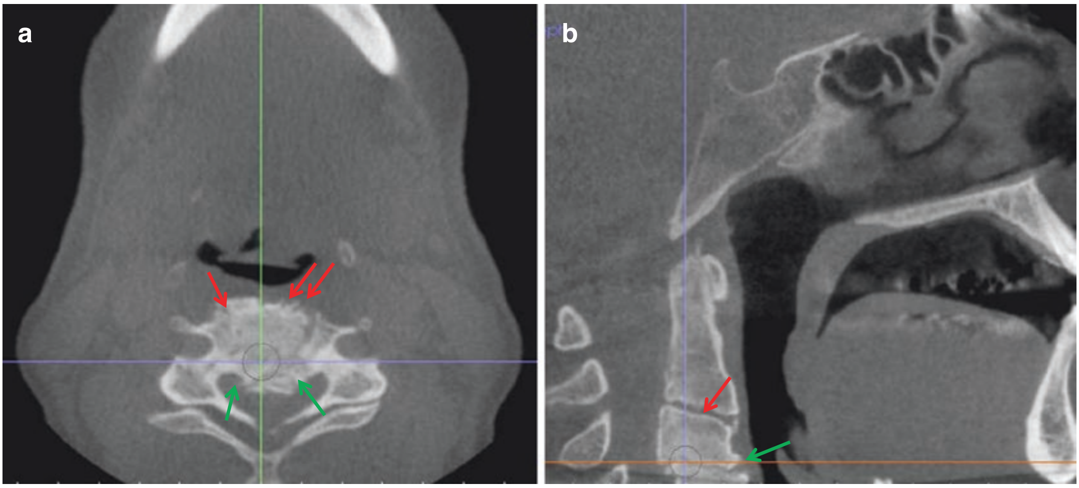

Fig. 11.37 Axial (**a**) and sagittal (**b**) orthogonal CBCT images of the upper cervical spine illustrating variable signs of degenerative changes including erosive changes (*red arrows*) and osteophyte formation (*green arrows*) resulting in gross changes in the contour of the vertebrae, narrowing of the intervertebral space and misalignment of the vertebral bodies

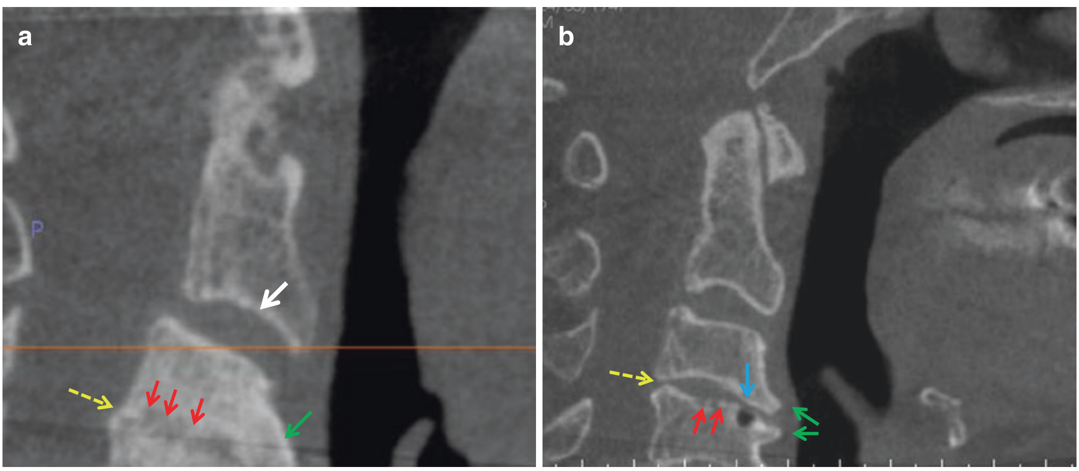

Fig. 11.38 Axial (**a**) and sagittal (**b**) orthogonal CBCT images of the upper cervical spine of two different patients illustrating various signs of degenerative changes including extensive erosion (*red arrows*), osteophyte formation (*green arrows*), intervertebral space narrowing (yellow dotted arrows), subchondral cyst (*white arrow*), and pneumatocyst formation (*blue arrow*). OA in individual (**a**) is severe as the intervertebral space is completely eliminated

findings include tophaceous peripheral deposits in the facet joints (osteophytes), flattening of the articulating surfaces, subarticular erosive changes in the cortical outline, subchondral cysts, pneumatocysts, and narrowing of the facet joint space (Richards 2005) (Figs. 11.37, 11.38, 11.39, 11.40, 11.41, 11.42, 11.43, and 11.44).

The extent of the relevant findings determines its severity. While numerous grading systems exist for OA (Kettler and Wilke 2006), clinicians often refer to severity in subjective terms such as mild, moderate, or severe.

11.2.8.4 Muscular, Ligamentous, and Tendon Calcifications

Calcification of the ligaments of the cervical spine may occur in the yellow ligament, anterior and posterior longitudinal ligaments, and inter-

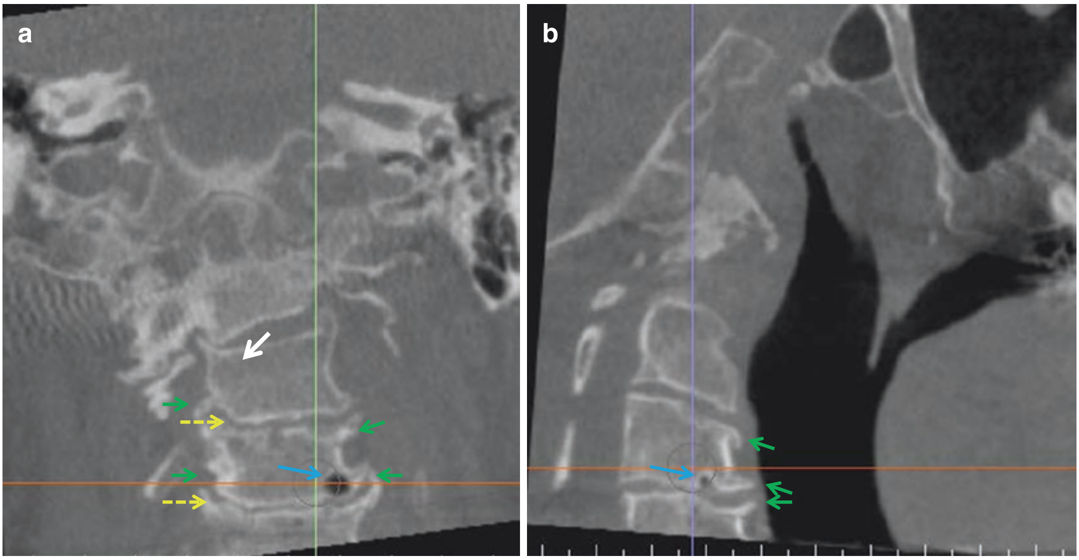

Fig. 11.39 Coronal (**a**) and sagittal (**b**) orthogonal CBCT images of the upper cervical spine of the same patient as in Fig. 11.38b with severe OA illustrating various signs of degenerative change including extensive erosive (*red arrows*), osteophyte formation (*green arrows*), intervertebral space narrowing (*yellow dotted arrows*), subchondral cyst (*white arrow*), and pneumatocyst formation (*blue arrow*)

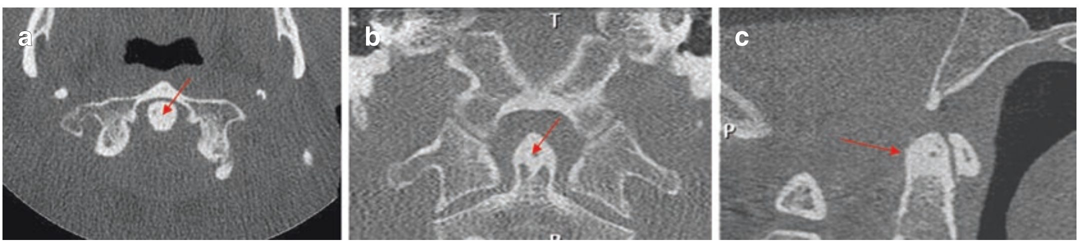

Fig. 11.40 Axial (**a**), coronal (**b**), and midsagittal (**c**) CBCT images of a 52-year-old woman with mild OA in the region of C1 and C2 showing sclerosis of the cranial portion of the odontoid process and faceting

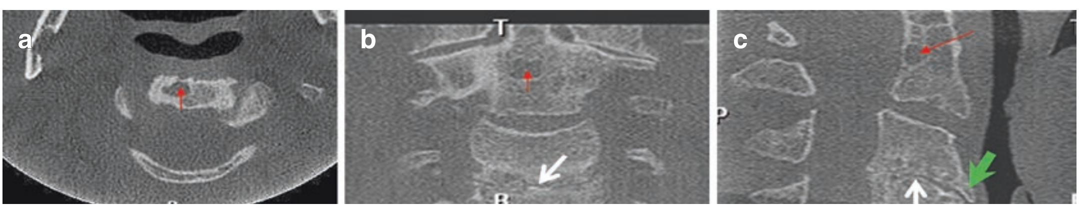

Fig. 11.41 Axial (**a**), coronal (**b**), and midsagittal (**c**) CBCT images of an 88-year-old man with severe OA in the region of C2 to C4 showing subchondral cyst formation (*red arrows*), the formation of anterior oesteophytes causing reduction in the upper airway space (*green arrow*) and the loss of intervertebral space (*white arrows*)

spinous ligament. These ligaments maintain the shape of the vertebral column and calcifications may affect the flexibility and range of motion of the spine and may be involved in neural disturbances pending on their location.

- **Calcified Alar and Transverse Ligaments.** The alar ligaments join the lateral margins of the sloping upper margin of the dens of C2 to the lateral margins of the foramen magnum (adjacent to the occipital condyles) and lie on

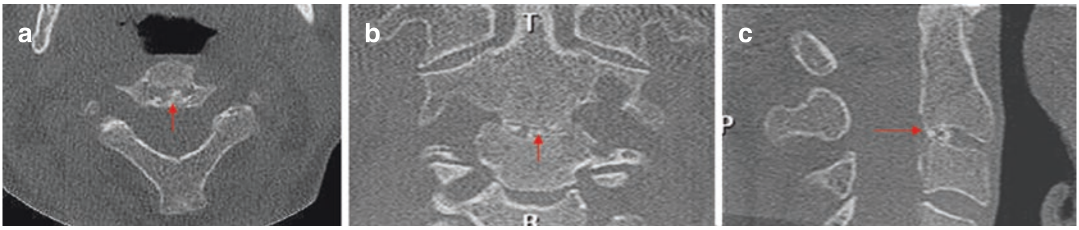

Fig. 11.42 Axial (**a**), coronal (**b**), and midsagittal (**c**) CBCT images of a 66-year-old woman with moderate OA showing a nodular calcification within and narrowing of intervertebral space between C2 and C3

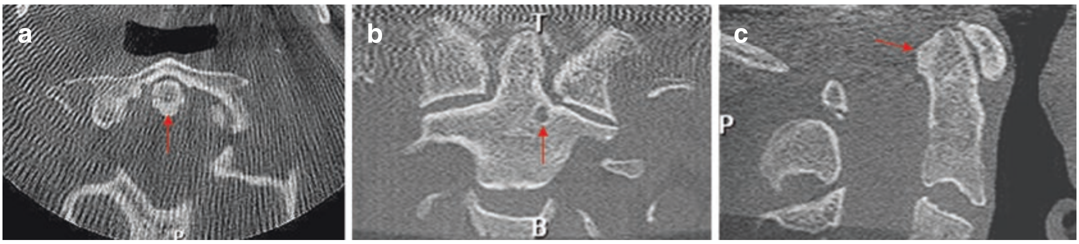

Fig. 11.43 Axial (**a**), coronal (**b**), and midsagittal (**c**) CBCT images of a 71-year-old woman with moderate OA in the region of C1 and C2 showing proliferative nodular sclerosis of the posterior aspect of the odontoid process reducing the spinal canal and subchondral cyst formation at the junction of the odontoid process and body

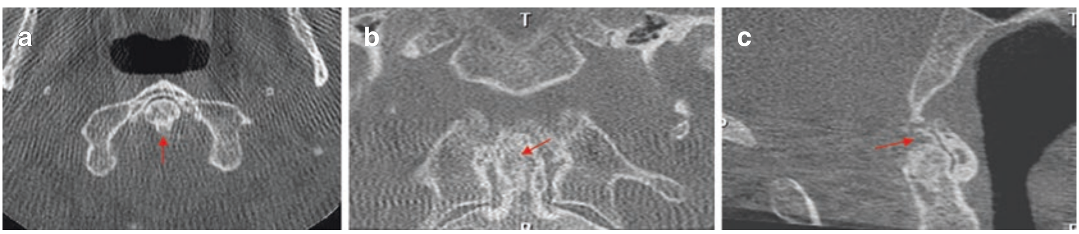

Fig. 11.44 Axial (**a**), coronal (**b**), and midsagittal (**c**) CBCT images of a 76-year-old woman with severe OA in the region of C1 and C2 showing collapse of the odontoid process of C2 into the base, alar ligament calcification and calcification of the medial facets of C1

either side of the apical ligament. They are paired ligaments that are very strong and limit rotation of the head. Calcification of the alar ligament is rare and associated with OA and can mimic an acute fracture of the craniovertebral junction (Fig. 11.45). The transverse ligament of C1 extends across the ring of the atlas, posterior to the odontoid process and retains the odontoid process in contact with the atlas. Calcification of the transverse ligament is an uncommon (5–7%) normal variant and more common in the elderly and those with advanced cervical OA (Fig. 11.46). This condition may be associated with neck pain, relieved by anti-inflammatory drugs and neck immobilization.

– *Crowned dens syndrome (CDS)*. CDS is an inflammatory condition resulting from crystal deposition in the cruciform and alar ligaments surrounding the odontoid process of C2, presenting as a hyper attenuating “crown” surrounding the top of the dens (Fig. 11.47). The term should be reserved to those patients presenting in pain and who demonstrate the present of increased inflammatory markers (e.g., erythrocyte sedimentation rate, C reactive protein, and white cell count).

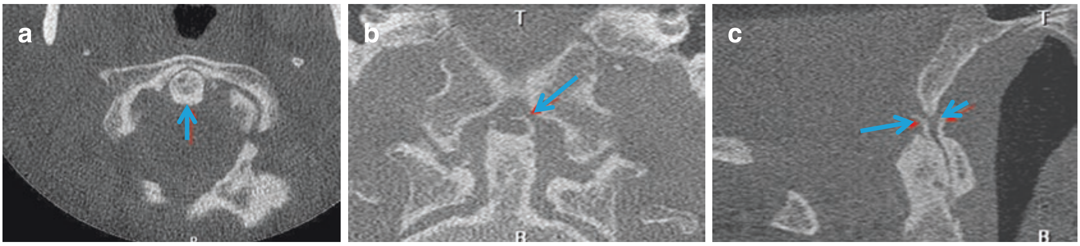

Fig. 11.45 Axial (**a**), coronal (**b**), and midsagittal (**c**) CBCT images of a 69-year-old man who presents with neck pain showing severe OA of C1 and C2 with concomitant calcifications of the alar ligaments of the odontoid process (*arrows*)

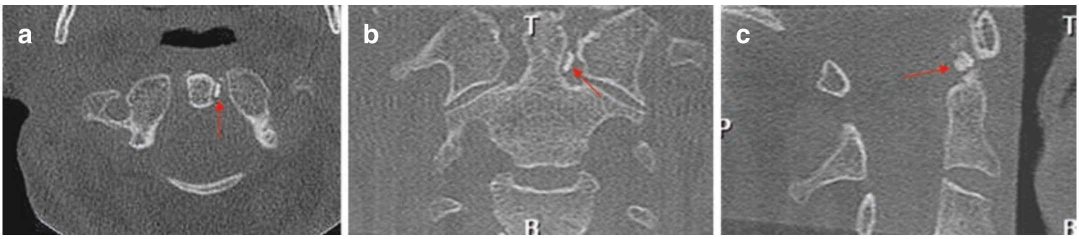

Fig. 11.46 Axial (**a**), coronal (**b**), and midsagittal (**c**) CBCT images of a 79-year-old woman with severe OA showing a nodular calcification in the right lateral intervertebral space (transverse ligament) between the odontoid process of C2 and the articular surface of C1

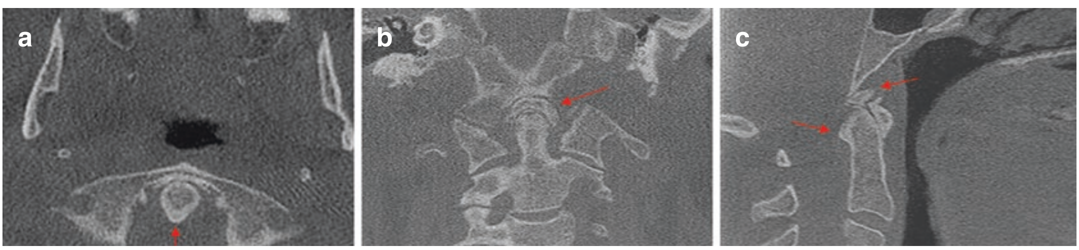

Fig. 11.47 Axial (**a**), coronal (**b**), and midsagittal (**c**) CBCT images of a 62-year-old woman referred for implant site assessment. Her medical history reveal with moderate neck pain and incidental findings showed a “halo” like calcification superior to the odontoid process. Note the associated posterior osteosclerosis and thickening of the cortex of the odontoid process of C2. This appearance is consistent with a working diagnosis of crowned dens syndrome. Patients presenting with this appearance should be referred to an appropriate physician for consultation

The condition presents predominantly in women with mean age of 60–70 years. Patients with CDS may be attributed to joint diseases such as rheumatoid arthritis, calcium pyrophosphate dihydrate crystal deposition disease (CPPD), systemic sclerosis, osteoarthritis, seronegative arthritis, osteoporosis, hematological disease, oncological disease, and trauma (Scutellari et al. 2007).

- **Calcific tendinitis of the longus colli muscle.** Prevertebral amorphous calcification within the posterior pharyngeal wall and immediately adjacent to the cervical vertebrae is consistent with calcific tendinitis of the longus colli muscle. This can occur anywhere along the path of this muscle (anterior arch of C1 to T3) but more typically in the proximal fibers of the longus colli (just inferior to the anterior arch of C1) (Fig. 11.48). This is an inflammatory/

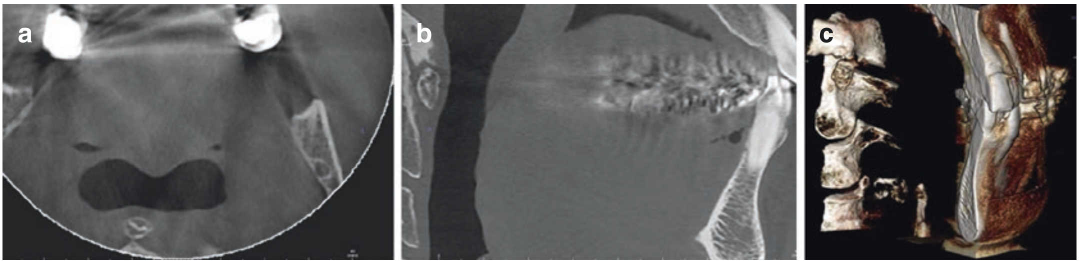

Fig. 11.48 Axial (**a**), midsagittal (**b**), and oblique volumetric rendering showing a smooth, mild thickening of the prevertebral soft tissues (7 mm), with a 1.3 cm focus of amorphous calcification anterior to the C2 vertebrae corresponding to superior oblique (proximal) tendon of the longus colli muscle

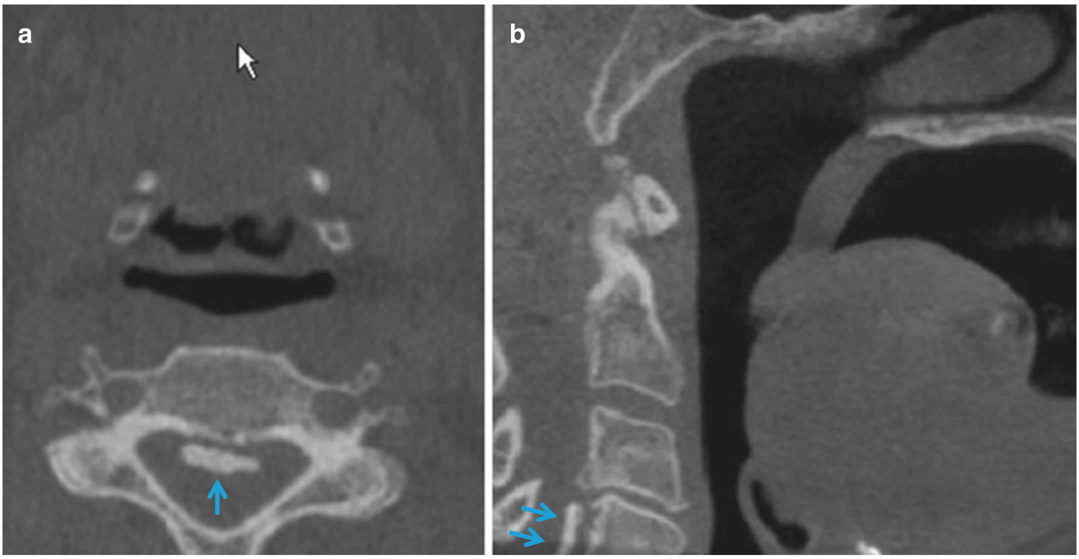

Fig. 11.49 Axial (**a**) and sagittal (**b**) CBCT images of the upper cervical spine from top (C1) to (C4) depicting an elongated, high density structure inside the vertebral canal (*blue arrows*); this is a calcified posterior longitudinal ligament which serves in the support of the dorsal aspect of the vertebral column along with the anterior longitudinal ligament on the ventral aspect. This calcification may result in neural disturbances in the cervical plexus

granulomatous response to deposition of calcium hydroxyapatite crystals in the tendons of the longus colli muscle. Patients can present with acute neck pain, stiffness, and odynophagia. In the absence of clinical symptoms, no further evaluation or follow-up is required. However if acutely symptomatic an MRI is recommended to distinguish between acute retropharyngeal tendinitis, which shows a prevertebral fluid collection/effusion, and retropharyngeal abscess, pharyngitis or perisonsilar abscess.

- **Ossification of the posterior longitudinal ligament (OPLL).** The posterior longitudinal ligament is located within the vertebral canal and extends adjacent to the posterior surfaces of the vertebral bodies from C2 to the sacrum. OPLL is rare with greater prevalence in males and in older adults. OPLL is often associated with other conditions including diffuse idiopathic skeletal hyperostosis and ankylosing spondylitis. Ossification most often occurs in the mid cervical region and results in reduction of the vertebral canal and varying degrees of spinal cord compression (Fig. 11.49). OPLL may present as continuous, segmental, mixed, or localized linear calcifications. Patients presenting with an incidental finding of OPLL should be referred for neurological examination. MRI T2 weighted sequences may be requested to evaluate the degree of compression and abnormal signal intensity of the spinal cord.

11.2.8.5 Foreign Bodies

Numerous metallic foreign bodies may present synchronously in maxillofacial CBCT scans. Fixation devices fusing cervical vertebrae are easily identified; however, other items include bullets and explosive fragments, dislocated screws or threads for vertebral stabilization and needles. As these bodies may potentially migrate if embedded within the soft tissue, confirmation of localization of the foreign body within the vertebral hard tissue is essential. A medical history should be elicited from the patient to confirm the etiology of the foreign body (Fig. 11.50).

11.3 The Hyoid Bone

The hyoid bone is a non-articulated, free-floating, U-shaped bone lying horizontally in the anterior neck located approximately at the level of C3 between the thyroid cartilage inferiorly

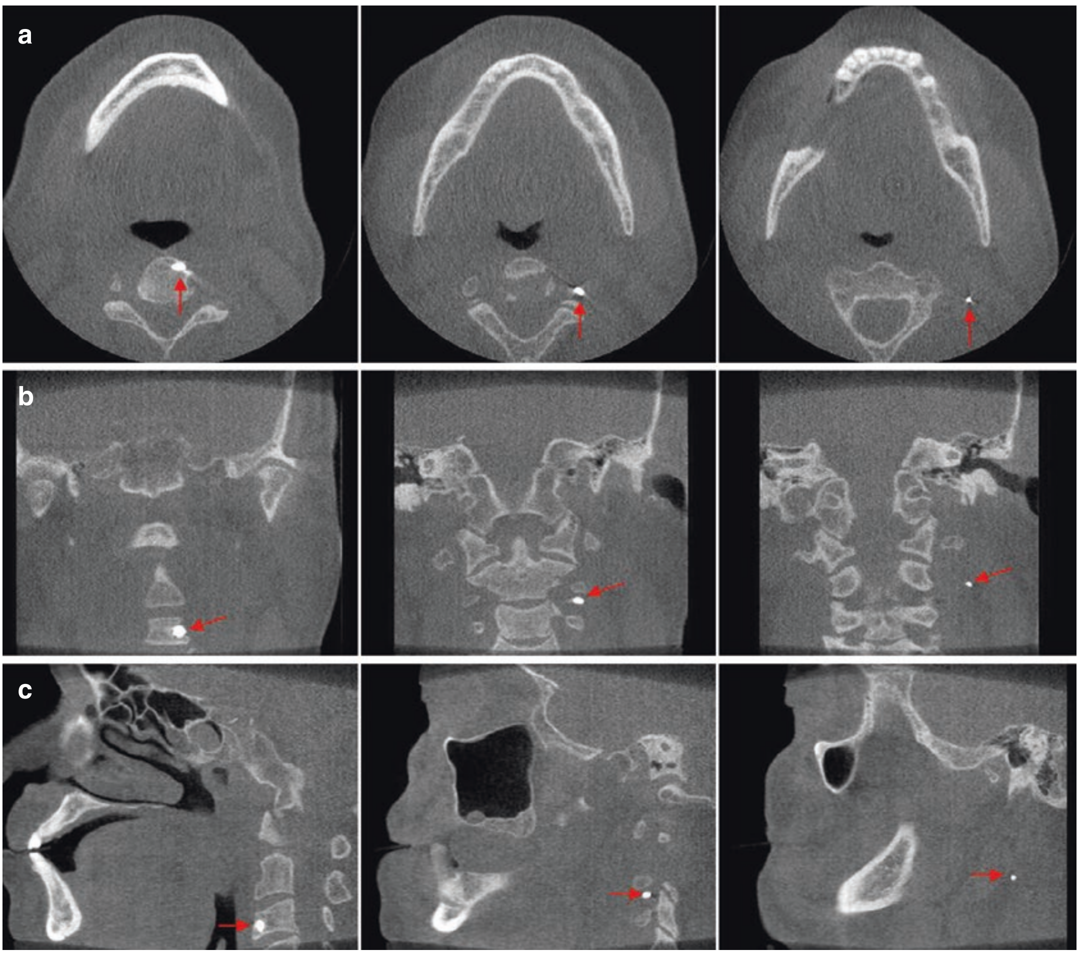

Fig. 11.50 Sequential axial (**a**), coronal (**b**), and sagittal CBCT images of a 64-year-old man with three metallic bodies. One is embedded within the body of C3, whereas two other fragments are located within the left lateral cervical soft tissues. This patient related a previous history of gunshot injury

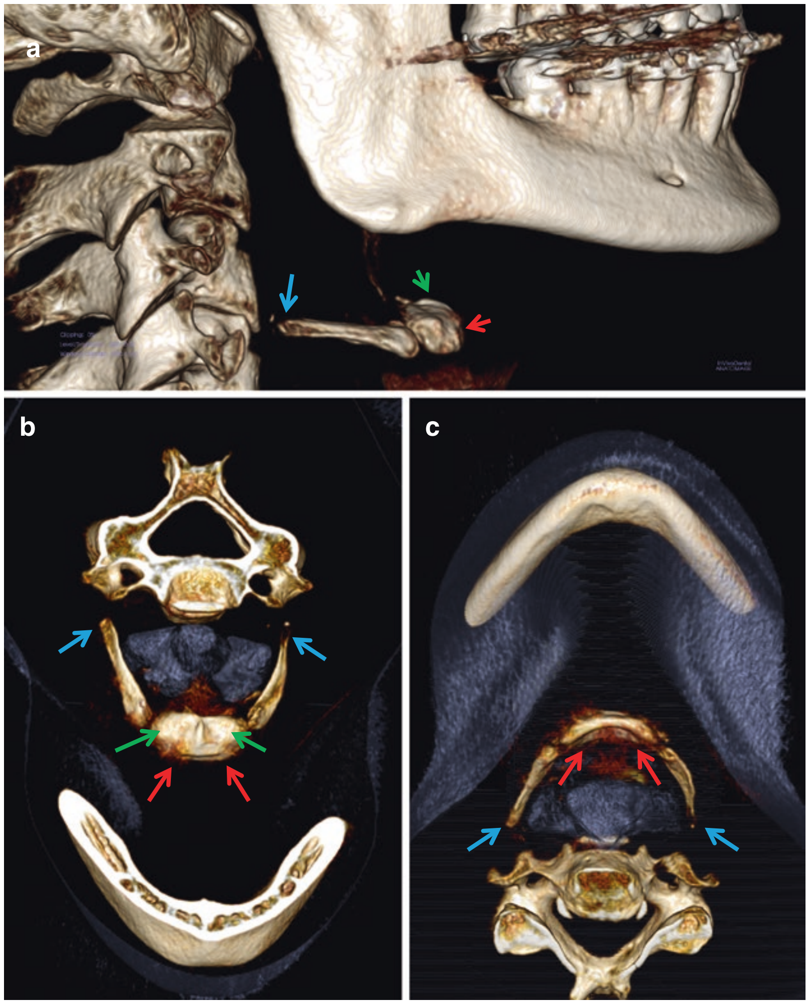

Fig. 11.51 Lateral (**a**), partial superior oblique (**b**), and inferior oblique (**c**) shaded surface rendering of upper neck illustrating the topographic features and spatial location of the hyoid bone in the upper neck in relation to the lower body of the mandible, upper airway and cervical spine including the body of the hyoid (*red arrows*), lesser horns (cornua) of the hyoid (*green arrows*), and greater horns (cornua) of the hyoid (*blue arrows*)

and the mandible superiorly (Fig. 11.51). The hyoid bone most commonly demonstrates a modular appearance but has considerable anatomical variation. It consists of three segments: the central body of the hyoid, the lesser horns, and the greater horns. The greater horns project postero-superiorly and laterally from the body, and the lesser horns project superiorly at the junction of the body and the greater horns (Fig. 11.52). It is suspended by the musculature that connects the mandible, styloid process, thyroid cartilage, manubrium, and scapulae. The hyoid bone is connected to the styloid processes by the stylohyoid ligaments. These may undergo partial calcification, usually from the styloid process inferiorly (see Chap. 17). The soft tissue regions adjacent to the hyoid in the antero-lateral neck can be divided vertically into suprahyoid and infrahyoid regions. The suprahyoid muscles consist of the stylohyoid, geniohyoid, mylohyoid, and digastric muscles, and connect the hyoid to the cranium.

There are two calcifications adjacent to the hyoid bone that are important to identify and distinguish from calcified carotid artery atheroma (CCAA) (see Chap. 17). They are calcifications of the triticeous cartilage and superior cornu (horn) of the thyroid cartilage. Both calcifications are located in the infrahyoid soft tissue, whereas the CCAA is located more laterally.

Physiologically the hyoid functions in association with the musculature in speech and

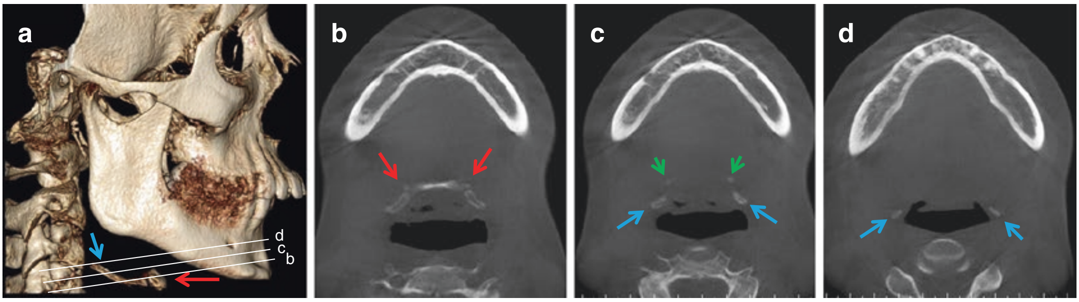

Fig. 11.52 Reference lateral (**a**) surface rendering identifying location of sequential axial orthogonal CBCT sections of the upper neck progressing caudal-cranially (**b**–**d**) depicting the features of the hyoid bone including the body of the hyoid (*red arrows*), lesser horns (cornua) of the hyoid (*green arrows*), and greater horns (cornua) of the hyoid (*blue arrows*)

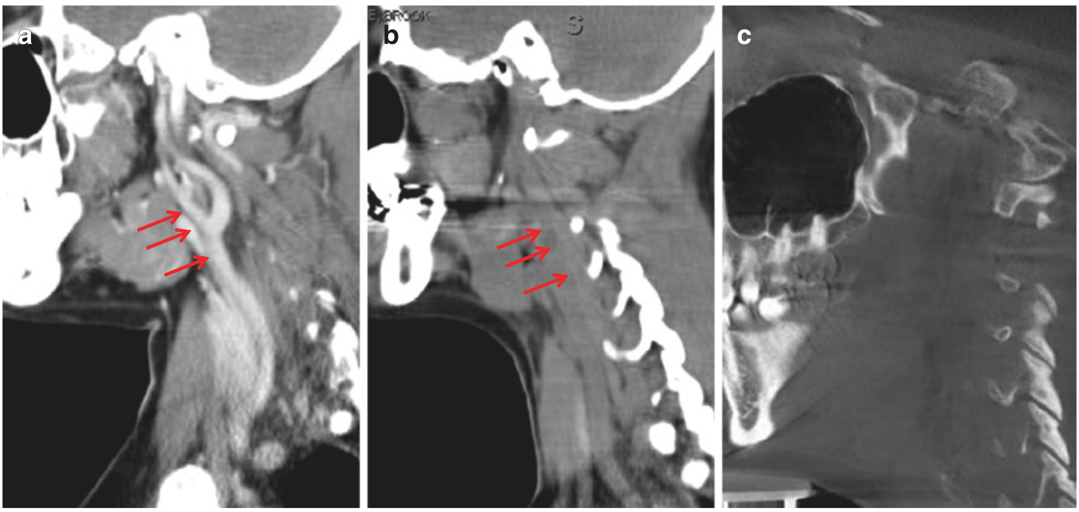

Fig. 11.53 MDCT left lateral neck sagittal section both with (**a**) and without (**b**) contrast and comparable CBCT sagittal section (**c**) illustrating the difference in the soft tissue contrast between these modalities. The common carotid artery (*red arrows*) is clearly visible in the MDCT with contrast (**a**) section and partially visible in the MDCT without contrast (**b**). This structure is not visualized in the CBCT section

deglutition. The two-dimensional position of the hyoid bone in relation to the cervical spine, mandible and maxilla and posterior pharyngeal airway on lateral projection images is important to consider as the distance of the hyoid bone to the posterior pharyngeal wall and to the posterior nasal spine has been correlated to indices of obstructive sleep apnea (Sforza et al. 2000). Lower hyoid bone position in relation to the mandibular plane has also been found to increase the individual tendency to pharyngeal collapse (Pracharktam et al. 1996; Sforza et al. 2000).

11.4 Soft Tissues of the Neck

The neck mainly consists of soft tissue structures and these dominate the CBCT volume and contents within orthogonal images. While soft tissue contrast on CBCT images may vary (to some degree) among different CBCT scanner, it is generally inadequate compared to multi-detector computed tomography either with or without contrast (MDCT) for the evaluation of or differentiation between soft tissues (see Chaps. 2 and 5) (Fig. 11.53). Occasionally soft tissue structures may be identified on orthogonal

CBCT images and these may provide crucial landmarks in localizing unusual features (Fig. 11.54).

The general scheme of soft tissue anatomy on axial images at and immediately caudal to the lower border of the mandible, approximately at the level of the 3rd and 4th cervical vertebrae (C3 and C4) for CBCT is shown in Fig. 11.54. Comparable MDCT axial images are shown in Figs. 11.55 and 11.56. This area on axial images is important because it is the region where the external (ECA) and internal carotid arteries (ICA) bifurcate from the common carotid artery (CCA). The ICA provides blood supply to the brain whereas the ECA supplies blood to the neck and face of either side. Cephalad (superior) to the bifurcation, the diameter of both vessels gradually reduces, making them less distinguishable. The relationship of the internal and external carotid arteries to the airway and other major neck muscles as well as the angle of bifurcation is inconsistent.

A basic understanding of orthogonal cross-sectional anatomy of the neck is important in regionally differentiating specific conditions that produce calcified material (Table 11.7) (Figs. 11.57, 11.58, 11.59, 11.60, 11.61, 11.62, 11.63, and 11.64) (see Chaps. 16 and 17). On CBCT imaging pathologic calcifications frequently seen in the neck (Table 11.7) are most often identified by their location rather than recognition of the tissue or organ of origin.

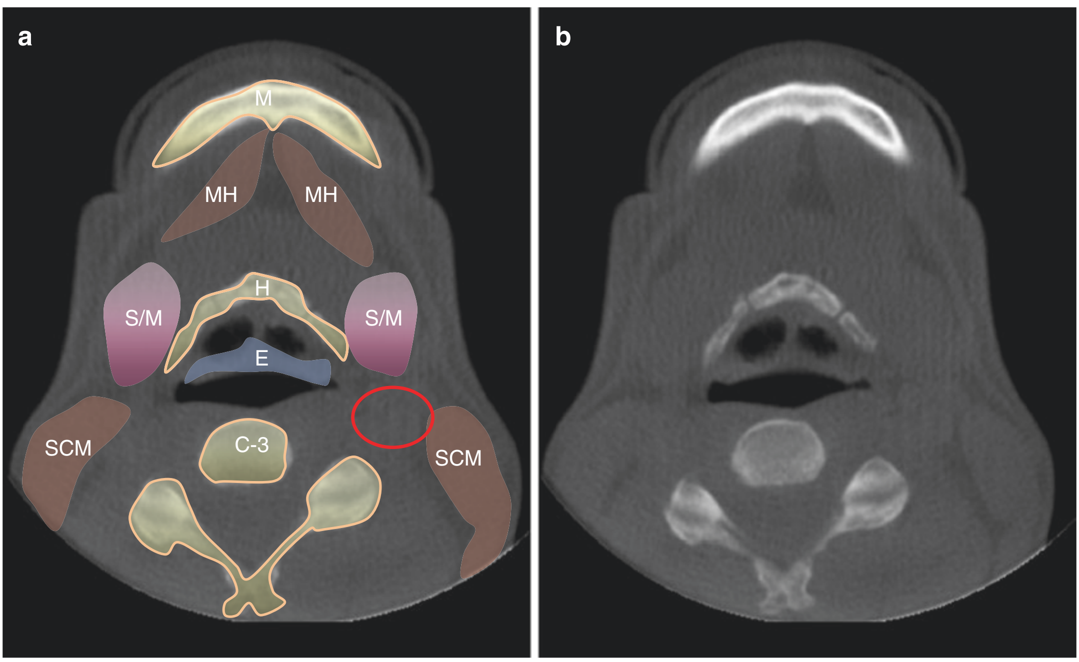

Fig. 11.54 Annotated (**a**) and clear (**b**) axial CBCT sections of the neck at the level of C3-C4 in identifying important osseous and muscular landmarks. The crescent-shaped osseous structure located ventrally, toward the superior border of axial cut, is the lower border of the anterior mandible and the structure to the dorsal of the image (*lower end*) is the vertebral body of 3rd cervical vertebra (*C3*). The thin, elongated, arch-shaped structure in the midline is the hyoid bone (*HB*). The nodular appearance of the HB can be misinterpreted as a fracture. Soft tissue structures at this level include sternocleidomastoid muscles (*SCM*) bilaterally, the mylohyoid muscles (*MH*) and submandibular space (*S/M*). The semicircular low-density void in the center of the image represents the patient's airway which is separated almost in two halves (a ventral and a dorsal) by a sickle-shaped soft tissue structure, the epiglottis (*E*). The approximate location of the carotid space at this level containing the common carotid artery, the internal carotid artery (medial), internal jugular vein (lateral), and the vagus nerve (posterior) is highlighted by the *red circle*

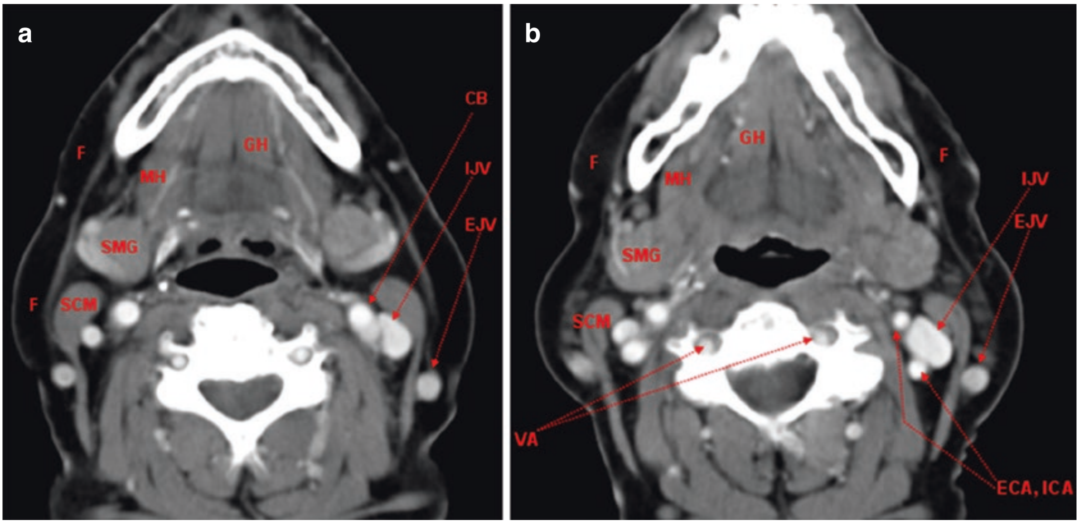

Fig. 11.55 MDCT axial images of the neck with IV contrast administration at the level of C3 (**a**) and C4 (**b**). Soft tissue contrast is adequate to identify soft tissue structures and anatomic landmarks within the neck and floor of the mouth. The contrast medium highlights blood vessels as high density round areas variable in diameter (*IJV* internal jugular vein, *EJV* external jugular vein, *ECA/ICA* external and internal carotid arteries, *VA* vertebral arteries, *GH* geneiohyoid muscle, *MH* mylohyoid muscle, *SCM* sternocleidomastoid muscle, *SMG* submandibular gland, *F* fat)

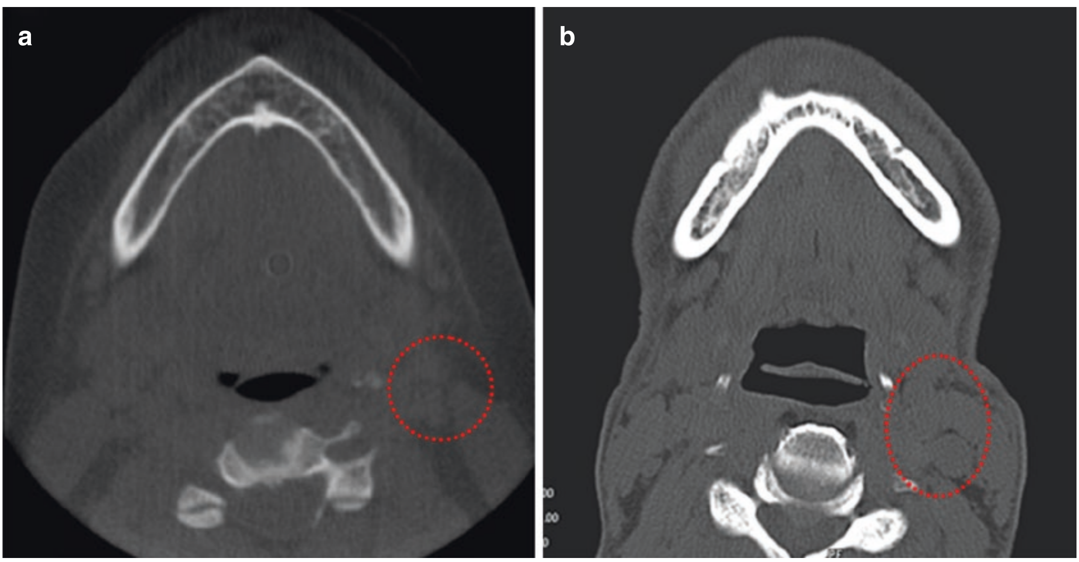

Fig. 11.56 Comparative axial CBCT (**a**) and MDCT (**b**) image of the neck at the level of C3/C4. The higher inherent contrast of MDCT images in comparison to the CBCT allows major blood vessels of the neck to be seen, even without contrast (*red circle* in **b**). The outline of the internal jugular vein, internal/external carotid arteries may be identified within the dotted ellipse. Usually, the widest in diameter vessel is the internal jugular vein

Table 11.7 Common physiologic and pathologic calcifications in the neck

Type	Tissue	Example	Axial level	Appearance
Physiologic	Ligaments	Stylohyoid (Figs. 11.57 and 11.58)	Variable (C4 to C1), superior to HB	Intermittent or continuous tubular hyperdensity directed supero-laterally from the LCHB
	Cartilage	Triticeous	C3/C4, immediately inferior and medial to GCHB	Small, single, bilateral, ovoid hyperdense calcification
		Thyroid (Fig. 11.59)	C3/C4, inferior to the triticeous cartilage	Diffuse chevron shaped, bilateral diffuse hyperdensity lateral to the postero-lateral walls of the oropharyngeal airway
Pathologic	Artery	Calcified carotid artery atheroma (Figs. 11.60, 11.61, and 11.62)	C3/C4	Rice grain sized varying to larger ring-like or tubular calcification antero-lateral to the anterior tubercle, postero-lateral to the parapharyngeal airway
	Salivary glands	Submandibular salivary gland stones (sialoliths) (Figs. 11.63 and 11.64)	LBM (ductal)	Single, elongated laminar calcification, medial to the lingual aspect of the mandible
			C3/C4 at level of HB (parenchymal)	Circular or diffuse calcifications antero-laterally to the HB
	Lymphoid	Tonsiloliths	C2/C3	Multiple, punctate hyperdensities in the superficial lateral parapharyngeal soft tissues
		Lymph node	C4, below LBM	Single, often "onion skinned" or lamellar hyperdensity, deep to the skin.

HB hyoid bone, *GCHB* greater cornu of the hyoid bone, *LBM* lower border of the mandible, *LCHB* lesser cornu of the hyoid bone, *C3* 3rd cervical vertebrae, *C4* 4th cervical vertebrae

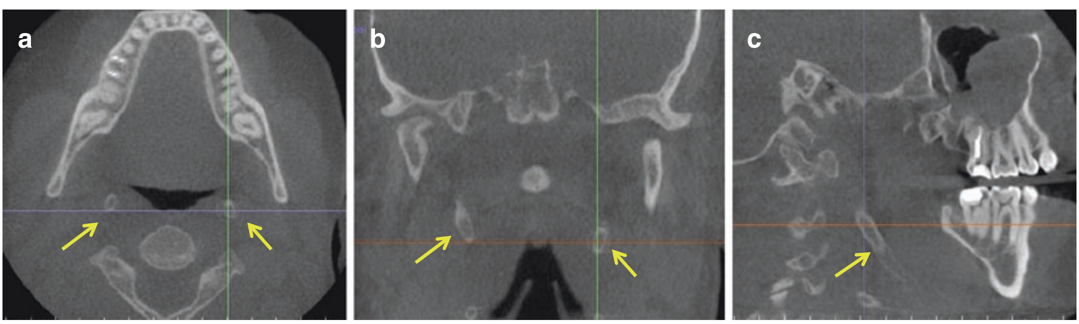

Fig. 11.57 Axial (**a**), coronal (**b**), and sagittal (**c**) CBCT sections of the neck at the level of the floor of the mouth depicting bilateral small, ring-like calcifications (*yellow arrows*) on either side of the airway, directed posterior/lateral to anterior/medial, consistent with calcified stylohyoid ligament

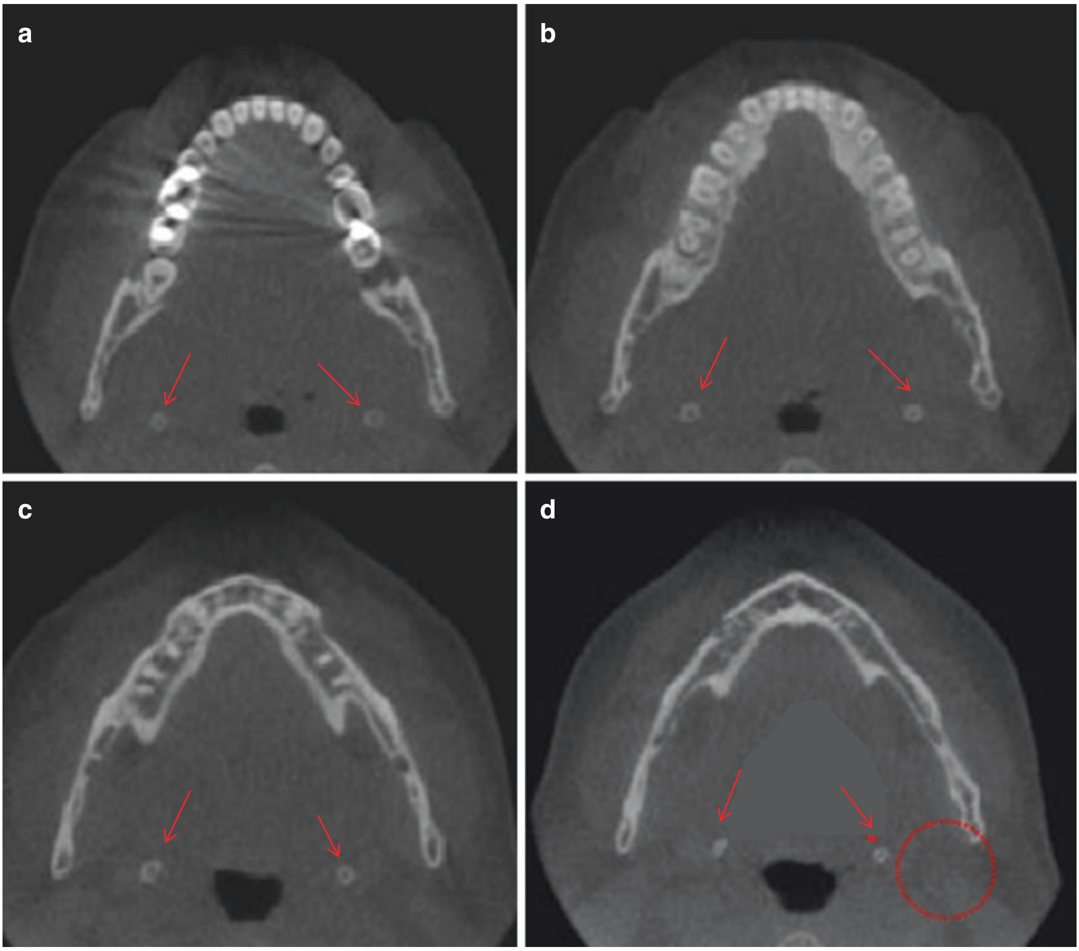

Fig. 11.58 Sequential, axial CBCT sections of the floor of the mouth and neck at the level of the crowns of the teeth (**a**), middle of the roots (**b**), apices of the teeth (**c**), and lower border of the mandible (**d**) showing the variable location of bilateral hyperdense tubular structures, consistent with calcified stylohyoid ligaments. Note the close proximity of the calcifications to the approximate anatomical region carotid space (*dotted red circle*)

11.5 Upper Airway

The upper airway (UA) is an important anatomical feature centrally located within the neck and often included with the imaging volume of CBCT scans. The UA is an air-filled, smooth-surfaced tube that extends for the dorsal aspect of the nasal cavity to the trachea. The shape of the UA is irregular due to anatomic restrictions along its path due to several muscles, cartilages, and ligaments. Cephalad the UA consists of two separate airway spaces, the nasal cavity and nasopharynx which become confluent with the oropharynx and eventually extend caudally to become the laryngopharynx.

Only a limited segment of the UA may be included in the FOV of a CBCT examination. Rarely is CBCT performed that provides imaging below the superior border of the thyroid cartilage. The UA is best evaluated in axial (Fig. 11.65) and sagittal CBCT sections of the head and neck and presents as a uniform, low-density (dark) space with sharp well-defined borders from the peripheral surrounding soft tissue (see Chap. 13 for details on the radiographic anatomy of the UA).

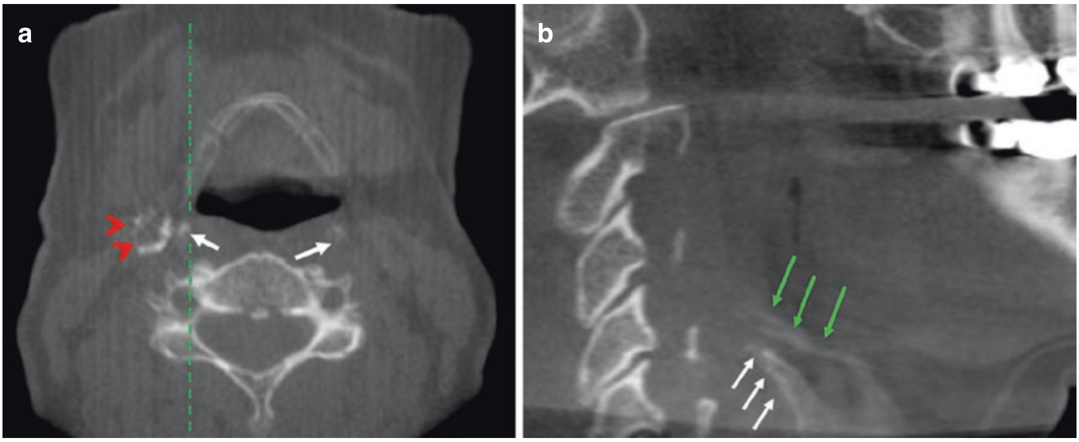

Fig. 11.59 Axial (**a**) and right sagittal (**b**) images of the neck at the level of C3/C4 vertebrae depicting the hyoid bone and the 3rd cervical vertebrae (C3). The calcified superior cornu of the thyroid cartilage (CSCTC) are shown as small round calcifications toward the dorsal/lateral walls of the airway (*white arrows*). Lateral to the right CSCTC there is a larger ring-like calcification (*red arrows*), consistent with calcified carotid artery atheroma (*red arrows*). The sagittal section depicts the hyoid bone (*green arrows*) and the right CSCTC (*white arrows*)

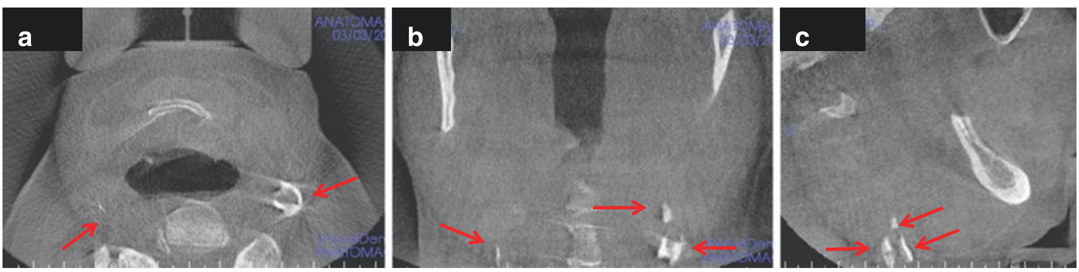

Fig. 11.60 Axial (**a**), coronal (**b**), and sagittal (**c**) CBCT images of the neck at the level of C3/C4 depicting bilateral curvilinear calcifications in the region of the carotid artery bifurcation, consistent with calcified carotid artery atheroma (CCAA)

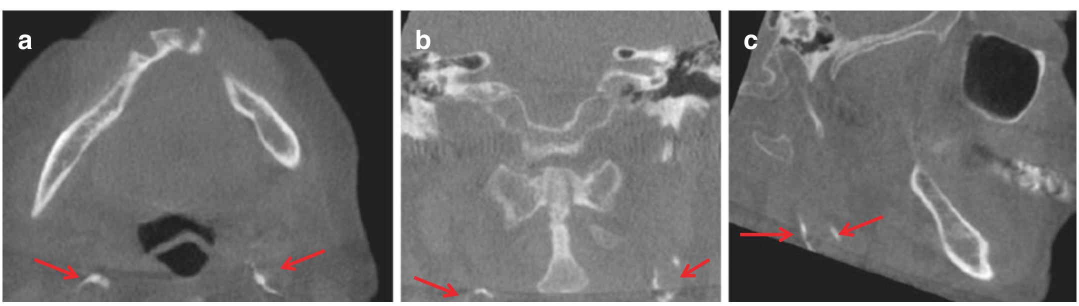

Fig. 11.61 Axial (**a**), coronal (**b**), and sagittal (**c**) CBCT images of the neck at the level of C3/C4 showing an incidental finding of bilateral curvilinear calcifications in the region of the carotid artery bifurcation, similar to those seen in Fig. 11.60, consistent with CCAA

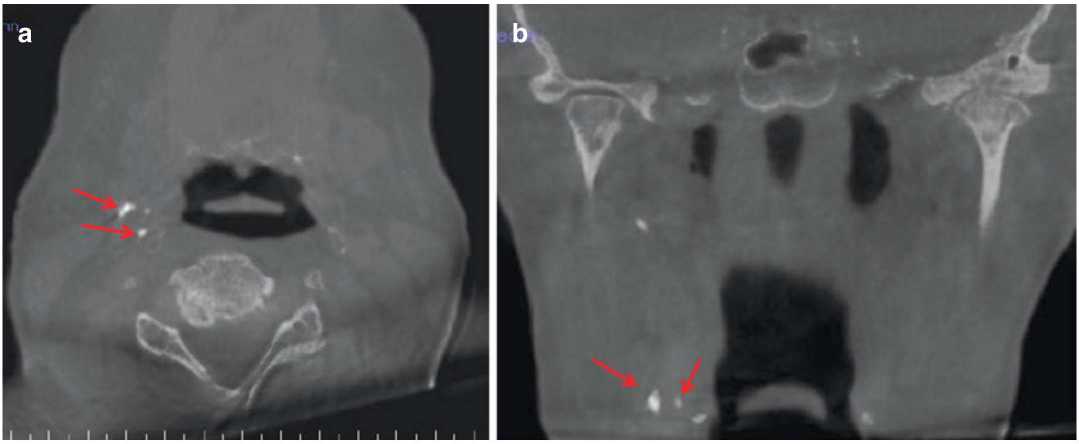

Fig. 11.62 Axial (**a**) and coronal (**b**) CBCT images of the neck at the level of C3/C4 depicting small "rice-grains" calcifications on the right side of the neck in the region of the carotid artery bifurcation, consistent with CCAA

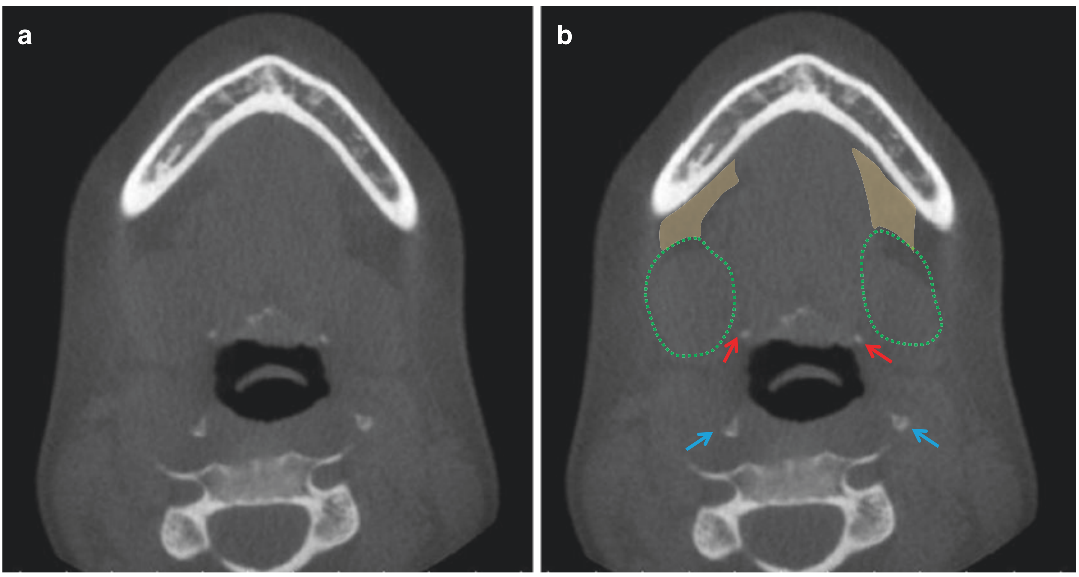

Fig. 11.63 Original (**a**) and annotated (**b**) axial CBCT image of the neck at the level of C3/C4 and hyoid bone depicting the outline of large ovoid soft tissue density structure bilaterally, antero-lateral to the hyoid bone consistent with the region of the submandibular salivary glands (SMSG). Greater (*blue arrows*) and lesser (*red arrows*) cornu of the hyoid. In the coronal plane (not shown) SMSG occupies a space from the mandibular angle to the level of the hyoid, below the mylohyoid muscle

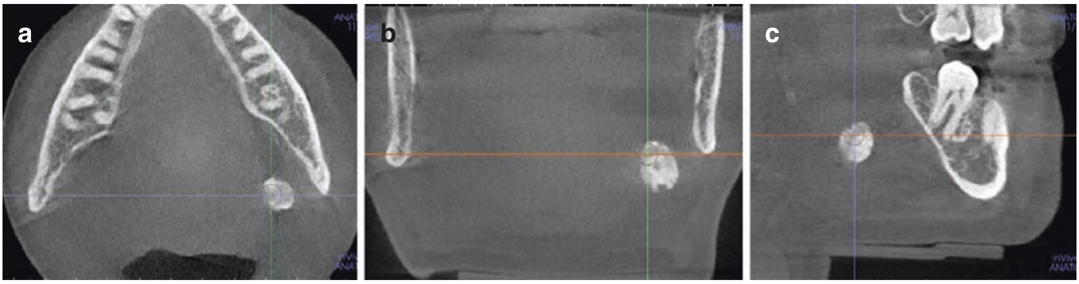

Fig. 11.64 Axial (**a**), coronal (**b**), and sagittal CBCT sections of the neck at the level of the floor of the mouth depicting a large sialolith in the body of the left submandibular salivary gland

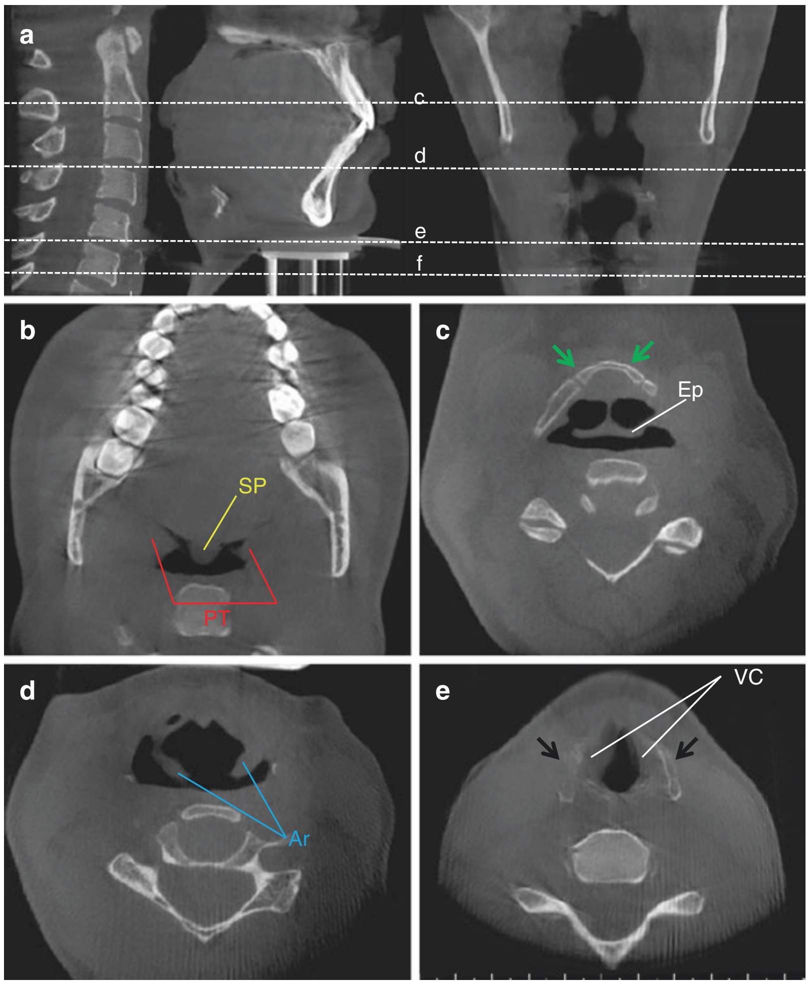

Fig. 11.65 Reference sagittal (*left*) and coronal (*right*) CBCT sections (**a**) identifying the level of various sequential cranio-caudal axial images (*dashed horizontal lines*) (**b**–**e**) at the most important constrictions of the upper airway (*SP* soft palate, *Ep* epiglottis, *Ar* arytenoid processes, *VC* vocal cords, *PT* palatine tonsils, thyroid cartilage (*black arrows*), hyoid bone (*green arrows*))

The importance of understanding the radiographic anatomy of the UA for dental clinicians is twofold. Constrictions present along the path of the UA are associated with specific anatomical landmarks such as the soft palate, dorsum and base of the tongue, tonsillar fauces, and epiglottis. The reduction in cross-sectional area due to a generalized increase in volume of the surrounding soft tissues (e.g., fat) or local phenomena (e.g., tonsillar hypertrophy) may result in changes in the airflow and be contributory to obstructive sleep apnea hypopnea syndrome (see Chap. 28 for details). UA shape alterations may also be due to adjacent impinging soft tissue pathology. Symmetrical changes are often the result of inflammation that affects a broader zone of the airway, whereas unilateral airway shape alterations may be suspicious for possible tumor development and may require further investigation and possibly biopsy.

References

Arvin B, Fournier-Gosselin MP, Fehlings MG (2010) Os odontoideum: etiology and surgical management. A review. Neurosurgery 66(Suppl 3):22–31

Baccetti T, Franchi L, JA MN Jr (2002) An improved version of the cervical vertebral maturation (CVM) method for the assessment of mandibular growth. Angle Orthod 72:316–323

Chen MY, Bohrer SP (1999) Radiographic measurement of prevertebral soft tissue thickness on lateral radiographs of the neck. Skelet Radiol 28:444–446

El-Khoury GY, Montgomery WJ, Bergman RA (2007) Sectional anatomy by MRI and CT. Churchill Livingstone, Philadelphia

Fishman LS (1982) Radiographic evaluation of skeletal maturation, a clinically oriented study based on hand-wrist films. Angle Orthod 52:88–112

Franquet T, Erasmus JJ, Giménez A, Rossi S, Prats R (2002) The retrotracheal space: normal an-atomic and pathologic appearances. A review. Radiographics 22:S231–S246

Guille JT, Sherk HH (2002) Congenital osseous anomalies of the upper and lower cervical spine in children. A review. J Bone Joint Surg Am 84-A:277–288

Hassel B, Farman AG (1995) Skeletal maturation evaluation using cervical vertebrae. Am J Orthod Dentofac Orthop 107:58–66

Jaqueira LM, Armond MC, Pereira LJ, Alcântara CE, Marques LS (2010) Determining skeletal maturation stage using cervical vertebrae: evaluation of three diagnostic methods. Braz Oral Res 24:433–437

Junewick JJ, Chin MS, Meesa IR, Ghori S, Boynton SJ, Luttenton CR (2011) Ossification patterns of the atlas vertebra. AJR Am J Roentgenol 197:1229–1234

Karwacki GM, Schneider JF (2012) Normal ossification patterns of atlas and axis: a CT study. AJNR Am J Neuroradiol 33:1882–1887

Kettler AA, Wilke H-JH (2006) Review of existing grading systems for cervical or lumbar disc and facet joint degeneration. Eur Spine J 15:705–718

Labrom RD (2007) Growth and maturation of the spine from birth to adolescence. A review. J Bone Joint Surg Am 89(Suppl 1):3–7

Lustrin ES, Karakas SP, Ortiz AO, Cinnamon J, Castillo M, Vaheesan K, Brown JH, Diamond AS, Black K, Singh S (2003) Pediatric cervical spine: normal anatomy, variants, and trauma. A review. Radiographics 23:539–560

Madden ME (2008) Introduction to sectional anatomy. Lippincott Williams & Wilkins, Philadelphia

O'Reilly M, Yanniello GJ (1988) Mandibular growth changes and maturation of cervical vertebrae—a longitudinal cephalometric study. Angle Orthod 58:179–184

Popat H, Drage N, Durning P (2008) Mid-line clefts of the cervical vertebrae – an incidental finding arising from cone beam computed tomography of the dental patient. Br Dent J 204:303–306

Pracharktam N, Nelson S, Hans MG, Broadbent BH, Redline S, Rosenberg C, Strohl KP (1996) Cephalometric assessment in obstructive sleep apnea. Am J Orthod Dentofacial Orthop 109:410–9

Richards PJ (2005) Cervical spine clearance: a review. Injury 36:248–269

Rosse C, Rosse PG (1997) Hollinshead's textbook of anatomy. 1997 Lippincott-Raven Publishers, Philadelphia

Scutellari PN, Galeotti R, Leprotti S, Ridolfi M, Franciosi R, Antinolfi G (2007) The crowned dens syndrome. Evaluation with CT imaging. Radiol Med 112:195–207

Seedat AK, Forsberg CD (2005) An evaluation of the third cervical vertebra (C3) as a growth indicator in black subjects. SADJ 60:156–160

Shi H, Scarfe WC, Farman AG (2007) Three-dimensional reconstruction of individual cervical vertebrae from cone-beam computed-tomography images. Am J Orthod Dentofac Orthop 131:426–432

Sforza E, Bacon W, Weiss T, Thibault A, Petiau C, Krieger J (2000) Upper airway collapsibility and cephalometric variables in patients with obstructive sleep apnea. Am J Respir Crit Care Med 161(2 Pt 1):347–52

Anatomy of the Nose and Paranasal Sinuses

12

Kivanç Kamburoğlu, Saulo L. Sousa Melo, Zhimin Li, Dirk Schulze, Sema Murat, Bruno Azevedo, Christos Angelopoulos, and William C. Scarfe

Contents

Kıvanç Kamburoğlu, D.D.S., M.Sc., Ph.D., B.P.A.
Department of Dentomaxillofacial Radiology, Faculty of Dentistry, Ankara University, Ankara, Turkey
e-mail: dtkivo@yahoo.com

S.L.S. Melo, D.D.S., M.S.D., Ph.D., M.S. (✉)
Department of Oral Pathology, Radiology and Medicine, University of Iowa College of Dentistry, Iowa City, IA, USA
e-mail: saulo-sousamelo@uiowa.edu

Z. Li, D.D.S., Ph.D.
Department of Oral Radiology, School and Hospital of Stomatology, Jilin University, Chang Chun, Jilin Province, China
e-mail: zhimin@jlu.edu.cn

D. Schulze, Priv. Doz. Dr. med. dent.
Digitales Diagnostik Zentrum, Freiburg, Germany
e-mail: dirk.schulze@ghostdoc.de

S. Murat, D.D.S., M.S., Ph.D.
Department of Prosthodontics, Faculty of Dentistry, Ankara University, Ankara, Turkey
e-mail: semamurat47@yahoo.com.tr

B. Azevedo, D.D.S., M.S. • W.C. Scarfe, B.D.S., F.R.A.C.D.S., M.S.
Division of Radiology and Imaging Science, Department of Surgical/Hospital Dentistry, University of Louisville School of Dentistry, Louisville, KY, USA
e-mail: Bruno.azevedo@louisville.edu; William.scarfe@louisville.edu

C. Angelopoulos, D.D.S., M.S.
Aristotle University of Thessaloniki, Thessaloniki, Greece

Columbia University, College of Dental Medicine, New York City, NY, USA
e-mail: angelopoulosc@gmail.com

W.C. Scarfe, C. Angelopoulos (eds.), *Maxillofacial Cone Beam Computed Tomography*,
https://doi.org/10.1007/978-3-319-62061-9_12

12.1 Introduction

Depending on the protocol used, some or all of the paranasal sinuses may be visible within the imaging field-of-view when CBCT is used for dental purposes. Correct interpretation therefore necessitates a knowledge of paranasal sinus anatomy and an understanding of the clinical significance of anatomical variants and pathologies (see Chap. 29) (Kamburoglu et al. 2011; Brullmann et al. 2011; Pazera et al. 2011).

Specifically, the assessment of normal paranasal sinuses on CBCT images should focus on the patency of the drainage pathway and anatomical variants (Kamburoglu et al. 2011; Brullmann et al. 2011; Pazera et al. 2011).

12.2 Anatomic Overview

The paranasal sinuses are a group of four paired, air-filled spaces located within the bones surrounding the nasal cavity that together with the nasal fossae constitute an anatomical and functional unit. The four paranasal sinuses take their names from the maxillofacial facial bones behind which they are located. From inferior to superior (Fig. 12.1):

- Maxillary sinuses
- Ethmoid sinuses (aircells)
- Sphenoid sinuses
- Frontal sinuses

Each sinus is an osseous cavity lined with respiratory mucosa (pseudo stratified, ciliated epithelium with small serous and mucinous glands (goblet cells)). This mucosa is a continuation of the nasal mucosa and is loosely attached to the underlying bone, containing relatively few vessels. Structurally each has an opening (ostium), through which it drains into the nasal meatus. The ostia are also the starting point for the development of the sinuses. The mastoid aircells are not considered paranasal sinuses as they have no direct communication with the nasal fossa.

The nasal fossa is an elongated pyramidal in shape cavity interposed between the maxillary sinuses and is separated from the oral cavity by a thin cortical wall which serves as its floor; the same wall also forms the hard palate. Its lateral walls are shared with the medial aspect of the maxillary sinuses with the medial aspect of the maxillary and, superiorly, the ethmoid sinuses. Attached to these sidewalls and extending into the fossa, there are three finger-like bony projec-

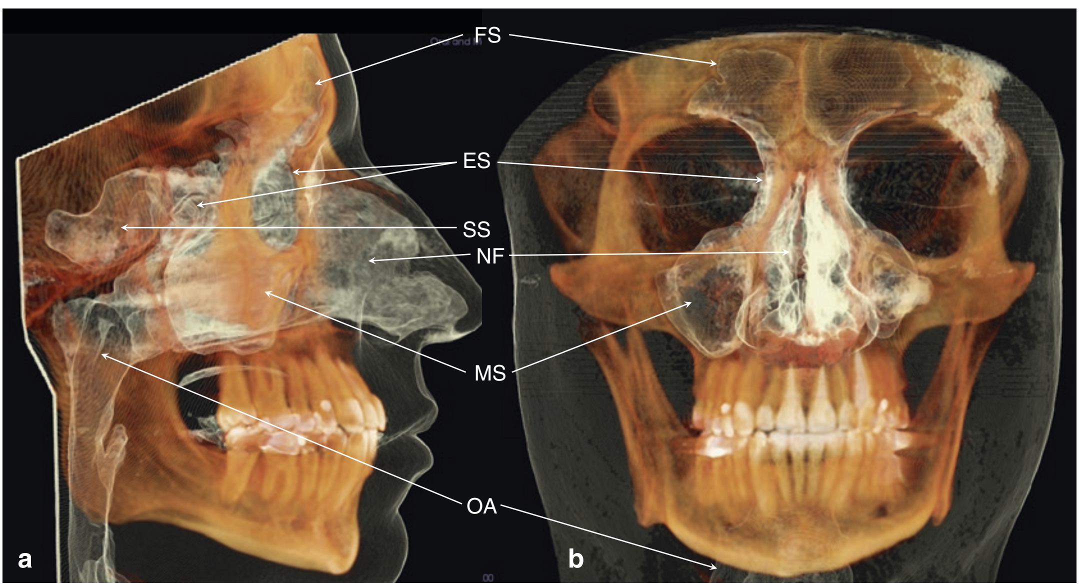

Fig. 12.1 Relationship of the four paranasal sinuses (**bold**) to the bones of the maxillofacial skeleton and the adjoining oropharyngeal airway (*OA*) and nasal fossa (*NF*) (*FS* frontal sinus, *ES* ethmoid sinus, *MS* maxillary sinus, *SS* sphenoid sinus, *OA* oropharyngeal airway, *NF* nasal fossa)

tions called *turbinates*. These create a series of "corridors" for the passage of air. The nasal fossa is divided by a vertical partition into a left and a right compartment by a midline septum. Three interconnecting components make up the septum (the nasal septum): the septal cartilage anteriorly, the perpendicular plate of the ethmoid superiorly, and a separate bone, the vomer posteriorly. The nasal fossa is contiguous with the cartilage of the nose anteriorly through the *anterior choanae* or *nasal aperture* and posteriorly with the nasopharynx through the *posterior choanae*.

12.2.1 Development

12.2.1.1 Paranasal Sinuses

The formation of the sinuses starts between the third and fifth months in utero as evaginations from the nasal mucosa. At birth they present as only slight recesses rather than complete sinuses. Complete pneumatization of a sinus is a long-term process and is only completed in early adulthood (18 years) (Fig. 12.2). Children therefore only demonstrate small or even no sinuses (Fig. 12.3). The adult sinuses are variable in their

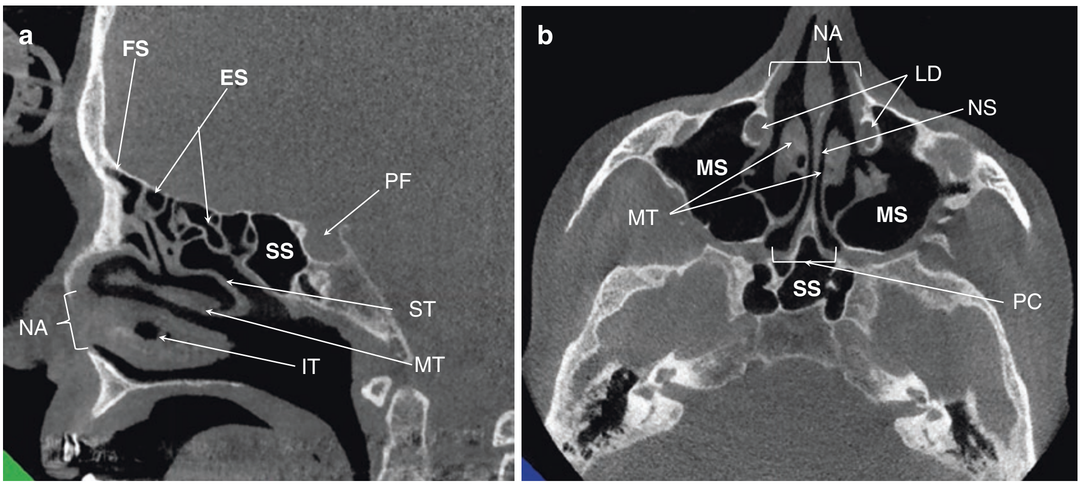

Fig. 12.2 Sagittal (**a**) and axial (**b**) CBCT images providing overview of upper maxillofacial region and relationship of paranasal sinuses in an adult. (*FS* frontal sinus, *ES* ethmoidal sinus, *SS* sphenoid sinus, *MS* maxillary sinus, *ST* superior turbinate, *MT* middle turbinate, *IT* inferior turbinate, *PF* pituitary fossa, *NA* nasal aperture (anterior choanae), *PC* posterior choanae, *NS* nasal septum, *LD* lacrimal duct)

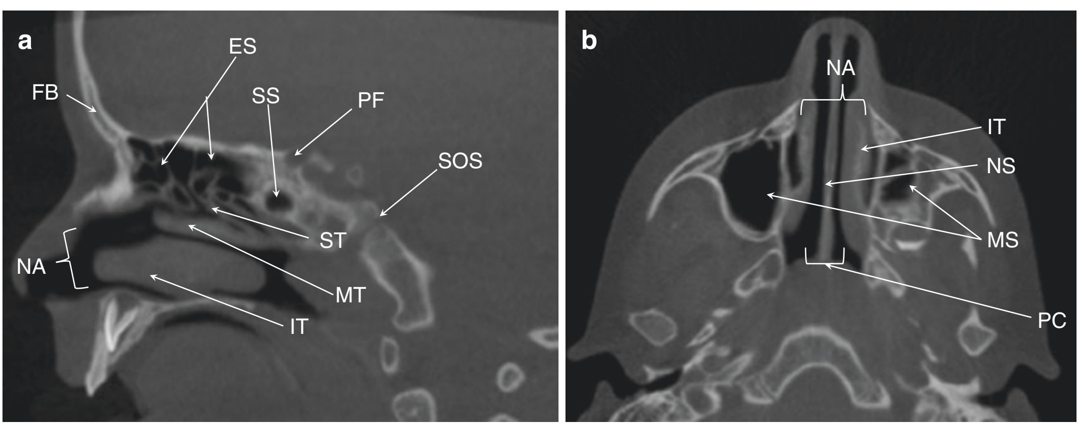

Fig. 12.3 Midsagittal (**a**) and axial (**b**) CBCT images providing overview of upper maxillofacial region and relationship of paranasal sinuses (**bold**) in a 4-year-old. (*FB* frontal bone, *SOS* spheno-occipital synchondrosis, *ES* ethmoidal sinus, *SS* sphenoid sinus, *MS* maxillary sinus, *ST* superior turbinate, *MT* middle turbinate, *IT* inferior turbinate, *PF* pituitary fossa, *NA* nasal aperture (anterior choanae), *PC* posterior choanae, *NS* nasal septum)

extensions (Snell 1995; Arıncı and Elhan 1997; Muranjan 1999; Pérez-Piñas et al. 2000). Knowledge of sinus development and variability is essential to prevent misdiagnosis (Smith et al. 1997). The development of each sinus varies:

- **Frontal.** Of the four paranasal sinuses, the frontal sinuses are the last to develop. They are the only paranasal sinuses absent at birth. Expansion of the sinus into the frontal bone begins at around 3.5 years of age and does not reach the frontal bone until about 6 years. It then proceeds slowly to age 11, and then more quickly until it reaches its full development between ages 14 and 16 years (Lang 1989; Muranjan 1999).
- **Ethmoid.** The ethmoidal sinuses develop as separate evaginations from the nasal cavity in the third to fifth month of gestation, are present at birth, and grow until late puberty.
- **Sphenoid.** The sphenoid sinuses develop as evaginations from the posterior nasal capsule in the fourth month in utero. They are present at birth as small cavities, and reach their adult configuration between ages 10 and 12 years.
- **Maxillary.** The maxillary sinuses begin as a lateral pouching of the ethmo-maxillary recess mucosa during the 10th to 12th week of gestation in association with the resorption of the surrounding tissue and growth of the maxillary pouch. The maxillary antrum is identifiable at the 16th week of gestation. Following the eruption of the upper teeth, pneumatization continues mainly in an inferior direction (Kalavagunta and Reddy 2003). The maxillary sinuses are the first of the paranasal sinuses to develop, and their growth ends with the eruption of the third molars at approximately 20 years of age.

12.2.1.2 Nasal Fossa

The nasal cavity and adjoining paranasal sinuses develop from a cartilaginous anlage called the *nasal capsule*. This appears between the seventh and eighth weeks in utero with the first cartilaginous area to develop being the nasal septal area. The lateral nasal wall development initiates with the cartilage of inferior turbinate (8th week), followed by middle turbinate (9th week), then the superior turbinates (12th week). Simultaneously the uncinate begins to develop during the ninth week. Nasal fossa development is then influenced by expansion of the ethmoidal bulla (12th week), anterior ethmoidal cells (22nd week), and finally the posterior ethmoid cells (40th week).

12.2.2 Function of the Nose and Paranasal Sinuses

The paranasal sinuses provide numerous functions including:

- A role in the establishment of equilibrium by decreasing the relative weight of the frontal bones.
- Contributes to the skeletal growth of the visceral maxillofacial skeleton and cranium by prolonged growth.
- Offer force absorption in case of trauma by acting as "airbags."
- Warm and humidify inspired air which directly links with our capability to smell and taste (Doty and Mishra 2001).
- Regulates the air pressure between paranasal sinuses, nasal meatus, pharynx, and middle ear.
- Provide adjustment of vocal resonance.

The physiological functions of the nose are chiefly olfactory and respiratory; however, the nasal septum acts as an "epiphyseal plate" and as such provides the growth center for the entire skeleton of the upper face particularly in the anteroposterior and vertical dimensions.

12.2.3 Drainage Pathways

The mucosa of the paranasal sinuses comprises mucous cells which produce mucus and incorporate cilia, small hair like structures which are oriented towards the ostia of each sinus (Figs. 12.4, 12.5, 12.6, and 12.7). Mucociliary drainage is dependent on the internal anatomic complexity and patency of the ostia. The mucus drainage pathway depends on the specific sinus:

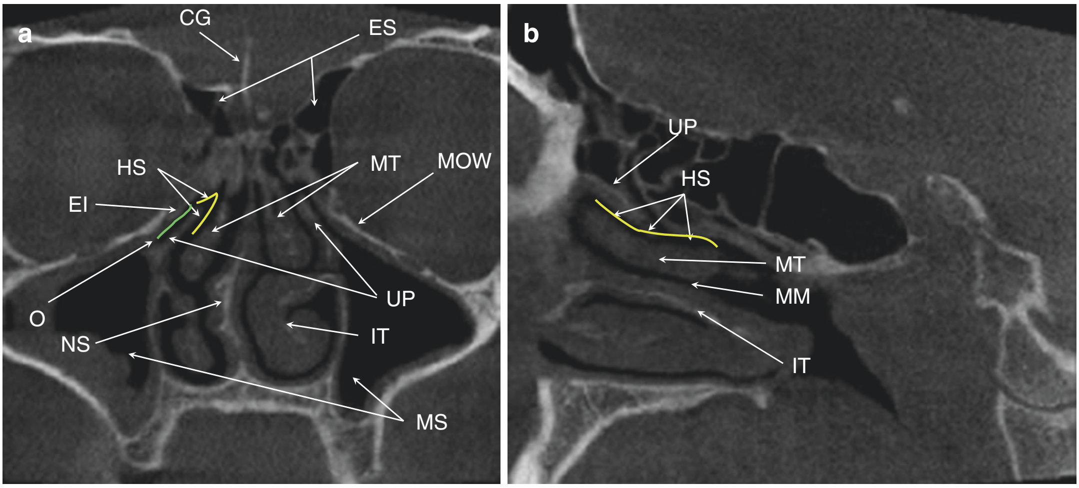

Fig. 12.4 Coronal (**a**) and lateral sagittal (**b**) CBCT images providing overview of upper maxillofacial region and depicting the most common drainage pathways of the maxillary sinus. (***ES*** ethmoid sinus, ***MS*** maxillary sinus, *MT* middle turbinate, *MM* middle meatus, *IT* inferior turbinate, *NS* nasal septum, *HS* hiatus semilunaris (*yellow dotted line*), *MOW* medial orbital wall, *CG* crista galli, *EI* ethmoid infundibulum (*green dotted line*), *O* ostium)

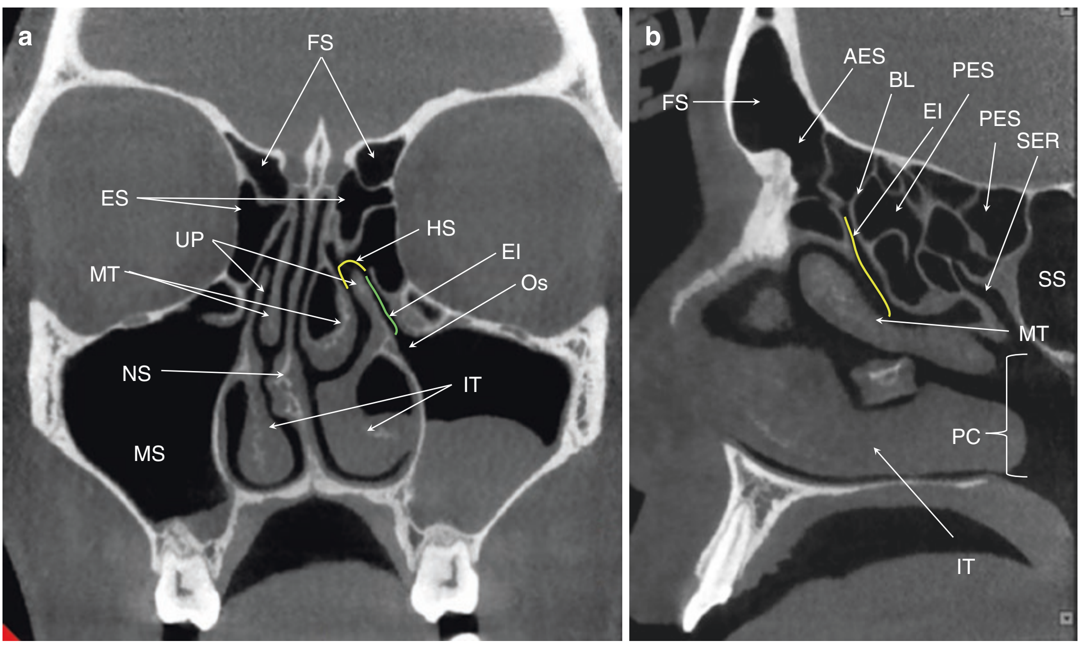

Fig. 12.5 Coronal (**a**) and sagittal (**b**) CBCT images providing overview of upper maxillofacial region and depicting the most common drainage pathways of the ethmoid sinuses. (***FS*** frontal sinus, ***AES*** anterior ethmoid sinus, ***PES*** posterior ethmoid sinus, ***PES*** posterior ethmoid sinus, *BL* basal lamina, ***MS*** maxillary sinus, ***SS*** sphenoid sinus, *MT* middle turbinate, *IT* inferior turbinate, *PC* posterior choanae, *NS* nasal septum, *SER* sphenoethmoidal recess, *UP* uncinate process, *HS* hiatus semilunaris (*yellow dotted line*), *EI* ethmoid infundibulum (*green dotted line*), *Os* maxillary ostium)

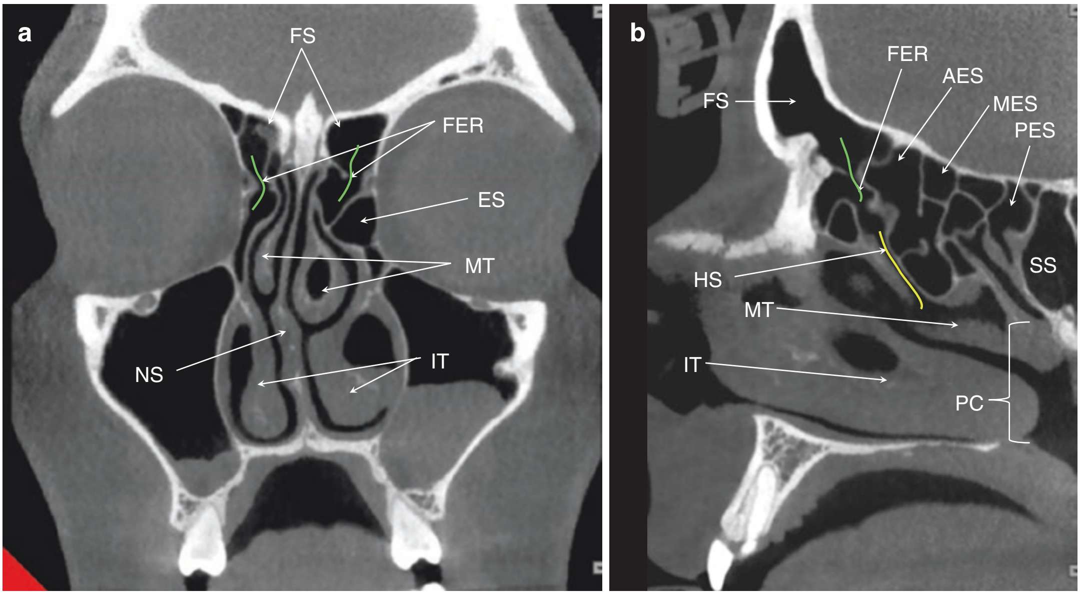

Fig. 12.6 Coronal (**a**) and lateral sagittal (**b**) CBCT images providing overview of upper maxillofacial region and depicting the most common drainage pathways of the frontal sinuses through the frontoethmoidal recess. (***FS*** frontal sinus, ***AES*** anterior ethmoid sinus, ***MES*** middle ethmoid sinus, ***PES*** posterior ethmoid sinus, ***SS*** sphenoid sinus, *MT* middle turbinate, *IT* inferior turbinate, *PC* posterior choanae, *NS* nasal septum, *FER* frontoethmoidal recess (*green dotted line*), *HS* hiatus semilunaris (*yellow dotted line*))

- The maxillary sinus communicates with the middle nasal meatus via the physiological ostium and the *ethmoid infundibulum*, which is situated between the uncinate process and the medial orbital wall (Fig. 12.4).
- The ethmoid sinus is located directly superior to the upper nasal meatus (Fig. 12.5). The anterior ethmoid drainage occurs via the hiatus semilunaris and middle meatus whereas the posterior ethmoid drainage occurs via the sphenoethmoidal recess and superior meatus.
- The frontal sinus has the most complex and variable drainage pathway of any of the paranasal sinuses. It communicates via the frontal recess and the anterior ethmoidal cells with the middle nasal meatus. Both drain regularly over the *frontoethmoidal recess* (duct) into the middle nasal meatus (approximately 60%) or *ethmoid infundibulum* (approximately 40%) through the frontal ostium (Fig. 12.6).
- The sphenoid sinus communicates with the upper nasal meatus via the sphenoethmoidal recess (Fig. 12.7) (Yousem 1993).

The ostiomeatal complex (OMC) (see later) plays a central role in drainage of the sinuses with obstruction in this area leading to a pansinusitis.

12.3 Nasal Cavity

12.3.1 Nasal Septum

The nasal septum is an osseo-cartilaginous structure that forms the medial extent of the nasal cavity and divides the nose into two halves (Fig. 12.8). Growth of the human nose, nasal cav-

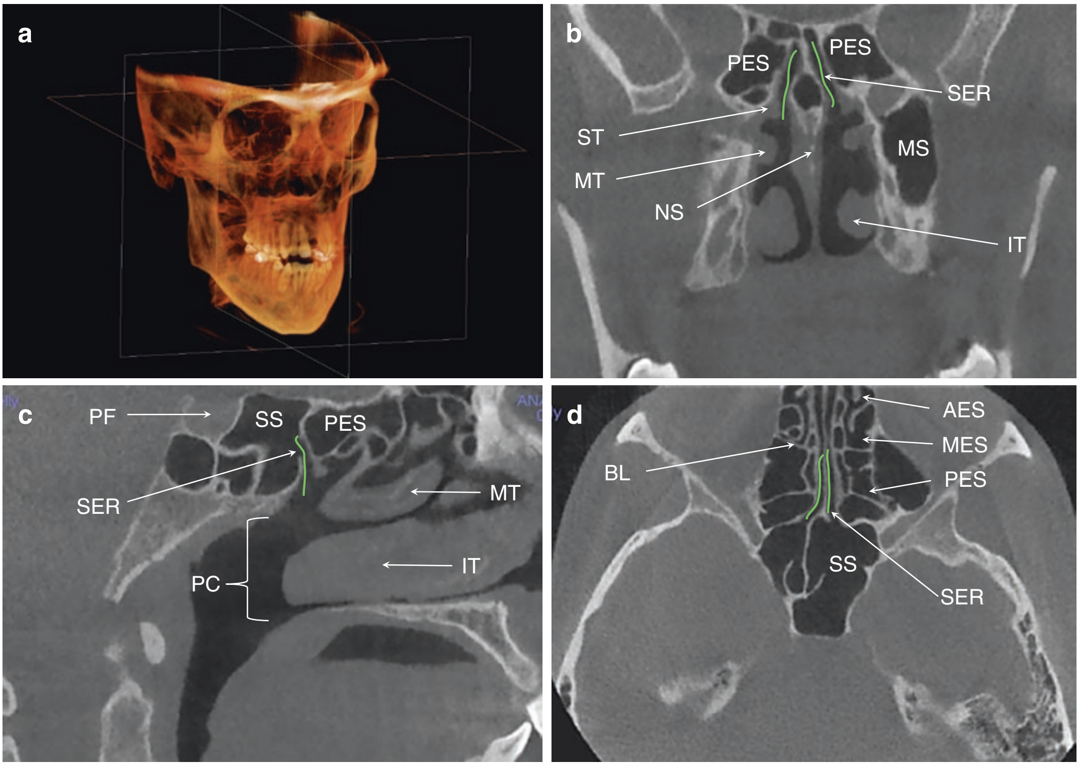

Fig. 12.7 Reference volumetric image (**a**) showing coronal (**b**) and sagittal (**c**) and axial (**d**) CBCT images providing overview of upper maxillofacial region and depicting the most common drainage pathways of the sphenoid and ethmoid sinuses through the sphenoethmoidal recess. (***FS*** frontal sinus, ***AES*** anterior ethmoid sinus, ***MES*** middle ethmoid sinus, ***PES*** posterior ethmoid sinus, *BL* basal lamina, ***SS*** sphenoid sinus, ***MS*** maxillary sinus, *PF* pituitary fossa, *ST* superior turbinate, *MT* middle turbinate, *IT* inferior turbinate, *PC* posterior choanae, *NS* nasal septum, *SER* sphenoethmoidal recess (*green dotted line*))

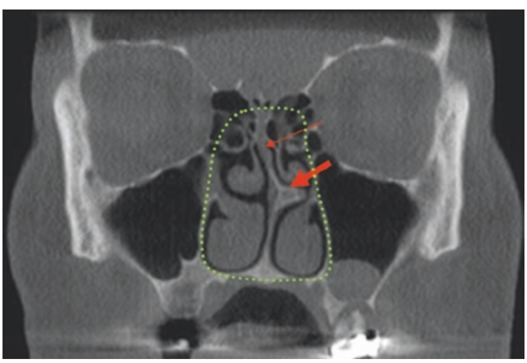

Fig. 12.8 Coronal CBCT image of the mid-face with nasal septum deviation along with a bone spur. *Thin arrow* shows septum deviation to left side and *thick arrow* shows the bone spur. *Dotted lines* show the boundary of the nasal cavity

ity, and face is largely dependent upon this structure (Muranjan 1999). The nasal septum consists of quadrangular cartilage extending to the perpendicular plate of the ethmoid bone posterosuperiorly and the vomer posteroinferiorly.

12.3.2 Lateral Wall of the Nose and the Turbinates

The lateral wall of the nose is a complex structure with three levels of scroll-like bony projections (conchae) covered with nasal mucosa identified by cranio-caudal position as the superior, middle, and inferior turbinates (and, on occasion, the supreme turbinate). The luminal space immediately inferior to each turbinate is referred to as the superior, middle, and inferior meatus, respectively. They are connected by the common meatus. Whereas the superior and middle turbinates are components of the ethmoid bone, the inferior turbinate is a separate bone (Fig. 12.9).

The superior turbinate is the smallest turbinate and overlies the superior meatus into which the posterior ethmoidal cells drain.

The middle turbinate forms an important landmark from the point of view of endoscopic sinus surgery (ESS) and should be preserved. The middle turbinate attaches superiorly to the skull base at the lamina cribrosa of the cribriform plate. The middle turbinate can be divided into anterior, middle, and posterior thirds. The anterior third courses vertically along the sagittal plane. The middle third turns coronally and laterally to enter the orbital lamina, and its coronal component, the basal lamella, represents the point of division between anterior and posterior ethmoid air cells. The posterior third of the middle turbinate turns toward the horizontal and posteroinferiorly attaches to the lateral nasal wall (Lang 1989; Earwaker 1993; Muranjan 1999; Vartanian 2010). A secondary middle turbinate may be occasionally present in the nasal cavity. Recognition of this variation is important, since it may narrow the ostiomeatal complex (OMC) and predispose to inflammatory sinus disease.

The inferior turbinate extends along the inferior lateral nasal wall posteriorly towards the nasopharynx above the inferior meatus, into which the nasolacrimal canal drains.

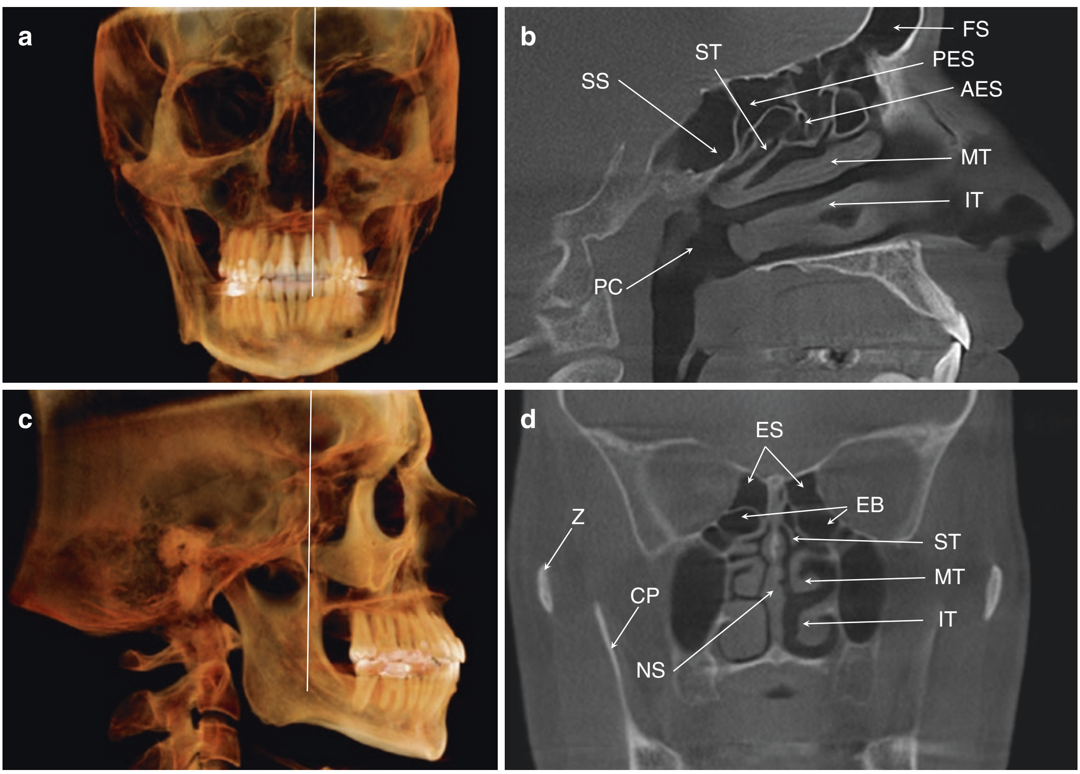

Fig. 12.9 Frontal (**a**) and right lateral (**b**) volumetric projections showing the location of left lateral wall (**c**) of the nasal fossa and coronal (**d**) CBCT images projections of the turbinates. (***ES*** ethmoid sinus, ***FS*** frontal sinus, ***AES*** anterior ethmoid sinus, ***PES*** posterior ethmoid sinus, ***SS*** sphenoid sinus, *ST* superior turbinate, *MT* middle turbinate, *IT* inferior turbinate, *PC* posterior choanae, *NS* nasal septum, *EB* ethmoid bulla, *Z* zygoma, *CP* coronoid process of the mandible)

12.4 Frontal Sinus

The frontal sinus is the second largest of the paranasal sinuses, after the maxillary sinuses. It is located between the medial and lateral laminas of the frontal bone, posterior to the superciliary arch and anterior cranial fossa and superior to the nose and orbit. It resembles an asymmetrical pyramid and can extend beyond the frontal bone into the orbital plate. The left and right frontal sinuses are separated by the *intersinus septum*. The superior segment of the *intersinus septum* is often characterized by marked deviation from the midline, unlike the inferior segment where deviation is extremely rare. Hence, the two frontal sinuses are rarely symmetrical. Each frontal sinus comprises a vertical component located in the frontal squama (*squama frontalis*) and a horizontal component located in the frontal bone (*pars orbitalis*). Within the *squama frontalis*, the frontal sinus drainage pathway (FSDP) has a wide superior component and an inferior compartment which is a narrow passageway formed by either the ethmoid infundibulum or the middle meatus. There is great individual variation in the size and shape of the frontal sinuses, which can range in volume from 5 to 30 cm^3 (Fig. 12.10) (Lang 1989; Snell 1995; Arıncı and Elhan 1997).

The frontal recess, the drainage pathway of the frontal sinus, usually drains into the middle meatus (semilunar hiatus) (62%) or into the ethmoidal infundibulum (38%). This pathway is

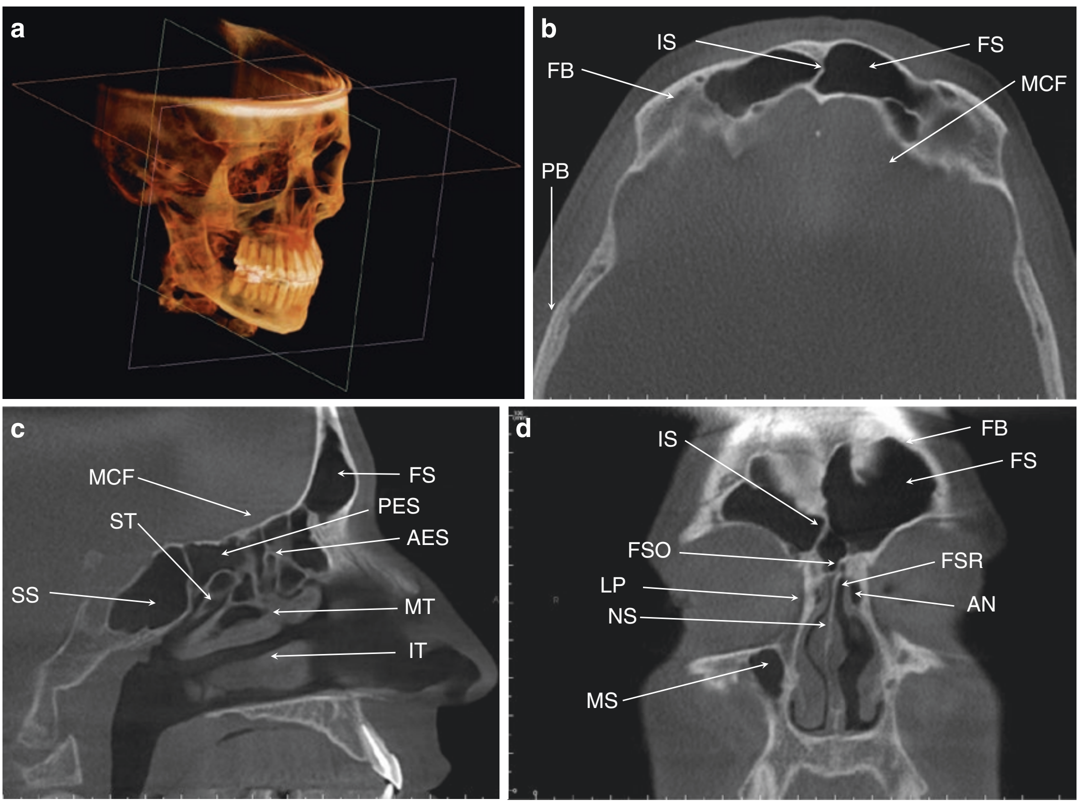

Fig. 12.10 Right supero-inferior volumetric rendering (**a**) showing location of axial (**b**), sagittal (**c**), and frontal (**d**) CBCT orthogonal sections of the frontal sinus. (*FS* frontal sinus, *FB* frontal bone, *IS* intersinus septum, *PB* parietal bone, *MCF* middle cranial fossa, ***MS*** maxillary sinus, *AES* anterior ethmoid sinus, *PES* posterior ethmoid sinus, *SS* sphenoid sinus, *ST* superior turbinate, *MT* middle turbinate, *IT* inferior turbinate, *NS* nasal septum, *FSO* frontal sinus ostium, *FSR* frontal sinus recess, *AN* agger nasi cell, *LP* lamina papyracea)

bordered by the *agger nasi* cell anteriorly, the orbital lamina laterally, the middle turbinate medially, and the anterior wall of the ethmoid bulla posteriorly. The frontal recess is affected by the development of anterior ethmoid cells, including the frontal or supraorbital cells, and enlargement or disease of any of these cells may contribute to blockage of the frontal sinus. On a coronal CT, the *agger nasi* cell, an extramural cell that represents the most anterior ethmoid cell, appears anterior and inferior to the frontal recess and lateral to the middle turbinate (Muranjan 1999; Tan and Chong 2001). The location of this cell makes it an important surgical landmark, and opening it usually provides an excellent view of the frontal recess. Depending on the degree of pneumatization, the agger nasi cell may extend laterally to the lacrimal fossa, resulting in a narrowing of the frontal recess (Fig. 12.10) (Vartanian 2010).

12.4.1 Frontoethmoidal Complex

The roof of the ethmoid is created by the frontal bone. Keros (1962) described three surgically important variations in the configuration of the ethmoid roof related to the length of the lateral lamella of the cribriform plate, the thinnest bone in the entire anterior skull base (Fig. 12.11).

- **Type 1.** The olfactory fossa is only 1–3 mm deep, the lateral lamella is almost nonexistent, and the ethmoid roof is located in almost the same plane as the cribriform plate.
- **Type 2**. The olfactory fossa is 4–7 mm deep, and the lateral lamella is somewhat longer.
- **Type 3.** The olfactory fossa is 8–16 mm deep, and the ethmoid roof lies significantly above the cribriform plate. This configuration represents the greatest concern for the surgeon because the increase in vertical height repre-

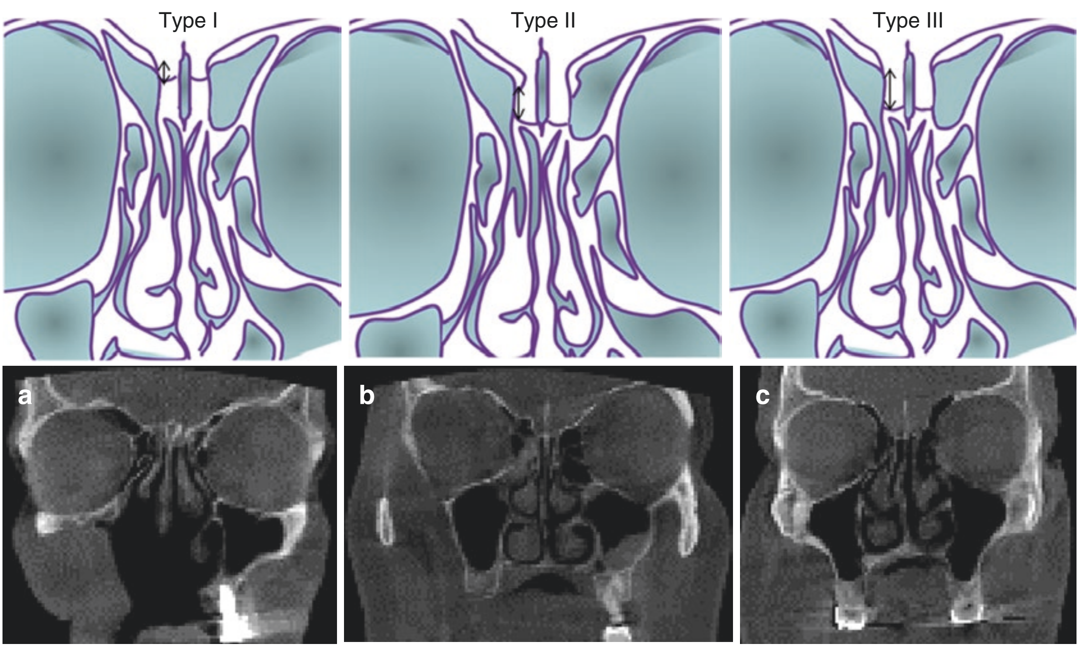

Fig. 12.11 Schematic representation and corresponding coronal CBCT image of Keros classifications Type I (**a**), Type II (**b**), and Type III (**c**)

sents an increased risk of anterior skull base damage as a result of instrument penetration of the thin and vulnerable lateral lamella (Fig. 12.11) (Stammberger and Kennedy 1995; Savvateeva et al. 2010).

12.5 Ethmoidal Sinuses

These thin-walled, air-filled cells occupy a position between the orbit laterally and the nasal cavity medially and comprise the bulk of the ethmoid bone (Fig. 12.12). The lateral wall separating each cell from the orbit is formed by the solid lacrimal bone anteriorly and the orbital lamina, a paper-thin bone situated behind the lacrimal bone. The ethmoidal sinuses are related to the anterior cranial fossa superiorly and the maxillary sinus inferiorly. The entire ethmoidal sinus structure measures 4–5 cm in length and 2.5–3 cm in height. A large number of ethmoid cells are coated with mucosa and separated by complete or incomplete thin lamellar bone with a variable pneumatization pattern.

The labyrinth of air cells is classified into two clusters according to their relation to the basal lamella and drainage patterns:

- The anterior ethmoidal cells lie anterior to the basal lamella and open onto the middle meatus.
- The posterior ethmoidal cells lie posterior to the basal lamella and open into the superior meatus.

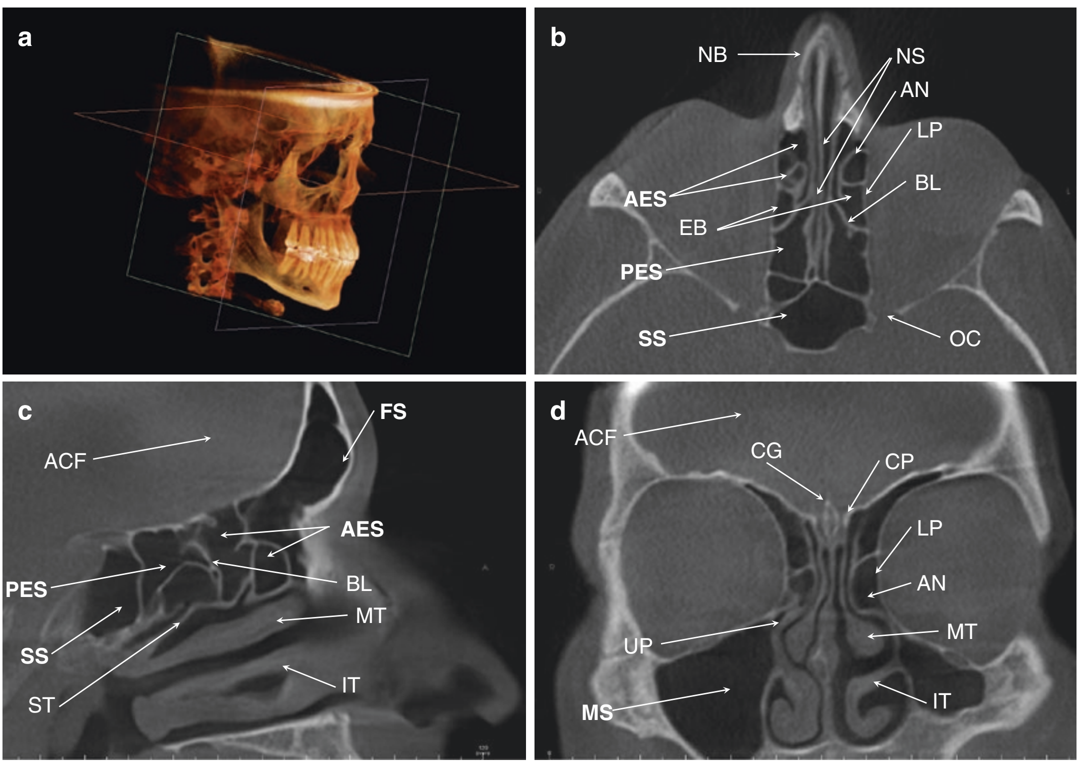

Fig. 12.12 Right supero-inferior volumetric rendering (**a**) showing location of axial (**b**), sagittal (**c**), and frontal (**d**) CBCT orthogonal sections of the ethmoid sinus. (*FS* frontal sinus, *ACF* anterior cranial fossa, *MS* maxillary sinus, ***AES*** anterior ethmoid sinus, ***PES*** posterior ethmoid sinus, ***SS*** sphenoid sinus, *ST* superior turbinate, *MT* middle turbinate, *IT* inferior turbinate, *AN* Agger Nasi, *CG* crista galli, *LP* lamina papyracea, *BL* basal lamina, *OC* optic canal, *CP* cribriform plate, *EB* ethmoid bulla, *UP* uncinate process)

The number of cavities is inversely proportional to their volume, with the anterior ethmoidal cells ranging from 4 to 17 and being smaller than the posterior cells, which range from 2 to 6 (Lang 1989; Earwaker 1993; Arıncı and Elhan 1997; Muranjan 1999; Vartanian 2010) (Fig. 12.12).

12.5.1 The Ostiomeatal Complex (OMC)

The OMC (also referred to as the *ostiomeatal unit*) is the most important area for normal sinus functioning. Any pathology in this area may disrupt physiologic function of this complex and lead to sinus dysfunction (Muranjan 1999). The complex comprises the maxillary sinus ostium, uncinate process, the ethmoidal infundibulum, the anterior ethmoid cells, and the frontal recess (Tan and Chong 2001) (Fig. 12.13).

The most anterior and key landmark of the OMC is the *uncinate process*, a hook-shaped bone attached anteriorly to the lacrimal bone and inferiorly to the ethmoidal process of the inferior turbinate. Superiorly, the uncinate process may attach to the middle turbinate, the orbital lamina, and/or the skull base (Vartanian 2010). The free edge of the uncinate process may be deviated medially or laterally, pneumatized, or bent. Lateral deviation may obstruct the infundibulum, whereas medial deviation may narrow the middle meatus (Cashman et al. 2011). If the uncinate process is attached superiorly to the skull base or the middle turbinate, the frontal sinus will open into the ethmoidal infundibulum, and infection in the infundibulum may affect the frontal, ethmoidal, and maxillary sinuses (Tan and Chong 2001).

Posterior to the uncinate process is a groove known as the *semilunar hiatus*, which leads into the *ethmoidal infundibulum* (Muranjan 1999), a structure bounded laterally by the inferomedial

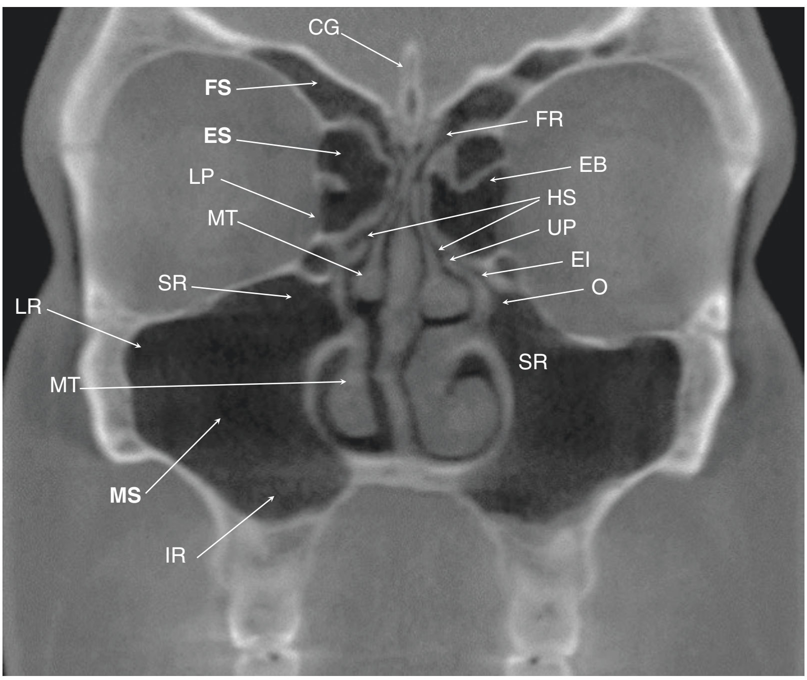

Fig. 12.13 Coronal CBCT image demonstrating the components of the ostiomeatal unit. The gap between the tip of the uncinate process (*UP*) and the ethmoid bulla (*EB*) constitutes the hiatus semilunaris (*HS*). (***FS*** frontal sinus, ***MS*** maxillary sinus, ***ES*** ethmoid sinus, *EB* ethmoid bulla, *MT* middle turbinate, *IT* inferior turbinate, *CG* crista galli, *LP* lamina papyracea, *UP* uncinate process, *HS* hiatus semilunaris, *SR* superior recess of the maxillary sinus, *LR* lateral recess of the maxillary sinus, *IR* inferior recess of the maxillary sinus, *O* ostium, *EI* ethmoid infundibulum, *FR* frontal recess)

wall of the orbit, superiorly by the semilunar hiatus and ethmoid bulla, and medially by the uncinate process. The maxillary sinus ostium and ethmoidal infundibulum constitute the common drainage for the anterior paranasal sinuses. The semilunar hiatus runs obliquely in a posteroinferior direction between the uncinate process and the ethmoid bulla. On orthogonal imaging, the semilunar hiatus appears bounded superiorly by the ethmoid bulla, laterally by the medial bony orbit, inferiorly by the uncinate process, and medially by the middle meatus. The semilunar hiatus is the final segment of the drainage pathway from the maxillary sinus and ethmoidal infundibulum to the middle meatus, and it communicates medially with the middle meatus (Tan and Chong 2001).

The ethmoid bulla is the most constant landmark and constitutes the most anterior ethmoidal air cell. The bulla extends laterally to the orbital lamina. The ethmoid bulla is bordered inferomedially by the infundibulum and the semilunar hiatus, laterally by the orbital lamina, and posterosuperiorly by the lateral sinus and basal lamina. The anterior ethmoid cells constitute an important part of the OMC, and obstruction here can also affect frontal and maxillary sinus drainage (Fig. 12.13) (Tan and Chong 2001). The radiologic appearance of the OMC has been categorized based on the characteristics of both the uncinated process and ethmoid bulla (Table 12.1).

Other cells that may originate from ethmoid cell development include frontal cells, supraorbital ethmoid cells, infraorbital cells (*Haller cells*), and sphenoethmoid cells (*Onodi cells*).

12.6 Sphenoidal Sinuses

The sphenoidal sinuses are the most posterior paranasal sinuses and situated within the body of the sphenoid bone, which is located superiorly to the nasopharynx and just anteroinferiorly to the *sella turcica*. A vertical osseous septum (*septum intersinuale sphenoidale*) divides each sphenoidal sinus into two asymmetrical spaces that vary in size and shape (Fig. 12.14). Additional partial or complete septa may also exist with, on occasion, a canal connecting the left and right sides.

Table 12.1 Radiographic categories of the OMC based on the orientation of the uncinate process and appearance of the ethmoid bulla (after Earwaker 1993)

Type	Uncinate process	Ethmoid bulla
I	Vertical	Enlarged
II	Vertical	Normal
III	Vertical	Absent/hypoplastic
IV	Horizontal	Enlarged
V	Horizontal	Normal
VI	Horizontal	Hypoplastic

The sphenoidal sinuses are located anteriorly adjacent to the optic chiasma and cerebral hypophysis and superiorly adjacent to the *Pterygoid* or *Vidian canal*. Laterally, the sphenoid sinuses are adjacent to the cavernous sinus and the structures that pass through it (e.g., internal carotid artery, oculomotor, trochlear, abducens nerve, ophthalmic, and maxillary nerve). Anteriorly, the sphenoid sinus is also related to the posterior ethmoid cell, with which it shares a common wall, the medial third of which is a freestanding surface within the nasal cavity (Snell 1995; Arıncı and Elhan 1997; Chong et al. 2000; Tan and Chong 2001; Vartanian 2010) known as the *sphenoethmoidal recess*. This recess is best observed in the sagittal and axial planes, although it may also be seen on coronal images (Fig. 12.14). The sphenoidal sinus opens into the sphenoethmoidal recess through the sphenoidal sinus aperture, a canal located in the superior portion of the anterior sinus wall. Posteriorly, the sphenoid sinus is separated from the posterior cranial fossa by a variable amount of bone (Fig. 12.15) (Snell 1995; Arıncı and Elhan 1997; Chong et al. 2000; Tan and Chong 2001; Vartanian 2010).

The carotid artery, the maxillary nerve, and the Vidian canal may project into the sphenoidal sinus, and they may be affected by sinus disease as well as at risk during ESS (Kantarci et al. 2004) (Fig. 12.16). Complete bony dehiscence of the optic and Vidian canal may occur in up to 8% of individuals.

Another anatomical variant is the sphenomaxillary plate (SMP), a triangular-shaped partition between the ethmoidal and maxillary sinuses

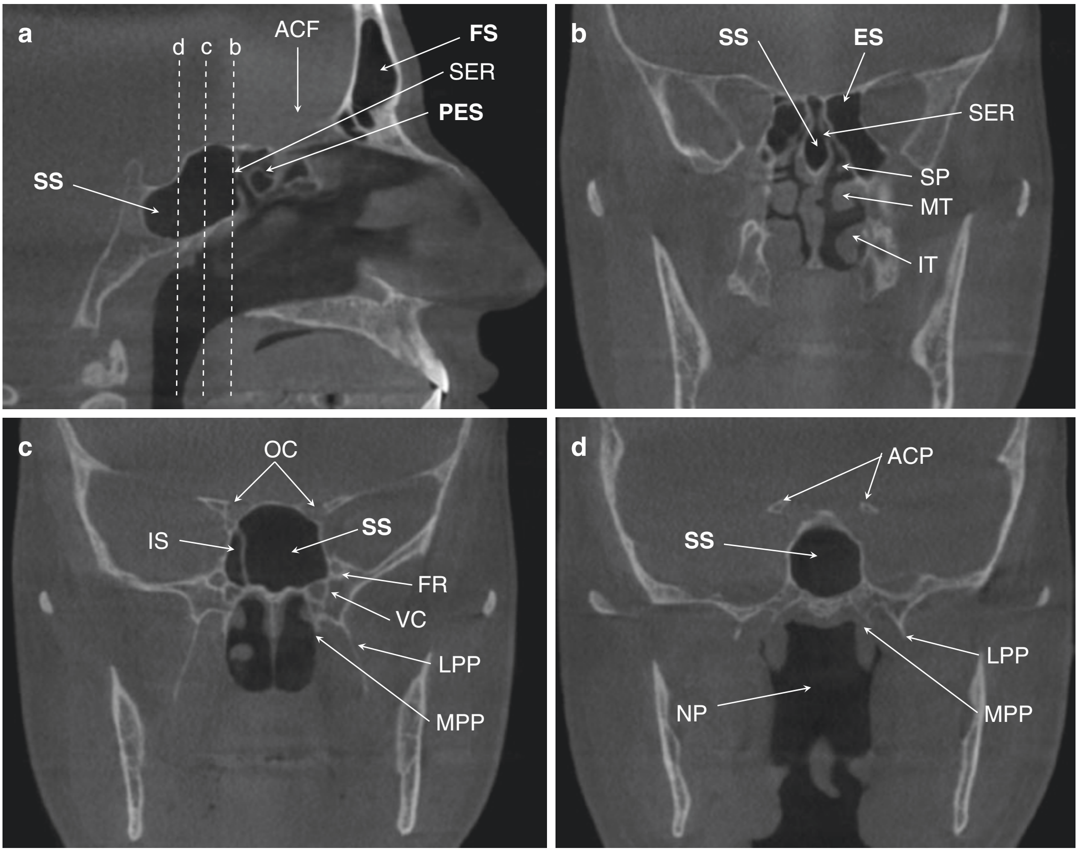

Fig. 12.14 Reference midsagittal (**a**) and anterior (**b**), middle (**c**), and posterior (**d**) coronal CBCT orthogonal sections of the anatomical features associated with the sphenoid sinus. (***FS*** frontal sinus, *ACF* anterior cranial fossa, *PES* posterior ethmoid sinus, *SS* sphenoid sinus, *SER* sphenoethmoidal recess, *VC* vidian canal, *FR* foramen rotundum, *IS* intersinus septum, *ACP* anterior clinoid process, *ST* superior turbinate, *MT* middle turbinate, *IT* inferior turbinate, *NP* nasopharynx, *OC* optic canal, ***ES*** ethmoid sinus, *LPP* lateral pterygoid process, *MPP* medial pterygoid process)

that has a reported incidence rate of 15%. Failure to identify this structure may lead to the sphenoidal sinus being mistaken for posterior ethmoidal cells during a transantral ethmoidectomy (Kantarci et al. 2004).

12.7 Maxillary Sinuses

The maxillary sinuses are the largest of the paranasal sinuses. Shaped like a pyramid, the maxillary sinus is situated entirely within the body of the maxilla, with the superior wall adjacent to the orbital floor, the curved inferior wall formed by the lower third of the medial wall and the buccoalveolar wall, and the floor formed by the maxillary alveolar process. In about half of the population, the maxillary sinus floor extends between adjacent teeth or individual roots, creating elevations in the antral surface that are commonly referred to as *hillocks* (Kilic et al. 2010). Rarely (approximately 2%), a dehiscence may be present in the floor of the sinus, bringing the roots of the teeth into close contact with the mucosa and facilitating the spread of infection (Muranjan 1999). It is even possible for the roots of the maxillary premolar, molar, and occasionally canine teeth to project into the maxillary sinus itself (Maillet et al. 2011). Clinicians must be aware of the exact relationship between the apical roots of the maxillary teeth and the maxillary sinus floor because of the implications this can have on sur-

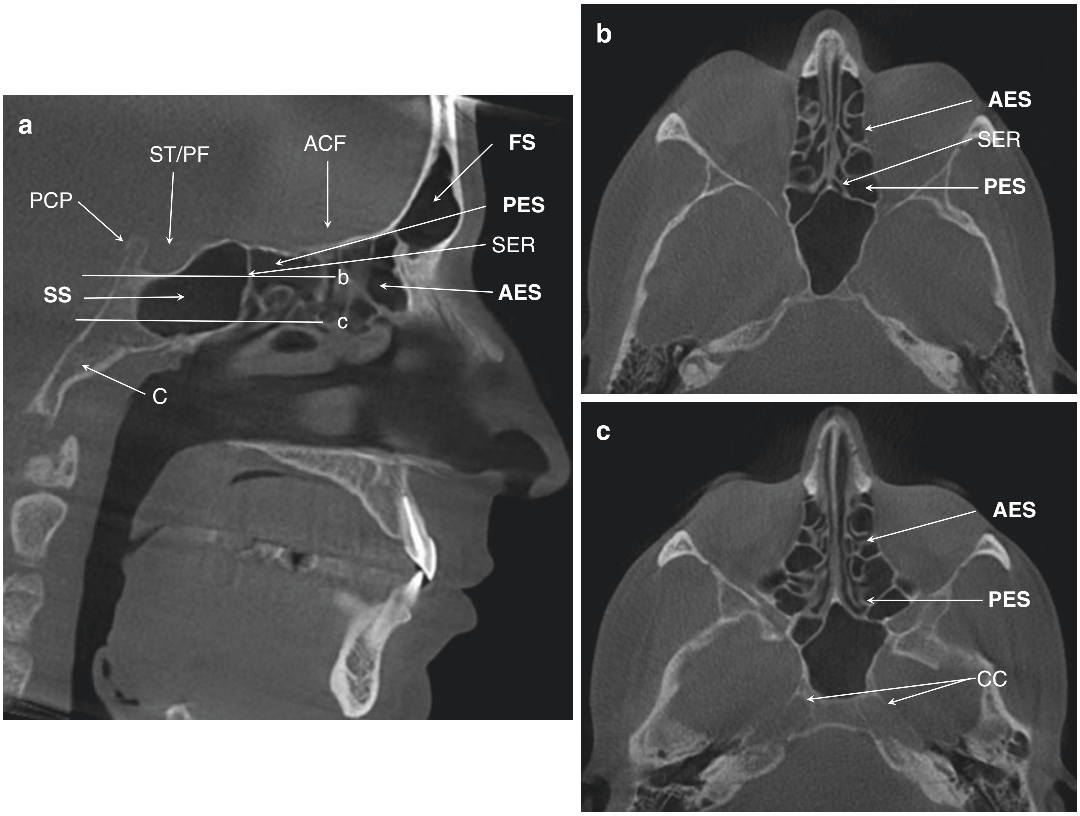

Fig. 12.15 Reference midsagittal (**a**) and superior (**b**), and inferior (**c**) axial CBCT orthogonal sections of the anatomical features associated with the sphenoid sinus. (*FS* frontal sinus, *ACF* anterior cranial fossa, ***PES*** posterior ethmoid sinus, *AES* anterior ethmoid sinus, *SS* sphenoid sinus, *SER* sphenoethmoidal recess, *ST/PF* sella turcica/pituitary fossa, *PCP* posterior clinoid process, *C* clivus, *CC* carotid canal)

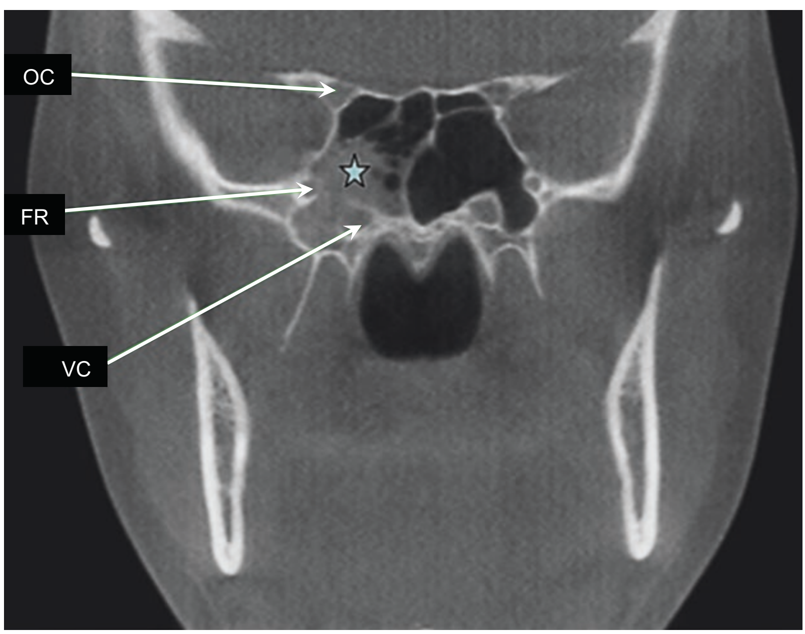

Fig. 12.16 Coronal CBCT image showing acute right sphenoid sinusitis (*star*) and adjacent important anatomic structures (*VC* vidian canal, *FR* foramen rotundum, *OC* optic canal)

gical procedures (Kilic et al. 2010). The apex of the maxillary sinus is situated in the maxillary zygomatic process.

The maxillary sinus drains into the nasal cavity through the maxillary sinus ostium, which is located high up in the medial wall and empties into the posterior aspect of the semilunar hiatus located in the middle meatus. Normal maxillary sinus ostia range from 7 to 11 mm in length and 2 to 6 mm in height. Accessory ostia are common (approximately 28%). Swelling of surrounding mucosa may cause significant blockage of the ostia (Muranjan 1999). The range of normal mucosal thickness on CBCT images varies in the sagittal (range, 1.21–1.68 mm) and coronal (1.18 mm) planes, with the highest values in the midsagittal plane. For edentulous patients, mean mucosal thicknesses is slightly higher (range, 2.1–2.7 mm) (Vogiatzi et al. 2014) (Fig. 12.17).

12.8 Anatomic Variations

The paranasal sinuses demonstrate great anatomic variability and numerous anomalies that can compromise inherently narrow drainage pathways, contribute towards obstruction, and as such predispose towards sinus disease, particularly in the region of the OMC. Awareness of the range of morphologic presentations and relative incidence for each sinus is important in radiologic interpretation by those performing CBCT

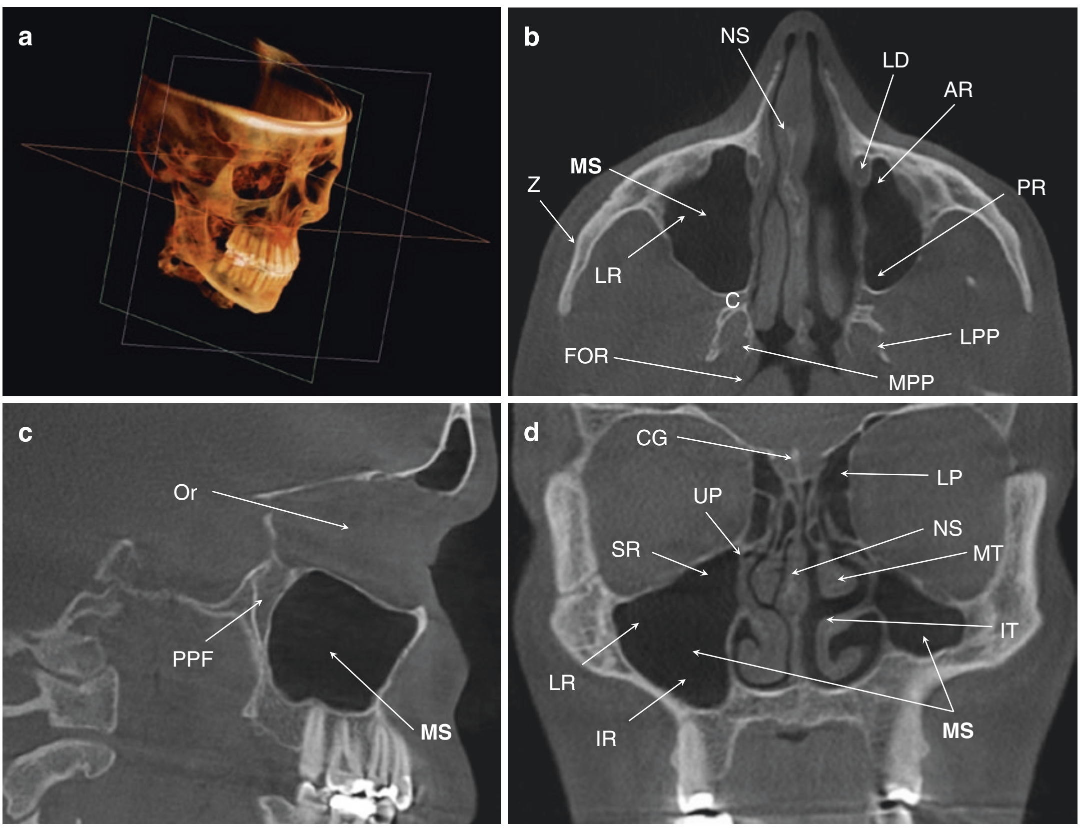

Fig. 12.17 Right supero-inferior volumetric rendering (**a**) showing location of axial (**b**), sagittal (**c**), and frontal (**d**) CBCT orthogonal sections of the maxillary sinus. (***FS*** frontal sinus, ***MS*** maxillary sinus, *MT* middle turbinate, *IT* inferior turbinate, *CG* crista galli, *LP* lamina papyracea, *LR* lateral recess, *UP* uncinate process, *LD* lacrimal duct, *PR* posterior recess, *AR* anterior recess, *IR* inferior recess, *SR* superior recess, *NS* nasal septum, *Z* zygoma, *LPP* lateral pterygoid plate, *MPP* medial pterygoid plate, *FOR* fossa of Rosenmuller, *PF* pterygopalatine fossa, *Or* orbit)

imaging and to assist in identification of those conditions that may predispose patients to increased risk of intraoperative complications such as functional endoscopic sinus surgery (FESS) or maxillary sinus elevation (MSE) and concomitant bone grafting procedures (Kantarci et al. 2004; Vallo et al. 2010; Ritter et al. 2011; Phothikhun et al. 2011).

The prevalence of specific developmental and anatomic anomalies varies greatly depending on the radiographic criteria applied (Kayalioglu et al. 2000; Zinreich 1998; Nitinavakarn 2005; Tao et al. 1998; Midilli et al. 2005; Lerdlum and Vachiranubhap 2005; William 1991; Tan and Chong 2001; Stallman 2004; Zinreich et al. 2003; Bolger et al. 1991; Pérez-Piñas et al. 2000); however, they can be rank ordered based on reported trends (Table 12.2).

12.8.1 Aplasia and Hypoplasia

For each of the paranasal sinuses, complete absence of development or agenesis of a paranasal sinus (aplasia) is rare. Reduction in the size of a sinus (hypoplasia) is more common, particularly in the frontal and sphenoid sinuses. Hypoplasia and aplasia have to be correlated with the patient's age assuming that sinus pneumatization has finished. Hypoplasia is frequently associated with sinonasal disease, particularly infections, because the physiologic apertures can be obstructed more easily (April et al. 1993).

Table 12.2 Approximate prevalence of most common nasal and paranasal sinus anatomic and developmental anomalies

Condition	Prevalence range (%)
Nasal septal deviation	40–96
Agger nasi	10–99
Conchae bullosa	9–55
Ethmoid bulla	70–90
Sphenoid pneumatization	13–43
Paradoxical middle turbinate	8–17
Hypoplastic frontal sinus	6.24–18
Haller cells	1.41–45
Onodi cells	0.4–24

- **Frontal.** Aplasia occurs most frequently in the frontal sinuses and occurs bilaterally in about 4% of the population. Typically, a frontal sinus can be identified if its borders rise higher than the orbital roof. Occasionally the ethmoidal cells can extend to the level of the frontal sinus and be misidentified. This frontal extension of ethmoid cells (*bulla frontalis*) may be observed in various degrees of development in approximately 17% of CT images (Fig. 12.18) (Lang 1989).
- **Sphenoid.** Complete agenesis of the sphenoidal sinus is extremely rare (Fig. 12.19) (Cakur et al. 2011). Hypoplasia has been defined as an oval-shaped sinus with pneumatization limited to the pre-sphenoid area, anterior to a vertical plane of the tuberculum sella (Fig. 12.20) (Cakur et al. 2011). Overall, sphenoid sinus hypoplasia is approximately 0.52% with unilateral hypoplasia and bilateral hypoplasia occurring with equal frequency (0.26%) (Fig. 12.21).
- **Ethmoid.** Aplasia and hypoplasia is rare in the ethmoidal cells.
- **Maxillary**. Aplasia of the maxillary sinus is extremely rare. Maxillary sinus hypoplasia (MSH) is an uncommon condition with a prevalence ranging from 2.5 to 6% (Kalavagunta and Reddy 2003). MSH has both developmental and acquired etiologies (Table 12.3).

Radiographic diagnosis of MSH requires that the following diagnostic imaging criteria be satisfied (Fig. 12.22, 12.23, and 12.24) (Geraghty and Dolan 1989):

– Vertical enlargement of the orbit
– Lateral position of infraorbital neurovascular canal
– Elevated canine fossa
– Enlargement of superior orbital and pterygopalatine fissure

Associated features include thickening of the anterior wall of the maxillary sinus (Pérez-Piñas et al. 2000), uncinate process hypoplasia and bulging of the lateral wall of the nasal fossa. Three distinct patterns of maxillary sinus

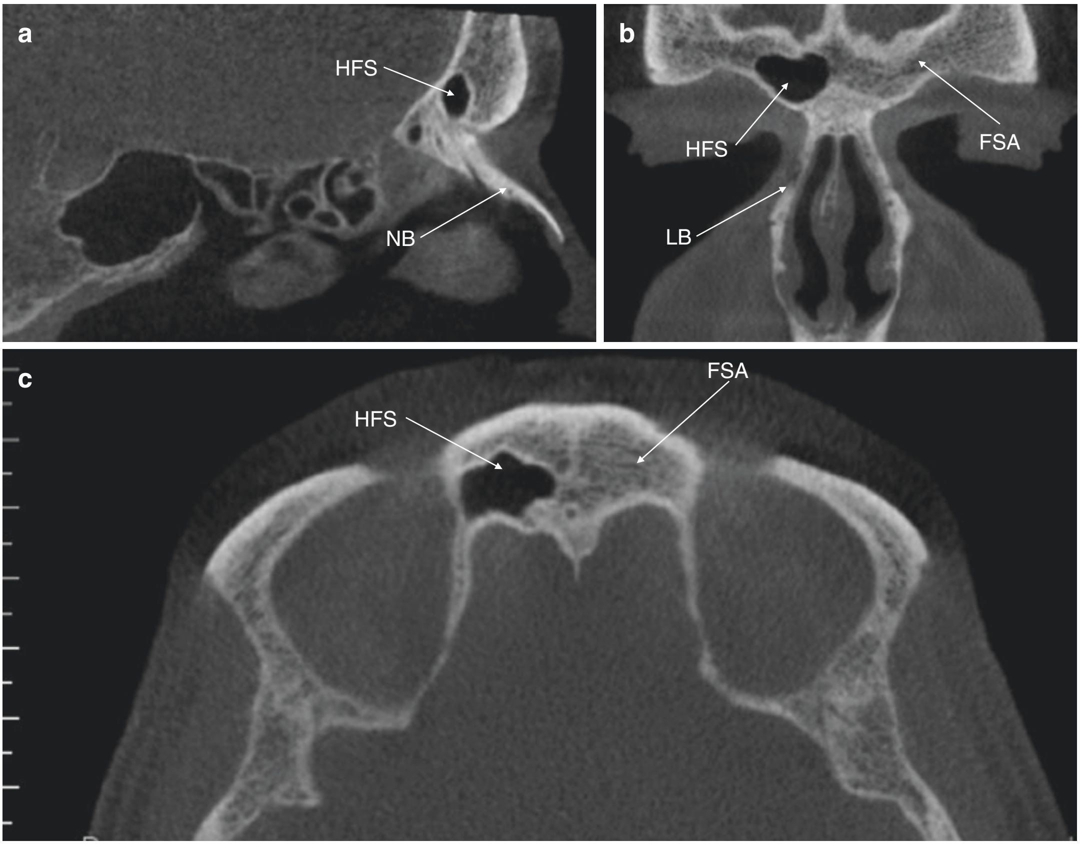

Fig. 12.18 Midsagittal (**a**), coronal (**b**), and axial (**c**) CBCT images of 63-year-old male with left frontal sinus aplasia (*FSA*) and right hypoplastic frontal sinus (HFS) (*NB* nasal bone, *LB* lacrimal bone)

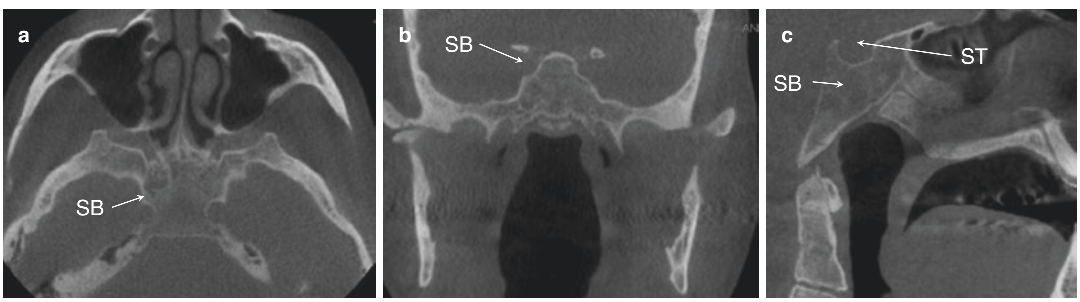

Fig. 12.19 Axial (**a**), coronal (**b**), and sagittal (**c**) CBCT sections showing absolute absence of sphenoid sinuses; the basi-spehenoid is solid without any sign of a sinus cavity. This appearance is consistent with aplasia or agenesis of the sphenoid sinuses. (*ST* sella turcica, *SB* sphenoid bone)

hypoplasia have been reported (Table 12.4) (Bolger et al. 1990; Sirikçi et al. 2000).

MSH may be misdiagnosed as chronic sinusitis and, especially in its severe form, can create difficulties in locating the maxillary sinus ostium during FESS.

12.8.2 Hyperplasia and Pneumatization

Overall increase in the size and extent of the paranasal sinuses (*hyperplasia*) is essentially as a result of increased aeration of the lumen of the

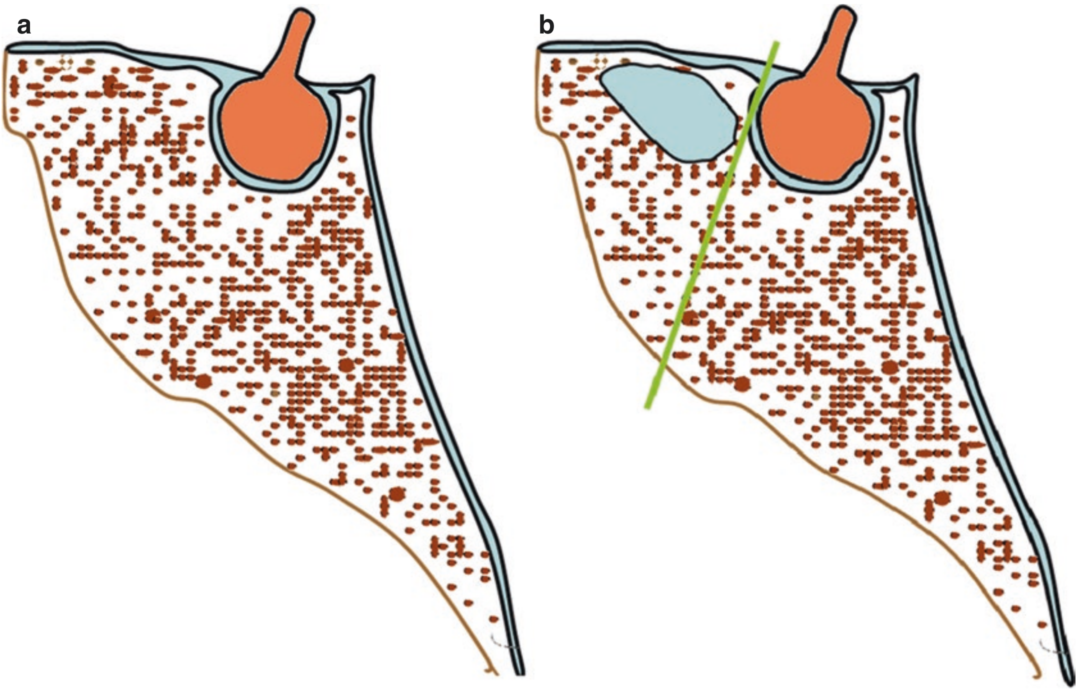

Fig. 12.20 Schematic representation of the appearance of sphenoid sinus agenesis (**a**) and hypoplasia (**b**) on a midsagittal CBCT image. Sphenoid sinus hypoplasia is defined to be present if any component or compartment of the sphenoid sinus lies anterior to the vertical plane of the tuberculum sella (*vertical line*) (Cakur et al. 2011)

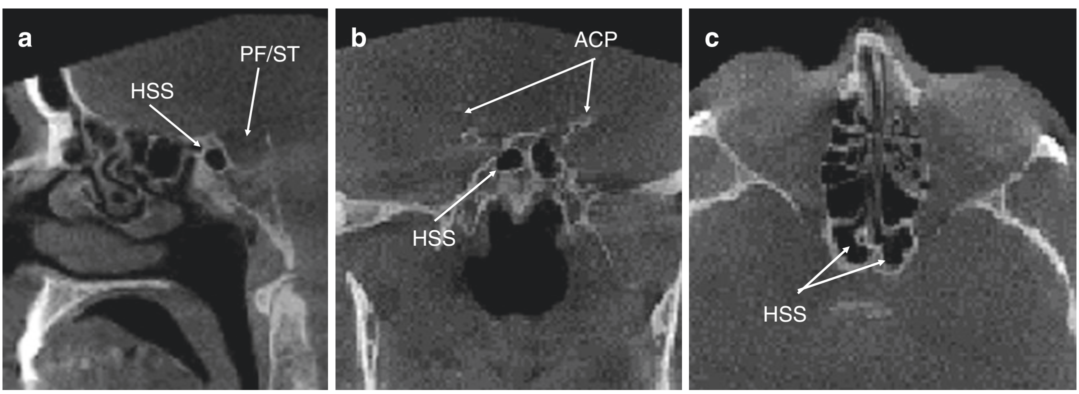

Fig. 12.21 Midsagittal (**a**), coronal (**b**), and axial (**c**) CBCT images demonstrating a hypoplastic sphenoid sinus (*HSS*) (*HSS* hypoplastic sphenoid sinus; *PF/ST* pituitary fossa/sella turcica, *ACP* anterior clinoid process)

sinus (*pneumatization*). Hyperplasia is common to frontal and maxillary sinuses and less common with the ethmoidal cells and sphenoid sinus. Although not a paranasal sinus, pneumatization of the mastoid air cells can extend to the articular eminence and even the zygomatic arch (Hofmann et al. 2001; Orhan et al. 2006). The presence of hyperplasia may contribute to a higher incidence of pathology, specifically sinusitis and or mucoceles.

12.8.2.1 Nasal Fossa

Hyperplasia of two elements of the nasal fossa can contribute to the most common pathology, rhinosinusitis. Midline septal deviation can occur due to a true hyperplasia of the cartilaginous and/

Table 12.3 Etiology of maxillary sinus hypoplasia

Developmental	Acquired
• Secondary to infection, trauma, or irradiation	• Trauma with deformity due to fracture of facial skeleton / surgery
• Developmental anomalies like facial dysostosis	• Inflammatory osteitis (Wegener's granuloma)
• Failure of development of the uncinated process	• Hypoplasia due to Thalassemia / cretinism
	• Neoplastic osteitis
	• Cystic fibrosis

or osseous components whereas hyperplasia of the structures of the lateral wall may occur due to increased aeration of the turbinates or mucosal hypertrophy.

Nasal Septal Deviation (NSD)

Midline NSD is common. Most often NSD occurs as a broad based curvature to one side of the midline in a single "C"-shaped or double "S"-shaped deviation (Fig. 12.25). While the deviation can occur throughout the length of the nasal fossa (approximately 25%), it is most often

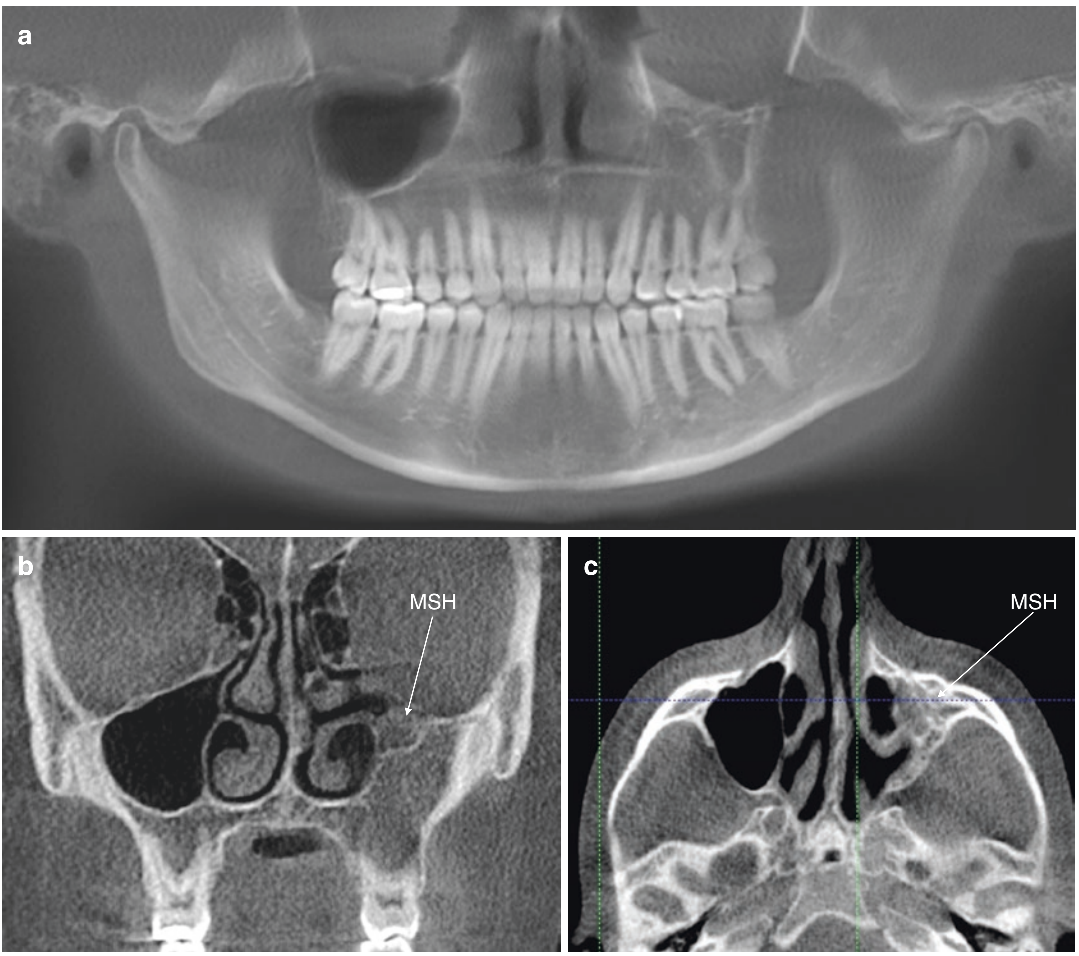

Fig. 12.22 Reformatted panoramic (**a**), coronal (**b**), and axial (**c**) CBCT images showing left maxillary sinus hypoplasia (*MSH*). Note the characteristic features of MSH Type III including aplasia of uncinated process, ipsilateral orbital enlargement and supplemental features of anterior wall thickening. Also note the compensatory hyperplasia of the alveolar process and bulge of the lateral wall of the left nasal fossa

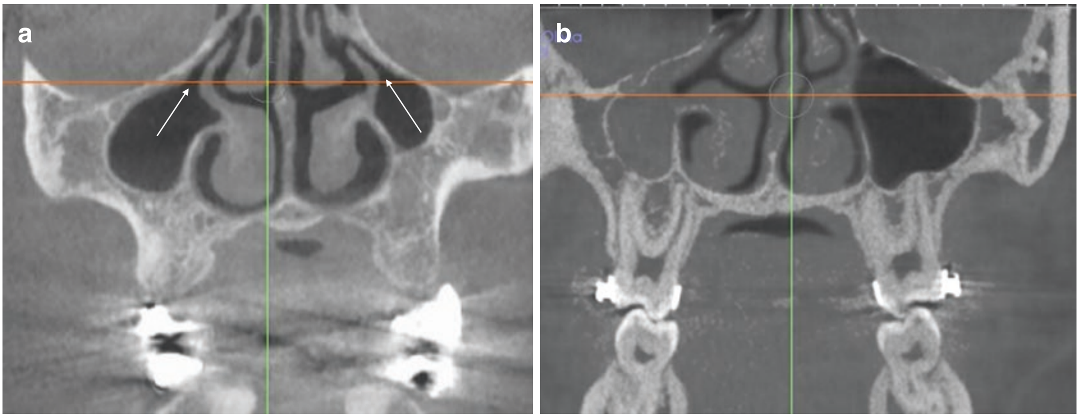

Fig. 12.23 CBCT coronal sections of two cases of maxillary sinus hypoplasia (MSH): (**a**) Mild MSH (type I); although there is some asymmetry between the right and left maxillary sinus, the sinus cavities are well aerated and the ostia are patent (*arrows*): (**b**) Mild to severe MSH (type II) with a hypoplasitc uncinate process, cleft-like right maxillary sinus and complete opacification of the sinus cavity

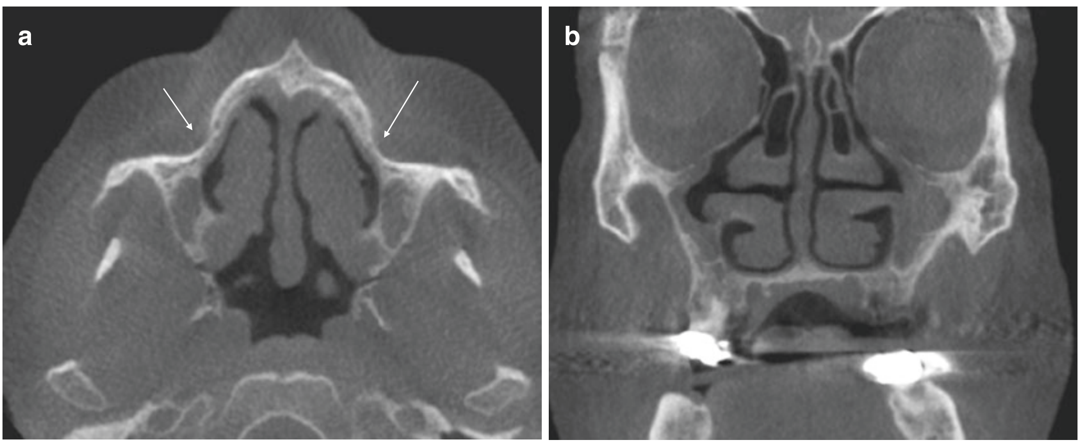

Fig. 12.24 CBCT axial (**a**) and coronal (**b**) sections of the maxillary sinuses showing severe maxillary sinus hypoplasia/aplasia (type III); the maxillary sinuses are almost completely absent, they show a cleft-like appearance and there is absence of the uncinate processes bilaterally. Note the marked depression of the infraorbital regions (*arrows*) and the enlarged orbits bilaterally

limited to anterior of the OMC. Radiographic criteria vary from any deviation of the nasal septum from the midline to midline discrepancies greater than 4 mm (Smith et al. 2010) where the midline is determined by a vertical line from the crista galli to the septal spur on the hard palate. Abnormal hard palate orientation such as upward tilts and lateral shifts as compared with the midline can be associated with NSD.

Localized NSD in the form of sharp angulations or osteophytes (bone spurs) may also be present at the chondro-vomerine junction (Fig. 12.26). While septal deviation may be due to trauma, in most of the cases it is a result of a developmental disturbance in the relationship of the three septal components (septal cartilage, perpendicular plate of the ethmoid and vomer). Nasal spurs are found more frequently on the convex side of the septum and a hypoplastic middle turbinate adjacent to the spur. Consecutively a hyperplastic or even pneumatized middle turbinate can be found collaterally.

Table 12.4 Types of maxillary sinus hypoplasia (*after* Bolger et al. 1990; Sirikçi et al. 2000)

Type	Category	Criteria
I	Mild MSH	• Normal uncinate process
		• Well-defined infundibular passage
		• Varying degrees of sinus mucosal thickening
II	Mild to severe MSH	• Ipsilateral orbital enlargement
		• Normal or hypoplastic uncinate process
		• Poorly defined or absent infundibulum
		• Total opacification of affected sinus
III	Severe MSH plus a cleft-like sinus with or without soft-tissue density opacifications	• Aplasia of the uncinate process
		• Ipsilateral orbital enlargement

In many cases NSD is associated with deformities and asymmetries of the adjacent conchae and nasal wall structures. Recognition of septal deviations is important because they may lead to significant nasal obstruction and can limit endoscopic visualization (Lang 1989; Earwaker 1993; Muranjan 1999; Pérez-Piñas et al. 2000; Vartanian 2010; Cashman et al. 2011).

Paradoxical Middle Turbinate

Usually the configuration of the turbinates is identical being convex medially; however, occasionally this convexity of the middle turbinate can be reversed and face laterally. This can occur uni- or bilaterally. This is called *paradoxical middle turbinate*—large paradoxical middle turbinates are often pneumatized (Fig. 12.27).

Concha Bullosa

A pneumatized middle turbinate is referred to as a *concha bullosa*, with a reported incidence ranging from 15 to 45%. Conchal aeration may result from pneumatization of one of the following:

- Anterior ethmoid cell into the middle meatus (55%)
- Posterior ethmoid cell from the upper meatus (45%)
- Anterior ethmoid cell from the frontal recess (5%)

Larger cells can develop in case of septal deviation and cause narrowing of the *infundibulum ethmoidale*. Concha bullosa are often asymptomatic and are not thought to have any significant role in the pathogenesis of chronic rhinosinusitis (Cashman et al. 2011). They may be large enough to cause obstruction in the middle meatus or the infundibulum. In most cases, a concha bullosa curves medially towards the nasal septum, but in 26% of patients, the convexity is directed laterally, resulting in a paradoxical middle turbinate (Tan and Chong 2001) that may obstruct and narrow the nasal cavity and middle meatus (Fig. 12.28). The three most common patterns of concha bullosa include (Fig. 12.29):

- **Lamellar.** Pneumatization of only the vertical lamella of the middle turbinate. This type is usually the most commonly occurring.
- **True concha bullosa.** This is extensive pneumatization of the entire middle turbinate.
- **Bulbous type.** Pneumatization of the inferior bulbous portion of the middle turbinate (Fig. 12.30).

Turbinate Mucosal Hypertrophy

Hypertrophy of the mucosa of the turbinates may result in generalized narrowing of the nasal meatus and should be distinguished from a nasal mass or polyp (Fig. 12.31). In patients with a significant allergic component to their symptoms, the inferior turbinates may be enlarged; however, enlarged turbinates may be obscured in CT scans and need to be correlated with the findings of physical examination (Tan and Chong 2001).

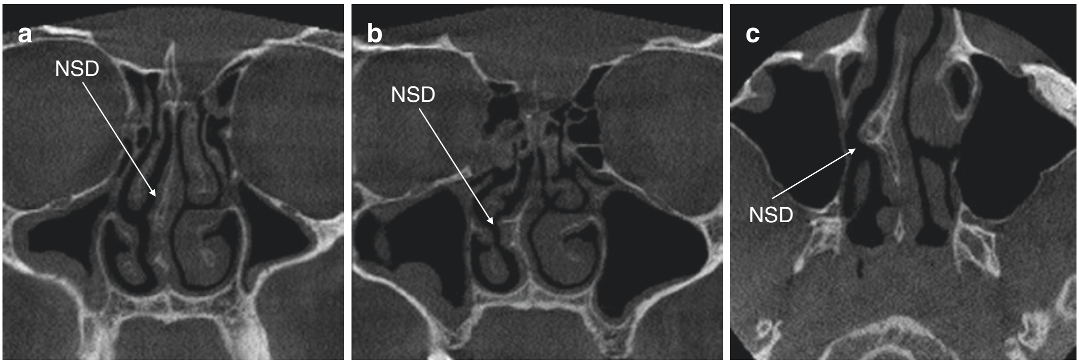

Fig. 12.25 Midsagittal (**a**), coronal (**b**), and axial (**c**) CBCT images demonstrating severe "C" shaped nasal septal deviation (*NSD*)

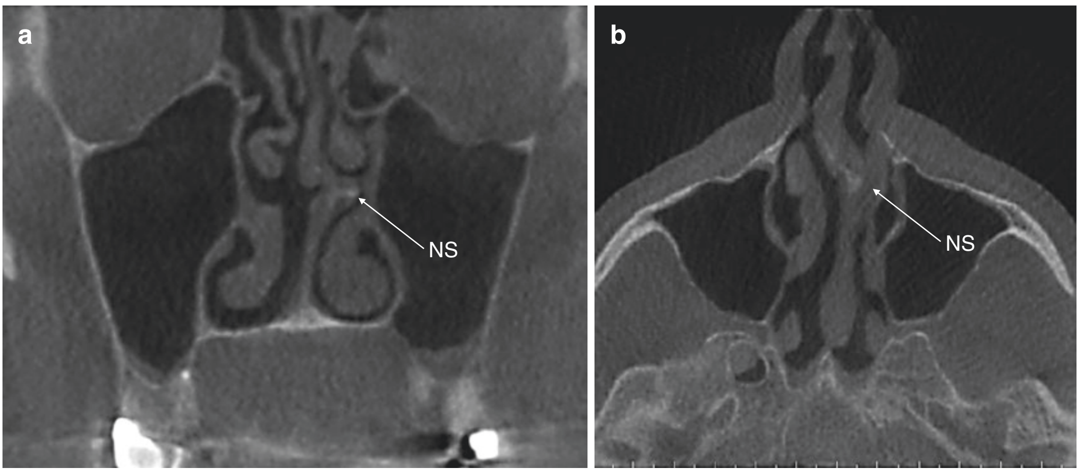

Fig. 12.26 Coronal (**a**) and axial (**b**) CBCT images of localized nasal septal deviation associated with a localized nasal spur (*NS*)

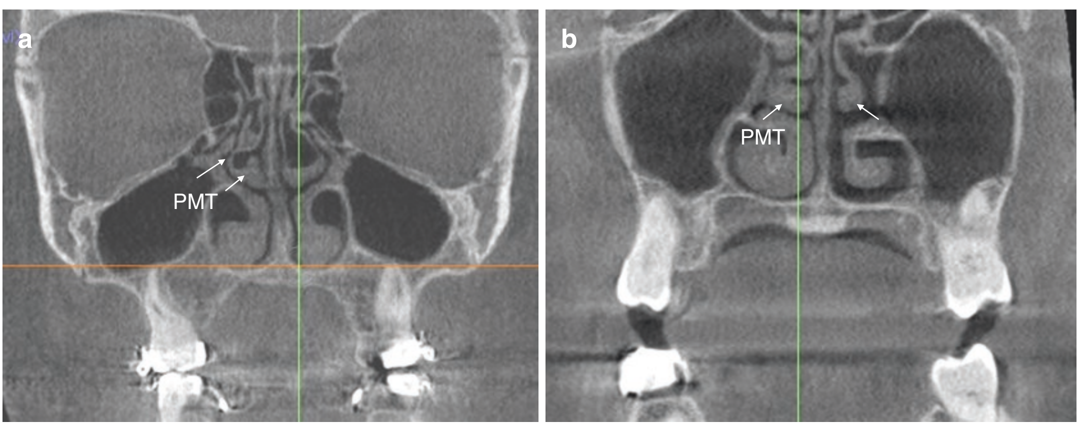

Fig. 12.27 CBCT coronal sections of the nasal cavity showing a unilateral paradoxical middle turbinate (*PMT*) (**a**) and (**b**) bilateral paradoxical middle turbinate (*PMT*)

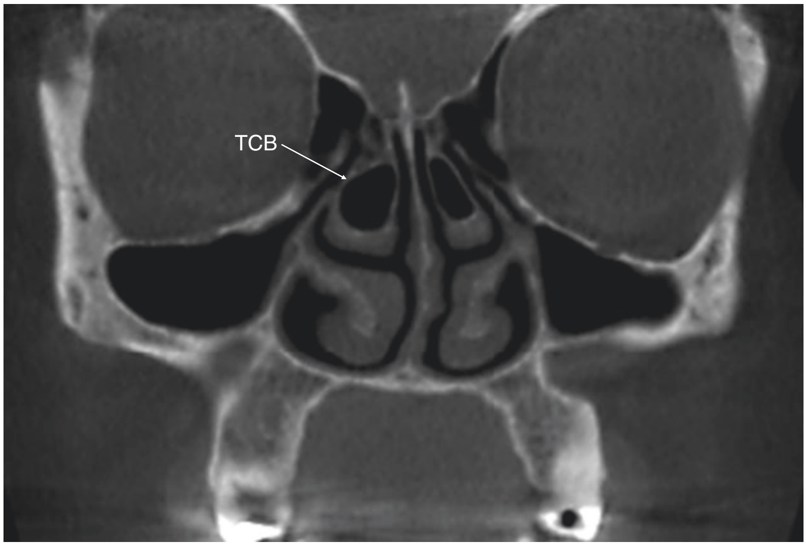

Fig. 12.28 Coronal CBCT image showing bilateral "true" concha bullosa (*TCB*) accompanied by a mild deviation of the nasal septum

Fig. 12.29 Coronal CBCT image demonstrating large right (*star*) "true" and moderate left (*dagger*) lamellar concha bullosa. Note the narrow configuration of the OMC bilaterally

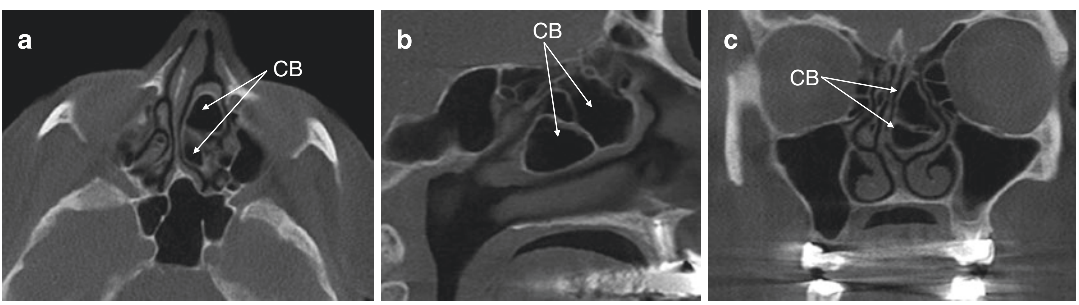

Fig. 12.30 Axial (**a**), midsagittal (**b**), and coronal (**c**) CBCT images of a large left unilateral bilobular "true" conchae bullosa (*CB*) with compensatory right nasal septal deviation

12.8.2.2 Paranasal Sinuses

Frontal

Pneumatization of the frontal sinus is usually asymmetric and may occur into the orbital plates, crista galli, and anterior ethmoids.

Another less common anomaly that may occur associated with the frontal sinus is *hyperostosis frontalis interna* (Fig. 12.32). This condition is characterized by irregular growth of the inner table of the frontal bone adjacent to the frontal sinus into the anterior cranial fossa. It most often presents as a benign, asymptomatic, and incidental finding, with a reported higher incidence in women (24%) as compared with men (5%). While the etiology is unknown, secondary causes of endocranial hyperostosis should be considered such as Paget's disease, acromegaly, and hyperparathyroidism. HFI has specific imaging features: it only affecting the frontal bone, grows symmetrically, has well-defined borders, is elongated, and never crosses the sagittal sinus area (She and Szakacs 2004).

Ethmoid

Extensions of the ethmoid cells that can occur to the frontal recess are intramural whereas those that extend to involve adjacent bones are referred to as extramural.

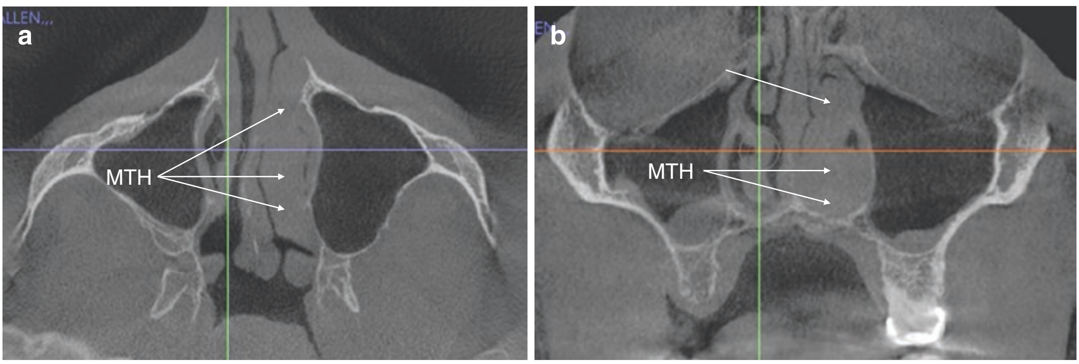

Fig. 12.31 Axial (**a**) and coronal (**b**) CBCT sections of the nasal cavity; the images show unilateral mucosal turbinate hypertrophy (*MTH*) (*solid arrows*). Note that the thickened mucosa has completely occluded the left nasal meatus. Thickened nasal mucosa is also noted in the left middle turbinate (*dotted arrows*). The size of the contralateral turbinates is within normal limits

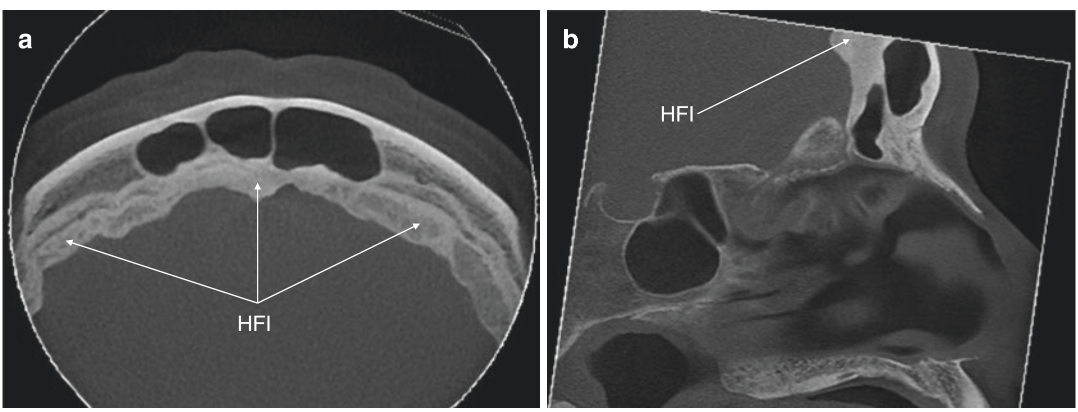

Fig. 12.32 Axial and midsagittal CBCT images demonstrating the location and appearance of hyperostosis frontalis interna (*HFI*)

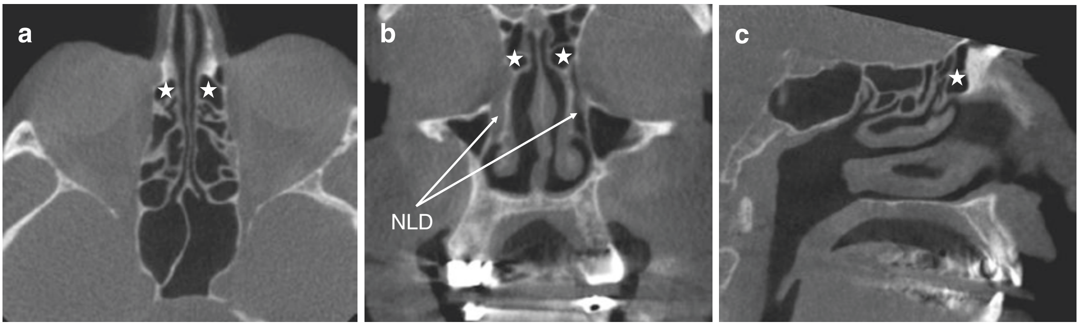

Fig. 12.33 Axial (**a**), coronal (**b**), and sagittal CBCT images demonstrating the appearance and location of Agger Nasi cells (*white stars*). Note their close proximity to the nasolacrimal duct (*NLD*)

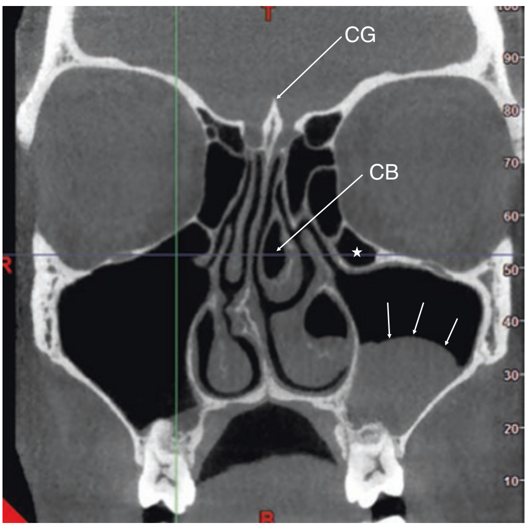

Fig. 12.34 Coronal CBCT image showing the location and appearance of a Haller cell (*white star*). Other anatomical structures identified are the crista galli (*CG*) and a pneumatized left middle basal concha (*CB* concha bullosa). Note the mucous retention cyst present on the floor of the left maxillary sinus (*dashed arrow*)

- **Agger Nasi.** Agger nasi cells are located anterior to the nasolacrimal duct; this can be evaluated in the coronal and sagittal plane (Fig. 12.33). The Agger nasi cells are connected with the anterior ethmoid cell group. Prevalence has been reported to range from 10 to almost 100% of the population, depending on definition (Bolger et al. 1991; Pérez-Piñas et al. 2000).
- **Supraorbital Cells.** These intramural cells extend from the anterior ethmoid cells into the orbital plates to lie medial to and above the adjacent posterior extensions of the frontal sinuses.
- **Middle Turbinate (Concha Bullosa).** See previously.
- **Haller cells.** Haller cells are irregular pneumatized cells in the orbital plate of the maxilla (Fig. 12.34). They can be detected at the orbital floor and in the surrounding of the infraorbital canal. Thus if opacified they can be misdiagnosed as the infraorbital canal. Moreover, a consecutive distortion or narrowing of the adjacent infundibulum ethmoidale can be seen. Haller cells grow into the bony orbital floor that constitutes the roof of the maxillary sinus, are differentiable from bulla, and have a potential pathophysiological relationship to a narrowed ethmoid infundibulum or maxillary sinus ostium.
- **Onodi Cells.** The Onodi cell is a posterosuperior ethmoidal air cell that is pneumatized laterally and to some degree superiorly to the sphenoidal sinus with a reported incidence of between 8 and 14% (Fig. 12.35). These cells may be some times in a close proximity to the optic canal and may even reach the anterior wall of the sella turcica (Tan and Chong 2001; Kantarci et al. 2004). The presence of an Onodi cell may increase the risk of accidental injury of the internal carotid artery and the optic nerve during endoscopic sinus surgery.
- **Ethmoid Bulla.** The degree of pneumatization varies considerably, ranging from failure ("torus ethmoidalis") to a giant ethmoid bulla insinuating between the middle turbinate and uncinate process and displacing the uncinate process medially, interfering with the OMC (Fig. 12.36). Enlargement of the ethmoid bulla is caused by a horizontal orientation and flattening of the uncinate process. Thus mucosal retention is frequently observed in an OMC adjacent to a large ethmoid bulla.

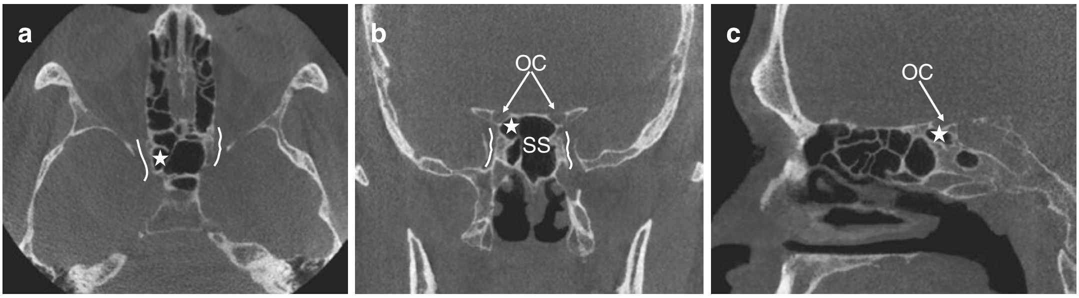

Fig. 12.35 Axial (**a**), coronal (**b**), and sagittal (**c**) CBCT images showing location and appearance of an Onodi cell (*white stars*). Note its close proximity to the optic canal (*OC*), superior orbital fissure (*dashed line*) and the sphenoid sinus (*SS*)

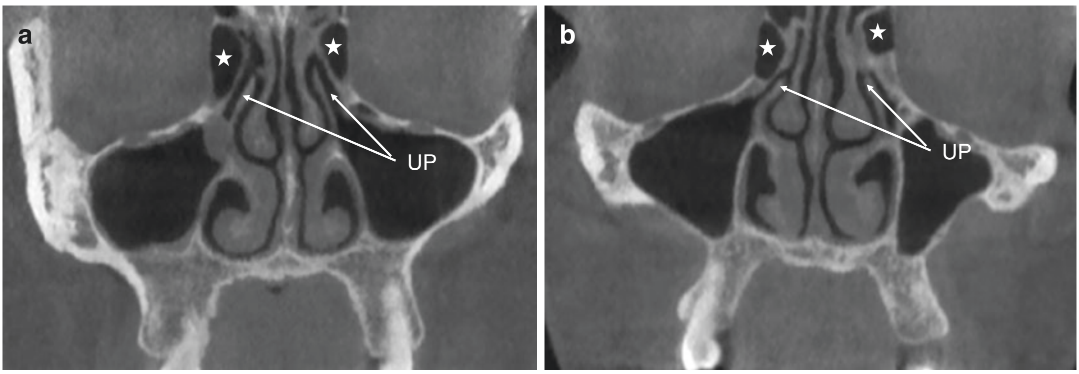

Fig. 12.36 Coronal CBCT sections of two different patients (**a**, **b**) depicting the anatomy of the anterior nasal cavity. The ethmoid bullae (*white stars*) are the most anterior ethmoid air cells and their location might have an impact on the shape and size of the uncinate process (*UP*)

Sphenoid

Pneumatization of the sphenoidal sinuses is extremely variable ranging from absence to extensive involvement into the pterygoid processes and the greater wings of the sphenoid bone. Because the sphenoidal sinus is located in the center of the cranial base and is surrounded by numerous neurovascular structures, pneumatization of this sinus provides a natural cavity through which wide areas of the cranial base may be accessed.

- **Sella Turcica.** Classification of the sphenoidal sinus pneumatization is based on the extent of aeration anteroposteriorly relative to the sella turcica (Figs. 12.37 and 12.38) (Wang et al. 2010) or laterally in the coronal plane.
  - *Conchal* (3%). A conchal sphenoid sinus has only rudimentary development of the sphenoid, with minimal pneumatization that does not extend into the sphenoid corpus. This configuration poses an anatomical challenge for endoscopic transphenoidal surgery.
  - *Presellar* (17%). A presellar configuration is situated in the anterior sphenoid bone, as far back as the anterior wall of the pituitary fossa. An additional but infrequent variation of this is the *postsellar* configuration, which shows a smaller pneumatization behind the sella. This pattern is important to recognize during extended intrasphenoidal approaches to the clivus (Singh et al. 2011).
  - *Sellar* (80%). A sellar sphenoid is pneumatized anterior and inferior to the sellar prominence.
- **Lateral Recess.** Sinus extensions can occur laterally into the greater wing, lesser wing, or pterygoid processes and in the midline through the rostral, caudal, vomeral, inferior, and superior clival processes (Fig. 12.39).

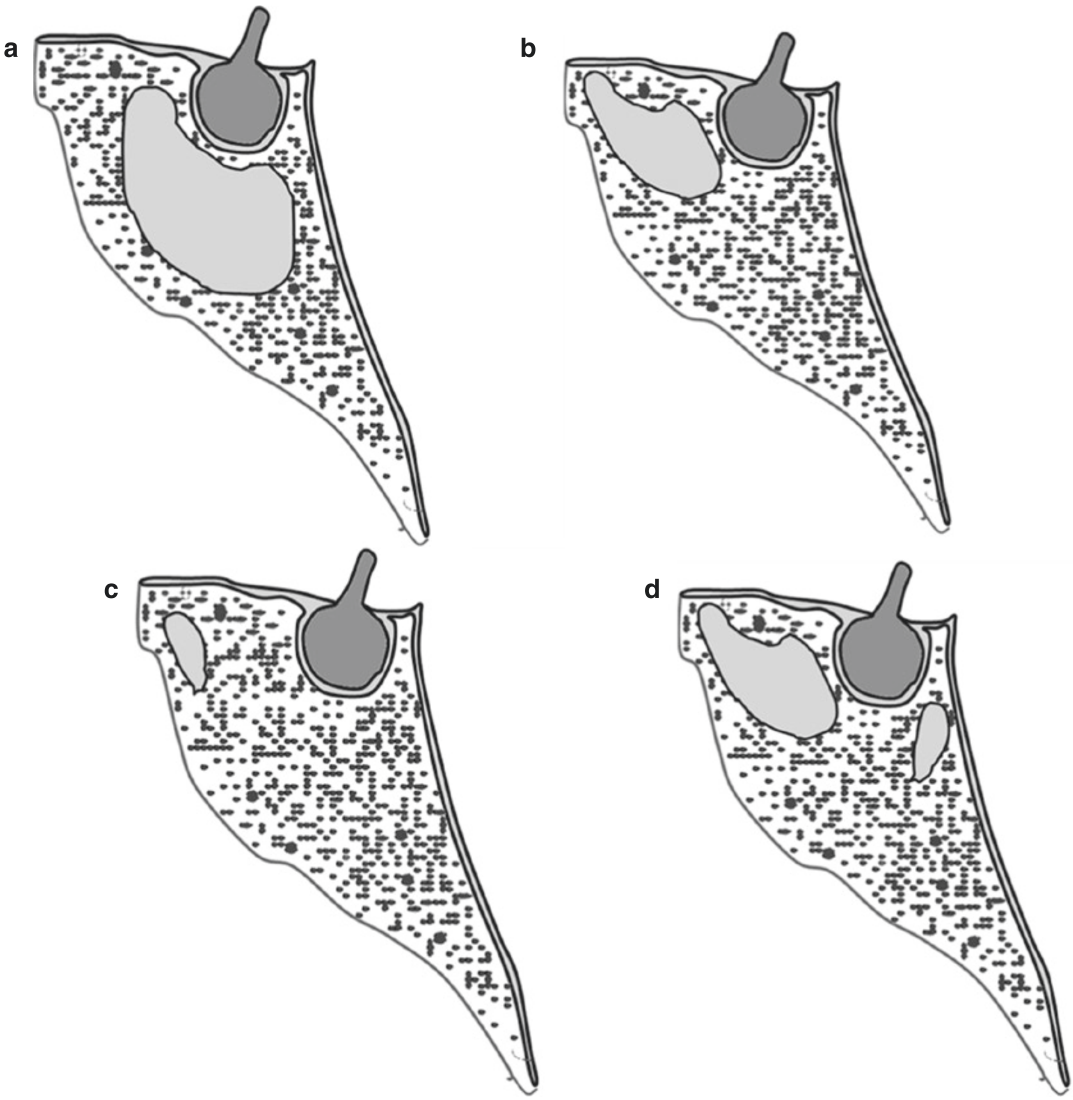

Fig. 12.37 Schematic representation midsagittal CBCT image for sellar (**a**), presellar (**b**), conchal (**c**), and postsellar (**d**) sphenoidal sinus pneumatization configurations

Anatomical variations of the sphenoidal sinuses have a major impact on the surgical access and possibility of complications in trans-sphenoid surgery, the standard approach to the surgical removal of pituitary adenomas. A non-pneumatized, conchal sphenoidal sinus has always been considered to be a contraindication to the trans-sphenoid approach to the sella, while a highly pneumatized sphenoidal sinus may distort the anatomical configuration of adjacent structures and attenuate the bone over the lateral wall, placing the optic nerve and carotid artery at greater risk (Hamid et al. 2008).

Maxillary

Extension of the maxillary sinus can occur in relation to four recesses and are almost always symmetrical:

- **Palatine.** The maxillary sinuses extend medially and involve the hard palate. Radiographically defined as the distance between the two recesses being less than half the width of the nose at the level of the inferior meatus (Earwaker 1993).
- **Alveolar**. Inferior extension and crenation below the roots of the premolar and molar teeth

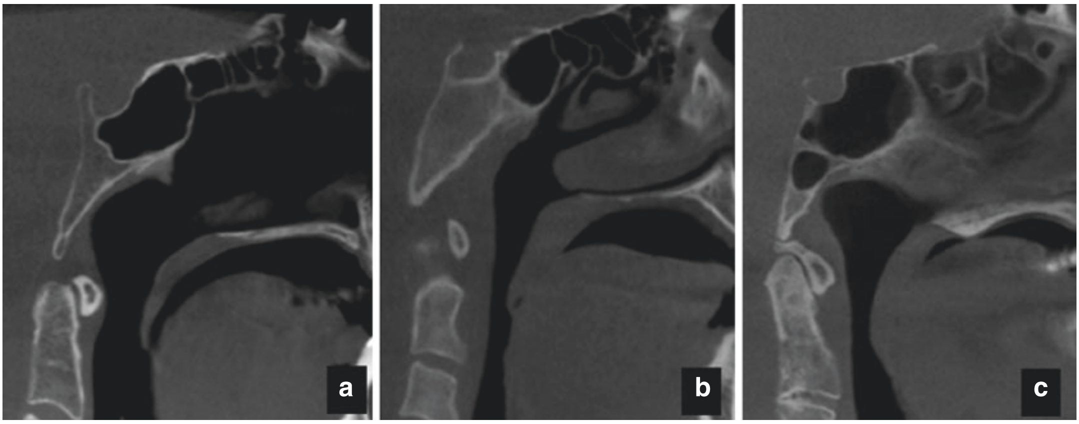

Fig. 12.38 Midsagittal CBCT images of different patients demonstrating sellar (**a**), presellar (**b**), and postsellar (**c**) sphenoid sinus pneumatization configurations

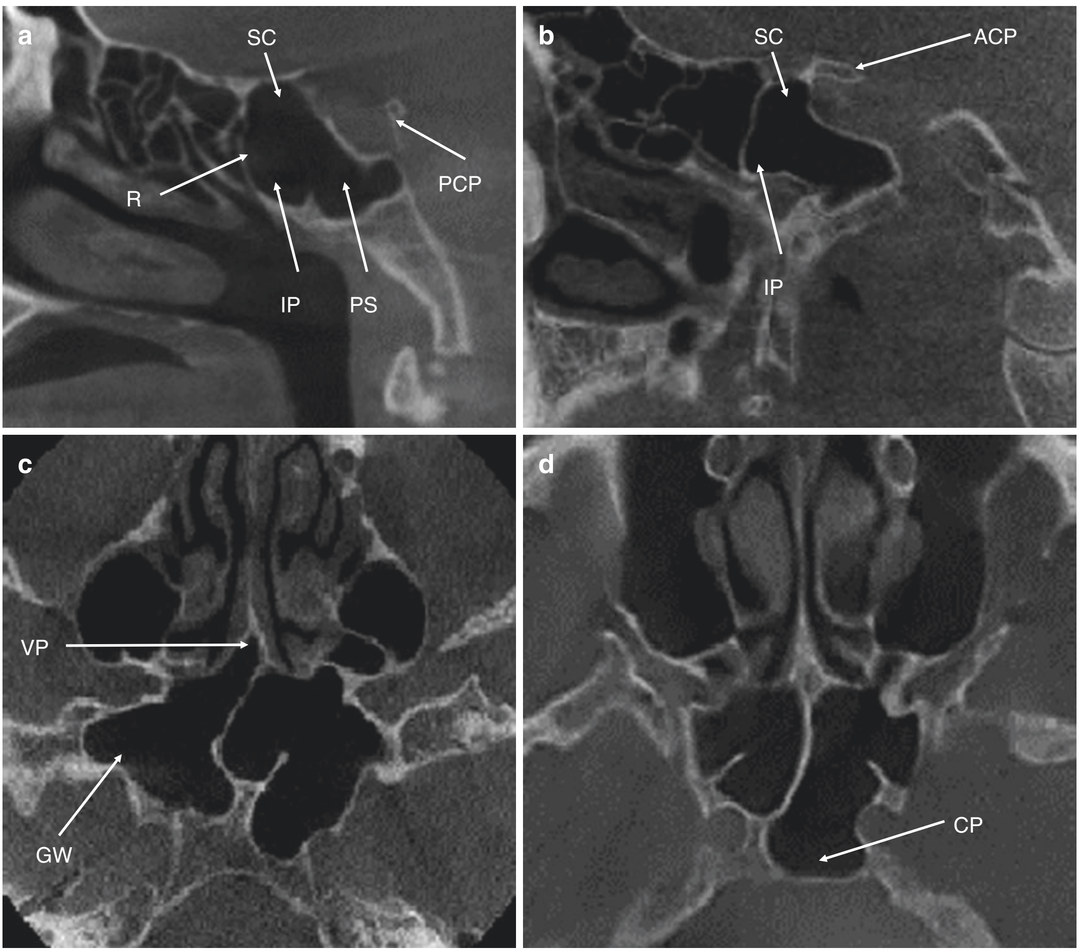

Fig. 12.39 Magnified and cropped midsagittal (**a**) and lateral (**b**) and axial images at the level of the orbit (**c**) and maxillary sinus (**d**) of a patient with extensive pneumatization of the sphenoid sinus involving post-sella (*PS*), superior clival (*SC*), rostral (*R*), caudal (*CP*), vomeral process (*VP*), inferior process (*IP*) and greater wing (*GW*) involvement (*PCP* posterior clinoid process, *ACP* anterior clinoid process)

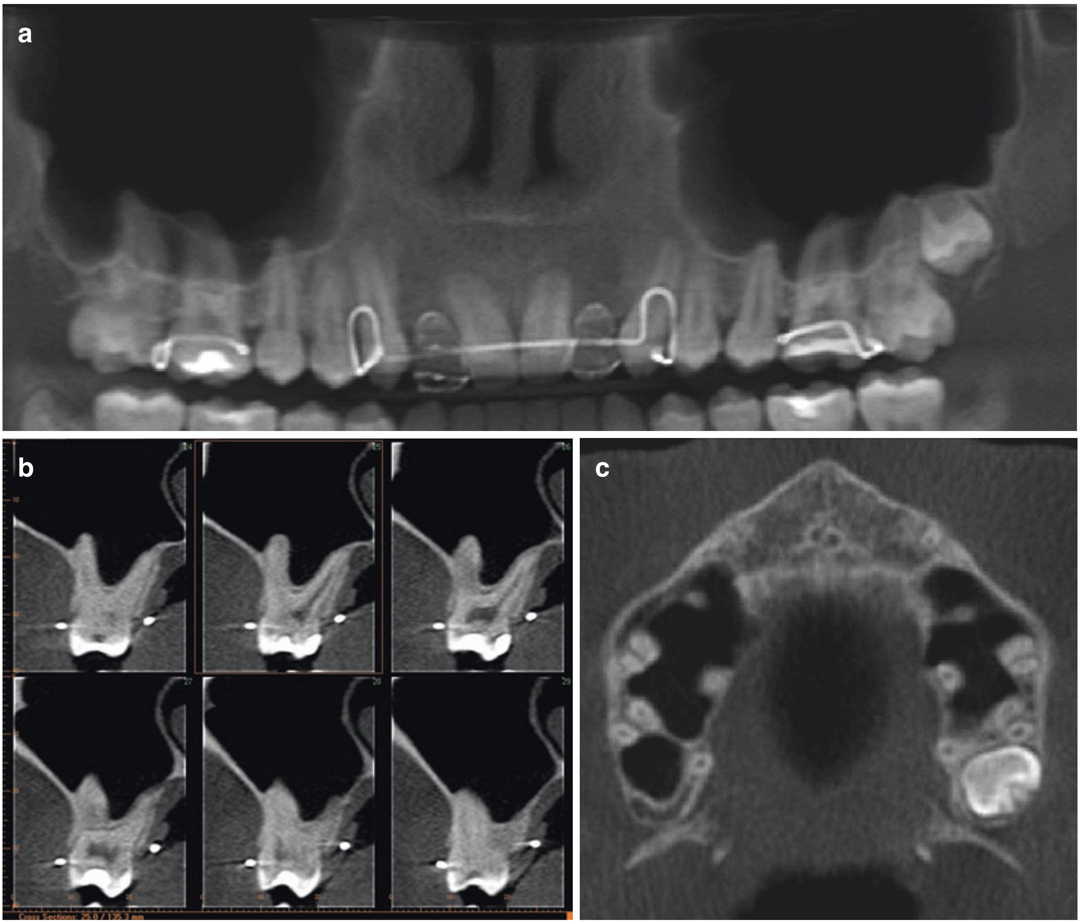

Fig. 12.40 Reformatted panoramic (**a**), right sequential cross-sectional (**b**), and axial (**c**) images showing alveolar maxillary sinus pneumatization with extensive crenation between the roots of the second premolar and molar teeth bilaterally

Table 12.5 Patterns of extensive maxillary sinus pneumatization (*after* Kalavagunta and Reddy 2003)

Type	Description	Features
I	Mild	Horizontal *or* vertical dimension of maxillary sinus ≥90% of the corresponding orbital dimension
II	Moderate	Horizontal *and* vertical dimension of maxillary sinus ≥90% of the corresponding orbital dimensions
III	Severe	Same as type II and, in addition, the presence of inter-maxillary plate, spheno-maxillary plate or extension into the frontal sinus

into the inter-radicular alveolar bone. The prevalence of alveolar pneumatization ranges from 50 to 83% (Lana et al. 2012) with most being bilateral (Fig. 12.40).

- **Intraorbital.** Aeration projects anteriorly along the roof of the maxillary sinus, most often medial to the infraorbital canal. Extension of the maxillary sinus in this region may indicate a possible risk of damage to the medial and inferomedial orbital wall during sinus surgery (Kalavagunta and Reddy 2003).

- **Zygomatic.** This comprises variable extension of the maxillary sinus into the zygomatic process. Three patterns of extensive maxillary sinus pneumatization (EMSP) have been described (Table 12.5) (Kalavagunta and Reddy 2003).

12.8.3 Additional Variations

12.8.3.1 Septae

The presence of intraluminal sinus bony projections (*septae*) can lead to incomplete compartmentalization, reducing the flow of nasal secretions and potentially predisposing to obstructive sinus disease. While occurring to a greater or lesser extent in specific sinuses, the significance of this anomaly is most important in dentistry when present in the maxillary sinus.

Septa are commonly found in the maxillary antrum (mean, 28%; range, 26.6–58%) with approximately bilateral distribution in 17.2% (Lana et al. 2012; Pommer et al. 2012; Vogiatzi et al. 2014) (Fig. 12.41). Multiple septa within the same sinus is rare (4.2%).

Septa arising from the floor of the maxillary sinus are referred to as Underwood's septa in acknowledgment of their first description in 1910 by Arthur S. Underwood, an anatomist at King's College in London (Underwood 1910). Septae are most often (mean, 54.6%) located in the middle region of the sinus (distal aspect of second premolar to distal aspect of second molar) (Pommer et al. 2012; Orhan et al. 2013). Interestingly prevalence is significantly higher in atrophic sinuses compared with dentate maxillae and are most often oriented transversely (Pommer et al. 2012). Average height of septae is 7.5 mm and complete septation is rare.

The identification of septae prior to maxillary sinus elevation and bone augmentation procedures is important. Both creation and inversion of the access window as well as sinus membrane elevation may be complicated by the presence of septae. In addition, the presence of septae may predispose to sinus membrane perforation during surgery, leading to the development of acute or chronic sinusitis and subsequent bone graft resorption.

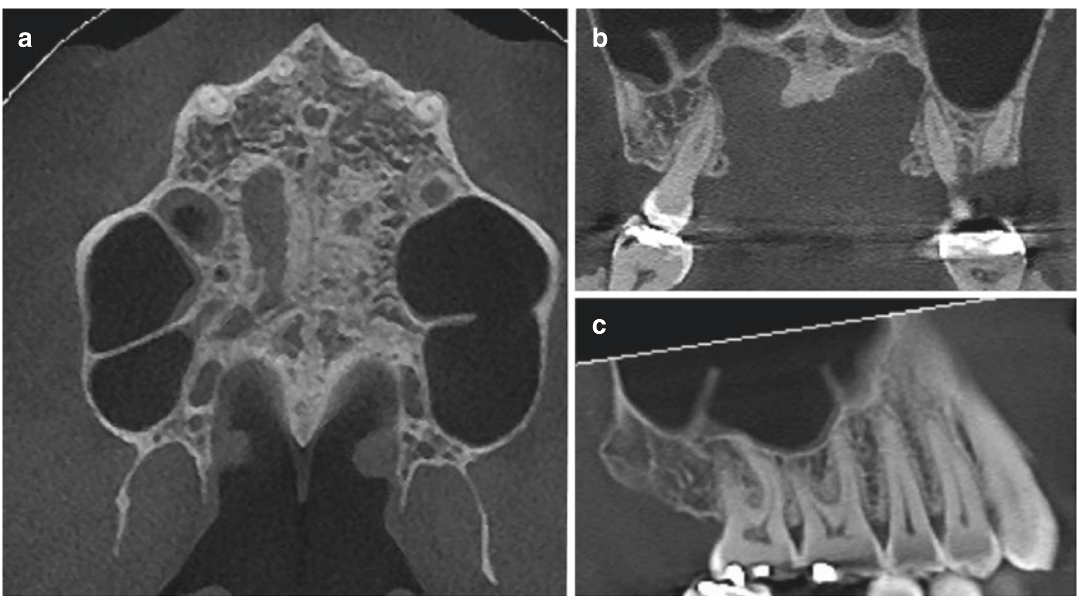

Fig. 12.41 Axial (**a**), coronal (**b**), and right para-sagittal (**c**) CBCT images showing left single and right double transverse maxillary septa arising from the floor of the maxillary sinus in the molar region (Underwood's septa)

References

April MM, Zinreich SJ, Baroody FM, Naclerio RM (1993) Coronal CT scan abnormalities in children with chronic sinusitis. Laryngoscope 103:985–990

Arıncı K, Elhan A (1997) Anatomi, 2nd edn. Güneş Kitabevi, Ankara

Bolger W, Butzin C, Parsons D (1991) Paranasal sinus bony anatomic variations and mucosal abnormalities: CT analysis for endoscopic sinus surgery. Laryngoscope 101:56–64

Bolger WE, Woodruff WW, Morehead J, Parsons DS (1990) Maxillary sinus hypoplasia: classification and description of associated uncinate process hypoplasia. Otolaryngol Head Neck Surg 103:759–765

Brüllmann DD, Schmidtmann I, Hornstein S, Schulze RK (2012) Correlation of cone beam computed tomography (CBCT) findings in the maxillary sinus with dental diagnoses: a retrospective cross-sectional study. Clin Oral Investig 16:1023–1029

Cakur B, Sümbüllü MA, Yılmaz AB (2011) A retrospective analysis of sphenoid sinus hypoplasia and agenesis using dental volumetric CT in Turkish individuals. Diagn Interv Radiol 17:205–208

Cashman EC, MacMahon PJ, Smyth D (2011) Computed tomography scans of paranasal sinuses before functional endoscopic sinus surgery. World J Radiol 3:199–204

Chong VF, Fan YF, Lau DP, Chee LW, Nguyen TM, Sethi DS (2000) Imaging the sphenoid sinus: pictorial essay. Australas Radiol 44:143–154

Doty RL, Mishra A (2001) Olfaction and its alteration by nasal obstruction, rhinitis, and rhinosinusitis. Laryngoscope 111:409–423

Earwaker J (1993) Anatomic variants in sinonasal CT. Radiographics 13:381–415

Geraghty JJ, Dolan KD (1989) Computed tomography of the hypoplastic maxillary sinus. Ann Otol Rhinol Laryngol 98:916–918

Hamid O, El Fiky L, Hassan O, Kotb A, El Fiky S (2008) Anatomic variations of the sphenoid sinus and their impact on trans-sphenoid pituitary surgery. Skull Base 18:9–15

Hofmann T, Friedrich RE, Wedl JS, Schmelzle R (2001) Pneumatization of the zygomatic arch on pantomography. Mund Kiefer Gesichtschir 5:173–179. (German)

Kalavagunta S, Reddy KT (2003) Extensive maxillary sinus pneumatization. Rhinology 41:113–117

Kamburoglu K, Kursun S, Akarslan ZZ (2011) Dental students' knowledge and attitudes towards cone beam computed tomography in Turkey. Dentomaxillofac Radiol 40:439–443

Kantarci M, Karasen RM, Alper F, Onbas O, Okur A, Karaman A (2004) Remarkable anatomic variations in paranasal sinus region and their clinical importance. Eur J Radiol 50:96–302

Kayalioglu G, Oyar O, Govsa F (2000) Nasal cavity and paranasal sinus bony variations: a computed tomographic study. Rhinology 38:108–113

Keros P (1962) On the practical value of differences in the level of the lamina cribrosa of the ethmoid. Z Laryngol Rhinol Otol 41:809–813

Kilic C, Kamburoglu K, Yuksel S, Ozen T (2010) An assessment of the relationship between the maxillary sinus floor and the maxillary posterior teeth root tips using dental cone-beam computerized tomography. Eur J Dent 4:462–467

Lana JP, Carneiro PMR, Machado VC, de Souza PEA, Manzi FR, Horta MCR (2012) Anatomic variations and lesions of the maxillary sinus detected in cone beam computed tomography for dental implants. Clin Oral Implants Res 23:1398–1403

Lang J (1989) Clinical anatomy of the nose, nasal cavity and paranasal sinuses. Georg Thieme Verlag, Stuttgart

Lerdlum S, Vachiranubhap B (2005) Prevalence of anatomic variation demonstrated on screening sinus computed tomography and clinical correlation. J Med Assoc Thail 88(Suppl 4):110–115

Maillet M, Bowles WR, McClanahan SL, John MT, Ahmad M (2011) Cone-beam computed tomography evaluation of maxillary sinusitis. J Endod 37:753–757

Midilli R, Aladag G, Erginoz E, Karci B, Savas R (2005) Anatomic variations of the paranasal sinuses detected by computed tomography and the relationship between variations and sex. Kulak Burun Bogaz Ihtis Derg 14:49–56

Muranjan S (1999) Special issue on sinusitis & it's management. Anatomy of the nose and paranasal sinuses. Bombay Hospital J 41(4):619–622. http://www.bhj.org/journal/1999_4104_oct99/special_toc.htm

Nitinavakarn B (2005) Anatomical variations of the lateral nasal wall and paranasal sinuses. J Med Assoc Thail 88:763–768

Orhan K, Seker BK, Aksoy S, Bayindir H, Berberoglu A, Seker E (2013) CBCT evaluation of maxillary sinus septa prevalence, height, location and morphology in children and an adult population. Med Princ Pract 22:47–53

Orhan K, Delilbasi C, Orhan AI (2006) Radiographic evaluation of pneumatized articular eminence in a group of Turkish children. Dentomaxillofac Radiol 35:365–370

Pazera P, Bornstein MM, Pazera A, Sendi P, Katsaros C (2011) Incidental maxillary sinus findings in orthodontic patients: a radiographic analysis using cone-beam computed tomography (CBCT). Orthod Craniofac Res 14:17–24

Pérez-Piñas I, Sabate J, Carmona A, Catalina-Herrera CJ, Jiménez-Castellanos J (2000) Anatomical variations in the human paranasal sinus region studied by CT. J Anat 197(Pt 2):221–227

Phothikhun S, Suphanantachat S, Chuenchompoonut V, Nisapakultorn K (2012) Cone beam computed tomographic evidence of the association between periodontal bone loss and mucosal thickening of the maxillary sinus. J Periodontol 83(5):557–564. doi:10.1902/jop.2011.110376

Pommer B, Ulm C, Lorenzoni M, Palmer R, Watzek G, Zechner W (2012) Prevalence, location and morphology of maxillary sinus septa: systematic review and meta-analysis. J Clin Periodontol 39:769–773

Ritter L, Lutz J, Neugebauer J, Scheer M, Dreiseidler T, Zinser MJ, Rothamel D, Mischkowski RA (2011) Prevalence of pathologic findings in the maxillary sinus in cone-beam computerized tomography. Oral Surg Oral Med Oral Pathol Oral Radiol Endod 111:634–640

Savvateeva DM, Güldner C, Murthum T, Bien S, Teymoortash A, Werner JA, Bremke M (2010) Digital volume tomography (DVT) measurements of the olfactory cleft and olfactory fossa. Acta Otolaryngol 130:398–404

She R, Szakacs J (2004) Hyperostosis frontalis interna: case report and review of literature. Ann Clin Lab Sci 34:206–208

Singh A, Wessell AP, Anand VK, Schwartz TH (2011) Surgical anatomy and physiology for the skull base surgeon. Oper Tech Otolaryngol 22:184–193

Sirikçi A, Bayazit Y, Gümüsburun E, Bayram M, Kanlikana M (2000) A new approach to the classification of maxillary sinus hypoplasia with relevant clinical implications. Surg Radiol Anat 22:243–247

Smith KD, Edwards PC, Saini TS, Norton NS (2010) The prevalence of concha bullosa and nasal septal deviation and their relationship to maxillary sinusitis by volumetric tomography. Int J Dent. doi:10.1155/2010/404982

Smith TD, Siegel MI, Mooney MP, Burrows AM, Todhunter JS (1997) Formation and enlargement of the paranasal sinuses in normal and cleft lip and palate human fetuses. Cleft Palate Craniofac J 34:483–489

Snell RS (1995) Clinical anatomy, 5th edn. Little Brown and Company, New York

Stallman J (2004) The incidence of concha bullosa and its relationship to nasal septal deviation and paranasal sinus diseases. Am J Neuroradiol 25:1613–1618

Stammberger HR, Kennedy DW (1995) Paranasal sinuses: anatomic terminology and nomenclature. Ann Otol Rhinol Laryngol Suppl 167:7–16

Tan HM, Chong V (2001) CT of the paranasal sinuses normal anatomy, variation and pathology. CME Radiology 2:120–125

Tao Y, Gao Q, Cui Y (1998) The evaluation of paranasal sinus coronal CT scanning in endoscopic sinus surgery. Lin Chuang Er Bi Yan Hou Ke Za Zhi 12(8):346

Underwood AS (1910) An inquiry into the anatomy and pathology of the maxillary sinus. J Anat Physiol 44:354–369

Vallo J, Suominen-Taipale L, Huumonen S, Soikkonen K, Norblad A (2010) Prevalence of mucosal abnormalities of the maxillary sinus and their relationship to dental disease in panoramic radiography: results from the health 2000 health examination survey. Oral Surg Oral Med Oral Pathol Oral Radiol Endod 109:e80–e87

Vartanian AJ. CT scan, paranasal sinuses. Updated 11 May 2010. http://emedicine.medscape.com/article/875244-overview

Vogiatzi T, Kloukos D, Scarfe WC, Bornstein MM (2014) Incidence of anatomical variations and disease of the maxillary sinuses as identified by cone beam computed tomography: a systematic review. Int J Oral Maxillofac Implants 29:1301–1314. doi:10.11607/jomi.3644.

Wang J, Bidari S, Inoue K, Yang H, Rhoton A Jr (2010) Extensions of the sphenoid sinus: a new classification. Neurosurgery 66:797–816

William EB (1991) Paranasal sinus bony anatomic variations and mucosal abnormalities: CT analysis for endoscopic sinus surgery. Laryngocope 101:56–64

Yousem DM (1993) Imaging of sinonasal inflammatory disease. Radiology 188:303–314

Zinreich S, Albayram S, Benson M, Oliverio P (2003) The ostiomeatal complex and functional endoscopic surgery. In: Som P (ed) Head and neck imaging, 4th edn. Mosby, St Louis, pp 149–173

Zinreich SJ (1998) Functional anatomy and computed tomography imaging of the paranasal sinuses. Am J Med Sci 316:2–12

The Upper Airway

13

Saulo Leonardo Sousa Melo, Zhimin Li,
Kivanç Kamburoğlu, and William C. Scarfe

Contents

S.L.S. Melo, D.D.S., M.S.D., Ph.D., M.S. (✉)
Department of Oral Pathology, Radiology and Medicine, University of Iowa College of Dentistry, Iowa City, IA, USA
e-mail: saulo-sousamelo@uiowa.edu

Z. Li, D.D.S., Ph.D.
Department of Oral Radiology, Jilin University, School and Hospital of Stomatology, Chang Chun, Jilin Province, China
e-mail: zhimin@jlu.edu.cn

K. Kamburoğlu, D.D.S., M.Sc., Ph.D.
Department of Oral and Maxillofacial Radiology, Faculty of Dentistry, Ankara University, Ankara, Turkey
e-mail: dtkivo@yahoo.com

W.C. Scarfe, B.D.S., M.S.
Division of Radiology and Imaging Science, Department of Surgical/Hospital Dentistry, University of Louisville School of Dentistry, Louisville, KY, USA
e-mail: william.scarfe@louisville.edu

13.1 Introduction

The upper airway (UA) is the mucosal lined fibromuscular tube that connects the nasal and oral cavities with the larynx and esophagus. The UA forms a dual pathway from the mouth for the flow of air to the lungs and passage of food to the stomach. It performs several different physiologic functions, including vocalization, deglutition, and respiration (Schwab 1998; Stevens and Jones 1995).

13.2 Development

During development the UA undergoes significant structural and functional changes that affect its size, shape, and mechanical properties. Structural changes include growth of the tissues, expansion of the maxillofacial elements, and development of the muscles comprising the UA whereas functional changes involve neuromuscular tone and ventilator drive. These factors result in anatomic dimensional changes of the UA during childhood (up to 12 years) that play an important role in maintaining airway patency. The linear anteroposterior, vertical, and transverse growth of the lower face during this period is mirrored by linear growth of each element of the soft tissue within the maxilla-skeletal boundary (Abramson et al. 2009). Children have smaller, rounder elliptical, more uniform, and more compact airways than adults (Arens et al. 2002).

W.C. Scarfe, C. Angelopoulos (eds.), *Maxillofacial Cone Beam Computed Tomography*,
https://doi.org/10.1007/978-3-319-62061-9_13

The structures within the UA with the greatest variability during childhood are the adenoids and tonsils. Adenoid size varies greatly with age from 0.8 to 23.8 mm (mean, 8.4 mm) (Fig. 13.1). The adenoids continued to enlarge throughout the first decade. The size of the adenoid pad is a maximum between the ages of 7–10 years of age group (mean, 14.59 ± 4.49 mm; range 6.6–22.2 mm) and then progressively diminishes until 60 years of age (Vogler et al. 2000; Isaacs and Sykes 2002).

The role of excessive adenoid tissue on breathing and craniofacial growth in the developing child is widely debated and still a controversial issue within orthodontics. It has been postulated that large adenoids lead to obstructed nasal breathing leading to mouth breathing and the stereotype of the adenoid face characterized by an incompetent lip seal, a narrow upper dental arch, increased anterior face height, a steep mandibular plane angle, and a retrognathic mandible (Subtelny 1954; Linder-Aronson et al. 1986).

13.3 Anatomy of the Upper Airway

The UA is approximately 15 cm long and extends from the base of the skull inferiorly to the inferior border of the cricoid cartilage (approximately at the sixth cervical vertebral level—C6) where it becomes continuous with the adventitia of the esophagus. Superiorly the UA is adjacent the sphenoid and occipital bones and posteriorly separated from the upper six cervical vertebrae by the prevertebral fascia and muscles. The UA is usually widest at the level of the hyoid bone and narrowest at its most inferior extent, where it becomes continuous with the esophagus posteriorly and trachea anteriorly (O'Rahilly et al. 1983; Isaacs and Sykes 2002; Auvenshine 2010).

The pharyngeal wall is composed of four layers:

- The internal layer comprises mucosal lining which changes from a ciliated columnar epithelium in the nasopharynx to a stratified columnar epithelium in the oro- and laryngopharynx.
- Adjacent to this is a fibrous layer, which forms the pharyngobasilar fascia and is attached superiorly to the skull.
- Next is a muscular layer composed of inner longitudinal and outer circular components.
- Finally, the external layer is loose connective tissue that forms the buccopharyngeal fascia. The buccopharyngeal fascia is continuous with the epimysium (deep surface) of the pharyngeal muscles, and it contains the pharyngeal plexus of nerves and veins (Fig. 13.2) (Auvenshine 2010).

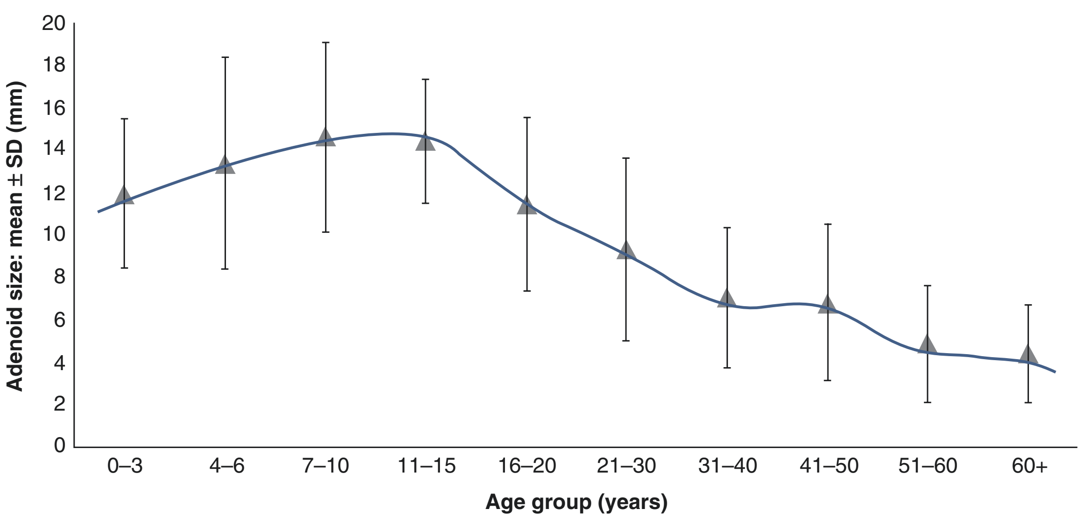

Fig. 13.1 Graph of adenoid measurement versus age (from Vogler et al. (2000))

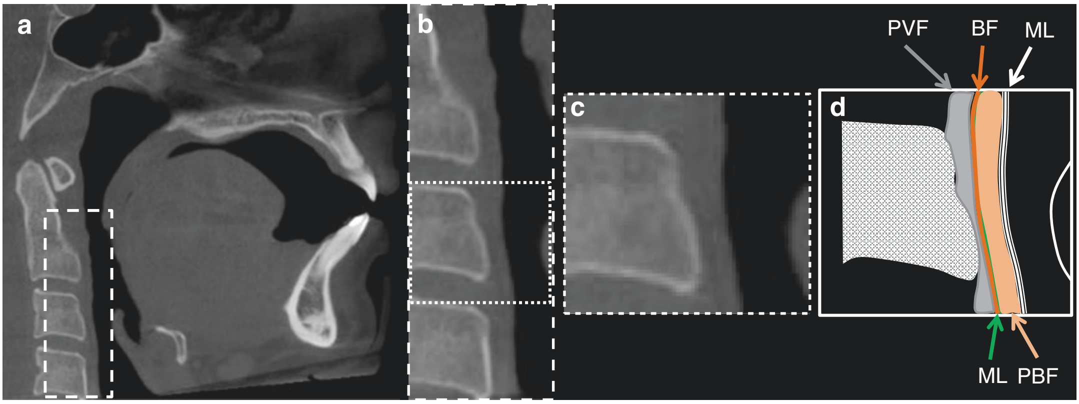

Fig. 13.2 Entire CBCT image of the head (**a**), magnified area of the upper cervical vertebrae (**b**), single cropped C3 vertebrae (**c**), and corresponding schematic (**d**) demonstrating the layers of the prevertebral/posterior pharyngeal soft tissue (*PVF* prevertebral fascia, *BF* buccopharyngeal fascia, *ML* muscular layer, *PBF* pharyngobasilar fascia, *ML* mucosal lining)

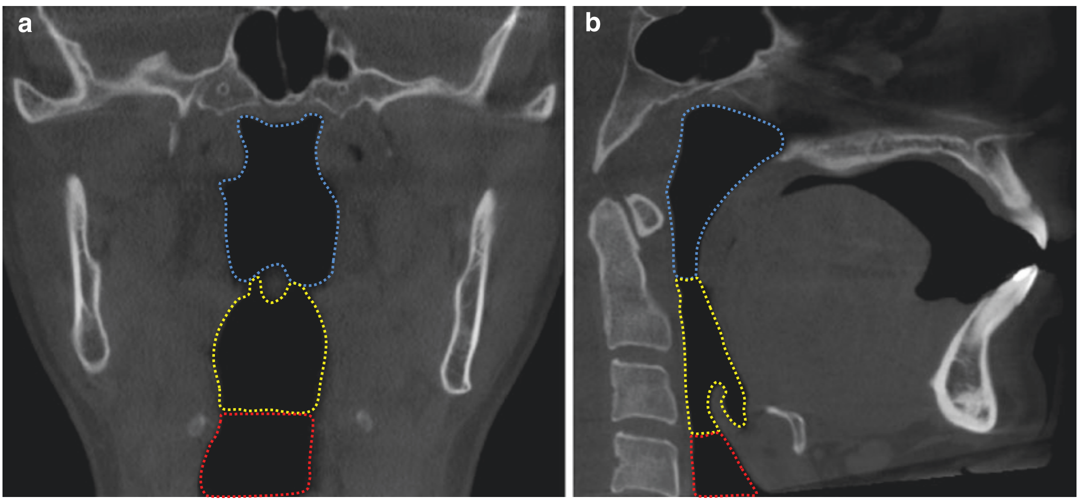

Fig. 13.3 Coronal (**a**) and sagittal (**b**) CBCT images identifying the three (3) anatomic boundaries of the upper airway including the nasopharynx (*blue*), oropharynx (*yellow*), and hypopharynx (*red*)

The upper airway can be subdivided into three anatomic parts (Fig. 13.3):

- The nasopharynx, a region between the posterior extent of the nasal cavity (the external nares) and tip of the inferior extent of the soft palate.
- The oropharynx, posterior to the oral cavity, from the tip of the soft palate to the base of the epiglottis.
- The hypo- or laryngopharynx, immediately posterior to the larynx, from the base of the epiglottis to the inferior border of the cricoid cartilage.

The nasal and the hypopharyngeal segments are supported by bony and cartilaginous structures, and are relatively rigid while the pharyngeal tissues are unsupported. These characteristics account for the fact that airflow resistance of the nasal and laryngeal segments is approximately linear (Hudgel 1986), whereas, within the oropharyngeal, airflow is highly variable due to the relative collapsibility of this structure.

Radiographically, the upper airway can be divided into the same segments; however, the boundaries are somewhat different based on the following cephalometric landmarks and planes (Park et al. 2010): The Frankfort horizontal (FH) plane, the most posterior point of the pterygomaxillary fissure (PT point), posterior nasal spine (PNS), and the third and the sixth cervical vertebrae (C3 and C6) (Fig. 13.4).

- The nasopharynx is defined as the airway space between a plane parallel to FH passing through the right and left PT points and a plane passing through the PNS.
- The oropharynx is defined as the airway space between a plane parallel to FH passing through PNS and a plane parallel to FH passing through C3.
- The hypopharynx is defined as the airway space between a plane parallel to FH passing through C3 and a plane parallel to FH passing through C6.

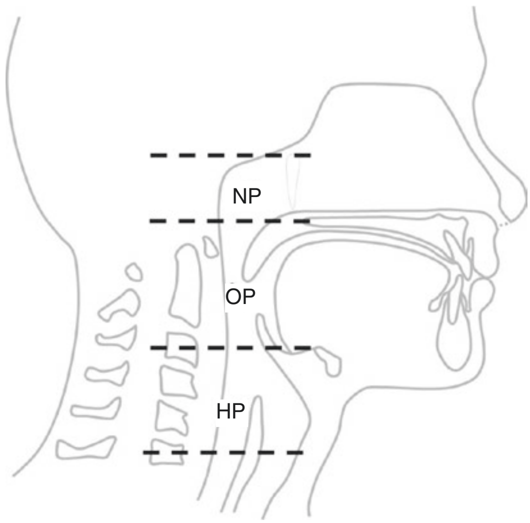

Fig. 13.4 Midsagittal diagram of the head and neck region demonstrating the three (3) radiographic divisions of the pharynx: nasopharynx (*NP*), oropharynx (*OP*), and hypopharynx (*HP*) (modified from Park et al. (2010))

13.4 Regional Anatomy

The anatomy of the upper airway and adjacent cervical, cranial, and maxillofacial bony confines is most often examined in coronal (Fig. 13.5) and midsagittal projections (Fig. 13.6). The interrelationships between these elements and specific anatomic details are best understood with respect to each of the radiographic divisions.

13.4.1 Nasopharynx

The nasopharynx is situated posterior to the nasal cavity, and superior to the soft palate (Fig. 13.7). It is contiguous with the nasal cavity through the posterior apertures, the bilateral nasal choanae, with the tympanic cavity through the bilateral Eustachian tubes and extends inferiorly to oropharynx. The posterior wall contains the pharyngeal tonsils. Essentially, the structure of the nasopharynx is defined by rigid walls with the superior-posterior aspect being formed by the body of the sphenoid and the basilar portion of the occipital bones of the skull base and the posterior aspect, limited by the cervical vertebrae. The transition between these elements occurs gradually, as the superior-posterior boundary slants posteriorly to continuous with the posterior nasopharyngeal wall. Furthermore, the posterior wall of the nasopharynx is separated from the upper cervical vertebrae by the rigid prevertebral and pharyngobasilar fasciae. The anterior boundary of the nasopharynx is nonrigid, comprising the soft palate, attached to the posterior hard palate and laterally to the walls of the pharynx. The superior-lateral walls are medial to the pterygoid processes. Inferiorly the lateral wall is unsupported with a contour which is concave outwards. A midline structure, the uvula, projects further posteriorly than the rest of the soft palate (Auvenshine 2010).

The mucous membranes of the roof of the nasopharynx contain a condensation of subepithelial lymphoid tissue named the adenoids, also referred to as the pharyngeal tonsil or nasopharyngeal tonsil. This tissue, together with the tubal tonsils (where the Eustachian tube opens in the nasopharynx), palatine tonsils, and lingual tonsils contributes to the immune-surveillance function of the structure known as Waldeyer's ring. The adenoids are important during the first years of life as an assistant in body's defense against incoming bacteria and viruses.

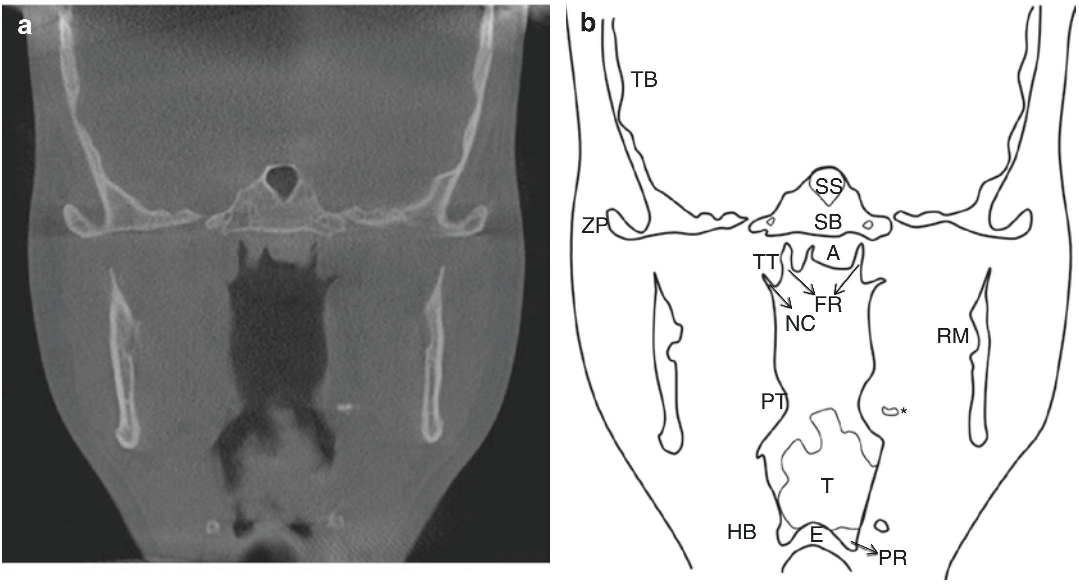

Fig. 13.5 Coronal CBCT image (**a**) and corresponding schematic (**b**) demonstrating anatomic features of the upper airway (*T* base of the tongue, *PT* palatine tonsils, *NC* nasal choanae, *TT* torus tubarius, *FR* fossa of Rosenmüller, *A* adenoid tonsils, *ZP* zygomatic process of temporal bone, *TB* temporal bone, *SS* sphenoidal sinus, *SB* sphenoidal bone, *RM* ramus of the mandible, *PR* piriform recess, *E* epligotis, *HB* hyoid bone, * tonsilolith)

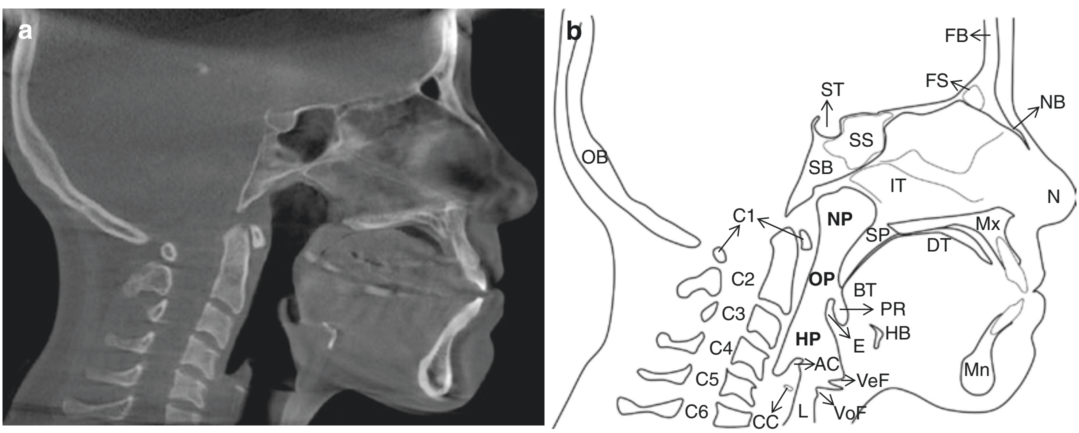

Fig. 13.6 Sagittal CBCT image (**a**) and corresponding schematic (**b**) demonstrating anatomic features of the upper airway (***NP*** nasopharynx, ***OP*** oropharynx, ***HP*** hypopharynx, *SP* soft palate, *Mx* maxilla, *Mn* mandible, *DT* dorsum of the tongue, *BT* base of the tongue, *PR* piriform recess, *HB* hyoid bone, *E* epiglottis, *VeF* vestibular fold, *VoF* vocal fold, *L* larynx, *CC* cricoid cartilage, *AC* arytenoid cartilage, *IT* inferior turbinate, *N* nose, *NB* nasal bone, *FB* frontal bone, *FS* frontal sinus, *SS* sphenoidal sinus, *SB* sphenoid bone, *ST* sella turcic, *OB* occipital bone, *C1* 1st cervical vertebra or atlas, *C2* 2nd cervical vertebra or axis, *C3* 3rd cervical vertebra, *C4* 4th cervical vertebra, *C5* 5th cervical vertebra, *C6* 6th cervical vertebra)

13.4.1.1 Topographic Features

There are numerous topographic structures associated with the walls of the nasopharynx (Figs. 13.8, 13.9 and 13.10).

The pharyngeal orifices of the Eustachian tube are located in the middle of the wall, posterior to the inferior turbinate. The tubal elevation (*torus tubarius*), formed by the elastic cartilage of the tube, is particularly prominent in its upper and posterior lip. The Eustachian tube helps to equalize middle ear and atmospheric pressure when opened by the specialized action of the palatal

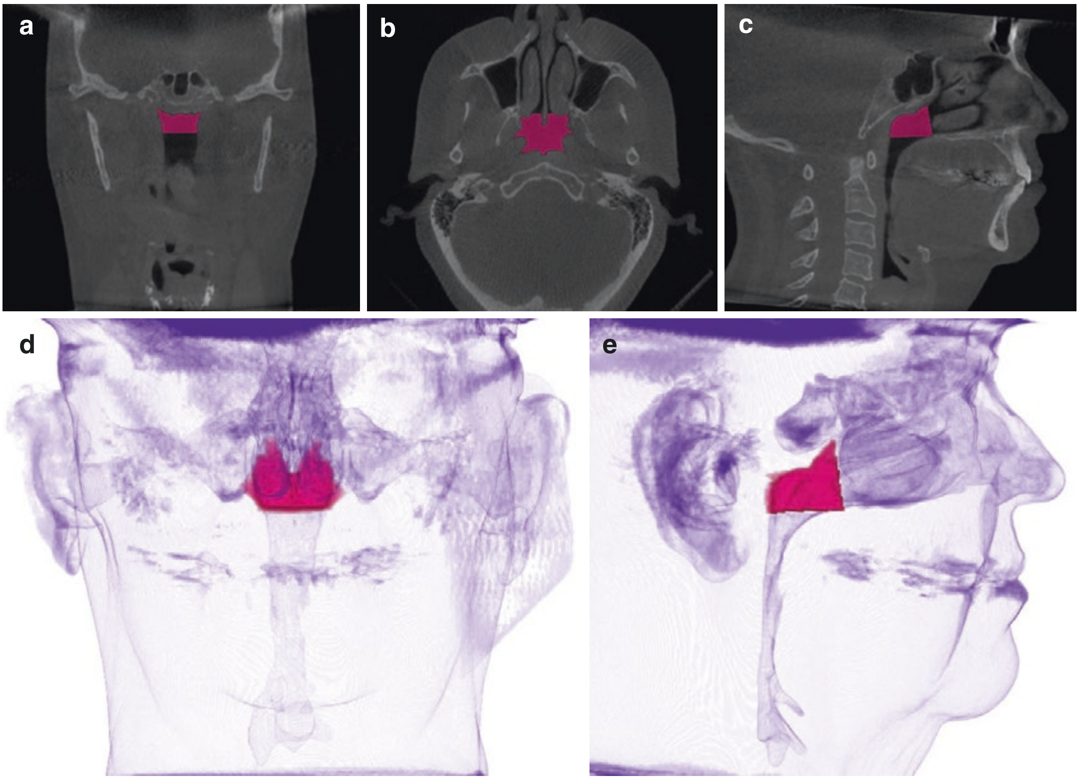

Fig. 13.7 Coronal (**a**), axial (**b**), and sagittal (**c**) orthogonal CBCT images and frontal (**d**) and right lateral (**e**) hollow volumetric renderings characterizing the airway volume of the nasopharyngeal division of the upper airway

muscles (Isaacs and Sykes 2002). The opening of the Eustachian tube is usually symmetrical and asymmetry should be treated with suspicion (Chong and Fan 2000).

Superior and posterior to the margin of the torus, between it and the pharyngeal wall is a fossa or recess, called the *pharyngeal recess* or *fossa of Rosenmüller*. Since the superior constrictor muscle does not reach the base of skull there is a lateral gap, called the *sinus of Morgagni*. At the base of this recess is the retropharyngeal lymph node (the *Node of Rouvier)*. The inverted "J" configuration of the torus tubarius results in the fossa appearing posterior (on axial images) and superior (on coronal images) to the Eustachian tube orifice. The shape of the fossa shows wide variation. The size and configuration depends on the amount of adenoid tissue and the prevertebral muscle mass. In the elderly, the loss of prevertebral muscle mass results in a shallow and wide recess. In children, the recess may be obliterated by adenoid tissue. The fossa of Rosenmüller may appear asymmetric. This is due to unequal air distension or an unequal amount of lymphoid tissue. The fossa of Rosenmüller is an important structure to identify, particularly in older individuals, as nasopharyngeal carcinoma (NPC) arises most often posterior-superiorly in the postnasal space in this region. The typical CT finding of NPC is asymmetry of the fossa of Rosenmüller manifested as blunting or obliteration. Widening of the preoccipital soft tissue area in the midline (Fig. 13.10) of more than 1.5 cm and up to 2.0 cm in the anterior-posterior plane should be viewed with a high index of suspicion (Hoe 1989a, b).

13.4.1.2 Soft Tissue Spaces

Progressing laterally from the surface, the soft tissues of the nasopharynx are delineated by fascial planes into anatomical spaces (Fig. 13.11):

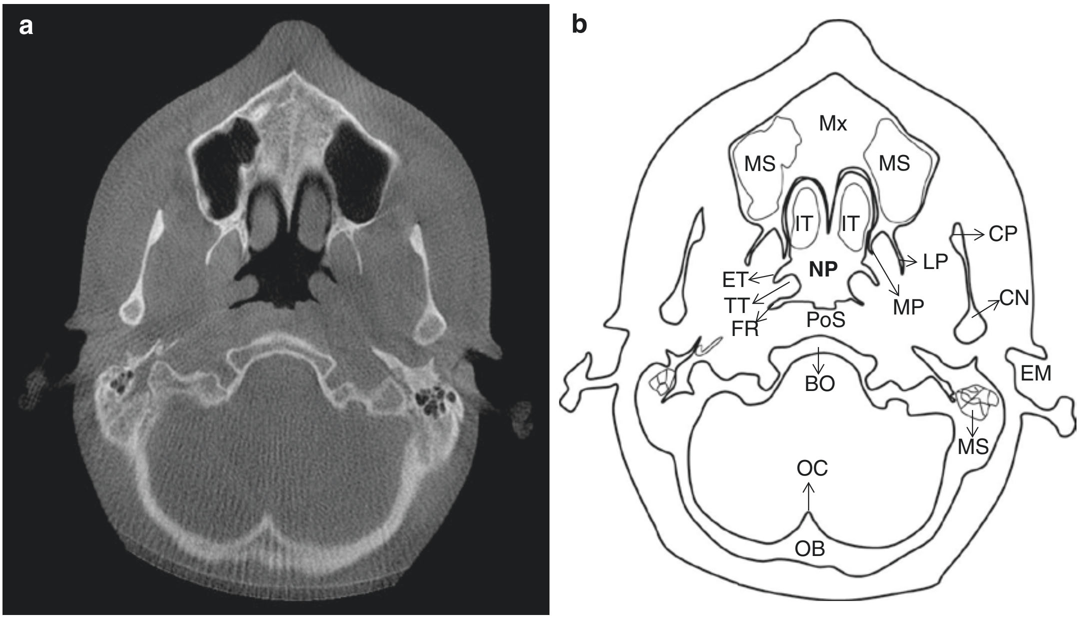

Fig. 13.8 Axial CBCT image (**a**) and corresponding schematic (**b**) demonstrating anatomic features of the upper airway (***NP*** nasopharynx, *PoS* preoccipital space, *FR* fossa of Rosenmüller, *TT* torus tubarius, *ET* Eustachian tube orifice, *IT* inferior nasal turbinate, *Mx* maxilla, *MS* maxillary sinus, *LP* lateral pterygoid plate, *MP* medial pterygoid plate, *CP* coronoid process of mandible, *CN* condylar neck, *EM* external auditory meatus, *MS* mastoid sinus or air cells, *BO* basilar portion of occipital bone, *OB* occipital bone, *OC* internal occipital crest

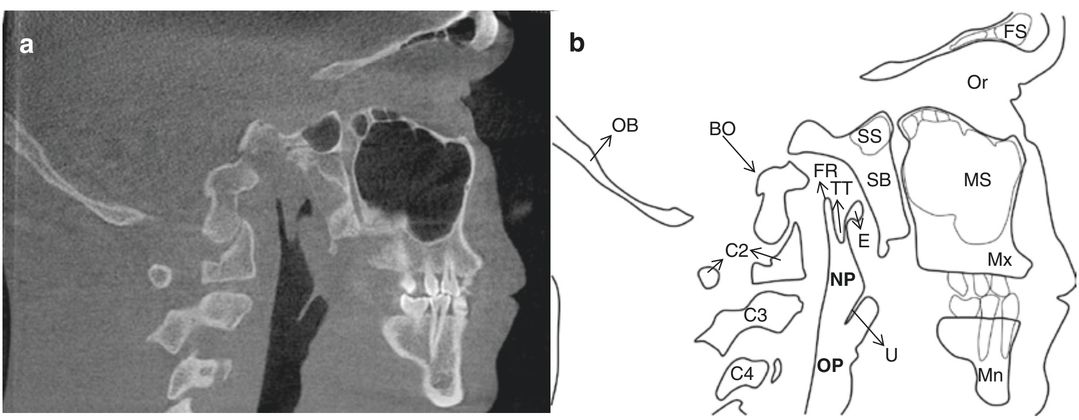

Fig. 13.9 Lateral sagittal CBCT image (**a**) and corresponding schematic (**b**) demonstrating anatomic features of the naso- and oropharynx. (***OP*** oropharynx, ***NP*** nasopharynx, *U* uvula, *FR* fossa of Rosenmüller, *TT* torus tubarius, *E* pharyngeal opening of Eustachian tube, *SB* sphenoidal bone, *SS* sphenoidal sinus, *MS* maxillary sinus, *Mx* maxilla, *Mn* mandible, *Or* orbit, *FS* frontal sinus, *OB* occipital bone, *BO* basilar portion of the occipital bone, *C2* 2nd cervical vertebra or axis, *C3* 3rd cervical vertebra, *C4* 4th cervical vertebra)

- **Pharyngeal mucosal space.** Immediately superficial to the pharyngeal mucosal walls this space includes Waldeyer's ring, the cartilaginous Eustachian tube, the pharyngobasilar fascia, the levator and constrictor muscles. The visceral (buccopharyngeal) fascia surrounds the nasopharyngeal mucosa and the constrictor muscles. This fascia separates the nasopharynx from the deep fascial spaces and is thought to be a barrier to deep spread of

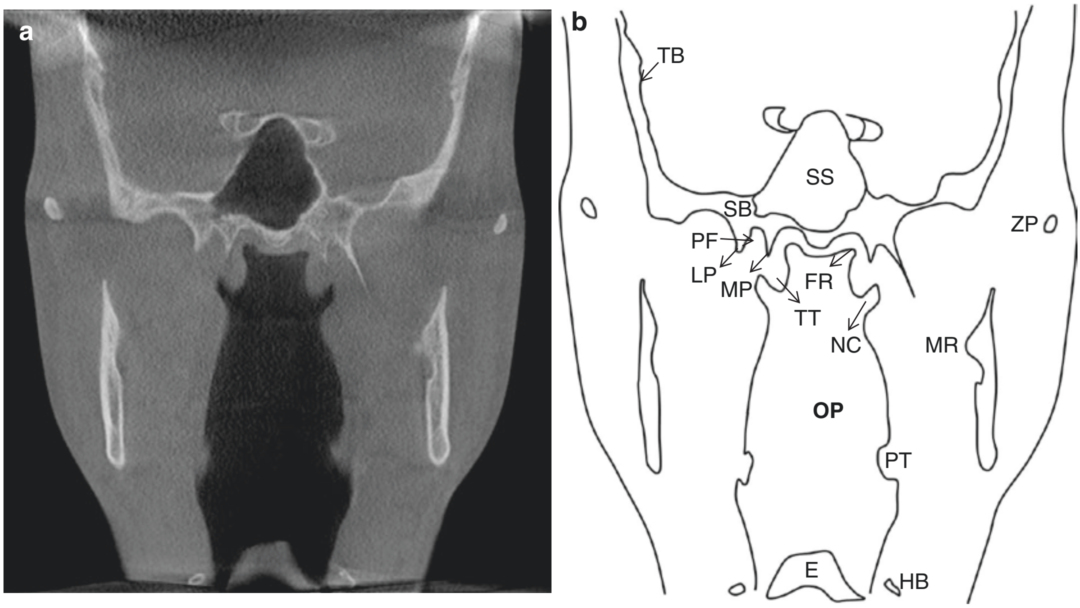

Fig. 13.10 Coronal CBCT image (**a**) and corresponding schematic (**b**) demonstrating anatomic features of the upper airway. (***OP*** oropharynx, *NC* nasal choanae, *TT* torus tubarius, *FR* fossa of Rosenmüller, *SS* sphenoidal sinus, *TB* temporal bone, *SB* sphenoidal bone, *LP* lateral pterygoid plate, *PF* pterygoid fossa, *MP* medial pterygoid plate, *ZP* zygomatic process of temporal bone, *MR* ramus of the mandible, *PT* base of the palatine tonsils, *HB* hyoid bone, *E* epligotis)

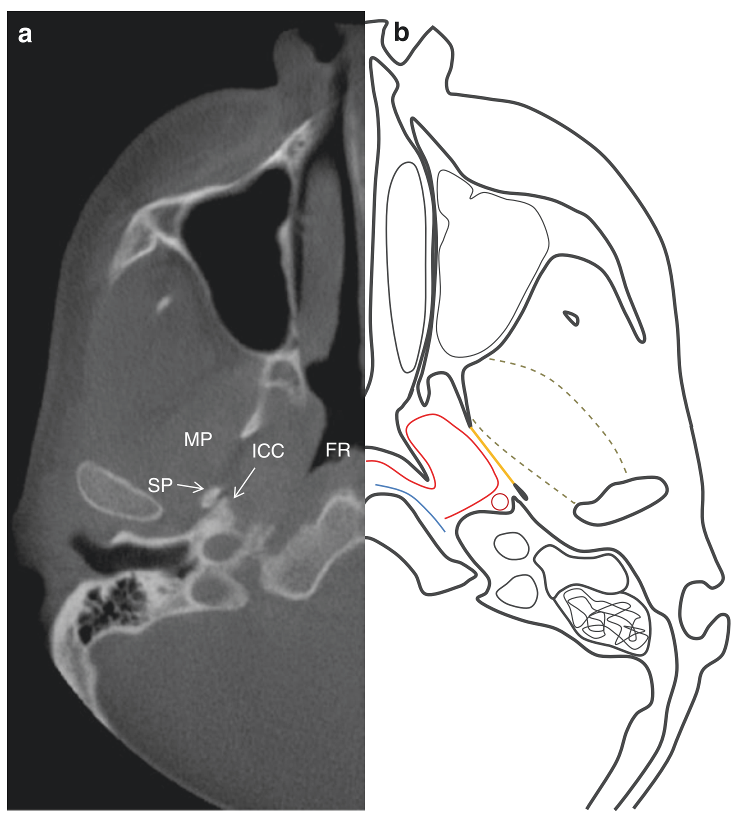

Fig. 13.11 Axial left CBCT image (**a**) and corresponding opposite schematic (**b**) image showing the lateral spaces and boundaries of the nasopharynx. The *orange line* is the *imaginary line* joining the medial pterygoid plate to the styloid process. The space in front of the line is the pre-styloid space and behind the post-styloid space. The *red line* is the pharyngobasilar fascia which joins with the fascia of the opposite side to form the median raphe. This fascia together with the prevertebral fascia (*blue line*) encloses the retropharyngeal space (*FR* fossa of Rosenmüller, *ICC* internal carotid artery, *MP* medial pterygoid muscle, *SP* styloid process)

infection and early malignancy. An extensive lymphatic plexus drains the nasopharynx, and this explains the high incidence of cervical nodal metastases associated with nasopharyngeal carcinomas. Primary nodal drainage is to the retropharyngeal nodes, which are usually not seen but may occasionally be identified as discrete 3–5 mm nodules (Chong and Fan 2000). However, the lymphatic pathways to these nodes are thought to become obliterated by adulthood secondary to the numerous pharyngeal infections that occur in childhood. As such, nasopharyngeal cancers often drain to the second-order nodes in levels II, III, and occasionally in level V (Mukherji 2002).

- **Parapharyngeal space.** The parapharyngeal space is immediately lateral to the pharyngeal mucosal space and contains primarily fat, branches of the trigeminal nerves, and the pterygoid veins. It extends from the skull base to the hyoid bone.
- **Masticator space.** The masticator space is situated anteriorly and contains the infratemporal fossa in its cephalic aspect. It is bounded medially and laterally by the superficial layer of deep cervical fascia and contains the muscles of mastication and body of the mandible.
- **Retropharyngeal/Prevertebral spaces.** Posteriorly the nasopharynx is bounded by the retropharyngeal and prevertebral spaces comprising a preoccipital space (Fig. 13.12). These posterior potential midline spaces can present a major pathway extending from the skull base inferiorly to the upper mediastinum (T3 level) and even the coccyx (prevertebral space).
- **Parotid space.** The parotid space is posterior-lateral to the parapharyngeal space and contains the parotid gland.
- **Carotid space.** The carotid space is formed by the carotid sheath; it contains the internal carotid artery and jugular vein and lymph nodes of the deep cervical chain and acts as a direct communication of spread of tumor or infection from the skull base superiorly to the aortic arch inferiorly.

13.4.2 Oropharynx

The oropharynx is part of the UA including the posterior wall of the oral cavity, communicating superiorly with the nasopharynx and inferiorly with the laryngopharynx. In fact, the oropharynx is continuous with the oral cavity through the oropharyngeal isthmus, and extends from the plane of the hard palate to the level of the hyoid

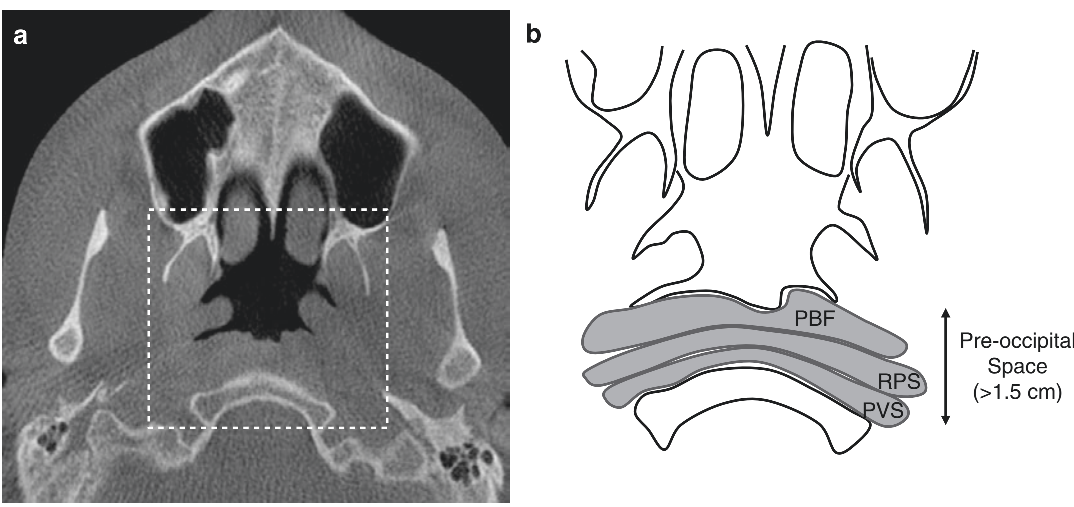

Fig. 13.12 Axial CBCT image (**a**) and schematic of highlighted area (**b**) at the level of the nasopharynx demonstrating the components of the preoccipital space: pharyngobasilar fascia (*PBF*); retropharyngeal space (*RPS*); prevertebral space (*PVS*). At this level, distances greater than 1.5 cm between the occipital bone/anterior vertebra and the posterior wall of the pharynx should be considered with suspicion (Hoe 1989a, b)

bone and epiglottic vallecula (a depression behind the root of the tongue between the glossoepiglottic folds in the throat) (Fig. 13.13).

The oropharynx can be subdivided into retropalatal and retroglossal regions (Fig. 13.14). The retropalatal region, also known as the velopharynx, extends from the level of the hard palate to the inferior margin of the soft palate (Fig. 13.15). The retroglossal region reaches from the inferior margin of the soft palate to the vallecula (Schwab 1998) (Fig. 13.16).

The oropharyngeal isthmus is a part of the oropharynx directly behind the mouth cavity, and it is composed by the soft palate, the tongue bounded by the circumvallate papillae, and the palatine arch. This arch is formed by two pairs of folds or pillars, whose names are derived from the muscles that form them—the palatoglossus and the palatopharyngeal folds. Between the pillars there is a depression, the tonsillar fossa, occupied by the palatine tonsil. In some children, the palatine tonsils may reach considerable size and actually obstruct exposure of the larynx. As it is commonly seen with the adenoid tonsil, the palatine tonsils usually involute after puberty (Isaacs and Sykes 2002).

The walls of the oropharynx are formed by a number of different structures. The anterior wall is formed by the soft palate and the tongue; the posterior wall by the pharyngeal constrictor muscles; and the lateral walls are defined as the tissue between the lateral edge of the airway, the parapharyngeal fat pads, and the mandible.

The lateral pharyngeal walls are made up of a number of muscles, in addition to lymphoid tissue (palatine tonsils). The muscles include the hypoglossus, styloglossus, stylohyoid, stylopharyngeus, palatoglossus, palatopharyngeus, and the pharyngeal constrictors (superior, middle, and inferior). The styloglossus, stylohyoid, and

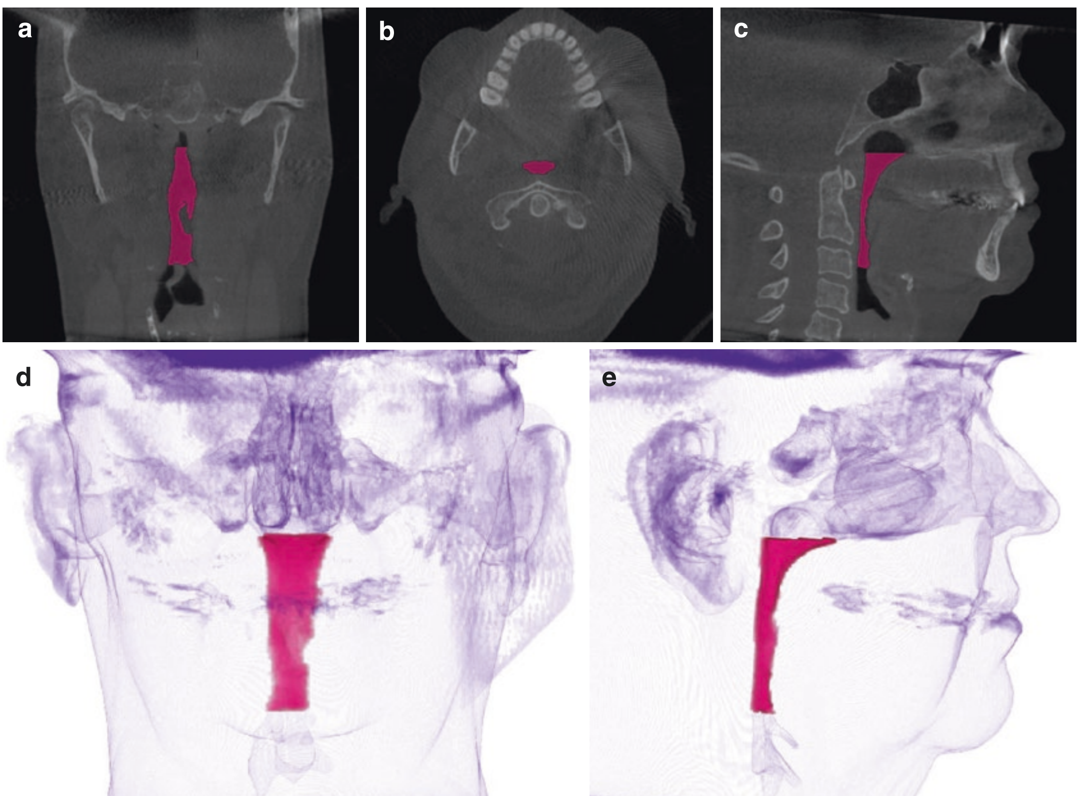

Fig. 13.13 Coronal (**a**), axial (**b**), and sagittal (**c**) orthogonal CBCT images and frontal (**d**) and right lateral (**e**) hollow volumetric renderings (**d**) characterizing the airway volume of the nasopharyngeal division of the upper airway

stylopharyngeus muscles arise from the styloid process and the hypoglossus, middle constrictor, and stylohyoid muscles insert on the hyoid bone (Schwab 1998).

The posterior wall is formed by the superior, middle, and inferior constrictor muscles (although those muscles also make up a portion of the lateral wall) in front of the second and third cervical vertebrae.

13.4.3 Hypopharynx

The hypopharynx, also called the laryngopharynx, is the part of the upper airway that lies below the aperture of the larynx and is continuous with the oropharynx superiorly and the esophagus inferiorly. It joins the oropharynx at the level of the superior border of the epiglottis, and then continues to the level of the sixth

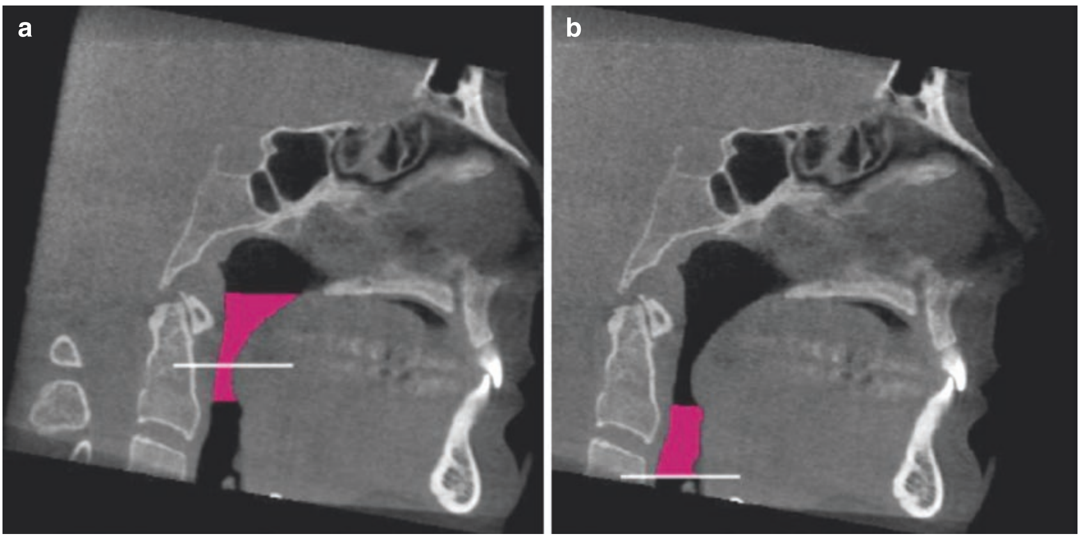

Fig. 13.14 Midsagittal CBCT images showing division (*pink areas*) of the oropharynx into retropalatal (**a**) and retroglossal (**b**) sections with horizontal marks identifying the region of minimal cross-sectional area in each

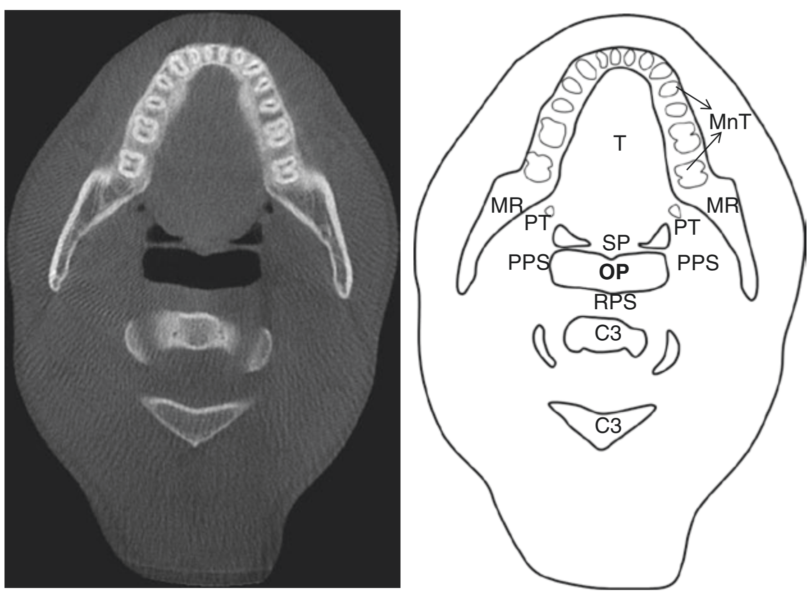

Fig. 13.15 Axial CBCT image (**a**) and corresponding schematic (**b**) demonstrating anatomic features of the oropharynx in the retropalatal region (*OP* oropharynx, *RPS* retropharyngeal space, *PPS* parapharyngeal space, *SP* soft palate, *T* tongue, *PT* palatine tonsils, *MnT* cross-section at the level of the cemento-enamel junction of the mandibular teeth, *MR* ramus of mandible, *C3* 3rd cervical vertebrae)

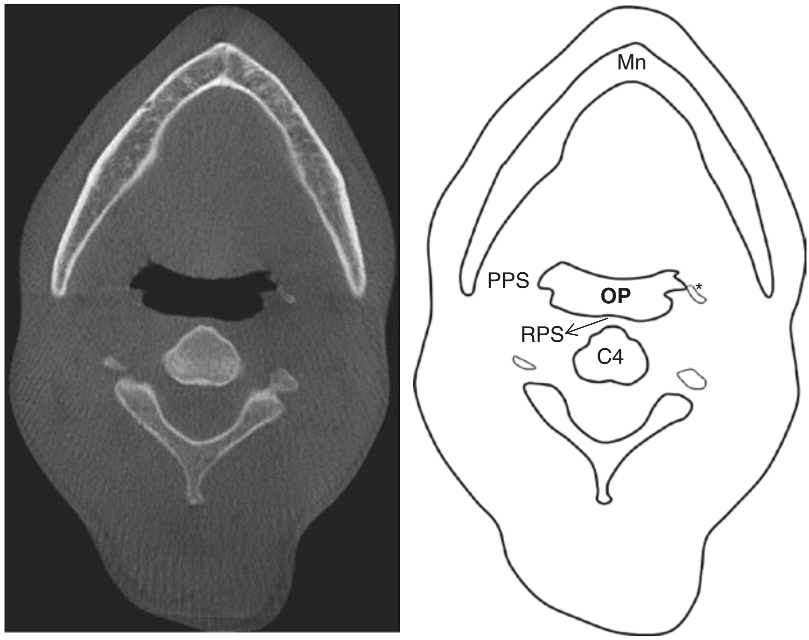

Fig. 13.16 Axial CBCT image (**a**) and corresponding schematic (**b**) demonstrating anatomic features of the oropharynx in the retroglossal region (*OP* oropharynx, *PPS* parapharyngeal space, *RPS* retropharyngeal space, *C4* 4th cervical vertebrae, *Mn* body of mandible)

cervical vertebra at the inferior border of the cricoid cartilage, where it becomes continuous with the esophagus. This specific anatomical area makes the circumferential size of the pharynx decrease rapidly from superior to inferior (O'Rahilly et al. 1983; Park et al. 2010) (Fig. 13.17).

The opening of the larynx is bounded anteriorly and superiorly by the upper portion of the epiglottis, laterally by the aryepiglottic folds, and posteriorly by the elevation of the arytenoid cartilages. Below the opening of the larynx, the anterior wall of the hypopharynx is formed by the posterior surfaces of the arytenoid cartilages and the posterior plate of the cricoid cartilage (Auvenshine 2010) (Figs. 13.18 and 13.19).

On each side of the inlet of the larynx, between the arytenoid cartilages, there is a recess termed the piriform recess, also referred to as the piriform sinus or fossa. The term "piriform," which means "pear-shaped," is also sometimes spelled "pyriform."

The piriform recess is bounded medially by the aryepiglottic fold and laterally by the thyroid cartilage and hyothyroid membrane. It extends from the lateral epiglottic fold to the upper portion of the esophagus (Auvenshine 2010). Deep to the mucous membrane of the piriform fossa lies the recurrent laryngeal nerve as well as the internal laryngeal nerve, a branch of the superior laryngeal nerve. The area is a common place for food to become trapped; if the internal laryngeal nerve is injured, it can give the sensation of food stuck in the throat (O'Rahilly et al. 1983). This distinction is important for head and neck cancer staging and treatment.

13.5 Radiologic Evaluation

13.5.1 Key Radiologic Features

Because CBCT imaging does not provide adequate distinction between soft tissue types, interpretation of images of the upper airway should include consideration of the following key radiologic features.

- **Asymmetry and loss of anatomic architecture.** Gross asymmetry of the morphology of the upper airway suggests the mass effect of

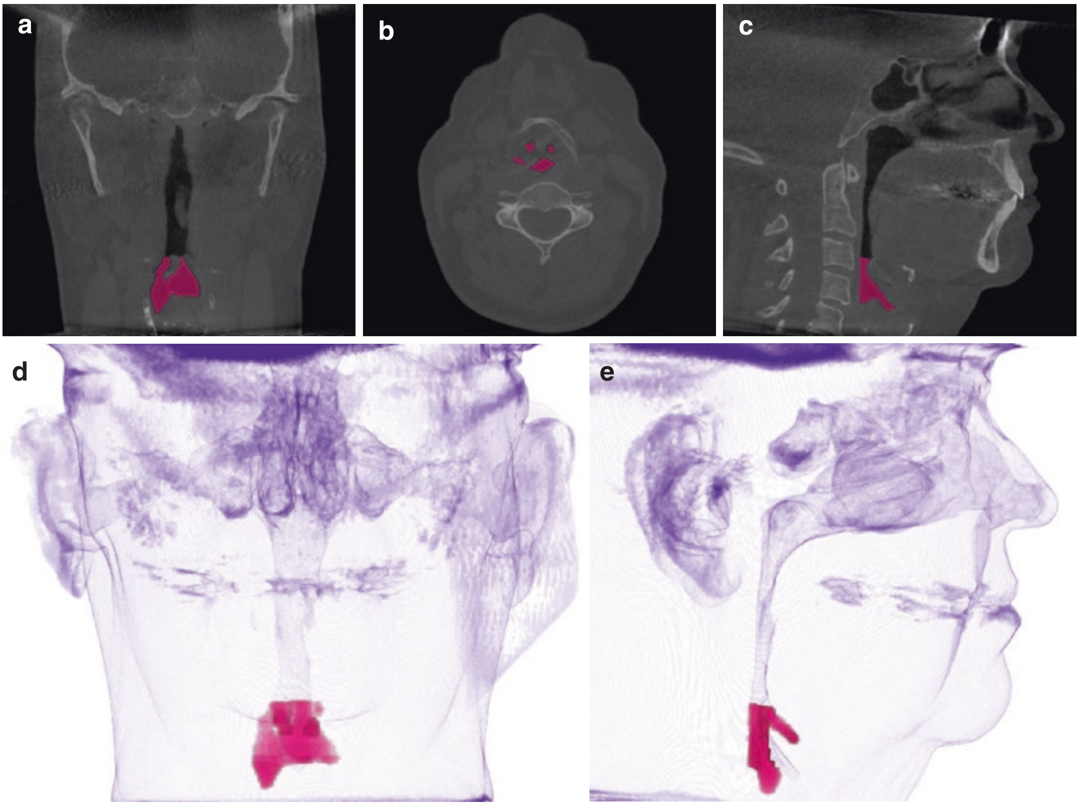

Fig. 13.17 Coronal (**a**), axial (**b**), and sagittal (**c**) orthogonal CBCT images and frontal (**d**) and right lateral (**e**) hollow volumetric renderings (**d**) characterizing the airway volume of the hypopharyngeal division of the upper airway

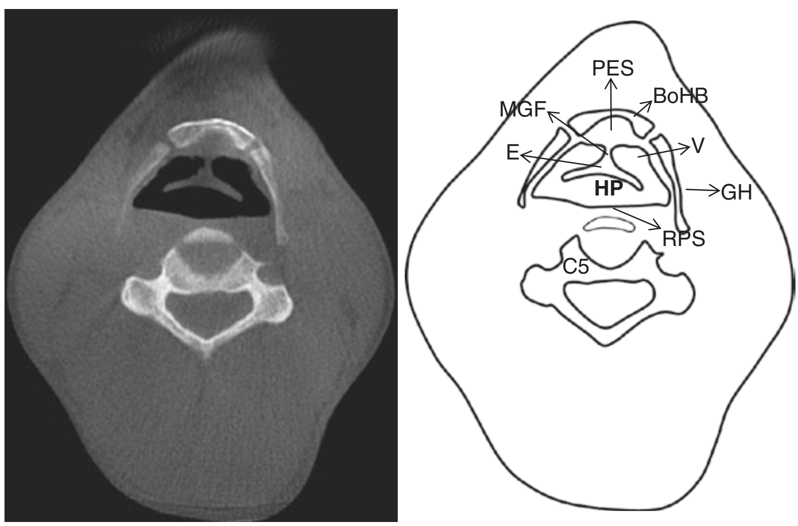

Fig. 13.18 Axial CBCT image (**a**) and corresponding schematic (**b**) demonstrating anatomic features of the hypopharynx (*HP* hypopharynx, *E* epiglottis, *MGF* median glossoepiglottic fold, *PES* pre-epiglottic space, *BoHB* body of the hyoid bone, *V* vallecula, *GH* greater horn of the hyoid bone, *RPS* retropharyngeal space, *C5* 5th cervical vertebra)

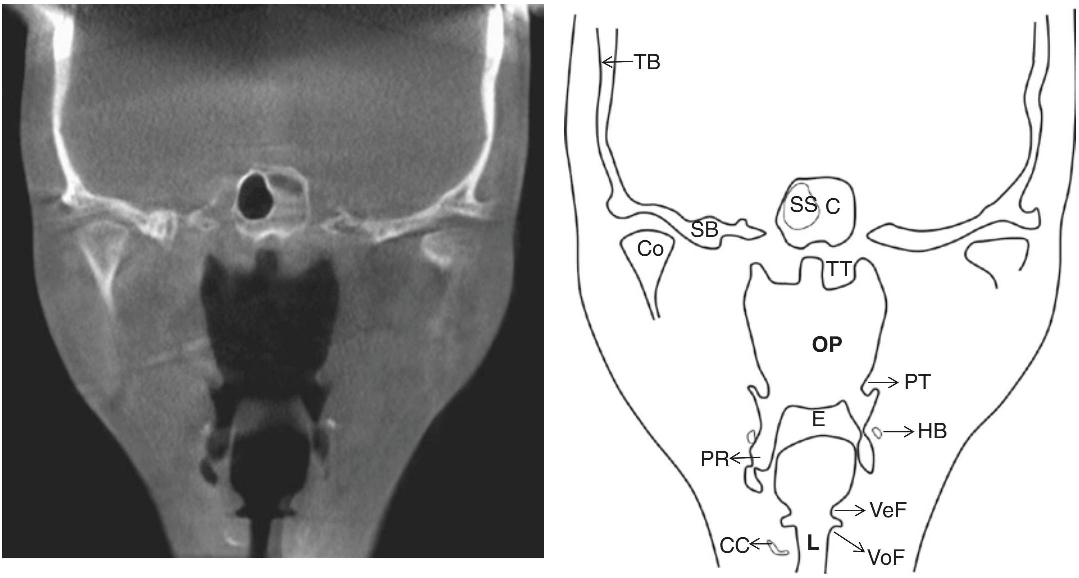

Fig. 13.19 Coronal CBCT image (**a**) and corresponding schematic (**b**) demonstrating anatomic features of the hypopharynx (*E* epiglottis, *OP* oropharynx, *TT* torus tubarius, *C* clivus, *SS* sphenoidal sinus, *SB* sphenoidal bone, *TB* temporal bone, *Co* mandibular condyle, *PT* palatine tonsil, *HB* hyoid bone, *PR* piriform recess, *CC* cricoid cartilage, *L* larynx, *VoF* vocal fold, *VeF* vestibular fold)

an adjacent entity. Differential diagnosis will depend on the site.

  – ***Nasopharyngeal mass.*** Adenoid hypertrophy, posterior extension of sino-nasal tumors.
  – ***Oropharyngeal mass***. Large submandibular gland sailolith, lymph node hypertrophy or calcification, parapharyngeal abscess, regional displacement due to a squamous cell carcinoma of the base of the tongue, tonsillar fauces or lateral oropharyngeal wall or deeper tumors within the pre- and post-styloid, carotid and parotid spaces.

- **Generalized reduction in airway cross-sectional dimensions.** There is great variability in the length and cross-sectional dimensions of the upper airway related to individual morphologic variability, age, body position when scanning, and position of mandibular and tongue. However, a reduction in the transverse dimension less than 17 mm either with or without an anteroposterior reduction less than 10 mm may suggest predilection to obstructive sleep apnea-hypopnea syndrome.
- **Obstruction.** Because of the poor tissue contrast provided by CBCT imaging, clinical correlation and possible referral for further investigation should be considered if soft tissue luminal obstruction or obliteration of anatomic architecture is observed.
- **Surface erosion**. Superficial benign and deep tumors may result in smooth surface localized expansions. However, any indication of surface irregularity or more specifically mucosal erosions are to be considered indicative of malignancy until proven otherwise. Referral to an ENT for further evaluation is highly advisable.

13.5.2 Clinical Significance

- The prevalence of congenital and acquired abnormalities that affect the UA is approximately 3% of the pediatric population (Schechter 2002).
- During development the configuration and function of the tongue largely dictates the patency of the oropharyngeal and hypopharyngeal airway.
- A number of craniofacial dysmorphologies including Pierre-Robin sequence and Apert's

and Treacher Collins' syndromes demonstrate underdevelopment of the maxilla both restricting and constricting UA development.

- Clinicians must be able to recognize incidental findings of non-significance, particularly in children such as the variability in the size of the tonsils and adenoids and the tendency of these structures to reduce in size with age.
- In older individuals, clinicians should recognize features and preferred locations of specific entities of significance such as the mass effect of nasopharyngeal carcinoma occurring most often in the fossa of Rosenmueller and the extension of both sinus and nasal lesions leading to reduced luminal dimensions or obstruction of the naso-, oro-, or hypopharyngeal airway.
- Imaging is important in assisting in the location of obstruction in obstructive sleep apnea hypopnea syndrome (OSAHS).

References

Abramson Z, Susarla S, Troulis M, Kaban L (2009) Age-Related Changes of the Upper Airway Assessed by 3-Dimensional Computed Tomography. J Craniofac Surg 20:657–663. doi:10.1097/SCS.0b013e318193d521

Arens R, McDonough JM, Corbin AM, Hernandez EM, Maislin G, Schwab RJ, Pack AI (2002) Linear dimensions of the upper airway structure during development: assessment by magnetic resonance imaging. Am J Respir Crit Care Med 165:117–122. doi:10.1164/rccm2107140

Auvenshine RC (2010) Anatomy of the airway: an overview. Sleep Med Clin 5:45–57

Chong VF, Fan YF (2000) Radiology of the nasopharynx: pictorial essay. Australas Radiol 44:5–13

Hoe JW (1989a) CT of nasopharyngeal carcinoma: significance of widening of the preoccipital soft tissue on axial scans. AJR Am J Roentgenol 153:867–872

Hoe JW (1989b) Computed tomography of nasopharyngeal carcinoma. A review of CT appearances in 56 patients. Eur J Radiol 9:83–90

Hudgel DW (1986) Variable site of airway narrowing among obstructive sleep apnea patients. J Appl Physiol 61:1403–1409

Isaacs RS, Sykes JM (2002) Anatomy and physiology of the upper airway. Anesthesiol Clin N Am 20:733–745

Linder-Aronson S, Woodside DG, Lundström A (1986) Mandibular growth direction following adenoidectomy. Am J Orthod 89:273–284

Mukherji SK (2002) Pharynx. In: Som PM, Curtin HD (eds) Head and neck imaging. Mosby, Missouri, pp 1465–1520

O'Rahilly R, Muller F, Carpenter S, Swenson R (1983) Basic human anatomy—a regional study of human structure. WB Saunders, Philadelphia

Park JW, Kim NK, Kim JW, Kim MJ, Chang YI (2010) Volumetric, planar, and linear analyses of pharyngeal airway change on computed tomography and cephalometry after mandibular setback surgery. Am J Orthod Dentofac Orthop 138:292–299

Schwab RJ (1998) Upper airway imaging. Clin Chest Med 19:33–54

Schechter MS (2002) Section on pediatric pulmonology, subcommittee on obstructive sleep apnea syndrome. Technical report: diagnosis and management of childhood obstructive sleep apnea syndrome. Pediatrics 109(4):e69

Stevens JJWM, Jones JG (1995) Functional anatomy and pathophysiology of the upper airway. Bailliere's Clin Anaesthesiol 9:213–234

Subtelny JD (1954) The significance of adenoid tissue in orthodontia. Angle Orthod 24:59–69

Vogler RC, Ii FJ, Pilgram TK (2000) Age-specific size of the normal adenoid pad on magnetic resonance imaging. Clin Otolaryngol Allied Sci 25:392–395

Temporal Bone

14

Mahi Sophia Mehr, Axel Ruprecht, and Kivanç Kamburoğlu

Contents

M.S. Mehr, D.D.S., M.Sc. (✉)
Department of Oral Pathology, Radiology and Medicine, The University of Iowa, College of Dentistry, Iowa City, Iowa, USA
e-mail: ddsmahit@gmail.com

A. Ruprecht, D.D.S., M.Sc.D.
Departments of Oral Pathology, Radiology and Medicine, Radiology, and Anatomy and Cell Biology, The University of Iowa, Iowa City, Iowa, USA

Department of Oral and Maxillofacial Diagnostic Sciences, The University of Florida, FL, USA
e-mail: axel-ruprecht@uiowa.edu

K. Kamburoğlu, D.D.S., M.Sc., Ph.D.
Department of Dentomaxillofacial Radiology, Faculty of Dentistry, Ankara University, Ankara, Turkey
e-mail: dtkivo@yahoo.com

14.1 Introduction

In comparison to traditional medical computed tomography (CT) systems, dental cone bean computed tomography (CBCT) units offer reduced effective radiation doses, shorter acquisition scan

W.C. Scarfe, C. Angelopoulos (eds.), *Maxillofacial Cone Beam Computed Tomography*,
https://doi.org/10.1007/978-3-319-62061-9_14

times, easier imaging, and lower costs. Applications have been extended to the face and skull base including the temporal bone. CBCT provides reliable morphologic assessment of the temporal bone with higher spatial resolution compared to multislice computed tomography (MSCT). Owing to its significantly reduced radiation dose, CBCT is becoming the method of choice in the diagnosis and follow-up of some temporal bone pathology (Dahmani-Causse et al. 2011). CBCT also revealed promising results for noninvasive intraoperative imaging to facilitate electrode array placement in the cochlea (Cushing et al. 2012; Barker et al. 2009). In addition, postoperative imaging is highly suggested in order to confirm electrode placement, typically with plain digital or film radiographs especially in the ossified or congenitally abnormal cochlea due to increased chance of poor implantation. However, assessment of electrode position can be difficult with two-dimensional radiographs, especially in bilateral implantation where the implants superimpose each other on lateral views (Barker et al. 2009). High-resolution and almost artifact-free multi-planar reconstruction images that allow assessment of the precise intra-cochlear position of the electrode and visualization of each of the individual contacts, make CBCT a perfect candidate for the postoperative assessment and follow-up of cochlear implantation electrodes (Ruivo et al. 2009). Considering the fact that CBCT imaging has the strong potential to replace medical CT for some applications related to otolaryngology, there is a trend towards including specific ear, nose, and throat imaging programs in CBCT systems.

14.2 Development

The development of the temporal bone and external and middle ear results from interaction between ectoderm, mesoderm, and endoderm. Migration of the neural crest cells gives rise to six pharyngeal or branchial arches by the fifth week of gestation. The tympanic cavity and the Eustachian tube develop from invagination of the first pharyngeal pouch (endoderm of tubotympanic recess). The ossicles and their supporting muscles and tendon develop from the mesoderm of the first and second branchial arches. The first branchial arch (mandibular arch or Meckel's cartilage) gives origin to the tensor tympani muscle, the head and the neck of malleus and the body and short process of incus. The long process of incus, the manubrium of malleus, the superstructure of stapes, and the stapedius muscle and tendon arise from the second branchial arch. The tympanic membrane arises from all three germ layers, endoderm medially, mesoderm in the middle, and ectoderm laterally. The external auditory canal and the auricles arise from the ectoderm of the first and second branchial arches. The *otic placode*, a thickening of the surface ectoderm located between the first branchial groove and hindbrain, gives rise to the inner ear (Swarts 2009; Fau et al. 2011; Swarts and Mukherji 2008). Embryology of the temporal bone and the auditory system is very complex; readers are referred to embryology text books for more detailed explanation.

14.3 Imaging Protocol

Two approaches to the imaging of the temporal bone should be adopted. The first involves depicting larger portions of the bone. This is best accomplished by the axial plane and reformatting the volumetric dataset in two orthogonal planes, the sagittal and coronal planes (Fig. 14.1). However some portions of the petrous part of the temporal bone contain anatomic structures that are not optimally depicted on these planes.

The more complex anatomy of the petrous portion of the temporal bone should be imaged by developing oblique planar images in relation to the long axis of the petrous part of the temporal bone. Oblique planar images can be obtained at a standard or corrected angulation according to the anatomy of each individual patient. Images obtained at a standard 45° angle to the midsagittal, and longitudinal to the petrous part of the temporal bone, simulate the plain radiograph skull projection known as the *Stenvers projection* (an occipitofrontal with the head rotated 45° and a 12° tilt away from the feet) The plane of the Stenvers sections is *perpendicular* to the course of the superior semicircular canal. Images perpendicular to this projection, providing cross-sectional images of the

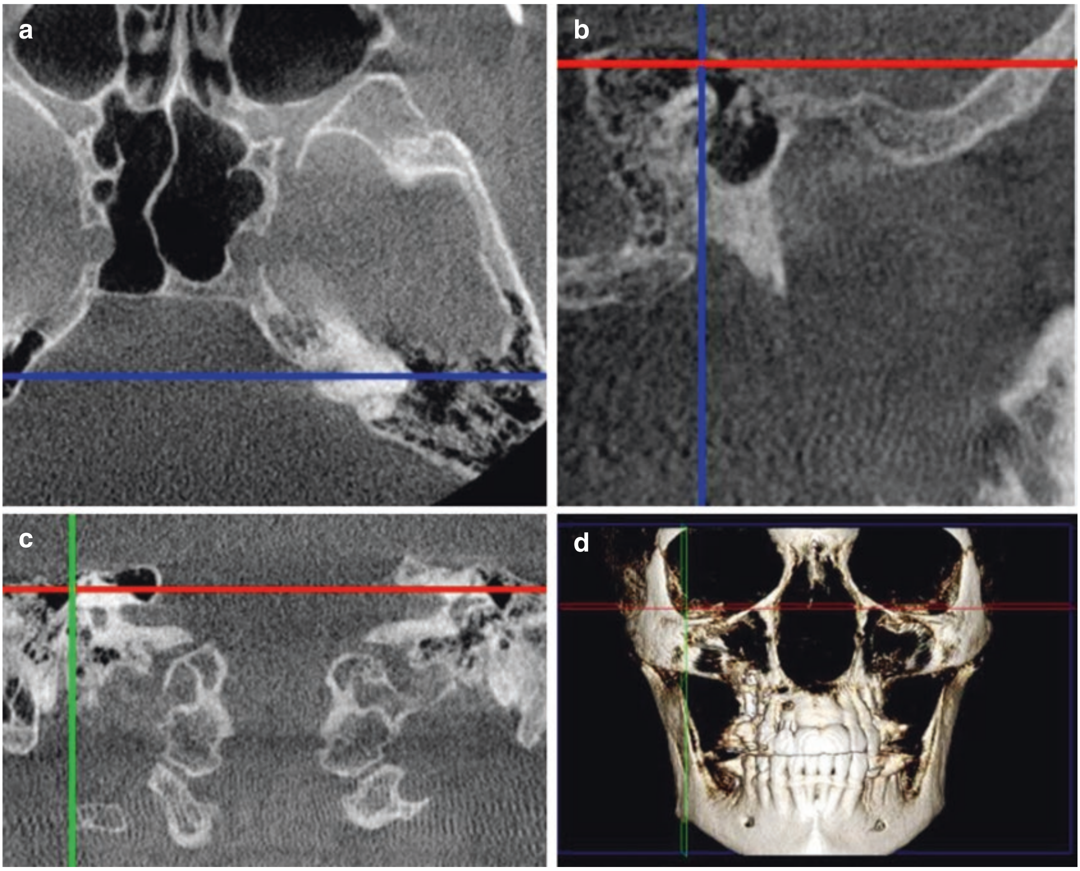

Fig. 14.1 Axial (**a**), sagittal (**b**), and coronal (**c**) CBCT planes and 3D reconstruction (**d**). The green lines indicate the location of the sagittal slice, the *blue lines* indicate the location of the coronal slice and the *red lines* indicate the location of the axial slice

petrous part of the temporal bone, simulate the plain radiograph skull projection known as the *Pöschl projection*, also called the axial projection of the pyramid or the transverse pyramidal plane (Figs. 14.2 and 14.3).

We recommend a *modified Stenvers projection* in which the oblique planar reconstruction is obtained by corrected adjustment of the Stenvers plane through the long axis of the petrous part of the temporal bone. This will subsequently provide *modified Pöschl views* (Fig. 14.4) (Lane et al. 2006; Branstetter et al. 2006).

In maxillofacial imaging, clinicians should be aware of the appearance of normal anatomy, anomalies, and common pathoses as they initially present on axial and coronal images. If further visualization is warranted, then corrected Stenvers and Pöschl views should be reconstructed.

14.4 Anatomy

The lateral aspects and base of the skull are formed partly by the temporal bones. Each temporal bone comprises five morphologically distinct parts: *squamous part* (anterosuperior), *tympanic part* (inferior and lateral), the *styloid process* (inferior), *petrous part* (medial), and *mastoid part* (posterior). The petrous and mastoid parts are sometimes considered to be a single unit referred to as the petromastoid part (Figs. 14.5, 14.6, 14.7, and 14.8) (Standring and Gray 2008).

When viewed from the lateral aspect, the temporal bone presents a smooth and convex surface that contributes to the lateral wall of the cranium and is composed of the squamous, tympanic, and mastoid parts. It articulates anteriorly with the greater wing of the sphenoid bone, superiorly with the parietal bone, and posteriorly with the

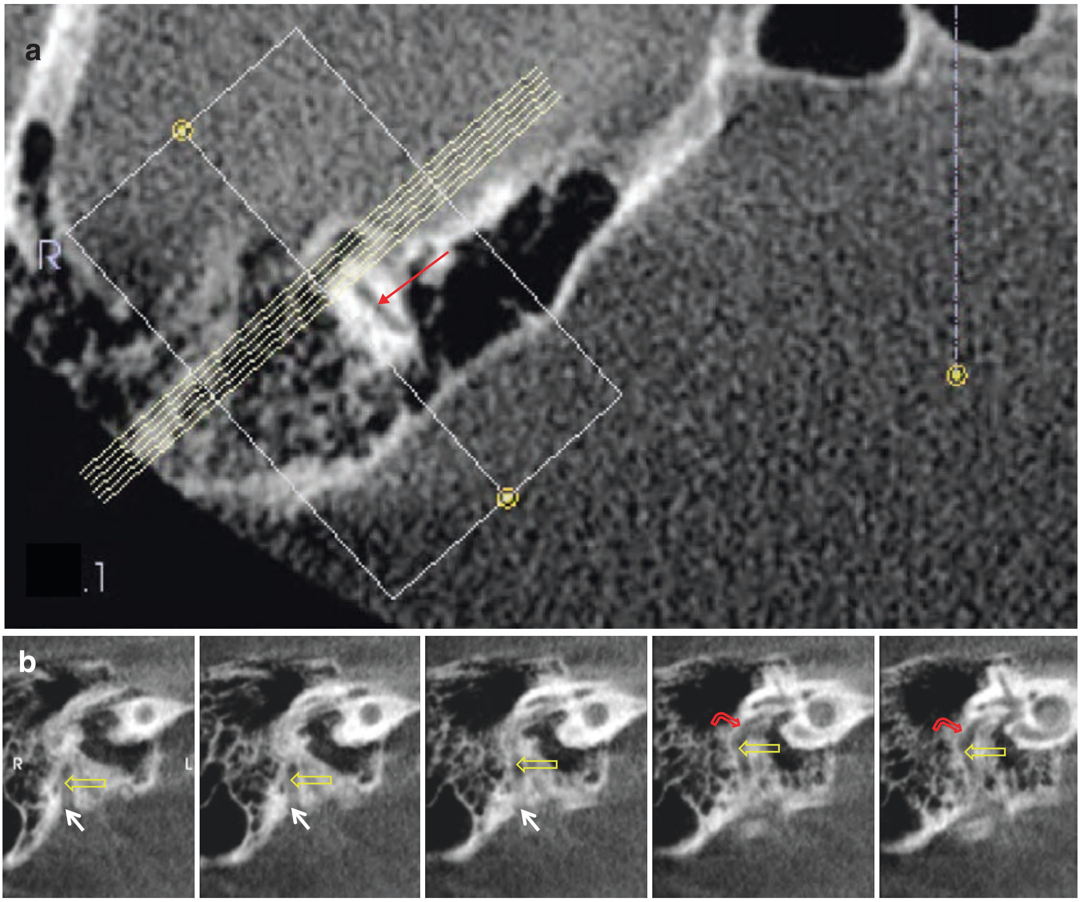

Fig. 14.2 Cropped CBCT axial image (**a**) shows the location and orientation (*green lines*) of the Stenvers slices reconstructed in a direction perpendicular to the course of the superior (anterior) semicircular canal (*red solid arrow*). The Stenvers sections (**b**) show the stylomastoid foramen (*white solid arrow*), the vertical or mastoid segment (*straight, yellow open arrow*) and the second genu of the facial nerve canal (*curved, red open arrow*)

occipital bone. The zygomatic process, mandibular fossa, articular eminence (tubercle), external auditory meatus (the opening to the external auditory canal), and styloid process are also visible from a lateral view (Figs. 14.5 and 14.7). When viewed from the medial aspect, the squamous, petrous, and mastoid parts of the temporal bone are visible. The petrous ridge is a wedge-like structure that contributes to the middle portion of the base of the skull and articulates anteriorly with the greater wing of the sphenoid bone and posteriorly with the occipital bone (Fig. 14.6) (Standring and Gray 2008).

The lateral surface of the skull can be subdivided into three regions: facial (anterior), temporal (middle), and occipital (posterior). The temporal region is bounded superiorly and posteriorly by the temporal lines and anteriorly by the frontal process of the zygomatic bone. Located on the temporal region is the zygomatic arch, deep to which the temporal and infratemporal spaces communicate. The *superior* and *inferior temporal lines* are two superiorly convex lines on the lateral surface of the skull, extending from the lateral aspect of the frontal bone posteriorly across the middle portion of the parietal bone. The superior line may become indistinct as it moves posteriorly, whereas the inferior temporal line becomes more prominent after it reaches the posterior part of the squamous portion of the

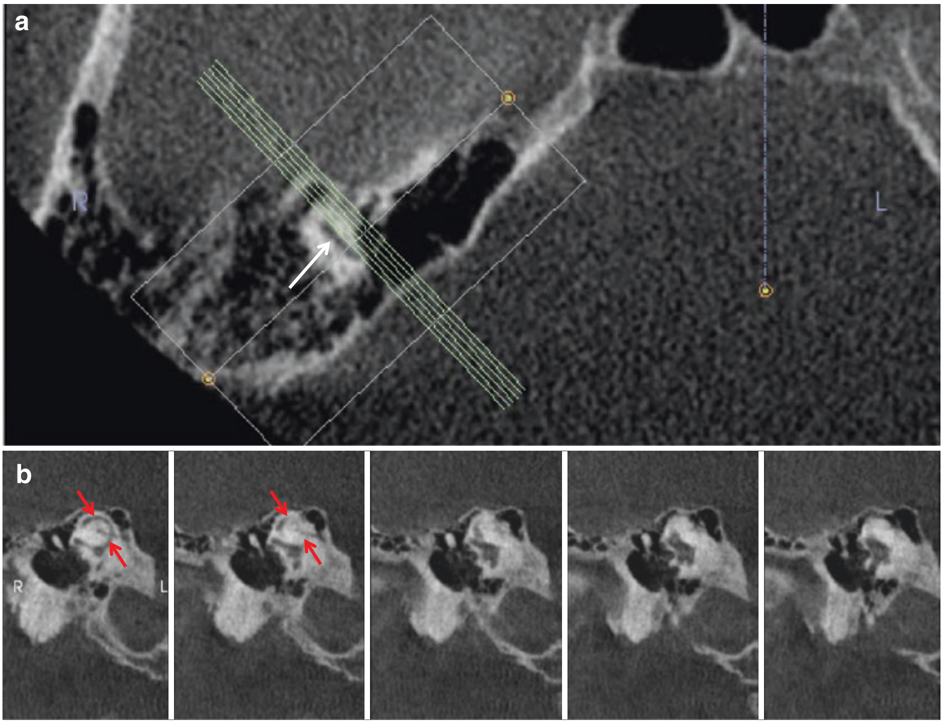

Fig. 14.3 Axial CBCT section (**a**) shows the location and orientation (*green lines*) of the Pöschl slices reconstructed in a direction parallel to the course of the superior (anterior) semicircular canal (*white arrow*). The superior semicircular canal (*red arrows*) can be optimally visualized on the Pöschl sections (**b**)

temporal bone where it curves anteroinferiorly to form the *supramastoid crest* at the base of the mastoid process. The superior temporal line provides attachment for the temporal fascia. The inferior temporal line is at the upper limit of the muscular origin of the temporalis muscle (Fig. 14.5) (Standring and Gray 2008).

14.4.1 Squamous

The squamous part of the temporal bone is a flat, thin, scale-like, and partially translucent structure that forms the anterosuperior part of the temporal bone and covers the temporal lobe of the brain laterally. It is composed of medial (*cerebral*), and lateral (*temporal*) surfaces as well as a small inferior (*infratemporal*) surface.

- **Temporal and Infratemporal surfaces**. The temporal surface has the *zygomatic process* and the *mandibular (glenoid) fossa*. The zygomatic process extends anteriorly from the anteroinferior aspect of the temporal surface and articulates with the temporal process of the zygomatic bone to form the *zygomatic arch*. The mandibular fossa (glenoid fossa) is a thin-walled depression on the anteroinferior aspect of the squamous part (infratemporal surface), posteromedial to the zygomatic process. This fossa is bounded anteriorly by the anterior articular eminene and posteriorly by the tympanic plate and posterior articular eminence. It forms the roof of the temporomandibular joint with which the condylar process of the mandible articulates (Figs. 14.5 and 14.7).
- **The internal or cerebral surface.** This part is concave and contains depressions that correspond to convolutions of the temporal lobe of the brain (Fig. 14.6) (Standring and Gray 2008).

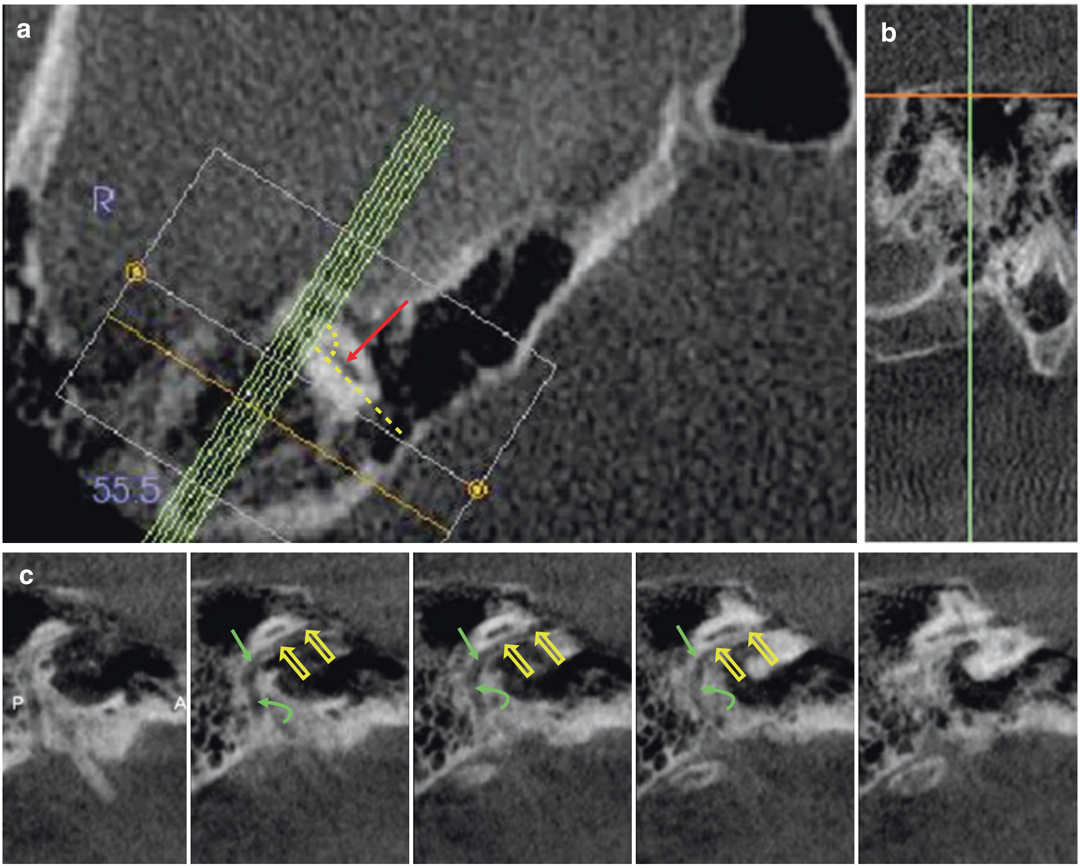

Fig. 14.4 The axial CBCT section (**a**) shows the direction and orientation (*green lines*) of the modified Stenvers slices reconstructed with a greater than 90° angle to the course of the superior (anterior) semicircular canal (*red arrow*); it also demonstrates the plane (*white rectangle*) of the modified Pöschl section (**b**). On the modified Stenvers slices (**c**), note that the tympanic part (*straight, yellow open arrows*) of the facial nerve canal is better visualized on the modified Stenvers sections than the standard Stenvers sections shown earlier. The vertical or mastoid portion (*curved green arrow*) and second genu (*straight green arrow*) of the facial nerve canal were also visualized on the standard Stenvers as shown earlier

14.4.2 Tympanic

The tympanic part of the temporal bone is shaped like an incomplete ring. It is situated inferior to the squamous part and anterior to the mastoid process and fuses medially with the petrous part. Its concave surface forms the anterior wall, floor, and part of the posterior wall of the bony portion of the external auditory canal (EAC) (Figs. 14.5 and 14.8). The tympanic membrane is attached to a narrow tympanic sulcus on its medial surface.

Located in the posterior aspect of the mandibular fossa, between the squamous part of the temporal bone and the tympanic plate is a fissure known as the *squamotympanic* fissure. Within this fissure lies a thin wedge of bone that divides it into *petrotympanic* and *petrosquamous* fissures (Fig. 14.9). The chorda tympani branch of the facial nerve (CN VII) travels through the petrotympanic fissure (Standring and Gray 2008).

14.4.3 The Styloid Process

The styloid process is situated anterior and medial to the mastoid process and gives attachment to several muscles and ligaments. It descends anteromedially and its tip usually extends to a point medial to the posterior margin of the mandibular ramus. It ranges in length from a few millimeters

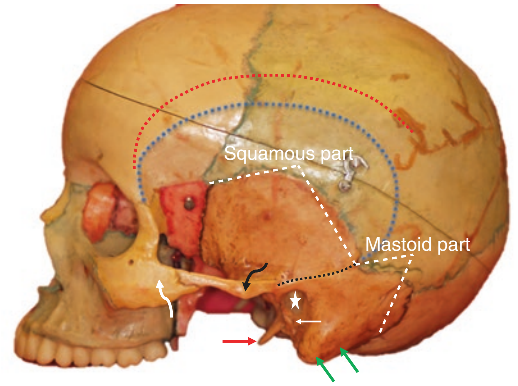

Fig. 14.5 Lateral view of the temporal bone shows the squamous and mastoid parts of the temporal bone (*white, dashed lines*), the tympanic part of the temporal bone (*straight white arrow*), the zygomatic process (*curved black arrow*), the styloid process (*red arrow*), the mastoid process (*green arrows*), the supramastoid crest (*black dotted line*), the external auditory meatus (*white star*), the location of the superior temporal line (*red dotted line*), the location of the inferior temporal line (*blue dotted line*). Note that the zygomatic arch is formed anteriorly by the temporal process of the zygomatic bone (*curved white arrow*) and posteriorly by the zygomatic process of the temporal bone (*curved black arrow*)

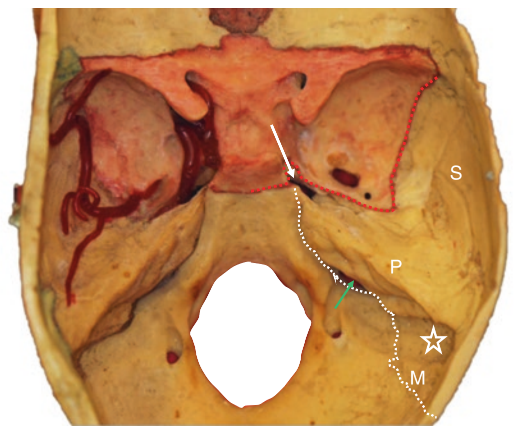

Fig. 14.6 Internal view of the skull shows the medial aspect of the squamous part (*S*), the petrous part (*P*), and the medial aspect of the mastoid part (*M*) of the right temporal bone. In addition, note the foramen lacerum (*white arrow*), a portion of the sigmoid sulcus situated on the mastoid part of the temporal bone (*white open star*), the border of the sphenoid bone (*red dotted line*), and the anterior border of the occipital bone (*white dotted line*). Note that the jugular foramen (*green arrow*) is formed by the articulation of the posterior border of the petrous part of the temporal bone and the anterior border of the occipital bone (*white dotted line*)

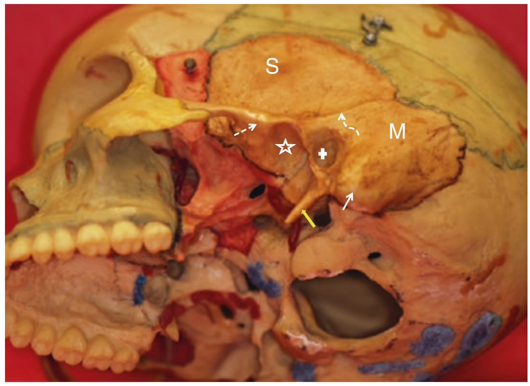

Fig. 14.7 Inferolateral view of the skull shows the mandibular or glenoid fossa (*white open star*), the anterior articular eminence (*straight, white dashed arrow*), the mastoid process (*straight, white solid arrow*), the styloid process (*yellow arrow*), the external auditory meatus (*white plus sign*), the supramastoid ridge (*curved, white dashed arrow*), and the mastoid (*M*) and squamous (*S*) parts of the temporal bone

to a few centimeters. The *stylomastoid foramen* lies between the styloid and mastoid processes. It represents the inferior end of the mastoid portion of the facial nerve canal through which the facial nerve exits the skull (Figs. 14.5, 14.7, 14.8 and 14.12) (Standring and Gray 2008).

14.4.4 Petromastoid

The petromastoid part of the temporal bone can be described as two separate parts, the *mastoid* and the *petrous* part (Fig. 14.10).

14.4.4.1 Mastoid

The mastoid part is the posterior region of the temporal bone from which the somewhat conical *mastoid process* projects inferiorly. This part of the temporal bone is larger in adult males than females. The sternocleidomastoid, splenius capitis, and longissimus capitis muscles are all attached to its lateral surface and the posterior belly of digastric is attached to its medial surface. On the medial surface of the mastoid part is a deep, curved sigmoid sulcus that houses the sigmoid venous sinus (Figs. 14.5, 14.6, 14.7, 14.8 and 14.10) (Standring and Gray 2008).

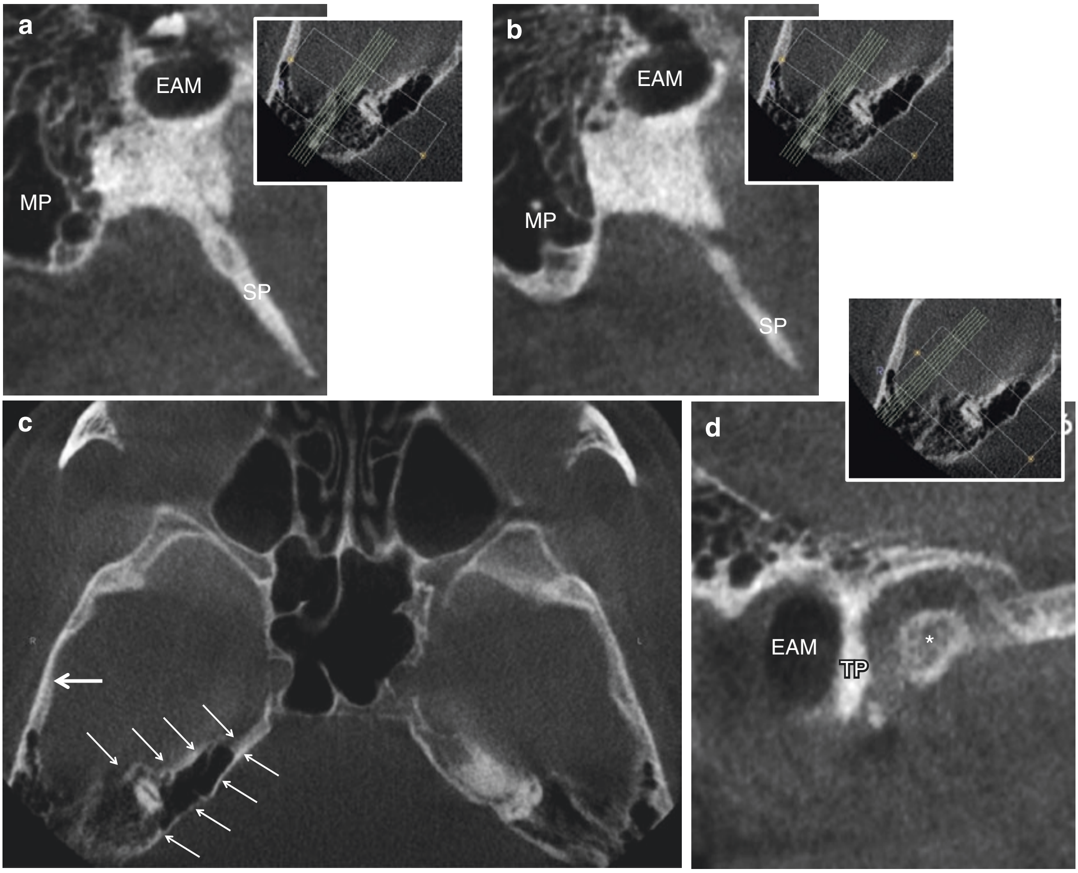

Fig. 14.8 Modified Stenvers slices (**a**, **b,** and **d**) of the right temporal bone with the small axial view on its top right shows the approximate location and orientation of the Stenvers section. The styloid process (*SP*), the mastoid process (*MP*), the tympanic part of the temporal bone (*TP*), the external auditory meatus (*EAM*), and the mandibular condyle (*asterisk*) can be visualized on these sections. An axial CBCT section (**c**) showing the petrous (*white thin arrows*) and the squamous (*white thick arrow*) parts of the temporal bone

The mastoid part houses the *mastoid air cells* (Figs. 14.9 and 14.11). This region is subdivided into the mastoid antrum, which communicates with the middle ear cavity through the aditus, and the peripheral mastoid air cells. A thin, vertical, osseous plate oriented along the sagittal plane, known as *Koerner's septum*, separates the aerated cells in the squamous part from the mastoid antrum. Koerner's septum is the remnant of the petrosquamous suture that extends from the glenoid fossa towards the mastoid tip and is situated lateral to the facial nerve canal (Fig. 14.12). It may be confused with the medial wall of the antrum by surgeons and lead to incomplete removal of disease (Swarts 2009; Virapongse et al. 1982). The extent of pneumatization of the temporal bone is dependent on the multiple factors including heredity, nutrition, and environment. There is a correlation between early onset diseases of the middle ear, such as infections, and poor development of the mastoid air cells (Tos et al. 1985; Valtonen et al. 2005).

Han et al. (2007) classified pneumatization of the temporal bone by the mastoid air cells into four groups using the sigmoid sinus, the labyrinth (superior semicircular canal), and the carotid canal as landmarks. In order to classify the pneumatization pattern with respect to the sigmoid sulcus, one needs an axial section of the temporal bone where the ice-cream cone structure (malleus and incus articulation; refer to the middle ear ossicles for detailed explanation) can be visualized. In group 1, pneumatization is confined to the anteromedial region of a line passing through the most anterior point of the sigmoid sinus; the line is drawn in an

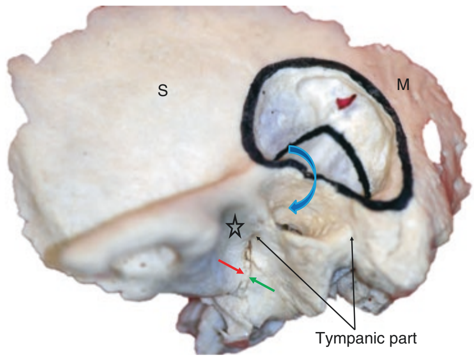

Fig. 14.9 The anterolateral view of the temporal bone shows the external auditory canal (*curved blue arrow*), the mandibular or glenoid fossa (*black open star*), the tympanic part of the temporal bone (*tympanic part*), the petrotympanic fissure (*green arrow*), the petrosquamous fissure (*red arrow*), the mastoid (*M*) and the squamous (*S*) parts of the temporal bone, and the opening created to access the mastoid air cells (*the area outlined by the black line*)

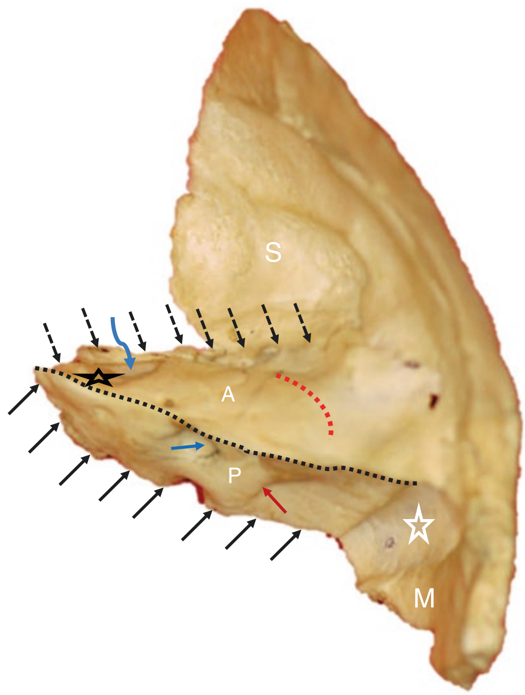

Fig. 14.10 Superior view of the temporal bone and petrous ridge shows the anterior surface (*A*), the posterior surface (*P*), the anterior border (*black dashed arrows*), the superior border (*black dotted line*) and the posterior border (*black solid arrows*) of the petrous ridge. In addition, the image shows the mastoid part (*M*), the sigmoid sulcus (*white open star*), the squamous part (*S*), the aperture of the carotid canal (*curved blue arrow*), internal auditory meatus (*straight blue arrow*), the arcuate eminence (*red dotted line*), the opening of the vestibular aqueduct (*red arrow*), and the trigeminal impression (*black open star*)

anterolateral direction such that it makes a 45° angle with the midsagittal plane. In group 2, pneumatization extends posteriorly between two lines drawn with the same 45° anterolateral direction passing through the most anterior part and the most lateral aspect of the sigmoid sulcus. In group 3, pneumatization extends posteriorly between two lines drawn with the same 45° anterolateral direction passing through the most lateral aspect and the most posterior point of the sigmoid sulcus. In group 4, pneumatization extends posterior to the line passing anterolaterally through the most posterior point of the sigmoid sulcus (Fig. 14.13).

Classification with respect to the labyrinth can be performed in an axial section through the superior semicircular canal (SSC). In group 1, there is no pneumatization medial to the SSC. In group 2, pneumatization involves less than half of the petrous portion medial to the SSC. In group 3, pneumatization involves more than half of the petrous portion medial to the SSC. In group 4, pneumatization extends to most of the petrous apex medial to the SSC (Fig. 14.13).

Classification with respect to the carotid canal can be achieved in an axial section in the inferior aspect of the petrous part of the temporal bone, through the vertical portion of the carotid canal, as follows: group 1, there is no pneumatization in the apex of the petrous portion near the carotid canal; group 2, pneumatization extends to an area in vicinity of the carotid canal; group 3, pneumatization extends to a point just lateral to the carotid canal; group 4, pneumatization extends medial to the carotid canal (Fig. 14.14) (Han et al. 2007).

Extensive pneumatization of the zygomatic process and the articular eminence may be found incidentally in CBCT images (Figs. 14.11, 14.12, 14.13, and 14.14) (Han et al. 2007). This may vary by population groups. Miloglu et al. (2011) reported pneumatization of the articular eminence in 8% of 514 subjects (Miloglu et al. 2011). However, Yavuz et al. (2009) found pneumatization of the articular eminence only in 1.03% of 8107 subjects (Yavuz et al. 2009).

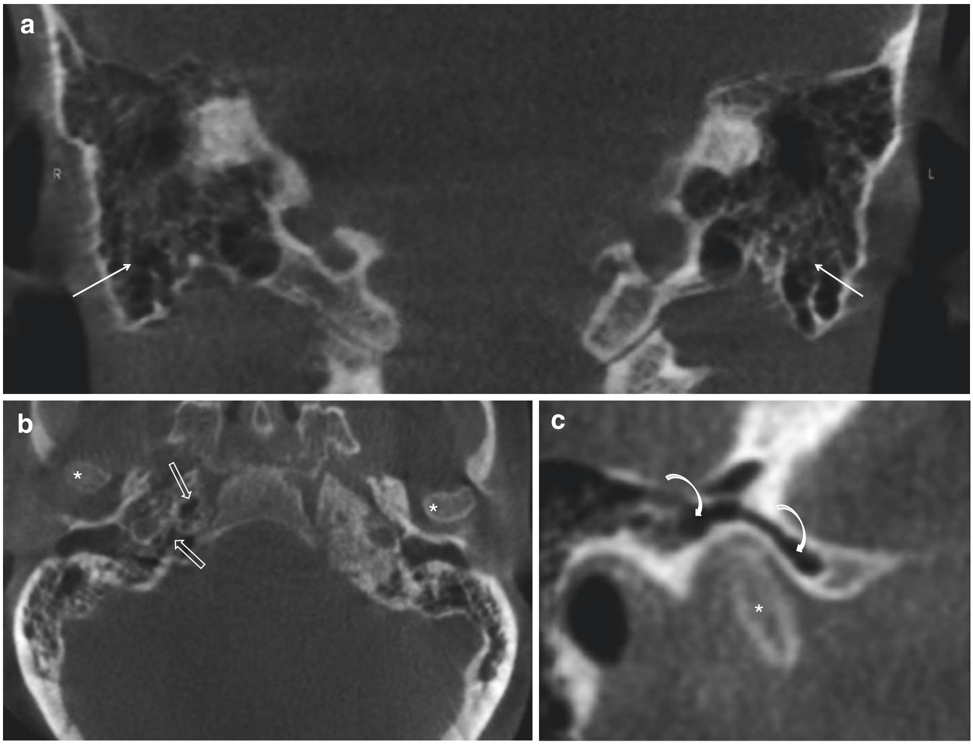

Fig. 14.11 The coronal CBCT section (**a**) of the mastoid air cells shows pneumatization of the mastoid processes (*straight solid arrows*). Axial CBCT section (**b**) shows pneumatization of the petrous apex (*open arrows*). Sagittal CBCT section (**c**) shows pneumatization of the temporal bone covering the mandibular or glenoid fossa (*curved solid arrows*). The mandibular condyle (*asterisk*) can be visualized in the axial and sagittal views (**b**, **c**).

14.4.4.2 Petrous

The petrous part encloses the *acoustic system* and contributes to the floor of the middle and posterior cranial fossae. It is a superiorly and anteromedially inclined, pyramid-shaped process that is wedged between the greater wing of the sphenoid bone and the occipital bone in the cranial base. It consists of a base, an apex, three surfaces (anterior, posterior, and inferior), and three borders (anterior, posterior, and superior). The anterior and posterior surfaces are, in fact, the cerebral surfaces and are visible from the internal aspect of the skull, whereas the inferior surface contributes to the external surface of the base of the skull (Figs. 14.6, 14.8, and 14.10).

The anterior surface of the petrous part is continuous with the cerebral surface of the squamous part and contributes to the part of the posterior floor of the middle cranial fossa. The aperture of the horizontal section of the *carotid canal*, which runs internally through the petrous apex in an anteromedial direction, can be visualized near the apex on the anterior surface of the petrous ridge. This portion of the carotid canal is often covered by a roof with deficient bone that has been replaced by fibrous tissue (Figs. 14.10, 14.14, 14.15, and 14.16). Located above the carotid canal, close to the petrous apex of the anterior surface, is a shallow impression known as the trigeminal impression, which provides a place for the trigeminal (semilunar or Gasserian) ganglion. Located approximately in the center of the anterior surface is the *arcuate eminence,* an elevation caused by the superior (anterior) semicircular canal which resembles a fingertip. Lateral to this eminence are two depressions. The anterior one is the roof of the middle ear cavity and the posterior one is the roof of the mastoid antrum. These depressions are made of an extremely thin layer of bone known as the tegmen tympani.

Immediately anterior and medial to the arcuate eminence is the *hiatus for the greater superficial petrosal nerve* that is a branch of the facial nerve. A shallow, thin groove runs anteromedially from

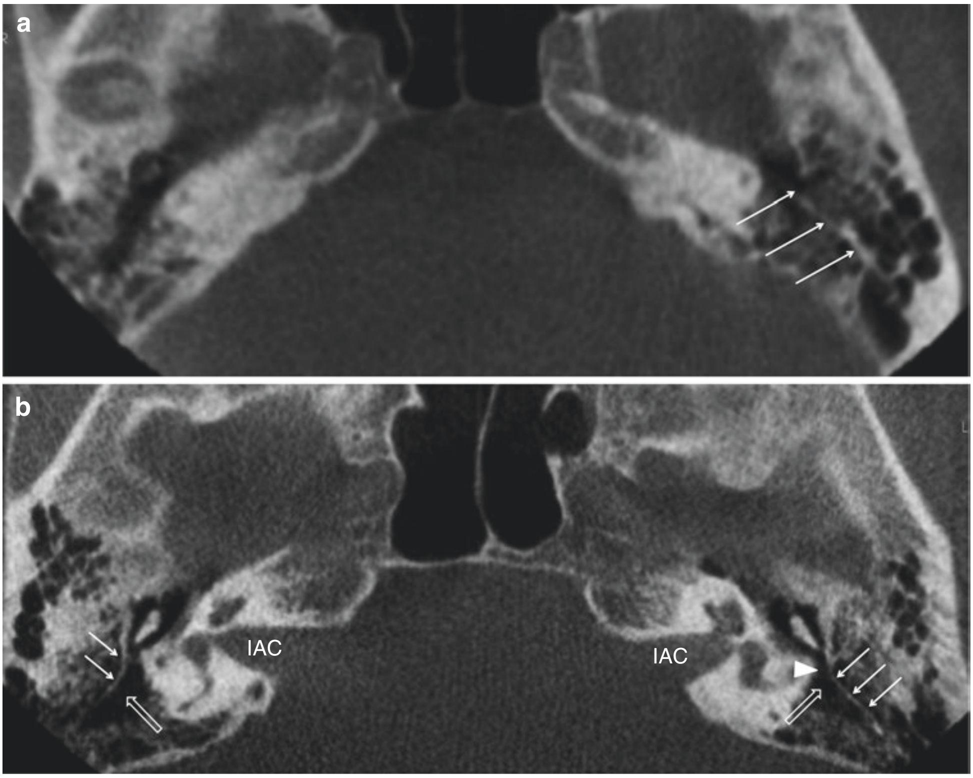

Fig. 14.12 Axial CBCT sections (**a**, **b**) show Koerner's septum (*solid arrows*), mastoid antrum (*open arrows*), internal auditory canal (*IAC*) and the aditus to the mastoid antrum (aditus ad antrum mastoideum) (*arrowhead*)

this hiatus which carries the greater superficial petrosal nerve towards the foramen lacerum where it joins with the deep petrosal nerve, a branch of the carotid sympathetic plexus, to form the vidian nerve or nerve of the pterygoid canal. *Foramen lacerum* is located in the middle cranial fossa, between the apex of the anterior surface of the petrous ridge and the attachment of the greater wing to the body of the sphenoid bone. A similar, but smaller hiatus and groove lateral to the hiatus of the greater superficial petrosal nerve runs to the foramen ovale and carries the *lesser superficial petrosal nerve* (Figs. 14.10 and 14.15).

The posterior surface of the petrous part is continuous with the internal surface of the mastoid part and forms the anterior part of the posterior cranial fossa. It contains the aperture of the *internal auditory canal* (IAC) approximately in its center (Figs. 14.10, 14.12, and 14.17). Posterolateral to this aperture is a small slit covered by a thin plate of bone which opens into the *vestibular aqueduct* (Figs. 14.10 and 14.17). The vestibular aqueduct is a narrow bony canal (aqueduct) that connects the inner ear (vestibule) to the cranial cavity. It contains the endolymphatic duct, a membranous "tube" filled with endolymph that terminates in the endolymphatic sac (Fig. 14.28). The sac protrudes into a space between the periosteum and dura mater, through the slit-like opening of the vestibular aqueduct. Located superiorly, halfway between the opening of the internal auditory canal and the vestibular aqueduct is the *subarcuate fossa,* a blind channel that extends anterolaterally to an area under the superior semicircular canal (Fig. 14.17). The *petromastoid canal* opens to the posterior surface of the petrous ridge through this fossa (Figs. 14.29, 14.30, and 14.32).

The inferior surface of the petrous part of the temporal bone contributes to the external surface of the cranial base. In the center of the inferior surface lies the large, *circular opening of the carotid canal*. Posterior to the opening of the carotid canal is a depression of variable length and depth known as the *jugular fossa*, which houses the superior jugular bulb. Between the jugular fossa and the opening of the carotid canal

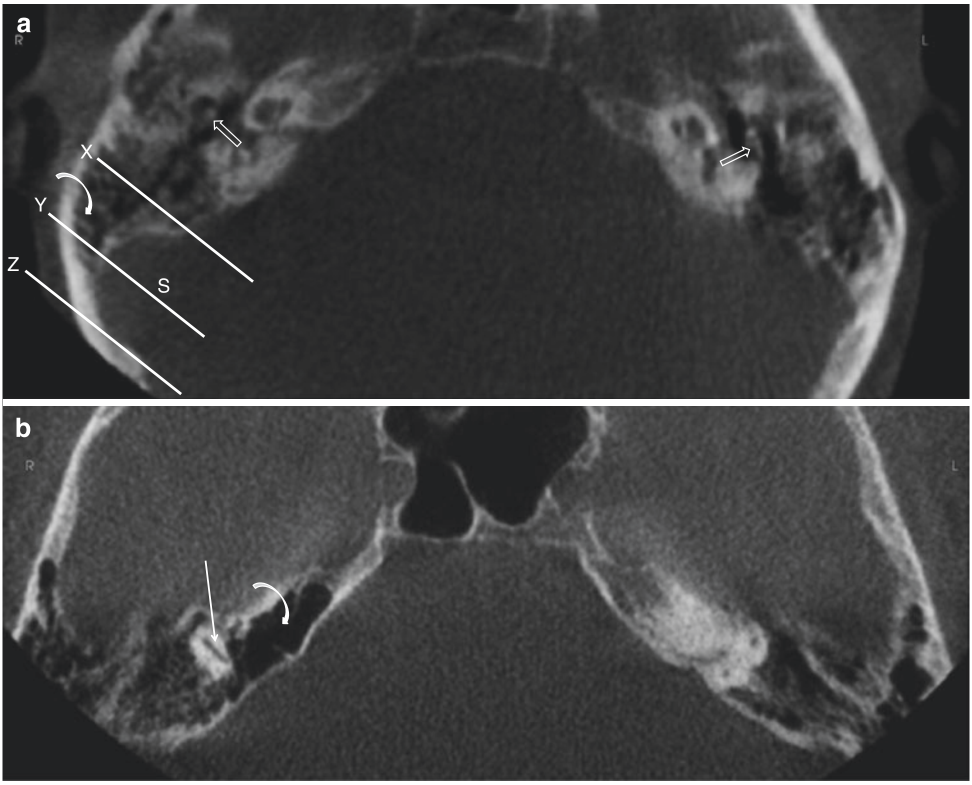

Fig. 14.13 Axial CBCT sections (**a**, **b**) shows pneumatization of the temporal bone with respect to the sigmoid sinus (s) and the labyrinth (*straight solid arrow*). The axial CBCT section at the level of the ice-cream cone of the head of malleus and body of incus (*straight open arrows*) (**a**) shows group 2 pneumatization of the temporal bone by the mastoid air cells (*curved solid arrow*) with respect to three lines passing through the most anterior (*line X*), the most lateral (*line Y*) and the most posterior (*line Z*) points of the sigmoid sinus (*S*) with 45 degree angle to the midsagittal plane. Another axial CBCT section (**b**) shows pneumatization of the temporal bone by the mastoid air cells (*curved solid arrow*) with respect to the superior semicircular canal (*straight solid arrow*)

is a small triangular depression, whose apex contains *a small opening onto the cochlear aqueduct* (Fig. 14.18). The cochlear aqueduct connects the inner ear (cochlea) to the cranial fossa and houses the *perilymphatic duct* (Fig. 14.32).

Of the three borders of the petrous part, the superior border is the longest. It is grooved by the superior petrosal sinus and crossed by the roots of the trigeminal nerve. Next in length is the posterior border, which contains the anterior part of the groove for the inferior petrosal sinus and the jugular fossa posterior to that. The jugular fossa, together with the basilar part of the occipital bone, contributes to the *jugular foramen* (Figs. 14.6 and 14.14).

The jugular foramen is subdivided into two parts by a fibrous or osseous bridge that connects the jugular spine on the petrous part of the temporal bone and the jugular process of the occipital bone. It has been likened to a *whale* with a smaller anteromedial part resembling the tail of the whale and the larger posterolateral part resembling the body of the whale. The smaller anteromedial part is called the *pars nervosa* and contains the glossopharyngeal (IX) nerve and the inferior petrosal sinus. The posterolateral part is called the *pars vascularis* or *pars venosa*, and contains the jugular bulb and the vagus (X) and spinal accessory (XI) nerves, as well as the posterior meningeal artery and meningeal branch of the ascending pharyngeal artery. The pars vascularis is usually larger on the right causing asymmetry of the jugular foramina (Fig. 14.16) (Daniels et al. 1984). It is variable in the literature where IX, X, and XI pass through.

At the junction of the anterior border of the petrous and squamous parts of the temporal bone

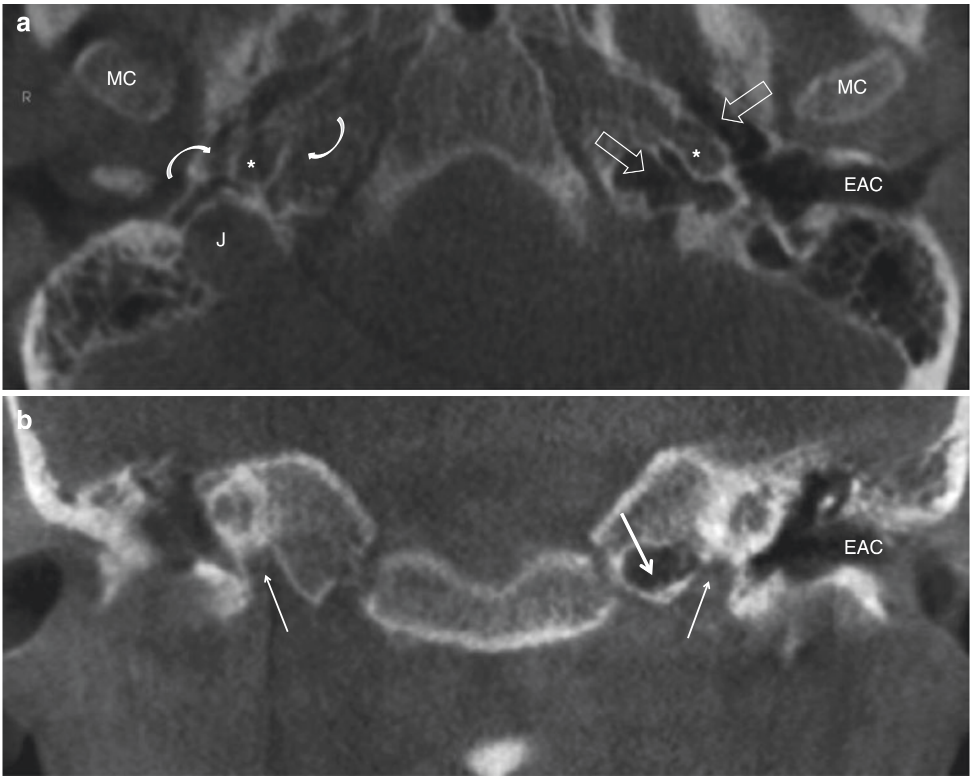

Fig. 14.14 Axial (**a**) and coronal (**b**) sections shows pneumatization of the temporal bone, with respect to the carotid canal. The axial CBCT section (**a**) shows the pneumatization of the temporal bone lateral and medial (*straight open arrows*) to the horizontal part of the carotid canal (*asterisk*) on the left side of the patient. Note that there is no pneumatization of the temporal bone around the carotid canal (*asterisk*) on the opposite side (*curved solid arrows*). The coronal CBCT section at the level of the vertical portion of the carotid canals (*straight, thin solid arrows*) (**b**) shows the pneumatization of the left temporal bone (*straight, thick solid arrow*) medial to the carotid canal. Other structures labeled on these sections include the external auditory canal (*EAC*), the jugular foramen (*J*), and the mandibular condyle (*MC*)

are two canals that extend from the tympanic cavity to the pharynx. These canals are located one above the other and are separated by a thin osseous plate. The upper canal contains the *tensor tympani muscle* and the lower canal carries the *pharyngotympanic tube* (*Eustachian tube*) (Fig. 14.25).

The petrous part of the temporal bone encloses the auditory system which is composed of three parts: the external ear, the middle ear, and the inner ear. These are described in detail in the following section (Standring and Gray 2008).

External Ear

The main function of the external ear is to collect sound waves and conduct them to the tympanic membrane. The external ear comprises the pinna or auricle (the outermost part of the ear) and the external auditory canal (EAC). The opening of the EAC is the external auditory meatus (EAM). It has a different embryological origin from the middle and inner ear, corresponding to its close location to the outer surface of the head. It also has a distinct spectrum of pathological conditions compared to the other two parts of the ear (Standring and Gray 2008).

External Auditory Canal

The EAC extends anteroinferiorly for 2.5 cm from the auricle to the tympanic membrane or ear drum. The outer third of the EAC is partly cartilaginous and partly fibrous, whereas, the medial two-thirds has a rigid bony wall. The bony part of the canal may contain an anteroinferior dehiscence called the *foramen of Huschke*. In the anterior part of the cartilaginous EAC are two or three deep fissures,

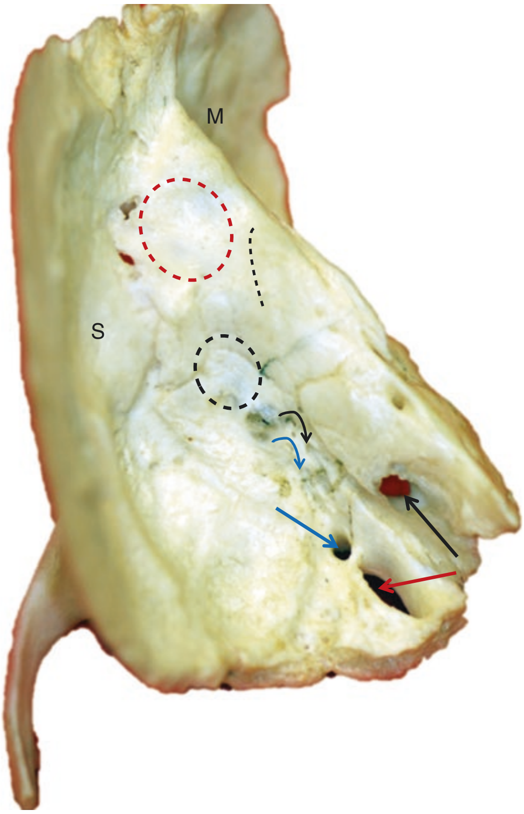

Fig. 14.15 Anterior view of the temporal bone and petrous ridge shows the squamous part of the temporal bone (*S*), the mastoid part (*M*), carotid canal (*straight black arrow*), foramen ovale (*red arrow*), foramen spinosum (*straight blue arrow*), hiatus for greater superficial petrosal nerve (*curved black arrow*), hiatus for lesser superficial petrosal nerve (*curved blue arrow*), arcuate eminence (*black dotted line*), tegmen tympani covering the middle ear cavity (*black dashed circle*), posterior extension of the tegmen tympani over the mastoid antrum (*red dashed circle*)

the *Santorini fissures*, through which tumors of the external acoustic meatus may escape the confines of the canal and spread into the adjacent soft tissues. At birth, the external auditory canal is very short and narrow and has no osseous part; it grows progressively till the age of 9 years when it achieves its typical S-shaped course and adult size with a variable diameter that is the widest at its lateral end (Standring and Gray 2008).

The EAC can be visualized in both axial and coronal sections with the anterior and posterior walls best visualized in the axial projection, and the roof and the inferior wall seen best in the coronal plane (Figs. 14.14 and 14.16) (Virapongse et al. 1982). The EAC should be *patent* and *air-filled* along its length. Within the EAC are two areas of narrowing, one between the fibro-cartilaginous and the bony portion known as the isthmus and the other adjacent to the tympanic membrane (Standring and Gray 2008; Kelly and Mohs 1996; Alvord and Farmer 1997). The ceruminous glands of the outer third of the EAC secrete cerumen or earwax which may be visible on the CBCT images.

Tympanic Membrane

The tympanic membrane is a thin, conical membrane, with a diameter of 9–10 mm that separates the external ear from the middle ear. It is situated in an oblique direction such that its lateral surface faces inferiorly and anteriorly. The tympanic membrane has a small, thin, triangular flaccid area on its superior aspect, known as the *pars flaccida*, which is located between the attachment of the lateral process of malleus and the superior margin of the tympanic membrane. Many primary acquired cholesteatomas of the middle ear originate from the pars flaccida. The remainder of the membrane, known as the *pars tensa*, is thick and more rigid. The thickened peripheral rim of the pars tensa where the connective tissue matrix of the membrane attaches to the bony tympanic sulcus is known as the *tympanic annulus*. Adjacent to the pars flaccida is a wedge-shaped, bony wall whose sharp inferior portion is known as the *outer attic wall* or *scutum* (Figs. 14.21 and 14.24) (Standring and Gray 2008; Kelly and Mohs 1996; Alvord and Farmer 1997).

Middle Ear

Located between the tympanic membrane and the inner ear, the middle ear is a narrow, air-filled chamber that contains the auditory ossicles (malleus, incus and stapes), the stapedius and tensor tympani muscles, the chorda tympani nerve (a branch of the facial nerve) and the tympanic plexus of the tympanic nerve (Standring and Gray 2008). The very small size of the middle ear cavity, sometimes referred to as the *tympanic cavity*, and the numerous structures found within it contribute to the complexity of this region. The anatomy of the middle ear and its appearance in computed tomography images are discussed below in three parts: the ossicles; the

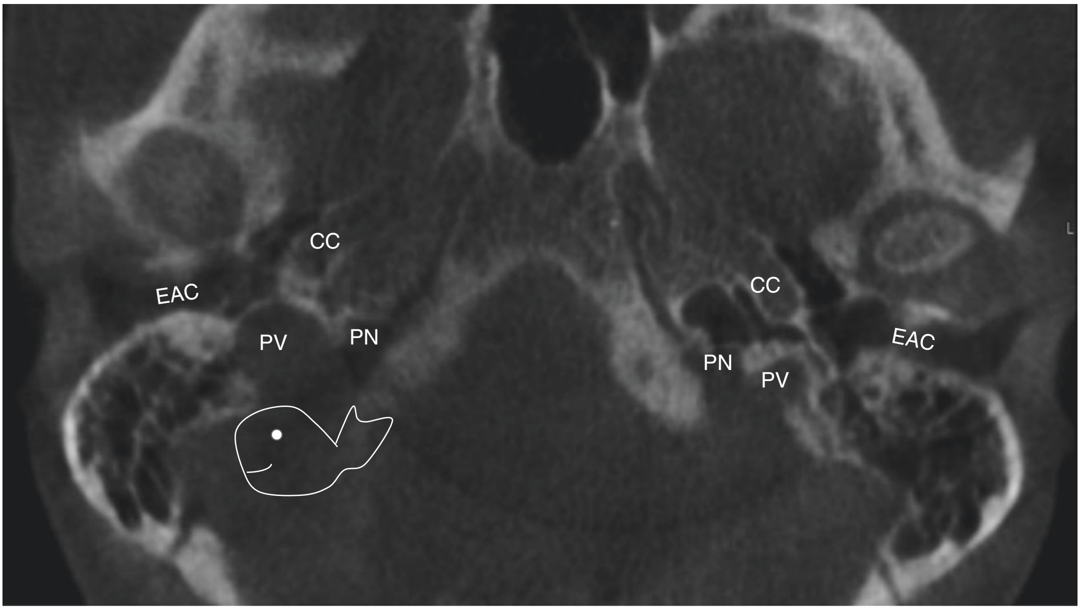

Fig. 14.16 Axial CBCT section shows the pars nervosa (*PN*) and pars vascularis (*PV*) parts of the jugular foramen, the external auditory canal (*EAC*), and the carotid canal (*CC*). Note the resemblance of the jugular foramen to a whale as drawn on the image

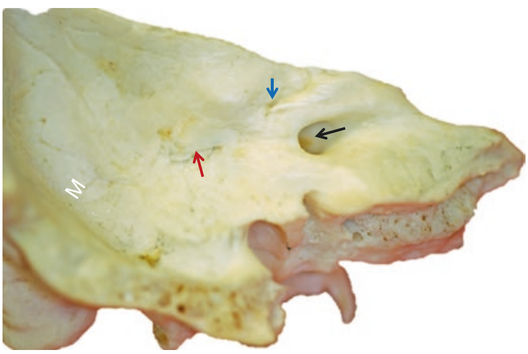

Fig. 14.17 The posterior surface of the petrous part shows the mastoid part (M) of the temporal bone, the internal auditory meatus (*black arrow*), the vestibular aqueduct (*red arrow*), and the subarcuate fossa (*blue arrow*)

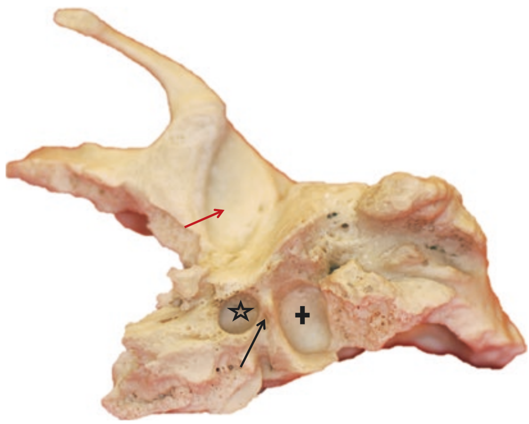

Fig. 14.18 The inferior surface of the petrous part of the temporal bone shows the carotid canal (*open star*), the jugular fossa (*plus sign*), the opening to the cochlear aqueduct (*black arrow*), and the mandibular or glenoid fossa (*red arrow*)

compartments of the middle ear cavity; and the walls of the tympanic cavity.

Ossicles

- **Malleus** (Latin: "hammer") is the largest of the ossicles and is shaped like a hammer. It is composed of a head, neck, handle (manubrium), and anterior and lateral processes. The head, an oval-shaped structure, lies in the epitympanic recess and articulates with the body of incus posteriorly at the malleoincudal or incudomalleolar joint (Figs. 14.19, 14.20, 14.21, 14.22, 14.23, and 14.24). Malleoincudal dislocation/subluxation, a complication sometimes observed in patients with trauma to the temporal bone, can best be visualized on axial and sagittal images (Standring and Gray 2008; Meriot et al. 1997). The neck, the narrowed part inferior to the head, lies against the flaccid

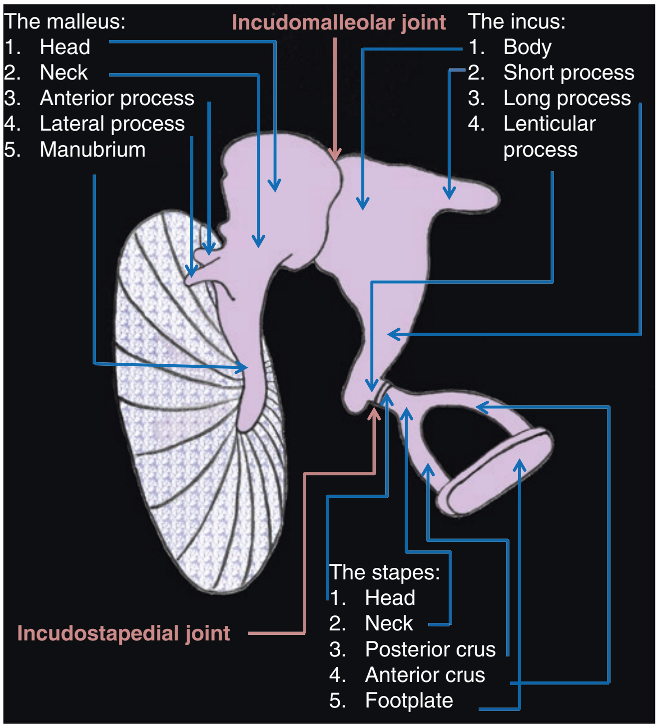

Fig. 14.19 The ossicles of the middle ear

part of the tympanic membrane. Inferior to the neck is an enlargement from which the anterior and lateral processes project. The anterior process connects to the petrotympanic fissure by ligamentous fibers. The lateral process projects laterally from the neck and is attached to the upper part of the tympanic membrane. The handle lies in the mesotympanum, and is embedded in the tympanic membrane with its tip at the umbo (Standring and Gray 2008). Malleus is supported by the lateral, superior, and anterior mallear ligaments as well as the tensor tympani muscle, the tendon of which inserts into the manubrium (handle) of malleus near the neck (Fig. 14.22). The lateral and superior mallear ligaments are best visualized on thin coronal sections whereas the anterior ligament is best seen on axial sections; the tensor tympani muscle can be visualized in both axial and coronal sections (Fig. 14.22) (Swarts 2009; Standring and Gray 2008) .

- **Incus** (Latin: "anvil") is shaped like an anvil and is located between malleus and stapes. It has a body, a short process, a long process, and a lenticular process. The body lies in the epitympanic recess and articulates with the head of malleus on its anterior surface. The long process, located in the mesotympanum, lies parallel to the handle of malleus. Its inferior end bends medially and terminates in a rounded lenticular process that articulates with the head of stapes at the incudostapedial joint (Figs. 14.19, 14.20, 14.21, 14.22, 14.23, and 14.24) (Standring and Gray 2008). The very fine structure of the long process and the lenticular process makes them the most vulnerable segment of the ossicular chain. This region is commonly eroded by inflammatory diseases (Swarts 2009). Incudostapedial disarticulation, the most common post-traumatic complication of the ossicular chain, occurs as a result of the very weak suspension of incus between the firmly anchored malleus and stapes and can be visualized on axial sections (Meriot et al. 1997).The short process is connected to the posterior wall of the tympanic cavity by a ligament. The chorda tympani nerve, a branch of the CN VII, passes through the space between the handle of malleus and the long process of incus (Swarts 2009).

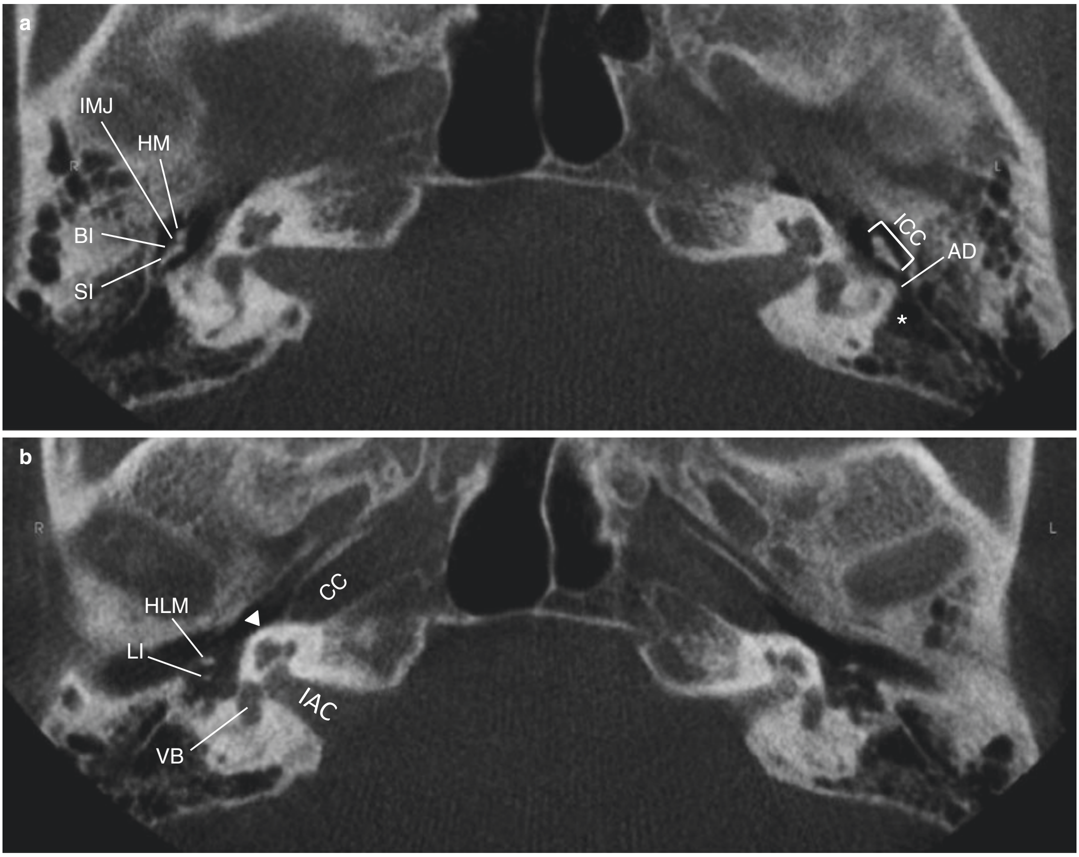

Fig. 14.20 Axial CBCT section through the level of the epitympanum (**a**) shows the ice-cream cone structure (*ICC*) made by the head of malleus (*HM*), body of incus (*BI*), the short process of incus (*SI*), and the incudomalleolar joint (*IMJ*); it also shows the aditus (*AD*) to the mastoid antrum (*). Note that the short process of incus (*SI*) points at the aditus (*AD*) to the mastoid antrum (*). Axial CBCT section through the mesotympanum (**b**) shows the handle of malleus (*HLM*), the long process of incus (LI), the internal auditory canal (*IAC*), the vestibule (*VB*), the cochlear promontory (*arrowhead*), and the carotid canal (*CC*)

- **Stapes** (Latin: "stirrup"), is the smallest bone in the body. It has a head (caput), neck, anterior crus, posterior crus, and a base or footplate. The head articulates laterally with the lenticular process of incus via the incudostapedial joint. The neck connects the head to the anterior and posterior crura. The tendon of the stapedius muscle is attached to the posterior surface of the neck. The crura diverge from the neck and are connected at their ends by the footplate. The space between the crura is known as the obturator foramen. The footplate is attached to and completely fills the oval window in the medial wall of the tympanic cavity through which it transmits the vibrations of the tympanic membrane and ossicles to the inner ear (Figs. 14.19, 14.20, 14.21, 14.22, 14.23, and 14.24) (Swarts 2009; Standring and Gray 2008).

In general, most parts of the ossicular chain can be visualized best on thin axial sections (Figs. 14.20, 14.22 and 14.26). These structures include the head of malleus, the body and short process of incus, the footplate and the crura of stapes, and malleoincudal and incudostapedial joints; however, it was not possible to identify the very fine structures of stapes on axial sections using dental CBCT images. Coronal and modified Poschl CT sections allow for better visualization of the handle of malleus, long process of incus and the right-angle junction of incus long and lenticular processes (Figs. 14.21, 14.22 and 14.24) (Swarts 2009; Clement and De

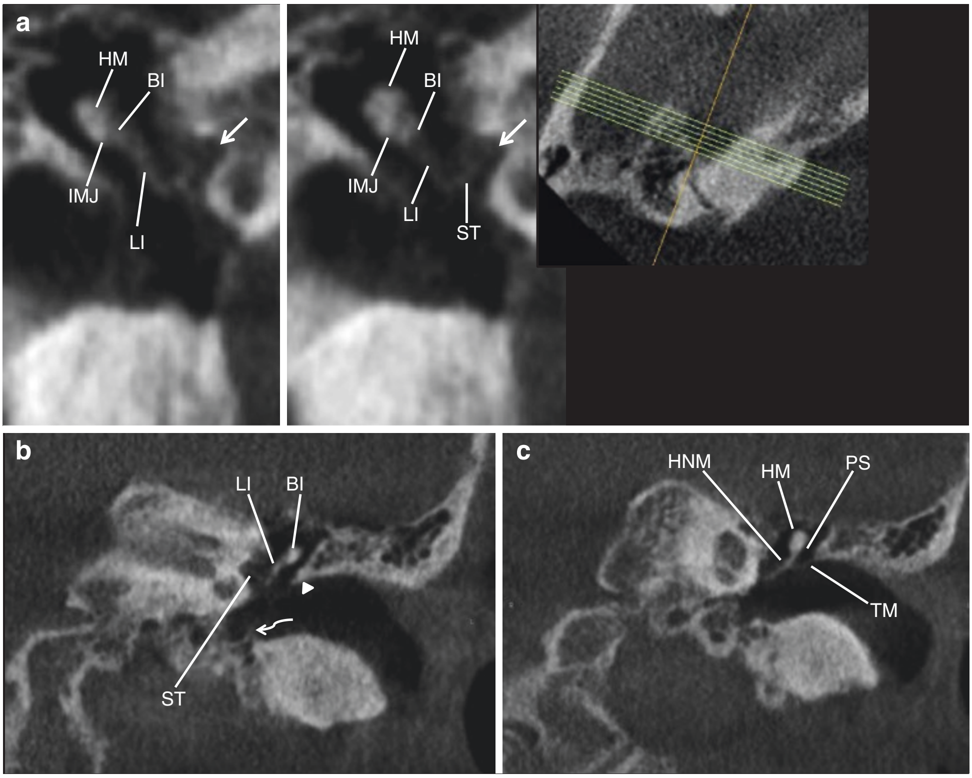

Fig. 14.21 Modified Pöschl views (**a**) of the ossicles of the middle ear with small axial view on the top right showing the location and orientation of the Pöschl planes, coronal CBCT section at the level of incus (**b**) and at the level of malleus (**c**) show the head of malleus (*HM*), the body of incus (*BI*), the incudomalleolar joint (*IMJ*), the long process of incus (*LI*), stapes (*ST*), the oval window (*straight arrow*), scutum (*arrowhead*), the bony annulus (*curved arrow*), the handle of malleus (*HNM*), Prussak's space (*PS*), and the tympanic membrane (*TM*). Note that stapes (*ST*) is hardly identifiable on these CBCT sections

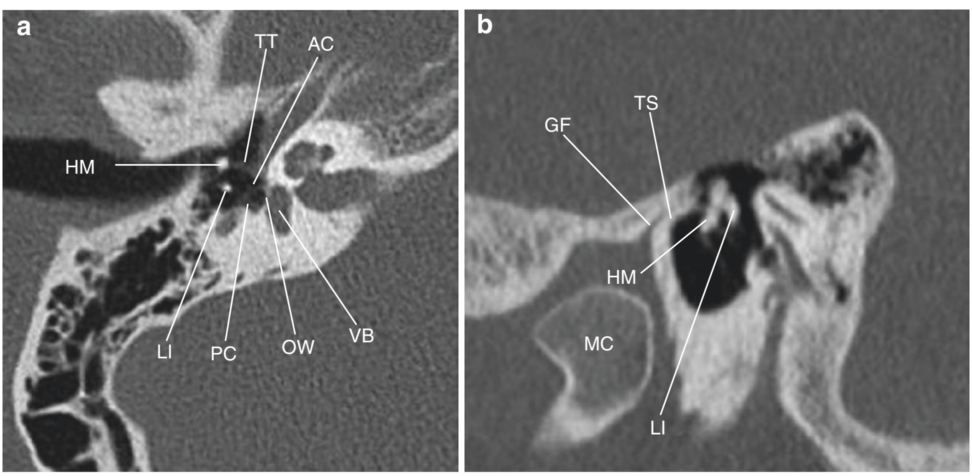

Fig. 14.22 Axial CT (**a**) shows the anterior crus of stapes (*AC*), the posterior crus of stapes (*PC*), the handle of malleus (*HM*), the long process of incus (*LI*), the tendon of the tensor tympani muscle (*TT*), the oval window (*OW*), and the vestibule (*VB*). The sagittal multislice CT (**b**) shows the classic molar tooth appearance made by the long process of incus (*LI*) and handle of malleus (*HM*), the tympanic spine (*TS*), the Glaserian or petrotympanic fissure (*GF*), and the mandibular condyle (*MC*)

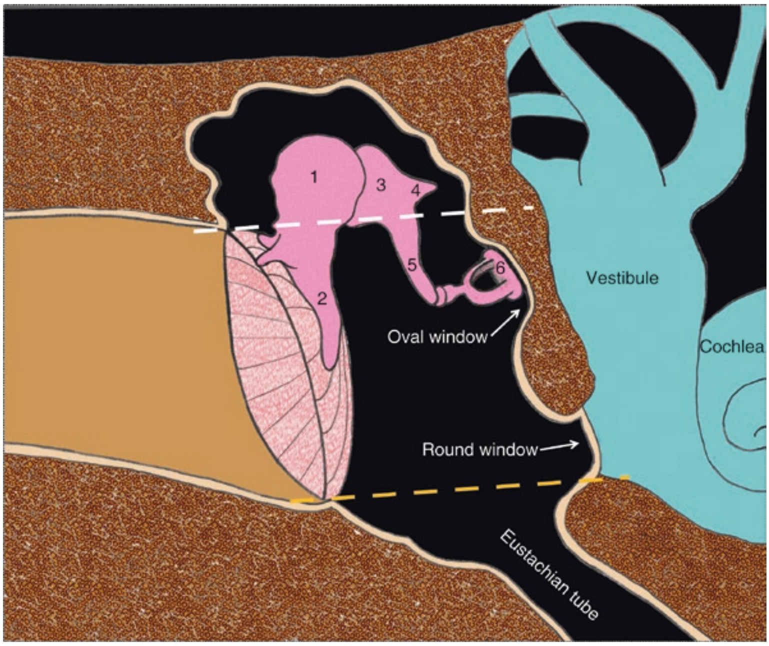

Fig. 14.23 Coronal graphic of the middle ear cavity shows the head of malleus (*1*), the handle (manubrium) of malleus (*2*), the body of incus (*3*), the short process of incus (*4*), the long process of incus (*5*), the footplate of stapes (*6*). The middle ear cavity is divided into three spaces by two lines, one passing through the superior margin of the tympanic membrane (*white dashed line*) and the other one drawn tangential to the lower margin of the tympanic membrane (*yellow dashed line*). Above the white dashed line is the epitympanum, below the yellow dashed line is the hypotympanum, and between the two lines is the mesotympanum

Smedt 1982). The malleoincudal articulation can also be visualized in sagittal CT sections with the classic "*molar tooth*" appearance (Fig. 14.22) (Swarts 2009).

Compartments of the Tympanic Cavity

The tympanic cavity is divided into three compartments in the coronal plane (the epitympanum, mesotympanum, and hypotympanum), and two compartments in the axial plane (the retrotympanum and protympanum) (Fig. 14.23).

- The **epitympanum** is composed of the *upper portion of the tympanic cavity* above the level of the tympanic membrane and also *Prussak's space*. Prussak's space lies between the pars flaccida of the tympanic membrane and the neck of malleus with the superior boundary being the lateral malleolar ligament (which extends from scutum to the neck of malleus) and the inferior boundary the lateral process of malleus (Fig. 14.21). This space is the most common site of first involvement by acquired cholesteatomas which may extend

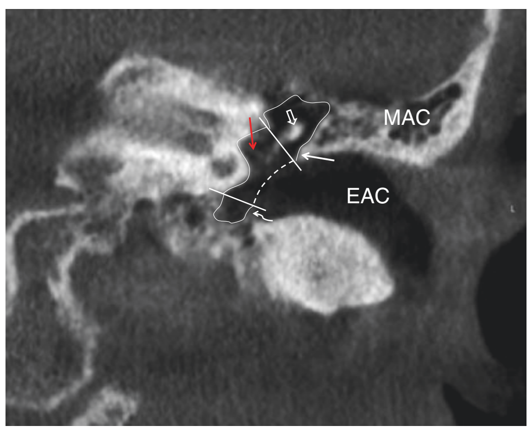

Fig. 14.24 Coronal CBCT section at the level of the middle ear cavity, with two white lines drawn tangential to the superior and inferior margin of the tympanic membrane, shows scutum (*solid straight arrow*), the bony annulus (*curved arrow*), the approximate location of the tympanic membrane (*white dashed line*), the hypotympanum (outlined space below the inferior *white line*), the epitympanum (outlined space above the superior *white line*), the mesotympanum (outlined space between two *white lines*), stapes (*red arrow*), the head of incus (*open straight arrow*), the external auditory canal (*EAC*), and the mastoid air cells (*MAC*). Note that stapes (*red arrow*) is hardly identifiable on this CBCT section

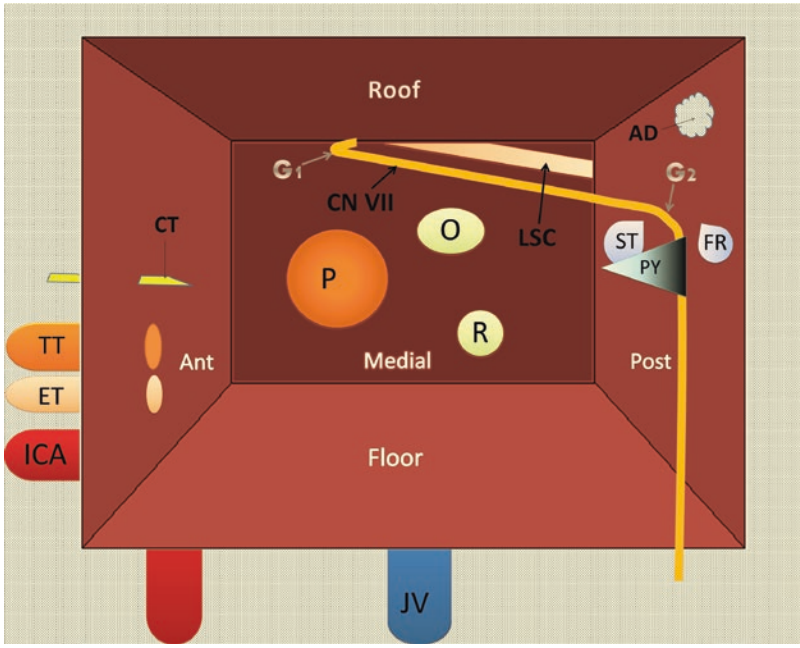

Fig. 14.25 Simplified anatomy of the left middle ear seen from the lateral, shows the internal carotid artery (*ICA*), the jugular vein (*JV*), the Eustachian tube (*ET*), the semicanal for tensor tympani muscle (*TT*), the chorda tympani nerve (*CT*), the cochlear promontory (*P*), the oval window (*O*), the round window (*R*), the facial nerve (*CN VII*), the first genu of the facial nerve (*G1*), the second genu of the facial nerve (*G2*), the lateral semicircular canal (*LSC*), the pyramidal eminence (*PY*), the sinus tympani (*ST*), the facial recess (*FR*), the aditus to the mastoid antrum (*AD*)

posteriorly into the attic, mastoid antrum and mastoid air cells and eventually erode into the middle cranial fossa through the tegmen tympani. The epitympanum contains the malleoincudal joint and communicates posteriorly with the mastoid antrum through the aditus. The *ice-cream cone structure* seen in the middle ear cavity on axial sections at the level of the epitympanum represents the head of malleus (the ice-cream) and the body of incus (the cone) with the tip of the cone (the short process of incus) pointing towards the aditus of the mastoid antrum (Figs. 14.20, 14.23, and 14.24) (Swarts 2009; Swartz and Varghese 1984; Nardis et al. 1992; Miyanaga and Morimitsu 1997; Gaurano and Joharjy 2004).

- The **mesotympanum** is the component of the tympanic cavity that lies against the tympanic membrane (Figs. 14.23 and 14.24).
- The **hypotympanum,** the smallest division**,** is an empty space in the inferior portion of the tympanic cavity below the level of the tympanic membrane (Figs. 14.23 and 14.24).
- The **retrotympanum** represents more than half of the tympanic cavity. It is located posterior to the bony annulus and cochlear promontory (a prominence in the medial wall of the tympanic cavity formed by the basal turn of the cochlea) and inferior to the mastoid antrum. Within the retrotympanum are the fossae or niches of the round and oval windows.
- The **protympanum** is the portion of the tympanic cavity located anterior to the bony annulus (Mazziotti et al. 2006; Pickett et al. 1995).

Walls of the Middle Ear Cavity

The middle ear is shaped like a box with six walls: the roof, the floor, and the anterior, posterior, medial, and lateral walls (Fig. 14.25).

- The **roof**, also known as **tegmen tympani**, separates the tympanic cavity from the middle cranial fossa (Figs. 14.15 and 14.27). It extends posteriorly as the roof of the mastoid antrum and anteriorly as the roof of the canal for the tensor tympani muscle and is best visualized on the coronal plane. The tegmen tympani can serve as a pathway for extension of middle ear infections into the epidural space (Fig. 14.54). Dehiscence of the tegmen tympani may cause an encephalocele with spontaneous cerebrospinal fluid (CSF) otorrhea. Fractures of the middle cranial fossa in the region of the petrous ridge commonly involve the tympanic roof (Schubiger et al. 1986; Kutz et al. 2008; Emir et al. 2009).

- The **anterior wall**, also known as the ***carotid wall***, separates the tympanic cavity from the carotid canal. The *Eustachian tube* (the auditory tube or pharyngotympanic tube) and the *semicanal for the tensor tympani muscle* also extend to the anterior wall of the tympanic cavity. The chorda tympani nerve travels posteroanteriorly within the tympanic cavity, passing through the space between the handle of the malleus and the long process of the incus, and leaves the cavity through the *canal of Huguier* at the medial end of the petrotympanic or glaserian fissure. The petrotympanic fissure opens just superior and anterior to the bony annulus (Fig. 14.22). The axial plane is best for visualizing the Eustachian tube, the tensor tympani canal, and the carotid canal (Fig. 14.26).
- The **medial wall**, also known as the **labyrinthine wall**, separates the tympanic cavity from the inner ear. There is a rounded prominence on this wall, the *cochlear promontory*, formed by the first turn of the cochlea. Located superoposterior to the promontory is the *oval window* (fenestra ovale, vestibular window) which connects the middle ear cavity to the vestibule of the inner ear. Inferoposterior to the promontory, and more posterior than the oval window, lies the *round window* (fenestra cochlea), which is an opening to the cochlea of the inner ear and is closed by a membrane. Located superoposterior to the oval window is the *prominence of the tympanic portion of the facial nerve*, and superior to that is the *prominence of the lateral semicircular canal* (Fig. 14.25).
- The **lateral wall**, also known as the **membranous wall**, separates the tympanic cavity from the external auditory canal. It is formed almost entirely by the *tympanic membrane* which has the *handle of malleus* embedded in it. It also contains the *bony annulus* which attaches the

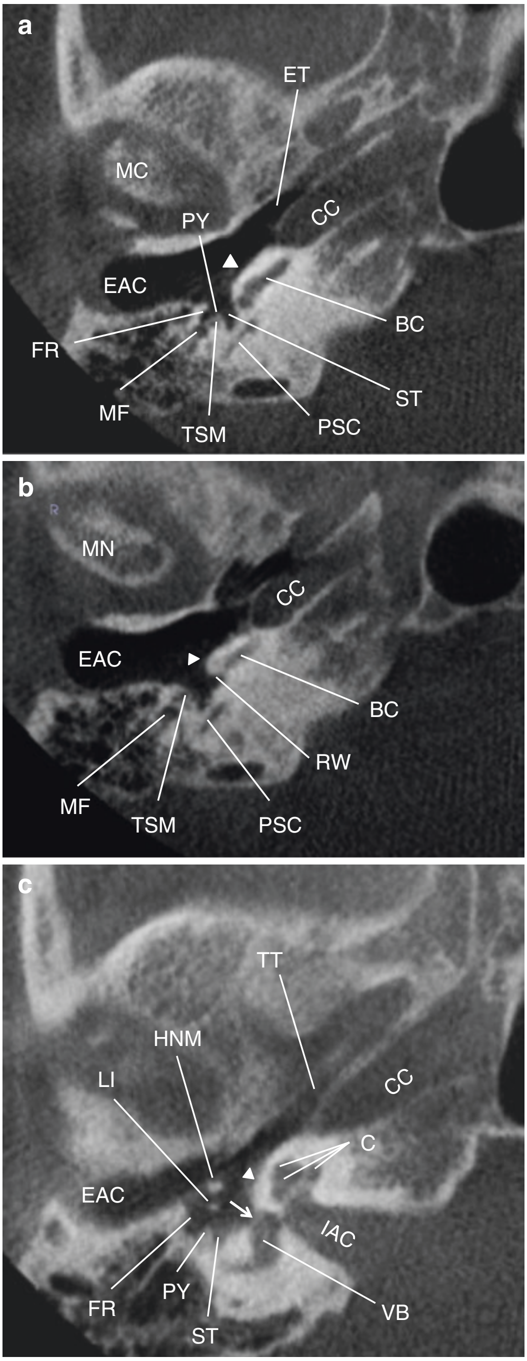

Fig. 14.26 The axial CBCT sections (**a**–**c**) show the structures on the posterior, anterior and medial walls of the middle ear, the mandibular condyle (*MC*), the external auditory canal (*EAC*), the carotid canal (*CC*), the cochlear promontory (*arrowheads*), the basal turn of the cochlea (*BC*), the pyramidal eminence (*PY*), the sinus tympani (*ST*), the facial recess (*FR*), the vertical or mastoid part of the facial nerve (*MF*), the posterior semicircular canal (*PSC*), the basal, middle and apical turns of the cochlea (*C*), Eustachian tube (*ET*), the semicanal for tensor tympani muscle (*TT*), round window (*RW*), oval window (*arrow*), long process of incus (*LI*), handle of malleus (*HNM*), the origin of the tendon of the stapedius muscle (*TSM*), and the internal auditory canal (*IAC*)

thickened peripheral rim of the tympanic membrane to the bony tympanic sulcus located on the medial end of the external auditory canal. The bony wall adjacent to the flaccid part of the tympanic membrane and lateral to the epitympanic recess is wedge-shaped in section and its sharp inferior portion is known as the *outer attic wall* or *scutum* (Figs. 14.21 and 14.24). Of importance to the radiologist is checking that scutum has a sharp point on CT scans. Blunting of this area is a sign of cholesteatoma (Fig. 14.54) (Swartz and Varghese 1984; Nardis et al. 1992; Gaurano and Joharjy 2004).

- The **floor**, also known as the **jugular wall**, separates the tympanic cavity from the *jugular bulb* whose superior border normally *lies inferior to the level of the hypotympanic recess* (Fig. 14.40).
- The **posterior wall**, also known as the **mastoid wall**, connects the tympanic cavity to the mastoid air cells through an opening in its superior part, the *aditus to the mastoid antrum* (aditus ad antrum mastoideum) (Figs. 14.12 and 14.20). Widening of the aditus is a sign of cholesteatoma (Gaurano and Joharjy 2004). The most prominent area in the posterior wall is a minute triangular-shaped spicule of bone, the *pyramidal eminence*, situated at the level of the oval window with its apex projecting towards the window. *The tendon of the stapedius muscle* emerges from its apex. The *vertical part of the facial nerve* canal is located in the posterior wall just posterior to the pyramidal eminence.

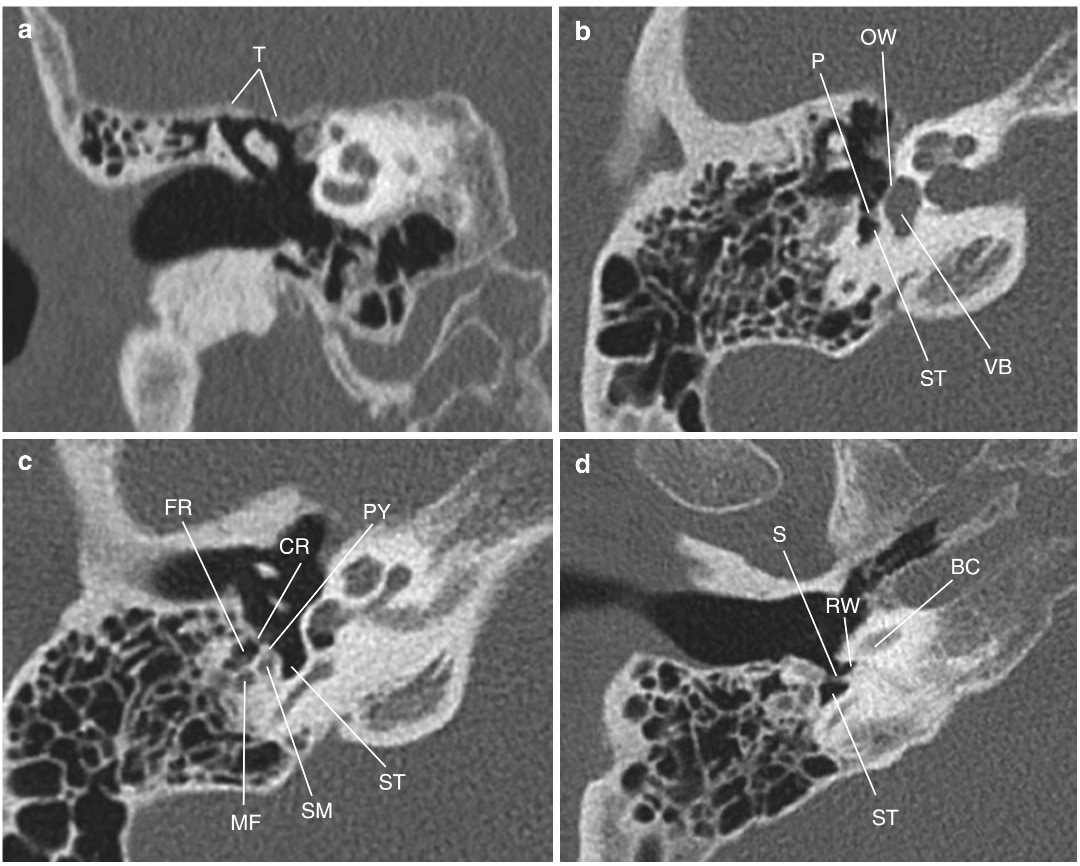

Fig. 14.27 The coronal CT section (**a**) shows the tegmen tympani (*T*). The axial CT sections (**b**–**d**) show the ponticulus (*P*), the oval window (*OW*), the sinus tympani (*ST*), the vestibule (*VB*), the facial recess (*FR*), the chordal ridge (*CR*), the pyramidal eminence (*PY*), the vertical or mastoid part of the facial canal (*MF*), the stapedius muscle (*SM*), the subiculum (*S*), the round window niche (*RW*), and the basal turn of the cochlea (*BC*). Note that the CT sections move inferiorly from **b** to **d**

There are recesses in the posterior wall which may be sites of occult extension of diseases of the middle ear cavity. These structures are visualized the best in axial sections but are hard to detect on the coronal sections (Figs. 14.26 and 14.27) (Mazziotti et al. 2006).

- The posterior wall is indented by two recesses that surround the pyramidal eminence and the facial canal. They can be localized by using the vertical or mastoid portion of the facial nerve canal which travels down the posterior wall of the tympanic cavity just behind the pyramidal eminence. Located lateral to the facial canal and the pyramidal eminence is the *facial recess* and medial to them is the *sinus tympani* (tympanofacial recess). The sinus tympani is usually the more developed one. Lateral to the facial recess, the chorda tympani branch of the facial nerve leaves the vertical portion of the facial nerve at the chordal eminence and moves towards the anterior wall of the tympanic cavity. The *chordal ridge* extends from the chordal eminence to the pyramidal eminence at the entry point for the stapedial tendon (Figs. 14.26 and 14.27).
  - The *ponticulus* is a bridge of bone extending from the pyramidal eminence to the superoposterior margin of the cochlear promontory. It separates the *oval window fossa (niche)* from the sinus tympani (Fig. 14.27). The fossa of the oval window is a relatively large depression containing the oval window which is in turn occupied by the footplate of stapes. The niche is bounded inferiorly by the promontory and the ponticulus and superiorly by the horizontal or tympanic part of the facial canal.
  - The *round window fossa (niche)* is a funnel-shaped depression containing the round window. It is situated under the free extremity of the basal turn of the cochlea with a posterior-lateral inclination. The sinus tympani is separated from the round window niche by the *subiculum*, a bony ridge extending from the inferoposterior aspect of the cochlear promontory to the inferior margin of the tympanic recess (Fig. 14.27).
  - The sinus tympani is situated between the ponticulus and subiculum. The round window is located inferior to the subiculum and the oval window is superior to the ponticulus. The tympanic sinus is bounded by the mastoid part of the facial canal laterally and the posterior semicircular canal medially. The relationship between the sinus tympani and the facial nerve canal, the oval window and the posterior semicircular canal can be evaluated in the axial sections of the temporal bone; this is of importance for the surgeons since the distance of these structures determines the surgical approach that should be employed to remove the disease in this region (Figs. 14.26 and 14.27) (Swarts 2009; Mazziotti et al. 2006; Pickett et al. 1995).

Inner Ear

The inner ear is situated in the petrous part of the temporal bone medial to the tympanic cavity. It is composed of the *bony* and the *membranous labyrinths* (Fig. 14.28). *The* bony labyrinth contains the sacs and ducts of the membranous labyrinth. The membranous labyrinth is filled with endolymph and separated from the bony labyrinth by the perilymph. The bony labyrinth is surrounded by the *otic capsule* which is made of a denser bone than the rest of the petrous part.

The Vestibule

The *vestibule* (Figs. 14.20, 14.22, 14.26, 14.27, 14.28, 14.29 and 14.30) is a somewhat ovoid cavity situated in the middle of the labyrinth, anterior to the semicircular canals and posterior to the cochlea. It is the largest cavity of the bony labyrinth, with an average anteroposterior and vertical dimension of 5 mm and medio-lateral dimension of 3 mm. It communicates medially with the middle ear cavity through the oval window. The internal auditory canal is located anterior to the vestibule and is separated from it by the lamina cribrosa through which the vestibular nerves pass. The vestibular aqueduct (Fig. 14.32) extends posteroinferiorly from the posterior surface of the vestibule to the posterior surface of the petrous ridge connecting the vestibule to the posterior cranial fossa.

Semicircular Canals

The *semicircular canals* (Figs. 14.3, 14.28, 14.29 and 14.30) are situated posterosuperior to the

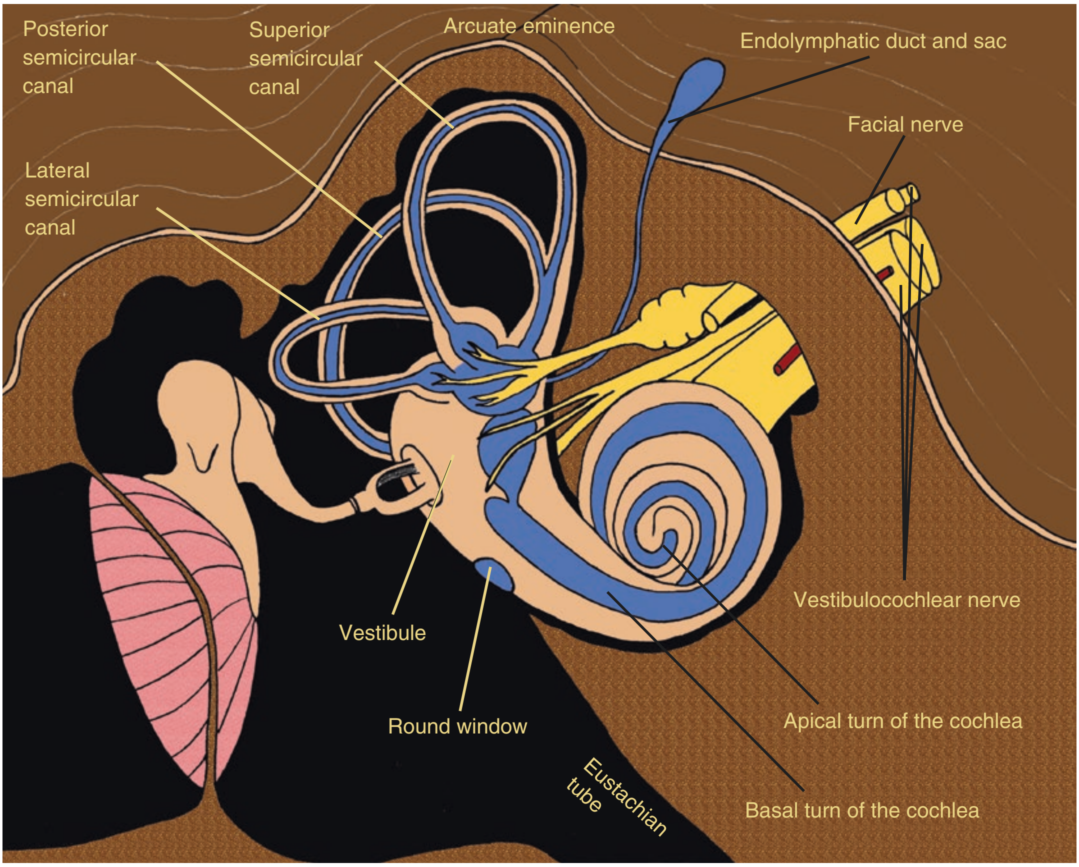

Fig. 14.28 Diagrammatic representation of the three parts of the bony and membranous labyrinths of the inner ear: the vestibule, the three semicircular canals, and the cochlea

vestibule and directly superior to the jugular bulb. Each canal forms two-third of a circle with one swollen end referred to as the osseous ampulla.

- The *superior semicircular canal* is vertically oriented and lies perpendicular to the long axis of the petrous portion. It has a non-ampullated posterior end which joins the non-ampullated end of the posterior semicircular canal laterally to form the *crus commune,* which in turn connects to the vestibule. The other end is ampullated and connects directly to the vestibule. As mentioned earlier, the arcuate eminence is a finger-like bony elevation on the anterior surface of the petrous ridge to accommodate the superior semicircular canal (Figs. 14.15 and 14.28).
- The *posterior semicircular canal* is vertically oriented and is parallel to the posterior surface of the petrous ridge. Its anterior end joins the crus commune and the ampullated posterior end connects directly to the vestibule.
- The *lateral semicircular canal* is horizontally oriented with its arch towards the lateral. Its anterior end is ampullated and connects to the vestibule just below the ampulla of the superior semicircular canal. Its other end connects to the vestibule above the ampulla of the posterior semicircular canal.

Cochlea

The *cochlea* (Figs. 14.26, 14.28, 14.29 and 14.30) is the most anterior part of the labyrinth and is located in the temporal bone inferior to the level of the semicircular canals. Inferior to the cochlea is the horizontal part of the carotid canal and posterior to it is the jugular bulb. It is a snail

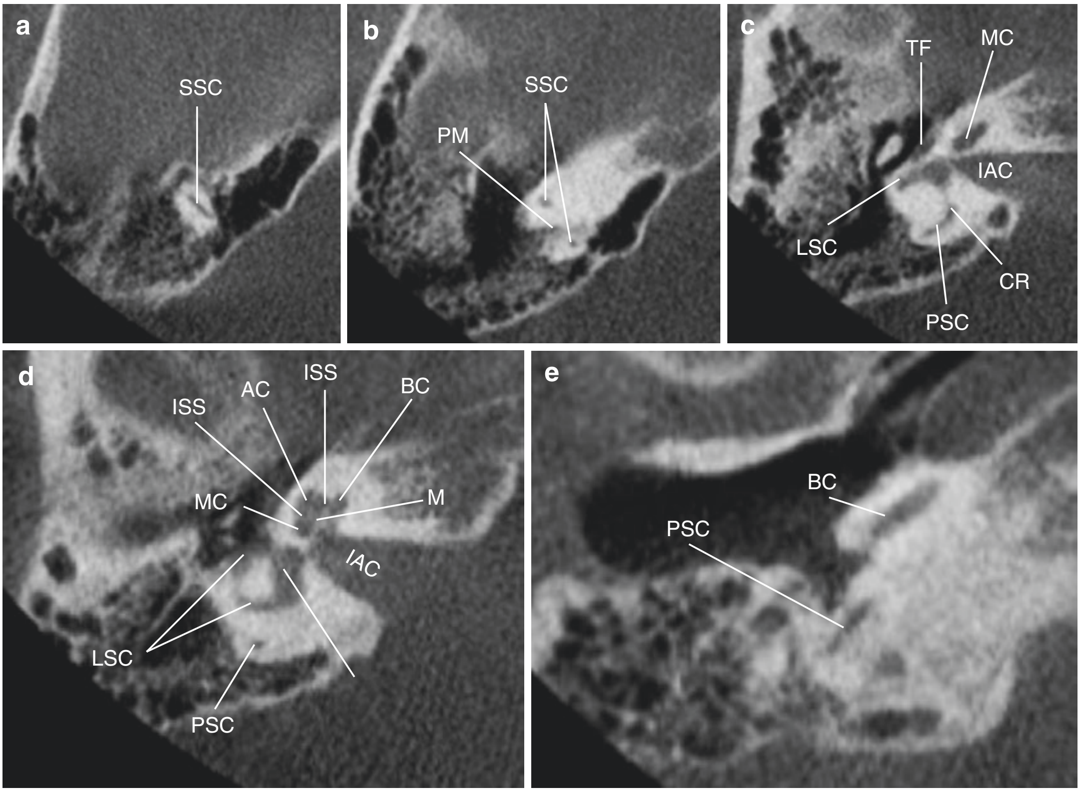

Fig. 14.29 Axial CBCT sections from superior to inferior (**a**–**e**), at the level of the semicircular canals, show the superior (anterior) semicircular canal (*SSC*); the crus commune (*CR*); the posterior semicircular canal (*PSC*); the lateral semicircular canal (*LSC*); the vestibule (*VB*); the internal auditory canal (*IAC*); the basal turn (*BC*); the middle turn (*MC*) and the apical turn (*AC*) of the cochlea; the modiolus (*M*); the interscalar septum (*ISS*); the tympanic segment of the facial nerve canal (*TF*); and the petromastoid canal (*PM*)]

shell-like cavity laid on its side which makes 2.5 turns around a horizontal axis called the *modiolus*. There is a central bony defect within the modiolus housing the cochlear nerve. A bony septum called *interscalar osseous septum* separates each turn from the other one.

The cochlea is located in the temporal bone with the modiolus tip pointing in an anterior, lateral, and slightly inferior direction. It measures 5 mm from base to apex and 9 mm across its base. The bulge of the basal turn forms the cochlear *promontory* (Figs. 14.25 and 14.26) on the medial wall of the middle ear cavity; the *cochlear aqueduct* (Figs. 14.18 and 14.32) extends posteromedially from the basal turn of the cochlea to an area between the jugular fossa and the opening of the carotid canal, on the inferior surface of the petrous ridge; it runs inferior and relatively parallel to the course of the internal auditory canal.

Internal Auditory Canal

The *internal auditory canal* transmits the *facial nerve* (CN VII) and the *vestibulocochlear nerve* (CN VIII) (Figs. 14.12, 14.17, 14.20, 14.26, 14.28, 14.29, 14.30, 14.31, 14.34 and 14.35). It is divided by a transverse osseous septum, the *crista falciformis*, into superior and inferior parts (Fig. 14.30). The superior part is further divided to an anterior and posterior part by a vertical crest of variably ossified arachnoid tissue known as *Bill's bar*. The facial nerve lies in the anterosuperior quadrant; the cochlear nerve and the superior and inferior vestibular nerves (branches of CN VIII) lie in the inferoanterior, superoposterior, and inferoposterior quadrants, respectively. The size of the internal auditory canal varies considerably; it may be unusually wide, narrow, or even duplicated. Asymmetric widening of this canal is commonly associated with schwannoma whereas bilateral widening may be encountered in patients with neurofibromatosis. Canals with a diameter of less than 2 mm are considered to be abnormal (Standring and Gray 2008; Baek et al. 2003; Salzman et al. 2001; Kew and Abdullah 2012; Egelhoff et al. 1987).

The *facial nerve* travels through the internal auditory canal, exiting through the anterosuperior aspect of the *internal acoustic opening (porus acusticus internus)*, where it enters the facial nerve canal. The facial nerve canal (fallopian canal) comprises three segments (labyrinthine, tympanic, and mastoid) and two genua (Figs. 14.2, 14.4, 14.25, 14.26, 14.27, 14.28, 14.30, 14.31, 14.33, and 14.35).

- The *labyrinthine segment* is the narrowest and shortest segment of the facial nerve and is located between the porus acusticus and the *first or anterior genu*. Anterior genu is a bend in which the geniculate ganglion, a bulbous enlargement of the canal, is located. The labyrinthine segment courses anterolaterally at a

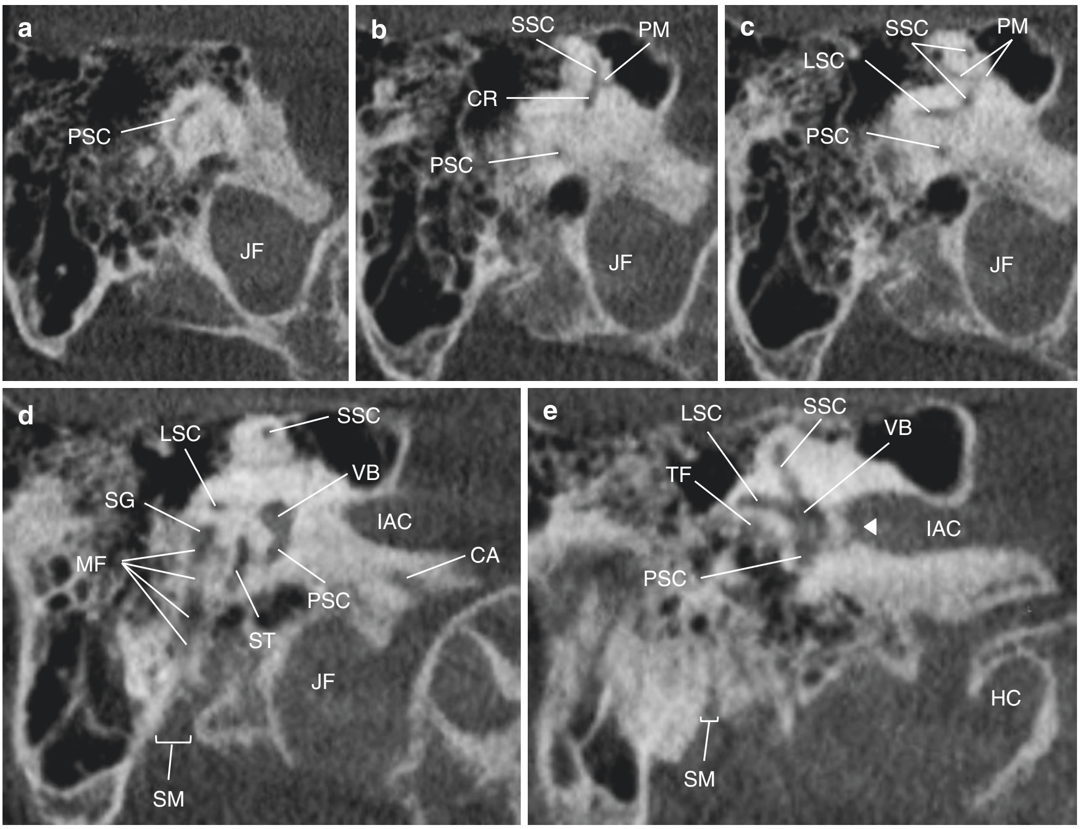

Fig. 14.30 Coronal CBCT sections from posterior to anterior (**a**–**e**), at the level of the inner ear, show the superior (anterior) semicircular canal (*SSC*); the crus commune (*CR*); the posterior semicircular canal (*PSC*); the lateral semicircular canal (*LSC*); the petromastoid canal (PM); the vestibule (*VB*); the mastoid segment of the facial nerve canal (*MF*); the second genu of the facial nerve canal (*SG*); the tympanic segment of the facial nerve canal (*TF*); the stylomastoid foramen (*SM*); the sinus tympani (*ST*); the internal auditory canal (*IAC*); the crista falciformis (*arrowhead*); the opening of the cochlear aqueduct (*CA*); the jugular foramen (*JF*); and the hypoglossal canal (*HC*). Continued coronal sections form posterior to anterior (**f-j**) show the external auditory canal (*EAC*); superior (anterior) semicircular canal (*SSC*); the lateral semicircular canal (*LSC*); the vestibule (*VB*); the oval window (*straight arrow*); the round window (*sigmoid arrow*); the tympanic (*TF*) and labyrinthine (*LT*) segments of the facial nerve canal; the internal auditory canal (*IAC*); the crista falciformis (*arrowhead*); the basal turn (*BC*); middle turn (*MC*) and apical turn (*AC*) of the cochlea; and the modiolus (*M*)

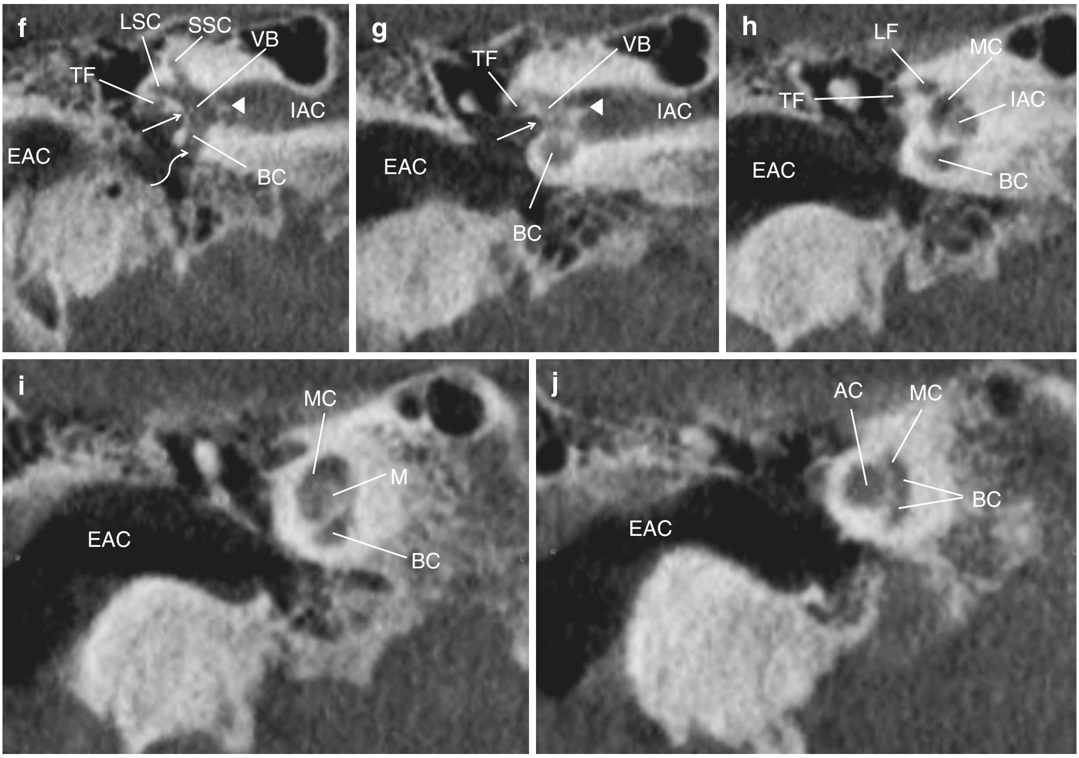

Fig. 14.30 (continued)

125° angle relative to the long axis of the internal auditory canal. It is best visualized on axial CT sections (Fig. 14.31).

- The *tympanic segment* (horizontal segment) exits posterolaterally from the geniculate ganglion, at the first genu, at an angle of 75° or less to the labyrinthine segment. The tympanic segment is approximately 10 mm in length and can be visualized on axial sections running anteroposteriorly along the superior portion of the medial wall of the tympanic cavity at the level of the ice-cream cone (Figs. 14.29 and 14.31). On coronal sections, the cross section of the facial nerve canal can be found between the lateral semicircular canal and the oval window (Fig. 14.30). Pathological conditions of the middle ear cavity such as cholesteatoma and otitis media may cause erosion of this segment of the canal and thereby cause facial palsy.

The *greater superficial petrosal nerve*, the first major branch of the facial nerve, also exits the geniculate ganglion and extends to the anterior surface of the petrous part of temporal bone; this can be occasionally visualized on axial high-resolution CT sections (Fig. 14.35). There is an accessory canal transmitting the *lesser petrosal nerve* branching off the geniculate ganglion as well. The lesser petrosal nerve consists of fibers from three nerves including the tympanic branch of glossopharyngeal nerve (Jacobson's nerve), the nervus intermedius of the facial nerve, and the auricular branch of vagus nerve (Arnold's nerve).

As the tympanic segment of the facial nerve extends posteriorly, it courses inferiorly and laterally towards the posterior wall of the tympanic cavity where it bends inferiorly with an angle of 95° to 125° to the horizontal segment; this bend is known as the *posterior* or *second genu*. The facial nerve canal then continues in the posterior wall as the *vertical or mastoid segment* of

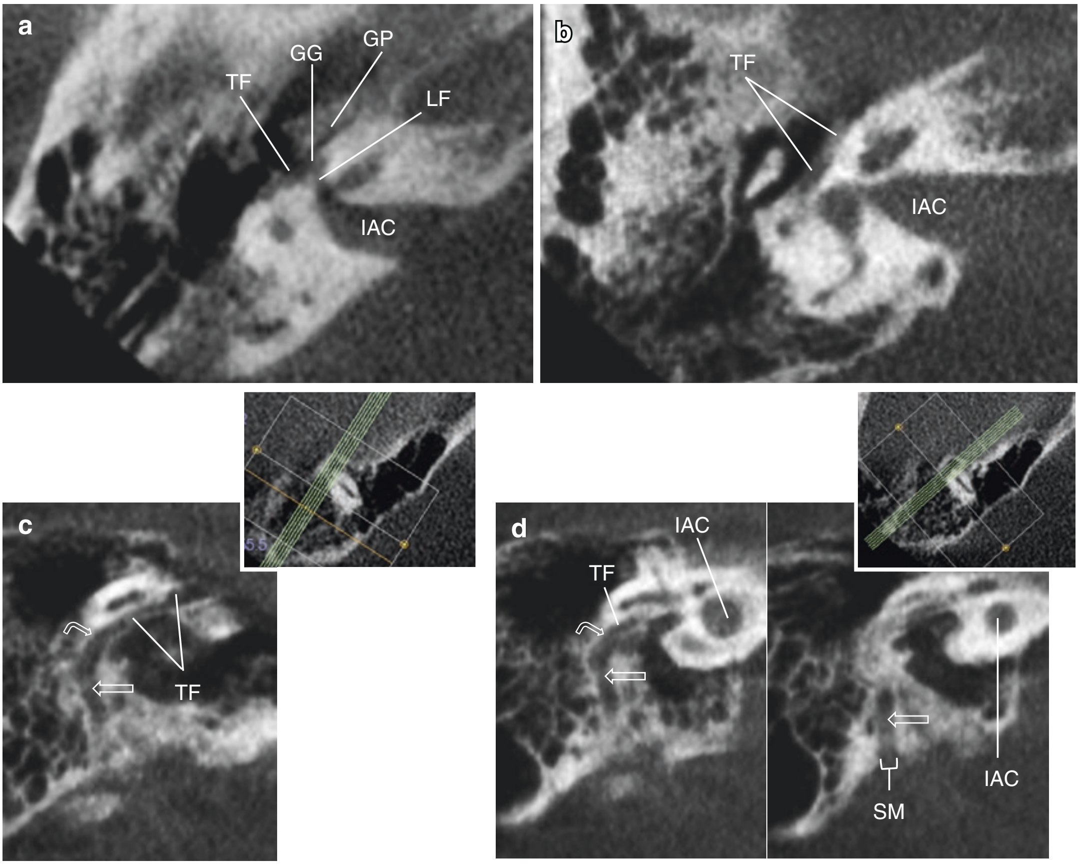

Fig. 14.31 Axial, (**a**, **b**), modified Stenvers (**c**) and Stenvers (**d**) CBCT sections of the facial nerve with a small axial section on the top right indicating the orientation and approximate location of the reconstructed Stenvers and modified Stenvers sections show the internal auditory canal (*IAC*); the labyrinthine segment of the facial nerve canal (*LF*); the geniculate ganglion (*GG*); the second genu of the facial nerve canal (*curved open arrow*); the canal of the greater petrosal nerve (*GP*); the tympanic segment of the facial nerve canal (*TF*); the mastoid segment of the facial nerve canal (*straight open arrow*); and the stylomastoid foramen (*SM*)]

the facial nerve for 13 mm and exits the cranium through the *stylomastoid foramen* (Figs. 14.2, 14.4, 14.30, and 14.31). This segment of the facial nerve is bounded medially by the sinus tympani, laterally by the facial recess, and anteriorly by the pyramidal eminence. Additional structures medial to this segment include the tendon of the stapedius muscle, the posterior semicircular canal, and the jugular bulb (Figs. 14.26, 14.27 and 14.30). The medial aspect of the mastoid segment may be either dehiscent or separated from the jugular bulb by a layer of bone measuring 7 mm or more in width. This part of the facial nerve may be compromised by erosive jugulotympanic paragangliomas in the region of the jugular fossa.

- Branching off the mastoid segment of the facial nerve are the *chorda tympani nerve* and the *nerve to the stapedius muscle*. At approximately 5 mm from the stylomastoid foramen, the chorda tympani nerve separates from the facial nerve and courses superiorly and anteriorly through the canaliculus chorda tympani, crossing the middle ear between the handle of the malleus and the long process of the incus. Eventually, the chorda tympani exits the cranium via the canal of Huguier, located in the anterior wall of the tympanic cavity at the medial end of the petrotympanic or glaserian fissure (Fig. 14.22) (Philips et al. 2008).

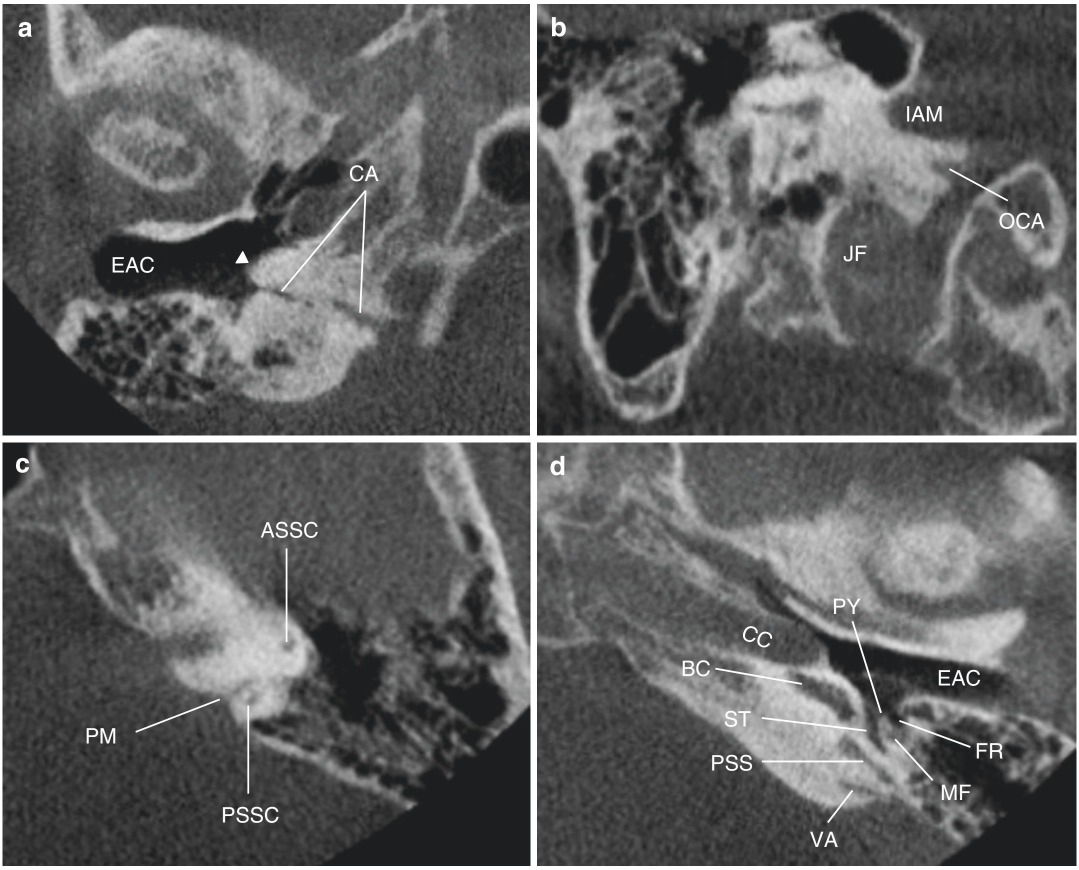

Fig. 14.32 Axial (**a**, **c,** and **d**) and sagittal (**b**) CBCT sections show the cochlear aqueduct (*CA*); opening of the cochlear aqueduct (*OCA*) inferior to the internal auditory meatus (*IAM*) and superior to the jugular foramen (*JF*); the petromastoid canal (*PM*) passing between the anterior (*ASSC*) and posterior (*PSSC*) limbs of the superior semicircular canal; and also the vestibular aqueduct (*VA*) running in the same direction as the posterior semicircular canal (*PSS*). Other structures labeled include the sinus tympani (*ST*); the pyramidal eminence (*PY*); the facial recess (*FR*); the mastoid or vertical part of the facial nerve canal (*MF*); the basal turn of the cochlea (*BC*); the carotid canal (*CC*); the external auditory canal (*EAC*); and the cochlear promontory (*arrowhead*)]

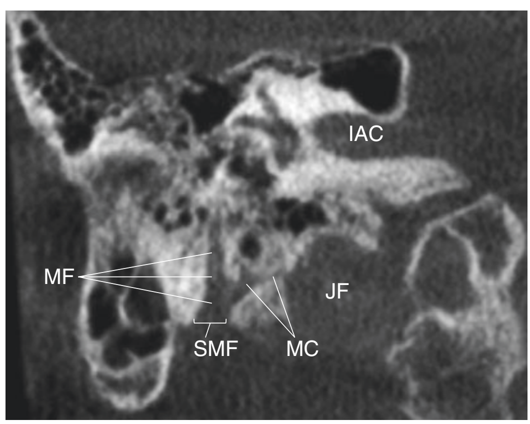

Fig. 14.33 Coronal CBCT section shows the mastoid canaliculus (*MC*) extending from the jugular foramen (*JF*) to the mastoid part of the facial nerve canal (*MF*). The internal auditory canal (*IAC*) and stylomastoid foramen (*SMF*) are also seen

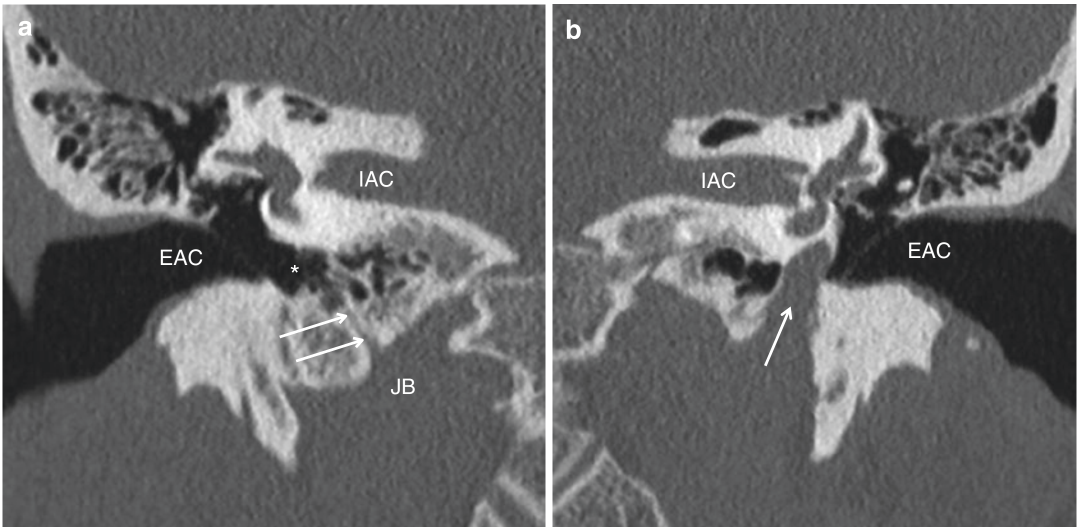

Fig. 14.34 Coronal multislice CT (**a**) section shows the inferior tympanic canaliculus (*white arrows*) extending from the jugular bulb (*JB*) to the medial wall of the hypotympanum (*asterisk*). The coronal multislice CT section at the same level on the opposite side (**b**) shows an enlarged inferior tympanic canaliculus (*white arrow*) caused by an aberrant internal carotid artery. The internal auditory canal (*IAC*) and the external auditory canal (*EAC*) are also seen

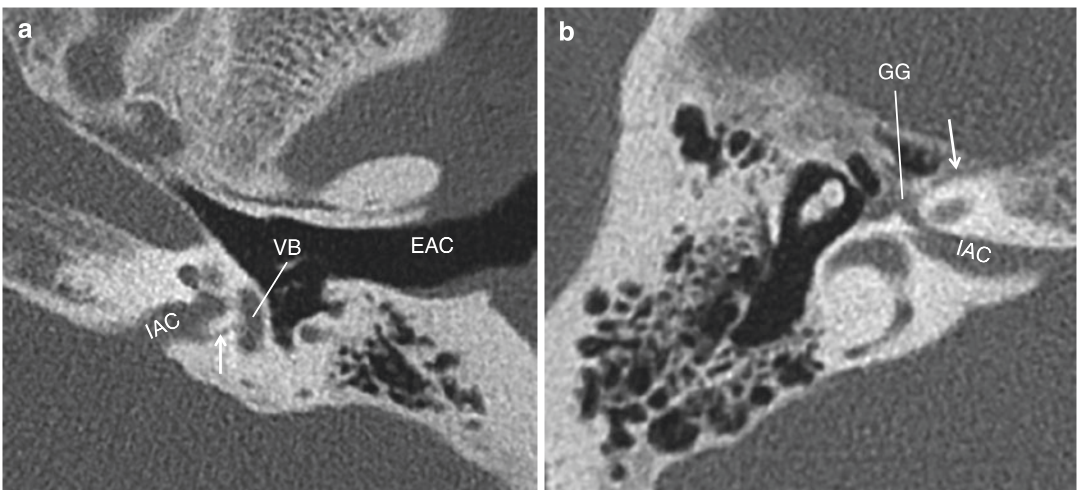

Fig. 14.35 Axial multislice CT section (**a**) shows the singular canal (*white arrow*) extending from the internal auditory canal (*IAC*) to the vestibule (*VB*). The axial multislice CT section (**b**) shows the canal for the superficial greater petrosal nerve (*white arrow*) extending from the geniculate ganglion (*GG*) anteriorly to the anterior surface of the petrous part of the temporal bone. The external auditory canal (EAC) is also labled

14.5 Normal Anatomic Variants

14.5.1 Anatomical Variants Simulating Other Conditions

14.5.1.1 Petromastoid Canal

The petromastoid canal (antrocerebellar canal of Chatellier, subarcuate canaliculus) is a thin channel containing the subarcuate artery/vein and also the prolongation of the dura mater. It extends from the mastoid antrum medially to the posterior cranial fossa, passing between the anterior and posterior limbs of the superior semicircular canal, with its medial orifice being the subarcuate fossa (Figs. 14.29, 14.30, and 14.32). The subarcuate fossa extends as a blind tunnel under the superior semicircular canal and opens to the posterior surface of the petrous part of the temporal bone (Fig. 14.17). It has been suggested to be a possible pathway for intracranial extension of the middle ear infections. Migirov and Kronenberg (2006) proposed the following classification of the width of the petromastoid canal: type I, an invisible channel; type II, a thin channel measuring less than 0.5 mm; type III, a thin channel measuring between 0.5 and 1 mm; and type IV, a channel wider than 1 mm. Their study showed that the type IV petromastoid channel is seen significantly more often in children less than 5 years of age and the type II in children older than 5 years of age. High-resolution CT with thin axial slices is the best modality for visualization of the petromastoid canal. This canal might mimic a fracture line in patients with a history of trauma to the temporal bone region (Migirov and Kronenberg 2006; Krombach et al. 2002; Connor et al. 2005).

14.5.1.2 Cochlear Aqueduct

The cochlear aqueduct is a communication between the perilymph and the cerebrospinal fluid. This can be visualized in coronal and axial CT sections as a canal extending obliquely and inferiorly from the junction of the basilar turn of the cochlea and the vestibule to an area anteromedial to the pars nervosa of the jugular foramen. This canal courses relatively parallel and inferior to the internal auditory canal (Fig. 14.32). It has a narrow lateral *otic capsule segment* and a medial *petrous apex segment*. The width of the otic capsule segment never exceeds 2 mm at maximal diameter. The petrous apex segment has a more variable width and has an average diameter of 4.5 mm. It widens progressively as it moves closer to its external opening on the posterior surface of the petrous bone. The normal diameter of this segment may be as great as 1 cm. A wide petrous apex segment should not be confused with the glossopharyngeal meatus through which the ninth cranial nerve enters the anteromedial jugular foramen. The cochlear aqueduct may also be mistaken for a fracture line (Connor et al. 2005; Swartz 2001; Koesling et al. 2005; Swartz 2004).

14.5.1.3 Vestibular Aqueduct

The vestibular aqueduct extends from the vestibule near the common crus, the junction of superior and posterior semicircular canals, to the posterior surface of the petrous ridge. This canal is identified on axial CT images as a thin radiolucent line which can be mistaken for a fracture line (Fig. 14.32) (Connor et al. 2005; Swartz 2001; Koesling et al. 2005).

14.5.1.4 Mastoid Canaliculus

The mastoid canaliculus is a canal connecting the jugular foramen to the vertical or mastoid part of the facial canal. It transmits the *nerve of Arnold* which is a branch of the vagus nerve. This can be seen on axial or coronal CT sections and needs to be differentiated from a fracture line (Fig. 14.33) (Connor et al. 2005; Swartz 2001).

14.5.1.5 Inferior Tympanic Canaliculus

The inferior tympanic canaliculus can be visualized on coronal CT section as a vertically oriented radiolucent line extending from the medial wall of the middle ear cavity to the jugular foramen. It transmits the *nerve of Jacobsen*, the inferior tympanic branch of the glossopharyngeal nerve, and the inferior tympanic artery. Knowledge of the anatomy of this canal is important since an *aberrant internal carotid artery* may cause an enlargement of this canal. It can also be confused with a fracture line (Fig. 14.34) (Connor et al. 2005; Swartz 2001).

14.5.1.6 Cochlear Cleft

The cochlear cleft is a C-shaped narrow space in the otic capsule located parallel and lateral to the basal turn of the cochlea and medial to the tympanic cavity. Chadwell et al. (2004) suggested that this cleft may be a space between the endosteal and outer periosteal layers of the otic capsule or closely related to the fissula ante fenestram which is an irregular ribbon-like space within the otic capsule, filled mostly with cartilage, extending from the vestibule anteriorly to the medial wall of the middle ear cavity. They also suggested that decreasing incidence of this space with age may be related to its replacement by bone. The cochlear cleft can be visualized on thin axial and coronal CT sections and may be mistaken for an otosclerotic focus (Chadwell et al. 2004; Dawes et al. 1983; Van Rompaey et al. 2011).

14.5.1.7 The Singular Canal

The singular canal is a thin channel which extends from the inferoposterior part of the internal auditory canal to the posterior semicircular canal. The singular canal transmits the *singular nerve* which is a branch of the inferior vestibular nerve. This can best be visualized on axial CT sections and should be distinguished from a fracture line (Figs. 14.35 and 14.45) (Connor et al. 2005; Swartz 2001).

14.5.1.8 Canal for the Superficial Greater Petrosal Nerve

The canal for superficial greater petrosal nerve extends from the geniculate ganglion anteriorly to the anterior surface of the petrous part of the temporal bone (Connor et al. 2005). This canal can be identified on axial CT sections and may be mistaken for a fracture line (Fig. 14.35).

14.5.1.9 Superior Petrosal Sinus

The superior petrosal sinus may groove the superior border of the petrous part of the temporal bone as it travels above it. This can be visualized on axial CT sections and needs to be distinguished from a fracture line in traumatized patients (Fig. 14.36) (Connor et al. 2005).

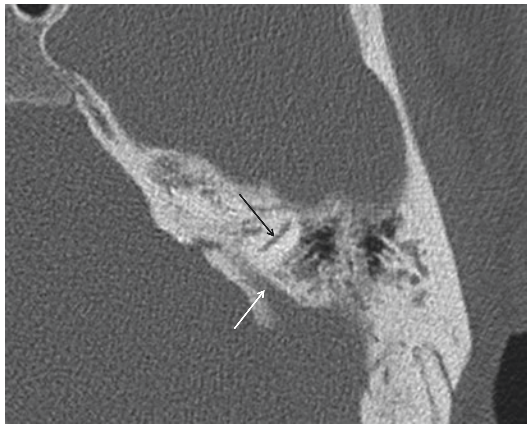

Fig. 14.36 Axial multislice CT section showing the superior petrosal sinus (*white arrow*) passing medial to the superior semicircular canal (*black arrow*)

14.5.1.10 Intrinsic and Extrinsic Fissures

The extrinsic fissures/sutures, where the temporal bone articulates with the neighboring bones, can mimic fracture lines in traumatized patients. Examples of these sutures include *petro-occipital*, *occipitomastoid*, *petrosphenoidal,* and *sphenosquamous* sutures. Located between different parts of the temporal bone (tympanic, squamous, mastoid, and petrous parts) are the intrinsic fissures. Examples of intrinsic fissures include *tympanosquamous*, *petrotympanic*, *petrosquamous,* and *tympanomastoid* fissures (Figs. 14.37 and 14.38). The tympanosquamous fissure is located along the anterior surface of the external auditory canal; a wedge-like bone divides this fissure to the petrotympanic and petrosquamous fissures (Figs. 14.9 and 14.39). The petrotympanic fissure or Glaserian fissure is bordered posteriorly by the anterior tympanic spine and contains the chorda tympani nerve and the anterior tympanic branch of the maxillary artery (Fig. 14.22).

These sutures can be appreciated on axial, coronal and sagittal CT sections. Knowledge of the normal appearance and position of these sutures is helpful in their differentiation from fracture lines (Connor et al. 2005; Swartz 2001; Furuya et al. 1984).

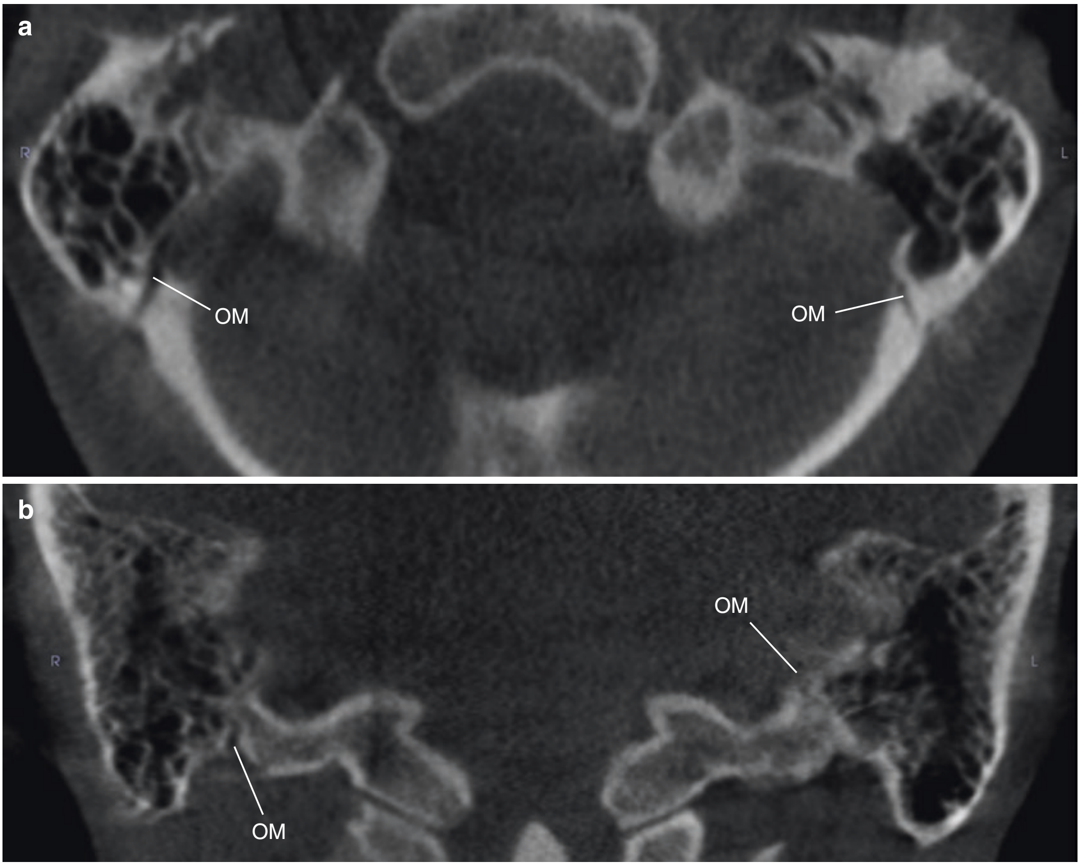

Fig. 14.37 Axial (**a**) and coronal (**b**) CBCT images showing the occipitomastoid suture (*OM*)

14.5.2 Possible Complications from Surgery

14.5.2.1 High-Riding Jugular Bulb

Normally, the superior border of the jugular bulb *lies below the level of the hypotympanic recess* (Fig. 14.40); a jugular bulb is considered *high riding* if it extends *superior to the floor of internal auditory canal* (IAC). It may be situated either medial or lateral to the otic capsule with the former protruding into the inner ear and the latter protruding into the middle ear cavity (Fig. 14.41). A high-riding jugular bulb protruding into the middle ear is associated with rhythmic pulsatile tinnitus waxing and waning with exercise or pressure over the internal jugular vein (Sayit et al. 2016; Friedmann et al. 2012; Huang et al. 2006). High-riding and dehiscent jugular bulbs protruding into the external ear canal have also been reported (Ball et al. 2010). Diverticulum formation may also accompany a high-riding jugular bulb extending medially to an area between the posterior wall of the IAC and the vestibular aqueduct which has a relatively weaker supporting bone than the dense otic capsule; this can be appreciated on CT images (Fig. 14.42) (Atilla et al. 1995; Van Rompaey et al. 2012). Atilla et al. (1995) reported a high jugular bulb in 20.3% and jugular bulb diverticulum in 7.9% of 700 temporal bones. Koesling et al. (2005) found a high jugular bulb in 6% of 223 temporal bones (Koesling et al. 2005).

14.5.2.2 Dehiscent Jugular Bulb

There should be a thin plate of bone covering the jugular bulb which can only be appreciated on thin slice bone algorithm CT. The jugular bulb rarely erodes into the middle ear cavity, vestibu-

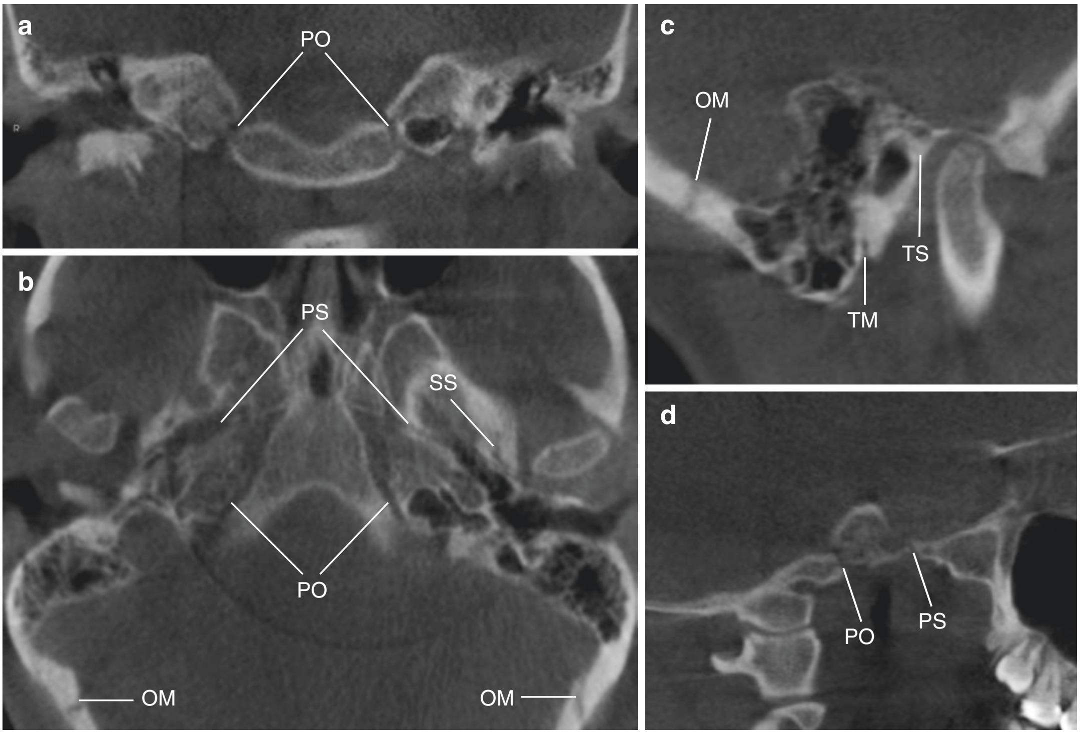

Fig. 14.38 Coronal (**a**), axial (**b**) and sagital (**c** and **d**) CBCT images show the occipitomastoid (*OM*), petro-occipital (*PO*), petrosphenoidal (*PS*), sphenosquamous (*SS*), tympanomastoid (*TM*), and tympanosquamous (*TS*) sutures

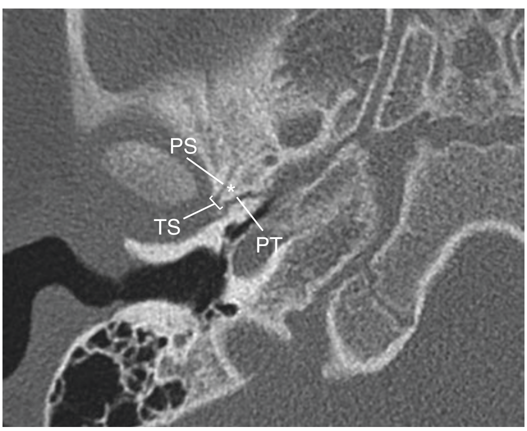

Fig. 14.39 An axial multislice CT section shows the tympanosquamous fissure (*TS*) subdivided into the petrotympanic (*PT*) and petrosquamous (*PS*) fissures by a wedge-shaped bony septum (*asterisk*)

lar aqueduct, facial nerve, and posterior semicircular canal. Patients with dehiscence in the inner ear may complain of pulsatile tinnitus, vertigo, and conductive hearing loss or may be asymptomatic. Atilla et al. (1995) reported dehiscent jugular bulb in 3.9% of 700 temporal bones; however, Koesling et al. (2005) found dehiscent jugular bulb in 1% of 223 temporal bones. As mentioned earlier, erosion of the jugular bulb into the external auditory meatus is uncommon (Friedmann et al. 2012; Ball et al. 2010).

14.5.2.3 Bulging Sigmoid Sinus

Occasionally, the sigmoid sinus may be located much more anteriorly and laterally than normal, making surgical procedures in this area more complicated with an increased risk of hemor-

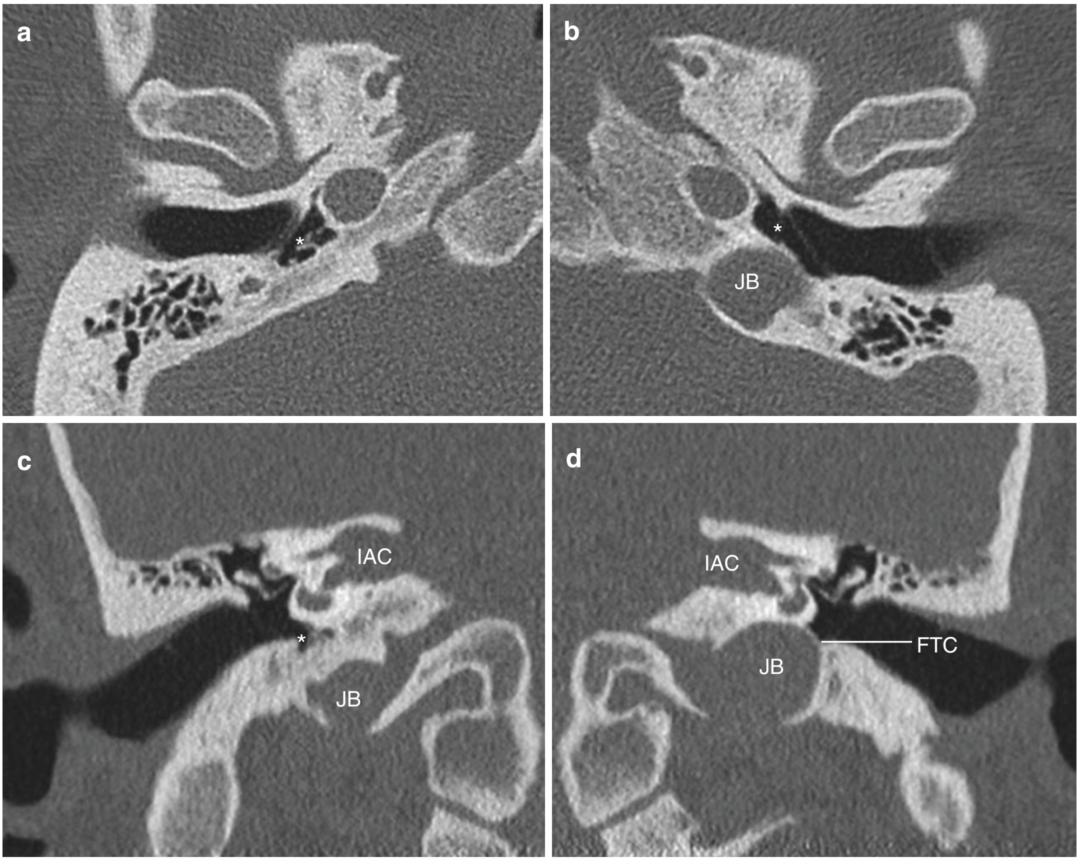

Fig. 14.40 The right axial multislice CT section (**a**) shows the absence of the right jugular bulb medial to the hypotympanum (*asterisk*) the left axial multislice CT section (**b**) at the same level shows the jugular bulb extending up to an area medial to the hypotympanum (*asterisk*). The right coronal multislice CT (**c**) shows a normal relationship between the jugular bulb (*JB*) and hypotympanum (*asterisk*), however the left coronal multislice CT (**d**) shows the jugular bulb (*JB*) extending superior to the floor of the tympanic cavity (*FTC*). Note that the enlarged jugular bulb on the left side of the patient does not reach the inferior border of the internal auditory canal (*IAC*) and is not considered to be high riding

rhage specifically if a postauricular approach is employed. Moreover the small size of the mastoid antrum, caused by the anterolateral location of the sigmoid sinus, may add to the complexity of the surgical procedure (Fig. 14.43) (Swarts 2009). The location of the sigmoid sinus can be evaluated measuring its distance from the external acoustic canal. Atilla et al. (1995) reported an average distance of 13.3 mm measured in 700 temporal bones with 12.4% of the cases having a distance of less than 10 mm. This condition is more commonly seen on the right side. Patients with bulging sigmoid sinus may complain of pulsatile tinnitus (Swarts 2009; Mehall et al. 1995; Otto et al. 2007).

14.5.2.4 Dehiscent Carotid Canal

The internal carotid artery passes by the middle ear cavity as it climbs up through the temporal bone. It is covered by a thin layer of bone which may be dehiscent and cause serious hemorrhage during middle ear surgery (Fig. 14.44) (Wang

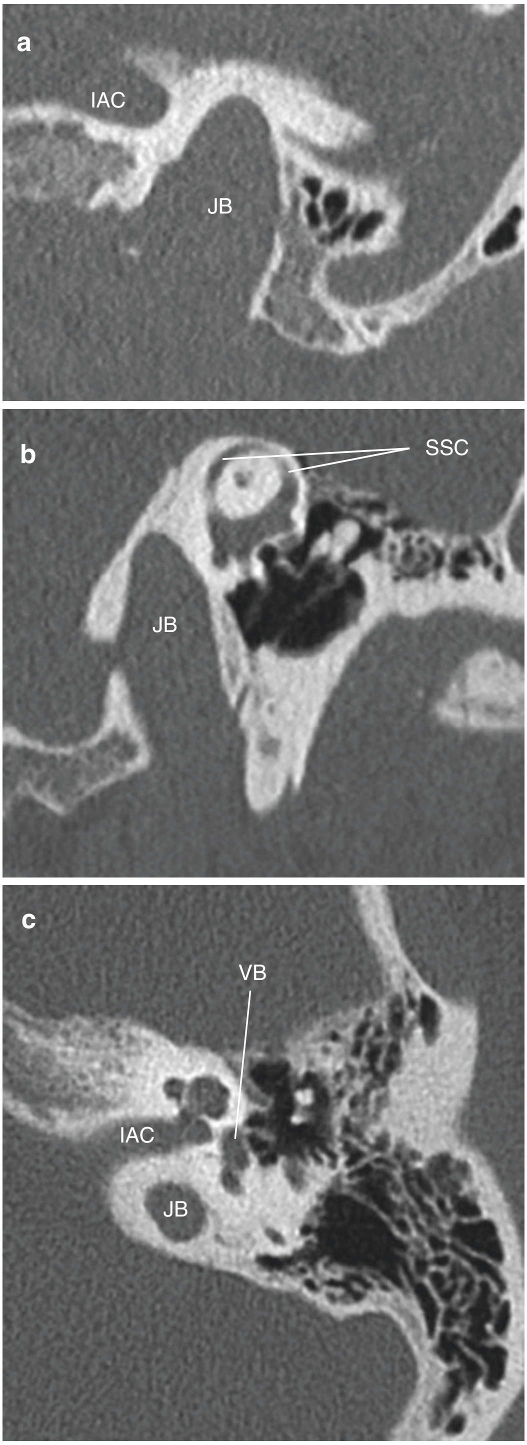

Fig. 14.41 Stenvers (**a**), Pöschl (**b**), and axial (**c**) multislice CT sections show a high-riding jugular bulb (*JB*) extending superior to the inferior border of the internal auditory canal (*IAC*), and medial the superior semicircular canal (*SSC*) and vestibule (*VB*)

et al. 2011). Wang et al. (2011) found dehiscence of the carotid canal adjacent to the middle ear cavity in 6.9% of 408 temporal bones.

14.5.2.5 Dehiscent Facial Canal

A dehiscent facial canal is a very serious surgical hazard which can lead to facial nerve injury and paralysis during removal of disease in the middle ear cavity. The bone covering the facial canal is very thin and may be dehiscent congenitally or eroded later in life by erosive lesions of the middle ear such as cholesteatomas (Magliulo et al. 2011; Nager and Proctor 1991; Di Martino et al. 2005). Moreano et al. (1994) reported congenital dehiscence of the facial canal in 55% of 1000 temporal bones with the most common location being *near the oval window* (Moreano et al. 1994). Protrusion of the facial nerve into the middle ear cavity through the dehiscence may also be encountered. This protrusion can occupy the oval window niche and may be mistaken for a lesion such as a schwannoma or congenital cholesteatoma (Swarts 2009).

14.5.2.6 Koerner's Septum

As described, Koerner's septum (petrosquamosal lamina) may be confused with the medial wall of the antrum and the surgeon may assume that the disease has been completely removed from the region (Fig. 14.12) (Swarts 2009; Virapongse et al. 1982).

14.5.2.7 Deep Sinus Tympani

The sinus tympani may extend posteriorly to an area medial to the vertical portion of the facial nerve canal, making it difficult for surgeons to remove the disease from this area (Fig. 14.45) (Pickett et al. 1995).

14.5.3 Congenital Anomalies

14.5.3.1 Large Vestibular Aqueduct

An enlarged vestibular aqueduct detected on CT or an enlarged endolymphatic duct and sac detected on MRI has been reported to be the most common imaging finding of the inner ear in patients with sensorineural hearing loss. This abnormality is often accompanied by other abnormalities of the inner ear

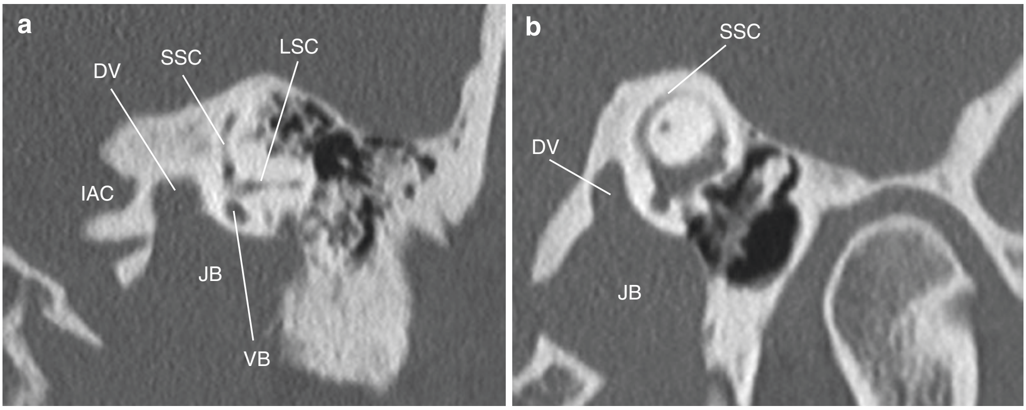

Fig. 14.42 Coronal (**a**) and Pöschl (**b**) multislice CT sections show diverticulum formation (*DV*) in the superior aspect of the jugular bulb (*JB*) between the internal auditory canal (*IAC*) and the labyrinth including the vestibule (*VB*), the superior (*SSC*) and lateral (*LSS*) semicircular canals

Fig. 14.43 Axial CBCT section shows that the right sigmoid sinus (*asterisk*) is laterally positioned compared to the left sigmoid sinus. Note the small size and more medially located left sigmoid sinus (*straight arrow*). The internal auditory canals (*curved arrows*) can also be visualized on this section

such as enlarged vestibule, enlarged lateral semicircular canal, dehiscent superior and/or posterior semicircular canal, and cochlear abnormalities. A vestibular aqueduct is considered to be enlarged when its diameter, as measured on CT images, is greater than 1.5 mm at the midpoint along its course, between the common crus and the opening of the aqueduct on the posterior surface of the petrous part of the temporal bone (Fig. 14.49) (Ma et al. 2009). One can also compare the width of the vestibular aqueduct to that of the simultaneously visualized posterior semicircular canal. They should be of approximately equal diameter under normal circumstances (Figs. 14.32 and 14.45) (Swartz 2004).

14.5.3.2 External Auditory Canal Atresia

A disturbance in the normal development of the first branchial arch can affect the external ear which leads to conductive hearing loss. These congenital malformations may be syndromic or nonsyndromic. Males are affected more often than females. These malformations are seen in 1 out of 10,000–20,000 births and are usually unilateral. Bilateral cases are usually syndromic.

Atresia of the EAC is one of the common features in patients with hemifacial microsomia, also known as *Goldenhar syndrome*, which is the second most common developmental craniofacial anomaly after cleft lip and cleft palate. Other malformations associated with this syndrome include deformity of the auricle, malformation of the tympanic cavity, and ossicular abnormalities. Atresia of the external ear can also occur in patients with *Treacher Collins* (Fig. 14.46), *Klippel-Feil*, *Rasmussen*, *Nager*, *Pfeiffer,* and *Pierre Robin* syndrome (Fau et al. 2011; Rosa et al. 2011; Yildirim et al. 2008; Julia et al. 2002; Wright 1997; Vallino-Napoli 1996; Katsanis and Jabs 2012; Kosling et al. 2009; Karmody and Annino 1995; Meyerson and Nisbet 1987; Gruen et al. 2005). Although *Crouzon* syndrome is more associated with malformation of the middle ear, atresia of the external auditory canal has been reported (Orvidas et al. 1999).

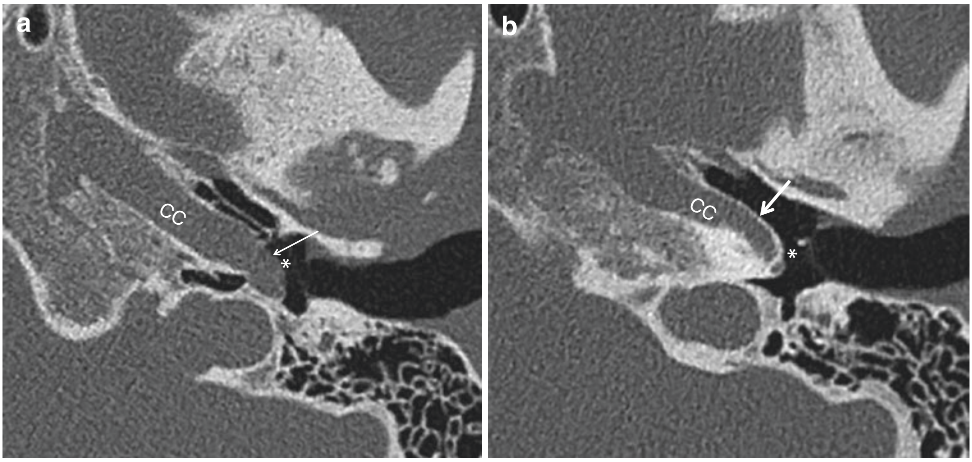

Fig. 14.44 Axial (**a**) multislice CT sections shows the dehiscence (*thin arrow*) of the carotid canal (*CC*) located adjacent to the middle ear cavity (*asterisk*). The axial multislice CT section (**b**) shows the presence of an intact cortical bone (*thick arrow*) covering the carotid canal (*CC*) that is located adjacent to the middle ear cavity (*asterisk*)

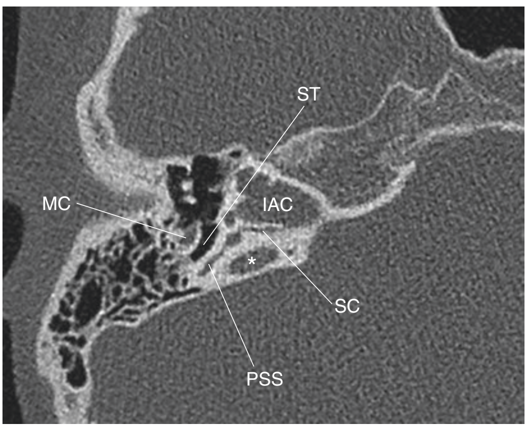

Fig. 14.45 Axial multislice CT section showing deep sinus tympani (*ST*) extending posteriorly between the mastoid or vertical portion of the facial nerve canal (*MC*) and the posterior semicircular canal (*PSS*). The singular canal (*SC*) can be seen running parallel to the course of the internal auditory canal (*IAC*) transferring the inferior vestibular nerve to the posterior semicircular canal (*PSS*). Also note the enlargement of the visualized portion of the vestibular aqueduct (*asterisk*)

Imaging findings depend on the severity of the malformation which may range from a mild microtia (a small auricle) to severe atresia of the EAC with malformation of the middle ear. Mild cases represent as a small and dysmorphic auricle with narrowing or stenosis of the EAC. As the condition becomes more severe, other malformations such as atresia of the EAC, thickened and calcified tympanic membrane, dysplasia, fusion or absence of the ossicles of the middle ear, a small or non-aerated middle ear cavity, and atresia of the round and oval windows may be found. An aberrant course of the facial nerve is commonly seen with more severe cases. The tympanic segment of the facial nerve may be dehiscent. The mastoid segment is usually displaced anterolaterally and may exit the skull base into the mandibular fossa or lateral to the styloid process. The inner ear and internal auditory canal may also be involved in very severe cases. Associated congenital cholesteatomas are less common. Malformation in the region of the external ear may manifest as stenosis, duplication of the EAC as well as cysts, sinuses and fistulas. The osseous malformation can be detected using CBCT images but soft tissue abnormalities such as cysts and fistulas are not discernible on CBCT images, and require further evaluation with MRI or MSCT (Fig. 14.47) (Castillo et al. 2009; Harnsberger et al. 2011). Osteomas and exostoses of the external auditory canal must be included in the differential diagnosis as these lesions can cause obstruction of the EAC (Fig. 14.47) (Kuczkowski et al. 2010).

14.5.3.3 Semicircular Canal Malformations

Semicircular canal (SCC) dysplasia may be syndromic or nonsyndromic. Examples of syndromes include *CHARGE*, *Alagille*, *Waardenburg*, *Apert,* and *Goldenhar syndrome*. Some SCC malformations are associated with cochlear malformation. Oval/round window atresia, cochlear nerve aper-

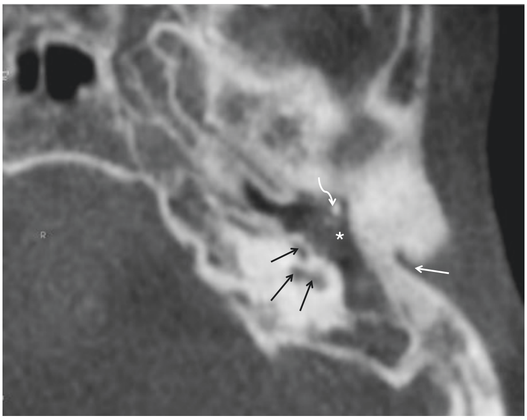

Fig. 14.46 An axial CBCT section of a patient with Treacher Collins syndrome shows atresia of the external auditory canal (*straight white arrow*), non-aerated middle ear cavity (*asterisk*) as well as severely malformed ossicles (*curved white arrow*) and labyrinth (*straight black arrow*)

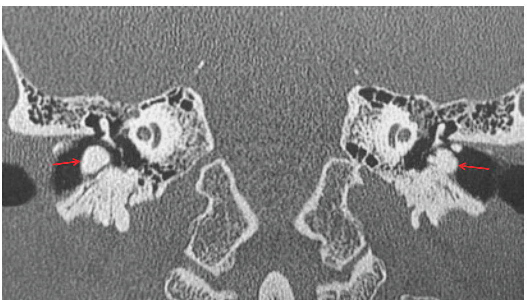

Fig. 14.47 Coronal reformatted MSCT section at the level of the external auditory canals (EAC) showing bilateral EAC osteomas; Note that the osteoma is continous with the normal cortical bone of the left external auditory meatus (Courtesy of Dr. Thomas Underhill)

ture atresia, facial nerve canal abnormalities, and middle ear deformity can be found in 70% of cases (Koch et al. 2006; Morimoto et al. 2006; Satar et al. 2003; Lemmerling et al. 2000; Higashi et al. 1992; Zhou et al. 2009).

Deformities of the lateral semicircular canal are relatively common and may be unilateral or bilateral. Familial cases accompanied by external and middle ear malformations have been reported (Johnson and Lalwani 2000; Matsunaga and Hirota 2003). Measurement of the bony island enclosed by this canal has been reported to be useful in determining the presence of a hypoplastic or hyperplastic lateral SCC. The normal range is between 2.6 and 4.8 mm (Chen et al. 2008).

Superior SCC dehiscence syndrome has been described as a very small defect in the bony wall of the superior SCC. This condition may be a result of erosion of the bone covering the canal by pathological conditions such as cholesteatoma of the petrous apex or subarcuate vascular malformation. Normally, the oval and round windows are the only openings to the inner ear. The SCCs are a hydraulically closed system with no substantial movement of fluid in response to the stapes vibrations. However, dehiscence of one of the SCCs serves as a *third window* and thereby causes slight movement of the endolymph within the membranous SCC in response to sound and vibration of the stapes. The brain interprets motion of the endolymph as movement of the body which may result in dizziness. Conductive hearing loss is another complication caused by this condition.

Pöschl and Stenvers CT sections optimally demonstrate the wall of the upper arc of the superior SCC. On Pöschl section, the superior SCC presents as a ring, with the entire arc of its outer wall visualized on one image. The Stenvers section also shows the superior cortex of the superior SCC in perfect cross section (Figs. 14.2, 14.3, and 14.48). Partial volume effect, when the structure is thinner and smaller than the individual voxel used to generate the CT image, can mimic a dehiscent superior SCC. For this reason, 1.0 or 0.5 mm collimation is required for optimal visualization of this defect (Curtin 2003).

14.5.3.4 Mondini Dysplasia

Mondini dysplasia refers to a rare deformity of the osseous labyrinth presenting as insufficient cochlear turns (1.5 turns instead of the normal 2.5–2.75 turns), an enlarged vestibule, and a large vestibular aqueduct. It may be unilateral or bilateral. Sensorineural hearing loss is the most common complication in these patients, but recurrent meningitis has also been reported. CT scan is the best modality for detecting this deformity. CT findings include a foreshortened cochlea along its modiolar axis with a normal basal turn and varying degrees of agenesis of the apical and middle turns, agenesis of the interscalar septum resulting in confluence of the apical and middle

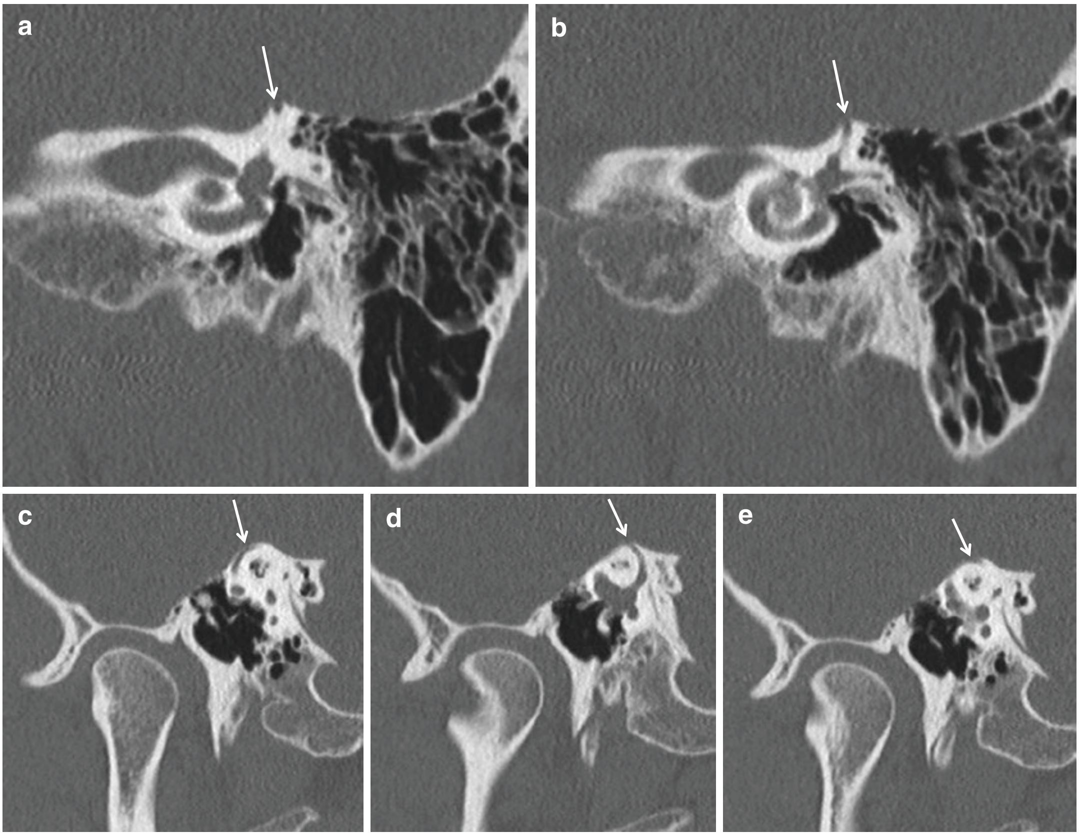

Fig. 14.48 Stenvers (**a**, **b**) and Pöschl (**c**–**e**) multislice CT reconstructions show dehiscence of the superior semicircular canal (*white arrows*)

turns of the cochlea and a cystic apex (Fig. 14.49) (Ma et al. 2009; Anandi et al. 2012; Ohlms et al. 1990; Urman and Talbot 1990).

14.5.3.5 Foreign Bodies

Cochlear Implant

A cochlear implant is a small, complex electronic device that is surgically implanted to provide a sense of sound perception through direct electrical stimulation. Multislice CT can be used as a valuable tool in the postoperative assessment of cochlear implant patients (Fig. 14.50) (Verbist et al. 2005).

Ossicular Prosthesis

Ossicular prostheses are commonly used in patients with destruction of the ossicular chain caused by pathological conditions such as cholesteatoma and otitis media or congenital malformations of the ossicles. Autografts and homografts were initially used to reconstruct the ossicles due to their biocompatibility; however, synthetic prostheses were developed later to overcome the difficulties encountered when using those grafts. Thin-section CT with contiguous 1-mm sections may help to evaluate the status of the prosthesis and remaining ossicles (Fig. 14.51) (Stone et al. 2000).

Tympanostomy Tubes

Tympanostomy tube is a miniature plastic or stainless steel ventilation tube which is surgically implanted into the eardrum to normalize intratympanic pressure and prevent accumulation of pus in the middle ear. Tympanostomy tubes are associated with certain complications such as permanent perforation of the tympanic membrane, otorrhoea, and tympanosclerosis (Hajiioannou

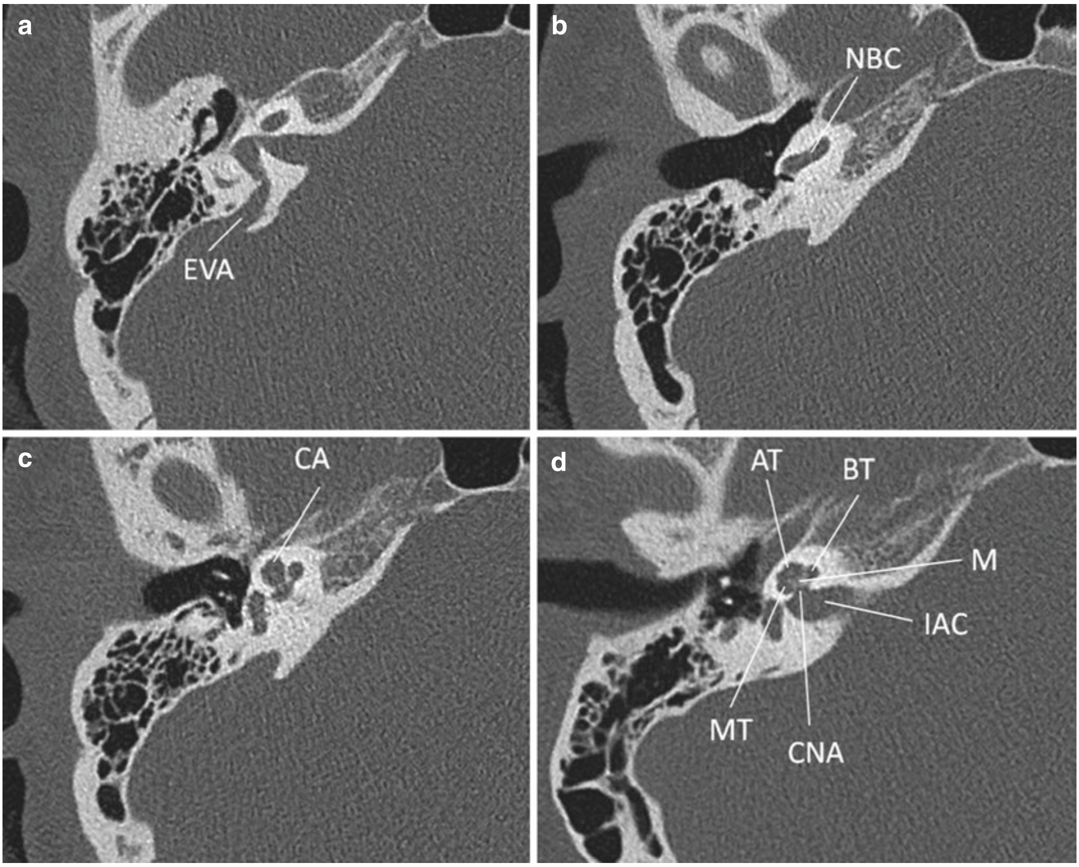

Fig. 14.49 Axial multislice CT sections (**a–c**) of a 26 year old female with Mondini dysplasia show an enlarged vestibular aqueduct (*EVA*), a normal basal turn of the cochlea (*NBC*) and a cystic apex (*CA*) of the cochlea resulting from coalescence of the middle and apical turns. Axial multislice CT section (**d**) shows normal turns of the cochlea; proximal basal turn (*BT*); middle turn (*MT*) and apical turn (*AT*) surrounding the modiolus (*M*); the cochlear nerve aperture *CNA*; and internal auditory canal (*IAC*)

et al. 2009; McDonald et al. 2008). The CT appearance of these ventilation tubes is usually characteristic, but the presence of surrounding fluid, technical problems such as motion and artifacts, or an atypical location may make it difficult to identify them (Fig. 14.52). It is important to properly report the presence of these tubes and differentiate them from foreign bodies or dislocated ossicles (Klein et al. 1988).

14.5.4 Common Pathology

14.5.4.1 Otitis Externa

Otitis externa refers to inflammation or infection of the external ear which can be acute or chronic. Acute cases can be caused by bacterial (90%) or fungal (10%) overgrowth after exposure to moisture or to local trauma. The chronic form is often part of a more generalized dermatologic (dermatitis, psoriasis, lupus, and infantile eczema) or allergic problem. Early acute and most chronic disease usually manifests as pruritus and local discomfort which can be exacerbated if left untreated. There is an increased risk of otomycosis in immunocompromised patients (Hamzany et al. 2011; Osguthorpe and Nielsen 2006; Daneshrad et al. 2002; Fau and Sataloff 2008; Krahl 1992). Ramsay Hunt syndrome, a rare complication of herpes zoster which can cause otalgia, auricular vesicles, and peripheral facial paralysis, is best evaluated by MRI (Castillo et al. 2009; Kim and Bhimani 2008).

Imaging has a limited role in the diagnosis of otitis externa unless there is an underlying

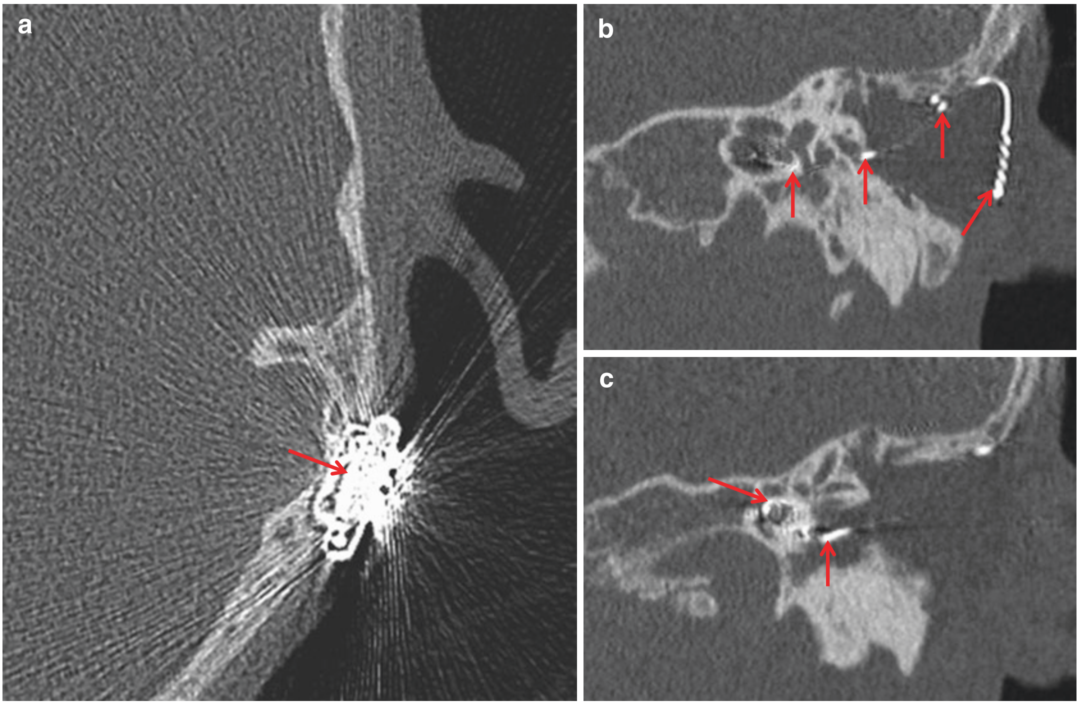

Fig. 14.50 Axial (**a**) and Stenvers (**b**, **c**) sections reconstructed using multislice CT show a cochlear implant (*red arrows*)

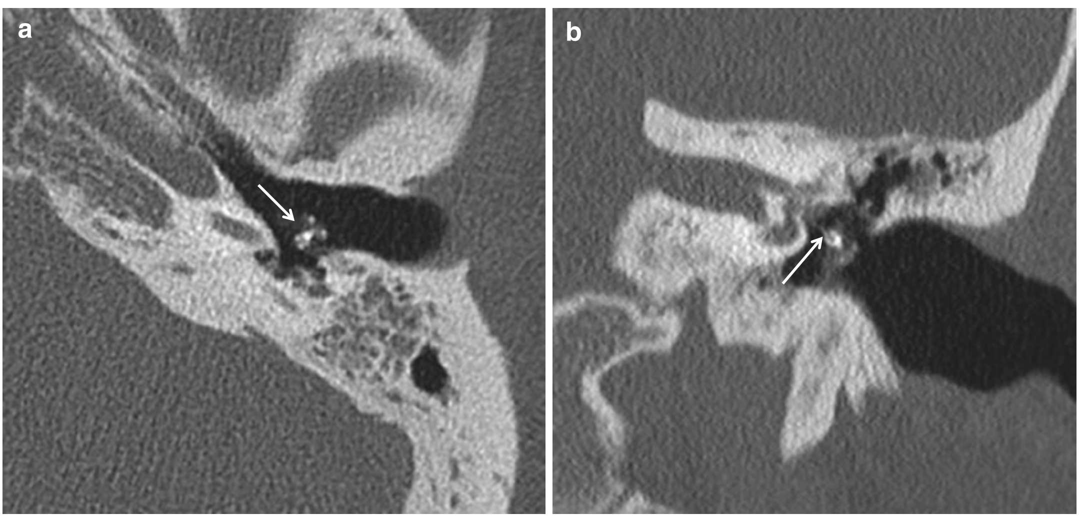

Fig. 14.51 Axial (**a**) and coronal (**b**) multislice CT sections show replacement of the ossicular chain by an ossicular prosthesis (*white arrows*)

condition such as a benign or malignant neoplasm, or an obstruction of the EAC which has caused infection of the external ear. CT can provide anatomical details in the case of obstruction. The presence of bony erosion can help with diagnosis of an underlying malignancy. Necrotizing external otitis, also known as malignant external otitis, is a severe invasive infection of the EAC

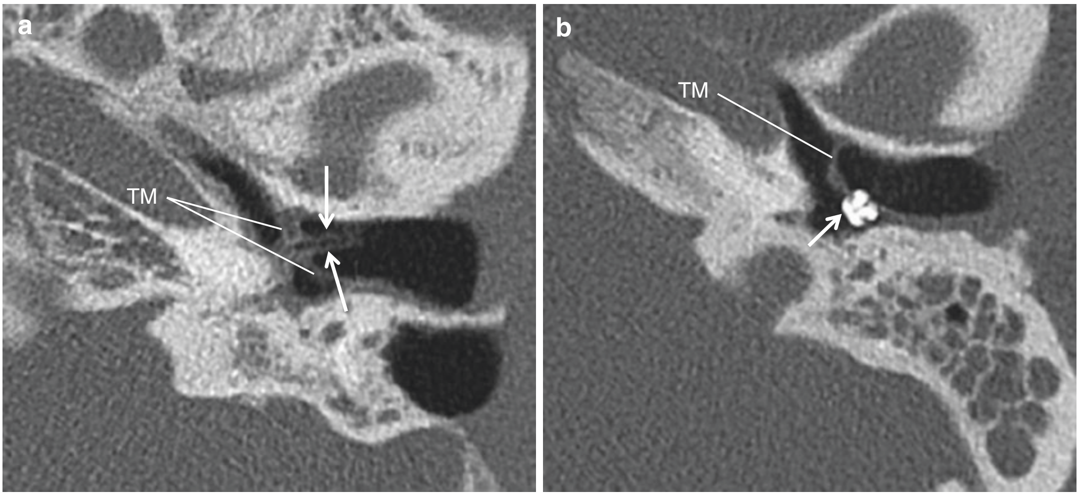

Fig. 14.52 Axial multislice CT sections shows two different types of tympanotomy tube (*white arrows*) on two separate patients (**a**, **b**). Note that the tympanic membrane (*TM*) is thickened in both cases

that causes bony erosion and swelling of the EAC soft tissue which may be mistaken for squamous cell carcinoma, cholesteatoma, keratosis obturans, chronic granulomatous disease, or Langerhans cell histiocytosis. Differentiation between these conditions may require microscopic evaluation (Castillo et al. 2009; Harnsberger et al. 2011).

14.5.4.2 Otitis Media and Mastoiditis

Otitis media is the second most common disease of childhood after upper respiratory tract infection. Otitis media is a more general term which refers to a spectrum of inflammatory conditions in the middle ear including *acute otitis media*, *otitis media with effusion*, and *chronic suppurative otitis media* (Morris and Leach 2009). The middle ear and mastoid air cells are considered to be extensions of the upper respiratory tract. The pharyngotympanic tube (Eustachian tube) serve as a pathway for the bacteria and infected secretions of the nasopharynx to reach the middle ear cavity and spread into the mastoid air cells, through the aditus of the mastoid antrum. Otomastoiditis may present as an acute or chronic infection. The acute form is usually caused by bacterial infection and the chronic form by long-standing pharyngotympanic tube (Eustachian tube) dysfunction. Although unusual, invasive mycotic and tuberculous otomastoiditis may occur especially in immunocompromised patients (Slack et al. 1999; Munoz et al. 2009; Mjoen et al. 1992).

A large number of patients with acute otomastoiditis are cured after a course of antibiotics, but nonspecific debris within the mastoid air cells and the middle ear, typically with several fluid levels may still be visualized on CT images. This appearance may also be found incidentally in 10–15% of children and a substantial percentage of adults with no history of otitis media. Therefore, radiologists *should not* interpret this common finding as necessarily an inflammatory condition or more specifically mastoiditis which is more of a clinical diagnosis. This appearance can simply be referred to as "*nonspecific debris.*" Integrity of the ossicular chain, mastoid septa, and the internal and external mastoid cortices are helpful in excluding inflammatory conditions. *Coalescent mastoiditis* is a term used for acute otomastoiditis when mucoperiosteal disease extends to involve the bone (Fig. 14.53) (Swarts 2009; Nemzek and Swarts 2003).

Complications of acute otomastoiditis include middle ear effusion, subperiosteal abscess, Bezold abscess (walled-off pus in and around the sternocleidomastoid and digastric muscle as a result of extension of the infection to the mastoid tip), facial nerve involvement, labyrinthitis, petrous apicitis, and intracranial involvement (meningitis,

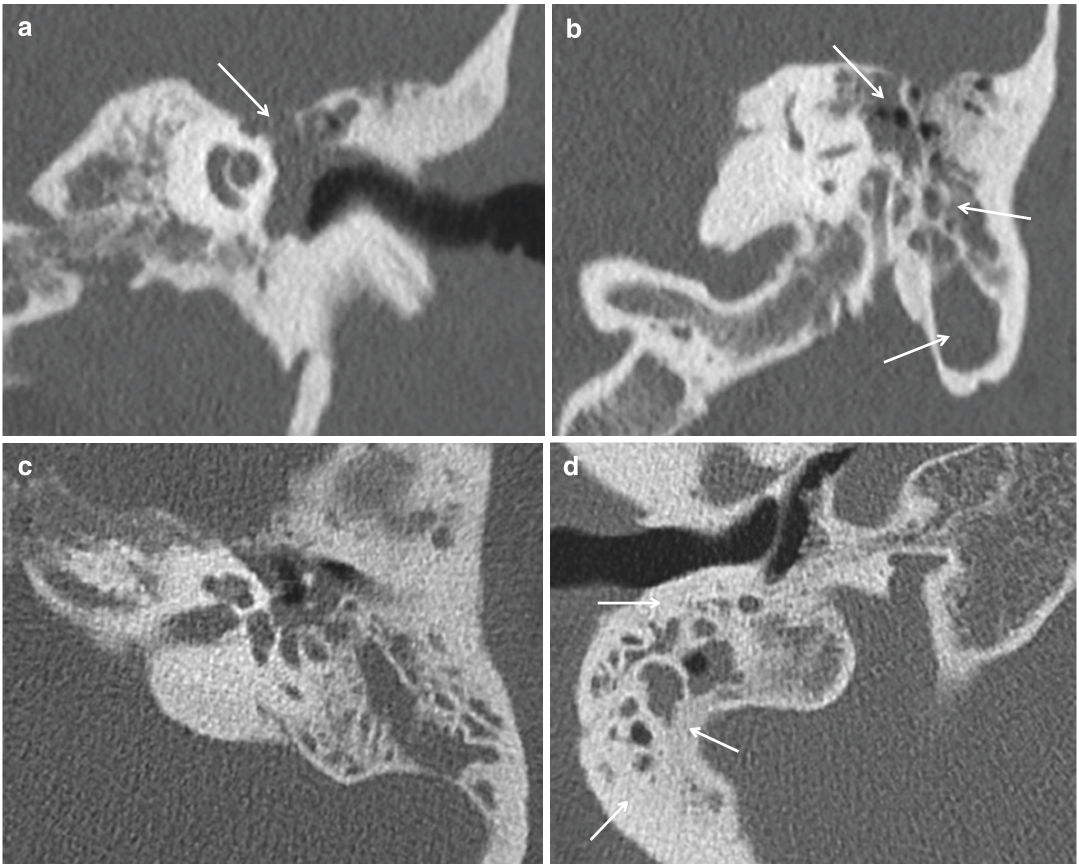

Fig. 14.53 Coronal (**a**, **b**) and axial (**c**) multislice CT sections of a case of coalescent mastoiditis show bone erosion and coalescence of the mastoid air cells in the left temporal bone (*white arrows*) as well as erosion of the ossicles in the middle ear cavity. Axial multislice CT section (**d**) of another patient shows sclerotic bone formation induced by chronic mastoiditis in the right temporal bone

abscess formation, and thrombosis). Chronic otomastoiditis can cause retraction and perforation of the tympanic membrane, acquired cholesteatoma, typical granulation tissue, cholesterol granuloma, ossicular fixation and erosion, and sclerosis of the surrounding bone (Fig. 14.53) (Swarts 2009). Granulation tissue formation in the middle ear is extremely common, both as an isolated phenomenon and a complication of other pathological conditions such as otitis media and cholesteatoma. Both the typical granulation tissue and cholesterol granuloma have a nonspecific CT appearance. However, the typical granulation tissue is vascularized and enhances after injection of contrast media unlike cholesterol granuloma and cholesteatoma. Magnetic resonance imaging (MRI) is helpful in differentiating these entities. Cholesterol granuloma has a tendency to bleed causing hemotympanum and has a bright signal on all pulse sequences (Swarts 2009; Pajor et al. 2006; Martin et al. 1990; Holliday 1989). Other conditions to be differentiated from otomastoiditis include cholesteatomas, temporal bone Langerhans histiocytosis, and temporal bone rhabdomyosarcoma (Harnsberger et al. 2011).

14.5.4.3 Cholesteatoma

Cholesteatoma is an erosive lesion composed of exfoliated keratin within stratified keratinizing squamous epithelium. It may be *acquired, congenital*, or *iatrogenic* (resulting as a late complication of tympanomastoid surgery). The acquired type is much more common and may be post-traumatic, post-obstructive or post-inflammatory (Park et al. 2009; Darrouzet et al. 2002; Louw 2010; Mills 2009; McKennan and Chole 1989; Preciado 2012). It affects individuals of all ages and is more common in males. The middle ear is a much more common location for cholesteatoma than the external auditory canal. CT is the modality of choice for detecting bony erosions; however, MRI is valuable when there is intracranial extension or involvement of the facial nerve (Swarts 2009; Mafee 1993).

Congenital cholesteatoma of the middle ear accounts for 2% of the cholesteatomas of this region and is found behind an intact tympanic membrane in a patient with no history of otitis media, otorrhea, or middle ear or mastoid surgery. The majority of acquired cholesteatomas of the middle ear arise primarily from the *pars flaccida* of the tympanic membrane and *Prussak's space* is the first place to be involved. As a Prussak's space cholesteatomas grows, it causes medial displacement of the ossicular chain and most commonly extends posteriorly to the epitympanum and the mastoid antrum (Fig. 14.54). Cholesteatomas

Fig. 14.54 Coronal (**a**) and axial (**b**) multislice CT sections demonstrate acquired cholesteatoma of the middle ear originating from the pars flaccida. The coronal multislice CT section (**a**) shows blunting of the scutum (*arrow*), erosion of the tegmen tympani (*open arrow*) and head (*HM*) and handle (*curved arrow* shows the location of the missing handle of malleus) of malleus. The axial multislice CT section (**b**) shows erosion of the head of malleus (*HM*), body of incus (*BI*), short process of incus (*SI*), erosion into the vestibule (*VB*) and posterior extension of cholesteatoma to the mastoid antrum and air cells (*M*). The coronal multislice CT section (**c**) shows extension of the lesion to the mastoid air cells (*M*) and the vestibule (*VB*) and complete erosion of the long process of the incus and stapes (*dashed arrows* show the location of the missing ossicles). The axial multislice CT section (**d**) of another case of cholesteatoma shows erosion of the lesion into the sigmoid sinus (SS)

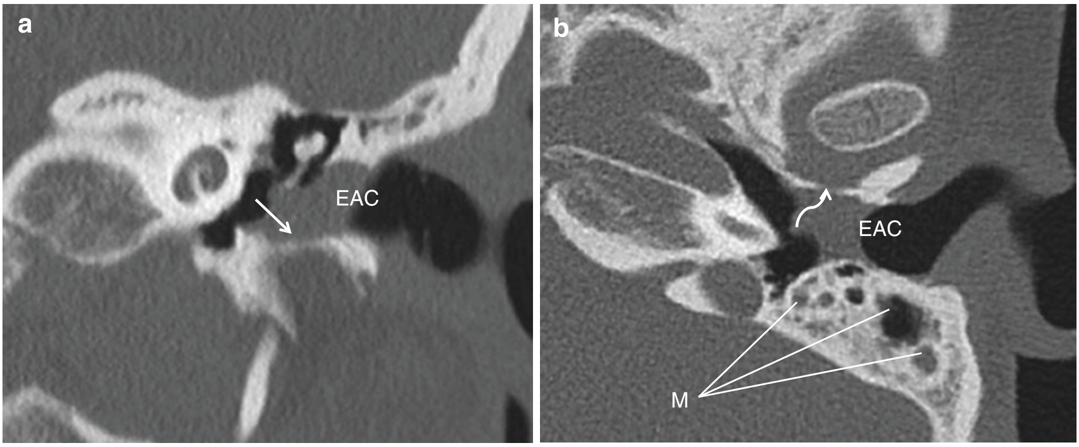

Fig. 14.55 Coronal (**a**) and axial (**b**) multislice CT sections of a cholesteatoma of the external auditory canal show erosion of the inferior (*straight arrow*) and anterior (*curved arrow*) walls of the external auditory canal (*EAC*). Note the extension of the lesion into the mastoid air cells (*M*)

originating from the pars tensa usually begin in the posterior tympanum and initially involve the more laterally located facial recess and subsequently extend to the more medially located sinus tympani. Extension to the mastoid antrum through the aditus can also occur. Widening of the aditus is an important diagnostic clue for identification of cholesteatomas. Many of cholesteatomas of the pars tensa grow to the medial of the ossicular chain and displace these structures laterally which is in contrast with the medial displacement of the ossicles caused by cholesteatomas of the pars flaccida. Cholesteatomas of the pars flaccida characteristically erode the head of malleus and the body and long process of the incus first, whereas cholesteatomas of the pars tensa erode the long process of the incus first, sparing the head of malleus and body of incus. On CT, cholesteatomas of the middle ear usually appear as a homogenous soft tissue mass with displacement of the adjacent structures as mentioned and also bony erosions (Fig. 14.54). Complications of middle ear cholesteatomas include secondary infections, facial nerve involvement and hearing loss, intracranial extension, involvement of the mastoid air cells, and subsequent extension to the petrous apex (Swarts 2009; Swartz and Varghese 1984; Holliday and Som 1991; Swartz 1984). Acquired cholesteatoma should be also differentiated from glomus tympanicum paraganglioma (Harnsberger et al. 2011).

The external auditory meatus is rarely involved by cholesteatomas. Computed tomographic findings of cholesteatomas of the external auditory meatus include smooth and irregular bony erosions caused by a soft tissue mass containing bony fragments (Fig. 14.55) (Swarts 2009; Dubach and Hausler 2008). Shin et al. (2010) classified the external auditory canal cholesteatomas (EACC) as follows: stage 1, the EACC lesion is limited to the external auditory canal; stage 2, the EACC lesion extends to the tympanic membrane and middle ear; stage 3, the EACC lesion creates a defect in the external auditory canal and involves the mastoid air cells; and stage 4, the EACC lesion extends beyond the temporal bone (Shin et al. 2010). In the external auditory meatus, it may be hard to differentiate cholesteatoma from squamous cell carcinoma, keratosis obturans, or necrotizing external otitis (Castillo et al. 2009; Harnsberger et al. 2011; Shin et al. 2010). Keratosis obturans is an abnormal accumulation of desquamated keratin in the EAC causing obstruction of the canal which is more common in young adults. Initially, keratosis obturans and external ear canal cholesteatoma were considered to be the same disease process. In contrast to cholesteatomas which rarely occur in the EAC, keratosis obturans is a much more common disease in this region which may explain why these names have been used interchangeably. However, these are two separate diseases and each requires different management. Unlike keratosis obturans, cholesteatoma is usually associated with osteonecrosis. Keratosis obturans may be cured once the keratin plug is removed and the underlying inflammation treated successfully, whereas most of the EAC cholesteatomas should undergo surgical removal of the entire cholesteatoma and necrotic bone to prevent progression and continuing erosion. Conservative treatment of external ear canal cholesteatoma may fail because of the unsuspected presence of osteonecrosis. Imaging characteristic of these two conditions are also different. Keratosis obturans is associated with a greatly widened ear canal resulting from circumferential remodeling of bone when compared to the bony erosion caused by the EAC cholesteatoma which is more localized and has an irregular pattern (Persaud et al. 2004).

Cholesteatomas can also involve the petrous bone medial to the otic capsule and are subdivided to five groups: supralabyrinthine, infralabyrinthine, massive labyrinthine, apical, and infralabyrinthine-apical (Sanna et al. 1993).

14.5.4.4 Otosclerosis

Otosclerosis (spongiosis) is an autosomal dominant disease with variable penetrance and expression (Saeed et al. 2007). The pathogenesis of this disease is still unknown (Bloch and Sorensen 2012; Markou and Goudakos 2009). This disease is characterized by pathological bone remodeling involving the otic capsule that can result in spongiosis and/or sclerosis of this region leading to progressive conductive, sensorineural, or mixed hearing loss. Conductive hearing loss is usually the result of impingement of abnormal bone on stapes footplate covering the oval window, known as *fenestral otosclerosis*. The fissula ante fenestram, which is a small cleft located in the bone just anterior to the oval window, is considered to be the most common location of involvement of otosclerosis. It is more common in women (2:1) and may be aggravated by pregnancy. It is reported to be bilateral in more than 80% of cases and often quite symmetrical. However, patients are not always symptomatic in both the ears simultaneously (Horner 2009; Lee et al. 2009).

The diagnosis in patients with uncomplicated conductive hearing loss is based on the characteristic clinical findings. These patients are often treated medically or surgically without imaging. High-resolution CT is often performed in cases with unexplained sensorineural or mixed hearing loss.

On high-resolution CT images of the temporal bone, sclerosis or spongiosis of the otic capsule in the region of the footplate of stapes, round/oval window, and cochlea can be detected. Otosclerosis of the otic capsule can be classified with respect to its location and severity as visualized on CT images: grade 1, solely fenestral involvement, appearing either as spongiotic or sclerotic thickening of stapes footplate, and/or decalcified, narrowed, or enlarged round or oval windows; grade 2, patchy localized cochlear involvement (with or without fenestral involvement) of either the basal cochlear turn (grade 2A), or the middle and apical turns (grade 2B), or both the basal turn and the middle and apical turns (grade 2C); and grade 3, diffuse confluent cochlear involvement (with or without fenestral involvement) (Fig. 14.56) (Lee et al. 2009; Marshall et al. 2005).

14.5.4.5 Glomus Jugulare Paraganglioma

This is a paragagnglioma (neuroendocrine neoplasm) of the head and neck which is confined to the jugular fossa. Glomus jugulare tumors are almost always benign and when growing they may expand towards the mastoid aircells, the middle ear, and the eusatchian tube. Their most common radiologic feature is erosive appearance of the jugular fossa and middle ear as well as the infratemporal fossa. Surgical removal is the most common treatment approach although recurrence and local invasion is common (Li and Dai 2015) (Fig. 14.57).

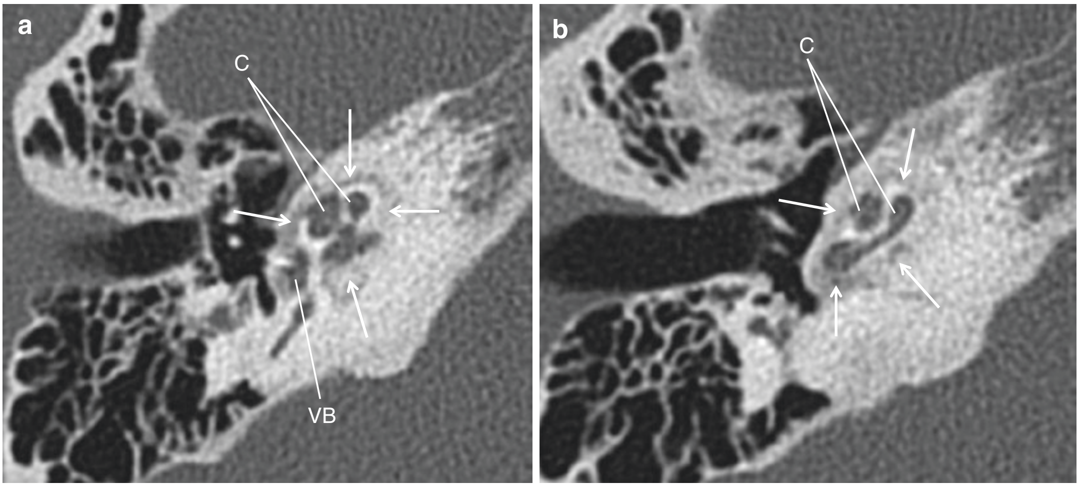

Fig. 14.56 Axial multislice CT sections (**a**, **b**) of grade 2C otosclerosis show replacement of the normal bone of the otic capsule by spongiotic bone (*white arrows*) extending anteriorly from an area anterior to the vestibule (*VB*) to the bone surrounding the basal, apical and middle turns of the cochlea (*C*)

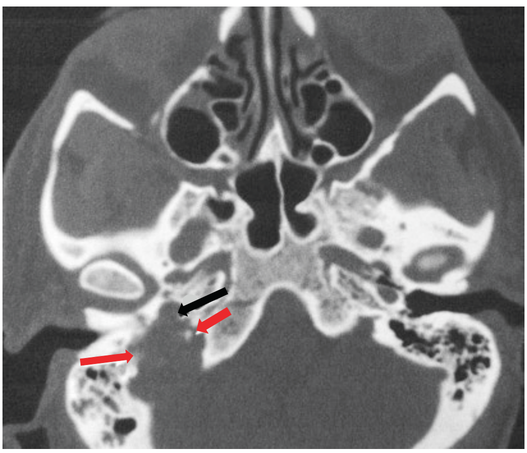

Fig. 14.57 Axial multislice CT section of the scull base showing a developing glomus jugulare in the right jugular fossa; note the eroded borders of the right jugular foramen (*red arrows*). Also note the eroded cortical outline of the right carotid canal (*black arrow*) (Courtesy of Dr. Thomas Underhill)

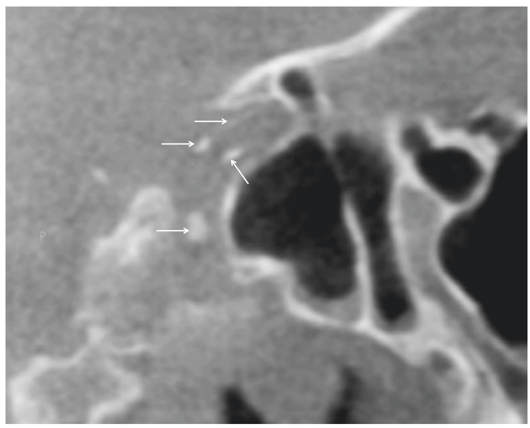

Fig. 14.58 Sagittal CBCT section showing thin discontinuous and punctate calcification (*arrows*) of the carotid artery in the carotid canal and parasellar region

14.5.4.6 Calcified Intracranial Internal Carotid Artery Atheroma (CIICAA)

Intracranial arterial wall calcifications are frequently reported on head computed tomography (CT) images (Sohn et al. 2004; Babiarz et al. 2005; Babiarz et al. 2003; Woodcock et al. 1999; Taoka et al. 2006). The appearance of ICCAC on CT can be categorized into three types (Suzuki et al. 2007); Type 1, thin discontinuous or punctate; Type 2, thin continuous or thick discontinuous; and Type 3, thick continuous or tubular with approximately equal distribution (Fig. 14.58). The identification of ICCAC is important in that the presence of arterial calcification seems to predict the existence of atheromatous plaque in the same artery. While the thickness of the calcification does not appear to correlate well with luminal stenosis, the shape of the calcification seemed to predict >50%

luminal stenosis. The incidence of stenosis in Type 1 calcification is low (2.2%), in Type 2 is mild (12.1%), and in Type 3 is moderate (39%) (Suzuki et al. 2007).

References

Alvord LS, Farmer BL (1997) Anatomy and orientation of the human external ear. J Am Acad Audiol 8:383–390

Anandi S, Tullu MS, Bhatia S, Agrawal M (2012) Mondini dysplasia as a cause for recurrent bacterial meningitis: an early diagnosis. J Child Neurol 27:1052–1055

Atilla S, Akpek S, Uslu S, Ilgit ET, Isik S (1995) Computed tomographic evaluation of surgically significant vascular variations related with the temporal bone. Eur J Radiol 20:52–56

Babiarz LS, Yousem DM, Bilker W, Wasserman BA (2005) Middle cerebral artery infarction: relationship of cavernous carotid artery calcification. AJNR Am J Neuroradiol 26:1505–1511

Babiarz LS, Yousem DM, Wasserman BA, Wu C, Bilker W, Beauchamp NJ Jr (2003) Cavernous carotid artery calcification and white matter ischemia. AJNR Am J Neuroradiol 24:872–877

Baek SK, Chae SW, Jung HH (2003) Congenital internal auditory canal stenosis. J Laryngol Otol 117:784–787

Ball M, Elloy M, Vaidhyanath R, Pau H (2010) Beware the silent presentation of a high and dehiscent jugular bulb in the external ear canal. J Laryngol Otol 124:790–792

Barker E, Trimble K, Chan H, Ramsden J, Nithiananthan S, James A, Bachar G, Daly M, Irish J, Siewerdsen J (2009) Intraoperative use of cone-beam computed tomography in a cadaveric ossified cochlea model. Otolaryngol Head Neck Surg 140:697–702

Bloch SL, Sorensen MS (2012) Otosclerosis: a perilabyrinthine threshold phenomenon. Acta Otolaryngol 132:344–348

Branstetter BF 4th, Harrigal C, Escott EJ, Hirsch BE (2006) Superior semicircular canal dehiscence: oblique reformatted CT images for diagnosis. Radiology 238:938–942

Castillo M, Jwells VL, Buchman C (2009) The external auditory canal and pinna. In: Swartz JD, Loevner LA (eds) Imaging of the temporal bone. Thieme Medical Publishers, New York, pp 25–57

Chadwell JB, Halsted MJ, Choo DI, Greinwald JH, Benton C (2004) The cochlear cleft. AJNR Am J Neuroradiol 25:21–24

Chen JL, Gittleman A, Barnes PD, Chang KW (2008) Utility of temporal bone computed tomographic measurements in the evaluation of inner ear malformations. Arch Otolaryngol Head Neck Surg 134:50–56

Sayit AT, Gunbey HP, Fethallah B, Gunbey E, Karabulut E (2016) Radiological and audiometric evaluation of high jugular bulb and dehiscent high jugular bulb. J Laryngol Otol 130:1059–1063

Clement PA, De Smedt E (1982) High-resolution computerized tomographic scans of the normal and abnormal ear. Am J Otolaryngol 3:286–294

Connor SE, Tan G, Fernando R, Chaudhury N (2005) Computed tomography pseudofractures of the mid face and skull base. Clin Radiol 60:1268–1279

Curtin HD (2003) Superior semicircular canal dehiscence syndrome and multi-detector row CT. Radiology 226:312–314

Cushing SL, Daly MJ, Treaba CG, Chan H, Irish JC, Blaser S, Gordon KA, Papsin BC (2012) High-resolution cone-beam computed tomography: a potential tool to improve atraumatic electrode design and position. Acta Otolaryngol 132(4):361–368

Dahmani-Causse M, Marx M, Deguine O, Fraysse B, Lepage B, Escude B (2011) Morphologic examination of the temporal bone by cone beam computed tomography: comparison with multislice helical computed tomography. Eur Ann Otorhinolaryngol Head Neck Dis 128:230–235

Daneshrad D, Kim JC, Amedee RG (2002) Acute otitis externa. J La State Med Soc 154:226–228

Daniels DL, Williams AL, Haughton VM (1984) Jugular foramen: anatomic and computed tomographic study. AJR Am J Roentgenol 142:153–158

Darrouzet V, Duclos JY, Portmann D, Bebear JP (2002) Congenital middle ear cholesteatomas in children: our experience in 34 cases. Otolaryngol Head Neck Surg 126:34–40

Dawes JD, Pearman K, Kochilas X (1983) Patent fissula ante fenestram. J Laryngol Otol 97:357–360

Di Martino E, Sellhaus B, Haensel J, Schlegel JG, Westhofen M, Prescher A (2005) Fallopian canal dehiscences: a survey of clinical and anatomical findings. Eur Arch Otorhinolaryngol 262:120–126

Dubach PF, Hausler R (2008) External auditory canal cholesteatoma: reassessment of and amendments to its categorization, pathogenesis, and treatment in 34 patients. Otol Neurotol 29:941–948

Egelhoff JC, Ball WS, Towbin RB, Seigel RS, Eckel CG (1987) Dural ectasia as a cause of widening of the internal auditory canals in neurofibromatosis. Pediatr Radiol 17:7–9

Emir H, Kaptan ZK, Gocmen H, Samim E (2009) Epidural abscess and encephalocele following tegmen defect due to mastoidectomy: a case report. Kulak Burun Bogaz Ihtis Derg 19:151–154

Johnson JM, Moonis G, Green GE, Carmody R, Burbank HN (2011) Syndromes of the first and second branchial arches, part 1: embryology and characteristic defects. AJNR Am J Neuroradiol 32:14–19

Fau RA, Sataloff RT (2008) Aspergillus otomycosis in an immunocompromised patient. Ear Nose Throat J 87:622–623

Friedmann DR, Eubig J, Winata LS, Pramanik BK, Merchant SN, Lalwani AK (2012) A clinical and histopathologic study of jugular bulb abnormalities. Arch Otolaryngol Head Neck Surg 138:66–71

Furuya Y, Edwards MS, Alpers CE, Tress BM, Ousterhout DK, Norman D (1984) Computerized tomography of cranial sutures. Part 1: comparison of suture anatomy in children and adults. J Neurosurgery 61:53–58

Gaurano JL, Joharjy IA (2004) Middle ear cholesteatoma: characteristic CT findings in 64 patients. Ann Saudi Med 24:442–447

Gruen PM, Carranza A, Karmody CS, Bachor E (2005) Anomalies of the ear in the Pierre Robin triad. Ann Otol Rhinol Laryngol 114:605–613

Hajiioannou JK, Bathala S, Marnane CN (2009) Case of perilymphatic fistula caused by medially displaced tympanostomy tube. J Laryngol Otol 123:928–930

Hamzany Y, Soudry E, Preis M, Hadar T, Hilly O, Bishara J, Nageris BI (2011) Fungal malignant external otitis. J Infect 62:226–231

Han SJ, Song MH, Kim J, Lee WS, Lee HK (2007) Classification of temporal bone pneumatization based on sigmoid sinus using computed tomography. Clin Radiol 62:1110–1118

Harnsberger HR, Glastonbury CM, Michel MA, Koch BL, Davidson AC, Shatzkes DR, Cornelius RS, Branstetter BF (2011) Diagnostic imaging: head and neck. Amirsys, Manitoba

Higashi K, Matsuki C, Sarashina N (1992) Aplasia of posterior semicircular canal in Waardenburg syndrome type II. J Otolaryngol 21:262–264

Holliday RA (1989) Inflammatory diseases of the temporal bone: evaluation with CT and MR. Semin Ultrasound CT MR 10:213–235

Holliday RA, Som PM (1991) Clinical radiology quiz. Pars tensa cholesteatoma. Am J Otolaryngol 12:54–55

Horner KC (2009) The effect of sex hormones on bone metabolism of the otic capsule—an overview. Hear Res 252:56–60

Huang BR, Wang CH, Young YH (2006) Dehiscent high jugular bulb: a pitfall in middle ear surgery. Otol Neurotol 27:923–927

Johnson J, Lalwani AK (2000) Sensorineural and conductive hearing loss associated with lateral semicircular canal malformation. Laryngoscope 110:1673–1679

Johnson JM, Moonis G, Green GE, Carmody R, Burbank HN (2011) Syndromes of the first and second branchial arches, part 1: embryology and characteristic defects. AJNR Am J Neuroradiol 32:14–19

Julia S, Pedespan JM, Boudard P, Barbier R, Gavilan-Cellie I, Chateil JF, Lacombe D (2002) Association of external auditory canal atresia, vertical talus, and hypertelorism: confirmation of Rasmussen syndrome. Am J Med Genet 110:179–181

Karmody CS, Annino DJ Jr (1995) Embryology and anomalies of the external ear. Facial Plast Surg 11:251–256

Katsanis SH, Jabs EW (2012) Treacher collins syndrome. In: Pagon RA, Adam MP, Ardinger HH, Wallace SE, Amemiya A, LJH B, Bird TD, Ledbetter N, Mefford HC, RJH S, Stephens K (eds) Gene reviews. [internet]. University of Washington, Seattle; 1993–2017. 2004 Jul 20 [updated 2012 Aug 30]

Kelly KE, Mohs DC (1996) The external auditory canal. Anatomy and physiology. Otolaryngol Clin North Am 29:725–739

Kew TY, Abdullah A (2012) Duplicate internal auditory canals with facial and vestibulocochlear nerve dysfunction. J Laryngol Otol 126:66–71

Kim DF, Bhimani M (2008) Ramsay hunt syndrome presenting as simple otitis externa. CJEM 10:247–250

Klein MA, Kelly JK, Eggleston D (1988) Recognizing tympanostomy tubes on temporal bone CT: typical and atypical appearances. AJR Am J Roentgenol 150:1411–1414

Koch B, Goold A, Egelhoff J, Benton C (2006) Partial absence of the posterior semicircular canal in Alagille syndrome: CT findings. Pediatr Radiol 36:977–979

Koesling S, Kunkel P, Schul T (2005) Vascular anomalies, sutures and small canals of the temporal bone on axial CT. Eur J Radiol 54:335–343

Kosling S, Omenzetter M, Bartel-Friedrich S (2009) Congenital malformations of the external and middle ear. Eur J Radiol 69:269–279

Krahl D (1992) Chronic otitis externa from the dermatologic viewpoint. Laryngorhinootologie 71:644–648

Krombach GA, Schmitz-Rode T, Prescher A, DiMartino E, Weidner J, Gunther RW (2002) The petromastoid canal on computed tomography. Eur Radiol 12:2770–2775

Kuczkowski JF, Potocka MF, Kobierska-Gulida GF, Przewozny TF, Dubaniewicz-Wybieralska M (2010) Osteomas and exostoses of external auditory canal in material of Otolaryngology Department Medical University of Gdansk. Otolaryngol Pol 64:365–369

Kutz JW Jr, Husain IA, Isaacson B, Roland PS (2008) Management of spontaneous cerebrospinal fluid otorrhea. Laryngoscope 118:2195–2199

Lane JI, Lindell EP, Witte RJ, DeLone DR, Driscoll CL (2006) Middle and inner ear: improved depiction with multiplanar reconstruction of volumetric CT data. Radiographics 26:115–124

Lee TC, Aviv RI, Chen JM, Nedzelski JM, Fox AJ, Symons SP (2009) CT grading of otosclerosis. AJNR Am J Neuroradiol 30:1435–1439

Lemmerling MM, Vanzieleghem BD, Mortier GR, Dhooge IJ, Kunnen MF (2000) Unilateral semicircular canal aplasia in Goldenhar's syndrome. AJNR Am J Neuroradiol 21:1334–1336

Li W, Dai C (2015) Lesions involving the jugular foramen:clinical characteristics and surgical management. Acta Otolaryngol 135:565–571

Louw L (2010) Acquired cholesteatoma pathogenesis: stepwise explanations. J Laryngol Otol 124:587–593

Ma X, Yang Y, Xia M, Li D, Xu A (2009) Computed tomography findings in large vestibular aqueduct syndrome. 129: 700–708

Mafee MF (1993) MRI and CT in the evaluation of acquired and congenital cholesteatomas of the temporal bone. J Otolaryngol 22:239–248

Magliulo G, Colicchio MG, Ciniglio M (2011) Facial nerve dehiscence and cholesteatoma. Ann Otol Rhinol Laryngol 120:261–267

Markou K, Goudakos J (2009) An overview of the etiology of otosclerosis. Eur Arch Otorhinolaryngol 266:25–35

Marshall AH, Fanning N, Symons S, Shipp D, Chen JM, Nedzelski JM (2005) Cochlear implantation in cochlear otosclerosis. Laryngoscope 115:1728–1733

Martin N, Sterkers O, Nahum H (1990) Chronic inflammatory disease of the middle ear cavities: Gd-DTPA-enhanced MR imaging. Radiology 176:399–405

Matsunaga T, Hirota E (2003) Familial lateral semicircular canal malformation with external and middle ear abnormalities. Am J Med Genet A 116A:360–367

Mazziotti S, Arceri F, Vinci S, Salamone I, Racchiusa S, Pandolfo I (2006) Role of coronal oblique reconstruction as a complement to CT study of the temporal bone: normal anatomy. Radiol Med 111:607–617

McDonald S, Langton Hewer CD, Nunez DA (2008) Grommets (ventilation tubes) for recurrent acute otitis media in children. Cochrane Database Syst Rev 4:CD004741

McKennan KX, Chole RA (1989) Post-traumatic cholesteatoma. Laryngoscope 99:779–782

Mehall CJ, Wilner HI, LaRouere MJ (1995) Pulsatile tinnitus associated with a laterally placed sigmoid sinus. AJNR Am J Neuroradiol 16:905–907

Meriot P, Veillon F, Garcia JF, Nonent M, Jezequel J, Bourjat P, Bellet M (1997) CT appearances of ossicular injuries. Radiographics 17:1445–1454

Meyerson MD, Nisbet JB (1987) Nager syndrome: an update of speech and hearing characteristics. Cleft Palate J 24:142–151

Migirov L, Kronenberg J (2006) Radiology of the petromastoid canal. Otol Neurotol 27:410–413

Mills R (2009) Cholesteatoma behind an intact tympanic membrane in adult life: congenital or acquired? J Laryngol Otol 123:488–491

Miloglu O, Yilmaz AB, Yildirim E, Akgul HM (2011) Pneumatization of the articular eminence on cone beam computed tomography: prevalence, characteristics and a review of the literature. Dentomaxillofac Radiol 40:110–114

Miyanaga S, Morimitsu T (1997) Prussak's space: chronological development and routes of aeration. Auris Nasus Larynx 24:255–264

Mjoen S, Grontved A, Holth V, Mair IW (1992) Tuberculous otomastoiditis. ORL J Otorhinolaryngol Relat Spec 54:57–59

Moreano EH, Paparella MM, Zelterman D, Goycoolea MV (1994) Prevalence of facial canal dehiscence and of persistent stapedial artery in the human middle ear: a report of 1000 temporal bones. Laryngoscope 104: 309–320

Morimoto AK, Wiggins RH 3rd, Hudgins PA, Hedlund GL, Hamilton B, Mukherji SK, Telian SA, Harnsberger HR (2006) Absent semicircular canals in CHARGE syndrome: radiologic spectrum of findings. AJNR Am J Neuroradiol 27:1663–1671

Morris PS, Leach AJ (2009) Acute and chronic otitis media. Pediatr Clin North Am 56:1383–1399

Munoz A, Ruiz-Contreras J, Jimenez A, Mate I, Calvo M, Villafruela M, del-Pozo G (2009) Bilateral tuberculous otomastoiditis in an immmunocompetent 5-year-old child: CT and MRI findings (2009: 3b). Eur Radiol 19:1560–1563

Nager GT, Proctor B (1991) Anatomic variations and anomalies involving the facial canal. Otolaryngol Clin North Am 24:531–553

Nardis PF, Bellelli A, D'Ottavi LR (1992) Cholesteatoma of the Prussak's space. Diagnosis with computerized tomography. Radiol Med 83:216–218

Nemzek WR, Swarts JD (2003) Temporal bone: inflammatory disease. In: Som PM, Curtin HD (eds) Head and neck imaging. Mosby, St. Louis, pp 1173–1230

Ohlms LA, Edwards MS, Mason EO, Igarashi M, Alford BR, Smith RJ (1990) Recurrent meningitis and Mondini dysplasia. Arch Otolaryngol Head Neck Surg 116:608–612

Orvidas LJ, Fabry LB, Diacova S, McDonald TJ (1999) Hearing and otopathology in Crouzon syndrome. Laryngoscope 109:1372–1375

Osguthorpe JD, Nielsen DR (2006) Otitis externa: review and clinical update. Am Fam Physician 74: 1510–1516

Otto KJ, Hudgins PA, Abdelkafy W, Mattox DE (2007) Sigmoid sinus diverticulum: a new surgical approach to the correction of pulsatile tinnitus. Otol Neurotol 28:48–53

Pajor A, Jankowski A, Danilewicz M, Durko T (2006) Evaluation of intensity of angiogenesis in granulation tissue in chronic otitis media—preliminary report. Otolaryngol Pol 60:571–576

Park KH, Park SN, Chang KH, Jung MK, Yeo SW (2009) Congenital middle ear cholesteatoma in children; retrospective review of 35 cases. J Korean Med Sci 24:126–131

Persaud R, Hajioff D, Thevasagayam M, Wareing M, Wright A (2004) Keratosis obturans and external ear canal cholesteatoma: how and why we should distinguish between these conditions. Clin Otolaryngol Allied Sci 29:577–581

Philips CD, Hanshisaki G, Veillon F (2008) Anatomy and developement of the facial nerve. In: Swarts JD, Loevner LA (eds) . Thieme, New York, pp 444–479

Pickett BP, Cail WS, Lambert PR (1995) Sinus tympani: anatomic considerations, computed tomography, and a discussion of the retrofacial approach for removal of disease. Am J Otol 16:741–750

Preciado DA (2012) Biology of cholesteatoma: special considerations in pediatric patients. Int J Pediatr Otorhinolaryngol 76:319–321

Rosa RF, da Silva AP, Goetze TB, Bier Bde A, de Almeida ST, Paskulin GA, Zen PR (2011) Ear abnormalities in patients with oculo-auriculo-vertebral spectrum (Goldenhar syndrome). Braz J Otorhinolaryngol 77:455–460

Ruivo J, Mermuys K, Bacher K, Kuhweide R, Offeciers E, Casselman JW (2009) Cone beam computed tomography, a low-dose imaging technique in the postoperative assessment of cochlear implantation. Otol Neurotol 30:299–303

Saeed SR, Briggs M, Lobo C, Al-Zoubi F, Ramsden RT, Read AP (2007) The genetics of otosclerosis: pedigree studies and linkage analysis. Adv Otorhinolaryngol 65:75–85

Salzman KL, Davidson HC, Harnsberger HR, Glastonbury CM, Wiggins RH, Ellul S, Shelton C (2001) Dumbbell schwannomas of the internal auditory canal. AJNR Am J Neuroradiol 22:1368–1376

Sanna M, Zini C, Gamoletti R, Frau N, Taibah AK, Russo A, Pasanisi E (1993) Petrous bone cholesteatoma. Skull Base Surg 3:201–213

Satar B, Mukherji SK, Telian SA (2003) Congenital aplasia of the semicircular canals. Otol Neurotol 24:437–446

Schubiger O, Valavanis A, Stuckmann G, Antonucci F (1986) Temporal bone fractures and their complications. Examination with high resolution CT. Neuroradiology 28:93–99

Shin SH, Shim JH, Lee HK (2010) Classification of external auditory canal cholesteatoma by computed tomography. Clin Exp Otorhinolaryngol 3:24–26

Slack CL, Watson DW, Abzug MJ, Shaw C, Chan KH (1999) Fungal mastoiditis in immunocompromised children. Arch Otolaryngol Head Neck Surg 125:73–75

Sohn YH, Cheon HY, Jeon P, Kang SY (2004) Clinical implication of cerebral artery calcification on brain CT. Cerebrovasc Dis 18:332–337

Standring S, Gray H (2008) Gray's anatomy [electronic resource]: the anatomical basis of clinical practice/editor. Churchill Livingstone/Elsevier, Edinburgh

Stone JA, Mukherji SK, Jewett BS, Carrasco VN, Castillo M (2000) CT evaluation of prosthetic ossicular reconstruction procedures: what the otologist needs to know. Radiographics 20:593–605

Suzuki M, Ozaki Y, Komura S, Nakanishi A (2007) Intracranial carotid calcification on CT images as an indicator of atheromatous plaque: analysis of high-resolution CTA images using a 64-multidetector scanner. Radiat Med 25:378–385

Swarts JD (2009) The middle ear and mastoid. In: Swartz JD, Loevner LA (eds) Imaging of the temporal bone. Thieme Medical Publishers, New York, pp 58–246

Swarts JD, Mukherji SK (2008) The inner ear and otodystrophies. In: Swarts JD, Loevner LA (eds) Imaging of the temporal bone. Thieme, New York, pp 298–411

Swartz JD (2004) An overview of congenital/developmental sensorineural hearing loss with emphasis on the vestibular aqueduct syndrome. Semin Ultrasound CT MR 25:353–368

Swartz JD (2001) Temporal bone trauma. Semin Ultrasound CT MR 22:219–228

Swartz JD (1984) Cholesteatomas of the middle ear. Diagnosis, etiology, and complications. Radiol Clin N Am 22:15–35

Swartz JD, Varghese S (1984) Pars flaccida cholesteatoma as demonstrated by computed tomography. Arch Otolaryngol 110:515–517

Taoka T, Iwasaki S, Nakagawa H, Sakamoto M, Fukusumi A, Takayama K, Wada T, Myochin K, Hirohashi S, Kichikawa K (2006) Evaluation of arteriosclerotic changes in the intracranial carotid artery using the calcium score obtained on plain cranial computed tomography scan: correlation with angiographic changes and clinical outcome. J Comput Assist Tomogr 30:624–628

Tos M, Stangerup SE, Andreassen UK (1985) Size of the mastoid air cells and otitis media. Ann Otol Rhinol Laryngol 94:386–392

Urman SM, Talbot JM (1990) Otic capsule dysplasia: clinical and CT findings. Radiographics 10:823–838

Vallino-Napoli LD (1996) Audiologic and otologic characteristics of Pfeiffer syndrome. Cleft Palate Craniofac J 33:524–529

Valtonen HJ, Dietz A, Qvarnberg YH, Nuutinen J (2005) Development of mastoid air cell system in children treated with ventilation tubes for early-onset otitis media: a prospective radiographic 5-year follow-up study. Laryngoscope 115:268–273

Van Rompaey V, Offeciers E, De Foer B, Somers T (2012) Jugular bulb diverticulum dehiscence towards the vestibular aqueduct in a patient with otosclerosis. J Laryngol Otol 126(3):313–315

Van Rompaey V, Potvin J, van den Hauwe L, Van de Heyning P (2011) Third mobile window associated with suspected otosclerotic foci in two patients with an air-bone gap. J Laryngol Otol 125:89–92

Verbist BM, Frijns JH, Geleijns J, van Buchem MA (2005) Multisection CT as a valuable tool in the postoperative assessment of cochlear implant patients. AJNR Am J Neuroradiol 26:424–429

Virapongse C, Rothman SL, Kier EL, Sarwar M (1982) Computed tomographic anatomy of the temporal bone. AJR Am J Roentgenol 139:739–749

Wang CH, Shi ZP, Liu DW, Wang HW, Huang BR, Chen HC (2011) High computed tomographic correlations between carotid canal dehiscence and high jugular bulb in the middle ear. Audiol Neurootol 16:106–112

Woodcock RJ Jr, Goldstein JH, Kallmes DF, Cloft HJ, Phillips CD (1999) Angiographic correlation of CT calcification in the carotid siphon. AJNR Am J Neuroradiol 20:495–499

Wright CG (1997) Development of the human external ear. J Am Acad Audiol 8:379–382

Yavuz MS, Aras MH, Gungor H, Buyukkurt MC (2009) Prevalence of the pneumatized articular eminence in the temporal bone. J Craniomaxillofac Surg 37:137–139

Yildirim N, Arslanoglu A, Mahirogullari M, Sahan M, Ozkan H (2008) Klippel-Feil syndrome and associated ear anomalies. Am J Otolaryngol 29:319–325

Zhou G, Schwartz LT, Gopen Q (2009) Inner ear anomalies and conductive hearing loss in children with Apert syndrome: an overlooked otologic aspect. Otol Neurotol 30:184–189

Part IV

Clinical Applications

Cone Beam Computed Tomography and Maxillofacial Diagnosis

15

David MacDonald, Christos Angelopoulos, and William C. Scarfe

Contents

D. MacDonald, M.Sc., D.D.S.(Edin.), F.R.C.D.C (✉)
Division of Oral and Maxillofacial Radiology, Faculty of Dentistry, University of British Columbia, Vancouver, BC, Canada
e-mail: dmacdon@dentistry.ubc.ca

C. Angelopoulos, D.D.S., M.S.
Aristotle University of Thessaloniki, Thessaloniki, Greece

Columbia University, College of Dental Medicine, New York City, NY, USA
e-mail: angelopoulosc@gmail.com

W.C. Scarfe, B.D.S., F.R.A.C.D.S., M.S.
Division of Radiology and Imaging Science, Department of Surgical/Hospital Dentistry, University of Louisville School of Dentistry, Louisville, KY, USA
e-mail: William.scarfe@louisville.edu

15.1 Fundamental Concepts in Diagnostic Radiologic Image Analysis

Diagnostic radiologic image analysis or interpretation is a critical stage in the diagnostic process for the assessment of any pathologic condition (Table 15.1). The role of imaging in this sequence is to: (1) assist and/or confirm a suspected diagnosis, (2) provide direction towards the appropriate management of the condition, (3) identify surgical parameters of importance (e.g., pathologic margins, involvement of important anatomical structures such as the inferior alveolar canal), and (4) determine the effectiveness of a specific management strategy treatments with

W.C. Scarfe, C. Angelopoulos (eds.), *Maxillofacial Cone Beam Computed Tomography*,
https://doi.org/10.1007/978-3-319-62061-9_15

Table 15.1 Stages in the diagnostic pathway

Stage	Purpose
Clinical/patient history	Establish signs and symptoms associated with the condition and establish individual patient context
Examine	Comprehensive extra- and intraoral evaluation of both the soft and hard tissues
Imaging	Select and perform appropriate imaging and interpret radiographic findings by describing the radiographic findings and determining significance
Nature of disease	Consolidate information to provide an overall categorization of the types of disease entities possible consistent with the clinical and radiographic presentation
Formulate differential diagnosis	Rank order the possible disease entities
Perform additional tests	Execute supplementary diagnostic tests or investigative procedures to confirm or rule out specific disease entities
Formulate working diagnosis	Refine the differential diagnosis according to the additional data
Manage and/or treat	Manage the patient and treat or observe and monitor entity based on the working diagnosis

Table 15.2 Universal differential diagnosis based on disease etiology using the Acronym V.I.N.D.I.C.A.T.E.

Letter	Pathologic etiology
V	Vascular
I	Infection
N	Neoplasms
D	Drugs
I	Inflammatory/idiopathic
C	Congenital
A	Autoimmune
T	Traumas
E	Endocrine/metabolic

Table 15.3 Disease taxonomy based on tissue (after Slootweg 2006)

Primary	Secondary	Tertiary	Quaternary
Dentition	Cysts	Odontogenic	Inflammatory
			Developmental
		Non-odontogenic	
	Tumors	Epithelial	Benign/malignant
		Mesenchymal	Benign/malignant
		Mixed	All benign
Bone	Hard tissue	Fibro-osseous	
		Giant cell lesions	
		Bone	
		Cartilage	
		Tissue elements within bone	Neurovascular, fibrous
	Soft tissue	Glandular	
		Neurovascular	
		Supportive	Fat, muscle

periodic assessment (postoperative follow-up radiographic examinations).

Accurate and consistent radiologic interpretation and development of a differential diagnosis requires:

- Images of diagnostic quality.
- Comprehensive working knowledge of osseous and soft tissue anatomy and correlative radiographic anatomy.
- An understanding of the basic nature and variability of the pathological process that affect the tissues maxillofacial region.
- The formulation of a differential radiologic diagnosis with the disease entities arranged in decreasing order of probability, determined by the strength of their supporting evidence.

A diagnosis of an osseous disease can rarely be rendered from radiographic appearance alone a so-called "pathognomonic" presentation—however the radiologic appearance can provide important clues as to the nature of the disease.

Cone beam CT with its multi-planar (MPR) imaging capabilities provides an enhanced approach to radiologic maxillofacial diagnosis because of its three-dimensional or multidirectional visualization of the diseased tissues.

Diseases are classified according to the nature of the process or the tissue involved. Bony lesions can therefore be classified based on etiology (pathologic or surgical) (Table 15.2) or tissue of origin (Table 15.3). However, it is difficult to use this scheme in actually arriving at a list of possible diagnoses based on imaging presentation. Much of this process involves the use of historical, clinical, surgical, and histopathologic information to arrive at a differential diagnosis. Imaging is sometimes used to merely provide information about the location and extent of the disease.

15.1.1 Role of CBCT

The advent of CBCT has significantly added to the diagnostic efficiency and accuracy of dental diagnostic imaging and had a positive impact on treatment outcomes. This becomes self-evident for many diagnostic tasks including surgical planning, placement of dental implants, detection of apical pathoses, etc. In these situations, diseased tissue effects on known anatomical areas and boundaries as well as adjacent structures are clearly depicted by CBCT. Previously available two-dimensional dental imaging (periapical, panoramic, and cephalometric radiography) provided limited opportunities for extracting meaningful interpretive information and developing a diagnostic solution. This is because of inherent two-dimensional (2D) limitations such as the inability to observe cross-section changes, geometric distortion and overlapping of the disease process with neighboring, dense anatomical structures, referred to as anatomical noise. The transition from projection-based to office-based dental and maxillofacial CBCT imaging is arguably the single-most important contribution of radiography to diagnostic efficiency and improved treatment outcomes, especially in surgery. Indeed, the ability to view and examine an area of concern or a potential surgical site in three-dimensions (3D) has provided several more pieces of information to the interpretive puzzle of diagnosis. Although conventional radiography is often the primary modality for initial detection and identification of entities affecting the face and jaws, CBCT involves three-dimensional acquisition providing volumetric and multiplanar display leading to accurate representation of the following:

- Lesional extent
- Involvement of adjacent anatomic structures
- Lesional borders
- Internal lesional details such as septae and peripheral crenations
- Presence and degree of root resorption, particularly on the buccal or lingual/palatal aspects of the lesion or tooth, respectively

Identification of many of these characteristics could potentially influence the differential diagnosis. For example, the presence of root resorption in association with a multilocular lesion is highly suggestive of neoplastic lesions, such as ameloblastomas and keratocystic odontogenic tumor (KCOT) (MacDonald 2011).

CBCT is very sensitive (91%) in the detection of invasion of adjacent bone by carcinoma, second only to that of MRI (94%) with specificity (100%) equal with both MRI and multidetector CT (Uribe et al. 2013). Nevertheless, lesions whose clinical and/or conventional radiological presentations are suggestive of either a malignancy or vascular anomaly are more appropriately imaged by multi-detector CT (MDCT) with or without contrast, MRI or both. The superior contrast resolution of the latter imaging modalities better display invasion (malignant lesions) or involvement (vascular anomalies) of adjacent structures. CBCT is also limited if larger benign lesions (e.g., ameloblastoma and KCOT) perforate cortical borders or involve adjacent soft tissues (e.g., osteomyelitis). CBCT is optimal for benign pathology due to better spatial resolution, availability, and lower financial and radiation dose cost.

15.1.2 Considerations Prior to Diagnostic Image Analysis

- **Is a CBCT scan necessary and, if so, what kind of a scan?** Cone beam CT is an optimal imaging modality for hard tissue assessment and should be prescribed when suspected disease involves in the osseous structures and/or teeth. The role of CBCT in soft tissue evaluation is limited to specific circumstances, such as the identification of the presence of luminal opacification in the paranasal sinuses and airway obstruction. A thorough clinical examination and review of available radiologic images is important to determine if a CBCT scan is needed by answering the clinical question, “Will the additional information gained add to the diagnosis?” If the answer to this initial question is “Yes,” then the second question is “What kind of a scan should be performed?” The answer to this question will provide guidance on the appropriate CBCT imaging protocol to be chosen.

Imaging protocol is determined by specific diagnostic concerns and results in developing task-specific imaging protocols—selection of available exposure and scanning parameters appropriate to the presenting situation. The imaging protocol includes the field of view (FOV) and the voxel resolution. The size of the pathological entity under investigation and the extent of the affected region will dictate the FOV to be selected (Scarfe and Farman 2008). Most CBCT scanners provide an adjustable FOV ranging from a projection area of exposure as small as 40 mm × 40 mm, appropriate for examining two to three teeth and their surrounding structures, to 150 mm × 150 mm, large enough to examine a large portion of the patient’s head (see Chap. 3). Extended or large FOV is appropriate for facial asymmetries, large developmental defects, and facial trauma whereas a smaller FOV is appropriate for edentulous sites for implant site assessment, single tooth impactions, endodontics, tooth defects, and periapical pathology (MacDonald 2017). Moreover, current CBCT scanners can acquire volumetric data with a voxel size between 0.08 and 0.4 mm nominal voxel resolution, which provide images with exceptional detail for hard tissue evaluation. Diagnostic tasks requiring high detail such as periapical pathology, missed and calcified canals external and internal root resorption, ankylosis, and root fractures almost always mandate choice of a small voxel resolution to achieve the needed image resolution.

CBCT scans, as well as other radiographic procedures, are also performed to assess the progression of disease or the outcome of a certain treatment or surgery (follow-up). The frequency of the follow-up examinations should be based on the suspected rate of the disease progression; certain pathological entities advance faster than others and no set rule exists as to the periodicity of these examinations. The follow-up clinical examination will determine how frequently scans should be acquired. Postsurgical follow-up or posttreatment scans are prescribed to assess the progress of treatment or surgery or healing. Osseous tissue healing is slow and these scans may be acquired every 6–12 months; they also may be substituted with simpler diagnostic images (e.g., panoramic or periapical radiography) if the clinician is satisfied by the progress of tissue healing. As always, the need for follow-up imaging and the selection of the appropriate type of imaging is determined after a clinical examination indicates that such an evaluation may be helpful. Progress of the treatment rendered is judged by comparing the follow-up radiographic examinations made at different time intervals after treatment or surgery with the initial radiographic examination.

While the above parameters provide some guidance on imaging procedures, a great deal of flexibility exists in the selection of the proper CBCT imaging protocol. The optimal protocol should ultimately be based on the clinician’s judgment, knowledge, and professional responsibility, with the clinical examination as the deciding factor.

Is the acquired scan of diagnostic quality? Poor image quality may obscure important details especially more subtle or early changes in the site under examination and this may compromise diagnosis. The association between high image quality and diagnostic efficiency is well established in the literature (White and Pharoah 2009).

The most frequent factors affecting image quality of a CBCT scan are patient motion during the scan acquisition and artifacts. Despite the fast acquisition time of CBCT scanners, patient motion may occur during the

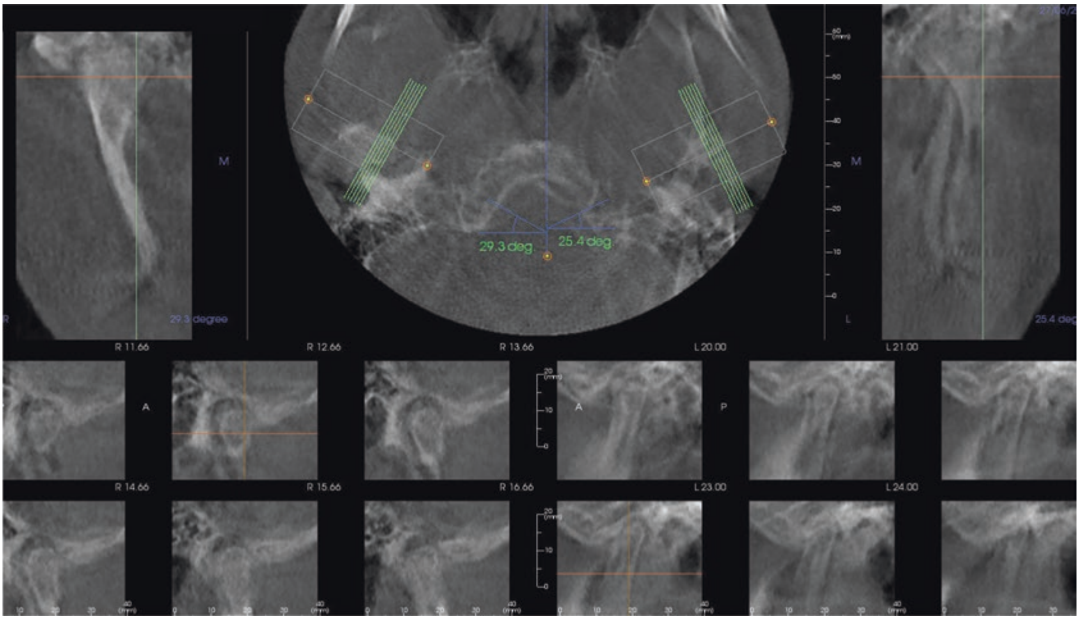

Fig. 15.1 Screen capture of a temporomandibular joint software display showing coronal sections of the right and left TMJ on either side of an axial section at the level of the condyles (*above*). These images are used for the reconstruction of a series of cross-sectional images of the right and left TMJs (*below*). All images show extensive patient motion artifacts that have compromised clarity of the mandibular condyles. The anatomical structures of interest are poorly visualized and the imaging procedure needs to be repeated

scan and may have a detrimental effect in image quality. Strict adherence to the manufacturer's recommendations on patient positioning and head stabilization in the scanner may reduce the likelihood of motion. A thorough review of the entire volumetric data immediately after the procedure—while the patient still is present—should be performed to identify signs of patient motion within the image. If there is evidence of patient motion, such as blurred images or double margins, that is likely to obscure diagnosis, the procedure should be repeated (Fig. 15.1).

The presence of artifacts in the CBCT scans may have an effect on image quality and diagnostic efficacy (Bechara et al. 2012). Metallic restorations are the most frequent cause of artifacts. They present with alternating bright and dark bands or a "sunray" appearance and may make it impossible to evaluate any areas of the scan that may overlap with the region of interest. They are most often present at the level of the crowns of the teeth and may have a detrimental effect especially in fine diagnostic tasks like the detection of crown and root fractures, early periodontal defects, and other defects adjacent to metallic restorations. Under these circumstances, a clinician's knowledge and experience will assist develop realistic expectations about the diagnostic efficiency of this exciting imaging modality.

- **What kind of image reconstructions should be applied?** Appropriate image reconstructions must provide a complete evaluation of the anatomical region of interest and address a specific diagnostic concern. MPR and interactive software applications offer tremendous opportunities for the clinician to unlock the diagnostic capabilities of CBCT. Application of specific reformatting options should be directed towards extracting the maximum diagnostic information. This demands a methodological approach and knowledge of the utility of specific reformatting methods.
- **Appreciate the limitations of CBCT Imaging.** While the inherent high spatial resolution of

CBCT imaging demonstrates osseous anatomy accurately, there are specific diagnostic tasks for which CBCT is not suited because of low contrast resolution. These include the following:

- Differentiation of the intralesional contents (e.g., fluid vs. tumor)
- Lesional extension through cortical perforation
- Adjacent soft tissue reaction (e.g., cellulitis associated with osteomyelitis)
- Intra-articular disorders (e.g., temporomandibular disc position, synovitis)

Overall and regional image quality can also be influenced by various factors including patient-related artifacts (Fig. 15.1) and inherent artifacts (e.g., radiolucent streaks and radiopaque scatter due to beam hardening).

15.2 Analysis of CBCT Images

Radiologic interpretation ascribes meaning to observations of imaging characteristics and results in the development of a differential diagnosis—a list of possible diagnoses, ranks in order, consistent with the radiologic and clinical findings. Interpretation involves a sequence of cognitive steps. The description of the imaging characteristics of a suspected pathology, identification of patterns of bony involvement and associated disease processes and subsequent categorization into groups providing a radiologic differential diagnosis is known as radiologic pattern recognition.

15.2.1 Collect All Available Diagnostic Information

The review of a CBCT scan is a step-by-step analysis of all abnormal radiographic findings or features with the goal of recognizing and collecting as much information as possible that is available in the various image reconstructions (White and Pharoah 2009). Described in detail earlier, the mechanics of radiologic analysis involves principally the methodological interactive display of the data set initially using orthogonal projections (i.e., axial, sagittal, and coronal) and then task-specific display protocols (e.g., reformatted panoramic and associated trans-axial images, volumetric rendering). Systematic review is necessary and requires multiple "sweeps" through the image sets focusing on different systems including:

- Gnathic
  - Maxilla and maxillary teeth
  - Maxillary sinus
  - Mandible and mandibular teeth
  - Temporomandibular joint
- Extra-gnathic
  - Nose and paranasal sinuses
  - Soft tissues of the neck
  - Cervical spine
  - Airway
  - Cranial vault

In reviewing each of the anatomical regions mentioned above, special attention should be paid to the "chief complaint" or the reason for the scan acquisition. The review may start from the region of concern, since one naturally is trying to identify "what's wrong" first. This is a common practice in most, if not all, disciplines of medicine and dentistry including oral and maxillofacial radiology. Modifications to the algorithm described above may be necessary depending on a clinician's individual approach.

15.2.2 Look for the Abnormality

A thorough review of the CBCT scan above should reveal the abnormality; this task may be guided by the reported patient history and the clinical findings. Key observation features that may indicate an abnormality include:

- **Changes in the appearance of known tissues and structures in the maxillofacial region.** Most dental practitioners are well acquainted with the normal appearance of the osseous structures of the maxillofacial region (shape and size, anatomical boundaries and

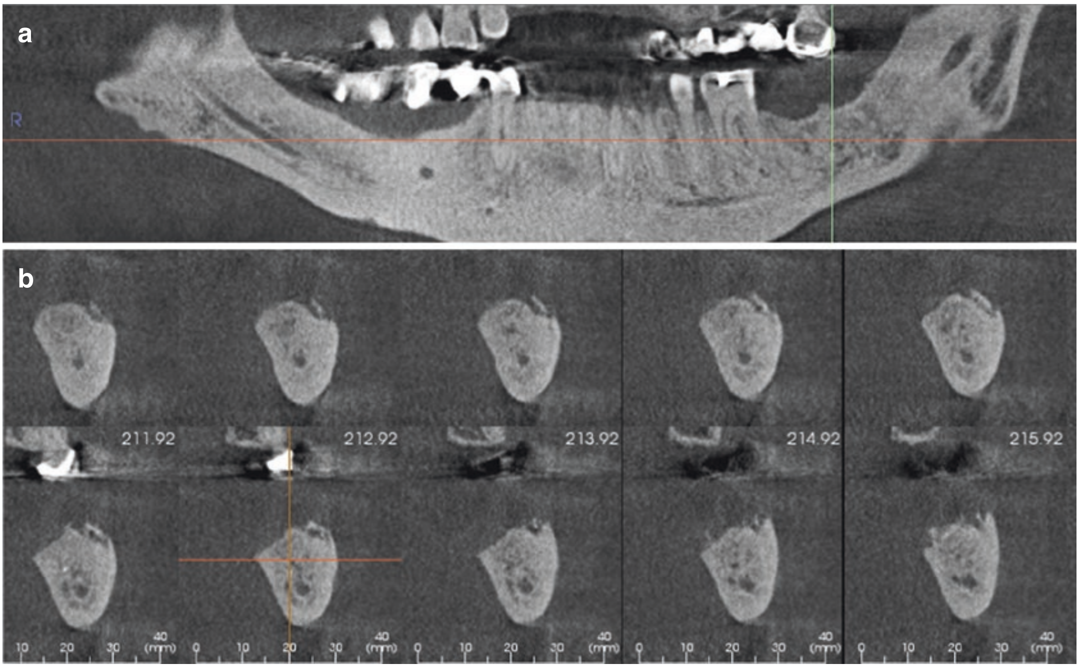

Fig. 15.2 Reformatted panoramic (**a**) and series of cross-sectional images (**b**) of the left mandible demonstrating homogenous high-density mandibular bone; the sclerotic cancellous bone is almost indistinguishable from the cortical bone. In addition, there are high-density sequestrations present in the left posterior mandible, adjacent to the alveolar crest. Together with the patient's history of bisphosphonate therapy and long-term clinically exposed bone in this region, this imaging presentation is consistent with a diagnosis of medication-related osteonecrosis of the jaws (MRONJ)

contours, etc.). Variations from normal patterns may be suspicious for developing abnormality or even pathology (Fig. 15.2).

- **Changes in the bone density**. These are a frequent indicator of disease development. The most common localized alteration of the cancellous bone pattern is associated with periapical pathosis (Fig. 15.3).
- **Asymmetry in known bilateral structures.** A deviation shape or form as compared to a contralateral structure is a sign of unilateral growth or atrophy and may indicate disease (Fig. 15.4). Differences between the right and left side in gross anatomical structures such as condylar heads, mandibular ramii, paranasal sinuses, and walls of the airway raise suspicion for abnormality as developing diseases tend to be unilateral. Anatomical variations tend to be bilateral. Anatomical variability between individuals and sometimes even within the same individual adds considerable difficulty in diagnosis. In these situations diagnosis may be assisted by viewing the radiologic abnormality in the light of clinical or historic findings.

15.2.3 Determine the Location of the Abnormality

Identifying the accurate location of the abnormality may be revealing as to the tissue or structure of origin or possible association with specific tissues. Most pathological entities in the maxillofacial region follow a domestic pattern: they develop and grow within the tissue from which they have originated. The only exceptions are metabolic conditions, systemic conditions, and metastatic disease. For example, if an intraosseous abnormality under assessment is located in tooth-bearing areas of the jaws, there is a high likelihood that it is of odontogenic origin (dental in origin)

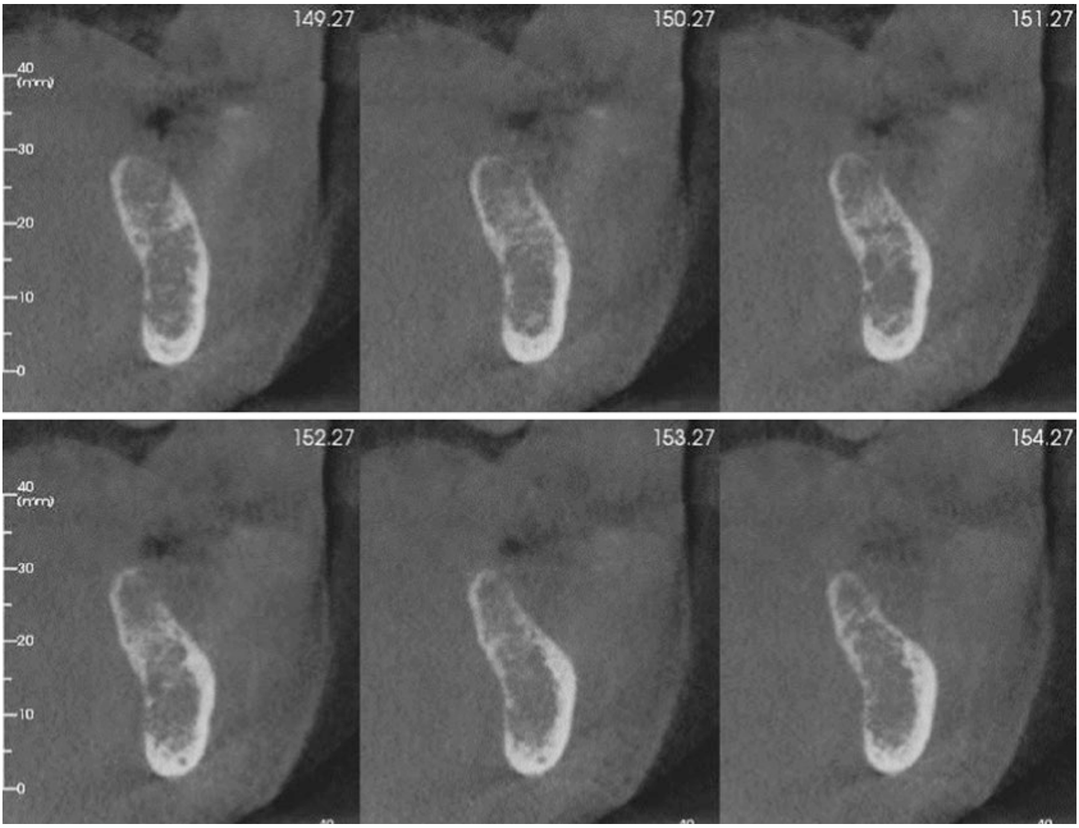

Fig. 15.3 A series of cross-sectional images in the left mandible showing an altered cancellous bone pattern. The mandibular cortices are thin with effacement of the internal margin and the trabeculae are sparce. The above findings are suspicious for osteoporosis

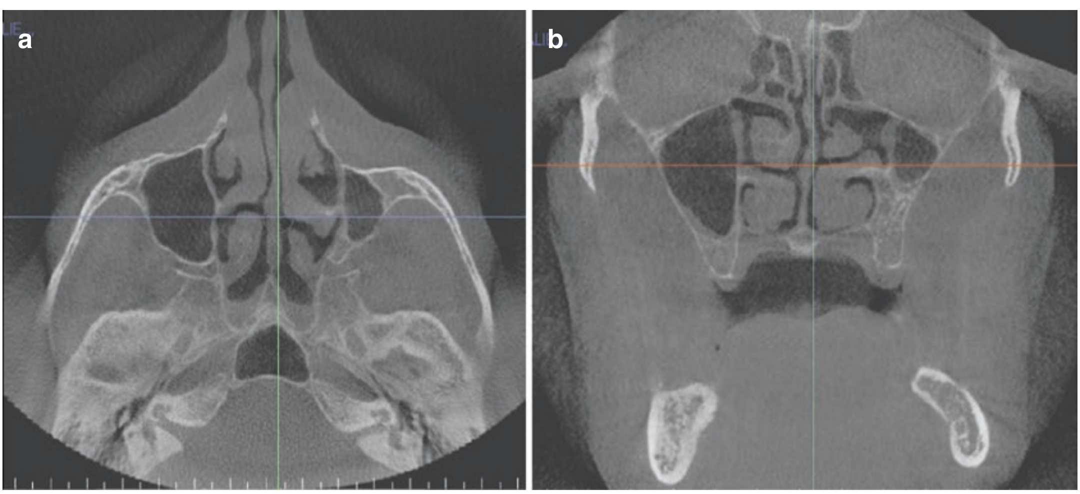

Fig. 15.4 An axial (**a**) and coronal (**b**) image depicting marked asymmetry between the right and left maxillary sinuses with the left one being considerably smaller in size. This imaging appearance is consistent with left unilateral maxillary sinus hypoplasia. This is a developmental defect that requires no attention

(Fig. 15.5). Similarly, if a lesion is located in a non-tooth-bearing area, there is a high likelihood that it is of non-odontogenic origin (Figs. 15.6 and 15.7). Tooth-bearing areas are the alveolar ridges in the maxilla and mandible. In the maxilla, the base of the alveolar bone is somewhat below the floor of the maxillary sinus and the floor of the nasal cavity. The mandibular alveolar bone is bordered by the mandibular canal in the posterior mandible and the mental ridge in the anterior mandible. These tooth-bearing zones (with the exception of the mandibular canal) are fairly

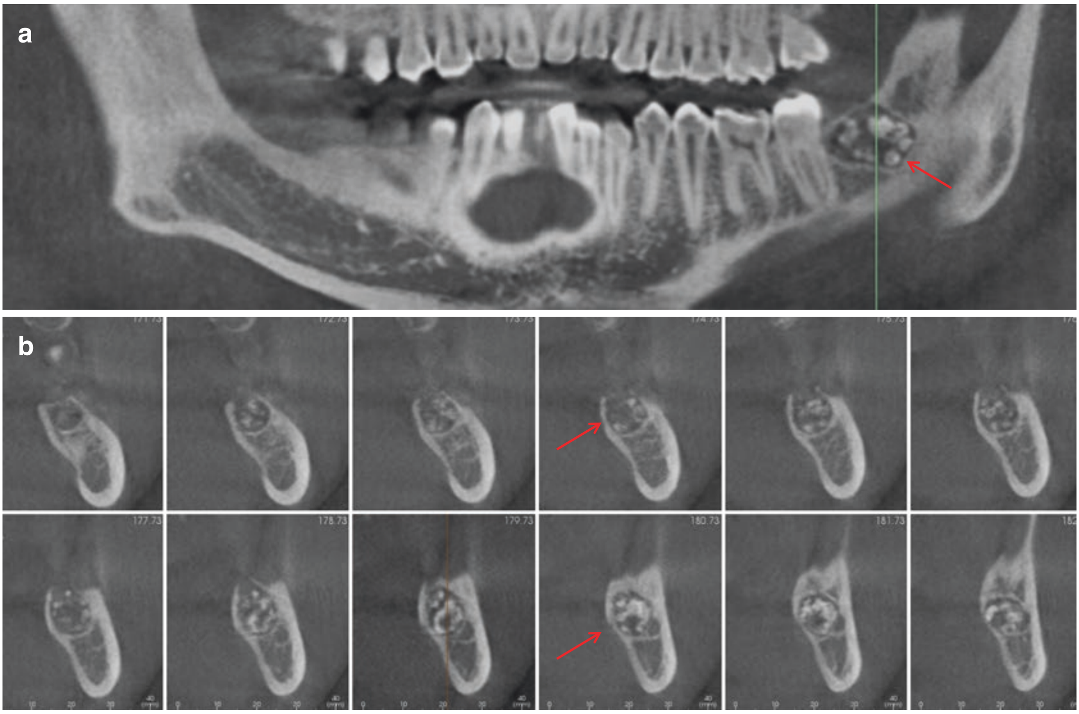

Fig. 15.5 A reformatted panoramic (**a**) and series of cross-sectional images (**b**) depicting a well-defined, mixed-density, unilocular entity in the left retromolar trigone. The lesion contains several small, high-density foci which look like tooth structures or tissues. The location of the lesion in question is above the left mandibular canal (tooth-bearing region) and suggests the entity is of odontogenic origin. The most likely diagnosis is compound odontoma

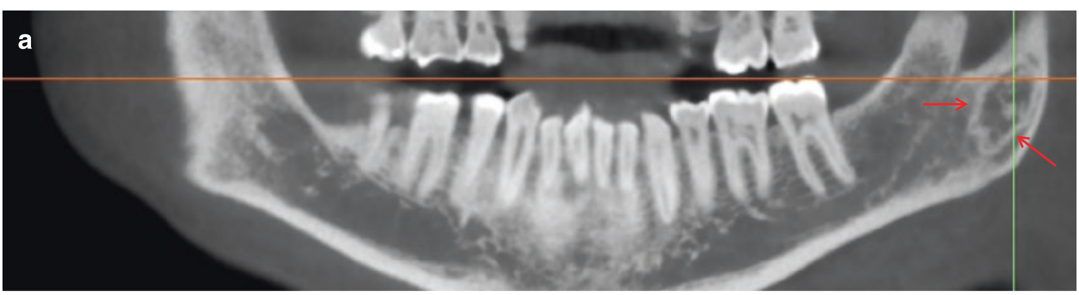

Fig. 15.6 Reformatted panoramic (**a**) and a series of cross-sectional images (**b**) depicting a well-defined, mixed density lesion in the left angle of the mandible. The entity is surrounded by an irregular and hyperostotic border and contains 2 to 3 high-density foci. The lesion is below the left mandibular canal (non-tooth-bearing region) which indicates a non-odontogenic origin (most likely). The imaging appearance is most consistent with a diagnosis of focal osseous dysplasia

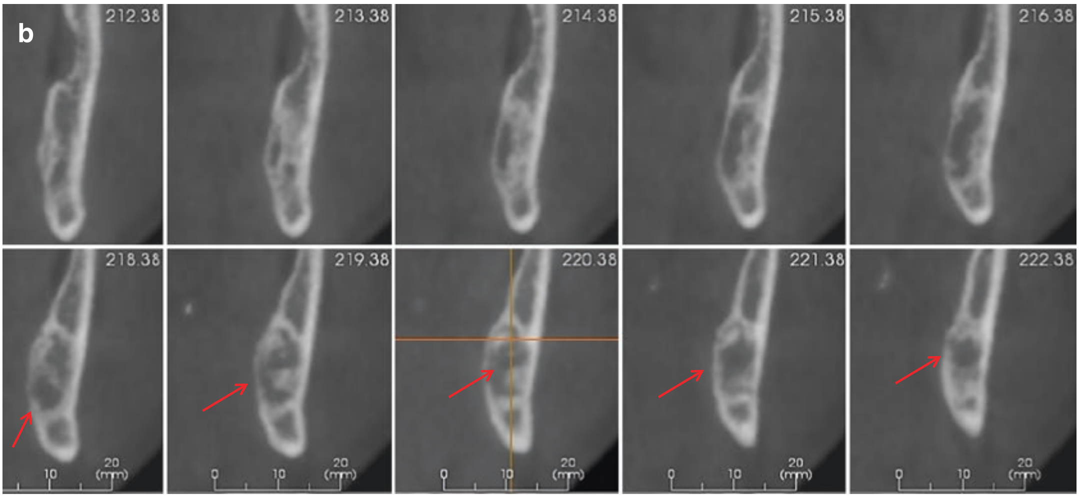

Fig. 15.6 (continued)

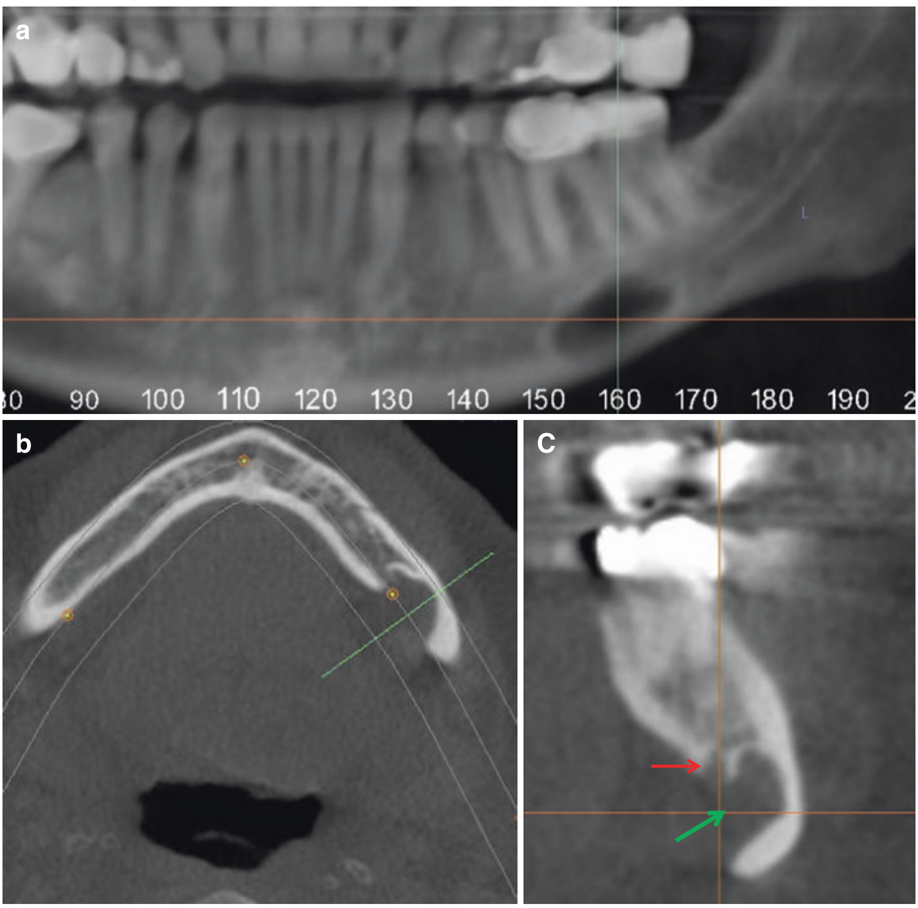

Fig. 15.7 Panoramic reformatted (**a**), axial reference (**b**) and cross-sectional (**c**) images of the left mandible showing a well-defined, semispherical defect in the lingual mandibular cortex in the molar region (*green arrow*). This defect extends to include the internal margin of the buccal cortex. The lesion is below the left mandibular canal (*red arrow*) which suggests a non-odontogenic origin. In this case, the imaging appearance and location are consistent with a lingual bone defect or Stafne bone cavity (anatomical variant)

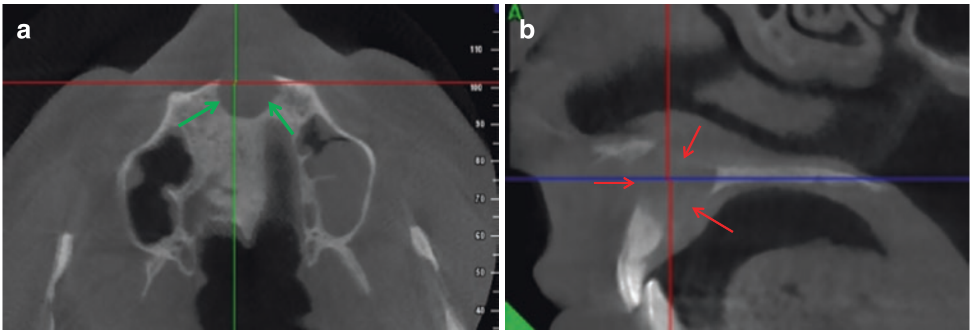

Fig. 15.8 Axial (**a**) and sagittal (**b**) orthogonal images of the anterior maxilla showing a well-defined, round, low-density unilocularity in the midline of the alveolar ridge between the central incisors (*green arrows*). While close to a tooth-bearing region, the lesion originated from the nasopalatine canal which appears to be eroded. The imaging appearance is consistent with a diagnosis of a nasopalatine duct cyst (non-odontogenic) which has eroded the labial and palatal cortices as well as the floor of the nasal cavity (*red arrows*)

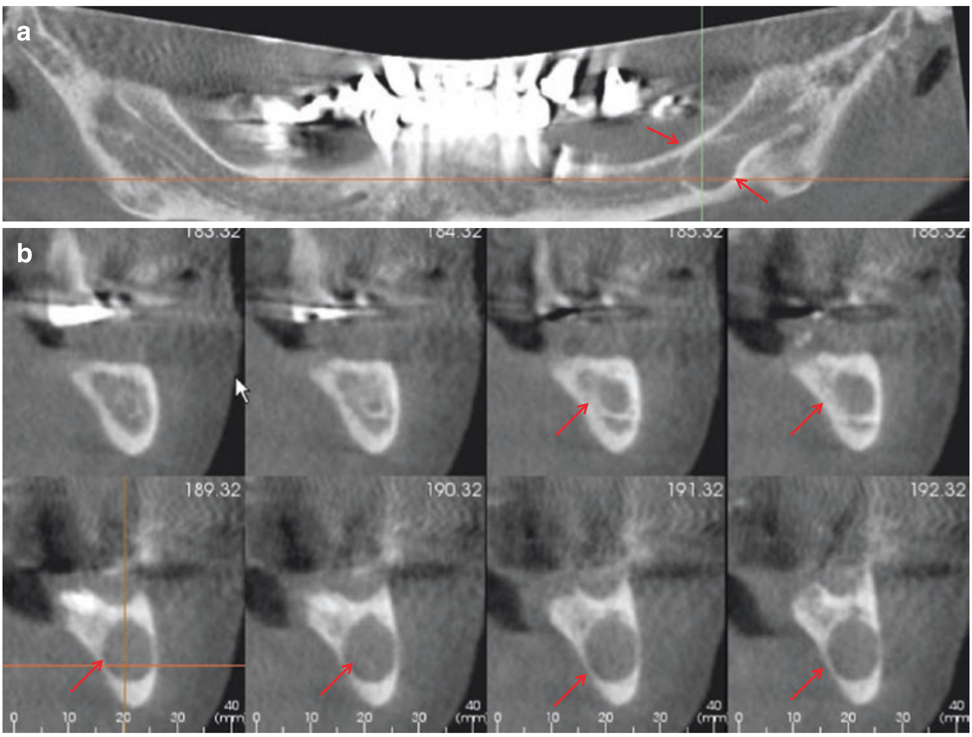

Fig. 15.9 Reformatted panoramic (**a**) and a series of cross-sectional images (**b**) of the mandible depicting a well-defined, unilocular, hypodense entity which coincides with the left mandibular canal. The cross-sectional images clearly demonstrate that there is a gradual increase in diameter of the mandibular canal (*red arrows*). This suggests an origin inside the mandibular canal of possible vascular or neural (non-odontogenic) origin

vague and this may cause some confusion as to the accurate localization of a lesion. In these situations, additional determinants may be employed.

The epicenter of the lesion may be of assistance in determining the tissue of origin (White and Pharoah 2009). If the epicenter of a lesion is inside the nasopalatine canal or inside the mandibular canal, the content of these canals should be linked to its origin (Figs. 15.8 and 15.9). If the epicenter of a lesion is inside the nasal cavity or the maxillary sinus, it is unlikely the lesion is of odontogenic origin. However if there is an osseous elevation arising

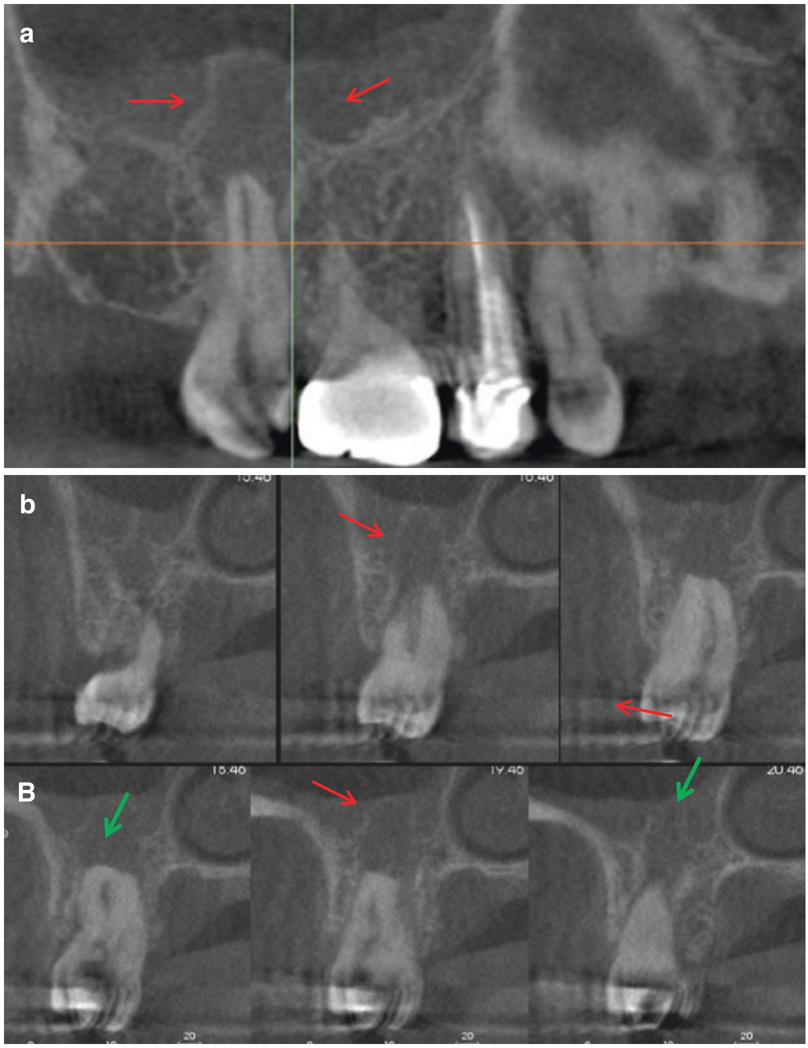

Fig. 15.10 A local reformatted panoramic (**a**) and series of cross-sectional images (**b**) of the right posterior maxillae depicting a well-defined, unilocular hypodense ovoid lesion in the apical region of the right second molar (*red arrows*). This has originated in the alveolar bone (apical pathology from pulpal necrosis) and as it progressed slowly, has caused an expansion of the floor of the right maxillary sinus. The *green arrows* show perforation of the maxillary sinus floor

from the floor of the maxillary sinus, this is suspicious of a lesion which has originated in the alveolar bone and is expanding superiorly (Fig. 15.10).

15.2.4 Determine and Describe Key Features of the Abnormality

Radiographic images alone, including those produced with CBCT, are seldom conclusively diagnostic. History, physical examination, and biopsy are usually prerequisites to final diagnosis. The various pathological entities that may present radiographically in the maxillofacial region differ in appearance. Various characteristics provide insight into the nature, growth pattern, aggressiveness, and progression of the lesions. These features have been studied in depth and are listed in several textbooks; however, most descriptions refer to previous 2D dental imaging, specifically intraoral and panoramic images. This has been changing gradually, with the growing utilization of CBCT for routine dental diagnosis; the collective experience of CBCT use by the authors is presented in this chapter.

It is important to acknowledge that soft tissue pathological entities are impossible to distinguish from CBCT images because of the poor soft tissue contrast. Unless such soft tissue lesions affect the normal shape and size of known neighboring anatomical structures (airway, nasal cavity) or invade osseous structures, they likely will be unidentifiable in CBCT scans and will continue to grow silently unless diagnosed clinically or by other diagnostic methods.

However, a thorough and comprehensive analysis of the radiographic characteristics is an important tool in categorizing the general nature of hard tissue lesions (Table 15.4).

Degree of Attenuation. In multi-detector computed tomography (MDCT), the overall presentation of an entity is described related to changes in attenuation due to loss or gain of osseous material. Because of the similarities with MDCT images, the three (3) general presentations of a lesion on CBCT images are characterized using similar language; low density/attenuating, high density/attenuating, and mixed density/attenuating (demonstrating both

Table 15.4 Summary of radiographic descriptors and their significance

Category			Significance
	Descriptor	Descriptor	
Attenuation	High		Generally slow growing and benign[a]
	Low		Locally destructive, may be fast or slow growing
	Mixed		Slow growing and benign
Border	Well-defined		Slow-growing lesion[b]
		High attenuating rim	Intact capsule surrounding the lesion, slow growing
		Sclerosis	Benign, very slow growing, peripheral reactive bone formation
	Indistinct/ ill-defined		Suggests an aggressive inflammatory (infectious) process or malignancy
Distribution	Association	Pericoronal, alveolar	Highly suggests odontogenic origin
		Intra-osseous	Possible odontogenic or non-odontogenic origin
		Extra-osseous	Neither of odontogenic or osseous origin, possible soft tissue entity
	Location	Maxilla	Consider intrinsic sinus pathology in posterior regions
		Mandible, ramus	Odontogenic lesions unlikely inferior to the mandibular canal
	Number	Single	Localized disease process
		Multiple	The presence of more than one entity, either lucent or opaque, in the jaws or in other bones (polyostotic) is highly suggestive of a congenital or systemic etiology[c]
Shape	Unilocular		Most common radiographic appearance, usually seen with developmental conditions, cysts, and infectious processes
	Multilocular[d]	Large locules (“soap bubble”), smaller locules (“honeycomb”)	Suggest a slow-growing, probably benign neoplasm
Internal architecture	Density		A homogeneous hypodensity is associated with odontogenic, non-odontogenic or “pseudo” cysts
	Nonhomogeneous	Calcifications	Associated with specific entities which are mostly pericoronal[e]
	Opacifications	Septae	Associated with specific entities[f]
		Residual bone	Associated with specific entities[g]
	Trabecular pattern	“Ground glass”	Very fine, grainy appearance of alveolar bone, associated with specific entities[h]
		“Cotton wool”	Suggestive of re-ossification of areas of low density may result in a “cotton wool” pattern[i]
		“Step ladder”	The formation of a few, coarse, horizontal trabeculae. Associated with specific entities[j]

(continued)

Table 15.4 (continued)

Category			Significance
	Descriptor	Descriptor	
Surrounding tissues	Dentition	Displacement	Associated with benign lesions and neoplasms, such as cysts and multilocular lesions
		"Floating teeth"	Destroy bone adjacent teeth without displacing teeth. Highly suggestive of malignancy[k] blood disorders[l] HX, diabetes and advanced periodontal disease
		Asymmetric PDL space widening	Associated with varying conditions including specific malignancies[m]
		"Knife-edged" root resorption	Usually is associated with pressure resorption from slowly growing lesions or benign neoplasms[n]
		"Spiked-root"	Highly suggestive of malignancy which erodes lateral surface of the roots
	Reactive response to bone	Expansion	Solid cortical expansion is indicative of benign cysts and tumors
		Lamellar	Associated with specific conditions[o]
		"Sunburst"	Associated with specific conditions[p]

MM multiple myeloma, *OS* osteosarcoma, *OM* odontogenic myxoma, *HE* hemangioma, *CS* chondrosarcoma, *HX* histiocytosis X, *AMB* ameloblastoma, *HPT* hyperparathyroidism, *ES* Ewing sarcoma, *CGCG* central giant cell granuloma, *ABC* aneurysmal bone cyst, *PDL* periodontal ligament space, *FD* fibrous dysplasia, *PD* Paget's disease, *AOT* adenomatoid odontogenic tumor, *SCC* squamous cell carcinoma, *ES* Ewing's sarcoma

[a]Exceptions include OS, CS, and ES—These lesion grow rapidly, cause destruction and paresthesia

[b]CS—Can be slow growing and cause cortication but is malignant; MM, HX—appear as "punched out," non-corticated

[c]Numerous conditions produce lesions in the jaws and other bones include HX, MM, metastatic carcinoma, Paget's disease, osteomas secondary to Gardner's syndrome, HPT, osteopetrosis, and acromegaly

[d]Examples include AMB, HE, CGCG, ABC, and OM

[e]Examples include AOT, ameloblastic fibro-odontoma, and calcifying epithelial odontogenic tumor

[f]Right angles (CGCG), increased width (sclerosing osteomyelitis, HE and neurofibroma), spindly (OM, CGCG, HE)

[g]Examples include OM, squamous cell carcinoma, AMB, and HE

[h]Characteristic of FD, HPT, and PD

[i]Characteristic of PG

[j]Associated with sickle cell anemia and thalassemia

[k]Examples include SCC and metastatic tumors

[l]Including leukemia, agranulocytosis, and cyclic neutropenia

[m]OS, CS, scleroderma, vertical root fracture, and orthodontic tooth movement

[n]Examples include AMB, cemento-ossifying fibroma, and arterio-venous malformation

[o]Includes OS, CS, Garre's osteomyelitis, and ES

[p]Includes OS, CS, ES, and hemangioma

low- and high-density features). Previously, in 2D maxillofacial imaging, the terms radiolucent, radiopaque, and radiomixed were used, respectively. These categories may show additional internal characteristics.

- **Shape and nature of the lesion's borders.** The shape and borders of a pathological entity will provide some suggestion as to its nature and even growth rate. Slow-growing pathological entities usually demonstrate a smooth border, whereas irregular borders often characterize more aggressive conditions. Cystic lesions usually are round or ovoid in shape within the constraints of the shape of the jaw in the region they have developed. The borders of a lesion require some special attention: They are characterized as "well defined," "moderately defined," or "poorly defined"

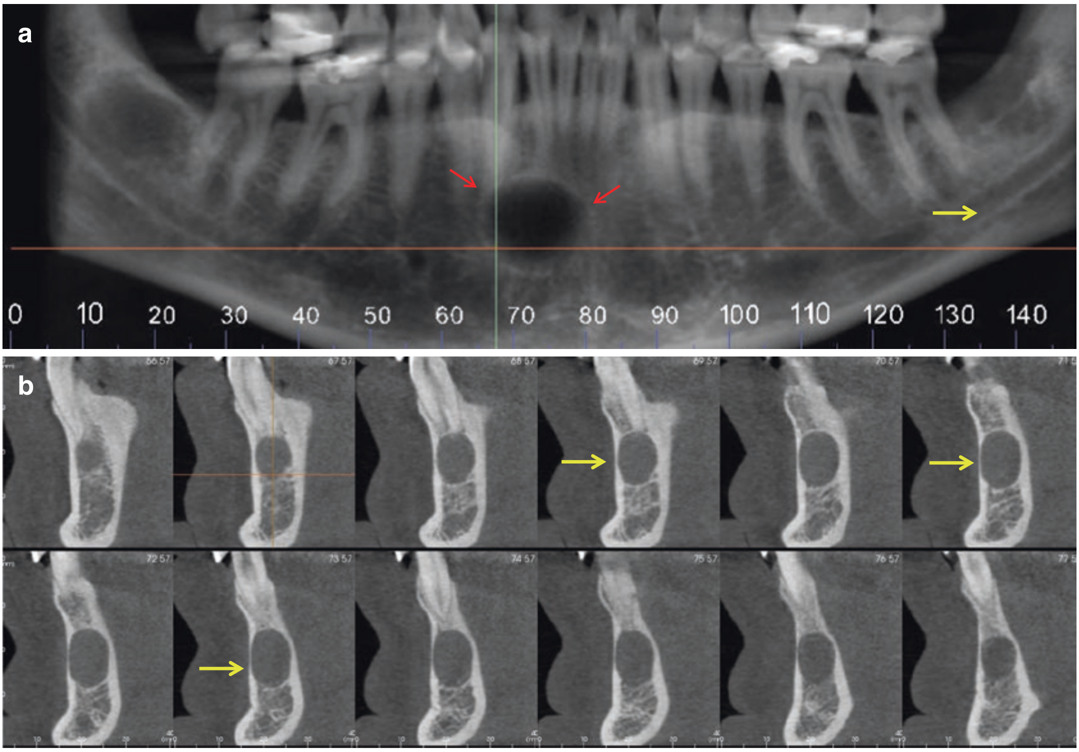

Fig. 15.11 Reformatted panoramic (**a**) and a series of cross-sectional images (**b**) of the mandible (B) depicting a well-defined, round, low-density, homogenous entity which is surrounded by a thin corticated border (*red arrows*). All features are characteristic of a benign, slow-growing lesion. Note the thinning of the labial cortical plate (*yellow arrows*) caused by the expanding cystic lesion. This lesion was associated with the apical region of the right mandibular canine and histologically confirmed as a radicular cyst

based on how clear the distinction is between the affected and unaffected by the lesion tissues. Well-defined entities are those in which there is absolute certainty about the margin of the lesion, with a definite line separating the diseased from the healthy tissue. Often, there may be a thin, high-density (corticated) line which borders the lesion (Fig. 15.11). This feature is characteristic of a benign, slow-growing lesion and is commonly found in cysts. Larger cystic lesions may expand and thin bony cortices, and, on some occasions, may perforate them. In such cases, it is possible that the lesion communicates with the oral cavity and becomes contaminated. Contaminated cystic lesions frequently behave like abscesses and may lose their clear delineation (Fig. 15.12).

In other occasions, the border is thicker, described as "sclerotic" or "hyperostotic": this is a feature of either very slow-growing lesions or reactive bone formation stimulated by the lesion like on chronic inflammation (Fig. 15.13). When there is no distinction between affected and unaffected osseous tissues, the border of these pathological entities is characterized as "poorly" defined (or ill-defined); in such cases, there is a gradual transition from the normal-appearing bone to the abnormal that it appears as if the border is blending (White and Pharoah 2009) This appearance is seen commonly in solid patho-

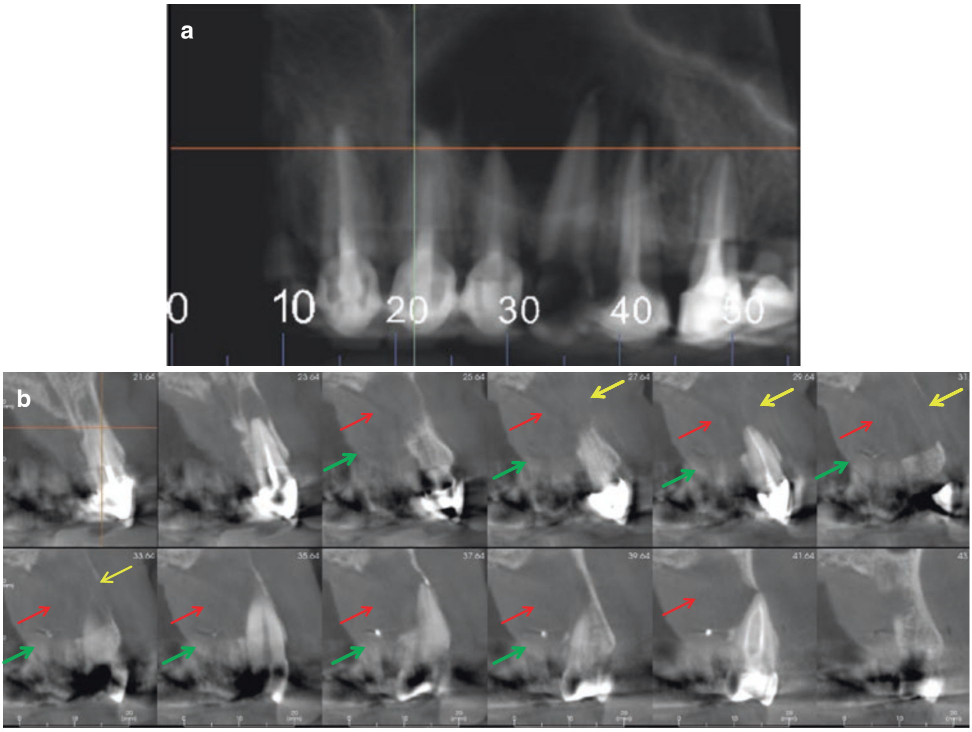

Fig. 15.12 Reformatted panoramic (**a**) and a series of cross-sectional images (**b**) of the left anterior maxilla depicting a moderately defined, homogenous, low-density lesion in the apical region involving multiple teeth. The entity has resulted in thinning and possible erosion of the palatal cortical plate (*red arrows*) and, to a lesser extent, thinning of the labial cortical plate (*yellow arrows*). These features are suggestive with a radicular cyst communicating with the oral cavity. If a cystic lesion communicates with oral cavity, it may become infected and may behave like an abscess. Note the marked soft tissue intraoral expansion involving the hard palate (*green arrows*)

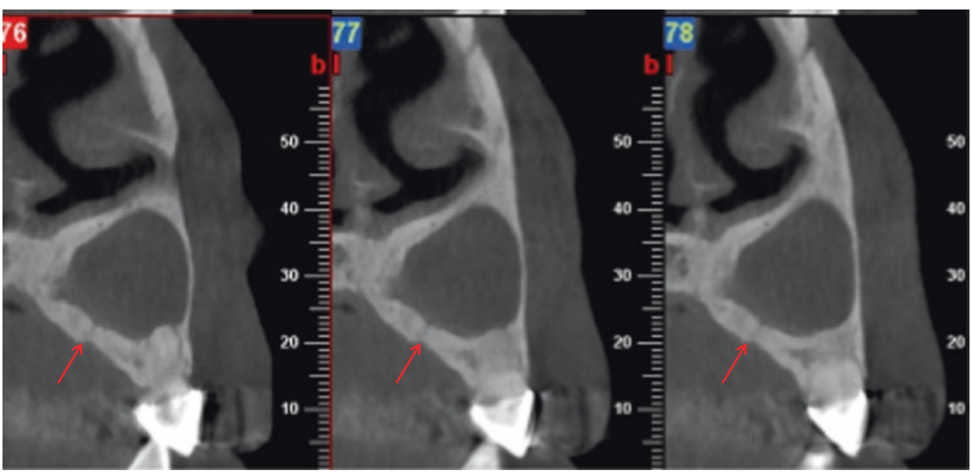

Fig. 15.13 A series of CBCT cross-sectional images of the maxillary left canine showing a large, homogenous, low-density, trapezoidal-shaped, cystic lesion. The thick-hyperostotic border noted is the result of reactive bone formation associated with chronic inflammation. The *red arrows* show a communication through which the lesion drained in the oral cavity. The imaging appearance is consistent with a radiologic diagnosis of radicular cyst with an "abscess"-like behavior

logical entities which are generally benign like fibrous dysplasia (Fig. 15.14). Lesions that demonstrate invasive, erosive, or permeative borders are rather aggressive and may be associated with rapid growth and tissue destruction. This is a characteristic of malignant lesions. In these lesions, the progression is not through expansion, as in benign lesions, but via destruction at the expense of trabeculae (White and Pharoah 2009) (Fig. 15.15).

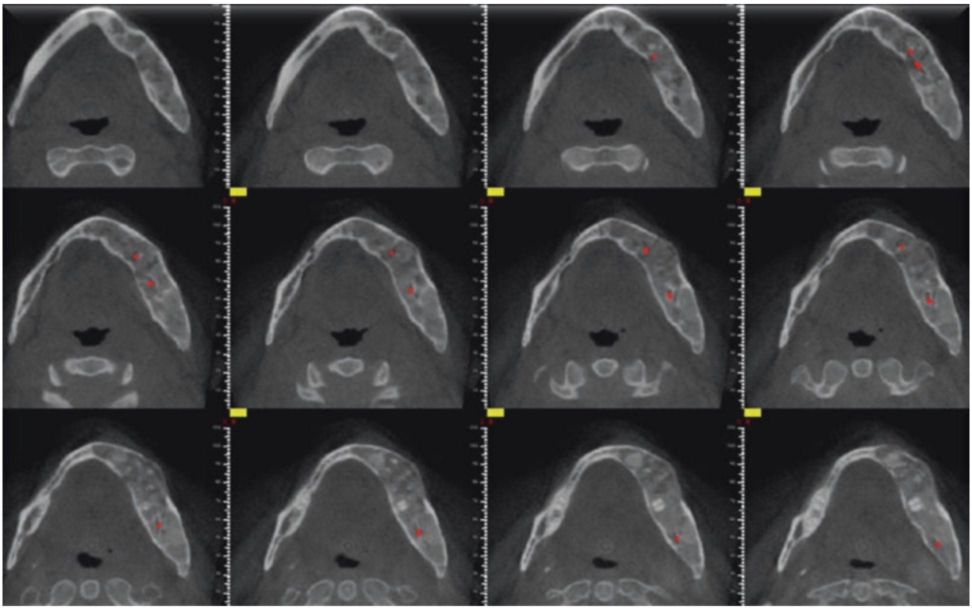

Fig. 15.14 A series of CBCT axial orthogonal sections showing marked asymmetry between the left and right posterior mandible. The left mandibular body shows marked expansion of the cortices and a "ground glass" appearance in an area the borders of which are not clearly determined (poorly defined lesion). The imaging findings are consistent with a diagnosis of fibrous dysplasia of the left mandible

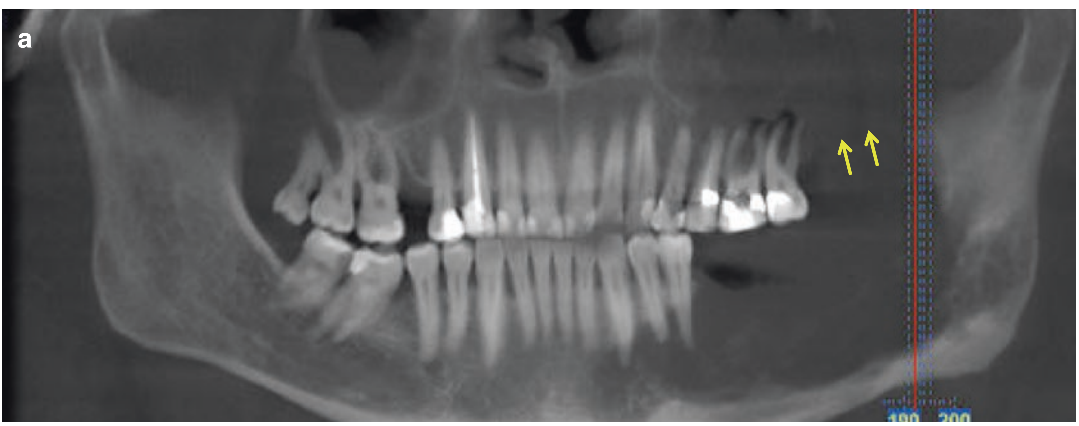

Fig. 15.15 Reformatted panoramic (**a**) and a series of cross-sectional images (**b**) of the left maxilla and mandible illustrating a large, ovoid, moderately defined, low-density lesion with rather irregular borders. Note the extensive destruction of the osseous tissues seen at the margins of the lesion (*red arrows*). Faint opacities seen within the lesion are most likely osseous remnants. These features are strongly suggestive of an aggressive, most likely malignant pathological entity. Also, note the destruction of the maxillary alveolar process (*yellow arrows*)

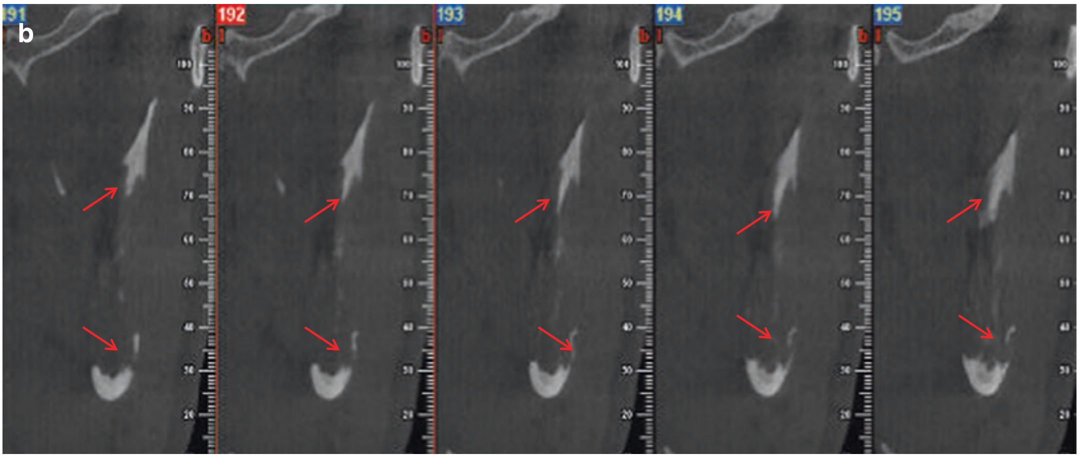

Fig. 15.15 (continued)

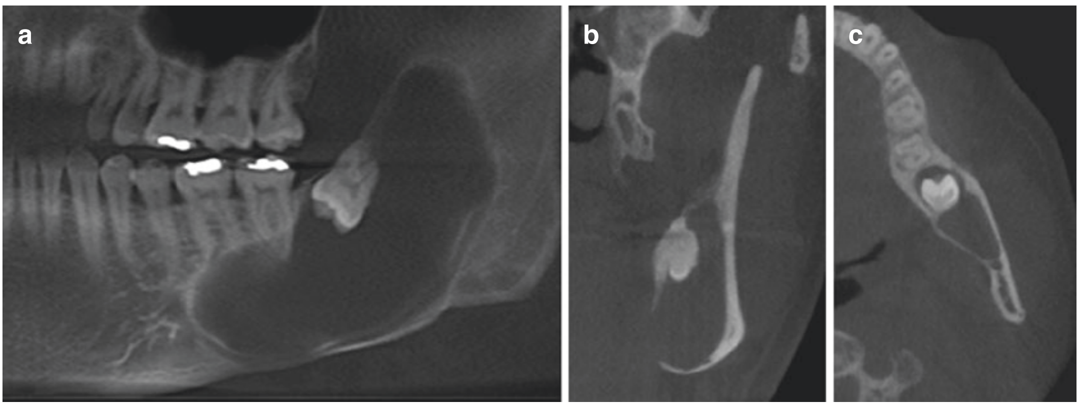

Fig. 15.16 Cropped reformatted panoramic (**a**), para-coronal (**b**), and axial (**c**) images of the left mandible showing a well-defined, ovoid lesion of uniform low density with a corticated border. Note the marked expansion of the bony cortices and thinning of the lingual and inferior cortex. This appearance is characteristic of a cyst and consistent with a dentigerous cyst. However, some solid lesions also mimic this appearance including ameloblastoma and keratocystic odontogenic tumor (KCOT)

- **Distribution**. The distribution of a pathologic entity can be described in relation to its association with the dentition (e.g., pericoronal, inter-radicular), jawbone, of intra- or extraosseous presentation, location within the jaws and number (Table 15.4).
- **Shape.** Studying the shape of the deformity made by a pathological entity often contributes to developing a differential diagnostic list; in fact, a broad distinction between some categories of pathological entities may be made based on the internal structure (like the differentiation between a solid mass and a cystic lesion). Lesions that demonstrate a uniform, low-density content and a single chamber (unilocular) are often cystic lesions (Fig. 15.16).

  Sometimes septae may divide the lesion into a series of smaller chambers called loculations. This appearance is referred to as multilocularity. Both solid benign tumors and some cysts may show multilocularity. The number of loculations and their shape and size are also of importance since they may

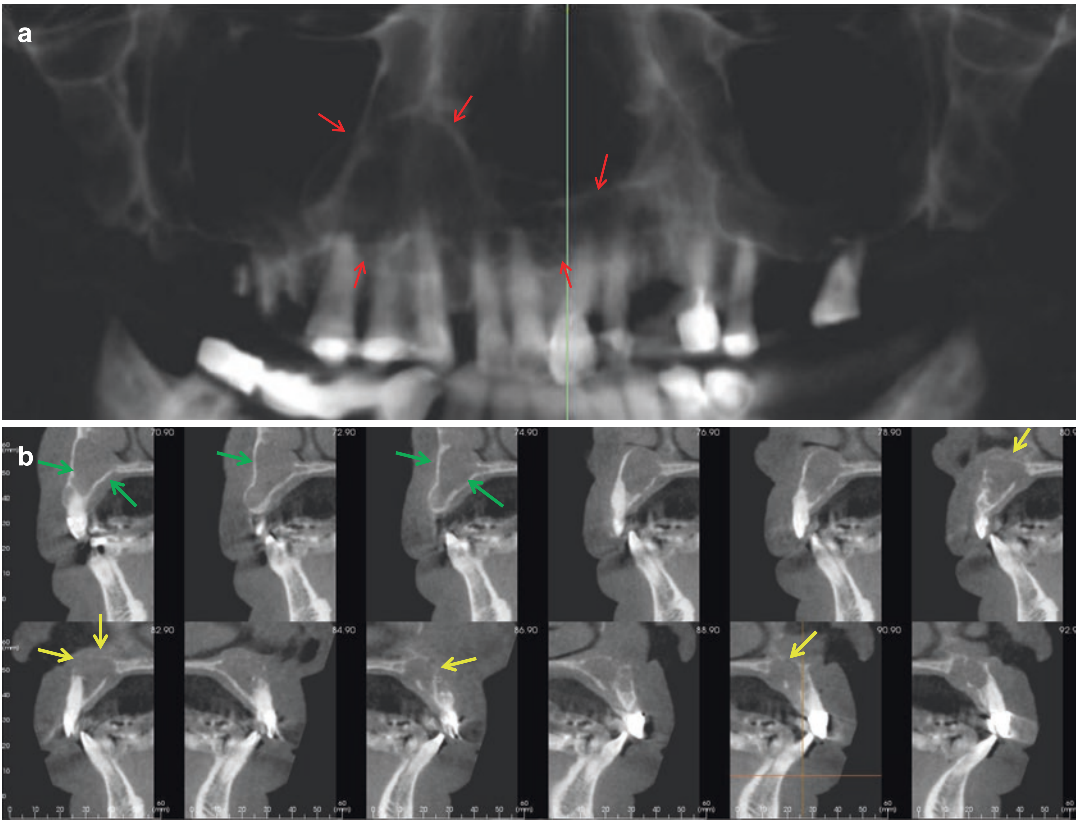

Fig. 15.17 Reformatted panoramic (**a**) and a series of cross-sectional images (**b**) of the maxilla depicting a well-defined, homogenous, multilocular, low-density lesion associated with the apical region the anterior and right premolar teeth occupying almost the entire anterior maxilla (*red arrows*). This has caused marked expansion and thinning of the labial and palatal cortices (*green arrows*) and erosion of the cortices in some areas (*yellow arrows*). The radiologic appearance is suggestive of a solid benign tumor such as an ameloblastoma (final diagnosis) or keratocystic odontogenic tumor (KCOT)

characterize certain pathological entities; benign tumors show frequently a multilocular internal pattern (more frequently than cysts). For example, an ameloblastoma (Figs. 15.17 and 15.18) may present with larger loculations which resemble a "soap-bubble" appearance (Fig. 15.19) whereas lesions with smaller loculations are referred to as "honeycomb."

- **Internal architecture.** The basic descriptors of the internal architecture of a lesion include a consideration of the homogeneity of the entity, the presence of calcifications or septae, and alterations in trabecular pattern. Some patterns are associated with specific entities (Table 15.4). In some cases the overall appearance of a lesion may be cystic containing high-density flecks or one or more high-density cores inside the lumen of the lesion. Despite the distinction, these fall in the broader category of mixed lesions and are mostly benign tumors or rarely some types of cysts (Figs. 15.20 and 15.21). High-density or mixed density lesions may also show variations in their internal structure that may be significant. High-density entities may be due to the formation of abnormal osseous tissue; in fact, if the trabecular pattern of healthy bone is altered and replaced by denser, smaller trabeculae, this will increase the overall density of the affected site. A mixture of bundles of denser,

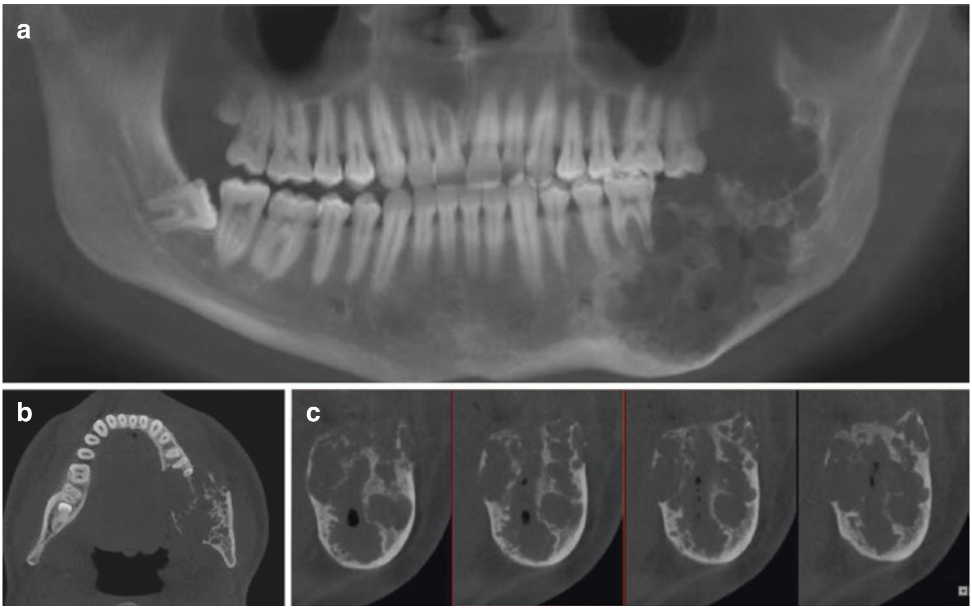

Fig. 15.18 Reformatted panoramic (**a**) axial (**b**), and a series of cross-sectional images(**c**) of the mandible (B) depicting an extensive, well-defined, multilocular, low-density lesion occupying almost the entire left posterior mandible. The loculations are small and the lesion shows a "soap-bubble" appearance. This has caused marked expansion and thinning of the buccal, lingual and inferior cortices. The imaging appearance is suggestive of ameloblastoma and keratocystic odontogenic tumor (histopathologic diagnosis)

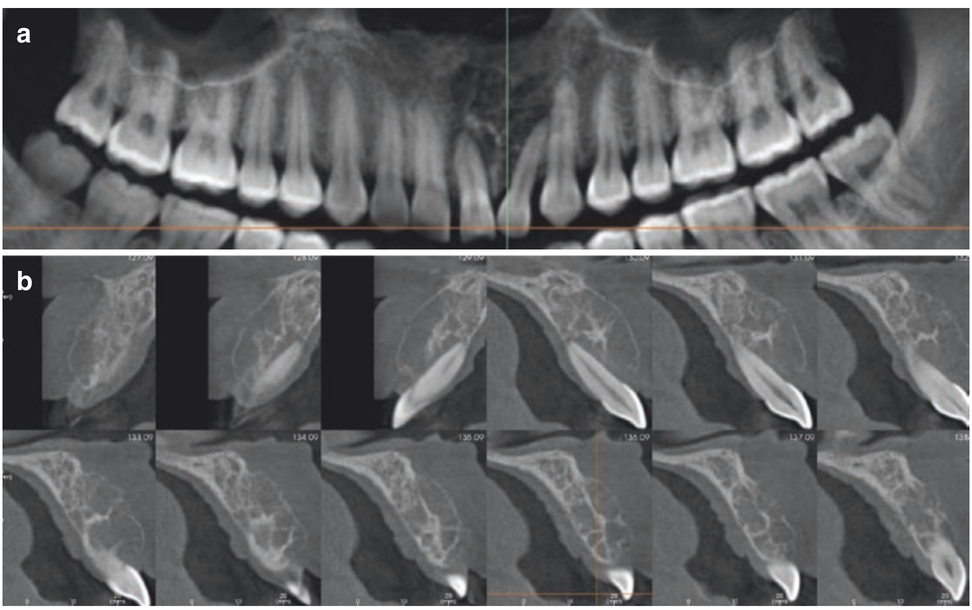

Fig. 15.19 Reformatted panoramic (**a**) and a series of cross-sectional images (**b**) depicting a moderately defined, expansile, multilocular mass in the anterior maxilla. Note that on the cross-sectional images (**b**) many of the trabecular are fine and angularly oriented demonstrating a "tennis racket" pattern with almost square loculations. The overall appearance is suggestive of benign tumor; the trabecular pattern may be associated with an odontogenic myxoma (histopathologic diagnosis)

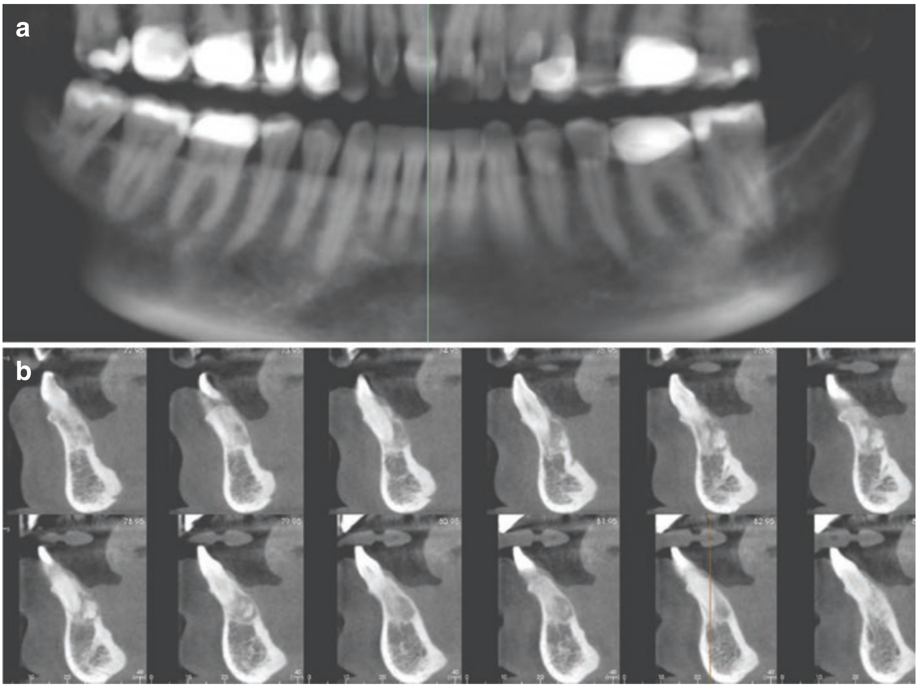

Fig. 15.20 Reformatted panoramic (**a**) and a series of cross-sectional images (**b**) depicting a well-defined, mixed attenuating lesion in the apical region of the right mandibular anterior teeth containing three to four small distinct globular hyperdensities with a hypodense periphery. The lesion has expanded and thinned the lingual mandibular cortex. These findings are suggestive of focal osseous dysplasia

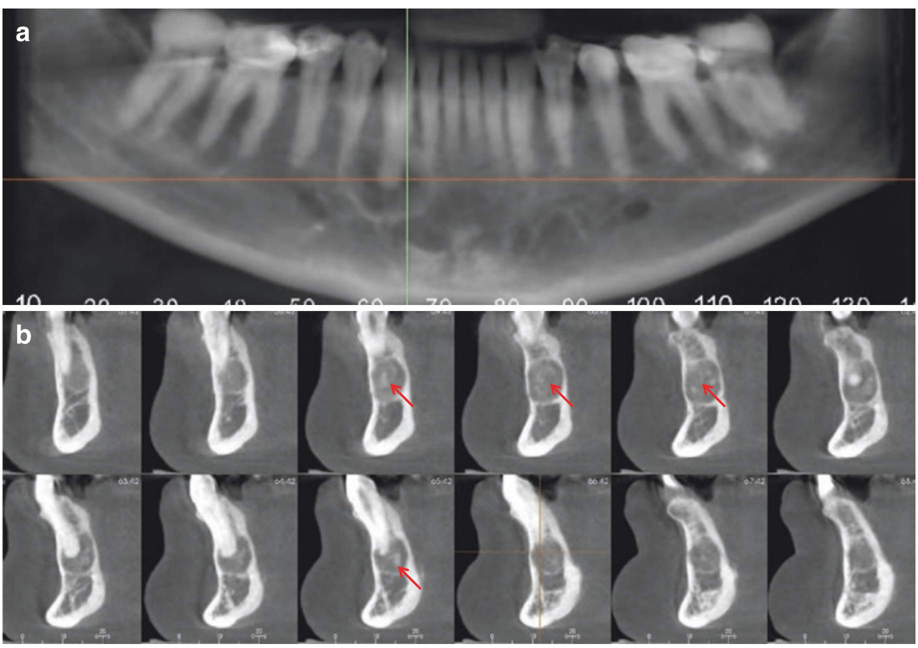

Fig. 15.21 Reformatted panoramic (**a**) and a series of cross-sectional images (**b**) of the mandible (B) depicting a single, well-defined, mixed attenuating lesion in the apical region of the right canine which contains high-density flecks (*red arrows*). The lesion has slightly expanded and thinned the labial and lingual mandibular cortex. In the absence of similar entities, these findings are suggestive of an ossifying fibroma

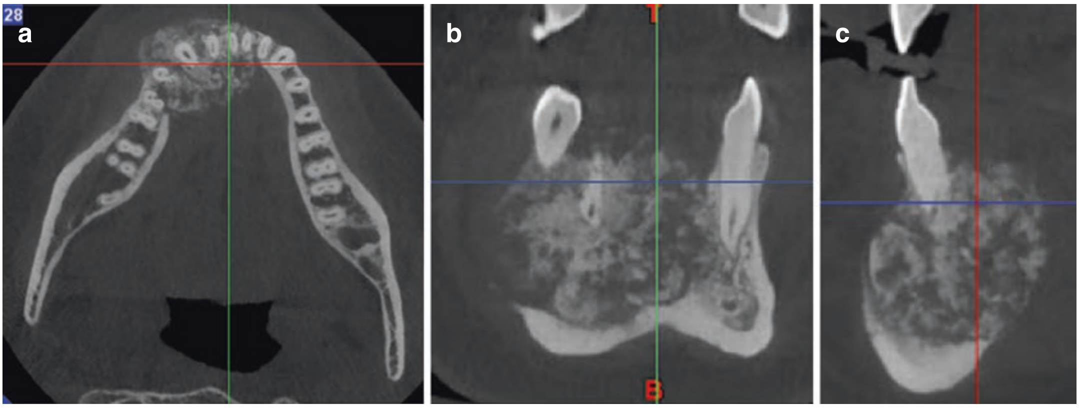

Fig. 15.22 Axial (**a**), coronal (**b**), and midsagittal (**c**) sections of the anterior mandible depicting a moderately defined, expansile, mixed attenuating, solid mass which has markedly expanded the mandibular cortices. These findings are suggestive of a benign tumor; the resorptive replacement resorption of the apex of the roots of some of the incisor teeth is suggestive of osteoblastoma (histopathologic diagnosis)

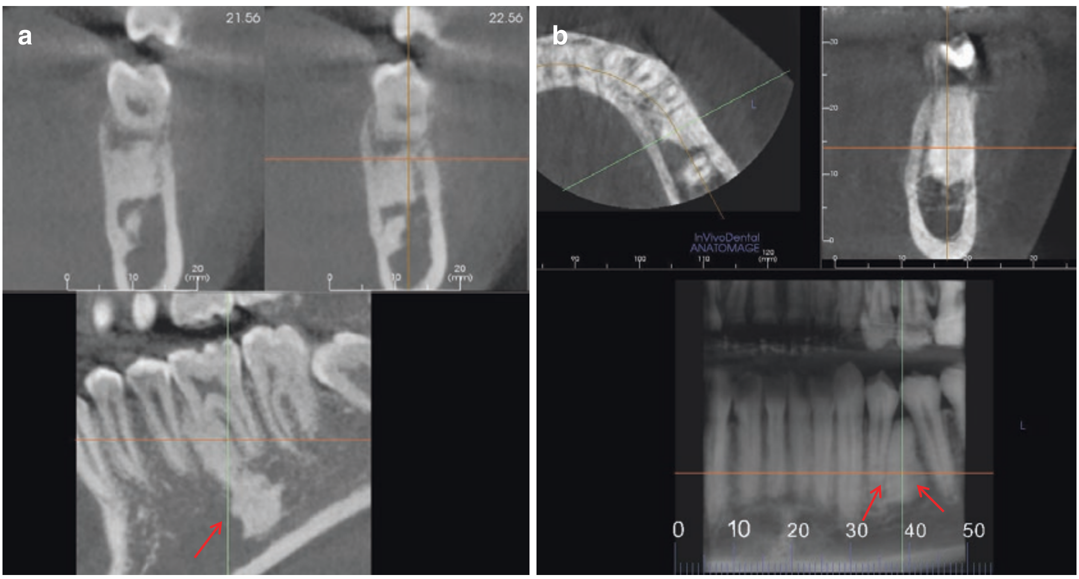

Fig. 15.23 Limited FOV CBCT image displays of two patients showing irregular, well-defined, homogenous, high-density lesions; one is in left posterior mandible resorbing or replacing the mesial root of the first molar and extending to almost the entire inferior mandibular cortex (*red arrows*) (**a**); the second hyperdensity is intraradicular and triangular in shape (*red arrows*), (**b**) apparently causing displacement of the roots of premolar teeth. The high-density appearance is an indication of a solid entity. The imaging appearance is consistent with idiopathic osteosclerosis in both cases

smaller trabeculae interchanged with layers of normal, healthy ones may reflect a mixed internal structure (Fig. 15.22). In all instances, a high-density or mixed appearance in a lesion under investigation is a strong indication of a solid mass (Figs. 15.22, 15.23, and 15.24).

- **Response of the surrounding tissue to the presence of the lesion.** The effects of the lesion on the surrounding tissues vary and will provide information about the behavior of the developing pathology. As they advance in size, slow-growing lesions gradually occupy more

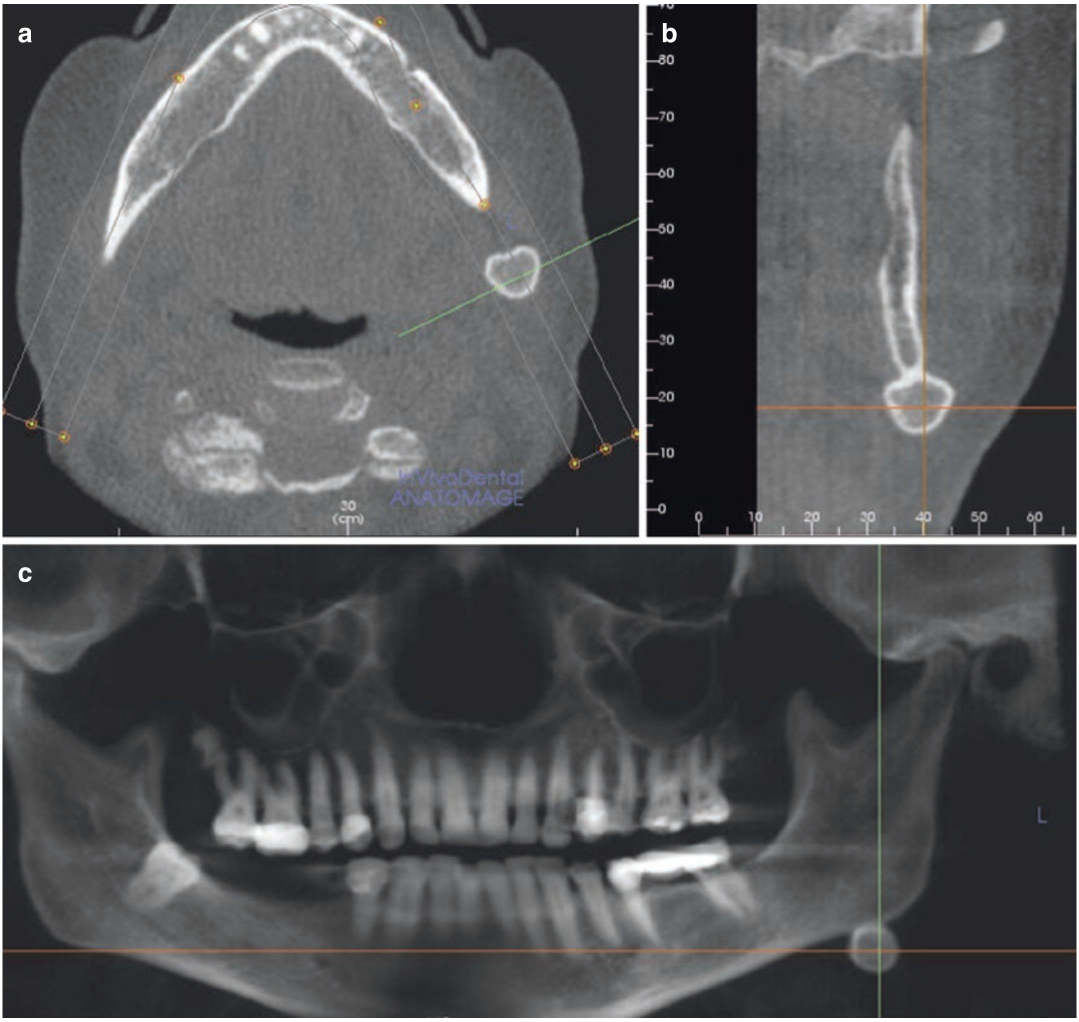

Fig. 15.24 Axial (**a**), cross-sectional (**b**) and reformatted panoramic (**c**) image sections showing a round, well-defined, pedunculated hyperdense, exophytic entity originating from the inferior mandibular cortex just anterior to the left mandibular angle (non-tooth-bearing region). Internally the density is similar to that of bone with a cancellous and a cortical component. The imaging appearance is consistent with a mandibular osteoma

space and in that process will often displace teeth (Fig. 15.25), may cause root resorption (Fig. 15.26), may expand bony cortices, and, in general, may displace anatomic structures in the vicinity. These may include the floor of the maxillary sinuses and nasal cavities, if they grow in the maxilla (Fig. 15.27), or the mandibular canal and mental foramen (Fig. 15.28), if they are developing in the mandible. While this commonly is seen in large lesions, it may be seen even in smaller ones causing what is known as the "halo effect" (Fig. 15.29). These findings are often associated with benign pathological entities such as cysts or benign neoplasms.

Fast-growing lesions, especially malignancies and inflammatory lesions, will cause significant peripheral destruction of the tissues or

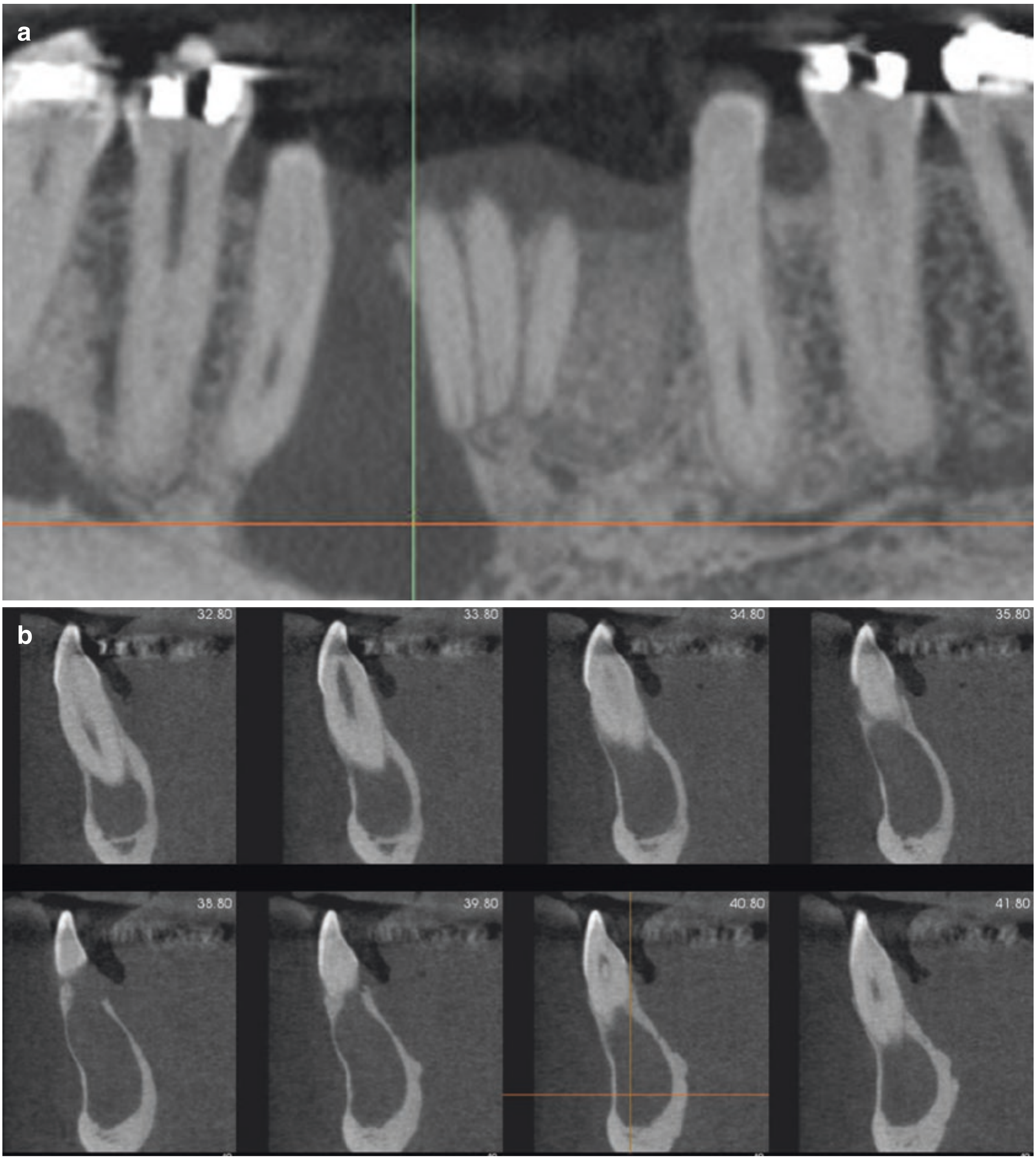

Fig. 15.25 Panoramic reformatted (**a**) and cross-sectional images (**b**) of the anterior mandible (limited FOV) showing a well-defined, pear-shaped homogeneous hypodense lesion causing displacement of the anterior central incisors. Displacement of teeth is a common phenomenon associated with the slow enlargement of benign pathological entities; this lesion histopathologically proven to be a unicystic ameloblastoma

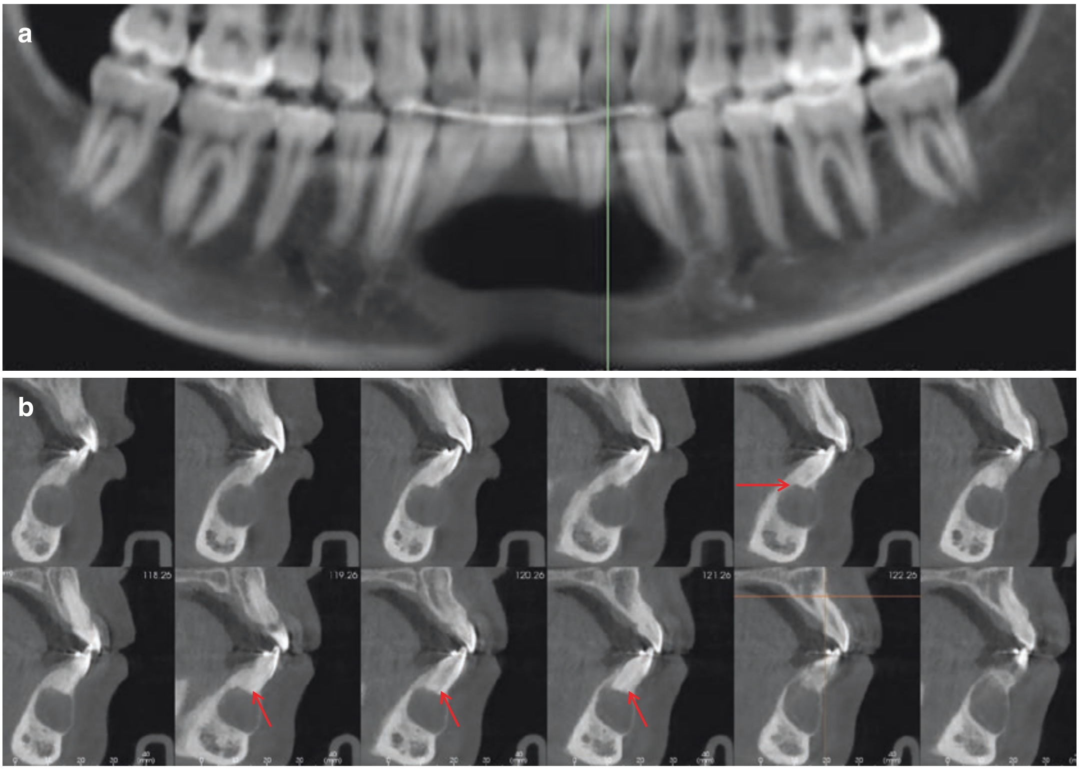

Fig. 15.26 Reformatted panoramic (**a**) and a series of cross-sectional images (**b**) of the mandible showing a well-defined, ovoid, homogenous low-density entity in the anterior mandible with displacement and "knife-edge" root resorption on multiple incisor teeth (*red arrows*). These features are typical of benign pathological entities with the pattern of root resorption being highly suggestive of ameloblastoma (histopathologic diagnosis)

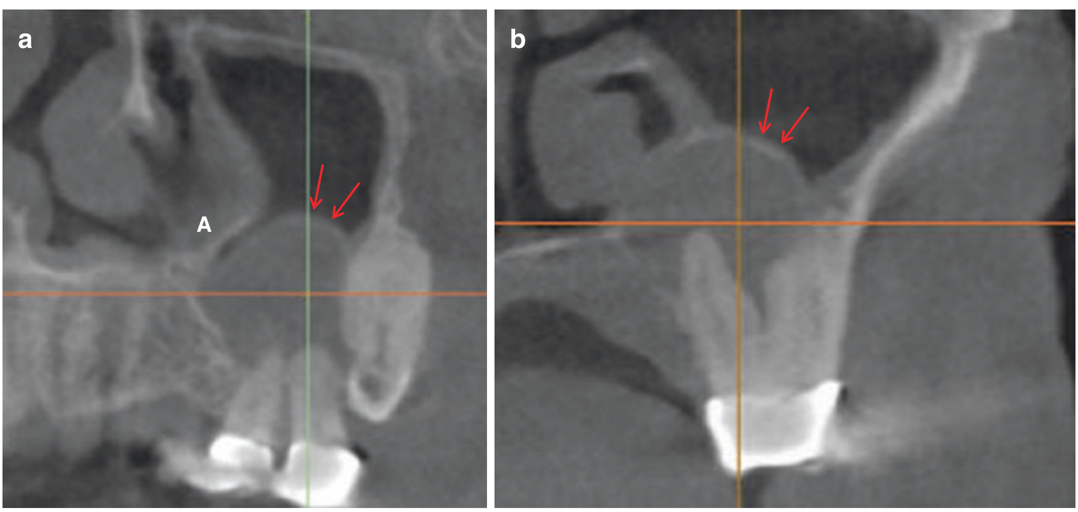

Fig. 15.27 Reformatted panoramic (**a**) and cross-sectional image (**b**) of the maxillary left molars showing the effects of a slow-growing superiorly expanding radicular cyst raising the floor of the left maxillary sinus (*arrows*)

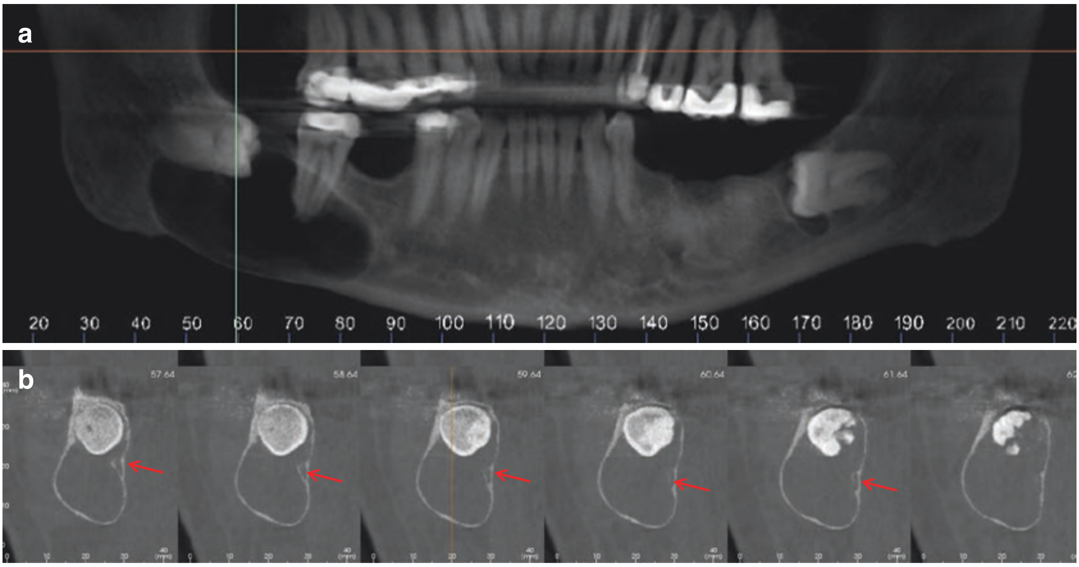

Fig. 15.28 Reformatted panoramic (**a**) and series of cross-sectional images (**b**) illustrating the marked expansion effects of a large pericoronal unilocular ovoid hypodensity on the mandibular cortices and associated lingual displacement of the mandibular canal (*red arrows*)

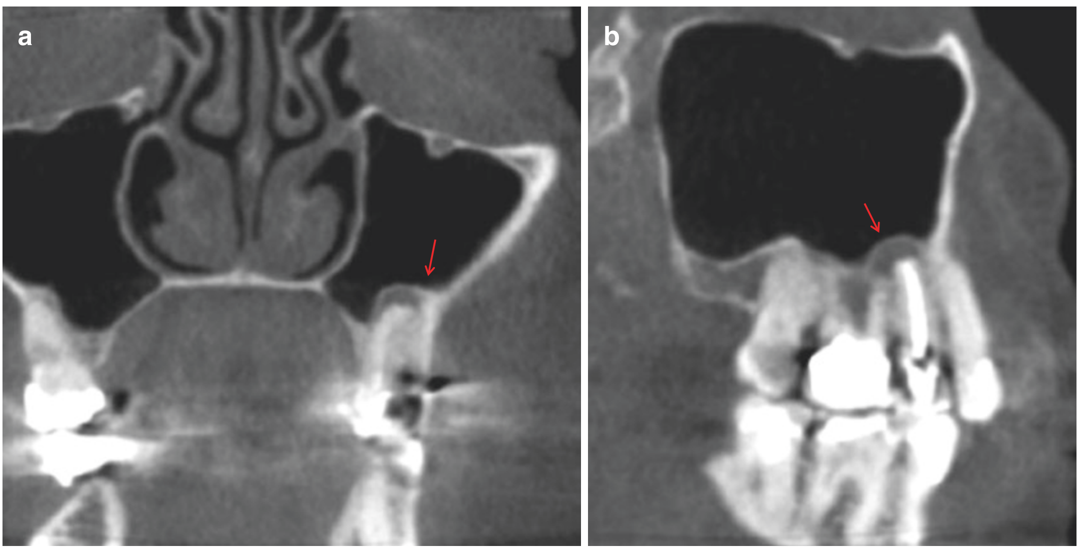

Fig. 15.29 Coronal (**a**) and parasagittal images (**b**) of the maxillary left premolars showing a elevation of the floor of the left maxillary sinus (*arrows*) immediately superior to the apex of the root of the second premolar caused by a local periapical inflammatory lesion; this is known as "halo effect," a sign of slow-growing lesions

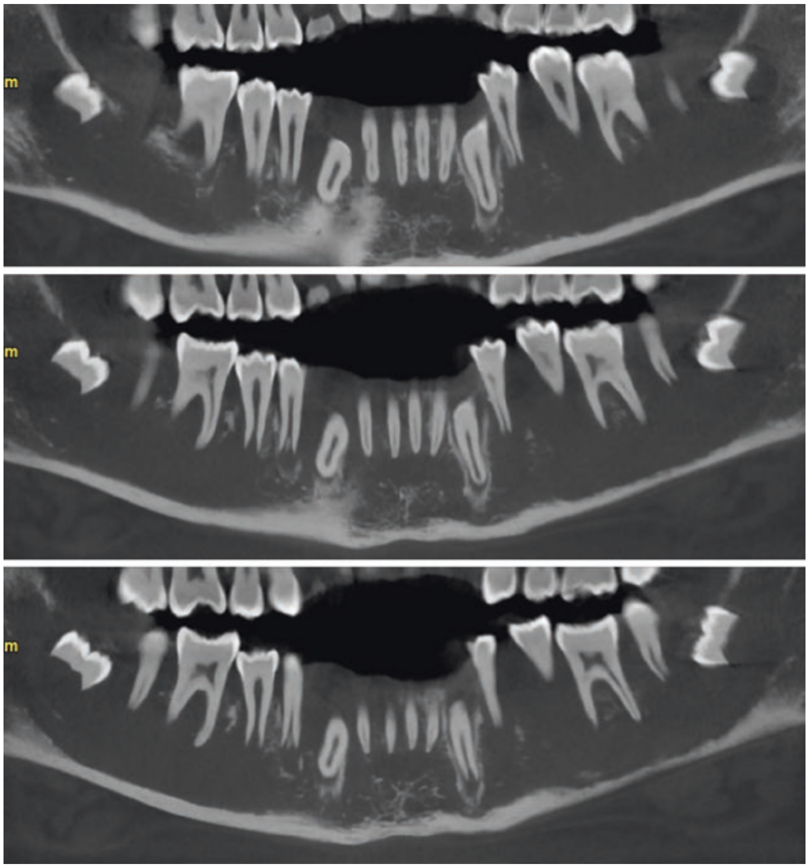

Fig. 15.30 Sequential thin slice reformatted panoramic images of the mandible of 12-year-old boy showing marked permeative destruction of the cancellous component of the mandibular bone including loss of lamina dura and trabeculation. These features highly suggestive of a malignancy (histologically diagnosed as a Burkitt lymphoma)

structures adjacent to the lesion rather than cause displacement. The most characteristic imaging findings suggesting a malignancy or inflammatory process include:

- Eroded or destroyed cortices.
- "Floating teeth" (the destruction of the supporting bone has made the teeth in the region to look like they float) (Fig. 15.30).
- Irregular widening or destruction of lamina dura.
- Invasion and destruction of the mandibular bone and bony cortices.
- Destruction of the walls of the mandibular canal and accompanying paresthesia (Fig. 15.31).
- "Moth-eaten" destruction pattern or borders of the affected bone (Fig. 15.32).

Numerous schemes have been proposed incorporating radiologic features to assist clinicians as an aide–mémoire including:

- L.E.S.I.O.N. (Gonzalez 2015): Acronym for lesion, edge, shape, internal, other structures, and number.
- "Lazy dental students surely become increasingly stupid" Pneumonic for location, (radio) density, shape, size, borders, internal structure, surrounding tissues.
- Five S's and Three D's (MacDonald 2011): Catch phrase for shade, shape, site, size, surroundings, diameter, density, and displacement.

Whichever scheme is used for radiologic data collection, the purpose of using radiographic

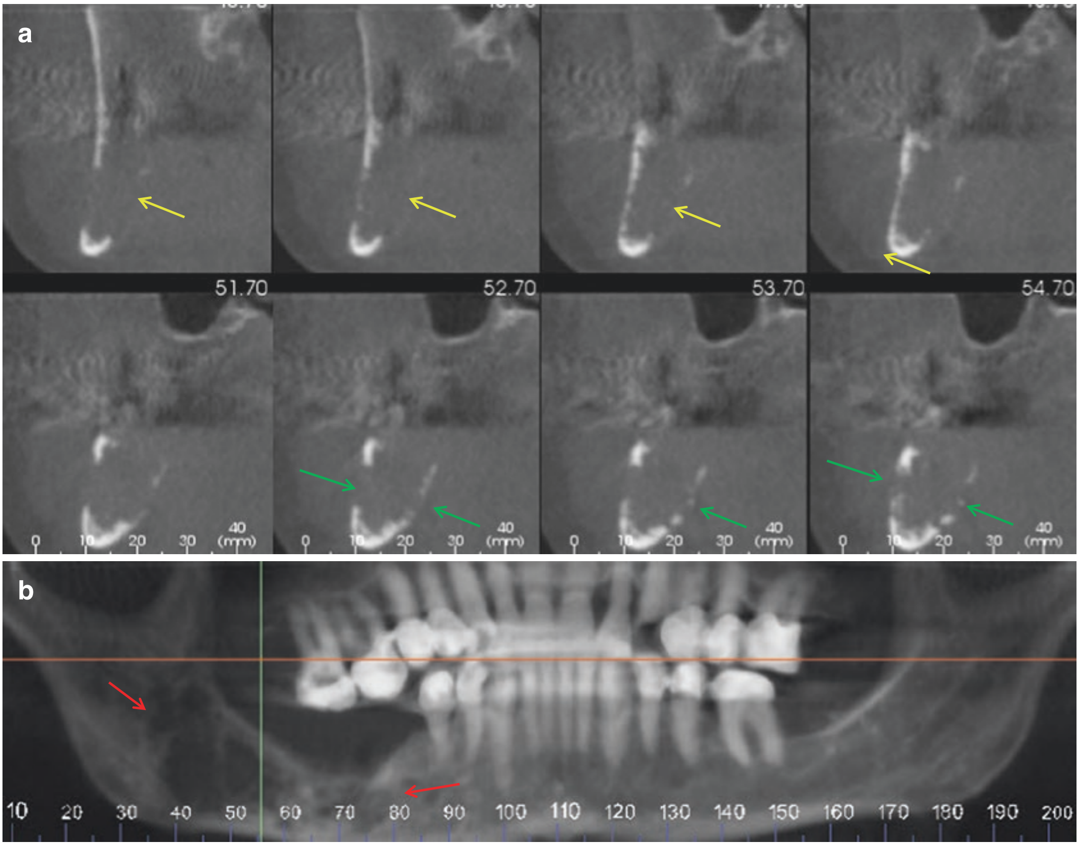

Fig. 15.31 Series of cross-sectional images (**a**) and a reformatted panoramic image (**b**) of the right posterior mandible illustrating the effects of poorly defined, aggressive lesion (*red arrows*) on the mandibular bone: Note the marked destruction in the cancellous component of the mandibular bone (showing as void in the cross-sections), destruction of the bony cortices (*yellow arrows*) and permeative signs (*green arrows*) as the lesion is invading the mandibular cortices. These are common features of aggressive or malignant pathological entities. The histopathologic diagnosis was osteomyelitis

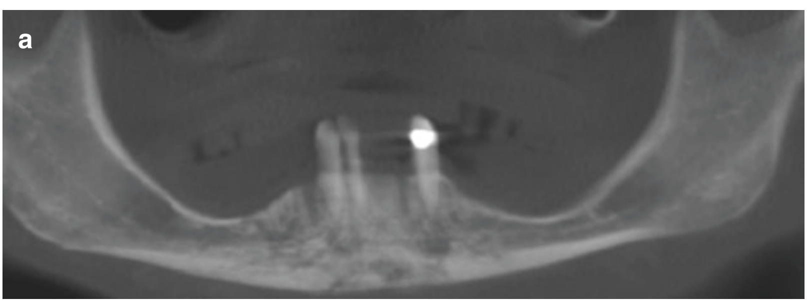

Fig. 15.32 Reformatted panoramic (**a**) and series of cross-sectional images (**b**) of the anterior mandible showing the characteristic "moth-eaten" pattern present on the lingual and inferior cortex. This feature is highly suggestive of an aggressive, invasive pathological entity. Correlated with moth the medical history (previous bisphosphonate use) and clinical presentation, the final diagnosis was medically related osteonecrosis of the jaw

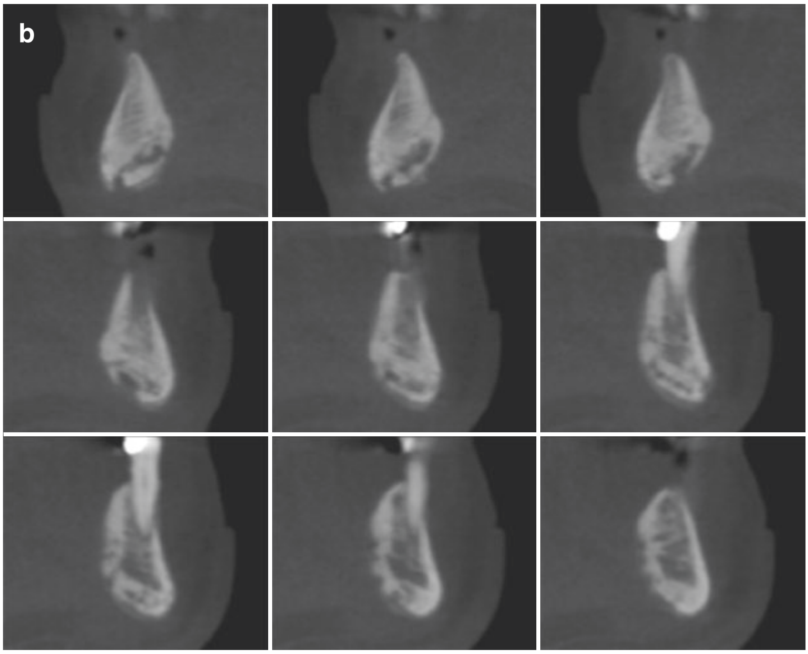

Fig. 15.32 (continued)

descriptors (Table 15.4) suggestive of specific disease processes is to match the imaging findings to radiologic patterns.

15.2.5 Putting Everything Together

Once the imaging of an entity has been reviewed in detail and all key features identified, the significance of each characteristic must be determined so that the entity can be categorized into a specific radiologic pattern. Radiologic patterns of tissue involvement are based principally on degree of attenuation, tooth association, number of entities present, lesion shape, and location of the entity with respect to the tooth. Use of this algorithm (Fig. 15.33) provides a manageable list of conditions that present with these characteristics. Further differentiation within these groups is dependent on knowledge of specific disease-related imaging characteristics.

In this process, the clinician must address the following considerations:

- **Is the suspected abnormality potentially a true pathological entity or an anatomical variant?** A knowledge of the radiologic appearance of possible anatomical variants that may look suspicious or imitate disease is an important step in the diagnostic process. This requires a sound knowledge of the anatomy of the maxillofacial region. This understanding is not trivial as there are a wide range of anatomic variability in the maxillofacial region.
- **Is the abnormality localized or generalized?** Generalized pathologic entities are usually the result of systemic, metabolic, or endocrine disorders; in this case the entire maxilla or mandible or more bones may be affected.
- **From where is the lesion originating (origin)?** This requires a thought related to two aspects; “Is the entity potentially developmental or acquired?” and “From which tissue (bone or soft tissue) and anatomical area is the most likely the origin of the lesion?”

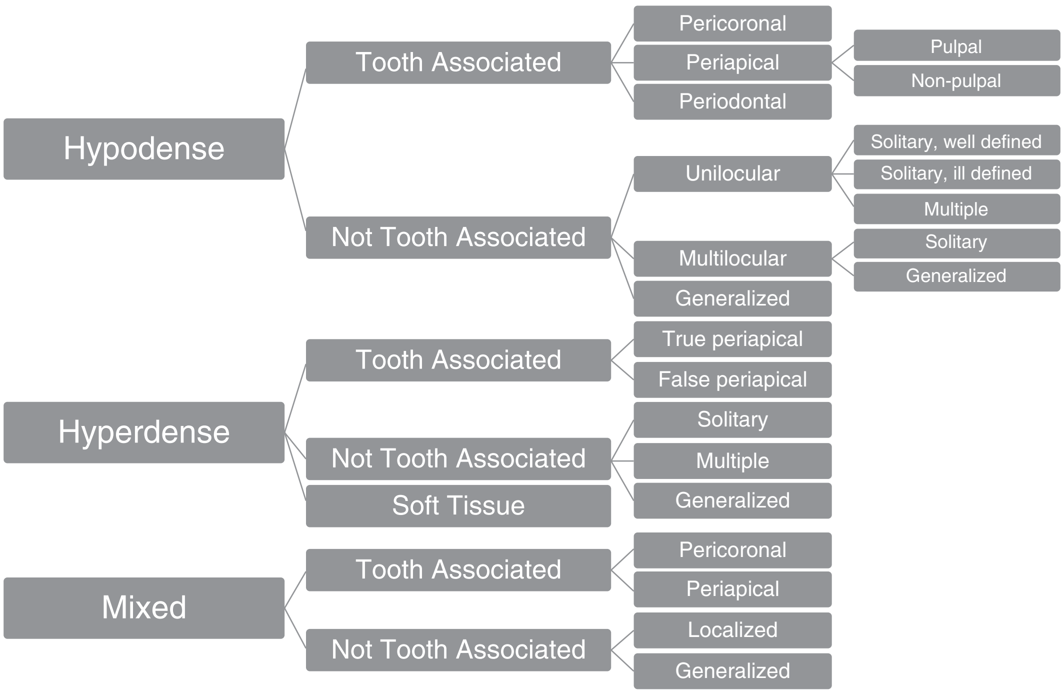

Fig. 15.33 Simplified three- and four-tier radiologic pattern description algorithm based on level of attenuation, tooth association, location, number, and shape

Alterations in the radiographic appearance of the affected region, determination of the lesional epicenter, changes in adjacent anatomical structures, and indirect effects within the surrounding tissues may reveal information as to whether the entity has an osseous or soft tissue origin. In dental and maxillofacial imaging, primary radiologic categorization and subsequent differential diagnosis is based on determining if the entity is tooth-associated or non-tooth-associated (Tables 15.5 and 15.6).

- **Is this possibly a benign or a malignant lesion?** Radiographic hallmarks of a malignancy include an irregular shape, evidence of fast growth, and an invasive and destructive behavior. In contrast, benign pathological entities such as cysts or benign tumors are slow growing and demonstrate round or ovoid-shaped well-defined lesions that displace and push the neighboring tissues instead of invading them (Table 15.7). The available clinical information may assist in determining possible metabolic, systemic, or inflammatory causality of a benign lesion.
- **Apart from the area of interest, is there anything else that should be reviewed?** An important step towards the completion of the diagnostic process includes the thorough review of the entire imaging volume to ensure that no incidental or synchronous disease is inadvertently omitted from consideration.
- **Are there any radiographic features present that could be considered as highly suggestive of a particular disease or act as a "red flag"?** Few pathological entities can be diagnosed from their radiographic features alone. In most cases, the clinician will formulate a list of possible diagnoses. Many entities are discovered serendipitously on an imaging examination usually performed for other purposes (e.g., assessment of third molars). Others may present as localized expansions. In formulating a differential diagnostic list,

Table 15.5 Differential diagnosis of tooth-associated entities

Descriptors			Examples
Hyopdense	Pericoronal	Homogeneous	Pericoronitis, dentigerous (follicular) cyst, eruption cyst, AMB, KCOT, ameloblastic fibroma
	Periapical	Pulpal	Apical periodontitis (acute and chronic), apical abscess, radicular cyst, residual cyst, apical scar, surgical defect
		Non-pulpal	Dentigerous cyst, POD, TBC, NPDC
	Periodontal		Periodontal pocket, lateral radicular cyst, lateral periodontal cyst
Hyperdense	Periapical		Condensing osteitis (focal sclerosing osteomyelitis), POD, unerupted tooth, foreign body, hypercementosis
	Alveolar		Unerupted and supernumerary teeth, odontoma, tori, exostoses, enostosis, retained root fragment, foreign body, mucous retention pseudocyst (maxillary sinus), ectopic calcifications
Mixed	Pericoronal	Calcific flecks	Ameloblastic fibro-odontoma, AOT, CEOT, keratinizing calcifying odontogenic cyst
		Globular calcifications	Odontoma
	Periapical		Condensing osteitis, POD, OF, benign cementoblastoma, central odontogenic fibroma

AMB ameloblastoma, *AOT* adenomatoid odontogenic tumor, *CEOT* calcifying epithelial odontogenic tumor, *OF* ossifying fibroma, *KCOT* keratocystic odontogenic tumor, *NPDC* nasopalatine canal duct cyst, *POD* periapical osseous dysplasia, *TBC* traumatic bone cavity

Table 15.6 Differential diagnosis of non-tooth-associated entities

Descriptor			Examples
Hypodense	Unilocular	Solitary, well-defined	Residual cyst, TBC, lingual salivary gland defect, NPDC, KCOT, AMB, CGCG, HPT, OF
		Solitary, ill defined	Infection (acute/chronic osteomyelitis), osteoradionecrosis, BRONJ, focal osteoporotic bone marrow defect, FD, malignancy, (SCC, metastatic tumor, OS, CS)
		Multiple	Nevoid basal cell carcinoma syndrome, MM, metastatic tumor, HX
	Multilocular	Solitary	AMB, CGCG, HPT, cherubism, OM, KCOT, ABC, vascular lesions (e.g., hemangioma), mucoepidermoid carcinoma
		Generalized	
	Generalized		HPT, osteoporosis, osteomalacia, hereditary hemolytic anemia, leukemia, HX, PD (early), MM
Hyperdense	Solitary		Tori, exostoses, enostosis, unerupted and supernumerary teeth, odontoma, retained root fragment, FOD, condensing osteitis (focal sclerosing osteomyelitis), POD, FD, diffuse sclerosing osteomyelitis, proliferative periosteitis ossifying subperiosteal hematoma
	Multiple		Tori, extoses, and osteomas, retained root fragments, socket sclerosis, POD, FOD, condensing osteitis (focal sclerosing osteomyelitis), unerupted (resorbed) tooth, cleidocranial dysplasia, hypercementosis, foreign bodies
	Generalized		FOD, osteopetrosis, PD
Mixed	Localized		Ossifying postsurgical defect
	Generalized		FOD

ABC aneurysmal bone cyst, *AMB* ameloblastoma, *BRONJ* bisphosphonate-related osteonecrosis of the jaw, *CGCG* central giant cell granuloma, *OF* ossifying fibroma, *CS* chondrosarcoma, *FOD* florid cemento-osseous dysplasia, *FD* fibrous dysplasia, *HPT* hyperparathyroidism, *HX* Langerhans cell histiocytosis X, *KCOT* keratocystic odontogenic tumor, *MM* multiple myeloma, *NPDC* nasopalatine canal duct cyst, *OM* Odontogenic myxoma, *OS* osteosarcoma, *PD* Paget's disease, *POD* periapical osseous dysplasia, *SCC* squamous cell carcinoma, *TBC* traumatic bone cavity

Table 15.7 Benign and malignant features associated with radiolucent and radiopaque entities

Appearance	Behavior	Feature	Comment
Radiolucent	Benign	Well-defined, smooth, sclerotic, distinct, or scalloped border	If multilocular, indicates aggressive process
		Resorption of tooth roots	Usually associated with slow-growing tumor or inflammatory lesion
		Tooth divergence or migration	Characteristic of benign, aggressive expanding entities
		Well-circumscribed, localized expansion confined by cortex or periosteum	Perforation is indicative of benign aggressive process
	Malignant	Absent or indistinct border	Border is referred to as having a "wide zone" of transition
		Shape and extent	Extensive intramedullary spread without expansion. Ill-defined irregular appearance varying from moth-eaten, permeative to mottled
		Cortical erosion and destruction	Associated with "floating teeth" surface "saucerization" is associated with peripheral infiltration of soft tissue malignancy
		Periosteal reaction	Lamellations ("onion skinning"), radiating spicules ("sunray"), or peripheral edge ("Codman's triangle") reactions
		Floating tooth	Radiolucency encompasses tooth root with no resorption. Sudden loosening of teeth
Radiopaque	Benign	Internal opacities	Large localized homogeneous distribution, central flecks or widely distributed internal calcification
		Radiolucent rim	Well-defined border
	Malignant	Ill-defined border	Disorganized, irregular or streaking or whirling pattern
		Tooth or alveolar extrusion	Displacement causing supra-eruption or elevation of the marginal alveolus

one should be aware of features and presentations that are highly suggestive of certain disease entities:

- Symptomatic presentation such as pain, altered sensation (paresthesia) should always alert the clinician to neurovascular infiltration by either infections or malignancy until proved otherwise.
  - Cysts have a number of "cardinal" radiographic features that when considered together assist in their differential diagnosis (Fig. 15.34).
  - Specific areas of the jaw are associated with the development of specific conditions, particularly cysts (Fig. 15.35).
  - Some well-defined lesions present predominantly in children (ameloblastic fibroma, ameloblastic fibro-odontoma) or young adults (traumatic bone cavity, adenomatoid odontogenic tumor) while others occur more commonly in males (traumatic bone cavity, ameloblastic fibro-odontoma)

Often times, there might be a need for further investigation: this may be either with additional advanced imaging, biopsy, possible treatment, or periodic evaluation (White and Pharoah 2009). Some pathological entities may require immediate attention whereas for others periodic observation may be a more appropriate. Consulting a specialist in oral and maxillofacial radiology may provide guidance not only when there is difficulty in diagnosis but also in developing management strategies.

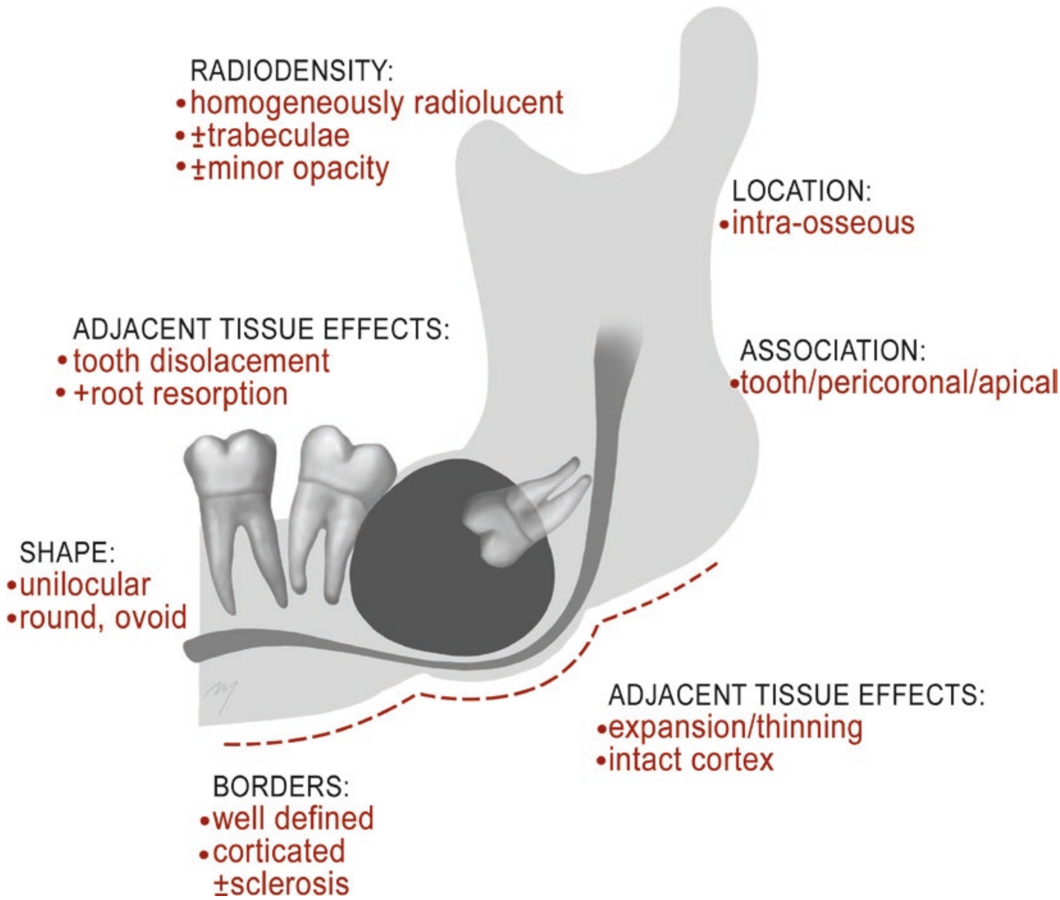

Fig. 15.34 Imaging features suggestive of cyst pathology

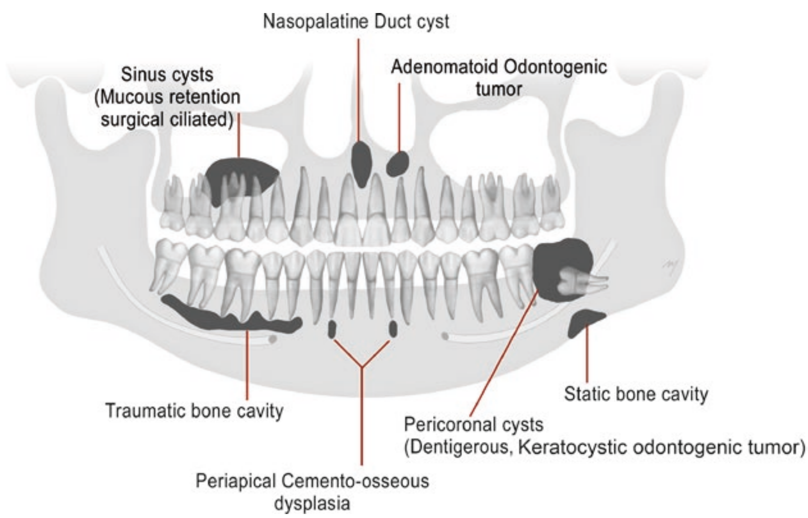

Fig. 15.35 Many solitary well-defined radiolucent lesions, especially cysts, tend to occur in specific areas. Traumatic bone cysts most frequently occur in the mandibular premolar area and extend between the apices of the teeth. Similarly, in the maxilla, incisive canal cysts only present in the incisive canal regions. The submandibular salivary gland developmental defect only presents coincident or below the mandibular canal

Finally formal documentation of all findings and notes of each reviewed CBCT volume provides an invaluable patient record for future use, enhances communication with other clinicians, and serves as a legal record. This will also provide documentation as to the progression of a pathological entity or the progress of certain treatments.

15.3 Key Considerations in Radiologic Presentation of Maxillofacial Pathology

15.3.1 Low-Density Lesions

The most common pathologic presentation for pathology in the jaw is that of a low-density lesion. While it is beyond the scope of this chapter to describe the clinical and distinctive radiographic features of radiolucent entities, they are numerous key points that should be appreciated.

- **The most frequent radiolucency of the jaws is of periapical inflammatory origin.** Smaller periapical lesions are as a result of chronic apical periodontitis whereas larger entities most often appear as a single, well-defined, unilocular, homogenous, low-density lesion arising secondary to necrosis of the dental pulp due to caries (Figs. 15.36 and 15.37) or trauma. Histologically these entities could be a granuloma, radicular cyst or abscess. Rosenberg and co-authors (2010) reported that CBCT findings cannot reliably distinguish a granuloma from a cyst. Tortorici et al. (2008) reported that 85% of dental cysts were radicular.
- **Not all lesions that present with a low-density appearance remain low density.** A number of entities such as focal osseous dysplasia (Figs. 15.38, 15.39 and 15.40) and ossifying fibroma progress radiographically from low-density to mixed density and finally mature to high-density lesions.
- **Two conditions are associated with multiple, bilateral multilocular low-density lesions.** Cherubism (Fig. 15.41) is easily identified presenting with bilateral, almost symmetrical, multilocular radiolucencies (giant cell lesions) affecting the posterior mandibular and commonly maxillary sextants in children, adolescents, or young adults. They generally undergo complete regression to lamella bone (MacDonald 2011). Multiple tumors keratocystic odontogenic tumors (KCOT) appear in approximately 2/3rds of patients with nevoid basal cell carcinoma syndrome (NBCCS)

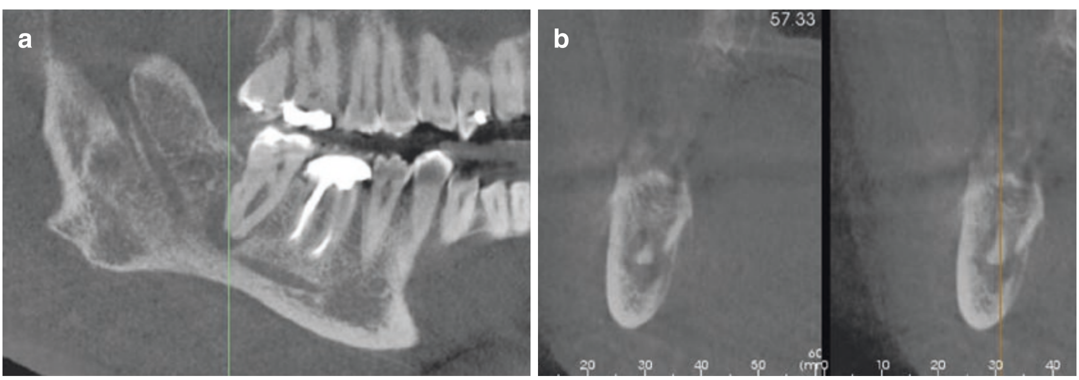

Fig. 15.36 Reformatted panoramic (**a**) and cross-sectional images (**b**) of the right posterior mandible depicting a small, well-defined, low-density lesion in the apical region of the second molar. This area of chronic apical periodontitis is most likely a result of pulpal necrosis. Periapical inflammatory lesions are the most common low-density lesions of the jaws

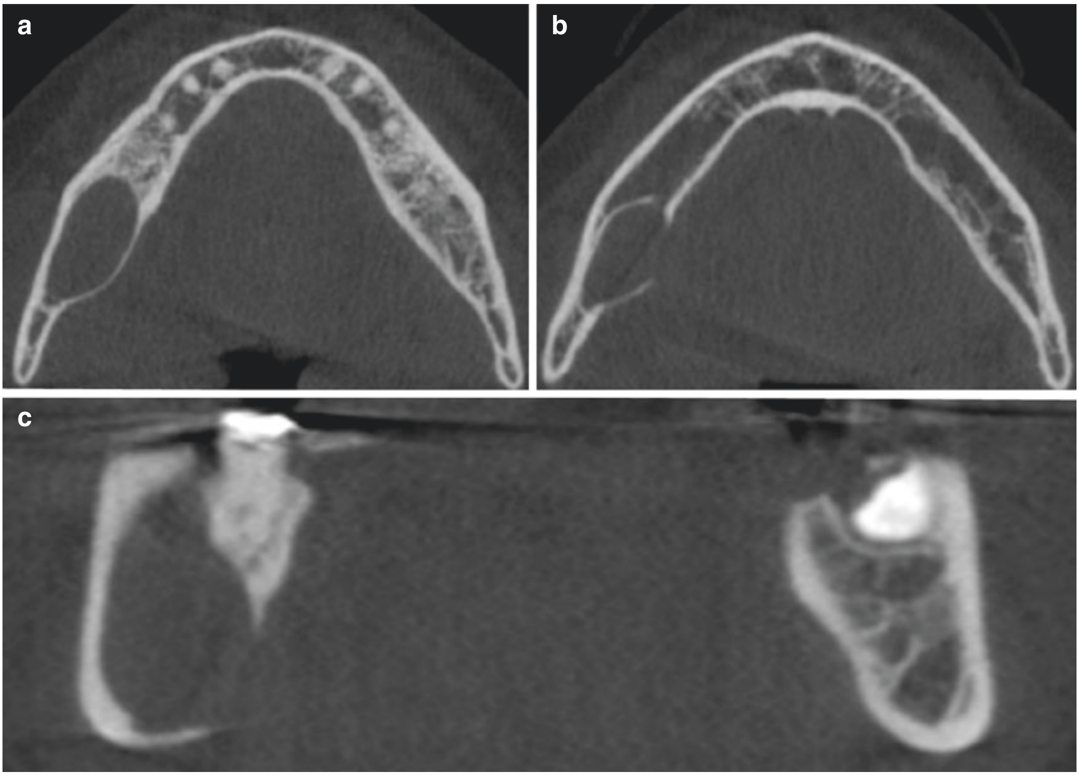

Fig. 15.37 Axial images at the alveolar (**a**) and basal (**b**) bone level and a posterior coronal (**c**) image showing a radicular cyst in the right posterior mandible associated with a carious molar tooth. The entity is unilocular, has expanded and eroded the lingual cortex, showing a fistulas tract in the alveolar crest, buccal to the carious tooth. (Images courtesy of Thomas Li, Elsevier (MacDonald 2016))

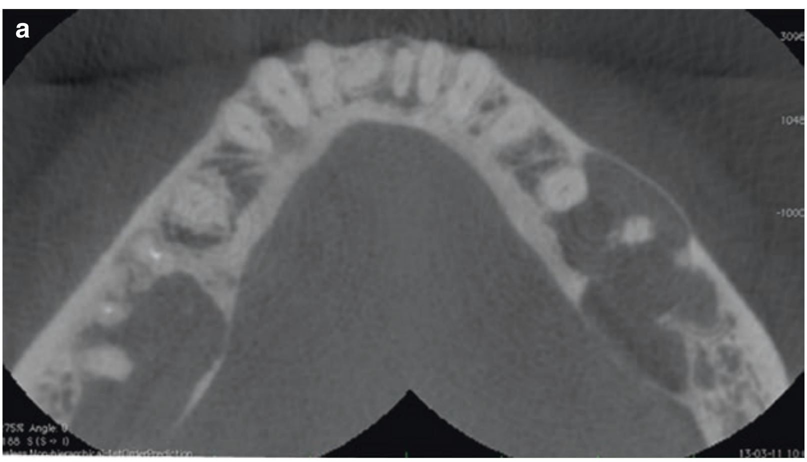

Fig. 15.38 Axial (**a**), posterior coronal (**b**), and anterior trans-axial (**c**) CBCT images of the mandible of florid osseous dysplasia in a middle-aged female of East Asian origin. Multiple radiolucencies are present throughout the mandible, the largest of which are present in the premolar-molar alveolus bilaterally, sparing the basal bone. These larger lesions exhibit a multilocularity and thin and erode the cortex with minimal expansion. The anterior lesions appear to arise as ill-defined discrete radiolucencies with small internal calcific foci associated with individual teeth (Images courtesy of Thomas Li, Elsevier (MacDonald 2015a))

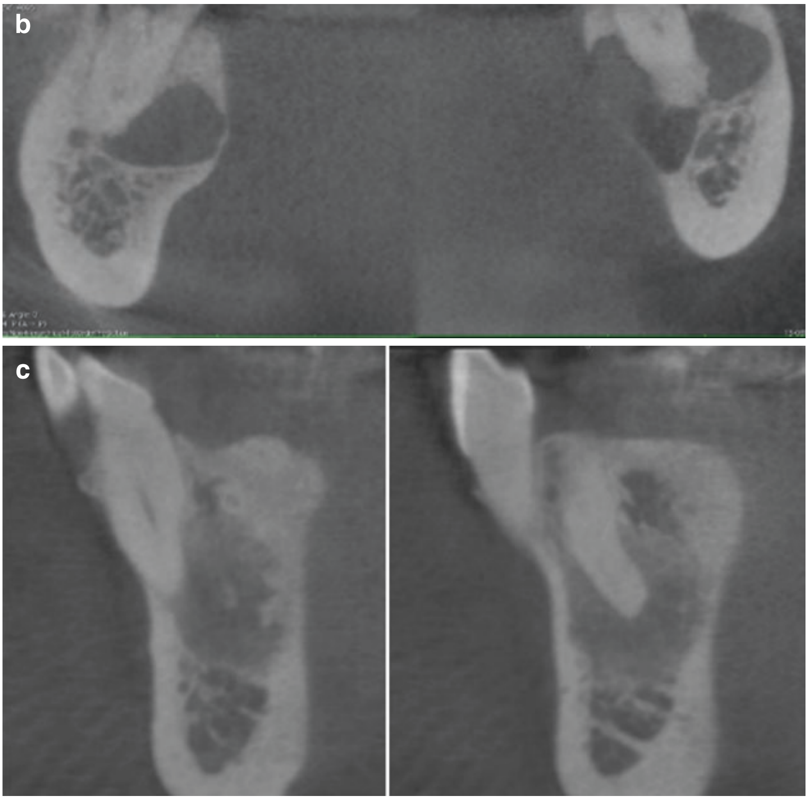

Fig. 15.38 (continued)

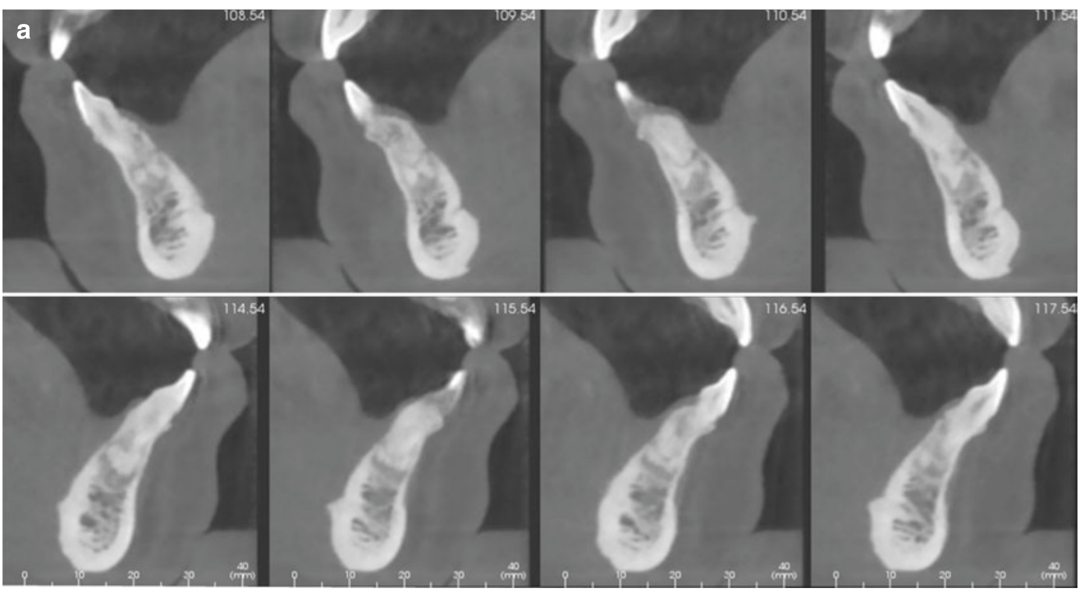

Fig. 15.39 Series of cross-sectional images (**a**) and a reformatted panoramic image (**b**) of the anterior mandible depicting multiple small, well-defined, low-density lesions in the apical region of anterior teeth with intralesional globular high-density areas. This appearance is consistent with periapical cento-osseous dysplasia (PCOD) of a mature stage. The entities start as low-density entities and gradually obtain high-density centrally located masses as they mature with time

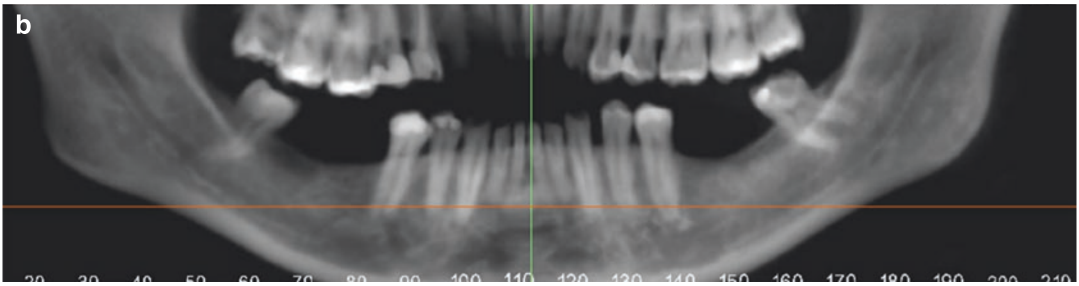

Fig. 15.39 (continued)

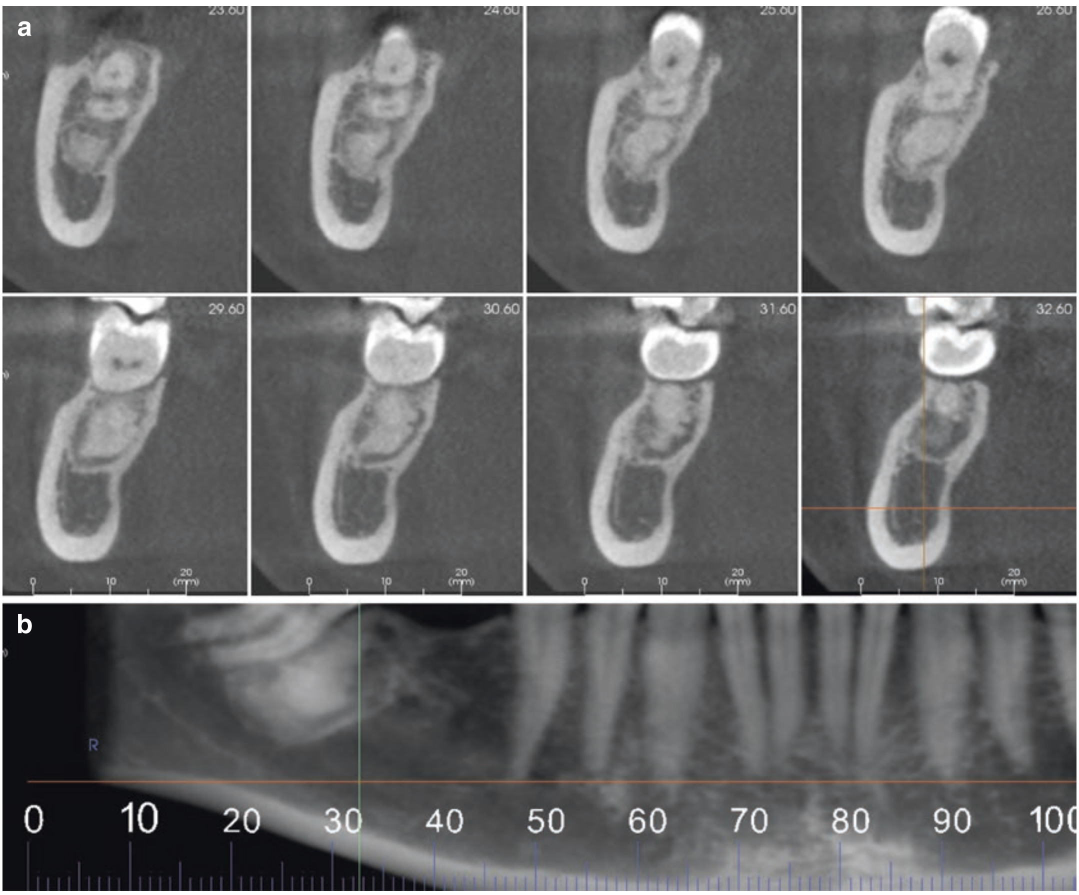

Fig. 15.40 Series of cross-sectional images (**a**) and a reformatted panoramic image (**b**) of the right posterior mandible depicting a large, well-defined, low-density entity surrounded by a corticated border associated with the mesial aspect the root of the visible molar. This contains a large high-density globular mass (mature stage). This imaging appearance is consistent with focal osseous dysplasia, a similar entity to POD entity, only in that it is solitary and may appear in any region of the maxilla and mandible and not necessarily limited to the apical region. This entity also undergoes radiographic transformation through different maturity stages

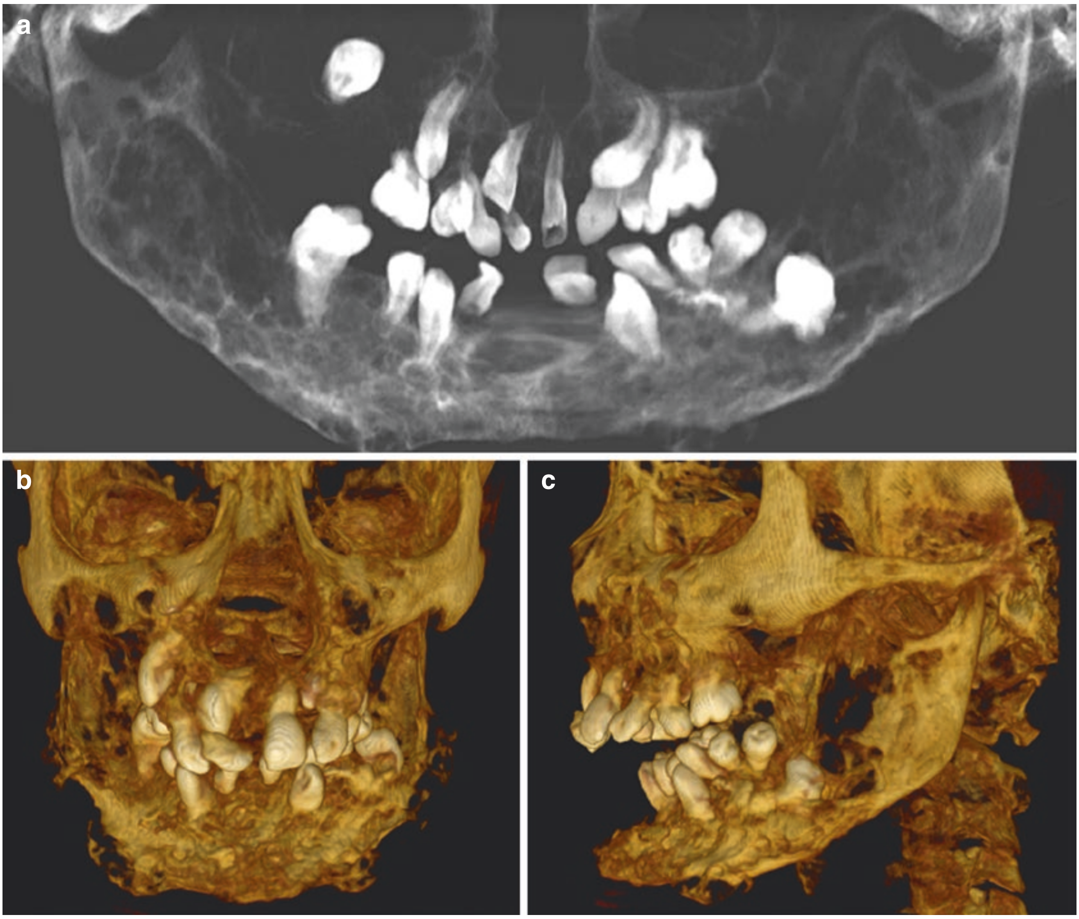

Fig. 15.41 Reformatted panoramic (**a**), facial 3D surface projection (**b**) and left lateral 3D surface projection (**c**) from CBCT data of a teenager with cherubism. The multilocular lesions affect the entire mandible and maxilla. The buccolingual expansion is symmetrical

(Fig. 15.42) (MacDonald 2011). These syndromic KCOTs present in the second and third decades, on average a full decade earlier than the solitary (non-syndromic) KCOTs. New lesions continue to form and since they are neoplasms, continue to grow.

- **Not all periapical unilocular low-density lesions should be considered of inflammatory origin.** In the anterior maxilla periapical inflammatory lesions (Fig. 15.43) must be distinguished from nasopalatine duct cysts (NPDC) (Fig. 15.44), particularly if they are associated with the central incisors. Although NPDC account for only 1% of all cysts of the jaws, if left untreated they can continue to grow and expand into the nasal cavity, distorting adjacent anatomy (Suter et al. 2011). Although the adjacent teeth are usually vital, these so-called fissural cysts may become secondarily infected (Faitaroni et al. 2011).
- Basal cell carcinomas present significantly more frequent in NBCCS cases in North Europeans in comparison to East Asians, whereas KCOTs present significantly more frequently in East Asians. PTCH was expressed significantly more frequently in syndromic KCOTs than in non-syndromic KCOTs (MacDonald 2015b). The recurrence rate of syndromic KCOTs was significantly greater than of the solitary KCOTs. The reader should note however that non-syndromic cases with multiple KCOTs could be more common in East Asians (MacDonald et al. 2015).
- **The most common odontogenic cyst is the radicular cyst.** This a unilocular, round or

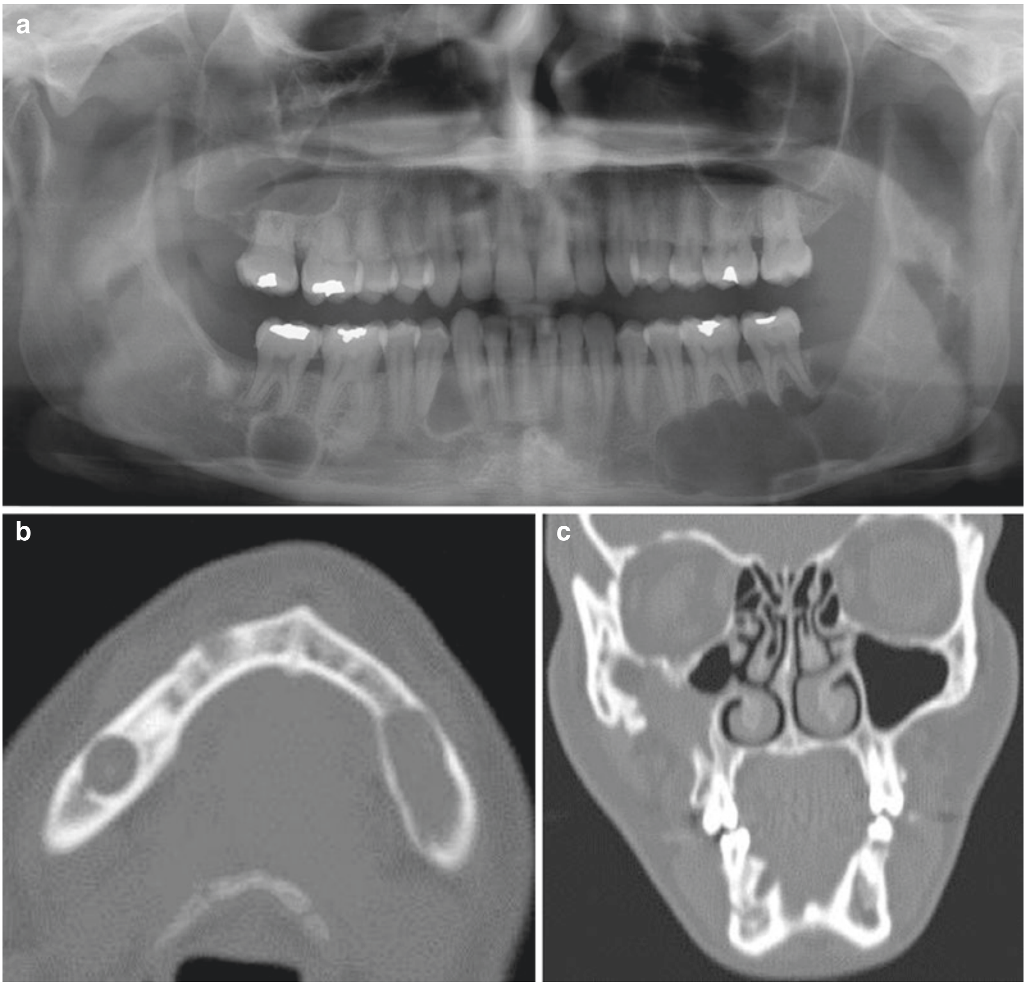

Fig. 15.42 Reformatted panoramic (**a**), axial (**b**), and coronal (**c**) CBCT images of a patient with Nevoid Basal Cell Carcinoma Syndrome (NBCCS). Note the multiple radiolucencies (KCOT) in the mandible bilaterally and one in the posterior right maxilla. Two of the mandibular lesions are unilocular with corticated margins, whereas one on the right is multilocular and demonstrates substantial thinning but minimal expansion of the lingual cortex. The maxillary lesion obliterates the lumen of the right maxillary sinus. (Images courtesy of Thomas Li, Elsevier (MacDonald et al. 2016)

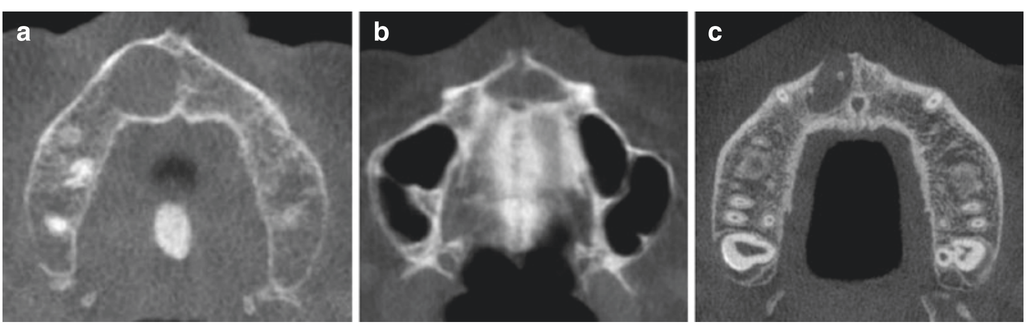

Fig. 15.43 Axial CBCT images from three individuals—(**a**, **b**, and **c**)—showing radicular cysts occurring in the anterior sextant of the maxilla. Images (**a**) and (**b**) show erosion and expansion of the buccal and palatal cortices and intimate but separate relationship to the nasopalatine canal. (Image (**a**) courtesy of Alexandre Khaireallah; images (**b**) and (**c**) courtesy of Thomas Li, Elsevier (MacDonald 2016))

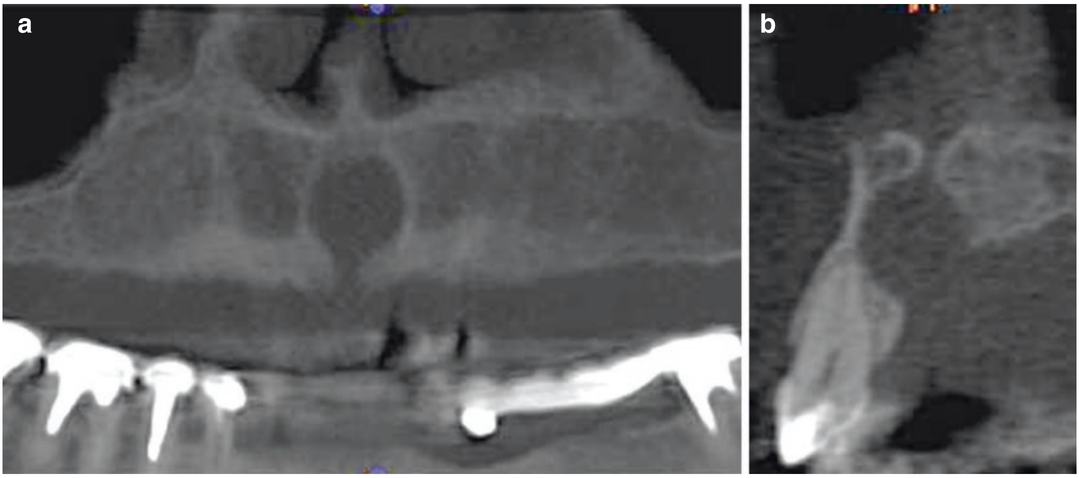

Fig. 15.44 Reformatted panoramic (**a**) and sagittal (**b**) image of maxillary edentulous patient with nasopalatine duct cyst. (Figure courtesy of Alexandre Khaireallah, Elsevier (MacDonald 2016))

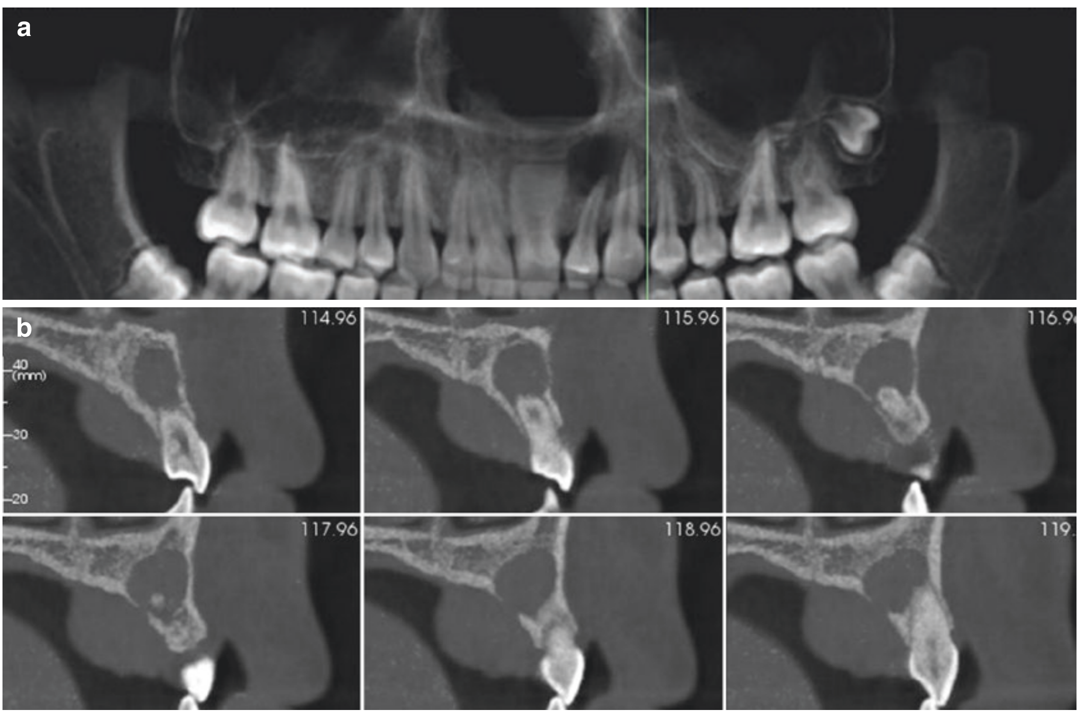

Fig. 15.45 Reformatted panoramic (**a**) and serial cross-sectional images (**b**) of the anterior maxilla depicting a round, well-defined, low-density entity in the apical region of the left lateral incisor with thinning of the palatal cortical plate. Together with the clinical history that this tooth was non-vital, the imaging appearance is most consistent with a radicular cyst

ovoid in shape, well-defined, uniform, low-density entity which is identified in the apical region of necrotic tooth and it is considered inflammatory in origin (Fig. 15.45). Most often it is circumscribed by a thin corticated border which may disappear if the osseous boundaries in which it is contained are compromised (Fig. 15.46) or may become thicker with chronic inflammation. It is the second most frequently seen periapical radiolucency after the periapical granuloma from which it is impossible to distinguish radiologically. It is generally accepted that larger lesions (greater than 16 mm in diameter) with the radiologic features described above are most often radicular cysts and smaller, with the same appearance, are most frequently periapical granulomas.

If the tooth involved in the origin of a radicular cyst is extracted and the radicular cyst is not removed, this cystic lesion may remain and continue to grow irrespective of the absence of the tooth that initiated it. While histologically identical to a radicular cyst, it is now referred to as a residual cyst (Fig. 15.47).

The glandular odontogenic cyst (GOC) is another lesion of growing importance, only recently described (Fig. 15.48). This is a rare, slow-growing entity which presents predominantly in the fifth decade most frequently in those of European or Middle-Eastern origin (Macdonald-Jankowski 2010). It can be either unilocular or multilocular in appearance and

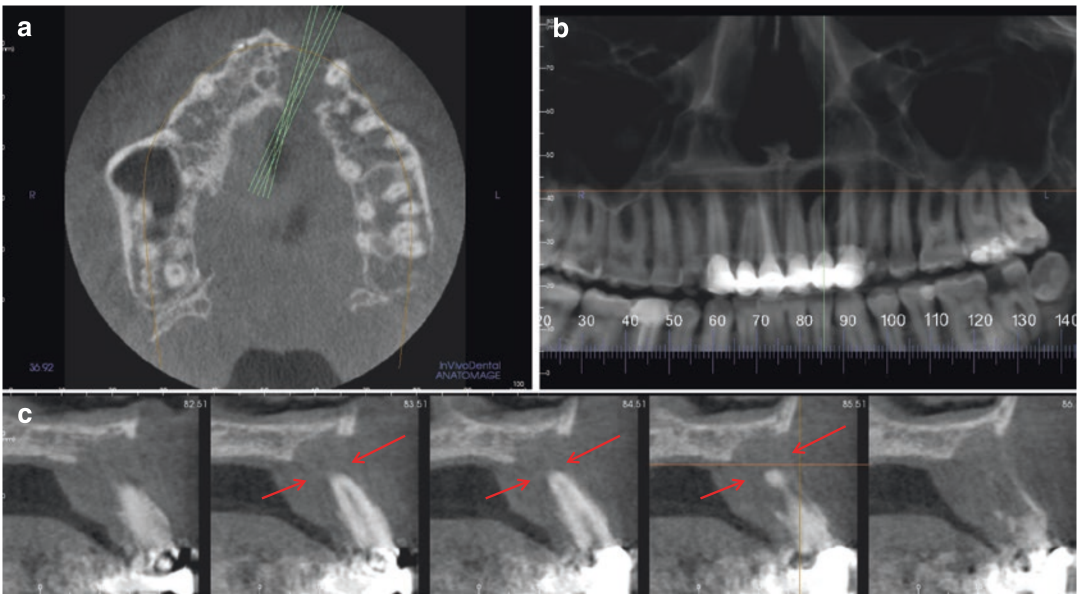

Fig. 15.46 Axial orthogonal image (**a**), reformatted panoramic image (**b**), and a series of cross-sectional images (**c**) of the anterior maxilla depicting a round, moderately defined, low-density entity in the apical region of the left lateral incisor with erosion of both buccal and palatal cortical plates. Despite the fact that this tooth appears to be "floating" due to lack of osseous support, the imaging presentation is most consistent with a radicular cyst

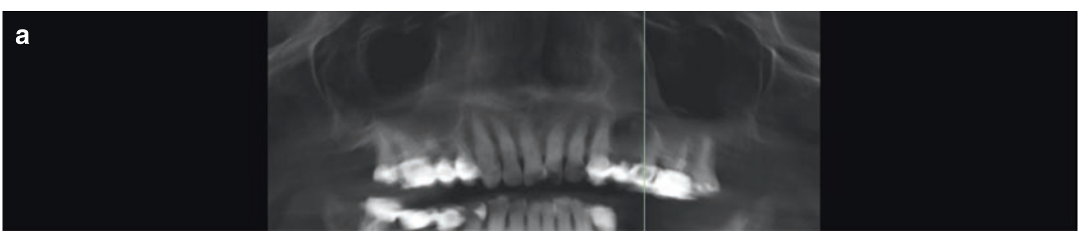

Fig. 15.47 Reformatted panoramic (**a**) and a series of cross-sectional images (**b**) of the left posterior maxilla depicting a round, well-defined, low-density entity in the premolar edentulous region. The lesion has a thin corticated border and expanded both buccal and palatal cortices. The imaging appearance is suggestive of a residual cyst

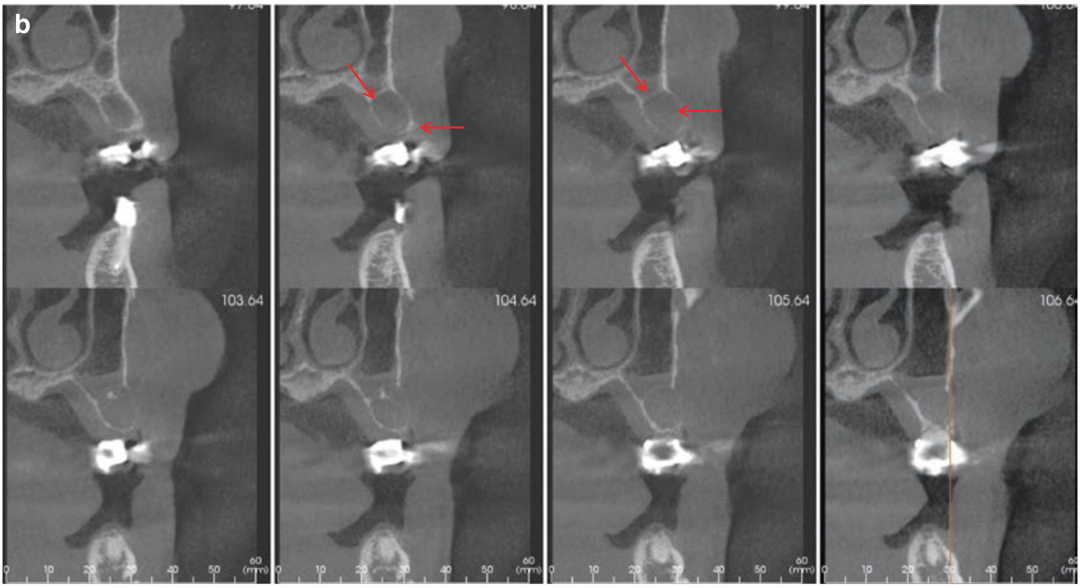

Fig. 15.47 (continued)

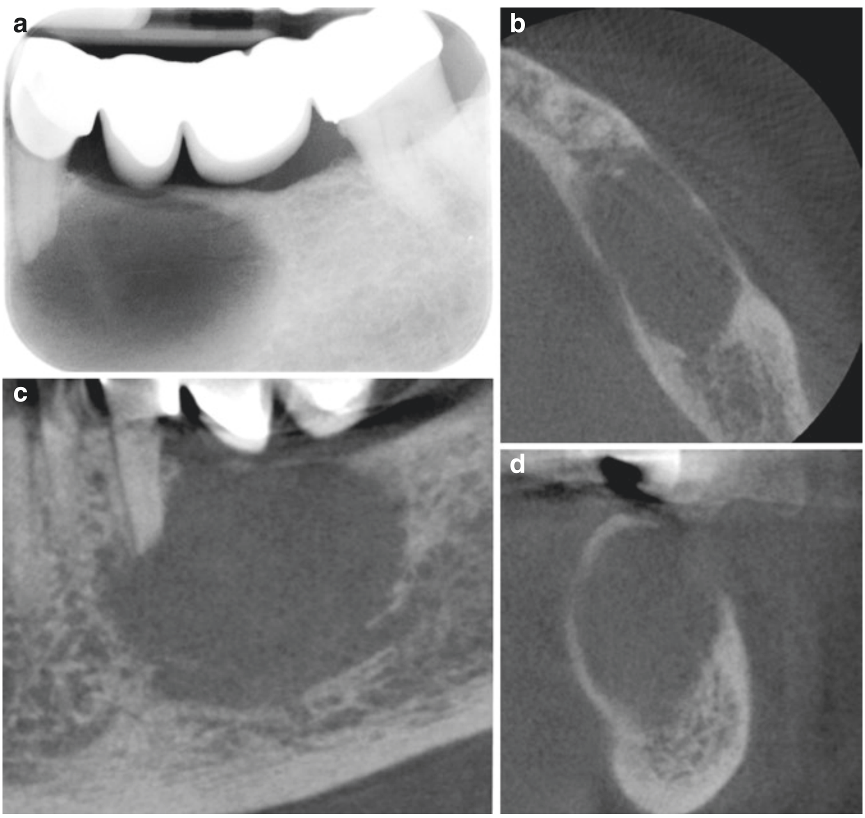

Fig. 15.48 Intraoral periapical (**a**), cropped reformatted panoramic (**b**), axial (**c**), and trans-axial (**d**) CBCT images of a glandular odontogenic cyst arising in the premolar-first molar area of the mandible. The lesion shows as a relatively ill-defined unilocular radiolucency, resorbing the apical half of the second premolar. There is some buccolingual expansion, extension from the alveolus into the basal process and erosion of the superior cortex posteriorly. The mandibular canal is displaced inferiorly (Images courtesy of Elsevier (MacDonald 2016))

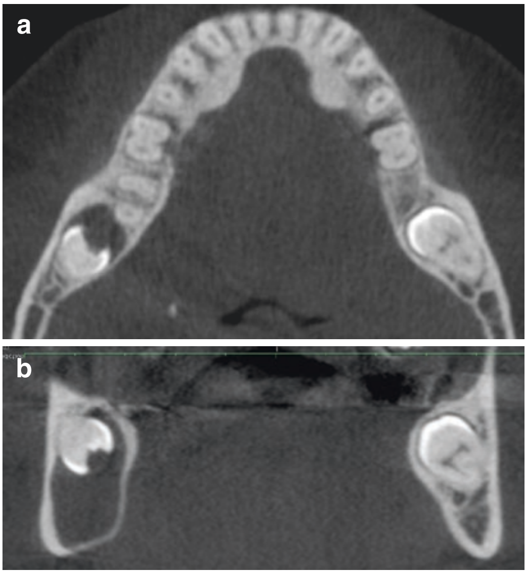

Fig. 15.49 Axial (**a**) and coronal (**b**) image of CBCT data showing a dentigerous cyst arising from the CEJ of an unerupted right mandibular molar. Note the bilateral mandibular tori arising adjacent to the pre molars (Images courtesy of Thomas Li)

most are well defined with almost 1/3rd presenting with root resorption. These features may resemble lesions like radicular cysts or unicystic ameloblastomas from which the differentiation of GOC is difficult. Approximately 18% recur (MacDonald 2011).

- **The most common pericoronal radiolucency is the dentigerous cyst (DC).** Dentigerous cysts are unilocular radiolucencies which are associated with the cemento-enamel junctions (CEJ) of unerupted and impacted teeth. They are the second most common cyst, after the radicular cyst. They may occasionally be symptomatic if secondarily infected or associated with fracture. They most often present in the second and third decades with a slight predilection for males. Approximately 50% occur in association with the mandibular third molars (Fig. 15.49). Other sites, in decreasing order of frequency, include the maxillary canines (Fig. 15.50), mandibular premolars, and maxillary third molars. They have a low recurrence rate. They present radiographically with all the hallmark features of a cyst including a well-defined, corticated unilocular homogeneous expansile radiolucency with displacement of involved teeth and root resorption of adjacent teeth. If a pericoronal space (normal value up to 3 mm wide) is greater than 3–5 mm, then a DC should be considered. In addition if the attachment of a pericoronal lesion is less than 1 mm apical to the cemento-enamel junction (CEJ), a DC is highly probable. The DC presents in one of the three radiographic patterns: Classical—symmetrical enveloping of the unerupted tooth; Lateral—arising from the side of a crown; and Circumferential—extension of the lesion below the CEJ. Possible sequelae include conversion of the cystic ling to KCOT, unicystic ameloblastoma, and rarely malignant neoplasm (squamous cell carcinoma or mucoepidermoid carcinoma). Dentigerous cysts are often associated with odontomas (MacDonald 2011).
- **The most common neoplasms associated with the alveolus and teeth are odontogenic in origin**. The most frequent neoplasm is the

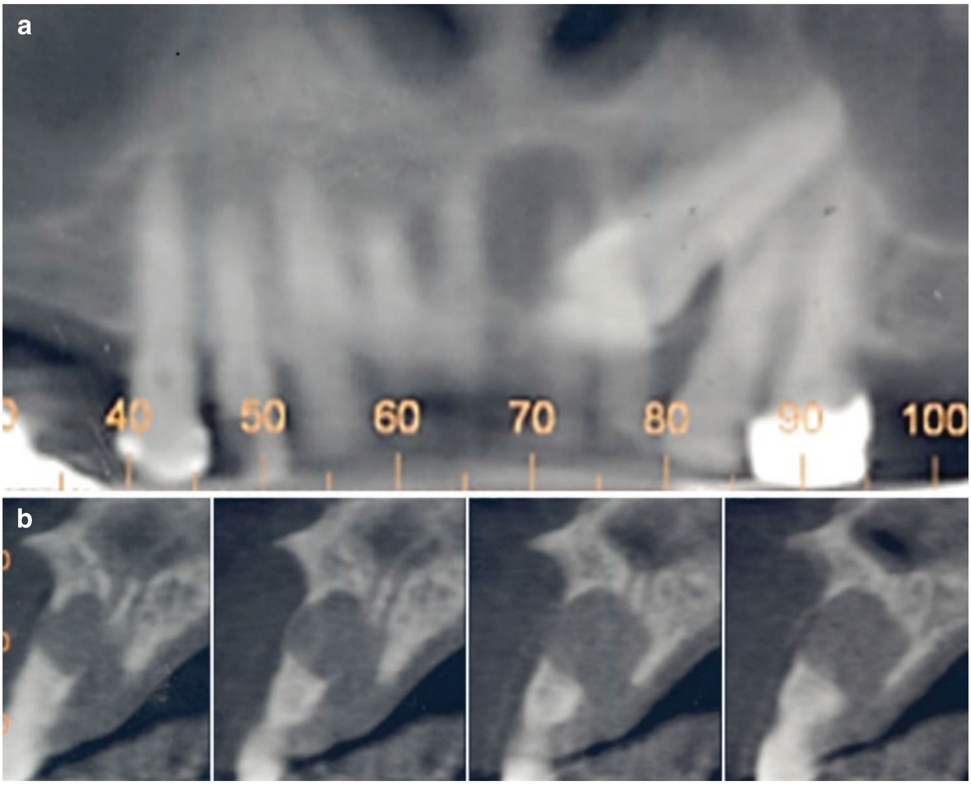

Fig. 15.50 Reformatted panoramic (**a**) and serial trans-axial images (**b**) of CBCT data showing a dentigerous cyst arising from a left unerupted maxillary canine. Note buccolingual expansion, and perforation of the labial (buccal) and palatal cortical plates (Figure courtesy of Wiley-Blackwell), (MacDonald 2011)

ameloblastoma and keratocystic odontogenic tumor (KCOT).

– ***Ameloblastoma.*** The vast majority of ameloblastomas present within the jaw bone and are sub-classified as solid (multilocular) (Fig. 15.51), unicystic (Fig. 15.52), and desmoplastic (Fig. 15.53). Root resorption is a prominent feature, especially "knife-edge" pattern. Root resorption is also associated with other jaw lesions, including KCOT, but with less severity (Fig. 15.54) and frequency (MacDonald 2011). Another feature of AMB is substantial buccolingual expansion (Figs. 15.2 to 15.54), which is more "ball-like" than that of KCOT (Fig. 15.55).
– ***Keratocystic Odontogenic tumor.*** The term keratocystic odontogenic tumor (KCOT) was introduced in 2005 by the 3rd WHO classification to replace the original term keratocystic odontgenic (OKC) to reflect its

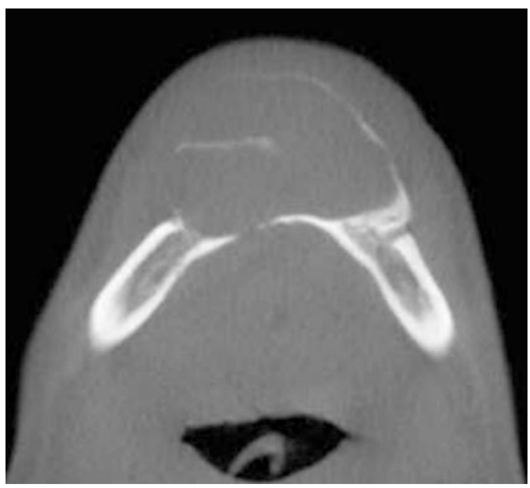

Fig. 15.51 Axial section of CBCT data showing an ameloblastoma (histopathologically solid type) in the anterior mandible. A single internal septa transects the lumen horizontally making this a multilocular lesion. The lesion demonstrates substantial displacement and erosion of the buccal cortex and some displacement and erosion of the lingual cortex. (Image courtesy of Jason Chen and Elsevier MacDonald D (2016))

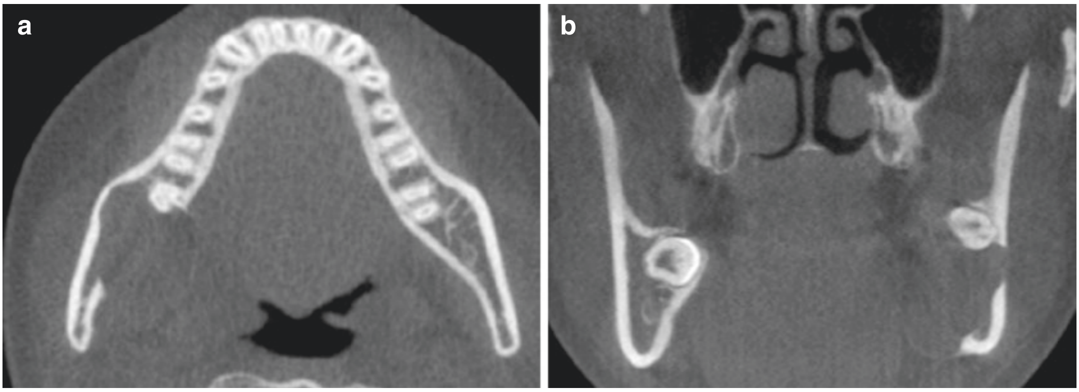

Fig. 15.52 Axial (**a**) and coronal (**b**) images of a unicystic ameloblastoma associated with an unerupted and impacted right mandibular third molar in a Chinese patient from Hong Kong. The lesion has significantly expanded and eroded the lingual cortex of the mandible to create an almost circular outline. The expanded lingual cortex has been displaced downward and past the lower border of the mandible, a feature previously reported on conventional images of this neoplasm (MacDonald 2011). Note that the buccal cortex is eroded at a single focus and the root of the second molar exhibits significant resorption. (Images courtesy of Thomas Li, Elsevier (MacDonald 2016))

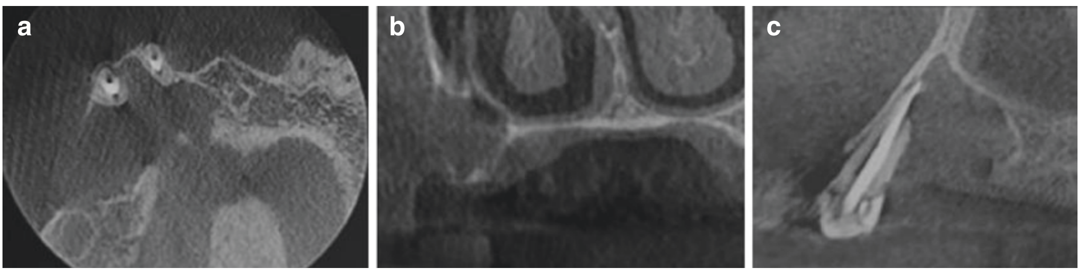

Fig. 15.53 Axial (**a**), cropped coronal (**b**), and trans-axial (**c**) CBCT images of a desmoplastic ameloblastoma in the right anterior maxilla. This neoplasm presents with an irregular, substantially corticated margin. Some broad-based septae are present and therefore the lesion is multilocular. It spares the anterior recess of the right maxillary sinus. Benign aggressive features include erosion of the palatal cortex of the alveolus, resorption of the distal aspect of the apical half of the root of the canine with irregular surface erosion on the palatal aspect of the cervical half of the root. (Image courtesy of Kenneth Chow, Elsevier (MacDonald 2016))

neoplastic attributes, which included a marked tendency to recur. Interestingly the author of this change was Philipsen, who originally coined the original term of OKC. The 4th edition of 2017 advocated that KCOT be changed back to OKC and that it no longer be considered to be a neoplasm, but rather a developmental cyst (Speight et al. 2017). Unfortunately this reasoning was largely based of out-dated publications. One of these initially indicated that the KCOT responded to marsupialisation, which was used by the WHO authors as evidence of the KCOT being a cyst rather than a neoplasm. Unfortunately, subsequent follow-up of these marsupialised cases revealed recurrences, which led not only to a partial retraction of the initial publications but the lead author (Pogrel) of that early work later showed by systematic review that the current preferred treatment for KCOT, namely enucleation with adjuvant treatment, was more effective that marsupialisation (Al-Moraissi et al. 2016). Therefore, the term KCOT will be retained.

- **Non-odontogenic conditions should always be considered in the differential diagnosis of low-density conditions.** Generally odontogenic

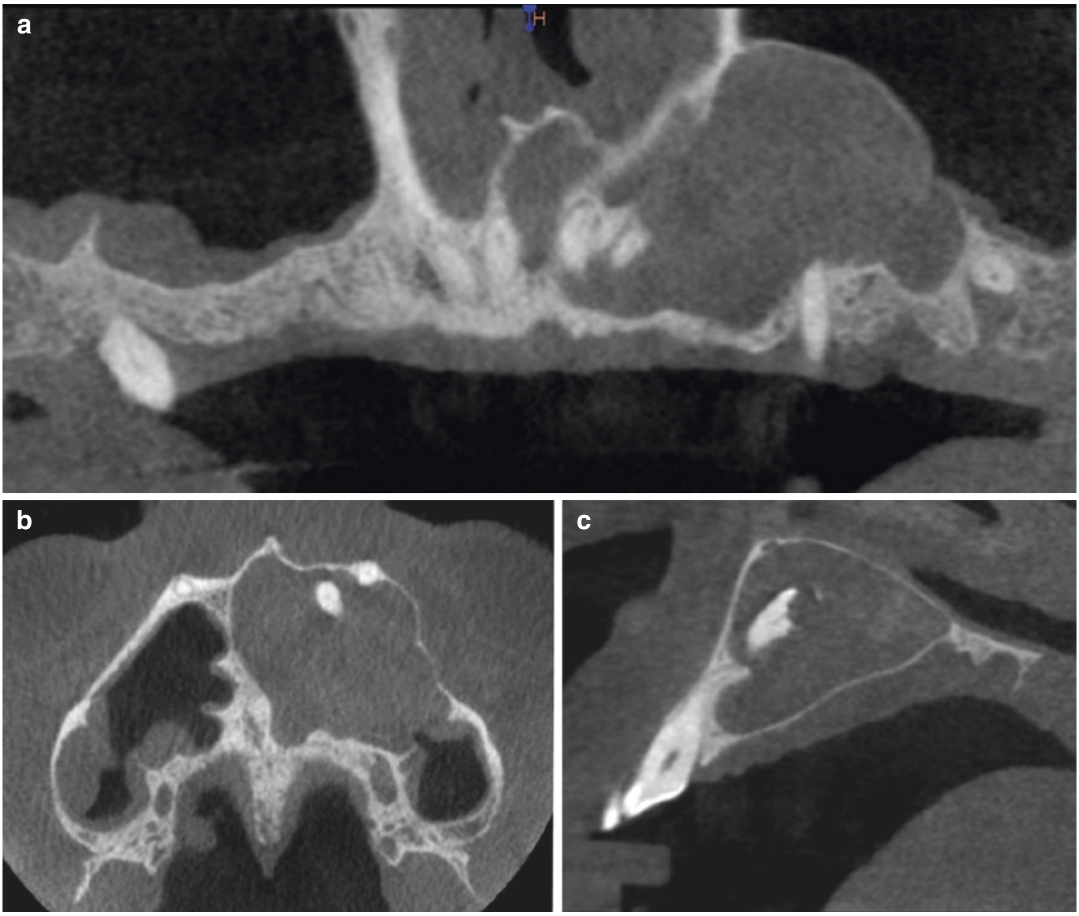

Fig. 15.54 Thin section reformatted panoramic (**a**), axial (**b**), and serial trans-axial (**c**) images of a keratocystic odontgenic tumor (KCOT) arising in the anterior maxilla. The lesion extends from the midline to the junction between the second premolar and first molar area with apparent occlusion of the superior half of the nasopalatine canal. The lesion has displaced and eroded the anterior wall and adjacent floor into the lumen of the left maxillary sinus. The buccolingual dimension is about half of that of its mesiodistal extent. Furthermore, although essentially unilocular, the expansion is variable. An unerupted tooth is observed within the neoplasm. (Images courtesy of Jason Chen, Elsevier (MacDonald 2016))

pathological entities may appear in the broader tooth-bearing zone of the maxilla and mandible (alveolar bone) whereas non-odontogenic lesions tend to present in both tooth-bearing and non-tooth-bearing areas of the maxillofacial region. These entities usually originate from the osseous tissues, however other origins should be considered. The diagnostic path for a differential diagnosis is somewhat clearer if these lesions appear in non-tooth-bearing areas (base of the alveolar bone, bony cortices, inside osseous canals, etc.). Developmental anomalies or anatomical variants may add some complexity to the diagnostic process.

– **Lingual bone defect (Stafne's bone cavity, Stafne's defect, submandibular gland depression).** Appearing as a distinct unilocular radiolucency on panoramic imaging, the lingual bone defect (LBD) shows as a specific well-defined lingual cortical discontinuity (Fig. 15.56). On the panoramic images most LBD present in the basal process of the posterior mandible, in relation to the submandibular fossa, below

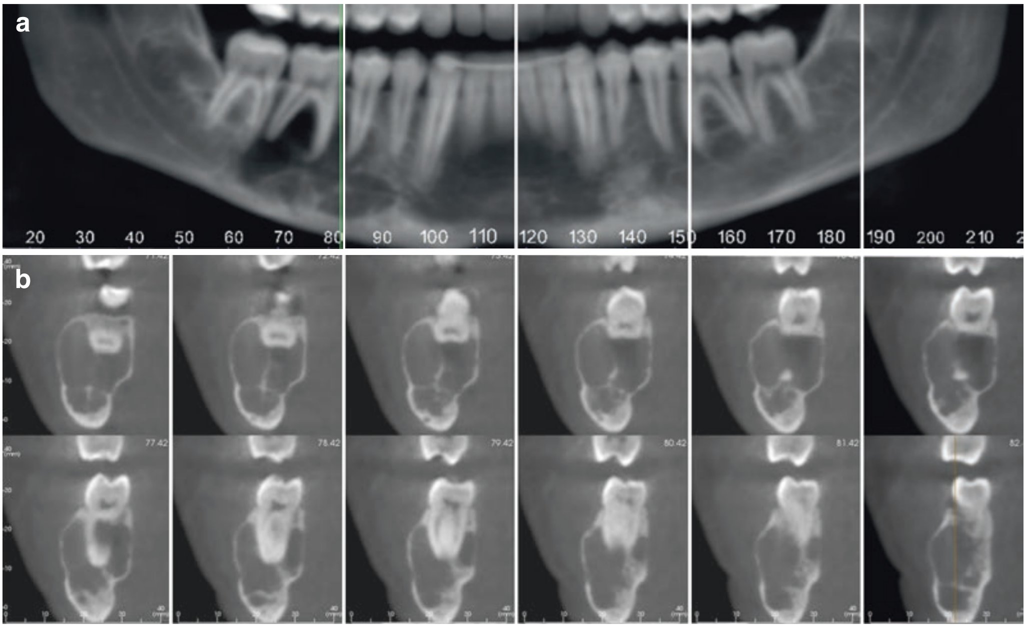

Fig. 15.55 Reformatted panoramic (**a**) and series of cross-sectional images (**b**) of the right posterior mandible depicting a multilocular, well-defined, low-density entity in the apical region of the premolar and molar teeth. The lesion has a thin corticated border and although expanded both buccal and palatal cortices. The imaging appearance is suggestive of KCOT in the region of the first molar

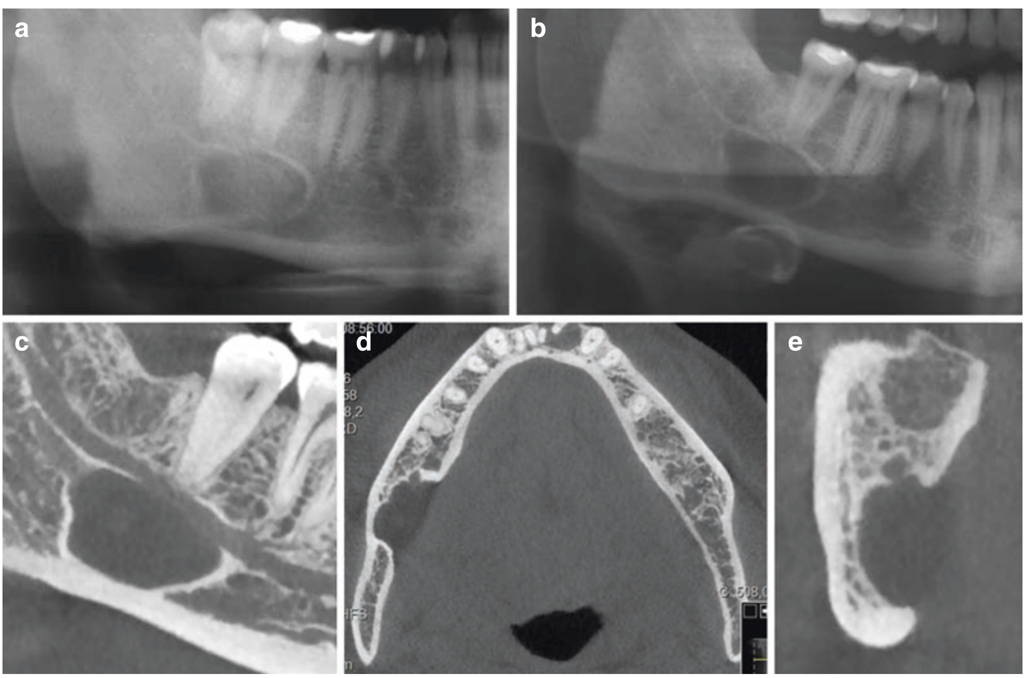

Fig. 15.56 Comparative panoramic images from 2010 (**a**) and 2013 (**b**) and 2013 parasagittal (**c**) axial (**d**) and trans-axial (**e**) CBCT images of a lingual bone defect LBD) appearing as a well-defined unilocular radiolucency in the right mandible. Minor extension of the entity is noted in the 2013 panoramic image associated with the removal of the third molar. CBCT images show upward displacement of the mandibular canal with a loss of its inferior cortex seen as a dehiscence of the canal in trans-axial sections. (Images courtesy of Lief Kullman, Elsevier (MacDonald 2016))

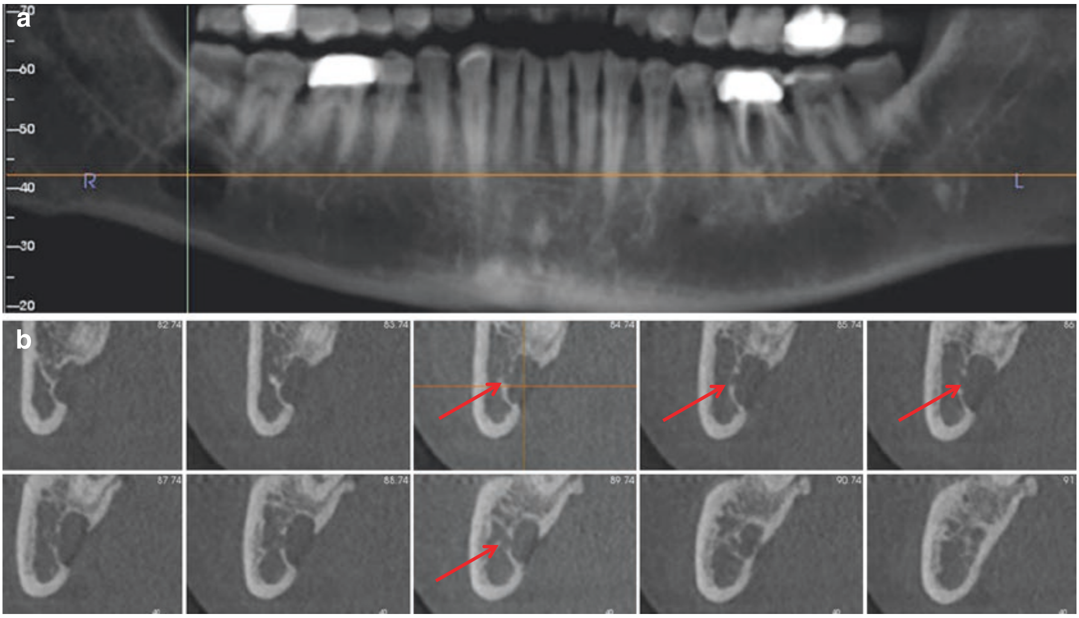

Fig. 15.57 Reformatted panoramic (**a**) and a series of cross-sectional images (**b**) of the right posterior mandible showing a deep lingual concavity which was diagnosed as a lingual bone defect (LBD). Diagnostic confusion may exist due to the fact that the entity is at the level of and appears to involve the left mandibular canal (*red arrows*)

or substantially below the mandibular canal. The location and corticated border of this entity on reformatted panoramic images raise the level of suspicion while the shape (semispherical concavity) in MPR images or cross-sectional images and location to the mandibular canal should confirm the pathognomonic presentation. On occasion, the LBD presents at the level of the mandibular canal or higher (Fig. 15.57). Although large LBDs may reduce the structural integrity of the mandibular body, pathologic fracture associated with this entity has not been reported. LBDs should be differentiated from aggressive, soft tissue pathological entities originating from the floor of the mouth and may be invading the lingual mandibular cortex (Fig. 15.58). LBD may present anteriorly adjacent the sublingual gland, where differential diagnosis includes simple bone cyst and periapical radiolucencies.

– ***Simple bone cyst (traumatic, idiopathic, or hemorrhagic bone cyst)***. (Fig. 15.59 and 15.60). Despite its name, the simple bone cyst (SBC) is not a true cystic lesion as it lacks an epithelial lining. It is a non-odontogenic condition of unknown etiology also occurring in the axial skeleton. In the maxillofacial region, the SBC occurs frequently in children, teenagers, and young adults with a possible relationship to previous trauma and orthodontic treatment (Velez et al. 2010). Mathew and co-authors (2012) have described the etiology of SBC in detail. The SBC is most frequently seen in the mandible (molar and premolar region) and as an incidental finding on routine panoramic radiographs. The SBC presents as a well-defined low-density cyst-like entity, round or ovoid in shape; it may be associated with the periapical area and extend superiorly between the roots of the teeth to involve the tooth-bearing areas producing a scalloped outline. The teeth involved are vital and show an intact lamina dura. In the jaws it may achieve considerable mesiodistal extension, but with little buccolingual expansion, although large lesions have been reported (Mathew et al. 2012). SBC must be

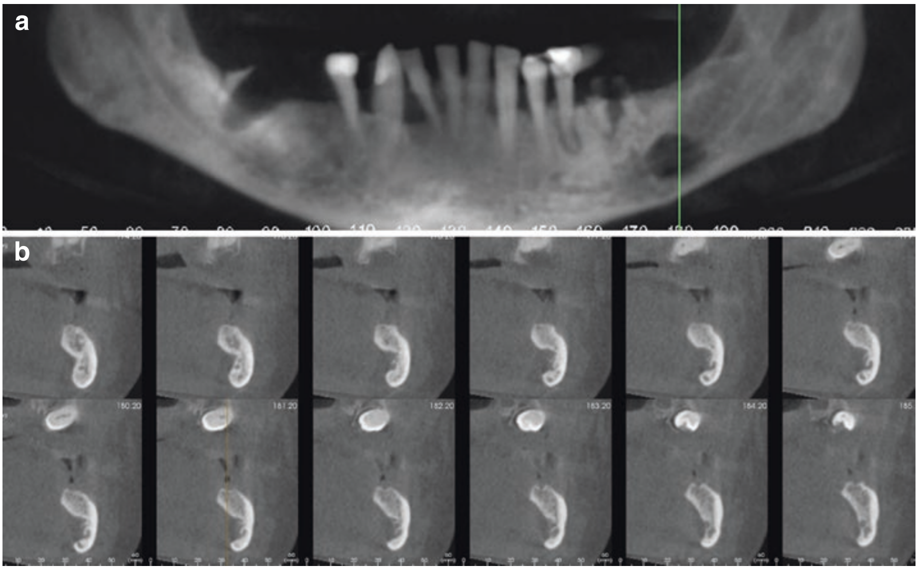

Fig. 15.58 Reformatted panoramic (**a**) and series of cross-sectional images (**b**) of the left posterior mandible depicting a lingual concavity occupying the lower half of the mandible in the molar region and appearing to involve the mandibular canal. The irregular internal border of this entity increases the level of suspicion towards an invasive soft tissue mass from the floor of the mouth. Clinical correlation and comparison to previous radiographic examinations confirmed this to be a lingual bone defect

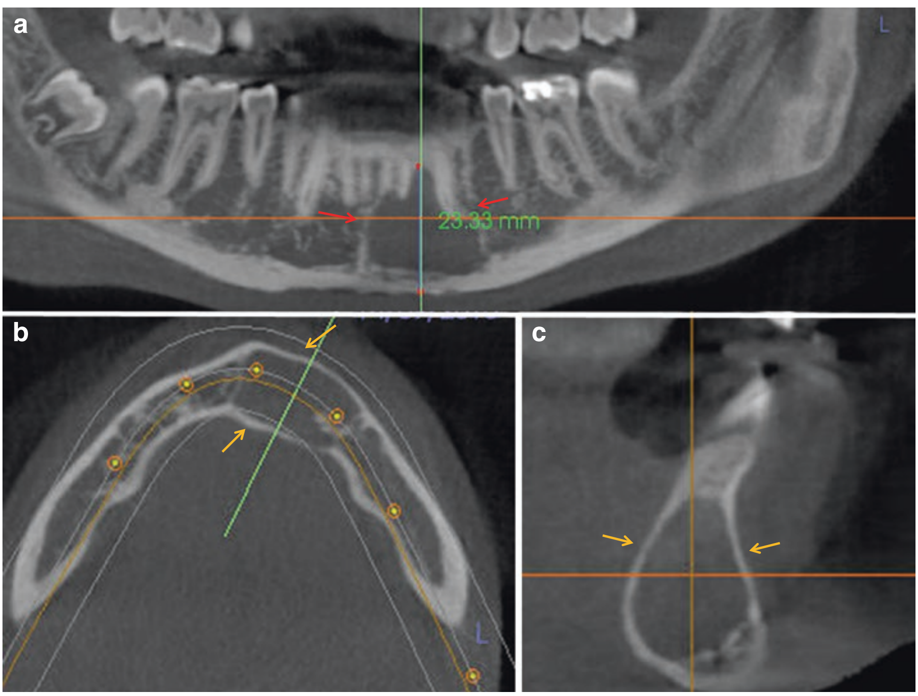

Fig. 15.59 Reformatted panoramic (**a**) axial (**b**) and cross-sectional image (**c**) in the region of the left anterior mandible showing a fairly well-defined, low-density, cystic entity which has caused uniform thinning and expansion of the lingual and labial cortex (*orange arrows*). Also note that the lesion is scalloping between the roots of involved incisor and canine teeth. The above features are suggestive of a SBC

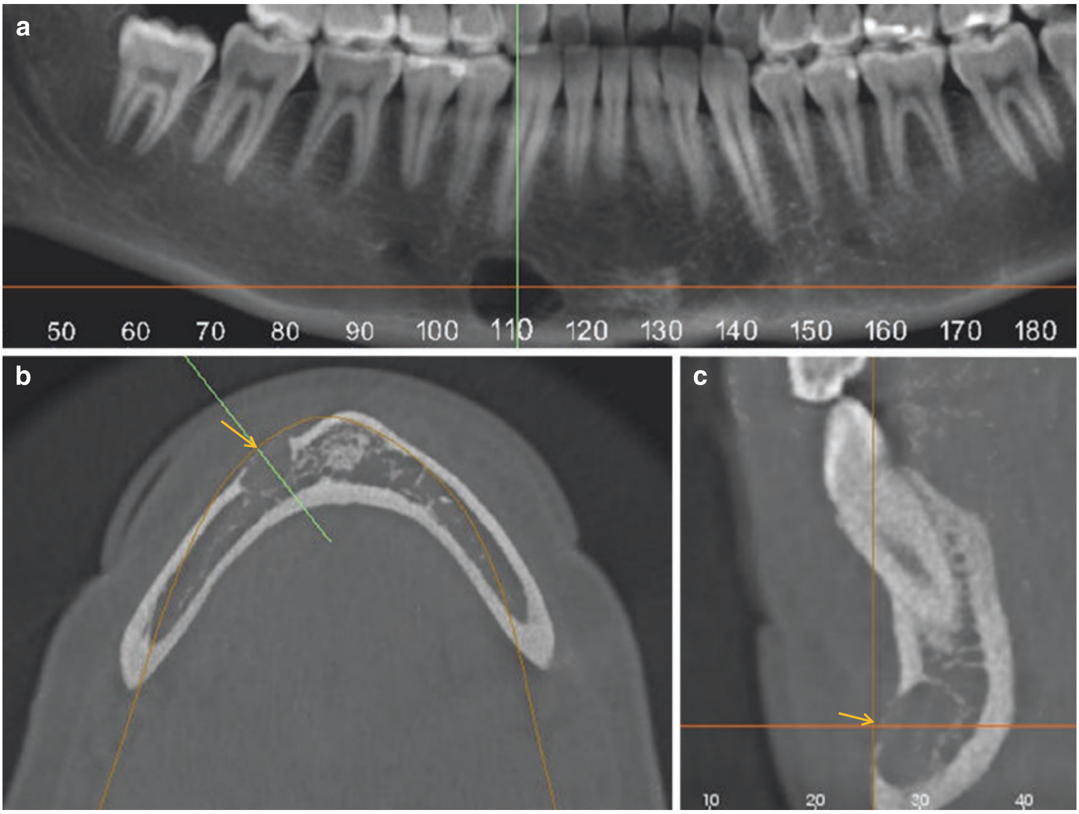

Fig. 15.60 Reformatted panoramic (**a**), axial (**b**), and single cross-sectional image (**c**) of the mandibular anterior region showing fairly well-defined, low-density, cystic entity inferior to the right canine which has resulted in thinning and expansion of the labial cortex (*orange arrows*). The lesion is clearly in a non-tooth-bearing area and its appearance consistent with a diagnosis of a SBC

distinguished from other lesions, such as the KCOTs, that require treatment. Commonly definitive diagnosis is only established at surgery when a cavity devoid of an epithelium is found. Recurrence rate is reported to be low in most, but not all reports (Suei et al. 2010) with multiple recurrences especially in middle-aged females (MacDonald-Jankowski 1995). Radiographic features associated with higher recurrence include loss of lamina dura, root resorption, nodular bone expansion, multilocularity and the concomitant presence of osseous dysplasia (Suei et al. 2010). Chadwick and co-authors (2011) report that while solitary SBCs occur equally in either gender in young individuals, those associated with osseous dysplasia occur in older almost exclusively female individuals. The reports of MacDonald-Jankowski would suggest that many of these patients may be of East Asian origin (MacDonald-Jankowski 1995).

– ***Brown tumor of hyperparathyroidism***. This is a rare cyst-like entity of the bone and represents a giant cell tumor as a result of abnormal calcium turnover in patients with hyperparathyroidism (primary or secondary). Although brown tumors may show in different bones (pelvis, femur, ribs, etc.) they are most common in the jaws; their radiologic appearance is that of a unilocular or multilocular low-density lesion, moderately or poorly defined which may present in any region of the jaws, both tooth- and non-tooth-bearing (Fig. 15.61). A case of a brown tumor was considered to be an ameloblastoma prior to biopsy (MacDonald 2012).

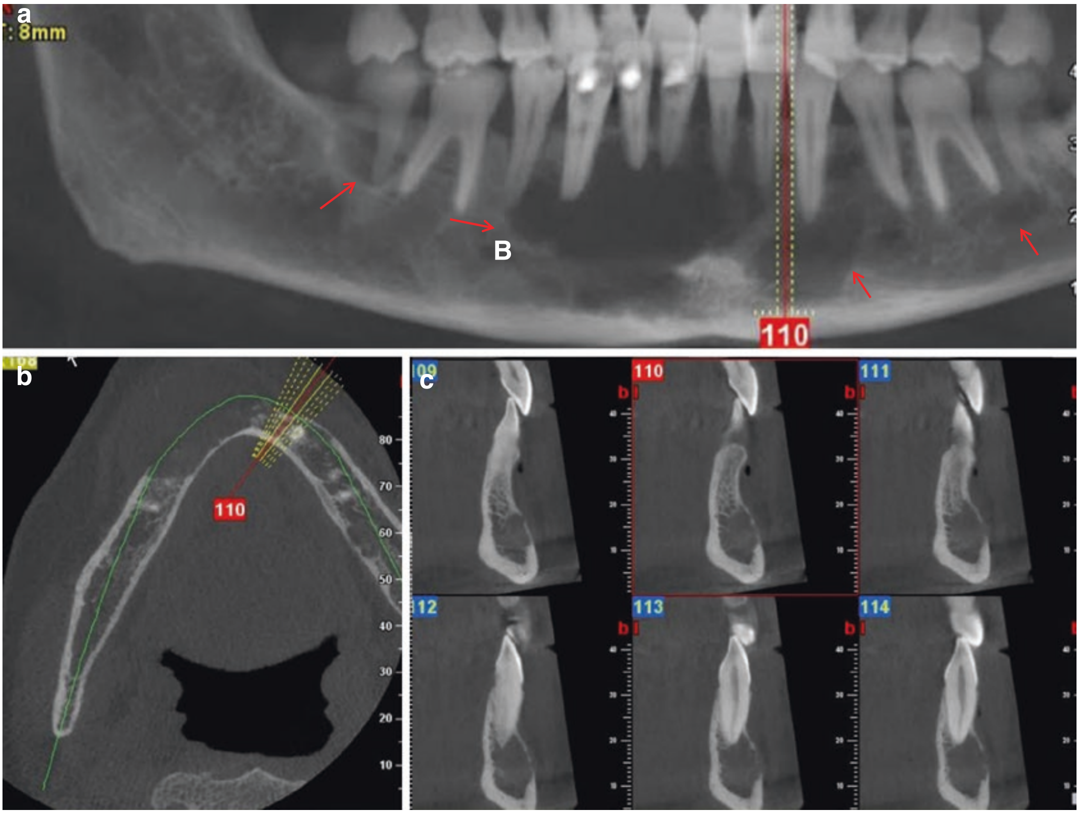

Fig. 15.61 Reformatted panoramic (**a**), axial (**b**), and a series of cross-sectional images (**c**) of the right mandible showing multiple, moderately well-defined, low-density entities, throughout the mandibular bone. Some of the lesions imitate periapical pathologies (*red arrows*), however there generalized presentation suggest a systemic or developmental condition. Based on the clinical presentation and medical history, a working diagnosis of giant cell tumors of primary hyperparathyroidism was established and subsequently confirmed

15.3.2 High-Density Lesions

Hyper-attenuating entities most often have well-defined borders that are associated with benign lesions representing slow-growing excessive formation of normal bone (e.g., exostoses and osteoma) or replacement of bone with odontogenic (e.g., odontoma, cementoblastoma) fibro-osseous (e.g., fibro-osseous lesions) or bone (e.g., enostosis, dense bone islands, osteoblastoma).

- **Odontomas are the most common benign odontogenic tumors of the jaws**. Odontomas present as an asymptomatic well-defined heterogeneous hyper-attenuating expansive mass, limited to the alveolus, with a radiolucent rim often associated with the failure of eruption of a permanent tooth. Most occur in the maxilla. Radiographically odontomas present in one of two patterns:
  - *Compound.* Multiple small tooth-like structures, not greater than the diameter of the associated tooth (Fig. 15.62).
  - *Complex*. A single radiopaque mass, tending to be round or ovoid with a round or smooth margin having density greater than bone (Fig. 15.63).

Presentation and location depends on type of radiographic pattern. Compound odontomas

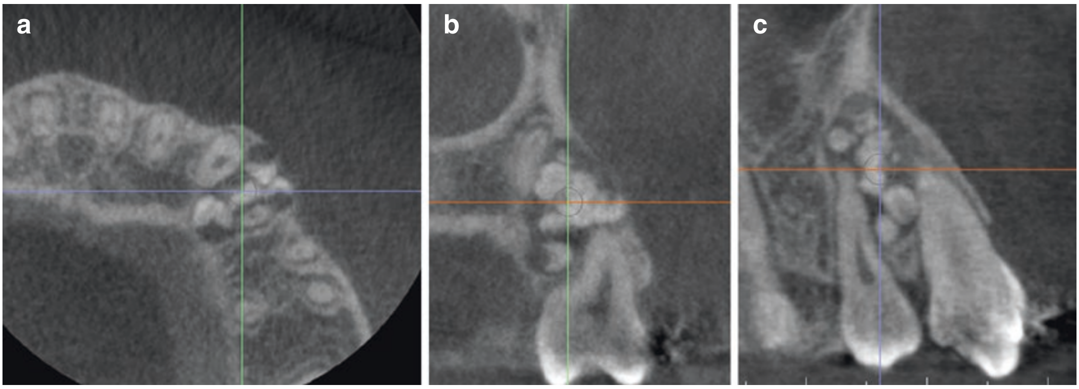

Fig. 15.62 Axial (**a**), cross-sectional (**b**), and parasagittal (**c**) images of the left anterior maxilla in the region of the premolar and canine showing multiple high-density, tooth-like structures surrounded by a wide low-density zone and a corticated border that resembles a tooth follicle. The lesion is slightly expansile and has thinned the buccal cortex. The imaging appearance is pathognomonic with a compound odontoma

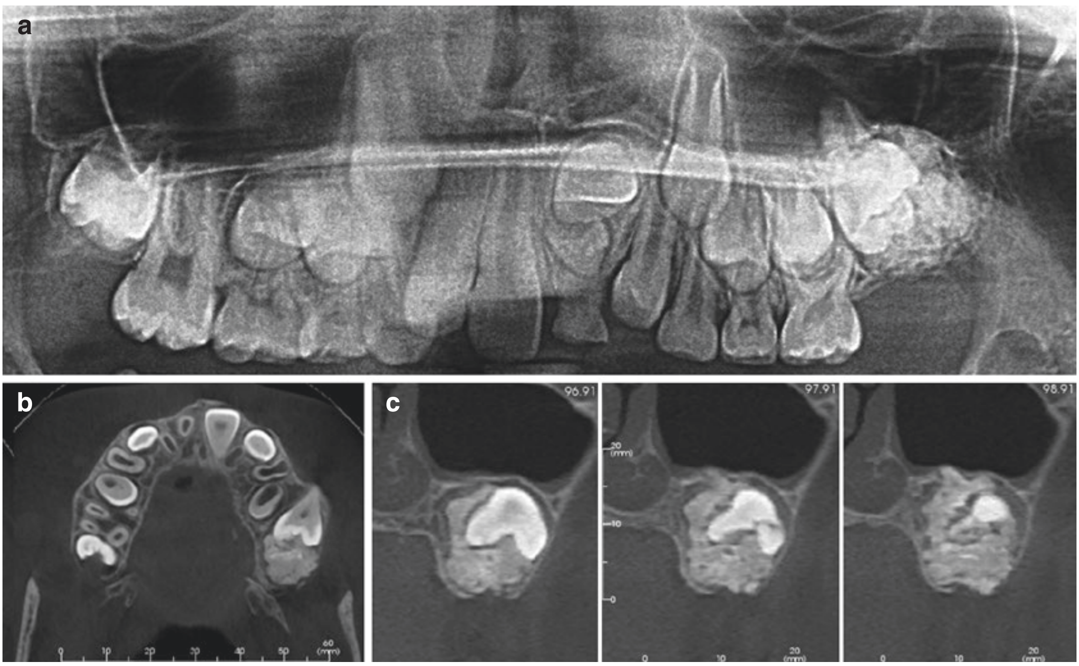

Fig. 15.63 Panoramic (**a**) and subsequent axial (**b**) and series of cross-sectional CBCT images (**c**) showing an amorphous globular high-density mass in the left posterior maxilla associated with the pericoronal aspect of a first molar. The mass is surrounded by a wide low-density zone and a corticated border with some expansion on the buccal and palatal cortices. The mass demonstrates varying densities, some of which correspond with the density of enamel. The imaging features are pathognomonic for a complex odontoma

more frequently occur in the anterior maxilla in teenagers whereas complex odontomas arise commonly in the posterior regions in young adults. If untreated, a high proportion develop into cysts (cystic odontoma) which may become secondarily infected (Fig. 15.64).

- **Exostoses are the most common benign non-odontogenic tumor of the jaws.**

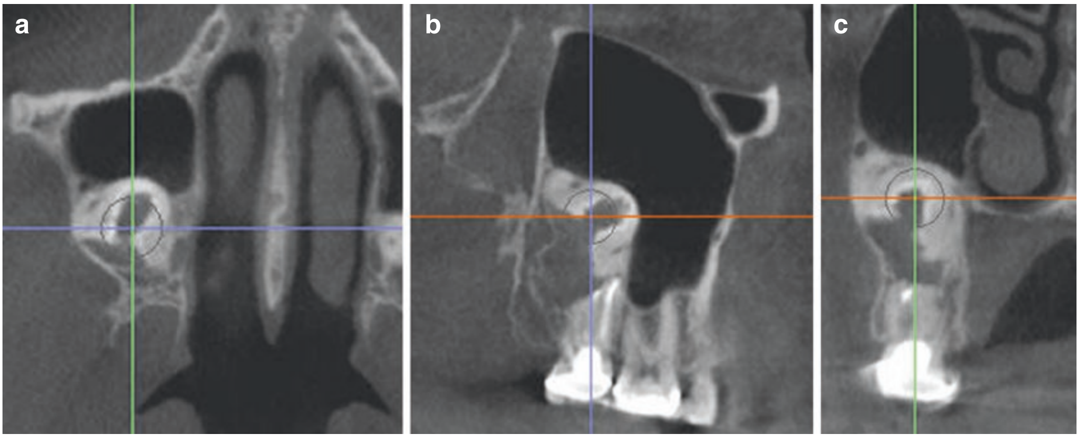

Fig. 15.64 Axial (**a**), parasagittal (**b**), and coronal images (**c**) of the right posterior maxilla showing an irregular, high-density mass that looks like a malformed tooth (contains both enamel and dentin elements) surrounded by a large cystic entity. Imaging appearance is similar to a resorbing third molar except for the irregularity of the enamel portion centrally. This imaging appearance is most consistent with a compound cystic odontoma

Fig. 15.65 Axial (**a**) and coronal (**b**) images showing large pedunculated osseous masses on the lingual aspect of the mandibular bone adjacent to the premolars, radiographically pathognomic for bilateral mandibular tori

Exophytic smooth surfaced self-limiting benign tumors of bone result in localized cortical exostosis which arise most often at three specific locations:

– *Mandibular Torus (MT).* MT are bilateral smooth surface well-defined exostoses arising from lingual alveolus of the mandible above the mylohyoid ridge in the region of the premolars (Fig. 15.65). Size may vary from small raised cortical bumps to large extensive pedunculated multi-nodular masses (Figs. 15.49 and 15.65). Rare in children and teenagers, MT is usually established by the fourth decade with a male predominance. It is a common with a variable incidence depending on ethnic group (range, 2–25%). Predominantly has a hereditary etiology (autosomal dominant) with contributing environmental factors such as occlusal stress associated with parafunctional habits and long-term use of phenytoin. MT is associated with other regional exophytic growths including buccal exostoses (up to 36%) and torus palatinus (up to 50%) which can be identified by clinical intraoral examination.
– *Torus palatinus (TP).*TP is a midline hard palate exostosis, more frequent than MT

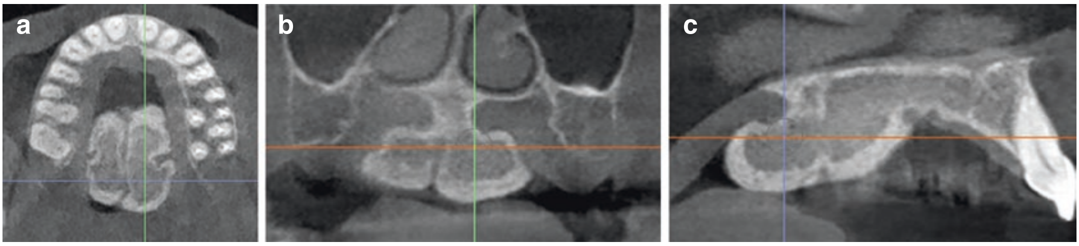

Fig. 15.66 Axial (**a**), coronal (**b**), and midsagittal (**c**) images of the maxillary palatal region showing a large pedunculated osseous mass along the midline of the hard palate, radiographically pathognomic for torus palatinus

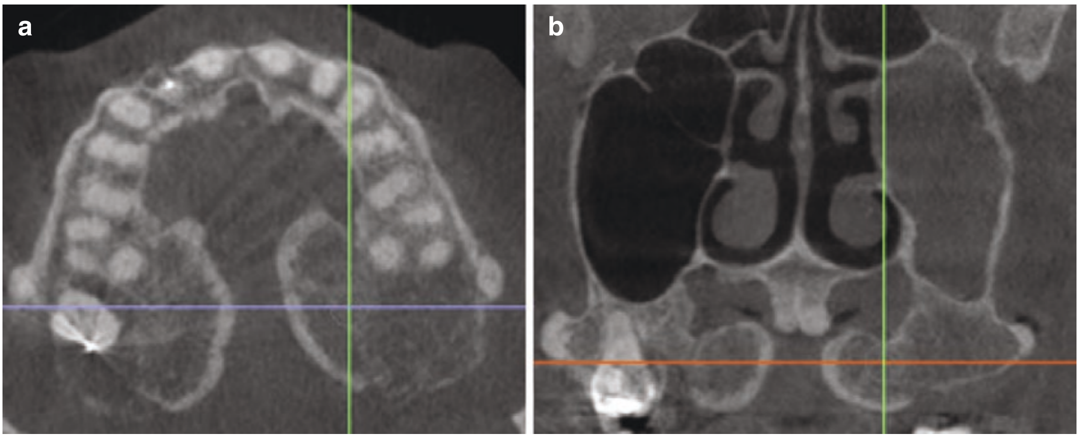

Fig. 15.67 Axial (**a**) and coronal (**b**) images showing large pedunculated bilateral osseous masses on the palatal aspect of the maxillary alveolus consistent with a diagnosis of buccal maxillary exostoses. Note also the torus palatinus in the coronal image

and more common in women. Typical radiographic patterns can be uni- or multi-lobulated, flat and spindle-shaped (Fig. 15.66).

– *Alveolar exostosis*. Alveolar exostoses can arise on the alveolus adjacent the cervical third of the roots of posterior teeth on either the palatal/lingual or, more commonly, the buccal aspect. Exostoses are more common in the maxilla than in the mandible (5.1:1) and prevalence increases with age. Exostoses are more common in men than in women and appear concurrently with MT than with TP (Fig. 15.67).

They present as asymptomatic exophytic masses that may increase in size slowly over time. Larger lesions may become nodular and can be multiple. They may appear as a uniformly homogeneously hyperdense expansion of the cortical plate (compact bone variant) or as an extension with an outer cortical plate and inner medullary bone (cancellous variant). Tightly bound thin mucosa may become traumatized.

- **Incidental high-density benign intramedullary entities are common.** These include:
  – *Idiopathic osteosclerosis (dense bone island)*. Idiopathic osteosclerosis (IO) is a benign entity characterized by uniformly dense bone (similar to that of cortical bone) which extends with variable shape and size within the intramedullary area between the cortical plates of the alveolus. While IO is often restricted in the alveolar bone, it may spread to the base of the maxillary or mandibular bone. IO is more frequently seen in mandible and of unknown etiology

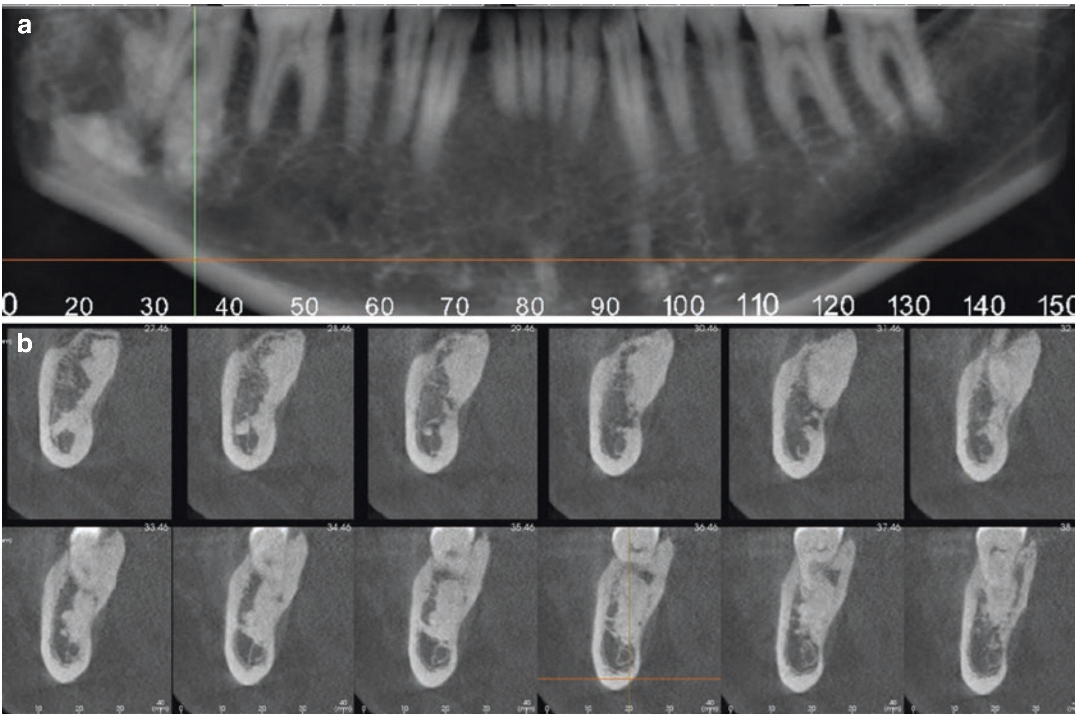

Fig. 15.68 Reformatted panoramic (**a**) and series of cross-sectional images (**b**) showing a large, irregularly shaped, homogenous, high-density lesion involving the roots of the right second molar extending below the alveolus. The imaging appearance is consistent with idiopathic osteosclerosis

(MacDonald-Jankowski 1999). IO may cause root displacement and sometimes even root resorption. IO should be differentiated from condensing osteitis and various forms of osseous dysplasia (OD) including mature periapical, focal, and florid osseous dysplasia. IO can occasionally present with radiographic features similar to osseous dysplasia or ossifying fibroma (OF) on conventional radiography. This may arise from the difficulty in discerning the "Mach band effect" (MacDonald 2011) adjacent to a central hyperdense lesion from a radiolucent border around OFs and most ODs (Figs. 15.68 and 15.69). A characteristic CBCT imaging feature is the presence of trabeculae extending from the periphery.

– *Condensing osteitis*. Condensing osteitis (CO) is characterized by the presence of sclerotic (dense) bone resulting from a local inflammatory response (McDonnell 1993), most commonly periapical in origin. The radiographic appearance of CO is similar to IO; however, CO is associated with mostly non-vital teeth with concomitant widening of the periodontal ligament space (Fig. 15.70)
– *Osteomas*. Osteomas are benign osseous masses that consist solely of cortical bone or a periphery of cortical bone and a central cancellous bone core. The most common are peripheral, and project from a bony surface, or they may be central, originating from the endosteum and projecting into the cancellous bone. They are uncommon and may also present in the frontal and ethmoid sinuses, maxillary sinuses, and in the mandible. Peripheral osteomas are readily

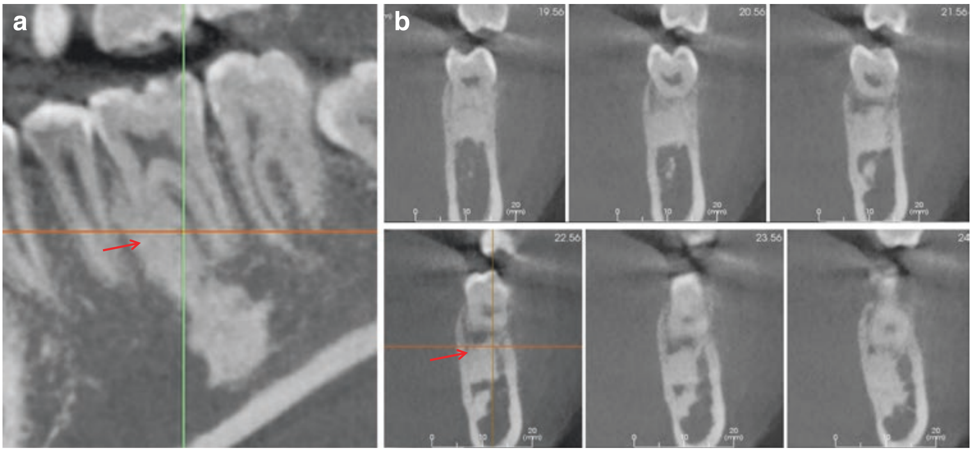

Fig. 15.69 Reformatted panoramic (**a**) and a series of cross-sectional images (**b**) of the mandibular left posterior region showing a localized elongated hyperdense area resorbing the mesial root of the first molar (*arrows*). The imaging appearance is consistent with idiopathic osteosclerosis

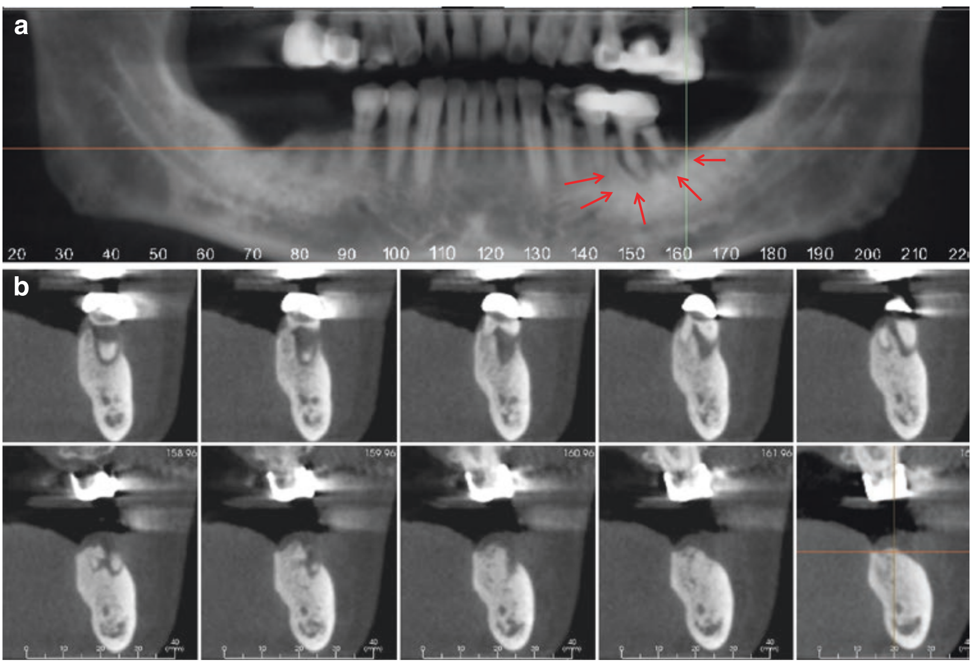

Fig. 15.70 Reformatted panoramic (**a**) and a series of cross-sectional images (**b**) of the mandible showing a large, diffuse, mostly homogenous high-density lesion, associated with the apices of the left first molar and pericircumferential alveolar bone loss associated with both roots. This is consistent with reactive sclerosis induced by chronic inflammation from this tooth. The imaging appearance is consistent with condensing osteitis

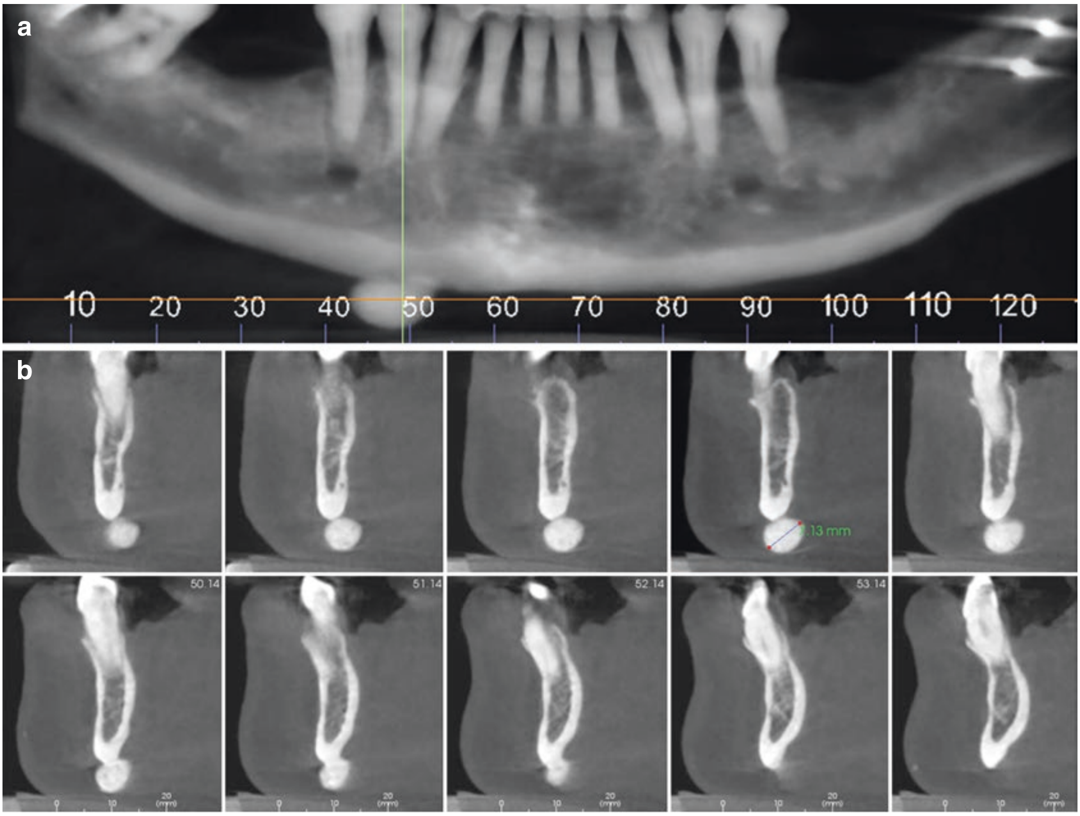

Fig. 15.71 Reformatted panoramic (**a**) and a series of cross-sectional images (**b**) of the mandible showing an exophytic, round, homogenous, high-density pedunculated mass extending from the lower border of the right mandible consistent with a radiologic diagnosis of osteoma

identified because of their exophytic nature, whereas central osteomas appear similar to IO, CO, and odontomas (Kaplan et al. 2008) (Fig. 15.71).

15.3.3 Mixed Density Lesions

Apart from the homogenous low-density and high-density entities addressed in earlier, there is a number of entities that demonstrate a mixed appearance; these may include cyst-like lesions (mostly low-density radiolucent) which contain high-density foci or lesions that demonstrate a mixture of different densities throughout the lumen of the lesion. The varying density levels may represent different degrees of mineralization for several of these entities; in fact, as some of these entities mature, they change in appearance from an initial low density to a mixed density and finally to high density as their content becomes gradually more mineralized. Some of these lesions are associated with teeth and others are not.

15.3.3.1 Tooth-Related Mixed Density Pathological Entities

Mixed density entities mat present in association with the crown of an impacted or unerupted tooth (pericoronal) or in the periapical region of the maxillary or mandibular teeth. Pericoronal

Table 15.8 Pericoronal entities with mixed density presentation

Entity	Presentation	Imaging features	Differential/management
Ameloblastic fibro-odontoma	Very rare	Well circumscribed, expansive, RL lesion with RO mass of small opacities	Larger lesions may be multilocular
	1^0 children (8–11 years)	Usually associated with unerupted teeth	DDx: Complex odontoma
	M > F (3:1)		
Adenomatoid odontogenic tumor (AOT)	Uncommon	Associated with U/E permanent tooth (75%)	Slow growing
	Teens	Two radiographic patterns: (1) round unilocular RL with no flecks. (35%)—Early; (2) round, central calcifications (65%) with well-defined regular RL rim, well corticated with tooth displacement and enveloping	
	"2/3 tumor"	Cortical perforation is rare	
	Mx canine most common		
Calcifying epithelial odontogenic tumor (CEOT)	Rare	Poorly defined, non-corticated, irregular RL ± calcifications, usually assoc. with UE/impacted tooth with expansion, root resorption, tooth displacement. Perforation not common	Unique histology
	2/3rd Mn, especially PM	Calcifications ("driven snow" or "snow storm") or RO masses of varying size which may coalesce near occlusal surface	Locally invasive (like ameloblastoma)
	Ave 40 years	Radiographic patterns: (1) Pericoronal (50%) ± calcification, (2) UL ± calcifications, (3) ML ± calcifications	
Keratinizing and calcifying odontogenic cyst (COC)	Very rare	Radiographic patterns: (1) Unilocular (most common), (2) Unilocular + calcification (21–40%), (3) calcifications: Clustered peripherally, resemble odontoma	Unique histology
	Neoplastic/cystic	20%—embedded or denticle structure	
	Painless	Expansion and perforation common	± assoc.: Complex odontoma, ameloblastic fibroma
	70% Mn Mol/ramus		

± with or without, 1^0 primarily, > greater than, *Ave* average age on presentation, *Mn* mandible, *ML* multilocular, *Mol* molar, *Mx* maxilla, *PM* premolar, *RL* radiolucent, *RO* radiopaque, *UE* unerupted, *UL* unilocular, *Syn* Synonym, *DDx* differential diagnosis, *assoc.* associated

entities that present as mixed density lesions are rare; however, many have characteristic demographics or imaging characteristics that help in diagnosis (Table 15.8).

Unlike their pericoronal counterparts, periapical mixed density lesions are relatively common.

- **Periapical osseous dysplasia (POD)**. The intermediate stage of POD presents as a mixed density periapical lesion which progresses to a high-density lesion when it is completely matured. Radiographic variation in presentation is related to the three stages

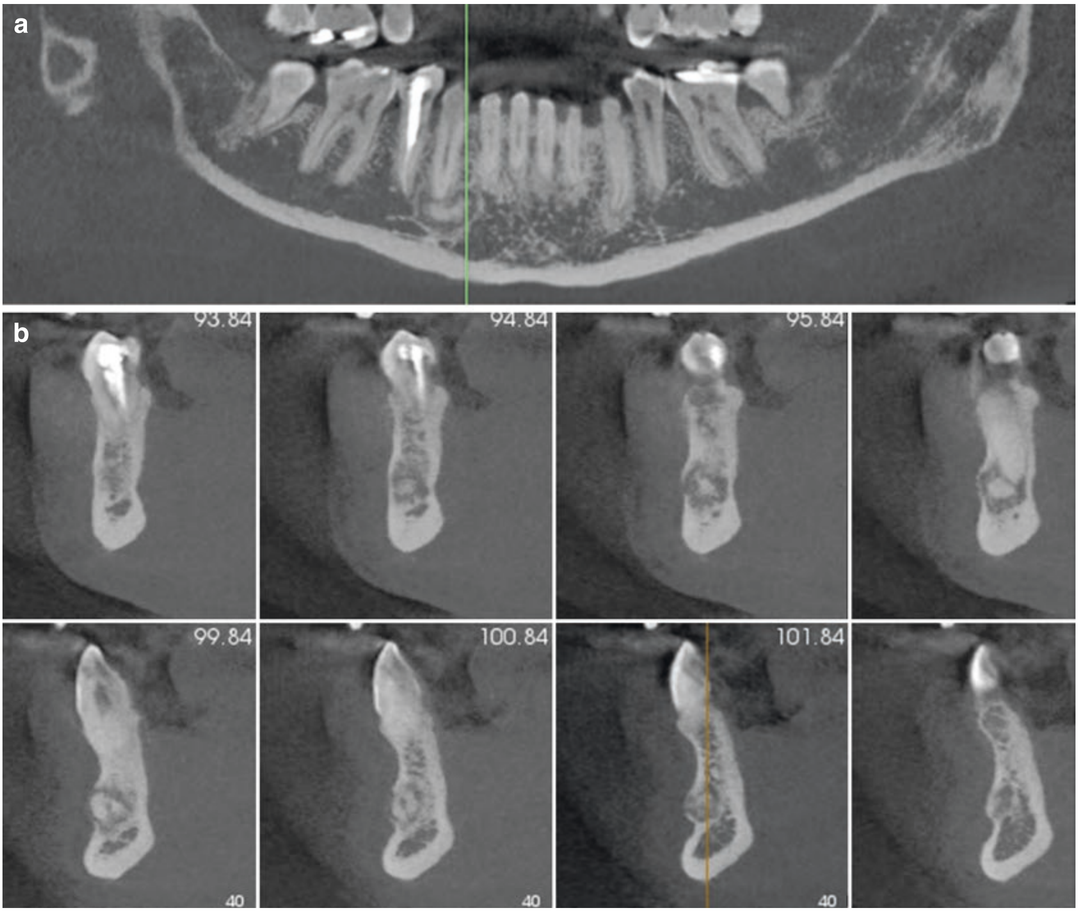

Fig. 15.72 Reformatted panoramic (**a**) and a series of cross-sectional images (**b**) of the mandible depicting a well-defined, mixed density lesion associated with the apex of the right premolar containing up to two discrete globular masses with a low-density uniform periphery. The lesion has expanded and thinned the lingual mandibular cortex. The radiologic findings are consistent with periapical osseous dysplasia

in the maturation of the lesion. POD is considered a localized form of osseous dysplasia and while the etiology is unknown, it is thought to be linked to elements within the periodontal ligament. Initially POD presents as a well-defined, low-density periapical area, sometimes surrounded by a corticated border. At this stage no expansion is observed. It is more common in the mandible affecting the anterior sextant only (Figs. 15.72, 15.73, 15.74, and 15.81). At the intermediate/mature stage, POD lesions contain high-density internal globular masses which may range in number and vary in form from tooth to tooth if multiple teeth are affected. The involved teeth are vital, however concurrent chronic apical periodontitis may occur minimal. At this stage POD may cause thinning or minimal expansion of the cortical plates locally and may affect more than one tooth. Any appreciable expansion of an OD should prompt consideration of expansive OD (Noffke et al. (2012). POD requires no treatment but periodic intraoral radiographic assessment to monitor transition is suggested.

- **Cementoblastomas.** Cementoblastomas are rare, benign odontogenic tumors which originate from the cementum of the root of a tooth; they

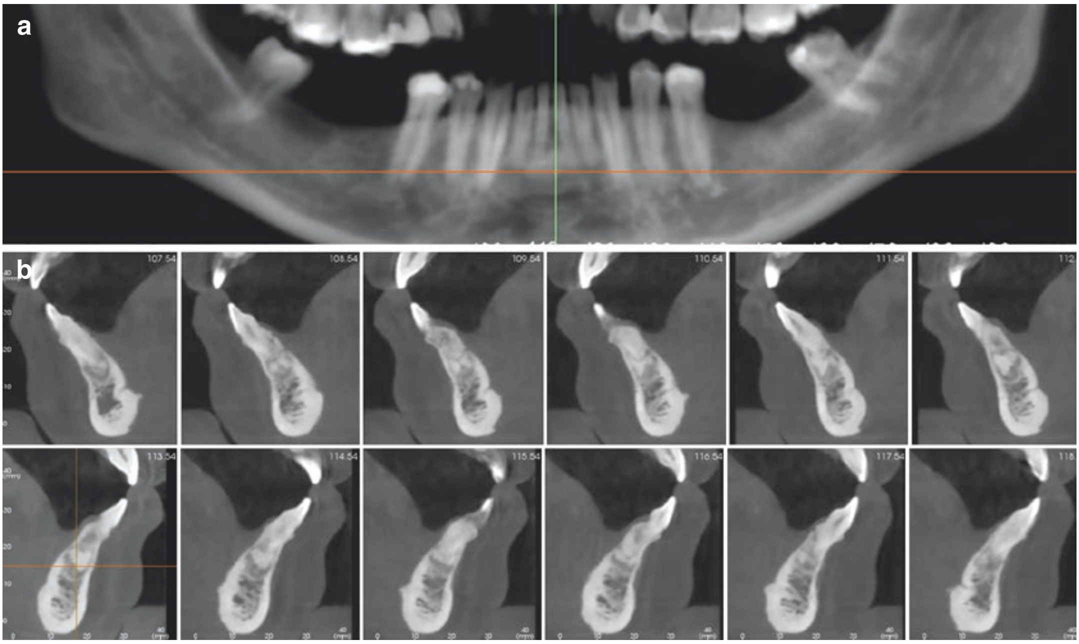

Fig. 15.73 Reformatted panoramic (**a**) and a series of cross-sectional images (**b**) of the mandible depicting multiple well-defined, mixed density lesions associated with the incisor teeth demonstrating central globular masses. Similar to the patient in Fig. 15.72, the lesions have expanded and thinned the lingual and labial mandibular cortex. The radiologic findings are consistent with periapical osseous dysplasia

appear as a well-defined and regularly shaped exophytic homogeneous mass of cementum or cementum-like tissues apparently fused to the root. They have a mixed or high-density presentation and may be surrounded by a thin hypodense peripheral rim. They are often round or ovoid in shape and may cause expansion of the jaw in the region they develop. They most frequently present associated with the roots of the mandibular premolars and molars (Figs. 15.75).

15.3.3.2 Mixed Density Jaw Pathology, Not Associated with Teeth

- **Fibro-osseous lesions (FOL).** FOL represent an important group of mixed or high-density lesions affecting the jaws. FOLs include fibrous dysplasia, ossifying fibroma, and osseous dysplasia. Until recently, large FOLs were most often imaged by MDCT. Smaller FOLs are often asymptomatic and discovered as an incidental finding on conventional dental radiography. With increasing availability of CBCT units in general and specialist dental offices, the radiographic features of FOLs are now being characterized on CBCT images. Regarding FOLs, the late Charles Waldron, state that:

> In absence of good clinical and radiological information a pathologist can only state that a given biopsy is consistent with a FOL. With adequate clinical and radiological information most lesions can be assigned with reasonable certainty into one of several categories.

Conversely, in the absence of such information, Eisenberg and Eisenbud stated (MacDonald-Jankowski 2004; MacDonald 2011):

> …pathologists today will often rightly decline to render a definitive diagnosis…. Instead, the pathologist will resort to the noncommittal designation of benign fibro-osseous lesions (their italics). This is the only acceptable approach considering the potential for inappropriate treatment otherwise.

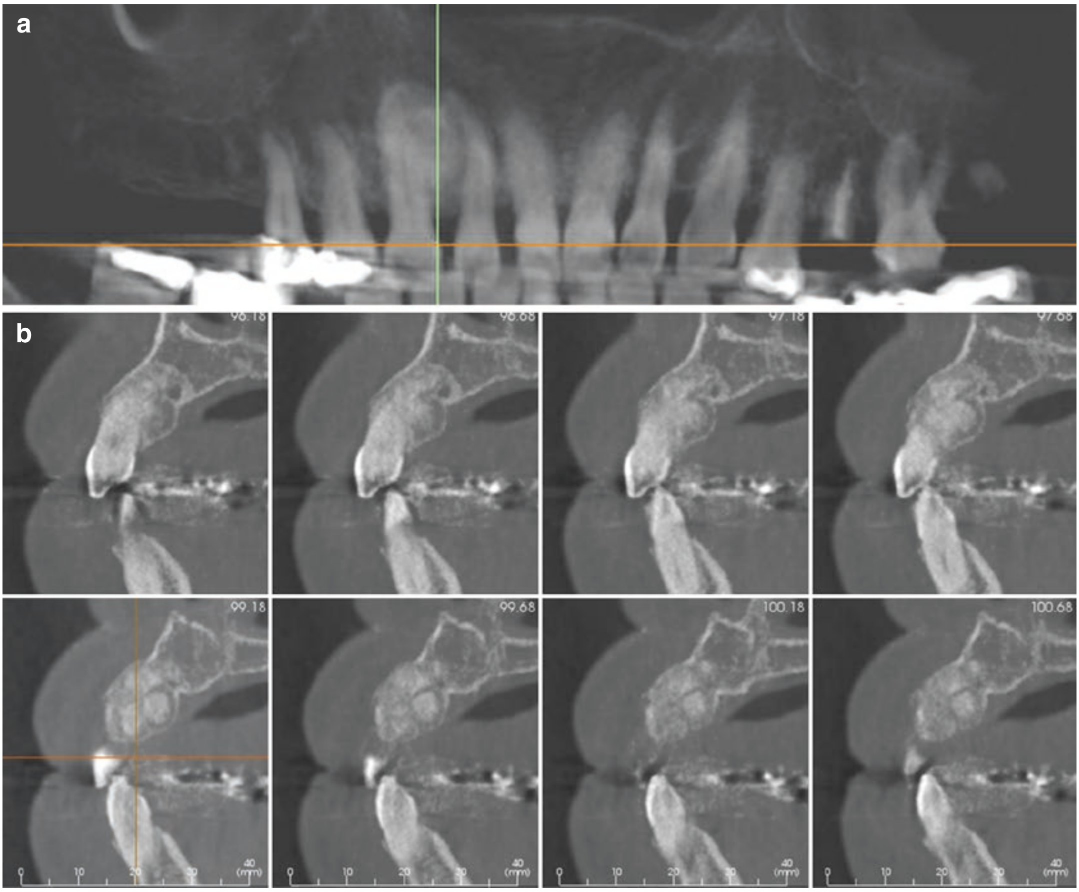

Fig. 15.74 Reformatted panoramic (**a**) and a series of cross-sectional images (**b**) of the anterior maxilla) depicting a single, well-defined, mixed density lesion associated with the root of the right canine demonstrating up to four central globular masses with a peripheral hypodense zone. The lesion has expanded and thinned the labial and palatal maxillary cortex. The radiologic findings are consistent with early expansive osseous dysplasia

– ***Fibrous Dysplasia (FD).*** FD is a slow-growing, usually self-limiting, benign fibro-osseous disease in which normal bone and marrow are replaced by fibrous tissue and irregularly distributed woven bone (Figs. 15.76 and 15.77). The most common locations are the craniofacial bones, proximal femur, and rib. Gnathic FD is referred to as a fibro-osseous lesion. Approximately 80% of individuals present with FD affecting one bone (monostotic) with the remaining affecting multiple bones (polyostotic) either with (McCune-Albright syndrome) or without endocrinopathies.

Polyostotic FD involving contiguous bones in the skull, such as the maxilla and zygoma, is referred to as craniofacial FD (Fig. 15.78). This disease is found in the third decade with a male predilection, especially in younger individuals (MacDonald-Jankowski 2009). Progression tapers with skeletal maturity however does not regress to lamellar bone and persists throughout life (MacDonald 2011). Most lesions become quiescent; however, the reactivation rate is approximately 18%.

Most commonly individuals present with painless, slow-growing asymptomatic facial swelling (MacDonald-Jankowski 2009) associated with uniform buccolingual expansion. Management is dependent on anatomic site, degree of involvement, patient's age and stage

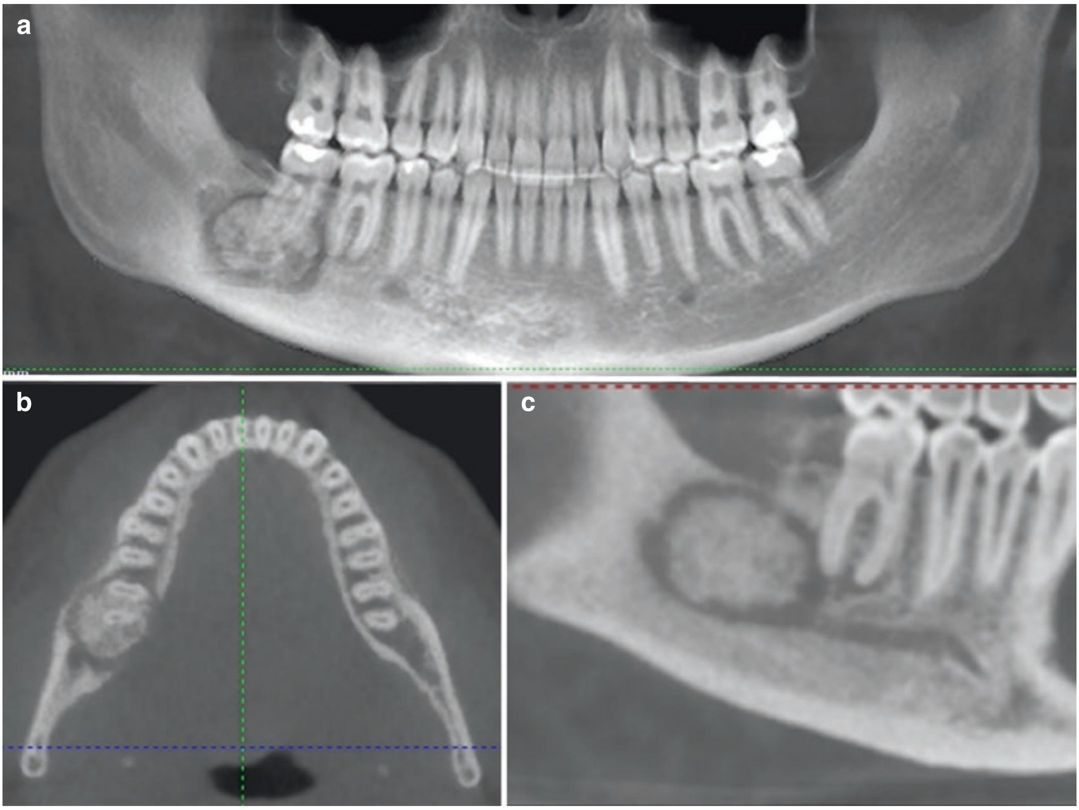

Fig. 15.75 Reformatted panoramic (**a**), axial (**b**), and parasagittal (**c**) image of the maxilla and mandible showing a large, round inhomogeneous spiculated globular mass associated with the roots of the right mandibular second molar surrounded by thin uniform hypodense rim. Although the radiologic findings are consistent with a benign cementoblastoma, the lack of root resorption and fusion with the root also prompt consideration of ossifying fibroma

of skeletal maturity and anticipated growth potential. Surgery is only indicated for esthetic reasons, impaired function (e.g., opening or tooth occlusion), pain due to constriction of neurovascular foraminae, or optic nerve encasement.

FD has poorly defined margins which distinguishes it from OF which has well-defined margins. This distinction is most clearly observed in the mandible and in the alveolus of the maxilla. Although not strictly necessary for a diagnosis of FD, a biopsy is necessary to confirm the diagnosis of OF since this lesion needs to be completely removed or resected, depending on size (MacDonald 2011).

– ***Ossifying Fibroma (OF).*** OF is a rare benign slow-growing neoplastic fibro-osseous lesion of the jaws, occasionally involving the mid-facial bones and paranasal sinuses (Figs. 15.79 and 15.80). It usually presents as an asymptomatic, unilateral hard facial swelling, often in the mandible. Maxillary sites often result in extensive sinus involvement. OF has a female predilection with the highest incidence of presentation in the second to fourth decades. The more aggressive, rapidly growing variant with intralesional psammomatous or trabecular calcifications and lack of radiographic capsule may occur in younger individuals (Juvenile OF). Presentation may be syndromic, associated with familial hyperparathyroidism or synchronous with other conditions such as aneurysmal bone cyst. Histopathologically presents as an encapsulated neoplasm of varying quantities of bone, osteoid and cementum-like material in a

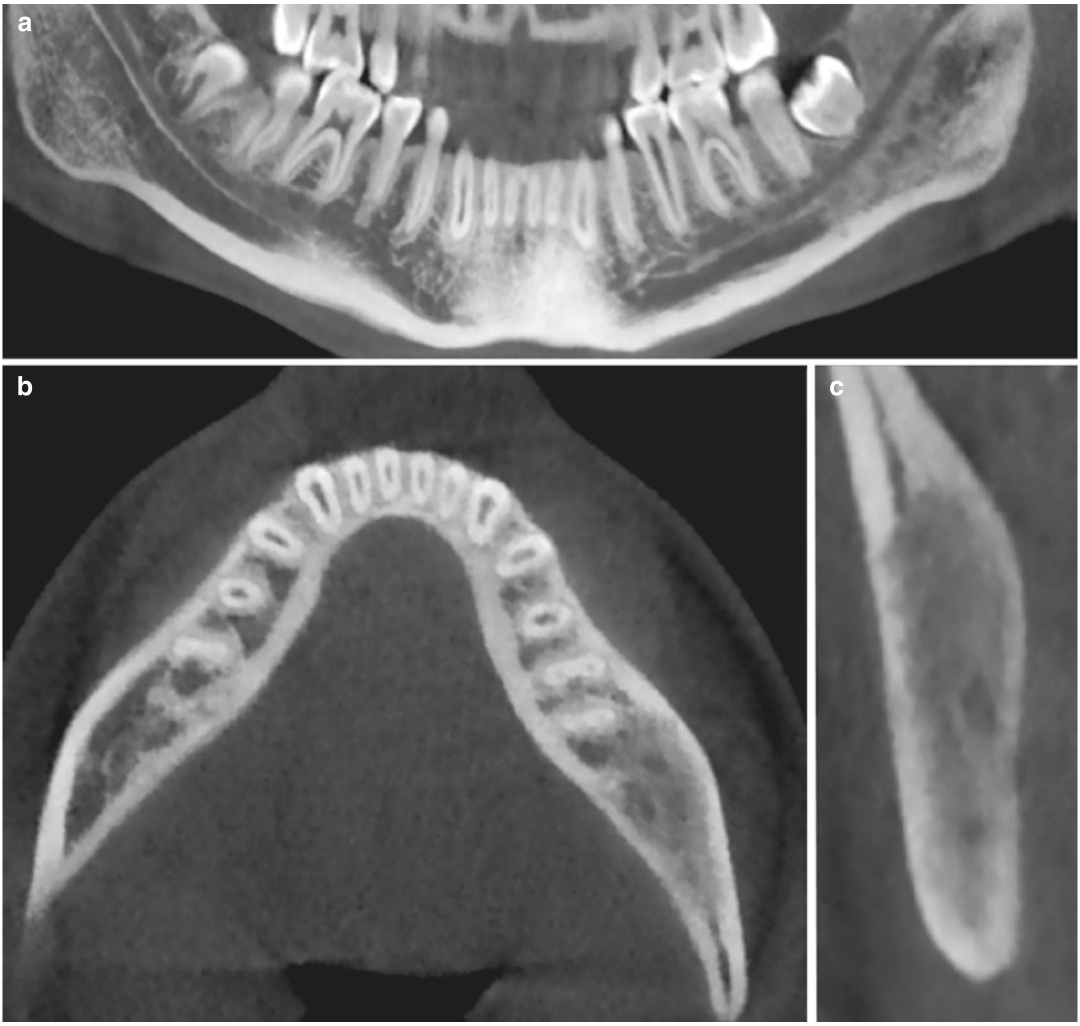

Fig. 15.76 Reformatted panoramic (**a**), axial (**b**), and coronal (**c**) CBCT images showing fibrous dysplasia in the left retromolar area involving the trigone and ramus with characteristic poorly defined margins. There is a little buccolingual expansion and the dysplastic bone has a ground glass appearance. (Images courtesy of Dr David Gane, Elsevier (MacDonald 2015))

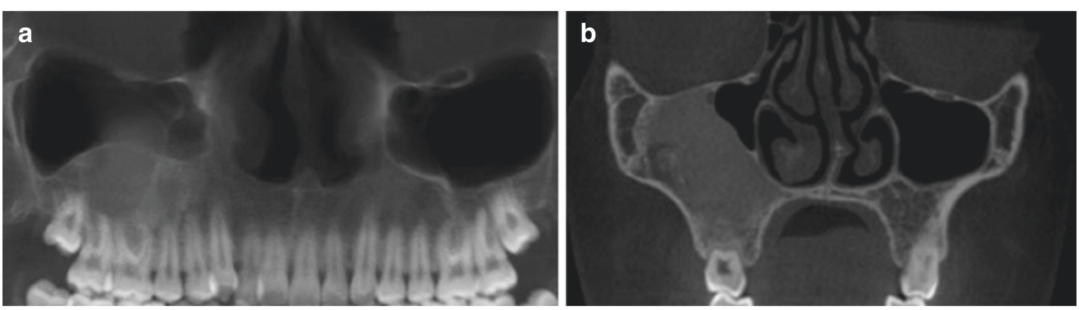

Fig. 15.77 Reformatted panoramic (**a**) and coronal (**b**) CBCT images of monostotic fibrous dysplasia in the right maxillary sinus in an asymptomatic 60-year-old female. The lesion shows an ill-defined ground glass lesion in the right posterior maxilla enveloping the apices of subjacent teeth with superior displacement of the floor of the maxillary sinus, obliterating the lateral aspect of the sinus. The infra-orbital canal is involved. (Images courtesy of Dr Allan Abuabara, Elsevier (MacDonald 2015))

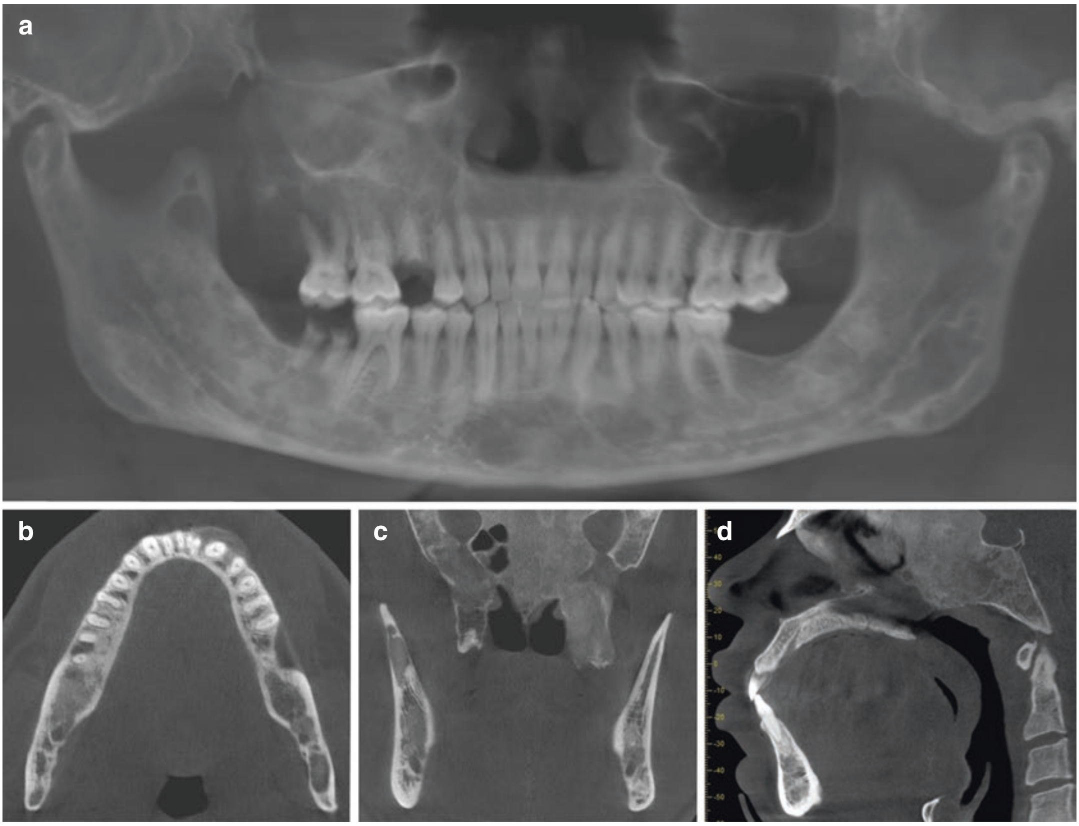

Fig. 15.78 Reformatted panoramic (**a**), axial image of the mandible (**b**), coronal image of the sphenoid bone (**c**), and midsagittal CBCT image (**d**) showing polyostotic high-density ill-defined ground glass expansion of multiple bones and invasion of the sphenoid and right maxillary sinus. The imaging appearance is radiologically pathognomonic for craniofacial fibrous dysplasia

fibrous connective tissue stroma. Recurrence rate is moderately high (up to 12%). Treatment involves surgical curettage or resection ± reconstruction.

Like other fibro-osseous lesions, OF has three radiographic patterns. OF presents initially and most commonly as a small to moderately sized, round to ovoid smooth expansile hypodensity with well-defined, egg-shell like sclerotic borders. Buccolingual expansion is symmetrical. The entity changes to mixed lesion with more prominent internal centrally located hyperdensity with increasing size ranging from fine, evenly distributed "snow flakes" to a fine, coarse or dense reticular pattern with or without globular dense opacities. Characteristic hypodense peripheral rimming occurs adjacent to the peripheral margin. Lesions can occur inter-radicularly, displacing teeth but not associated with root resorption. In the mandible, the inferior alveolar canal is displaced inferiorly. There is no perforation or associated periosteal reaction.

– ***Osseous Dysplasia (OD).*** Two well-recognized variants of OD exist with radiographic presentations so distinctive that biopsies are rarely required. Histopathology confirmation of an OD lesion only becomes available when an infected lesion needs to be surgically removed (MacDonald 2011).

Florid Osseous Dysplasia (FOD). The multiple sextant involvement of OD is a well-recognized radiological phenomenon particularly among middle-to-old aged females of sub-Saharan African or East Asian (Fig. 15.81).

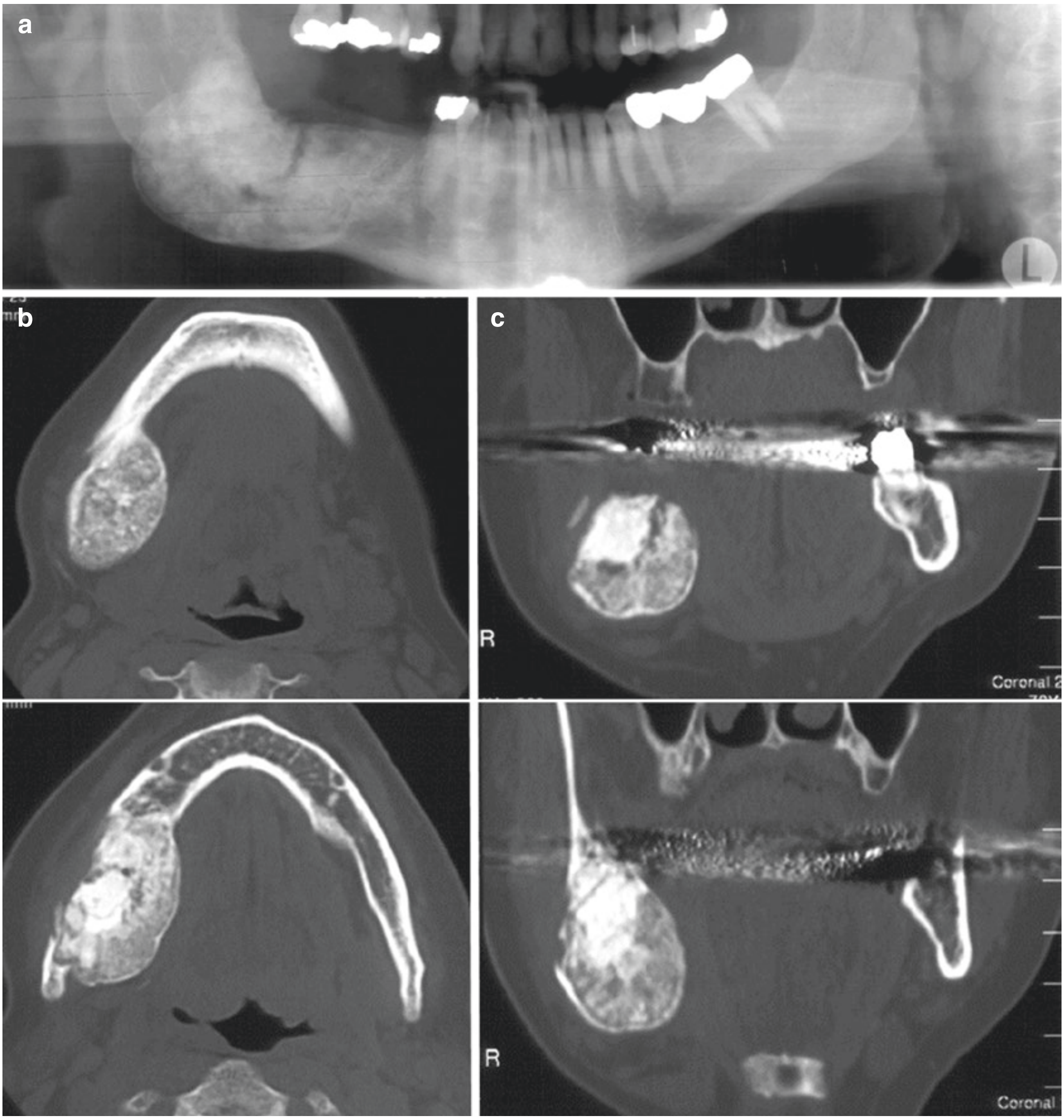

Fig. 15.79 Conventional panoramic (**a**) and axial (**b**), and coronal (**c**) MDCT images of the right mandible showing a well-defined high-density spherical expansion of the right posterior body, associated edentulous alveolus and angle of the mandible. There is smooth expansion and egg-shell like thinning of both buccal and lingual cortices concentrically. Internally there are two regions of hyper-density, separated from the peripheral cortical bone by a thin hypodense rim. The inferior alveolar canal is intact and displaced inferiorly within the entity. The imaging appearance is consistent with ossifying fibroma (Images courtesy of George Kushner)

Focal Osseous Dysplasia (FocOD). Another form of OD, which may be multiple, but localized to a single sextant is especially distinctive if confined to the lower anterior sextant (Figs. 15.82, 15.83 and 15.84) (previously *periapical cemental dysplasia*).

The differential diagnosis of FOLs is challenging. The radiological challenge in the diagnosis of FOLs is greatest when attempting to distinguish between OF and FocOD, particularly when the lesion is small (Fig. 15.85). Although OFs are associated with root resorption, this is not a consistent feature, especially

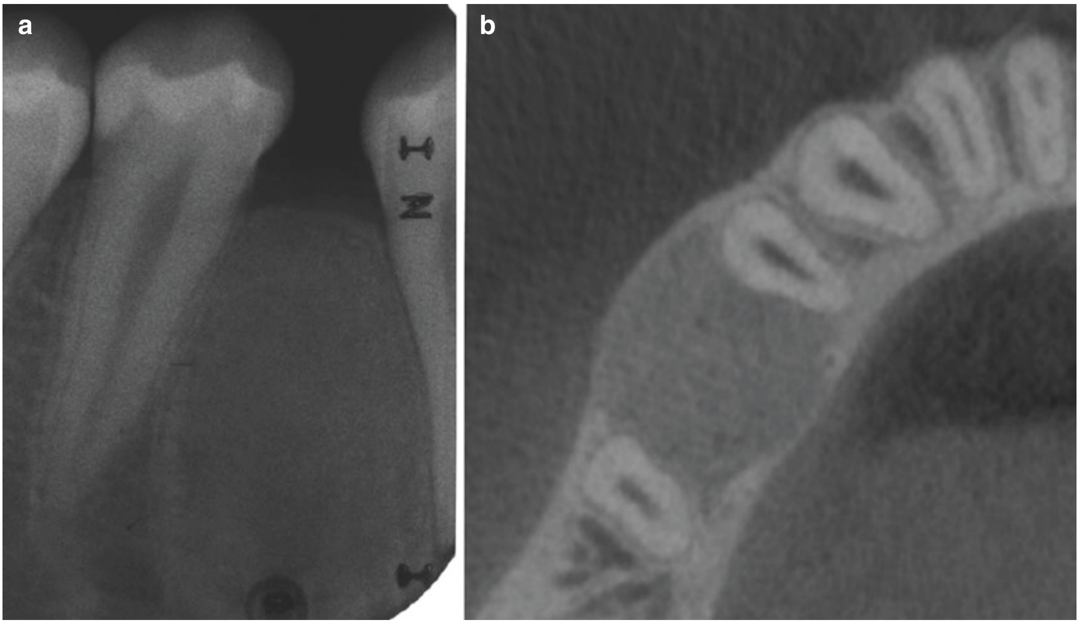

Fig. 15.80 Periapical (**a**) and axial (**b**) CBCT images of the right mandibular region showing a well-defined ground glass high-density egg-shaped lesion displacing the adjacent premolar teeth. Both buccal and lingual cortices are eroded and there is buccal expansion. The lesion is separated from the normal adjacent bone by a thin radiolucent space. The imaging appearance is consistent with ossifying fibroma. (Images courtesy of Kenneth Chow, Elsevier (MacDonald 2015))

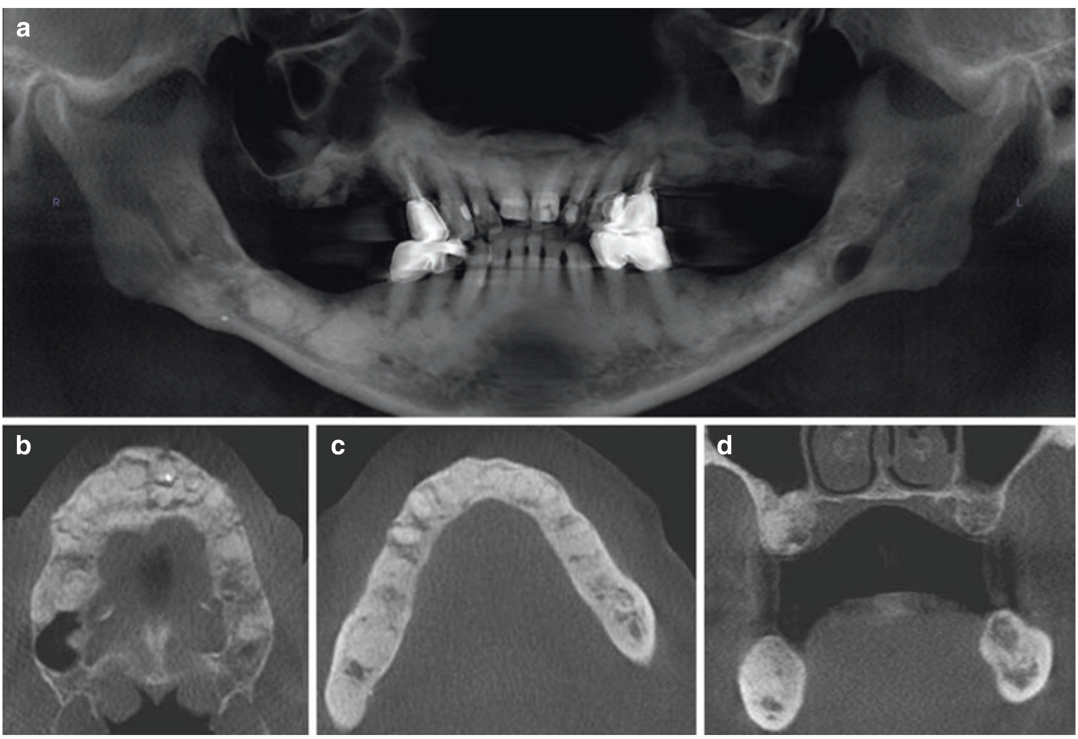

Fig. 15.81 Reformatted panoramic (**a**), maxillary (**b**), and mandibular axial (**c**) images and coronal image (**d**) showing generalized globular masses in the alveolus of both jaws. The imaging appearance is radiologically pathognomonic for florid osseous dysplasia

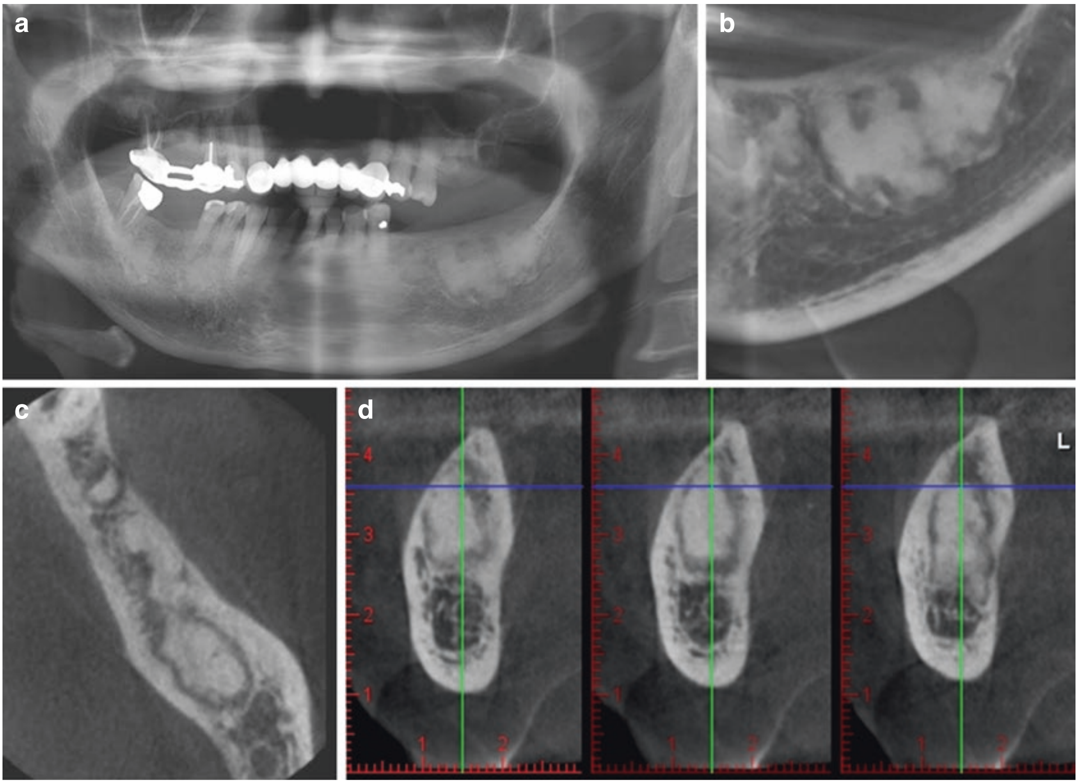

Fig. 15.82 Conventional panoramic (**a**), reconstructed panoramic (**b**), axial (**c**), and serial trans-axial (**d**) images of florid osseous dysplasia in the left mandible of 60-year-old Chinese woman. There are multiple well-defined globular hyperdensities bilaterally within the alveolus of the mandible (**a**). On the right mandible the globular hyperdensities are all above the mandibular canal and do not demonstrate buccolingual expansion. All lesions are separated from their adjacent normal bone by a radiolucent rim and variable cortication. (Images courtesy of Raman Sumanth, Elsevier (MacDonald 2015))

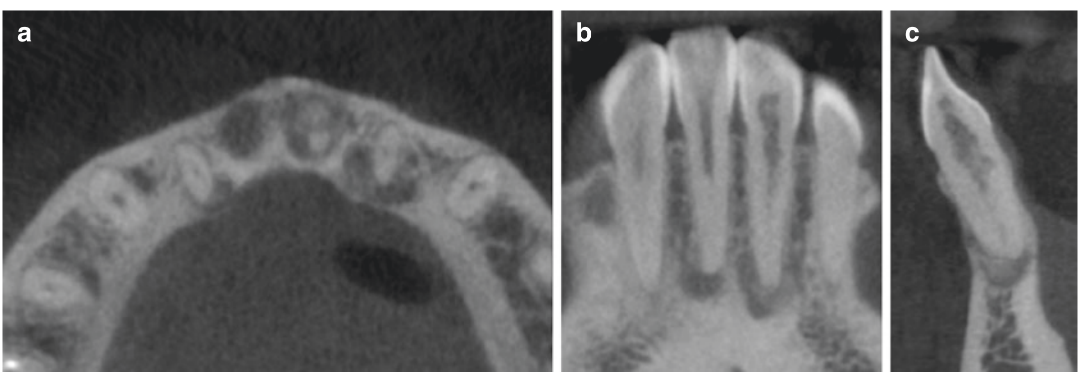

Fig. 15.83 Axial (**a**), coronal (**b**), and cross-sectional (**c**) CBCT images of multiple periapical osseous dysplastic lesions in the anterior mandible in a female. The lesions comprise small diameter central hyperdensities within hypodensities. There is little buccolingual expansion. (Images courtesy of Michael Matwychuk, Elsevier (MacDonald 2015))

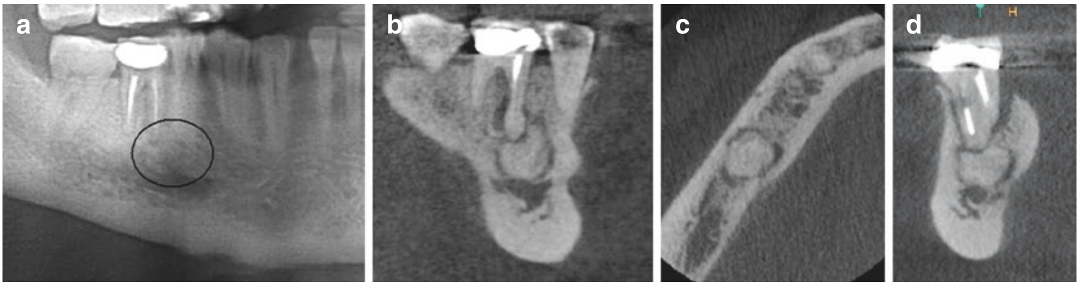

Fig. 15.84 Conventional panoramic (**a**) and parasagittal (**b**), axial (**c**), and trans-axial (**d**) CBCT images of focal osseous dysplasia associated with the right mandibular second premolar and the mesial root of the first molar. The lesion comprises a central hyperdensity separated from normal adjacent bone by a hypodense periphery. There is no buccolingual expansion or root resorption however there is effacement of the internal margin of the buccal and lingual cortices. (Images courtesy of Jason Chen, Elsevier (MacDonald 2015))

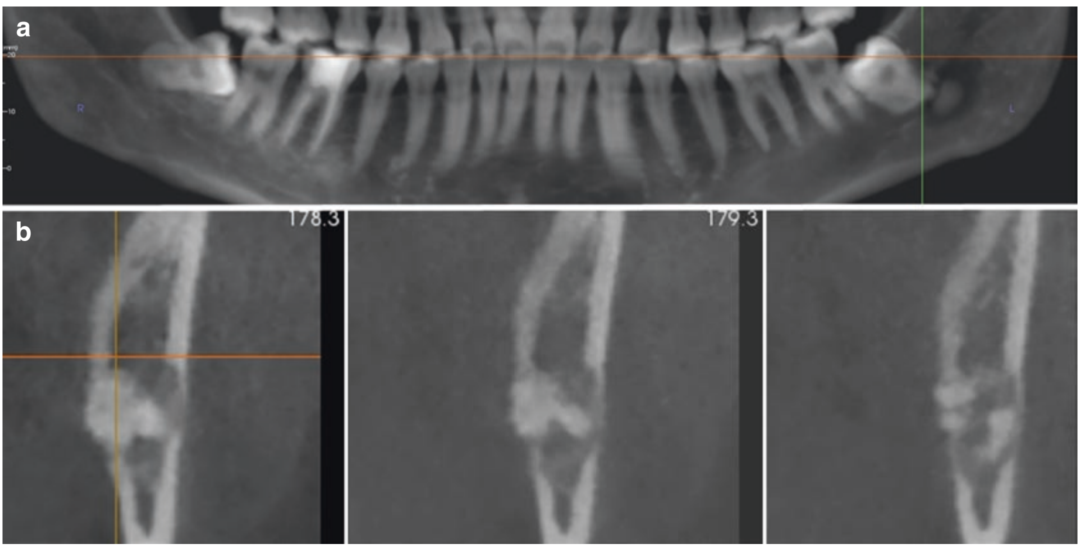

Fig. 15.85 Reformatted panoramic (**a**) and trans-axial (**b**) CBCT images of an OD associated with the apex of the left unerupted and impacted third molar. The lesion presents as a central opacity within a radiolucent periphery inferior to the mandibular canal. There is minimal buccolingual expansion, but considerable erosion of both buccal and lingual cortices

in small lesions. This may present the clinician with a diagnostic dilemma in that a OD misdiagnosed as a FocOD may require surgery latter. The following may assist the clinician is differentiating between FOLs.

CBCT provides valuable information in distinguishing OD from OF and FD. Specifically, CBCT imaging identifies the position of the lesion within the alveolar bone and its effect on the cortex. Both OF and OD can cause erosion and displacement of the cortex. Although this is usually minimal, exceptions can arise. OF can be distinguished from the other entities by tooth displacement and root resorption only when the lesion has achieved considerable size. OD rarely increases to such large dimensions (MacDonald 2011). Such lesions when affecting one or more sextants in young individuals of either gender or any ethnic

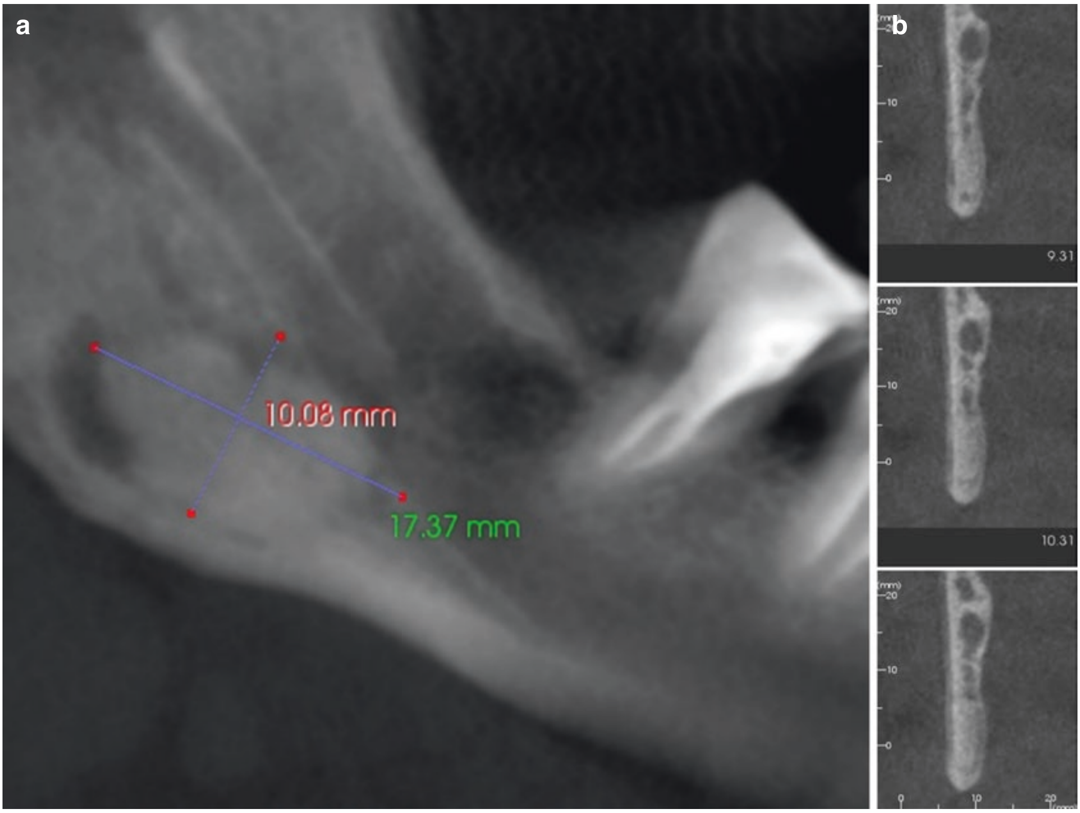

Fig. 15.86 Reformatted panoramic (**a**) and serial trans-axial CBCT images (**b**) of an osseous dysplastic lesion within the right ramus of the mandible below the mandibular canal. The lesion comprises a central hyperdensity within a hypodense periphery. Although the lesion is nearly 2 cm in diameter, it is associated with minimal buccolingual expansion

origin (MacDonald 2011) have been called gigantiform cementomas. The term familial is added to these if there is a familial history. The more appropriate term, expansive osseous dysplasia, has been proposed by Noffke et al. (2012).

A major feature of OD is that it is most frequently confined to the alveolus, above the mandibular canal in the mandible or below the image of the hard palate in the maxilla (MacDonald-Jankowski 2009). Occasionally, the OD may appear below the mandibular canal (Fig. 15.85) and even unassociated with a tooth (Fig. 15.86). Although the absence of a buccolingual expansion and a well-defined periphery with a radiolucent rim is diagnostic of OD, the diagnosis can only be confirmed at follow-up if there is no increase in size, tooth displacement, or root resorption. Asymptomatic OD in edentulous sites should be left alone unless they occur in a site required for an implant. Then they should be first removed by lateral trepanation to preserve the alveolar ridge and the surgical defect allowed to heal (MacDonald 2011).

There is a lack of information on the long-term progression of FD. There are few long-term follow-up studies of FD. The largest study in a Hong Kong Chinese population (MacDonald-Jankowski and Li 2009) reports reactivation of FD in 3 out of 17 cases, with two presenting after 10 years. Therefore, FD, once detected, should have long-term, perhaps life-long follow-up

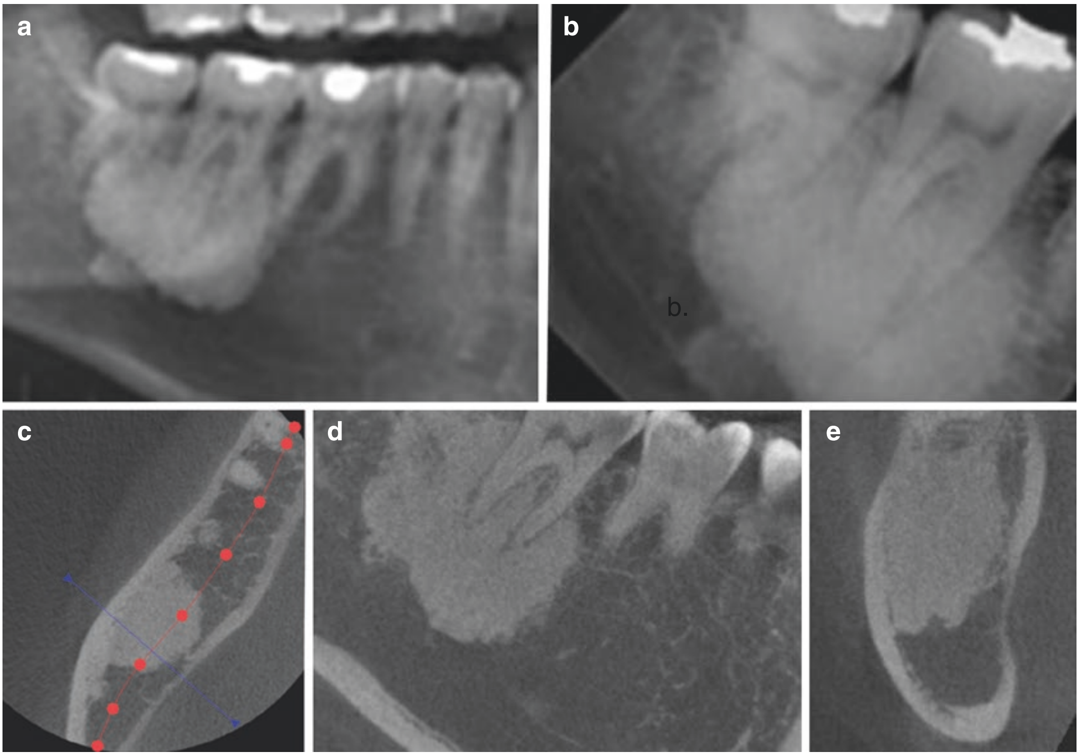

Fig. 15.87 Conventional panoramic (**a**) and periapical (**b**) images of a large dense bone island (also called idiopathic osteosclerosis) associated with a second molar inthe right mandible. Initially the lesions was considered to have a radiolucent rim (**a**) representing a follicular space. Axial (**c**), parasagittal (**d**), and cross-sectional (**e**) CBCT imaging was performed only after a incisional biopsy reported a histopathologic diagnosis of "cortical bone." CBCT clearly demonstrates the continuity of the lesion and normal trabeculae throughout

as they may be reactivated by a life event such as pregnancy. While panoramic radiography may be adequate for most cases of FD affecting the mandible, in the maxilla CBCT is likely the modality of choice when clinically indicated (MacDonald 2011).

While sarcomatous transformation in FD can be induced by radiation therapy, it is rare in the jaws (MacDonald-Jankowski and Li 2009; MacDonald-Jankowski 2009). However, it may occur in up to 1% of cases of FD affecting the face and skull (Cheng et al. 2012; Ruggieri et al. 1994).

- **Other entities may appear radiographically similar to FOL.** The differential diagnosis of FOL includes idiopathic osteosclerosis (Fig. 15.87) and medication-related osteonecrosis of the jaw (MRONJ).

  – ***Medication-related osteonecrosis of the jaw (MRONJ).*** This condition presents radiographic similarities to OD and OF, from which it needs to be distinguished (Fig. 15.88). This is usually achieved with a positive history of bisphosphonate therapy for previous bone cancer (bone metastasis and multiple myeloma) or other diseases such as osteoporosis (Kühl et al. 2012; Treister et al. 2010). Although any lesion that becomes exposed to the oral environment can become infected, suspicion of MRONJ must be entertained of clinical exposed bone for longer than 8 weeks, an accompanying history of bisphosphonate and no prior radiation therapy (Treister et al. 2010). CBCT is superior to panoramic radiography (Treister et al. 2010).

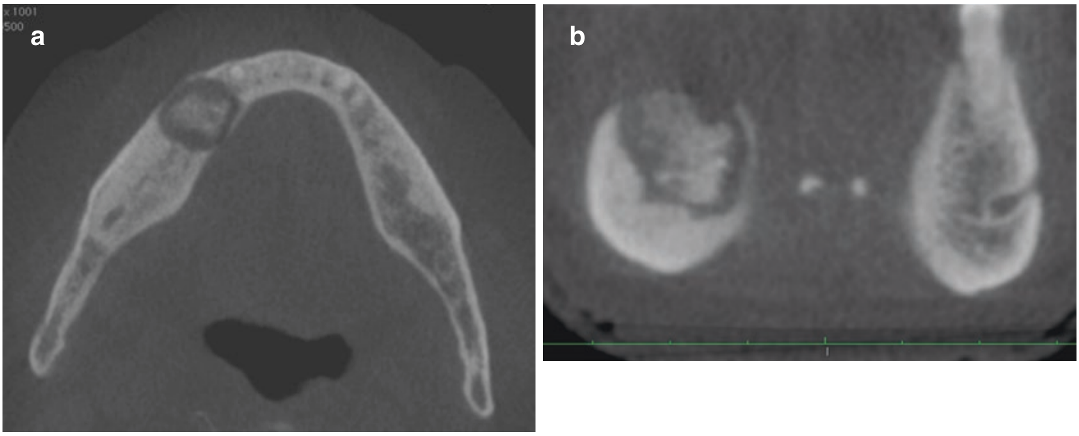

Fig. 15.88 Axial (**a**) and coronal (**b**) CBCT images of a patient with medication-related osteonecrosis of the jaws (MRONJ). The right para-symphyseal region of the mandible side shows expansion and sclerosis of the bone adjacent to the sequestrum. The "expansion" represents a periosteal reaction with the creation of 'new bone' or involucrum. Note: the two circular small hyperdensities in the midline of the coronal image (**b**) are the genial tubercles

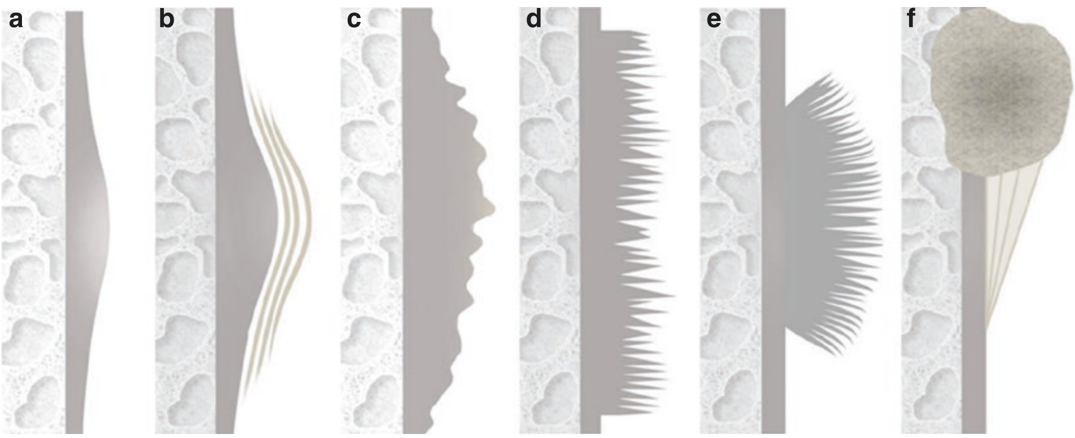

Fig. 15.89 Diagrammatic representation of patterns of periosteal include solid periosteal (**a**), multi-layer or "onion skin" (**b**), thick irregular (**c**), spiculated "hair on end" (**d**), and "sunburst" (**e**) as well as the "Codman's triangle" (**f**) (Adapted from Rana et al. 2009)

15.3.4 Periosteal Reaction

Periosteal reaction refers to the reactive bone formation underneath the periosteum as a result of any kind of stimulus. Bone formation under the periosteum may demonstrate certain patterns based on the type of induction stimulus. The pattern of new bone formation in the cortical bone observed on CBCT images may be able to suggest whether the underlying process is of a benign or an aggressive nature. These different patterns of bone formation are based mainly on how fast the stimulating abnormal process progresses; thus the detected radiologic differences broadly called periosteal reaction are a reflection of the speed at which new bone is formed (Fig. 15.89) (Rana et al. 2009).

The speed of new bone formation and thus the detected periosteal reaction is a determinant of the aggressiveness of the stimulating pathological entity and this is why it is important to the diagnostician.

- **Solid.** A solid periosteal reaction is associated with benign, non-aggressive, slow-growing conditions like osteoid osteoma and healing osteomyelitis. Radiologically this appears as thin or thick layers of bone (Fig. 15.90).
- **Multi-layer.** A faster more aggressive entity may induce a laminated or "onion skin" pattern of periosteal reaction; in this cases multiple layers of bone are noted and this is considered an "interrupted" pattern (Figs. 15.91, 15.92, and 15.93).
- **Spiculated**. This pattern of periosteal reaction characterizes very aggressive and fast developing entities, like sarcomas. In this pattern, thin osseous fibers may appear to be spreading out of the bony surface. Spicules may originate either perpendicular to the bone ("hair on end") or may diverge ("sunburst") (Figs. 15.94 and 15.95).
- **Codman's triangle.** This pattern is associated with rapidly advancing pathological and results in an elevation of the periosteum at a sharp angle at the periphery of the lesion. This may also be seen in sarcoma.

15.3.5 The Diagnostic Challenge of the Aggressive Lesion

The most important concern of the clinician in radiologic analysis of CBCT images is to ensure that no serious pathological condition within the volume is missed. Therefore, the distinction between a malignant and a benign lesion is of utmost priority.

Albeit the key imaging features of malignant lesions were characterized previously, it should be noted there is considerable overlap in presentation between benign and malignant conditions that may be difficult to distinguish. These pathological entities include:

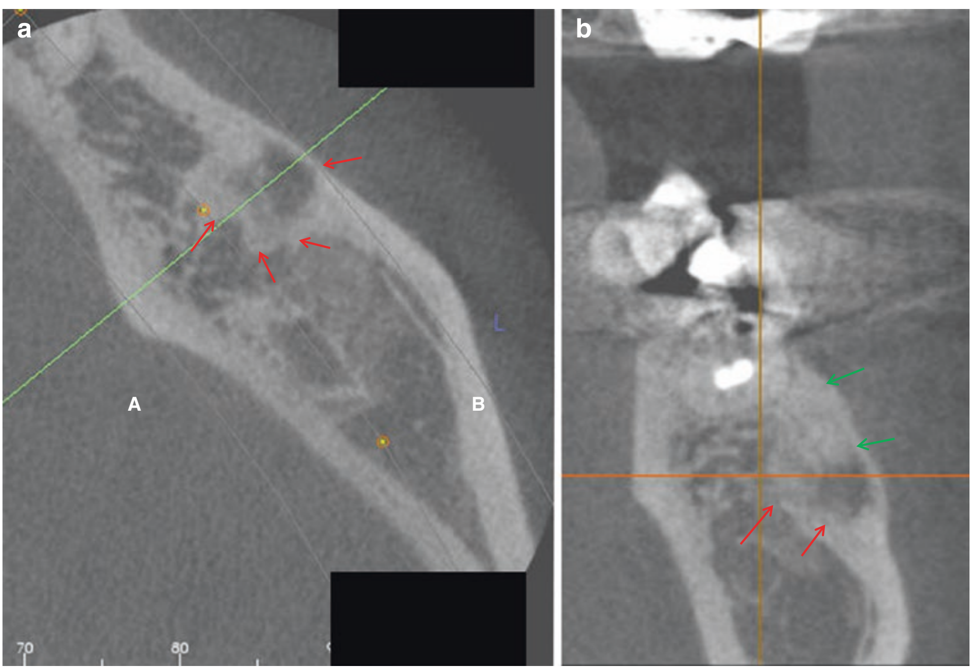

Fig. 15.90 Axial (**a**) and cross-sectional (**b**) CBCT images of a limited FOV scan of the left mandible depicting a "solid type" of periosteal (*green arrows*). Note the central hypodense region surrounded by a thick hyperdense border. The imaging appearance is suggestive of a long-term local inflammatory reaction, possibly related to the previous apical pathology on the adjacent, now root canal filled, tooth

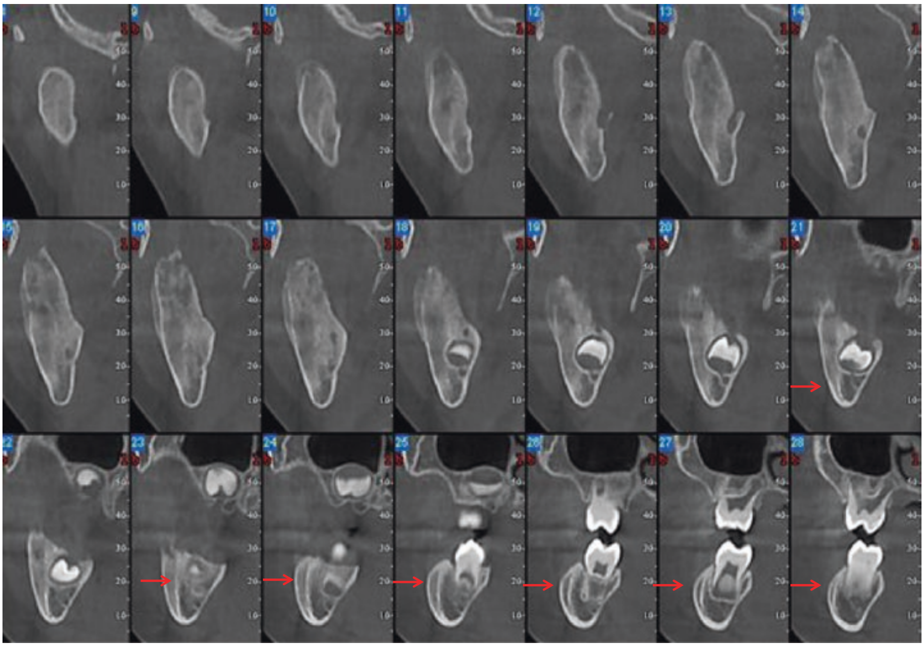

Fig. 15.91 A series of cross-sectional images of the right posterior mandible illustrating “multi-layer” bone deposition on the buccal aspect of the mandible (*red arrows*). This type of periosteal reaction characterizes a more aggressive pathological entity than that of the solid type as in Fig. 15.90. Considering the clinical presentation and access to previous radiography, the imaging features are consistent with the diagnosis of Garre’s osteomyelitis

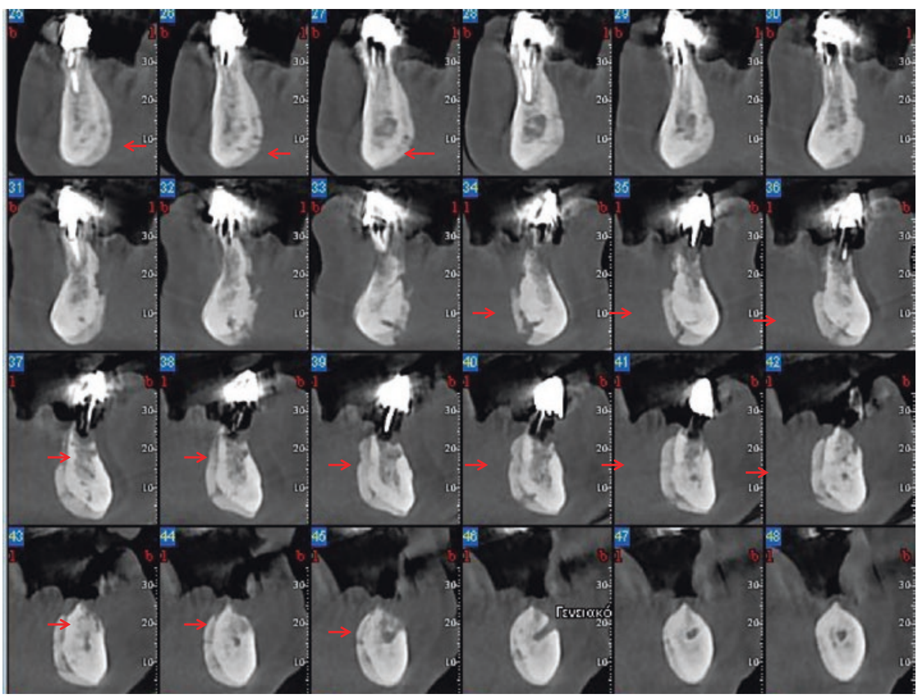

Fig. 15.92 A series of cross-sectional images of the left anterior mandible illustrating “multi-layer” periosteal reaction on the lingual aspect of the mandible (*red arrows*). Bone deposition is interrupted at specific locations suggesting a rapid and disorganized growth. Considering the clinical presentation and medical history, the imaging features are consistent with the diagnosis of medication-related osteonecrosis of the jaws (MRONJ)

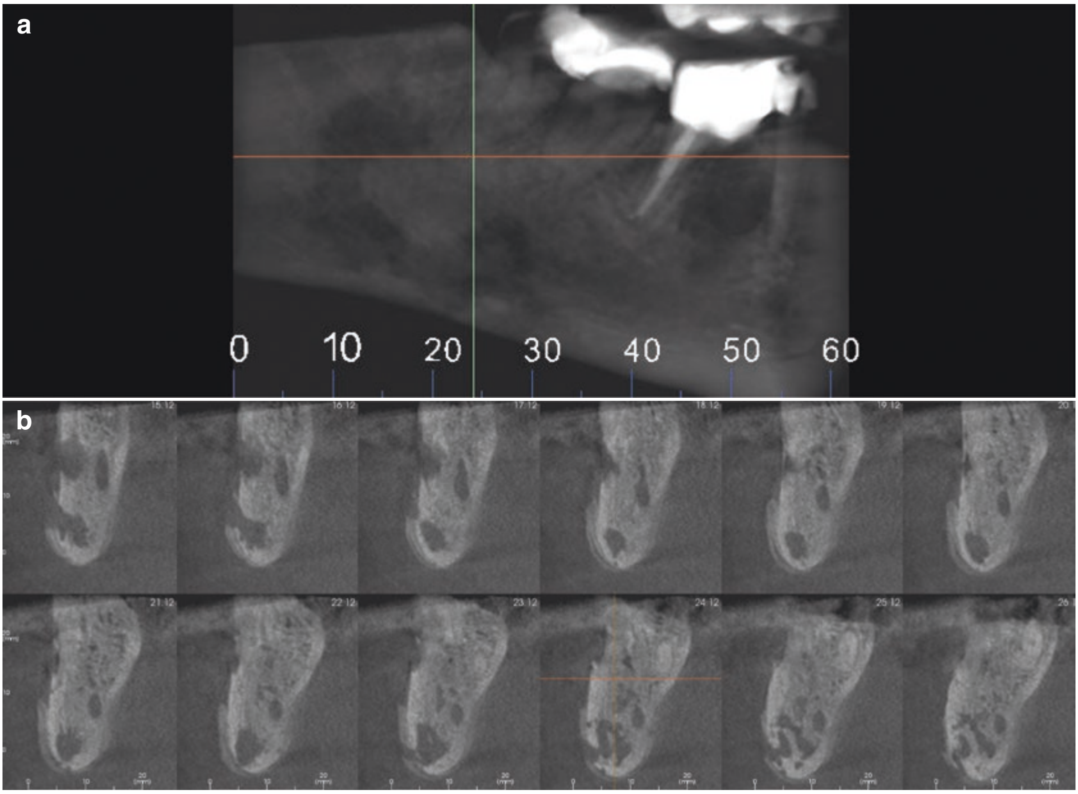

Fig. 15.93 Reformatted panoramic (**a**) and a series of cross-sectional images (**b**) of the right posterior mandible showing interrupted "multi-layer" periosteal reaction on the buccal/inferior cortex combined with extensive destruction of the mandibular bone. This appearance is suggestive of a high level of aggressiveness. Considering the clinical presentation and medical history, the imaging features are consistent with the diagnosis of osteomyelitis

Osteomyelitis (Figs. 15.96 and 15.97)

- Osteoradionecrosis
- Medication related osteonecrosis of the jaw (MRONJ) (Fig. 15.98)
- Malignant lesions (primary or metastatic) (Figs. 15.99 and 15.100)

All of the above pathological entities may demonstrate the following radiologic features:

- Mixed or low-density appearance showing areas of destruction
- Irregular, invasive, permeative borders
- "Moth-eaten" appearance
- Periosteal reaction
- Rapid growth
- Possible paresthesia if they are present in the posterior mandible

The reported medical history, clinical examination, and the history of the present illness must always be applied to imaging findings to direct the most appropriate diagnosis. For example, if a medical history reveals that there was a previous episode of cancer, metastatic disease should always be included on the differential of conditions

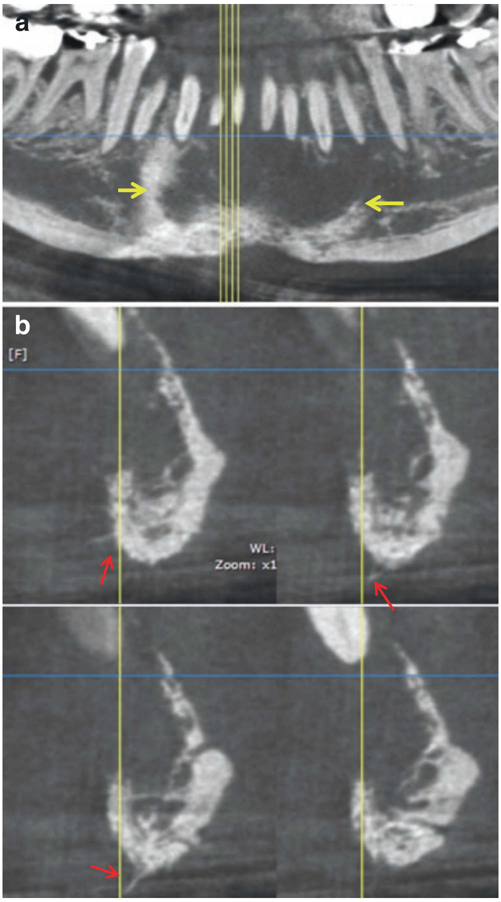

Fig. 15.94 Thin slice reformatted panoramic (**a**) and a series of cross-sectional images of the anterior mandible (**b**) showing a large, irregular, poorly defined, destructive lesion (*yellow arrows*). Note the moth-eaten appearance of the mandibular cortex as well as the fine spicules originating from the cortical plate (*red arrows*). This appearance and periosteal reaction are consistent with a very aggressive entity. Considering the clinical presentation and medical history and biopsy, the imaging features are consistent with the diagnosis of Langerhans cell histiocytosis

producing an ill-defined imaging presentation. Similarly, if the patient presents with clinical signs of inflammation, osteomyelitis may be the first choice. If there is a history of treatment with bisphosphonate medications, medically related osteonecrosis of the jaws should be considered.

15.3.6 Systemic, Metabolic, and Endocrine Disorders

Systemic, metabolic, and endocrine-related pathologic conditions may cause changes in the osseous tissues of the maxillofacial region depicted in CBCT studies. These changes are usually generalized rather than localized and not usually pathognomonic.

The most characteristic radiologic findings are those typically associated with osteoporosis which may present with wide bone marrow spaces or voids in the mandibular bone, thinning of the mandibular cortices and "moth-eaten appearance" of the mandibular cortices (Fig. 15.101). The association of certain radiological indices of the mandibular cortices and osteoporosis has been extensively reported in the literature (Horner et al. 2007; Devlin et al. 2007).

Though not pathognomonic, certain hematologic disorders may present with radiologic findings in the jaws (Figs. 15.102 and 15.103).

Endocrine disorders that may affect calcium balance nay present with radiologic findings in the jaws; hyperparathyroidism, although rarely, may cause marked changes in maxillary and mandibular bone, like brown tumors and osteomalacia (Fig. 15.104).

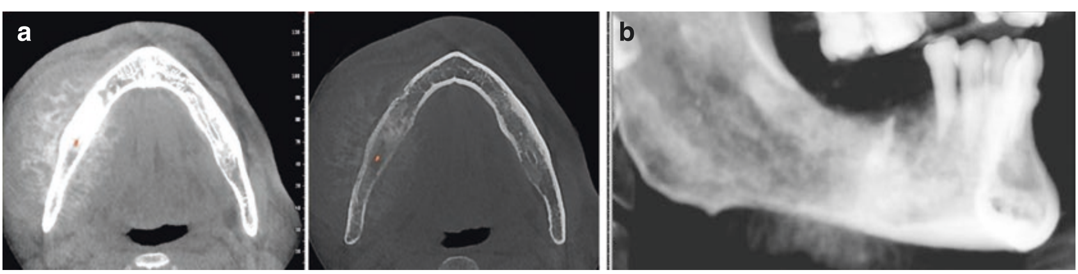

Fig. 15.95 Axial section (soft tissue window—*left*; bone window—*right*) (**a**) and MIP reconstruction (**b**) of the right posterior mandible illustrating a "sunburst" type of periosteal reaction, suggestive of the highest level of lesion aggression. Considering the clinical presentation, medical history and biopsy, the imaging features confirmed the histopathologic diagnosis of osteogenic sarcoma

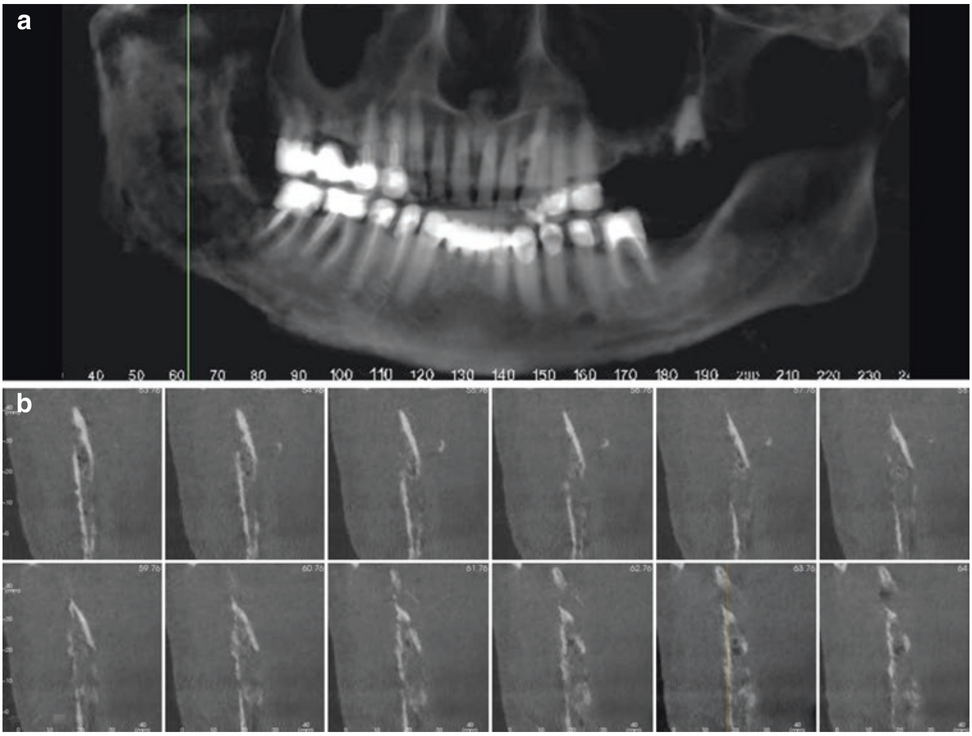

Fig. 15.96 Reformatted panoramic (**a**) and series of cross-sectional images (**b**) illustrating a massive, poorly defined, mixed lesion occupying the entire right mandibular ramus; note the "moth-eaten" appearance and extensive destruction. This was proven to be osteomyelitis, although a malignant lesion could be considered, based on imaging findings alone

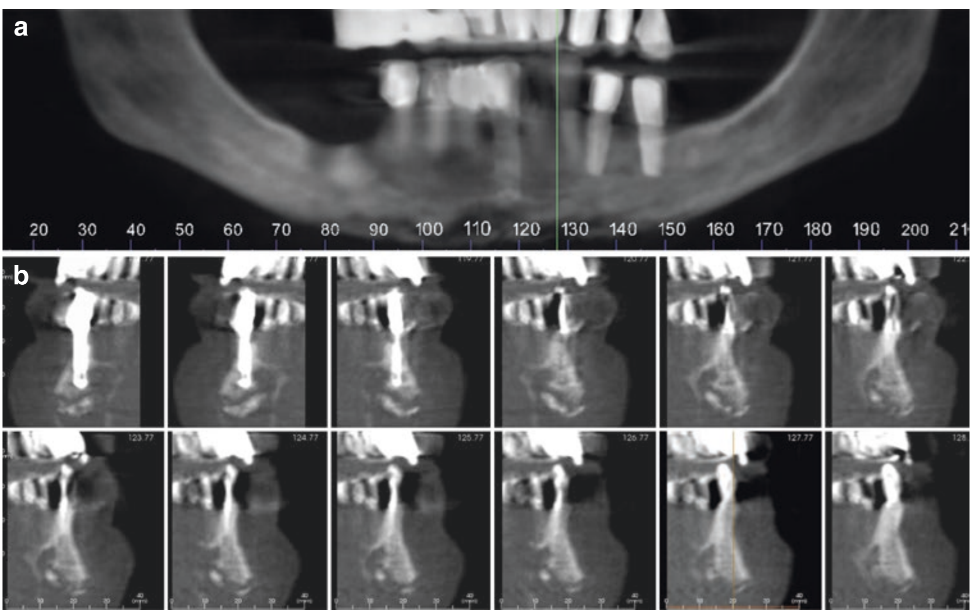

Fig. 15.97 Reformatted panoramic (**a**) and a series of cross-sectional images (**b**) illustrating a massive, poorly defined, mixed lesion occupying the entire anterior mandible. Note the erosion of the inferior cortex and extensive destruction of the mandibular bone. Based on clinical presentation, the imaging features suggest osteomyelitis, which was confirmed by biopsy

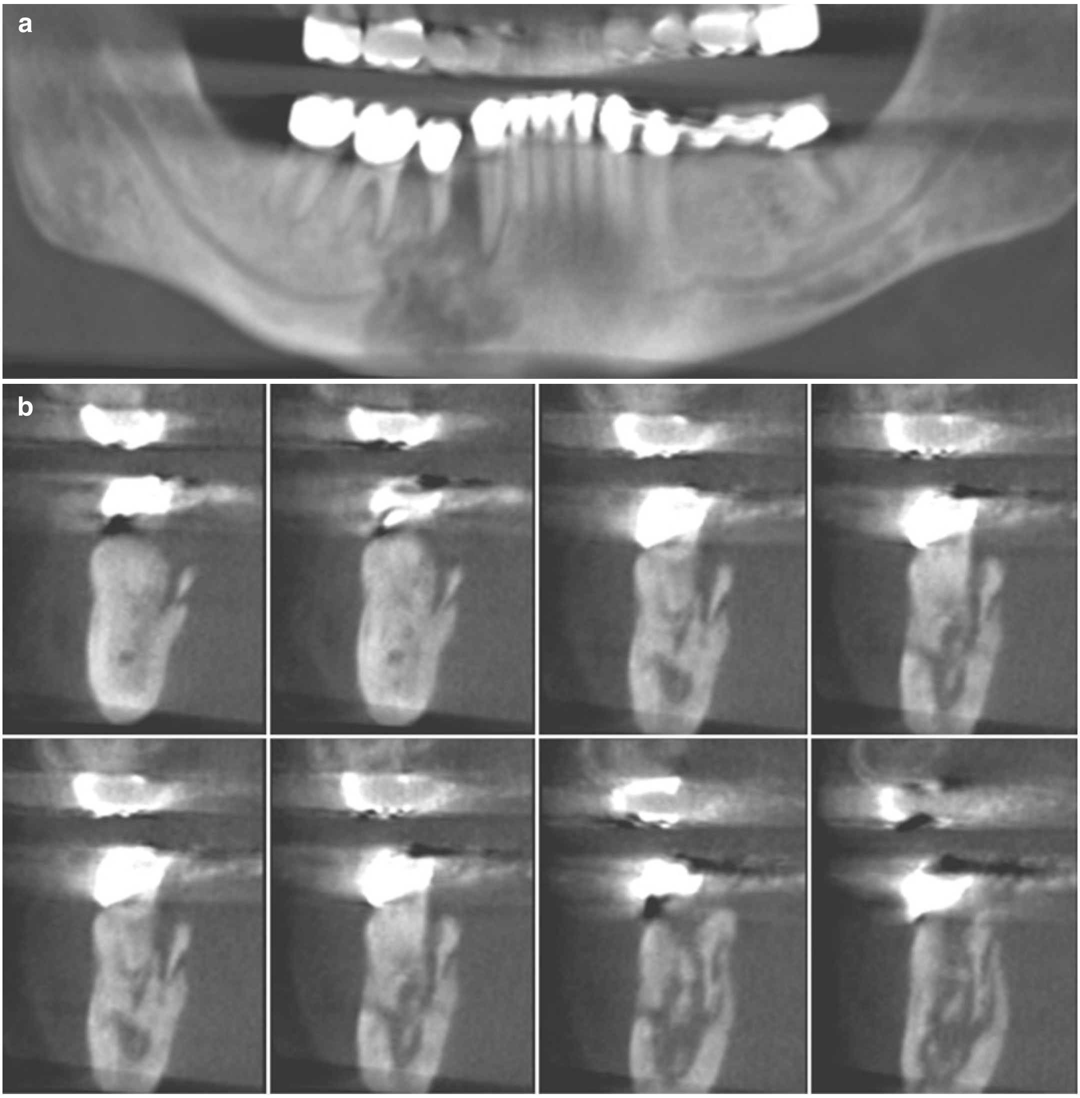

Fig. 15.98 Reformatted panoramic (**a**) and a series of cross-sectional images (**b**) illustrating a large, poorly defined, mixed density lesion in the mandibular right canine/premolar region. Note the localized destruction of the mandibular bone and the diffuse sclerosis extending throughout the mandible. Based on clinical presentation and medical history, the imaging features suggest medication-related osteonecrosis of the jaws (MRONJ), which was confirmed by biopsy

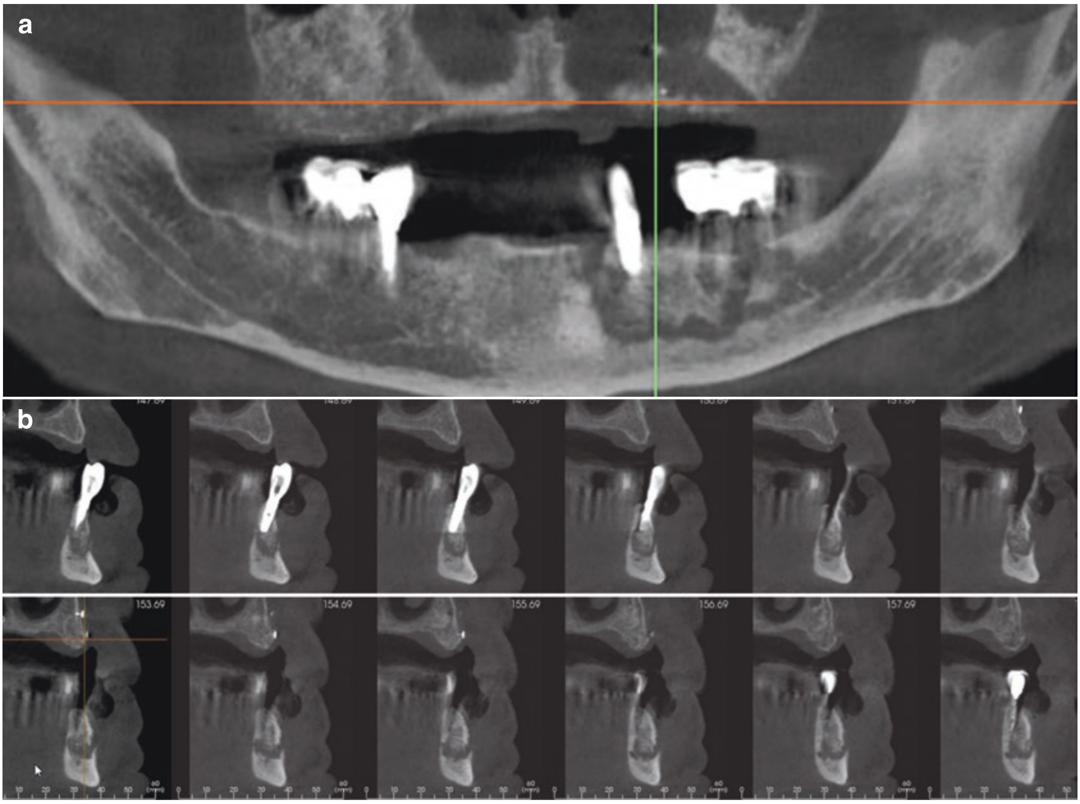

Fig. 15.99 Reformatted panoramic (**a**) and a series of cross-sectional images (**b**) illustrating a large, poorly defined, mixed density lesion in the mandibular left premolar/molar region. The entity appears to be surrounded by a wide irregular low-density zone whereas there are signs of considerable destruction of the osseous tissue in the affected area. Inferior alveolar nerve paresthesia was reported. Although similar to the imaging findings presented in Figs. 15.96, 15.97, and 15.98, based on biopsy the final diagnosis was s metastatic carcinoma from the lung

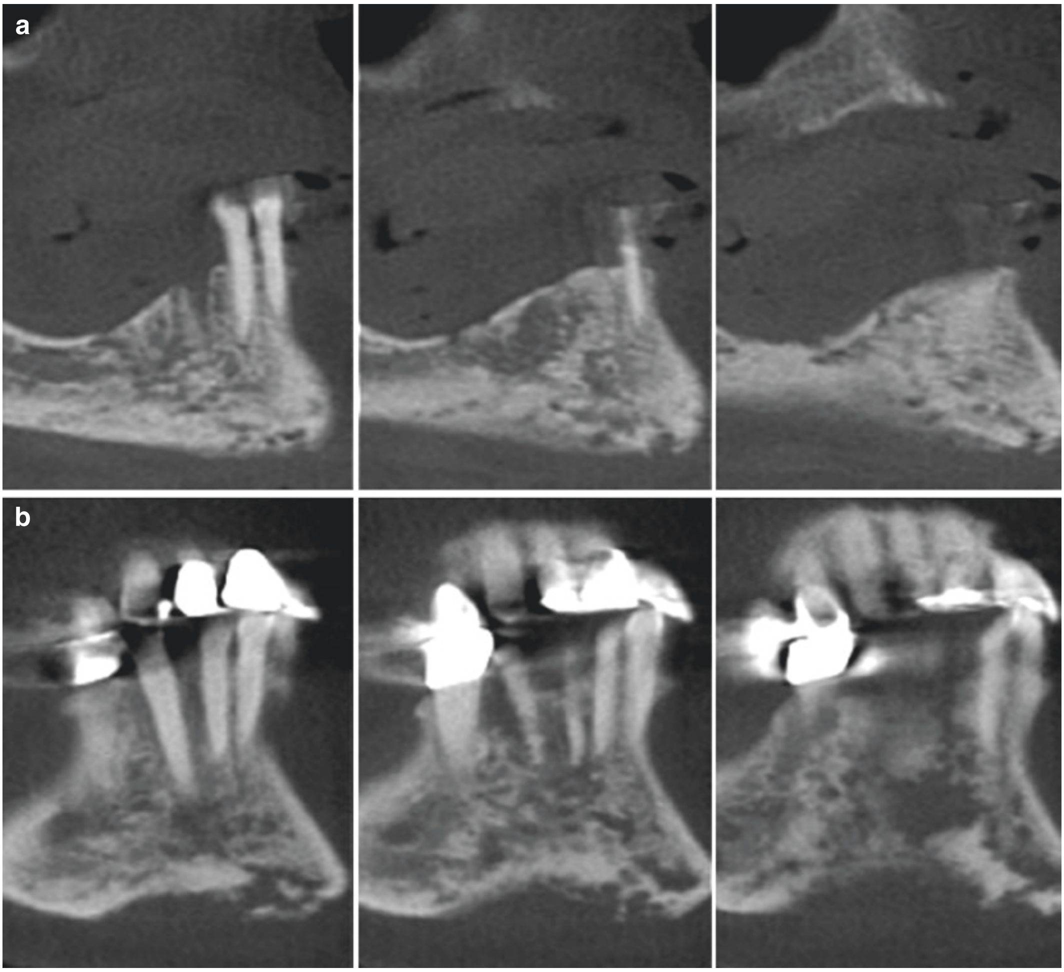

Fig. 15.100 Sagittal (**a**) sections of the anterior mandible illustrating the "moth-eaten" appearance of the mandibular bone for a patient diagnosed with medication-related osteonecrosis of the jaws. Coronal (**b**) images of a different patient in the same area demonstrating almost identical radiologic findings. However in the latter case, histopathologic diagnosis was metastatic cancer

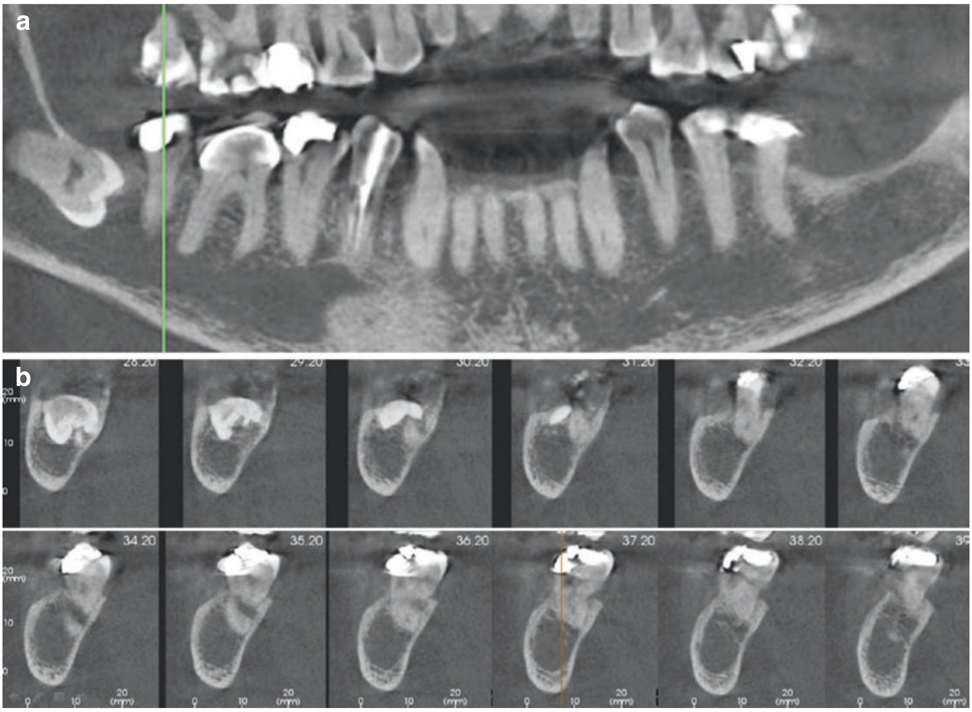

Fig. 15.101 Reformatted panoramic (**a**) and a series of cross-sectional images (**b**) showing generalized thinning of the mandibular cortex, large voids in the cancellous component of the mandibular bone and a "moth-eaten" appearance. The imaging findings are consistent with osteoporosis of the mandible

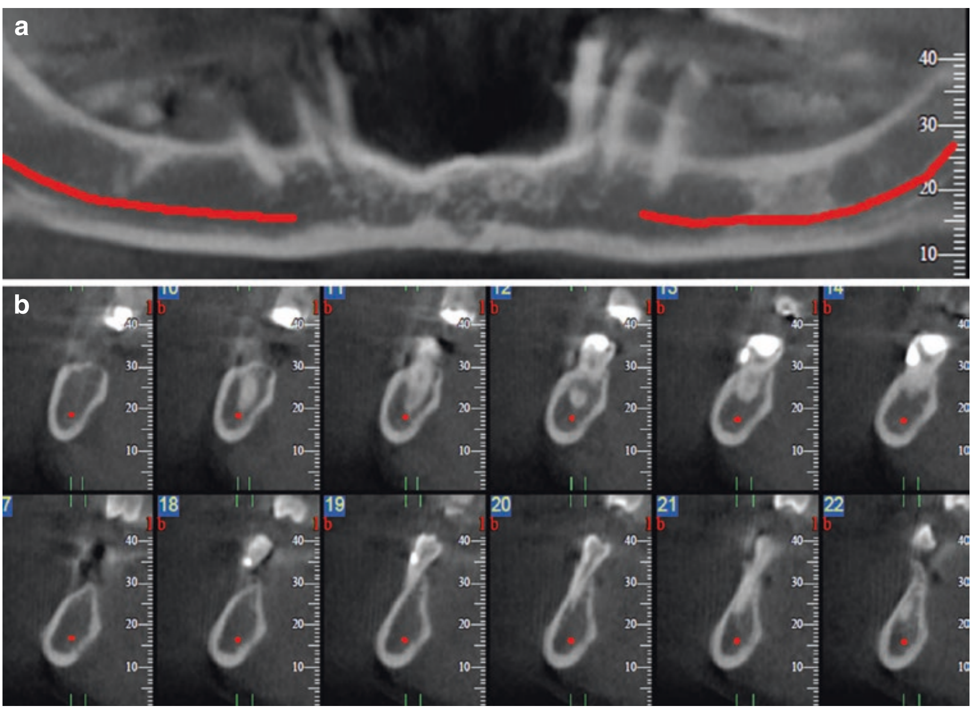

Fig. 15.102 Reformatted panoramic (**a**) and a series of cross-sectional images (**b**) of a patient diagnosed with sickle cell anemia. Note the generalized rarefaction of the mandible; however, this is not a distinctive feature of the disease

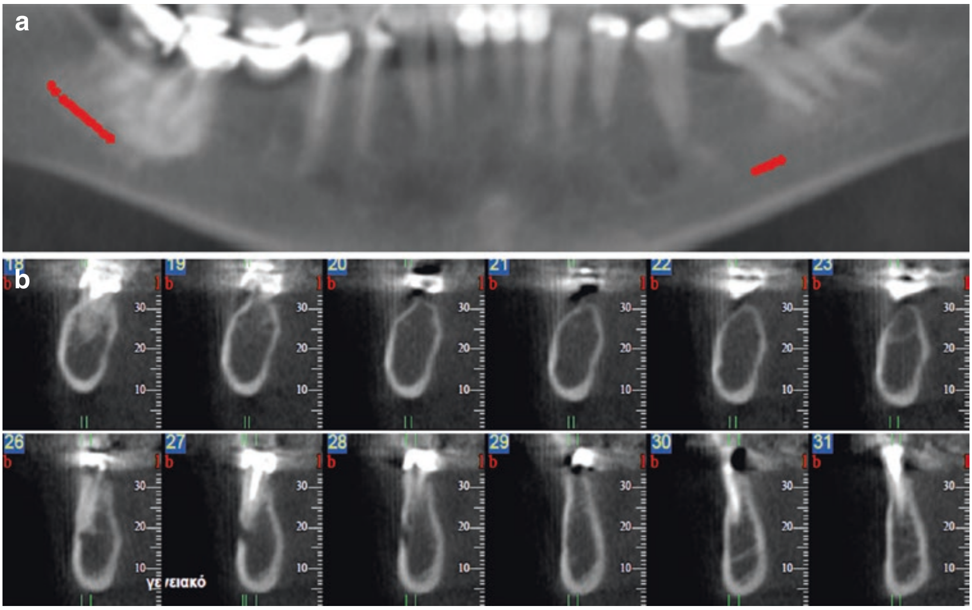

Fig. 15.103 Reformatted panoramic (**a**) and a series of cross-sectional images (**b**) of a patient diagnosed with thalassemia illustrating generalized rarefaction of the mandible, however, this is not a distinctive feature of the disease

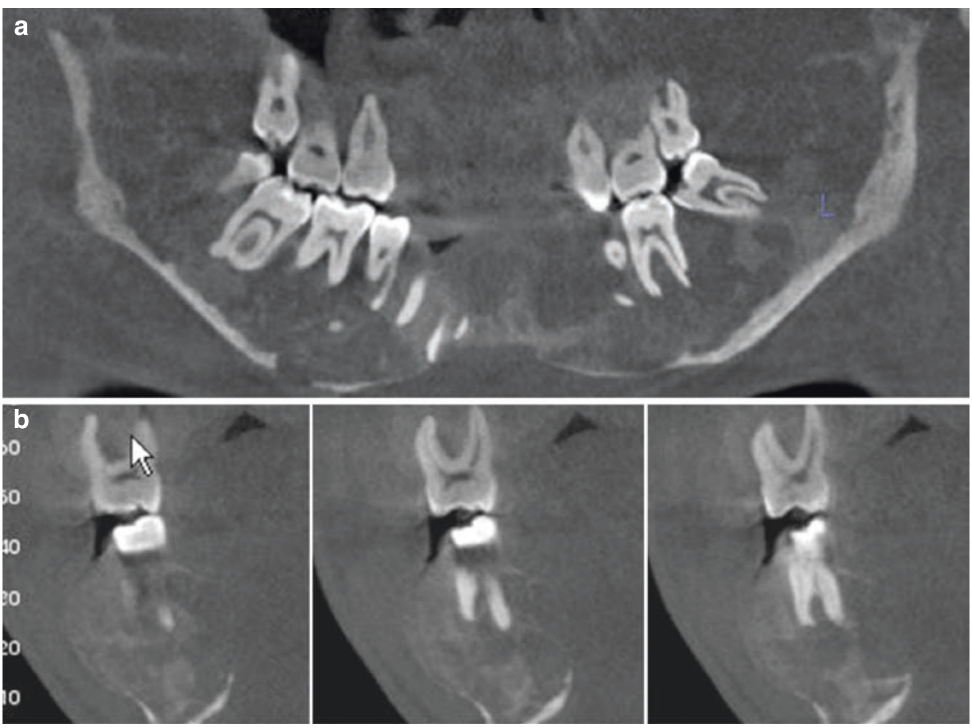

Fig. 15.104 Reformatted thin panoramic (**a**) and a series of cross-sectional images (**b**) of a patient in chronic renal failure and secondary hyperparathyroidism. Note the extensive changes in the appearance of the maxillary and mandibular bones, with bicortical expansion and loss of bone density due to osteomalacia

Acknowledgments Some figures are reproduced with permission from Wiley-Blackwell, the British Journal of Radiology and Elsevier (Clinical Radiology).

References

Al-Moraissi EA, Pogrel MA, Ellis E 3rd (2016) Enucleation with or without adjuvant therapy versus marsupialization with or without secondary enucleation in the treatment of keratocystic odontogenic tumors: A systematic review and meta-analysis. J Craniomaxillofac Surg 44:1395–403

Bechara B, McMahan CA, Geha H, Noujeim M (2012) Evaluation of a cone beam CT artefact reduction algorithm. Dentomaxillofac Radiol 41:422–8

Chadwick JW, Alsufyani NA, Lam EW (2011) Clinical and radiographic features of solitary and cemento-osseous dysplasia associated simple bone cysts. Dentomaxillofac Radiol 40:230–235

Cheng J, Wang Y, Yu H, Wang D, Ye J, Jiang H, Wu Y, Shen G (2012) An epidemiological and clinical analysis of craniomaxillofacial fibrous dysplasia in a Chinese population. Orphanet J Rare Dis 7:80–86

Devlin H, Karayianni K, Mitsea A, Jacobs R, Lindh C, van der Stelt P, Marjanovic E, Adams J, Pavitt S, Horner K (2007) Diagnosing osteoporosis by using dental panoramic radiographs: the OSTEODENT project. Oral Surg Oral Med Oral Pathol Oral Radiol Endod 104:821–828

Faitaroni LA, Bueno MR, Carvalhosa AA, Mendonça EF, Estrela C (2011) Differential diagnosis of apical periodontitis and nasopalatine duct cyst. J Endod 37:403–410

Gonzalez SM (2015) Describing radiographic lesions at: https://oralradiology.wordpress.com/describing-radiographic-lesions/. Accessed 6 Mar 2015

Horner K, Karayianni K, Mitsea A, Berkas L, Mastoris M, Jacobs R, Lindh C, van der Stelt P, Marjanovic E, Adams J, Pavitt S, Devlin H (2007) The mandibular cortex on radiographs as a tool for osteoporosis risk assessment: the OSTEODENT project. J Clin Densitom 10:138–146

Kaplan I, Nicolaou Z, Hatuel D, Calderon S (2008) Solitary central osteoma of the jaws: a diagnostic dilemma. Oral Surg Oral Med Oral Pathol Oral Radiol Endod 106:e22–e29

Kühl S, Walter C, Acham S, Pfeffer R, Lambrecht JT (2012) Bisphosphonate-related osteonecrosis of the jaws—a review. Oral Oncol 48:938–947

MacDonald D (2011) Oral and maxillofacial radiology: a diagnostic approach. Wiley-Blackwell, Hoboken, pp 1–39

MacDonald DS, Zhang L, Gu Y (2012) Calcification of the external carotid arteries and their branches. Dentomaxillofac Radiol 41:356–61.

MacDonald D, Gu Y, Zhang L, Poh C (2013) Can clinical and radiological features predict recurrence in solitary odontogenic keratocysts? Oral Surg Oral Med Oral Pathol Oral Radiol 115:263–271

MacDonald DS, Li TK, Goto TK (2015) A consecutive case series of nevoid basal cell carcinoma syndrome affecting the Hong Kong Chinese. Oral Surg Oral Med Oral Pathol Oral Radiol 120:408–15

MacDonald DS (2015a) Maxillofacial fibro-osseous lesions. Clin Radiol 70:25–36

MacDonald DS (2015b) A systematic review of the literature of nevoid basal cell carcinoma syndrome affecting East Asians and North Europeans. Oral Surg Oral Med Oral Pathol Oral Radiol 120:396–407

MacDonald D (2016) Lesions of the jaws presenting as radiolucencies on cone-beam CT. Clin Radiol 71:972–85

MacDonald D (2017) Cone-beam computed tomography and the dentist. J Investig Clin Dent 8(1). doi: 10.1111/jicd.12178.

MacDonald-Jankowski DS (1995) Traumatic bone cysts in the jaws of a Hong Kong Chinese population. Clin Radiol 50:787–791

MacDonald-Jankowski DS (1999) Idiopathic osteosclerosis in the jaws of Britons and of the Hong Kong Chinese: radiology and systematic review. Dentomaxillofac Radiol 28:357–63

MacDonald-Jankowski DS (2004) Fibro-osseous lesions of the face and jaws. Clin Radiol 59:11–25

MacDonald-Jankowski DS, Li TK (2009) Fibrous dysplasia in a Hong Kong community: the clinical and radiological features and outcomes of treatment. Dentomaxillofac Radiol 38:63–72

MacDonald-Jankowski D (2009) Fibrous dysplasia: a systematic review. Dentomaxillofac Radiol 38:196–215

MacDonald-Jankowski DS (2010) Glandular odontogenic cyst: systematic review. Dentomaxillofac Radiol 39:127–139

Mathew R, Omami G, Gianoli D, Lurie A (2012) Unusual cone-beam computerized tomography presentation of traumatic (simple) bone cyst: case report and radiographic analysis. Oral Surg Oral Med Oral Pathol Oral Radiol 113:410–413

McDonnell D (1993) Dense bone island. A review of 107 patients. Oral Surg Oral Med Oral Pathol 76:124–128

Noffke CE, Raubenheimer EJ, MacDonald D (2012) Fibro-osseous disease: harmonizing terminology with biology. Oral Surg Oral Med Oral Pathol Oral Radiol 114:388–192

Rana RS, Wu JS, Eisenberg RL (2009) Periosteal reaction. AJR Am J Roentgenol 193:259–272

Rosenberg PA, Frisbie J, Lee J, Lee K, Frommer H, Kottal S, Phelan J, Lin L, Fisch G (2010) Evaluation of pathologists (histopathology) and radiologists (cone beam computed tomography) differentiating radicular cysts from granulomas. J Endod 36:423–428

Ruggieri P, Sim FH, Bond JR, Unni KK (1994) Malignancies in fibrous dysplasia. Cancer 73:1411–1424

Scarfe WC, Farman AG (2008) What is cone-beam CT and how does it work? Dent Clin N Am 52:707–30

Slootweg PJ (2006) Chapter 4. Maxillofacial bone and teeth. In: Cardesa A, Slootweg PJ (eds) Pathology of the head and neck. Springer, Heidelberg, pp 104–131

Speight P, Fantasia JE, Neville BW. (2017) Oodontogenic and non-odontogenic development cysts. In El-nagger AK, Chan JK, Grandis JR, Takata T, Slootweg PJ.

(Eds.), WHO classification of head and neck tumours. 4th ed., Lyon: International Agency for research on Cancer. pp. 235–7

Suei Y, Taguchi A, Nagasaki T, Tanimoto K (2010) Radiographic findings and prognosis of simple bone cysts of the jaws. Dentomaxillofac Radiol 39:65–71

Suter VG, Büttner M, Altermatt HJ, Reichart PA, Bornstein MM (2011) Expansive nasopalatine duct cysts with nasal involvement mimicking apical lesions of endodontic origin: a report of two cases. J Endod 37:1320–1326

Tortorici S, Amodio E, Massenti MF, Buzzanca ML, Burruano F, Vitale F (2008) Prevalence and distribution of odontogenic cysts in Sicily: 1986-2005. J Oral Sci 50:15–18

Treister NS, Friedland B, Woo SB (2010) Use of cone-beam computerized tomography for evaluation of bisphosphonate-associated osteonecrosis of the jaws. Oral Surg Oral Med Oral Pathol Oral Radiol Endod 109:753–764

Uribe S, Rojas L, Rosas C (2013) Accuracy of imaging methods for detection of bone tissue invasion in patients with oral squamous cell carcinoma. Dentomaxillofac Radiol 42:20120346

Velez I, Siegel MA, Mintz SM, Rolle R (2010) The relationship between idiopathic bone cavity and orthodontic tooth movement: analysis of 44 cases. Dentomaxillofac Radiol 39:162–166

White S, Pharoah M (2009) Oral radiology: principles and interpretation, 7th edn. Mosby, St. Louis

Wright JM, Vered M (2017) Update from the 4th edition of the World Health Organization classification of head and neck tumours: odontogenic and maxillofacial bone tumors. Head Neck Pathol 11:68–77

16 Incidental Findings on CBCT

Jie Yang, William C. Scarfe,
and Christos Angelopoulos

Contents

J. Yang, D.D.S., M.Med.Sc., M.S., D.M.D. (✉)
Division of Oral and Maxillofacial Radiology, Department of Oral and Maxillofacial Pathology, Medicine, and Surgery, Temple University Kornberg School of Dentistry, Philadelphia, PA, USA
e-mail: jieyang@temple.edu

W.C. Scarfe, B.D.S., F.R.A.C.D.S., M.S.
Division of Radiology and Imaging Science, Department of Surgical/Hospital Dentistry, University of Louisville School of Dentistry, Louisville, KY, USA
e-mail: William.scarfe@louisville.edu

C. Angelopoulos, D.D.S., M.Sc.
Aristotle University of Thessaloniki, Thessaloniki, Greece

Columbia University, College of Dental Medicine, New York City, NY, USA
e-mail: angelopoulosc@gmail.com

16.1 Introduction

An incidental finding is a generic term applied in radiology to describe an occult entity discovered unexpectedly on an imaging examination performed for an unrelated reason. Some incidental findings on CBCT images are readily identifiable based on radiologic presentation and location (e.g., tonsilloliths) whereas others may be inconclusive and may present as a radiologic diagnostic dilemma. It is not uncommon for many physiological features, normal variants, minor developmental anomalies, and imaging artifacts to be misidentified as potential pathology by untrained or inexperienced observers. The latter may result in unnecessary concern for the patient and result in inappropriate and costly supplemental tests and imaging.

One area that has received little attention in oral and maxillofacial (OMF) CBCT imaging thus far is the professional, ethical, clinical, and

W.C. Scarfe, C. Angelopoulos (eds.), *Maxillofacial Cone Beam Computed Tomography*,
https://doi.org/10.1007/978-3-319-62061-9_16

legal issues involved in the recognition and management of incidental disease or findings, particularly those where diagnosis is indeterminate. The availability and use of CBCT imaging continues to expand into all areas of dentistry giving rise to more and more imaging studies. Not surprisingly, the growing number of these studies is partly responsible for a commensurate increase in incidental findings. However, other factors such as the greater image resolution of CBCT units, growing knowledge of practitioners, and heightened awareness of medicolegal issues also contribute to the perceived rise in incidental findings.

As the numbers of clinicians who own and operate CBCT equipment and interpret their own images continues to overshadow those with formal training in OMF radiology guidance on recognition, interpretation, and appropriate management of these findings is necessary.

16.2 Incidental Findings on Medical Diagnostic Images

16.2.1 Prevalence

The prevalence of occult disease or findings in imaging diagnostic tests in medical radiology is surprisingly high. Lumbreras et al. (2010) performed a systematic review of the available evidence on the frequency and management of incidental findings in medical imaging diagnostic tests. From the 26 included CT articles they found the mean frequency of incidental findings was 31.1% (95% confidence interval, 20.1–41.9%). They proposed a simplistic, albeit subjective, classification system of the incidental findings detected according to their clinical importance: major, moderate, and minor.

Two recent studies have quantified the prevalence of significant findings for advanced imaging involving the head, from a medical radiology perspective. In the largest study to date, involving almost 16,000 CT scans of children involved in blunt trauma, Rogers et al. (2013) reported 4% (95% confidence interval: 3.8–4.5%) of children had incidental findings on their CT scans unrelated to their injury. 30% of children with incidental findings warranted immediate intervention or outpatient follow-up with 4% required immediate attention (tumors) and 26% required follow-up (mainly sinus conditions).

16.2.2 Significance

Incidental findings identified on medical radiological studies present a dilemma. In medical radiology practice, failure to report what is believed to be occult disease of equivocal or carrying some degree of clinical significance may well have medical-legal ramifications (Berlin 2011). On the other hand, reporting clinically insignificant incidental entities can result in **overdiagnosis**; *this means the diagnosis of a condition* that would otherwise not go on to cause morbidity or mortality or even not being present. In other words, diagnosing insignificant entities, or even non-existing ones. This may lead to a cascade of unnecessary tests and may overwhelm and distress patients if their having the information will provide no obvious benefit. A patient's right to autonomy must be balanced with the ethical obligations of physicians to do good for patients (beneficence) and to not harm them (non-maleficence) (Epstein et al. 2010)). Individual radiologists should report the incidental findings they detect and use existing evidence-based recommendations when possible (Brown 2013); however, agreement is lacking between individuals, departments, institutions nationally and internationally for the management of commonly encountered incidental findings (Johnson et al. 2011).

Concern among the medical radiology community in the United States has reached a level where various "white" papers have been developed to provide guidance to radiologists on specific topics such as abdominal CT (Berland et al. 2010), adnexal (Patel et al. 2013), vascular (Khosa et al. 2013), splenic and nodal (Heller et al. 2013), and gallbladder and biliary findings (Sebastian et al. 2013). While not specifically pertinent to oral and maxillofacial radiology, they do provide a methodology incorporating classification based on description of the lesion and algorithms involving steps that involve further data gathering to affect management (e.g., categorization, demographics, history) or action (e.g., performing an additional imaging study, following up, or intervening with a biopsy or surgery). The identification of incidental findings on the images of research subjects has received particular attention (Ballantyne 2008) from not only the medical (Booth et al. 2010) but also the legal profession (Tovino 2008) with even the development of management pathways and disclosure recommendations (Wolf et al. 2008).

In the United States, broad recommendations for handling incidental and secondary findings in clinical, research, and direct-to-consumer settings have been proposed (Presidential Commission for the Study of Bioethical Issues 2013):

- Practitioners should inform potential recipients about the possibility of incidental or secondary findings, and if and how those findings will be disclosed, before the start of a test or procedure. Informed consent and open communication between providers and potential recipients is essential.
- Professional representative groups should develop guidelines that categorize findings likely to arise from each diagnostic modality, and develop best practices for managing them.
- Research should be performed to keep abreast of the rapidly evolving types and frequency of findings; potential costs, benefits, and harms; and recipient and practitioner preferences about incidental and secondary findings.
- Public and private entities should prepare materials and enhance education of all stakeholders, including practitioners, institutional review boards, and potential recipients about the ethical, practical, and legal considerations raised by incidental and secondary findings.

In the clinical context, these recommendations can be applied to the consent process and present specific guidelines:

- Patients should be alerted that a particular test or procedure could or will give rise to anticipatable incidental and secondary findings before testing occurs so that patients have the opportunity to express preferences regarding their disclosure and subsequent management.
- Patients should be notified about the possibility that unanticipated findings could arise that could lead to additional diagnostic testing or clinical care.
- Patients should be given the opportunity to ask questions, state reservations, and express preferences about the return and management of incidental and secondary findings.
- Patients should be allowed the opportunity to "opt out" of information that is not pertinent to their immediate well-being.

16.3 CBCT Incidental Findings

16.3.1 Prevalence

Compared to advanced medical imaging modalities, where soft tissue differences are discernible, one might expect CBCT imaging to be less likely to result in the identification of incidental findings. However numerous authors have reported on the frequency of incidental findings on CBCT. While these vary widely depending on age groups, population studied, study purpose, field of view, and category of findings, they are consistently approximately 50% (Miles 2005; Arnheiter et al. 2006; Cha et al. 2007; Pliska et al. 2011; Drage et al. 2013; Pette et al. 2012; Price et al. 2012; Çağlayan and Tozoğlu 2012; Allareddy et al. 2012; Balshi et al. 2013) (Tables 16.1, 16.2, and 16.3). In order to systematically review CBCT images, incidental findings can be classified based on anatomic locations and clinical significances. Depending on field of view and study purpose, CBCT images may cover dental structures in the maxilla and mandible, paranasal sinuses, nasal fossa, pharyngeal airway, TMJ, skull base and temporal bone, cervical spine and neck soft tissues. Clinical significance can be classified into low, intermediate, and high significance (Table 16.1). Findings with a low significance normally do not require a clinical and radiographic follow-up while an intermediate significance may do. High significant findings usually require an immediate clinical and therapeutic intervention.

Table 16.1 Categorization and reported prevalence of incidental findings of low potential clinical significance on CBCT according to anatomic location

Location	Entity	Example(s)	Prevalence Range
Dental/jaws	Enostosis/osteosclerosis	Fig. 16.1	14.1%[a]/6.7%[b]/1.9%[c]/3.5%[d]
	Torus/exostosis	Figs. 16.2 and 16.3	10.6%[b]
Paranasal sinuses	Mucosal thickening	Fig. 16.4	31.3%[e]/17.6%[f]/19.41%[c]/34.9%[g]/15%[b]/62.6%[h]/23.7%[i]/48.5%[j]/25.5%[k]/35.6%[d]
	Retention pseudocysts	Fig. 16.5	2.9%[e]/16.4%[k]/5.8%[b]/19.4%[i]/21.4%[h]/6.89%[c]/11.5%[d]
	Hypoplasia	Fig. 16.6	2.1%[a]/4.8%[h]/1.68%[l]
	Antral septations		44.4%[h]/20.6%[j]
	Pneumatization of sinuses	Fig. 16.7	2.7%[d]
Nasal fossa	Deviated nasal septum	Fig. 16.8	12.6%[e]/5.2%[f]/5.34%[c]/9.4%[k]/19.5%[d]
	Conchae bullosa	Figs. 16.5 and 16.9	3.9%[e]/1.4%[f]/3.56%[c]/7.4%[b]/7.6%[k]/3.4%[d]
Pharyngeal airway	Tonsillar hypertrophy and anomalies	Fig. 16.10, 16.11, and 16.12	10.7%[a]/18.3%[c]
	Tonsilloliths	Fig. 16.13	9.2%[a]/4.9%[b]/10.1%[k]
TMJ	DJD	Fig. 16.14	8.2%[e]/15.8%[a]/6.28%[c]/6.17%[g]/15.3%[b]/27.1%[k]/32.6%[d]
	Remodeling		5.3%[d]
	Bifid condyle	Fig. 16.15	2.9%[e]/0.12%[c]
Skull base/brain	Pineal gland calcification	Fig. 16.16	14.7%[a]/19.2%[k]
Cervical spine	Degenerative changes	Fig. 16.17	24%[a]/1.3%[c]/4.93%[g]/45.6%[k]/12.6%[d]
	Non-segmentation C2–3		0.2%[a]
	Fixation hardware		0.3%[a]
Neck soft tissues	Stylohyoid ligament calcification	Fig. 16.18	9%[b]/3.1%[k]
	Calcified thyroid cartilage/ triticeous cartilage	Fig. 16.19	3.9%[b]

TMJ temporomandibular joint, *DJD* degenerative joint disease (osteoarthrosis), *C2* 2nd cervical vertebrae, *C3* 3rd cervical vertebrae
[a]Allareddy et al. (2012)
[b]Price et al. (2012)
[c]Edwards et al. (2014)
[d]Balshi et al. (2013)
[e]Çağlayan and Tozoğlu (2012)
[f]Doğramaci et al. (2014)
[g]Drage et al. (2013)
[h]Lana et al. (2012)
[i]Pazera et al. (2011)
[j]Dobele et al. (2013)
[k]Pette et al. (2012)
[l]Edwards et al. (2013)

Considering the penetration of CBCT imaging into dental practices, most studies report findings from a relatively small sample (less than 400 subjects). Only one study attempted to classify incidental disease into groups regarding their potential clinical significance and found that while 16.1% required follow-up or referral, this was mostly in regard to questionable periapical status (Price et al. 2012). Only one study has reported for a sample size of 1000 subjects, within which three malignancies were identified incidentally (Allareddy et al. 2012).

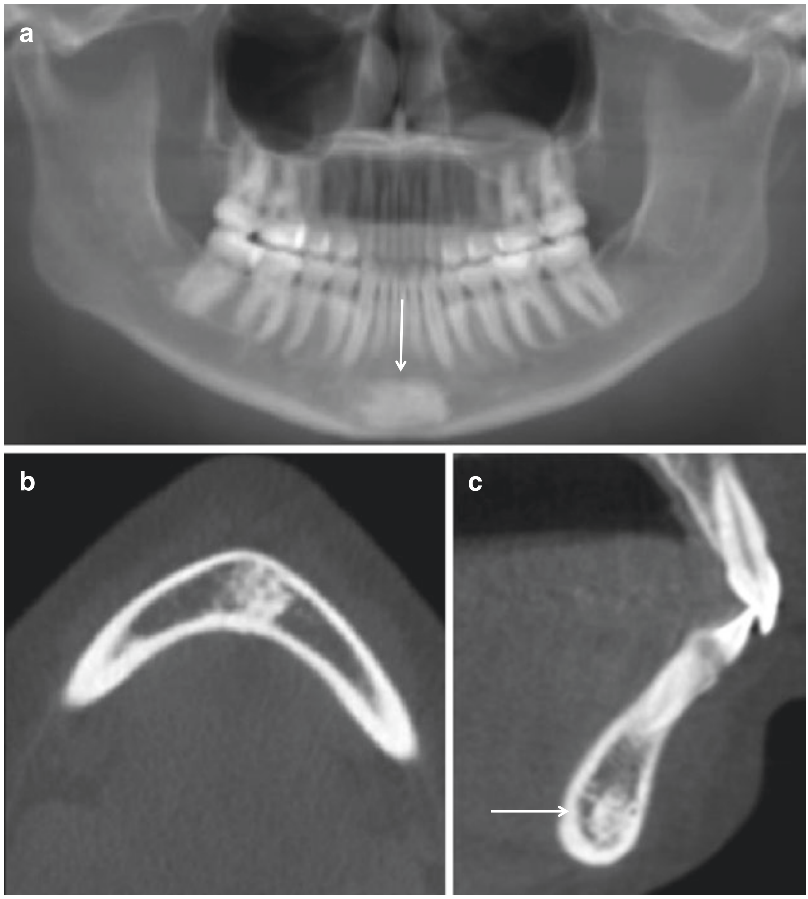

Fig. 16.1 Reformatted panoramic (**a**), axial (**b**), and sagittal (**c**) images show a hyper attenuating area in the anterior mandible. The attenuation approximates that of cortical bone. The entity is located between the buccal and lingual cortical plates, and blends into the surrounding bone. The appearances are consistent with enostosis or idiopathic osteosclerosis

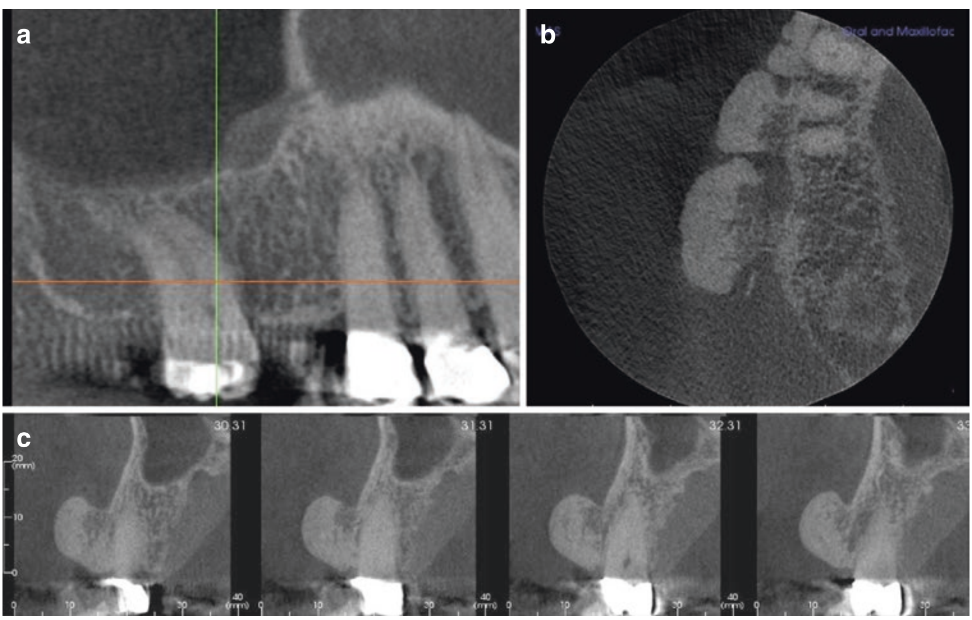

Fig. 16.2 Cropped reformatted panoramic (**a**), axial (**b**), and serial cross-sectional (**c**) CBCT images of the maxillary right posterior dental alveolus showing a massive pedunculated buccal exostoses adjacent to the premolar and molar areas

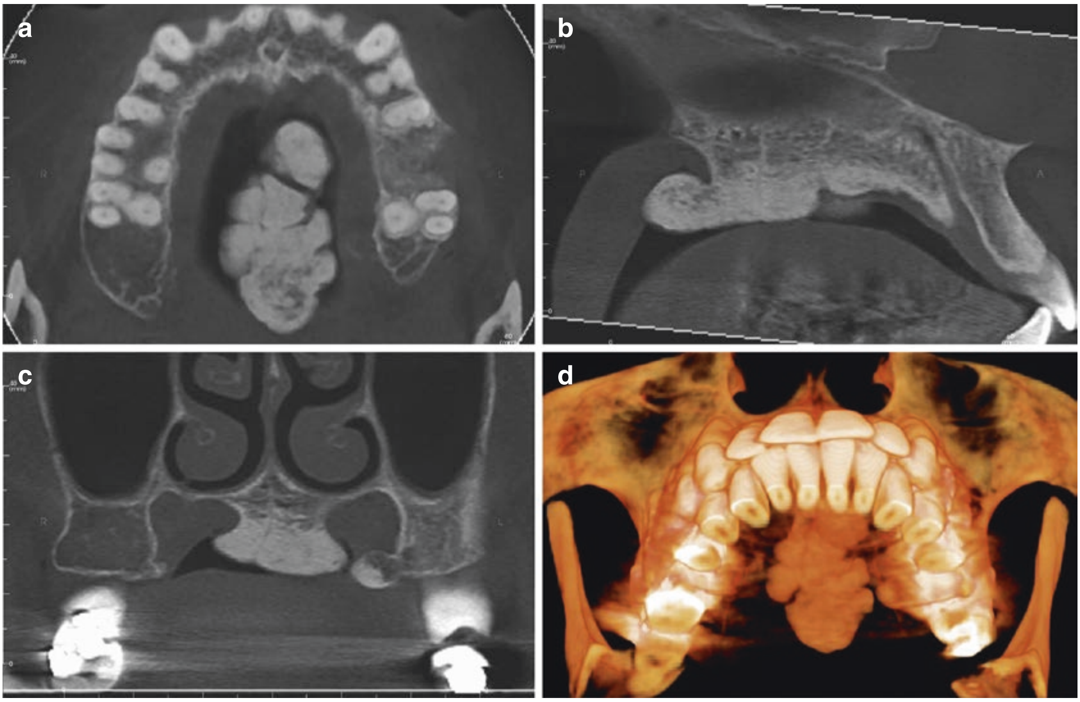

Fig. 16.3 Axial (**a**), midsagittal (**b**), coronal (**c**), and infero-oblique volumetric (**d**) CBCT images showing a large midline palatal torus and localized left palatal alveolar exostosis in the region adjacent to the premolars/molars

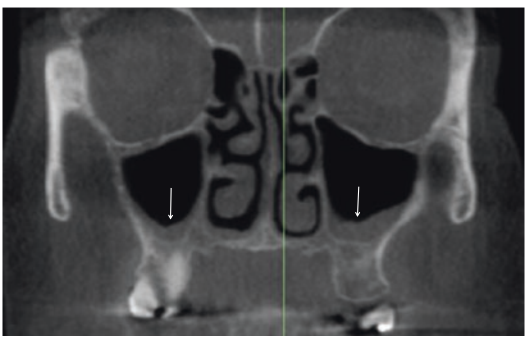

Fig. 16.4 Coronal image shows mucosal thickening of the maxillary sinuses (*thin arrows*). The floor of the maxillary sinuses bilaterally is intact

Fig. 16.5 Coronal CBCT image shows a dome-shaped, non-corticated, and homogenous soft tissue density in the right maxillary sinus (*thin arrow*). The sinus floor is intact. The appearances are consistent with a mucous retention pseudocyst. There are bilateral concha bullosa (pneumatized nasal conchae (*thick arrows*)), a common anatomic anomaly of the middle turbinates

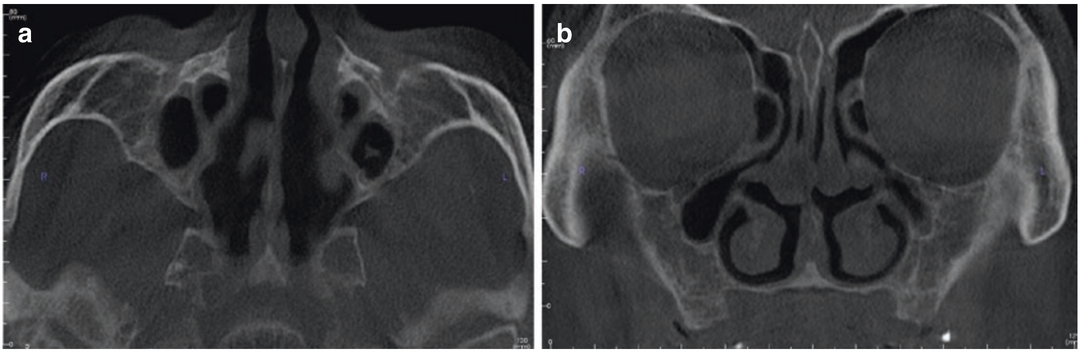

Fig. 16.6. Axial (**a**) and coronal (**b**) CBCT images showing bilateral maxillary sinus hypoplasia

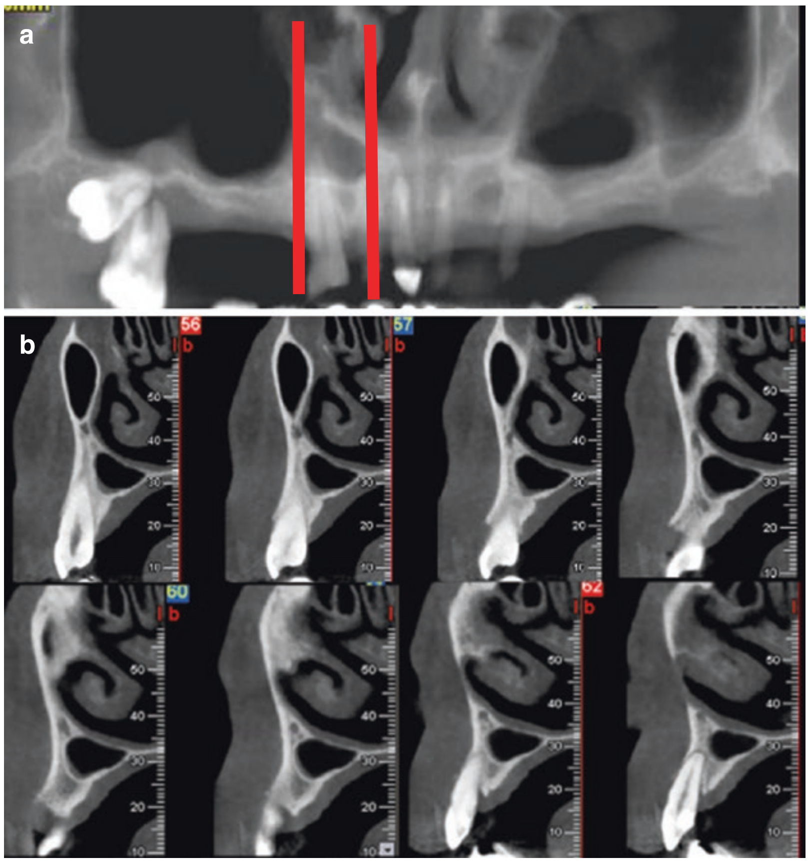

Fig. 16.7 Reformatted panoramic (**a**) and cross-sectional (**b**) CBCT images of the right canine and incisor area (between the *red lines*), showing extensive pneumatization of the maxillary sinuses bilaterally and extension to the palatal aspect of the anterior maxillary teeth

Fig. 16.8 Coronal CBCT image shows that the nasal septum is deviated to the left with a bone spur (*arrow*). There is another incidental finding of mucous retention pseudocyst in the left maxillary sinus

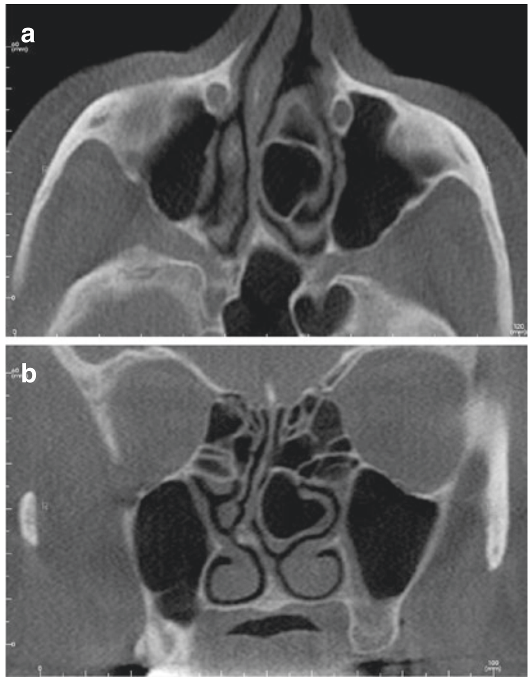

Fig. 16.9 Axial (**a**) and coronal (**b**) CBCT images showing a large round left unilateral concha bullosa with associated right nasal septal deviation

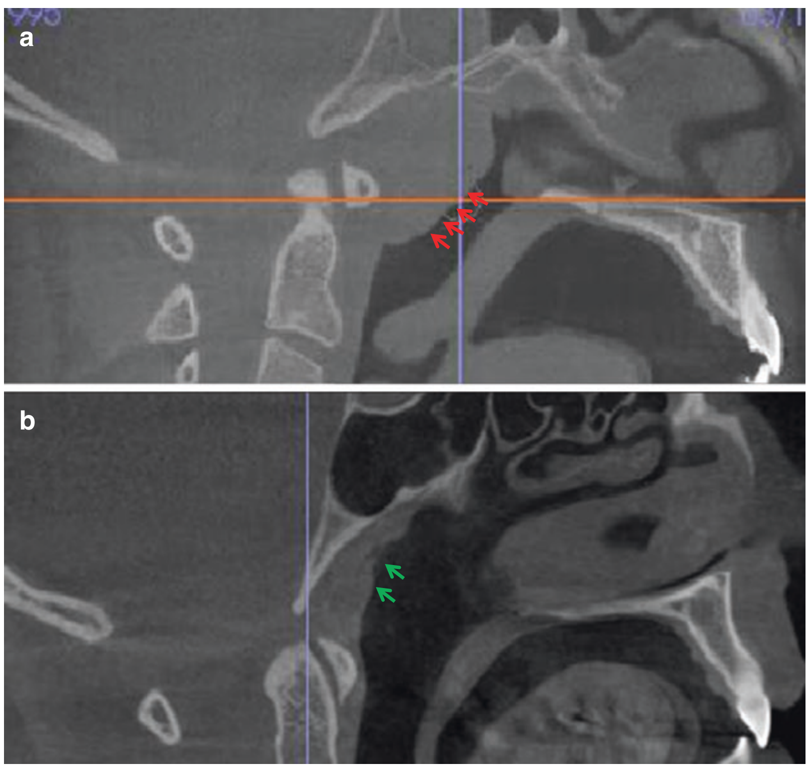

Fig. 16.10 Sagittal section of the nasopharynx (**a**) showing a large soft tissue projection of the posterior pharyngeal wall (*red arrows*). This occludes a large portion of the nasopharynx and is consistent with posterior pharyngeal tonsillar hypertrophy (hypertrophic adenoids). A similar midsagittal section in an individual without hypertrophy (**b**) (*green arrows*)

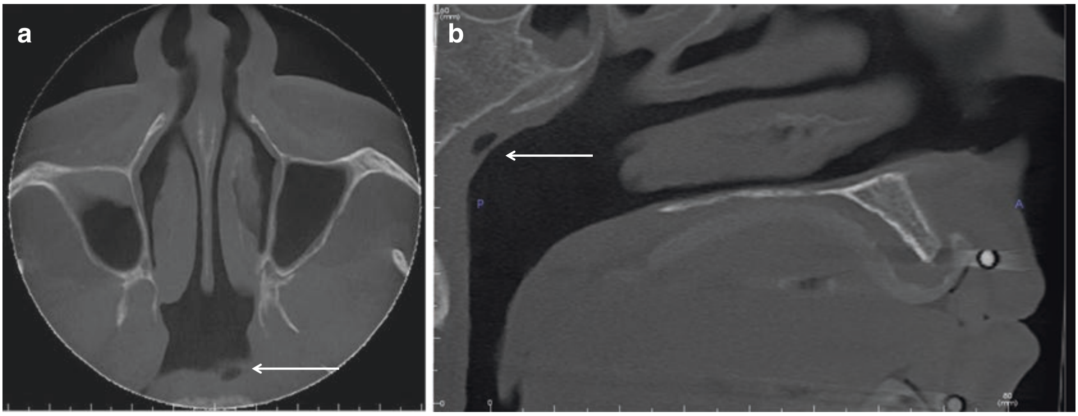

Fig. 16.11 Axial (**a**) and midsagittal (**b**) CBCT images of a completely edentulous maxilla with an air hypodensity within the submucosal consistent with a submucosal cyst of the nasopharynx. In the absence of any symptoms, this requires no treatment or follow-up. This appearance should be differentiated from a Tornwaldt cyst, a submucosal cyst that occurs in the midline

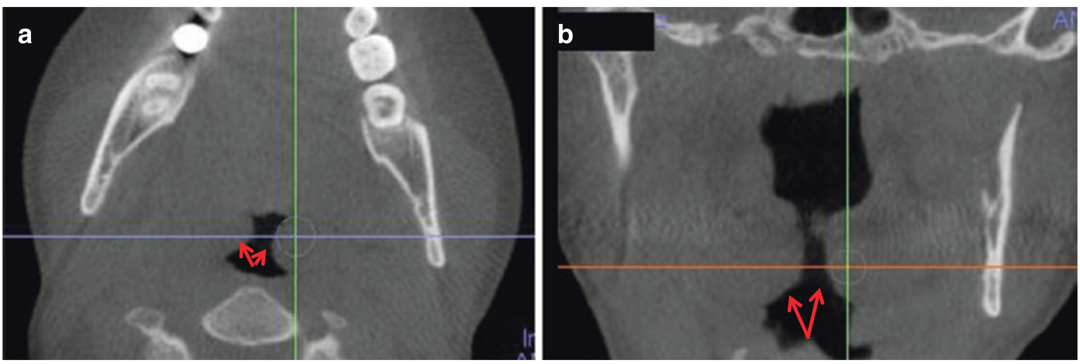

Fig. 16.12 Axial (**a**) and coronal (**b**) CBCT orthogonal images showing large, bilateral, soft tissue projections (*arrows*) at the level of the floor of the mouth; these findings are consistent with bilateral hypertrophic tonsillitis

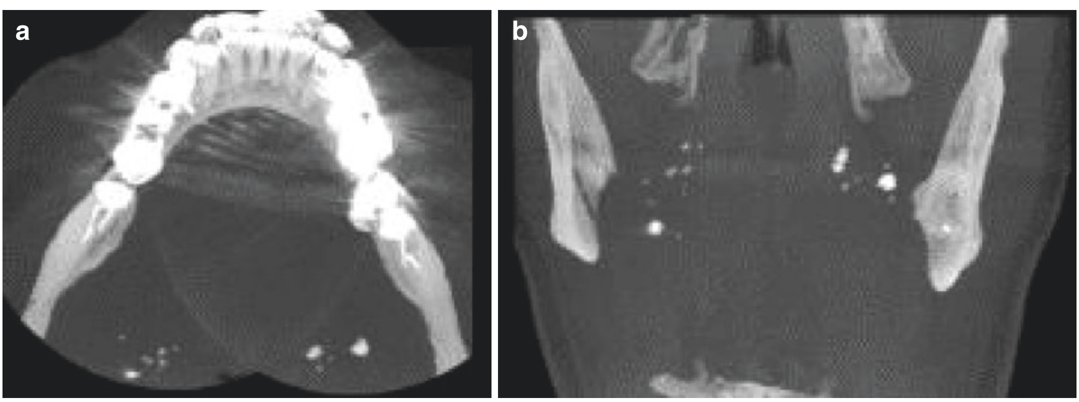

Fig. 16.13 Thin section axial (**a**), coronal (**b**), and full sectional infero-oblique (**c**) maximum intensity projection CBCT images and a volumetric rendering (**d**) showing the characteristic appearance and location of parapharyngeal calcifications in the palatine tonsils consistent with tonsilloliths (images courtesy, Marcelo Sales)

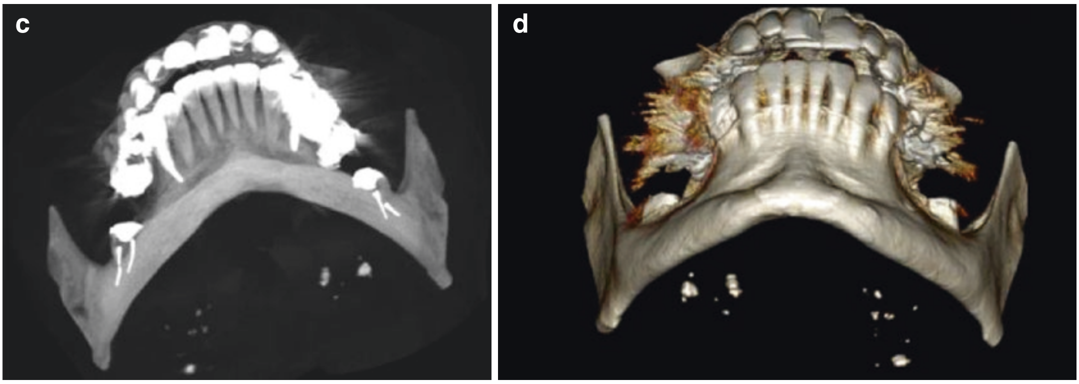

Fig. 16.13 (continued)

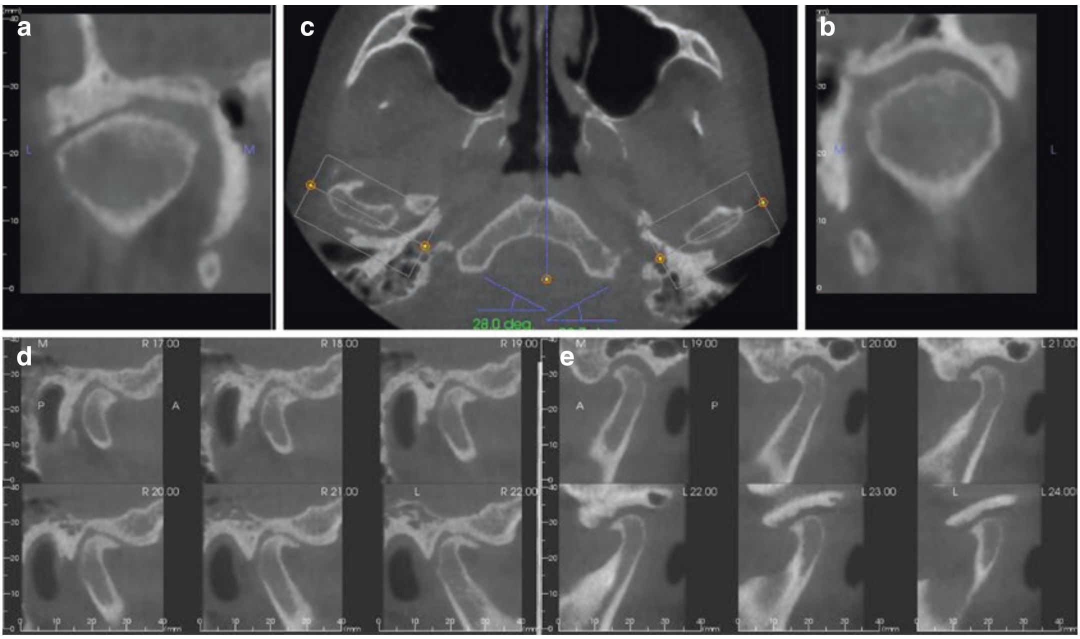

Fig. 16.14 Right (**a**) and left (**b**) corrected para-coronal TMJ images with reference axial (**c**) and right (**d**) and left (**e**) serial parasagittal sections of a 59-year-old asymptomatic male with degenerative joint disease (DJD). The superior surfaces of the condyles demonstrate signs of flattening, sclerosis, and anterior osteophyte formation. The posterior slopes of the articular eminence show signs of flattening and sclerosis. There is narrowing of the right joint space

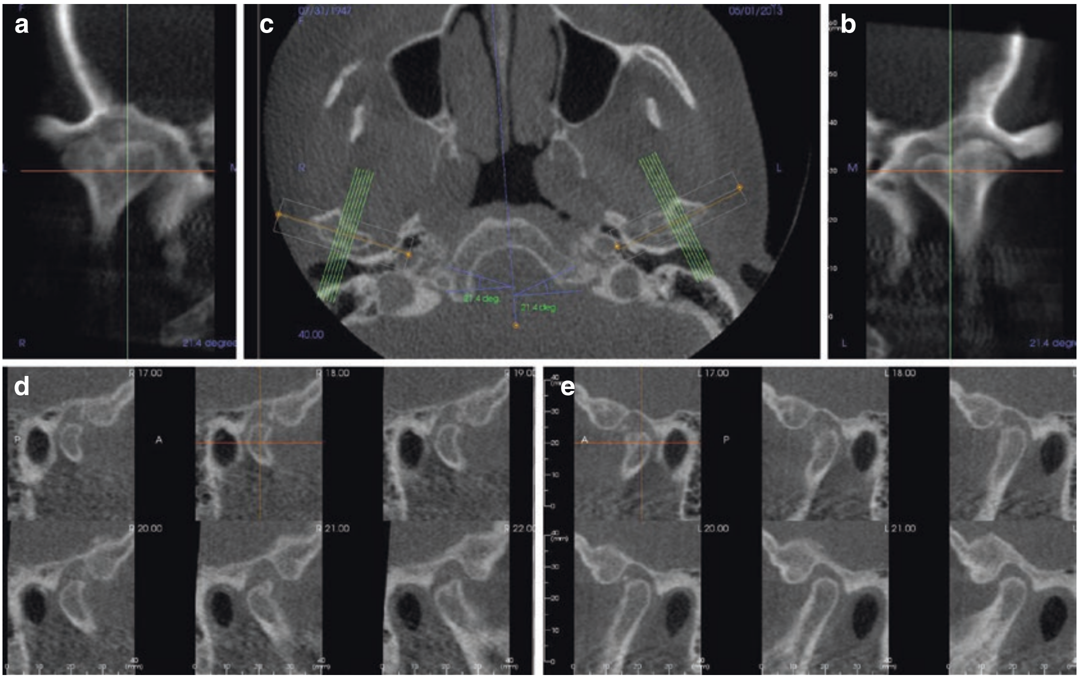

Fig. 16.15 Right (**a**) and left (**b**) corrected para-coronal TMJ images with reference axial (**c**) and right (**d**) and left (**e**) serial parasagittal sections demonstrating bilateral bifid condyles

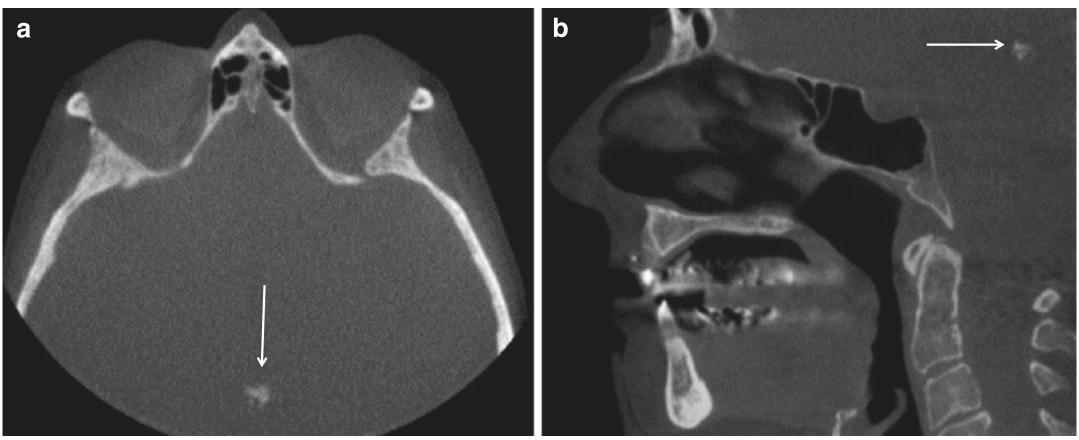

Fig. 16.16 Axial (**a**) and sagittal (**b**) images depict a physiological midline intracranial calcification in the region of the pineal gland (*arrow*)

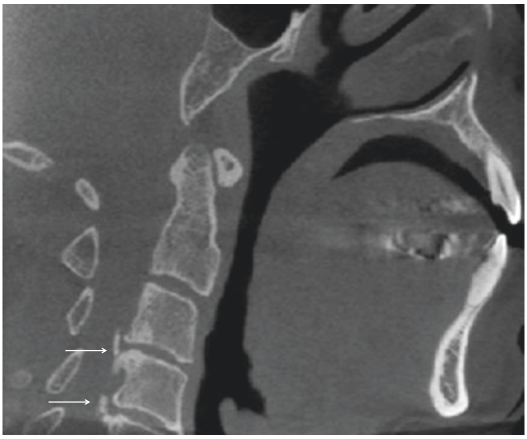

Fig. 16.17 Sagittal CBCT image shows sclerosis, calcifications of the posterior longitudinal ligament, and osteophyte formation on the dorsal aspect of C3–5 vertebrae. These findings are consistent with degenerative changes of the cervical spine (*arrows*)

16.3.2 Incidental Findings with Low to Intermediate Clinical Importance

16.3.3 Incidental Findings with Potentially High Clinical Importance

A number of incidental findings of intermediate (Table 16.2) and high (Table 16.3) potential clinical significnace may require referral to an oral and maxillofacial radiologist or other competent diagnostician for confirmation or direct referral for immediate management.

16.3.3.1 Cystic Lesions and Tumors of the Jaws

Benign neoplastic disease (odontogenic and non-odontogenic in origin) is rare although cys-

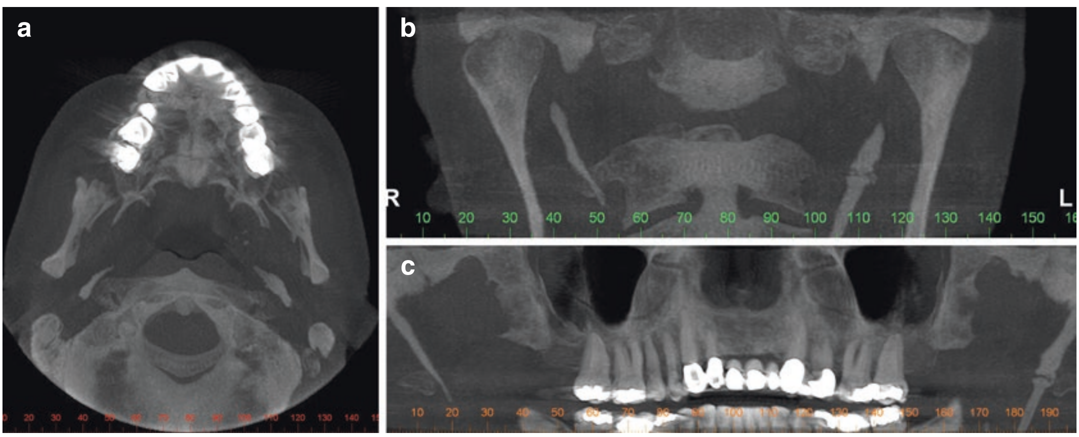

Fig. 16.18 Axial (**a**), coronal (**b**), and reformatted panoramic (**c**) 10 mm thick maximum intensity projection images demonstrating bilateral calcification of the stylohyoid chain on an asymptomatic female. Note the pseudoarticulation of the left stylohyoid calcification

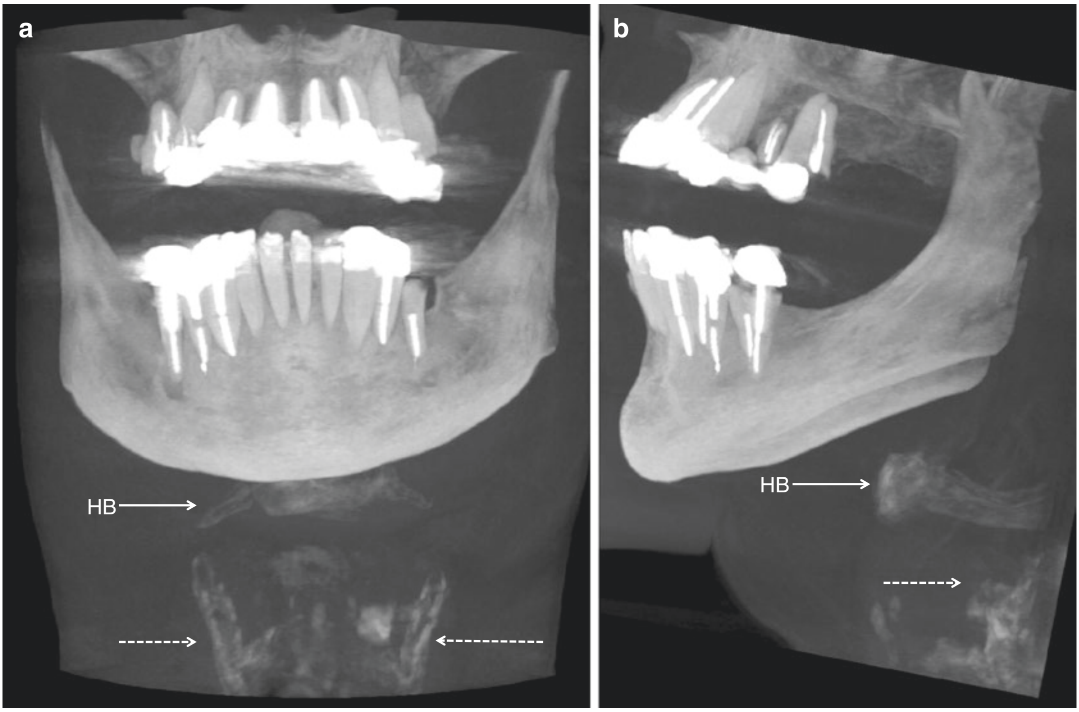

Fig. 16.19 Frontal (**a**) and left lateral (**b**) full thickness maximum intensity projections showing calcifications within the thyroid cartilage (*dashed arrows*) (HB, hyoid bone)

tic lesions of the jaws (odontogenic or not) are more common (Fig. 16.33). Both may occur as incidental findings because they are asymptomatic and have a slow progression. They can be depicted on CBCT scans performed for dental implants, endodontic and orthodontic treatment planning. Radicular and dentigerous cysts are most common as incidental findings among cystic lesions. Keratocystic odontogenic tumor (KCOT) and other benign tumors or lesions, such as ameloblastomas, myxomas, adenomatoid odontogenic tumors, central giant cell granulomas, and hemangiomas have also been reported. As discussed in detail in Chap. 15, CBCT may be useful in determining the origin and nature of these pathological entities and to develop a radiologic differential diagnosis. In fact, CBCT can depict the extent of the lesions, the exact location, the effect on buccal and lingual cortices and the relationship with adjacent teeth, important neurovascular structures, and sinonasal cavities. Knowledge of each of these features may assist in directing the next stage of management of such entities.

Table 16.2 Categorization and reported prevalence of incidental findings of intermediate potential clinical significance on CBCT according to anatomic location

Location	Entity	Example(s)	Prevalence range
Dental/jaws	Periapical pathology (AP, CO, RR, HC)	Fig. 16.20	4.3%[a]/35.3%[b]/11.1%[c]
	Variations		8.9%[b]/14.6%[d]/9.22%[e]
	Impaction	Fig. 16.21	21.7%[a]/6.6%[b]/3.33%[e]
	Cemento-osseous lesion	Fig. 16.22	1.8%[b]
	Root fragments		10.0%[b]/1.7%[d]
	Odontoma		2%[d]
	Cleft palate		0.5%[b]
	Osteoporosis/osteopenia		2.83%[f]
	Root fracture		0.2%[c]
Paranasal sinus	Mucosal thickenings and sclerotic changes of sinus wall	Figs. 16.23, 16.24 and 16.25	3.8%[g]
	Blocked ostiomeatal complex	Figs. 16.25 and 16.34	1.31%[e]/6.29%[f]/8.8%[h]
	Total opacification	Figs.16.25 and 16.34	2.9%[i]
	Discontinuity of sinus floor/antro-oral fistula	Fig. 16.25	17.4%[g]
	Foreign body	Fig.16.26	1.6%[g]
	Antral calcifications/antroliths		3.2%[g]
	Air-fluid level		4.4%[g]/3.6%[j]
	Antral polyps	Fig. 16.27	1.4%[d]/5.2%[c]/4.2%[h]
	Accessory ostia		0.12%[k]
Nasal fossa	Conchal hypertrophy		11.1%[a]
	Rhinitis/nasal polyposis	Fig. 16.28	3.09%[e]/1.9%[f]
Pharyngeal airway	Airway obstruction	Fig. 16.29	7.86%[f]/6.9%[h]
	Tonsillar hypertrophy		7.48%[e]
TMJ	Osteoma		0.1%[c]
	Coronoid hyperplasia		1.7%[b]
	Condylar hyper-/hypoplasia		0.5%[b]/1.9%[e]
Skull base/brain			
Temporal bone/ear	Opacification of middle ear		4.5%[l]
	Opacification of mastoid air cells		3.0%[l]
Cervical spine	Herniation of an invertebral disc		0.4%[h]
Neck soft tissues	Foreign body, sialoliths	Figs.16.30, 16.31 and 16.32	0.4%[b]/1%[f]
Other	Proptosis		0.4%[h]

AP apical periodontitis, *CO* condensing osteitis, *RR* root resorption, *HC* hypercementosis
[a]Çağlayan and Tozoğlu (2012)
[b]Allareddy et al. (2012)
[c]Price et al. (2012)
[d]Doğramaci et al. (2014)
[e]Edwards et al. (2014)
[f]Pette et al. (2012)
[g]Lana et al. (2012)
[h]Balshi et al. (2013)
[i]Dobele et al. (2013)
[j]Pazera et al. (2011)
[k]Edwards et al. (2013)
[l]Drage et al. (2013)

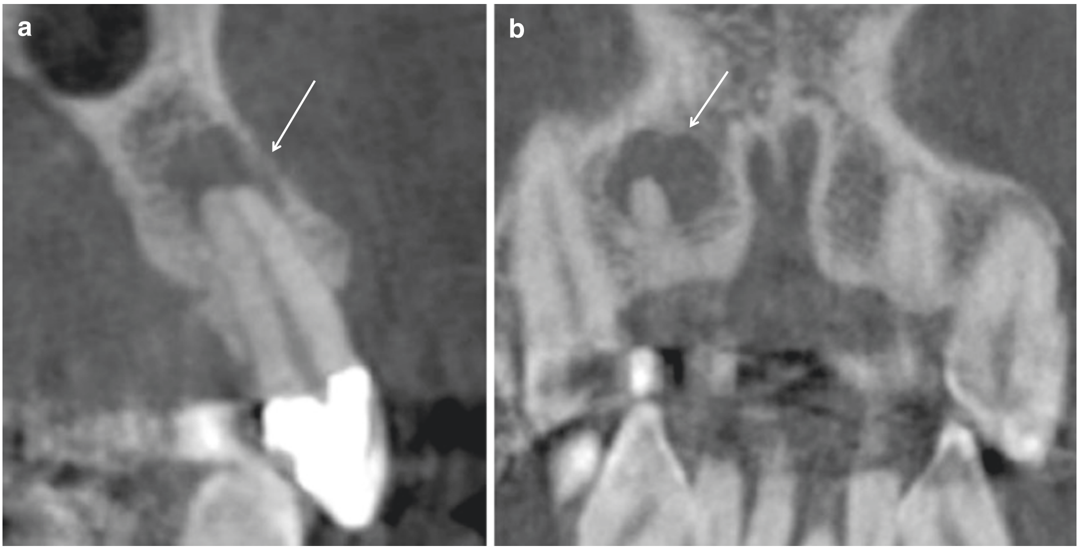

Fig. 16.20 Cross-sectional (**a**) and coronal (**b**) images showing a periapical radiolucent area (*arrow*) in association with the maxillary right lateral incisor. The tooth has a coronal restoration. There is evidence of apical root resorption of the tooth. The appearances are consistent with chronic apical periodontitis (apical inflammatory lesion)

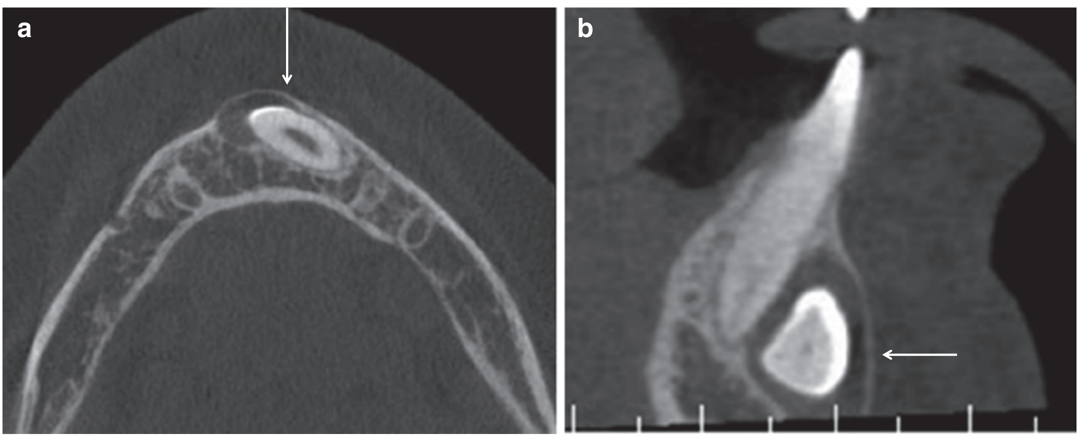

Fig. 16.21 Axial (**a**) and sagittal (**b**) images showing an impacted mandibular canine. The follicle of the impacted tooth is enlarged with expansion of the labial cortices (*arrow*). The appearance is consistent with a dentigerous cyst

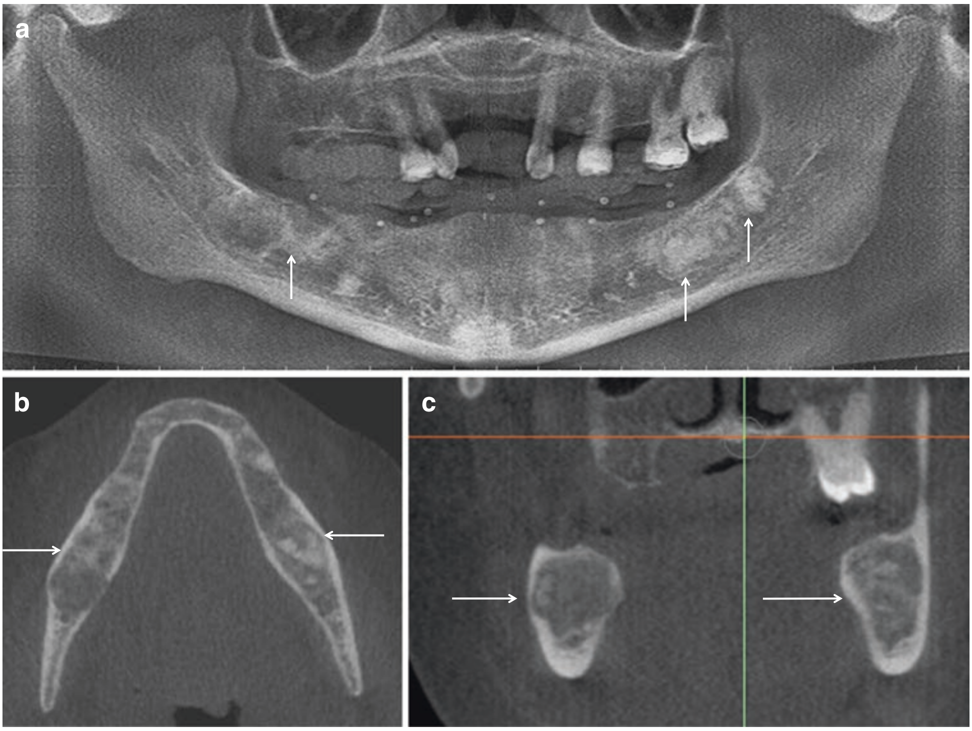

Fig. 16.22 Reformatted panoramic (**a**), axial (**b**), and coronal (**c**) CBCT images of a 45-year-old black female who presented for dental implants in her edentulous mandible. Multiple mixed radiolucent and radiopaque areas are seen in the mandible, consistent with florid cemento-osseous dysplasia. Implant insertion is contraindicated in these regions

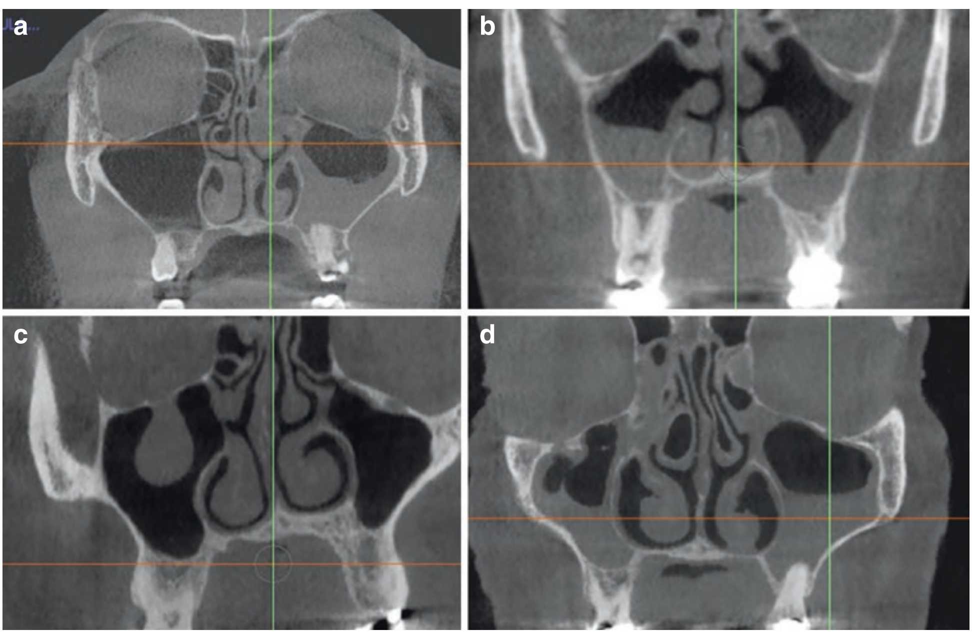

Fig. 16.23 Coronal CBCT images of four different patients (**a**-**e**) showing different degrees of incidental inflammatory changes in the maxillary sinuses of asymptomatic patients: unilateral left maxillary and ethmoid sinus inflammation (**a**); bilateral sinus inflammation (**b**); sinus polyp in the right maxillary sinus (**c**); and bilateral maxillary and ethmoid sinuses' inflammatory changes (**d**)

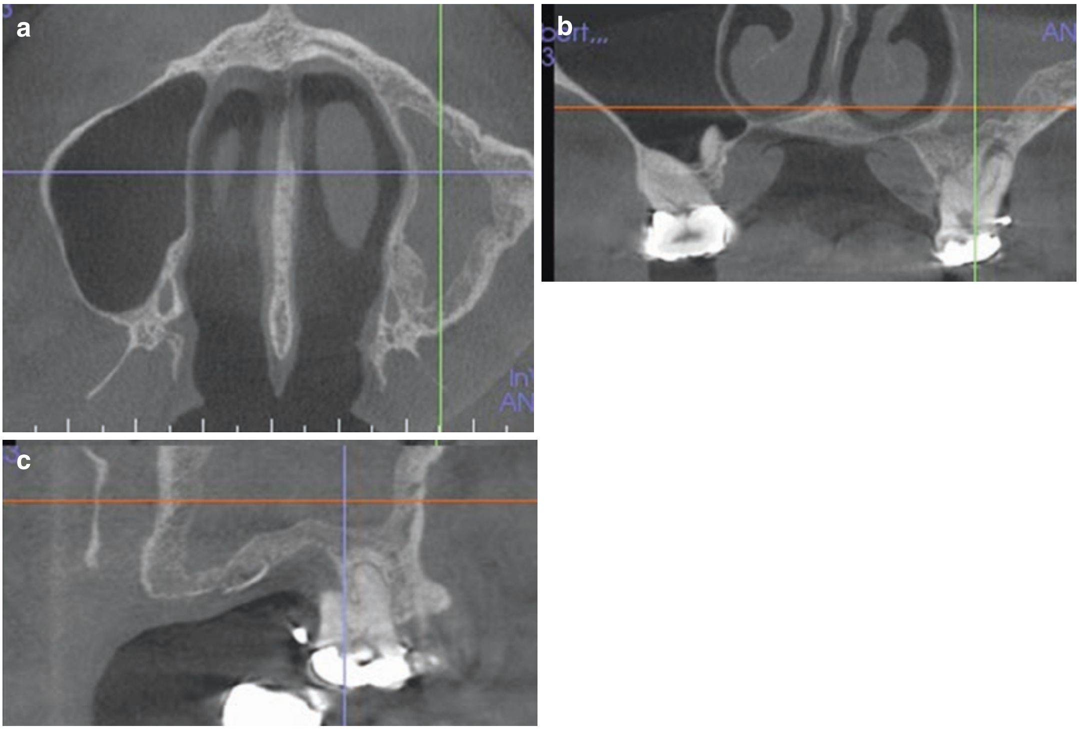

Fig. 16.24 Axial (**a**), coronal (**b**), and sagittal (**c**) images of the maxillary sinuses showing presence of inflammatory tissue in the left maxillary sinus and rather thick (sclerotic) walls of the affected sinus cavity; this is consistent with chronic inflammatory changes (sinusitis). Surprisingly, often times such pathological conditions may be unattended for long time and may be an incidental finding

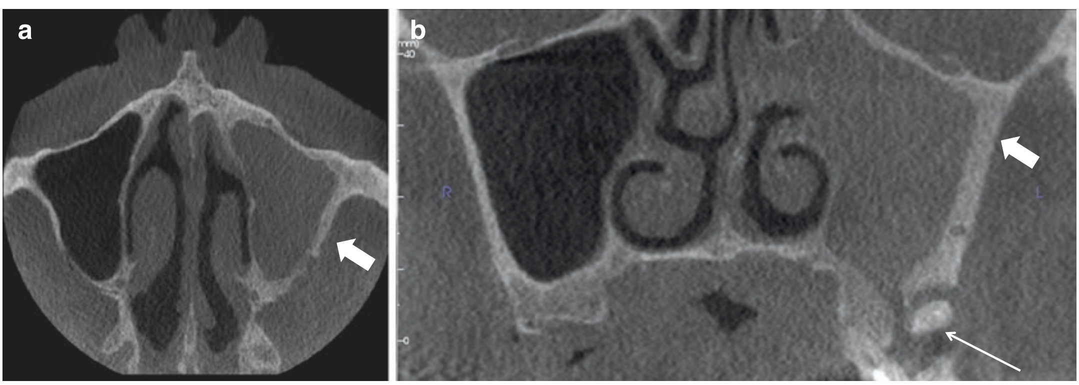

Fig. 16.25 Axial (**a**) and coronal (**b**) images of the maxillary sinuses showing complete opacification of the left maxillary sinus, sclerotic sinus walls (*thick arrow*) and occluded ostiomeatal complex. The inflammatory changes seem to have originated from a chronic periapical abscess around the left maxillary second molar (*white narrow arrow*). The appearances are consistent with chronic sinusitis of odontogenic origin

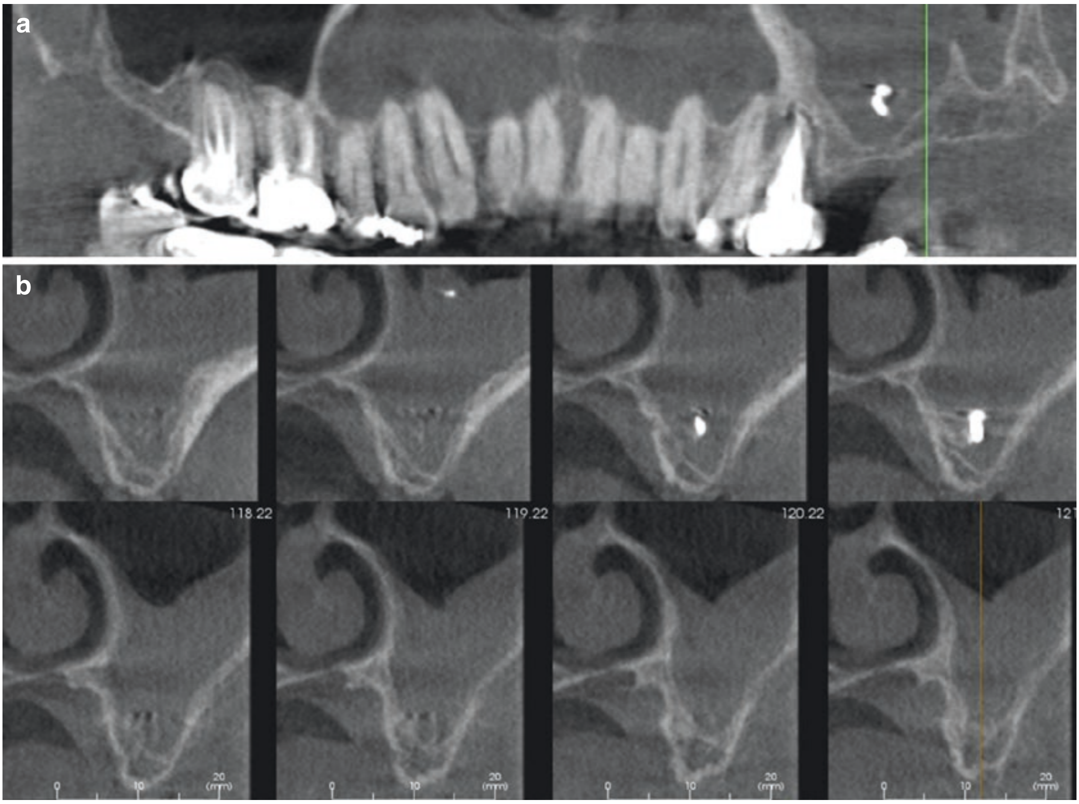

Fig. 16.26 Reformatted panoramic (**a**) and serial cross-sectional (**b**) images of the left maxillary sinus demonstrating a high density foreign object suspended in the soft tissue in the sinus

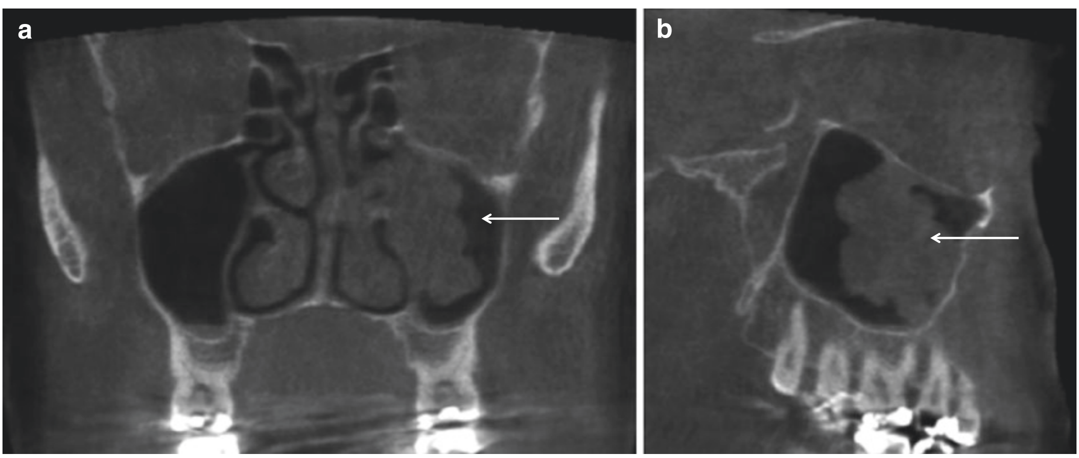

Fig. 16.27 Coronal (**a**) and sagittal (**b**) images showing multiple polypoidal, "grape-shaped" soft tissue densities in the left maxillary sinus consistent with antral polyps. The polyps may block the left ostiomeatal complex

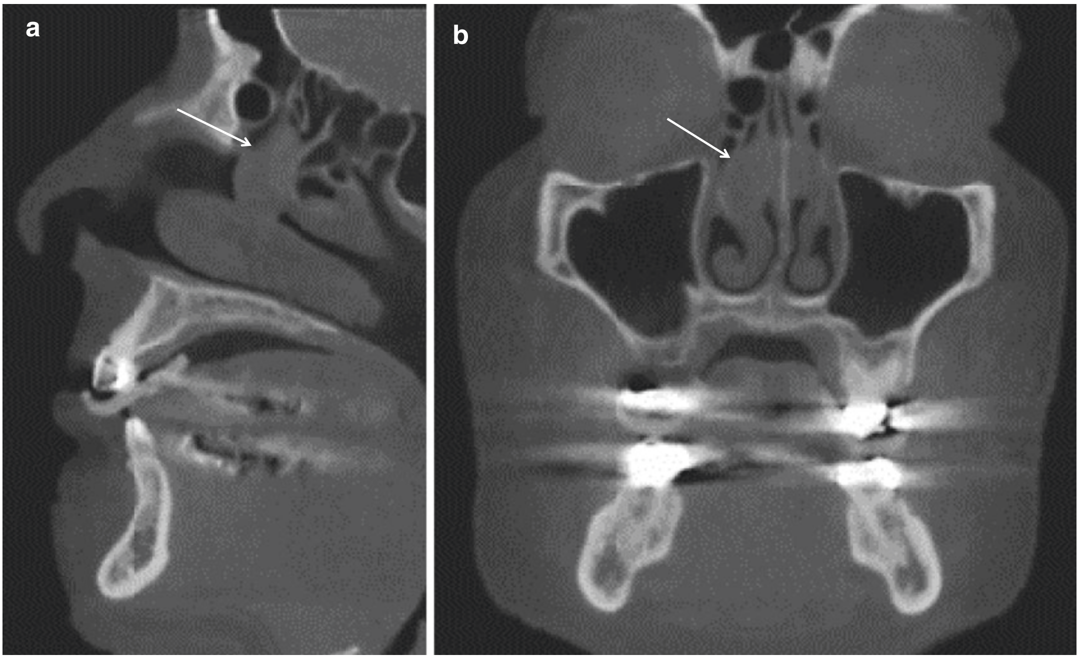

Fig. 16.28 Sagittal (**a**) and coronal (**b**) images of the nasal cavity showing a pear-shaped soft tissue mass in the right nasal fossa consistent with a nasal polyp

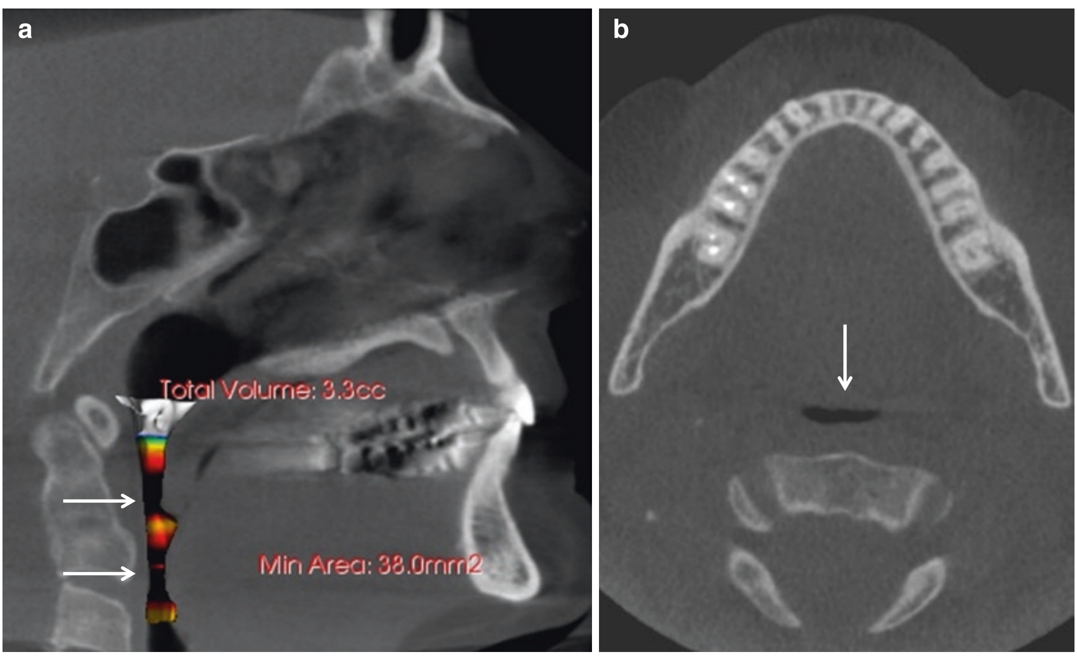

Fig. 16.29 Sagittal (**a**) and axial (**b**) images show narrowing of the airway in the retropalatal and retroglossal areas (*arrows*). The measurements of minimal cross section area (38 mm^2) and total volume (3.3 cm^3) of the airway noted on the sagittal image (**b**) indicate a risk factor for obstructive sleep apnea

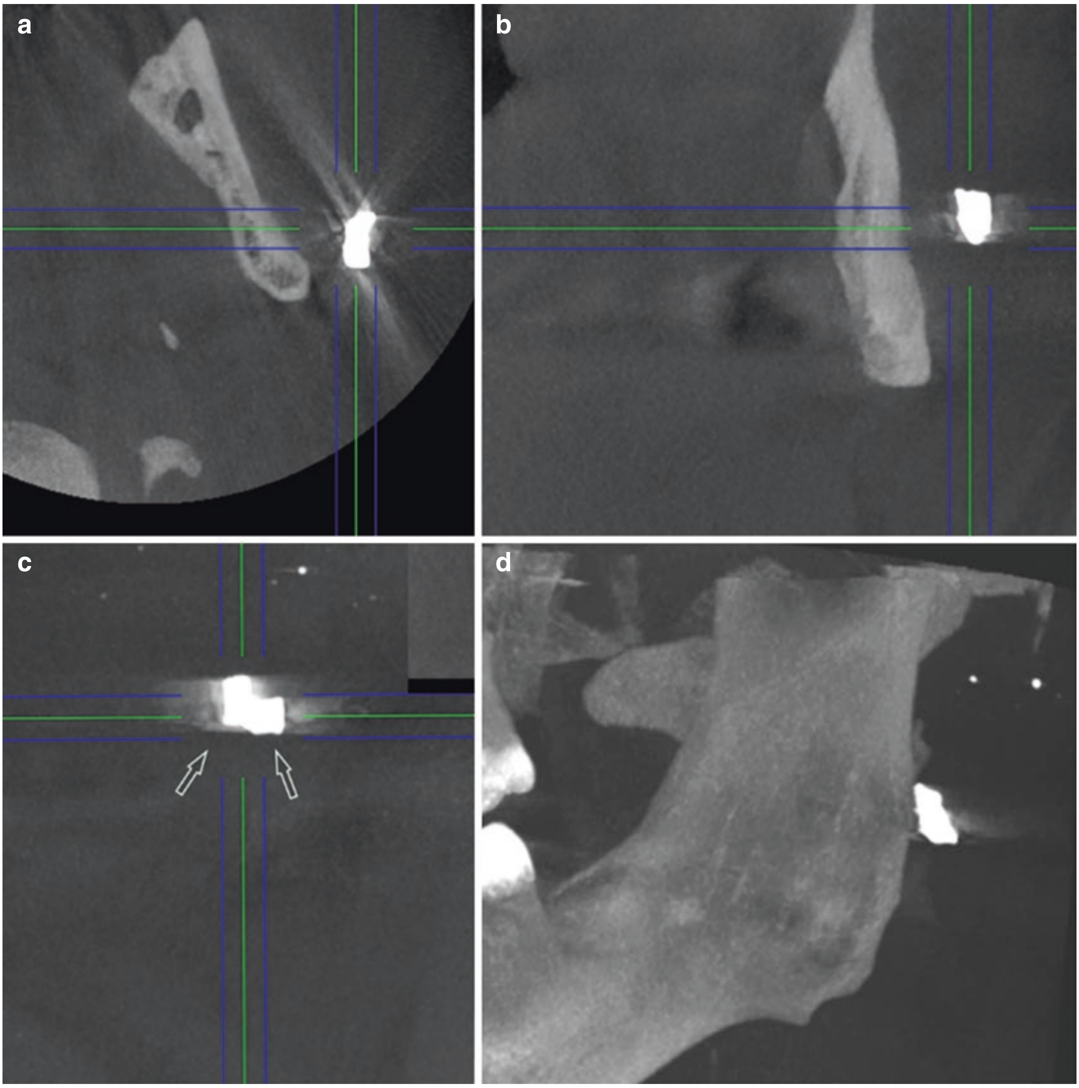

Fig. 16.30 Thin section axial (**a**), coronal (**b**), and sagittal maximum intensity projections (**c**) and thick section reformatted panoramic MIP section (**d**) showing the location and appearance of a high attenuating foreign body in the left masseteric space adjacent the posterior border of the left ramus consistent with a metallic fragment (*bullet*) from a shotgun to the face (Image courtesy, Marcelo Sales)

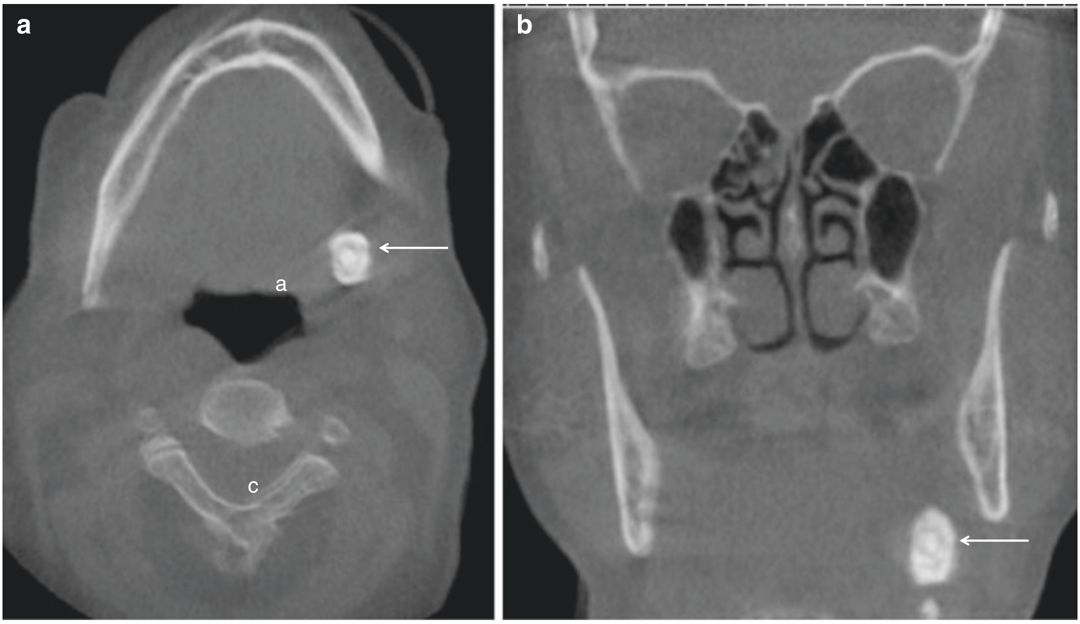

Fig. 16.31 Axial (**a**) and coronal (**b**) images showing a large laminated calcification, located in the soft tissue of the left submandibular triangle, consistent with a submandibular salivary gland sialolith

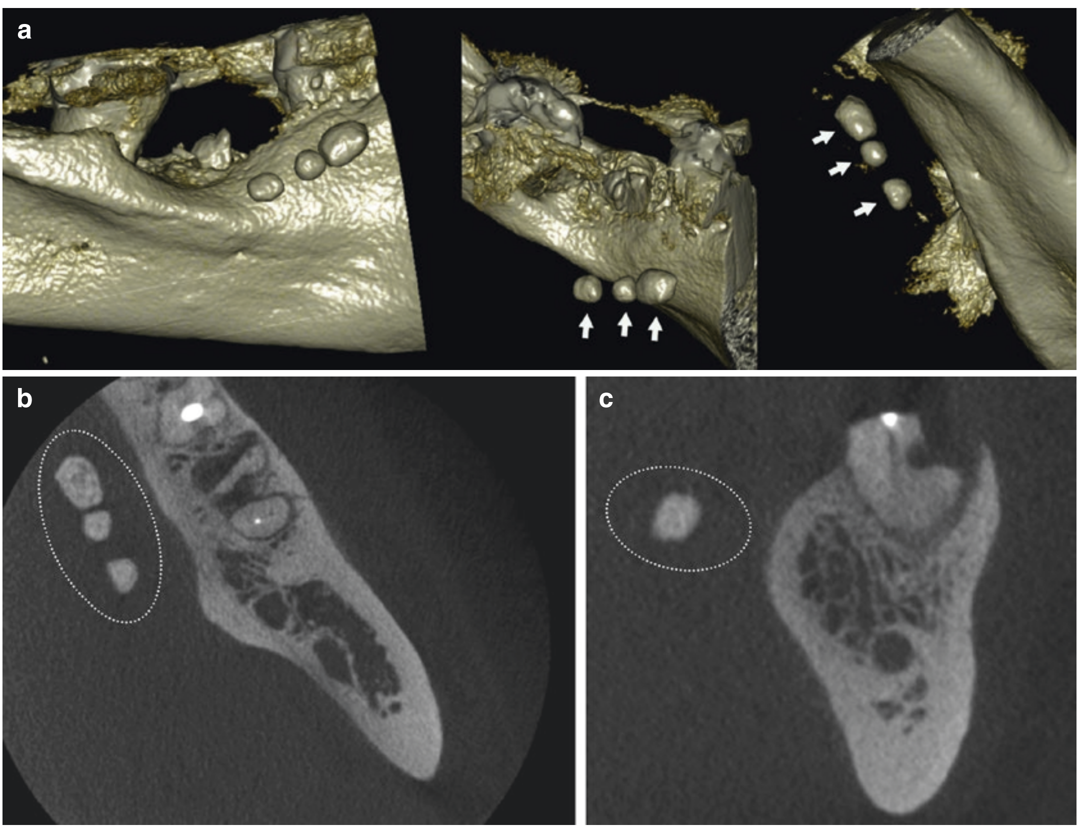

Fig. 16.32 Multiple volumetric projections (**a**) and axial (**b**) and coronal (**c**) CBCT images showing a series of three salivary gland calculi distributed along the duct of the left submandibular gland (Images courtesy, Marcelo Sales)

Table 16.3 Categorization and reported prevalence of incidental findings of high potential clinical significance on CBCT according to anatomic location

Location	Entity	Example(s)	Prevalence range
Dental/jaws	Cysts/benign tumors	Fig. 16.33	3.0%[a]/4.6%[b]/6.6%[c]
	Osteomyelitis/osteonecrosis		0.4%[a]/2.83%[c]
	Malignant tumors		0.3%[a]
Nasal fossa/maxillary sinus	Soft tissue mass/tumor	Fig. 16.34 and 16.35	0.31%[c]
Pharyngeal airway	Soft tissue mass/tumor		0.31%[c]/0.4%[d]
Skull base/brain	Intracranial CCAA	Figs. 16.44 and 16.45	33.26[e]/57.11%[e]/60.1%[f]/17.93%[c]
	Enlarged sella turcica/ pituitary/tumor	Figs. 16.36 and 16.37	0.34%[g]/0.94%[c]
	Non-CCAA calcification/ meningioma	Fig 16.38	1.5%[d]
Temporal bone/ear	Cholesteatoma		1.5%[h]/1.1%[d]
Cervical spine	Tumor/tumor-like lesion	Fig. 16.39	1%[i]
Neck soft tissues	Extracranial CCAA	Figs. 16.40, 16.41, 16.42, 16.43 and 16.44	30.99[e]/42.88%[e]/39.9%[f]/5.7%[a]/ 11.6%[c]/5.66%[c]/6.5%[d]
	Soft tissue mass/tumor		0.4%[d]
Other	Calcified vertebral artery atheroma	Figs. 16.45, 16.46 and 16.47	2%[i]

CCAA calcified carotid artery atheroma
[a]Allareddy et al. (2012)
[b]Doğramaci et al. (2014)
[c]Pette et al. (2012)
[d]Balshi et al. (2013)
[e]Damaskos et al. (2015a)
[f]Damaskos et al. (2015b)
[g]Edwards et al. (2014)
[h]Drage et al. (2013)
[i]Yang (2015)

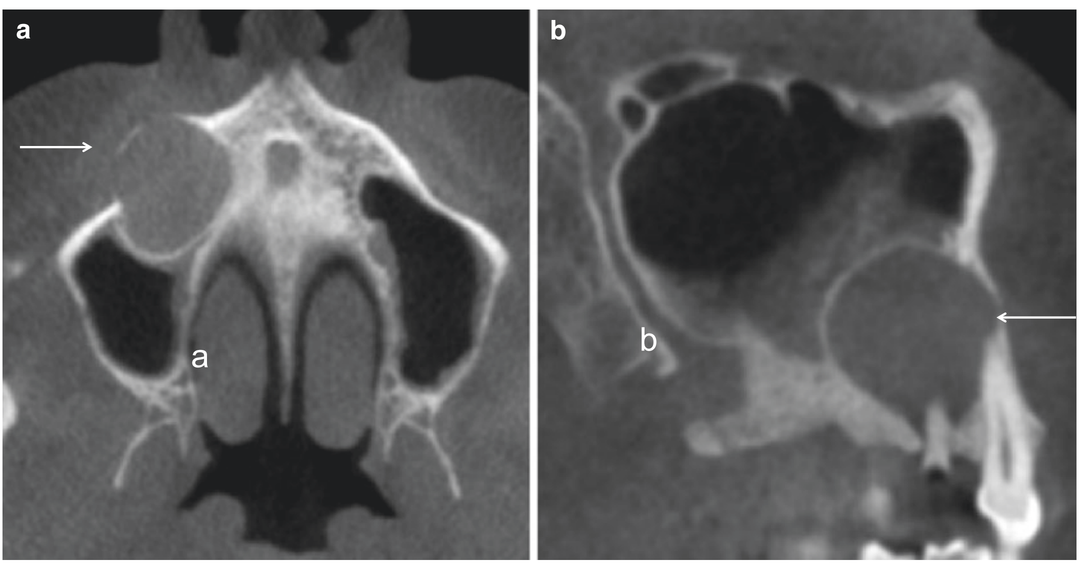

Fig. 16.33 Axial (**a**) and sagittal (**b**) CBCT images of a 60-year-old female who presented for a dental implant in the mandibular left molar region. The images demonstrate a large, well-defined radiolucency in association with a retained root fragment of the maxillary right first premolar. The entity encroaches the maxillary sinus with a well-corticated border. The imaging appearance is consistent with a radicular cyst

16.3.3.2 Complete Opacification of the Paranasal Sinuses

The most common incidental findings in the paranasal sinuses are mucosal thickenings and mucosal retention cysts/pseudocysts (Figs 16.4, 16.5, 16.8, and 16.22). These conditions have a relatively low significance. However, complete opacification of the paranasal sinuses should be considered differently (Fig. 16.34). This presentation signifies that the entire maxillary sinus cavity (or cavities) or any other paranasal sinuses is completely occupied by inflammatory tissue. This is often associated with blockage of the draining pathway of the maxillary sinus. Surprisingly, patients with this imaging feature may present without significant symptoms; however, a clinical history of sinus pressure or sinus headaches should be elicited in these cases. In some cases, the extensive presence of inflammation and blockage may lead to development of a mucocele (Fig. 16.34) and may cause severe damage of adjacent structures. In the early stages of mucocele development, the patient may have no symptoms. When sinus infection persists and the ostiomeatal complex is completely occluded, the patient (especially those with a low immune resistance) may develop a fast-growing, expansile, and destructive entity. Erosion of the sinus walls, mimicking the radiographic appearance of a malignant lesion, may be seen (Fig. 16.35). In rare occasions, this pathological entity may spread to other paranasal sinuses such as the frontal and ethmoid sinuses and may even invade the endocranium. Such a mucocele may result in severe complications, or even death, if not treated in time.

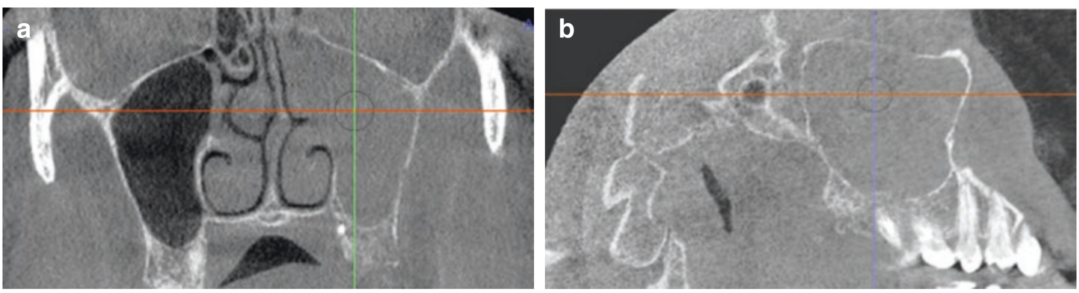

Fig. 16.34 Coronal (**a**) and sagittal (**b**) CBCT sections of the left maxillary sinus showing complete opacification of the sinus cavity; this is consistent with extensive inflammatory changes (sinusitis) and blockage of the ostiomeatal complex. In association with the mottling of the sinus walls and loss of the bony architecture of the medial wall of the sinus, immediate referral to and ENT is warranted

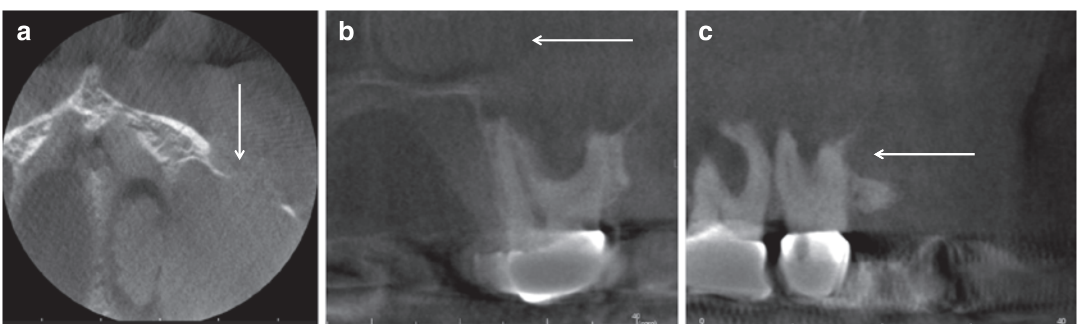

Fig. 16.35 Axial (**a**), coronal (**b**), and sagittal (**c**) CBCT images of a patient who presented to an endodontist for root canal treatment. The images show complete opacification of the left maxillary sinus and partial missing inferior, medial, and lateral walls of the sinus. The appearance is most consistent with a benign space occupying lesion, although a malignant lesion cannot be ruled out. Referral to and subsequent evaluation by an ENT physician provided a diagnosis of sinus mucocele

Practitioners should be alert because complete opacification of the maxillary sinus or other sinuses may be present as incidental disease. Its recognition on CBCT images is important and may require immediate attention. A referral to the proper physician (most often an ear, nose, throat (ENT) physician) may be necessary.

16.3.3.3 Space Occupying or Destructive Lesions in the Skull Base

As reported elsewhere in this book, soft tissue pathology cannot be accurately depicted in CBCT images because of inherent low soft tissue contrast. Therefore, different soft tissues cannot be distinguished and relevant pathological entities may not be visible. In some cases, a growing soft tissue mass may affect surrounding anatomical boundaries by pushing, displacing, remodeling, or even eroding neighboring tissues or structures. If these structures are osseous, the changes may be seen on CBCT. In fact, it is not uncommon to suspect such a developing pathological entity by its impact in the structures in the vicinity.

An example of this phenomena is osseous remodeling of the sella turica (or pituitary fossa) due to changes in the pituitary gland. The pituitary gland is an important endocrine gland which is located in the middle cranial fossa and is nestled in the sella turcica of the sphenoid bone. The hormones produced by this gland control growth, blood pressure, and other important body functions, such as reproduction, metabolism, fluid balance, temperature regulation, and pain relief. The pituitary gland is approximately 17 mm in diameter and of soft tissue density and therefore cannot be distinguished from adjacent soft tissues on CBCT images. The gland is therefore defined and depicted by the shape and size of the sella turcica. Pathological changes in the pituitary gland may alter the shape and size of the gland and sometimes its density. These changes may be reflected by alterations in the shape and size of the sella turcica (Fig. 16.36). Depending on the nature and aggressiveness of the developing pathologies, the size of the sella turcica may be increased, its cortical outline may be eroded or remodeled or even completely destroyed in aggressive entities. While the gland itself is not identifiable, changes within it involving calcifications (Fig. 16.37) or its effects on the neighboring structures might be on CBCT images (Fig. 16.36). This may be applicable to any kind of soft tissue density alterations which may indicate disease (Fig. 16.38).

16.3.3.4 Malignant Lesions in the Head and Neck

Although the chance discovery of a malignant lesion in the maxilla and mandible and other

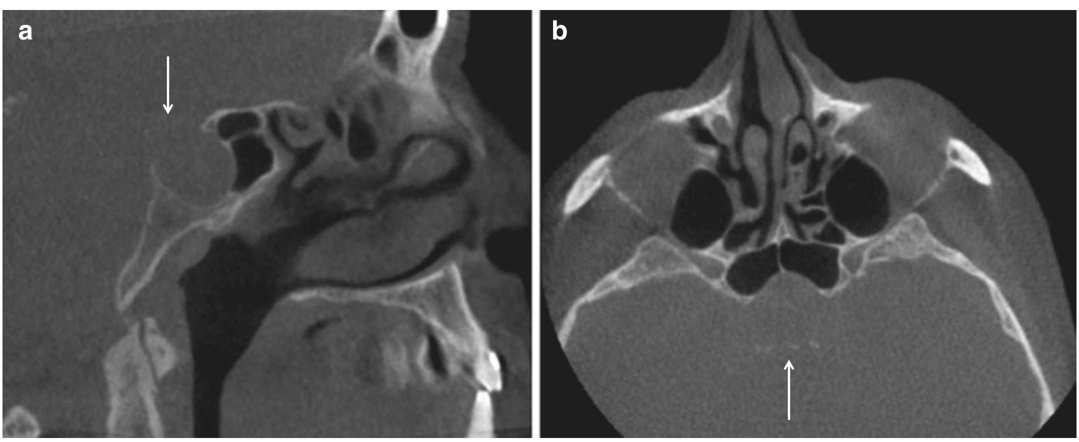

Fig. 16.36 Sagittal (**a**) and axial (**b**) CBCT images of a 71-year-old male who presented for dental implants showing an enlarged sella turcica with considerable expansion of the anterior and inferior walls of the sella. The imaging appearance is consistent with a pituitary gland adenoma

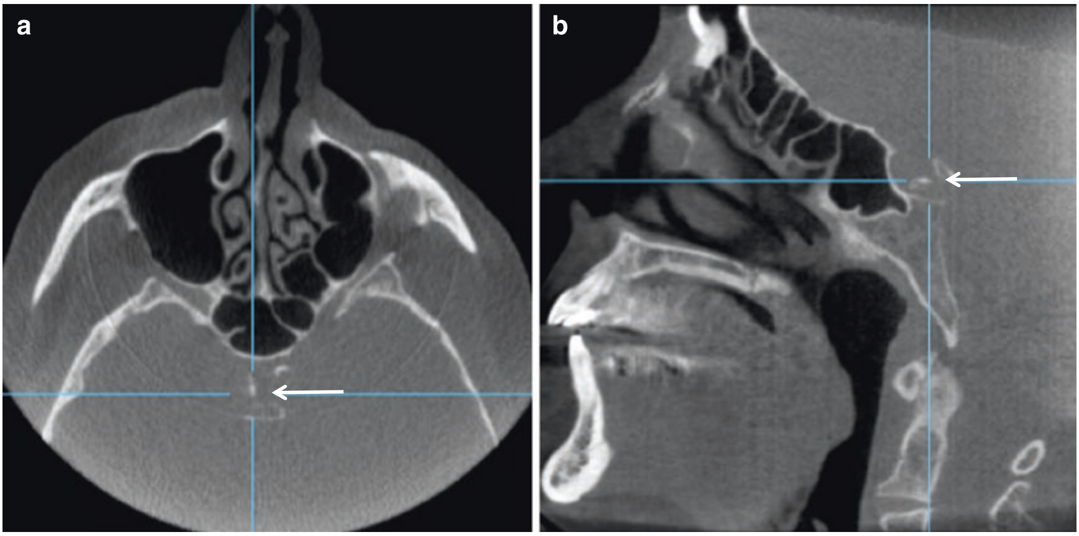

Fig. 16.37 Axial (**a**) and sagittal (**b**) CBCT images of a 68-year-old female who presented for a dental implant showing a calcification in the middle of the sella turcica with erosion of the dorsum sella (*arrow*). The appearances are consistent with a space occupying lesion. Further medical examination confirmed a craniopharyngioma

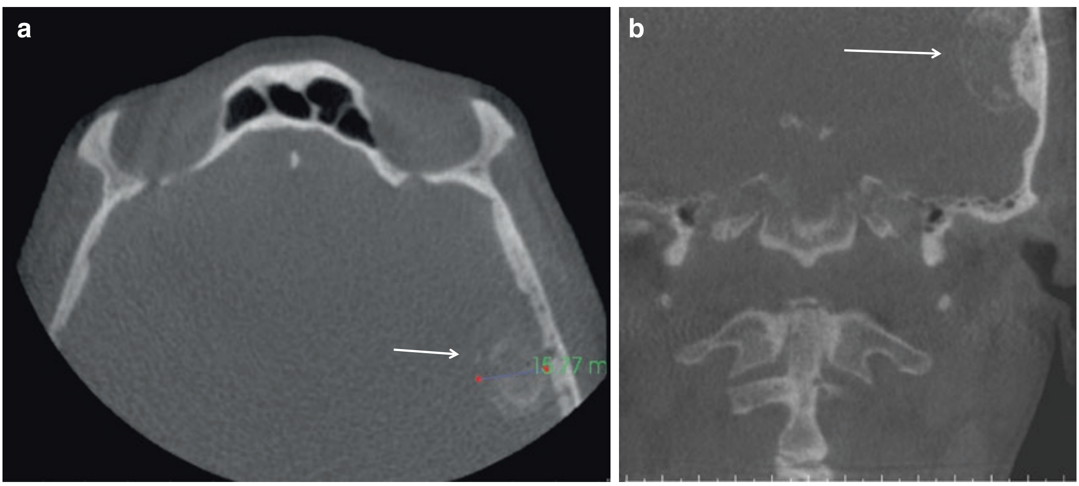

Fig. 16.38 Axial (**a**) and coronal (**b**) CBCT images of a 74-year-old male who presented for a dental implant showing a large circular and heterogeneous calcification in the left temporal lobe. The imaging appearance is consistent with an intracranial meningioma

adjacent anatomic structures is rare, the clinical and individual impact of failure to diagnose or a misdiagnosis is high. Failure to discover or recognize the lesion will lead to severe consequences, and occasionally even patient death.

To recognize a malignancy, the practitioner must be familiar with associated radiologic findings and, in particular, hallmark features. If a malignancy is located in the hard tissues, such as the maxilla and mandible, it usually presents as an ill-defined, non-corticated hypodensity, or occasionally, a hyperdensity. It may invade or destroy anatomical boundaries such as buccal and lingual cortices, the inferior alveolar canal and mental foramen, sinus and nasal cavity walls. Early suspicious imaging features may be simple

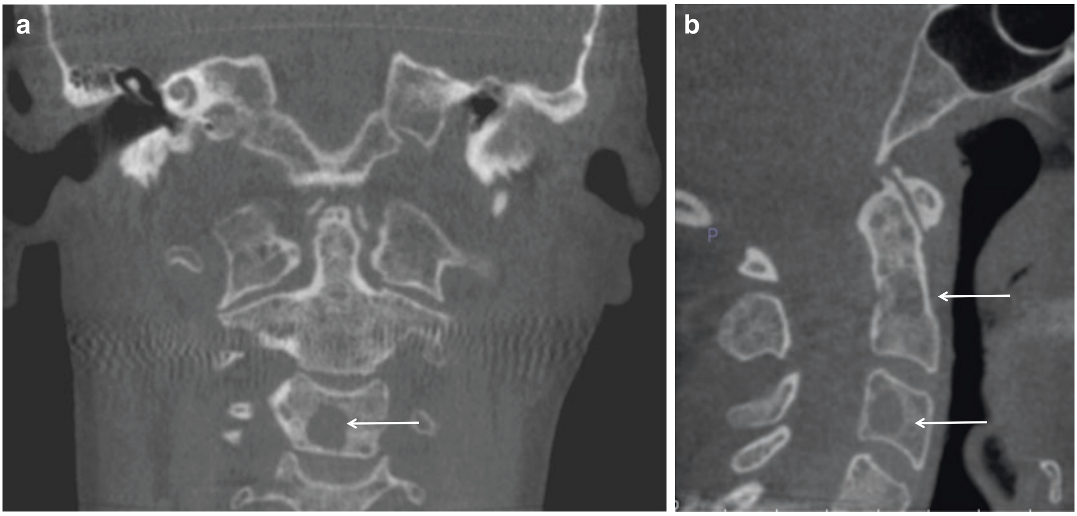

Fig. 16.39 Coronal (**a**) and sagittal (**b**) images of a 48-year-old female who presented for dental implants showing multiple osteolytic (punched-out) lesions involving multiple cervical vertebrae (C2–4). Further medical evaluation confirmed a diagnosis of multiple myeloma

as widening of the periodontal ligament (PDL) space, in which case it may mimic the inflammatory changes of periodontal disease. Sometimes malignancies present as multiple hypodensities and may affect more than one bone; in such instances the lesions look "punched out" or erosive (Fig. 16.39).

Malignant tumors in the head and neck soft tissues are more difficult to detect since the soft tissue contrast of CBCT images is poor. However, the effects of a growing mass on adjacent soft tissues may be a clue to an astute clinician, especially if detailed clinical information is available. These effects may include asymmetry, displacement or infiltration of known osseous boundaries, changes in the density of the affected soft tissue or soft tissue space.

While these observations may lead to a suspicion of a malignancy, CBCT is not the appropriate diagnostic modality for full assessment of these conditions, irrespective of its origin (hard or soft tissue). When malignant lesion is suspected in the hard or soft tissue of the maxillofacial region, a thorough clinical examination and further imaging, such as medical CT with contrast and magnetic resonance imaging (MRI), are strongly recommended. If multiple lesions are seen and lymph node involvement is suspected or detected, positron emission tomography/computed tomography (PET/CT) may be the recommended imaging modality. Prescription of these imaging studies should be performed after confirmation with a radiologist and referral to an appropriate surgical specialist.

16.3.3.5 Extracranial Calcified Carotid Artery Atheromatosis (Carotid Artery Calcifications)

Atherosclerosis or atheromatosis is a pathological condition of the blood vessels in which, due a variety of reasons, intralumenal plaques are formed, especially at areas of greatest shear force and turbulence such as the bifurcation of the common carotid artery (CCA) to the internal (ICA) and external carotid artery (ECA). Since the common carotid artery provides the main blood supply to the brain, atherosclerotic conditions of the carotid artery may lead to brain tissue ischemia (inadequate provision oxygen to the brain) thus resulting in a cerebrovascular accident (CVA), or stroke. When atheromatic plaques are of high density, they are in most cases identifiable in radiogaphic examinations which include parts of the neck. Atheroma-related formations of thrombi and emboli in the carotid artery is the most frequent cause of stroke (American Heart Association/American Stroke Association 2008). Stroke is a significant public health issue with both morbidity and mortality costs (Tegos et al. 2001; Gorelick et al. 1999).

Extracranial calcified carotid artery atheromatosis presents frequently with carotid artery calcifications (CAC) and has been discussed extensively in the literature (Carter et al. 1997; Friedlander and Lande 1981; Friedlander et al. 2002; Friedlander et al. 2005; Friedlander and Golub 2006; Friedlander et al. 2013). CAC not only can be seen on CBCT, but can also be depicted on panoramic radiographs. On the panoramic radiograph the prevalence of the incidental findings ranges from 3.6 to 4.2% in a general dental population (Carter et al. 1997; Friedlander et al. 2005). The prevalence could be much higher in patients with cardiovascular diseases, diabetes mellitus, obstructive sleep apnea, hyperparathyroidism, and many other endocrine and metabolic diseases (Friedlander et al. 2002; Friedlander et al. 2005; Friedlander and Golub 2006; Friedlander et al. 2013;). On CBCT imaging the prevalence of CAC in a general dental population has been reported to range from 5.6 to 6.4% (Allareddy et al. 2012; Pette et al. 2012; Balshi et al. 2013). In other dental populations, the prevalence of CAC is reported to be as high as 39–42% (Damaskos et al. 2015a; Damaskos et al. 2015b).

When present, CACs are most often found in the carotid bifurcation region, where the common carotid artery is divided into the internal and external carotid arteries. Anatomically, the carotid bifurcation is most often located towards the superior border of the thyroid cartilage (level of C3-C4 cervical vertebrae) and posterolaterally to the thyroid cartilage. However, the thyroid cartilage is soft tissue radiodensity and not always seen in CBCT scans, blending with the surrounding soft tissues. The most frequently used reference landmark to approximate the location of the carotid bifurcation is the level of C3/C4 vertebrae on coronal and sagittal images (Fig. 16.40). These anatomical “bearings” are almost always

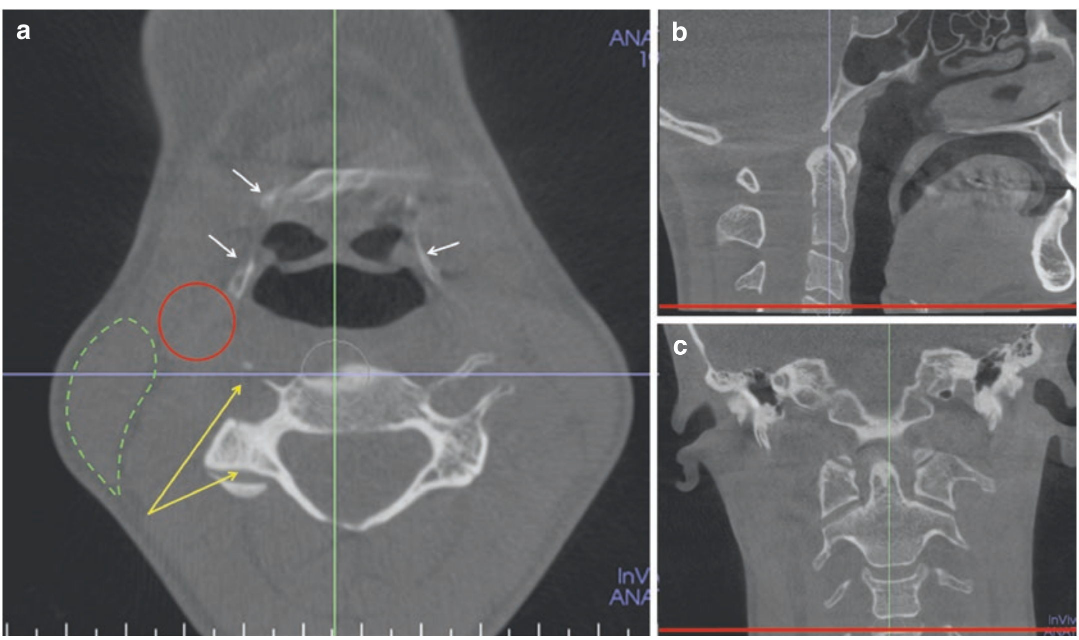

Fig. 16.40 Axial section (**a**) at the level of C3/C4 vertebrae depicting the anatomical landmarks for the carotid artery calcifications (CAC). The *red line* in the sagittal (**b**) and coronal (**c**) CBCT sections indicates the level of the axial section (**a**). (*yellow arrows*, the right transverse process of C4; *white arrows*, the outline of the hyoid bone; *green dotted outline*, the right sternocleidomastoid muscle; *red circle*, approximate location of the CCA close to its bifurcation to the ECA and ICA. This is the region that most CAC occur)

included in extended field of view (FOV) scans of the maxillofacial region or limited FOV scans of the mandible; thus possible presence of calcified plaques is evident within the margins of the imaging volume and should not be missed.

Axial CBCT sections of the upper neck are the most important projections in identifying the landmarks discussed above and are of great use in the identification of CACs. In these sections, the carotid arteries are located posterolaterally or laterally to the airway, anterolaterally to the ipsilateral transverse process of C3 or C4 vertebrae and medially to the anterior aspect of the sternocleidomastoid muscle (SCM) (Fig. 16.40). Blood vessels are not identifiable in CBCT images because they are radiographically indistinguishable from radiodensity of adjacent soft tissue structures. However, when carotid calcified plaques are calcified, they may be depicted because of their high density in the characteristic region described previously. Their shape and size vary; sometimes they are larger and line the lumen of the blood vessel and other times appear as smaller "rice-grain" hyperdensities, but more or less in the same location (Fig. 16.41). Exceptions do exist, and infrequently, calcified plaques may show caudal to the carotid bifurcation and even cephalad (rarely) after the branching to the external (ECA) and internal (ICA) arteries.

In the axial sections, CAC may have a ring-like appearance (continuous or interrupted). In coronal or sagittal views, they seem more curvilinear or irregular (Figs. 16.42 and 16.43). CACs can be unilateral but are more often bilateral. The

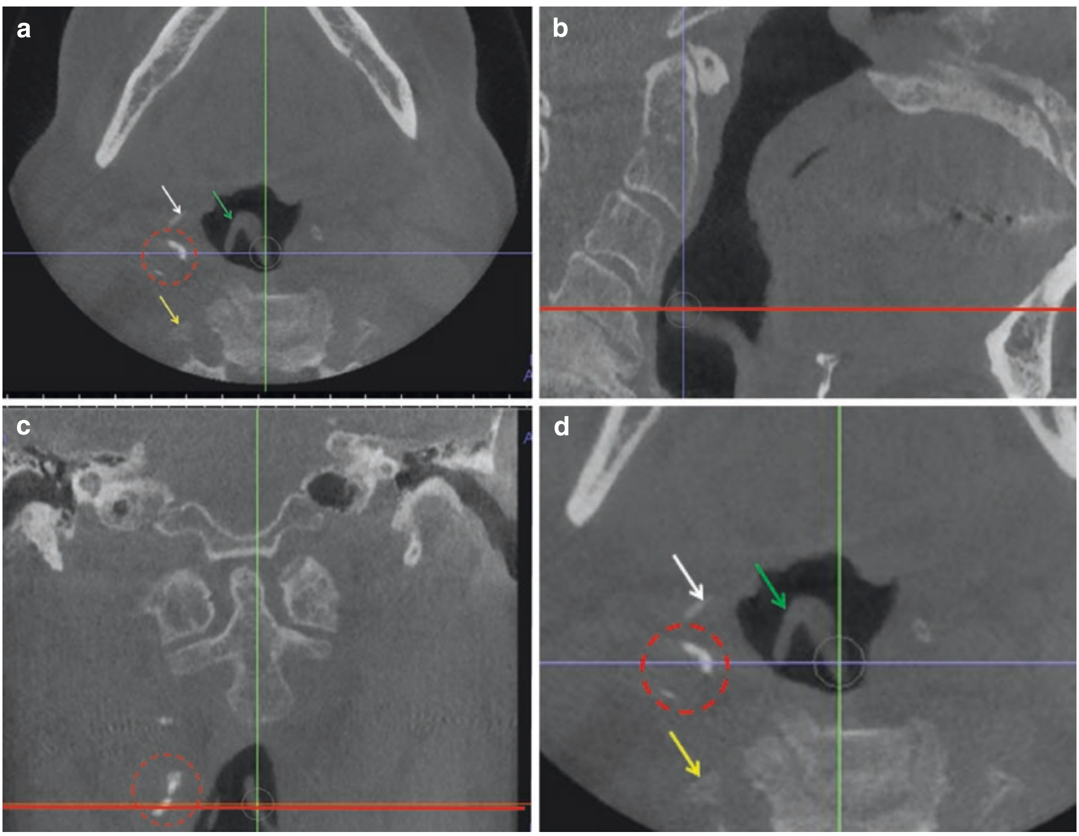

Fig. 16.41 Axial (**a**), sagittal (**b**), and coronal sections (**c**) demonstrating the typical location and appearance of CAC on CBCT (*red line* (**b**) and (**c**) indicates the level of the axial section). A cropped, magnified portion (**d**) of the axial section (**a**) is shown to demonstrate the details. Note the location of the CAC (*red dotted circle*) which is found laterally to the airway, anterolaterally to the ipsilateral transverse process of C3 (*yellow arrow*) and dorsally to the hyoid bone (*white arrow*). The *green arrow* shows the epiglottis

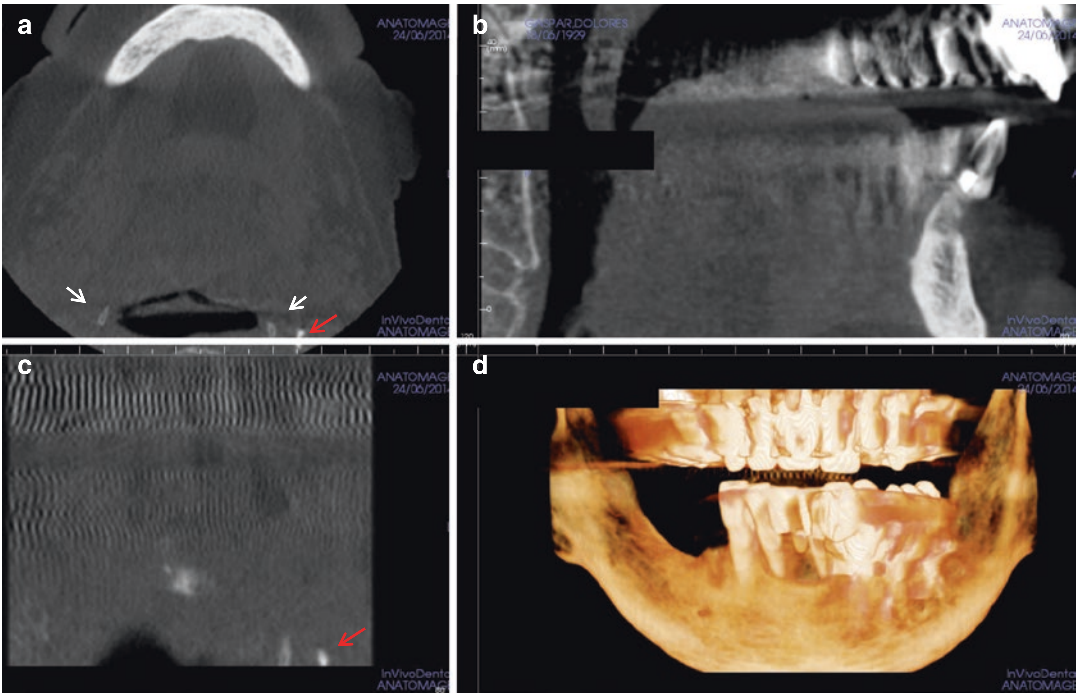

Fig. 16.42 Axial (**a**), coronal (**b**), sagittal (**c**), and volume rendered (**d**) images of a limited FOV CBCT scan on a patient who presents for implant site assessment of the right posterior mandible. The axial (**a**) and coronal (**b**) views revealed the presence of a CAC (*red arrows*), lateral to the hyoid bone (*white arrows*). Significant findings, such as these, may be present even in smaller FOVs

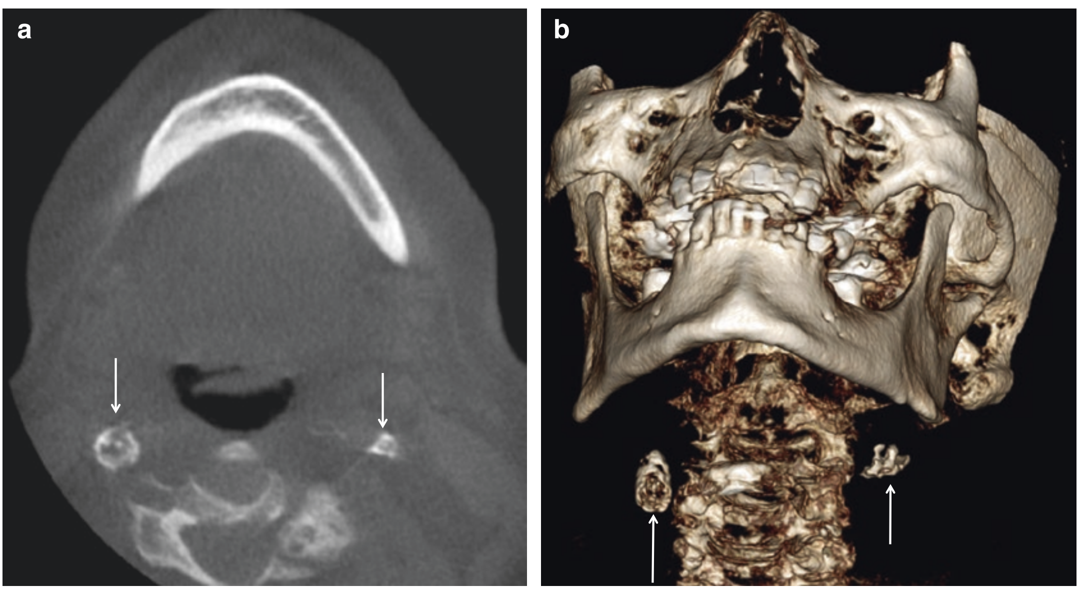

Fig. 16.43 Axial (**a**) and volumetric infero-frontal projection (**b**) CBCT images showing large heterogeneous bilateral curvilinear and circular calcifications on either side of the neck consistent with bilateral carotid artery calcifications (CACs)

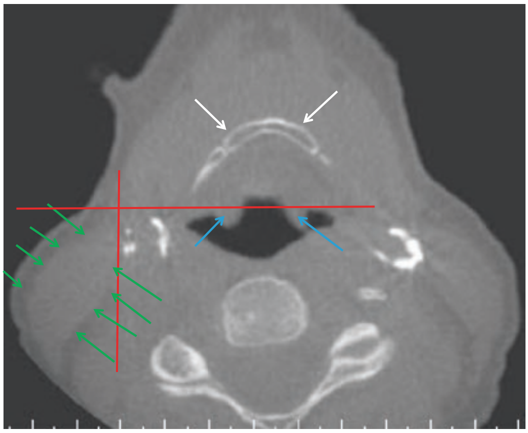

Fig. 16.44 Axial section at the level of C3/C4 vertebrae demonstrating an empirical yet simple way to explore the origin of an unknown calcification of the lateral neck. A vertical line is drawn tangential to the anteromedial aspect of the SCM muscle (*green arrows*), and a horizontal line along the epiglottis (*blue arrows*) which is almost always identifiable at that level. If the unknown calcification lies on the lower right quadrant of the "cross-hair" formed by the above lines, it is likely that the calcification is a CAC. (*white arrows*, hyoid bone)

differential diagnosis of CAC includes calcifications in the thyroid cartilage complex, such as triticeous cartilage, calcifications in the thyroid cornu or even the hyoid bone (see Chap. 17 for a detailed description).

An alternate, simple, anecdotal method to verify the origin of an unknown neck calcification as a potential CAC is explained in Fig. 16.44.

16.3.3.6 Intracranial Internal Carotid Artery Calcifications

Carotid calcifications may also occur within any of the seven anatomical segments (Bouthillier classification) of the internal carotid artery (ICA), of which six are intracranial: (1) cervical, (2) petrous (horizontal), (3) lacerum, (4) cavernous, (5) clinoid, (6) ophthalmic (supraclinoid), and (7) communicating (terminal) segments (Bouthillier et al. 1996). Most commonly, calcifications are observed in the cavernous segment and carotid siphon (the curve of the ICA) within the petrous portion (petrous and lacerum segments) (Fig. 16.45)

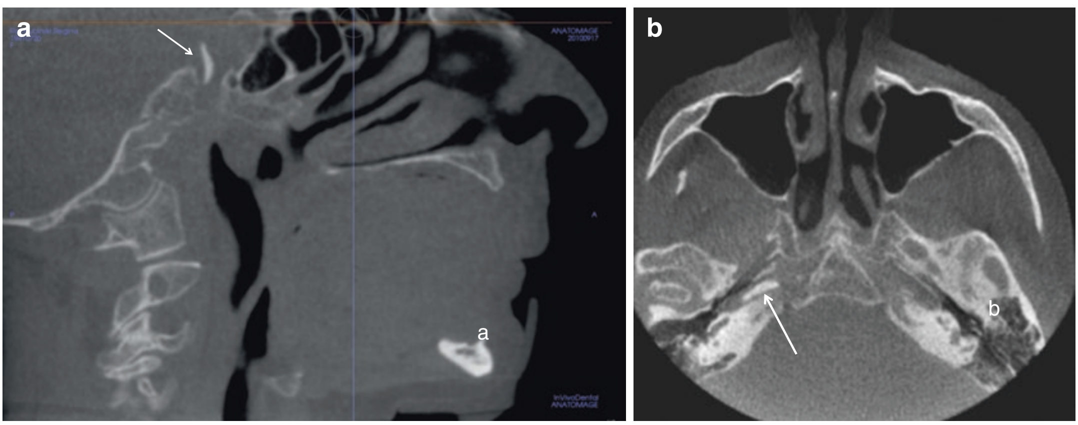

Fig. 16.45 Sagittal (**a**) and axial (**b**) images in the region of the skull base showing curvilinear calcifications consistent with of intracranial petrous segment of internal carotid artery calcifications

(Bouthillier et al. 1996). Once again, alterations in the blood flow in the ICA may induce or attract deposits on the arterial walls and consequently plaque formation.

The CBCT imaging characteristics of ICA calcifications vary and depend on the image projection (mostly because of the multi-directional course of the ICA) and size (Çağlayan and Tozoğlu 2012). In most cases the ICA calcifications appear as single or multiple "rice grains" or variable in thickness tubular or curvilinear, continuous or interrupted, high density linear or oblique structures, lateral to the pituitary fossa and extending from the anterior to the posterior clinoid process (Figs. 16.45 and 16.46).

The overall prevalence of ICA calcifications can be high (82.2%) in older adults, especially in white males and has been reported to be higher than that of extracranial CAC on CBCT images (Damaskos et al. 2015a, Damaskos et al. 2015b).

The relationship of internal CAC and age and its association with traditional cardiovascular risk factors (smoking, hypercholesterolemia, and a history of cardiac and ischemic cerebrovascular disease) is well established in the literature (Woodcock et al. 1999; de Weert et al. 2009; Çağlayan and Tozoğlu 2012; Bos et al. 2012). However, internal CACs are also seen frequently even in pediatric populations; Koch reported 25% of children aged 18 years or less had definitive calcifications within the wall of the ICA with a 6% prevalence in children younger than 2 years and 28% prevalence in children 12–19 years of age (Koch et al. 2007). Admittedly, the formation of these calcifications has been attributed to a physiologic response to turbulent flow at natural bends in the artery rather than secondary to underlying disease predisposing to early atherosclerotic calcifications.

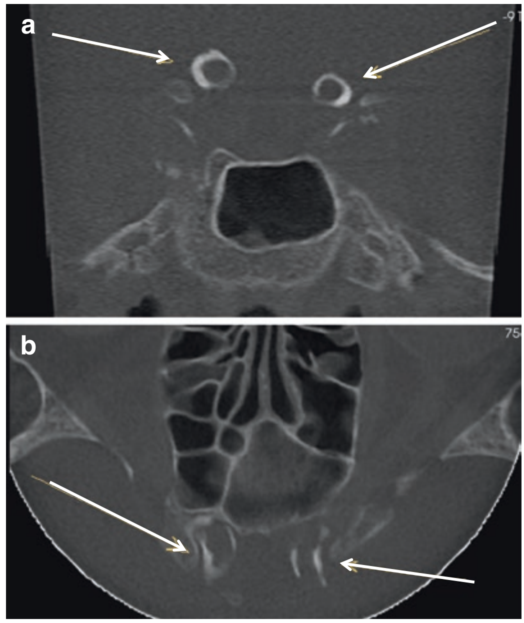

Fig. 16.46 Two millimeter (2 mm) thick, MIP coronal (**a**) and axial (**b**) images in the region of the middle cranial fossa at the level of the pituitary fossa showing large, heterogeneous, bilateral curvilinear and circular calcifications within the intracranial cavernous and clinoid segments of internal carotid artery

Currently the possible association of internal CACs and intracranial arterial stenosis and an increased risk of stroke is unclear. Although, it appears that there is a link between intracranial arterial stenosis and cerebrovascular ischemic disease, the relationship between ICACs and stenosis is, as yet, undetermined.

The following management principles are currently regarded as best practice in CBCT imaging if the presence of internal CAC is suspected:

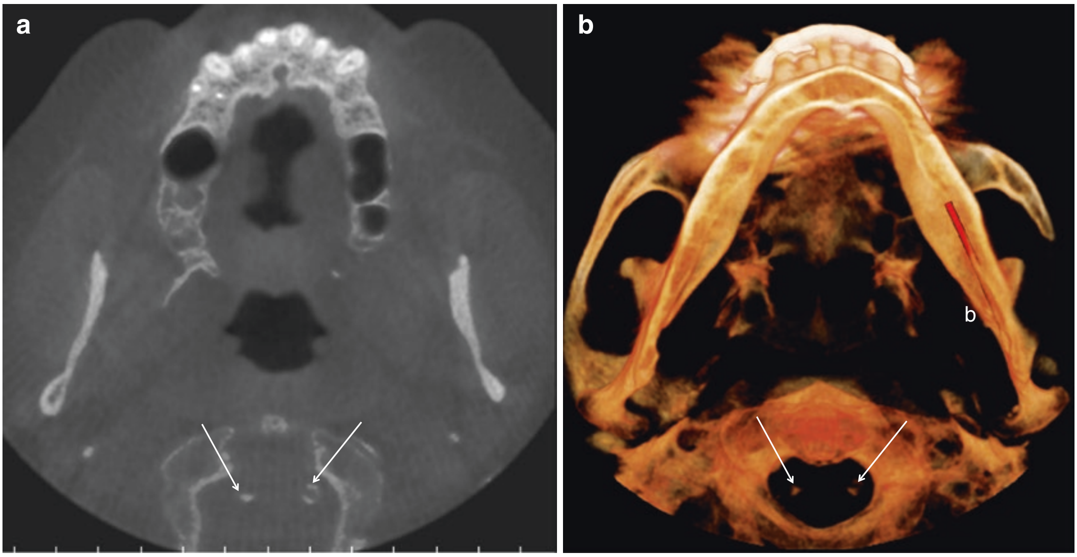

Fig. 16.47 Axial CBCT section at the level of C1 (atlas) (**a**) and submentovertex volume rendering projection (**b**) depicting two small calcifications within the foramen magnum (*arrows*). These are calcifications in the vertebral arteries

- If the CBCT FOV includes the skull base, the presence of intracranial CAC should be considered and investigated, especially when extracranial calcified CAC are identified (Damaskos et al. 2015b).
- When internal CACs are identified on CBCT images, a consultation with a knowledgeable colleague is recommended, noting the imaging findings and a suggestion to substantiate the diagnosis and determine the extent of stenosis (Schulze and Friedlander 2013; Friedlander et al. 2014).

Apart from carotid artery calcifications, other vascular calcifications may be observed on CBCT images, including those of the vertebral/basilar arteries whose prevalence ranges between 1 and 2% (Fig. 16.47).

16.4 To Report or Not to Report…?

Without clear professional guidelines, clinicians face a dilemma. Currently there is a continuum of professional opinion as to the reporting of incidental disease in medical radiology, representative of the thoughts of oral and maxillofacial (OMF) radiologists. At one end of the spectrum is the notion that superfluous medical information is potentially harmful and that the patient would be better off not knowing all incidental findings. Those in this camp insist that radiologists should have discretion to ignore unsolicited incidental findings on imaging studies if they appear benign, if the disclosure of such findings provides little or no benefit to patients and potentially expose them to considerable psychological distress (Welch et al. 2011; Volk and Ubel 2011). Indeed, some insist that unfiltered reporting of occult pathological entities, especially to zealous practitioners, is tantamount to over diagnosis, having the potential to harm the patient by exposing them to overtreatment including supplemental imaging or clinical procedures including biopsy.

On the opposite end of the spectrum, others content that practitioners have the ethical and legal duty to disclose all relevant medical information to patients (American Medical Association Council on ethical and judicial affairs, 2010). In a litigious medical environment, where patient autonomy is valued and where there is no interpretive reporting standard on what constitutes a relevant or legitimate incidental finding, subscribers to this opinion content that the patient's "right to know" trumps all professional considerations and that it is ultimately for the patient to decide on how much risk they themselves should tolerate. To do otherwise would be malpractice (Brown 2013).

16.5 Recommendations for Management

As there is no consensus guideline providing those who perform and interpret CBCT images with a "usual and customary manner" in which to deal with incidental findings, practitioners must decide for themselves how to deal with them. We believe practitioners have a responsibility to develop individual management protocols to deal with unexpected findings in CBCT imaging. The following provides a management strategy for dealing with incidental findings in clinical practice.

1. **Systematically review the entire CBCT volumetric dataset and report on relevant findings.** Numerous medical professional bodies' guidelines (American College of Radiology-ACR 2011; Board of Faculty of Clinical Radiology, Royal College of Radiologists 2006) recommend that all imaging procedures and now specifically CBCT (Carter et al. 2008) should include an expert opinion from a radiologist, given by means of a written report or comment. While some discrepancies such as omissions of insignificant findings, typographical errors, and errors in interpretive opinion are likely to occur, frank errors including exclusion of obvious overt findings of significance and lack of description of incidental findings of potentially moderate to high significance while inevitable, must be minimized. Workload can be a significant factor in increasing the likelihood of errors in CBCT. "Reckless reads," where too many cases are viewed superficially, potentially has great legal implications (Berlin 2000) Comprehensive radiologic assessment and interpretation of takes time and must be considered integral to the performance of CBCT imaging.
2. **Report all relevant incidental findings.** The ACR guidelines for CT reporting (American College of Radiology 2014) form the basis for government reimbursement of CBCT examinations in the United States, and therefore to some extent offer a minimal *defacto* standard for CBCT reporting.

   A report should have four essential elements including sections describing demographics, relevant clinical information, the body of the report, and radiologic impression. Incidental findings should be described as a section within the findings of the body of the report and, if they are potentially significant, they should be highlighted in the radiologic impression. In addition, it is there where follow-up or additional diagnostic studies to clarify or confirm the impression should be suggested or recommend, when appropriate. However, it appears that there is a general lack of agreement concerning how radiologists report incidental findings on multi-detector CT (Johnson et al. 2011). The same is most likely true for CBCT reports. This may be due, at least in part, to a lack of or inconsistency in standards in disclosing or reporting incidental findings.
3. **Familiarity with the incidence, location, and presentation of common incidental disease.** Depending on experience and training, the knowledge base in identification and characterization of common incidental findings will vary for each practitioner. Practitioners are strongly encouraged to become familiar with the current scientific literature (e.g., case reports and series in journals, books) and attend continuing dental education courses on CBCT interpretation. These courses offer opportunities at developing baseline competency in understanding the relative incidence and radiographic features of the more common incidental findings as well as opportunities to network with OMF radiologists.
4. **When in doubt, refer.** When an incidental finding remains undetermined and becomes a diagnostic dilemma, one should consider "the

second opinion" option. This is equally true for generalists and other dental specialists as it is for oral and maxillofacial radiologists. Referral should first be to a specialist who is most knowledgeable about the radiologic appearance of maxillofacial disease or a medical radiologist. If unavailable, an oral pathologist with expertise in advanced imaging should be considered next. This is likely the most cost-effective referral route as these individuals usually have a wealth of experience and expertise on which to draw. The practice of providing specific image "screen-shots" for comment, while likened by many to a "corridor consultation," is akin to handicapping the radiologist not to mention now being a litigious minefield, especially if forwarded as an e-mail attachment. An opinion request should be accompanied by inclusion of the entire volumetric dataset and some basic information about patient demographics, clinical findings, and reason for the scan acquisition. The OMF radiology professional network is extensive and OMF radiologists readily seek the opinions of colleagues including head and neck radiologists and neuro-radiologists. An essential role of the OMF radiologist is act as a collaborative resource for clinicians to assist on deciding if an incidental imaging feature is normal, an anatomic variant or has a low, intermediate or high level of potential significance and in guiding appropriate management follow-up. Management recommendations provided by radiologists include:

– Ignore (in the case of identification or low level of significance).
– Comparison to available prior relevant imaging examinations.
– Correlation with current clinical presentation.
– Further evaluation (intraoral radiography of specific teeth, repeat CBCT with extended FOV, referral for advanced imaging including MDCT or MRI).
– Periodic surveillance (observe until some changes are observed or a threshold is reached).
– This is often communicated within the written radiologic interpretation report and may initiate further discussion by telephone or e-mail.

16.6 Future Directions

At this stage there is a need for multi-variant analysis of a much larger (perhaps multi-center) study sample enrolling up to 10,000 subjects to provide a clearer understanding of the prevalence of significant incidental disease and providing associative guidance on identification.

While practitioners may be aware of the prevalence of incidental findings in specific groups, currently this relationship has no roadmap, no consensus direction on the most appropriate management protocol. Professional recommendations, with input from specific specialties and disciplines, are needed to develop clinical decision management algorithms for specific incidental entities such as:

- The asymptomatic presence of chronic apical periodontitis on root canal filled teeth.
- Intracranial calcifications.
- Sinus opacifications.
- Vertebral entities.

One such algorithm is available for the management of the incidental finding of carotid artery calcifications due to atheromatosis on dental images (MacDonald et al. 2012).

Acknowledgments Sections of this chapter are reproduced from Scarfe WC (2014) with permission from Elsevier.

References

Allareddy V, Vincent SD, Hellstein JW, Qian F, Smoker WR, Ruprecht A (2012) Incidental findings on cone beam computed tomography images. Int J Dent 2012:871532

American College of Radiology (2011) ACR practice guideline for communication of diagnostic imaging findings. http://wwwacrorg/~/media/

C5D1443C9EA4424AA12477D1AD1D927Dpdf. Accessed 30 Dec 2013
American College of Radiology (2014) ACR practice parameter for communication of diagnostic imaging findings. Revised 2014 (Resolution 11). Available at: http://www.acr.org/~/media/C5D1443C9EA4424AA12477D1AD1D927D.pdf. Accessed August 28, 2017
American Heart Association/American Stroke Association, Heart Disease and Stroke Statistics (2008) Update, Dallas, TX
American Medical Association Council on ethical and judicial affairs (2010) Code of medical ethics 2010–2011 edition.8.082. Withholding information from patients, 269–270
Arnheiter C, Scarfe WC, Farman AG (2006) Trends in maxillofacial cone beam computed tomography usage. Oral Radiol 22:80–85
Ballantyne C (2008) To know or not to know. Nat Med 14:797
Balshi T, Wolfinger G, Yang J, Wulc D, Balshi S (2013) Prevalence of non-dental pathology in cone beam computed tomography studies for dental implants. JIACD, J Implant Adv Clin Dent 5(3):21–26
Berland LL, Silverman SG, Gore RM, Mayo-Smith WW, Megibow AJ, Yee J, Brink JA, Baker ME, Federle MP, Foley WD, Francis IR, Herts BR, Israel GM, Krinsky G, Platt JF, Shuman WP, Taylor AJ (2010) Managing incidental findings on abdominal CT: white paper of the ACR incidental findings committee. J Am Coll Radiol 7:754–773
Berlin L (2000) Liability of interpreting too many radiographs. AJR Am J Roentgenol 175:17–22
Berlin L (2011) The Incidentaloma: A Medicolegal Dilemma. Radiol Clin N Am 49:45–255
Board of Faculty of Clinical Radiology. Royal College of Radiologists (2006) Standards for the reporting and interpretation of imaging investigations. BRCR (06)1 Roy Coll Radiol. http://www.rcr.ac.uk/docs/radiology/pdf/Standardsfor Reporting and Inetrpwebvers.pdf. Last accessed 31 Dec 2013
Booth TC, Jackson A, Wardlaw JM, Taylor SA, Waldman AD (2010) Incidental findings found in "healthy" volunteers during imaging performed for research: current legal and ethical implications. Br J Radiol 83:456–465
Bos D, van der Rijk MJ, Geeraedts TE, Hofman A, Krestin GP, Witteman JC, van der Lugt A, Ikram MA, Vernooij MW (2012) Intracranial carotid artery atherosclerosis prevalence and risk factors in the general population. Stroke 43:1878–1884
Bouthillier A, van Loveren HR, Keller JT (1996) Segments of the internal carotid artery: a new classification. Neurosurgery 38(3):425–433
Brown S (2013) Professional norms regarding how radiologists handle incidental findings. J Am Coll Radiol 10:253–257
Cağlayan F, Tozoğlu U (2012) Incidental findings in the maxillofacial region detected by cone beam CT. Diagn Interv Radiol 18:159–163
Carter L, Farman AG, Geist J, Scarfe WC, Angelopoulos C, Nair MK, Hildebolt CF, Tyndall D, Shrout M, American Academy of Oral and Maxillofacial Radiology (2008) American Academy of Oral and Maxillofacial Radiology executive opinion statement on performing and interpreting diagnostic cone beam computed tomography. Oral Surg Oral Med Oral Pathol Oral Radiol Endod 106:561–562
Carter LC, Haller AD, Nadarajah V, Calamel AD, Aguirre A (1997) Use of panoramic radiography among an ambulatory dental population to detect patients at risk of stroke. J Am Dent Assoc 128:977–984
Cha JY, Mah J, Sinclair P (2007) Incidental findings in the maxillofacial area with 3-dimensional cone-beam imaging. Am J Orthod Dentofacial Orthop 132:7–14
Damaskos S, Aartman IH, Tsiklakis K, van der Stelt P, Berkhout WE (2015a) Association between extra- and intracranial calcifications of the internal carotid artery: a CBCT imaging study. Dentomaxillofac Radiol 44:20140432
Damaskos S, Tsiklakis K, Syriopoulos K, Stelt P v d (2015b) Extra- and intra-cranial arterial calcifications in adults depicted as incidental findings on cone beam CT images. Acta Odontol Scand 73(3):202–209
de Weert TT, Cakir H, Rozie S, Cretier S, Meijering E, Dippel DW, van der Lugt A (2009) Intracranial internal carotid artery calcifications: association with vascular risk factors and ischemic cerebrovascular disease. AJNR Am J Neuroradiol 30:177–184
Dobele I, Kise L, Apse P, Kragis G, Bigestans A (2013) Radiographic assessment of findings in the maxillary sinus using cone-beam computed tomography. Stomatologija 15:119–122
Doğramacı EJ, Rossi-Fedele G, McDonald F (2014) Clinical importance of incidental findings reported on smallvolume dental cone beam computed tomography scans focused on impacted maxillary canine teeth. Oral Surg Oral Med Oral Pathol Oral Radiol 118:e205–e209
Drage N, Rogers S, Greenall C, Playle R (2013) Incidental findings on cone beam computed tomography in orthodontic patients. J Orthod 40:29–37
Edwards R, Altalibi M, Flores-Mir C (2013) The frequency and nature of incidental findings in cone-beam computed tomographic scans of the head and neck region: a systematic review. J Am Dent Assoc 144:161–170
Edwards R, Alsufyani N, Heo G, Flores-Mir C (2014) The frequency and nature of incidental findings in large-field cone beam computed tomography scans of an orthodontic sample. Prog Orthod 15:37–49
Epstein RM, Korones DN, Quill TE (2010) Withholding information from patients: when less is more. N Engl J Med 362:380–381
Friedlander AH, Aghazadehsanai N, Chang TI, Harada N, Garrett NR (2013) Prevalence of calcified carotid artery atheromas on panoramic images of individuals with primary hyperparathyroidism. Dentomaxillofac Radiol 42(8):20130118

Friedlander AH, Garrett NR, Chin EE, Baker JD (2005) Ultrasonic confirmation of carotid artery atheromas diagnosed via panoramic radiography. J Am Dent Assoc 136:635–640

Friedlander AH, Garrett NR, Norman DC (2002) The prevalence of calcified carotid artery atheromas on the panoramic radiographs of patients with type 2 diabetes mellitus. J Am Dent Assoc 133:1516–1523

Friedlander AH, Golub MS (2006) The significance of carotid artery, atheromas on panoramic radiographs in the diagnosis of occult metabolic syndrome. Oral Surg Oral Med Oral Pathol Oral Radiol Endod 101:95–101

Friedlander AH, Lande A (1981) Panoramic radiographic identification of carotid arterial plaques. Oral Surg Oral Med Oral Pathol 52:102–104

Friedlander AH, Liebeskind DS, Tran HQ, Mallya SM (2014) What are the potential implications of identifying intracranial internal carotid artery atherosclerotic lesions on cone-beam computed tomography? A systematic review and illustrative case studies. J Oral Maxillofac Surg 72:2167–2177

Gorelick PB et al (1999) Prevention of a first stroke: a review of guidelines and a multidisciplinary consensus statement from the National Stroke Association. J Am Med Assoc 281:1112–1120

Heller MT, Harisinghani M, Neitlich JD, Yeghiayan P, Berland LL (2013) Managing incidental findings on abdominal and pelvic CT and MRI, part 3: white paper of the ACR Incidental Findings Committee II on splenic and nodal findings. J Am Coll Radiol 10:833–839

Johnson PT, Horton KM, Megibow AJ, Jeffrey RB, Fishman EK (2011) Common incidental findings on MDCT: survey of radiologist recommendations for patient management. J Am Coll Radiol 8:762–767

Khosa F, Krinsky G, Macari M, Yucel EK, Berland LL (2013) Managing incidental findings on abdominal and pelvic CT and MRI, part 2: white paper of the ACR incidental findings committee II on vascular findings. J Am Coll Radiol 10:789–794

Koch B, Blackham A, Jones B (2007) Incidental internal carotid artery calcifications on temporal bone CT in children. Pediatr Radiol 37:141–144

Lana JP, Carneiro PM, Machado Vde C, de Souza PE, Manzi FR, Horta MC (2012) Anatomic variations and lesions of the maxillary sinus detected in cone beam computed tomography for dental implants. Clin Oral Implants Res 23:1398–1403

Lumbreras B, Donat L, Hernández-Aguado I (2010) Incidental findings in imaging diagnostic tests: a systematic review. Br J Radiol 83:276–289

MacDonald D, Chan A, Harris A, Vertinsky T, Farman AG, Scarfe WC (2012) Diagnosis and management of calcified carotid artery atheroma: dental perspectives. Oral Surg Oral Med Oral Pathol Oral Radiol 114:533–547

Miles DA (2005) Clinical experience with conebeam volumetric imaging report of findings in 381 cases. Comput Tomogr 20:416–424

Patel MD, Ascher SM, Paspulati RM, Shanbhogue AK, Siegelman ES, Stein MW, Berland LL (2013) Managing incidental findings on abdominal and pelvic CT and MRI, part 1: white paper of the ACR incidental findings committee II on adnexal findings. J Am Coll Radiol 10:675–681

Pazera P, Bornstein MM, Pazera A, Sendi P, Katsaros C (2011) Incidental maxillary sinus findings in orthodontic patients: a radiographic analysis using cone-beam computed tomography (CBCT). Orthod Craniofac Res 14:17–24

Pette GA, Norkin FJ, Ganeles J, Hardigan P, Lask E, Zfaz S, Parker W (2012) Incidental findings from a retrospective study of 318 cone beam computed tomography consultation reports. Int J Oral Maxillofac Implants 27:595–603

Pliska B, DeRocher M, Larson BE (2011) Incidence of significant findings on CBCT scans of an orthodontic patient population. Northwest Dent 90:12–16

Presidential Commission for the Study of Bioethical Issues (2013) Anticipate and communicate: ethical management of incidental and secondary findings in the clinical, research, and direct-to-consumer contexts (December 2013 Report of the Presidential Commission for the Study of Bioethical Issues. http://bioethicsgov/sites/default/files/FINALAnticipateCommunicate_PCSBI_0pdf. Accessed 16 Dec 2015

Price JB, Thaw KL, Tyndall DA, Ludlow JB, Padilla RJ (2012) Incidental findings from cone beam computed tomography of the maxillofacial region: a descriptive retrospective study. Clin Oral Implants Res 23:1261–1268

Rogers AJ, Maher CO, Schunk JE, Quayle K, Jacobs E, Lichenstein R, Powell E, Miskin M, Dayan P, Holmes JF, Kuppermann N (2013) Pediatric emergency care applied research network. Incidental findings in children with blunt head trauma evaluated with cranial CT scans. Pediatrics 132:e356–e363

Scarfe WC (2014) Incidental findings on CBCT images. A Pandora's box? Oral Surg Oral Pathol Oral Med Oral Radiol 117:537–540

Schulze R, Friedlander AH (2013) Cone beam CT incidental findings: intracranial carotid artery calcification—a cause for concern. Dentomaxillofac Radiol 2:20130347

Sebastian S, Araujo C, Neitlich JD, Berland LL (2013) Managing incidental findings on abdominal and pelvic CT and MRI, part 4: white paper of the ACR incidental findings committee II on gallbladder and biliary findings. J Am Coll Radiol 10:953–956

Tegos TJ et al (2001) The genesis of atherosclerosis and risk factors: a review. Angiology 52:89–98

Tovino SA (2008) Incidental findings: a common law approach. Account Res 15:242–261

Volk ML, Ubel PA (2011) Better off not knowing: improving clinical care by limiting physician access to unsolicited diagnostic information. Arch Intern Med 171:487–488

Welch HG, Schwartz LM, Woloshin S (2011) Overdiagnosed: making people sick in the pursuit of health. Beacon Press, Boston, pp 90–101

Wolf SM, Lawrenz FP, Nelson CA, Kahn JP, Cho MK, Clayton EW, Fletcher JG, Georgieff MK, Hammerschmidt D, Hudson K, Illes J, Kapur V, Keane MA, Koenig BA, Leroy BS, McFarland EG, Paradise J, Parker LS, Terry SF, Van Ness B, Wilfond BS (2008) Managing incidental findings in human subjects research: analysis and recommendations. J Law Med Ethics 36:219–248, 211.

Woodcock RJ Jr, Goldstein JH, Kallmes DF, Cloft HJ, Phillips CD (1999) Angiographic correlation of CT calcification in the carotid siphon. AJNR Am J Neuroradiol 20:495–499

Yang J (2015) Unpublished data

Soft Tissue Hyperdensities

17

William C. Scarfe, Allan G. Farman, and Christos Angelopoulos

Contents

W.C. Scarfe (✉)
Radiology and Imaging Science, Department of Surgical, Hospital Dentistry, University of Louisville School of Dentistry, Louisville, KY, USA
e-mail: William.scarfe@louisville.edu

A.G. Farman, B.D.S., Ph.D., D.Sc., M.B.A.
Emeritus Professor, The University of Louisville School of Dentistry, Louisville, KY, USA

Independent Consultant in Maxillofacial Imaging Science, Chicago, IL, USA
e-mail: allanfarman@aol.com

C. Angelopoulos, D.D.S., M.Sc.
Aristotle University of Thessaloniki, Thessaloniki, Greece

Columbia University, College of Dental Medicine, New York City, NY, USA
e-mail: angelopoulosc@gmail.com

17.1 Introduction

Calcifications of soft tissue structures located in the head and neck region are a relatively common occurrence. These calcifications are often detected on traditional imaging used in dental practice, particularly panoramic radiography. However, many

W.C. Scarfe, C. Angelopoulos (eds.), *Maxillofacial Cone Beam Computed Tomography*, https://doi.org/10.1007/978-3-319-62061-9_17

of the structures in the head and neck are in close proximity to one another which makes localization and identification difficult. This potentially leads to both false positive and false negative detection of some calcifications of significance in certain areas in this region such as calcified atheromatic plaques within the carotid arteries.

17.1.1 Etiology of Soft Tissue Hyperdensities

Calcifications can occur either as physiological or pathological mineralizations (Kirsch 2006). Physiological mineralization is restricted to specific sites in skeletal tissues, including growth plate cartilage (Fig. 17.1), bones, and teeth whereas pathological mineralization can occur in any soft tissue, particularly in articular cartilage, cardiovascular tissues, ligaments, and glandular tissues and are usually associated with chronic inflammation or scarring. The mineralization of arteries leads to morbidity and may contribute, in some cases, to mortality, whereas mineralization of articular cartilages, and often ligaments, can lead to their destruction and joint stiffness.

The two most important mechanisms of calcification are dystrophic and metastatic calcification.

- **Dystrophic.** Dystrophic calcification occurs in soft tissues that normally do not contain such deposits and may occur as the result of chronic inflammation, necrosis, or scarring. The deposition of mineral salts in dead or degenerating tissues is referred to as dystrophic calcification.
- **Metastatic.** In contrast, metastatic calcification is the process by which normal undamaged tissues may become calcified due to hypercalcemia such as that which occurs in hyperparathyroidism. The minerals deposited in the tissues may not necessarily be calcium salts exclusively.

17.1.2 Calcifications in the Maxillofacial Region

In the craniofacial region, dystrophic calcifications can occur associated with various tissues in the cranial vault, the soft tissues adjacent the jaws, the neck and parapharyngeal structures or the orbit (Table 17.1).

17.1.3 Clinical Significance

Calcifications of soft tissue structures are a relatively common occurrence on cross-section CT images. Approximately 35% of CBCT scans may show some form of soft tissue calcification with most (90%) in the neck region (Khan et al. 2008). The most common soft tissue calcifications, with an almost equal distribution, are carotid artery calcifications, calcifications of the triticeous cartilage, or tonsillar calcifications (Khan et al. 2008). Detection and differentiation of these calcifications on traditional (conventional or digital) radiographic images used in dental practice is problematic because these images are flat two-dimensional (2-D) representations of complex three-dimensional (3-D) objects. With the increasing use and availability of CBCT, the incidental discovery of these calcifications is most likely to increase.

Knowledge of the CBCT imaging characteristics of a calcification combined with accurate localization will guide the clinician towards considering the tissue of origin; this assists in developing a differential diagnosis and facilitates appropriate management. Most calcifications in the maxillofacial region are relatively benign in nature and are associated with few negative outcomes; however, a few, mainly in the neck and endocranium, are potentially serious (like carotid artery calcifications due to atheromatic disease) and could contribute to morbidity. Therefore, the clinician should be able not only to identify and recognize different calcifications on CBCT imaging but also be aware of their relative incidence rate in certain age groups (like older individuals as far as it concerns carotid artery calcifications), and have a solid foundation in distinguishing the most common radiographic appearance of calcifications and their location to the various structures. Because CBCT has poor tissue contrast, the location of a calcification is usually described in relation adjacent bony structures such as the cervical vertebrae, the hyoid bone and pharyngeal airway.

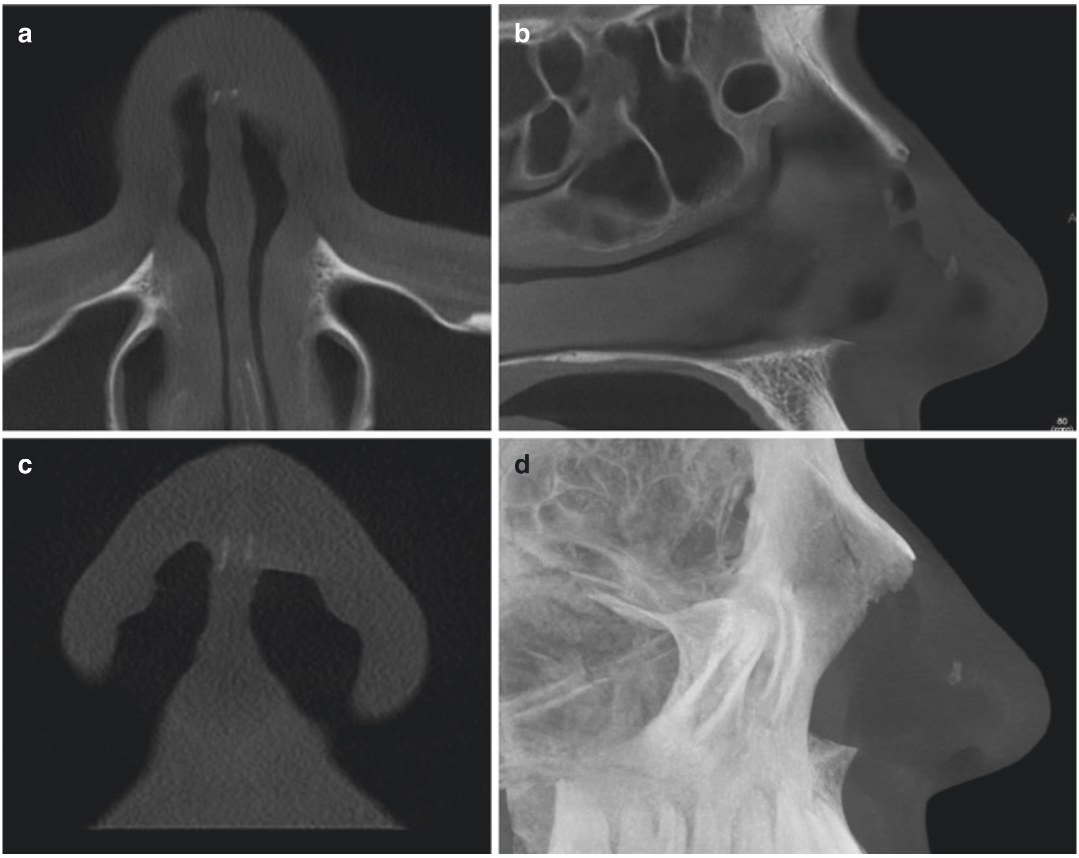

Fig. 17.1 The nose is constructed from paired and singular midline cartilages: The midline cartilage is the vomeronasal cartilage forming the base and the septal cartilage; bilateral paired cartilages include the major alar cartilage comprising the tip, the minor alar cartilages forming the base, and the lateral nasal cartilages extending inferiorly from the nasal bones bilaterally. Accessory (sesamoid) alar cartilages separate the lateral portion of the greater and lateral nasal cartilages. Axial (**a**), magnified axial (**b**), sagittal thin section (**c**), and maximum intensity projection (**d**) CBCT images demonstrate physiologic calcifications on the medial crus (junction) of the greater alar cartilage

17.1.4 Radiologic Evaluation

Task specific image display protocols should be used to demonstrate the presence and location of soft tissue calcifications. Because the key to differential diagnosis is determining the anatomic location of the calcification, an appropriate display mode should be used to provide the optimal viewing. Triangulation of the unknown calcification with multi-planar reformated (MPR) images in the three standard planes of section (axial, coronal, sagittal) will assist in the accurate localization of the calcification in relationship with known, neighboring anatomical structures. However, these images require at least some familiarity and considerable knowledge of the anatomy of the maxillofacial region (Fig. 17.2). An alternative image viewing protocol includes the use of medium thickness slice (20–40 mm) maximum intensity projection (MIP) images (Scarfe and Farman 2007). This technique is faster and less expensive than direct volumetric reconstruction (Fig. 17.3) and, when used in all three orthogonal projections, provides adequate three-dimensional information for diagnosis.

Table 17.1 Most common dystrophic calcifications according to maxillofacial regional location

Soft tissue	Cranial vault	Jaws and adjacent soft tissue	Neck	Orbit
Vascular	Atheromas in the intracranial internal carotid artery	Lingual arteries	Atheromas at the bifurcation of the common carotid artery	
			Phleboliths	
Ligamentous	Petroclinoid and interclinoid ligaments	Stylomandibular	Stylohyoid chain	Superior oblique
	Falx	Ligament	Prevertebral longus colli	
Glandular	Pineal gland	Submandibular and sublingual salivary glands	Calcifications in the tonsillar tissue	
	Choroid plexus	Subdermal fascia		
Cartilage		Alar cartilage	Thyroid cartilage	
			Triticeous cartilage	
Lymph nodes		Submental/submandibular lymph nodes	Supra-clavicular lymph nodes	
Muscular		Myositis ossificans	Prevertebral	
Foreign bodies		Radiopaque dermal fillers/inserts/implants	Carotid stent	Ocular prosthetics
		Subdermal implants		

Moreover, it is contributory for gross localization of the calcification in question and rather educational for the patient.

Apart from the above, any kind of reconstructed image (planar or curved) that may be of assistance to the examining should be employed in order to facilitate diagnosis.

17.2 Cranial Vault

Intracranial calcifications (IC) may be detected within the cranial vault, especially when large FOVs are used. It is important to consider the possible etiology of IC and recognize characteristic locational and structural features which may indicate specific pathological entities and guide towards appropriate management. IC can be categorized according to three broad potential etiologies (Kıroğlu et al. 2010).

- **Physiologic and age related.** Calcifications on a number of brain and dural structures may occur as a result of neurodegenerative, age-related changes at various sites including the pineal gland (small endocrine gland located along the midbrain producing melatonin), habenula (small group of nerve cells located near the pineal gland which seem to be closely associated with the pineal gland), choroid plexus (a network of capillaries close to the cerebellum that produce cerebrospinal fluid-CSF), basal ganglia dura (multiple subcortical nuclei on either side of the midbrain which are associated with a number of functions including voluntary motor movements, procedural learning, routine behaviors or habits), and clinoid ligaments. These are the most common intracranial calcifications and can usually be identified by the location, morphology, and symmetry.
- **Congenital.** Numerous congenital conditions are associated with intracranial calcifications. They are commonly associated with Sturge–Weber syndrome (SWS) and tuberous

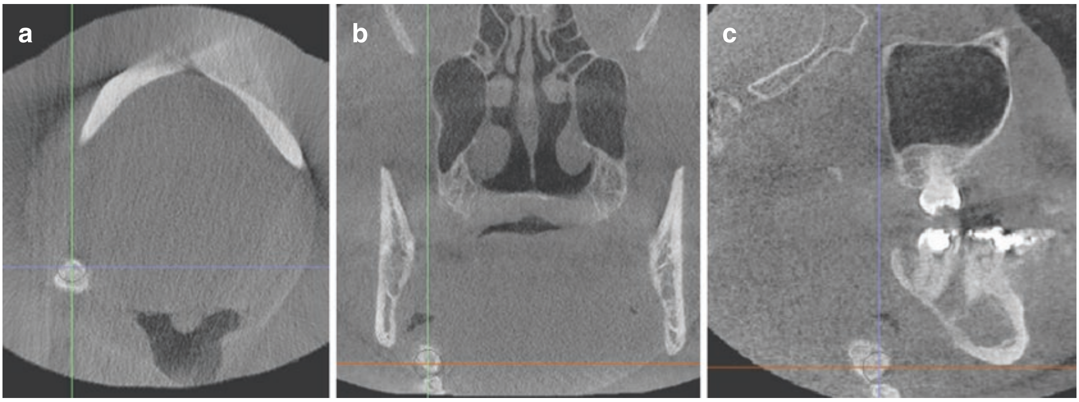

Fig. 17.2 "Triangulation" of a large calcification in axial (**a**), coronal (**b**), and sagittal (**c**) CBCT images indicates that it is located inferomedially to the angle of the right mandible. This region corresponds to the submandibular space and the calcification is most likely a sialolith in the body of the right submandibular salivary gland

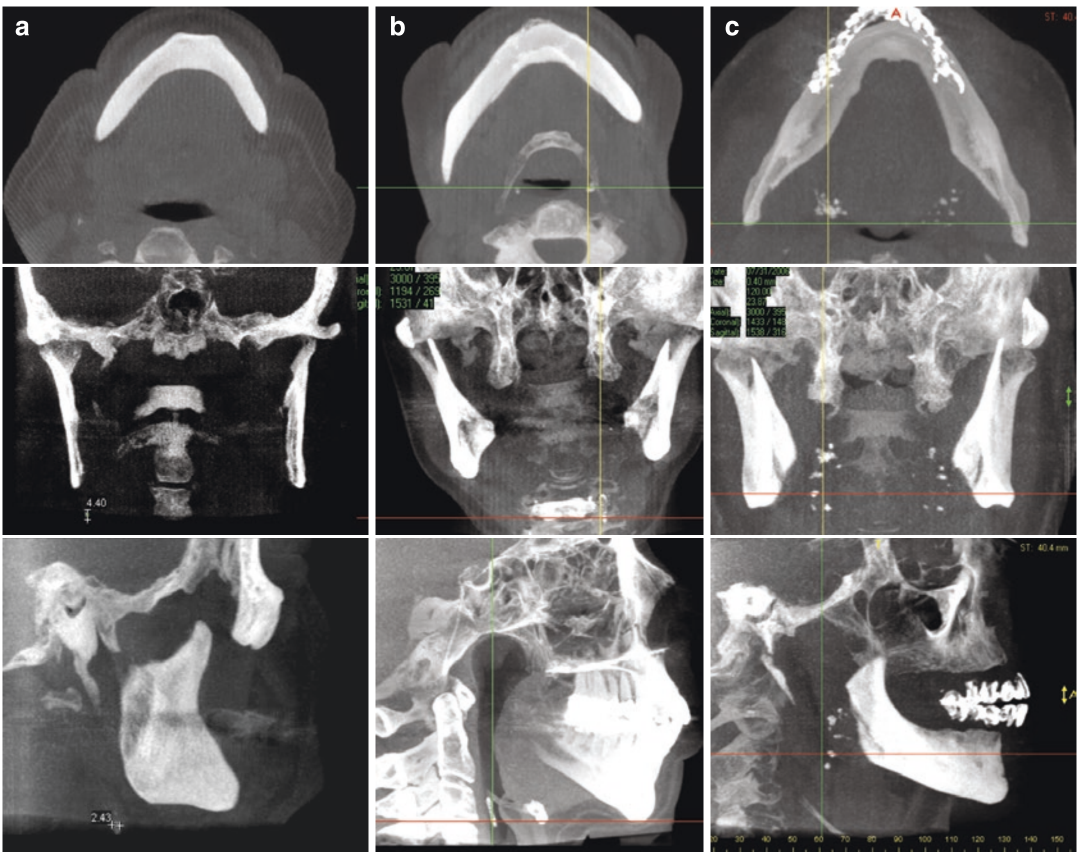

Fig. 17.3 Differences in the pattern and location of a calcified common carotid artery atheromatic plaque (**a**), a triticeous cartilage calcification (**b**), and tonsillar tissue calcifications (**c**) are clearly demonstrated using a standard imaging protocol including axial (*top row*), coronal (*middle row*), and sagittal (*lower row*) 10 mm thick MIP images

sclerosis (TS) and less frequently in other conditions (e.g., neurofibromatosis, nevoid basal cell carcinoma syndrome (NBCCS), arteriovenous malformations (AVM), and hemangiomas). Characteristic patterns of calcification are associated with SWS (linear gyral calcifications), TS (calcified globular subependymal nodules commonly located along the caudothalamic groove and atrium), NBCCS (calcified falx cerebri), and vascular abnormalities such as AVM (serpentine calcifications). Other conditions usually present as asymmetric globular hyper-attenuating masses.

- **Pathologic.** Pathological calcifications are rare but knowledge of the common imaging appearance of physiologic calcifications and an understanding of the distinguishing features of pathologic calcifications may assist in appropriate management which may include nothing or referral to a neurologist. Pathologic calcifications are usually larger, nonsymmetrical, abnormal in shape with irregular borders and located at non-physiologic locations (Sedghizadeh et al. 2012).
  - *Infectious.* Congenital TORCH (toxoplasmosis, rubella, Cytomegalovirus, and Herpes simplex virus) diseases are associated with scattered or nodular calcifications. Other conditions include granulomatous infections and chronic viral encephalitis.
  - *Endocrine and metabolic.* Since the parathyroid glands are concerned with maintenance of plasma calcium levels, diseases such as hypoparathyroidism, hyperparathyroidism, and pseudohypoparathyroidism may result in intracranial calcifications.
  - *Vascular.* Causes of vascular calcifications include primary atherosclerosis (see Sect. 17.2.2), aneurysm, arteriovenous malformation (AVM), and cavernous malformation.
  - *Neoplastic.* The prevalence and appearance of calcification associated with cerebral tumors depends on the type of tumor (Table 17.2). Benign slow growing tumors are more likely to calcify than malignant tumors.

The overall incidence of physiologic intracranial calcifications in CBCT imaging has been reported to be 35.2% (Mean age 52 years, range 13–82 years) (Sedghizadeh et al. 2012). CBCT (Sedghizadeh et al. 2012) and CT (Daghighi et al. 2007) studies indicate that the most common intracranial calcifications are age-related physiologic calcifications (pineal gland range, 71–80%; choroid plexus range, 12–66%; and dural or ligamentous range 7.3–8%).

The various types of calcifications discussed next are approached by means of significance and importance to the clinician as well as frequency of appearance.

17.2.1 Physiologic Calcifications

These are the most common intracranial calcifications and occur as a result of age-related physiologic and neurodegenerative processes. All are incidental findings that are not associated with a specific disease entity.

- **Pineal gland.** The pineal gland (epiphysis or conarium) is a small endocrine gland which lies near the center of the brain inside the epithalamus. It produces melatonin; this hormone affects sleeping patterns. Calcification of the pineal gland can occur in up to 2/3rd of the adult population and increases with age. They usually present as a single well-demarcated, irregular in shape or “pine-cone”-shaped, homogenous or mixed in appearance, high-density mass with a mean diameter of 4 mm (range, 1–7 mm) (Sedghizadeh et al. 2012) (Fig. 17.4). Calcification over 1 cm in diameter or detection in individuals under 9 years of age may be suspicious of a neoplasm (Deepak and Jayakumar 2005).

Table 17.2 Prevalence of calcifications in specific intracranial tumors and radiologic appearance

Tumor	Location	Prevalence of calcification	Common radiographic presentation
Craniopharyngioma	Midsagittal, immediately superior to sella turcica	50–80%	Mostly children
			Range from few punctate specks to a densely calcified mass
			Curvilinear calcification may be observed if the tumor is cystic
			May deform sella
Oligodendroglioma	Frontal lobe	70–90%	Nodular or clumped
Germ cell tumors	Sella turcica and suprasellar region	60–80%	Children or adults, 2:1 males-to-females
Pineal gland tumor	In sella turcica	60–80%	Heterogeneous calcified mass
Astrocytoma	Suprasella or posterior fossa	10–20%	Most common pediatric brain tumor
			Homogeneous hyper-attenuating large mass with smooth borders
Ependymoma	4th ventricle, posterior fossa	50%	10% of all pediatric brain tumors
Meningioma	Asymmetric	10%	Elderly
			Range from speckled or nodular to more characteristic "ball-like" and amorphous
			Adjacent bony hyperostosis
			Increased peripheral meningeal markings
Dermoid	Posterior fossa, base of skull	5%	Arc of calcification
			May be associated with characteristic small central defect in the occipital bone

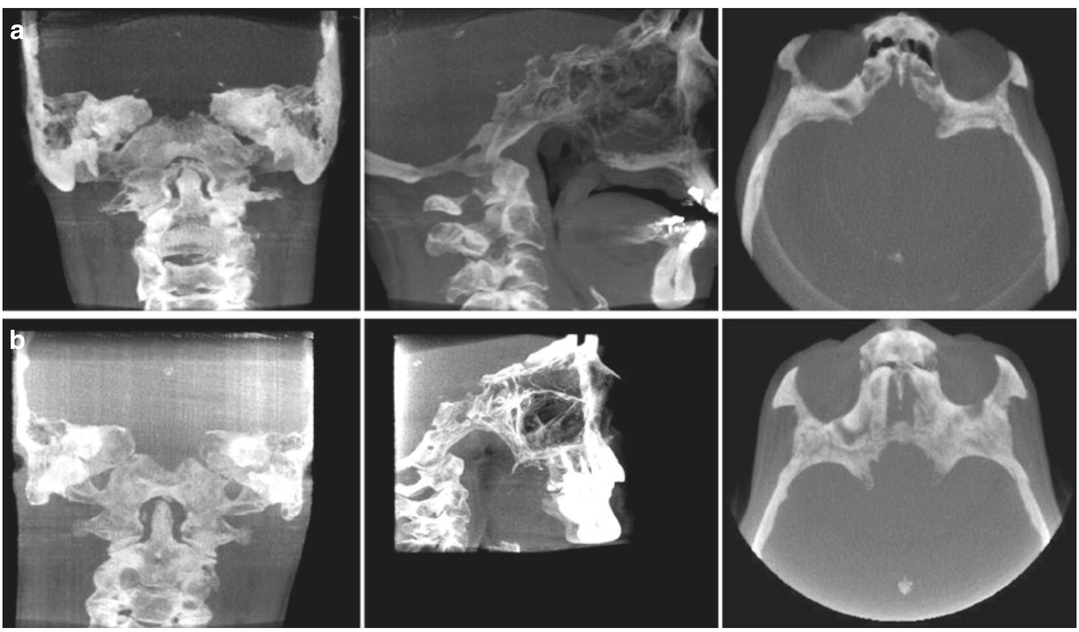

Fig. 17.4 Coronal (*left column*) sagittal (*middle column*), and axial (*right column*) 10 mm thick MIP CBCT images of two patients (**a**, **b**) demonstrating the typical appearance and location of calcified pineal gland/habenula

- **Habenula.** These paired nuclei (small group of nerve cells) lie on each side and slightly anterior to the midline pineal gland which seem to be associated with the pineal gland. It has a central role in the regulation of the limbic system and may calcify in up to 15% of the adult populations. When calcified, in CBCT images it appears as a small irregular in shape (some time curvilinear) dense structure lying a few millimeters anterior and inferior to the pineal body (Fig. 17.5).
- **Choroid Plexus.** These are complex vessel or capillary networks inside the brain ventricles (four of them exist, one in each brain ventricle) close to the cerebellum. Their main function is the production of CSF and acting as a filtration system (blood-CSF barrier). Calcifications of the choroid plexuses are frequent usually in the atrial portions of the lateral ventricles. They usually present as bilateral, round to curvilinear faint, high-density masses (Figs. 17.6 and 17.7). Note that calcification in the third or fourth ventricle (midline ventricles) or in patients less than 9 years of age is uncommon and should prompt referral to a neurological specialist.
- **Basal ganglia.** These are multiple subcortical nuclei on either side of the midbrain which are associated with a number of functions including voluntary motor movements, procedural learning, routine behaviors or habits like bruxism, etc. Calcifications of the basal ganglia are an uncommon (up to 1.5%) finding with an increasing incidence with age. They may present as a relatively hyperdense punctate or coarse conglomerated symmetrical pattern. They are usually an idiopathic finding in older individuals but, if present in individuals under

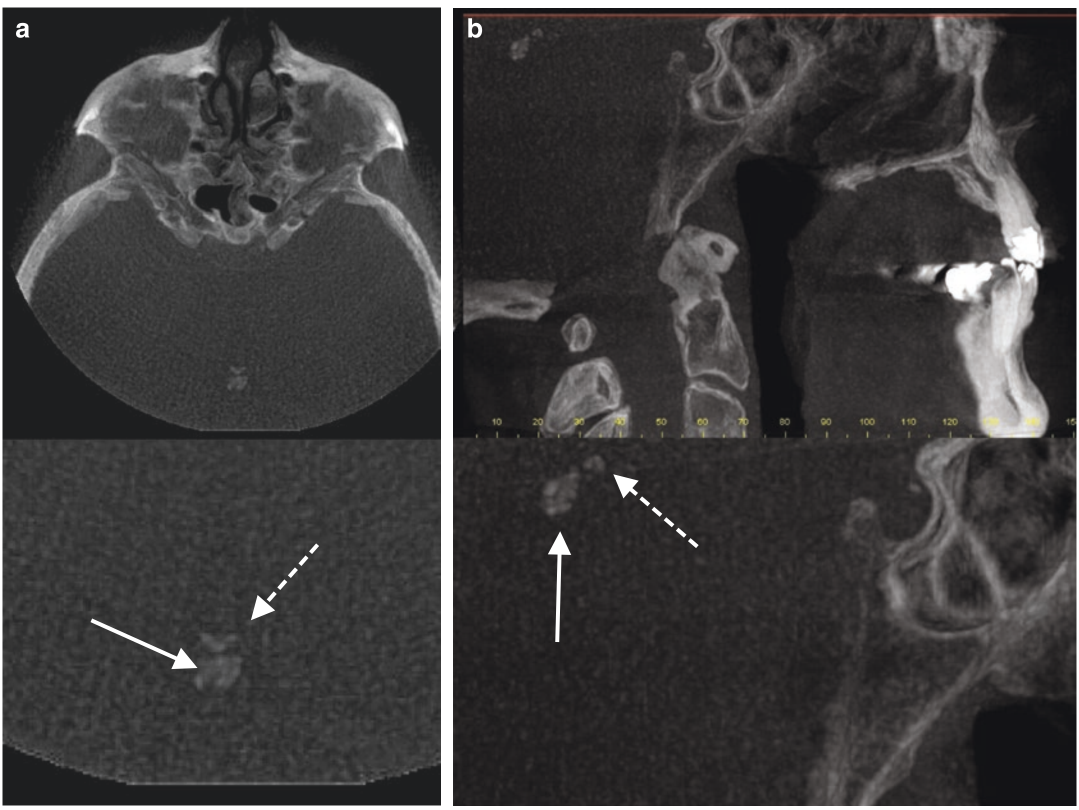

Fig. 17.5 Axial (**a**) and sagittal (**b**) 10 mm thick MIP CBCT images and magnified cropped areas (lower images) showing two posterior midline intracranial calcifications. Based on location and calcification pattern, they represent a calcified pineal gland (*solid arrow*) and habenula (*dashed arrow*)

Fig. 17.6 Coronal (**a**), left sagittal (**b**), and axial (**c**) 10 mm thick MIP CBCT images showing two bilateral symmetrically positioned faint high-density intracranial calcifications consistent with the choroid plexus (Image courtesy, Jack Fisher)

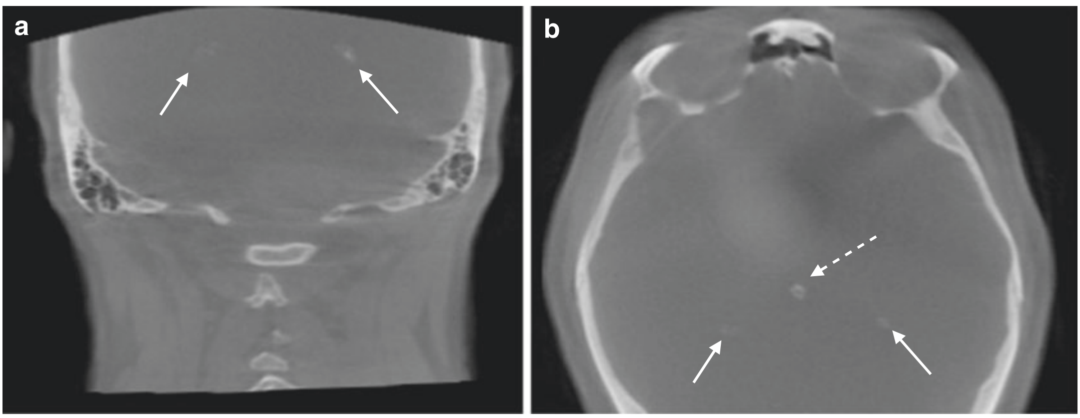

Fig. 17.7 Coronal (**a**) and axial (**b**) 2 mm thick CBCT sections demonstrating the typical location and diffuse appearance of choroid plexus (*solid arrow*). Concomitant calcification of the pineal gland/habenula is also observed (**b**)

40 years of age, should be considered pathologic until proved otherwise. Their appearance is associated with toxicity (carbon monoxide and lead poisoning), infections (CNS tuberculosis, neurocysticerosis and toxoplasmosis), and metabolic diseases (e.g., hyper- and pseudohyperparathyroidism).

- **Falx, dura matter, and tentorium cerebelli.** Calcification of these structures occur in up to 10% of elderly adults. Calcifications of the falx are usually seen as a lamellar hyperdensity in the midsagittal cerebral plane and horizontal plane in the posterior fossa, respectively (Fig. 17.8). Calcification of the falx cerebri can occur intermittently. Extensive calcification of the falx cerebri is one of the major diagnostic criteria of NBCCS.
- **Petroclinoid and interclinoid ligaments**. Two ligaments arise from the posterior clinoid process. Anteriorly, the interclinoid (or fibrous) ligament connects the posterior to the anterior clinoid process and serves as the connective tissue roof of the sella turcica. Posterolaterally the petroclinoid ligament (also known as the petroclinoid dural fold or sphenopetrosal ligament) connects the posterior clinoid process with the apex of the petrous portion of the temporal bone. Both ligaments may be calcified and observed on CBCT imaging as an incidental finding; these should be differentiated from calcifications of the internal carotid artery (ICA), which is also adjacent and lateral to the sella turcica (Fig. 17.9).

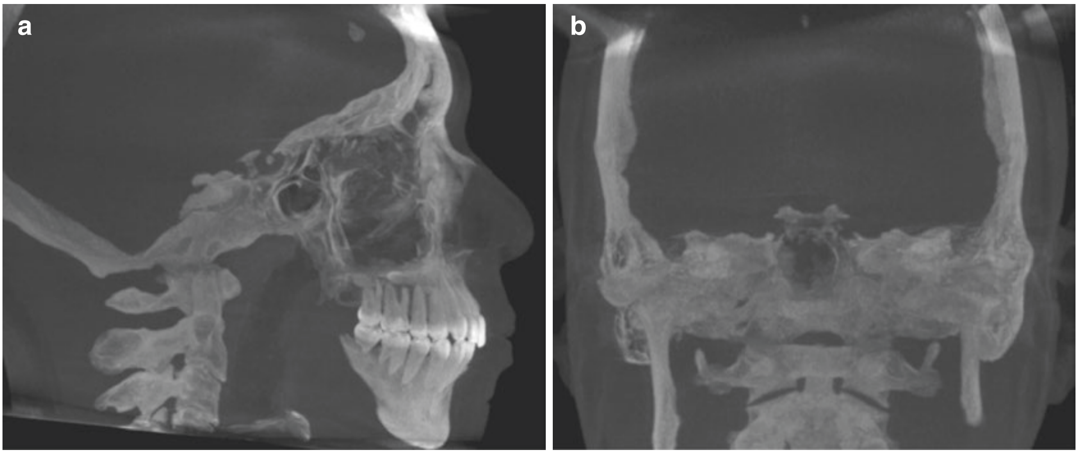

Fig. 17.8 Midsagittal (**a**) and coronal (**b**) 10 mm thick MIP CBCT images showing a midsagittal triangular-shaped lamellar calcification in the anterior intracranial fossa consistent with partial calcification of the falx cerebri

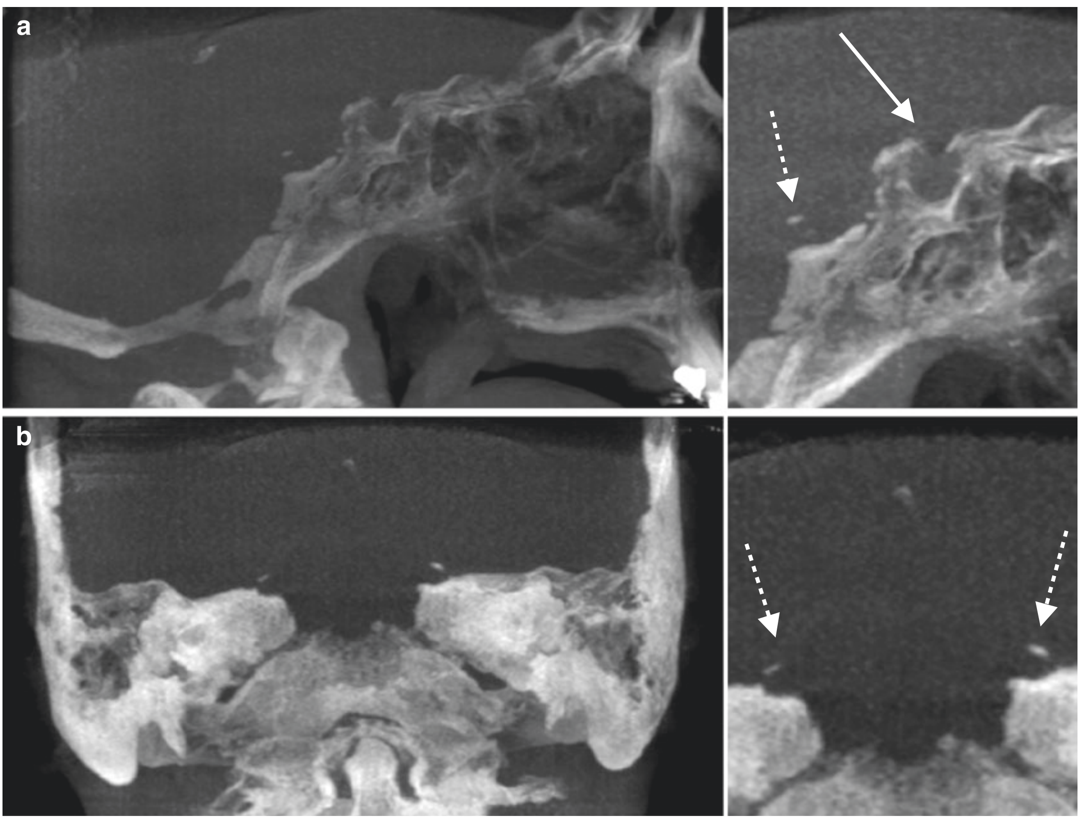

Fig. 17.9 Midsagittal (**a**) and coronal (**b**) 10 mm thick MIP CBCT images and corresponding magnified cropped areas (*right*) showing interclinoid (*solid arrow*) calcification resulting in "sella bridging" and petroclinoid ligament calcification (*dashed arrow*)

– *Calcified interclinoid ligament.* Calcification of the interclinoid ligament (or "bridged sella") is reported to occur frequently (5–10%) in radiographic or autopsy studies. While most represent a typical anatomical anomaly or are associated with NBCCS, suggested links to other conditions, such as diabetes or epilepsy are yet to be proven (Cederberg et al. 2003). Radiographically this is observed as a thin, partial or complete linear, hyper-attenuating streak connecting the anterior and posterior clinoid processes.
– *Calcified petroclinoid ligament.* Calcification of this ligament is rare and also considered to be an anatomic anomaly. It has been reported as a radiographic feature of basal cell carcinoma syndrome and systemic fluorosis. On CBCT imaging it appears as two linear, wispy, hyper-attenuating streaks extending lateral and inferior to the posterior clinoid process, adjacent to the pituitary fossa.

17.2.2 Pathologic Calcifications

Based on origin, pathologic IC calcifications include infectious, metabolic, neoplastic, and vascular. Infectious and metabolic calcifications are rare and are associated with bacterial or viral infections and metabolic or endocrine disorders, respectively. Neoplastic calcifications result from certain type of tumors developing in the brain and dural layers. Discussion of these tumors is beyond the scope of this book.

On the contrary, vascular calcifications in the endocranium and skull base are not uncommon and may be present in CBCT scans of the maxillofacial region due to the close topographic relationship of the skull base and anterior/middle cranial fossa to the maxillofacial skeleton.

17.2.2.1 Vascular Calcifications

Calcifications of the intracranial vasculature are most commonly associated with arterial primary atherosclerosis and occur most commonly in the internal carotid artery but also appear in the vertebral (20%), basilar (5%), and middle cerebral (5%) arteries.

Intracranial Vertebrobasilar Artery Calcification

Calcification of the intracranial vertebrobasilar artery (VBA) has a low overall prevalence of 3.4% in individuals over the age of 40 years (Katada et al. 1983). In the fifth decade the incidence of calcified VBA is low (0.7%) and increases to 16.7% in the ninth decade. In older ischemic stroke patients, the prevalence can be as high as 54.6% and is associated with male gender and diabetes (Pikija et al. 2013). Most of the calcifications are found at the level of the foramen magnum, whereas they sometimes present at the craniocervical junction, more distally in the vertebral artery or extend upward to involve the basilar artery. On imaging, the pattern of calcification varies widely from focal (spotty and nodular), crescent (e.g., curvilinear), and circular (tubular) presentations (Figs. 17.10 and 17.11). While no significant relationship has been identified between the VBA calcification and ischemic infarction of the cerebellum and brainstem (Chawalparit and Chareewit 2013), intracranial VBA calcification is an independent risk factor of ischemic stroke (Chen et al. 2007). Identification of this entity, particularly in the absence of a previous history of cardiovascular or cerebrovascular disease, warrants a cardiovascular consultation.

Intracranial Internal Carotid Artery (ICA)

Atherosclerotic calcifications in the intracranial internal carotid arteries (ICA) are frequent findings in computed tomography studies in the general population with an overall prevalence in the elder white population (>65 years) of approximately 82% increasing with age to over 90% in individuals greater than 80 years (Bos et al. 2012). In this population, the presence of calcifications of the intracranial ICA in men is associated with excessive alcohol intake and smoking and in women is associated with diabetes and hypertension.

Intracranial ICA calcifications are common finding on temporal bone CT studies in children. Koch reported 25% of children aged 18 years or less had definitive calcifications within the wall of the ICA with a 6% prevalence in children

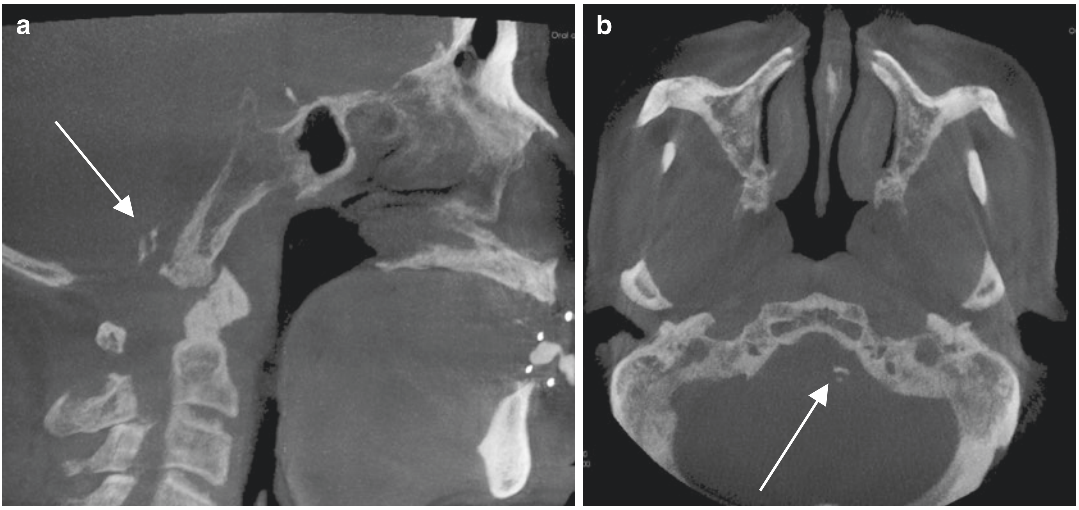

Fig. 17.10 5 mm thick sagittal (**a**) and axial (**b**) MIP images shows a curvilinear structure adjacent to the left basal occipital bone consistent with intracranial calcification of atheroma in the basilar artery

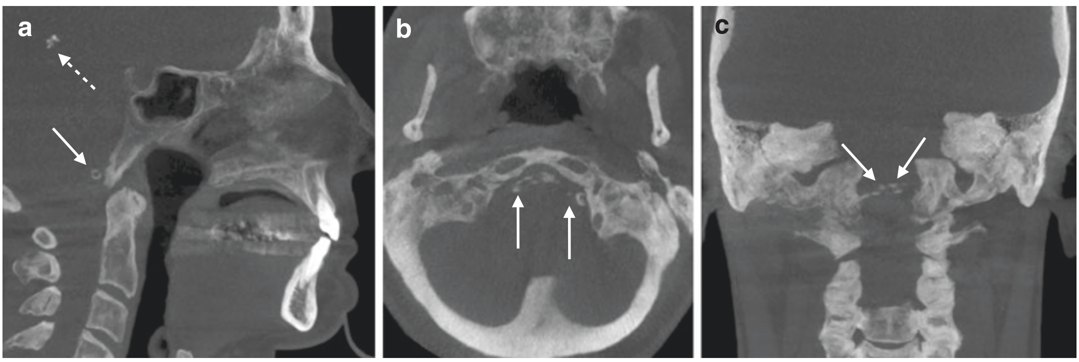

Fig. 17.11 Midsagittal (**a**), axial (**b**), and coronal (**c**) 5 mm thick MIP CBCT images of a 67-year-old female patient with a history of controlled blood pressure and cardiovascular disease with bilateral circular calcifications of the intradural section (V4) of the vertebral artery—the bilateral intracranial portion of the vertebral artery just before it becomes the basilar artery. The midsagittal superoposterior intracranial hyperdensity (*dashed arrow*) (**a**) is consistent with pineal gland calcification

younger than 2 years and 28% prevalence in children 12–19 years of age (Koch et al. 2007). However, the etiology of these calcifications is most likely a physiologic response to turbulent flow at natural bends in the artery rather than secondary to underlying disease predisposing to early atherosclerotic calcification.

In a dental population seeking implant therapy (mean age approximately 63 years, range 16–91 years), the prevalence rate of calcifications in the intracranial ICA has been reported to be 17% (Pette et al. 2012).

There are seven segments (Bouthillier classification) in the course of the ICA (six of them are intracranial): the cervical, petrous (horizontal), lacerum, cavernous segment, clinoid, ophthalmic (supraclinoid), and communicating (terminal) segments (Bouthillier et al. 1996). Most commonly calcifications are observed in the cavernous segment (Figs. 17.12, 17.13, 17.14, 17.15, and 17.16) and carotid siphon (the curve of the ICA) (Fig. 17.17) within the petrous portion (petrous and lacerum segments).

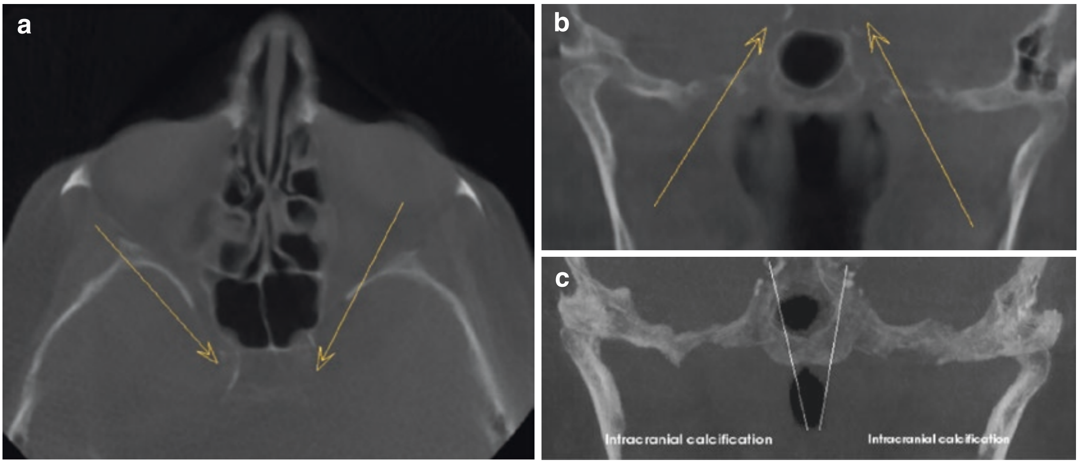

Fig. 17.12 5 mm thick axial (**a**) and coronal (**b**) images demonstrating small, heterogeneous, hyperdensities adjacent to the pituitary fossa indicating internal carotid artery dystrophic calcifications. 10 mm thick coronal MIP image (**c**) clearly shows the curvilinear structure and confirms the radiologic impression of Type 1 (thin, discontinuous or punctate) intracranial ICA calcifications

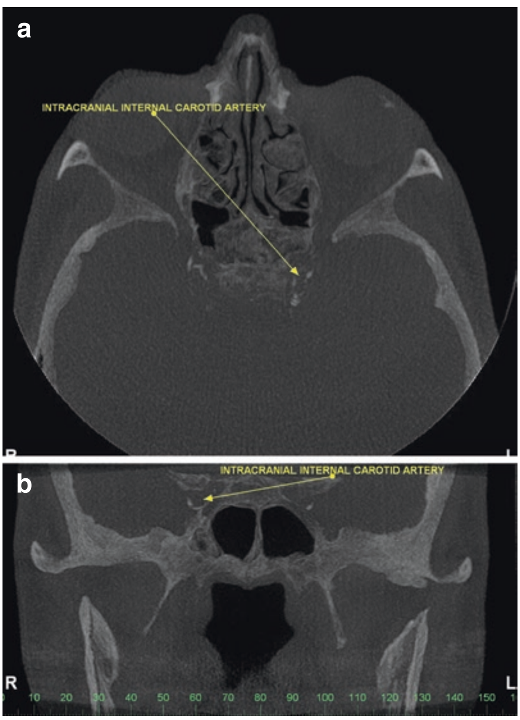

Fig. 17.13 Axial (**a**) and coronal (**b**) 10 mm thick MIP orthogonal images demonstrating small, heterogeneous, bilateral curvilinear foci of intracranial calcifications adjacent to the pituitary fossa consistent with Type 2 (thin continuous or thick discontinuous) intracranial ICA calcifications

The pattern of calcification of intracranial ICA for the cavernous segments (Erbay et al. 2007) and carotid siphon (Suzuki et al. 2007) have been described (Woodcock et al. 1999):

- **Type 1**—thin, discontinuous or punctate
- **Type 2**—thin continuous or thick discontinuous
- **Type 3**—thick continuous or tubular

The presence of intracranial ICA calcifications is associated with smoking, hypercholesterolemia, and a history of cardiac and ischemic cerebrovascular disease (de Weert et al. 2009). However, current literature is equivocal as to whether the presence and degree of calcifications of the intracranial ICA is associated with luminal stenosis or an increased incidence of stroke in the general population (Woodcock et al. 1999; Suzuki et al. 2007). Stenosis may be more correlated with the pattern of calcification as approximately 40% of individuals with a previous history of stroke with continuous, concentric thick calcification show >50% stenosis (Suzuki et al. 2007). Despite this, the detection of the presence of calcifications in the ICA can be considered as a marker of systemic atherosclerotic disease (de Weert et al. 2009) and may be an indicator of arterial stenosis.

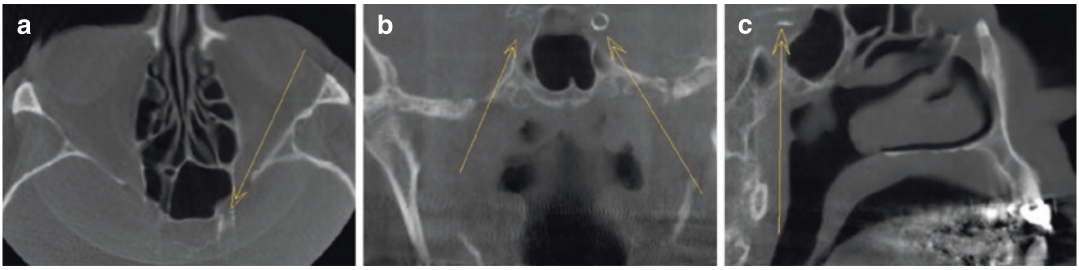

Fig. 17.14 5 mm thick axial (**a**), coronal (**b**), and sagittal (**c**) images demonstrating circular heterogeneous hyperdensities adjacent to the pituitary fossa consistent with of Type 2 intracranial ICA calcifications

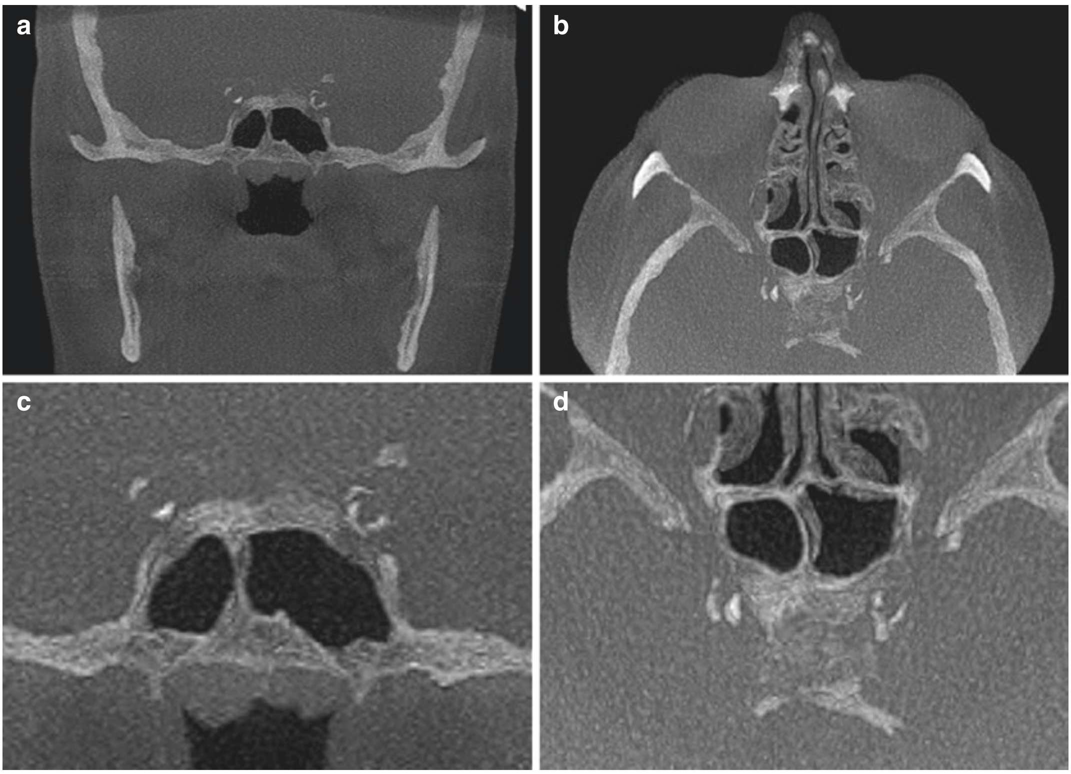

Fig. 17.15 Coronal (**a**) and axial (**b**) MIP (10 mm) orthogonal sections with cropped magnified images (**c** and **d**, respectively) depicting bilateral intracranial Type 2 (thick discontinuous) calcification within the cavernous segment of the ICA

When identified on CBCT images a consultation with a knowledgeable colleague is recommended, noting the imaging findings and a suggestion to substantiate the diagnosis and determine the extent of stenosis (Schulze and Friedlander 2013; Friedlander et al. 2014). Certainly in the absence of a clinical history of cardiovascular disease, evaluation by a cardiovascular specialist is highly advisable.

17.2.3 Foreign Bodies

Intracranial foreign bodies are rare and can be present as a result of gunshot or traumatic injury or surgical intervention (Figs. 17.18 and 17.19). Although their appearance is rather impressive, their investigation and diagnosis is uncomplicated with a detailed medical and surgical history including a history of trauma.

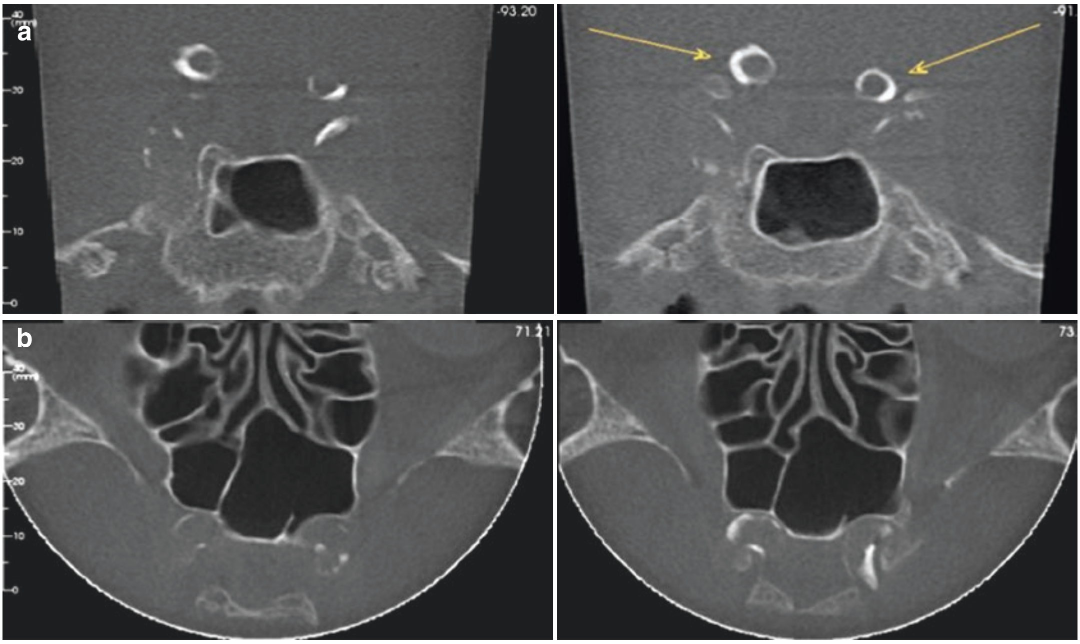

Fig. 17.16 Coronal (**a**) and axial (**b**) MIP (5 mm) orthogonal sections depicting bilateral intracranial Type 3 (thick continuous) calcification within the cavernous segment of the ICA

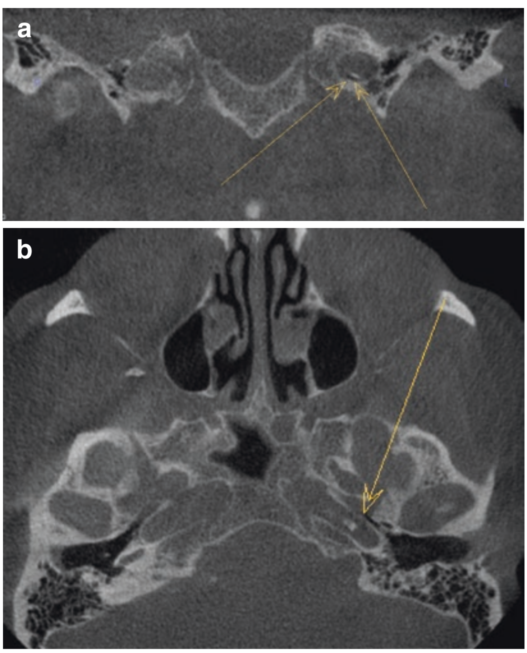

Fig. 17.17 Coronal (**a**) and axial (**b**) thin (1 mm) orthogonal sections depicting intracranial Type 1 (thin discontinuous calcification) within the carotid siphon of the ICA within of the right petrous segment

Fig. 17.18 Coronal 10 mm thick MIP CBCT image showing intracranial internal and left carotid artery vascular stents

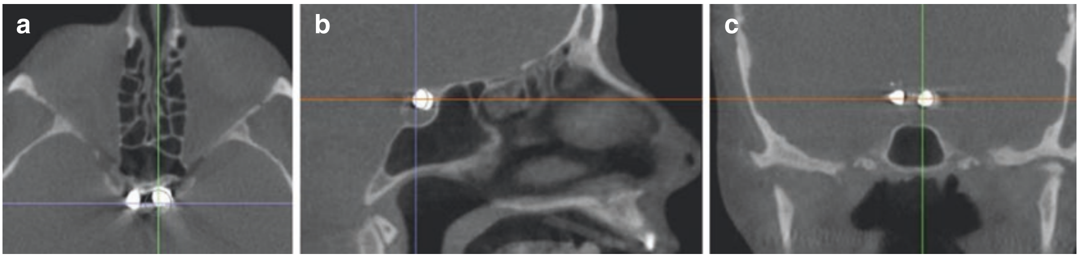

Fig. 17.19 Axial (**a**), sagittal (**b**), and coronal (**c**) 1 mm CBCT images from an extended FOV scan depicting two discrete round, high-density (metallic structures) adjacent and lateral to the sella turcica. This imaging appearance is consistent with carotid stents

17.3 Orbit

Physiologic calcifications within the orbit are relatively common incidental, asymptomatic findings, occurring in approximately 8% of the population (Murry 1995). They should be distinguished from high-density intraorbital foreign bodies and rarer pathologic conditions of clinical significance that may also produce calcifications.

17.3.1 Physiologic Calcifications

Physiologic calcifications can be identified because they occur at specific soft tissue sites and have a characteristic appearance.

- **Scleral plaques**. Scleral plaques are seen in elderly patients greater than 70 years old, are often bilateral, and are located at the insertion sites of the medial and lateral rectus muscles (Moseley 2000).
- **Cataracts**. A cataract is defined as an abnormal opacity of any portion of the lens of the eye and may present with or without changes in visual acuity. This can occur as a result of direct trauma to the globe, due to longstanding inflammations (uveitis) or associated with age-related changes (senile cataract). On CBCT it appears as a well-defined, biconvex homogeneous hyper-attenuating disk, posterior to the cornea.
- **Trochlear calcifications**. The trochlear apparatus is a U-shaped piece of fibrocartilage attached to the medial orbital wall, supporting the distal tendon of the superior oblique, the longest extraocular eye muscle, as it turns laterally and inserts into the sclera below the superior rectus. Calcification of this fibrocartilage usually occurs in adults as a normal age-related process and is present in approximately 25–30% of individuals over the age of 50 years. However, if observed in individuals less than 40 years, may be associated with autoimmune disease, particularly diabetes mellitus (Hart et al. 1992). Other associations include CKD, HIV infection, or a history of alcoholism. Radiographically these calcifications present as small and focal curvilinear homogeneous hyperdensities, at point of superior oblique angulation, adjacent to the medial orbital wall (Fig. 17.20).

17.3.2 Pathologic Calcifications

- **Phthisis bulbi (non-functioning eye).** This condition describes the atrophy of the globe as a result of infection, inflammation, and trauma and appears as a shrunken globe with ocular calcification. It is the sequela of a wide variety of pathologic ocular processes, including.
- **Optic Nerve Head Drusen.** These are yellow, opalescent, hyaline excrescences from degen-

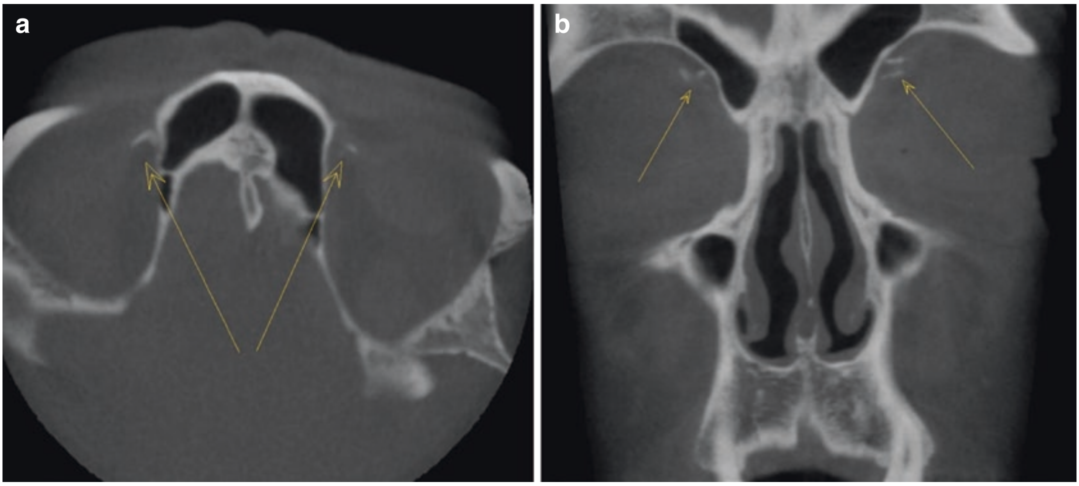

Fig. 17.20 5 mm thick axial (**a**) and coronal (**b**) orthogonal images of a 56-year-old male demonstrating curvilinear calcifications in the right and left orbits arising from the superior aspect of the right and left lamina papyracea at the level of the superior oblique muscles consistent with calcified trochlear apparatus

erated nerve fibers present on the surface of the optic disc and are a cause of benign (and usually bilateral) pseudopapilledema. They are typically seen in patients with age-related macular degeneration; however, they also may be seen in relatively young patients. They may present as small, well-defined, punctate calcifications, located in the optic disc, anterior to the lamina cribrosa. They are often undetected as their average size ranges from less than 1 mm to 3 mm.

- **Tumor-related calcifications.** Some tumors of the eye present as intraorbital calcifications. Most are tumors of childhood and while it is unlikely that the condition is unknown to the parents or guardians of these individuals, physiologic calcifications should be distinguished from these entities. These include optic nerve meningioma and retinoblastoma. Although rare (approximately 200 cases per year in the United States), retinoblastoma is the most common malignancy involving the globe in the pediatric patient. Most are diagnosed by the age of 4 years. On CBCT retinoblastoma may present as characterized by enhancing intermediate-density soft tissue mass or masses, with varying degrees of calcification.

17.3.3 Foreign Bodies

Numerous foreign bodies can present radiographically in the orbital tissues such as projectiles, surgical devices (e.g., palpebral springs, eyelid weights, orbital wall reconstruction materials), and ocular implant prostheses, often with characteristic locations and shapes.

- **Nasolacrimal Duct Stent**. Nasolacrimal duct stents or Jones tubes and other lacrimal drainage bypass devices have been used to treat dacryostenosis and epiphora. These devices are usually composed of polyurethane or nitinol in the form of tubular structures with a "mushroom" that secures the stent at the orifice of the nasolacrimal duct or dacryocystorhinostomy (Ginat et al. 2012) (Fig. 17.21).
- **Ocular Implant Prosthesis**. Numerous implants are available to occupy the volume of tissue when a globe is removed from the orbit. These can be based on their degree of soft tissue integration. Non-integrated implants are usually made of a solid material, such as a polymethylmethacrylate sphere wrapped in a mesh, to which the muscles are attached. Integrated implants are made of a porous material such as hydroxyapatite, high-density

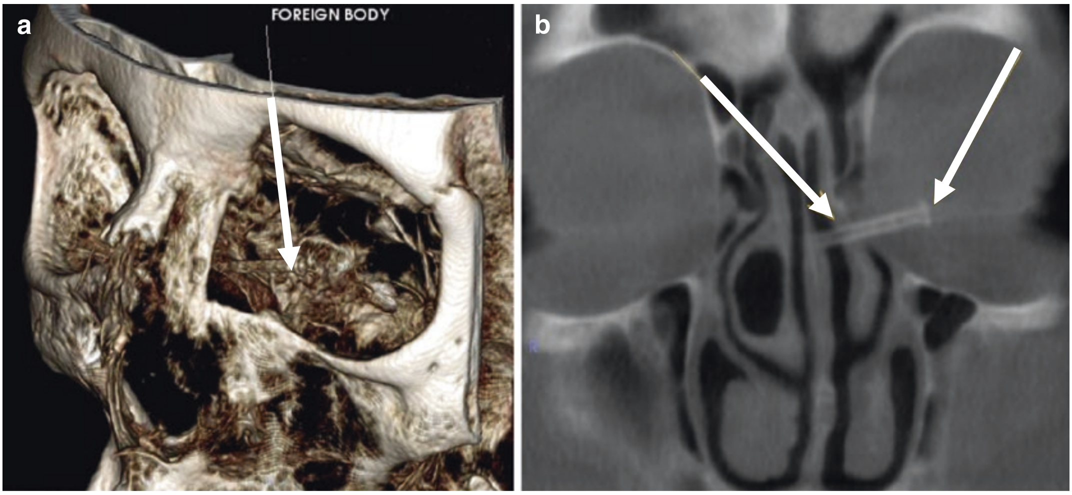

Fig. 17.21 Volumetric rendering (**a**) and coronal (**b**) CBCT image of a tubular relative hyperdensity with flattened terminal edge originating in the globe, projecting through the lamina papyracea and terminating in the nasal fossa. The imaging appearance is consistent with a Jones tube

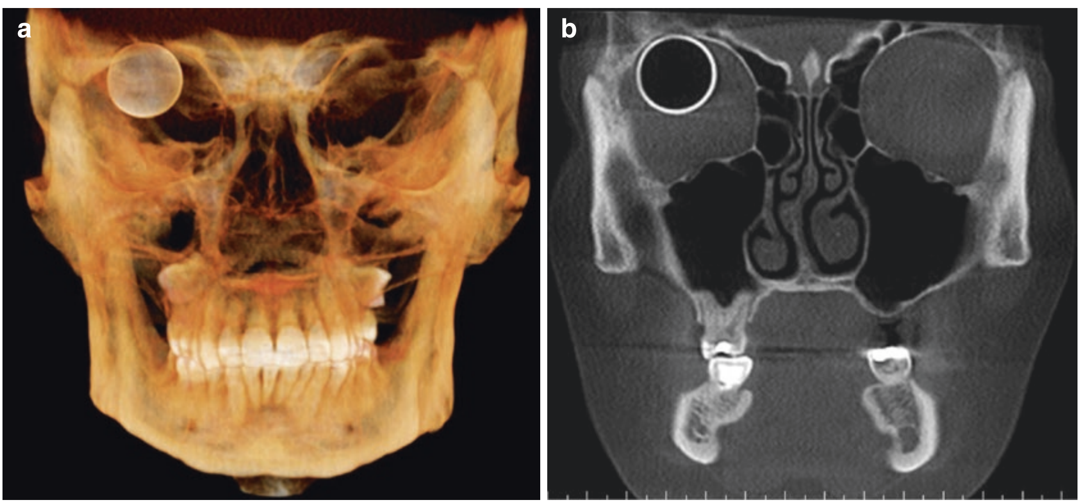

Fig. 17.22 Volumetric rendering (**a**) and coronal (**b**) CBCT image of a spherical hollow glass ocular implant prosthesis in the right orbit replacing the globe

porous polyethylene (Medpor), and aluminum oxide (Bioceramic) into which grows the tissue in the eye socket (Figs. 17.22 and 17.23).

17.4 Jaws and Adjacent Soft Tissue

Calcifications in the oral and perioral tissues are not uncommon; however, the vast majority are not associated with pathologic processes. Foreign bodies in the maxillofacial region and various types of inserts/implants or grafts are also frequently seen in CBCT scans of the jaws.

Physiologic calcifications (the result of function of the various tissues) in the oral cavity and surrounding soft tissues are rare if not nonexistent; therefore, emphasis will be placed in the pathologic calcifications of the oral cavity and perioral tissues which are common.

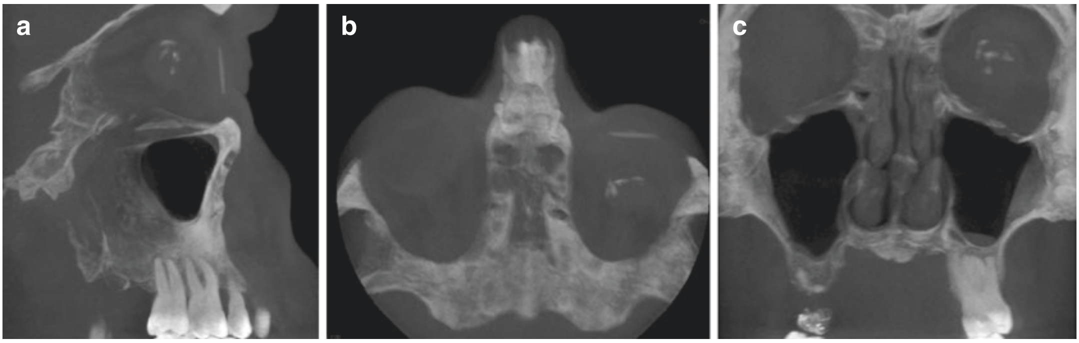

Fig. 17.23 10 mm thick MIP sagittal (**a**), axial (**b**), and coronal (**c**) CBCT images showing a round partially hyperdense ocular prosthesis (most likely methylmethacrylate) in the left orbit replacing the globe. Superficial to this is a prosthetic eye, seen as a separate hyperdense curvilinear “shell”

17.4.1 Pathologic Calcifications

Several pathologic calcifications are seen in and around the oral cavity; sialoliths, antroliths (calcifications in the paranasal sinuses), and tonsillar calcifications are some of the more common.

17.4.1.1 Sialolithiasis

Sialolithiasis is an aggregation of calcified material in the salivary glands secondary to chronic inflammation or status of saliva. The overall incidence in the general population is about 1% which may not be symptomatic. Sialoliths (salivary gland stones) may be found within glandular tissue (intra-parenchymal) or in the ductal system of major salivary glands. Sialoliths are also called salivary stones or salivary gland calculus. Disturbances in calcium metabolism, dehydration, altered acidity of the saliva, and inflammation are all possible causes of sialolithiasis. The most common complication of sialoliths is obstruction of the duct or ducts leading to salivary gland fluid stasis (ductal stenosis) and secondary sequelae including glandular inflammation, known as sialadenitis. However, sialolithiasis may be asymptomatic and present as an incidental imaging finding.

- **Intraparenchymal.** These salivary gland calcifications are not common. Their presentation may be associated with lymphatic malformations, immune-mediated diseases (such as HIV/AIDS and autoimmune parotitis), and tumors (e.g., pleomorphic adenoma as well as low-grade mucoepidermoid carcinoma). Radiographically they may appear as diffuse localized aggregation (Figs. 17.24 and 17.25) or multiple, scattered punctate small sialoliths (Fig. 17.26). Bilateral parenchymal calcifications, especially in the parotid glands, may indicate systemic involvement such as Sjögren’s syndrome or sarcoidosis (Fig. 17.26).
- **Ductal**. Sialoliths are most commonly present in the submandibular gland (approx. 80%). Salivary gland stones in Wharton’s duct (draining duct of the submandibular salivary gland) may be one or more (multiple stones are present in approximately 25% of sialolithiasis) and may be occurring within intraglandular ductal tributaries or within the main ducts especially near the hilum of the gland or in the proximal portion of the ductal system. Depending on the position of the hyoid bone at the time of the CBCT, a sialolith may appear to be present within the superior neck. They appear as single linear or globular ovoid homogeneous opacities medial to the angle of the mandible (Fig. 17.27).

17.4.1.2 Calcified Acne

Acne is a long-term skin disease which is characterized by multiple white, red, or black small lesions originating around the hair follicles. The areas affected the most are the face, chest, and upper back. Acne may result in scarring which sometimes

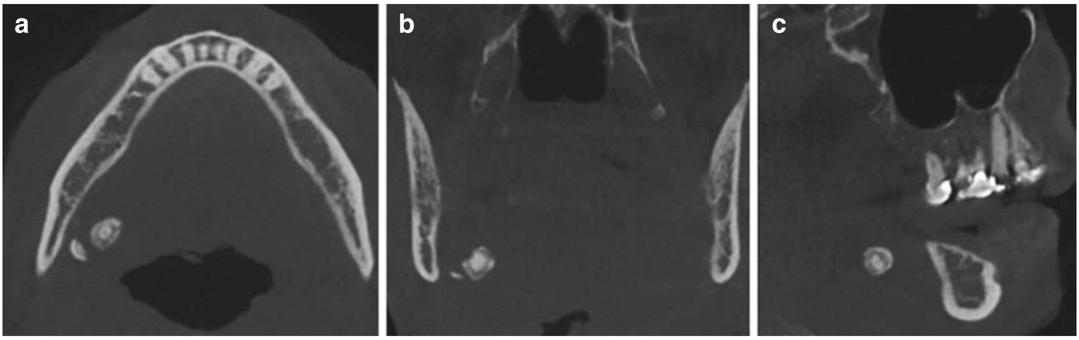

Fig. 17.24 Axial (**a**), coronal (**b**), and sagittal (**c**) CBCT images at the level of the floor of the mouth depicting two localized discrete concentric hyperdensities located medial to the right mandibular angle, corresponding to the anatomical location of the right submandibular gland. The imaging appearance is consistent with paired sialoliths in the parenchyma of the right submandibular salivary gland

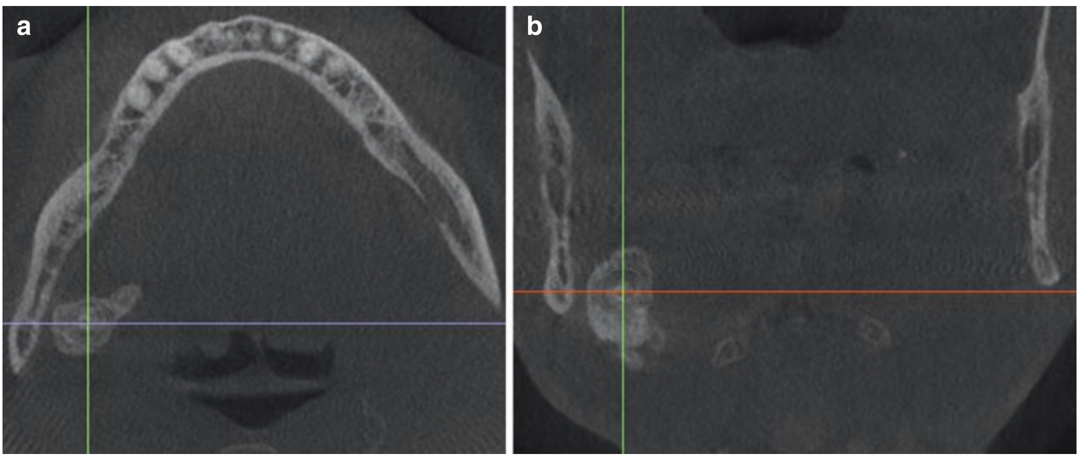

Fig. 17.25 Axial (**a**) and coronal (**b**) CBCT sections at the level of the floor of the mouth showing a very large localized concentric pair-shaped hyperdensity associated with two smaller hyperdensities inferomedially corresponding to the anatomical location of the right submandibular gland. The imaging appearance is very similar to that in Fig. 17.24 and consistent with in the parenchyma of the right submandibular salivary gland

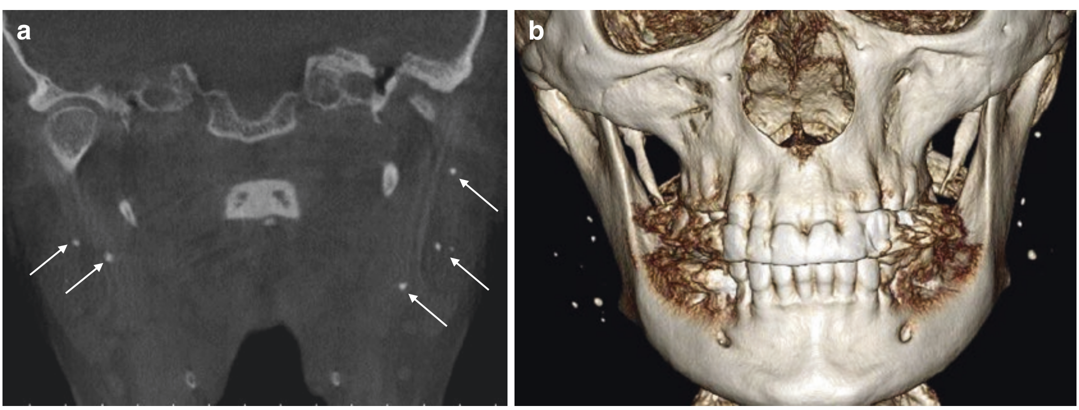

Fig. 17.26 Coronal section at the level of the condyles (**a**) and volumetric rendering (**b**) depicting multiple bilateral punctate calcifications lateral to the mandibular rami corresponding to the anatomical parotid space in a patient diagnosed with Sjögren's syndrome consistent with sialoliths

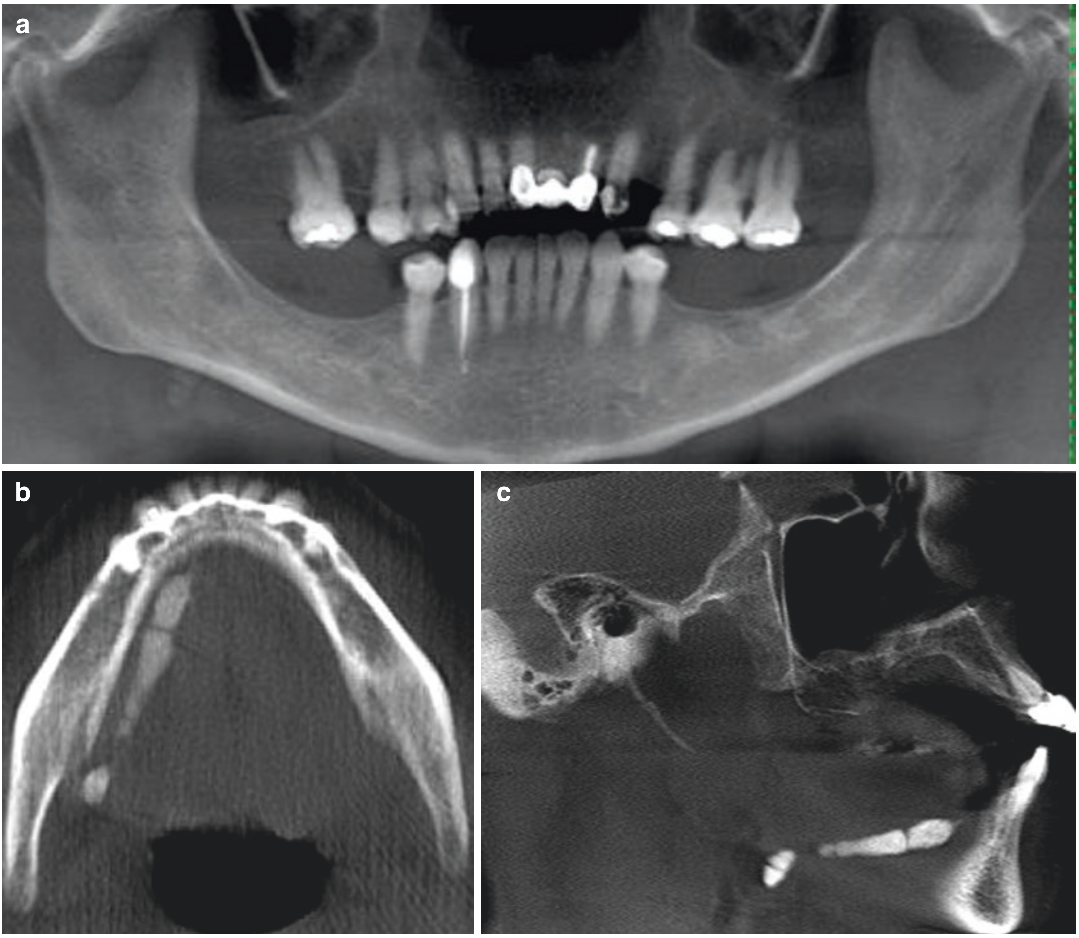

Fig. 17.27 Reformatted panoramic (**a**), 10 mm thick MIP axial (**b**) and sagittal CBCT images showing large pseudo articulated right submandibular ductal sialoliths in an asymptomatic patient with previous history of removal of left submandibular gland

may calcify. Calcified acne lesions are dystrophic calcifications which may show in CBCT scans of the maxillofacial region as small, numerous, superficial (inside the skin), high-density entities located sub-dermally around the face and neck (Fig. 17.28).

17.4.1.3 Phleboliths

A phlebolith is a calcified vascular thrombus that is most frequently associated with a vein, venule, or hemangioma not contained within bone. Their formation is thought to be as a result of vascular anomaly, which induces thrombus formation. The end result is calcium deposit with eventual stone formation. The presence of a phlebolith is highly suggestive of either a hard of soft tissue hemangioma (Altuğ et al. 2007) either isolated or in association with vascular anomalies including arteriovenous malformations or syndromic conditions such as Sturge–Weber syndrome. They are usually multiple, laminated spherical hyperdensities with an "onion-like" appearance (Fig. 17.29) in the superficial and deep soft tissue of the face. It may be necessary to refer patients who present with this condition to a vascular specialist for further assessment.

17.4.1.4 Heterotopic Ossifications (Bone Formation)

Calcifications within the soft tissues of the face and mouth other than the vasculature and ligaments are extremely rare. They may be present in articulations such as the cervical vertebrae or temporomandibular joint (chondrocalcinosis), or may be the result of metastatic calcification (due to parasitic infections such as cysticercosis), tumoral calcinosis, primary or metastatic malignancies (e.g., osteosarcoma), or heterotopic ossification.

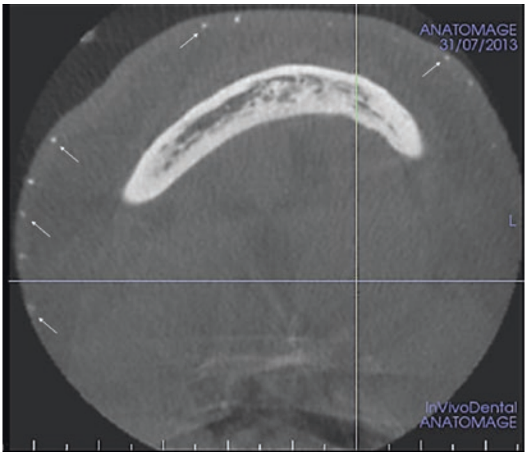

Fig. 17.28 Axial section at the level of the inferior border of the mandible depicting very small, superficial, round calcifications (*arrows*) in the periphery of the face just underneath the dermal layer consistent with calcified acne

Heterotopic ossification refers to the process of bone formation outside of its usual location and is often the result of an inflammatory process, trauma or other kind of stimulus which eventually stimulates the formation of bone. This may occur in the soft tissue (mostly muscle) as well as in connective or epithelial tissue. The paranasal sinuses, the orbits, and the floor of the mouth have been reported as areas of heterotopic bone formation (Fig. 17.30).

The term *myositis ossificans* (MO) refers to bone formation inside muscular tissue. Most cases occur in the soft tissues around the pelvis, knee, and femur. Four distinct types of MO have been described: fibrodysplasia ossificans

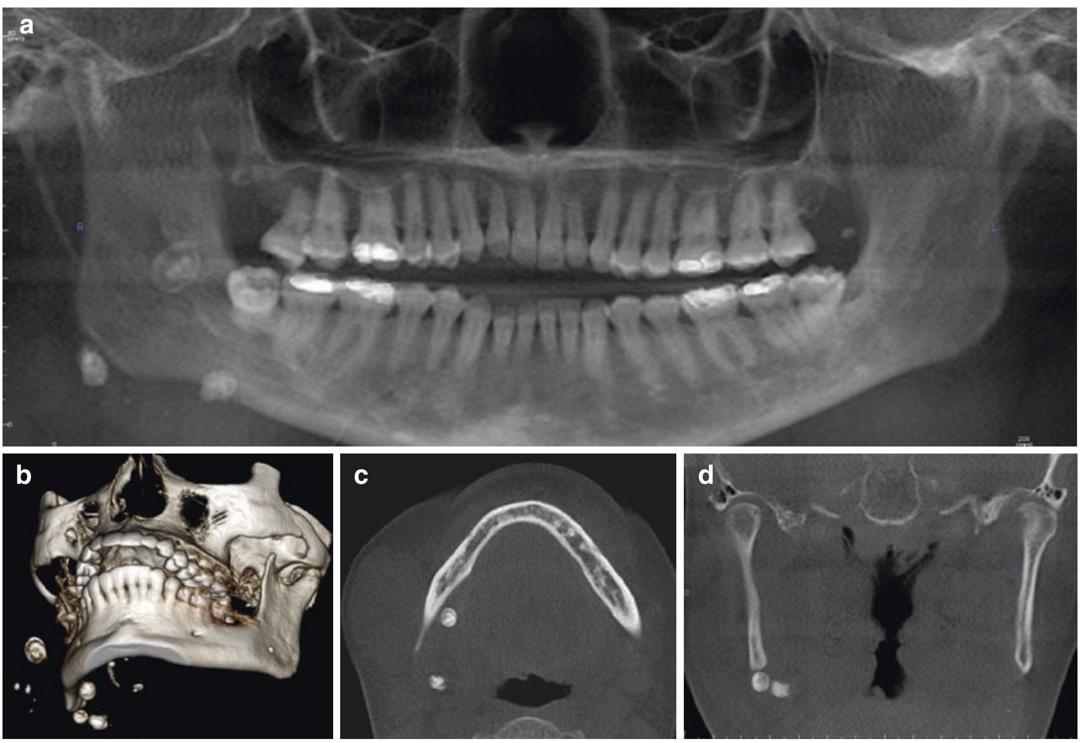

Fig. 17.29 Reformatted panoramic image (**a**) demonstrating circular hyperdensities adjacent to and superimposed on the right mandibular ramus. Volumetric rendering (**b**), axial (**c**) and coronal (**d**) multiple discrete circular lamellar "donut-shaped" dystrophic calcifications in the sublingual and masseteric soft tissue spaces consistent with phleboliths associated with soft tissue hemangioma. Note the substantial associated soft tissue expansion in the right masseteric space (**c**)

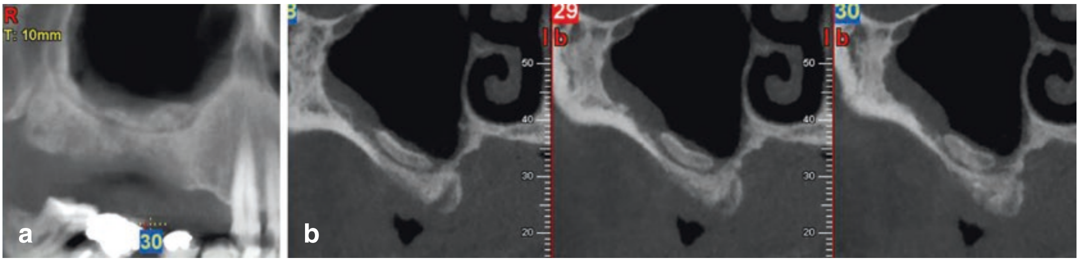

Fig. 17.30 Reformatted panoramic (**a**) and serial cross-sectional (**b**) images showing a well-defined high-density structure on the floor of the right maxillary sinus. The density and structure of the entity is similar to that of the osseous tissue with a peripheral cortical and central cancellous core and consistent with a diagnosis of hetertropic bone ossification. It is located entirely in the thickened mucosa of the sinus cavity and has no contact with the floor of the maxillary sinus

progressive, an autosomal dominant disorder involving several muscular groups; traumatic MO (MO circumscripta), limited to a single muscle and associated with previous injury; pseudo-malignant MO, limited to soft tissue and not associated to any trauma; and MO associated with paraplegia. In the facial region, the muscles of mastication (temporalis, masseter, medial and lateral pterygoids), buccinators muscle, platysma muscle, and the sternocleidomastoid muscle have all been reported with MO. Different phases of MO have been described that correlate well to the radiologic findings (Shirkhoda et al. 1995). The most typical radiographic appearance of MO is that of a localized circumferential calcification with a hypodense center, and a hypodense cleft (string sign) that separates the lesion from the cortex of the adjacent bone. This appearance must be differentiated from soft tissue osteosarcoma. Extensive calcification may be associated with soft tissue facial asymmetry or limited mandibular opening.

17.4.2 Foreign Bodies

Objects and materials foreign to the human body may be present in the soft tissues of the maxillofacial region either intentionally or accidentally. In the former case, the insertion of foreign structures is the result of surgery and serves to reconstruct, augment deficient soft tissue or enhance the appearance of a certain anatomical region. In the latter case, the insertion of the foreign objects is the result of an accident or iatrogenic event.

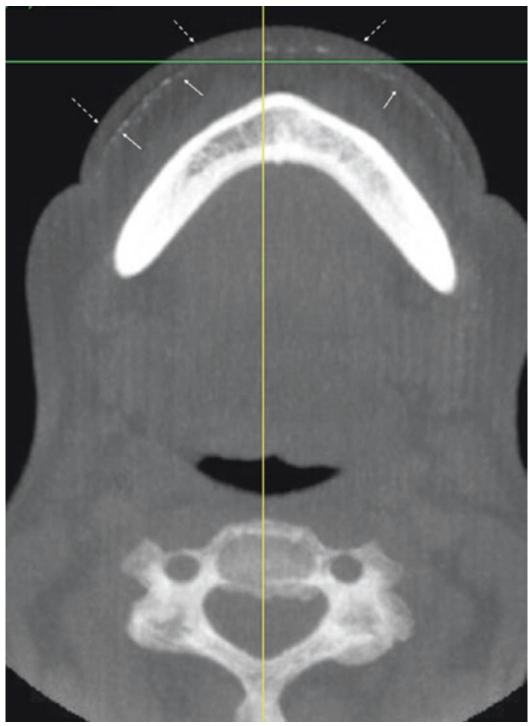

Fig. 17.31 Axial medium slice (10–20 mm) maximum intensity orthogonal projections demonstrating multiple small peripheral punctate hyperdensities on the superficial surface of the skin (*solid arrows*) consistent with cosmetic accumulation in the surface imperfections and pores of the skin. The uniform semi-circular layer covering the opaque lamination (*dashed arrows*) represent the plastic chin holder of the CBCT unit

17.4.2.1 Inserts-Implants (Cosmetic Enhancements)

- **Cosmetics.** Cosmetics often contain metallic substrates which when used to mask facial skin imperfections can accumulate and present as multiple punctate surface hyperdensities (Fig. 17.31).

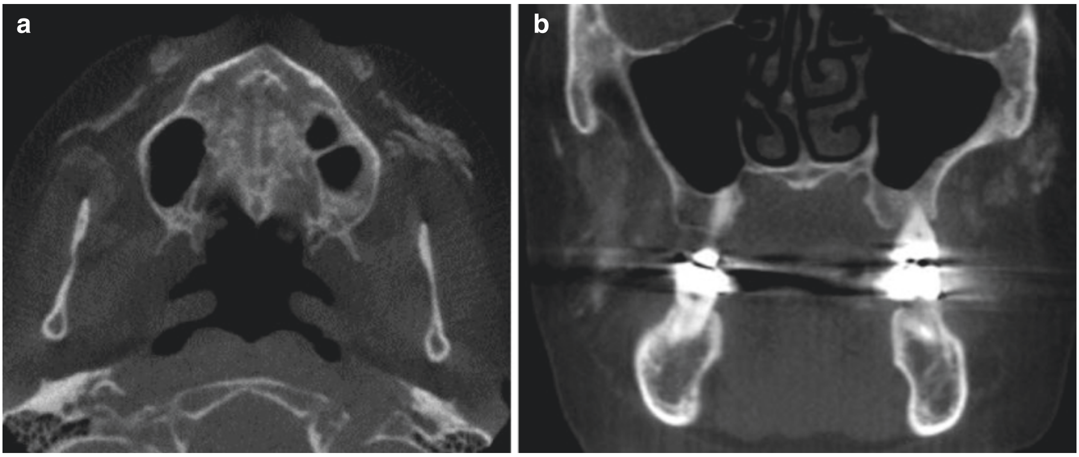

Fig. 17.32 Axial (**a**) and coronal (**b**) orthogonal images showing buccal and masseteric fascial globular and linear soft tissue low attenuations. This appearance is however most consistent with dermatologic soft tissue augmentation (filler), possibly calcium hydroxyapatite

- **Subdermal Fillers.** Various materials have been approved for use as dermal and subdermal injectable fillers for facial rejuvenation, some of which are hyper-attenuating on CBCT imaging (Ginat and Schatz 2013). Injectable calcium hydroxylapatite (Radiesse) was approved in 2006 for the treatment of facial lipoatrophy and wrinkles. This material appears on CT and CBCT imaging as hyper-attenuating linear streaks or clumps, mostly in the cheek soft tissues. While this material gradually resorbs, it can last for at least 2 years or more (Figs 17.32, 17.33, 17.34, and 17.35). Liquid silicone (polydimethylsiloxane; Silikon, AdatoSil) has been used for over 50 years for facial augmentation and the treatment of acne scars. On imaging, it appears as multiple highly attenuating small globular foci within the bilateral cheek. Expanded polytetrafluoroethylene (Gore-Tex) has been approved for facial augmentation since the mid-1990s. On imaging it appears as linear hyper-attenuation at specific sites such as the lips, nasolabial folds, and glabella.
- **Facial implants and grafts.** Cosmetic surgery and, to a lesser extent, maxillofacial reconstruction of dento-facial deformities involving soft tissue deficiencies incorporate the use of synthetic soft tissue graft materials for the nose, cheek, lip, and chin augmentation. A variety of material have been used including silicone (Silastic), expanded polytetrafluoroethylene (Gore-Tex),

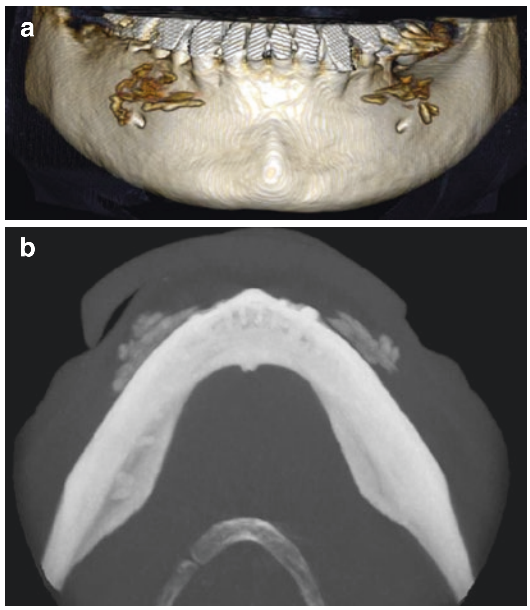

Fig. 17.33 Volumetric surface rendering (**a**) and axial 20 mm thick MIP image (**b**) demonstrating the location of bilateral subdermal hyper-attenuating liner globular masses in the parasymphyseal regions consistent with dermatologic soft tissue augmentation (filler)

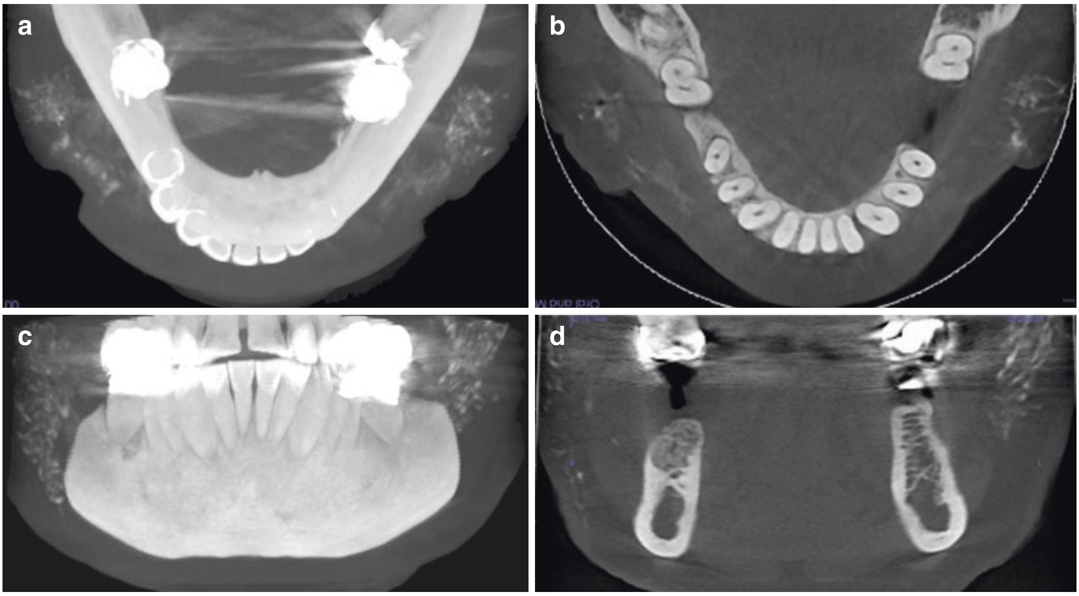

Fig. 17.34 10 mm thick axial MIP (**a**) / thin section (**b**) and coronal 10 mm thick MIP (**c**) / thin section (**d**) images demonstrating the location of bilateral subdermal hyperattenuating globular masses in the subdermal sift tissue superficial to the bucccinator muscle consistent with dermatologic soft tissue augmentation (filler)

hydroxyapatite, and porous polyethylene (Medpor). On CBCT imaging these implants may be identified incidentally. Many of these grafts have a distinctive shape and radiologic imaging features and should not be misinterpreted as pathology. Schatz and Ginat (2013) provide an excellent pictorial review of the available graft augmentation materials and corresponding CT imaging appearance. Non-bone-derived grafts, such as Silastic, Gore-Tex, Teflon, and Medpor, have variable attenuation, usually denser than soft tissue, but less dense than bone. Cosmetic implants have a relatively low complication rate necessitating removal, depending on location (Range, 1.9–4.9%) (Wang 2003), and includes infection, migration or displacement, extrusion, foreign body reaction, heterotopic bone formation (Fig. 17.36), and bone erosion.

- **Hair artifacts.** Two types of relative hyperdense artifact can be associated with the imaging of hair on CBCT images. The first is described as *pseudolesions*, when hair is bound in pigtails, twisted, braided, wet or naturally curled and appear as tiny, diffuse opacities. These may resemble tuberculous foci or microcalcifications. A second pattern presents as radiopaque streaking patterns adjacent to the cranial vault and neck region due to superimpositions of strongly braided hair such as dreadlocks or Rasta hair, from natural origin or synthetic extensions (Fig. 17.37) (Scheifele et al. 2003).

17.4.2.2 Foreign Bodies Due to Accident

Not infrequently, foreign bodies may be accidentally inserted or displaced into the soft tissues of the oral cavity and maxillofacial region. These include dental (e.g., restorative materials, endodontic fillers, dental implants, teeth) (Figs. 17.38 and 17.39) and non-dental (Figs. 17.40, 17.41, and 17.42) objects. While CBCT imaging presentation may be impressive, recognition is usually uncomplicated if supplemented by a thorough medical and surgical patient history.

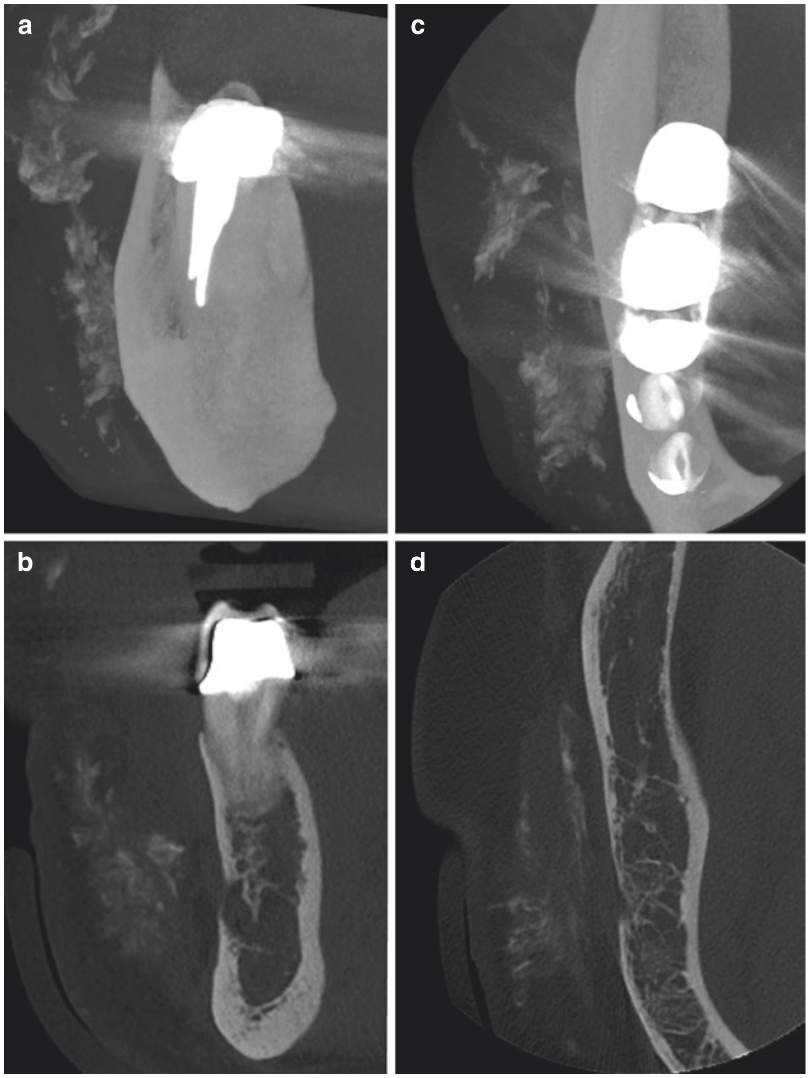

Fig. 17.35 Frontal full thickness MIP (**a**) and coronal 2 mm section (**b**) and axial full thickness MIP (**c**) with corresponding axial section (**d**) of the right mandibular body of a 54-year-old female demonstrating the typical features of hyper-attenuating globular masses in the subdermal soft tissue superficial to the bucccinator muscle consistent with dermatologic soft tissue augmentation (filler) (Image courtesy, Marcelo Sales)

17.5 Neck and Parapharyngeal Soft Tissues

There are many entities that appear as hyperdensities in the neck and parapharyngeal regions (MacDonald et al. 2012). These range from variants of normal anatomy, such as calcification of the stylohyoid complex, triticeous cartilage, and thyroid cartilage (in older patients) to localized concrescences such as sialoliths and tonsilloliths to those that are pathologic or are potentially of some concern including calcified lymph nodes and calcified carotid artery atheroma. CBCT imaging features can be used to assist locating, characterizing, and differentiating between these entities (Fig. 17.42) (MacDonald et al. 2012).

17.5.1 Physiologic Calcifications

17.5.1.1 Elongated Styoid Process and Stylohyoid Ligament Calcifications

The styloid process (SP) is a slender osseous projection that arises from the inferior surface of the temporal bone just beneath the external auditory meatus. The normal length in an adult is considered to be between 20 mm (Miller 1997) and 30 mm (Feldman 2003; Eagle 1962). Within the

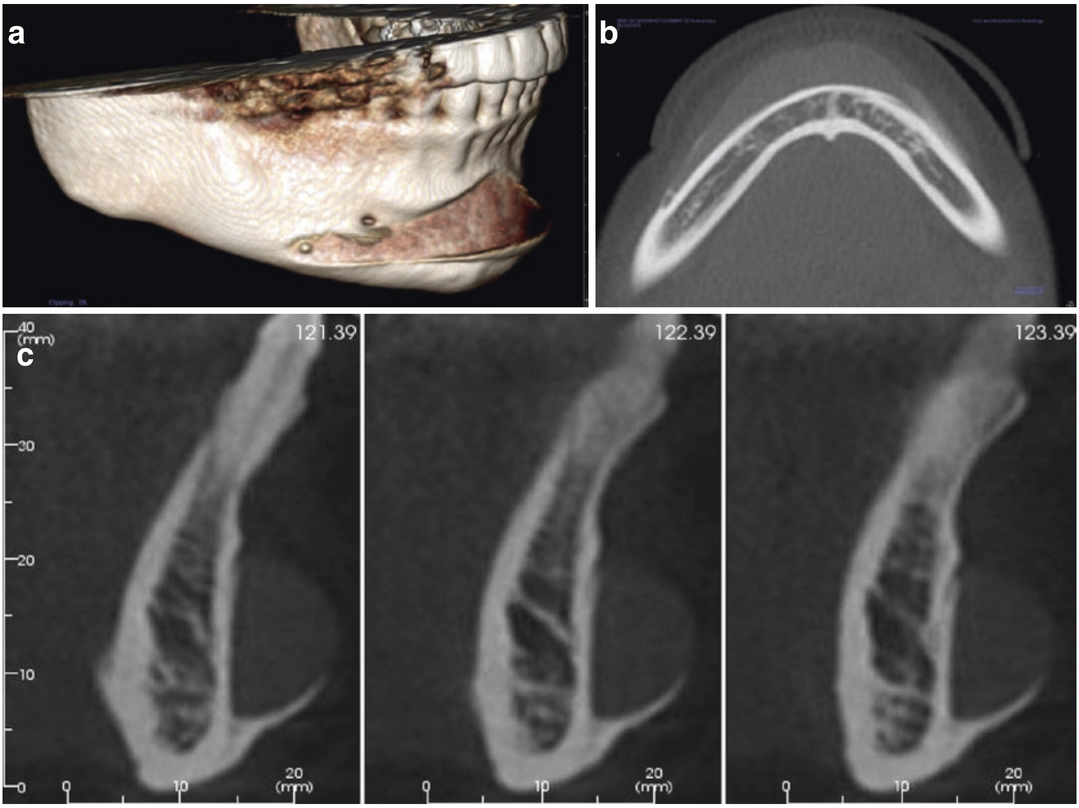

Fig. 17.36 Lateral oblique volumetric rendering (**a**), axial (**b**), and trans-axial (**b**) CBCT images of a midline crescent-shaped hyper-attenuated alloplastic silicone implant used for chin augmentation positioned in the symphysis, inferior to the mental foramina. Note that there is secondary thin lamellar heterotopic bone formation along the inferior peripheral margin of the implant secondary to subperiosteal elevation. This is of no clinical significance

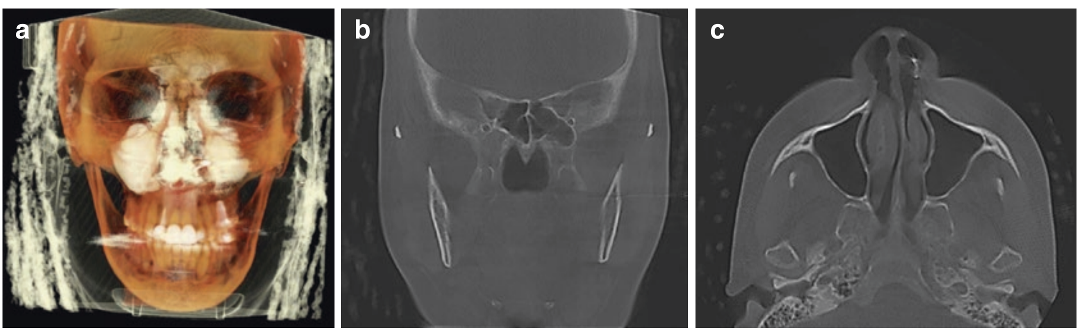

Fig. 17.37 Volumetric rendering (**a**) with soft tissue algorithm and frontal (**b**) and axial (**c**) orthogonal images of a 46-year-old black female referred for orthodontic assessment demonstrating the tight isolated relative hyper-attenuating artifacts peripheral to the soft tissue integument associated with synthetic hair brad extensions

neck, the SP extends inferomedially towards the pharyngeal wall, lateral to the tonsillar fossa (Fig. 17.43).

There are several ligaments (stylohyoid and stylomandibular) and muscles (styloglossus, stylohyoid, and stylopharyngeus) that originate from the SP which together act to stabilize the hyoid bone during normal oropharyngeal functions. In particular, the stylohyoid ligament (SHL) arises from the tip of the SP and attaches

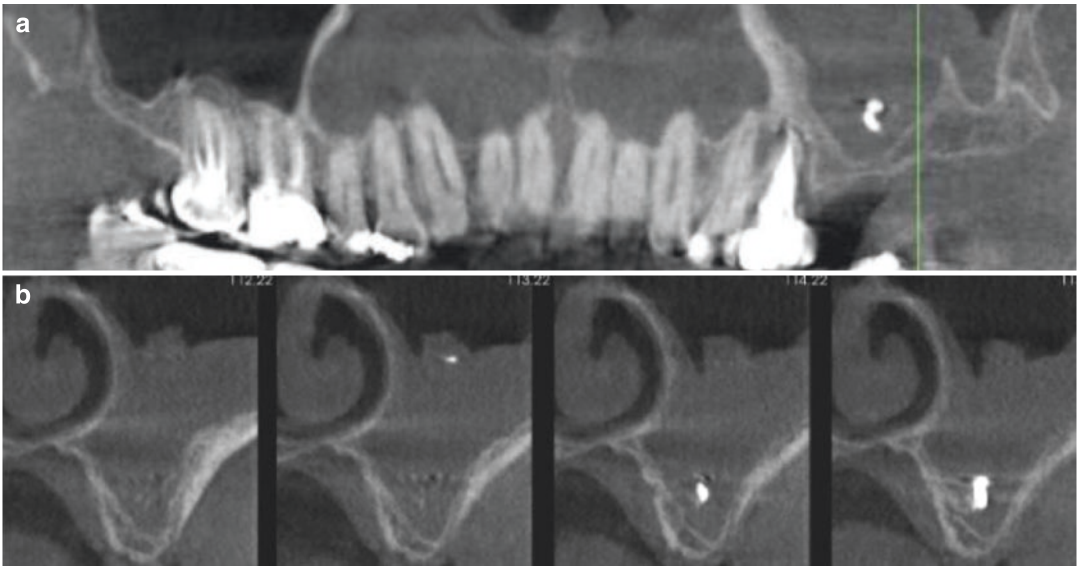

Fig. 17.38 Reformatted panoramic image (**a**) and serial cross-sectional images (**b**) of the left maxilla showing two small high-density structures embedded within the soft tissue of the mucosa of the floor of the maxillary sinus consistent with either previously displaced endodontic filler or other restorative material residue. Concomitant polypoidal mucosal sinusitis may be secondary to the presence of these materials

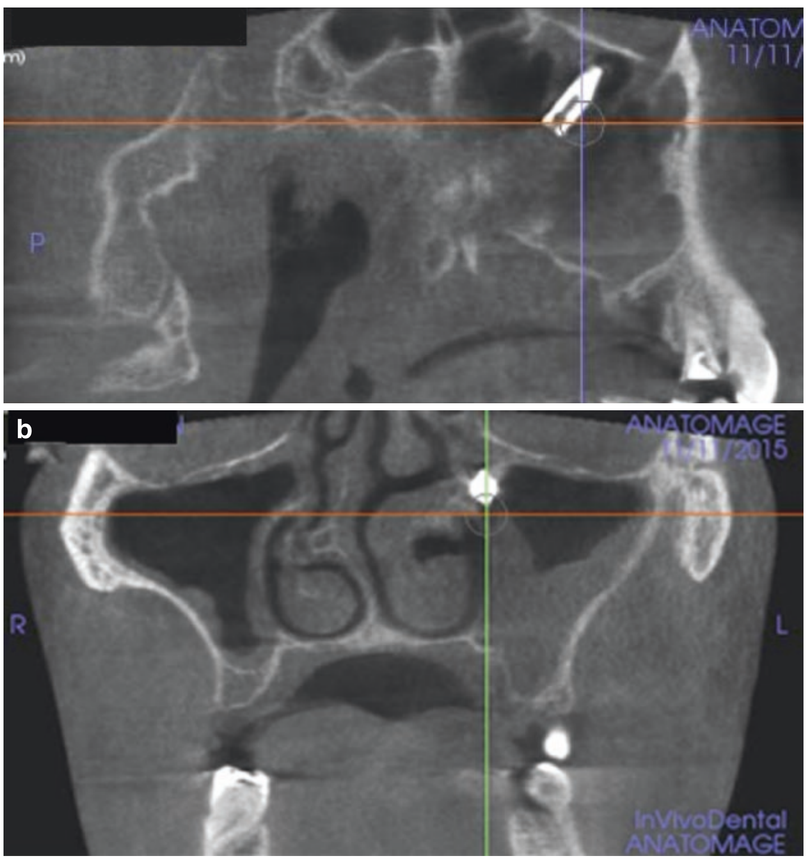

Fig. 17.39 Sagittal (**a**) and coronal (**b**) CBCT image sections show a well-defined cylindrical high-density (metallic) object embedded in the ostium of the left maxillary sinus. The patient reported that a dental implant was displaced through the alveolar bone in the left posterior region during surgery and never retrieved. The polypoidal mucosal thickening of the left maxillary sinus is most likely secondary to the presence of the dental implant occluding the drainage pathway of the ipsilateral sinus

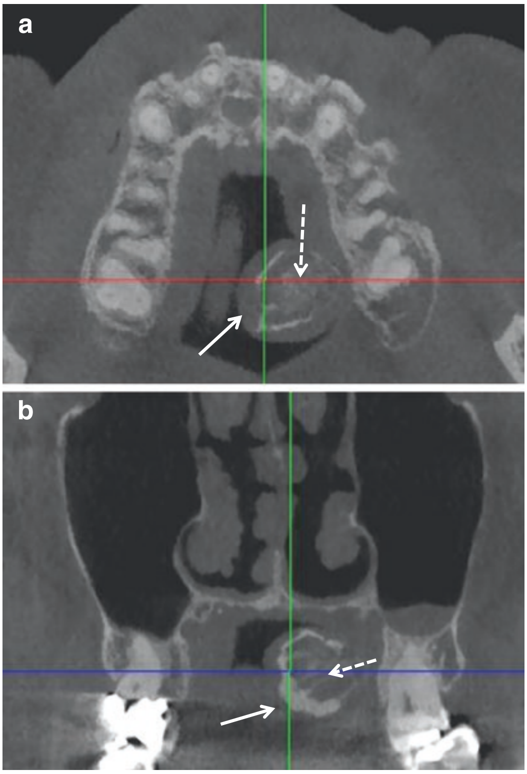

Fig. 17.40 Axial (**a**) and coronal (**b**) CBCT images of the maxillary arch depicting a mixed attenuating structure consisting of a mixed hyperdensity homogeneous core (*dashed arrow*) and peripheral hyperdense shell (*solid arrow*) arising from the soft tissue of the left palatal gingivae. There is no apparent connection to the osseous tissue of the hard palate. The patient's history revealed the unintentional insertion of a rock into the gingiva as a child. Biopsy confirmed the peripheral hyperdense shell to be heterotopic bone and the homogeneous core to be a small piece of rock

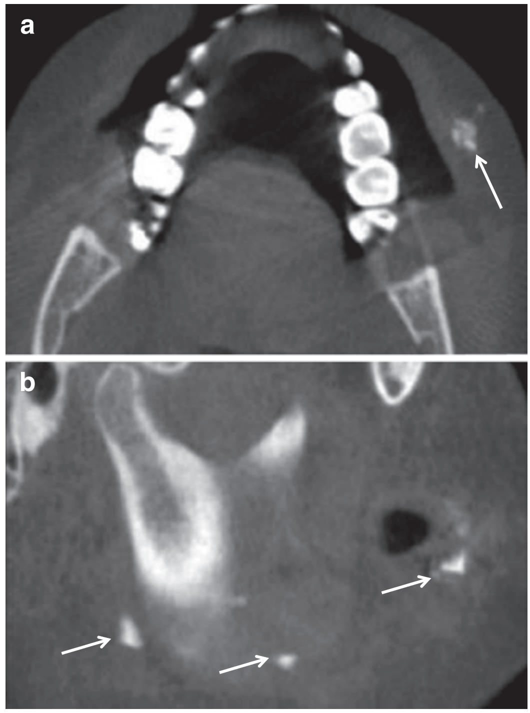

Fig. 17.41 Axial (**a**) and sagittal (**b**) CBCT images showing multiple, calcifications of variable size within the soft tissues of the right cheek. The patient's history revealed a previous fall in a bicycle accident and multiple facial soft tissue abrasions suggesting that the foreign bodies were embedded debris (several small rocks)

to the lesser cornu of the hyoid bone. This anatomic arrangement is collectively referred to as the stylohyoid chain (SHC).

Excessive or abnormal calcification of SHC components includes elongation of the SP (Keur et al. 1986; Ilguy et al. 2005) and calcification of the stylohyoid ligament (Carmada et al. 1989; Langlais et al. 1986; Ferrario et al. 1990). Depending on the population sample, between approximately 1.4% (Gossman and Tarsitano 1977) and 30% (Keur et al. 1986) of individuals have radiographic evidence of calcification of the SHC, most of which (75%) are bilateral (Ilguy et al. 2005). Most patients are asymptomatic; however, a small proportion, reported ranging from 1% (Langlais et al. 1986) to 10% (Keur et al. 1986), may have clinical symptoms due to the rigid stylohyoid compression of the nearby structures, such as the carotid artery (Winkler et al. 1981). The presence of specific symptoms associated with SHC ossification (neck stiffness, difficulty in swallowing, etc.) has been referred to as "Eagle's" or "Elongated Styloid Process" syndrome.

On conventional projections or panoramic images, the calcification of the SHC typically appears as an elongated slender bony projection that continues from the SP and extends towards, and occasionally appearing continuous with, the lesser cornu of the hyoid bone. Calcification may present in 1 of 12 patterns (Okabe et al. 2006) incorporating incomplete ossification, segmentation, pseudo-articulation with variations in thickness and/or angulation. Because of the caudal, medial, and anterior progression of the ligament

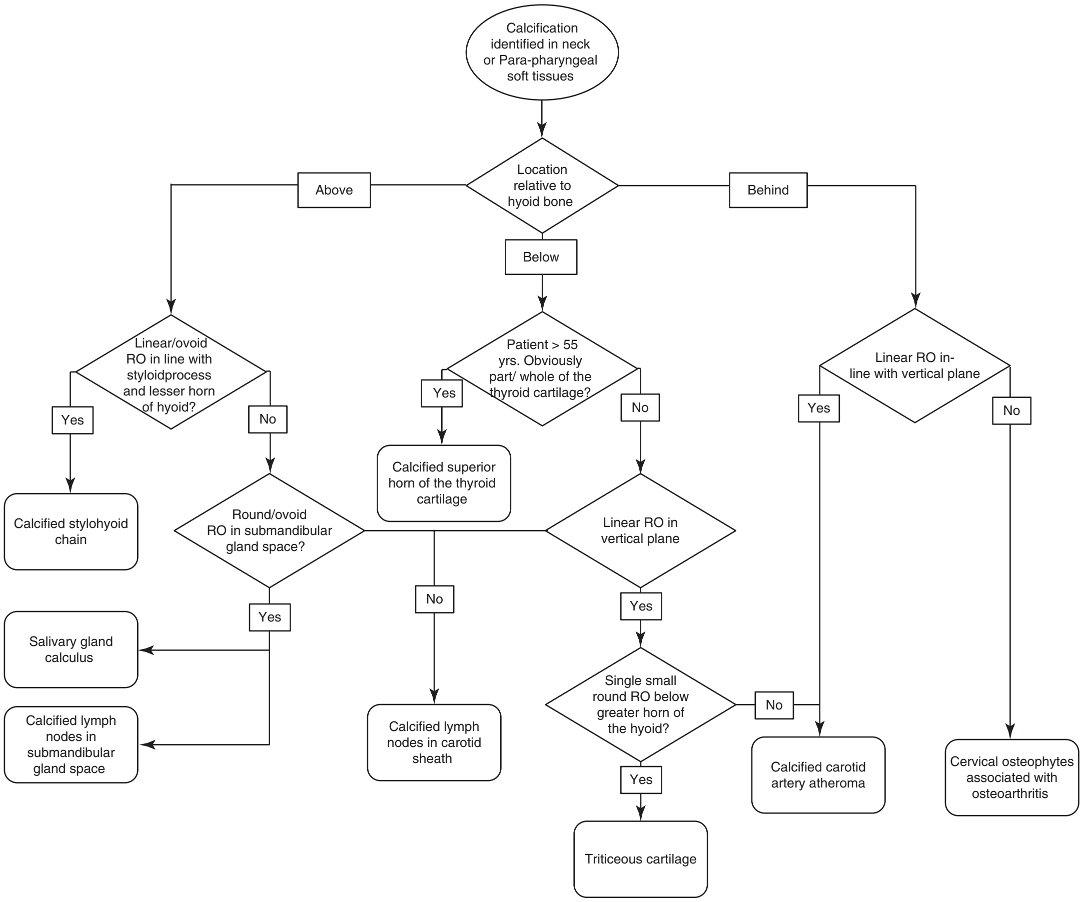

Fig. 17.42 Diagnostic flow chart to characterize the appearance of calcifications in the lateral neck and parapharyngeal soft tissues on presentation on CBCT imaging. Initial decisions involve determining the location of the calcification relative to the hyoid bone and further characterization relative to other structures or appearance (modified from MacDonald et al. (2012). Used with permission from Elsevier)

within the lateral parapharyngeal space, the imaging appearance of calcified SHC on axial orthogonal CBCT images vary. While they consistently present as circular corticated opacifications, their relative position within the section becomes more anterior and medial (Figs. 17.44 and 17.45).

Coronal images are not useful in the evaluation of the calcified SHC because they are not parallel to a laterally deviated complex. If CSC is suspected, the optimal viewing protocol is maximum intensity projection (MIP) images (Fig. 17.46) or volumetric surface renderings (Fig. 17.47) to provide definition of the extension, course, shape, and degree of ossification.

17.5.1.2 Calcification of the Posterior/Anterior Longitudinal Ligaments (Cervical Spine)

The anterior and posterior longitudinal ligaments are long flattened bundles of fibers of connective tissue which assist to support the shape and provide the flexibility of the vertebral column. The anterior longitudinal ligament runs down the ventral aspect of the vertebral bodies and intervertebral disks.

The posterior longitudinal ligament is thicker and extends along the dorsal surfaces of the vertebral bodies from the axis to the sacrum. These ligaments may calcify and present as elongated or irregularly shaped high-density entities in this

Fig. 17.43 Shaded surface lateral volumetric rendering demonstrating elongated styloid process

location. Their identification is crucial because they may be involved in spinal stenosis and neural disturbances (especially the posterior longitudinal ligament) (Figs. 17.48 and 17.49).

17.5.1.3 Calcified Triticeous Cartilage

The triticeous cartilages are small, bilateral, ovoid structures that are part of a complex of structures comprising the laryngeal skeleton. Each cartilage is located just below the hyoid bone, inside the ipsilateral lateral thyrohyoid ligament at the level of C3-C4 (approximately). Clinically, the triticeous cartilage has no known function, although recently it has been suggested that it might help reinforce the lateral thyrohyoid ligament (Carter 2000). Calcification of these structures is benign and is a common finding on panoramic radiographs, with a prevalence ranging from 5 to 29% (Ahmad et al. 2005). The triticeous cartilages present on panoramic images as faint, single, rice grain-sized opacifications immediately inferior to the tip of the greater cornu (horn) of the hyoid bone (GCHB) (Fig. 17.50). Recognition of this appearance and location is necessary so that they may be differentiated from other dystrophic soft tissue calcifications including calcified atheromatic plaques in the common carotid artery (CCA).

On CBCT images, calcified triticeous cartilages most often appear as small ovoid, bilateral, homogeneously dense, “rice grain”-sized structures. Their consistent appearance and location on orthogonal projections coinciding with the anatomic location differentiates them from calcifications in the common carotid artery or tonsillar calcifications (Fig. 17.51). On axial sections, single discrete calcifications are always located medio-dorsal to the most distal extent of the greater cornu of the hyoid bone and in the vicinity of the superficial soft tissue in the lateral prevertebral space immediately adjacent but dorsal to the maximum width of the oropharyngeal airspace (Fig. 17.52). On coronal images, calcified triticeous cartilage are immediately inferior to the greater cornu of the hyoid bone (Fig. 17.53). On sagittal images, they are immediately inferior and slightly ventral to the greater cornu of the hyoid bone (Fig. 17.51c).

17.5.1.4 Calcified Superior Cornu of the Thyroid Cartilage

All three major cartilages of the larynx—the thyroid, cricoid, and arytenoids may undergo physiologic (dystrophic) calcification, endochondral ossification, or both and become visible radiographically (Salman and Kinney 1990). The thyroid is the largest and most superior cartilage, suspended immediately below the hyoid bone by the thyrohyoid membrane, median and lateral thyrohyoid ligaments. The latter extend from the terminal portion of the greater cornu of the hyoid bone caudally to lateral/cephalad projections of the thyroid cartilage known as the superior cornu of the thyroid cartilage. Calcifications in the laryngeal cartilages are initially seen in the

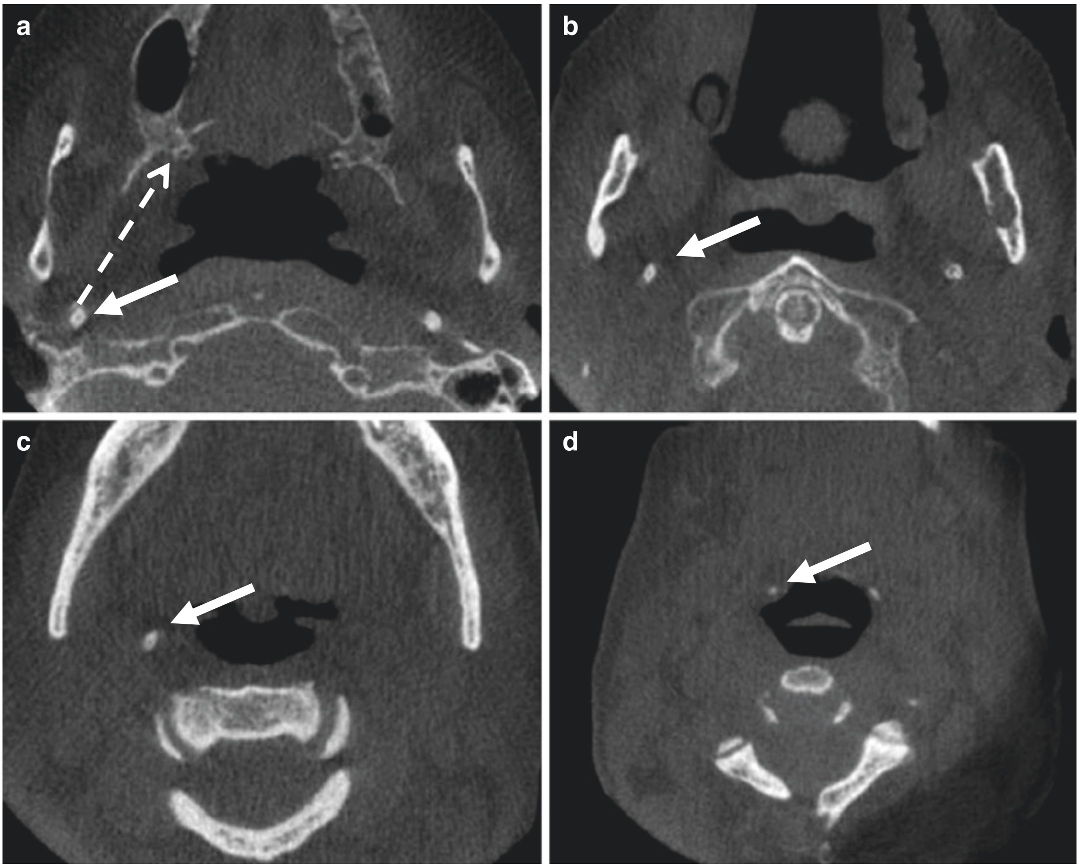

Fig. 17.44 Sequence of axial CBCT images progressively inferiorly from the level of the sigmoid notch (**a**), level of the mid ramus o the mandible/C1 (**b**), mid mandible/C2 (**c**), and immediately suprahyoid (**d**) showing the changing location of calcified stylohyoid chain (SHC) on axial images (*solid arrow*). At the level of the sigmoid notch (**a**), discrete circular opacities are present posterior and lateral to the pharyngeal airspace, anterior to the petrous temporal bone and posterior and medial to the distal border of the ramus. More inferiorly, the location of the opacity changes along a medial anterior path (*dashed arrow*) such that immediately suprahyoid (**d**) the opacities are anterior to the airway. Because of the close approximation to the carotid sheath, they may be easily confused with common carotid artery calcifications due to atheromatosis

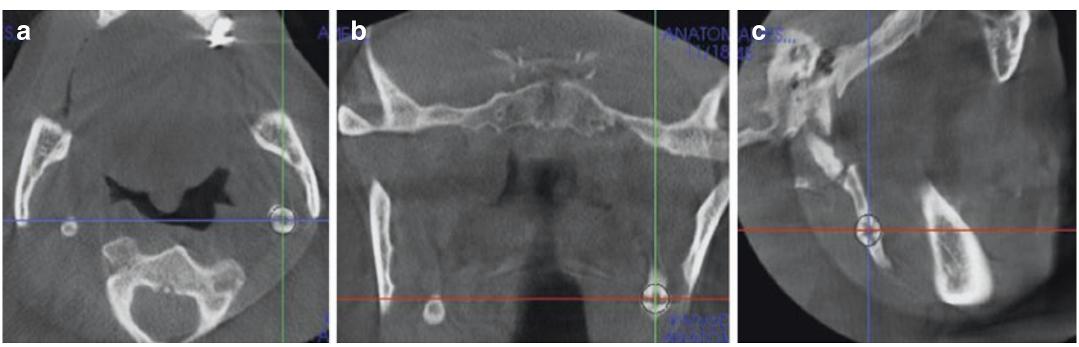

Fig. 17.45 Axial (**a**), coronal (**b**), and sagittal (**c**) sections "triangulating" a tubular structure with a cortical outline in the left neck, medial to the posterior border of the ramus. The sagittal image demonstrates the supero-inferior and anteroposterior orientation, characteristic of a calcified SH ligament. Note the similar appearance of a smaller calcification on the contralateral side

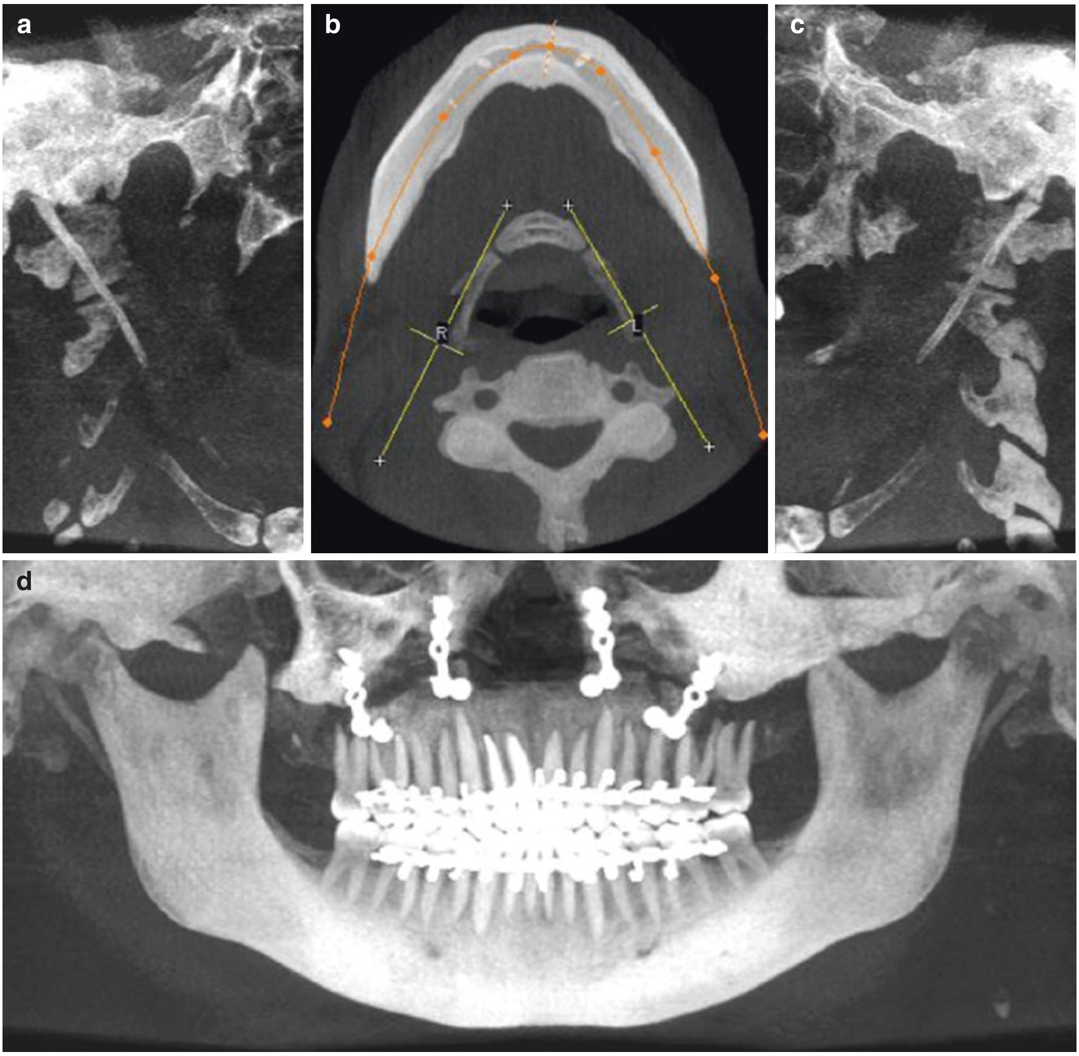

Fig. 17.46 Definitive characterization of the calcified styloid chain (CSC) is provided by bilateral oblique linear medium thickness (40 mm) MIP images (**a**, **c**). These are produced by MPR bisector alignment with the outer periphery of the hyoid bone demonstrated by an axial 40 mm thick MIP image at the level of the mandible (**b**—*yellow line*). A reformatted panoramic image (**d**) created from the axial view (**b**—*orange line*) may be useful.

thyroid, followed by the cricoid and the arytenoids. Thyroid cartilage calcification usually commences at the posterior border, the lower margin, and the inferior cornu and is completed around the age of 70 years (Hately et al. 1965). Consequently, calcification of the superior cornu of the thyroid cartilage (SCT) may present on panoramic images in older individuals (Monsour et al. 1991). Moreover, because of its location, it is important to differentiate it among other juxtapositioned calcifications such as the CTC and, more importantly, common carotid artery calcifications (Carter 2000).

On CBCT imaging, the calcified superior cornu of the thyroid cartilage (SCT) most often appears immediately inferior to the lower border of the greater cornu of the hyoid, unilaterally or bilaterally (Fig. 17.54). The localization of these calcifications on orthogonal projections just lateral to the posterolateral walls of the oropharyngeal airway at the level of C3/C4 vertebrae is an important differentiating feature.

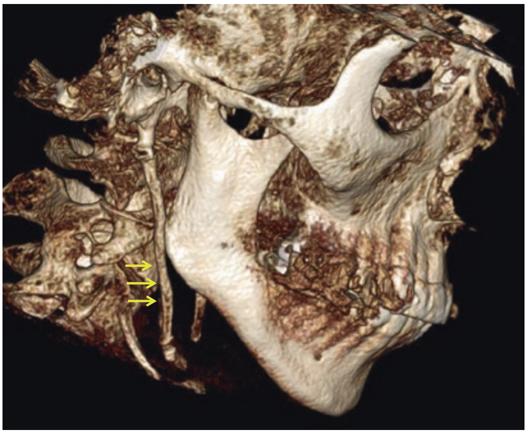

Fig. 17.47 Surface rendering reconstruction (3D image) showing the right side of this patient's neck. The arrows (*yellow arrowheads*) point out an elongated, tubular osseous structure which seems to be the extension of the styloid process to the hyoid bone (calcified SHC). Often along these calcifications knots or nodules may be seen (*white arrows*) indicative of pseudo-articulations

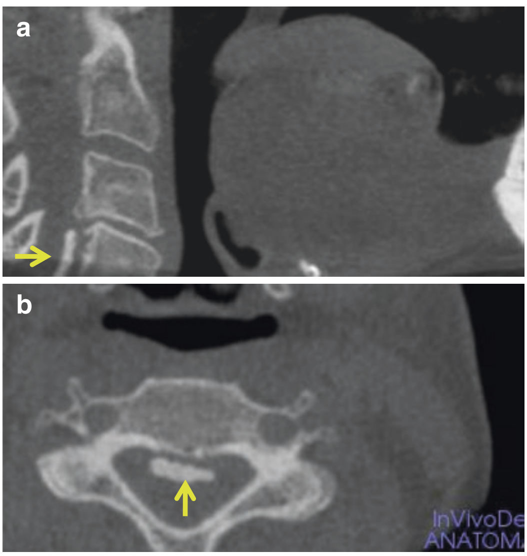

Fig. 17.48 Sagittal (**a**) and axial (**b**) CBCT sections at the level of the 4th cervical vertebra (C4). A flattened, elongated, high-density structure is seen adjacent to the dorsal aspect of the vertebral bodies, inside the spinal canal. This imaging appearance is consistent with a calcified posterior longitudinal ligament

On axial images, the calcified SCT appears as a small, single, distinct, round, high-density structure, present unilaterally or bilaterally, immediately posterior to the greater cornu of the hyoid bone (Fig. 17.55). This projection may be most helpful in distinguishing calcifications in the SCT from those in the triticeous cartilage, which always appear medial to the most posterior extent of the greater cornu of the hyoid (Fig. 17.55). Axial images are best in differentiating these benign calcifications (SCT and CTC) from carotid artery calcifications frequently seen in the lateral neck at the level of C3/C4. Other distinguishing imaging features of carotid artery calcifications compared to SCT and CTC include: they are often larger in size and more irregular in shape, they are more lateral, and they are found in a somewhat less consistent location in the axial plane (Fig. 17.56).

On coronal projections, calcified SCT appears as a linear cylindrical opacification extending inferior from the greater cornu of the hyoid. Occasionally another "rice grain" size opacification is interposed between calcified SCT and the hyoid bone, the calcified triticeous cartilage (CTC) (Fig. 17.57).

On sagittal sections, calcified SCT appear as a single peripherally corticated hyperdensity located along a line projected inferiorly and slightly anterior to the most posterior extent of the greater cornu of the hyoid bone. Separation of the calcified SCT from the greater cornu of the hyoid bone is evident, albeit, sometimes, a single more densely calcified structure, the calcified triticeous cartilage, is interposed between these structures (Fig. 17.58).

17.5.2 Pathologic Neck and Para-Pharyngeal Calcifications

17.5.2.1 Tonsillar Calcifications (Tonsilloliths)

The palatine tonsils are paired bilateral lymphoid tissue located in the lateral wall of the oropharynx adjacent lateral to the terminal sulcus of the tongue. In combination with the pharyngeal (adenoids), tubal, and lingual tonsils, they form a ring of lymphatic tissue known as Waldeyer's tonsillar ring.

Tonsiloliths are small individual areas of calcified matter which form in the tonsillar crypts. They may grow or coalesce to a large size (de Moura et al. 2007). They may be associated with

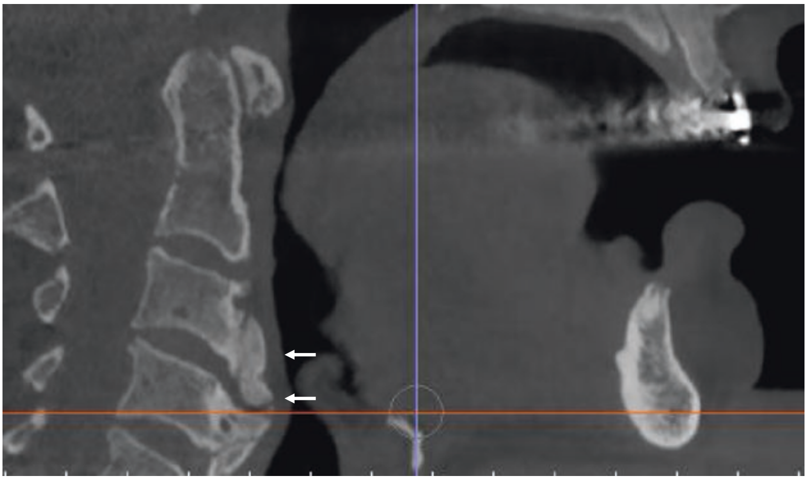

Fig. 17.49 Midsagittal CBCT section at the level of 3rd (C3) and 4th cervical vertebra (C4) showing an irregular, high-density mass, attached to the ventral aspect of the vertebral bodies of C3 and C4. This is consistent with partial calcification of anterior longitudinal ligament. Note the marked obliteration of the airway caused by the calcification. Most often these kind of calcifications are asymptomatic. In rare occasions, presenting symptoms may include dysphagia or airway obstruction or even sleep apnea

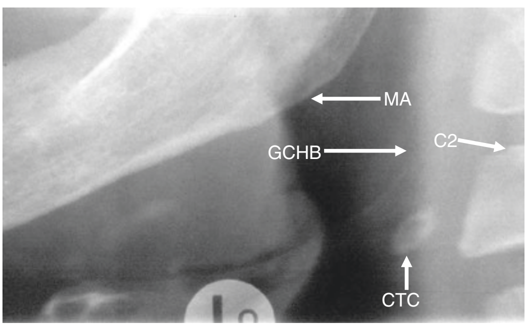

Fig. 17.50 Cropped panoramic image of the lower left mandibular angle (MA) demonstrating relationship of the calcified triticeous cartilage (CTC) to the greater cornu of the hyoid (GCH) and 2nd cervical vertebrae (C2)

recurrent tonsillitis, retention of bacterial debris or as a result of stasis of saliva in the efferent ducts of the accessory salivary gland, secondary to mechanical obstruction arising from post-tonsillectomy scars or chronic inflammation (Pruet and Duplan 1987). Patients may be asymptomatic or complain of persistent throat irritation, foul taste and odor, otalgia, or foreign body sensation. Tonsilloliths are a common incidental finding on CT imaging, presenting in from 16% (Aspestrand and Kolbenstvedt 1987) to up to 39% of patients (Takahashi et al. 2014). They are often visible on panoramic images as small

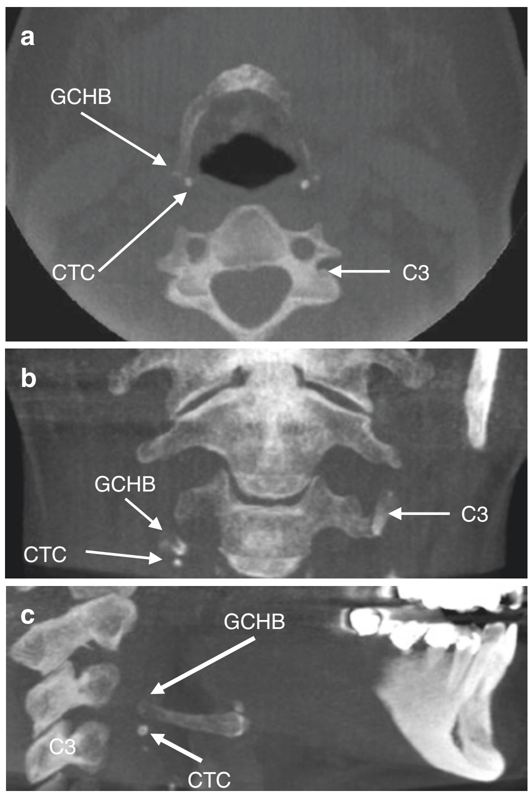

Fig. 17.51 Medium slice (10–20 mm) MIP axial (**a**), coronal (**b**), and sagittal (**c**) CBCT images demonstrating the consistent location and appearance of the calcified triticeous cartilage (CTC) in relation to the greater cornu of the hyoid bone (GCHB) and the 3rd cervical vertebrae (C3)

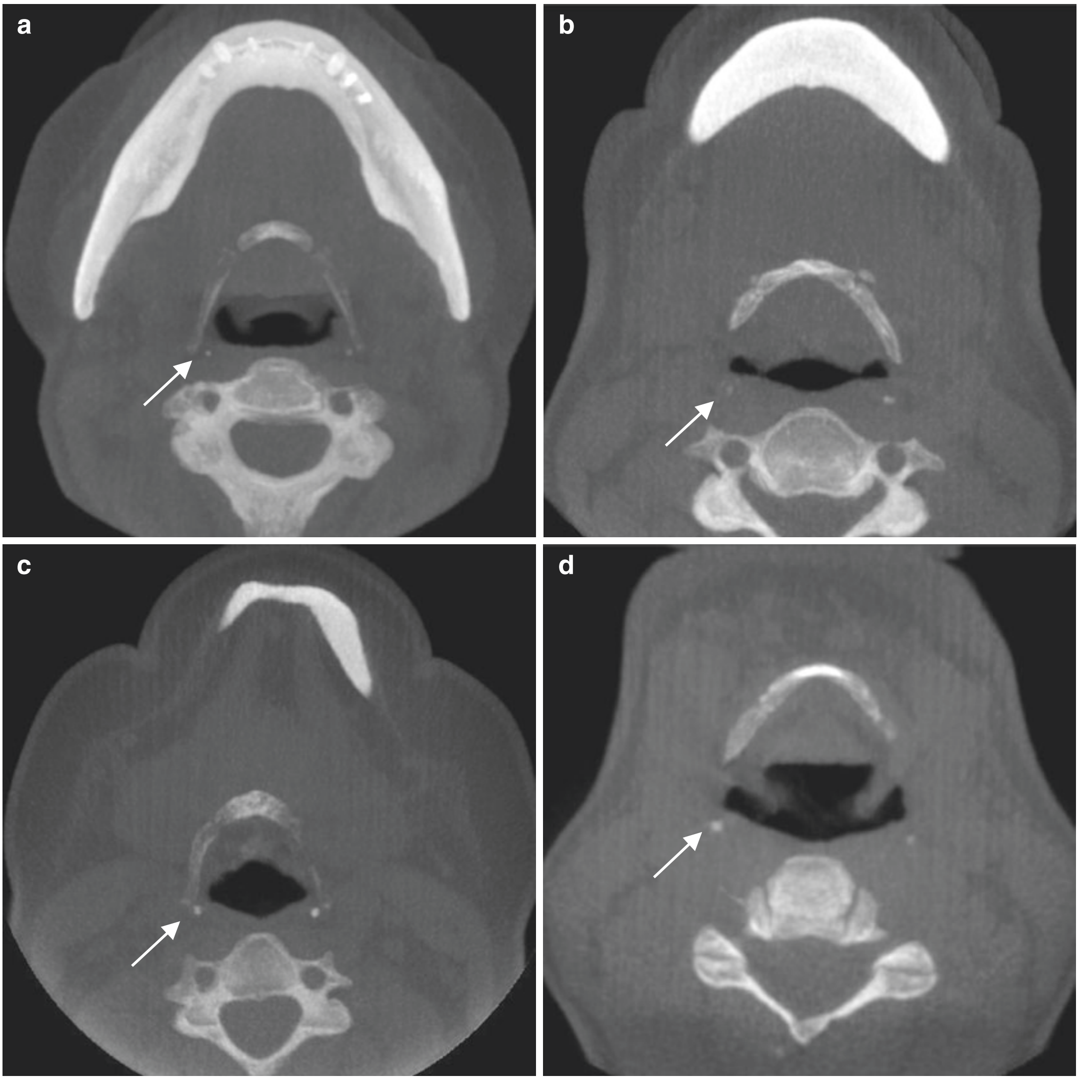

Fig. 17.52 Axial medium slice (10–20 mm) MIP CBCT images from four different patients (**a**–**d**) demonstrating the consistent location and appearance of the CTC (*arrow*)

opaque masses in soft tissues near the anterior border of the oropharyngeal airway space. This location reflects the palatine tonsils which are the mostly affected.

On CBCT images, tonsillar calcifications may appear as a medium-sized single (Fig. 17.59), but more often multiple, clustered "rice grain"-like (Fig. 17.60), homogeneous, high-density structures, ranging in size from 1 to 5 mm or more in diameter, identified superficially inside the mucosal lining of the parapharyngeal airway either uni- or bilaterally Their superficial location at the level of the floor of the mouth distinguishes them from carotid calcifications or calcified triticeous cartilage.

On axial CBCT sections, tonsilloliths present as multiple small opacifications located anterolateral to the oropharyngeal airway space immediately medial to the mandibular angle or mandibular ramus. The depth of the calcifications with respect to the surface of the airway space can be variable. On coronal sections these calcifications may be identified in a zone which extends

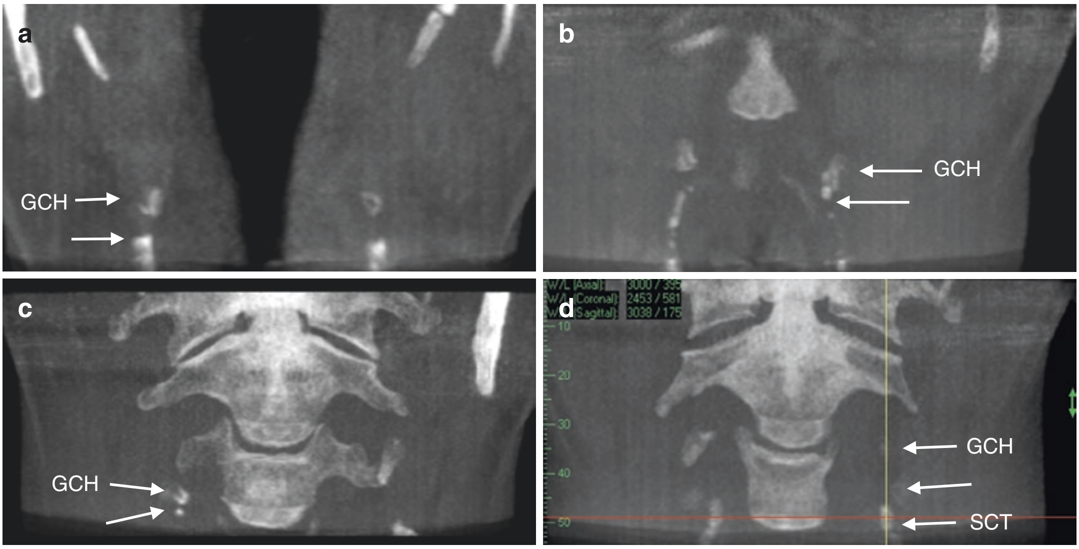

Fig. 17.53 Coronal medium slice (10–20 mm) MIP CBCT images from four different patients (**a**–**d**) demonstrating the consistent location and appearance of the CTC (*dashed arrow*) immediately inferior to the maximal extension of the greater cornu of the hyoid bone (GCH). Note that in (**d**) an additional calcified structure is present inferior to the CTC on coronal image—this is the calcified superior cornu of the thyroid cartilage (SCT)

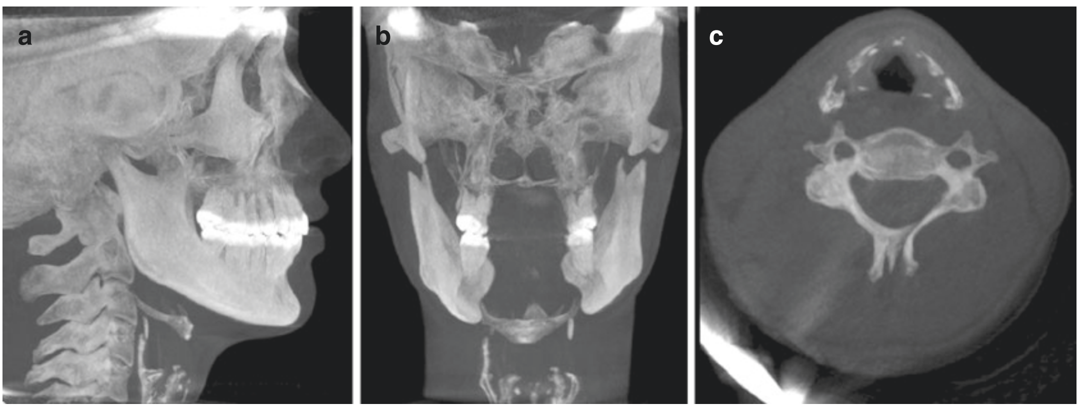

Fig. 17.54 Full thickness lateral (**a**), 40 mm thickness coronal (**b**), and 20 mm thickness axial MIP CBCT images demonstrating the characteristic appearance of the calcified SCT and its relationship to the hyoid bone inferiorly and airway superficially

from the floor of the mouth or lower to the lateral pharyngeal walls. Finally, on sagittal sections, the tonsillar calcifications are most often found at the junction of the soft palate with the root of the tongue either uni- or bilaterally.

Calcifications in tonsillar tissues other than the palatine tonsils (lingual, pharyngeal) are not as common (Fig. 17.61).

17.5.2.2 Carotid Artery Calcifications

Atherosclerosis or atheromatosis is a pathological condition of the vasculature where intra-lumenal vascular plaques form, especially at areas of greatest shear force and turbulence. In the head and neck region this most commonly occurs at the bifurcation of the common carotid artery (CCA) to the internal (ICA) and external carotid artery (ECA),

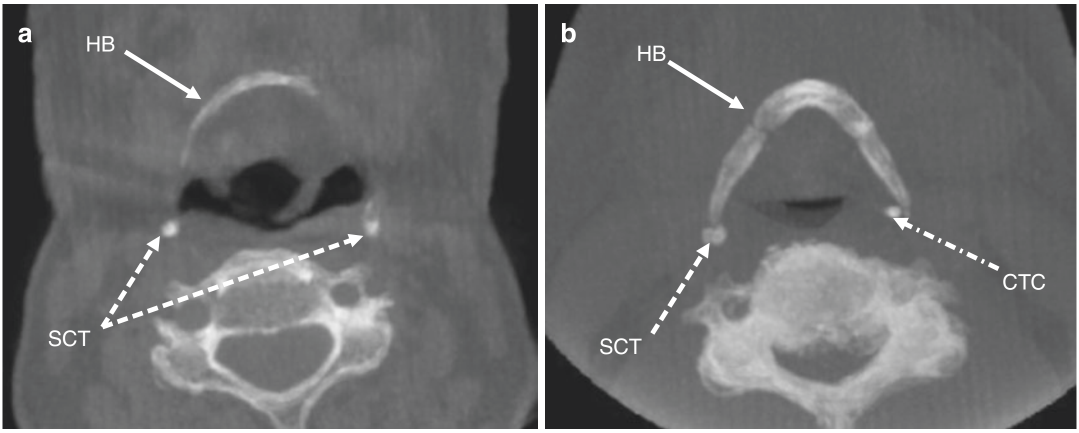

Fig. 17.55 Cropped axial medium slice (10–20 mm) maximum intensity orthogonal projections demonstrating the location and appearance of the calcified superior cornu of the thyroid cartilage (SCT) on axial images for two patients (**a**, **b**). The calcified triticeous cartilage (CTC) can be differentiated from the SCT on these images as being medial to the greater cornu of the hyoid bone (HB) (**b**)

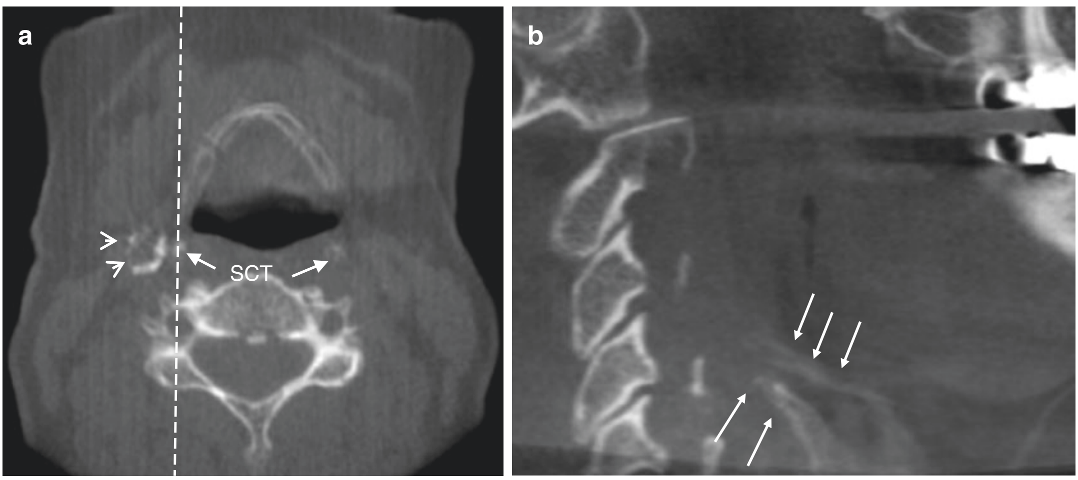

Fig. 17.56 Thin (1 mm) axial (**a**) section of the neck at the level of C3/C4 vertebrae with sagittal reference line (*dashed white*) and corresponding sagittal image (**b**) depicting the hyoid bone and a vertebra. The small round calcifications towards the dorsal/lateral walls of the airway (**a**) are calcifications of the superior cornu of the thyroid (SCT) (*thick arrows*). In the same region, just laterally to the right superior cornu, there is a larger ring-like calcification (*arrowheads*). This is a carotid artery calcification due to atheromatic disease. The hyoid bone (*thin arrows*) and the right superior cornu of the thyroid (*dashed arrows*) are depicted

located lateral and inferior to the hyoid bone. Since the CCA provides the main blood supply to the brain, atherosclerotic conditions of the carotid artery may lead to neural ischemia (inadequate oxygen to the brain) thus resulting in a cerebrovascular accident (CVA), or stroke. Atheroma-related formations of thrombi and emboli in the carotid artery is the most frequent cause of stroke (American Heart Association/American Stroke Association 2008). Stroke is a significant public health issue with both morbidity and mortality costs (Tegos et al. 2001; Gorelick et al. 1999).

Not all atheromatic plaques are calcified; calcification is a morphologic complication in the evolution of atheromatous plaque enabling potential detection by diagnostic imaging. Since

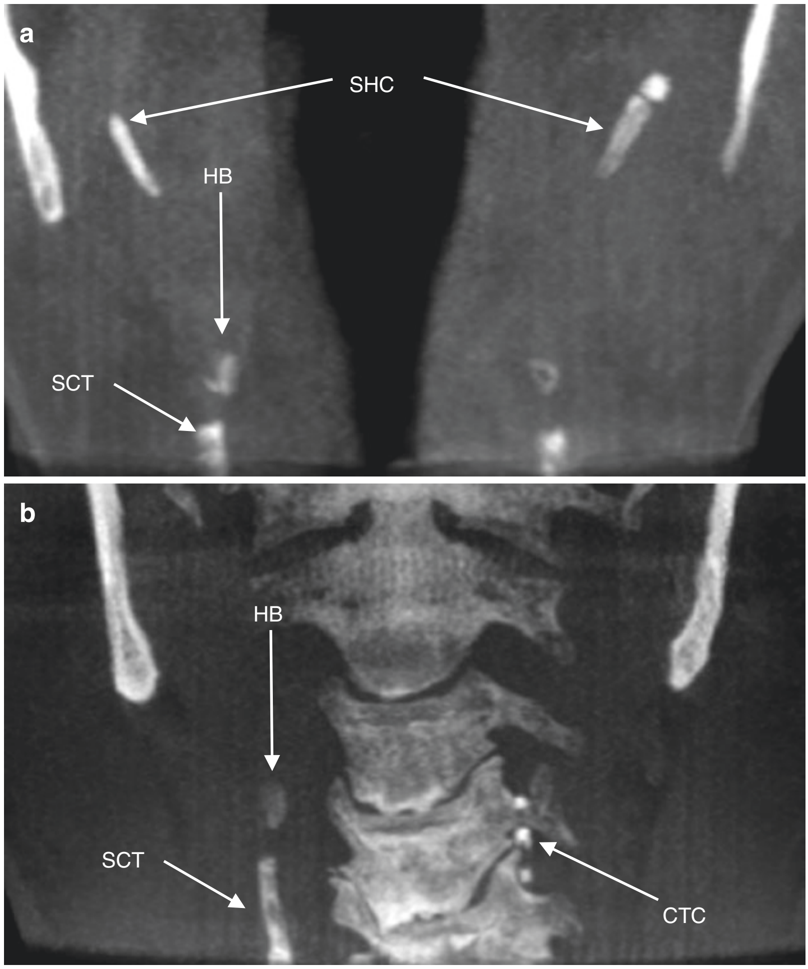

Fig. 17.57 Coronal medium slice (10–20 mm) MIP projections of two patients (**a**, **b**) demonstrating the location and appearance of the calcified SCT in relation to the hyoid bone (HB). A calcified triticeous cartilage (CTC) can be differentiated from a calcified SCT on these images as immediately inferior and more medial to the greater cornu with a higher attenuating "rice grain" appearance (**b**)

1981, calcified atherosclerotic lesions at the bifurcation of the CCA have been reported on panoramic images. They appear as curvilinear irregular parallel radiopacities, about 1.5–2.5 cm inferior-posterior to the angle of the mandible adjacent to the cervical spine at or below the third and fourth cervical vertebra and inferior and lateral to the hyoid bone (Friedlander and Lande 1981; Friedlander and August 1998).

The prevalence of carotid artery calcifications (CAC) on panoramic images in the general dental population over 50 years varies from 0.1 to 3.2%, increasing with age and is substantially higher (22–37%) in populations exhibiting atherosclerotic (hypertension, cardiovascular disease, past stroke/CVA, transient ischemic attacks, or diabetes) or other (hypercholesterolemia, obesity and physical inactivity, cigarette smoking, sleep apnea, head and neck radiation therapy, and male gender) risk factors.

The appearance of the CAC may vary in size and shape. Larger calcifications may be an indicator of the severity of the obstruction. They range in shape greatly from small linear or curved dense structures to more "ring"-like or "tube"-like structures that follow the periphery of the blood vessel. This may be associated with the progression and severity of the obstruction. Their common feature is their location which, in the vast majority of the presentations, is adjacent to the carotid artery bifurcation, with a few only exceptions.

The CCA has a short straight cephalad course from the sternoclavicular joint to the superior border of the thyroid cartilage where it branches

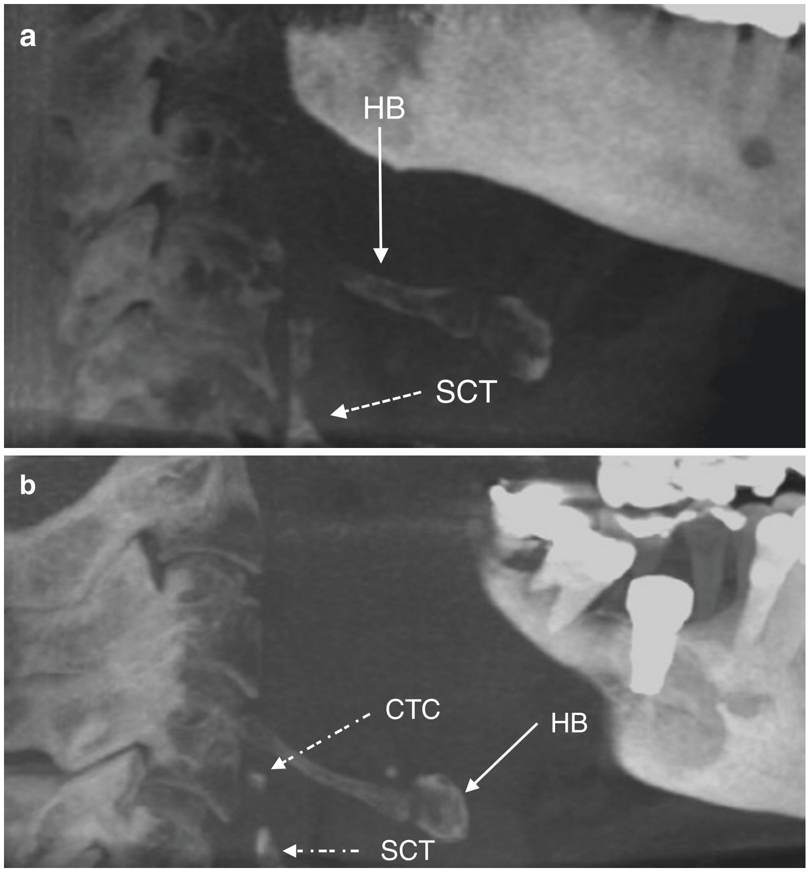

Fig. 17.58 Medium slice (10–20 mm) MIP sagittal projections of two patients (**a**, **b**) demonstrating the location and appearance of the calcified SCT in relation to the hyoid bone (HB). A calcified triticeous cartilage (CTC) can be differentiated from the SCT in (**b**) as immediately inferior to the greater cornu, rice grain-like, and higher attenuating

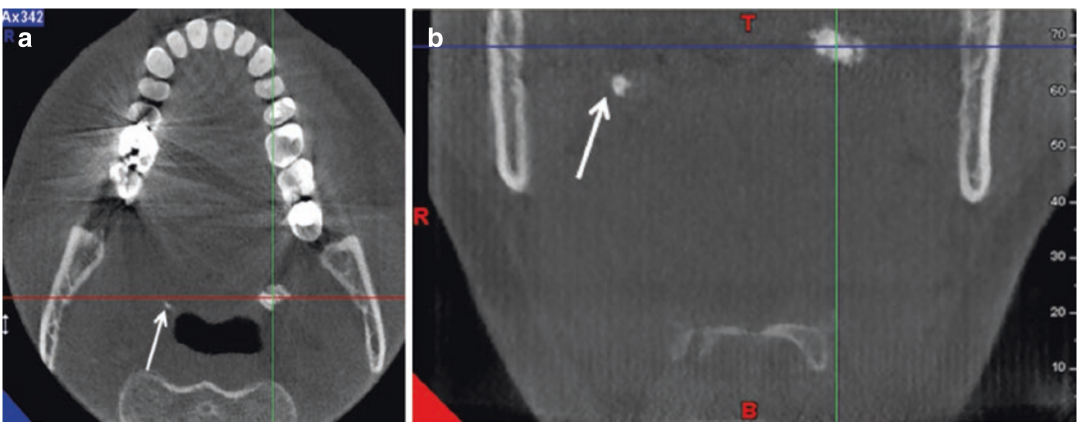

Fig. 17.59 Axial (**a**) and coronal (**b**) CBCT sections of the mandible and suprahyoid neck depicting bilateral tonsilloliths: a large tonsilloliths (approx. 10 mm diameter) in the left palatine tonsil and a smaller one (*white arrows*) in the right palatine tonsil. Note their superficial location on the anterolateral walls of the airway (**a**)

to the ICA which takes a deeper course and provides blood supply to the brain and the ECA which provides blood supply to the head and neck (excluding the brain). It is suspected that non-laminar blood flow in the bifurcation region contribute to the formation of atheromatic plaques. Another anatomical landmark that has been used to determine the carotid artery bifurcation apart from the superior border of the thyroid cartilage is the level of C3/C4 vertebrae.

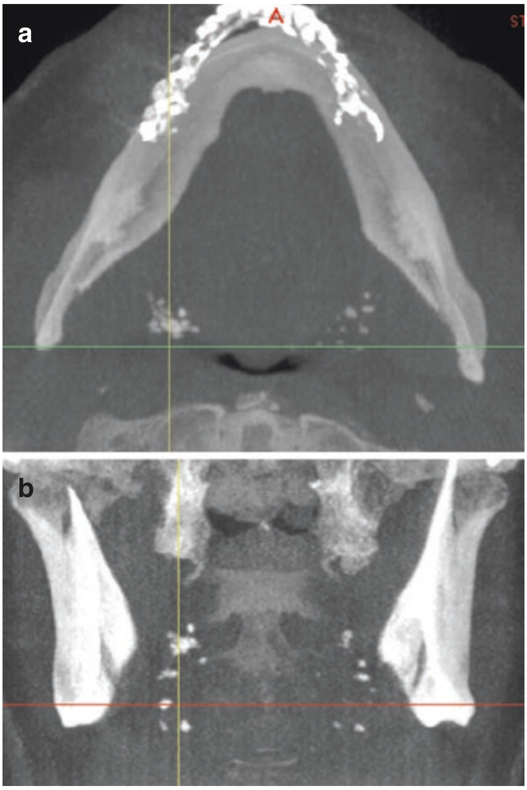

Fig. 17.60 Axial (**a**) and coronal (**b**) thick (10–20 mm) MIP CBCT images of bilateral calcifications of tonsillar tissue (palatine tonsils). The axial section (**a**) demonstrates calcifications anterolateral to the oropharyngeal airway space and medial to angle or ramus of the mandible (**a**). The coronal section (**b**) demonstrates clusters of opacifications dispersing on the soft tissue medial to the mandible inside the lateral walls of the airway

Axial sections are the most appropriate for the recognition of CAC. Current CT and CBCT interactive software programs facilitate the assessment of all orthogonal sections (multiplanar sections) simultaneously; location can thereby be confirmed using triangulation.

On axial sections, CAC initially present as single or multiple “rice grains”-shaped linear, or curvilinear homogeneous opacifications (Fig. 17.62). As these calcifications increase in size, they often tend to form larger coalescing masses. Curvilinear calcifications presented with a crescent shape or extended into a “C” shape with a few almost completely encompassing the vessel forming a circle or appeared to occlude the soft tissue region. CAC are most commonly located in the soft tissue approximately 0–10 mm anterolaterally to the transverse process of the ipsilateral vertebra, lateral or more often posterolaterally to the greater cornu of the hyoid bone (Fig. 17.63). They are always posterolateral to the pharyngeal airway space. On some occasions, depending on the window and level settings, it is possible to delineate the soft tissue vessel within which the calcification occurred within the carotid space (Fig. 17.64).

On coronal sections, CAC are lateral to the transverse processes of the cervical vertebrae. In this projection, CAC present as linear, linear

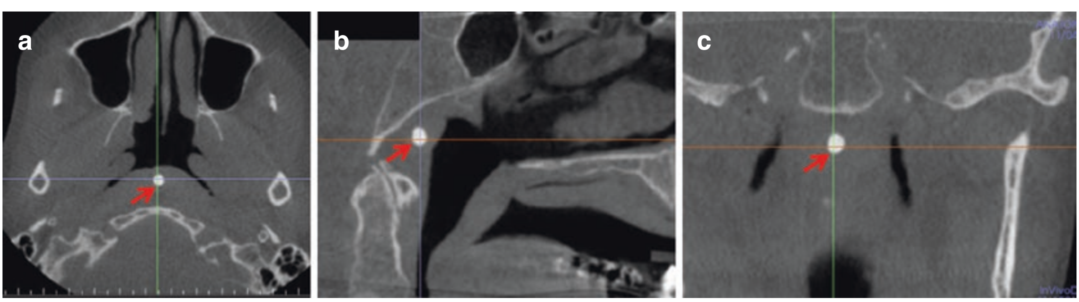

Fig. 17.61 Axial (**a**), midsagittal (**b**), and coronal (**c**) CBCT sections showing a single, round tonsilolith in the pharyngeal tonsil (adenoids) (*red arrow*)

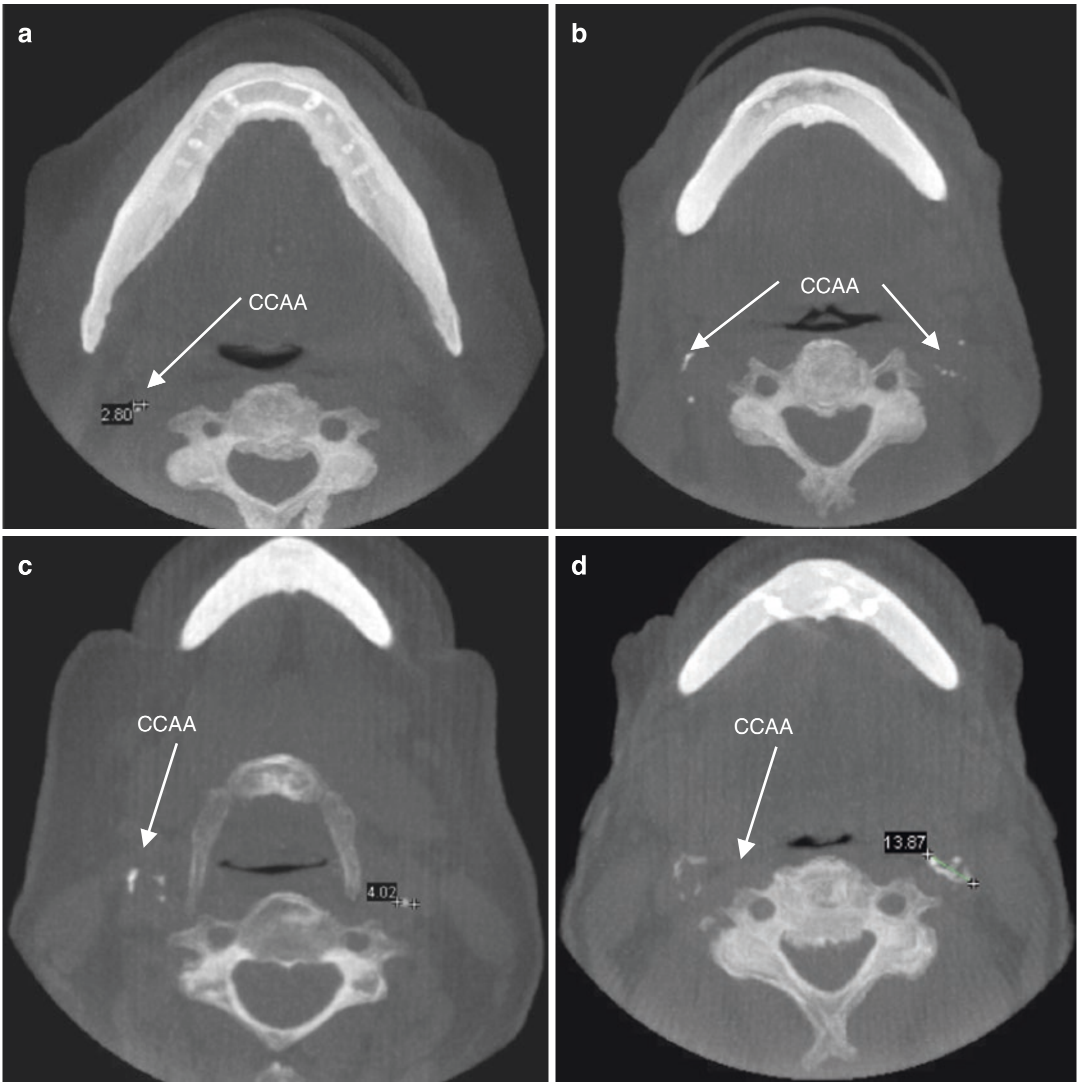

Fig. 17.62 Axial projections demonstrating the varying presentations of calcified carotid artery atheroma (CCAA) as single rice grain (**a**), multiple "rice grains" (**b**—*right*), linear (**b**—*left*; **c**—*right*), or curvilinear (**c**—*left*; **d**—*left*) homogeneous opacifications. Often as the size of the CCAA increase, the number of ipsilateral opacifications also increases (**d**—*left*) tending to form larger coalescing masses (**d**—*right*) (with permission from MacDonald et al. (2012))

globular, globular, or irregular in shape calcifications (Fig. 17.65).

On sagittal sections, CAC are most often medial and inferior to the angle of the mandible, lateral or anterolateral to the transverse processes of the respective cervical vertebrae (most often C3 or C4) with vertical position varying from C3 to C5. Most are either at or below the level of the superior cornu of the hyoid bone (level of C3/C4); however, some may be above that level (Fig. 17.66). Presentation may range from linear to linear oblique to globular homogeneous opacifications (Fig. 17.67). Sometimes multiple discontinuous globular opacifications are evident (Fig. 17.68).

While the vast majority of calcifications in the neck region are physiologic (e.g., stylohyoid chain calcifications, triticeous cartilage calcifications and

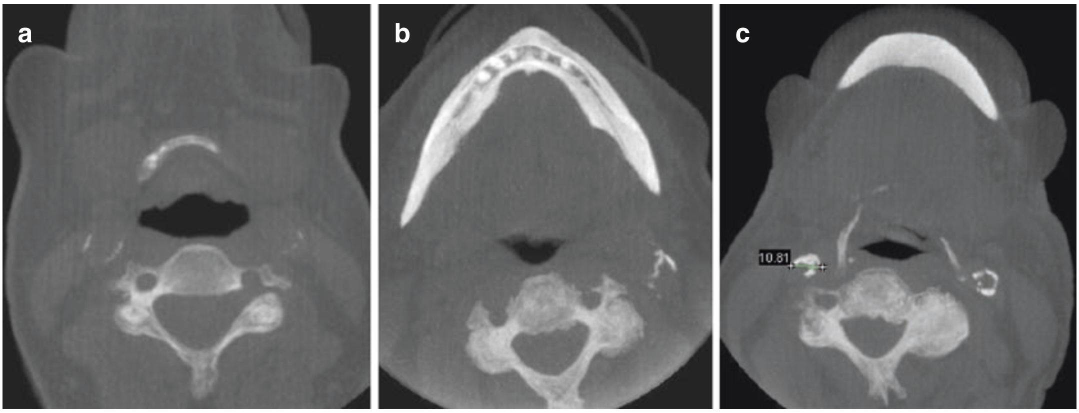

Fig. 17.63 Axial medium slice (10–20 mm) MIP images of three patients (**a**, **b**, and **c**) demonstrating presentation of curvilinear calcified carotid artery atheroma as a crescent shape (**a**), extended into a “C” (**b**) or almost completely forming a circle (**c**)

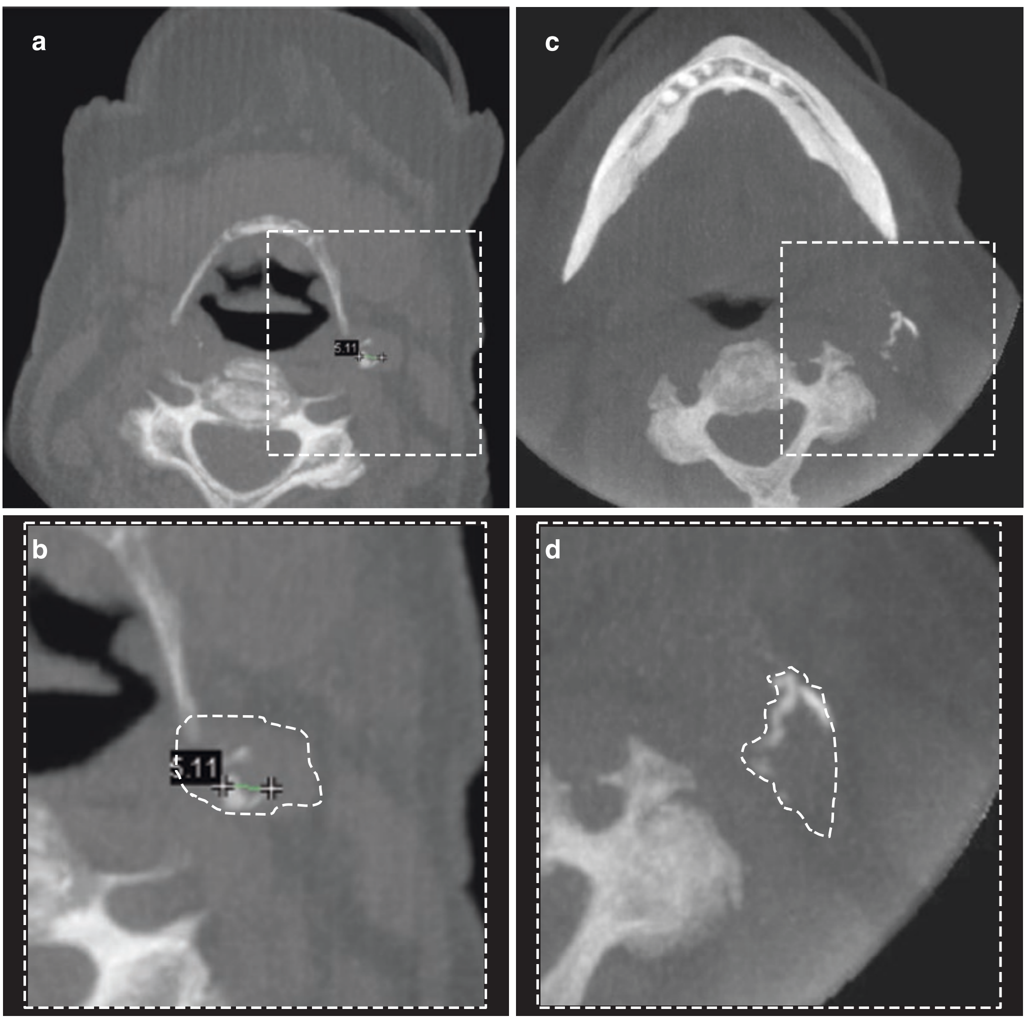

Fig. 17.64 Two (**a/c**) axial medium slice (10–20 mm) MIP orthogonal projection demonstrating correlation of calcified carotid artery atheroma (CCAA). Magnified images (**b/d**) show the boundary with soft tissue outline

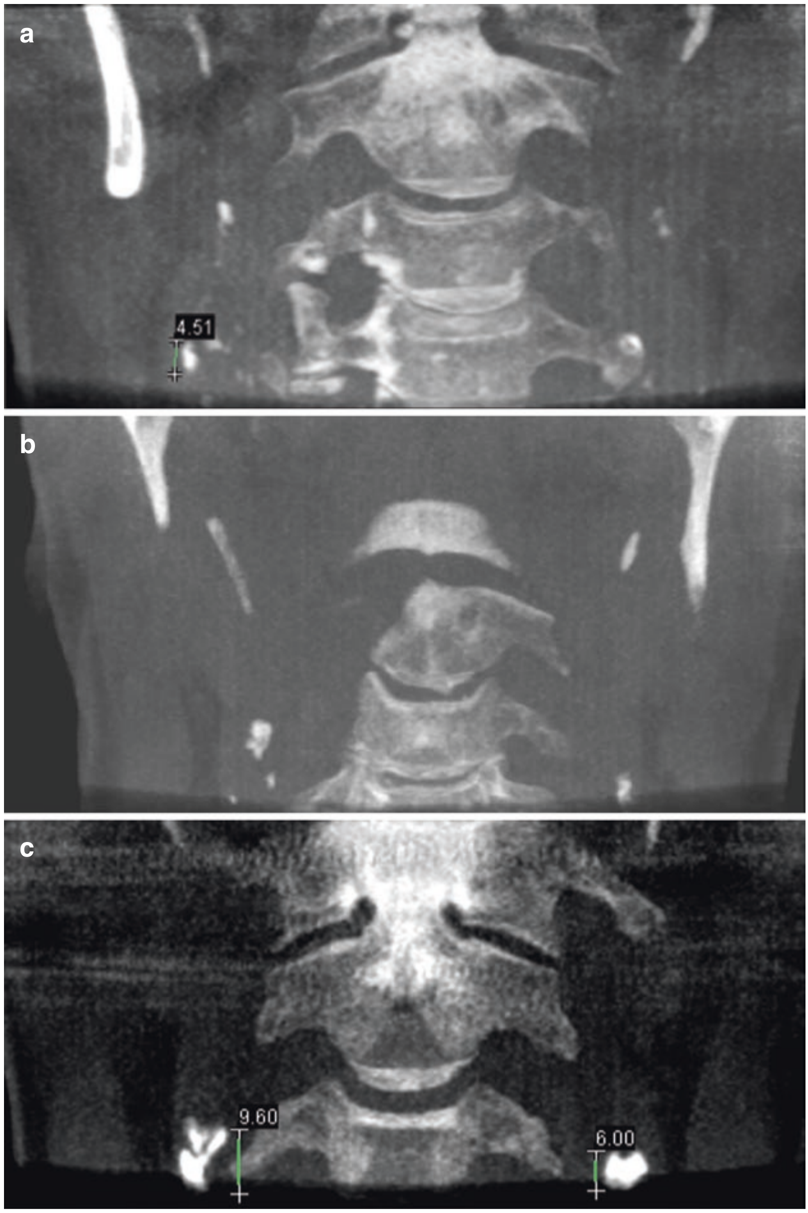

Fig. 17.65 Coronal medium slice (10–20 mm) MIP orthogonal projections of three patients (**a**, **b**, and **c**) demonstrating the characteristic location of calcified carotid artery atheroma lateral to the cervical vertebrae and variation in presentation from linear (**a**), linear globular (**b**), to globular calcifications (**c**)

calcifications of the thyroid cornu), the morbidity and potential mortality of CACs necessitate radiographic differentiation of these entities (Table 17.3).

Simultaneous assessment of any suspicious calcification in the lateral neck by triangulation is strongly advised to determine the location and nature of the entity.

When CAC is suspected on CBCT images, initial management is based on the patient's history and clinical presentation. For neurologically symptomatic individuals, referral to an appropriate physician for a complete evaluation of the carotid bifurcation and the extent of the blockage is recommended for every patient (Ricotta et al. 2011). This should be accompanied by a summary of the specific imaging findings on which the referral is based.

The course of action for patients who are neurologically asymptomatic is somewhat controversial. Maxillofacial CBCT is excellent for demonstrating hard tissues, but weak in delineation of soft tissues. As such, it provides little information on the degree of possible stenosis as soft tissue plaque accumula-

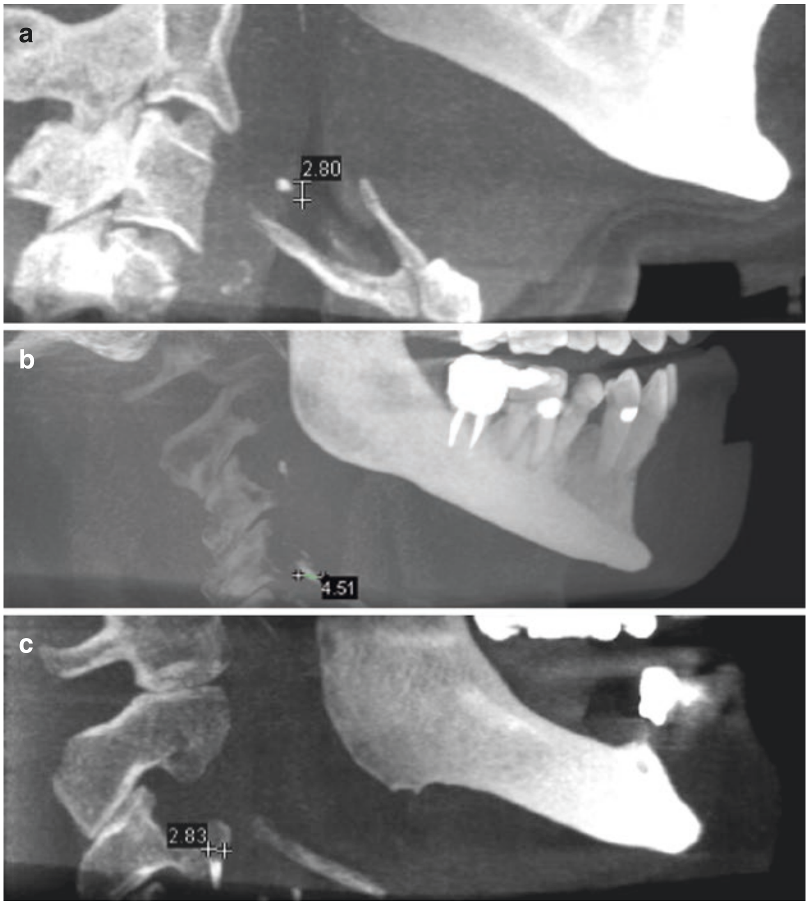

Fig. 17.66 Sagittal medium slice (10–20 mm) MIP orthogonal projections of three patients (**a**, **b**, and **c**) demonstrating location of calcified carotid artery atheroma in relation to the hyoid bone as either above (**a**), at the level of (**b**) or below (**c**) the hyoid bone

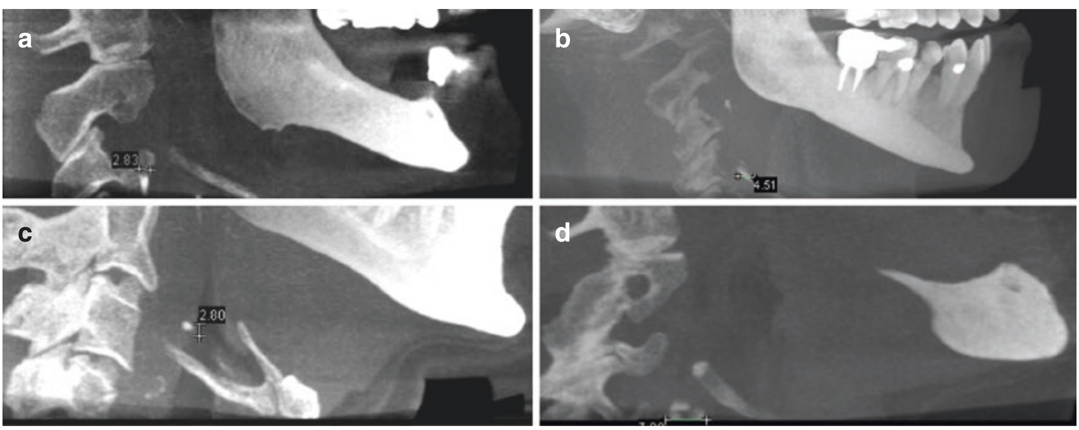

Fig. 17.67 Sagittal medium slice (10–20 mm) MIP orthogonal projections of four patients (**a**, **b**, **c**, and **d**) demonstrating appearance of CAC as linear (**a**), oblique linear (**b**), globular (**c**) or coalescing globules (**d**)

tion is not demonstrated. Since the presence of CAC is not only a risk factor for CVA but myocardial infarction (Friedlander and Cohen 2007; Prabhakaran et al. 2007), confirmed radiographic findings may have consequence to the systemic health of the patient. For asymptomatic patients who present with high-risk factors (e.g., high blood pressure, known coronary artery disease, diabetes,

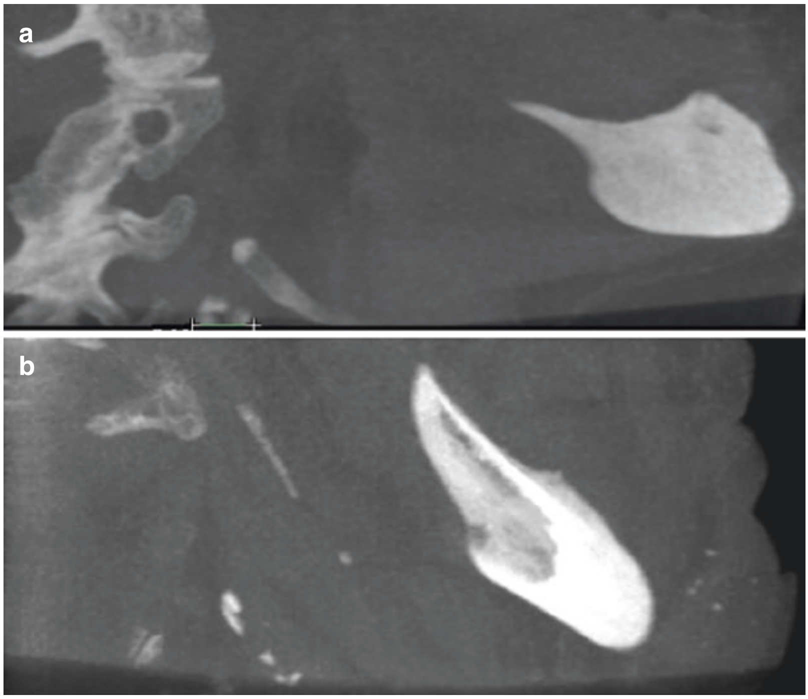

Fig. 17.68 Right sagittal medium slice (10–20 mm) MIP orthogonal projections of two patients (**a**, **b**) demonstrating multiple discontinuous globular calcification appearance of CAC

Table 17.3 Differential diagnosis of calcified carotid artery atheroma

Features		Carotid Artery	Stylohyoid chain	Triticeous Cartilage	Thyroid Cartilage	Tonsils
Clinical		Over 55 years	–	–	↑ with age	+ve history of tonsillitis
Location	Hyoid bone	Posterior and adjacent or inferior	Superior	Immediately inferior to GCHB	Inferomedial to GCHB	Superior
	Oropharynx	Retropharyngeal	Variable			Lateral wall, superficial
	Cervical vertebrae	Anterolateral C3-C4	Anterior lateral C1-C3	Anterior C4	Anterior C4-C5	C2 or superior
Presentation		Curvilinear, globular, with irregular margins	Discontinuous linear	Small, single, ovoid, smooth, well-defined corticated border	Linear parallel	Multiple, punctate

smoking, or hypercholesterolemia), referral to an appropriate physician for an opinion and possible further imaging investigation is recommended (MacDonald et al. 2012) (Fig. 17.69). If a patient consistently exhibits high blood pressure or is not under the care of a physician, it is recommended that the patient be further evaluated by a physician using procedures specific to cardiovascular study to confirm the presence and degree of stenosis of the lumen (e.g., angiography and/or Doppler ultrasonography) combined with a thorough clinical examination. If the patient's blood pressure is <140 (systolic) or the patient is currently undergoing management of their blood pressure, then the need for referral should be determined by contacting the physician.

17.5.2.3 Calcified Lymph Nodes

The presence of calcified lymph nodes is an indication of nodal disease, either active or a sequela of previous disease (Eisenkraft and Som 1999). There are several groups of lymph nodes present in the

__/__/_____ (*Insert date of referral*)

Dr. ____ (*Insert referring clinician name*)
____
____

RE: ____ (*Insert prefix, first and last name of patient*)
Report #: _______________________ (*Insert internal chart/record #*)

Dear Dr. ____, (*Insert referring clinician name*)

On _________________ (*Insert date imaging performed),* I had the pleasure of seeing the above patient in our office for maxillofacial cone beam computed tomographic imaging (CBCT). He/She is a ______ (*Insert age*) year old man/woman with a history of
____
(*list any risk factors for development of atherosclerosis, history of TIAs, carotid bruit, prior cardiovascular or cerebrovascular events*)

CBCT examination revealed irregular, heterogeneous foci of calcification in the lateral soft tissues of the __________ (*insert left/right/both*) side(s) of the neck in a vertico-linear orientation inferior to the angle of the mandible and adjacent to the hyoid bone in the approximate region of the carotid space at the level of the third and fourth cervical vertebrae.

My radiographic impression of this appearance is that of calcified atherosclerotic plaque in the _________________________________ (insert left/right/bilateral) extracranial carotid vasculature at the level of the bifurcation of the internal and external carotid artery.

Maxillofacial cone beam CT is excellent for demonstrating hard tissues, but poor in delineation of soft tissues. Furthermore, it provides little information on the degree of possible stenosis as soft tissue plaque accumulation is not visible.

We are requesting a cerebro-vascular evaluation of Mr./Mrs./Ms.________________________ (insert patient name) since the findings may might have consequence to the systemic health of the patient in so much as carotid calcifications have been linked to coronary vascular disease (Lancet 1996;348:766) and stroke.

Please forward copies of reports to the address indicated on the letterhead. Thanking you in advance for assistance in the care of this patient.

Respectfully yours.

Fig. 17.69 Example of the text of a letter to be used to refer a patient with suspected CAC identified on a CBCT image to a physician

general head and neck region and often some are within the FOV of the maxillofacial CBCT scan.

Lymph nodes are present in the neck in the submandibular, submental, pre-auricular, and cervical areas. Nodal calcification is generally asymptomatic and mostly associated with granulomatous disease such as sarcoidosis and tuberculosis (Fig. 17.70). Although the majority of cases of cervical nodal calcifications are attributed to tuberculosis, these occur after the treatment of the disease. Some neoplastic diseases have been reported to cause lymph node calcifications (lymphoma, metastatic thyroid carcinoma, etc.).

Radiographically these calcifications usually appear as distinct, irregularly shaped, consolidated opacities, characteristically described as "cauliflower-like" (Figs. 17.70 and 17.71). As cervical lymph nodes are grouped both superficially

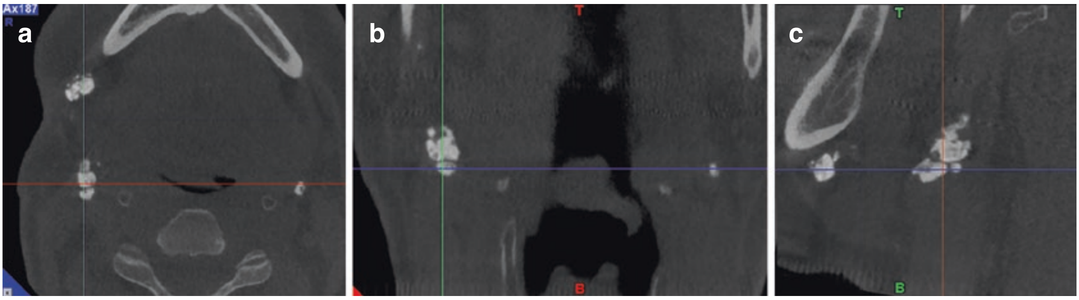

Fig. 17.70 Axial (**a**), coronal (**b**), and sagittal (**c**) 1 mm sections at the level of the C3 vertebral body. Two clusters of "cauliflower-like" high-density structures are depicted in the right submandibular and lateral neck region. Their appearance and location is characteristic for calcified cervical/submandibular lymph nodes secondary to tuberculosis (scrofula; also known as tuberculous cervical lymphadenitis)

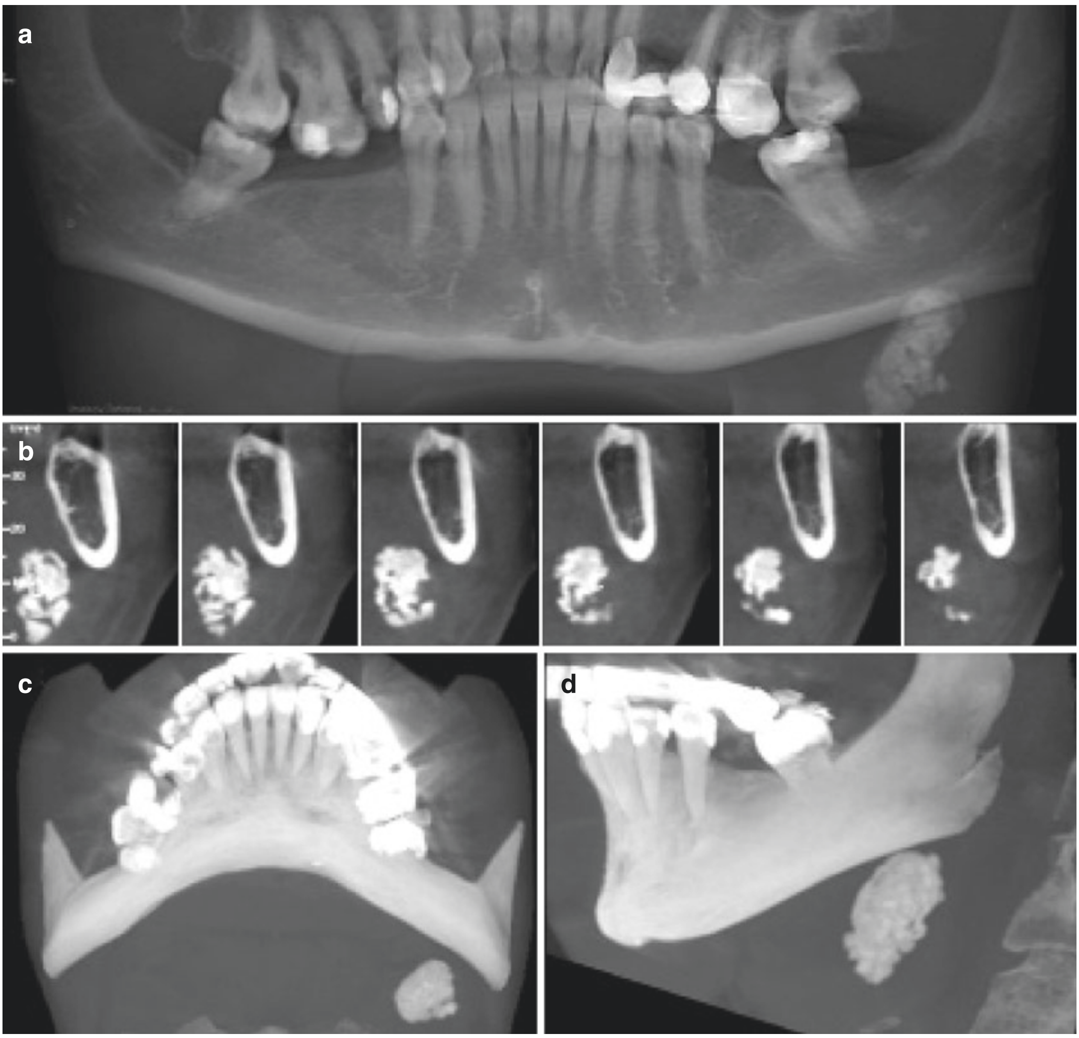

Fig. 17.71 Reformatted panoramic (**a**) and serial cross-sectional (**b**) CBCT images of the left mandibular region showing coalescence of punctate calcifications (multiple calcifications <2 mm in size) located inferomedial to the lower border of the left mandible. 50 mm thick MIP infero-oblique frontal (**c**) and left lateral CBCT images confirming the location and calcification pattern consistent with consolidated calcification of the left submandibular gland lymph node

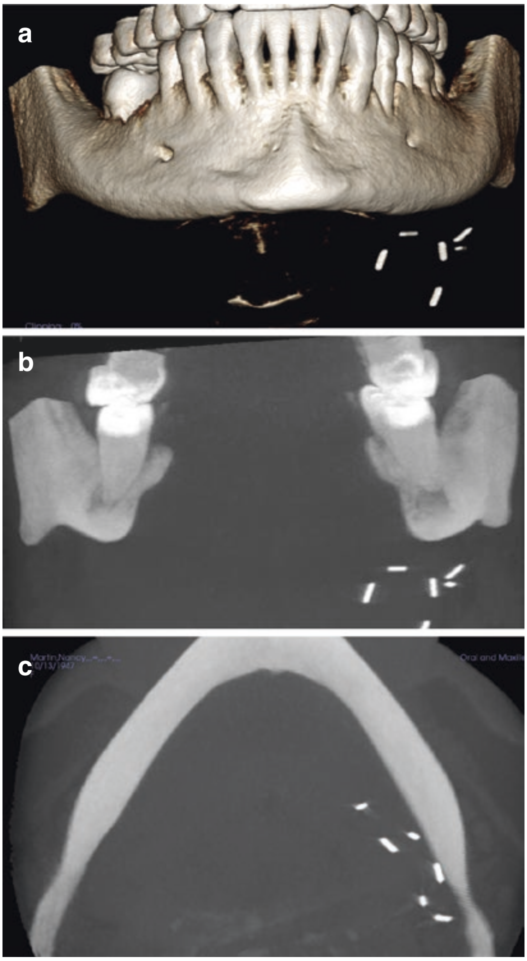

Fig. 17.72 Frontal volumetric rendering (**a**), coronal 20 mm thick maximum intensity projection (**b**) and axial 20 mm thick MIP (**c**) projection of brachytherapy seeds

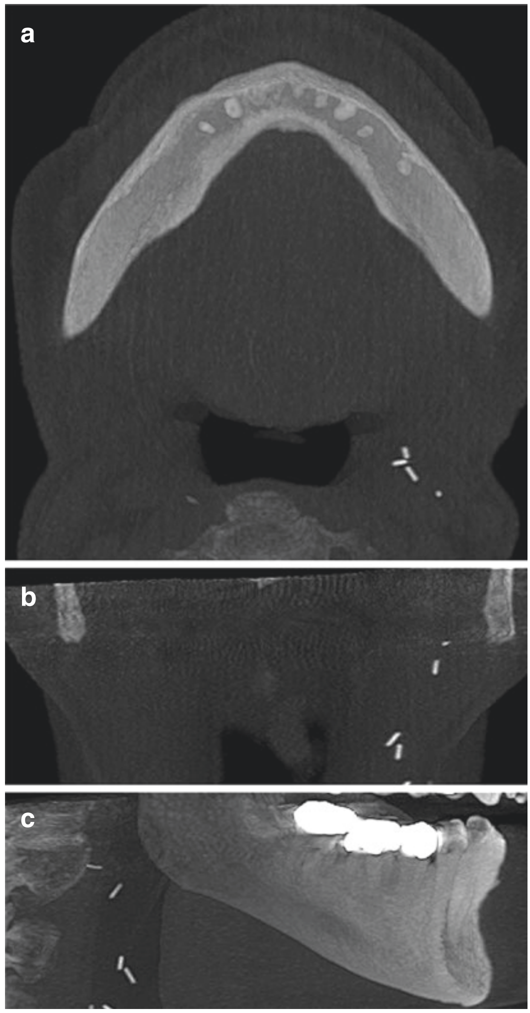

Fig. 17.73 20 mm thick MIP axial (**a**), coronal (**b**), and sagittal (**a**) orthogonal images showing multiple small cylindrical metallic foreign bodies in the region of the left carotid space. This is consistent with the carotid endarterectomy surgical clips and confirmed by the patient's history of this procedure on this side

and deep to the neck, imaging differentiation is most often based on appearance.

17.5.3 Foreign Bodies

The majority of foreign bodies identified in the neck are associated with prior surgical procedures, other medical or dental intervention and sometimes trauma. Despite their peculiar appearance, their recognition is not difficult in conjunction with a detailed patient history. Some examples of foreign bodies found in the neck include:

- Brachytherapy Seeds (Fig. 17.72)
- Endarterectomy Clips (Figs. 17.73 and 17.74)
- Surgical Stents (Fig. 17.75)
- Cotton rolls (Fig. 17.76)

Acknowledgments Figures 17.62, 17.63, 17.64, 17.65, 17.66, 17.67, 17.68, and 17.69 are reproduced from:

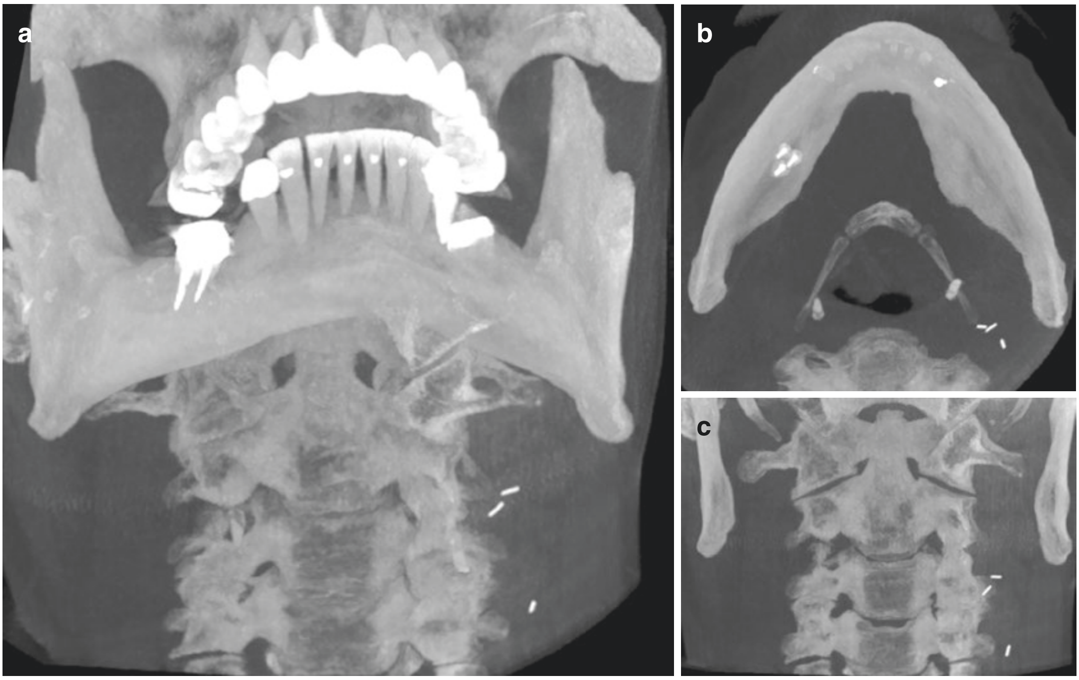

Fig. 17.74 Infero-oblique frontal full thickness (**a**), 20 mm thick axial (**b**) and coronal (**c**) MIP orthogonal images showing multiple small cylindrical metallic foreign bodies in the region of the left carotid space. This is consistent with the carotid endartectomy surgical clips and confirmed by the patient's history of this procedure

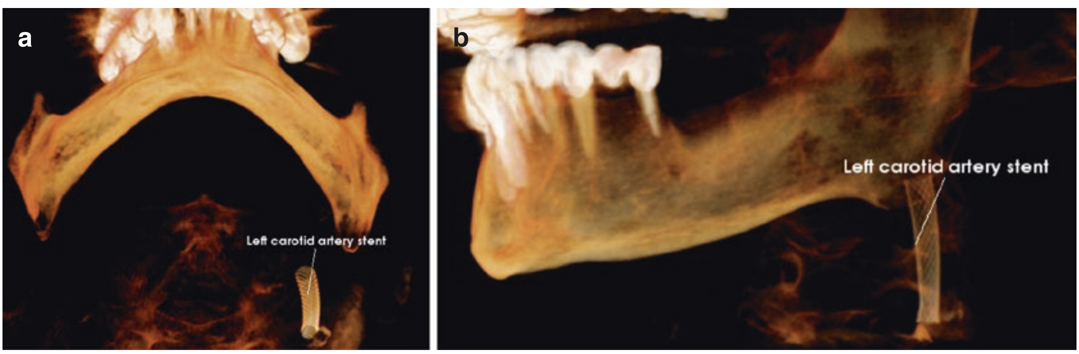

Fig. 17.75 Infero-oblique frontal (**a**) and left sagittal (**b**) volumetric images demonstrating a metallic mesh surgical stent in the left carotid space associated with previous endarterectomy

MacDonald D, Chan A, Harris A, Vertinsky T, Farman AG, Scarfe WC (2012) Diagnosis and management of calcified carotid artery atheroma: dental perspectives. Oral Surg Oral Med Oral Pathol Oral Radiol 114:533–47. With kind permission from Elsevier Inc., Atlanta, Georgia USA.

Sections of this chapter are reproduced from: Scarfe WC, Farman AG (2008) Soft tissue calcifications in the neck: Maxillofacial CBCT presentation and significance. Australasian Dental Practice 19:102-108. With kind permission from Main Street Publishing Pty Ltd., Cammeray, New South Wales, Australia.

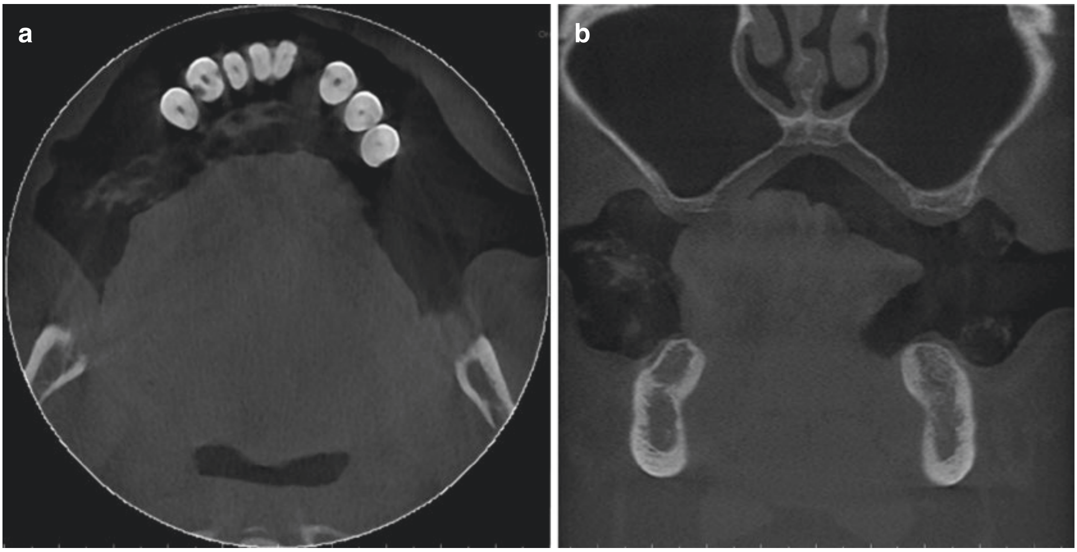

Fig. 17.76 Axial (**a**) and coronal (**b**) CBCT images with cotton rolls placed in the oral cavity in the buccal vestibules to retract the soft tissues away from the attached mucosa. The cotton rolls appear as heterogeneous swirls in the hypodense buccal spaces

References

Ahmad M, Madden R, Perez L (2005) Triticeous cartilage: prevalence on panoramic radiographs and diagnostic criteria. Oral Surg Oral Med Oral Pathol Oral Radiol Endod 99:225–230

Altuğ HA, Büyüksoy V, Okçu KM, Doğan N (2007) Hemangiomas of the head and neck with phleboliths: clinical features, diagnostic imaging, and treatment of 3 cases. Oral Surg Oral Med Oral Pathol Oral Radiol Endod 103:e60–e64

American Heart Association/American Stroke Association, Heart Disease and Stroke Statistics 2008 Update. Dallas, TX

Aspestrand F, Kolbenstvedt A (1987) Calcifications of the palatine tonsillary region: CT demonstration. Radiology 165:479–480

Bos D, van der Rijk MJ, Geeraedts TE, Hofman A, Krestin GP, Witteman JC, van der Lugt A, Ikram MA, Vernooij MW (2012) Intracranial carotid artery atherosclerosis: prevalence and risk factors in the general population. Stroke 43(7):1878–1884

Bouthillier A, van Loveren HR, Keller JT (1996) Segments of the internal carotid artery: a new classification. Neurosurgery 38(3):425–433

Carmada AJ, Deschamps C, Forest D (1989) Stylohyoid chain ossification: a discussion of etiology. Oral Surg Oral Med Oral Pathol 67:508–514

Carter LC (2000) Discrimination between calcified triticeous cartilage and calcified carotid atheroma on panoramic radiography. Oral Surg Oral Med Oral Pathol Oral Radiol Endod 90:108–110

Cederberg RA, Benson BW, Nunn M, English JD (2003) Calcification of the interclinoid and petroclinoid ligaments of sella turcica: a radiographic study of the prevalence. Orthod Craniofac Res 6(4):227–232

Chawalparit O, Chareewit S (2013) Ischemic cerebrovascular disease and calcified intracranial vertebrobasilar artery: a case-control study by using cranial CT. J Med Assoc Thail 96:346–350

Chen XY, Lam WW, Ng HK, Fan YH, Wong KS (2007) Intracranial artery calcification: a newly identified risk factor of ischemic stroke. J Neuroimaging 17:300–303

Daghighi MH, Rezaei V, Zarrintan S, Pourfathi H (2007) Intracranial physiological calcifications in adults on computed tomography in Tabriz, Iran. Folia Morphol (Warsz) 66:115–117

de Moura MD, Madureira DF, Noman-Ferreira LC, Abdo EN, de Aguiar EG, Freire AR (2007) Tonsillolith: a report of three clinical cases. Med Oral Pathol Oral Cir Bucal 12:E130–E133

de Weert TT, Cakir H, Rozie S, Cretier S, Meijering E, Dippel DW, van der Lugt A (2009) Intracranial internal carotid artery calcifications: association with vascular risk factors and ischemic cerebrovascular disease. AJNR Am J Neuroradiol 30:177–184

Deepak S, Jayakumar B (2005) Intracranial calcifications. J Assos Physicians India 53:948

Eagle WW (1962) The symptoms, diagnosis and treatment of the elongated styloid process. Am Surg 28:1–5

Eisenkraft BL, Som PM (1999) The spectrum of benign and malignant etiologies of cervical node calcification. AJR Am J Roentgenol 172:1433–1437

Erbay S, Han R, Baccei S, Krakov W, Zou KH, Bhadelia R, Polak J (2007) Intracranial carotid artery calcification on head CT and its association with ischemic changes on brain MRI in patients presenting with stroke-like symptoms: retrospective analysis. Neuroradiology 49:27–33. Epub 2006 Nov 7

Feldman VB (2003) Eagle's syndrome: a case of symptomatic calcification of the stylohyoid ligaments. J Can Chiropr Assoc 47:21–27

Ferrario VF, Sigurta D, Daddona A, Dalloca L, Miani A, Tafuro F et al (1990) Calcification of the stylohyoid ligament: incidence and morphoquantitave evaluations. Oral Surg Oral Med Oral Pathol 69:524–529

Friedlander AH, Cohen SN (2007) Panoramic radiographic atheromas portend adverse vascular events. Oral Surg Oral Med Oral Pathol Oral Radiol Endod 103:830–835

Friedlander AH, Lande A (1981) Panoramic radiographic identification of carotid arterial plaques. Oral Surg Oral Med Oral Pathol 52:102–104

Friedlander AH, Liebeskind DS, Tran HQ, Mallya SM (2014) What are the potential implications of identifying intracranial internal carotid artery atherosclerotic lesions on cone-beam computed tomography? A systematic review and illustrative case studies. J Oral Maxillofac Surg 72:2167–2177

Friedlander AH, August M (1998) The role of panoramic radiography in determining an increased risk of cervical atheromas in patients treated with therapeutic irradiation. Oral Surg Oral Med Oral Pathol Oral Radiol Endod 85:339–344

Ginat DT, Moonis G, Hayden BC, Singh AD (2012) Chapter 2. Imaging the postoperative orbit. In: Ginat DT, PLA W (eds) Atlas of postsurgical neuroradiology. Springer-Verlag, Berlin, pp 33–73

Ginat DT, Schatz CJ (2013) Imaging features of midface injectable fillers and associated complications. AJNR Am J Neuroradiol 34:1488–1495

Gorelick PB et al (1999) Prevention of a first stroke: a review of guidelines and a multidisciplinary consensus statement from the National Stroke Association. JAMA 281:1112–1120

Gossman JR Jr, Tarsitano JJ (1977) The styloid-stylohyoid syndrome. J Oral Surg 35:555–560

Hart BL, Spar JA, Orrison WW Jr (1992) Calcification of the trochlear apparatus of the orbit: CT appearance and association with diabetes and age. Am J Roentgenol 159:1291–1294

Hately W, Evison G, Samuel E (1965) The pattern of ossification in the laryngeal carti-lages: a radiological study. Brit J Radiol 38:585–591

Ilguy M, Ilguy D, Guler N, Bayirli G (2005) Incidence of the type and calcification patterns in patients with elongated styloid process. J Int Med Res 33:96–102

Katada K, Kanno T, Sano H, Shinomiya Y, Koga S (1983) Calcification of the vertebral artery. AJNR Am J Neuroradiol 4:450–453

Keur JJ, Campbell JP, McCarthy JF, Ralph WJ (1986) The clinical significance of the elongated styloid process. Oral Surg Oral Med Oral Pathol 61:399–404

Khan Z, Wells A, Scarfe W, Farman A (2008) Cone Beam CT isolation of calcifications in the maxillofacial and cervical soft tissues: a retrospective analysis. Int J Computer Assist Radiol Surg 3(Suppl 1):S221–S222

Kıroğlu Y, Callı C, Karabulut N, Oncel C (2010) Intracranial calcifications on CT. Diagn Interv Radiol 16:263–269

Kirsch T (2006) Determinants of pathological mineralization. Curr Opin Rheumatol 18:174–180

Koch B, Blackham A, Jones B (2007) Incidental internal carotid artery calcifications on temporal bone CT in children. Pediatr Radiol 37:141–144

Langlais RP, Miles DA, Van Dis ML (1986) Elongated and mineralized styholyoid ligament complex: a proposed classification and report of a case of Eagle's syndrome. Oral Surg Oral Med Oral Pathol 61:527–532

MacDonald D, Chan A, Harris A, Vertinsky T, Farman AG, Scarfe WC (2012) Diagnosis and management of calcified carotid artery atheroma: dental perspectives. Oral Surg Oral Med Oral Pathol Oral Radiol 114:533–547

Miller DB (1997) Eagle's syndrome and the trauma patient. Funct Ortho 2264:916–925

Monsour PA, Romaniuk K, Hutchings RD (1991) Soft tissue calcifications in the differential diagnosis of opacities superimposed over the mandible by dental panoramic radiography. Aust Dent J 36:94–101

Moseley I (2000) Spots before the eyes: a prevalence and clinicoradiological study of senile scleral plaques. Clin Radiol 55:198–206

Murry J (1995) Incidental asymptomatic orbital calcifications. J Neuro-Ophthalmol 15:203–208

Okabe S, Morimoto Y, Ansai T, Yamada K, Tanaka T, Awano S, Kito S, Takata Y, Takehara T, Ohba T (2006) Clinical significance and variation of the advanced calcified stylohyoid complex detected by panoramic radiographs among 80-year-old subjects. Dentomaxillofac Radiol 35:191–199

Pette GA, Norkin FJ, Ganeles J, Hardigan P, Lask E, Zfaz S, Parker W (2012) Incidental findings from a retrospective study of 318 cone beam computed tomography consultation reports. Int J Oral Maxillofac Implants 27:595–603

Pikija S, Magdič J, Hojs-Fabjan T (2013) calcifications of vertebrobasilar arteries on CT: detailed distribution and relation to risk factors in 245 ischemic stroke patients. Biomed Res Int 2013:918970

Prabhakaran S, Singh R, Zhou X, Ramas R, Sacco RL, Rundek T (2007) Presence of calcified carotid plaque predicts vascular events: the Northern Manhattan study. Atherosclerosis 195:e197–e201

Pruet CW, Duplan DA (1987) Tonsil concretions and tonsilloliths. Otolaryngol Clin North Am 20:305–9

Ricotta JJ, Aburahma A, Ascher E, Eskandari M, Faries P, Lal BK, Society for Vascular Surgery (2011) Updated Society for Vascular Surgery guidelines for management of extracranial carotid disease. J Vasc Surg 54:e1–31. Erratum in J Vasc Surg 2012; 55:894

Salman RA, Kinney LA (1990) Calcified thyroid cartilage. Oral Surg Oral Med Oral Pathol 70:806–807

Scarfe WC, Farman AG (2007) Voxel vision using maxillofacial CBCT: clinical applications of the maximum intensity projection. X-ray Lab and Imaging Currents. (AADRT Newsletter); Summer:1–25
Schatz CJ, Ginat DT (2013) Imaging of cosmetic facial implants and grafts. AJNR Am J Neuroradiol 34:1674–1681
Scheifele C, Lemke AJ, Reichart PA (2003) Hair artefacts in the head and neck region. Dentomaxillofac Radiol 32:255–257
Schulze R, Friedlander AH (2013) Cone beam CT incidental findings: intracranial carotid artery calcification—a cause for concern. Dentomaxillofac Radiol 42(10):20130347
Sedghizadeh PP, Nguyen M, Enciso R (2012) Intracranial physiological calcifications evaluated with cone beam CT. Dentomaxillofac Radiol 41:675–678
Shirkhoda A, Armin AR, Bis KG, Makris J, Irwin RB, Shetty AN (1995) MR imaging of myositis ossificans: variable patterns at different stages. J Magn Reson Imaging 5:287–292
Suzuki M, Ozaki Y, Komura S, Nakanishi A (2007) Intracranial carotid calcification on CT images as an indicator of atheromatous plaque: analysis of high-resolution CTA images using a 64-multidetector scanner. Radiat Med 25:378–385
Takahashi A, Sugawara C, Kudoh T, Uchida D, Tamatani T, Nagai H, Miyamoto Y (2014) Prevalence and imaging characteristics of palatine tonsilloliths detected by CT in 2,873 consecutive patients. Sci World J 2014:940960
Tegos TJ, Kalodiki E, Sabetai MM, Nicolaides AN (2001) The genesis of atherosclerosis and risk factors: a review. Angiology 52:89–98
Wang TD (2003) Multicenter evaluation of subcutaneous augmentation material implants. Arch Facial Plast Surg 5:153–154
Winkler S, Sammartino FJ, Monari JH (1981) Stylohyoid syndrome. Oral Surg Oral Med Oral Pathol 51:215–217
Woodcock RJ, Goldstein JH, Kallmes DF, Cloft HJ, Phillips CD (1999) Angiographic correlation of CT calcification in the carotid siphon. Am J Neuroradiol 20:495–499

Applications of CBCT in Orthodontics

18

William E. Harrell Jr, William C. Scarfe, Lucas Rodrigues Pinheiro, and Allan G. Farman

Contents

W.E. Harrell Jr, D.M.D. (✉)
Harrell Orthodontics, Alexander City, AL, USA
e-mail: drh@drharrell.com

W.C. Scarfe, B.D.S., F.R.A.C.D.S., M.S.
Division of Radiology and Imaging Science, Department of Surgical/Hospital Dentistry, University of Louisville School of Dentistry, Louisville, KY, USA
e-mail: William.Scarfe@louisville.edu

L.R. Pinheiro, D.D.S., Ph.D.
Oral and Maxillofacial Radiology, Faculdade de Odontologia (FO), Universidade de São Paulo (USP), São Paulo, Brazil
e-mail: lucasrpin@hotmail.com

A.G. Farman, B.D.S., Ph.D., E.dS., M.B.A., D.Sc.
Emeritus Professor, The University of Louisville School of Dentistry, Louisville, KY, USA

Independent Consultant in Maxillofacial Imaging Science, Chicago, IL, USA
e-mail: allanfarman@aol.com

W.C. Scarfe, C. Angelopoulos (eds.), *Maxillofacial Cone Beam Computed Tomography*,
https://doi.org/10.1007/978-3-319-62061-9_18

18.1 The Role of Imaging in Orthodontics

Radiographic imaging is an integral component of the overall assessment of the orthodontic patient. The purpose of imaging in orthodontics is to provide additional information supporting the clinical diagnosis of skeletal and dental conditions, soft tissues and their interrelationships.

Orthodontic diagnosis and development of treatment plans, the evaluation of growth and development, assessment of treatment progress and outcomes have traditionally been achieved from the integration of clinical data with findings obtained from two-dimensional (2D) extraoral radiography such as panoramic and lateral cephalometric images, associated analytical tracings along with 2D photographs. In addition to these static records, the only true documentation that has been used routinely for decades with three-dimensional (3D) information are plaster study models of the maxillary and mandibular dental arches. Now numerous digital reflective light-based technologies are emerging for recording and storing virtual 3D models of the dentition (e.g., indirect scanning of the plaster study model(s) or impressions or direct scanning of the teeth intraorally) used to create various orthodontic appliances to move teeth and 3D facial surface capture.

From an individual practitioner's perspective, each clinician must clearly be able to answer the question: "What are my goals for imaging?" While some structures are adequately represented by traditional 2D imaging, others may need to be represented with anatomic accuracy in three dimensions (e.g., maxillofacial skeleton, facial surface, airway, temporomandibular joints (TMJs)) or even temporally, in four dimensions (4D) over time. Selection of imaging modalities or combinations thereof must fulfill these imaging goals and at a reasonable financial and radiation dose cost based on clinical evaluation of the patient.

For an increasing number of orthodontic patients, an understanding of the complex anatomic relationships and surrounding structures of the maxillofacial skeleton is necessary for orthodontic planning and management so that the most appropriate therapy from the wider array of available treatment options is selected.

18.1.1 The Goals of Imaging in Orthodontics

The rationale for the use of imaging in orthodontics depends on the stage of therapy at which it is considered. There are three stages of orthodontic therapy:

- **Diagnostic Stage.** Initially, imaging is used as an adjunctive diagnostic modality to provide a pretreatment assessment of the orthodontic patient. Radiography can assist in determining the contribution of each of the osseous and dental elements to the malocclusion or craniofacial anomaly. Information may also be obtained about the relationship of the soft tissue envelope to the underlying hard tissue and determine the possible contribution of the soft tissue to the development or stability of the malocclusion. In addition to clinical data, radiographic images assist the clinician in the process of formulating a provisional diagnosis and a tentative treatment plan.
- **Treatment Stage.** Imaging may be performed during treatment to monitor the effects of therapy on the development of the jaws, position of the teeth including dental root angulation, and the influence of orthopedic and orthodontic therapies on facial profile. This is especially important prior to initiation of the surgical phase of orthognathic surgery.
- **Posttreatment Stage.** Imaging after therapy may be used to measure the immediate outcome of treatment and to monitor the stability of the dentition over time. Imaging may provide feedback to the clinician by comparing the posttreatment result to a pretreatment predicted outcome.

18.1.2 Clinically Based Imaging Selection

The use of radiography in orthodontics should never be routine in clinical practice, as it involves the use of ionizing radiation, a known carcinogen. For each patient, the potential benefits of the imaging series should be weighed against the known risks. The current known radiation risks of radiography and CBCT imaging in particular are described in Chap.

3. Determining the potential benefits of a radiographic technique for an orthodontic patient involves consideration of four sequential issues:

1. **Will the radiograph complement or supplement the clinical findings?** The initial decision to perform radiography is governed by the individual practitioner's need to support a clinical diagnosis or provide additional information to confirm or improve a clinical impression. Justifying every radiographic exposure is never a matter of routine and involves consideration of the individual patient's initial physical presentation as determined by a thorough clinical examination, their chief complaint, a comprehensive medical and dental history, an analysis of study models and identification of preliminary treatment goals based on a working diagnosis.
2. **What specific imaging modality or series of radiographic examinations will provide me with anatomically valid, clinically useful information?** Once the decision is made to image the patient to augment clinical findings, the next decision is to choose the radiographic procedure that provides the necessary information with the minimum patient radiographic exposure. This necessitates that the practitioner understands the advantages, indications for, and limitations of specific radiographic procedures.
3. **What are the best exposure settings for the chosen imaging procedure?** Once the most appropriate radiographic procedure is chosen, the next decision is practical and involves correct selection of exposure parameters to provide an image of optimal diagnostic quality. The appropriate choice of radiographic procedure and selection of optimal exposure factors for a specific technique to address a clinical problem is universal in all fields of radiology and is referred to as the "as low as reasonably achievable" (ALARA) principle.
4. **What does the image show?** Finally, a systematic interpretation of the radiographic series should be performed. This is especially critical in the case of volumes acquired from CBCT where specific images are generated, and, if necessary, a quantitative analysis performed. In the case of CBCT imaging, appropriate image formatting should be applied towards answering the specific clinical question that prompted the use of the radiographic procedure in the first place.

Patient selection criteria should always be applied for any radiographic imaging modality for every patient in orthodontics. Because of the ease with which CBCT scans can be performed and the attraction of finding some potentially important additional diagnostic information, some advocate that current conventional imaging modalities such as panoramic and lateral cephalometric radiography should be replaced by CBCT for standard orthodontic diagnosis and treatment (Hechler 2008; Mah et al. 2010; Larson 2012). This is based on illustrative, but anecdotal, case reports, without support of the current published evidence base nor does it adequately address the risks involved, particularly those associated with radiation exposure. While there is no doubt that CBCT provides greater clinician decision confidence in specific clinical orthodontic circumstances (Alqerban et al. 2014) and provides additional diagnostic information (see Specific Indications to follow), there is limited, albeit growing evidence that such information has a clinical impact such as to adjust treatment approach as compared to conventional imaging for specific clinical scenarios (Haney et al. 2010; Botticelli et al. 2011; Alqerban et al. 2013; Hodges et al. 2013; Alqerban et al. 2014).

18.2 The Advantages in CBCT Imaging in Orthodontics

CBCT imaging provides many unique features and advantages to orthodontic practice over conventional extraoral imaging, such as panoramic and lateral cephalometric radiography.

18.2.1 Clinical Imaging Efficiency

Full field of view (FOV) CBCT imaging provides volumetric data acquisition of the entire maxillofacial skeleton in a single radiographic procedure. This data can be easily reformatted to provide simulated images (e.g., lateral and posterior-anterior cephalometric, panoramic) currently used in orth-

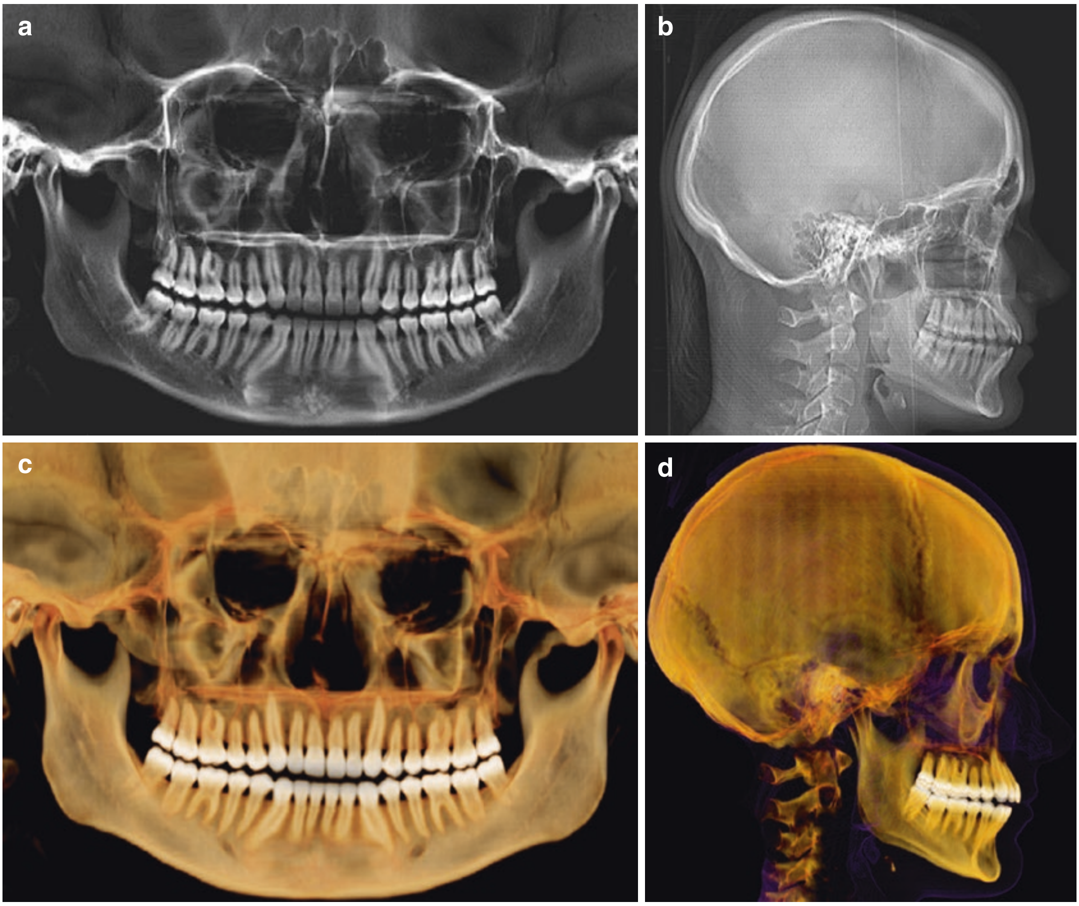

Fig. 18.1 Example of simulated projection panoramic (**a**) and lateral cephalometric (**b**) radiographic and comparable volumetric rendered panoramic (**c**) and lateral (**d**) images generated from CBCT data

odontic diagnosis, cephalometric analysis, and treatment planning (Fig. 18.1). This provides for greater clinical imaging efficacy. However, some suggest that this level of imaging may not be necessary, particularly in less complex situations (Silling et al. 1979; Atchison et al. 1991: Atchison et al. 1992; Bruks et al. 1999; Pae et al. 2001; Nijkamp et al. 2008; Devereux et al. 2011; Mah et al. 2011).

18.2.2 Volumetric Visualization

CBCT data can be reconstructed to provide unique, interrelational, undistorted orthogonal (i.e., axial, sagittal, and coronal) images previously unavailable in orthodontic practice (Fig. 18.2). Other imaging processing can also be performed such as maximum intensity projection (MIP) and surface or volumetric rendering that provides an interactive virtual model. Virtual maxillofacial models provide visualization and interrelationship of craniofacial structures including the maxillofacial skeleton and soft tissue boundaries such as the airway and facial outline.

18.2.3 Anatomic Accuracy

The advantage of CBCT is that volumetric renderings and reformatted images represent the radiographic “anatomic truth” of the morphology and inter-relatiobships of the teeth, the maxillofacial skeleton, and accompanying soft tissue (Harrell et al. 2002).

Volumetric rendering facilitates enhanced 3D visualization using motion parallax by rotation around any axis. Depth information can also be augmented by using stereoscopic binocular vision with the aid of stereoscopic eyewear and

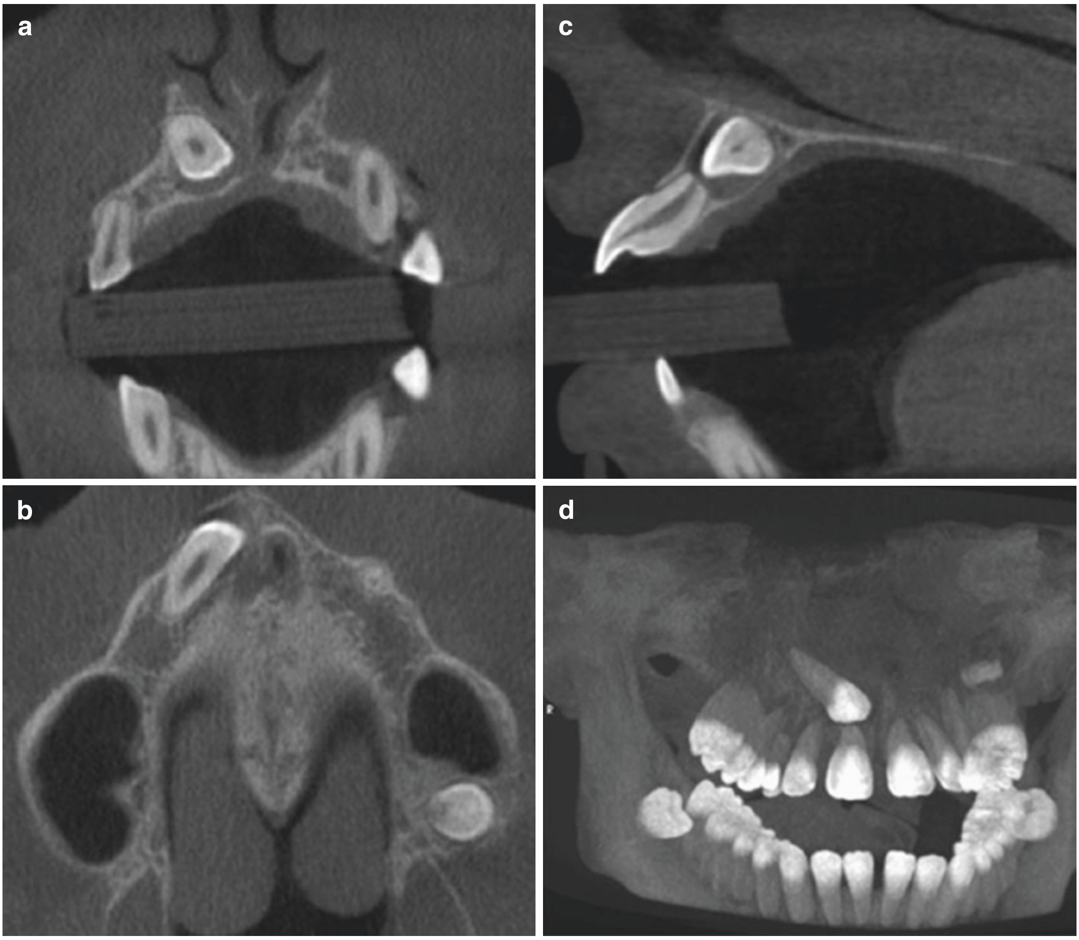

Fig. 18.2 Coronal (**a**), axial (**b**), and sagittal (**c**), interrelational, undistorted orthogonal images showing the orientation of an ectopically positioned, unerupted, and impacted right maxillary lateral canine and apical root resorption of the maxillary right central incisor. The reconstructed maximum intensity projection (MIP) (**d**) provides a translucent "glass-like" image clearly showing location of the canine, its ectopic position, and relationship to the erupted teeth in the dentition

even MicroSoft Hololens (Microsoft Corp., Redmond, Washington, USA) technology for a virtual reality (VR) experience.

The co-registration of an optical facial scan over the CBCT surface model gives an accurate skin surface to make improved diagnosis and treatment planning for early growth guidance and orthognathic surgery cases. Two-dimensional photographic warping techniques that stretch flat planar images comprising an area array of 2D pixels over the volumetric surface of the CBCT do not currently provide the necessary accuracy.

Unlike traditional extraoral and panoramic radiography, CBCT images are almost anatomically true (1:1 in size) representations, from which slices can be displayed at any angle for any part of the maxillofacial skeleton. Therefore, measurements can be obtained without the need for considerations of magnification or projection discrepancies. Linear and angular accuracy is approximately less than 5% for hard tissues and less than 10% for soft tissues and is dependent on scan resolution and intra- and interobserver error.

18.2.4 Data Integration

The concept of a holistic approach to three-dimensional diagnosis and treatment planning in orthodontics is not a revolution, merely an evolution facilitated by the recent rapid emergence and availability of technological developments, particularly

CBCT. In the early twentieth century, Case (1908) and Van Loon (1915a, b) integrated the use of plaster facial masks along with plaster dental study models for diagnosis and treatment planning. Van loon (1915b) stated:

> "…that for meaningful diagnosis and treatment planning, a three-dimensional system was required to determine the relation of the dentition to the face."

Orthodontics and orthopedics involves considerations of not only the maxillofacial skeleton but also the dentition and soft tissue integument—the facial mask. The concept of image integration relies on the notion of the development of a Patient Specific Anatomic Reconstruction (PSAR) (Lane and Harrell 2008; Schendel et al. 2011a, b). It is more than just a repository of 3D data from CBCT and other sources—moreover, it is a central database containing various inputs regarding the muscles, teeth, bone, and soft tissues, perhaps separately acquired but dynamically integrated that can be manipulated, moved, and changed individually, creating a true interactive, patient-specific simulation. The availability of dynamic PSARs would facilitate rapid and accurate diagnoses, determine treatment options, monitor changes over time, predict and display final treatment results, and more accurately measure treatment outcomes on the basis of a patient's actual morphogenic characteristics and an understanding of craniofacial growth and development. 3D models would also help the clinician to communicate with an interdisciplinary treatment team as well as with patients and their parents/guardians.

Currently CBCT data may be used as a platform onto which other inputs can be fused with acceptable clinical accuracy. These data sources include light-based surface data such as photographic facial images (Jayaratne et al. 2012) or high resolution 3D surface models of the dentition produced by direct scans intraorally or indirectly by scanning impressions or study models (Fig. 18.3). The integration of hard and soft

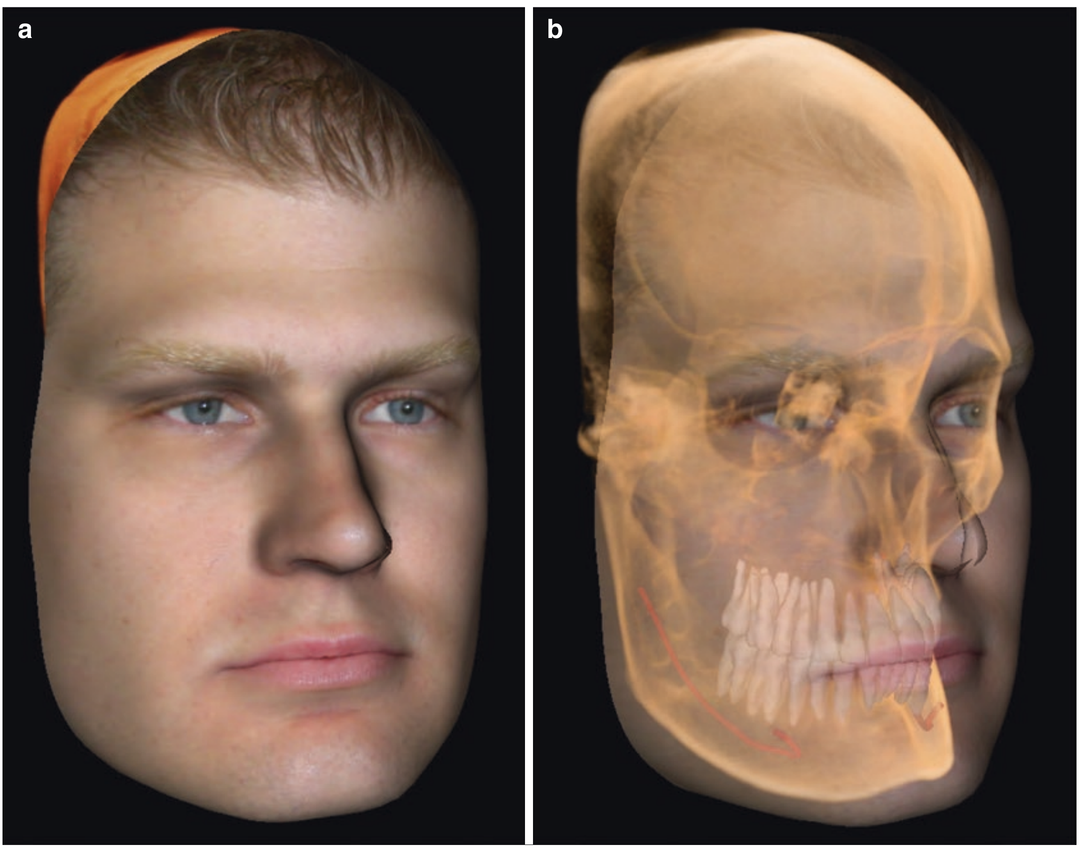

Fig. 18.3 Right lateral oblique profile rendered volumetric patient composite (**a**) from integration of surface photograph (**a**) and CBCT data (**b**) (Images courtesy, Anatomage)

tissues can provide a greater understanding of the interrelationship of the dentition and soft tissues to the underlying osseous frame and vice versa.

18.2.5 3D Cephalometry

18.2.5.1 Historical Perspectives

Further to the work of Pacini (1922), who introduced the concept of a fixed distance for head radiography, Broadbent (1931) in the United States and Horfrath (1931) in Germany simultaneously published techniques for cephalometric radiography. While slight variations are present between the two techniques, both used standardized projection geometry to produce perspective head radiographs in both the anterior (frontal) and lateral views at a known magnification. These images, in turn, facilitated the development of 2D radiographic cephalometry—the measurement of dimensions between various anatomic and reference landmarks, the construction of planes between these points and determination of angular variation between planes.

Two-dimensional (2D) cephalometry has been the standard radiographic documentation upon which numerous diagnostic analyses have been developed since the early 1950s. They include Downs (1952), Steiner (1960), Tweed (1954), Ricketts (1957, 1961), Jacobson (1975), McNamara (1984), and many others. The principles and details of these analyses have been summarized in numerous authoritative texts (Athanasiou 1995; Jacobson and Jacobson 2006). Additional multiplanar analyses with emphasis on the frontal analysis, such as Grummons and Kappeyne van de Coppello (1987), Ricketts and Grummons (2003) and Grummons and Ricketts (2004), were subsequently introduced to aid in the understanding of anatomy and asymmetry from the frontal (transverse) dimension.

Despite the myriad of analyses, the inherent limitations in the analysis of planar radiographic projections for maxillofacial assessment in orthodontics have been recognized for decades and have called into doubt the validity of assessments obtained from them (Adams et al. 2004; Sarver 1998; Johnston 1968; Baumrind et al. 1976; Moyers and Bookstein 1979; Johnston 2011). In particular, lateral cephalometric radiography, used as the principle imaging modality in cephalometry, while demonstrating a composite of anterior posterior and vertical relations, provides little information on unilateral or transverse aspects of malocclusions or craniofacial anomalies.

Cephalometric measurements are subject to errors due to magnification, disproportional distortion, projective superimposition of anatomical details, errors and artifacts due to X-ray projection and patient positioning, and cephalometric measurement errors due to inherent difficulties in landmark identification (Baumrind and Frantz 1971a; Baumrind and Frantz 1971b; Major et al. 1994; Athanasiou 1995; Largravere and Major 2005; Ludlow et al. 2009). Enlow predicted that the advent of computer-based 3D imaging, coupled with increased understanding of the biology of craniofacial development would *"…turn craniofacial diagnosis inside out*." (Enlow and Hans 1996; Enlow 2000). His vision that *"… an individual's own craniofacial growth and development… will be determined by a 3-dimensional evaluation based on that person's actual morphogenic characteristics, not simply developmentally irrelevant radiographic landmarks"* is now becoming a reality, assisted by CBCT imaging.

18.2.5.2 3D Cephalometric Software

To compensate for the drawbacks of 2D cephalometry, numerous techniques and related procedures were introduced in the 1970s and 1980s to improve landmark identification and analysis in three dimensions. These techniques include the Orientator (Broadbent et al. 1975), the coplanar stereometric system (Baumrind et al. 1983a, b), the multiplane cephalometric analysis (Grayson et al. 1983), the basilar multiplane cephalometric analysis (Grayson et al. 1985), and the biplanar cephalometric stereoradiography (Trocme et al. 1990). While these efforts have helped lay the foundation on which to build an anatomically accurate 3D analysis, they still lacked the integration of dimensional information from multiple planes.

Subsequent developments in CT and now the availability of CBCT have enabled the provision of multiple co-relational orthogonal images of the maxillofacial region in all three dimensions

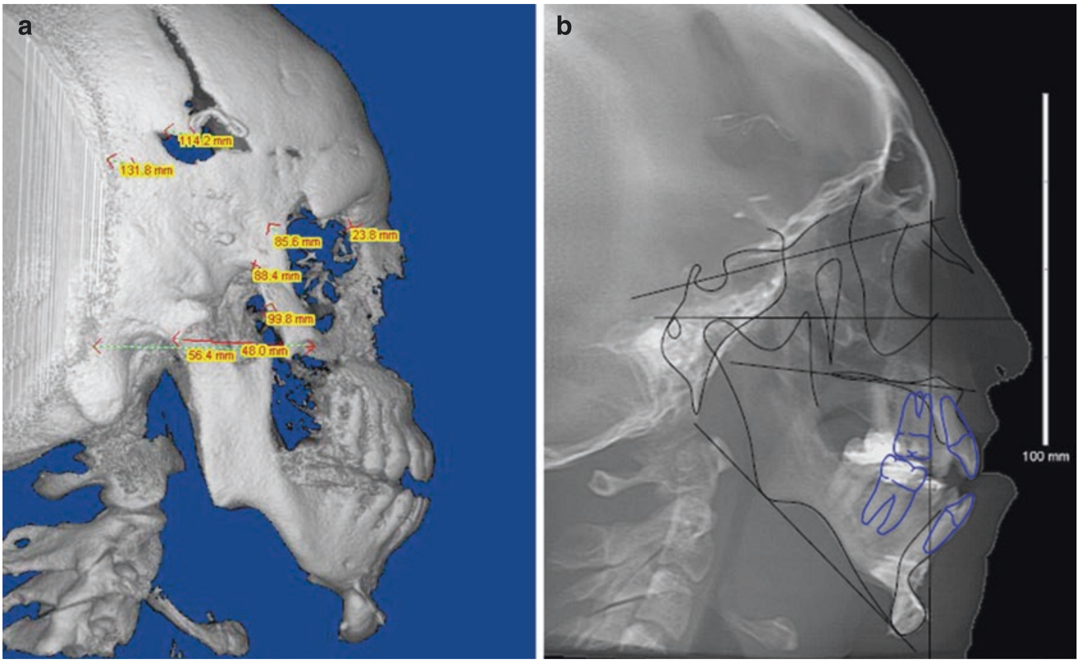

Fig. 18.4 Lateral volumetric shaded surface rendering (**a**) with 3D cephalometric measurements of patient with corrected craniofacial deformity and comparable lateral cephalometric image with tracing (**b**) both created from CBCT data

simultaneously. In addition, standardization and acceptance of a digital format for medical images, the DICOM (Digital Imaging and Communications in Medicine) file format, allows importation of CBCT data into third party software capable of visualization of the dataset and volumetric 3D cephalometric analysis (Fig. 18.4). Currently available software includes:

- 3dMD Vultus (3dMD, Atlanta, Georgia, USA)
- Dolphin 3D (Dolphin Imaging, Chatsworth, California, USA)
- InVivoDental (Anatomage, San Jose, California, USA)
- ACRO 3D software (Cliniques universitaires Saint-Luc- Université Catholique de Louvain)
- ViewBox4 (dHAL software, Kifissia, Greece)
- Beta NemoStudio software (Software Nemotec SL, Madrid, Spain)
- Maxilim (Medicim, Mechelen, Belgium)
- MIMICS 10.02 (Materialise, Belgium)
- CMF application software (CMFapp; M.E. Müller Institute for Surgical Technology and Biomechanics, University of Bern, Switzerland)

18.2.5.3 Accuracy and Precision of 3D Cephalometry

Numerous authors have confirmed the accuracy and precision of linear and angular measurements between anatomic landmarks using various 3D software programs for both CT (Hildebolt et al. 1990; Richtsmeier et al. 1995; Kragskov et al. 1997; Cavalcanti and Vannier 1998; Kim et al. 2002; Cavalcanti et al. 2004) and CBCT (Frongia et al. 2012; Schlicher et al. 2012). Results from these and other investigators (Lou et al. 2007) indicate:

- Landmarks are more difficult to locate on 2D slices than rendered volumes alone (Richtsmeier et al. 1995; Kragskov et al. 1997; Cavalcanti and Vannier 1998).
- Each landmark exhibits a characteristic pattern of error that contributes to measurement inaccuracy, and with repeated practice of landmark identifications, the error can be reduced to within 0.5 mm for 2D CT (Lou et al. 2007; Delamare et al. 2010).
- The most reliable bony landmarks are those in the midline and on surfaces (e.g., A Point, B Point, Anterior nasal spine, Pogonion, Gnathion,

Menton, maxillary and mandibular incisal edge), those associated with sutures (e.g., frontozygomatic sutures), and as those on the surface of the cranium (e.g., Nasion, Basion, Sella and Porion).

- The most unreliable landmarks are bilateral and either associated with surface curves (e.g., Gonion, Orbitale, and Superior oblique), the TMJ (e.g., Condylion) or thin bone (e.g., posterior nasal spine) (Zamora et al. 2012).
- The accuracy and reliability of a quantitative 3D cephalometric analysis will depend on the choice of landmarks. However, 3D landmark identification using CBCT can offer consistent and reproducible data if a protocol for operator training and calibration is followed (de Oliveira et al. 2009; Delamare et al. 2010).
- Linear percentage accuracy is approximately 1% to 2% for hard tissues and 2% for soft tissues and is less than 1mm to 2 mm from actual measurements whereas angular measurement accuracy ranges from −3.2° to −1.18° (Ward and Jamison 1991; Cavalcanti et al. 2004; Matteson et al. 1989; Hildebolt et al. 1990; Cavalcanti et al. 1999; Cavalcanti and Vannier 1998; Nawaratne et al. 1997; Xia et al. 2000; de Oliveira et al. 2009; Oz et al. 2011; Tulunoglu et al. 2011).
- Intra-observer measurement error, in general, is higher than 1mm to 2 mm.
- The degree of measurement accuracy is dependent on CT type (multidetector, CBCT) as well as data acquisition parameters (e.g., slice thickness and interval of the reconstruction for MDCT; acquisition and display voxel resolution for CBCT) (Richtsmeier et al. 1995; Cavalcanti and Vannier 1998; Cavalcanti et al. 2002; Kim et al. 2002). Low dose protocols involving the reduction of mA, kVp, and basis images (for CBCT) do not appear to reduce landmark identification accuracy (Olszewski et al. 2008).
- The greatest accuracy and reliability of 3D landmark identification is provided by use of a combination of 3D virtual rendering and

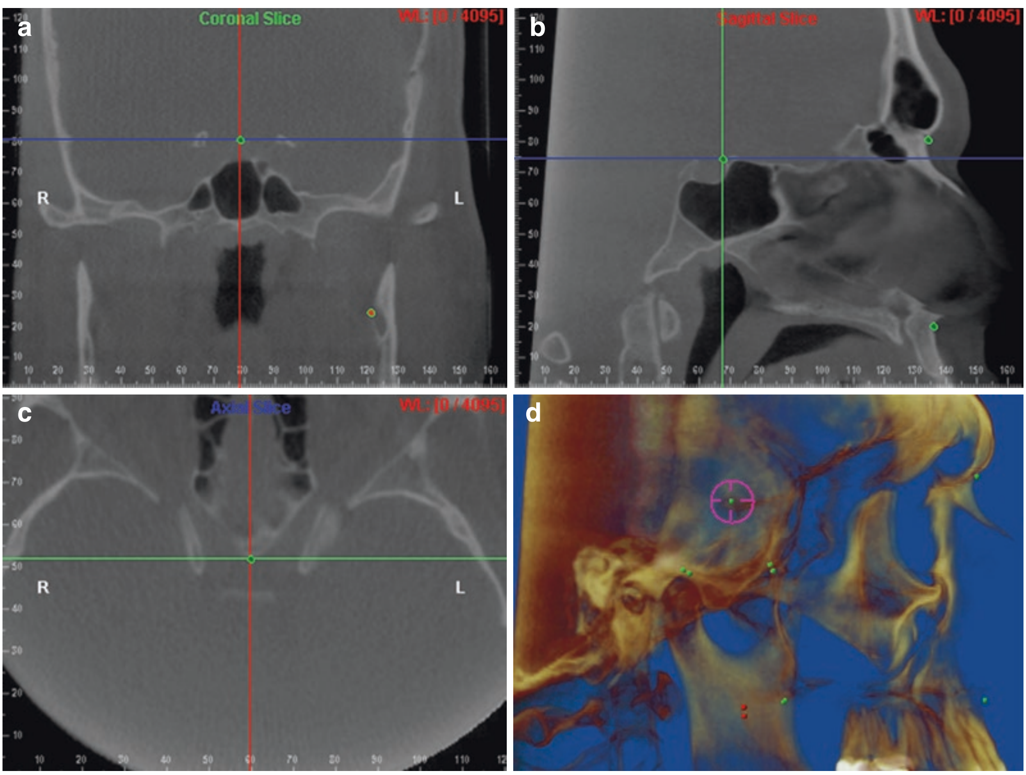

Fig. 18.5 Example of identification of 3D cranial base landmark (TS) in three dimensions using combination of coronal (**a**) sagittal (**b**), axial (**c**) orthogonal slices and virtual rendering (**d**) in three planes of space. (*TS* tuberculum sellae point located on the midsagittal plane at the most posterior superior point of the clinoid process)

cross-sectional slices in the 3 planes of space (de Oliveira et al. 2009) (Fig. 18.5).
- The interobserver error and accuracy of measurements from CBCT-generated and simulated lateral cephalograms is the same as for conventional projection cephalograms except for dimensions that are oblique to the midsagittal plane (e.g., Gonion-Menton, Condylion-Gnathion).
- The accuracy and interobserver accuracy of many measurements from CBCT-generated and simulated frontal cephalograms is significantly different and may be important in the assessment of patients with craniofacial deformities involving asymmetries such as cleft lip and palate.

18.2.5.4 Types of 3D Cephalometric Analyses

Several 3D cephalometric analyses have been proposed for maxillofacial skeletal measurements, each comprising a subset of anatomic landmarks (Table 18.1) and reference planes.

Techniques in the *Diagnostic Stage* are directed towards identifying and quantifying deviations from values obtained from a representative “normal” comparative group. Techniques in the *Posttreatment Stage* are used to compare results with the representative “normal” comparative group as well as to compare with the analysis of the individual patient pretreatment (see Chap. 20 for technical details).

Three (3) general methods are possible for volumetric cephalometric analysis depending on the stage of treatment at which it is to be used:

- **Dimensional Analysis.** A dimensional analysis compares linear or angular measurements of different craniofacial structures to a line or a reference plane. It can be used at diagnostic and posttreatment stages.
- **Topographical Analysis.** A topological analysis compares the proportions of various craniofacial structures. It can be used at diagnostic and posttreatment stages.
- **Volumetric Superimposition.** Superimposition of rendered volumetric images (Cevidanes et al. 2010, 2011a, b), particularly between pre- and post-orthognathic surgery, can provide both a visual demonstration of changes and a quantitative analysis (see Chap. 20).

Summary of 3D Analyses

Pittayapat et al. (2014) provide an excellent systematic review of the literature providing summarizing the details of published CT/CBCT cephalometric analyses.

Cavalcanti et al. (1999) reformatted spiral CT data in 3D on a workstation and measured 20 linear distances between 17 conventional craniofacial anthropometric landmarks described by Farkas (1981) and originally used by Hildebolt et al. (1990). Kusnoto et al. expanded this 3D approach to include 22 linear and 10 angular measurements based on similar landmarks (1999).

Treil et al. (1999) developed a 3D cephalometric orthodontic analysis on 2D CT slices based on eight cranial landmarks related to the trigeminal neuromatrical axis of facial growth (heads of the mallei, supraorbital, suborbital, and submental points) and has subsequently refined the analysis to include a dentoalveolar component (Faure et al. 2002). Their analysis involves the geometrical construction of a maxillofacial frame, as well as computation of angles, distances, areas, volumes, center of gravity, and axes of inertia.

Hayashi (2003) proposed a 3D analysis based on CT data to quantify the relationship between the cranial base and the maxillofacial morphology in an effort to overcome the shortcomings of the 2D-based parameters (e.g., SNA, SNB, ANB, and Angle’s classification). The basis of the analysis is that the anterior cranial base is chiefly determined by Sella (S) whereas the posterior cranial base is determined largely by length and inclination of the posterior cranial base, which is related to Basion (Ba) and the position of the glenoid fossa. Computations are based on orientation with respect to three planes: The X-axis, a line parallel to the FH plane passing point S; the Y-axis, a line perpendicular to the X-axis passing point S; and the Z-axis, a line perpendicular to the X- and Y-axes passing point S. The position of eight landmarks structures in the midsagittal plane (S, N, SE, Ba, A point, ANS, PNS, and B point), and the glenoid fossa in both the sagittal and coronal planes relative to a perpendicular

Table 18.1 Definitions of specific 3D cephalometric landmarks

Landmark (Abbreviation)	Definition
Alare (al)	Maximum width of nasal opening
Alveolare/subspinale (A point)	Most posterior point on curve between ANS and prosthion (Pr)
Antegonion (Ag)	Deepest point of antegonial notch of mandible
Anterior nasal spine (ANS)	Most anterior point of nasal floor
Anterior ramus point (R)	Deepest point at anterior border of ramus
Atlas (at)	Most anterior border of atlas arch in 3D
B point (supramentale)	Most posterior point of bony curvature of mandible below infradentale and above Pog
Basion (Ba)	Anterior midpoint of foramen magnum
Bregma (Br)	Junction of the sagittal and coronal sutures
Buccale (Bc)	Point on external surface of each zygomatic arch where arch turns medially and directly starts on backward sweep
Canine eminence (CE)	Point on the surface of the maxilla corresponding to the canine root apex
Condylion lateralis (Cd_{lat})	Most lateral point of condyle head
Condylion medius (Cd_{med})	Most medial point of condyle head
Condylion posterioris (co/CP/Cd_{pos}	Most upper and posterior aspect of condyle
Condylion superius (Cd_{sup})	Most superior aspect of condyle
Crista Galli (cg)	Most superior point of crista galli of ethmoid bone
Dacyron (D)	Point at which the frontal, maxillary, and lacrimal bones meet
Endomolare (Enm)	Medial point of the alveolar ridge at the second molar
Foramen rotundum (Fr_{rt}, Fr_{lt})	Lower wall of foramen rotundum; proximal to pterygopalatine fossa (bilateral)
Frontomaxillar (Fm_{rt}, Fm_{lt}, Fm_{mid})	Junction of frontomaxillary sutures at mid distance between anterior and posterior tops of maxillary process (left and right with additional point being midpoint between bilateral Fm)
Glabella (G)	Most anterior point of the skull in sagittal plane
Glenoid fossa (Gf)	Most superior point of the glenoid fossa (bilateral)
Gnathion (Gn)	Lowest anterior inferior point on the mandible on the anterior symphysis in the midline
Gonion inferius (Go_{inf})	Most inferior point of gonion area
Gonion lateralis (Goi_{lat})	Most lateral point of gonion area
Gonion posterius (Go_{post})	Most posterior point of gonion area
Gonion1 (Go1)	Most posterior point of posterior border of ramus
Gonion2 (Go2)	Midpoint of posterior border of mandibular angle/point of intersection between right ramal plane and right mandibular plane
gonion3 (Go3)	Most inferior point of posterior border of ramus
Infradentale (I)	Tip of the mandibular alveolar bone between the central incisors
Mandibular body curve (MBC)	Most convex point on the curvature, midway between the inner and outer borders of the mandibular body
Maxillare (mx)	Zygomaticoalveolar crest, points show maximum concavity on contour of maxilla around molars and lower contour of maxillozygomatic process
Maxillary tuberosity (max. T)	The most inferior and lateral point on the maxillary tuberosity
Mentale (Mn)	Most anterior point on the mental foramen
Menton (me)	Most inferior point on the mandibular symphysis in the midline
Mrt, Mlt, Mmid	Junction of maxillary, nasal, and frontal sutures (left and right with additional point being midpoint between bilateral M)
Nasion (Na/N)	Most posterior point on curvature between frontal bone and nasal bone in midsagittal plane/medial point between the nasofrontal suture and the nasal origin in midsagittal plane

(continued)

Table 18.1 (continued)

Landmark (Abbreviation)	Definition
Nasoesphinale (ns)	Highest point on nasal spine
Nasopalatine foramen (Np_{rt}, Np_{lt}, Np_{mid})	Anterior wall of nasopalatine foramen, at the level of nasal floor (left and right with additional point being midpoint between bilateral Np)
Odontoid (od)	Posterosuperior border of odontoid process
Opisthion (op)	Most posterior point on posterior margin of foramen magnum in the midsagittal
Opisthocranion (op)	Most posterior part of skull in midsagittal plane
Optic (Optrt, Optlt)	Anterior and lower wall of optic foramen (bilateral)
Or (orbitale)	Lowest point on infraorbital margin of each orbit
Orbital rim (OR)	Most lateral extent of the orbital rim (bilateral)
PNS (posterior nasal spine)	Most posterior and middle point on contour of bony palate
Pogonion (Pog)	Most anterior midpoint of symphysis of mandible
Porion, anatomical (Po)	Highest midpoint on roof of external auditory meatus
Posterior clinoid process (Pcp_{rt}, Pcp_{lt}, Pcp_{mid})	Lateral, anterior and superior top of posterior clinoid process
Prechiasmatic groove (P)	Vertical and transverse midpoint of prechiasmatic groove
Prosthion (Pr)	Point of maxillary alveolar process between left and right maxillary incisors
Pterygoid inferior (Pti_{rt}, Pti_{lt}, Pti_{mid})	Junction of palatine bone and pterygoid process of sphenoid bone (left and right with additional point being midpoint between bilateral Pti)
Sella (S)	Middle of sella turcica in the midsagittal plane
Sigmoid notch (sig)	Deepest point on the sigmoid notch
Sphenooccipital synchondrosis (SOS)	Middle of the sphenooccipital synchondrosis on the caudal side of the sphenooccipital junction
Staphylion (S)	Point where a line tangent to the two curves at the posterior of the palate cross
Supraorbitale (SOr_{rt}, SOr_{lt})	Internal wall of foramen supraorbitale on the roof of the orbit (bilateral)
Upper /lower incisor apex ($U1_{Apx}$/ $L1_{Apx}$)	The root apex of the central incisors (bilateral)
Upper/lower first molar (U6, L6)	Upper or lower first molars (bilateral)
Zygion point (ZP/Zy)	Most lateral point where zygomatic arch is widest
Zygomatic point (Z)	The point on orbital rim showing the frontozygomatic suture
Zygomaticotemporal (Zyg)	Point of junction between the zygomatic bone and the suture of the temporal bone (bilateral)
Zygomaxillary (Zm/ZMX)	Lowest point on the suture between the zygomatic and maxillary bones/ central point of right zygomatic suture

Lat lateral, *inf* inferior, *post* posterior, *Rt* right, *lt* left, *mid* midpoint, *Apx* apex

plane intersections formed the basis for the analysis.

Harun et al. (2005) proposed a method of 3D landmark identification and measurement in which coordinates were located, created, and stored as templates of 3D CAD files for subsequent analysis. They measured 25 measurements involving 20 landmarks in the coronal, axial, and sagittal planes, within each of four structures including the mandible, orbits, zygoma, and maxilla in order to develop a craniofacial database and found no measurement differences between 3D renderings and actual measurements to be greater than 2 mm.

Bettega et al. (2000) and Olszewski et al. (2003, 2006, 2007) adapted the Delaire's 2D cephalometric analysis (Delaire et al. 1981) and developed a 3D CT cephalometric topological analysis, ACRO 3D. While the Delaire analysis is based on 19 cranial reference landmarks and 12 reference lines, ACRO 3D compared the proportions of different craniofacial structures of a subject and tried to provide a facial and mandibular topology. It incorporates three cranial planes (C1 to C3) and nine craniofacial planes (F1 to F8). Olszewski et al. (2007) reported absolute differences between measured and reference values to range from 0.75 to 0.991 mm and a greater reproducibility than the 3D–Swennen analysis (2010).

Park et al. (2006) proposed a 3D analysis comprising 19 measurements examining the zygoma, maxilla, mandible, and facial convexity and provided a 3D chart on which to record measurements. They constructed eight (8) reference planes from which to measure angular and linear deviations: (1) a horizontal reference plane parallel to the FH plane, which was constructed on both sides of Po and left of Or, passing through Na, (2) a midsagittal plane perpendicular to the horizontal plane passing through Na and P, (3) a coronal plane at right angles to the horizontal and midsagittal plane passing through Na, (4) a maxillary plane was made by the right and left Mx and ANS, (5) a mid-maxillary plane perpendicular to the maxillary plane passing through ANS and PNS, (6) a mandibular plane constructed by Me and both sides of Go2, (7) a mid-mandibular plane perpendicular to the mandibular plane passing through Me and the midpoint of right and left Go2(Go2M), and (8) a ramal plane on both sides of the ramus formed by R, Go1, and CP. They commented that some limitations occur with a 3D technique in that there are relatively large errors in the vertical position (z-coordinate) of coordinates compared with the anteroposterior (y-coordinate) and transverse (x-coordinate). They provided normative values for Korean males and females (Park et al. 2006).

Lagravère and Major (2005) proposed a reference landmark for use in three-dimensional cephalometric analyses with 3-dimensional volumetric images from CBCT datasets. They introduced the point ELSA—located equidistant between both foramen spinosum as the reference landmark ($x = 0$, $y = 0$, $z = 0$ coordinates) from which linear and angular measurements were made. They found that the foramina spinosum had a low identification error in both the vertical and horizontal planes. They chose this landmark because these foramina appear as small circles when viewed axially and it is easy to locate by using the condyle and the glenoid fossa as guides. Subsequently (Lagravère and Major 2005; Lagravère et al. 2010), they defined a 3D anatomical reference coordinate system based on the left and right auditory external meatus (AEM) and the dorsum foramen magnum (DFM). They defined an axial-horizontal plane (x-y plane) by using both left and right AEM points and ELSA whereas a sagittal-vertical plane (z plane) was determined perpendicular to the x-y plane and passing through points ELSA and DFM. Furthermore, they reported that landmarks forming the standardized reference system all presented with excellent intrareliability in all axes however serial registration of CBCT datasets using these four cranial base landmarks produces unacceptable uncertainty in coordinate system alignment (Lagravère et al. 2010).

Swennen et al. (2005, 2006) described a dimensional analysis using a specific software that combines a 3D CT surface model of a skull with two orthogonal 2D X-ray cephalograms. Reference landmarks were similarly identified and measurements were performed on lateral and frontal cephalograms as well as on 3D CT surface rendering of the skull. They validated their system by comparing individual measurements to the classical cephalometric lateralis and frontalis norms.

Chan et al. (2007) reported on the accuracy of eight measurements ((sagittal (Sella-Nasion, ANS-PNS), transverse (biorbital, bicoronoidal, and palatal width) and vertical (upper, lower, and posterior facial height)) between 12 commonly used craniometric landmarks using CBCT. Using 6-in, 9-in, and 12-in FOV images, they found differences of 0.53 ± 0.46 mm, 0.48 ± 0.44 mm, and 0.46 ± 0.45 mm, respectively, as compared to 3.34 ± 4.55 mm for 2D cephalometry. They concluded that linear measurement accuracy improved as voxel size decreased.

Kamiishi et al. (2007) proposed a 3D analysis using two types of surface renderings: 3D-cephalogram I comprised a lateral view with the right half of the skull removed to allow identification of conventional anatomic landmarks whereas 3D-cephalogram II comprised an entire lateral surface rendering except for removal of the right lateral temporal area to allow visualization of sella turcica.

Farronato et al. (2010) proposed a 10-point 3D analysis of CBCT images directly digitized on the rendered view of the volume and centroid of the maxilla and mandible. They evaluated the reliability and reproducibility of their method and compared their results to 2D data. They did not report norms of the variables in their study, most likely as their sample was small and had a wide range in age.

Cheung et al. (2011) proposed a 3D cephalometric analysis scheme for orthognathic surgery based on the Cartesian 3D Cephalometric Reference System according to Swennen et al. (2006). In addition, they combined hard tissue and soft tissue stereophotography, introducing a new reference plane (supraorbital margin plane or 3D Frankfurt Horizontal) for midfacial assessment. In addition, they provided normative values for a Chinese population.

Bayome et al. (2013) proposed a 3D analysis performed on the reorientation of the head according to a coordinate system with Nasion was selected as the origin of the X, Y, and Z coordinates. They defined the horizontal plane as passing through N and parallel to the plane defined through the right and left orbitales (Or) and the left porion (Po); the midsagittal plane (Y) was defined as the perpendicular plane passing through the origin N and anterior nasal spines (ANS); and the vertical plane (Z) was defined as a perpendicular to both X and Y passing through N. They divided landmarks into maxillary, ramal and condylar, mandibular body and calculated linear and angular dimensions. They also defined a mandibular and maxillary body curve (MBC) length and provided normative values based on 38 young adults with Class I skeletal occlusion.

3D Analysis of Facial Asymmetry

Most individuals have some degree of facial asymmetry, especially those with Class II skeletal malocclusions. However facial asymmetry caused by facial skeletal imbalances can be camouflaged by dental or soft tissue compensation or change of head posture. A variety of 3D CT analyses have been proposed to assess and quantify facial asymmetry.

Table 18.2 3D CT-based classification of facial asymmetry using asymmetry indices (after Maeda et al. (2006))

Group		Region		
Main	Subgroup	Maxilla	Mandibular body	Mandibular ramus
I		–	–	–
II	A	–	+	–
	B	–	+	+
III	A	+	–	–
	B	+	+	+

– hypoplasia, + hyperplasia

Katsumata et al. (2005) and Maeda et al. (2006) (Table 18.2) defined a number of anatomical landmarks on axial images modified from orthodontic craniometric (cephalometric) points. They defined 3 orthogonal places, to provide a 3D reference: The midsagittal (x) reference plane was formed by joining points S, N, and Dent (the tip of the odontoid process); the coronal (y) plane, perpendicular to the midsagittal plane passed through Dent, whereas the axial reference plane included points S and N. They measured the distances between each anatomical point each plane in millimeters and defined them as dx, dy, and dz. The *asymmetry index* of each bilateral point, the length of 3D vector, was calculated formulaically. Both investigators developed a diagrammatic chart with a baseline quantifying three levels of asymmetry (Fig. 18.6).

Hwang et al. (2006) used three reference planes in their 3D asymmetry analysis: (1) the midsagittal reference plane connecting three midsagittal landmarks (opisthion (Op), crista galli (Cg), and anterior nasal spine (ANS)), (2) the Frankfort horizontal (FH) plane connecting right and left porion and orbitale of 1 side, and (3) the mandibular plane connecting right and left antegonion and menton. They also provided a suggested 3D projection protocol to demonstrate asymmetry. Their analysis is based on the assertion that the causes of chin deviation are right and left differences in (1) maxillary height, (2) ramus length, (3) ramal inclination from a frontal view, (4) ramal inclination from a lateral view, (5) mandibular body length, and (6) mandibular body height (Fig. 18.7).

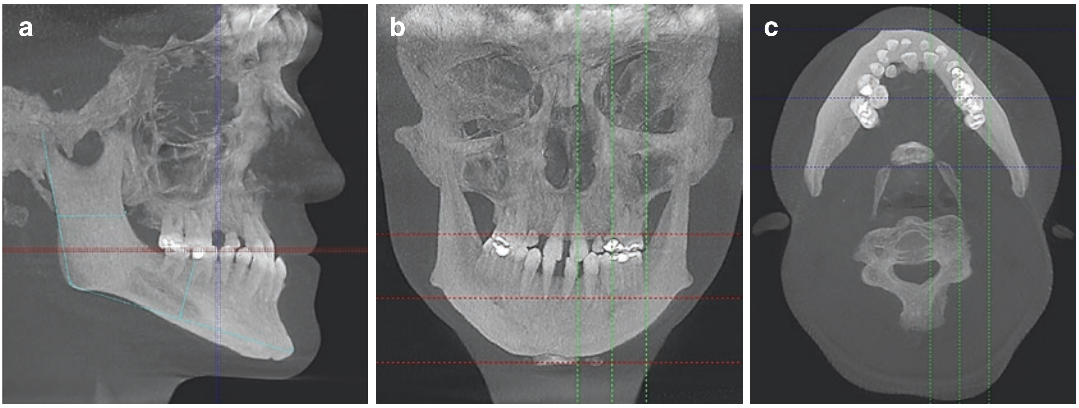

Fig. 18.6 Right lateral (**a**), anteroposterior (**b**), and submentovertex (**c**) maximum intensity projections showing an adult with a Class III skeletal facial pattern with mandibular prognathism (hyperplasia), maxillary deficiency (hypoplasia) resulting in a posterior crossbite and reverse overbite and overjet. In the PA dimension, there is mandibular asymmetry associated with left maxillary and mandibular body relative hyperplasia. According to Maeda et al. (2006), this facial asymmetry would be classified as II A

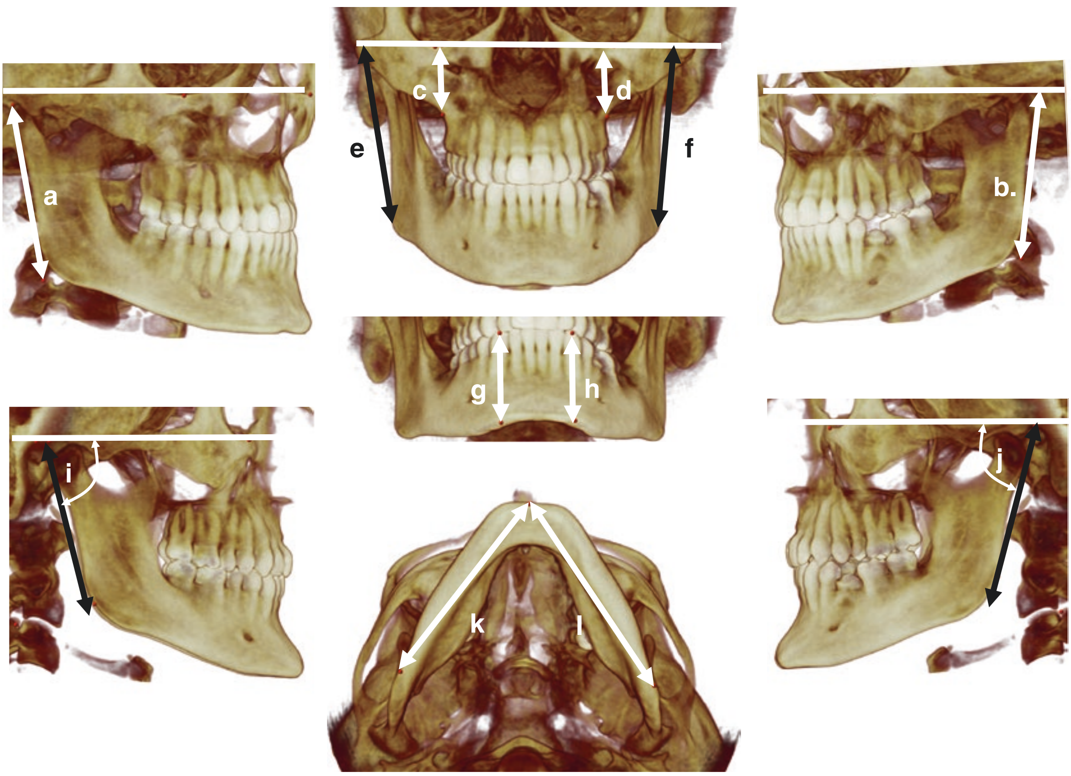

Fig. 18.7 Visual display of 3D volumetric renderings of 3D asymmetry analysis (after Hwang et al. 2006) demonstrating the contributing factors to chin deviation: Right (**a**) and left (**b**) ramus length, right (**c**) and left (**d**) maxillary height, right (**e**) and left (**f**) frontal ramal inclination, right (**g**) and left (**h**) mandibular body height, right (**i**) and left (**j**) lateral ramal inclination, and right (**k**) and left (**l**) mandibular body length. The solid horizontal line represents the 3D Frankfurt Horizontal

Kwon et al. (2006) provided another method for the assessment of facial asymmetry using 3D volumetric reconstructions including soft tissue landmarks. Their technique is based on asymmetry indices developed from deviations of maxillary (ANS, U1I, Or, Po, and U1M,), mandibular body (L1I, Me, and L1M), and mandibular ramus region (Co, CoP, and Go) landmarks from three orthogonal reference planes. The midsagittal (X-) reference plane was defined as the plane containing the points S, N, and Dent, the axial (Z-) plane was defined as the plane perpendicular to the X-plane and included the points S and N, and the coronal (Y-) plane was defined as the plane perpendicular to the X- and Z-planes that included the S point. In addition, by comparing their 3D-derived metrics to normal subjects, they were able to provide a classification of asymmetry.

Based on the premise that the mandible appears to be the dominant factor in facial asymmetry, You et al. (2010) analyzed the contribution of ten skeletal units grouped according to alveolar process, coronoid process, angular process, body, condylar process, and chin to mandibular asymmetry. They found significantly shorter condylar and body unit lengths and coronoid unit length on the non-deviated side than on the deviated side with no differences in chin unit length and suggested that both condylar and body units contribute to mandibular asymmetry, with the condylar influence being the most prominent.

Kim et al. (2011a, b, 2013) investigated the differences in the assessment of facial asymmetry as determined by jaw deviation between using facial MSP (defined as the sagittal plane which crossed crista galli (CG) and also vertically bisected a line formed by the frontozygomatic suture on both sides) and cranial MSP (defined as the sagittal plane crossing CG, the midpoint between foramina ovale bilaterally and the midpoint between foramina spinosum). For Class III subjects, they found that facial asymmetry was significantly inconsistent depending on the reference determination of midsagittal plane. Damstra et al. (2012) reported that clinically significant difference exists between 3D cephalometric midsagittal planes and the true plane of symmetry determined by the visible facial features were clinically relevant.

Using maxillary (upper midline deviation, maxilla canting, and arch form discrepancy) and mandibular (menton deviation, gonion to midsagittal plane, ramus height, and frontal ramus inclination) asymmetry indices on CBCT surface renderings, Baek et al. (2012) introduced an asymmetry categorization based on cluster analysis of patients (Table 18.3).

Because of the time necessary to perform the analysis, the high cost of software, the lack of an acceptable standardized analytical methodology, and limited evidence for the diagnostic efficacy of this approach (Pittayapat et al. (2014), the

Table 18.3 Characteristic patterns of facial asymmetry based on CBCT analysis (after Baek et al. (2012))

Group	Type	Distribution (%)	Jaw component of asymmetry	
			Mandible	Maxilla
1	Mandibular body asymmetry	44	Essentially horizontal deviation of the body of the mandible	Little to no asymmetry
2	Universal lateral condylar hyperplasia asymmetry	39	Greatest discrepancy in ramus height	Greatest upper midline deviation, moderate maxillary canting, and arch form discrepancy
3	Atypical asymmetry	12	Prominent opposite side with the ramus was more medially tilted on the deviated side	Reverse maxillary occlusal cant plane tilted towards the opposite side (away from the deviated me)
4	C-shaped asymmetry	5	Greatest degree of midline deviation mandibular angular and ramus inclination	Greatest degree of maxillary canting and arch form discrepancy

application of 3D cephalometry is currently limited to research and the presurgical analysis of patients with complex maxillofacial abnormalities. The value of 3D cephalometry to orthodontic treatment outcomes is not yet supported by the evidence of randomized controlled trials.

Transitioning from 2D to 3D Cephalometry

Practitioners who are accustomed to working with traditional 2D cephalograms may be hesitant towards 3D analysis as navigation of most currently available software requires moderate computer skills. However, 2D conventional measurements do not have to be abandoned when moving to 3D implementation. As analysis shifts forwards towards 3D analysis, it will still be necessary to allow comparisons to previously acquired 2D cephalometric databases to correlate established superimposition protocols and evaluate growth changes. For example, 3D measurements can be applied to the Ricketts/Grummons 2D Frontal Analysis (Ricketts and Grummons 2003; Grummons and Ricketts 2004) (Fig. 18.8).

Three-dimensional data can be rendered as a 2D projection resembling a planar cephalometric projection facilitating traditional analyses or customary cephalometric points can also be identified in 3D on the volumetric rendering itself. Two approaches have been proposed.

- Ray-sum MPR volume reformation has been reported to be a potential method to simulate lateral cephalometric images from CBCT datasets (Farman et al. 2005a, b; Schuytser and Van Cleynenbreugel 2005; Scarfe et al. 2006; Farman and Scarfe 2006). The ray-sum method includes two-dimensional cephalometric reconstructions developed by increasing the slice thickness of the midsagittal plane, hence providing an image composed of the summed voxels. This approach has been termed the *virtual cephalogram* (Schuytser and Van Cleynenbreugel 2005) or *synthesized lateral cephalograms* (Kumar et al. 2007). The accuracy and precision of planar images produced by this method have been found to be as precise and accurate as 2D transmission images (Moshiri et al. 2007), especially if an orthogonal reconstruction rather than a perspective approach is used (Kumar et al. 2007).
- Swennen et al. (2005, 2006) proposed a voxel-based 3D cephalometry method as a bridge between conventional cephalometry and 3D analysis. From a single computed tomography (CT) dataset, virtual lateral and frontal cephalograms are computed and linked with both hard and soft tissue 3D surface representations. They demonstrated that this approach allows the development of a precise and reproducible

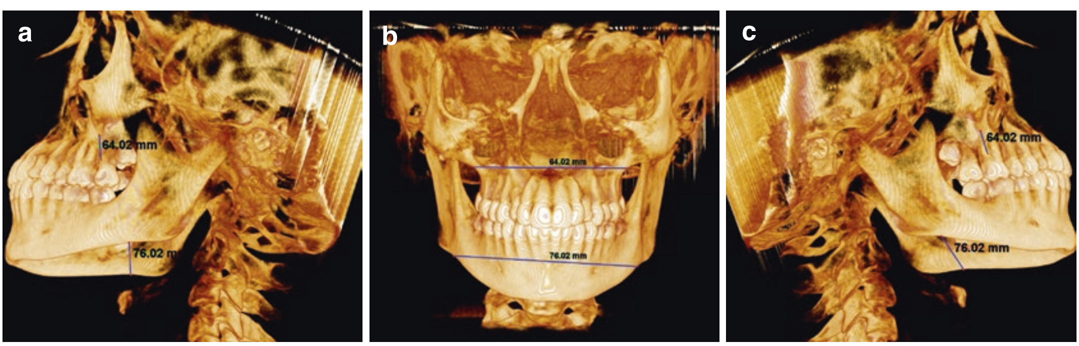

Fig. 18.8 Right infero-lateral (**a**), frontal (**b**), and left infero-lateral (**c**) 3D volumetric renderings showing maxillary (J – J′ = 64.02 mm) and mandibular (Agrt – Aglt = 76.02 mm) width measurements in 3D space to Ricketts and Grummons (2003) and Grummons and Ricketts (2004). The resultant ratio of maxillary width:mandibular width is 84.2%. According to Grummons and Ricketts (2004) this value should be approximately 80% when measured from the 2D frontal plane and indicates excessive maxillary width, reduced mandibular width or a disparity resulting from a combination of both

3D cephalometric reference and provides accurate and reliable definition of 3D cephalometric hard and soft tissue.

Challenges to 3D Cephalometry

While there has been an enormous interest in the 3D topographic approach to maxillofacial CBCT imaging analysis, this technique is prone to limitations and unique methodological problems.

- **Development and consensus on 3D reference landmarks.** Transition from 2D to 3D cephalometry will require the development and establishment of 3D reference landmarks of either embryological, (e.g., sphenooccipital synchondrosis) or morphologic significance (e.g., suture or neural foramina). It may also demand that some 2D landmarks may be abandoned as they are impossible to transpose into 3D space. This may be because they are the center of anatomical structures defined on a profile of a space (e.g., Sella Turcica,) radiography (e.g., landmark “Sella” or “S”), or defined by the process of crossing the radiological shadows on the 2D lateral radiography (e.g., Articulare or “Ar”). In addition, it is likely that there will be more landmarks to identify as the same reference landmark is present on the right and left side of the anatomical structure of interest. In the interest of time it may be necessary to identify a “representative” side for symmetric patients or to construct midpoints between these landmarks. Currently there is no consensus agreement on operational descriptions for the location of relevant 3D cephalometric landmarks. Very little age-related normative data currently exist to provide race or gender normative correlational databases.
- **Measurement error must be quantified and taken into consideration.** There are at least four aspects of measurement error in 3D analysis: the magnitude of error associated with multiple observers/repeated measurements (precision); the degree of congruence between the device and more established techniques (accuracy); the tendency of the device to systematically under- or overestimate values (bias); and the device’s ability to capture data in a consistent manner (reproducibility) (Kohn and Cheverud 1992; Weinberg and Kolar 2005). The clinical significance of the magnitude of landmark identification error depends on the level of accuracy required. If the goal is to assess growth changes, then the error must be smaller than the dimensional changes recorded in either comparison between values at two time points in time or between values for one image to a set of ethnic standardized norms. Therefore, the development of 3D analyses must incorporate landmarks that are able to be reliably identified and may involve consideration of landmarks that may be novel and different from the traditional cephalometric landmarks currently used (Lou et al. 2007).
- The image resolution of CT machines is generally reported to be sufficient for linear measurements (Harun et al. 2005; Kwon et al. 2006; Togashi et al. 2002; Richtsmeier et al. 1995). Reproducibility of the length measurement, which is landmark dependent, may account for greater than 98% of measurement error inaccuracy (Richtsmeier et al. 1995). Kragskov et al. (1997) investigated the reliability of the anatomic cephalometric points used in 3-D CT and compared them to conventional cephalograms. They found interobserver variations less than 1 mm for most points on conventional images compared to about 2 mm for 3-D CT. These findings are consistent with those reported by Cavalcanti et al. (1999) who found a mean error of 0.87 mm and a maximum error of 2 mm. Rocha et al. (2003) found that measurement standard error percentage was low, ranging between 0.85% and 3.09% whereas interobserver error was 1.95% and 1.61%, for bone and soft tissue measurements, respectively. Muramatsu et al. (2008) quantified landmark coordinate error with varying resolution and found that among five landmarks frequently used as 3D reference points, Ba showed the

Table 18.4 95% linear (mm) confidence distances in three planes for 3D CT landmarks for 1 mm slice thicknesses (after Muramatsu et al. (2008))

		Plane		
Landmark (abbreviation)	Definition on 3D CT	XY	YZ	ZX
Sella (S)	Center of the pituitary fossa	3.35	4.35	5.42
Nasion (N)	Nasofrontal structure at the midline	3.56	3.98	4.32
Basion (Ba)	Anterior inferior margin of the foramen magnum	0.63	0.34	0.38
Orbitale (or)	The midpoint of the infraorbital margin	6.31–7.02	2.23–1.77	7.96–6.65
Porion (Po)	Center of the narrowest segment of the external auditory meatus	9.96–8.16	2.78–4.05	11.06–21.85
Anterior nasal spine (ANS)	The most anterior point of the anterior nasal spine	2.75	4.25	4.25
Condyle (cd)	The most superior point of the condyle	2.74–4.57	0.88–0.85	1.88–2.41
Coronoid process (CP)	The most superior point of the coronoid process	1.90–1.04	0.63–1.08	0.75–1.22
Gonion go (go)	The most inferior and posterior point of the mandibular angle	12.11–11.96	15.36–18.99	14.82–9.6
Menton (me)	The lowest border of the mid-mandibular suture	3.37	10.66	4.05
Upper first molar (U6)	The most superior point of the mesial buccal cusp of the maxillary first molar	2.35–1.98	4.49–1.12	2.72–0.86
Upper incisor (U1)	The midpoint between the mesial angles of maxillary central incisors	1.02	3.66	2.64
Lower incisor (L1)	The midpoint between the mesial angles of mandibular central incisors	1.89	2.56	6.39

smallest areas for all three coordinate axes, whereas Porion and Orbital showed the highest (Table 18.4).

- Williams and Richtsmeier (2003) reported that for the mandible, constructed (a point whose location is determined by constructing a line tangent to another landmark or bony edge (Bookstein 1991)) and fuzzy (i.e., that the definition of the landmark is larger than a single point within the observers' range of view (Valeri et al. 1998)) landmarks generally exhibit relatively more error than biological landmarks. Fuzzy landmarks include gnathion, pogonion, posterior and lateral mandibular condyle, superior anterior ramus, and inferior anterior ramus whereas constructed landmarks include the alveolar and inferior border of the body of the mandible, gonion and the inferior posterior ramus. Dimensional intra-observer reliability for 3D dimensions has been reported to be greater than for 2D measurements. Olszewski et al. (2007) reported intra-class coefficients to range from 0.972 to 0.998 as compared to 0.133 to 0.841 for 2D cephalometry.

3D CBCT-Based Facial Assessment

> Appearance is the most public part of the self. It is our sacrament, the visible self that the world assumes to be the mirror of the invisible, inner self (Etcoff 1999).

Facial appearance, or esthetic, is the outward expression of facial soft tissue supported by the bones, teeth, muscles, etc. Facial soft tissue may play an important aspect of orthodontic and, increasingly, orthognathic surgical treatment plans. Numerous 2D and 3D soft tissue analyses have been proposed including Farkas (1981, 1994), Farkas and Muro (1987), Farkas/Mayes (Personal Communication Dr. Joe Mayes), Arnett

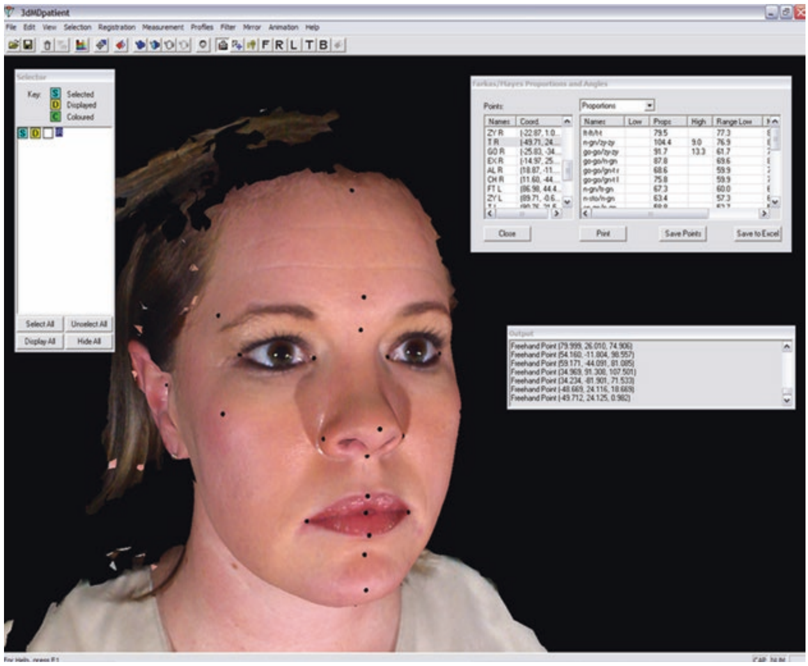

Fig. 18.9 Topographic landmarks placed on a patient's face for the Farkas/Mayes Proportional Analysis (FMA). Images acquired on a 3dMD Vultus system (3dMD, Atlanta, Georgia, USA)

and Bergman (1993), Sarver (1998), and Idiculla et al. (2006) (Fig. 18.9). A 3D facial soft tissue analysis not only evaluates the profile but any projections of the face (i.e., frontal, superior, inferior, ¾ views, oblique views).

3D stereo-photogrammetry systems (SPS) (e.g., 3dMD™ Cranial System, Atlanta, GA, USA) have been used successfully in orthodontics and orthognathic surgery for both clinical and research purposes for diagnosis, surgery simulation, and postoperative comparisons (Popat et al. 2010; Tzou et al. 2014) (Fig. 18.10). These devices capture high resolution color facial surface data quickly and instantaneously. They also offer software for accurate measurement, evaluation, treatment planning, progress monitoring (surface comparison analysis), and outcomes evaluation using user-guided interactive landmark localization.

Untextured soft tissue CBCT surface renderings can be used for these analyses; however, the surface data lacks accuracy as compared to SPS (Moerenhout et al. 2009; Metzger et al. 2014). Some SPS systems can map CBCT surface renderings onto their 3D textured surface-imaging data (Maal et al. 2008; Naudi et al. 2012) either separately (superimposition accuracy range 0.3–0.9 mm) or simultaneously (superimposition accuracy range 0.4 mm). However, registration and fusion of these datasets may produce inaccuracies due to changes in facial expression, spatial soft tissue changes, and differences in the patient's positioning (Nahm et al. 2014).

18.2.6 Virtual 3D Study Casts

In addition to a thorough clinical intraoral, radiographic, and photographic examination, dental study casts of the dentition of both jaws are often acquired and articulated to analyze the relationship of the maxillary to the mandibular dentition. Digital study casts can now be created virtually by numerous methods:

- Indirect
  - 3D Laser, optical or CT scanning of plaster casts.
  - CT/CBCT scanning of the patient impressions which are then reversed to create the "positive" study cast.

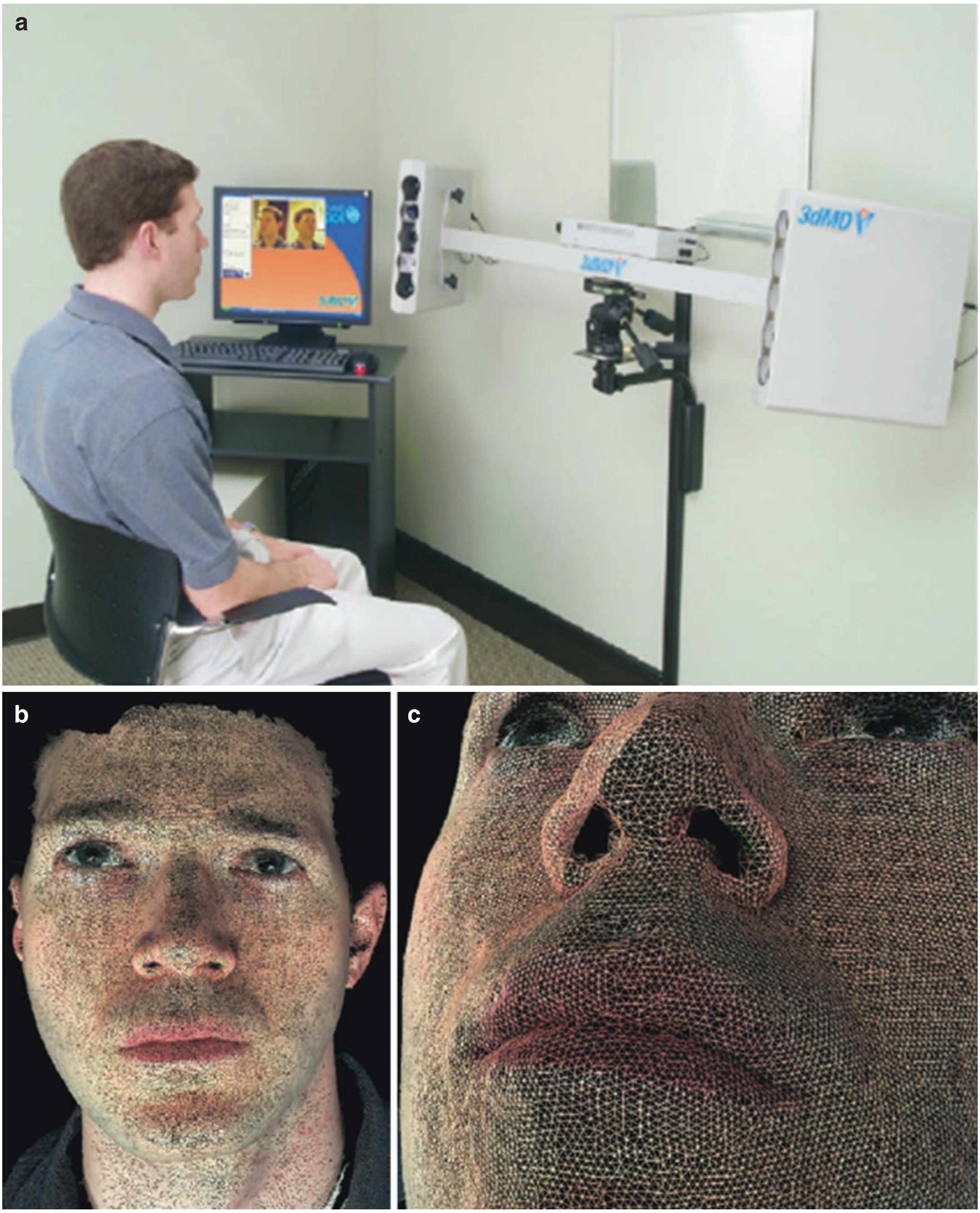

Fig. 18.10 The 3dMDface system (**a**) consists of 6 medical-grade, machine-vision cameras that are synchronized to image a subject in 1.5 ms, enabling geometry to be processed as a continuous point cloud; a single raw dataset with 1 coordinate system (no stitching) providing ear-to-ear coverage. 3dMD raw data mesh, both with (**b**) and without (**c**) texture shows a continuous *x*, *y*, and *z* coordinate system generated from 2 separate viewpoints—left and right sides of face. (Images courtesy of Chris Lane and Kelly Duncan)

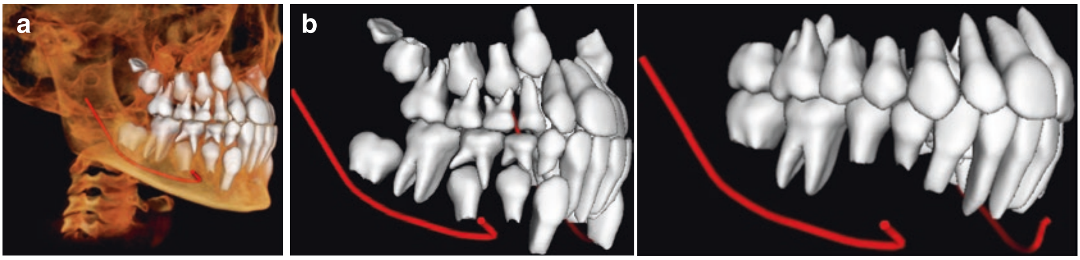

Fig. 18.11 Identification and isolation of the teeth from the CBCT data (**a**) via the process of segmentation allows separation of the dentition and creation of 3D virtual study casts of the dentition (**b**). Because it is time consuming and technically demanding, virtual segmentation and creation of models is often provided as an additional service. (Images courtesy, Anatomage)

- Direct
  - Thresholding of CBCT data to segment the dentition (Fig. 18.11) and create surface study casts.
  - Intraoral optical scanning of the patient's dentition.

Digital study casts offer advantages that include ease of storage and retrieval, ease of interoffice transferability, and possibly equal or better diagnostic capabilities. While a number of authors have reported a statistically but clinically insignificant difference between linear dental anatomic measures obtained from digital to plaster study casts (Garino and Garino 2002; Zilberman et al. 2003: 73), they are equally as efficacious as clinical records (Rheude et al. 2005; Stevens et al. 2006; Mullen et al. 2007). Most orthodontic software programs can be used to create virtual 3D models of the maxillofacial region for manipulation and visualization within the program (Fig. 18.5).

In vitro (laboratory) investigations show that surface virtual study casts are very accurate for most CBCT units (98.9% of measurements being within 1 mm deviation and 92.8% within 0.5 mm) (Vandenberghe et al. 2012) and comparable to optical scanning of dental impressions (Kau et al. 2010; White et al. 2010). CBCT exposure factors, mostly scan time and voxel size, have been reported to have had a limited influence on surface model accuracy (Vandenberghe et al. 2012). However, the separation of bony or tooth structures from the volumetric dataset, a process referred to as segmentation, is a time-consuming technique, prone to artifacts, and may result in clinical levels of inaccuracy of 3D surface models particularly in regions of thin bone such as the condylar region and lingual cortex of the mandible (Fourie et al. 2012; Engelbrecht et al. 2013).

Digital study casts can be used for both analysis (e.g., Bolton Tooth Size Discrepancy, Arch Length Analysis and Moyers Mixed Dentition Analysis) and therapy in the production of removable clear aligners (e.g., Invisalign, Align Technology Inc., Sunnyvale, CA, USA), positioning of orthodontic brackets or customizing the shape of arch wires (SureSmile, OraMetrix, Richardson, Texas, USA).

The use of CBCT as an imaging modality for the production of digital study casts alone or to fabricate appliances is unwarranted at the present time as the effective doses produced using acquisition parameters necessary to provide adequate resolution and image quality approximate almost twice that for a comparable scan for diagnostic purposes (Grünheid et al. 2012). "Going digital"—substitution of CBCT imaging for both diagnosis and impression modality over a course of treatment may result in up to a 3.75 times higher radiation burden (approximately 272.6 μSv) compared to a conventional radiographic series involving panoramic and cephalometric imaging with analog impressions (73.5 μSv) (Grünheid et al. 2012). This approach also violates Recommendation 1.3 of the AAOMR clinical recommendations regarding use of cone beam computed tomography in orthodontics (AAOMR 2013).

Avoid using CBCT on patients to obtain data that can be provided by alternate nonionizing modalities (e.g., to produce virtual orthodontic study models).

18.2.7 Predictive Simulations

Ricketts coined the term “Visual Treatment Objective” (VTO) to describe the individual prediction of tooth movement due to the expected influence of orthodontic treatment and growth as analyzed on lateral cephalometric images (Ricketts et al. 1979). Similarly, a virtual 3D VTO is a predictive computer-assisted simulation using CBCT data to provide a pictorial digital 3D representation of the optimal post-therapy treatment results based on virtual repositioning of either dental and/or maxillofacial skeletal components (Fig. 18.12).

Establishing a virtual 3D VTO is potentially important in clinical orthodontics in that it facilitates a determination of the proposed treatment feasibility, optimizes case management, and increases the patient’s understanding and acceptance of a proposed treatment. Final location of these hard tissue elements is based on orthodontic and orthopedic principles. However, soft tissue response to these movements, especially involving the skeletal envelope or facial mask, is multifactorial (Kolokitha and Chatzistavrou 2012) and is simulated by software based on preprogrammed hard-to-soft tissue ratios, which differ among available programs. Facial mask simulations are particularly important in prediction of the esthetics of orthognathic surgery. Fusion of photogrammetric facial optical (3dMD Inc., Atlanta, Georgia) and CBCT data provides a highly accurate simulation with differences between most soft tissue measurements being smaller than 0.5 mm (Schendel et al. 2013). In addition, 4D real-time surface acquisition capture is now being used for the assessment of facial expression, chewing, and craniofacial dysmorphology (e.g., 3dMDhead Temporal System, 3dMD, Atlanta Georgia, USA).

Several software programs are available for lateral cephalometric treatment simulations (Smith et al. 2004; Kaipatur and Flores-Mir 2009). Proprietary dental software for treatment simulations for both tooth-related (e.g., AnatoModel, Anatomage, Inc. San Jose, California, USA) and skeletal conditions (e.g., 3DMDvultus, 3DMD, Atlanta, Georgia, USA; Maxilim, Medicim,

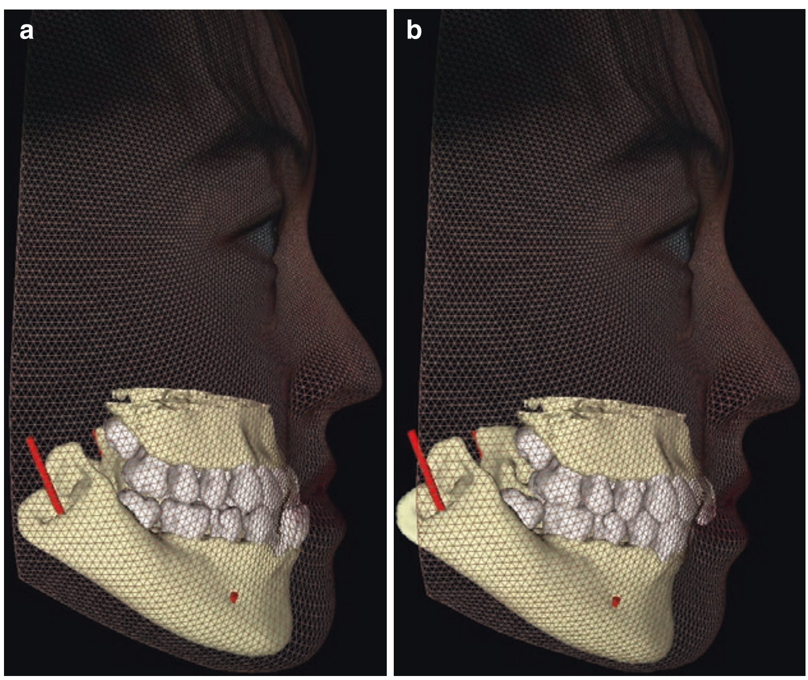

Fig. 18.12 Presurgical facial surface image integrated with CBCT-derived virtual models of the jaws with highlighted mandibular neurovascular contents (**a**) shows the effect of Class III skeletal relationship to the dental profile. Predictive orthognathic virtual surgery of the 3D models shows the predicted effect on the facial profile (**b**) (Images courtesy, Anatomage)

Mechelen, Belgium; Dolphin Imaging, Dolphin Imaging & Management Solutions, Chatsworth, California, USA; InVivoDental, Anatomage, San Jose, California, USA and SimPlant OMS, Materialise, Leuven, Belgium) for CBCT data are also available. Initial reports indicate high reliability between post-therapy results and those predicted by surgical simulation software for craniofacial and orthognathic surgery (Tucker et al. 2010; Cevidanes et al. 2010).

18.3 Specific Indications

CBCT imaging has indications in the diagnostic phase of orthodontic treatment of patients with maxillofacial orthodontic and orthopedic anomalies for the assessment of a number of specific conditions (Kau et al. 2005; Korbmacher et al. 2007; Hechler 2008; Merrett et al. 2009; Kapila et al. 2011; van Vlijmen et al. 2011; American Academy of Oral and Maxillofacial Radiology 2013).

18.3.1 Dental Structural Anomalies

Developmental anomalies of tooth structure can lead to disturbances in maxillary and mandibular dental arch lengths, occlusal arch discrepancies resulting in crowding and poor esthetics, and inter-arch differences producing malocclusions. The effects that these anomalies may have can be local, producing regional disturbances, or generalized creating more widespread problems. Recognition of the presence of these conditions is important in that it may complicate orthodontic treatment planning. CBCT imaging facilitates arch length analysis in these situations and provides qualitative data from which extraction or non-extraction techniques can be implemented. The reported prevalence and distribution of dental anomalies varies widely (5–74%) depending on population sampling and different diagnostic criteria (Altug-Atac and Erdem 2007). Developmental dental abnormalities can be categorized in three broad categories (Katheria et al. 2010; Leuzinger et al. 2010; Van Elslande et al. 2010; Shemesh et al. 2011; Sherrard et al. 2010; Treil et al. 2009; Liedke et al. 2009; Liu et al. 2007, 2008):

- **Variations in tooth morphology** (e.g., fusion, gemination, microdontia (peg-shaped maxillary and mandibular lateral incisors), macrodontia, dilacerated roots, and transposed teeth) (Figs. 18.13, 18.14, and 18.15).
- **Variations in tooth number** (e.g., oligodontia, hypodontia (congenitally missing maxil-

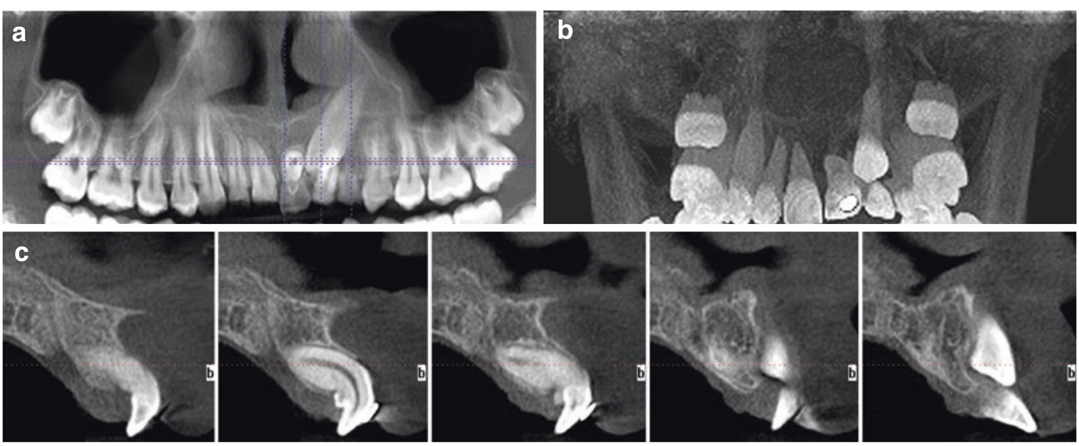

Fig. 18.13 Reformatted simulated panoramic (**a**), frontal maximum intensity projection (**b**), and 1 mm thick sequential cross-sectional images (**c**) showing fully dentate young adult with failure of orthodontic movement of the maxillary left central incisor. Severe facio-palatal dilaceration at the middle of the root of this tooth is preventing controlled movement and alignment

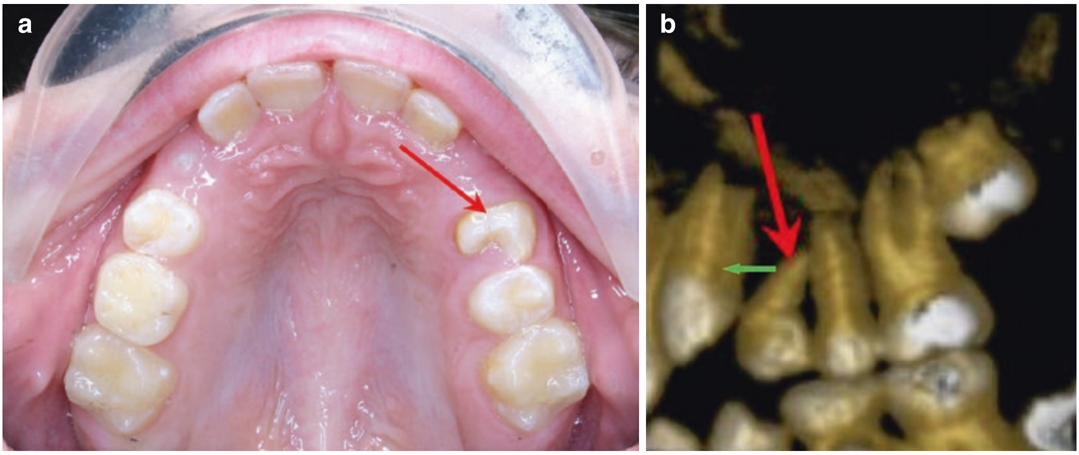

Fig. 18.14 Intraoral occlusal photo (**a**) and cropped volumetric rendering (**b**) of an 11-year-old male patient with a distally tipped maxillary left first bicuspid. The clinical impression suggests bicuspid up righting however unexpected dilacerated root (*red arrow*) is present. This tooth was retained and actually upright mesially to parallel it with the adjacent roots (*green arrow*) until such time that it could be removed and replaced

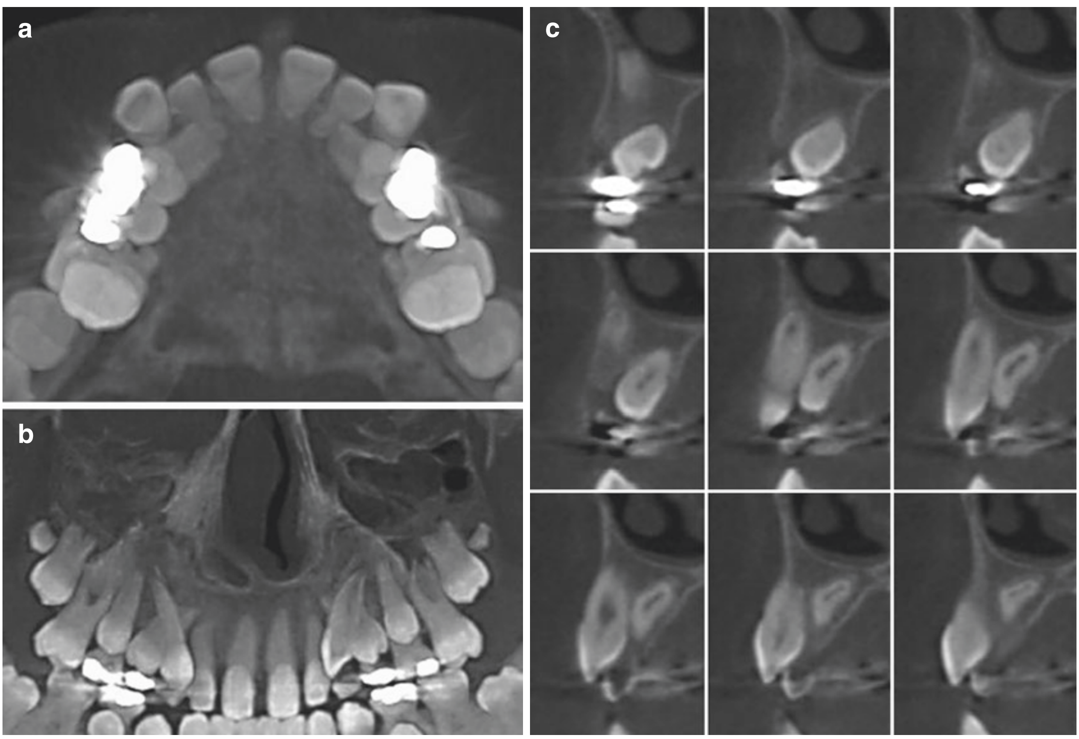

Fig. 18.15 Axial (**a**), panoramic (**b**) maximum intensity projections (MIP), and cross-sectional (**c**) CBCT images of an 11-year-old female with transposed roots of the maxillary cuspids and 1st bicuspids. In the cross-sectional views (**c**), the cuspid root is buccal to the 1st bicuspid root. Knowing the true position and location of the roots can aid the orthodontist in planning bracket placement, in addition to calculating the force systems and force vectors needed to upright the roots without damage to adjacent teeth

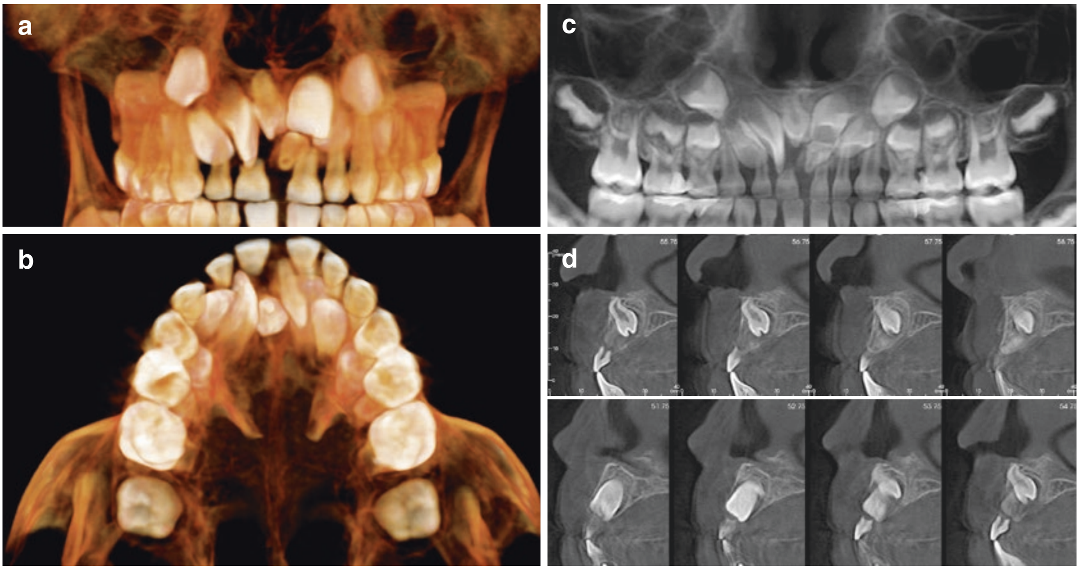

Fig. 18.16 Frontal (**a**) and submentovertex (**b**) volumetric renderings with reconstructed simulated panoramic (**c**) and 1 mm sequential cross-sectional images (**d**) of the right maxillary anterior region of a child in the early mixed dentition phase. The images show crowding of the anterior incisor teeth due to the presence of two impacted and unerupted midline microdontic supernumerary teeth either side of the midline (mesiodens)

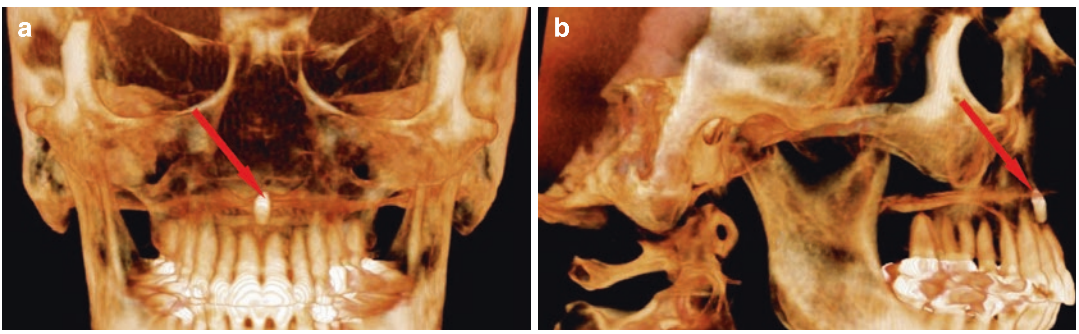

Fig. 18.17 Frontal (**a**) and right lateral (**b**) volumetric images demonstrating a high location of a single, mid-sagittal mesiodens located just inferior to the anterior nasal spine with negligible effect on the dentition

lary lateral incisors, mandibular incisors and canines, maxillary and mandibular premolars), and hyperdontia (supernumerary teeth)) (Figs. 18.16, 18.17, and 18.18). The location of supernumerary teeth, particularly the mesiodens, is important in the premaxillary region. Supernumerary teeth often present effects that compromise orthodontics such as delayed or failure of eruption of permanent teeth rotation or displacement of permanent teeth, persistence of a median diastema and even cystic changes around the unerupted supernumerary tooth (Nik-Hussein 1990; von Arx 1992).

- **Variations in tooth structure** (e.g., internal root resorption or congenital conditions affecting the entire dentition such as amelogenesis or dentinogenesis imperfect) (Fig. 18.19).

18.3.2 Anomalies in Dental Position

Imaging can play an important role in the evaluation of common impacted teeth such as the third molars or maxillary canines (Fig. 18.20), the presence of unerupted and impacted supernumeraries (e.g., mesiodens) (Fig. 18.21), anomalies in dental eruption sequence, and ectopic eruption

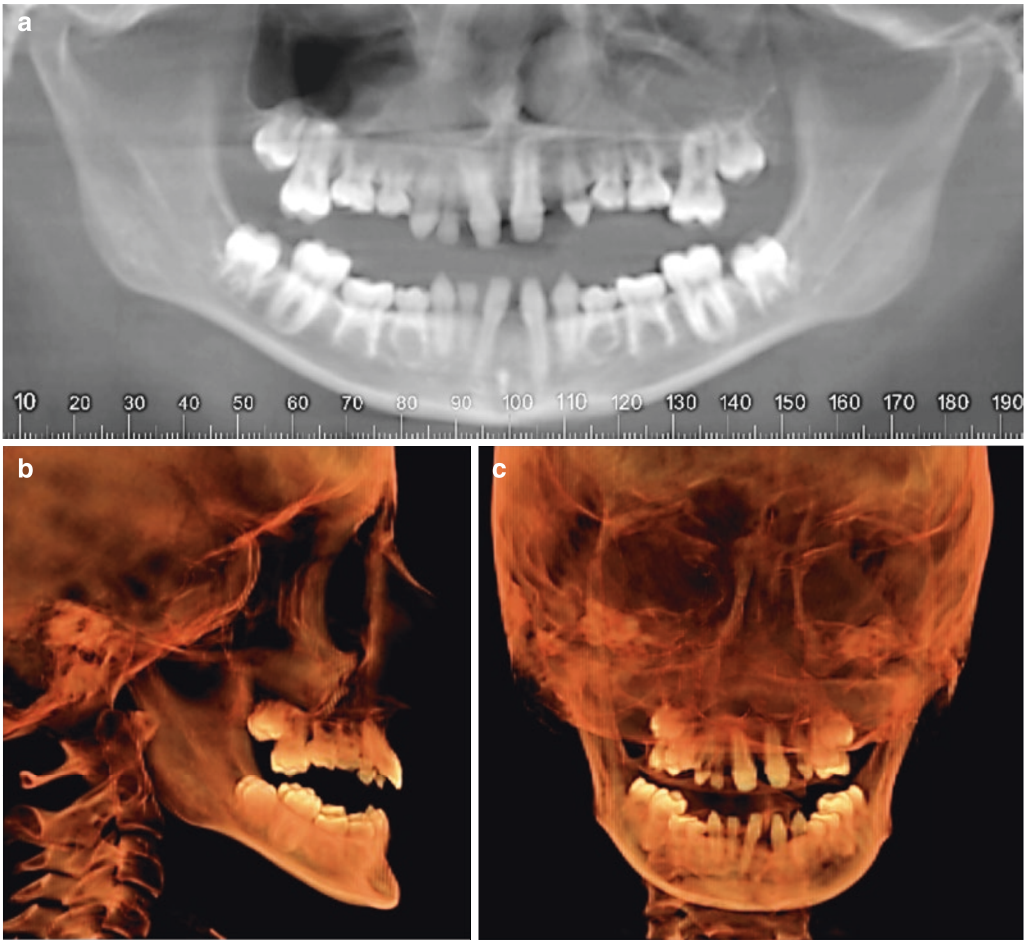

Fig. 18.18 Reformatted panoramic (**a**), lateral (**b**), and frontal (**c**) volumetric renderings of a skeletal Class III patient with Witkop syndrome, a form of ectodermal dysplasia primarily presenting with dysplasia of nails and hypodontia, with unaffected sweat gland function. Maxillofacial images demonstrate partial hypodontia of the permanent dentition (specifically premolars, canines, and lateral incisors) and retention of the deciduous teeth

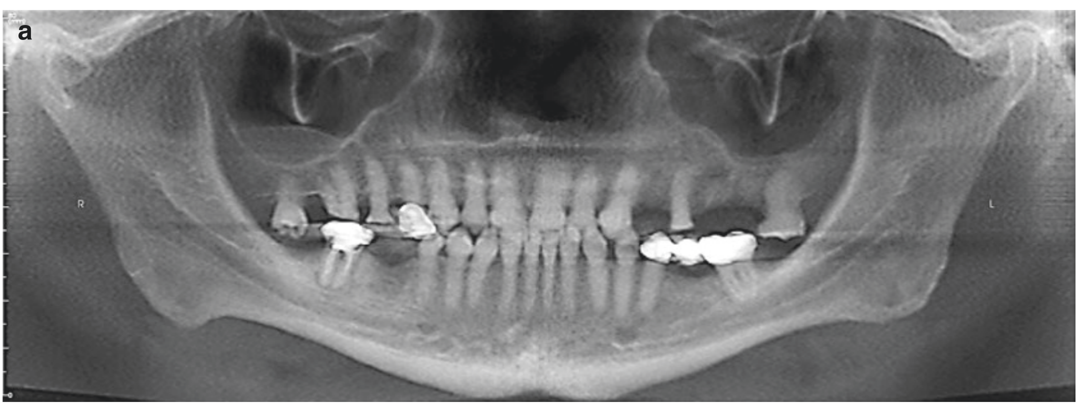

Fig. 18.19 Reformatted panoramic (**a**) and serial 1 mm thick/2.5 mm interval cross-sectional (**b**) images of the central incisors of a patient with dentinogenesis imperfect demonstrating typical radiographic features including bulbous crowns with constricted short roots and pulpal obliteration

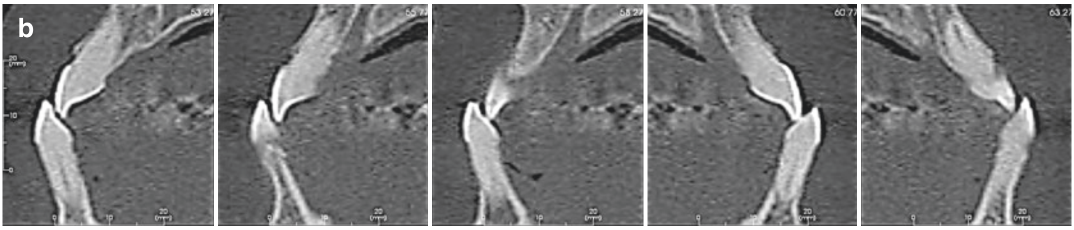

Fig. 18.19 (continued)

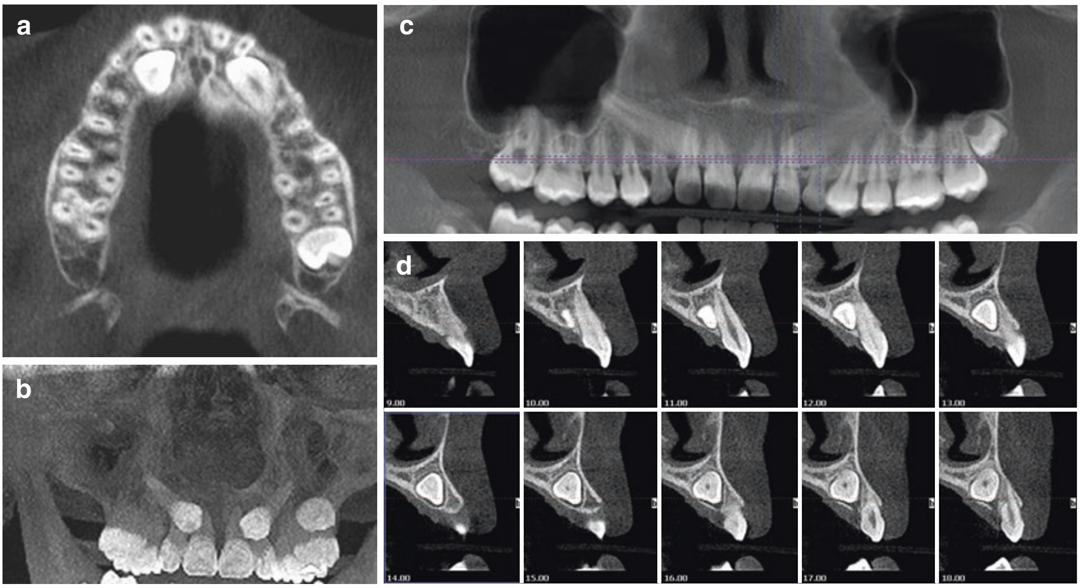

Fig. 18.20 Axial (**a**), frontal maximum intensity projection rendering (**b**), reformatted panoramic (**c**), and multiple cross-sectional 1 mm thick sections (**d**) of the left anterior region demonstrating the location, orientation, and position of the severely mesioangular, palatally positioned, completely bony impacted, and unerupted maxillary canines bilaterally

(including teeth associated with clefts) (Fig. 18.22). The information gained from this assessment can assist the clinician in decisions such as whether or not to remove the tooth and if so on surgical approach and technique.

Specific information includes (Katheria et al. 2010; Tamimi and ElSaid 2009; Becker et al. 2010; Liu, et al. 2008; Chaushu et al. 2004; Botticelli et al. 2011; Walker et al. 2005; Oberoi and Knueppel 2012; Hofmann et al. 2011; Hofmann et al. 2013):

- Determining the size of the crown of the tooth
- Localizing the position of the tooth (e.g., inclination of the long axis of the tooth, relative buccal and palatal positions, amount of the bone covering the tooth) (Fig. 18.23)
- Determining the effect on adjacent teeth (e.g., resorption of the roots of adjacent teeth, the condition of adjacent teeth) (Figs. 18.24 and 18.25)
- Identifying local anatomic surgical considerations (e.g., location of the nasopalatine canal, mental foramen, or inferior alveolar canal)
- Determining the overall stage of dental development
- Assessment of associated pathology (Fig. 18.26)

18.3.3 Dentoalveolar Morphology

The width of the alveolar bone within the dental arches provides the clinician with an understanding of the anatomic facio-palatal/lingual bound-

Fig. 18.21 Reformatted panoramic maximum intensity projection (MIP) (**a**), axial (**b**), cross-sectional (**c**), and rendered volumetric virtual model (**d**) demonstrating location and position of two maxillary, partially formed, supernumerary teeth displacing and preventing the eruption of the maxillary central incisors labially

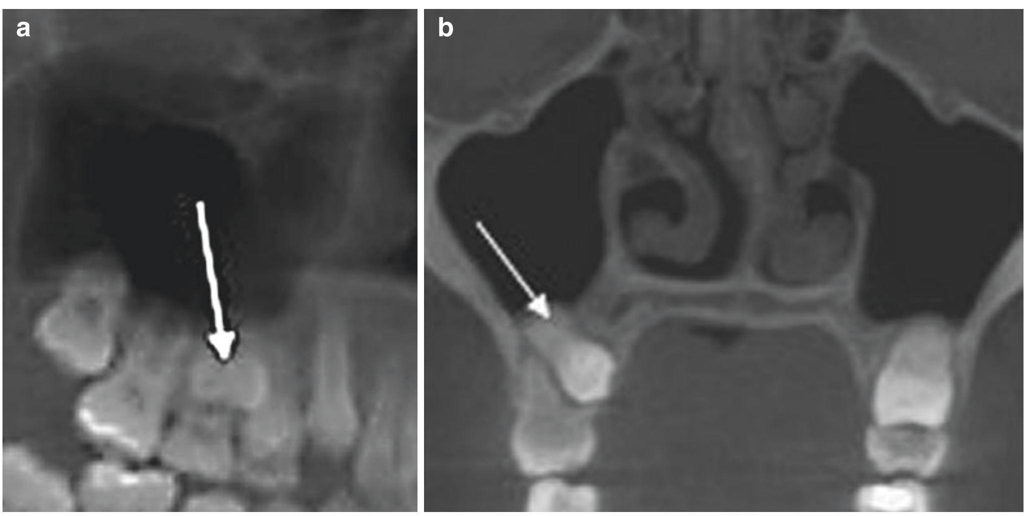

Fig. 18.22 Cropped right panoramic (**a**) reformatted image and coronal MIP (**b**) image of an ectopically palatally erupting maxillary right 2nd bicuspid. The lingual position is not evident from the panoramic view; however, the coronal view shows the lingual position clearly

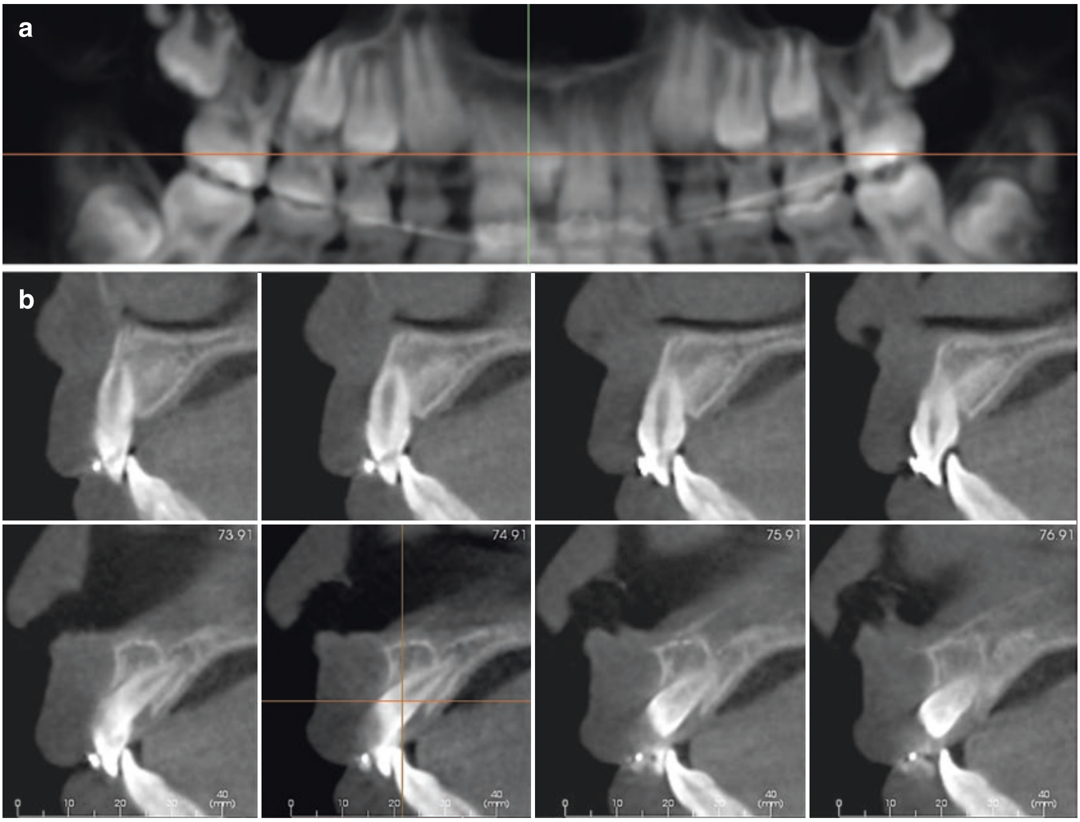

Fig. 18.23 Reformatted panoramic image (**a**) and series of cross-sectional images (**b**) of the maxillary right anterior regions showing a transposed, ectopic location for the lateral incisor

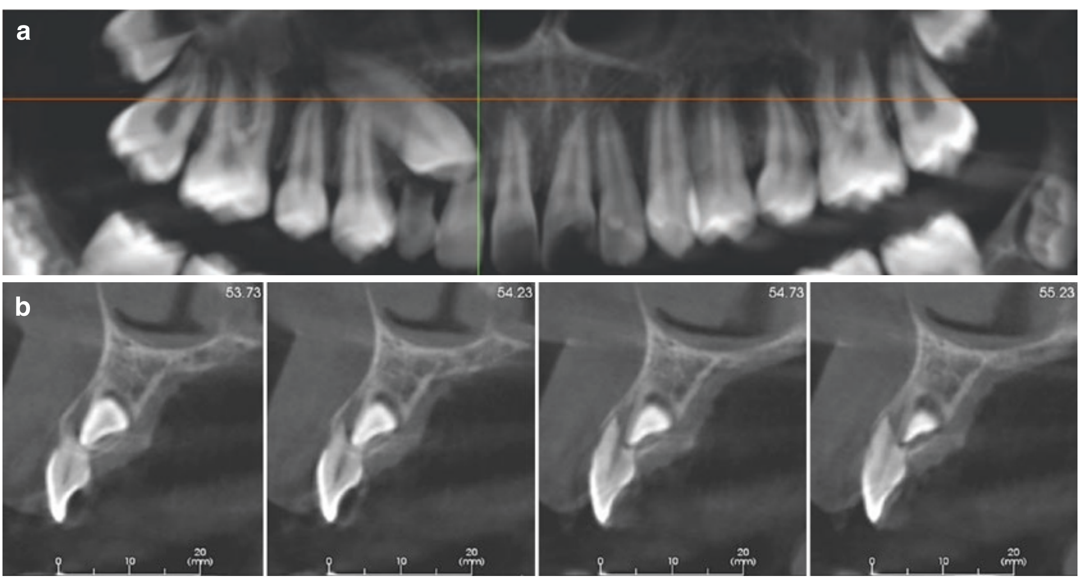

Fig. 18.24 Reformatted panoramic image (**a**) and series of cross-sectional images (**b**) of the maxillary right anterior region showing severe apical and middle third root resorption on the lateral incisor associated with the mesio-angular, ectopically positioned completely bony impacted canine

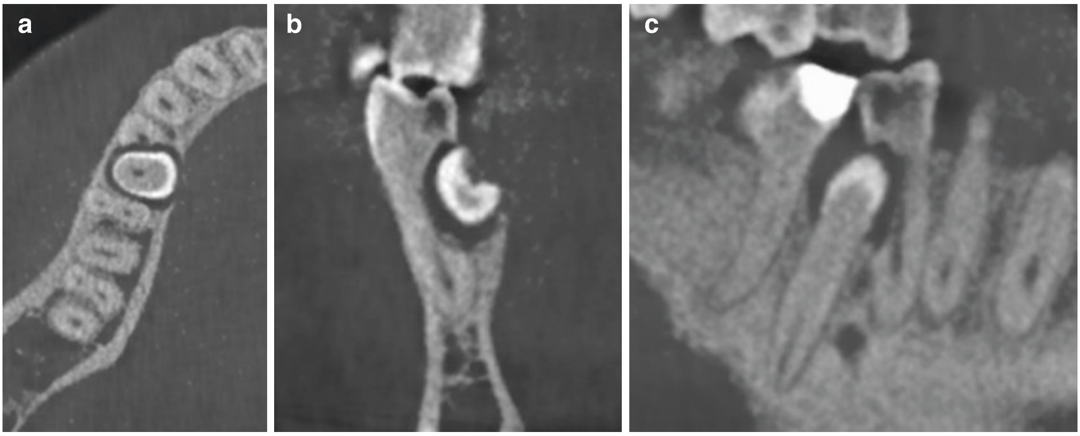

Fig. 18.25 Axial (**a**), cross-sectional (**b**), and corrected sagittal (**c**) CBCT images of the right posterior mandible showing a supernumerary impacted premolar causing severe root resorption on the distal aspect of the root of the second premolar

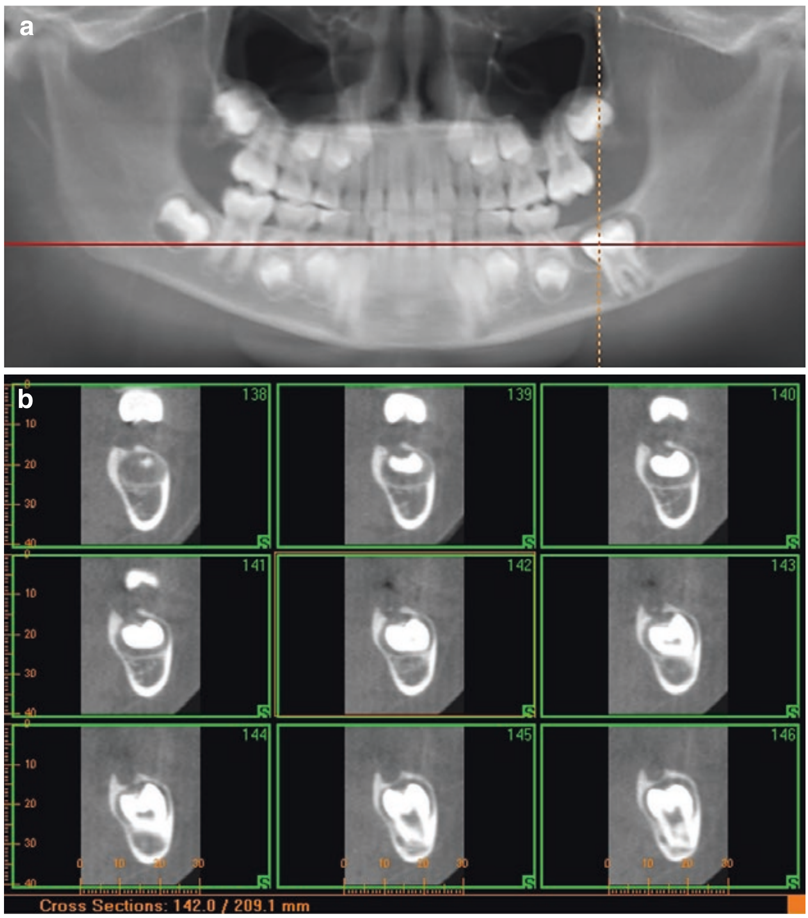

Fig. 18.26 Reformatted panoramic (**a**) and serial cross-sectional (**b**) CBCT images of pericoronal cyst preventing the eruption of the left mandibular first molar in a 10-year-old female

aries available for orthodontic torque movement of teeth (i.e., retraction, arch expansion or labial movement of incisors) (Fig. 18.27). Evaluation of fenestrations and dehiscence on the buccal and lingual surfaces can be an important consideration in certain patients such as those with bimaxillary protrusion, compromised periodontal status, and/or clefts of the alveolus (Molen

2010; Yagci et al. 2012; Timock et al. 2011; Leung et al. 2010; Loubele et al. 2008; Rungcharassaeng et al. 2007). Narrow transverse maxillary dimension can occur with or without crossbite (Vanarsdall 1999) and be an unrecognized source for fenestrations and dehiscence (Fig. 18.28). In addition, determination of dento-alveolar volume is important for patients who are

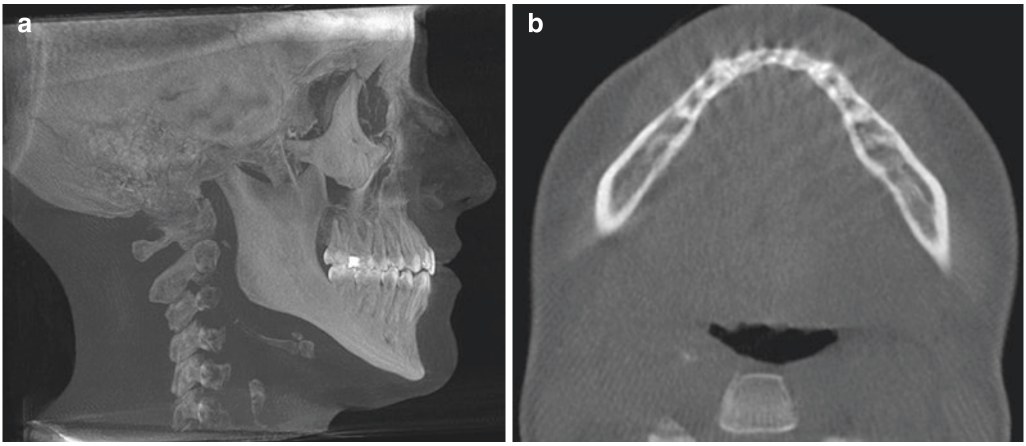

Fig. 18.27 Maximum intensity projection lateral cephalometric image reformatted from CBCT data (**a**) demonstrating anterior open bite and excessive interincisal angle between the maxillary and mandibular incisors requiring a change in the position of the anterior mandibular incisors. The axial image (**b**) shows a very thin alveolar bone width associated with the roots of the mandibular incisor teeth. This restricts the range of orthodontic movement possible for the mandibular anterior incisors without dehiscence or fenestration of the roots through the cortical plate

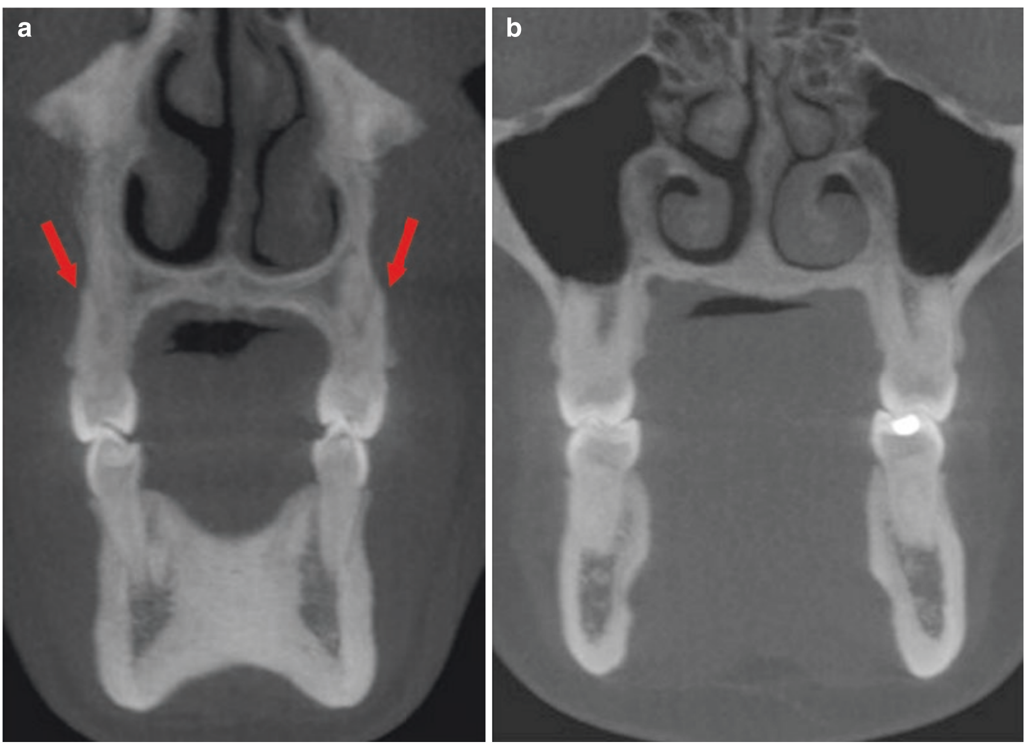

Fig. 18.28 Coronal 2 mm thick maximum intensity projection (MIP) image through the first premolars (**a**) and first molar (**b**) region showing reduced transverse maxillary dimension without crossbite. Note lingual inclination of maxillary teeth and close proximity of the buccal roots to the buccal plate (*red arrows*)

potential candidates for dental implants, bone grafts, or temporary anchorage devices (Kapila et al. 2011; Mah et al. 2010; White and Pae 2009).

18.3.3.1 Dental Arch Length and Form Evaluation

Plaster study casts are often used in orthodontics to assess symmetry, arch form, severity of the curves of Spee and Wilson, axial inclinations of teeth as well as perform dental tooth analyses such as Peck and Peck, Bolton and Tooth Size-Arch Length Discrepancy. Often a space analysis is performed to determine whether extractions are necessary to accommodate teeth in the dental arch. Tooth size-arch length discrepancies are calculated by determining the space available (basal region available in the dental arch) and subtracting the space required (sum of mesiodistal diameters of existing teeth). Correctly oriented CBCT axial and reformatted panoramic images provide highly accurate means of space analysis (Fig. 18.29). In addition, 1:1 axial images can be used to customize arch form wires (Fig. 18.30).

18.3.4 Dentofacial Deformities and Craniofacial Anomalies

Volumetric rendering is a particularly useful imaging tool for the analysis of severe skeletal discrepancies producing facial or mandibular asymmetry, anteroposterior, vertical and transverse deficiencies as well as an assessment of their dental effects (Agarwal 2011; Behnia et al. 2012; Dalessandri et al. 2011; Ebner et al. 2010; Edwards 2010; Jayaratne et al. 2010a, b; Kim et al. 2011a; Abou-Elfetouh et al. 2011; Lloyd et al. 2011; Gateno et al. 2011; Almeida et al. 2011; Scolozzi and Terzic 2011; Heymann et al. 2010; Cevidanes et al. 2010; Tucker et al. 2010; Orentlicher et al. 2010; Jayaratne et al. 2010a, b; Popat and Richmond 2010; Carvalho et al. 2010; Schendel and Lane 2009) (Figs. 18.31 and 18.32). Appreciation of the complexity of these abnormalities demands visualization of the interrelationships of the dental, skeletal, and soft tissue elements. CBCT data can be exported to specific software programs that can be used for virtual treatment simulations to plan orthopedic corrections such as orthognathic surgery or distraction osteogenesis.

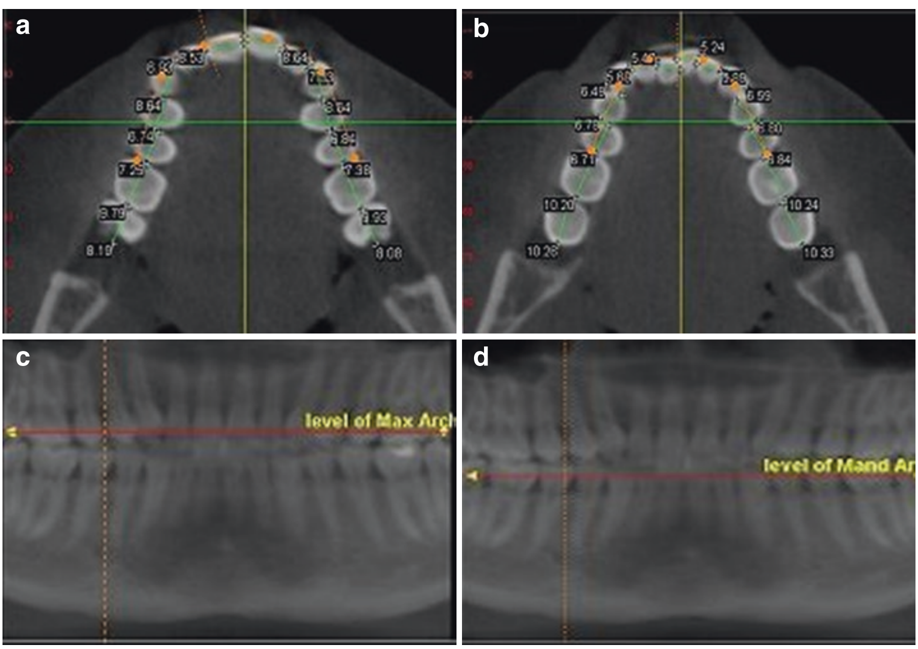

Fig. 18.29 Maxillary (**a**) and mandibular (**b**) axial and corresponding maxillary (**c**) and mandibular (**d**) reformatted panoramic (**b**) images of a patient with each tooth in the dental arch measured along the greatest mesiodistal width. A parabolic arch form is also created and the measurement compared to the sum of the individual tooth measurements and arch length discrepancies noted

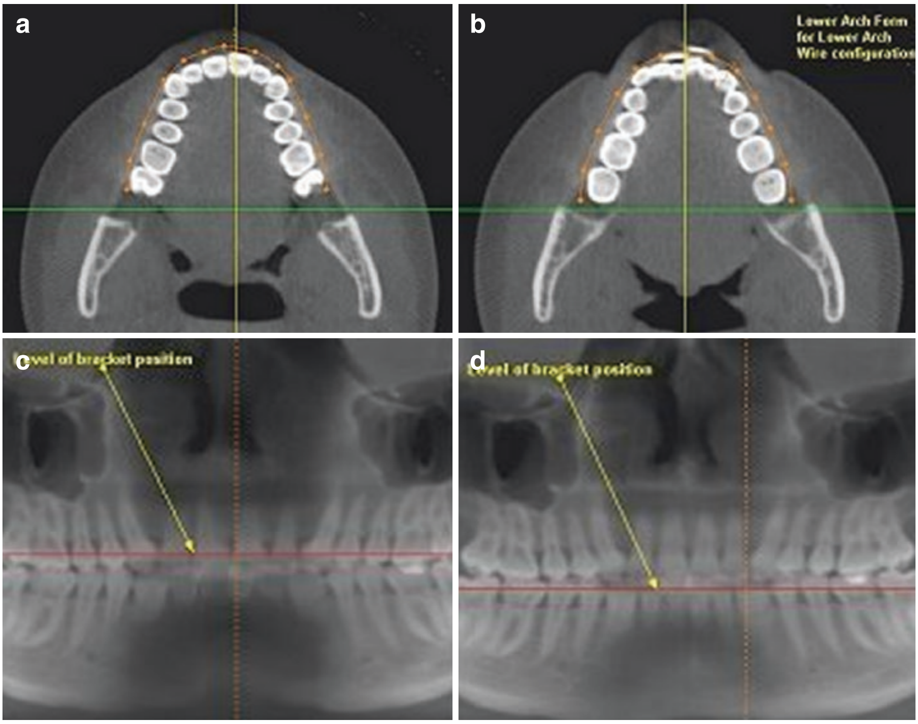

Fig. 18.30 Maxillary (**a**) and mandibular (**b**) axial and corresponding maxillary (**c**) and mandibular (**d**) reformatted panoramic (**b**) of patient with parabolic line drawn to facilitate arch wire configuration

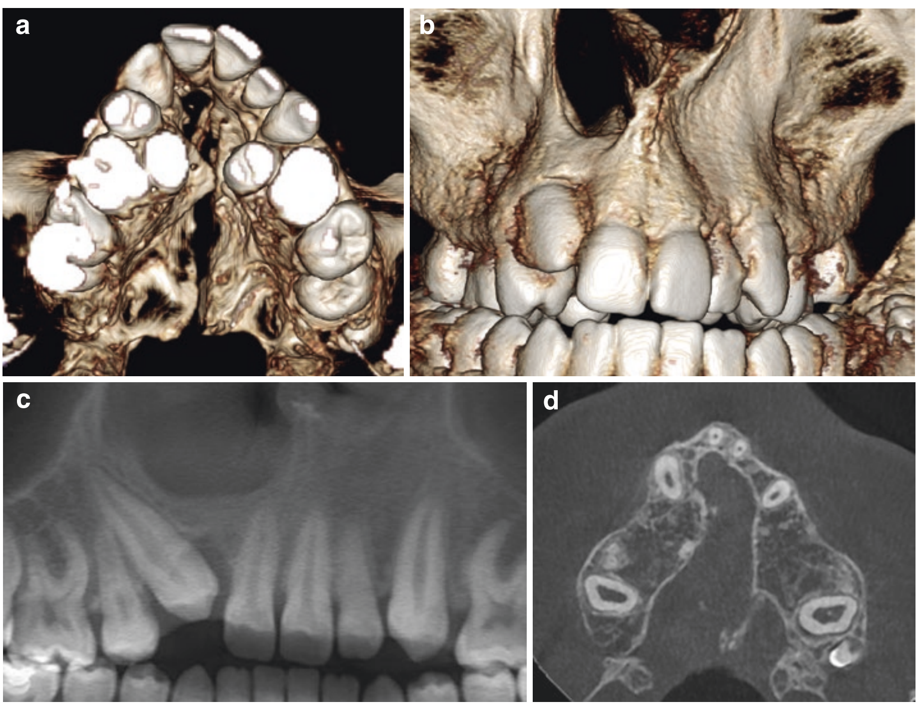

Fig. 18.31 Inferior (**a**) and frontal (**b**) 3D surface renderings, reformatted cropped reconstructed panoramic (**c**) and axial section (**d**) small FOV high resolution CBCT images of a 16-year-old male with failure of orthodontic therapy associated with repaired right maxillary unilateral cleft

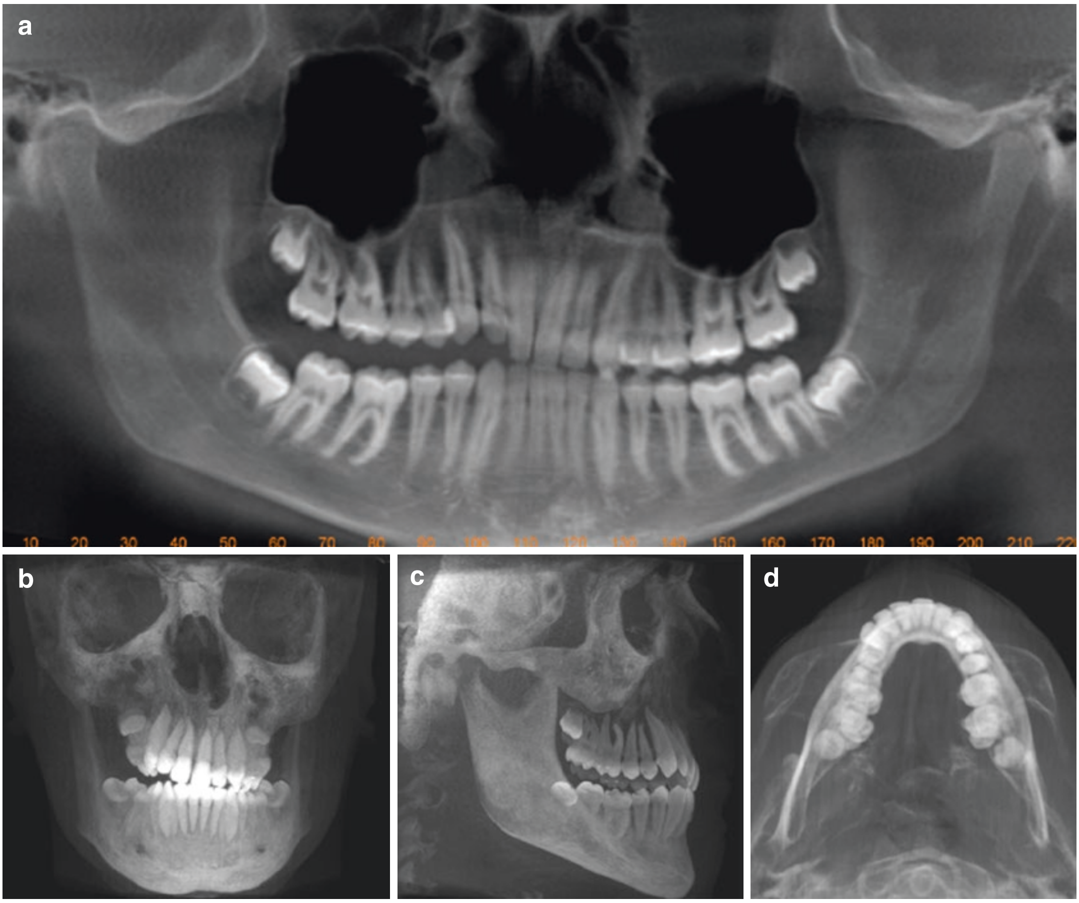

Fig. 18.32 Reformatted panoramic (**a**) and frontal (**b**), right lateral (**c**) and submentovertex (**d**) MIPs showing facial asymmetry with maxillary transverse deficiency and right vertical maxillary deficiency with severe right sided anterior and posterior open bite associated with right unilateral maxillary hypoplasia

18.3.5 Malocclusions, Dental and Skeletal Discrepancies

Identification of Class II and Class III skeletal malocclusions (Almeida et al. 2011; Cevidanes et al. 2010; Gateno et al. 2011; Heymann et al. 2010; Kim et al. 2011b; Lloyd et al. 2011; Orentlicher et al. 2010; Tucker et al. 2010), increased or decreased vertical facial height and asymmetry (Sievers et al. 2012; Al Hadidi et al. 2011; de Moraes et al. 2011; Damstra et al. 2013; Veli et al. 2011; Kook and Kim 2011; Cevidanes et al. 2011a, b), either alone or in combination involves an appreciation of the contribution of maxillary and mandibular anterior-posterior, vertical, and transverse discrepancies (Fig. 18.33). These are well visualized with CBCT images. These anomalies may present clinically as chin or mandibular deviation, dental midline deviation, and/or occlusal cant discrepancies, anterior open bite, deep overbite, skeletal lingual or buccal crossbites, or excessive dental compensation of the buccolingual inclination of posterior teeth.

18.3.5.1 Facial Asymmetry

There are numerous osseous structural conditions in the sagittal, vertical, and transverse plane that may influence dental arch shape and result in dental asymmetry. Dental asymmetries have been grouped into four types: diverging occlusal planes, asymmetric left-to-right buccal occlusion, unilateral crossbite, and asymmetric arch form (Van Steenbergen and Nanda 1995) (Fig. 18.34).

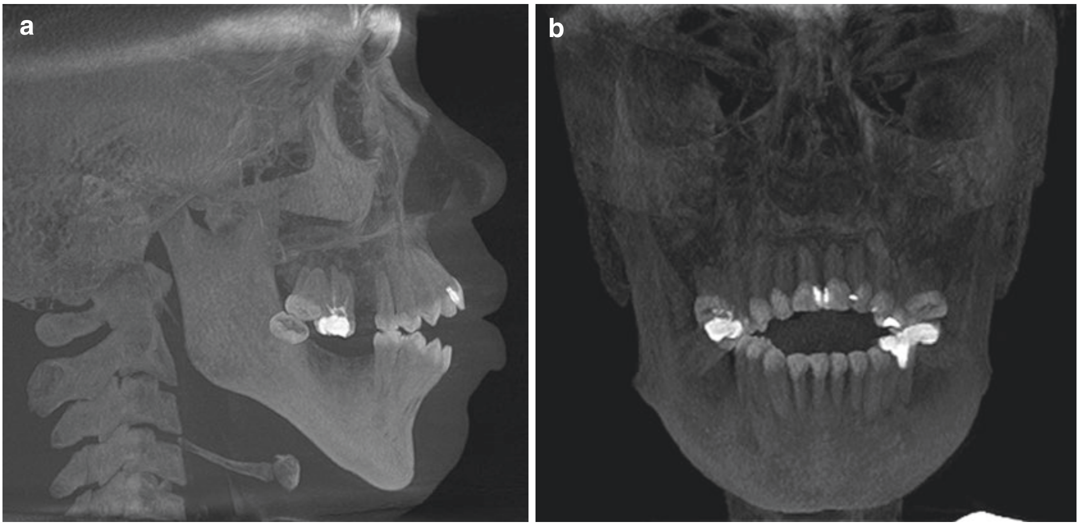

Fig. 18.33 Right lateral (**a**) and frontal (**b**) MIPs showing severe Class II skeletal with anterior open bite due to maxillary insufficiency and high mandibular plane

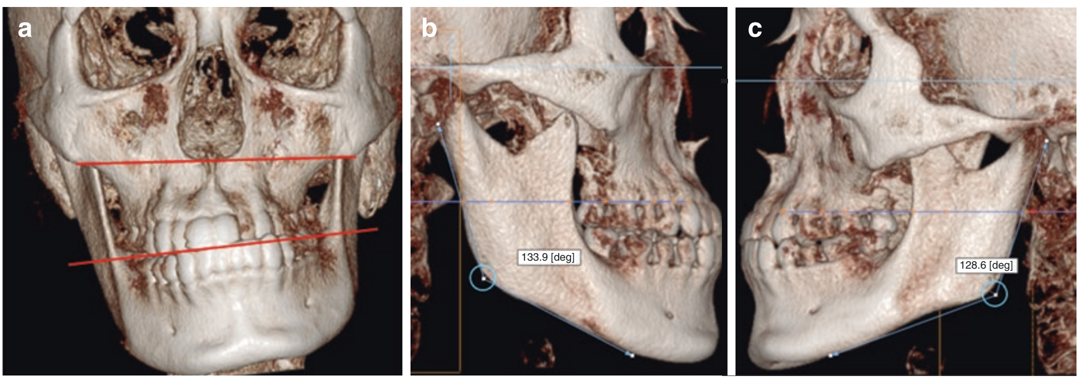

Fig. 18.34 AP frontal (**a**), right (**b**), and left (**c**) lateral volumetric surface renderings of a female orthodontic patient. Note the marked asymmetry evidenced by the altered occlusal plane, shift in the mandibular midline to the left and unilateral left anterior and posterior crossbite. This was caused by a right hemi-mandibular hyperplasia; the mandibular angles (**b**, **c**) confirm and quantify this skeletal discrepancy

18.3.6 The Temporomandibular Joint (TMJ)

Visualizing the morphology of the TMJ articulation may be necessary if orthopedic treatment is anticipated that may affect structural development during growth (e.g., head gear, functional appliances such as a Herbst appliance), or if the patient relates a history of previous condylar trauma.

TMJ pathologies that result in alterations in the size, form, quality, and spatial relationships of the osseous joint components may lead to skeletal and dental discrepancies such as progressive bite changes including bite opening and limitation, deviation upon opening or closing, changes in tooth position and occlusion, and changes in the TMJ of the non-affected side. Such TMJ instabilities can lead to unpredictable orthodontic outcomes. Affected joints are particularly important to image in patients with diminishing quality of life issues, such as persistent pain or limited opening. Important TMJ conditions include developmental disorders such as condylar hyperplasia, hypoplasia or aplasia (Figs. 18.35 and 18.36), and moderate to severe arthritic degeneration as well as fractures (Fig. 18.37) (Alexiou et al. 2009; Helenius et al. 2005; Koyama et al. 2007; Ahmad et al. 2009;

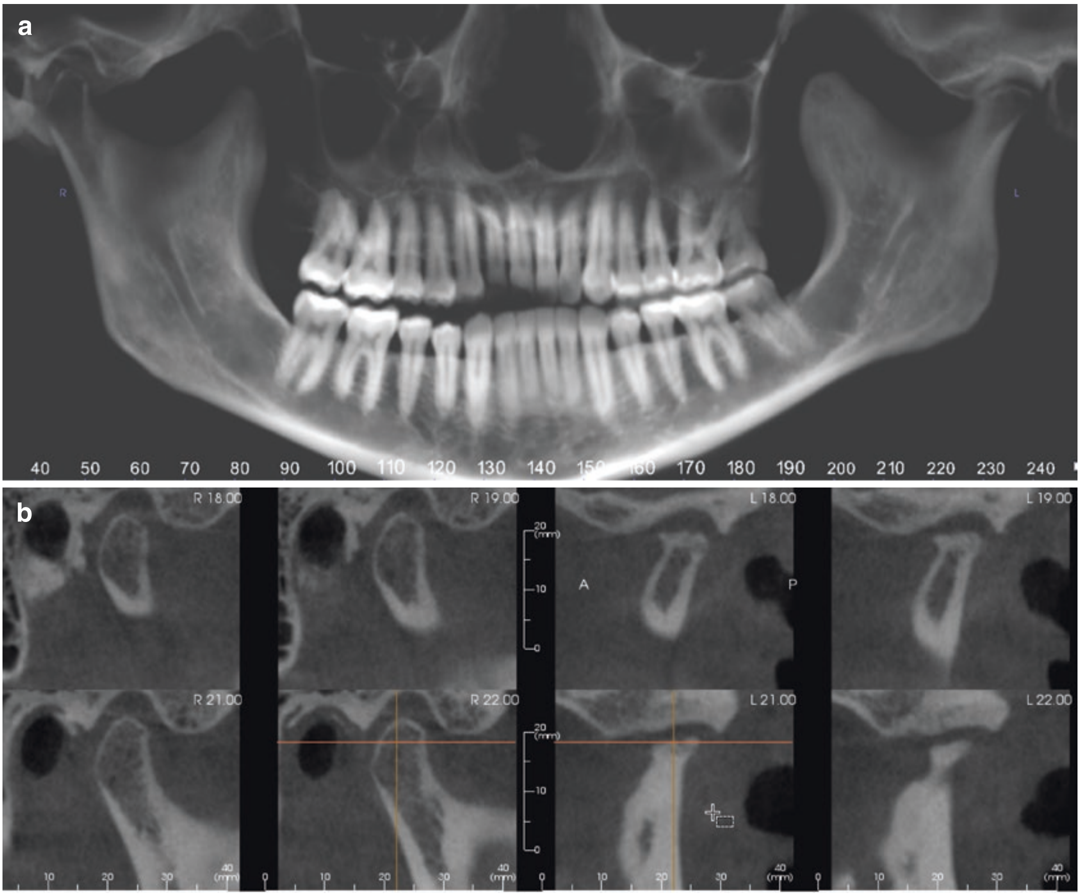

Fig. 18.35 Reformatted panoramic (**a**) and serial cross-sectional (**b**) CBCT images of the right and left TMJs of a younger patient presenting for orthodontic therapy to correct a right posterior open bite. Images demonstrate an asymmetry between the right and left mandible due to left condylar hypoplasia. Failure to diagnose such an association may result in unpredictable orthodontic outcomes

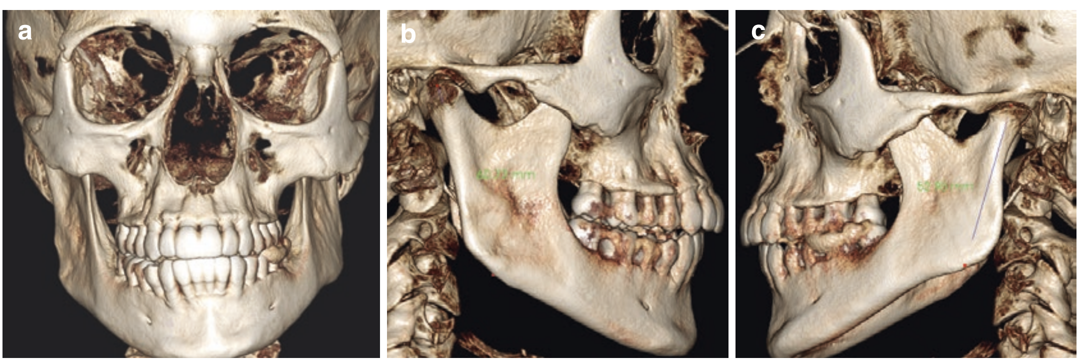

Fig. 18.36 Frontal AP (**a**), right (**b**), and left (**c**) lateral volumetric surface renderings of the same patient as in Fig. 18.35, clearly demonstrating the asymmetry and left condylar hypoplasia with reduced left ramal length

Dworkin and LeResche 1992; Schiffman et al. 2010a, b; Truelove et al. 2010; Bryndahl et al. 2006). In these situations, CBCT imaging provides additional diagnostic information such as the size, shape, and position of mandibular condyle heads in established positions and the presence of active disease that may influence management.

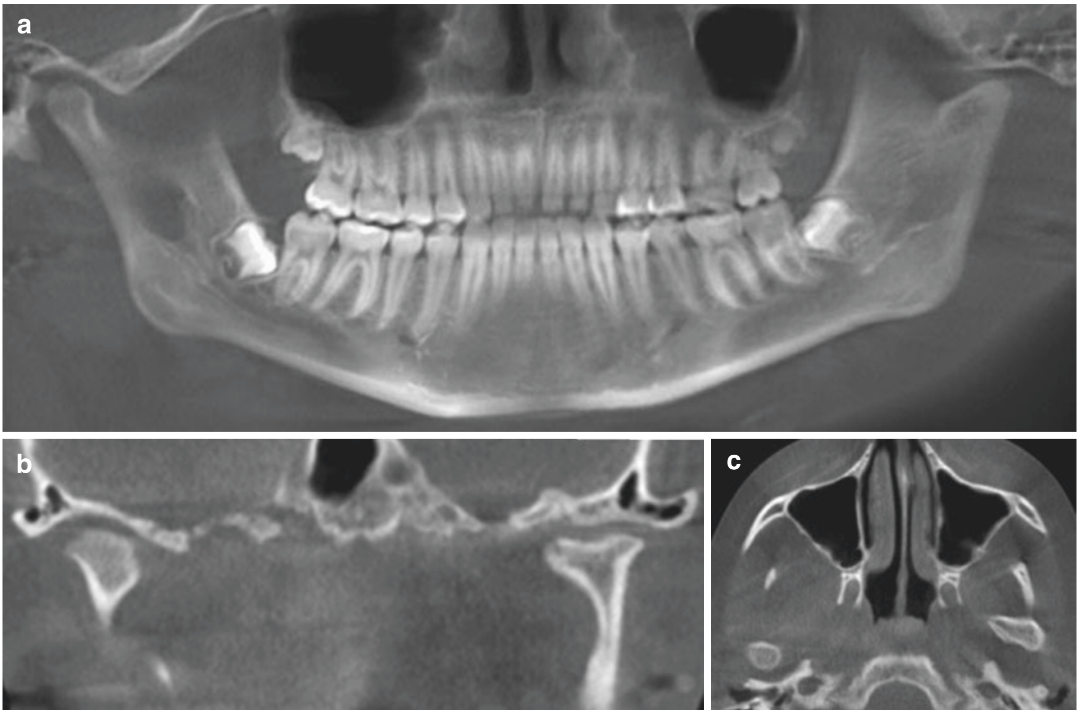

Fig. 18.37 Reformatted panoramic (**a**), 2 mm thick orthogonal coronal (**b**), and axial (**c**) sections through the mandibular condyles showing left healed and remodeled condylar fracture. Note the remodeling of both the temporal glenoid fossa and mandibular condylar components such that there is no overall vertical discrepancy on the left side

18.3.7 Post-therapy Assessment

CBCT may be useful in assessing the treatment outcomes of orthognathic surgery, grafting procedures, and use of nonsurgical devices to affect vertical or transverse discrepancies (Fig. 18.38) (Kapila et al. 2011; Mah et al. 2010; Merrett et al. 2009). For technical details on the use of specific software for post-therapy assessment, see Chap. 20.

18.3.7.1 Assessment of Alveolar Cleft and Palate Defects

Cleft lip and palate (CLP) is the most common craniofacial anomaly and requires an integrated multi-disciplinary and staged approach to management. Orthodontic involvement is typically at about 9 years of age when often a rapid palatal expansion is required to correct maxillary transverse deficiencies. CBCT assessment of the CLP patient at this time is highly advisable to: (1) determine the need for secondary alveolar bone grafting (SABG), (2) localize the presence and position of unerupted and impacted teeth, especially the maxillary canines, (3) monitor the movement of teeth adjacent the cleft, and (4) assess the status of the alveolar bone if dental implant restoration is anticipated.

SABG provides bony support to the teeth adjacent to the cleft, stabilizes the maxillary arch, particularly in bilateral clefts and, closes any oronasal fistulae present. The procedure is usually performed as one of many “revision” surgeries at an age of between 9 and 11 years. This is based on the assumption that growth of the anterior region of the maxilla is largely complete at this age and that scarring would not compromise future maxillary growth. Unfortunately, there is only fair to good treatment outcome after SABG with 34% providing good bone support with deficiencies in bone filling were noticed in palatal or apical areas. (Suomalainen et al. 2014).

The Bergland system (Bergland et al. 1986) is a radiographic-based qualitative classification system applied to intraoral periapical images and

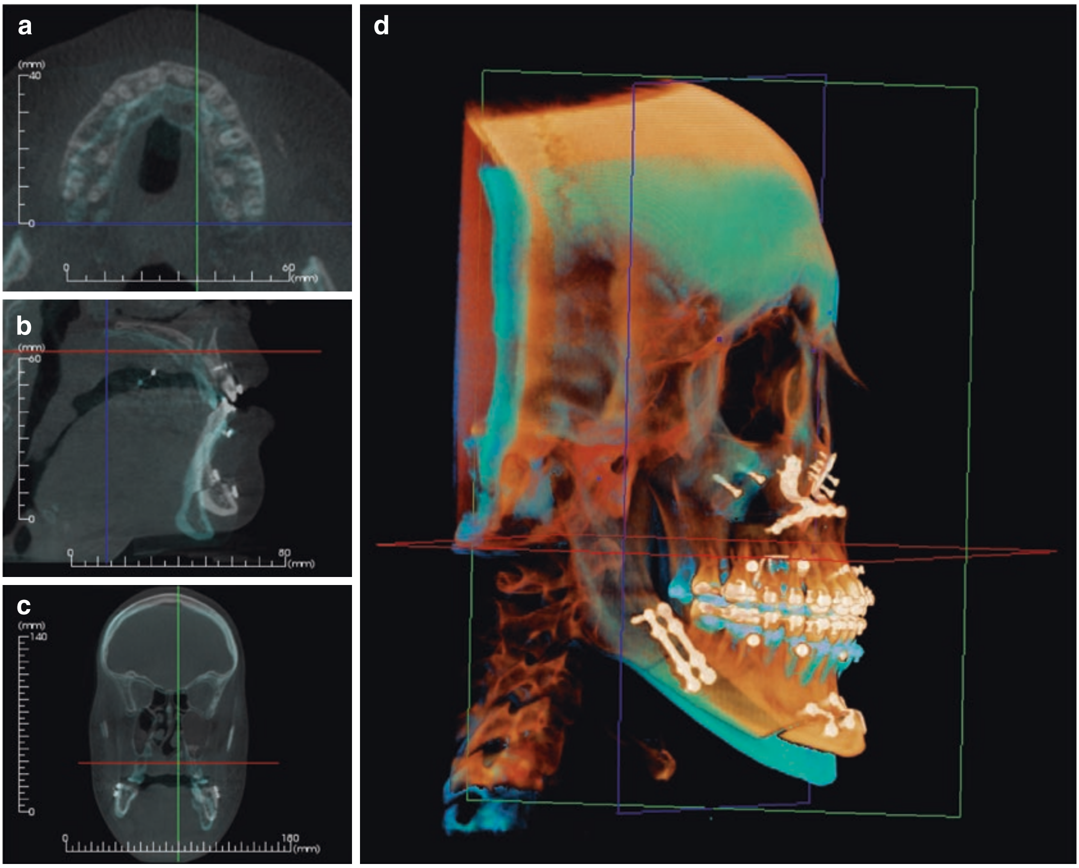

Fig. 18.38 Screen shot of computer program allowing superimposition of initial CBCT data (*blue*) with post-orthognathic treatment CBCT data (*orange*). Superimposition of reference anatomic landmarks in axial (**a**), sagittal (**b**), and coronal (**c**) reference planes provides a 3D volumetric representation (**d**). (Images courtesy, Anatomage)

quantifies the height of the interalveolar septum height in CLP individuals according to four types: Type I—height approximately normal, Type II—at least 3/4 of normal height, Type III—less than 3/4 of normal height, and Type IV—no bone, failure. However, this system is based on the eruption of the canine adjacent the cleft and does not provide a quantitative assessment.

Suomalainen et al. (2014) proposed a CBCT-based assessment of the CLP defect based on the amount of residual bone in two planes at three root levels of the adjacent teeth: cervical, middle, and apical third:

- **Vertical plane.** Incorporating parasagittal images, the presence or absence of the bone graft at each root level is classified as:
  - 1 = poor (i.e., no detectable bone).
  - 2 = fair (i.e., the bony bridge extends in part to the height of the given section of the roots of the adjacent teeth).
  - 3 = good (i.e., the bony bridge fills the total height of the given section).
  - NA = not assessable due to artifacts caused by metallic orthodontic appliances.
- **Horizontal plane.** Using axial images, the labio-palatal thickness of the bone at each root level is classified as:
  - 1 = poor (i.e., no detectable bone).
  - 2 = fair (i.e., bone width in horizontal dimension is less than the width of the roots of the teeth adjacent to the cleft).
  - 3 = good (i.e., the width of the bony bridge is as wide as or wider than the width of the roots of the teeth adjacent to the cleft.

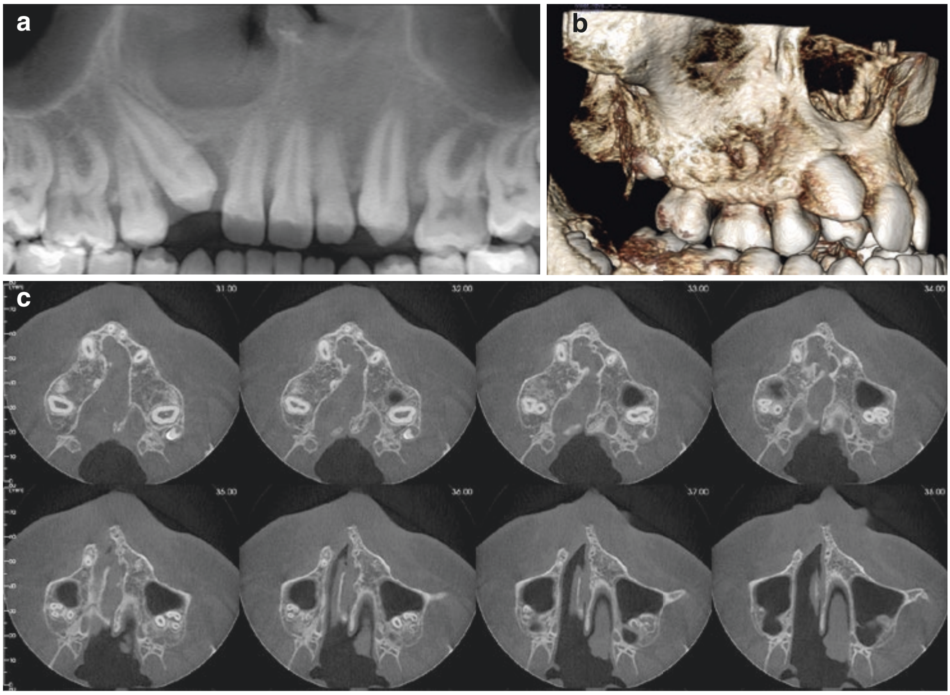

Fig. 18.39 Reformatted panoramic (**a**), right lateral solid surface rendering (**b**), and sequential axial images (**c**) of a patient with maxillary hypoplasia with transverse deficiency and complete right unilateral cleft with medial displacement of the right segment. A small bone "bridge" is present inferior to the right piriform nasal aperture at the apical level between the right maxillary central incisor and the canine. Marginally adequate bone is present to facilitate orthodontic alignment of the teeth adjacent the cleft, however a residual bony defect will persist and may be accompanied by mucosal recession

CBCT imaging is advisable prior to orthodontic treatment, prior to and after secondary alveolar bone grafting (SABG) (Figs. 18.39 and 18.40). Specifically, CBCT images assist in (1) visualizing and characterizing the volume of the alveolar defect and, therefore, the amount of bone needed, (2) determining the postoperative bone fill, (3) assessing the orthodontic considerations such as amount of available bone and path of eruption associated with commonly occurring impacted canines (Oberoi et al. 2010).

18.3.8 Airway Assessment

CBCT imaging can be considered as a tool for the purpose of assessing the airway but findings should be interpreted with caution. This is particularly so for patients suffering from obstructive sleep apnea/hypopnea syndrome (OSA), who often present with a multifactorial etiology. For these individuals, CBCT images of the airway are most often acquired in the standing or seated position whereas ideally imaging should be made with the patient in the supine position. Although a number of studies have measured airway linear and volumetric airway dimensions (Fig. 18.41) and changes over time (particularly with regard to OSA), the validity of such measurements present a number of challenges. The boundaries of the nasopharynx with the maxillary/paranasal sinuses and the boundaries of the oropharynx with the oral cavity are not consistent among subjects and image acquisitions, and airway shapes and volumes vary markedly with dynamic processes such as breathing and head postures (El and Palomo 2010; Oh et al. 2011; Abramson et al. 2011; Schendel et al. 2011a, b; Iwasaki et al. 2011; Conley 2011; Lenza et al. 2010; El and Palomo 2010; Schendel and

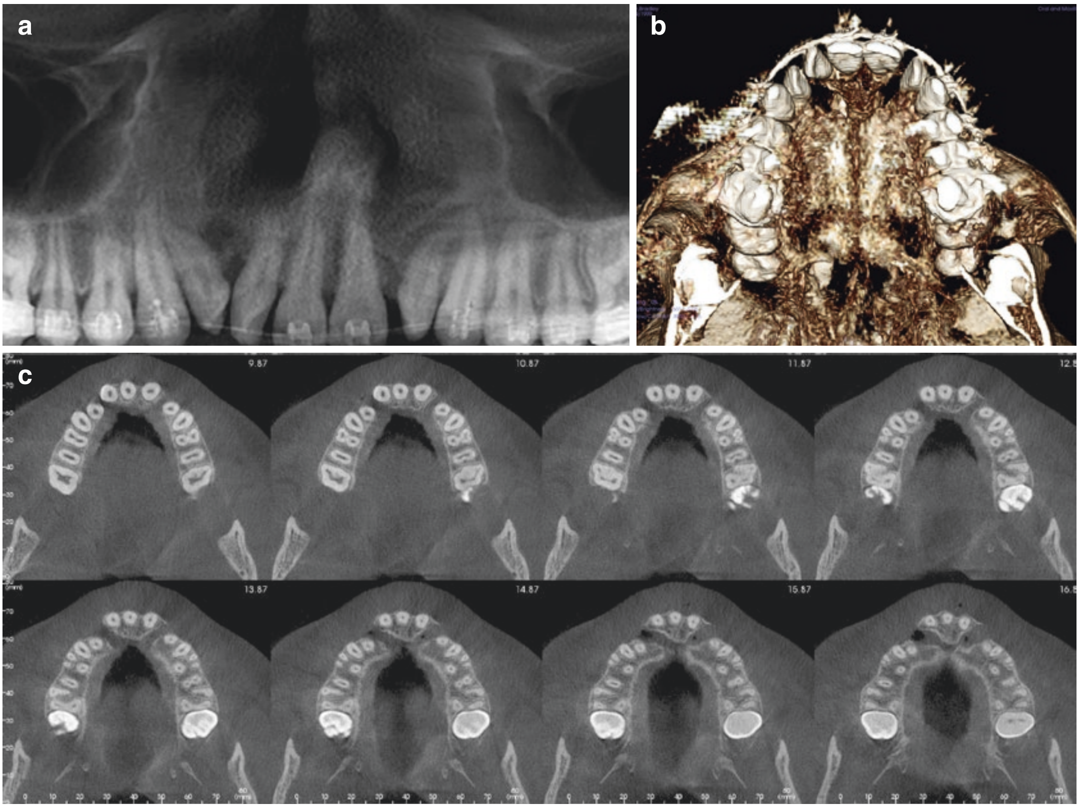

Fig. 18.40 Reformatted panoramic (**a**), inferior maxilla solid surface rendering (**b**), and sequential axial images (**c**) of a patient with bilateral complete maxillary alveolar clefts. The remaining premaxillary segment is suspended by a superior bony bridge attached to the nasal spine. Inadequate bone is present to facilitate orthodontic alignment of the teeth adjacent the cleft

Hatcher 2010; Tso et al. 2009; Strauss and Burgoyne 2008; Osorio et al. 2008; Ogawa et al. 2005; Aboudara et al. 2003; Sera et al. 2003). However, special attention should be paid towards airway assessment especially in orthodontic patients who are suspected of mouth breathing, adenoid hypertrophy, or OSA (El et al. 2011). Specifically, airway patency and nasal morphology including the turbinates should be assessed.

18.3.9 Pathology

CBCT imaging demonstrates the location, size, shape, extent, and full involvement of pathology of the jaws. Various conditions may be encountered, most commonly benign cysts and tumors of the jaws, however some infections (Fig. 18.42) and malignancies are more prevalent in children. All potentially require surgical intervention prior to orthodontic therapy.

18.3.9.1 Incidental Findings on Orthodontic Patients

Unlike conventional imaging, CBCT images demonstrate large areas that are free from blurring and overlapping of adjacent structures and clearly depict the sinus, TMJ relationships, and airway anatomy. In orthodontics it is therefore expected that the use of CBCT will provide a higher prevalence of incidental findings—observations that appear unrelated to the scan's original purpose (see Chap. 17). These incidental findings might raise concern as they may not necessarily be insignificant.

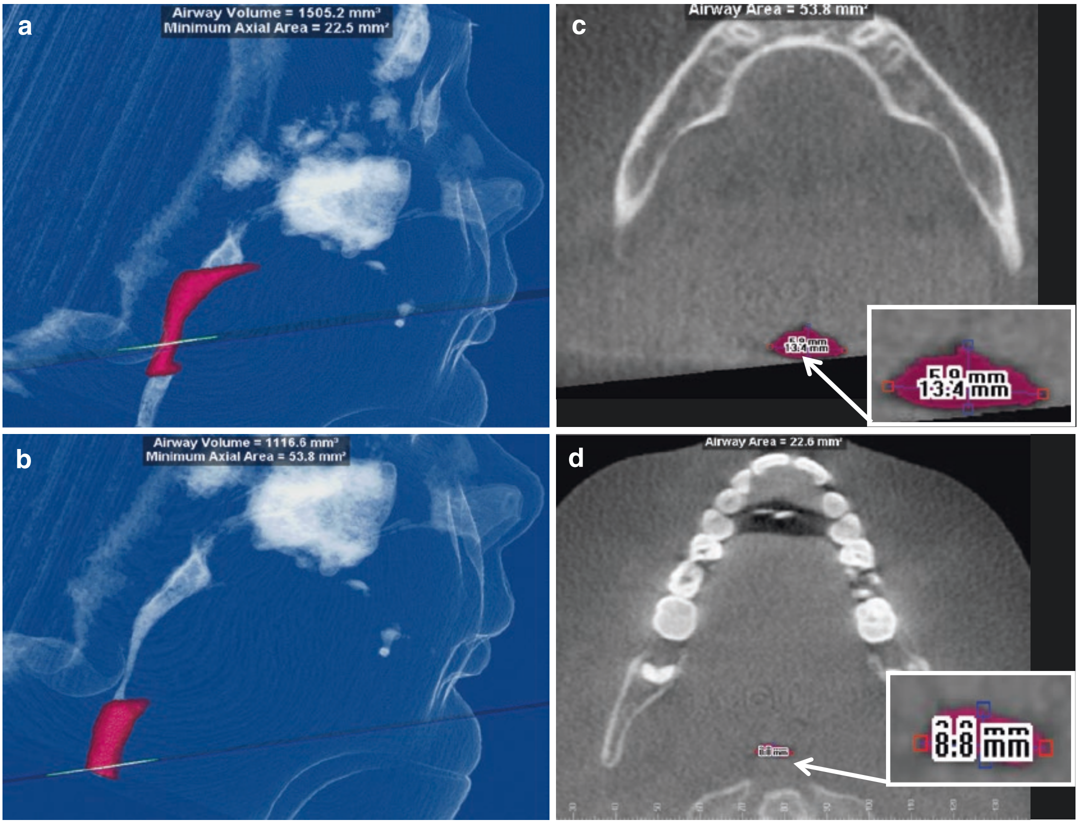

Fig. 18.41 Lateral 3D images of the segmented airway of a patient with OSA showing the segmented volumes of retroglossal (**a**) and retropalatal (**b**) airway space. The software algorithm identifies and displays the axial images at which the minimum cross-sectional area is present (**c**, **d**) and allows for measurement of anteroposterior and transverse dimensions (insert). (Images created using Dolphin 3D)

There are limited retrospective studies describing the incidence of various findings in an orthodontic population (Table 18.5) (Cha et al. 2007a; Pazera et al. 2011; Gracco et al. 2012; Doğramacı et al. 2014; Drage et al. 2013; Edwards et al. 2014; Kuijpers et al. 2014). While the prevalence varies depending on the population sample, it appears that the most common findings are related to the airway and include enlarged airway masses (Fig. 18.43) sinusitis, retention cysts and sinus polyps and sinus developmental conditions (Fig. 18.44).

However, there are occasions where significant findings are discovered which influence not only the orthodontic management of the patient may require medical intervention or advanced imaging such as multi slice computed tomography with contrast or magnetic resonance imaging such as including skull base entities (Newaz et al. 2015) and cervical conditions (Fig. 18.44).

18.3.10 Biomechanical Assessments

> The design of an orthodontic appliance depends on a thorough understanding of both biological and physical variables. It is an area wherein concepts of both biology and physics can be wedded into a true biomechanical discipline (Burstone 1985).

The ability to create 3D maxillofacial virtual "solid" structures from CBCT datasets provides opportunities for clinicians to apply the principles of biomechanics including vector analysis in regard to the entire gnathologic system as well as local tooth movement.

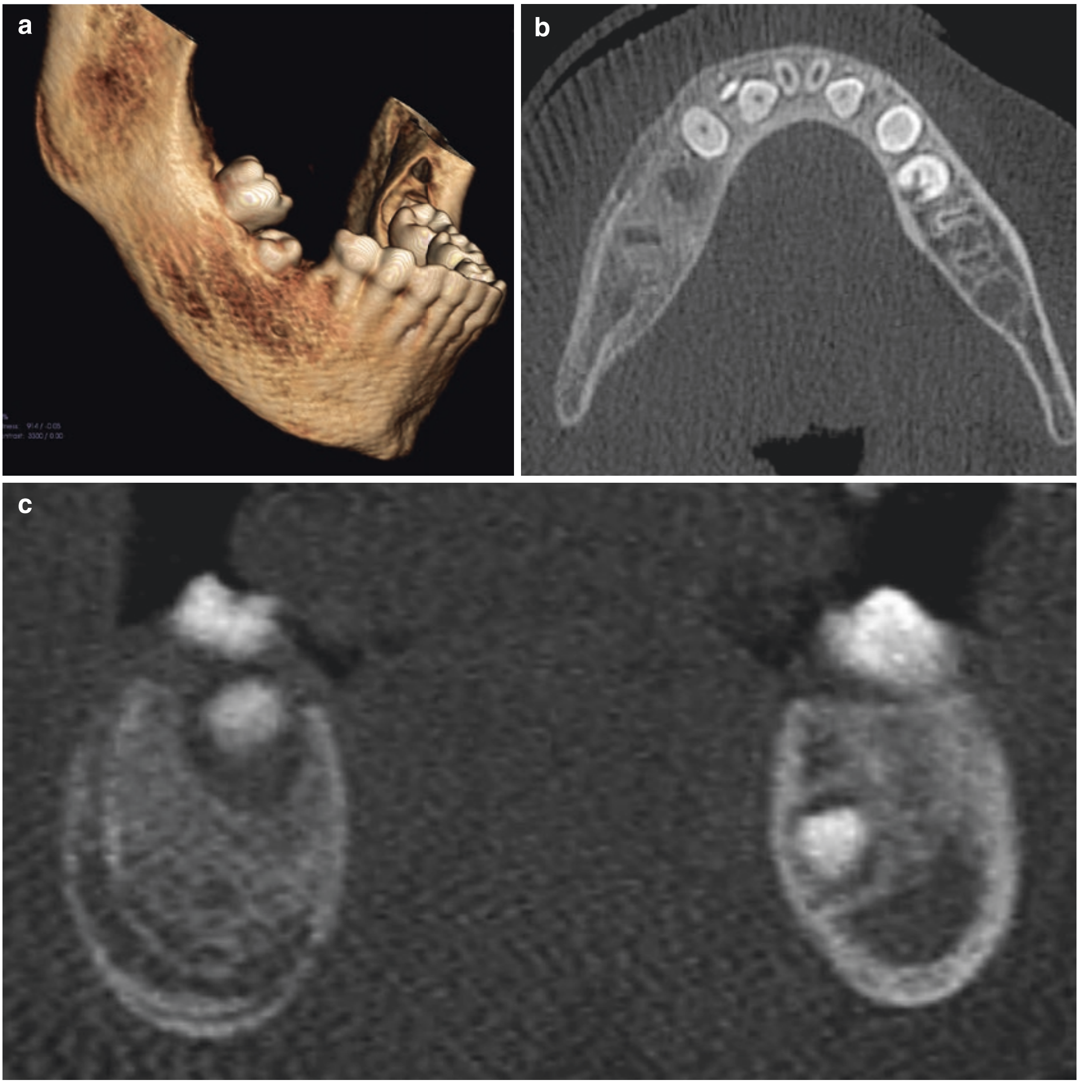

Fig. 18.42 Volumetric rendering (**a**), axial (**b**), and coronal (**c**) images of a young patient with expansion of the right mandibular body and pain after failure of eruption of the right mandibular second molar with removal of an infected deciduous tooth. In view of the patient history, the regional intra-medullary sclerosis and "onion-skin" cortical laminations are suggestive of an exaggerated response to the infection, Garre's osteomyelitis with proliferative periostitis

18.3.10.1 Temporary Skeletal Anchorage Device Placement

The movement of teeth is based on the establishment of an invariant fulcrum (known as anchorage) against which a force vector is applied. This can be in relation to a single tooth, a group teeth, or an entire dental arch. Mini-screws (mini-implants) have been used as temporary skeletal anchorage devices (TSADs) in orthodontics to establish anchorage and not only increased how far teeth can be moved, but also allowed more treatment options to patients. They have been used in the retraction of anterior teeth or the whole dentition, distalization of molars, in lingual orthodontics, for the protraction of molars or the whole dentition, in orthopedics, for the intrusion or extrusion of

Table 18.5 Summary of reported prevalence of incidental findings on CBCT for orthodontic samples

	Reference						
	1	2	3	4	5	6	7
Sample							
Number	252	139	513	183	329	427	187 (CLP)
Mean age (years)	18.6	UR	UR	18.3	14.5	14.2	11.7
Range (years)	UR	UR	12–60	9–60	UR	5–46	6.9–45
FOV	Large	Medium	Large	Small	Medium	Large	Medium
Incidental findings (%)							
Maxillary sinus (overall) (%)	14.3	46.8	50.3	33.8	37.6	30.9	80.3
Mucosal thickening (%)	7.5	23.7	40.1	17.6	23.6	18.1	39
Pseudocysts	5.8%	19.4	10.1%	1.7%	7.8%	6.89%	31%
ARS	–	3.6%	–	2.9	3.4%	1.3%	10.3%
Nasal	–	–	–	–	–	42.3%	–
Cervical spine	–	–-	–	–	4.5%	1.3%	–
Periapical lesion	2.3%	–	–	2.6%	4.5%	–	–
Cysts	–	–	–	3.5%	–	–	–
TMJ	4.3%	–	–	–	6.1%	6.4%	–

CLP cleft lip and palate, *UR* unreported
1 Cha et al. (2007a), *2* Pazera et al. (2011), *3* Gracco et al. (2012), *4* Doğramacı et al. (2014), *5* Drage et al. (2013), *6* Edwards et al. (2014), *7* Kuijpers et al. (2014)

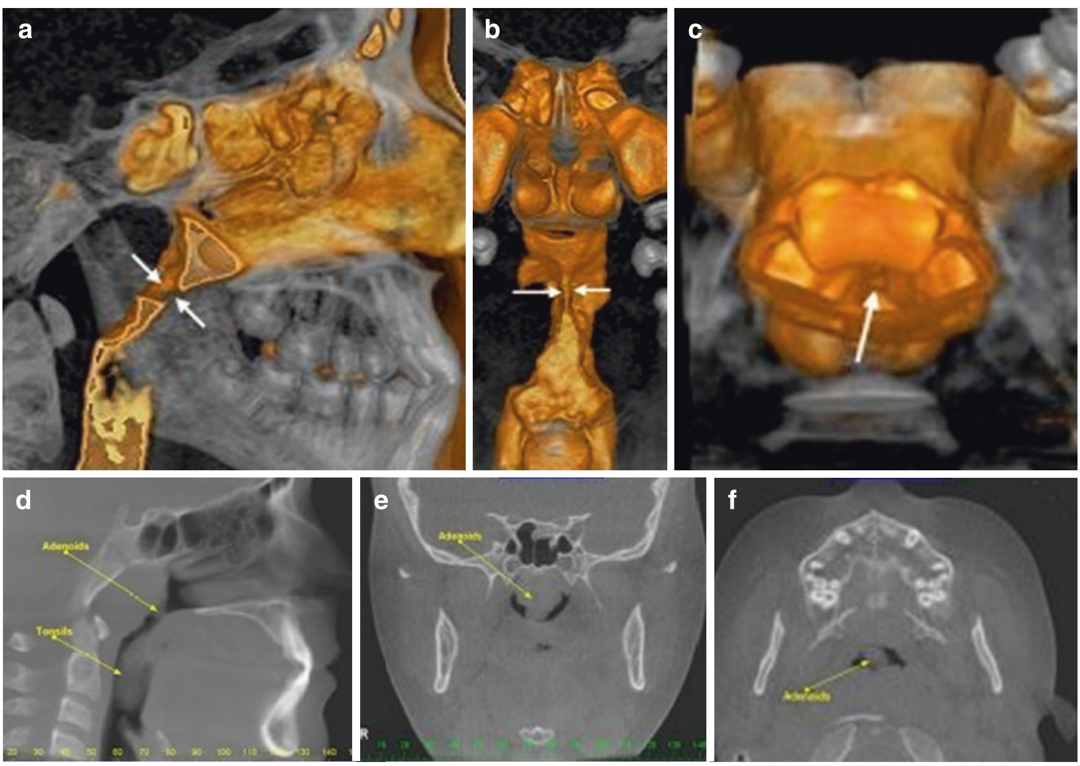

Fig. 18.43 Sagittal (**a**), coronal (**b**), and axial (**c**), hollow rendered airway with corresponding sagittal (**d**), coronal (**e**), and axial (**f**) CBCT images of patient with enlarged adenoids and tonsils and severe constriction of the retro-palatal airway

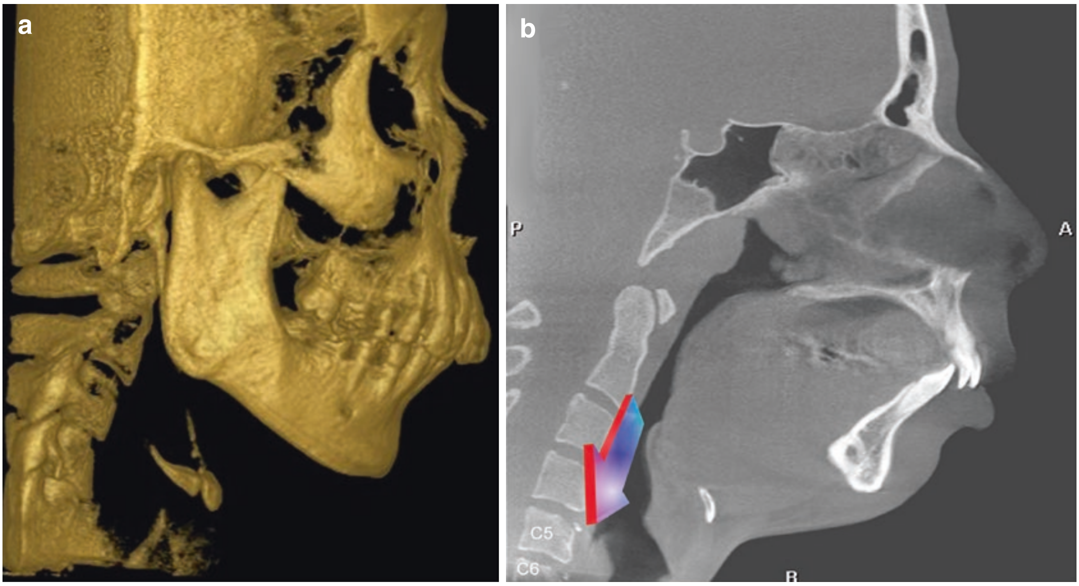

Fig. 18.44 Right lateral volumetric surface rendering (**a**) and midsagittal orthogonal image (**b**) of a 16-year-old with severe Class II malocclusion presented for "correction of his bite." In addition, a kyphosis of the cervical spine was noted. The patient was subsequently referred to a physician who diagnosed Scheuermann's kyphosis (Scheuermann's disease). Congenital kyphosis is a term used to describe a forward curvature of the spine. A dowager's hump or hunchback is often caused by collapse of the spinal vertebrae. Note the forward head posture and the fracture of the anterior region of C5 and C6

individual teeth, palatal expansion and molar uprighting. The ideal positioning of TSADS should avoid tooth roots which can result in potential loss of vitality and mechanical ankylosis as well as vital structures including the sinus and nerve canals. Placement depends on the type of anchorage required (Papadopoulos and Tarawneh 2008) and while most are inserted through the buccal alveolus alternate insertion sites include the palatal alveolus, palate and zygoma. While current literature does not support the routine use of CBCT imaging for the placement of TSADs (van Vlijmen et al. 2012), volumetric imaging can be useful in situations where there is concern for cortical bone thickness and density, areas of questionable bone quantity (Fig. 18.45), where intraoral placement is difficult such as the palate and zygomatic arch and postoperatively, especially when patients are symptomatic (Fig. 18.46).

18.3.10.2 Biomechanical Modeling

Dynamic functional biomechanical modeling of the jaw, masticatory system and the TMJ articulation by muscular kinetic simulations was pioneered and developed by Dr. Allan Hannam (2003). He and his colleagues created a dynamic biomechanical model of the human jaw and laryngeal structures through data extraction from high resolution cone beam CT imaging of a representative 35-year-old male subject. The model incorporated multiple dynamic parameters including mandibular muscle properties, taken from published literature. The model included rigid-body skeletal components for the mandible, maxilla, hyoid, thyroid, and cricoid, point-to-point, hill-type muscle models, La Grangian rigid-body constraints for the TMJ and bite contact and spring networks for laryngeal connective tissue (Hannam et al. 2008; Stavness et al. 2014) (Fig. 18.47).

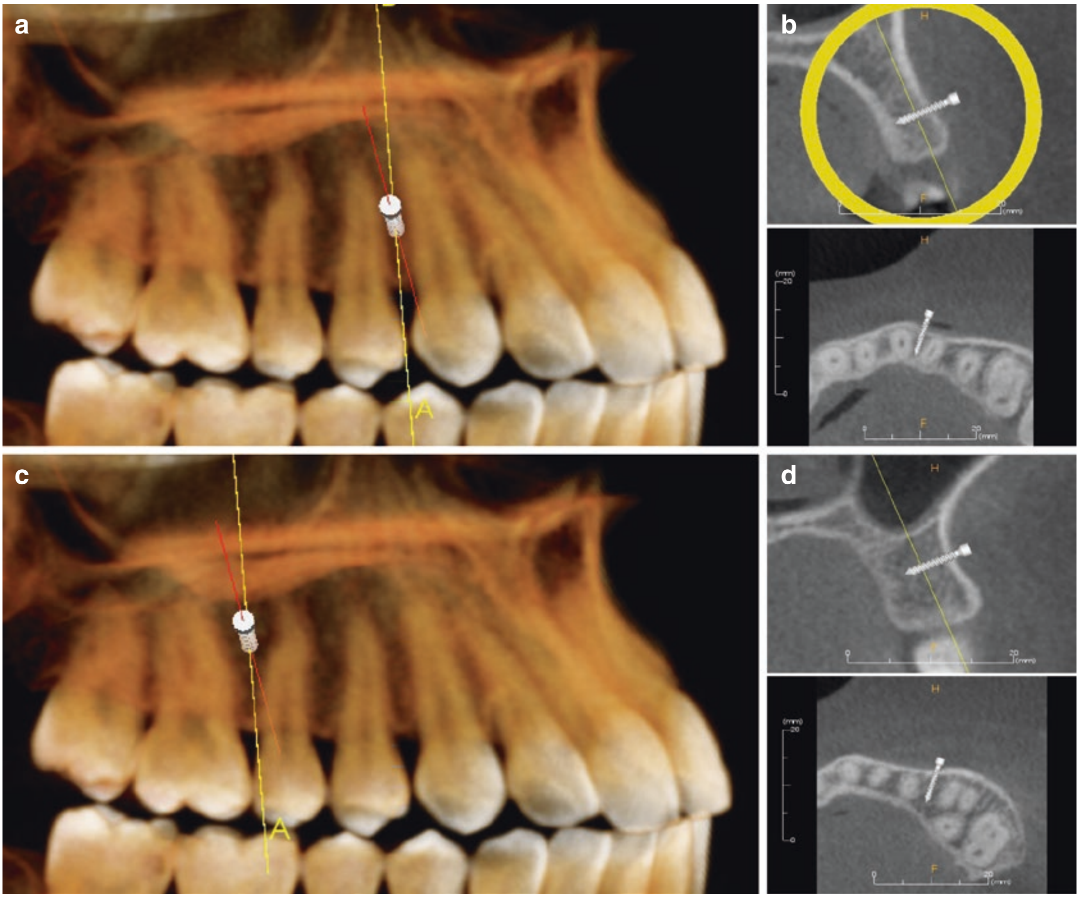

Fig. 18.45 Right volumetric rendering (**a**) and corresponding cross-sectional and axial images (**b**) showing planned buccal placement of TSAD in the alveolus distal to the right maxillary canine. While there appears to be adequate buccal bone, the palatal bone is markedly reduced because of the distal rotation of the adjacent first bicuspid. Left volumetric rendering (**c**) and corresponding cross-sectional and axial images (**d**) showing planned buccal placement of TSAD in the alveolus distal to the right maxillary 2nd bicuspid with adequate interradicular bone present

Based on this work, individualized models for specific patients can be created online using a Java platform, ArtiSynth (http://artisynth.magic.ubc.ca/artisynth/ (Langenbach and Hannam 1999; Lloyd et al. 2012). The models can be used to predict muscular, occlusal, and articular biomechanical events during simulated function and to examine deviations in form and function. Active tongue posture can also be biomechanically modeled for analysis (Stavness et al. 2011; Gerard et al. 2003) (Fig. 18.48). Volume measurements of the tongue could provide a more objective assessment of size, to aid in the diagnosis of open bites, tongue thrust, and arch-width discrepancies. These functional dynamic models may give additional information and understanding on airway dynamics and its effect on craniofacial growth and tongue posture. Obstructive airway issues are becoming of greater interest in medicine and dentistry. Obstructive airway, allergy, and altered tongue function need to be evaluated early in life when we have the best chance to normalize facial growth and airway function.

18.3.11 4D Analysis

Temporal, or 4D assessment of maxillofacial bony or soft tissue changes related to treatment or growth is an important component in predicting changes associated with treatment, the effects of development, and treatment stability.

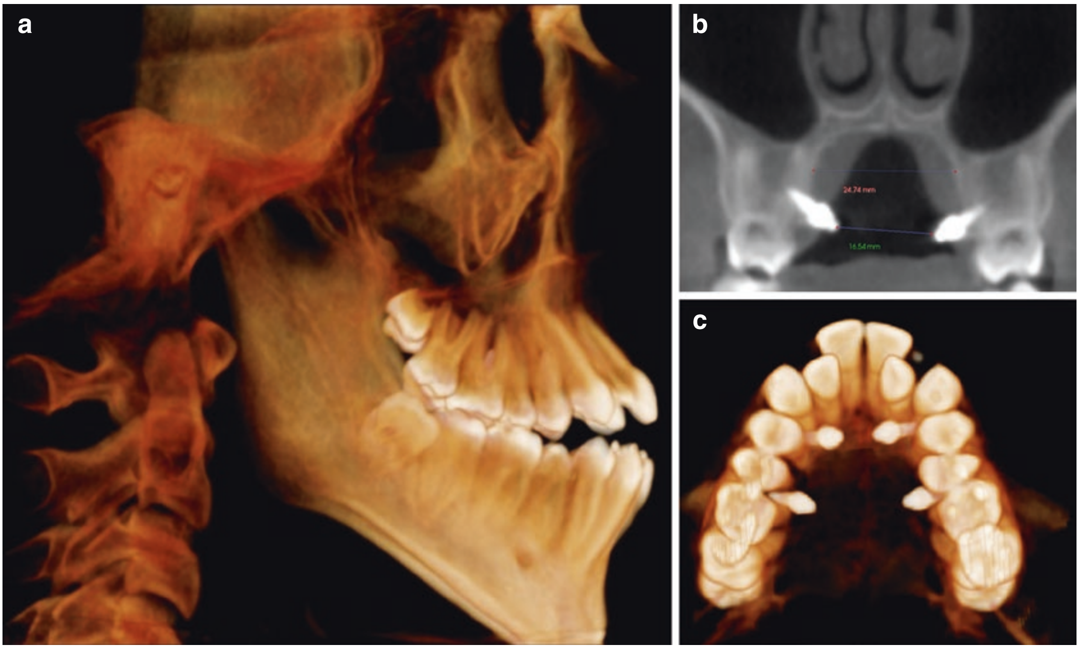

Fig. 18.46 Right lateral volumetric rendering of Class III skeletal patient with maxillary deficiency and anterior open bite. Coronal (**b**) and interior maxillary volumetric rendering (**c**) showing placement of palatal TSADS used as anchorage for bilateral posterior maxillary segmental intrusion (Images courtesy, Jack Fisher)

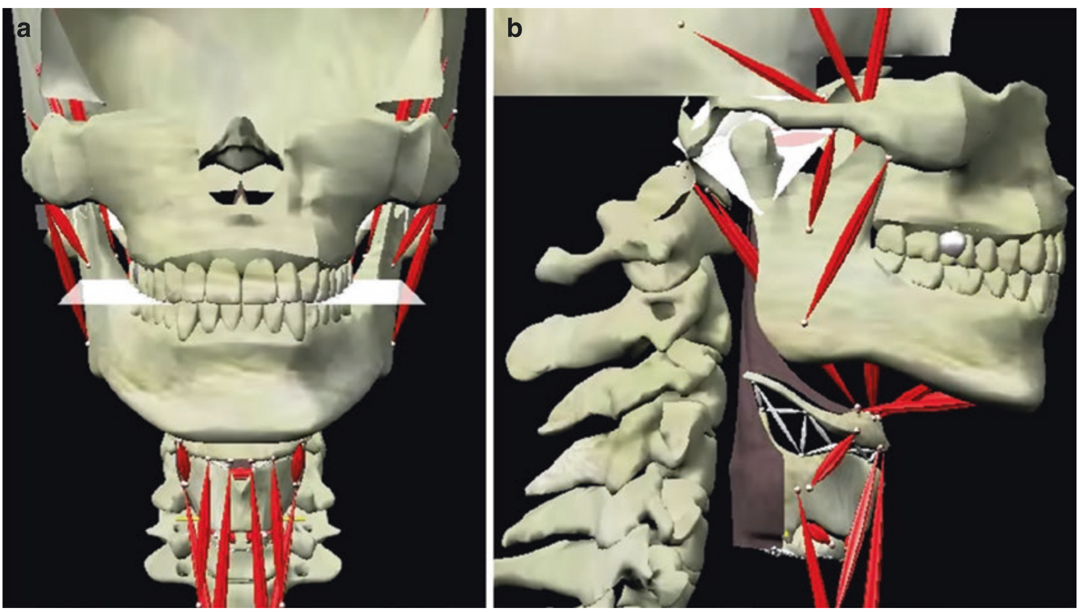

Fig. 18.47 Frontal (**a**) and right lateral (**b**) screenshots of a dynamic biomechanical model of the human jaw, hyoid, and laryngeal structures (Images courtesy Drs. A Hannam and GEJ Langenbach, (Hannam et al. 2008; Stavness et al. 2006; Lloyd et al. 2012))

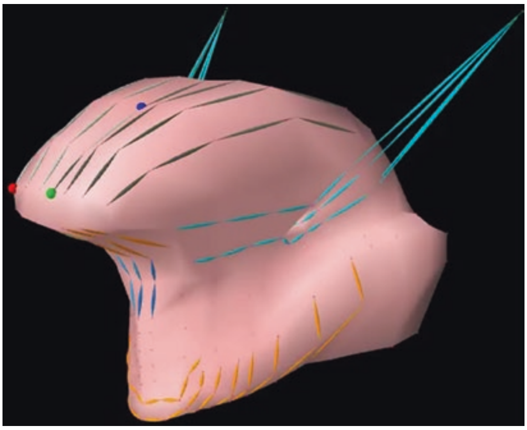

Fig. 18.48 Left oblique screenshot of a dynamic biomechanical 3D tongue model (Vogt et al. 2006) with fast 3D finite element method (FEM) and methods to connect to other models (Lloyd et al. 2012)

4D analysis can be performed by comparison of specific metrics obtained from 2D or 3D reconstructions between temporal stages or provided visually. Both methods require the superimposition of landmarks, planes, or structures to align 3D CBCT datasets at different time points. The computed registration is then applied to the segmented structures to measure changes with time or treatment procedures. The most common method to compare such datasets include the construction, registration, and superimposition of virtual 3D models using software that allows visual and quantitative assessment of the location and magnitude of changes over time providing a 3D graphic display where the regional magnitude of the displacement is color coded (Cevidanes et al. 2005, 2006, 2007) (Fig. 18.49). See Chap. 20 for specific details.

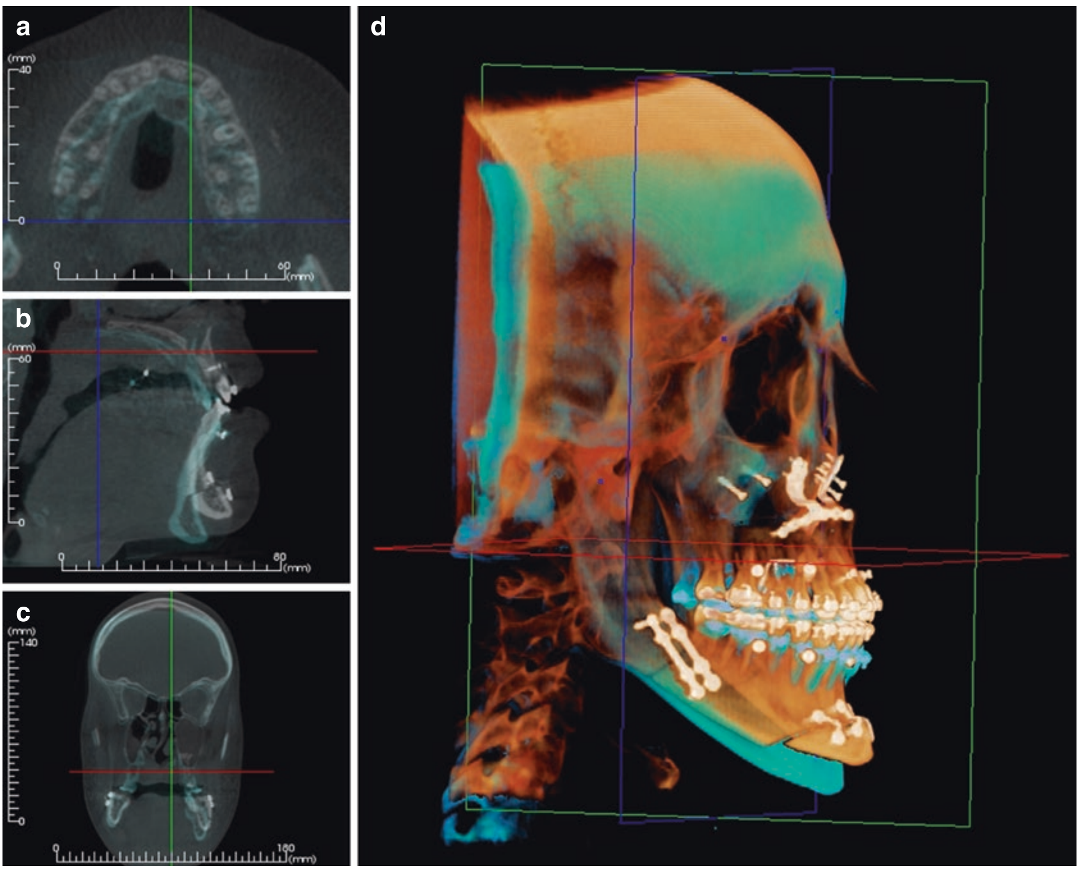

Fig. 18.49 Screen shot of superimposition of initial CBCT data (*blue*) with post-orthognathic treatment CBCT data (*orange*). Superimposition of reference anatomic landmarks in axial (**a**), sagittal (**b**), and coronal (**c**) reference planes provides a 3D volumetric representation (**d**) (Images courtesy, Anatomage)

18.4 Radiographic Imaging Guidelines for Orthodontics

The first set of recommendations for appropriate radiographic examinations for dentistry in the United States, referred to as "*selection criteria,*" were based on patient presentation and initially published in 1987 (Matteson et al. 1987) with the latest version in 2006 (Greenblatt et al. 2006). They were the result of work of a panel consisting of representatives from general dentistry and various disciplines convened by the Food and Drug Administration (FDA) in 1983. These guidelines suggest that for monitoring growth and development for children and adolescents:

> …clinical judgment be used in determining the need for, and type of radiographic images necessary for, evaluation and/or monitoring of dentofacial growth and development (Greenblatt et al. 2006).

While outlining broad principles, this document provides little specific direction as to appropriate radiographic protocols for patients with growth or dental anomalies presenting for orthodontic opinion.

In the European Union (Janssens et al. 2003) and in the United Kingdom, (Isaacson et al. 2008), guidelines for orthodontic imaging state that there are no orthodontic indications for taking radiographs routinely before a clinical examination nor taking a series of radiographs for all orthodontic patients. The latter document provides clinical decision algorithms based on the age of the patient (less than or over 9 years of age) and clinical presentation such as delayed or ectopic eruption, crowding and anteroposterior discrepancies such as anterior overjet or overbite.

18.4.1 Guidelines for the Use of CBCT in Orthodontics

Farman and Scarfe (2006) were among the first to publically urge the development of appropriate imaging sequence selection criteria for CBCT imaging to reinforce the "*as low as reasonably achievable*" (ALARA) principle to ensure that orthodontic patients were not exposed to ionizing radiation unnecessarily. Subsequently White and Pae (2009) proposed an algorithm for obtaining radiographs for the patient requiring orthodontic care, including consideration of CBCT. They recommended CBCT for patients presenting with specific clinical conditions:

- Severe facial asymmetry or facial disharmony.
- Sleep apnea.
- Impacted maxillary cuspids.
- Minidental implants are being considered.

The British Society of Orthodontics (Isaacson et al. 2008) suggested the use of CBCT be limited to highly selected cases where conventional radiography cannot supply satisfactory diagnostic information for conditions such as:

- Cleft palate patients
- Unerupted teeth, particularly when resorption is a concern
- Orthognathic surgery planning
- TMJ articulation, but only if the additional information obtained was likely to influence management or subsequent treatment

This Group along with the French (Haute Autorité de Santé, 2009) and German (Leitlinie der DGZMK 2009) dental authorities specifically indicate that the routine use of CBCT for all orthodontic patients could not be recommended in the absence of adequate scientific evidence for diagnostic utility and cost-effectiveness.

The SEDENTEXCT Project (2008–2011), funded by The Seventh Framework Programme of the European Atomic Energy Community (Euratom), developed evidence-based guidelines dealing with justification, optimization, and referral criteria for users of dental CBCT (European Commission, 2012). The presented an evidence-based assessment of the indications for CBCT imaging for the developing child including orthodontics (Table 18.6). This group, representing countries of the European Union, also stated that large volume CBCT should not be used routinely for orthodontic diagnosis. They

Table 18.6 SEDENTEXCT consensus assessment of evidence-based potential applications of CBCT imaging in orthodontics

Region	Potential application	Level of evidence[a]	Comment
Localized	Cleft palate	GP	Where the current imaging method of choice is MSCT, CBCT may be preferred if radiation dose is lower
	Unerupted tooth localization	GP	Where the current imaging method of choice is MSCT, CBCT may be preferred because of reduced radiation dose
	Localization of and external resorption related to unerupted teeth	C	CBCT may be indicated when the information cannot be obtained adequately by lower dose conventional (traditional) radiography
	Bone dimensions	NR	Limited evidence
	Temporary orthodontic anchorage using mini-implants	GP	Not normally indicated
	Rapid maxillary expansion	NR	Limited evidence
Generalized	3D cephalometry	NR	Limited evidence
	Surface imaging integration	NR	Limited evidence
	Airway assessment	NR	Limited evidence
	Age assessment	NR	Limited evidence
	Orthodontic related paresthesia	NR	Limited evidence
	Craniofacial abnormalities	GP	For complex cases of skeletal abnormality, particularly those requiring combined orthodontic/surgical management
	Orthognathic surgery	C	Where bone information is required, in orthognathic surgery planning, for obtaining three-dimensional datasets of the craniofacial skeleton

[a]*C* a body of evidence including studies rated as 2+, directly applicable to the target population and demonstrating overall consistency of results; or extrapolated evidence from studies rated as 2++. *D* evidence level 3 or 4; or extrapolated evidence from studies rated as 2+. *GP* Good Practice based on clinical expertise of the guideline group and consensus of stakeholders. *NR* no recommendation, inadequate evidence

concluded that while some clinical indications exist, that research is needed to define robust guidance on clinical selection for large volume CBCT in orthodontics, based upon quantification of benefit to patient outcome.

Recommendations from the American Dental Association Council on Scientific Affairs (ADA-CSA) (American Dental Association Council on Scientific Affairs 2012) state that CBCT imaging should be performed:

> …only when they (sic. The dental practitioner) expects that the diagnostic yield will benefit patient care, enhance patient safety or improve clinical outcomes significantly (ADA-CSA 2012).

The ADA-CSA also indicate that:

> CBCT should be considered as an adjunct to standard oral imaging modalities (ADA-CSA 2012).

Concerning the appropriateness of CBCT imaging in orthodontics, the ADA-CSA states:

> Dentists should use professional judgment in the prescription and performance of CBCT examinations by consulting recommendations from available CBCT guidelines and by considering the specific clinical situation and needs of the individual patient (ADA-CSA 2012).

The American Academy of Oral and Maxillofacial Radiology (AAOMR) summarized the potential benefits and risks of maxillofacial CBCT use in orthodontic diagnosis, treatment, and outcomes (American Academy of Oral and Maxillofacial Radiology 2013). They provide clinical guidelines developed by a consensus panel of board-certified orthodontists and oral and maxillofacial radiologists for use of CBCT in orthodontics based on analysis of the available published evidence. Specific recommendations are grouped under four (4) general principles.

- **Image Appropriately According to Clinical Condition.** Factors to be considered if CBCT imaging is appropriate for a particular patient include the patient's history, clinical examination, and the patient's presenting clinical condition. To assist clinicians with their choice, specific imaging selection guidelines based on stage of treatment on initial presentation, potential treatment complexity, and the presence of modifying factors are provided. For various clinical scenarios, practitioners are provided with an index of the strength of the available evidence and recommendations on the most appropriate field of view (FOV) (Fig. 18.50).
- When patients present with an orthodontic condition, the first decision is to determine the phase of treatment (pre-, during, or post-treatment). If the patient is currently undergoing treatment or is posttreatment, then it should be determined if a previous CBCT scan is available. If it is available in these circumstances, then taking a CBCT is likely not indicated (III).
- If a CBCT is not available, the second stage is to assess the treatment difficulty. Mild difficulty includes patients who present with dental malocclusions, with or without minimal anterior-posterior, vertical, or transverse skeletal discrepancies. For these patients, CBCT is likely not indicated (III). Moderate difficulty includes patients who present with dental and skeletal discrepancies that are treated orthodontically and/or orthopedically only including bimaxillary proclination, open bite, and compensated Class III malocclusion. For these patients, CBCT may be indicated in certain circumstances (II). Severe difficulty patients are those who present with skeletal conditions including, but not limited to, complicated skeletal discrepancies, craniofacial anomalies (e.g., cleft lip and palate, craniofacial synostosis), sleep apnea, speech disorders, and postsurgical/trauma. For these patients, CBCT is likely indicated (I).
- Finally, CBCT of various fields of view (FOV) are most likely (I) or possibly indicated in certain circumstances (II) with the presence of additional skeletal and dental conditions.
- More specifically the AAOMR document provides a number of common sense recommendations for the use of CBCT in orthodontics including:
  - CBCT should be considered only when lower-dose conventional dental radiography (i.e., panoramic, intraoral, or cephalometric imaging) or alternate nonionizing imaging modalities cannot provide the necessary information to answer a specific clinical question. One such example is when orthodontic therapy on a submerged/impacted tooth produces no movement. In this case, small FOV, high resolution (<0.2 mm nominal voxel size) CBCT imaging would be indicated to identify the periodontal ligament space. No other modality is able to provide an accurate representation of possible ankylosis.
  - The use of CBCT should be avoided as the sole method to create virtual models of the dentition when non-radiographic imaging methods are available. CBCT can practically be used as a "virtual impression" material to assist in the placement of orthodontic appliances including aligners, brackets, or custom arch wires. However, such techniques are often performed at higher resolutions and/or at a greater exposure with an increased radiation dose to the patient than would otherwise be necessary for a diagnostic scan (Grünheid et al. 2012).
  - CBCT exposures should be task specific and tailored to the patient's specific presenting circumstances. This may include adjustments in exposure (mA and kVp), image-quality parameters (e.g., number of basis images, resolution), and reduction of

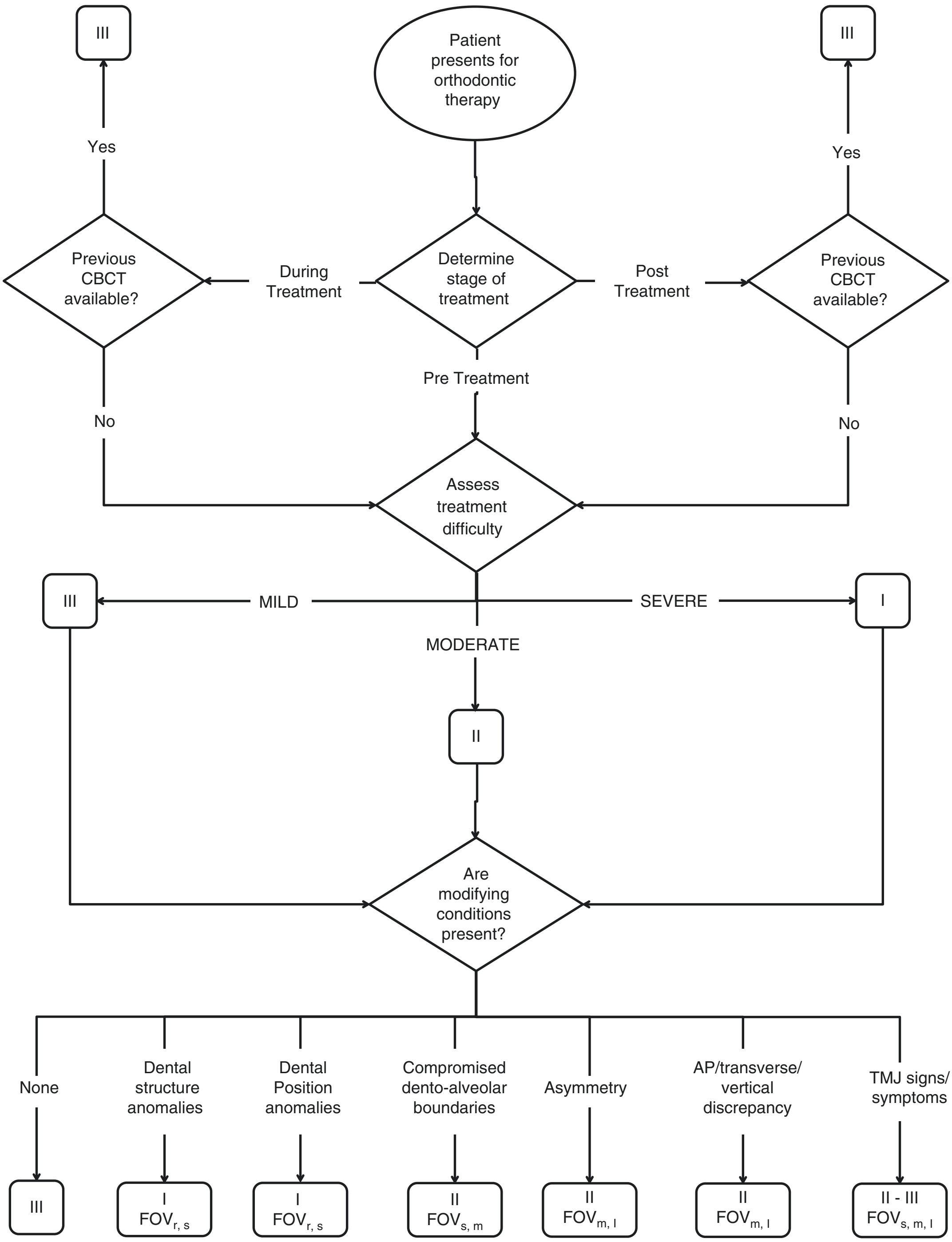

Fig. 18.50 Decision summary of the recommendations for appropriate selection of CBCT imaging in orthodontics (American Academy of Oral and Maxillofacial Radiology, 2013) *FOV_l* large FOV, *FOV_m* medium FOV, *FOV_s* small FOV, *FOV_r* reduced FOV, (*asterisks*) currently commercially available

the FOV to visualize adequately the region of interest.

- **Assess the Radiation Dose Risk.** Dental practitioners should be knowledgeable of the radiation risk when performing CBCT imaging in orthodontics and must communicate this risk to their patients beforehand. This risk is currently expressed by the Effective Dose, described previously (Chap. 4). This is particularly important for children, whose risk is conservatively 3–5 times higher than an adult for the same CBCT procedure according to assumptions made in current guidelines. One should carefully note that these assumptions are based on population averages rather than the individual who might be more or less resistant to radiation than the average. The child risk compared to the adult depends on the age of the child and that of the adult and can be an order of magnitude if compared to an elderly patient imaged for dental implant site assessment. The AAOMR panel suggests the use of Relative Radiation Risk (RRL), developed by the American College of Radiology (American College of Radiology 2013) as being useful for assessment of orthodontic radiation dose risk. Practitioners should also be mindful that a course of orthodontic therapy often incorporates multiple radiographic examinations (e.g., pre-, peri-, and posttreatment imaging) and every effort should be made to reduce the effective radiation dose to the patient not only for a single exposure, but more so for the cumulative dose over time.
- Recently, a number of manufacturers have introduced CBCT units capable of providing medium or even full FOV CBCT acquisition using "low dose" protocols. By adjustments to rotation arc, mA, kVp, or number of basis images or a combination thereof, CBCT imaging can be performed at effective doses comparable with conventional panoramic examinations (range, 14–24 μSv) (Ludlow and Walker 2013; Al-Okshi et al. 2015; Ludlow et al. 2015; Ludlow and Koivisto 2015). Hoverer, this is accompanied by significant reductions in image quality. Bear in mind that even at this level, child doses have been reported to be, on average, 36% greater than adult doses (Ludlow and Walker 2013). The use of low dose protocols may be adequate for low level diagnostic tasks such as the assessment of root angulations. Currently no data is available evaluating the effect of low dose protocols on diagnostic accuracy of other orthodontic tasks such as identifying or determining the degree of root resorption.
- **Minimize Patient Radiation Exposure.** There are numerous methods to reduce the radiation exposure to patients when CBCT imaging is used. The simplest method is to reduce the field of view (FOV) of the CBCT unit to cover a specific region of interest by collimating the X-ray beam, thereby limiting the area of exposure. Exposure settings, number of basis projection images and resolution, depending on the equipment type and operator preferences, can also be chosen to reduce exposure (Palomo et al. 2008). However, the patient radiation dose for an equivalent FOV examination can vary on different CBCT units by as much as tenfold (Ludlow and Ivanovic 2008). Avoiding regions of high relative radiation risk (eyes, thyroid glands, etc.) can also reduce the risk to patients. The use of patient protective shielding such as lead torso aprons and thyroid shields (Tsiklakis et al. 2005; Qu et al. 2012) is recommended, when possible, to minimize exposure to radiosensitive organs outside the field of view of the exposure.
- **Maintain professional competency in performing and interpreting CBCT studies.** Any radiographic procedure, including CBCT, may reveal information that is important to the management or general health of the patient. Incidental findings in CBCT images of orthodontic patients are common (Cha et al. 2007a; Pliska et al. 2011; Pazera et al. 2011) and some may be critical to the health of the patient (Rogers et al. 2011). Clinicians who order or perform CBCT for orthodontic patients are responsible for interpreting the entire image volume (Carter et al. 2008;

American Dental Association Council on Scientific Affairs 2012; American Academy of Oral and Maxillofacial Radiology 2013). Qualified specialists including oral and maxillofacial radiologists should be consulted to assist diagnostically when practitioners are unwilling to accept the responsibility to review the entire exposed tissue volume (Carter et al. 2008). Clinicians should regularly attend continuing educational/professional development program courses to become familiar with the technical and operational aspects of CBCT and to maintain current knowledge of scientific advances and health risks associated with the use of CBCT.

18.5 Imaging Protocols

There is a myriad of possible exposure, technical and display options available for acquiring and displaying CBCT images when investigating conditions of orthodontic interest. Not all are available to each practitioner using the OEM (original equipment manufacturer) software with specific CBCT units. However, it is possible to develop a set of nominal scanning and specific image formats—*imaging protocols*—that provide the clinician with guidance on appropriate parameter choice.

As with all CBCT imaging applied for a specific clinical application, orthodontic CBCT imaging should be task specific—adjusted to answer specific clinical questions. Tables 18.7, 18.8, 18.9, and 18.10 provide general task-specific imaging protocol suggestions, based on the 10-year experience of the authors, for the most common orthodontic applications (Figs. 18.51, 18.52, 18.53, 18.54, and 18.55).

18.6 Summary

CBCT is a valuable supplemental imaging modality to 2D radiography for the assessment and diagnosis of many specific conditions in the

Table 18.7 Task-specific imaging protocol—3D cephalometry/craniofacial analysis (Fig. 18.51)

Technical		Image display			
		Orientation		Reconstructions	
Acquisition	Rationale	Reference planes	Rationale	Reformats	Rationale
1 or 2 scans (CO ± CR)	Confirm teeth in CO ± CR	Midsagittal plane parallel to the middle of the hard palate and nasal septum	Minimize asymmetry to enable comparison of skeletal elements	Pano MPR with serial XS	Demonstrate individual teeth and anomalies, arrangement of the teeth in the dental arch, intermaxillary and craniofacial interrelationships
1st scan—Full FOV/mod res	Minimize dose for 2nd scan	FH (volume) parallel to the axial plane		Coronal and axials	
2nd scan—full or limited FOV/low res	ROI to include entire facial ST profile	Interorbital line (volume) parallel to the axial plane		MIP/ray sum (AP, lateral, SMV cephalometric images and analysis)	
				3D–S, 3D–V renderings (static ± dynamic)	
				± surgical simulations	
				Airway hollow modeling	

Table 18.8 Task-specific imaging protocol—TMJ assessment (Fig. 18.52)

Technical		Image display			
		Orientation		Reconstructions	
Acquisition	Rationale	Reference planes	Rationale	Reformats	Rationale
2 or 3 scans (CO, open, stent)	Demonstrate translation with motion or condylar position with stent in position	Midsagittal plane should be parallel to the nasal septum/vomer at the level of the TMJ	To minimize asymmetry and enable comparison of condylar morphology	Axial	Demonstrate anatomic structure ± pathology
1st scan—Full FOV/MR	Confirm relationship of teeth in CO	Imaginary line between the articular eminence and the middle of the external auditory meatus should be parallel to the axial plane	To allow establishment of condylar axis using linear MPR	Linear MPR XS (P-S/P-C)	Confirm relationship of teeth in CO
2nd and 3rd scan—limited FOV/LR	Minimize dose for 2nd and 3rd scan	Imaginary line between the roof of the glenoid fossae should be parallel to the axial plane		Pano MPR with serial XS	Assess craniofacial relationship
				MIP/ray sum	
				3D–S, 3D–V renderings (static and dynamic)	

MR moderate resolution (e.g., <0.4 mm voxel size, >300 basis images), *LR* low resolution (e.g., up to 0.5 mm voxel size, <300 basis images), *P-S* parasagittal, *P-C* para-coronal, *Pano* reformatted panoramic; *MPR* multiplanar reformatted, *MIP* maximum intensity projection, *3D-S* surface rendering, *3D-V* volumetric rendering, *Limited FOV* 6 cm high, *Full FOV* height to include nasion to hyoid, *XS* cross-sectional images, *ROI* region of interest, *ST* soft tissue

Table 18.9 Task-specific imaging protocol—impacted/unerupted tooth (e.g., Maxillary canine, third molar, supernumerary tooth) (Figs. 18.53 and 18.54)

Technical		Image display			
		Orientation		Reconstructions	
Acquisition	Rationale	Reference planes	Rationale	Reformats	Rationale
Restricted or limited FOV/HR	Resolution required to be < PDL space (0.2 mm)	CEJ should be parallel to the axial plane such that sagittal plane transects M/D root long axis, coronal plane transects F/P root long axis	To re-orient the volumetric dataset such that the tooth is perpendicular to trans-axial, coronal and sagittal planes	Axial	Localize position in jaw, show crown/root morphology, demonstrate relationship to adjacent structures, show dental effects (e.g., ankylosis and adjacent tooth root resorption
	ROI should ideally cover 3–5 teeth and 10–25 mm superior to the root apices			Modified XYZ orthogonal slices	
				Pano MPR with serial XS	
				MIP/ray sum 3D–S, 3D–V renderings (static and dynamic)	
				± annotations (e.g., IAC tracing)	

HR high resolution (e.g., <0.2 mm voxel size, >400 basis images), *P-S* parasagittal, *P-C* para-coronal, *Pano* reformatted curved planar panoramic, *MPR* multiplanar reformatted, *MIP* maximum intensity projection, *3D-S* 3D surface rendering, *3D-V* 3D volumetric rendering, *Restricted FOV* <4 cm high, *Limited FOV* 4–6 cm high, *XS* cross-sectional images, *ROI* region of interest, *ST* soft tissue, *PDL* periodontal ligament space, *M/D* mesial/distal, *FP* facial/palatal, *CEJ* cemento-enamel junction, *IAC* inferior alveolar canal

Table 18.10 Task-specific imaging protocol—airway assessment (Fig. 18.55)

Technical		Image display			
		Orientation		Reconstructions	
Acquisition	Rationale	Reference planes	Rationale	Reformats	Rationale
1 or 2 scans (CO, diagnostic appliance)	Resolution required is low	Axial plane should be parallel to line from PNS to basion	To re-orient the volumetric dataset such that the cross-sectional, linear and volumetric hollow airway measurements are standardized	Linear MPR XS (P-S/P-C)	Demonstrate intermaxillary and craniofacial interrelationships
Full FOV/LR	Confirm relationship of teeth in CO or with diagnostic appliance	Midsagittal plane parallel to the middle of the hard palate and nasal septum		Pano MPR with serial XS	Provide metrics of retropalatal and retroglossal minimal XS airway area and AP and transverse dimensions
Standardize head position (NHP or Mueller maneuver[a])	Minimize dose for 2nd scan	Interorbital line (volume) parallel to the axial plane		MIP/ray sum (AP, lateral, SMV cephalometric images and analysis)	
	ROI to include entire facial ST profile and airway from superior extent of nasal fossa to the level of the epiglottis including the hyoid bone			3D–V renderings (static HT and ST hollow modeling)	

LR low resolution (e.g., ≥ 0.4 mm voxel size, > 150 basis images), *NHP* natural head position, *P-S* parasagittal, *P-C* paracoronal, *Pano* reformatted curved planar panoramic, *MPR* multiplanar reformatted, *MIP* maximum intensity projection, *3D-S* 3D surface rendering, *3D-V* 3D volumetric rendering, *Restricted FOV* <6 cm high XS, cross-sectional images, *ROI* region of interest, *ST* soft tissue, *PDL* periodontal ligament space, *M/D* mesial/distal, *FP* facial/palatal, *CEJ* cemento-enamel junction, *IAC* inferior alveolar canal, *AP* anterio-posterior image, *SMV* submentovertex image, *lateral* lateral cephalometric image

[a]After a forced expiration, the patient attempts inspiration with closed mouth and nose, creating a negative pressure in the airway. Use in assessment of obstructive sleep apnea syndrome is equivocal (Soares et al. 2009)

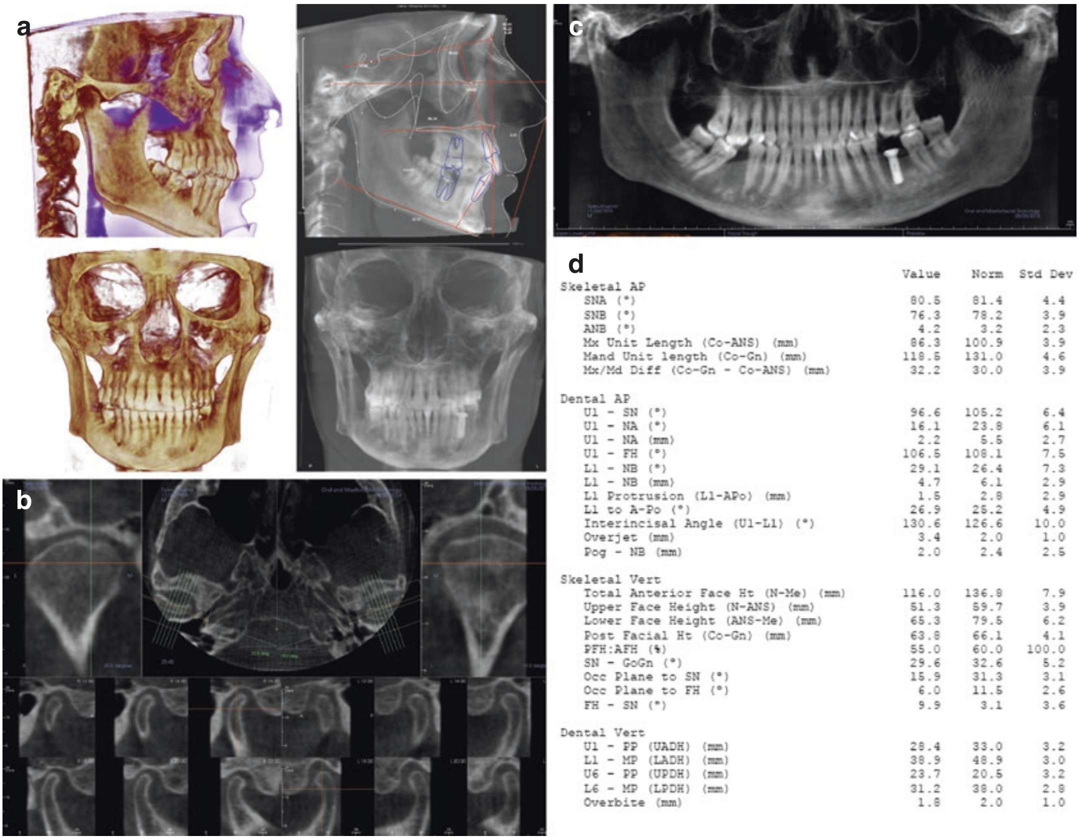

	Value	Norm	Std Dev
Skeletal AP			
SNA (°)	80.5	81.4	4.4
SNB (°)	76.3	78.2	3.9
ANB (°)	4.2	3.2	2.3
Mx Unit Length (Co-ANS) (mm)	86.3	100.9	3.9
Mand Unit length (Co-Gn) (mm)	118.5	131.0	4.6
Mx/Md Diff (Co-Gn - Co-ANS) (mm)	32.2	30.0	3.9
Dental AP			
U1 - SN (°)	96.6	105.2	6.4
U1 - NA (°)	16.1	23.8	6.1
U1 - NA (mm)	2.2	5.5	2.7
U1 - FH (°)	106.5	108.1	7.5
L1 - NB (°)	29.1	26.4	7.3
L1 - NB (mm)	4.7	6.1	2.9
L1 Protrusion (L1-APo) (mm)	1.5	2.8	2.9
L1 to A-Po (°)	26.9	25.2	4.9
Interincisal Angle (U1-L1) (°)	130.6	126.6	10.0
Overjet (mm)	3.4	2.0	1.0
Pog - NB (mm)	2.0	2.4	2.5
Skeletal Vert			
Total Anterior Face Ht (N-Me) (mm)	116.0	136.8	7.9
Upper Face Height (N-ANS) (mm)	51.3	59.7	3.9
Lower Face Height (ANS-Me) (mm)	65.3	79.5	6.2
Post Facial Ht (Co-Gn) (mm)	63.8	66.1	4.1
PFH:AFH (%)	55.0	60.0	100.0
SN - GoGn (°)	29.6	32.6	5.2
Occ Plane to SN (°)	15.9	31.3	3.1
Occ Plane to FH (°)	6.0	11.5	2.6
FH - SN (°)	9.9	3.1	3.6
Dental Vert			
U1 - PP (UADH) (mm)	28.4	33.0	3.2
L1 - MP (LADH) (mm)	38.9	48.9	3.0
U6 - PP (UPDH) (mm)	23.7	20.5	3.2
L6 - MP (LPDH) (mm)	31.2	38.0	2.8
Overbite (mm)	1.8	2.0	1.0

Fig. 18.51 Montage of images representing some components of a typical craniofacial assessment protocol performed using moderate full FOV CBCT including volumetric and ray-sum lateral and anteroposterior projections (**a**), TMJ MPR (**b**), reformatted panoramic (**c**), and cephalometric analysis (**d**)

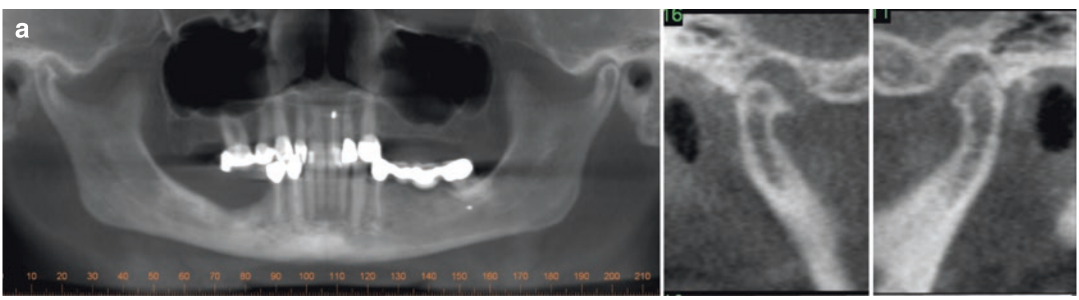

Fig. 18.52 Montage of images representing some components of a typical TMJ protocol performed using moderate and low resolution, full and restricted FOV CBCT. In this case imaging was performed in centric occlusion (**a**), with a stent in place at a desired occlusal vertical dimension (**b**), and with maximum unassisted opening. Reformatted panoramic and right and left mid-condylar sections demonstrate moderate degenerative joint disease and marked posteroinferior positioning in CO and with the stent in position. CBCT images in the open position (**c**) show limited translation and excessive inter-articular space, suggestive of anterior disc displacement without reduction

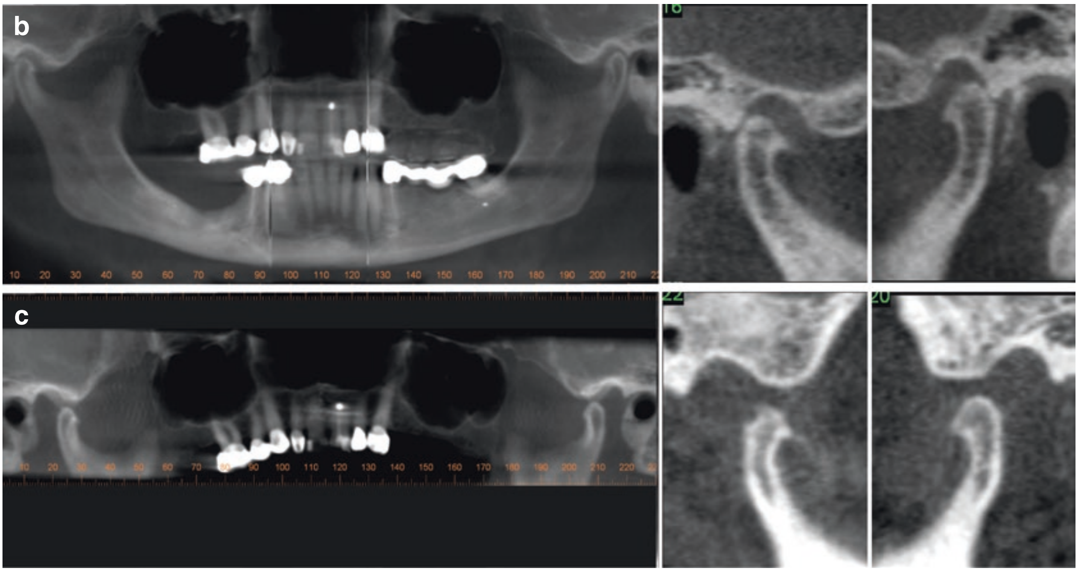

Fig. 18.52 (continued)

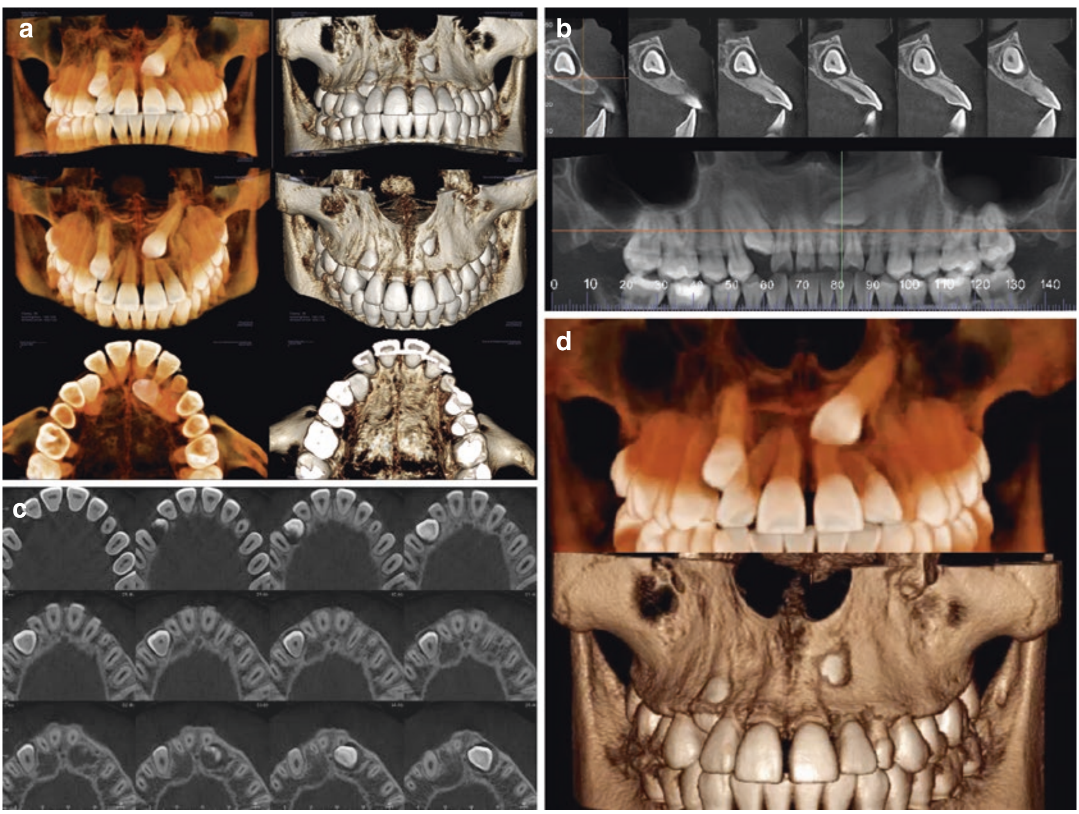

Fig. 18.53 Montage of images representing typical maxillary canine imaging protocol performed using high resolution, restricted FOV. Multiple projections 3D–S and 3D–V static renderings (**a**), axial (**b**), reformatted panoramic MPR with serial XS (**c**), and 3D–S and 3D–V dynamic renderings (movies) (**d**)

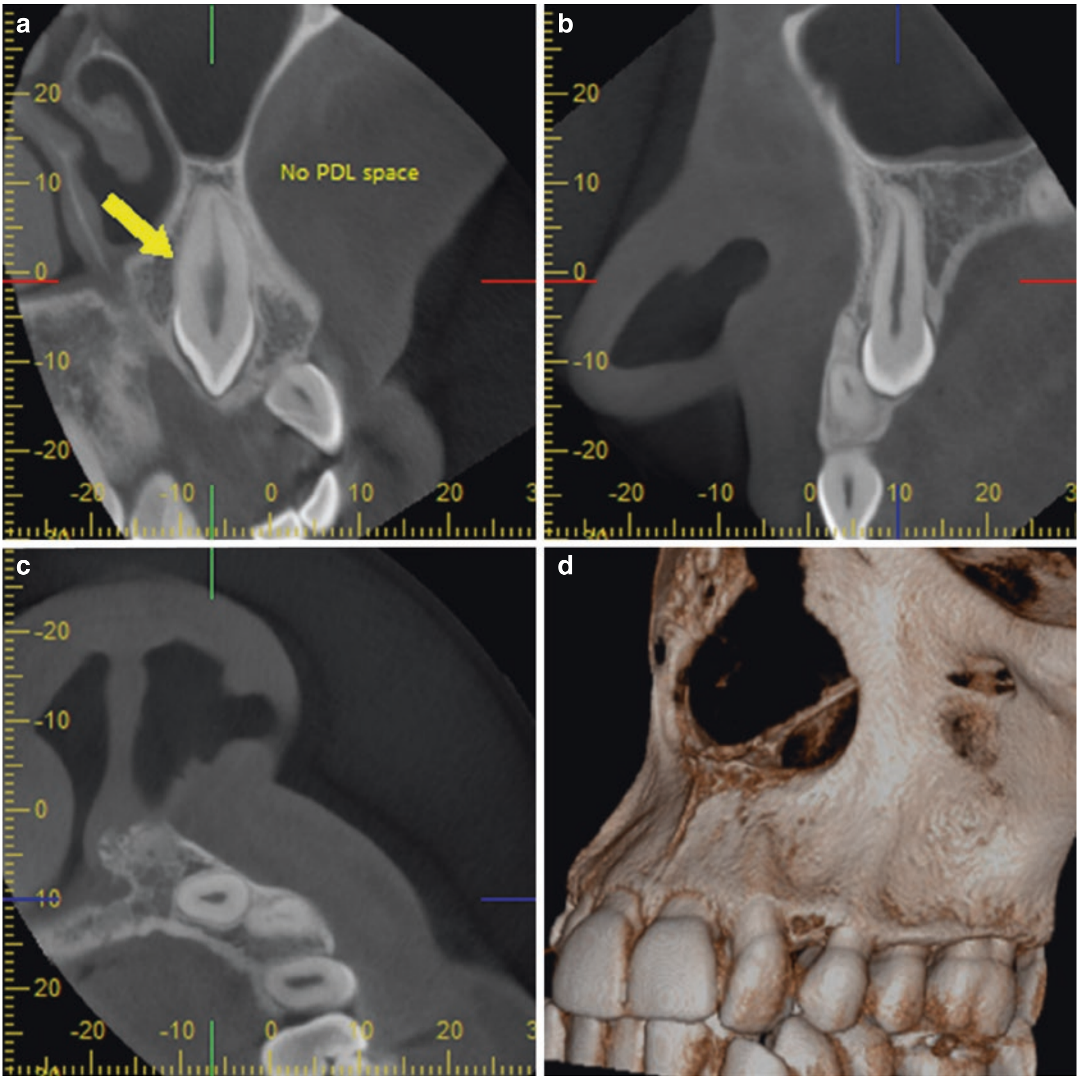

Fig. 18.54 Modified XYZ display for a patient with a palatally impacted and unerupted left maxillary canine achieved by re-orienting the coronal (**a**), sagittal (**b**) planes to be aligned with to transect the facio-palatal and mesiodistal long axes of the root of the tooth. The resulting axial image (**c**) allows assessment of the PDL space and determination of possible ankylosis. The surface volumetric rendering (**d**) demonstrates complete buccal cortical plate coverage

orthodontic patient with many promising and emerging applications. While it is the responsibility of each practitioner to make a decision, along with the patient/family, as to what imaging is considered to be in the patient's best interest, consensus derived, evidence-based clinical guidelines are available to assist the dental practitioner in the decision-making process. Specific recommendations provide selection guidance based on variables such as phase of treatment, clinically assessed treatment difficulty, presence of dental and/or skeletal modifying conditions, and pathology.

Current scientific evidence is lacking to recommend CBCT imaging as a replacement for extraoral (lateral cephalometric and panoramic) radiography in orthodontics. CBCT imaging in orthodontics should always be considered wisely, as children have conservatively On average a three to five times greater radiation risk than that of adults for the same exposure.

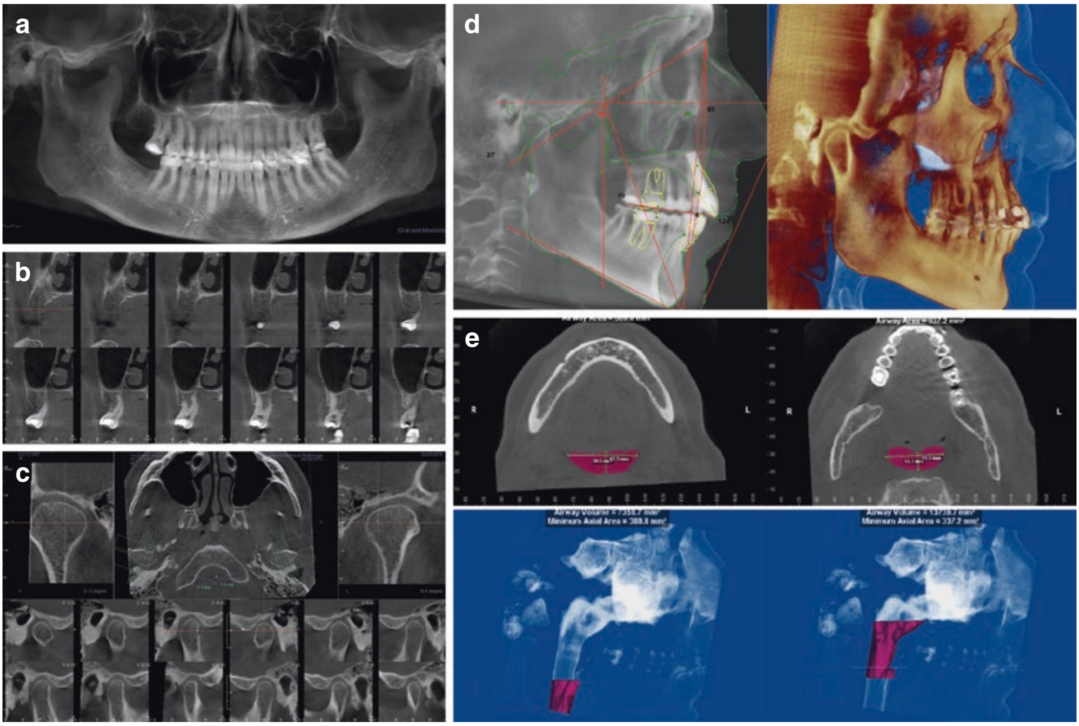

Fig. 18.55 Montage of images representing typical airway assessment imaging protocol performed using low resolution, full FOV. Reformatted panoramic MPR (**a**) with serial XS images (**b**), TMJ series (**c**), lateral cephalometric images with analysis and corresponding 3D–V hard tissue and soft tissue hollow static renderings (**d**), and retroglossal and retropalatal axial and hollow surface renderings with minimum cross-sectional airway area, AP, transverse dimensions and volumetric calculations (**e**)

Acknowledgments Figure 20.10 images courtesy of Chris Lane and Kelly Duncan, 3dMD, Atlanta, Georgia, USA) previously published (Lane and Harrell 2008), and used with permission. The authors acknowledge the valuable contributions of the Drs. Carla Evans, Lucia Cevidanes, Martin Palomo, Kirt Simmons, Stu White, John Ludlow, and Mansur Ahmad as members of a panel convened by the AAOMR providing clinical recommendations regarding use of cone beam computed tomography in orthodontics (American Academy of Oral and Maxillofacial Radiology, 2013). Sections of this chapter have also been published as a series of articles entitled “Cone Beam Computed Tomography and the Orthodontic Patient,” “Indications for CBCT Use,” and “Strategies for the Safe Use of CBCT” in *Dimensions of Dental Hygiene*, and are reproduced with permission by Belmont Publications, Inc.

References

Aboudara CA, Hatcher D, Nielsen IL, Miller A (2003) A three-dimensional evaluation of the upper airway in adolescents. Orthod Craniofac Res 6(Suppl 1):173–175

Abou-Elfetouh A, Barakat A, Abdel-Ghany K (2011) Computed-guided rapid-prototyped templates for segmental mandibular osteotomies: a preliminary report. Int J Med Robot 7:187–192

Abramson Z, Susarla SM, Lawler M, Bouchard C, Troulis M, Kaban LB (2011) Three-dimensional computed tomographic airway analysis of patients with obstructive sleep apnea treated by maxillomandibular advancement. J Oral Maxillofac Surg 69:677–686

Adams GL, Gansky SA, Miller AJ, Harrell WE, Hatcher DC (2004) Comparison between traditional 2-dimensional cephalometry and a 3-dimensional approach on human dry skulls. Am J Orthod Dentofac Orthop 126:397–409

Agarwal R (2011) Anthropometric evaluation of complete unilateral cleft lip nose with cone beam CT in early childhood. J Plast Reconstr Aesthet Surg 64:e181–e182

Ahmad M, Hollender L, Anderson Q, Kartha K, Ohrbach RK, Truelove EL, John MT, Schiffman EL (2009) Research diagnostic criteria for temporomandibular disorders (RDC/TMD): development of image analysis criteria and examiner reliability for image analysis. Oral Surg Oral Med Oral Pathol Oral Radiol Endod 107:844–860

Alexiou K, Stamatakis H, Tsiklakis K (2009) Evaluation of the severity of temporomandibular joint osteoarthritic changes related to age using cone beam computed tomography. Dentomaxillofac Radiol 38:141–147

AlHadidi A, Cevidanes LH, Mol A, Ludlow J, Styner M (2011) Comparison of two methods for quantitative assessment of mandibular asymmetry using cone beam computed tomography image volumes. Dentomaxillofac Radiol 40:351–357

Almeida RC, Cevidanes LH, Carvalho FA, Motta AT, Almeida MA, Styner M, Turvey T, Proffit WR, Phillips C (2011) Soft tissue response to mandibular advancement using 3D CBCT scanning. Int J Oral Maxillofac Surg 40:353–359

Al-Okshi A, Lindh C, Salé H, Gunnarsson M, Rohlin M (2015) Effective dose of cone beam CT (CBCT) of the facial skeleton: a systematic review. Br J Radiol 88(1045):20140658

Alqerban A, Hedesiu M, Baciut M, Nackaerts O, Jacobs R, Fieuws S (2013) SedentexCT consortium, Willems G. Pre-surgical treatment planning of maxillary canine impactions using panoramic vs cone beam CT imaging. Dentomaxillofac Radiol 42(9):20130157

Alqerban A, Willems G, Bernaerts C, Vangastel J, Politis C, Jacobs R (2014) Orthodontic treatment planning for impacted maxillary canines using conventional records versus 3D CBCT. Eur J Orthod 36(6):698–707

Altug-Atac AT, Erdem D (2007) Prevalence and distribution of dental anomalies in orthodontic patients. Am J Orthod Dentofacial Orthop 131:510–514

American Academy of Oral and Maxillofacial Radiology (2013) Clinical recommendations regarding use of cone beam computed tomography in orthodontics. (corrected). Position statement by the American Academy of Oral and Maxillofacial Radiology. Oral Surg Oral Med Oral Pathol Oral Radiol 116:238–257. Erratum in: Oral Surg Oral Med Oral Pathol Oral Radiol 2013;116:661

American College of Radiology (2013) ACR appropriateness criteria®. Radiation dose assessment introduction. http://www.acr.org/~/media/a27a29133302408bb86888eafd460a1f.pdf. Accessed 21 Jan 2014

American Dental Association Council on Scientific Affairs (2012) The use of cone-beam tomography in dentistry. An advisory statement from the American Dental Association Council on Scientific Affairs. J Am Dent Assoc 143:899–902

Arnett GW, Bergman RT (1993) Facial keys to orthodontic diagnosis and treatment planning. Part I. Am J Orthod Dentofacial Orthop 103:299–312

Atchison KA, Luke LS, White SC (1991) Contribution of pretreatment radiographs to orthodontists' decision making. Oral Surg Oral Med Oral Pathol 71(2):238–245

Atchison K, Luke L, White SC (1992) An algorithm for ordering pretreatment orthodontic radiographs. Am J Orthod Dentofac Orthop 102:29–44

Athanasiou AE (1995) Orthodontic cephalometry. Mosby-Wolfe, London

Baek C, Paeng JY, Lee JS, Hong J (2012) Morphologic evaluation and classification of facial asymmetry using 3-dimensional computed tomography. J Oral Maxillofac Surg 70:1161–1169

Baumrind S, Frantz RC (1971a) The reliability of head film measurements. 1. Landmark identification. Am J Orthod 60:111–127

Baumrind S, Frantz RC (1971b) The reliability of head film measurements. 2. Conventional angular and linear measures. Am J Orthod 60:505–517

Baumrind S, Miller D, Molthen R (1976) The reliability of head film measurements. 3. Tracing superimposition. Am J Orthod Dentofac Orthop 70:617–644

Baumrind S, Moffitt FH, Curry S (1983a) The geometry of three-dimensional measurement from paired coplanar x-ray images. Am J Orthod 84:313–322

Baumrind S, Moffitt FH, Curry S (1983b) Three-dimensional x-ray stereometry from paired coplanar images: a progress report. Am J Orthod 84:292–312

Bayome M, Park JH, Kook YA (2013) New three-dimensional cephalometric analyses among adults with a skeletal class I pattern and normal occlusion. Korean J Orthod 43:62–73

Becker A, Chaushu C, Casap-Caspi N (2010) Cone-beam computed tomography and the orthosurgical management of impacted teeth. J Am Dent Assoc 141:14S–18S

Behnia H, Khojasteh A, Soleimani M, Tehranchi A, Atashi A (2012) Repair of alveolar cleft defect with mesenchymal stem cells and platelet derived growth factors: a preliminary report. J Craniomaxillofac Surg 40:2–7

Bergland O, Semb G, Abyholm FE (1986) Elimination of the residual alveolar cleft by secondary bone grafting and subsequent orthodontic treatment. Cleft Palate J 23:175–205

Bettega G, Payan Y, Mollard B, Boyer A, Raphael B, Lavallee S (2000) A simulator for maxillofacial surgery integrating 3D cephalometry and orthodontia. Comput Aided Surg 5:156–165

Bookstein FL (1991) Morphometric tools for landmark data. Cambridge University Press, New York. 455 pp

Botticelli S, Verna C, Cattaneo PM, Heidmann J, Melsen B (2011) Two- versus three-dimensional imaging in subjects with unerupted maxillary canines. Eur J Orthod 33:344–349

Broadbent BH (1931) A New x-ray technique and its applications to orthodontia. Angle Orthod 1:45–66

Broadbent BH Sr, Broadbent BH Jr, Golden WH (1975) Bolton standards of dentofacial developmental growth. Mosby, St Louis

Bruks A, Enberg K, Nordqvist I, Hansson AS, Jansson L, Svenson B (1999) Radiographic examinations as an aid to orthodontic diagnosis and treatment planning. Swed Dent J 23:77–85

Bryndahl F, Eriksson L, Legrell PE, Isberg A (2006) Bilateral TMJ disk displacement induces mandibular retrognathia. J Dent Res 85:1118–1123

Burstone CJ (1985) Applications of bioengineering to clinical orthodontics, Chapter 3. In: Graber TM, Swain BF (eds) Orthodontics: current principles and techniques. CV Mosby, St. Louis

Carter L, Farman AG, Geist J, Scarfe WC, Angelopoulos C, Nair MK, Hildebolt CF, Tyndall D, Shrout M (2008)

American Academy of oral and maxillofacial radiology. American Academy of oral and maxillofacial radiology executive opinion statement on performing and interpreting diagnostic cone beam computed tomography. Oral Surg Oral Med Oral Pathol Oral Radiol Endod 106:561–562

Carvalho Fde A, Cevidanes LH, da Motta AT, Almeida MA, Phillips C (2010) Three-dimensional assessment of mandibular advancement 1 year after surgery. Am J Orthod Dentofac Orthop 137(4 Suppl):S53.e1–12

Case CS (1908) A practical treatise on the techniques and principles of dental orthopedia. CS Case, Chicago

Cavalcanti MG, Vannier MW (1998) Quantitative analysis of spiral computed tomography for craniofacial clinical applications. Dentomaxillofac Radiol 27:344–350

Cavalcanti MG, Haller JW, Vannier MW (1999) Three-dimensional computed tomography landmark measurement in craniofacial surgical planning: experimental validation in vitro. J Oral Maxillofac Surg 57:690–694

Cavalcanti MGP, Ruprecht A, Vannier MW (2002) 3D volume rendering using multislice computed tomography for dental implants. Dentomaxillofac Radiol 31:218–223

Cavalcanti MG, Rocha SS, Vannier MW (2004) Craniofacial measurements based on 3D-CT volume rendering: implications for clinical applications. Dentomaxillofac Radiol 33:170–176

Cevidanes LH, Bailey LJ, Tucker GR Jr, Styner MA, Mol A, Phillips CL, Proffit WR, Turvey T (2005) Superimposition of 3D cone-beam CT models. Dentomaxillofac Radiol 34:369–375

Cevidanes LH, Styner MA, Proffit WR (2006) Image analysis and superimposition of 3-dimensional cone-beam computed tomography models. Am J Orthod Dentofacial Orthop 129:611–618

Cevidanes LH, Bailey LJ, Tucker SF, Styner MA, Mol A, Phillips CL, Proffit WR, Turvey T (2007) Three-dimensional cone-beam computed tomography for assessment of mandibular changes after orthognathic surgery. Am J Orthod Dentofacial Orthop 131:44–50

Cevidanes LH, Tucker S, Styner M, Kim H, Chapuis J, Reyes M, Proffit W, Turvey T, Jaskolka M (2010) Three-dimensional surgical simulation. Am J Orthod Dentofac Orthop 138(3):361–371

Cevidanes LH, Alhadidi A, Paniagua B, Styner M, Ludlow J, Mol A, Turvey T, Proffit WR, Rossouw PE (2011a) Three-dimensional quantification of mandibular asymmetry through cone-beam computerized tomography. Oral Surg Oral Med Oral Pathol Oral Radiol Endod 111:757–770

Cevidanes LH, Oliveira AE, Grauer D, Styner M, Proffit WR (2011b) Clinical application of 3D imaging for assessment of treatment outcomes. Semin Orthod 17(1):72–80

Cha JY, Mah J, Sinclair P (2007) Incidental findings in the maxillofacial area with 3-dimensional cone-beam imaging. Am J Orthod Dentofac Orthop 132:7–14

Chaushu S, Chaushu G, Becker A (2004) The role of digital volume tomography in the imaging of impacted teeth. World J Orthod 5:120–132

Cheung LK, Chan YM, Jayaratne YS, Lo J (2011) Three dimensional cephalometric norms of Chinese adults in Hong Kong with balanced facial profile. Oral Surg Oral Med Oral Pathol Oral Radiol Endod 112:e56–e73

Conley RS (2011) Evidence for dental and dental specialty treatment of obstructive sleep apnoea. Part 1: the adult OSA patient and part 2: the paediatric and adolescent patient. J Oral Rehabil 38:136–156

Dalessandri D, Laffranchi L, Tonni I, Zoti F, Piancino MG, Paganelli C, Bracco P (2011) Advantages of cone beam computed tomography (CBCT) in the orthodontic treatment planning of cleidocranial dysplasia patients: a case report. Head Face Med 27:7–6

Damstra J, Fourie Z, De Wit M, Ren Y (2012) A three-dimensional comparison of a morphometric and conventional cephalometric midsagittal planes for craniofacial asymmetry. Clin Oral Investig 16:285–294

Damstra J, Fourie Z, Ren Y (2013) Evaluation and comparison of postero-anterior cephalograms and cone-beam computed tomography images for the detection of mandibular asymmetry. Eur J Orthod 35(1):45–50

Delaire J, Schendel SA, Tulasne JF (1981) An architectural and structural craniofacial analysis: a new lateral cephalometric analysis. Oral Surg Oral Med Oral Pathol 52:226–238

Delamare EL, Liedke GS, Vizzotto MB, da Silveira HL, Ribeiro JL, Silveira HE (2010) Influence of a programme of professional calibration in the variability of landmark identification using cone beam computed tomography-synthesized and conventional radiographic cephalograms. Dentomaxillofac Radiol 39(7):414–423

Devereux L, Moles D, Cunningham SJ, McKnight M (2011) How important are lateral cephalometric radiographs in orthodontic treatment planning? Am J Orthod Dentofac Orthop 139:175–181

Doğramacı EJ, Rossi-Fedele G, McDonald F (2014) Clinical importance of in-cidental findings reported on small-volume dental cone beam computed tomography scans focused on impacted maxillary canine teeth. Oral Surg Oral Med Oral Pathol Oral Radiol 118:e205–e209

Downs WB (1952) The role of cephalometrics in orthodontic case analysis and diagnosis. Am J Orthod 38:162

Drage N, Rogers S, Greenall C, Playle R (2013) Incidental findings on cone beam computed tomography in orthodontic patients. J Orthod 40:29–37

Dworkin SF, LeResche L (1992) Research diagnostic criteria for temporomandibular disorders: review, criteria, examinations, and specifications, critique. J Craniomandib Disord 6:301–355

Ebner FH, Kürschner V, Dietz K, Bültmann E, Nägele T, Honegger J (2010) Craniometric changes in patients with acromegaly from a surgical perspective. Neurosurg Focus 29:E3

Edwards SP (2010) Computer-assisted craniomaxillofacial surgery. Oral Maxillofac Surg Clin North Am 22:117–134

Edwards R, Alsufyani N, Heo G, Flores-Mir C (2014) The frequency and nature of incidental findings in large-field cone beam computed tomography scans of an orthodontic sample. Prog Orthod 15:37. https://doi.org/10.1186/s40510-014-0037-x

El H, Palomo JM (2010) Measuring the airway in 3 dimensions: a reliability and accuracy study. Am J Orthod Dentofacial Orthop 137(4 Suppl):S50.e1–9; discussion S50–2

El AS, El H, Palomo JM, Baur DA (2011) A 3-dimensional airway analysis of an obstructive sleep apnea surgical correction with cone beam computed tomography. J Oral Maxillofac Surg 69:2424–2436

Engelbrecht WP, Fourie Z, Damstra J, Gerrits PO, Ren Y (2013) The influence of the segmentation process on 3D measurements from cone beam computed tomography-derived surface models. Clin Oral Investig 17:1919–1927

Enlow D (2000) Discussion. Am J Orthod Dentofac Orthop 117:147

Enlow D, Hans MG (1996) Essentials of facial growth. W. B. Saunders Co., Philadelphia

Etcoff NL (1999) Survival of the prettiest: the science of beauty. Anchor Books/Random House, New York, NY. 325 pp

European Commission (2012) Publication no. 172 (SEDENTEXCT). Cone beam CT for dental and maxillofacial radiology: evidence based guidelines. Office for Official Publications of the European Communities, Luxembourg. http://ec.europa.eu/energy/nuclear/radiation_protection/doc/publication/172.pdf

Farkas LG (1981) Anthropometry of the head and face in medicine. Elsevier—North Holland Inc., New York, NY. 293 pp

Farkas LG (ed) (1994) Anthropometry of the head and face, 2nd edn. Raven Press, New York, NY. 427 pp

Farkas LG, Muro IR (1987) Anthropometric facial proportions in medicine. Charles C. Thomas, Springfield, IL. 337 pp

Farman AG, Scarfe WC (2006) Development of imaging selection criteria and procedures should precede cephalometric assessment with cone-beam computed tomography. Am J Orthod Dentofac Orthop 130:257–265

Farman AG, Scarfe WC, Hilgers MJ, Bida O, Moshiri M, Sukovic P (2005a) Dentomaxillofacial cone-beam CT for orthodontic assessment. Int Congr Ser 1281:1187–1190

Farman AG, Scarfe WC, Hilgers MJ, Bida O, Moshiri M, Sukovic P (2005b) Dentomaxillofacial cone-beam CT for orthodontic assessment. In: Lemke HU, Inamura K, Doi K, Vannier MK, Farman AG (eds) Computer assisted radiology and surgery. Proceedings of the 19th international congress on computer assisted radiology and surgery, Berlin, Germany, June 22–25, 2005. Elsevier, Amsterdam, pp 1187–1190

Farronato G, Garagiola U, Dominici A, Periti G, de Nardi S, Carletti V, Farronato D (2010) "Ten-point" 3D cephalometric analysis using low-dosage cone beam computed tomography. Prog Orthod 11:2–12

Faure J, Treil J, Borianne P, Casteigt J, Baron P (2002) 3-dimensional cephalometry in orthodontics. The current possibilities of Cepha 3DT software. Orthod Fr 73:19–37. [French]

Fourie Z, Damstra J, Schepers RH, Gerrits PO, Ren Y (2012) Segmentation process significantly influences the accuracy of 3D surface models derived from cone beam computed tomography. Eur J Radiol 81(4):e524–e530

Frongia G, Piancino MG, Bracco P (2012) Cone-beam computed tomography: accuracy of three-dimensional cephalometry analysis and influence of patient scanning position. J Craniofac Surg 23(4):1038–1043

Garino F, Garino GB (2002) Comparison of dental arch measurements between stone and digital casts. World J Orthod 3:250–254

Gateno J, Xia JJ, Teichgraeber JF (2011) New 3-dimensional cephalometric analysis for orthognathic surgery. J Oral Maxillofac Surg 69:606–622

Gerard JM, Wilhelms-Tricarico R, Payan Y, Perrier P (2003) A 3D biomechanical tongue model to simulate speech movements. Arch Physiol Biochem 111:7

Gracco A, Incerti Parenti S, Ioele C, Alessandri Bonetti G, Stellini E (2012) Prevalence of incidental maxillary sinus findings in Italian orthodontic patients: a retrospective cone-beam computed tomography study. Korean J Orthod 42:329–334

Grayson BH, McCarthy JG, Bookstein F (1983) Analysis of craniofacial asymmetry by multiplane cephalometry. Am J Orthod 84:217–224

Grayson BH, LaBatto FA, Kolber AB, McCarthy JG (1985) Basilar multiplane cephalometric analysis. Am J Orthod 88:503–516

Greenblatt C, Berryman R, Brooks SL, Burton B, Murdoch-Kinch CA, Rachlin JA, et al. (2006) The selection of patients for dental radiographic examinations. American dental association and U.S. Department of Health and Human Services. http://www.fda.gov/cdrh/radhlth/adaxray-1.html

Grummons DC, Kappeyne van de Coppello MA (1987) Frontal asymmetry analysis. J Clin Orthod 21:448–465

Grummons D, Ricketts RL (2004) Frontal Cephalometrics: practical applications, part 2. World J Orthod 5:99–119

Grünheid T, Kolbeck Schieck JR, Pliska BT, Ahmad M, Larson BE (2012) Dosimetry of a cone-beam computed tomography machine compared with a digital x-ray machine in orthodontic imaging. Am J Orthod Dentofac Orthop 141:436–443

Haney E, Gansky SA, Lee JS, Johnson E, Maki K, Miller AJ, Huang JC (2010) Comparative analysis of traditional radiographs and cone-beam computed tomography volumetric images in the diagnosis and treatment planning of maxillary impacted canines. Am J Orthod Dentofac Orthop 137(5):590–597

Hannam AG (2003) Dynamic modeling and jaw biomechanics. Orthod Craniofac Res 6(Suppl 1):59–65

Hannam AG, Stavness I, Lloyd JE, Fels S (2008) A dynamic model of jaw and hyoid biomechanics during chewing. J Biomech 41:1069–1076

Harrell WE, Hatcher DC, Bolt RL (2002) In search of anatomic truth: 3-dimensional digital modeling and the future of orthodontics. Am J Orthod Dentofacial Orthop 122:325–330

Harun WARW, Rajion ZA, Aziz IA, Samsudin AR (2005) 3D CT landmark analysis for development of Malaysian craniofacial database. In: 27th Annual international conference of the engineering in medicine and biology society, 2005. IEEE-EMBS Shanghai, China, September 1–4, pp 817–820

Haute Autorité de Santé (2009) Tomographie Volumique a Faisceau Conique de la Face (Cone Beam Computerized Tomography). Rapport d'évaluation Technologique. Service évaluation des actes professionnels. Haute Autorité de Santé, Saint-Denis La Plaine. http://www.has-sante.fr

Hayashi I (2003) Morphological relationship between the cranial base and dentofacial complex obtained by reconstructive computer tomographic images. Eur J Orthod 25:385–391

Hechler SL (2008) Cone-beam CT: applications in orthodontics. Dent Clin N Am 52:753–759

Helenius LM, Hallikainen D, Helenius I, Meurman JH, Könönen M, Leirisalo-Repo M, Lindqvist C (2005) Clinical and radiographic findings of the temporomandibular joint in patients with various rheumatic diseases: a case control study. Oral Surg Oral Med Oral Pathol Oral Radiol Endod 99:455–463

Heymann GC, Cevidanes L, Cornelis M, De Clerck HJ, Tulloch JFC (2010) Three-dimensional analysis of maxillary protraction with intermaxillary elastics to miniplates. Am J Orthod Dentofac Orthop 137:274–284

Hildebolt CF, Vannier MW, Knapp RH (1990) Validation study of skull three-dimensional computerized tomography measurements. Am J Phys Anthropol 82:283–294

Hodges RJ, Atchison KA, White SC (2013) Impact of cone-beam computed tomography on orthodontic diagnosis and treatment planning. Am J Orthod Dentofac Orthop 143(5):665–674

Hofmann E, Medelnik J, Keller T, Steinhäuser S, Hirschfelder U (2011) Measuring mesiodistal width of impacted maxillary canines: CT-assisted determination. J Orofac Orthop 72(1):33–44

Hofmann E, Medelnik J, Fink M, Lell M, Hirschfelder U (2013) Three-dimensional volume tomographic study of the imaging accuracy of impacted teeth: MSCT and CBCT comparison—an in vitro study. Eur J Orthod 35(3):286–294

Horfrath H (1931) Bedeutung der Roentrenfern und Abstands Aufnahme fur die Diagnostik der Kieferanomalien. Fortschr der Orthod 1:231–258. [German]

Hwang HS, Hwang CH, Lee KH, Kang BC (2006) Maxillofacial 3-dimensional image analysis for the diagnosis of facial asymmetry. Am J Orthod Dentofac Orthop 130:779–785

Iculla AJ, Harrell WE, Secchi AG, Ayala J, Katz SH (2006) 3-dimensional morphometric facial analysis to determine the effects of altering the occlusal vertical dimension [thesis]. University of Pennsylvania, Philadelphia PA

Isaacson KG, Thom AR, Horner K, Whaites E (2008) Orthodontic radiographs—guidelines for the use of radiographs in clinical orthodontics, 3rd edn. British Orthodontic Society, London

Iwasaki T, Saitoh I, Takemoto Y, Inada E, Kanomi R, Hayasaki H, Yamasaki Y (2011) Evaluation of upper airway obstruction in class II children with fluid-mechanical simulation. Am J Orthod Dentofac Orthop 139:e135–e145

Jacobson A (1975) The "WITS" appraisal of jaw disharmony. Am J Orthod 67:125–138

Jacobson A, Jacobson RL (2006) In: Jacobson A, Jacobson RL (eds) Radiographic Cephalometry from basics to 3D imaging. Quintessence Publishing, Hanover Park

Janssens A, Horner K, Rushton V, et al (2003) Radiation protection: European guidelines on radiation protection in dental radiology—the safe use of radiographs in dental practice. http://www.sefm.es/docs/otros/raddigUE.pdf. Accessed 20 Apr 2006

Jayaratne YSN, Zwahllen RA, Lo J, Cheung LK (2010a) Three-dimensional color maps: a novel tool for assessing craniofacial changes. Surg Innov 17:198–205

Jayaratne YS, Zwahlen RA, Lo J, Tam SC, Cheung LK (2010b) Computer-aided maxillofacial surgery: an update. Surg Innov 17:217–225

Jayaratne YS, McGrath CP, Zwahlen RA (2012) How accurate are the fusion of cone-beam CT and 3-D stereophotographic images? PLoS One 7(11):e49585

Johnston LE (1968) A statistical evaluation of cephalometric prediction. Angle Orthod 38(4):284–304

Johnston LE Jr (2011) A few comments on an elegant answer in search of useful questions. Semin Orthod 17:13–14

Kaipatur NR, Flores-Mir C (2009) Accuracy of computer programs in predicting orthognathic surgery soft tissue response. J Oral Maxillofac Surg 67(4):751–759

Kamiishi H, Miyasato Y, Kosaka M (2007) Development of the 3D-cephalogram: a technical note. J Craniomaxillofac Surg 35:258–260

Kapila S, Conley RS, Harrell WE Jr (2011) The current status of cone beam computed tomography imaging in orthodontics. Dentomaxillofac Radiol 40:24–34

Katheria BC, Kau CH, Tate R, Chen J-W, English J, Bouquot J (2010) Effectiveness of impacted and supernumerary tooth diagnosis from traditional radiography versus cone beam computed tomography. Pediatr Dent 32:304–309

Katsumata A, Fujishita M, Maeda M, Ariji Y, Ariji E, Langlais RP (2005) 3D-CT evaluation of facial asymmetry. Oral Surg Oral Med Oral Pathol Oral Radiol Endod 99:212–220

Kau CH, Richmond S, Palomo JM, Hans MG (2005) Three-dimensional cone beam computerized tomography in orthodontics. J Orthod 32:282–923

Kau CH, Littlefield J, Rainy N, Nguyen JT, Creed B (2010) Evaluation of CBCT digital models and traditional models using the Little's index. Angle Orthod 80:435–439

Kim DO, Kim HJ, Jung H, Jeong HK, Hong SI, Kim KD (2002) Quantitative evaluation of acquisition parameters in three dimensional imaging with multidetector computed tomography using human skull phantom. J Digit Imaging 15(Suppl 1):254–257

Kim TY, Baik JS, Park JY, Chae HS, Huh KH, Choi SC (2011a) Determination of midsagittal plane for evaluation of facial asymmetry using three-dimensional computed tomography. Imaging Sci Dent 41:79–84

Kim YI, Park SB, Son WS, Hwang DS (2011b) Midfacial soft-tissue changes after advancement of maxilla with le fort I osteotomy and mandibular setback surgery: comparison of conventional and high le fort osteotomies by superimposition of cone-beam computed tomography volumes. J Oral Maxillofac Surg 69:e225–e233

Kim EJ, Ki EJ, Cheon HM, Choi E, Kwon KH (2013) 3-dimensional analysis for class III malocclusion patients with facial asymmetry. J Korean Assoc Oral Maxillofac Surg 39:168–174

Kohn L, Cheverud J (1992) Calibration, validation, and evaluation of scanning systems: anthropometric imaging system repeatability book series electronic imaging of the human body. In: Vannier MW, Yates RE Whitestone JJ, CSERIAC (series ed.), Proceedings of a working group. Dayton, OH, pp 114–123

Kolokitha OE, Chatzistavrou E (2012) Factors influencing the accuracy of cephalometric prediction of soft tissue profile changes following orthognathic surgery. J Maxillofac Oral Surg 11:82–90

Kook YA, Kim Y (2011) Evaluation of facial asymmetry with three-dimensional cone-beam computed tomography. J Clin Orthod 45:112–115

Korbmacher H, Kahl-Nieke B, Schöllchen M, Heiland M (2007) Value of two cone-beam computed tomography systems from an orthodontic point of view. J Orofac Orthop 68:278–289

Koyama J, Nishiyama H, Hayashi T (2007) Follow-up study of condylar bony changes using helical computed tomography in patients with temporomandibular disorder. Dentomaxillofac Radiol 36:472–477

Kragskov J, Bosch C, Gyldensted C, Sindet-Pedersen S (1997) Comparison of the reliability of craniofacial anatomic landmarks based on cephalometric radiographs and three-dimensional CT scans. Cleft Palate Craniofac J 34:111–116

Kuijpers MA, Pazera A, Admiraal RJ, Bergé SJ, Vissink A, Pazera P (2014) In-cidental findings on cone beam computed tomography scans in cleft lip and pal-ate patients. Clin Oral Investig 18:1237–1244

Kumar V, Ludlow JB, Mol A, Cevidanes L (2007) Comparison of conventional and cone beam CT synthesized cephalograms. Dentomaxillofac Radiol 36:263–269

Kusnoto B, Evans CA, BeGole EA, de Rijk W (1999) Assessment of 3-dimensional computer-generated cephalometric measurements. Am J Orthod Dentofac Orthop 116:390–399

Kwon TG, Park HS, Ryoo HM, Lee SH (2006) A comparison of craniofacial morphology in patients with and without facial asymmetry—a threedimensional analysis with computed tomography. Int J Oral Maxillofac Surg 35:43–48

Lagravère MO, Major PW (2005) Proposed reference point for 3-dimensional cephalometric analysis with cone-beam computerized tomography. Am J Orthod Dentofac Orthop 128:657–660

Lagravère MO, Major PW, Carey J (2010) Sensitivity analysis for plane orientation in three-dimensional cephalometric analysis based on superimposition of serial cone beam computed tomography images. Dentomaxillofac Radiol 39:400–408

Lane C, Harrell W Jr (2008) Completing the 3-dimensional picture. Am J Orthod Dentofac Orthop 133:612–620

Langenbach GEJ, Hannam AG (1999) The role of passive muscle tensions in a three-dimensional dynamic model of the human jaw. Arch Oral Biol 44:557–573

Largravere MO, Major PW (2005) Proposed reference point for 3-dimensional cephalometric analysis with cone-beam computerized tomography. Am J Orthod Dentofac Orthop 128:657–660

Larson BE (2012) Cone-beam computed tomography is the imaging technique of choice for comprehensive orthodontic assessment. Am J Orthod Dentofacial Orthop 141(4):402, 404, 406 passim

Leitlinie d DGZMK (2009) Dentale Volumentomographie (DVT)—S1 Empfehlung. Dtsch Zahnarztl Z 64:490–496

Lenza MG, Lenza MM, Dalstra M, Melsen B, Cattaneo PM (2010) An analysis of different approaches to the assessment of upper airway morphology: a CBCT study. Orthod Craniofac Res 13:96–105

Leung CC, Palomo L, Griffith R, Hans MG (2010) Accuracy and reliability of cone-beam computed tomography for measuring alveolar bone height and detecting bony dehiscences and fenestrations. Am J Orthod Dentofac Orthop 137(4 Suppl):S109–S119

Leuzinger M, Dudic A, Giannopoulou C, Killaridis S (2010) Root-contact evaluation by panoramic radiography and cone-beam computed tomography of super-high resolution. Am J Orthod Dentofac Orthop 137:389–392

Liedke GS, Dias de Silveira HE, Dias de Silveira HL, Dutra V, Poli de Figueiredo JA (2009) Influence of voxel size in the diagnostic ability of cone beam tomography to evaluate simulated external root resorption. J Endod 35:233–235

Liu D, Zhang W, Zhang z WY, Ma X (2007) Three-dimensional evaluations of supernumerary teeth using cone-beam computed tomography for 487 cases. Oral Surg Oral Med Oral Pathol Oral Radiol Endod 103:403–411

Liu D, Zhang W, Zhang z WY, Ma X (2008) Localization of impacted maxillary canines and observation of adjacent incisor resorption with cone-beam computed tomography. Oral Surg Oral Med Oral Pathol Oral Radiol Endod 105:91–98

Lloyd TE, Drage NA, Cronin AJ (2011) The role of cone beam computed tomography in the management of unfavourable fractures following sagittal split mandibular osteotomy. J Orthod 38:48–54

Lloyd JE, Stavness I, Fels S (2012) ArtiSynth: a fast interactive biomechanical modeling toolkit combining multibody and finite element simulation. In: Soft tissue biomechanical modeling for computer assisted surgery. Springer, New York, pp 355–394

Lou L, Lagravere MO, Compton S, Major PW, Flores-Mir C (2007) Accuracy of measurements and reliability of landmark identification with computed tomography (CT) techniques in the maxillofacial area: a systematic review. Oral Surg Oral Med Oral Pathol Oral Radiol Endod 104:402–411

Loubele M, Van Assche N, Carpentier K, Maes F, Jacobs R, Van Steenberghe D, Suetens P (2008) Comparative localized linear accuracy of small-field cone-beam CT and multislice CT for alveolar bone measurements. Oral Surg Oral Med Oral Pathol Oral Radiol Endod 105:512–518

Ludlow JB, Ivanovic M (2008) Comparative dosimetry of dental CBCT devices and 64-slice CT for oral and maxillofacial radiology. Oral Surg Oral Med Oral Pathol Oral Radiol Endod 106:106–114

Ludlow JB, Koivisto J (2015) Dosimetry of Orthodontic Diagnostic FOVs using Low dose CBCT protocols. J Dent Res 94(Spec Iss A):0920. http://www.iadr.org

Ludlow JB, Walker C (2013) Assessment of phantom dosimetry and image quality of i-CAT FLX cone-beam computed tomography. Am J Orthod Dentofac Orthop 144:802–817

Ludlow JB, Gubler M, Cevidanes L, Mol A (2009) Precision of cephalometric landmark identification: cone-beam computed tomography vs conventional cephalometric views. Am J Orthod Dentofac Orthop 136(3):312.e1–10; discussion 312–3

Ludlow JB, Timothy R, Walker C, Hunter R, Benavides E, Samuelson DB, Scheske MJ (2015) Effective dose of dental CBCT-a meta analysis of published data and additional data for nine CBCT units. Dentomaxillofac Radiol 44:20140197

Maal TJ, Plooij JM, Rangel FA, Mollemans W, Schutyser FA, Bergé SJ (2008) The accuracy of matching three-dimensional photographs with skin surfaces derived from cone-beam computed tomography. Int J Oral Maxillofac Surg 37:641–646

Maeda M, Katsumata A, Ariji Y, Muramatsu A, Yoshida K, Goto S, Kurita K, Ariji E (2006) 3D-CT evaluation of facial asymmetry in patients with maxillofacial deformities. Oral Surg Oral Med Oral Pathol Oral Radiol Endod 102:382–390

Mah JK, Huang JC, Choo H (2010) Practical applications of cone-beam computed tomography in orthodontics. J Am Dent Assoc 141(Suppl 3):7S–13S

Mah JK, Yi L, Huang RC, Choo H (2011) Advanced applications of cone beam computed tomography in orthodontics. Semin Orthod 17:57–71

Major PW, Johnson DE, Hesse KL, Glover KE (1994) Landmark identification error in posterior anterior cephalometrics. Angle Orthod 64:447–454

Matteson SR, Joseph LP, Bottomley W, Finger HW, Frommer HH, Koch RW, et al (1987) The selection of patients for X-ray examinations: dental radiographic examinations. In: Center for Devices and Radiological Health (ed), US Department of Health and Human Services, Public Health Service, Food and Drug Administration

Matteson SR, Bechtold W, Phillips C (1989) A method for three dimensional image reformation for quantitative cephalometric analysis. J Oral Maxillofac Surg 47:1053–1061

McNamara JA Jr (1984) A Method of cephalometric evaluation. Am J Orthod 86:449–469

Merrett SJ, Drage NA, Durning P (2009) Cone beam computed tomography: a useful tool in orthodontic diagnosis and treatment planning. J Orthod 36:202–210

Metzger TE, Kula KS, Eckert GJ, Ghoneima AA (2014) Orthodontic soft-tissue parameters: a comparison of cone-beam computed tomography and the 3dMD imaging system. Am J Orthod Dentofac Orthop 144:672–681

Moerenhout BA, Gelaude F, Swennen GR, Casselman JW, Van Der Sloten J, Mommaerts M (2009) Accuracy and repeatability of cone-beam computed tomography (CBCT) measurements used in the determination of facial indices in the laboratory setup. J Craniomaxillofac Surg 37:18–23

Molen AD (2010) Considerations in the use of cone-beam computed tomography for buccal bone measurements. Am J Orthod Dentofac Orthop 137(4 Suppl):S130–S135

de Moraes ME, Hollender LG, Chen CS, Moraes LC, Balducci I (2011) Evaluating craniofacial asymmetry with digital cephalometric images and cone-beam computed tomography. Am J Orthod Dentofac Orthop 139:e523–e531

Moshiri M, Scarfe WC, Hilgers ML, Scheetz JP, Silveira AM, Farman AG (2007) Accuracy of linear measurements from imaging plate and lateral cephalometric images derived from cone-beam computed tomography. Am J Orthod Dentofacial Orthop 132:550–560

Moyers RE, Bookstein FL (1979) The inappropriateness of conventional cephalometrics. Am J Orthod Dentofac Orthop 75:599–617

Mullen SR, Martin CA, Ngan P, Gladwin M (2007) Accuracy of space analysis with emodels and plaster models. Am J Orthod Dentofacial Orthop 132:346–352

Muramatsu A, Nawa H, Kimura M, Yoshida K, Maeda M, Katsumata A, Ariji E, Goto S (2008) Reproducibility of Maxillofacial Anatomic Landmarks on 3-Dimensional Computed Tomographic Images Determined with the 95% Confidence Ellipse Method. Angle Orthod 78:396–340

Nahm KY, Kim Y, Choi YS, Lee J, Kim SH, Nelson G (2014) Accurate registration of cone-beam computed tomography scans to 3-dimensional facial photographs. Am J Orthod Dentofac Orthop 145:256–264

Naudi KB, Benramadan R, Brocklebank L, Ju X, Khambay B, Ayoub A (2012) The virtual human face: superimposing the simultaneously captured 3D photorealistic skin surface of the face on the untextured skin

image of the CBCT scan. Int J Oral Maxillofac Surg 42:393–400
Nawaratne S, Fabiny R, Brien JE, Zalcberg J, Cosolo W, Whan A, Morgan DJ (1997) Accuracy of volume measurement using helical CT. J Comput Assist Tomogr 21:481–486
Newaz ZA, Barghan S, Katkar RA, Bennett JA, Nair MK (2015) Incidental findings of skull-base abnormalities in cone-beam computed tomography scans with consultation by maxillofacial radiologists. Am J Orthod Dentofac Orthop 147:127–131
Nijkamp P, Habets L, Aartman I, Zentner A (2008) The influence of cephalometrics on orthodontic treatment planning. Eur J Orthod 30:630–635
Nik-Hussein NN (1990) Supernumerary teeth in the premaxillary region: its effects on the eruption and occlusion of the permanent incisors. Aust Orthod J 11:247–250
Oberoi S, Knueppel S (2012) Three-dimensional assessment of impacted canines and root resorption using cone beam computed tomography. Oral Surg Oral Med Oral Pathol Oral Radiol Endod 113:260–267
Oberoi S, Gill P, Chigurupati R, Hoffman WY, Hatcher DC, Vargervik K (2010) Three-dimensional assessment of the eruption path of the canine in individuals with bone-grafted alveolar clefts using cone beam computed tomography. Cleft Palate Craniofac J 47:507–512
Ogawa T, Enciso R, Memon A, Mah JK, Clark GT (2005) Evaluation of 3D airway imaging of obstructive sleep apnea with cone-beam computed tomography. Stud Health Technol Inform 111:365–368
Oh KM, Hong JS, Kim YJ, Cevidanes LS, Park YH (2011) Three-dimensional analysis of pharyngeal airway form in children with anteroposterior facial patterns. Angle Orthod 81:1075–1082
de Oliveira AE, Cevidanes LH, Phillips C, Motta A, Burke B, Tyndall D (2009) Observer reliability of three-dimensional cephalometric landmark identification on cone-beam computerized tomography. Oral Surg Oral Med Oral Pathol Oral Radiol Endod 107:256–265
Olszewski R, Nicolas V, Macq B, Reychler H (2003) ACRO 4D: universal analysis for four-dimensional diagnosis; 3D planning and simulation in orthognathic surgery. CARS Proc 1256:1235.e1240
Olszewski R, Cosnard G, Macq B, Mahy P, Reychler H (2006) 3D CT-based cephalometric analysis: 3D cephalometric theoretical concept and software. Neuroradiology 48:853–862
Olszewski R, Zech F, Cosnard G, Nicolas V, Macq B, Reychler H (2007) Three-dimensional computed tomography cephalometric craniofacial analysis: experimental validation in vitro. Int J Oral Maxillofac Surg 36:828–833
Olszewski R, Reychler H, Cosnard G, Denis JM, Vynckier S, Zech F (2008) Accuracy of three-dimensional (3D) craniofacial cephalometric landmarks on a low-dose 3D computed tomograph. Dentomaxillofac Radiol 37:261–267
Olszewski R, Tanesy O, Cosnard G, Zech F, Reychler H (2010) Reproducibility of osseous landmarks used for computed tomography based three-dimensional cephalometric analyses. J Craniomaxillofac Surg 38:214–221
Orentlicher G, Goldsmith D, Horowitz A (2010) Applications of 3-dimensional virtual computerized tomography technology in oral and maxillofacial surgery: current therapy. J Oral Maxillofac Surg 68:1993–1959
Osorio F, Perilla M, Doyle DJ, Palomo JM (2008) Cone beam computed tomography: an innovative tool for airway assessment. Anesth Analg 106:1803–1807
Oz U, Orhan K, Abe N (2011) Comparison of linear and angular measurements using two-dimensional conventional methods and three-dimensional cone beam CT images reconstructed from a volumetric rendering program in vivo. Dentomaxillofac Radiol 40(8):492–500
Pacini AJ (1922) Roentgen ray anthropometry of the skull. J Radiol 3:230–231. 322-331, 418-426
Pae EK, McKenna GA, Sheehan TJ, Garcia R, Kuhlberg A, Nanda R (2001) Role of lateral cephalograms in assessing severity and difficulty of orthodontic cases. Am J Orthod Dentofacial 120:254–262
Palomo JM, Rao PS, Hans MG (2008) Influence of CBCT exposure conditions on radiation dose. Oral Surg Oral Med Oral Pathol Oral Radiol Endod 105:773–782
Papadopoulos MA, Tarawneh F (2008) The use of miniscrew implants for temporary skeletal anchorage in orthodontics: a comprehensive review. Oral Surg Oral Med Oral Pathol Oral Radiol Endod 103:e6–15
Park SH, HS Y, Kim KD, Lee KJ, Baik HS (2006) A proposal for a new analysis of craniofacial morphology by 3-dimensional computed tomography. Am J Orthod Dentofac Orthop 129:600.e23–34
Pazera P, Bornstein MM, Pazera A, Sendi P, Katsaros C (2011) Incidental maxillary sinus findings in orthodontic patients: a radiographic analysis using cone-beam computed tomography (CBCT). Orthod Craniofac Res 14:17–24
Pittayapat P, Limchaichana-Bolstad N, Willems G, Jacobs R (2014) Three-dimensional cephalometric analysis in orthodontics: a systematic review. Orthod Craniofac Res 17:69–91
Pliska B, DeRocher M, Larson BE (2011) Incidence of significant findings on CBCT scans of an orthodontic patient population. Northwest Dent 90:12–16
Popat H, Richmond S, Drage NA (2010) New developments in: three-dimensional planning for orthognathic surgery. J Orthod 37:62–71
Qu XM, Li G, Sanderink GC, Zhang ZY, Ma XC (2012) Dose reduction of cone beam CT scanning for the entire oral and maxillofacial regions with thyroid collars. Dentomaxillofac Radiol 41:373–378
Rheude B, Sadowsky PL, Ferriera A, Jacobson A (2005) An evaluation of the use of digital study models in orthodontic diagnosis and treatment planning. Angle Orthod 75:300–304
Richtsmeier JT, Paik CH, Elfert PC, Cole TM III, Dahlman HR (1995) Precision, repeatability, and validation of the localization of cranial landmarks using computed tomography scans. Cleft Palate Craniofac J 32:217–227

Ricketts RM (1957) Planning treatment on the basis of the facial pattern and an estimate of its growth. Angle Orthod 27:14–37

Ricketts RM (1961) Cephalometric analysis and synthesis. Angle Orthod 31:141–156

Ricketts RL, Grummons D (2003) Frontal Cephalometrics: Practical Applications, Part 1. World J Orthod 4:297–316

Ricketts RM, Bench RW, Gugino CF, Hilgers JJ, Schulhof RJ (1979) Bioprogressive therapy. Rocky Mountain® Orthodontics, Denver, pp 35–54. Visual treatment objective or V.T.O

Rocha S, Ramos D, Cavalcanti M (2003) Applicability of 3D-CT facial reconstruction for forensic individual identification. Pesqui Odontol Bras 17:24–28

Rogers SA, Drage N, Durning P (2011) Incidental findings arising with cone beam computed tomography imaging of the orthodontic patient. Angle Orthod 81:350–355

Rungcharassaeng K, Caruso JM, Kan JY, Kim J, Taylor G (2007) Factors affecting buccal bone changes of maxillary posterior teeth after rapid maxillary expansion. Am J Orthod Dentofac Orthop 132:428.e1–8

Sarver DM (1998) Esthetic orthodontics and orthognathic surgery. Mosby, St. Louis

Scarfe WC, Farman AG, Sukovic P (2006) Clinical applications of cone beam computed tomography in dental practice. J Can Dent Assoc 72:75–80

Schendel SA, Hatcher D (2010) Automated 3-dimensional airway analysis from cone-beam computed tomography data. J Oral Maxillofac Surg 68:696–701

Schendel SA, Lane C (2009) 3D orthognathic surgery simulation using image fusion. Semin Orthod 15:48–56

Schendel SA, Duncan KS, Lane C (2011a) Image fusion in preoperative planning. Facial Plast Surg Clin North Am 19:577–590

Schendel S, Powell N, Jacobson R (2011b) Maxillary, mandibular, and chin advancement: treatment planning based on airway anatomy in obstructive sleep apnea. J Oral Maxillofac Surg 69:663–676

Schendel SA, Jacobson R, Khalessi S (2013) 3-dimensional facial simulation in orthognathic surgery: is it accurate? J Oral Maxillofac Surg 71:1406–1414

Schiffman EL, Ohrbach R, Truelove EL, Tai F, Anderson GC, Pan W, Gonzalez YM, John MT, Sommers E, List T, Velly AM, Kang W, Look JO (2010a) The research diagnostic criteria for temporomandibular disorders. V: methods used to establish and validate revised Axis I diagnostic algorithms. J Orofac Pain 24:63–78

Schiffman EL, Truelove EL, Ohrbach R, Anderson GC, John MT, List T, Look JO (2010b) The research diagnostic criteria for temporomandibular disorders. I: overview and methodology for assessment of validity. J Orofac Pain 24:7–24

Schlicher W, Nielsen I, Huang JC, Maki K, Hatcher DC, Miller AJ (2012) Consistency and precision of landmark identification in three-dimensional cone beam computed tomography scans. Eur J Orthod 34(3):263–275

Schuytser FA, Van Cleynenbreugel J (2005) From 3-D volumetric computer tomography to 3-D cephalometry. In: Swennen GJ, Schuytser FA, Hausamen JE (eds) Three dimensional cephalometry: a color atlas and manual. Springer GmbH Berlin, Germany p, pp 2–11

Scolozzi P, Terzic A (2011) "Mirroring" computational planning, navigation guidance system, and intraoperative mobile C-arm cone-beam computed tomography with flat-panel detector. J Oral Maxillofac Surg 69:1697–1707

Sera T, Fujioka H, Yokota H, Makinouchi A, Himeno R, Schroter RC, Tanishita K (2003) Three-dimensional visualization and morphometry of small airways from microfocal X-ray computed tomography. J Biomech 36:1587–1594

Shemesh H, Cristescu RC, Wesslink PR, M-K W (2011) The use of cone-beam computed tomography and digital periapical radiographs to diagnose root perforations. J Endod 37:513–516

Sherrard JF, Rossouw PE, Benson BW, Carrillo R, Buschang PH (2010) Accuracy and reliability of tooth and root lengths measured on cone-beam computed tomographs. Am J Orthod Dentofac Orthop 137(4 Suppl):S100–S108

Sievers MM, Larson BE, Gaillard PR, Wey A (2012) Asymmetry assessment using cone-beam CT a class I and class II patient comparison. Angle Orthod 82(3):410–417

Silling G, Rauch MA, Pentel L, Garfinkel L, Halberstadt G (1979) The significance of cephalometrics in treatment planning. Angle Orthod 49:259–262

Smith JD, Thomas PM, Proffitt WR (2004) A comparison of current prediction imaging programs. Am J Orthod Dentofac Orthop 125(5):527–536

Soares MC, Sallum AC, Gonçalves MT, Haddad FL, Gregório LC (2009) Use of Muller's maneuver in the evaluation of patients with sleep apnea—literature review. Braz J Otorhinolaryngol 75:463–466

Stavness I, Hannam AG, Lloyd JE, Fels S (2006) An Integrated Dynamic Jaw and Laryngeal Model Constructed from CT Data. In: Harders M, Székely G (eds) Biomedical Simulation. ISBMS 2006. Lecture Notes in Computer Science, vol 4072. Springer, Berlin, Heidelberg, pp 169–177

Stavness I, Lloyd J, Payan Y, Fels S (2011) Coupled hard-soft tissue simulation with contact and constraints applied to jaw-tongue-hyoid dynamics. Int J Numer Method Biomed Eng 27:367–390

Stavness I, Nazari M, Flynn C, Perrier P, Payan Y, Lloyd JE, Fels S (2014) Coupled biomechanical modeling of the face, jaw, skull, tongue, and hyoid bone. In: Magnenat-Thalmann N, Ratib O, Choi H-F (eds) 3D Multiscale physiological human. Springer-Verlag, London, pp 253–274. Chapter 11

Steiner CC (1960) The use of cephalometrics as an aid to planning and assessing orthodontic treatment. Am J Orthod 46:721

Stevens DR, Flores-Mir C, Nebbe B, Raboud DW, Heo G, Major PW (2006) Validity, reliability, and reproducibility of plaster vs digital study models: comparison of peer assessment rating and Bolton analysis and their constituent measurements. Am J Orthod Dentofacial Orthop 129:794–803

Strauss RA, Burgoyne CC (2008) Diagnostic imaging and sleep medicine. Dent Clin N Am 52:891–915

Suomalainen A, Åberg T, Rautio J, Hurmerinta K (2014) Cone beam computed tomography in the assessment of alveolar bone grafting in children with unilateral cleft lip and palate. Eur J Orthod 36:603–611

Swennen GR, Schutyser FA, Hausamen JE (eds) (2005) Three dimensional cephalometry: a color atlas and manual. Springer, Berlin

Swennen GR, Schutyser F, Barth EL, De Groeve P, De Mey A (2006) A new method of 3-D cephalometry part I: the anatomic Cartesian 3-D reference system. J Craniofac Surg 17:314e325

Tamimi D, ElSaid K (2009) Cone beam computed tomography in the assessment of dental impactions. Semin Orthod 15:57–62

Timock AM, Cook V, McDonald T, Leo MC, Crowe J, Benninger BL, Covell DA Jr (2011) Accuracy and reliability of buccal bone height and thickness measurements from cone-beam computed tomography imaging. Am J Orthod Dentofac Orthop 140:734–744

Togashi K, Kitaura H, Yonetsu K, Yoshida N, Nakamura T (2002) Three-dimensional cephalometry using helical computer tomography: measurement error caused by head inclination. Angle Orthod 72:513–520

Treil J, Casteigt J, Borianne P, Madrid C, Jaeger M, de Bonnecaze P (1999) The architectural balance of the face: a 3D cephalometric concept. Rev Stomatol Chir Maxillofac 100:111–122. [French]

Treil J, Braga J, Loubes J-M, Maza E, Inglese J-M, Casteigt J, Waysenson B (2009) 3D tooth modeling for orthodontic assessment. Semin Orthod 15:42–47

Trocme MC, Sather AH, An KN (1990) A biplanar cephalometric stereoradiography technique. Am J Orthod Dentofac Orthop 98:168–175

Truelove E, Pan W, Look JO, Mancl LA, Ohrbach RK, Velly AM, Huggins KH, Lenton P, Shiffman EL (2010) The research diagnostic criteria for temporomandibular disorders. III: validity of axis I diagnoses. J Orofac Pain 24:35–47

Tsiklakis K, Donta C, Gavala S, Karayianni K, Kamenopoulou V, Hourdakis CJ (2005) Dose reduction in maxillofacial imaging using low dose cone beam CT. Eur J Radiol 56:413–417

Tso HH, Lee JS, Huang JC, Maki K, Hatcher D, Miller AJ (2009) Evaluation of the human airway using cone-beam computerized tomography. Oral Surg Oral Med Oral Pathol Oral Radiol Endod 108:768–776

Tucker S, Cevidanes LHS, Styner M, Kim H, Reyes M, Proffit W, Turvey T (2010) Comparison of actual surgical outcomes and 3-dimensional surgical simulations. J Oral Maxillofac Surg 68:2412–2421

Tulunoglu O, Esenlik E, Gulsen A, Tulunoglu I (2011) A comparison of three-dimensional and two-dimensional cephalometric evaluations of children with cleft lip and palate. Eur J Dent 5(4):451–458

Tweed CH (1954) The Frankfort Mandibular Incisor Angle (FMIA) in orthodontic diagnosis, treatment planning, and prognosis. Angle Orthod 24:121–169

Tzou CH, Artner NM, Pona I, Hold A, Placheta E, Kropatsch WG, Frey M (2014) Comparison of three-dimensional surface-imaging systems. J Plast Reconstr Aesthet Surg 67:489–497

Valeri CJ, Cole TM, Lele S, Richtsmeier JT (1998) Capturing data from three-dimensional surfaces using fuzzy landmarks. Am J Phys Anthropol 107:113–124

Van Elslande D, Heo G, Flores-Mir C, Carey J, Major PW (2010) Accuracy of mesiodistal root angulation projected by cone-beam computed tomographic panoramic-like images. Am J Orthod Dentofac Orthop 137(4 Suppl):S94–S99

Van Loon JAW (1915a) A New method for indicating normal and abnormal relationships of the teeth to facial lines. Dent Cosmos 57:973–983

Van Loon JAW (1915b) A new method in dento-facial orthopedia, parts 1 and 2. Dent Cosmos 57:1093–1101, 1229–1235

Van Steenbergen E, Nanda R (1995) Biomechanics of orthodontic correction of dental asymmetries. Am J Orthod Dentofacial Orthop 107:618–624

Vanarsdall RL Jr (1999) Transverse dimension and long-term stability. Semin Orthod 5:171–180

Vandenberghe B, Luchsinger S, Hostens J, Dhoore E, Jacobs R, SEDENTEXCT Project Consortium (2012) The influence of exposure parameters on jawbone model accuracy using cone beam CT and multislice CT. Dentomaxillofac Radiol 41(6):466–474

Veli I, Uysal T, Ozer T, Ucar FI, Eruz M (2011) Mandibular asymmetry in unilateral and bilateral posterior crossbite patients using cone-beam computed tomography. Angle Orthod 81:966–974

van Vlijmen OJ, Rangel FA, Bergé SJ, Bronkhorst EM, Becking AG, Kuijpers-Jagtman AM (2011) Measurements on 3D models of human skulls derived from two different cone beam CT scanners. Clin Oral Investig 15:721–727

van Vlijmen OJ, Kuijpers MA, Bergé SJ, Schols JG, Maal TJ, Breuning H, Kuijpers-Jagtman AM (2012) Evidence supporting the use of cone-beam computed tomography in orthodontics. J Am Dent Assoc 143:241–252

Vogt F, Lloyd J, Buchaillard S, Perrier P, Chabanas M, Payan Y, Fels S (2006) Efficient 3D finite element modeling of a muscle-activated tongue. Lecture Notes Comput Sci 4072:19–28

Von Arx T (1992) Anterior maxillary supernumerary teeth: a clinical and radiographic study. Aust Dent J 37:189–195

Walker L, Enciso R, Mah J (2005) Three-dimensional localization of maxillary canines with cone-beam computed tomography. Am J Orthod Dentofac Orthop 128:418–423

Ward RE, Jamison PL (1991) Measurement precision and reliability in craniofacial anthropometry: implications and suggestions for clinical applications. J Craniofac Genet Dev Biol 11:156–164

Weinberg SM, Kolar JC (2005) Three-Dimensional Surface Imaging: Limitations and Considerations From the Anthropometric Perspective. J Craniofac Surg 16:847–845

White SC, Pae E-K (2009) Patient image selection criteria for cone beam computed tomography imaging. Semin Orthod 15:19–28

White AJ, Fallis DW, Vandewalle KS (2010) Analysis of intra-arch and interarch measurements from digital models with 2 impression materials and a modeling process based on cone-beam computed tomography. Am J Orthod Dentofac Orthop 137:456.e1–9; discussion 456–7

Williams FL, Richtsmeier JT (2003) Comparison of mandibular landmarks from computed tomography and 3D digitizer data. Clin Anat 16:494–500

Xia J, Ip HH, Samman N, Wang D, Kot CS, Yeung RW, Tideman H (2000) Computer-assisted three-dimensional surgical planning and simulation: 3D virtual osteotomy. Int J Oral Maxillofac Surg 29:11–17

Yagci A, Veli I, Uysal T, Ucar FI, Ozer T, Enhos S (2012) Dehiscence and fenestration in skeletal class I, II, and III malocclusions assessed with cone-beam computed tomography. Angle Orthod 82:67–74

You KH, Lee KJ, Lee SH, Baik HS (2010) Three-dimensional computed tomography analysis of mandibular morphology in patients with facial asymmetry and mandibular prognathism. Am J Orthod Dentofac Orthop 138:540.e1–e8

Zamora N, Llamas JM, Cibrián R, Gandia JL, Paredes V (2012) A study on the reproducibility of cephalometric landmarks when undertaking a three-dimensional (3D) cephalometric analysis. Med Oral Patol Oral Cir Bucal 17:e678–e688

Zilberman O, Huggare JAV, Parikakis KA (2003) Evaluation of the validity of tooth size and arch width measurements using conventional and threedimensional virtual orthodontic models. Angle Orthod 73:301–306

Orthodontic and Orthognathic Surgery Planning and Simulation Software

19

Lucia H.S. Cevidanes, Antonio C.O. Ruellas, and William C. Scarfe

Contents

L.H.S. Cevidanes, D.D.S., M.S., Ph.D. (✉)
Department of Orthodontics and Pediatric Dentistry, School of Dentistry, University of Michigan, Ann Arbor, MI, USA
e-mail: luciacev@umich.edu

A.C.O. Ruellas, D.D.S., M.S., Ph.D.
Department of Orthodontics, Dental School, Federal University of Rio de Janeiro, Rio de Janeiro, Brazil
e-mail: antonioruellas@yahoo.com.br

W.C. Scarfe, B.D.S., F.R.A.C.D.S., M.S.
Division of Radiology and Imaging Science, Department of Surgical/Hospital Dentistry, University of Louisville School of Dentistry, Louisville, KY, USA
e-mail: william.scarfe@louisville.edu

19.1 Introduction

Since the introduction of dental and maxillofacial CBCT imaging in the United States in 2001, volumetric reconstructions providing three-dimensional (3-D) visualizations of complex craniofacial skeletal, dental, and soft tissue conditions have been applied to assess the effects of dental tooth loss, dentofacial deformities, craniofacial anomalies, and airway obstructions associated

W.C. Scarfe, C. Angelopoulos (eds.), *Maxillofacial Cone Beam Computed Tomography*,
https://doi.org/10.1007/978-3-319-62061-9_19

with obstructive sleep apnea/hypopnea syndrome. In particular, 3-D assessment of facial morphology provides the diagnostic basis for rational clinical decisions for the treatment of patients that require combined orthodontic and surgical correction. Surgical and orthodontic treatment planning involving multiple procedures is now based on computer-assisted assessment and virtual simulations using volumetric images, virtual models, and 3-D printed splints rather than two-dimensional (2-D) radiographic images and plaster-based surgical simulations. Studies on the 3-D bone remodeling, surgical simulations, and comparisons with postoperative outcomes have helped clarify clinical questions on the variability of outcomes of surgery (Cevidanes et al. 2005; Carvalho et al. 2010; Tucker et al. 2010).

CBCT imaging offers the potential to develop diagnostic and treatment planning skills in regard to orthodontic and orthognathic surgical planning but requires an understanding of 3-D image analyses procedures associated with surface modeling, superimpositions, surgical simulations, and imager-guided navigation.

19.2 3-D CBCT-Based Orthodontic and Orthognathic Surgery Diagnosis and Treatment Planning

The availability of volumetric CBCT images providing 3-D representations of the maxillofacial skeleton has aided in the diagnosis and treatment planning of many clinical orthodontic and orthognathic conditions.

19.2.1 Tooth Development and Relative Position Within the Alveolar Bone

Small or medium field of view (FOV) high-resolution images reveal anatomic details of unerupted tooth development, the position of these teeth relative to adjacent teeth, and the effect of these teeth on adjacent structures. These findings may lead to modifications in the treatment planning including the need for extraction or additional anchorage using bone plates and mini-screws, more precise surgical guides, reduced treatment duration, and reduction in the contribution of orthodontic tooth movement to root resorption (Tamimi and El Said 2009; Treil et al. 2009; Becker et al. 2010; Katheria et al. 2010; Leung et al. 2010; Molen 2010; Sherrard et al. 2010; Tai et al. 2010; Van Elslande et al. 2010; Botticelli et al. 2011; Shemesh et al. 2011; Evans et al. 2013).

19.2.2 Temporomandibular Joint Morphology, Spatial and Functional Relationships

Temporomandibular (TM) anomalies and pathologies may result in deformities to the size and form, and alterations in the spatial and functional relationships of the elements of the joint. Such variations can lead to progressive musculoskeletal changes and dental and skeletal compensations that may ultimately affect jaw and tooth positions and related occlusion. Small FOV, high-resolution acquisition of the TM joints separately yields the best image quality for TM joint assessments. Imaging data currently are recommended to help differentiate the diagnosis of disc displacement and arthralgia, osteoarthritis, and osteoarthrosis. Panoramic radiography and magnetic resonance imaging (MRI) have only poor to marginal sensitivity for detecting osseous changes in the TM joint (Ahmad et al. 2009). CBCT imaging has recently replaced other imaging modalities as the modality of choice to investigate suspicious osseous changes in the TM articulation (Helenius et al. 2005; Koyama et al. 2007; Alexiou et al. 2009).

The Research Diagnostic Criteria for Temporomandibular Disorders (RDC/TMD) (Dworkin and LeResche 1992) was revised recently to include image analysis criteria for various imaging modalities (Ahmad et al. 2009). The RDC/TMD validation project concluded that revised clinical criteria alone, without recourse to imaging, are inadequate for valid diagnosis of TM disorders and had previously underestimated the prevalence of bony changes in the TM joint (Schiffman et al. 2010a, b; Truelove et al. 2010). In affected condyles, altered growth or bone remodeling involving resorption and apposition can lead to progressive bite changes that are accompanied by compensations in the maxilla,

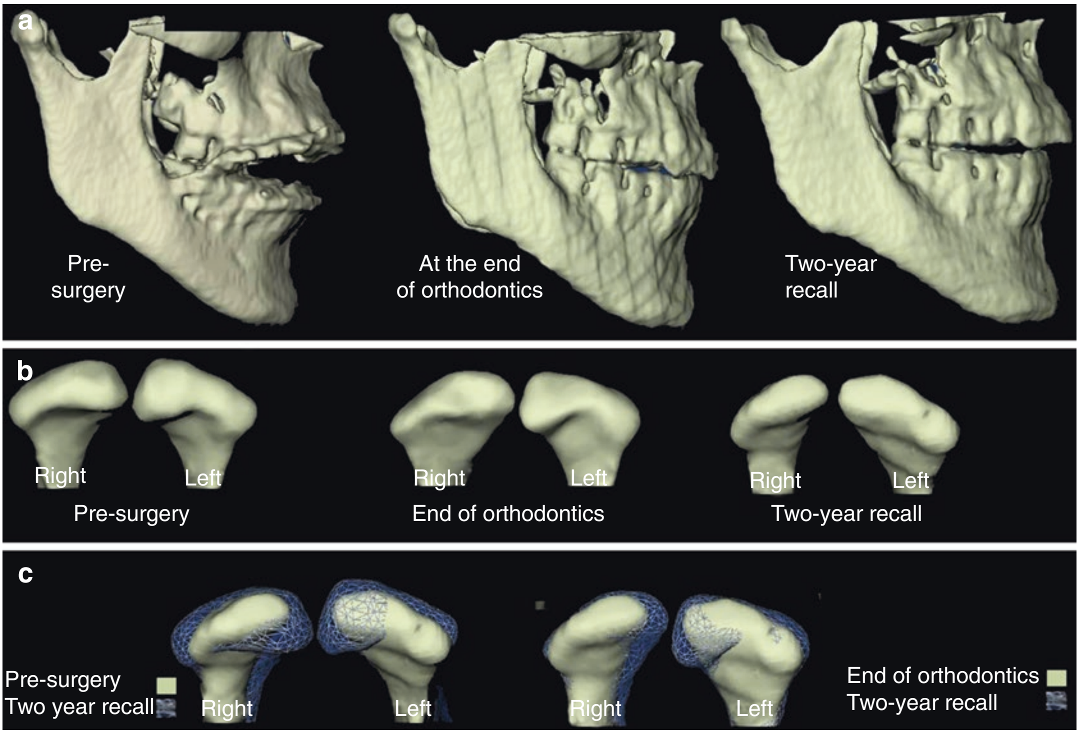

Fig. 19.1 (**a**) CBCT-based surface renderings at presurgery, end of orthodontic treatment and 2-year postsurgery recall (**b**) with magnified views of the condylar morphology at these time points for a patient who was treated with maxillary impaction for correction of open bite. Condylar regional superimposition (**c**) showing the progression of condylar resorptive changes in more detail. These images demonstrate that the patient initially presented presurgically with generalized condylar flattening of the lateral poles and bony projection of the anterior surface of the medial pole

"non-affected" side of the mandible, tooth position, occlusion, and the articular fossa with unpredictable orthodontic outcomes (Bryndahl et al. 2006; Kapila et al. 2011) (Fig. 19.1).

The TM articulation is prone to pathologies often described as "degenerative" and "proliferative" pathologies. The threshold between functional physiologic stimulus with its positive biochemical effects on the TM joint and joint overloading that leads to degenerative or inflammatory proliferative changes is beyond current knowledge (Scott and Athanasiou 2006; Verteramo and Seedhom 2007; Blumberg et al. 2008; Burgin and Aspden 2008; Gallo et al. 2008; Ishida et al. 2009; Roemhildt et al. 2010). Such threshold is influenced by the joint loading vectors, patient genetic and mostly epigenetic factors, including hormonal and autoimmune imbalances. Bone scintigraphy and positron emission tomography (PET-CT) are highly sensitive to detect pathological conditions in a cross-sectional diagnostic assessment. However, they do not have enough specificity, as there are no standard normal values for baseline assessments.

Longitudinal 3-D quantification using volumetric CBCT imaging offers a relatively low cost/low radiation dose technology (compared to PET-CT and bone scintigraphy) and can make a significant difference on treatment planning as an additional imaging marker or risk factor tool. The use of imaging markers to aid in diagnosis of those patients with TM joint disorders is very promising. Several biomarkers, including C-reactive protein, have previously been identified in blood and in synovial fluid biopsies of patients with TMJ condylar bone resorption and related to the pathological progress (Alstergren and Kopp 2000; Nordahl et al. 2001; Fredriksson et al. 2006). These techniques, while still currently restricted to research, are promising to complement imaging modalities that are already part of clinical protocols.

19.2.3 Airway Morphology and Respiration

Impairment of respiration in obstructive sleep apnea has recently been assessed with CBCT images (El and Palomo 2010; Lenza et al. 2010; Schendel and Hatcher 2010; Abramson et al. 2011; Conley 2011; Iwasaki et al. 2011; Schendel et al. 2011).

Challenges in the CBCT assessments of the airway include the definition of consistent boundaries of the nasopharynx superiorly with the maxillary and paranasal sinuses, anteriorly with the oral cavity anteriorly, and inferiorly with the larynx. In static CBCT image acquisitions, the airway shape and volume vary markedly with the functional stage of the dynamic process of breathing (inspiration and expiration physiology) and head posture. If head posture is not correctly reproduced during image acquisition in longitudinal studies, differences in head posture will lead to variability in the assessment of airway dimensions. Longitudinal assessments of mandibular setback have not shown consistent reduction of airway space nor have mandibular propulsion devices shown enlargement of the airway space that might be helpful for obstructive breathing conditions (Fig. 19.2).

19.2.4 Dentofacial Deformities and Craniofacial Anomalies

Complex deformities, discrepancies, or anomalies of the maxillofacial skeleton include skeletal, dental, and soft tissue components of the face and cranium. Diagnosis and treatment planning requires assessment of positional and morphological discrepancies among these craniofacial components in the anteroposterior, vertical, and transverse

Airway changes in CBCT cross-sections and 3D surfaces

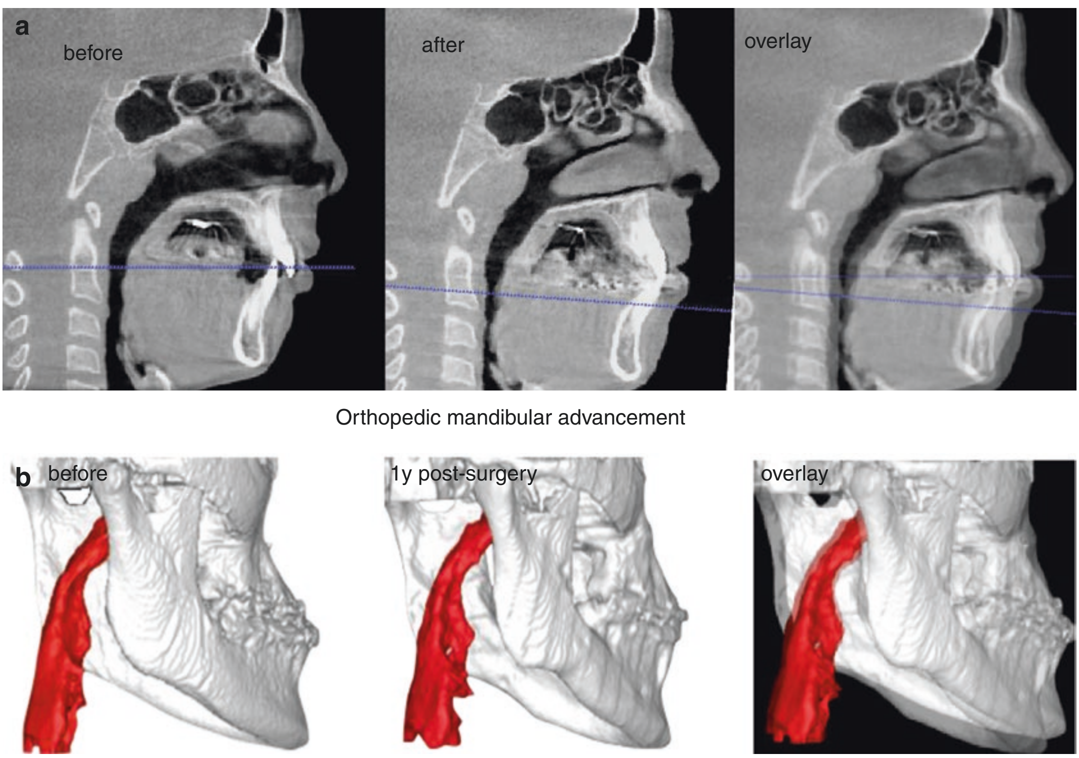

Orthopedic mandibular advancement

Surgical mandibular setback/ maxillary advancement

Fig. 19.2 Midsagittal cross-sectional views (**a**) for a growing patient treated with an orthopedic appliance for mandibular advancement. 3-D airway surface models (**b**) before and 1 year after mandibular setback surgery demonstrates that the airway appears much narrower after orthopedic mandibular advancement. Note that the head posture or the stage of inspiration/expiration during image acquisition may account for the unexpected narrowing of the airway dimensions at presentation, after intervention as well as at temporal intervals. Computer-aided jaw surgery (CAS) is increasingly being used because of a high level of precision in accurately transferring virtual plans into the operating room. In complex cases, follow-up CBCT acquisitions, for growth observation, treatment progress, and post-treatment observations, may be helpful to assess stability of the correction overtime (Agarwal and Muranjan 2008; Ebner et al. 2010; Edwards 2010; Dalessandri et al. 2011; Behnia et al. 2012). CAS systems in jaw surgery include procedures from image scanners and registration of the occlusion to the CBCT or CT scans to the operating room. CAS is described in more detail in Sect. 19.4 of this chapter (Fig. 19.3).

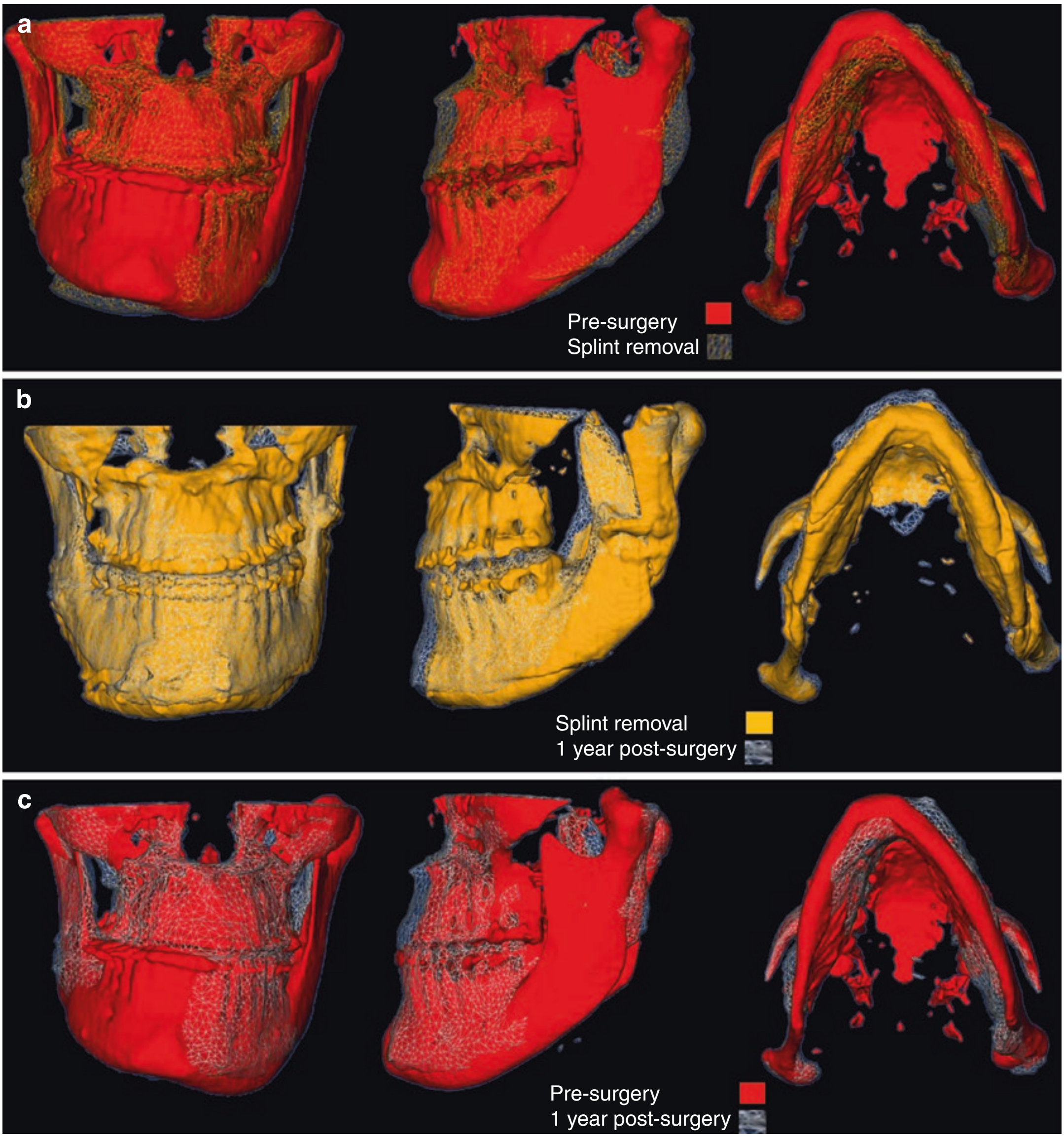

Fig. 19.3 Superimposed volumetric surface renderings for a patient diagnosed with left hemi-mandibular hypertrophy registered to the patient cranial base. (**a**) Overlay of presurgical (*red*) and splint removal (*gray speckled*); (**b**) Overlay of splint removal (*yellow*) and 1 year postoperative (*gray speckled*); (**c**) Overlay of presurgical (*red*) and 1 year postoperative (*gray speckled*). Note how the surgical correction addressed the yaw and roll positional asymmetries as well as improvement of differences in right and left ramus morphology, with surgical shaving of the left condylar surface to decrease ramus length on the hypertrophic side

19.3 3-D Image Analysis Procedures for Clinical and Research Assessments

3-D image analysis is a complex set of procedures that involves a sequence of steps. We have proposed a methodological approach that can be applied to most clinical and research evaluations that includes (Ruellas et al. 2016a):

- Volume or surface image acquisition
- Construction of volumetric label maps
- Conversion of volumetric datasets to surface models
- Establishment of a common coordinate system
- Image registration
- Visual analytics with graphic display and quantification of location, directions and magnitude of 3-D morphological variability and/or changes

These steps can be applied when using any volumetric dataset including CBCT, CT, and MRI. Contour or surface rendering acquired by optical or laser scanners don't require construction of 3-D volumetric label maps and 3-D surface models, enabling registration immediately after their acquisition.

19.3.1 Acquisition of 3-D Diagnostic Records

Diagnosis, virtual treatment planning and simulations are based on the integration of 2 or more sources of 3-D digital data including clinical examination, 3-D photographs, CBCT, CT, MRI, and optically scanned dental study casts. Volumetric datasets (acquired from CBCT, CT, and/or MR images) are saved in file formats such as DICOM, gipl, or nrrd. To simplify the description of image analysis procedures, this chapter specifically describes 3-D analysis of images acquired with CBCT.

DICOM images from CBCT scans can be visualized in various software (Table 19.1).

Table 19.1 Representative examples of Analytical Orthognathic/Orthodontic Software capable of importing multiple file formats, including DICOM

Availability	Name	Manufacturer
Proprietary	3-DMDvultus	3-DMD Atlanta, Georgia USA (3-Dmd 2015)
	Maxilim	Medicim, Mechelen, Belgium (Maxilim 2015)
	Dolphin Imaging	Dolphin Imaging & Management Solutions, Chatsworth, California USA (Dolphin Imaging 2015)
	InVivo Dental	Anatomage, San Jose, California USA (Invivo 2015)
	SimPlant OMS or Mimics	Materialise, Leuven, Belgium (Simplant 2015)
Open source	TurtleSeg	(Turtleseg 2015)
	ITK-SNAP	(Itksnap 2015)
	SlicerCMF	(3-Dslicer 2015)

Within each software, DICOM files can be visualized in various display formats including (Fig. 19.4): (1) as cross-sectional slices; (2) as 3-D projected images (volumetric rendering); and (3) as construct 3-D volumetric files and/or 3-D surface models of specific anatomic structures of interest.

The assessments based on the visualization of multi-planar cross-sectional slices is limited to 2-D evaluations of each slice and poses challenges toward standardization of which cross section to analyze (Molen 2010). More commonly, CBCT volumes are visualized as volumetric renderings that are 3-D representations of the craniofacial anatomy. This allows visual and quantitative assessments of the anatomic surfaces reconstructed from CBCT volumetric dataset without the construction of surface models. However, these renderings should be used only for perspective visualizations and not for quantitative assessments, because they are simply projected images (Fig. 19.4b), transparent, and do not present with solid surface meshes (Fig. 19.4d). Proper quantitative assessment requires the construction of 3-D surface meshes or 3-D surface models generated from the 3-D volumetric label maps (Fig. 19.4d).

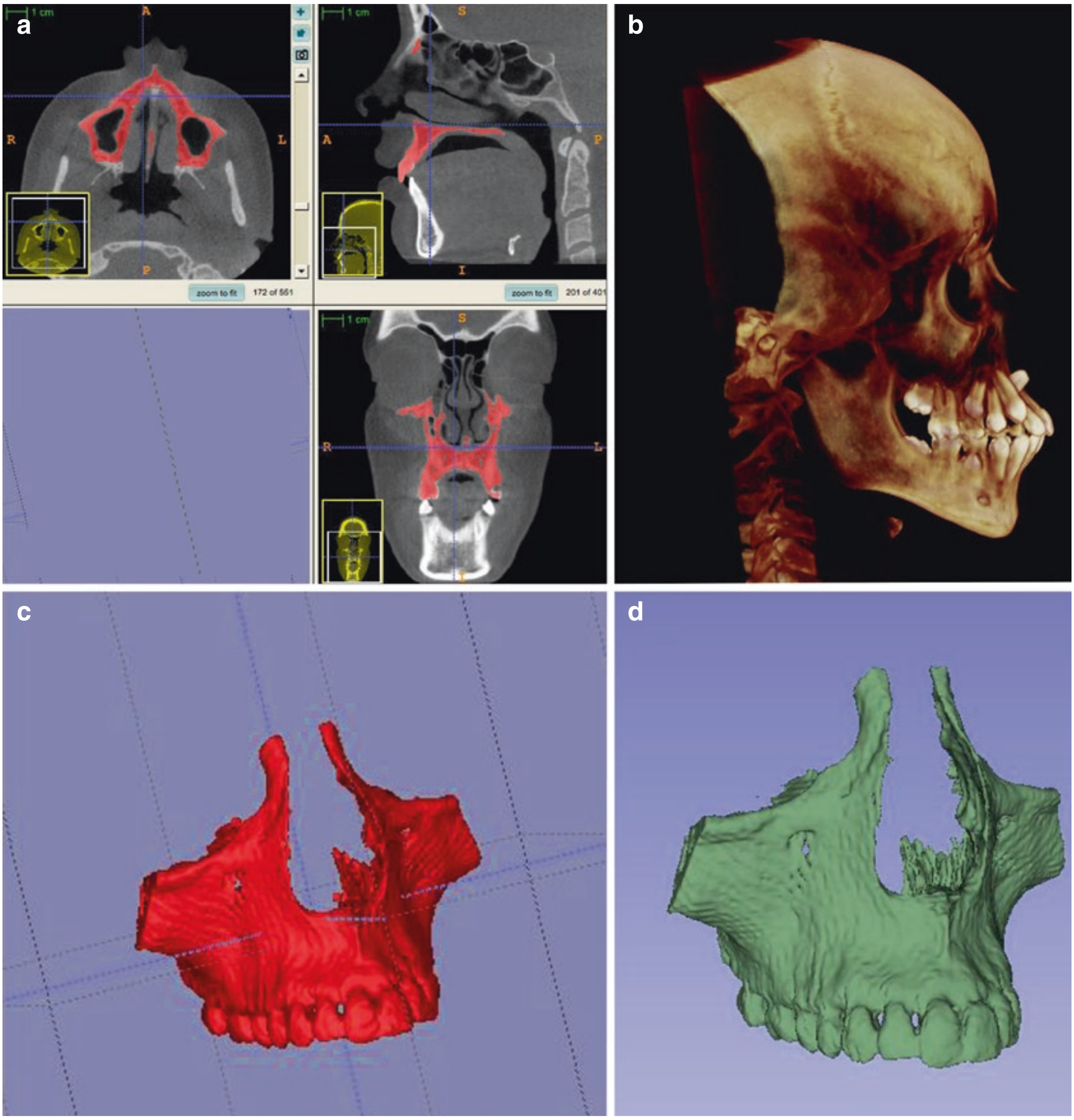

Fig. 19.4 Examples of various display formats used to demonstrate DICOM data in Orthodontic/Orthognathic analytical software include visualization as cross-sectional slices (**a**), 3-D projected images (3-D renderings) (**b**), as a 3-D volumetric label map (**c**), and as 3-D surface models (**d**)

19.3.2 Construction of 3-D Volumetric Label Maps (Segmentation)

3-D surface meshes or surface models provide additional diagnostic information on size and shape of a structure (Kapila and Nervina 2015) and are generated from 3-D volumetric label maps (Fig. 19.5). This process is called *image segmentation*. This procedure allows identification and labeling of the anatomical structures of interest in the acquired CBCT volume. 3-D volumetric label map files are useful in that they provide a visualization of the hard and soft tissues. The representation of fine anatomic details by examining cross sections of a volumetric dataset remains to be one of the most time-consuming steps in image processing and it is a challenge (Lie, 1995; Ma and Manjunath 2000; Moon et al. 2002).

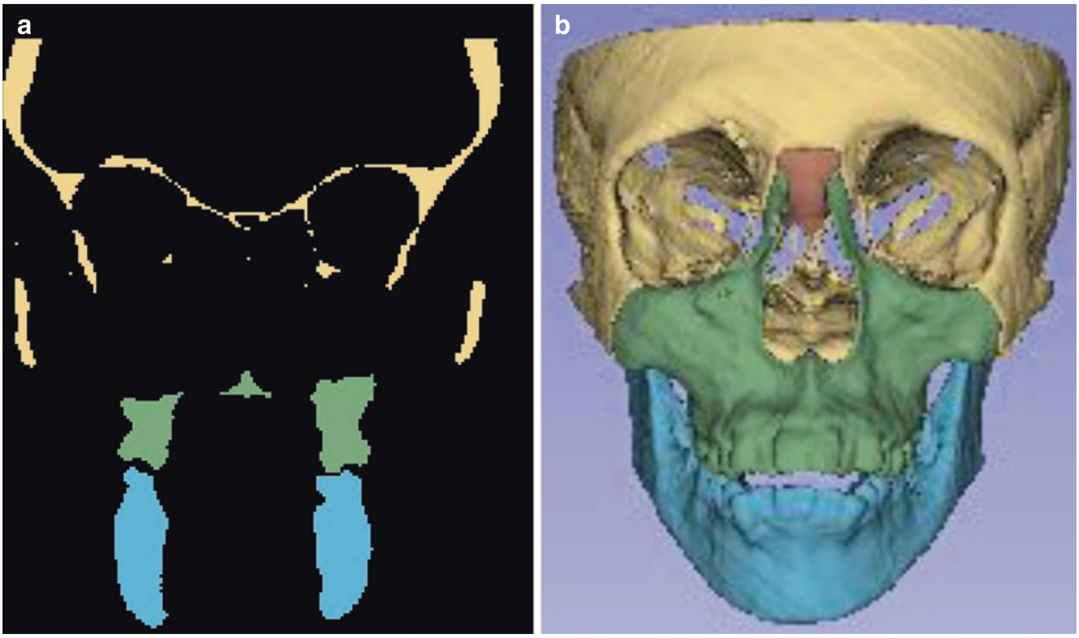

Fig. 19.5 Comparison of a 3-D volumetric label map in a coronal section at the level of the middle of the orbits (**a**) and a 3-D surface model or surface mesh model (**b**)

A major challenge of segmentation with CBCT data is that hard and soft tissues in different regions of the same structure (e.g., the mandibular condyle, cortical plate of the maxillary tuberosity, or the teeth) have no corresponding Hounsfield units. Within a single CBCT dataset from the same individual, similar structures may have different intensity levels depending on their location within the volume and their relationship to adjacent anatomy. No standard segmentation method can be expected to work equally well for all tasks.

Many commercial software incorporates intensity thresholding algorithms to accomplish segmentation. From our research, we have found that in many instances this global approach may segment much of the data, if may not adequately segment other anatomically desirable elements. Therefore, we have developed a segmentation technique using a two-stage approach, incorporating different tools from two open source software (DCBIA VT 2015).

- **Slicer software**. Within this software, the tool *Intensity Segmenter* allows labeling of different structures of different intensities with different labels. It is an automatic segmentation, guided by the information contained in a file (range file) that specified which label will be designed for different ranges of intensities.
- **ITK-SNAP software**. In order to best capture the structure anatomy, our method of choice for individualized segmentation procedures utilizes the automatic segmentation procedures in this software which utilizes active contour methods to compute feature images based on the CBCT image gray level intensity and boundaries. ITK-SNAP is versatile because it allows the adjustment of the parameters for automatic detection of intensities and boundaries as well as enables user interactive editing of contours.

The 3-D volumetric label map generated from this two-step procedure has basically two functions: (1) to be used as a mask to identify which regions within the data should be used for corresponding voxels in voxel-based image registration, and (2) to generate 3-D surface (or mesh) models.

19.3.3 Conversion of 3-D Volumetric Label Maps to 3-D Surface Models

After segmentation, the 3-D volumetric label map can be saved or converted as a 3-D triangular/polygonal mesh model (3-D surface model). Different file formats can be used, with corresponding extensions such as .STL, .OBJ, .PLY, .VTK, or .3UD, and can be visualized in various viewer software. For longitudinal comparisons, the 3-D surface model will be generated only for the initial, referred to as the first time interval (T1), surface models which can be used to establish a common coordinate system across subjects, performing the head orientation.

19.3.4 Establishment of a Common Coordinate System Across Subjects

Establishing a common coordinate system allows for group comparisons and consistent measurements across subjects (Ruellas et al. 2016b). Quantification of directional changes (Fig. 19.6) in each plane of the 3-D space (3-D components) can be obtained by the distances between projections of the 3-D landmarks and require a standardized common x, y, z coordinate system across time points and all patients, (Fig. 19.7). 3-D orientation of the data can be achieved by using standard intracranial reference planes defined by at least three landmarks or two landmarks and a plane (Ludlow et al. 2009): Frankfurt horizontal, midsagittal, and transporionic planes.

As an example, Slicer software displays a fixed 3-D coordinate system (within a cube) that can be used as reference to orient the −3-D models. Using axial, coronal, and sagittal views of the 3-D models, the T1 model can be moved to orient the midsagittal plane (crista galli, glabella, and foramen magnum) vertically and coincident with the vertical (sagittal) plane of the 3-D coordinate

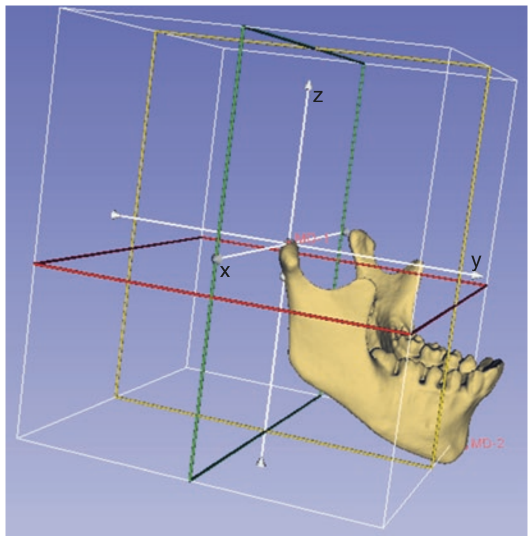

Fig. 19.6 An example of a mandibular model in Slicer software within a standardized common x, y, z coordinate system that allows for consistent measurements between scans acquired at different time points

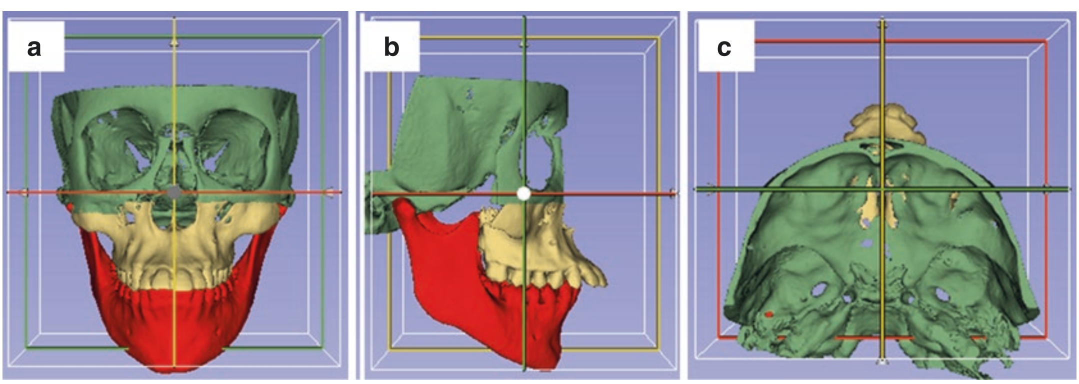

Fig. 19.7 3-D standardized orientation achieved by using intracranial reference planes: Frankfurt horizontal, midsagittal, and transporionic planes in Slicer software as seen in the coronal (**a**), sagittal (**b**), and axial (**c**) views

system. The Frankfurt horizontal plane can be oriented to match with the horizontal (axial) plane. The horizontal transporionic line can be oriented to be coincident with the intersection between the axial plane and the posterior border of the cube in both sides of the head. Then, the matrix generated from this step must be applied to the T1 CBCT scan and T1 3-D volumetric label map, obtaining the same head orientation. The same procedure of head orientation should be repeated for each temporally acquired dataset for specific individuals with the goal of obtaining a common coordinate system for quantitative evaluations.

19.3.5 Image Registration

Registering and superimposing a volumetric image of an individual at a second time interval (T2) over an initial volume (T1) used as a reference necessitates 3-D surface models to be based on the same common coordinate system. The registration procedure requires the use of invariant, stable anatomic regions of reference to be used as a baseline for the superimposition. Various fiducial reference areas have been suggested including the cranial base (Cevidanes et al. 2009a), maxilla (Ruellas et al. 2016a), and mandible (Ruellas et al. 2016c). Different areas and sources of reference for registration will lead to different interpretations of the results (Fig. 19.8).

The registration procedures can be based on landmarks, surface models, or voxel gray intensity for craniomaxillofacial registration (https://sites.google.com/a/umich.edu/dentistry-image-computing/) (DCBIA VT 2015).

Both commercial and open source software can be used to perform this registration step. From our research, we have found that the most consistent and reliable voxel-based registrations result from a two-stage procedure:

- **Approximation of T2 and T1 Scans.** Although the head position should be standardized during CBCT imaging acquisition, usually the T2 and T1 scans are not similarly oriented. Therefore, we recommend that the T2 scan should be approximately realigned in relation to the oriented T1, using a visual "best fit" of the outlines of the reference region as a guide. In some software (e.g., Slicer software) (3-Dslicer 2015), the approximation can be visualized in each of the 3-D multi-planar cross sections (see http:/www.youtube.com/user/DCBIA (DCBIA VT 2015).
- **Voxel-Based Registration for Longitudinal Assessments.** The voxel-based registration

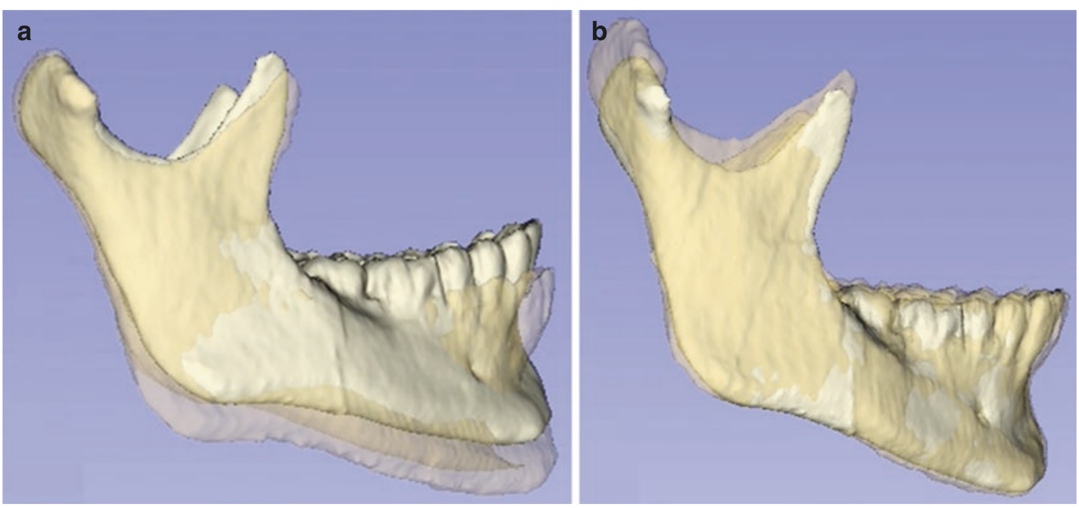

Fig. 19.8 When T1 (*solid*) and T2 (*transparent*) mandibular overlays are superimposed based on the cranial base (**a**) or mandible (**b**) different areas of change are identified

methods compare the gray-level values of the two regions of reference in T2 and T1 volumes voxel by voxel to calculate the rotational and translational parameters that will reorient them to make them coincident. The process of registration involves computing transformations. These are mathematical operation that applies a matrix file containing the information about how much to move a 3-D image in multiple planes in space to make it coincident with the target image used as reference. The image registration computes the translational (anteroposterior, transverse, and vertical) and rotational displacements (pitch, roll, and yaw) in a procedure known as *rigid registration* (Thompson et al. 1997). The image registration can also compute differences in scale (size changes with growth and/or treatment) and/or shape if nonrigid registration is selected. However if nonrigid registration is used, the resultant 3-D models can be deformed (Maes et al. 1997)**.** To avoid distorting or morphing the images, nonrigid registration should be used. In these instances, linear transformations considering scale and shape differences are applied and then apply only the rigid transformation (rotation and translation) to preserve the actual scale and shape features (Cevidanes et al. 2006, 2009b).

We have developed a sequence of fully automated voxel-wise rigid registration techniques for two clinical scenarios: the cranial base for overall facial assessments relative to cranial structures that complete their growth early in childhood (Cevidanes et al. 2009a), and: regionally to assess maxillary and mandibular bone remodeling (Ruellas et al. 2016a, c).

After the registration procedures, the registered 3-D volumetric label maps can then be saved as a 3-D surface model. All image registration procedures and conversion from 3-D volumetric label maps to 3-D surfaces models can be accomplished in SlicerCMF (DCBIA VT 2015). They were initially developed as part of the National Alliance of Medical Image Computing (NA-MIC, NIH Roadmap for Medical Research), and have been widely used internationally.

19.3.6 Visualization and Quantification of Changes Overtime

Different software offers different tools for assessment of changes due to growth and/or treatments. Our group has developed tools for 3-D visualization and quantification in SlicerCMF (DCBIA VT 2015). This software offers different tools for quantification, such as model to model distance, shape population viewer, angle planes, mesh statistics, pick and paint and Q3-DC.

19.3.6.1 Visual Analytics with Graphic Display of 3-D Morphological Changes

- **Semitransparent overlays.** For visualization of morphological differences between two time points, registered surface models can be visualized using contrasting opaque or semi-transparent colors. The overlays provide visual qualitative assessment of the location and direction of changes or morphological differences (Fig. 19.9).
- **Model to model distance and color-coded map:** The surface distances between two time points (computed by model to model distance tool in Slicer software, for example) can also be graphically displayed with color-coded maps. The graphical display of color-coded or "heat" maps (Fig. 19.10) may contain information computed by using closest or corresponding surface points, statistical significance p-values maps of group and interaction comparisons and vector maps and displayed within Slicer CMF (DCBIA VT 2015).

  Model to model distance generate files (color-coded map file) that store the differences between two superimposed time points. The software offers the options of computing closest or corresponding distances between two superimposed models. This is an important aspect for interpretation of results because corresponding point method measures distances between corresponding anatomical regions on two or more images. Closest point refers to the point on T2 surface that is closest to the point on T1 surface. The Closest Point

Fig. 19.9 Overlay of the maxillae providing visual qualitative assessment of the location and direction of changes before and after treatment. Observe incisors retraction and intrusion of the maxillary teeth

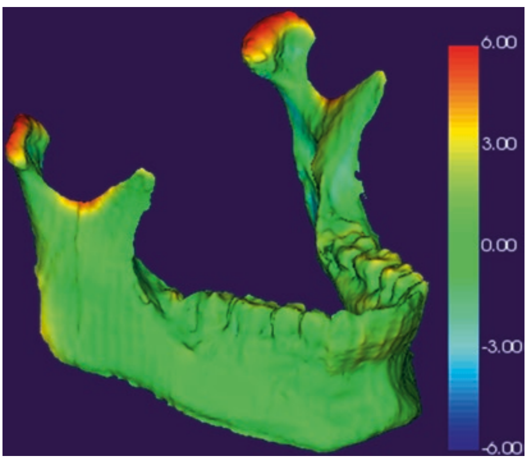

Fig. 19.10 Color-coded or "heat" map displaying the surface distances between two time points (computed by model to model distance tool in Slicer software)

method measures the closest 3-D linear distances between surfaces. Figure 19.11 displays corresponding and closest Condylion points at T1 and T2. For identification of corresponding points, it is necessary that T1 and T2 have the same number of vertices (Fig. 19.12), evenly distributed. By running the models using the Spharm tool in 3-Dslicer, a parameterization of the triangles will be reached. Then, for corresponding points computation it is mandatory to process the models in Spharm tool before running them in model to model distance tool.

- **Shape correspondence.** As computed using the SPHARM-PDM module (Gerig et al. 2001) in the 3-DSLicer software, this algorithm computes point-based surface models, where all models have the same number of triangular meshes and vertices in corresponding (homologous) locations (Fig. 19.12a, b). Corresponding surface distances and vectors can then be calculated and graphically displayed in SlicerCMF (DCBIA VT 2015).

The pattern for non-corresponding meshes is very different (Fig. 19.12c, d). By using the meshes on the Fig. 19.12a, b, the software will compute corresponding distances, and closest distances will be computed using models from Fig. 19.12c, d.

The color-coded map file, generated from model to model distance tool, that stored the differences between two time points can be visualized (Fig. 19.10) using shape population viewer tool in Slicer software and can be used for quantification using the Pick and Paint tool, as well.

19.3.6.2 Quantitative Measurements

- **Volume.** Volume (Thompson et al. 1997) can be measured in Slicer, ITK-SNAP, Dolphin, or Invivo. Changes in volume can reflect overall changes or to calculate volume of specific structures, such as airway, sinus, and bone graft. But volume assessment does not reveal the location or direction of such changes. This information is clinically important as to ascertain post treatment proliferative or resorptive changes.
- **3-D Linear Surface Distances in Triangular Meshes.** Using linear and angular measurements based on landmarks alone on virtual models can camouflage bone remodeling and may lead to confusion and does not take into account rotational changes, changes in shape

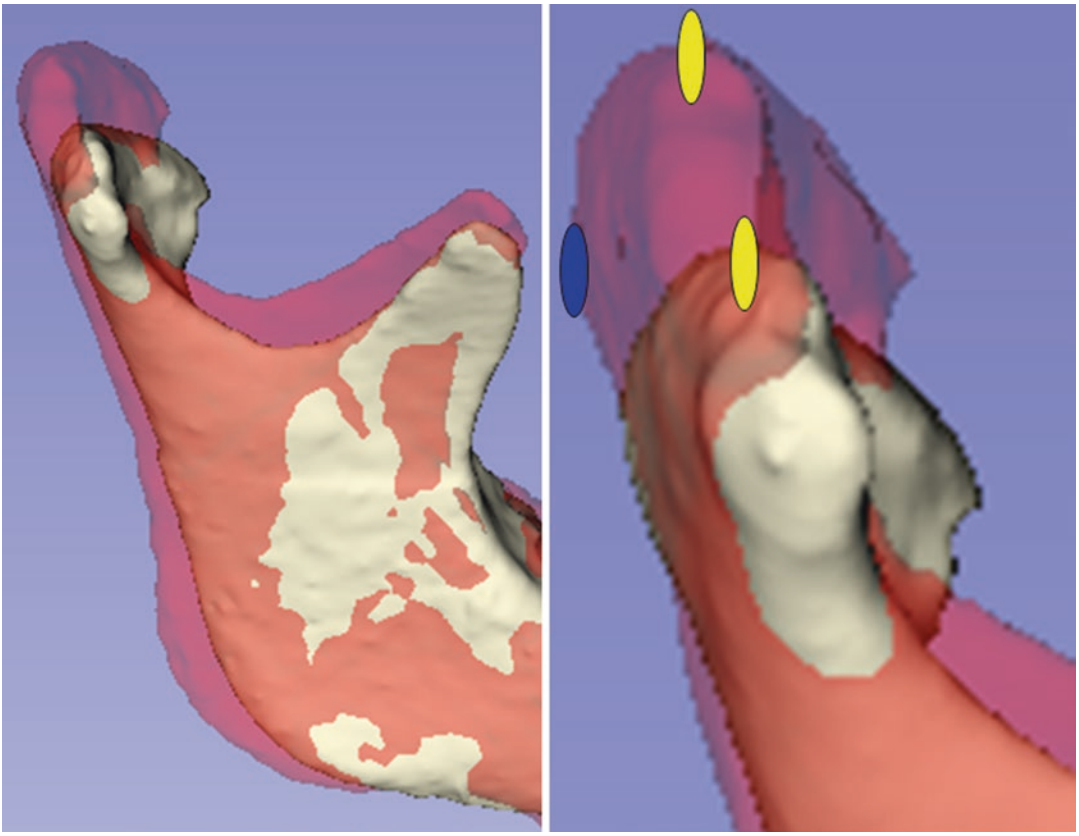

Fig. 19.11 Mandibular overlay resulting from mandibular superimposition highlighting the difference between corresponding and closest points. *Green* landmark corresponds to the condylion point at T1; *yellow* landmark corresponds to the condylion point at T2 (corresponding point in relation to the condylion point at T1); *blue* landmark corresponds to the closest point (on T2 surface) in relation to the condylion point at T1

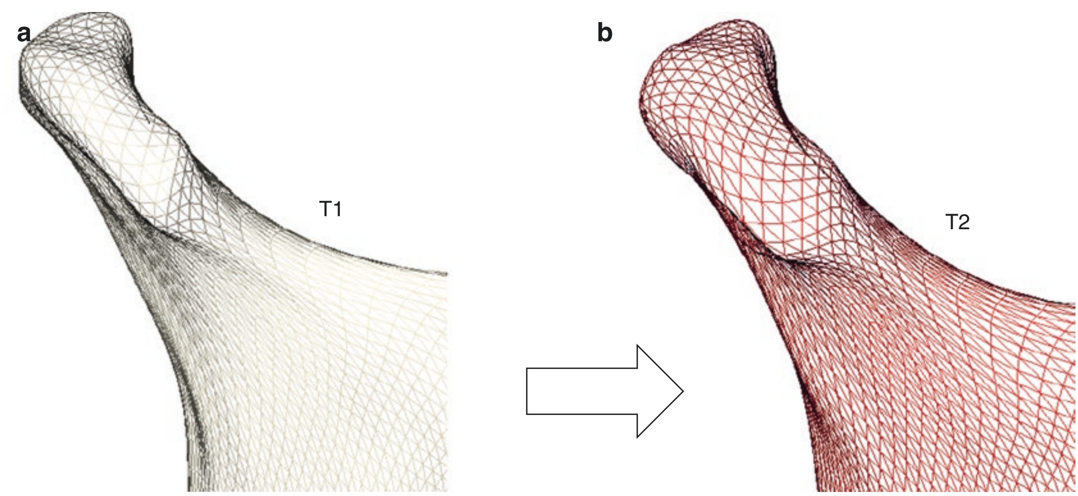

Fig. 19.12 Different patterns of meshes: T1 (**a**) and T2 (**b**) triangular meshes evenly distributed resulting in vertices on homologous locations due to the shape correspondence methodology; T1 (**c**) and T2 (**d**) non-corresponding meshes that will be used for closest distances computation

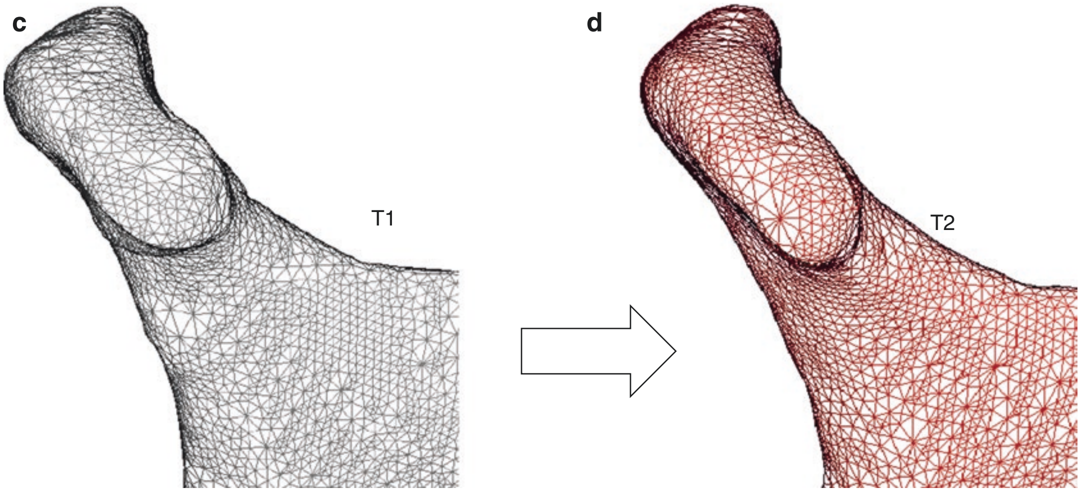

Fig. 19.12 (continued)

as opposed to those of size, and registering angles on landmarks as vertices (Bookstein 1991). Locating 3-D landmarks on complex curving structures can affect the representation of the craniofacial form (Dean et al. 2000). There continues to be a lack of literature about suitable operational definitions for the landmarks in the three (3) planes of space (coronal, sagittal, and axial), which leads to errors and variability in landmark location (Bookstein, 1991). The studies of Subsol et al. (1998) and Andresen et al. (2000) provided clear advances toward studies of curves or surfaces in 3-D, referring to tens of thousands of 3-D points to define geometry. Although 3-D linear distances are a simplification of complex morphological changes, they still provide relevant clinical information of changes in the space related to differences between time points.

- **Quantification of directional changes in each plane of the 3-D space (3-D components).** 3-D distances and 3-D components can be measured based on: (1) observer defined landmarks (Rohr 2001), or (2) automatically defined points. The distances between corresponding coordinates of corresponding landmarks can be quantified in the transversal (*x* axis), anteroposterior (*y* axis), and vertical (*z* axis) direction (Ruellas et al. 2016b) using Slicer software (Fig. 19.13).

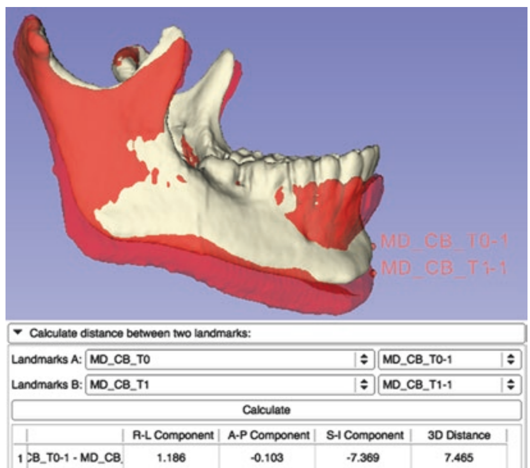

Fig. 19.13 Mandibular displacement calculated by distances between corresponding coordinates of corresponding landmarks before and after treatment based on the cranial base registration and assessed in the transversal (*x* axis), anteroposterior (*y* axis), and vertical (*z* axis) axes using Slicer software

  – *Based on observer defined landmarks:* 3-D landmarks should be pre-labeled (Ruellas et al. 2016a, b, c) in ITK-SNAP software that makes possible the identification of them using all 3 views (axial, sagittal, and coronal) and using as reference a 3-D surface model (3-D volumetric label map) for consistency of landmark location

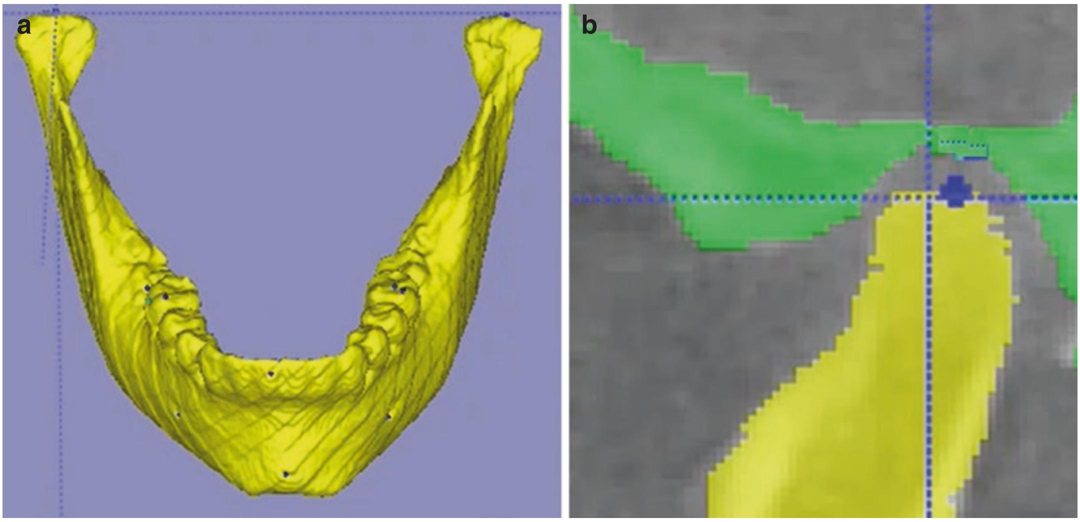

Fig. 19.14 (**a**) While landmark placement can be seen and verified in the 3D surface models, (**b**) the pre-labeling procedure in ITK-Snap software allows precise identification in the multi-planar cross-sectional views

(Fig. 19.14). Different 3-D surface mesh models can be loaded simultaneously, for example, in the Slicer software, and the landmark coordinates (*x*, *y*, and *z*) are generated and displayed for each landmark on T1 and the registered T2 surface models. Quantitative assessment of the differences between landmarks can be performed: (1) At one-time point (baseline or follow-up) for characterization of dimensions, for example, prior to treatment; (2) Differences between two time points (T1 and T2) for measuring displacements of the maxilla and/or mandible (Fig. 19.13).

– *Based on thousands points in triangular meshes automatically defined on the surface models:* 3-D surface distances computed at the vertices of the triangular meshes can be stored as color-coded 3-D linear distances within .obj, .ply, or .vtk file formats in the user software of choice, such as Paraview (2015) or within Slicer in shape population viewer tool (DCBIA VT 2015). Localized measurements in color-coded maps can be made from point to point or at any radius defined around the landmark (Fig. 19.15).

- **3-D Angular Measurements**. 3-D angular measurements between lines or planes defined in a common 3-D coordinate system can be used to quantify pitch, roll, and yaw of the whole skull or the mandible or maxilla separately. Evaluations using each of the three views (sagittal, coronal, or axial) allow these angles be measured by the intersection of two lines based on the coordinates of landmarks (Fig. 19.16a) or by the intersection of two planes passing through specific structures (Fig. 19.16b). Positive and negative values can be used to indicate rotations in different directions, such clockwise or counterclockwise rotation. The selection of landmarks or planes depends on which kind of evaluation researchers would perform to answer their aims. For example, maxillary pitch rotations between two time points can be measured as the angle obtained by the intersection of the planes through the palatal plane (PNS-ANS) in each time point or by the intersection of two lines through the PNS and ANS in the sagittal view. The cant of the occlusal plane can be calculated as a roll rotation and measured by the intersection of two lines through the right and left tip of the molar in the coronal view. Yaw of the dentition can be calculated by the intersection of two lines through the right and left tip of the molar in the axial view.

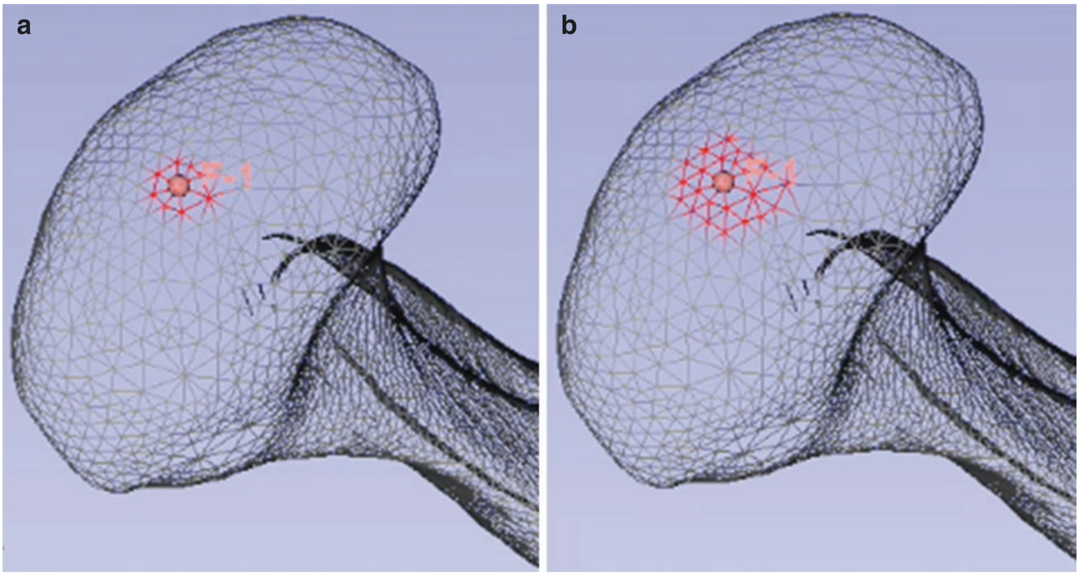

Fig. 19.15 Measurements based on color-coded maps and made from point to point at a radius of 1 (**a**) and a radius of 2 (**b**) around a specific landmark. In this case the landmark is the most superior point on the curvature of the mandibular condyle

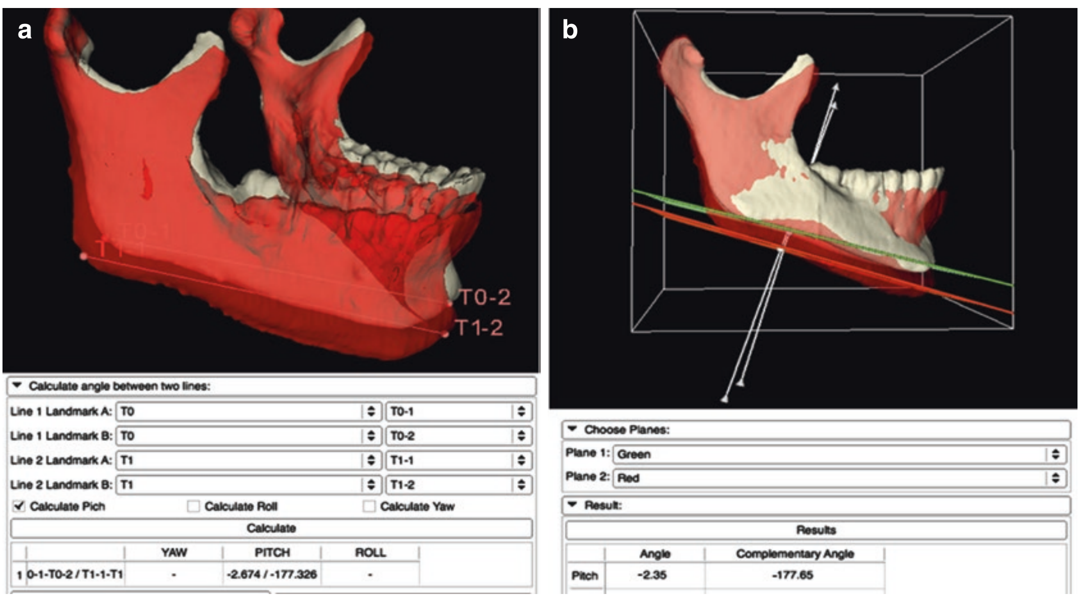

Fig. 19.16 Example of the calculation of mandibular plane rotation (pitch) before and after treatment using two methods based on the difference between the intersection of two lines mandibular planes created joining the coordinates of gonion and mental landmarks. Angular measurement can be calculated as the deviation between the two mandibular planes (**a**) or by the intersection of two planes passing through the mandibular plane (**b**)

19.4 Treatment Planning with Computer-Assisted Surgery (CAS)

There are a number of commercially available computer-assisted surgical treatment planning and simulation software available for orthognathic or jaw surgery (Table 19.2). In the United States the use of CAS software for orthognathic surgery necessitates that the software has been approved by the U.S. FDA (United States Food and Drug Administration) as a Class III medical device within a specific treatment pathway.

Orthognathic treatment planning and simulation software is expensive and proficiency in use requires considerable expertise. Therefore, companies such as AccuPlan (MedCAD, Dallas, Texas, USA), Virtual Surgical Planning (VSP) Orthognathics (3D Systems, Littleton, Colorado, USA, formerly Medical Modeling, Medical Modeling Inc., Golden, Colorado, Medical Modeling 2015), and Maxilim (Medicim, Mechelen, Belgium) provide planning services that can be used by the surgeon case by case. The process involves a number of sequential stages (Table 19.3). The benefit to the clinician is that orthognathic planning does not require purchase of the software, lost clinical time or time associated with gaining computer expertise. For a service fee, the planning service constructs surface models from CBCTs and impressions/or digital dental casts, registers the optical surface data to the CBCT, perform the osteotomies and virtual surgery and print surgical splints.

Table 19.2 Examples of commercially available computer-assisted orthognathic surgical treatment planning and simulation software

Name	Manufacturer
3dMDvultus	3dMD Atlanta, Georgia USA (3dMD 2015)
InVivo Dental	Anatomage, San Jose, California USA (Invivo 2015)
Maxilim	Medicim, Mechelen, Belgium (Maxilim 2015)
MIMICS	Materialise N.V., Leuven, Belgium
NemoCeph 3D–OS	Nemotec, Madrid, Spain
Orthognathic Surgical Planning	Dolphin Imaging and Management Solutions, Chatsworth, California USA (Dolphin Imaging 2015)
PROPLAN CMF/Simplant Pro/OMS/Synthes ProPlan	Materialise N.V., Leuven, Belgium (Simplant 2015)

Table 19.3 Sequential workflow steps associated with planning service facilitated orthognathic treatment planning

Stage	Description
Data acquisition	Various digital (e.g., CBCT, intra- and extraoral optical scans and/or analog (impressions, bite registrations or stone casts) inputs are acquired
Data submission	Digital and/or analog inputs are provided to the planning service either electronically or via mail with an order or "prescription" describing the anticipate procedure
Preliminary or "working" treatment plan developed	A biomedical engineer creates digital versions of analog inputs and fuses all digital components to create a composite 3-D virtual rendering demonstrating the dentition, the inter-arch relationship (occlusion), skeletal base and facial surface features. A preliminary 3-D VTO is created by the biomedical engineer using the planning software based on the orthognathic prescription
Conference call	The surgeon or orthognathic team are presented with the "working" VTO and, in real time (e.g., web conference), communicate with the biomedical engineer to modify the final design, if necessary. Details such as the type of osteotomy, splint types and style and confirmation of rotation (roll, pitch or yaw) (Fig. 19.17) and translation of each surgical element are confirmed
Final plan submission and approval	Based on the input from the surgeon or orthognathic team during the conference call a formal report/plan is presented and approved
Surgical splints are fabricated and delivered	The surgical splints are fabricated in the appropriate autoclavable resin, usually by 3-D printing, and forwarded to the surgeon

VTO virtual treatment objective

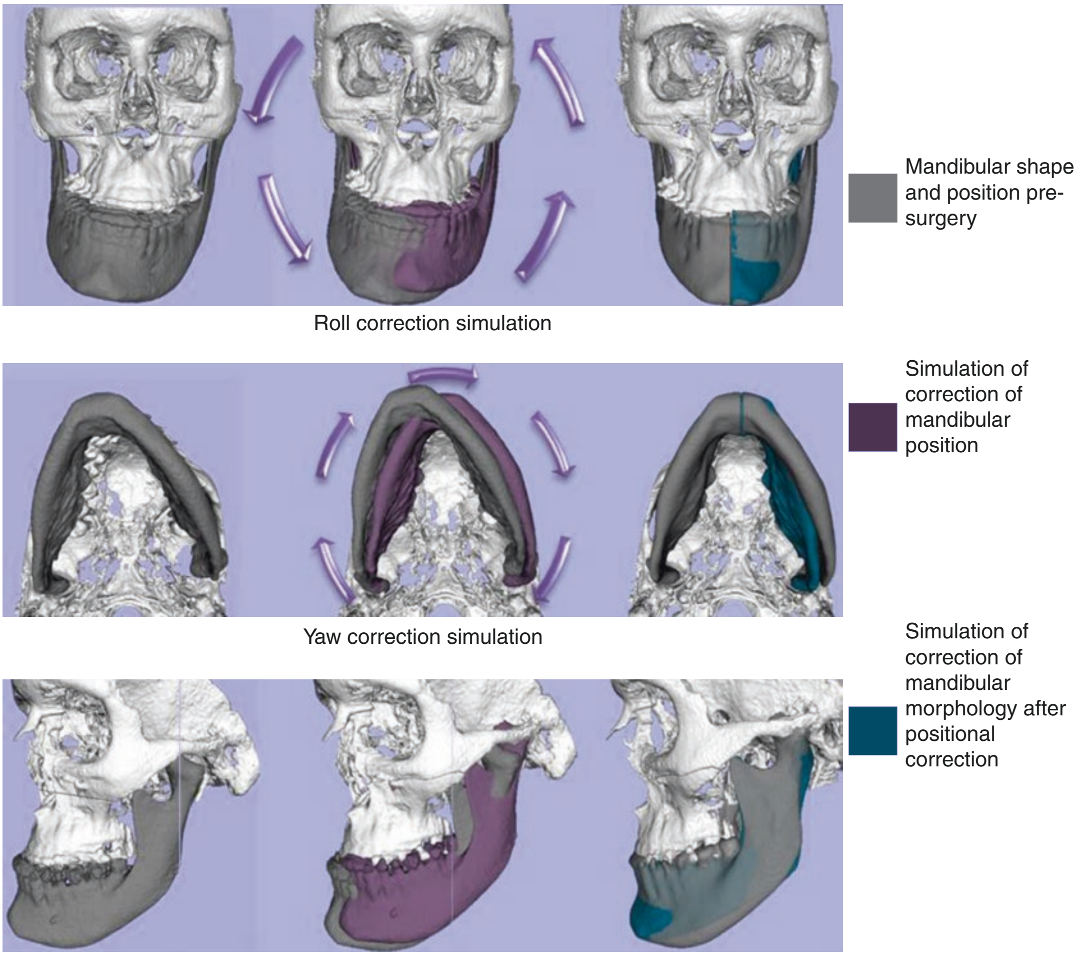

Fig. 19.17 Virtual simulation allows clinicians to diagnose the rotational components of mandibular asymmetry. Simulation steps where mandibular 3-D rotational displacements are virtually corrected prior to the use of mirroring techniques. Such procedures allow the assessment of true left and right shape differences. The *white* and *gray* models display the patient actual facial structures. The purple models are the virtually simulated correction of yaw and roll. In the virtual simulation, the mandible was reoriented with the left condyle as the center of rotation before mirroring to correct asymmetrical mandibular yaw and roll, in an attempt to place the chin in a clinically acceptable location while preserving the facial width. The overlays between the *purple/gray* and *green/gray* models help clinicians plan surgical displacements

19.4.1 Treatment Planning and Simulation Software

The CAS procedure using orthognathic treatment planning and simulation software requires a methodological approach and therefore incorporates a series of procedural steps. A typical treatment planning and simulation sequence is illustrated using an orthognathic case planned using VSP Orthognathics (3D Systems, Littleton, Colorado USA).

19.4.1.1 Data Acquisition

The basis data for any orthognathic surgical planning and simulation is maxillofacial skeletal DICOM data (Fig. 19.18). This can be acquired from a MDCT or CBCT device. Additional digital data is necessary of the dentition and occlusal relationships (centric relation, centric occlusion, or both) using bite registration (Fig. 19.19). This can be done directly with the use of intraoral high-resolution surface scan or via digitization of analog (stone casts, impressions, and/or bite registrations)

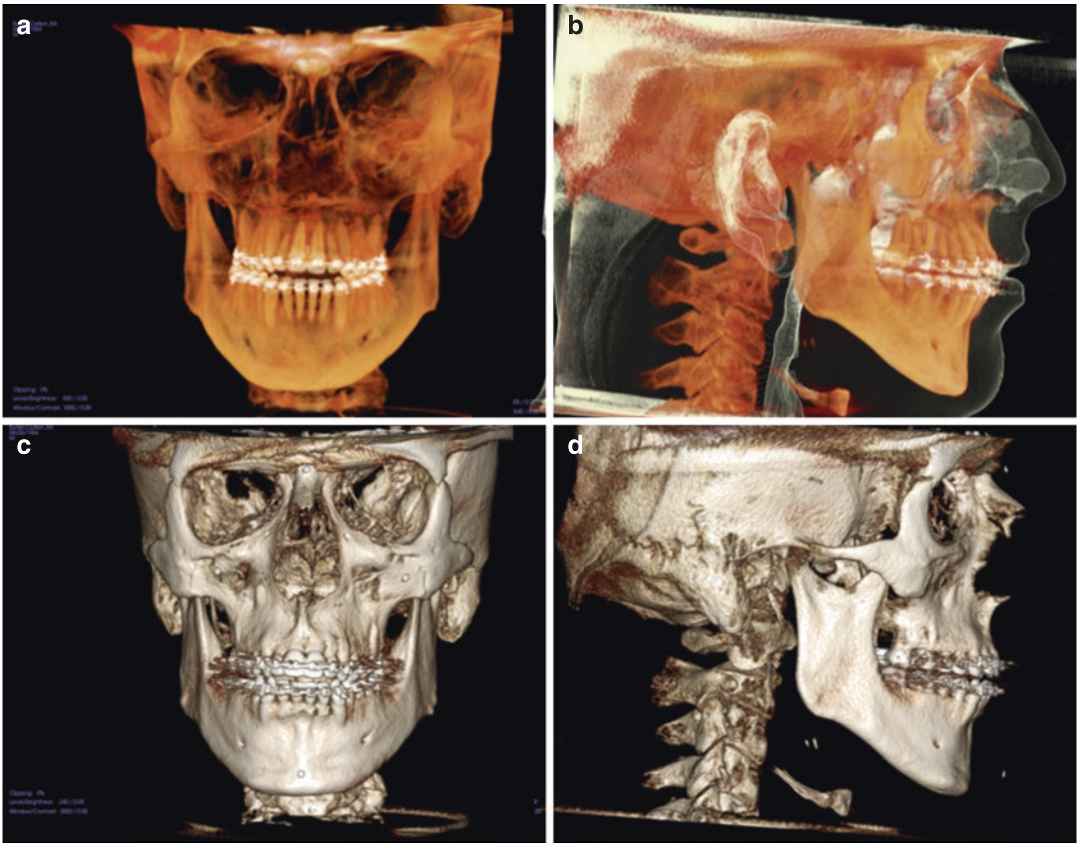

Fig. 19.18 Volumetric AP (**a**) and lateral (**b**) and surface rendering AP (**c**) and lateral with soft tissue and airway outline (**d**) of imported DICOM data of a CBCT scan of a 27-year-old male patient with multiple breathing issues immediately pre-orthognathic surgery. The patient presents with a convex facial profile, Class II (*right*) and Class I (*left*) dental malocclusion, mandibular retrognathia, anterior and posterior open bite, and maxillary transverse deficiency with posterior cross bite

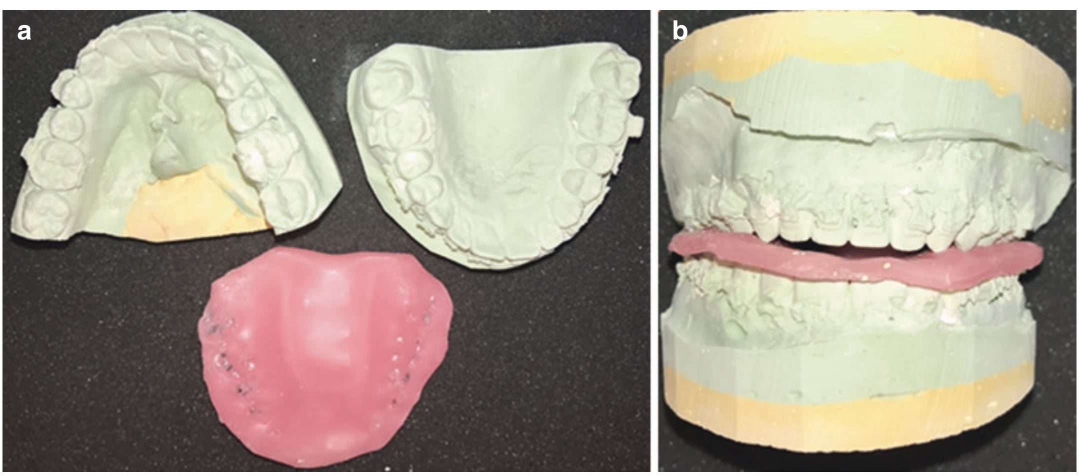

Fig. 19.19 (**a**) Maxillary and mandibular study casts with separate wax bite registration of the patient in Fig. 19.18 and analog components articulated (**b**) as provided to an orthognathic planning service

inputs. Supplementary digital data may include facial surface optical scans with the patient in repose with teeth closed or smiling.

19.4.1.2 Integration of Diagnostic Data

The skeletal MDCT/CBCT data is used to create a virtual scaffold or framework upon which additional digital 3-D are layered or fused producing a composite virtual 3-D model. This is the most technically demanding phase and requires precise registration and superimposition of digitized casts of the maxillary and mandibular dentition to corresponding fiducial landmarks within the CBCT scan. The MDCT/CBCT volumetric data may be reoriented to specific reference planes in the sagittal (e.g., natural head position, Frankfurt horizontal), axial (e.g., transporionic), and coronal (e.g., perpendicular to crista galli to basion) planes. Various individual elements can be visualized individually as a solid surface or translucent rendering or together as a composite image.

19.4.1.3 Image Segmentation

For specific technical details on image segmentation, see the section on *Step-by-Step Image Analysis Procedures* in this chapter. Specific software approaches the process of segmentation differently.

Because CBCT images often have scatter or beam hardening artifacts associated with high density materials (e.g., amalgams, crowns) and orthodontic brackets and wires used in initial orthodontic compensation, it may be necessary to fine tune or clean up CBCT/MDCT images to remove artifacts prior to planning and treatment simulation. This can facilitate the identification of fiducial corresponding landmarks on CBCT/MDCT data necessary for image fusion, superimposition and registration of concordance with high-resolution scans of the dentition (Fig. 19.20).

19.4.1.4 Virtual Planning and Treatment Simulation

– *Virtual osteotomies.* Depending on the skeletal presentation of the patient and preferred surgical intervention, orthognathic surgery requires standard operating approaches to create osteotomies (Table 19.4).

  Virtual osteotomies allow for planning of cuts, position, and size of fixation screws and plates, taking into account the intrinsically complex cranial anatomy. Challenges in planning the cuts include regions of thin (or absent) bone, such as the maxillary sinus anterior wall, that create discontinuities in the surface mesh that inadvertently separate segments virtually that are actually continuous. Other challenges include the difficulty in placing osteotomy cuts that do not involve intraosseous anatomic and vital structures (e.g., tooth roots, mandibular nerve canal).
– *Segment repositioning*. After the virtual osteotomy, virtual surgery with relocation of the bony segments can be performed (Figs. 19.21,

Fig. 19.20 Left lateral (**a**), frontal (**b**), and right lateral (**c**) preoperative final composite solid surface rendering of the patient in Fig. 19.18 incorporating the CBCT skeletal and digital maxillary and mandibular study cast data. Note the high detail of the dentition incorporating the fixed orthodontic appliance therapy and lack of beam hardening artifact

Table 19.4 Most common surgical considerations, decisions, and approaches used in orthognathic surgery

Primary decisions	Secondary decision	Considerations	Approach
Number of jaws involved	Single jaw		Which jaw surgery is to be performed first?
	Double jaw		
Maxillary surgery	Jaw segments		LeForte I (1, 2 or 3 piece)
			LeForte II
			LeForte III
	Anterior esthetic correction	Vertical change in central incisor	Impaction
			Down fracture
		Midline correction	Left
			Right
	Occlusal plane	Change in angulation	Increase
			Decrease
		Change in posterior molar position	Molar impaction
			Molar down fracture
	Horizontal translational movement		Advancement
			Setback
Mandibular surgery	Bilateral		Sagittal split
	Unilateral		Vertical ramus
			Inverted L
	Chin augmentation		Sliding Genioplasty
			Alloplastic chin implant

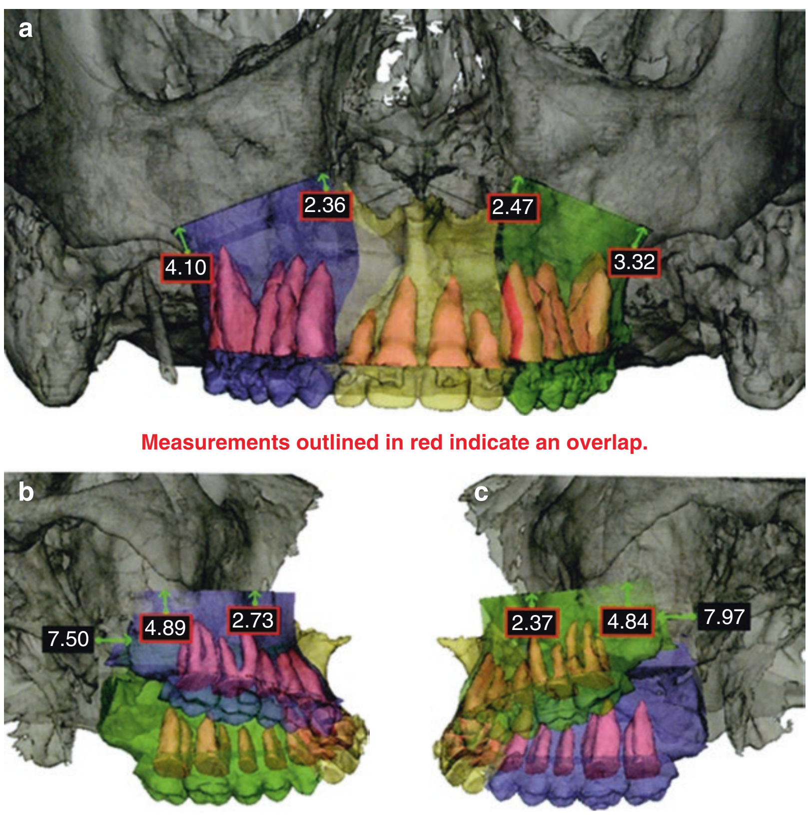

Fig. 19.21 Frontal (**a**) right (**b**) and left oblique composite transparent surface rendering of the maxilla of the patient shown in Fig. 19.18 showing location of 3-piece segmental LeFort I osteotomy sites and lateral and pre-maxillary segment repositioning. The segment vector direction and displacement magnitude are shown after maxillary impaction (2.36 mm [right] and 2.47 mm [left] in the premolar region and 4.1 mm [right] and 3.32 mm [left] in the molar regions) and advancement (7.5 mm [right] and 7.97 mm [left]). Note that measurement outlined in red indicates overlap due to impaction

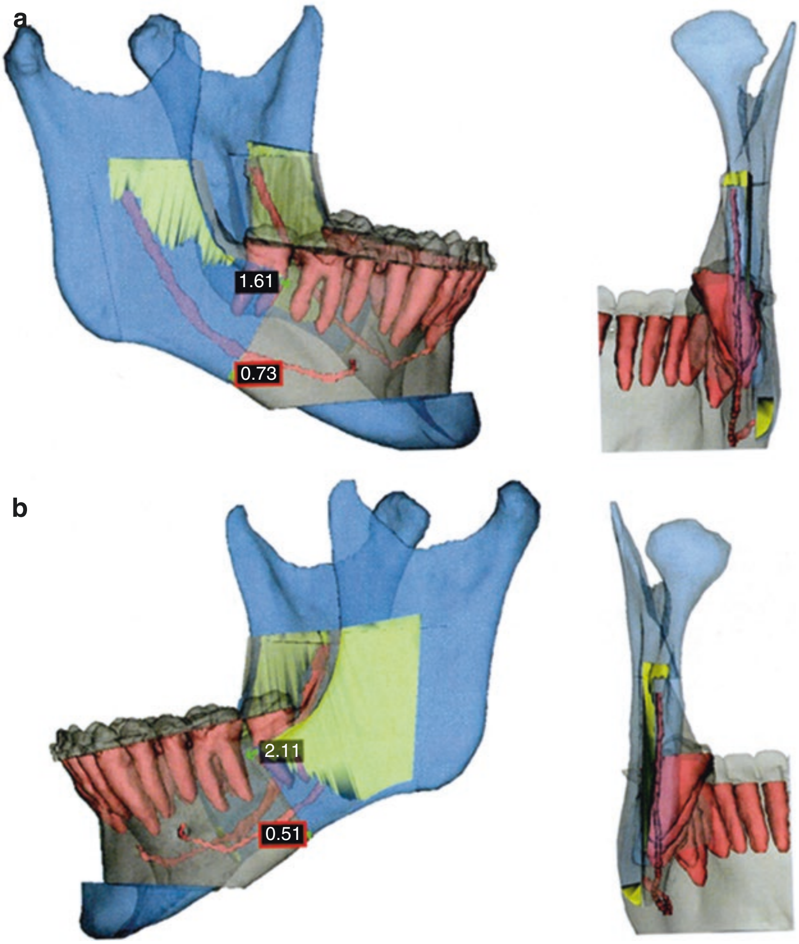

Fig. 19.22 Right (**a**) and left (**b**) oblique composite transparent surface rendering of the mandible of the patient shown in Fig. 19.18 showing location of bilateral sagittal split osteotomy sites and segment repositioning. The segment vector direction and displacement magnitude are shown after mandibular advancement (1.61 mm [right] and 2.11 mm [left] in the occlusal region and 0.73 mm [right] and 0.51 mm [left] in the lower mandibular body regions). Note that measurement outlined in red indicates overlap due to impaction

19.22, and 19.23) with quantification of the planned surgical movements (De Momi et al. 2006; Chapuis et al. 2007). Relocation of the anatomical segments allows for the correction of the skeletal discrepancy for a given patient and simultaneous tracking of measurements of *X*, *Y*, and *Z* translation and rotation around each of these axes. In the maxilla specific considerations include occlusal adjustment and occlusal plane leveling, anterior and posterior rotation and anterior and posterior intrusion.

– *Grafting*. Two types of orthognathic schemes are possible. Corrective interventions are those surgeries that involve repositioning of existing osteotomy segments whereas reconstructive procedures require addition of an extrinsic graft. The latter procedures may require more extensive planning, particularly in the positioning of surgical mesh, dental implants, or plates. In reconstructive procedures, problems

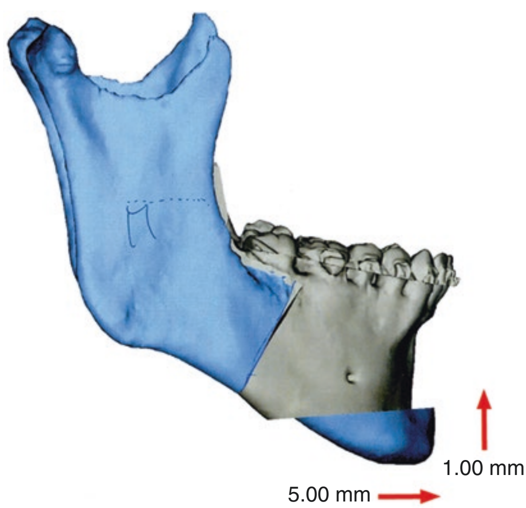

Fig. 19.23 Right lateral solid surface rendering of the patient shown in Fig. 19.18 showing location of mandibular symphysis osteotomy site and segment repositioning after a virtual simulated genioplasty. The segment vector direction and displacement magnitude are shown

often present in determining the desired implant or graft shape. Implants and prosthesis require selection of the proper device and reshape it, or to fabricate an individual device from a suitable biocompatible material. With a graft, the difficulties lie in choosing the harvesting site, shaping the graft, and placing the implant or graft in the appropriate location (Chapuis 2006).

– *Soft Tissue Predictions.* Prediction of soft tissue changes remains challenging. Challenges to predict soft tissue changes overtime include the individual surgical skeletal changes and postsurgical adaptations, aging, weight gain or loss, and postsurgical adaptations of the muscles and connective tissues. Prediction of facial soft tissue changes that result from skeletal reshaping often utilize approximation models, since direct formulation and analytical resolution of the equations of continuum mechanics is not possible with such geometrical complexity. Different types of approximation models have been proposed: displacements of soft tissue voxels are estimated with the movements of neighboring hard tissue voxels (Schutyser et al. 2000), bone displacement vectors are simply applied on the vertices of the soft tissue mesh (Xia et al. 2000), multilayer mass-spring models (Teschner et al. 2001), finite element models (Chabanas et al. 2003; Westermark et al. 2005), and mass tensor models (Keeve et al. 1998) that assume biological properties of soft tissue response. Comparisons of the soft tissue simulations with the postoperative facial surface have not yet been performed. Surgical planning functions generally do not fulfill the requirements enumerated above for preparation of quantitative facial tissue simulation for surgical planning. Other functionalities that have been incorporated into different software systems include: simulation of muscular function (Zachow et al. 2001), distraction osteogenesis planning (Gladilin et al. 2004), and 4-D surgery planning (Gateno et al. 2003).

19.4.1.5 Quantitative Analysis

After completion of the virtual surgery, quantitative measures can be used as a "working" plan for comment by members of the orthognathic team and as a tool to create multiple simulation scenarios and establish achievable surgical treatment goals for each patient (Fig. 19.24).

19.4.1.6 Surgical Guide Design and Fabrication

The ultimate outcome for the use of orthognathic treatment planning and surgical simulation software is to translate the virtual treatment objective to surgical reality. The most common method of achieving this is with the use of interim and final resin occlusal splints. These intraoral devices are used either during surgery to act as a template for repositioning of osteotomy segments (interim) or finally in inter-maxillary fixation to confirm and stabilize the relationship between the maxillary and mandibular dentition. Based on the approved virtual treatment plan, occlusal splints can be designed (Fig. 19.25) and exported in industry-standard STL (standard tessellation language) format for 3D printing either by an external service or in house (Fig. 19.26).

19.4.2 Intraoperative Guidance: Surgical Navigation

Surgical navigation systems have been developed to help accurately transfer treatment plans to the operating room. In complex surgical procedures, segments must often be moved with very limited visibility, under swollen skin, the desired bone segment realignment is limited by adjacent soft and hard tissue structures. Surgical approaches that do not utilize surgical navigation rely largely on the clinician's experience and intuition. In maxillary repositioning, for example, a combination of dental splints, compass, ruler, and intuition is used to determine the final position. It has been shown that in the vertical direction (in which the splint exerts no constraint), only limited control is achieved (Vandewalle et al. 2003). While the surgical splint guides the position of the maxilla relative to the mandible, in two-jaw surgeries the spatial position of the two jaws relative to the face is influenced by the splint precision and the trans-surgical vertical assessment. As the splints are made over teeth and guide bone changes away from those teeth, small splint inaccuracies may reflect in significant bone position inaccuracies.

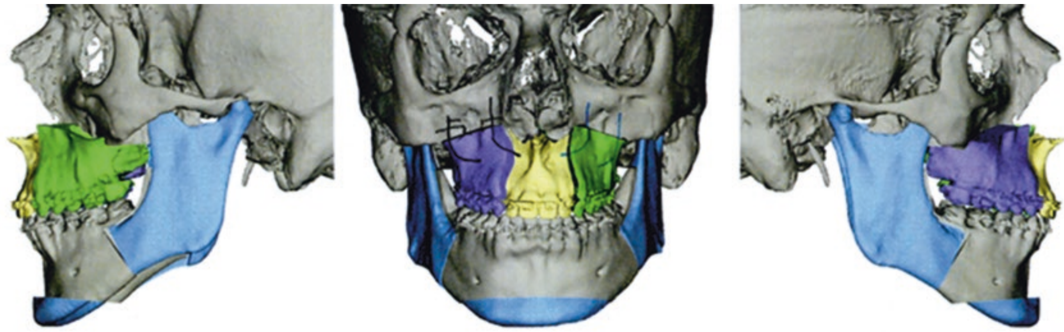

Point	Name	Anterior/Posterior	Left/Right	Up/Down
ANS	Anterior Nasal Spine	6.93 mm Anterior	0.69 mm Left	0.67 mm Down
A	A Point	6.52 mm Anterior	0.74 mm Left	0.41 mm Down
ISU1	Midline of Upper Incisor	6.00 mm Anterior	0.00	0.50 mm Down
U3L	Upper Left Canine	5.62 mm Anterior	1.36 mm Left	0.78 mm Up
U6L	Upper Left Anterior Molar (mesiobuccal cusp)	5.58 mm Anterior	0.52 mm Left	3.03 mm Up
U3R	Upper Right Canine	5.34 mm Anterior	1.61 mm Right	1.41 mm Up
U6R	Upper Right Anterior Molar (mesiobuccal cusp)	6.02 mm Anterior	2.49 mm Right	2.89 mm Up
ISL1	Midline of Lower Incisor	6.37 mm Anterior	0.38 mm Right	2.35 mm Up
L6L	Lower Left Anterior Molar (mesiobuccal cusp)	6.78 mm Anterior	0.02 mm Right	3.25 mm Up
L6R	Lower Right Anterior Molar (mesiobuccal cusp)	6.07 mm Anterior	0.03 mm Right	3.10 mm Up
B	B Point	5.39 mm Anterior	0.19 mm Right	2.63 mm Up
Pog.	Pogonion	10.05 mm Anterior	0.00	3.62 mm Up

Fig. 19.24 Left lateral, frontal, and right solid surface renderings of the patient shown in Fig. 19.18 showing osteotomy sites and final position of segments after virtual orthognathic surgery comprising a segmental LeFort I, bilateral sagittal split osteotomy, and genioplasty. Quantitative vectored (anterior/posterior, left/right, up/down) linear displacements of specific cephalometric landmarks relative to the original spatial location are provided

The predictability of precise osteotomies with consequent controlled fractures during surgeries such as the pterygoid plates, sagittal split osteotomies, or interdental cuts are a concern. In reconstructive procedures, the problems of shaping and placing a graft or implant in the planned location also arises (Fig. 19.27).

19.4.2.1 Tracking Technology

Tracking of the displacement of the bone fragments in the course of surgery can utilize different tracking technologies (Langlotz 2004):

1. Ultrasound, where an array of three ultrasound emitters is mounted on the object to be

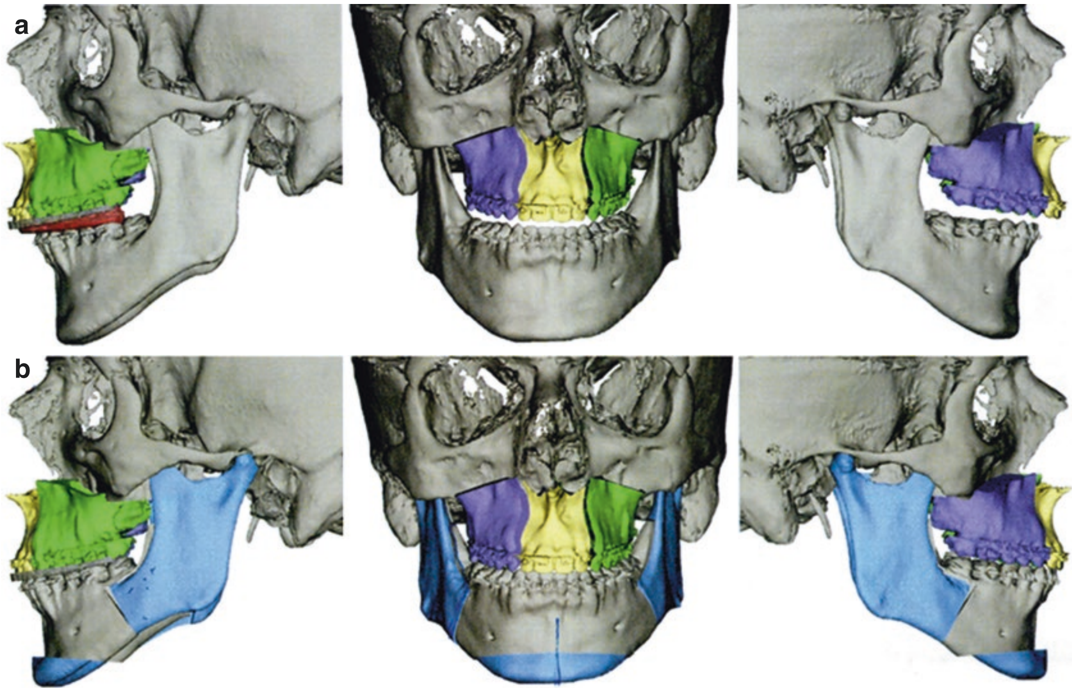

Fig. 19.25 Left lateral, frontal, and right lateral solid volumetric renderings after Le Forte I osteotomy and virtual simulation (**a**) and after BSSO with genioplasty. The relationship of the dentition after the Le Forte I is used to design and finally fabricate an interim surgical splint (*red* wafer separating the maxillary and mandibular dentition in (**a**)). A second final surgical splint is designed to fit the maxillary teeth and act as a key for the mandibular dentition after the BSSO (*gray* wafer separating the maxillary and mandibular dentition in (**b**))

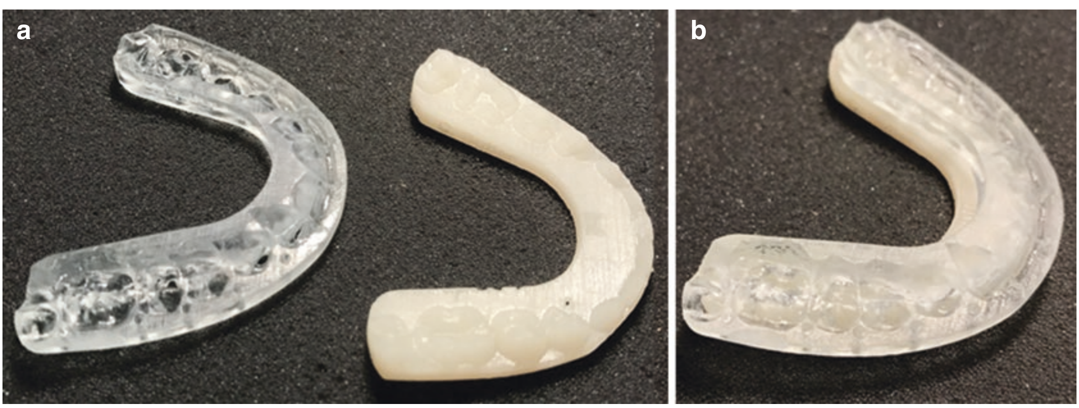

Fig. 19.26 Maxillary (clear) interim and mandibular (opaque) final perioperative surgical splints printed by external orthognathic planning service in sterilizable Class IV resin (**a**). The maxillary splint (clear) is positioned on the dentition of the unoperated mandible and the maxillary occlusal scheme used to position and then stabilize the maxillary segments. After stabilization of the maxillary segments, the mandibular splint (opaque) is inserted into the maxillary splint (**b**) and this composited splint used to position and then stabilize the mandibular BSSO segments

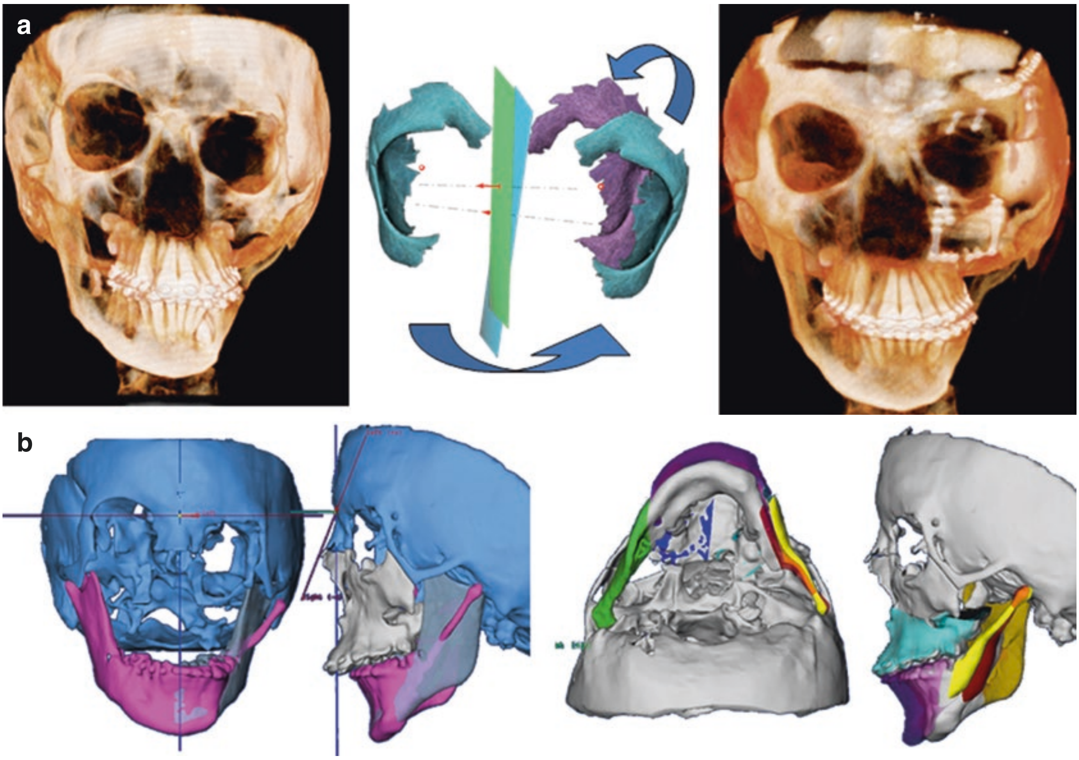

Fig. 19.27 CAS simulation prior to surgery required surgical navigation for the complex corrections for a patient with degree 3 of craniofacial macrosomia consisting of an orbital reconstruction planning (**a**) and mandibular advancement planning (**b**)

tracked, but the speed of sound value can vary with temperature changes and the calibration procedure is very delicate.

2. Electromagnetic tracking, where a homogeneous magnetic field is created by a generator coil. Ferromagnetic items such as implants, instruments, or the operation table can interfere strongly with these systems, distorting the measurements in an unpredictable way. Newer systems claim reduction of these effects and feature receivers the size of a needle head possibly announcing a renewal of interest for electromagnetic tracking in surgical navigation (examples are the 3-D guidance trackstar, Ascension, Burlington, Vermont USA; StealthStation® AXIEM, Medtronic, Louisville, Colorado USA, and: Aurora, Northern Digital Inc., Ontario, Canada).
3. Infrared (IR) optical tracking devices rely on pairs or triplets of charged coupled devices that detect positions of IR markers and in these device between the cameras and markers, a free line-of-sight is required.

References

3-DSLICER. http://www.slicer.org. Accessed 30 Apr 2015

Abramson Z, Susarla SM, Lawler M, Bouchard C, Troulis M, Kaban LB (2011) Three-dimensional computed tomographic airway analysis of patients with obstructive sleep apnea treated by maxillomandibular advancement. J Oral Maxillofac Surg 69:677–686

Agarwal RL, Muranjan MN (2008) Diagnostic practice for organic acidemias: barriers to early diagnosis. Arch Dis Child 93:1000

Ahmad M, Hollender L, Anderson Q, Kartha K, Ohrbach R, Truelove EL et al (2009) Research diagnostic criteria for temporomandibular disorders (RDC/TMD): development of image analysis criteria and examiner reliability for image analysis. Oral Surg Oral Med Oral Pathol Oral Radiol Endod 107:844–860

Alexiou K, Stamatakis H, Tsiklakis K (2009) Evaluation of the severity of temporomandibular joint osteoarthritic changes related to age using cone beam computed tomography. Dentomaxillofac Radiol 38: 141–147

Alstergren P, Kopp S (2000) Prostaglandin E2 in temporomandibular joint synovial fluid and its relation to pain and inflammatory disorders. J Oral Maxillofac Surg 58:180–186. discussion 186-188

Andresen PR, Bookstein FL, Conradsen K, Ersbøll BK, Marsh JL, Kreiborg S (2000) Surface-bounded growth modeling applied to human mandibles. IEEE Trans Med Imaging 19:1053–1063

Becker A, Chaushu S, Casap-Caspi N (2010) Cone-beam computed tomography and the orthosurgical management of impacted teeth. J Am Dent Assoc 141(Suppl 3):14S–18S

Behnia H, Khojasteh A, Soleimani M, Tehranchi A, Atashi A (2012) Repair of alveolar cleft defect with mesenchymal stem cells and platelet derived growth factors: a preliminary report. J Craniomaxillofac Surg 40:2–7

Blumberg TJ, Natoli RM, Athanasiou KA (2008) Effects of doxycycline on articular cartilage GAG release and mechanical properties following impact. Biotechnol Bioeng 100:506–515

Bookstein F (1991) Morphometric tools for landmark data. Cambridge University Press, Cambridge

Botticelli S, Verna C, Cattaneo PM, Heidmann J, Melsen B (2011) Two- versus three-dimensional imaging in subjects with unerupted maxillary canines. Eur J Orthod 33:344–349

Bryndahl F, Eriksson L, Legrell PE, Isberg A (2006) Bilateral TMJ disk displacement induces mandibular retrognathia. J Dent Res 85:1118–1123

Burgin LV, Aspden RM (2008) Impact testing to determine the mechanical properties of articular cartilage in isolation and on bone. J Mater Sci Mater Med 19:703–711

Carvalho FA, Cevidanes LH, da Motta AT, Almeida MA, Phillips C (2010) Three-dimensional assessment of mandibular advancement 1 year after surgery. Am J Orthod Dentofacial Orthop 137:S53.e1–12; discussion S53–55

Cevidanes LH, Bailey LJ, Tucker GR, Styner MA, Mol A, Phillips CL et al (2005) Superimposition of 3-D cone-beam CT models of orthognathic surgery patients. Dentomaxillofac Radiol 34:369–375

Cevidanes LH, Heymann G, Cornelis MA, DeClerck HJ, Tulloch JF (2009a) Superimposition of 3-dimensional cone-beam computed tomography models of growing patients. Am J Orthod Dentofac Orthop 136:94–99

Cevidanes LH, Styner M, Proffit WR (2009b) Three-dimensional superimposition of the skull base for the longitudinal evaluation of the effects of growth and of treatment. Orthod Fr 80:347–357

Cevidanes LH, Styner MA, Proffit WR (2006) Image analysis and superimposition of 3-dimensional cone-beam computed tomography models. Am J Orthod Dentofac Orthop 129:611–618

Chabanas M, Luboz V, Payan Y (2003) Patient specific finite element model of the face soft tissues for computer-assisted maxillofacial surgery. Med Image Anal 7:131–151

Chapuis J, Schramm A, Pappas I, Hallermann W, Schwenzer-Zimmerer K, Langlotz F et al (2007) A new system for computer-aided preoperative planning and intraoperative navigation during corrective jaw surgery. IEEE Trans Inf Technol Biomed 11:274–287

Chapuis J (2006) Computer-aided cranio-maxillofacial surgery. University of Bern, Bern

Conley RS (2011) Evidence for dental and dental specialty treatment of obstructive sleep apnoea. Part 1: the adult OSA patient and part 2: the paediatric and adolescent patient. J Oral Rehabil 38:136–156

Dalessandri D, Laffranchi L, Tonni I, Zotti F, Piancino MG, Paganelli C et al (2011) Advantages of cone beam computed tomography (CBCT) in the orthodontic treatment planning of cleidocranial dysplasia patients: a case report. Head Face Med 7:6

DCBIA VT. http://www.youtube.com/user/DCBIA: Videos Tutoriais DCBIA; 30 Apr 2015

De Momi E, Chapuis J, Pappas I, Ferrigno G, Hallermann W, Schramm A et al (2006) Automatic extraction of the mid-facial plane for cranio-maxillofacial surgery planning. Int J Oral Maxillofac Surg 35:636–642

Dean D, Hans MG, Bookstein FL, Subramanyan K (2000) Three-dimensional Bolton-Brush growth study landmark data: ontogeny and sexual dimorphism of the Bolton standards cohort. Cleft Palate Craniofac J 37:145–156

Dworkin SF, LeResche L (1992) Research diagnostic criteria for temporomandibular disorders: review, criteria, examinations and specifications, critique. J Craniomandib Disord 6:301–355

Ebner FH, Kürschner V, Dietz K, Bültmann E, Nägele T, Honegger J (2010) Craniometric changes in patients with acromegaly from a surgical perspective. Neurosurg Focus 29:E3

Edwards SP (2010) Computer-assisted craniomaxillofacial surgery. Oral Maxillofac Surg Clin North Am 22:117–134

El H, Palomo JM (2010) Measuring the airway in 3 dimensions: a reliability and accuracy study. Am J Orthod Dentofac Orthop 137:S50.e51–59; discussion S50–52

Evans C, Scarfe W, Ahmad M, Cevidanes L, Ludlow J, Palomo J et al (2013) Clinical recommendations regarding use of cone beam computed tomography in orthodontic treatment. Position statement by the American Academy of Oral and Maxillofacial Radiology. Oral Surg Oral Med Oral Pathol Oral Radiol 116:238–257

Fredriksson L, Alstergren P, Kopp S (2006) Tumor necrosis factor-alpha in temporomandibular joint synovial fluid predicts treatment effects on pain by intra-articular glucocorticoid treatment. Mediat Inflamm 2006:59425

Gallo LM, Gössi DB, Colombo V, Palla S (2008) Relationship between kinematic center and TMJ anatomy and function. J Dent Res 87:726–730

Gateno J, Teichgraeber JF, Xia JJ (2003) Three-dimensional surgical planning for maxillary and midface distraction osteogenesis. J Craniofac Surg 14:833–839

Gerig G, Jomier M, Chakos M. 2001 Valmet: a new validation tool for assessing and improving 3-D object segmentation. In: Niessen W, Viergever M (eds) MICCAI 2001: Proceedings of the international society and conference serien on medical image computing and computer-assisted intervention, Berlin, pp 516–528

Gladilin E, Zachow S, Deuflhard P, Hege HC (2004) Anatomy- and physics-based facial animation for craniofacial surgery simulations. Med Biol Eng Comput 42:167–170

Helenius LM, Hallikainen D, Helenius I, Meurman JH, Könönen M, Leirisalo-Repo M et al (2005) Clinical and radiographic findings of the temporomandibular joint in patients with various rheumatic diseases. A case-control study. Oral Surg Oral Med Oral Pathol Oral Radiol Endod 99:455–463

Dolphin Imaging. http://www.dolphinimaging.com: Dolphin Imaging; 30 Apr 2015.

Invivo. http://dental.anatomage.com/specialty/orthodontist: Invivo; 30 Apr 2015

Ishida T, Yabushita T, Soma K (2009) Effects of a liquid diet on temporomandibular joint mechano-receptors. J Dent Res 88:187–191

ITKSNAP. http://www.itksnap.org/pmwiki/pmwiki.php: ITKSNAP; 30 Apr 2015

Iwasaki T, Saitoh I, Takemoto Y, Inada E, Kanomi R, Hayasaki H et al (2011) Evaluation of upper airway obstruction in Class II children with fluid-mechanical simulation. Am J Orthod Dentofac Orthop 139:e135–e145

Kapila S, Conley RS, Harrell WE (2011) The current status of cone beam computed tomography imaging in orthodontics. Dentomaxillofac Radiol 40:24–34

Kapila SD, Nervina JM (2015) CBCT in orthodontics: assessment of treatment outcomes and indications for its use. Dentomaxillofac Radiol 44:20140282

Katheria BC, Kau CH, Tate R, Chen JW, English J, Bouquot J (2010) Effectiveness of impacted and supernumerary tooth diagnosis from traditional radiography versus cone beam computed tomography. Pediatr Dent 32:304–309

Keeve E, Girod S, Kikinis R, Girod B (1998) Deformable modeling of facial tissue for craniofacial surgery simulation. Comput Aided Surg 3:228–238

Koyama J, Nishiyama H, Hayashi T (2007) Follow-up study of condylar bony changes using helical computed tomography in patients with temporomandibular disorder. Dentomaxillofac Radiol 36:472–477

Langlotz F (2004) Localizers and trackers for computer assisted freehand navigation. In: Picard F, Noite L, Digiola A, Jaramaz B (eds) Hip and knee surgery—navigation, robotics, and computer assisted surgical tools. Oxford University Press, Oxford, pp 51–53

Lenza MG, Lenza MM, Dalstra M, Melsen B, Cattaneo PM (2010) An analysis of different approaches to the assessment of upper airway morphology: a CBCT study. Orthod Craniofac Res 13:96–105

Leung CC, Palomo L, Griffith R, Hans MG (2010) Accuracy and reliability of cone-beam computed tomography for measuring alveolar bone height and detecting bony dehiscences and fenestrations. Am J Orthod Dentofac Orthop 137:S109–S119

Lie WN (1995) Automatic target segmentation by locally adaptive image thresholding. IEEE Trans Image Process 4:1036–1041

Ludlow JB, Gubler M, Cevidanes L, Mol A (2009) Precision of cephalometric landmark identification: cone-beam computed tomography vs conventional cephalometric views. Am J Orthod Dentofacial Orthop 136:312.e1–10; discussion 312–313

Ma WY, Manjunath BS (2000) EdgeFlow: a technique for boundary detection and image segmentation. IEEE Trans Image Process 9:1375–1388

Maes F, Collignon A, Vandermeulen D, Marchal G, Suetens P (1997) Multimodality image registration by maximization of mutual information. IEEE Trans Med Imaging 16:187–198

Maxilim. http://www.medicim.com/en/products: Maxilim; Accessed 30 Apr 2015

Medical Modeling.. http://www.medicalmodeling.com: Medical Modeling; 30 Apr 2015

Molen AD (2010) Considerations in the use of cone-beam computed tomography for buccal bone measurements. Am J Orthod Dentofac Orthop 137:S130–S135

Moon N, Bullitt E, Leemput K, Gerig G. Model-based brain and tumor segmentation. In: Casturi R, Laurendeau D, Suen C (eds) Proceeding of 16th International Conference on Pattern recognition ICPR 2002, Aug 2002, IEE Computer Society, pp 528–531

Nordahl S, Alstergren P, Eliasson S, Kopp S (2001) Radiographic signs of bone destruction in the arthritic temporomandibular joint with special reference to markers of disease activity. A longitudinal study. Rheumatology (Oxford) 40:691–694

Paraview. http://www.paraview.org: Paraview; 30 Apr 2015

Roemhildt ML, Coughlin KM, Peura GD, Badger GJ, Churchill D, Fleming BC et al (2010) Effects of increased chronic loading on articular cartilage material properties in the lapine tibio-femoral joint. J Biomech 43:2301–2308

Rohr R (2001) Landmark-based image analysis: using geometric and intensity models. Kluwer Academic, London

Ruellas AC, Huanca Ghislanzoni LT, Gomes MR, Danesi C, Lione R, Nguyen T et al (2016a) Comparison and reproducibility of 2 regions of reference for maxillary regional registration with cone-beam computed tomography. Am J Orthod Dentofac Orthop 149:533–542

Ruellas AC, Tonello C, Gomes LR, Yatabe MS, Macron L, Lopinto J et al (2016b) Common 3-dimensional coordinate system for assessment of directional changes. Am J Orthod Dentofac Orthop 149:645–656

Ruellas AC, Yatabe MS, Souki BQ, Benavides E, Nguyen T, Luiz RR et al (2016c) 3-D mandibular superimposition: comparison of regions of reference for voxel-based registration. PLoS One 11:e0157625
Schendel S, Powell N, Jacobson R (2011) Maxillary, mandibular, and chin advancement: treatment planning based on airway anatomy in obstructive sleep apnea. J Oral Maxillofac Surg 69:663–676
Schendel SA, Hatcher D (2010) Automated 3-dimensional airway analysis from cone-beam computed tomography data. J Oral Maxillofac Surg 68:696–701
Schiffman EL, Ohrbach R, Truelove EL, Tai F, Anderson GC, Pan W et al (2010a) The research diagnostic criteria for temporomandibular disorders. V: methods used to establish and validate revised Axis I diagnostic algorithms. J Orofac Pain 24:63–78
Schiffman EL, Truelove EL, Ohrbach R, Anderson GC, John MT, List T et al (2010b) The research diagnostic criteria for temporomandibular disorders. I: overview and methodology for assessment of validity. J Orofac Pain 24:7–24
Schutyser F, Poorten VV, Van Cleynenbreugel J, Delaere P, Suetens P (2000) An image-based 3-D planning environment for hemicricolaryngectomy and reconstruction by tracheal autotransplantation. Comput Aided Surg 5:166–174
Scott CC, Athanasiou KA (2006) Mechanical impact and articular cartilage. Crit Rev Biomed Eng 34:347–378
Shemesh H, Cristescu RC, Wesselink PR, Wu MK (2011) The use of cone-beam computed tomography and digital periapical radiographs to diagnose root perforations. J Endod 37:513–516
Sherrard JF, Rossouw PE, Benson BW, Carrillo R, Buschang PH (2010) Accuracy and reliability of tooth and root lengths measured on cone-beam computed tomographs. Am J Orthod Dentofac Orthop 137:S100–S108
Simplant. http://www.dentsply.com/en-uk-implants/digital-solutions/simplant.html/Implants/Digital-solutions/SIMPLANT/Software/c/3000106.html: Simplant; 30 Apr 2015
Software 3-DMD. http://www.3-Dmd.com/3-Dmd-software/: 3-DMD Vultus; Accessed 30 Apr 2015
Subsol G, Thirion JP, Ayache N (1998) A scheme for automatically building three-dimensional morphometric anatomical atlases: application to a skull atlas. Med Image Anal 2:37–60
Tai K, Hotokezaka H, Park JH, Tai H, Miyajima K, Choi M et al (2010) Preliminary cone-beam computed tomography study evaluating dental and skeletal changes after treatment with a mandibular Schwarz appliance. Am J Orthod Dentofacial Orthop 138:262.e1–262.e211; discussion 262–263
Tamimi D, El Said K (2009) Cone beam computed tomography in the assessment of dental impactions. Semin Orthod 15:57–62
Teschner M, Girod S, Girod B (2001) 3-D simulation of craniofacial surgical procedures. Stud Health Technol Inform 81:502–508
Thompson PM, MacDonald D, Mega MS, Holmes CJ, Evans AC, Toga AW (1997) Detection and mapping of abnormal brain structure with a probabilistic atlas of cortical surfaces. J Comput Assist Tomogr 21:567–581
Treil J, Braga J, Aït Ameur A (2009) 3-D representation of skull and soft tissues. Usefulness in orthodontic and orthognathic surgery. J Radiol 90:634–641
Truelove E, Pan W, Look JO, Mancl LA, Ohrbach RK, Velly AM et al (2010) The research diagnostic criteria for temporomandibular disorders. III: validity of Axis I diagnoses. J Orofac Pain 24:35–47
Tucker S, Cevidanes LH, Styner M, Kim H, Reyes M, Proffit W et al (2010) Comparison of actual surgical outcomes and 3-dimensional surgical simulations. J Oral Maxillofac Surg 68:2412–2421
Turtleseg. http://www.turtleseg.org. Turtleseg; 30 Apr 2015
Van Elslande D, Heo G, Flores-Mir C, Carey J, Major PW (2010) Accuracy of mesiodistal root angulation projected by cone-beam computed tomographic panoramic-like images. Am J Orthod Dentofac Orthop 137:S94–S99
Vandewalle P, Schutyser F, Van Cleynenbreugel J, Suetens P (2003) Modeling of facial soft tissue growth for maxillofacial surgery planning environments. IS4TH:27–37
Verteramo A, Seedhom BB (2007) Effect of a single impact loading on the structure and mechanical properties of articular cartilage. J Biomech 40:3580–3589
Westermark A, Zachow S, Eppley BL (2005) Three-dimensional osteotomy planning in maxillofacial surgery including soft tissue prediction. J Craniofac Surg 16:100–104
Xia J, Samman N, Yeung RW, Shen SG, Wang D, Ip HH et al (2000) Three-dimensional virtual reality surgical planning and simulation workbench for orthognathic surgery. Int J Adult Orthodon Orthognath Surg 15:265–282
Zachow S, Gladilin E, Zeilhofer H, Sader R (2001) Improved 3-D osteotomy planning in craniomaxillofacial surgery. Medical image computing and computer-assisted intervention 4th International Conference Ultrecht, The Netherlands

Dental Implants

20

Reinhilde Jacobs and William C. Scarfe

Contents

R. Jacobs, D.D.S., Ph.D., M.S., Dr., H.C. (✉)
Omfsimpath Research Group, Department of Imaging and Pathology, Faculty of Medicine, Katholieke Universiteit Leuven, Leuven, Belgium

Dentomaxillofacial Radiology Center, Oral and Maxillofacial Surgery, University Hospitals Leuven, Leuven, Belgium

Department of Dental Medicine, Karolinska Institutet, Stockholm, Sweden
e-mail: reinhilde.jacobs@kuleuven.be

W.C. Scarfe, B.D.S., F.R.A.C.D.S., M.S.
Division of Radiology and Imaging Science, Department of Surgical/Hospital Dentistry, University of Louisville School of Dentistry, Louisville, KY, USA
e-mail: William.scarfe@louisville.edu

20.1 Introduction

The use of dental implants to replace the dentition and restore oral form, function, and esthetics in partially and fully edentulous patients has revolutionized dental treatment. Four basic types of dental implants have been available over the years: (1) subperiosteal (Fig. 20.1), (2) blade, (3) transosseous, and (4) endosseous (Fig. 20.1). Only endosseous dental implants are retained in the jaws by osseointegration (Brånemark et al. 1977). Based on excellent

W.C. Scarfe, C. Angelopoulos (eds.), *Maxillofacial Cone Beam Computed Tomography*,
https://doi.org/10.1007/978-3-319-62061-9_20

long-term clinical success rates (Albrektsson et al. 1986; Adell et al. 1990; Shearer 1995), endosseous type dental implants are now considered the optimal treatment for tooth replacement.

20.1.1 Dental Implant Components

Osseointegrated implants comprise three components that, together, serve as a dental implant system (Fig. 20.2) (Laney 2007; ISO 2014):

- *Dental implant body*. This is the portion of the dental implant that is surgically embedded in the osseous tissue of the jaw. A root form endosseous implant body is usually titanium based and essentially cylindrical in shape and may be solid, hollow, or vented. The surface of the implant may present with or without screw threads. The distance between recurring threads is the thread pitch. The *endosseous zone* is that part of the surface that contacts the bone and promotes osseointegration. The surface may be coated (usually with ceramic) or blasted resulting in an increased

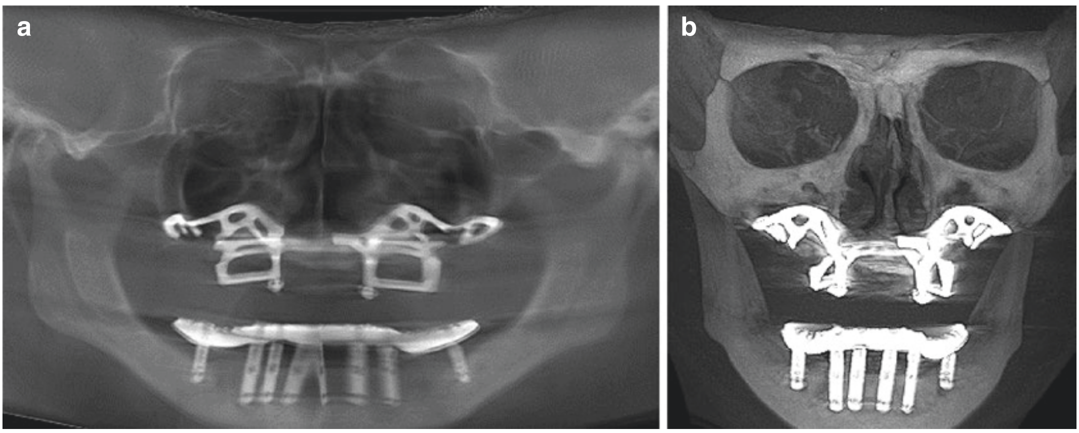

Fig. 20.1 Reformatted panoramic (**a**) and frontal maximum intensity projection (**b**) of completely edentulous jaws restored with bilateral subperiosteal implants in the maxilla and multiple endosseous implants in the mandible

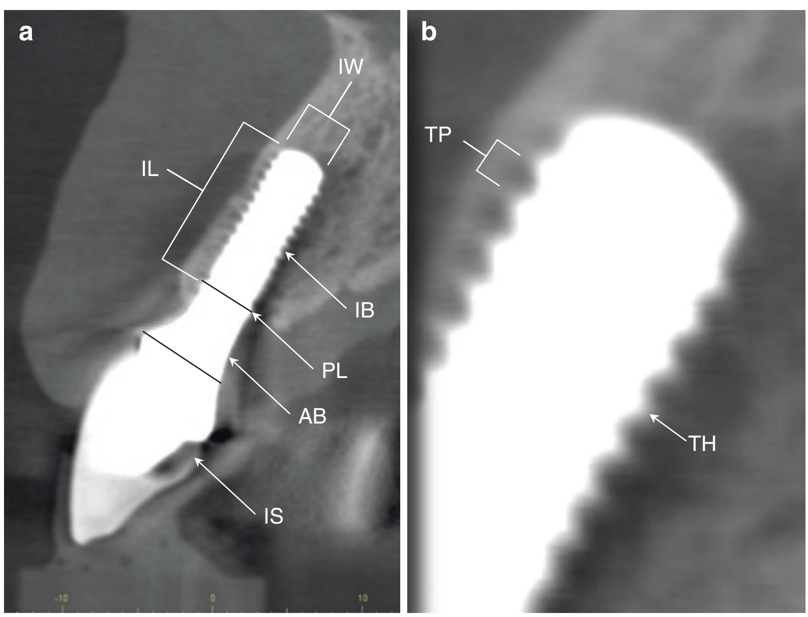

Fig. 20.2 Cross-sectional CBCT image of a single maxillary central incisor (**a**) and magnified apical portion of the implant body (**b**) illustrating the components of a conventional endosseous titanium implant system (*IB* implant body, *EZ* endosseous zone of the implant body, *AB* abutment, *TH* thread, *TP* thread pitch, *PL* platform, *IL* implant length, *IW* implant width, *IS* implant suprastructure)

surface roughness with improved bone response. Implant sizes are manufacturer dependent, typically ranging from 3 to 5 mm in diameter (implant width) and 5 mm to over 15 mm in length (implant length). The portion of the implant body that connects with the abutment is known as the *connective platform*. Titanium may have an endosseous zone extending all the way to the platform, in which case the implant is placed with the platform level with the bone (bone level implant). Alternately titanium may be polished or "machined" approximately 2–3 mm inferior to the platform, in which case the implant is placed with the platform level with the mucosa (tissue level implant)

- *Dental abutment*. This is the portion of the dental implant system that serves to connect the implant body with the implant superstructure by protruding through the mucosa. It connects to the implant body through a connecting interface. The abutment may have a central long axis coincident with (straight implant abutment) or divergent from (angled implant abutment) the implant body. An abutment screw is used to attach the implant abutment to the implant body.
- *Implant Superstructure*. This is the prosthetic restoration. While initially dental implants were mainly used for anchorage of a full support fixed prostheses, their application has now expanded to support overdentures or to replace single missing teeth. The superstructure may be screw or cement retained.

20.1.2 Surgical Approaches

Two dental implant surgical approaches are possible.

- *Two Stage Procedure*. The original surgical treatment protocol for endosseous implants, proposed by Brånemark (1985), consisted of two stages. In the first stage, the implant body is placed in bone either after flap elevation or flapless through the mucosa and a healing abutment inserted (Fig. 20.3) (van Steenberghe et al. 2002, 2004, 2005). After an appropriate healing period to allow for secondary stability (approximately 3 (mandible) to 6 (maxilla) months), a second-stage surgery uncovers the

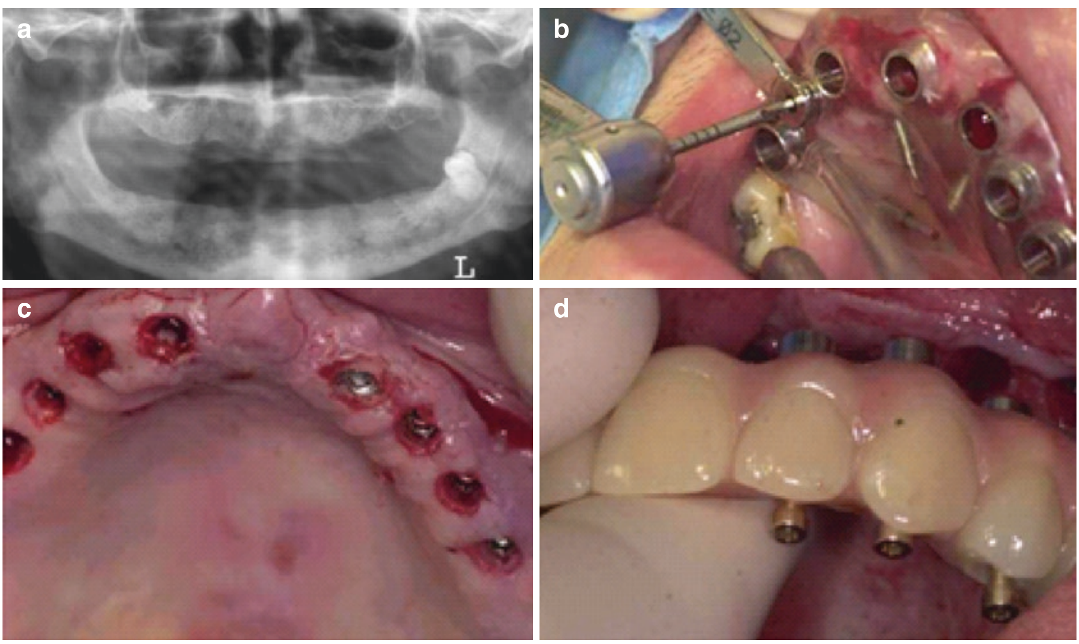

Fig. 20.3 Preoperative panoramic image (**a**) and sequential clinical photographs using a surgical guide to create initial drill hole osteotomies (**b**), immediately postoperatively after flapless surgical placement of eight cylindrical implants (**c**), and after insertion of the complete fixed prosthesis (**d**)

dental implant body and an abutment and subsequent suprastructure is fabricated and the implant restored.

- *Single Stage Procedure*. Alternately the implant is placed such that it projects into the oral cavity immediately after placement. The dental implant in this case may be placed into function within a maximum of 72 h after placement (immediate loading) or restored after a prescribed healing period.

20.2 Role of Imaging in Implant Therapy

Imaging has a specific role in each of the three phases of implant therapy.

20.2.1 Presurgical Assessment and Planning

This phase involves analysis of the actual alveolar bone foundation based on prosthesis design considerations in regard to function and esthetics. In addition to a thorough clinical examination, imaging assessment is essential to estimate the regional morphologic characteristics of the proposed implant site and the location of anatomical structures. Various imaging options are available for the evaluation of the recipient site such as panoramic, intraoral, and cross-sectional modalities including cone beam computed tomography (CBCT). Panoramic radiographs provide information on the gross anatomy of the jaws and related anatomical structures; however, due to inherent distortion, these images are less well suited for estimating the amount of alveolar bone, particularly in the horizontal planes. Intraoral periapical images are valuable for an estimate of the mesiodistal dimension of the potential implant site, as well as a preliminary estimate of the vertical dimensions. Unlike cross-sectional techniques, neither provides information on the buccolingual width or angulation and irregularities in the alveolar process. Images are often performed using intraoral appliances incorporating radiopaque materials as *radiographic templates* to either calibrate linear measurements or provide specific information on the location or angulation of proposed implant body placement. These guides are often used to derive or are converted into *surgical guides*. The role of CBCT in facilitating interrelationship of prosthetic, surgical, and diagnostic components of implant therapy using computer-assisted operative strategies cannot be underrated.

20.2.2 Perioperative Treatment

This phase involves all surgical and clinical aspects of dental implant and superstructure placement including pre-prosthetic surgery (e.g., bone augmentation), operative (e.g., access, soft tissue flap design, osteotomy, osseous surgical technique), and prosthetic considerations (e.g., abutment and final superstructure placement and management). Initially, a small osteotomy is prepared with a narrow (approximately 2 mm in diameter) drill. The recipient osteotomy site is sequentially broadened using drills of increasing widening diameter. Site location, depth, and parallelism of the initial osteotomy site may be confirmed by imaging a metallic graded marker of comparable diameter placed into the surgical site. This procedure incorporating direct digital intraoral radiography has been called *image-assisted implant placement* (Jeffcoat 1993). Panoramic radiography may also be used with multiple interarch surgical site preparations. Cross-sectional imaging, including CBCT, is usually not indicated at this stage because of dose considerations and limitations in accuracy due to metallic artifacts created by the pilot drill marker.

20.2.3 Postoperative Maintenance

This phase involves periodic review of the osseointegration integrity of the implant body and prosthetic success and application of maintenance therapies. Implant performance relies on clinical assessment (e.g., implant mobility, signs of gingival inflammation, periodontal attachment loss, and pocket formation); however, periapical imaging may be used for evaluation of marginal alveolar and endosseous peri-implantitis.

20.3 Presurgical Planning Considerations

While the surgical aspects of implant therapy are usually straightforward, dental implant location is critical. Rather than being dependent on the availability of adequate alveolar bone volume (surgically driven), placement is now determined by the esthetic, biomechanical, and functional demands of the final prosthesis (prosthetically driven). Based on this concept, thorough preoperative planning of implant treatment is a prerequisite for a successful treatment outcome (Jacobs and van Steenberghe 1997).

Planning comprises obtaining an adequate medical and social history in combination with an extensive extra and intraoral clinical evaluation. Clinical assessment of the nature of the edentulism must consider prosthetic rehabilitation strategies to reestablish form, function, and esthetics. Once possible restorative strategies are established, assessment should be directed towards:

Determining the appropriate number of implants to be inserted.

Selecting the optimal dental implant type (e.g., bone vs. tissue level).

Determining the optimal length, width, and orientation of each implant at each site.

Assessing the possible need for additional treatment before or during implant placement, such as bone augmentation.

Diagnostic imaging provides an indispensable technique on addressing these considerations. The choice of technique(s) depends on a balance between the need for additional information on the jawbone and cost, both financially and in terms of radiation dose to the patient. Imaging should provide accurate assessments of alveolar bone quantity as well as the quality. In addition, imaging reduces the morbidity of the procedure by providing essential information on the location of vital anatomical structures such as the inferior alveolar nerve and the extension of the maxillary sinus (Fig. 20.4). Numerous recommendations and indications for the choice of radiographic method related to pre-implant imaging have been proposed (Schwarz et al. 1989; Quirynen et al. 1990; Williams et al. 1992; Faculty of General Dental Practitioners (UK) and the Royal College of Surgeons of England 1998; Jacobs and van Steenberghe 1997; Tyndall and Brooks 2000; White et al. 2001: Harris et al. 2002; Academy of Osseointegration 2010; Harris et al. 2012; SEDENTEXCT Project 2011; ARö DGZMK 2009; European Commission 2012; Superior Health Council 2011; Benavides et al. 2012; DGZMK 2012; Tyndall et al. 2012). Cross-sectional imaging is often preferred to conventional imaging alone as it provides necessary information in the third dimension such as buccolingual width, inclination, and morphology along with crucial information on the spatial relationship of the anatomical structures at the recipient site (Fig. 20.5).

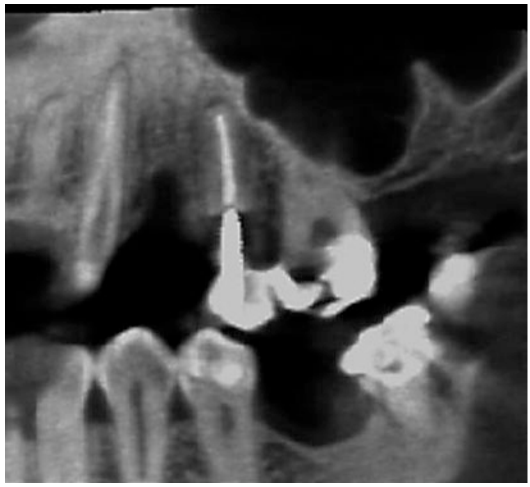

Fig. 20.4 Thin slice (1 mm) reformatted panoramic image of the left maxillary posterior quadrant showing the post extraction pneumatization and inferior alveolar extension of floor of the maxillary sinus in the region of the second molar

Planning involves two major considerations: prosthetic and surgical. CBCT imaging and its

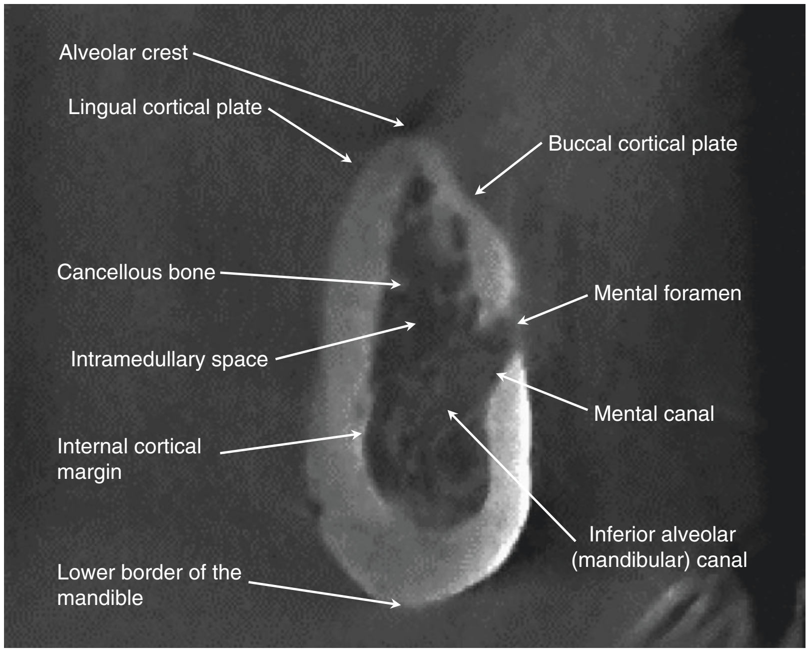

Fig. 20.5 1 mm thick cross-sectional CBCT image in the region of the left mandibular premolar edentulous region showing representative cross-sectional morphologic macro-anatomy, regional topography, bone quality, bone quantity, and localization of the mental canal, mental foramen, and inferior alveolar canal

associated techniques and software applications facilitate the integration of these determinants and support the concept of prosthetically driven implant placement. The role of CBCT imaging in the preoperative and planning phase is to assist in the assessment, support the planning, and ultimately guide surgical implant placement based on prosthetic and anatomic considerations.

20.3.1 Prosthetic Considerations

There are a number of characteristics associated with osseointegrative and prosthetic success that direct implant selection and placement.

- *Implant length*. Numerous investigators have reported a direct association between implant length and diameter and success (Bahat 1993; Buser et al. 1997; Goodacre et al. 1999; Scurria et al. 1998; Duyck and Naert 1998; Alsaadi et al. 2007). Implants with longer length and wider diameter may provide greater initial and secondary stability; however, implants longer than 15 mm may increase the risk for thermal trauma and local bone necrosis (Alsaadi et al. 2007). Recent modifications to the endosseous zone has diminished the need for longer implants (Alsaadi et al. 2008), yet still yield excellent outcomes.
- *Implant angulation*. Non-axial loading of a dental implant may contribute to peri-implant bone loss and have an adverse effect on osseointegration (Barbier and Schepers 1997; Isidor 1996). Ideally an implant should be placed such that its long axes coincide with those of the prosthetic teeth and occlusal table of the final prosthesis (Sethi and Sochor 1995). While non-axial loading may be tolerable within certain limits (Koutouzis and Wennström 2007), inappropriate inclination of implants may also lead to a poor esthetic result or necessitate the use of angulated abutments.
- *Adequate alveolar bone at prosthetically important sites*. The minimal osseous support requirements for a dental implant body is a 1–2 mm thickness of alveolar bone pericircumferentially covering the endosseous zone and separating it from adjacent vital structures such as the mandibular canal, maxillary sinus, and nasal fossa (Del Balso et al. 1994). This dimension accounts for the tolerance of clinical placement and provides enough bone material for osseointegration. While multiple anatomic and individual variations that affect

these tolerances, planning should be directed towards identifying volumes of alveolar bone within these constraints.

At prosthetically important sites with inadequate alveolar bone volume, bone augmentation procedures should be considered. These include local surgical (e.g., ridge expansion osteotomy, crestal split technique, guided bone regeneration (GBR), and distraction osteogenesis) and bone grafting procedures (e.g., the use of autogenous bone grafts harvested from intraoral or extraoral sources, autogenous platelet rich fibrins and order blood derived biomaterials and alloplasts, alloplastic bone substitutes and xenografts to replace bone).

20.3.1.1 Prosthetic Prerequisites

Apart from the morphology of the residual ridge, certain regional dental conditions may provide significant limitations in restoring, as well as placing, dental implants.

Following the removal of teeth, not only are there changes in the shape of the alveolar ridge, but there are potential inter- and intra-arch changes that can encroach on the available bone. If teeth are unopposed in the dental arch (i.e., immediately superior (in the maxilla) or inferior (in the mandible) to a region of edentulism), they have a tendency to continue to *supraerupt* into the mouth. This may limit the amount of interarch distance between the teeth and the alveolar ridge when the teeth are in occlusion. Radiologically the distance between the biting (occlusal) surface of the teeth and the alveolar ridge should be enough to allow for the soft tissue interface around the abutment (approx. 2 mm) and a restoration of adequate height above the soft tissue (approx. 4 mm) (Fig. 20.6). Therefore, an interarch distance between the occlusal surface and the alveolar crest should be 6 mm or more.

In addition, teeth posterior to an alveolar ridge have a tendency to bodily *mesially drift* and moreover *mesially tilt* into the edentulous space. Less commonly teeth anterior to the alveolar ridge migrate distally. Both phenomena can result in teeth adjacent to an edentulous bounded space reducing the available intercoronal space. Teeth are naturally shaped as an inverted bell (i.e., wider

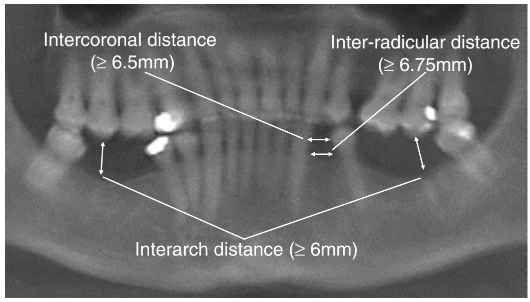

Fig. 20.6 Reformatted panoramic CBCT of a partially dental mandible with the patient scanned in maximum intercuspation (centric occlusion) analyzed for dental relationships which may limit implant placement. The interarch distance must be adequate to allow for the mucosal interface and a prosthesis conforming to functional and esthetic priorities. The intercoronal distance must be wide enough to allow a taper to the abutment/body junction. The interradicular distance should be adequate to allow for 1.5 mm of alveolar bone between the adjacent tooth root and the implant fixture

at the occlusal plane and narrower at the fixture/abutment attachment). The minimum distance intercoronally between the nearest curvatures of the tooth crown should be approximately equal to the width of the shoulder of the implant fixture (approx. 3.75–4.1 mm) plus an adequate taper to the region where the crowns are to make interproximal contact (approx. 1.25 mm either side), therefore, a distance of approximately 6.5 mm.

Finally, the interradicular distance between roots may also be compromised by tooth malposition. Ideally a tooth root should be approximately 1.5 mm from an implant surface at its narrowest. Therefore, the minimum interradicular space should be approximately equal to the implant diameter plus 3 mm (approx. 6.75–7.1 mm).

20.3.2 Anatomic Considerations

Once prosthetic requirements are satisfied, consideration should be directed regionally to the assessment of alveolar bone morphology and regional anatomic considerations.

20.3.2.1 Alveolar Bone Morphology

The alveolar bone available for dental implant placement can be compromised by variations in bone quantity or quality. Assessment of bone quality involves consideration of overall bone volume and morphology. Bone quality involves consideration of trabecular bone pattern, cortical thickness, and bone density (Fig. 20.7). Alterations to bone quality or quantity can be local or due to systemic conditions (Fig. 20.8) and should be considered during the preoperative planning phase. Finally, the relationship of the implant fixture to important anatomical structures, such as neurovascular bundles, tooth roots, the nasal floor, and maxillary sinus, can significantly affect the morbidity of the surgical procedure and influence the final prosthetic outcome.

There are substantial and progressive morphologic changes of the alveolar process following the removal of teeth. This post-extraction physiologic resorptive phenomenon, *residual ridge reduction* (RRR) (Atwood 1971), is a major determinant of the morphology and quantity of the alveolar bone available for implant fixture placement and consequently limits the choice and orientation of the implant with respect to the planned prosthesis. Subsequent bone loss may increase the crown-to-implant body ratio and loading conditions of the implant-retained restoration, both considerations for overall implant success (Duyck and Naert 1998). Loss of the

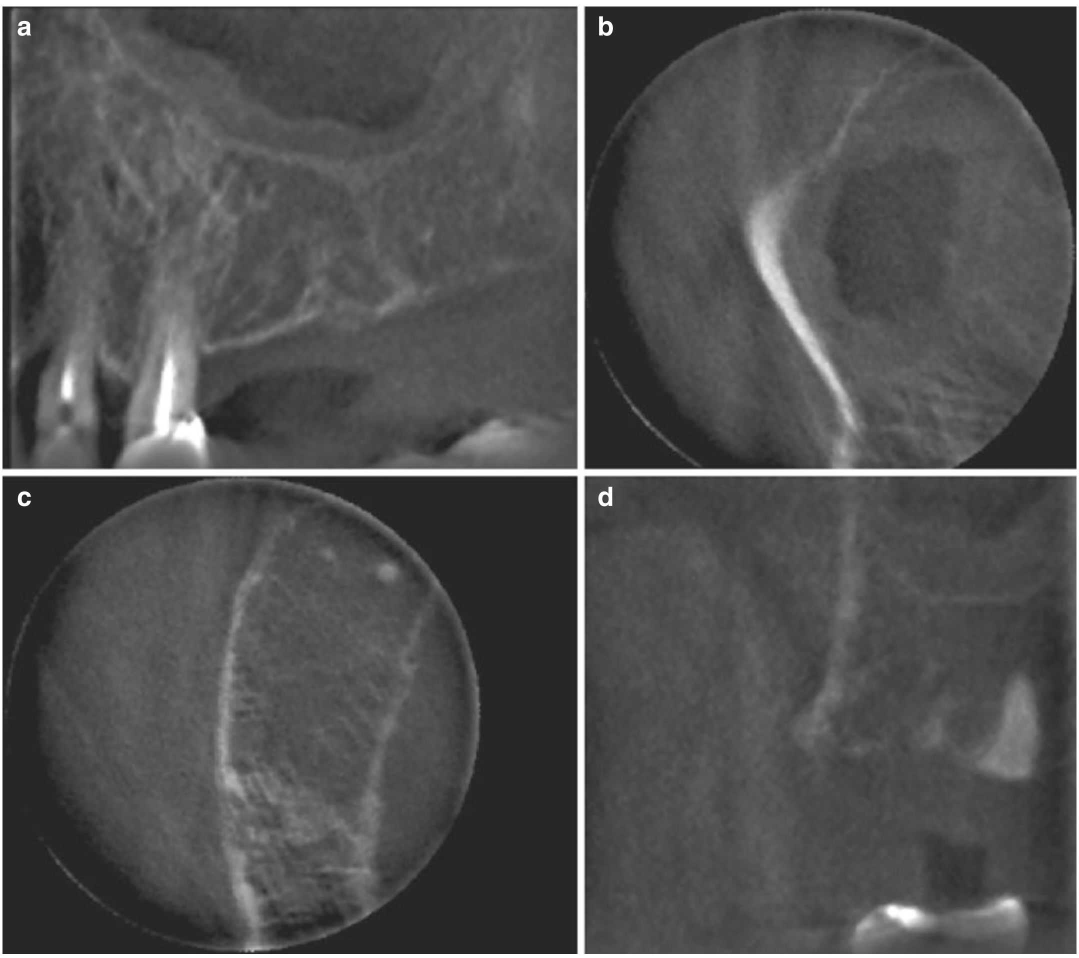

Fig. 20.7 Parasagittal (**a**), high (**b**) and low (**c**) axial and cross-sectional (**d**) CBCT images showing a partially dentate left maxillary posterior edentulous free-end region. Note the lack of cortication and poor intramedullary bone density (sparse trabecular pattern) consistent with Type IV bone (Lekholm and Zarb 1985). In addition, there is concomitant generalized moderate polypoidal thickening of the floor and walls of the left maxillary sinus consistent with chronic sinusitis. Retained root fragments are embedded in the alveolus identified in images (**c**) and (**d**)

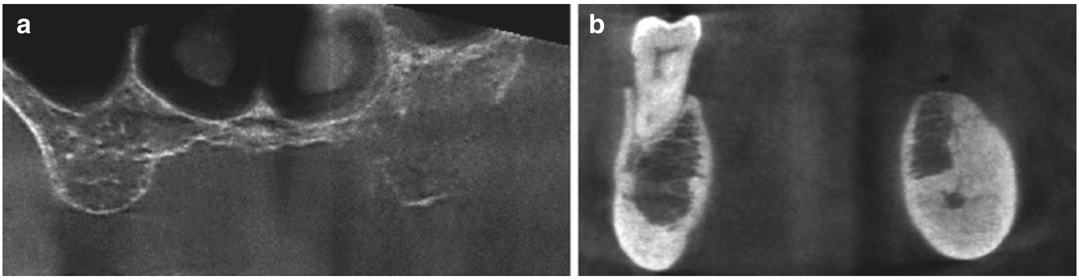

Fig. 20.8 Maxillary (**a**) and mandibular (**b**) coronal CBCT images of a patient with a completely edentulous maxilla and partially dentate mandible showing generalized rarefaction and loss of cortical outline of the left maxillary posterior region and osteosclerotic changes of the left mandible in a patient with a history of intravenous bisphosphonate therapy consistent with medication-related osteonecrosis of the jaw (maxilla)

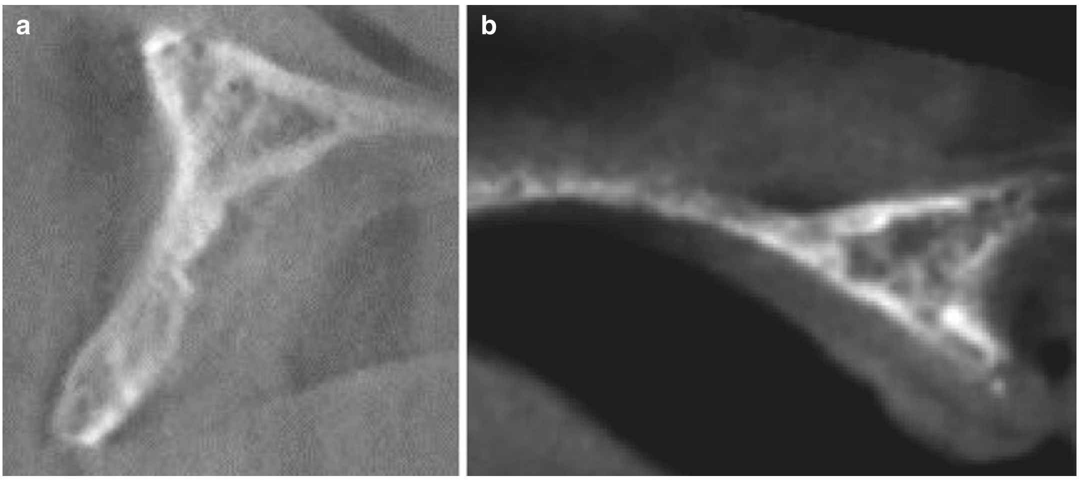

Fig. 20.9 Anterior left (**a**) and left posterior (**b**) cross-sectional CBCT images of a completely edentulous maxilla showing a narrow "knife-edge" ridge with inadequate alveolar bone for implant placement

labial or facial wall of the alveolus, due to surgical extraction or RRR, may only permit placement of an implant in a region outside the occlusal perimeter of the existing teeth and may compromise the final esthetic result.

Extensive ridge resorption often leads to a "knife-edge" ridge (Denissen et al. 1993) of the alveolar bone and is inappropriate for implant placement. This condition must be reduced to a level so as to provide a platform at least equivalent to the platform diameter of the implant body. This may also necessitate the use of narrow implants and increase the risk of exposure of the surface of the implant via fenestration (Fig. 20.9). Reduction in the height of the alveolus also leads to potential encroachment on anatomical structures.

Totally edentulous dental arches present with numerous anatomical characteristics compromising implant placement. If tooth loss has occurred in the early adulthood, RRR may be so pronounced resulting in severe atrophy of the maxilla or mandible (Fig. 20.10). In these

Fig. 20.10 Panoramic image of a completely edentulous maxilla showing an extremely atrophic ridge in conjunction with severe maxillary sinus pneumatization. These anatomic confinements restricted implant placement to the canine areas bilaterally and limited prosthetic options to a bar-supported removable overdenture

circumstances, the pattern of ridge resorption is arch and region dependent and presents with specific limitations related to bone morphology, alveolar bone angulation with respect to the basal bone, buccolingual width, and crestal bone shape. Preoperative assessment might also lead to recommendations of pre-prosthetic ridge augmentation procedures such as bone grafting (Fig. 20.11), sinus augmentation (Fig. 20.12), or even orthognathic surgery.

Assessment

Comprehensive imaging assessment of alveolar bone morphology should comprise consideration of the following:

Alveolar Bone Volume

Alveolar bone resorption after tooth extraction is a progressive process and occurs most rapidly during the first few years. The cause for resorption of alveolar bone after tooth loss has been assumed to be due to disuse atrophy, decreased blood supply, localized inflammation, or unfavorable prosthesis pressure. Even implant placement cannot always prevent further bone resorption (Jacobs et al. 1992, 1993; Araújo et al. 2006). In general, loss in vertical height is greatest anteriorly. The pattern of RRR in the maxilla is more complex than in the mandible.

The maxilla shows, on average, 25% of alveolar bone reduction after a period of 7 years. The majority of the bone loss occurs from the buccal aspect in the upper jaw anteriorly and from the palatal aspect posteriorly resulting in a reduction in palatal width and length, as well as height. Ultimately this resorptive pattern results in a maxilla that is smaller in all dimensions (Atwood 1971; Cawood and Howell 1988). Loss has been estimated to be 40–60% during the first 3 years decreasing to 0.25–0.5% annually thereafter.

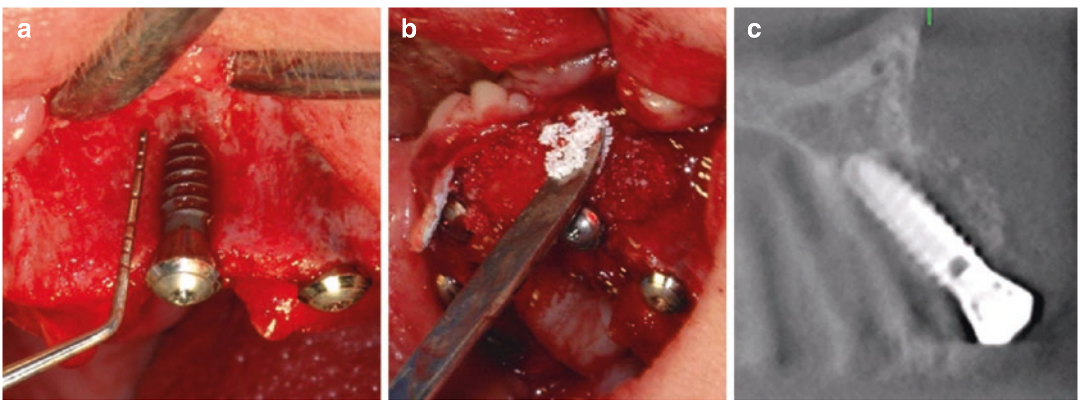

Fig. 20.11 Clinical intraoral photographs of dental implant with large buccal vestibular dehiscence before (**a**) and after (**b**) alveolar bone augmentation procedure using allograft material with corresponding postoperative cross-sectional CBCT image (images courtesy, Marc Quirynen)

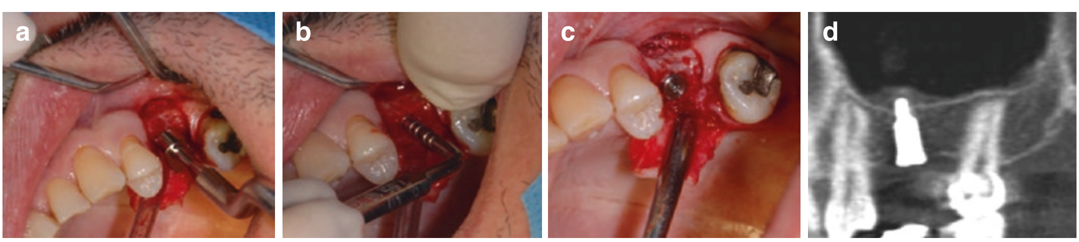

Fig. 20.12 Clinical photographs showing osteotomy preparation (**a**), sinus elevation (**b**), postoperative implant position (**c**), and corresponding parasagittal CBCT image (**d**) of an osteotome sinus floor elevation (Summers 1994) and implant placement in the region of the right maxillary second premolar (images courtesy, Marc Quirynen)

In the mandible, the anterior alveolar processes resorb lingually and the posterior alveolar process resorbs bucally. Since the mandible demonstrates a greater width at its inferior border, the residual ridge appears wider posteriorly after resorption has occurred.

As resorption progresses, a discrepancy develops between the edentulous jaws, with the maxilla becoming significantly smaller than the mandible, leading to a Class III relation with a differential arch width of approximately 7 mm (measured immediately anterior to the retromolar and tuberosity areas bilaterally, respectively).

In the pediatric dentition, loss of deciduous teeth, without permanent tooth replacement has also been associated with bone loss. Ridge width decreases up to 25% within the first 3 years after deciduous tooth removal with continual reduction of a further 4% annually over the next 3 years.

Qualitative Assessment

Three general approaches have been used to classify the alveolar ridge preoperatively in edentulous spaces prior to implant placement.

- *Morphology of ridge defect*. The first method has been to describe specific ridge defects according to morphologic form, severity, and extent.
  - Seibert (1983) classified alveolar ridge defects broadly into three morphologic presentations: buccolingual loss, apicocoronal loss, and a combination of both.
  - Allen et al. (1985) provided a descriptive definition of alveolar ridge resorption indicating that resorption can be considered mild if less than 4 mm, moderate if 4–6 mm, and extensive when greater than 6 mm.
  - The most commonly used classification for presurgical implant assessment is perhaps the Lekholm and Zarb index (1985) for bone quality and bone quantity (Fig. 20.13).
  - Misch and Judy (1987) describe four divisions of available bone with treatment options based on the amount of available bone height, width, and angulation.
  - Based on orthoradial CT data, Cawood and Howell (1988) classified jaw morphology and the AR associated with jaw atrophy according to six classes. In general, after extraction of a tooth (Class 2), a continuous reduction of bone occurs until the alveolar crest demonstrates a “knife-edge” appearance (Class 4). If atrophy continues, further bone height is lost until only the jaw base remains.
  - Studer et al. (1997) proposed a simple classification system based on vertical and horizontal alveolar ridge changes (Table 20.1).
- *In relation to surgical treatment*. A second approach has been to describe the bone defect in relation to surgical treatment plan implications (Sabri 1999).
  - Tinti and Parma-Benfenati (2003) introduced a clinical classification of bone defects. They categorized “the envelope of bone” into five categories: extraction wounds, fenestrations, dehiscences, horizontal ridge deficiencies, and vertical ridge deficiencies. They also proposed treatment based on this classification.
  - Wang and Al-Shammari (2002) described the HVC classification, a modification of Seibert’s system. Horizontal (H), vertical (V), and combination (C) defects are subdivided into small (S), medium (M), and large (L) subcategories. Treatment options are described based on this classification system.
  - The ITI SAC (International Team for Implantology Straightforward, Advanced and Complex) (Chen et al. 2009) system of bone volume assessment provides clinicians with a simple classification of ridge deficiency incorporating both horizontal and vertical bone deficiencies. Bone volume is classified as: (1) sufficient, (2) deficient horizontally but allowing simultaneous augmentation, (3) deficient horizontally requiring prior or bone augmentation, and (4) deficient vertically and/or horizontally, requiring prior bone augmentation. This classification system is unique in that it also implements bone grafting as being done prior to the implant placement or allowing simultaneous

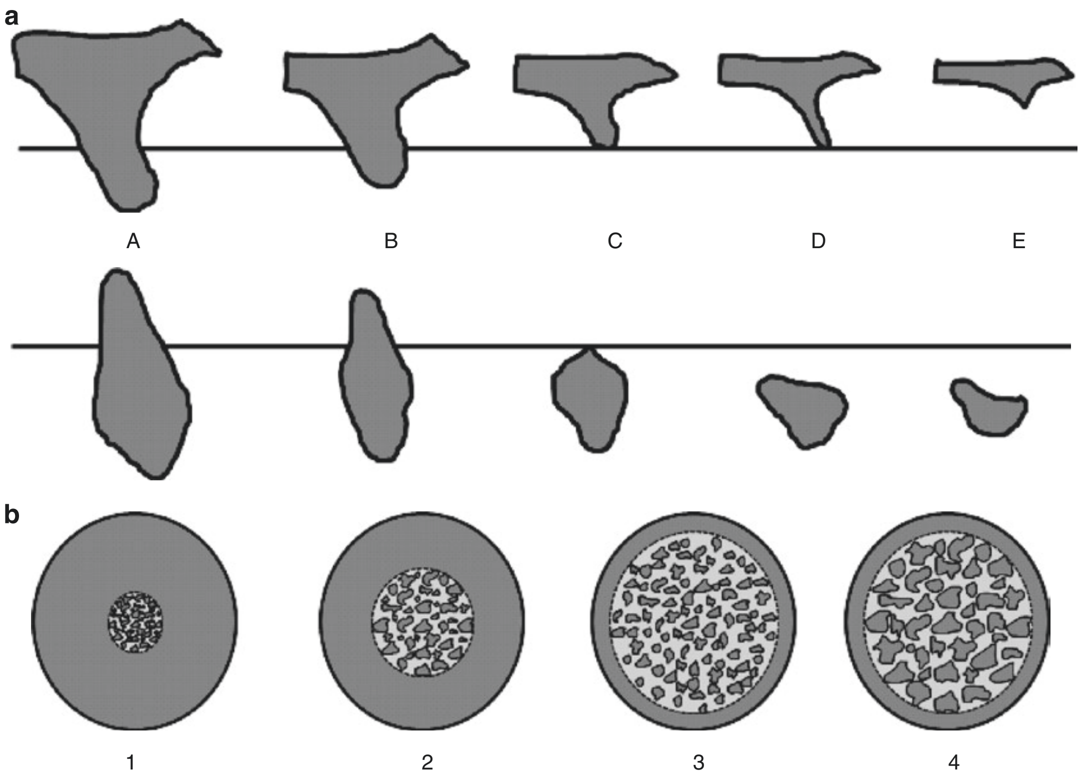

Fig. 20.13 Schematic diagram of the cross-sectional morphologic patterns of the edentulous maxilla and mandible (**a**) and bone quality (**b**) modified from Lekholm and Zarb (1985). The shape of the maxilla and mandible in cross section is scored alphabetically from A to E, based on the severity of the alveolar ridge resorption, with E being the worst. Bone quality (**b**) is scored from 1 to 4 with the least dense pattern, Type 4 (low density of the trabecular bone combined with a very thin cortical ridge). Implant failure is associated with bone quality Type 4 and bone quantity E

Table 20.1 Bone quantity classification (after Studer et al. (1997))

Class	Study type
I/B defect	A defect limited exclusively to the buccolingual direction with normal ridge height
II/A defect	A bone one loss running in the apico-coronal direction only
III/C defect	A defect that has a combination buccolingual and apico-coronal resorption of alveolar bone resulting in loss of ridge height and width

augmentation with the placement of the implant. This system is useful in that it provides an indication of the degree of anatomical reconstruction required to be replaced simultaneously or prior to implant placement.

- *In relation to optimal implant position*. A third approach has been proposed by Park et al. (2009) and specifically describes ridge therapy based on ideal implant restorative position as determined by implant simulation on cross-sectional images. They classified the morphology into five categories. The categories start with the implant completely surrounded by bone, and progress to describe dehiscence only and fenestration only and both dehiscence and fenestration. Subcategories describe the defect in the buccal or palatal direction or both.

Quantitative Assessment

Vertical bone height, horizontal width, and edentulous saddle length determine the amount of bone volume available for implant fixture placement. This information is necessary to correlate the available bone dimensions with the selection of the number and physical dimensions of the fixture. Moderate deficiencies in horizontal and vertical bone may be corrected by augmentation procedures at the time of the osteotomy and fixture placement whereas severe deficiencies will require prior surgical procedures, such as ridge augmentation. Similarly, excessive or irregular vertical alveolar bone may require pre-prosthetic or simultaneous alveoloplasty.

Quantitative analysis of the alveolar ridge using CBCT is facilitated by cursor driven measurement algorithms available with both proprietary and third party software programs providing sub-millimeter accuracy. These are applied to reformatted images, most often in three planes.

- *Axial plane*. This image provides information on implant position with respect to the shape of the available alveolar ridge in a horizontal plane.

  For completely edentulous jaws, assessment in this plane allows for consideration of the position of multiple implants according to provide symmetrical support of the prosthesis maximum posterior extension of the most distal implant to provide the maximum resistance to displacement of the prosthesis, a concept called *indirect retention*. The axial image can therefore be used to map the ideal position of the implant fixture with respect to stability and retention of the final prosthesis. Implant location will vary depending on the type of final prosthesis.
- *Implant supported.* The prosthesis is completely supported by implants and fixed to the implants and not to be removed by the patient. For this type of prosthesis, it is desirable to position the implants at least at the site of the previous first molar teeth.
- *Implant retained.* This refers to a removable prosthesis which obtains additional retention from a mechanical interlocking mechanism between the prosthesis and the implants individually or a suprastructure linking the fixtures. For this type of prosthesis implants should be positioned at the site of the canine or the first or second premolar to provide for optimal retention and support.

For partially dentate situations, the vertical position of the axial plane should be at the level of the alveolar crest. This enables a precise evaluation of the linear distance of the available alveolar ridge in a mesiodistal (anterior-posterior) dimension between adjacent tooth roots (interradicular dimensions). This view also provides a tool for implant placement in relation to the curvature of the dental arch form. Optimal implant placement should be in alignment with an imaginary line connecting adjacent teeth and coinciding with the alveolar arch form.

- *Curved Oblique Plane*. This MPR image provides clinicians with a familiar display simulating images obtained from panoramic radiography (Fig. 20.14). In bounded edentulous regions, angular and dimensional distortion is minimized if the panoramic spline is constructed with reference to adjacent teeth.

  For completely edentulous dental arches, this image allows for consideration of the elevation and shape of the ridge (Fig. 20.15). The vertical position of multiple implants should be such that the platform of the implant body is approximately in the same horizontal plane as adjacent implants. This provides optimum superior-inferior placement and facilitates consideration of necessary pre-prosthetic surgical modifications to the ridge. In addition, this view allows for the assessment of anterior-posterior tilt or parallelism between multiple implant fixtures or between adjacent teeth and a proposed implant. Parallelism is desirable because it facilitates loading along the long axis of the implant and a parallel path of insertion of the final prosthesis, otherwise prosthetic compromises may occur. These compromises include segmenting the restoration into multiple components, the use of custom abutments, telescopic copings or alteration from a fixed to a removable design involving fabrication of trans-implant bars. In addition, potential placement of implants can be assessed in regard to symmetry and support.

  For partially edentulous situations, this image allows for the placement of the fixture at

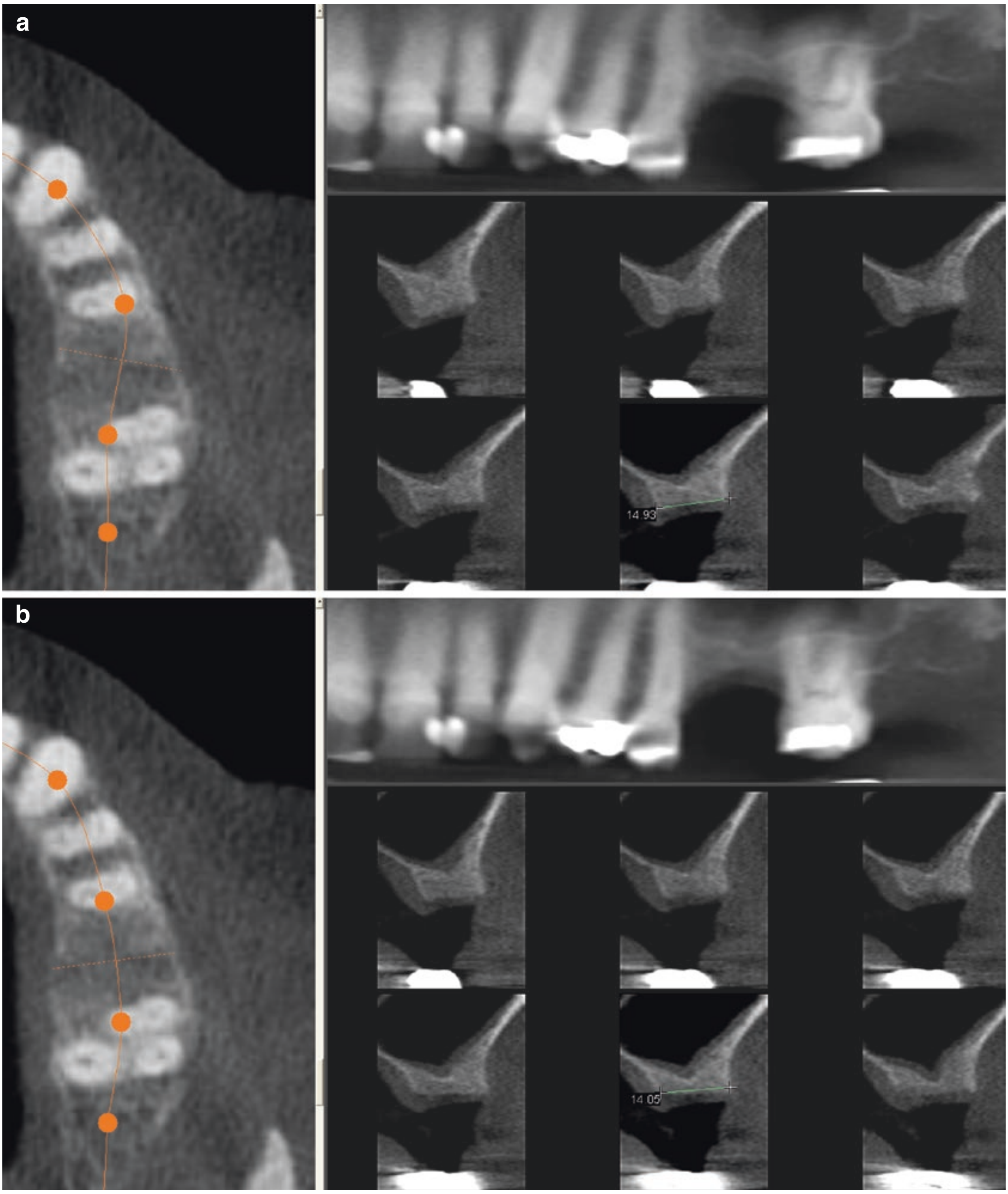

Fig. 20.14 Comparative sets of axial reference, reformatted panoramic and serial 1 mm thick cross-sectional images of the same left maxillary edentulous bounded space when the panoramic spline is constructed without (**a**) and with (**b**) reference to the position of the adjacent teeth. Substantial parallax error is evident in the shape and dimensions of the cross-sectional images when the spline is constructed without reference to the dentition (**b**)

an optimal distance (at least 1.5 mm) from the root surfaces of adjacent teeth and an adequate distance from anatomic landmarks either in the maxilla (e.g., nasal fossa, incisive canal, and maxillary sinus) or the mandible (e.g., mental foramen and inferior alveolar canal).

- *Cross-sectional* (*serial transaxial*) *plane.* Multiple, sequential, contiguous, thin slice

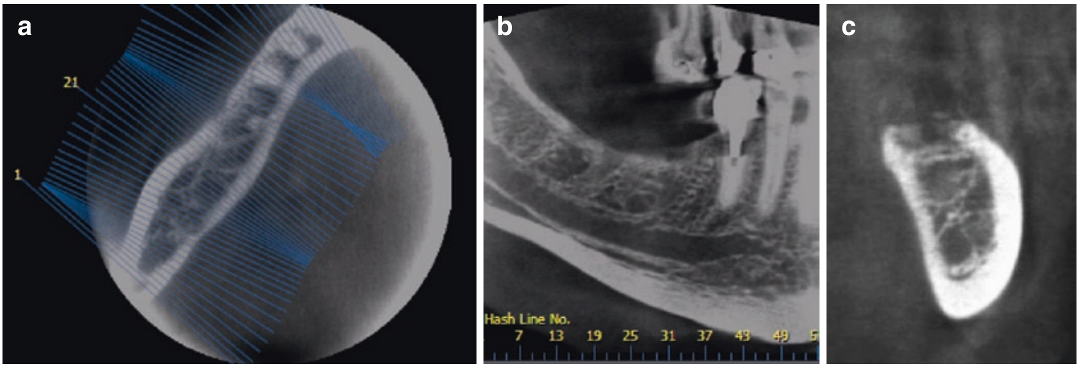

Fig. 20.15 Axial (**a**), reformatted panoramic generated from a curved oblique plane (**b**), and representative cross-sectional image (**c**) of the mandibular right posterior edentulous free-end saddle. The axial image for creation of the panoramic spline is level is typically selected at the level of the basal axial plane to obtain perpendicular cross-sectional slices

(1–2 mm) cross-section images provide the regional views necessary for the analysis of individual implant sites (Fig. 20.16). Proposed implant sites should be considered with respect to maximal available alveolar bone between the buccal and lingual cortical plates, the superior-inferior constraints of the alveolar crest and any local anatomic structure. In addition, this view can provide a visualization of the potential implant and prosthetic placement with respect to the buccolingual angulation and the necessity of pre-prosthetic preparation, especially important in the anterior maxillary esthetic zone (Leblebicioglu et al. 2007). In this region an implant should be surrounded with at least 1 mm of bone thickness on both the buccal and palatal aspects. The potential for bone loss decreases significantly and bone apposition is more likely to occur when a mean facial bone thickness of 1.8 mm or larger is present (Spray et al. 2000). Also an implant body should be aligned with adjacent teeth as well as with respect to the dentition in the opposing arch. The orientation of the implant body determines the long axis trajectory of the implant and is commonly referred to as the *emergence profile*. To assure optimal esthetic outcome, an implant body divergence from the long axis of the restoration should not exceed 25° (Sethi and Sochor 1995; Belser et al. 2004). In addition, a ridge deficiency at an implant site should be within 3 mm of its optimal contour to allow the clinician to modify the soft tissues suitably. In bounded edentulous spaces, placement of the implant platform should be no greater than 3–5 mm from the cementoenamel junction of the adjacent tooth (Hermann et al. 2001; Hartman and Cochran 2004).

These applications provide linear dimensions between anatomic features providing the physical boundaries within which the implant fixture can be positioned.

Minimal Prosthetic Requirements

Measurements with respect to the planned implant fixture site should be obtained in three dimensions and compared to the prosthetic parameters of optimal implant placement:

- *Vertical*. The primary image for determining vertical height is the cross-sectional image; however, it is advisable that this information be supplemented and confirmed with measurements from the curved oblique panoramic MPR image. Initially the maximum distance from the alveolar crest inferiorly or superiorly should be determined. In the maxilla, this distance would be along the long axis of the proposed implant fixture, from the crest to the maximum inferior extension of the nasal fossa or maxillary sinus (Fig. 20.17). In the mandible, posterior to the mental foramen, this

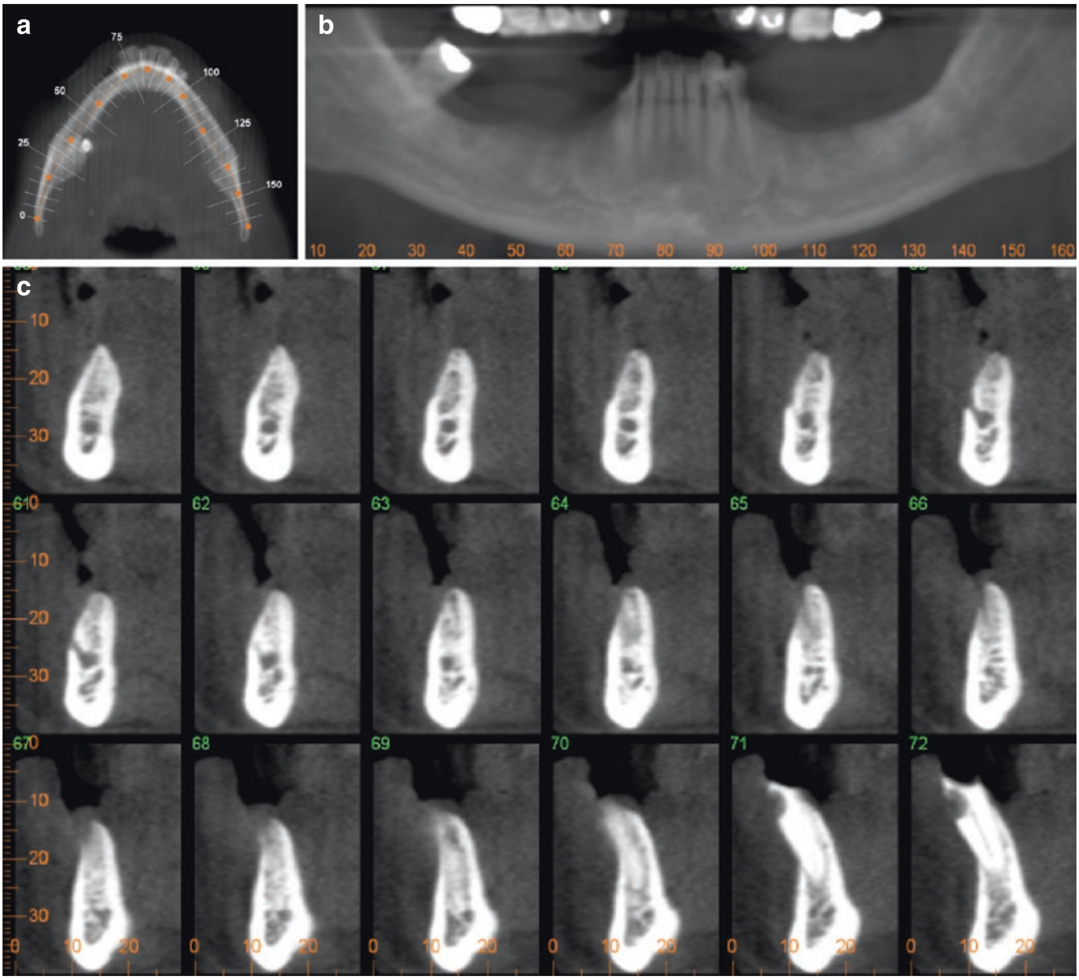

Fig. 20.16 Axial ray sum reference image (**a**), reformatted ray sum thick section panoramic reference (**b**), and multiple sequential contiguous thin slice (1 mm), perpendicular cross-sectional views of the left mandibular premolar region. Section location in the upper left side of each cross-sectional image (green number) designates the corresponding location on the axial and panoramic image

measurement would also be from the alveolar crest but would extend to the maximum superior extent of the corticated outline of the inferior alveolar canal (Fig. 20.18). In the area of the mental foramen, two measurements should be performed. The first is from the alveolar crest to the most inferior extent of the mental foramen as it ascends from the IAC. The second measurement is from the crest to the most superior buccal extent of the exit of the mental foramen (Fig. 20.19). Knowledge of both measurements provides a range of maximum and minimum distances within which there is a decreasing margin of error. Anterior to the mental foramen, measurement should be performed inferiorly in line with the angulation of the proposed implant fixture to the inferior border of the mandible. If the anterior loop of the IAC is identified, then an additional measurement from the crest to this structure should be made. If the marginal alveolar crest is not rounded or flat and presents with a "knife-edge" or tapering morphology, then an additional measurement should be made. In these circumstances, the measurement of the maximum available alveolar bone should be

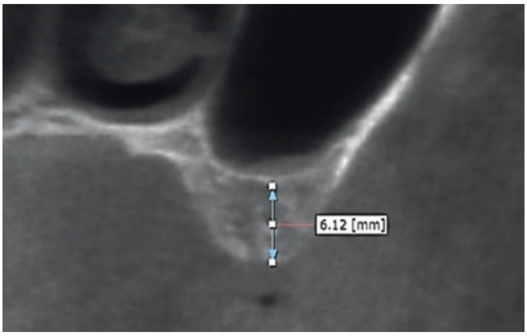

Fig. 20.17 Cross-section image of the left posterior quadrant of a completely edentulous maxilla showing the vertical distance (6.12 mm) from the alveolar crest to the maximum inferior extension of the maxillary sinus

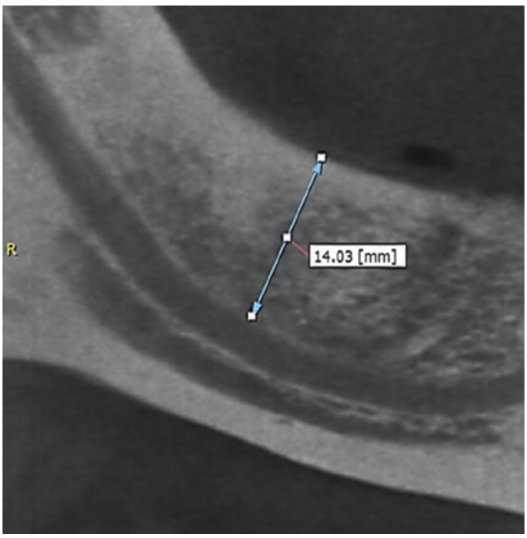

Fig. 20.18 Cropped medium thickness (10 mm) reformatted panoramic image of the right posterior quadrant of an edentulous mandible showing the vertical distance from the alveolar crest to the maximum superior extent of the corticated outline of the inferior alveolar canal

Fig. 20.19 Cross-sectional CBCT image of the left mental foramina in a completely edentulous mandible showing the distance from the alveolar crest to the most inferior extent of the mental foramen as it ascends from the IAC (*yellow arrow*) and to the most superior buccal extent of the exit of the mental foramen (*white arrow*)

reduced such that the crest of the marginal ridge provides the implant body with a width equivalent to the dimensions of the implant platform plus adequate alveolar bone on both the buccal and lingual/palatal surfaces. This is equal to implant platform width plus (2×) 1.5 mm or approximately 6–7 mm. These measurements can be used to determine the length of the implant fixture given the available bone dimensions and requirements for peripheral bone necessary for adequate anchorage and osseointegration. Maximum fixture length should always be considered to be approximately 1–2 mm shorter than the maximum measured vertical alveolar bone. This is because when the osteotomy for the fixture is made, the tapering of the cutting edge of the drill extends approximately 1–1.5 mm longer than the maximum length; therefore injury of anatomic structures can occur even if the final implant does not reach these structures (Fig. 20.20).

- *Mesiodistal*. The principal view for determining mesiodistal width is the reformatted curved oblique "panoramic" MPR image, usually supplemented with the axial view. For the majority of edentulous arches, the most important dimensions are the available

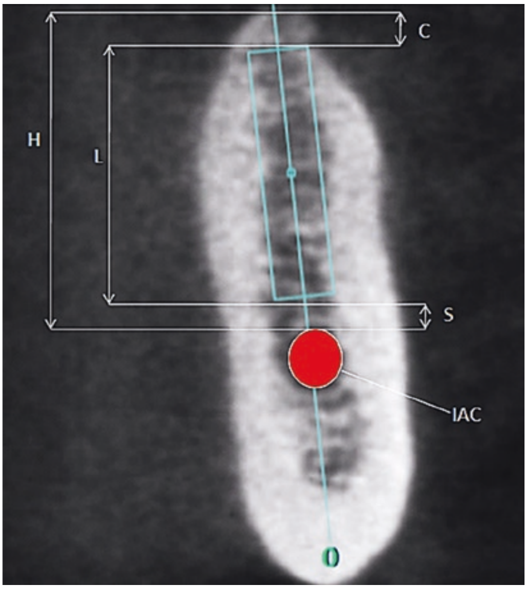

Fig. 20.20 Cross-sectional CBCT image posterior to the left mental foramina in a completely edentulous mandible showing the main dimensions necessary to assess residual alveolar ridge volume. The outline of a virtual cylindrical implant bone level avatar is superimposed over the image at the same magnification (*light blue*) with a corresponding long axis of the implant. IAC (*red circle*), a cross section of the inferior alveolar canal; H, total height of bone apparently available for implant placement above the IAC; C, crestal bone reduction necessary to place implant such that the implant platform is positioned at bone level; S, safety zone of bone (approximately 2 mm) between apical portion of the implant and the IAC necessary for surgical tolerance; L, actual implant length allowable at this site

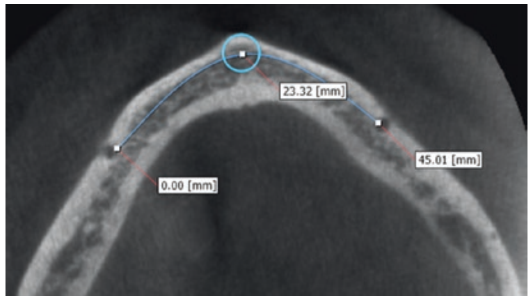

Fig. 20.21 Axial CBCT image at the level of the exit of the mental foraminae bilaterally showing the available inter-mental foraminae distance along the residual arch in a completely edentulous mandible. In this example, the inter-mental foramina distance is 45 mm. If implants of 4 mm diameter are anticipated, then the maximum number of implants in the anterior symphyseal region can be calculated ((inter-mental foraminae distance (45 mm) –2× (surgical tolerance anterior to the mental foramina (5 mm)/(implant diameter (4 mm) + safety zone of bone necessary for each implant (3 mm)) = 35/7 = 5 implants maximally)

inter-mental foraminae distance along the residual arch in the mandible and the intercanine eminence distance along the residual arch in the maxilla (Fig. 20.21). The latter is usually inferior to a line extended from the anterior border of the maxillary sinus as depicted in the curved oblique "panoramic" image. Assuming a minimum clearance of 3–4 mm between adjacent implants, and approximately 5 mm safe zone anterior to mental foraminae, then the maximum number of implants in these anterior symphyseal region can be calculated.

If implants are positioned between teeth or in consideration of existing teeth, then three measurements should be made. The first mesiodistal dimension is the distance between the greatest extent of the enamel of adjacent crowns. This dimension provides for an assessment of the available space for the final restoration(s). The second dimension is slightly below the cementoenamel junctions of adjacent teeth at the level of the alveolar crest. Considering a minimum of 1.5–2 mm of clearance is required between implant and adjacent tooth for proper osseointegration, decreased risk of damage to adjacent teeth and allowing for fabrication of contact points between crowns, knowledge of this distance helps in choosing the width of the implant, particularly in edentulous regions bounded by teeth. For example, if the mesiodistal distance at this level between adjacent teeth is 16 mm and the prosthetic plan requires for two crowns, then the maximum width of each implant would be 16/(2 + 4 + 2) = 4 mm. The final mesiodistal distance is measured between the middle of the roots of adjacent teeth, approximately 5 mm inferior to the alveolar crest. If the dimensions are less than that available at the level of the alveolar crest, then this indicates convergence of the roots of the adjacent teeth and reduction of the available

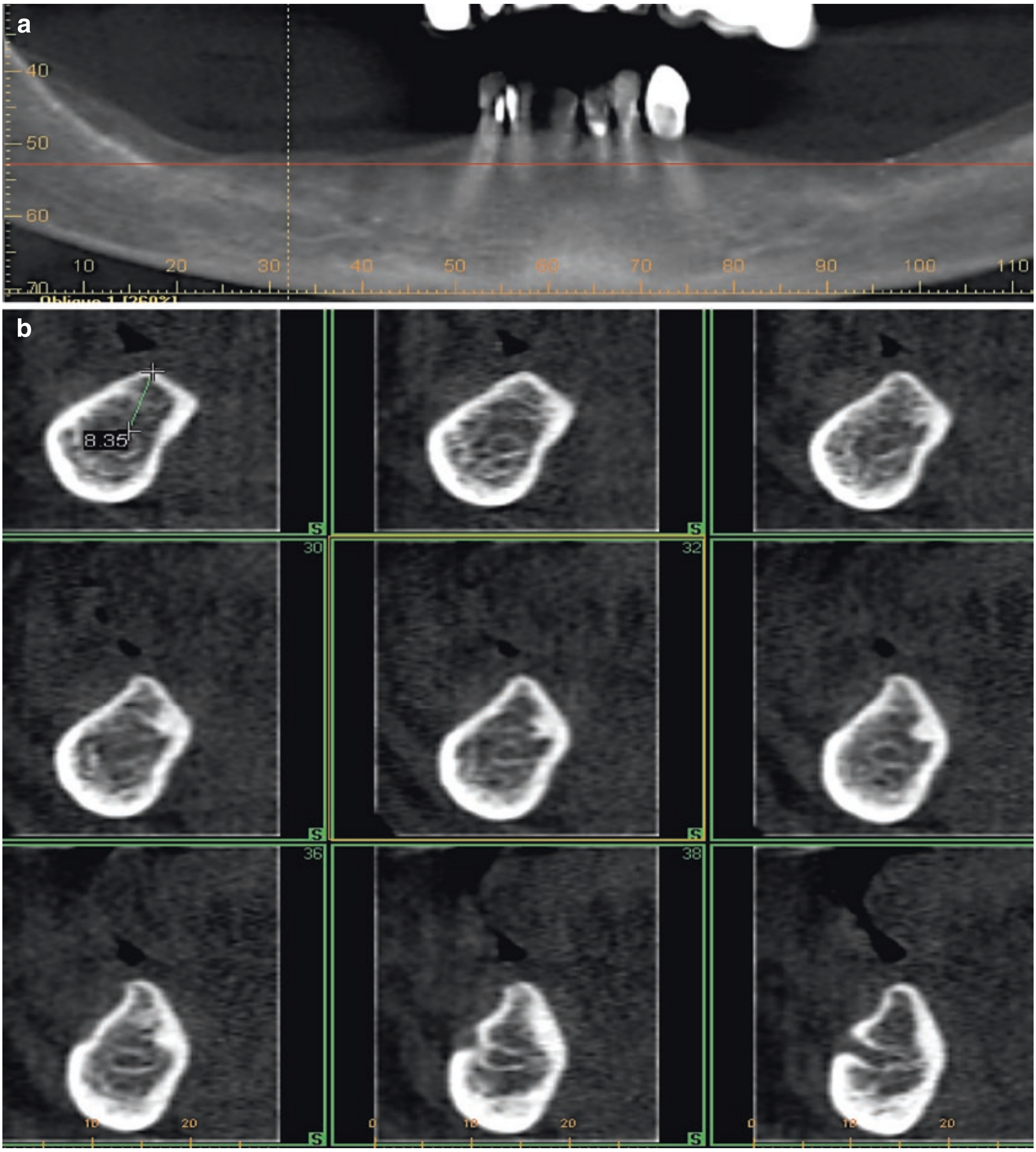

Fig. 20.22 Cross-sectional CBCT image of the left maxillary canine region showing the maximum buccolingual dimension of the alveolar ridge

interradicular alveolar bone. In this situation tapering implant should be considered.

- *Buccolingual*. The primary image for determining buccolingual depth is the cross-sectional view. Occasionally this may be supplemented with the axial image. At each proposed implant site, two dimensions should be measured.

The first measurement should be the maximum buccolingual dimension at the alveolar crest (Fig. 20.22). The minimal thickness of bone on both buccal and lingual aspects of a dental implant is 1 mm. Therefore, the minimal alveolar crest requirement is approximately 6 mm (2 mm + implant platform width). If this minimal requirement is not satisfied because of the shape of the alveolar crest, then a linear distance of 6 mm should be provided on the cross-sectional image as close to the crest as possible. Depending upon the vertical distance from this line showing the amount of available height, this provides a visual and quantitative indication of either the amount of bone that must be removed prior to fixture placement or alternately that must be augmented to the ridge.

A second buccolingual measurement should be performed at the narrowest portion of the cortical plates. This dimension is particularly important in regional areas where the anatomy creates depressions of either the buccal (e.g., lateral incisor region in the maxilla) or lingual (e.g., submandibular gland fossa in the mandible) cortical plate. The use of tapering implants may be considered in areas of marginal width.

From a prosthetic viewpoint, one of the most important measurements rarely performed is the buccolingual/palatal emergence profile. This is the angle between the long axis of the implant fixture and the long axis of the proposed prosthetic crown. It should be less than 25°. As the position of the prosthetic crown is determined by its relationship between adjacent teeth as well as its occlusion with the dentition in the opposing arch (Kim et al. 2005), these factors also determine the position of the platform of the implant fixture buccolingually. Once this is established, then the optimum buccolingual angulation of the implant fixture can be determined within the confines of the available alveolar bone and the emergence profile. These considerations are particularly important in the anterior maxillary area because of the high esthetic demands in this region.

Alveolar Bone Quality

Numerous authors have reported an increased implant failure rate associated with low density bone, particularly Type IV (Engquist et al. 1988; Jemt et al. 1992; Jaffin and Berman 1991; Triplett et al. 1991; Truhlar et al. 1997; Molly 2006; Farré-Pagés et al. 2011; Marquezan et al. 2012). Furthermore, in areas with local poor bone quality, apart from increased implant failure, marginal bone level tends to decrease (Merheb et al. 2015). Thus, bone quality assessment should be strongly recommended during presurgical implant planning. This can be realized using CBCT, as it is a widely available, and a noninvasive method to presurgically assess jaw bone quality. Yet, in practice, implant surgeons may have difficulty to determine the preoperative quality of cancellous bone that is able to offer proper implant bone support.

While a number of subjective rating scales have been proposed to provide a preoperative assessment of jawbone quality, they are not routinely applied in clinical practice. There is no single universally accepted and unbiased system for classifying jaw bone quality (Lekholm and Zarb 1985; Ribeiro-Rotta et al. 2010, 2011). Results from such scorings are highly variable and subjective, while correlation with bone density show a wide variation (Ribeiro-Rotta et al. 2010; Merheb et al. 2010). Most are grading scales based on the characterization of cross-sectional morphology with respect to the trabecular pattern (Lindh et al. 1996) and cortical bone thickness (Benson et al. 1991). The most traditional preoperative method for bone quality assessment is that of Lekholm and Zarb (1985) (Fig. 20.11). This system categorizes bone quality into four groups according to the degree of corticalization and the trabecular bone morphology based on the premise that osseointegrative potential and therefore bone quality is associated with thicker cortical density and smaller trabecular spaces. This assertion has been supported in that higher implant failure rates are reported in type IV bone, whereas type II and III bone have the lowest failure rate (Engquist et al. 1988; Jemt et al. 1992; Jaffin and Berman 1991; Bass and Triplett 1991). Difficulties in applying this scheme occur with intra-observer variation and distinction between type II and III bone.

Evaluation of regional trabecular density by analysis of Hounsfield units has been proposed. The availability of these measurement parameters have lent themselves to associations with the quality scale of Lekholm and Zarb (Lekholm and

Zarb 1985; Norton and Gamble 2001) (Table 20.2). The most favorable osseointegration is thought to occur only in certain types of bone (Misch 1990). Although there is no single universally accepted system for classifying bone quality in the maxilla and mandible, the Misch system (Misch 1990), based on the radiographic appearance of bone and correlated with HU values, has been widely used by clinicians.

The Misch system divides bone into four subdivisions (D-1 to D-4) based on measured bone density. D-1 and D-2 bones generally have dense cortical plates with coarse trabeculae and small bone marrow spaces, with D-1 (atrophic anterior mandible) being denser than D-2 (anterior maxilla, anterior and posterior mandible). D-3 (anterior and posterior maxilla) and D-4 (posterior maxilla) bones range from poorly mineralized or thin trabeculae to complete paucity of mineralized trabeculae (D-3 being denser than D-4).

A factor complicating the use of CBCT for clinical bone density assessment is the lack of standardized gray value distribution. Hounsfield units (HU) have been designed for medical CT, but do not apply for CBCT (Loubele et al. 2006, 2007). Compared to HU units for medical CT, the reliability of CBCT-based jaw bone density assessment was found unreliable over time and with significant variations influenced by device, imaging parameters and positioning (Nackaerts et al. 2011). However, density measurement variations recorded within the same jaw scan reflect local bone density variations with lower values for poor bone quality (e.g., tuberosity region).

While lack of HU standardization is a major deficiency for most CBCT devices, the presence of a healthy vascularized bone structure may be important. Therefore, bone structural analysis, as is available in microCT software, may become a more important CBCT imaging metric. Structural analysis has already been validated to be used

Table 20.2 Correlation between subjective classification (Lekholm and Zarb 1985) and quantitative CT-derived bone quality indices

		Correlations		
			CT Attenuation (HU)	
Category[a]	Description	Bone density[b]	Misch[c]	Norton and Gamble[d]
Quality I	Almost entire jaw is comprised of homogenous compact bone	76.54 ± 16.19%	> +1250 HU (D1)	> +850HU
Quality II	A thick layer of compact bone surrounds a core of dense trabecular bone	66.78 ± 15.82%	+850 to +1250 HU (D2)	+500 to +850HU
Quality III	A thin layer of cortical bone surrounds a core of dense trabecular bone	59.61 ± 19.55%	+350 to +850 HU (D3)	+500 to +850HU
Quality IV	A thin layer of cortical bone surrounds a core of low density trabecular bone	28.28 ± 12.02%	+150 to +350 HU (D4) < +150 HU (D5)	0HU to +500HU < 0HU (failure zone)

HU Hounsfield Unit
[a]Lekholm and Zarb (1985)
[b]Trisi and Rao (1999)
[c]Misch (1990)
[d]Norton and Gamble (2001)

with CBCT (Huang et al. 2014; Van Dessel et al. 2013) and has a clinical potential for presurgical assessment of bone quality.

20.3.2.2 Anatomic Structures

The placement of endosseous titanium implants in the maxillofacial region is limited by the presence of numerous anatomic structures in the maxilla and mandible.

Mandible

In the mandible, the most important structures associated with implant morbidity include the inferior alveolar canal (IAC) and submandibular fossa in the posterior region, the mental foramen in the premolar region, and interforaminal vascular and anatomic morphological anomalies in the symphyseal region.

Inferior Alveolar Canal (IAC)

The IAC or *mandibular canal* (MC) is the bony channel containing the inferior alveolar neurovascular bundle as it progresses anteriorly from its entrance at the mandibular foramen on the lingual cortical bone of the ramus. The inferior alveolar nerve continues within the IAC to the midsagittal region. In the parasymphyseal region, the IAC divides into two terminal branches; the *incisive* branch, which progresses anteriorly within the incisive canal (Jacobs et al. 2002) and the *mental* branch which exits though the buccal cortical bone through the *mental foramen* (Fig. 20.23). In the dentate mandible, the mental foramen is usually located between first and second premolar. While the IAC can be visualized in most cross-sectional images, the presence of cortication forming the wall of the canal is variable.

The intraosseous course of the inferior alveolar neurovascular bundle within the IAC is not always straightforward (Anderson et al. 1991), so the chance for surgical trauma may vary accordingly. The canal usually progresses inferoanteriorly as it progresses towards the mental foramen (Fig. 20.24); however, it may dive steeply or assume a parabolic shape, allowing more room for implants above the canal. Bifid mandibular

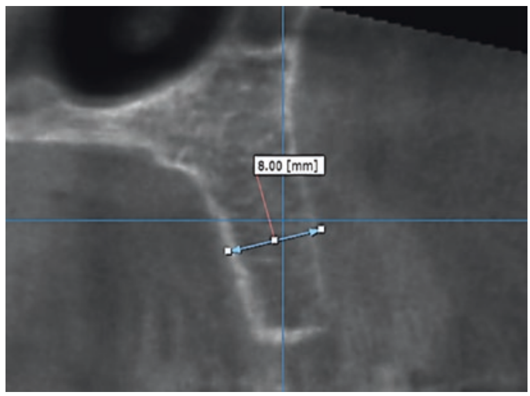

Fig. 20.23 Reformatted panoramic (**a**) CBCT image of a partially dentate mandible and serial 1 mm thick cross-sectional images (**b**) of the right parasymphyseal region showing the location of the corticated IAC and exit through the mental foramen

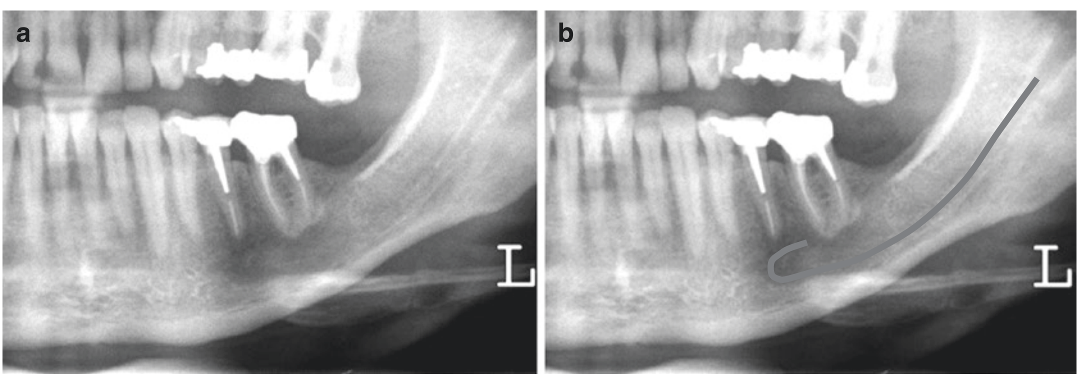

Fig. 20.24 Left cropped panoramic image without (**a**) and with (**b**) tracing (*gray line*) of the IAC. This demonstrates the anterior looping of the mental canal seen in approximately 10% of panoramic images, presenting potential risks for neurosurgical trauma (Jacobs et al. 2007)

canals, although rare (less than or equal to 1%) (Nortje et al. 1977; Rouas et al. 2007), present additional limitations for implant placement. The identification and localization of the mandibular canal is of importance in the planning of implant fixture placement in the posterior mandible (Jacobs and van Steenberghe 1997) as incorrect placement and overextension of the osteotomy site has the potential risk of significant inferior alveolar nerve injury and can compromise treatment outcome (Jacobs et al. 2002; Quirynen et al. 2003; Greenstein and Tarnow 2006).

When identification of the IAC on cross-sectional images is obscured, two methods can be used to assist in location.

- As the mandibular neurovascular bundle traverses anteriorly through the mandible, it progresses from the lingual to the buccal cortex. In the region of the second and particularly the third molar teeth it can create a concave defect or indentation of the internal margin of the lingual cortical plate, known as the *cortical niche sign* (Wyatt and Pharoah 1998), and is most commonly seen on cross-sectional images (Fig. 20.25). While it may not be present in all cases, it can be of assistance in the location of the IAC. The niche sign should be observed as a continuous defect on multiple cross-sectional images before the location of the IAC can be verified.
- The second method comprises identifying and cross-correlating features on multiple images (e.g., cross-sectional, curved oblique "panoramic") via use of the scale marker on the images to relate an anatomic structure seen on one view with its location on another view. This is referred to as *triangulation* (Wyatt and Pharoah 1998). The most common features are the absence of trabeculation, the apical extent of the roots of the adjacent teeth, and relative radiolucencies within trabecular bone.

Incisive Canal

The mandibular incisive canal is an extension of the mandibular canal in the region of the mental foramina containing the terminal branch of the inferior alveolar neurovascular bundle (Fig. 20.26). It can be identified in 93% of the conventional CT scans of the lower jaw and has a mean internal diameter of 1.1 mm ± 0.3 mm (range, 0.5 mm ± 2.3 mm) (Jacobs et al. 2002) (Fig. 20.27). The size of the canal may suggest the presence of a large well-defined incisive neurovascular bundle which should, if possible, be avoided to prevent possible postoperative sensory disturbances.

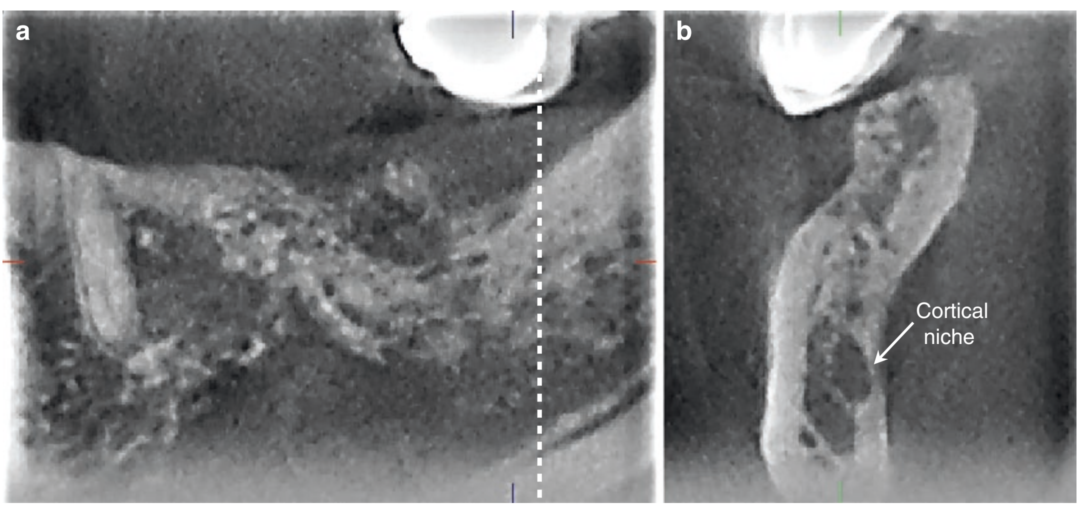

Fig. 20.25 Parasagittal image of the partially dentate left mandible (**a**) and corresponding cross-sectional image (**b**) showing a cortical niche sign

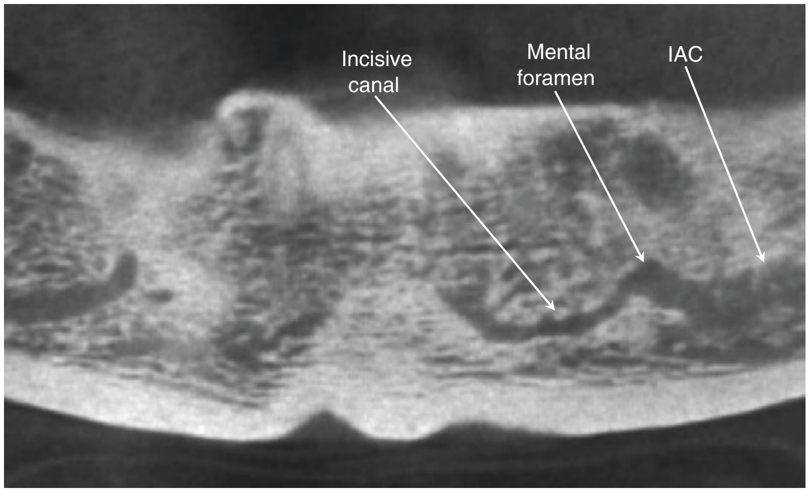

Fig. 20.26 Thin section panoramic CBCT image demonstrating the extension of the IAC anterior to the mental foramen as the incisive canal

Lingual Canal

The lingual canal is a bony channel on the lingual cortical aspect in the midline of the mandible, at the level of, or superior to, the mental spines (Fig. 20.28) and can be seen on CT imaging in over 80% of the mandibles (Jacobs et al. 1992). Radiologically it appears as a corticated radiolucency extending diagonally from the middle of the mandibular bone superior-lingually to exit at the lingual foramen. Recognition of this feature is important as the associated lingual artery could be of sufficient size induce an intraosseous or adjacent hemorrhage soft tissue during osteotomy (Darriba and Mendonca-Cardad 1997).

Accessory Canals and Foraminae

Occasionally accessory branches of the sublingual artery may anastomose with the incisive artery and penetrate the lingual cortical plate, creating accessory anterior lingual mandibular channels and foramina. The most common of these is the median lingual foramina (Fig. 20.28) with a secondary inferior midline foramen, below the genial tubercles occurring in up to 76% of individuals (Shiller and Wiswell 1954). Lateral lingual foramina are located posterior to the anterior midline and include the interalveolar medial foramen (between the central and lateral incisors), the interalveolar lateral foramen (located between the lateral incisors and canines), as well foramina further posteriorly (Fig. 20.29).

Mental Foramen and Anterior Loop

The mental foramen is the exit for the mental branch of the inferior alveolar nerve. It is normally a single structure, but double or even multiple foramina have been reported (Serman 1987; Toh et al. 1992) (Fig. 20.30). It may be oval or round and is located on the buccal parasymphyseal cortex. Typically, the foramen is located halfway between the alveolar crest and the lower border of the mandible, between the first and second premolars. However, it may be found as far anterior as the canine or as far posterior as the first and even second molar teeth. The mental nerve may extend more anteriorly within the mandibular bone as it ascends, a feature called *the anterior loop* (Fig. 20.31). Postsurgical complications such as neurosensory damage, disturbed sensory feeling, or pain (Bavitz et al. 1993) may occur if this anatomic is not identified and iatrogenic injury occurs (Arzouman et al. 1993). The average diameter (Uchida et al. 2007) and length of the anterior loop of the mental nerve ranges from 3 to 7 mm (Arzouman et al. 1993; Misch and Crawford 1990; Tatum and Lebowitz 1991; Rosenquist 1996). A 2 mm anterior safety zone between an implant body and the most coronal aspect of the nerve has been recommended to avoid nerve injury during surgery (Greenstein and Tarnow 2006).

The anterior region of the mandible has always been considered to be a relative “safe zone” for the use of oral implants. However, implant place-

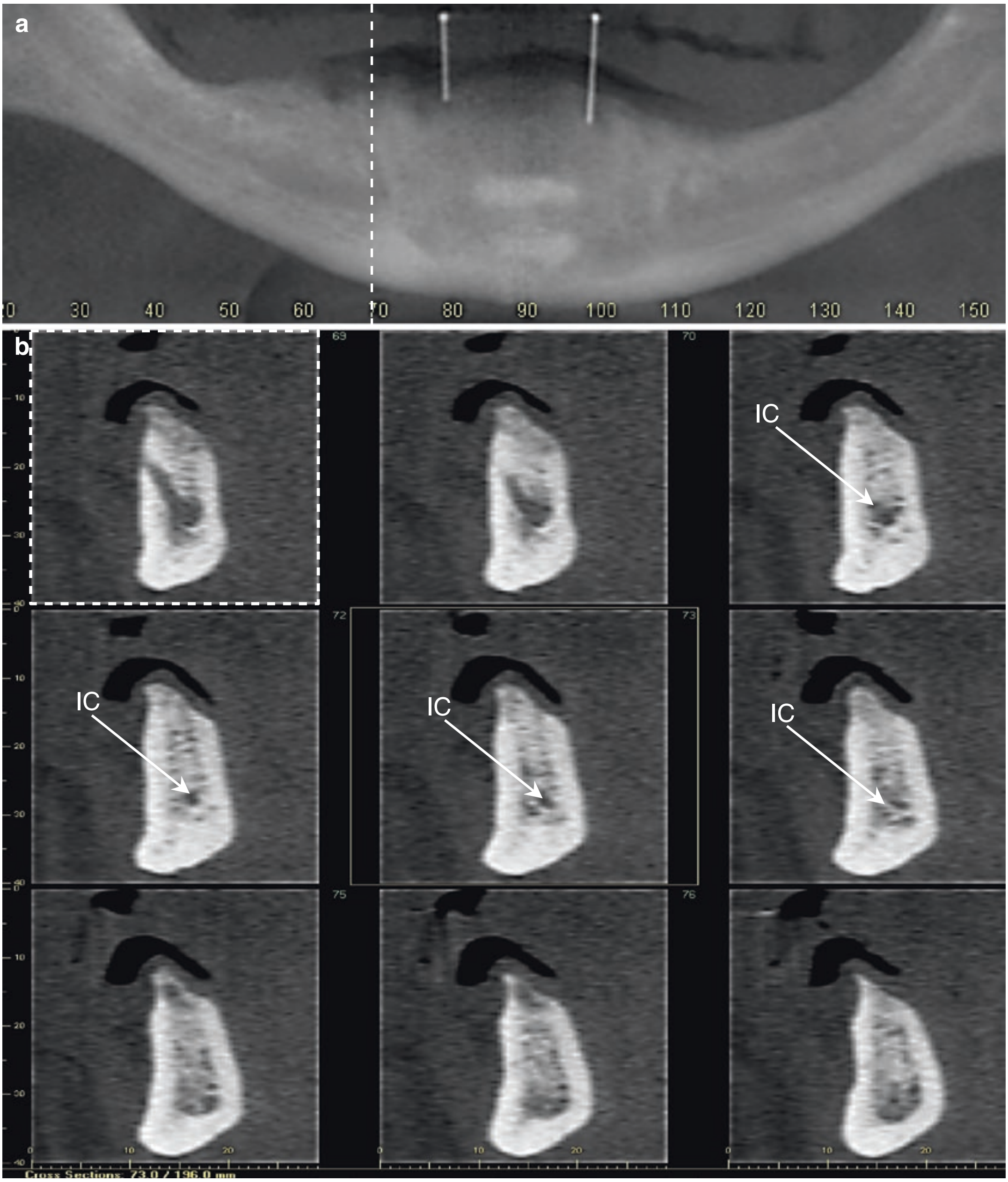

Fig. 20.27 Reformatted panoramic CBCT image (**a**) and serial 1 mm thick cross-sectional CBCT images of the right parasymphyseal region progressing anteriorly from the mental foramen (*dashed line*). The mandibular incisive canal (IC) is clearly visible 4–5 mm anterior to the mental foramen

ment in this region is associated with a high incidence (31–35%) of postoperative neurosensory disturbances (Abarca et al. 2006; Ellies 1992; Ellies and Hawker 1993). Severe surgical complications such as neurological deficits due to penetration of the lingual incisive canal (Ellies and Hawker 1993; Wismeijer et al. 1997; Dao and Mellor 1998; Walton 2000), severe hemorrhage into the floor of the mouth potentially resulting in life-threatening obstruction of the

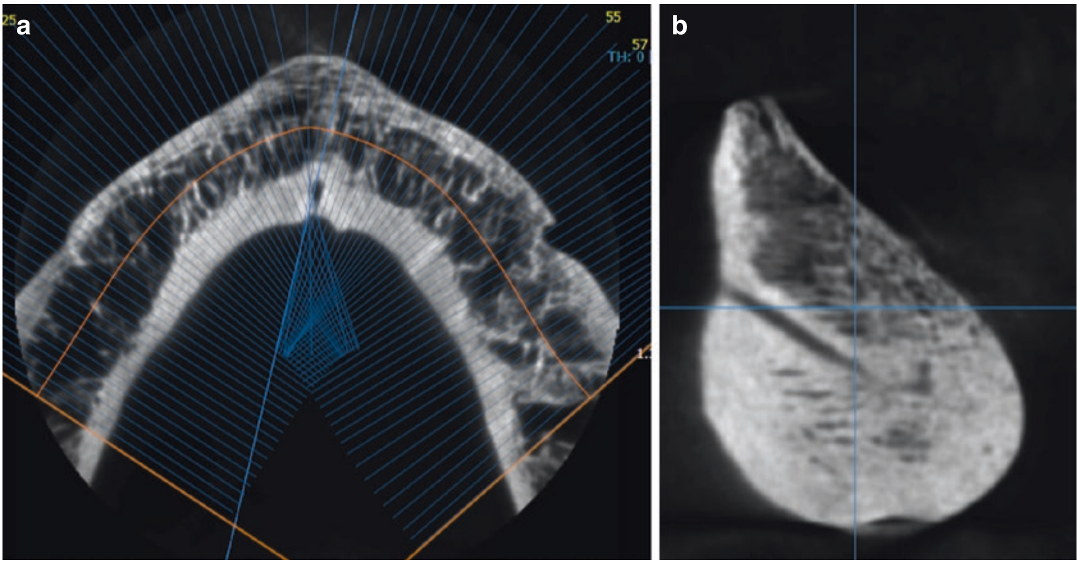

Fig. 20.28 Axial (**a**) and midsagittal cross-section (**b**) CBCT image of a completely edentulous mandible showing a single midline lingual canal exiting through the lingual cortical plate as the lingual foramen

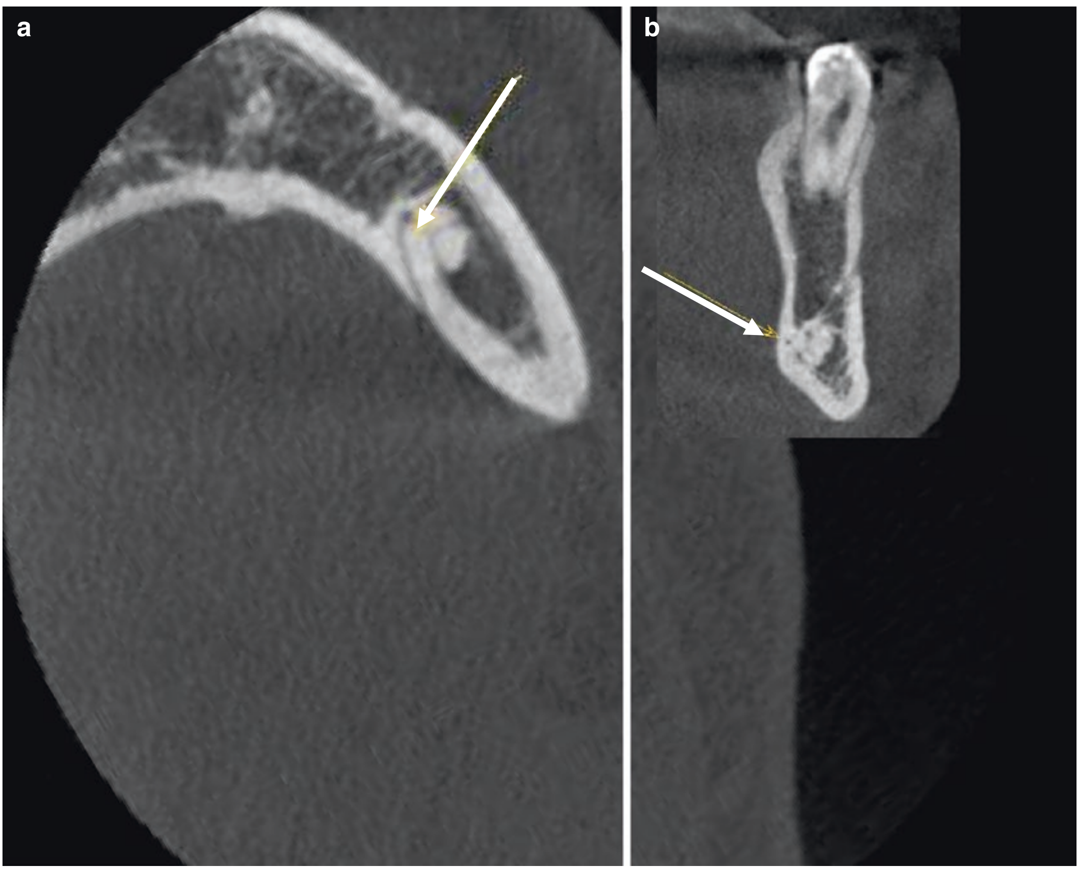

Fig. 20.29 Axial (**a**) and cross-section (**b**) CBCT image of an accessory lateral lingual canal and foraminae through the lingual cortical bone as far posteriorly as the left premolar region

Fig. 20.30 Volumetric rendering of the left partially dentate mandible demonstrating the presence of a double mental foramen and an accessory canal more superiorly

upper respiratory tract (ten Bruggenkate et al. 1993; Tepper et al. 2001) after perforation of the lingual cortex, and even fracture of the jaw bone after implant insertion into extremely resorbed mandibles (Carls et al. 1996; Kan et al. 1997) have been associated with implant placement in the anterior mandibular area. Three morphological categories have been described, each associated with varying risk of implant perforation (Quirynen et al. 2003).

- *Type I (2%)*. A lingual concavity. Associated with a potential for increased risk of lingual perforation during implant placement, particularly with selection of wider implants (Fig. 20.32).
- *Type II (28%)*. With a nearly constant width but a clear lingual slope. Risks of perforation are more closely related to the degree of tilting/inclination of the bone (linguoversion). The lower the slope (thus the lower angle), the higher the risk of a lingual perforation.
- *Type III (70%)*. Bone widening in the caudal direction.

Maxilla

In contrast to the mandibular posterior region, all of the available bone height in the maxilla can be used for implant placement. In fact, anchoring the terminal end of the implant body into the cortical bone of either the maxillary sinus or nasal fossa may enhance primary implant stability. In the maxilla structures such as the nasopalatine canal, nasal fossa or maxillary sinus may impede and influence implant success; however, violation of these structures does not usually result in serious sequelae. Assessment of the posterior maxilla not only involves an assessment of the amount of bone available from the marginal crest to the most inferior extent of the nasal fossa or maxillary sinus, but also an evaluation of potential implant placement sites such as the maxillofacial buttresses and the presurgical access and postsurgical success of sinus augmentation procedures.

Nasopalatine Foramen and Canal

The *nasopalatine* or *incisive* canal (NPC) is a corticated structure that originates as the *nasopalatine* or *incisive* foramen on the palatal aspect of the maxillary alveolus in the midline, immediately posterior to the central incisor teeth and adjacent to the alveolar crest, and ascends superoposteriorly to enter the nasal fossa (Fig. 20.33). Two terminal lateral canals are usually visible (incisive canals) at the nasal floor level, exiting as the *foraminae of Stenson* (Fig. 20.34). Occasionally two additional minor foraminae are present, *the foraminae of Scarpa*. These canals contain the nasopalatine nerve and the terminal branch of the nasopalatine artery.

The NPC may show important anatomical variations, both with regard to morphology and dimensions. The NPC morphology may present as three shapes: "Y" (67%), canal with four (4) foraminae (9%), and a cylinder (24%) (Mraiwa et al. 2004) (Fig. 20.33). The mean length of the canal is 8.1 mm ± 3.4 mm with a mean internal incisive foramen width of 4.6 mm ± 1.8 mm. If the diameter of the nasopalatine foramen exceeds 10 mm, pathological conditions should be suspected (Swanson et al. 1991). The incidence of

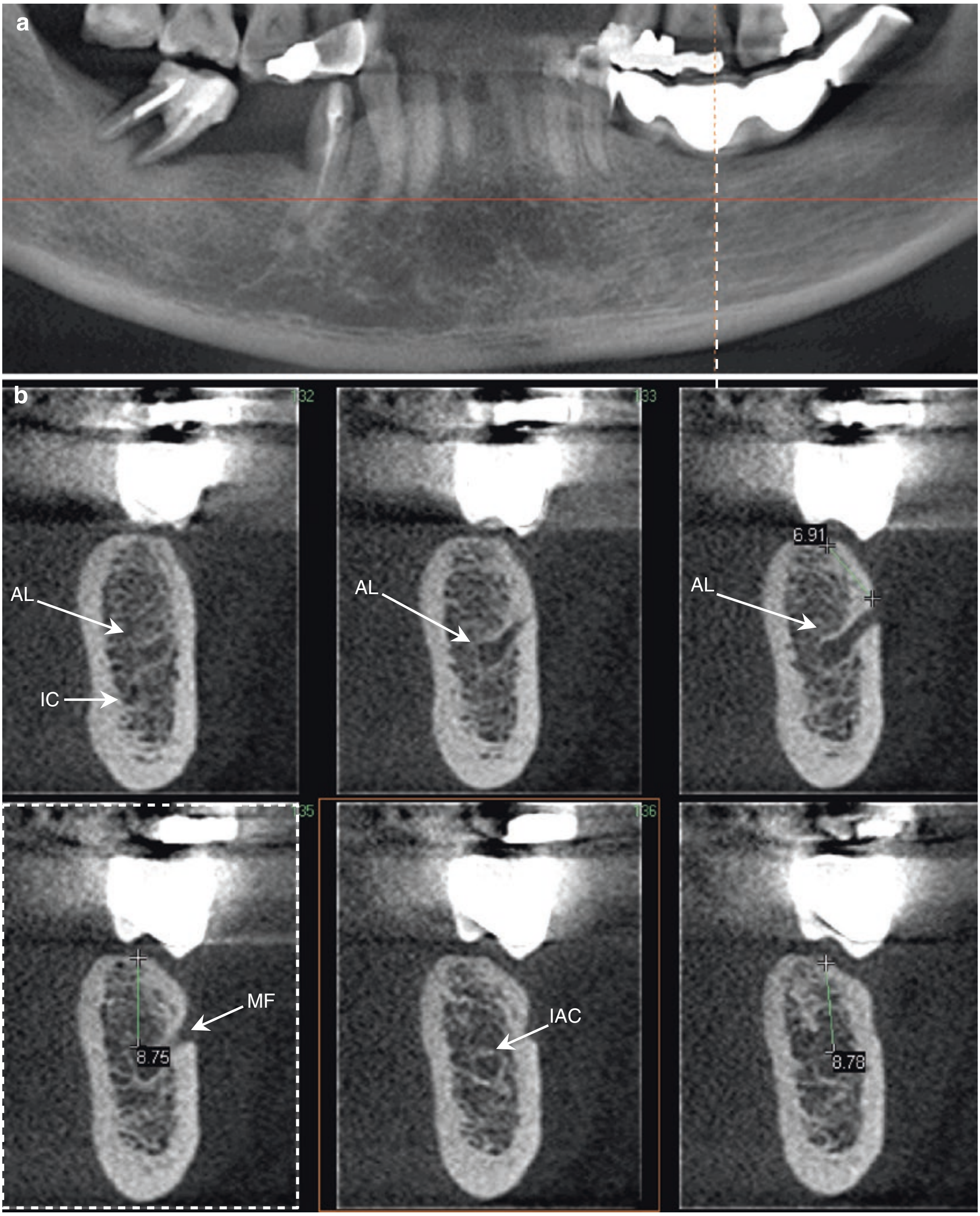

Fig. 20.31 Reformatted panoramic CBCT image (**a**) and serial 1 mm thick cross-sectional CBCT images (**b**) of the left parasymphyseal region progressing anteriorly from the mental foramen (MF) (*dashed line*). The anterior loop of the mental branch (AL) extends 3 mm anterior to the MF. The anterior incisive branch continues anteriorly through the mandibular incisive canal (IC)

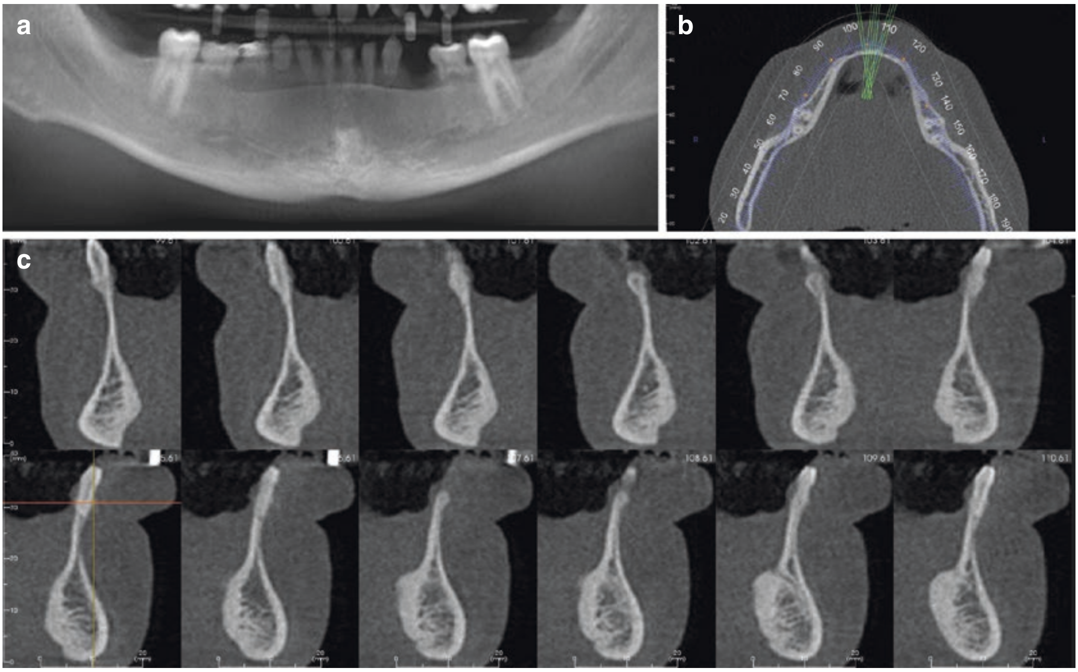

Fig. 20.32 Reformatted panoramic (**a**), axial (**b**), and multiple cross-sectional images of the anterior mandible of a patient with ectodermal dysplasia showing Type I jaw bone (lingual concave morphology)

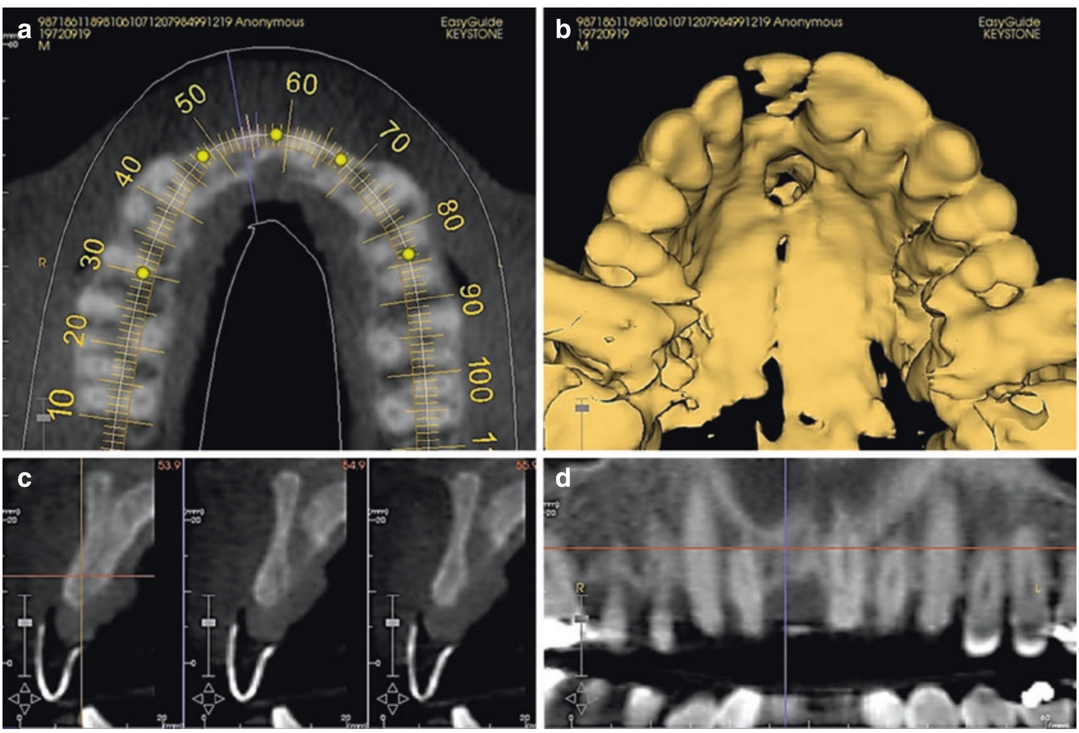

Fig. 20.33 Axial (**a**), inferior projection of volumetric shaded surface rendering (**b**), serial cross-sectional 1 mm thick images of the right central incisor region (**c**) and reformatted thin slice panoramic (**d**) of a maxillary right anterior bounded edentulous space. The size and location of the nasopalatine canal markedly reduces the available alveolar bone width for implant placement in this region

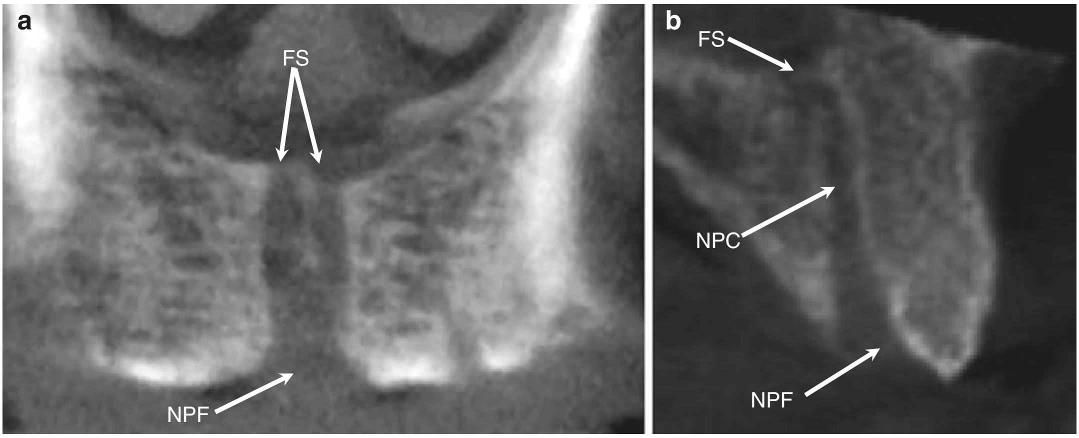

Fig. 20.34 Coronal thin section (**a**) and midline cross-sectional (**b**) CBCT image through the nasopalatine canal (NPC) of an edentulous anterior maxilla demonstrating the typical Y-form including the Foraminae of Stenson (FS) and nasopalatine fossa (NPF)

nasopalatine duct cysts is about 1% and should be recognized and treated prior to implant surgery (Swanson et al. 1991). Insertion of implants in the immediate vicinity of the nasopalatine canal has been associated with higher failure rates (Scher 1994) and may prevent placement in up to 4% of cases (Kraut and Boyden 1998). Contact of the implant surface with the contents of the canal (fat) may prevent osseointegration or lead to sensory dysfunction. In such cases, Artzi et al. (2000) propose a surgical technique in which implant placement in the central incisor region is achieved by adjusting a bone graft to fit the foramen while pushing back the soft tissue content.

Nasal Fossa and Maxillary Sinus

A partially or completely edentulous and atrophic upper jaw, especially with pneumatization of the maxillary sinuses and the presence of the nasal fossae, may present limitations for implant placement. While implant placement often involves engagement of the cortical boundaries of these structures, frank penetration potentially reduces initial implant stability and limits osseointegrative potential. In addition, both areas are potentially septic and may contribute to peri-implantitis and implant failure. Rehabilitation solutions include ridge and sinus augmentation or the use of shorter and wider diameter (*wide body*) implants. Before these procedures, imaging should consist of an assessment of three natural areas of thickened bone.

- The *fronto-maxillary* or *canine buttress* originates in the alveolus of the upper canine, following along the lateral margin of the piriform aperture, forming the frontal process of the upper jaw and merging with the medial margin of the supraorbital arch. This region normally presents a compact cortical layer and dense medullary bone—thus allowing the placement of long implants with para-sinusal angulation (Tulasne 1989). Implants may be inserted in this region with a distal angulation, after the use of osteodilators to prepare the osteotomy site. Alternately distally tilted implants can be used (Krekmanov et al. 2000). This idea, when used with immediate loading, has been developed as the "All-on-4" concept (Nobel Biocare, Kloten, Switzerland) (Fig. 20.35) (Malo et al. 2003).
- The *frontozygomatic buttress* is located in the region of the upper first molar, forming the so-called zygomatico-alveolar crest, which continues laterally along a concave trajectory to the zygomatic process of the maxillary bone and, posteriorly, to the zygomatic bone. Two surgical approaches utilize this naturally occurring area of thickened bone. In the first,

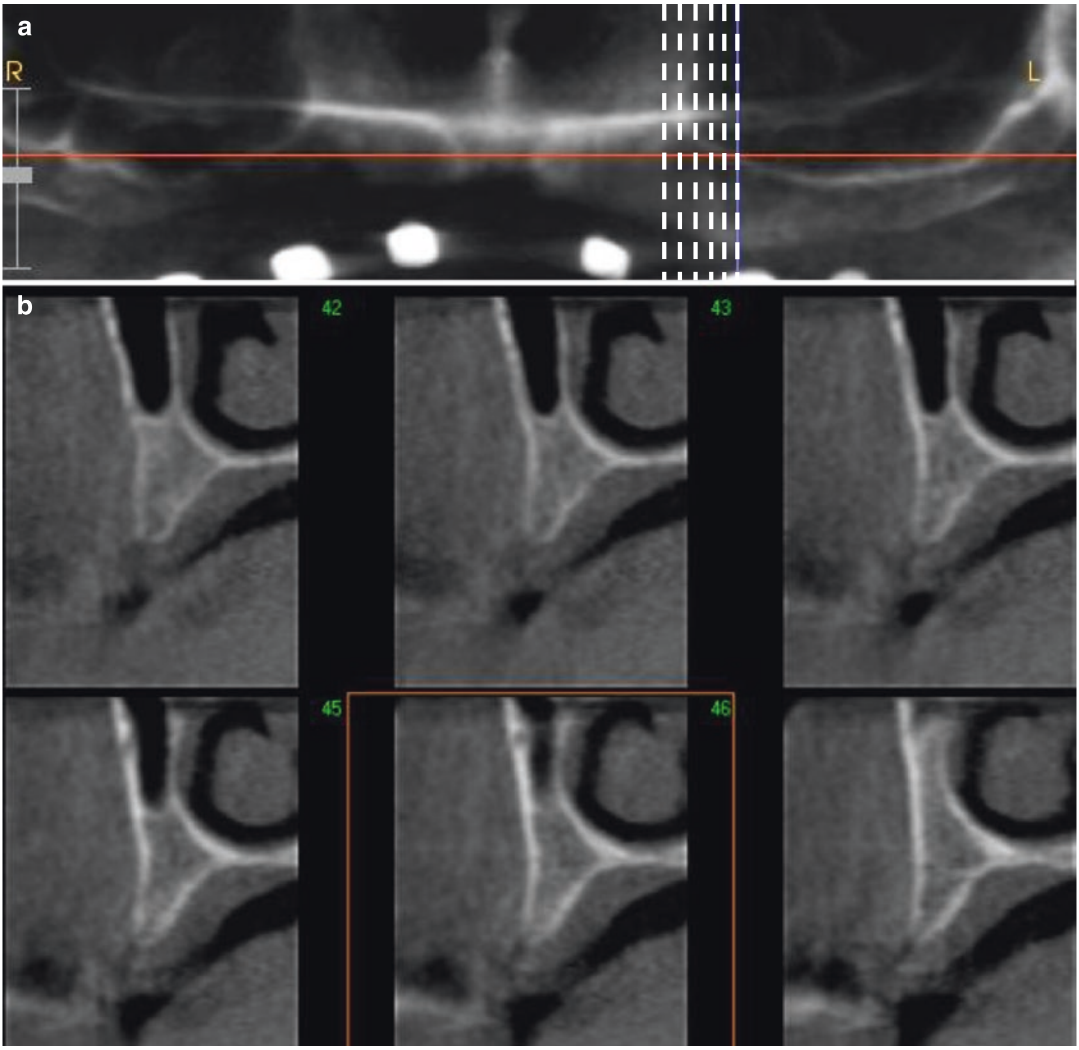

Fig. 20.35 Reformatted panoramic (**a**) and serial 1 mm thick/1 mm interval cross-sectional (**b**) CBCT images of a moderately atrophic completely edentulous maxilla showing the increased thickness and width of alveolar bone available in the residual alveolar ridge in the left fronto-maxillary buttress region

an angled implant is placed in the region of the first molar engaging the palatal vault. In the second, trans zygomatic (aka *zygomaticus* or *zygoma)* implants 35–55 mm in length are inserted in the palatal region of the second premolar and anchored in the zygomatic bone via an intrasinusal trajectory (Fig. 20.36) (Stella and Warner 2000; Balshi et al. 2006; Kahnberg et al. 2007). Currently this procedure is always performed bilaterally and in conjunction with at least two implants in the anterior region, splinted by the prosthetic superstructure. Because of the length of the implants, curved anatomy of the maxillary sinus and the variability and relatively small size of the zygoma, accurate implant trajectory is mandatory as even minute angular deviations lead to significant discrepancies at the extremity. While positioning may be facilitated by prosthetic and/or surgical guides manufactured on plaster models, CBCT-based techniques potentially provide greater accuracy. These include surgical navigation or the fabrication of custom surgical

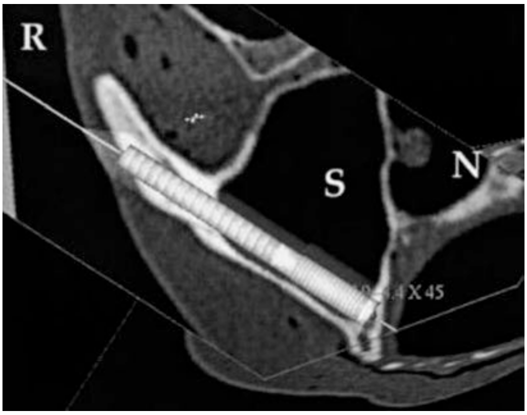

Fig. 20.36 Right corrected cross-sectional image of the frontozygomatic buttress and zygomatico-alveolar crest of a completely edentulous maxilla superimposed with a virtual zygomaticus implant. (*N* nasal cavity, *S* maxillary sinus) (with permission from van Steenberghe et al. 2003, Wiley-Blackwell publishing)

drilling guides based on implant planning software (see later).

- The posterior *pterygomaxillary buttress* comprises three structures: the tuberosity, the pyramidal process of the palatal bone, and the pterygoid process of the sphenoid bone. While the tuberosity is usually composed of scantly dense medullary bone with a very thin cortical layer, both the pyramidal process of both the palatal and sphenoid bone, located in the posterior and medial zone of the tuberosity, are composed of cortical bone and may provide sufficient bone for implant placement. Placement of an implant in this region requires an implant of between 15 and 20 mm in length directed posterior, superior and medial to anchor in the pterygoid process or even traverse the latter—avoiding the posterior portion of the sinus and major palatal duct (Tulasne 1989).

Specific Considerations for Maxillary Sinus Augmentation

A common method for creating bone in the maxilla is the *sinus lift technique*. Boyne and James (1980) first described this technique as a combination of a lateral window osteotomy followed by elevation of the floor of the maxillary sinus and insertion of a bone like graft material. Variations of this technique include the osteotome sinus floor elevation (Summers 1994), crestal core elevation (Toffler 2001), and the localized management of the sinus floor (Bruschi et al. 1998).

The site for the access osteotomy should be approximately 3–4 mm above the apical base of the maxillary sinus through the buccal plate. This ensures optimal access for proper elevation of the *Schneiderian membrane* from the medial wall of the sinus. Adequate buccal cortical plate should be available to allow dissection of the inferior aspect of the membrane from the floor of the maxillary sinus and to elevate it upward to create a space in the floor of the sinus for the bone graft material. Cross-section CBCT imaging provides location-specific measurements to optimize this access. Ideally the sinus should be disease free or have minimal mucosal thickening (<3 mm), which would potentially compromise vascularity and healing. The ostia should be patent (Fig. 20.37). Arterial vessels in the lateral antral wall (*posterior superior alveolar*) should be identified so that they are avoided during surgery (Mardinger et al. 2007) (Fig. 20.38). In addition, any condition that could lead to obstruction of the ostium and therefore drainage of the maxillary sinus may be a possible contraindication to the procedure. This includes localized mucosal thickening of the ostium and concha bullosa (pneumatized inferior turbinate). While mucosal thickening of the inferior medial or lateral wall of the maxillary sinus associated with chronic sinusitis is not a contraindication to the procedure, careful consideration should be given to situations in which elevation of a thickened mucosa may lead to a mechanical obstruction of the ostium (Figs. 20.39 and 20.40).

Because of the variability of the maxillary sinus volume, software measurements on CBCT panoramic and cross-sectional imaging can provide potential volume estimates of the graft material to be used. This guards against the possibility of overfilling the maxillary sinus and occluding the ostium. Third party software is available that provides excellent tools to assist in planning for the volume of bone graft material necessary for a specific sinus (Fig. 20.41).

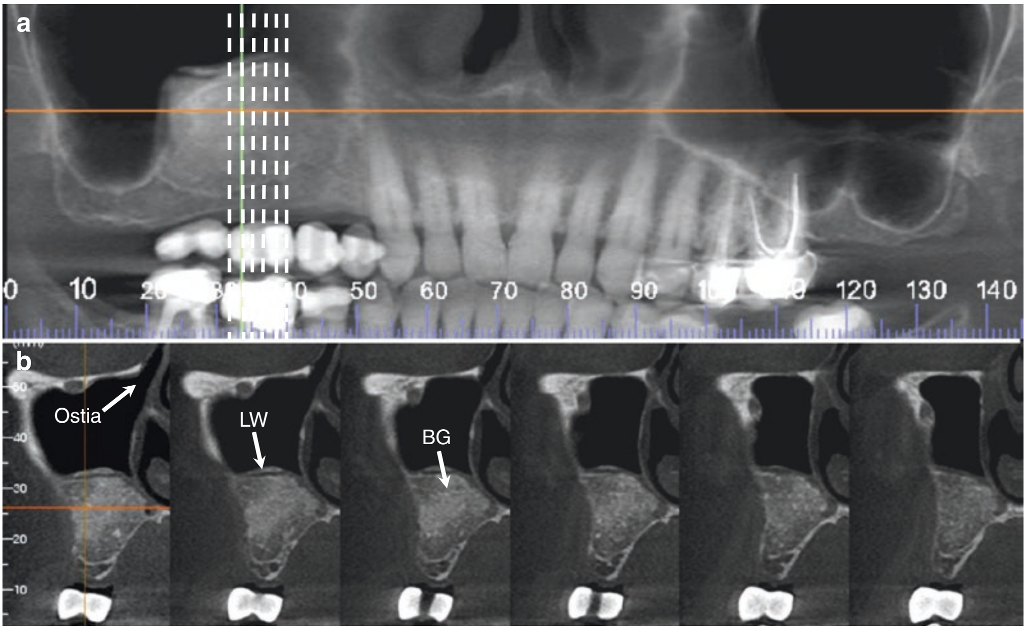

Fig. 20.37 Coronal cross-sectional CBCT image showing patent ostia bilaterally with no mucosal thickening

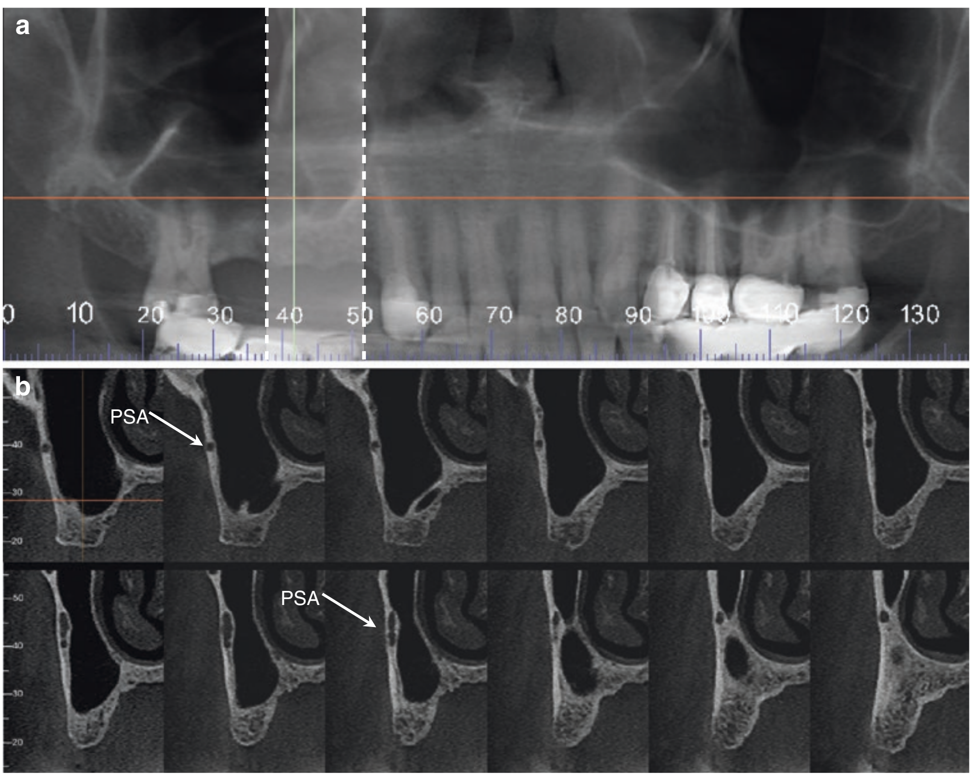

Fig. 20.38 Reformatted panoramic (**a**) and serial 1 mm thick/1 mm interval cross-sectional (**b**) CBCT images of a maxillary right moderately atrophic bounded residual alveolar ridge where a sinus lift is planned showing the a large posterior superior alveolar (PSA) canal embedded in the lateral wall of the sinus

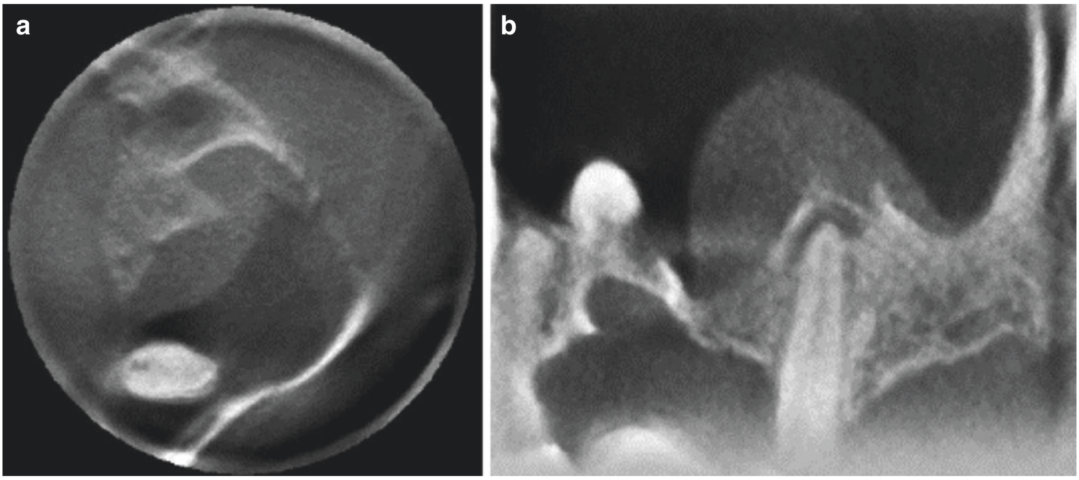

Fig. 20.39 Axial (**a**) and parasagittal (**b**) CBCT images of the left partially edentulous maxilla showing a local endo-sinus condition with severe swelling of the mucosa at the level of the apically involved premolar. Note that there is an intra-sinus osteoma anteriorly arising from the floor of the maxillary sinus

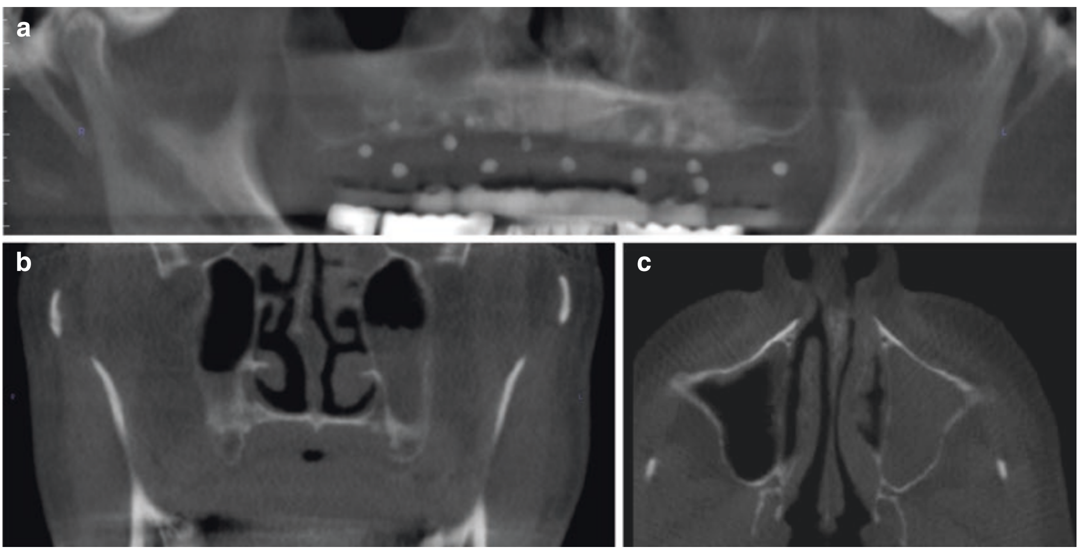

Fig. 20.40 Reformatted panoramic (**a**), coronal (**b**), and axial (**c**) CBCT images of a completely edentulous maxilla with a radiographic template inserted during the scan (notice the multiple radiopaque markers). There is soft tissue opacification occupying approximately 2/3rds of the left maxillary sinus with an irregular surface consistent with chronic sinusitis. This patient was scheduled for bilateral sinus augmentation procedure; however, as addition of bone graft material would most probably elevate the soft tissue material to occlude the left ostia, the procedure was delayed until after resolution of the condition

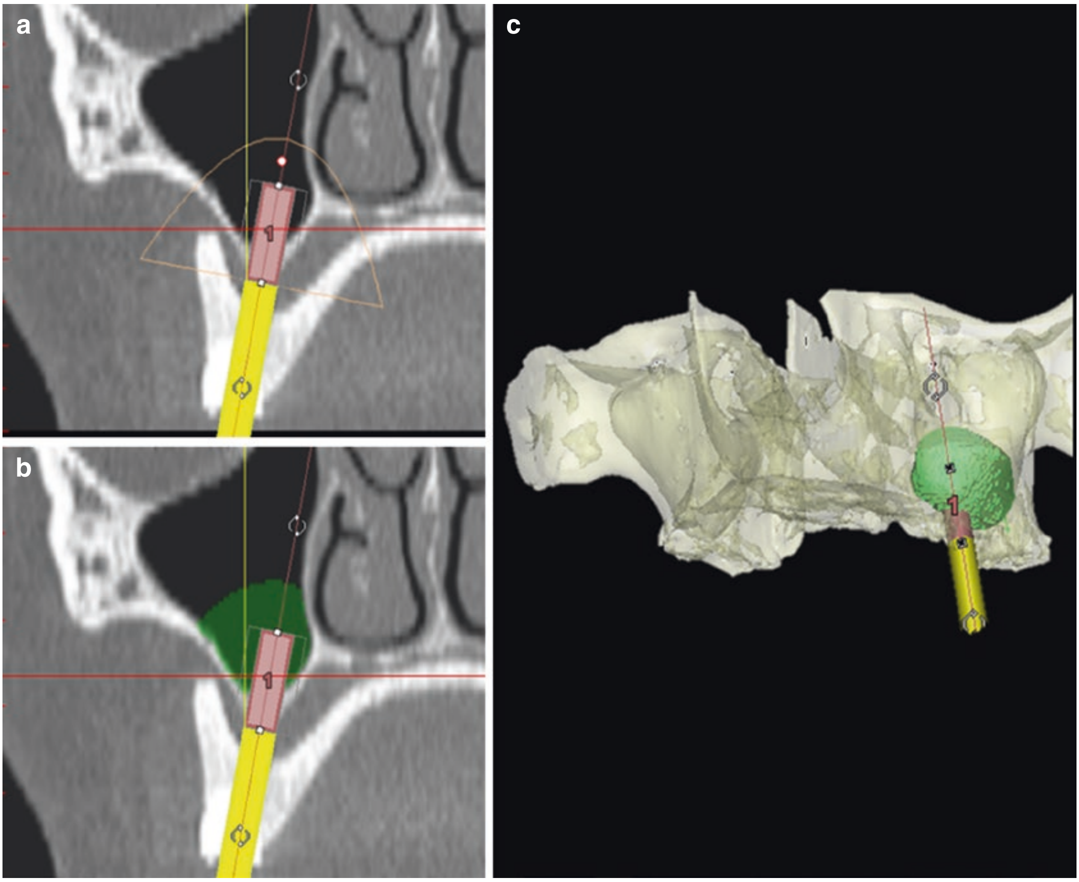

Fig. 20.41 Cross-sectional CBCT image (**a**) superimposed with a virtual implant (*pink*) and prosthetic emergence profile (*yellow*) positioned in the left posterior region in a severely atrophic completely edentulous maxilla (Dentsply Implants, Leuven, Belgium). Corresponding cross-sectional (**b**) and volumetric rendered (**c**) images with virtual sinus grafting material (*green*)

20.4 Preoperative Assessment Strategies

Cone beam CT-based imaging provides clinicians with two broad approaches to preoperative assessment of potential implant sites (Fig. 20.42).

Whichever approach is used and no matter how sophisticated and elaborate preoperative site evaluation and simulation software may be, it is always necessary that the prosthetically driven plan is transferred to the surgical field within a clinically and medico-legally acceptable level of accuracy. Several techniques are available to facilitate this transfer including the use of diagnostic radiographic templates, surgical guides, and surgical navigation—all of which mandate the use of CBCT imaging.

20.4.1 Software Independent Approach

Two software independent techniques to share CT or CBCT derived data to facilitate implant planning are possible.

20.4.1.1 Hard and Soft Media

Presurgical planning of implant placement from conventional CT acquisition was typically performed by secondary reformatting using

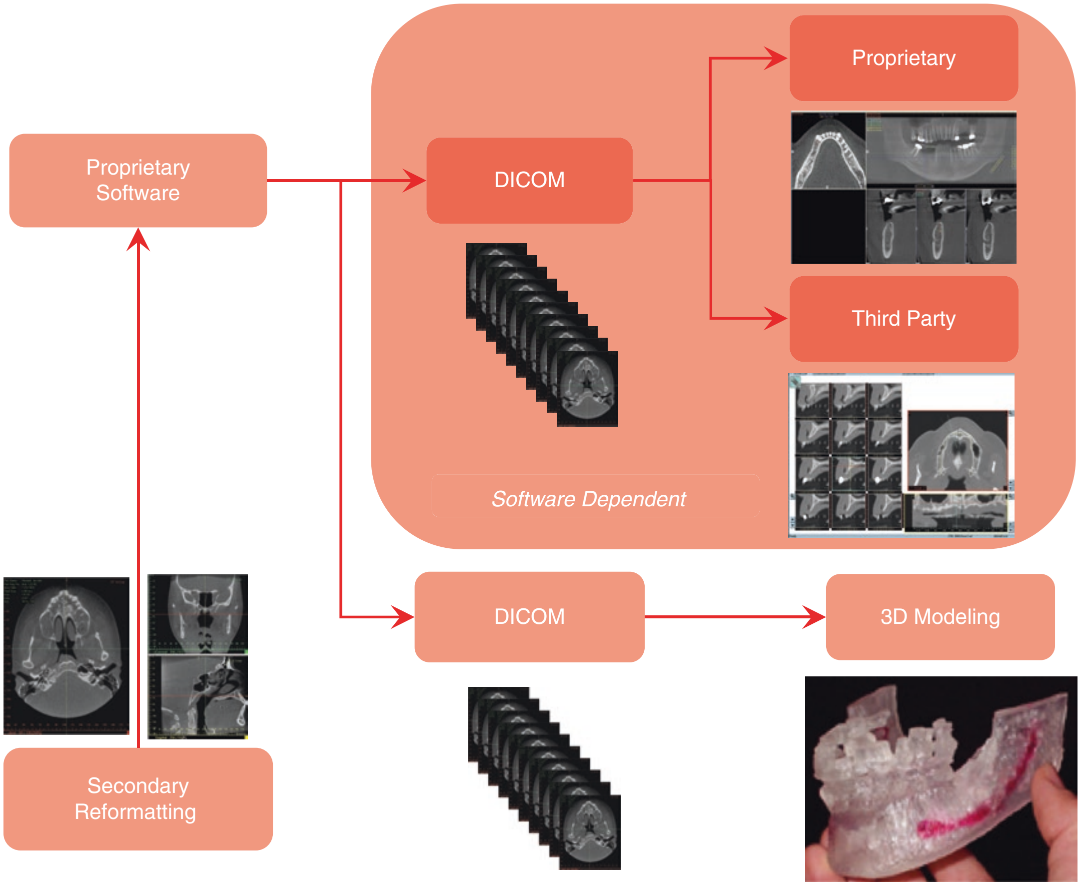

Fig. 20.42 Schematic illustrating preoperative CBCT-based implant assessment strategies. After image acquisition and inspection of the orthogonal display via secondary reconstruction, the data can be analyzed using one of two strategies. The software-independent method involves export of DICOM data and manufacture of a physical model. Alternately the data can be analyzed after DICOM export using either proprietary or third party software

dedicated workstation software. For each CT manufacturer, specific proprietary reformatting software is used. For example, scans performed with Siemens spiral CT are reconstructed using the Dental CT® software (Siemens, Erlangen, Germany), while CT data acquired via a General Electric MSCT, are typically reconstructed using Dentascan® software (GE, Medical systems, Milwaukee, USA) (Jacobs and van Steenberghe 1998). While institutions distribute images internally via their PACS (Picture Archival and Communication System) system, external distribution of images can be achieved either as hard or soft (electronic) copy.

Early implementation of CT and CBCT in implant planning often involved printing reformatted images in life size on large transparency film (e.g., 17 in. × 14 in.) for external distribution (Fig. 20.43). With the introduction of CBCT, hard copy distribution of images transitioned to archival quality photographic paper in familiar sizes (e.g., A4 or US Letter) and then electronically, often in PDF format. This distribution approach has advantages in that images are life size with no magnification or distortion, images are preformatted and measurements can be obtained directly.

The distinct disadvantage of hard and soft copy distribution is an inability to interact with the data. The clinician is reliant on the expertise of the operator providing appropriate image sectioning and specific reformatting addressing

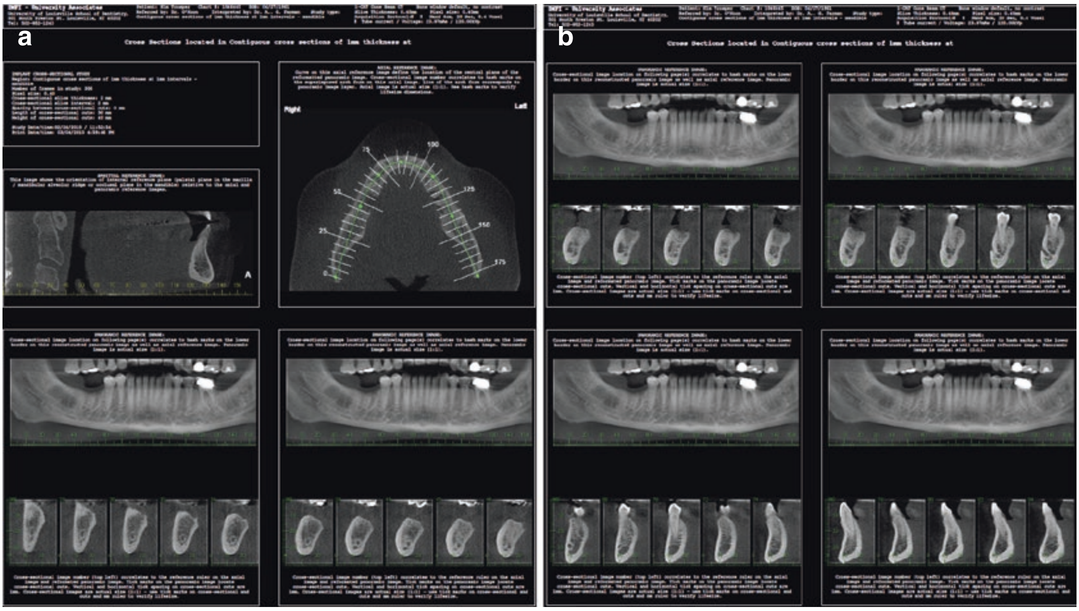

Fig. 20.43 Reference (**a**) and subsequent pages (**b**) in 17-in. × 14-in. hard copy format for distribution of CBCT images at 1:1 for implant planning

prosthetic and surgical considerations. Various authors have reported that measurement errors occur in CT images for implant assessment related to poor patient head positioning (Dantas et al. 2005) and gantry angle, which results in *parallax error* on cross-sectional images from non-perpendicular sectioning to the structure of interest (Choi et al. 2002). Inaccuracy may also result from inappropriate construction of the panoramic MPR, particularly if the panoramic curve is positioned along the line of the dental arch rather than the residual alveolar bone. Parallax error is more prominent in regions where there is greatest divergence between the dental arch shape and the shape of the residual ridge, particularly in the mandibular posterior region.

20.4.1.2 Provision of Biomodels

While not common practice, some clinicians request the production of physical solid biomodels from CBCT data. Biomodels provide accurate, tactile, three-dimensional representations of the patient's maxillofacial anatomy useful for direct visualization, surgical planning and simulation and allow for the fabrication of surgical guides which can be used as to direct osteotomy location at the time of surgery. This concept as applied to implant planning has been commercialized by Biomedical Modeling, Inc. (Boston, MA) as the BioDental Model System™ (Fig. 20.44).

20.4.2 Software Dependent Assessment

In 1988, Columbia Scientific, Inc. (Columbia, MD, USA) developed a dental software program that worked with standard GE CT scanners. In 1993, SimPlant™ for Windows was introduced allowing clinicians to utilize personal computers (PC) to manipulate, analyze, and interactively plan implant fixture placement on a graphic user interface. This development was facilitated by the establishment of a non-proprietary image file format for CT data export—the Digital Imaging and Communications in Medicine (DICOM) standard. Substantial increases in PC processor computing power, improved image storage options and further standardization and refinement of the DICOM interoperability standard

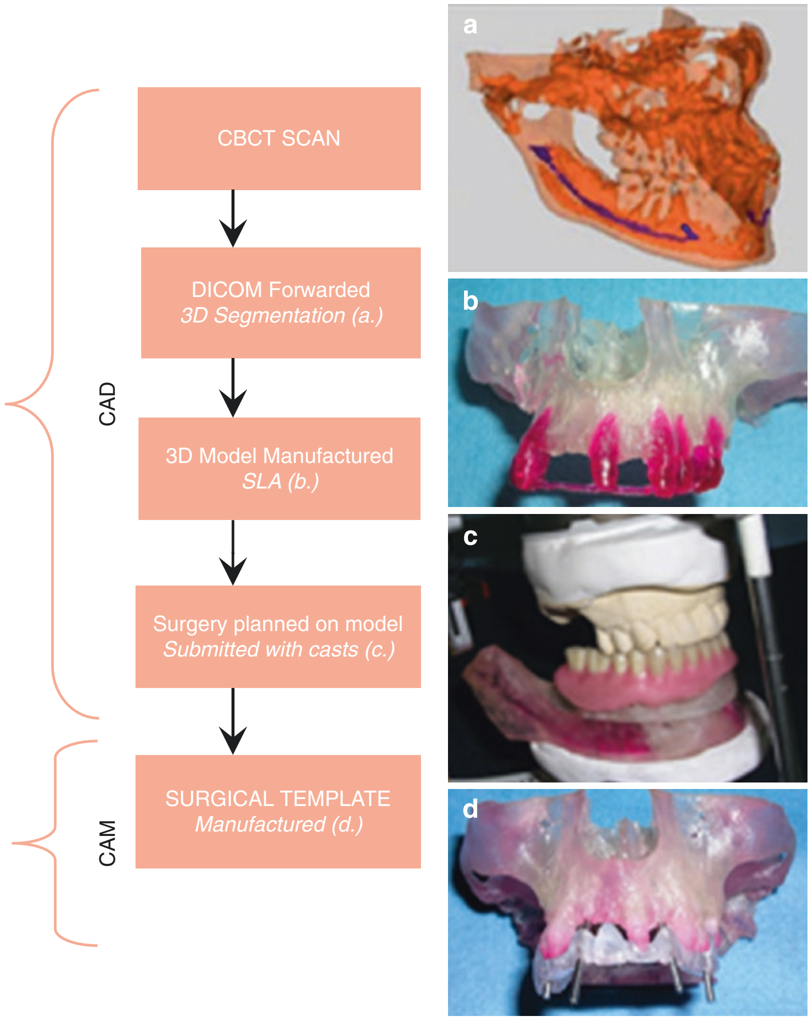

Fig. 20.44 Software independent implant planning using biomodels has two phases—computer-aided design (CAD) and computer-aided manufacture (CAM). The computer-assisted design phase involves implant planning based on biomodels fabricated from DICOM CBCT datasets. After a volumetric computer graphic virtual model is constructed by an imaging facility via segmentation techniques and reviewed by the clinician as static images or in *.stl format using a specific viewer, a stereolithographic model is authorized and forwarded to assist in hands-on implant simulation. The model can be opaque; however, transparent models are often used employing selected coloring of vital anatomic structures (e.g., IAC). Implant treatment planning can be performed by marking or drilling the osteotomy sites either free hand or using an opposing mounted plaster model with prosthetic setup. In addition, it is possible to fabricate a custom surgical guide/drill guide based on submitted simulated surgery and prosthetic design elements

fueled an explosion in the commercial availability of PC-based third party software for implant assessment and analysis.

PC-based computer planning software is now the most common approach in utilizing CBCT data for implant assessment (Fig. 20.45). The distribution of free viewing software capable of reformatting DICOM datasets and providing displays useful for implant site assessment from CBCT manufacturers has expanded the availability of software dependent implant assessment. In addition to vendor-specific products, numerous

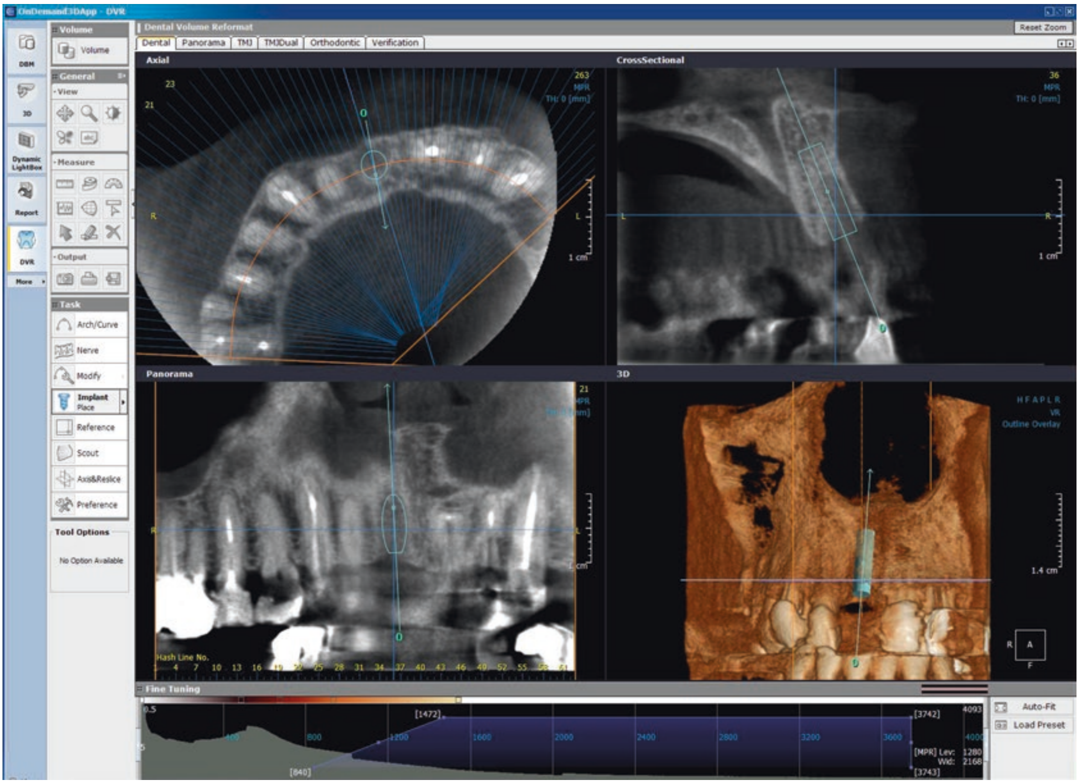

Fig. 20.45 Example of preoperative implant planning software screen virtual simulated placement of an endosseous implant to replace the maxillary right central incisor (OnDemand 3D, Cybermed, Seoul, Korea). Virtual planning software typically has multiple panels on a window including axial, cross-sectional, panoramic, and volumetric rendering which provide inter-relational images related to virtual implant placement and allow facilitate comprehension of implant position in relation to anatomic and prosthetic considerations

specific third party software programs are available for planning implant surgery in the jaws capable of importing DICOM data from any CBCT scanner (Table 20.3).

20.4.2.1 Implant Planning Software Display Formats

Software display formats of conventional CT data to generate curved MPR images for imaging of the jaw specifically for implant imaging was first reported by Schwarz et al. (1987a, b) who referred to it as *dental CT*.

Creating an Implant Image Series

Despite minor functionality differences between CBCT proprietary and third party software programs, reformatting CBCT data to create a standard image display for implant planning involves a two-step protocol:

- *Reorientation of the volumetric dataset*. The volumetric data is reoriented before reformatting to ensure that cross-sectional images are perpendicular to structures of prosthetic (e.g., occlusal plane) or anatomic importance (e.g., inferior alveolar canal or edentulous alveolar crest topography) (Figs. 20.46 and 20.47).
- *Creating a panoramic MPR and cross-sectional images*. Each software usually provides a separate window or screen presenting a pane showing axial reference images. Often the slice thickness of these images is the default acquisition resolution of the CBCT dataset or another arbitrary thickness. While

Table 20.3 Some representative third party implant planning software applications

Name	Vendor
Simplant®, Facilitate, Surgicase®	Dentsply Implants, Leuven, Belgium
InVivo	Anatomage, Inc., San Jose, CA, USA
Nobel Clinician	Nobel Biocare, Kloten, Switzerland
OnDemand	Cybermed, Seoul, South Korea
Romexis	Planmeca OY, Helsinki, Finland
NNT viewer	QR Verona, Verona, Italy
Galileos Implant Software	Sirona, Bensheim, Germany
Blue Sky Plan	Blue Sky Bio, LLC Grayslake, IL, USA
Artma Virtual Implant™	Artma Medical Technologies AG, Vienna, Austria
360dps	360imaging, Atlanta, GA, USA
Scan2Guide	iDent, Ft. Lauderdale, FL, USA
Med 3D®	Med3D GmbH, Heidelberg, Germany
Virtual Implant Placement (VIP)	Biohorizons, Birmingham, AL, USA
RoboDent DICOM-Viewer	RoboDent GmbH, Ismaning, Germany
EasyGuide	Keystone Dental, Burlington, MA, USA
Implant 3D	Media Lab Srl, Follo, Italy
coDiagnostiX®	Dental Wings, Inc., Montreal, Canada

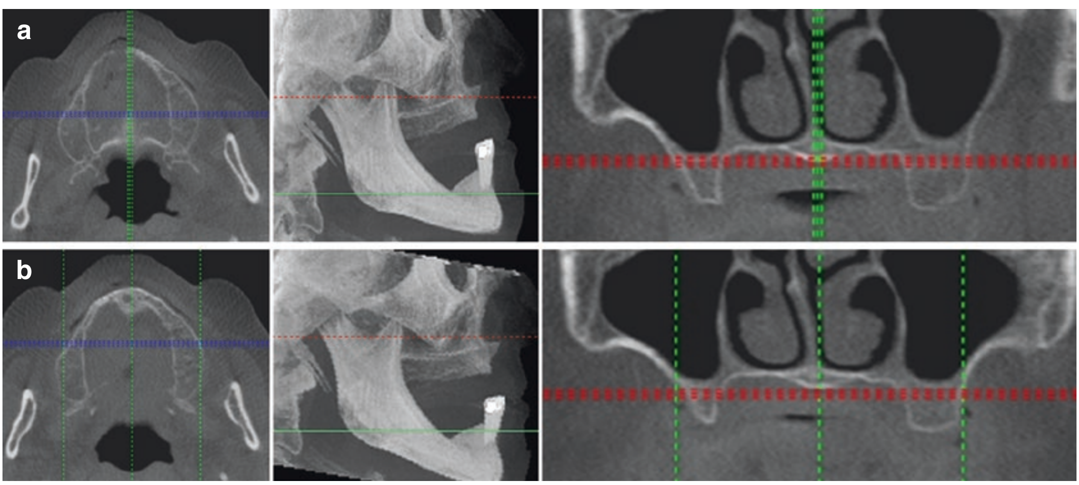

Fig. 20.46 Sequence of original (from *left* to *right*) axial, lateral MIP and coronal images before (**a**) and after (**b**) reorienting the volumetric dataset such that the maxillary edentulous residual alveolar ridge is parallel to the occlusal plane. Note the substantial difference in alveolar bone height at the same section between original and reoriented coronal images

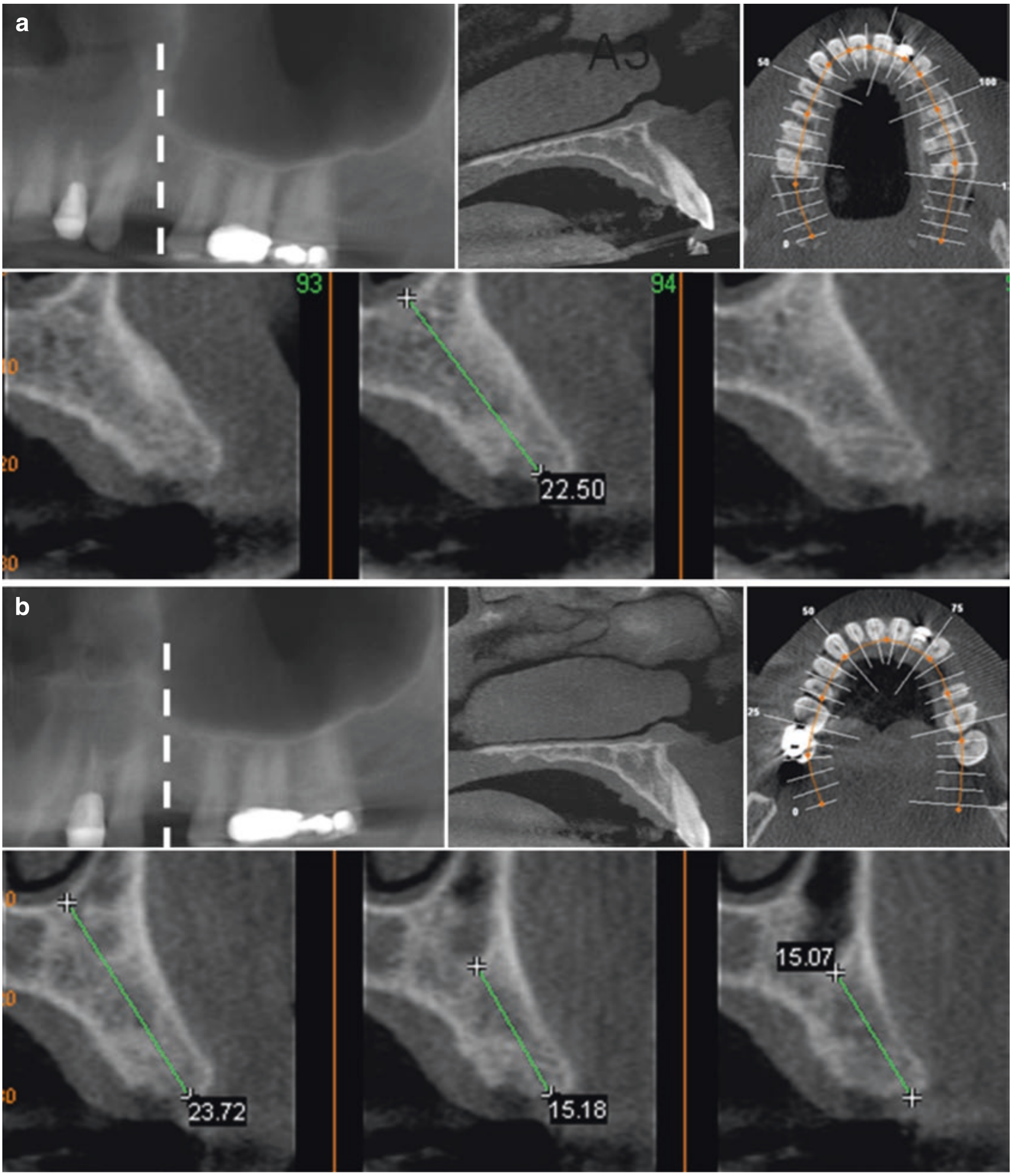

Fig. 20.47 Sequence of original (from *left* to *right*) reformatted panoramic, midsagittal, axial and serial cross-sectional images before (**a**) and after (**b**) reorienting the volumetric dataset such that the cross-sectional slices are parallel to the long axes of the adjacent teeth in the left maxillary bounded edentulous space. Note the substantial difference in alveolar bone height measurements and relationship of the maxillary sinus with respect to the alveolar bone at the proposed implant site at the same section between original and reoriented cross-sectional images

thin sections provide sharp, high contrast images from which anatomic measurements can be obtained, features that may be outside the plane thickness providing additional information which can contribute to prosthetic or surgical considerations may not be included (Fig. 20.48). Therefore, it is desirable that software allow user selection in the thickness of the reference images to provide “thick slab” visualization.

The cursor is used to draw a panoramic planning line or *spline* manually along the centerline of the jaw arch of either the maxilla or mandible using a series of *nodes* and is superimposed on axial views as they are scrolled caudally. Increasing the number of nodes used to designate the spline assures that the cross-sectional images are reconstructed perpendicular to the buccal and lingual/palatal alveolar bone (Fig. 20.49). This line designates the trans-axial curved re-slicing plane used to generate the panoramic and cross-sectional images. The resulting perpendicular cross-sectional views are numbered consecutively, corresponding to numbers on the reference panoramic image and planning plane.

While seemingly easy, lack of attention to a specific protocol can result in images with parallax errors in multiple planes (Fig. 20.50). The spline is drawn on the axial image at the CEJ for partially edentulous jaws or within

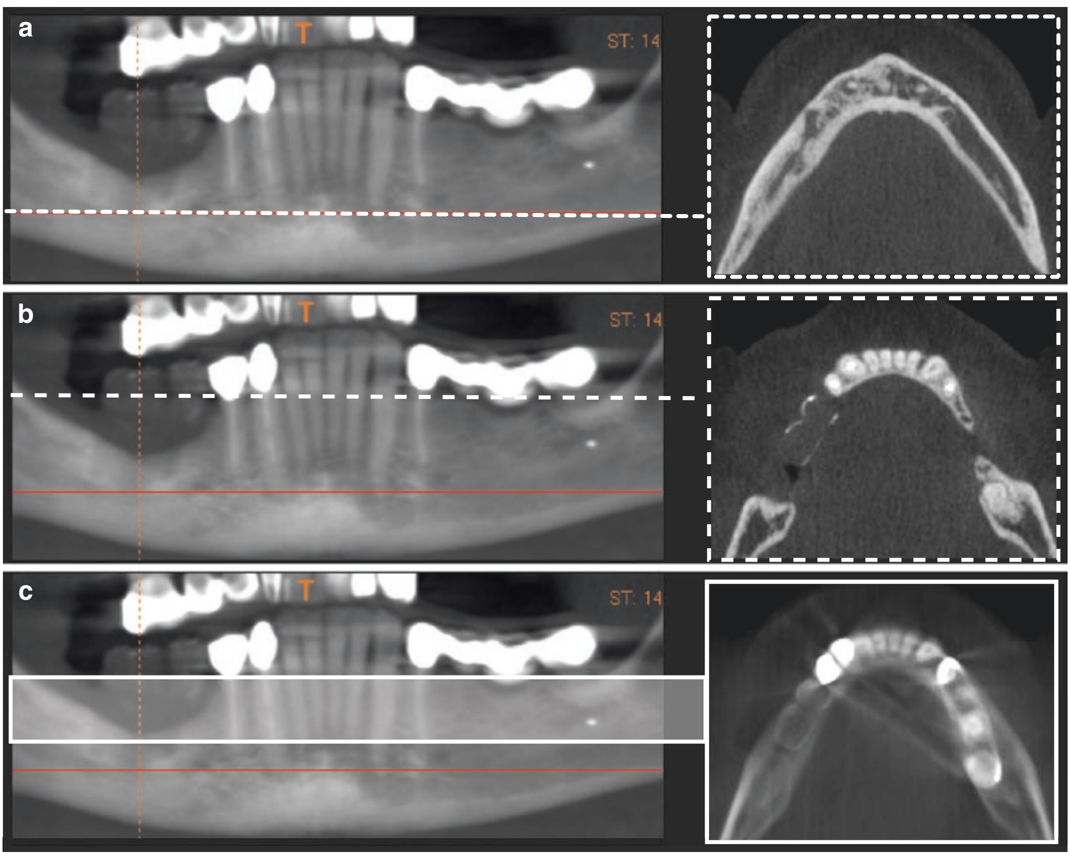

Fig. 20.48 Reference reformatted panoramic image with a thin section reference axial image at the level of the roots of the teeth (**a**), a thin section reference image at the alveolar crest (**b**) and a thick section reference image below the CEJ and above the roots of the teeth. Thin section images show the shape of the mandibular arch (**a**) and radiopaque markers on the radiographic template (**b**); however, thick section axial images show both prosthetic (markers) and anatomic (jaw shape) features and is optimal for generating a panoramic spline

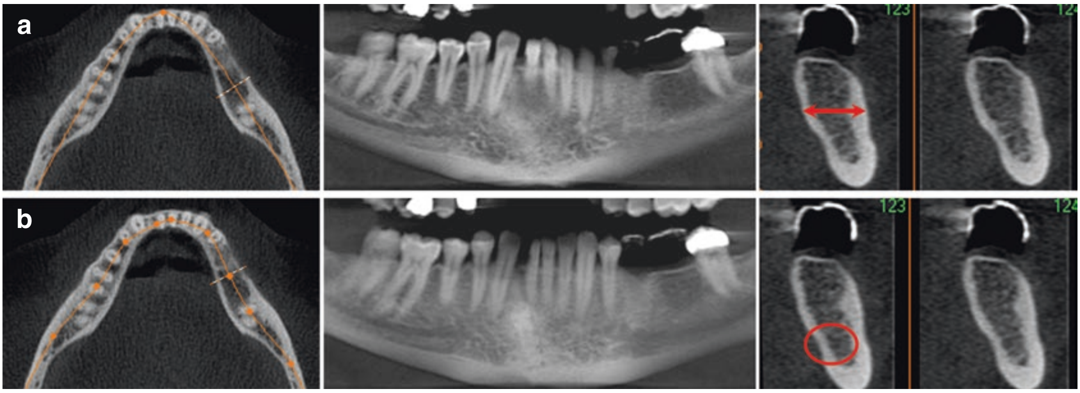

Fig. 20.49 A sequence (*left* to *right*) of axial, reformatted panoramic, and cross-sectional images developed using 3 (**a**) and multiple (**b**) spline nodes. Producing a panoramic image using a spline from multiple nodes (**b**) on the axial image provides more representative cross-sectional images. Note the reduced alveolar width of the alveolar crest and increased visibility of the IAC in cross-sectional images when multiple modes are used

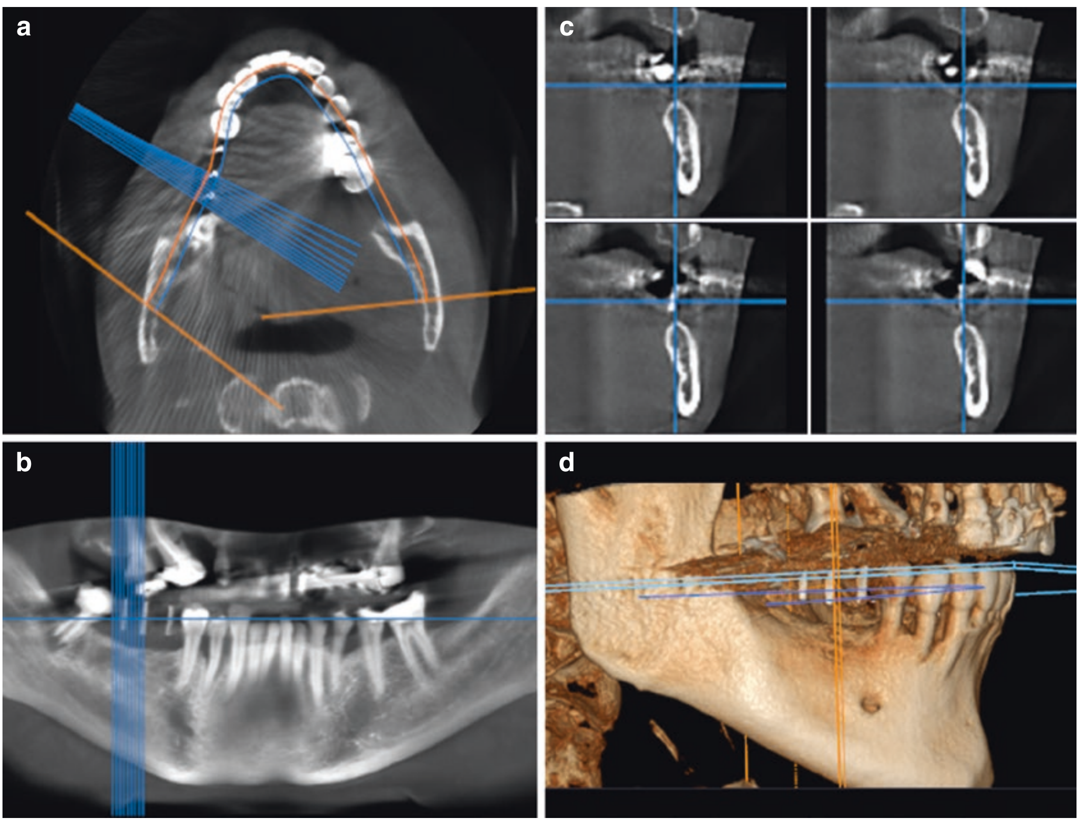

Fig. 20.50 Preoperative implant planning software screen (OnDemand 3D, Cybermed, Seoul, Korea) with axial (**a**), reformatted panoramic (**b**), cross-sectional (**c**), and volumetric rendering (**d**) CBCT images. There are multiple errors in the panoramic reformatting which contribute to parallax error in the cross-sectional images; (1) The mandibular horizontal plane has not been adjusted such that the marker of the radiographic template are parallel to the cross-sectional images; (2) The panoramic spline has been created at the level of the occlusal plane of the anterior teeth rather than at the alveolar crest and vary from the position of the radiopaque markers and therefore the ortho-radial images are not true cross-sectional images to the alveolus

5 mm of the alveolar crest for a completely edentulous jaw. If both jaws are contained within the FOV, then two (2) panoramic images are often created, each corresponding to the shape of either the maxilla or mandible (Fig. 20.51).

The Implant Display Protocol

- *Axial Image*. The axial image is an essential view of the display protocol as it shows the shape of the dental arch and the planning line with multiple numbered perpendicular lines defining the orientation of the reformatted cross-sectional images. These lines allow correlation with the reformatted panoramic and cross-sectional images by indicating their position (Fig. 20.51).
- *Custom MPR Panoramic Image*. Panoramic reconstructions are generated conforming to the panoramic spline. Some software programs provide multiple additional panoramic cuts parallel to the central spline, which are positioned closer to the buccal (outer) and lingual (inner) side from the planning line at specific distances (usually approximately 1–2 mm) (Fig. 20.52). Often this image will provide a reference marker system, corresponding to the perpendicular numbered lines on the axial display and cross-sectional images, providing correlative information.
- *Cross-sectional* (*synonyms include transaxial or orthoradial*). Contiguous (without deficit or overlap) cross-sectional slices perpendicular to the panoramic planning line provide a series of thin slice, limited field images, essential for accurate diagnosis. The distance between the cross-sectional images can be varied; in general, a spacing of 1–2 mm is used, similar to the *inter-slice interval* in CT terminology. Most planning software allows for varying both slice thickness and slice interval, often with defaults at 1 mm slice interval and 0 mm slice thickness. Some clinicians prefer 2 mm as the number of cross-sectional slices as this is the clinical order of accuracy that most can provide in clinical practice. In the mandible, these images demonstrate the mandibular canal and mental foraminae and allow assessment of the buccolingual width and contour of the jaw. In the maxilla pertinent anatomic structures confines to implant fixture placement can be visualized. Beam hardening

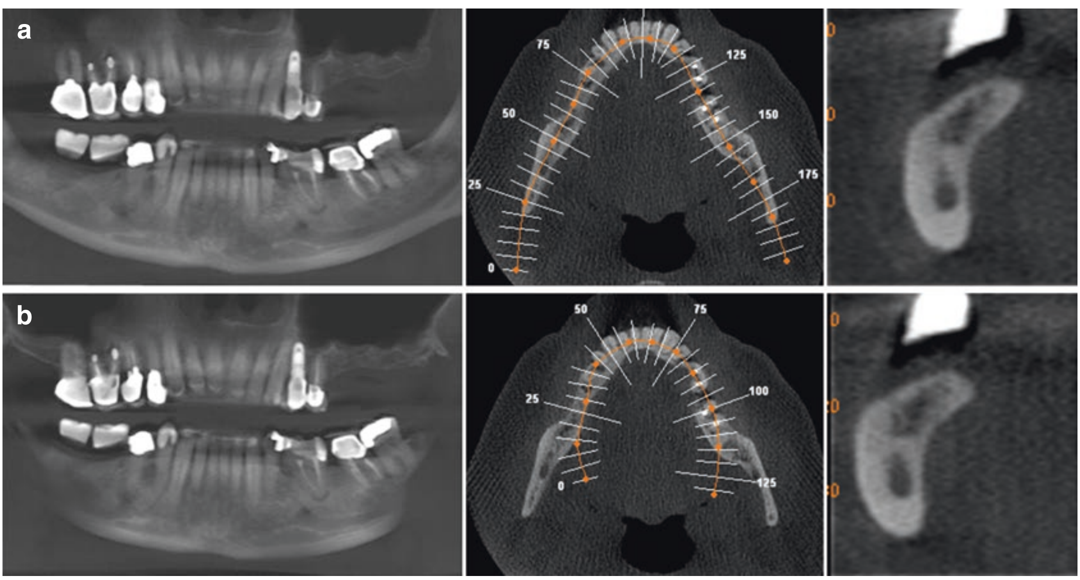

Fig. 20.51 A sequence (*left* to *right*) of reformatted panoramic, axial, and right mandibular molar cross-sectional image demonstrating the effect of a mandibular (**a**) and maxillary (**b**) panoramic spline on cross-sectional images relative to the opposite arch. Using the mandibular spline (**a**) produces cross-sectional images perpendicular to the alveolus whereas using a maxillary spline and layering this over the mandible (**b**) creates cross-sectional images with substantial distortion in the right mandible due to parallax error

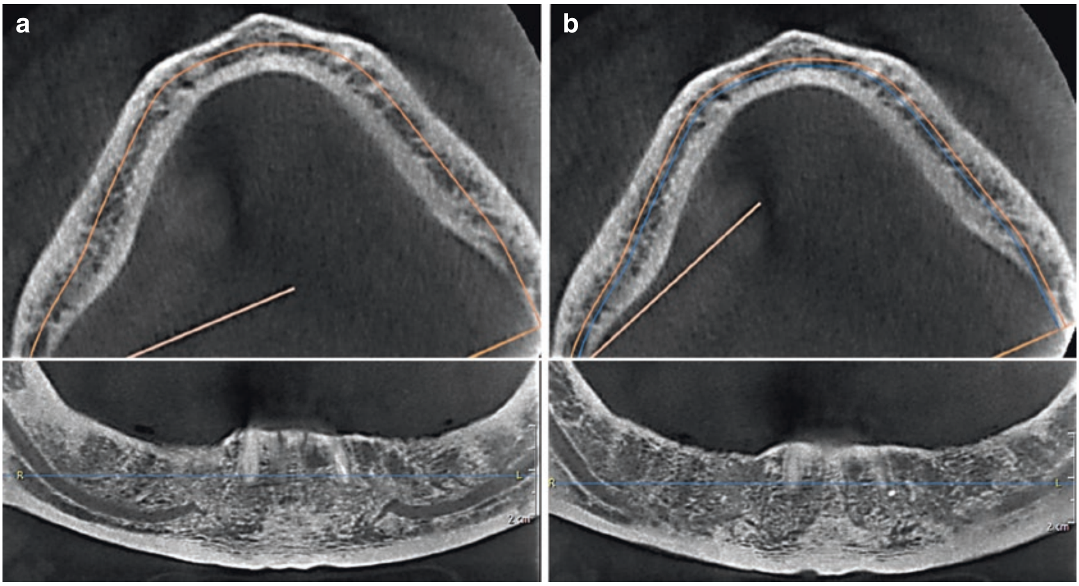

Fig. 20.52 Axial and reformatted panoramic image set showing the primary (*orange* – (**a**)) and secondary (*blue* – (**b**)) panoramic spline with corresponding thin section panoramic images. Note the loss of mental foraminae when the thin section spline is positioned lingually (**b**)

artifacts from coronal restorations do not interfere with visualization as these effects are predominantly seen in axial images at the level of the occlusal plane. However, these artifacts are prominent within the alveolar bone adjacent to teeth restored with root canal filling materials and, in particular, edentulous spaces adjacent to titanium implants (Fig. 20.53).

Implant Software Display Parameters

Most dental implant planning software programs provide a similar image display format comprising various arrangements of panes with axial, panoramic, and cross-sectional images. Many of the default image attributes may be adjusted by varying specific parameters of the display (Fig. 20.54).

- *Display Layout*. The montage of panes displayed within the implant task window usually includes axial and panoramic reference images and a series of cross-sectional views; however, numerous permutations and combinations of these images are possible.
- *Specific Image Parameters*
  - *Cross-sectional Images.* A number of elements contributing to the individual and group appearance of cross-sectional images can be modified including the number of contiguous cross-sectional images displayed on the screen, the physical dimensions of each cross-sectional image including width and height, the section thickness and spacing or interval between each image.
  - *Panoramic Image(s).* The group appearance of panoramic MPR images can be modified by adjusting the number of panoramic splines displayed and the increment between the splines, while the appearance of each individual panoramic may be altered by changing the thickness of the MPR and by application of a display algorithm such as MIP or composite ray sum, providing a conventional "radiographic" view.
  - *Axial Image(s).* Most often only a single axial image is included in the layout for reference purposes. If an image is to be deleted from the display interface layout, it will most commonly be the axial image. Possible modifications to this image include increasing the thickness of the slice to provide both anatomic and prosthetic

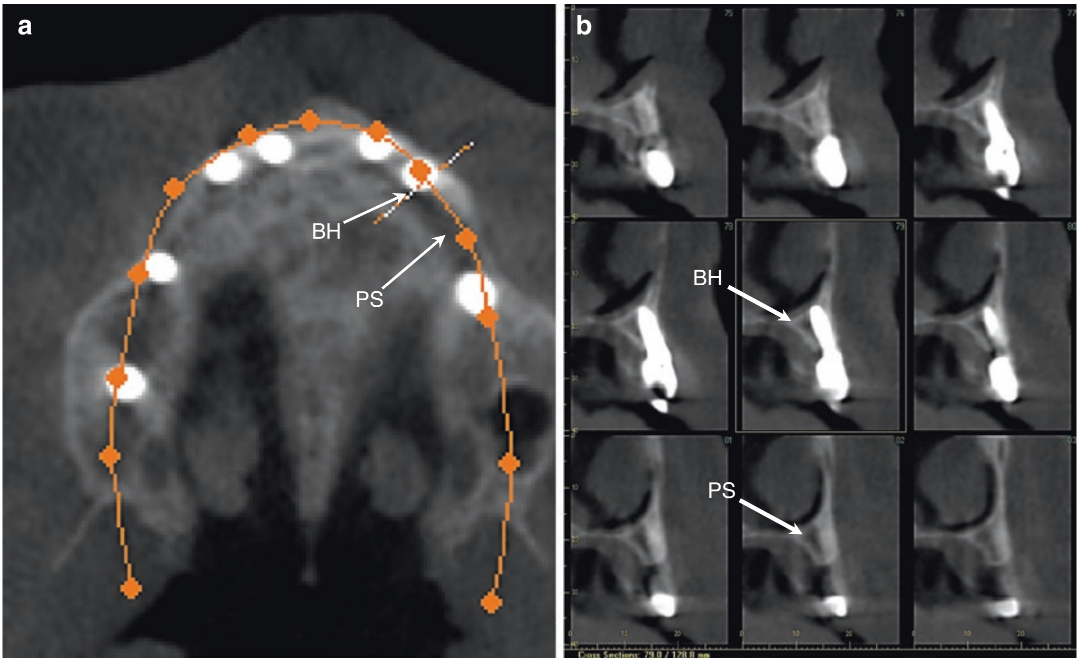

Fig. 20.53 Axial image with reformatted panoramic nodes and spline (**a**) and cross-sectional CBCT images of a completely edentulous maxilla in the region of the left canine. Beam hardening artifact (BH) is seen on the palatal aspect of the implant in the left maxillary canine region. Photon starvation artifact (PS) from lack of data presents as a peri-implant defect on the distal aspect of the canine implant and a relatively hypodense intramedullary "shadow" on the palatal aspect of the alveolar crest

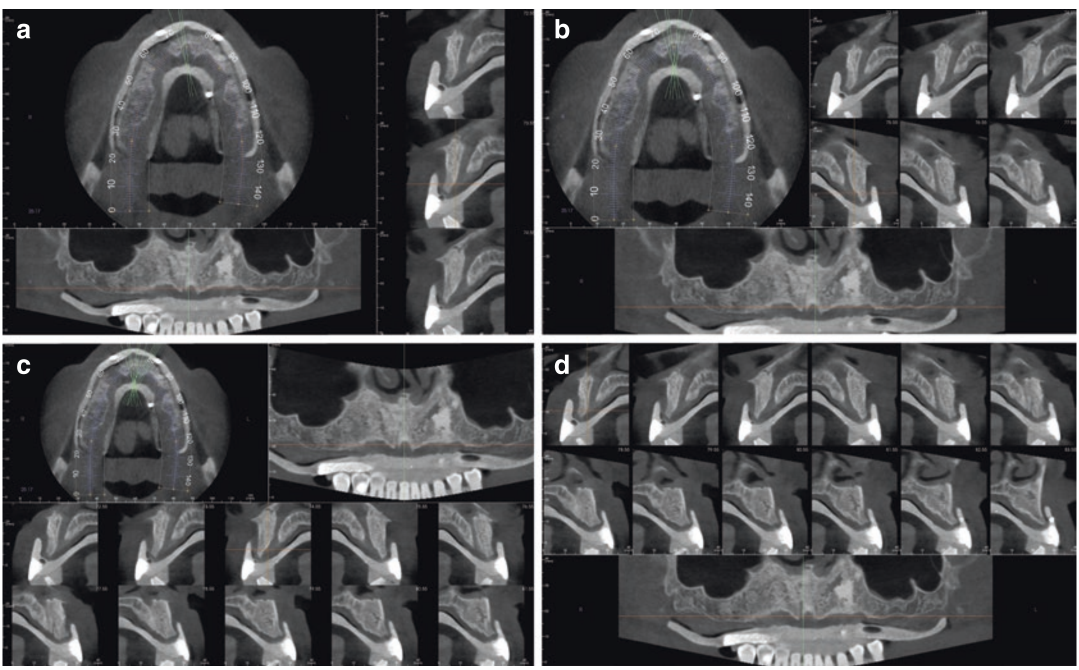

Fig. 20.54 Screen captures of four representative window pane formats ((**a**)–(**d**)) from a specific dental implant software program (InVivo, Anatomage, San Jose, CA, USA) showing different arrangements of axial, reformatted panoramic, and cross-sectional image window displays for a completely edentulous maxilla with a radiographic template

reference guides and the application of display algorithms such as the MIP or composite ray sum method.

20.4.2.2 Levels of Software Integration

The common feature of all PC-based implant planning software is that it allows the clinician to interact with CBCT data to achieve *image-guided surgery (IGS)*. This interactivity occurs at five hierarchical levels of software integration within the implant therapy process, depending on the level of functionality of the software (Fig. 20.55).

Computer-Aided Assessment

The first level of integration is dental implant software that provides essential display formats and measurement tools. Software at this level allows basic quantitative assessment of the implant site(s), is usually easy to use, and provides a standard display interface format. Proprietary CBCT viewers usually provide this functionality and may operate on proprietary image file formats rather than DICOM. Proprietary viewers do not allow import of external DICOM datasets. While the use of a radiographic template is desirable to relate available bone quantity to the planned prosthetic restauration (see later), it is not necessary. The primary requirement for software at this level is that it should add dynamic interactivity with the images. The basic viewing tool may offer tools for reslicing and measuring and also for implant placement simulated in volumetric rendered and combined environments. Computer-aided assessment software is characterized by the following features:

- *Reorientation of the volumetric dataset*. It is not always possible for a patient to be positioned within a scanner such that prosthetic

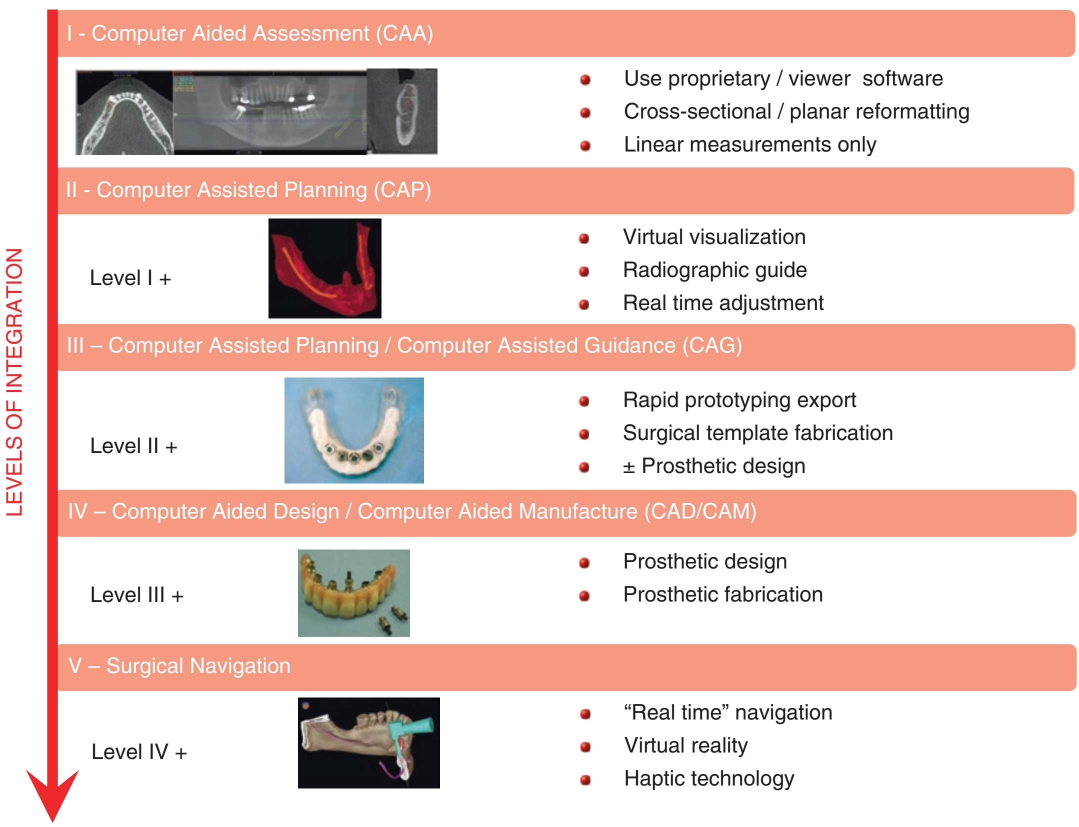

Fig. 20.55 Schematic diagram showing system analysis of five (5) levels of software integration to facilitate image-guided surgery using CBCT DICOM datasets for implant assessment, planning, guidance, design and manufacture, and surgical navigation depending on sophistication and functionality

and anatomic reference landmarks on reformatted images are ideally aligned. Analysis of maxillary and mandibular jaws requires reorientation of the dental arch in each to specific reference planes depending on degree of edentulism and presence of radiographic template. In the partially dentate maxilla or mandible the patient's occlusal plane should be parallel to the axial orthogonal reconstruction and perpendicular to the midsagittal plane. Alternately the axial plane should be adjusted as such to assure parallelity with the edentulous basal bone, ideally with a perpendicular orientation to the teeth bouding the edentulous saddle perpendicular is parallel to teeth bounding the edentulous saddle. The presence of a radiographic template facilitates these realignments. These restrictions minimize potential parallax error on transaxial cross-sectional images. Therefore, it is highly desirable that software allows for reorientation of the volumetric dataset such that the three orthogonal planes are correctly aligned with specific prosthetic or surgical reference planes.

- *"Cine" visualization of the entire cross-sectional region*. Identification of the panoramic spline on the axial image identifies the curved oblique MPR plane along which multiple reformatted contiguous trans-axial cross-sectional slices are created. If a 1 mm slice thickness is used, then potentially 50–120 slices can be generated. It is impractical to display all slices on one display format, so it is essential that software allows review of cross-sectional images by scrolling. The location of each cross-sectional slice is identified on both reformatted panoramic and reconstructed axial reference images. As scrolling is performed, the viewer should focus on one cross-sectional image as a cinematic progression occurs from one extent of the alveolar ridge to another. This visualization technique provides a dynamic method to efficiently assess the changes in topology and internal morphology of the available alveolar bone in the region of interest.
- *"Thick slab" visualization of reference images*. Often the slice thickness of axial and panoramic reference images is the default acquisition resolution of the CBCT dataset—submillimeter. This provides a sharp, high contrast image from which anatomic measurements can be obtained; however, features that may be outside the plane thickness providing additional information which can contribute to prosthetic or surgical considerations may not be included. This includes the presence of radiopaque markers on radiographic templates indicating desirable implant fixture placement. On axial images minimal slice thickness will not include these markers. It is desirable that software allow selection of the thickness of the reference images to provide "thick slab" visualization.
- *Cursor-driven measurements*. Quantitative analysis is an integral component of the assessment of available bone volume in implant site evaluation. This is usually performed using a measurement tool which allows a line to be drawn between two identified reference positions (e.g., the floor of the maxillary sinus and the crest of the edentulous alveolar bone) and displays the linear distance between them. Implant planning software should also allow to make multiple linear measurements on cross-sectional as well as axial and simulated panoramic MPR images (Fig. 20.56).
- *Image enhancement for optimal viewing*. Adjustment of image slice thickness for reference axial and panoramic images is highly desirable; however, it should be recognized that window level and width adjustments may be necessary (Fig. 20.57). In addition, the use of edge enhancement filters or features such as MIP may provide greater contrast to assist in the detection of fine osseous structures (e.g., cortication of the walls of the IAC) (Fig. 20.58). It is desirable that planning software allows for specific image enhancements to each display panel optimizing visualization.

Computer-Assisted Planning

Software at this and subsequent levels of integration provide additional functions to assist in the planning of implant therapy via simulation of the implant placement and, with the superimposition of prosthetic elements, demonstrate the interaction between planned surgical scenarios and

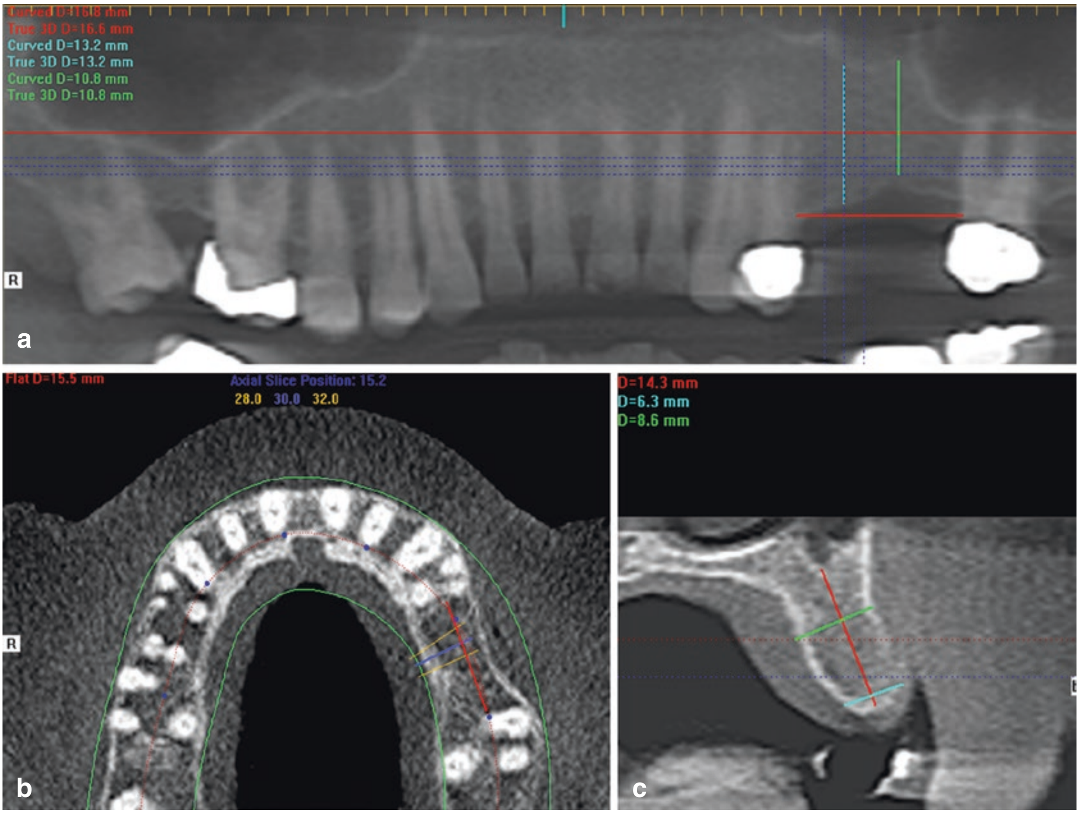

Fig. 20.56 Example of software providing reformatted panoramic (**a**), axial (**b**), and individual cross-sectional (**c**) CBCT images showing the use of cursor-driven linear measurement. The dashed lines on the upper frame of the panoramic MPR image (**a**) provides the location of a 1 mm thick cross-sectional image (**c**) in the maxillary left posterior molar region. The reference axial (**b**) is located at the apical third of the root surfaces. Numerous color-coded linear measurements of the height and width of the alveolar ridge at this location have been performed on the cross-sectional images. In addition, measurements have been made on the axial and the panoramic images for cross-reference. The actual dimensions are displayed in the upper left hand corner of the image

prosthetic implications. The use of software at this level is more complicated as more options and preferences are available. The display screen format of software is often similar to that for computer-aided assessment but adds a level of sophistication requiring greater expertise.

Dental implant planning software at this level fulfills a dual role in displaying the data and allowing insertion of graphic elements into the data (implant body or prosthetic elements). Image file formats may be proprietary and incorporate an additional "processing" stage into one of two workflow strategies.

- *Software-based DICOM conversion*. In this strategy, the software converts the DICOM data at the time of import. This is optimal as it makes the processing phase seamless within the workflow. Most vendors incorporate this feature into their software intuitively whereas others offer two levels of software—a stand-alone product capable of converting the data or as a less expensive, functionally identical version without conversion capabilities.
- *Data Conversion Service*. The second strategy involves conversion of the DICOM data into the proprietary format by a third party provider, which may be the vendor themselves. This strategy is the least preferred as there is usually a delay between forwarding the DICOM data for conversion via secure internet transfer and receipt of the reformatted data.

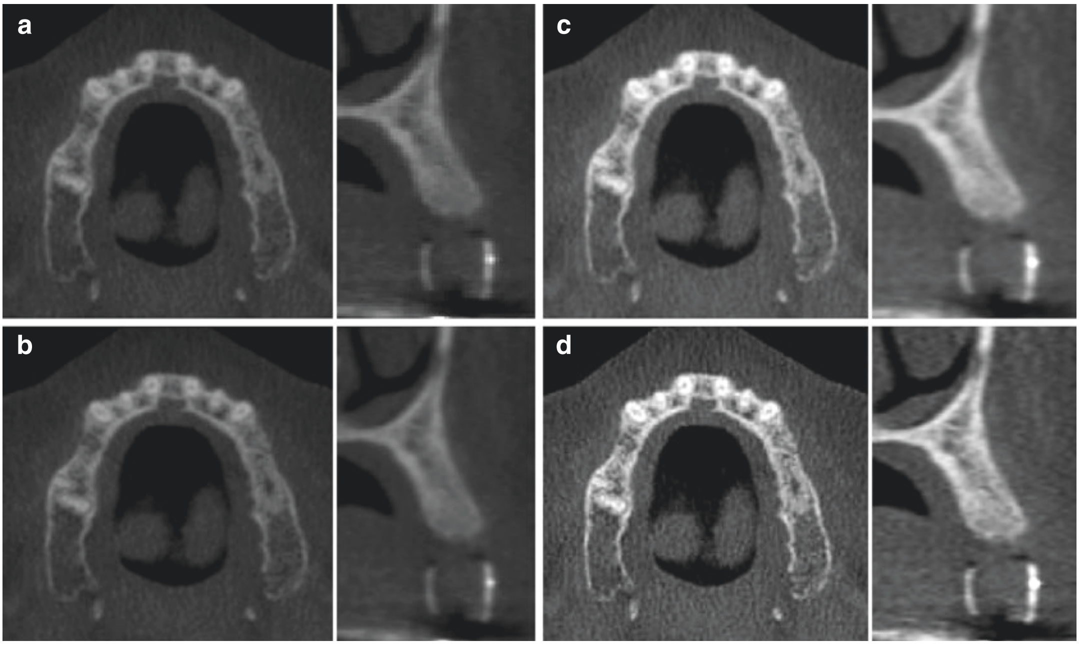

Fig. 20.57 Axial and cross-sectional CBCT image pairs showing default (**a**) and application of progressive interpolation (**b**), contrast and brightness (**c**) and edge sharpening (**d**) image enhancements to optimize visualization

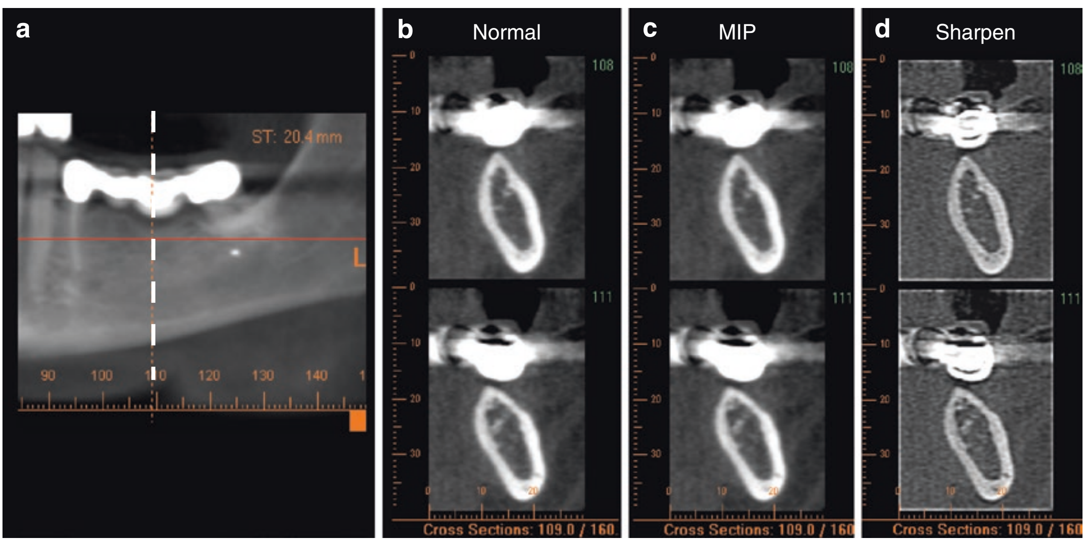

Fig. 20.58 Cropped reformatted panoramic (**a**) and two sequential cross-sectional CBCT images located in the left posterior mandible (*dashed line*) with normal (**b**), maximum intensity projection (**c**) and edge sharpen (**d**) image enhancements. With a normal cross-sectional image (**b**) the IAC is difficult because of the lack of cortical outline and blurring of the trabeculae associated with superimposed structural noise. The application of the MIP algorithm reduces the noise, increases the contrast slightly and further defines the edge. The application of the sharpen algorithm however has the most marked effect. While reducing contrast, the algorithm clearly accentuates the internal trabecular within the cortical confines and allows discernment of a trabeculae void adjacent to the inferior buccal cortical plate most consistent with the location of the IAC. Note also that "voids" within the buccal and inferior cortical plate are now clearly visualized

Because the hallmark of this software is simulated placement of the implant fixture, the use of a radiographic template is highly desirable. The radiographic template indicates the optimal position of the prosthetic restoration and anticipated location and angulation of the osteotomy site. Without this prosthetic element, transfer of any virtual plan to the clinical situation is extremely difficult. The primary requirement for software operating at this level is that it should add elements of surgical and prosthetic simulation and planning, complementing visualization of the images.

Basic Views

The fundamental display format of software in this category is similar to that described in computer-aided assessment and usually intuitive to use.

- *MPR panoramic view.* Often the buccolingual position of this image can be interactively altered.
- *Axial view*. This offers a perspective from a caudal direction.
- *Cross-sectional views*. This allows a mesial/distal cross-sectional perspective of the arch. This is helpful in determining bone thickness, demonstrating anatomic structures and is the optimal view to correlate the position of a radiographic template to the bone. All three views are correlational, so when a marker is moved on one, it corresponds to the other two views.
- *Volumetric rendering perspective*. Computer-assisted planning software is distinguished by providing an overall final perspective of the surgical, prosthetic and anatomic elements in a volumetric rendition.

Visualization Tools

Ideally planning and simulation is performed in the software with interactive virtual implant placement on planar cross-sectional slices and visual feedback on volumetric renderings showing prosthetic parameters.

- *Simulated virtual implant placement in correlated images*. While the selection and positioning tool varies depending on the software, simulated implant placement in the virtual environment is prosthetically driven and should incorporate a radiographic template. The process involves the following phases (Fig. 20.59).
  - The cross-sectional region where the proposed implant fixture site has been identified by the radiographic marker is located. Reference markers on the correlated axial and panoramic images adjust automatically to identify this region on these views.
  - The implant selection tool is activated and approximate dimensions of the implant are selected. Initial dimensions will depend on the original assessment of the available bone volume. An initial length of 10 mm and width of 4 mm satisfies most prosthetic requirements in the posterior region and 3.3 mm width and 10 mm length in the anterior region.
  - The implant selection tool is moved to the cross-sectional image that best correlates with the radiographic marker and the tool is activated. A graphic representation of an implant is then superimposed on the cross-sectional image. This graphic representation is shown on the correlated images to various degrees, depending on the level at which the planar image bisects the implant.
  - The position of the implant is then adjusted within the alveolar bone volume on the cross-sectional image according to several guidelines: (1) The long axis of the implant should be as parallel to the long axis of the crown of the proposed prosthetic unit as possible, (2) The implant should be positioned such that the buccal and palatal/lingual cortex covers the surface of the implant by approximately 1.5 mm, and (3) The implant should be positioned into the alveolar bone such that the abutment platform of the implant body is level with the marginal or crestal alveolar ridge. If the ridge is knife-edge, then either the implant should be positioned lower to achieve this, requiring ridge reduction at the time of surgery, or the implant can be positioned more coronally if ridge augmentation is considered. If the implant is placed in an edentulous

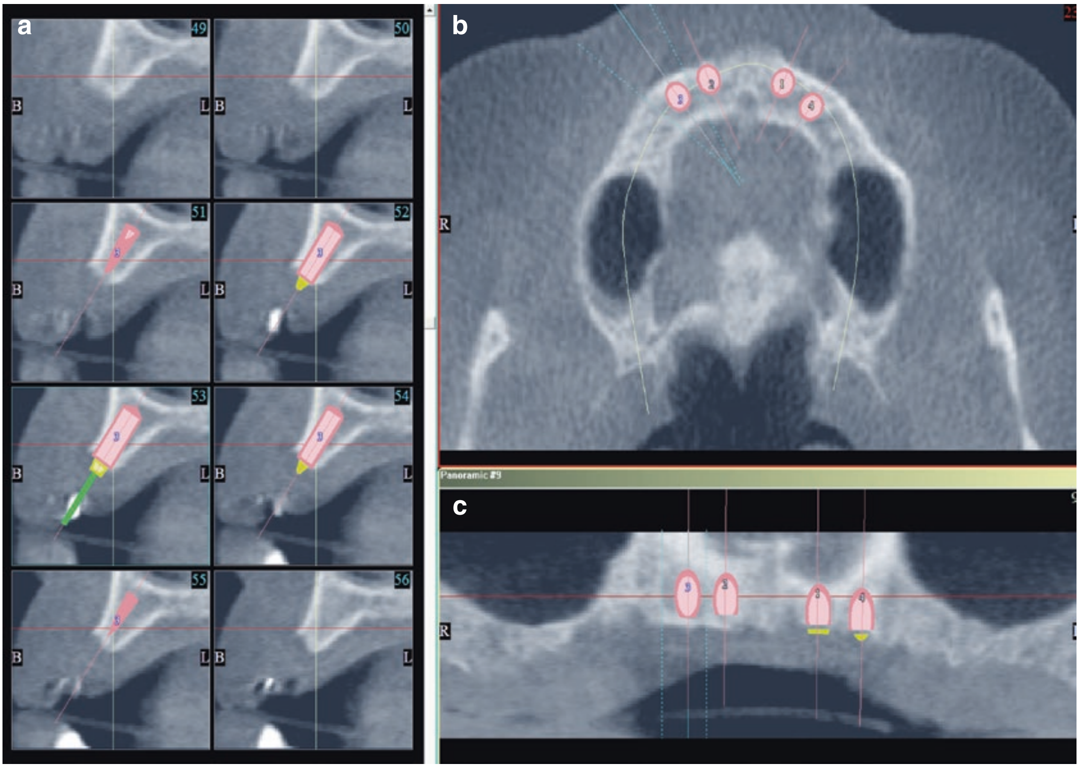

Fig. 20.59 Screen display of simulated virtual implant (pink cylinder) placement in correlated cross-sectional (**a**), axial (**b**), and thin section panoramic CBCT images in the anterior region of an edentulous maxilla. The cross-sectional images (**a**) show the bucco-palatal emergence profile. The axial image (**b**) provides a visualization of the anteroposterior position of this implant relative to adjacent virtual implants placed in the arch. The panoramic image (**c**) shows the relative parallelism of the implants with respect to each other

bounded area, especially in the anterior esthetic zone, then the apico-coronal position of the abutment platform should be no lower than 2 mm from the cementoenamel junction of the adjacent teeth.

– The position of the implant is then adjusted in the horizontal direction on the axial image. This image provides a representation of the shape of the available arch and guides implant placement such that prosthetic retention, balance, and support are optimized. This is particularly important when multiple fixtures are anticipated and when dental or osseous structures confine or limit mesiodistal location.
– The position of the implant is further adapted in the panoramic image. This display allows adjustment of the mesiodistal orientation of the fixture and adjustment of the level of the fixture collar with respect to adjacent teeth or implants.
– The implant position is finally fine-tuned in the cross-sectional image. At this stage the physical parameters of the implant can be adjusted to optimize fixture surface area now that implant position has been established.

- *Volumetric visualization*. The above approach allows for independent considerations for implant placement but does not provide an overall visualization, taking into account both clinical and esthetic considerations. Most software at this level of integration provide a display where the final implant fixture placement can be visualized in volumetric renderings and also adjusted (Fig. 20.60).

Volumetric visualization can be extremely useful in partially dentate situations where

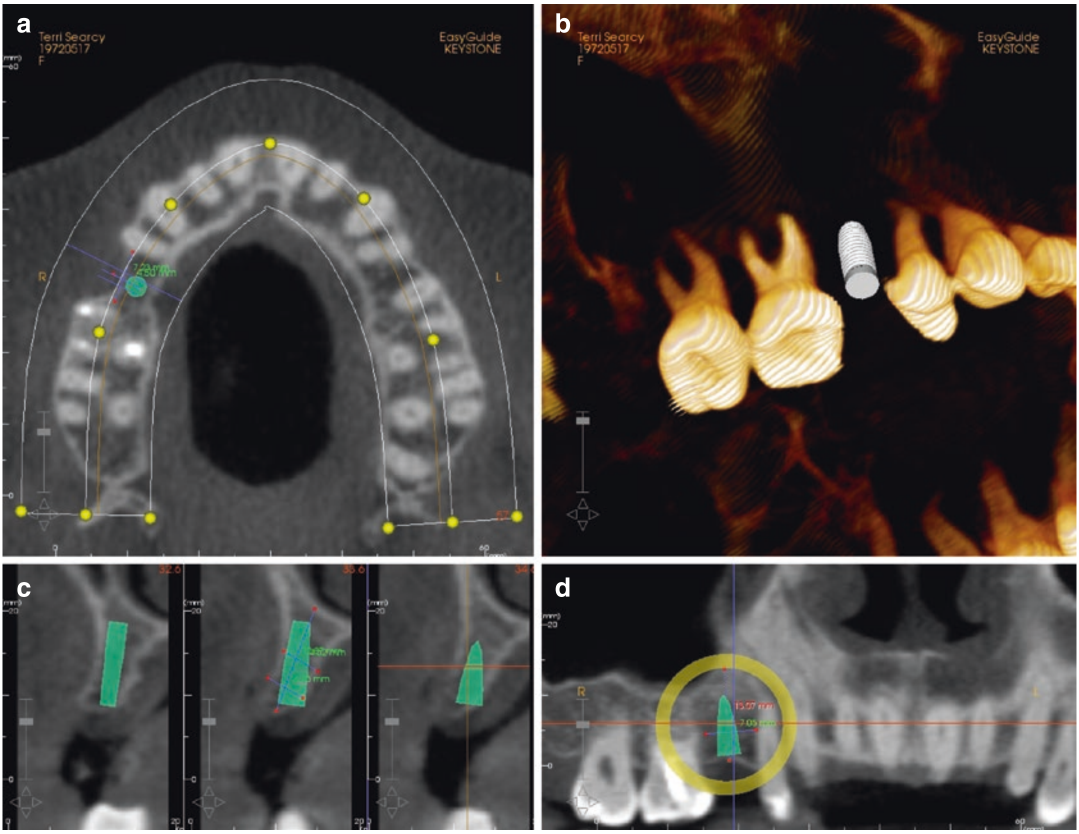

Fig. 20.60 Axial (**a**), volumetric rendering (**b**), cross-sectional (**c**), and reformatted panoramic (**d**) CBCT images demonstrating perspectives of virtual implant simulation for replacement of a right maxillary second premolar in both correlated planar images and volumetric perspective. The axial image (**a**) allows for repositioning in the buccolingual dimension or horizontally taking into consideration the dental arch curvature according to the position of the roots of the remaining teeth. The cross-section images (**b**) allow for adjustment of the emergence profile and the panoramic image (**d**) allows for rotation of the fixture relative to the adjacent teeth. The overall orientation and position of the implant relative to the anatomic boundaries of the edentulous space and prosthetic considerations is most clearly visualized by the volumetric rendering perspective view (**b**)

implant placement is anticipated to support replication of tooth position. Implant placement can be superimposed in bone and various clipping tools can be used to more clearly demonstrate the implant fixture position with respect to the existing tooth position (Fig. 20.61).

Volumetric renderings can provide either a surface (SSD) or volumetric rendition (VR) of the anatomy. Surface virtual models are optimal in demonstrating topographical features of the bony anatomy (e.g., mental and nasopalatine foraminae) and morphology of the alveolar crest whereas VR images demonstrate internal features more clearly (e.g., the IAC) and show more clearly the position of the implant fixture with respect to prosthetic determinants. Some software is capable of providing both types of volumetric renderings.

Surgical Tools

- *Inferior Alveolar Canal (IAC) Marker*. Software at this level provides tools that trace the location of the IAC in the mandible and show this structure on correlated and volumetric image displays (Fig. 20.62).

  Two methods of identifying the IAC are available.

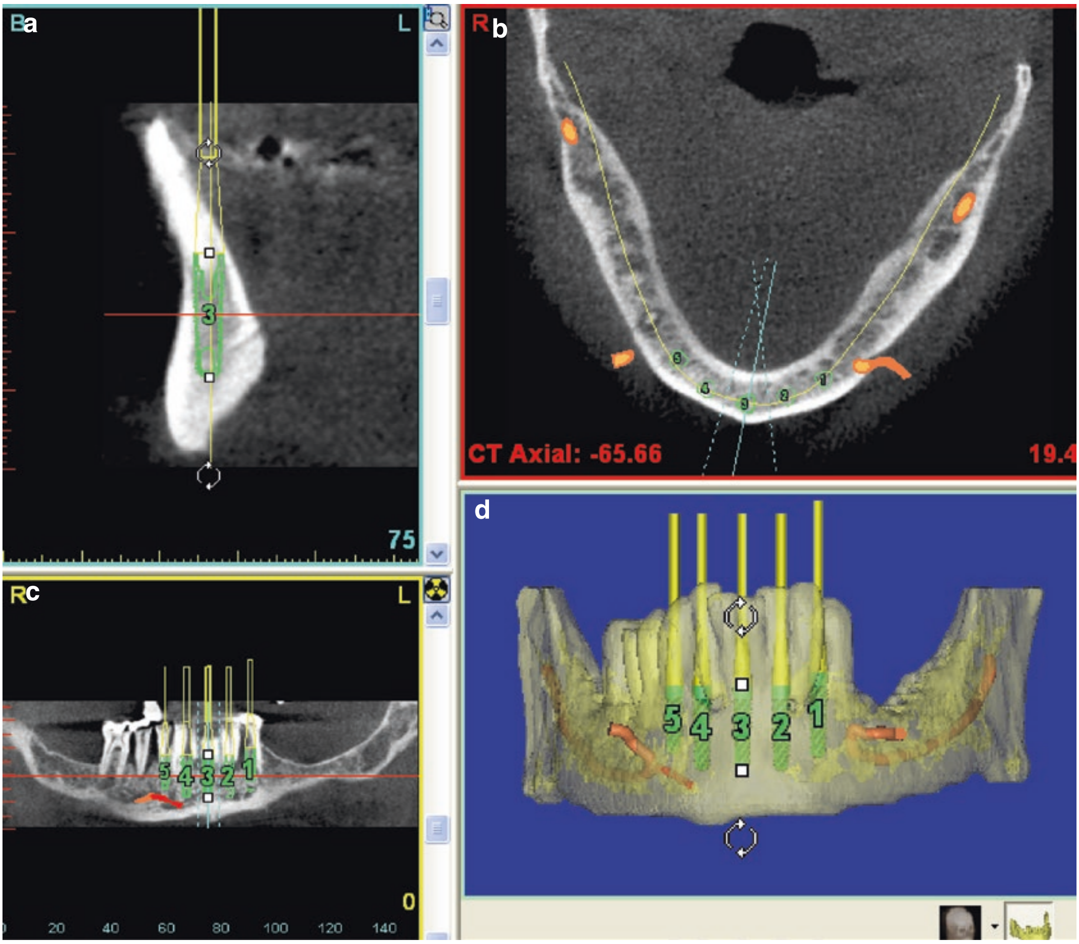

Fig. 20.61 Cross-sectional (**a**), axial (**b**), thin section reformatted panoramic (**c**), and volumetric rendering demonstrate the utility of 3D visualization in implant fixture placement when multiple teeth are to be removed and the prosthesis based on current tooth position. The panoramic view (**c**) reveals advanced periodontal disease and associated bone loss. All teeth are scheduled for removal. The cross-sectional view (**a**) is used to plan the position of the replacement implants (*green*) at specific sites with abutment projection (*yellow*) positioned for screw-retained hybrid restoration. The volumetric rendition (**d**) demonstrates the tooth position in relation to the proposed implant position(s). (Images courtesy, Scott D. Ganz)

- *Method 1*. Cross-sectional images either in the mental foramen region or posterior to the implant site are located. The marker tool is selected and the position of the IAC is identified. Subsequent cross-sectional images are scrolled and the procedure is repeated either progressing anteriorly or posteriorly until all cross-sectional images in the region of interest are marked. As consecutive cross-sectional images are marked, a line is drawn between the positions and is displayed on the supplementary correlated and the 3D representation views (Fig. 20.63).
- *Method 2*. A narrow slice section for the panoramic MPR is defined (1–2 mm) and adjusted buccolingually to highlight the path of the corticated border of the IAC. This defines the location of the IAC in regard to depth. The marker tool is then used to identify the location of the mandibular canal on the panoramic image. As this image is marked, a line is drawn between the locations and is displayed

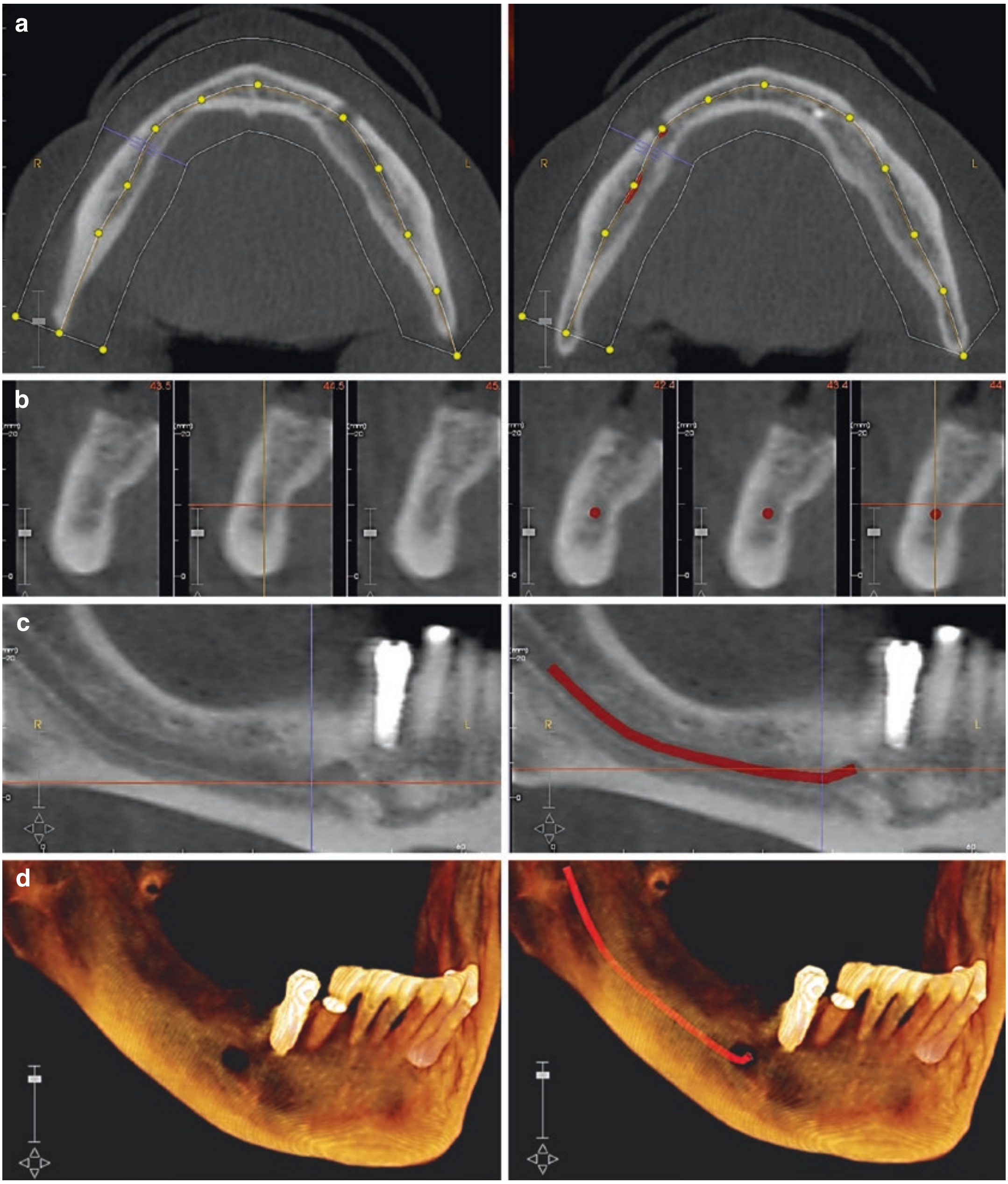

Fig. 20.62 Axial (**a**), serial cross-sectional (**b**), reformatted thin section panoramic (**c**), and volumetric rendering showing before (*left*) and after (*right*) IAC tracing

on the correlated images and the volumetric rendered representations (Fig. 20.64).

- *Graft Simulation*. Some software allows addition of solid material into either cross-sectional or panoramic images. This is most commonly performed to simulate bone augmentation in the maxillary sinus associated with a sinus lift procedure. This is applied by either designating the confines within which the material is to be added or simply painted in successive

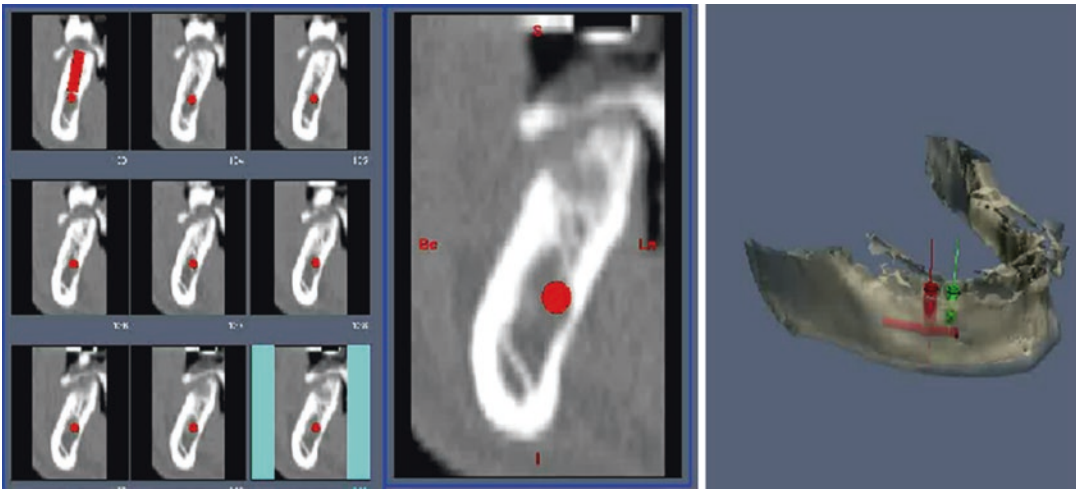

Fig. 20.63 Screen capture of software that uses a single cross-sectional image (*center*) to identify the location of the IAC as it progresses through the mandible (*left*). The resultant tracing can be used to demonstrate the position of the IAC in relation to important anatomic structures and simulated implant position virtually

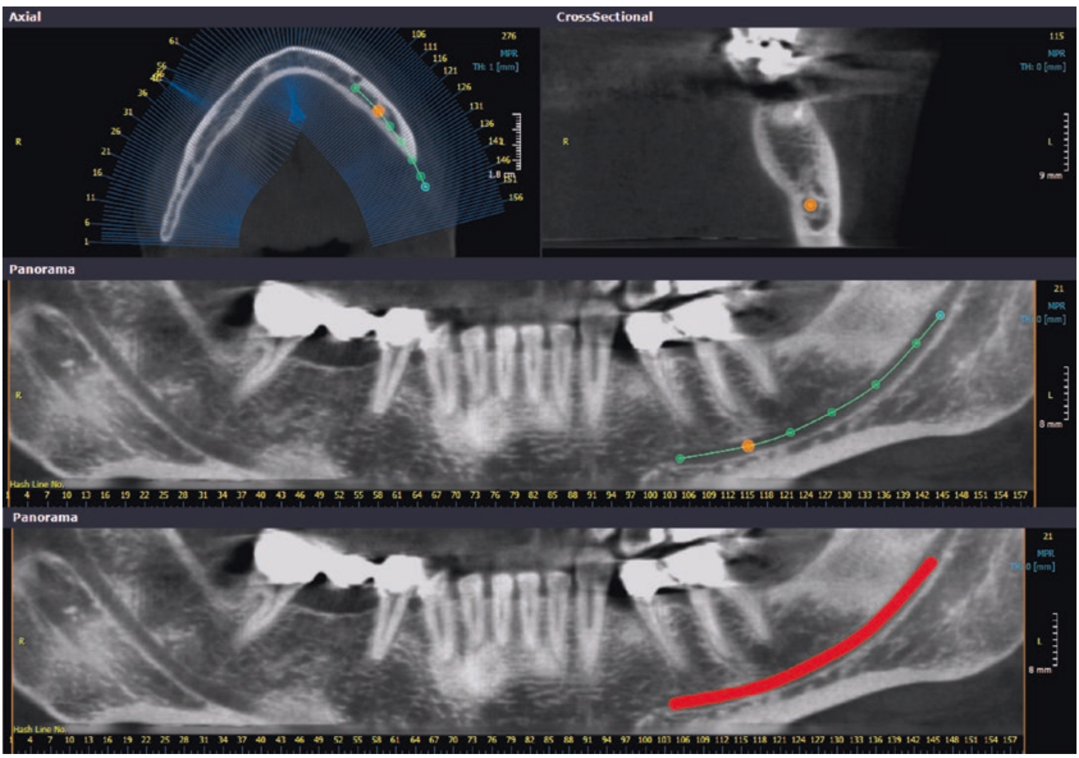

Fig. 20.64 Screen capture of software that uses the reformatted panoramic (*middle*) and axial (*upper left*) images to identify nodes to mark the location of the IAC as it progresses serial cross-sectional images through the mandible (*upper right*). After the position of the IAC is confirmed (*green dots*), the final tracing (*red*) is generated (*lower*)

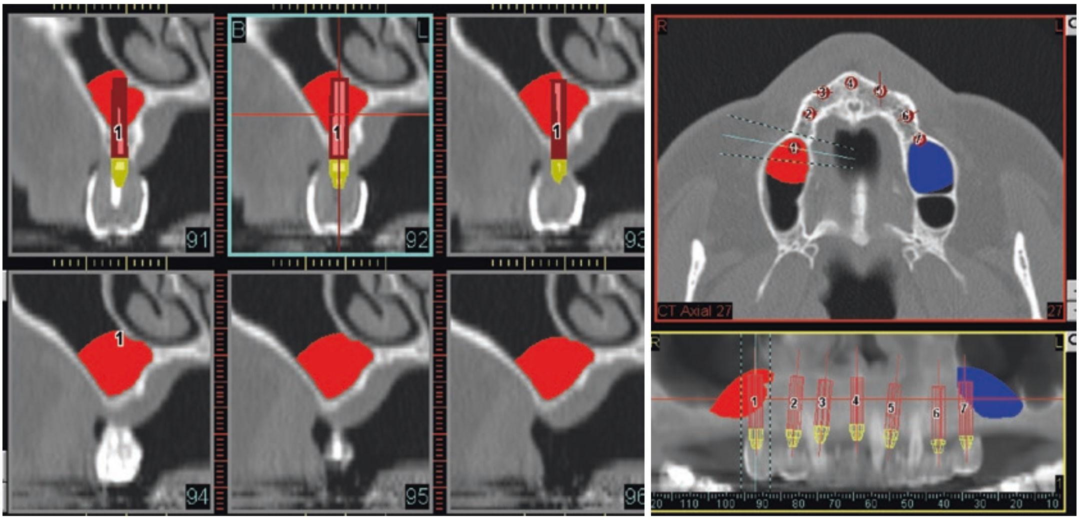

Fig. 20.65 Screen capture of completely edentulous maxilla with radiographic template showing simulated virtual placement of multiple implants. The most posterior implants bilaterally are positioned into the anterior recess of the maxillary sinus. The *red* and *blue* volumes indicate anticipated bone graft material required for successful sinus lift and bone augmentation procedure

axial or cross-sectional contiguous frames. Qualitative dimensions both linearly and volumetrically can be derived from these simulations to assist preoperatively in defining the limits of bone harvest material or amount of synthetic bone that is needed to bone placement to ensure against over- and underfilling (Fig. 20.65).

- *Implant Property Selection*. Two methods are available to define the shape and size of the implant graphic appearance.
- An optimal generic or custom implant can be developed and used based on the confines of the available alveolar bone. Numerous implant characteristics can be adjusted such as implant length, shape (cylinder or tapered apically), and width. For tapering implants, both the platform width and the apical diameter can be adjusted. The disadvantage of this approach is that once the "ideal" implant is fabricated it is necessary then to compare these dimensions to those commercially available. As few surgeons use more than two or three manufacturers' implants, the process reduces to comparing the optimal properties of the implant to those which are used by the specific surgeon.
- More commonly, vendor-specific implant graphics are chosen from an implant catalogue that correspond to the design dimensions of various manufactured implants. These are able to be selected from a list or vendor-specific library (Figs. 20.66).
- *Surgical Confidence Limit Indication*. A safety zone of bone should be considered to envelope an implant considering the inherent surgical tolerance of the dental implant placement. Software commonly allows the application of a variable virtual peri-circumferential zone around the endosseous zone of the implant body prompting the surgeon to consider the biological requirements for implant osseointegration. The tool has various designations including *collision detection* or *proximity detection*. The buffer zone layer can be adjusted by altering the preferences. The zone can be visualized as a solid color on planar images or as a transparency on volumetric rendered images. Options include the following:
- *Implant perimeter surgical confidence limit*. This provides a fixed dimensional thickness increase around the body of the implant, usually 1.5 mm (Figs. 20.67).

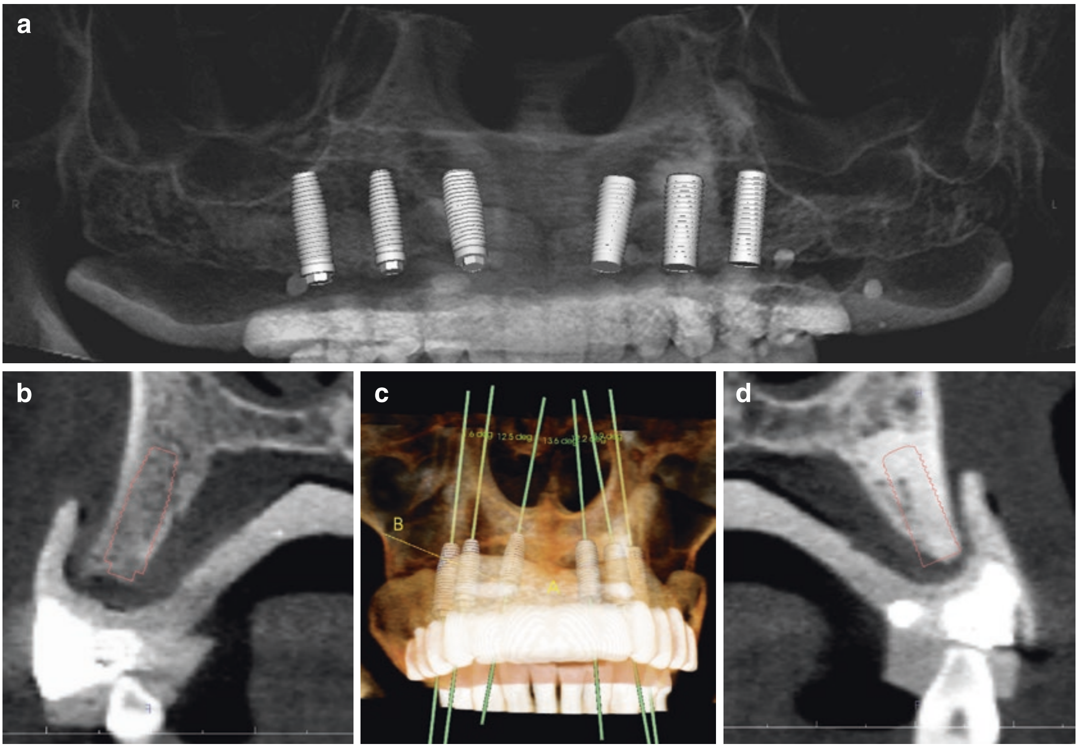

Fig. 20.66 Reformatted panoramic (**a**), volumetric rendered image (**b**) and right (**b**) and left cross-sectional CBCT images of the corresponding implant sites in the canine region bilaterally of a completely edentulous maxilla scanned with a radiographic template. Six virtual implants were chosen and a simulation performed using generic (*left*) and proprietary (*right*) bone level implants. Specific features of each implant are identified in each implant outline superimposed on the cross-sectional images

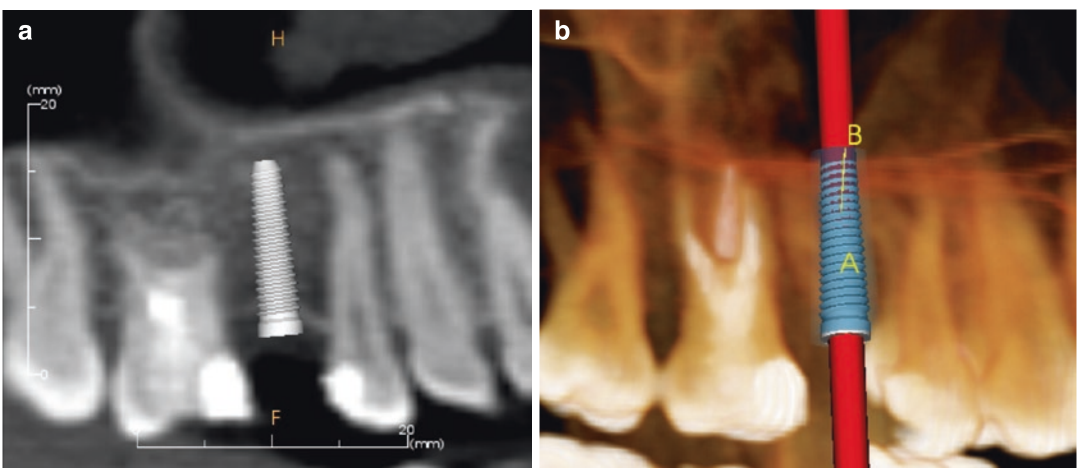

Fig. 20.67 Cropped reformatted panoramic image (**a**) and corresponding volumetric rendering (**b**) of a virtual tapering endosseous implant positioned in the bounded edentulous region of the maxillary right second premolar. The volumetric rendering (**b**) shows implant endosseous zone "coated" with a surgical confidence zone (transparent blue)

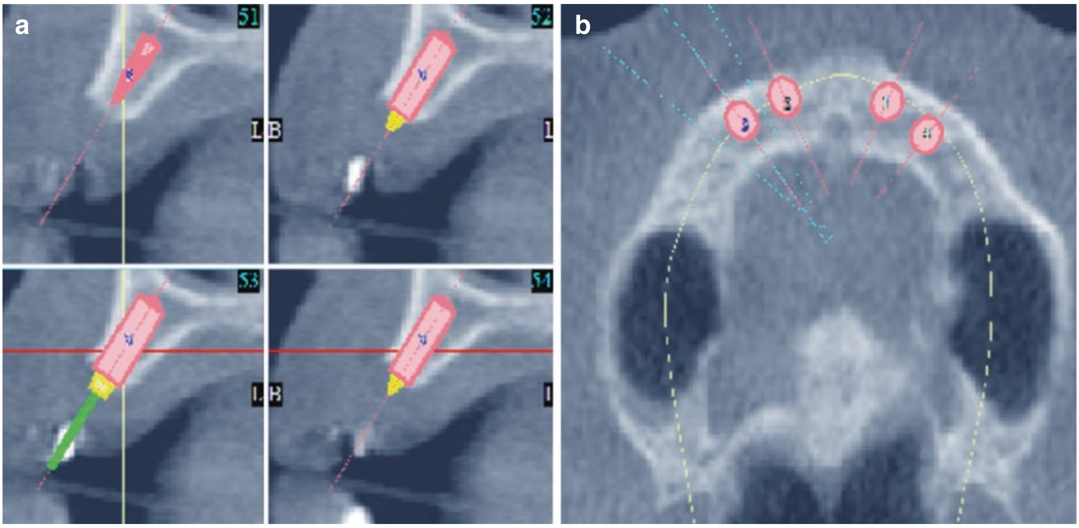

Fig. 20.68 Serial cross-sectional (**a**) and axial (**b**) CBCT images showing the virtual position of four implants planned for an edentulous maxilla. The cross-sectional images (**a**) show the position and emergence profile of the right most posterior implant. The implant bodies themselves are indicated by a light pink whereas the surgical confidence zone of 0.5 mm is indicated by a dark pink. Note the separate tapering drill tolerance limit, shown on the apical portion of the implant

- *Apical drill tolerance.* While the apical end of most implants is flat, the drill that is used for the surgical osteotomy is usually tapered and extends beyond the apical extent of the placed implant. Therefore, the osteotomy is usually prepared in a tapering shape approximately 1.5 mm apical to the implant. The apical drill tolerance feature provides a tapering thickness zone at the apical end of the implant which represents the taper of the surgical drill (Fig. 20.68).

Prosthetic Tools.
One of the most useful and highly efficient interactive tools available in implant planning software is the ability to add virtual prosthetic elements associated with implant simulation (Jacobs et al. 1999a, b). Various specific tools are available.

- *Implant Long Axis*. Visualization of the long axis of the implant body is important is aligning multiple implants to each other or adjacent teeth and in defining the angular deviation between the implant body and long axis of the abutment. If inclination implant body to the abutment is within the range of 12–15°, stress distribution within the implant system is similar to that of a parallel implant (Papavasiliou et al. 1996). The angular offset between the two should not be greater than 25°, otherwise there is a risk of failure due to non-axial forces. This tool also provides information that can be used to select the most appropriate abutment. Angular divergence between implant body and abutment can be compensated for by an offset abutment. These abutments are usually pre-fabricated at specific angles (stock), can be custom made or prepared. Determination of the correct type using simulation can substantially reduce chairside time and optimize crown fabrication.
- *Abutment Space*. The distance between the implant platform and the marginal soft tissue alveolar ridge is referred to as the *tissue depth* or *trans-mucosal tissue height*. Tissue depth varies greatly depending on the location of the implant in the dentition and between individuals and ranges from less than 2 mm to greater than 4 mm. Abutments are available in variable heights and should be chosen based on assessment of the cross-sectional image. An abutment that is too short will ultimately result in a restoration that blanches cervical

tissues and is prone to inflammation, whereas one that is too long can provide for a poor esthetic result, especially in the anterior aesthetic zone. Measurement of the tissue height prior to implant placement can assist greatly in selection of the abutment with the most appropriate height.

- *Restorative Elements.* Numerous biomechanical parameters can be measured in relation to the abutment that may direct the fabrication of the final prostheses and modify or anticipate implant placement (Fig. 20.69). Analysis of these factors may aid in the CAD/CAM design of the implant-supported prosthetic restorations (Bellaïche 2001).
- *Transition angle.* The angle that is formed by the long axis of the crown with a line that is perpendicular to the occlusal plane. Ideally this angle is less than 30° and should not exceed 60–70°.
- *Buccolingual cantilever.* The linear distance between the center of the implant emergence and the most buccal extent of the prosthesis. Ideally this distance should be less than 7 mm.
- *Crown height.* The distance between the occlusal extent of the final planned prosthesis and the gingival crown emergence plane.
- *Prosthesis:implant ratio.* The ratio of the distance between the combined length of the crown and the abutment height and the length of the implant body. This dimension should be similar to the crown:root ratio of the dentition to be replaced and should not exceed 1.
- *Moment.* Based on the previous dimensions it is possible to calculate vectors of force transmitted non-axially along the implant fixture. One method of quantifying this is the moment of the force or the rotational result of occlusal forces transmitted to the implant by the prosthesis.
- *Lateral Forces.* In addition, the percentage of the occlusal forces transmitted to the abutment/implant interface can be calculated and is referred to as the lateral force.

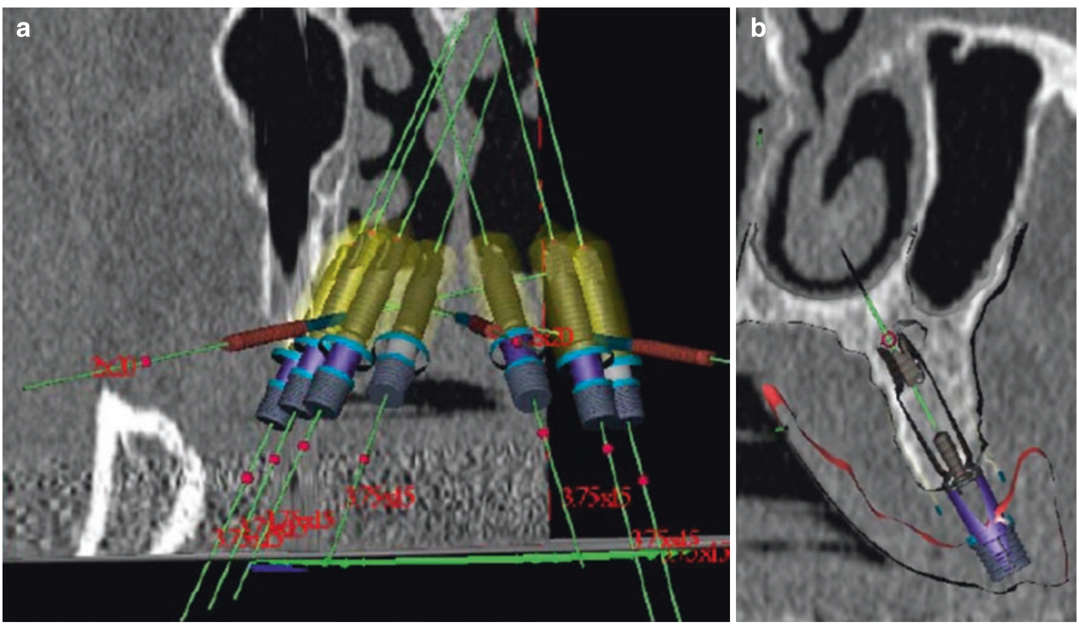

Fig. 20.69 Right coronal (**a**) with volumetric virtual implant placement overlay and representative cross-sectional (**b**) image with implant and prosthetic outline for a completely edentulous maxilla (**a**) The cross-sectional image visualizes location of the implant body with regard to available cortical and trabecular bone and adjacent anatomic boundaries (nasal fossa and left maxillary sinus) A transparent safety zone (*yellow*) surrounds the endosseous zone of the implant body. Esthetics are optimized by implant placement in relation to the occlusal level of the prosthesis and abutment designed by considering the mucosal thickness. Overall biomechanics (spread, parallelism, axial loading, etc.) can be confirmed by verifying the entire setup with and without prosthetic and bone models

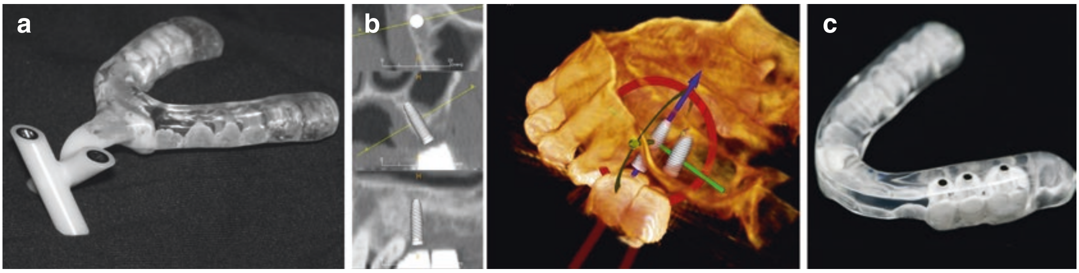

Fig. 20.70 A radiographic template including an X-marker fiduciary system for spatial orientation (**a**) is scanned in the patients mouth and a simulated implant plan using virtual implants created (**b**) The virtual plan is then transferred via a computer-driven milling table to the radiographic template which is transformed to the surgical guide (**c**) (Image courtesy, Thomas Fortin)

Computer-Assisted Planning/Computer-Assisted Guidance

Once interactive implant planning has been performed it is necessary to transfer the virtual implant plan to surgery. Many clinicians use free-hand surgical navigation based on mental transference of the visualized implant plan or alternately a surgical guide modified from a radiographic template. Although providing surgical freedom, this approach increases variability and decreases predictability of virtual simulations especially with advanced and complex surgical procedures.

Implant planning software at this level of integration incorporates the functionality of the previous levels and, in addition, the production of surgical guides to directly guide implant placement. The use of software at this level requires greater prosthetic design competency. There are essentially two systems capable of providing surgical guides. Appropriate software selection necessitates an understanding of their application within each specific system.

Software Directed Drilling

In this system the patient is scanned with a radiographic template in position and a virtual implant treatment plan developed. The plan is exported and, together with the radiographic template and mounted diagnostic casts, sent to a third party provider. The third party provider uses the virtual plan to convert the existing radiographic template into a surgical guide using a computer-driven milling table. As the radiographic template becomes the surgical guide, the cost in fabrication is somewhat reduced. Examples of this approach include the intraoperative drilling template using Med3D® (Med3D GmbH, Heidelberg, Germany), Compu-Guide using Virtual Implant Placement (Biohorizons, Birmingham, AL, USA) and Easy Guide® (Keystone, MN, USA) (Fig. 20.70).

Virtual Modeling

The alternate system is a totally virtual approach in which all phases of surgical and prosthetic planning from diagnostic cast wax up to surgical guide design and fabrication can be performed by software integrating prosthetic, esthetic, and surgical anatomic inputs. Virtual modeling can be modified, adjusted, and approved by various clinicians involved in the procedure. Thereafter, a computer-aided manufacturing may guarantee an accurate transfer to a surgical guide. Alternatively, the planning may be used for computer-aided surgical navigation.

Computer-Aided Design/Computer-Aided Manufacture (CAD/CAM)

In the mid-1990s van Steenberghe and coworkers introduced a CAD/CAM procedure creating both surgical guides and a full prosthesis for a completely edentulous arch using a double CT scan procedure (Verstreken et al. 1996a, b, 1998). A radiographic template, created from an existing approved full prosthesis with small gutta-percha spheres as fiducial markers is scanned in the mouth and separately. The two data sets are then fused and superimposed using specific software on the basis of the radiopaque gutta-percha markers and an implant placement plan generated.

A stereolithographic technique was used to fabricate a jaw bone model and a surgical guide from the CT data. Implants were then placed and immediately loaded using the original prosthesis. This original concept was initially termed Litorim (Leuven Information Technology-based Oral Rehabilitation by means of Implants) with the software later commercialized under the name Nobelguide® (Nobel Biocare, Kloten, Switzerland) and the procedure involving immediate loading by means of a CAD/CAM prefabricated fixed denture, Teeth-in-an-Hour™ (Nobel Biocare, Kloten, Switzerland) (van Steenberghe et al. 2005) (Fig. 20.71). Since then, similar concepts have been developed by other implant manufacturers. Despite some differences, the primary concept remains the integration of biomechanical, aesthetic, and anatomic information in a virtual environment facilitating integration of implant surgical and prosthesis design (Vercruyssen et al. 2015).

The clinical efficacy of this approach is dependent on the additive maximum deviations observed associated with all elements involved in process including the data acquisition and planning phases (e.g., accuracy of CBCT data, errors associated with superimposition of multiple datasets), fabrication variability (CAM tolerances), and surgical technique.

Image-Guided Surgery and Navigation

IGS in implant therapy has undergone significant evolution and rapid technological advancements in recent years. IGS levels of integration previously described range from fundamental preoperative planning using computer-assisted assessment to CAD/CAM procedures. At higher integration levels, planning information is used to fabricate surgical guides containing drill guides that transfer the virtual planned implant position to the operating field of the patient. These techniques are referred to as *static systems* (Jung et al. 2009). *Dynamic systems*, on the other hand, communicate the selected implant positions to the operative field with visual imaging tools on a computer monitor, instead of rigid intraoral surgical guides. These include surgical navigation and computer-aided navigation technologies, and allow the surgeon to alter the surgical procedure and implant position in real time using the anatomical information available from the virtual preoperative plan generated from CBCT data.

Surgical navigation systems typically consist of a virtual plan transferred to the operation theatre using a reference frame and optical tracking system. CT or CBCT images of a patient are obtained with a dedicated fiduciary splint and preoperative virtual treatment plan developed. At the time of surgery, the patient wears the same splint to localize and spatially match the actual position of the patient to the CBCT data. Both splint and dental hand piece are equipped with strategically located infrared emitters communicating with various camera detectors placed in the operation room. These infrared emitters guar-

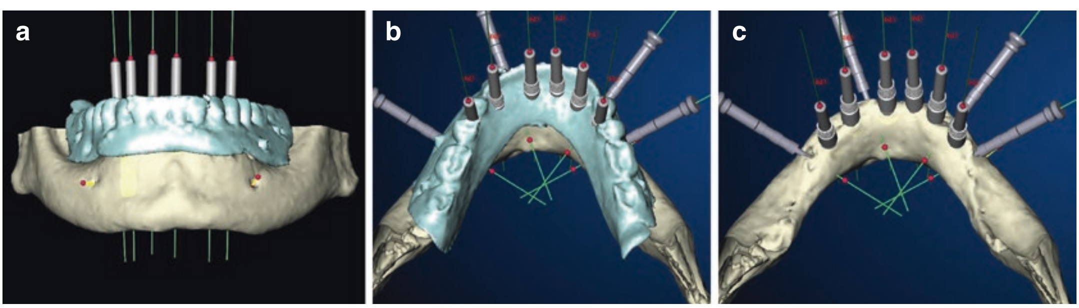

Fig. 20.71 Frontal (**a**) and oblique occlusal volumetric rendering with (**b**) and without (**c**) superimposed previously scanned implant supported mandibular prosthesis of a completely edentulous mandible showing prosthetic and anatomic elements and simulated implant plan using virtual implants. The surgical and prosthetic plan is exported and a surgical guide will be fabricated and fixed to the mandible during the transmucosal osteotomies using anchor pins. The final prosthesis will also be fabricated and inserted immediately after implant insertion (images courtesy, Luc Vrielinck)

antee accurate tracking of movements of the jaw and the handpiece during surgery. This arrangement allows for real-time feedback and continuous tracking of the drillhead and actual implant locations in relation to the jaw bone and the virtual placed implants. Dynamic systems provide real-time virtual surgical guidance that may be altered according to the conditions encountered during surgery.

The first image-guided surgical navigation system for implant surgery, Image-guided Implantology (IGI®, Image Navigation Ltd., New York, NY, USA) was introduced and validated in 2002 (Wanschitz et al. 2002). Since then multiple systems have been introduced including RoboDent NaviPanel (RoboDent GmbH, Ismaning, Germany) (Meyer et al. 2003), Vector Vision 2, (BrainLAB, Munich, Germany) (Mischkowski et al. 2006), IGI (DenX Advanced Dental Systems, Moshav Ora, Israel) (Casap et al. 2005), VISIT® (Vienna General Hospital, University of Vienna, Vienna, Austria) (Wanschitz et al. 2002), and StealthStation S7 Treon navigation system (Medtronic, MN, USA) (Widmann et al. 2005). Examples of currently available systems are shown in Table 20.4 (Bordin et al. 2016).

Table 20.4 Examples of currently available dynamic navigation systems for implant dentistry

Name	Components	Operation
DenX Image Guided Implantology System[a]	Hand piece attachment Patient jaw attachment (IGI horseshow) Mobile cart with cameras, monitor, computer, and software	An intraoral one splint is used to position and secure the IGI horseshoe reference and the patient tracker The CBCT scan is taken with the splint with the IGI horseshoe containing ceramic reference markers in the mouth Virtual planning is performed Tracking guide is attached to IGI shorseshow and registered prior to surgery Camera is calibrated to ceramic markers
XGuide Dynamic 3D Navigation[b]	Three (3) components, as above	CBCT is performed with jaw attachment in place Virtual planning is performed Prior to surgery, the hand piece attachment is secured to the hand piece and the jaw attachment to a patient splint
Navident[c]	Notebook Universal hand piece attachment comprising removable metal clamp and plastic "drill tag" Customizable jaw attachment comprising a stent (JawRef) and plastic tag (JawTag) Optical sensor reporting real-time position of DrillTag and jaw tag	JawRef is fitted to dentition and CBCT performed Virtual planning is performed JawRef is placed in the mouth and the DrillTag is latched on the drill clamp
Inliant[d]	Two proprietary cameras Hand piece has laser engraved markers Special markers attached to patient stent	Cameras are attached to existing dental light No hand piece attachment Perioperative use of special markers attached to stent.

CBCT cone beam computed tomographic imaging
[a]Image Navigation, Jerusalem, Israel
[b]X–Nav Technologies, Lansdale, USA
[c]ClaroNav, Toronto, Canada
[d]Inliant Dental Technologies, Vancouver, Canada

Some of these systems may not have US FDA approval, which is necessary for use in the United States.

Numerous technical issues exist to this approach including bulkiness of the handpiece with the attached fiducial apparatus and the need for multiple calibrations during the procedure to prevent signal loss which result in reduced implant placement accuracy compared to static system techniques (1 mm up to 3 mm).

20.5 Radiographic Templates

Various techniques have been proposed to facilitate the transfer of clinical information related to the proposed implant position and orientation to CT imaging. Most involve the fabrication of a radiographic template. A number of types of diagnostic radiographic templates have been described in the literature (Burns et al. 1998; Higginbottom and Wilson 1996; Almog et al. 2002; Meitner and Tallents 2004) and include tooth outline-type templates, spherical type markers, wire overlay type markers, or cylindrical markers (Fig. 20.72).

- The original denture can be coated with high density barium varnish. The ideal implant placement is determined based on the visualization of the bone-volume and the barium-coated crowns. A surgical guide is fabricated by duplicating the existing denture. The position of the implants can be marked on the guide by means of holes, extending to form grooves (Israelson et al. 1992).
- Alternately a duplicate of the existing denture (Verde and Morgano 1993) or diagnostic wax-up can be fabricated and gutta-percha spheres, gutta-percha or silicone (Tsuchida et al. 2004) filled location holes can be placed at the desired location of each implant fixture. More recently precision milled cylinders have been used with this purpose (Kopp et al. 2003; Pontual et al. 2004; Sammartino et al. 2004).
- Verstreken et al. (1996a, b) describe a dual scanning technique, enabling the complete prosthetic visualization on CT or CBCT images in which there is principally no need for a replica of the prosthesis or a new diagnostic setup. This technique is unique as it can make use of the existing prosthesis, if it has a satisfactory prosthetic setup and can be relined to guarantee optimal mucosal fit. Alternatively, a replica or new diagnostic wax-up can be made. In each case, at least 6 gutta-percha points, spheres, or even glass balls are optimally spread to serve as orientation markers for repositioning the prosthesis on the patient's anatomic model. This is possible by scanning the jaw with the prosthesis in situ, ideally fitting with the mucosa and/or neighboring teeth and then making a scan of the scan prosthesis alone at a low exposure parameter protocol.
- Based on a diagnostic wax-up, a plastic radiographic template can be constructed and gutta-percha applied in a buccal groove parallel to the occlusal plane and in a groove parallel to the long axis. This represents the ideal implant position according to the prosthesis. The patient is scanned with the device inserted and analysis of this site(s) is performed using implant placement software. The original radiological guide is then transformed into a surgical guide by cutting a lingual or palatal window through the acrylic resin plate (Klein et al. 1993; Pesun and Gardner 1995). This method can also be performed using an initial patient acceptance prosthesis (Amet and Ganz 1997). An alternate method is to construct a radiopaque barium sulfate radiographic template and cut buccal grooves or place location holes in the template at the proposed implant site prior to scanning. The full contour radiopaque template enables the clinician to visualize the outline of the planned restoration in

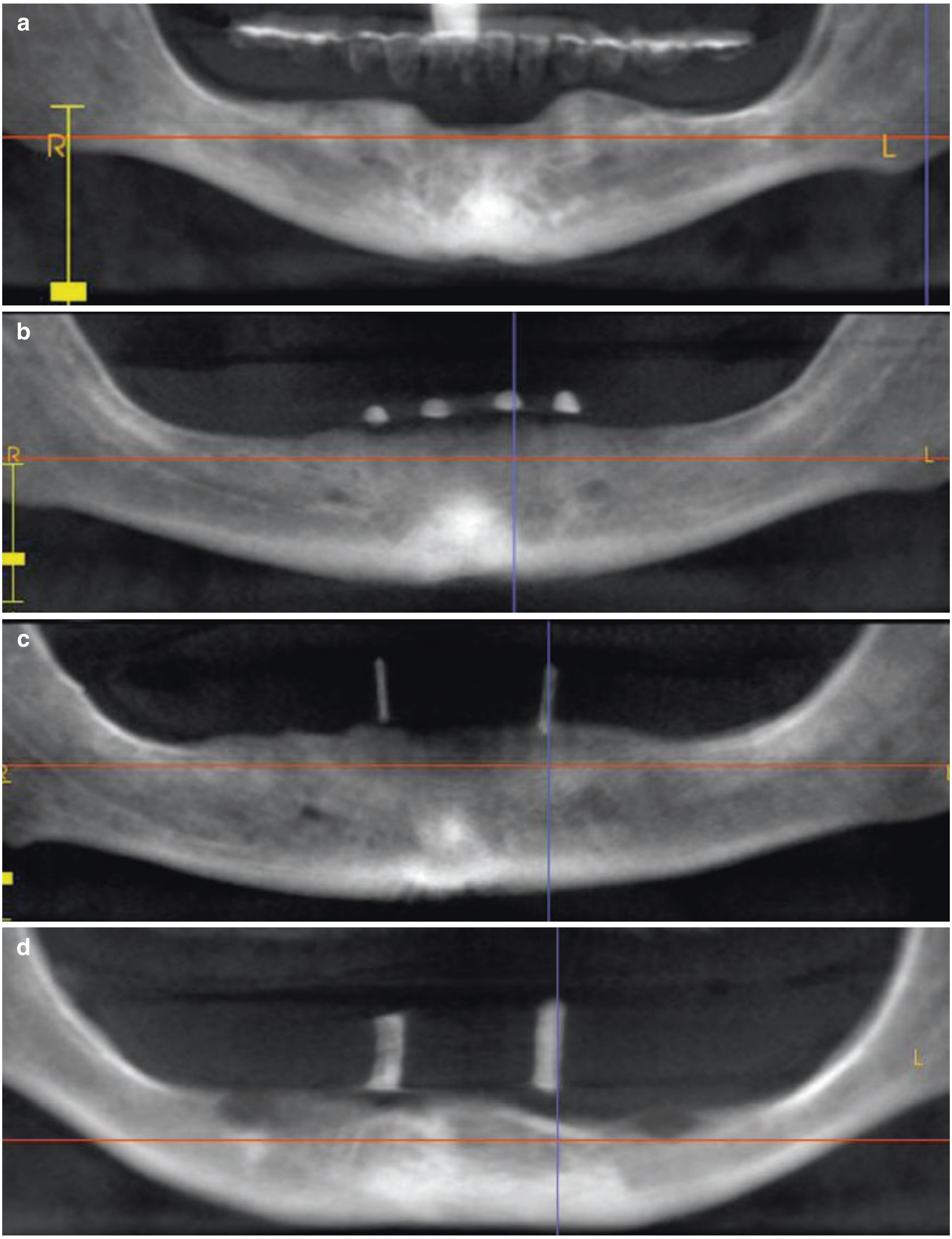

Fig. 20.72 Reformatted 20 mm panoramic CBCT images demonstrating appearance of tooth outline markers (**a**), spherical markers (**b**), wire onlay type markers (**c**), and cylindrical markers (**d**) used in radiographic templates to designate the potential location of implants according to a prosthetic plan for a completely edentulous mandible

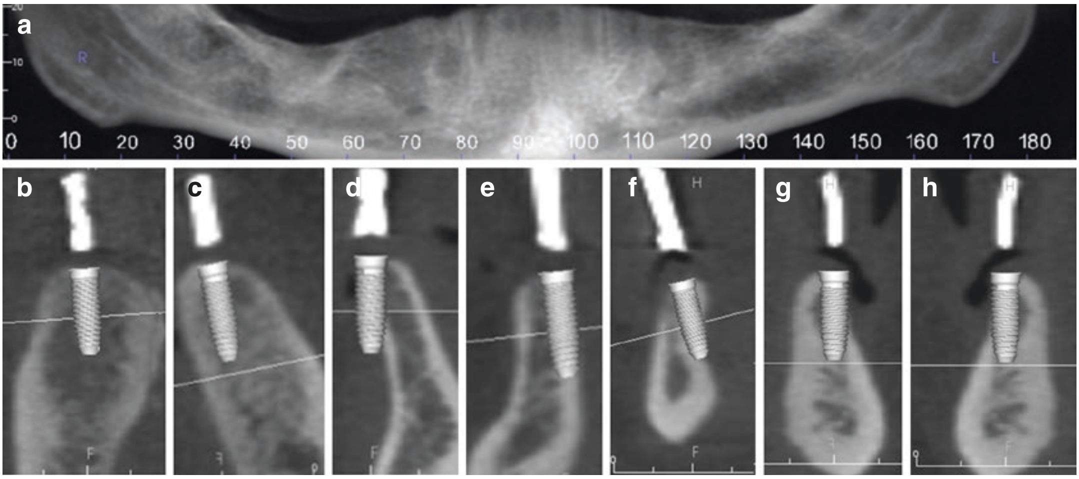

Fig. 20.73 Reformatted panoramic (**a**) with radiographic template with cylindrical radiopaque markers identifying restoratively projected position of the implants for implant-retained mandibular overdentures based on visual inspection, diagnostic casts, and panoramic radiography only. Representative cross-sectional images showing possible variations between projected and surgically acceptable virtual implant positions—ideal position (b – 6.4%), minor adjustment necessary (c – 20.2%), buccally displaced (d – 7.8%), lingually displaced (e – 1.8%), lingually fenestrated (f – 6.4%), lingual dehiscence (g – 9.3%), and buccal dehiscence (h – 47.1%) (Scarfe et al. 2012)

relation to the bone structures (Basten 1995; Basten and Kois 1996).

- Weinberg and Kruger (1998, 1999) present a system using both radiographic and photographic data. A radiographic template is fabricated and vertical orientation pins are placed at the crest of the alveolar ridge, representing the ideal implant position. Once the CT is taken, a photographic duplicate is made. A vertical line through the center of the pin is drawn. Another line is drawn through the starting point of the osteotomy, but now representing the ideal position according to the available bone volume. The difference between both is measured in degrees and transferred to the cast by means of a dual-axes table. The ideal inclination for implant placement is then transferred to the surgical guide by means of guide tubes (5 mm).
- Tomotake et al. (2002) describe the fabrication of a plastic life-size skull model by a photocurable plastic modeling system. This technique provides three-dimensional modeling of anatomic structures from computed tomography. The model is mounted in the articulator. Planning of the implants is done, using CT data, the model, and clinical examination. An individual template is designed, and implant replicas are placed in the plastic model, allowing to preoperatively fabricate the framework of the prosthesis. Thus immediate loading of the implants can be achieved while offering a rigid splinting of them.

Radiographic templates are useful in planning implants for implant supported mandibular overdentures (Scarfe et al. 2012a) (Fig. 20.73) and especially for bounded regions in the anterior maxilla—the anterior esthetic zone (Fig. 20.74).

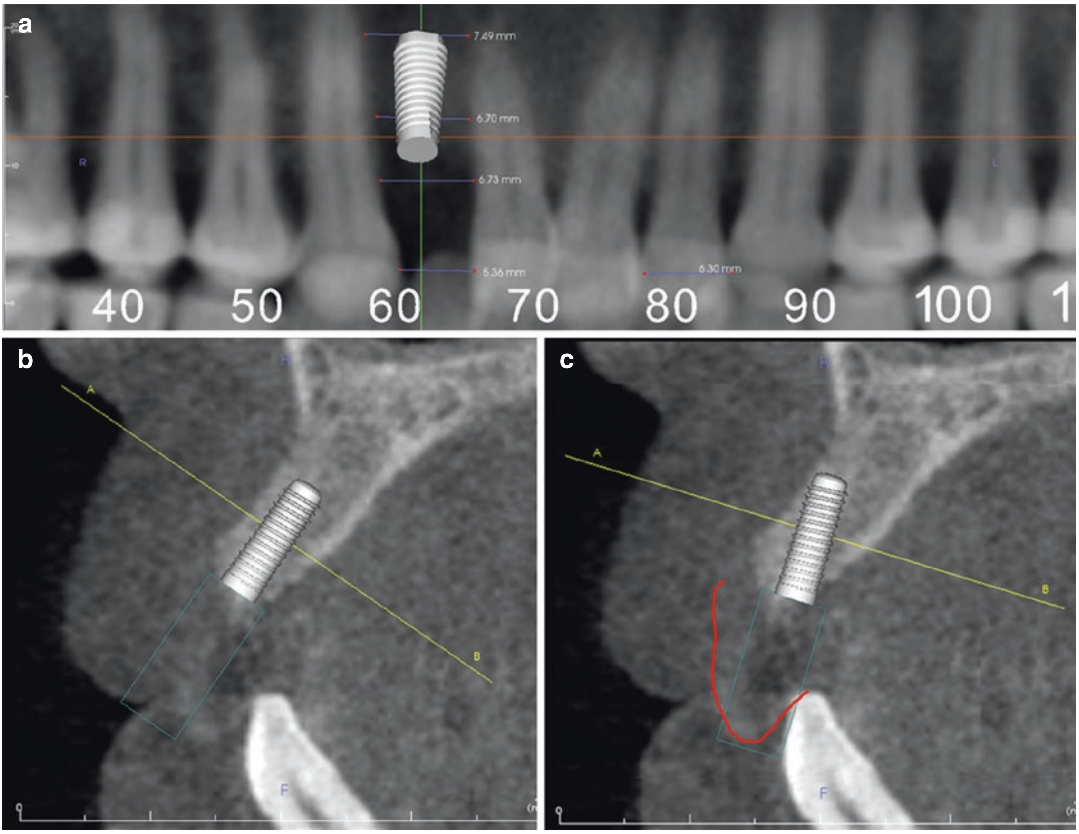

Fig. 20.74 Reformatted panoramic CBCT image (**a**) with appropriately sized, screw retained, bone level virtual implant positioned in the edentulous bounded space of the previous maxillary right lateral incisor with an optimal 1.5 mm of bone between the implant and adjacent tooth roots. Cross-sectional image with virtual implant positioned optimally surgically ((**b**)—within the available bone) and optimally prosthetically ((**c**)—platform corresponding to within 2 mm of the adjacent tooth CEJ level and angled such that the emergence profile is directed towards the palatal aspect of the crown). Optimal implant positioning for a screw retained prosthesis requires bone grafting

20.6 Clinical Efficacy of Image-Guided Implant Therapy

20.6.1 Use of Virtual Implant Treatment Planning

A number of authors have reported on the effect of the preoperative use of cross-sectional imaging, such as CBCT, and implant treatment planning, on preoperative assessment, treatment, or outcome (Table 20.5). Various outcome measures have been reported including choice of implant length, implant width, or both, change in treatment plan, or necessity for bone grafting or sinus augmentation surgery. Early reports present equivocal data, whereas more recent studies demonstrate a clear benefit. While systematic analysis of the current data shows no clear evidence for the use of cross-sectional imaging or virtual treatment planning for the assessment of all dental implant sites (Shelley et al. 2014), the increasing adoption of CBCT and virtual implant treatment planning clearly outpaces our ability to describe and quantify the benefits to clinical practice.

Table 20.5 Summary of studies reporting the clinical efficacy of the availability of cross-sectional imaging, including CBCT, or virtual implant planning

Author (year)	Study			Conclusions
	Patients	Implants	Modalities	
Correa et al. (2014)	71	103	Pan vs. CBCT	• CBCT predicts narrower and shorter implants in premolar areas
Guerrero et al. (2014a)	108	365	Pan vs. CBCT	• CBCT predicts need for bone graft augmentation and perioperative complications • CBCT predicts use of shorter implant length in posterior
Guerrero et al. (2014b)	105	619	Pan vs. CBCT	• CBCT predicts use of shorter implant length in posterior but not anterior region
Schropp et al. (2011)	121	121	Pan vs. XS	• Implant choice differed in 89% • Implants planned on XS were longer than those planned on pans in 47% and narrower in 30%
Diniz et al. (2008)	29	113	ST vs. pa + Pan	• CT results in change in choice of implant length (39.8%) and width (18.8%) • In 15.8% and 5.3% of cases bone grafting and other procedures were planned only after CT
Frei et al. (2004)	50	77	ST Vs. pan + clinical	• Very minor impact (approx. 4%) on implant choice in mandibular molar and premolar areas
Schropp et al. (2001)	46	46	ST vs. pa + Pan	• XS results in change in choice of implant in 70% of the cases
Jacobs et al. (1999a)	33	139	Pan vs. pan + CT	• Addition of CT changes choice of implant length 66%
Jacobs et al. (1999b)	100	416	CT vs. surgery	• Longer implants are planned in 20% of cases in the maxilla and 35% in the mandible • CT is poor for predicting anatomical complications

Pan panoramic radiography, *XS* cross-sectional tomograms, *pa* periapical radiographs, *ST* spiral linear tomography, *CT* computed tomography, *nr* not reported

20.6.2 Use and Fabrication of Static Surgical Guides

Numerous methodologies for CBCT-based implant planning using a fabricated surgical guide have been reported and recently summarized (Vercruyssen et al. 2015). Two principal manufacturing methodologies can be distinguished—those that convert the radiographic template into a surgical guide and those that fabricate a separate stereolithographic surgical guide. Static image-guided systems can also be differentiated in regard to their respective design for the drill guidance through the template; some systems use multiple surgical guides with sleeves of an increasing diameter, others use of drill keys inserted into base sleeves within the guide, which guide the consecutive drills with increasing diameters. Particular systems foresee special drills or drill stops to allow depth control, while other systems use indication lines on the drills. Some systems allow a guided insertion of the implant (fully guided implant placement), while for other systems, the template has to be removed to allow freehanded implant insertion. A guide can be tooth, bone, or mucosa supported. The choice is primarily made on the number of remaining teeth for support of the guide and on the appropriateness of a flapless approach.

Van Assche et al. (2012), Tahmaseb et al. (2014), and Bornstein et al. (2014) summarized the published evidence defining the accuracy clinical performance, limitations, and complications of surgical guides in static systems in image-guided surgical implant dentistry. Between static surgical guiding systems, significant variations can be observed (Van Assch et al. 2012). From 14 clinical and 10 in vitro studies Tahmaseb et al. (2014) found results for nine computer-guided systems, the majority of which reported results for the NobelGuide. Overall they found the mean error at the implant entry to be 1.12 mm, with a maximum of 4.5 mm, a mean error at the apex of 1.39 mm, with a maximum of 7.1 mm, and an average angular deviation was 3.89° with a maximum of 21.16°. They also reported statistically higher accuracy for the flapless (c.f. flap) approach, guided (c.f. freehand) placement, and the use of tooth supported mucosa or mucosa and pin supported guides (c.f. bone supported).

Guided implant surgery reduces clinical inaccuracy in transferring the virtual implant position planned using software and the actual final position of the implant. While applicable to any implant situation, current systems all involve multiple stages within the workflow, each with inherent error. Cumulative error results from radiographic imaging, image measurement and segmentation, the virtual plan, surgical guide fabrication, the positioning of the template, and the surgical procedure itself.

Nevertheless, IGS-specific indications are situations that involve minimal invasive surgery, require high tolerance for implant planning and positioning such as esthetic cases and many immediate loading procedures (Hämmerle et al. 2015).

20.7 Guidelines and Recommendations

There is a continuous and rapid evolution of techniques, protocols, and procedures related to specific software and prosthetic manufacturing technologies. Numerous authors, societies, organizations, and government agencies have provided guidelines for the use of cross-sectional radiography, specifically CBCT imaging, for the pre- and/or postoperative assessment of potential dental implant sites (Table 20.6).

Table 20.6 Summary of guidelines for the use of CBCT for the assessment of potential dental implant sites

Author (year)	Organization		
	Name	Type	Country
Dula et al. (2015)	SGDMFR	PO (S)	Switzerland
Hämmerle et al. (2015)	EAO	PO (MD)	European
Bornstein et al. (2014)	ITI	PO (MD)	International
Tyndall et al. (2012)	OMFR	PO (S)	USA
Harris et al. (2012)	EAO	PO (MD)	European
DGZMK (2012)	DGZMK	PO (MD)	Germany
Benavides et al. (2012)	ICOI	PO (MD)	International
EC (2012)	EC	GA (I)	European
SHC (2011)	SHC	GA (N)	Belgium
SEDENTEXCT (2011)	SEDENTEXCT	GA (I)	European
AO (2010)	AO	PO (MD)	International
ARö (2009)	German dental association	PO (G)	Germany

AAOMR American Association of Oral and Maxillofacial Radiology, *AO* Academy of Osseointegration, *ARö* Association for Radiology, *EADMFR* European Academy of Dentomaxillofacial Radiology, *EAO* European Academy of Osseointegration, *EC* European Commission, *ICOI* International Congress of Oral Implantologists, *DGZMK* German Society of Dental Sciences, *OMFR* Oral and Maxillofacial Radiology, *SEDENTEXCT* Safety and Efficacy of a New and Emerging Dental X-ray Modality Computer Tomography, *SGDMFR* Swiss Society of Dentomaxillofacial Radiology, *SHC* Superior Health Council, *PO* (*S*) dental professional organization, specialty, *PO* (*G*) dental professional organization, general, *PO* (*MD*) dental professional organization, multi discipline, *GA* (*I*): government agency, international, *GA* (*N*) government agency, national

The reported indications for CBCT use in implant dentistry vary from preoperative analysis regarding specific anatomic considerations, site development using grafts, and computer-assisted treatment planning to postoperative evaluation focusing on complications due to damage of neurovascular structures. Recommendations are most often consensus-based or derived from a limited methodological approach with only partial retrieval and/or analysis of the literature or contain even generalized or non-case-specific statements. These statements vary from recommendations for widespread to selected use. However, certain underlying principles for CBCT use in implant therapy are common.

- When cross-sectional information is considered necessary, CBCT is preferable to MDCT as the imaging modality of choice.
- Cross-sectional radiographic techniques are to be considered an adjunctive imaging modality with the need for CBCT imaging e based on the clinical examination, the treatment requirements, and information obtained from standard imaging modalities.
- CBCT imaging should be specifically considered preoperatively for the following clinical situations:
  - Where there is clinical doubt of alveolar bone volume or morphology.
  - In specific regions of the jaws where there is concern that anatomic structures may

compromise implant placements such as: (1) anterior maxilla (nasal floor, naso-palatine canal, anterior superior alveolar canal), (2) posterior maxilla (maxillary sinus and related structures, posterior superior alveolar canal, maxillary tuberosity, pterygoid plates, (3) anterior mandible (lingual foramen, incisive canal, genial tubercles), (4) posterior mandible (inferior alveolar nerve canal, mental foramina, anterior loop, retromolar foramen, sublingual fossa (lingual undercut), mylohyoid undercut, lingula of ascending ramus), and (5) zygomatic region (orbital floor, infraorbital foramen, zygomatic bone).
  - Anterior esthetic region.
  - When site development is anticipated (e.g., sinus augmentation block or particulate bone grafting ramus or symphysis grafting).
  - When concomitant pathology is observed or a history of previous traumatic injury.
  - When CAD/CAM procedures are planned.
- CBCT imaging should be specifically considered postoperatively to assess the success of augmentation procedures and integration of graft materials, when implant retrieval is considered and when patients present with surgically related implant complications (e.g., including altered sensation, infection/postoperative integration failure, implant mobility, and concomitant rhinosinusitis).
- CBCT should be provided using dose optimization protocols involving exposure (mA and kVp), image-quality parameters (e.g., number of basis images, resolution), and field of view restrictions to the region of interest such that images are provided with patient radiation doses as low as diagnostically acceptable (ALADA).
- The use of a radiographic template is advisable to maximize surgical and prosthetic information.

Most guidelines do not offer evidence-based action statements developed for specific case scenarios. The International Team for Implantology (ITI) has recommended the SAC classification to categorize implant treatment procedures into three levels of difficulty: straightforward, advanced, and complex. This system provides general and site-specific criteria in defining case types as regards surgical degree of difficulty (Chen et al. 2009). As CBCT imaging provides information in the surgical domain regarding bone volume, anatomic risk, esthetic risk, and surgical complexity, it is reasonable to designate CBCT imaging appropriateness for specific clinical scenarios. Based on the SAC classification, a hierarchy of imaging need for CBCT imaging in implant therapy can be developed based on potential preoperative contribution relative to diagnostic and surgical value (Scarfe 1998):

- *Level I* (*LI*). CBCT is an essential and necessary imaging modality providing valuable diagnostic information in most clinical situations. All SAC complex cases should be designated Level I.
- *Level II* (*LII*). CBCT is a highly desirable imaging modality providing valuable diagnostic information in many clinical situations. All SAC advanced cases should be designated Level II.
- *Level III* (*LIII*). CBCT is an appropriate imaging modality that may contribute to diagnostic information in some clinical situations. All SAC simple cases should be designated Level I.

Applying this hierarchy to site-specific surgical scenarios as defined by ITI (Chen et al. 2009) provides logical, clinically based guidelines for the necessity of CBCT imaging in implant dentistry (Table 20.7).

Table 20.7 Necessity of CBCT imaging according to SAC classification of bone volume using the ITI SAC surgical clinical case system (after Scarfe et al. (2012a, b))

Surgical classification			CBCT imaging necessity			
Region to be restored	Esthetic risk	Example	Sufficient	Horizontally deficient, possible simultaneous augmentation	Horizontally deficient, prior grafting possible	Vertically and/or horizontally deficient
Single tooth	Low	Mn PM/M 1	LIII (S)	LII (A)	LI (C)	LI (C)
	High	Max central, Inc.	LII (A)	LII (A)	LI (C)	LI (C)
Short edentulous space	Low	Mn PM/M	LIII (S)	LII (A)	LI (C)	LI (C)
	High	Three Mx ant teeth	LII (A)	LII (A)	LI (C)	LI (C)
Extended edentulous space	Low	Mx post posterior	LIII (S)	LII (A)	LI (C)	LI (C)
	High	Mx ant teeth	LII (A)	LII (A)	LI (C)	LI (C)
Full arch	Low	Edent man, 2 implants	LIII (S)	LII (A)	LI (C)	LI (C)
		Edent man, 4 or more implants	LII (A)	LI (A)	LI (C)	LI (C)
	High	Edent Mx, 4 implants	LIII (S)	LII (A)	LI (C)	LI (C)
		Edent Mx, 4 or more implants	LII (A)	LI (C)	LI (C)	LI (C)
Single rooted tooth, immediate replacement	Low	Man PM	LIII (S)	LII (A)	LI (C)	LI (C)
	High	Mx/Mn In and Can	LI (C)	LI (C)	LI (C)	LI (C)
Multi rooted tooth, immediate replacement	Low	Mx PM1	LII (A)	LI (C)	LI (C)	LI (C)

S Simple *A* advanced, *C* Complex, *LI* Level I Imaging, *LII* Level II Imaging, *LIII* Level III Imaging, *Ant* anterior, *Can* canines, *Edent* edentulous, *PM1* first premolar, *In incisors*, *Man* mandibular, *Mx* maxillary, *M* molar, *Post* posterior, *PM* premolar

20.8 Postoperative Assessment

The assessment of postoperative implant performance primarily relies on clinical evaluations such as the detection of mobility, the clinical signs of gingival inflammation, periodontal attachment loss, and pocket formation, supplemented with imaging to define the degree of bone loss. Progressive peri-implant bone changes may occur at the alveolar crest. Traditional implant success criteria include an acceptable marginal bone loss of ≤0.5 mm in the first year and <0.2 mm annually thereafter (Albrektsson et al. 1986; Smith and Zarb 1989). Recently, however, there have been suggestions for these criteria to be revised, indicating that a more acceptable bone loss for modern implant systems would be 0.3 mm over 5 years.

CBCT imaging is inappropriate for postoperative marginal bone loss assessment because it lacks the necessary resolution to monitor this level of change. In these cases, the diagnosis of an ailing or failing implant is usually based on periodic implant mobility testing or spontaneous complaints. Intraoral periapical radiography

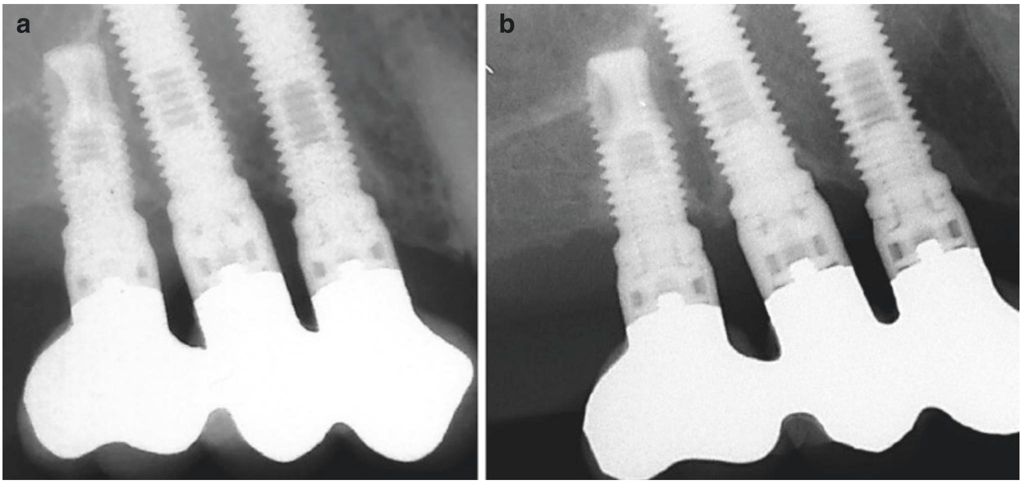

Fig. 20.75 Periapical images of dental implants in the maxillary right posterior region at time of restoration (**a**) and after 12 years (**b**) without evidence of marginal bone loss. Note marginal bone densification, which is more pronounced in the stress-bearing areas (mesial and distal borders of the bridge)

using the long cone paralleling technique remains the method of choice for postoperative radiographic follow-up (Fig. 20.75). Many implant materials induce metal image artifacts in alveolar bone adjacent to the implants, reducing the visualization of implant-to-bone contact and marginal alveolar bone height. Although rare, most dental implant body failures tend to occur early due to lack of osseointegration and cluster in patients with common profiles or risk factors (van Steenberghe et al. 2002). Patient factors, such as uncontrolled diabetes type II and smoking, are important risk factors. Long-term radiographic assessment may demonstrate local densification of the bone adjacent the implant, presumably a result of positive stress-induced reactive bone (Fig. 20.75).

While periapical radiography at specific intervals is currently the principal modality for radiographic assessment, CBCT should be considered in specific circumstances, such as failure of sinus lift and bone augmentation, the presence of large defects associated with implant failure or if reconstructive techniques are anticipated. CBCT imaging provides valuable information on the extent of the regional bone destruction in these situations.

20.8.1 Bone Augmentation

Survival rates for implants placed using the sinus lift technique are greater than 90% (Del Fabbro et al. 2004); however, sometimes postsurgical radiographic evaluation of the maxillary sinus is advisable (Tyndall et al. 2012).

Evaluation of the results of the sinus augmentation procedure 6 months to 8 months after placement of the graft material and prior to implant placement is advisable to confirm the presence of adequate bone. Graft material has a porous structure and gains radiodensity on CBCT as osseointegration and osteogenesis progresses. Imaging appearance will depend on the technique used. The most typical appearance associated with the sinus lift technique is a dome-shaped homogeneous radiopacity with or without flecks filling the floor of the maxillary sinus with an associated indentation, concavity or defect on the adjacent lateral wall of the maxillary sinus (Fig. 20.76). With the osteotome technique, a similar appearance to the sinus lift is observed, but the amount of graft material in the base of the sinus floor will be less, usually only a thin layer of graft material is observed (Fig. 20.77). If onlay grafting is performed, there will be no change in

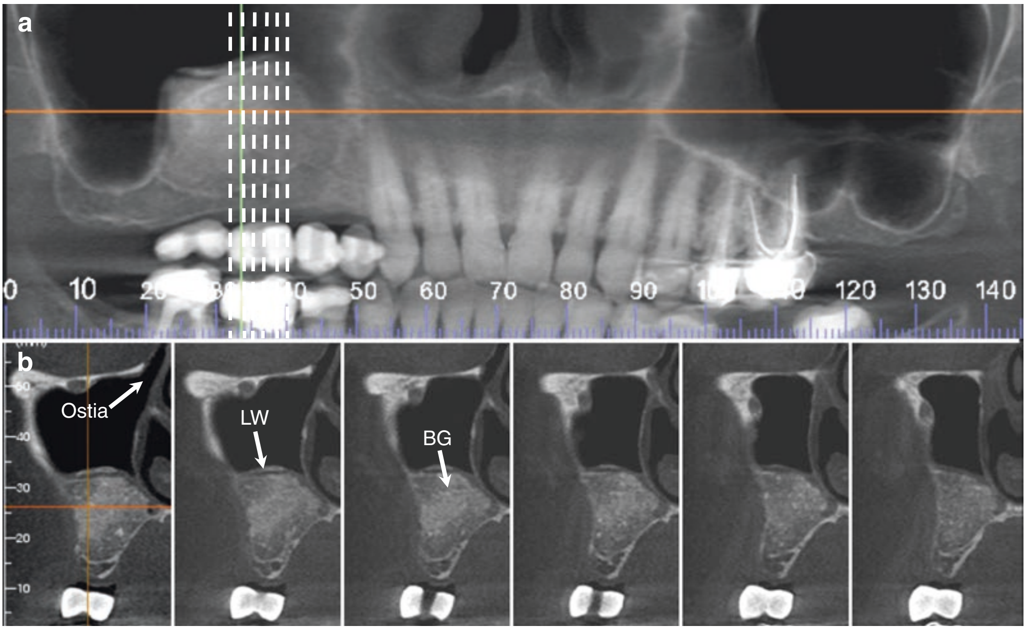

Fig. 20.76 Reformatted panoramic (**a**) with serial 1 mm thick cross-sectional CBCT images (**b**) showing homogeneous hyperdense bone graft (BG) material immediately below the cortical plate of the lateral window (LW) in the maxillary right molar region

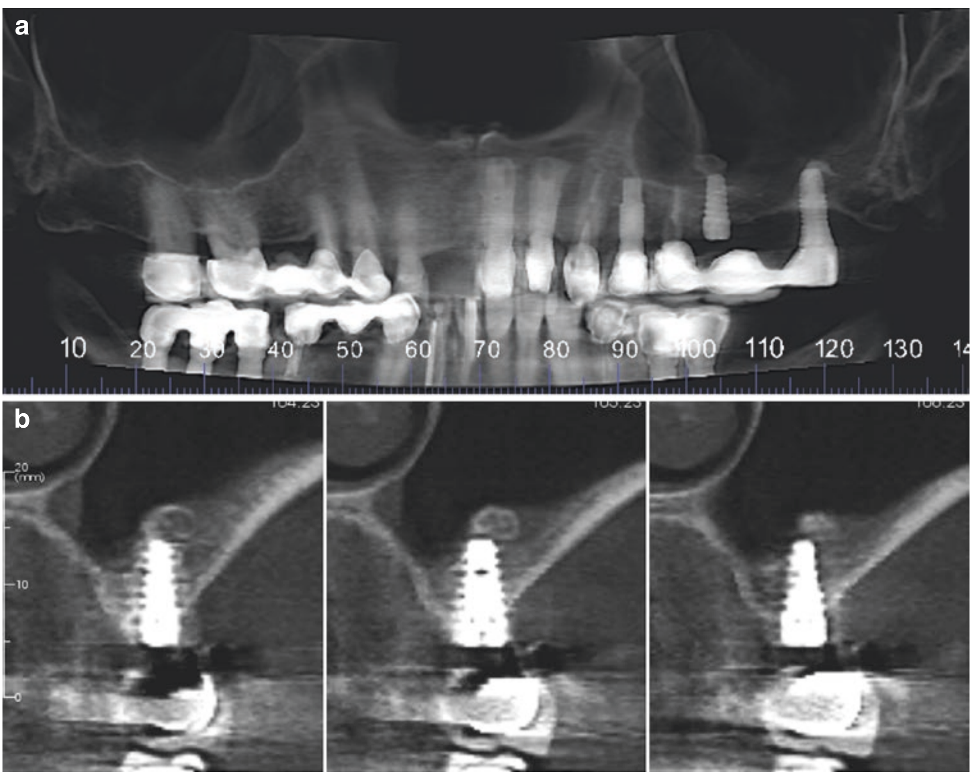

Fig. 20.77 Reformatted panoramic (**a**) and serial 1 mm thick cross-sectional CBCT images (**b**) of a successful maxillary sinus osteotome technique associated with an endosseous dental implant placed in the maxillary left second premolar previous tooth position

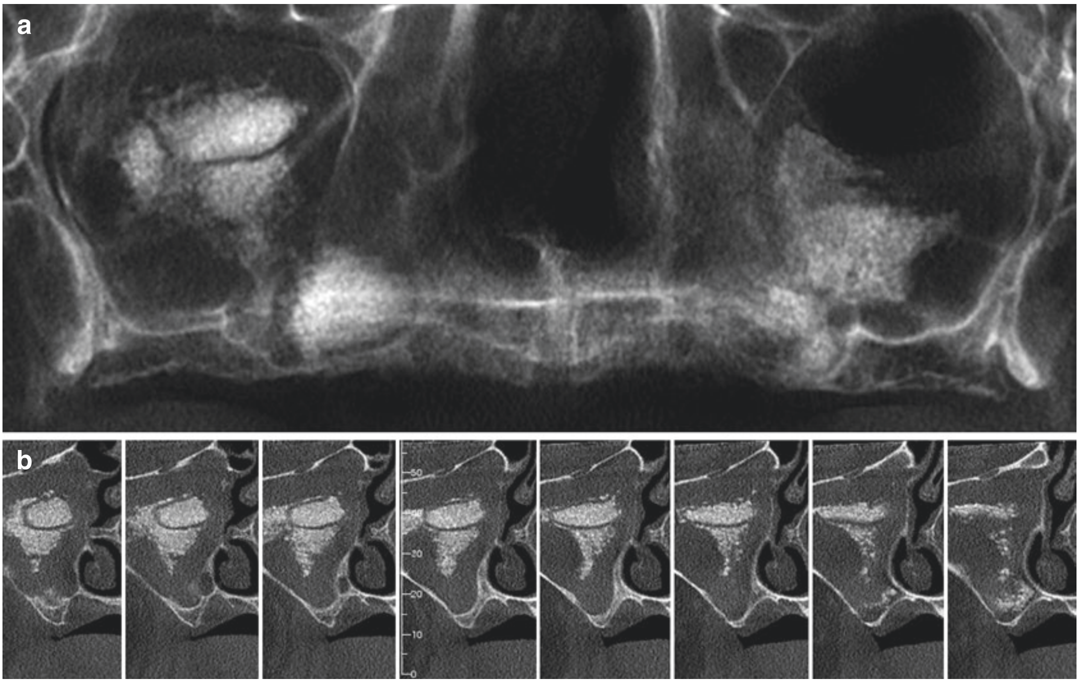

Fig. 20.78 Reformatted panoramic (**a**) and serial 1 mm thick cross-sectional CBCT images (**b**) of a completely edentulous maxilla showing complete right maxillary sinus postoperative infection with supero-lateral displacement and dispersion of hyperdense bone graft material in the maxillary right molar region associated with a sinus lift procedure

the sinus floor and the graft material will be observed superior or buccal to the alveolar bone. Imaging may also demonstrate postoperative sequelae such as acute sinusitis, graft infection, or formation of an oroantral communication (Fig. 20.78). Graft material scattered or displaced within the sinus can mean failure of incorporation of the graft material (Fig. 20.79).

20.8.2 Implant Complications

While dental implant therapy is a high predictable procedure with a well-documented long-term success rate, complications and failures do occur. Implant complications can be either mechanical or biological in origin. Mechanical complications occur when the fatigue strengths of the dental implant or restorative components are reached and breakdown occurs resulting in material failure. Biologic complications involve pathosis of the peri-implant tissues resulting in loss of supporting bone integration on the implant body itself.

20.8.2.1 Early Complications

Initial non-osseointegration of the dental implant is unusual and occurs along the endosseous zone of the implant body in the early phase after implant placement (Fig. 20.80).

Hemorrhage and neurovascular disturbances are amongst the most common and most severe immediate postoperative sequelae (Fig. 20.81) (Jacobs et al. 2007). A major complication is perforation of the implant into the mandibular canal, which can lead to paresthesia of the mental region and loss of vitality of the more mesially located teeth. Implants may also be placed such that they extend beyond the alveolar bone volume and perforate adjacent structures. The morbidity of these perforations include esthetic, functional, and structural considerations (Fig. 20.82).

Other complications are to be anticipated when perforating an infected maxillary sinus or

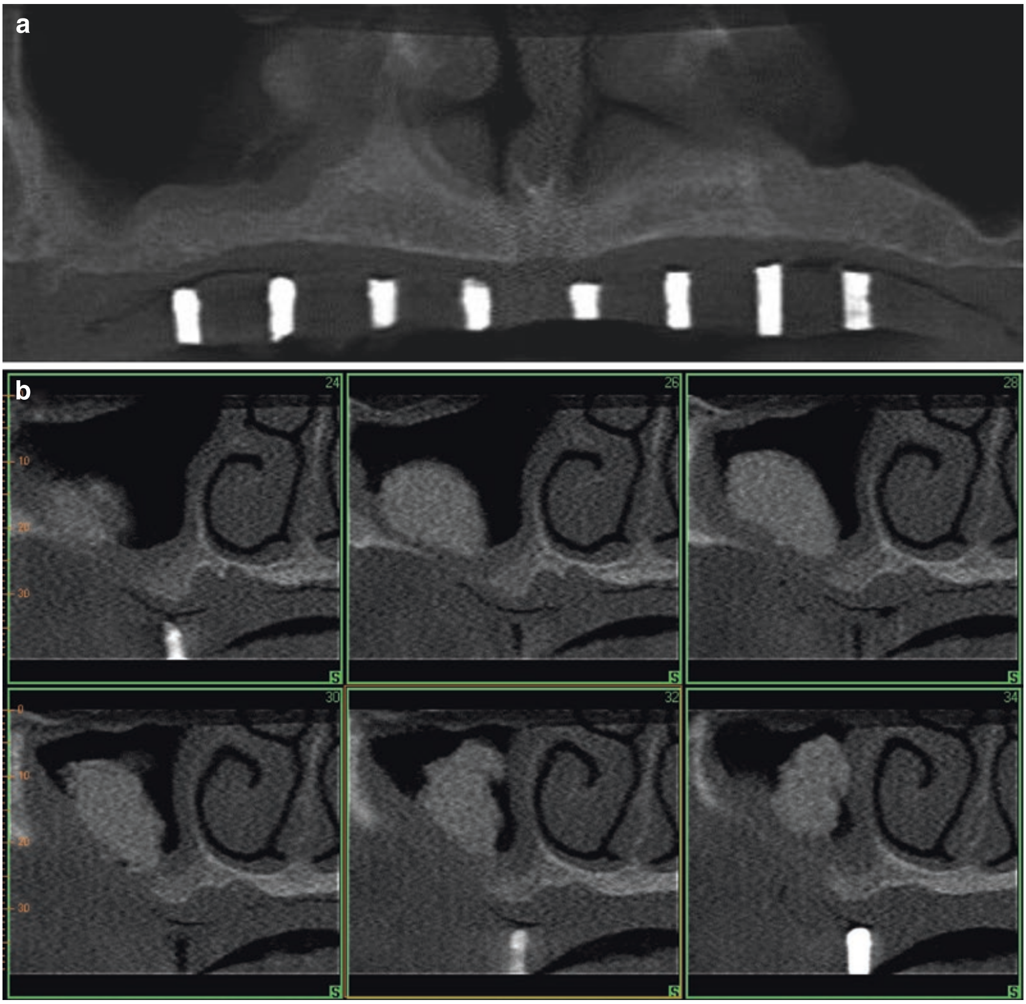

Fig. 20.79 Reformatted panoramic (**a**) and serial 1 mm thick coronal CBCT images (**b**) of a completely edentulous maxilla showing postoperative supero-lateral displacement of hyperdense bone graft material placed in the maxillary right premolar/molar region associated with a sinus lift procedure. The bone graft material is not visible on the panoramic image because of this displacement

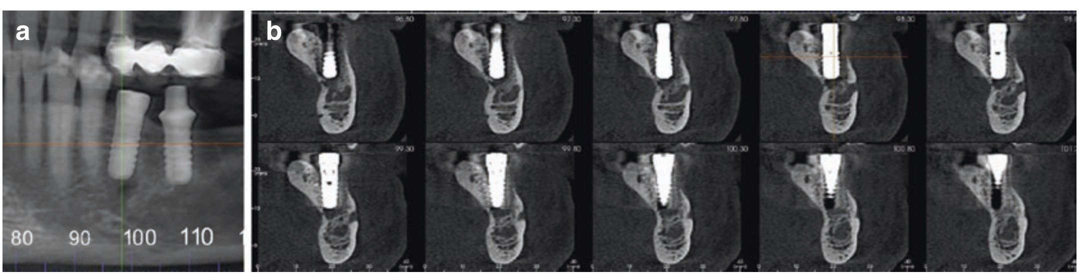

Fig. 20.80 Reformatted panoramic (**a**) and 1 mm thick serial cross-sectional images (**b**) of the left mandibular edentulous region 3 months after insertion of two dental implants at the sites of previous molar and second molar teeth taken after clinical mobility of the implant at the second premolar site was discovered. Cross-sectional images show a lack of continuity of the alveolar crest on the buccal aspect of the implant at the premolar site with lack of peri-implant medullary integration on the buccal aspect extending to the base of the implant, highly suggestive of biological failure

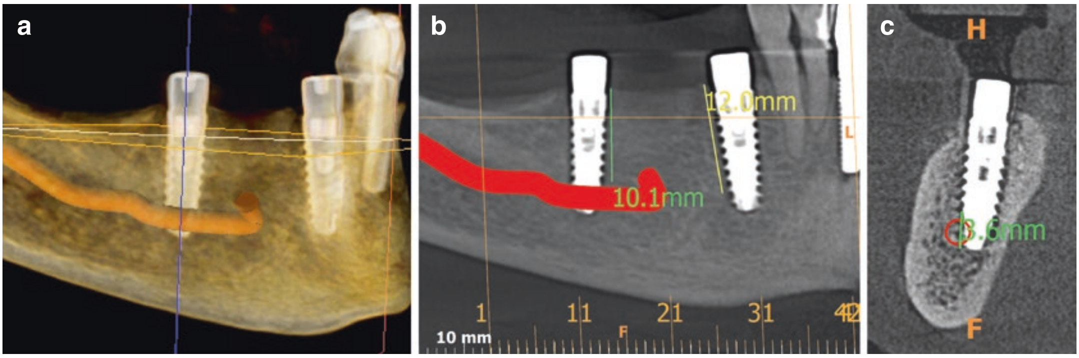

Fig. 20.81 Volumetric rendering (**a**), reformatted panoramic (**b**), and cross-sectional image (**c**) of the mandibular right posterior edentulous region taken after implant placement of a patient reporting postoperative paresthesia to the right lip. The cross-sectional image shows penetration of the apical third of the implant into the superior and lingual cortex of the right IAC

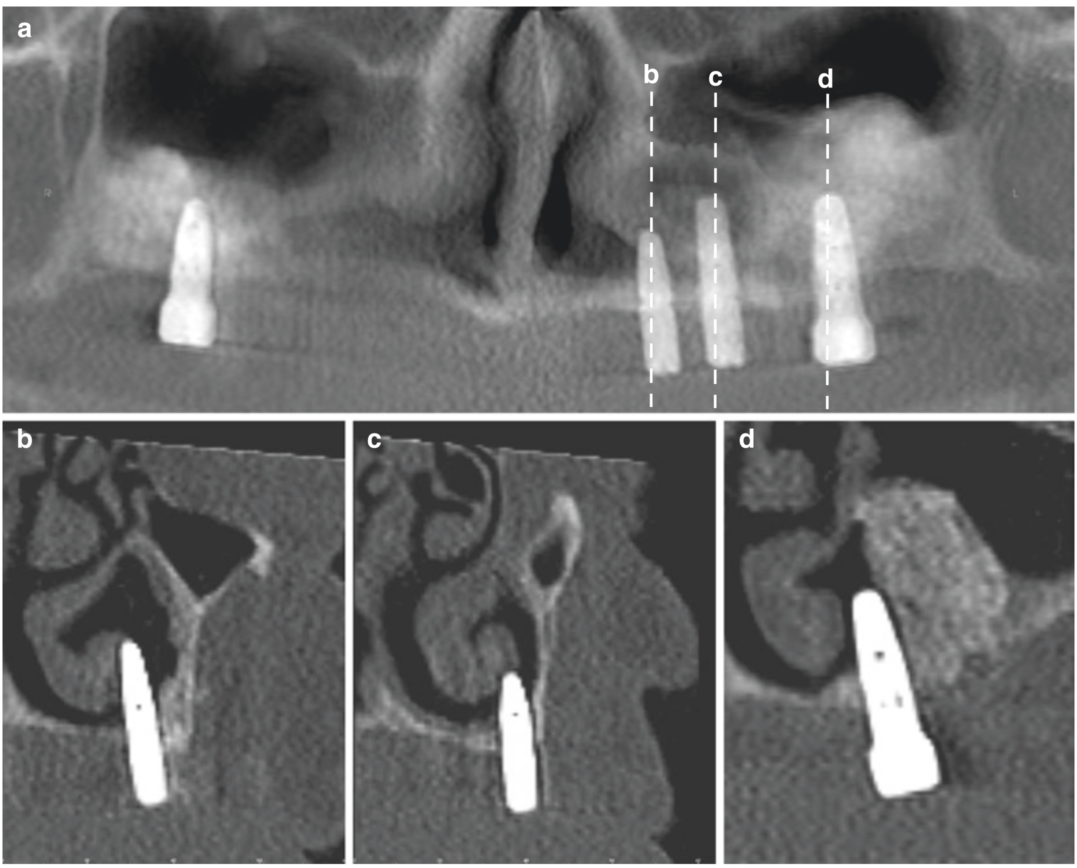

Fig. 20.82 Reformatted panoramic (**a**) of a 59-year-old female with a totally edentulous maxilla referred for assessment of the maxillary right premolar region after previous bilateral maxillary sinus elevation and bone augmentation. Previous dental implants are noted. Cross-section images of the dental implants at designated locations (*dashed lines*) demonstrate all implants perforate the nasal floor and engagement of the inferior turbinates ((**b**), (**c**)). In addition, the implant at site (**d**) is palatally positioned relative to the bone graft material

when placing implants in a bone with a priori bad bone conditions such as local osteomyelitis. Intravenous bisphosphonate therapy or previous radiotherapy is amongst contraindications for implant placement, as these could cause major postoperative problems because of a severely compromised host bone.

20.8.2.2 Late Complications

Late complication of dental implants occurs after osseointegration and delivery of the final prosthesis. Appreciation of the possible biologic or mechanical causes of late complications can lead to early recognition and correction. Late biologic complications are those in which the peri-implant soft and hard tissues are affected. Peri-implant mucositis is the reversible inflammatory reaction of the mucosa adjacent to an implant. Peri-implantitis is defined as the inflammatory process that affects the tissues around an osseointegrated implant which results in loss of supporting bone. Postoperative failure of osseointegration necessitating removal of the implant is unusual but can result from incorrect positioning (Fig. 20.83),

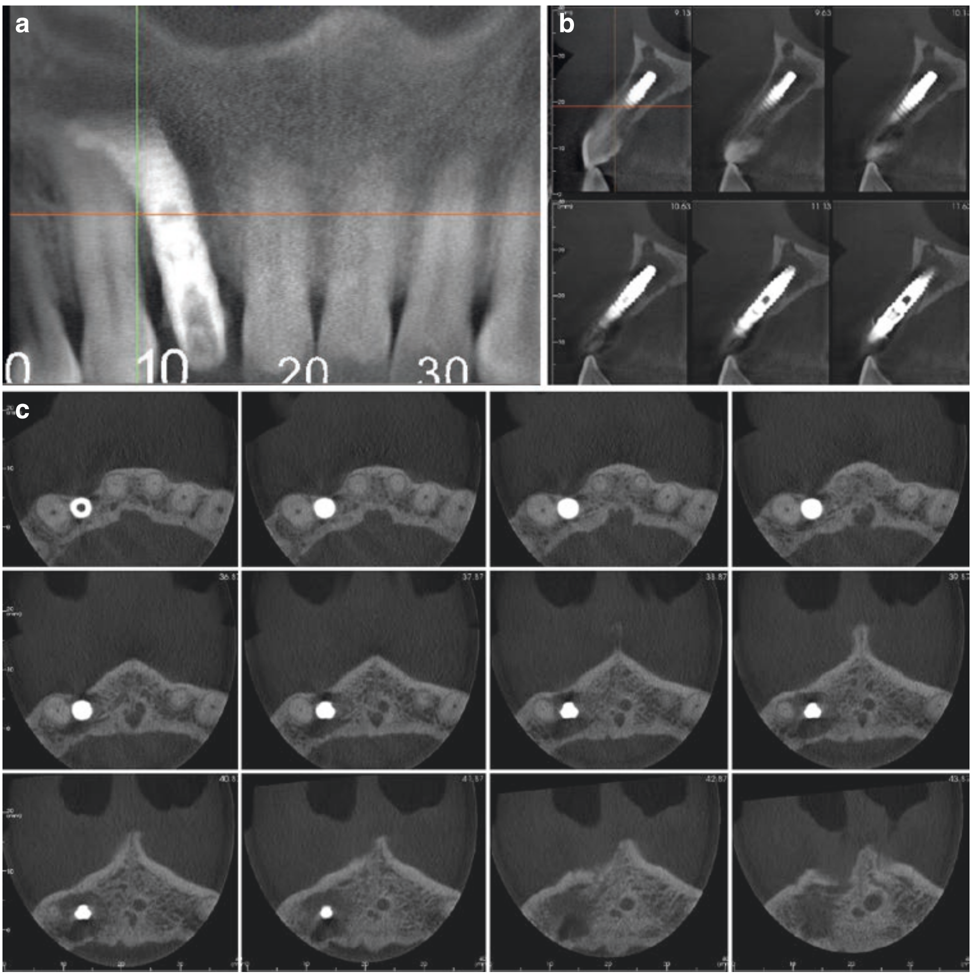

Fig. 20.83 Reformatted panoramic (**a**), serial 1 mm thick/1 mm interval cross-sectional (**b**), and serial 1 mm thick/1 mm interval axial (**c**) CBCT images showing a single implant replacement of the right maxillary lateral incisor contacting the mesial surface of the adjacent canine. There is a large intramedullary rarefaction extending to both the labial and palatal cortical plates and involving almost the entire implant. All teeth are unrestored; however, the maxillary right canine was non-vital. Implant failure was a result of the loss of necrosis of pulp of this tooth and subsequent chronic apical periodontitis most likely due to trauma at the time of the osteotomy

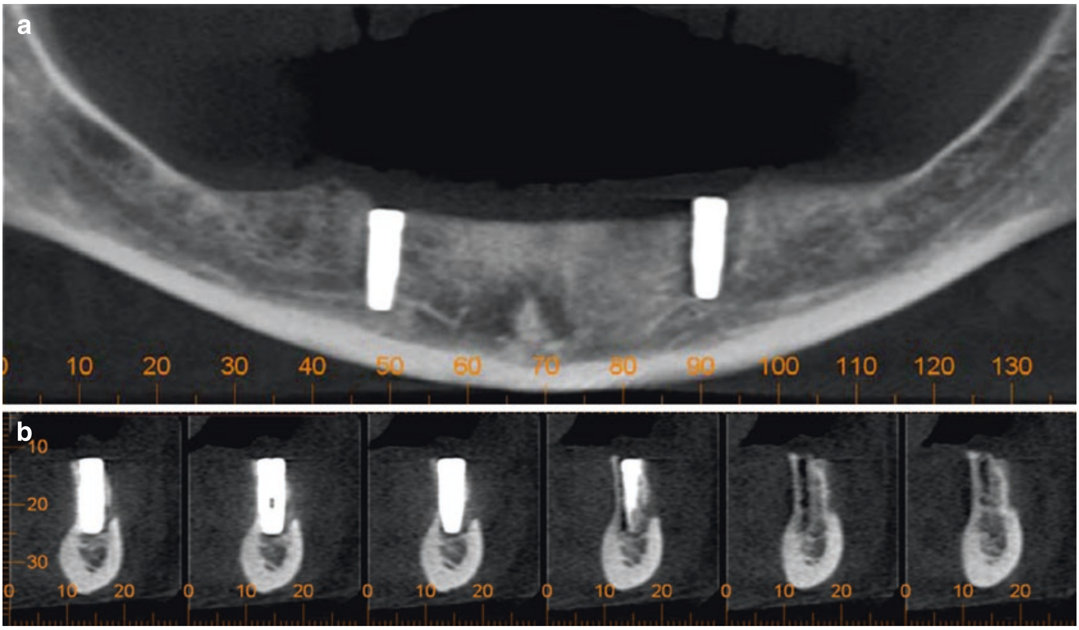

Fig. 20.84 Reformatted panoramic (**a**) and serial 1 mm thick/1 mm interval cross-sectional (**b**) CBCT images of a completely edentulous mandible of a patient who presents with looseness of a left mandibular implant 5 years after implant placement. There are two dental implants in the parasymphyseal region bilaterally used to support a complete mandibular prosthesis however, note a peripheral zone of rarefaction (loss in relative density) in the reformatted panorama image (**a**) associated with the left implant. Cross-sectional images (**b**) show complete loss of buccal cortical bone and thinning or perforation of the implant through the lingual cortical plate. Overloading of the left implant together with a lack of bone volume contributed to the late failure of this implant

insufficient bone density or volume, excessive loading or overloading (Fig. 20.84), damage to surrounding tissues, external force/sudden impact or fracture.

Conclusions

CBCT provides clinicians with a cost efficient volumetric imaging modality and, together with DICOM compliant software, has significantly contributed to presurgical assessment of alveolar bone prior to dental implant surgery. Accurate cross-sectional and volumetric rendered interactive images provide visualization of existing osseous anatomy important in developing and planning prosthetic treatment options. CBCT-based interactive virtual implant planning software facilitates consideration of more diverse and complex prosthetic design and implant fixture placement treatment options requiring higher degrees of accuracy and clinical confidence including bone augmentation procedures and surgical guidance.

References

Abarca M, van Steenberghe D, Malevez C, De Ridder J, Jacobs R (2006) Neurosensory disturbances after immediate loading of implants in the anterior mandible: an initial questionnaire approach followed by a psychophysical assessment. Clin Oral Investig 10:269–277

Academy of Osseointegration (2010) 2010 Guidelines of the Academy of Osseointegration for the provision of dental implants and associated patient care. Int J Oral Maxillofac Implants 25:620–627

Adell R, Eriksson B, Lekholm U, Brånemark PI, Jemt T (1990) A long-term follow-up study of osseointegrated implants in the treatment of totally edentulous jaws. Int J Oral Maxillofac Implants 5:347–359

Albrektsson T, Zarb G, Worthington P, Eriksson B (1986) Long-term efficacy of currently used dental implants: a review and proposed criteria of success. Int J Oral Maxillofac Implants 1:11–25

Allen EP, Gainza CS, Farthing GG, Newbold DA (1985) Improved technique for localized ridge aug-mentation. A report of 21 cases. J Periodontol 56:195–199

Almog M, Moss ME, Meitner SW, LaMar F (2002) Use of imaging guides in preimplant tomography. Oral Surg Oral Med Oral Pathol Oral Radiol Endod 93:483–487

Alsaadi G, Quirynen M, Komárek A, van Steenberghe D (2007) Impact of local and systemic factors on the incidence of oral implant failures, up to abutment connection. J Clin Periodontol 34:610–617

Alsaadi G, Quirynen M, Michiels K, Teughels W, Komárek A, van Steenberghe D (2008) Impact of local and systemic factors on the incidence of failures up to abutment connection with modified surface oral implants. J Clin Periodontol 35:51–57

Amet ME, Ganz SD (1997) Implant treatment planning using a patient acceptance prothesis, radiographic record base, and surgical guide. Part 1: Presurgical phase. Implant Dent 6:193–197

Anderson LC, Konsikik TF, Mentag PJ (1991) A review of the intraosseous course of the nerves of the mandible. J Oral Implantol 17:394–403

Araújo MG, Sukekava F, Wennström JL, Lindhe J (2006) Tissue modeling following implant placement in fresh extraction sockets. Clin Oral Implants Res 17:615–624

Arbeitsgemeinschaft für Röntgenologie (ARö), Deutsche Gesellschaft für Mund- und Kief-erheilkunde (DGZMK) (2009) 5.5 Implantologie In: Dentale Volumentomographie (DVT) - S1 Empfehlung (in German). http://www.dgzmk.de/uploads/tx_szdgzmkdocuments/S1_Empfehlung_Dentale_Volumentomographie.pdf. Accessed 10 Dec 2015

Artzi Z, Nemcovsky CE, Bitlitum I, Segal P (2000) Displacement of the incisive foramen in conjunction with implant placement in the anterior maxilla without jeopardizing vitality of nasopalatine nerve and vessels: a novel surgical approach. Clin Oral Implants Res 11:505–510

Arzouman MJ, Otis L, Kipnis V, Levine D (1993) Observation of the anterior loop of the inferior alveolar canal. Int J Oral Maxillofac Implants 8:295–300

Atwood DA (1971) Reduction of residual ridges: a major oral disease entity. J Prosthet Dent 26:266–279

Bahat O (1993) Treatment planning and placement of implants in the posterior maxillae: report of 732 consecutive Nobelpharma implants. Int J Oral Maxillofac Implants 8:151–161

Balshi SF, Wolfinger GJ, Balshi T (2006) Surgical planning and prosthesis construction using computer technology and medical imaging for immediate loading of implants in the pterygomaxillary region. Int J Periodontics Restorative Dent 26:239–247

Barbier L, Schepers E (1997) Adaptive bone remodeling around oral implants under axial and nonaxial loading conditions in the dog mandible. Int J Oral Maxillofac Implants 12:215–223

Bass SL, Triplett RG (1991) The effects of preoperative resorption and jaw anatomy on implant suc-cess. A report of 303 cases. Clin Oral Implant Res 2:193–198

Basten CH (1995) The use of radiopaque templates for predictable implant placement. Quintessence Int 26:609–612

Basten CH, Kois JC (1996) The use of barium sulfate for implant templates. J Prosthet Dent 76:451–454

Bavitz JB, Harn SD, Hansen CA, Lang M (1993) An anatomical study of the mental neurovascular bundle-implant relationships. Int J Oral Maxillofac Implants 8:563–567

Bellaïche N (2001) Imaging in oral implantology. In: Scortecci GM, Misch CE, Benner KU (eds) Implants and restorative dentistry. Taylor and Francis, London, p 194

Belser UC, Schmid B, Higginbottom F, Buser D (2004) Outcome analysis of implant restorations located in the anterior maxilla: a review of the recent literature. Int J Oral Maxillofac Implants 19(Suppl):30–42

Benavides E, Rios HF, Ganz SD et al (2012) Use of cone beam computed tomography in implant dentistry: the international congress of oral Implantologists consensus report. Implant Dent 21:78–86

Benson BW, Prihoda TJ, Glass BJ (1991) Variations in adult cortical bone mass as measured by a panoramic mandibular index. Oral Surg Oral Med Oral Pathol 1:349–356

Bordin TB, Refahi P, Karimbux N, Dragan IF (2016) Dynamic navigation in implant dentistry. In: Newman M (ed) Trends in clinical periodontology and implant dentistry. Elsevier, Amsterdam. http://www.Trendsperioimplantresourcecenter.Com/Content/Dynamic-Navigation-Implant-Dentistry. Accessed 10 Dec 2016

Bornstein MM, Al-Nawas B, Kuchler U, Tahmaseb A (2014) Consensus statements and recommended clinical procedures regarding contemporary surgical and radiographic techniques in implant dentistry. Int J Oral Maxillofac Implants 29(Suppl):78–82

Boyne PJ, James RA (1980) Grafting of the maxillary sinus floor with autogenous marrow and bone. J Oral Surg 38:613–616

Brånemark P-I (1985) Introduction to osseointegration. In: Brånemark P-I, Zarb G, Albrektsson T (eds) Tissue-integrated prostheses. Osseointegration in clinical dentistry. Quintessence Publishing Co, Chicago, pp 11–76

Brånemark P-I, Hansson BO, Adell R, Breine U, Lindström J, Hallén O, Ohman A (1977) Osseointegrated implants in the treatment of the edentulous jaw. Experience from a 10-year period. Scand J Plast Reconstr Surg Suppl 16:1–132

Bruschi GB, Scipioni A, Calesini G, Bruschi E (1998) Localized management of the sinus floor with simultaneous implant placement: a clinical report. Int J Oral Maxillofac Implants 13:219–226

Burns DR, Crabtree DG, Bell DH (1998) Template for positioning and angulation of intraosseous implants. J Pros Dent 60:479–483

Buser D, Mericske-Stern R, Bernard JP, Behneke A, Behneke N, Hirt HP, Belser UC, Lang NP (1997)

Long-term evaluation of non-submerged ITI implants. Part 1: 8-year life table analysis of a prospective multi-center study with 2359 implants. Clin Oral Implants Res 8:161–172

Carls FR, Pajarola G, Sailer HF (1996) Mandibular fractures due to implant management—incidence, mechanism of injury and therapeutic characteristics. Fortschr Kiefer Gesichtschir 41:106–108

Casap N, Wexler A, Persky N, Schneider A, Lustmann J (2005) Navigation surgery for dental implants: assessment of accuracy of the image guided implantology system. J Oral Maxillofac Surg 62:116–119

Cawood JI, Howell RA (1988) A classification of the edentulous jaws. Int J Oral Maxillofac Surg 17:232–236

Chen S, Buser D, Cordaro L (2009) Chapter 3.3 Surgical modifying factors. In: Dawson A, Chen S (eds) The SAC classification in implant dentistry. Quintessence Publishing Co, Berlin, pp 18–20. isbn:978-1-85097-188-7

Choi SC, Ann CH, Choi HM, Heo MS, Lee SS (2002) Accuracy of reformatted CT image for measuring the pre-implant site: analysis of the image distortion related to the gantry angle change. Dentomaxillofac Radiol 31:273–277

Correa LR, Spin-Neto R, Stavropoulos A, Schropp L, da Silveira HE, Wenzel A (2014) Planning of dental implant size with digital panoramic radiographs, CBCT-generated panoramic images, and CBCT cross-sectional images. Clin Oral Implants Res 25:690–695

Dantas JA, Montebello Filho A, Campos P (2005) Computed tomography for dental implants: the influence of the gantry angle and mandibular positioning on the bone height and width. Dentomaxillofac Radiol 34:9–15

Dao TT, Mellor A (1998) Sensory disturbances associated with implant surgery. Int J Prosthodont 11:462–469

Darriba MA, Mendonca-Cardad JJ (1997) Profuse bleeding and life-threatening airway obstruction after placement of mandibular dental implants. J Oral Maxillofac Surg 55:1328–1330

Del Balso AM, Greiner FG, Licata M (1994) Role of diagnostic imaging in the evaluation of the dental implant patient. Radiographics 14:699–719

Del Fabbro M, Testori T, Francetti L, Weinstein R (2004) Systematic review of survival rates for implants placed in the grafted maxillary sinus. Int J Periodontics Restorative Dent 24:565–577

Denissen HW, Kalk W, Veldhuis HA, van Waas MA (1993) Anatomic consideration for preventive implantation. Int J Oral Maxillofac Implants 8:191–196

Deutsche Gesellschaft für Zahn-, Mund- und Kieferheilkunde (DGZMK) (2012) Indikationen zur implantologischen 3D–Röntgendiagnostik und navigationsgestützten Implantologie. S3-k-Leitlinie. AWMF-Registriernummer: 083–111. http://www.dgzmk.de/uploads/tx_szdgzmkdocuments/20120508_Leitlinie_navigierte_Implantatinsertion.pdf. Accessed 6 Dec 2015

Diniz AF, Mendonça EF, Leles CR, Guilherme AS, Cavalcante MP, Silva MA (2008) Changes in the pre-surgical treatment planning using conventional spiral tomography. Clin Oral Implants Res 19:249–253

Dula K, Benic GI, Bornstein M, Dagassan-Berndt D, Filippi A, Hicklin S, Kissling-Jeger F, Luebbers HT, Sculean A, Sequeira-Byron P, Walter C, Zehnder M (2015) SADMFR guide-lines for the use of cone-beam computed tomography/digital volume tomography. Swiss Dent J 125:945–953

Duyck J, Naert I (1998) Failure of oral implants: aetiology, symptoms and influencing factors. Clin Oral Investig 2:102–114

Ellies LG (1992) Altered sensation following mandibular implant surgery: a retrospective study. J Prosthet Dent 68:664–671

Ellies LG, Hawker PB (1993) The prevalence of altered sensation associated with implant surgery. Int J Oral Maxillofac Implants 8:674–679

Engquist B, Bergendal T, Kallis T, Linden U (1988) A retrospective multicenter evaluation of osse-ointegrated implant supporting overdentures. Int J Oral Maxillofac Implants 3:129–134

European Commission (EC) (2012) Item 4.4.2 Implant Dentistry. In: Protection Radiation No 172. Cone beam CT for dental and maxillofacial radiology (Evidence-based guidelines). http://ec.europa.eu/energy/nuclear/radiation_protection/doc/publication/172.pdf. Accessed 14 Dec 2015

Faculty of General Dental Practitioners (UK) (1998) The Royal College of Surgeons of England. Selection criteria for dental radiography. Nottingham, UK: Penn Advertising and Marketing

Farré-Pagés N, Augé-Castro ML, Alaejos-Algarra F, Mareque-Bueno J, Ferrés-Padró E, Hernández-Alfaro F (2011) Relation between bone density and primary implant stability. Med Oral Patol Oral Cir Bucal 16:e62–e67

Frei C, Buser D, Dula K (2004) Study on the necessity for cross-section imaging of the posterior mandible for treatment planning of standard cases in implant dentistry. Clin Oral Implants Res 15:490–497

Goodacre CJ, Kan JY, Rungcharassaeng K (1999) Clinical complications of osseointegrated implants. J Prosthet Dent 81:537–552

Greenstein G, Tarnow D (2006) The mental foramen and nerve: clinical and anatomical factors related to dental implant placement: a literature review. J Periodontol 77:1933–1943

Guerrero ME, Noriega J, Jacobs R (2014a) Preoperative implant planning considering alveolar bone grafting needs and complication prediction using panoramic versus CBCT images. Imaging Sci Dent 44:213–220

Guerrero ME, Noriega J, Castro C, Jacobs R (2014b) Does cone-beam CT alter treatment plans? Comparison of preoperative implant planning using panoramic versus cone-beam CT images. Imaging Sci Dent 44:121–128

Hämmerle CH, Cordaro L, van Assche N, Benic GI, Bornstein M, Gamper F, Gotfredsen K, Harris D, Hürzeler M, Jacobs R, Kapos T, Kohal RJ, Patzelt SB, Sailer I, Tahmaseb A, Ver-cruyssen M, Wismeijer D (2015) Digital technologies to support planning, treatment, and fabrication processes and outcome assessments in implant dentistry. Summary and con-sensus statements. The 4th EAO consensus conference 2015. Clin Oral Implants Res 26(Suppl 11):97–101

Harris D, Buser D, Dula K, Gröndahl K, Harris D, Jacobs R, Lekholm U, Nakielny R, van Steenberghe D, van der Stelt P (2002) EAO Guidelines for the use of diagnostic imaging in implant dentistry. Clin Oral Impants Res 13:566–570

Harris D, Horner K, Gröndahl K et al (2012) EAO guidelines for the use of diagnostic imaging in implant dentistry 2011: a consensus workshop organized by the European Association for Osseointegration at the Medical University of Warsaw. Clin Oral Implants Res 23:1243–1253

Hartman GA, Cochran DL (2004) Initial implant position determines the magnitude of crestal bone remodeling. J Periodontol 75:572–577

Hermann JS, Buser D, Schenk RK, Schoolfield JD, Cochran D (2001) Biologic width around one- and two-piece titanium implants: a histometric evaluation of unloaded nonsubmerged and submerged implants in the canine mandible. Clin Oral Implants Res 12:559–571

Higginbottom FL, Wilson TG (1996) Three-dimensional templates for placement of root-form dental implants: a technical note. Int J Oral Maxillofac Implants 11:787–793

Huang Y, Van Dessel J, Liang X, Depypere M, Zhong W, Ma G, Lambrichts I, Maes F, Jacobs R (2014) Effects of immediate and delayed loading on Peri-implant trabecular structures: a cone beam CT evaluation. Clin Implant Dent Relat Res 16(6):873–883. doi:10.1111/cid.12063

International Standards Organization (ISO) (2014) ISO/FDIS 16443 dentistry—vocabulary of oral implantology. ISO Copyright Office. Geneva, Switzerland, pp 1–12

Isidor F (1996) Loss of osseointegration caused by occlusal load of oral implants. A clinical and radiographic study in monkeys. Clin Oral Implants Res 7:143–152

Israelson H, Plemons JM, Watkins P, Sory C (1992) Barium-coated surgical stents and computer-assisted tomography in the preoperative assessment of dental implant patients. Int J Periodontics Restorative Dent 12:53–61

Jacobs R, van Steenberghe D (1997) Radiographic planning and assessment of endosseous oral implants, 1st edn. Springer, Berlin

Jacobs R, Schotte A, van Steenberghe D, Quirynen M, Naert I (1992) Posterior jaw bone resorption in osseointegrated implant-supported overdentures. Clin Oral Implants Res 3:63–70

Jacobs R, van Steenberghe D, Nys M, Naert I (1993) Maxillary bone resorption in patients with mandibular implant-supported overdentures or fixed prostheses. J Prosthet Dent 70:135–140

Jacobs R, Adriansens A, Verstreken K, Suetens P, van Steenberghe D (1999a) Predictability of a three-dimensional planning system for oral implant surgery. Dentomaxillofac Radiol 28:105–111

Jacobs R, Adriansens A, Naert I, Quirynen M, Hermans R, Van Steenberghe D (1999b) Predictability of reformatted computed tomography for pre-operative planning of endosseous implants. Dentomaxillofac Radiol 28:37–41

Jacobs R, Mraiwa N, van Steenberghe D, Gijbels F, Quirynen M (2002) Appearance, location, course, and morphology of the mandibular incisive canal: an assessment on spiral CT scan. Dentomaxillofac Radiol 31:322–327

Jacobs R, Lambrichts I, Liang X, Martens W, Mraiwa N, Adriaensens P, Gelan J (2007) Neurovascularization of the anterior jaw bones revisited using high-resolution magnetic resonance imaging. Oral Surg Oral Med Oral Pathol Oral Radiol Endod 103:683–693

Jaffin RA, Berman CL (1991) The excessive loss of Brånemark fixtures in type IV bone: a 5 year analysis. J Periodontol 62:2–4

Jeffcoat MK (1993) Application of digital radiography to implantology. J Dent Sym 1:30–33

Jemt T, Book K, Linden B, Urde G (1992) Failures and complications in 92 consecutively inserted overdentures supported by Brånemark implants in severely resorbed edentulous maxillae: a study from prosthetic treatment to first annual check-up. Int J Oral Maxillofac Implants 7:162–167

Jung RE, Schneider D, Ganeles J, Wismeijer D, Zwahlen M, Hämmerle CH, Tahmaseb A (2009) Computer technology applications in surgical implant dentistry: a systematic review. Int J Oral Maxillofac Implants 24(Suppl):92–109

Kahnberg KE, Henry PJ, Hirsch JM, Ohrnell LO, Andreasson L, Brånemark PI, Chiapasco M, Gynther G, Finne K, Higuchi KW, Isaksson S, Malevez C, Neukam FW, Sevetz E Jr, Urgell JP, Widmark G, Bolind P (2007) Clinical evaluation of the zygoma implant: 3-year follow-up at 16 clinics. J Oral Maxillofac Surg 65:2033–2038

Kan JY, Lozada JL, Boyne PJ, Goodacre CJ, Rungcharassaeng K (1997) Mandibular fracture after endosseous implant placement in conjunction with inferior alveolar nerve transposition: a patient treatment report. Int J Oral Maxillofac Implants 12:655–659

Kim Y, Oh TJ, Misch CE, Wang HL (2005) Occlusal considerations in implant therapy: clinical guidelines with biomechanical rationale. Clin Oral Implants Res 16:26–35

Klein M, Cranin AN, Sirakian A (1993) A computerized tomography (CT) scan appliance for opti-mal presurgical and preprosthetic planning of the implant patient. Pract Periodontics Aesthet Dent 5:33–39. quiz 39

Kopp KC, Koslow AH, Abdo OS (2003) Predictable implant placement with a diagnostic/surgical guide and advanced radiographic imaging. J Prosthet Dent 89:611–615

Koutouzis T, Wennström JL (2007) Bone level changes at axial- and non-axial-positioned implants supporting fixed partial dentures. A 5-year retrospective longitudinal study. Clin Oral Implants Res 18:585–590
Kraut RA, Boyden DK (1998) Location of incisive canal in relation to central incisor implants. Implant Dent 7:221–225
Krekmanov L, Khan M, Rangert B, Lindström A (2000) Tilting of posterior mandibular and maxil-lary implants for improved prosthesis support. Int J Oral Maxillofac Implants 15:405–414
Laney WR (2007) Glossary of oral and maxillofacial implants (GOMI). Quintessence Publishing Co, Ltd., Berlin, p 199
Leblebicioglu B, Rawal S, Mariotti A (2007) A review of the functional and esthetic requirements for dental implants. J Am Dent Assoc 138:321–329
Lekholm U, Zarb G (1985) Patient selection and preparation. In: Brånemark P-I, Zarb GA, Albrektsson T (eds) Tissue-integrated prostheses: osseointegration in clinical dentistry. Quintessence Publ Co, Chicago, pp 199–209
Lindh C, Nilsson M, Klinge B, Petersson A (1996) Quantitative computed tomography of trabecular bone in the mandible. Dentomaxillofac Radiol 25:146–150
Loubele M, Maes F, Schutyser F, Marchal G, Jacobs R, Suetens P (2006) Assessment of bone segmentation quality of cone-beam CT versus multislice spiral CT: a pilot study. Oral Surg Oral Med Oral Pathol Oral Radiol Endod 102:225–234
Loubele M, Guerrero ME, Jacobs R, Suetens P, van Steenberghe D (2007) A comparison of jaw dimensional and quality assessments of bone characteristics with cone-beam CT, spiral tomography, and multi-slice spiral CT. Int J Oral Maxillofac Implants 22:446–454
Malo P, Rangert B, Nobre M (2003) "All-on-Four" immediate-function concept with Brånemark system implants for completely edentulous mandibles: a retrospective clinical study. Clin Implant Dent Relat Res 5(Suppl. 1):2–9
Mardinger O, Abba M, Hirshberg A, Schwartz-Arad D (2007) Prevalence, diameter and course of the maxillary intraosseous vascular canal with relation to sinus augmentation procedure: a ra-diographic study. Int J Oral Maxillofac Surg 36:735–738
Marquezan M, Osório A, Sant'Anna E, Souza MM, Maia L (2012) Does bone mineral density influence the primary stability of dental implants? A systematic review. Clin Oral Implants Res 23(7):767–774. doi:10.1111/j.1600-0501.2011.02228.x
Meitner SW, Tallents RH (2004) Surgical guides for prosthetically guided implant placement. J Pros Dent 92:569–574
Merheb J, Van Assche N, Coucke W, Jacobs R, Naert I, Quirynen M (2010) Relationship between cortical bone thickness or computerized tomography-derived bone density values and implant stability. Clin Oral Implants Res 21:612–617
Merheb J, Graham J, Coucke W, Roberts M, Quirynen M, Jacobs R, Devlin H (2015) Prediction of implant loss and marginal bone loss by analysis of dental panoramic radiographs. Int J Oral Maxillofac Implants 30:372–377
Meyer U, Wiesmann HP, Runte C, Fillies T, Meier N, Lueth T, Joos U (2003) Evaluation of accuracy of insertion of dental implants and prosthetic treatment by computer-aided navigation in minipigs. Br J Oral Maxillofac Surg 41:102–108
Misch CE (1990) Density of bone: effect on treatment plans, surgical approach, healing and progressive bone loading. Int J Oral Implant 6:23–31
Misch CE, Crawford EA (1990) Predictable mandibular nerve location. A clinical zone of safety. Int J Oral Implantol 7:37–40
Misch CE, Judy KW (1987) Classification of partially edentulous arches for implant dentistry. Int J Oral Implantol 4:7–13
Mischkowski RA, Zinser MJ, Neugebauer J, Kubler AC, Zöller JE (2006) Comparison of static and dynamic computer-assisted guidance methods in implantology. Int J Comput Dent 9:23–35
Molly L (2006) Bone density and primary stability in implant therapy. Clin Oral Implants Res 17:124–135
Mraiwa N, Jacobs R, Van Cleynenbreugel J, Sanderink G, Schutyser F, Suetens P, van Steenberghe D, Quirynen M (2004) The nasopalatine canal revisited using 2D and 3D CT imaging. Dentomaxillofac Radiol 33:396–402
Nackaerts O, Maes F, Yan H, Couto Souza P, Pauwels R, Jacobs R (2011) Analysis of intensity variability in multislice and cone beam computed tomography. Clin Oral Implants Res 22:873–879
Nortje CJ, Farman AG, Grotepass FW (1977) Variation in the normal anatomy of the inferior dental (mandibular) canal. J Oral Maxillofac Surg 15:55–63
Norton MR, Gamble C (2001) Bone classification: an objective scale of bone density using the computerised tomography scan. Clin Oral Implants Res 12:79–84
Papavasiliou G, Tripodakis A, Kamposiora P, Strub JR, Bayne SC (1996) Finite element analysis of ceramic-abutment restoration combinations for osseointegrated implants. Int J Prosthodont 9:254–260
Park SH, Brooks SL, Oh TJ, Wang HL (2009) Effect of ridge morphology on guided bone regeneration outcome: conventional tomographic study. J Periodontol 80:1231–1236
Pesun IJ, Gardner FM (1995) Fabrication of a guide for radiographic evaluation and surgical place-ments of implants. J Prosthet Dent 73:548–552
Pontual MA, Freire JN, Souza DC, Ferreira CF, Bianchini MA, Magini RS (2004) A newly designed template device for use with the insertion of immediately loaded implants. J Oral Implantol 30:325–329
Quirynen M, Lamoral Y, Dekeyser C, Peene P, van Steenberghe D, Bonte J, Baert AL (1990) CT scan standard reconstruction technique for reliable jaw bone volume determination. Int J Oral Maxillofac Implants 5:384–389
Quirynen M, Mraiwa N, van Steenberghe D, Jacobs R (2003) Morphology and dimensions of the mandibular jawbone in the interforaminal region in patients requir-

ing implants in the distal areas. Clin Oral Implants Res 14:280–285
Ribeiro-Rotta RF, Pereira AC, Oliveira GH, Freire MC, Leles CR, Lindh C (2010) An exploratory survey of diagnostic methods for bone quality assessment used by Brazilian dental implant specialists. J Oral Rehabil 37:698–703
Ribeiro-Rotta RF, Lindh C, Pereira AC, Rohlin M (2011) Ambiguity in bone tissue characteristics as presented in studies on dental implant planning and placement: a systematic review. Clin Oral Implants Res 22:789–801
Rosenquist B (1996) Is there an anterior loop of the inferior alveolar nerve? Int J Periodontics Restorative Dent 16:40–45
Rouas P, Nancy J, Bar D (2007) Identification of double mandibular canals: literature review and three case reports with CT scans and cone beam CT. Dentomaxillofac Radiol 36:34–38
Sabri R (1999) Management of missing maxillary lateral incisors. J American Dent Assoc 130:80–84
Sammartino G, Della Valle A, Marenzi G, Gerbino S, Martorelli M, di Lauro AE, di Lauro F (2004) Stereolithography in oral implantology: a comparison of surgical guides. Implant Dent 13:133–139
Scarfe WC (1998) A common sense approach to TMJ and implant imaging. Ann R Australas Coll Dent Sur 14:48–61
Scarfe W, Vaughn WS, Farman AG, Harris BT, Paris MM (2012a) Comparison of restoratively projected and surgically acceptable virtual implant position for mandibular overdentures. Int J Oral Maxillofac Implants 27:111–118
Scarfe WC, Farman AG, Ruskin JD (2012b) Is cone beam computed tomography really necessary for performing dental implant surgery? Forum Implantologicum 8:63–73
Scher EL (1994) Use of the incisive canal as a recipient site for root form implants: preliminary clinical reports. Implant Dent 3:38–41
Schropp L, Wenzel A, Kostopoulos L (2001) Impact of conventional tomography on prediction of the appropriate implant size. Oral Surg Oral Med Oral Pathol Oral Radiol Endod 92:458–463
Schropp L, Stavropoulos A, Gotfredsen E, Wenzel A (2011) Comparison of panoramic and conventional cross-sectional tomography for preoperative selection of implant size. Clin Oral Implants Res 22:424–429
Schwarz MS, Rothman SL, Rhodes ML, Chafetz N (1987a) Computed tomography. I. Preoperative assessment of the mandible for endosseous implant surgery. Int J Oral Maxillofac Implants 2:137–141
Schwarz MS, Rothman SL, Rhodes ML, Chafetz N (1987b) Computed tomography. II. Preoperative assessment of the maxilla for endosseous implant surgery. Int J Oral Maxillofac Implants 2:143–148
Schwarz MS, Rothman SL, Chafetz N, Rhodes M (1989) Computed tomography in dental implantation surgery. Dent Clin N Am 33:555–597
Scurria MS, Morgan ZV IV, Guckes AD, Li S, Koch G (1998) Prognostic variables associated with implant failure: a retrospective effectiveness study. Int J Oral Maxillofac Implants 13:400–406
SEDENTEXCT Project (2011) Chapter 4, Justification and referral criteria. Surgical applications. Implant dentistry. In: Radiation protection: Cone Beam CT for Dental and Maxillofacial Radiology. Evidence based guidelines 2011 (v2.0 Final).. http://www.eadmfr.info/sites/default/files/guidelines_final.pdf. Accessed 14 Jan 2013.
Seibert JS (1983) Reconstruction of deformed, partially edentulous ridges, using full thickness Onlay grafts, part I: technique and wound healing. Compend Contin Educ Dent 4:437–453
Serman NJ (1987) Differentiation of double mental foramina from extra bony coursing of the incisive branch of the mandibular nerve—an anatomic study. Refuat Hashinayium 5:20–22
Sethi A, Sochor P (1995) Predicting esthetics in implant dentistry using multiplanar angulation: a technical note. Int J Oral Maxillofac Implants 10:485–490
Shearer BH (1995) Osseointegrated implants: a review of the literature. Int Dent J 45:261–266
Shelley AM, Glenny AM, Goodwin M, Brunton P, Horner K (2014) Conventional radiography and cross-sectional imaging when planning dental implants in the anterior edentulous man-dible to support an overdenture: a systematic review. Dentomaxillofac Radiol 43:20130321
Shiller WR, Wiswell OB (1954) Lingual foramina of the mandible. Anat Tec 119:387–390
Smith DE, Zarb GA (1989) Criteria for success of osseointegrated dental implants. J Prosthet Dent 62:67–72
Spray JR, Black CG, Morris HF, Ochi S (2000) The influence of bone thickness on facial marginal bone response: stage 1 placement through stage 2 uncovering. Ann Periodontol 5:119–128
Stella JP, Warner MR (2000) Sinus slot technique for simplification and improved orientation of zy-gomaticus dental implants: a technical note. Int J Oral Maxillofac Implants 15:889–893
Studer S, Naef R, Schärer P (1997) Adjustment of localized alveolar ridge defects by soft tissue transplantation to improve mucogingival esthetics: a proposal for clinical classification and an evaluation of procedures. Quintessence Int 28:785–805
Summers RB (1994) The osteotome technique: part 3—less invasive methods of elevating the sinus floor. Compend Contin Educ Dent 15:698–708
Superior Health Council (2011) Section 2.3 Indications for and part played by dCBCT in imaging the dental and maxillofacial region. In Advisory Report from the Superior Health Council No 8705. Dental Cone Beam Computed Tomography. http://health.belgium.be/internet2Prd/groups/public/@public/@shc/documents/ie2divers/19068321_en.pdf. Accessed 14 Dec 2015
Swanson KS, Kaugars GE, Gunsolley JC (1991) Nasopalatine duct cyst: an analysis of 334 cases. J Oral Maxillofac Surg 49:268–271
Tahmaseb A, Wismeijer D, Coucke W, Derksen W (2014) Computer technology applications in surgical implant

dentistry: a systematic review. Int J Oral Maxillofac Implants 29(Suppl):25–42
Tatum OH Jr, Lebowitz MS (1991) Anatomic consideration for dental implants. J Oral Implantol 17:16–21
ten Bruggenkate CM, Krekeler G, Kraaijenhagen HA, Foitzik C, Oosterbeek HA (1993) Hemorrhage in the floor of the mouth resulting from lingual perforation during implant placement: a clinical report. Int J Oral Maxillofac Implants 8:329–334
Tepper G, Hofschneider UB, Gahleitner A, Ulm C (2001) Computed tomographic diagnosis and localization of bone canals in the mandibular interforaminal region for prevention of bleeding complication during implant surgery. Int J Oral Maxillofac Implants 16:68–72
Tinti C, Parma-Benfenati S (2003) Clinical classification of bone defects concerning the placement of dental implants. Int J Periodontics Restorative Dent 23:147–155
Toffler M (2001) Site development in the posterior maxilla using osteocompression and apical alveolar displacement. Compend Contin Educ Dent 22:775–790
Toh H, Kodama J, Yanagisako M, Ohmori T (1992) Anatomical study of the accessory mental foramen and the distribution of its nerve. Okajimas Folia Anat Jpn 69:85–88
Tomotake Y, Ishida O, Kanitani H, Ichikawa T (2002) Immediate implant-supported oral rehabilitation using a photocurable plastic skull model and laser welding. A technical note on the screw-retained type: part 1. Int J Prosthodont 15:303–306
Triplett RG, Mason ME, Alfonso WF, McAnear JT (1991) Endosseous cylinder implants in severely atrophic mandibles. Int J Oral Maxillofac Implants 6:264–269
Trisi P, Rao W (1999) Bone classification: clinical-histomorphometric comparison. Clin Oral Implants Res 10:1–7
Truhlar RS, Orenstein IH, Morris HF, Ochi S (1997) Distribution of bone quality in patients receiving endosseous dental implants. J Oral Maxillofac Surg 55(12 suppl 5):38–45
Tsuchida F, Hosoi T, Imanaka M, Kobayashi K (2004) A technique for making a diagnostic and sur-gical template. J Prosthet Dent 91:395–397
Tulasne J (1989) Implant treatment of missing posterior dentition. In: Albrektsson T, Zarb GA (eds) The Brånemark Osseointegrated implant. Quintessence, Chicago, pp 103–115
Tyndall DA, Brooks SL (2000) Selection criteria for dental implant site imaging: a position paper of the American Academy of oral and maxillofacial radiology. Oral Surg Oral Med Oral Pathol Oral Radiol Endod 89:630–637
Tyndall DA, Price JB, Tetradis S, Ganz SD, Hildebolt C, Scarfe WC (2012) Position statement of the American Academy of oral and maxillofacial radiology on selection criteria for the use of radiology in dental implantology with emphasis on cone beam computed tomography. Oral Surg Oral Med Oral Pathol Oral Radiol 113:817–826
Uchida Y, Yamashita Y, Goto M, Hanihara T (2007) Measurement of anterior loop length for the mandibular canal and diameter of the mandibular incisive canal to avoid nerve damage when installing endosseous implants in the interforaminal region. J Oral Maxillofac Surg 65:1772–1779
Van Assche N, Vercruyssen M, Coucke W, Teughels W, Jacobs R, Quirynen M (2012) Accuracy of computer-aided implant placement. Clin Oral Implants Res 23:112–123
Van Dessel J, Huang Y, Depypere M, Rubira-Bullen I, Maes F, Jacobs R (2013) A comparative evaluation of cone beam CT and micro-CT on trabecular bone structures in the human mandible. Dentomaxillofac Radiol 42:20130145
van Steenberghe D, Jacobs R, Desnyder M, Maffei G, Quirynen M (2002) The relative impact of local and endogenous patient-related factors on implant failure up to the abutment stage. Clin Oral Implants Res 13:617–622
van Steenberghe D, Ericsson I, Van Cleynenbreugel J, Schutyser F, Brajnovic I, Andersson M (2004) High precision planning for oral implants based on 3-D CT scanning. A new surgical technique for immediate and delayed loading. Appl Osseointegration Res 4:39–42
van Steenberghe D, Glauser R, Blombäck U, Andersson M, Schutyser F, Pettersson A, Wen-delhag I (2005) A computed tomographic scan-derived customized surgical guide and fixed prosthesis for flapless surgery and immediate loading of implants in fully edentulous maxillae: a prospective multicenter study. Clin Implant Dent Relat Res Suppl 1:S111–S120
Vercruyssen M, Laleman I, Jacobs R, Quirynen M (2015) Computer-supported implant planning and guided surgery: a narrative review. Clin Oral Implants Res 26(Suppl 11):69–76
Verde MA, Morgano MS (1993) A dual-purpose stent for the implant-supported prosthesis. J Prosthet Dent 69:276–280
Verstreken K, Van Cleynenbreugel J, Marchal G, Naert I, Suetens P, van Steenberghe D (1996a) Computer-assisted planning of oral implant surgery: a three-dimensional approach. Int J Oral Maxillofac Implants 11:806–810
Verstreken K, Van Cleynenbreugel J, Marchal G, Suetens P, van Steenberghe D (1996b) Computer-assisted planning of oral implant surgery. An approach using virtual reality. Stud Health Technol Inform 29:423–434
Verstreken K, Van Cleynenbreugel J, Martens K, Marchal G, van Steenberghe D, Suetens P (1998) An image-guided planning system for endosseous oral implants. IEEE Trans Med Imaging 17:842–852
Walton JN (2000) Altered sensation associated with implants in the anterior mandible: a prospective study. J Pros Dent 83:443–449
Wang HL, Al-Shammari K (2002) HVC ridge deficiency classification: a therapeutically oriented classification. Int J Periodontics Restorative Dent 22:335–343

Wanschitz F, Birkfellner W, Watzinger F, Schopper C, Patruta S, Kainberger F, Figl M, Kettenbach J, Bergmann H, Ewers R (2002) Evaluation of accuracy of computer-aided intraoperative positioning of endosseous oral implants in the edentulous mandible. Clin Oral Implants Res 13:59–64

Weinberg LA, Kruger B (1998) Three-dimensional guidance system for implant insertion: part I. Implant Dent 7:81–93

Weinberg LA, Kruger B (1999) Three-dimensional guidance system for implant insertion: part II. Dual axes table-problem solving. Implant Dent 8:255–262

White SC, Heslop EW, Hollender LG, Mosier KM, Ruprecht A, Shrout MK (2001) American Academy of oral and maxillofacial radiology, ad hoc committee on parameters of care. Parameters of radiologic care: an official report of the American Academy of oral and maxillofacial radiology. Oral Surg Oral Med Oral Pathol Oral Radiol Endod 91:498–511

Widmann G, Widmann R, Widmann E, Jaschke W, Bale RJ (2005) In vitro accuracy of a novel registration and targeting technique for image-guided template production. Clin Oral Implants Res 16:502–508

Williams MY, Mealey BL, Hallmon WW (1992) The role of computerized tomography in dental implantology. Int J Oral Maxillofac Implants 7:373–380

Wismeijer D, Van Waas MA, Vermeeren JI, Kalk W (1997) Patients' perception of sensory disturb-ances of the mental nerve before and after implant surgery: a prospective study of 110 patients. Brit J Oral Maxillofac Surg 35:254–259

Wyatt CC, Pharoah MJ (1998) Imaging techniques and image interpretation for dental implant treatment. Int J Prosthodont 11:442–452

Planning and Assessment of Bone Reconstruction for Dental Implants

21

George A. Mandelaris, Christos Angelopoulos, Reinhilde Jacobs, Robert A. Levine, and William C. Scarfe

Contents

G.A. Mandelaris, D.D.S., M.S., F.A.C.D., F.I.C.D. (✉)
Periodontal Medicine and Surgical Specialists, Oakbrook Terrace, Park Ridge and Chicago, IL, USA

Adjunct Clinical Assistant Professor, Department of Graduate Periodontics, College of Dentistry, University of Illinois, Chicago, IL, USA
e-mail: GMandelaris@PeriodontalMedicine.org

C. Angelopoulos, D.D.S., M.S.
Aristotle University of Thessaloniki, Thessaloniki, Greece

Columbia University, College of Dental Medicine, New York City, NY, USA
e-mail: angelopoulosc@gmail.com

R. Jacobs, D.D.S., Ph.D., M.S., Dr. H.C.
Omfsimpath Research Group, Faculty of Medicine, Department of Imaging and Pathology, Katholieke Universiteit Leuven, Leuven, Belgium

Dentomaxillofacial Radiology Center, Oral & Maxillofacial Surgery, University Hospitals Leuven, Leuven, Belgium
e-mail: reinhilde.jacobs@kuleuven.be

R.A. Levine, D.D.S., F.C.P.P.
Pennsylvania Center for Dental Implants and Periodontics, Philadelphia, PA, USA

Department of Periodontics and Implantology, Kornberg School of Dentistry, Temple University, Philadelphia, PA, USA
e-mail: RLevine@padentalimplants.com

W.C. Scarfe, B.D.S., F.R.A.C.D.S., M.S.
Department of Surgical/Hospital Dentistry, Division of Radiology and Imaging Science, University of Louisville School of Dentistry, Louisville, KY, USA
e-mail: William.scarfe@louisville.edu

W.C. Scarfe, C. Angelopoulos (eds.), *Maxillofacial Cone Beam Computed Tomography*,
https://doi.org/10.1007/978-3-319-62061-9_21

21.1 The Edentulous Residual Alveolar Ridge

Tooth loss leads to many challenges in order to restore the dentition for esthetics and function. These challenges range in complexity from engineering the appropriate type of prosthesis and supporting teeth to advanced surgical, planning and therapies to maintain the alveolar ridge dimensions or construct the anatomy which has lost normal contours. The ultimate goal is directed towards compensating for tooth loss and supporting structures with dental implants, when appropriate. While shape and size of the residual ridge are important for function and esthetics in fixed and removable prosthetics, these become critical when dental implants are used to restore an edentulous space. In these circumstances, maintenance of the native bone or construction of the atrophic jaw is mandatory.

The long-term success of dental implants relies on the fact that they must be embedded in a prosthetically driven location and within a structually sound and vital bone organ unit responding favorably to biomechanical demands. As described in *Chap.* 19, adequate cortical and pericircumferential bone coverage around implants is of utmost importance. When this is compromised, the esthetic and biological osseointegrative success of the implant is compromised.

After tooth loss, the alveolar bone in the edentulous space undergoes progressive remodeling. In most cases, remodeling occurs slowly and gradually. Several factors have been identified as contributory to post-tooth extraction *alveolar bone resorption*, a term that includes all changes that may occur after tooth loss. These factors include the age of the individual, the extent of the deficient alveolar ridge (determined by the number of teeth extracted and the size of the residual defects), the time elapsed since tooth loss, and the jaw (maxilla or mandible).

21.1.1 Evaluating and Intercepting Alveolar Bone Resorptive Patterns

When tooth replacement is considered using fixed or removable partial prosthetics, post tooth extraction alveolar bone resorption is expected, let alone bone reconstructive strategies considered. However, if tooth replacement by implant supported restorations are considered, implementing therapies to intercept and prevent alveolar bone loss either prior to or immediately after tooth extraction may delay resorption or alter resorptive patterns that may reduce the need for possible future therapeutic or surgical interventions.

The evaluation of the degree of atrophy for an established residual alveolar ridge in a partially or completely edentulous patient is necessary to classify the existing resorption and comprehend the available alveolar bone volume. As described in detail in *Chap.* 19, both qualitative and quantitative approaches are possible to characterize the morphology of the residual alveolar ridge defect. While the most extensive descriptive categorization has been proposed by Cawood and Howell (1988), the ITI SAC (International Team for Implantology Straightforward, Advanced and Complex) (Chen et al. 2009) system describing the bone defect in relation to surgical treatment plan implications has greater clinical application. In summary, alveolar bone volume is classified as: (1) sufficient, (2) deficient horizontally but allowing simultaneous augmentation, (3) deficient horizontally requiring prior or bone augmentation, and (4) deficient vertically and/or horizontally, requiring prior bone augmentation.

In addition to classifying residual alveolar ridge morphology as to the amount of available bone volume (height and width) and potential need for osseous reconstruction, the clinician should consider the following questions:

- Is the site of interest present in a partially or completely edentulous location?
- What is the quality of the alveolar bone in the sites under examination?
- What is the alveolar ridge morphology?
- What specific local bone deficiencies exist (compromised cortical plates, anatomic or cortical deficient concavities, etc.)?
- What is the integrity of cortical plates, particularly at recent tooth extraction sites?
- What is the degree of healing that has occurred at recent extraction sites?

After evaluating and classifying the residual alveolar ridge and taking specific considerations into account then decisions regarding the need for augmentation (based on the morphologic features of the alveolar bone), the type of augmentation procedure necessary, and the use of graft types most suitable for certain types of deficiencies can be made and the prognosis of a successful augmentation determined.

21.1.2 The Role of Cone Beam Computed Tomography

Cone Beam Computed Tomography (CBCT) is the imaging modality of choice to evaluate, classify, and address specific clinical diagnostic concerns regarding the residual alveolar bone in an edentulous space and often for the periodic evaluation of any grafting procedure.

CBCT provides outstanding detail and anatomic accuracy necessary for the assessment of the osseous structures of the maxillofacial region and their anatomical boundaries. Potential osseous defects can be analyzed from all perspectives including volumetric three-dimensional (3D) representations of alveolar resorption patterns. The internal trabecular structure and quality of cancellous bone, and peripheral cortical thickness is readily discernible with CBCT. If the scan is performed with the patient's dentition closed and the FOV extends to the teeth of the opposite dental arch, CBCT may also reveal the available restorative space. More detailed analysis of the contribution of CBCT in the assessment of the alveolar bone is beyond the scope of this chapter (See *Chap.* 19).

21.2 Materials and Methods Used to Reconstruct the Residual Alveolar Ridge

21.2.1 Autogenous Grafts and Bone Substitutes (Allografts, Xenografts, and Alloplasts)

Thorough implant treatment planning should also consider the possibility of alveolar reconstructive options when deficiencies exist in the alveolar bone at prosthetically important sites. A variety of materials has been used for that goal. Autogenous bone remains the "gold standard" of grafting materials.

Allografts are tissue grafts originating from donors of the same species but different genotype and are mostly human cadaveric material. They possess some osteoinductive capability, and may be combined with BMPs (Bone Morphogenetic Proteins), rPDGF (recombinant platelet-derived growth factor), and other biomolecules that induce bone growth, that are native to the bone filler material or mixed with it.

Xenografts are grafts that originate from donors of a different species whereas alloplasts are minerals like hydroxyapatite, which are naturally present in bone. These graft materials are primarily vehicles of *osteoconduction* and *creeping substitution* (Becker et al. 1994; van Steenberghe et al. 2000; Maréchal et al. 2005; Molly et al. 2006).

On CBCT images, autogenous bone and allograft materials will appear relatively hypodense, whereas a xenograft will appear hyperdense and generally possesses greater dimensional stability, which is one of its advantages. Functionally, the key to successful xenograft placement is vascularized bone, so a xenograft may be more stable as a scaffold. However, because the resorptive properties of these grafts are poor, they may be more prone to infection or react as a foreign body. Their physical stabilizing property also helps preserve microarchitecture and prevent resorption once well incorporated.

Another class of bone grafting materials includes a reverse-phase putty-based combination of demineralized human bone matrix, naturally occurring growth factors, and BMPs that can be molded and packed into an irregularly shaped defect (Accell Connexus®, Keystone Dental, Burlington, MA, USA). This material may have a bone like appearance on CBCT (Figs. 21.1 and 21.2).

Choices of bone augmentation materials are driven by a combination of individual practitioner's preference, appraisal of the available literature as well as objective clinical experience and results obtained with specific techniques and materials.

Vital bone volume is an important consideration in guided bone regeneration (Buser 2009). A bone substitute material used in alveolar ridge preservation or reconstruction should resorb and remodel similarly to new bone to facilitate implant placement. Low substitution-rate or nonresorbable material such as an inorganic bone matrix xenograft (e.g., BioOss®, Geistlich Pharma North America, Inc., Princeton, NJ, USA) or alloplasts (e.g., Perioglas®, Novabone, Jacksonville, FL, USA) may offer advantages in certain applications, such as in esthetic sites (Buser 2009). These materials control dimensional aspects of sites with high esthetic demand by adding structural support to underlying bone, in support of esthetically critical soft tissue architecture (Buser 2009).

21.2.1.1 Tissue Engineering

Tissue engineering is the use of a combination of cells, engineering, materials, methods, and suitable biochemical and physicochemical factors to improve or replace biological functions. Tissue engineering involves the use of a scaffold for the formation of new viable tissue for a medical purpose. Its objective is the de novo bone formation by recapitulating fetal intramembranous bone growth. There are different ways for this to be accomplished:

- Use of biomolecules like protein-peptides where the therapeutic state of the art exists today, best exemplified by recombinant human bone morphogenetic protein 2 (rhBMP-2).
- Use of mitogens (proteins that induce cell division).

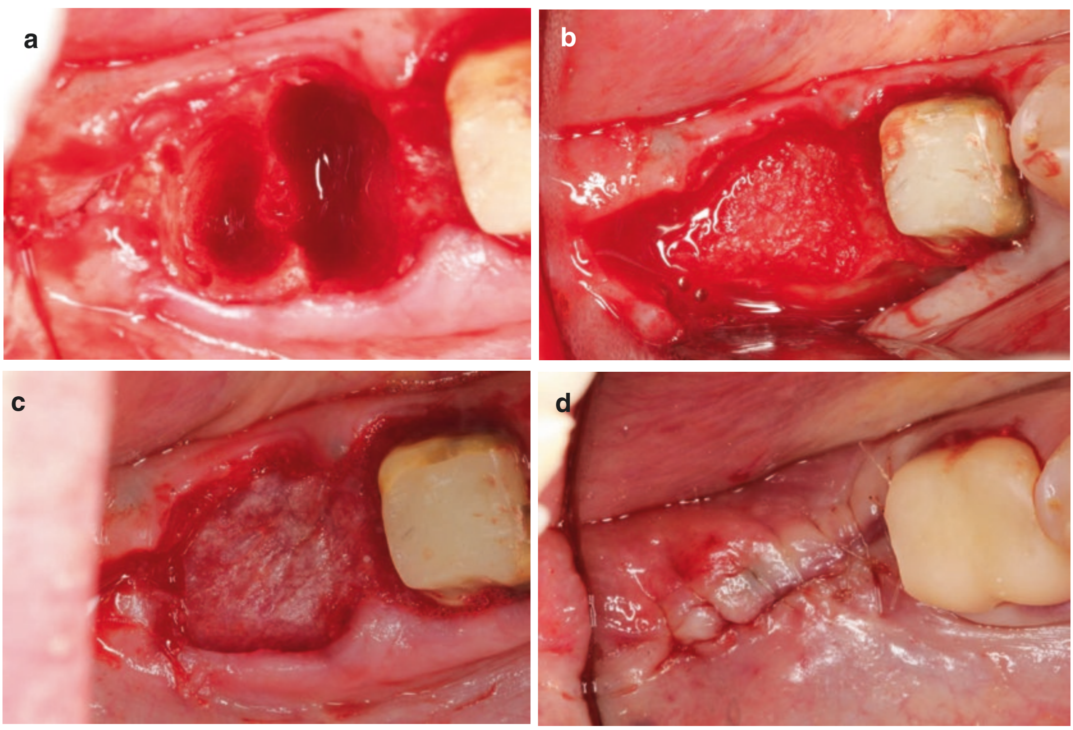

Fig. 21.1 Sequence of intraoral clinical photographs demonstrating the use of Accell Connexus® as an allograft graft material for the ridge preservation after removal of the mandibular right second molar. Appearance of socket immediately after tooth extraction (**a**), with graft material inserted (**b**), with placement of a resorbable biomembrane (**c**), and after soft tissue closure (**d**)

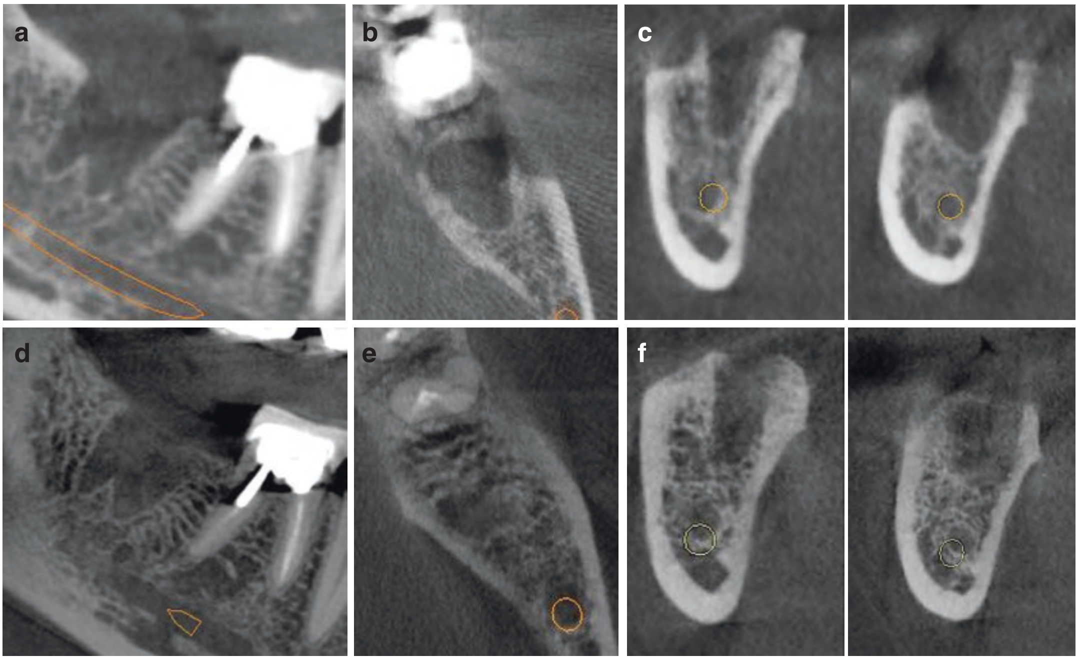

Fig. 21.2 Sagittal (**a**), axial (**b**), and cross-sectional (**c**) CBCT images of the mandibular right second molar extraction site illustrated clinically in Fig. 21.1 24 h after tooth removal and insertion of graft material. Note that the grafting material used shows minimal density and may not be identifiable unless reported by the clinician to the radiologist. Corresponding sagittal (**d**), axial (**e**), and cross-sectional (**f**) images 4 months after tooth extraction and simultaneous grafting procedure. At this time there is only subtle differences in the imaging appearance of the extraction socket with relatively increased hyperdensity. This appearance suggests successful osteoinductive capacity. Unless the type of the procedure, grafting material, and time interval postsurgery are known, it is almost impossible to draw conclusions about the healing process and progress of integration

- Cell-based therapy. This includes the use of mesenchymal stem cells, such as those available from the iliac crest at the time of surgery for oncologic as well as oral and maxillofacial surgical procedures.
- Gene-based/RNA therapeutic strategies (Rios et al. 2011).
- Scaffold fabrication technology.
- Laser technology.

Most applicable techniques of tissue engineering in alveolar bone augmentation seem to be the utilization of molecules like rhBMP-2 or mitogens like platelet-rich plasma (PRP), plasma-rich growth factor (PRGF), platelet-rich fibrin (PRF), and platelet-derived growth factor (PDGF). These materials accelerate angiogenesis and favorable bone formation. Emerging regenerative approaches for periodontal reconstruction has been recently published by Cochran et al. (2015).

21.2.2 Graft Techniques

A number of osseoconductive surgical procedures have been designed to increase the amount of bone available locally without bone grafting (Table 21.1). Bone grafting has been used to maintain or reshape the atrophic alveolar bone and restore the dimensional morphology of the residual ridge. These along with proper bone quality are considered the foundations for successful implant placement. The use of osteoconductive materials such as growth factors, bone morphogenetic proteins, and cytokines have been tested in animal studies (Preti et al. 2007; Stadlinger et al. 2008).

21.2.2.1 Alveolar Bone Maintenance/ Extraction Socket Preservation

After tooth extraction, the alveolar bone usually undergoes rapid morphologic changes after heal-

Table 21.1 Methods to reconstruct deficient alveolar ridges

Category	Type	Description	Application
Local surgical procedures	Ridge expansion osteotomy	Osteocondensation technique to expand alveolus buccolingually	Increase width of alveolar bone, facilitate sinus wall elevation
	Crestal split technique	Uses osteotomes and chisels to produce a "greenstick fracture" at the base of the alveolus. Alveolar plates are expanded buccolingually	Widen alveolar ridge
	Guided bone regeneration (GBR)	Uses resorbable or nonresorbable membranes to prevent soft tissue growth into surgical sites. Allows bone to regenerate	Maintain alveolar ridge height and width, prior to or in association with tooth extraction
	Distraction osteogenesis	Contiguous force on healing surgically created fracture segment generates a distraction gap which, as it increases in height, fills with callus which later matures into bone	Limited regional vertical augmentation of 4 mm to 7 mm. Overcorrection is recommended
Bone grafting procedures	Autogenous	Cortical and cancellous bone grafting harvested from the same individual. Most common cortical harvesting sites include ribs, the iliac crest, ascending ramus, and mandibular symphysis. Cancellous harvesting mostly from iliac crest	Cortical used to onlay large areas such as decreased vertical or horizontal alveolar ridges. Cancellous used to fill defects associated with alveolar clefts and maxillary sinus floor augmentations
	Allografts	Non-vital osseous tissue harvested from one individual and transferred to another individual of the same species. There are three forms of allogeneic bone: Fresh frozen (not used now), freeze-dried and demineralized bone (FDDBM) Demineralized bone matrix (DBM) is incorporated into carriers such as collagen or selected polymers to form putties	Freeze dried used to onlay areas or as a crib to retain autogenous bone graft. DBM is most commonly used in extraction sites to prevent ridge resorption, alveolar ridge reconstruction and bone expansion (e.g., sinus augmentation)
	Xenografts	Skeletal tissue harvested from one species (mammalian bones such as bovine, porcine, equine or murine or coral exoskeletons) transferred to the recipient site of another species. Usually powder	Fill defect or extraction site to preserve alveolar ridge. May require retentive structure (e.g., membrane, miniscrews)
	Alloplastic bone substitutes	Synthetic substances (hydroxyapatite, other ceramics and polymers)	Used as fillers and expanders often in association with autogenous bone grafts

ing is established and present as resorption of the alveolar ridge. Various anatomic, metabolic, and functional factors affect the rate of resorption and final morphology of the alveolar process (Atwood 1957). Generally, the labial cortical plates are most affected and undergo resorption reducing bone volume and altering the buccal contour, resulting in the reduction of the alveolar bone width (Araujo et al. 2015a, b). This is most likely as a result of the reduced thickness of the cortical plate and the higher incidence of dehiscence associated with the tooth roots (Irinakis 2006). Bone volume reduction is principally caused by horizontal alveolar changes rather than a reduction in vertical height (Araujo et al. 2015a, b).

The time after tooth extraction is an important determinant of the residual ridge resorption rate. Most loss of tissue contour in the alveolus involving narrowing of the ridge occurs within the first 6 months after tooth extraction. These changes occur at a greater rate in the maxilla than the mandible (Araujo et al. 2015a, b). At the completion of healing, alveolar bone height is often reduced as compared to pre-extraction levels (Irinakis 2006).

Understanding of the pattern of alveolar bone resorption underscores the need for atraumatic extraction and appreciation of the available strategies to preserve ridge volume overall (Araujo et al. 2015a, b). It is now acceptable practice that to arrest the effects of ridge resorption immediately after the removal of a tooth, the fresh extraction socket should be treated with grafting material, a barrier membrane, or both (Isaella et al. 2003; Artzi et al. 2000). Araujo et al. (2015a) proposed a ridge preservation strategy involving xenograft placement in fresh maxillary extraction sockets that resulted in a significant reduction in post-extraction hard tissue cross-sectional area on CBCT at 4 months (3%) versus a control (25%) (Figs. 21.1 and 21.2).

Value of CBCT Imaging

The role of CBCT is crucial in the initial assessment of the pre-extraction site for the periodic evaluation of the graft integration or maturation. CBCT is the only dental imaging modality that provides the detail necessary to assess the integrity of the facial and lingual/palatal cortical plates adjacent to the tooth to be extracted. Specifically, CBCT can provide information on the thickness of the cortical plates and risk of possible fracture, and presence of fenestrations or dehiscences that may compromise the cortical plates. Postoperatively CBCT provides useful information about the progress of integration of the graft, graft stability, and possible complications (Fig. 21.3).

Many different types of grafting materials are available for socket preservation. The imaging appearance of grafted sites on CBCT depends on its type, composition, and the time elapsed since the procedure was performed. Rarely are these features reported to the maxillofacial radiologist. Autografts often appear as osseous fragments, similar to the adjacent cortical bone. Some grafts consist of different sizes of granules and demonstrate a particulate hyperdense appearance, a heterogeneous conglomerate of medium to high opacity and attenuation within the defect (e.g., alloplasts such as hydroxyapatite-based Perioglas®) (Fig. 21.4). Others graft materials (e.g., xenografts composed of inorganic bone matrix) are smoother and show a more homogenous lower density appearance (e.g., BioOss®). It is crucial for the clinician who seeks expert interpretive consultation to provide all relevant clinical information to facilitate assessment of the status of a bone graft.

While no standardized radiographic features have been defined to assess the success of a grafted site, some parameters are useful to consider when a socket preservation graft (or any graft) is evaluated with CBCT:

- Has the graft contributed in maintaining (preserving) the dimensional stability of the grafted site (extraction socket)? Specifically, has the alveolar bone maintained the initial shape and size after the grafting procedure?
- Is the grafted site homogenous in density and how does it compare to the surrounding native

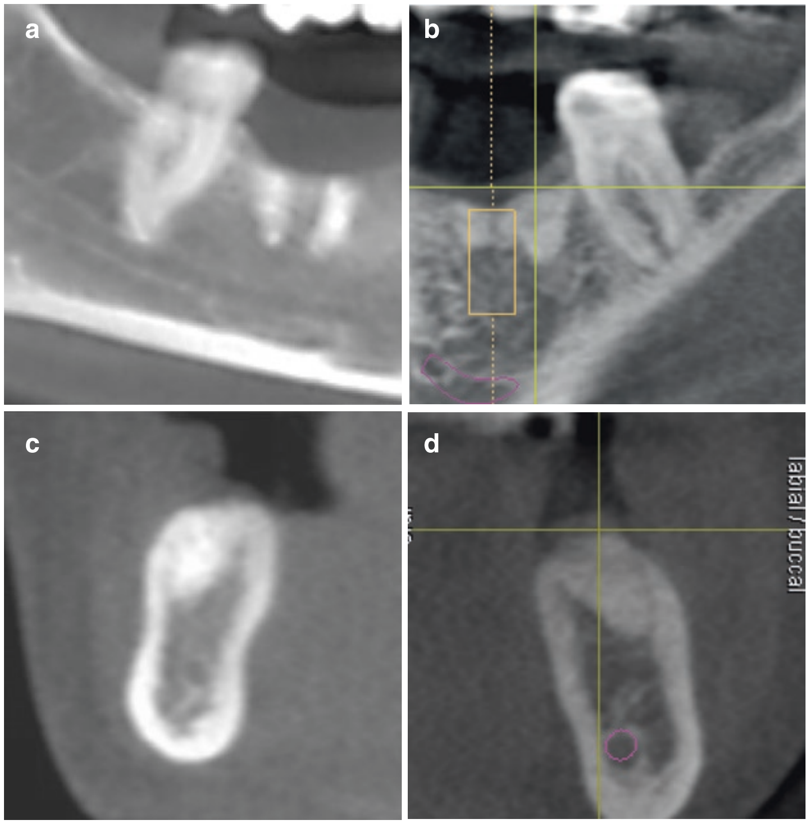

Fig. 21.3 Cropped right (**a**) and left (**b**) panoramic and corresponding cross-sectional right (**c**) and left (**d**) CBCT images of the mandibular first molar region for two patients 6 months postoperatively demonstrating successfully integrated socket grafts. Note the relative differences in hyperdensity of the graft indicating different material used at each site. Note the intimate contact interface between the graft material and the intramedullary cancellous bone

bone? Are any voids present or areas of density similar to that of soft tissue?
- Is there any part (or parts) of the graft which is separated from the main body of the graft?
- What is the contact interface of the graft to the surrounding bone (or extraction socket)? Is there a tight contact between the graft and the native bone or there are areas separated?
- In the case of a graft which has been placed to preserve a socket with a compromised buccal/lingual plate, has the graft achieved to establish a stable buccal/labial boundary? Does this maintain the natural contours of the bone with a smooth and rounded outline?

A successful socket preservation graft usually maintains the anatomical contours of the alveolar ridge even if dehiscences are present. These grafts are usually homogenous hyperdensity without any voids. Depending on the material used, some grafts may be of a somewhat lower density than that of the surrounding cancellous bone. If granulated, the grafting material granules should demonstrate even distribution without any soft tissue inter-dispersed. Finally, the graft should demonstrate a very tight contact with the extraction socket with no separation from inner aspect of the socket wall (lamina dura).

Socket preservation procedures involving grafting is fairly straightforward surgical procedure with a high success rate (Apostolopoulos and Darby 2016; Covani et al. 2014). Given the reliability of this procedure to maintain the dimensional morphology of the alveolar ridge, it is likely that CBCT will be used more often for site assessment and graft evaluation prior to implant osteotomy.

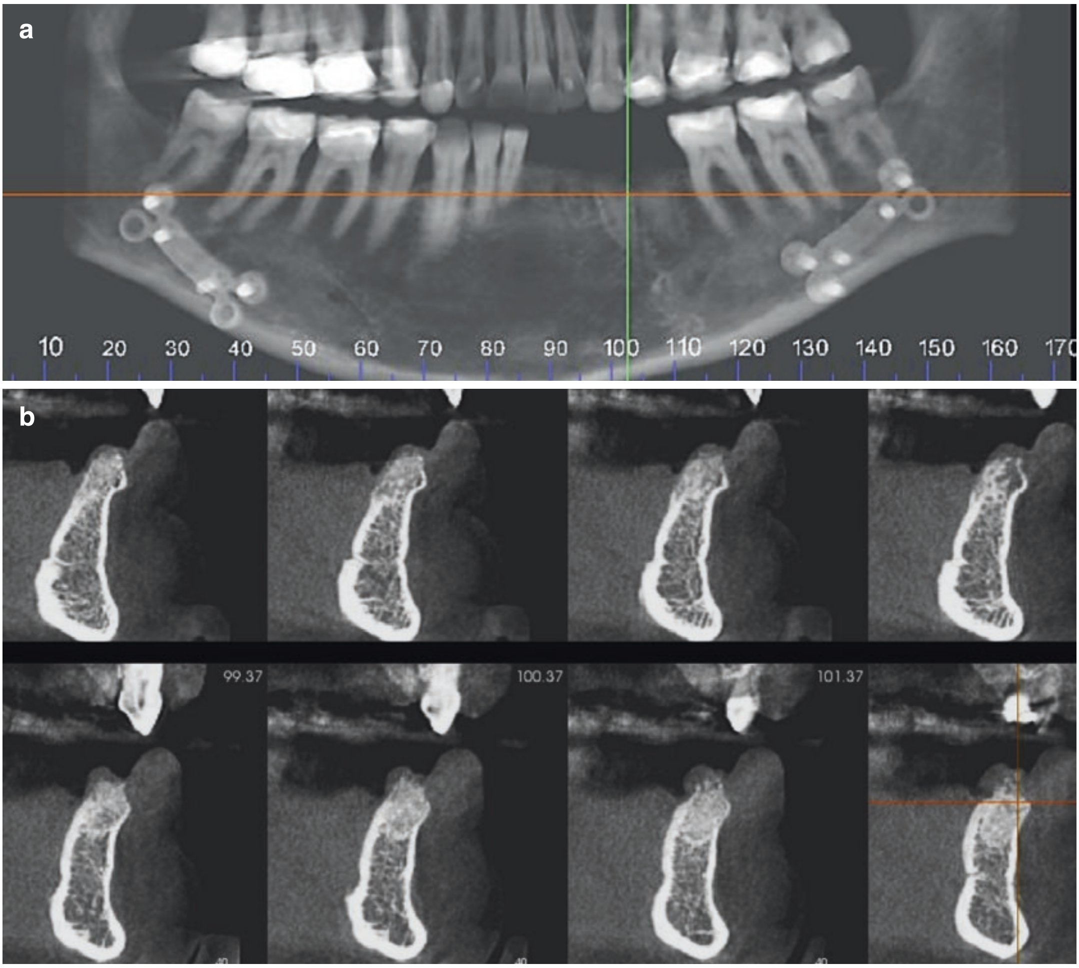

Fig. 21.4 Reformatted panoramic (**a**) and serial cross-sectional (**b**) (CBCT images) of two socket grafts in the areas of the mandibular left premolars. The panoramic also demonstrates a patient who has undergone orthognathic surgery in the mandible where fixation plates are present bilaterally. The grafting material used is granulated and of high density. Note the fairly homogenous appearance and the close contact with the extraction socket, indicating a satisfactory fill of the socket

21.2.2.2 Horizontal and Vertical Alveolar Ridge Augmentation

Restoring the anatomical contours of the severely atrophic alveolar crest of either the maxilla or mandible is challenging. The pattern of resorption in these situations is such that the alveolar ridges are no longer representative of the location of teeth. In fact, since the tooth-bearing bone is no longer present, the spatial relationship between existing teeth (in the partially dentate edentulous space) and the residual bone available for implant placement is markedly discordant. This implies that not only is there insufficient alveolar bone available to place a dental implant based on the occlusal considerations of the implant retained prosthesis, but also, pending on the extent and severity of resorption, there is most likely inadequate facial contours to provide soft tissue support (Figs. 21.5 and 21.6).

In partially dentate situations, the existing occlusal scheme determines the type and amount of reconstructive surgery necessary to restore a deficient alveolar ridge. In completely edentulous situations, the redesigned occlusal platform and scheme will dictate the location of implants

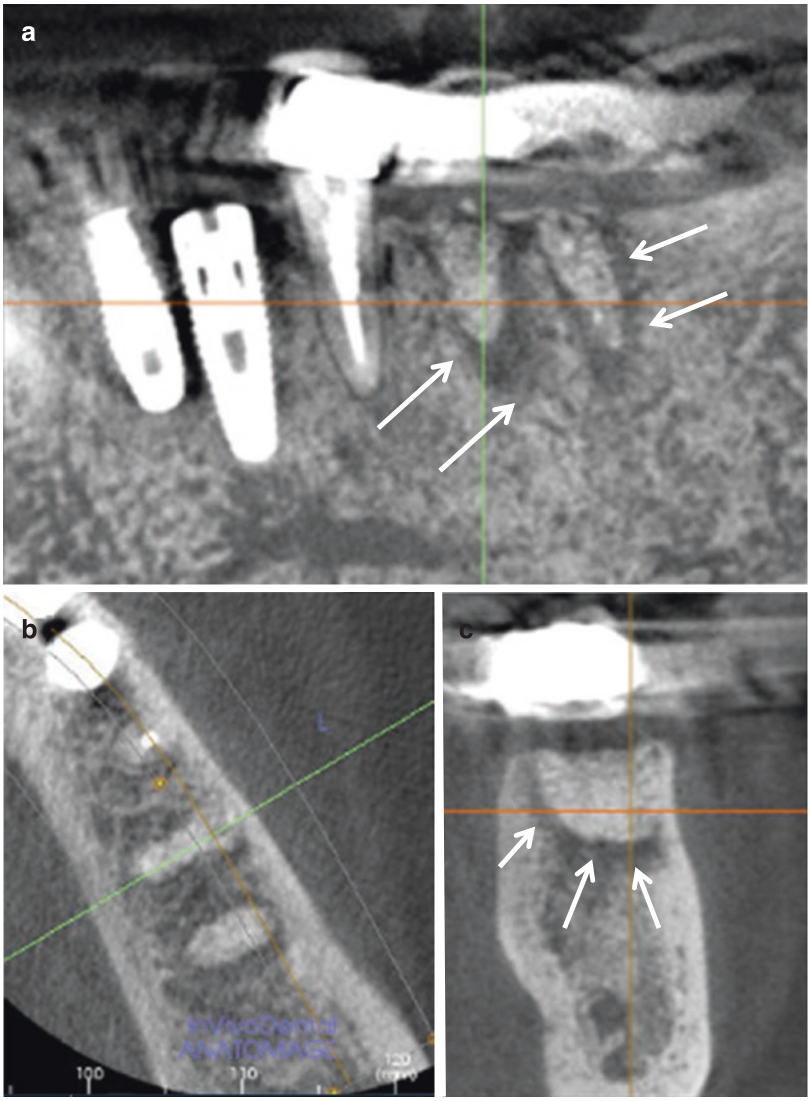

Fig. 21.5 Reformatted panoramic (**a**), axial (**b**), and cross-sectional (**c**) CBCT images of a socket graft in the region the left mandibular first molar. Note the wide, low density zone surrounding the graft (*arrows*). This zone may indicate a layer of soft tissue proliferating between the graft and the socket raising concerns about its stability and integration. This appearance should be correlated to clinical history and surgical timeline. Naturally, this needs to be verified by correlation with the post-operative period after the grafting procedure and, if necessary, surgical exploration

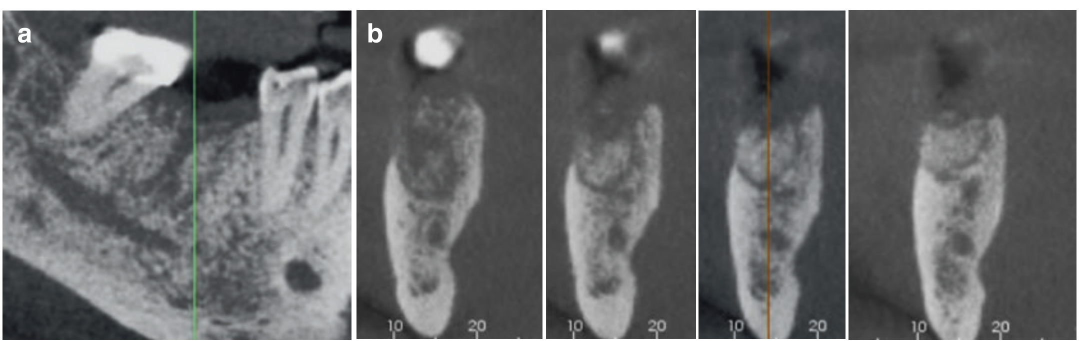

Fig. 21.6 Reformatted cropped panoramic image (**a**) and CBCT cross-sectional images (**b**) of a socket preservation graft in the area of the right mandibular first molar. Note the thin low density separation between the graft material and alveolar bone, the void inside the graft which seems to be reducing the superior extent of the graft and dispersing fragments or granules of the graft towards the crest. This appearance is suggestive of graft failure

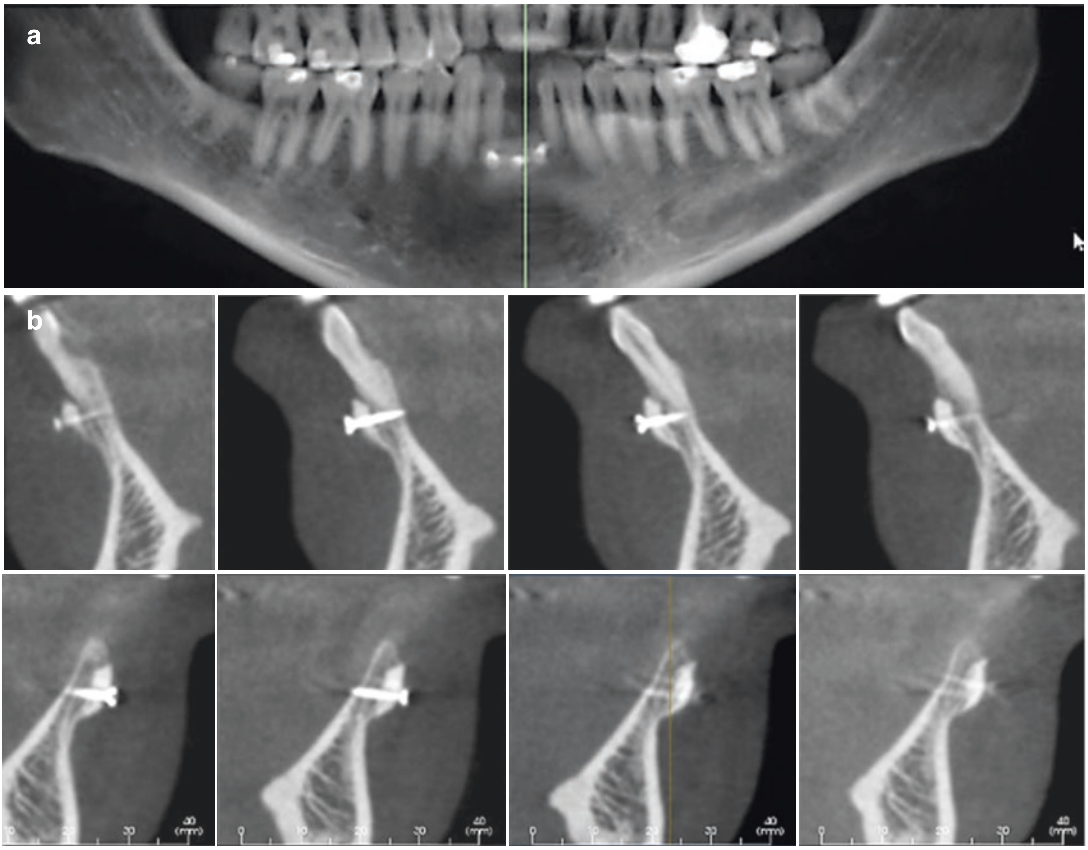

Fig. 21.7 Reformatted panoramic (**a**) and serial cross-sectional (**b**) CBCT images of the anterior mandible showing a cortical, hyperdense, onlay block graft stabilized to the labial aspect of alveolar ridge with a fixation miniscrew. The contact of the graft to mandibular bone is satisfactory and the graft has increased the thickness of the bone towards the crest

and therefore the kind of ridge augmentation needed to facilitate implant positioning. Alveolar ridge augmentation may be necessary in the horizontal dimension to increase the width of the alveolar bone, in the vertical dimension to increase the height of the alveolar bone, or in both dimensions. The more extensive the grafting procedure, the more complex and challenging it becomes.

Several methods have been described for the augmentation of the bone height and/or width of the deficient alveolar ridge (Table 21.1). These include guided bone regeneration (GBR) with and without particulate grafting materials, alveolar ridge splitting, distraction osteogenesis, and the utilization of block "onlay" grafts. Both particulate and block grafts can be used for either horizontal or vertical augmentation.

Onlay Block Grafts

Donor sites for "onlay" grafts may be intraoral or extraoral from the patient themselves or from cadaveric donors (Toscano et al. 2010). The most common intraoral sources are the mandibular symphysis (chin region) and the anterior border of the ascending mandibular ramus whereas the most common extraoral sources include the iliac crest, parietal cranial bone (calvarium), tibial plateau, and ribs (Indrontino and Valente 2016). Block grafts are not as widely used as particulate grafts which tend to vascularize more quickly and with the advent of tissue engineering techniques. Onlay grafts are commonly retained with narrow diameter, self-tapering fixation miniscrews (Figs. 21.7 and 21.8) Cortical-cancellous onlay grafts (e.g., symphysis) are preferred as the presence of the cancellous component facilitates

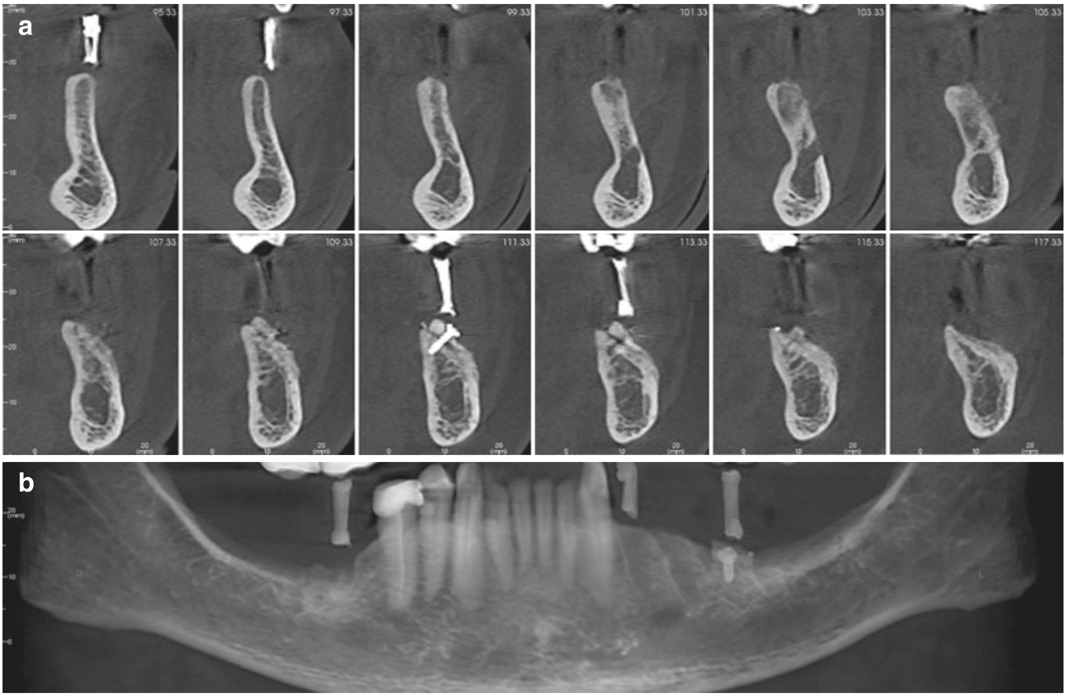

Fig. 21.8 Sequential 1 mm thickness cross-sectional CBCT images at 2 mm intervals (**a**) and a reference reformatted panoramic image (**b**) of the left mandible showing use of both particulate graft (left second premolar region) and miniscrew fixated, block onlay graft (first molar region) material throughout the edentulous space in the region of the left mandibular premolar and first molar. Both techniques increase or restore the horizontal bone volume necessary for implant placement

faster vascular in growth after placement, faster integration (osteogenesis) and less potential resorption after healing (Hammack and Enneking 1960). When cortical grafts are used they may be fixated using a miniscrew with a "filler" of autogenous graft material (e.g., bone marrow). In this situation cortical bone is used for space maintenance and stability whereas the autogenous graft material is osseoinductive. Failure of this grafting technique may involve either the cortical onlay component or lack of osseoinductive "fill" of the autogenous graft (Fig. 21.9).

Particulate Grafts

Particulate grafts are more commonly used in dentoalveolar regenerative procedures because they are more easily vascularized and pose less morbidity for the patient. Small-particle autogenous grafts can be combined with cortico-cancellous allograft, xenograft, or tissue engineering, as with the use of BMP-2 (Mandelaris et al. 2015) and physically retained with biomembrane with or without miniscrew "tenting" technique (Figs. 21.10 and 21.11) or miniscrew retained metallic mesh (Figs. 21.12, 21.13, 21.14, and 21.15). The production of inexpensive biomodels can be used to preshape and prebend mesh, saving considerable intraoperative time (Figs. 21.16 and 21.17).

Despite the fact that CBCT imaging has markedly enhanced the three-dimensional assessment of bone for "onlay" grafts, no radiologic standardized criteria exist regarding the successful integration of these types of grafts. The large number and different types of grafting materials used, their different origin and properties, different forms (variability in size granules and consistence such as putty or paste), their different

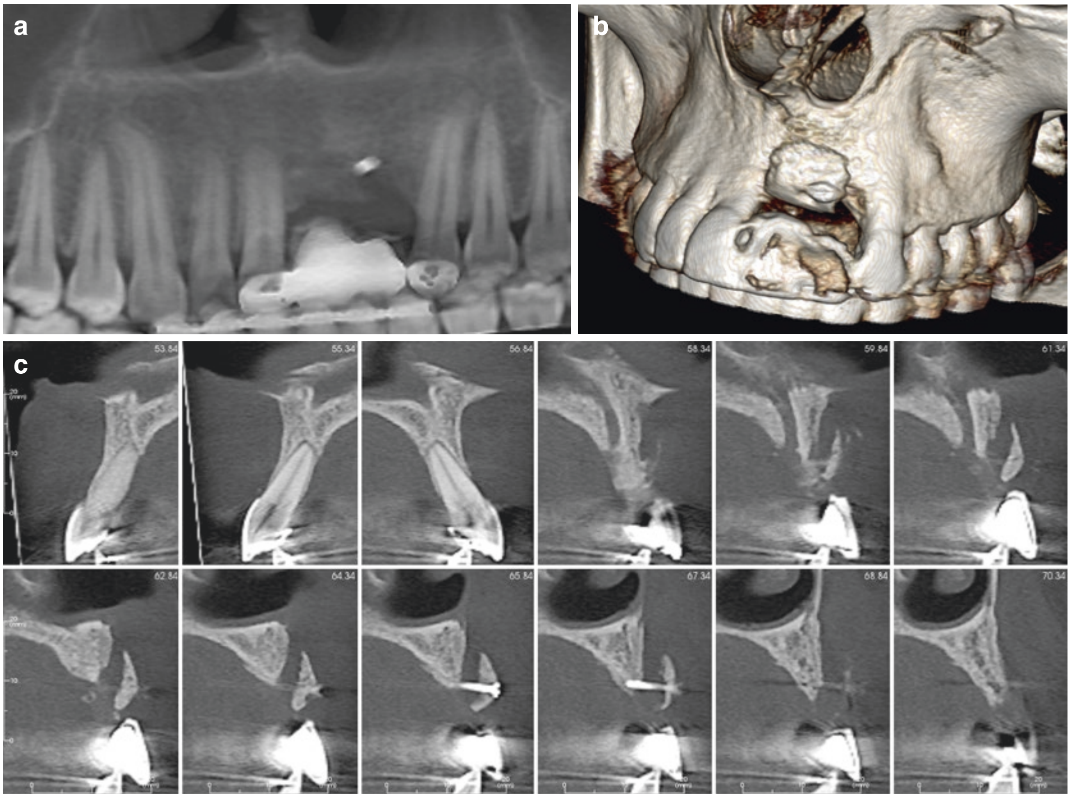

Fig. 21.9 Reformatted panoramic (**a**) and serial cross-sectional 1 mm thickness and 1 mm intervals (**b**) CBCT images showing the 5-month postoperative imaging appearance of the left maxillary anterior region. The patient presents with an extensive history of left facial trauma with root canal therapy and ultimate loss of the left maxillary left central and then lateral incisor teeth. Initially particulate bone grafting was performed which failed. Most recently a tibia graft was performed to reconstruct the edentulous alveolar defect. There is a single labial miniscrew present supporting a well-defined onlay graft; however, a hypodense uniform void is present between the graft material and labial surface of the existing alveolar ridge with multiple small irregular osseous curvilinear fragments intermittently dispersed within the alveolar soft tissues on the labial and palatal aspects adjacent to the graft and residual ridge. The imaging appearance is consistent with inadequate integration of the graft

density and mechanism of action (e.g., scaffolding, osseoconduction, osseoinduction), and degree of maturation make it difficult to identify characteristic radiographic features that suggest success or failure. Although periodic radiologic assessment of an alveolar bone graft is not specifically contraindicated (especially those applied to extensive areas of the ridge), conclusions should not be drawn about the integration or bone formation progress at early stages after surgery, especially if the postoperative progress is uneventful and without complications (Bornstein et al. 2014; Harris et al. 2012). Therefore, it is recommended that bone augmentation be evaluated by CBCT after the completion of bone maturation (4 months to 6 months for most graft materials). At that time, the anatomical contours of the deficient bone should have been reshaped, the graft is fairly homogenous in density and that the contact between the graft and the native bone is "tight" and continuous without any soft tissue undermining the graft (Figs. 21.18 and 21.19). These radiologic findings are highly suggestive of a successful ridge augmentation. However,

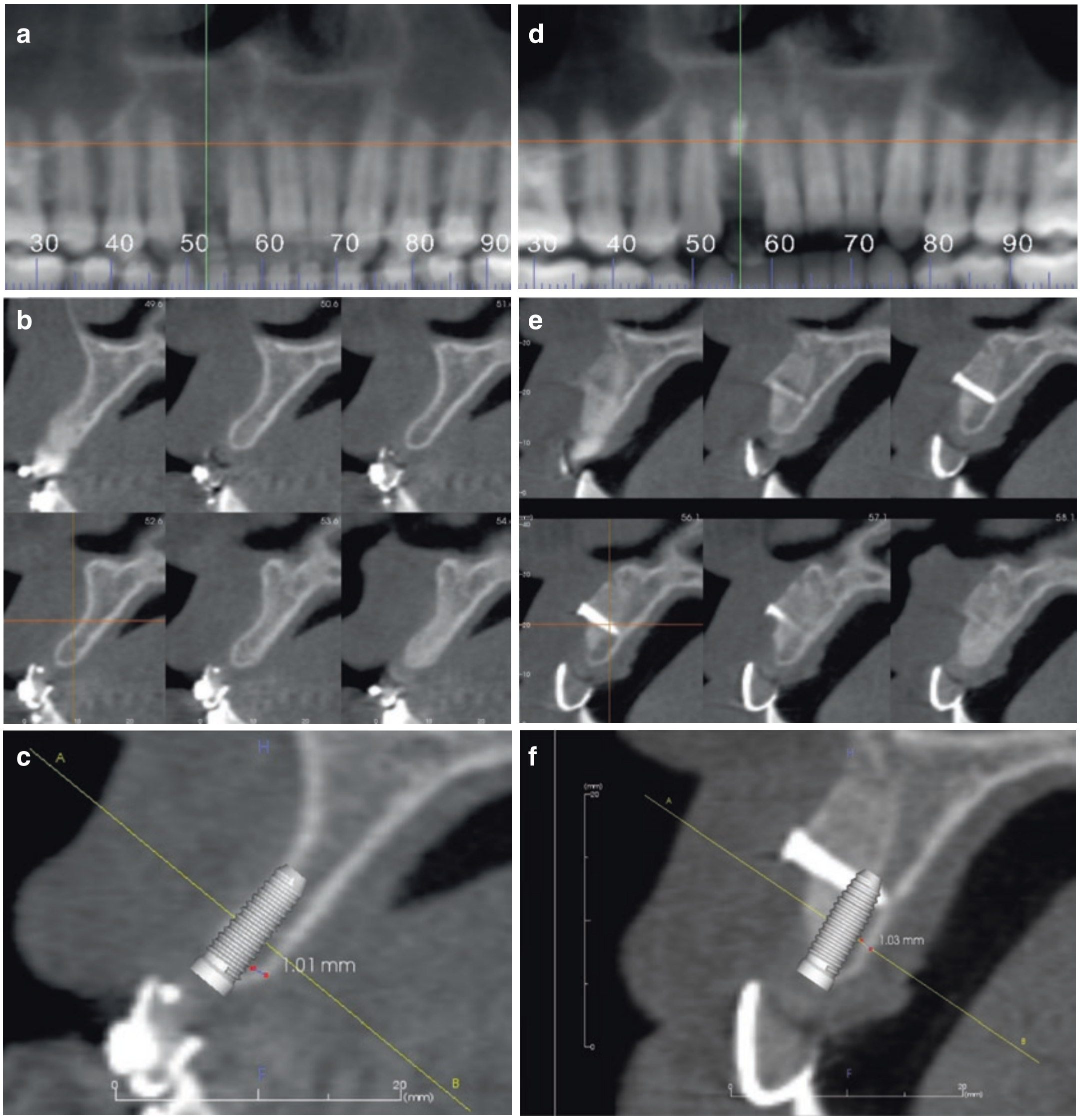

Fig. 21.10 Reformatted panoramic (**a**), serial 1 mm thick cross-sectional (**b**) images and virtual implant simulation on cross-sectional image of and edentulous maxillary right lateral incisor region showing a deficiency in alveolar bone width necessary for implant placement. Corresponding reformatted panoramic (**d**), serial 1 mm thick cross-sectional (**e**) images and virtual implant simulation on cross-sectional image 6 months after screw retained autogenous graft with bioresorbable membrane (**f**). Note the marked increase in alveolar bone width adequate for dental implant placement and excellent adaptation of graft material to the buccal cortical plate

ultimately, the successful grafting procedure is judged mostly by the end result determined clinically and at the time of implant osteotomy. This includes considerations of the stability of the graft, its homogeneous nature, gross appearance, and its density. A core biopsy of the graft, where the percentage of newly formed osseous tissue is calculated, appears to be a generally accepted objective method to assess true success.

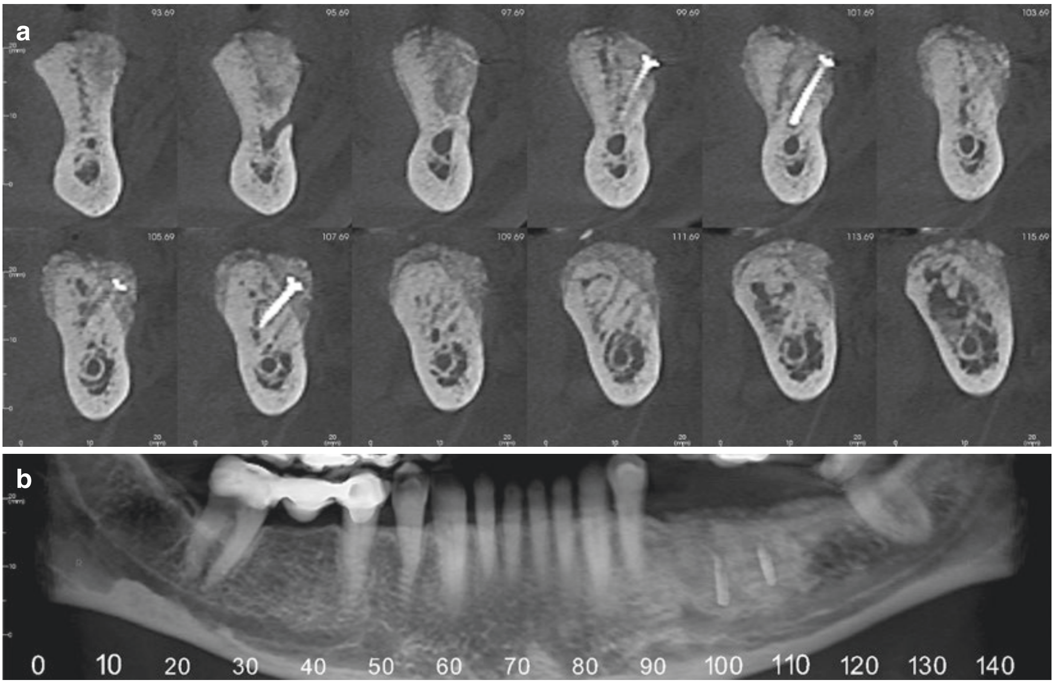

Fig. 21.11 Sequential 1 mm thickness cross-sectional CBCT images at 2 mm intervals (**a**) and a reference reformatted panoramic image (**b**) showing and extensive particulate graft extending through the edentulous space in the region of the left mandibular premolar and first molar. Note that there are two bucally inclined miniscrews used to provide support for a biomembrane (tenting) under which a well-consolidated homogeneous hyperdensity is closely adhered to the buccal cortical plate posteriorly and labial bone defect adjacent the area of the mental foramen. This graft increases the horizontal bone volume necessary for implant placement

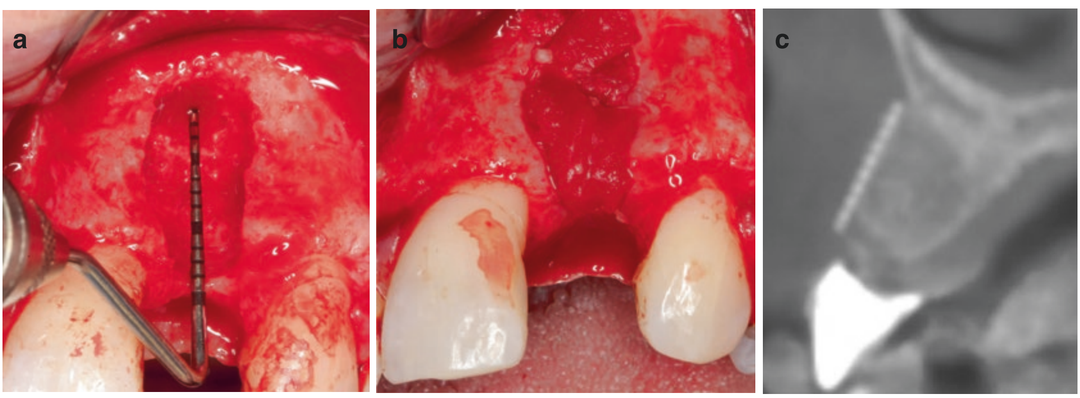

Fig. 21.12 Clinical photograph of extensive labial and cancellous defect at the site of the left maxillary lateral incisor arising from a failed graft/implant (**a**). In fact, only the palatal cortical plate was intact. Clinical photograph of the defect immediately after grafting with rhBMP-2 and cancellous allograft combination therapy (**b**). Subsequently, a titanium mesh was used to maintain space and provide stability for wound healing. Cross-sectional CBCT image (**c**) of the grafted site 9 months postoperatively; note the newly formed bone marrow suggesting successful de novo bone formation

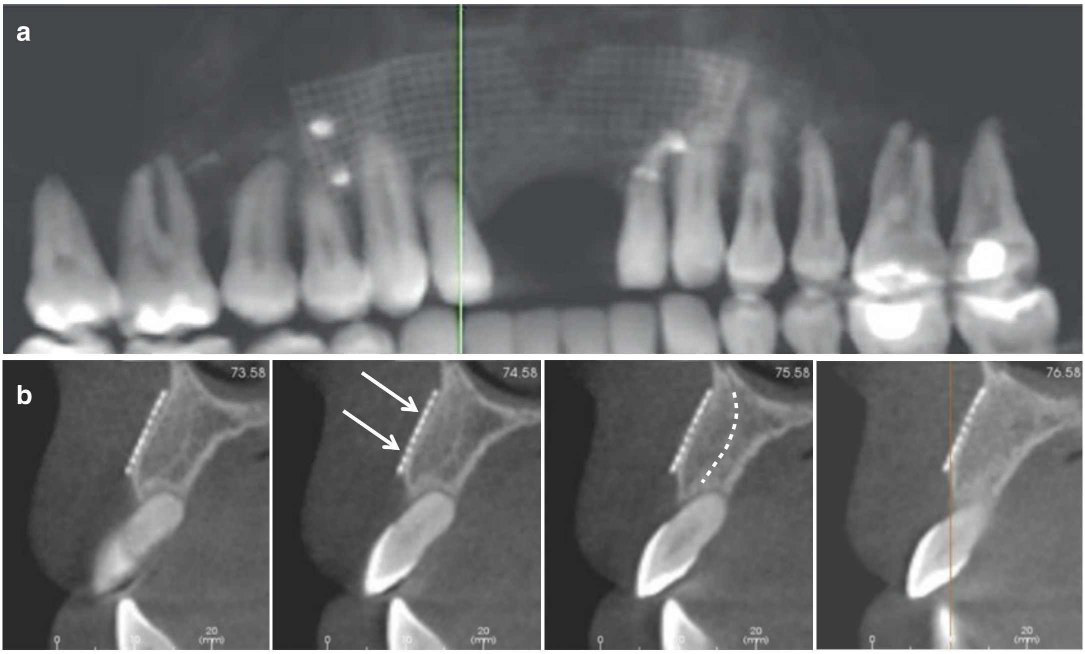

Fig. 21.13 Reformatted panoramic (**a**) and serial cross-sectional CBCT (**b**) images of the maxillary anterior edentulous region showing a mature alveolar ridge on lay grafted site with cancellous bone formation underneath a titanium mesh applied on the labial aspect of the alveolar ridge to maintain the graft. Note the initial bone thickness (*dotted line*) and the intimate contact interface between the graft and the residual bone (*arrows*). The alveolar ridge width is almost doubled after the procedure

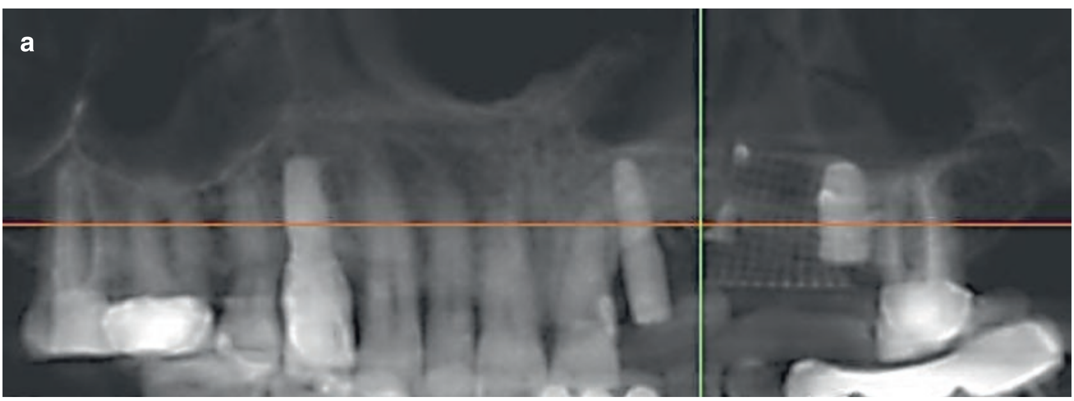

Fig. 21.14 Reformatted panoramic (**a**) and serial cross-sectional CBCT ((**b**), (**c**), and (**d**)) images of the maxillary left posterior edentulous bounded region showing the initial appearance of the grafted site with underneath a titanium mesh fixated with miniscrews on both the labial and palatal aspects of the alveolar ridge to maintain the graft. The graft is designed to increase both alveolar residual ridge height and width

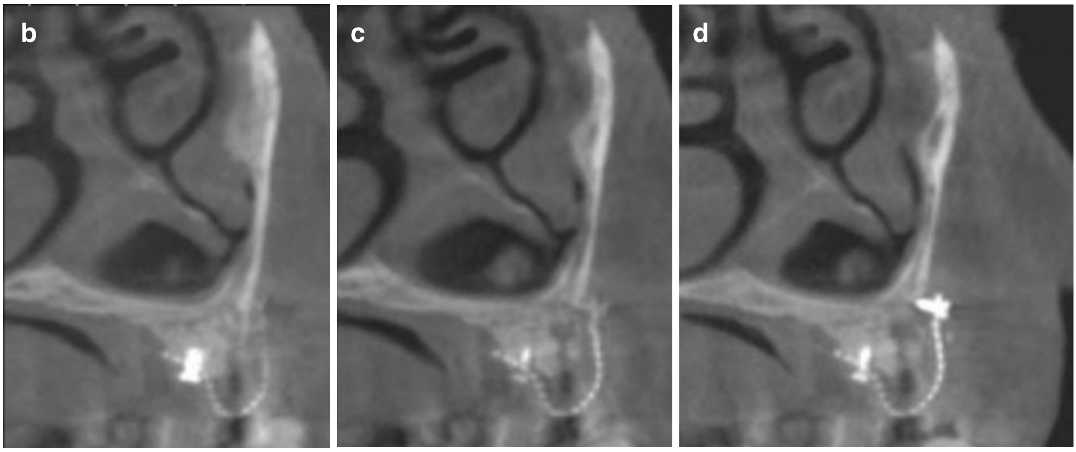

Fig. 21.14 (continued)

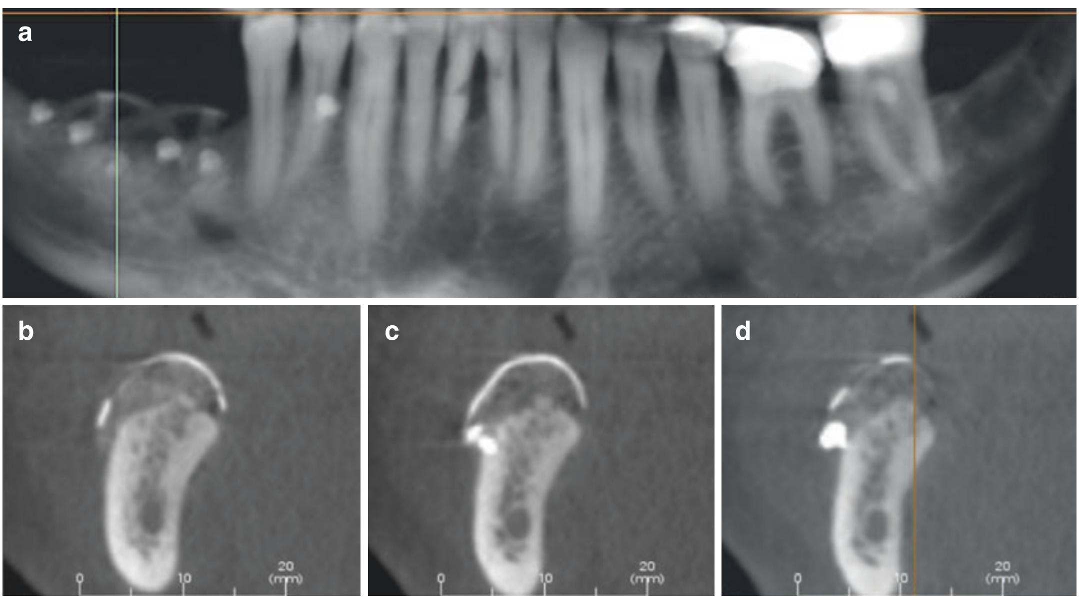

Fig. 21.15 Reformatted panoramic (**a**) and serial cross-sectional CBCT ((**b**), (**c**), and (**d**)) images of the mandibular right posterior edentulous free-end region showing the initial appearance of the grafted site underneath two "X"-shaped, miniscrew fixated titanium barriers. The graft is designed to increase both alveolar residual ridge height and width

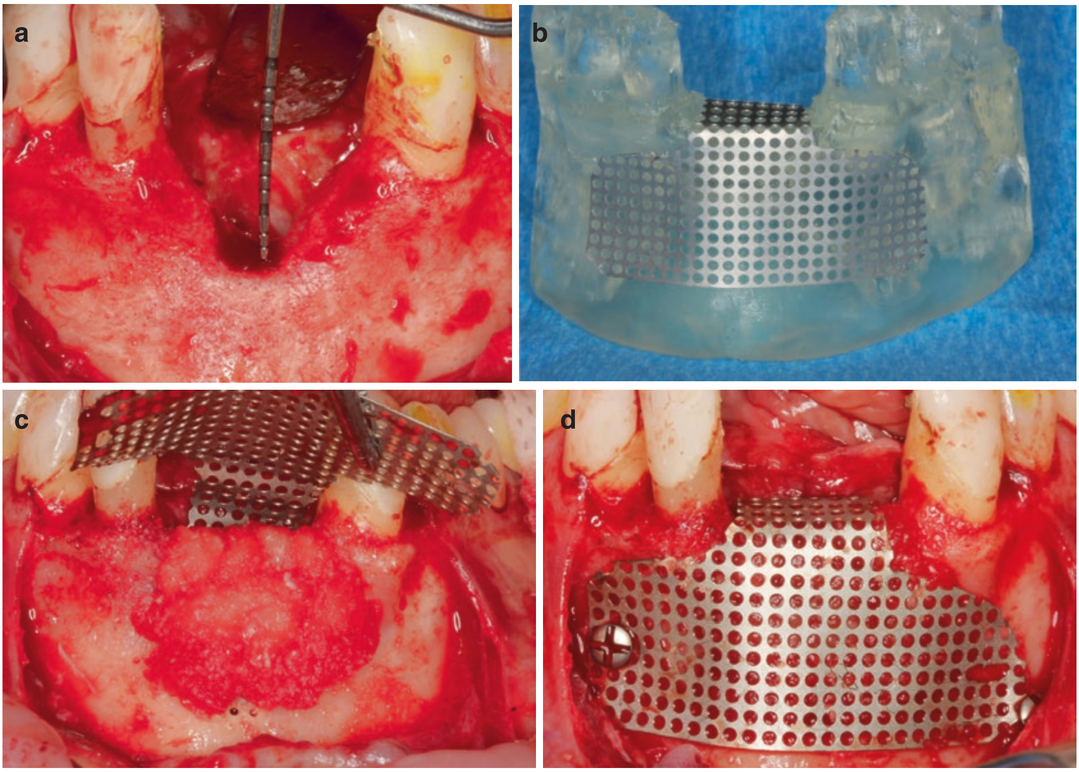

Fig. 21.16 Clinical intraoral photograph (**a**) of a large combined vertical and horizontal defect in the anterior mandible with a compromised labial cortical plate. A mandibular biomodel was printed using CBCT presurgical data and a titanium mesh pre-sculptured to the desired shape of the alveolus (**b**). The defect was reconstructed with tissue engineering combination therapy (rhBMP-2+ cancellous allograft) (**c**) which was secured in place by fixating the custom preformed titanium mesh with miniscrews (**d**)

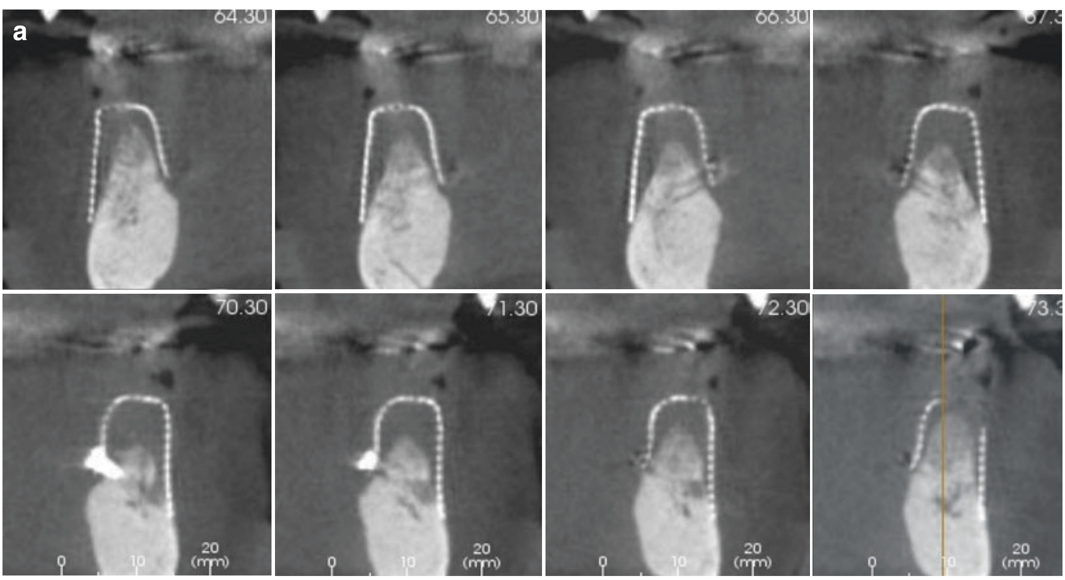

Fig. 21.17 Immediately postoperative cross-sectional (**a**) and reformatted panoramic (**b**) CBCT images of the patient in Fig. 21.16. Note the minimal density of the graft underneath the titanium mesh

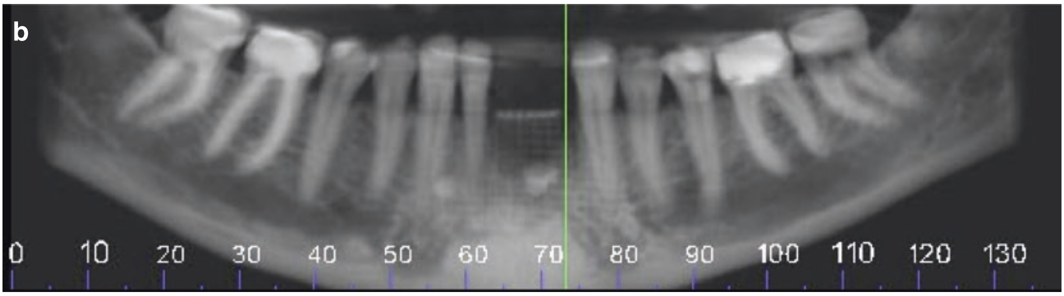

Fig. 21.17 (continued)

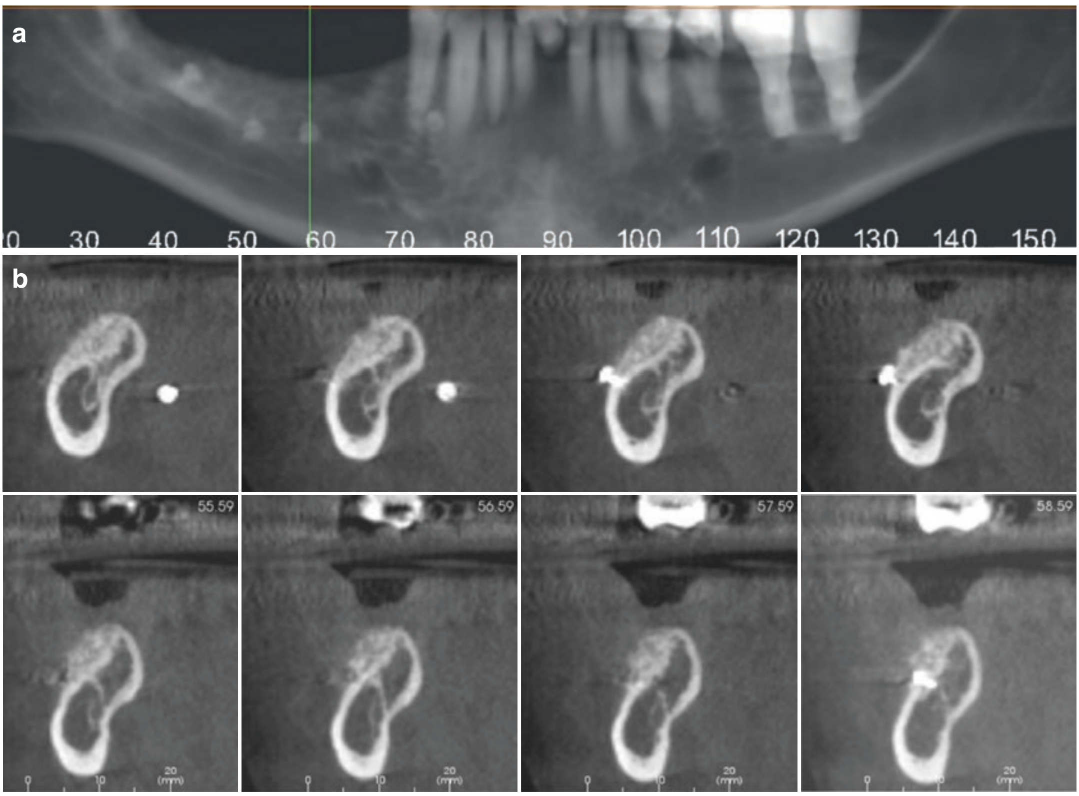

Fig. 21.18 5-month postoperative reformatted panoramic (**a**) and serial cross-sectional (**b**) CBCT images of the patient with an extensive resorbable biomembrane, miniscrew fixated particulate graft on the buccal aspect of the mandibular right posterior free-end edentulous region increasing the horizontal width of the residual alveolar ridge. Note the homogenous density of the graft, intimate contact between the graft and the native bone and well-defined supero-buccal alveolar crest, all features indicative of a successful horizontal augmentation procedure

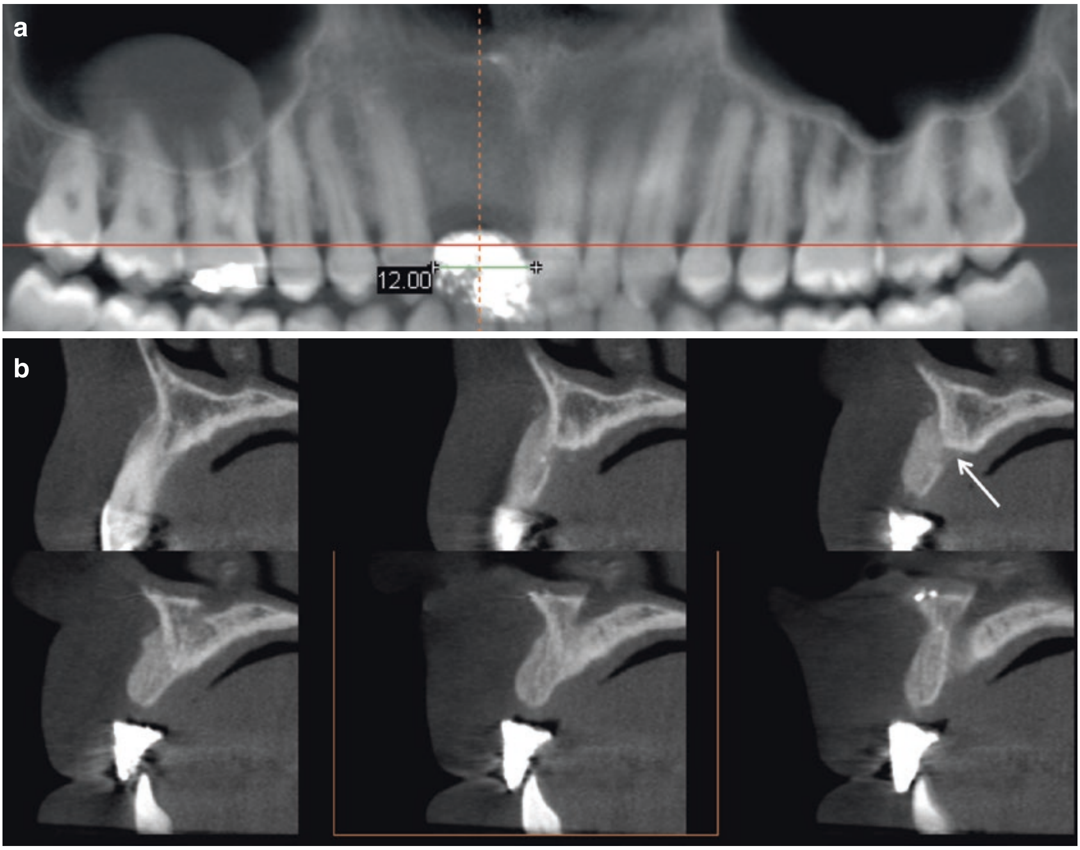

Fig. 21.19 7-month postoperative reformatted panoramic (**a**) and serial cross-sectional (**b**) CBCT images of the maxillary right anterior region to assess the integration of a mandibular symphysis particulate autograft which was reshaped to match the anatomy of the alveolar crest. The margin of the native bone and the size of the defect are clearly seen; however, there is no separation evident. This was considered a successful grafting procedure although there was a small gap on the palatal aspect (*arrow*)

21.3 Maxillary Sinus Elevation and Grafting (MSEG)

For almost 30 years MSEG has been the mainstay of implant-directed maxillary reconstruction in situations in the posterior maxilla with inadequate bone height (Tatum 1986). The *sinus lift technique* was first described by Boyne and James (1980) as a combination of a lateral window osteotomy followed by elevation of the floor of the maxillary sinus and insertion of a bone like graft material.

Two surgical approaches can be used either to simply raise the sinus lining or to additionally introduce bone regenerative material under the Schneiderian membrane.

21.3.1 Techniques

- *Lateral Window Approach* (*LWA*). The technique is essentially a lateral antrostomy which involves the creation of a rectangular osseous window through the lateral wall of the maxillary sinus which is elevated as a hinge superiorly (Tatum 1986). Careful elevation of the mucoperiosteum of the maxillary sinus (Schneiderian membrane) is performed creating a soft tissue pocket below which bone augmentation material is compacted (Fig. 21.20). The amount of bone augmentation material placed depends on the amount of existing residual ridge resorption of the edentulous space and

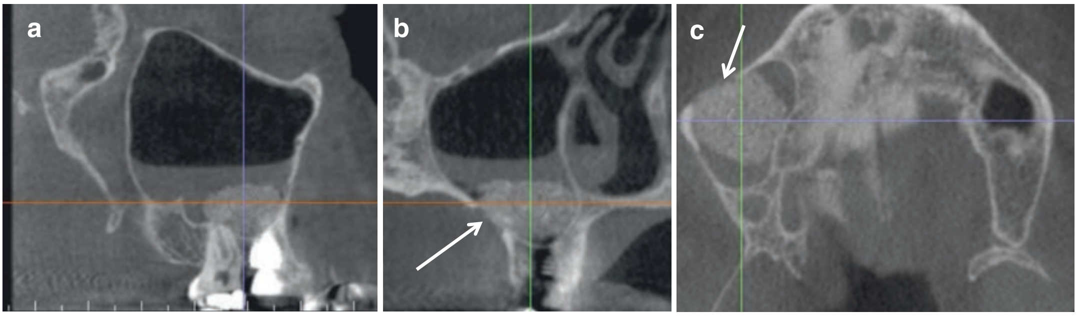

Fig. 21.20 Postoperative sagittal (**a**), coronal (**b**), and axial (**c**) CBCT images of a LWA MSEG procedure homogeneous consolidation of hyperdense bone graft material adjacent to the maxillary right second premolar edentulous space now restored with a dental implant. A localized defect in the lateral cortical plate of the maxillary sinus (*arrows*) corresponds to the antrostomy site. Moderate concomitant mucosal thickening is present; however, this is not near the right ostia

the length of the planned implant. This technique is usually performed for multiple implant sites. Various modifications of the technique have been reported without the creation of a bony hinge, and implants are either placed simultaneously or in a delayed procedure following bony remodeling of the augmentative material (Bornstein et al. 2008).

- *Trans-Alveolar Osteotomy* (*TAO*). A more conservative approach used is a trans-alveolar osteotomy which uses osteotomes through the crestal bone to raise the Schneiderian membrane and perform a ridge expansion osteotomy superiorly (Summers 1994). In general, xenograft particulate graft materials are more compatible with this approach, because of their greater visibility. This technique is usually performed for a single implant site, however variations include crestal core elevation (Toffler 2001), and the localized management of the sinus floor (Fig. 21.21) (Bruschi et al. 1998).

Survival rates for implants placed using either of these procedures are greater than 90% (Del Fabbro et al. 2004); however, presurgical and sometimes postsurgical radiographic evaluation of the maxillary sinus is advisable (Tyndall et al. 2012).

21.3.2 Presurgical CBCT Assessment

Assessment of the maxillary sinus condition with consideration of the integrity of Schneiderian membrane prior to MSEG is important to minimize possible postoperative complications. Even in maxillary sinuses with absent signs of disease (e.g., mucosal thickening), minor postoperative sequelae are expected as MSEG surgical procedures may impair physiological maxillary drainage into the middle meatus by inducing transient inflammatory periostial swelling or other mechanisms predisposing to acute maxillary sinusitis. However, sinus mucosa most often recovers well after MSEG surgery, with a prompt return to normal homeostasis, especially if sinus drainage is good (Stammberger 1986; Jensen et al. 1998; Timmenga et al. 2003).

Compared to panoramic radiography, CBCT imaging provides a significantly higher detection rate of sinus mucosal hypertrophy with a concomitant increase in surgical confidence and a significantly better prediction of complications (Caciut et al. 2013).

21.3.2.1 Surgical Considerations

- *Access*. The site for the access osteotomy should be approximately 3–4 mm above the apical base of the maxillary sinus through the buccal plate. This ensures optimal access for proper elevation of the *Schneiderian membrane* from the medial wall of the sinus.
- *Buccal cortical plate*. Adequate buccal cortical plate should be available to allow dissection of the inferior aspect of the membrane from the floor of the maxillary sinus and to elevate it upward to create a space in the floor

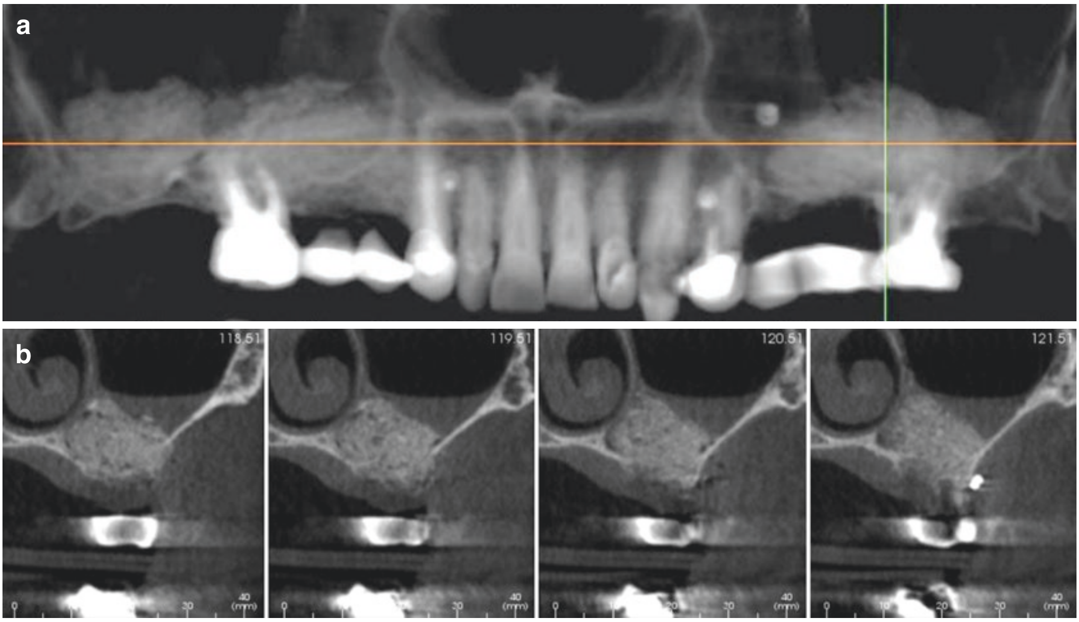

Fig. 21.21 6-month postoperative reformatted panoramic (**a**) and serial cross-sectional (**b**) CBCT images of the left posterior maxillary bounded edentulous region where simultaneous sinus bone grafting was required in conjunction with immediate post-extraction socket bone grafting. This illustrates the concomitant use of the TAO approach associated with the extraction and localized, more extensive sinus floor management adjacent the edentulous space required using the LWA

of the sinus for the bone graft material. Cross-section or coronal CBCT imaging provides location specific measurements to optimize this access.

- *Schneiderian Membrane Thickness*. In both techniques, a possible major complication is perforation of the Schneiderian membrane during the surgical procedure. Perforation increases the possible side effects of graft loss, infection that causes disruption of sinus function, and even implant survival (Viña-Almunia et al. 2009). Ideally the sinus should be disease free or have minimal mucosal thickening (<3 mm), which would potentially compromise vascularity and healing. Assessment of sinus membrane thickness prior to MSEG provides a potential index of perforation. For both the LWA (Lin et al. 2016) and TAO (Wen et al. 2015) techniques, lowest perforation rates occur when the membrane thickness as measured on CBCT images is 1–1.5 mm and higher when membranes are thicker (≥2 mm) or thinner (<1 mm).
- *Local anatomy*. Intraosseous canals containing arterial vessels such as in the lateral antral wall (*posterior superior alveolar*) and on the palatal aspect of the maxillary canine should be identified so that they are avoided during surgery (Mardinger et al. 2007). Compared to CBCT imaging, panoramic radiography is unable to detect these canals and underscores the mesiodistal distance of available bone in the upper premolar region (mean 2.9 mm, range 0.1–7.5 mm) (Temmerman et al. 2011).
- *Patency of the maxillary sinus ostia*. In addition, any condition that could lead to obstruction of the ostium and therefore drainage of the maxillary sinus may be a possible contraindication to the procedure. The ostia should be patent (Fig. 21.22); however, localized mucosal thickening of the ostium and concha bullosa (pneumatized inferior turbinate) should be noted. While mucosal thickening of the inferior medial or lateral wall of the maxillary sinus associated with chronic sinusitis is not a contraindication to the procedure, care-

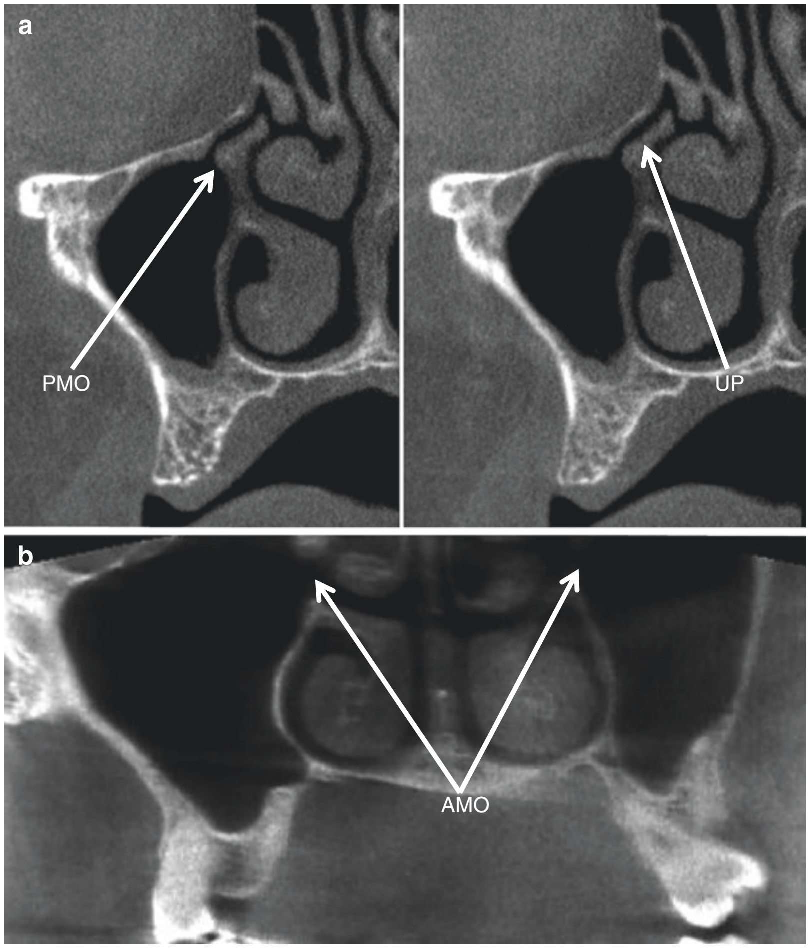

Fig. 21.22 Serial coronal cross-sectional CBCT images (**a**) showing patent right primary maxillary sinus ostia (PMO) and uncinate process (UP) with mild mucosal thickening of the floor of the maxillary sinus. Additional coronal image of another patient (**b**) showing accessory maxillary ostia (AMO). AMO have been reported to occur in the lateral wall of the nasal fossa and should not be confused with PMO (Alyea 1936; Myerson 1958; Walter et al. 1976; Stammberger and Kennedy 1995; Kumar et al. 2001)

ful consideration should be given to situations in which elevation of a thickened mucosa will lead to a mechanical obstruction of the ostium (Figs. 21.23 and 21.24).

21.3.2.2 Clinical Contraindications

From the otolaryngologist's (Pignataro et al. 2008; Torretta et al. 2013) and maxillofacial surgeon's (Ozyuvaci et al. 2005) perspectives, many common anatomical alterations, such as mild nasal septal deviation, small concha bullosa or paradoxical middle turbinate not associated with history or evidence of sinus disease are not contraindications to MSEG. However, it is important to identify maxillary sinus conditions that are treatable and potentially reversible from those that are irreversible and are likely to jeopardize a successful outcome and need management or surgical treatment prior to MSEG.

Relative Contraindications

Many conditions are present in the maxillary sinuses that are a low risk for MSEG related complications. Many are anatomic in nature, potentially compromising sinus ventilation, whereas others are pathologies, presumably reversible either pharmacologically (e.g., by the use of preoperative topic steroid therapy or nasal irrigants) or by functional endoscopic sinus surgery (FESS) before MSEG. These include:

- Conditions impairing the maxillary sinus drainage pathways. Nasal septal deviation, paradoxical bending of the middle turbinate, and concha bullosa.
- Inflammatory conditions. Allergic rhinitis.
- Conditions causing mild luminal opacification (less than 1/3rd to ½ luminal opacification.

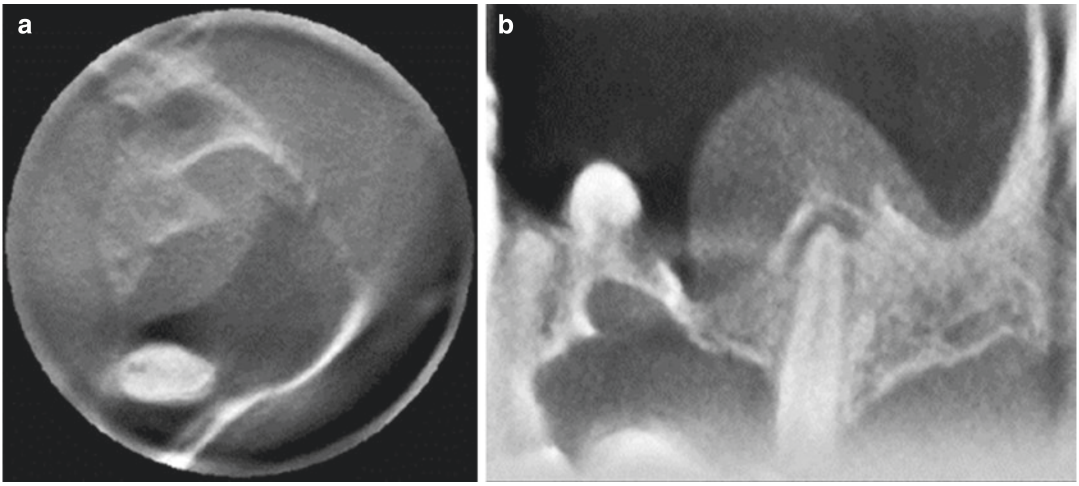

Fig. 21.23 Axial (**a**) and parasagittal (**b**) CBCT images of the left partially edentulous maxilla showing a local endo-sinus condition with severe swelling of the mucosa at the level of the apically involved premolar. Note that there is an intra-sinus osteoma anteriorly arising from the floor of the maxillary sinus, most probably associated with a history of previous tooth extraction

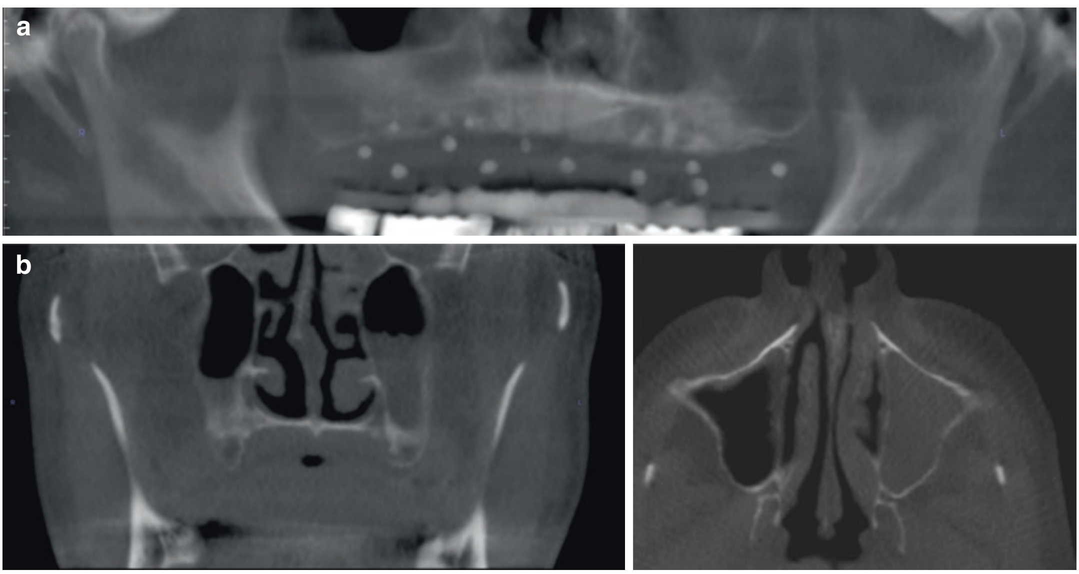

Fig. 21.24 Reformatted panoramic (**a**), coronal (**b**), and axial (**c**) CBCT images of a completely edentulous maxilla with a radiographic template inserted during the scan (notice the multiple radiopaque markers). There is soft tissue opacification occupying approximately 2/3rds of the left maxillary sinus with an irregular surface consistent with chronic sinusitis. This patient was scheduled for bilateral sinus augmentation procedure; however, as addition of bone graft material would most probably elevate the soft tissue material to occlude the left ostium, the procedure was delayed until after resolution of the condition

Presence of polypoidal mucosal thickening, CRS, or retention pseudocysts (Kara et al. 2010) on the floor or walls that, with elevation, are unlikely to obstruct the maxillary ostia.

Absolute Contraindications

Conditions that require treatment prior to MSEG procedures include any condition that occludes the ostia or has the potential to occlude the ostia including:

- Patients with ARS.
- Conditions causing moderate to severe luminal opacification (greater than 1/3rd to ½ luminal opacification. Presence of polypoidal mucosal thickening, CRS, or retention pseudocysts (Kara et al. 2010) on the floor or walls that, with elevation, are likely to obstruct the maxillary ostia.
- Suspected benign or malignant sinonasal neoplasms.
- Concomitant presence of odontogenic pathology. Odontogenic cysts, tumors, or periapical infections of odontogenic origin.

21.3.2.3 Graft Simulation

Because of the variability of the maxillary sinus volume, software measurements on CBCT panoramic and cross-sectional imaging can provide potential volume estimates of the graft material to be used. This guards against the possibility of overfilling the maxillary sinus and occluding the ostium.

Some software allows addition of solid material into either cross-sectional or panoramic images (Fig. 21.25). This is most commonly

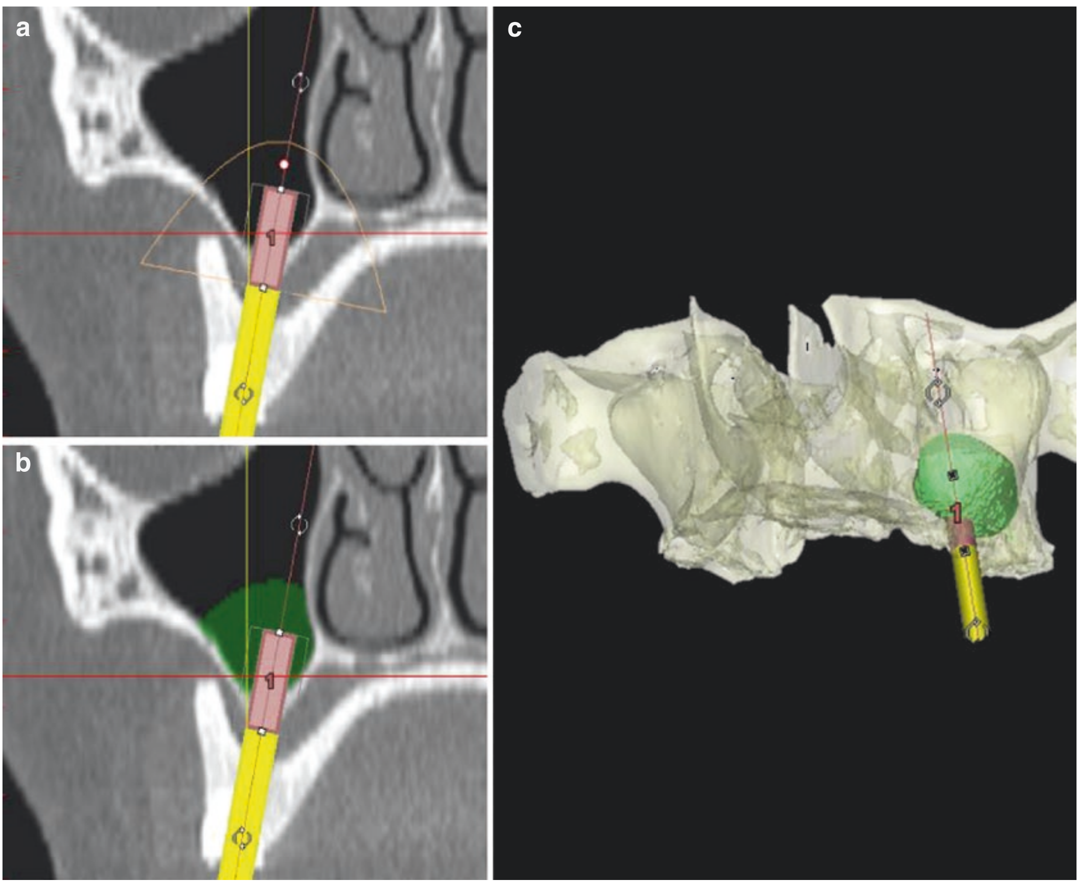

Fig. 21.25 Cross-sectional CBCT image (**a**) superimposed with a virtual implant (*pink*) and prosthetic emergence profile (*yellow*) positioned in the left posterior region in a severely atrophic completely edentulous maxilla (Dentsply Implants, Leuven, Belgium). Corresponding cross-sectional (**b**) and volumetric rendered (**c**) images with virtual sinus grafting material (*green*)

performed to simulate bone augmentation in the maxillary sinus associated with a sinus lift procedure. This is applied by either designating the confines within which the material is to be added or simply painted in successive axial or cross-sectional contiguous frames. Qualitative dimensions both linearly and volumetrically can be derived from these simulations to assist preoperatively in defining the limits of bone harvest material or amount of synthetic bone that is needed to bone placement to ensure against over- and underfilling (Fig. 21.26).

21.3.3 Postoperative Radiographic Patterns

Evaluation of the results of the sinus augmentation procedure 6 months to 8 months after placement of the graft material and prior to implant placement is advisable to confirm the presence of adequate bone. Graft material has a porous structure and gains radiodensity on CBCT as osseointegration and osteogenesis progresses. CBCT radiographic imaging appearance appearances of the postsurgical MSEG maxillary sinus depends on the technique used and degree of condensation of graft material.

- *TAO*. The osteotome technique results in a small, dome-shaped homogeneous dense radiodensity arising from the base of the sinus floor adjacent to the apical portion of the implant (Fig. 21.27).
- *LWA*.
  - *Globular, well-condensed, homogeneous, particulate hyperdense mass*. A hyperdense mass juxtaposed the potential dental osteotomy site in the edentulous alveolar region exhibiting excellent adaptation to the floor and walls (Fig. 21.28). This finding suggests well-condensed bone augmentation material with optimal osseoinductive effect. There may be mild to moderate mucosal thickening immediately superior to the graft material. Primary dental implant stability (achievable insertion torque) is likely optimal.
  - *Irregular heterogeneous particulate hyperdense mass with irregular areas of soft tissue/fluid hypodensity*. Incomplete or partial condensation of the bone augmentation

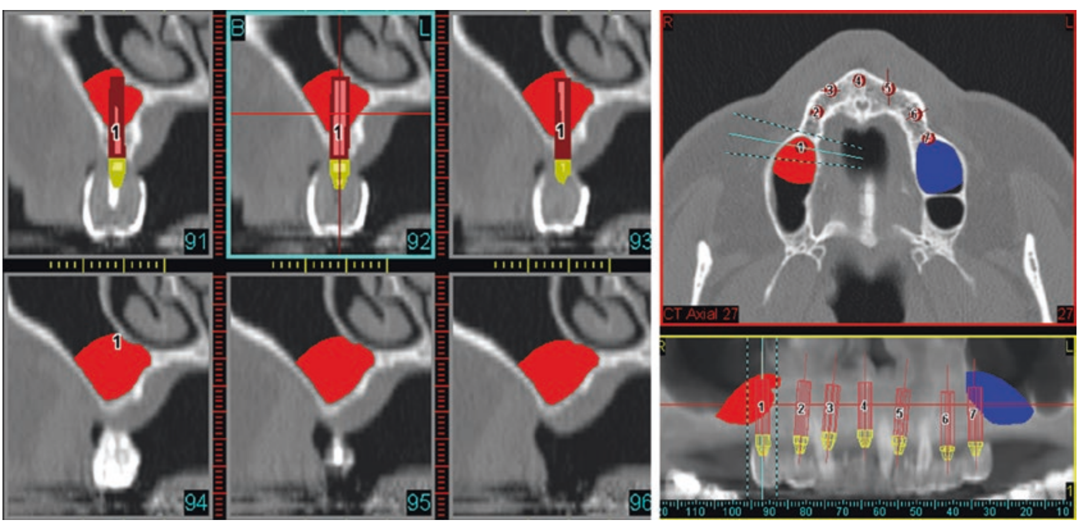

Fig. 21.26 Screen capture of completely edentulous maxilla with radiographic template showing simulated virtual placement of multiple implants. The most posterior implants bilaterally are positioned into the anterior recess of the maxillary sinus. The *red* and *blue* volumes indicate anticipated bone graft material required for successful sinus lift and bone augmentation procedure

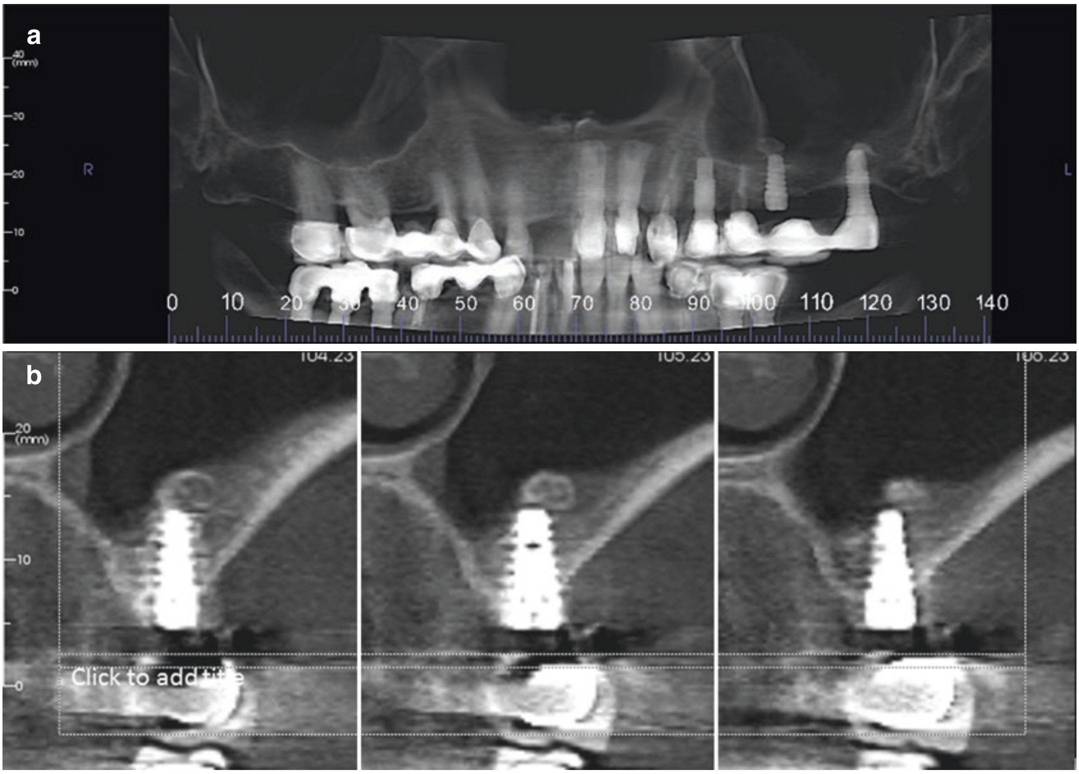

Fig. 21.27 Reformatted panoramic (**a**) and serial 1 mm thick cross-sectional CBCT images (**b**) of a successful maxillary sinus osteotome technique associated with an endosseous dental implant placed in the maxillary left second premolar previous tooth position

material adjacent to the potential dental osteotomy site suggests a poorly condensed host graft material with compromised osteogenic potential and possible bone microbial contamination (Fig. 21.29). Adaptation to the floor and walls is intermittent. Bone volume and primary dental implant stability may be less than optimal.

– *Diffuse particulate hyperdense aggregates within soft tissue/fluid hypodensity***.** Incomplete or partial condensation of the bone augmentation material adjacent spread out over the floor or within the lumen of the maxillary sinus with poor adaptation to the floor and walls (Figs. 21.30 and 21.22). Bone volume is likely inadequate for dental implant placement and primary dental stability is expected to be poor (Fig. 21.31).
– *Completely dispersed or displaced hyperdense mass within soft tissue/fluid hypodensity***.** Lack of bone augmentation with minimal accumulation adjacent the potential dental osteotomy site (Fig. 21.32). Completely detached hyperdense mass “floating” within soft tissue/fluid or scattered particulate hyperdensities throughout the sinus indicate lack of bone augmentation material condensation and integration.
– *Loss of integrity or collapse of the lateral wall.* Lack of stability of the graft material, infection, or biomembrane collapse due to external forces can result in physical displacement of the graft material further into the maxillary sinus lumen and loss of desired morphology of the residual alveolar ridge (Fig. 21.33).

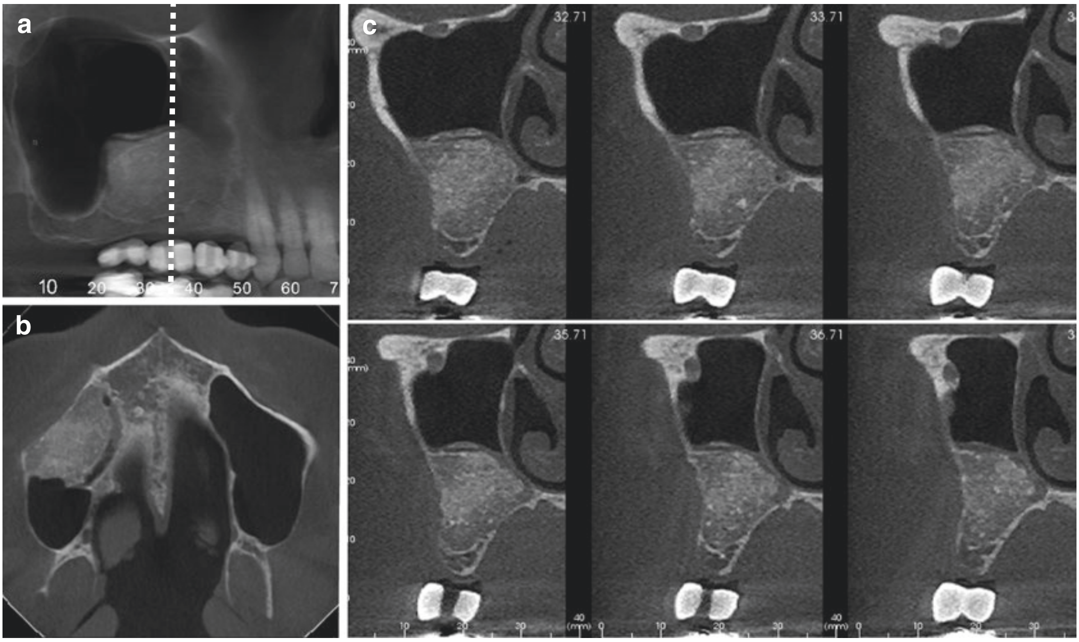

Fig. 21.28 Cropped reformatted panoramic (**a**), axial (**b**), and right ((**c**)—*small dashed*) cross-sectional images demonstrating globular, well-condensed, homogeneous, particulate hyperdense mass with minimal superimposed mucosal thickening. This represents the optimal postoperative radiographic appearance of MSEG procedures

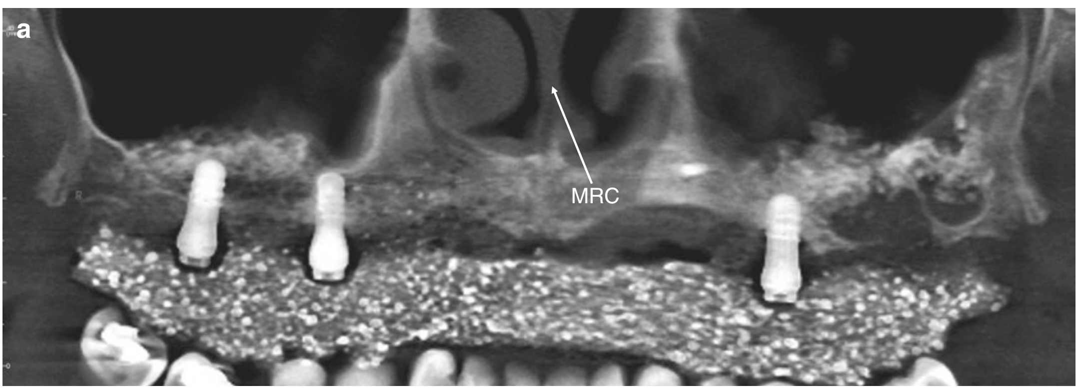

Fig. 21.29 Thin section (10 mm) reformatted panoramic (**a**), coronal (**b**), and axial (**c**) CBCT images of a 52-year-old female with a completely edentulous maxilla reporting failure and recent removal of a dental implant in the left posterior region. The images demonstrate variable heterogeneity and intermittent condensation of the hyperdense particulate bone graft material adjacent the floor of the left maxillary sinus with a hypodense alveolar defect related to the removal of a dental implant. Note: the images visualize a scanning prosthesis fabricated by adding barium sulfate to the traditional metylmethacrylate

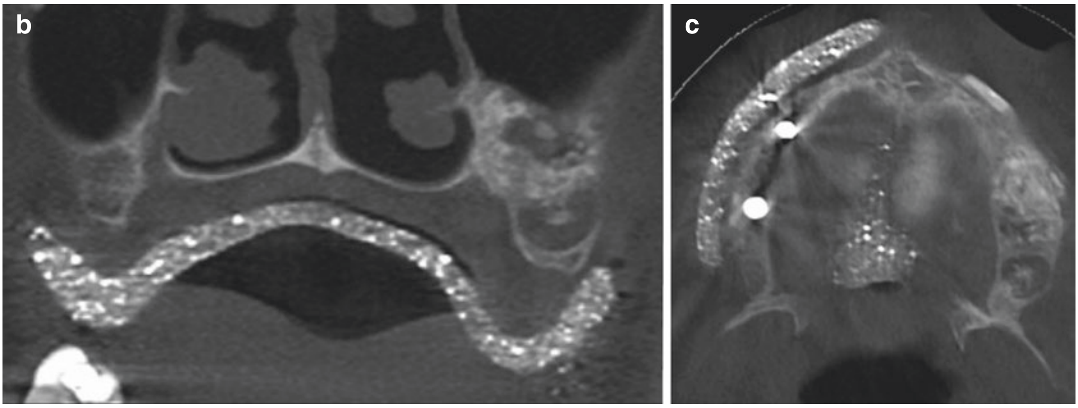

Fig. 21.29 (continued)

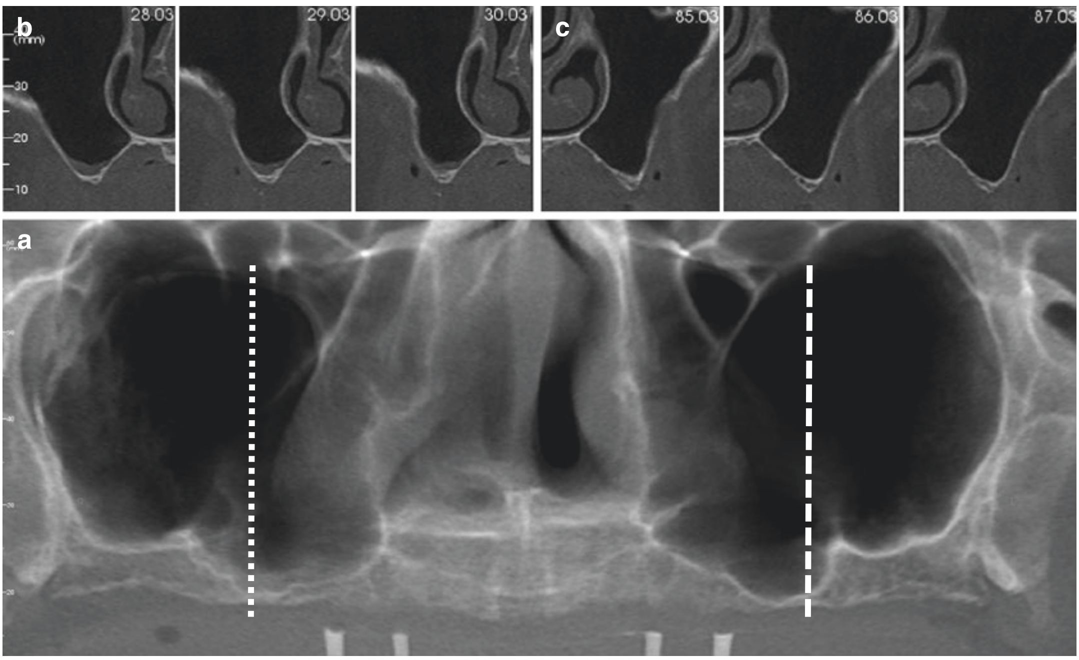

Fig. 21.30 Preoperative reformatted panoramic (**a**) and right ((**b**)—*small dashed*) and left ((**c**)—*heavy dashed*) cross-sectional images demonstrating clear, normal maxillary sinus bilaterally

21.3.3.1 Long-Term Changes in Graft Volume

Few studies have evaluated the stability of the height and volume of the bone graft over the long term (Hallman et al. 2002; Hatano et al. 2004; Harris et al. 2012; Baciut et al. 2013; McCrea 2014; Kim et al. 2014). Reports generally indicate that MSEG bone graft height is progressively lost postoperatively and, in some instances, may even resorb to the level of the original sinus height. Most resorption usually occurs within the first 3 years after the bone graft. Average bone height loss is approximately 3.2 mm (Kim et al. 2014) or up to 32% volumetric loss after almost 3 years postoperatively. Type of graft material (e.g., autogenous bone±bone substitute), surgical method (LWA or TOA) and stages of surgery (one- vs. two-stage

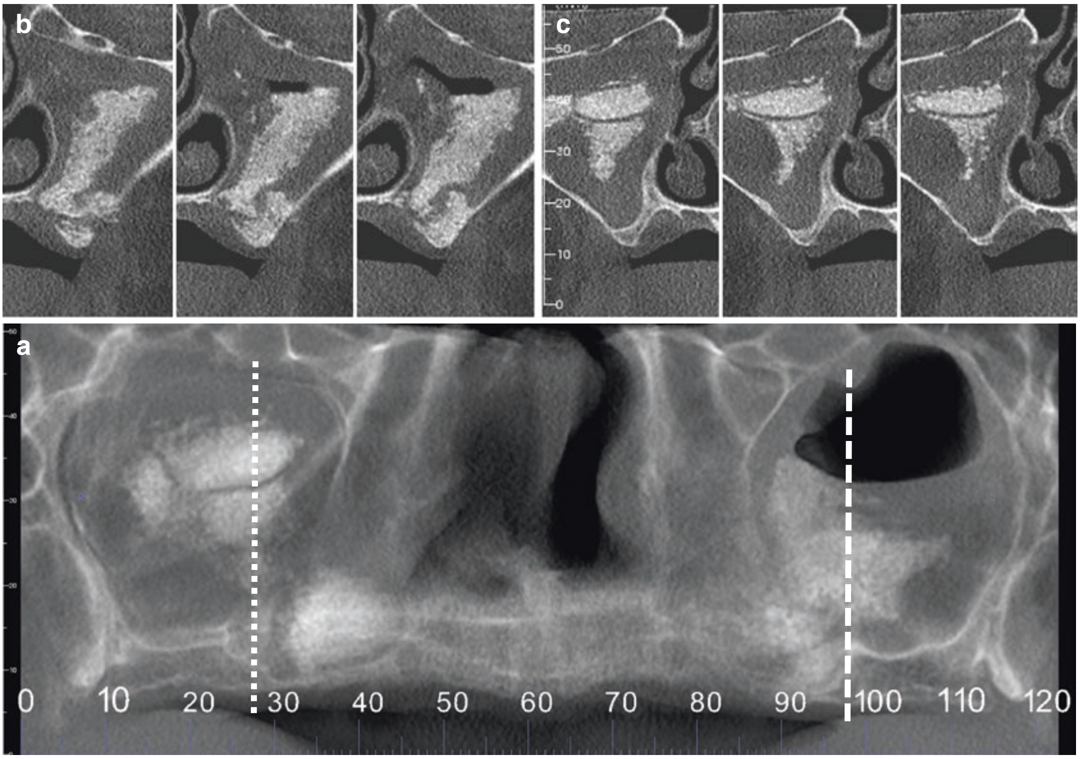

Fig. 21.31 Postoperative reformatted panoramic (**a**) and right ((**b**)—*small dashed*) and left ((**c**)—*heavy dashed*) cross-sectional images of the same patient as shown in Fig. 21.30 demonstrating bilateral postoperative acute sinusitis. Some consolidation of the graft material occurs in the anterior recess; however, the bulk of the material shows diffuse particulate hyperdense aggregates within soft tissue/fluid hypodensity

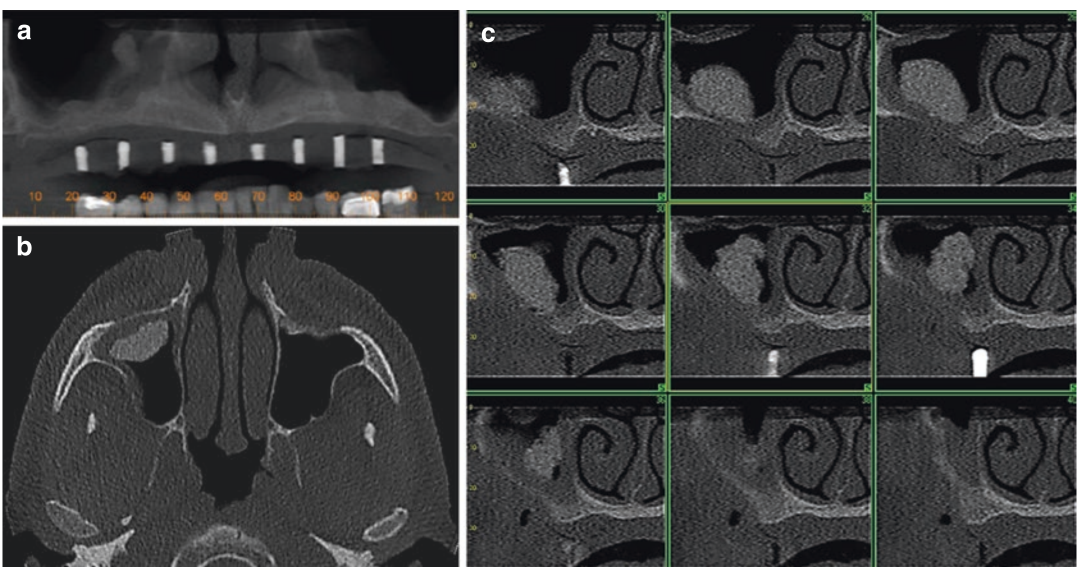

Fig. 21.32 Reconstructed panoramic (**a**), axial (**b**), and sequential cross-sectional (**c**) images demonstrating completely detached hyperdense bone graft material mass "floating" within soft tissue/fluid with minimal accumulation adjacent the proposed implant site suggestive of a lack of bone augmentation material condensation and integration

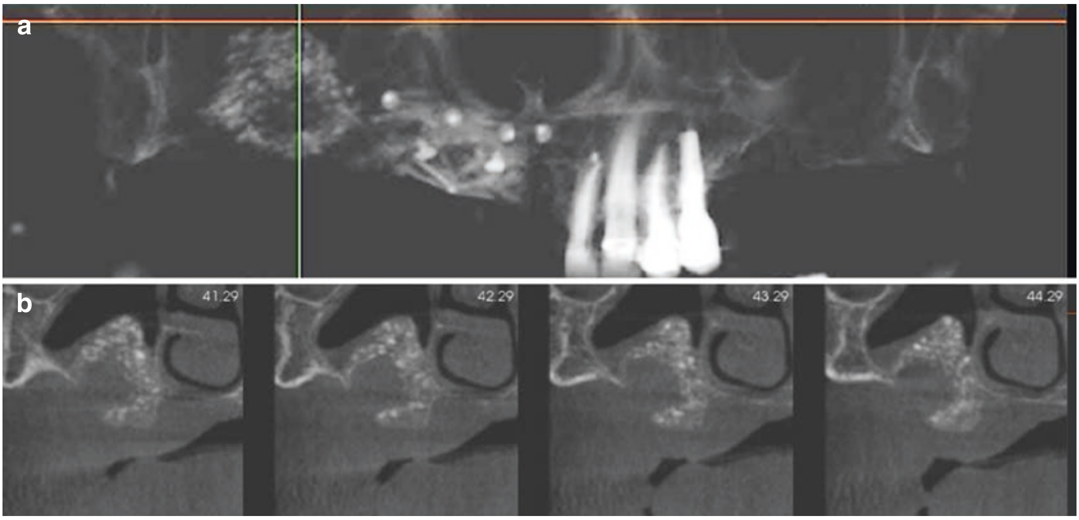

Fig. 21.33 Reformatted panoramic (**a**) and serial cross-sectional (**b**) CBCT images of the right maxillary free-end edentulous region demonstrating extensive anterior mesh retained graft reconstruction in the premolar, canine, and incisor region and a MSEG in the molar region. The cross-sectional images demonstrate localized medial displacement of the graft material and creation of a regional void or "pocket" within the graft volume

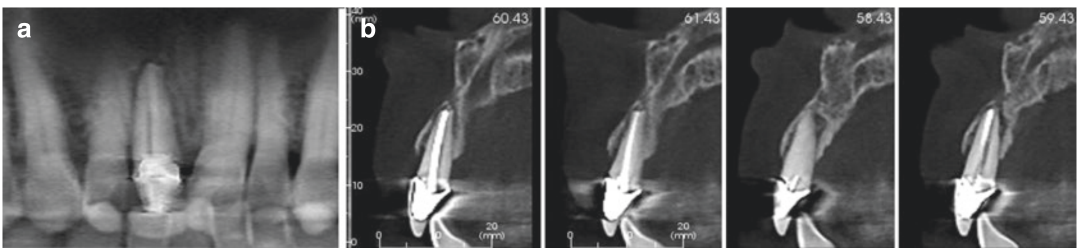

Fig. 21.34 Reformatted panoramic (**a**) and cross-sectional (**b**) CBCT images of the maxillary right central in a 58-year-old female which is to be removed and an implant immediately inserted. This tooth demonstrates generalized pericircumferential periodontal ligament space widening and, in the panoramic projection, appears that there is separation between the distal aspect of the tooth and the root canal material highly suggestive of vertical root fracture. The maxillary central incisor demonstrates a Type I sagittal root position (Kan et al. 2013). Note that there is marked reduction in the width of the alveolus in the apical region associated with the presence of a prominent buccal concavity and the nasopalatine fossa

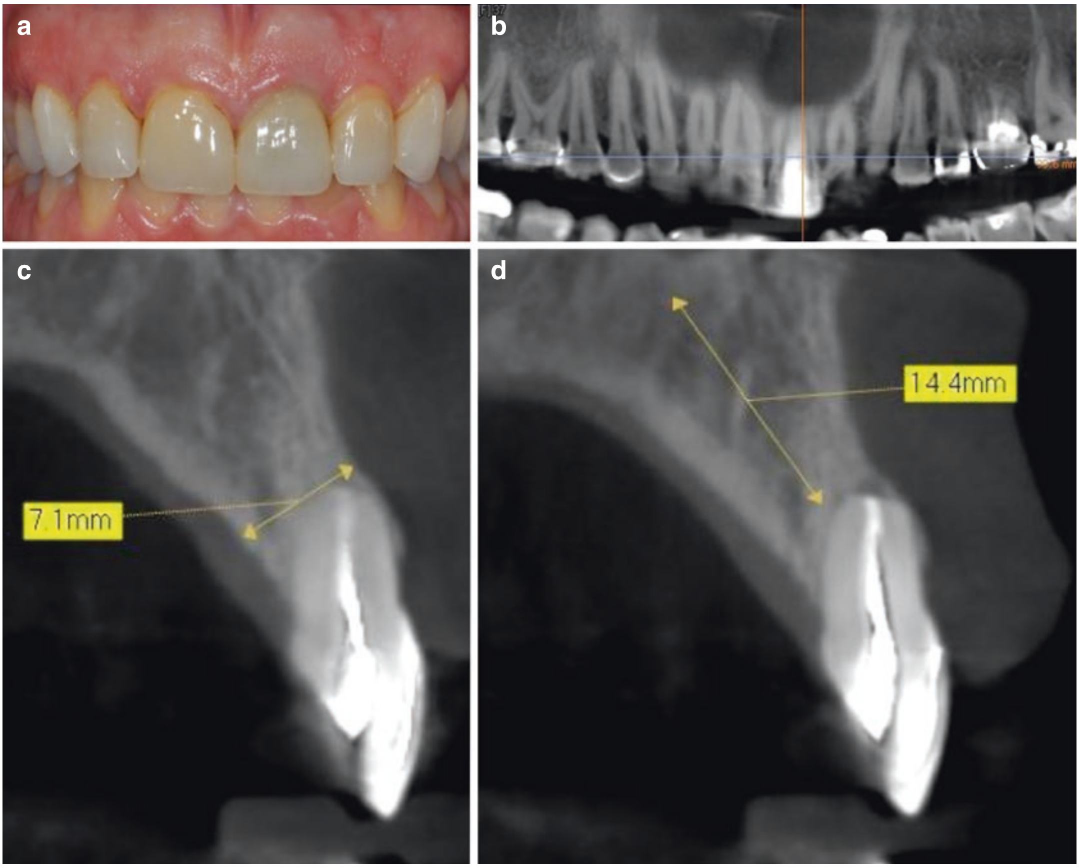

Fig. 21.35 Clinical intraoral photograph (**a**), reformatted panoramic (**b**) and cross-sectional (**b**) CBCT images in a female with a chief complaint of poor esthetics associated with root canal filled maxillary left central incisor. The patient presents with an excessive gingival display and poor esthetics and altered passive eruption of the anterior teeth (Levine and McGuire 1997). The left central incisor is to be removed and an implant immediately inserted. The maxillary left central incisor demonstrates a Type I sagittal root position (Kan et al. 2013). This tooth was extracted and an implant immediately inserted with guided bone regeneration procedure used to fill the buccal gap along with connective tissue grafting under the buccal gap for "perio biotype conversion" (Kan et al. 2011). The implant together with all anterior teeth were subsequently restored with fixed prostheses

surgery) and residual alveolar bone height may all influence total resorption and resorption rates (Peng et al. 2013).

21.4 Immediate Implant Placement

Immediate implant placement (IIP) and restorative provisionalization for single maxillary anterior failing teeth is a Complex SAC procedure (Dawson and Chen 2009) with high success rates if specific clinical guidelines are adopted. These include the maintenance of intact labial cortical bone, absence of adjacent infection, the use of adjunctive soft and hard tissue graft material and planning the positioning of the implant to achieve primary stability by engaging the palatal aspect of the socket and bone 4–5 mm apical to the base of the socket. In addition, a buccal gap is desired of at least 2 mm facial to the implant which helps in determining the implant width to be used. A presurgical CBCT is very important in determining the feasibility of IIP by assessing root length, sagittal root position (SRP), and the morphology of the residual alveolar housing (Levine et al. 2014a, b, c; Chung et al. 2011; Tsuda et al. 2011).

21.4.1 Sagittal Root Position

Assessment and classification of SRP of maxillary anterior teeth (Table 21.2) (Kan et al. 2013) prior to IIP and restorative provisionalization is a valuable aid in team communication and treatment planning. Most anterior teeth at all sites present with a Class I SRP and are most favorable locations for IIP because they present with a considerable amount of bone present on the palatal aspect and potentially allow minimal intrusion on the labial plate. At sites with teeth presenting with Class III SRP, implant stability relies mostly on engagement of the labial cortical bone. In these situations, there is more labial bone remodeling and a greater incidence of labial dehiscence and fenestration. When teeth are centered within the alveolus (Class II), bone volume is usually reduced compared to Class I and III sites. For Class II sites, labial bone grafting may need to be considered and adequate alveolar bone beyond the socket base (up to 5 mm) necessary to ensure primary implant stability. Approximately one out of every ten maxillary anterior tooth sites demonstrate the most unfavorable SRP, Class IV where the tooth occupies the entire bone volume. Often these sites are considered to be a contraindication for IIP and need adjunctive bone grafting procedures (Kan et al. 2013).

Based on reviews of the limited studies in the literature (Levine et al. 2014a, b, c) and general consensus (Morton et al. 2014), ideally a minimum of 2 mm of buccal bone wall (and preferably more than 2 mm) is necessary in the anterior maxilla once the implant osteotomy has been prepared in a healed site to ensure proper soft tissue support and to avoid resorption of the buccal bone wall following restoration. If this bone volume is not present clinically, contour augmentation (contour grafting) is recommended to create this adequate zone facial to the implant (Jensen et al. 2014). If soft tissue thickness is not adequate (<2 mm) considerations to augment should also be determined (Kan et al. 2009; Yoshino et al. 2015; Puisys et al. 2015).

Table 21.2 Classification and frequency distribution of sagittal root position of anterior teeth on cross-sectional CBCT Images (Kan et al. 2013)

Class	Description	Maxillary tooth CI	LI	C	Overall frequency distribution
I	Root is positioned against the labial cortical plate (Figs. 21.34 and 21.35)	86.5%	76%	81%	81.1%
II	Root is centered in the middle of the alveolar housing with or without engaging either the labial or palatal cortical plates at the apical third.	5%	8.5%	6	6.5%
III	The root is positioned against the palatal cortical plate	0.5%	1.5%	0	0.7%
IV	At least 2/3^{rds} of the root engages both the labial and palatal cortical plates.	8%	14%	13%	11.7%

CI central incisor, *LI* lateral incisor, *C* canine

21.5 Implant Removal and Alveolar Reconstruction

While the long-term prognosis of dental implants is excellent, they may need to be removed for various reasons including early or late failure of osseointegration, fracture or initial inappropriate three-dimensional placement resulting in poor esthetics (Figs. 21.36, 21.37, and 21.38). While trephines, burs, piezoelectric devices, and various forceps have been used, these techniques often result in defects in bone. More and more commonly implant removal systems (e.g., Neobiotech NEO FR fixture remover, Neobiotech

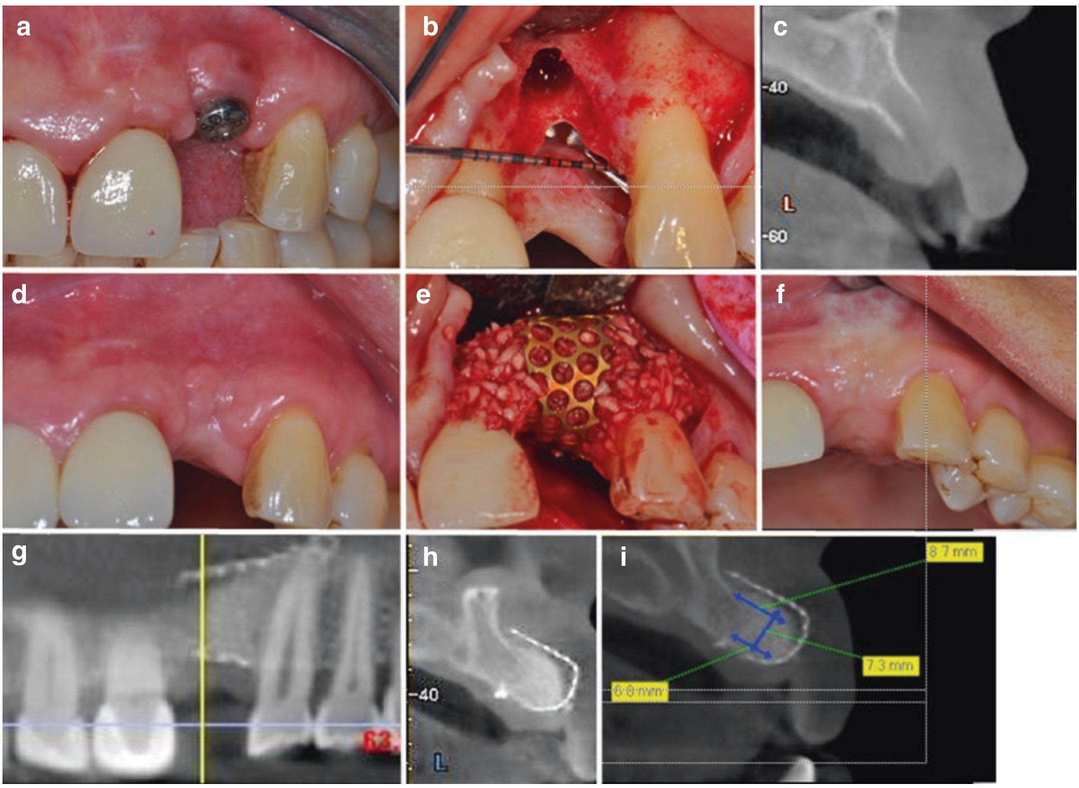

Fig. 21.36 Implant removal and alveolar reconstruction of the left maxillary lateral incisor site for (**a**) 50-year-old female whose implant was placed too far labially with multiple soft tissue procedures attempted to correct for poor esthetics. Initial intraoral presentation of implant (**a**) and subsequent implant retrieval (**b**) and immediate postoperative CBCT cross-sectional image (**c**) demonstrate large osseous vertical and horizontal alveolar deficiency. After healing (**d**) the site was re-entered and Gem-21 (Luitpold Pharmaceuticals, Inc., Shirley, NY, USA), a highly purified recombinant human platelet-derived growth factor (rhPDGF-BB) with an osteoconductive matrix (beta tricalcium phosphate, β-TCP) with Puros cortical bone graft (Zimmer Dental, Inc., Carlsbad, CA, USA) was secured using a titanium mesh (DePuy Synthes, West Chester, PA, USA) fixated using miniscrews (**e**). 5-month post-op intraoral (**f**) and reformatted panoramic (**g**) and cross-sectional CBCT image (**h**) shows substantial reconstruction of the alveolus in both height and width with Type IV bone. Analysis on the cross-sectional image (**i**) shows adequate bone volume for implant placement

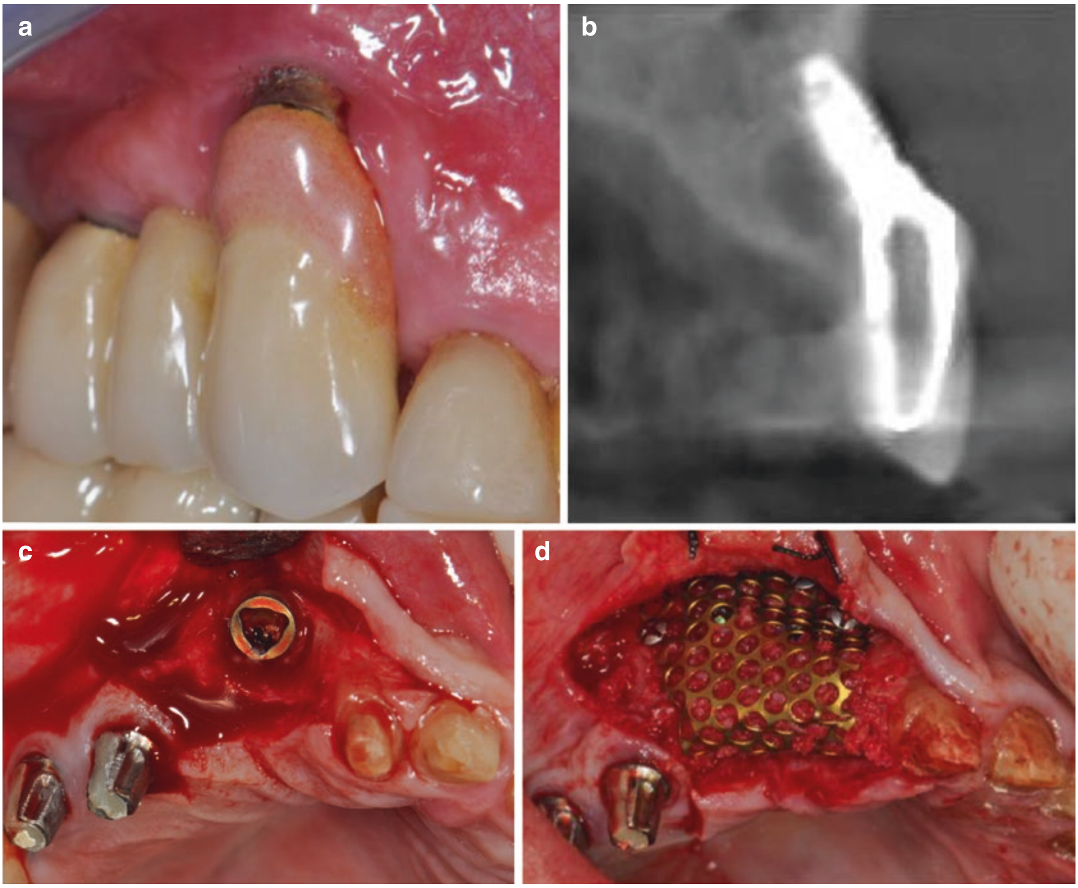

Fig. 21.37 Intraoral clinical photograph (**a**) and corresponding cross-sectional CBCT image of (**b**) a right maxillary implant placed outside (labial) to the available bone volume. Removal of the abutment and adjacent crowns on the right posterior premolar and molars reveals the excessive labial location of the implant (**c**). The implant was removed, the cortical bone bed prepared and Osteocel (human adult stem cell; Nuvasive®, Inc.) graft was secured using Synthes mesh which was retained using miniscrews (**d**) (Levine and McAllister 2016)

USA, Los Angeles, CA, USA) that act to derotate the implant by application of reverse torque are being used, especially for integrated implants. Often graft procedures are required to reconstruct bone loss from the surgical retrieval procedure or due to inadequate bone. Mean survival rate for implant replacement at the second attempt has been reported to be 89% with a range from 71 to 95% (Zhou et al. 2016).

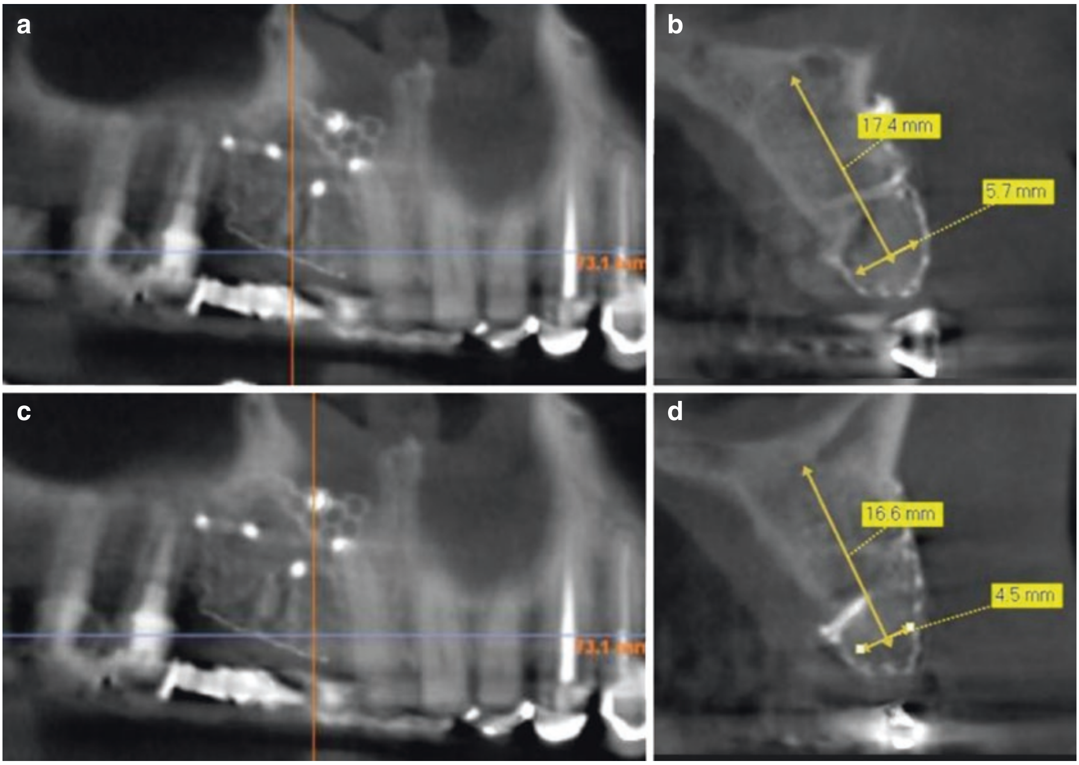

Fig. 21.38 CBCT imaging 6-months post GBR of the patient identified in Fig. 21.37. Reformatted panoramic (**a**) with site reference (*orange vertical line*) and corresponding cross-sectional image (**b**) at the second premolar region and reformatted panoramic (**c**) with site reference (*orange vertical line*) and corresponding cross-sectional image (**d**) at the first premolar region. Measurements confirm establishment of adequate bone volume for insertion of implant in correct prosthetically driven location

References

Alyea OE (1936) The ostium maxillare. Anatomic study of its surgical accessibility. Arch Otolaryngol 24:553–569

Apostolopoulos P, Darby I (2016) Retrospective success and survival rates of dental implants placed after a ridge preservation procedure. Clin Oral Implants Res 28(4):461–468. doi:10.1111/clr.12820

Araujo MG, da Silva JC, de Mendonca AF, Lindhe J (2015a) Ridge alterations following grafting of fresh extraction sockets in man. A randomized clinical trial. Clin Oral Implants Res 26:407–412

Araujo MG, Silva CO, Misawa M, Sukekava F (2015b) Alveolar socket healing: what can we learn? Periodontol 68:122–134

Artzi Z, Tal H, Dayan D (2000) Porous bovine bone mineral in healing of human extraction sockets. Part 1: histomorphometric evaluations at 9 months. J Periodontol 71:1015–1023

Atwood DA (1957) A cephalometric study of the clinical rest position of the mandible. Part II. The variability in the rate of bone loss following the removal of occlusal contacts. J Prosthet Dent 7:544–552

Baciut M, Hedesiu M, Bran S, Jacobs R, Nackaerts O, Baciut G (2013) Pre- and postoperative assessment of sinus grafting procedures using cone-beam computed tomography compared with panoramic radiographs. Clin Oral Implants Res 24:512–516

Becker W, Dahlin C, Becker BE, Lekholm U, van Steenberghe D, Higuchi K, Kultje C (1994) The use of e-PTFE barrier membranes for bone promotion around titanium implants placed into extraction sockets: a prospective multicenter study. Int J Oral Maxillofac Implants 9:31–40

Bornstein MM, Chappuis V, von Arx T, Buser D (2008) Performance of dental implants after staged sinus floor elevation procedures: 5-year results of a prospective study in partially edentulous patients. Clin Oral Implants Res 19:1034–1043

Boyne PJ, James RA (1980) Grafting of the maxillary sinus floor with autogenous marrow and bone. J Oral Surg 38:613–616

Braut V, Bornstein MM, Belser U, Buser D (2011) Thickness of the anterior maxillary facial bone wall-a retrospective radiographic study using cone beam computed tomography. Int J Periodontics Restorative Dent 31:125–131

Bruschi GB, Scipioni A, Calesini G, Bruschi E (1998) Localized management of the sinus floor with simultaneous implant placement: a clinical report. Int J Oral Maxillofac Implants 13:219–226

Buser D (2009) 20 years of guided bone regeneration in implant dentistry, 2nd edn. Quintessence Pub Co, Hanover Park

Cawood JI, Howell RA (1988) A classification of the edentulous jaws. Int J Oral Maxillofac Surg 17:232–236

Chen S, Buser D, Cordaro L (2009) Chapter 3.3. Surgical modifying factors. In: Dawson A, Chen S (eds) The SAC classification in implant dentistry. Quintessence Publishing Co, Berlin, pp 18–20. isbn:978-1-85097-188-7

Chung S, Rungcharassaeng K, Kan JY, Roe P, Lozada JL (2011) Immediate single tooth replacement with subepithelial connective tissue graft using platform switching implants: a case series. J Oral Implantol 37:559–569

Cochran DL, Cobb CM, Bashutski JD, Chun YH, Lin Z, Mandelaris GA, BS MA, Murakami S, Rios HF (2015) Emerging regenerative approaches for periodontal reconstruction: a consensus report from the AAP regeneration workshop. J Periodontol 86(2 Suppl):S153–S156

Covani U, Canullo L, Toti P, Alfonsi F, Barone A (2014) Tissue stability of implants placed in fresh extraction sockets: a 5-year prospective single-cohort study. J Periodontol 85:e323–e332

Dawson A, Chen S (eds) (2009) The SAC classification in implant dentistry. Quintessence Publishing Co, Berlin, p 8

Del Fabbro M, Testori T, Francetti L, Weinstein R (2004) Systematic review of survival rates for implants placed in the grafted maxillary sinus. Int J Periodontics Restorative Dent 24:565–577

Hallman M, Hedin M, Sennerby L, Lundgren S (2002) A prospective 1-year clinical and radiographic study of implants placed after maxillary sinus floor augmentation with bovine hydroxyapatite and autogenous bone. J Oral Maxillofac Surg 60:277–284

Hammack BL, Enneking WF (1960) Comparative vascularization of autogenous and homogenous bone transplants. J Bone Joint Surg 42:811

Harris D, Horner K, Gröndahl K, Jacobs R, Helmrot E, Benic GI, Bornstein MM, Dawood A, Quirynen M (2012) E.A.O. Guidelines for the use of diagnostic imaging in implant dentistry 2011. A consensus workshop organized by the European Association for Osseointegration at the Medical University of Warsaw. Clin Oral Implants Res 23:1243–1253

Hatano N, Shimizu Y, Ooya K (2004) A clinical long-term radiographic evaluation of graft height changes after maxillary sinus floor augmentation with a 2:1 autogenous bone/xenograft mixture and simultaneous placement of dental implants. Clin Oral Implants Res 15:339–345

Iasella JM, Greenwell H, Miller RL, Hill M, Drisko C, Bohra AA, Scheetz JP (2003) Ridge preservation with freeze-dried bone allograft and a collagen membrane compared to extraction alone for implant site development: a clinical and histologic study in humans. J Periodontol 74:990–999

Idrontino G, Valente NA (2016) Intraoral and extraoral autologous bone block graft echniques: a review of the recent literature. Int J Contemp Dent Med Rev 2016:1–5

Irinakis T (2006) Rationale for socket preservation after extraction of a single-rooted tooth when planning for future implant placement. J Can Dent Assoc 72:917–922

Jensen OT, Shulman LB, Block MS, Iacono VJ (1998) Report of the sinus consensus conference of 1996. Int J Oral Maxillofac Implants 13(Suppl):11–45

Jensen SS, Bosshardt DD, Gruber R, Buser D (2014) Long-term stability of contour augmentation in the esthetic zone: histologic & histomorphometric evaluation of 12 human biopsies 14 to 80 months after augmentation. J Periodontol 85:1549–1556

Kan JYK, Rungcharassaeng K, Morimoto T, Lozada J (2009) Facial gingival tissue stability after connective tissue graft with single immediate tooth replacement in the esthetic zone: Consecutive case report. J Oral Maxillofac Surg 67:40–48

Kan JY, Rungcharassaeng K, Lozada JL, Zimmerman G (2011) Facial gingival tissue stability following immediate placement and provisionalization of maxillary anterior single implants: a 2- to 8-year follow-up. Int J Oral Maxillofac Implants 26:179–187

Kan JY, Roe P, Rungcharassaeng K, Patel RD, Waki T, Lozada JL, Zimmerman G (2013) Classification of sagittal root position in relation to the anterior maxillary osseous housing for immediate implant placement: a cone beam computed tomography study. Int J Oral Maxillofac Implants 26:873–876

Kara IM, Küçük D, Polat S (2010) Experience of maxillary sinus floor augmentation in the presence of antral pseudocysts. J Oral Maxillofac Surg 68:1646–1650

Kim YK, Lee J, Yun JY, Yun PY, Um IW (2014) Comparison of autogenous tooth bone graft and synthetic bone graft materials used for bone resorption around implants after crestal approach sinus lifting: a retrospective study. J Periodontal Implant Sci 44:216–221

Kumar H, Choudhry R, Kakar S (2001) Accessory maxillary ostia: topography and clinical application. J Anat Soc India 50:3–5

Levine RA, McAllister B (2016) Implant site development using Ti-Mesh & cellular allograft in the esthetic zone for restorative-driven implant placement: a case report. Int J Perio Rest Dent 36(3):373–381

Levine RA, McGuire M (1997) The diagnosis and treatment of the gummy smile. Compend Contin Ed Dent 18:757–764

Levine RA, Huynh-Ba G, Cochran DL (2014a) Soft tissue augmentation procedures for mucogingival defects in esthetic sites. Int J Oral Maxillofac Implants 29(Suppl):155–185

Levine RA, Manji A, Faucher J, Present S (2014b) Use of titanium mesh in implant site development for restorative-driven implant placement: case report from a consecutive case series of 77 titanium mesh in 62 patients treated in private practice. Part I: restorative protocol for single-tooth esthetic zone sites. Compend Contin Dent 35(4):264–273

Levine RA, Manji A, Faucher J, Fava PL (2014c) Use of titanium mesh in implant site development for restorative-driven implant placement: case report from a Consecutive case series of 77 titanium mesh in 62 patients treated in private practice. Part II: surgical protocol for single-tooth esthetic zone sites. Compend Contin Dent 35:324–333

Lin YH, Yang YC, Wen SC, Wang HL (2016) The influence of sinus membrane thickness upon membrane perforation during lateral window sinus augmentation. Clin Oral Implants Res 27:612–617

Mandelaris GA, Lu M (2015) Extraction socket preservation prior to implant placement. Dent Today 34:78–79

Mandelaris GA, Spagnoli DB, Rosenfeld AL, McKee J, Lu M (2015) Tissue engineering for lateral ridge augmentation with recombinant human bone morphogenetic protein 2 combination therapy: a case report. Int J Periodontics Restorative Dent 35:325–333

Mardinger O, Abba M, Hirshberg A, Schwartz-Arad D (2007) Prevalence, diameter and course of the maxillary intraosseous vascular canal with relation to sinus augmentation procedure: a radiographic study. Int J Oral Maxillofac Surg 36:735–738

Maréchal M, Luyten F, Nijs J, Postnov A, Schepers E, van Steenberghe D (2005) Histomorphometry and micro-computed tomography of bone augmentation under a titanium membrane. Clin Oral Implants Res 16:708–714

McCrea SJ (2014) Coalescence of inter: osteotomy bone graft material inserted via separate transcrestal sinus osteotomies: a case report and concise review of the literature. Eur J Dent 8:553–558

Molly L, Quirynen M, Michiels K, van Steenberghe D (2006) Comparison between jaw bone augmentation by means of a stiff occlusive titanium membrane or an autologous hip graft: a retrospective clinical assessment. Clin Oral Implants Res 17:481–487

Morton D, Chen ST, Martin WC, Levine RA, Buser D (2014) Consensus statements and recommended clinical procedures regarding optimizing esthetic outcomes in implant dentistry. Int J Oral Maxillofac Implants 29(Suppl):216–220

Myerson MC (1958) Irrigation of the maxillary sinus through the middle meatus. Laryngoscope 68:1555–1565

Ozyuvaci H, Aktas I, Yerit K, Aydin K, Firatli E (2005) Radiological evaluation of sinus lift operation: what the general radiologist needs to know. Dentomaxillofac Radiol 34:199–204

Peng W, Kim IK, Cho HY, Pae SP, Jung BS, Cho HW, Seo JH (2013) Assessment of the autogenous bone graft for sinus elevation. J Korean Assoc Oral Maxillofac Surg 39:274–282

Pignataro L, Mantovani M, Torretta S, Felisati G, Sambataro G (2008) ENT assessment in the integrated management of candidate for (maxillary) sinus lift. Acta Otorhinolaryngol Ital 28:110–119

Preti G, Martinasso G, Peirone B, Navone R, Manzella C, Muzio G, Russo C, Canuto RA, Schierano G (2007) Cytokines and growth factors involved in the osseointegration of oral titanium implants positioned using piezoelectric bone surgery versus a drill technique: a pilot study in minipigs. J Periodontol 78:716–722

Puisys A, Vindaisute E, Linkevciene L, Linkevicius T (2015) The use of acellular dermal matrix membrane for vertical soft tissue augmentation during submerged implant placement: a case series. Clin Oral Impl Res 26:465–470

Rios HF, Lin Z, Oh B, Park CH, Giannobile WV (2011) Cell- and gene-based therapeutic strategies for periodontal regenerative medicine. J Periodontol 82:1223–1237

Stadlinger B, Pilling E, Huhle M, Mai R, Bierbaum S, Scharnweber D, Kuhlisch E, Loukota R, Eckelt U (2008) Evaluation of osseointegration of dental implants coated with collagen, chondroitin sulphate and BMP-4: an animal study. Int J Oral Maxillofac Surg 37:54–59

Stammberger H (1986) Endoscopic endonasal surgery—concepts in treatment of recurring rhinosinusitis. Part I. Anatomic and pathophysiologic considerations. Otolaryngol Head Neck Surg 94:143–147

Stammberger HR, Kennedy DW, Anatomic Terminology Group (1995) Paranasal sinuses: anatomic terminology and nomenclature. Ann Otol Rhinol Laryngol Suppl 167:7–16

Summers RB (1994) The osteotome technique: part 3—less invasive methods of elevating the sinus floor. Compend Contin Educ Dent 15:698–708

Tatum H Jr (1986) Maxillary and sinus implant reconstructions. Dent Clin North Am 30:207–229

Temmerman A, Hertelé S, Teughels W, Dekeyser C, Jacobs R, Quirynen M (2011) Are panoramic images reliable in planning sinus augmentation procedures? Clin Oral Implants Res 22:189–194

Timmenga NM, Raghoebar GM, Liem RS, van Weissenbruch R, Manson WL, Vissink A (2003) Effects of maxillary sinus floor elevation surgery on maxillary sinus physiology. Eur J Oral Sci 111:189–197

Toffler M (2001) Site development in the posterior maxilla using osteocompression and apical alveolar displacement. Compend Contin Educ Dent 22:775–790

Torretta S, Mantovani M, Testori T, Cappadona M, Pignataro L (2013) Importance of ENT assessment in stratifying candidates for sinus floor elevation: a prospective clinical study. Clin Oral Implants Res 24(Suppl A100):57–62

Toscano N, Shumaker N, Holtzclaw D (2010) The art of block grafting a review of the surgical protocol for reconstruction of alveolar ridge deficiency. J Implant Adv Clin Dent 2:45–66

Tsuda H, Rungcharassaeng K, Kan JY, Roe P, Lozada JL, Zimmerman G (2011) Peri-implant tissue response following connective tissue and bone grafting in conjunction with immediate single-tooth replacement in the esthetic zone: a case series. Int J Oral Maxillofac Implants 26:427–436

Tyndall DA, Price JB, Tetradis S, Ganz SD, Hildebolt C, Scarfe WC, American Academy of Oral and Maxillofacial Radiology (2012) Position statement of the American Academy of oral and maxillofacial radiology on selection criteria for the use of radiology in dental implantology with emphasis on cone beam computed tomography. Oral Surg Oral Med Oral Pathol Oral Radiol 113:817–826

van Steenberghe D, Callens A, Geers L, Jacobs R (2000) The clinical use of deproteinized bovine bone mineral on bone regeneration in conjunction with immediate implant installation. Clin Oral Implants Res 11:210–216

Viña-Almunia J, Peñarrocha-Diago M, Peñarrocha-Diago M (2009) Influence of perforation of the sinus membrane on the survival rate of implants placed after direct sinus lift. Literature update. Med Oral Patol Oral Cir Bucal 14:E133–E136

Walter P, Stebler S, Schaffer P, Vetter JM, Guerbaoui M (1976) Cylindrical epithelioma of nasal cavities and accessory sinuses. Anatomoclinical study of 26 cases. Ann Anat Pathol (Paris) 21:463–476. (In French)

Wen SC, Lin YH, Yang YC, Wang HL (2015) The influence of sinus membrane thickness upon membrane perforation during transcrestal sinus lift procedure. Clin Oral Implants Res 26:1158–1164

Yoshino K, Ito K, Kuroda M, Sugihara N (2015) Prevalence of vertical root fracture as the reason for tooth extraction in dental clinics. Clin Oral Investig 19:1405–1409

Zhou W, Wang F, Monje A, Elnayef B, Huang W, Wu Y (2016) Feasibility of dental implant replacement in failed sites: a systematic review. Int J Oral Maxillofac Implants 31:535–545

Endodontic Applications of CBCT

22

Scott L. Doyle, Bruno Azevedo, Martin D. Levin, David Gane, Allan G. Farman, and William C. Scarfe

Contents

S.L. Doyle, D.D.S., M.S. (✉)
Metropolitan Endodontics, Eden Prairie, MN, USA

Metropolitan Endodontics, Inver Grove Heights, MN, USA

Metropolitan Endodontics, Woodbury, MN, USA

Metropolitan Endodontics, Burnsville, MN, USA

Division of Endodontics, Department of Restorative Sciences, University of Minnesota School of Dentistry, Minneapolis, MN, USA
e-mail: scottdoyle45@gmail.com

B. Azevedo, D.D.S., M.S.
Division of Radiology and Imaging Science, Department of Surgical/Hospital Dentistry, University of Louisville School of Dentistry, Louisville, KY, USA
e-mail: bruno.deazevedo@louisville.edu

M.D. Levin, D.M.D.
Department of Endodontics, School of Dental Medicine, Univeristy of Pennsylvania, Philadelphia, PA, USA
e-mail: mlevin@dental.upenn.edu

D. Gane, B.Sc. (hons), D.D.S.
LED Medical Diagnostics, Inc., Vancouver, BC, Canada
e-mail: david.gane@leddental.com

A.G. Farman, B.D.S., Ph.D., M.B.A., D.Sc.
Emeritus Professor, The University of Louisville School of Dentistry, Louisville, KY, USA

Independent consultant in Maxillofacial Imaging Science, Chicago, IL, USA
e-mail: allanfarman@aol.com

W.C. Scarfe, B.D.S., F.R.A.C.D.S., M.S.
Division of Radiology and Imaging Science, Department of Surgical/Hospital Dentistry, University of Louisville School of Dentistry, Louisville, KY, USA
e-mail: william.scarfe@louisville.edu

W.C. Scarfe, C. Angelopoulos (eds.), *Maxillofacial Cone Beam Computed Tomography*,
https://doi.org/10.1007/978-3-319-62061-9_22

22.1 Introduction

Endodontics is the specialty of dentistry concerned with the morphology, physiology, and pathology of the human dental pulp and periradicular tissues. Its study and practice encompasses the basic and clinical sciences including the biology of the normal pulp and the etiology, diagnosis, prevention, and treatment of diseases and injuries of the pulp and associated periradicular conditions (American Association of Endodontists 2012).

22.2 Imaging in Endodontics

Endodontics is an image-guided specialty, relying on radiographic assessments for diagnosis, treatment planning, management, and follow-up assessment of pulpal and periradicular disease. Conventional radiography has historically been the principle imaging modality used throughout the stages of clinical endodontics (Walton 2008; Basrani 2012):

1. *Preoperative Assessment*. According to a joint statement by the American Association of Endodontists (AAE) and American Academy of Oral and Maxillofacial Radiology (AAOMR) (AAE/AAOMR 2015):

   > Intraoral radiographs should be considered the imaging modality of choice in the evaluation of the endodontic patient.

   Intraoral images serve as an indispensable adjunct to endodontic examination (Gröndahl and Huumonen 2004), providing visualization of dental morphology such as information on the location and number of canals, pulp chamber size and degree of calcification, root structure, length, and curvature. In addition, the effects of pulpal and periradicular disease can be determined, including the degree of root resorption and characteristics of periradicular osteolysis.
2. *Intraoperative Assessment*. Working images with a rubber dam in place are used during treatment to assess canal location, curvature, and length. Although electronic apex locators are very accurate in determining working length (Martins et al. 2014), the adjunctive use of intraoperative radiographs is generally recommended. Working length images with files or master cones in place can help verify that the canal is prepared and obturated to the desired apical extent. Though controversial, it is commonly accepted that instrumentation and obturation should be terminated at the apical terminus (Ng et al. 2008).
3. *Postoperative Management*. A post-obturation intraoral image is acquired to assess the length, density, and taper of the root canal obturant. This image is also used as a baseline for clinical outcome analysis. Periodic checkup examinations should be performed to monitor the status of the apical tissues. The peak incidence of healing or emerging apical periodontitis is seen 1 year after treatment but complete healing may require as long as 4 years (Orstavik 1996). Most orthograde treated cases show radiographic signs of healing within 1 year of treatment, although some cases may require longer follow-up intervals (Huumonen and Orstavik 2002). Imaging is also important when considering nonsurgical or surgical management of teeth with posttreatment disease.

22.2.1 Limitations of Radiographic Intraoral Imaging

Conventional two-dimensional (2D) radiographic imaging provides limited information in endodontics due to variation in exposure (e.g., density and contrast), geometric distortion (Gröndahl and Huumonen 2004), superimposition of structures, and misrepresentation, particularly when the anatomy of the teeth and surrounding tissues is complex. The limitations of planar imaging can contribute to shortcomings related to diagnosis, access preparation, cleaning and shaping, obturation and post-space preparation. Intraoral imaging has limitations in each of the following clinical situations:

- *Visualization of Root Canal Anatomy*. Tooth morphology in the permanent dentition is complex. Teeth show a wide range of variation, such as the number of roots/canals, configurations, curvature, and length (Vertucci 1984). Superimposition of anatomic structures and image distortion can impair canal identification and possible associated pathoses. 2D images limit visualization to the mesiodistal plane, with buccolingual and buccopalatal features often absent. Multiple periapical images from slightly varying angles are often exposed to assist in visualization (Brynolf 1970; Walton 1973; Martinez-Lozano et al. 1999; Gröndahl and Huumonen 2004).

- *Detection of Periapical Pathosis*. An apical lesion often requires extensive decalcification of the cortical plate to be detected radiographically on conventional 2D images (Bender and Seltzer 1961a, b; Bender 1982), with cancellous lesions being more difficult to detect (Schwartz and Foster 1971; Folk et al. 2005) and often underestimated in size (Shoha et al. 1974; Lee and Messer 1986; Barbat and Messer 1998; Scarfe et al. 1999; Marmary et al. 1999).
- *Assessment of Periradicular Tissue Healing*. Periapical radiography has historically been used to monitor changes in the periradicular tissues in order to assess outcomes following endodontic treatment. Favorable outcomes depend on healing of the supporting bone. Repair of periradicular tissues consists of a complex regeneration involving bone, periodontal ligament, and cementum (Huumonen and Orstavik 2002). Accurate determination of the true status of periapical tissues is limited with conventional radiography (Peters and Peters 2012). Healing of periradicular lesions is assessed by interpretation of periodic checkup radiographs but there is a great degree of variability within and among observers when determining the outcome of treatment (Goldman et al. 1972, 1974).

22.2.2 Advantages of CBCT in Endodontics

CBCT imaging, especially limited field of view (FOV), high resolution modalities, overcome many of the limitations of conventional imaging in contemporary endodontic practice by producing undistorted and geometrically accurate three-dimensional images. This influences how clinicians diagnose, treatment plan, manage (Ee et al. 2014), and assess treatment outcomes (Figs. 22.1, 22.2, 22.3, 22.4, and 22.5).

Specific advantages of CBCT for endodontics include:

- Images are interactive and interrelational in three orthogonal planes (axial, sagittal, and coronal).
- The ability to reorient data such that coronal and sagittal images are parallel with, and axial images perpendicular, to the long axis of the root.
- Multi-planar reformation (MPR) images can be used to highlight specific anatomic regions in relation to endodontic investigation (Figs. 22.1 and 22.2).
- Enhancements including zoom or magnification, window/level adjustments, and annota-

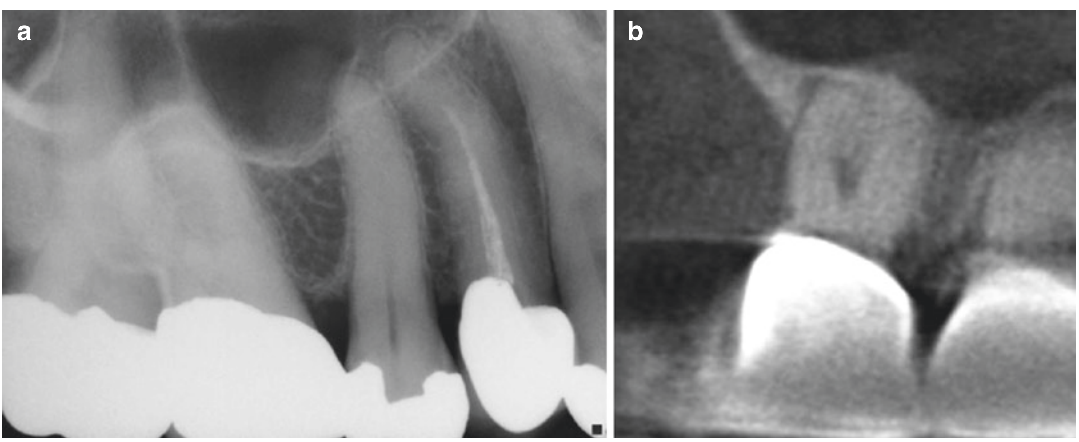

Fig. 22.1 The periapical image of the maxillary right second molar (**a**) in an asymptomatic patient is unremarkable and shows lack of coverage of this tooth with marked superimposition of the distal root of the first molar over the mesial root of the second molar. The corresponding cropped sagittal thin section CBCT image (**b**) demonstrates a furcal area of low density and associated periradicular periodontitis. Subsequent clinical investigation found the pulp in this tooth to be necrotic

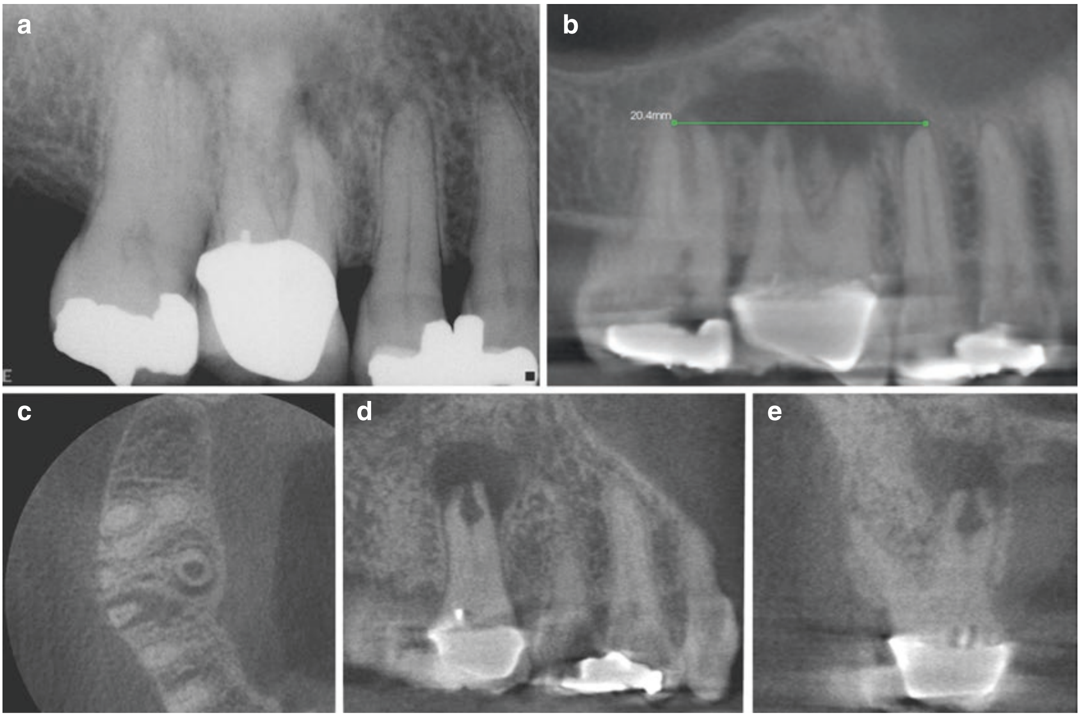

Fig. 22.2 A periapical image (**a**) of the maxillary right posterior region in a patient presenting with discomfort extending from the nose to the ear, local buccal swelling and induration. All teeth tested vital except the maxillary right first molar. Periapical image (**a**) shows an area of low density at the apices of the first and second molars. 10 mm curved planar (**b**), axial (**c**), sagittal (**d**), and cross-sectional (**e**) CBCT images demonstrate a much larger (21.4 mm maximum length) unilocular area of low density centered on the palatal root of the maxillary first molar, and extending to each tooth either side. Note the internal resorptive defect at the junction of the apical and middle thirds of the palatal root of the maxillary first molar, not visible on the periapical image. Biopsy confirmed the lesion to be a periapical granuloma with abscess formation at the time of root canal treatment and surgery

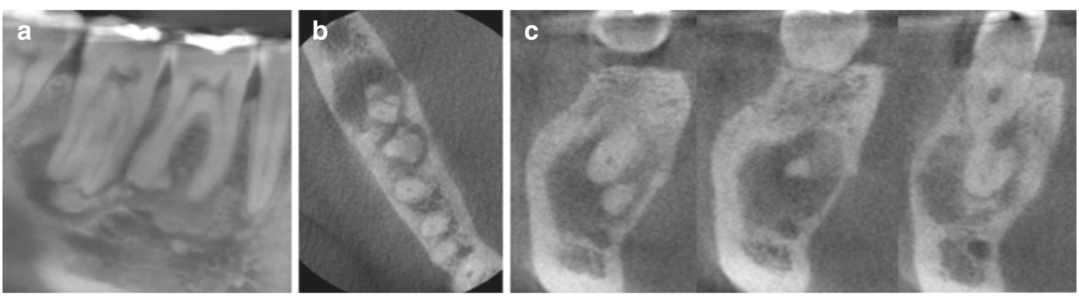

Fig. 22.3 Parasagittal (**a**), axial (**b**), and correlated multiple cross-sectional (**c**) images of a 52-year-old Caucasian female presenting for assessment of multiple periapical areas associated with the mandibular right first and second molars. There are areas of mixed central opacity and peripheral radiolucency associated with the apices of the teeth however no expansion, tooth resorption or displacement is evident. All teeth in this quadrant tested vital. A digital panoramic image (**d**) revealed similar bony patterns in the left posterior maxilla and mandible and confirmed the working diagnosis of florid cemento-osseous dysplasia and concomitant hypercementosis on the right mandibular first molar. Management of this patient comprised CBCT radiographic checkup at 6 months to assess the progression of the hyperdensities

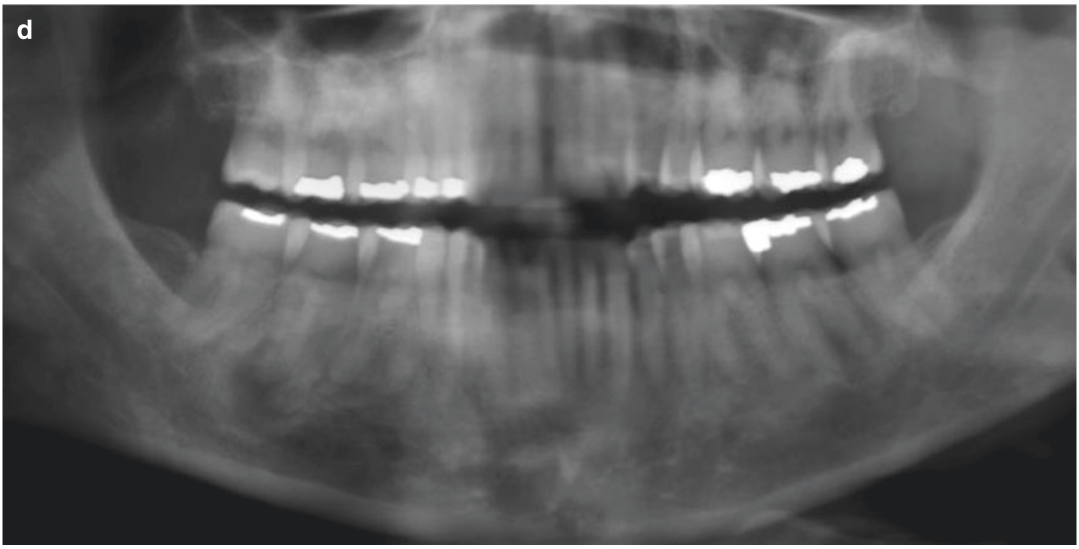

Fig. 22.3 (continued)

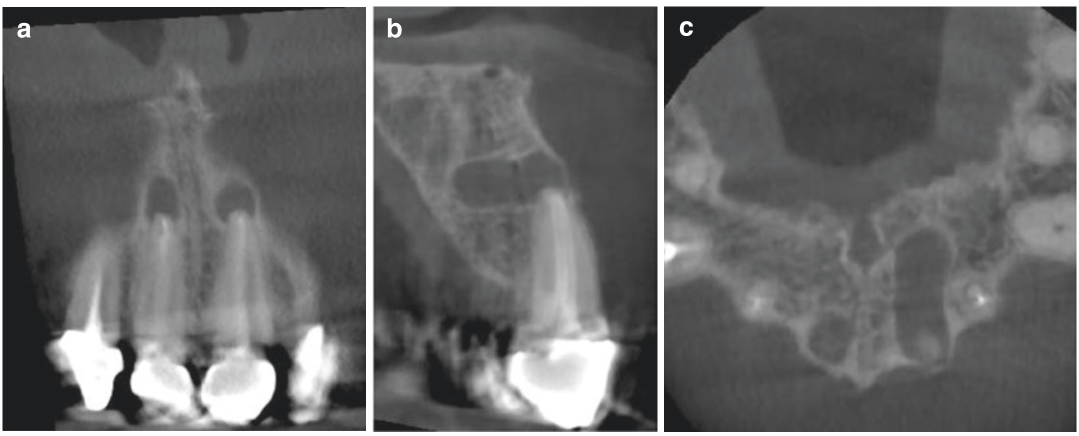

Fig. 22.4 Coronal CBCT image (**a**) showing moderately sized periapical areas of low density associated with both endodontically treated maxillary central incisors. Cross-sectional (**b**) and axial (**c**) images demonstrate the palatal extension associated with the maxillary left central incisor, important if surgery is to be performed

tion (text and arrows) can all be applied to the images.

- Interactive, on-screen measurements provide dimensions free from distortion and magnification (Fig. 22.2).
- Assessment of a quadrant or sextant of teeth and supporting bone in one image, which may reduce radiation exposure compared to multiple intraoral images.
- Extraoral imaging in trauma cases where placement of an intraoral detector would be problematic.
- Quantification of volumetric data such as amount of bony change and healing.

22.2.3 Challenges of CBCT for Use in Endodontics

22.2.3.1 Technical

- *Spatial resolution*. The spatial resolution of CBCT images (0.4–0.075 mm voxel size, equivalent to 1.25–6.6 line pairs per mm^{-1}(lp.mm^{-1})) is inferior to film-based (approx. 20 lp.mm^{-1}) or digital (ranging from 8–23 lp.mm^{-1}) intraoral radiography. The optimal resolution for CBCT images in endodontics is task specific, invariably involving imaging of inherently small structures. Liedke et al. (2009) recommend a minimal voxel resolution of 0.3 mm (1.6 lp.mm^{-1}) for the

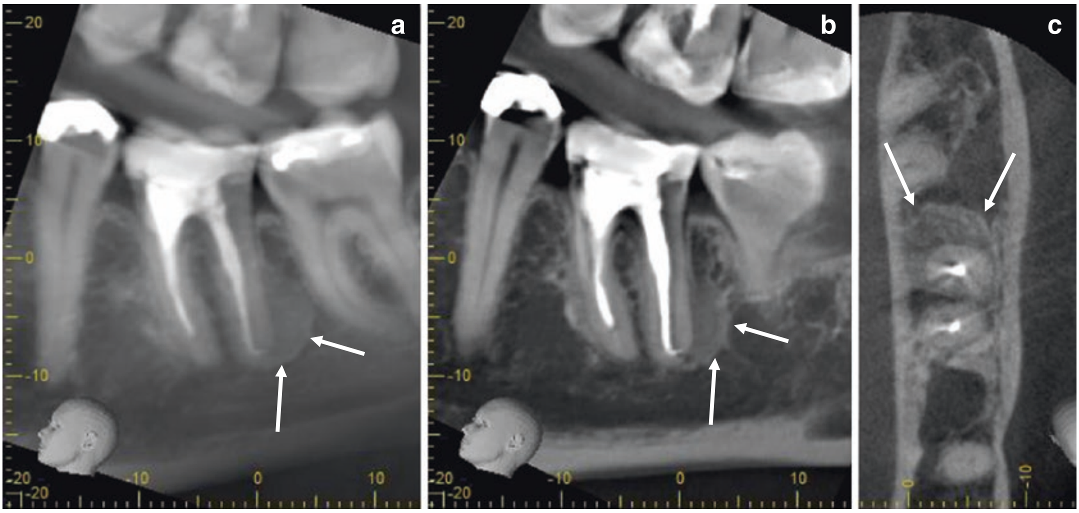

Fig. 22.5 Thick section (10 mm) sagittal (**a**), thin section sagittal (**b**), and axial image (**c**) showing a unilocular, well-defined, tear-shaped relative hyperdensity associated with the distal aspect of a left mandibular root canal treated first molar. The patient was asymptomatic and referred for an opinion with a concern for a possible cementoblastoma, suggested by the loss of lamina dura and PDL space. No previous imaging was available, however the patient did report that endodontic therapy on this tooth was performed approximately 2–3 years previously. The homogeneous nature and confluence with adjacent intramedullary bone is most consistent with sclerotic healing

detection of external root resorption. Bauman et al. (2011) investigated the effect of varying isotropic voxel dimensions on the detection of secondary canals in the mesiobuccal root of the maxillary first permanent molar. They showed that observer inter-rater reliability and detection of mesiobuccal canals improves with increasing resolution from 60.1% (0.4 mm/1.25 lp.mm^{-1}) to 93.3% (0.125 mm/4 lp.mm^{-1}). The diagnosis of subtler conditions (e.g., early stages of apical periodontitis) involving the periodontal ligament (PDL) space, which has an average dimension of 0.2 mm, may demand resolution at or below 0.2 mm voxel size (2.5 lp.mm^{-1}) (Scarfe et al. 2009).

- *The presence of artifacts*. CBCT images, like those from other imaging modalities, are susceptible to artifacts that affect fidelity (*see Chap.* 2). The presence of radiopaque metal objects and root canal filling materials in the field of view (FOV) can lead to severe beam hardening and streaking artifacts. In clinical endodontic practice, CBCT scanners with a limited FOV may provide clearer images as they can avoid scanning structures outside the region of interest susceptible to beam hardening (e.g., metallic restorations, dental implants). Cropping the FOV of the scan to the root portion of the tooth may also negate the effect of metallic artifacts. New algorithms and flat-panel detectors promise to reduce scatter and beam hardening artifacts in the future (Dang et al. 2015).
- *Contrast resolution*. CBCT images also lack the ability to record subtle changes in attenuation of soft tissues. This feature would be of potential importance in distinguishing the nature of periapical (e.g., abscess vs. cyst vs. granuloma) or sinus soft tissue contents. Current CBCT imaging is primarily limited to the assessment of the dentition and osseous structures.

22.2.3.2 Interpretation

Interpretation of CBCT images requires considerable experience and training. The clinician is responsible for the evaluation of the entire image volume, not only the tooth or pathosis in the volume of interest. If a clinician has a concern regarding image interpretation, the case should be referred to an oral and maxillofacial radiologist.

22.3 Specific Applications

Numerous authors have published reviews illustrating the applications of CBCT imaging in endodontics (Cohenca et al. 2007a, b; Nair and Nair 2007; Cotton et al. 2007; Patel et al. 2007; Tyndall and Rathore 2008; Scarfe et al. 2009; Patel 2009, 2010a; American Association of Endodontists 2011; Tyndall and Kohltfarber 2012; Ball et al. 2013; Venskutonis et al. 2014; Todd 2014a, b; McClammy 2014; Mao and Neelakantan 2014; Cohenca and Shemesh 2015; Patel et al. 2015; Nair et al. 2015).

22.3.1 Clinical Use Guidelines

The American Association of Endodontists (AAE) together with the American Academy of Oral and Maxillofacial Radiology (AAOMR) (AAE/AAOMR 2011; AAE/AAOMR 2015) and The European Society of Endodontology (ESE) (2014) have provided evidence-based, case-specific indications for CBCT use in endodontics (Table 22.1).

In addition, both organizations provide specific parameters of care including:

- *Justification*. Patient exposure should be justified such that the total potential diagnostic and therapeutic benefits are greater than the individual detriment radiation exposure might cause. CBCT should not be considered a replacement for standard digital radiographic applications. Rather, CBCT is a complementary modality for specific applications.
- *Optimization*. Practitioners follow professional judgment in minimizing the radiation dose to the patient to that which is necessary for diagnosis and treatment guidance.
  - *FOV.* Optimal FOV should be selected based on disease presentation. Smaller scan volumes generally produce higher resolution images and reduce radiation dose.
  - *Spatial resolution.* A discerning task in endodontics is the detection and charac-

Table 22.1 Comparison of indications for Use of CBCT in Endodontics from The American Association of Endodontists and American Academy of Oral and Maxillofacial Radiology (AAE/AAOMR 2015) and European Society of Endodontology (2014)

Indication	Example	Organization	
		AAE/AAOMR	ESE
Diagnosis of periapical pathosis when there are contradictory or nonspecific signs and/or symptoms	Symptomatic teeth with no signs of pathosis, anatomic superimposition	✓	✓
Confirmation of nonodontogenic causes of pathosis	Sinusitis of maxillary origin	✓	✓
Assessment and/or management of complex dento-alveolar trauma	Severe luxation injuries, suspected alveolar fractures, horizontal root fractures	✓	✓
Appreciation of complex root canal systems prior to endodontic management	Dens invaginatus, accessory canals, root curvature, root canal system anomalies	✓	✓
Retreatment—nonsurgical	Untreated MB2, complex root canal anatomy	✓	✓
Assessment of endodontic treatment complications	Post and root canal perforations, calcified canals, separated endodontic instruments	✓	✓
Assessment and/or management of root resorption	Internal or external resorption	✓	✓
Assessment prior to complex periradicular surgery	Location of pathologic lesion, determine optimal surgical access, locate vital anatomical structures	✓	✓
Presurgical dental implant planning	Immediate implant placement	✓	

AAE/AAOMR The American Association of Endodontists and the American Academy of Oral and Maxillofacial Radiology, *ESE* European Society of Endodontology, *MB2* second canal of the mesiobuccal root of the maxillary first molar terization of disruptions in the PDL space, small resorptive defects and localization of calcified canals; an optimal resolution of approximately 0.125 μm or less is preferred.

- *Exposure settings.* The lowest mA setting and the shortest exposure time in conjunction with a pulsed exposure mode of acquisition are recommended.
- *Dose.* Depending on the equipment used, CBCT exposure may expose a patient to comparable or slightly higher radiation doses. This is especially important when considering 3D imaging for children (up to 18 years old) and pregnant patients.
- *Task-specific imaging*. Depending on the diagnostic objective of the imaging study, selecting a larger voxel size, 180° instead of 360° rotation, or lower kVp and/or mA can reduce radiation dose to the patient (e.g., temporal imaging of the same area to assess gross changes). Exposure parameters can be reduced when acquiring a series of radiographs to monitor bony changes during checkup, as opposed to endodontic assessments which generally require high resolution, and hence increased exposure parameters.

22.3.2 Clinical Efficacy: Effect on Diagnosis and Treatment Planning

The diagnostic efficacy hierarchical model is used to appraise the efficacy levels for an imaging modality (Fryback and Thornbury 1991). The model presents six levels of imaging efficacy: Level 1—Technical, Level 2—Diagnostic accuracy, Level 3—Diagnostic thinking, Level 4—Therapeutic, Level 5—Patient outcome, and Level 6—Societal efficacy. Systematic reviews (European Commission SEDENTEXCT 2012; Rosen et al. 2015; Kruse et al. 2015) on the diagnostic efficacy of CBCT imaging in endodontics report that most studies have a low level of efficacy (levels 1, 2, or 3), with none at level 6. However, recent Level 4 studies suggest that preoperative CBCT imaging provides additional diagnostic and treatment planning information (Figs. 22.6 and 22.7).

Mota de Almeida et al. (2014a) compared therapy plan changes before and after CBCT imaging on 53 patients (81 teeth) referred from specialty endodontic practices. The primary reasons for referral were differentiating pathosis from normal anatomy (47%) and presurgical assessment (25%). Treatment plan changes were made in 53% of patients after CBCT imaging. In a related study using the same database, the authors found that use of CBCT imaging led to diagnostic changes in 41% of patients and 35% of teeth (Mota de Almeida et al. 2014b).

Ee et al. (2014) compared the relative diagnostic value of preoperative periapical images alone to CBCT image findings on 30 patients in a private practice setting. They used a preliminary diagnosis and treatment plan based on clinical diagnosis and the interpretation of both imaging modalities as the diagnostic "gold" standard. They found sensitivity to be 36.6–40% when using periapical images alone and 76.6–83.3% when CBCT imaging was used. The examiners altered their treatment plan in 62.2% of the cases after viewing the CBCT scan and concluded that availability of a preoperative CBCT can directly influence a clinician's treatment plan.

It is important to emphasize that evaluation of the patient's chief complaint, history, clinical and radiographic findings are all considered essential to the formulation of a diagnosis and treatment plan.

22.3.3 Preoperative Assessment

There are numerous situations in the assessment phase of endodontics where CBCT imaging can assist in the diagnosis and subsequent treatment planning of endodontic disease and in the evaluation of dental features that may affect therapy. Teeth with anatomical variations and complex morphology may be indications for 3D imaging. CBCT is significantly better in terms of sensitivity, positive or negative predictive values, and

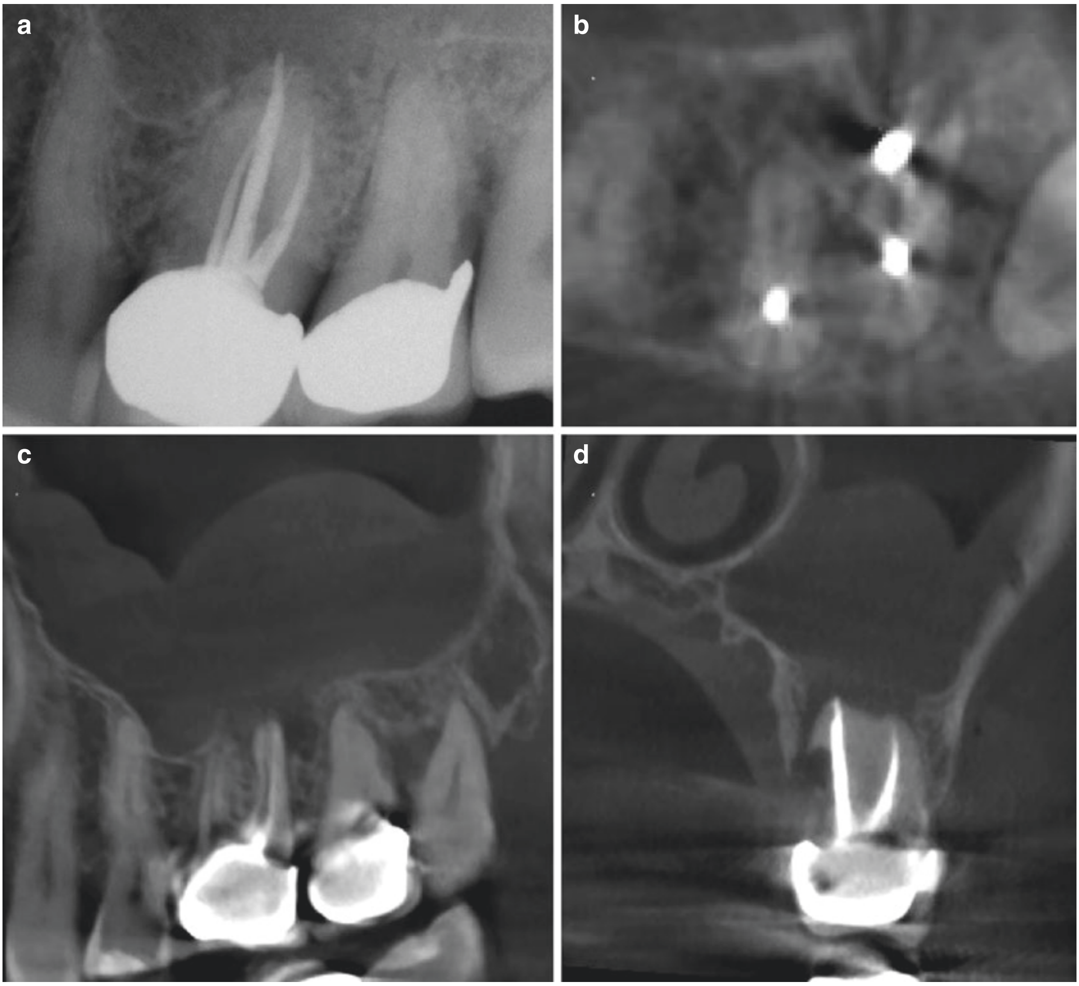

Fig. 22.6 Periapical image (**a**) of symptomatic maxillary left first molar showing a periapical radiolucency suggesting an untreated MB2 canal. Axial (**b**) CBCT image confirms the presence of an untreated MB2. Parasagittal (**c**) and cross-sectional (**d**) CBCT images demonstrate an apical area of low density, cortical bone resorption of the maxillary sinus floor, secondary soft tissue involvement and a mid-root palatal resorptive defect. While nonsurgical retreatment may have been recommended based on the periapical image, CBCT imaging substantially changes the prognosis and treatment recommendation

diagnostic accuracy than digital or conventional radiographs (Peters and Peters 2012) with the exception of the assessment of vertical root fractures of root-treated teeth (Talwar et al. 2016).

22.3.3.1 Tooth Root Anatomy

Anatomical variations exist with each tooth and root type. The success of endodontic treatment depends on the identification of all root canal systems so that they can be accessed, cleaned, shaped, and obturated (Vertucci 1984). A thorough understanding of specific root canal anatomy is essential prior to initiating treatment.

Multiple in vitro (ex vivo) studies have validated the use of CBCT in identifying root canal systems compared to multiple intraoral images (Matherne et al. 2008; Neelakantan et al. 2010). These studies report high detection rates compared to histologic sections (Michetti et al. 2010) and similar detection rates to staining and clearing techniques on extracted teeth (Neelakantan et al. 2010) (Fig. 22.8).

Fig. 22.7 Periapical image (**a**) of patient with vague pain in the right mandibular area for several years with inconclusive clinical and microscopic findings. This image demonstrates extensive calcification of the unrestored first molar. Axial (**b**), mesial (**c**), and distal (**d**) coronal CBCT images show a significant mesial-distal fracture

Additional Canals and Roots

Maxillary molars have been frequently investigated because of their complex root anatomy and canal morphology. Many studies have reported the presence of a second mesiobuccal canal (MB2) in the mesiobuccal root of the maxillary first and second molars (Weine et al. 1969; Pineda and Kuttler 1972; Kulild and Peters 1990; Fogel et al. 1994; Buhrley et al. 2002) and limitations of intraoral radiography in identifying them (Pineda 1973; Nance et al. 2000; Ramamurthy et al. 2006; Domark et al. 2013).

The frequency of MB2 is reported with varying methodology and results (Cleghorn et al. 2006). Contemporary instruments, enhanced magnification, illumination, and experience are critical to successful treatment. A clinical study using the dental operating microscope reported MB2 identification in more than 90% of maxillary first molars and 60% of maxillary second molars

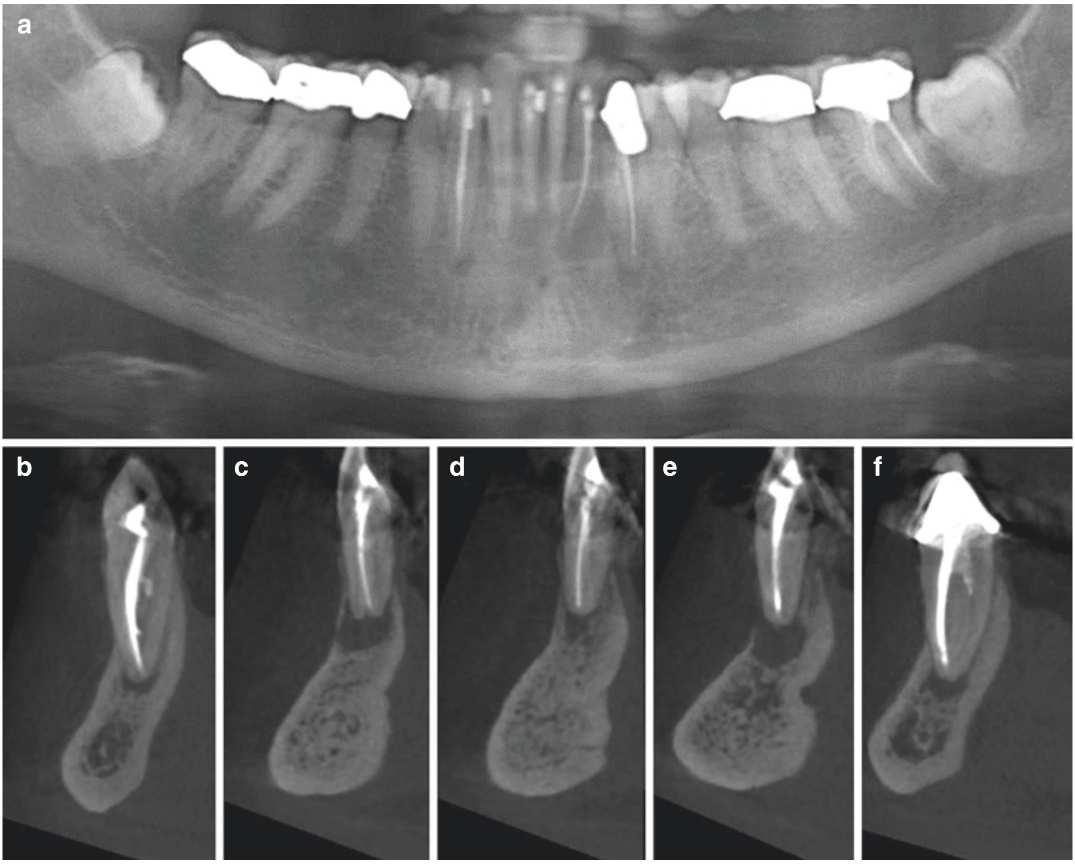

Fig. 22.8 Cropped panoramic image (**a**) of a patient who presented with pain/swelling in the mandibular anterior region after multiple root canal treatments of the mandibular teeth. Coronal CBCT images of the right canine (**b**), right (**c**) and left (**d**) central incisors, left lateral incisor (**e**) and left canine (**f**) illustrate areas of low density with asymmetry of the previous filling material and evidence of untreated canal space

(Stropko 1999). Clinicians should be aware that untreated MB2 canals likely have a negative impact on the outcome of endodontic treatment (Wolcott et al. 2005; Huumonen et al. 2006).

Barato Filho et al. (2009) investigated the internal morphology of extracted maxillary first molars using ex vivo sections, CBCT and clinical treatment using an operating microscope. Results showed that when an additional canal was present, it was located in the MB root 92.85–95.63% of the time. Additional canals were also located in the DB and palatal roots, though much less frequently. The authors concluded that CBCT provides a good method for the initial evaluation of maxillary first molar internal morphology. The location and identification of the root canals were facilitated by the combined use of an operating microscope and CBCT.

Blattner et al. (2010) assessed extracted maxillary molars for the prevalence of MB2 canals. They found an 80% correlation between the results using CBCT and tooth sectioning. Vizzotto et al. (2013) showed CBCT to have higher mean values of specificity and sensitivity when compared to intraoral radiographs in the detection of the MB2 canal.

Bauman et al. (2011) investigated the effect of increasing voxel resolution on the detection rate of multiple observers of the MB2 on 24 maxillary first molars by CBCT. Compared to the overall prevalence of MB2 (92%), CBCT detection rates increased from 60 to 93.3% with increasing resolution, suggesting that if CBCT is to be used then resolutions in the order of 0.12 mm or less are optimal (Figs. 22.9 and 22.10).

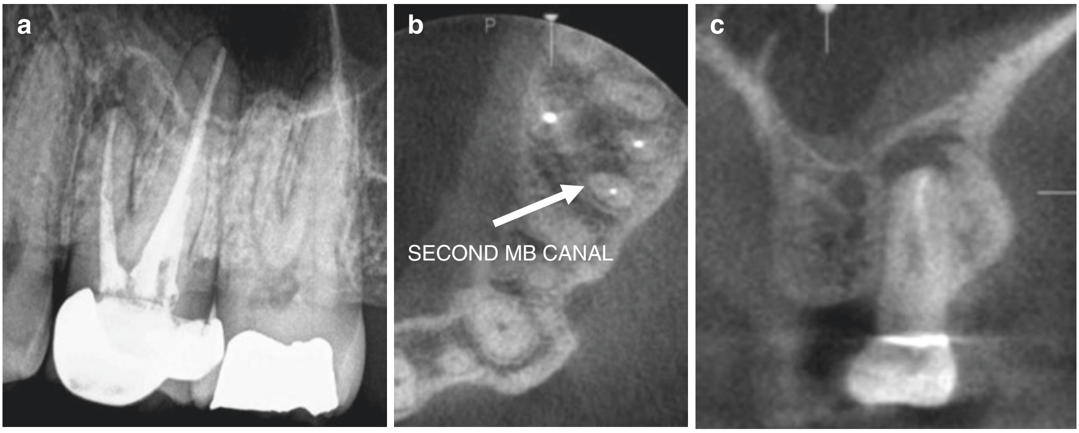

Fig. 22.9 A periapical image of a previously treated maxillary left first molar (**a**) with geometric distortion in the horizontal plane shows a periapical radiolucency associated with the mesiobuccal root. High resolution axial (**b**) and cross-sectional (**c**) CBCT imaging demonstrates an untreated MB2 canal

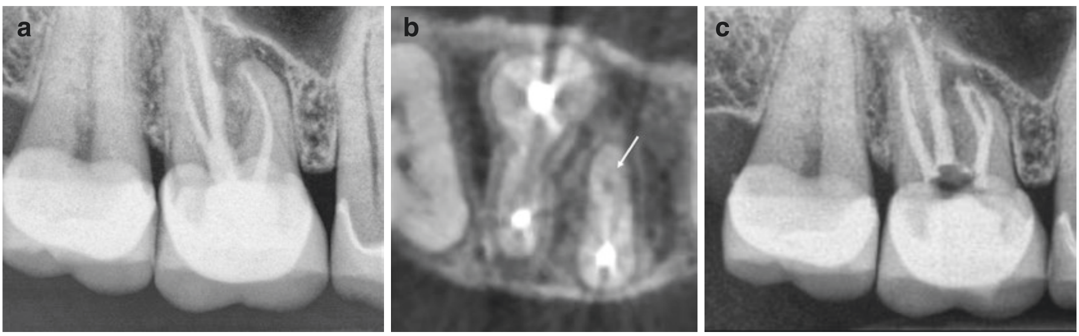

Fig. 22.10 A periapical image of a previously treated maxillary right first molar (**a**) shows a periapical radiolucency associated with the mesiobuccal root. High resolution axial (**b**) CBCT imaging demonstrates an untreated MB2 canal. Postoperative periapical image (**c**) shows complete obturation of both mesiobuccal root canal systems

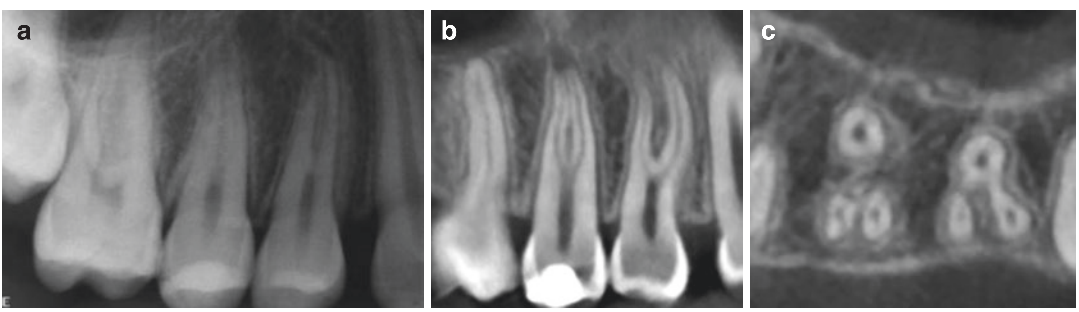

Fig. 22.11 Periapical image (**a**) with corresponding parasagittal (**b**) and axial (**c**) CBCT images demonstrating right maxillary first and second premolars with three distinct canal systems

All teeth types have the possibility for variations in roots and root canal anatomy (de Pablo et al. 2010; Silva et al. 2013; Llena et al. 2014; Paes da Silva Ramos Fernandes et al. 2014; Silva et al. 2014; Abella et al. 2015) (Fig. 22.11). An additional disto-lingual root (radix entomolaris) with significant curvature can be present in mandibular molars (Tu et al. 2007, 2009; Abella et al. 2011).

CBCT scans may also be used as an adjunct for determination of estimated working length in select cases and have similar or greater accuracy to periapical radiographs for maxillary posterior teeth (Metska et al. 2014) or electronic apex locators (Janner et al. 2011; Jeger et al. 2012). If a preexisting scan is available, length measurements can be used as an estimate prior to treatment. Canal curvature may also be assessed with CBCT images (Estrela et al. 2008a) and is particularly useful for detecting curvature in the buccolingual or buccopalatal plane.

The AAE/AAOMR (2015) state:

> Limited FOV CBCT should be considered the imaging modality of choice for initial treatment of teeth with the potential for extra canals and suspected complex morphology.

In addition to identifying canals, determining the configurational relationship of multiple canals within a root can also affect treatment decisions. Accurate preoperative assessment may allow for more conservative access and canal preparations, reducing the possibility of iatrogenic errors during preparation.

22.3.3.2 Developmental Anomalies

Dental developmental anomalies are common and many have endodontic significance (Ezoddini et al. 2007). CBCT imaging provides accurate assessment of these conditions.

Dens Invaginatus (Dens in Dente)

Dens invaginatus is a malformation of individual teeth that results from an invagination of the dental papilla during development with a reported frequency of 0.04–10% (Hovland and Block 1977). It most commonly affects the maxillary lateral incisors which accounts for 43% of all cases (Grahnen et al. 1959) (Figs. 22.12 and 22.13), often bilaterally, but may occur in various maxillary and mandibular teeth (Grahnhen et al. 1959; Hülsmann 1997; Hamasha and Alomari 2004) (Fig. 22.14). Dens invaginatus presents with varying degrees of complexity and severity, classified by Oehlers (1957) into three types:

- *Type I*: The minimal and enamel-lined invagination is confined to the crown of the tooth and does not extend beyond the level of the external cementoenamel junction (CEJ) (Fig. 22.12).

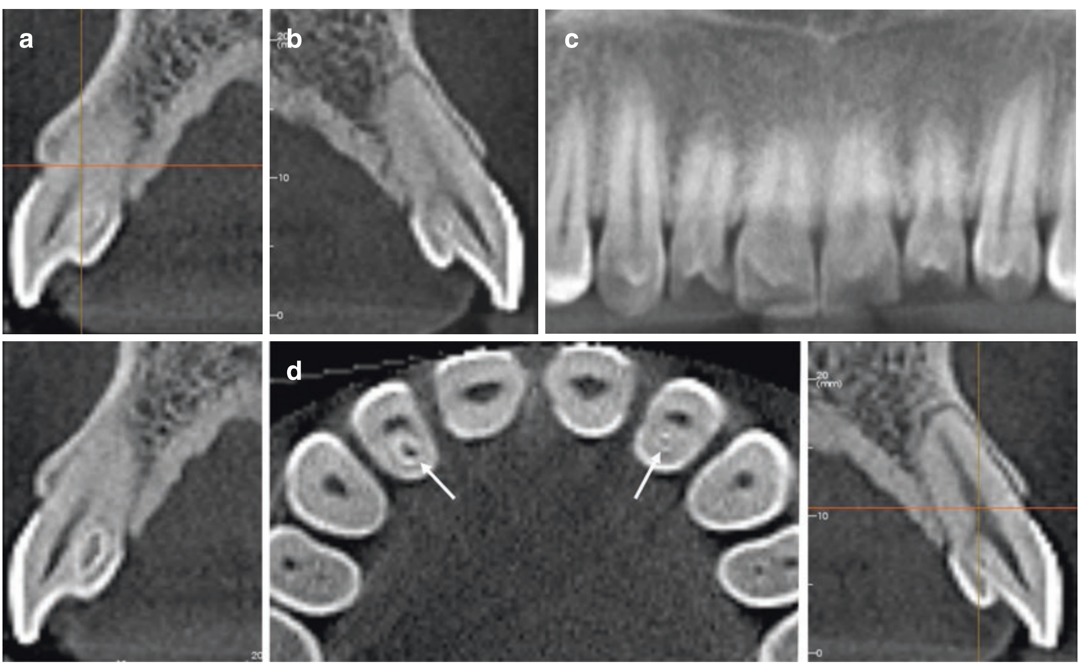

Fig. 22.12 Right (**a**) and left (**b**) serial cross-sectional images of the lateral incisors with reformatted cropped panoramic (**c**) and axial CBCT images showing Type II (**a**) and Type I (**b**) dens in dente on an asymptomatic female patient

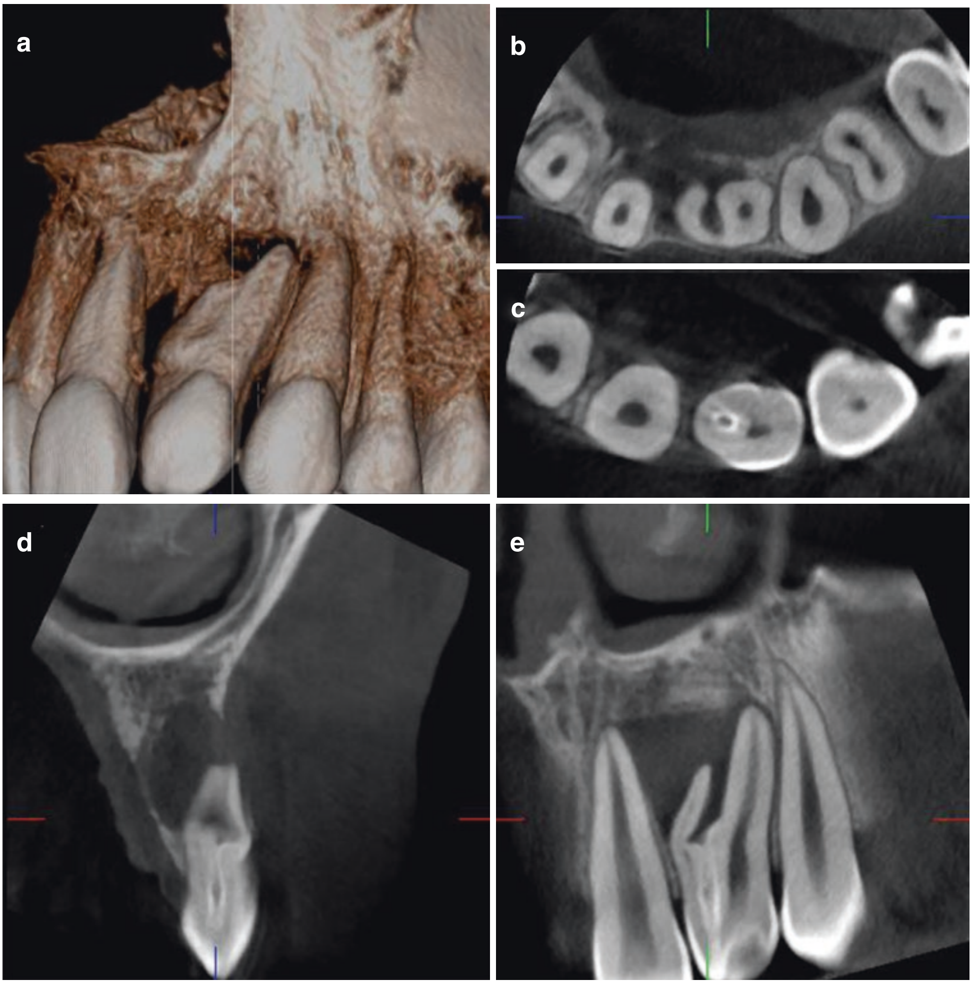

Fig. 22.13 The complexity of Type III dens invaginatus is demonstrated in by preoperative volumetric surface rendered (**a**), axial ((**b**), (**c**)), cross-sectional (**d**) and parasagittal (**e**) CBCT images of this necrotic, asymptomatic left lateral incisor

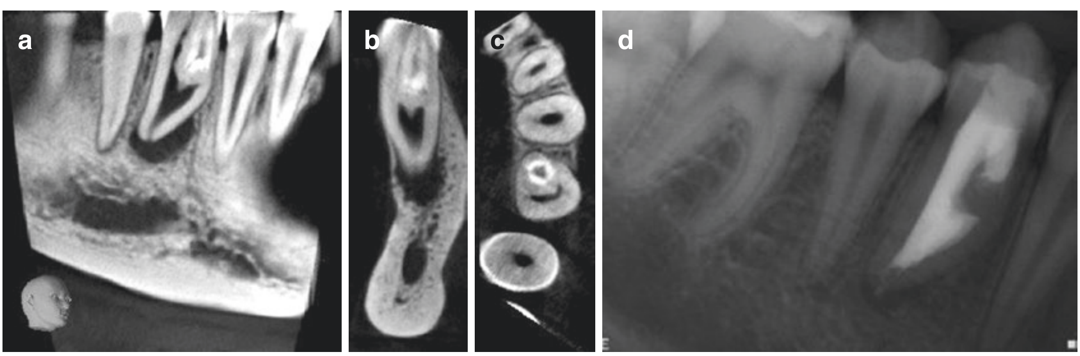

Fig. 22.14 Preoperative parasagittal (**a**), cross-sectional (**b**), and axial (**c**) CBCT images showing the complexity of dens invaginatus in a mandibular right first premolar with pulp necrosis and symptomatic apical periodontitis. Checkup image shows healing of the supporting bone following orthograde root canal treatment

- *Type II*: The deeper and enamel-lined invagination extends below the CEJ but remains within the root, ending in a blind sac. The pulp shows no direct communication with the periodontal ligament (Fig. 22.12).
- *Type III*: The severe invagination extends through the root to form an additional apical (IIIA) or lateral (IIIB) foramen (Fig. 22.13). There is usually no direct communication with the pulp. The invagination may be completely lined by enamel but cementum may also be present. In Type III variations, any infection within the invagination can lead to an inflammatory response within the periodontal tissues giving rise to a "peri-invagination periodontitis."

A recent retrospective study using CBCT found type I to be the most commonly observed (65.9%), followed by type II (29.5%) and type III (4.6%) (Capar et al. 2015).

Teeth affected by dens invaginatus are prone to developing caries within the invagination that may result in pulp necrosis and subsequent periradicular periodontitis (Figs. 22.13 and 22.14). Successful endodontic treatment depends on characterization of the anatomical variations of the anomaly including the irregular shape of the root canal system and appreciation of the degree of involvement of the pulp and/or invagination (John 2008).

Taurodontism

The characteristic features of teeth with this condition include an enlarged pulp chamber, apical displacement of the pulpal floor and no constriction at the level of the CEJ (Jafarzadeh et al. 2008). The prevalence of taurodontism has been reported to range from 0.5 to 46.4% depending on the population studied, with most authors reporting from 5 to 10%. The trait has been reported to be inherited as autosomal recessive and associated with numerous syndromes and conditions including cleft lip and palate (Laatikainen and Ranta 1996), tricho-dento-osseous syndrome, Klinefelter's, Williams, McCune-Albright syndromes, and probably most often with Down syndrome. CBCT provides important information characterizing this anomaly, potentially important in endodontic treatment considerations (Nawa et al. 2008; Borges et al. 2014).

Dilaceration

Dilaceration is a root anomaly with an abrupt change in direction of the long axis of the root of the tooth in relation to the crown. The defining criteria vary from a deviation of 20° in the apical part of the root to a 90° or greater angle. It can occur as a result of trauma, or occur spontaneously and has been associated with some developmental syndromes. It can occur in both deciduous and permanent teeth, more commonly in posterior teeth and in the maxilla. The presence of a dilaceration can severely complicate endodontic treatment (Jafarzadeh and Abbott 2007).

Gemination/Fusion

Both gemination and fusion are developmental disorders of individual teeth associated with abnormalities in the differentiation of dental lamina. Gemination occurs when two teeth develop from one enamel organ producing a single root structure with two partial or completely separated crowns. Fusion is a union of two teeth, normally with separated enamel organs leading to the formation of a joined tooth with the confluence of dentin. The clinician benefits from a knowledge of the root canal system provided by CBCT for treatment of both conditions.

22.3.3.3 Dental Periapical Pathosis

Apical periodontitis (AP) is generally considered to be a sequelae of pulp necrosis and subsequent microbial infection and results in local inflammation, resorption of hard tissues, destruction of other periapical tissues, and eventual formation of various histopathological entities such as granulomas, cysts, or abscesses (Bhaskar 1968; Nair 2004). Because radiographic distinction between these entities is difficult, the bony destruction observed radiographically associated with AP is commonly referred to as a periapical lesion.

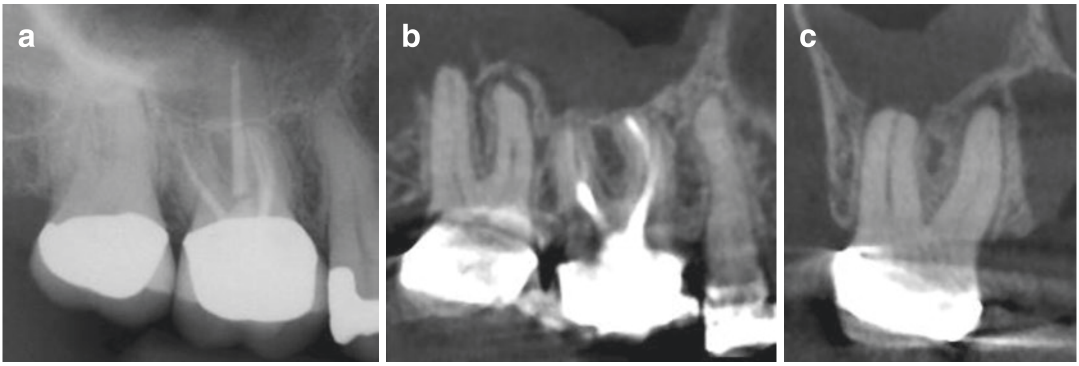

Fig. 22.15 Periapical image (**a**) of patient with pain in the maxillary right quadrant, initially referred for retreatment of the first molar. Parasagittal (**b**) and cross-sectional (**c**) CBCT images of the second molar indicate areas of low density associated with all root apices and concomitant sinus mucosal thickening

22.3.3.4 Early Radiographic Changes

During the early stages of the inflammatory process, there may be minimal or no periradicular radiographic changes (Barthel et al. 2004). Periapical symptoms may or may not be present. Eventually the periodontal ligament (PDL) space, which appears as an approximately 200 μm-wide, low density feature surrounding the root, becomes wider (thickened). PDL widening may progress to a more defined radiolucency. PDL space widening due to AP must be distinguished from other causes including trauma from occlusion, orthodontic treatment, tooth extrusion, root formation (dental papilla), wide marrow space superimposed on a tooth apex, or superimposition of a tooth apex on radiolucent anatomical structures (such as a nasal fossa, maxillary sinus, mental foramen, or submandibular fossa).

Mature Radiographic Presentation

Most periapical lesions are asymptomatic, associated with teeth having necrotic pulps and appear radiolucent on radiographs. Condensing osteitis is the most common radiopaque lesion found in the jaws and represents a localized bony reaction to a low-grade inflammatory stimulus, usually associated with root apices (American Association of Endodontists 2012). Periapical lesions of endodontic origin usually have the following radiographic characteristics (Walton and Fouad 2015):

- Radiolucent
  - The lamina dura is absent apically.
  - The hypodensity remains at the apex of the tooth and tends to resemble a hanging drop (Fig. 22.15).
  - The cause of pulp necrosis is usually evident (e.g., dental caries, trauma, large restoration).
- *Radiopaque* (Condensing osteitis or focal sclerosing osteomyelitis)
  - Radiolucent apical epicenter associated with the inflammatory lesion (Green et al. 2013).
  - Diffuse radiopaque border.

CBCT Detection

Ex vivo (Stavropoulos and Wenzel 2007; Ozen et al. 2009; Soğur et al. 2009; Patel et al. 2009a) and invivo (Lofthag-Hansen et al. 2007; Low et al. 2008; Estrela et al. 2008b; de Paula-Silva et al. 2009a, b; Patel et al. 2012a; Abella et al. 2014) studies indicate CBCT imaging (range; 61–100%) has an 18.8–54.2% higher AP detection rate than periapical radiography (range, 24.8–44%), particularly for smaller lesions (Estrela et al. 2008b; Abella et al. 2012) (Figs. 22.15 and 22.16). Periapical radiography frequently underestimates the size of the radiolucency compared to CBCT (Tsai et al. 2012; Estrela et al. 2008b; Christiansen et al. 2009).

Some authors suggest that true apical cysts require surgical treatment, as they are less likely

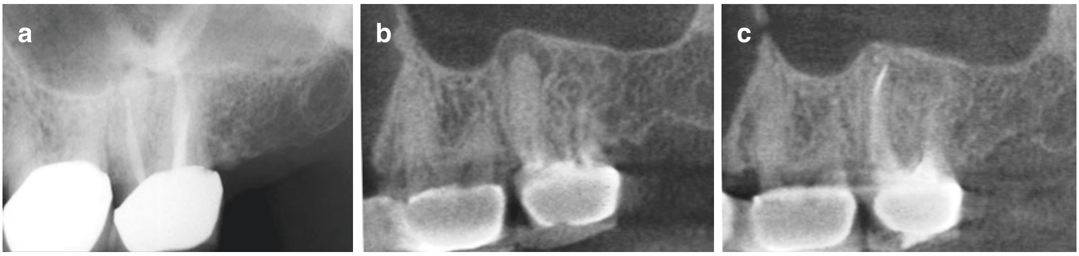

Fig. 22.16 Periapical radiograph of the maxillary left second molar (**a**) shows an area of low density surrounding the mesial root with unfilled canal space. A parasagittal CBCT image (**b**) shows a chronic periradicular osteoperiostitis, or "halo lesion," where the apical periodontitis has caused displacement of the periosteum but does not penetrate the antral floor. Three months after retreatment, CBCT imaging (**c**) demonstrates complete apical resolution

to resolve following nonsurgical root canal treatment (Natkin et al. 1984; Nair 2003; Nair et al. 1993). Numerous investigators have suggested that specific radiographic features can be used to differentiate between cysts and granulomas. These include:

- Cysts may be associated with a well-defined hypodensity that may slowly enlarge and ultimately cause expansion of the cortical plates.
- The peripheral border of radicular cysts may be hyperostotic (sclerotic or corticated), whereas the border of an apical abscess may be diffuse and irregular.

However, differentiation between these entities based on these and other features on CBCT imaging presentation have proven unreliable (Simon et al. 2006; Rosenberg et al. 2010; Guo et al. 2013). Surgical biopsy and histopathological examination remains the current standard for definitive diagnosis.

The AAE and AAOMR (2015) state:

> Limited FOV CBCT should be considered the imaging modality of choice for diagnosis in patients who present with contradictory or nonspecific clinical signs and symptoms associated with untreated or previously endodontically treated teeth.

When patients present with poorly localized symptoms or suspected pathosis with limited radiographic findings using conventional imaging, CBCT may reveal the presence of previously undetected disease. CBCT may also be indicated to help confirm the absence of an odontogenic etiology when managing nonodontogenic causes of pain (Patel et al. 2015). Examples may include patients with sinusitis or neuropathic pain-related symptoms.

Residual (Persistent) Periapical Pathosis

Most apical lesions treated by nonsurgical root canal therapy heal with hard tissue regeneration, resulting in elimination or reduction of the periapical radiolucency. However, in a proportion of cases, asymptomatic radiolucencies persist after root canal treatment. These may be due to persistent intraradicular infection, extraradicular infection (principally actinomycosis), extruded root canal filling or other exogenous materials causing a foreign body reaction, the accumulation of endogenous cholesterol crystals that irritate the periapical tissue, true cystic lesions, and scar tissue healing of the lesion (Nair 2006). Radiographically, a scar may appear as incomplete bone fill with a radiopaque periphery and an internal radiolucency. Scar tissue is most commonly found following apical surgery where there is a perforation of both the buccal and lingual or palatal cortex. While most surgical sites heal successfully within 12 months (Maddalone and Gagliani 2003), some require longer periods of time for complete resolution of the radiolucency (von Arx et al. 2001; Testori et al. 1999). CBCT may be considered for healing assessment following apical surgery (Tanomaru-Filho et al. 2015) (Figs. 22.17 and 22.18).

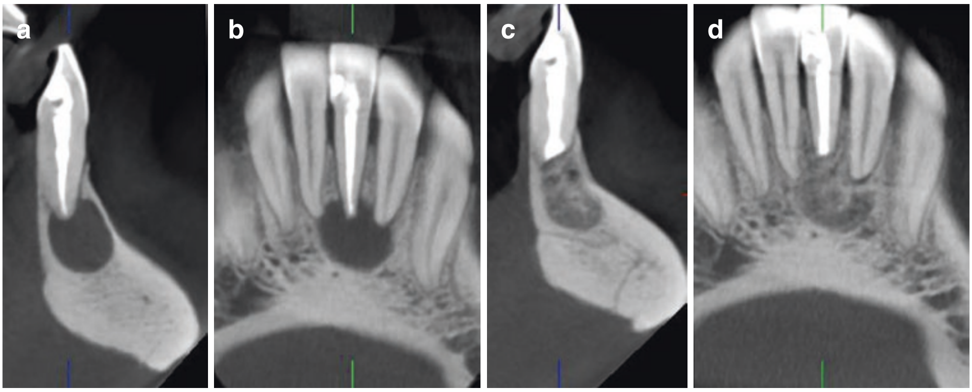

Fig. 22.17 Cross-sectional (**a**) and parasagittal (**b**) CBCT images of a patient with a large well-defined residual apical area of low density after root canal treatment of the mandibular right central incisor. Cross-sectional (**c**) and parasagittal (**d**) CBCT images 12 months after root end resection and root end filling shows healing. The biopsy revealed a periapical cyst. The adjacent teeth remain responsive to vitality testing

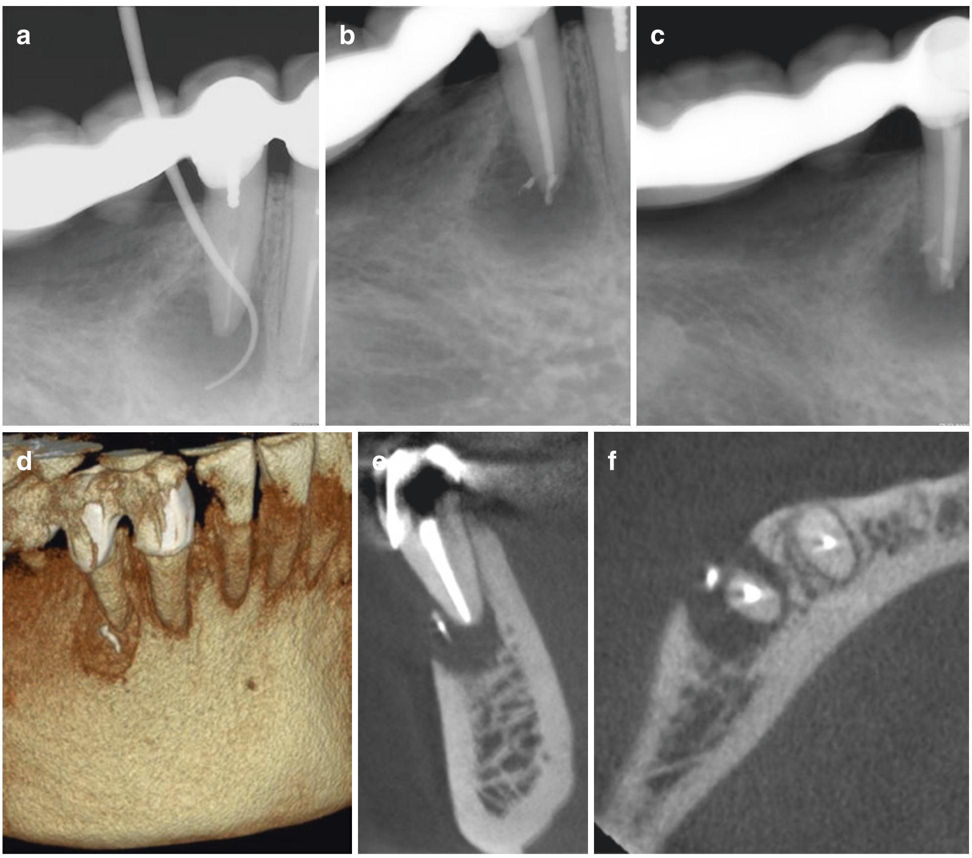

Fig. 22.18 Initial intraoral periapical image (**a**) of a patient presenting with localized right mandibular swelling and fistula tract. The image shows a first premolar acting as a bridge abutment with a large diffuse hypodensity (shown with gutta percha). A periapical image of the tooth with orthograde retreatment 6 weeks later (**b**). The patient presented 4 months later with similar signs and symptoms with no apical resolution demonstrable on periapical images (**c**). CBCT volumetric (**d**), cross-sectional (**e**), and axial (**f**) CBCT images taken at the time of the second presentation show complete loss of buccal cortical plate and floating hyperdense, presumably extruded material. In the absence of a fracture, surgical curettage, apicoectomy, retrograde endodontic treatment and guided tissue regeneration was planned based on this second imaging presentation

22.3.3.5 Traumatic Injury

Numerous classification systems for describing tooth injury have been proposed based on factors such as etiology, anatomic involvement of the tooth, pathosis, prognosis, and therapy. These range from basic (e.g., Ellis and Davey Classification (Ellis and Davey 1970)) to comprehensive (e.g., Sanders Classification (Sanders et al. 1979)) categorizations. The most widely used system, adopted by the World Health Organization, is the Andreasen classification system (Andreasen and Andreasen 1994). This system divides dentoalveolar injury into four major categories: dental tissues and pulp, periodontal tissues, supporting bone, and gingival and oral mucosa. Within the dental hard tissue and pulp division, injuries are classified as:

- *Crown infraction*. Incomplete fracture or crack without loss of tooth structure.
- *Uncomplicated crown fracture*. Fracture confined to enamel and/or involving dentin without pulp exposure.
- *Complicated crown fracture*. Enamel and/or dentin fracture with pulp involvement.
- *Complicated crown-root fracture*. Involves enamel, dentin, and cementum with pulp exposure.
- *Root fracture*. A fracture of the root involving dentin, cementum, and pulp (Figs. 22.19 and 22.20).

Intraoral periapical imaging is often sufficient to assess many of these conditions. CBCT imaging is useful in the diagnosis of horizontal root fracture and luxation injuries such as concussion, subluxation, extrusive luxation, lateral luxation, intrusive luxation, and avulsion (Bakland and Andreasen 2004) (Fig. 22.21).

Root fractures due to trauma account for 0.5–7% of dental impact injuries (Andreasen et al. 2007). Traumatically induced tooth fractures are usually horizontal whereas those related to previous root canal therapy or posts are vertical. Horizontal root fractures (HRF) can be classified according to the location of the fracture line (cervical, middle and apical thirds of the root). HRFs in the middle third of the root are the most common (Andreasen 1989) (Fig. 22.19) and those located in the cervical third appear to have the least favorable prognosis (Cvek et al. 2001, 2008).

Periapical radiography has limitations in the assessment of HRFs (Cohenca et al. 2007a; Palomo and Palomo 2009). The fracture line is visible radiographically only if the X-ray beam

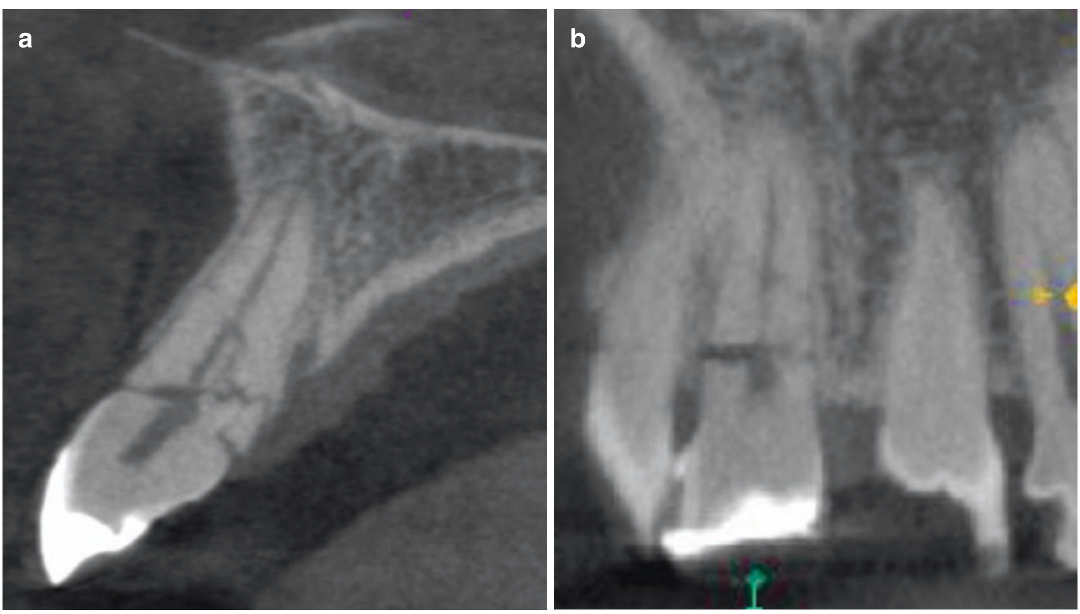

Fig. 22.19 Thin sectional cross-sectional (**a**) and sagittal (**b**) high-resolution CBCT images shows cervical horizontal comminuted radiolucent lines and displacement of the palatal root fragments

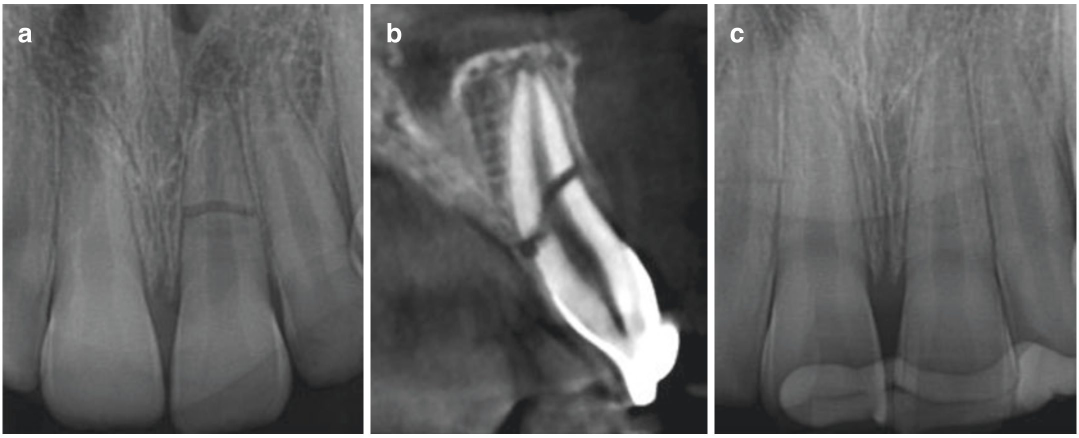

Fig. 22.20 Periapical (**a**) and cross-sectional CBCT image of an adolescent showing a middle third horizontal root fracture of the left maxillary central incisor sustained due to a playground accident. The tooth was repositioned and splinted with follow-up periapical image (**c**) showing excellent approximation of the segments

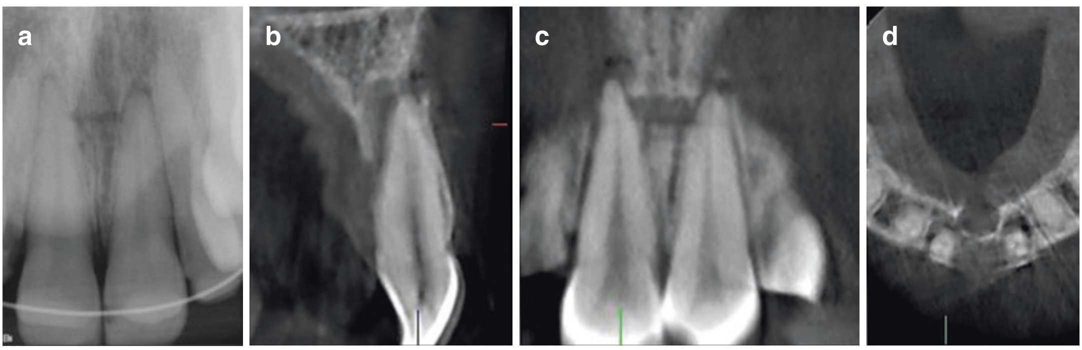

Fig. 22.21 Periapical image (**a**) of an adolescent who suffered from a traumatic blow to the anterior dentition. A discontinuity of the interradicular bone between the maxillary central incisors and slight widening of the PDL space is noted. Thin cross-sectional (**b**), sagittal (**c**), and axial (**d**) CBCT images show antero-medial lateral luxation with displacement of the crown lingually and the root facially. There is a concomitant alveolar fracture. Compared to the findings of the periapical image (**a**), CBCT provides more information regarding the tooth displacement and associated alveolar fracture, which can lead to better repositioning of the traumatized teeth

passes directly through the fracture (Patel et al. 2015). Since root fractures often have an oblique component in the sagittal plane (Andreasen et al. 2007), multiple radiographs from varying angles are recommended to maximize the likelihood of detection (Flores et al. 2007; International Association of Dental Traumatology 2012).

Numerous authors have illustrated the usefulness of CBCT in the diagnosis (Figs. 22.16, 22.17, and 22.18) and management of dento-alveolar trauma, including root fractures (Tsukiboshi 2006; Cohenca et al. 2007a; Tyndall and Rathore 2008; Patel 2009; Bornstein et al. 2009; Iikubo et al. 2009; May et al. 2013). Clinical outcomes depend on the exact location of the fracture, extent of displacement, and potential communication of the fracture to the oral cavity.

The AAE and AAOMR (2015) state:

> Limited FOV CBCT should be considered the imaging modality of choice for diagnosis and management of limited dento-alveolar trauma, root fractures, luxation, and/or displacement of teeth and localized alveolar fractures, in the absence of other maxillofacial or soft tissue injury that may require other advanced imaging modalities.

22.3.3.6 Root Resorption

Root resorption is defined by the American Association of Endodontists (2012) as:

> A condition associated with either a physiologic or pathologic process resulting in a loss of dentin, cementum, and/or bone.

It may result from traumatic luxation injuries, orthodontic tooth movement, or chronic infections of the pulp and/or periodontal structures (Ne et al. 1999). Since root resorption is usually asymptomatic, radiographic examination is critical to determine the presence, extent, and location of the defect. Based on the location in relation to the root surface, root resorption can be classified as external or internal (Gartner et al. 1976; Tronstad 1988).

CBCT is reported to be superior to periapical radiography in the detection and localization of external and internal resorptive defects (da Silveira et al. 2007; Estrela et al. 2009; Patel et al. 2009c; Bernardes et al. 2012; Kamburoğlu et al. 2011; D'Addazio et al. 2011; Durack et al. 2011). Others have presented selected cases illustrating the utility of CBCT in the detection of small lesions, localizing and differentiating the resorption from other conditions, classification of the lesion, determining prognosis and directing treatment (Cotton et al. 2007; Patel and Dawood 2007; Maini et al. 2008; Cohenca et al. 2007b; Patel et al. 2009c; Hahn et al. 2009). The accuracy of CBCT in the detection of surface defects, while higher than conventional imaging modalities, is not perfect (Hahn et al. 2009) and may improve with increasing voxel resolution.

The AAE and AAOMR (2015) state:

> Limited FOV CBCT is the imaging modality of choice in the localization and differentiation of external and internal resorptive defects and the determination of appropriate treatment and prognosis.

External Root Resorption (ERR)

ERR is a process that initiates in the periodontium and affects the external surface of the root (Andreasen 1985). Specific types include:

- *Surface (repair-related)*. Transient process involving small areas of the root surface following luxation and avulsion injuries. In the absence of bacteria, the resorption is reversible (Tronstad 1988). This generally has little clinical significance.
- *Inflammatory (infection-related)*. This is a common complication following traumatic luxation and avulsion injuries (Andreasen and Vestergaard Pedersen 1985; Andreasen et al. 1995). Early detection is critical, as the process can have a rapid onset and aggressive progression. External inflammatory resorption is dependent on the presence of infected necrotic pulp tissue within the root canal space; therefore, it is responsive to endodontic treatment (Andreasen 1985). Radiographically, the resorptive defect on the root surface has irregular borders and the surrounding bone may have radiolucent areas.
- *Replacement (ankylosis-related)*. Replacement resorption (ankylosis) occurs as a complication following trauma to the PDL, especially in luxation injuries such as avulsion. The root surface is resorbed and replaced with bone. Radiographically, the PDL space is absent and has a characteristic "moth-eaten" appearance (Tronstad 1988) (Figs. 22.22 and 22.23).
- *External Cervical Resorption*. External cervical resorption (Bakland and Andreasen 2004), also referred to as invasive cervical resorption (Heithersay 1999a), is a pathologic condition occurring immediately below the epithelial attachment of the tooth in the cervical region. The pulp is not involved in the etiology and often occurs in a tooth with a vital pulp (Patel et al. 2009b). Predisposing factors include a history of orthodontic treatment, dental trauma, intracoronal bleaching, prior surgical procedures, and periodontal therapy. Many teeth have multiple associations. However, cervical resorption is often idiopathic (Heithersay 1999a, b, 2004). Clinical signs are often absent in the early stages. However, the appearance of a pinkish color in the tooth crown is highly suggestive of late stage external resorption as the highly vascular resorptive tissue becomes visible through thin residual tooth structure. External cervical resorption is commonly misdiagnosed and confused with caries and internal resorption on periapical images (Fig. 22.24).

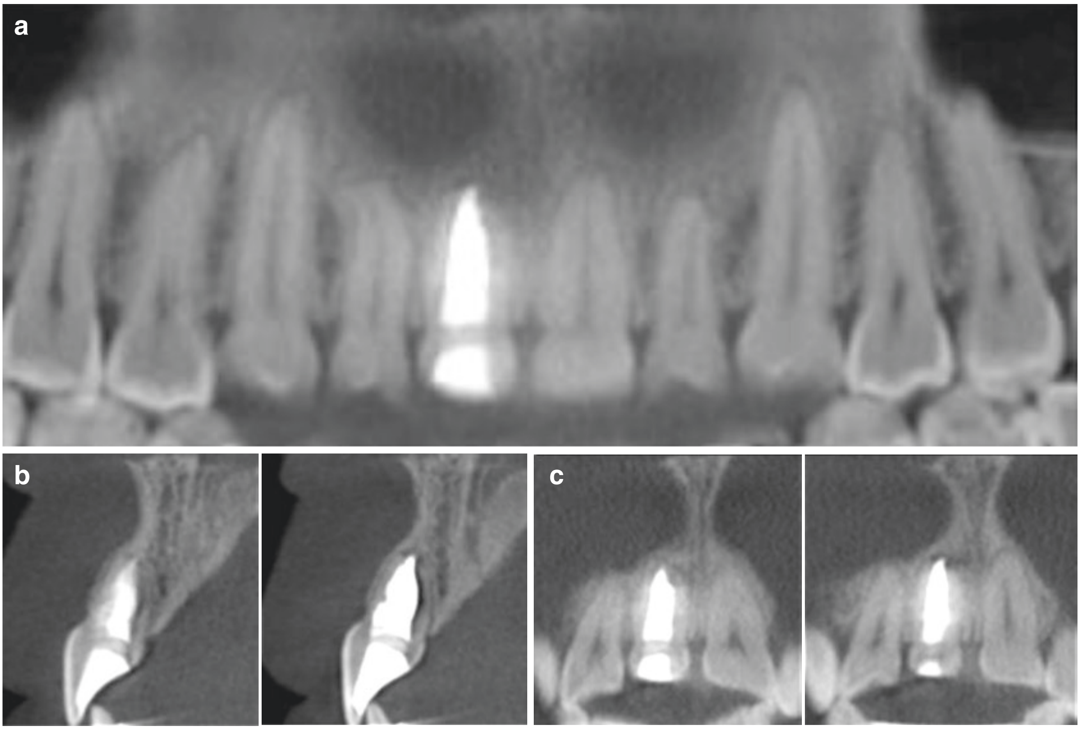

Fig. 22.22 Reformatted panoramic (**a**), and serial cross-sectional (**b**) and coronal (**c**) CBCT images of a root-filled maxillary right central incisor with a previous history of trauma. The images show bone trabecular-like replacement of the superior and palatal aspects of the apex consistent with external replacement resorption

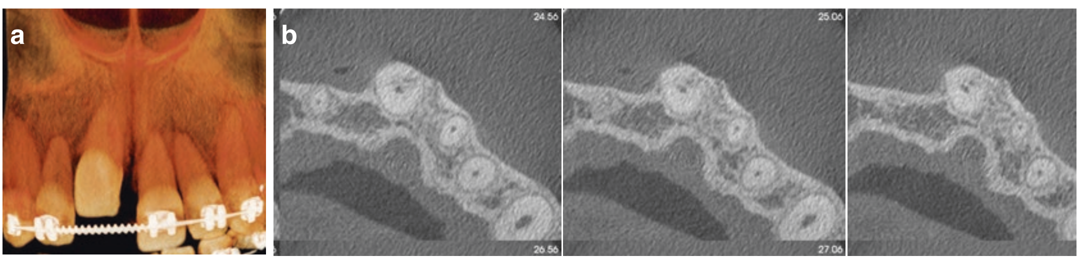

Fig. 22.23 Rendered volumetric image (**a**) of 14-year-old with a history of luxation of the deciduous maxillary right central incisor and failure of eruption of the associated permanent central incisor. Sequential axial images (**b**) show the irregularity of the mesial surface this tooth and loss of PDL space suggestive of replacement resorption. Note concomitant external root resorption extending to the pulp canal

Heithersay (2004) reported a clinical classification of invasive cervical root resorption based on increasing severity (Table 22.2).

Internal Root Resorption (IRR)

IRR is an inflammatory process that initiates within the pulp space and results in the loss of internal tooth structure. Compared with ERR, IRR is relatively rare (Haapasalo and Endal 2006). IRR has been associated with a history of trauma, caries and periodontal infections, pulpal inflammation and orthodontic treatment (Haapasalo and Endal 2006; Caliskan and Turkun 1997; Patel et al. 2010b). Accurate assessment is essential as treatment regimens may vary. Differentiating between IRR and ERR may be challenging using periapical radiography alone.

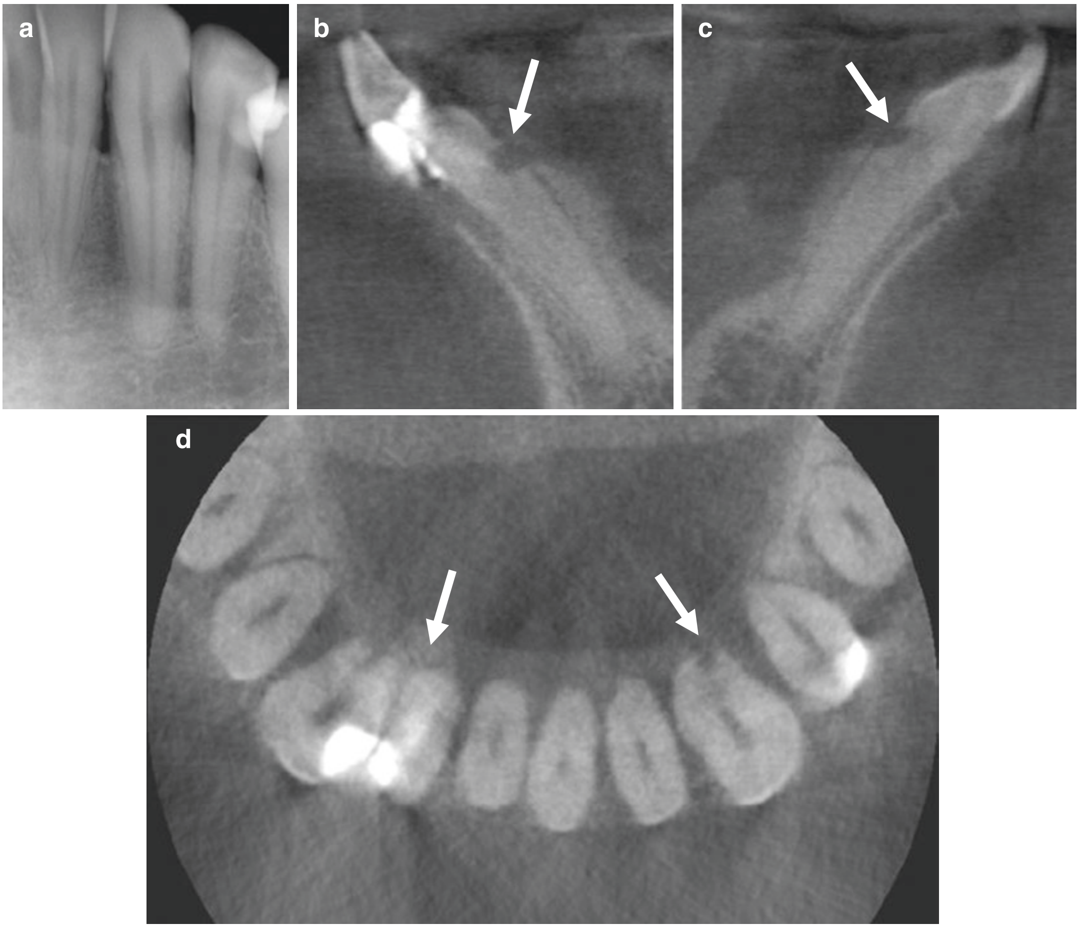

Fig. 22.24 Unremarkable periapical image of the mandibular left anterior teeth (**a**) of a patient with history of previous orthodontic revision for mandibular anterior crowding. Right (**b**) and left (**c**) cross-sectional and axial (**d**) CBCT images showing early (Class I) ERR on the left and right canines

Table 22.2 Classification of invasive cervical resorption (Heithersay 2004)

Classification	Description
Class 1	Small, invasive resorptive lesion characterized by shallow penetration into the dentin near the cervical area
Class 2	Well-defined, invasive resorptive lesion that has penetrated close to the coronal pulp chamber but has little or no extension into the radicular dentin
Class 3	Deeper invasion of the dentin that involves the coronal dentin and extends into the coronal third of the root (Figs. 22.25 and 22.26)
Class 4	Large invasive resorptive process that has extended beyond the coronal third of the root

On CBCT, characterization of root resorption is determined by location of the resorptive defect. IRR usually appears as a round or oval-shaped radiolucent "ballooning-out" of the root canal and has smooth, well-defined regular margins (Figs. 22.26, 22.27, 22.28, and 22.29).

22.3.3.7 Periapical Non-dental Associated Conditions

Anatomic Features

Numerous anatomic landmarks of the jaws may resemble periapical pathoses of dental origin, most of which are low density. The most important radiologic differential feature is whether the

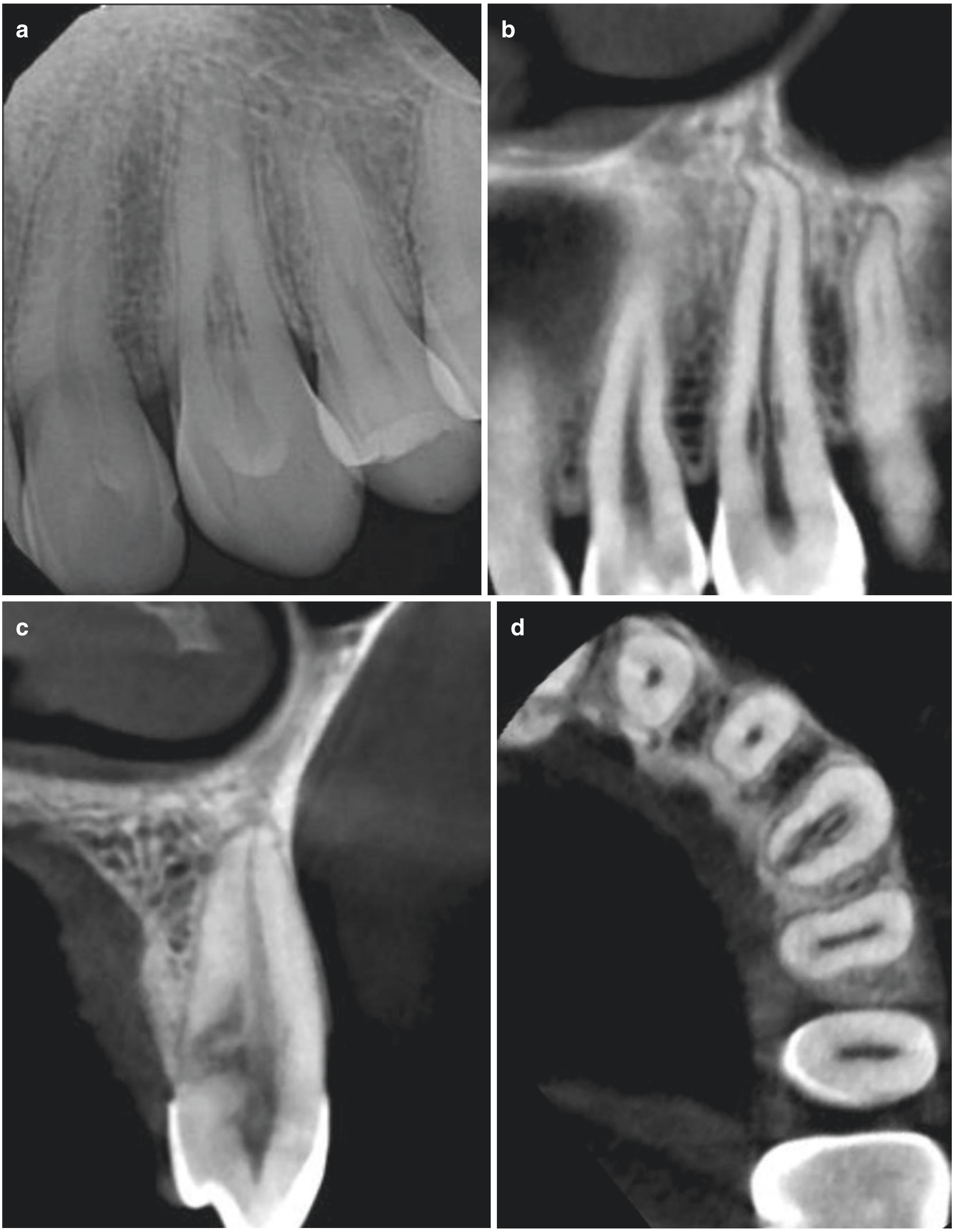

Fig. 22.25 Periapical image (**a**) of an asymptomatic patient referred for evaluation of possible internal resorption of the left maxillary canine. Parasagittal (**b**), cross-sectional (**c**), and axial (**d**) CBCT images demonstrate Class 3 external cervical root resorption

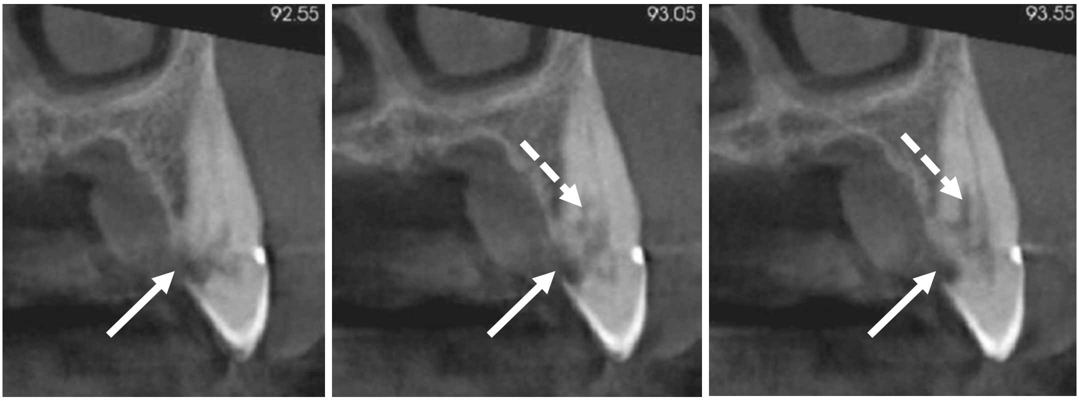

Fig. 22.26 A series of cross-sectional images of the left maxillary canine (#11) showing a lesion of invasive cervical external root resorption (*solid arrow*) combined with an internal resorptive site (*dashed arrow*)

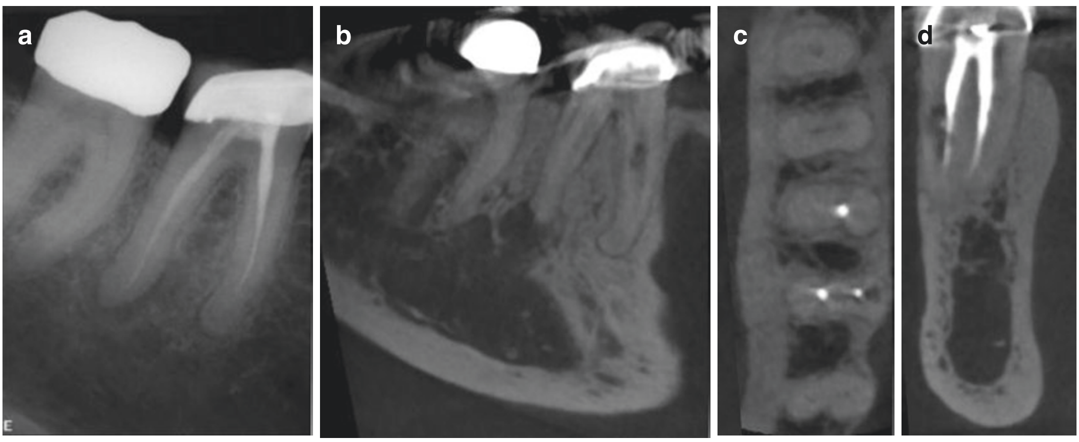

Fig. 22.27 Periapical image (**a**) of the right mandibular first molar referred for retreatment showing periapical hypodensity on the distal root. Parasagittal (**b**), axial (**c**), and cross-sectional (**d**) CBCT images show mid-root facial internal resorption

periodontal ligament (PDL) space is intact. Acute dental inflammatory conditions eventually result in widening of this space and are clinically associated with pain, particularly on dental occlusion or percussing the tooth. With chronic dentally related periapical pathoses, pain may or may not be a symptom; however, there is generally a remodeling of the apical periodontal space with an apical radiolucency having walls that merge with the lamina dura. By way of comparison, normal anatomic landmarks are superimposed on the undisturbed PDL space. CBCT imaging clearly identifies anatomical structures associated with the periapical regions including the inferior alveolar canal, the mental foramen and nutrient canals in the mandible, and the incisive fossa and the maxillary sinus in the maxilla. The incisive fossa may contain the foramina of Stenson and Scarpa, adding additional uncertainty when these features are projected on the apices of the maxillary central incisors using intraoral periapical radiography.

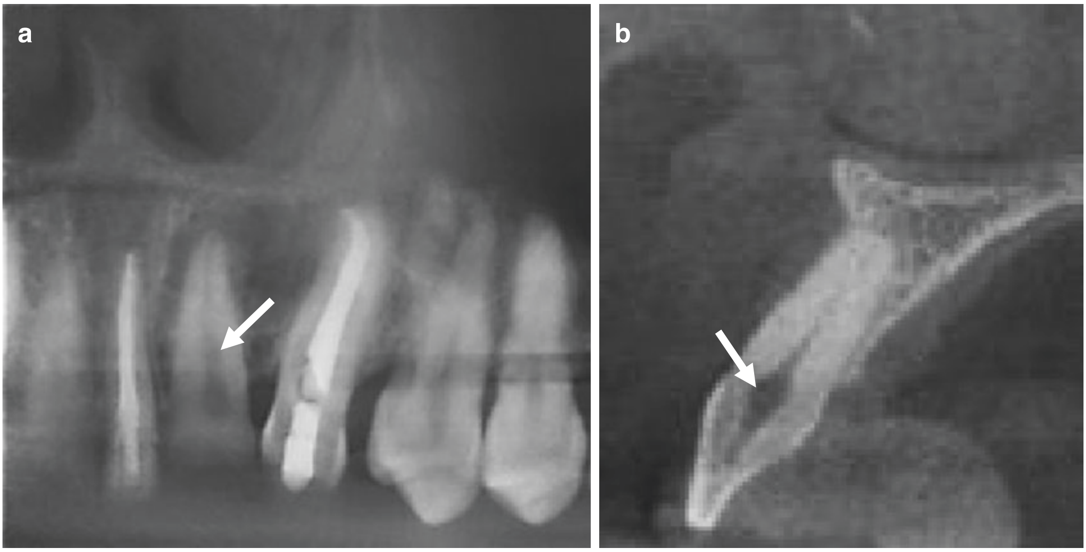

Fig. 22.28 Reformatted cropped panoramic (**a**) and cross-sectional (**b**) CBCT images of the left maxillary central incisor showing internal resorption

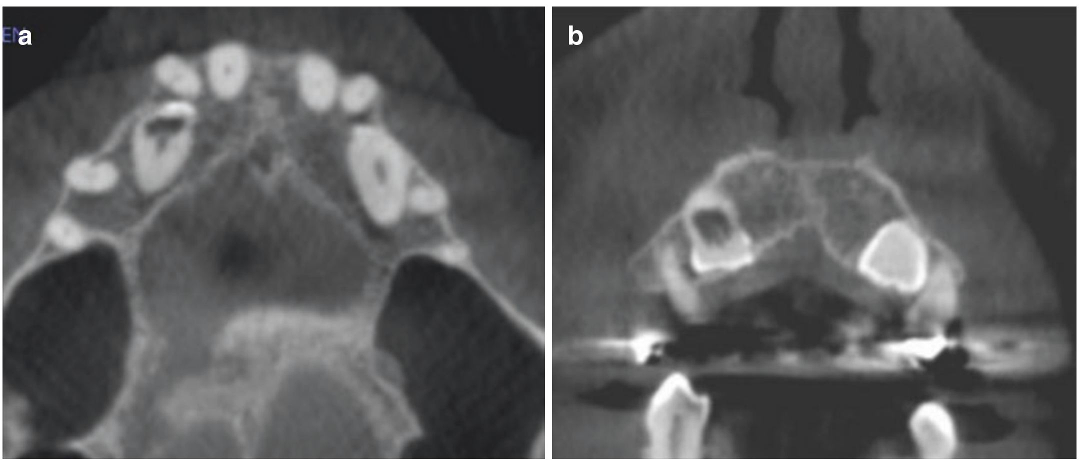

Fig. 22.29 Axial (**a**) and coronal (**b**) CBCT sectional images of the anterior maxilla showing a large internal resorptive lesion (IRR) on the impacted right lateral incisor

Anomalies

There are numerous anomalies of the tooth-bearing areas of the jaws, most of which present as a single separate hyperdensity, that may be superimposed on the root system of the teeth. CBCT can assist in the differentiation of these conditions from pathologic entities.

- *Exostosis*. An exostosis is a hyperplastic, localized, exophytic benign growth of cortical bone. It is self-limiting and consists of either compact or spongy type bone. They are important in endodontics as they may simulate the appearance of intraosseous conditions and complicate the provision of treatment or limit surgical access. Three variants exist:
  - *Torus Palatinus.* These are common single exostoses that develop along the midsagittal suture line of the posterior hard palate, and

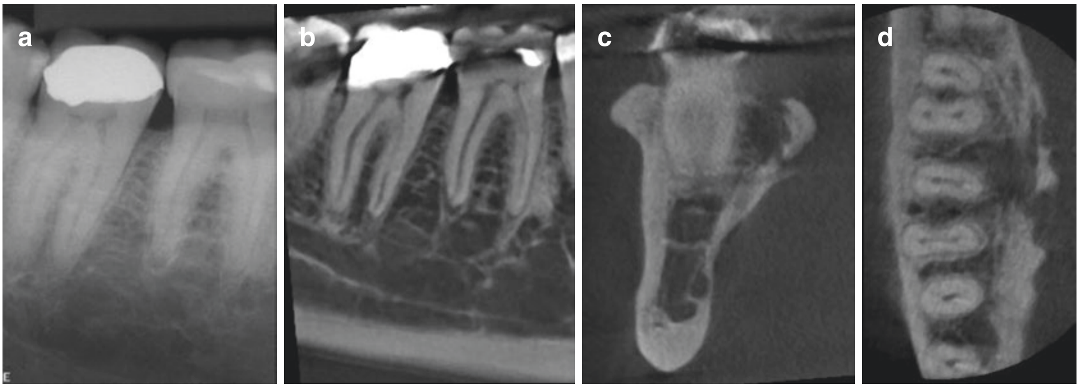

Fig. 22.30 Periapical intraoral image (**a**) and parasagittal (**b**), cross-sectional (**c**) and axial (**d**) CBCT images of a patient referred for evaluation due to discomfort in right mandibular area. Clinic examination and vitality testing were all normal with the exception of palpation tenderness on the lingual of molars. CBCT images demonstrate an area of low density on the lingual aspect of the distal root involving the lingual exostosis. Also note the buccal exostosis. Biopsy confirmed necrotic bone consistent with sequestra. The teeth have remained vital at the 2-year checkup

while usually round, may be flat, spindle-shaped, nodular or lobular in shape.

– *Mandibular Torus.* These occur on third as frequently as torus palatinus and present as bilateral exostoses on the lingual alveolar crestal surface, adjacent the mandibular premolars.
– *Alveolar Exostoses*. Other less common exostoses of the alveolar cortical plate include palatal (palatal aspect of the maxillary alveolus) or buccal (buccal alveolus of either jaw) (Fig. 22.30) (Jainkittivong and Langlais 2000; Horning et al. 2000).

- *Enostosis*. An enostosis is an intramedullary growth of compact bone or a mixture of compact and cancellous bone from the inner aspect of the facial and lingual cortical plates, often occurring in the mandibular canine and premolar area inferior to the apices of teeth. While radiographically indistinguishable from osteosclerosis, it may simulate other more aggressive conditions such as osteosarcoma.
- *Idiopathic Osteosclerosis*. This condition, also called focal periapical osteopetrosis or dense bone islands, is an infrequently occurring (range, 4.1–6.7% (Geist and Katz 1990; MacDonald-Jankowski 1999) localized intramedullary well-defined irregular hyperdensity located in the mandibular molar and premolar areas and usually associated with a tooth having a vital pulp. They may present radiographically as (Yonetsu et al. 1997):
  – *Enostosis (E type).* This present as a localized homogeneous thickening of either the buccal or lingual cortical bone in a particular area.
  – *Central sclerosis (CS type).* This may present as a solitary radiopacity in the medullary bone without attachment to the internal margin of the cortical bone. This type can be further divided into homogeneous and heterogeneous subtypes.
- *Impacted tooth elements*. Numerous entities in proximity to or superimposed on the roots of the dentition include impacted and submerged retained root fragments (deciduous or permanent), microdontic teeth or developing teeth (Fig. 22.31). Most present radiographically as a homogeneous hyperdensity with the shape of a tooth or root, a thin pericoronal or PDL space, and a central linear hypodensity suggestive of a root canal space.

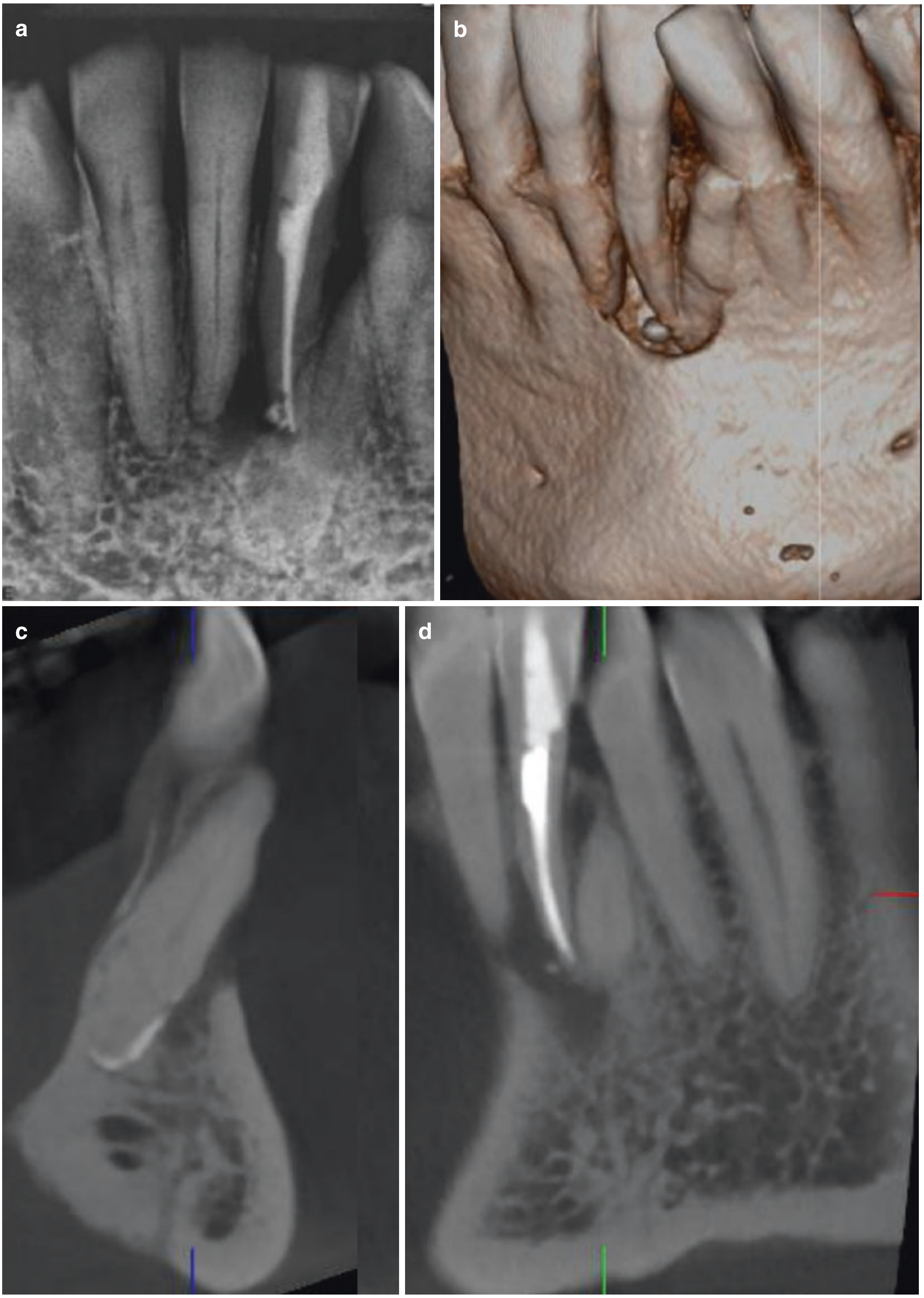

Fig. 22.31 Periapical image (**a**) of root-filled left mandibular central incisor with apical radiolucency and buccal cortical perforation involving a completely inverted and bony impacted canine. Volumetric rendering (**b**), cross-sectional (**c**), and coronal (**d**) CBCT images of the canine showing the loss of buccal cortical plate, lingual positioning of the crown and association with the apex of the central incisor

22.3.3.8 Tooth-Associated Pathology (Not Necessarily Odontogenic in Origin)

Various cysts and neoplasms can also be superimposed over the apices of teeth, and may result in resorption of the lamina dura and tooth roots (Table 22.3). CBCT can assist in differentiating these conditions from inflammatory conditions. In many instances the teeth concerned remain vital to pulp testing. Several conditions are relatively common, self-limiting, and require minimal intervention; however, consideration should always be given to those conditions that exhibit aggressive growth patterns or have a high recurrence rate. Radiographically, these conditions present as either radiolucencies (usually benign but locally destructive), mixed and radiopaque lesions (usually slow growing and benign) with either uni- or multilocular borders (Table 22.3).

22.3.3.9 Maxillary Sinus Disease

A detailed description of specific diseases of the maxillary sinus is presented in *Chap.* 29. As the roots of the posterior maxillary teeth may be intimately associated with the maxillary sinus, radiographic differentiation between conditions of intrinsic or extrinsic origin is important from an endodontic perspective.

Intrinsic Sinus Disease

Incidental mucosal thickenings are common imaging findings in asymptomatic individuals (range, 14.3–82%) (Harar et al. 2007; Kanagalingam et al. 2009; Vogiatzi et al. 2014). Radiographic patterns on CBCT imaging include:

- *Generalized polypoidal thickening*. Regular or irregular (polypoidal) soft tissue thickening (> 3 mm) with partial or complete coverage of the periphery of the maxillary sinus.
- *Localized polyps*. Localized soft tissue mass appearing as somewhat pedunculated polyps with a smooth outline usually originating from the roof or lateral walls of the maxillary sinus (Vogiatzi et al. 2014) (Fig. 22.35)This imaging appearance is similar for three (3) different entities: antral mucosal pseudocyst, mucous retention cyst (which occur near the ostium), and mucocele (complete opacification associated with peripheral bony erosion).
- *Rhinosinusitis*. Rhinosinusitis presents as partial or complete sinus soft tissue opacification with surface air locules and peripheral convexity (acute). It may also be associated with peripheral sclerosis and osteoblastic osteitis (linear calcifications adjacent the cortical border), both of which suggest chronic rhinosinusitis. Allergic rhinosinusitis often has generalized bilateral and adjacent mucosal (nasal) thickening.
- Fungal sinusitis, while uncommon, is of particular importance in endodontics. Based on the radiographic pattern of bone involvement and presence of central calcifications, fungal

Table 22.3 Examples of pathology associated with tooth apices, not necessarily odontogenic in origin.

Border	Radiolucent	Radiopaque	Radiomixed
Unilocular	• Nasopalatine canal duct cyst	• Odontoma (compound and complex)	• Focal COD (intermediate) (Fig. 22.34)
	• Lateral periodontal cyst (Botryoid odontogenic cyst)	• Focal cemento-osseous dysplasia (mature)	• Cementoblastoma
	• KOT (early) (Fig. 22.32)		• Osteoblastoma
	• Central giant cell granuloma (Fig. 22.33)		• Osteosarcoma
	• Aneurysmal bone cyst		
	• Traumatic bone cavity		
	• Focal COD (osteolytic)		
Multilocular	• Keratocystic odontogenic tumor	• Florid COD (mature)	• Florid COD (mature)
	• Ameloblastoma		
	• Central giant cell granuloma		
	• Odontogenic myxoma		

KOT keratocystic odontogenic tumor, *COD* cemento-osseous dysplasia

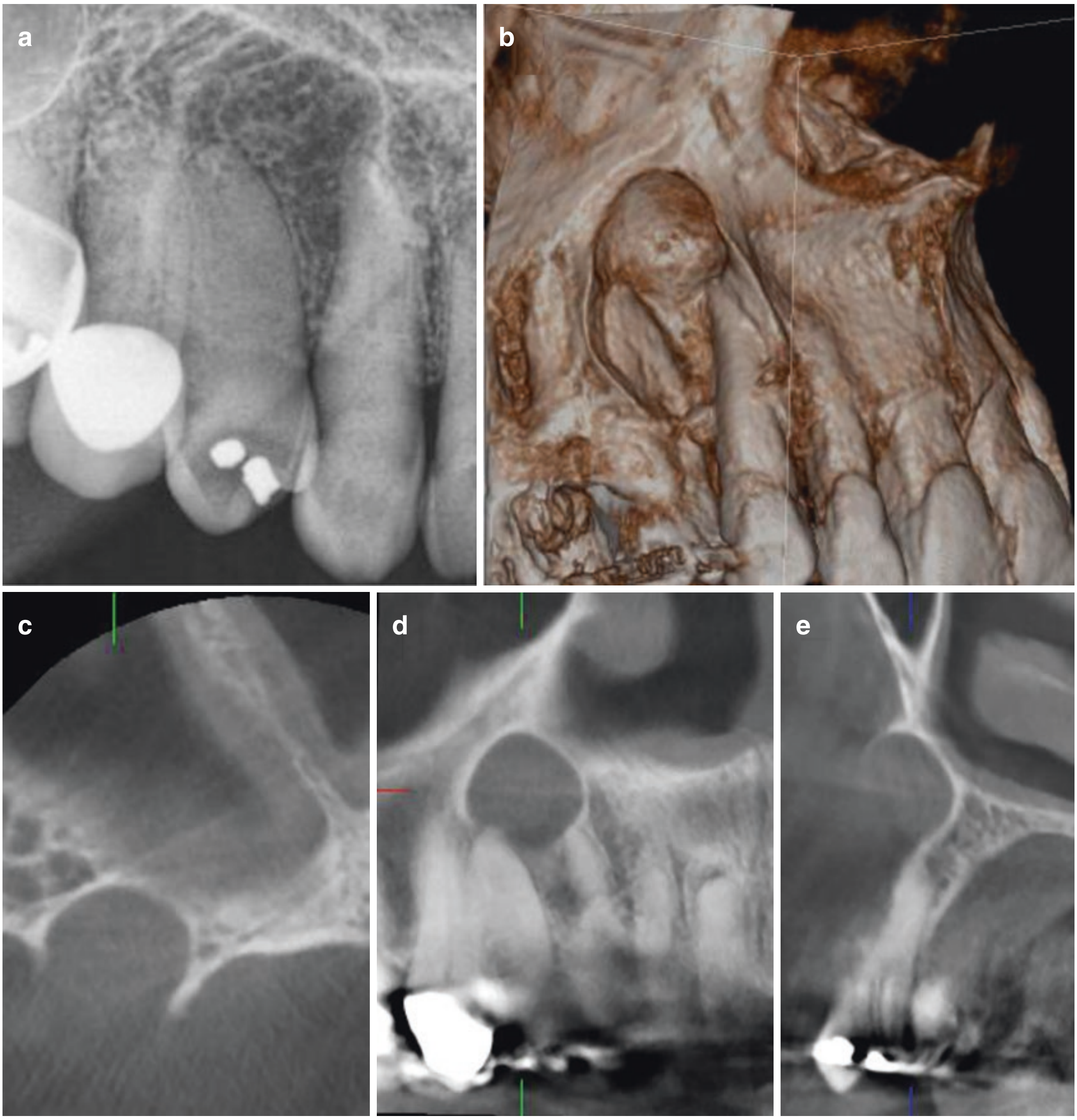

Fig. 22.32 Periapical image (**a**) of patient referred for evaluation of soft tissue swelling in the maxillary right canine area. Pulp testing was normal. Volumetric rendering (**b**), axial (**c**), parasagittal (**d**), and cross-sectional (**e**) CBCT images demonstrate a unilocular apical area of low density with buccal cortical perforation (radiographic sign of aggression) with no change in PDL space. Histopathology reveals a keratocystic odontogenic tumor. Entities in this region, with various histopathology, had previously been referred to as "globulomaxillary cyst"

sinusitis can be classified into two types (Aribandi et al. 2007):

- Noninvasive or *allergic fungal sinusitis*, usually presents with involvement of multiple sinuses, mimicking pansinusitis and associated rhinitis, with near-complete opacification. Peripheral bony expansion with erosion is an important imaging feature.
- Fungus ballor fungal mycetoma is an extramucosal fungal proliferation, mostly caused by *Aspergillus* spp., often involving the maxillary sinus (Pagella et al. 2007). Many patients present with a history of facial pain or rhinorrhea and a history of previous endodontic treatment. Aspergillosis of the maxillary sinus has been reported in association with

Fig. 22.33 Premolar (**a**) and molar (**b**) periapical images of an asymptomatic patient undergoing active orthodontic therapy referred for evaluation of the mandibular right quadrant. These images show a generalized area of rarefaction in the interradicular bone between the first molar and second premolar but no changes in the lamina dura. Pulp testing was within normal limits. Parasagittal (**c**), axial (**d**), and cross-sectional (**e**) CBCT images show a large, well-defined, non-corticated periapical area of low density with buccal cortical expansion, furcation involvement and thinning. Histopathology reported a central giant cell granuloma

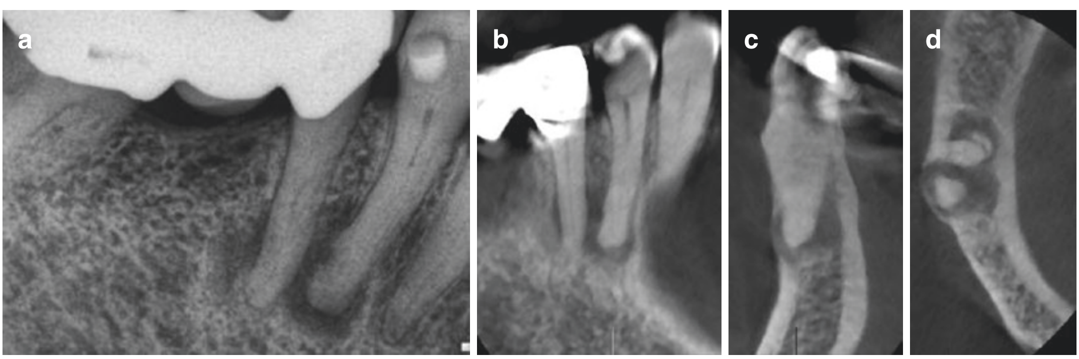

Fig. 22.34 Periapical image (**a**) of asymptomatic middle-aged African-American female referred for evaluation of mixed hyper- and hypodensity associated with the apices of both mandibular right premolars. Parasagittal (**b**), cross-sectional (**c**), and axial (**d**) images show associated buccal expansion without perforation of the cortical plate. Together with the history, the imaging appearance is most consistent with focal cemento-osseous dysplasia (intermediate)

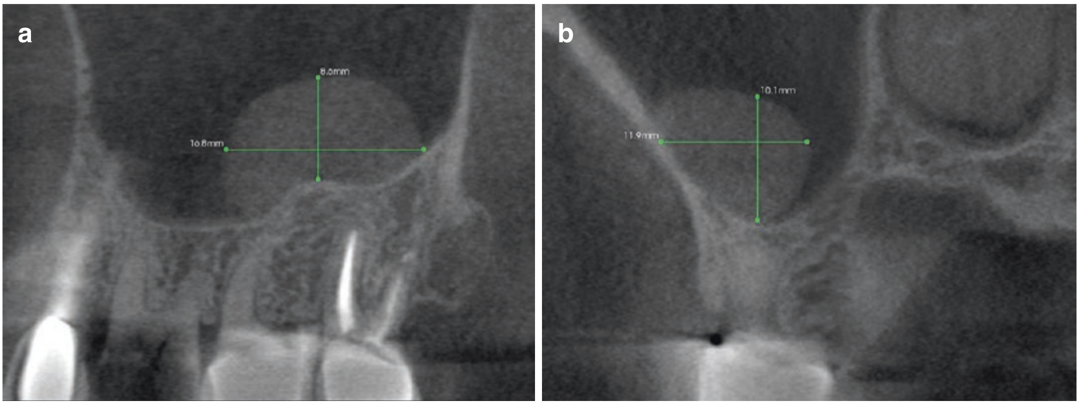

Fig. 22.35 Parasagittal (**a**) and cross-sectional (**b**) CBCT images showing typical homogeneous dome-shaped appearance of an antral mucosal pseudocyst. Unlike periapical mucositis, which is associated with a periapical lesion, antral mucosal pseudocysts do not disrupt the floor of the sinus nor expand superiorly from the apices of the roots of adjacent teeth

extrusion of root canal material with certain cements (Khongkhunthian and Reichart 2001; Giardino et al. 2006). There is almost total opacification of the sinus, with sclerosis and thickening or expansion and thinning with focal areas of erosion from pressure necrosis occurring in approximately 1/3rd of cases. The unique appearance of metallic or highly calcified central, punctate, hyperdense calcifications within an opacified sinus cavity is considered a characteristic finding.

Extrinsic Sinus Disease

Dental infection may often be a major predisposing factor in the development of maxillary sinusitis. This may be due to an oroantral fistula, secondary to periapical, periodontal or pericoronal disease or associated with endodontic treatment (Engström and Ericson 1964; Legert et al. 2004).

- *Endo-Antral Syndrome (EAS)* (Selden 1989, 1994, 1999). This results from the spread of pulpal disease beyond the apex into the maxillary sinus. CBCT clearly demonstrates the features of EAS (Angelopoulos 2008; Patel et al. 2007b; Shanbhag et al. 2013), which is characterized by one or more of the following:
  – Associated with a tooth having pulpal disease whose apices approximate the floor of the maxillary sinus.
  – The presence of a periapical radiolucency with the involved tooth (periapical osteoperiostitis).
  – Radiographic loss of the lamina dura at the inferior border of the maxillary sinus over the involved tooth.
  – *Periapical mucositis.* Localized reactive, relatively hyperdense soft tissue swelling and thickening of the sinus mucosa above the apex of a pulpally involved tooth. The apical lesion may displace periosteum resulting in a "halo" of thin peripheral layer of new bone (Bornstein et al. 2012; Vogiatzi et al. 2014) (Fig. 22.36).
  – *Maxillary sinusitis of dental origin (MSDO).* MSDO (Bauer 1943) has been reported to account for approximately 5–10% (Maloney and Doku 1968; Mehra and Murad 2004; Vogiatzi et al. 2014) and even more than 50% (Malliet et al. 2011; Lu et al. 2012) of all cases of sinusitis and presents as partial or complete opacification of the lumen of the maxillary sinus (Fig. 22.37).

Fig. 22.36 Periapical image (**a**) of a patient referred for endodontic evaluation of maxillary left first molar shows loss of lamina dura of the palatal root and possible sclerotic apical radiolucency concentrically located over the apex. Axial (**b**), parasagittal (**c**), and cross-sectional (**d**) CBCT images show palatal apical periodontitis with large cortical “halo” expanding superiorly into the lumen with concomitant periapical mucositis

Resolution of MSDO cannot occur until the identified tooth is endodontically treated or extracted. Currently, there is a lack of evidence to suggest that complete resolution of localized mucosal thickening will occur after extraction or endodontic treatment. Mucosal thickening may persist for more than 3 months postoperatively (Nurbakhsh et al. 2011; Yoo et al. 2011).

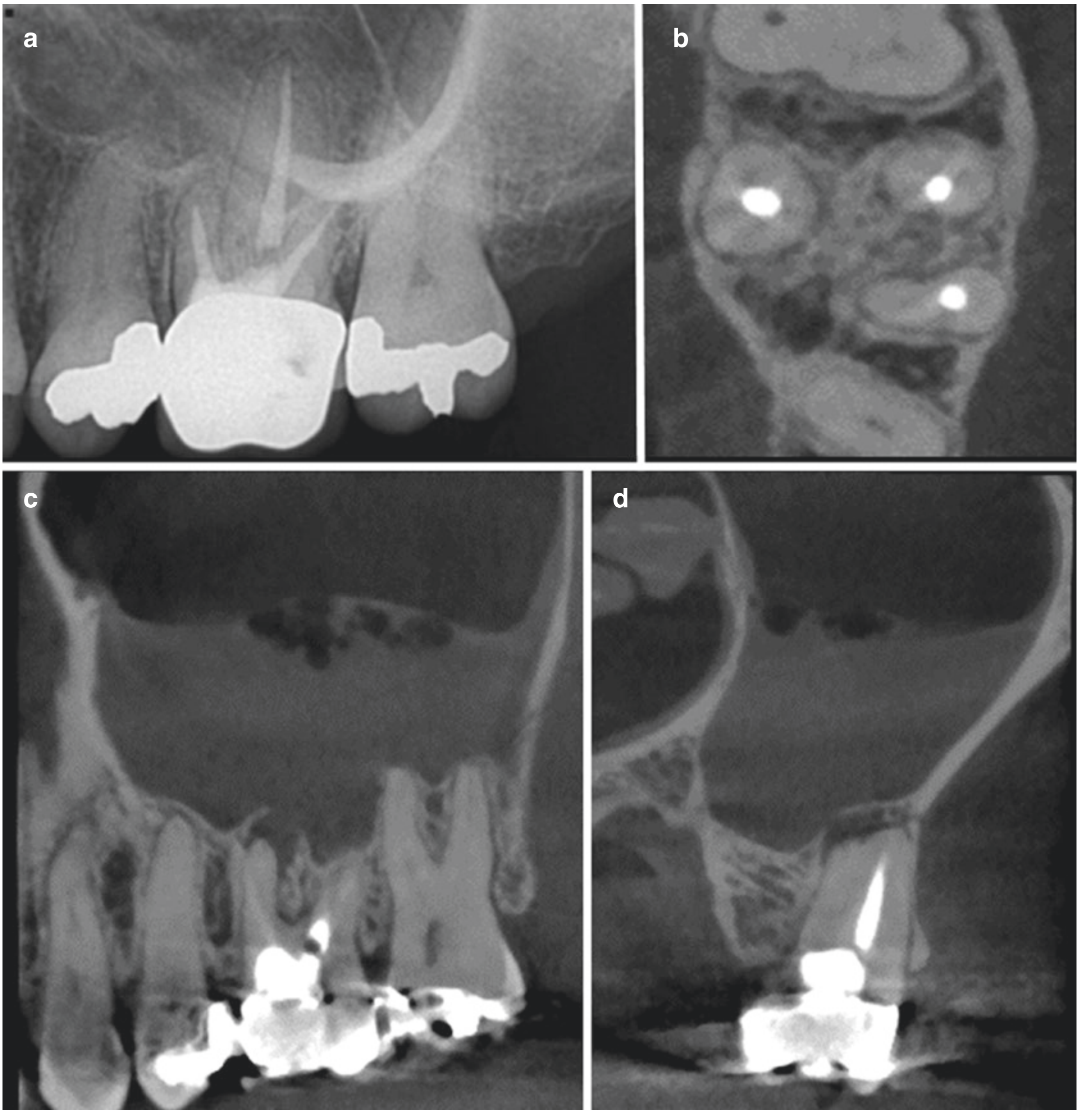

Fig. 22.37 Periapical image (**a**) of a patient with left maxillary pain shows partial elevation of the floor of the maxillary sinus and loss of lamina dura adjacent to the apex of the mesiobuccal root of the endodontically treated first molar. Axial (**b**), parasagittal (**c**), and cross-sectional (**d**) CBCT images show a periapical hypodensity associated with an untreated MB2. The lack of cortical integrity superior to the MB root and accompanying partial opacification with surface air locules is consistent with acute MSDO

22.3.4 Intraoperative Applications

Limited FOV CBCT may be useful in difficult cases requiring surgical or nonsurgical endodontic treatment and those presenting with intraoperative complications such as:

- *Location of calcified canals*. CBCT can assist in determining the extent of obstruction of calcified canals and by providing information on the location, angle, and depth to access the patent portion (Fig. 22.38). CBCT may also identify completely calcified canals that may not be accessible to nonsurgical treatment. Unnecessary removal of tooth structure, especially in the absence of apical pathosis, may be avoided and the risk of perforation reduced (Cohenca and Shemesh 2015).

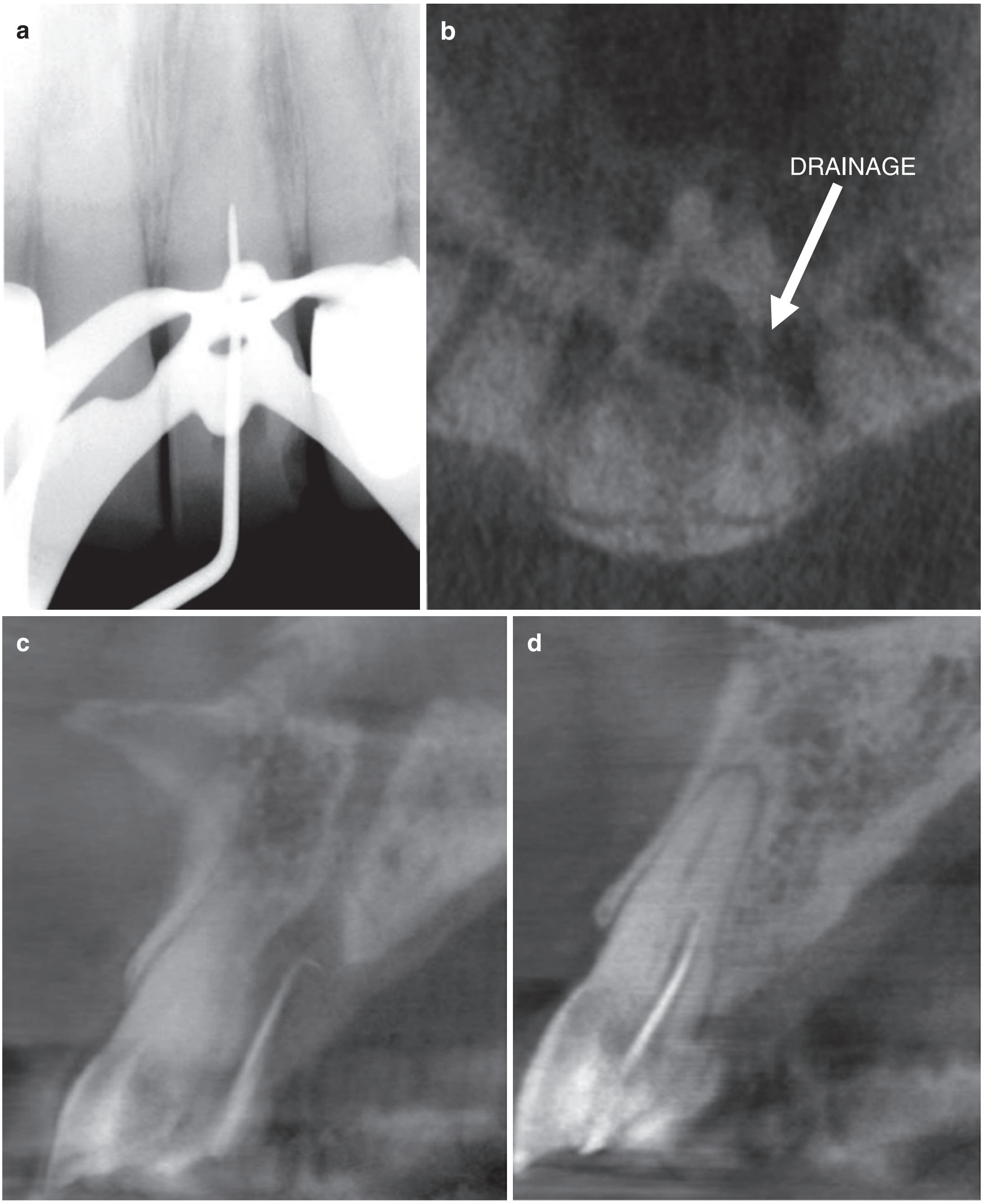

Fig. 22.38 Intraoperative periapical image (**a**) of a maxillary left central incisor with an instrument inserted into the root canal after initial mechanical preparation through a calcified obstruction in the mid third of the root. Axial (**b**) and cross-sectional (**c**) CBCT images with gutta percha placed in the palatal sinus tract shows involvement of the incisive canal. A cross-sectional CBCT image (**d**) with gutta percha inserted into the canal shows the mechanical preparation was directed palatally. The access was redirected facially, resulting in negotiation of the canal to the apex

- *Evaluation of unexpected anatomic findings*.
- *Identification of missed canals in endodontic retreatment*.
- *Evaluation of root resorption and root fractures*.
- *Assessment of possible iatrogenic errors such as perforation, fractured instruments, and extruded obturation materials* (Figs. 22.39 and 22.40).

The benefits of the additional diagnostic information provided by intraoperative CBCT in select cases justify the risk associated with the limited level of radiation exposure (Ball et al. 2013). The AAE and AAOMR (2015) state:

> If a preoperative CBCT has not been taken, limited FOV CBCT should be considered as the imaging modality of choice for intra-appointment identification and localization of calcified canals.

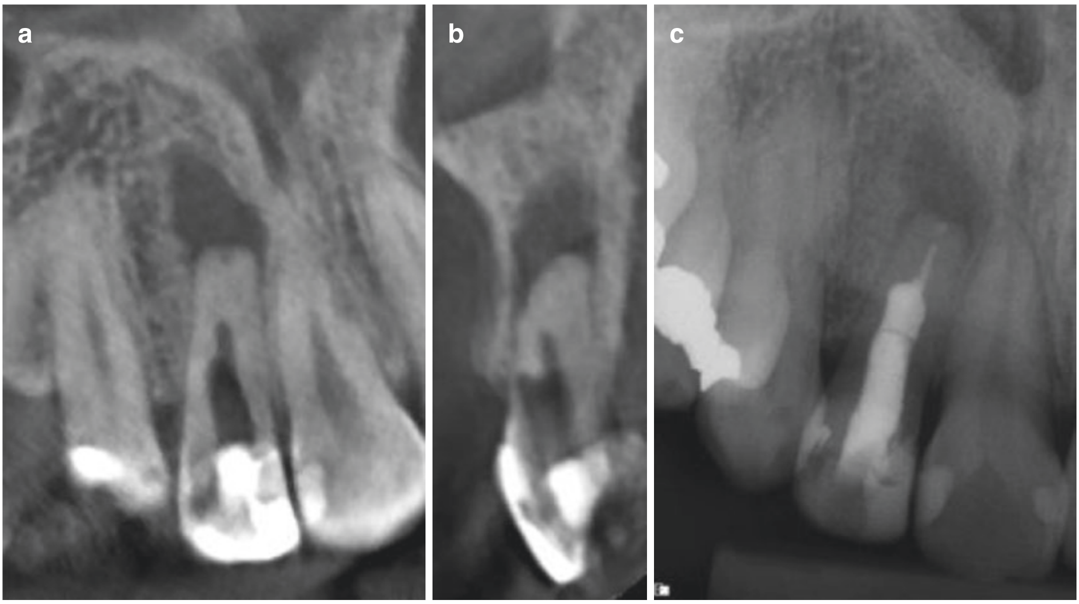

Fig. 22.39 Coronal CBCT image (**a**) of patient referred for completion of root canal treatment on maxillary right lateral incisor showing area of low density. Cross-sectional CBCT image (**b**) shows facial direction of initial access, however no perforation. Periapical image (**c**) shows completed root canal treatment

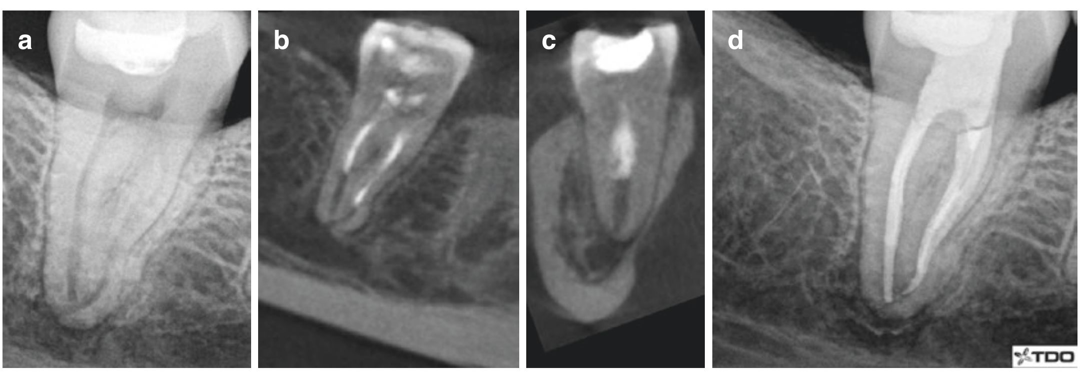

Fig. 22.40 Cropped periapical image (**a**) of a mandibular right second molar with moderately sized low density apical area in close approximation to the mandibular canal. Intraoperative parasagittal (**b**) and cross-sectional (**c**) CBCT images used after placement of calcium hydroxide to confirm containment within the canal. Periapical image (**d**) shows completed treatment with filling material confined to the canal

22.3.5 Postoperative Evaluation

The assessment of outcome is important in endodontics, especially in medically complex patients, such as patients with prosthetic heart valves, orthopedic prostheses, at risk of medication-related osteonecrosis of the jaw (MRONJ), or immunocompromised, to name a few. A favorable outcome for root canal treatment is dependent on appropriate diagnosis, effective instrumentation and disinfection, obturation of the root canal system, and subsequent coronal seal and restoration. Outcome measures have historically incorporated a strict combination of radiographic and clinical criteria to define "success" and "failure" (Strindberg 1956). The absence of clinical symptoms and apical lesions is an indicator of successful root canal treatment. Apical periodontitis is frequently asymptomatic and can often only be detected radiographically (Huumonen and Orstavik 2002).

The European Society of Endodontology (2006) defines a favorable outcome as the absence of pain, swelling, and other symptoms, no sinus tract, no loss of function, and radiological evidence of a normal periodontal ligament space around the root. As an alternative to the concepts implied by the terms "success" and "failure," the American Association of Endodontists (2012) has proposed the following terms:

- *Healed*: Functional, asymptomatic teeth with no or minimal radiographic periradicular pathosis (radiolucency).
- *Nonhealed*: Nonfunctional, symptomatic teeth with or without radiographic periradicular pathosis.
- *Healing*: Teeth with periradicular pathosis, which are asymptomatic and functional, or teeth with or without radiographic periradicular pathosis which are symptomatic but whose intended function is not altered.
- *Functional*: A treated tooth or root that is serving its intended purpose in the dentition.

Postoperative endodontic assessment should include clinical examination and intraoral periapical radiographic imaging immediately posttreatment and until complete healing is observed. The recommended timeframe for checkup examinations varies but follow-ups at regular intervals for a minimum observation period of one year is generally suggested (Orstavik 1996; Reit 1987; European Society of Endodontology 2006). Endodontic treatment options for teeth with persistent signs and symptoms following initial treatment include orthograde retreatment, endodontic microsurgery, and removal of the tooth with or without replacement.

While conventional intraoral radiography often provides adequate imaging for postoperative assessment, CBCT has a unique role in monitoring lesion resolution for certain cases, diagnosis and management of endodontic complications, imaging prior to periradicular surgery and for planning alternate treatments.

22.3.5.1 Outcome Assessment for Select Cases

Monitoring the resolution of apical lesions is an important aspect of postoperative assessment in endodontics (Figs. 22.41 and 22.42). The AAE and AAOMR (2015) indicate:

> Intraoral radiographs should be considered the imaging modality of choice for immediate postoperative imaging.

They are also used routinely to assess the outcome of endodontic treatment. However, interpretation of apical healing on periapical images has limitations and a great degree of variability. Preoperative factors such as the presence and true size of periapical lesions play an important role in determining endodontic treatment outcome. It is generally accepted that prevention of apical periodontitis is more predictable than the treatment of apical periodontitis. Success, when measured by radiographic criteria, is higher when teeth are endodontically treated before radiographic signs of periapical disease are detected (Friedman 2002). Therefore, radiographic identification of early periapical radiographic changes may result in earlier diagnosis and treatment and in faster or more complete healing (Patel et al. 2007b, 2009a). On average, apical lesions on periapical radiographs are at

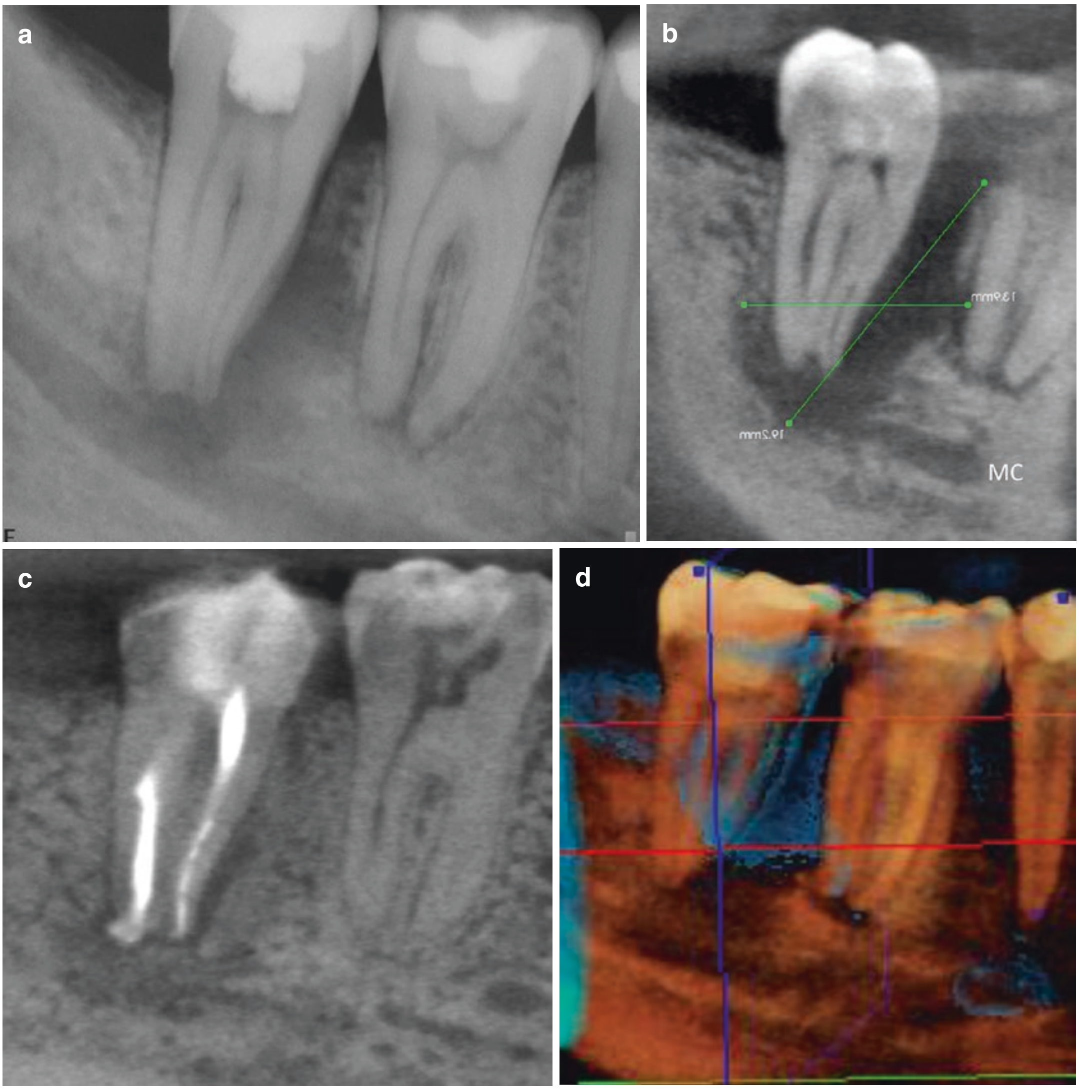

Fig. 22.41 Periapical image (**a**) of patient who presented with dysesthesia associated in the right posterior mandible showing a large apical and interradicular rarefaction adjacent to the mandibular canal (mc). Parasagittal (**b**) CBCT image confirms the extent and proximity of the lesion to the mc. Postoperative parasagittal (**c**) CBCT image and digital subtraction composite image (**d**) at 6 months shows bony healing (*blue*)

least 10% smaller on CBCT (Tsai et al. 2012; Estrela et al. 2008b; Christiansen et al. 2009; Peters and Peters 2012).

Periapical images may therefore result in an overestimation of favorable outcomes (Wu et al. 2009). The use of CBCT provides a more objective representation of dynamic osseous changes over time (Pinsky et al. 2006; Patel et al. 2007b, 2015; Kaya et al. 2012). However, outcome assessment may be complicated as some healthy teeth demonstrate a widened PDL space on CBCT (Pope et al. 2014). In addition, investigators have shown that healed rate for CBCT is much lower than for periapical images (Patel et al. 2012b).

Various indices and scales to assess outcomes with CBCT have been proposed (Estrela et al. 2008c; Venskutonis et al. 2015) including apical lesion area or volumetric analysis (Alhowalia et al. 2013; Van der Borden et al. 2013; Metska et al. 2013) which appear to provide reliable results. Other factors affecting treatment outcomes such as root canal length and radiodensity (Ng et al. 2008) can also be determined. Liang et al. (2011) found 80% of apparently short apical

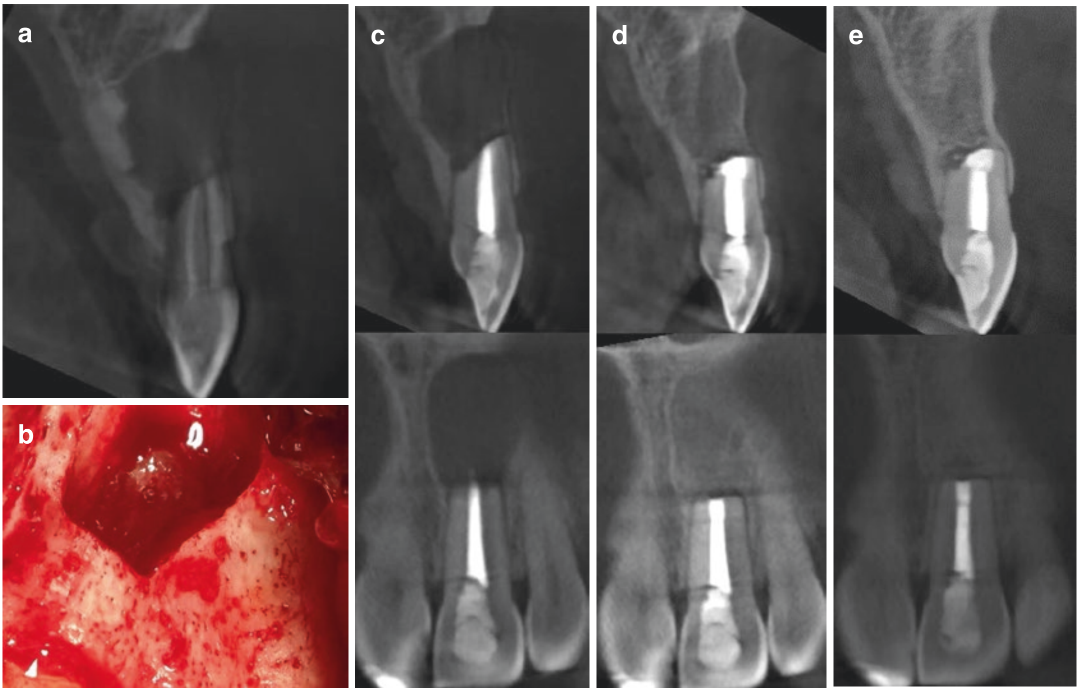

Fig. 22.42 Cross-sectional CBCT image (**a**) and surgical photograph (**b**) of a symptomatic patient showing a large periapical lesion associated with an endodontically treated maxillary left central incisor. After apical microsurgery with bone graft, cross-sectional and parasagittal CBCT images immediately postoperative (**c**), 6 months and 3.5 years (**d**) after surgery show excellent healing

treatments on intraoral radiographs correspond to the apical terminus on CBCT images. In addition, they found CBCT identified the presence of voids in almost 3× as many teeth as periapical images. CBCT will likely become more important for assessing the dynamics of periapical disease; however, currently studies are limited (Cohenca and Shemesh 2015).

22.3.5.2 Complications Associated with Endodontically Treated Teeth

Vertical Root Fracture (VRF)

VRF is a longitudinal fracture of an endodontically treated tooth root that develops over time due to predisposing and/or iatrogenic factors (Tamse 2006; Kishen 2006). Associated variable signs, symptoms, and radiographic findings can make diagnosis difficult.

VRF usually initiate apically but may develop at variable locations along the root and propagate either apically or coronally. VRFs originate from the root canal wall and expand laterally, often occurring in the faciolingual or faciopalatal plane. Fractures may be either incomplete (involving one side of the root) or complete (both root surfaces). Complete fractures are typically more easily detected as root segments separate. Incomplete fractures are more difficult to detect because they are often not visible until further progression (American Association of Endodontists 2008). Traditionally, the diagnosis of VRF is based on both clinical examination and periapical radiographic interpretation (Table 22.4) (Fig. 22.43) and largely empirical, without evidence-based data (Tsesis et al. 2010). An exploratory flap surgery may be necessary to confirm and directly visualize a VRF (Meister et al. 1980). While any root-filled tooth may present with a VRF, the most common are the maxillary and mandibular premolars and the mesial roots of mandibular molars (Tamse 2006).

It is important to differentiate a VRF from similar conditions such as endodontic disease (sinus tract draining through the gingival sulcus) or a localized periodontal defect, since the treatment and prognosis may be very different (Cohen

Table 22.4 Common clinical and radiographic findings associated with vertical root fractures (Testori et al. 1993; Nicopoulou-Karayianni et al. 1997; Tamse et al. 1999a, b, 2006; Fayad et al. 2012)

Clinical	Imaging	
	pa	CBCT
• Isolated deep periodontal probing defect	• "Halo or J-shaped" periapical and perilateral radiolucency around the root	• Loss of bone in the mid-root area with intact bone coronal and apical to the defect (mid-root fracture)
• Crestally located sinus tract(s)	• Lateral periodontal radiolucency alongside the root	• Absence/loss of the entire buccal plate
• Root-filled tooth	• Angular radiolucency from the crestal bone that terminate along the side of the root	• Periradicular radiolucency at the terminus of a post (mid apical root fracture)
		• Radiolucency between the cortical plates and the root surface

pa intraoral periapical radiography, *CBCT* cone beam computed tomography

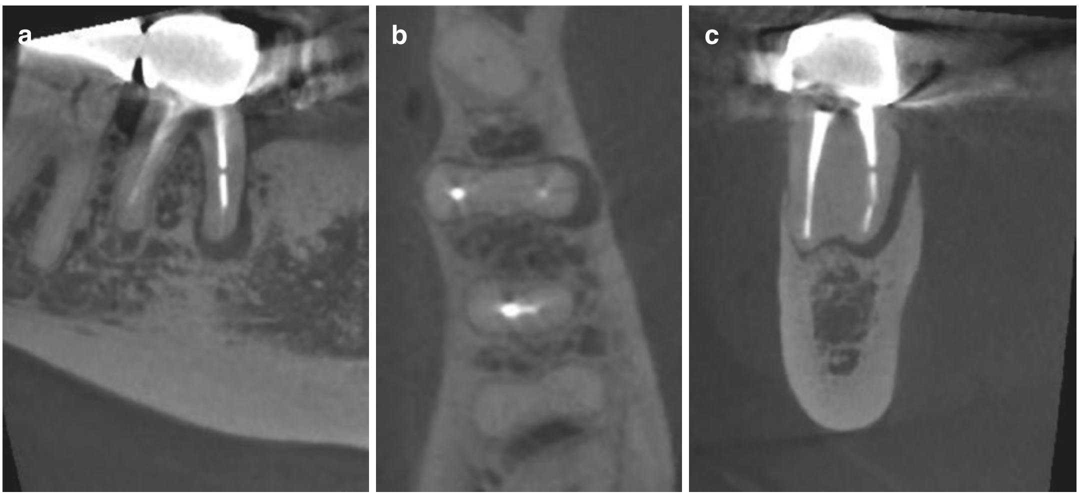

Fig. 22.43 Parasagittal (**a**), axial (**b**), and cross-sectional (**c**) CBCT images of right mandibular molar demonstrating multiple radiographic features consistent with incomplete VRF of the mesial root (confirmed after extraction)

et al. 2003). Early diagnosis and treatment is critical, since VRF can have a rapid and extensive effect on the surrounding periodontium and osseous bone (Walton et al. 1984).

Numerous ex vivo (in vitro) experiments (Hassan et al. 2009, 2010; Melo et al. 2010; Ozer 2011; da Silveira et al. 2013; Patel et al. 2013; Brady et al. 2014; Junqueira et al. 2013; Jakobson et al. 2014), clinical (in vivo) studies (Edlund et al. 2011; Wang et al. 2011; Metska et al. 2012), and case series (Bernardes et al. 2009) have compared the efficiency of CBCT and intraoral radiography for the detection of VRFs. These studies indicate that CBCT has similar specificity (the ability to detect the absence of VRF) but higher sensitivity (the ability to detect confirmed VRF) than periapical radiography, particularly when a voxel size smaller than 0.2 mm is used (Ozer 2011; Corbella et al. 2014). In addition, CBCT with smaller fields of view have higher accuracy and sensitivity for detecting VRF than larger fields of view (Bechara et al. 2013). The type of CBCT scanner may also affect the reproducibility and accuracy of VRF detection (Hassan et al. 2010; Metska et al. 2012).

The presence of radiopaque obturation materials and/or posts in the root canals of endodontically treated teeth may cause radiographic artifacts such as beam hardening and streak artifacts that can interfere with the definitive identification of a fracture (Junqueira et al. 2013;

Corbella et al. 2014; Jakobson et al. 2014; Neves et al. 2014). In these situations, removal of canal materials may potentially enhance the detection of VRFs (Ball et al. 2013).

Despite the limitations of CBCT, it can be a valuable adjunct for the diagnosis of VRF (Patel et al. 2015; Corbella et al. 2014; Chavda et al. 2014; Chang et al. 2016). The usefulness of CBCT may be more likely related to specific changes in the periradicular bone patterns associated with an undetected VRF than in the actual visualization of the fracture in the root structure. The authors of a recent meta-analysis of the role of CBCT in the diagnosis of VRF stated that CBCT scans showed better sensitivity and specificity than periapical radiography in unfilled teeth, especially when with a voxel size of 0.2 mm. CBCT showed low pooled sensitivity in detecting VRF in root-filled teeth (Talwar et al. 2016). In regard to the use of CBCT for VRF, the AAE and AAOMR (2015) state:

> Limited FOV CBCT should be considered the imaging modality of choice if clinical examination and 2-D intraoral radiography are inconclusive in the detection of VRF.

Further research is needed to investigate the effect of changes in periradicular bone patterns, the experience of observers, the resolution of the CBCT images, and image interval thickness in the radiographic diagnosis of VRF (Cohenca and Shemesh 2015).

Perforation

Iatrogenic root perforations are complications that may occur during endodontic treatment (Fig. 22.44) or subsequent post preparation or pin

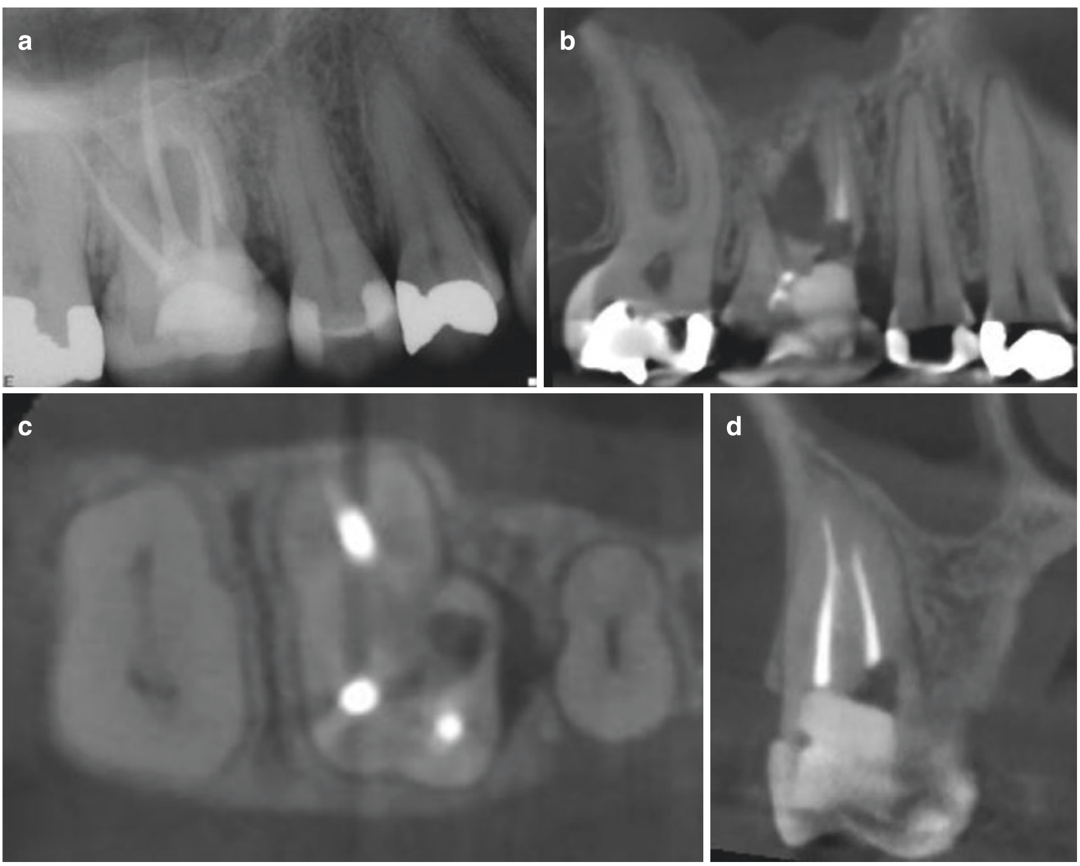

Fig. 22.44 Periapical image (**a**) of endodontically treated maxillary right first molar with intermittent symptoms. Sagittal (**b**), axial (**c**), and cross-sectional (**d**) CBCT images demonstrate furcal perforation due to misguided access during attempt to negotiate the MB2 canal and mesial vertical marginal alveolar defect. The patient opted for extraction and symptoms resolved

insertion (Fig. 22.45). Treatment involves immediate sealing of the perforation and prevention of infection using nonsurgical, surgical, or a combination of approaches. Prognosis depends on the time of occurrence, size, location, and material used to repair the perforation (Fuss and Trope 1996; Siew et al. 2015).

Radiographic detection of perforations involving the labial or lingual root surface is challenging, even using a tube shift technique (Goerig and Neaverth 1987). CBCT may facilitate in the determination of the nature of a perforation, prognosis, and subsequent treatment (Young 2007; Shemesh et al. 2011; Kamburoğlu et al. 2015). Dynamic visualization by axial image scrolling or "map reading" (Bueno et al. 2011) may provide an optimal interpretation strategy.

In regard to detection of endodontic complications, the AAE and AAOMR (2015) state:

> Limited FOV CBCT should be the imaging modality of choice for nonsurgical retreatment to assess endodontic treatment complications, such as overextended root canal obturation material, separated endodontic instruments, and localization of perforations.

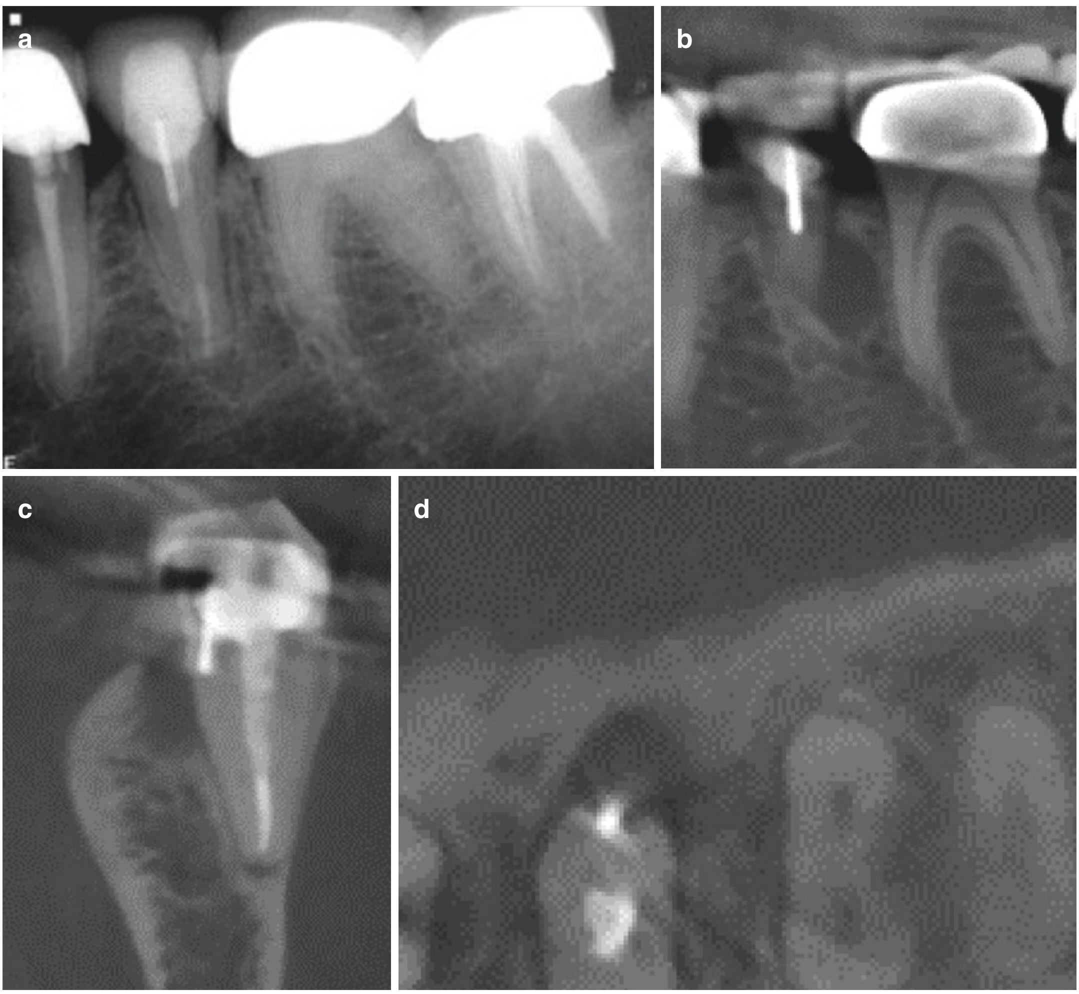

Fig. 22.45 Periapical image (**a**) of a patient who presents with a low-grade ache and mild tenderness to percussion associated with the left second mandibular premolar. Sagittal (**b**), cross-sectional (**c**), and axial (**d**) CBCT images demonstrate an area of low density lingually and perforation of a restorative pin

22.3.5.3 Endodontic Retreatment Options: Nonsurgical and Surgical

Despite endodontic retention rates up to 97% (Salehrabi and Rotstein 2004; Chen et al. 2007; Lazarski et al. 2001; Ng et al. 2010; de Chevigny et al. 2008), some root-filled teeth may require additional procedures to address residual post-treatment apical periodontitis. The AAE and AAOMR (2015) state:

> Limited FOV CBCT should be the imaging modality of choice when evaluating the nonhealing of previous endodontic treatment to help determine the need for further treatment, such as nonsurgical, surgical or extraction.

Causes for residual AP include additional canal(s), variations in canal morphology, poor obturation, incorrect position of intracanal post, perforations, resorptions, and size and location of apical lesion (Cohenca and Shemesh 2015). Nonsurgical retreatment is often the first choice if the etiology can be addressed (Gorni and Gagliani 2004) with selective root retreatment (Nudera 2015) proposed as a conservative option.

Endodontic microsurgery has evolved to provide a predictable option to retain diseased teeth (Niemczyk 2010; Setzer et al. 2010; Torabinejad et al. 2015). In regard to surgical planning for microsurgery, the AAE and AAOMR (2015) state:

> Limited FOV CBCT should be considered as the imaging modality of choice for presurgical treatment planning to localize root apex/apices and to evaluate the proximity to adjacent anatomical structures.

In this regard, CBCT imaging should involve assessment of the following (Tsurumachi and Honda 2007; Mao and Neelakantan 2014):

- Positional relationship of root apices and periapical lesions with critical vital anatomical structures such as the mandibular canal (Kim et al. 2010; Kovisto et al. 2011; Bornstein et al. 2011), mental foramen (von Arx et al. 2013; Carruth et al. 2015), and the maxillary sinus (Rigolone et al. 2003; Low et al. 2008; Bornstein et al. 2012; Kurt et al. 2014).
- Thickness and architecture of the cortical plate and the cancellous bone.
- Inclination of roots.
- Root canal morphology.
- Untreated root canals.
- Cracks and fractures.
- Location and extent of periapical pathoses (Nakata et al. 2006; Patel et al. 2012a).

22.3.5.4 Dental Implant Therapy

The predictability of dental implant therapy has had profound effects on endodontic, periodontal, and prosthodontic treatment planning for the rehabilitation of edentulous spaces and for teeth with an unfavorable prognosis. With appropriate usage and case selection, implant dentistry provides a viable option for the replacement of missing teeth (American Association of Endodontists 2015; Iqbal and Kim 2007). Radiographic examination, particularly cross-sectional imaging, is crucial for the assessment of available bone volume (Tyndall and Kohltfarber 2012). Limited FOV CBCT should be considered as the imaging modality of choice for surgical placement of implants (AAOMR/AAE 2015).

Conclusion

Radiography is an essential imaging adjunct for diagnosis, treatment planning, management and follow-up assessment of pulpal and periradicular disease. CBCT imaging overcomes many of the limitations of intraoral radiography, offering significant benefits in all phases of endodontic therapy in many clinical situations. With judicious use, CBCT influences how clinicians diagnose, treatment plan, and treat patients. Future CBCT research should be directed towards improvements in diagnostic capabilities and assessment of clinical efficacy towards more predictable management of patients with endodontic disease.

Acknowledgments The authors wish to thank Dr. Scott Hetz, Dr. William Nudera, Dr. David Landwehr, Dr. Michael Ribera and all partners at Metropolitan Endodontics (Eden Prairie, Inver Grove Heights, Woodbury and Burnsville, Minnesota USA) for their support in the development of this chapter.

References

Abella F, Mercadé M, Duran-Sindreu F, Roig M (2011) Managing severe curvature of radix entomolaris: three-dimensional analysis with cone beam computed tomography. Int Endod J 44:876–885

Abella F, Patel S, Duran-Sindreu F, Mercad M, Bueno R, Roig M (2012) Evaluating the periapical status of teeth with irreversible pulpitis by using cone-beam computed tomography scanning and periapical radiographs. J Endod 38:1588–1591

Abella F, Patel S, Durán-Sindreu F, Mercadé M, Bueno R, Roig M (2014) An evaluation of the periapical status of teeth with necrotic pulps using periapical radiography and cone-beam computed tomography. Int Endod J 47:387–396

Abella F, Teixidó LM, Patel S, Sosa F, Duran-Sindreu F, Roig M (2015) Cone-beam computed tomography analysis of the root canal morphology of maxillary first and second premolars in a Spanish population. J Endod 41:1241–1247

Ahlowalia MS, Patel S, Anwar HM, Cama G, Austin RS, Wilson R, Mannocci F (2013) Accuracy of CBCT for volumetric measurement of simulated periapical lesions. Int Endod J 46:538–546

American Association of Endodontists (2008) Colleagues for Excellence. Cracking the cracked tooth code: detection and treatment of various longitudinal fractures

American Association of Endodontists (2011) Colleagues for Excellence. Cone beam-computed tomography in endodontics

American Association of Endodontists (2012) Glossary of endodontic terms. American Association of Endodontists, Chicago

American Association of Endodontists (2015) Colleagues for Excellence. Treatment planning: retention of the natural dentition and the replacement of missing teeth

American Association of Endodontists; American Academy of Oral and Maxillofacial Radiology (2011) Use of cone-beam computed tomography in endodontics joint position statement of the American Association of Endodontists and the American Academy of oral and maxillofacial radiology. Oral Surg Oral Med Oral Pathol Oral Radiol Endod 111:234–237

American Association of Endodontists; American Academy of Oral and Maxillofacial Radiology (2015) Use of cone-beam computed tomography in endodontics 2015 update AAE and AAOMR joint position statement. J Endod 41:1393–1396

Andreasen JO (1985) External root resorption: its implications in dental traumatology, paedodontics, periodontics, orthodontics and endodontics. Int J Endod 8:109–118

Andreasen J (1989) Prognosis of root-fractured permanent incisors: prediction of healing modalities. Endod Dent Traumatol 5:11–22

Andreasen JO, Andreasen FM (1994) Classification, etiology and epidemiology. In: Andreasen JO, Andreasen FM (eds) Textbook and color atlas of traumatic injuries to the teeth, 3rd edn. Munksgaard, Copenhagen, pp 151–216

Andreasen FM, Vestergaard Pedersen B (1985) Prognosis of luxated permanent teeth—the development of pulp necrosis. Endod Dent Traumatol 1:207–220

Andreasen JO, Borum MK, Jacobsen HL, Andreasen FM (1995) Replantation of 400 avulsed permanent incisors. 4. Factors related to periodontal ligament healing. Endod Dent Traumatol 11:76–89

Andreasen FM, Andreasen JO, Cvek M (2007) Root fractures. In: Andreasen JO, Andreasen FM, Andersson L (eds) Textbook and color atlas of traumatic injuries to the teeth. Munksgaard, Kopenhagen, Denmark, pp 337–371

Angelopoulos C (2008) Cone beam tomographic imaging anatomy of the maxillofacial region. Dent Clin N Am 52:731–752

Aribandi M, McCoy VA, Bazan C III (2007) Imaging features of invasive and noninvasive fungal sinusitis: a review. Radiographics 27:1283–1296

Bakland LK, Andreasen JO (2004) Dental traumatology: essential diagnosis and treatment planning. Endod Topics 7:14–34

Ball RL, Barbizam JV, Cohenca N (2013) Intraoperative endodontic applications of cone-beam computed tomography. J Endod 39:548–557

Baratto Filho F, Zaitter S, Haragushiku GA, de Campos EA, Abuabara A, Correr GM (2009) Analysis of the internal anatomy of maxillary first molars by using different methods. J Endod 35(3):337–342

Barbat J, Messer HH (1998) Detectability of artificial periapical lesions using direct digital and conventional radiography. J Endod 24:837–842

Barthel CR, Zimmer S, Trope M (2004) Relationship of radiologic and histologic signs of inflammation in human root-filled teeth. J Endod 30:75–79

Basrani B (2012) Radiographic considerations during the endodontic treatment. In: Basrani B (ed) Endodontic radiology. Wiley, Ames, Iowa, pp 193–217

Bauer WH (1943) Maxillary sinus of dental origin. Am J Orthod Oral Surg 29:133–151

Bauman R, Scarfe W, Clark S, Morelli J, Scheetz J, Farman A (2011) Ex vivo detection of mesiobuccal canals in maxillary molars using CBCT at four different isotropic voxel dimensions. Int Endod J 44:752–758

Bechara B, McMahan CA, Noujeim M, Faddoul T, Moore WS, Teixeira FB, Geha H (2013) Comparison of cone beam CT scans with enhanced photostimulated phosphor plate images in the detection of root fracture of endodontically treated teeth. Dentomaxillofac Radiol 42:20120404

Bender IB (1982) Factors influencing the radiographic appearance of bony lesions. J Endod 8:161–170

Bender IB, Seltzer S (1961a) Roentgenographic and direct observation of experimental lesions in bone. Part 1. J Am Dent Assoc 62:152–160

Bender IB, Seltzer S (1961b) Roentgenographic and direct observation of experimental lesions in bone. Part 2. J Am Dent Assoc 62:708–716

Bernardes RA, de Moraes IG, Duarte MA, Azevedo BC, de Azevedo JR, Bramante CM (2009) Use of cone-beam volumetric tomography in the diagnosis of root fractures. Oral Surg Oral Med Oral Pathol Oral Radiol Endod 108:270–277

Bernardes RA, de Paulo RS, Pereira LO, Duarte MA, Ordinola-Zapata R, de Azevedo JR (2012) Comparative study of cone beam computed tomography and intraoral periapical radiographs in diagnosis of lingual-simulated external root resorptions. Dental Traumatol 28:268–272

Bhaskar SN (1968) Oral pathology in the dental office: survey of 20,575 biopsy specimens. J Am Dent Assoc 76:761–766

Blattner TC, Goerge N, Lee CC, Kumar V, Yelton CDJ (2010) Efficacy of CBCT as a modality to accurately identify the presence of second mesiobuccal canals in maxillary first and second molars: a pilot study. J Endod 36:867–870

Borges AH, Mamede-Neto I, Volpato LE, Pedro FL, Bueno MR, Estrela C (2014) Using cone beam computed tomography images to diagnose multiple taurodontisms. Gen Dent 62:20–22

Bornstein MM, Wölner-Hanssen AB, Sendi P, von Arx T (2009) Comparison of intraoral radiography and limited cone beam computed tomography for the assessment of root-fractured permanent teeth. Dent Traumatol 25:571–577

Bornstein MM, Lauber R, Sendi P, von Arx T (2011) Comparison of periapical radiography and limited cone-beam computed tomography in mandibular molars for analysis of anatomical landmarks before apical surgery. J Endod 37:151–157

Bornstein MM, Wasmer J, Sendi P, Janner SF, Buser D, von Arx T (2012) Characteristics and dimensions of the Schneiderian membrane and apical bone in maxillary molars referred for apical surgery: a comparative radiographic analysis using limited cone beam computed tomography. J Endod 38:51–57

Brady E, Mannocci F, Brown J, Wilson R, Patel S (2014) A comparison of cone beam computed tomography and periapical radiography for the detection of vertical root fractures in nonendodontically treated teeth. Int Endod J 47:735–746

Brynolf I (1970) Roentgenologic periapical diagnosis. II. One, two or more roentgenograms? Sven Tandlak Tidskr 63:345–350

Bueno MR, Estrela C, Figueiredo JAP, Azevedo BC (2011) Map-reading strategy to diagnose root perforations near metallic intracanal posts by using cone beam computed tomography. J Endod 37:85–90

Buhrley LJ, Barrows MJ, BeGole EA, Wenckus CS (2002) Effect of magnification on locating the MB2 canal in maxillary molars. J Endod 28:324–327

Calişkan MK, Türkün M (1997) Prognosis of permanent teeth with internal resorption: a clinical review. Endod Dent Traumatol 13:75–81

Capar ID, Ertas H, Arslan H, Tarim Ertas E (2015) A retrospective comparative study of cone-beam computed tomography versus rendered panoramic images in identifying the presence, types, and characteristics of dens invaginatus in a Turkish population. J Endod 41:473–478

Chang E, Lam E, Shah P, Azarpazhooh A (2016) Cone-beam computed tomography for detecting vertical root fractures in Endodontically treated teeth: a systematic review. J Endod 42(2):177–189

Chavda R, Mannocci F, Andiappan M, Patel S (2014) Comparing the in vivo diagnostic accuracy of digital periapical radiography with cone-beam computed tomography for the detection of vertical root fracture. J Endod 40:1524–1529

Chen SC, Chueh LH, Hsiao CK et al (2007) An epidemiologic study of tooth retention after nonsurgical endodontic treatment in a large population in Taiwan. J Endod 33:226–229

Christiansen R, Kirkevang L-L, Gotfredsen E, Wenzel A (2009) Periapical radiography and cone beam computed tomography for assessment of the periapical bone defect 1 week and 12 months after root-end resection. Dentomaxillofac Radiol 38:531–536

Cleghorn BM, Christie WH, Dong CC (2006) Root and root canal morphology of the human permanent maxillary first molar: a literature review. J Endod 32:813–821

Cohen S, Blanco L, Berman L (2003) Vertical root fractures—clinical and radiographic diagnosis. J Am Dent Assoc 134:434–441

Cohenca N, Shemesh H (2015) Clinical applications of cone beam computed tomography in endodontics: a comprehensive review. Quintessence Int 46:465–480

Cohenca N, Simon JH, Roges R, Morag Y, Malfaz JM (2007a) Clinical indications for digital imaging in dento-alveolar trauma. Part 1: traumatic injuries. Dental Traumatol 23:95–104

Cohenca N, Simon JH, Mathur A, Malfaz JM (2007b) Clinical indications for digital imaging in dento-alveolar trauma. Part 2: root resorption. Dent Traumatol 23:105–113

Corbella S, Del Fabbro M, Tamse A, Rosen E, Tsesis I, Taschieri S (2014) Cone beam computed tomography for the diagnosis of vertical root fractures: a systematic review of the literature and meta-analysis. Oral Surg Oral Med Oral Pathol Oral Radiol 118:593–602

Cotton TP, Geisler TM, Holden DT, Schwartz SA, Schindler WG (2007) Endodontic applications of cone-beam volumetric tomography. J Endod 33:1121–1132

Cvek M, Andreasen JO, Borum MK (2001) Healing of 208 intra-alveolar root fractures in patients aged 7-17 years. Dent Traumatol 17:53–62

Cvek M, Tsilingaridis G, Andreasen JO (2008) Survival of 534 incisors after intra-alveolar root fracture in patients aged 7–17 years. Dent Traumatol 24:379–387

D'Addazio PS, Campos CN, Ozcan M, Teixeira HGC, Passoni RM, Carvalho ACP (2011) A comparative study between cone-beam computed tomography and periapical radiographs in the diagnosis of simulated endodontic complications. Int Endod J 44:218–224

da Silveira HL, Silveira HE, Liedke GS, Lermen CA, Dos Santos RB, de Figueiredo JA (2007) Diagnostic ability of computed tomography to evaluate external root resorption in vitro. Dentomaxillofac Radiol 36:393–396

da Silveira PF, Vizzotto MB, Liedke GS, da Silveira HL, Montagner F, da Silveira HE (2013) Detection of vertical root fractures by conventional radiographic examination and cone beam computed tomography-dan in vitro analysis. Dent Traumatol 29:41–46

Dang H, Stayman JW, Sisniega A, Xu J, Zbijewski W, Wang X, Foos DH, Aygun N, Koliatsos VE, Siewerdsen JH (2015) Statistical reconstruction for cone-beam CT with a post-artifact-correction noise model: application to high-quality head imaging. Phys Med Biol 60:6153–6175

de Chevigny C, Dao TT, Basrani BR et al (2008) Treatment outcome in endodontics: the Toronto study—phase 4: initial treatment. J Endod 34:258–263

de Pablo OV, Estevez R, Péix Sánchez M, Heilborn C, Cohenca N (2010) Root anatomy and canal configuration of the permanent mandibular first molar: a systematic review. J Endod 36:1919–1931

de Paula-Silva FW, Wu M-K, Leonardo MR, da Silva LA, Wesselink PR (2009a) Accuracy of periapical radiography and cone-beam computed tomography scans in diagnosing apical periodontitis using histopathological findings as a gold standard. J Endod 35:1009–1012

de Paula-Silva FW, Santamaria M, Leonardo MR, Consolaro A, da Silva LA (2009b) Cone-beam computerized tomographic, radiographic, and histologic evaluation of periapical repair in dogs' post-endodontic treatment. Oral Surg Oral Med Oral Path Oral Radiol Endod 108:796–805

Domark JD, Hatton JF, Benison RP, Hildebolt CF (2013) An ex vivo comparison of digital radiography and cone-beam and micro computed tomography in the detection of the number of canals in the mesiobuccal roots of maxillary molars. J Endod 31:901–905

Durack C, Patel S, Davies J, Wilson R, Mannocci F (2011) Diagnostic accuracy of small volume cone beam computed tomography and intraoral periapical radiography for the detection of simulated external inflammatory root resorption. Int Endod J 44:136–147

Edlund M, Nair MK, Nair UP (2011) Detection of vertical root fractures by using cone-beam computed tomography: a clinical study. J Endod 37:768–772

Ee J, Fayad MI, Johnson BR (2014) Comparison of endodontic diagnosis and treatment planning decisions using cone-beam volumetric tomography versus periapical radiography. J Endod 40:910–916

Ellis RG, Davey KW (1970) The classification and treatment of injuries to the teeth of children, 5th edn. Year Book Medical Publishers, Inc, Chicago

Engström B, Ericson S (1964) Roentgenological-clinical follow-up study of perforations of the maxillary sinus via root canals. Od Revy 15:404–413

Estrela C, Bueno MR, Sousa-Neto MD, Pécora JD (2008a) Method for determination of root curvature radius using cone-beam computed tomography images. Braz Dent J 19:114–118

Estrela C, Bueno MR, Leles CR, Azevedo B, Azevedo JR (2008b) Accuracy of cone beam computed tomography and panoramic and periapical radiography for detection of apical periodontitis. J Endod 34:273–279

Estrela C, Bueno MR, Azevedo BC, Azevedo JR, Pécora JD (2008c) A new periapical index based on cone beam computed tomography. J Endod 34:1325–1331

Estrela C, Reis Bueno M, Alencar AHG et al (2009) Method to evaluate inflammatory root resorption by using cone beam computed tomography. J Endod 35:1491–1497

European Commission (2012) Radiation protection no 172 cone beam CT for dental and maxillofacial radiology (evidence-based guidelines). The SEDENTEXCT Project, Luxembourg

European Society of Endodontology (2006) Quality guidelines for endodontic treatment: consensus report of the European Society of Endodontology. Int Endod J 39:921–930

European Society of Endodontology, Patel S, Durack C, Abella F, Roig M, Shemesh H, Lambrechts P, Lemberg K (2014) European Society of Endodontology position statement: the use of CBCT in endodontics. Int Endod J 47:502–504

Ezoddini AF, Sheikhha MH, Ahmadi H (2007) Prevalence of dental developmental anomalies: a radiographic study. Community Dent Health 24:140–144

Fayad MI, Ashkenaz PJ, Johnson BR (2012) Different representations of vertical root fractures detected by cone-beam volumetric tomography: a case series report. J Endod 38:1435–1442

Flores MT, Andersson L, Andreasen JO et al (2007) Guidelines for the management of traumatic dental injuries: I—fractures and luxations of permanent teeth. Dent Traumatol 23:66–71

Fogel HM, Peikoff MD, Christie WH (1994) Canal configuration in the mesiobuccal root of the maxillary first molar: a clinical study. J Endod 20:135–137

Folk RB, Thorpe JR, McClanahan SB, Johnson JD, Strother JM (2005) Comparison of two different direct digital radiography systems for the ability to detect artificially prepared periapical lesions. J Endod 31:304–306

Friedman S (2002) Prognosis of initial endodontic therapy. Endod Topics 2:59–98

Fryback DG, Thornbury JR (1991) The efficacy of diagnostic imaging. Med Decis Mak 11:88–94

Fuss Z, Trope M (1996) Root perforations: classification and treatment choices based on prognostic factors. Endod Dent Traumatol 12:255–264

Gartner AH, Mack T, Somerlott RG, Walsh LC (1976) Differential diagnosis of internal and external root resorption. J Endod 2:329–334

Geist JR, Katz JO (1990) The frequency and distribution of idiopathic osteosclerosis. Oral Surg Oral Med Oral Pathol 69:388–393

Giardino L, Pontieri F, Savoldi E, Tallarigo F (2006) Aspergillus mycetoma of the maxillary sinus secondary to overfilling a root canal. J Endod 32:692–694

Goerig AC, Neaverth EJ (1987) A simplified look at the buccal object rule in endodontics. J Endod 13:570–572

Goldman M, Pearson AH, Darzenta N (1972) Endodontic success—who's reading the radiograph? Oral Surg Oral Med Oral Pathol 33:432–437

Goldman M, Pearson AH, Darzenta N (1974) Reliability of radiographic interpretations. Oral Surg Oral Med Oral Pathol 38:287–293

Gorni FG, Gagliani MM (2004) The outcome of endodontic retreatment: a 2-yr follow-up. J Endod 30:1–4

Grahnhen H, Lindahal B, Omnell K (1959) Dens invaginatus, part I: a clinical roentgenological and genetical study of permanent upper lateral incisors. Odontol Rev 10:115–137
Green TL, Walton RE, Clark JM, Maixner D (2013) Histologic examination of condensing osteitis in cadaver specimens. J Endod 39:977–979
Gröndahl H-G, Huumonen S (2004) Radiographic manifestations of periapical inflammatory lesions. Endod Topics 8:55–67
Guo J, Simon JH, Sedghizadeh P, Soliman ON, Chapman T, Enciso R (2013) Evaluation of the reliability and accuracy of using cone-beam computed tomography for diagnosing periapical cysts from granulomas. J Endod 39:1485–1490
Haapasalo M, Endal U (2006) Internal inflammatory root resorption: the unknown resorption of the tooth. Endod Topics 14:60–79
Hahn W, Fricke-Zech S, Fricke J, Gruber RM, Dullin C, Zapf A, Hannig C, Kubein-Meesenburg D, Sadat-Khonsari R (2009) Detection and size differentiation of simulated tooth root defects using flat-panel volume computerized tomography (fpVCT). Oral Surg Oral Med Oral Pathol Oral Radiol Endod 107:272–278
Hamasha AA, Alomari QD (2004) Prevalence of dens invaginatus in Jordanian adults. Int Endod J 37:307–310
Harar RP, Chadha NK, Rogers G (2007) Are maxillary mucosal cysts a manifestation of inflammatory sinus disease? J Laryngol Otol 121:751–754
Hassan B, Metska ME, Ozok AR, van der Stelt P, Wesselink PR (2009) Detection of vertical root fractures in endodontically treated teeth by a cone beam computed tomography scan. J Endod 35:719–722
Hassan B, Metska ME, Ozok AR, van der Stelt P, Wesselink PR (2010) Comparison of five cone beam computed tomography systems for the detection of vertical root fractures. J Endod 36:126–129
Heithersay GS (1999a) Clinical, radiographic, and histopathological features of invasive cervical resorption. Quintessence Int 30:27–37
Heithersay GS (1999b) Invasive cervical resorption: an analysis of potential predisposing factors. Quintessence Int 30:83–95
Heithersay GS (2004) Invasive cervical resorption. Endod Topics 7:73–92
Horning GM, Cohen ME, Neils TA (2000) Buccal alveolar exostoses: prevalence, characteristics, and evidence for buttressing bone formation. J Periodontol 71:1032–1042
Hovland EJ, Block RM (1977) Nonrecognition and subsequent endodontic treatment of dens invaginatus. J Endod 3:360–362
Hülsmann M (1997) Dens invaginatus: aetiology, classification, prevalence, diagnosis, and treatment considerations. Int Endod J 30:79–90
Huumonen S, Ørstavik D (2002) Radiological aspects of apical periodontitis. Endod Topics 7:3–25
Huumonen S, Kvist T, Gröndahl K, Molander A (2006) Diagnostic value of computed tomography in retreatment of root fillings in maxillary molars. Int Endod J 39:827–833
Iikubo M, Kobayashi K, Mishima A et al (2009) Accuracy of intraoral radiography, multi- detector helical CT, and limited cone-beam CT for the detection of horizontal tooth root fracture. Oral Surg Oral Med Oral Pathol Oral Radiol Endod 108:70–74
International Association of Dental Traumatology (2012) International Association of Dental Traumatology guidelines for the management of traumatic dental injuries: 1. Fractures and luxations of permanent teeth. Dental Traumatol 28, 2–12
Iqbal MK, Kim S (2007) For teeth requiring endodontic treatment, what are the differences in outcomes of restored endodontically treated teeth compared to implant-supported restorations? Int J Oral Maxillofac Implants 22(Suppl):96–116
Jafarzadeh H, Abbott PV (2007) Dilaceration: review of an endodontic challenge. J Endod 33:1025–1030
Jafarzadeh H, Azarpazhooh A, Mayhall JT (2008) Taurodontism: a review of the condition and endodontic treatment challenges. Int Endod J 41:375–388
Jainkittivong A, Langlais RP (2000) Buccal and palatal exostoses: prevalence and concurrence with tori. Oral Surg Oral Med Oral Pathol Oral Radiol Endod 90:48–53
Jakobson SJ, Westphalen VP, Silva Neto UX, Fariniuk LF, Schroeder AG, Carneiro E (2014) The influence of metallic posts in the detection of vertical root fractures using different imaging examinations. Dentomaxillofac Radiol 43:20130287
Janner SF, Jeger FB, Lussi A, Bornstein MM (2011) Precision of endodontic working length measurements: a pilot investigation comparing cone-beam computed tomography scanning with standard measurement techniques. J Endod 37:1046–1051
Jeger FB, Janner SF, Bornstein MM, Lussi A (2012) Endodontic working length measurement with preexisting cone-beam computed tomography scanning: a prospective, controlled clinical study. J Endod 38:884–888
John V (2008) Non-surgical management of infected type III dens invaginatus with vital surrounding pulp using contemporary endodontic techniques. Aust Endod J 34:4–11
Junqueira RB, Verner FS, Campos CN, Devito KL, do Carmo AM (2013) Detection of vertical root fractures in the presence of intracanal metallic post: a comparison between periapical radiography and cone-beam computed tomography. J Endod 39:1620–1622
Kamburoğlu K, Kursun S, Yuksel S, Oztas B (2011) Observer ability to detect ex vivo simulated internal or external cervical root resorption. J Endod 37: 168–175
Kamburoğlu K, Yeta EN, Yılmaz F (2015) An ex vivo comparison of diagnostic accuracy of cone-beam computed tomography and periapical radiography in the detection of furcal perforations. J Endod 41:696–702
Kanagalingam J, Bhatia K, Georgalas C, Fokkens W, Miszkiel K, Lund VJ (2009) Maxillary mucosal cyst is not a manifestation of rhinosinusitis: results of a pro-

spective three-dimensional CT study of ophthalmic patients. Laryngoscope 119:8–12
Kaya S, Yavuz I, Uysal I, Akkus Z (2012) Measuring bone density in healing periapical lesions by using cone beam computed tomography: a clinical investigation. J Endod 38:28–31
Khongkhunthian P, Reichart PA (2001) Aspergillosis of the maxillary sinus as a complication of overfilling root canal material into the sinus: report of two cases. J Endod 27:476–478
Kim TS, Caruso JM, Christensen H, Torabinejad M (2010) A comparison of cone-beam computed tomography and direct measurement in the examination of the mandibular canal and adjacent structures. J Endod 36:1191–1194
Kishen A (2006) Mechanisms and risk factors for fracture predilection in endodontically treated teeth. Endod Top 13:57–83
Kovisto T, Ahmad M, Bowles WR (2011) Proximity of the mandibular canal to the tooth apex. J Endod 37:311–315
Kruse C, Spin-Neto R, Wenzel A, Kirkevang LL (2015) Cone beam computed tomography and periapical lesions: a systematic review analysing studies on diagnostic efficacy by a hierarchical model. Int Endod J 48:815–828
Kulild JC, Peters DD (1990) Incidence and configuration of canal systems in the mesiobuccal root of maxillary first and second molars. J Endod 16:311–317
Kurt SN, Üstün Y, Erdogan Ö, Evlice B, Yoldas O, Öztunc H (2014) Outcomes of periradicular surgery of maxillary first molars using a vestibular approach: a prospective, clinical study with one year of follow-up. J Oral Maxillofac Surg 72:1049–1061
Laatikainen T, Ranta R (1996) Taurodontism in twins with cleft lip and/or palate. Eur J Oral Sci 104(2(part 1)):82–86
Lazarski MP, Walker WA III, Flores CM et al (2001) Epidemiological evaluation of the outcomes of nonsurgical root canal treatment in a large cohort of insured dental patients. J Endod 27:791–796
Lee S-J, Messer HH (1986) Radiographic appearance of artificially prepared periapical lesions confined to cancellous bone. Int J Endod 19:64–72
Legert KG, Zimmerman M, Stierna P (2004) Sinusitis of odontogenic origin: pathophysiological implications of early treatment. Acta Otolaryngol 124:655–663
Liang Y-H, Li G, Wesselink PR, Wu M-K (2011) Endodontic outcome predictors identified with periapical radiographs and cone-beam computed tomography scans. J Endod 37:326–331
Liedke GS, da Silveira HE, da Silveira HL, Dutra V, de Figueiredo JA (2009) Influence of voxel size in the diagnostic ability of cone beam tomography to evaluate simulated external root resorption. J Endod 35:233–235
Llena C, Fernandez J, Ortolani PS, Forner L (2014) Cone-beam computed tomography analysis of root and canal morphology of mandibular premolars in a Spanish population. Imaging Sci Dent 4:221–227
Paes da Silva Ramos Fernandes LM, Rice D, Ordinola-Zapata R, Alvares Capelozza AL, Bra-mante CM, Jaramillo D, Christensen H (2014) Detection of various anatomic patterns of root canals in mandibular incisors using digital periapical radiography, 3 cone-beam com-puted tomographic scanners, and micro-computed tomographic imaging. J Endod 40:42–45
Lofthag-Hansen S, Huumonen S, Gröndahl K, Gröndahl HG (2007) Limited cone-beam CT and intraoral radiography for the diagnosis of periapical pathology. Oral Surg Oral Med Oral Pathol Oral Radiol Endod 103:114–119
Low KM, Dula K, Bürgin W, von Arx T (2008) Comparison of periapical radiography and limited cone-beam tomography in posterior maxillary teeth referred for apical surgery. J Endod 34:557–562
Lu Y, Liu Z, Zhang L, Zhou X, Zheng Q, Duan X, Zheng G, Wang H, Huang D (2012) Associations between maxillary sinus mucosal thickening and apical periodontitis using cone-beam computed tomography scanning: a retrospective study. J Endod 38:1069–1074
MacDonald-Jankowski DS (1999) Idiopathic osteosclerosis in the jaws of Britons and of the Hong Kong Chinese: radiology and systematic review. Dentomaxillofac Radiol 28:357–363
Maddalone M, Gagliani M (2003) Periapical endodontic surgery: a 3-year follow-up study. Int Endod J 36:193–198
Maini A, Durning P, Drage N (2008) Resorption: within or without? The benefit of cone-beam computed tomography when diagnosing a case of an internal/external resorption defect. Br Dent J 204:135–137
Malliet M, Bowles WR, McClanahan SL, John MT, Ahmad M (2011) Cone-beam computed tomography evaluation of maxillary sinusitis. J Endod 37:753–757
Maloney PL, Doku HC (1968) Maxillary sinusitis of odontogenic origin. J Can Dent Assoc 34:591–603
Mao T, Neelakantan P (2014) Three-dimensional imaging modalities in endodontics. Imaging Sci Dent 44:177–183
Marmary Y, Koter T, Heling I (1999) The effect of periapical rarefying osteitis on cortical and cancellous bone. A study comparing conventional radiographs with computed tomography. Dentomaxillofac Radiol 28:267–271
Martinez-Lozano MA, Forner-Navarro L, Sanchez-Cortes JL (1999) Analysis of radiologic factors in determining premolar root canal systems. Oral Surg Oral Med Oral Pathol Oral Radiol Endod 88:719–722
Martins JN, Marques D, Mata A, Caramês J (2014) Clinical efficacy of electronic apex locators: systematic review. J Endod 40:759–777
Matherne RP, Angelopoulos C, Kulild JC, Tira D (2008) Use of cone-beam computed tomography to identify root canal systems in vitro. J Endod 34:87–89
McClammy TV (2014) Endodontic applications of cone beam computed tomography. Dent Clin N Am 58:545–559
Mehra P, Murad H (2004) Maxillary sinus disease of odontogenic origin. Otolaryngol Clin N Am 37:347–364

Meister F, Lommel TJ, Gerstein H (1980) Diagnosis and possible causes of vertical root fractures. Oral Surg Oral Med Oral Pathol 49:243–253

Melo SL, Bortoluzzi EA, Abreu M Jr, Correa LR, Correa M (2010) Diagnostic ability of a cone-beam computed tomography scan to assess longitudinal root fractures in prosthetically treated teeth. J Endod 36:1879–1882

Metska ME, Aartman IH, Wesselink PR, Ozok AR (2012) Detection of vertical root fractures in vivo in endodontically treated teeth by cone-beam computed tomography scans. J Endod 38:1344–1347

Metska ME, Parsa A, Aartman IH, Wesselink PR, Ozok AR (2013) Volumetric changes in apical radiolucencies of endodontically treated teeth assessed by cone-beam computed tomography 1 year after orthograde retreatment. J Endod 39:1504–1509

Metska ME, Liem VM, Parsa A, Koolstra JH, Wesselink PR, Ozok AR (2014) Cone-beam computed tomographic scans in comparison with periapical radiographs for root canal length measurement: an in situ study. J Endod 40:1206–1209

Michetti J, Maret D, Mallet J-P, Diemer F (2010) Validation of cone beam computed tomography as a tool to explore root canal anatomy. J Endod 36:1187–1190

Mota de Almeida FJ, Knutsson K, Flygare L (2014a) The effect of cone beam CT (CBCT) on therapeutic decision-making in endodontics. Dentomaxillofac Radiol 43:20130137

Mota de Almeida FJ, Knutsson K, Flygare L (2014b) The impact of cone beam computed tomography on the choice of endodontic diagnosis. Int Endod J 48:564–572

Nair PNR (2003) Non-microbial etiology: periapical cysts sustain post-treatment apical periodontitis. Endod Topics 6:96–113

Nair PN (2004) Pathogenesis of apical periodontitis and the causes of endodontic failures. Crit Rev Oral Biol Med 15:348–381

Nair PNR (2006) On the causes of persistent apical periodontitis: a review. Int Endod J 39:249–281

Nair MK, Nair UP (2007) Digital and advanced imaging in endodontics: a review. J Endod 33:1–6

Nair PNR, Sjögren U, Schumacher E, Sundqvist G (1993) Radicular cysts affecting a root-filled human tooth: a long-term post-treatment follow-up. Int Endod J 26:225–233

Nair M, Levin M, Nair U (2015) Chapter 2. Radiographic interpretation. In: Hargreaves KM, Berman L (eds) Cohen's pathways of the pulp, 11th edn. Mosby Elsevier, St. Louis, pp 33–70

Nakata K, Naitoh M, Izumi M, Inamoto K, Ariji E, Nakamura H (2006) Effectiveness of dental computed tomography in diagnostic imaging of periradicular lesion of each root of a multirooted tooth: a case report. J Endod 32:583–587

Nance R, Tyndall D, Levin LG, Trope M (2000) Identification of root canals in molars by tuned-aperture computed tomography. Int Endod J 33:392–396

Natkin E, Oswald RJ, Carnes LI (1984) The relationship of lesion size to diagnosis, incidents and treatment of periapical cysts and granulomas. Oral Surg Oral Med Oral Pathol 57:82–94

Nawa H, Oberoi S, Vargervik K (2008) Taurodontism and van der Woude syndrome. Is there an association? Angle Orthod 78:832–837

Ne RF, Witherspoon DE, Gutmann JL (1999) Tooth resorption. Quintessence Int 30:9–25

Neelakantan P, Subbarao C, Subbarao CV (2010) Comparative evaluation of modified canal staining and clearing technique, cone-beam computed tomography, peripheral quantitative computed tomography, spiral computed tomography, and plain and contrast medium-enhanced digital radiography in studying root canal morphology. J Endod 36:1547–1551

Neves FS, Freitas DQ, Campos PS, Ekestubbe A, Lofthag-Hansen S (2014) Evaluation of cone-beam computed tomography in the diagnosis of vertical root fractures: the influence of imaging modes and root canal materials. J Endod 40:1530–1536

Ng YL, Mann V, Rahbaran S, Lewsey J, Gulabivala K (2008) Outcome of primary root canal treatment: systematic review of the literature - part 2. Influence of clinical factors. Int Endod J 41:6–31

Ng YL, Mann V, Gulabivala K (2010) Tooth survival following non-surgical root canal treatment: a systematic review of the literature. Int Endod J 43:171–189

Nicopoulou-Karayianni K, Bragger U, Lang NP (1997) Patterns of periodontal destruction associated with incomplete root fractures. Dentomaxillofac Radiol 26:321–326

Niemczyk SP (2010) Essentials of endodontic microsurgery. Dent Clin N Am 54:375–399

Nudera WJ (2015) Selective root retreatment: a novel approach. J Endod 41:1382–1388

Nurbakhsh B, Friedman S, Kulkarni GV, Basrani B, Lam E (2011) Resolution of maxillary sinus mucositis after endodontic treatment of maxillary teeth with apical periodontitis: a cone-beam computed tomography pilot study. J Endod 37:1504–1511

Oehlers FA (1957) Dens invaginatus. I. Variations of the invagination process and associated anterior crown forms. Oral Surg Oral Med Oral Pathol 10:1204–1218

Ørstavik D (1996) Time-course and risk analyses of the development and healing of chronic apical periodontitis in man. Int Endod J 29:150–155

Ozen T, Kamburoğlu K, Cebeci AR, Yüksel SP, Paksoy CS (2009) Interpretation of chemically created periapical lesions using 2 different dental cone-beam computerized tomography units, an intraoral digital sensor, and conventional film. Oral Surg Oral Med Oral Pathol Oral Radiol Endod 107:426–432

Ozer SY (2011) Detection of vertical root fractures by using cone beam computed tomography with variable voxel sizes in an in vitro model. J Endod 37:75–79

Pagella F, Matti E, De Bernardi F, Semino L, Cavanna C, Marone P, Farina C, Castelnuovo P (2007) Paranasal sinus fungus ball: diagnosis and management. Mycoses 50: 451–456

Palomo L, Palomo JM (2009) Cone beam CT for diagnosis and treatment planning in trauma cases. Dent Clin N Am 53(717–27):vi–vii

Patel S (2009) New dimensions in endodontic imaging: part 2. Cone beam computed tomography. Int Endod J 42:463–475

Patel S, Dawood A (2007) The use of cone beam computed tomography in the management of external cervical resorption lesions. Int Endod J 40:730–737

Patel S, Dawood A, Ford TP, Whaites E (2007) The potential applications of cone beam computed tomography in the management of endodontic problems. Int Endod J 40:818–830

Patel S, Dawood A, Mannocci F, Wilson R, Pitt Ford T (2009a) Detection of periapical bone defects in human jaws using cone beam computed tomography and intraoral radiography. Int Endod J 42:507–515

Patel S, Kanagasingam S, Pitt Ford T (2009b) External cervical resorption: a review. J Endod 35:616–625

Patel S, Dawood A, Wilson R, Horner K, Mannocci F (2009c) The detection and management of root resorption lesions using intraoral radiography and cone beam computed tomography – an in vivo investigation. Int Endod J 42:831–838

Patel S, Kanagasingam S, Mannocci F (2010a) Cone beam computed tomography (CBCT) in endodontics. Dent Update 37:373–379

Patel S, Ricucci D, Durak C, Tay F (2010b) Internal root resorption: a review. J Endod 36:1107–1121

Patel S, Wilson R, Dawood A, Mannocci F (2012a) The detection of periapical pathosis using periapical radiography and cone beam computed tomography – part 1: pre-operative status. Int Endod J 45:702–710

Patel S, Wilson R, Dawood A, Foschi Mannocci F (2012b) The detection of periapical pathosis using digital periapical radiography and cone beam computed tomography – part 2: a 1-year post-treatment follow-up. Int Endod J 45:711–723

Patel S, Brady E, Wilson R, Brown J, Mannocci F (2013) The detection of vertical root fractures in root filled teeth with periapical radiographs and CBCT scans. Int Endod J 46:1140–1152

Patel S, Durack C, Abella F, Shemesh H, Roig M, Lemberg K (2015) Cone beam computed tomography in Endodontics – a review. Int Endod J 48:3–15

Peters CI, Peters OA (2012) Cone beam computed tomography and other imaging techniques in the determination of periapical healing. Endod Topics 26:57–75

Pineda F (1973) Roentgenographic investigation of the mesiobuccal root of the maxillary first molar. Oral Surg Oral Med Oral Pathol 36:253–260

Pineda F, Kuttler Y (1972) Mesiodistal and buccolingual roentgenographic investigation of 7,275 root canals. Oral Surg Oral Med Oral Pathol 33:101–110

Pinsky HM, Dyda S, Pinsky RW, Misch KA, Sarment DP (2006) Accuracy of three-dimensional measurements using cone-beam CT. Dentomaxillofac Radiol 35:410–416

Pope O, Sathorn C, Parashos P (2014) A comparative investigation of cone-beam computed tomography and periapical radiography in the diagnosis of a healthy periapex. J Endod 40:360–365

Ramamurthy R, Scheetz JP, Clark SJ, Farman AG (2006) Effects of imaging system and exposure on accurate detection of the second mesio-buccal canal in maxillary molar teeth. Oral Surg Oral Med Oral Pathol Oral Radiol Endod 102:796–802

Reit C (1987) Decision strategies in endodontics: on the design of a recall program. Endod Dent Traumatol 3:233–239

Rigolone M, Pasqualini D, Bianchi L, Berutti E, Bianchi SD (2003) Vestibular surgical access to the palatine root of the superior first molar: “low-dose cone-beam” CT analysis of the pathway and its anatomic variations. J Endod 29:773–775

Rosen E, Taschieri S, Del Fabbro M, Beitlitum I, Tsesis I (2015) The diagnostic efficacy of cone-beam computed tomography in endodontics: a systematic review and analysis by a hierarchical model of efficacy. J Endod 41:1008–1014

Rosenberg P, Frisbie J, Lee J, Lee K, Frommer H, Kottal S, Phelan J (2010) Evaluation of pathologists (histopathology) and radiologists (cone beam computed tomography) differentiating radicular cysts from granulomas. J Endod 36:423–428

Salehrabi R, Rotstein I (2004) Endodontic treatment outcomes in a large patient population in the USA: an epidemiological study. J Endod 30:846–850

Sanders B, Brady FA, Johnson R (1979) Injuries. In: Sanders B (ed) Pediatric oral and maxillofacila surgery, 1st edn. CV Mosby, St. Louis, p 330

Scarfe WC, Czerniejewski VJ, Farman AG, Avant SL, Molteni R (1999) In vivo accuracy and reliability of color-coded image enhancements for the assessment of periradicular lesion dimensions. Oral Surg Oral Med Oral Pathol Oral Radiol Endod 88: 603–611

Scarfe WC, Levin MD, Gane D, Farman AG (2009) Use of cone beam computed tomography in endodontics. Int J Dent 2009:634567

Schwartz SF, Foster JK (1971) Roentgenographic interpretation of experimentally produced bone lesions. Oral Surg Oral Med Oral Pathol 32:606–612

Selden HS (1989) The endo-antral syndrome: an endodontic complication. J Am Dent Assoc 119(397–8): 401–402

Selden HS (1994) Diagnostic radiographic findings and symptom free teeth. J Endod 20:100–102

Selden HS (1999) Endo-antral syndrome and various endodontic complications. J Endod 25:389–393

Setzer FC, Shah SB, Kohli MR, Karabucak B, Kim S (2010) Outcome of endodontic surgery: a meta-analysis of the literature - part 1: comparison of traditional root-end surgery and endodontic microsurgery. J Endod 36:1757–1765

Shanbhag S, Karnik P, Shirke P, Shanbhag V (2013) Association between periapical lesions and maxillary sinus mucosal thickening: a retrospective cone-beam computed tomographic study. J Endod 39:853–857

Shemesh H, Cristescu RC, Wesselink PR, Wu M-K (2011) The use of cone-beam computed tomography and digital periapical radiographs to diagnose root perforations. J Endod 37:513–516

Shoha RR, Dowson J, Richards AG (1974) Radiographic interpretation of experimentally produced bone

lesions. Oral Surg Oral Med Oral Pathol Oral Radiol Endod 38:294–303
Siew K, Lee A, Cheung G (2015) Treatment outcome of repaired root perforation: a systematic review and meta-analysis. J Endod 41:1795–1804
Silva EJ, Nejaim Y, Silva AV, Haiter-Neto F, Cohenca N (2013) Evaluation of root canal configuration of mandibular molars in a Brazilian population by using cone-beam computed tomography: an in vivo study. J Endod 39:849–852
Silva EJ, Nejaim Y, Silva A, Haiter-Neto F, Zaia AA, Cohenca N (2014) Evaluation of root canal configuration of maxillary molars in a Brazilian population using cone-beam computed tomographic imaging: an in vivo study. J Endod 40:173–176
Simon JH, Enciso R, Malfaz JM, Roges R, Bailey-Perry M, Patel A (2006) Differential diagnosis of large periapical lesions using cone-beam computed tomography measurements and biopsy. J Endod 32:833–837
Soğur E, Baksı BG, Gröndahl H-G, Lomcali G, Sen BH (2009) Detectability of chemically induced periapical lesions by limited cone beam tomography, intra-oral digital and conventional film radiography. Dentomaxillofac Radiol 40:458–464
Stavropoulos A, Wenzel A (2007) Accuracy of cone beam dental CT, intraoral digital and conventional film radiography for the detection of periapical lesions. An ex vivo study in pig jaws. Clin Oral Investig 11:101–106
Strindberg LZ (1956) The dependence of the results of pulp therapy on certain factors. An analytic study based on radiographic and clinical follow-up examinations. Acta Odontol Scand 14(Suppl 21):1–175
Stropko JJ (1999) Canal morphology of maxillary molars: clinical observations of canal configurations. J Endod 25:446–450
Talwar S, Utneja S, Nawal RR, Kaushik A, Srivastava D, Oberoy SS (2016) Role of cone-beam computed tomography in diagnosis of vertical root fractures: a systematic review and meta-analysis. J Endod 42:12–24
Tamse A (2006) Vertical root fractures in endodontically treated teeth: diagnostic signs and clinical management. Endod Top 13:84–94
Tamse A, Fuss Z, Lustig J, Kaplavi J (1999a) An evaluation of endodontically treated vertically fractured teeth. J Endod 25:506–508
Tamse A, Fuss Z, Lustig J, Ganor Y, Kaffe I (1999b) Radiographic features of vertically fractured, endodontically treated maxillary premolars. Oral Surg Oral Med Oral Pathol Oral Radiol Endod 88:348–352
Tamse A, Kaffe I, Lustig J, Ganor J, Fuss Z (2006) Radiographic features of vertically fractured endodontically treated mesial roots of mandibular molars. Oral Surg Oral Med Oral Pathol Oral Radiol Endod 101:797–802
Tanomaru-FIlho M, Jorge ÉG, Guerreiro-Tanomaru JM, Reis JM, Spin-Neto R, Gonçalves M (2015) Two- and tridimensional analysis of periapical repair after endodontic surgery. Clin Oral Investig 19:17–25
Testori T, Badino M, Castagnola M (1993) Vertical root fractures in endodontically treated teeth: a clinical survey of 36 cases. J Endod 19:87–91
Testori T, Capelli M, Milani S, Weinstein RL (1999) Success and failure in periradicular surgery: a longitudinal retrospective analysis. Oral Surg Oral Med Oral Pathol Oral Radiol Endod 87:493–498
Todd R (2014a) Cone beam computed tomography updated technology for endodontic diagnosis. Dent Clin N Am 58:523–543
Todd R (2014b) Dental imaging – 2D to 3D: a historic, current, and future view of projection radiography. Endod Topics 31:36–52
Torabinejad M, Landaez M, Milan M et al (2015) Tooth retention through endodontic microsurgery or tooth replacement using single implants: a systematic review of treatment outcomes. J Endod 41:1–10
Tronstad L (1988) Root resorption - etiology, terminology and clinical manifestations. Endod Dent Traumatol 4:241–252
Tsai P, Torabinejad M, Rice D, Azevedo B (2012) Accuracy of cone-beam computed tomography and periapical radiography in detecting small periapical lesions. J Endod 38:965–970
Tsesis I, Rosen E, Tamse A, Taschieri S, Kfir A (2010) Diagnosis of vertical root fractures in endodontically treated teeth based on clinical and radiographic indices: a systematic review. J Endod 36:1455–1458
Tsukiboshi M (2006) Optimal use of photography, radiography and micro computed tomography scanning in the management of traumatized teeth. Endod Topics 14:4–19
Tsurumachi T, Honda K (2007) A new cone beam computerized tomography system for use in endodontic surgery. Int Endod J 40:224–232
Tu M-G, Tsai C-C, Jou M-J et al (2007) Prevalence of three-rooted mandibular first molars among Taiwanese individuals. J Endod 33:1163–1166
Tu MG, Huang HL, Hsue SS, Hsu JT, Chen SY, Jou MJ, Tsai CC (2009) Detection of permanent three-rooted mandibular first molars by cone-beam computed tomography imaging in Taiwanese individuals. J Endod 35:503–507
Tyndall DA, Kohltfarber H (2012) Application of cone beam volumetric tomography in endodontics. Aust Dent J 57(Suppl 1):72–81
Tyndall DA, Rathore S (2008) Cone-beam CT diagnostic applications: caries, periodontal bone assessment, and endodontic applications. Dent Clin N Am 52:825–841
Tyndall DA, Price JB, Tetradis S, Ganz SD, Hildebolt C, Scarfe WC (2011) Position statement of the American Academy of oral and maxillofacial radiology on selection criteria for the use of radiology in dental implantology with emphasis on cone beam computed tomography. Oral Surg Oral Med Oral Pathol Oral Radiol 113:817–826
van der Borden WG, Wang X, Wu MK, Shemesh H (2013) Area and 3-dimensional volumetric changes of periapical lesions after root canal treatments. J Endod 39:1245–1249
Venskutonis T, Plotino G, Juodzbalys G, Mickevičienė L (2014) The importance of cone-beam computed tomography in the management of endodontic problems: a review of the literature. J Endod 40:1895–1901

Venskutonis T, Plotino G, Tocci L, Gambarini G, Maminskas J, Juodzbalys G (2015) Periapical and endodontic status scale based on periapical bone lesions and endodontic treatment quality evaluation using cone-beam computed tomography. J Endod 41:190–196

Vertucci FJ (1984) Root canal anatomy of human permanent teeth. Oral Surg Oral Med Oral Pathol 58: 589–599

Vizzotto MB, Silveira PF, Arus NA, Montagner F, Gomes BP, da Silveira HE (2013) CBCT for the assessment of second mesiobuccal (MB2) canals in maxillary molar teeth: effect of voxel size and presence of root filling. Int Endod J 46:870–876

Vogiatzi T, Kloukos D, Scarfe WC, Bornstein MM (2014) Incidence of anatomical variations and disease of the maxillary sinuses as identified by cone beam computed tomography: a systematic review. Int J Oral Maxillofac Implants 29:1301–1314

von Arx T, Gerber C, Hardt N (2001) Periradicular surgery of molars: a prospective clinical study with a one-year follow-up. Int Endod J 34:520–525

Walton RE (1973) Endodontic radiographic technics. Dent Radiogr Photogr 46:51–59

Walton RE (2008) Diagnostic imaging. A endodontic radiography. In: Ingle JI, Bakland LK, Baumgartner JC (eds) Ingles' endodontics, 6th edn. BC Decker Inc, Hamilton, ON, p 554

Walton RE, Fouad AF (2015) Endodontic radiography. In: Torabinejad M, Walton RE, Fouad AF (eds) Endodontics: principles and practice, 5th edn. Elsevier Saunders, St. Louis, pp 198–217

Walton RE, Michelich RJ, Smith GN (1984) The histopathogenesis of vertical root fractures. J Endod 10:48–56

Wang P, Yan XB, Lui DG, Zhang WL, Zhang Y, Ma XC (2011) Detection of dental root fractures by using cone-beam computed tomography. Dentomaxillofacial Rad 40:290–298

Weine FS, Healey HJ, Gerstein H, Evanson L (1969) Canal configuration in the mesiobuccal root of the maxillary first molar and its endodontic significance. Oral Surg Oral Med Oral Pathol 28:419–425

Wolcott J, Ishley D, Kennedy W, Johnson S, Minnich S, Meyers J (2005) A 5-year clinical investigation of second mesiobuccal canals in endodontically treated and retreated maxillary molars. J Endod 31: 262–264

Wu M-K, Shemesh H, Wesselink PR (2009) Limitations of previously published systematic reviews evaluating the outcome of endodontic treatment. Int Endod J 42:656–666

Yonetsu K, Yuasa K, Kanda S (1997) Idiopathic osteosclerosis of the jaws: panoramic radiographic and computed tomographic findings. Oral Surg Oral Med Oral Pathol Oral Radiol Endod 83:517–521

Yoo JY, Pi SH, Kim YS, Jeong SN, You HK (2011) Healing pattern of the mucous membrane after tooth extraction in the maxillary sinus. J Periodontal Implant Sci 41:23–29

Young GR (2007) Contemporary management of lateral root perforation diagnosed with the aid of dental computed tomography. Aust Endod J 33:112–118

Periodontal Disease

23

William C. Scarfe, Bruno Azevedo,
Lucas Rodrigues Pinheiro, Menik Priaminiari,
and Marcelo Augusto Oliveira Sales

Contents

W.C. Scarfe, B.D.S., F.R.A.C.D.S., M.S. (✉)
B. Azevedo, D.D.S., M.S.
Division of Radiology and Imaging Science,
Department of Surgical/Hospital Dentistry,
University of Louisville School of Dentistry,
Louisville, KY, USA
e-mail: William.scarfe@louisville.edu

L.R. Pinheiro, D.D.S., Ph.D.
Oral and Maxillofacial Radiology, Faculdade de Odontologia (FO), Universidade de São Paulo (USP), São Paulo, Brazil

M. Priaminiari, D.D.S., Ph.D.
Department of Dentomaxillofacial Radiology, Faculty of Dentistry, Universitas Indonesia, Jakarta, Indonesia

M.A.O. Sales, D.D.S., Ph.D.
Department of Clinical and Social Dentistry, Universidade Federal da Paraíba, João Pessoa, Paraíba, Brazil

23.1 Introduction

Periodontal disease is a bacterially induced, host mediated inflammatory pathology (Loe 1994) resulting in loss of connective soft tissue attachment of the dentition and supporting marginal alveolar bone. Initial assessment of both soft and hard tissue elements of the periodontal apparatus provides a diagnostic baseline and may direct specific treatment approaches. Ongoing periodic evaluation provides comparative clinical data to determine the success of therapies or monitor the progression of the disease. While soft tissue measurements such as pocket depth and bleeding indices are important clinical indicators, radiography is widely used for the assessment of hard tissue

W.C. Scarfe, C. Angelopoulos (eds.), *Maxillofacial Cone Beam Computed Tomography*,
https://doi.org/10.1007/978-3-319-62061-9_23

status and response to therapy. Imaging provides diagnostic information on general and localized alveolar bone levels, plaque retention factors, caries, furcation defects, subgingival calculus, and additional pathology. However, evidence of the clinical efficacy of radiographs in influencing treatment decisions and increasing treatment outcomes has been limited (Tugnait et al. 2004).

Two-dimensional (2-D) planar images from intraoral and panoramic radiography are the most commonly used imaging modalities to identify the location, quantify the amount, and determine the pattern of alveolar bone loss. This is evaluated by comparing radiographic bone height (RBH) measurements to normative or baseline values. However, dimensions obtained from these assessments provide information in only the parasagittal plane, adjacent the mesial and distal aspects of the teeth, and may not accurately reflect the actual three-dimensional (3-D) osseous morphology of the alveolar crest. Contemporary periodontal therapy has evolved to become more interdisciplinary and increasingly involves more complex treatments including bone and soft tissue regenerative procedures. These therapeutic options require an imaging modality or combination of techniques capable of measuring smaller increments of change, both loss and additive, comparable over time providing 3-D morphologic information of the periodontal apparatus (Halperin-Sternfeld and Levin 2013).

23.2 Two-Dimensional Imaging

Conventional intraoral (periapical and bitewing) and panoramic radiography are the most commonly used imaging technologies in dental clinical practice to determine the status of the periodontal apparatus including the alveolar crestal bone, the periodontal ligament (PDL) space, and lamina dura. In addition, contributory factors such as restoration contours (e.g., overhangs) and subgingival calculus can be identified. Assessment of periapical and panoramic images usually involves a measurement of interproximal alveolar bone height (ABH). Radiographic bone height (RBH) on panoramic and intraoral images is calculated by measuring the vertical distance between the alveolar crest and cementoenamel junction (CEJ) parallel to the long axis of the adjacent tooth. Based on 95% confidence intervals (range, 0.4–1.9 mm), bone loss should be considered if the RBH is greater than 1.9 mm (Hausmann et al. 1992).

23.2.1 Intraoral Radiography

Intraoral radiography, specifically periapical and bitewing techniques, remain the most commonly used imaging modality for alveolar bone assessment in clinical dental practice. While these images provide the highest spatial resolution of all radiographic modalities, they are only bidimensional representations of interproximal bone, with marked limitation in the visualization of facial/buccal or lingual/palatal aspects. Even when performed correctly, the limitations of intraoral dental radiography for periodontal diagnosis have been well documented (Suomi et al. 1968; Renvert et al. 1981; Akesson et al. 1992). Intraoral radiographs underestimate the extent of alveolar bone loss by 0.3 ± 2.0 mm to 0.8 ± 1.9 mm (Benn 1990; Eickholz et al. 1999) and vertical bone loss by approximately 1.5 ± 2.6 mm (Eickholz and Hausmann 2000). Defects smaller than 3 mm are generally not seen on radiographs (Pauls and Trott 1966; Pepelassi et al. 2000).

Inaccuracy arises due to image density and contrast variability associated with inadequate exposure, processing or kilovoltage (Douglass et al. 1986), and intra-and interobserver variability. In clinical dental practice, intraoral radiography is highly dependent on the standardization of technical and geometric factors such as the orientation of the image sensor in relation to the anatomic site and of both to the X-ray beam projection (Fig. 23.1) (Grondahl et al. 1984). For periapical radiography, the paralleling technique rather than the bisecting angle

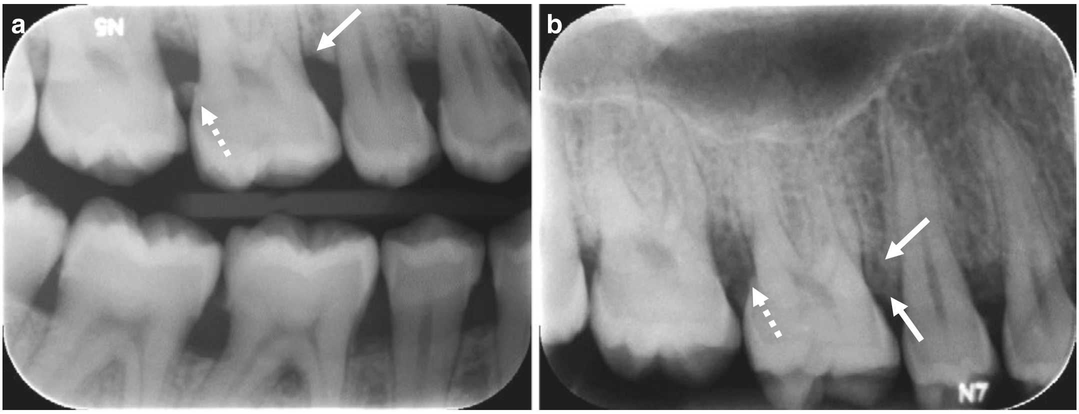

Fig. 23.1 Comparison of the radiologic features of periodontal disease on bitewing (**a**) and long cone periapical (**b**) intraoral radiography. The alveolar bone height level (*solid arrow*) and the presence and location of calculus (*dotted arrow*) is more easily visualized on the bitewing image

technique provides a geometric configuration with the least amount of distortion. Bitewing radiography, performed by default as a paralleling technique, is also useful in that it provides visualization of the alveolar crestal bone in both dental arches simultaneously. Overall diagnostic accuracy can be increased, particularly in regard to the detection of intrabony and furcation defects, if multiple 2-D modalities are used (Muhammed and Manson-Hing 1982; Galal et al. 1985; Rohlin et al. 1989; Akesson et al. 1989). A number of methodologies for computerized analysis of digital intraoral images have been introduced for the detection of periodontal alveolar bone loss. These include specific image enhancements either individually or in series, line density functions, gray scale value assessment of region of interest or application of digital subtraction radiography (DSR) techniques.

23.2.2 Panoramic Radiography

Rotational panoramic radiography (PR) is a low-dose, low-cost, readily available modality that produces a single curved planar tomographic image of the dentition and alveolus of both jaws and adjacent maxillofacial structures in one procedure. PR image generation is designed to provide a static, in-focus image layer corresponding to the average shape of the mandibular dental arch. Imaging requires that the patient's dentition is aligned within a specific three-dimensional space and therefore resultant images often demonstrate positioning errors and artifacts due to tomographic acquisition producing misrepresentation of anatomic structures, and dense structures resulting in ghosting. PR has numerous disadvantages including the superimposition of anatomical structures, and positioning errors that result in disproportionate image magnification, distortion, and blur.

The accuracy of PR for the determination of horizontal bone loss associated with periodontal disease is equivocal. Many authors report that bitewing or periapical radiography are the most accurate methods of bone assessment for both alveolar and intrabony defects as compared to PR (Akesson et al. 1992; Pepelassi and Diamanti-Kipioti 1997), particularly for mild bone loss (Semenoff et al. 2011; Ziebolz et al. 2011); however, others report similar accuracy between PR and periapical radiography (Persson et al. 2003; Langlois Cde et al. 2011; Takeshita et al. 2014), or bitewing and PR for intrabony defects (Gedik et al. 2008). Recent developments such as multi-later panoramic radiography (Figs. 23.2 and 23.3) may improve visualization of marginal alveolar bone height and provide greater utility for this modality.

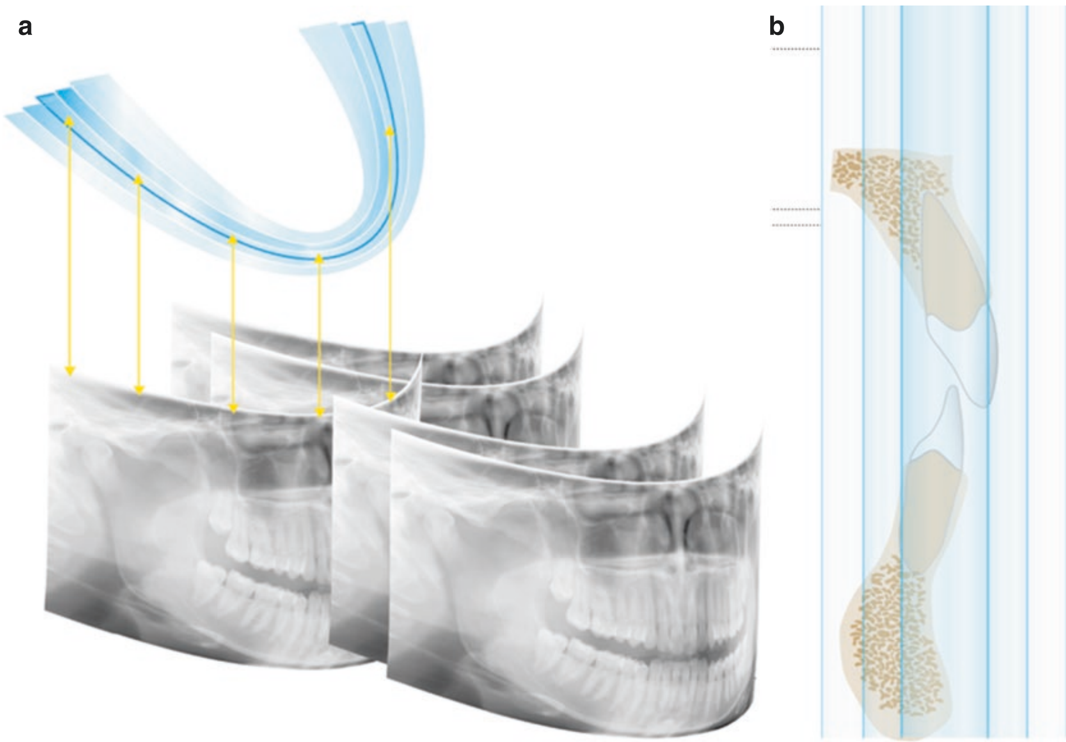

Fig. 23.2 Multi-later panoramic radiography provides up to five images at various horizontal depths with a wide focal trough with only one scan and comparable radiation dose as traditional imaging (**a**). The image layer which corresponds most closely to the vertical location of the teeth and alveolar bone (**b**) is then selected, producing the sharpest panoramic image. (Images courtesy, Instrumentarium Dental)

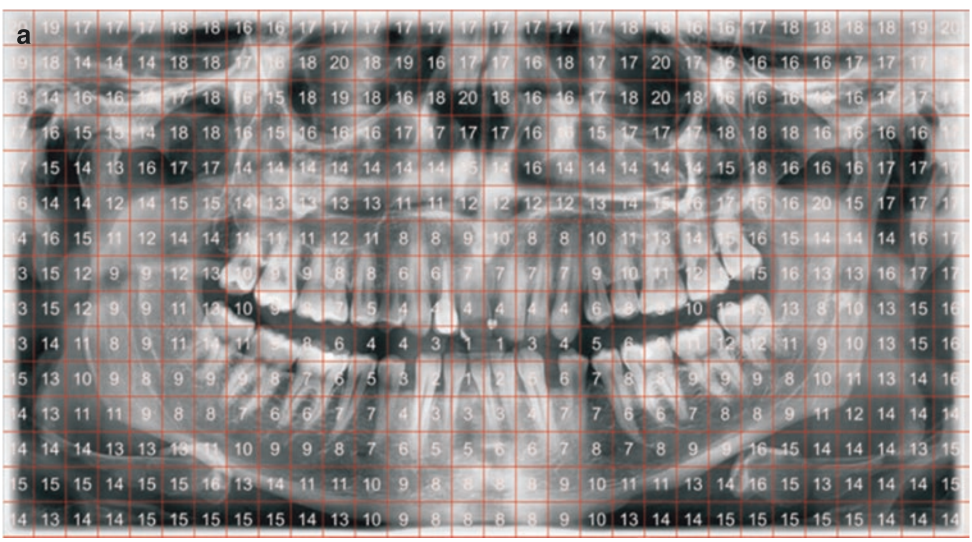

Fig. 23.3 Construction and representation of the panoramic image from multiple layer in-focus segments (ProVecta S-Pan, Air Techniques, Inc., Melville, NY, USA). Example of one of the 20 layers within the depth of the focal trough divided into row and column area segments (**a**). Within each of the 1000 area segments, the depth of the in-focus element is identified numerically. Comparative representative anterior image of panoramic system with conventional focal trough (**b**), optimal image from a multi-layer panoramic system (**c**) and image generated from automatic assembly of 20,000 in-focus segments (**d**). (Images courtesy, Air Techniques, Inc.)

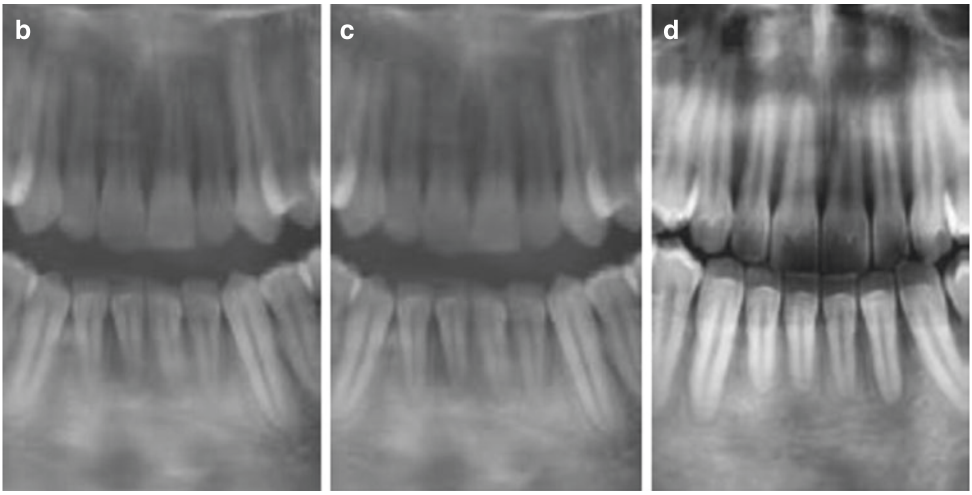

Fig. 23.3 (continued)

23.3 Cone Beam Computed Tomography

Panoramic and intraoral projection images, while being useful, provide only 2D information. Various 3D imaging technologies have been introduced which have potential application to the diagnosis of the hard tissue effects of periodontal disease including Tuned Aperture Computed Tomography (TACT) and panoramic tomosynthesis (Fig. 23.4) (Ogawa et al. 2010, 2011; Katsumata et al. 2011; Kitai et al. 2013). However only cone beam computed tomography (CBCT) has had widespread adoption into clinical dental practice since the early years of the current millennium.

23.3.1 Advantages in Periodontal Diagnosis

CBCT imaging offers specific advantages for periodontal diagnosis with the ability to accurately assess alveolar bone on the facial/buccal and lingual/palatal surfaces of all teeth as well as the mesial and distal aspects. Similar to panoramic radiography, image acquisition is extraoral, rapid, and technically easy to perform. Data is reconstructed volumetrically and images can be developed in linear or curved planes eliminating structural superimposition. Images can also be rendered volumetrically to demonstrate specific 3-D anatomic structures with geometric accuracy. Collimation of the X-ray beam by adjusting the irradiated FOV to the region of interest (ROI) allows considerable reduction in dose and improves, to some extent, image quality by minimizing scatter radiation. Depending on the manufacturer, acquisition parameters such as the exposure settings (e.g., mA and kVp), rotation angle, and number of basis images can also be adjusted by the operator to improve image quality. Almost all CBCT units produce voxels are that are isotropic, providing sub-millimeter spatial resolution up to a current theoretical nominal 0.076 mm. Spatial resolution is primarily a function of detector nominal pixel size and fill factor, however many factors such as beam projection geometry, patient X-ray scatter, detector and patient motion blur, X-ray generator focal spot size, number of basis images and reconstruction algorithm all contribute to the final maximum achievable resolution.

23.3.2 Limitations for Periodontal Diagnosis

While CBCT is capable of producing images with higher resolutions than that for panoramic

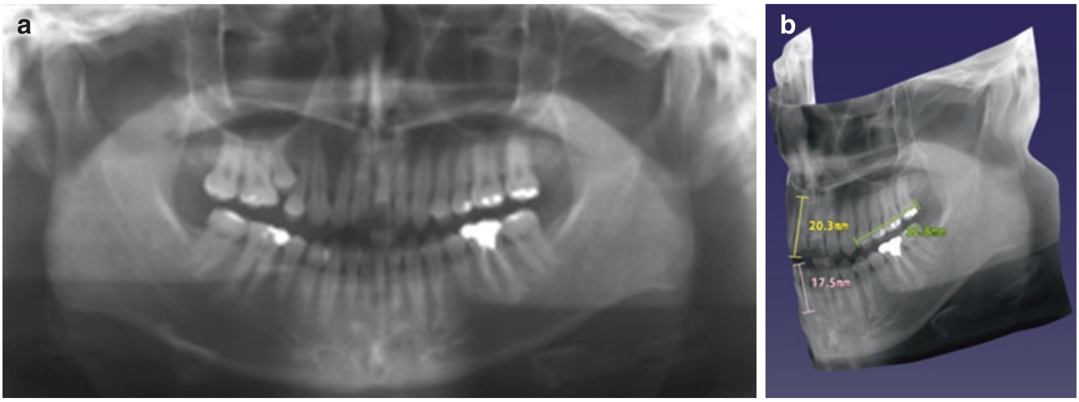

Fig. 23.4 A combination of cadmium-telluride semiconductor detector and a shift-and-add tomosynthesis methodology can convert a 2D panoramic image (**a**) into a narrow 3D geometric panoramic image (**b**) based upon information acquired from the patient's arch shape and tooth position. (Images courtesy, QRmaster-P, Telesystems Co. Ltd.)

radiography, both are inferior to intraoral radiography. CBCT is ideal for imaging relatively high attenuating bony structures such as teeth and bone but contrast resolution is limited. Contrast resolution allows the distinction between tissues with minor differences in tissue attenuation and to display them with different gray density levels. Gray scale intensity values measured on CBCT images do not directly represent Hounsfield units (HU), the relative density of body tissues according to a calibrated gray-level scale (Molteni 2013). As a consequence, cortical or intramedullary measurements of gray scale values cannot be considered as accurate or reliable indicators of bone mineral density.

23.3.3 Influences on Periodontal Diagnosis

There is a dearth of evidence on the influence of acquisition factors on CBCT image quality in relation to various aspects of periodontal disease diagnosis.

23.3.3.1 Image Acquisition Parameters

Of particular interest is the number of acquired projections and the projection arc. These vary greatly from manufacturer to manufacturer and may be fixed or variable, depending on machine. Reduction in either or both results in a reduction in the number of X-ray beam photons and data comprising the volumetric dataset and therefore increases the noise in tomographic images. Alteration in both parameters has been found to reduce diagnostic accuracy in the detection of root fractures (Costa et al. 2014).

Another factor that influences alveolar bone measurement accuracy (Sun et al. 2011) and buccal cortical defect detection (de-Azevedo-Vaz et al. 2013) is voxel size. Smaller voxel sizes are associated with better spatial resolution, however also result in higher image noise. To mitigate this effect, higher resolution scans may require higher exposures and higher number of projections (frames) in order to improve SNR (signal-to-noise ratio), however this results in greater patient radiation dose. Discernment of the PDL space, in particular, requires resolutions capable of less than 0.2 mm (Liang et al. 2010; Kamburoğlu et al. 2011).

23.3.3.2 Artifacts

Numerous authors have investigated the relative efficacy of CBCT imaging in detection and measurement of marginal alveolar bone height or localized defects as compared to intraoral or panoramic imaging using cadaver or skull samples with unrestored dentition (Vandenberghe et al.

2007, 2008a, b; Fleiner et al. 2015). However, the presence of artifacts produced in association with the interaction of the X-ray beam with high density materials (HDM), for example, titanium implants, amalgam, composite or gold restorations or root canal filling materials are a major cause of image degradation. HDM artifacts are a result of scatter and beam hardening and present at the horizontal level of the material as radiolucent and radiopaque streaks as well as distortion of adjacent structures. In areas of adjacent HDM, beam hardening may be additive resulting in dark voids, known as extinction artifacts. These artifacts are more pronounced on CBCT images because these systems have lower mean kilovoltage compared to multi-detector CT.

Another source of artifacts in clinical practice is patient motion during the CBCT gantry rotation. This can cause misregistration of data and commonly results in loss of spatial resolution that appears as a "double contour" on orthogonal or cross-sectional images. The influence of these artifacts on the detection of changes in or measurement of alveolar bone height has yet to be investigated.

23.4 Clinical Applications of CBCT in Periodontics

23.4.1 Crestal Alveolar Bone Morphology and Horizontal Bone Loss

The early detection and monitoring of crestal alveolar bone loss is important because it provides a hard tissue index for the presence of, or effects of preventative and corrective therapies for, periodontal disease. Changes in radiodensity and the outline of the crestal alveolar bone are the earliest signs of the osseous effects of periodontal disease and precede the loss of vertical height of the alveolar crest. The ideal radiographic imaging modality to record and monitor radiodensity and subtle morphology changes in the crestal bone should be cost efficient and easy to perform with high interobserver reliability and reproducibility. Images should demonstrate the circumferential morphology of the alveolar crestal bone and have a measurement accuracy of clinical relevance (approximately 10% of the CEJ to CAB distance or 0.2 mm or less spatial resolution) and able to discern nominal density differentials (approximately 10% or less). Despite the introduction of volumetric imaging, currently no radiographic modality exists that satisfies all of these requirements. Some have assumed that volumetric imaging is inherently better than conventional 2-D imaging simply because the anatomy of the patient is three-dimensional and crestal alveolar bone destruction occurs in 3-D. Although CBCT imaging can provide critical information for diagnosis and treatment planning in some cases, this is not always so.

23.4.1.1 Bone Mapping

One ultimate goal of CBCT image reconstructions in the diagnosis and assessment of therapies in periodontology is to provide morphologic or 3D mapping of the alveolar bone (Naito et al. 1998; Vandenberghe et al. 2008b) and or to visualize the topography of specific locations (Fig. 23.5). This is important given the variable and potentially complex resorption patterns of bone in response to periodontal disease.

The use of a 5.1 mm thick ray-sum CBCT reconstructed panoramic images for measuring periodontal bone levels (mean error 0.47 mm) has been reported to be at least as accurate as intraoral digital radiography (mean error 0.56 mm) (Vandenberghe et al. 2008a, b; Mol and Balasundaram 2008; de Faria Vasconcelos et al. 2012) and more accurate than panoramic radiography (Fig. 23.6) (Takeshita et al. 2014; Georgescu et al. 2010).

Fleiner et al. (2015) describe a 6-site (mesial, central, and distal aspects on the oral and vestibular surfaces) technique for tooth specific radiographic quantification of circumferential periodontal bone level (Fig. 23.7). They found a range of concordance between radiographic and manual measurements of 0.36–0.69 mm, with 83% of all results less than 0.5 mm. This methodology, together with the comments of others (Vandenberghe and Sarment 2013), highlights that the reliability and precision of bone loss

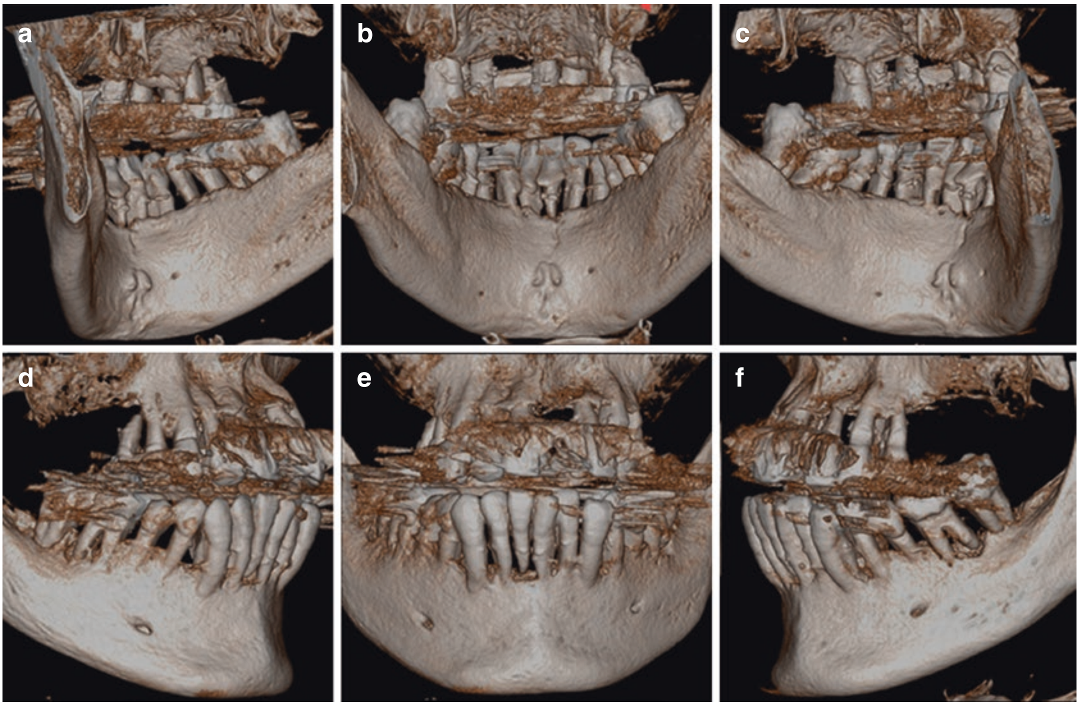

Fig. 23.5 3D morphologic bone mapping for periodontal assessment can involve various projections of shaded surface volumetric 3D image incorporating both lingual ((**a**)–(**c**)) and facial ((**d**)–(**f**)) aspects. Note the horizontal streaks at the coronal aspect in both dental arches indicative of beam hardening artifact. Additional artifacts associated with thresholding and segmentation are present particularly in the right maxillary posterior alveolar region showing the second molar "floating" in space

measurements related to specific teeth on CBCT orthogonal and cross-sectional images is highly dependent on the orientation of the sectional plane relative to individual teeth. Therefore, it is recommended sectioning be individualized according to the long axis of each tooth to provide accurate and reliable measurements of bone loss on specific teeth. Using this technique, mean height discrepancies ranging from 0.13 mm (Mengel et al. 2005) to 0.91 mm to 1.95 mm (Mol and Balasundaram 2008) compared to actual dimensions can be obtained. Comparative mean height discrepancies for intraoral radiography are approximately double this value (0.29 mm (Mengel et al. 2005) to 1.16 mm to 2.24 mm (Mol and Balasundaram 2008)).

Accuracy can be improved by using submillimeter section thickness of both reconstructed panoramic and cross-sectional planes (Vandenberghe et al. 2008a); however, image quality is somewhat degraded due to an increase in the noise of the image. While this technique produces clinically acceptable, reliable, and accurate data, it is extremely time consuming. In addition, the clinical efficacy of this technique specifically in the translation of greater overall measurement accuracy to improved clinical outcome measures such as choice of treatment regime and therapeutic result has not, as yet, been reported in the literature.

CBCT-based periodontal bone charting comprising morphologic mapping involving quantitative measurements of 3D virtual models is currently not a "one click" automated feature on any dental software and requires a knowledge of imaging concepts such as thresholding and segmentation as well as an expertise in interpreting the resultant images (Fig. 23.5). Despite technical difficulties, it would be highly desirable to quantify three-dimensional bony changes to compare the ability of different treatment modalities to arrest progression of bone destruction or even to visualize the effect of surgical interventions.

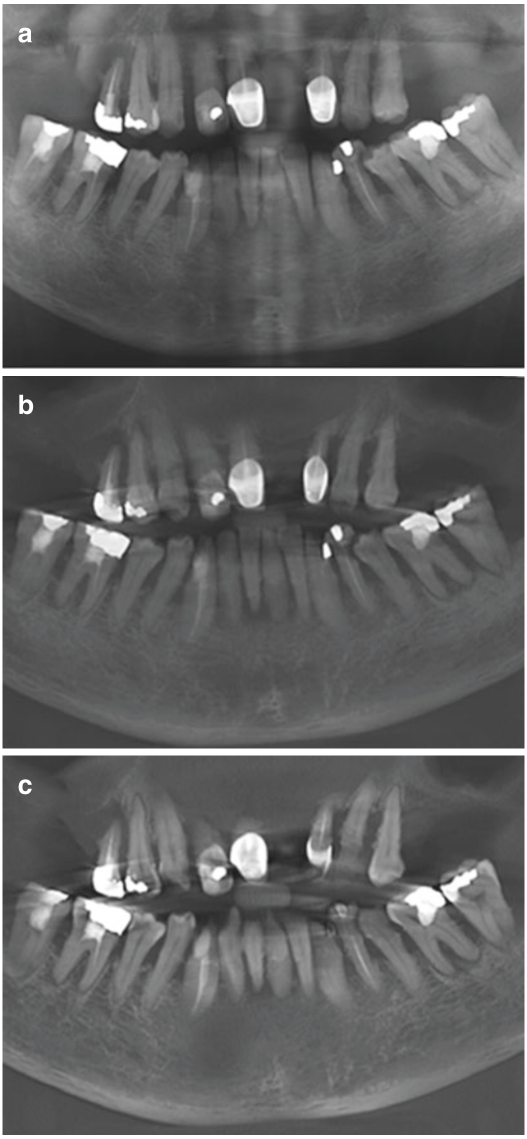

Fig. 23.6 Conventional (**a**) panoramic image of a patient with generalized moderate with localized severe marginal alveolar bone loss associated with adult periodontitis compared to reformatted simulated panoramic images with a 15 mm (**b**) and 5 mm (**c**) focal depth corresponding to the shape of the dental arch at the level of the cementoenamel junction. Reduction in image layer thickness sharpens the image and allows for greater visualization of the marginal alveolar bone however regions not corresponding to the shape or width of the image layer (e.g., maxillary anterior teeth and alveolus) are obscured

As described previously, repetitive measures at multiple specific sites on serial CBCT images is tedious and fraught with opportunities for reader error. One possible methodology, currently used in the assessment of the effect of orthognathic surgery on the maxillofacial skeleton (Cevidanes et al. 2010) and to record the effects of osteoarthritis on the mandibular condyle (Cevidanes et al. 2010; Schilling et al. 2014), is CBCT shape correspondence analysis. This method involves the superimposition and registration of consecutive CBCT volumes and the application of pseudo color maps to provide quantitative visualization of differences.

23.4.2 Localized Intrabony Defects

Localized intrabony defects usually present as isolated vertical "V" shaped defects often adjacent one surface of the tooth and are considered an indicator of a regional advanced active periodontitis (Fig. 23.8). They may be associated with an exacerbating condition(s), such as traumatic occlusion or fracture and most likely progress if left untreated. The defect angle, as determined by the angular discrepancy between the alveolar outline of the defect and adjacent tooth root surface measured at the apex of the base of the defect, has been used as a radiographic prognostic indicator of treatment success, especially for regenerative therapy (Tonetti et al. 1993; Klein et al. 2001). Angular ranges have been used to qualitatively distinguish narrow from wide defects (narrow range, ≤26° to ≤36°) (Klein et al. 2001; Eickholz et al. 2004).

The surgical treatment of intrabony defects using bone replacement grafts, guided tissue regeneration (GTR) and regenerative therapies such as enamel matrix derivative and recombinant human platelet derived Growth Factor-BB with β-tri-calcium phosphate has been shown to produce long-term (>10 years) intrabony defect fill. Selection and appropriate use of these therapies is based on modifying factors (e.g., smoking, oral hygiene) and local factors, particularly tooth mobility and defect morphology (Reynolds et al. 2015). Numerous authors have reported CBCT imaging to be superior to conventional intraoral or panoramic radiography for the detection (Mol and Balasundaram 2008; Mengel et al. 2005;

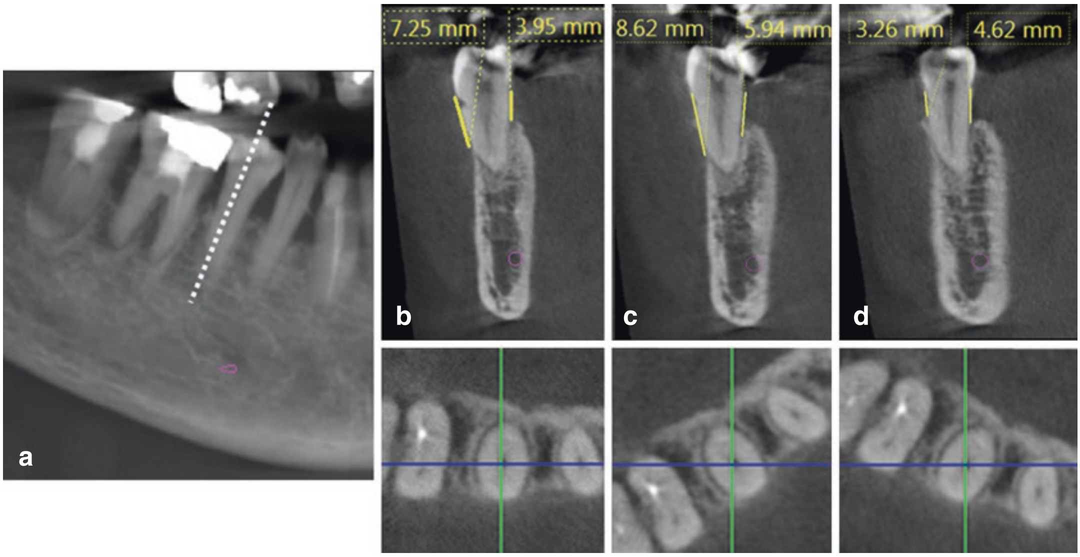

Fig. 23.7 Six site marginal alveolar bone height measurement protocol as described by Fleiner et al. (2013). Cropped reformatted panoramic image (**a**) of the right mandibular posterior region patient with generalized moderate generalized with localized moderate-to-severe alveolar bone loss with sequential cross-sections through the long axis of the second premolar at 90° (**b**), 45° distal (**c**), and 45° mesial (**d**) axial angulations. This approach provides six standardized sites for periodic measurement of the alveolar bone per tooth

Misch et al. 2006; Noujeim et al. 2009) and quantification (Vandenberghe et al. 2007; Fleiner et al. 2015; Vandenberghe et al. 2008b) of localized intrabony defects both in vitro and, more recently, in vivo (Raichur et al. 2012; Grimard et al. 2009) with up to 100% detection rate for CBCT as compared to intraoral radiography (Range, 21–67%) varying depending on lesion size (Fig. 23.9). Interestingly, clinical in vivo studies suggest that the CBCT radiographic measurement between the CEJ and base of the defect is underestimated compared to surgical measurements (Range, 0.4–1 mm). Unlike for overall periodontal bone loss mapping, the use of CBCT to assess localized defects has been reported to influence and direct treatment decisions (Walter et al. 2009) and improve clinical efficacy in regard to treatment cost and time (Walter et al. 2012).

23.4.3 Buccal Cortical Plate Defects

The facial alveolar bone adjacent the tooth root surface is prone to isolated perforations, called fenestrations, and deficiencies in alveolar bone height, referred to as a dehiscence. The prevalence of dehiscence and/or fenestration defects is high in both anterior (range, 9.9–51.6%) and posterior (range, 13.9–84.5%) regions (Zekry et al. 2014). Maxillary canines and first premolars most commonly demonstrate these defects (Evangelista et al. 2010). While most inflammatory related periodontal bone loss occurs on the mesial and distal aspects of the alveolar crest of teeth, when involved with progressive periodontal bone loss, a fenestration or dehiscence can lead to a substantial and immediate reduction in alveolar tooth support (Fig. 23.10).

Rapid maxillary expansion involving torquing of the roots of the posterior teeth can result in the reduction of the buccal cortical bone thickness as well as fenestration and/or dehiscence in the buccal aspects of the maxillary teeth (Garib et al. 2005; Wainwright 1973; Baysal et al. 2013). The presence of fenestrations and dehiscence is therefore important as a prognostic indicator of available alveolar bone for patients with periodontal disease or those undergoing orthodontic therapy especially those with previous periodontal bone loss. CBCT imaging has been shown to be mark-

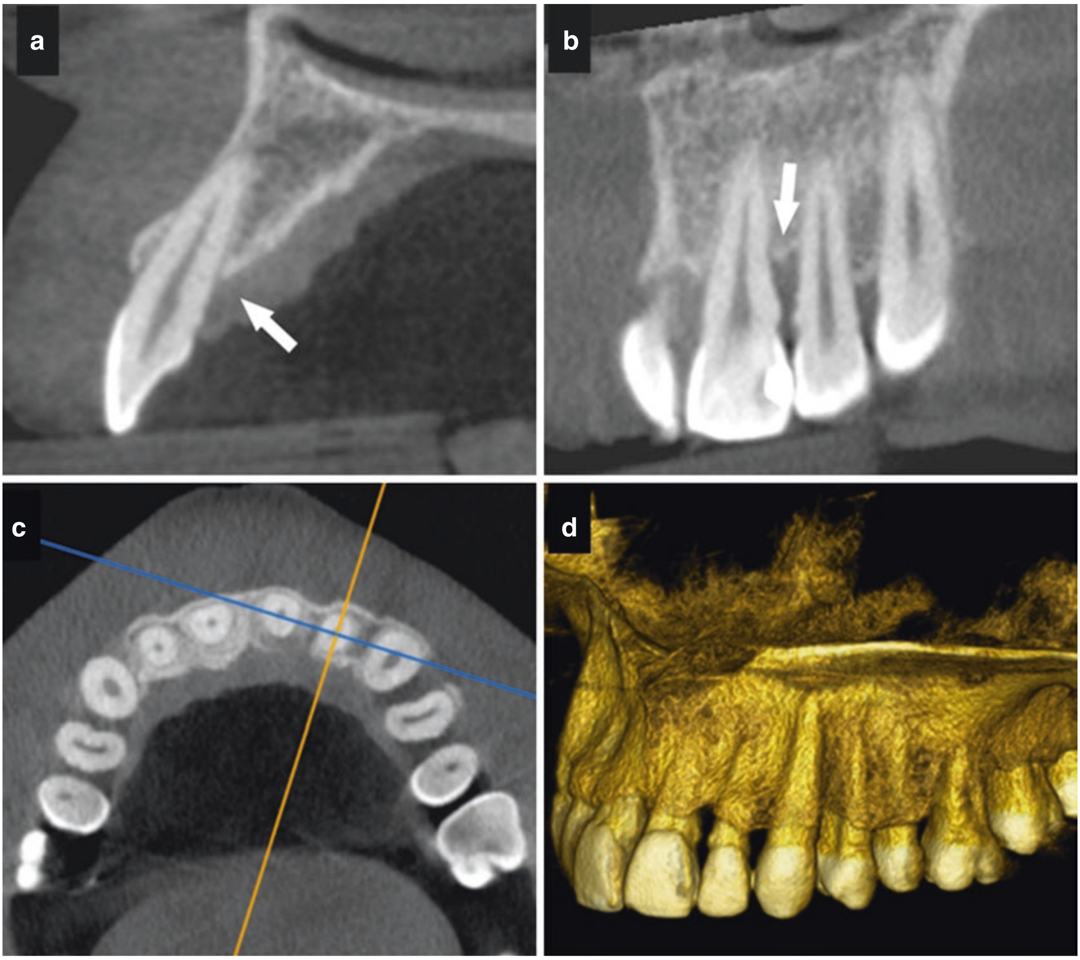

Fig. 23.8 Sagittal (**a**), para-coronal (**b**), axial reference (**c**), and 3D volumetric surface reconstructed images (**d**) of a patient with mild generalized horizontal marginal periodontitis. A localized deep 7 mm pocket with excessive bleeding and suppuration was identified clinically on the distal aspect of the right maxillary central incisor. CBCT imaging demonstrates irregular moderate intrabony defect associated with the disto-palatal this tooth. The interproximal alveolar crest in this region is diffuse (**c**) and extensive subgingival calculus is seen (**b**)

edly superior to intraoral imaging in the detection of anatomic (Zekry et al. 2014; Leung et al. 2010) or simulated (Braun et al. 2014) dehiscence and fenestration. In high esthetic risk zones, such as the maxillary canine, knowledge of dehiscence is valuable in planning regenerative soft tissue procedures.

23.4.4 Molar Furcation Involvement

Furcation involvement and associated bone loss associated with multi-rooted teeth, particularly maxillary first molars, present complex diagnostic challenges and can be addressed using various surgical therapeutic methods, depending on the degree of involvement and overall prognosis. These include selective root amputation, hemi- or tri-sectioning and apically repositioning of gingival flaps with or without tunnel preparations. Molars with interradicular loss of hard tissue have an increased risk of additional attachment loss with an impaired long-term prognosis. CBCT imaging has been reported to be superior to intraoral radiography for the identification (CBCT range, 83–100%; periapical range,

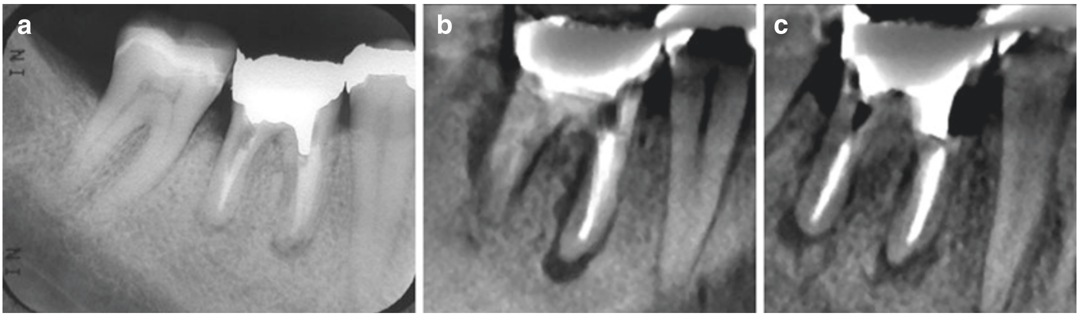

Fig. 23.9 Intraoral periapical image (**a**) of the mandibular right posterior region shows a root canal filled restored mandibular first molar with residual apical hypo-densities and a localized mild vertical alveolar bone loss on the distal aspect of the root. Sequential buccal (**b**) and mid-tooth (**c**) thin slice (1 mm thick) corrected parasagittal CBCT images demonstrate well-defined apical lesions with extensive localized marginal alveolar bone loss on the distal surface of the mesial root and pericircumferentially on the distal root not visualized on intraoral imaging. The pattern of involvement of both roots is suggestive of a furcation root fracture

56–73%) (Figs. 23.11 and 23.12) (Vandenberghe et al. 2008a; Noujeim et al. 2009; Umetsubo et al. 2012) and classification of furcation involvements (Laky et al. 2013; Qiao et al. 2014). Higher detection rates for CBCT are related to increased visualization on the bucco-facial and linguo-palatal aspects (Mengel et al. 2005). CBCT imaging has been found to be useful to determine the degree of bone loss associated with furcations in maxillary molar teeth, particularly on patients with existing generalized chronic periodontitis and clinical evidence of Class I furcation involvement (horizontal loss of periodontal tissue support up to 3 mm) (Walter et al. 2009, 2010). In fact, for almost 75% of patients, CBCT indicated that the degree of osseous furcation involvement determined clinically was either overestimated (29%) or underestimated (44%). Knowledge of the osseous anatomy of Class I furcation lesions as determined by CBCT imaging resulted in a change in treatment approach in more than 50% of cases (Range, 59–82%) depending on whether a conservative or aggressive approach to therapy (Walter et al. 2009, 2010).

CBCT analyses can also identify several morphological variations and pathologic observations pertinent to the decision-making process including fusion of partial or the entire surface of the adjacent roots, reduced interradicular space, concomitant periapical pathology, the presence of combined contiguous periodontal-endodontic lesions, root perforation, fenestration, and inadequate root canal obturation (Walter et al. 2011). The clinical efficacy of CBCT for furcation assessment has been demonstrated to provide a positive benefit-to-cost ratio for over 60% of cases with an overall reduction in treatment cost (approximating 25%) and time (approximately 136 ± 217 min), being greater for more invasive procedures (Walter et al. 2012). Emerging consensus appears to be that CBCT is becoming an important radiographic diagnostic tool for furcation assessment, particularly when more complex surgical treatment therapies are anticipated (Takane et al. 2010; Caminiti et al. 1998).

23.4.5 Surgical Exposure of Maxillary Canines

The prevalence of maxillary canine impaction ranges from 0.8 to 2.8%, depending on population studied with almost 75% of teeth being palatally impacted. The correction of impacted, unerupted maxillary canines, may require surgical and adjunctive orthodontic therapies. Two techniques are commonly used: one involves single surgical exposure of the crown of the tooth allowing for passive eruption—this is often used for labially positioned teeth; the second also involves exposure however, in addition, an orthodontic bracket with a ligature is attached to the crown of the

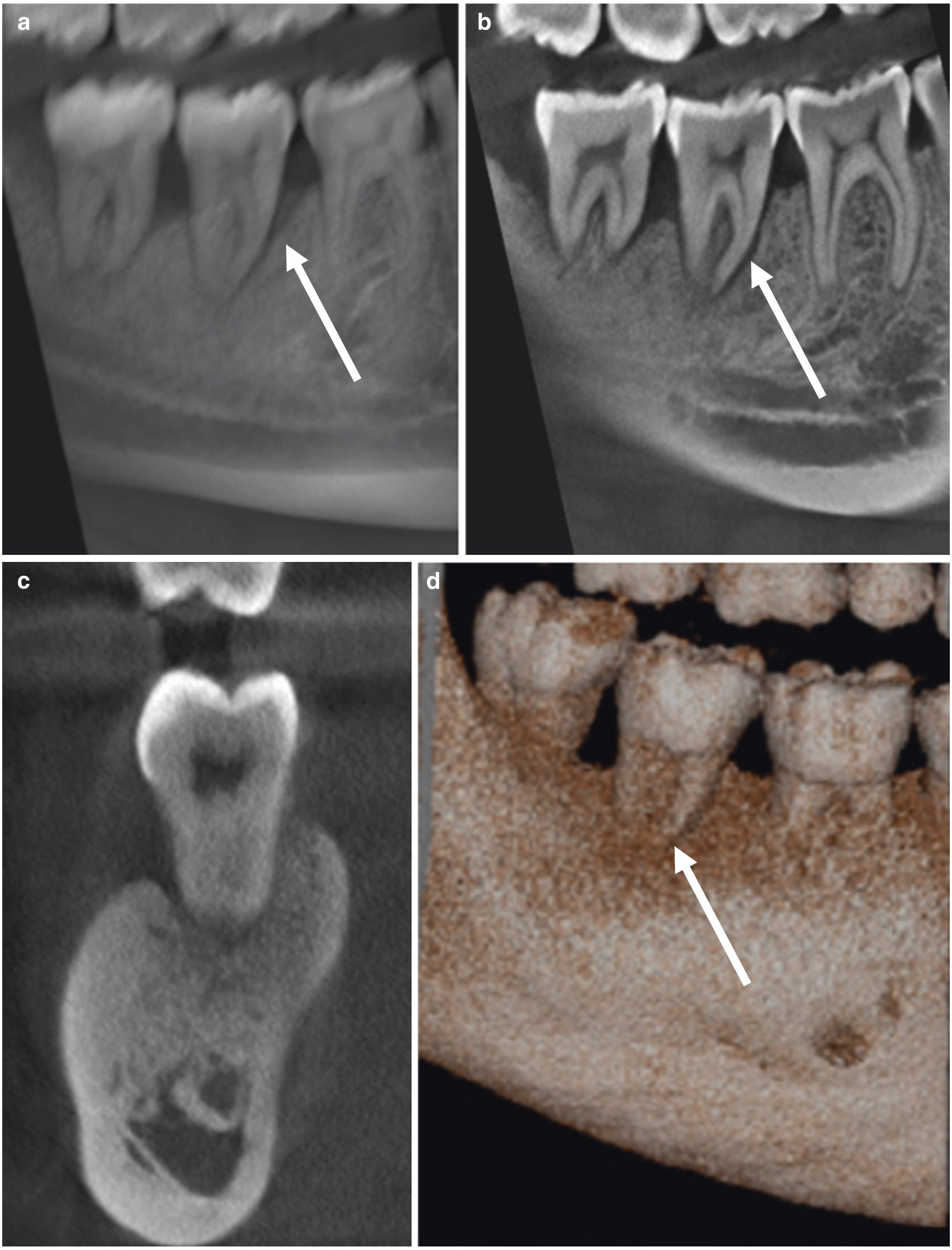

Fig. 23.10 Cropped panoramic image (**a**) of the mandibular right posterior molar region showing localized vertical defect and PDL space widening associated with the mesial aspect of the second molar. Small field of view CBCT sagittal (**b**), cross-sectional (**c**), and shaded surface volumetric rendering (**d**) showing PDL space widening but no mesial defect. However, there is a substantial buccal cortical dehiscence reducing overall alveolar support and contributing to the PDL space widening

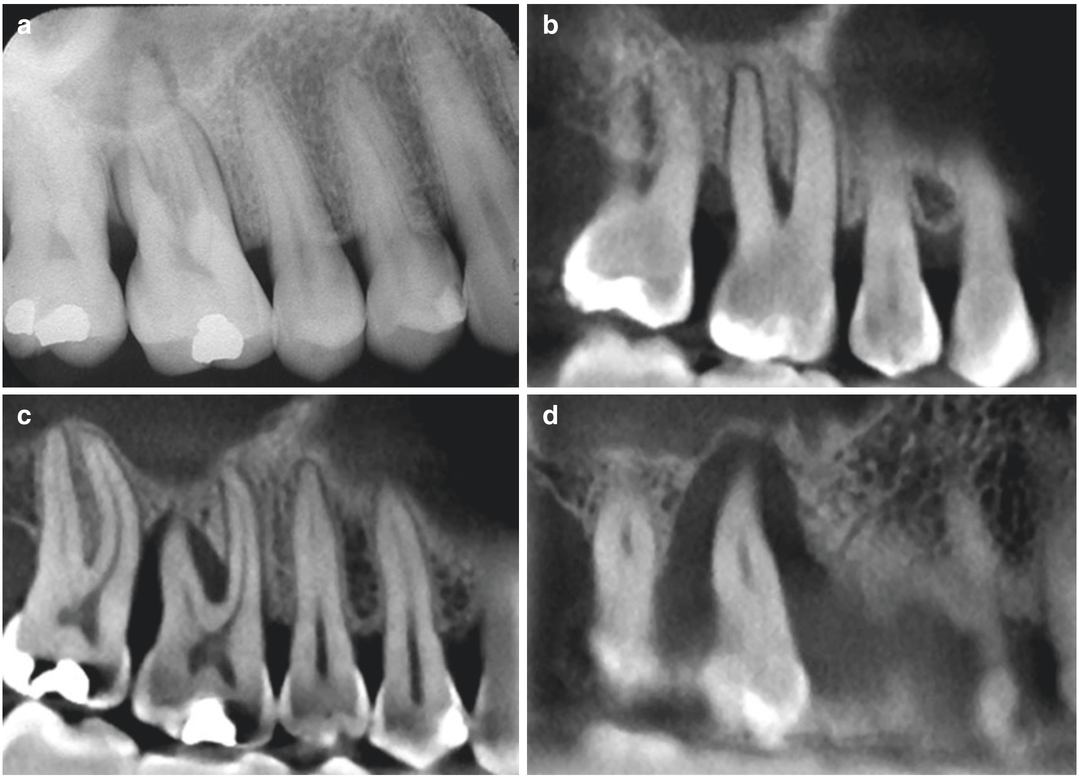

Fig. 23.11 Intraoral periapical image (**a**) of the maxillary right posterior region shows a minimally restored maxillary first molar with clinical mobility and shows generalized moderate PDL space widening and some loss of lamina dura. A buccal (**b**) corrected thin slice (1 mm thick) corrected parasagittal CBCT image confirms the findings of the intraoral image. However sequential mid-tooth (**c**) and palatal (**d**) parasagittal CBCT images demonstrate extensive Class III furcation involvement and severe localized pericircumferential alveolar bone loss on the palatal root not appreciated on intraoral imaging. (Images courtesy, Dr. José Ribamar Azevedo)

tooth to which an orthodontic force is applied providing active eruption into the dental arch. Periodontists as well as oral and maxillofacial surgeons are often requested to assist in surgically exposing the crown. The success of these treatments is variable, with up to 15% of simple surgical cases and 30.7% requiring re-exposure (Caminiti et al. 1998; Pearson et al. 1997). Numerous radiographic factors can affect the surgical approach and orthodontic management including the facial/palatal and anteroposterior location, the amount of bone covering the crown, the edentulous space available for eruption, the angulation of the canine to the midline, canine root anomalies, overlap of the adjacent lateral incisor root (Fig. 23.13), and degree of root formation (Motamedi et al. 2009). The detection and confirmation of the extent of external root resorption of adjacent teeth, especially the lateral incisor, is an important finding affecting management. Ankylosis has been reported to affect up to almost 30% of canines (Motamedi et al. 2009). CBCT images have found to be valuable in the identification of these factors (Alqerban et al. 2011; Botticelli et al. 2011) and substantially influence treatment decisions especially when canine inclination on the panoramic image exceeds 30°, when root resorption of adjacent teeth is suspected, and/or when the canine apex is not clearly discernible (Haney et al. 2010; Wriedt et al. 2012).

23.4.6 Periradicular Pathology

Increasingly periodontal therapies include the identification and treatment of periradicular

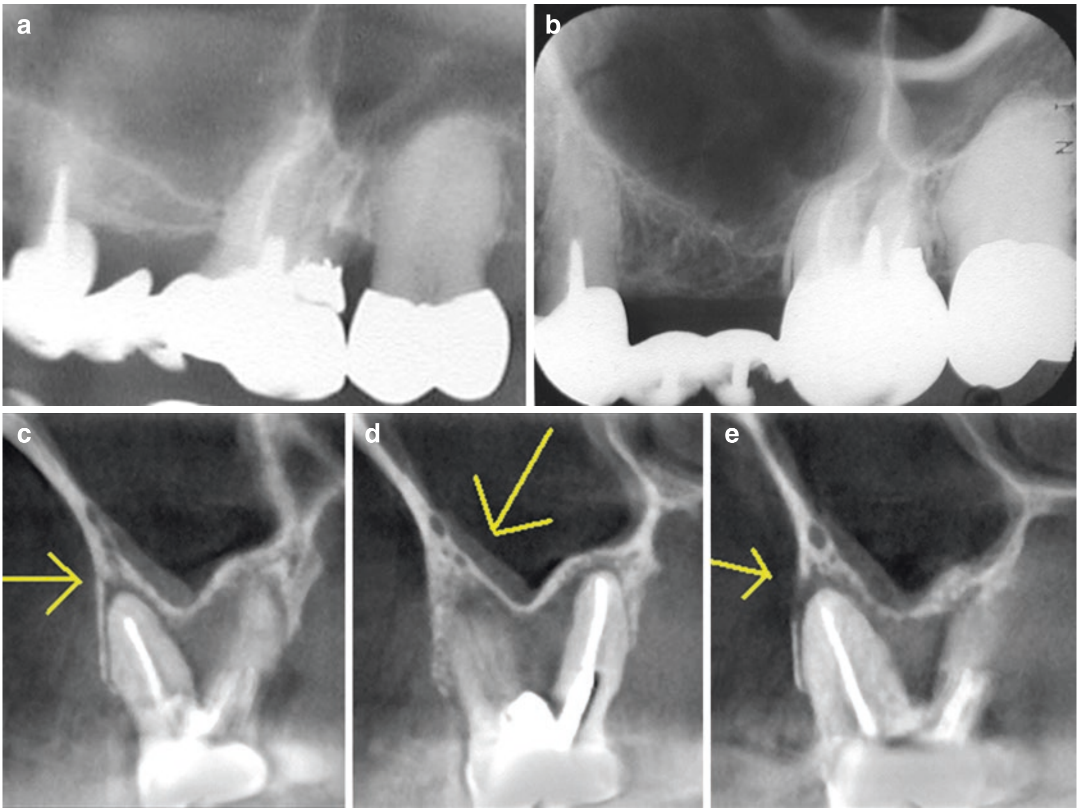

Fig. 23.12 Cropped panoramic (**a**) and corresponding intraoral periapical (**b**) images of the left maxillary posterior region with a root canal filled first molar acting as a fixed prosthesis abutment. The patient reported mobility of the bridge. Sequential cross-sectional images through the mesio-buccal (**c**), palatal (**d**), and disto-buccal (**e**) roots demonstrating severe Class III furcation involvement involving the apices of all teeth and perforating through the buccal cortical plate of the disto-buccal root. Note the secondary reactive mucosal thickening of the floor of the maxillary sinus (*arrow* in (**d**)) and apparent perforation of restorative material through the floor of the pulp canal in the furcation (**d**). (Images courtesy, Dr. José Ribamar Azevedo, Brazilia, Brazil)

pathologies involving the marginal alveolar bone and overlying gingival mucosa.

23.4.6.1 External Root Resorption

External root resorption (ERR) is an osteoclastic process on the root surface of teeth that most frequently occurs in the region of the cervical third. ERR can be classified as surface resorption, external inflammatory resorption, external replacement resorption, external (or invasive) cervical resorption (ECR), and transient apical breakdown (Patel and Ford 2007). Appropriate therapeutic approaches are directed towards differentiating the process of ECR from internal root resorption (IRR) and correct classification. Numerous predisposing factors have been suggested as initiating factors of ECR including orthodontics, trauma, intracoronal bleaching, surgical procedures and periodontal therapy and idiopathic etiologies (Patel et al. 2009; Kandalgaonkar et al. 2013). CBCT imaging is extremely useful in identifying, quantifying, and distinguishing ECR from IRR (Fig. 23.14) (Patel and Dawood 2007; Estevez et al. 2010). On imaging, ECR presents as a well-defined, irregular bordered mottled root surface hypodense defect, potentially confused with dental caries. The extent and involvement of the lesion is classified according to Heithersay (1999). In the early and intermediate stages, a hyperdense zone, representing secondary responsive predentin, often separates the defect from the root canal. Periodontal management involves

Fig. 23.13 Left anterosuperior oblique view of a volumetric 3D rendering (**a**) showing bilateral ectopically positioned maxillary buccal impacted and unerupted canines. Both (**a**) and the cross-sectional image through the root of the left maxillary lateral incisor (**b**) show bucco-apical root resorption associated with the coronal aspect of the left lateral canine

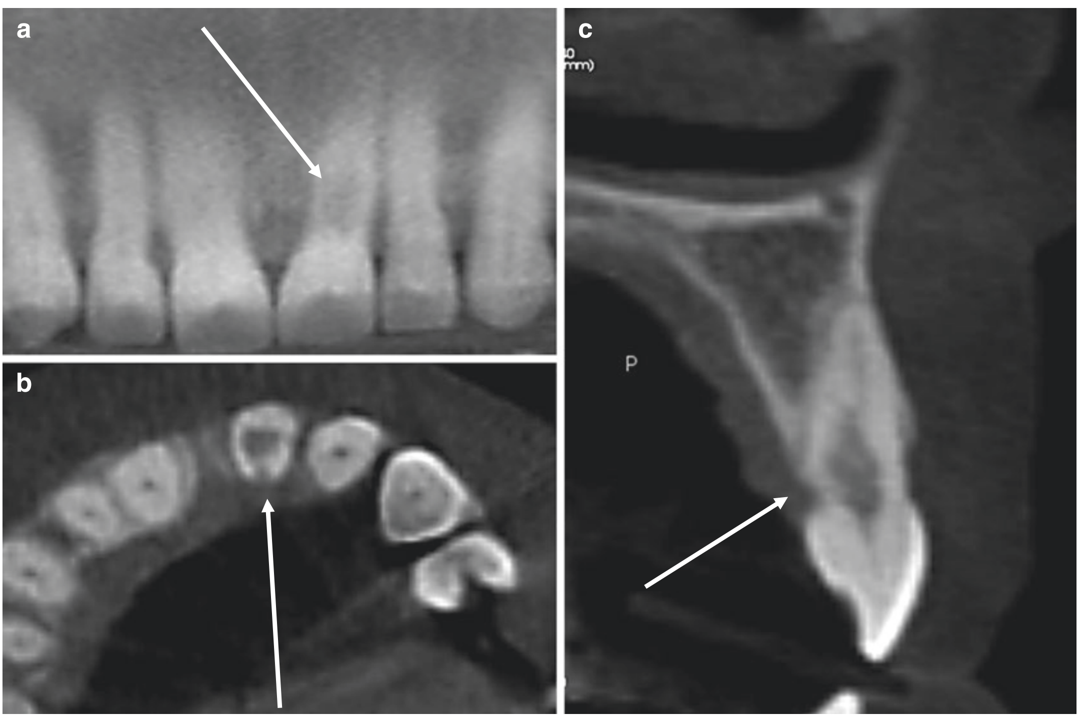

Fig. 23.14 CBCT reformatted panoramic image (**a**) of the anterior maxilla demonstrating (*arrow*) apparent internal root resorption on the left central incisor. Axial (**b**) and cross-sectional (**c**) images confirm the presence of internal root resorption but also shows an area of external cervical resorption on the palatal aspect, below the CEJ. Appropriate management involves both endodontic and periodontal therapies

mucoperiosteal flap access, debridement, and restoration with concurrent endodontic therapy if root canal involvement is identified.

23.4.6.2 Periodontal Abscess

The periodontal abscess is the third most common cause of a dental emergency after acute dentoalveolar abscess and pericoronitis, accounting for approximately 7% of patients presenting with pain (Herrera et al. 2000). A periodontal abscess is a localized region of periodontal breakdown located within the gingival wall of a periodontal pocket usually beyond the mucogingival line, occurring over a short period of time producing a localization of pus. A periodontal abscess may develop in the absence of periodontal disease, often associated with the impaction of a foreign body (e.g., popcorn kernel, orthodontic elastic). When associated with concurrent periodontitis, it is usually an indication of localized exacerbation of active bone destruction. Clinically a periodontal abscess presents as a painful ovoid elevation of the gingiva along the lateral part of the root with suppuration sometimes associated with tooth mobility and sensitivity to palpation. Imaging may reveal a normal marginal alveolar bone or variable localized bone loss ranging from widening of the periodontal space to a dramatic radiographic bone loss. Differential diagnosis, particularly when signs and symptoms are ambiguous or when standard treatments (incision, drainage, local debridement and antibiotic therapy) are ineffective, include vertical root fracture, periodontic-endodontic lesions, lateral periodontal cyst, local osteomyelitis (Parrish et al. 1989) and tumors such as eosinophilic granuloma or even malignancy such as gingival squamous cell carcinoma. Left untreated a periodontal abscess may become an odontogenic source of cellulitis (Schuknecht et al. 2008). CBCT imaging may be useful in quantifying the degree and pattern of localized bone loss (Fig. 23.15), serving as a

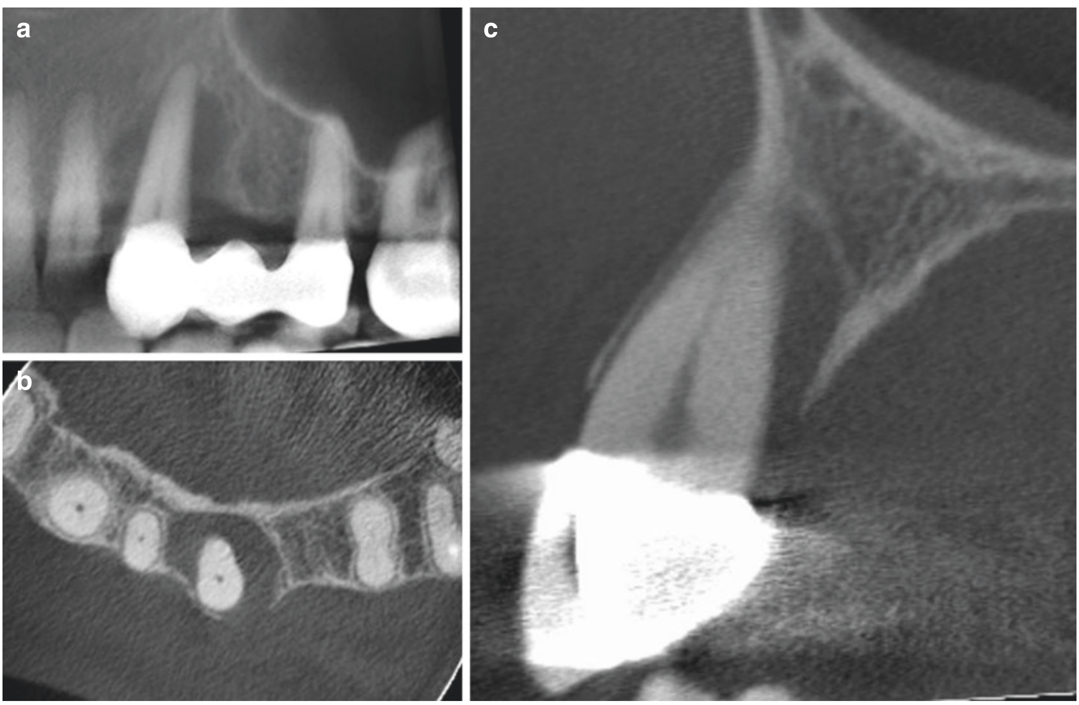

Fig. 23.15 Small volume CBCT showing a reformatted panoramic (**a**), axial (**b**) and cross-sectional (**c**) images of a large pericircumferential alveolar defect associated with the left canine which is an abutment for a fixed partial prosthesis. The lack of apical involvement and expansion, thinning and perforation of the buccal cortical plate on the distal aspect of the tooth together with the clinical presence of a parulis are consistent with a periodontal abscess

baseline for therapy and exclusion of other pathologic entities, as described previously.

23.4.6.3 Lateral Periodontal Cyst

Although uncommon, the lateral periodontal cyst is an odontogenic cyst of developmental origin arising from the epithelial rest of Malassez within the periodontal ligament space or within the bone between the roots of adjacent teeth. Often asymptomatic, they present as incidental findings on radiographic examination as small (less than 1 cm in diameter) well-defined, round, oval or tear-dropped shaped unilocular hypodensity, most often located between the lateral surface of the tooth root between the alveolar crest and the root apex (Fig. 23.16). Adjacent teeth are usually vital, unless root canal filled. Up to 75% of cases are found in the mandible, most frequently in the canine to premolar region. Larger lesions may result in root divergence; however, expansion or perforation of the facial or lingual cortical plates is rare. A multilocular variant of the LPC, but with a much higher recurrence rate (range, 15–33%), is the botryoid odontogenic cyst. Differential diagnosis should include a consideration of a lesion of pulpal origin. The LPC is a progressively slow growing lesion which requires surgical excision. While most heal within 6–12 months, lesions should be monitored radiographically for several years for recurrence. Although rare, ameloblastoma and squamous cell carcinoma has been reported to occur in association with LPC.

23.4.7 Third Molar Pericoronal Pathology

Pericoronitis is an inflammatory response to an infection of the soft tissue covering the coronal aspect of partially unerupted and impacted third molars resulting in pain, localized swelling, and trismus (Punwutikorn et al. 1999). It is the most common pathology associated with impacted third molars (Doğan et al. 2007; McNutt et al. 2008). Pericoronitis can be a significant quality of life issue (McNutt et al. 2008) and is second most common reason for dental emergencies. Recurrent episodes may result in localized infection of the follicular space and the adjacent bone,

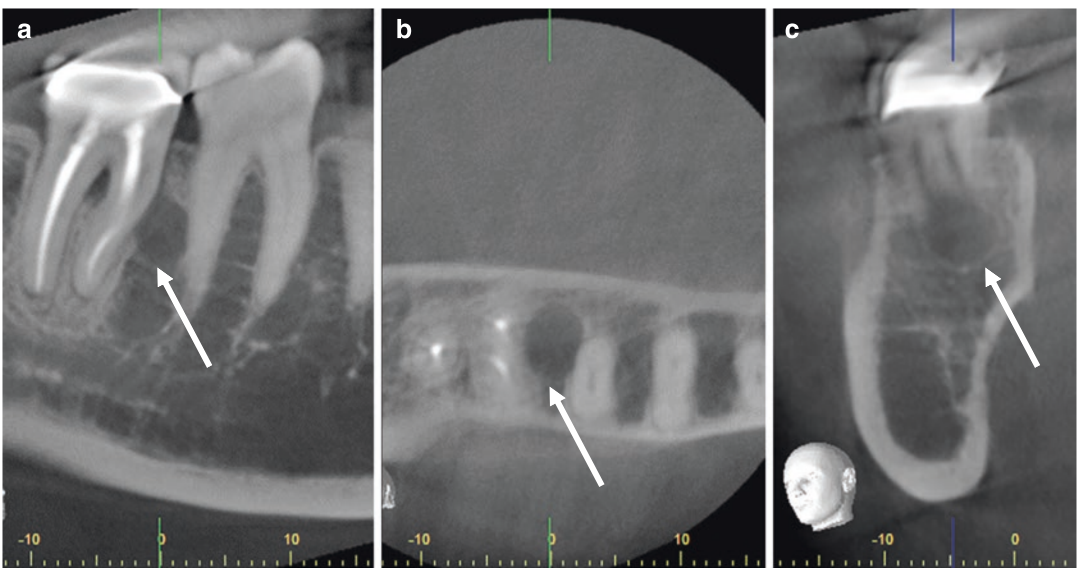

Fig. 23.16 Small field of view CBCT sagittal (**a**), axial (**b**), and cross-sectional (**c**) images of the right posterior mandible showing a well-defined, unilocular hypodensity in the interradicular bone adjacent the mesial root of the right second molar and distal root of the first molar consistent with a lateral periodontal cyst. Secondary PDL space widening is seen on the upper third of the mesial root of the second molar

referred to as osteitis. Surgical management therapies may involve soft tissue procedures involving the removal of the operculum (e.g., laser) or, more commonly, hard tissue procedures particularly if osteitis is identified. Surgical techniques include extraction of the third molar, coronectomy (Monaco et al. 2012) if the proximity of the mandibular inferior alveolar canal to the tooth roots is such that nerve damage may result. Presurgical risk assessment of third molars using CBCT prior to removal can identify the presence of osteitis, assess the location of the IAC in relation to the tooth roots and identify incidental pericoronal pathology that may compromise the alveolar support on the distal aspect of the second molars including dentigerous cysts (Fig. 23.17) or odontogenic tumors such as ameloblastoma or keratocystic odontogenic tumor. CBCT has also been found to modify surgical approach as compared with panoramic radiography (Ghaeminia et al. 2011).

23.4.8 Osteomyelitis

Osteomyelitis of the jaws can theoretically occur by direct spread and extension of chronic marginal periodontitis or localized periodontal infection into the medullary cavity; however, this is a rare sequelae of periodontal disease (Parrish et al. 1989; Waalkens 1984; Tomaselli et al. 1993). Patients usually have systemic comorbidities affecting either the immune-suppressive response such as end stage renal disease or compromising vascularity including diabetes or bone dyscrasias such as Osteopetrosis, Paget's disease, or fibrous dysplasia. Diagnosis is based on the patient's clinical symptoms (pain), clinical signs (swelling, previous recent periodontal therapy, fenestration), and radiographic features (diffuse osteolysis of the interdental septum with subsequent extension to the apical region) in addition to the failure of response to conservative antibiotic therapy and debridement (Fig. 23.18).

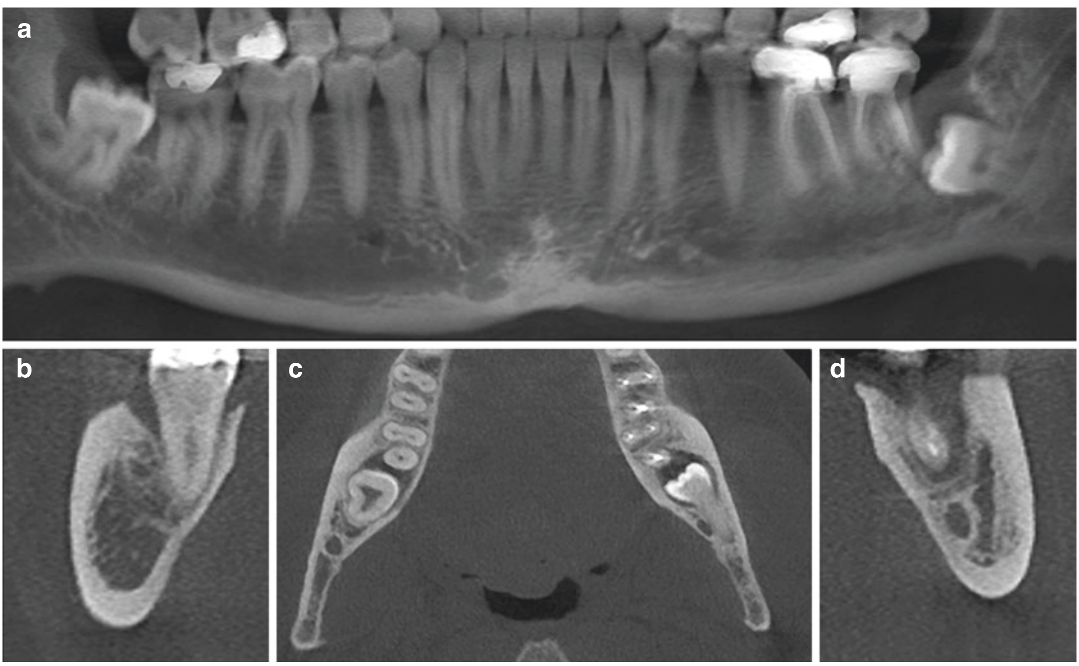

Fig. 23.17 Reformatted panoramic image (**a**) of mandibular arch demonstrating bilateral mesio-angular completely bony impacted and unerupted third molars with involvement of the distal aspect of the second molars. There is widening of the right follicular space (>3 mm) typical of pericoronitis with osteitis and loss of distal alveolar bone involving approximately half of the root as confirmed on the right cross-sectional (**b**) and axial image (**c**). The pericoronal osteolysis is more substantial, suggestive of a dentigerous cyst on the left side and extends to involve the entire distal and apical portion of the root of the root canal filled left second molar

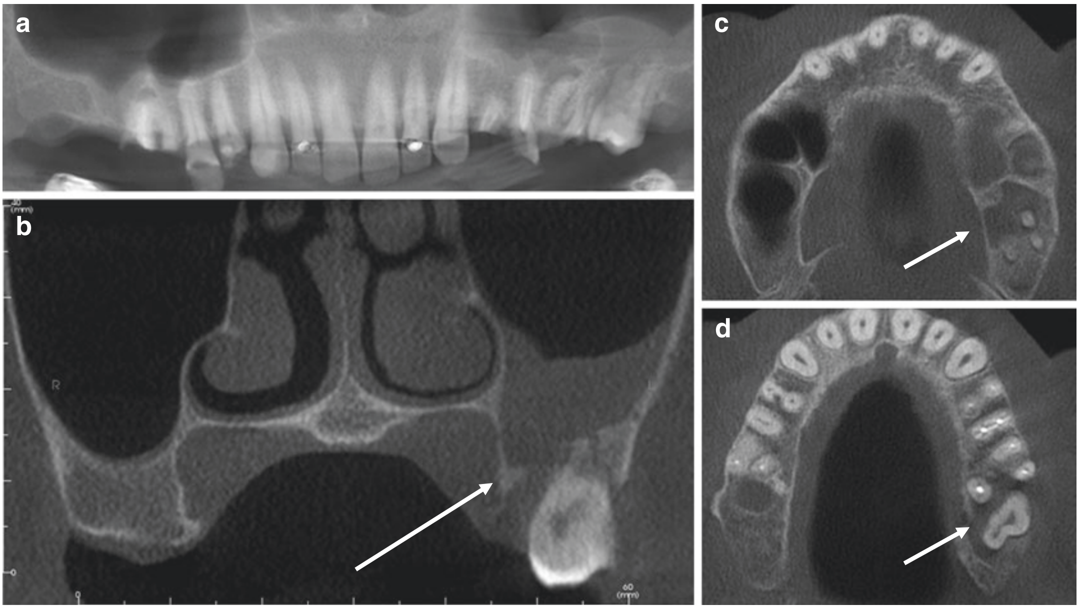

Fig. 23.18 Sagittal (**a**), para-coronal (**b**), axial reference (**c**), and 3D volumetric surface reconstructed images (**d**) of a patient with mild generalized horizontal marginal periodontitis. A localized deep 7 mm pocket with excessive bleeding and suppuration was identified clinically on the distal aspect of the right maxillary central incisor. CBCT imaging demonstrates irregular moderate intrabony defect associated with the disto-palatal this tooth. The interproximal alveolar crest in this region is diffuse (**c**) and extensive subgingival calculus is seen (**b**)

23.4.9 Combined Periodontic-Endodontic Lesions

There are three potential sequelae resulting in simultaneous inflammatory involvement of periodontal and pulpal/apical tissues (Simon et al. 2013) referred to as periodontic-endodontic lesions. All sequelae may lead to the initiation and progression of bone loss; however, the pattern of this loss and associated osteolytic entities can assist in distinguishing the etiology and therefore direct treatment therapies. A primary endodontic lesion results from a periapical inflammatory response to pulpal necrosis with subsequent fistula formation coronally through the periodontal ligament from the apex or a lateral canal. Clinically the involved tooth is nonvital; radiographically this may present as a periradicular radiolucency in multi-rooted teeth, similar in appearance to a furcation involvement with loss of lamina dura or as apical radiolucency with diffuse but uniform PDL space widening on any aspect of the tooth. A primary periodontic lesion results from an inflammatory response to chronic marginal periodontitis at the alveolar crest progressing through the PDL to the apical region. Clinically the involved tooth is usually vital with involvement of the cervical root surface; radiographically this may also present as a furcation-like lesion or loss of lamina dura and diffuse PDL space widening on any aspect of the tooth. The final sequelae involve concurrent inflammatory events at the cervical margin and apically to produce a "True" combined lesion. Two possibilities exist: the primary endodontic lesion may have secondary periodontic involvement (Fig. 23.19) or the primary periodontic lesion may have secondary endodontic involvement (Fig. 23.20). Radiographically the bone destructive processes are demonstrated separated until they coalesce.

Alternate classification systems have been proposed by Torabinejad and Trope based on the origin of the periodontal pocket (Torabinejad and Rotstein 2014) and at the World workshop for Classification of Periodontal Diseases (Armitage

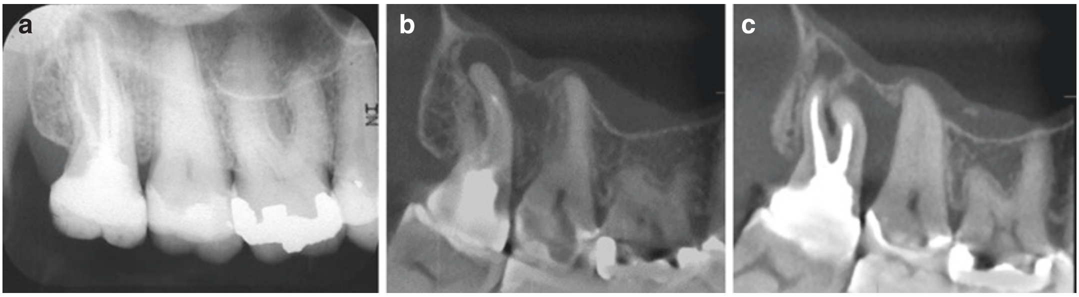

Fig. 23.19 Intraoral periapical image (**a**) of the maxillary right posterior region of a patient who presents with acute pain in this region. The image shows a root canal filled maxillary third molar with indistinct apical integrity but apparently intact alveolar crestal bone. Sequential buccal (**b**) and mid-tooth (**c**) thin slice (1 mm thick) corrected parasagittal CBCT images demonstrate well-defined apical lesions on both the mesio-buccal and disto-buccal apices with a endodontic-periodontic lesion with extensive localized alveolar bone loss on the mesial surface of the mesio-buccal root involving the distal surface of the second molar. This degree of bone loss is not seen on intraoral imaging. The pattern of involvement of both roots is suggestive of a furcation root fracture

1999). Clinical diagnosis relies on pulp testing and periodontal probing however imaging can provide details on the size and extent of the periodontal defect or apical lesion and degree and pattern of involvement of the PDL space and adjacent lamina dura. The radiographic appearance of periodontic-endodontic lesions may appear similar to the bony responses elicited by vertical root fracture. CBCT imaging may assist in identifying these fractures as well as other contributing factors such as inadequate endodontic treatment, root perforations, and developmental malformations.

23.4.10 Regenerative Procedures

Digital subtraction radiography provides a relatively sensitive measure of osseous response to regenerative therapies in periodontics (Guimarães et al. 2010; Kyriazis et al. 2012; Mardas et al. 2011); however, as a technique it is almost exclusively employed as a noninvasive research assessment tool. CBCT imaging has been used to assess bone augmentation or preservation procedures for ridge development prior to or simultaneously with implant placement; however, few studies have reported its use in the postoperative evaluation of regenerative periodontal therapies in vitro (Grimard et al. 2009). With the increasing use of guided tissue regenerative (GTR) membranes and emerging availability of inexpensive 3D model fabrication, it is plausible that reasonably priced additive models of the dentition and surrounding alveolar morphology can be derived from CBCT datasets and used in pre-forming and customizing GTR membranes providing adequate 3–5 mm extension of the barrier beyond the defect with concomitant savings in surgical time (Takane et al. 2010).

23.4.11 Soft Tissue Assessment

Periodontal disease is not just a pathologic process affecting the supporting hard tissues but presents with adjacent soft tissue inflammatory mediated changes of the gingival mucosal. These present clinically as loss of gingival attachment levels relative to the physiologic norms, edema as measured by periodontal pocket probing depth, and bleeding on probing. All of these signs are used to establish disease extent and monitor progression or resolution with therapy. Unfortunately, operator inconsistency and differences in methodology result in a limitation of the accuracy of clinical quantitative indices (Range, 1–3 mm). Poor correlation exists between clinical measurements and radiographic bone height which may reflect different milieu of periodontal destruction and periodontal healing (Cury et al. 2004) or inaccuracies in measurement methodology.

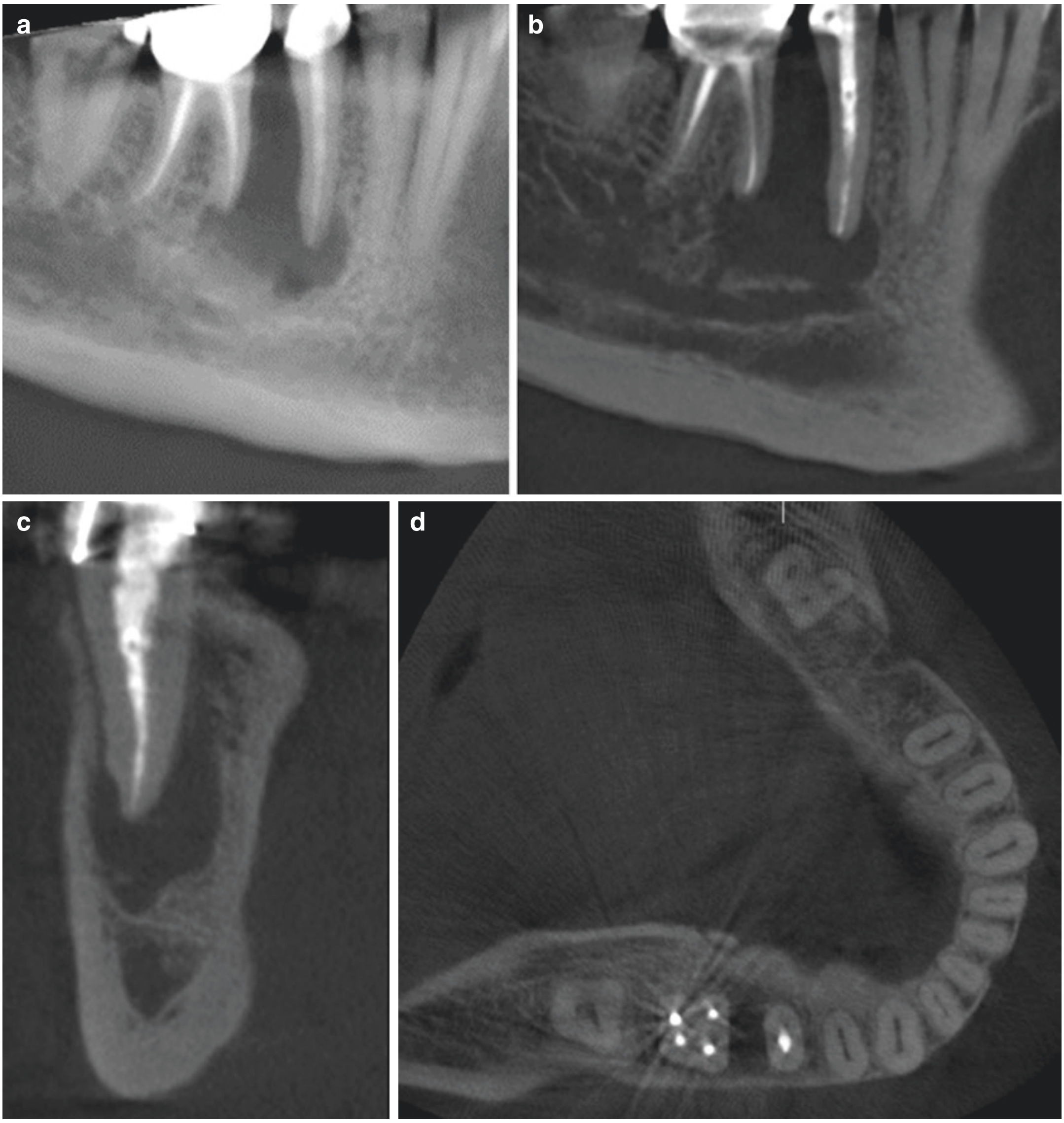

Fig. 23.20 Simulated panoramic image of the right mandibular molar region showing large localized osteolytic alveolar defect in a patient with an otherwise normal periodontal bone level. The lesion involves the apices of two adjacent root canal filled teeth; the second premolar and the mesial root of the first molar. Based on this image alone, the defect involves the entire interradicular bone and suggests a one walled defect with poor prognosis. Small field of view CBCT sagittal (**b**), cross-sectional (**c**), and axial (**d**) images demonstrate an apical focus and intact buccal and lingual cortical plates with intramedullary destruction suggesting a primary endodontic origin with secondary periodontic involvement

Both conventional intraoral radiographic and CBCT imaging are able to discern air/soft tissue boundaries; however, in clinical practice, this is not usually appreciated. The soft tissue mucosal shadow of the alveolar crest is infrequently observed in edentulous regions in intraoral radiography because of the preference for most practitioners for high contrast, overall dense (dark) images. In CBCT, visualization of the bucco-facial or linguo-palatal surfaces of the gingival soft tissues are obscured by the collapse of and contact with the surface of the cheeks, lips, and tongue. A technique protocol referred to as soft tissue CBCT (ST-CBCT) has been reported to facilitate visualization of the soft tissue profile on the facial/buccal aspect of the alveolus and dentition (Fig. 23.21) (Januario et al. 2008). This technique involves scanning of the patient while using lip/cheek retractors to prevent these soft tissues from contacting the dentition and mucosa of the buccal alveolus. This enables identification of both the hard tissue of the alveolar crest and dentition (e.g., CEJ) and adjacent gingival soft tissue and facilitates precise measurement of clinical parameters such as the position of the gingival margin to both the alveolar crest and CEJ as well as the mucosal thickness adjacent the tooth as well the buccal alveolar bone.

This technique has also been modified to include wooden spatulas to position the tongue away from the palate to provide a clear soft tissue interface over the palatal tissues (Barriviera et al. 2009). Knowledge of the thickness of the palatal masticatory mucosa is potentially important in identifying optimal donor areas for periodontal soft tissue grafts requiring keratinizing mucosa such as those covering exposed root surfaces.

23.5 Summary

In situations where conventional imaging involving a combination or panoramic and intraoral radiography is unable to answer a specific diagnostic question, CBCT imaging provides a simple, relatively low dose imaging procedure capable of accurately demonstrating the quantity and pattern marginal alveolar bone loss associated with periodontitis on all surfaces of the dentition in one procedure. However, there is no current evidence to suggest that, for routine use, CBCT

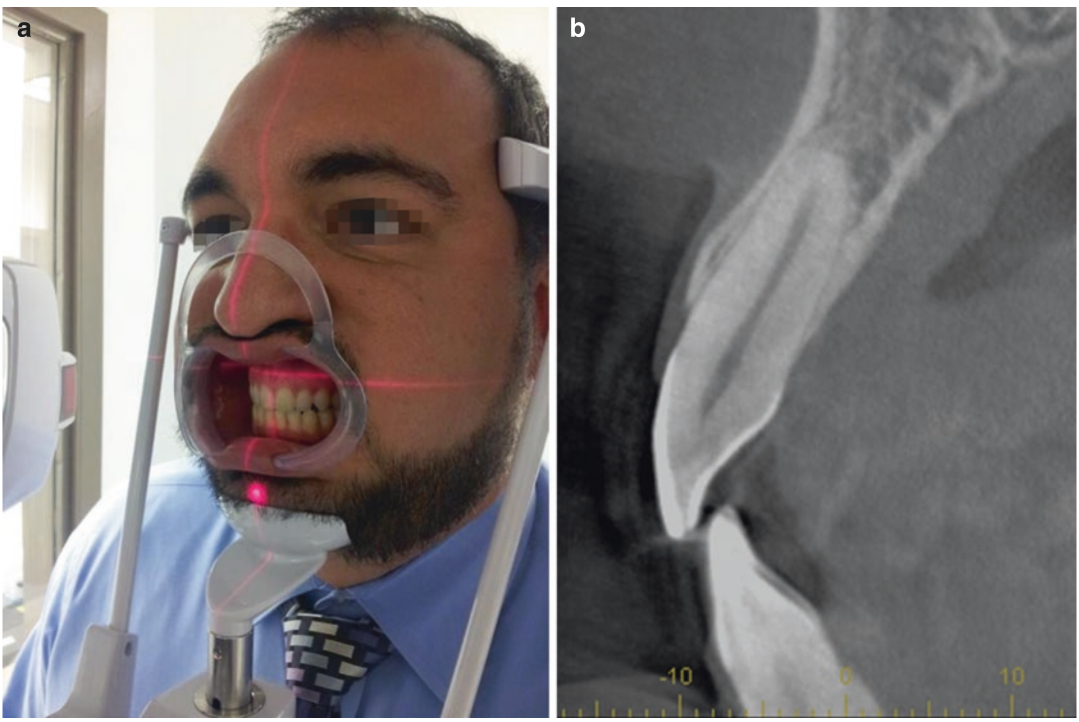

Fig. 23.21 Soft tissue CBCT (ST-CBCT) technique with the patient positioned in CBCT unit using lip/cheek retractors (e.g., Free Access II, J Morita Corp., Kyoto, Japan) to prevent these soft tissues from contacting the dentition and mucosa of the buccal alveolus (**a**). Cross-sectional 1 mm CBCT image (**b**) showing the buccal and palatal hard tissue of the alveolar crest and adjacent gingival soft tissue. This technique allows measurement of the gingival margin to both the alveolar crest and CEJ, mucosal thickness adjacent the tooth as well the thickness of the buccal alveolar bone

imaging for 3D bone mapping provides any clinical advantages to current intraoral and panoramic radiography. Supplemental CBCT imaging of localized defects such as furcation involvement, intrabony vertical, and buccal/lingual defects have been shown to be clinically efficacious, particularly in the assessment of the effects of regenerative therapy. In these situations, limited field of view, high resolution protocols are indicated.

Acknowledgments Portions of this chapter are reproduced from Scarfe WC et al. (2016) with permission from John Wiley & Sons.

References

Akesson L, Rohlin M, Håkansson J, Håkansson H, Näsström K (1989) Comparison between panoramic and posterior bitewing radiography in the diagnosis of periodontal bone loss. J Dent 17:266–271

Akesson L, Hakansson J, Rohlin M (1992) Comparison of panoramic and intraoral radiography and pocket probing for the measurement of marginal bone level. J Clin Periodontol 19:326–332

Alqerban A, Jacobs R, Fieuws S, Willems G (2011) Comparison of two cone beam computed tomographic systems versus panoramic imaging for localization of impacted maxillary canines and detection of root resorption. Eur J Orthod 33:93–102

Armitage GC (1999) Development of a classification system for periodontal diseases and conditions. Ann Periodontol 4:1–6

Barriviera M, Duarte WR, Januário AL, Faber J, Bezerra AC (2009) A new method to assess and measure palatal masticatory mucosa by cone-beam computerized tomography. J Clin Periodontol 36:564–568

Baysal A, Uysal T, Veli I, Ozer T, Karadede I, Hekimoglu S (2013) Evaluation of alveolar bone loss following rapid maxillary expansion using cone-beam computed tomography. Korean J Orthod 43:83–95

Benn DK (1990) A review of the reliability of radiographic measurements in estimating alveolar bone changes. J Clin Periodontol 17:14–21

Botticelli S, Verna C, Cattaneo PM, Heidmann J, Melsen B (2011) Two- versus three-dimensional imaging in subjects with unerupted maxillary canines. Eur J Orthod 33:344–349

Braun X, Ritter L, Jervøe-Storm PM, Frentzen M (2014) Diagnostic accuracy of CBCT for periodontal lesions. Clin Oral Investig 18:1229–1236

Caminiti MF, Sandor GK, Giambattistini C, Tompson B (1998) Outcomes of the surgical exposure, bonding and eruption of 82 impacted maxillary canines. J Can Dent Assoc 64:572–574, 576–579

Cevidanes LH, Hajati AK, Paniagua B, Lim PF, Walker DG, Palconet G, Nackley AG, Styner M, Ludlow JB, Zhu H, Phillips C (2010) Quantification of condylar resorption in temporomandibular joint osteoarthritis. Oral Surg Oral Med Oral Pathol Oral Radiol Endod 110:110–117

Costa FF, Pinheiro LR, Umetsubo OS, Santos Júnior OD, Gaia BF, Cavalcanti MG (2014) Influence of cone-beam computed tomographic scan mode for detection of horizontal root fracture. J Endod 40:1472–1476

Cury PR, Araújo NS, Bowie J, Sallum EA, Jeffcoat M (2004) The relationship between radiographic and clinical parameters in periodontal maintenance in class II furcation defects. Braz Oral Res 18:116–120

de Faria Vasconcelos K, Evangelista KM, Rodrigues CD, Estrela C, de Sousa TO, Silva MA (2012) Detection of periodontal bone loss using cone beam CT and intraoral radiography. Dentomaxillofac Radiol 41:64–69

de-Azevedo-Vaz SL, Vasconcelos Kde F, Neves FS, Melo SL, Campos PS, Haiter-Neto F (2013) Detection of periimplant fenestration and dehiscence with the use of two scan modes and the smallest voxel sizes of a cone-beam computed tomography device. Oral Surg Oral Med Oral Pathol Oral Radiol 115:121–127

Doğan N, Orhan K, Günaydin Y, Köymen R, Okçu K, Uçok O (2007) Unerupted mandibular third molars: symptoms, associated pathologies, and indications for removal in a Turkish population. Quintessence Int 38:e497–e505

Douglass CW, Valachovic RW, Wijesinah A (1986) The clinical efficacy of dental radiography in the detection of dental caries and periodontal disease. Oral Surg Oral Med Oral Pathol 62:330–339

Eickholz P, Riess T, Lenhard M, Hassfeld S, Staehle HJ (1999) Digital radiography of interproximal bone loss; validity of different filters. J Clin Periodontol 26:294–300

Eickholz P, Hausmann E (2000) Accuracy of radiographic assessment of interproximal bone loss in intrabony defects using linear measurements. Eur J Oral Sci 108:70–73

Eickholz P, Hörr T, Klein F, Hassfeld S, Kim TS (2004) Radiographic parameters for prognosis of periodontal healing of infrabony defects: two different definitions of defect depth. J Periodontol 75: 399–407

Estevez R, Aranguren J, Escorial A, de Gregorio C, De La Torre F, Vera J, Cisneros R (2010) Invasive cervical resorption Class III in a maxillary central incisor: diagnosis and follow-up by means of cone-beam computed tomography. J Endod 36:2012–2014

Evangelista K, Vasconcelos Kde F, Bumann A, Hirsch E, Nitka M, Silva MA (2010) Dehiscence and fenestration in patients with Class I and Class II division 1 malocclusion assessed with cone-beam computed tomography. Am J Orthod Dentofac Orthop 138:133.e1–133.e7

Fleiner J, Hannig C, Schulze D, Stricker A, Jacobs R (2015) Digital method for quantification of circum-

ferential periodontal bone level using cone beam CT. Clin Oral Investig 17:389–396
Galal A, Manson-Hing L, Jamison H (1985) A comparison of combinations of clinical and radiographic examinations in evaluation of a dental clinic population. Oral Surg Oral Med Oral Pathol 60:553–561
Garib DG, Henriques JF, Janson G, Freitas MR, Coelho RA (2005) Rapid maxillary expansion-tooth tissue borne versus tooth-borne expanders: a computed tomography evaluation of dentoskeletal effects. Angle Orthod 75:548–557
Gedik R, Marakoglu I, Demirer S (2008) Assessment of alveolar bone levels from bitewing, periapical and panoramic radiographs in periodontitis patients. West Indian Med J 57:410–413
Georgescu CE, Mihai A, Didilescu AC, Moraru R, Nimigean V, Nimigean VR et al (2010) Cone beam computed tomography as a method of quantitative and qualitative analysis of alveolar crest in the frontal mandibular area. Romanian J Morphol Embryol 51:713–717
Ghaeminia H, Meijer GJ, Soehardi A, Borstlap WA, Mulder J, Vlijmen OJ, Bergé SJ, Maal TJ (2011) The use of cone beam CT for the removal of wisdom teeth changes the surgical approach compared with panoramic radiography: a pilot study. Int J Oral Maxillofac Surg 40:834–839
Grimard BA, Hoidal MJ, Mills MP, Mellonig JT, Nummikoski PV, Mealey BL (2009) Comparison of clinical, periapical radiograph, and cone-beam volume tomography measurement techniques for assessing bone level changes following regenerative periodontal therapy. J Periodontol 80:48–55
Grondahl H-G, Grondahl K, Webber RL (1984) Influence of variations in projection geometry on the detectability of periodontal bone lesions. J Clin Periodontol 11:411–420
Guimarães Mdo C, Passanezi E, Sant'Ana AC, Grechi SL, Taba Junior M (2010) Digital subtraction radiographic analysis of the combination of bioabsorbable membrane and bovine morphogenetic protein pool in human periodontal infrabony defects. J Appl Oral Sci 18:379–384
Halperin-Sternfeld M, Levin L (2013) Do we really know how to evaluate tooth prognosis? A systematic review and suggested approach. Quintessence Int 44:447–456
Haney E, Gansky SA, Lee JS, Johnson E, Maki K, Miller AJ, Huang JC (2010) Comparative analysis of traditional radiographs and cone-beam computed tomography volumetric images in the diagnosis and treatment planning of maxillary impacted canines. Am J Orthod Dentofac Orthop 137:590–597
Hausmann E, Allen K, Carpio L, Christersson LA, Clerehugh V (1992) Computerized methodology for detection of alveolar crestal bone loss from serial intraoral radiographs. J Periodontol 3:657–662
Heithersay GS (1999) Invasive cervical resorption: an analysis of potential predisposing factors. Quintessence Int 30:83–95
Herrera D, Roldán S, Sanz M (2000) The periodontal abscess: a review. J Clin Periodontol 27:377–386
Januario AL, Barriviera M, Duarte WR (2008) Soft tissue cone-beam computed tomography: a novel method for the measurement of gingival tissue and the dimensions of the dentogingival unit. J Esthet Restor Dent 20:366–373, discussion, p. 374
Kandalgaonkar SD, Gharat LA, Tupsakhare SD, Gabhane MH (2013) Invasive cervical resorption: a review. J Int Oral Health 5:124–130
Kamburoğlu K, Murat S, Kolsuz E, Kurt H, Yüksel S, Paksoy C (2011) Comparative assessment of subjective image quality of cross-sectional cone-beam computed tomography scans. J Oral Sci 53:501–508
Katsumata A, Ogawa K, Inukai K, Matsuoka M, Nagano T, Nagaoka H, Yamakawa T (2011) Initial evaluation of linear and spatially oriented planar images from a new dental panoramic system based on tomosynthesis. Oral Surg Oral Med Oral Pathol Oral Radiol Endod 112:375–382
Kitai N, Mukai Y, Murabayashi M, Kawabata A, Washino K, Matsuoka M, Shimizu I, Katsumata A (2013) Measurement accuracy with a new dental panoramic radiographic technique based on tomosynthesis. Angle Orthod 83:117–126
Klein F, Kim TS, Hassfeld S, Staehle HJ, Reitmeir P, Holle R, Eickholz P (2001) Radiographic defect depth and width for prognosis and description of periodontal healing of infrabony defects. J Periodontol 72:1639–1646
Kyriazis T, Gkrizioti S, Mikrogeorgis G, Tsalikis L, Sakellari D, Lyroudia K, Konstantinides A (2012) Crestal bone resorption after the application of two periodontal surgical techniques: a randomized, controlled clinical trial. J Clin Periodontol 39:971–978
Laky M, Majdalani S, Kapferer I, Frantal S, Gahleitner A, Moritz A, Ulm C (2013) Periodontal probing of dental furcations compared with diagnosis by low-dose computed tomography: a case series. J Periodontol 84:1740–1746
Langlois Cde O, Sampaio MC, Silva AE, Costa NP, Rockenbach MI (2011) Accuracy of linear measurements before and after digitizing periapical and panoramic radiography images. Braz Dent J 22:404–409
Leung CC, Palomo L, Griffith R, Hans MG (2010) Accuracy and reliability of cone-beam computed tomography for measuring alveolar bone height and detecting bony dehiscences and fenestrations. Am J Orthod Dentofac Orthop 137(4 Suppl):S109–S119
Liang X, Jacobs R, Hassan B, Li L, Pauwels R, Corpas L, Souza PC, Martens W, Shahbazian M, Alonso A, Lambrichts I (2010) A comparative evaluation of cone beam computed tomography (CBCT) and multi-slice CT (MSCT) part I. On subjective image quality. Eur J Radiol 75:265–269
Loe H (1994) Periodontal disease as we approach the year 2000. J Periodontol 65(5 Suppl):464–467
Mardas N, D'Aiuto F, Mezzomo L, Arzoumanidi M, Donos N (2011) Radiographic alveolar bone changes

following ridge preservation with two different biomaterials. Clin Oral Implants Res 22:416–423
McNutt M, Partrick M, Shugars DA, Phillips C, White RP Jr (2008) Impact of symptomatic pericoronitis on healthrelated quality of life. J Oral Maxillofac Surg 66:2482–2487
Mengel R, Candir M, Shiratori K, Flores-de-Jacoby L (2005) Digital volume tomography in the diagnosis of periodontal defects: an in vitro study on native pig and human mandibles. J Periodontol 6:665–673
Misch KA, Yi ES, Sarment DP (2006) Accuracy of cone beam computed tomography for periodontal defect measurements. J Periodontol 77:1261–1266
Mol A, Balasundaram A (2008) In vitro cone beam computed tomography imaging of periodontal bone. Dentomaxillofac Radiol 37:319–324
Molteni R (2013) Prospects and challenges of rendering tissue density in Hounsfield units for cone beam computed tomography. Oral Surg Oral Med Oral Pathol Oral Radiol 116:105–119
Monaco G, de Santis G, Gatto MR, Corinaldesi G, Marchetti C (2012) Coronectomy: a surgical option for impacted third molars in close proximity to the inferior alveolar nerve. J Am Dent Assoc 143:363–369
Motamedi MH, Tabatabaie FA, Navi F, Shafeie HA, Fard BK, Hayati Z (2009) Assessment of radiographic factors affecting surgical exposure and orthodontic alignment of impacted canines of the palate: a 15-year retrospective study. Oral Surg Oral Med Oral Pathol Oral Radiol Endod 107:772–775
Muhammed AH, Manson-Hing LR (1982) A comparison of panoramic and intraoral radiographic surveys in evaluating a dental clinic population. Oral Surg Oral Med Oral Pathol 54:108–117
Naito T, Hosokawa R, Yokota M (1998) Three dimensional alveolar bone morphology analysis using computed tomography. J Periodontol 69:584–589
Noujeim M, Prihoda T, Langlais R, Nummikoski P (2009) Evaluation of high-resolution cone beam computed tomography in the detection of simulated interradicular bone lesions. Dentomaxillofac Radiol 38: 156–162
Ogawa K, Langlais RP, McDavid WD, Noujeim M, Seki K, Okano T et al (2010) Development of a new dental panoramic radiographic system based on a tomosynthesis method. Dentomaxillofac Radiol 39:47–53
Ogawa K, Langlais RP, McDavid WD, Noujeim M, Seki K, Okano T, Yamakawa T, Sue T (2011) Pre-clinical evaluation of a new dental panoramic radiographic system based on tomosynthesis method. Dentomaxillofac Radiol 40:42–46
Parrish LC, Kretzschmar DP, Swan RH (1989) Osteomyelitis associated with chronic periodontitis: a report of three cases. J Periodontol 60:716–722
Patel S, Dawood A (2007) The use of cone beam computed tomography in the management of external cervical resorption lesions. Int Endod J 40:730–737
Patel S, Ford TP (2007) Is the resorption external or internal? Dent Update 34:218–229
Patel S, Kanagasingam S, Ford TP (2009) External cervical resorption: a review. J Endod 35:616–625
Pauls V, Trott JR (1966) A radiological study of experimentally produced lesions of bone. Dent Pract 16(7):254
Pearson MH, Robinson SN, Reed R, Birnie DJ, Zaki GA (1997) Management of palatally impacted canines: the findings of a collaborative study. Eur J Orthod 19:511–515
Pepelassi EA, Diamanti-Kipioti A (1997) Selection of the most accurate method of conventional radiography for the assessment of periodontal osseous destruction. J Clin Periodontol 24:557–567
Pepelassi EA, Tsiklakis K, Diamanti-Kipioti A (2000) Radiographic detection and assessment of the periodontal endosseous defects. J Clin Periodontol 27:224–230
Persson RE, Tzannetou S, Feloutzis AG, Brägger U, Persson GR, Lang NP (2003) Comparison between panoramic and intra-oral radiographs for the assessment of alveolar bone levels in a periodontal maintenance population. J Clin Periodontol 30(9):833
Punwutikorn J, Waikakul A, Ochareon P (1999) Symptoms of unerupted mandibular third molars. Oral Surg Oral Med Oral Pathol Oral Radiol Endod 87:305–310
Qiao J, Wang S, Duan J, Zhang Y, Qiu Y, Sun C, Liu D (2014) The accuracy of cone-beam computed tomography in assessing maxillary molar furcation involvement. J Clin Periodontol 41:269–274
Raichur PS, Setty SB, Thakur SL, Naikmasur VG (2012) Comparison of radiovisiography and digital volume tomography to direct surgical measurements in the detection of infrabony defects. J Clin Exp Dent 4:e43–e47
Renvert S, Badersten A, Nilveius R, Egelberg J (1981) Healing after treatment of periodontal intraosseous defescts. I. Comparative study of clinical methods. J Clin Periodontol 8:387–399
Reynolds MA, Kao RT, Camargo PM, Caton JG, Clem DS, Fiorellini JP, Geisinger ML, Mills MP, Nares S, Nevins ML (2015) Periodontal regeneration: intrabony defects: a consensus report. J Periodontol 86(2 Suppl):S105–S107
Rohlin M, Akesson L, Hakansson J, Hakansson H, Nasstrom K (1989) Comparison between panoramic and periapical radiography in the diagnosis of periodontal bone loss. Dentomaxillofac Radiol 18:72–76
Schilling J, Gomes LC, Benavides E, Nguyen T, Paniagua B, Styner M, Boen V, Gonçalves JR, Cevidanes LH (2014) Regional 3D superimposition to assess temporomandibular joint condylar morphology. Dentomaxillofac Radiol 43:20130273
Schuknecht B, Stergiou G, Graetz K (2008) Masticator space abscess derived from odontogenic infection: imaging manifestation and pathways of extension depicted by CT and MR in 30 patients. Eur Radiol 18:1972–1979
Semenoff L, Semenoff TA, Pedro FL, Volpato ER, Machado MA, Borges AH, Semenoff-Segundo A (2011) Are pan-

oramic radiographs reliable to diagnose mild alveolar bone resorption? ISRN Dent 2011:363578
Simon JH, Glick DH, Frank AL (2013) The relationship of endodontic-periodontic lesions. J Endod 39:e41–e46
Sun Z, Smith T, Kortam S, Kim DG, Tee BC, Fields H (2011) Effect of bone thickness on alveolar bone-height measurements from cone-beam computed tomography images. Am J Orthod Dentofac Orthop 139:e117–e127
Suomi JD, Plumbo J, Barbano JP (1968) A comparative study of radiographs and pocket depths in periodontal disease evaluation. J Periodontol 39:311–315
Takane M, Sato S, Suzuki K, Fukuda T, Asano Y, Honda K, Arai Y, Ito K (2010) Clinical application of cone beam computed tomography for ideal absorbable membrane placement in interproximal bone defects. J Oral Sci 52:63–69
Takeshita WM, Vessoni Iwaki LC, Da Silva MC, Tonin RH (2014) Evaluation of diagnostic accuracy of conventional and digital periapical radiography, panoramic radiography, and cone-beam computed tomography in the assessment of alveolar bone loss. Contemp Clin Dent 5:318–323
Tomaselli DL Jr, Feldman RS, Krochtengel AL, Fernandez P (1993) Osteomyelitis associated with chronic periodontitis in a patient with end-stage renal disease: a case report. Periodontal Clin Investig 15:8–12
Tonetti MS, Pini-Prato G, Cortellini P (1993) Periodontal regeneration of human intrabony defects. IV. Determinants of healing response. J Periodontol 64:934–940
Torabinejad M, Rotstein H (2014) Endodontic and periodontal interrelationships. In: Torabinejad M, Fouad A, Walton RE (eds) Principles and Practice of Endodontics. Elsevier, St. Louis, MO, pp 106–120
Tugnait A, Clerehugh V, Hirschmann PN (2004) Use of the basic periodontal examination and radiographs in the assessment of periodontal diseases in general dental practice. J Dent 32:17–25
Umetsubo OS, Gaia BF, Costa FF, Cavalcanti MG (2012) Detection of simulated incipient furcation involvement by CBCT: an in vitro study using pig mandibles. Braz Oral Res 26:341–347
Vandenberghe B, Sarment D (2013) Chapter 11. Periodontal disease diagnosis using cone beam computed tomography. In: Sarment D (ed) Cone beam computed tomography: oral and maxillofacial diagnosis and applications. Wiley, Chichester
Vandenberghe B, Jacobs R, Yang J (2007) Diagnostic validity (or acuity) of 2D CCD versus 3D CBCT-images for assessing periodontal breakdown. Oral Surg Oral Med Oral Pathol Oral Radiol Endod 104:395–401
Vandenberghe B, Jacobs R, Yang J (2008a) Detection of periodontal bone loss using digital intraoral and cone beam computed tomography images: an in vitro assessment of bony and/or infrabony defects. Dentomaxillofac Radiol 37:252–260
Vandenberghe B, Jacobs R, Yang J (2008b) Use of CBCT as a replacement charting system. Dentomaxillofac Radiol 37:252–260
Waalkens CC (1984) Periodontal abscess/osteomyelitis: a case report. J N Z Soc Periodontol 58:14–15
Wainwright WM (1973) Faciolingual tooth movement: its influence on the root and cortical plate. Am J Orthod 64:278–302
Walter C, Kaner D, Berndt DC, Weiger R, Zitzmann NU (2009) Three-dimensional imaging as a pre-operative tool in decision making for furcation surgery. J Clin Periodontol 36:250–257
Walter C, Weiger R, Zitzmann NU (2010) Accuracy of three-dimensional imaging in assessing maxillary molar furcation involvement. J Clin Periodontol 37:436–441
Walter C, Weiger R, Zitzmann NU (2011) Periodontal surgery in furcation-involved maxillary molars revisited—an introduction of guidelines for comprehensive treatment. Clin Oral Investig 15:9–20
Walter C, Weiger R, Dietrich T, Lang NP, Zitzmann NU (2012) Does three-dimensional imaging offer a financial benefit for treating maxillary molars with furcation involvement? A pilot clinical case series. Clin Oral Implants Res 23:351–358
Wriedt S, Jaklin J, Al-Nawas B, Wehrbein H (2012) Impacted upper canines: examination and treatment proposal based on 3D versus 2D diagnosis. J Orofac Orthop 73:28–40
Zekry A, Wang R, Chau AC, Lang NP (2014) Facial alveolar bone wall width—a cone-beam computed tomography study in Asians. Clin Oral Implants Res 25:194–206
Ziebolz D, Szabadi I, Rinke S, Hornecker E, Mausberg RF (2011) Initial periodontal screening and radiographic findings—a comparison of two methods to evaluate the periodontal situation. BMC Oral Health 11:3

CBCT and the Diagnosis of Temporomandibular Joint Disease

24

Christos Angelopoulos, William C. Scarfe, Ghabi Kaspo, Kostas Tsiklakis, and Wael M. Aboelmaaty

Contents

C. Angelopoulos, D.D.S., M.S. (✉)
Aristotle University of Thessaloniki, Thessaloniki, Greece

Columbia University, College of Dental Medicine, New York City, NY, USA
e-mail: angelopoulosc@gmail.com

W.C. Scarfe, B.D.S., F.R.A.C.D.S., M.S.
Division of Radiology and Imaging Science, Department of Surgical/Hospital Dentistry, University of Louisville School of Dentistry, Louisville, KY, USA

G. Kaspo, D.D.S.
Facial Pain and Sleep Center, Troy, MI, USA

K. Tsiklakis, D.D.S., M.S., Ph.D.
Department of Oral Diagnosis and Radiology, National and Kapodestrian University of Athens, Athens, Greece

W.M. Aboelmaaty, B.D.S., M.Sc.
Department of Oral Medicine and Periodontology, Faculty of Dentistry, Mansoura University, Mansoura, Egypt

24.1 Introduction

The temporomandibular joint (TMJ) is susceptible to the same pathologic processes that affect other joints in the body. Temporomandibular

W.C. Scarfe, C. Angelopoulos (eds.), *Maxillofacial Cone Beam Computed Tomography*,
https://doi.org/10.1007/978-3-319-62061-9_24

disorders (TMDs) are a diverse group of conditions, often with multifactorial etiology, which can affect one or all of the components of the TMJ including the osseous and soft tissue (e.g., articular disc and capsule) elements and supportive and functional elements such as the muscles of mastication and ligamentous attachments. TMD is the most common cause of extraoral pain with varied presentations including muscular, preauricular and TMJ pain, headache, earache, joint sounds such as clicking and popping, and limited or asynchronous jaw opening. Approximately 40–75% of those in the general adult population are asymptomatic but show at least one sign of articular dysfunction (noise, disturbances of mandibular movements, etc.). Approximately 33% of those with articular dysfunction report at least one symptom (Rugh and Soldberg 1985; Dworkin et al. 1990). The most commonly reported symptom is either noise or irregular mouth opening and the least frequent is difficulty in mouth opening (Jerolimov 2009). A higher incidence of TMDs is reported for females (Maixner et al. 2011) and those between 20 and 40 years of age (Isberg et al. 1998). Children, adolescents, and those over 60 years of age rarely complain of the symptoms of TMDs (Jerolimov 2009).

Most individuals with TMD experience signs or symptoms that they do not report and are essentially clinically insignificant. However, for a few individuals, their TMJ dysfunction and related symptomatology is severe enough to affect masticatory function, produce chronic pain, and restrict mouth opening. The etiology of TMDs is multifactorial, so if therapeutic intervention is anticipated, diagnostic CBCT imaging may be indicated prior to treatment to confirm clinical suspicion or rule out the contribution of the osseous elements of the TMJ articulation. CBCT imaging should also be considered for those who present with radiographic evidence of severe dysmorphology or a high index of suspicion for disease (Fig. 24.1).

24.1.1 Role of Diagnostic Imaging

Diagnostic imaging plays an important role in the evaluation of the osseous and soft tissue elements of the TMJ. The goal of TMJ imaging is to provide information in support of a working diagnosis based on a thorough medical history and extra- and intraoral examination.

Numerous authors have reviewed the relative contribution of specific imaging modalities for TMJ evaluation (Bag et al. 2014; Suenaga et al. 2016; Morales and Cornelius 2016). While internal derangement (ID) (abnormal positional and functional relationship of the articular disc) is the most common TMD, confirmatory imaging by magnetic resonance imaging (MRI) is expensive and usually only performed when surgery is considered or symptoms are severe. Degenerative osteoarthritis (OA) or degenerative joint disease (DJD) is the second most common TMD and often identified on maxillofacial imaging. Unlike ID, DJD is often asymptomatic. Panoramic imaging has been used extensively to assess OA of the TMJ, sometimes as a radiographic screening examination. However, related to inherent geometric distortions associated with image acquisition, the accuracy of panoramic imaging in detecting morphologic changes in the TMJ is low, especially for mild or moderate conditions (Honey et al. 2007; Hintze et al. 2009), and is not recommended (Winocur et al. 2010). Computerized tomography may be considered if the suspected findings might affect diagnosis and potentially influence management. Multidetector computed tomography (MDCT) has shown great value for the three-dimensional assessment of the integrity of the bony cortices of the articulating surfaces and the presence of erosions or osteophytes. Several authors have demonstrated that CBCT provides excellent multiplanar images of the TMJ structures (Terakado et al. 2000; Honda et al. 2001a, b, 2006; Tsiklakis et al. 2004; Hintze et al. 2007; Honey et al. 2007) including normal cortical bone (Fig. 24.2), condylar osteophytosis (Fig. 24.3), and condylar erosion (Fig. 24.4) and is now the imaging modality of choice for the assessment of possible osseous changes in the TMJ articulation. De Boer et al. (2014) found that the availability of CBCT for patients with disorders of the TMJ led to changes in primary diagnosis (25%), management (45%), and treatment (12%).

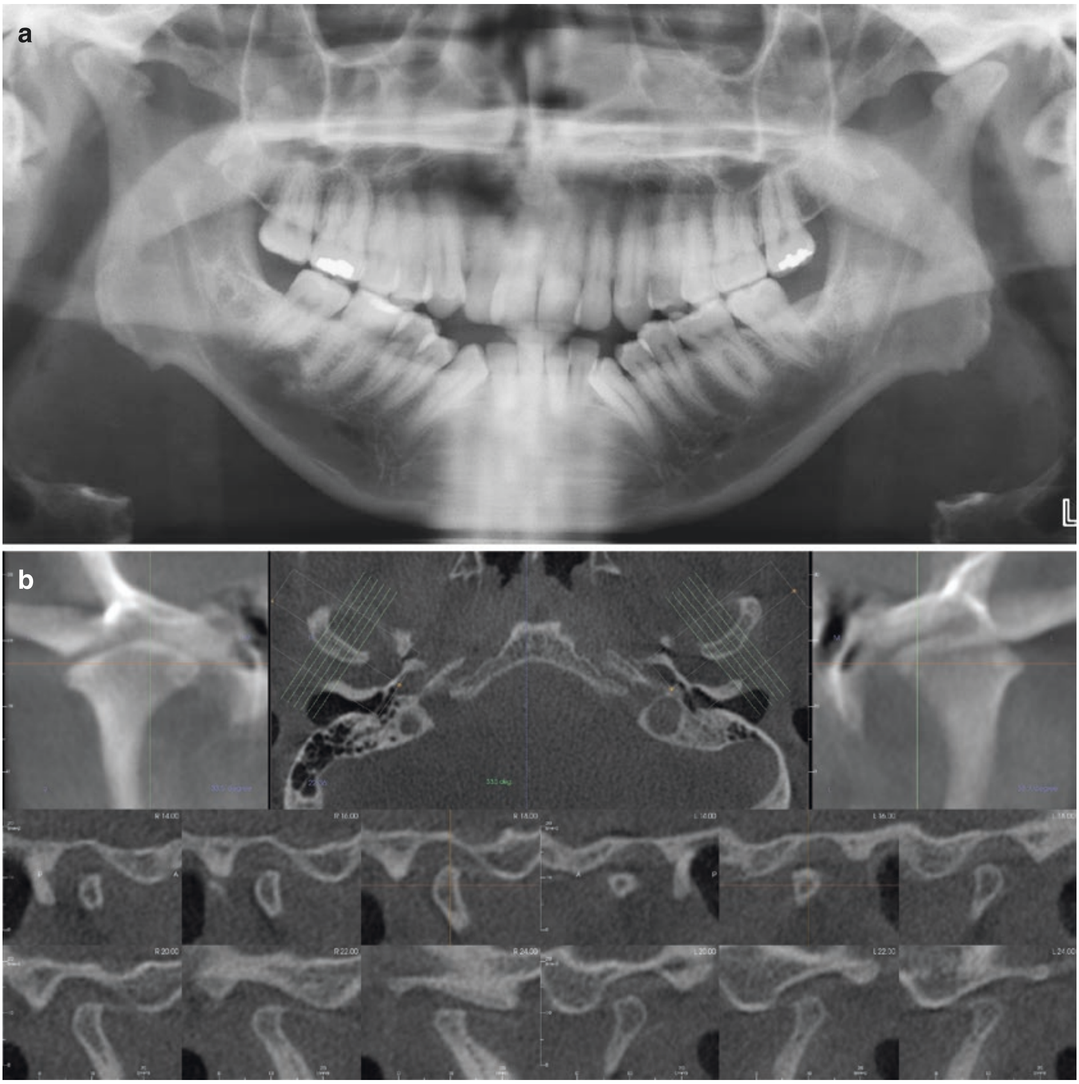

Fig. 24.1 Conventional panoramic image (**a**) of a 31-year-old male with Class III skeletal and dental malocclusion and anterior open bite showing possible resorption and collapse of the condylar heads bilaterally. Based on this initial imaging presentation and clinical examination, CBCT imaging was performed founded on a high index of suspicion of condylar resorption or severe osteoarthritis. Standard TMJ reformatted display incorporating coronal, axial reference and serial cross-sectional images (**b**) shows the mandibular condyles bilaterally are angular in shape and demonstrate mild osteoarthritic degenerative joint change. However, there is no evidence of resorption of either condyle. The panoramic presentation is most likely due to projection artifact as the intercondylar angle of both condyles on the axial projection is extremely high (approximately 60°)

It is important to reiterate that *CBCT is inadequate to demonstrate the soft tissue elements of the TMJ* (e.g., articular disk, ligaments, muscles of mastication and surrounding fascia) because of inherently poor contrast resolution. MRI or single or double joint space CBCT TMJ arthrography (Figs. 24.5, 24.6, 24.7 and 24.8) (Honda et al. 2004; Honda and Bjørnland 2006) should be considered if imaging is considered to confirm clinical suspicion of or detect soft tissue disorders such as ID, disc perforations, joint effusion, or synovitis.

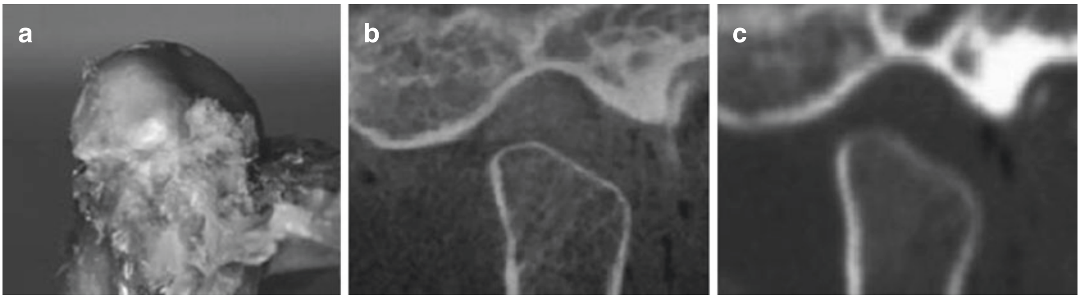

Fig. 24.2 Comparison of appearance of a normal left mandibular condyle on an anatomic specimen (**a**), parasagittal CBCT (**b**), and helical CT parasagittal (**c**) images (Images courtesy of Kazuya Honda)

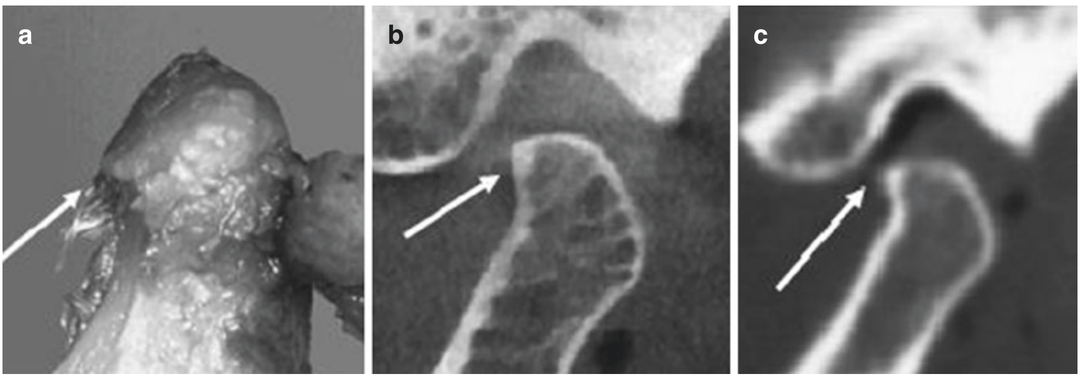

Fig. 24.3 Comparison of appearance of minor osteophyte (*arrow*) on the left mandibular condyle on an anatomic specimen (**a**), parasagittal CBCT (**b**), and helical CT parasagittal (**c**) images (Images courtesy of Kazuya Honda)

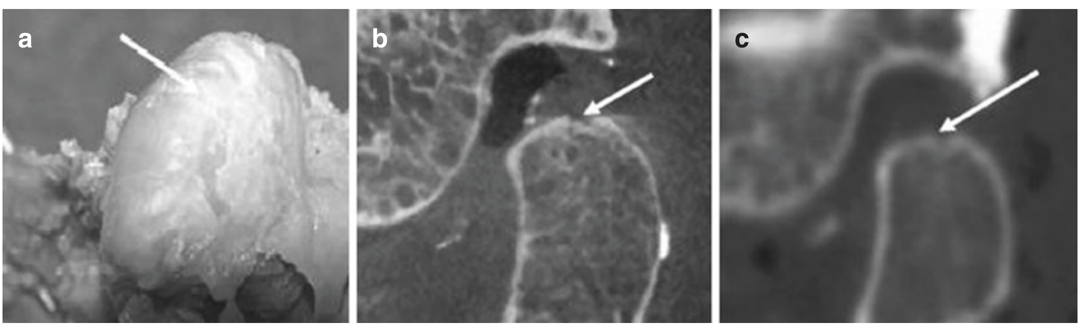

Fig. 24.4 Comparison of appearance of minor erosion (*arrow*) on the left mandibular condyle on anatomic specimen (**a**), parasagittal CBCT (**b**), and helical CT parasagittal (**c**) images (Images courtesy of Kazuya Honda)

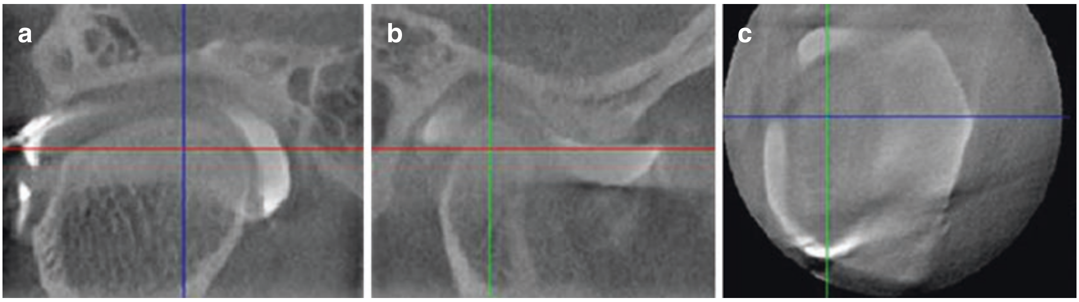

Fig. 24.5 Single contrast small volume CBCT arthrogram of the right TMJ articulation showing the normal morphology of the upper joint space on para-coronal (**a**), parasagittal (**b**), and axial (**c**) images (Images courtesy of Kazuya Honda)

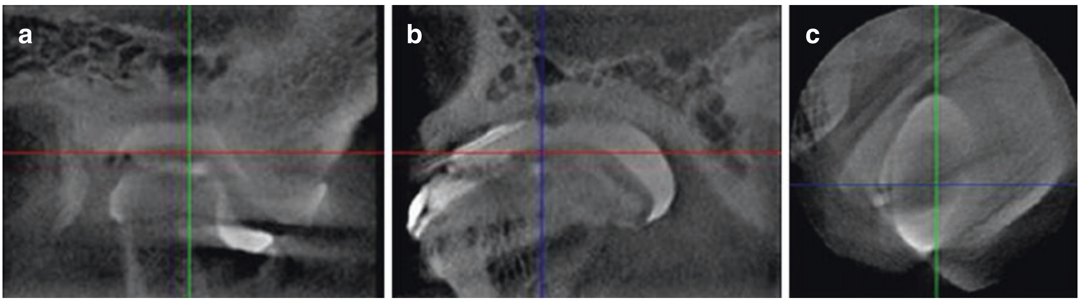

Fig. 24.6 Parasagittal (**a**), para-coronal (**b**), and axial (**c**) images from a single contrast small volume CBCT arthrogram of the right TMJ articulation of a 36-year-old female who presents with pain and difficulty with mouth opening but no pain on palpation. The maximum mouth opening accompanied by pain was 24 mm with no evidence of joint sounds. No abnormalities of the TMJ were observed on an initial panoramic radiograph; however, the CBCT arthrogram shows that the articular disk had slight anterior displacement, the disk configuration is biconcave, and perforation of the disk was present (as evidenced by extension of radiopaque contrast material from the superior into the inferior joint space) (Images courtesy of Kazuya Honda)

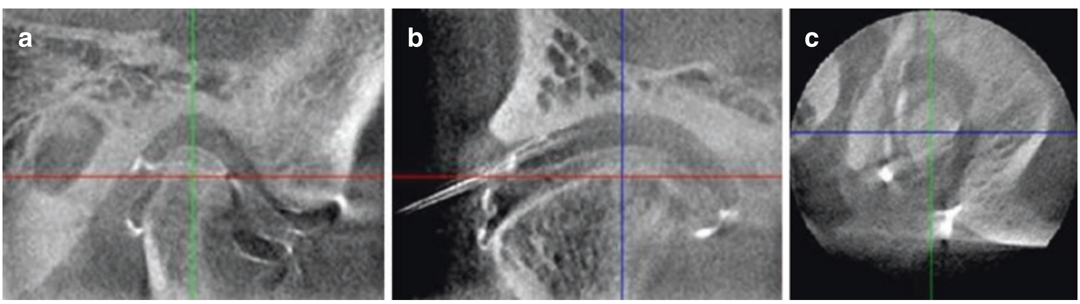

Fig. 24.7 Parasagittal (**a**), para-coronal (**b**), and axial (**c**) images of a double contrast arthrography of the same patient as in Fig. 24.6 demonstrating disk perforation of the right TMJ in the lateral part of condyle (Images courtesy of Kazuya Honda)

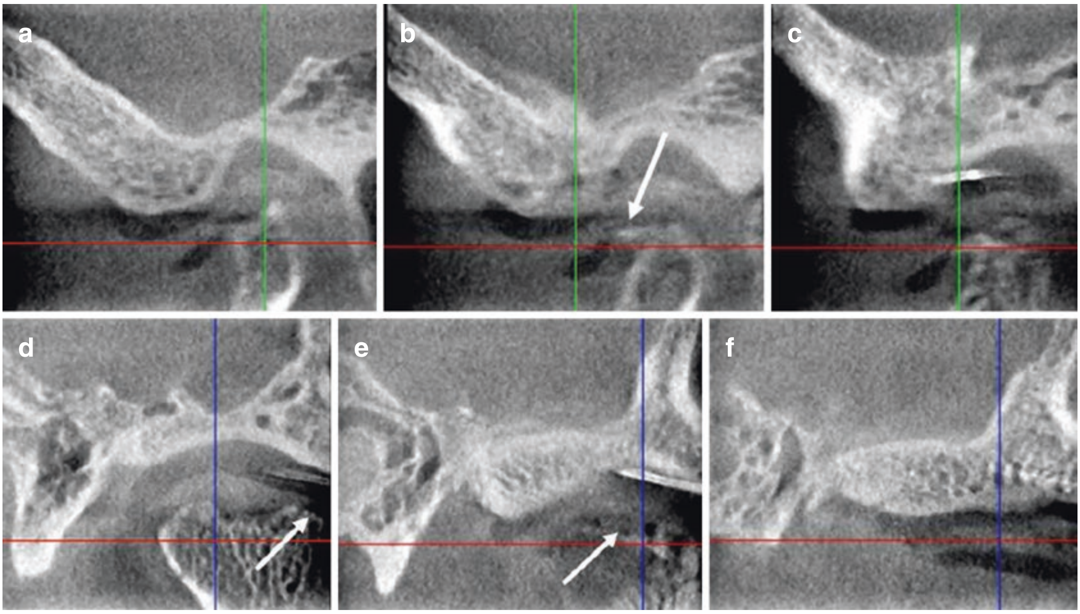

Fig. 24.8 Sequential medial (**a**), central (**b**), and lateral (**c**) parasagittal and posterior (**d**), central (**e**), and anterior (**f**) para-coronal small volume CBCT images of a 54-year-old female who presented with pain and difficulty with mouth opening and closing in the left TMJ for the past year. The patient had experienced numerous adverse effects associated with the prior use of iodine contrast medium on conventional MDCT. The central frontal image (**e**) shows adhesion of the lower joint space (*arrow*) and suspicious disk perforation of the lateral pole. The posterior frontal image (**d**) shows adhesion of the lower joint space and disk perforation of the lateral pole (*arrow*). The medial sagittal image (**a**) shows anterior displacement and the disk configuration was biconcave. The central sagittal image (**b**) shows slight anterior displacement, the disk configuration was biconcave, and the mandibular condyles has osteophytes (*arrow*). The lateral sagittal image (**c**) shows anterior displacement (Images courtesy of Kazuya Honda)

24.2 Radiographic Correlative Anatomy of the TMJ

The temporomandibular articulation or joint (TMJ) is a diarthrodal synovial joint. It comprises the condyle of the mandible and the glenoid fossa formed by the squamous part of the temporal bone (Fig. 24.9).

The glenoid fossa comprises two functional components: a convex articular eminence anteriorly into which the condyle articulates and a concave articular fossa posteriorly onto which the condyle translates (Fig. 24.10). Similar to the other synovial joints in the body, the TMJ has a disk, articular surfaces, fibrous capsule, synovial fluid, synovial membrane, and ligaments. The TMJ differs from most other synovial joints of the human body by having its articular surface made of fibrous connective tissue instead of hyaline cartilage.

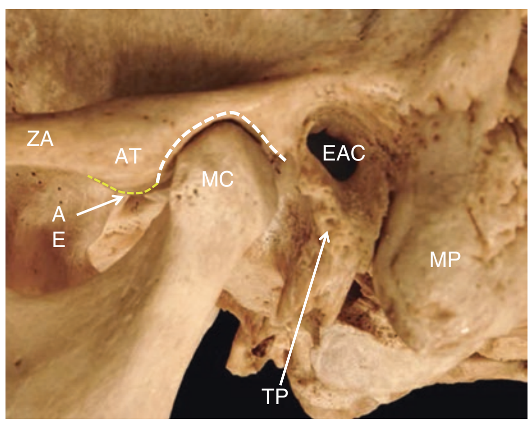

Fig. 24.9 Lateral view of the left temporomandibular articulation of a skull identifying key topographic features. *ZA* zygomatic arch, *AE* articular eminence (*yellow dotted line*), *AT* articular tubercle, *EAC* external auditory canal, *MP* mastoid process, *TP* tympanic plate of the temporal bone, *MC* mandibular condyle, *curved dotted line*, glenoid fossa

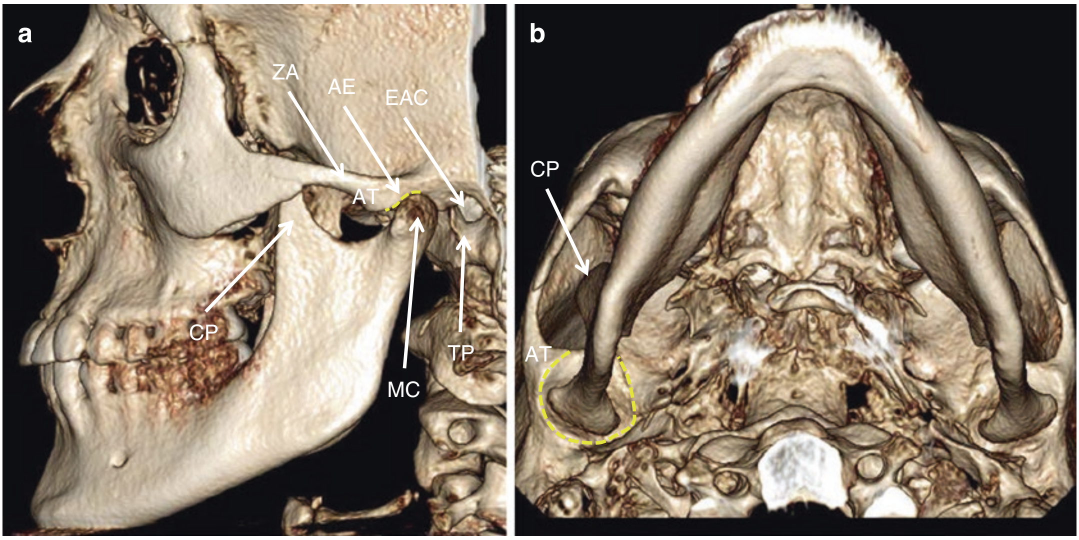

Fig. 24.10 Left lateral (**a**) and inferior (submentovertex) (**b**) CBCT 3D volumetric projections identifying the osseous elements of the TMJ. Note the spatial relationship of the mandibular condyle (MC) and coronoid process (CP) to the skull base and zygomatic arch (ZA). *AE* articular eminence (*yellow dotted line*), *AT* articular tubercle, *EAC* external auditory canal, *MP* mastoid process, *TP* tympanic plate of the temporal bone, *MC* mandibular condyle, *curved dotted line*, glenoid fossa

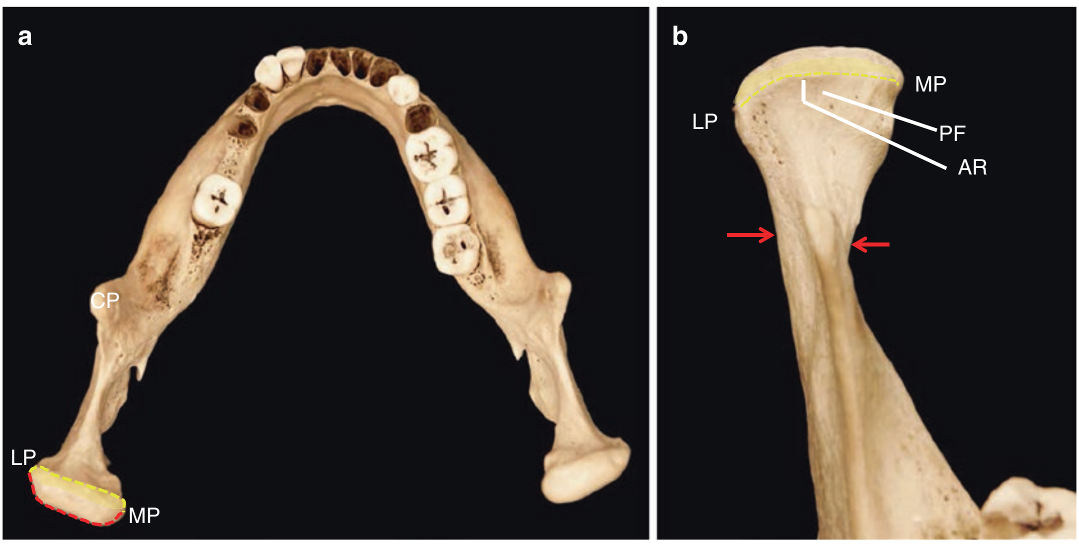

Fig. 24.11 Axial view of the mandible (**a**) and cropped, magnified frontal view of the right mandibular condyle (**b**) of a skull identifying key topographic features. *LP* lateral pole, *MP* medial pole, *CP* coronoid process, *yellow dotted line* anterior articulating ridge of the condylar head, *red dotted line* posterior articulating ridge of the condylar head, *yellow shading* anterosuperior surface of the articulating ridge of the condylar head, *PF* pterygoid fovea (slight concavity just below the anterior ridge which serves as a muscle attachment point), *red arrows* condylar neck

24.2.1 The Mandibular Condyle

There are two posterior cephalad (superior) extensions of the mandibular ramus: the mandibular condyle and the coronoid process. The mandibular condyle comprises two components, the condylar neck and the condylar head (Fig. 24.11).

In the adult, the head of the normal condyle is usually ovoid or elliptical in shape when viewed from above (axially), although variation is common including curvilinear (or "banana") shaped or irregular (Fig. 24.12) (Solberg and Hansson 1985).

The articulating surface of the condylar head is bordered by an anterior and posterior ridge (Fig. 24.11). The average mediolateral dimensions of the condylar head in the adult are approximately 21.8 ± 1.93 mm for males and 18.7 ± 1.57 mm for females. Anteroposterior dimensions for males (10.1 ± 0.83 mm) and females (9.8 ± 1.31 mm) are remarkably similar (Solberg and Hansson 1985). During childhood, the mandibular condyle changes significantly in size and shape. As the condyles increase in size, they change from a round to a more ovoid shape with a concomitant decrease in the horizontal condylar angle (Karlo et al. 2010). During this period, condylar shape transitions through the following morphologies as observed in the parasagittal projection (Karlo et al. 2010):

- **Type I**. Smooth, round, finger-like shape, most frequently seen in children aged up to 5 years (Fig. 24.13).
- **Type II**. Beginning of angularity with the development of an anterior beak, most often observed in children aged 5–10 years.
- **Type III**. Terminal tufting with flattening of the condyle's anterior surface, occurring in children older than 10 years (Fig. 24.14).

When viewed from below, the long axes of the mandibular condyles, formed from a perpendicular through the medial and lateral poles, create a

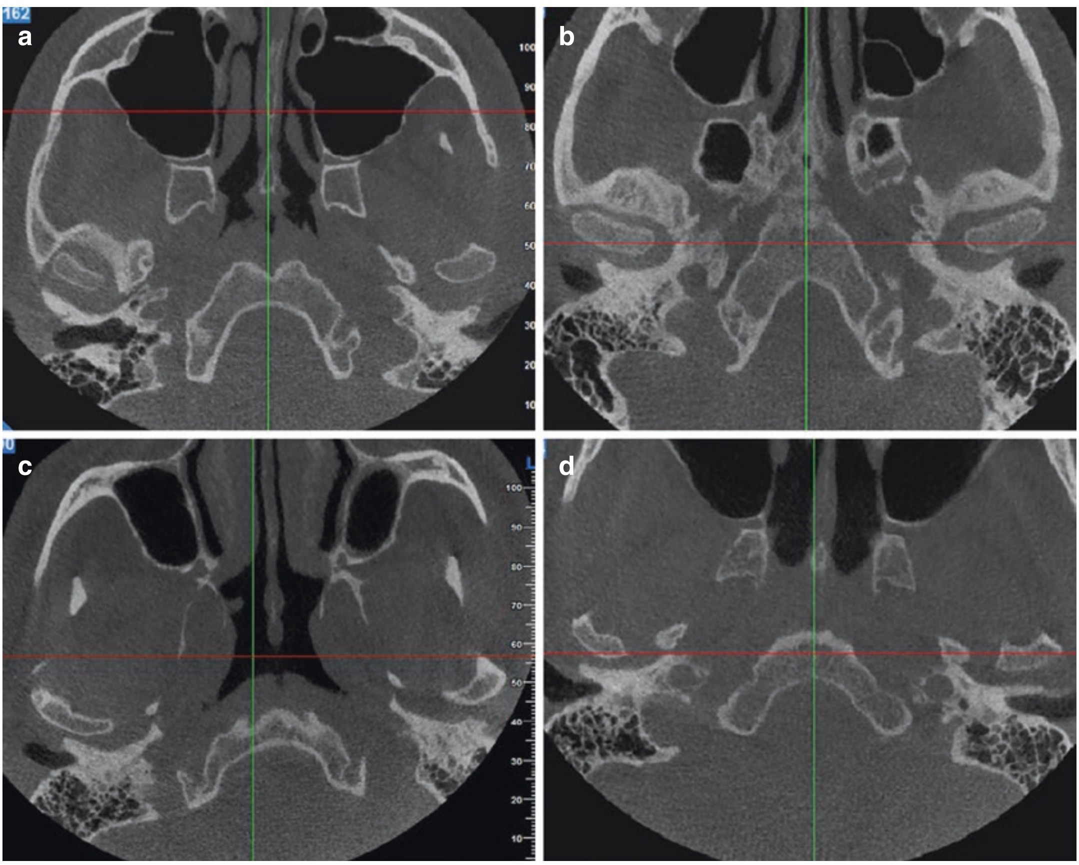

Fig. 24.12 Axial orthogonal CBCT sections of four individuals (**a**–**d**) at the level of the mandibular condyles/zygomatic arch. The images show marked differences in size and shape of the condylar heads in the axial plane, ranging from ovoid or elliptical (**a**), bean shaped (**b**), crescent shaped (**c**), and irregular (**d**)

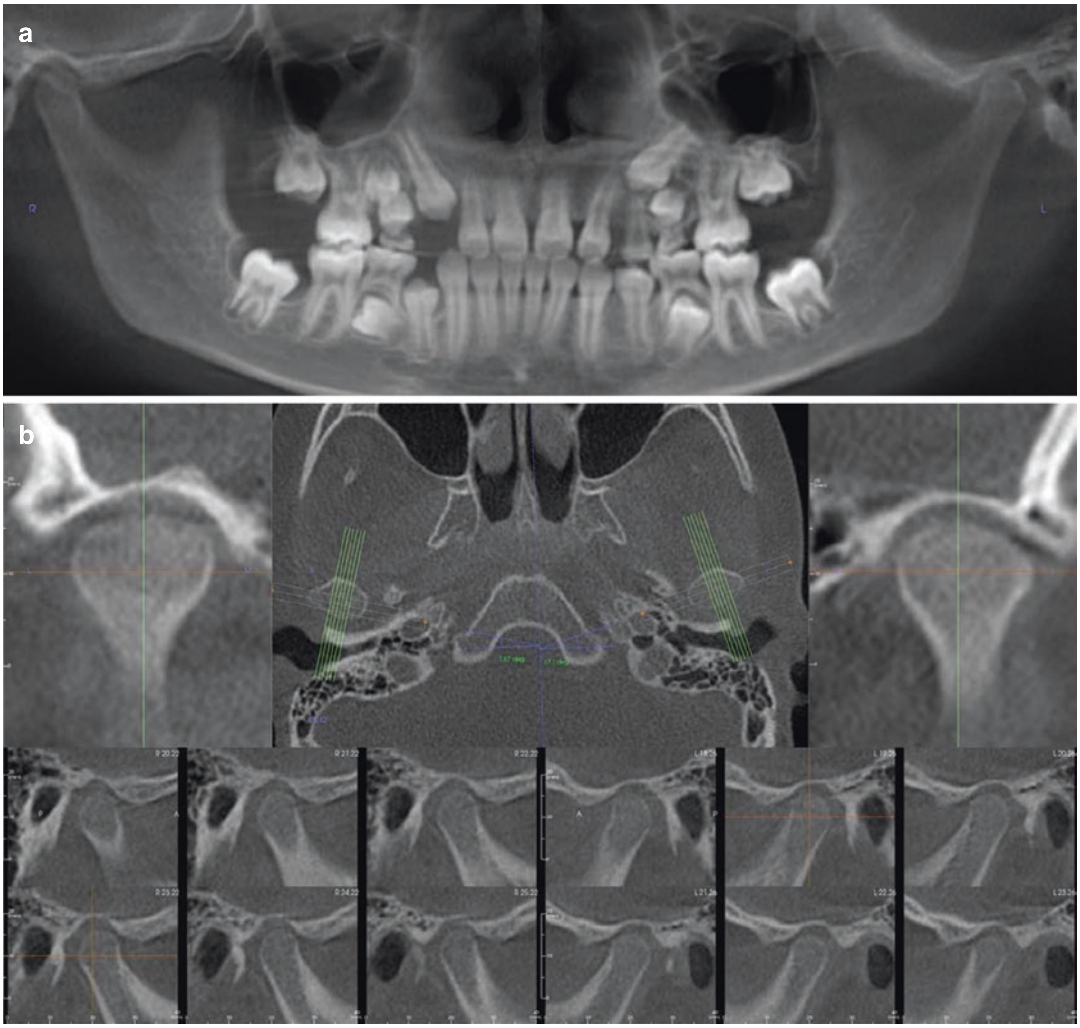

Fig. 24.13 Reformatted panoramic (**a**) and standard TMJ reformatted display incorporating coronal, axial reference and serial cross-sectional images (**b**) of a 7-year-old female shows Type I (Karlo et al. 2010) mandibular condyles bilaterally

narrow angle with respect to the coronal plane, known as the horizontal condylar or ante-version angle. On average this angle is between 15° and 19° (Fig. 24.15). The lateral pole of the condyle is located approximately 1–1.5 cm beneath the skin.

The mandibular condyle demonstrates great variability in shape. Based on the frontal profile of autopsy specimens, the shape of the condylar head can be described according to one of the four types (in order of frequency): convex, flattened, angled (or gable), and rounded (Yale et al. 1966; Solberg and Hansson 1985; Christiansen et al. 1987). The morphology of mandibular condyle shape on 2D reconstructed oblique coronal CT images, and thus CBCT images, presents with five (5) patterns (Fig. 24.16) (Cimen et al. 1999; Ueda et al. 2003). Interestingly condylar shape is symmetrical in only up to 56% of individuals.

Parasagittal shapes of the mandibular condyle were initially reported in terms of increasing angularity by Solberg and Hansson (1985) who described convex, local concavity, and wedge shaped. Using MRI, Lemke et al. (2005) described four types of mandibular condyles in the parasagittal projection including round (normal), flat, osteophytic, and with cortical thickening.

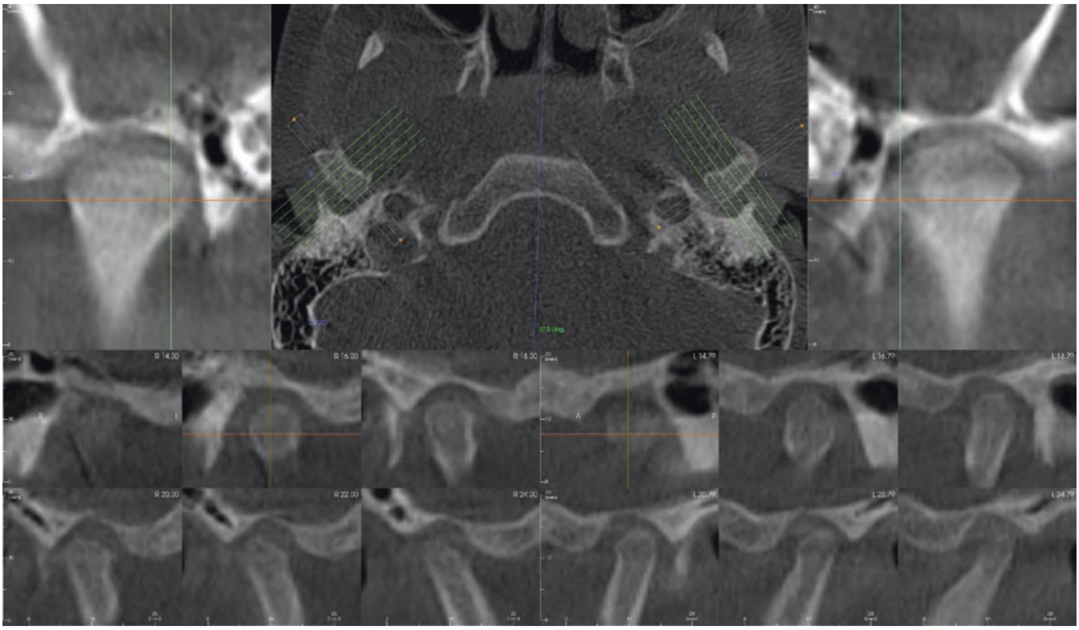

Fig. 24.14 Standard TMJ reformatted display incorporating coronal, axial reference and serial cross-sectional images (**b**) of a 10-year-old individual shows Type III (Karlo et al. 2010) mandibular condyles bilaterally

Fig. 24.15 An inferior view of the mandibular condyles (*blue dotted line*) articulating in the glenoid fossa of a skull illustrating the horizontal condylar or "ante-version" angle formed between the long axis of the mandibular condyle (*red dotted line*) and the coronal plane (*yellow line*)

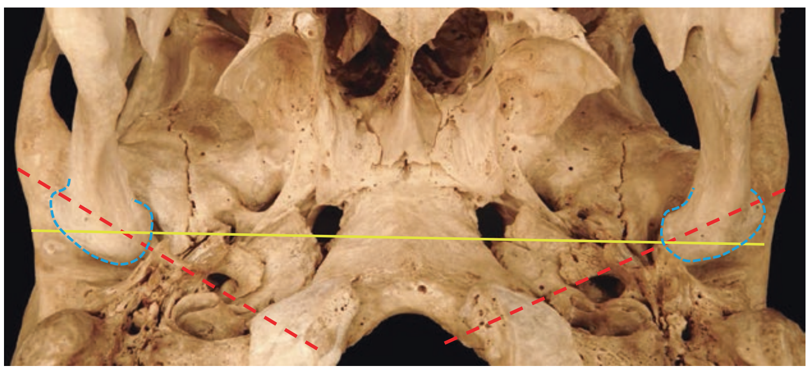

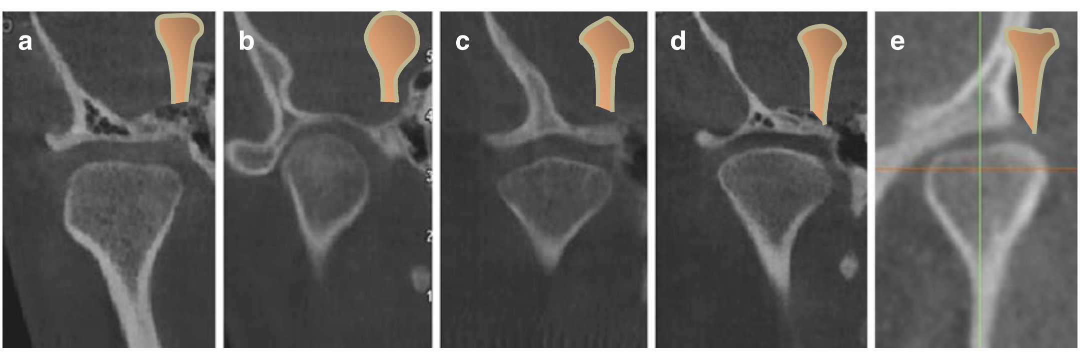

Fig. 24.16 Para-coronal CBCT sections with accompanying schematic illustrating the different patterns of condylar head morphology described by Cimen et al. (1999) including flat (**a**), round (**b**), angled (**c**), convex (**d**), and concave (**e**)

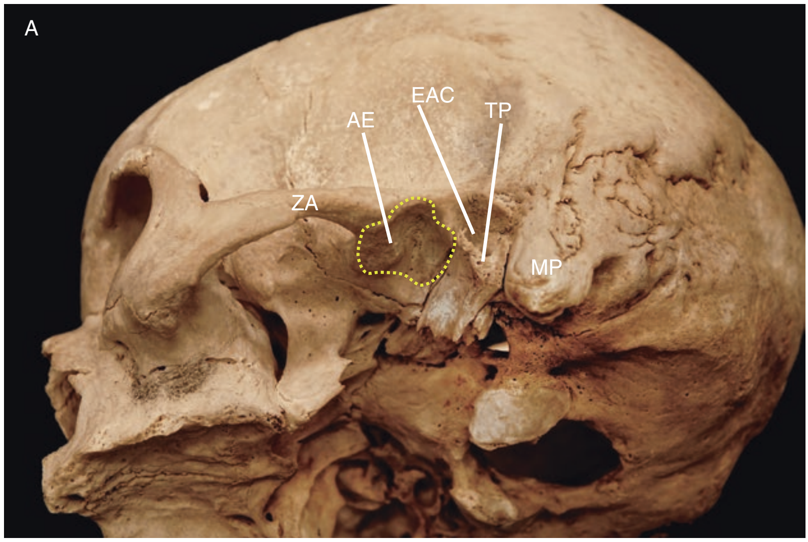

Fig. 24.17 Topographic anatomy of the left glenoid fossa (*yellow dotted line*) and relationship to adjacent maxillofacial bones on a skull. *ZA* zygomatic arch, *AE* articular eminence, *EAC* external auditory canal, *TP* tympanic process, and *MP* mastoid process

24.2.2 The Glenoid Fossa

The glenoid (or mandibular) fossa is a shallow concavity on the skull base which articulates with the mandibular condyle; it forms the cranial component of the joint (Fig. 24.17). The glenoid fossa is formed entirely by the squamous portion of the temporal bone. It is bordered by the tympanic plate and the external auditory canal posteriorly and the articular eminence anteriorly. The posterior part of the articular fossa is elevated to form the posterior articular ridge. In most individuals, the posterior articular ridge becomes thicker on the lateral aspect and forms a cone-shaped projection known as postglenoid process (PGP), comparable to the anterolateral projection, the anterior tubercle. The squamotympanic fissure lies at the posterior and lateral part of the glenoid fossa, between the squamous and tympanic portion of the petrous bone and separates the articular surface from the nonarticular surface of the glenoid fossa. Along the medial aspect of the glenoid fossa is the petrotympanic fissure. The articular eminence (AE) forms the anterior boundary of the glenoid fossa. The AE is a transverse bony bar anterior to the glenoid fossa and medial to the posterior margin of the zygomatic process, the anterior tubercle. The anterior slope of the AE is known as the preglenoid plane (PEP) and rises gently from the infratemporal surface of the squamous bone (Bag et al. 2014). When viewed from the parasagittal projection, the average angle of the articular eminence is approximately 60°. The temporal component of the TMJ measures approximately 23 mm, both in mediolateral and in anteroposterior dimension. Medially, the fossa narrows considerably and is bounded by an osseous plate that prevents the condyle from being displaced medially. The minimum thickness of the roof of the normal glenoid fossa varies greatly between 0.1 and 3.6 mm, with an average of 1 mm (Fig. 24.18) (Eckerdal and Ahlqvist, 1979).

Just as the normal morphology of the mandibular condyle varies, so too does the shape of the glenoid fossa. Most commonly these shapes are described from the sagittal projection and while corresponding to condylar morphology, their incidence varies. Katsavrias (2006) found that the percentages for the fossa shapes in Class I Division II patients were: round, 7.3%, oval, 58.3%, triangular, 18.8%, and trapezoidal, 15.6%. However, he found that only 52% of TMJs had matching condylar and fossa shapes, of which 41% were oval and 8% were round (Katsavrias 2006). For Class II Division 1, Class II Division 2, and Class III malocclusions Katsavriasa and Halazonetisb (2005) found that the shape variability of the condyle was mainly related to inclination of the condylar head

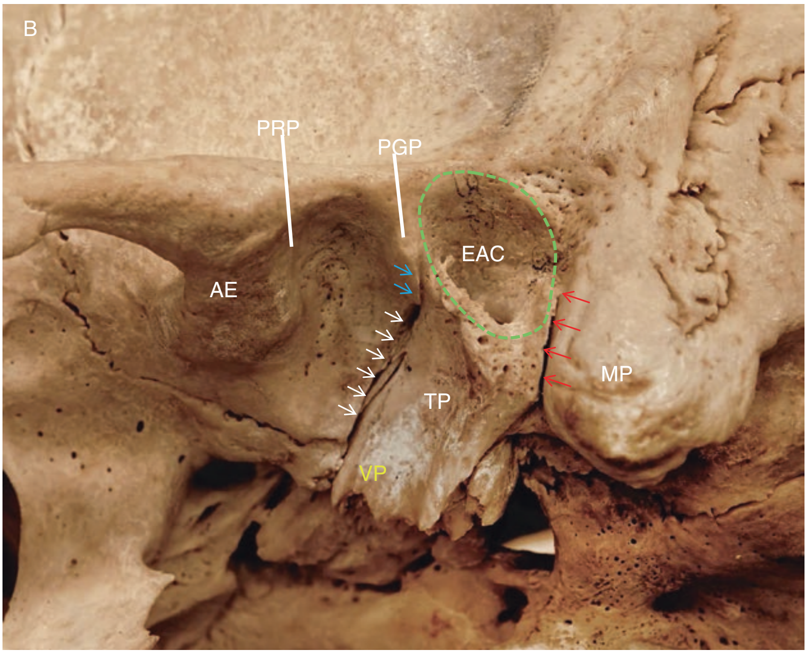

Fig. 24.18 Infero-lateral projection of the left glenoid fossa of a skull showing the anatomical boundaries of the fossa as well as relevant significant landmarks. *AE* articular eminence, *EAC* external auditory canal, *MP* mastoid process, *TP* tympanic plate, *VP* vaginal process of the tympanic plate, *PRP* preglenoid process—this is a slight ridge marking the anterior end of the fossa, *PGP* postglenoid process, a ridge that marks its posterior end, *white arrows* petrotympanic fissure, *blue arrows* squamotympanic fissure—separates the roof from the posterior wall of the fossa, *red arrows* tympanomastoid fissure)

whereas variability of the fossa was related to inclination of the eminence and fossa height. In addition, they reported a tendency for older Class III individuals to have larger fossa. They also found that Class III individuals had a condylar head that was more elongated and anteriorly inclined and more superiorly positioned with a wider and shallower fossa. They also found that in Class II Division 1 individuals the condyle was situated more anteriorly in the fossa (Katsavriasa and Halazonetisb 2005).

24.2.2.1 Pneumatization

Pneumatization refers to the development of air-filled cavities or cells within bone. Within the maxillofacial skeleton, accessory air cells can occur in many locations including the major paranasal sinuses, as well as the temporal bone, either singly or in clusters. Pneumatization of the temporal bone occurs in five regions, each of which is subdivided into areas. The primary regions consist of the middle ear, mastoid (squamomastoid), perilabyrinthine, petrous apex, and accessory. The squamomastoid region comprises two key areas of pneumatization related to the TMJ articulation—the mastoid antrum (including the central tract) and the periantral area. The tegmental periantral cells lie superior to the mastoid antrum and may pass upward into the squamous temporal region or extend into the zygomatic arch (Fig. 24.19). In association with the TMJ, pneumatization can occur in association with the roof of the glenoid fossa, articular eminence, zygomatic process, and *peritubal* area (region adjacent to the auditory tube located anterior and lateral to the carotid canal). The *zygomatic air cell defect* (ZACD) (Tyndall and Matteson 1987) or *pneumatized articular eminence or tubercule* (PAT) (Tyndall and Matteson 1985) is specifically used to describe accessory air cells which occur in the root of the zygomatic arch and in the articular eminence of the

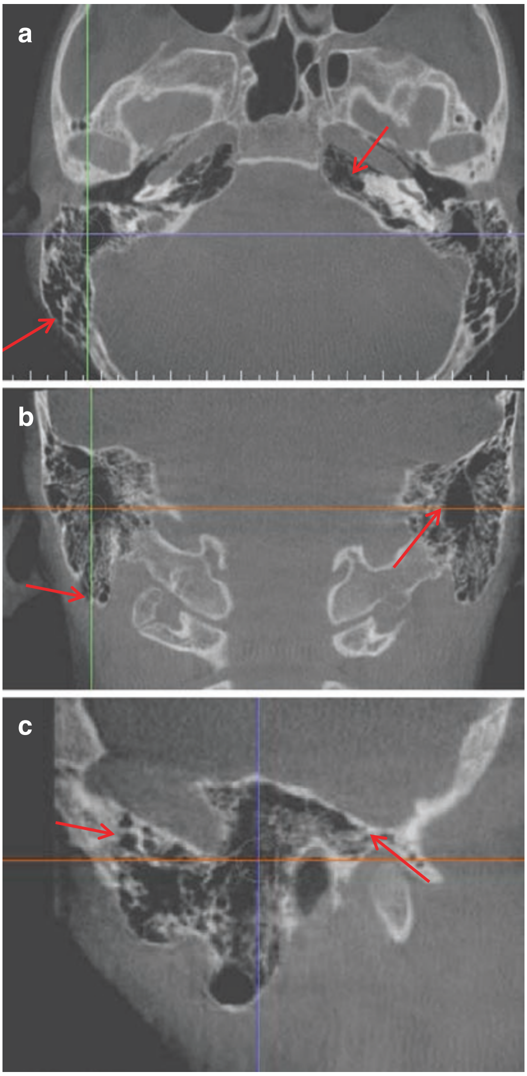

Fig. 24.19 Axial (**a**), coronal (**b**), and right lateral sagittal (**c**) CBCT sections showing pneumatization of the entire temporal bone (*red arrows*) including the mastoid with periantral cells

temporal bone, respectively (Fig. 24.20). Pneumatization may occur as a unilocular hypodense oval defect with well-defined bony borders or as multilocular air cells appearing as numerous hypodense small cavities. The incidence ranges from 1% to 2.6% on panoramic radiographs (Tyndall and Matteson 1985; Carter et al. 1999), with approximately equal distribution between uni- and multilocular variants (Tyndall and Matteson 1985). However CT demonstrates a high incidence of pneumatization of the temporal bone from the mastoid bone extending into the roof (51%), articular eminence (12%), and even to the root of the zygomatic process (5%) (Fig. 24.19) (Groell and Fleischmann 1999). In addition, air cells in the peritubal area extend into the medial wall of the glenoid fossa in 53% of patients (Groell and Fleischmann 1999). While the differential diagnosis of uni- or multilocular distinct hypodensities in this region include aneurysmal bone cyst, osseous hemangioma, chondroblastoma, fibrous dysplasia, giant cell tumor, eosinophilic granuloma, and metastatic tumor, only PAT presents with non-expansile, nondestructive features.

24.2.2.2 Foramen Tympanicum

The *foramen tympanicum*, or *foramen of Huschke*, is an anatomic structure present during embryological development in the tympanic portion of the temporal bone that is normally closed by 5 years of age (Weissman et al. 1991). It is located on the anterior-inferior aspect wall of the external auditory canal on the tympanic portion of the temporal bone, posteromedial to the TMJ. It therefore exists as a communication between the external acoustic canal and the mandibular fossa (Fig. 24.21). It may persist into adulthood as an anatomical anomaly in between 4.6% (Lacout et al. 2005) and 9.9% of individuals with a significantly higher incidence in females (Faig-Leite and Horta Júnior 1999; Wang et al. 1991). The foramen tympanicum is a variant of ossification that transmits no neural or vascular structures. It is not a true foramen; it may be more appropriately termed a bony or osseous defect or dehiscence. Reported mean dimensions are 4.2 mm axially and 3.6 mm sagittally (Lacout et al. 2005).

The foramen tympanicum may predispose individuals to conditions with clinical relevance. It may permit spontaneous herniation of soft tissue from the TMJ into the EAC, which can cause TMJ pain and dysfunction (Heffez et al. 1989). Herniation of the posterior and deep insertions of the TMJ meniscus through the foramen tympanicum into the EAC has also been reported (Hawke et al. 1987). Herniations are characteristic and

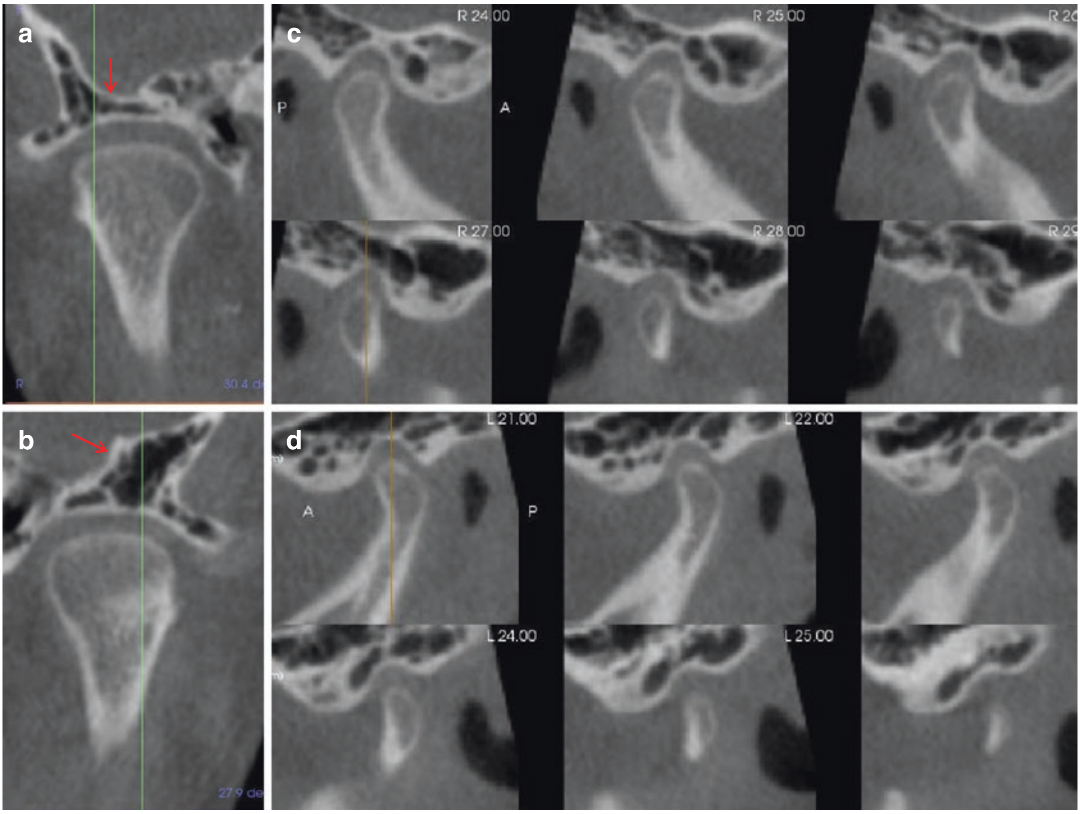

Fig. 24.20 Right (**a**) and left (**b**) para-coronal and right (**c**) and left (**d**) serial cross-sectional images demonstrating pneumatized articular eminence or tubercule (PAT) (*red arrows*)

fairly easy to identify because they usually retract out of the EAC after anterior translation of the TMJ that occurs with opening of the mouth. Otologic complications include spontaneous salivary gland (Lacout et al. 2005; Sharma and Dawkins 1984) and synovial TMJ fistulas (Hawke et al. 1988) as well as possible TMJ post-arthroscopic otologic complications including tympanic membrane rupture, dislocation of the incus, injury to the tympanic segment of the facial nerve, labyrinthine disruption, and ear infection (Herzog and Fiese 1989).

24.2.3 The Interarticular Joint Space

In the closed position, the average normal interarticular joint space varies depending on the CBCT image projection.

- On the sagittal projection, the space from the condyle to the glenoid fossa varies from approximately 1.75 to 2 mm to the articular slope, 3 to 3.5 mm to the deepest part of the fossa and 1 to 1.5 mm to the tympanic plate (Fig. 24.22).
- Coronally, the space is uniformly approximately 3–3.5 mm.
- Axially, the distance varies depending on the level of the section but is approximately 2.5 mm anteriorly to 1.5 mm posteriorly. This results from variability in the thickness of the fibrocartilage, meniscus, and synovial space.

The articular surfaces of the condyle and fossa bone are separated by an articular disk, which divides the joint cavity into two small spaces (Figs. 24.23 and 24.24). The articular disk, also known as the meniscus, is a biconcave, fibrocartilaginous structure, which provides the gliding surface for the mandibular condyle, resulting in smooth joint movement. The meniscus has three parts—a thick anterior band, a thin intermediate zone, and a thick posterior band. As the jaw opens,

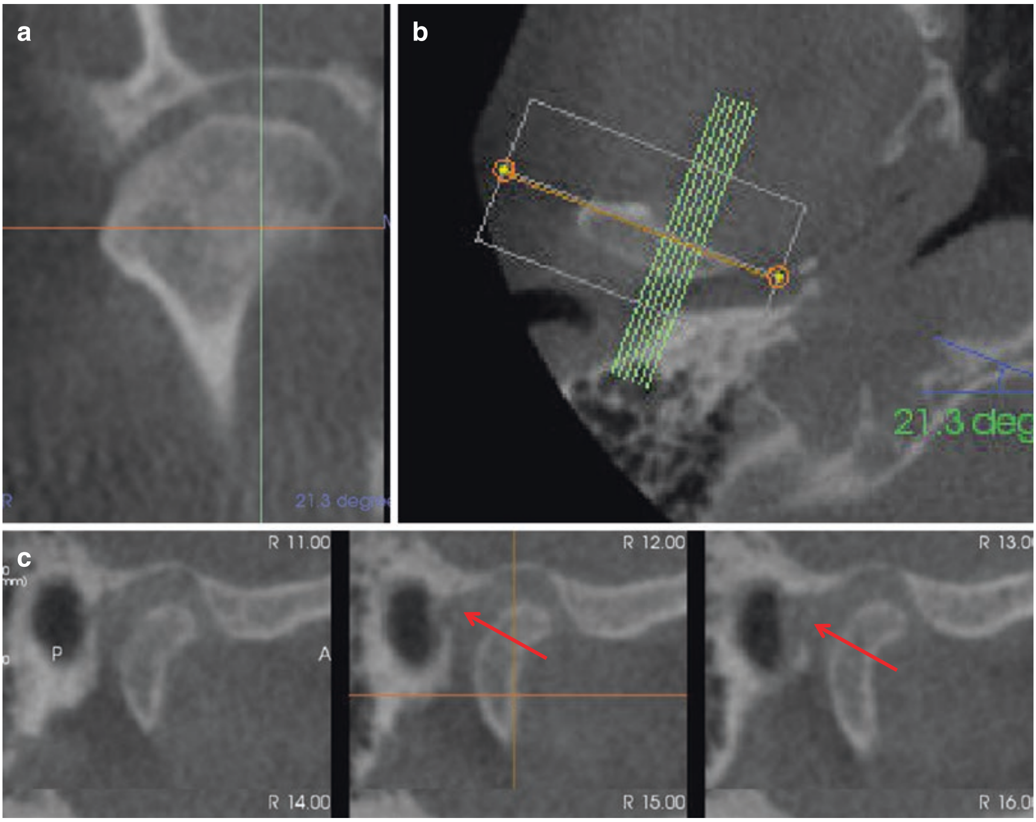

Fig. 24.21 Para-coronal (**a**), axial reference (**b**), and serial parasagittal (**c**) CBCT views of the right TMJ articulation illustrating the presence of a foramen tympanicum (*red arrows*) with herniation of intra-articular contents into the external auditory meatus

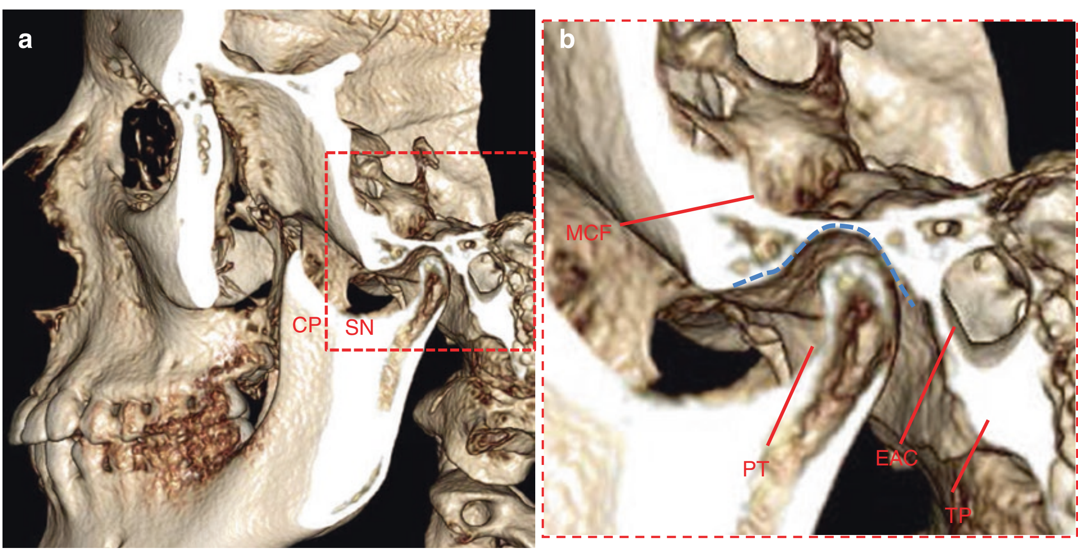

Fig. 24.22. Left lateral view of a shaded surface rendering (**a**) of an individual in maximum intercuspation (centric occlusion) with the squamous part of the temporal bone removed to reveal the left joint space. The insert (**b**) is a magnified view of the TMJ articulation to show the joint space and the position of the condylar head relative to the fossa (*blue dotted line*). Note the relatively retruded position of the condylar head. The joint space is occupied by the articular disk and synovial fluid. *CP* coronoid process, *EAC* external auditory canal, *TP* tympanic plate, *SN* sigmoid notch, *MCF* middle cranial fossa, *PT* pterygoid fovea

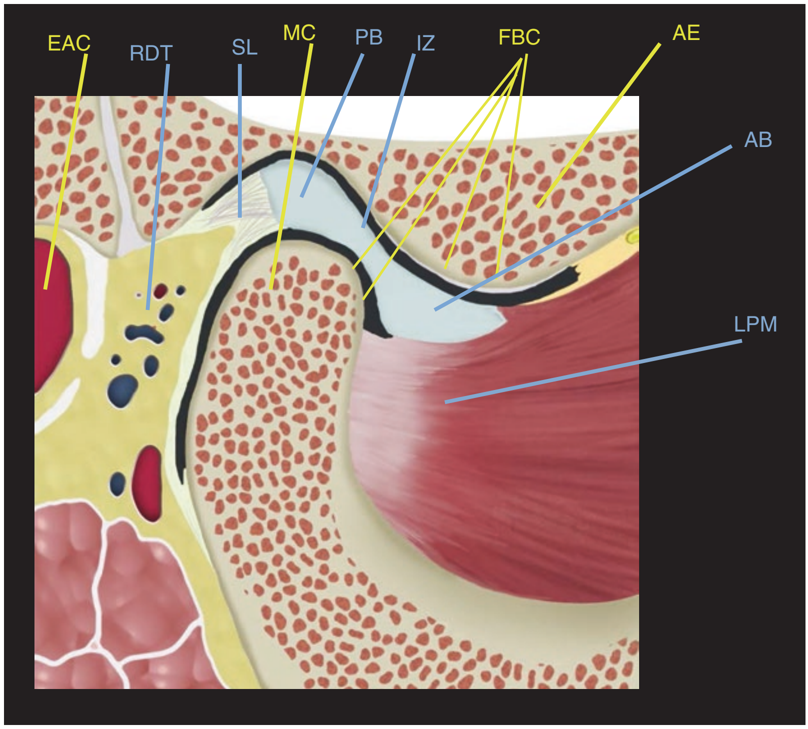

Fig. 24.23 Sagittal schematic of the right TMJ illustrating the hard and soft tissue elements of the TMJ. The dark curved zones noted superior and inferior to the articular disc represent the superior and inferior joint spaces (on either side of the disc). *EAC* external auditory canal, *MC* mandibular condyle, *AE* articular eminence, *FBC* fibrocartilage of the condylar head and fossa, *LPM* lateral pterygoid muscle, *AB* anterior band of the articular disc, *PB* posterior band of the disc, *IZ* intermediate zone of the disc, *RT* retrodiscal tissues-attachment points, *SL* superior lamina—temporal posterior attachment

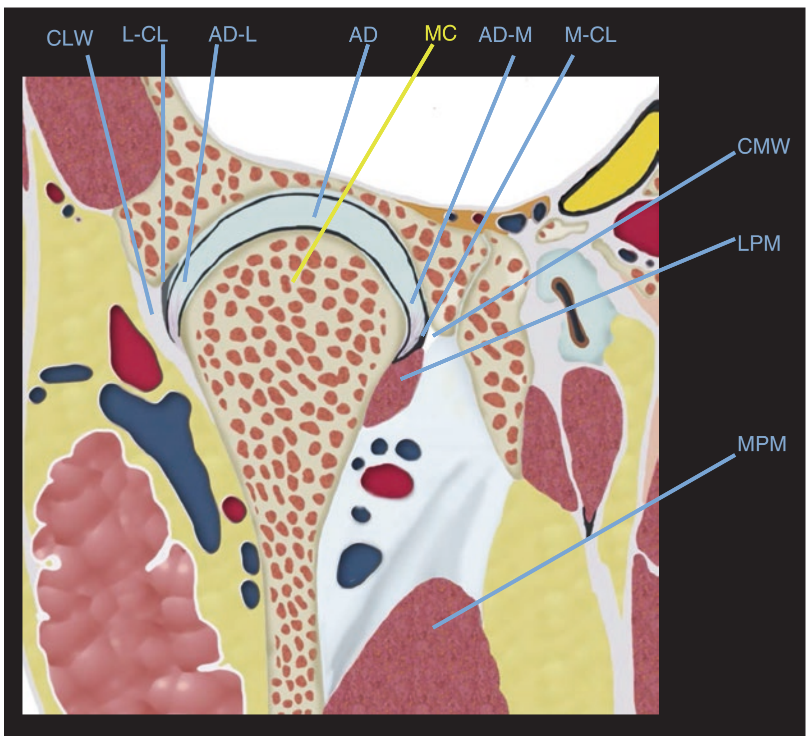

Fig. 24.24 Coronal schematic of the right TMJ illustrating the hard and soft tissue elements of the TMJ. The thin, dark curved zones noted superior and inferior to the articular disc represent the superior and inferior joint spaces on either side of the disc. *MC* mandibular condyle, *LPM* lateral pterygoid muscle, *MPM* medial pterygoid muscle, *AD* articular disc, *AD-L* lateral aspect of disc, *AD-M* medial aspect of disc, *CLW* capsular lateral wall, *CMW* capsular medial wall, *L-CL* lateral collateral ligament, *M-CL* medial collateral ligament

the condyle initially rotates within the fossa on the thick posterior band and translates to the apex of the eminence or beyond such that the condyle is separated from the articular eminence of the temporal bone by the thin intermediate zone.

The articular disk is round or ovoid, biconcave, avascular fibrocartilage between the condyle and glenoid fossa. The disk is considerably thinner centrally in the intermediate zone. The triangular anterior band is approximately 2 mm in thickness and blends with the joint capsule. The posterior band is approximately 3 mm in thickness and continues as bilaminar zone (also known as retrodiscal region and posterior attachment), which consists of superior fibroelastic layer (also known as temporal lamina) that attaches to PGP and an inferior fibrous layer (also known as the inferior lamina) that attaches to the posterior condylar neck. The superior layer prevents slipping of the disk during wide mouth opening and the inferior layer prevents excessive rotation of the disk over the condyle. Both the lamina are separated by loose elastic fibers with blood vessels and nerves. These fibers attach to the posterior joint capsule and augments disk retraction during mouth closing. The bands are longer in the mediolateral dimension than in the anteroposterior dimension. The smaller anterior band attaches anteriorly to the joint capsule, condylar head, and AE. Some patients have an additional anteromedial attachment to the superior belly of the lateral pterygoid muscle. Unlike its anterior and posterior attachments, the disk is not attached to the joint capsule medially and laterally. Instead, the disk is firmly attached to the medial and lateral poles of the mandibular condyle. This allows simultaneous movements of the disk and the condyle.

The thickness of the fibrocartilage layer of the condylar head and fossa varies considerably. For the condyle it may range from 0.3 to 0.5 mm thick. The fibrocartilaginous layer within the glenoid fossa is relatively uniform and approximately 0.3 mm thick, whereas for the articular eminence it may increase in thickness to 0.75 mm. Like the articular disc, it is not radiographically discernable (Fig. 24.25). Therefore, it is possible that the radiographic outline of the glenoid fossa and condyle varies from the actual anatomic, functional size of these structures. Consequently, the radiographic position of the condyle within the fossa may not reflect the actual position of the anatomic elements.

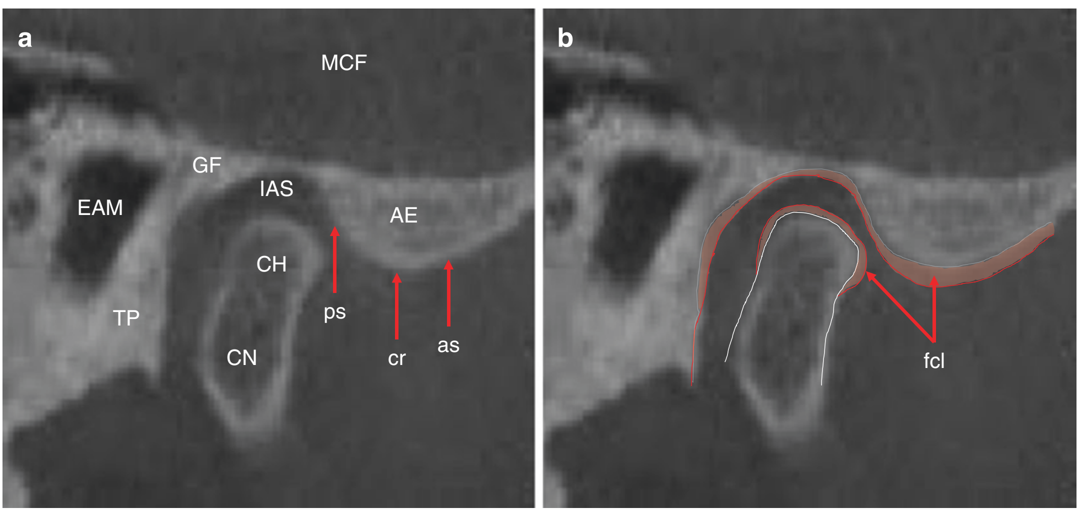

Fig. 24.25 Parasagittal CBCT section of the right TMJ articulation showing radiographic (**a**) appearance and schematic overlay (**b**) showing anatomic functional appearance after consideration of the fibrocartilage layer superimposed on the articulating elements. *GF* glenoid fossa, *AE* articular eminence, *TP* tympanic plate, *IAS* interarticular space, *EAM* external auditory meatus, *MCF* middle cranial fossa, *CH* condylar head, *CN* condylar neck, *fcl* (*red* transparent space) fibrocartilage layer, *ps* posterior slope of the articular eminence, *cr* crest of the articular eminence, *as* anterior slope of the articular eminence, *white solid line* cortical outline, *red solid line* anatomic functional shape

24.3 Radiographic Imaging of the TMJ

CBCT imaging is indicated to characterize the morphology of the TMJ when there is suspicion of disease or limitation of opening from either clinical examination or other radiographic modalities such as panoramic radiography. The osseous components of the TMJ comprise the glenoid fossa, formed by the squamous part of the temporal bone, into which the condyle of the mandible articulates. The articular surfaces of the condyle and glenoid fossa are separated by the interarticular space which appears hypo-dense on CBCT imaging. The interarticular space not only reflects the space occupied by the articular disk but also represents the noncalcified and therefore non-radiographically observed variable thickness of the fibrocartilage covering the mandibular condyle, glenoid fossa, and articular eminence (Fig. 24.25).

24.3.1 Protocols

Various authors underline the importance of the selected image acquisition protocols and the type of the CBCT scanner as parameters of performance in regard with accuracy (Patel et al. 2014; Librizzi et al. 2011; Zhang et al. 2014).

24.3.1.1 Scan Protocol

Comprehensive radiographic examination of the TMJ should be performed using two or occasionally three scans:

- **Mouth closed scan**. This scan is acquired to determine the position of the condyle within the mandibular fossa in a functional, tooth defined position. The first scan should be of moderate resolution (0.3 mm nominal voxel size or less) with the teeth in either maximum intercuspation or centric relation, depending on clinician preference. Ideally, the field of view (FOV) should include 1 cm superior to the base of the glenoid fossa (approximately at the mid-orbital level) and extend to include the mandibular dentition to confirm the occlusal relationship of the teeth. If changes in the articular surface are suspected, then the voxel resolution should be increased (0.25–0.125 nominal voxel size). Head position during the scan should be stabilized to reduce the loss of cortical definition associated with motion artifact.
- **Mouth open scan**. This scan is acquired to determine the range of motion of the condylar head on opening. Low resolution, reduced dose exposure settings should be used with a narrow FOV to include the base of the glenoid fossa and neck of the translated mandibular condyle. Stability of the patient's jaw during an open scan is mandatory. Two possible positions can be used:
  - *Custom maximum unstrained opening.* Mouth opening devices such as Burnett opening device (Burnett BiDirectional TMJ device; Medrad, Pittsburgh, PA, USA) may be used for incremental opening of the mouth controlled by the patient. Some may consider this to be passive mouth opening and not representative of a true physiologic opening given the possible role of the lateral pterygoid muscle in disc stabilization during mouth opening. An alternate method is to ask the patient to bite into an apple. This titrated position is determined by the patient and is most often the maximum opening a patient can perform without pain.
  - *Standard opening.* A bite jig can be used (e.g., multiple Styrofoam blocks) to standardize interincisal opening. The advantage of this approach is that a fixed interincisal opening is used to compare condylar translation.
- **Mouth closed scan with oral orthotic device in position**. Occasionally it may be advisable to perform an additional scan with a diagnostic or therapeutic orthotic oral appliance in position to determine or confirm condylar-fossa relationships.

24.3.1.2 Image Reformatting Protocol

The anatomical variation in the shape and size of the osseous components of the TMJ in cross-sectional images necessitates a standardized approach to reconstructing and displaying TMJ images. In this way at least, the influence of parallax error on image display is minimized. In addition, a standardized display enables comparison of images between patients or within patients at different time intervals. TMJ image reformatting protocols should provide a complete assessment of the articulation in standard jaw positions (like mouth closed or opened) eliminating the chance that important diagnostic information might be disregarded or discovered (Tsiklakis et al. 2004). The application of a "TMJ" protocol for a radiologic examination does not preclude the formation of additional images (e.g., volumetric or shaded surface renderings, maximum intensity projections (MIP)); it merely sets a minimum approach required for thorough interpretation.

The basis for image reconstruction of the TMJ articulation is the construction of an oblique sagittal (or parasagittal) multiplanar reformatted (MPR) images perpendicular to the line between medial and lateral pole of the condyle (i.e., the condylar axis or plane) based on the axial plane (Figs. 24.26 and 24.27).

- **Axial plane**. This horizontal plane should provide a cross-sectional view of both condyles at the greatest inter-polar dimension. For large FOV CBCT units, this may require reorientation of the volumetric dataset. While a native resolution slice provides cortical detail, a medium slice thickness may be valuable in comparing intercondylar angulation with respect to the midsagittal plane and determining the relative size and shape of the condyle.
- **Corrected sagittal plane (parasagittal) plane**. This projection provides multiple sequential cross-sectional images perpendicular to the intercondylar axis. Comparison

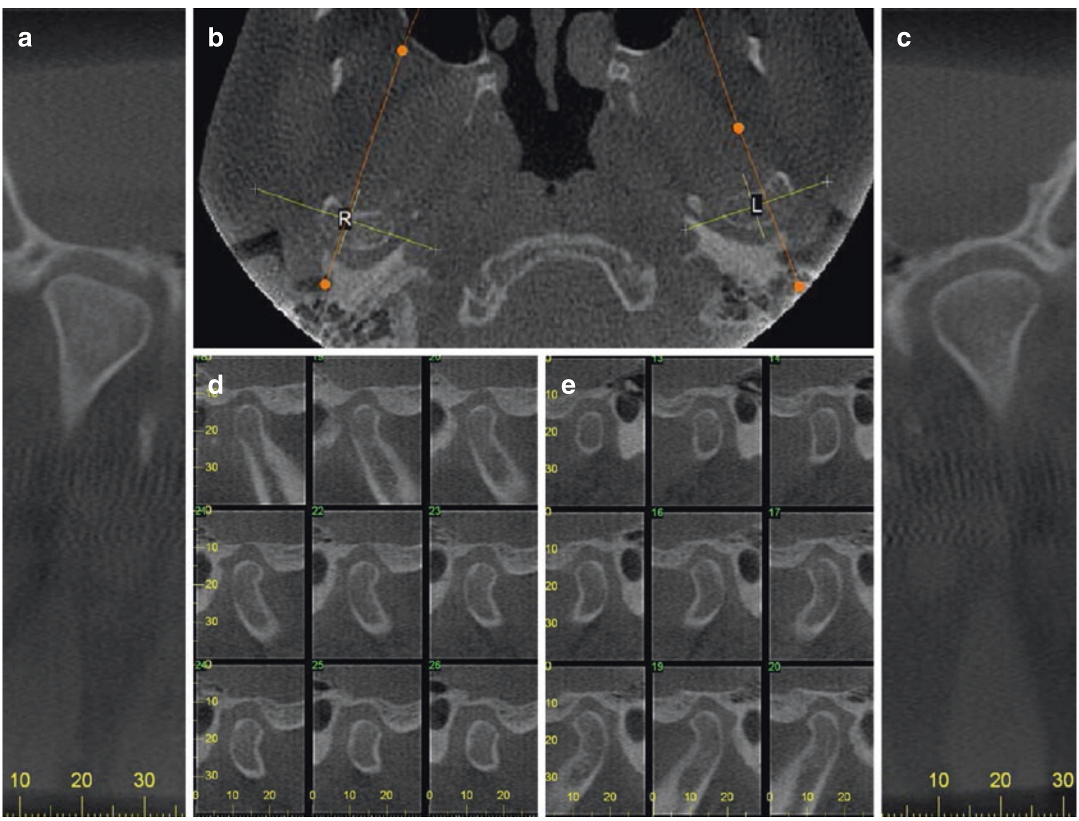

Fig. 24.26 Standard TMJ format for displaying corrected sagittal images with the jaw in the closed position incorporates right (**a**) and left (**c**) para-coronal and axial (**b**) reference images and a series of right (**d**) and left (**e**) parasagittal images at a 1 mm thickness and either 1 mm or 2 mm interval spacing

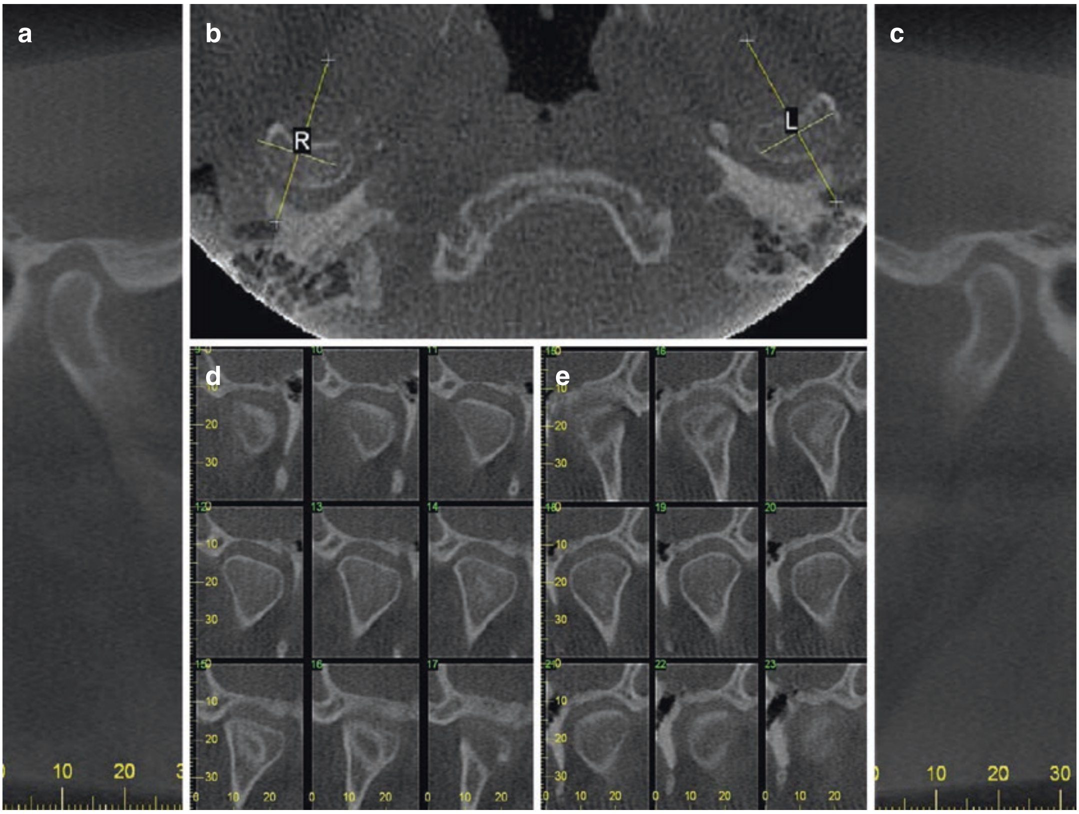

Fig. 24.27 Standard TMJ format for displaying corrected coronal images with the jaw in the closed position incorporates right (**a**) and left (**c**) parasagittal and axial (**b**) reference images and a series of right (**d**) and left (**e**) paracoronal images at a 1 mm thickness and 1 mm interval spacing

of the symmetry of the interarticular space may provide insight into the relative position of the mandibular condyle within the glenoid fossa in the closed position. The view provides the most commonly used projection in the assessment of degenerative changes of the TMJ articulation, particularly the thickness of the glenoid fossa (Fig. 24.26).

- **Corrected coronal (para-coronal) plane**. This projection provides mediolateral appreciation of the condylar and glenoid fossa morphology at the level of the greatest width of the condyle. Comparison of the symmetry of the interarticular disc space may provide insight into the position of the mandible at either centric occlusion (CO) or centric relation (CR). The view provides an invaluable projection of condylar displacement especially in relation to fracture (Fig. 24.27).

24.3.2 Strategies for Image Interpretation

A thorough interpretation of the TMJ articulation is based on a methodological approach. The following strategy is based on an assessment of the anatomic components of the TMJ as a microfunctional unit and the influence of this to the jaw overall as a macrofunctional unit.

24.3.2.1 Individual Elements Within and Between Functional Units

Because each TMJ articulation is composed of two anatomic osseous components, the specific imaging features of each should be assessed individually at the macroscopic level. Identification of specific presentations, particularly in light of clinical presentation and historical perspective, are often useful in diagnosis and management. The features demonstrated on left and right sides should be compared.

Condyle

The morphology of the condyle is described with regard to its overall topographic morphology and surface features.

- **Size**. Condylar size increases with increasing age more so in mediolateral as compared to the anteroposterior dimension. There is often some degree of anatomic variability in condylar size not only within an individual but between individuals. Gender also influences condylar size with males having a slightly larger condyle in all dimensions by approximately 1 mm. Reduction in condylar horizontal dimensions has also been associated with internal derangement (Kurita et al. 2002). While hypo- and hyperplasia are relative terms, it is important to realize that mandibular asymmetry may be the result of either accelerated growth of the mandibular condyle on one side or decreased growth on the opposite side (Tallents et al. 1991). The size of the condyle should complement the size of the glenoid fossa.
- **Shape**. There is great variability in normal condylar form. Condylar shape can be qualitatively described from the sagittal perspective as either round, elliptical, flattened, compressed, or triangular (gabled). From the coronal perspective, condyles can be described as flat, round, angled (or gabled), concave, or convex. Superimposed on these normal morphological forms, condylar shape may be altered by the process of remodeling—the physiological response of the condyle to functional load. Therefore, it is advisable to compare the shape of the condyle between functional units (viz. between the left and right side). It is important when doing so to realize that condylar shape symmetry occurs only in approximately 50% of individuals. Therefore, it is almost equally likely that condylar shapes bilaterally will be different. Remodeling may present as a flattening of a particular surface or compression of the condyle with some degree of condylar neck widening.
- **Surface**. Variations in the condylar surface such as irregularities, erosion, discontinuity, or interruption are likely to represent a pathologic process. Single or localized subchondral defects, referred to as "Ely's cysts," can occur and appear very destructive. This feature is most often associated with osteoarthritis and signifies an active disease process. Thickening of the cortex may be generalized (sclerosis) or localized, principally on the anterior superior condylar surface. Substantial localized cortical thickening and hyperplasia can produce localized "spur-like" deformities (osteophytes). Erosive changes produce a localized area of decreased density of the condylar surface and adjacent subcortical bone. In the condyle, this can create substantial dysmorphology and usually occur in joints with advanced disc displacement, (Kurita et al. 2001) as the articular disc can then no longer act as a kind of shock absorber for the stress in the TMJ.

Glenoid Fossa

The shape and depth of the glenoid fossa as well as the angle of the posterior slope of the articular eminence may potentially be of importance in the mechanical considerations of mandibular motion.

- **Thickness of the roof**. The normal minimal thickness of the glenoid fossa usually determined from parasagittal projections is 0.7 ± 0.12 mm (Tsuruta et al. 2003). Sclerosis and bone formation in the roof of the glenoid fossa has been proposed as a compensatory mechanism to withstand the increased stress in the articulation accompanying DJD. It is often accompanied by a commensurate reduction in condylar height.
- **Depth**. The shape of the glenoid fossa varies from childhood to adulthood, gradually increasing in depth. Fossa depth can be described according to its relationship to the superior portion of the external auditory meatus (EAM):
  - *Shallow*. Extends to less than half way to the level of the EAM

- *Moderate*. Extends to just above the most superior aspect of the EAM
- *Deep*. Extends substantially above the most superior aspect of the EAM

- **Size and Shape**. Glenoid fossa shape is usually assessed from the sagittal projection and, in order of decreasing frequency, described as oval, triangular, trapezoidal, or round. Only about half of TMJ articulations have matching condylar and fossa shapes (Katsavrias 2006). For Class II Division 1, Class II Division 2, and for Class III malocclusions there is tendency for older Class III individuals to have larger fossa (Katsavriasa and Halazonetisb 2005).
- **Posterior Slope of the Articular Eminence**. The articular eminence can be described according to the relative degree of the slope of posterior portion as viewed from sagittal projection. The posterior slope can be nearly flattened (≤45°), acute (45°–65°), moderately acute (65°–80°), and abrupt (80°–90°) eminence.

24.3.2.2 Relationships of the Elements as a Functional Unit

Comparisons of the condylar/glenoid fossa relationship in both a closed reference position (CO or CR) and with the jaw in an opened position may assist in the evaluation of the functional interactions of the mandible as a unit.

- **Anterior–Posterior**. The parasagittal projection provides the best view of demonstrating this relationship.
- **Mediolateral Relationships**. The paracoronal projection provides the optimal view of this relationship. This is particularly important in the open position where the relative changes in interarticular dimensions can suggest mandibular shift.

24.3.2.3 The Effects of the TMJ Functional Unit on the Maxillofacial Skeleton

Three-dimensional images of the condyle and surrounding structures facilitate analysis and diagnosis of bone morphology, joint space and dynamic function, critical keys to providing appropriate treatment outcomes in patients with TMJ signs and symptoms. While surface changes are difficult to discern, MIP and volumetric rendering techniques, in conjunction with MPR images, are well suited at demonstrating severe and often complex morphologic changes of the condyle and temporal articulation associated with severe degenerative joint disease or ankylosis (Ciccarelli et al. 1998). Developmental anomalies and their effects on related but distal structures such as the occlusion can also be clearly visualized as can structural impediments to mandibular opening.

24.3.3 Characteristics of the Normal Temporomandibular Joint

Taking into account the variability in the shape and size of the condylar head and the glenoid fossa discussed earlier (Fig. 24.28), healthy (unaffected) osseous structures of the TMJ present some common radiologic features:

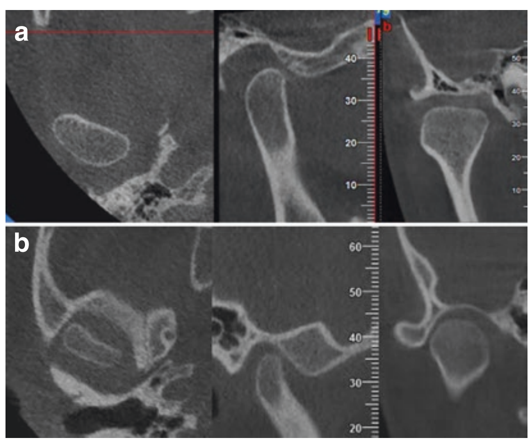

Fig. 24.28 Comparison of shape if the left TMJ articulation for two individuals (**a**, **b**) with normal morphology showing (from left to right) axial, parasagittal and paracoronal images

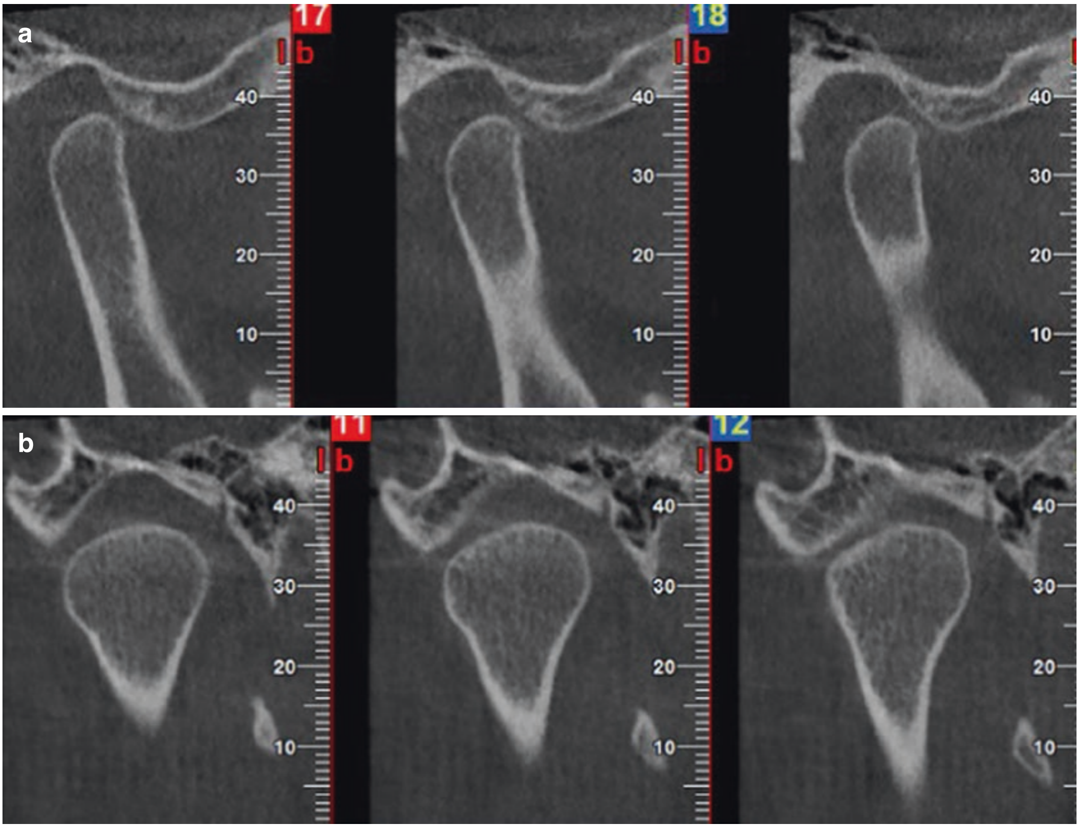

Fig. 24.29 Serial parasagittal (**a**) and coronal (**b**) CBCT images of an individual in the mouth open position showing normal morphology of the right TMJ articulation including no gross shape alterations of the articulating surfaces, a smooth and rounded contour, a thin and uninterrupted cortical outline with fairly clear distinction between the cortical and cancellous bone

- No gross shape alterations of the articulating surfaces (beyond the reported variation) (Figs. 24.29 and 24.30)
- A smooth and rounded contour of both articulating surfaces (condyle and fossa) (Figs. 24.29 and 24.30)
- A thin and uninterrupted cortical outline for both articulating surfaces (Figs. 24.29 and 24.30)
- A fairly clear distinction between the cortical and cancellous bone especially for the condylar head (Figs. 24.29 and 24.30)
- A fairly concentric position of the condyle in the fossa (in the mouth closed position) (Fig. 24.31)
- An interarticular joint space of approximately 2–3 mm (Fig. 24.31)
- The mandibular condyle translates to the tip of the articular eminence (in the mouth opened position) (Fig. 24.32)

When the above characteristics are present in a symptomatic TMJ, the clinician may be suspicious of soft tissue origin of the patient's symptoms and exclude osseous tissues as origin.

24.4 Disorders of the TMJ

Three groups have developed diagnostic classification systems for TMD—The American Academy of Orofacial Pain (Leeuw 2008), the International Consortium for RDC/TMD-based

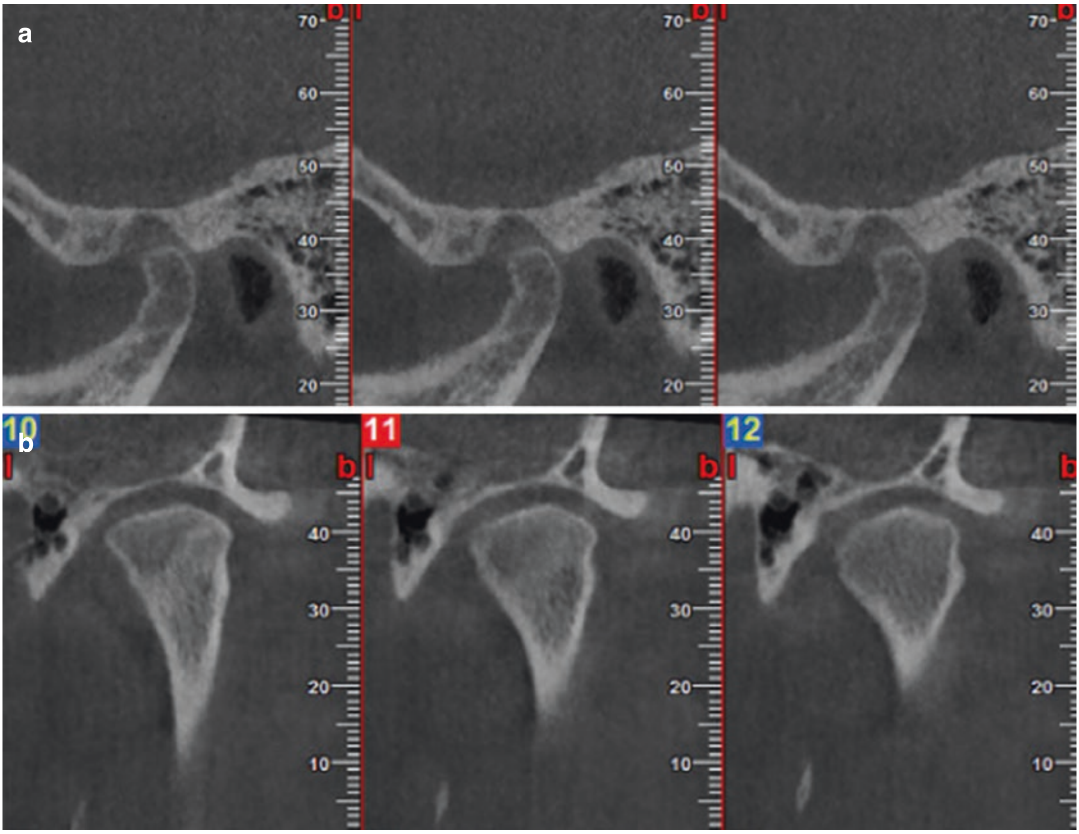

Fig. 24.30 Serial parasagittal (**a**) and coronal (**b**) CBCT images of an individual in the closed jaw position showing normal morphology of the left TMJ articulation. Note two differences that may have clinical significance: (1) The condylar angle relative to the neck shows moderate deviation—this may be due to remodeling of the condyle, and (2) posterior and inferior position of the condyle within the fossa. Both may be in response to anatomic or habitual chronic retrusion of the mandible

Research (Petersson 2010), and the American Society of Temporomandibular Joint Surgeons (American Society of Temporomandibular Joint Surgeons 2003). These classification systems are not identical but are substantially similar (John et al. 2005). Clinically TMJ disorders are categorized based on the anatomic origin of the problem: intra-articular disorders include the articular surface, intra-articular disc, or articulating bones whereas extra-articular disorders are concerned with the musculoskeletal and nervous system elements (Table 24.1).

Most intra-articular disorders affect either the size and/or shape of the mandibular condyle due to congenital or development conditions, neoplasia or arthritides, with noninflammatory degenerative joint disease (DJD) being the most common. Severe TMJ morphologic deformity is associated with ankylosis or condylar resorption. Heterotopic ossification, a major complication of TMJ-related surgery, is rare in the maxillofacial region, but may result in varying degrees of restricted mandibular movement or eventual ankylosis.

24.4.1 Congenital and Developmental Conditions

Congenital and developmental anomalies of the TMJ are relatively uncommon. The more common entities include condylar agenesis, condylar aplasia, condylar hypoplasia, condylar hyperplasia, and manifestations associated with craniofacial conditions such as hemifacial

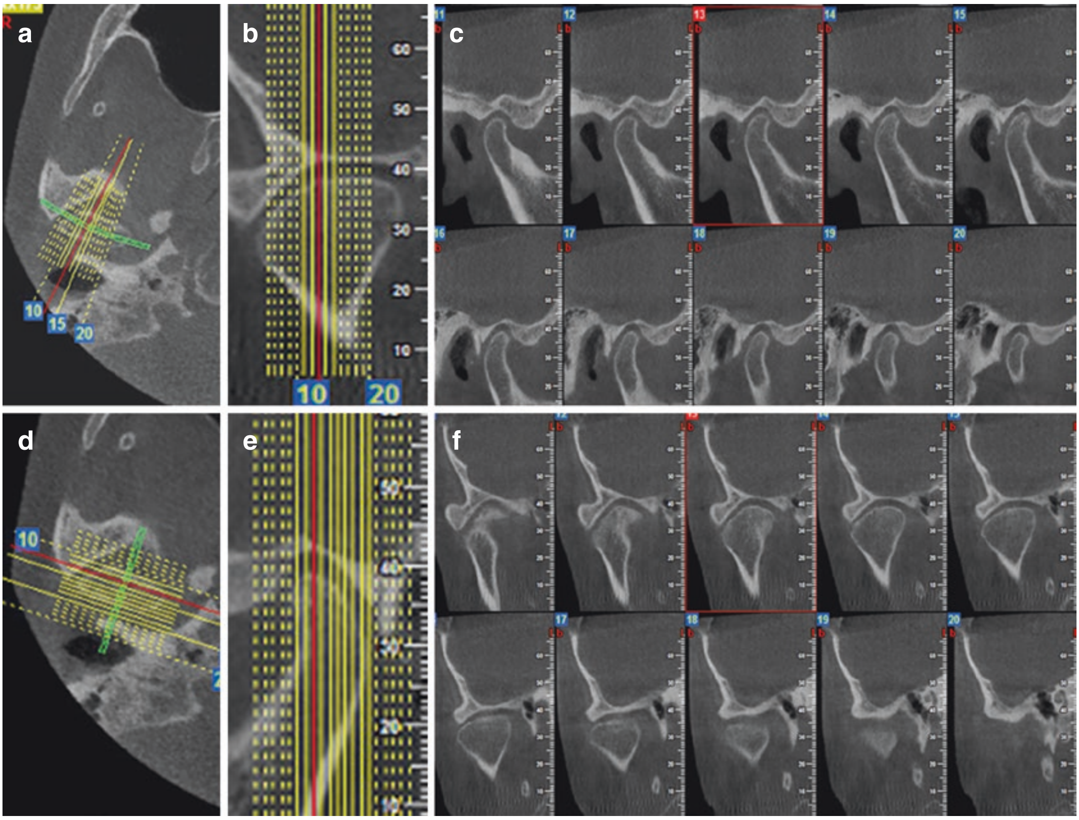

Fig. 24.31 Axial (**a**) and para-coronal (**b**) reference and serial parasagittal CBCT images of a normal right TMJ articulation in the mouth closed position with corresponding axial (**d**) and parasagittal (**e**) reference and serial para-coronal (**f**) CBCT images. While the mandibular condyle is concentrically positioned, the relative location of the condyle within the fossa and interarticular space varies substantially on the image section slice

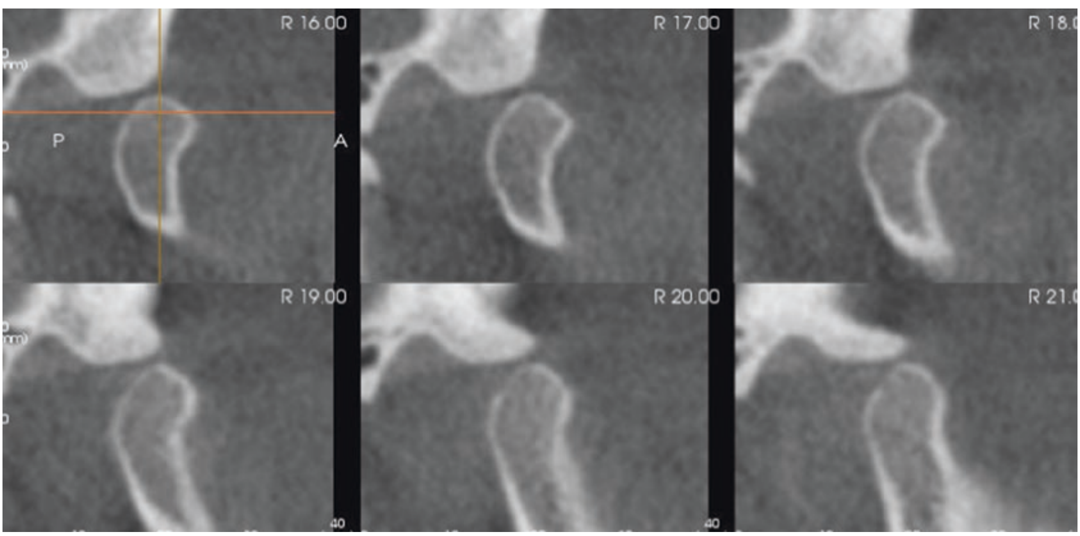

Fig. 24.32 Serial parasagittal CBCT images of the right TMJ articulation showing the translation of the mandibular condyle beyond the crest to lie on the anterior slope of the articular eminence

microsomia. These disorders may present as a progressive facial or mandibular asymmetry. Of all the developmental conditions, condylar hyperplasia is the one most likely to be surgically treated.

24.4.1.1 Bifid Mandibular Condyle

The bifid mandibular condyle (BMC) is a rare condition (Gundlach et al. 1987) and usually has no significant presenting symptoms or clinical features (Hersek et al. 2004). Although this type of morphologic change is generally considered to be developmental, conditions such as trauma, teratogenic drug use, genetic inheritance, infection, and exposure to radiation can also cause this anomaly (Fig. 24.33). According to Blackwood (1957), two articulating surfaces of the BMC are divided by a groove and can be orientated mediolaterally or anteroposteriorly, characterizing a specific entity.

24.4.1.2 Condylar Hyperplasia

Condylar hyperplasia is a slowly developing idiopathic malformation of non-neoplastic origin characterized by increased thickness of the entire cartilaginous and pre-cartilaginous layers of the mandibular condyle. It usually occurs unilaterally and is accompanied by varying degrees of hyperplasia of the ipsilateral mandible. The condition is often an incidental radiographic finding on teenagers and young adults. Therefore, it has been proposed to arise as a result of an acceleration of physiologic condylar growth in young patients or as an unpredictable growth spurt in adults. Individuals may present with one or more of the following signs or symptoms: mandibular asymmetry, chin deviation to the opposite side, an increase in vertical dimension of ramus, mandibular body or alveolar process of same side, unilateral posterior open bite on the affected side, TMJ dysfunction, or restricted mouth opening. Imaging findings include:

- **Morphologic condylar changes**. Enlargement of the overall size of the condyle with maintenance of shape (Fig. 24.34). Occasionally the outline may be irregular. Often there is elongation of condylar neck and lateral curvature. Cortical thickness and trabecular pattern is normal—this feature differentiates it from condylar osteochondroma.

Table 24.1 Diagnostic classification of TMJ and related musculoskeletal disorders (After American Society of Temporomandibular Joint Surgeons 2003)

Category	Common examples
Intra-articular disorders of the TMJ	
Articular disc	• Internal derangement with/without reductions
Disc attachments	• Perforation • Fibrosis
Synovium	• Inflammation/effusion • Arthritides (rheumatoid, degenerative) • Synovial chondromatosis • Neoplasia
Articular fibrocartilage	• Hypoplasia/hypertrophy
Mandibular condyle and glenoid fossa	• Osteoarthritis (osteoarthrosis, degenerative joint disease) • Condylar resorption • Hypertrophy • Fibrous and bony ankylosis • Fracture/dislocations • Others (e.g., avascular necrosis, implant arthropathy)
Extra-articular disorders	
Musculoskeletal	• Bone (temporal, mandible, styloid) • Anomalous development (hypoplasia, hypertrophy, malformation, ankylosis) • Fracture • Metabolic disease • Systemic inflammatory disease (connective tissue/arthritides) • Infection • Dysplasias • Neoplasia
	• Masticatory muscles • Local myalgia (unclassified) • Myofascial pain and myospasm
Central nervous system	• Reflex sympathetic dystrophy

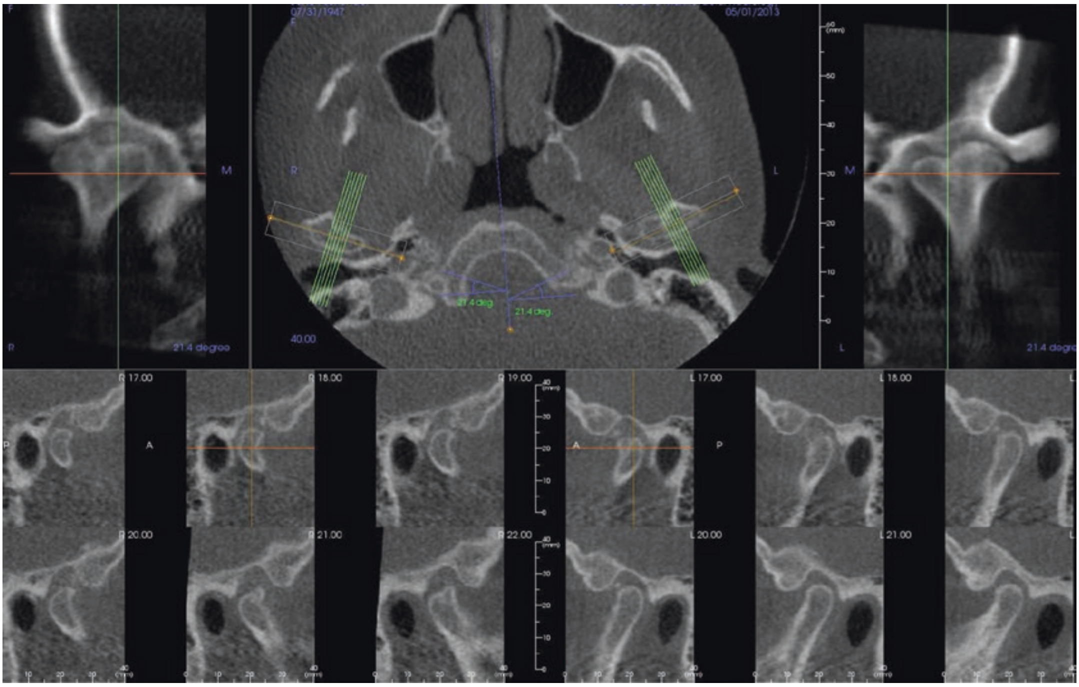

Fig. 24.33 Standard TMJ reformatted display incorporating coronal, axial reference and serial cross-sectional images demonstrating bilateral bifid mandibular condyles with an anteroposterior groove

- **Associated ipsilateral changes**. Enlargement of the glenoid fossa, ramus, and body of mandible on the affected side.
- **Secondary findings**. Malocclusion related to cross-bite of the teeth and a shift in the position of the mandibular midline to the unaffected side.

24.4.1.3 Condylar Hypoplasia

Condylar hypoplasia is usually a unilateral condition producing a smaller size of condylar neck and head compared to normal. Condylar hypoplasia is most commonly the result of a postnatal insult, such as trauma, infection, or radiation that produces a disturbance in the condylar growth centers (Proffit et al. 1980). When an affected side fails to grow downward and forward, a three-dimensional asymmetry is produced. As a result of the hypoplasia, the mandibular skeletal midline deviates to the affected side, a lack of vertical growth on the same side produces a cant of the occlusal plane, and there is mandibular retrognathia. The lower border of the mandibular body and angle on the contralateral side is usually flattened. The severity of the deformity depends on the degree of hypoplasia—the more severe the deformity, the greater the probability that it will worsen with growth. Imaging features include:

- **Altered TMJ articulation morphology**. Well-corticated, smooth and normal condyle which is markedly smaller than the contralateral side (Fig. 24.35). Ankylosis may also be associated. The glenoid fossa may also be smaller and shallower.
- **Altered mandibular morphology**. Shallow sigmoid notch, a short ramus and reduced mandibular body length.
- **Soft-tissue abnormalities**. Deficiencies in the external ear, are not a feature of condylar hypoplasia

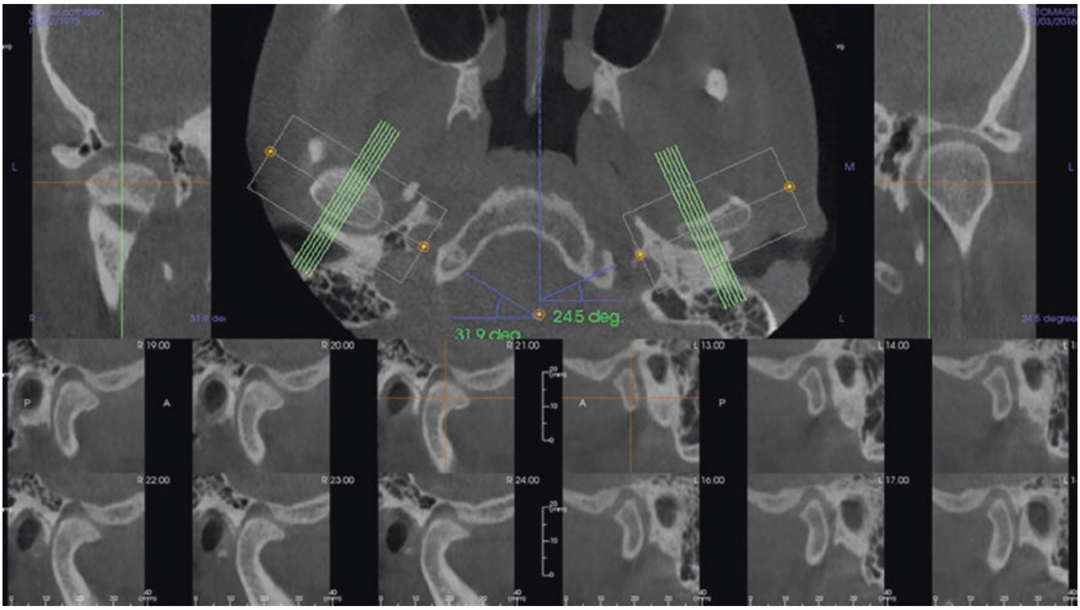

Fig. 24.34 Standard TMJ reformatted display incorporating coronal, axial reference and serial cross-sectional images demonstrating features consistent with hyperplasia of the right mandibular condyle

Condylar hypoplasia occurs in Hurler's syndrome (mucopolysaccharidosis type I), a genetic disorder that results in the deficiency of alpha-L iduronidase. Therefore, depending on presentation, it may be advisable to request a urine analysis to determine chondroitin sulfate B and heparin sulfate, both of which are elevated. A "J-shaped" sella turcica may also be present in these individuals. In addition, patients with condylar hypoplasia have significantly greater incidence and severity of morphological deviations of the cervical column (Sonnesen et al. 2007).

24.4.1.4 Coronoid Hyperplasia

Coronoid hyperplasia is a rare condition characterized by an enlarged mandibular coronoid process. Patients usually present with painless progressive reduction in jaw opening due to impingement of the coronoid process on the posterior aspect of the zygomatic bone. Hyperplasia may be unilateral or bilateral. Unilateral hyperplasia is often secondary to a proliferative hypertrophy of the coronoid process associated with TMJ dysfunction (Fig. 24.36) whereas bilateral hyperplasia presents in adolescence and is developmental (Fig. 24.37). In unilateral cases, there may be facial asymmetry with deviation on opening to the affected side. Coronoid hyperplasia appears to be a disorder predominately of young male adults, with peak age of presentation in the middle of the third decade (McLoughlin et al. 1995). Isberg et al. (1987) suggested that the temporal muscle may play a role in the reactive elongation of the coronoid process. Imaging features include:

- **Coronoid process features**: Tip of the coronoid process projects more than 1 cm above lower edge of zygomatic arch; pointed shape of process.
- **Mandible ramus**: Associated mandibular angle hypertrophy has been described in a subgroup of patients reported as "square mandible" (Murakami et al. 2000).

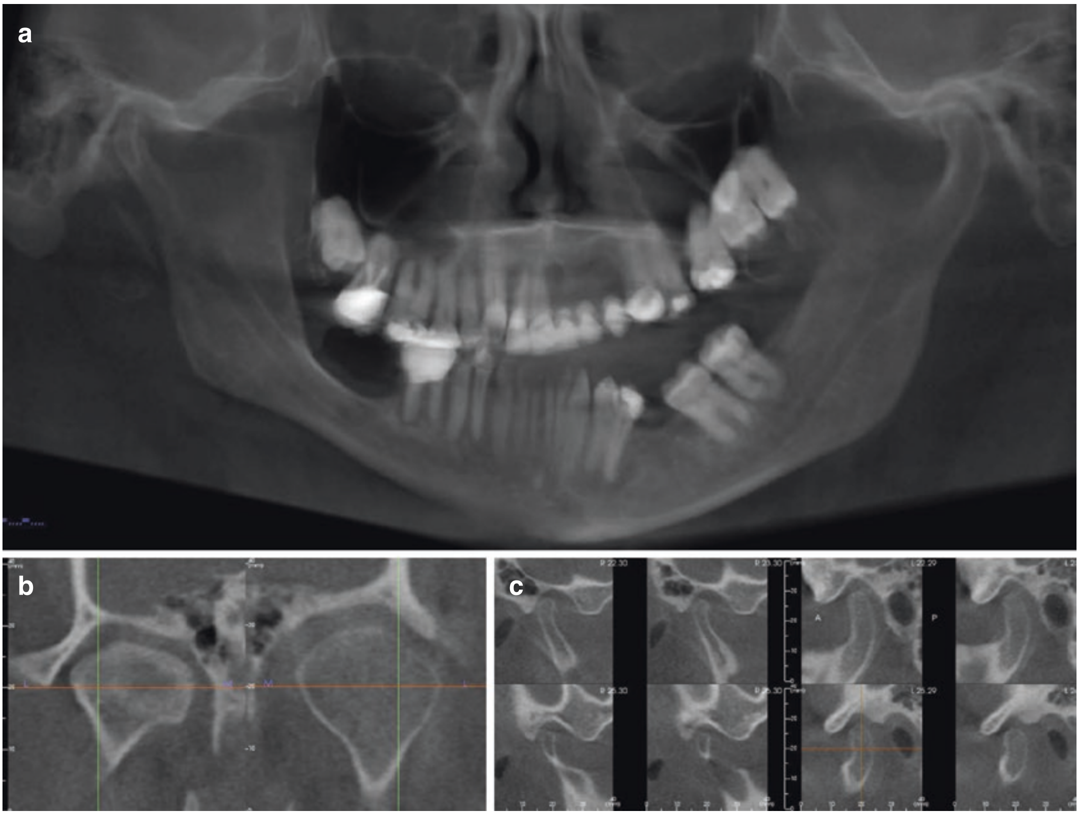

Fig. 24.35 Reformatted panoramic (**a**), left and right coronal (**b**), and left and right parasagittal (**c**) images showing right condylar hypoplasia. Note the smaller size of the right condylar head compared to the normal sized glenoid fossa

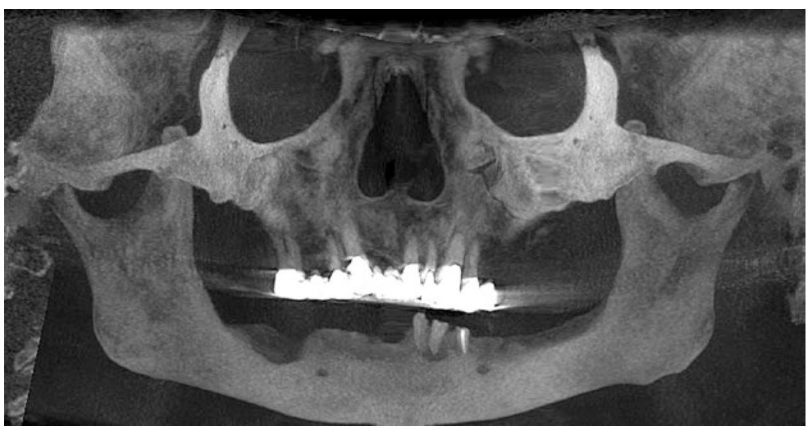

Fig. 24.36 Reformatted maximum intensity projection (MIP) panoramic projection of an 83-year-old male with middle (Izumi et al. 2005) vertical bilateral coronoid proliferative hypertrophy, most likely secondary to chronic TMJ dysfunction or as a result of marked decrease in occlusal vertical dimension resulting in overclosure

Izumi et al. (2005) categorized the morphologic cross-sectional configuration of the coronoid process on the axial slice at the level of the superior border of the zygomatic arch as being either angular (31%), round (62%), or stick shaped (7%). In addition, they classified the vertical extension above the zygomatic arch as high (7%), middle (86%), and low (7%).

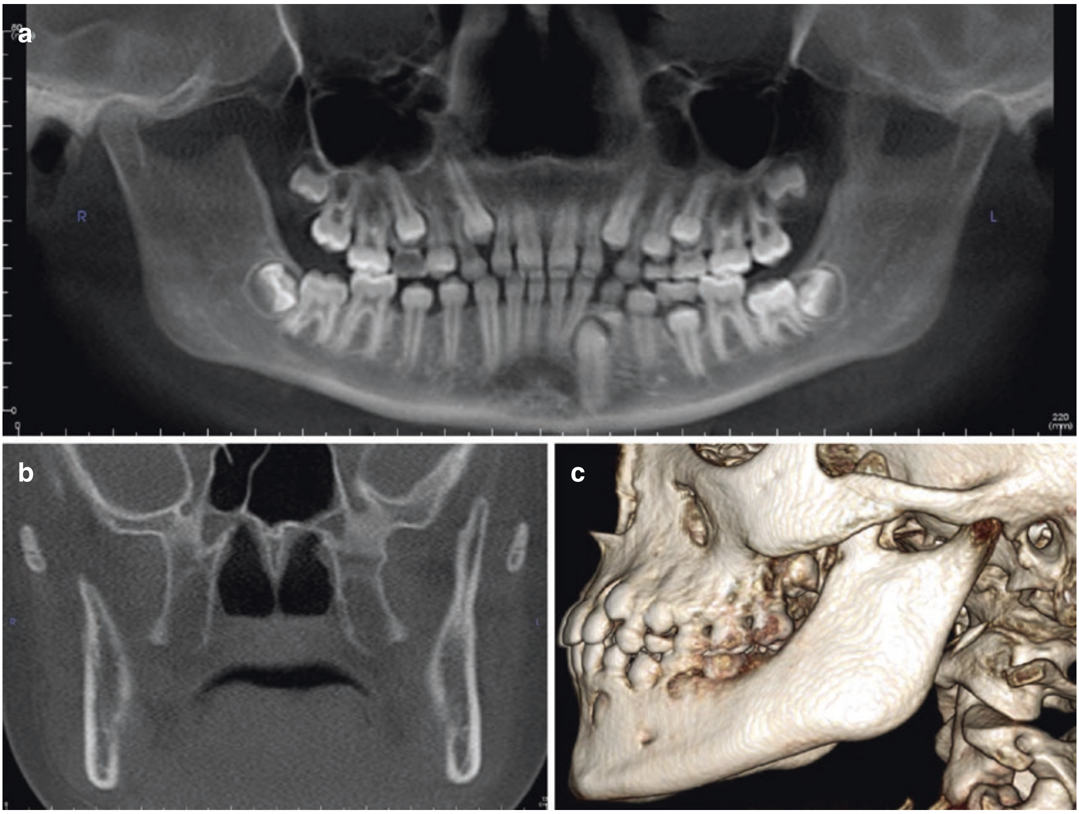

Fig. 24.37 Reformatted panoramic (**a**), coronal (**b**), and left lateral shaded surface volumetric rendering (**c**) of a 12-year old female with progressive limited maximal interincisal opening of 25 mm. who reports a previous bilateral coronoidotomy at 5 years of age. The imaging demonstrates a well-defined osseous, pedunculated "finger-like" ovoid projection extending superiorly from the residual apex of the left coronoid process above the superior border of the zygomatic process to the level of the left orbital rim within the infratemporal fossa. These findings are consistent with a developmental coronoid hyperplasia

Imaging should be performed both in closed and maximal jaw opening. The latter is performed to evaluate the degree of interference between the coronoid processes and the zygomatic bone and for the surgical planning. In cases of reduced jaw opening, surgical correction by coronoidectomy or coronoidotomy eliminates coronoid-malar interference. Relapse may occur, with regrowth of the coronoid process (Fig. 24.38).

24.4.2 Condylar Fracture

Fracture of the condyle itself, the neck or the subcondylar region accounts for between 20% and almost 50% of all mandible fractures. Up to 50% of condylar fractures involve other elements of the mandible and maxillofacial complex including midfacial fractures. Unilateral condylar fractures are the most common, occurring in approximately 75%. Patients usually present with a history of direct or indirect trauma and a varying degree of limitation of mandibular movement, mandibular deviation to the injured side on opening and de novo occlusal prematurities and discrepancies. Patients may present many years after the injury with condylar dysmorphology (Figs. 24.38 and 24.39). Condylar fractures in children are particularly important, especially prior to completion of growth (less than 4 years of age), as such injury may predispose to growth disturbances and asymmetry at multiple facial levels, including the orbits, cheeks, maxilla, and

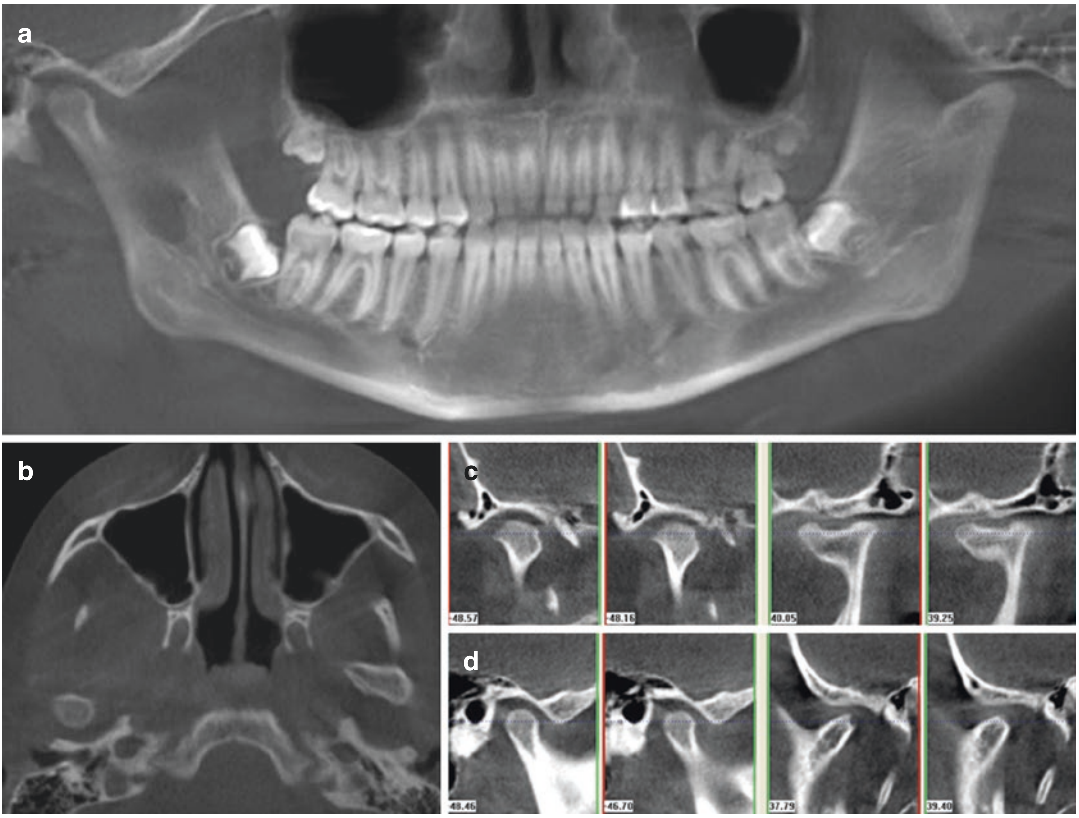

Fig. 24.38 Reformatted panoramic (**a**), axial (**b**), and left and right coronal (**c**) and parasagittal (**d**) CBCT images of an adolescent with a history of a motor vehicle accident with fracture of the left mandibular condyle approximately 5 years previously. The patient was initially treated with intermaxillary fixation and then fixed orthodontic appliances for 1 year. The images show marked dysmorphology and hyperplasia of the left condyle with pseudo articulation on the left articular eminence consistent with a healed medially displaced uncorrected subcondylar fracture

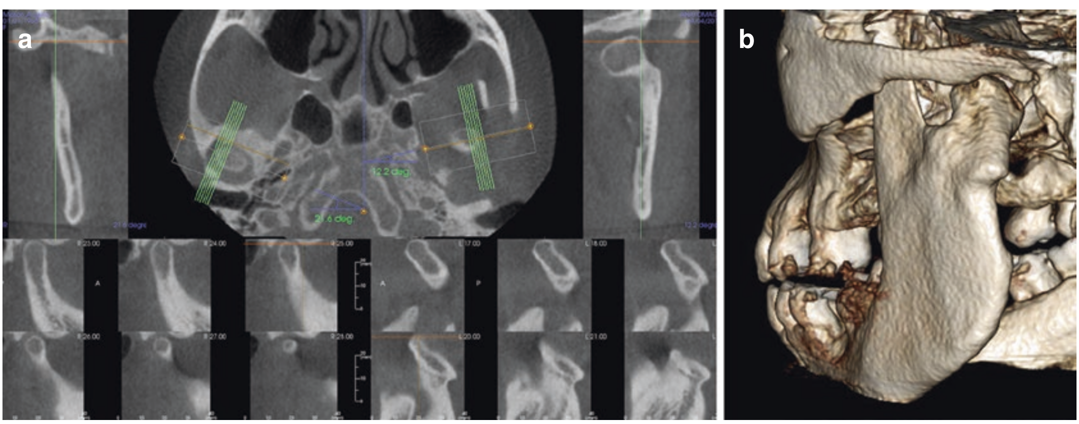

Fig. 24.39 Standard TMJ reformatted display incorporating coronal, axial reference and serial cross-sectional images (**a**) and a left posterior oblique shaded surface rendering (**b**) of a 46-year-old female with a history of blunt facial trauma approximately 10 years previously. The images show marked dysmorphology and malunion of the anteromedially rotated condylar segment. Note that the morphology of the right TMJ articulation and the occlusion are within normal limits

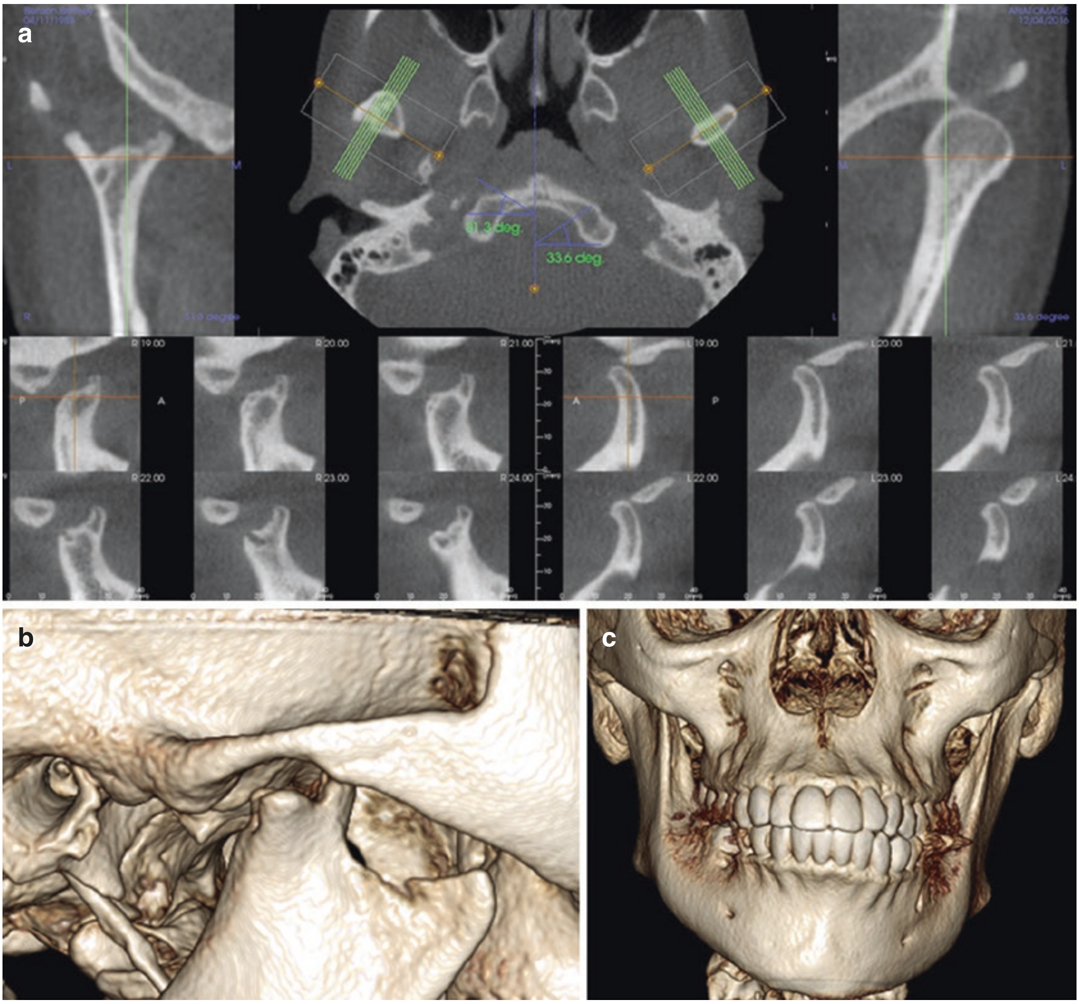

Fig. 24.40 Standard TMJ reformatted display incorporating coronal, axial reference and serial cross-sectional images in closed position (**a**), right lateral shaded surface rendering in the open position (**b**) and frontal shaded surface rendering in the closed position (**c**) of a 28-year-old female with a history of motor vehicle accident when a child. The patient presents with mandibular asymmetry associated with erosive remodeling and formation of a pseudo articulation of the right mandibular condyle with loss of ipsilateral ramal vertical dimension

mandible (Fig. 24.40). Injury in children may also predispose to local disorders such as ankylosis and dysfunction, malocclusion, chronic dislocation, and pain on the injured as well as the non-injured side.

Condylar fractures are best described according to the following considerations:

- The element of the mandibular component involved; intracapsular (Fig. 24.41) or extracapsular (condylar neck or subcondylar).
- Type of deformity; undisplaced, deviated, or displaced (with medial or lateral overlap, or complete separation).
- Degree of dislocation; displacement in relation to the glenoid fossa (Table 24.2).

Lindahl and Hollender (1977) classify condylar head fractures into horizontal, vertical, and compression types. Nineteen per cent of the condylar fractures are undisplaced, 12% deviated, and 69% displaced. Fifty-six per cent of the dis-

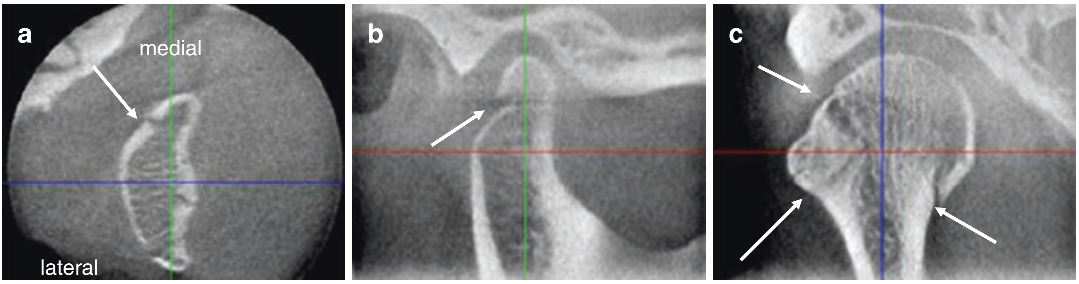

Fig. 24.41 Limited area CBCT axial (**a**), parasagittal (**b**), and coronal (**c**) orthogonal images of 33-year-old female who complained of pain in her right TMJ after trauma. Images demonstrate minimally displaced intracapsular fracture (*white arrows*) through the lateral and medial poles of the condyle

Table 24.2 Classification of condylar fracture based on severity with respect to condylar head displacement

Type	Description
I	Involves the neck of the condyle with relatively slight displacement of the head. The angle between the head and the axis of the ramus varies from 10° to 45°
II	Involves the neck of the condyle to produce an angle from 45° to 90°, resulting in tearing of the medial portion of the joint capsule
III	Fragments are not in contact, and the head is displaced medially and forward. Fragments are confined within the area of the glenoid fossa. The capsule is torn, and the condylar head is outside the capsule
IV	Fragments of the condylar head articulate on or in a forward position with regard to the articular eminence
V	Multiple vertical or oblique fractures through the head of the condyle

placed fractures demonstrate some form of overlap (77% medial and 23% lateral), 37% demonstrate anteroposterior override, and in 6% of the cases there is no contact. Nineteen per cent of the condylar fractures are dislocated (Zachariades et al. 2006).

Imaging features are usually associated with anteromedial displacement of the fragments to varying degrees by the medial pterygoid muscle. Based on this, condylar fractures are categorized in order of increasing severity (Table 24.2).

Alternately, classification can be based on location of the fracture location and degree of displacement (Table 24.3) (Spiess and Schroll 1972).

Table 24.3 Classification of condylar fracture based on location and displacement (Spiess and Schroll 1972)

Type	Description
I	Condylar fracture without displacement
II	Low condylar fracture with displacement
III	High condylar fracture with displacement
IV	Low condylar fracture with dislocation
V	High condylar fracture with dislocation
VI	Condylar head fracture

Table 24.4 Classification of condylar fracture based on location and displacement (Loukota et al. 2005)

Type	Description
Diacapitular fracture	Fracture through the head of the condyle: The fracture line starts in the articular surface and may extend outside the capsule
Condylar neck	The fracture line starts somewhere above a perpendicular line through the sigmoid notch to the tangent of the ramus
Condylar Base	The fracture line runs behind the mandibular foramen and, in more than half, below a perpendicular line through the sigmoid notch to the tangent of the ramus

The Strasbourg Osteosynthesis Research Group (SORG) proposed a simplified classification system based on anatomic considerations (Table 24.4) (Loukota et al. 2005). They also defined minimal displacement to be displacement of less than 10° or overlap of the bone ends of less than 2 mm, or both.

While there is no absolute protocol governing treatment of condylar fractures. However, correct determination of condylar fracture location and degree of displacement via CBCT imaging is essential in determining diagnosis (Fig. 24.41) and, if necessary, directing surgical intervention towards open or closed reduction. While conservative therapy is usually preferred, surgery may be considered in the adult in the following situations: severely displaced condyles; dislocated subcondylar or condylar neck fractures that lie out of the glenoid fossa or interfere with mechanical mandibular function; medial or lateral override resulting in significant loss of vertical ramus height, that cannot be compensated in any other way; to avoid intermaxillary fixation associated with panfacial injury and/or comminuted maxillary fractures; displacement of the condyle into the middle cranial fossa; compound fractures; and associated foreign bodies.

24.4.3 Arthritides

Arthritic changes are the most frequent condition affecting the TMJ; however, most often patients are asymptomatic. All types occur, but degenerative (osteoarthrosis) and inflammatory (e.g., rheumatoid arthritis) are the most common.

24.4.3.1 Degenerative

Osteoarthritis (OA) or degenerative joint disease (DJD) of the TMJ is a noninflammatory disorder characterized by reduction in the synthesis and destruction of the articular cartilage and also by new bone formation at the joint surfaces. The disease may be primary, as a condition associated with advancing age, or secondary following trauma or chronic bruxism.

Osteoarthritis (OA) is common and has been found to affect between 27% and 50% of individuals by the fifth decade (Öberg et al. 1971; Toller 1973). Degenerative changes are also often observed in younger individuals (Ogus 1979), especially those who present with symptoms (Katzberg et al. 1985) suggesting that some subjects are at risk for the degeneration of the joints. Classical imaging features include (Figs. 24.42, 24.43, 24.44, 24.45, 24.46, 24.47, 24.48, 24.49, 24.50, 24.51, and 24.52):

- **Interarticular space**. Joint "space" is reduced because of loss of articular cartilage.
- **Condylar changes**. The conventional classifications of condylar bone change on conventional radiography were proposed by Uemura et al. (1979) and include:
  - Surface changes of the cortical bone comprising localized erosions (subcortical or subchondral voids, referred to as or *Ely cysts*), thickened cortical outlines (eburnation) and sclerosis
  - Deformity comprising osteophyte formation (marginal anterior superior bone proliferation resulting in bony exostoses, eburnation, or bone lipping—producing a "bird beak" appearance on parasagittal images) and faceting (flattening of superior anterior surface of the condylar head).
- **Glenoid fossa changes**. While OA changes most often occur on the mandibular condyle, they may also involve the glenoid fossa or articular eminence. These are predominantly eburnation and sclerosis. The thickness of the roof of the glenoid fossa has been reported to increase significantly with osteoarthritis (Tsuruta et al. 2003).

Degenerative osseous changes are broadly characterized as mild, moderate, and severe based on the extent and severity of the observed changes in the osseous components of the TMJ.

24.4.3.2 Inflammatory

This group of conditions comprises systemic disorders affecting the synovial membrane in multiple joints and includes rheumatoid arthritis, and rare conditions such as infective or psoriatic arthritis (Table 24.5). In general, all conditions demonstrate cortical erosions of both the condyle and fossa/eminence with accompanying osteoarthritic changes. The most common presenting features are preauricular edema, pain, and trismus. It is not possible to differentiate between rheumatic diseases based on imaging alone, although bone production seems to be more pronounced in ankylosing spondylitis (Wenneberg et al. 1990; Larheim et al. 2015).

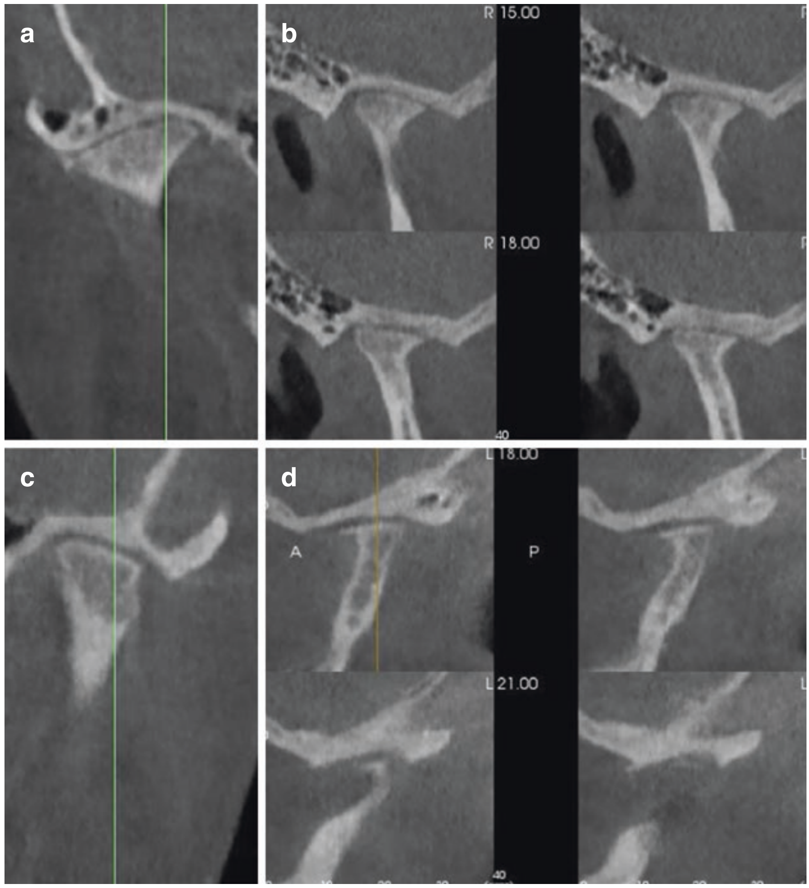

Fig. 24.42 Right (**a**) and left (**c**) para-coronal reference CBCT images and right (**b**) and left (**d**) consecutive 1 mm thick parasagittal images demonstrating bilateral severe TMJ OA. Imaging features include loss of interarticular space, condylar flattening, osteophyte formation and loss of depth and sclerosis of the glenoid fossa

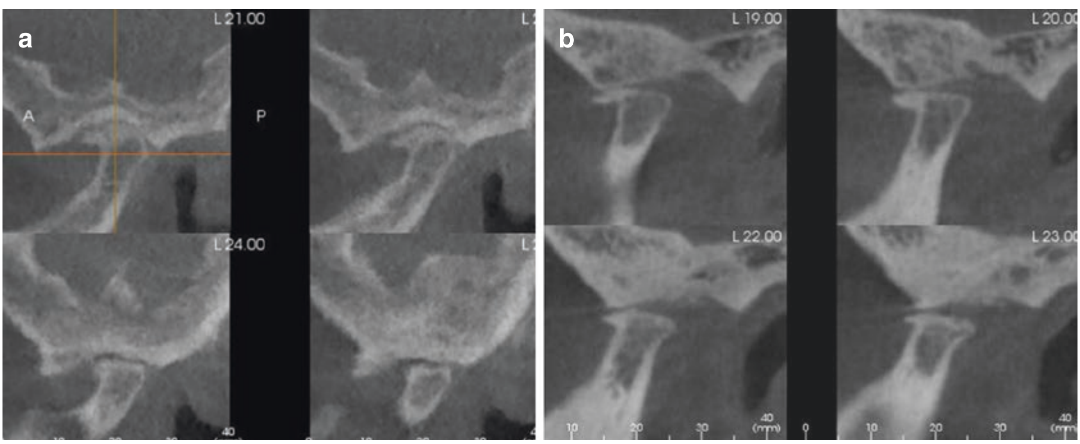

Fig. 24.43 Serial cross-sectional parasagittal images of the left TMJ in the mouth closed (**a**) and mouth open (**b**) positions demonstrating limited range of motion of the mandibular condyle and various representations of severe OA of the TMJ. Imaging features include loss of interarticular space, condylar flattening, osteophyte formation and flattening and marked sclerosis of the glenoid fossa

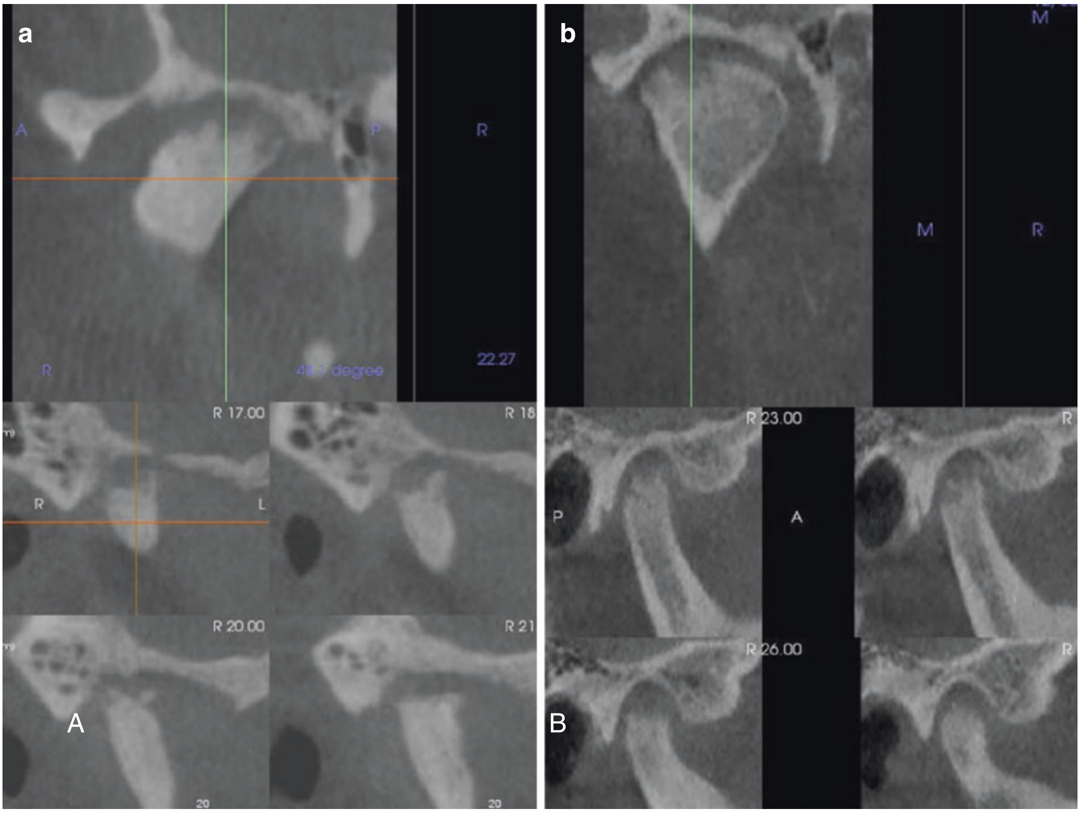

Fig. 24.44 Coronal (*upper*) and serial parasagittal images (*lower*) of two individuals (**a** and **b**) demonstrating severe OA of the TMJ featuring condylar and glenoid fossa sclerosis (**a**), loss of cortication and irregular surface changes and erosions (**a** and **b**)

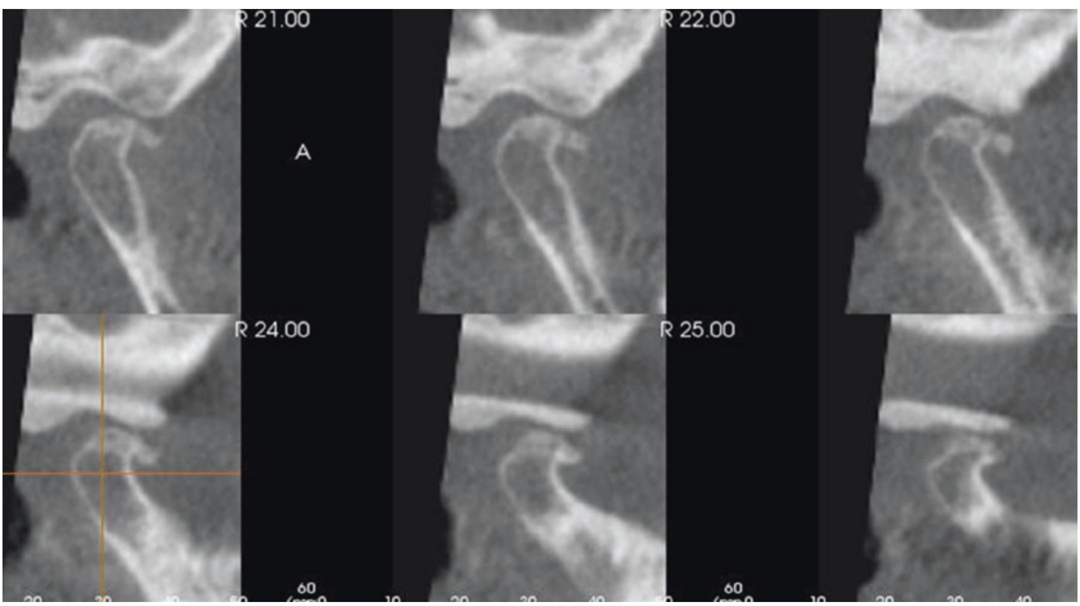

Fig. 24.45 Serial parasagittal images demonstrating moderate OA of the right TMJ articulation featuring osteophyte formation on the anterosuperior surface of the condylar head and sclerosis of the glenoid fossa

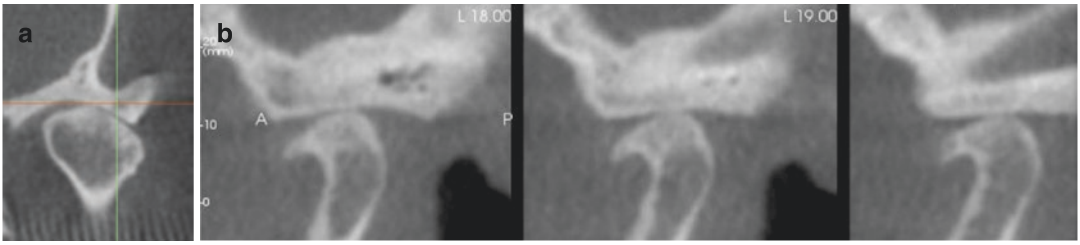

Fig. 24.46 Para-coronal reference image (**a**) and serial parasagittal images (**b**) of the left TMJ demonstrating moderate OA of the TMJ featuring osteophyte formation on the anterosuperior surface of the condylar head, sclerosis of the glenoid fossa and loss of interarticular space

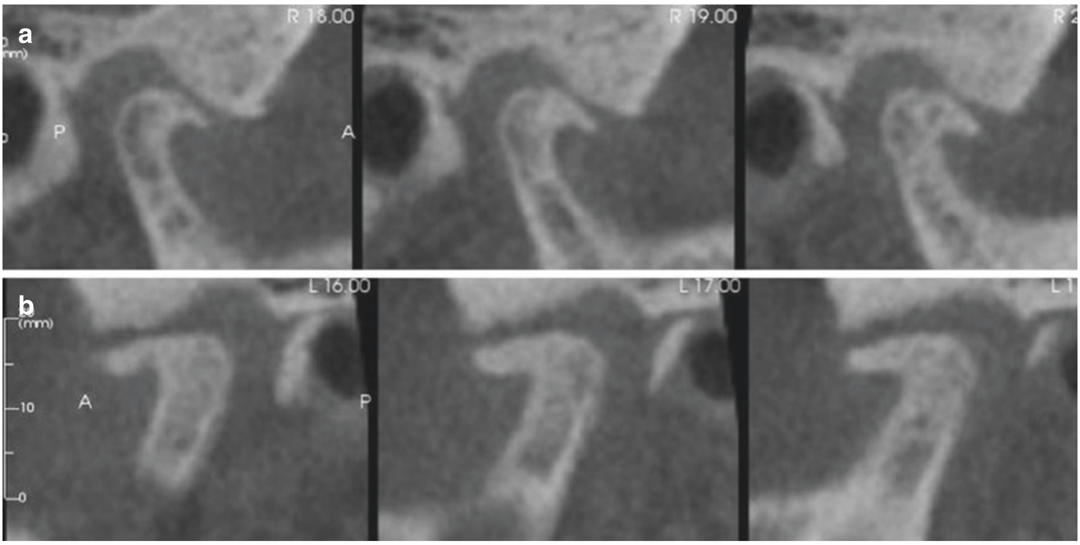

Fig. 24.47 Right (**a**) and left (**b**) sequential 1 mm thick parasagittal images of bilateral TMJs with severe OA featuring marked osteophyte formation and condylar head and glenoid fossa. Note that unlike the appearance of the left TMJ articulation in Fig. 24.46, the interarticular space is still observed

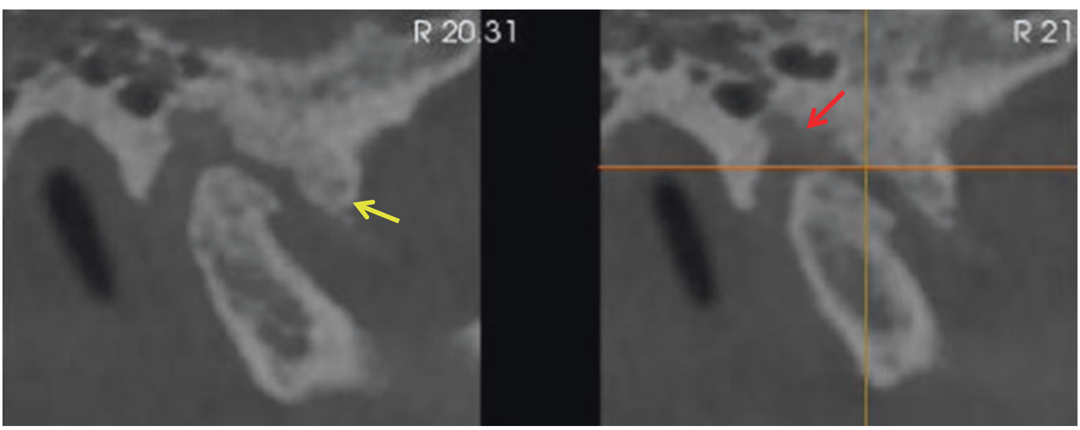

Fig. 24.48 Serial parasagittal image of the right TMJ showing severe OA featuring sclerosis, subchondral cyst formation in the base of the glenoid fossa (*red arrow*) and osteophyte formation on the crest of the articular eminence (*yellow arrow*)

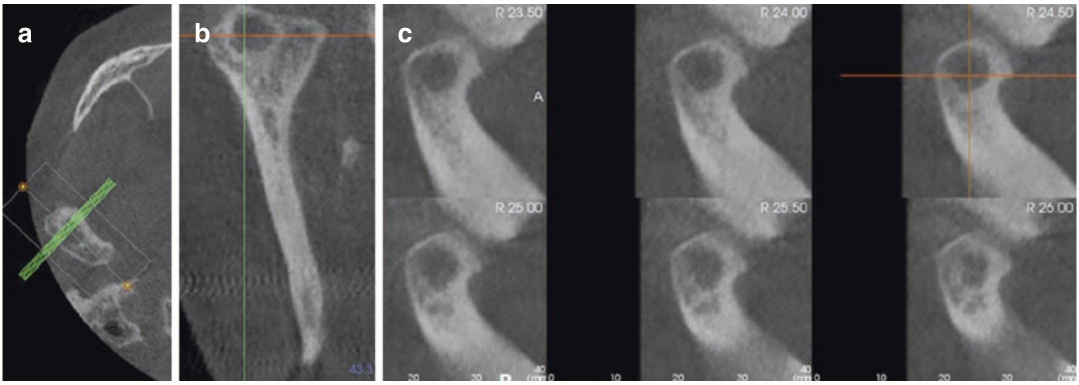

Fig. 24.49 Axial (**a**) and para-coronal (**b**) reference images and serial parasagittal sections (**c**) of the right mandibular condyle showing a large, well defined and intermittently corticated unilocular intramedullary hypodensity immediately below the superior surface of the cortical outline of the condyle consistent with a subchondral cyst (Ely's cyst)

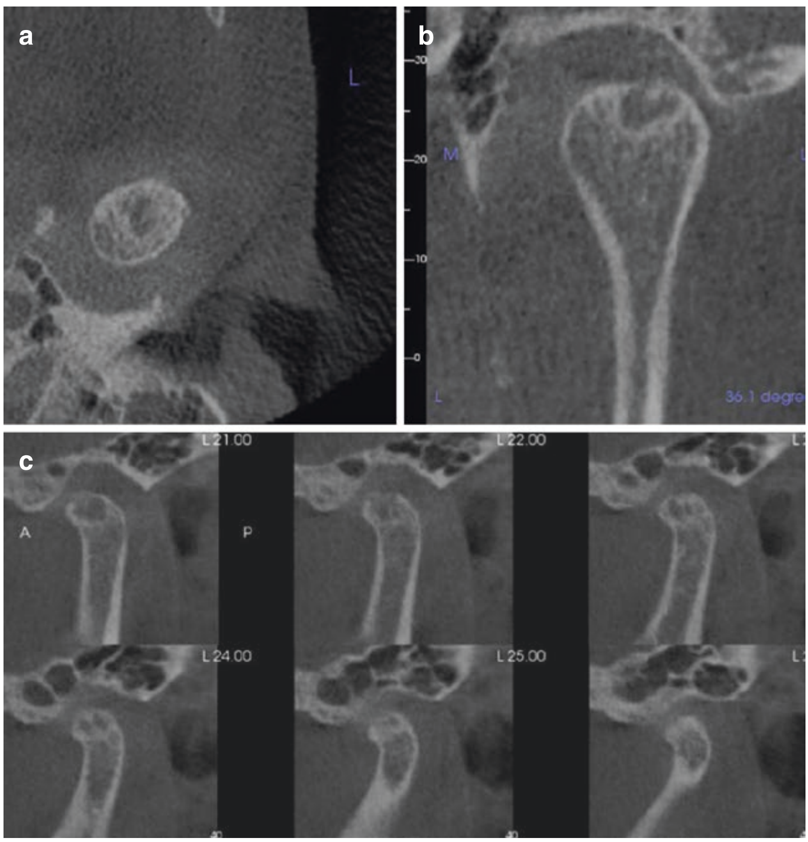

Fig. 24.50 Axial (**a**) and para-coronal (**b**) reference images and serial parasagittal sections (**c**) of the left mandibular condyle showing a large, well defined and intermittently corticated bilobular intramedullary hypodensity immediately below and perforating the superior surface of the cortical outline of the condyle consistent with a subchondral cyst (Ely's cyst). Note that the glenoid fossa is within normal limits and demonstrates extensive pneumatization extending into the articular eminence

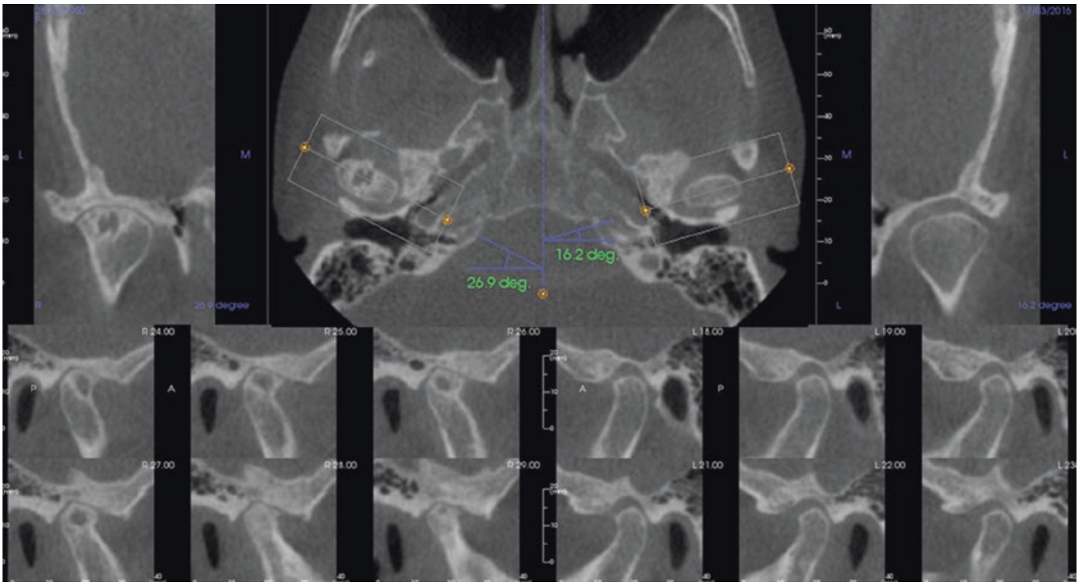

Fig. 24.51 Standard TMJ reformatted display incorporating coronal, axial reference and serial cross-sectional images demonstrating severe OA of the right TMJ with a normal left TMJ for comparison. Imaging features include loss of interarticular space, faceting of the supero-anterior surface of the condylar head, subchondral cyst formation and changes in the glenoid fossa such as flattening and sclerosis

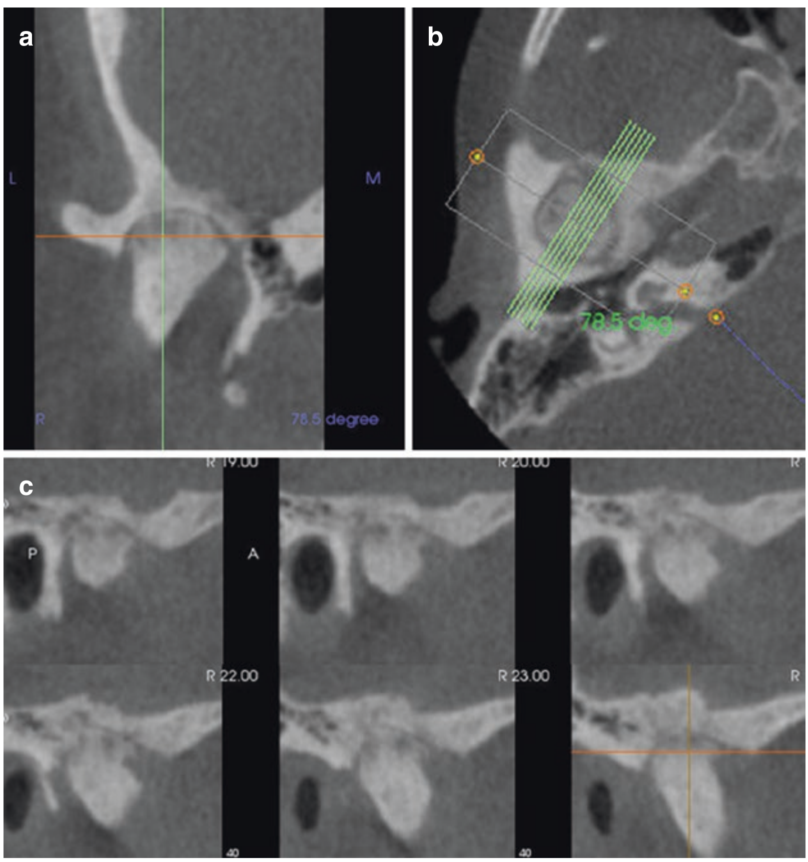

Fig. 24.52 Para-coronal (**a**) and axial (**b**) reference images and serial parasagittal sections (**c**) of the right mandibular condyle showing a multiple, well defined intramedullary hypodensity immediately below and perforating the superior surface of the homogeneously sclerotic condyle consistent with a subchondral cysts (Ely's cyst). Note that the glenoid fossa is also irregular, sclerotic and the posterior slope is flat; the intra-articular space is absent

Table 24.5 Comparison of features of infective and psoriatic arthritis

Feature	Infective	Psoriatic
Frequency of TMJ signs	Less than RA, but up to 38%	Low, 2.6–7%%
Etiology	Local or hematogenous spread of Staphylococcus aureus, Neisseria gonorrhea, and Haemophilus influenzae	Chronic, genetic, noncontagious skin disorder
Age	Adults	Adults
Presentation	Concomitant exacerbating local or systemic factors Most often in one location, usually the hips and knees No skin lesions	Dermal cutaneous plaques and nail psoriasis precede arthritis in approximately 5–24% of individuals Polyarthritis including spondylitis, axial skeleton, knee, hip, and fingers and toes
Distinguishing features	Diffuse soft-tissue swelling involving the preauricular region	TMJ correlates well with changes in the finger joints such as erosion, dislocation, and ankylosis
Rheumatoid factor	Seronegative	Usually seronegative

Rheumatoid Arthritis

Rheumatoid arthritis (RA) is a chronic multisystem disease of unknown etiology. The current hypothesis is that an unknown antigen triggers an autoimmune response in a genetically susceptible individual. The predominant pathological change is that of an inflammatory synovitis, characterized by subsequent bone and cartilage destruction. Rheumatoid arthritis usually presents in other joints prior to TMJ involvement, although, on occasion, it may be the first joint affected. Afflicted TMJ articulations with RA may produce pain, joint stiffness, and difficulties in opening the mouth. In particular, the presence of a gradually increasing anterior open bite, especially in adolescents, should always be considered ominous and suggestive of RA. The reported prevalence of TMJ involvement in those individuals with RA varies widely, with up to 88% incidence (Ardic et al. 2006).

There are no specific pathognomonic TMJ CBCT imaging findings in RA patients (Goupille et al. 1993; Akerman et al. 1988)—findings are similar to those with OA. However a reduction in joint space usually occurs, particularly with increasing morphologic change. In end-stage rheumatoid arthritis of the TMJ, the joint space obliteration results in an anterior open bite. In juvenile rheumatoid arthritis with TMJ involvement, end-stage disease can result in destruction of the condylar growth plate.

While imaging alone cannot provide a diagnosis, consideration of the following associated features may increase the level of suspicion of a diagnosis of RA compared to OA:

- The incidence of erosions and cysts of the mandibular condyle are significantly higher in patients with rheumatoid arthritis.
- The progression of radiographic changes of the temporomandibular joint (TMJ) occurs quickly with RA (over approximately 12–18 months) and has been correlated to raised levels of C-reactive protein (Nordahl et al. 2001).
- Patients with RA changes in the TMJ have comparable findings in the metacarpophalangeal and metatarsophalangeal joints of the hands and feet (Akerman et al. 1988). Therefore, hand-wrist imaging is recommended, particularly in younger individuals with severe TMJ changes. Evaluation of the hand-wrist image should be according to Sharp's scoring method (Sharp et al. 1985)
- Because arthritic change of the cervical spine is often associated with patients with severe RA of the TMJ (Redlund-Johnell 1987), CBCT investigation of the TMJ with suspicion of RA should also involve imaging of the upper cervical spine.
- Condylar resorption is a common finding in children with juvenile chronic RA (Pedersen et al. 2001) (Figs. 24.53 and 24.54) and therefore RA should be considered if there is any condylar arthritic change in children or adolescents.

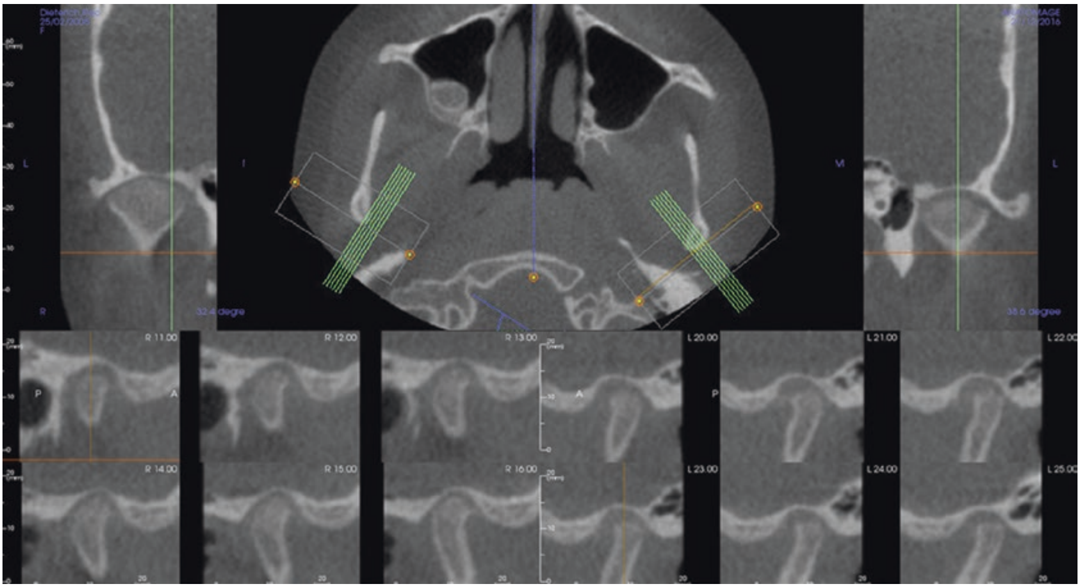

Fig. 24.53 Standard TMJ reformatted display incorporating coronal, axial reference and serial cross-sectional images of an 11 year old girl demonstrating reduction in interarticular joint space on the right and loss of superior cortication and evidence of irregular cortical margin on the left suggestive of grade II (Rohlin and Petersson 1989) juvenile RA (clinically confirmed)

Several scoring systems are proposed to quantify the radiographic changes of joints in RA (Larsen et al. 1977; Sharp et al. 1971). For assessment of the TMJ, the scoring system by Larsen et al. (1977) has been modified by Rohlin and Petersson (1989) (Table 24.6).

24.4.4 Cysts and Tumors, Osteomyelitis, and Neoplasia

Odontogenic or non-odontogenic cysts and tumors, osteomyelitis, and neoplasia involving the TMJ are rare. Any element of the articulation can give rise to these conditions including the bone of the mandibular condyle or articular fossa, the joint capsule or the articular disc (Tables 24.7 and 24.8). The most common TMJ tumors are benign: they include osteomas (Lew et al. 1999), chondromas, and osteochondromas. Rarely, fibrous dysplasia (Fig. 24.55), giant cell granuloma, traumatic bone cyst, aneurysmal bone cyst, ossifying fibroma, glomus tumor, and chondroblastoma may be associated with the mandibular condyle. Even odontogenic infections (e.g., osteomyelitis) (Fig. 24.56) as well as odontogenic cysts and tumors (e.g., keratocystic odontgenic tumour and ameloblastoma) (Fig. 24.57) that involve the posterior aspect of the mandible can ascend the ramus and, in some instances, involve the condylar head. Malignant tumors of the TMJ are exceedingly rare. They may be primary in origin or direct extensions of local neoplasms. Primary malignant tumors include chondrosarcoma (Sesenna and Tullio 1997), synovial sarcoma, and fibrosarcoma of the joint capsule. Carcinomas occasionally metastasize to the mandibular condyle (Fig. 24.58) and include oral squamous carcinoma, breast, lung, and skin (melanoma).

24.4.5 Ankylosis

Ankylosis of the TMJ articulation is a slowly progressive condition whereby there is gradual reduction in function and modality of the TMJ articulation either due to intra-articular (true) or extra-articular causes. Intra-articular ankylosis can occur due to fibrous or more commonly osseous union of mandibular condyle with temporal bone. CBCT or MDCT are equally efficacious at detecting and characterizing the morphology or

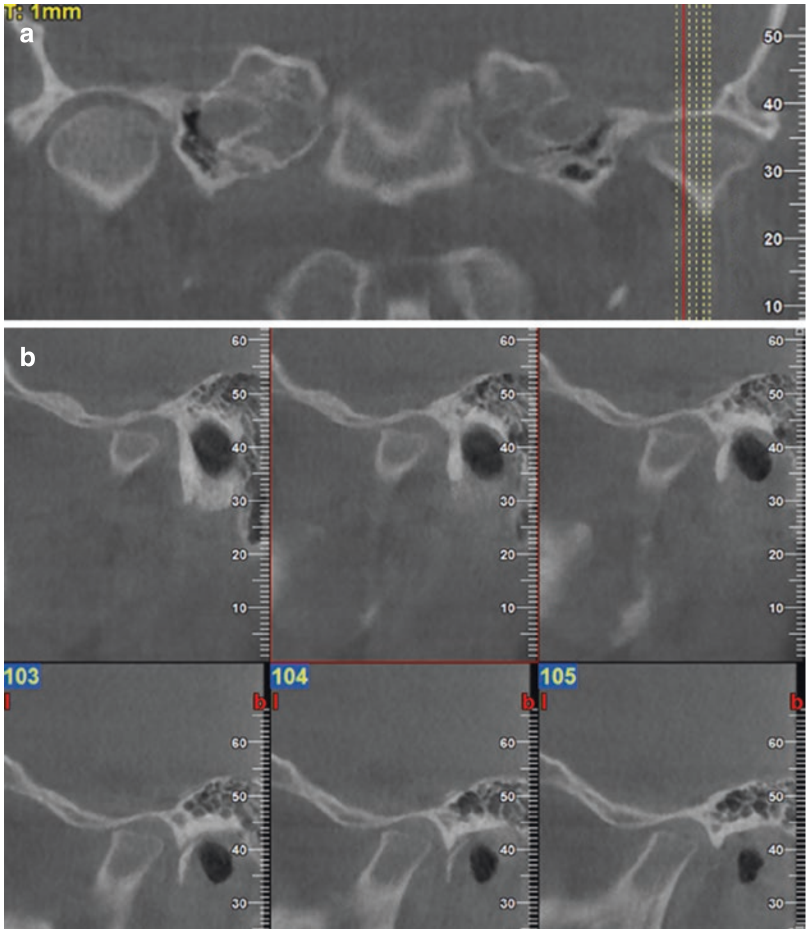

Fig. 24.54 Coronal (**a**) and serial parasagittal CBCT sections (**b**) of a 10 year old girl demonstrating reduction in interarticular joint space on the left, and condylar dysmorphology associated with moderate erosion and flattening of the condyle suggestive of grade III (Rohlin and Petersson 1989) juvenile RA (clinically confirmed)

Table 24.6 Classification of TMJ changes with RA (Rohlin and Petersson 1989)

Grade	Description
0	Normal: Well-defined cortical outline of the condyle
I	Mild: Presence of cortical destruction and irregular margin of the condyle
II	Moderate: Bony destruction or erosion of the condyle or evident flattening, with deviation from normal joint morphology
III	Severe: Complete or almost complete destruction of the condyle

ankylosis; however if TMJ reconstruction with a titanium prosthesis is anticipated, MDCT is preferable in that it provides images with less noise which makes segmentation easier for biomodel fabrication (Fig. 24.60).

The etiology of osseous intra-articular ankylosis has been associated with condylar fracture with involvement of the articular surface, advanced arthritis, and trauma from obstetric forceps. Presentation will depend on the age of onset. Long-standing, early-onset ankylosis in childhood results in marked facial asymmetry, whereas maxillofacial changes may be more local rather than region minimal if it occurs during adolescence or the patient has early treatment. Patients usually present with gradual immobility of joint and lack of translation on opening. Imaging findings include bony union of mandibular condyle with temporal bone and lack of demonstrable joint space on imaging. Specifically bony union can extend from the lateral aspect of the zygomatic arch medially as far as the foramen spinosum and carotid canal in some cases. Other additional findings include displacement of the sigmoid notch and the coronoid process upward behind the zygomatic

Table 24.7 Classification and features of primary benign neoplasms of the TMJ

Tissue	Type	Description
Bone	Osteoma	Formation of compact or cancellous bone Most commonly occur in mandibular body Result in asymmetry or change in occlusion May occur in association with Gardner syndrome
	Osteoid Osteoma	Rare, mixed tumor rarely >2 cm Mostly occurs in young adulthood, rarely over the age of 30 years; mostly males Characteristic spontaneous pain, initially mild and intermittent progressing to severe and constant A central small oval or round area of relative hypodensity (the nidus) surrounded by a dense hyperdense border of reactive bone sclerosis
	Osteoblastoma	Similar radiographically to osteoid osteoma however usually grows larger than 2 cm, is painless and shows greater hyperdensity
Cartilage	Chondroma	Exceeding rare in TMJ[a] Two types: Enchondroma, within the medullary cavity and; or periosteal or juxtacortical chondroma, that develop adjacent to the cortical surface of the bone, but beneath the periosteum Presents as expansile hypo-attenuating lesion with internal calcific foci varying from powder-like to dense aggregates Difficult to distinguish from low-grade chondrosarcoma
	Osteochondroma (Fig. 24.59)	Rare in the jaws[b] Most affect the coronoid process followed by the condyle Occur after 40 years of age, with a higher incidence in females May present with difficulty in opening (coronoid type) or TMD like symptoms (condylar type)I Imaging shows pedunculated or sessile, exophytic and lobulated dome-shaped hyper-attenuating mass with a smooth, regular surface, often with irregular internal calcifications

[a]do Egito Vasconcelos et al. (2007)
[b]Vezeau and Fridrich (1995)

Table 24.8 Classification and features of primary malignant neoplasms of the TMJ

Tissue	Type	Description
Bone	Osteosarcoma	Extremely rare in TMJ; the body and the angle of the mandible are the most commonly affected sites Three radiographic patterns[a]; osteolytic, osteoblastic and lamellar "sunburst" appearance of osteosarcoma is not pathognomonic MRI imaging is recommended
Cartilage	Chondrosarcoma	Present insidiously as nonspecific preauricular swelling Imaging shows as soft tissue mass with calcifications within TMJ sometimes with erosion of adjacent structures

[a]Bianchi and Boccardi (1999)

arch, reduced vertical height of the ramus, accentuated antegonial notching and in advanced cases, mandibular recession. Sawhney (1986) described the severity of intra-articular ankylosis based on imaging presentation (Table 24.9) (Figs. 24.61 and 24.62).

El-Hakim and Metwalli (2002) proposed an alternate surgically relevant classification based on the relation of the ankylosed mass to the surrounding vital structures, including the maxillary artery and base of the skull (Table 24.10) (Figs. 24.61 and 24.62).

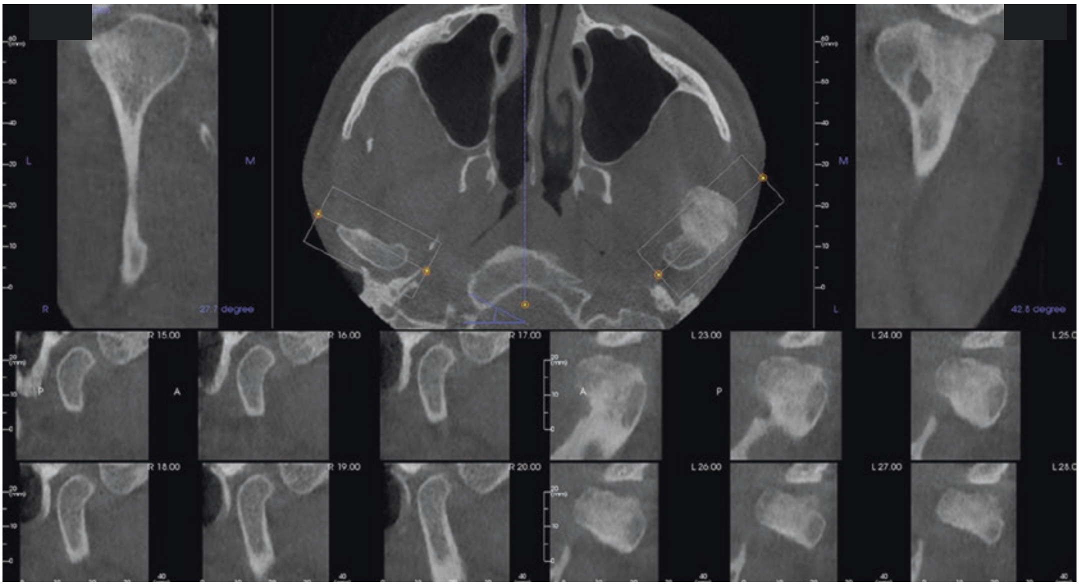

Fig. 24.55 Standard TMJ reformatted display incorporating coronal, axial reference and serial cross-sectional images demonstrating severe dysmorphology of the left mandibular condyle with a well-defined hyperdense irregular exophytic mass associated with the lateral pole. The internal trabecular is ground glass with a medial and distal hypodensity suggestive of fibrous dysplasia (histopathologically confirmed)

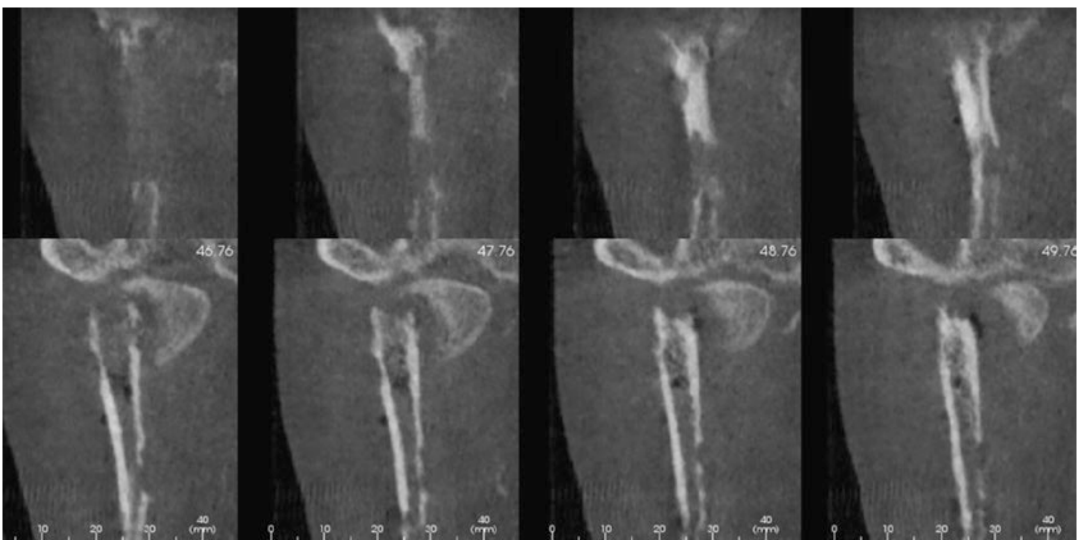

Fig. 24.56 Serial para-coronal images of the right TMJ and ascending ramus showing mottling of the cortical plate of the ascending ramus, medial displacement of a rarefied condylar fragment (pathologic condylar fracture) and collapse of the condylar neck superiorly into the glenoid fossa associated with osteomyelitis involving the entire right mandible

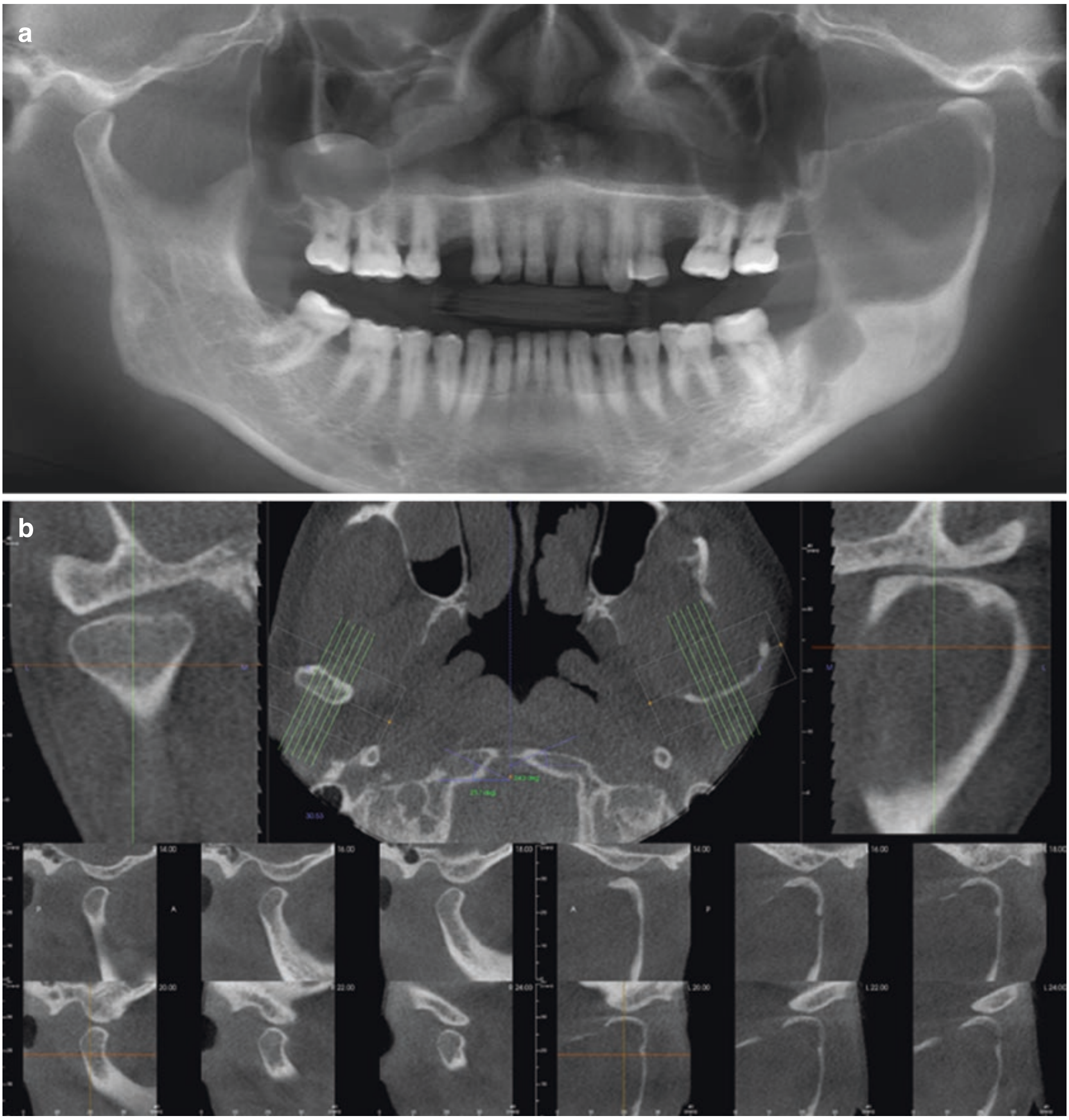

Fig. 24.57 Reformatted panoramic (**a**) and standard TMJ reformatted display incorporating coronal, axial reference and serial cross-sectional images (**b**) demonstrating a large expansile multilocular well defined hypo attenuating lesion involving the left ramus and extending superiorly from the retromolar trigone to involve the coronoid process, neck and head of the left mandibular condyle. The imaging appearance is suggestive of an odontogenic cyst or tumor. The entity was histologically confirmed as keratocystic odontgenic tumour (Images courtesy of Juliana R.V. Mussi)

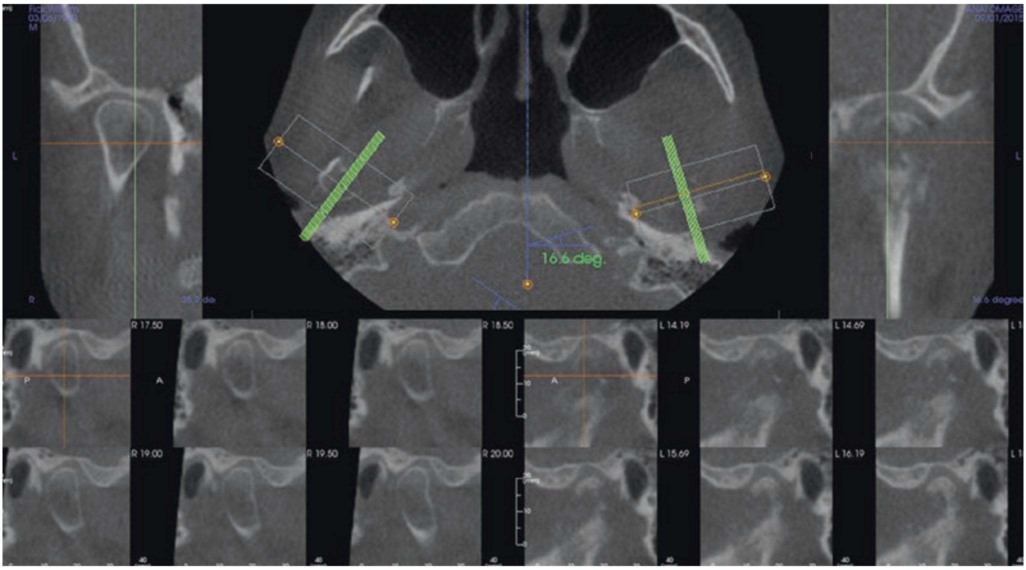

Fig. 24.58 Standard TMJ reformatted display incorporating coronal, axial reference and serial cross-sectional images demonstrating localized but extensive mottled erosion and expansion of the left mandibular condyle in an 85-year-old male with a history of prostate cancer. This appearance is suggestive of either primary or secondary malignant neoplasia until proven otherwise. The working radiologic diagnosis was secondary metastatic disease (histopathologically confirmed)

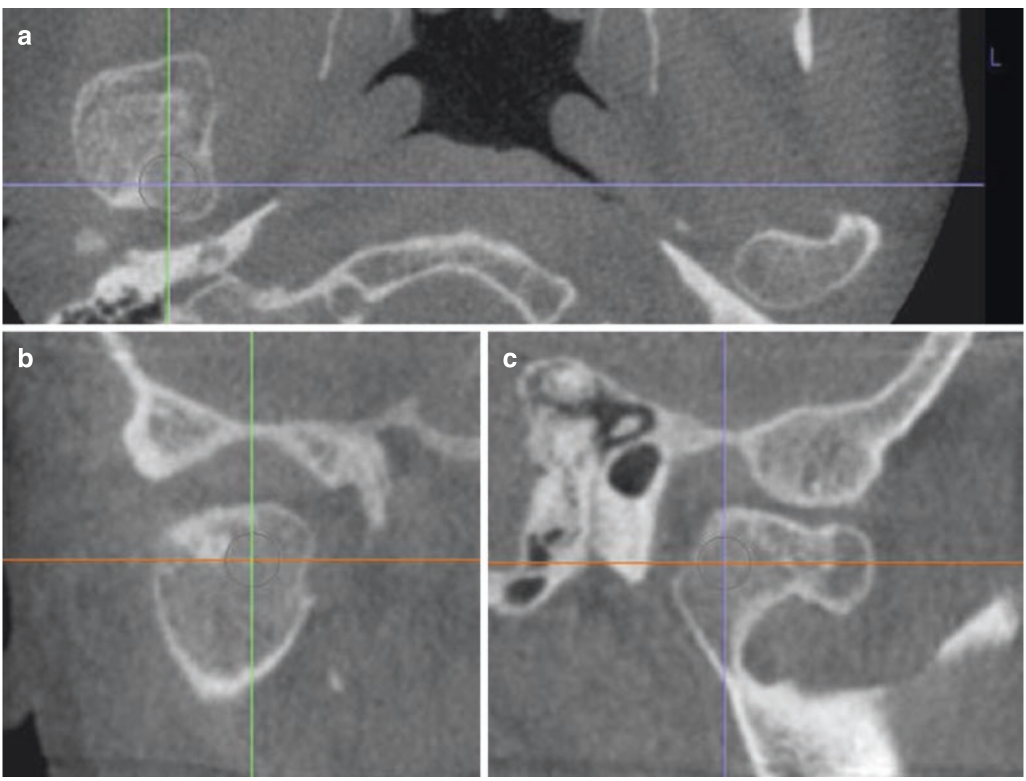

Fig. 24.59 Axial (**a**), para-coronal (**b**), and parasagittal (**c**) sectional CBCT images (**b**) demonstrating severe dysmorphology of the right mandibular condyle with a well-defined hyperdense irregular lobulated expansion, predominantly anteriorly. The cortical plate is intact and the internal trabeculae is slightly hyperdense, imaging features suggestive of osteochondroma (histopathologically confirmed)

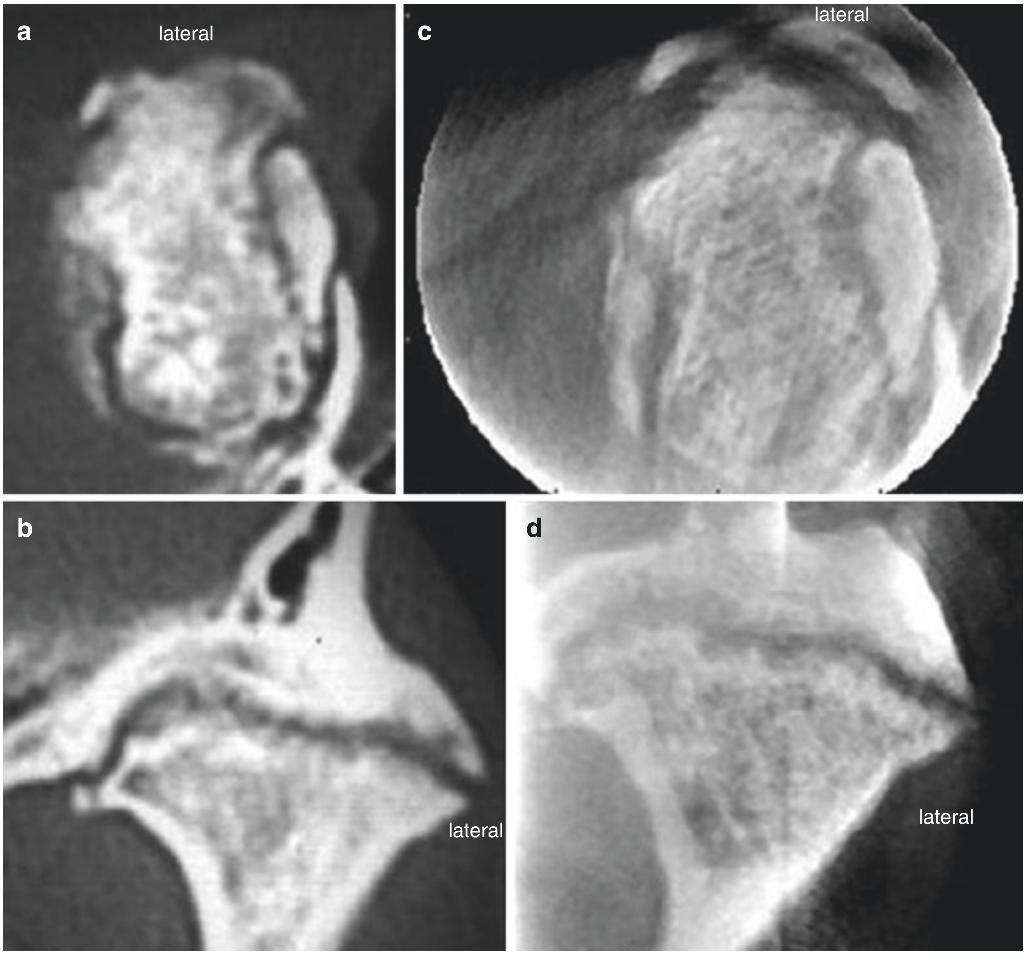

Fig. 24.60 Comparison of conventional MDCT axial (**a**) and para-coronal (**b**) and limited area CBCT axial (**c**) and para-coronal (**d**) images of a 66-year-old female who complained of severe trismus. Images show a narrow and irregular joint space and surface irregularities (erosions, osteophytes, and sclerosis) in the mandibular condyle and the temporal component. Both images are indicative of fibro-osseous ankylosis. Note that the CBCT images have greater noise ("salt and pepper" or mottled appearance)

Table 24.9 Classification of TMJ ankylosis based on severity of imaging presentation (Sawhney 1986)

Type	Description
I	The condyle is medially angulated and associated with a deformed articular fossa together with a mild-to-moderate amount of new bone formation
II	No recognizable condyle or fossa but instead a large mass of new bone extending from the ramus to the base of the skull
III	Ankylosis usually results from a medially displaced fracture dislocation with bone bridging the mandibular ramus to the zygomatic arch
IV	Joint architecture is replaced completely by bone with fusion of the condyle, sigmoid notch and coronoid process to the zygomatic arch and glenoid fossa

24.4.6 Condylar Resorption

Condylar resorption (CR) is the generic radiographic term used to describe the change in mandibular condylar morphology associated with initial osteolytic erosion with resultant loss of cortical surface integrity leading to an overall dysmorphic shape and reduction in relative overall size. Patients may present with jaw deformities, malocclusions, TMJ and jaw dysfunction, pain, and headaches; however up to 25% are asymptomatic and are discovered on incidental panoramic imaging. Numerous pathologic abnormalities can cause CR including (Mercuri 2008; Wolford and Gonçalves 2015):

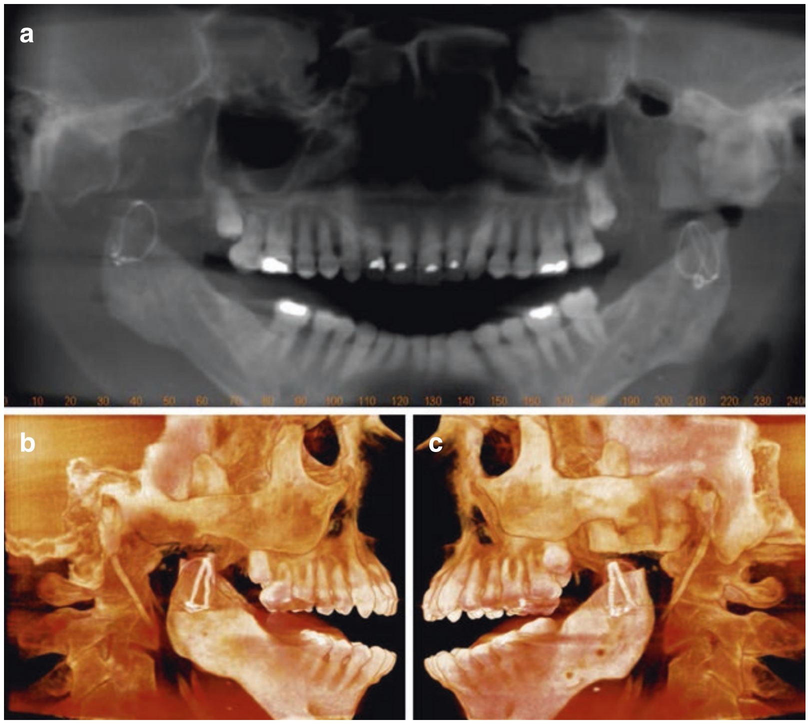

Fig. 24.61 Reformatted panoramic (**a**) and right (**b**) and left (**c**) volumetric renderings of a 39 year old male after partial ramus resections of the mandible bilaterally to treat bony ankylosis of the mandibular condyles to the glenoid fossae. Both mandibular rami have been separated from the condylar process at a level in line with the upper border of the mandibular body. The ankylosed bony elements at the TMJ level are intact

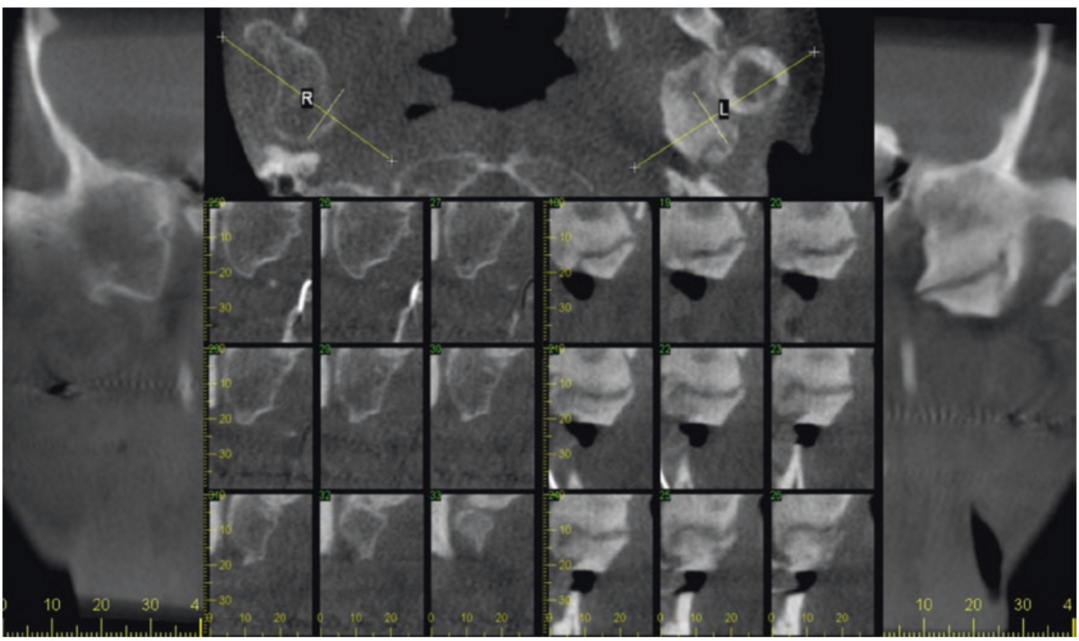

Fig. 24.62 Standard TMJ reformatted display incorporating coronal, axial reference and serial cross-sectional images of the individual shown in Fig. 24.61 demonstrating Type II (Sawhney 1986) or Class III (El-Hakim and Metwalli 2002) ankylosis

Table 24.10 Classification of TMJ ankylosis based on relation of the ankylosed mass to the surrounding vital structures (El-Hakim and Metwalli 2002)

Class	Description
I	Unilateral and bilateral fibrous ankylosis. The condyle and glenoid fossa retain their original shape, and the maxillary artery is in normal anatomical relation to the ankylosed mass
II	Unilateral or bilateral bony fusion between the condyle and the temporal bone. The maxillary artery lies in normal anatomical relation to the ankylosed mass
III	The distance between the maxillary artery and the medial pole of the mandibular condyle is less on the ankylosed than in the normal side or the maxillary artery runs within the ankylotic bony mass
IV	The ankylosed mass appears fused to the base of the skull and there is extensive bone formation, especially from the medial aspect of the condyle to the extent that the ankylosed bony mass is in close relationship to the vital structures at the base of the skull such as the pterygoid plates, the carotid and jugular foramina and foramen spinosum and no joint anatomy can be defined from the imaging study

1. ***Adolescent internal condylar resorption (AICR)***. Also referred to as idiopathic condylar resorption (ICR), idiopathic condylysis, condylar atrophy, and progressive condylar resorption (PCR) (Figs. 24.63 and 24.64). It occurs in a female:male ratio of 8:1, mostly frequently in the pubertal growth phase, rarely before age 11 or after the age of 15 years. Because female patients who present often report participating in sports activities, it has been referred to as *cheerleader syndrome*. Although the specific cause of the condition is, as yet, unknown it is considered to be hormonally mediated process. AICR is usually a slowly progressing, bilateral condition with periods of remission. Conditions in which joint loading is excessive (e.g., orthodontics, trauma, para-functional habits, orthognathic surgery) may contribute to exacerbation of the process. Characteristic associations include high occlusal plane angle facial morphology, Class II occlusion with or without an anterior open bite,

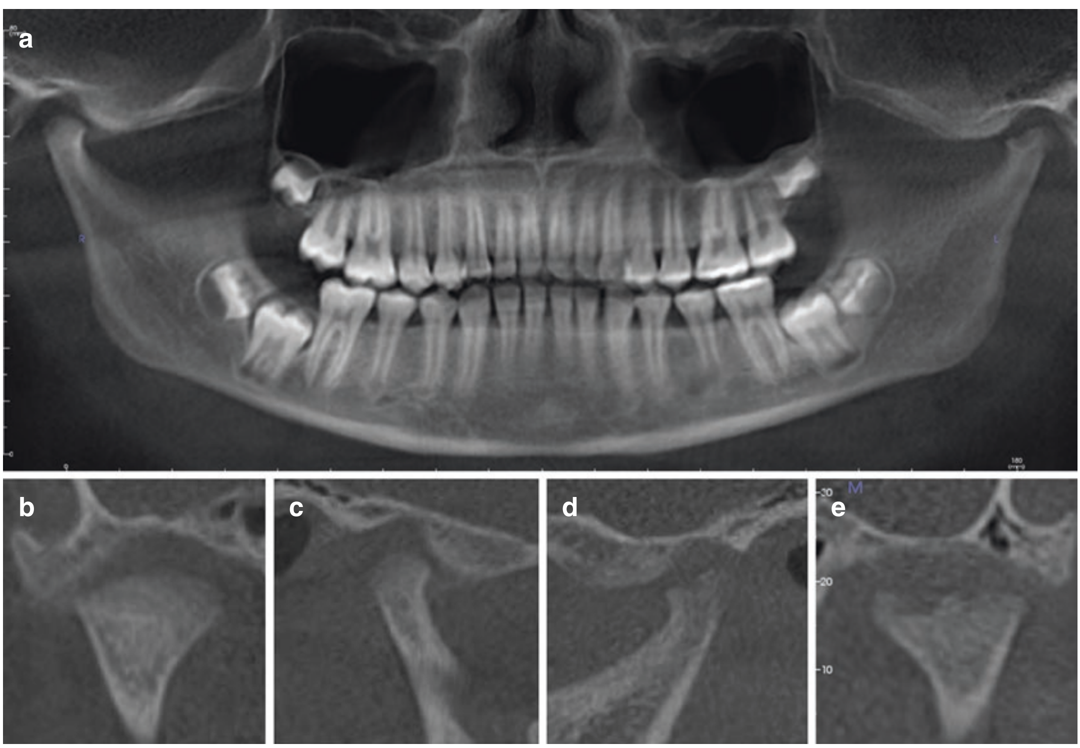

Fig. 24.63 Reformatted panoramic (**a**), right coronal (**b**) and parasagittal (**c**), and left parasagittal (**d**) and coronal (**e**) CBCT images showing severe erosion of the left mandibular condyle in an 11-year old female patient prior to orthodontic therapy with a history of nonspecific left TMJ soreness of 3 months duration. The imaging appearance is consistent with adolescent internal condylar resorption

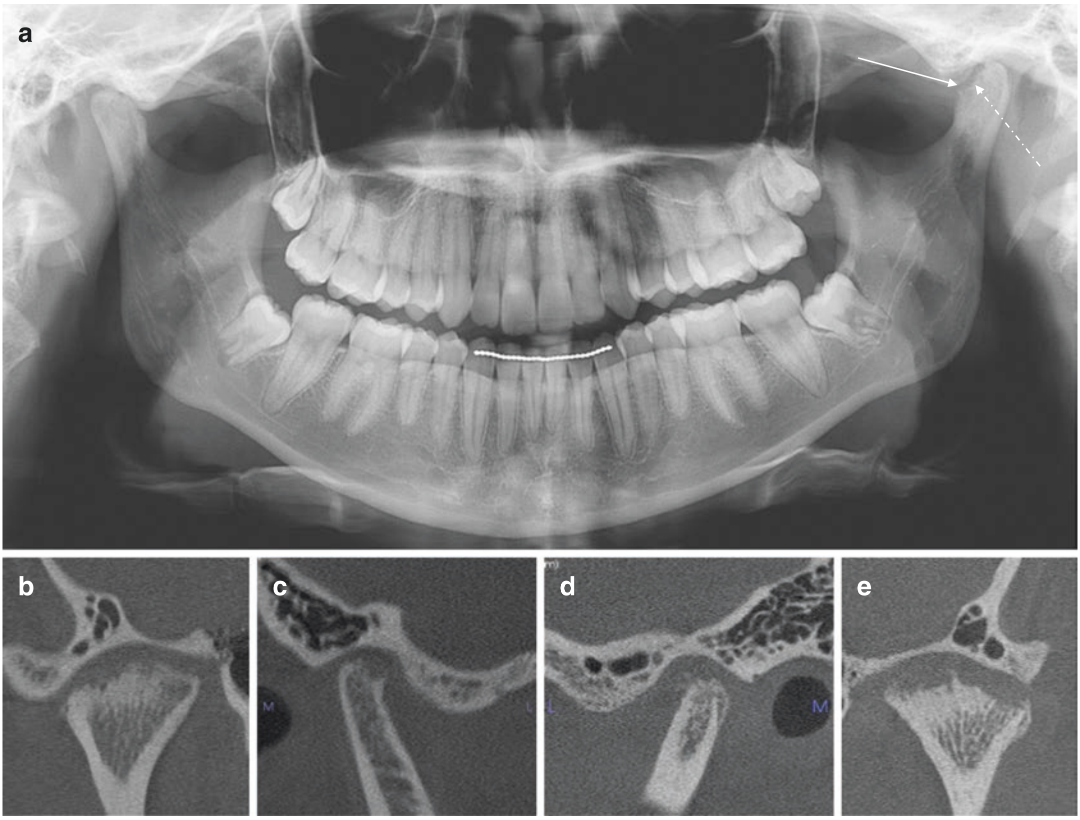

Fig. 24.64 Conventional panoramic (**a**), and right para-coronal (**b**), parasagittal (**c**) and left parasagittal (**d**) and para-coronal (**e**) CBCT images showing bilateral idiopathic condylar resorption on a 20 year old female. Note that while there is evidence of possible resorption visible on the left condyle on the panoramic image (*white arrows*), resorption is not observed on the panoramic image on the right

absence of other joint or systemic involvement and non-contributory medical history.

2. ***Reactive arthritis (RA)***. Also called seronegative spondyloarthropathy, RA is an inflammatory process associated with bacterial (e.g., Chlamydia, Mycoplasma, Borrelia (Lyme disease), Salmonella, Shigella, Yersina, and Campylobacter species) or viral (e.g., Herpes, Epstein-Barr, Cytomegalovirus, and Varicella species) pathogens. The condition usually occurs bilaterally however with less severe CR with other joint involvement. MR imaging shows joint effusion and inflammation on T2-weighted images.
3. ***Autoimmune and connective tissue diseases (AI/CT)***. CR may occur in association with specific AI/CT diseases such as rheumatoid arthritis, juvenile idiopathic arthritis (JIA), psoriatic arthritis, ankylosing spondylitis, Sjogren syndrome, systemic lupus erythematosus, and scleroderma. Onset is usually in adult patients, relatively slow and is co-incident with multiple systemic involvement.
4. ***Other end-stage TMJ pathologic abnormalities***. These include conditions such as neoplasms, multiple operated joints, failed TMJ autogenous grafts or alloplastic implants, traumatic injuries, avascular necrosis, and metabolic diseases.

In cases where the specific cause is unknown, the presentation is generically referred to as idiopathic condylar resorption (ICR) (Figs. 24.65 and 24.66). The term progressive condylar resorption (PCR) is a more general term describing conditions resulting in loss of condylar height, including those of known etiology (1–4 above).

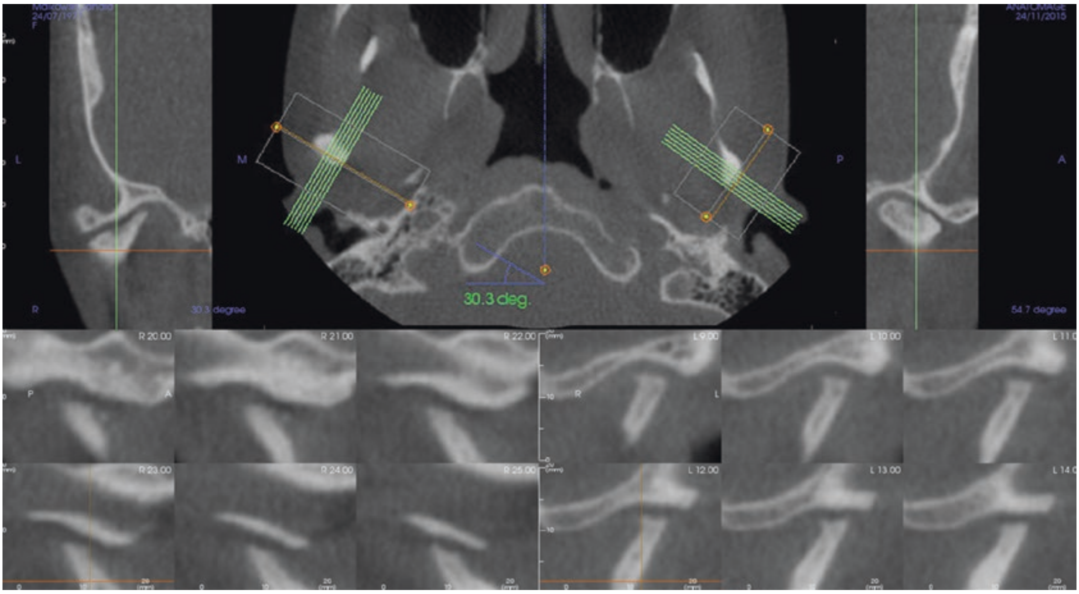

Fig. 24.65 Standard TMJ reformatted display incorporating coronal and axial reference (*above*) and serial cross-sectional (*below*) images demonstrating severe progressive condylar resorption of the right and left mandibular condyles

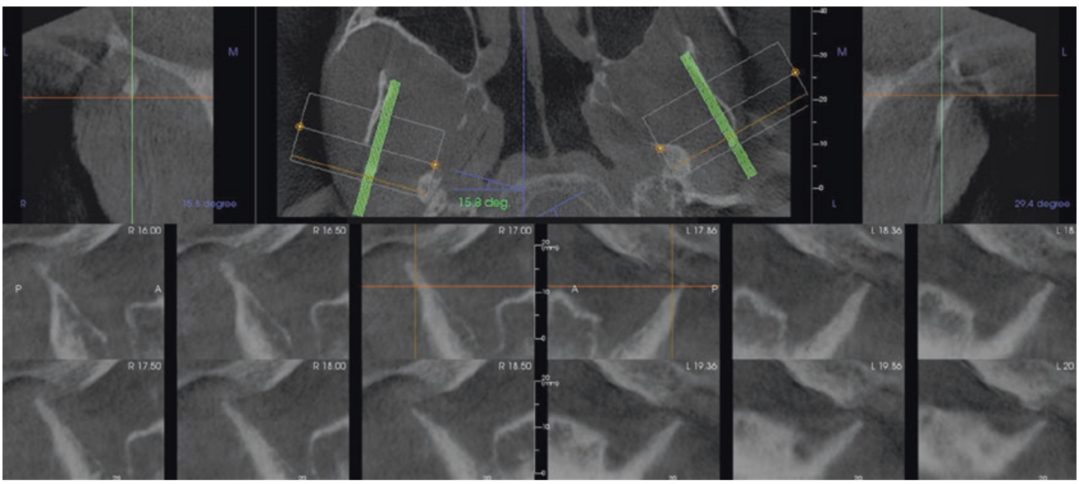

Fig. 24.66 Standard TMJ reformatted display incorporating coronal, axial reference and serial cross-sectional images (**b**) demonstrating severe progressive condylar resorption of the both mandibular condyles—in fact, the condyles are almost completely resorbed

The patient may initially present with a gradually increasing shift of the mandible towards the affected side (unilateral) or anterior open bite (bilateral) and associated occlusal discrepancies such as cross-bite and posterior prematurities and musculoskeletal instability, which may result in the TMJ symptoms and pain. While numerous authors have documented an association with orthodontic treatment and orthognathic surgery, this may be coincidental rather than a causal relationship. In addition ICR has been associated with a number of facial characteristics including a dolicocephalic facial morphology (high occlusal and mandibular plane angle) and mandibular plane angle and Angle Class II skeletal relationships. Similarly ICR rarely occurs in patients with brachyocephalic facial types or Angle Class III skeletal relationships. CBCT imaging features include:

- ***Craniofacial Associations***. Skeletal and occlusal class II deformity, anterior open bite, high occlusal and mandibular plane angle, decreased vertical height of the ramus (loss of posterior facial height), ± overangulation of the lower incisors. Narrowing of the oro-pharyngeal airway associated with mandibular retruded positioning.
- ***Local Regional TMJ***. Condylar hypoplasia and dysmorphology due to severe condylar surface resorption with progressive loss of the mandibular condyles. Normal or excessive interarticular joint space.

Symptoms associated with the condition may be managed using splint therapy to "unload" the condyles and anti-inflammatory medications. Immediate management should include a consultation with a rheumatologist is highly recommended to rule out systemic cause. An MRI should also be considered. MRI of AICR will often show early anterior disc displacement initially with and, then latter, without reduction, reduction in condylar size and amorphous appearing tissue possibly surrounding the condyle, with or without an increased joint space. For ICR other than AICR, erosion in both mandibular and glenoid fossa components, a reactive pannus with T2-weighted images often showing joint effusion and inflammation.

Definitive treatment options include arthroscopic lysis and lavage, orthognathic (corrective) jaw surgery (Posnick and Fantuzzo, 2007) with or without disc repositioning (Wolford and Gonçalves 2015), orthodontics, and restorative dentistry but only after resorption has been demonstrated to be stable or has "burnt out" for at least 1 year. Others suggest that because the end-point of the disease is unknown, management should include removal of the affected condyle and reconstruction with a costochondral (rib) graft or alloplast (total joint replacement).

24.4.7 TMJ Implants

Numerous materials and techniques have been used to reconstruct the TMJ articulation, particularly the mandibular condyle, as a result of surgical intervention. Autogenous tissues such as temporalis muscle (Su-Gwan 2001), fascia lata (Paterson and Shepherd 1992), cartilage, dermis, full thickness skin, perichondrium, metatarsal, sternoclavicular, and ulnar heads have all been used as interposition materials as a replacement for the absent disc in patients with advanced degenerative TMJ disease. For partial joint reconstruction, various allogenic prostheses have been reported. All autogenous materials have the disadvantage of an extra donor site morbidity and some risk of resorption. Costochondral grafts have also been used especially in children due to their capacity for growth, although this is not predictable (Guyuron and Lassa 1992). Artificial materials like silicone, titanium, proplast, ticonium, stainless steel, acrylic, vitallium, and Medpor have been used as interpositional materials (Morgan 1992). For replacement of the disc, allogenic materials including various silicone products have been used with disappointing outcomes. Dacron-reinforced silicone in particular (e.g., Proplast/Teflon, Silastic (Dow Corning Inc., Midland, MO) and Vitek-Kent products (Vitek Inc., Houston, TX)) have been found to induce a reactive synovitis which produces destructive lesions of the mandibular condyles and have been removed from the market. (Mercuri 1998, VanLoon et al. 1995).

TMJ reconstruction can be accomplished using a hemi-joint replacement technique where either the fossa-eminence or condyle are replaced and function against a native condyle or eminence, respectively (e.g., Christensen metal fossa-eminence implant, Christensen TMJ Implant System; TMJ Implant Inc., Golden, CO), or a total joint reconstruction, where both the fossa-eminence and condyle are replaced. Examples of the temporomandibular joint (TMJ) total joint prostheses include the Christensen prosthesis (TMJ Inc., Golden, CO) (Fig. 24.67)

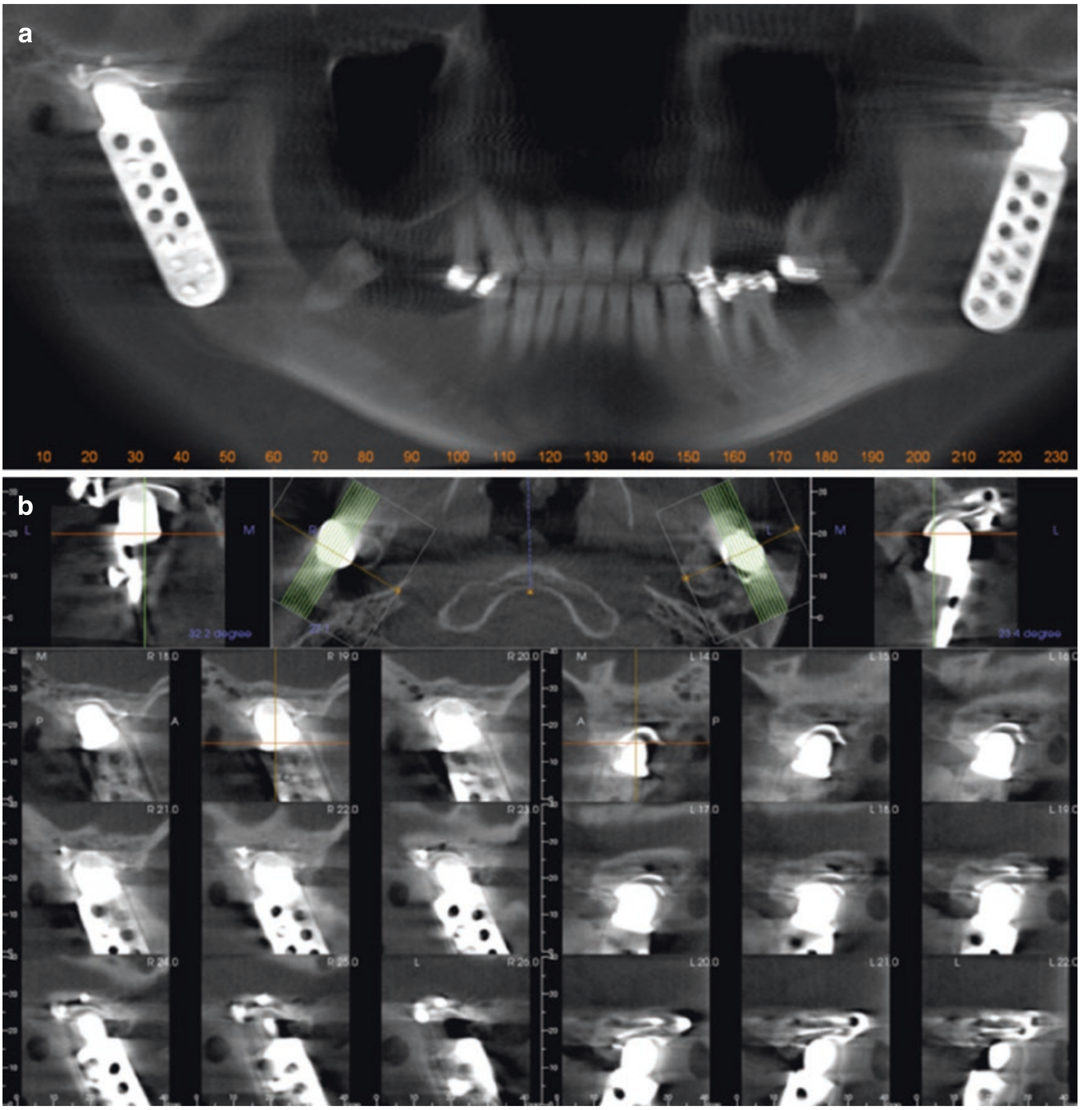

Fig. 24.67 Reformatted panoramic (**a**) and standard TMJ reformatted, high resolution (0.2 mm voxel size) display incorporating reference coronal and axial images and serial cross-sectional images (**b**) of a 38-year-old female who reports constant extreme preauricular pain 15 years after bilateral TMJ titanium replacement due to motor vehicle accident. The images demonstrate excellent adaptation of the right metallic fossa to the temporal bone but discontinuity of the outline of the left metallic fossa consistent with fracture and displacement of the glenoid fossa element. Specifically the most superior portion of the left glenoid fossa element demonstrates superior displacement as a "step" defect with intimate contact between the condylar and fossa portion anteriorly and posteriorly but markedly increased interarticular space superiorly. In the closed position, the right condyle is concentrically positioned within the glenoid fossa whereas the left condyle is inferiorly and anteriorly positioned

and the TMJ Concepts prosthesis (TMJ Concepts Inc., Camarillo, CA). Both prostheses consist of a fossa and a mandibular component. The former appliance is an off-the-shelf product and choice is based on a "best-fit" comparison of proposed replacement morphology with a choice of over

30 pre-fabricated sizes and shape. The TMJ Concepts prosthesis is a custom-made and custom-fitted device derived from computed tomography (CT) data using computer-aided design/computer-aided manufacture stereolithography technology, fabricating an accurate anatomic plastic model of the patient's jaws and TMJs. The TP fossa component becomes osseointegrated to the fossa, whereas the CP fossa is mechanically stabilized to the zygomatic arch with bone screws.

24.4.7.1 CBCT Imaging Protocol and Assessment

Multidetector computed tomography (MDCT) is usually acquired for the presurgical assessment and planning of patients who are to undergo hemi- or full joint replacement with a titanium prosthesis. While CBCT may provide a volume with greater resolution, MDCT is preferable to CBCT because of reduced image noise. Titanium prosthetic reconstruction requires the creation of a virtual simulation and then a physical biomodel, the contrast resolution of MDCT data enables more reliable and easier thresholding and segmentation than CBCT.

It may be necessary to provide images of patients with these prostheses post operatively or because of symptoms (Figs. 24.67, 24.68, and 24.69). A three-scan protocol is recommended:

- **Full field of view (FOV) maxillofacial scan at nominal resolution (0.3–0.4 mm nominal voxel size) in the closed position (i.e., centric occlusion)**. The scan should extend from approximately 3 cm above the base of the glenoid fossa (approximately at the horizontal level of the middle of the orbits) to approxi-

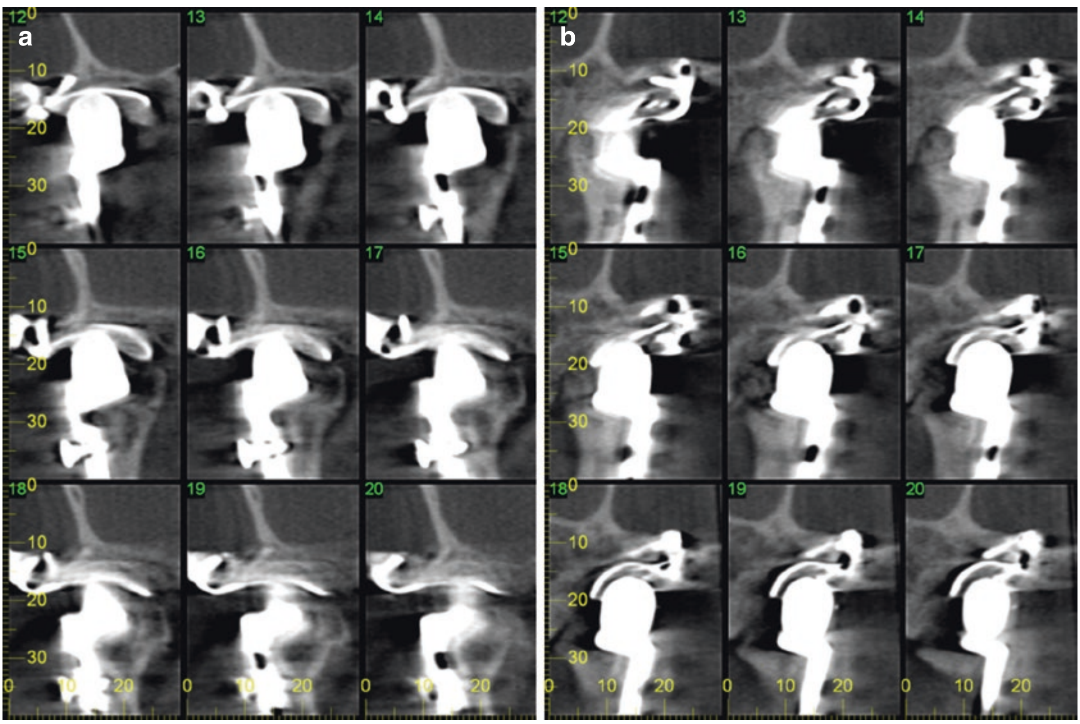

Fig. 24.68 Right (**a**) and left (**b**) high resolution (0.2 mm voxel size) para-coronal images of the same individual as in Fig. 24.67 in the closed position demonstrating excellent adaptation of the right glenoid component to the temporal bone; however, on the left, there is medial superior and lateral inferior displacement and separation of the prosthesis from the glenoid fossa. The imaging appearance is consistent with fracture of the left glenoid element with displacement

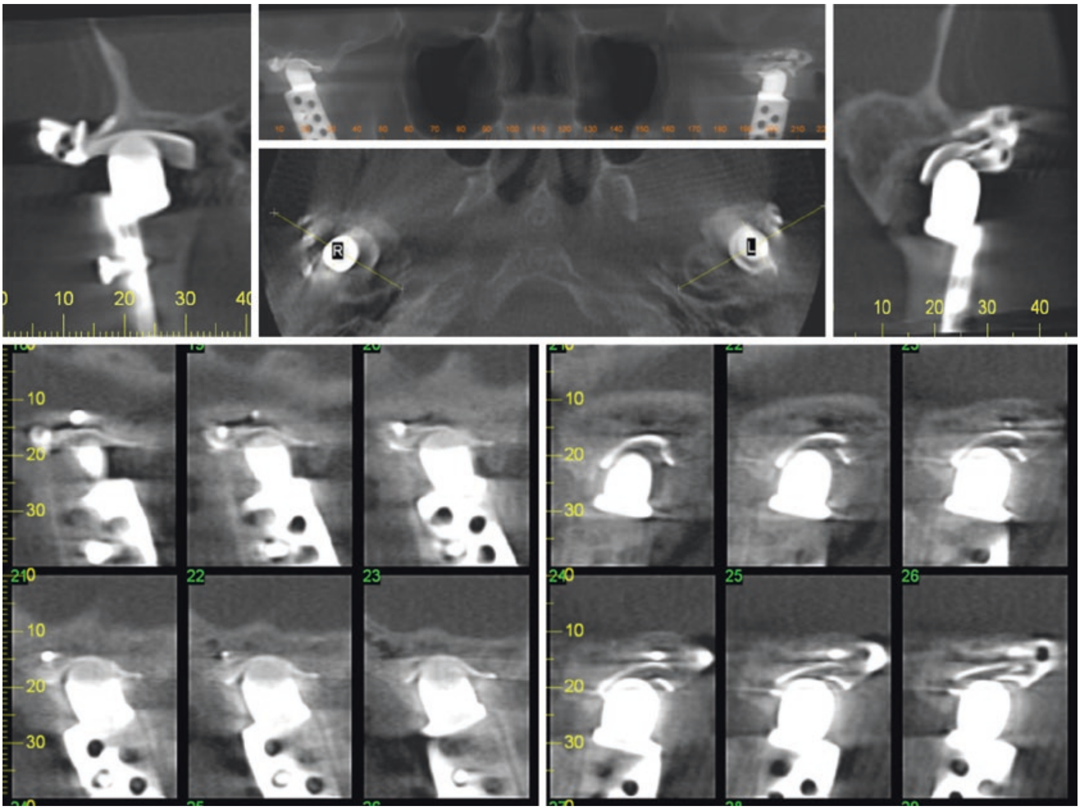

Fig. 24.69 Standard TMJ reformatted, high resolution (0.2 mm voxel size) display incorporating reference coronal, panoramic and axial images and serial cross-sectional images of the same individual as in Fig. 24.67 in the open position; there is no translation of the right condylar element, however there is a slight anterior and inferior translation of the left condylar element

mately 1 cm below the inferior extent of the lower border of the mandible. This scan provides an overview of the relationship of the condylar and temporal elements of the prosthesis and effects on the mandibular body and position of the dentition at maximum intercuspation.

- **Limited FOV at nominal resolution (0.3–0.4 mm nominal voxel size) at maximum unforced opening**. The scan should be centered on the TMJ articulation and extend from approximately 3 cm above the base of the glenoid fossa (approximately at the horizontal level of the middle of the orbits) to include the lower extent of the prosthesis. This scan provides an overview dynamic interaction, both in terms of rotation and translation, of the mandibular and temporal elements in addition to an assessment of the range of motion. To some degree, this also separates the metallic components and reduces beam-hardening artifacts in the horizontal plane so that the articulating elements can be more clearly assessed.
- **Limited FOV at high resolution (0.2 mm or less nominal voxel size) in the closed position (i.e., centric occlusion)**.The vertical range of the scan should be similar to that taken at maximum unforced opening, approximately 4–6 cm. This scan provides higher detail of the metallic components, including the retaining screws, and the integrity of the adjacent bone.

Evaluation should include an assessment of the adaptation of the prosthesis to the existing osseous morphology, continuity and symmetry of the mandibular prosthesis with the residual jaw and arch form. The integrity and adaptation of screws should also be assessed. Because of the possibility of metallic artifacts degrading 2D planar and 3D image quality, intermediate thickness MIP images in at least two projections often provide helpful images for assessment.

24.4.8 Periarticular Calcifications

The radiographic appearance of single or multiple preauricular hyperdense entities juxtapositioned to the TMJ articulation on CBCT imaging is useful when developing a radiologic differential diagnosis and in management of such conditions. The most common loose body occurs because of fracture and displacement of condylar (Figs. 24.70 and 24.71) and, less frequently, glenoid fossa (Fig. 24.72) osteophytes related to severe DJD or previous intracapsular fracture (Fig. 24.73). Multiple intra-articular mineralizations (referred to as “loose bodies” or “joint mice”) can arise from local benign conditions or as a presentation of systemic disease (Table 24.11). Intra-articular calcifications can be asymptomatic and discovered as an incidental radiographic finding or present as a preauricular swelling and pain, crepitus of the joint, changes in occlusion or imitation of motion. The role of CBCT is to locate and characterize the presentation of the condition as well as identify the presence of intracranial extension. If a systemic origin is suspected, then the diagnostic workup should involve serum calcium phosphorus and alkaline phosphatase levels. Apart from detached osteophytes, osteochondritis dissecans and synovial chondromatosis are considered the most common causes of loose bodies within the joints of the body.

24.4.8.1 Synovial Chondromatosis

Synovial chondromatosis (SC) is an uncommon benign monoarticular arthropathy characterized by chondrometaplasia of the synovial membrane, in which cartilaginous nodules form and may become pedunculated and/or detach from the synovial

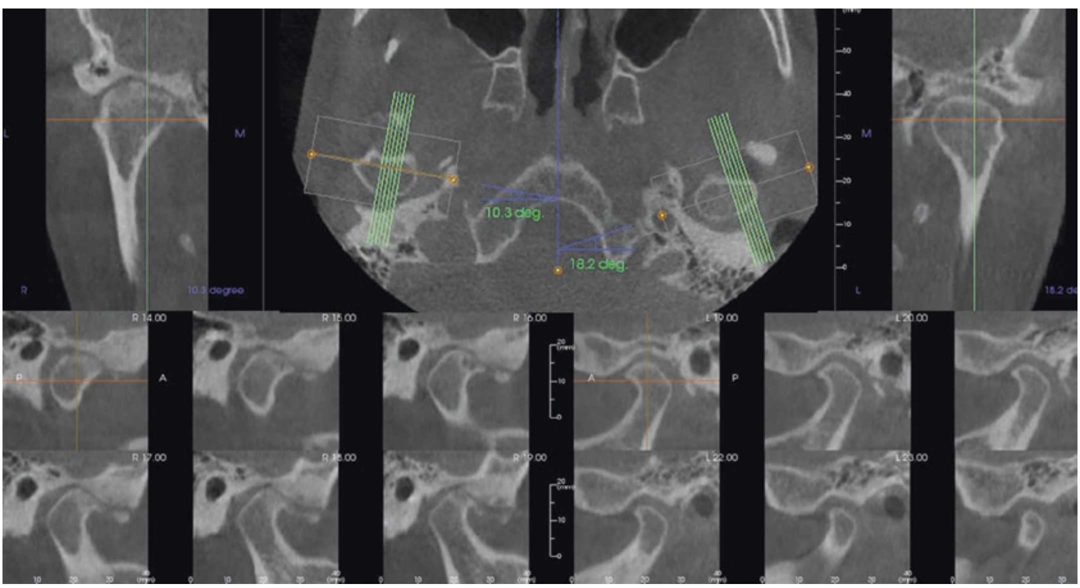

Fig. 24.70 Standard TMJ reformatted display incorporating coronal and axial reference (*above*) and serial cross-sectional (*below*) images demonstrating severe right, and mild (*left*) osteoarthritis of the mandibular condyles. Note that there is a large singular, curvilinear hyper atenuating loose body adjacent to the anterior osteophyte of the right mandibular condyle consistent with a detached osteophyte

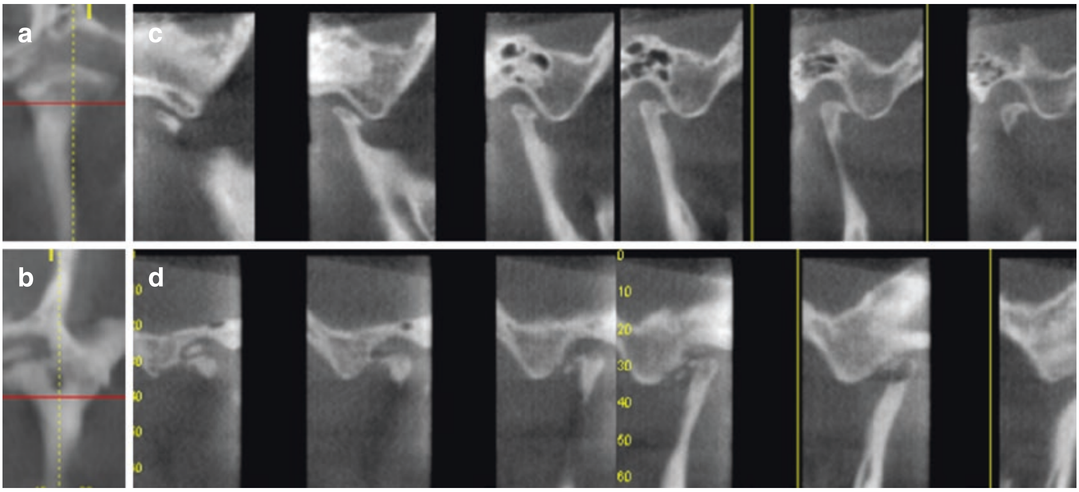

Fig. 24.71 Left (**a**) and right (**b**) para-coronal reference CBCT sections and serial right (**c**) and left (**d**) parasagittal images of an individual with severe bilateral osteoarthritis with a small loose body adjacent to the anterior osteophyte and superior to the medial pole of the left mandibular condyle consistent with a detached osteophyte. This patient was suffering from generalized osteoarthritis (GOA), a condition that affects more than 3–5 articulations simultaneously

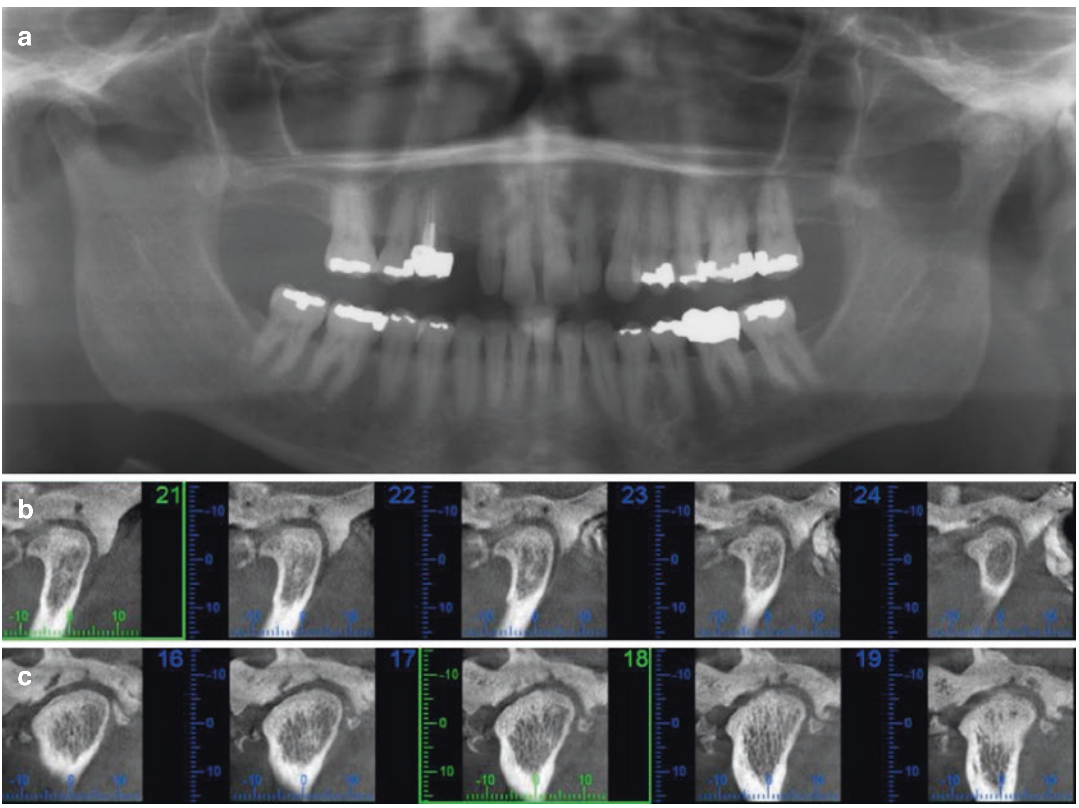

Fig. 24.72 Conventional panoramic image (**a**) showing a large radiopaque mass associated with the left TMJ articulation and relative hypertrophy of the condylar head. The morphology of the contralateral condylar head is within normal limits. Serial parasagittal (**b**) and para-coronal (**c**) CBCT images of the left TMJ articulation demonstrates severe OA with sclerosis and faceting of both the glenoid fossa and mandibular condyle. Note that there are multiple irregular hyper attenuating loose bodies anterior, medial, and lateral to the condylar head which are most likely fragments of osteophytes from both the glenoid fossa and condyle

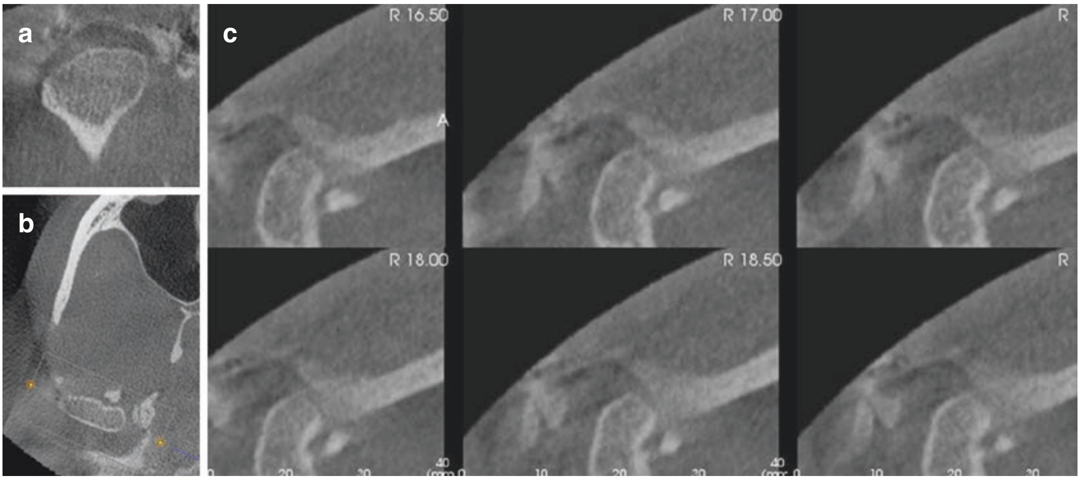

Fig. 24.73 Para-coronal (**a**), axial (**b**), and serial parasagittal images of the right TMJ articulation demonstrating a single small loose body, anterio-medial to the anterior articular ridge of the condyle. Note that the morphology of the condylar head is within normal limits however, the medial aspect of the articular eminence (**c**) is indistinct. The loose body is triangular in shape and comprises compact bone (**b**) and is most likely a fractured and dislodged tip of tympanic plate, comprising the medial portion of the glenoid fossa. The condition is not likely to be synovial chondromatosis because it is singular and not associated with the upper joint space

membrane, becoming loose bodies within the joint space. Synonyms include synovial chondrometaplasia, synovial chondrosis, and periarticular tenosynovial chondrometaplasia. SC usually affects single larger joints such as the knee, hip, and elbow. While the disease is rare in the TMJ articulation, it is an important entity to diagnose since it can potentially destroy the floor of the middle cranial fossa and invade the intracranial structures. Intracranial extension may lead to neurological deficits such as facial nerve paralysis.

Imaging features of SC in the TMJ articulation (Noyek et al. 1977; Yu et al. 2004) involve both mandibular condyle and skull base changes with intracranial extension (Mupparapu 2005) and, in decreasing frequency, include:

- Localized soft tissue swelling
- Articular changes
- Loose small, punctate, or irregular loose calcified bodies in the soft tissue of the TMJ (Fig. 24.74)
- Widening of the interarticular joint space
- Sclerosis of the glenoid fossa and/or head the mandibular condyle
- Thinning or resorption of the glenoid fossa

CBCT is the imaging modality of choice in the evaluation of SC as it depicts the above features well but can further demonstrate soft tissue swelling; define size, shape, and locations of the loose calcified bodies; and show possible change of the articular surface of the temporal bone at the skull base, as well as intracranial extension. Yu et al. (2004) categorized SC into three presentations (Table 24.12).

While SC is a local, non-neoplastic, self-limiting process, postsurgical recurrence and malignant transformation to synovial chondrosarcoma mandate regular postoperative imaging follow-up.

24.4.9 Heterotopic Bone Formation

Heterotopic ossification (HTO) is the formation of highly organized mature ectopically located lamellar bone in soft tissue due to trauma, rare

Table 24.11 Differential diagnosis of periarticular calcifications

Type	Condition	Distinguishing features
Local	Detached osteophytes (Figs. 24.70, 24.71, and 24.72)	Associated with OA of the TMJ Few in number Usually anterior to the condylar head but can also be associated with the glenoid fossa With opening, the association of the osteophyte fragment with the condyle may be confirmed
	Intracapsular fracture (Fig. 24.73)	Often single fragment, displaced but adjacent to condylar head with corresponding defect May be associated with condylar head or articular eminence
	Osteochondritis dissecans	Rare, condylar necrosis followed by healing Single or limited number of osteochondral fragments with corresponding bone defect of the condylar head Often associated with trauma Condylar head shows findings similar to avascular necrosis on MRI
	Synovial chondromatosis (see 24.4.8.1)	Rare, but may erode the base of the skull Multiple small loose bodies, limited to superior joint space Minimal joint effusion
	Pigmented villonodular synovitis	Extremely rare, benign but locally destructive solitary nodule locally destructive involving the infratemporal fossa and subtemporal skull base
	Tumoral calcinosis	Rare, characterized by periarticular soft tissue hyperplasia and calcification Most common in teenagers and black patients Joint effusion is unusual
Systemic	Crystal deposition diseases	Three types: (1) urate deposition (gout), (2) calcium pyrophosphate dihydrate deposition (CPPD or pseudogout), and (3) hydroxyapatite deposition (calcific periarthritis) Extremely rare, bit may erode the base of the skull Evenly distributed, fine particulate hyperdense amorphous chondrocalcinosis initially progressing to globular diffusely calcified mass with adjacent remodeling of the condyle and adjacent structures Medical and clinical history are important in diagnosis
	Chronic renal failure	Periarticular soft tissue calcification

*synovitis (S), acne (A), palmoplantar pustulosis (P), hyperostosis (H), and osteitis (O)
[a]Chamot et al. (1987)
[b]Marsot-Dupuch et al. (2004); OA, osteoarthritis

genetic conditions, or idiopathic or pathologic processes. It is rare in the maxillofacial region, but may include ossification of the tissues adjacent to the TMJ and the muscles used in mastication, resulting in varying degrees of restricted mandibular movement. Heterotopic ossification is a rare but major complication of TMJ-related surgery leading to eventual ankylosis of the condylar and glenoid fossa elements (Lindqvist et al. 1992, Westermark et al. 2006) (Fig. 24.75). The pathogenesis of HTO is unknown but it has been suggested that immediately postoperatively pluripotential mesenchymal cells are stimulated to differentiate into osteoblastic and chondroblastic stem cells. While the mechanism of this stimulation is unknown, a factor in the bone matrix is considered to be the most likely agent. As other theories have also been reported, the causes may be multifactorial. While the precise incidence of HTO in patients who undergo TMJ surgical pro-

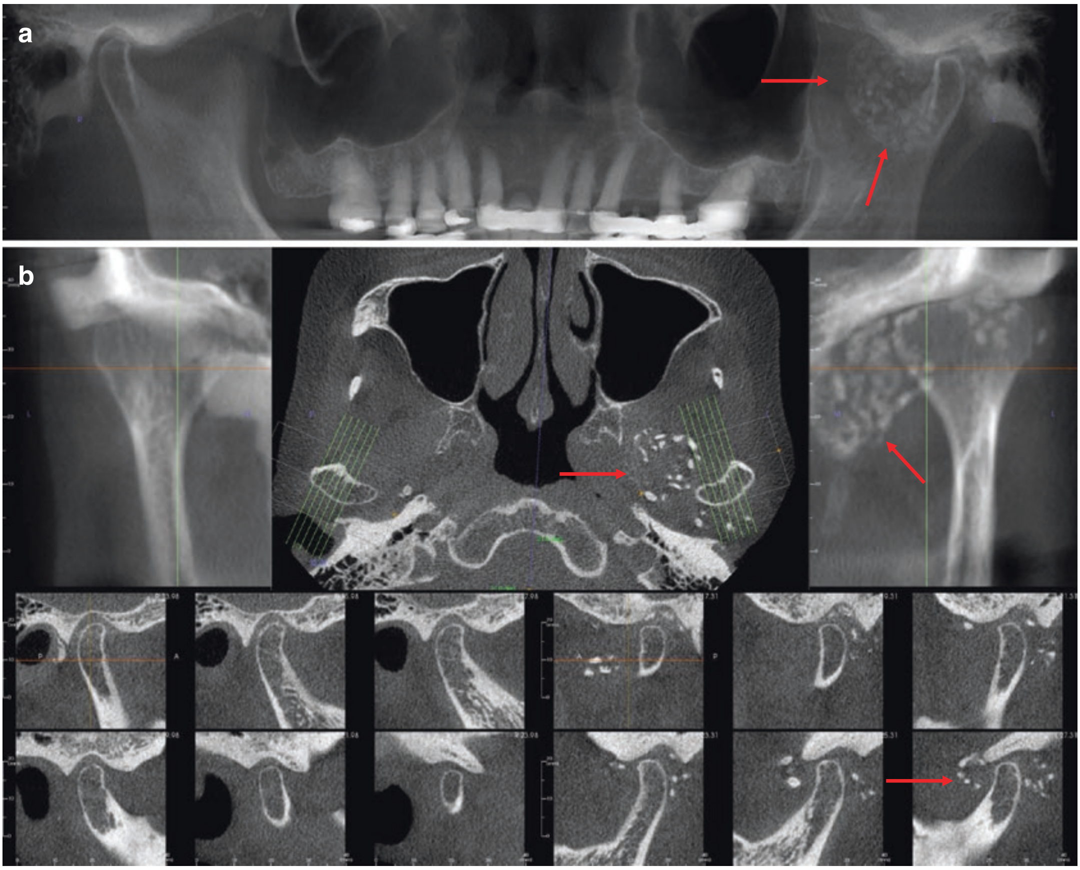

Fig. 24.74 Reformatted panoramic (**a**) and standard TMJ reformatted display incorporating coronal, axial reference and serial cross-sectional images (**b**) demonstrating multiple localized rice grain sized hyperdensities located within the anterior posterior and medial joint space (*red arrows*) causing displacement of the left mandibular condyle. Note localized sclerosis of the associated glenoid fossa. The imaging appearance is consistent with Type 3 (Yu et al. 2004) synovial chondromatosis (histologically confirmed) (Images courtesy of Ryan Lee)

cedures will is unknown, risk factors include existing ectopic bone and a history of previous trauma. HTO is also associated with a number of conditions including hypertrophic osteoarthritis, diffuse idiopathic skeletal hyperostosis, and ankylosing spondylitis. Imaging findings include:

Table 24.12 Classification of synovial chondromatosis (after Yu et al. 2004)

Type	Description
1	Active intrasynovial disease only—soft tissue swelling without detached cartilaginous bodies
2	Transitional lesion—soft tissue swelling with detached cartilaginous bodies
3	Multiple detached cartilaginous bodies—Free osteochondral bodies surrounding the TMJ but no soft tissue swelling

- Generalized formation of cortical bone leading to dysmorphology of condylar and temporal bone elements equally.
- Extensive lace-like pattern of bone within the soft tissues overlying the bony elements.
- Gradual reduction and eventual elimination of interarticular space leading ultimately to fusion and ankylosis.

Heterotopic bone formation in the TMJ articulation has been categorized by two authors. Durr et al. (1993) characterized HBF into 1 of 4 grades (Table 24.13). This system was adapted from an earlier classification published by Brooker et al. (1973), who graded heterotopic bone formation around the hip. Grades 1, 2, and 3 are further classified as symp-

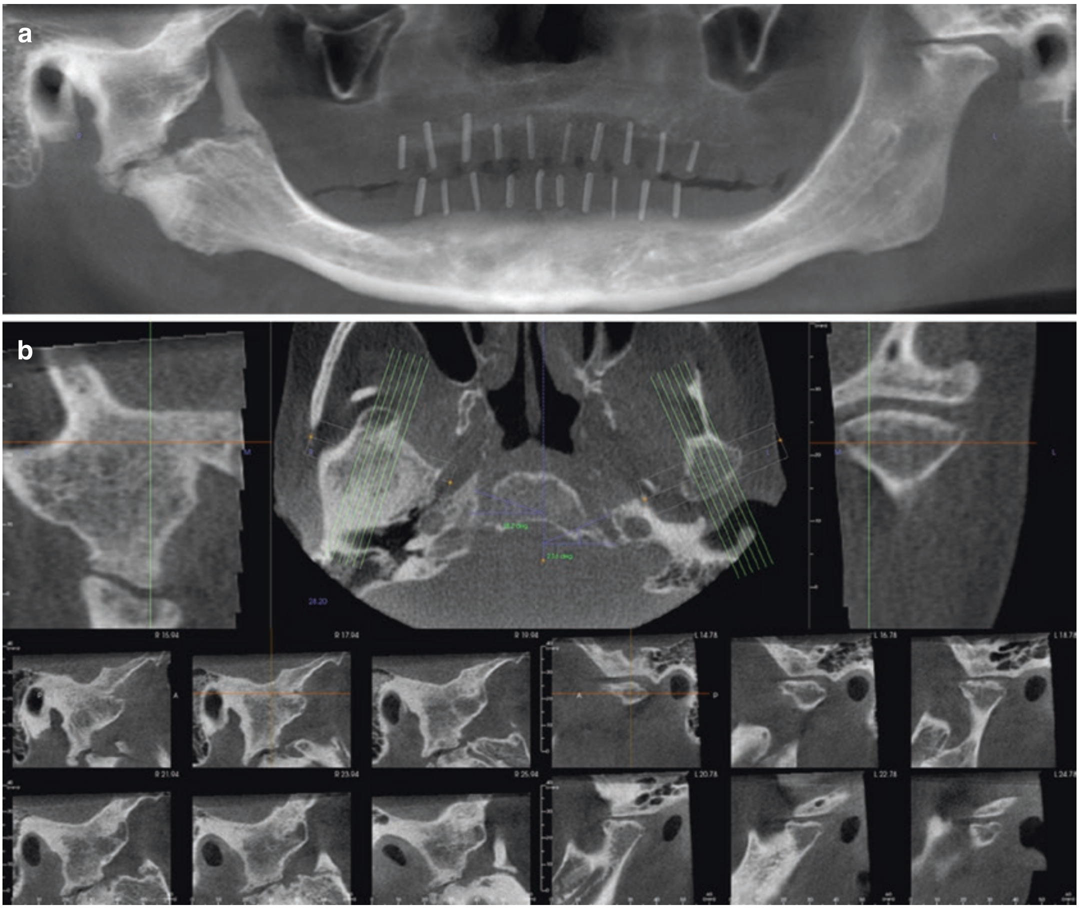

Fig. 24.75 Reformatted panoramic (**a**) and standard TMJ reformatted display incorporating coronal, axial reference and serial cross-sectional images (**b**) demonstrating grade V (Garrett and Abbey 2000) heterotopic bone formation of the right mandibular condyle with the temporal process. A surgical separation has been performed at the level of the mid ramus of both the condylar and coronoid portion. This has created a pseudoarticulation on the right. Note that the scan was performed with a radiographic template in position for potential implant site assessment

Table 24.13 Turlington-Durr classification of heterotopic ossification in the temporomandibular joint

Grade[a]	Description[b]	Subdivisions[b]
0	No bone islands visible	
1	Islands of bone visible within soft tissues around joint	A/S
2	Periauricular bone formation	A/S
3	Apparent bone ankylosis	A/S

[a]Modified from the classification of heterotopic ossification in the hips described by Brooker et al. (1973)
[b]A = asymptomatic; S = symptomatic. Symptomatic ossification includes severe pain, decreased interincisal opening (15 mm or less), closed locking of the jaw, or decreased lateral or protrusive movement

tomatic (S) and asymptomatic (A). Symptomatic ossification includes severe pain, decreased interincisal opening (15 mm or less), closed locking of the jaw, or decreased lateral or protrusive movement.

Garrett and Abbey (2000) expanded on this system based on CT data to try to increase the accuracy of classifying patients and to identify those at greatest risk (Table 24.14).

They indicated that as CT imaging provides the most accurate diagnosis of the amount of heterotopic bone that has formed it should be mandatory in the preoperative planning phase for patients with this condition. Based on their experience with treating patients with HBF they suggested

Table 24.14 Garrett/Abbey grading system based on CT examination and treatment protocol recommendations based on multiply operated patients with heterotopic ossification

Grade	Description	Treatment protocols	
		Radiation	Surgical
I	Ossification present histologically, but not visible on CT or surgical dissection	None	Full surgical protocol (total joint as needed)
II	Small islands of ossified material within joint space visible on CT, but without bridging across joint space between condyle and fossa, some ossification noted at surgery	None	Full surgical protocol (total joint as needed)
III	Moderate formation of bone viable on CT with bridging medially, excessive bone and union of condyle with medial aspect of fossa easily detected at surgery	Patient choice—yes if more than 5 previous surgeries	Full surgical protocol (total joint as needed)
IV	Severe bone formation on CT with bridging medially and laterally, joint space still visible with separation apparent on CT between condyle and fossa. Joint space discernable at surgery, but gross bone formation and union of condyle and fossa in more than one spot seen	10 Gy, fractionated	Full surgical protocol (total joint replacement)
V	No discernable joint space, complete fusion of condyle and fossa on CT with total ankylosis present. At surgery, total union of condyle or graft with fossa noted, no dissectible joint space	10 Gy, fractionated	Full surgical protocol (total joint replacement)

treatment protocols involving both surgery and radiation therapy based on disease classification.

The classical treatment for HTO has been surgical. A number of procedures have been described, all directed at the production of a pseudoarthrosis. These surgical procedures have been categorized into five groups: osteoarthrotomy, osteoarthrectomy, gap arthroplasty, costochondral grafting, and total joint prosthesis. Unfortunately, the success rates for each of these procedures are variable and notoriously unpredictable. Recurrence of HTO within the joint space has been a significant postoperative complication with between 53 and 100% recurrence (Topazian 1966; Popescu and Vasiliu 1977).

References

Akerman S, Kopp S, Nilner M, Petersson A, Rohlin M (1988) Relationship between clinical and radiologic findings of the temporomandibular joint in rheumatoid arthritis. Oral Surg Oral Med Oral Pathol 66:639–643

American Society of Temporomandibular Joint Surgeons (2003) Guidelines for diagnosis and management of disorders involving the temporomandibular joint and related musculoskeletal structures. Cranio 21:68–76

Ardic F, Gokharman D, Atsu S, Guner S, Yilmaz M, Yorgancioglu R (2006) The comprehensive evaluation of temporomandibular disorders seen in rheumatoid arthritis. Aust Dent J 51:23–28

Bag AK, Gaddikeri S, Singhal A, Hardin S, Tran BD, Medina JA, Curé JK (2014) Imaging of the temporomandibular joint: an update. World J Radiol 6:567–582

Bianchi SD, Boccardi A (1999) Radiological aspects of osteosarcoma of the jaws. Dentomaxillofacial Radiol 28:42–47

Blackwood HJ (1957) The double-headed mandibular condyle. Am J Phys Anthropol 15:1–8

de Boer EW, Dijkstra PU, Stegenga B, de Bont LG, Spijkervet FK (2014) Value of cone-beam computed tomography in the process of diagnosis and management of disorders of the temporomandibular joint. Br J Oral Maxillofac Surg 52:41–46

Brooker AF, Bowerman JW, Robinson RA, Riley LH (1973) Ectopic ossification following total hip replacement: incidence and a method of classification. J Bone Joint Surg Am 55:1629–1632

Carter LC, Haller AD, Calamel AD, Pfaffenbach A (1999) Zygomatic air cell defect (ZACD). Prevalence and characteristics in a dental clinic outpatient population. Dentomaxillofac Radiol 28:116–122

Chamot AM, Benhamou CL, Kahn MF, Beraneck L, Kaplan G, Prost A (1987) Le syndrome acne' pustulose hyperostose oste'ite (SAPHO): re'sultats d'une enqueˆte nationale-85 observations. Rev Rhum Mal Osteoartic 54:187–196 (In French)

Christiansen EL, Chan TT, Thompson JR, Hasso AN, Hinshaw DB Jr, Kopp S (1987) Computed tomography of the normal temporomandibular joint. Scand J Dent Res 95:499–509

Ciccarelli R, Di Salle F, Guidi G, Lavorgna G, Sagliocco R, Rotondo A, Smaltino F (1998) Three-dimensional imaging with computerized tomography. Etiologic considerations and methods for studying temporomandibular joints. Radiol Med 95:417–423 (in Italian)

Cimen M, Işik AO, Gedik R (1999) A radiological method on the classification of human mandibular condyles. Okajimas Folia Anat Jpn 76:263–272

Durr ED, Turlington EG, Foote RL (1993) Radiation treatment of heterotopic bone formation in the temporomandibular joint articulation. Int J Radiat Oncol Biol Phys 27:863–869

Dworkin SF, LeResche L, Von Korff MR (1990) Diagnostic studies of temporomandibular disorders: challenges from an epidemiologic perspective. Anesth Prog 37:147–154

Eckerdal O, Ahlqvist J (1979) Thin bony walls of the temporomandibular joint: morphologic properties and tomographic reproduction. Acta Radiol Diagn 20:385–392

do Egito Vasconcelos BC, Porto GG, Bessa-Nogueira RV (2007) Rare benign tumors of the mandibular condyle: report of 2 cases and literature review. J Oral Maxillofac Surg 65:1830–1835

El-Hakim IE, Metwalli SA (2002) Imaging of temporomandibular joint ankylosis. A new radiographic classification. Dentomaxillofac Radiol 31:19–23

Faig-Leite H, Horta Júnior JAC (1999) Persistence of the foramen of Huschke. Dent Res 77:1177

Garrett WR, Abbey PA (2000) Protocol for the treatment of heterotopic bone formation in the Temporomandibular joint. Surg Technol Int 8:332–339

Goupille P, Fouquet B, Goga D, Cotty P, Valat JP (1993) The temporomandibular joint in rheumatoid arthritis: correlations between clinical and tomographic features. J Dent 21:141–146

Groell R, Fleischmann B (1999) The pneumatic spaces of the temporal bone: relationship to the temporomandibular joint. Dentomaxillofac Radiol 28:69–72

Gundlach KK, Fuhrmann A, Beckmann-Van der Ven G (1987) The double headed mandibular condyle. Oral Surg Oral Med Oral Pathol 64:249–253

Guyuron B, Lassa CI (1992) Unpredictable growth pattern of costochondral graft. Plast Reconstr Surg 90:880–886

Hawke M, Kwok P, Mehta M, Wang RG (1987) Bilateral spontaneous temporomandibular joint herniation into the external auditory canal. J Otolaryngol 16:387–389

Hawke M, Kwok P, Shankar L, Wang RG (1988) Spontaneous temporomandibular joint fistula into the external auditory canal. J Otolaryngol 17:29–31

Heffez L, Anderson D, Mafee M (1989) Developmental defects of the tympanic plate: case reports and review of the literature. J Oral Maxillofac Surg 47:1336–1340

Hersek N, Ozbek M, Tasar F, Akpinar E, Firat M (2004) Bifid mandibular condyle: a case report. Dent Traumatol 20:184–186

Herzog S, Fiese R (1989) Persistent foramen of Huschke: possible risk factor for otologic complications after arthroscopy of the temporomandibular joint. Oral Surg Oral Med Oral Pathol 68:267–270

Hintze H, Wiese M, Wenzel A (2007) Cone beam CT and conventional tomography for the detection of morphological temporomandibular joint changes. Dentomaxillofac Radiol 36:192–197

Hintze H, Wiese M, Wenzel A (2009) Comparison of three radiographic methods for detection of morphological temporomandibular joint changes: panoramic, scanographic and tomographic examination. Dentomaxillofac Radiol 38:134–140

Honda K, Bjørnland T (2006) Image-guided puncture technique for the superior temporomandibular joint space: value of cone beam computed tomography (CBCT). Oral Surg Oral Med Oral Pathol Oral Radiol Endod 102:281–286

Honda K, Larheim TA, Johannessen S, Arai Y, Shinoda K, Westesson P-L (2001a) Ortho cubic super-high resolution computed tomography (ortho-CT): a new radiographic technique with application to the temporomandibular joint. Oral Surg Oral Med Oral Pathol Oral Radiol Endod 91:239–243

Honda K, Larheim TA, Sano T, Hashimoto K, Shinoda K, Westesson P-L (2001b) Thickening of the glenoid fossa in osteoarthritis of the temporomandibular joint: an autopsy study. Dentomaxillofac Radiol 30:10–13

Honda K, Matumoto K, Kashima M, Takano Y, Kawashima S, Arai Y (2004) Single air contrast arthrography for temporomandibular joint disorder using limited cone beam computed tomography for dental use. Dentomaxillofac Radiol 33:271–273

Honda K, Larheim TA, Maruhashi K, Matsumoto K, Iwai K (2006) Osseous abnormalities of the mandibular condyle: diagnostic reliability of cone beam computed tomography compared with helical computed tomography based on an autopsy material. Dentomaxillofac Radiol 35:152–157

Honey OB, Scarfe WC, Hilgers MJ, Klueber K, Silveira AM, Haskell BS, Farman AG (2007) Accuracy of cone-beam computed tomography imaging of the temporomandibular joint: comparisons with panoramic radiology and linear tomography. Am J Orthod Dentofacial Orthop 132:429–438

Isberg A, Isacsson G, Nah KS (1987) Mandibular coronoid process locking: a prospective study of frequency and association with internal derangement of the temporomandibular joint. Oral Surg Oral Med Oral Pathol 63:275–279

Isberg A, Hägglund M, Paesani D (1998) The effect of age and gender on the onset of symptomatic temporomandibular joint disk displacement. Oral Surg Oral Med Oral Pathol Oral Radiol Endod 85:252–257

Izumi M, Isobe M, Toyama M, Ariji Y, Gotoh M, Naitoh M, Kurita K, Ariji E (2005) Computed tomographic features of bilateral coronoid process hyperplasia with special emphasis on patients without interference between the process and the zygomatic bone. Oral Surg Oral Med Oral Pathol Oral Radiol Endod 99:93–100

Jerolimov V (2009) Temporomandibular disorders and orofacial pain. Rad 504 Med Sci 33:53–77

John MT, Dworkin SF, Mancl LA (2005) Reliability of clinical temporomandibular disorder diagnoses. Pain 118:61–69

Karlo CA, Stolzmann P, Habernig S, Müller L, Saurenmann T, Kellenberger CJ (2010) Size, shape and age-related changes of the mandibular condyle during childhood. Eur Radiol 20:2512–2517

Katsavrias EG (2006) Morphology of the temporomandibular joint in subjects with class II Division 2 malocclusions. Am J Orthod Dentofacial Orthop 129:470–478

Katsavriasa EG, Halazonetisb DJ (2005) Condyle and fossa shape in Class II and Class III skeletal patterns: a morphometric tomographic study. Am J Orthod Dentofacial Orthop 128:337–346

Katzberg RW, Tallents RH, Hayakawa K, Miller TL, Goske MJ, Wood BP (1985) Internal derangement of the temporomandibular joint: findings in the pediatric age group. Radiology 154:125–127

Kurita H, Otsuka A, Kobayashi H, Kurashina K (2001) Resorption of the lateral pole of the mandibular condyle in temporomandibular disc displacement. Dentomaxillofac Radiol 30:88–91

Kurita H, Ohtsuka A, Kobayashi H, Kurashina K (2002) Alteration of the horizontal mandibular condyle size associated with temporomandibular joint internal derangement in adult females. Dentomaxillofac Radiol 31:373–378

Lacout A, Marsot-Dupuch K, Smoker WR, Lasjaunias P (2005) Foramen tympanicum, or foramen of Huschke: pathologic cases and anatomic CT study. AJNR Am J Neuroradiol 26:1317–1323

Larheim TA, Abrahamsson AK, Kristensen M, Arvidsson LZ (2015) Temporomandibular joint diagnostics using CBCT. Dentomaxillofac Radiol 44:20140235

Larsen A, Dale K, Eek M (1977) Radiographic evaluation of rheumatoid arthritis and related conditions by standard reference films. Acta Radiol Diagn (Stockh) 18:481–491

Leeuw RD (2008) American Academy of Orofacial pain. Orofacial pain: guidelines for assessment, diagnosis, and management, 4th edn. Quintessence Publishing, Chicago

Lemke AJ, Griethe M, Peroz I, Lange KP, Felix R (2005) Morphometric analysis of the temporomandibular joint with MRI in 320 joints. Rofo 177:217–228

Lew D, DeWitt A, Hicks RJ, Cacalcanti MGP (1999) Osteomas of the condyle associated with Gardner's syndrome causing limited mandibular movement. J Oral Maxillofac Surg 57:1004–1009

Librizzi ZT, Tadinada AS, Valiyaparambil JV, Lurie AG, Mallya SM (2011) Cone-beam computed tomography to detect erosions of the temporomandibular joint: effect of field of view and voxel size on diagnostic efficacy and effective dose. Am J Orthod Dentofacial Orthop 140:25–30

Lindahl L, Hollender L (1977) Condylar fractures of the mandible. A radiographic study of remodelling processes in the temperomandibular joint. Int J Oral Surg 6:153–165

Lindqvist C, Söderholm AL, Hallikainen D, Sjövall L (1992) Erosion and heterotopic bone formation after alloplastic temporomandibular joint reconstruction. J Oral Maxillofac Surg 50:942–949

Loukota RA, Eckelt U, De Bont L, Rasse M (2005) Subclassification of fractures of the condylar process of the mandible. Br J Oral Maxillofac Surg 43:72–73

Maixner W, Diatchenko L, Dubner R, Fillingim RB, Greenspan JD, Knott C, Ohrbach R, Weir B, Slade GD (2011) Orofacial pain prospective evaluation and risk assessment study—the OPPERA study. J Pain 12(11 Suppl.):T4–11.e1-2

Marsot-Dupuch K, Smoker WRK, Gentry LR, Cooper KA (2004) Massive calcium pyrophosphate dihydrate crystal deposition disease: a cause of pain of the temporomandibular joint. AJNR Am J Neuroradiol 25:876–879

McLoughlin PM, Hopper C, Bowley NB (1995) Hyperplasia of the mandibular coronoid process: an analysis of 31 cases and a review of the literature. Oral Maxillofac Surg 53:250–255

Mercuri LG (1998) Alloplastic temporomandibular joint reconstruction: review article. Oral Surg Oral Med Oral Pathol 85:631–637

Mercuri LG (2008) Osteoarthritis, osteoarthrosis, and idiopathic condylar resorption. Oral Maxillofac Surg Clin North Am 20:169–183

Morales H, Cornelius R (2016) Imaging approach to temporomandibular joint disorders. Clin Neuroradiol 26:5–22

Morgan DH (1992) Development of alloplastic materials for temporomandibular joint prosthesis: a historical perspective with clinical illustrations. Cranio 10:192–204

Mupparapu M (2005) Synovial chondromatosis of the temporomandibular joint with extension to the middle cranial fossa. J Postgrad Med 51:122–124

Murakami K, Yokoe Y, Yasuda S, Tsuboi Y, Iizuka T (2000) Prolonged mandibular hypomobility patient with a "square mandible" configuration with coronoid process and angle hyperplasia. Cranio 18:113–119

Nordahl S, Alstergren P, Eliasson S, Kopp S (2001) Radiographic signs of bone destruction in the arthritic temporomandibular joint with special reference to markers of disease activity. A longitudinal study. Rheumatology 40:691–694

Noyek AM, Holgate RC, Fireman SM, Rosen P, Pritzker KPH (1977) The radiological findings in synovial chondromatosis (chondrometaplasia) of the temporomandibular joint. J Otolaryngol 6:45–48

Öberg T, Carlsson GE, Fajers CM (1971) The temporomandibular joint. A morphometric study on a human autopsy material. Acta Odontol Scand 29:349–384

Ogus H (1979) Degenerative disease of the temporomandibular joint in young persons. Br J Oral Surg 17:17–24

Patel A, Tee BC, Fields H, Jones E, Chaudhry J, Sun Z (2014) Evaluation of cone-beam computed tomography in the diagnosis of simulated small osseous defects in the mandibular condyle. Am J Orthod Dentofacial Orthop 145:143–156

Paterson AW, Shepherd JP (1992) Fascia lata interpositional arthroplasty in the treatment of temporomandibular joint ankylosis caused by psoriatic arthritis. Int J Oral Maxillofac Surg 21:137–139

Pedersen TK, Jensen JJ, Melsen B, Herlin T (2001) Resorption of the temporomandibular condylar bone according to subtypes of juvenile chronic arthritis. J Rheumatol 28:2109–2115

Petersson A (2010) What you can and cannot see in TMJ imaging—an overview related to the RDC/TMD diagnostic system. J Oral Rehabil 37:771–778

Posnick JC, Fantuzzo JJ (2007) Idiopathic condylar resorption: current clinical perspectives. J Oral Maxillofac Surg 65:1617–1623

Popescu V, Vasiliu D (1977) Treatment of temporo-mandibular ankylosis with particular reference to the interposition of full-thickness skin autotransplant. J Maxillofac Surg 5:3–14

Proffit WR, Vig KWL, Turvey TA (1980) Early fracture of the mandibular condyles: frequently an unsuspected cause of growth disturbances. Am J Orthod 78:1–24

Redlund-Johnell I (1987) Severe rheumatoid arthritis of the temporomandibular joints and its coincidence with severe rheumatoid arthritis of the cervical spine. Scand J Rheumatol 16:347–353

Rohlin M, Petersson A (1989) Rheumatoid arthritis of the temporomandibular joint: radiologic evaluation based on standard reference films. Oral Surg Oral Med Oral Pathol 67:594–599

Rugh JD, Solberg WK (1985) Oral health status in the United States: temporomandibular disorders. J Dent Educ 49:398–406

Sawhney C (1986) Bony ankylosis of the temporomandibular joint: follow up of 70 patients treated with arthroplasty and acrylic spacer interposition. Plast Reconstr Surg 77:29–38

Sesenna E, Tullio A, Ferrari S (1997) Chondrosarcoma of the temporomandibular joint: a case report and review of the literature. J Oral Maxillofac Surg 55:1348–1352

Sharma PD, Dawkins RS (1984) Patent foramen of Huschke and spontaneous salivary fistula. J Laryngol Otol 98:83–85

Sharp JT, Lidsky MD, Collins LC, Moreland J (1971) Methods of scoring the progression of radiologic changes in rheumatoid arthritis. Correlation of radiologic, clinical and laboratory abnormalities. Arthritis Rheum 14:706–720

Sharp JT, Young DY, Bluhm GB, Brook A, Brower AC, Corbett M, Decker JL et al (1985) How many joints in the hands and wrists should be included in a score of radiologic abnormalities used to assess rheumatoid arthritis? Arthritis Rheum 28:1326–1335

Solberg WK, Hansson TL, Nordstrom BB (1985) The temporomandibular joint in young adults at autopsy: a morphologic classification and evaluation. J Oral Rehabil 12:303–321

Sonnesen L, Pedersen CE, Kjaer I (2007) Cervical column morphology related to head posture, cranial base angle, and condylar malformation. Eur J Orthod 29:398–403

Spiess B, Schroll K (1972) Gelenkfortsatz- und Gelenkköpfchenfrakturen. In: Nigst H (ed) Spezielle Frakturen- und Luxationslehre. Bd. I/II, Thieme, Stuttgart. (in German)

Su-Gwan K (2001) Treatment of temporomandibular joint ankylosis with temporalis muscle and fascia flap. Int J Oral Maxillofac Surg 30:189–193

Suenaga S, Nagayama K, Nagasawa T, Indo H, Majima HJ (2016) The usefulness of diagnostic imaging for the assessment of pain symptoms in temporomandibular disorders. Jpn Dent Sci Rev 52:93–106

Tallents RH, Guay JA, Katzberg RW, Murphy W, Proskin H (1991) Angular and linear comparisons with unilateral mandibular asymmetry. J Craniomandib Disord 5:135–142

Terakado M, Hashimoto K, Arai Y, Honda M, Sekiwa T, Sato H (2000) Diagnostic imaging with newly developed ortho cubic super-high resolution computed tomography (Ortho-CT). Oral Surg Oral Med Oral Pathol Oral Radiol Endod 89:509–518

Toller PA (1973) Osteoarthrosis of the mandibular condyle. Br Dent J 134:223–231

Topazian RG (1966) Comparison of gap and interpositional arthroplasty in the treatment of temporomandibular joint ankylosis. J Oral Surg 28:603

Tsiklakis K, Syriopoulos K, Stamatakis H (2004) Radiographic examination of the temporomandibular joint using cone beam computed tomography. Dentomaxillofac Radiol 33:196–201

Tsuruta A, Yamada K, Hanada K, Hosogai A, Tanaka R, Koyama J, Hayashi T (2003) Thickness of the roof of the glenoid fossa and condylar bone change: a CT study. Dentomaxillofac Radiol 32:217–221

Tyndall DA, Matteson RS (1985) Radiographic appearance and population distribution of the pneumatized articular eminence of the temporal bone. J Oral Maxillofac Surg 43:493–497

Tyndall DA, Matteson RS (1987) The appearance of the zygomatic air cell defect (ZACD) on panoramic radiographs. Oral Surg Oral Med Oral Pathol 64:373–376

Ueda M, Yonetsu K, Ohki M, Yamada T, Kitamori H, Nakamura T (2003) Curvature analysis of the mandibular condyle. Dentomaxillofac Radiol 32:87–92

Uemura S, Nakamura M, Iwasaki H, Fuchihata H (1979) A roentgenological study on temporomandibular joint disorders. Morphological changes of TMJ in arthrosis. Dent Radiol 19:224–237. (in Japanese)

VanLoon JP, DeBont LGM, Boering G (1995) Evaluation of temporomandibular joint prostheses: review of the literature for 1946–1994 and implications for future designs. J Oral Maxillofac Surg 53:984–996

Vezeau PJ, Fridrich KL, Vincent SD (1995) Osteochondroma of the mandibular condyle. Literature review and report of two atypical cases. J Oral Maxillofac Surg 53:954–963

Wang RG, Bingham B, Hawke M, Kwok P, Li JR (1991) Persistence of the foramen of Huschke in the adult: an osteological study. J Otolaryngol 20:251–254

Weissman JL, Hirsh BE, Chan K, Tabor EK, Curtin HD (1991) Dehiscent temporomandibular joint. Radiology 180:211–213

Wenneberg B, Könönen M, Kallenberg A (1990) Radiographic changes in the temporomandibular joint of patients with rheumatoid arthritis, psoriatic, arthritis, and ankylosing spondylitis. J Craniomandib Disord 4:35–39

Westermark A, Koppel D, Leiggener C (2006) Condylar replacement alone is not sufficient for prosthetic reconstruction of the temporomandibular joint. Int J Oral Maxillofac Surg 35:488–492

Winocur E, Reiter S, Krichmer M, Kaffe I (2010) Classifying degenerative joint disease by the RDC/

TMD and by panoramic imaging: a retrospective analysis. J Oral Rehabil 37:171–177

Wolford LM, Gonçalves JR (2015) Condylar resorption of the temporomandibular joint: how do we treat it. Oral Maxillofac Surg Clin North Am 27:47–67

Yale SH, Allison BD, Hauptfuehrer JD (1966) An epidemiological assessment of mandibular condyle morphology. Oral Surg Oral Med Oral Pathol 21:169–177

Yu Q, Yang J, Wang P, Shi H, Luo J (2004) CT features of synovial chondromatosis in the temporomandibular joint. Oral Surg Oral Med Oral Pathol Oral Radiol Endod 97:524–528

Zachariades N, Mezitis M, Mourouzis C, Papadakis D, Spanou A (2006) Fractures of the mandibular condyle: a review of 466 cases. Literature review, reflections on treatment and proposals. J Craniomaxillofac Surg 34:421–432

Zhang ZL, Shi XQ, Ma XC, Li G (2014) Detection accuracy of condylar defects in cone beam CT images scanned with different resolutions and units. Dentomaxillofac Radiol 43:20130414

25 CBCT Sialography

Fatima M. Jadu and Ernest W.N. Lam

Contents

F.M. Jadu, BDS, MSc., PhD, FRCD(C) (✉)
Division of Oral and Maxillofacial Radiology,
Department of Oral Diagnostic Sciences,
Faculty of Dentistry, King Abdulaziz University,
Jeddah, Saudi Arabia
e-mail: fatima.jadu@gmail.com

E.W.N. Lam, DMD, MSc., PhD, FRCD(C)
Discipline of Oral and Maxillofacial Radiology,
Faculty of Dentistry, University of Toronto,
Toronto, ON, Canada
e-mail: Ernest.Lam@dentistry.utoronto.ca

25.1 Introduction

The salivary glands are exocrine glands with the sole purpose of producing and secreting saliva into the oral cavity to maintain the health and well-being of the oral tissues. They are divided into major and minor glands. The major salivary glands are large paired glands located outside the oral cavity that deliver their secretions to the oral cavity via ductal systems. The minor salivary glands are small and numerous, and scattered throughout the oral submucosa. They too deliver their secretions through ducts but the ducts are numerous and short.

A wide variety of conditions can affect the salivary glands from infections to tumors, and more often than not, imaging of the glands is necessary for diagnosis, management, and follow-up purposes. Many imaging modalities have been used to image the major salivary glands including plain (projection) radiography, ultrasonography (US), multi-detector computed tomography (MDCT), magnetic resonance imaging (MRI), and scintigraphy. Some modalities (namely plain radiography and computed tomography) have also been paired with the injection of iodinated contrast media into the ducts of the major salivary glands, a method referred to as sialography. Recently, we and others have paired cone beam computed tomography (CBCT) with sialography (Drage and Brown 2009; Jadu and Lam 2013; Abdel-Wahed et al. 2013; Shahidi and Hamedani 2014).

W.C. Scarfe, C. Angelopoulos (eds.), *Maxillofacial Cone Beam Computed Tomography*,
https://doi.org/10.1007/978-3-319-62061-9_25

25.2 Major Salivary Gland Anatomy

There are three pairs of major salivary glands located outside the oral cavity. Their secretions are delivered to the oral cavity through a sophisticated system of ducts and when combined, contribute to the bulk of the saliva secreted per day.

25.2.1 Parotid Gland

The paired parotid glands are the largest of the major salivary glands. The body of each gland is located caudal to the external auditory meatus, extending from the zygomatic arch superiorly to near the angle of the mandible inferiorly, and overlying the posterior borders of the masseter muscle and mandibular ramus (Fig. 25.1).

Each gland weighs approximately 14–28 grams, and is divided into superficial and deep lobes. The separation of the two lobes is controversial with some believing the plane of division to be the facial nerve and its five terminal branches while others believe it to be the lateral border of the mandibular ramus (Holsinger and Bui 2007). As well, approximately 20% of the population has accessory parotid tissue found anterior to the superficial lobe and superior to the main duct, overlying the zygomatic process of the temporal bone.

Branches from the carotid artery provide the blood supply to the parotid glands, and innervation is controlled by parasympathetic fibers which control secretion and sympathetic fibers that control vasoconstriction. Parasympathetic innervation of the parotid gland is received from the glossopharyngeal nerve (cranial nerve IX) via the auriculotemporal nerve, and sympathetic innervation is received from the sympathetic plexus of the carotid artery. Lymphatic drainage from the parotid nodes, which are intimately associated with the gland tissue, drains into level II A and level II B lymph nodes.

The primary duct of the parotid gland, Stensen's duct, is the main excretory duct for the gland. This duct is approximately 6–7 cm long, and has an average lumen caliber of 1–2 mm. The duct leaves the anterior border of the gland, and runs parallel and inferior to the zygomatic process of the temporal bone then it pierces the buccal fat pad and buccinator muscle at the anterior border of the masseter muscle to enter the oral cavity opposite the maxillary second molar.

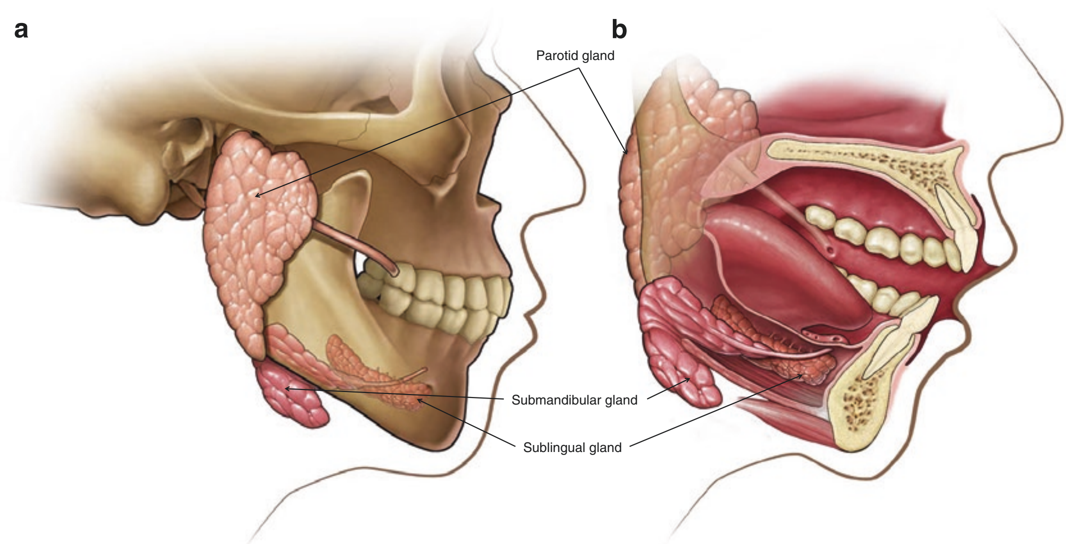

Fig. 25.1 Sagittal schematic of the maxillofacial region from the lateral (**a**) and medial (**b**) views demonstrating the anatomic location of the three major salivary glands and their respective excretory ducts

Within the gland, the primary duct branches extensively into smaller ducts finally ending in numerous terminal secretory end pieces (acini) which make up the parenchymal part of the gland. The acini of the parotid glands predominantly secrete a serous type of saliva, contributing to nearly 45% of the total saliva volume produced per day (450–675 mL/day).

25.2.2 Submandibular Gland

The paired submandibular glands are the second largest of the major salivary glands. Each gland weighs between 10 and 15 gm. Like the parotid gland, the submandibular gland is divided into superficial and deep lobes by the posterior free border of the mylohyoid muscle. The superficial lobe lies inferior to the mylohyoid muscle in the submandibular gland fossa while the deep lobe lies superior to the mylohyoid muscle in the posterior floor of the mouth (Fig. 25.1).

The external maxillary and lingual arteries provide the blood supply to the submandibular glands. Innervation by the chorda tympani branch of the facial nerve (cranial nerve VII) provides parasympathetic innervation via the lingual nerve while the sympathetic plexus of the carotid artery provides sympathetic innervation for the submandibular glands. The submandibular lymph nodes drain into the deep cervical and jugular chain nodes.

The main excretory duct of the submandibular gland is known as Wharton's duct. The 5 cm long duct leaves the deep lobe of the gland and courses anteriorly and superiorly to a small opening in the anterior floor of mouth, lateral to the lingual frenum. The lumen of Wharton's duct ranges in diameter between 1 and 3 mm. The acini of the submandibular gland parenchyma are composed of both mucous- and serous-secreting acini; mucous tubules capped with serous demilunes and serous acini. Consequently, the saliva produced by the submandibular glands is more mucinous compared to the saliva produced by the parotid glands. The contribution, however, of the submandibular glands to the daily total saliva volume is similar to the parotid glands.

25.2.3 Sublingual Gland

The sublingual glands are the smallest of the major salivary glands. Each gland weighs between 2 and 4 gm. They are located on either side in the anterior floor of the mouth between the mandibular body laterally and the genioglossus muscle medially (Fig. 25.1). The blood supply to the sublingual glands is derived from the lingual artery, and the nerve supply is identical to that of the submandibular gland. The submental and submandibular lymph nodes receive the lymph drainage of the sublingual glands.

The sublingual glands have several small excretory ducts called the *ducts of Rivinus* that open like pores upwards into the sublingual fold. The acini of the sublingual gland are like those of the submandibular gland; they are mixed but with predominantly mucous tubules and some mucous tubules capped with serous demilunes. This mixture of acini results in sublingual secretions that are more viscous than the other major salivary glands. The daily contribution of the sublingual glands to the total saliva volume is 50–75 mL (5%).

25.3 Salivary Gland Disease

The salivary glands can be affected by a wide range of diseases and conditions that span several pathophysiologies. Broadly, these conditions can be divided into three major categories: inflammatory, noninflammatory, and space occupying masses (Mandel 2014).

25.3.1 Inflammatory Conditions

Inflammation is the most common pathologic condition to affect the salivary glands. The inflammatory process may involve the parenchyma of the gland (sialadenitis) (Fig. 25.2) or it may affect the ductal structures of the gland (sialodochitis) (Fig. 25.3). Simultaneous involvement of both parts of the gland is also possible

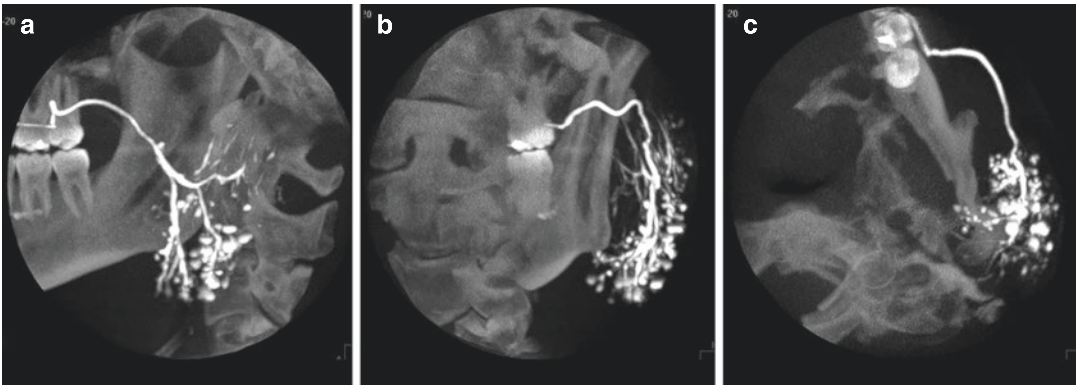

Fig. 25.2 Reformatted sagittal (**a**), coronal (**b**), and axial (**c**) maximum intensity projection (MIP) CBCT sialography images of the left parotid gland. The images demonstrate multiple collections of contrast media of various sizes predominantly in the inferior portion of the gland. These collections represent the formation of abscesses within the gland parenchyma due to sialadenitis

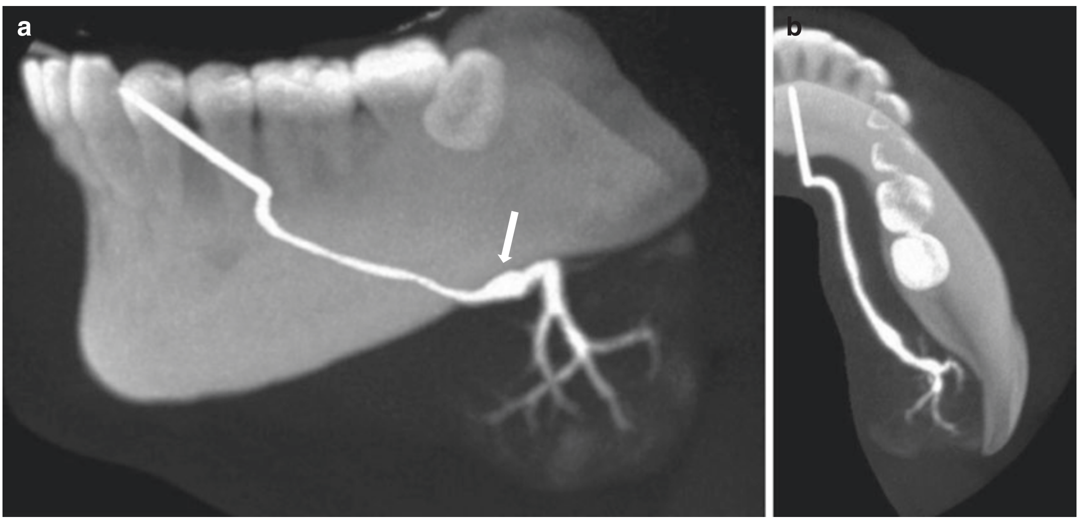

Fig. 25.3 Reformatted sagittal (**a**) and axial (**b**) MIP sialography CBCT images of a 26-year-old female patient presenting with a single painful episode of swelling in the area of the left submandibular gland. These images demonstrate sialectasia in the primary duct (*arrow*)

(Fig. 25.4). Regardless of the gland structure involved, the clinical signs and symptoms of inflammation that can be observed include swelling, pain, and xerostomia (the subjective feeling of dry mouth usually due to a decrease in the quantity of saliva produced) (Jadu and Lam 2014; Mandel 2014).

Acute inflammation of the salivary glands is most often caused by bacterial or viral infections. Bacterial infections are usually caused by one of the following organisms: *Staphylococcus aureus, Streptococcus viridans, Streptococcus pneumonia, Haemophilus influenzae, Streptococcus pyogenes, and Escherichia coli*. These bacteria are found in the oral cavity, and can infect the salivary glands through retrograde movement when there is a decrease in salivary flow. Therefore, dehydration is considered the primary etiology of acute bacterial infections of the salivary glands. The parotid glands are most commonly infected because Stensen's duct orifice is larger than that of the other salivary glands, and because parotid

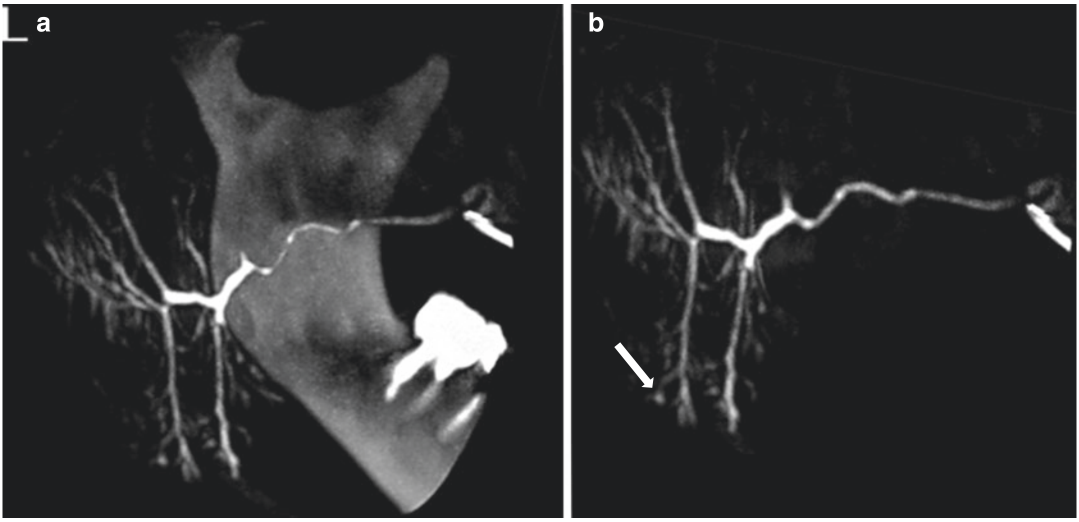

Fig. 25.4 Reformatted sagittal MIP CBCT sialography images of the left parotid gland with (**a**) and without (**b**) the adjacent osseous structures. The images demonstrate sialectasia of the secondary and tertiary ducts of the gland in addition to small collections of contrast in the inferior portion of the gland (*arrow*). These findings are consistent with sialodochitis accompanied with sialadenitis

serous secretions are not as rich as mucinous secretions with antibacterial substances such as immunoglobulin A (IgA) and lysosomes. Tender swelling of the gland and adjacent lymph nodes is a typical presentation. Pus may also be noted at the orifice of the main excretory duct.

Viral infections are less common than bacterial infections with the exception of mumps, which is considered the most common condition to affect the salivary glands in children. This contagious disease is caused by a ribonucleic acid (RNA) paramyxovirus, and the parotid glands can be affected bilaterally. Less commonly, the submandibular and sublingual glands may be affected as well. Mumps is characterized by painful swellings that may be preceded by a prodromal period of general malaise. Some cases of mumps are subclinical and other cases, especially in adults, may develop serious complications such as thyroiditis and orchitis.

The most common cause of chronic inflammation of the salivary glands is obstruction, although there may be primary and secondary causes. Primary causes of obstruction include salivary stones (sialoliths), ductal narrowing (strictures), and mucous plugs. In contrast, secondary causes of obstruction can include trauma to the ductal structures and space occupying lesions impinging on gland ducts. Sialoliths are estimated to affect nearly 1% of the general population, and are by far the most common cause of obstruction, and the most common cause of chronic inflammation of the salivary glands (Fig. 25.5). Sialoliths may be single or multiple, unilateral or bilateral, intraglandular or within the ductal system of the gland. The majority (83%) of sialoliths (sialolithiasis) form in the submandibular gland ducts because of the more viscous nature of submandiublar saliva, its high mineral content, high pH, and the long, tortuous upward path of Wharton's duct toward a relatively narrow orifice. Strictures are the second most common cause of primary obstruction accounting for nearly 23% of all cases of obstruction. The etiology of strictures is not known but several hypotheses have been proposed including ductal injury secondary to sialoliths, recurrent infections, and minor trauma. Obstruction, regardless of the cause, eventually leads to saliva accumulation within the ducts especially during meal times when copious amounts of saliva are produced rapidly. With saliva build-up over time, there may be permanent distension of the ducts (sialectasia) and this in turn leads to saliva stagnation in the

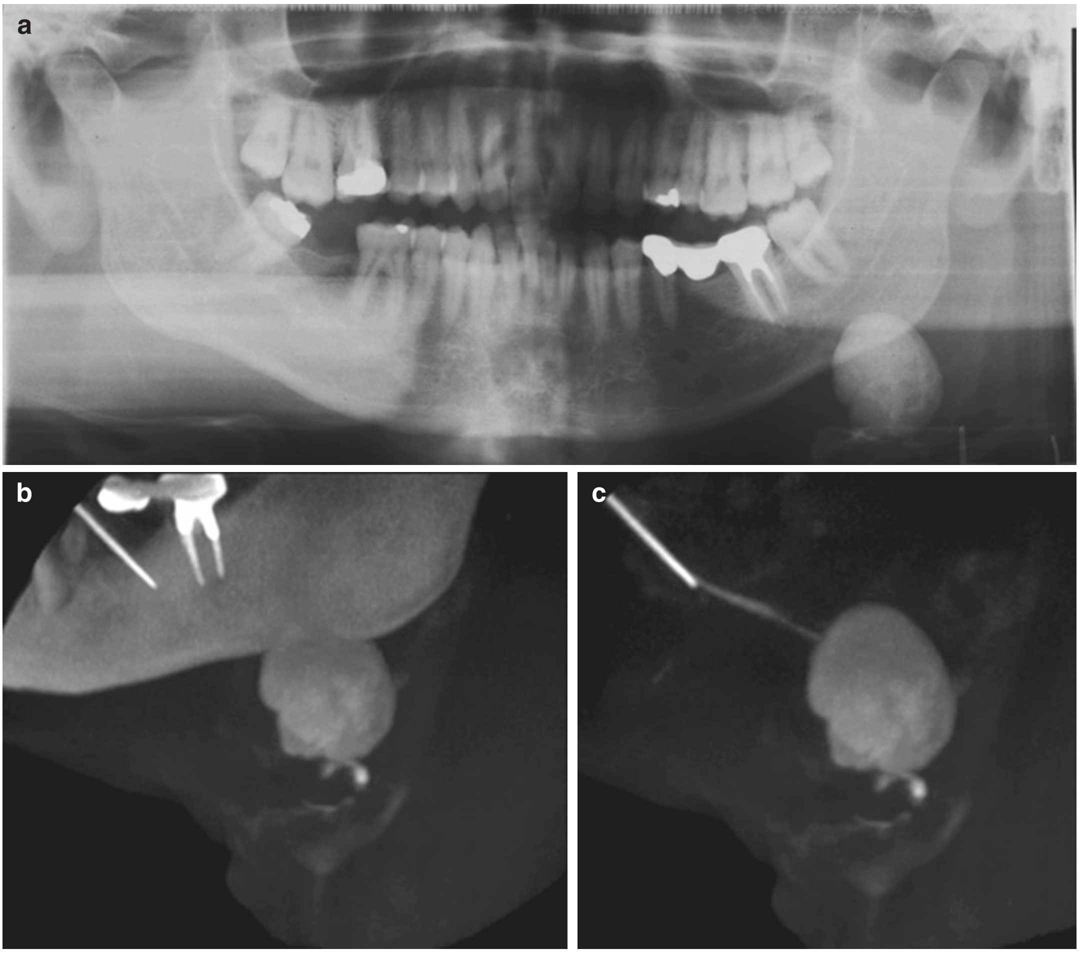

Fig. 25.5 Panoramic (**a**) and reformatted sagittal MIP CBCT sialography images (**b**) with and without (**c**) adjacent osseous structures of a 45-year-old male who complained of several episodes of meal time swelling. Imaging shows a large calcified sialolith in the proximal portion of the primary duct of the left submandibular gland. There is minimal fill of the ductal structures which indicates fibrosis of the ducts secondary to long-standing chronic inflammation

distended portions of the ducts, predisposing the gland to repeated retrograde infections. Patients with obstruction typically present with a history of intermittent, tender unilateral gland swelling, especially at meal times.

25.3.2 Space Occupying Conditions

Space occupying conditions of the salivary glands include both cysts and neoplasms. Cysts of the salivary glands, whether developmental or acquired, are relatively uncommon representing less than 5% of all salivary gland masses. The developmental cysts include branchial, lymphoepithelial, and dermoid or epidermoid cysts. These cysts usually present later in life despite being present at birth, and typically manifest as a unilateral painless swelling. Histopathologic examination is the diagnostic gold-standard for such cysts.

Sialocysts and acquired immune deficiency syndrome (AIDS) related parotid cysts (ARPC) are classified as acquired entities. Sialocysts occur when obstruction of the salivary ducts leads to retention of saliva within the ducts with

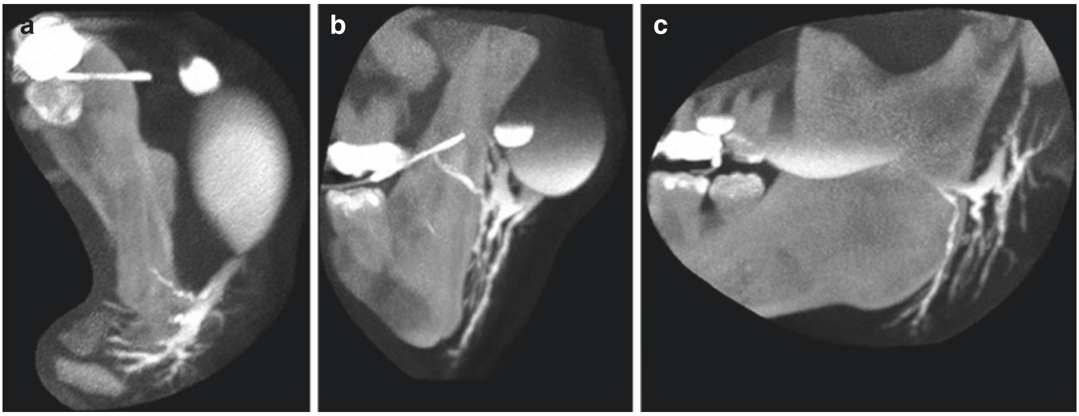

Fig. 25.6 Reformatted axial (**a**), coronal (**b**), and sagittal (**c**) MIP CBCT sialography images of the left parotid gland in a 60-year-old complaining of a left facial swelling. The images demonstrate two fusiform areas of dilatation in Stensen's duct; a smaller one distally (nearer the gland orifice) and a larger one proximally (nearer the gland parenchyma). Contrast material pools in the inferior portions of both dilated sections, and the secondary and tertiary ducts. These findings are consistent with a sialocyst

exuberant dilatation (Fig. 25.6). This should not be confused with a sialocele which develops from injury to a salivary duct and extrusion of saliva into the adjacent connective tissue forming a pseudocyst. The sialocyst is also known by several other terms, including retention cyst, mucus retention cyst, ductal cyst, and salivary ductal cyst. In contrast, the sialocele which is an extravasation phenomenon is commonly seen in minor salivary glands, and is known as a mucocele. The terminology of these two conditions is used interchangeably in the literature and is therefore confusing but their differing pathophysiologies are well understood and documented. The term ranula is reserved for the sublingual glands. It can be classified as a true cyst when it is located in the oral cavity or a pseudocyst when plunging below the mylohyoid muscle into the cervical region.

ARPC may be the first manifestation of HIV infection. These cysts typically involve the parotid glands bilaterally, even when only unilateral swelling is clinically evident. Multiple cysts that vary in size between 0.5 and 5.0 cm may be seen on imaging, confined to the superficial lobes of the parotid glands. The pathophysiology of ARPC is controversial but their frequencies have decreased with the advent of highly active antiretroviral therapy (HAART).

Tumors of the salivary glands are generally rare accounting for less than 3% of all head and neck neoplasms. Eighty percent of all salivary gland tumors are encountered in the parotid glands, and this is followed by the submandibular, and then the sublingual glands. Fortunately, the larger the size of the salivary gland, the more likely the tumor occurring within it is benign. The most common tumor in adults is pleomorphic adenoma, accounting for 75% of all tumors affecting both the major and minor salivary glands. Warthin tumor (papillary cystadenoma lymphomatosum) is the second most common benign neoplasm, and can uniquely affect salivary glands bilaterally. Mucoepidermoid carcinoma is the most common malignant neoplasm to affect the salivary glands accounting for approximately 30% of all cases, while adenoid cystic carcinoma frequently affects the submandibular glands and has a strong propensity for perineural spread. Because most tumors of the salivary glands are either benign or low-grade malignancies, they tend to present as slow growing, relatively painless masses. With high-grade malignancies, facial nerve deficits and cervical lymphadenopathy are common. In children, the most common neoplasm is hemangioma of the parotid gland (Fig. 25.7).

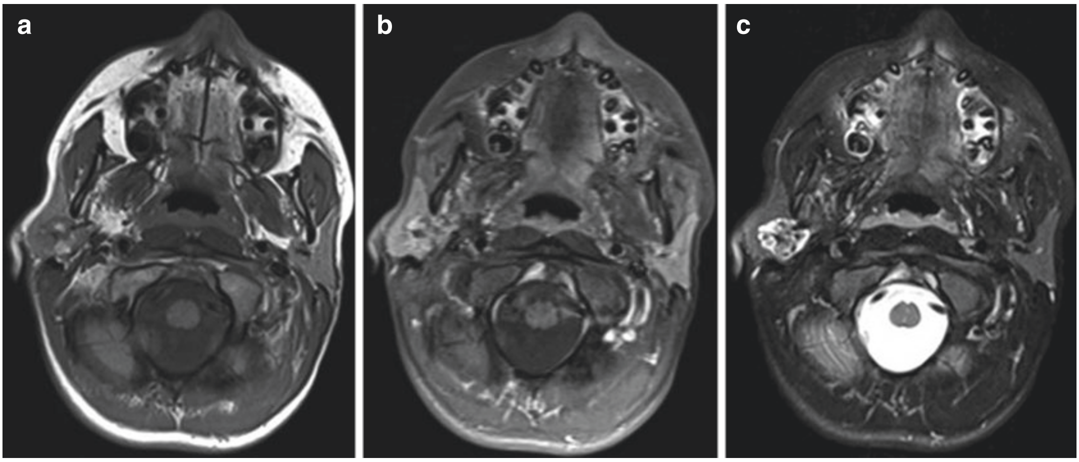

Fig. 25.7 T1-weighted (**a**), T1-weighted post-contrast (**b**), and T2-weighted (**c**) MR images of a 16-year-old male. The images demonstrate a well-defined mass in the superficial lobe of the right parotid gland with a high T2 signal and flow voids consistent with a hemangioma

25.3.3 Noninflammatory Conditions

Noninflammatory conditions of the salivary glands include sialadenosis, autoimmune conditions such as Sjögren's syndrome, and postradiation sialadenitis. These three conditions are of particular interest because they are often confused with primary inflammatory conditions of the salivary glands because their presenting signs and symptoms can be similar. Other conditions in this category are immunoglobulin G4 (IgG4)-related sialadenitis, pneumoparotid, and sarcoidosis. The conditions in this category result in secretory abnormities (xerostomia) and require further investigation in the form of imaging.

Xerostomia is the subjective feeling of dry mouth. An objective decrease in the quantity of saliva, however, is determined by measuring the amount of stimulated or unstimulated whole saliva collected per unit time. Normal levels of stimulated whole saliva range between 1 and 2 mL/min and normal unstimulated saliva levels range between 0.3 and 0.5 mL/min. If the amount of unstimulated saliva decreases to 0.1 mL/min or the amount of stimulate saliva decreases to less than 1.5 mL/15 min, the patient is said to have hyposalivation. Patients with hyposalivation complain of soreness, difficulty swallowing altered or loss of taste, and a burning sensation in the oral cavity. The oral soft tissues are often erythematous, the tongue fissured, and saliva difficult to illicit. These patients also suffer from extensive cervical caries and repeated infections of *Candida albicans*.

- *Sialadenosis*. Also known as sialosis, this is a condition caused by hypertrophy of salivary gland acini. The condition often presents as a chronic bilateral painless swelling of the glands. Although the parotid glands are most commonly affected, the involvement of other major salivary glands is also possible. A number of underlying diseases can cause sialosis including endocrine disorders such as diabetes mellitus and nutritionally related abnormalities such as chronic alcoholism, bulimia nervosa, and anorexia. Certain medications including nonsteroidal anti-inflammatory drugs (NSAID) and a number of antibiotics also can cause sialosis as a side effect.
- *Sjögren's syndrome*. This condition is considered to be the second most common autoimmune condition after rheumatoid arthritis. This disorder targets the exocrine glands, with a predilection for the salivary and lacrimal glands, resulting in dry mouth (xerostomia) and dry eyes (xerophthalmia). There is a remarkable female predilection (90–95%) to

this condition, with a peak incidence after the fifth decade of life. The primary form of Sjögren's syndrome affects only the salivary and lacrimal glands, and is also known as Sicca syndrome. A secondary form of Sjögren's syndrome presents with the triad of salivary gland involvement, lacrimal gland involvement, and another autoimmune condition such as rheumatoid arthritis, systemic lupus erythematosus (SLE), or progressive systemic sclerosis (scleroderma). Patients with Sjögren's syndrome are at a significantly greater risk of developing mucosa-associated lymphoid tissue (MALT) lymphoma, a subtype of non-Hodgkin's lymphoma in intraparotid and extra-parotid sites.

- *Postirradiation sialadenitis*. This is an inflammatory condition of the salivary glands following either external beam radiation (EBR) therapy to the head and neck or treatment with radioactive iodine 131 (^{131}I). In both cases, the parotid glands are more commonly and more severely affected because they are the most radiosensitive of the salivary glands. The disease mechanism involves an intense inflammatory reaction in the parenchyma of the gland that impinges on the ductal structures causing obstruction. This results in a build-up of saliva that manifests as a bilateral painful swelling. Gradually, the salivary glands undergo atrophy and fibrosis, and salivary production diminishes significantly a few months after treatment.
- *Sarcoidosis*. This is an inflammatory disorder of unknown etiology characterized by noncaseating granuloma formation. The granulomas can form in any organ but have a predilection for the lungs and the intra-thoracic lymph nodes. Involvement of the minor salivary glands is common in approximately 58% of cases. Ten to thirty percent of patients, however, suffer from parotid gland involvement which may be the initial presentation of the disease. These patients present with persistent painless swelling of both parotid glands. The triad of salivary gland sarcoidosis, uveitis, and facial nerve paralysis in known as Heerfordt's syndrome.
- *IgG4-related sialadenitis*. This is a recently recognized disease featuring periductal sclerosis, acinar atrophy, and lymphocyte infiltration of primarily the submandibular glands. Typically, both submandibular glands are persistently swollen and may or may not be painful. Both Milkulicz disease and Kuttner tumor are now considered manifestations of this disease.
- *Pneumoparotid*. Also known as a pneumocele is an uncommon condition in which air is forced into Wharton's duct in a retrograde manner, causing dilatation of the ductal structures, and an associated painless swelling. This condition is often seen in wind-instrument musicians and glass blowers as a result of constant increases to intraoral pressure associated with the practice of their art. Eliciting saliva from the glands will characteristically reveal aerated saliva at the duct orifice.

25.4 Imaging

Diagnostic imaging plays a pivotal role in the diagnosis of patients with salivary glands disorders. Imaging can provide vital information about the nature of the abnormality, its cause, the extent of glandular involvement, and the effect on the adjacent surrounding structures. Several imaging modalities have been utilized for salivary gland imaging (Yousem et al. 2000; Curtin 2007; Burke et al. 2011; Abdullah et al. 2013):

- *Projection radiography*. Occlusal and panoramic images can demonstrate calcified sialoliths, especially when there are signs or symptoms of mealtime swelling. The advantages of plain images are that they are readily available, relatively inexpensive and are accompanied by relatively low patient radiation doses.
- *High-Resolution Ultrasonography* (*HRUS*). This is primarily used for initial assessment of the parotid and submandibular glands and to guide biopsies and further imaging choices. Provided such entities are contained within the more superficial aspects of the major

salivary glands, cysts can be differentiated from tumors quite accurately using HRUS, and benign lesions can be differentiated from malignant ones. Recent technological advances have also made HRUS more specific at detecting conditions such as Sjögren's syndrome but its diagnostic accuracy for detecting sialoliths is still comparably low. The major advantage of HRUS is its relative safety because it does not utilize ionizing radiation.

- *Multidetector CT* (*MDCT*). MDCT is often used to image inflammatory conditions of the salivary glands because it specifically demonstrates characteristic changes such as enlargement, peripheral enhancement, soft tissue "streaking," thickening of subcutaneous tissues, and lymph node involvement. With regard to sialoliths, MDCT images can easily depict relatively large, calcified sialoliths but not smaller noncalcified ones. Strictures, however, are not easily depicted using MDCT. The sensitivity of MDCT for tumors of the salivary glands is almost perfect but its specificity is less optimal. The lack of specificity renders MDCT unreliable in being able to distinguish between benign and malignant neoplasia. Additionally, MDCT is limited in availability, and both costs and radiation doses can be high.
- *Magnetic Resonance Imaging* (*MRI*). MRI is the imaging modality of choice for soft tissue neoplasms of the salivary glands because of its superior contrast resolution. Changes in MRI signal are also helpful in differentiating edema from inflammatory infiltrate in cases of salivary gland inflammation. MRI is also the imaging method of choice for assessing intracranial and perineural spread of salivary gland neoplasms. Like HRUS, MRI does not utilize ionizing radiation, however, its disadvantages include low spatial resolution, long acquisition times and signal voids associated with calcified structures such as sialoliths. Like MDCT, cost and accessibility are further limitations of MRI.
- *Scintigraphy*. This is a functional examination of salivary gland physiology rather than the morphology. Scintigraphy of the salivary glands utilizes radiopharmaceutical agents such as technetium-99 m (^{99m}Tc) pertechnetate (TPT) because of its selective uptake by the salivary glands (MacDonald and Burrell 2009). Salivary gland disorders can be identified on the basis of uptake and clearance of TPT. For example, inflammation, ductal obstruction, and Sjögren's syndrome can all affect the uptake and excretion of TPT. In addition, Warthin tumor uniquely concentrates TPT. This functional examination yields highly sensitive results but suffers from low specificity and poor resolution.
- *Sialography*. This technique combines the benefits of morphologic imaging with function of the major salivary glands. This technique involves the introduction of an iodinated contrast agent into the gland ductal structures, then imaging is performed using plain imaging, CT, or fluoroscopy. The contrast material fills the ductal structures of the gland, attenuating the incident radiation, rendering them radiopaque. Filling of the glandular acini may also be visualized. The rate of clearance of the contrast material from the gland is then used to assess glandular function, with longer retention times signaling reduced gland function. Sialography may also be performed with MRI. With this modality, the need for an iodinated contrast material is eliminated because the patient's own saliva is used as a contrast agent, and heavily weighted T2 images provide image contrast.
- *Sialendoscopy*. This is a minimally invasive examination technique that allows the direct visualization of the major ducts of the parotid and submandibular glands. First performed in 1990, this examination has revolutionized not only the diagnosis but also the management of obstructive conditions of the salivary glands (Jadu and Jan 2014). Sialoscopes can be equipped with stone retrieval and stricture dilatation devices that have facilitated the management of these conditions with success rates of 96–98%. The only contraindication for sialendoscopy is acute inflammation of the gland of interest due to the associated pain.

25.5 CBCT Sialography

Sialography is a well-established technique for examining the parotid and submandibular glands, and has been performed since 1902 (Yousem et al. 2000; Burke et al. 2011; Abdullah et al. 2013). Over the years, sialography has been paired with plain imaging, MDCT, fluoroscopy, and MRI. Unfortunately, each of these imaging techniques has its own limitations, and these have affected the availability, success, and diagnostic accuracy of sialography.

Plain images suffer from anatomical structures that overlap glandular ductal anatomy. Consequently, the sensitivity of the examination in detecting subtle abnormalities can be reduced. Fluoroscopy also suffers from overlapping anatomical structures even though this imaging modality offers real-time imaging of the glands. MDCT and MRI sialography offer the advantage of three-dimensional (3D) images, circumventing the problem of overlapping anatomical structures, but their spatial resolution limits their abilities to detect small sialoliths, strictures, and subtle changes to the delicate ductal anatomy. Cost, accessibility, and lengthy imaging times are further limitations of MDCT and MRI sialography.

CBCT sialography has been reported by numerous authors as a highly sensitive and cost-effective technique for depicting changes in the delicate ductal anatomy because of its relatively high spatial resolution and relatively low radiation dose (compared with MDCT) (Drage and Brown 2009; Jadu et al. 2010; Jadu et al. 2011; Li et al. 2011 Jadu and Lam 2013; Abdel-Wahed et al. 2013).

25.5.1 Indications/Contraindications

The primary indication for CBCT sialography is obstructive conditions of the parotid and submandibular glands. Not only does CBCT sialography provide high sensitivity but has also demonstrated high specificity for identifying the cause, location, and number of obstructions. Other indications include suspected sialosis, postirradiation sialadenitis especially in the early stages of this condition, and Sjögren's syndrome. Occasionally, sialography is therapeutic, flushing ducts and dislodging small obstructions (Drage et al. 2000; Brown et al. 2002; Drage et al. 2002).

There are, however, several contraindications to sialography. In acute inflammation, pain can increase during injection of the contrast material. Moreover, the potential for introducing an infective organism deeper into the gland is also potentially problematic. Immediately anticipated thyroid function tests are also considered a contraindication because some of the iodine in the contrast material is uptaken by the thyroid glands, and this can interfere with the results of a thyroid function test.

Finally, an allergy to iodine, which for many years was regarded as a contraindication for sialography, is no longer considered a contraindication. Most allergic patients can safely undergo a sialography procedure provided they are premedicated with appropriately dosed and timed corticosteroid (Liccardi et al. 2008). Antihistamines may also be administered prophylactically for control of the allergic reaction.

25.5.2 Types of Contrast Agents

Advancements in the composition of iodinated contrast agents have made them safer and more tolerable for human use, but this does not negate the occurrence of adverse reactions. Most adverse reactions are, however, mild, and result in skin-surface urticaria or itchiness. Therefore, clinicians choosing to use radiologic contrast agents must be familiar with their indications, possible side effects, and management of adverse reactions.

Iodinated contrast agents used in sialography are based on a tri-iodinated benzene ring. The older agents were monomeric (a single benzene ring) and ionized in water; these were termed high osmolar contrast media (HOCM). Monomeric nonionic agents were then developed, and these dissolved in water with dissociation; these were termed low osmolar contrast media (LOCM). The most recent development in contrast technology is a dimer of two benzene rings. These dimer agents are nonionic and are known as iso-osmolar contrast media (IOCM). As contrast agent technology has advanced, and as they have approached serum osmolar levels, the toxicity of these agents has decreased. Another significant improvement in contrast agents has been increasing the ratio of iodine atoms to particles in solution, nearly doubling from 3.0 in LOCM to 6.0 in IOCM making more iodine available for uptake.

25.5.3 Technique

Sialography requires special armamentarium, adequate training and detailed knowledge of the anatomy of the major salivary glands and their ducts. The equipment needed includes a series of metal probes of increasing diameter for dilatation of the duct orifice, catheters of different diameters to accommodate variations in ductal diameter amongst patients, and an iodinated contrast agent. The procedure starts by locating the orifice of the main duct of the gland of interest. This is achieved by drying the area where the duct orifice is located, and examining it carefully for a dark spot that usually represents the duct opening. If the orifice remains elusive then the gland under examination can be gently massaged, and the area of the duct orifice can be closely observed in anticipation of the first drop of saliva to appear, indicating the exact location of the duct opening.

A series of probes of increasing diameter are then used to gently dilate the duct orifice so that an appropriately sized catheter can be fitted snugly a short distance beyond the duct orifice and into the distal part of the major duct (Fig. 25.8). A snug fit will ensure that the catheter will not dislodge during injection of the contrast material, and that contrast material will not leak out. Care must be taken that there are no air bubbles in the catheter or the syringe containing the contrast material. When these assurances have been confirmed, the contrast material is gradually and gently injected until the patient reports maximum

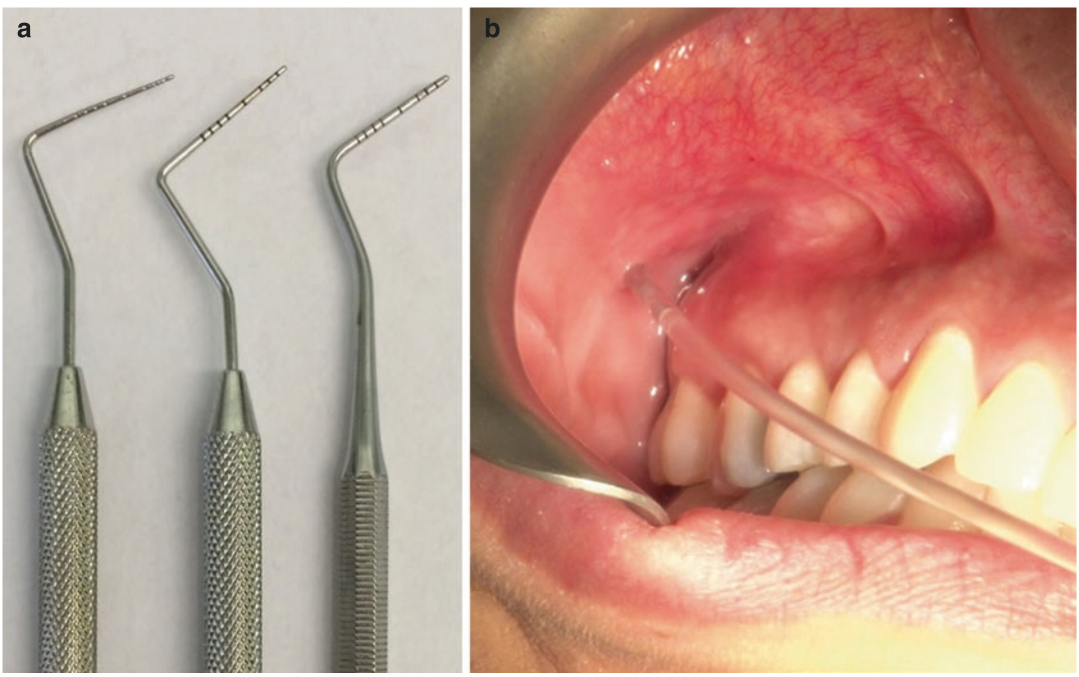

Fig. 25.8 A series of three metal probes of increasing diameter are used to locate and dilate the orifice of the primary duct of the gland (**a**). Choosing an appropriately sized catheter ensures self-retentiveness within the gland orifice and the distal portion of the duct during the procedure (**b**). In this clinical photograph, a catheter is self-retained in the right Stensen's duct

tolerance to a feeling of pressure in the examined gland. A scout image (which at our institution is a single plain image) may be performed at this point to ensure adequate fill of the gland with contrast material (Fig. 25.9).

Imaging is then performed by placing the patient in the CBCT machine with the occlusal plane parallel to the floor and the gland of interest centered in the imaging field of view (Fig. 25.10). The choice of imaging parameters (field of view size, peak kilovoltage, filament current) is based on a balance between diagnostic quality and radiation risk. After imaging, the catheter is removed and it is beneficial at this point to ask the patient if the procedure recreated his or her symptoms. Guiding questions of this sort will help determine whether the original symptoms are related to saliva accumulation, and recreated by the injection of contrast. Because sialography is also a functional examination, a second plain image is made a few minutes after catheter removal to assess the rate of contrast clearance (Fig. 25.9).

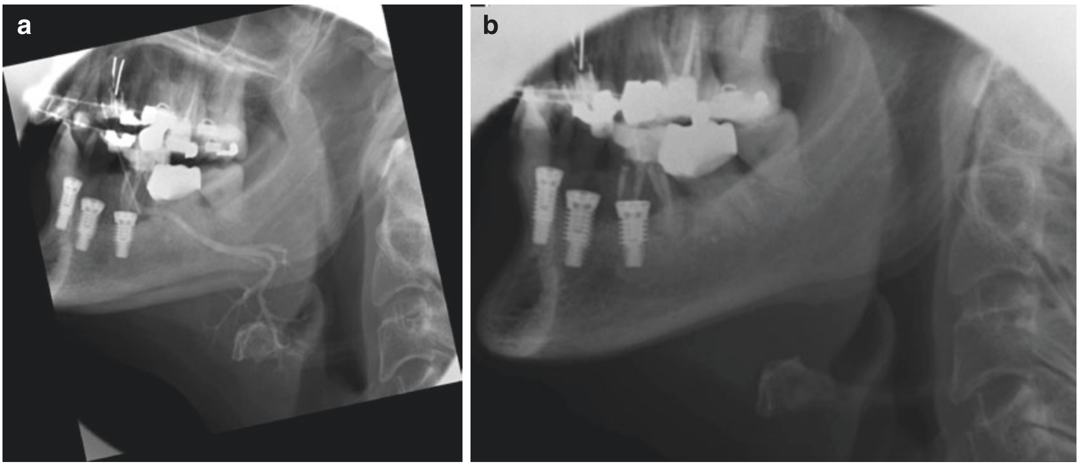

Fig. 25.9 Lateral skull plain radiographs acquired following contrast injection (**a**) to ensure adequate fill prior to CBCT imaging. A second image (**b**) is acquired 5 min after catheter removal to monitor the rate of contrast clearance and to indirectly assess gland function

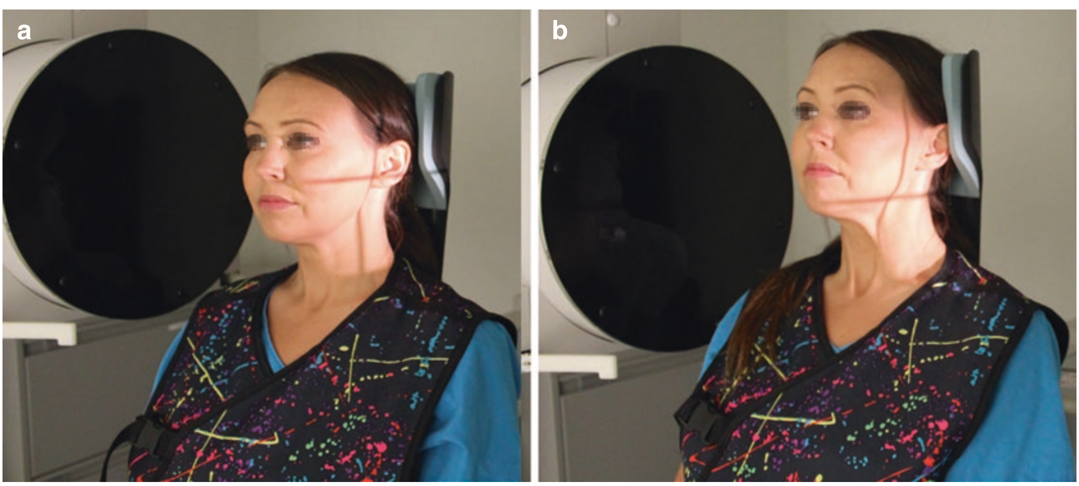

Fig. 25.10 Clinical photographs of a patient in the CBCT unit oriented so that the occlusal plane is parallel to the floor. In photograph (**a**), the localizer cross-hairs shows the field of view (FOV) centered on the parotid gland. In photograph (**b**) the localizer cross-hairs shows the FOV centered on the submandibular gland

25.5.4 Adverse Effects

Most patients who undergo sialography will experience mild discomfort and swelling of the gland during and shortly following the procedure due to injection of the contrast material. Fortunately, these symptoms are transient and subside 24–48 h after removal of the catheter.

Adverse effects of sialography are either related to the minimally invasive nature of the procedure or to the contrast material used. Sialography carries the risk of infection but this risk is minimal especially if the appropriate infection control procedures are followed. Usually, the continuous flow of saliva prevents the occurrence of retrograde infections into the salivary glands even after a minimally invasive procedure like sialography. Therefore, hydration is important, and all patients are instructed to remain well hydrated after the procedure. Antibiotics are prescribed for patients who develop infections.

Adverse reactions to iodinated contrast agents are divided into anaphylactoid and non-anaphylactoid reactions such as nephrotoxicity and neurotoxicity. In sialography, allergic reactions are rare (2–10% of patients), and these are typically mild if they occur at all because the contrast material is not injected intravenously. Mild adverse reactions can include nausea, vomiting, rash, hives, headaches, dizziness, and swelling of the eyes and face. These reactions are typically self-limiting, and require observation and reassurance. Patients with these signs and symptoms must not be dismissed but rather should be observed until their symptoms subside because these reactions can become more severe. If the patient develops signs and symptoms of hypotension, hypertension, laryngeal spasm, bronchospasm, or dyspnea, then medical attention is needed. Most reactions take place shortly after contrast administration; however, there are reactions that develop several hours after contrast injection. Delayed adverse reactions are more common in patients with a previous history of allergic reactions to contrast.

25.5.5 Radiation Dose Considerations

The risk of radiation-induced damage from low diagnostic doses of radiation remains a concern for both healthcare practitioners and their patients. The head and neck area is especially concerning because of the radiosensitive structures that reside within it such as the thyroid gland. As a result, radiologists are continually striving to develop and utilize dose-sparing protocols that do not compromise the diagnostic quality of the images.

One of the most important points that must be considered when acquiring diagnostic images is that many technical variables can substantially alter the radiation dose. For CBCT, depending on the vintage, make, and model of the system, these variables can include the X-ray tube peak kilovoltage (kVp), the filament current (mA) setting, the size and location of the imaging field of view (FOV), and the choice of voxel size (Ludlow et al. 2006). Several authors have consistently demonstrated that reducing kVp and mA significantly reduces the radiation dose to the patient (Ludlow et al. 2006; Jadu et al. 2010). However, care must be taken when altering these factors because as the amount of radiation decreases, the image signal-to-noise ratio increases reducing the quality of the images.

The size and location of the imaging FOV may be the most significant factor affecting patient radiation dose because this changes the percentage of each organ or tissue within in the primary radiation field. For example, a smaller FOV centered on the mandible will result in less radiation dose to the brain than a larger FOV extending from the skull vertex to the hyoid bone. Similarly, centering the FOV on the submandibular gland results in a greater radiation dose to thyroid tissue than centering the FOV on the parotid gland.

Some CBCT systems allow the operator a choice of voxel size. Voxel sizes can range from as small as 0.076 mm to as large as 0.40 mm, although most larger FOV systems generally offer voxel sizes in the 0.20–0.30 mm range. The larger the voxel size, the poorer the spatial resolution of the images, but this also reduces patient radiation dose. This is an important consideration when assessing the risk versus benefit balance of the diagnostic task. The choice of voxel size for CBCT sialography needs to be small enough to resolve the delicate nature of the ductal structures.

The effective dose for the collective series of plain images (one panoramic, two anterior–posterior skull and four lateral skull images) made during sialography compares favorably to low dose protocol (15 cm FOV, 80 kVp, 10 mA) CBCT sialography for the parotid (65 μSv vs. 60 μSv) and submandibular glands (156 μSv vs. 148 μSv) (Jadu and Lam 2013).

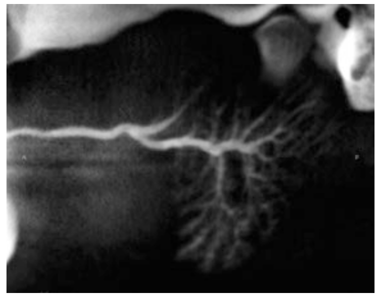

Fig. 25.11 Reformatted MIP image of a right parotid CBCT sialogram demonstrating the normal branching pattern of the ductal structures

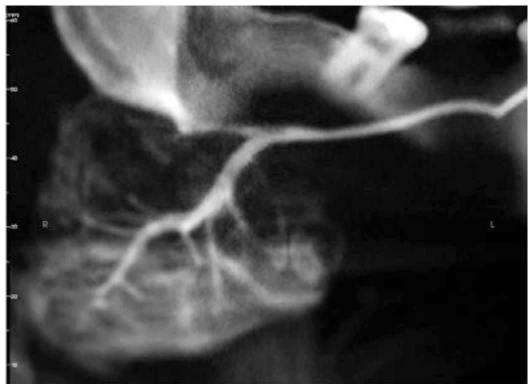

Fig. 25.12 Reformatted MIP image of a normal right submandibular CBCT sialogram demonstrating the normal branching pattern of the ductal structures. The image also demonstrates fill of the acini with contrast material causing parenchymal blush and outlining the body of the gland

25.6 CBCT Imaging Patterns

25.6.1 Normal Ductal Structure

A diagnostic sialogram should have contrast material completely fill the ductal structures of the gland being examined; the primary duct, its branches and its sub-branches resulting in an appearance similar to that of a branching tree. The ducts should appear regular and uniform in caliber, tapering gently as they branch toward their terminal acini (Figs. 25.11 and 25.12) (Nahlieli et al. 2001; Ngu et al. 2007; Jadu and Lam 2013). As the contrast agent fills the ductal structures, the acini become filled, and the tree is said to "bloom"; an appearance termed *parenchymal blush* (Fig. 25.12). This is a feature more commonly seen with submandibular gland sialography than parotid sialography.

25.6.2 Pathologic Patterns

With disease, changes to the morphology of the ductal structures and terminal acini can be readily appreciated. Inflammation of the gland ducts typically occurs between the gland parenchyma and the point of an obstruction. In some instances, the obstruction can be a sialolith, a stricture, or a mucous plug. The chronic and cyclic nature of saliva accumulating at this location (i.e., proximal to the obstruction) results in permanent dilatation of the duct. When several intermittent points of obstruction exist together with areas of dilatation, the ducts assume a "sausage-like" appearance (Fig. 25.13) (Nahlieli et al. 2001; Ngu et al. 2007; Jadu and Lam 2013). In the instance where abscesses may form within the gland in this process, contrast material pools within the abscess cavities and appears as globular collections of contrast material visible in the parenchymal part of the gland. These globular collections can vary in number, size, and distribution and are pathognomonic of sialadenitis (Fig. 25.14). In more advanced cases of inflam-

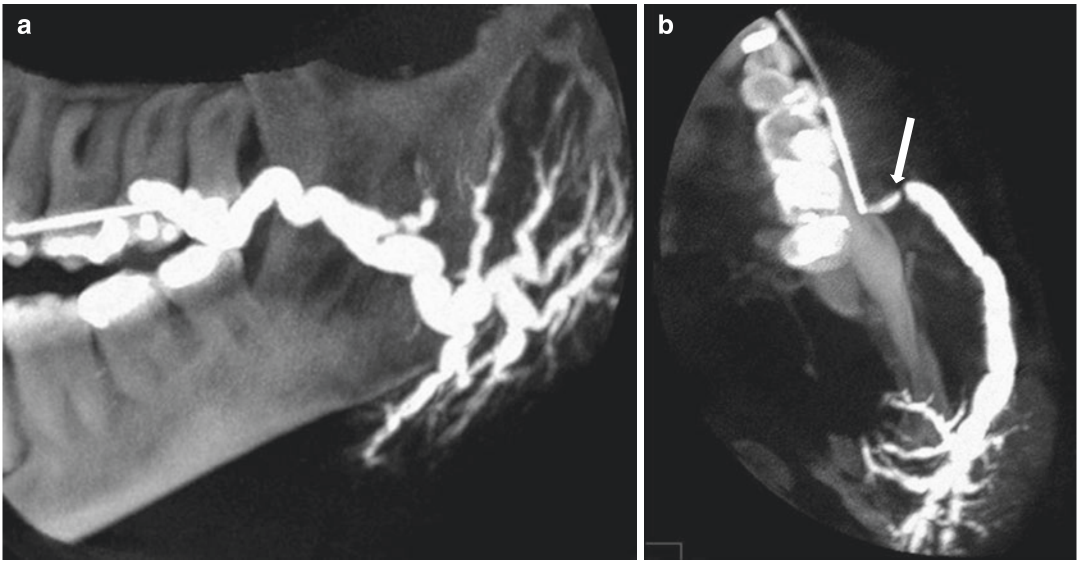

Fig. 25.13 Reformatted sagittal (**a**) and axial (**b**) MIP CBCT sialography images of a 51-year-old female patient complaining of intermittent swelling and soreness in the left parotid gland area. The images demonstrate the characteristic "sausage-like" appearance of sialodochitis. A noncalcified sialolith immediately proximal to the duct orifice is noted (*arrow*)

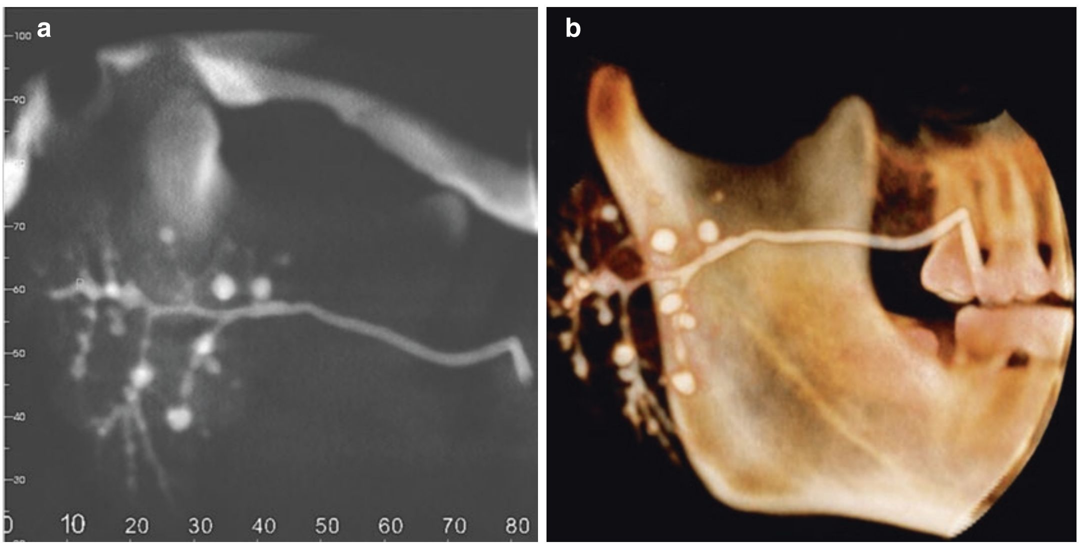

Fig. 25.14 Reformatted sagittal MIP (**a**) and 3D volume rendering (**b**) of CBCT sialography image of the right parotid gland. The images demonstrate multiple globular collections of contrast media in the parenchyma of the glands. These variable collections are consistent with sialadenitis

mation where acinar atrophy has taken place, the ducts leading to the atrophied acini become narrow to the degree where they become not visible on imaging. This appearance is termed "pruning of the tree" (Fig. 25.15).

In cases of autoimmune diseases, such as Sjögren's syndrome, the contrast material accumulates in the damaged acini of the glands. These collections of contrast are relatively equal in size and evenly distributed throughout the gland

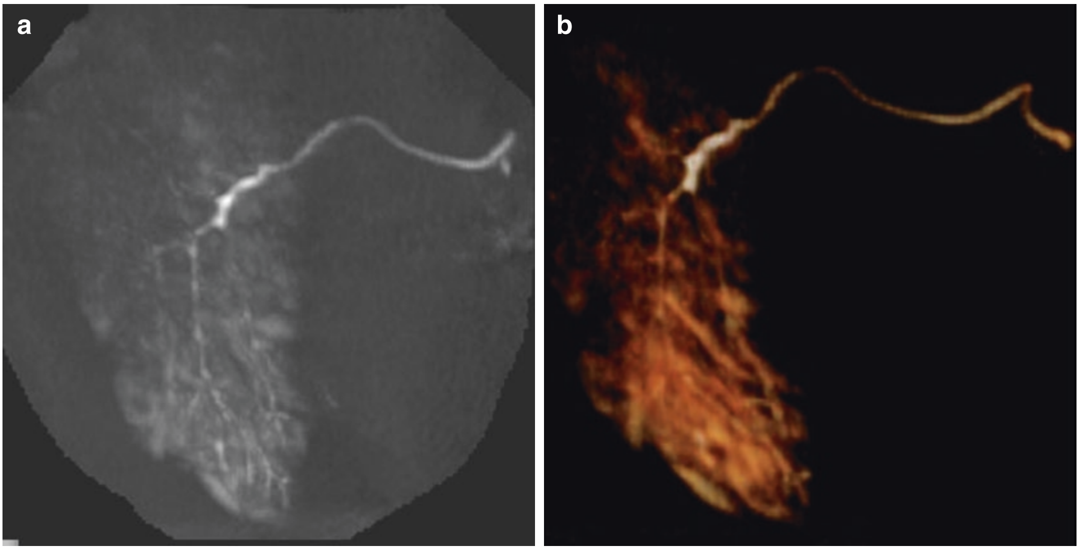

Fig. 25.15 Reformatted sagittal MIP CBCT sialography image (**a**) and 3D volume rendering (**b**) of the right parotid gland. The images demonstrate pruning of the secondary and tertiary ducts secondary to long-standing sialodochitis

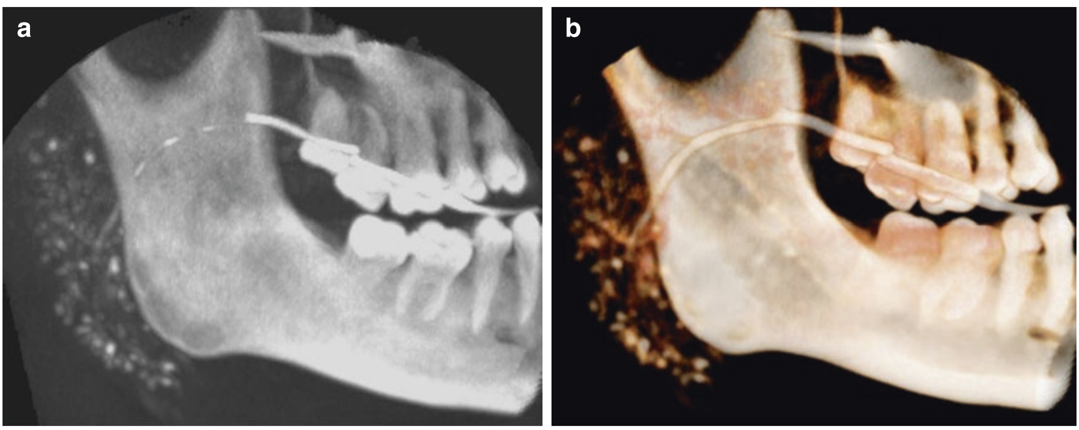

Fig. 25.16 Reformatted sagittal MIP CBCT sialography image (**a**) and 3D volume rendering image (**b**) of the right parotid gland. The images demonstrate equally sized and evenly distributed contrast collections characteristics of the "branchless fruit laden tree" appearance

parenchyma. In earlier stages of the disease, the collections are small and punctate. With time, these collections become larger and globular. In the later stages of the condition, the collections of contrast material become large and cavitated. The ducts of the gland also become progressively narrower with time until eventually they become indiscernible on imaging. This results in an appearance termed "branchless fruit laden tree" where the ducts are not visible and the contrast material is retained in the damaged acini (Fig. 25.16) (Nahlieli et al. 2001; Ngu et al. 2007; Jadu and Lam 2013). Retention of the contrast material in the damaged acini of Sjögren's patients remains for many years after the examination especially when oil based contrast agents are used (Fig. 25.17).

Sialadenosis reveals a normal ductal system that may be slightly splayed due to glandular enlargement and a normal parenchymal blush

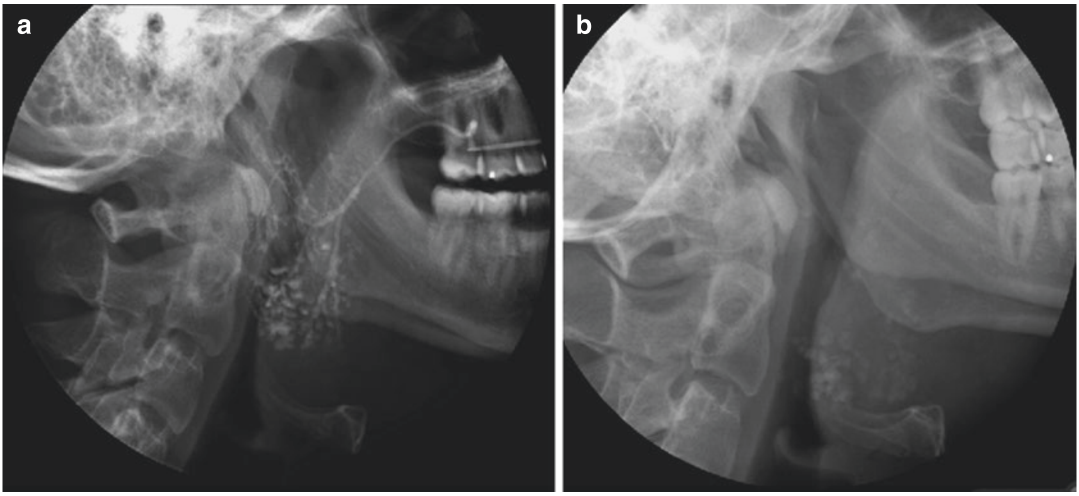

Fig. 25.17 Lateral skull radiographs after catheterization and contrast injection (**a**) and 5 min after catheter removal (**b**). Retention of the contrast material is noted especially in the inferior portion of the gland. This finding indirectly indicates reduced salivary function

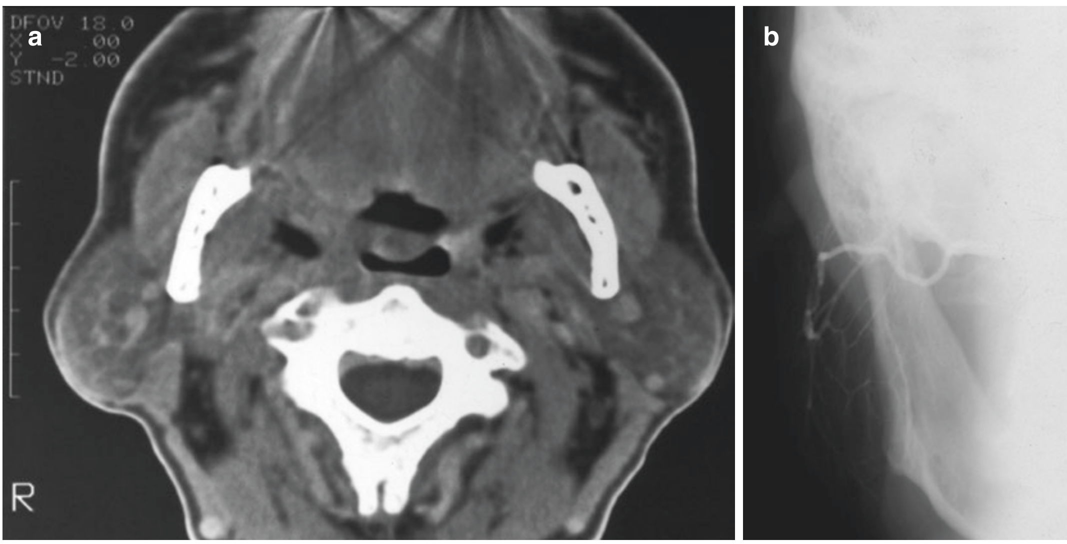

Fig. 25.18 Axial soft tissue window MDCT image (**a**) at the level of the parotid glands in a 59-year-old male. The image demonstrates bilateral enlargement of otherwise normal parotid glands. The anteroposterior skull image post-contrast injection of a right parotid gland sialogram (**b**). The caliber and branching pattern of the ducts are normal but they are splayed laterally (Courtesy of Dr. M.J. Pharoah)

(Fig. 25.18). These noted changes are significantly different than changes noted with sialodochitis, sialadenitis, and Sjögren's syndrome. Similarly, the sialographic findings of postirradiation salivary glands are specific in the early stages after irradiation and demonstrate fill voids where acini have atrophied. Such changes can occur with both external beam radiation as well as radioactive iodine therapy. Sialography is not helpful in the later stages of radiation injury because of gland fibrosis; the fibrotic glands cannot be infused with contrast material.

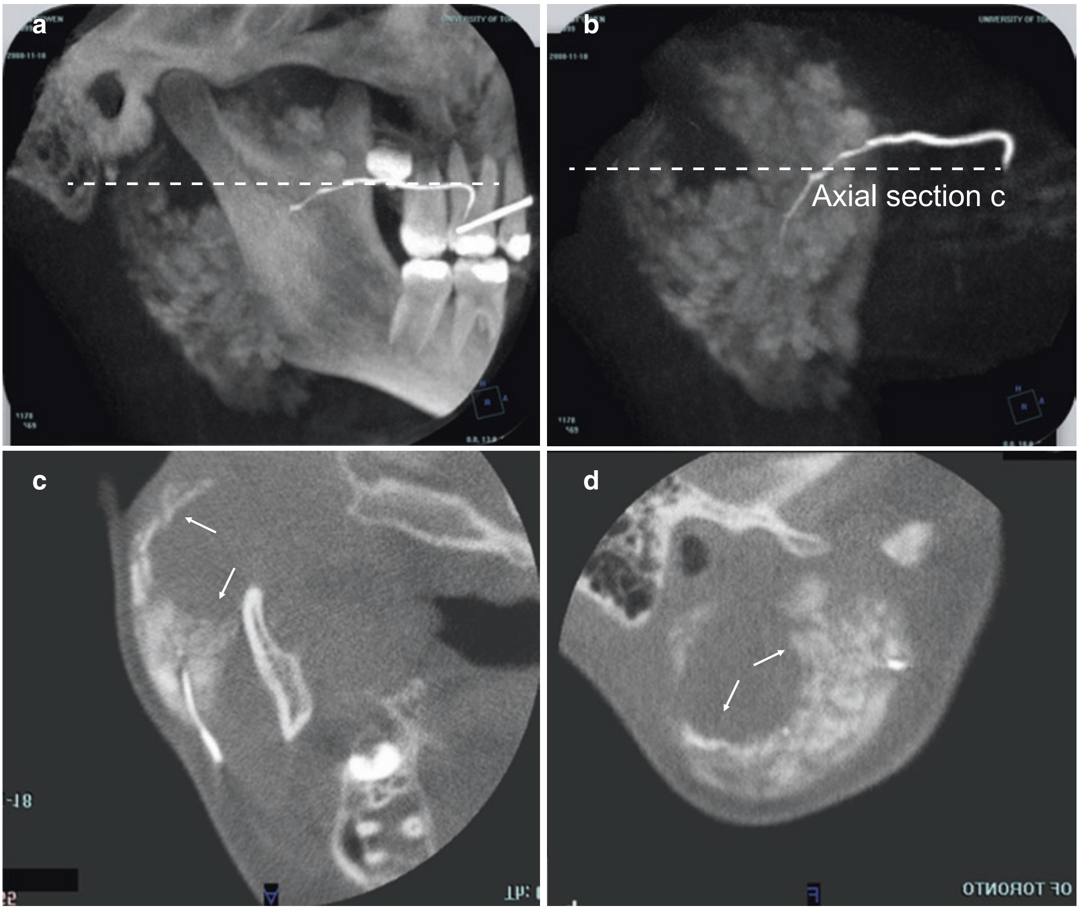

Fig. 25.19 Right sagittal thick (40 mm) (**a**) and moderate (20 mm) (**b**) thickness maximum intensity CBCT sialography projections of the right parotid gland with corresponding axial (**c**) and sagittal (**d**) thin projections demonstrating a "ball in hand" type of fill void in the superior part of the gland. This appearance is characteristic of a benign, space occupying lesion within the gland

Benign, space occupying lesions such as tumors involving the salivary glands, although generally rare, demonstrate a characteristic displacement or splaying of the ducts adjacent to the mass lesion (Nahlieli et al. 2001; Ngu et al. 2007; Jadu and Lam 2013; Shahidi and Hamedani 2014). This effect is seen in sialography images as a characteristic "ball in hand" appearance where the ducts wrap around the periphery of the tumor as normal parenchyma is displaced (the "hand"). As well, a filling void may be visible in the parenchyma (the "ball") as a result of the space occupying lesion (Fig. 25.19).

References

Abdel-Wahed N, Amer ME, Abo-Taleb NS (2013) Assessment of the role of cone beam computed sialography in diagnosing salivary gland lesions. Imaging Sci Dent 43:17–23

Abdullah A, Rivas FF, Srinivasan A (2013) Imaging of the salivary glands. Sem Roentgenol 48:65–74

Brown JE, Drage NA, Escudier MP, Wilson RF, McGurk M (2002) Minimally invasive radiologically guided intervention for the treatment of salivary calculi. Cardiovasc Intervent Radiol 25:352–355

Burke CJ, Thomas RH, Howlett D (2011) Imaging the major salivary glands. Brit J Oral Maxillofac Surg 49:261–269

Curtin HD (2007) Chapter 2. Imaging of the salivary glands. In: Myers EN, Ferris RL (eds) Salivary gland disorders. Springer, Berlin, pp 1–16. ISBN:978–3–540-47070-0

Drage NA, Brown JE (2009) Cone beam computed sialography of sialoliths. Dentomaxillofac Radiol 38:301–305

Drage NA, Brown JE, Escudier MP, McGurk M (2000) Interventional radiology in the removal of salivary calculi. Radiology 214:139–142

Drage NA, Brown JE, Escudier MP, Wilson RF, McGurk M (2002) Balloon dilatation of salivary duct strictures: report on 36 treated glands. Cardiovasc Intervent Radiol 25:356–359

Holsinger FC, Bui DT (2007) Chapter 1. Anatomy function and evaluation. In: Myers EN, Ferris RL (eds) Salivary gland disorders. Springer, Berlin, pp 1–16. ISBN:978–3–540-47070-0

Jadu FM, Jan AM (2014) A meta-analysis of the efficacy and safety of managing parotid and submandibular sialoliths using sialendoscopy assisted surgery. Saudi Med J 35:1188–1194

Jadu FM, Lam EWN (2013) A comparative study of the diagnostic capabilities of 2D plain radiograph and 3D cone beam CT sialography. Dentomaxillofac Radiol 42:20110319

Jadu FM, Lam EWN (2014) The mystery of meal time swellings revealed. Oral Health 104:33–35

Jadu FM, Yaffe MJ, Lam EWN (2010) A comparative study of the effective radiation doses from cone beam computed tomography and plain radiography for sialography. Dentomaxillofac Radiol 39:257–263

Jadu FM, Hill ML, Yaffe MJ, Lam EW (2011) Optimization of exposure parameters for cone beam computed tomography sialography. Dentomaxillofac Radiol 40:362–368

Li B, Long X, Cheng Y, Wang S (2011) Cone beam CT sialography of Stafne bone cavity. Dentomaxillofac Radiol 40:519–523

Liccardi G, Lobefalo G, Di Florio E, Di Iorio C, Occhiochiuso L, Romano L, Savoia G, Massa RM, D'Amato G, Cardarelli Hospital Radiocontrast Media, Anesthetic-Induced Anaphylaxis Prevention Working Group (2008) Strategies for the prevention of asthmatic, anaphylactic and anaphylactoid reactions during the administration of anesthetics and/or contrast media. J Invest Allerg Clin Immunol 18:1–11

Ludlow JB, Davies-Ludlow LE, Brooks SL, Howerton WB (2006) Dosimetry of 3 CBCT devices for oral and maxillofacial radiology: CB Mercuray, NewTom 3G and i-CAT. Dentomaxillofac Radiol 35:219–226

MacDonald A, Burrell S (2009) Infrequently performed studies in nuclear medicine: part 2. J Nuc Med Technol 37:1–13

Mandel L (2014) Salivary gland disorders. Medical Clin North Am 98:1407–1449

Nahlieli O, Shacham R, Yoffe B, Eliav E (2001) Diagnosis and treatment of strictures and kinks in salivary gland ducts. J Oral Maxillofac Surg 59:484–492

Ngu RK, Brown JE, Whaites EJ, Drage NA, Ng SY, Makdissi J (2007) Salivary duct strictures: nature and incidence in benign salivary obstruction. Dentomaxillofac Radiol 36:63–67

Shahidi S, Hamedani S (2014) The feasibility of cone beam computed tomographic sialography in the diagnosis of space-occupying lesions: report of 3 cases. Oral Surg Oral Med Oral Pathol Oral Radiol 117:e452–e457

Yousem DM, Kraut MA, Chalian AA (2000) Major salivary gland imaging. Radiology 216:19–29

Image-Guided Surgical Navigation

26

Georg Eggers

Contents

G. Eggers, M.D., D.M.D.
Department of Oral and Cranio-Maxillofacial Surgery, Weinheim Head Center, Dürrestrasse 2, Weinheim 69469, Germany
e-mail: Georg.Eggers@med.uni-heidelberg.de

26.1 Introduction

Registration is the transfer of geometrical knowledge from the outside, be it a general anatomical atlas, or individual image data, and the patient's anatomy into a common coordinate system. First attempts to register atlas-based knowledge into intraoperative physical space were performed 100 years ago (Al-Rodhan and Kelly 1992). With the availability of medical image data, patient individual information was registered to the patient (Spiegel and Wycis 1962). With the possibility of registering patient individual anatomical information into the operative environment, methods were developed to transfer also a preoperative surgical planning that was performed based on the image data. From this point on we can call the whole process "image-guided surgery." The tasks of a system for image-guided surgery based on patient individual image data are:

- To give a coordinate system to the physical body, hence creating a patient space.
- To give a coordinate system to the image data, hence creating an image space.
- To create a transform, that accurately assigns a point in image space to the corresponding anatomical point in patient space. This process is called *registration.*

Today, two technical concepts for the realization of these tasks are known: stereotactic frames

W.C. Scarfe, C. Angelopoulos (eds.), *Maxillofacial Cone Beam Computed Tomography*,
https://doi.org/10.1007/978-3-319-62061-9_26

and frameless stereotactic systems (navigation systems).

26.2 Frame-Based Stereotaxy

Chronologically, frame-based stereotactic systems were the first approach to image-guided surgery and the concept is still in use today. The development was initiated by Horsley and Clarke, who also coined the term "stereotaxy." One hundred years ago they attached a stereotactic frame to the head of animals. This frame had an own coordinate system and hence allowed to measure coordinates on the head (Horsley and Clarke 1908). It was used in experiments to measure positions of extracranial landmarks on animals. With these coordinates the prospective coordinates of intracranial anatomical structures of interest were calculated using previously obtained anatomical knowledge. Since this knowledge was about the general anatomy of the species investigated, we can call this atlas-based knowledge.

The next step in the development of stereotaxy was to use patient individual image data rather than general anatomical knowledge. Hence the development of stereotactic frames advanced. The new frames could be attached to the head of the patient and defined a coordinate system in patient space. Furthermore, these frames were designed in a way, that they would also define a coordinate system in the image data of the patient. Radiopaque rulers and landmarks were attached that allowed to measure coordinates in the image data (Kelly et al. 1988). The transformation from a set of coordinates in image data to the corresponding coordinates in the patient's head was defined by the construction of the stereotactic frame. The first stereotactic frames of this kind were designed in the 1940s for use with X-ray imaging. They required two strictly orthogonal X-ray films of the head to calculate positions in physical space. Later, with advances in imaging methods, stereotactic frames were developed, that were used with computer tomography (CT) or magnetic resonance imaging (MRI) (Leber et al. 1995; Lunsford et al. 1986). The stereotactic frame was equipped with localizers containing vertical and diagonal rods. In an axial CT-image slice of the head, these rods appeared as spots whose distribution allowed a definite allocation of the image slice in patient space (Pell et al. 1994).

This concept proved to be reliable and accurate, and is still in use in neurosurgery. However, there are a few disadvantages: The stereotactic frame must not be dislocated between imaging and surgery and hence has to remain attached to the patient's head. It is designed to approach intracranial positions via the calvarium. If other positions are to be reached, e.g., in the viscerocranium, the frame may impede rather than support the surgeon. Finally, moving the head on the operating table is cumbersome and restricted. Stereotactic frames were developed especially for the use in maxillofacial surgery (Fialkov et al. 1992). However, due to these restrictions, there was little use of this methodology in the area of maxillofacial surgery.

26.3 Frameless Stereotaxy

With the progress of computer technology and imaging, stereotactic concepts were developed, that intended to avoid these problems by making the stereotactic frame obsolete. Hence this new class of devices, the "Navigation Systems" are also referred to as "frameless stereotaxy" or "neuronavigation" systems (Watanabe et al. 1987). A prerequisite were volume image data without geometric distortion, like CT or MRI, in contrast to projection image data like conventional X-ray. In volume image data three-dimensional coordinates could be measured.

The primary idea was to replace the stereotactic frame by fiducial markers that could be freely distributed on the patient's body. In contrast to a stereotactic frame that has a given geometry, in frameless stereotaxy the geometric configuration of the markers is always different. Hence their position in image data as well as on the patient has to be measured using a targeting device. The markers are designed in a way that they also can be identified in image data, to perform the registration between image space and physical space.

The transform of these "registration points" that calculates their coordinates from image space to physical space and back, is the transform, that can be applied to any point in physical space to be transformed into image space and vice versa (Maurer and Fitzpatrick 1993). Using a computer system that holds all image data, the position of this pointing device in the hand of the surgeon is tracked. After successful registration, the position of this pointing device is displayed in real time in the image data on the computer screen. De-facto standard today is infrared (IR) tracking. A stereoscopic infrared camera system is set up towards the patient's head. One dynamic reference frame (DRF) each, reflecting or emitting IR-light, is attached rigidly to the patient and the surgeon's instrument (Wiles et al. 2004). The main shortcoming is the "line-of-sight problem": if the camera view to a DRF is obstructed, tracking is impossible. Hence the surgeon always has to consider his position relatively to patient, camera, and his tracked instrument.

Two technical concepts for patient-to-image registration are in use in image-guided surgery today: pair-point registration and surface-based registration (Maurer et al. 1997; Eggers et al. 2006).

26.3.1 Pair-Point Registration

If there are at least three markers on the body of the patient that are linearly independent (e.g., not lying on a line), they create a definite coordinate system of the patient's body. The same three points also create a definite coordinate system in the image data.

These two coordinate systems can be unambiguously registered, by correlating these two sets of points in image data (identifying them on the computer screen) and patient space (by touching them with the tracked pointing device). Using an optimization algorithm, the navigation system calculates a least-square solution for the transformation matrix that optimally transfers the set of points from one coordinate system into the other. Assuming that the image data is not distorted, the navigation system can now transfer any point in image physical space into the coordinates in image data and vice versa.

Various methods are in use to define the registration points. Markerless pair-point registration relies on the identification of characteristic points ("anatomical landmarks," e.g., tragus, spina nasalis) in image data as well as on the patient (Strasters et al. 1997). The main advantage is that no dedicated imaging with attached markers is necessary. However, since anatomical landmarks are not always that definite, or can be moved by swelling, the accuracy of this method is limited (Hassfeld et al. 1995).

The attachment of fiducial markers to the patient's body prior to imaging (Barnett et al. 1999) is a safer method. The markers have to be clearly identifiable in image data as well as on the patient's body and it is of importance for the accuracy of registration that their position remains unchanged between preoperative imaging and intraoperative registration.

Adhesive skin markers can be attached without being invasive. However, markers can be dislocated by swelling, or get lost accidentally. Hence, registration accuracies are less than optimum with this method (Ecke et al. 2003). Bone-mounted fiducial markers usually consist of a titanium screw that is drilled into the cranial bone under local anesthesia. They are the gold standard in registration accuracy, yet invasive. A combination of little invasiveness with high registration accuracy are devices that are connected to the dentition of the upper jaw, for example, individual templates with integrated titanium markers. This concept has proven its accuracy for the surgery of the maxilla, face, orbit, and anterior skull base. It is the standard registration method in image-guided dental implant placement using navigation systems. For more remote regions of surgery however, the oral template lacks registration accuracy (Eggers et al. 2005a).

26.3.2 Surface Registration

Instead of aligning a small number of well-defined point-pairs as in pair-point registration, in surface registration, two large sets of points (hundreds, thousands, or more) describing corresponding surfaces of patient body and image data are used. Surface information in image data is calculated using contouring algorithms that extract, e.g., the skin surface from image data. As in pair-point registration using anatomical landmarks, no additional imaging (e.g., CT-scan) with attached registration markers is required but retrospective image data can be used. Surface data of the patient can be extracted using the tracked pointer of the navigation system (Kall et al. 1996) or optical systems, e.g., laser surface scanners (Marmulla et al. 2003).

However, there is no correspondence of single points in the image space and the surface from patient space. Both surfaces as a whole are aligned optimally, e.g., using an "Iterative Closest Point algorithm" (ICP) so that the residual distance between the points of the two surfaces is at a minimum (Besl and McKay 1992). However, registration accuracy is lower than pair-point registration (Schlaier et al. 2002) and deteriorates in the occipital region (Raabe et al. 2002).

26.3.3 Planning and Transfer

After successful registration, a navigation system can be useful for the surgeon to give him intraoperative orientation. When he inserts the tracked pointing device into the patient's body, the real-time display of the pointer's position in image data helps him to avoid certain structures or to find others. But navigation systems can give additional assistance. Commercially available systems contain a more or less elaborate software, that allows to perform preoperative surgical planning. A planning can consist of the position of a foreign body to be retrieved, the labelling of a structure that has to be avoided to avoid morbidity, or the definition of a safe path to the surgical target. With this planning data, the navigation system can provide additional assistance intraoperatively: The distance and direction of the instruments tip towards the foreign body can be displayed, the surgeon can be warned when he approaches an anatomically important structure, or the system indicates the orientation of the instrument for alignment to the preoperatively planned path, e.g., the correct orientation of the drill for an implant burr hole. With these methods the navigation system not only locates the surgeon's tool but also assists in transferring a preoperative planning into the surgical situs.

While technical progress is still ongoing in the field, image-guided surgery has become a routine method beyond the field of neurosurgery. With the availability of frameless stereotaxy, image-guided surgery has become more and more available in the fields of oral and maxillofacial surgery, dental implant placement, and ENT surgery.

26.4 Specific CBCT Requirements for IGS

In order to define the requirements for CBCT image data to be used in image-guided surgery, we can use the experience from the use of conventional CT image data.

26.4.1 Field of View

First of all, the field of view of the image data must cover the region where surgery is performed, as well as the features that are used for image to patient registration, e.g., anatomical landmarks, fiducial markers, or the surface of the face. Hence devices with a small field of view—e.g., 1st generation Accuitomo (Morita, Kyoto, Japan) with a field of view of 30 mm × 40 mm (Lofthag-Hansen et al. 2007)—are less likely to be useful for CBCT-guided surgery. On the other hand, there are a growing number of CBCT devices that are constructed with a larger fields of view, up to 12 in. (Ludlow et al. 2006). Devices with a field of view of 9 in. are sufficient for image-guided oral surgery. For surgery in the viscerocranium, this field of view is also sufficient for most tasks, but the patient has to be positioned carefully to make sure that the region of interest and registration markers are within the imaging volume. A reduced field of view can also impede surface registration, when the surface of the face is clipped (Fig. 26.1). A possible approach to increase the image volume when using a CBCT device with limited field of view is stitching:

Fig. 26.1 Axial slice of a CBCT image data set. Due to the limited field of view, the nose is truncated

merging two adjacent subvolumes using the overlap between the two. There are reports that stitching may be accurate (Egbert et al. 2015), however there is no data on its use in image-guided surgery.

26.4.2 Geometric Accuracy

Secondly, geometric accuracy of the image data has to be good. The algorithms that are in use in current navigation systems for patient to image registration of CT or CBCT data are based on the concept of rigid registration: The assumption is that the geometry of the image data and of the patient's body are the same. Hence, after registration it can be assumed, that the coordinates of a voxel in image data reflect the respective coordinates in the patient's body. If this requirement of geometric accuracy is not met, registration and targeting errors will occur.

Recent studies on the geometric accuracy of CBCT systems indicate that the geometric accuracy of CBCT devices is generally good for the Newtom 9000 (Marmulla et al. 2005), the i-CAT (Pinsky et al. 2006), and the Galileos (Mischkowski et al. 2007a). LaScala et al. (2004) found that distances in the skull base are underestimated using the Newtom 9000, while the accuracy in the facial region was better. This would be in accordance with own measurements indicating that the geometric accuracy of the Newtom 9000 is better in the center of the volume and deteriorates to the margins (Eggers et al. 2008).

26.4.3 Resolution and Contrast

Image resolution and contrast are important for two reasons in image-guided surgery: On the one hand, they add to the diagnostic image quality and should ease the identification of structures that may be the target of an image-guided intervention or are to be avoided (Rouas et al. 2007). Furthermore, information is needed to create a geometric model of the site of surgery. With some deviations from the gold standard CT, this can be achieved with the image data from existing CBCT systems (Loubele et al. 2006). Furthermore, CBCT data can be used to assess bone quality for dental implant planning (Lee et al. 2007).

The identification of markers for fiducial marker registration is usually a simple task since these markers are designed to have a distinct high-contrast appearance in image data (Kozak et al. 2002). However, when registration is to be performed using surface matching, the surface of the face has to be reconstructed against the surrounding air. If the contrast is not sufficient, surface reconstruction gives invalid results that make surface registration impossible (Fig. 26.2).

The image resolution influences registration accuracy as well. This is due to the fact that the accuracy of targeting with a navigation system depends on the accuracy of the identification of registration markers in the image data (Fitzpatrick et al. 1998). A higher image resolution can result in higher navigation accuracy (Bartling et al. 2007). The reconstructed spatial resolution of current CBCT devices is comparable to conventional CT scanners.

26.4.4 Artifacts

Dental metal artifacts are a common finding in CT involving the oral cavity. The affected slices of the image data set can sometimes be utterly useless for diagnostic purposes when streak artifacts obscure

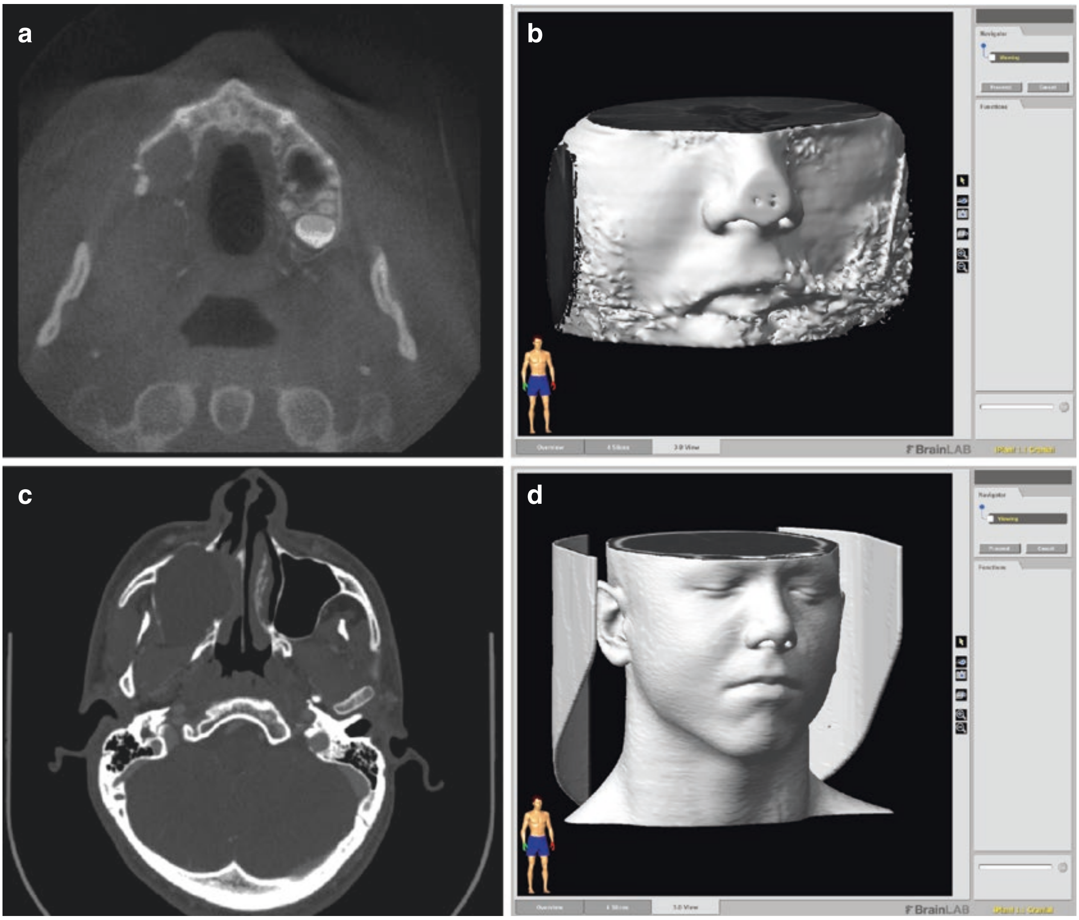

Fig. 26.2 Axial slice of a CBCT image data set (**a**) with surface reconstruction of facial soft tissues (**b**) and corresponding axial slice of a multidetector CT image data set (**b**) with surface reconstruction of facial soft tissues (**d**). Note that for the CBCT data set, the border between facial soft tissue and surrounding air is blurred by artifacts at the air-tissue border (**b**) with the clipping of the nose whereas the MDCT scan provides a large field of view, a high-contrast data set with a distinctive air–soft tissue margin

the anatomy. Furthermore, the detectability of fiducial registration markers can be reduced when they are mounted intraorally, e.g., using a maxillary template. In contrast to conventional CT, streak artifacts in CBCT are lower (Holberg et al. 2005). Beam hardening artifacts can be observed in CBCT image data (Draenert et al. 2007) but are not critical for fiducial marker identification.

Motion artifacts are a common phenomenon in medical imaging. They occur more likely when image acquisition takes a longer period of time (Lell et al. 1999). The problem for image-guided surgery is that motion artifacts are not always noticeable when there was motion of the patient during the scan (Wagner et al. 2003). This can have a detrimental effect on navigation accuracy (Petterson et al. 2012), because the geometry of the image data set no longer reflects the true geometry of the patient's body (Marmulla and Mühling 2006). Hence a short scanning time is desirable. The development in CBCT devices towards shorter examination times is beneficial in this context and the scanning times of current CBCT devices are comparable to spiral CT scanners (Scarfe et al. 2006). It has still to be evaluated, if motion artifacts are lower in CBCT devices where the patient is supine during image data acquisition, as compared to devices, where the patient is sitting.

26.5 IGS for Dental Implants

The main use of CBCT imaging in image-guided surgery is the image-guided planning (Sato et al. 2004; Hatcher et al. 2003) and image-guided placement (Heurich et al. 2002) of dental implants. Dental implant placement is a surgical task that contains all elements of image-guided surgery: There is a highly individual anatomy that has to be considered when placing the implants. This refers to the bone available for implant placement and also to the location of structures that are at risk during surgery, e.g., the mandibular nerve. Hence diligent planning is necessary. CT is superior to panoramic radiography in implant planning and assessment of risk-structures (Reddy et al. 1994; Lindh et al. 1995; Bou Serhal et al. 2001; Bou Serhal et al. 2002; Eufinger et al. 1997) and can help to improve implant size planning (Schropp et al. 2001) at the cost of higher radiation dose (Hassfeld et al. 1998).

However, with an optimum planning of implant positions in image data there is still the need for an accurate transfer of this planning. Various techniques have been described to transfer an implant planning into the patient's mouth (Fortin et al. 2002; Kopp et al. 2003; Tardieu et al. 2003; Brief et al. 2005).

Over the years two concepts for image-guided dental implant placement have been developed. They originally based on CT image data, and are in successful clinical use today: on the one hand there are template-based systems. On the other hand, there are dedicated navigation systems that implement the concept of frameless stereotaxy in image-guided implantology (Mischkowski et al. 2006b). Today, both concepts of image-guided implantology are in use based on CBCT image data as well (Heurich et al. 2002; Hümmeke et al. 2004).

26.5.1 Template-Based Image-Guided Implantology

Today various systems by different manufacturers exist that base on the concept of template-based IGI and the number of vendors is growing. All systems have in common that the dental implant planning is performed virtually in a computerized planning system on a computer screen, based on patient individual volume image data.

Based on the numerical planning data, a patient individual drilling template (the surgical template) is created. This template contains tubular holes that indicate the direction of the pilot burr holes for the planned implants. The template is inserted onto the mandible, or maxilla, respectively, and all the surgeon has to do is to insert the pilot drill into the guidance holes and to drill the pilot burr hole. The subsequent dilation steps and the actual placement of the implant can be performed free-handedly using the guidance from the existing pilot burr hole. Alternatively, a set of templates with guidance holes of increasing diameters is provided to accommodate the burrs with increasing diameter in the course of the implantation. The various systems differ in the technology that is applied to create the surgical template from the planning data.

On the one hand there are systems, where a resin-template is created from an impression of the jaw (e.g., Med3D, Heidelberg, Germany). The template is equipped with a registration marker and inserted into the patient's mouth for CT or CBCT imaging (Fig. 26.3). The image data

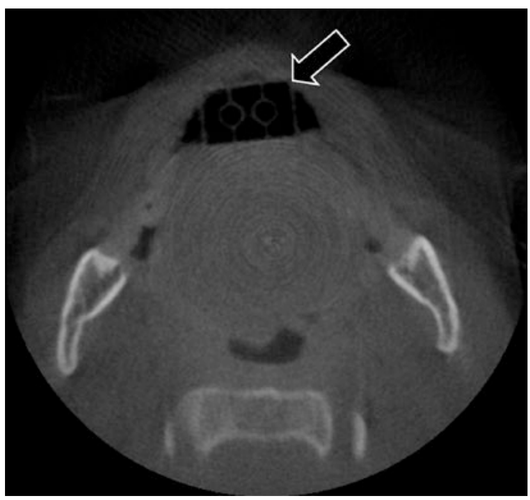

Fig. 26.3 Axial slice of a CBCT image data set showing a registration marker (LEGO®-Brick—arrow) that is embedded in the radiographic template

is imported into a planning software (Fig. 26.4). The registration markers are located in the image data and the implant positions are defined in the software planning system. The planning data (implant positions and registration marker positions) together with the template are sent to the dental technician. The template is then equipped with the metal sleeves using the planning data: Thus the imaging template is transformed into a surgical template (Fig. 26.5). The template is returned to the surgeon for implantation.

In this concept the drilling template has all characteristics of an individual stereotactic frame: The template with registration marker is worn during imaging and gives a coordinate sys-

Fig. 26.5 The radiographic template is transformed into the surgical template by placement of the burr sleeves according to the planning data

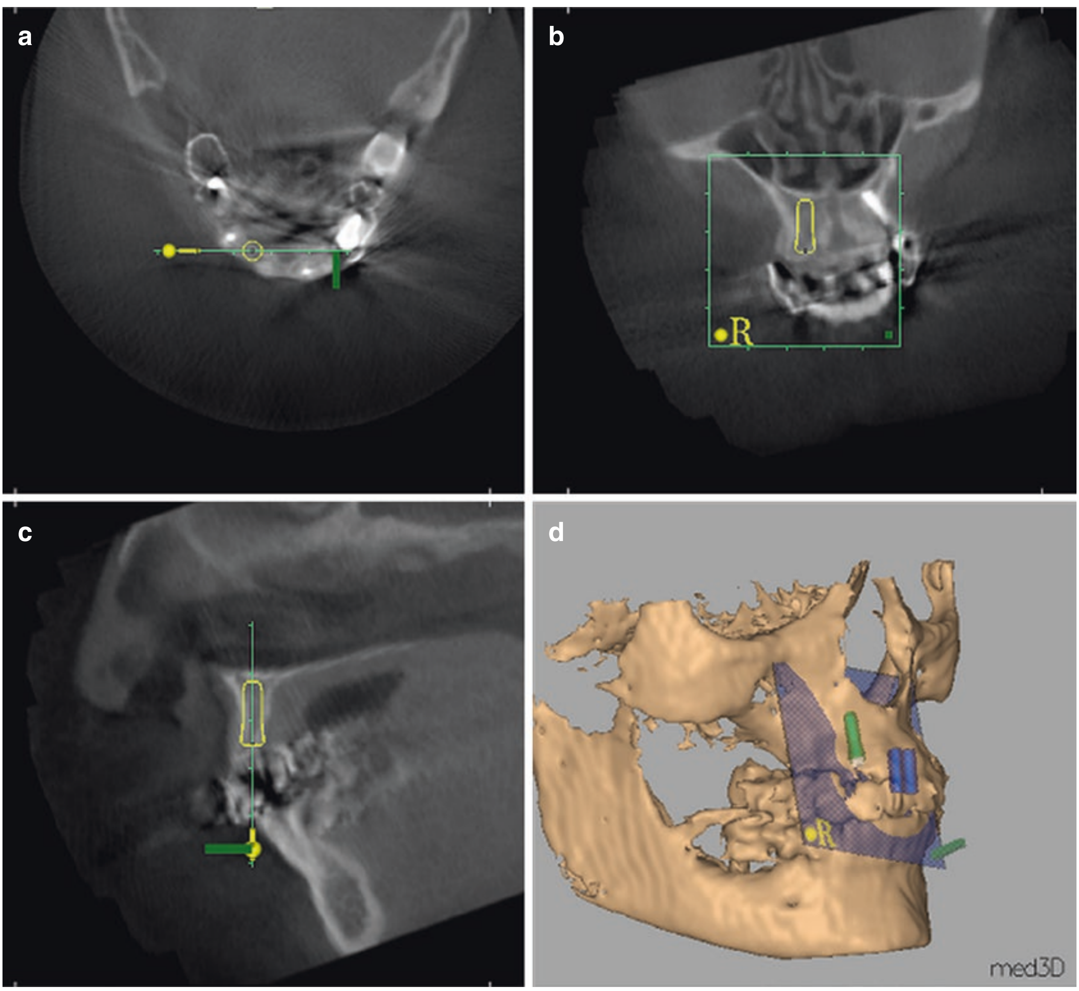

Fig. 26.4 Virtual dental implant positioning in the planning software on reformatted CBCT image data and a 3D reconstruction of the bone

tem to the image data. The same template, after being equipped with the drill guides and inserted into the mouth again, establishes the patient's coordinate system.

Alternately systems are available that create a surgical template directly from image data using rapid prototyping techniques (SurgiGuide, Materialise, Leuven, Belgium): The CT or CBCT scan is performed before any template exists. The image data is then imported into a planning software and implant positions are planned. Then it has to be decided whether the template to be produced shall sit on the mucosa, a remaining dentition, or the bone of the mandible. The image data and the planning data are then sent to the manufacturer of the templates. Using a computerized rapid prototyping process (stereolithography), a template is created from the image data fitting to the desired oral surface (tooth/mucosa/bone). Simultaneously, holes are provided in the template that will later guide the surgeon (Tardieu et al. 2007). The template is then returned to the surgeon for implantation. It is obvious that the correct identification of the respective surface in the image data in the segmentation process is of paramount importance for the correct fit of the template intraorally, and hence for the accuracy of the guidance provided by the template (Stumpel 2012).

26.5.2 Navigation Systems for Image-Guided Implantology

For the surgical task of dental implant placement, systems have been developed, that contain all components of a standard navigation system.

Image-guided surgical navigation for implant surgery was introduced, demonstrated, and validated by a group in Vienna (Wanschitz et al. 2002). Soon thereafter, two other systems where commercially introduced. The Robodent system was one of the first developed by T. Lueth and J. Bier at the Charité, Humboldt-Universität Berlin (Vector Vision 2, BrainLAB, Munich, Germany) (Mischkowski et al. 2006a, b). The second is known as IGI (Image Navigation Ltd., New York, NY, USA formerly DenX Advanced Dental Systems, Moshav Ora, Israel) (Casap et al. 2004).

Since then multiple navigation systems have been developed and/or validated (Table 26.1) (Fig. 26.6). The systems differ in marker technology, configuration of the dynamic reference frames, registration procedure, and user interface. However, they all follow the same basic concept.

These systems typically consist of a virtual 3D-based planning transferred to the operation theatre using a reference frame and optical tracking system. On an impression of maxilla or mandible, a resin template is created and equipped with registration-markers, provided by the manufacturer of the respective system (Fig. 26.7). The patient is scanned with this dedicated fiduciary splint allowing a 3D matching of the prepoperative virtual treatment plan and the actual localization of the jaw bone during surgery. CT or CBCT

Table 26.1 Representative commercially available systems for image-guided implantology

System	Manufacturer
Image-guided Implantology (IGI®)	Image Navigation Ltd., New York, NY, USA
RoboDent®	Vector Vision 2, BrainLAB, Munich, Germany[a]
VISIT®	Vienna General Hospital, University of Vienna, Vienna, Austria[b]
SMN® system	Zeiss, Oberkochen, Germany[c]
Vector vision® compact	VVC, BrainLAB, Heimstetten, Munich, Germany[d]
Stealth Station Treon navigation system	Medtronic, Minnesota, USA[e]
X-Guide	X-Nav Technologies, Lansdale, PA, USA
Inliant Clinical™ Dental Navigation System	Navigate Surgical Technologies, Vancouver, BC, Canada
Mona dent (Med3D)	Mona_X, Dortmund, Germany

[a]Meyer et al. 2003
[b]Wanschitz et al. 2002
[c]Gaggl et al. 2001
[d]Siessegger et al. 2001
[e]Widmann et al. 2005

Fig. 26.6 Example of a system for navigated dental implant placement (RoboDent GmbH, Garching, Germany). The infrared camera (*arrow*) tracks the positions of the drill and the patient

Fig. 26.7 Axial slice of a CBCT image data set showing fiducial markers (*bright dots*) embedded in the radiographic template for image patient registration

image data is acquired and imported into the planning software. Virtual implant placement is performed and the registration marker positions are determined.

For surgery, the template is equipped with a DRF for the infrared tracking camera. The handpiece with the drill is equipped with a DRF as well. The infrared-camera is adjusted to the mouth of the patient and pair-point registration is performed. Now, the infrared camera tracks the position of the patient and the handpiece with the drill for the pilot burr hole (Fig. 26.8). On a computer screen, the surgeon is informed how to adjust the position of the handpiece in order to create a pilot burr hole in accordance with the planning. Overall, this setup allows for real-time feedback and continuously updating of the drill and/or actual implant locations in relation to the jaw bone and the virtual placed implants, with an accuracy in the same range or slightly above the surgical template technique (1 up to 3 mm) (Wanschitz et al. 2002).

26.5.2.1 Accuracy

High accuracy of the implant position is necessary for an optimum in function and aesthetics. Current expertise about the accuracy of image-guided dental implant systems is mainly derived from studies based on CT image data. In phan-

Fig. 26.8 Implant placement using the Robodent system: The surgeon holds the drill with the attached tracking body. Another tracking body is attached to the oral template in the patient's mouth. Using a display, the system guides the surgeon to the planned implant positions

tom studies the positions of image-guided pilot bore holes or dental implants were measured using 3D digitizer arms (Brief et al. 2005) or CT scans of the phantoms (Wanschitz et al. 2002). In patient studies, the gold standard for the assessment of the accuracy is postoperative CT scan of the patient after image-guided dental implant placement (Di Giacomo et al. 2005). Phantom studies for navigation-based systems found average spatial errors between 0.35 mm and 0.97 mm (Casap et al. 2004; Hoffmann et al. 2005). The average angular error in the latter study was 1.35°. These values are better than the accuracy of non-guided implant placement (Hoffmann et al. 2005) with average deviations of 1.35 mm (entry point) to 1.89 mm (apex point) (Brief et al. 2005). Studies for stereolithographic template-based systems found average spatial errors between 0.9 mm in a phantom study (Sarment et al. 2003) and up to 2.99 mm in a patient study (Di Giacomo et al. 2005). Both studies found that the accuracy of the implant positions was higher at the implant shoulder than at the implant apex. In a phantom study, Mischkowski et al. (2006a) achieved dental implant placement with an accuracy better than 1 mm and did not find apparent differences in the accuracy of either concept.

Accuracy studies based on Newtom 9000 data found a translational error of less than 0.2 mm and an angular error of less than 1.1° for the recovery of target sleeves in a phantom (Fortin et al. 2002). However, this was only an indication of the accuracy of burr sleeve positions in the template. In a phantom study using stereolithographic drill guides created on the basis of the 3D Accuitomo FPD (J. Morita, Kyoto, Japan), linear errors of 1.1 mm (entry) to 2.0 mm (apex) were measured, with an average angular error of 2° (Van Assche et al. 2007). In a phantom study, stereolithographic drill guides that were created based on CBCT image data allowed significantly higher accuracy of burr hole placement than conventional drill guides (Sukovic 2003).

The results of the studies on accuracy show that the in-vivo accuracy is lower than the results of the phantom studies. This can be related to difficulties with the fixation of the template, movement by surgeon or patient, and the line-of-sight problem when navigation systems are used (Hümmeke et al. 2004). Hence the temporary fixation of the template during surgery using screws was suggested (Holst et al. 2007).

26.5.2.2 Workflow

Since the literature so far does not indicate a significant difference in accuracy of either methodology, workflow considerations become important (Mischkowski et al. 2006a).

One advantage of navigation-based systems is that there is no need for a dental technician to transform the imaging template into a surgical template. Furthermore, the flexibility is higher: if a planning turns out to be inappropriate intraoperatively, there is the possibility to modify the planned implant positions in the planning software and execute the new planning immediately (Hümmeke et al. 2004). Template-based systems would require action by the dental technician in such a situation.

The disadvantage is, however, that there is a considerable financial investment for the technical equipment. Furthermore, the intraoperative situation requires from the surgeon to handle technology: tracking bodies have to be attached to patient and handpiece. A registration procedure has to be performed after insertion of the template. Finally, the transfer of the information from the navigation system into the correct position of the drill has to be performed free-handedly and is not supported by a sleeve in the template. At the same time, the line of sight of the tracking camera must not be interrupted.

In contrast, the handling of template-based systems in the intraoperative situation is particularly simple and straightforward (Mischkowski et al. 2006a). The template is attached to the dentition and the dental surgeon is guided intuitively by the drilling guide that also gives some mechanical support. Since the registration of planning data and the patient's body is in effect done by the dental technician when creating the template, the surgeon is relieved from this task. However, he has to check the accuracy of the technicians work prior to implant placement.

26.5.2.3 Conclusion

The imaging properties of CBCT are appropriate for dental implant planning. The importance of this modality in image-guided dental implantology is rising continuously (Arnheiter et al. 2006). Many manufacturers of the guidance systems defined standard protocols for CBCT imaging and endorse the use of CBCT images for their planning systems. With the lower radiation dose and cost, CBCT is a good replacement for conventional CT.

26.6 Image-Guided Maxillofacial Surgery

The use of navigation systems in maxillofacial surgery has been described for numerous applications. Today, CT is the most important imaging modality for image-guided maxillofacial surgery (Mischkowski et al. 2007b). The clinical applications include the therapy of space occupying lesions (Hoffmann et al. 2004), Reconstructive surgery (Gellrich et al. 2002; Hohlweg-Majert et al. 2005), Orthognathic surgery (Mischkowski et al. 2006b), traumatology (Westendorff et al. 2006; Eggers et al. 2009a), and foreign body removal (Eggers et al. 2005b). The most widespread registration methods are pair-point registration based on anatomical markers, fiducial marker screws, and maxillary templates. Surface registration methods are applied less frequently.

With the close relation of CBCT imaging to conventional CT one could expect similar indications and methods to be used based on CBCT image data. However, in the current literature the scope of clinical applications and methods of CBCT-based image-guided surgery is limited. This can be attributed to the fact that CBCT imaging is comparably young and the availability of imaging devices is sparse in comparison to the ubiquitous CT scanners. Furthermore, due to the particularities of CBCT image data, clinical as well as technical restrictions apply that limit the use in image-guided surgery.

Clinical indications are limited by image contrast issues. CT image data has a better soft tissue contrast, and it can be further enhanced by contrast agents or by matching with MR image data (Hoffmann et al. 2002). Furthermore, the field of view of some CBCT device is limited and could prove to be insufficient for a clinical case. While there may be differences in geometric accuracy between CBCT and CT, this does not affect the effective registration—and hence navigation—accuracy of CBCT-based navigation (Eggers et al. 2009b).

Technical problems with CBCT in image-guided surgery occur in the step of patient to image registration. Sufficient dentition provided, maxillary splints with fiducial markers work without problems (Figs. 26.9, 26.10, 26.11, 26.12, and 26.13). However, there are some difficulties with skull mounted fiducial markers for pair-point registration. Firstly, the number of fiducial markers available for registration can be reduced: firstly due to the reduced field of view. Secondly in systems with automated detection of the fiducials in image data, the detection rate is lower due to the lower image quality (Mischkowski et al. 2007b). The reduced field of view can also be a problem in registration using head sets or head gears that easily reach beyond the field of view (Mischkowski et al. 2007b). Finally, surface registration methods do not work well. This can be due to restrictions in field of view and air–soft tissue contrast.

However, applications for CBCT-based image-guided surgery include the removal of foreign bodies (Pohlenz et al. 2007), orbital recon-

Fig. 26.9 Maxillary template for image-guided maxillofacial surgery. The template is made of a light curing resin. Titanium screws are used as fiducial markers

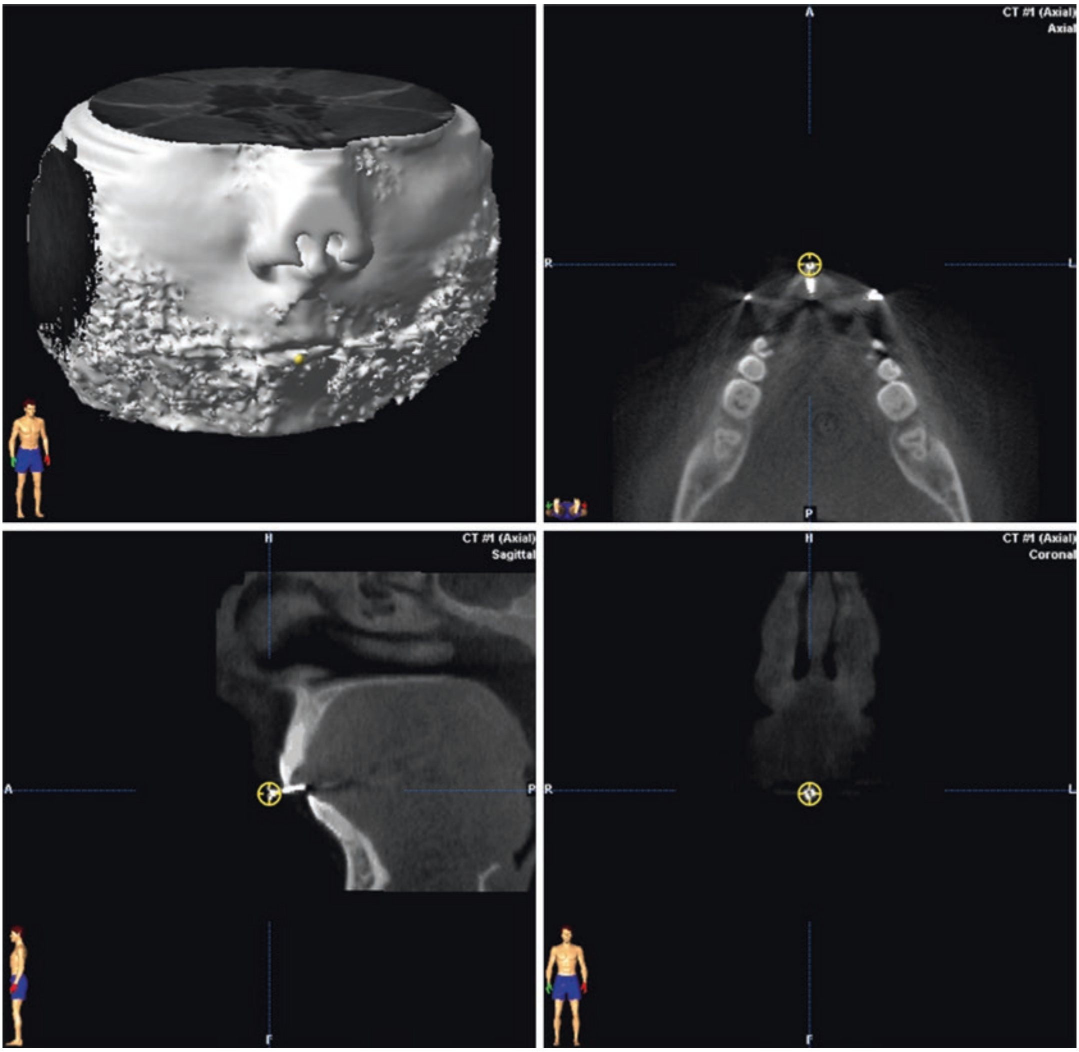

Fig. 26.10 Screen capture of navigation system CBCT image data set of a patient with the maxillary template. The positions of the fiducial marker screws are identified for registration

struction (Zizelmann et al. 2007), and surgery of osseous lesions (Mischkowski et al. 2007b).

26.6.1 Intraoperative Imaging

Another interesting application of CBCT is intraoperative image data acquisition. A major problem in image-guided surgery is the fact that the moment of imaging is not the moment of surgery. Changes that occur in between are not reflected by image data. This could, e.g., be the swelling of the patient or the change of a position of a foreign body. Furthermore, during the course of the surgical procedure, the surgical situs is altered and hence the difference between surgical situs and image data grows (Heiland et al. 2004a).

The solution for this problem is the update of the navigation system with intraoperatively acquired image data. The first application of intraoperative volume data acquisition was magnetic resonance imaging (MRI) in neurosurgery (Wirtz et al. 1997: Black et al. 1997). Later, intraoperative CT was introduced in maxillofacial surgery (Hölzle et al. 2001;

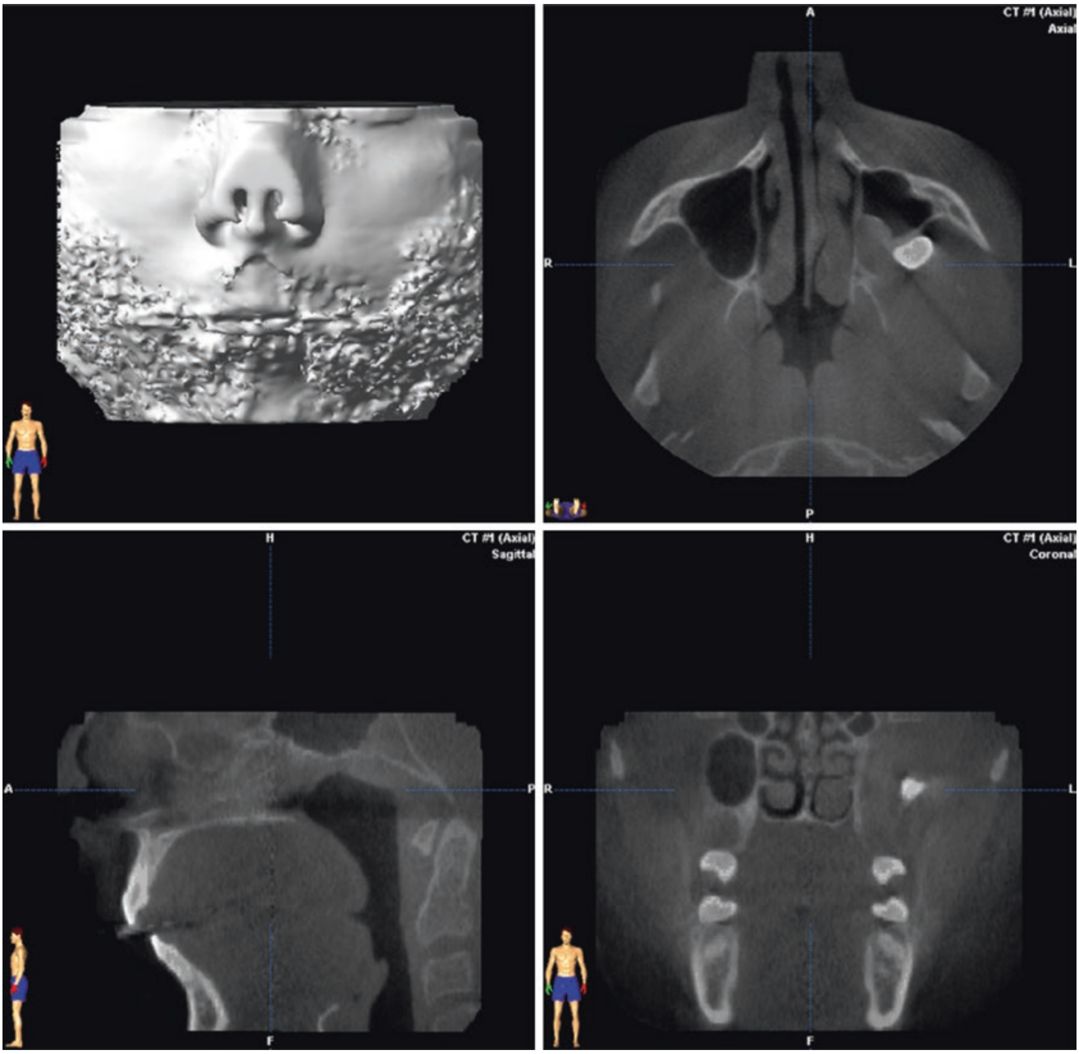

Fig. 26.11 Surgical planning on the CBCT image data set: Identification of the position of a dislocated third molar in the image data

Fig. 26.12 At the beginning of the surgical intervention, the maxillary template that could be removed after image data acquisition, is attached again into the patient's mouth for registration

Hoffmann et al. 2002), later also CBCT devices (Heiland et al. 2004b; Heiland et al. 2005). Recently CBCT devices have been used successfully for intraoperative imaging with direct link to a navigation system (Heiland et al. 2008, Gröbe et al. 2009). However these were not dedicated CBCT devices for maxillofacial imaging but isocentric 3D C-arm devices that are in use for, e.g., orthopedic surgery as well (Mischkowski et al. 2007b). More recent developments are mobile CBCT devices (e.g., xCAT, Xoran Technologies, Ann Arbor, Michigan USA) dedicated for intraoperative image data acquisition of the head. The use of these devices has been demonstrated for skull base surgery

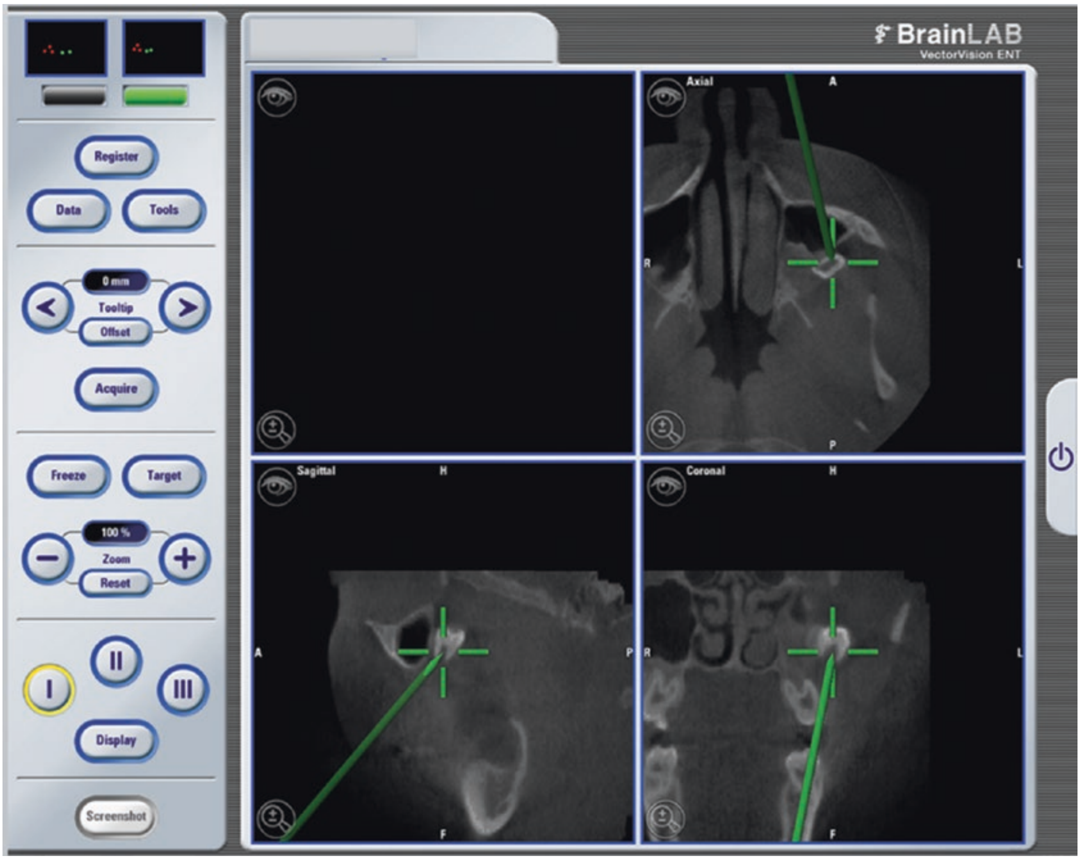

Fig. 26.13 Intraoperative screenshot from the navigated removal of the dislocated molar based on CBCT image data. The crosshairs indicate the current position of the pointing device in the surgeons hand, who just identified the position of the dislocated tooth

(Batra et al. 2011) and facial trauma surgery (Rabie et al. 2011), including intraoperative update of navigation system image data (Woodworth et al. 2008).

Conclusion

CBCT has a more and more important role in image-guided maxillofacial surgery, as the devices become more and more available. The technical constraints concerning the registration procedure will continuously disappear with the spread of devices with a larger field of view and better image contrast. Except for surgery of soft tissue tumors, it can be expected that CBCT will develop to an equivalent alternative to conventional CT for image-guided maxillofacial surgery.

References

Al-Rodhan NR, Kelly PJ (1992) Pioneers of stereotactic neurosurgery. Stereotact Funct Neurosurg 58:60–66

Arnheiter C, Scarfe WC, Farman AG (2006) Trends in maxillofacial cone-beam computed tomography usage. Oral Radiol 22:80–85

Barnett GH, Miller DW, Weisenberger J (1999) Frameless stereotaxy with scalp-applied fiducial markers for brain biopsy procedures: experience in 218 cases. J Neurosurg 91:569–576

Bartling SH, Leinung M, Graute J, Rodt T, Dullin C, Becker H, Lenarz T, Stover T, Majdani O (2007) Increase of accuracy in intraoperative navigation through high-resolution flat-panel volume computed tomography: experimental comparison with multislice computed tomography-based navigation. Otol Neurotol 28:129–134

Batra PS, Manes RP, Ryan MW, Marple BF (2011) Prospective evaluation of intraoperative computed tomography imaging for endoscopic sinonasal and skull-base surgery. Int Forum Allergy Rhinol 1:481–487

Besl PJ, Mckay ND (1992) A method for registration of 3-D shapes. IEEE Trans Pattern Anal Mach Intell 14:239–256

Black PM, Moriarty T, Alexander E III, Stieg P, Woodard EJ, Gleason PL, Martin CH, Kikinis R, Schwartz RB, Jolesz FA (1997) Development and implementation of intraoperative magnetic resonance imaging and its neurosurgical applications. Neurosurgery 41: `831–842

Bou Serhal CB, van Steenberghe D, Quirynen M, Jacobs R (2001) Localisation of the mandibular canal using conventional spiral tomography: a human cadaver study. Clin Oral Implants Res 12:230–236

Bou Serhal C, Jacobs R, Flygare L, Quirynen M, van Steenberghe D (2002) Perioperative validation of localisation of the mental foramen. Dentomaxillofac Radiol 31:39–43

Brief J, Edinger D, Hassfeld S, Eggers G (2005) Accuracy of image-guided implantology. Clin Oral Implants Res 16:495–501

Casap N, Wexler A, Persky N, Schneider A, Lustmann J (2004) Navigation surgery for dental implants: assessment of accuracy of the image guided implantology system. J Oral Maxillofac Surg 62:116–119

Di Giacomo GA, Cury PR, de Araujo NS, Sendyk WR, Sendyk CL (2005) Clinical application of stereolithographic surgical guides for implant placement: preliminary results. J Periodontol 76:503–507

Draenert FG, Coppenrath E, Herzog P, Müller S, Mueller-Lisse UG (2007) Beam hardening artefacts occur in dental implant scans with the NewTom cone beam CT but not with the dental 4-row multidetector CT. Dentomaxillofac Radiol 36:198–203

Ecke U, Maurer J, Boor S, Khan M, Mann WJ (2003) Fehlerquellen der Navigation in der lateralen Schädelbasischirurgie. Darstellung von Einflussfaktoren in der Praxis. HNO 51:386–393

Egbert N, Cagna DR, Ahuja S, Wicks RA (2015) Accuracy and reliability of stitched cone-beam computed tomography images. Imaging Sci Dent 45(1):41–47

Eggers G, Mühling J, Marmulla R (2005a) Template-based registration for image guided maxillofacial surgery. J Oral Maxillofac Surg 63:1330–1336

Eggers G, Haag C, Hassfeld S (2005b) Image-guided removal of foreign bodies. Br J Oral Maxillofac Surg 43:404–409

Eggers G, Mühling J, Marmulla R (2006) Image-to-patient registration techniques in head surgery. Int J Oral Maxillofac Surg 35:1081–1095

Eggers G, Klein J, Welzel T, Mühling J (2008) Geometric accuracy of digital volume tomography and conventional computed tomography. Br J Oral Maxillofac Surg 46:639–644

Eggers G, Mühling J, Hofele C (2009a) Clinical use of navigation based on cone-beam com-puter tomography in maxillofacial surgery. Br J Oral Maxillofac Surg 47:450–454

Eggers G, Senoo H, Kane G, Mühling J (2009b) The accuracy of image guided surgery based on cone beam computer tomography image data. Oral Surg Oral Med Oral Pathol Oral Radiol Endod 107:e41–e48

Eufinger H, König S, Eufinger A (1997) The role of alveolar ridge width in dental implantology. Clin Oral Investig 1:169–177

Fialkov JA, Phillips JH, Gruss JS, Kassel EE, Zuker RM (1992) A stereotactic system for guiding complex craniofacial reconstruction. Plast Reconstr Surg 89:340–345

Fitzpatrick JM, West JB, Maurer CR Jr (1998) Predicting error in rigid-body point-based registration. IEEE Trans Med Imaging 17:694–702

Fortin T, Champleboux G, Bianchi S, Buatois H, Coudert JL (2002) Precision of transfer of preoperative planning for oral implants based on cone-beam CT-scan images through a robotic drilling machine. Clin Oral Implants Res 13:651–656

Gaggl A, Schultes G, Kärcher H (2001) Navigational precision of drilling tools preventing damage to the mandibular canal. J Craniomaxillofac Surg 29:271–275

Gellrich NC, Schramm A, Hammer B, Rojas S, Cufi D, Lagrèze W, Schmelzeisen R (2002) Computer-assisted secondary reconstruction of unilateral post-traumatic orbital deformity. Plast Reconstr Surg 110:1417–1429

Gröbe A, Weber C, Schmelzle R, Heiland M, Klatt J, Pohlenz P (2009) The use of navigation (BrainLAB Vector vision(2)) and intraoperative 3D imaging system (Siemens Arcadis Orbic 3D) in the treatment of gunshot wounds of the maxillofacial region. Oral Maxillofac Surg 13(3):153–158

Hassfeld S, Mühling J, Zöller J (1995) Intraoperative navigation in oral and maxillofacial surgery. Int J Oral Maxillofac Surg 24:111–119

Hassfeld S, Streib S, Sahl H, Stratmann U, Fehrentz D, Zöller J (1998) Low-dose-Computertomographie des Kieferknochens in der präimplantologischen Diagnostik. Mund Kiefer Gesichtschir 2:188–193

Hatcher DC, Dial C, Mayorga C (2003) Cone beam CT for pre-surgical assessment of implant sites. J Calif Dent Assoc 31:825–833

Heiland M, Habermann CR, Schmelzle R (2004a) Indications and limitations of intraoperative navigation in maxillofacial surgery. J Oral Maxillofac Surg 62:1059–1063

Heiland M, Schmelzle R, Hebecker A, Schulze D (2004b) Intraoperative 3D imaging of the facial skeleton using the SIREMOBIL Iso-C3D. Dentomaxillofac Radiol 33:130–132

Heiland M, Schulze D, Blake F, Schmelzle R (2005) Intraoperative imaging of zygomaticomaxillary complex fractures using a 3D C-arm system. Int J Oral Maxillofac Surg 34:369–375

Heiland M, Pohlenz P, Blessmann M, Werle H, Fraederich M, Schmelzle R, Blake FA (2008) Navigated implantation after microsurgical bone transfer using intraoperatively acquired cone-beam computed tomography data sets. Int J Oral Maxillofac Surg 37:70–75

Heurich T, Stein W, Brief J, Mühling J, Hassfeld S (2002) Computergestützte dentale Implantatplanung auf der Basis volumentomographischer Bildgebung und deren operative Umsetzung mittels computerunterstützt erstellter Bohrschablonen. Biomed Tech (Berl) 47(Suppl. 1):25–28

Hoffmann J, Dammann F, Reinert S (2002) Initial experience with intraoperative computed tomography in maxillofacial surgery. Biomed Tech (Berl) 47(Suppl. 1):470–473

Hoffmann J, Westendorff C, Troitzsch D, Ernemann U, Reinert S (2004) Bilddatengestützte Navigation zur Steuerung der interstitiellen Lasertherapie von vaskulären Malformationen im Kopf- und Halsbereich. Biomed Tech (Berl) 49:199–201

Hoffmann J, Westendorff C, Schneider M, Reinert S (2005) Accuracy assessment of image guided implant surgery: an experimental study. Int J Oral Maxillofac Implants 20:382–386

Hohlweg-Majert B, Schön R, Schmelzeisen R, Gellrich NC, Schramm A (2005) Navigational maxillofacial surgery using virtual models. World J Surg 29:1530–1538

Holberg C, Steinhäuser S, Geis P, Rudzki-Janson I (2005) Cone-beam computed tomography in orthodontics: benefits and limitations. J Orofac Orthop 66:434–444

Holst S, Blatz MB, Eitner S (2007) Precision for computer-guided implant placement: using 3D planning software and fixed intraoral reference points. J Oral Maxillofac Surg 65:393–399

Hölzle F, Klein M, Schwerdtner O, Lüth T, Albrecht J, Hosten N, Felix R, Bier J (2001) Intraoperative computed tomography with the mobile CT Tomoscan M during surgical treatment of orbital fractures. Int J Oral Maxillofac Surg 30:26–31

Horsley VA, Clarke RH (1908) The structure and functions of the cerebellum examined by a new method. Brain 31:45–124

Hümmeke S, Voßhans J, Esser E (2004) Navigierte Implantatchirurgie im klinischen Einsatz. Z Zahnärztl Impl 20:80–85

Kall BA, Goerss SJ, Stiving SO, Davis DH, Kelly PJ (1996) Quantitative analysis of a noninvasive stereotactic image registration technique. Stereotact Funct Neurosurg 66:69–74

Kelly P, Kall B, Goerss S (1988) Results of computed tomography-based computerassisted stereotactic resection of metastatic intracranial tumors. Neurosurgery 22:7–17

Kopp KC, Koslow AH, Abdo OS (2003) Predictable implant placement with a diagnostic/surgical template and advanced radiographic imaging. J Prosthet Dent 89:611–615

Kozak J, Nesper M, Fischer M, Lutze T, Goggelmann A, Hassfeld S, Wetter T (2002) Semiautomated registration using new markers for assessing the accuracy of a navigation system. Comput Aided Surg 7:11–24

Lascala CA, Panella J, Marques MM (2004) Analysis of the accuracy of linear measurements obtained by cone beam computed tomography (CBCT-NewTom). Dentomaxillofac Radiol 33:291–294

Leber KA, Eder HG, Pendl G (1995) Localization of superficial cerebral lesions using a magnetic resonance imagingguided localizer. Minim Invasive Neurosurg 38:87–89

Lee S, Gantes B, Riggs M, Crigger M (2007) Bone density assessments of dental implant sites: 3. Bone quality evaluation during osteotomy and implant placement. Int J Oral Maxillofac Implants 22: 208–212

Lell M, Baum U, Koester M, Nömayr A, Greess H, Lenz M, Bautz W (1999) Morphologische und funktionelle Diagnostik der Kopf-Hals-Region mit Mehrzeilen-Spiral-CT. Radiologe 39:932–938

Lindh C, Petersson A, Klinge B (1995) Measurements of distances related to the mandibular canal in radiographs. Clin Oral Implants Res 6:96–103

Lofthag-Hansen S, Huumonen S, Gröndahl K, Gröndahl HG (2007) Limited cone-beam CT and intraoral radiography for the diagnosis of periapical pathology. Oral Surg Oral Med Oral Pathol Oral Radiol Endod 103:114–119

Loubele M, Maes F, Schutyser F, Marchal G, Jacobs R, Suetens P (2006) Assessment of bone segmentation quality of cone-beam CT versus multislice spiral CT: a pilot study. Oral Surg Oral Med Oral Pathol Oral Radiol Endod 102:225–234

Ludlow JB, Davies-Ludlow LE, Brooks SL, Howerton WB (2006) Dosimetry of 3 CBCT devices for oral and maxillofacial radiology: CB Mercuray, NewTom 3G and i-CAT. Dentomaxillofac Radiol 35:219–226

Lunsford LD, Martinez AJ, Latchaw RE (1986) Stereotaxic surgery with a magnetic resonance- and computerized tomography-compatible system. J Neurosurg 64:872–878

Marmulla R, Mühling J (2006) The influence of computed tomography motion artifacts on computer-assisted surgery. J Oral Maxillofac Surg 64:466–470

Marmulla R, Hassfeld S, Lüth T, Mühling J (2003) Laser-scan-based navigation in cranio-maxillofacial surgery. J Craniomaxillofac Surg 31:267–277

Marmulla R, Wörtche R, Mühling J, Hassfeld S (2005) Geometric accuracy of the NewTom 9000 cone beam CT. Dentomaxillofac Radiol 34:28–31

Maurer CR, Fitzpatrick JA (1993) Review of medical image registration. In: Maciunas RJ (ed) Interactive image-guided neurosurgery. American Association of Neurological Surgeons, Park Ridge, pp 17–44

Maurer CR Jr, Fitzpatrick JM, Wang MY, Galloway RL Jr, Maciunas RJ, Allen GS (1997) Registration of head volume images using implantable fiducial markers. IEEE Trans Med Imaging 16:447–462

Meyer U, Wiesmann HP, Runte C, Fillies T, Meier N, Lueth T, Joos U (2003) Evaluation of accuracy of insertion of dental implants and prosthetic treatment by computer-aided navigation in minipigs. Br J Oral Maxillofac Surg 41:102–108

Mischkowski RA, Zinser MJ, Neugebauer J, Kübler AC, Zöller JE (2006a) Comparison of static and dynamic computer-assisted guidance methods in implantology. Int J Comput Dent 9:23–35

Mischkowski RA, Zinser MJ, Kübler AC, Krug B, Seifert U, Zöller JE (2006b) Application of an augmented reality tool for maxillary positioning in orthognathic surgery—a feasibility study. J Craniomaxillofac Surg 34:478–483

Mischkowski RA, Pulsfort R, Ritter L, Neugebauer J, Brochhagen HG, Keeve E, Zöller JE (2007a) Geometric accuracy of a newly developed cone-beam device for maxillofacial imaging. Oral Surg Oral Med Oral Pathol Oral Radiol Endod 104:551–559

Mischkowski RA, Zinser MJ, Ritter L, Neugebauer J, Keeve E, Zöller JE (2007b) Intraoperative navigation in the maxillofacial area based on 3D imaging obtained by a cone-beam device. Int J Oral Maxillofac Surg 36:687–694

Pell MF, Thomas DGT, Cosman E (1994) Development and technical features of the Cosman-Roberts-wells (CRW) stereotactic system. In: Pell MF, Thomas DGT (eds) Handbook of Stereotaxy using the CRW apparatus. Williams & Wilkins, Baltimore, pp 1–52

Pettersson A, Komiyama A, Hultin M, Näsström K, Klinge B (2012) Accuracy of virtually planned and template guided implant surgery on edentate patients. Clin Implant Dent Relat Res 14:527–537

Pinsky HM, Dyda S, Pinsky RW, Misch KA, Sarment DP (2006) Accuracy of three-dimensional measurements using cone-beam CT. Dentomaxillofac Radiol 35:410–416

Pohlenz P, Blessmann M, Blake F, Heinrich S, Schmelzle R, Heiland M (2007) Clinical indications and perspectives for intraoperative cone-beam computed tomography in oral and maxillofacial surgery. Oral Surg Oral Med Oral Pathol Oral Radiol Endod 103: 412–417

Raabe A, Krishnan R, Wolff R, Hermann E, Zimmermann M, Seifert V (2002) Laser surface scanning for patient registration in intracranial image-guided surgery. Neurosurgery 50:797–801

Rabie A, Ibrahim AM, Lee BT, Lin SJ (2011) Use of intraoperative computed tomography in complex facial fracture reduction and fixation. J Craniofac Surg 22:1466–1467

Reddy MS, Mayfield-Donahoo T, Vanderven FJ, Jeffcoat MK (1994) A comparison of the diagnostic advantages of panoramic radiography and computed tomography scanning for placement of root form dental implants. Clin Oral Implants Res 5:229–238

Rouas P, Nancy J, Bar D (2007) Identification of double mandibular canals: literature review and three case reports with CT scans and cone beam CT. Dentomaxillofac Radiol 36:34–38

Sarment DP, Sukovic P, Clinthorne N (2003) Accuracy of implant placement with a stereolithographic surgical guide. Int J Oral Maxillofac Implants 18:571–577

Sato S, Arai Y, Shinoda K, Ito K (2004) Clinical application of a new cone-beam computerized tomography system to assess multiple two-dimensional images for the preoperative treatment planning of maxillary implants: case reports. Quintessence Int 35:525–528

Scarfe WC, Farman AG, Sukovic P (2006) Clinical applications of cone-beam computed tomography in dental practice. J Can Dent Assoc 72:75–80

Schlaier J, Warnat J, Brawanski A (2002) Registration accuracy and practicability of laser-directed surface matching. Comput Aided Surg 7:284–290

Schropp L, Wenzel A, Kostopoulos L (2001) Impact of conventional tomography on prediction of the appropriate implant size. Oral Surg Oral Med Oral Pathol Oral Radiol Endod 92:458–463

Siessegger M, Schneider BT, Mischkowski RA, Lazar F, Krug B, Klesper B, Zöller JE (2001) Use of an image-guided navigation system in dental implant surgery in anatomically complex operation sites. J Craniomaxillofac Surg 29:276–281

Spiegel E, Wycis H (1962) Stereoencephalotomy. Grune & Stratton, New York

Strasters KC, Little JA, Buurman J, Hill DLG, Hawkes DJ (1997) Anatomical landmark image registration: validation and comparison. Lect Notes Comput Sci 1205:161–170

Stumpel LJ (2012) Deformation of stereolithographically produced surgical guides: an obser-vational case series report. Clin Implant Dent Relat Res 14:442–453

Sukovic P (2003) Cone beam computed tomography in craniofacial imaging. Orthod Craniofac Res 6(Suppl. 1):31–36

Tardieu PB, Vrielinck L, Escolano E (2003) Computer-assisted implant placement. A case report: treatment of the mandible. Int J Oral Maxillofac Implants 18:599–604

Tardieu PB, Vrielinck L, Escolano E, Henne M, Tardieu AL (2007) Computer-assisted implant placement: scan template, simplant, surgiguide, and SAFE system. Int J Periodontics Restorative Dent 27: 141–149

Van Assche N, van Steenberghe D, Guerrero ME, Hirsch E, Schutyser F, Quirynen M, Jacobs R (2007) Accuracy of implant placement based on pre-surgical planning of three-dimensional cone-beam images: a pilot study. J Clin Periodontol 34:816–821

Wagner A, Schicho K, Kainberger F, Birkfellner W, Grampp S, Ewers R (2003) Quantification and clinical relevance of head motion during computed tomography. Investig Radiol 38:733–741

Wanschitz F, Birkfellner W, Watzinger F, Schopper C, Patruta S, Kainberger F, Figl M, Kettenbach J, Bergmann H, Ewers R (2002) Evaluation of accuracy of computer-aided intraoperative positioning of endosseous oral implants in the edentulous mandible. Clin Oral Implants Res 13:59–64

Watanabe E, Watanabe T, Manaka S, Mayanagi Y, Takakura K (1987) Threedimensional digitizer (neuronavigator): new equipment for computed tomography-guided stereotaxic surgery. Surg Neurol 27: 543–547

Westendorff C, Gülicher D, Dammann F, Reinert S, Hoffmann J (2006) Computer-assisted surgical treatment of orbitozygomatic fractures. J Craniofac Surg 17:837–842

Widmann G, Widmann R, Widmann E, Jaschke W, Bale RJ (2005) In vitro accuracy of a novel registration and targeting technique for image-guided template production. Clin Oral Implants Res 16:502–508.

Wiles AD, Thompson DG, Frantz DD (2004) Accuracy assessment and interpretation for optical tracking systems. In: Galloway RL Jr (ed) Medical imaging 2004: visualization, image-guided procedures, and display. Proceedings of the SPIE volume 5367, pp. 421–432

Wirtz CR, Bonsanto MM, Knauth M, Tronnier VM, Albert FK, Staubert A, Kunze S (1997) Intraoperative magnetic resonance imaging to update interactive navigation in neurosurgery: method and preliminary experience. Comput Aided Surg 2:172–179

Woodworth BA, Chiu AG, Cohen NA, Kennedy DW (2008) Real-time computed tomography image update for endoscopic skull base surgery. J Laryngol Otol 122:361–365

Zizelmann C, Gellrich NC, Metzger MC, Schoen R, Schmelzeisen R, Schramm A (2007) Computer-assisted reconstruction of orbital floor based on cone beam tomography. Br J Oral Maxillofac Surg 45:79–80

CBCT-Based Image Guidance for Sinus and Skull Base Surgery

27

Bradford A. Woodworth, Sri Kiran Chennupati, and Alexander G. Chiu

Contents

B.A. Woodworth, M.D. (✉)
Department of Otolaryngology—Head and Neck Surgery, University of Alabama at Birmingham, Birmingham, AL, USA
e-mail: bwoodworth@uabmc.edu

S.K. Chennupati, M.D.
Pediatric Otolaryngology, Division of Pediatric Surgery, Lehigh Valley Health Network, Allentown, PA, USA
e-mail: chennups@gmail.com

A.G. Chiu, M.D.
Department of Otorhinolaryngology—Head and Neck Surgery, University of Kansas Medical Center, Kansas City, MO, USA
e-mail: Achiu@kumc.edu

27.1 Introduction

The field of otolaryngology—head and neck surgery encompasses the diagnosis and treatment of a wide variety of disease processes involving the ear, nose, and throat (ENT). In particular, surgeries involving the paranasal sinuses and skull base demand a high level of imaging accuracy because of the complexity of the regional anatomy and intimate association with both neurovascular, ocular and cerebral tissues. Improvements in the field of diagnostic imaging have driven a number of technological advancements in operative techniques, especially stereotactic surgical navigation. Image-guided systems (IGS) monitor surgical instruments relative to known patient anatomic landmarks. This chapter will discuss the origins and utility of this modality and highlight the particular use of in-office and intraoperative CBCT imaging for endoscopic paranasal sinus and skull base surgery.

27.2 Imaging in Otolaryngology

Multi-detector computed tomography (MDCT) is presently the core modality of diagnostic imaging in ENT applications. The fine bone detail provided by high-resolution MDCT scanners can assist in determining the status of the inner ear after temporal bone trauma and provide accuracy paranasal sinus imaging necessary to develop a

W.C. Scarfe, C. Angelopoulos (eds.), *Maxillofacial Cone Beam Computed Tomography*,
https://doi.org/10.1007/978-3-319-62061-9_27

"road map" for sinus surgery. With the advent of MDCT, direct coronal imaging for temporal bones and sinuses are essentially examinations of the past. Coronal and sagittal plane reconstructions from data obtained from fast MDCT scans are exceptionally reliable (Phelps et al. 2000).

Magnetic resonance imaging (MRI), although unsatisfactory for demonstrating the middle ear, is now the imaging modality of choice for inner ear lesions and their central connections. The cranial nerves in the internal auditory meatus can be reliably depicted as well as the contents of the scalae of the cochlea (Phelps et al. 2000). Magnetic resonance angiography is also a noninvasive modality to demonstrate the major vessels of the head and neck. MRI is particularly useful for tumors and meningoencephaloceles of the skull base and paranasal sinuses. MRI can identify brain parenchyma and CSF that have herniated into the sinus. However, MRI lacks fine bony detail of the skull base, which limits its accuracy in localizing cerebrospinal fluid (CSF) leaks and characterizing the bony paranasal sinuses needed for intraoperative image guidance.

27.2.1 Emerging Role of CBCT Imaging in ENT

The first application of cone beam computed tomography (CBCT) outside the dentomaxillofacial region was as an in-office volumetric scanner for ENT clinical situations (Fig. 27.1). Portable CBCT units such as Xoran xCAT (XoranTechnologies Inc., Ann Arbor, MI) and Medtronic O-ARM (Medtronic Inc., Minneapolis, MN) are now emerging for intraoperative use (Fig. 27.2) (Conley et al. 2011).

CBCT imaging offers numerous advantages over CT in ENT applications:

- **Less expensive**. The use of flat-panel detector technology in CBCT units rather than a detector array for MDCT reduces the cost of the equipment substantially.
- **Compact size**. The overall size of in-office units and the "C" arm configuration of intraoperative units have an extremely small footprint compared to medical CT units which provide greater physical constraints of the operating environment.
- **Low Dose**. Although CBCT units do not have dose modulation throughout the scan, they operate at lower kilovoltage and mAs providing up to 59% less effective dose (Conley et al. 2011)
- **High resolution**. CBCT have higher submillimeter spatial resolution (range, 0.4–0.83 mm) than MDCT (approximately 0.625 mm) (Conley et al. 2011).

Fig. 27.1 Volumetric cone-beam CT scanners acquire multiple slices in one pass of the gantry. Office-based versions, such as the MiniCAT™ (Xoran Technologies, Ann Arbor, MI) shown here, allow convenient CT scanning in a clinic setting. Preoperative CT scans are performed expeditiously for download into any available image-guidance system

Fig. 27.2 Image-guided surgical navigation during endoscopic sinus surgery (*white arrow*). Stereotactic information is portrayed in the coronal, axial, and sagittal planes (BrainLab™, Munich, Germany)

CBCT imaging provides data volumetrically in one pass of the gantry, without translation, so that patients can be scanned faster than on MDCT scanners (Fig. 27.1). With the dramatic increase in image processing and the ongoing development of digital imaging, the use of volumetric imaging is adding a previously unknown level of diagnostic support to otolaryngologists (Siewerdsen and Jaffray 2001; Sukovic 2003). CBCT produces the equivalent of MDCT bone window images at a greatly reduced radiation dose (Aldrich et al. 2006; Cohnen et al. 2006) as well as section thickness, and is on the verge of revolutionizing CT imaging for otolaryngology.

27.2.2 Sinus Surgery

The origins of sinus surgery can be traced to ancient Egypt (Reardon 2002). In the nineteenth century, Caldwell and Luc independently described techniques to specifically address maxillary sinusitis. The Caldwell-Luc approach, as well as other external approaches, aimed to eradicate diseased mucosa of affected sinuses (Reardon 2002). In 1967, Messerklinger described localized disruptions of mucociliary clearance occurring in areas of mucosal contact (Messerklinger 1967; Kennedy et al. 1985). He felt that inflammation was most likely to occur in the narrow channel of the middle meatus and ethmoid air cells (Kennedy et al. 1985). With the advent of high resolution optics and endoscopes, functional endoscopic sinus surgery (FESS) was developed as a means to correct the underlying pathology of the osteomeatal unit (OMU) (Kennedy et al. 1985). Zinreich et al. (1987) noted that coronal computed tomography (CT) is the best imaging technique to examine the OMU. With the complimentary techniques of nasal endoscopy and CT imaging, the anatomic spatial relationships of the paranasal sinuses can now be appreciated like never before.

27.2.2.1 Functional Endoscopic Sinus Surgery

Functional endoscopic sinus surgery (FESS) has now become one of the most common otolaryngologic surgical procedures in ENT (Wise and DelGaudio 2005). The success rate of FESS has been reported to be as high as 80–90% (Kennedy and Senior 1997). Endoscopic sinus techniques have evolved from diagnosis and treatment of inflammatory disease into approaches for a variety of neoplastic and skull base lesions. Endoscopic approaches are now widely utilized for the management of mucoceles, skull base defects, CSF leaks of the anterior skull base, benign tumors, orbital and optic nerve decompression, and dacryocystorhinostomies. Furthermore, the boundaries for the endoscopic approach to the sinuses have been expanded to include the endoscopic resection of appropriately selected paranasal sinus malignancies and pituitary tumors. Basic techniques for the treatment of inflammatory disease have evolved as a result of increasing recognition of the importance of mucoperiosteal preservation and improving knowledge with regard to disease pathogenesis and management. Because of the variability of the anatomy and the critical relationships of the sinuses to the orbit and brain, endoscopic surgical techniques require a detailed knowledge of the anatomy and embryology to avoid potentially disastrous complications.

Complications of Endoscopic Sinus Surgery

Despite the increasing popularity of endoscopic sinus surgery, the procedure is fraught with potential morbidity due to orbital and intracranial complications. Complications of FESS are either major or minor (Kennedy et al. 1994). Major complications include CSF leak or intracranial injury, orbital hematoma, blindness, diplopia, extraocular muscle injury, or death. Minor complications include nasolacrimal duct injury, adhesions, or hemorrhage. While there is a less than 1% incidence of complications with FESS, it is one of the most commonly litigated procedures in otolaryngology (Wise and DelGaudio 2005). Ways to decrease complications and improve surgical accuracy are needed.

27.2.2.2 Image-Guided Sinus Surgery

The development of new technologies for endoscopic sinus surgery has increased the ability for the surgeon to maneuver safely through diseased or surgically altered sinus anatomy. In particular, the development of image-guidance or computer-aided systems provides a method for sinus surgeons to monitor surgical instruments relative to a preoperative CT scan and navigate skull base and orbital walls with more precision (Fig. 27.2). Image-guided surgery (IGS) links the patient's radiographic and endoscopic images (Fried and Morrison 1998). High-resolution preoperative axial images are reformatted and registration links the space defined by the virtual space of the reformatted images (Fried and Morrison 1998; Wise and DelGaudio 2005). These computer systems provide continuous information in the coronal, axial, and sagittal planes.

History

Image-guidance has its origins within the field of neurosurgery. In the 1970s, neurosurgeons began to first use IGS to target specific areas of the brain to eliminate tremors, drain abscesses, and treat pain (Fried and Morrison 1998; Palmer and Kennedy 2005; Wise and DelGaudio 2005). They utilized rigid frame fixation of patients' heads and plain film radiographs for anatomic localization. The bulky frames often obstructed access to patients and made procedures cumbersome. In addition, the use of two-dimensional plain radiographs lacked precision. By 1976, the incorporation of CT with IGS resulted in a system that allowed for improved three-dimensional visualization of the paranasal sinuses and skull base. Repeat CT imaging was performed using a CT-dependent frame with diagonal rods that served as fiducial markers for the computer (Perry et al. 1980). Stereotactic ability was conveyed by the CT scanner itself so that repeat scans could be obtained during surgery to confirm the position of the probe tip. Because of the impractical nature of using large CT scanners in the operating room and associated high radiation exposures, intraoperative imaging was abandoned for one preoperative imaging sequence that could be applied to a CT-dependent frame. Subsequently, frameless stereotactic image-guidance systems were developed and incorporated into neurosurgical procedures.

Because neurosurgical procedures ultimately involve soft tissue, anatomic shift decreases the utility of this technology for neurosurgical purposes. However, the limits of dissection in endoscopic sinus surgery are the bony boundaries of the skull base and orbit—stable structures with no anatomic shift. Therefore, image-guidance systems were aptly suited for this type of surgery. Frameless, stereotactic image-guidance systems were incorporated into endoscopic sinus surgery for skull base and orbital wall navigation in an attempt to make the procedure safer and more complete.

Accuracy

The popularity of this image-guidance technology has led to the development of many systems which are now in common practice. Each system has a method of anatomical point registration, a localization device, and a computerized interface that will determine the anatomic accuracy of image-guidance during the procedure. The incorporation of real-time endoscopic views as part of the navigation screen is an added benefit.

Despite these advantages, the accuracy of image-guidance systems is the most crucial factor in an area where a few millimeters separate the sinonasal cavity from the brain and eye (Woodworth et al. 2005).

The accuracy of these systems has been studied by numerous investigators, with results reporting accuracy within a few millimeters (Kato et al. 1991; Anon et al. 1994; Fried and Morrison 1998; Metson et al. 1998; Woodworth et al. 2005). However, these systems are ultimately dependent on registered anatomical reference points entered into the system. Registration of patient landmarks is one of the most important steps in using this technology. Most techniques currently used are based on either paired-point registration methods or surface-based methods. Point-based methods determine spatial coordinates of corresponding points in different images and physical space and calculate a geometric transformation between the volumes (Schlaier et al. 2002). This method usually uses extrinsic fiducial markers and an electromagnetic tracking system. Surface-based systems fit numerous points derived from contours in one image set to surface models of coordinates from the patient's face or head. Since accuracy typically degrades over the course of a procedure by almost 1 mm (Maciunas et al. 1992), frequent intraoperative comparison of known anatomic landmarks to the registered output from the IGS system will ensure higher reliability during the procedure.

Technology Innovations for IGS

Recent updates to this technology include the integration of CT angiogram and CT/MRI fusion techniques into computer-aided systems. Because CT scans do not provide detailed anatomy of the intracranial vasculature, the incorporation of CT angiograms is a large improvement in imaging technology for skull base surgery. CT/MRI fusion facilitates delineation of soft tissue tumors, while providing the necessary bony anatomic boundaries and landmarks for intraoperative navigation (Figs. 27.3, 27.4 and 27.5). Although some authors have

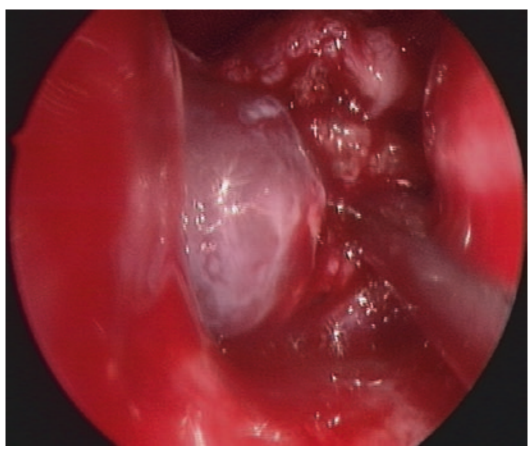

Fig. 27.3 Endoscopic image of juvenile nasopharyngeal angiofibroma

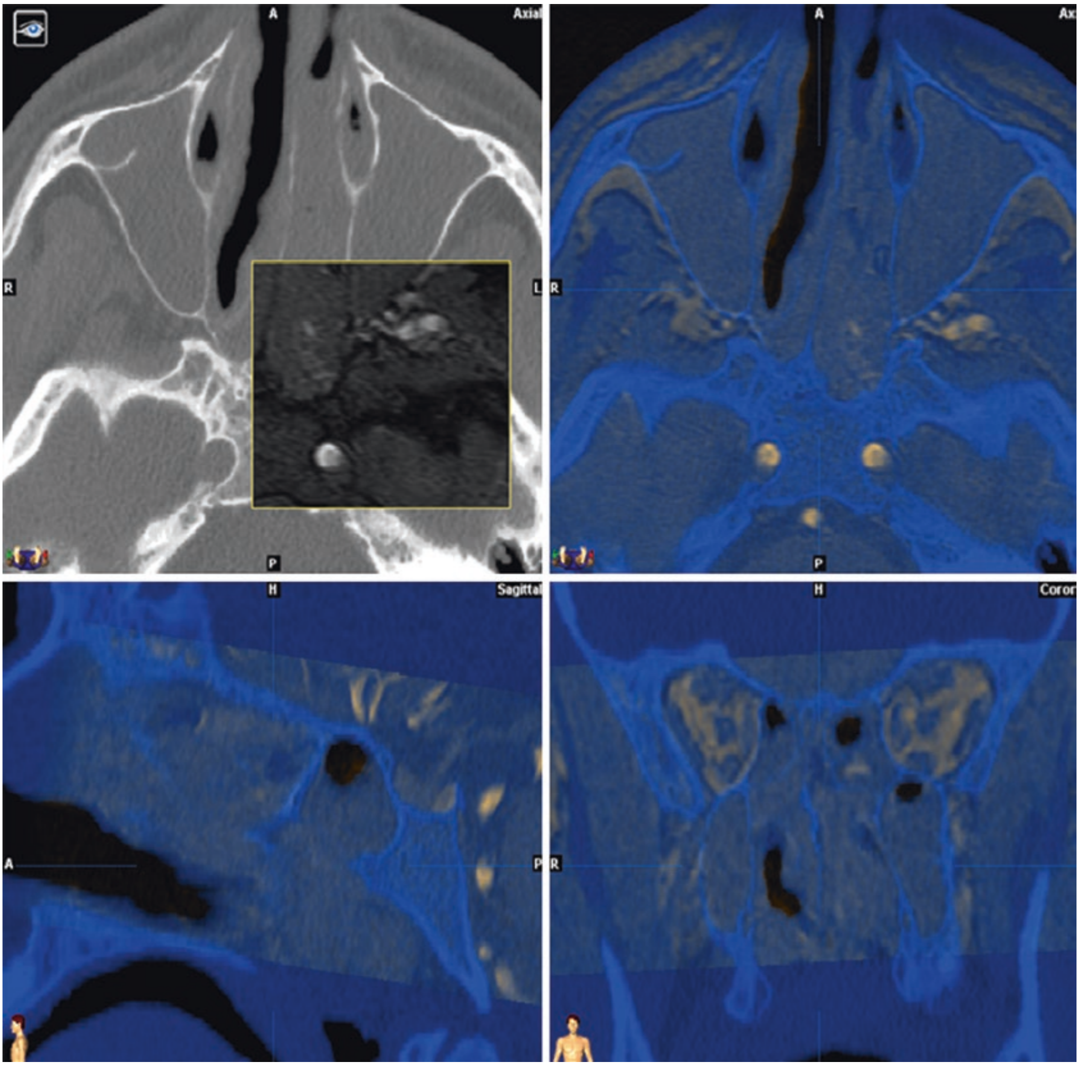

Fig. 27.4 Same patient as Fig. 27.3 (juvenile nasopharyngeal angiofibroma) showing preoperative fusion of CT and MRI (*insert*) images on image-guided software program. Superimposition of MRI image assists in distinguishing tumor from surrounding inflammatory disease

proposed MRI surgical navigation alone in both sinus and skull base surgery (Pergolizzi et al. 2001; Suzuki et al. 2005), CT/MRI fusion techniques are likely superior due to the ability to combine the best aspects of each technology.

Historically, conventional image-guidance systems do not provide true real-time updated imaging while the patient is still on the operating table. Once data has been acquired for these navigation systems, they do not provide the opportunity for any modification of the data sets themselves.

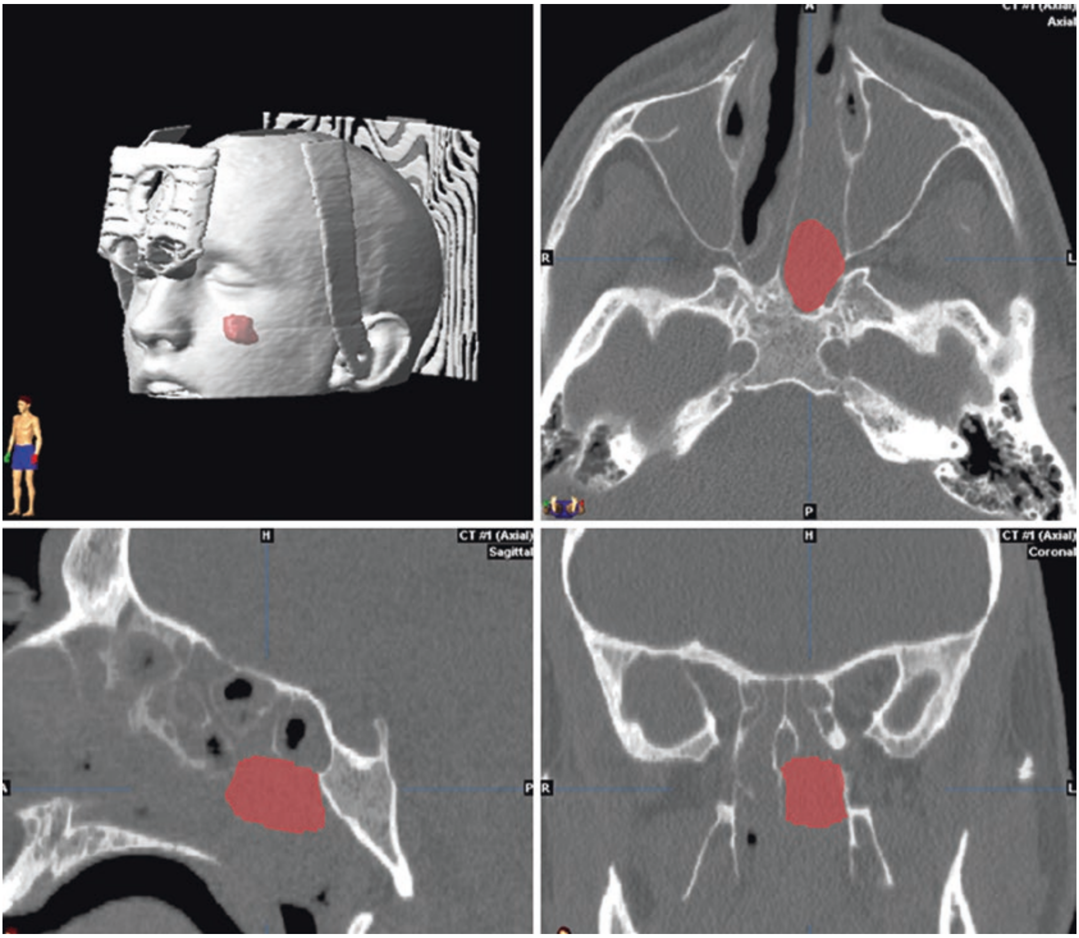

Fig. 27.5 Same patient as Fig. 27.3 (juvenile nasopharyngeal angiofibroma) showing marking technology to outline the tumor seen on image fusion. The tumor is shaded in *red*

One such attempt to remedy this problem is through the application of Eraser software (BrainLab, Germany). This software provides the ability to digitally erase sinus disease or tumor from the preoperative CT scan based upon intraoperative tracking of the surgical instruments (Fig. 27.6). This technology is very useful if the disease or tumor is confined by the bony anatomy of the sinuses and skull base where the surgeon obtains a virtual image update of the actual surgical progress. However, the utility of this software decreases dramatically when surgery extends beyond the bony boundaries of the sinuses into soft tissue (i.e., pituitary surgery). Soft tissue collapse and anatomic shift effectively limits this technology. Therefore, updating the actual MRI or CT images in the IGS could eliminate these shortcomings (Figs. 27.7 and 27.8).

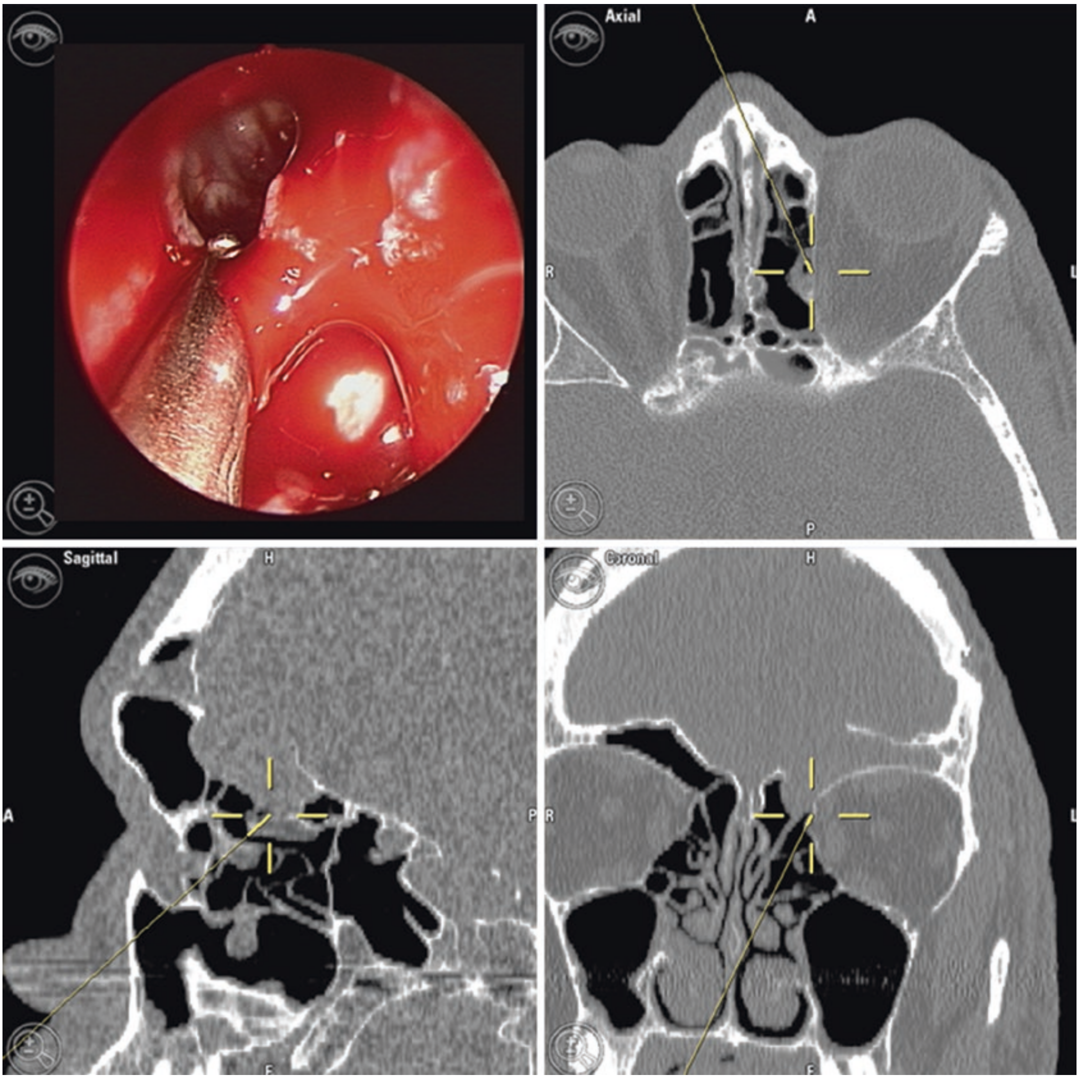

Fig. 27.6 An intraoperative endoscopic view with triplanar CT imaging of a patient with a left supraorbital ethmoid mucocele and corresponding skull base erosion

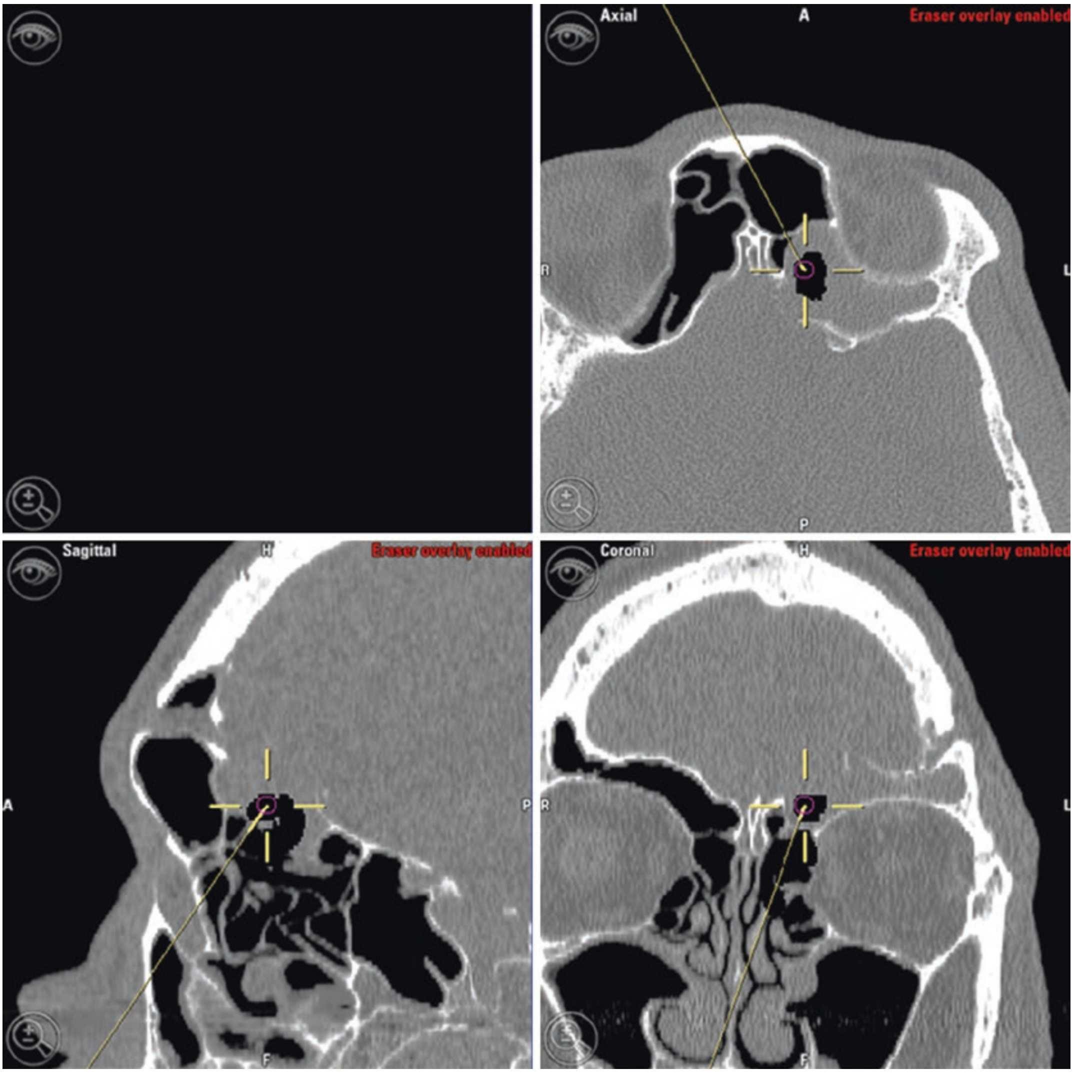

Fig. 27.7 Same patient as Fig. 27.6 (supraorbital ethmoid mucocele). Upon entering the mucocele, the Eraser software program begins to digitally "erase" the mucocele based on the path of the instrument

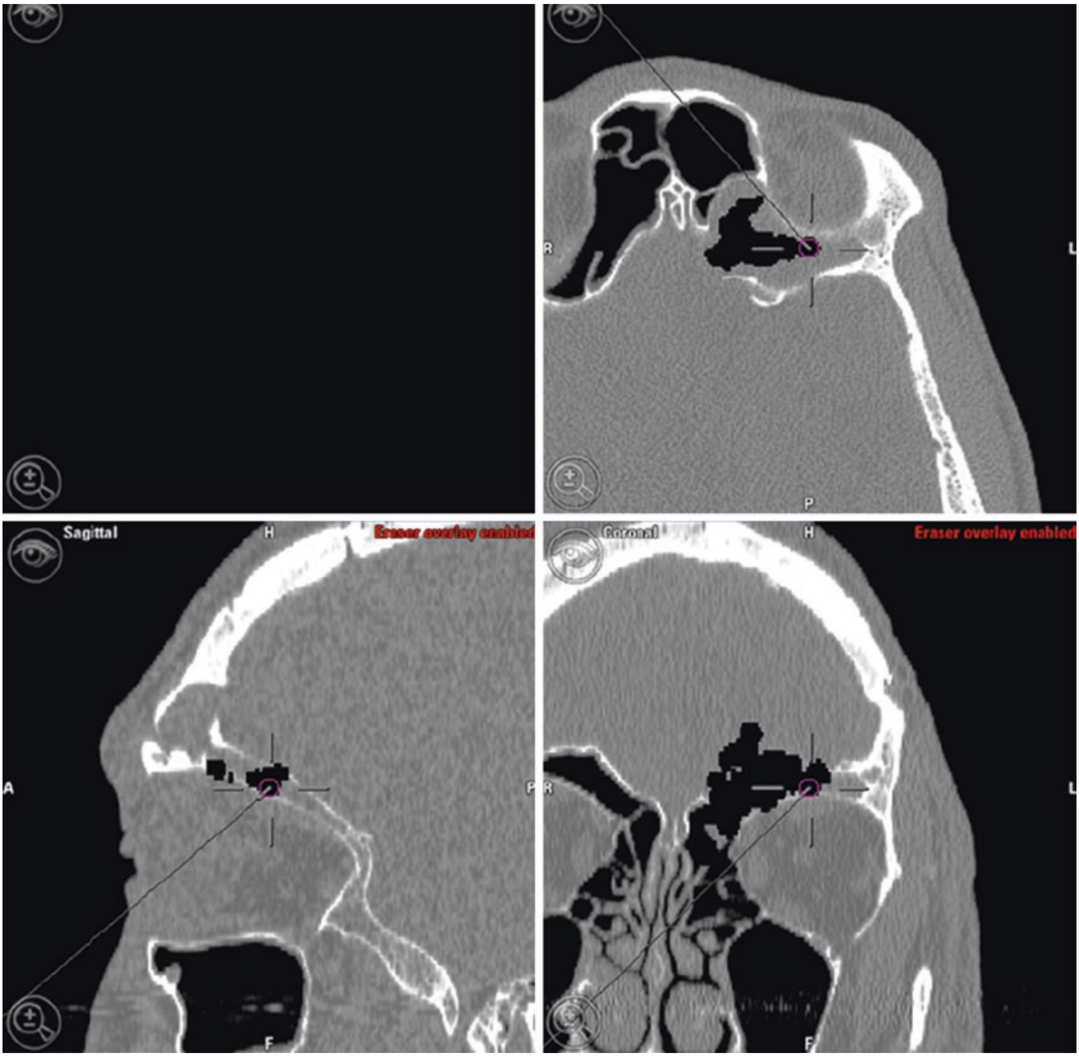

Fig. 27.8 Same patient as Fig. 27.6 (supraorbital ethmoid mucocele triplanar CT imaging with extensive digital simulated "erasure" reveals the full extent of the mucocele beyond the skull base

27.3 Intraoperative Imaging for IGS

Intraoperative imaging acquisition with both CT and MRI during sinus or skull base surgery is not a novel concept (Fried et al. 1998a, b; Cartellieri and Vorbeck 2000; Pergolizzi et al. 2001). Previously, Cartellieri and Vorbeck (2000) published a report of six patients who underwent intraoperative conventional CT scanning during endoscopic sinus surgery in order to provide an update to their image-guidance system. Unfortunately, this study required additional staff to operate the CT, the operation to be performed on a CT table, and a complete CT data set for updating the three-dimensional navigation system. This resulted in prolonged anesthesia ranging from 20 to 60 min.

New compact, portable CT scanners (xCAT™, Xoran Technologies, Ann Arbor, MI) can now provide intraoperative CT scans of the sinuses and skull-base for real-time update of image-guidance systems (Fig. 27.9).

This volumetric cone-beam CT scanner contains an X-ray source and detector mounted on a

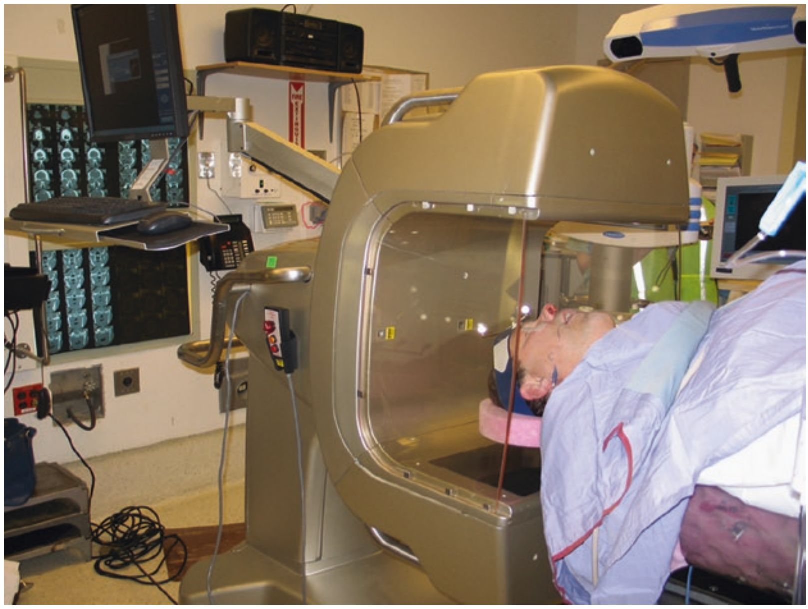

Fig. 27.9 Intraoperative CT with the xCAT—a mobile cone-beam scanner. A special head rest allows rotation of the gantry for image acquisition. CT scans are then transferred into the surgical navigation system of preference for a real-time update of the images

rotating scanning arm, a personal computer with an integrated wide screen monitor, and an image-processing unit. During one rotation of the scanning arm, the detector collects the flux of X-rays that have passed through the patient. Cone-beam CT scanners utilize a two-dimensional multi-row detector, which allows for a single rotation of the gantry to generate a scan of the entire head, as compared to conventional, full body "fan-beam" CT scanners whose multiple "slices" must be stacked to obtain a complete image. Thus, this system displays scans on its integrated monitor in less than 3 min. Cone-beam technology utilizes X-rays much more efficiently, requires far less electrical energy, and allows for the use of more compact X-ray components than fan-beam technology (Perry et al. 1980; Siewerdsen and Jaffray 2001; Sukovic 2003). The effective radiation dose to the patient is as low as 0.25 millisievert (mSV), while the radiation dose from a full-body CT scanner is an average of 10 times higher (Aldrich et al. 2006; Cohnen et al. 2006).

With the practicality of a mobile, CT scanner and the ability to obtain slice thickness as little as 0.2 mm, real-time updates of intraoperative image guidance systems can be performed in as little as 10 min. Numerous authors have reported that this feature allows for endoscopic sinus surgeons to check the thoroughness of surgery to either extirpate sinus cells or fully resect bony and soft tissue lesions of the sinuses and skull base (Fig. 27.10). Jackman et al. (2008) showed that intraoperative CT scanning performed at the conclusion of FESS surgery lead to an alteration in the surgical plan in 30% of patients. Jeon et al. (2013) used intraoperative CT to determine the extent of resection of tumor, degree of hematoma removal, confirmation of catheter placement, and monitoring unexpected complications and found that overall 7% of surgeries required additional surgical procedures based on imaging.

27.3.1 Does IGS Increase Safety in Sinus Surgery?

Although IGS has been used in sinus surgery for over a decade, the real value of IGS in sinus surgery remains to be determined. Randomizing a cohort of subjects to a therapeutic intervention that could place them at an increased risk is unethical. Thus, there are no randomized, controlled trials on whether IGS contributes to the safety of surgery. Furthermore, the quality of information that is available is very poor and

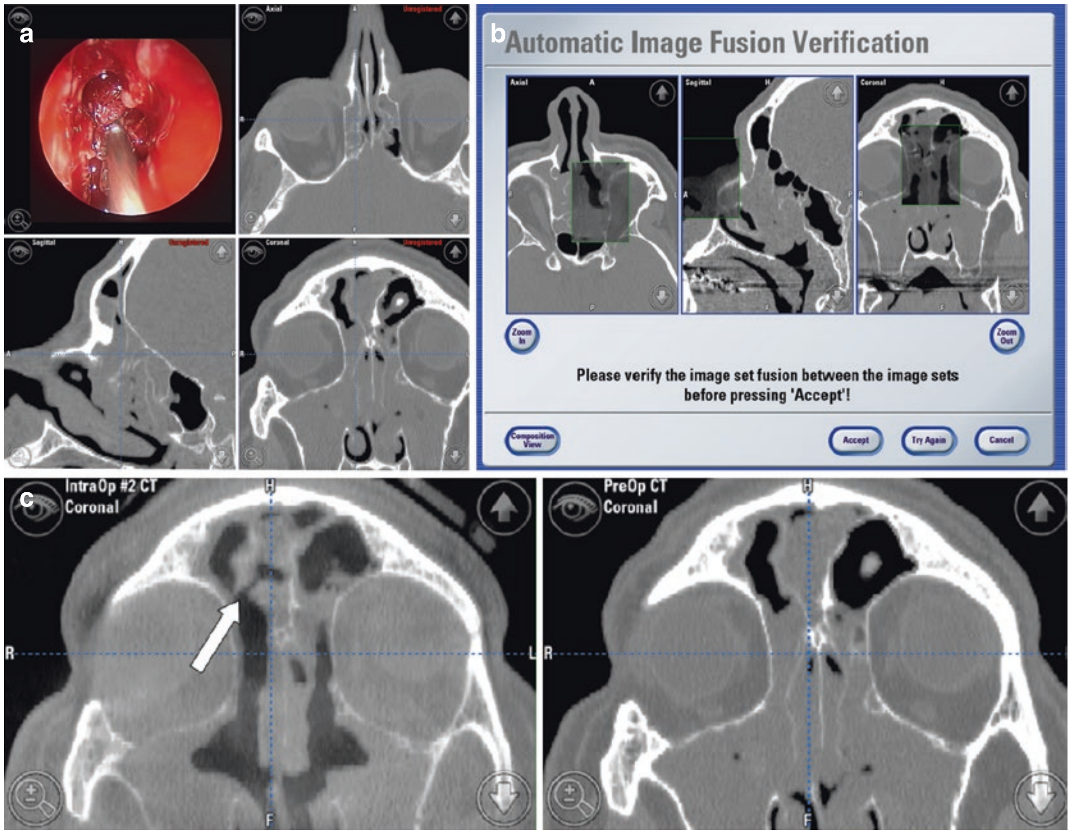

Fig. 27.10 Intraoperative endoscopic view and triplanar CT imaging of a patient with bilateral nasal polyposis and a right frontal recess cell extending into the frontal sinus (type III) (**a**). During real-time update of image-guidance with the xCAT CT scan, it is possible to superimpose images (*boxes*) (**b**) Clearance of polyps and bone in the frontal recess is evident with the initiation of the type III frontal cell dissection on the left hand image (*arrow*) (**c**)

limited to retrospective case series and expert opinion. Practicing otolaryngologists gave their views regarding image-guided sinus surgery in a survey study published by Hepworth et al. (2006). Approximately 75% of otolaryngologists stated that IGS was used in all or some of their cases, while the remaining 25% never used IGS. The chief reason cited for not using IGS was cost (34%). Although 80% of respondents felt that IGS increased safety, this reflects an opinion and does not indicate the actual impact of IGS on safety outcomes during sinus surgery. Yet, despite the differences in opinion, the overwhelming majority (84%) believed that IGS had a role in a subset of surgical cases.

Currently, the American Academy of Otolaryngology-Head and Neck Surgery feels there is sufficient expert consensus opinion and evidence in the literature to endorse the use of IGS in appropriately selected cases (Marple and Setzen 2006). The Academy is also of the opinion that it is impossible to corroborate this with Level 1 evidence. Appropriate indications purportedly include revision surgery, extensive polyposis, disease involving the skull base, post-traumatic, benign or malignant tumors, and pathology involving the frontal, posterior ethmoid and sphenoid sinuses.

27.3.2 Other Applications for IGS

Despite the acceptance and widespread use of image-guidance in endoscopic sinus surgery, this technology has not been universally incorporated into other fields within otolaryngology. In otology and neurotology, image-guidance systems have been used for middle cranial fossa surgery, aural atresia, cochlear implantation, and approaches to the petrous apex (Sargent and Bucholz 1997; Caversaccio et al. 2003; Van Havenbergh et al. 2003; Miller et al. 2006; Rafferty et al. 2006). However, the use of these systems is rare and not generally accepted as beneficial for routine use by otologic and neurotologic surgeons. Other applications within otolaryngology have been limited to needle biopsies and facial trauma (Fried et al. 1998a, b; Kokoska et al. 2003; Stuck et al. 2012). As always, the system itself cannot be used in place of detailed, thorough knowledge of head and neck anatomy.

27.4 Future Directions

In the future, the development of compact, intraoperative MRI scanners will provide real-time up-to-date registrations for image guidance systems. This will be most beneficial in the fields of skull base surgery and neurosurgery, because the anatomic shift of soft tissue during procedures will become a non-factor in the accuracy of the system. Other future possibilities include combined systems (CT with IGS, MRI with IGS) as well as intraoperative imaging and IGS applications for soft tissue surgery in the head and neck.

Conclusion

While technological advances will continue to increase the clinical utility of image-guided surgery systems, the ultimate responsibility for accuracy and anatomic localization in any procedure lies with the surgeon. This technology does not eliminate potential intracranial or orbital complications and is no substitute for expert knowledge of the anatomy and sound surgical training. However, IGS does provide additional information for intraoperative decision-making, especially in the absence of normal anatomic landmarks.

References

Aldrich JE, Bilawich AM, Mayo JR (2006) Radiation doses to patients receiving computed tomography examinations in British Columbia. Can Assoc Radiol J 57:79–85

Anon JB, Lipman SP, Oppenheim D, Halt RA (1994) Computer-assisted endoscopic sinus surgery. Laryngoscope 104(7):901–905

Cartellieri M, Vorbeck F (2000) Endoscopic sinus surgery using intraoperative computed tomography imaging for updating a three-dimensional navigation system. Laryngoscope 110(2 Pt 1):292–296

Caversaccio M, Romualdez J, Baechler R, Nolte LP, Kompis M, Häusler R (2003) Valuable use of computer-aided surgery in congenital bony aural atresia. J Laryngol Otol 117:241–248

Cohnen M, Wittsack HJ, Assadi S, Muskalla K, Ringelstein A, Poll LW, Saleh A, Mödder U (2006) Radiation exposure of patients in comprehensive computed tomography of the head in acute stroke. AJNR Am J Neuroradiol 27:1741–1745

Conley DB, Tan B, Bendok BR, Batjer HH, Chandra R, Sidle D, Rahme RJ, Adel JG, Fishman AJ (2011) Comparison of intraoperative portable CT scanners in Skull Base and endoscopic sinus surgery: single center case series. Skull Base 21:261–270

Fried MP, Morrison PR (1998) Computer-augmented endoscopic sinus surgery. Otolaryngol Clin N Am 31(2):331–340

Fried MP, Topulos G, Hsu L, Jalahej H, Gopal H, Lauretano A, Morrison PR, Jolesz FA (1998a) Endoscopic sinus surgery with magnetic resonance imaging guidance: initial patient experience. Otolaryngol Head Neck Surg 119:374–380

Fried MP, Hsu L, Jolesz FA (1998b) Interactive magnetic resonance imaging-guided biopsy in the head and neck: initial patient experience. Laryngoscope 108(4 Pt 1):488–493

Hepworth EJ, Bucknor M, Patel A, Vaughan WC (2006) Nationwide survey on the use of image-guided functional endoscopic sinus surgery. Otolaryngol Head Neck Surg 135:68–73

Jackman AH, Palmer JN, Chiu AG, Kennedy DW (2008) Use of intraoperative CT scanning in endoscopic sinus surgery: a preliminary report. Am J Rhinol 22:170–174

Jeon JS, Lee SH, Son YJ, Yang HJ, Chung YS, Jung HW (2013) Mobile computed tomography: three year clinical experience in Korea. J Korean Neurosurg Soc 53:39–42

Kato A, Yoshimine T, Hayakawa T, Tomita Y, Ikeda T, Mitomo M, Harada K, Mogami H (1991) A frameless, armless navigational system for computer-assisted neurosurgery. Technical note. J Neurosurg 74:845–849

Kennedy DW, Senior BA (1997) Endoscopic sinus surgery. A review. Otolaryngol Clin N Am 30:313–330

Kennedy DW, Zinreich SJ, Rosenbaum AE, Johns ME (1985) Functional endoscopic sinus surgery. Theory and diagnostic evaluation. Arch Otolaryngol 111:576–582

Kennedy DW, Shaman P, Han W, Selman H, Deems DA, Lanza DC (1994) Complications of ethmoidectomy: a survey of fellows of the American Academy of Otolaryngology—Head and Neck Surgery. Otolaryngol Head Neck Surg 111(5):589–599

Kokoska MS, Hardeman S, Stack BC, Citardi MJ (2003) Computer-aided reduction of zygomatic fractures. Arch Facial Plast Surg 5:434–436

Maciunas RJ, Galloway RL Jr, Fitzpatrick JM, Mandava VR, Edwards CA, Allen GS (1992) A universal system for interactive image-directed neurosurgery. Stereotact Funct Neurosurg 58(1–4):108–113

Marple BF, Setzen M (2006) Image-guidance technology: what type of information best guides its appropriate use? Otolaryngol Head Neck Surg 135:173–175

Messerklinger W (1967) On the drainage of human paranasal sinuses under normal and pathologic conditions. 2. The frontal sinus and its evacuation systemMonatsschr Ohrenheilkd Laryngorhinol 101:313-326. [German]

Metson R, Gliklich RE, Cosenza M (1998) A comparison of image guidance systems for sinus surgery. Laryngoscope 108(8 Pt 1):1164–1170

Miller RS, Hashisaki GT, Kesser BW (2006) Image-guided localization of the internal auditory canal via the middle cranial fossa approach. Otolaryngol Head Neck Surg 134:778–782

Palmer JN, Kennedy DW (2005) Historical perspective on image-guided sinus surgery. Otolaryngol Clin N Am 38:419–428

Pergolizzi RS Jr, Nabavi A, Schwartz RB, Hsu L, Wong TZ, Martin C, Black PM, Jolesz FA (2001) Intraoperative MR guidance during trans-sphenoidal pituitary resection: preliminary results. J Magn Reson Imaging 13:136–141

Perry JH, Rosenbaum AE, Lunsford LD, Swink CA, Zorub DS (1980) Computed tomography/guided stereotactic surgery: conception and development of a new stereotactic methodology. Neurosurgery 7:376–381

Phelps P, Savy L, Richards P (2000) The future of imaging in otolaryngology. J Laryngol Otol 114:659–660

Rafferty MA, Siewerdsen JH, Chan Y, Daly MJ, Moseley DJ, Jaffray DA, Irish JC (2006) Intraoperative cone-beam CT for guidance of temporal bone surgery. Otolaryngol Head Neck Surg 134:801–808

Reardon EJ (2002) Navigational risks associated with sinus surgery and the clinical effects of implementing a navigational system for sinus surgery. Laryngoscope 112(7 Pt 2 Suppl 99):1–19

Sargent EW, Bucholz RD (1997) Middle cranial fossa surgery with image-guided instrumentation. Otolaryngol Head Neck Surg 117:131–134

Schlaier J, Warnat J, Brawanski A (2002) Registration accuracy and practicability of laser-directed surface matching. Comput Aided Surg 7:284–290

Siewerdsen JH, Jaffray DA (2001) Cone-beam computed tomography with a flat-panel imager: magnitude and effects of X-ray scatter. Med Phys 28:220–231

Stuck BA, Hülse R, Barth TJ (2012) Intraoperative cone beam computed tomography in the management of facial fractures. Int J Oral Maxillofac Surg 41:1171–1175

Sukovic P (2003) Cone beam computed tomography in craniofacial imaging. Orthod Craniofac Res 6(Suppl 1):31–36. discussion 179–182

Suzuki M, Sakurai H, Seno S, Kitanishi T, Shimizu T, Nishida Y, Morikawa H, Inubushi T, Kitano H (2005) Use of real-time magnetic resonance image guidance in endoscopic sinus surgery. Minim Invasive Ther Allied Technol 14:376–384

Van Havenbergh T, Koekelkoren E, De Ridder D, Van De Heyning P, Verlooy J (2003) Image guided surgery for petrous apex lesions. Acta Neurochir 145(9):737–742; discussion 742

Wise SK, DelGaudio JM (2005) Computer-aided surgery of the paranasal sinuses and skull base. Expert Rev Med Devices 2:395–408

Woodworth BA, Davis GW, Schlosser RJ (2005) Comparison of laser versus surface-touch registration for image-guided sinus surgery. Am J Rhinol 19(626):623

Zinreich SJ, Kennedy DW, Rosenbaum AE, Gayler BW, Kumar AJ, Stammberger H (1987) Paranasal sinuses: CT imaging requirements for endoscopic surgery. Radiology 163:769–775

Obstructive Sleep Apnea Hypopnea Syndrome

28

Saulo L. Sousa Melo, Zhimin Li, Kivanç Kamburoğlu, Yuko Shigeta, Takumi Ogawa, Reyes Enciso, and William C. Scarfe

Contents

Saulo L. Sousa Melo, D.D.S., M.S.D., Ph.D., M.S (✉)
Department of Oral Pathology, Radiology and Medicine, University of Iowa College of Dentistry, Iowa City, IA, USA
e-mail: saulo-sousamelo@uiowa.edu

Z. Li, D.D.S., Ph.D.
Department of Oral Radiology, Jilin University, School and Hospital of Stomatology, Chang Chun, Jilin Province, China
e-mail: zhimin@jlu.edu.cn

K. Kamburoğlu, D.D.S., M.Sc., Ph.D.
Faculty of Dentistry, Department of Oral and Maxillofacial Radiology, Ankara University, Ankara, Turkey
e-mail: dtkivo@yahoo.com

Y. Shigeta, D.D.S., Ph.D. • T. Ogawa, D.D.S., Ph.D.
Department of Fixed Prosthodontic, School of Dental Medicine, Tsurumi University, Yokohama, Japan
e-mail: shigeta-y@tsurumi-u.ac.jp, ogawa-t@tsurumi-u.ac.jp

R. Enciso, Ph.D.
Department of Dental Public Health and Pediatric Dentistry, Herman Ostrow School of Dentistry, University of Southern California, Los Angeles, CA, USA
e-mail: renciso@usc.edu

William C. Scarfe, B.D.S., M.S.
Division of Radiology and Imaging Science, Department of Surgical/Hospital Dentistry, University of Louisville School of Dentistry, Louisville, KY, USA
e-mail: william.scarfe@louisville.edu

W.C. Scarfe, C. Angelopoulos (eds.), *Maxillofacial Cone Beam Computed Tomography*,
https://doi.org/10.1007/978-3-319-62061-9_28

28.1 Introduction

Sleep-disordered breathing (SDB) describes a group of disorders characterized by a disturbance in normal respiratory pattern during sleep. Those related to increased upper airway resistance include snoring, respiratory effort related arousals (RERA), upper airway resistance syndrome (UARS), and sleep apnea. Sleep apnea is defined simply as a cessation of airflow for 10 or more seconds; however, there are a number of types based on etiology. Obstructive sleep apnea–hypopnea syndrome (OSAHS) is a type of sleep apnea in which there is interrupted breathing during sleep due to collapse of the airway when the pharyngeal and tongue muscles relax resulting in an obstructive event. Sleep apnea also can occur if the neurons that control breathing malfunction during sleep (central sleep apnea).

OSAHS is a specific disorder characterized by snoring, repetitive total or partial collapse of the pharyngeal airway during sleep and the need for arousal to resume ventilation. Airway obstruction is manifested by a reduction in airflow, termed hypopnea, or a complete cessation of airflow, termed apnea, despite ongoing inspiratory effort.

Hypopnea is defined in adults as a 10-s event where, despite continued breathing effort, there is reduction of airflow below 70% for 10 s or longer with a 4% or greater blood oxygen desaturation (Iber et al. 2007). Apnea is total cessation of airflow for at least 10 s. Both result in a reduction of oxygen saturation levels in the blood, detectable with oximetry. This results in involuntary and unconscious cerebral activity triggering the upper airway musculature and opening the upper airway. The person may snort or gasp, then resume snoring. This cycle may be repeated several hundred times a night.

The prevalence of SDB is common, with at least 10% of the population suffering from a clinically significant sleep disorder and therefore this is an important public health concern. In a study of 6139 individuals of US population, over the age of 16, the prevalence of physician-diagnosed sleep apnea was 4.2%. The prevalence by age and gender is shown in the figure below (Fig. 28.1). A peak in prevalence occurs among 50–59-year-olds (7.1%), with gradual reductions to 3% among 80-year-olds (Ram et al. 2010). SDB is not a condition exclusive to adults. Approximately 2% of children have SDB. Prevalence increases in children between 2 and 7 years and is between 2.5 and 6% among adolescents, with a higher predilection for boys (Rosen et al. 2003; Greenfield et al. 2003; Johnson and Roth 2006; Wildhaber and Moeller 2007).

The early effects of repeated disrupted sleep are waking somnolence, impaired mental function, delayed reaction time, and difficulty maintaining concentration. In children numerous authors have reported increased daytime

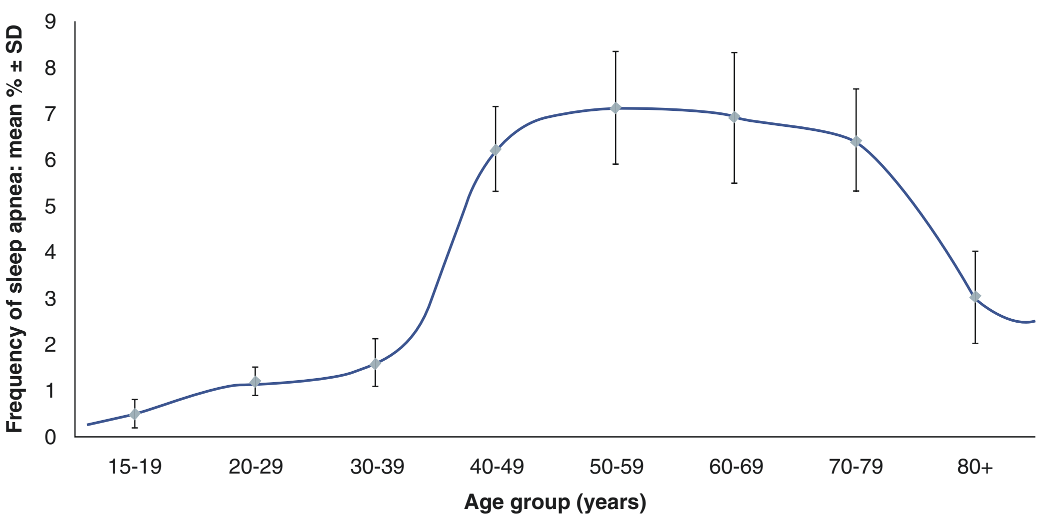

Fig. 28.1 Average prevalence (with standard deviation bars) of physician-diagnosed sleep disorders by age group (data from Ram et al. 2010)

sleepiness and sleep problems which have been correlated to an increased risk of hyperactivity and learning problems and attention-deficient/hyperactivity disorder (Corkum et al. 1999; Chervin et al. 2002; Chan et al. 2004; O'Brien et al. 2004). Long-term effects of moderate and severe OSAHS result in potentially severe medical consequences. Morbidity has been associated with weight gain, learning and memory difficulties, increased sick time, poor job performance, depression, irritability, impotence, and headaches. Patients with OSAHS also have a higher probability of accidents (sometimes fatal) either on the job site (Roth et al. 1988) or while driving (Findley et al. 1988). More importantly OSAHS has been associated with cardiovascular conditions such as hypertension (systemic hypertension is observed in 50–70% of patients with OSA), heart disease, congestive heart failure, pulmonary hypertension, cardiac arrhythmia, ischemic heart disease, and stroke (Yamashiro and Kryger 1994).

28.2 Presentation and Predictors of OSAHS

Sleep apnea is not always easily diagnosed as symptoms might not be evident, either to the patient or others. Common symptoms of sleep apnea are snoring, witnessed apneas, gasping for air, and choking sensations during sleep. Daytime symptoms may include somnolence, daytime fatigue and tiredness, and poor concentration. Factors contributing to the presence and severity of OSAHS are multifactorial and include:

Physical reduction in airway space. This includes reduced upper-airway (UA) anatomy and physical nasal obstruction, enlarged tongue, adenotonsillar hypertrophy (particularly in children and young adults), uvula size, and tonsillar occlusion, qualitatively assessed by the Mallampati score (Fig. 28.2). On average, for every 1-point increase in the Mallampati score, the odds of having an AHI greater than or equal to 5 increases more than twofold (Nuckton et al. 2006).

- **The presence and distribution of body fat**. Being even moderately overweight is the most common risk factor, especially a body mass index or BMI (weight in kilograms divided by height in meters squared) greater than 28.
- **Upper airway collapsibility**. UA collapsibility increases during sleep compared to wakefulness and is significantly higher in sleep apnea patients compared to controls

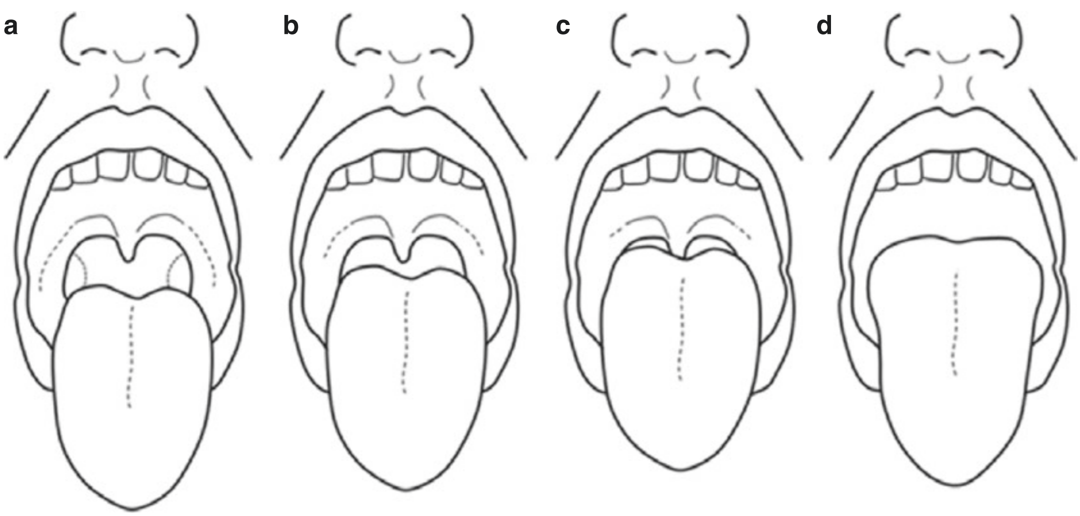

Fig. 28.2 Diagram of Mallampati scoring system for clinical assessment of upper airway space viewed intraorally: (**a**) Class I, full visibility of tonsils, uvula, and soft palate; (**b**) Class II, visibility of hard and soft palate, upper portion of tonsils, and uvula; (**c**) Class III, soft and hard palate and base of the uvula are visible; and (**d**) Class IV, only hard palate visible (modified from Mallampati et al. 1985)

(Malhotra et al. 2001). Also, UA collapsibility during wakefulness correlates highly with UA collapsibility during sleep. Upper airway collapsibility is defined as the pressure difference between the choanae and the epiglottis during the pressure pulse:

$$\text{Collapsibility} = \frac{P_{cho} - P_{epi}}{P_{cho}} \times 100$$

The physiological basis for the continuous positive airway pressure (CPAP) treatment of OSAHS is based on the observation in patients with obstructive sleep apnea that the critical pressure (Pcrit) can be defined experimentally as the level of nasal pressure below which maximal inspiratory airflow ceases. Schwartz et al. (1988) demonstrated that the normal human upper airway during sleep is characterized by a negative Pcrit and that occlusion may be induced when nasal pressure is decreased below this Pcrit. In patients with OSAHS, complete occlusion of the upper airway accompanies the cessation of airflow during apneas while they sleep.

- **Neck circumference**. A neck circumference greater than 43 cm (17 in.) in men and 37 cm (15 in.) in women is a good prognosticator of OSAHS.
- **Craniofacial skeletal abnormalities**. These are of particular importance in nonobese adults and children and include large overjet, micrognathia, or retrognathia.

28.3 Diagnosis and Treatment

Diagnosis of OSAHS is made through a sleep study that is generally performed at a sleep laboratory. Various physiologic functions related to sleep are recorded using a polysomnogram, a compilation of tests including an electroencephalogram, electrooculogram, electromyogram, and pulse oximetry.

The severity of the OSAHS is indexed using the Apnea/Hypopnea Index (AHI) calculated by adding the total number of apneas and hypopneas and dividing by the number of hours of observed sleep. Another metric is the Respiratory Disturbance Index (RDI). Some diagnosticians use AHI and RDI interchangeably. While similar, the RDI also includes respiratory events such as RERA's that do not technically fit the definitions of apnea or hypopnea but do disrupt sleep. Severity of OSAHS is generally defined using the ratio AHI/RDI. An AHI/RDI of 5–15 is considered mild; 16–25 moderate; and greater than 26 severe. Exact boundaries are somewhat fluid, leading to terms such as "Mild to Moderate" to better describe clinical reality. The upper boundary of "Severe" is relatively open ended, with AHI/RDI's greater than 100 being well known.

Therapies of OSAHS are primarily directed at pneumatically splinting the airway open or secondarily adjusting the airway in making it less apt to collapse. The primary therapy available for the treatment of OSAHS is nightly use of a device called Continuous Positive Airway Pressure (CPAP) (Giles et al. 2006). No matter where the obstruction in the upper airway occurs, this treatment has been shown to be very effective in most cases. In this treatment method, the patient wears a mask at night (Fig. 28.3) attached to a machine that continuously forces air through the entire airway. This keeps the pharynx patent due solely to increased air pressure as if it is being blown up like a balloon. It is usually provided in association with behavioral changes such as avoiding alcohol, smoking, and medicines that cause sleepiness, and altered sleep posture

Fig. 28.3 Example of CPAP device with patient wearing full face mask

or nutritional and dietary counseling to reduce weight. Unfortunately, CPAP is a cumbersome modality with approximately 25–50% of patients with OSAHS either refusing CPAP therapy or unwilling to tolerate it (Zozula and Rosen 2001).

Secondary therapy for patients suffering from OSAHS who cannot tolerate CPAP is directed towards physically widening the pharyngeal airway. This can be performed reversibly by the use of removable oral appliances (OAs) or permanently by surgery.

Oral appliances are recommended by the American Academy of Sleep Medicine as a primary treatment for use in patients with mild to moderate OSAHS who prefer them to continuous positive airway pressure (CPAP) therapy, those who do not respond to, are not appropriate candidates for, or who fail treatment attempts with CPAP (Kushida et al. 2006). The US Food and Drug Administration (FDA) has approved the use of these devices only for individuals 18 years and older. Although oral appliances are being used for the treatment of children, there is currently a lack of evidence on the clinical efficacy of OAs in the pediatric population.

OAs are categorized by the method used to improve the patency of the airway space. There are many different types of appliance design, but no official criteria exist for the ideal amount of mandibular protrusion, nor for the amount of vertical opening to be associated with it. Success rates of these devices vary.

The most common OAs are mandibular advancement devices (MAD) designed to protrude the mandible anteriorly and pull the muscles of the oropharynx forward (Fig. 28.4), and tongue retaining devices (TRD) that aim at holding the tongue in a protrusive position. Devices protrude the mandible either as fixed amount or are titrated to the individual, usually at 75% of maximal protrusion. The most common MAD devices operate by capitalizing on the attachment of the mandible to the tongue, pharyngeal dilator muscles, and indirectly the soft palate. By moving the mandible anteriorly, these structures are moved forward as well, thereby increasing the airway space (Battagel et al. 1998; Clark et al. 1993; Lowe 1993; Tsuiki et al. 2001, 2004a, b) (Fig. 28.5). These devices can be titrated to best fit the patient for comfort and efficiency (Fig. 28.4).

OA appliances are therapeutic only if selected appropriately for the specific site(s) of upper airway obstruction, which varies between individuals (Shepard et al. 1991; Launois et al. 1993). In children, rapid maxillary expansion (RME) (Villa et al. 2007, 2011), sometimes in combination with adenoidectomy (Guilleminault et al. 2011), has been found to be an effective appliance for treating children with OSAHS (Fig. 28.6).

For patients with severe AHI and comorbidities (e.g., significant bradycardia, severe hypercarbia, cor pulmonale, and extreme hypersomnolence) on whom CPAP is not a viable option, surgery

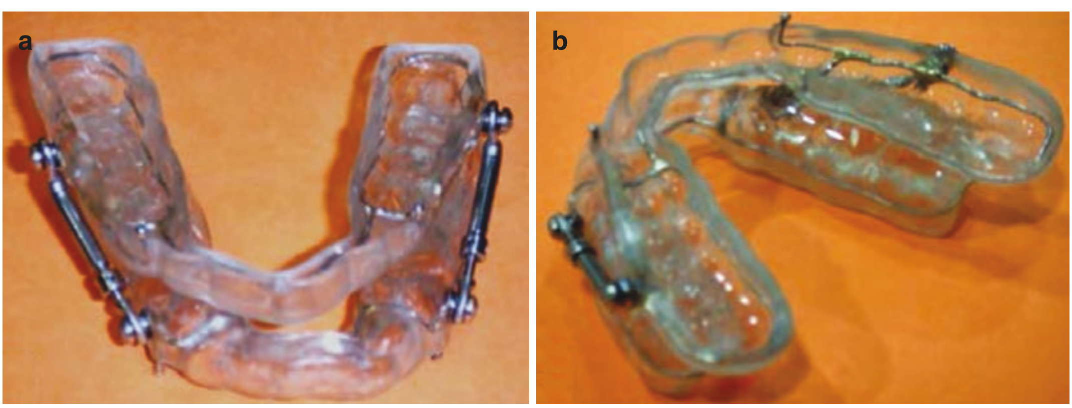

Fig. 28.4 Anterior (**a**) and posterior (**b**) views of a Herbst design MAD device allowing titratable mandibular advancement using a bilateral piston system comprised of rods and sleeves

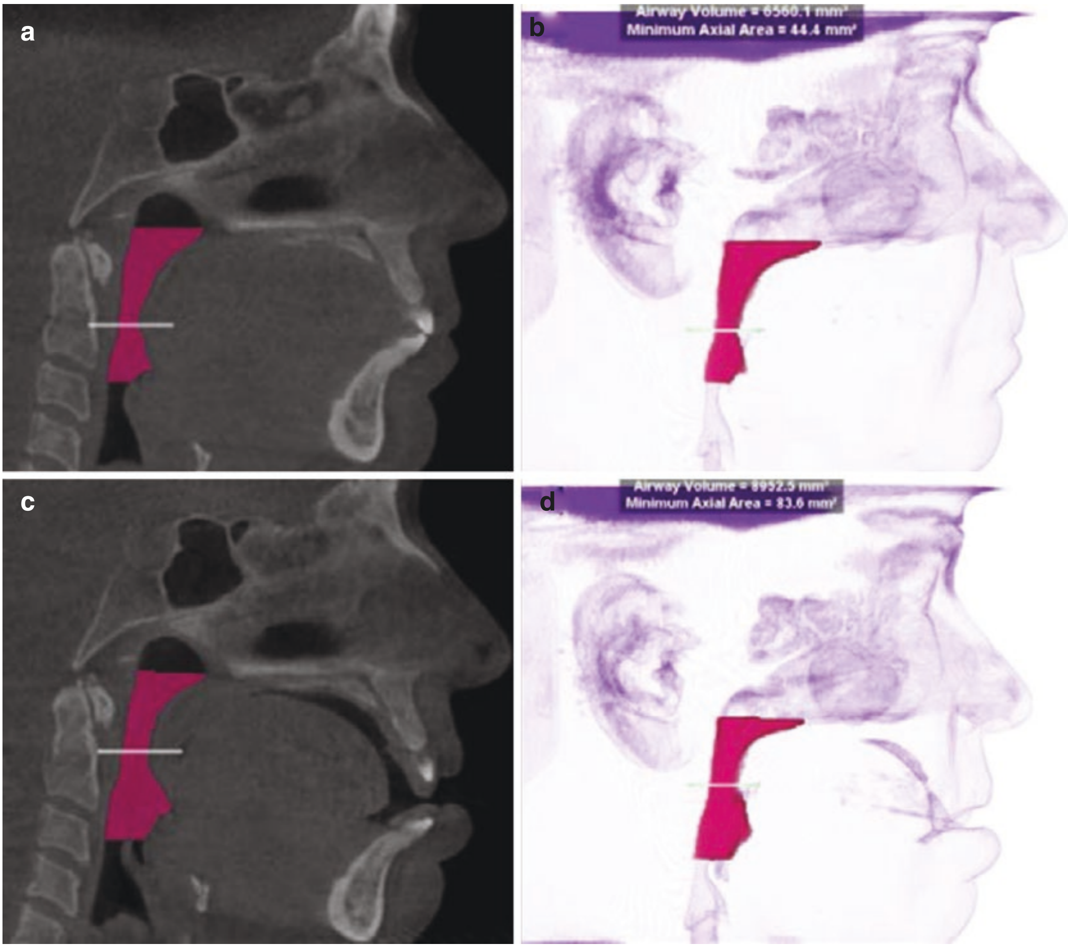

Fig. 28.5 Comparison of midsagittal CBCT image (**a**) and volumetric rendering (**b**) of a patient with OSAHS before and midsagittal CBCT image (**c**) and volumetric rendering (**d**) after MAD device inserted. Oropharyngeal airway (*purple*) shows improvement in anterior–posterior, overall volume, and minimal cross-sectional area with MAD in position (Images created using Dolphin 3D V.11, Dolphin Imaging and Management Solutions Chatsworth, CA)

may be considered. Surgery options include soft or hard tissue correction as well as combination therapies. A number of soft tissue procedures have been used to enlarge the pharyngeal space and prevent airway collapse. These include tonsillectomy, adenoidectomy, radiofrequency ablation of the tongue or soft palate (somnoplasty), uvulopalatopharyngoplasty (UPPP), laser-assisted UPPP, and reduction in tongue size. These therapies are reported to have a relatively low (50%) success rate (Sher et al. 1996).

Orthognathic surgery to position the mandible anteriorly has also been used to improve upper airway caliber. The rationale of this approach is that anterior positioning of the mandible pulls the tongue forward and away from the posterior wall of the oropharynx, thus opening the airway. These procedures include inferior sagittal mandibular osteotomy, maxillomandibular (bimaxillary) osteotomy and advancement and either separate or combined genioglossal advancement with hypoid myotomy. Recently, maxillary and mandibular expansion has also been found to successfully treat sleep apnea (Conley and Legan 2006; Rachmiel et al. 2005). Procedures to improve upper airway patency are successful

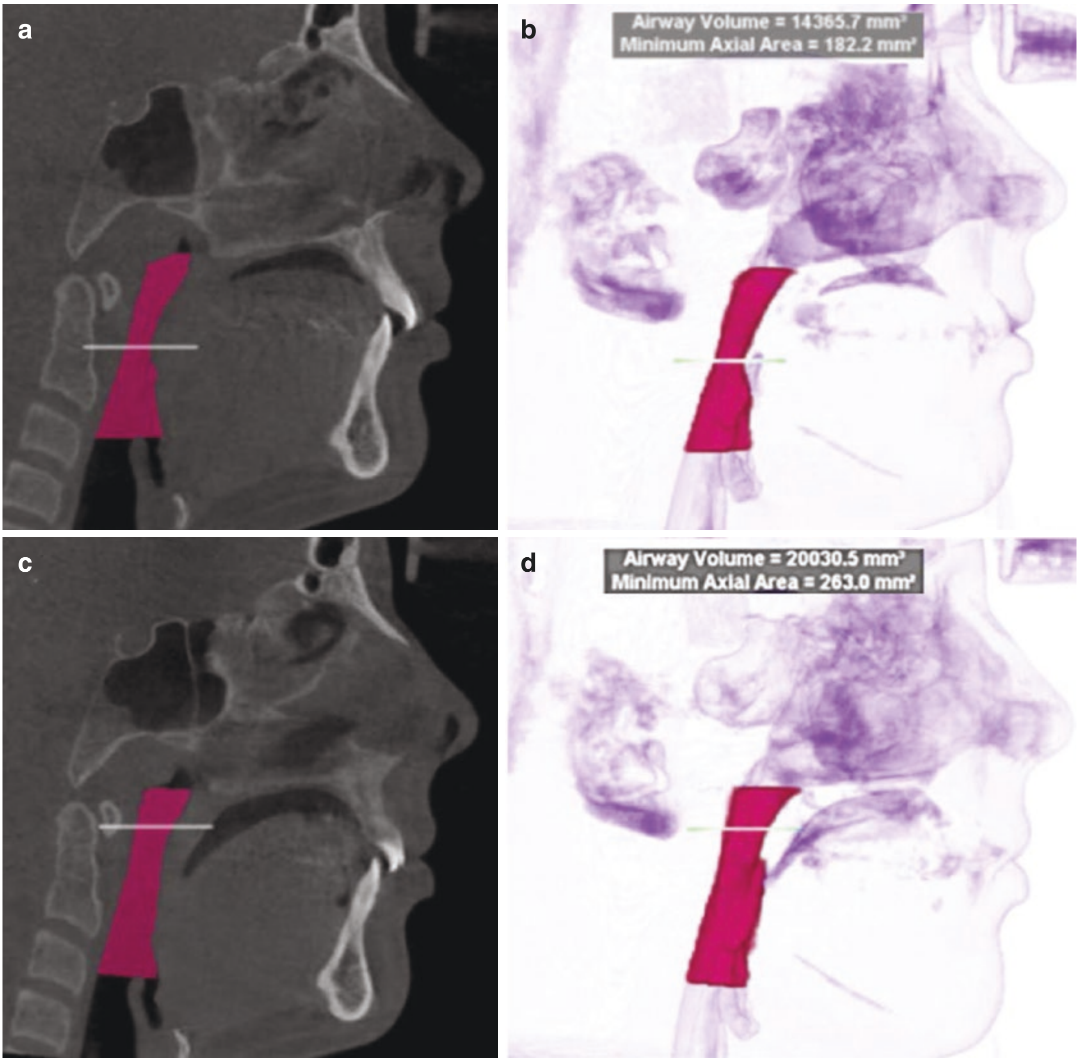

Fig. 28.6 Comparison of midsagittal CBCT image (**a**) and volumetric rendering (**b**) of a patient before and midsagittal CBCT image (**c**) and volumetric rendering (**d**) after RME. Oropharyngeal airway (*purple*) shows improvement in anterior–posterior, overall volume, and minimal cross-sectional area with MAD in position. Images created using Dolphin 3D software (Dolphin Imaging and Management Solutions Chatsworth, CA)

in certain subsets of patients, but some do not achieve desired relief (Veasey et al. 2006).

If secondary treatments are necessary, the site of the oropharyngeal obstruction must be identified such that appropriate therapy can be applied. Numerous supplemental tests can be performed to determine the site of reduction in airway caliber including fiberoptic nasopharyngoscopy (Hsu et al. 2005a, b; Johal et al. 2005), acoustic pharyngometry (Bradley et al. 1986; Hatzakis et al. 2003), rhinomanometry, and optical coherence tomography (Armstrong et al. 2006). The most common method for determining the morphology of the upper airway is radiography.

28.4 Radiographic Imaging for OSAHS

The specific roles of diagnostic imaging in evaluating the upper airway are to determine the site and degree of pharyngeal obstruction

Table 28.1 Upper airway anatomic abnormalities associated with OSAHS

Region	Structure	Condition
Nasal cavity	Turbinate	Hypertrophy, polyps, mucosal thickening, hypersecretion
	Septae	Deviated
Maxillofacial skeletal	Mandible	Relative hypoplasia, deficiency, cross-bite, mandibular tori
	Maxilla	Relative hypoplasia, deficiency, cross-bite
	Hyoid	Caudal displacement relative of the cervical spine and mandible
Upper airway	Soft palate	Excessive length, low lying position
	Tongue	Macroglossia, short length, loss of muscle tone
	Nasopharynx	Hypertrophic adenoids, fatty lumen
	Oropharynx	Hypertrophic tonsils, lumen thickening, fat pad accumulation
	Hypopharynx	Lumen thickening
	Larynx	Abnormal vocal cord anatomy, paralysis of vocal cords

and to identify potential causative conditions (Table 28.1) and anatomic characteristics that may be predictive of therapeutic efficacy.

While most obstructions in OSAHS occur in the region of the oropharynx, a common point of airway blockage is the nasopharynx. Hypertrophied adenoids are a common source of obstruction of the upper airway. This type of obstruction may directly cause OSAHS if the sufferer is not able to breathe through the mouth during sleep, or it can result in mouth breathing. If a patient is still growing, mouth breathing can alter the development of skeletal structures in a growing individual (Major et al. 2006).

There are numerous mechanisms postulated linking maxilloskeletal anomalies with decreased oropharyngeal patency and OSAHS. A skeletal Class II configuration is caused by the maxilla being too far anterior relative to the mandible. It may be caused by the mandible being positioned too far posteriorly, or simply underdeveloped. It may also be due to the maxilla being positioned too far anteriorly, or any combination of these problems in either jaw. In skeletal Class II patients with OSAHS, the problem is likely caused by a posteriorly oriented mandible that is displacing the soft tissues attached to it, impinging on the airway space (Conley and Legan 2006). Retrognathia has also been identified as a contributing factor in OSAHS, with patients having a shorter mandibular body length, with a significantly shorter distance from their posterior pharyngeal wall to the lingual surface of their lower incisors (Johal and Conaghan 2004). A shorter anterior–posterior face length and specifically a lower-positioned hyoid is also a contributing factor (Choi et al. 2000; Fogel et al. 2003; Johal et al. 2007). This anomaly is related to posteriorly displaced tongue because the muscles that connect the tongue to the hyoid, such as the hyoglossus, would pull the tongue posteriorly when the hyoid is more inferior. Soft tissue anomalies such as a larger and longer soft palate, a smaller pharynx, and a larger tongue can also be soft tissue contributors (Johal et al. 2007). The pharyngeal dilator muscles seem to be less effective in preventing pharyngeal lumen collapse in these soft tissue anatomical anomalies.

28.4.1 Dynamic Imaging

During normal sleep, the tone of the pharyngeal musculature is decreased, the airway dimension is narrowed, and the resistance to breathing is increased. If resistance to breathing occurs, inspiratory effort must intensify which increases the possibility of collapse and thereby obstruction of the nonrigid portion of the upper airway—namely, the velopharynx and oropharynx. Obstruction occurs when the relative negative airway pressure of inspiration is greater than the force produced by the abductor and dilator muscles of the pharynx.

In imaging the upper airway collapsibility, three parameters can be measured:

1. The percent change in diameter or cross-sectional area of the oropharyngeal airway

during breathing cycle at a pre-defined anatomical structure (usually at the hard palate, tip of the epiglottis, or tip of the uvula).
2. The smallest cross-section area (usually in the retro-palatal area).
3. The percentage change in volume at different times during the breathing cycle.

Two modalities have been used in research to describe changes in the upper airway during normal sleep and in individuals with SDB:

- **Cine-MRI**. During natural sleep changes in anterior–posterior (AP) and lateral width of the airway observed in the retro-palatal (RP) region (between hard palate and tip of the uvula) are substantially greater than changes in the retro-glossal (RG) region (from the tip of the uvula to the top of the epiglottis) (Trudo et al. 1998). Reduction in the RP airway area results from posterior movement of the soft palate, thickening of the lateral pharyngeal walls, and an increase in tongue oblique distance. As compared to normal patients, patients with OSAHS show greater reduction in the diameter and cross-sectional area of the oropharynx between nasopharynx (Ciscar et al. 2001) or both the nasopharynx and hypopharynx. In children, Arens et al. (2005) found significantly larger percentage change in upper airway cross-sectional area during a tidal breath in OSAHS subjects and significant narrowing of lateral dimension both at different levels of the upper airway and from inspiration to expiration.
- **Fast-CT**. Also named cine-CT or dynamic CT, fast-CT is a two-dimensional technique that provides cross-sectional images of the airway at different breathing phases, in some cases every 0.4 s. Studies using these techniques have found that in OSAHS patients (1) when awake, the airway is narrowed and shows increased collapsibility (Stein et al. 1987), (2) in early inspiration there is an enlargement of airway due to increased activity of upper airway muscles while at the end expiration there is narrowing of upper airway, approaching the fully occluded position (Schwab et al. 1993), and (3) in patients with severe OSAHS there is significantly reduction in cross-sectional area at the level of uvula in expiration, but not during tidal breathing or inspiration (Yucel et al. 2005).

28.4.2 Static Imaging

28.4.2.1 Lateral Cephalometric Radiography

Lateral cephalometric radiography (LCR) has long been used in clinical practice to quantify anatomic differences in OSAHS patient to both identify and characterize patients with the condition and measure treatment outcome. LCR is inexpensive, readily available and widely used with low radiation dose to the patient. However, the images are only two-dimensional, providing anterior–posterior information. Consequently, medial-lateral dimensions cannot be measured (Fig. 28.7). Numerous authors have reported a

Fig. 28.7 Comparison of conventional lateral cephalometric (**a**), CBCT ray sum generated simulated lateral cephalometric image (**b**), and lateral view of maximum intensity projection (**c**) of the same patient

variety of craniofacial anatomical abnormalities associated with OSAHS on LCR including reduced retroglossal airway linear dimensions, a long, bulky soft palate, an inferiorly placed hyoid bone, and mandibular deficiency (Riley et al. 1983; Rivlin et al. 1984; Hochban and Brandenburg 1994; Tangugsorn et al. 1995a, b; Cistulli 1996; Johal and Conaghan 2004). Unfortunately, studies vary in quality (Miles et al. 1996). Specifically, many of the control groups are not matched populations and frequently the sample size is small. Despite numerous studies providing cephalometric measurements attempting to correlate facial morphology with OSAHS, there is no consistent agreement regarding which specific anatomic markers have the best correlation (Miles et al. 1996). Other disadvantages associated with cephalometric imaging include considerations that the technique is usually performed in an upright posture and a lateral view of airway does not demonstrate the width of the airway.

28.4.2.2 Computed Tomography and Magnetic Resonance Imaging

Computed tomography and magnetic resonance imaging have been used in the research environment in both awake and sleeping subjects to provide three-dimensional metrics of the naso-, oro-, and hypo-pharyngeal regions such as minimal cross-sectional area, minimal antero-posterior/lateral dimensions, and airway volumes.

The results from these studies indicate that the upper airway is significantly narrowed among patients with OSAHS compared to controls, but that the site of narrowing varies among OSAHS patients. Using CT in a limited number of awake patients, Suratt et al. (1983) demonstrated that the narrowest section of the airway in patients compared to control subjects was the region posterior to the soft palate. Sforza et al. (2000) reported a significant association between airway collapsibility and both soft palate length and hyoid bone position. Kato et al. (2000) reported that airway collapsibility was inversely proportional to the amount of mandibular advancement, thus establishing a direct causal relationship between airway volume and collapsibility. Schwab et al. (1995) found with MRI in awake subjects at the minimum airway area, that the thickness of the lateral pharyngeal muscular walls rather than enlargement of the parapharyngeal fat pads was the predominant anatomic factor causing airway narrowing in apneic subjects. In a follow-up study using MRI, Schwab et al. (2003) found a significantly increased risk of sleep apnea the larger the volume of the tongue, lateral pharyngeal walls, and total soft tissue. Chen et al. (2002) found that the anteroposterior and the lateral diameters of the retropalatal (RP) region, as well as the smallest area of the RP region, are significantly smaller in subjects with OSAHS.

28.4.2.3 Cone Beam Computed Tomography

CBCT has particular application in the diagnosis and assessment of therapy in OSAHS patients and has the potential to eliminate the need for additional static imaging. A main advantage of using CBCT to image the oropharynx is the low dosage of radiation relative to conventional spiral computed tomography The resulting volume of digital data can be manipulated to allow the clinician three-dimensional (3D) images that can be reoriented in all three axes to correspond to anthropometric reference planes (Fig. 28.8), and can be selectively contrasted, emphasized, or reduced to visualize certain anatomical structures such as the craniofacial skeleton or airway (Fig. 28.9).

Data can be exported as Digital Imaging and Communications in Medicine (DICOM) format dataset and imported into proprietary orthodontic image and analysis programs (e.g., InVivoDental, Anatomage, San Jose, CA; Dolphin 3D, Dolphin Imaging and Management Solutions Chatsworth, California, USA; Amira software, FEI Visualization Sciences Group, Hillsboro, Oregon, USA; OnDemand3D, CyberMed Inc., Torrance, California, USA; 3dMDvultus, 3dMD Atlanta, Georgia, USA) which have specific modules capable of measuring linear and volumetric parameters of the airway and its surrounding structures (Figs. 28.10 and 28.11). These programs offer practitioners opportunities to interact with the data and allow visualization of both untreated obstruction tendencies and potentially of changes in the airway by treatment modality. In this way

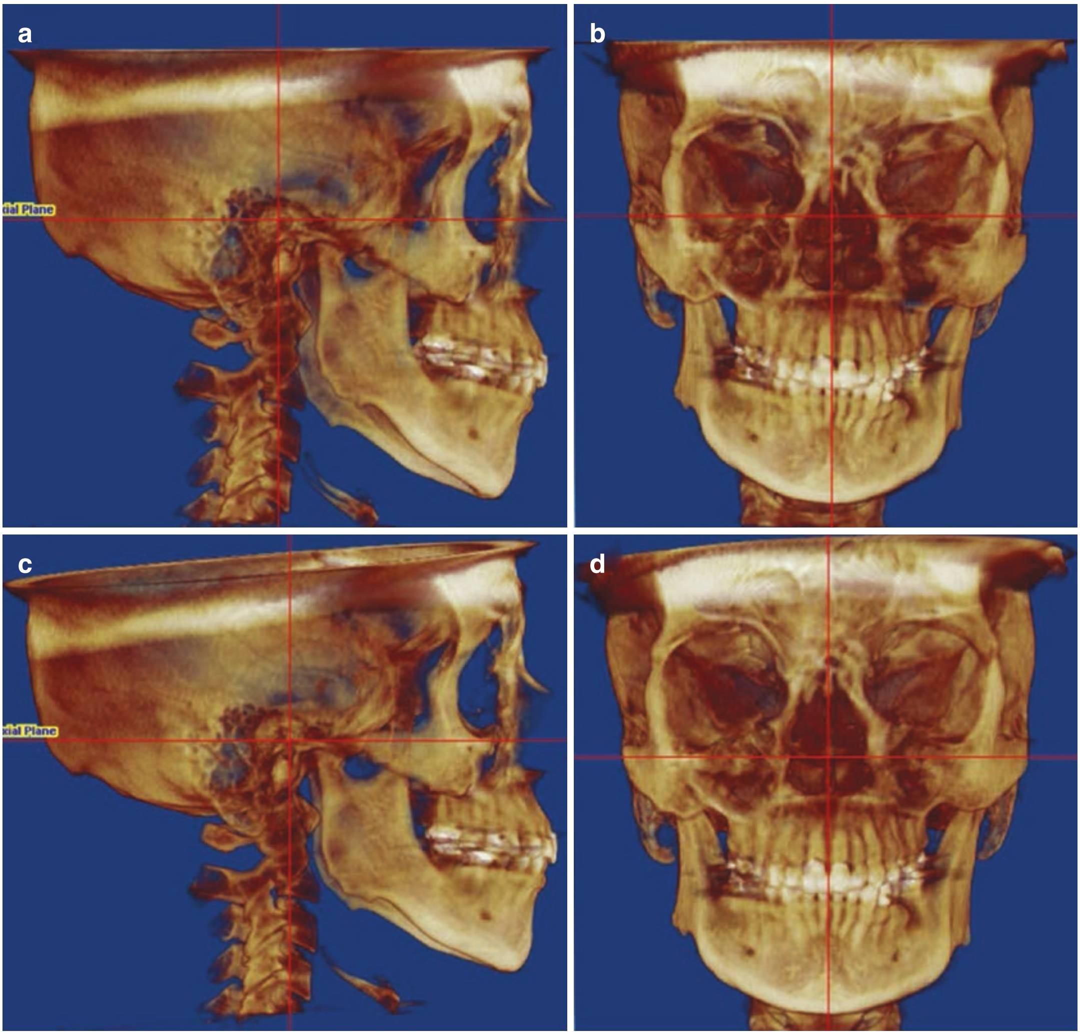

Fig. 28.8 Reorientation of volumetric data to adjust patient head position during scan to anthropomorphic standard reference planes. Lateral (**a**) and frontal (**b**) volume rendering show that the patient originally scanned with the head tilted down and towards the left. Comparable lateral (**c**) and frontal (**d**) volumetric rendering with adjusted data to position Frankfurt horizontal (FH) parallel to floor and the midsagittal plane perpendicular to FH

it may help identify those subsets of patients who may or may not benefit from a choice of treatment modalities.

Potential Limitations

There are a number of considerations that should be taken into account when interpreting metrics obtained from software analysis of the airway.

- **Validity**. The greatest reduction in the airway space occurs when the patient is asleep and supine; however, most CBCT units acquire images of the airway upright in either the standing or seated position (Tsuiki et al. 2003, 2005). In addition, the tonicity of the musculature is very different when the patient is supine as compared to when they are awake and influences upper airway anatomic characteristics (Tsuiki et al. 2003). Therefore, while CBCT measurements should not be considered absolute and only a relative index of airway obstruction.
- **Patient Jaw Position and Instructions During the Scan**. The position of the jaw during the scan can greatly influence the airway measurements obtained. Performing the scan in centric occlusion (maximum dental inter-

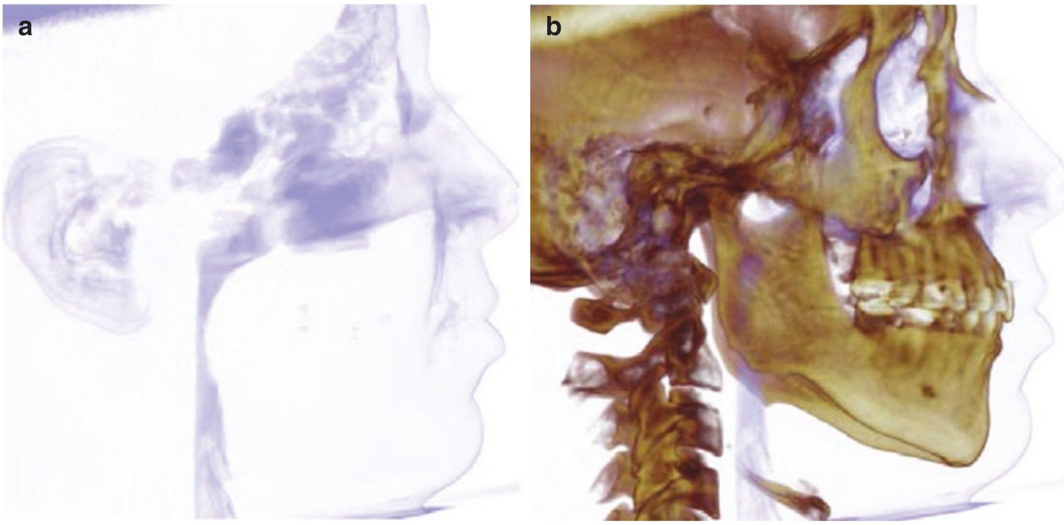

Fig. 28.9 Volumetric rendering of the right side of an OSAHS patient demonstrating airway only (**a**) and with maxillofacial skeleton overlay (**b**). This is performed by selective thresholding and segmentation procedures

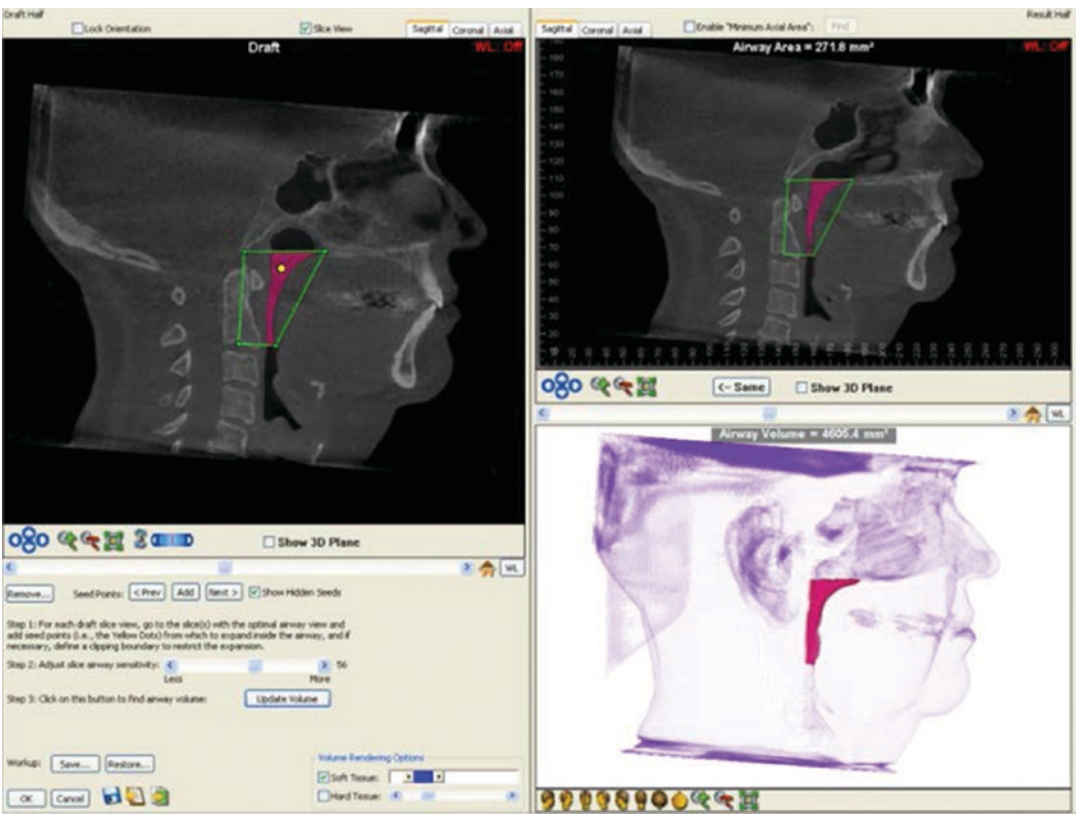

Fig. 28.10 Screen capture of airway assessment module from Dolphin 3D software (Dolphin Imaging and Management Solutions Chatsworth, California, USA)

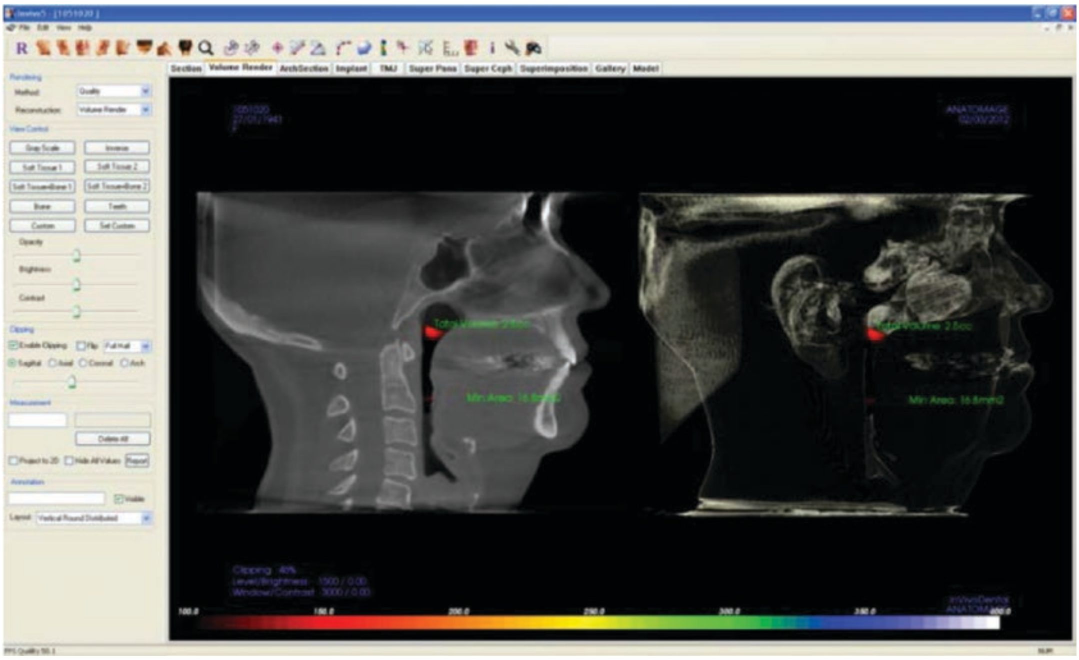

Fig. 28.11 Composite screen capture of airway assessment module from InVivo software (Version 5, Anatomage, San Jose, California, USA)

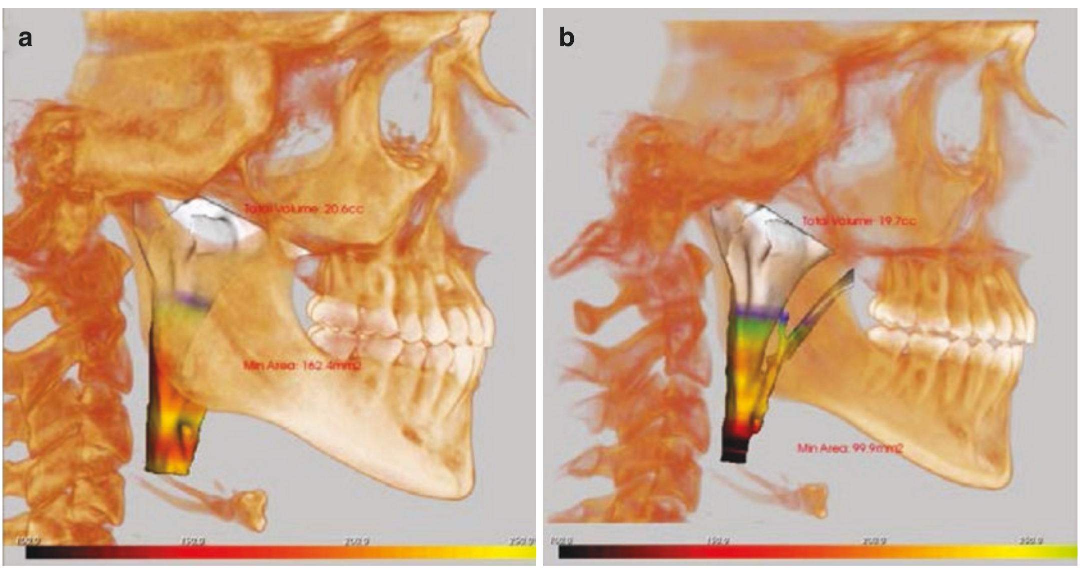

Fig. 28.12 Comparative midsagittal airway volume in centric occlusion (**a**) (minimal cross-sectional area = 162.4 mm²) and centric relation (**b**) (minimal cross-sectional area = 99.9 mm²) of 16-year-old female with TMJ pain, Epworth score of 10, and difficulty in jaw movement for 2 years. The minimal cross-sectional area discrepancy between the two positions is 39%

cuspation), centric relation (Fig. 28.12), or with a dental orthotic in position (Tsuiki et al. 2001, 2004a) (Fig. 28.13) can influence volumetric and area measurements. In addition, it is advisable to provide with some guidance on what to do with their tongue during the scan as retroposition of the tongue can reduce the airway space and influence the position of

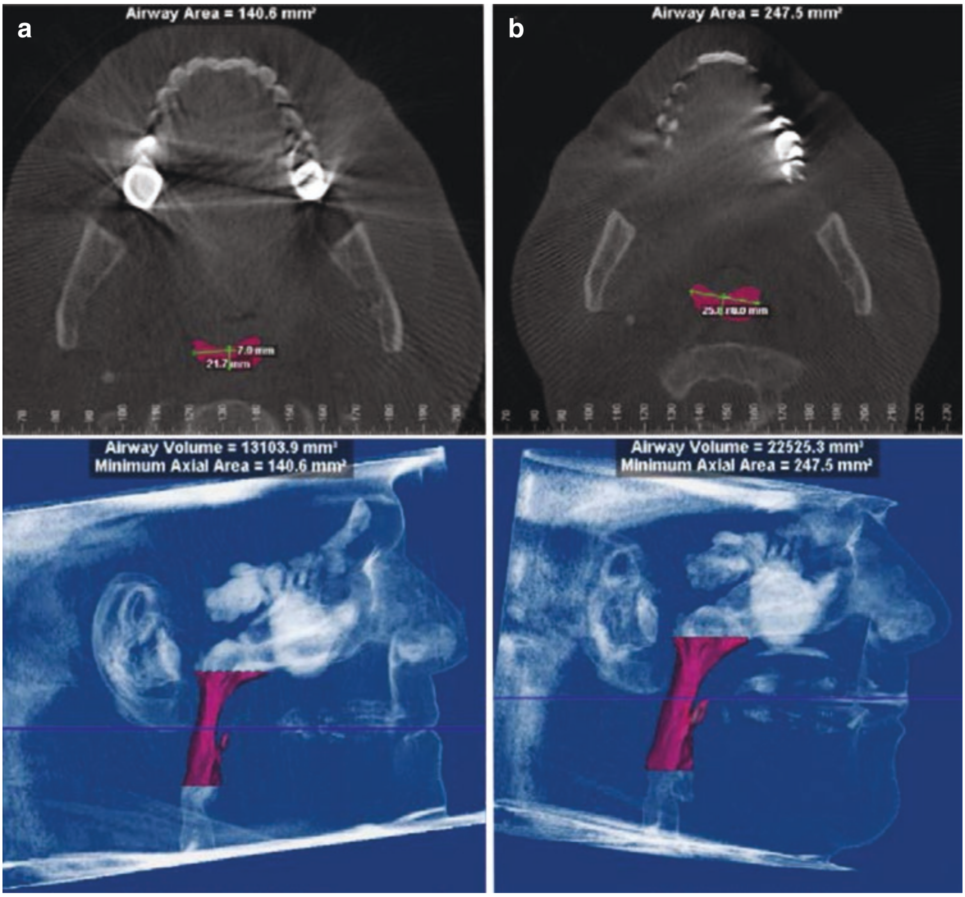

Fig. 28.13 Comparative axial (*upper*) and hollow volumetric (*lower images*) in centric occlusion (**a**) (minimal cross-sectional area = 140.6 mm^2) and with a maxillary anterior guided orthotic (MAGO) in position (**b**) (minimal cross-sectional area = 247.5 mm^2) of 68-year-old male with TMJ pain. Note that both antero-posterior and transverse linear dimensions increase with the MAGO in. Images created using Dolphin 3D software (Dolphin Imaging and Management Solutions Chatsworth, California, USA)

the hyoid (Camacho et al. 2014). Therefore, it is advisable to ensure that the position of the jaw is standardized and patients are provided with instructions on what to do when scanning is performed. As tongue positioning may determine the size of the airway, CBCT studies demonstrating air space between the tongue and hard palate may signify posterior positioning of the tongue (Fig. 28.14). Some have suggested that the Mueller Manoeuvre be performed by patients during the scan. This is performed by asking the patient to make a maximum inspiratory effort with a closed mouth and nostrils occluded. This procedure attempts to simulate the collapsibility of the upper airway at the base of the tongue.

- **Software Accuracy and Reliability**. While the reliability of individual software packages is high overall (Souza et al. 2013), accuracy is variable with all software underestimating volume from 2% for interactive thresholding-based software (e.g., Mimics, Materialise, Leuven, Belgium; Dolphin3D, Dolphin Imaging & Management Solutions, Chatsworth, California, USA; OnDemand3D CyberMed, Seoul, Korea; OsiriX, Pixmeo, Geneva, Switzerland; and ITK-Snap, www.itksnap.org) to 11% for fixed threshold interval-based software (e.g., InVivo Dental, Anatomage, San Jose, California, USA; Mimics; Ondemand3D; OsiriX; and ITK-Snap) (Weissheimer et al. 2012), suggesting systematic errors (El and Palomo 2010).

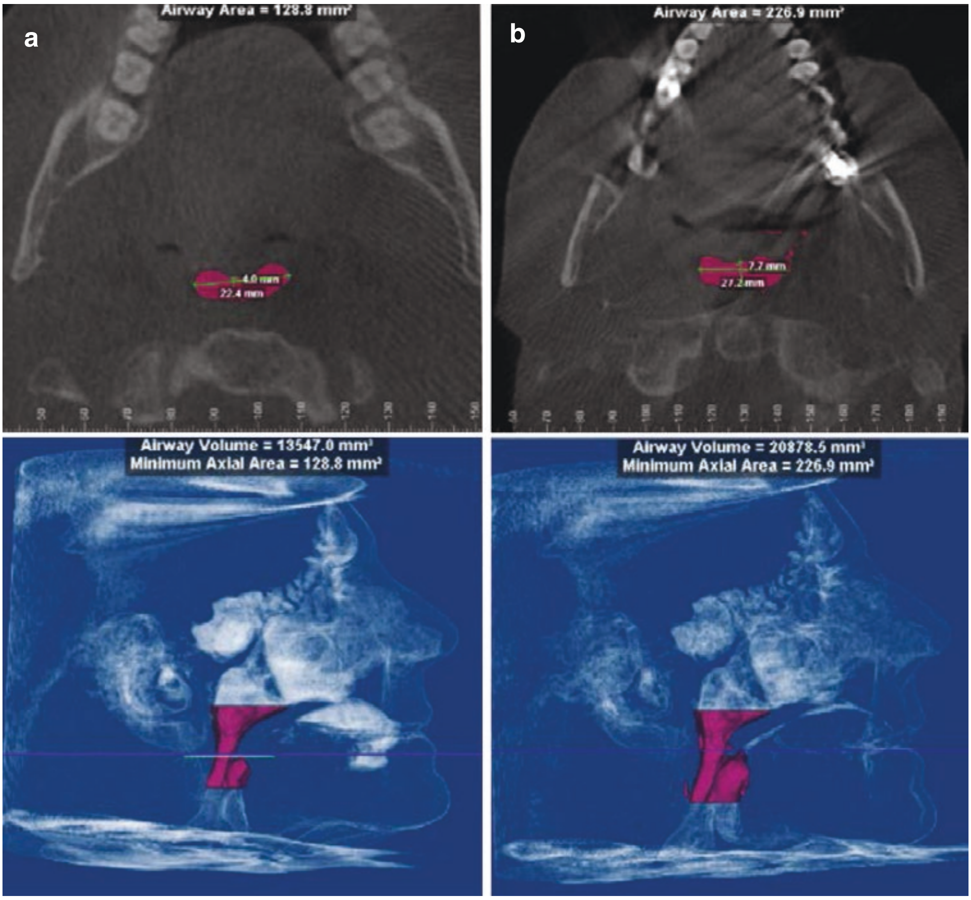

Fig. 28.14 Comparative axial (*upper*) and hollow volumetric (*lower images*) in centric occlusion (**a**) (minimal cross-sectional area = 128.8 mm^2) and with a maxillary anterior guided orthotic (MAGO) in position (**b**) (minimal cross-sectional area = 226.9 mm^2) of 72-year-old male with TMJ pain. However, note that the hollow rendering in centric occlusion (**a**—lower image) demonstrates a substantial space between the dorsum of the tongue and the palate suggesting retroposition of the tongue during the scan. The hollow rendering with MAGO in (**b**—lower image) shows minimal airway space between the tongue and the palate. The difference in minimal cross-sectional airway dimensions between the closed and MAGO in may be, in part, due to differences in tongue posture. Images created using Dolphin 3D software (Dolphin Imaging and Management Solutions Chatsworth, California, USA)

28.5 CBCT Imaging Protocol

28.5.1 Reorient the Volumetric Dataset to an Established Orientation Reference Plane

CBCT volumetric data can be reoriented to any internal or external reference plane prior to analysis. Ogawa et al. (2005) defined the upper and lower aspects of the airway by two lines parallel to the Frankfort Horizontal: one through the most distal point of the hard palate, and one through the most anterior-inferior point of the second vertebrae. Alternately the hard palate can be realigned as an internal reference point and the most superior extent of the nasopharynx defined as a line projected through anterior nasal spine and posterior nasal spine (ANS-PNS) (Fig. 28.15).

28.5.2 Cross-Sectional Assessment

This involves interpretation of sequential axial and coronal images (1 mm thickness/3 mm interval). These conventional orthogonal

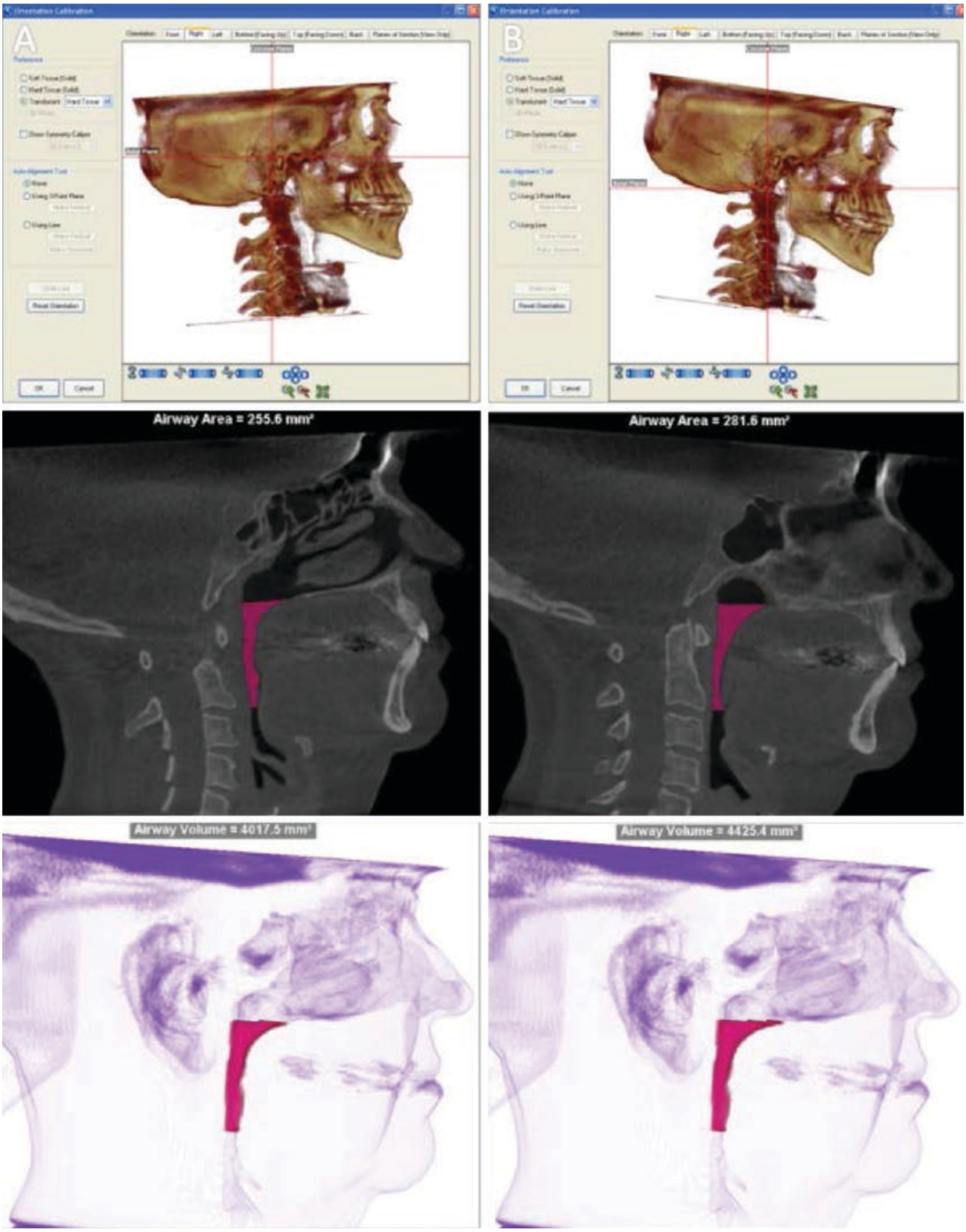

Fig. 28.15 Representative example of the effect of reorientation of CBCT dataset on airway volume calculations. Initial volumetric rendering orientation (**a**), midsagittal analysis (**b**), and final hollow surface rendering (**c**) without regard to standardized internal or external orientation. Corresponding volumetric rendering (**d**), midsagittal (**e**), and hollow surface rendering (**f**) images reoriented to align the palatal plane horizontally. This allows standardization of the construction of boundaries for airway segmentation. Note that the volume calculation before (4017 mm^2) and after (4425 mm^2) is 10% different between orientations. The ANS-PNS line and inferior anteroinferior point of the second cervical vertebrae provide the superior and inferior limits of the oropharyngeal volume. Both lines are parallel to each other. Images created using Dolphin 3D software (Dolphin Imaging and Management Solutions Chatsworth, California, USA)

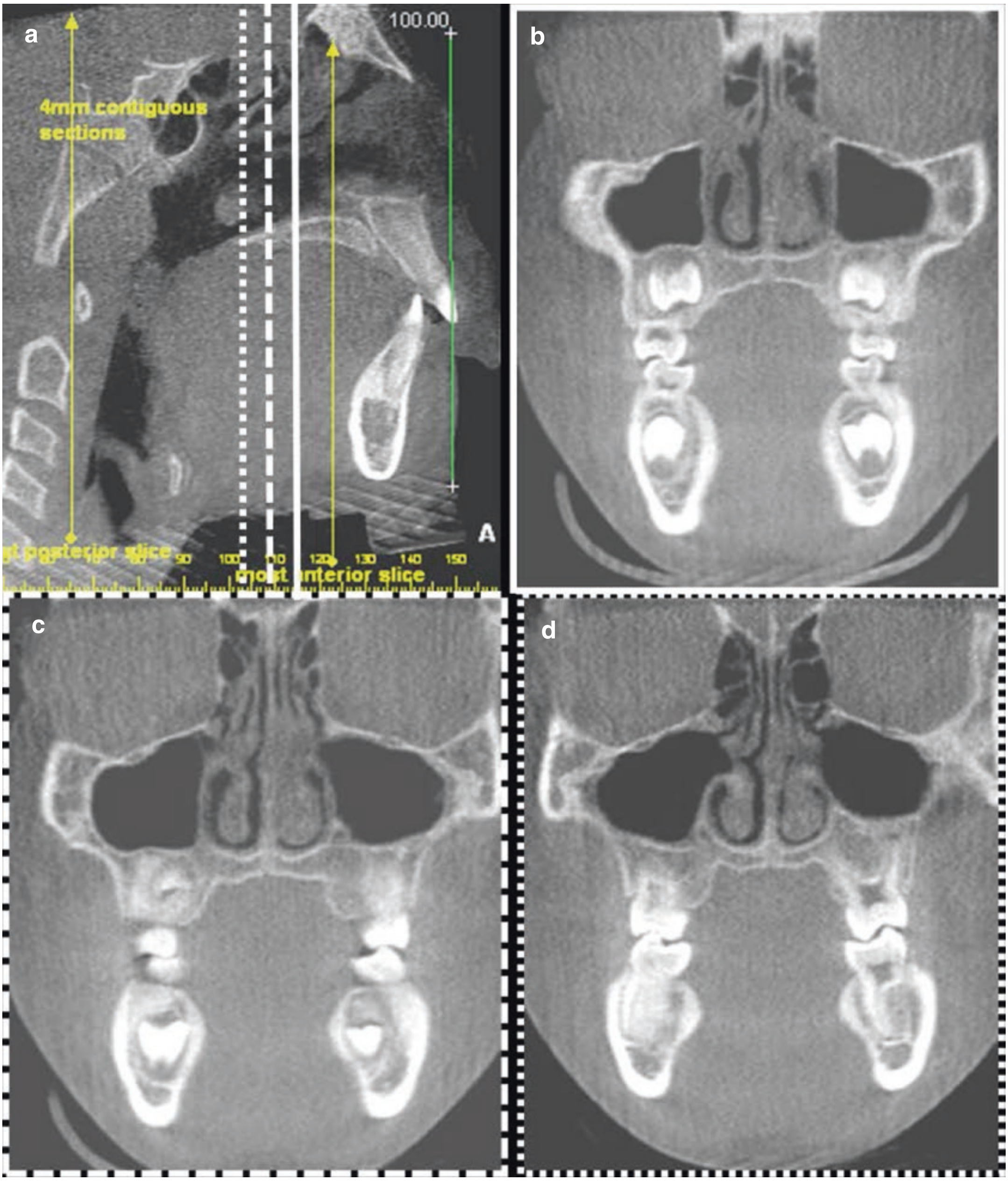

Fig. 28.16 Reference sagittal orthogonal image at 0.4 mm (**a**) of pediatric OSAHS patient demonstrating coronal scans at progressively posterior locations (*solid line* (**b**), *hashed line* (**c**), *dotted line* (**d**)). Note the generalized mucosal thickening of the turbinates of the right nasal fossa and marked reduction and partial occlusion in nasal cavity space

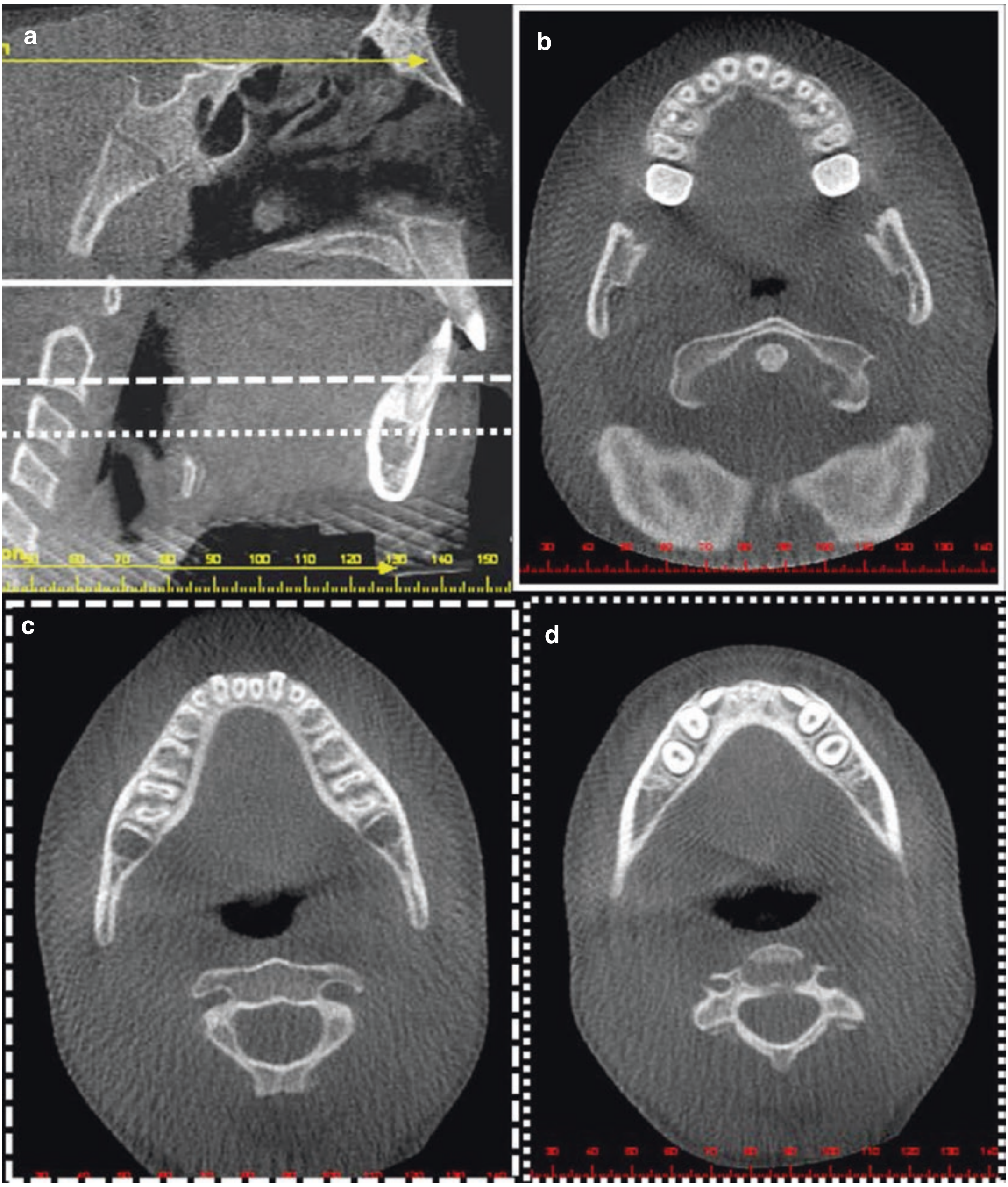

Fig. 28.17 Reference sagittal orthogonal image at 0.4 mm (**a**) of pediatric OSAHS patient demonstrating axial scans at progressively inferior locations; high retro-palatal (*solid line*—**b**); lower retro-palatal (*hashed line*—**c**); and retroglossal (*dotted line*—**d**). Note the marked reduction in the upper retropalatal airway space (**b**)

images enable visualization of potential nasal (Figs. 28.16 and 28.17), oropharyngeal, and anatomic structures that may contribute to obstructions (Table 28.2) and provide an overview of the maximum and minimal caliber of the airway space. Because of the relatively poor contrast resolution of CBCT imaging potential specific soft tissue factors (e.g.,

Table 28.2 Qualitative classification of velohypopharyngeal airway obstruction (after Fujita 1987)

Type	Subtype	Description
I		Retropalatal or velopharyngeal
II		Combined retropalatal and hypopharyngeal/retroglossal (base of tongue)
	IIa	Predominantly retropalatal
	IIb	Predominantly retroglossal
III		Isolated retroglossal or hypopharyngeal (base of tongue)

muscular hypertrophy, redundant fat pads) are unable to be visualized. The airway should be assessed regionally using a "cine" approach axially and coronally. Special attention should be given to the presence of a "mass effect" from encroachment of adjacent soft tissue masses on the nasal cavity and airway lumen resulting in asymmetry (Fig. 28.18) and airway narrowing (Figs. 28.17 and 28.19).

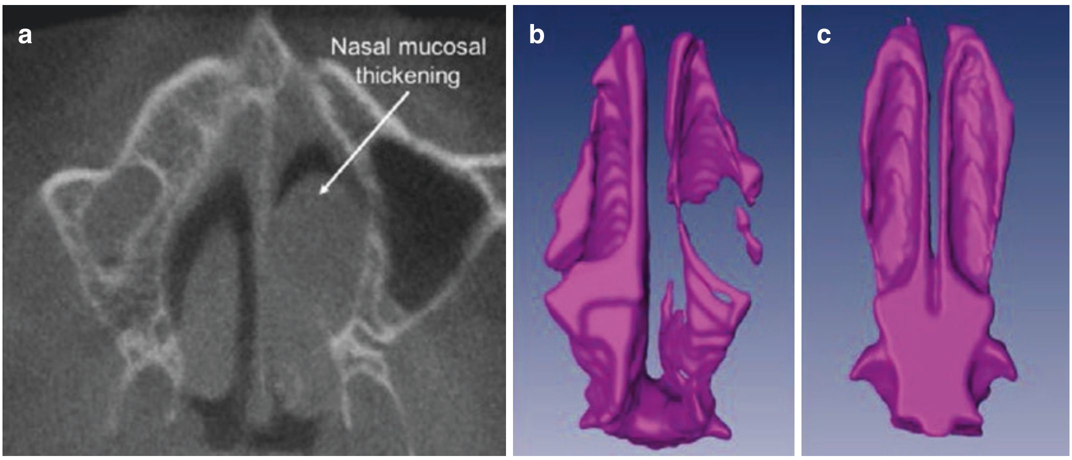

Fig. 28.18 Axial image of a patient with OSAHS (**a**) demonstrating mucosal thickening of the nasal mucosa of the left inferior turbinate obliterating part of the nasal meatus. Reconstructed solid 3D rendering of the nasal airway (*purple*) shows an asymmetric configuration due to a nasal mucosa thickening on the right side (**b**) compared to an asymptomatic patient (**c**). Images created using Amira software (FEI Visualization Sciences Group, Hillsboro, Oregon, USA) (Reprinted from Shigeta et al. (2007), with permission from Springer)

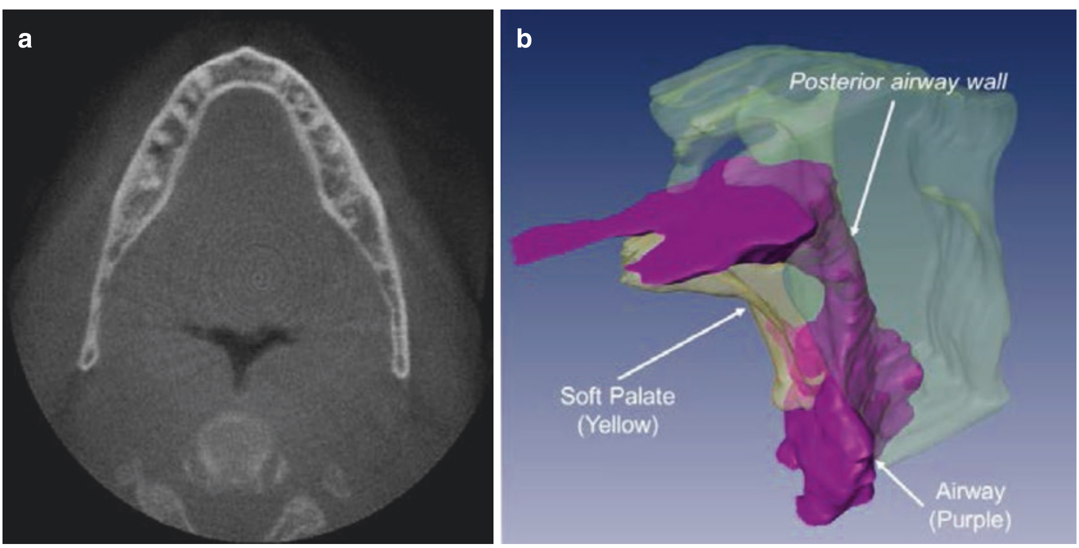

Fig. 28.19 Axial image (**a**) and combination volumetric hollow rendering (**b**) demonstrating compression and reduction in the retropalatal and retroglossal airway space (*purple*) by the palate (*yellow*) against the soft tissues of the posterior pharyngeal wall compress (*green*) (Images created using Amira software (FEI Visualization Sciences Group, Hillsboro, Oregon, USA) (Reprinted from Shigeta et al. (2007), with permission from Springer)

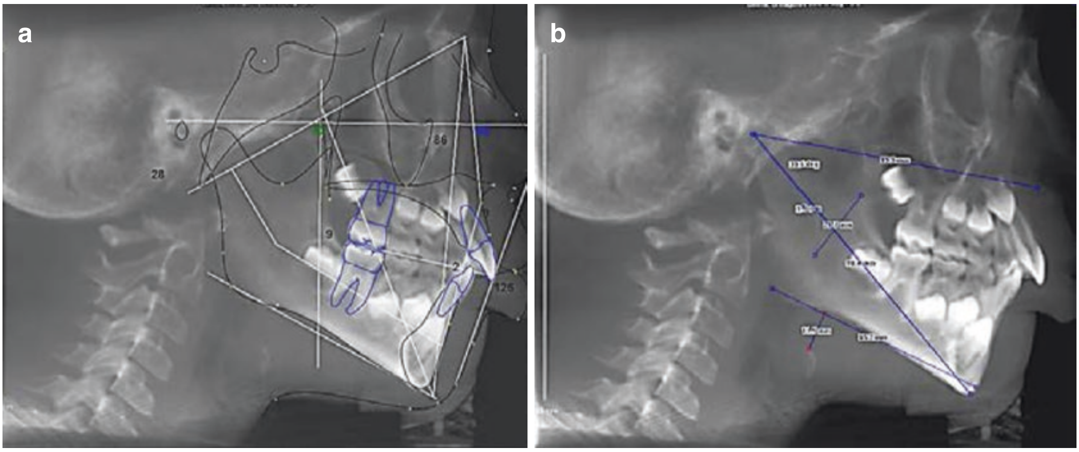

Fig. 28.20 Ray sum simulated lateral cephalometric images (**a** and **b**) demonstrating tracing of soft and hard tissue measurements using specific orthodontic analysis software. Images created using Dolphin software (Dolphin Imaging and Management Solutions Chatsworth, California, USA)

28.5.3 Planar Assessment

Construction and analysis of ray sum simulated and maximum intensity projection panoramic, lateral cephalometric, postero-anterio, and submentovertex images from CBCT data remains an important transitional modality in the assessment of the upper airway in orthodontics as airway morphology can be characterized in relation to skeletal type, growth, and development (Fig. 28.20). Orthopedic or positional changes (e.g., orthognathic surgery or use of mandibular advancement device) can also be related to modifications to the airway (Figs. 28.5 and 28.6).

28.5.4 Three-Dimensional Maxillofacial Assessment

A number of proprietary and third party commercial DICOM compliant medical (e.g., Amira software, FEI Visualization Sciences Group, Hillsboro, Oregon, USA) and dental software (e.g., Dolphin3D, Dolphin Imaging & Management Solutions, Chatsworth, CA; InVivoDental, Anatomage, San Jose, California, USA; OnDemand3D, CyberMed, Seoul, Korea; 3dMDvultus, 3dMD Atlanta, Georgia, USA) are available for volumetric airway depiction and analysis. Volumetric rendering can demonstrate global deficiencies of the maxillofacial skeleton in all three orthogonal planes that may identify potential contributors to OSAHS (e.g., retrognathia, maxillary cross-bite, mandibular asymmetry, palatal soft tissue length and thickness) and allow visualization and measurement of parameters that have been reported to be associated with OSAHS.

- **Three-dimensional analysis of upper airway**. Concomitant segmentation of hard tissue maxillofacial skeleton, airway space, and facial soft tissue surfaces provides visualization of the interrelationship of these structures on airway obstruction. Airway visualization can be achieved by surface isodensity reconstruction to delineate and remove all other surrounding structures to provide a clearer analysis and visualization of the airway (Figs. 28.21, 28.22, and 28.23). Segmentation of the airway can be done either manually slice by slice (Ogawa et al. 2007, b) or automatically. Automatic segmentation is performed by differentiating the low density airway space from the surrounding soft tissue. The range of included voxel gray scale values included in the segmentation, referred to as the threshold values, can be preset in automatic segmentation or manually adjusted. Small changes in this process can have dramatic changes of the calculated volume of the airway (Fig. 28.24).

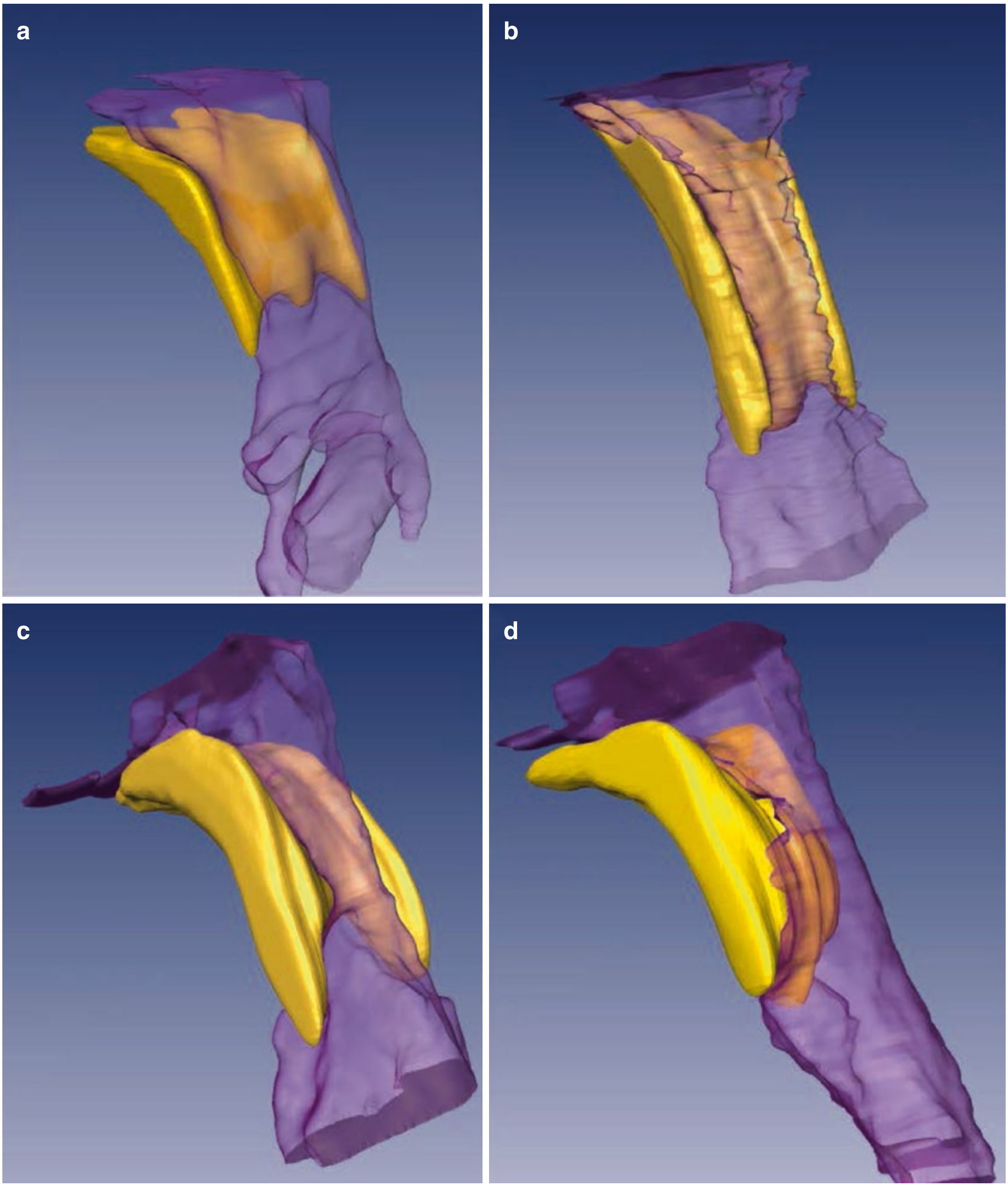

Fig. 28.21 Volumetric solid soft tissue segmentation of the soft palate combined with surface isodensity reconstruction of the oropharyngeal airway in a control (**a**) patient and patients with OSAHS (**b**, **c**, and **d**). Images created using Amira software (FEI Visualization Sciences Group, Hillsboro, Oregon, USA) (Reprinted from Shigeta et al. (2007), with permission from Springer)

The surface isodensity reconstruction and the segmentation of the airway facilitate identification and classification of the level of the obstruction (Table 28.2) and quantitative analysis of linear, area, and volumetric parameters (Fig. 28.25). These images also provide superior visualization of airway shape and caliber under influence of soft tissue elements such as the epiglottis, soft

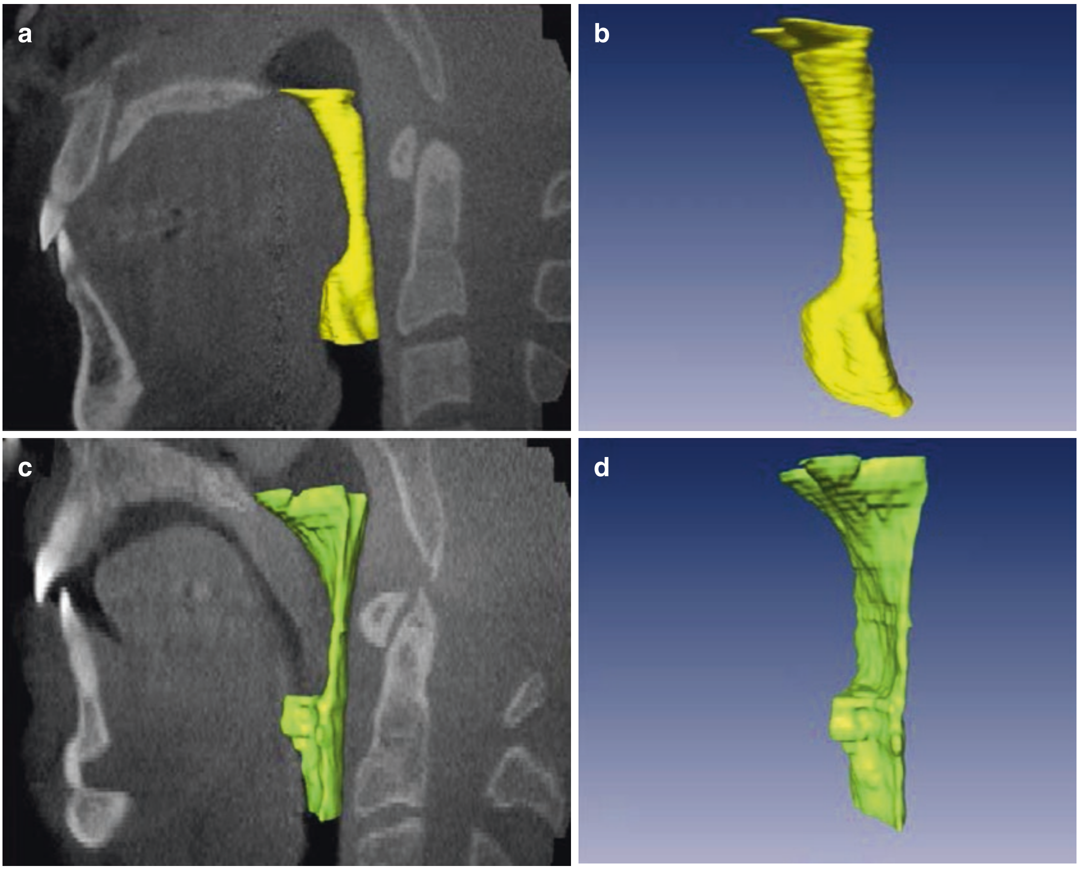

Fig. 28.22 The oropharyngeal airway volume superimposed on the sagittal image for a control (**a**) and OSAHS patient (**b**). The solid volumetric renderings of the control (**c**) and OSAHS patient (**d**) can be separated from the CBCT data, viewed and analyzed separately. Images created using Amira software (FEI Visualization Sciences Group, Hillsboro, Oregon, USA) (Reprinted from Ogawa et al. 2007, b, with permission from Elsevier)

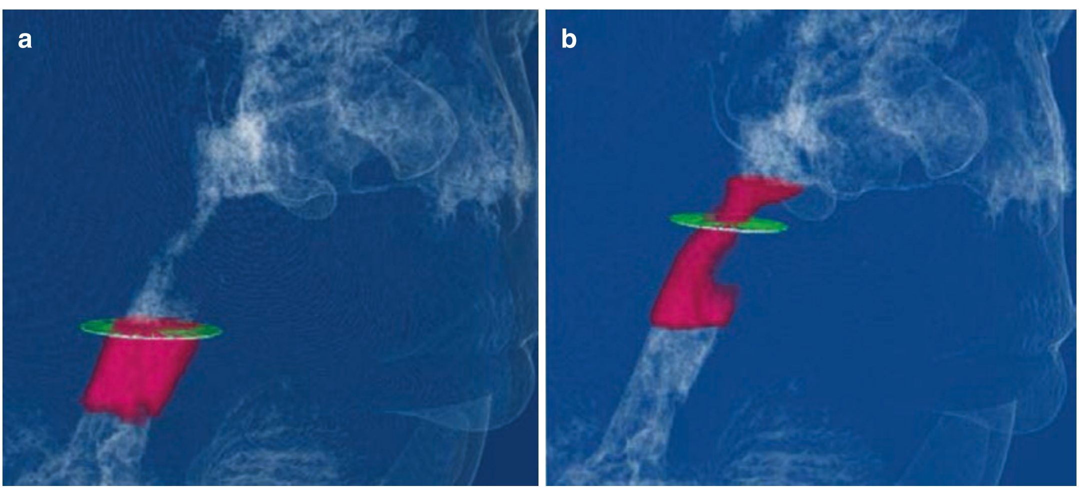

Fig. 28.23 Lateral oblique volumetric surface and airway hollow images of an OSAHS patient after application of software algorithm to identify the volume of specific portions of the oropharyngeal airway. Retroglossal (**a**) and retropalatal (**b**) volumes are identified by a purple solid; the level of the minimum cross-sectional airway within the segment is identified as a radial disc. Images created using Dolphin 3D software (Dolphin Imaging and Management Solutions Chatsworth, California, USA)

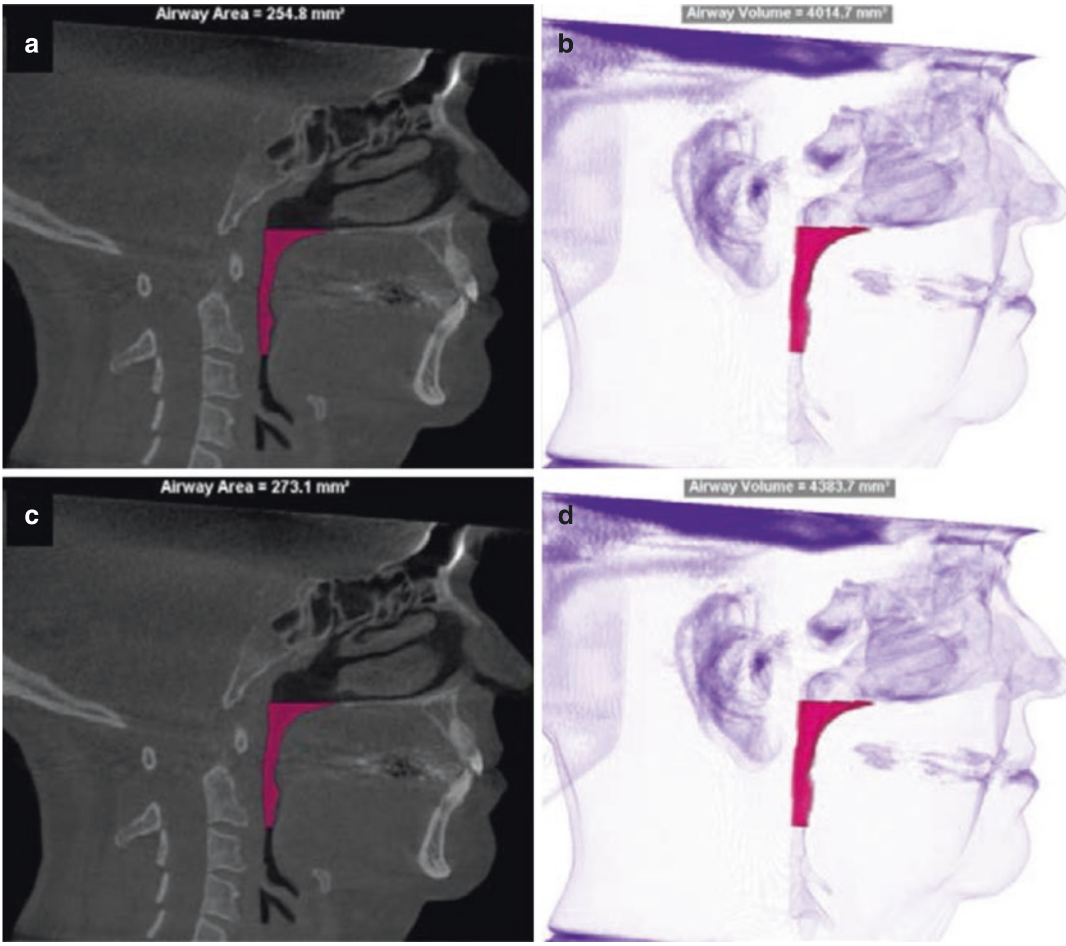

Fig. 28.24 Effects of variation in threshold values from 45% sensitivity (**a**—airway area, 254.8 mm^2; airway volume, 4014.7 mm^3) to 55% sensitivity (**b**—airway area, 273.1 mm^2; airway volume, 4383.7 mm^3) on airway volumetric renderings on the midsagittal (*left*) and volumetric result (*right*). Note that the difference in calculated volume is almost 10%. Images created using Dolphin 3D software (Dolphin Imaging and Management Solutions Chatsworth, California, USA)

palate (Fujita 1987) and mass effects caused by variations in hard tissue (Figs. 28.26, 28.27, 28.28, and 28.29).

28.5.5 Regionally Corrected Temporomandibular Joint Images

Visualization of the temporomandibular joint (TMJ) articulation provides information of the relative stability of morphology of this determinant of mandibular position. Active degenerative joint disease (DJD) either osteoarthritic, autoimmune, or idiopathic in nature can reduce mandibular ramal length resulting in an anterior open bite and produce substantial inferior and posterior positional changes in the location of the associated soft tissue (Fig. 28.30).

28.5.6 Comparison of Pre- and Posttreatment Effects

Most simplistically, comparison of airway changes as a result of specific therapies can be performed by observation of differences in metrics before and after intervention (Figs. 28.13

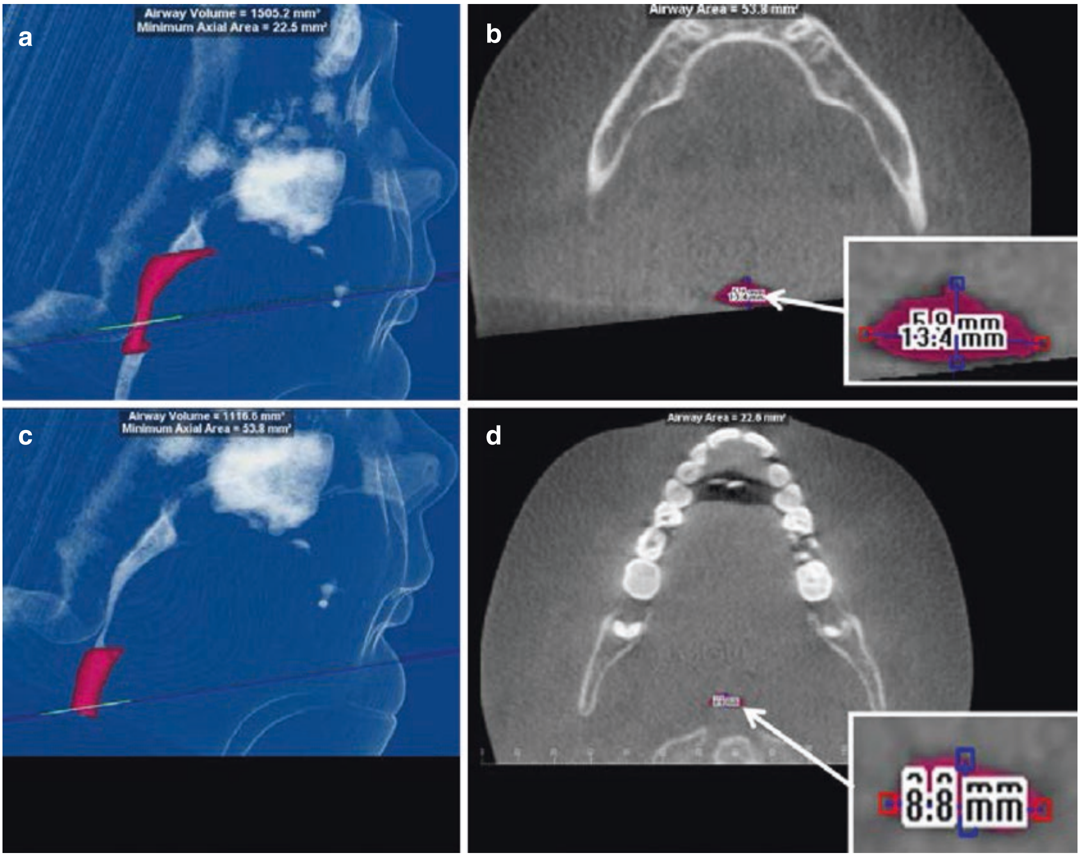

Fig. 28.25 Lateral volumetric images of the segmented airway of an OSAHS patient demonstrating the specific volumes of retroglossal (**a**) and retropalatal (**b**) airway space. The software algorithm identifies and displays the corresponding axial images at which the minimum cross-sectional area is present in the respective regions (**c** and **d**) and allows for measurement of antero-posterior and transverse dimensions. Images created using Dolphin 3D software (Dolphin Imaging and Management Solutions Chatsworth, California, USA)

and 28.14). Some software is capable of more sophisticated volumetric superimposition of CBCT datasets and can provide either qualitative (Fig. 28.31) or quantitative (Schendel and Hatcher 2010) (Fig. 28.32) comparative data.

28.5.7 Dynamic Visualization

In addition to the static imaging protocol presented above it is possible to generate video frame of reference "fly through" reconstructions (e.g., Osiris Imaging Software. V3.1, University Hospital of Geneva, Switzerland; OnDemand3D, CyberMed Inc., Seoul, Korea; 3dMDvultus, 3dMD, Atlanta, Georgia, USA). While images produced by this technique demonstrate the static airway, this noninvasive approach serves as a potential method to create virtual fiberoptic nasopharyngoscopy visualizations (Fig. 28.33).

28.6 Radiographic Image Analysis

28.6.1 Lateral Cephalometric

Many measurements from lateral cephalometric (LC) image can be made that attempt to describe the maxillofacial skeletal relationship or the upper airway.

The maxillofacial skeleton on LCR can be described by the measurement of numerous

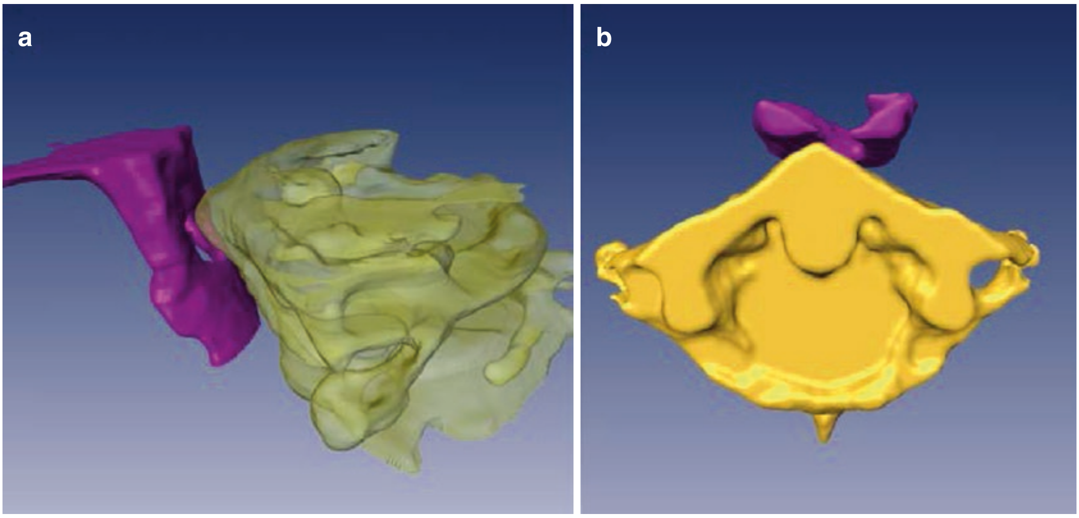

Fig. 28.26 Lateral (**a**) and axial (**b**) view of a solid volumetric rendering of the airway (*purple*) and transparent rendering of the first cervical vertebra (*yellow*) showing a large osteophyte of the first vertebra compressing the prevertebral soft tissues resulting in an obstruction of the airway space. Images created using Amira software (FEI Visualization Sciences Group, Hillsboro, Oregon, USA) (Reprinted from Shigeta et al. (2007), with permission from Springer)

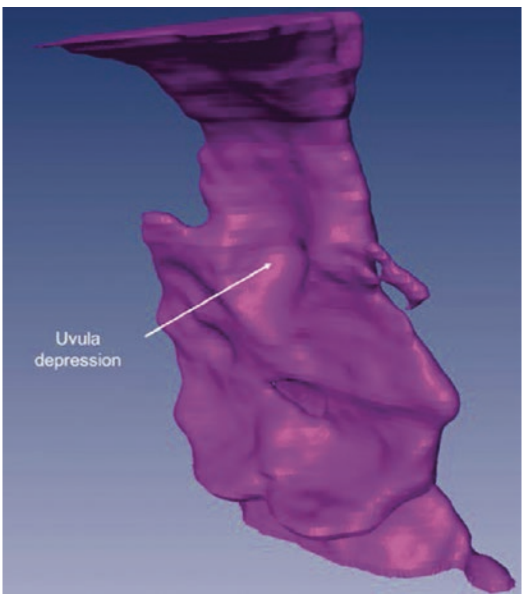

Fig. 28.27 Lateral oblique view of a solid volumetric rendering showing the effect of a large uvula narrowing the retropalatal airway space. Images created using Amira software (FEI Visualization Sciences Group, Hillsboro, Oregon, USA) (Reprinted from Shigeta et al. (2007), with permission from Springer)

parameters related to the cranial base, vertical and horizontal aspects of the maxilla and mandible, the intermaxillary and interdental relationships. A number of measurements have been identified as being particularly useful (Mayer and Meier-Ewert 1995; Hsu et al. 2005a, b; Liu et al. 2001; Kim et al. 2012; Ng et al. 2012). Consideration should also be given to cranio-cervical posture (Solow and Tallgren 1976).

28.6.2 Cone Beam CT

28.6.2.1 Nasopharyngeal

Linder-Aronson (1970) provides a list of nasopharyngeal airway dimensions including:

- **Linder-Aronson 1:** The distance from PNS to the nearest adenoid tissue in a line from PNS to Basion.
- **Linder-Aronson 2:** The distance from PNS to the nearest adenoid tissue in a line from PNS perpendicular to Sella-Basion.

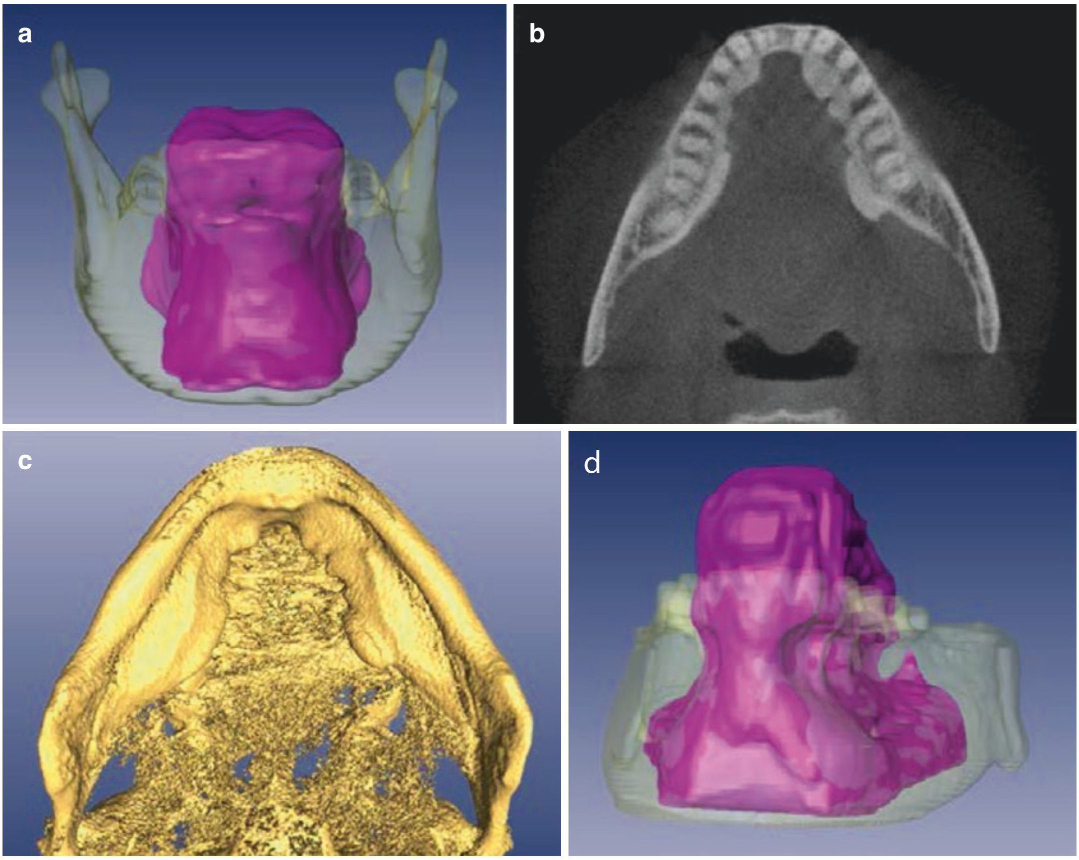

Fig. 28.28 Volumetric rendering of a control patient demonstrating a separately segmented transparent mandible and solid tongue (**a** - *purple*). Axial (**b**), solid 3D rendering of the mandible (**c**), and volumetric rendering of a separately segmented transparent mandible and solid tongue (**d**) demonstrating the displacement effect of large bilateral mandibular tori on the position of the tongue and subsequent reduction in retroglossal airway space. Images created using Amira software (FEI Visualization Sciences Group, Hillsboro, Oregon, USA) (Reprinted from Shigeta et al. (2007), with permission from Springer)

Similarly, Solow et al. (1996) report a comprehensive oropharyngeal airway analysis scheme involving measurements of the soft palate and hyoid bone vary depending on age, sex, ethnic origins, and size of tissue mass.

28.6.2.2 Oropharyngeal

The main area of interest in the upper airway is the oropharynx (from the posterior nasal spine to the tip of the epiglottis) which is most prone to obstruction. Airway volume, shape, length, and uniformity are greatly influenced by age (Chiang et al. 2012). The following measurements may provide useful metrics:

Soft Palatal Dimensions

One local airway factor that has been proposed as causative agent of OSAHS is a long soft palate. Several studies report increased size of the soft palate in apnea patients versus non-apnea subjects (Rodenstein et al. 1990; Schwab et al. 1995). More specifically, patients with OSAHS have a longer soft palate (Yu et al. 2003; Ciscar et al. 2001; Johal and Conaghan 2004). Namyslowski et al. (2005) found excessive flaccidity and muscular atrophy in the soft palate and uvula in patients with snoring and OSAHS and this suggests that the soft palate can change shape with time and disease. Malhotra et al. (2006)

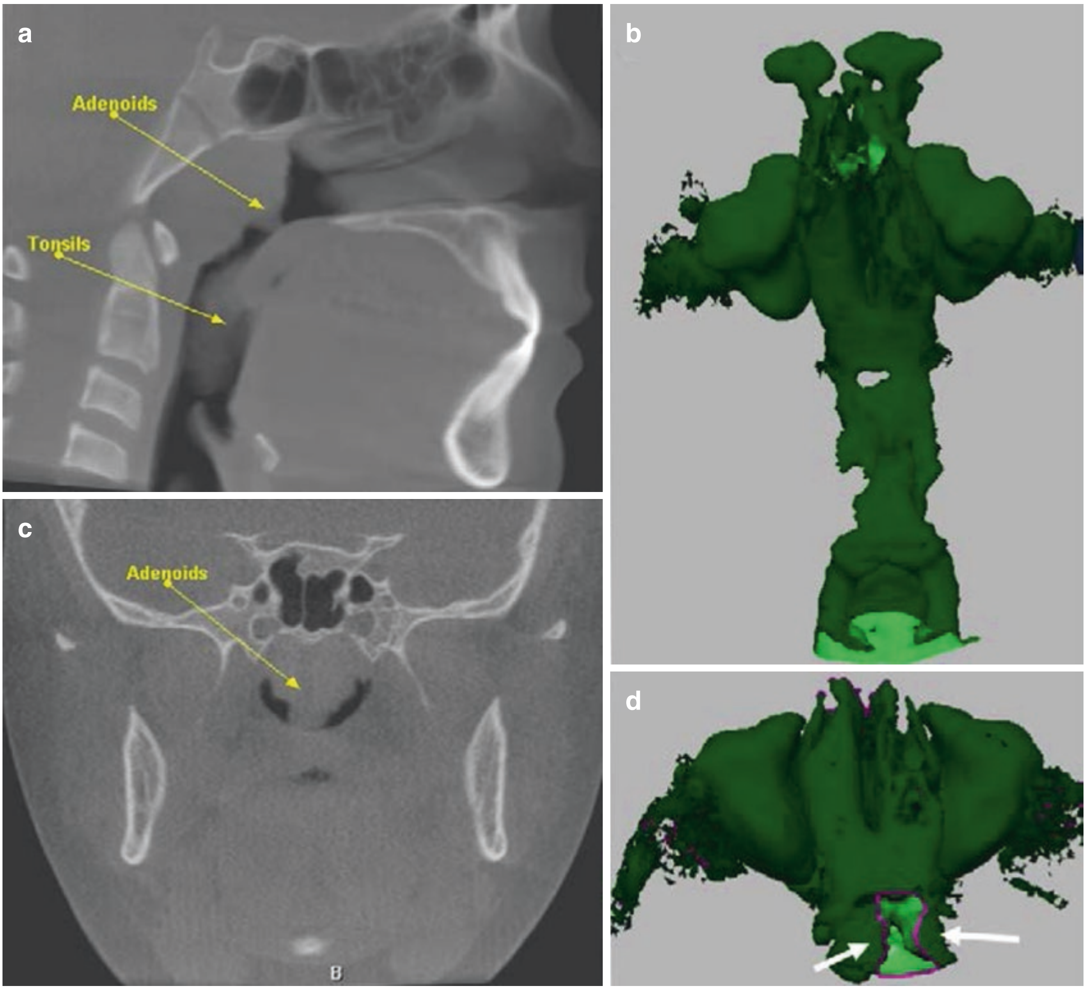

Fig. 28.29 Midsagittal (**a**) and coronal (**b**) CBCT images of 9-year-old female with enlarged adenoids and tonsils (labelled) with frontal projection (**c**) and minimal cross-sectional area, superior view (**d**) hollow volumetric rendering of the naso- and oro-pharyngeal airway. Indentations from the hypertrophic tonsils are clearly evident on the superior hollow volumetric rendering at the level of the retroglossal airway space (*arrows*). Images created using 3dMDvultus software (3dMD, Atlanta, Georgia, USA). (Images courtesy William Harrell)

reported that the soft palate length also increased progressively with aging but only in women. This is somewhat paradoxical since apnea prevalence is higher in men. Comparing OSAHS patients with controls, Enciso et al. (2006) found differences in cross-sectional area of the soft palate in midsagittal whereas Shigeta et al. (2010) found soft palate length, measured as a percent of oropharyngeal airway length was significantly larger. Most recently, soft palate length has been found to be significantly larger in OSAHS patients (42.2 ± 5.19 mm) compared to controls (38.6 ± 6.57 mm), and in men (42.5 ± 5.76 mm) compared to women (36.4 ± 4.2 mm) (Shigeta et al. 2010). Based on these studies, we suggest that the following are measured:

- Maximum length of the soft palate in the midline (Fig. 28.34).
- Maximal cross-sectional area in a midsagittal image (Fig. 28.34).
- Vertical and oblique length of the soft palate as a proportion of the total oropharynx length (Fig. 28.35).

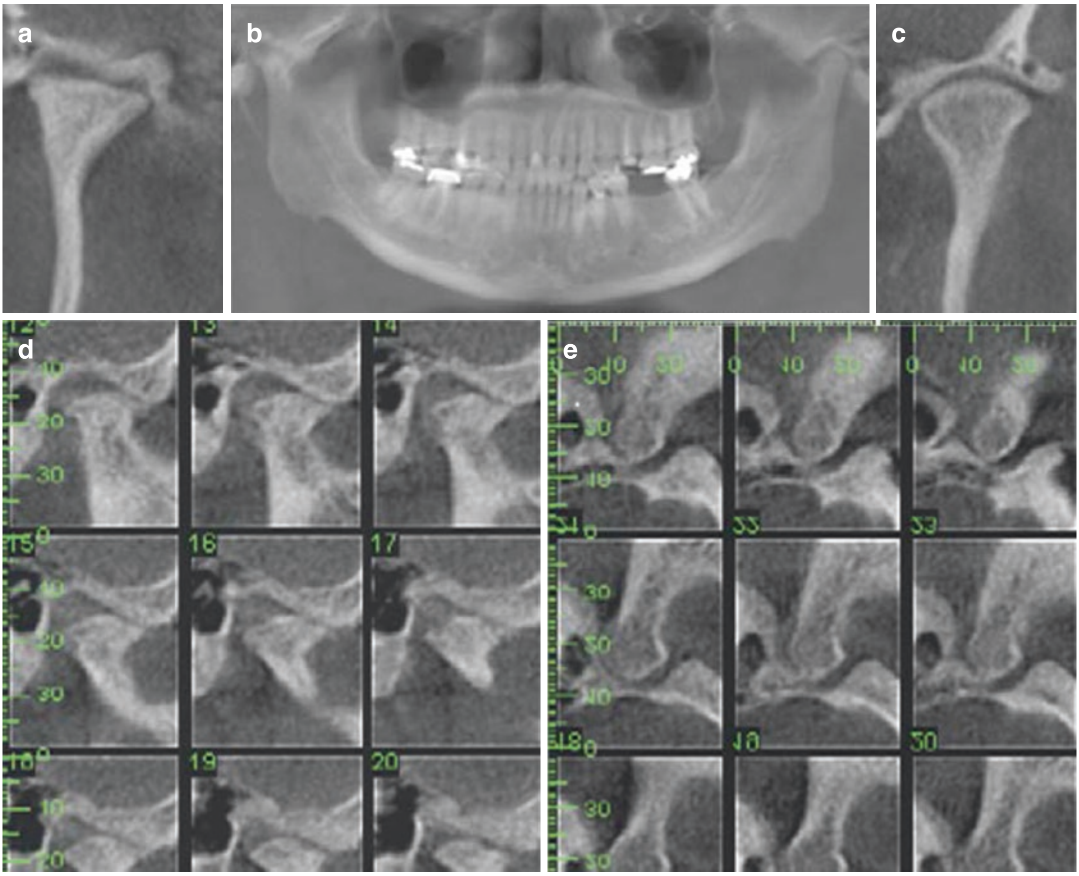

Fig. 28.30 Temporomandibular image protocol demonstrating ray sum reformatted panoramic (**b**), 5 mm thick para-sagittal (**a** and **b**) and sequential 1 mm cross-sectional right (**d**) and left (**e**) images. Note the marked osteoarthritic degenerative joint disease of the right TMJ articulation in this OSAHS patient contributing to reduction in mandibular ramal length and asymmetry of the mandible

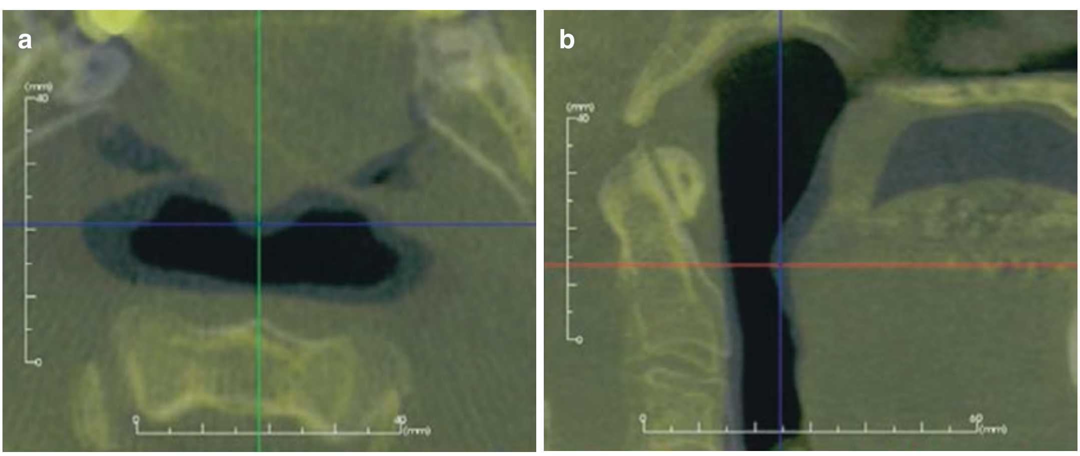

Fig. 28.31 Superimposition of CBCT data providing qualitative color-contrasted differences between CBCT scans with insertion of MAD device. Axial (**a**), sagittal (**b**), and coronal (**c**) views of original (*gray*) and post-therapy images (*yellow*) using skeletal fiducial points demonstrate improvement in airway patency. Volumetric image superimposition (**d**) shows original position of the mandible (*orange*) and position of mandible with MAD device in position (*blue*). Images created using InVivo Dental (Anatomage, San Jose, CA)

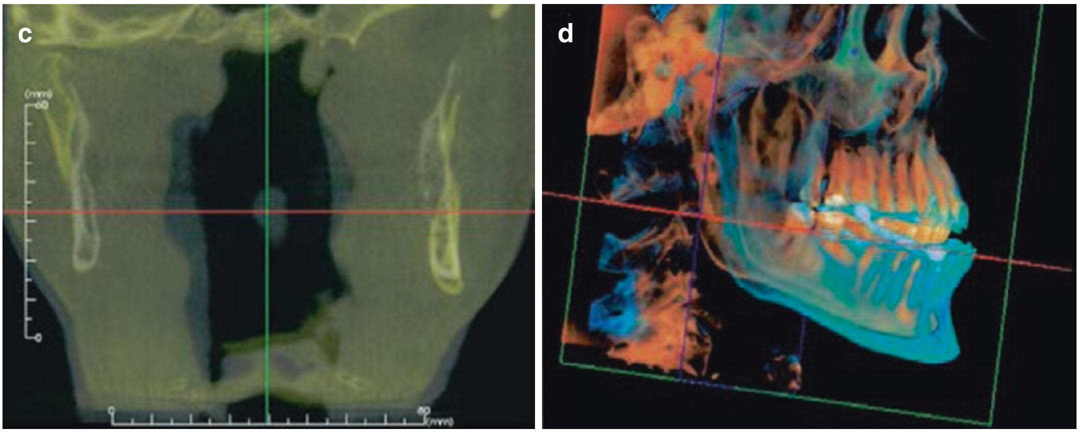

Fig. 28.31 (continued)

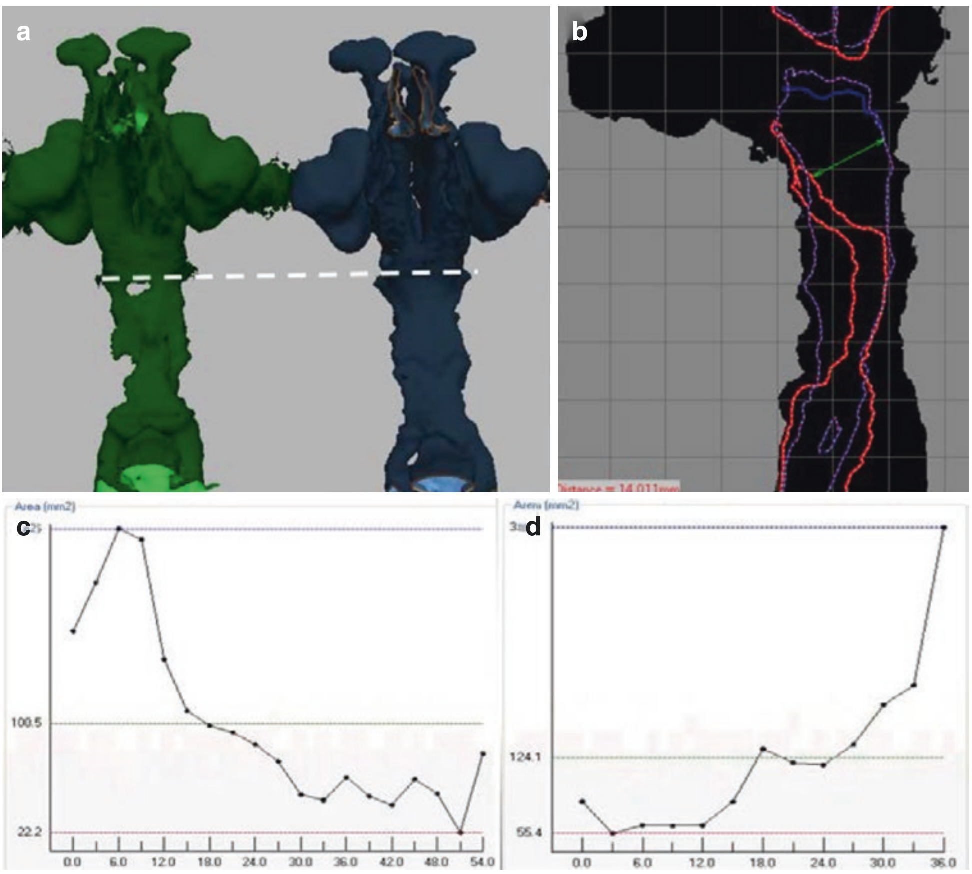

Fig. 28.32 CBCT quantitative analysis of airways space of 9-year-old female with enlarged adenoids and tonsils (as in Fig. 28.29) before and after rapid palatal expansion and adenoidectomy and tonsillectomy. Comparative hollow volumetric airway images (**a**) before (*green*) and after treatment with minimal cross-sectional area (*dashed line*) identified. Midsagittal qualitative analysis of the entire upper airway after coregistration and superimposition of CBCT volumes (**b**) before (*red*) and after (*blue*) treatment. Continuous plots of minimal cross-sectional area (*y*-axis) vs. distance from inferior to superior (*x*-axis) before (**c**) and after (**d**) treatment. Retropalatal minimal cross-sectional area increases from 100.5 mm² initially to 124.1 mm² post-treatment. Images created using 3dMDvultus software (3dMD, Atlanta, Georgia, USA) (Images courtesy William Harrell)

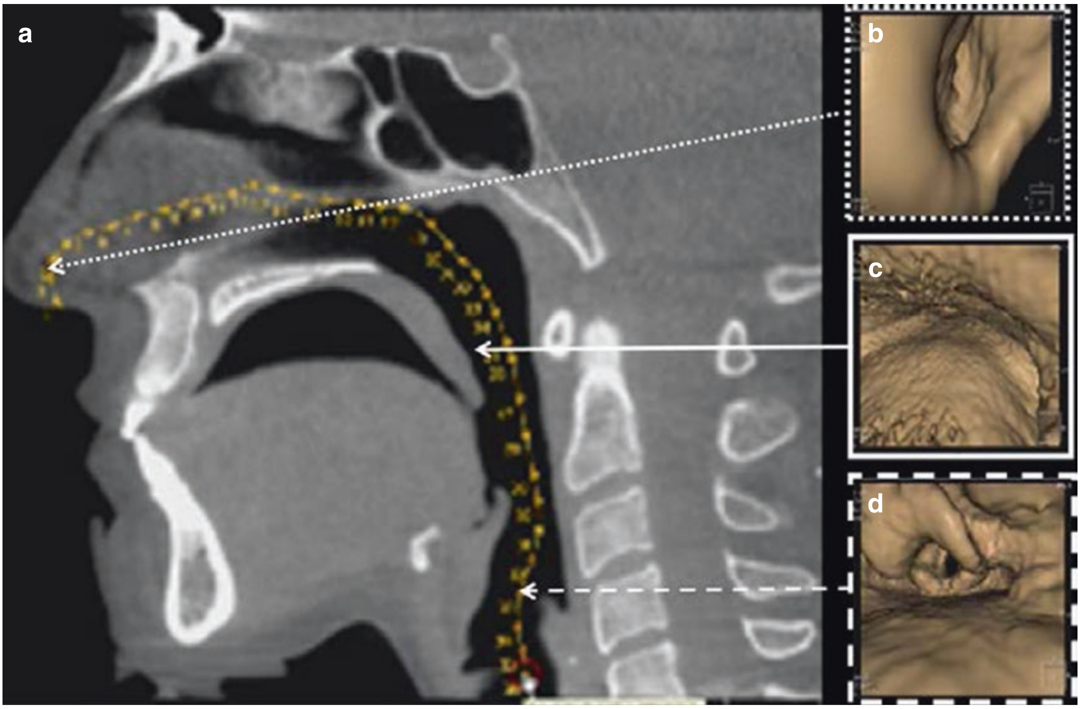

Fig. 28.33 Initial sagittal reference image demonstrating "fly-through" path (**a**) and sequential screen capture of "virtual" nasopharyngoscopy video from at the level of the nares (**b**—*dotted line*), velo- (**c**—*solid line*), and hypo-pharyngeal (**d**—*dashed*) regions

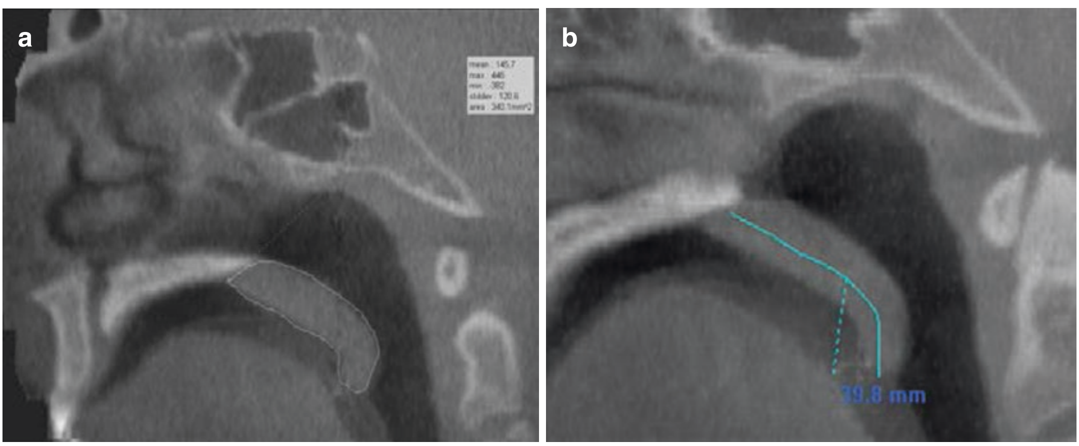

Fig. 28.34 Midsagittal CBCT image of the maxilla, naso- and oro-pharyngeal airway space showing the cross-sectional area of the soft palate (**a**) and a magnified image of the same region centered on the soft palate showing the centerline length measuring the soft palatal length (**b**) (Enciso et al. 2006)

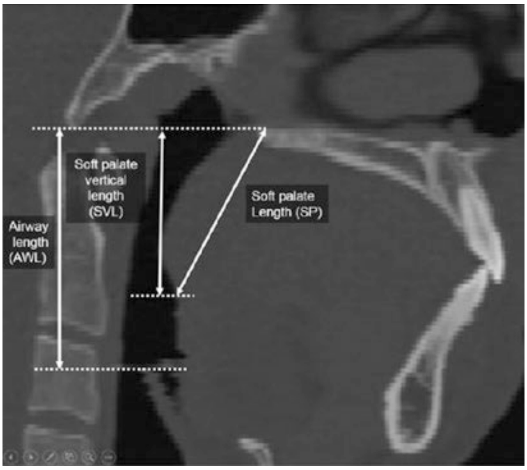

Fig. 28.35 The most common soft palate measurements on midsagittal CBCT (and cephalometric images) include airway length (AWL—vertical height between posterior nasal spine and tip of soft palate), soft palate length (SP—distance between posterior nasal spine and tip of soft palate), and vertical soft palate length (SVL—vertical height between posterior nasal spine and top of epiglottis) (Reprinted from Shigeta et al. (2010), with permission from Springer

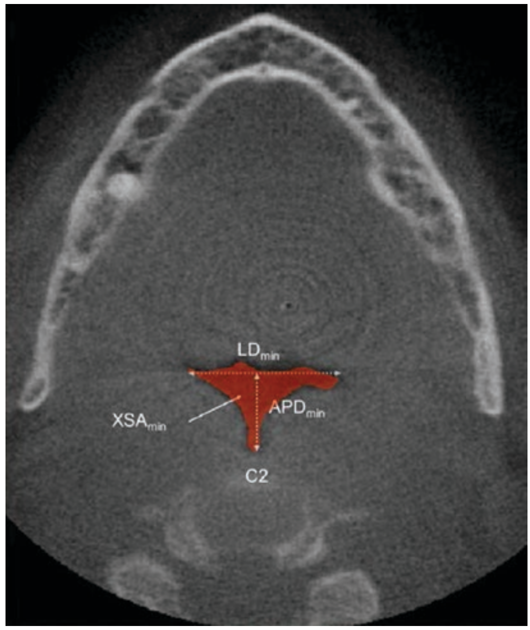

Fig. 28.36 Axial CBCT image shows the configuration of the retrognathic airway space at the level of the minimal cross-sectional airway area (*red*) (XSA_{min}). The minimum antero-posterior dimension (APD_{min}) and lateral dimension (LD_{min}) are also determined at this location

Airway Linear Dimensions

The most common measurements used to compare the static morphology of the upper airway are recorded at either the retro-palatal (RP) or retroglossal (RG) regions (Cosentini et al. 2004) (Fig. 28.36)

- *Minimum Anterior–Posterior Dimension (APD_{min})* (Rodenstein et al. 1990; Schwab et al. 1993). This dimension can be measured at the RP (RG APD_{min}) or RG (RP APD_{min}) regions. Patients with OSAHS demonstrate significantly smaller APD_{min} than controls (Ogawa et al. 2007, b).
- *Minimum Lateral Dimension (LD_{min})* (Rodenstein et al. 1990; Schwab et al. 1993). Similarly, this dimension can be measured at the RP (RP LD_{min}) or RG (RG LD_{min}) regions. Patients with OSAHS demonstrate significantly smaller LD_{min} than controls which always occurs retropalatally (Ogawa et al. 2007, b).
- *APDmin/LDmin Ratio (AP:LD)*. This ratio is a descriptor of airway shape. Three metrics are possible: RP AP:LD, RG AP:LD, ffigand C2 AP:LD. Ogawa et al. (2007, b) found that the LD_{min} dimension is usually greater than the APD_{min} which makes the airway slightly more concave or elliptic in shape for patients with OSAHS. Others have reported that OSAHS patients have a more spherical shape (Mayer and Meijer-Ewert 1995) or even no correlation between OSAHS and airway shape (Cosentini et al. 2004).
- *Minimal Cross-Sectional Area (XSA_{min})*. The smallest cross-section area is the location within the UA where the airflow is theoretically most constricted. The minimal cross-sectional area can be measured empirically within the retropalatal (RP) and retroglossal (RG) regions in relation to reorientation of the CBCT dataset to a reference or in relation to a regional structure such as C2. Therefore three metrics are possible: RP XSA_{min}, RG XSA_{min}, and C2 XSA_{min}.
- Li et al. (2003) demonstrated a relationship between the airway area and the likelihood of

OSAHS. Using MDCT they reported that the probability of severe OSAHS is high with an airway area less than 52 mm^2, intermediate if the airway is 52–110 mm^2, and low if the airway is greater than 110 mm^2.

- However, it must be noted that XSA_{min} can vary substantially depending on skeletal malocclusion. Jayaratne and Zwahlen (2016) reported the average surface area of both RG and RP regions were significantly larger in patients with skeletal class III (RP XSA_{min}, 304.75 ± 166.03 mm^2; RG XSA_{min}, 276.4 ± 116.17 mm^2) than skeletal Class II (RP XSA_{min}, 211.2 ± 81.44 mm^2; RG XSA_{min}, 186.2 ± 64.2 mm^2). The most constricted area in the RG and RP airway was significantly larger in individuals with skeletal class III deformity.
- *Dimensions at a fixed location*. APD_{min}, LD_{min}, and AP:LD can also be measured in relation to a fixed anatomic location, usually the anterior-inferior border of the second cervical vertebrae (C2) (Fig. 28.37). These dimensions provide a measurement of how the caliber at the same point within the UA changes (Fig. 28.38).

Airway Volume (AV)

Three volumetric measurements can be made of the airway volume (Fig. 28.20), retropalatal airway volume (AV_{rp}), retroglossal airway volume (AV_{rg}), and the total airway volume (AV_t) ($AV_{rp} + AV_{rg}$).

Rostrocaudal Airway Length (RL)

Maximum rostrocaudal length of the airway is usually defined as the length of the upper airway space between the palatal plane and parallel constructed plane at the level of the lowermost border of C4. In an orthodontic sample of patients, the length of the airway was found to increase for female patients up to the age of 15 to 66.75 ± 4.8 mm (Chiang et al. 2012). In the same group, the length of the airway in male patients increased throughout the entire age range to 70.75 ± 9.7 mm and does not appear to plateau (Chiang et al. 2012). Abramson et al. (2010) demonstrated that the presence of OSAHS is associated with an increase in airway length (76.7 ± 11.1 mm) as compared to controls (66.3 ± 10.1 mm).

Airway Shape

Patients with OSAHS present with a concave- or elliptic-shaped airway as compared to non-OSAHS controls who demonstrate a concave-, round-, or square-shaped airway (Ogawa et al. 2007, b; Abramson et al. 2010).

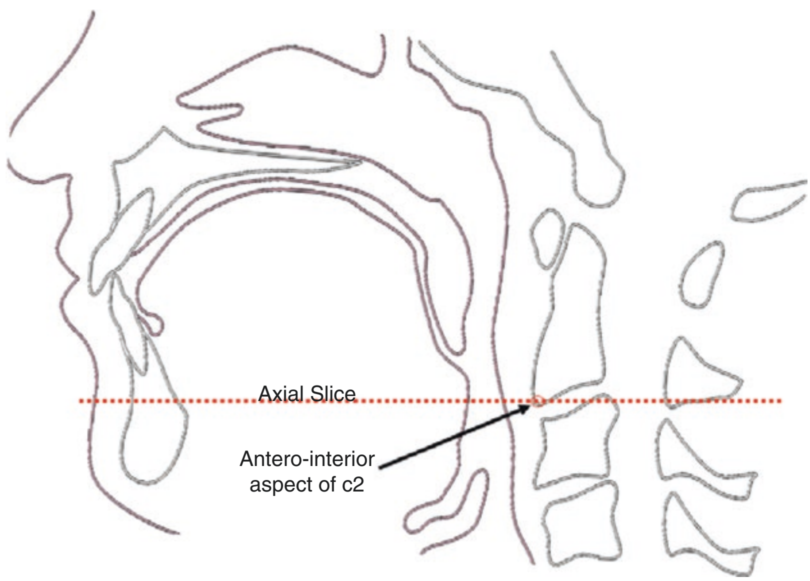

Fig. 28.37 Schematic of midsagittal CBCT section showing the axial level at which linear and area airway measurements are determined in relation to C2 (Reprinted from Shigeta et al. (2008), with permission from Springer)

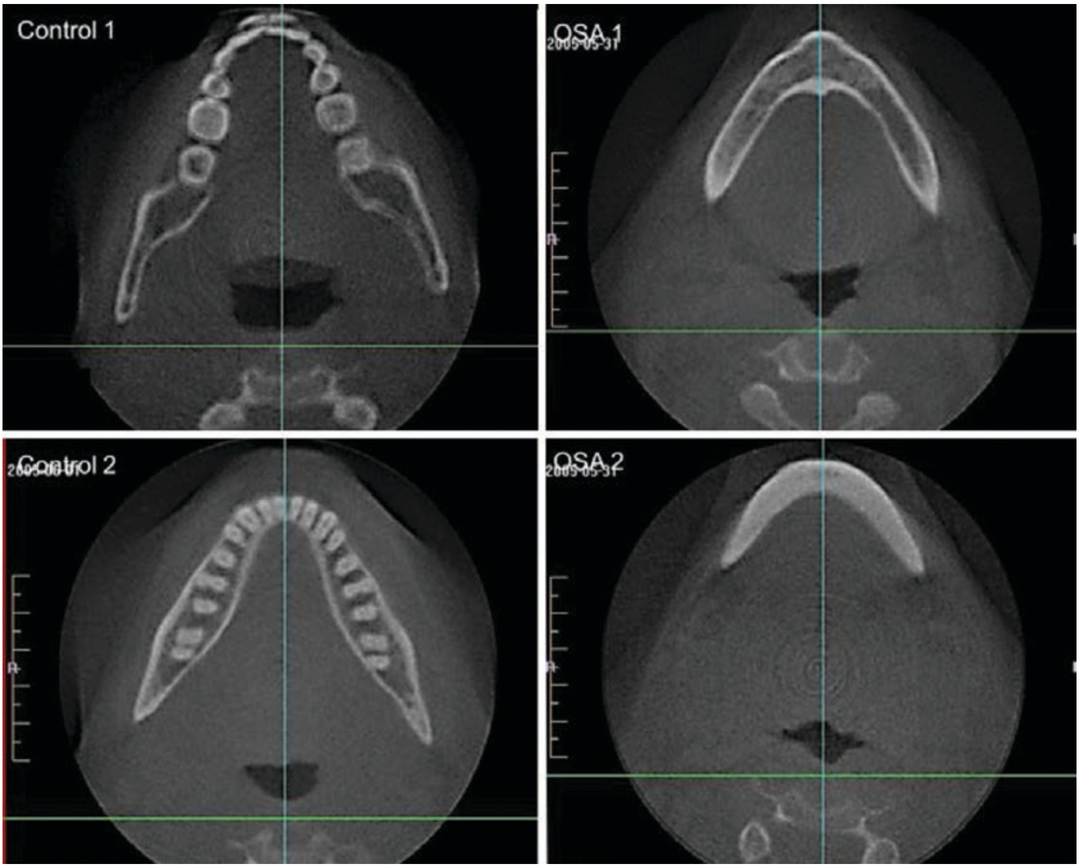

Fig. 28.38 Comparison of the airway shape at the level of the anterior-inferior corner of second vertebra (C2) between two controls (*left*) and two OSAHS patients (*right*) (Reprinted from Shigeta et al. (2008), with permission from Springer)

28.7 Current Status and Future Directions

Research in this area can be categorized as (Guijarro-Martinez and Swennen 2011):

- **Clinical applications**. Most publications provide information on the specific applications of CBCT imaging including evaluation of sinus anatomy and pathology (Enciso et al. 2012), the relationship between upper airway and dentomaxillofacial morphology, effects of surgical-orthodontic treatment, the relationship between upper airway and obstructive sleep apnea, and upper airway evaluation in normal subjects.
- **Accuracy and reliability of CBCT imaging of the upper airway**. Studies in this area compare the anatomic information on the nasopharyngeal airway between lateral cephalometric images and CBCT, or evaluate the accuracy of linear measurements, cross-sectional areas, and/or volumes (Weissheimer et al. 2012).
- **Technical reports**. These studies deal with practical features that have relevant clinical implications in methodology and the interpretation of results, such as the response of oropharyngeal structures to gravity and the quality of airway imaging with different acquisition times.
- **Accuracy and reliability of various DICOM viewers**. According to Guijarro-Martinez

and Swennen (2011), important challenges remained, including the impact of respiration phase, influence of tongue position and mandible morphology on the longitudinal and cross-sectional assessment of upper airway, and 3D CBCT definition of the anatomical boundaries of the upper airway.

- We concluded that there are three main areas in CBCT imaging and OSAHS that require further research:
- **Predicting sleep apnea based on imaging and family history**. While OSAHS is a multifactorial disease, it would be desirable to predict which patients have a proclivity to develop OSAHS. This may include the identification of specific static airway predictors, either alone or in combination with basic questionnaires for family and medical history (Enciso et al. 2010; Enciso and Clark 2011). Knowledge of these "markers" could direct preventative strategies such as behavioral changes and/or minor surgery that could influence the development of the disease.
- **Modeling**. Huang et al. (2007) have developed a finite element computer model of the upper airway to explore the effect of palatal resection, mandibular advancement, and palatal stiffening. This model was derived from signal averaged sagittal MRI scans of normal, non-OSAHS individuals with a normal upper airway and provides a baseline for assessment of patients with OSAHS. Moreover, Lucey et al. 2010 described a methodology to determine fluid dynamics of the upper airway based on an endoscopic optical technique. Their simulations reveal flow mechanisms that produce low-pressure regions on the sidewalls of the pharynx and on the soft palate within the pharyngeal section of minimum area. Correlations between pressure and airway deformation indicated that clinicians should make quantitative prediction of the low-pressure regions for their patients. CBCT hollow modeling provides a relatively low dose method of creating static volumes which could be used with this method. Such a technique could allow investigators to compare the effects of treatment options and, ultimately, to predict the best therapy tailored to a specific patient's site(s) of upper airway collapse.
- **Predicting surgical and interventional outcomes**. The predictability of response to surgical and other interventional techniques is one of the most challenging research areas in OSAHS and is an area of priority for research (Marcus et al. 2009). Previous literature presents mixed results in determining which patients are likely to respond to various surgical techniques, including uvulopalatopharyngoplasty. These studies potentially provide a paradigm for matching patient presentation with a specific treatment option based on measurable anatomic variables, as opposed to the AHI and patient preference. However, there are numerous difficulties in carrying out such research, especially given the variety of surgical procedures, oral appliances, and variations in the imaging modalities used to evaluate and predict efficacy.

Acknowledgments Figures 28.18, 28.19, 28.21, 28.26, and 28.28 are reprinted from Shigeta et al. (2007) with permission from Springer. Figure 28.22 is reprinted from Ogawa et al. 2007, b with permission from Elsevier. Figure 28.35 is reprinted from Shigeta et al. (2010) with permission from Springer. Figure 28.37 is reprinted from Reprinted from Shigeta et al. (2008) with permission from Springer.

References

Abramson Z, Susarla S, August M, Troulis M, Kaban L (2010) Three-dimensional computed tomographic analysis of airway anatomy in patients with obstructive sleep apnea. J Oral Maxillofac Surg 68:354–362

Arens R, Sin S, McDonough JM, Palmer JM, Dominguez T, Meyer H, Wootton DM, Pack AI (2005) Changes in upper airway size during tidal breathing in children with obstructive sleep apnea syndrome. Am J Respir Crit Care Med 171:1298–1304

Armstrong JJ, Leigh MS, Sampson DD, Walsh JH, Hillman DR, Eastwood PR (2006) Quantitative upper airway imaging with anatomic optical coherence tomography. Am J Respir Crit Care Med 173: 226–233

Battagel JM, L'Estrange PR, Nolan P, Harkness B (1998) The role of lateral cephalometric radiography and fluoroscopy in assessing mandibular advancement in sleep-related disorders. Eur J Orthod 20:121–132

Bradley TD, Brown IG, Grossman RF, Zamel N, Martinez D, Phillipson EA, Hoffstein V (1986) Pharyngeal size in snorers, nonsnorers, and patients with obstructive sleep apnea. N Engl J Med 315:1327–1331

Camacho M, Capasso R, Schendel S (2014) Airway changes in obstructive sleep apnoea patients associated with a supine versus an upright position examined using cone beam computed tomography. J Laryngol Otol 128:824–830

Chan J, Edman JC, Koltai PJ (2004) Obstructive sleep apnea in children. Am Fam Physician 69:1147–1154

Chen NH, Li KK, Li SY, Wong CR, Chuang ML, Hwang CC, Wu YK (2002) Airway assessment by volumetric computed tomography in snorers and subjects with obstructive sleep apnea in a far-east Asian population (Chinese). The Laryngoscope 112:721–726

Chervin RD, Archbold KH, Dillon JE, Panahi P, Pituch KJ, Dahl RE, Guilleminault C (2002) Inattention, hyperactivity, and symptoms of sleep-disordered breathing. Pediatrics 109:449–456

Chiang CC, Jeffres MN, Miller A, Hatcher DC (2012) Three-dimensional airway evaluation in 387 subjects from one university orthodontic clinic using cone beam computed tomography. Angle Orthod 82:985–992

Choi JK, Goldman M, Koyal S, Clark G (2000) Effect of jaw and head position on airway resistance in obstructive sleep apnea. Sleep Breath 4:163–168

Ciscar MA, Juan G, Martínez V, Ramón M, Lloret T, Mínguez J, Armengot M, Marín J, Basterra J (2001) Magnetic resonance imaging of the pharynx in OSA patients and healthy subjects. Eur Respir J 17:79–86

Cistulli PA (1996) Craniofacial abnormalities in obstructive sleep apnoea: implications for treatment. Respirology 1(3):167–174

Clark GT, Arand D, Chung E, Tong D (1993) Effect of anterior mandibular positioning on obstructive sleep apnea. Am Rev Respir Dis 147:624–629

Conley RS, Legan HL (2006) Correction of severe obstructive sleep apnea with bimaxillary transverse distraction osteogenesis and maxillomandibular advancement. Am J Orthod Dentofac Orthop 129:283–292

Corkum P, Moldofsky H, Hogg-Johnson S, Humphries T, Tannock R (1999) Sleep problems in children with attention-deficit/hyperactivity disorder: impact of subtype, comorbidity, and stimulant medication. J Am Acad Child Adolesc Psychiatry 38:1285–1293

Cosentini T, LeDonne R, Mancini D, Colavita N (2004) Magnetic resonance imaging of the upper airway in obstructive sleep apnea. Radiol Med 108:404–416

El H, Palomo JM (2010) Measuring the airway in 3 dimensions: a reliability and accuracy study. Am J Orthod Dentofacial Orthop 137:S50.e1–S50.e9

Enciso R, Clark GT (2011) Comparing the berlin and the ARES questionnaire to identify patients with obstructive sleep apnea in a dental setting. Sleep Breath 15:83–89

Enciso R, Shintaku W, Clark G (2006) Soft palate length and area (mid-sagittal view) in obstructive sleep apnea versus non-snoring controls. In: 15th annual meeting of the Academy of Dental Sleep Medicine (abstract)

Enciso R, Nguyen M, Shigeta Y, Ogawa T, Clark GT (2010) Comparison of cone-beam CT parameters and sleep questionnaires in sleep apnea patients and control subjects. Oral Surg Oral Med Oral Pathol Oral Radiol Endod 109:285–293

Enciso R, Shigeta Y, Nguyen M, Clark GT (2012) Comparison of cone-beam computed tomography incidental findings between patients with moderate/severe obstructive sleep apnea and mild obstructive sleep apnea/healthy patients. Oral Surg Oral Med Oral Pathol Oral Radiol 114:373–381

Findley L, Unverzadt M, Suratt P (1988) Automobile accidents in patients with obstructive sleep apnea. Am Rev Respir Dis 138:337–340

Fogel RB, Malhotra A, Dalagiorgou G, Robinson MK, Jakab M, Kikinis R, Pittman SD, White DP (2003) Anatomic and physiologic predictors of apnea severity in morbidly obese subjects. Sleep 26:150–155

Fujita S (1987) Pharyngeal surgery for management of snoring and obstructive sleep apnea. In: Fairbanks DN, Fujita S, Ikematsu T (eds) Snoring and obstructive sleep apnea. Raven Press, New York, pp 101–128

Giles TL, Lasserson TJ, Smith BJ, White J, Wright J, Cates CJ (2006) Continuous positive airways pressure for obstructive sleep apnoea in adults. Cochrane Database Syst Rev 1:CD001106

Greenfeld M, Tauman R, DeRowe A, Sivan Y (2003) Obstructive sleep apnea syndrome due to adenotonsillar hypertrophy in infants. Int J Pediatr Otorhinolaryngol 67:1055–1060

Guijarro-Martinez R, Swennen GRJ (2011) Cone-beam computerized tomography imaging and analysis of the upper airway: a systematic review of the literature. Oral Maxillofac Surg 40:1227–1237

Guilleminault C, Monteyrol PJ, Huynh NT, Pirelli P, Quo S, Li K (2011) Adeno-tonsillectomy and rapid maxillary distraction in pre-pubertal children, a pilot study. Sleep Breath 15:173–177

Hatzakis GE, Karsan N, Cook J, Schloss M, Davis GM (2003) Acoustic reflectance of pharyngeal structures in children. Int J Pediatr Otorhinolaryngol 67:373–381

Hochban W, Brandenburg U (1994) Morphology of the viscerocranium in obstructive sleep apnoea syndrome ± cephalometric evaluation of 400 patients. J Craniomaxillofac Surg 22:205–213

Hsu PP, Tan AK, Chan YH, PK L, Blair RL (2005a) Clinical predictors in obstructive sleep apnoea patients with calibrated cephalometric analysis—a new approach. Clin Otolaryngol 30:234–241

Hsu PP, Tan BY, Chan YH, Tay HN, PK L, Tan AK, Blair RL (2005b) 10th Yahya Cohen memorial lecture: clinical predictors in obstructive sleep apnoea patients with computer-assisted videoendoscopic upper airway analysis. Ann Acad Med Singap 34:703–711

Huang Y, White DP, Malhotra A (2007) Use of computational modeling to predict responses to upper airway surgery in obstructive sleep apnea. Laryngoscope 117:648–653

Iber C, Ancoli-Israel S, Chesson A, Quan SF (2007) The AASM manual for the scoring of sleep and associated events: rules, terminology and technical specifications. Westchester, American Academy of Sleep Medicine, p 56

Jayaratne YS, Zwahlen RA (2016) The Oropharyngeal airway in young adults with skeletal class II and class III deformities: a 3-D morphometric analysis. PLoS One 11:e0148086

Johal A, Conaghan C (2004) Maxillary morphology in obstructive sleep apnea: a cephalometric and model study. Angle Orthod 74:648–656

Johal A, Battagel J, Kotecha B (2005) Sleep nasoendoscopy: a diagnostic tool for predicting treatment success with mandibular advancement splints in obstructive sleep apnea. Eur J Orthod 27:607–614

Johal A, Patel SI, Battagel JM (2007) The relationship between craniofacial anatomy and obstructive sleep apnea: a case-controlled study. J Sleep Res 16:319–326

Johnson EO, Roth T (2006) An epidemiologic study of sleep-disordered breathing symptoms among adolescents. Sleep 29:1135–1142

Kato J, Isono S, Tanaka A, Watanabe T, Araki D, Tanzawa H, Nishino T (2000) Dose-dependent effects of mandibular advancement on pharyngeal mechanics and nocturnal oxygenation in patients with sleep-disordered breathing. Chest 117:1065–1072

Kim SJ, Kim YS, Park JH, Kim SW (2012) Cephalometric predictors of therapeutic response to multilevel surgery in patients with obstructive sleep apnea. J Oral Maxillofac Surg 70(6):1404–1412

Kushida CA, Morgenthaler TI, Littner MR, Alessi CA, Bailey D, Coleman J, Friedman L, Hirshkowitz M, Kapen S, Kramer M, Lee-Chiong T, Owens J, Pancer JP (2006) Practice parameters for the treatment of snoring and obstructive sleep Apnoea with oral appliances: an update for 2005. Sleep 29:240–243

Launois SH, Feroah TR, Campbell WN, Issa FG, Morrison D, Whitelaw WA, Isono S, Remmers JE (1993) Site of pharyngeal narrowing predicts outcome of surgery for obstructive sleep apnea. Am Rev Respir Dis 147:182–189

Li HY, Chen NH, Wang CR, Shu YH, Wang PC (2003) Use of 3-dimensional computed tomography scan to evaluate upper airway patency for patients undergoing sleep-disordered breathing surgery. Otolaryngol Head Neck Surg 129:336–342

Linder-Aronson S (1970) Adenoids. Their effect on mode of breathing and nasal airflow and their relationship to characteristics of the facial skeleton and the dentition. Acta Otolaryngol 265:1–132

Liu Y, Lowe AA, Fleetham JA, Park YC (2001) Cephalometric and physiologic predictors of the efficacy of an adjustable oral appliance for treating obstructive sleep apnea. Am J Orthod Dentofac Orthop 120:639–647

Lowe AA (1993) Can we predict the success of dental appliance therapy for the treatment of obstructive sleep apnea based on anatomic considerations? Sleep 16:S93–S95

Lucey AD, King AJC, Tetlow GA, Wang J, Armstrong JJ, Leigh MS, Paduch A, Walsh JH, Sampson DD, Eastwood PR, Hillman DR (2010) Measurement, reconstruction, and flow-field computation of the human pharynx with application to sleep apnea. IEEE Trans Biomed Eng 57:2535–2548

Major MP, Flores-Mir C, Major PW (2006) Assessment of lateral cephalometric diagnosis of adenoid hypertrophy and posterior upper airway obstruction: a systematic review. Am J Orthod Dentofac Orthop 130:700–708

Malhotra A, Pillar G, Edwards J, Beauregard J, Fogel R, White DP (2001) Upper airway collapsibility: measurement and sleep effects. Chest 120:156–161

Malhotra A, Huang Y, Fogel R, Lazic S, Pillar G, Jakab M, Kikinis R, White DP (2006) Aging influences on pharyngeal anatomy and physiology: the predisposition to pharyngeal collapse. Am J Med 119:72.e9–72.14

Mallampati SR, Gatt SP, Gugino LD, Desai SP, Waraksa B, Freiberger D, Liu PL (1985) A clinical sign to predict difficult tracheal intubation: a prospective study. Can Anaesth Soc J 32:429–434

Marcus CL, Smith RJ, Mankarious LA, Arens R, Mitchell GS, Elluru RG, Forte V, Goudy S, Jabs EW, Kane AA, Katz E, Paydarfar D, Pereira K, Reeves RH, Richtsmeier JT, Ruiz RL, Thach BT, Tunkel DE, Whitsett JA, Wootton D, Blaisdell CJ (2009) Developmental aspects of the upper airway: report from an NHLBI workshop. Proc Am Thorac Soc 15:513–520

Mayer G, Meier-Ewert K (1995) Cephalometric predictors for orthopaedic mandibular advancement in obstructive sleep apnea. Eur J Orthod 17:35–43

Miles PG, Vig PS, Weygand RJ, Forrest TD, Rockette HE (1996) Craniofacial structure and obstructive sleep apnea syndrome: a qualitative analysis and meta-analysis of the literature. Am J Orthod Dentofac Orthop 109:163–172

Namyslowski G, Scierski W, Zembala-Nozynska E, Nozynski J, Misiolek M (2005) Histopathologic changes of the soft palate in snoring and obstructive sleep apnea syndrome patients. Otolaryngol Pol 59:13–19

Ng AT, Darendeliler MA, Petocz P, Cistulli PA (2012) Cephalometry and prediction of oral appliance treatment outcome. Sleep Breath 16:47–58

Nuckton TJ, Glidden DV, Browner WS, Claman DM (2006) Physical examination: Mallampati score as an independent predictor of obstructive sleep apnea. Sleep 29:903–908

O'Brien LM, Mervis CB, Holbrook CR, Bruner JL, Smith NH, McNally N, McClimment MC, Gozal D (2004) Neurobehavioral correlates of sleep-disordered breathing in children. J Sleep Res 13:165–172

Ogawa T, Enciso R, Memon A, Mah JK, Clark GT (2005) Evaluation of 3D airway imaging of obstructive sleep apnea with cone-beam computed tomography. Stud Health Technol Inform 111:365–368

Ogawa T, Enciso R, Shintaku WH, Clark GT (2007) Evaluation of cross-section airway configuration of obstructive sleep apnea. Oral Surg Oral Med Oral Pathol Oral Radiol Endod 103:102–108

Rachmiel A, Aizenbud D, Pillar G, Srouji S, Peled M (2005) Bilateral mandibular distraction for patients with compromised airway analyzed by three-dimensional CT. Int J Oral Maxillofac Surg 34:9–18
Ram S, Seirawan H, Kumar SKS, Clark GT (2010) Prevalence and impact of sleep disorders and sleep habits in the United States. Sleep Breath 14:63–70
Riley R, Guilleminault C, Herran J, Powell N (1983) Cephalometric analyses and flow volume loops in obstructive sleep apnoea patients. Sleep 6:303–311
Rivlin J, Hoffstein V, Kalbfleisch J, McNicholas W, Zamel N, Bryan AC (1984) Upper airway morphology in patients with idiopathic obstructive sleep apnea. Am Rev Respir Dis 129:355–360
Rodenstein DO, Doom G, Thomas Y, Liistro G, Stanescu DC, Culee C, Aubert-Tulkens G (1990) Pharyngeal shape and dimension in healthy subjects, snorer and patients with obstructive sleep apnea. Thorax 45:722–727
Rosen CL, Larkin EK, Kirchner HL, Emancipator JL, Bivins SF, Surovec SA, Martin RJ, Redline S (2003) Prevalence and risk factors for sleep-disordered breathing in 8- to 11-year-old children: association with race and prematurity. J Pediatr 142:383–389
Roth T, Roehrs TA, Conway WA (1988) Behavioral morbidity of apnea. Sem Respir Med 9:554–559
Schendel SA, Hatcher D (2010) Automated 3-dimensional airway analysis from cone-beam computed tomography data. J Oral Maxillofac Surg 68:696–701
Schwab RJ, Gefter WB, Hoffman EA, Gupta KB, Pack AI (1993) Dynamic upper airway imaging during awake respiration in normal subjects and patients with sleep disordered breathing. Am J Respir Crit Care Med 148:1385–1400
Schwab RJ, Gupta KB, Gefter WB, Metzger LJ, Hoffman EA, Pack AI (1995) Upper airway and soft tissue anatomy in normal subjects and patients with sleep-disordered breathing. Significance of the lateral pharyngeal walls. Am J Respir Crit Care Med 152:1673–1689
Schwab RJ, Pasirstein M, Pierson R, Mackley A, Hachadoorian R, Arens R, Maislin G, Pack AI (2003) Identification of upper airway anatomic risk factors for obstructive sleep apnea with volumetric magnetic resonance imaging. Am J Respir Crit Care Med 168:522–530
Schwartz AR, Smith PL, Wise RA, Gold AR, Permutt S (1988) Induction of upper airway occlusion in sleeping individuals with subatmospheric nasal pressure. J Appl Physiol 64:535–542
Sforza E, Bacon W, Weiss T, Thibault A, Petiau C, Krieger J (2000) Upper airway collapsibility and cephalometric variables in patients with obstructive sleep apnea. Am J Respir Crit Care Med 161:347–352
Shepard JW Jr, Gefter WB, Guilleminault C, Hoffman EA, Hoffstein V, Hudgel DW, Suratt PM, White DP (1991) Evaluation of the upper airway in patients with obstructive sleep apnea. Sleep 14:361–371
Sher AE, Schechtman KB, Piccirillo JF (1996) The efficacy of surgical modifications of the upper airway in adults with obstructive sleep apnea syndrome. Sleep 19:156–177
Shigeta Y, Enciso R, Ogawa T, Shintaku WH, Clark GT (2007) Upper airway alterations/abnormalities in a case series of obstructive sleep apnea patients identified with cone-beam CT. Int J Comput Assist Radiol Surg 2:402–404
Shigeta Y, Enciso R, Ogawa T, Shintaku WH, Clark GT (2008) Correlation between retroglossal airway size and body mass index in OSA and non-OSA patients using cone beam CT imaging. Sleep Breath 12:347–352
Shigeta Y, Ogawa T, Tomoko I, Clark GT, Enciso R (2010) Soft palate length and upper airway relationship in OSA and non-OSA subjects. Sleep Breath 14:353–358
Solow B, Tallgren A (1976) Head posture and craniofacial morphology. Am J Phys Anthropol 44:417–436
Solow B, Skov S, Ovesen J, Norup PW, Wildschiødtz G (1996) Airway dimensions and head posture in obstructive sleep apnoea. Eur J Orthod 18:571–579
Souza KR, Oltramari-Navarro PV, Navarro Rde L, Conti AC, Almeida MR (2013) Reliability of a method to conduct upper airway analysis in cone-beam computed tomography. Braz Oral Res 27:48–54
Stein MG, Gamsu G, de Geer G, Golden JA, Crumley RL, Webb WR (1987) Cine CT in obstructive sleep apnea. Am J Roentgenol 148:1069–1074
Suratt PM, Dee P, Atkinson AL, Armstrong P, Wilhol SC (1983) Fluoroscopic and computed tomographic features of the pharyngeal airway in obstructive sleep apnea. Am Rev Respir Dis 127:487–492
Tangugsorn V, Skatvedt O, Krogstad O, Lyberg T (1995a) Obstructive sleep apnoea: a cephalometric study. Part I. Cervico-craniofacial skeletal morphology. Eur J Orthod 17:45–56
Tangugsorn V, Skatvedt O, Krogstad O, Lyberg T (1995b) Obstructive sleep apnoea: a cephalometric study. Part II. Uvulo-glossopharyngeal morphology. Eur J Orthod 17:57–67
Trudo FJ, Gefter WB, Welch KC, Gupta KB, Maislin G, Schwab RJ (1998) State-related changes in upper airway caliber ans surrounding soft-tissue structures in normal subjects. Am J Respir Care Med 158:1259–1270
Tsuiki S, Hiyama S, Ono T, Imamura N, Ishiwata Y, Kuroda T, Lowe AA (2001) Effects of titratable oral appliance on supine airway size in awake non-apneic individuals. Sleep 24:554–560
Tsuiki S, Almeida FR, Bhalla PS, A Lowe AA, Fleetham JA (2003) Supine-dependent changes in upper airway size in awake obstructive sleep apnea patients. Sleep Breath 7:43–50
Tsuiki S, Lowe AA, Almeida FR, Fleetham JA (2004a) Effects of an anteriorly titrated mandibular position on awake airway and obstructive sleep apnea severity. Am J Orthod Dentofac Orthop 125:548–555
Tsuiki S, Lowe AA, Almeida FR, Kawahata N, Fleetham JA (2004b) Effects of mandibular advancement on airway curvature and obstructive sleep apnoea severity. Eur Respir J 23:263–268

Tsuiki S, Almeida FR, Lowe AA, Su J, Fleetham JA (2005) The interaction between changes in upright mandibular position and supine airway size in patients with obstructive sleep apnea. Am J Orthod Dentofac Orthop 128:504–512

Veasey SC, Guilleminault C, Strohl KP, Sanders MH, Ballard RD, Magalang UJ (2006) Medical therapy for obstructive sleep apnea: a review by the medical therapy for obstructive sleep apnea task force of the standards of practice Committee of the American Academy of sleep Medicine. Sleep 29:1036–1044

Villa MP, Malagola C, Pagani J, Montesano M, Rizzoli A, Guilleminault C, Ronchetti R (2007) Rapid maxillary expansion in children with obstructive sleep apnea syndrome: 12-month follow-up. Sleep Med 8:128–134

Villa MP, Rizzoli A, Miano S, Malagola C (2011) Efficacy of rapid maxillary expansion in children with obstructive sleep apnea syndrome: 36 months of follow-up. Sleep Breath 15:179–184

Weissheimer A, Menezes LM, Sameshima GT, Enciso R, Pham J, Grauer D (2012) Imaging software accuracy for 3-dimensional analysis of the upper airway. Am J Orthod Dentofac Orthop 142:801–813

Wildhaber JH, Moeller A (2007) Sleep and respiration in children: time to wake up! Swiss Med Wkly 137:689–694

Yamashiro Y, Kryger M (1994) Why should sleep apnea be diagnosed and treated? Clin Pulm Med 1:250–259

Yu X, Fujimoto K, Urushibata K, Matsuzawa Y, Kubo K (2003) Cephalometric analysis in obese and nonobese patients with obstructive sleep apnea syndrome. Chest 124:212–218

Yucel A, Unlu M, Haktanir A, Acar M, Fidan F (2005) Evaluation of the upper airway cross-sectional area changes in different degrees of severity of obstructive sleep apnea syndrome: cephalometric and dynamic CT study. Am J Neuroradiol 26:2624–2629

Zozula R, Rosen R (2001) Compliance with continuous positive airway pressure therapy: assessing and improving treatment outcomes (review). Curr Opin Pulm Med 7:391–398

Dental Impactions

29

Dania Tamimi, Birgitta Warvarovsky,
Sarah Lawson, William C. Scarfe,
and Christos Angelopoulos

Contents

29.1 Introduction

The normal human dentition comprises two sets of teeth which gradually emerge or *erupt* into the oral cavity; the first set comprises 20 primary or *deciduous* teeth and the second set which gradually replace the deciduous teeth comprise 32 permanent teeth. The teeth are equally divided among the maxilla and the mandible and between sides.

The primary dentition includes a central and lateral incisor, a canine, and two molars in each quadrant. The permanent dentition includes a

D. Tamimi, B.D.S., D.M.Sc. (✉)
Private Practice in Oral and Maxillofacial Radiology, Orlando, FL, USA

Adjunct Assistant Professor, Department of Comprehensive Dentistry, University of Texas, San Antonio, TX, USA
e-mail: daniatamimi@hotmail.com

B. Warvarovsky, D.D.S., M.S.
Private Practice in Oral and Maxillofacial Radiology, Sacramento, CA, USA

Department of Biomedical Sciences, Arthur A. Dugoni School of Dentistry, University of the Pacific, San Francisco, CA, USA
e-mail: beerwarflys@gmail.com

S. Lawson, D.D.S.
Private Practice in Oral Surgery, Sacramento, CA, USA
e-mail: sarah.t.lawson@gmail.com

W.C. Scarfe, B.D.S., F.R.A.C.D.S., M.S.
Division of Radiology and Imaging Science, Department of Surgical/Hospital Dentistry, University of Louisville School of Dentistry, Louisville, KY, USA
e-mail: william.scarfe@louisville.edu

C. Angelopoulos, D.D.S., M.S.
Aristotle University of Thessaloniki, Thessaloniki, Greece

Columbia University, College of Dental Medicine, New York City, NY, USA
e-mail: angelopoulosc@gmail.com

W.C. Scarfe, C. Angelopoulos (eds.), *Maxillofacial Cone Beam Computed Tomography*,
https://doi.org/10.1007/978-3-319-62061-9_29

central and lateral incisor, a canine, two premolars (identified by their distance from the midline as the first and second premolars), and three molars (identified by their distance from the midline as the first, second, and third molars) in each quadrant. The deciduous teeth provide masticatory function for the developing child and act as space maintainers for the generally larger permanent teeth. The primary incisors, canines, and first and second molars are replaced by the permanent incisors, canines, and the first and second premolars, respectively. The permanent molars do not have predecessors and erupt posterior to the deciduous teeth in the dental arch. When there is an imbalance in this normal sequence due to jaw or dental abnormalities, the permanent teeth and, less commonly, the primary teeth may become impacted.

29.1.1 Dental Eruption Sequence

The dental eruption sequence is remarkably similar for most individuals although the chronological timing may vary between tooth type and dental arch (Table 29.1). A general appreciation of the sequence and timings is necessary, particularly in the transition period between the exfoliation of the deciduous teeth and eruption of the permanent teeth, to anticipate the possibility of tooth crowding and implement therapy towards preventing possible dental impaction.

The first teeth to erupt into the oral cavity are usually the primary central and lateral incisors. These are followed by the primary canines and the primary molars. The first permanent tooth to erupt into the oral cavity is the permanent 1st molar (“6-year molar”). The primary incisors then exfoliate associated with the eruption of the

Table 29.1 Primary and permanent dentition calcification, eruption, and exfoliation timings

Arch	Location	Type	Time		
			Calcification[a]	Erupt	Exfoliation
Maxilla	Central incisor	D	4th mo. IU	8–12 mo.	6–7 yr.
		P	3–4 mo.	7–8 yr.	
	Lateral incisor	D	4th mo. IU	9–13 mo.	7–8 yr.
		P	10–12 mo.	8–9 yr.	
	Canine	D	4th mo. IU	16–22 mo.	10–12 yr.
		P	4–5 mo.	11–12 yr.	
	1st molar	D	4th mo. IU	13–19 mo.	9–11 yr.
		P (1st premolar)	18–24 mo.	10–11 yr.	
	2nd molar	D	4th mo. IU	25–33 mo.	10–12 yr.
		P (2nd premolar)	24–30 mo.	10–12 yr.	
	1st molar	P	Birth	6–7 yr.	
	2nd molar	P	30–36 mo.	12–13 yr.	
	3rd molar	P	7–8 yr.	17–21 yr.	
Mandible	Central incisor	D	4th mo. IU	6–10 mo.	6–7 yr.
		P	3–4 mo.	6–7 yr.	
	Lateral incisor	D	4th mo. IU	10–16 mo.	7–8 yr.
		P	3–4 mo.	7–8 yr.	
	Canine	D	4th mo. IU	17–23 mo.	9–12 yr.
		P	4–5 mo.	9–10 yr.	
	1st molar	D	4th mo. IU	14–18 mo.	9–11 yr.
		P (1st premolar)	18–24 mo.	10–12 yr.	
	2nd molar	D	4th mo. IU	23–31 mo.	10–12 yr.
		P (2nd premolar)	24–30 mo.	11–12 yr.	
	1st molar	P	Birth	6–7 yr.	
	2nd molar	P	30–36 mo.	11–13 yr.	
	3rd molar	P	8–10 yr.	17–21 yr.	

[a]Follicle formation; *IU* in utero, *D* Deciduous, *P* Permanent, *yr.* years, *mo.* months

permanent incisors. The permanent premolars then erupt, either after or simultaneously with the second molars. The final teeth to erupt into the oral cavity are the permanent maxillary canines (11–13 years) followed by the third molars (18 years), if present.

Root development of the permanent teeth is completed approximately 2.5–3 years after eruption. For example, if the permanent first molars and the permanent mandibular central incisors erupt at around 6 years, the root formation of these teeth should be complete by around 9 years of age. The eruptive potential of a tooth is greatest during this period. Dental age can be correlated to chronological age to determine if a tooth is erupting in normal time, or will probably become impacted.

29.1.2 Gubernacular Tract

The gubernacular tract (GT), also known as *gubernaculum dentis*, is a bony channel between a developing dental follicle and the overlying gingiva on unerupted maxillary and mandibular teeth. It is proposed to act as an eruptive pathway from the dental follicle to the gingiva for permanent teeth. On cross-sectional CBCT imaging, the GT appears as a well-defined low-density tract (Figs. 29.1 and 29.2). While rarely seen on panoramic images, GTs are often observed on CBCT images with detection rates varying depending on jaw and tooth location (Table 29.2).

On axial images, GTs for incisors and canines are visualized as distinct, corticated rounded (approximately 1 mm diameter) areas with low density on the palatal and lingual side of the respective deciduous predecessors in the maxilla and mandible, respectively. In the molar region, the GT appear as narrow, rounded areas with low density immediately coronal to the dental follicles. As teeth erupt, GTs become shorter and wider. GTs are rarely associated with mesiodens (Nishida et al. 2015). Approximately two-thirds of teeth with obstructed eruption show deformation and/or obliteration of the GT. An odontoma may develop within the GT of the unerupted permanent successor, at the base of the GT within the dental follicle immediately adjacent the occlusal surface, or independently with or without a separate GT (Oda et al. 2016).

29.1.3 Stages in the Development of the Dentition

There are four (4) stages in the development of the human dentition, each associated with a specific eruptive pattern (McNamara and Brudon 2001). They include:

1. **Primary dentition:** Beginning in infancy with the eruption of the first tooth, usually about 6 months of age, and complete from approximately 3–6 years of age when all primary teeth are erupted.
2. **Mixed dentition:** From approximately age 6–13 years, primary and permanent teeth are present in the mouth.

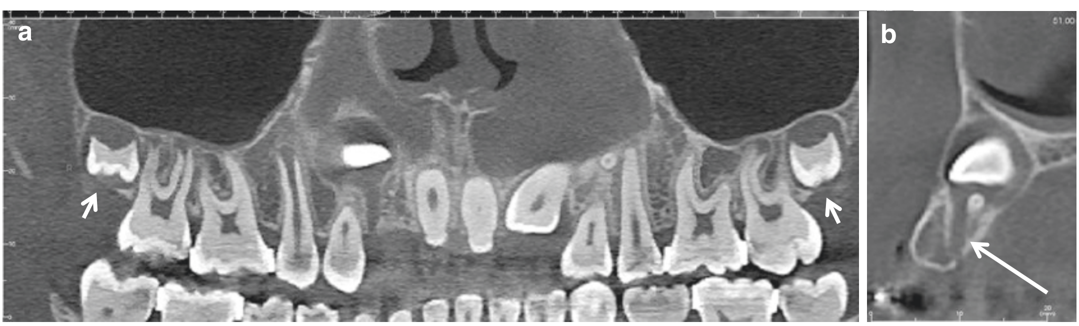

Fig. 29.1 Reformatted panoramic (**a**) showing gubernaculum tracts associated with the unerupted maxillary third molars (*arrows*) and right maxillary canine. Cross-sectional image (**b**) showing the gubernaculum tract associated with the maxillary right canine

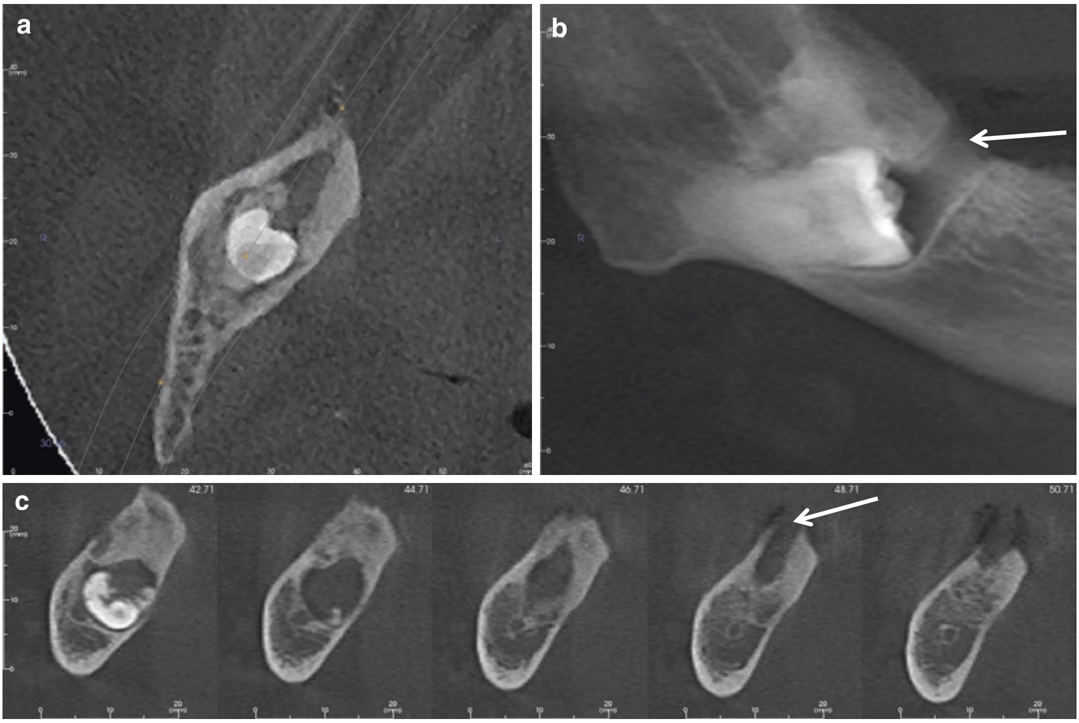

Fig. 29.2 Axial (**a**), reformatted panoramic (**b**), and serial cross-sectional (**c**) CBCT images demonstrating the presence of a gubernaculum tract associated with an unerupted and impacted right mandibular third molar in an edentulous patient

Table 29.2 Detection rates of gubernaculum dentis in unerupted maxillary and mandibular teeth (Nishida et al. 2015)

Tooth	Maxilla (%)	Mandible (%)
Central incisor	87.8	100
Lateral incisor	91.3	100
Canine	87.2	86.1
1st premolar	58.1	97
2nd premolar	43.7	80
1st molar	94.1	100
2nd molar	98.2	100
3rd molar	100	100

3. **Adolescent dentition:** All primary teeth have exfoliated, second permanent molars may be erupted or erupting, and third molars have not erupted.
4. **Adult dentition:** All permanent teeth are present and eruptive growth is complete.

These stages may further be divided as "early" and "late" (e.g., early primary, late primary, early mixed, late mixed).

29.2 Etiology of Dental Impaction

An impacted tooth is one with completed root formation that is either totally or partially covered by bone that has failed to erupt into occlusion at its correct location within the expected normal time (usually beyond the third decade). An unerupted tooth is an embedded tooth that will probably erupt by the middle of the third decade. Generally, a tooth begins to erupt into the oral cavity with approximately three-quarters of its final root length. An unerupted tooth that demonstrates more than this degree of root development may potentially become impacted. Failure of eruption may be due to one or a combination of soft or hard tissue factors including the size of adjacent teeth, the presence of jaw obstructions (e.g., anterior border of the ramus occlusal to an impacted mandibular third molar), osseous pathology, or dense soft tissue. The tooth root should be fully formed with complete apex formation to be defined as "impacted." If the tooth root is still developing, the tooth is called *unerupted* although its position may imply future impaction. An impacted tooth with a fully formed root tends to have a root that is curved, most notably in the apical third. There are numerous causes for dental impaction. The impaction of deciduous teeth is rare (Bianchi and Roccuzzo 1991).

- **Jaw abnormalities, skeletal malocclusion, and dental malocclusion**. Discrepancies between the size of a developing jaw or jaws and size of the teeth may provide a dental arch length discrepancy that can result in dental impactions (Fig. 29.3). For example, in Skeletal Class II malocclusions there is a higher chance of malalignment and possible impactions in the lower jaw as the mandible tends to be smaller.

Genetics may play a predominant role in the etiology of some palatally impacted canines, impacted mandibular second molars (autosomal dominant), and impacted mandibular canines (primary tooth germ displacement and angulation).

Developmental disturbances of the jaws can also result in dental impaction including cleft palate (impaction occurring in the anterior region), Crouzon's (maxillary hypoplasia) and other craniofacial synostosis syndromes, hemifacial microsomia (impaction

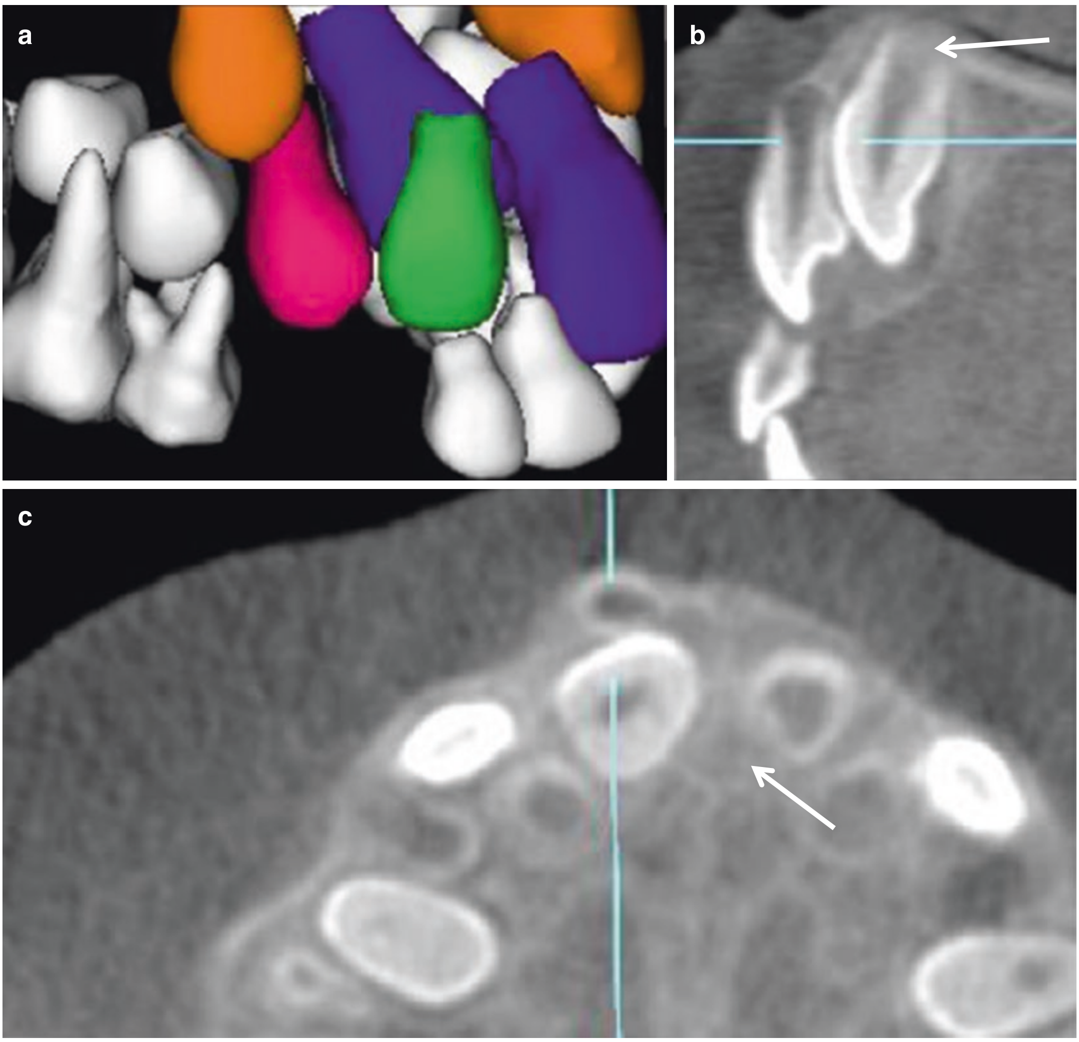

Fig. 29.3 Surface rendering segmentation (**a**), cross-sectional (**b**), and axial (**c**) images of the right maxillary dentition in a 7-year-old shows a supero-palatally positioned, unerupted right maxillary central (*purple tooth*) due to a ectopically positioned lateral incisor (*green tooth*). The developing root of the unerupted right maxillary incisor is within the floor of the nasal cavity (**b**) and palatal to the lateral incisor (**b**, **c**)

occurring on the affected side), Treacher Collin's syndrome (hypoplasia of the maxilla and, more so, the mandible), and segmental odontodysplasia.

- **Supernumerary Teeth**. A supernumerary tooth (hyperdontia) is an additional tooth to the normal dental complement of 20 deciduous and 32 permanent teeth. The presence of a supernumerary in the path of eruption of a tooth may lead to impaction or ectopic eruption of the normal tooth. Supernumerary teeth are often single, small, and impacted, the most common of which in decreasing order of prevalence are the mesiodens (Fig. 29.4) often resulting in impaction of the central incisors (Chaushu et al. 2014), an extra premolar (particularly in the mandible) (Fig. 29.5), a 4th molar, a paramolar, and, rarely, an extra canine. The presence of multiple supernumerary teeth may be part of a developmental disorder such as cleft lip and palate, cleidocranial dysostosis (Fig. 29.6), Gardner's syndrome, Ehlers–Danlos syndrome, or incontinentia pigmenti.

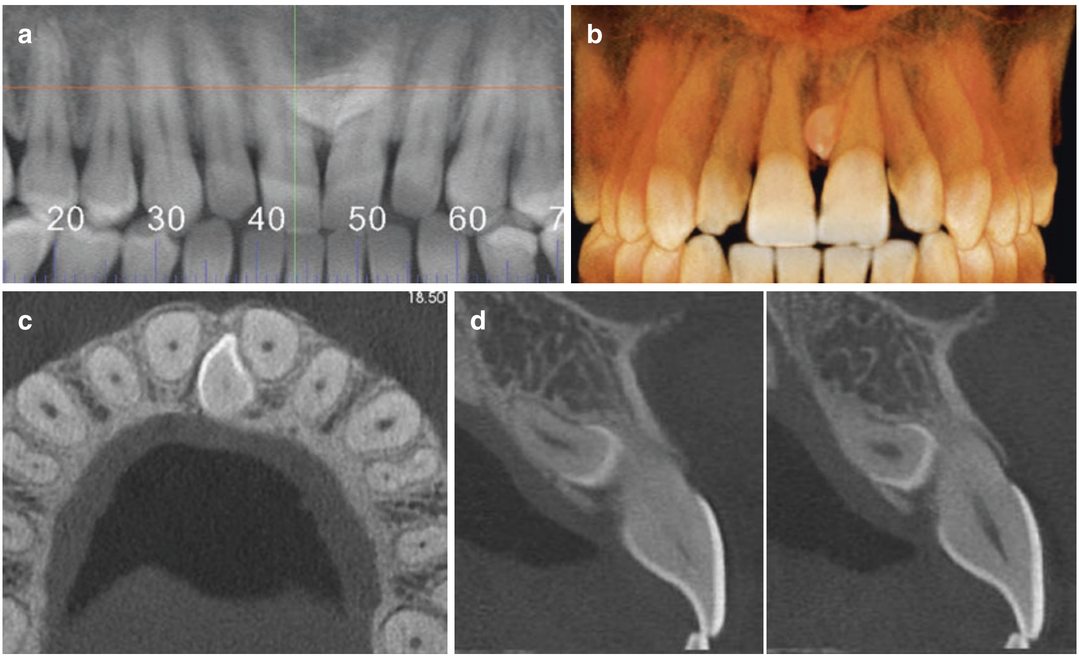

Fig. 29.4 Reformatted CBCT panoramic (**a**) volumetric rendering (**b**), axial (**c**), and sequential 1 mm thick cross-sectional (**d**) images showing a single, fully formed, microdontic supernumerary palatally impacted and unerupted in the alveolar bone between the maxillary central incisors

Fig. 29.5 Reformatted CBCT panoramic image (**a**) shows developing bilateral supernumerary premolars present inter-radicular to the mandibular canines and first premolars. Right thin section parasagittal image (**b**) shows the more lingually located supernumerary premolar

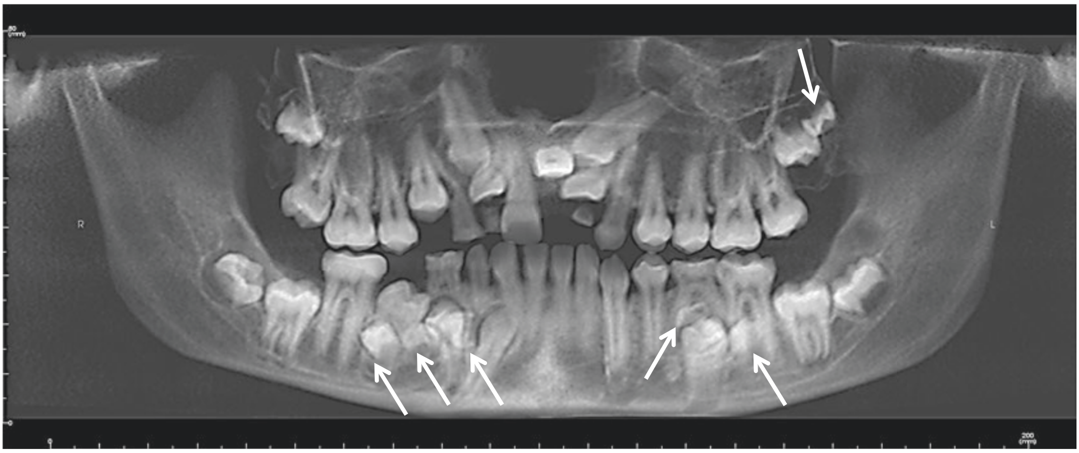

Fig. 29.6 Reformatted CBCT panoramic image of 16-year-old patient with cleidocranial dysplasia demonstrating multiple unerupted and impacted teeth (*arrows*)

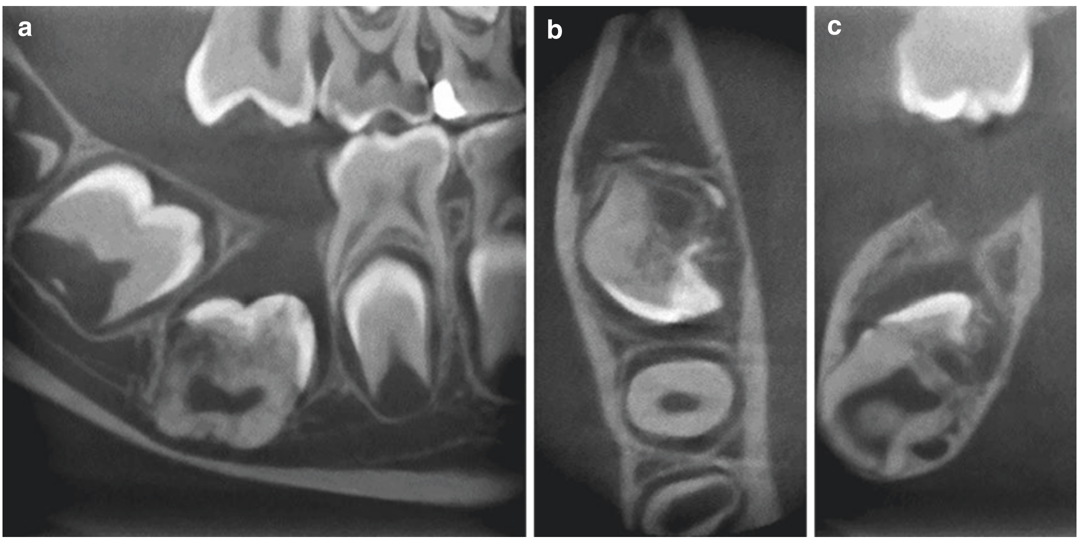

Fig. 29.7 Sagittal (**a**), axial (**b**), and cross-sectional (**c**) CBCT images of the right mandibular posterior region in a child demonstrating bony replacement external resorption leading to ankylosis and subsequent submersion and impaction of the crown of a partially formed mandibular first molar

- **Pathology**. The presence of pathology directly affecting (Fig. 29.7), adjacent to (Fig. 29.8), or involving the pericoronal space (e.g., dentigerous cysts, adenomatoid odontogenic tumor, keratocystic odontogenic tumor) (Fig. 29.9) can result in tooth impaction. Inflammatory pathology in the periapical or furcation area of primary teeth may also delay the eruption of the permanent successor as well as delay the normal resorption pattern of the primary tooth roots. Some systemic diseases manifest dentally as delayed eruption or impaction of teeth, such as hypoparathyroidism, hypopituitarism, hyperthyroidism, Rickets, and osteopetrosis.
- **Ankylosis**. The dental-alveolar process, or *gomphosis,* should be carefully evaluated when no obvious cause for a dental

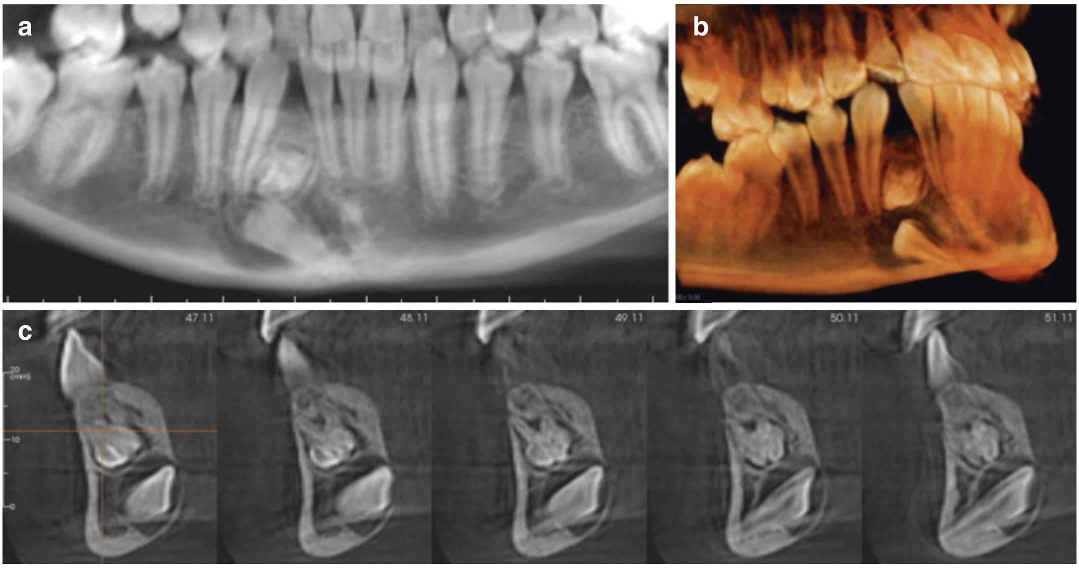

Fig. 29.8 Reformatted CBCT panoramic (**a**), volumetric rendering (**b**), and serial 1 mm thick cross-sectional (**c**) CBCT images of the anterior mandible shows an inter-radicular compound odontoma between the right canine and lateral permanent incisor causing impaction of and lingually and posteriorly displacing the right mandibular second incisor

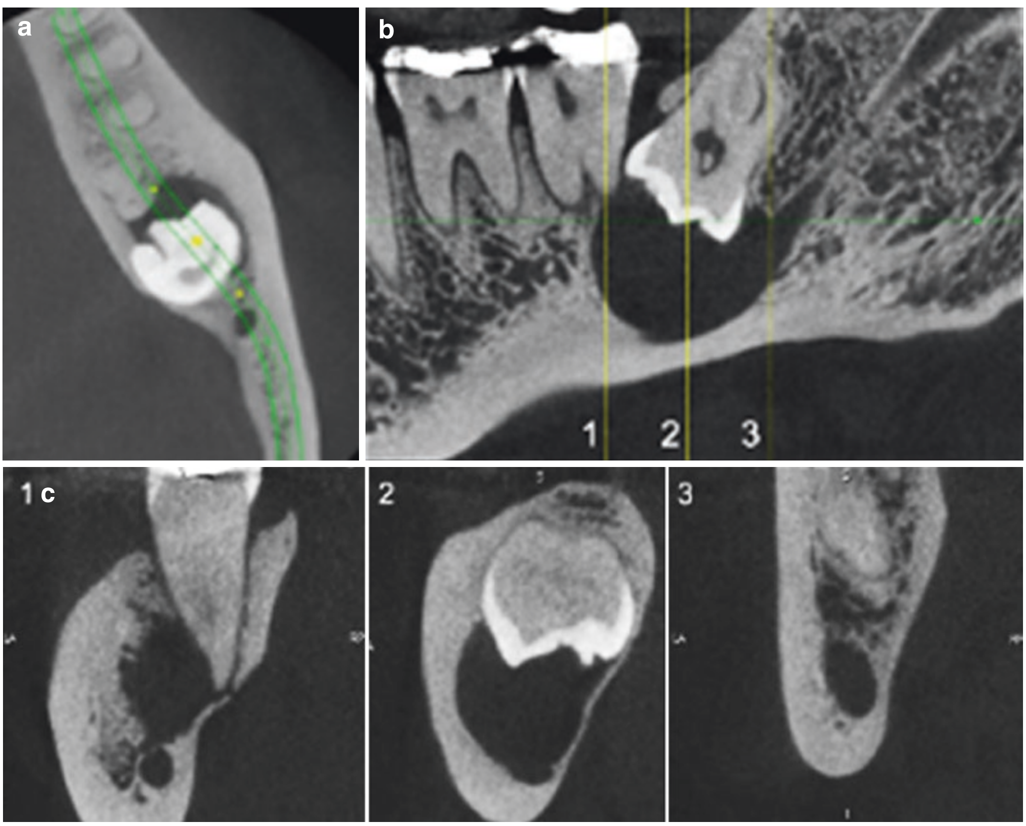

Fig. 29.9 Axial reference (**a**), sagittal (**b**), and multiple cross-sectional (**c**) CBCT images of the left mandibular retromolar area showing and inverted and completely bony impacted third molar with a well-defined unilocular pericoronal hypodensity. Cross-sectional images (**c**) show infero-lingual displacement of the inferior alveolar canal and surface resorption of the disto-buccal aspect of the distal root of the second molar

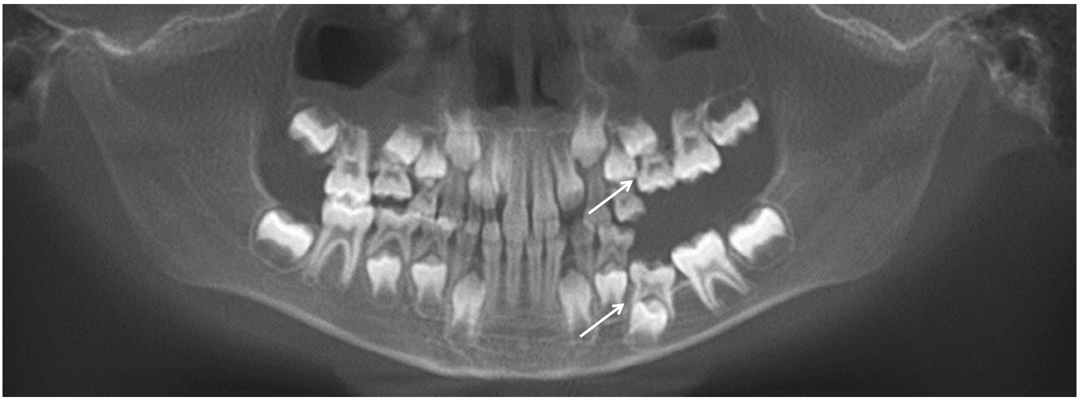

Fig. 29.10 Panoramic reconstruction from CBCT of an 8-year-old shows ankylosis of primary second molars on the left side teeth. Primary failure of eruption must be considered as the permanent teeth in the adjacent alveolar base have also not erupted/ are delayed relative to the contralateral side and the patient's age

impaction is identified. Ankylosis is most common in the permanent dentition although, in rare cases, has been observed in the primary dentition (Fig. 29.10). Ankylosis of primary teeth is very rare, occurring most commonly with the primary molars (Fig. 29.10). The normal fibrous connective tissue portion of a dental-alveolar joint, radiographically appearing as the periodontal ligament (PDL) space, presents as a uniform low density or radiolucent rim adjacent to the roots of teeth that is approximately 0.18 mm wide. These fibrous connective tissues may become non-vital for various reasons such as trauma, ectopic development of an adjacent tooth, or unknown cause. When this happens, bony replacement of the fibers occurs and direct attachment of the tooth to bony socket or dental alveolus is observed. Ankylosis is the loss of this PDL space due to bony-dental root fusion, and may be partial or complete. Ankylosis therefore may prevent tooth eruption and result in impaction (Fig. 29.11).

Gentle manipulation of a tooth with suspected ankylosis using a periosteal elevator can either confirm or reject suspicion of ankylosis. This is important for orthodontic treatment, particularly with impacted canines, as no movement of canine during surgery may signify poor response to orthodontic guided eruption.

A second type of clinical ankylosis, *pseudo- or mechanical ankylosis* of the maxillary canine may result in failure of response to orthodontic guided eruption when the apical one third of the root has a severe dilaceration or curvature (Fig. 29.12). Severe dilacerations act to mechanically lock the tooth into the alveolar bone and respond minimally or not at all to orthodontic forces. Clinically these teeth will typically respond to orthodontic guidance status post apicoectomy of the dilacerated portion of the apical third of the root.

Primary failure of eruption is another form of ankylosis and is characterized by nondevelopment of the alveolar processes and a resultant exaggerated open bite. This is a genetic disorder caused by PTH1R gene mutation and 50% of cases are familial.

- **Early extraction of the primary predecessor**. Premature extraction of primary teeth due to dental caries or trauma may cause drifting of the remaining teeth and loss of space necessary for the permanent successor. Malalignment of the dental follicle creates a deviation from the normal eruption path of the tooth and makes it more difficult for the tooth to make its way to the occlusal plane. The impacted teeth may be well aligned, and there may be adequate space (usually maintained with a space maintainer), but due to the development of a thick mucosa overlying the teeth after very early extraction

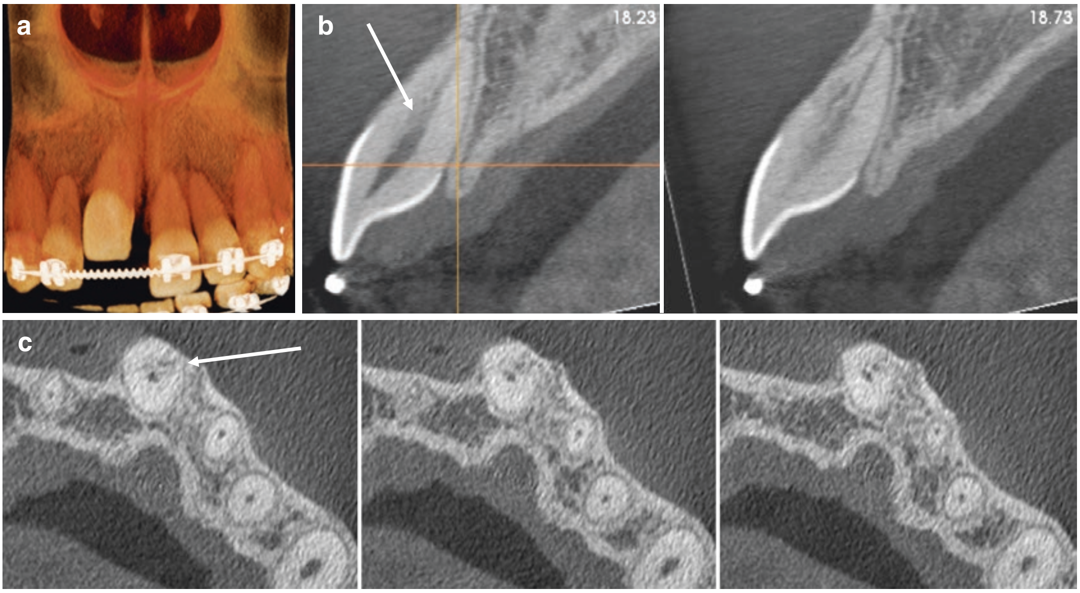

Fig. 29.11 Volumetric rendering (**a**), contiguous cross-sectional (**b**), and 0.5 mm thick /0.5 mm interval axial sections (**c**) of a 15-year-old African American female demonstrating an impacted, facially ectopically positioned, infra-erupted right maxillary central incisor located at the level of CEJs of the adjacent maxillary anterior teeth. The patient had received previously unsuccessful active orthodontic fixed appliance therapy directed towards repositioning this tooth into the dentition. There is internal root resorption in the mid root area (**b**). The PDL space is well defined on the distal and palatal aspect; however, the mesial surface of the tooth #8 is irregular and appears to be contiguous with the adjacent alveolar bone highly suggestive of ankylosis. There is minimal, if any, facial cortical plate covering the cervical to mid third of the root of this tooth (**b**)

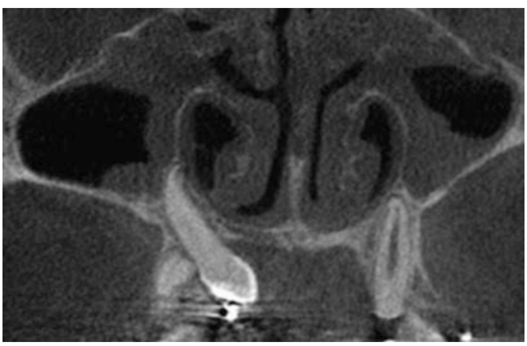

Fig. 29.12 Coronal CBCT image demonstrating palatally erupted maxillary right canine unresponsive to fixed orthodontic appliance therapy. There is marked dilaceration of the apical third of the root of this tooth and engagement of the junction of the medial wall of the maxillary sinus and the floor of the nasal cavity consistent with a mechanical or *pseudo-ankylosis*

of a primary molar, the premolar may become impacted or may be delayed in eruption.

- **Idiopathic**. Sometimes there is no obvious reason for a dental impaction. The tooth follicle may have developed ectopically, become mal-aligned during development, or may be in correct alignment, but fails to erupt.

29.3 Consequences of Dental Impaction

29.3.1 Tooth Resorption

Resorption is a function of increased odontoclast activity, and may occur on the external surface of the tooth (odontoclasts in the PDL), originate from the internal surface of the tooth (odontoclasts in the pulp), or both. All mineralized dental structures (cementum, dentin, and enamel) may resorb, although enamel tends to be slightly more resistant due to the higher mineral content and only undergoes resorption by odontoclastic action if it has not erupted. If the tooth is partially erupted, the resorption may either superimpose on a carious lesion or be confused with it. An impacted tooth can undergo resorption itself (either internal or external), or may affect adjacent teeth that are in direct contact causing pressure resorption.

- **Internal Resorption**. The pattern of internal resorption usually associated with an impacted tooth is called *replacement* or *metaplastic* resorption as there is no inflammatory etiology that may cause inflammatory internal resorption. Portions of the dentinal structures are resorbed and replaced with woven-bone or cementum-like bone that fuses with the adjacent dentin, and appear radiographically as an enlargement of the canal which is filled with a material that is less radiodense than the surrounding dentin (Figs. 29.7 and 29.13). Because a central zone of the pulp is replaced

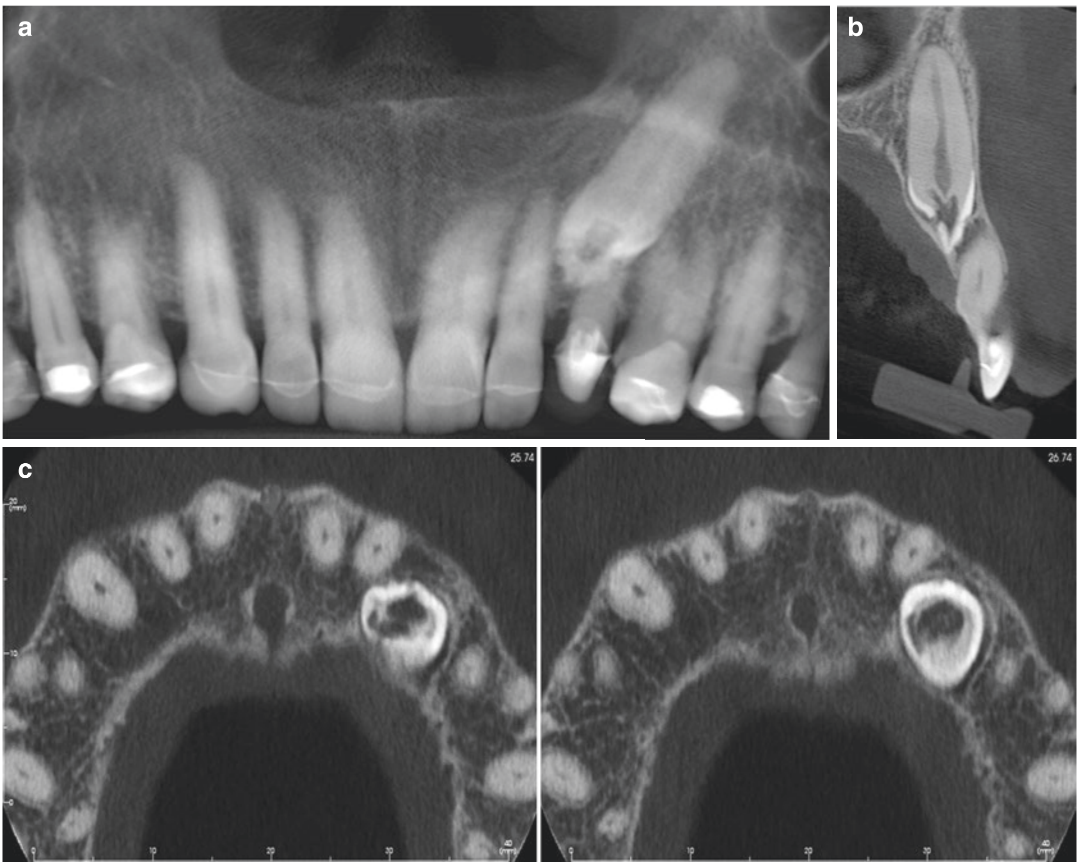

Fig. 29.13 Reformatted CBCT panoramic (**a**), cross-sectional (**b**), and axial (**c**) images of the maxillary anterior dentition showing a mesioangular, complete bony impacted, palatally positioned, and unerupted left maxillary canine with coronal internal pathologic resorption. Note that there is no root resorption of the retained left maxillary deciduous canine or adjacent permanent teeth

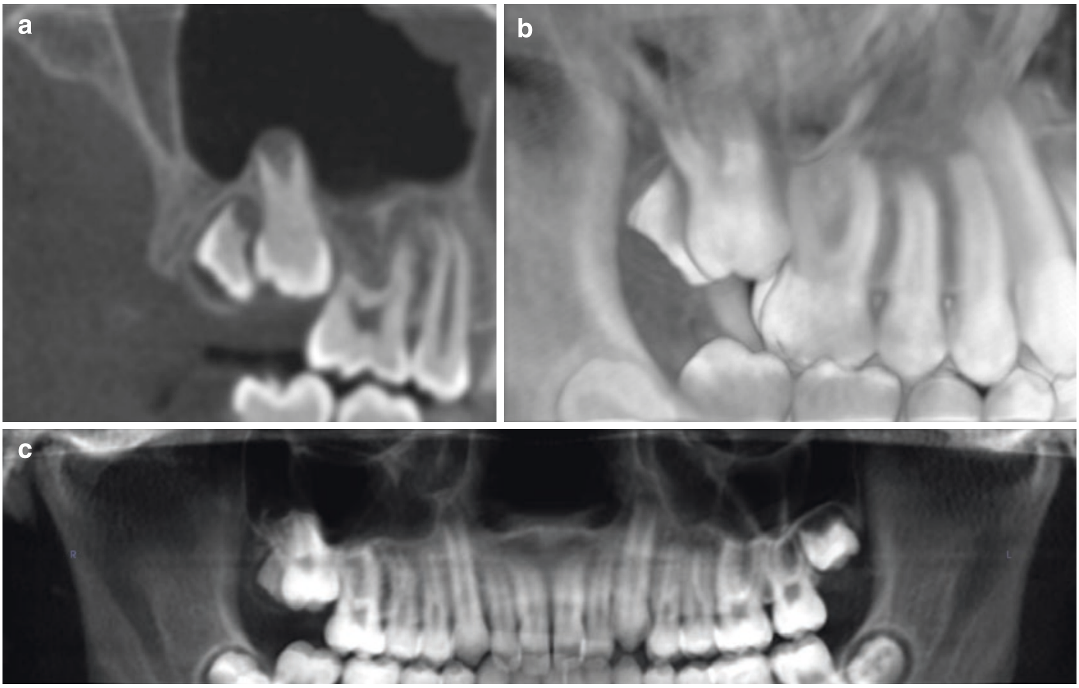

Fig. 29.14 Reformatted CBCT panoramic (**a**), parasagittal (**b**), and volumetric (**c**) images of the maxillary right posterior dentition showing a vertically completely impacted and unerupted right second molar advancing into the developing root and crown of the right third molar causing external resorption in its crown and root

with bone, the radiographic appearance often demonstrates partial obliteration of the canal. This most often occurs with the coronal aspect of the impacted tooth.

- **External Resorption**. The reduced enamel epithelium surrounding the completed crown of a tooth separates the crown from the surrounding tissues. With age, this intact epithelial covering may degenerate if the tooth remains unerupted. This allows the bone and connective tissue to come into direct contact with the crown of the tooth. In time, osteoclastic activity will lead to replacement resorption of the enamel and its substitution by bone which may grow into these resorptive lesions, leading to a mechanical ankylosis. Over a long period of time, serial radiographic examination will show progressive loss of definition of the tooth outline. The pattern of external resorption in an impacted tooth usually appears moth-eaten and irregular on the external surface of the tooth (Fig. 29.14). External resorption of teeth adjacent to the impacted teeth usually results from pressure of the impacted tooth on the resorbing tooth, and usually manifests as loss of mineral density of the affected tooth localized to the point of contact with the impacted tooth (Fig. 29.15). This may occur at any point along the root of the affected tooth, and may be severe enough to extend to the pulp and compromise the tooth structure.

29.3.2 Pathology

While the impaction of a tooth does not cause the development of odontogenic pathology, the lack of eruption of a tooth is often the first sign that a tooth may have associated pathology. It has been stipulated that dentigerous cysts and other pericoronal pathology are associated with the teeth that are most commonly impacted, i.e., the maxillary canine and the third molars in both jaws. Although pathology is rarely associated with impacted teeth in children and young adults, numerous reports have documented an

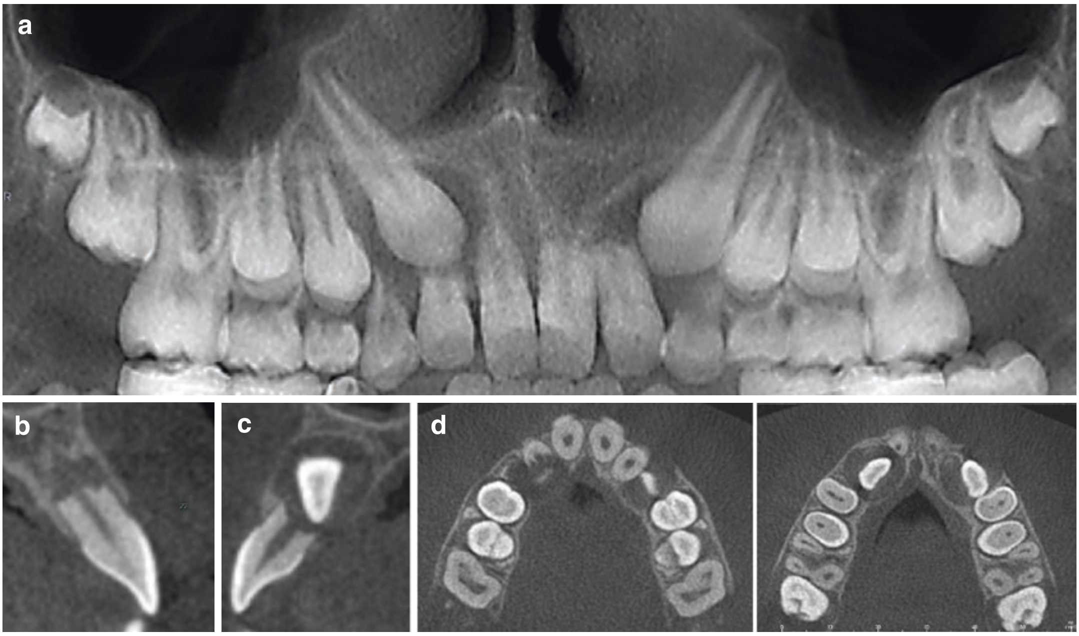

Fig. 29.15 Reformatted CBCT panoramic (**a**), right (**b**) and left (**c**) cross-sectional, and axial (**d**) images of the maxillary anterior dentition of a dentate 12-year-old child in the mixed dentition demonstrating substantial apical root resorption associated with the maxillary lateral and central incisors associated with an unerupted mesioangular impacted maxillary canines, both demonstrating pericoronal space widening. Note that there is marked apical blunting of the roots of the maxillary central incisors

increased prevalence of problems later on. Thus, an impacted tooth that is not extracted should be followed up long term to rule out the development of pathology in later years.

- **Inflammatory**. A partially erupted but impacted tooth may be prone to inflammatory pericoronal soft (pericoronitis) and later hard (localized osteitis) tissue pathology as well as coronal dental caries. If untreated, the latter may lead to pulpal and subsequent periapical involvement. The periapical region of a partially erupted third molar should be examined for signs for periapical rarefying osteitis, ranging from periapical widening of the PDL space to a frank hypodensity.

  Localized pericoronal osteitis is often secondary to soft tissue pericoronitis and manifests as sclerosis of the bone surrounding the submerged parts of the tooth follicle and possible parts of the tooth together with widening of the tooth follicular space (Fig. 29.16). Chronic inflammation around these lesions may induce sclerosis of the adjacent bone (Fig. 29.17). This has also been called the *paradental cyst of the third molar*. Acute suppuration may occur and be extremely painful with regional cellulitis leading to trismus or limitation of movement.

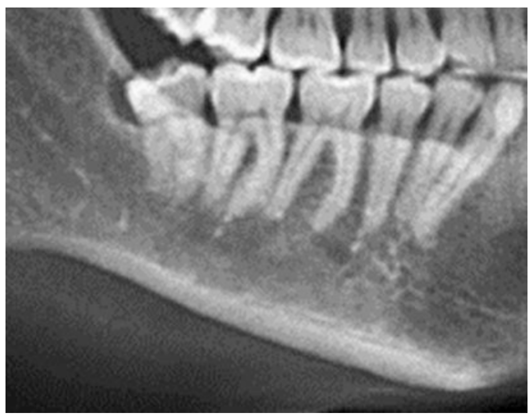

Fig. 29.16 Reformatted panoramic CBCT image of a 22-year-old patient showing a widening of the follicular pace of a distoangular, partially bony impacted mandibular right third molar

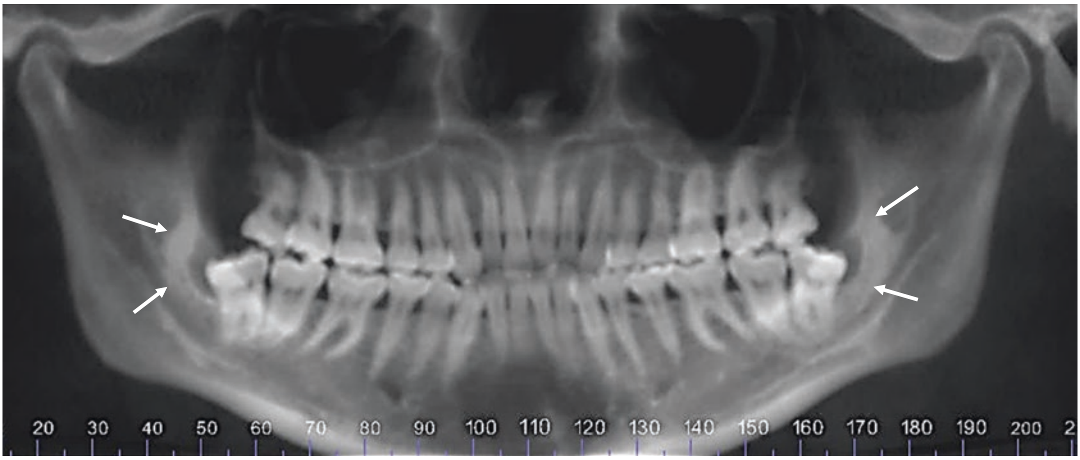

Fig. 29.17 Reformatted panoramic CBCT image of a young adult showing a widening of the follicular space of distoangular, partially bony impacted mandibular right and left third molars. Note the localized sclerosis adjacent to the widened follicles indicating reactive sclerosis suggestive of chronic inflammation

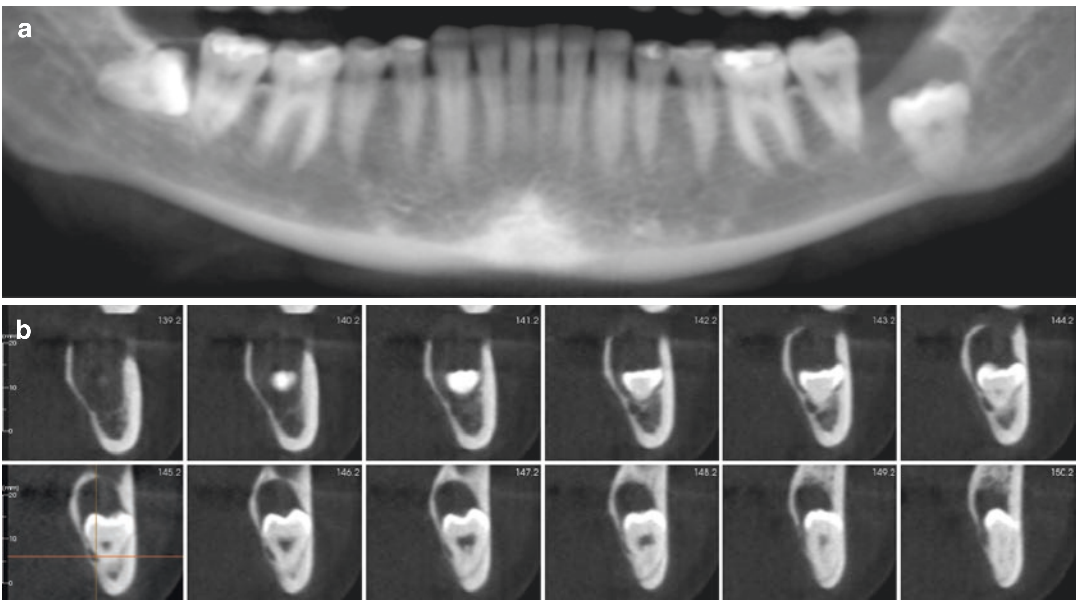

Fig. 29.18 Reformatted panoramic (**a**) and multiple serial 1 mm thick cross-sectional (**b**) images showing a horizontally impacted right vertically displaced left mandibular third molars. The left mandibular molar is associated with a moderately sized pericoronal unilocular radiolucency histopathologically confirmed as a dentigerous cyst

- **Odontogenic Cysts**. Failure of eruption of a tooth is often the first clinical presentation of an associated pericoronal pathology. Pericoronal pathology is rarely associated with impacted teeth in children and young adults; however, there is increased prevalence in impacted permanent teeth in the later decades.

An impacted tooth that is not extracted should be followed up long term to monitor the possible development of pathology in later years (Curran et al. 2002).

Dentigerous cysts are associated with the pericoronal follicle of unerupted teeth, most commonly mandibular third molars (Figs. 29.9

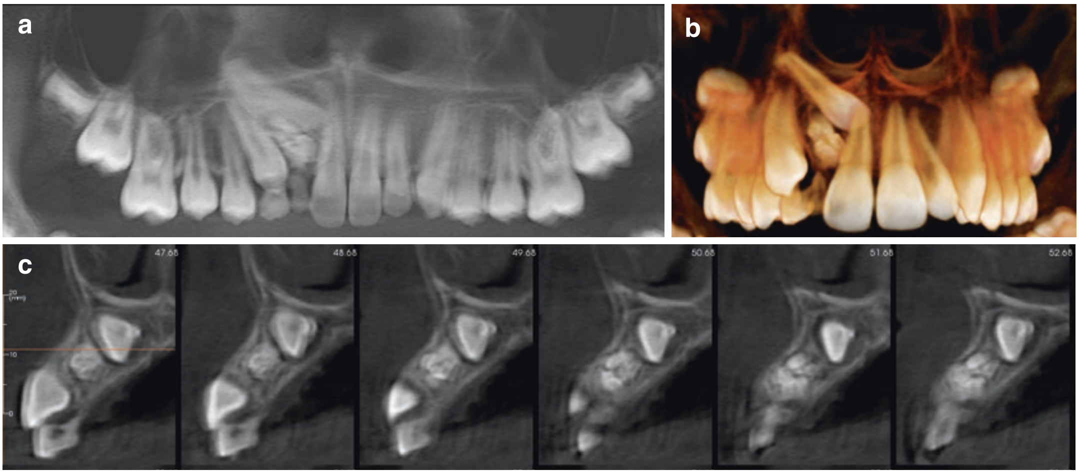

Fig. 29.19 Reformatted panoramic (**a**), volumetric rendering (**b**) and sequential 1 mm thick cross-sectional CBCT images (**c**) demonstrating compound odontoma occupying the inter-radicular alveolus between the maxillary right canine and central incisor. This entity produces an impaction and displaces the right lateral incisor mesiopalatally

and 29.18) followed by maxillary canines, maxillary third molars, and mandibular second premolars. On occasion, a dentigerous cyst may develop around the crown of an unerupted permanent tooth secondary to apical inflammation from an overlying primary tooth. Development of an inflammatory cyst along the buccal aspect of a partially erupted first molar is called the paradental cyst, juvenile paradental cyst, mandibular infected buccal cyst, or buccal bifurcation cyst. This often appears as a well-defined, semi-lunar or ovoid-shaped hypodensity associated with the buccal surface of the coronal aspect of the third molar, occasionally with cortical expansion

- **Benign Odontogenic Tumors**. Most benign neoplasias associated with impacted teeth are odontogenic in nature. Odontomas are most common and may be found either pericoronal (Fig. 29.19) or adjacent to the root altering the position of the tooth or impeding eruption. Other entities that are commonly associated with impacted teeth are keratocystic odontogenic tumors, ameloblastomas, ameloblastic fibromas and fibro-odontomas, adenomatoid odontogenic tumor (in 75% of cases reported were associated with an unerupted maxillary canine), and calcifying epithelial odontogenic tumor (most common in mandibular third molar region).

29.3.3 Malocclusion

The impaction of a tooth or multiple teeth may delay or impede the proper alignment of other teeth in the dental arch. This malocclusion may be further confounded by a deficient arch length. The treatment of mal-alignment may require extraction of the impacted tooth and orthodontic treatment.

29.4 Imaging Protocols for the Evaluation of Impacted Teeth

Due to the timing of eruption sequence, it is not surprising that the third molars and maxillary canines are the first and second most common teeth to be crowded, erupt ectopically or become impacted.

The American Association of Oral and Maxillofacial Surgeons (2012) lists numerous indications for the removal of impacted teeth and, more specifically, third molars. Many are likely to require radiographic imaging (Table 29.3).

Table 29.3 Indications for the removal of impacted teeth (after American Association of Oral and Maxillofacial Surgeons 2012)

Indication	Teeth other than third molars	Third molars	
		Partially erupted	Unerupted/impacted
Pain	✓	✓	✓
Clinical findings including: Dental caries, periodontal disease, periapical pathology, non-restorable tooth, internal or external resorption of tooth or adjacent teeth, infection, failure of the tooth to spontaneously erupt, ectopic eruption of a tooth	✓	✓	✓
Orthodontic abnormalities (e.g., arch length/ tooth size discrepancies, ankylosis)	✓	✓	✓
Medical or surgical condition or treatment for which removal of teeth is prophylactic	✓	✓	✓
Adjunct to prosthetic rehabilitation	✓	✓	✓
Teeth in line of osseous fracture	✓	✓	✓
Pathology associated with tooth follicle (e.g., cysts, tumors)	✓	✓	✓
Teeth associated with pathologic lesions	✓	✓	✓
Facilitation of management in trauma or orthognathic surgery	✓	✓	✓
Insufficient space to accommodate erupting tooth or teeth	✓	✓	✓
Traumatic injury to the tooth	✓	✓	✓
Anatomical position causing potential damage to adjacent teeth	✓	✓	✓
Pericoronitis		✓	
Facilitation of the management or limitation of periodontal disease		✓	✓
Abnormalities of tooth size/shape precluding normal function		✓	✓
Facilitation or orthodontic tooth movement and promotion of dental stability		✓	✓

29.4.1 Third Molars

Fully erupted, functional, and easily cleansable third molars are uncommon in modern humans. Retention of third molars is associated with local morbidity (Huang and Rue 2006; Ventä 2012; Huang et al. 2014), especially with increasing age (Haug et al. 2005). In industrialized nations, the vast majority of third molars, including those that are asymptomatic, are eventually removed. In the United States, 50% of those insured undergo third molar extraction by the age of 20 years. Pretreatment surgical planning involving radiographic evaluation is mandatory (Flygare and Ohman 2008) especially since most third molars are clinically unerupted or at least partially impacted. According to the AAOMS (2012):

> A panoramic radiograph is recommended for management of third molars, although periapical, maxillary, and/or mandibular radiographs and computed tomography may also be used. Indications for cone beam computed tomography for routine third molar surgery should be documented before ordering scans and follow the principles of ALARA (as low as reasonably achievable).

CBCT imaging may be necessary to assess conditions that may affect surgical approach or potentially affect morbidity. This includes the presence of multiple roots (Fig. 29.20), involvement with the lingual plate (Fig. 29.21), and the path of the inferior alveolar canal (IAC) in

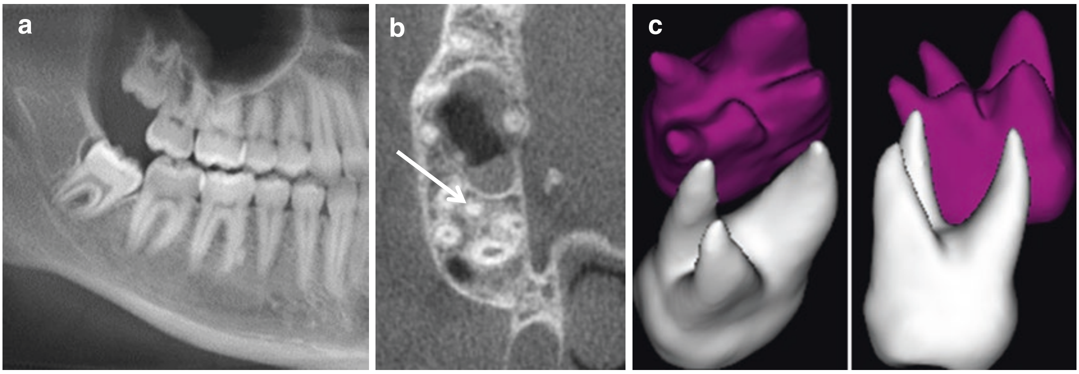

Fig. 29.20 Reformatted panoramic (**a**), axial (**b**), and segmented tooth surface models (**c**) of a 17-year-old showing a vertically impacted, completely formed maxillary right third molar. While not shown on the panoramic image (**a**), the axial (**b**) and segmented models (**c**) demonstrate a supernumerary mesial root

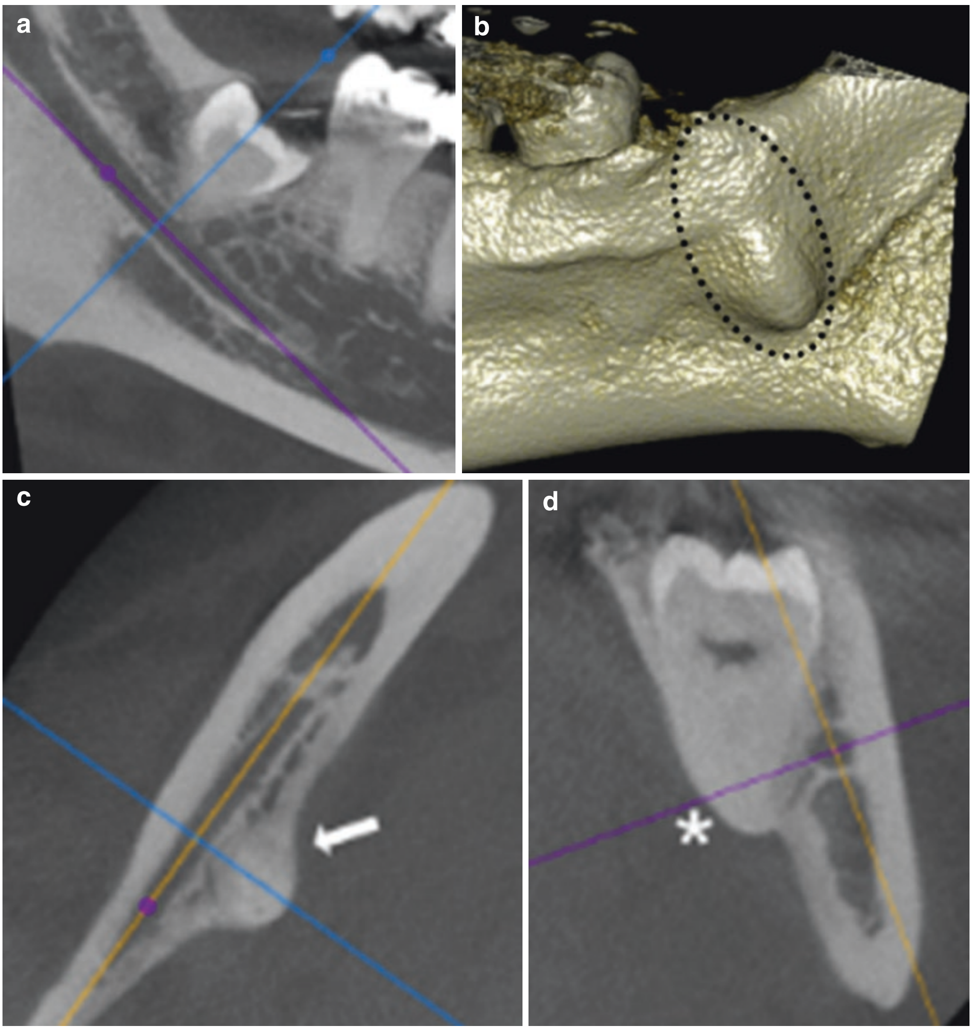

Fig. 29.21 Sagittal (**a**), lingual projection of shaded surface volumetric rendering (**b**), axial (**c**), and cross-sectional (**d**) CBCT images of the right mandibular retromolar area showing completely bony mesioangular impacted third molar with localized expansion of the lingual cortical plate covered by the root of the tooth. The asterisk in (**d**) indicates the submandibular fossa

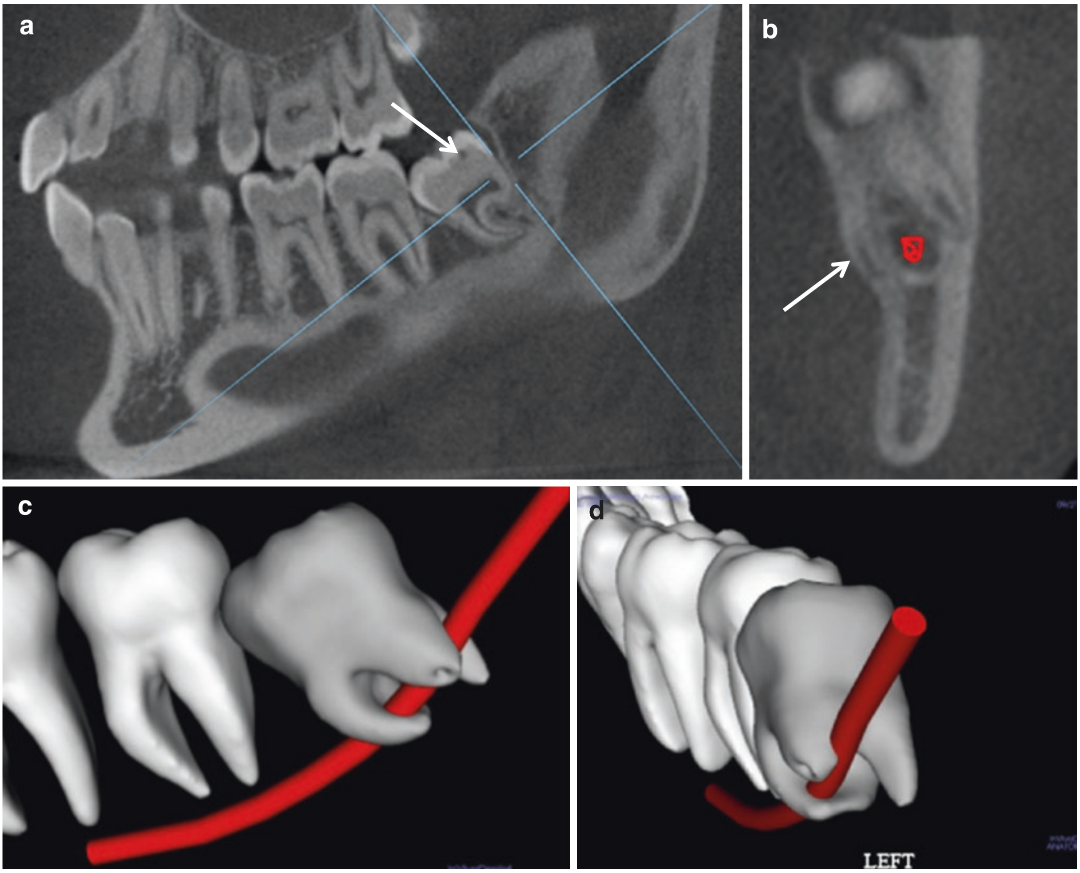

Fig. 29.22 Parasagittal (**a**), cross-sectional (**b**) CBCT images and lateral (**c**) and posterior oblique (**d**) segmented tooth surface models showing a mesioangularly impacted, fully formed left mandibular third molar impacted with possible occlusal carious lesion (*arrow*). The disto-lingual root engages the lingual cortex (*arrows* on (**b**)). Three roots are present with the IAC passing through the mesial root and the furcation of the distal roots. The extraction of this tooth presents with possible morbidity and alternate approaches, such as coronectomy, may be considered as an option in this case

relation to the tooth roots (Fig. 29.22). However, recent clinical studies do not demonstrate a greater *overall* clinical efficacy for the use of CBCT as compared to panoramic radiography in reducing the risk of inferior alveolar nerve injury or other postoperative complications prior to mandibular third molar removal (Guerrero et al. 2014; Ghaeminia et al. 2015). CBCT may be suggested when one or more signs for a close contact between the tooth and the mandibular canal are present in conventional imaging (Neves et al. 2012), particularly if it is believed that CBCT will change the treatment or the treatment outcome for the patient (Matzen and Wenzel 2015).

29.4.1.1 Surgical Difficulty of Removal

Historically the Pell and Gregory (1933) impaction severity classification and Winter angulation criteria (1926) have been applied to panoramic images to assess the difficulty of third molar removal and used practically in determining the number of surgical minutes to allocate for the procedure, the necessary surgical equipment and armamentarium, and use of local anesthesia, sedation, or general anesthesia (Komerik et al. 2014). Additional features that may complicate surgical difficulty include the presence of dilacerated or bulbous roots, poorly visualized periodontal ligament space suggesting possible ankylosis, enlarged, abnormal, or nonexistent follicle, dental caries or restorations on adjacent teeth, relative size and location of tooth to the body, inferior border and ramus, supernumerary teeth, endodontic treatment, "stand-alone" molars, evidence of limited opening from temporomandibular anatomy, hyper or hypo-dense bone, adjacent lesions, fractured or missing crown, lingual tori, maxillary sinus proximity, and evidence of previous trauma or hardware.

At least as critical as an assessment of surgical difficulty is determination of the individual patient's risk of specific complications, based largely on collective professional experience and ongoing evidence-based inquiry. Informed consent should call attention to any unique anatomy or conditions that may increase specific risks. Panoramic radiography is sufficient to estimate distance from a non-intimate inferior alveolar nerve as well as potential for sinus perforation, root or lesion exposure on adjacent teeth, and displacement of questionable restorations and orthodontic devices in contact with the third molar. Rood and Shehab (1990) proposed five radiographic criteria on panoramic images associated with the potential for inferior alveolar nerve injury:

1. Linear radiolucency across the roots of the third molar
2. Deviation of the mandibular canal
3. Interruption of the white line of the canal
4. Deflection of the third molar roots by the canal
5. Narrowing of the third molar root

Subsequent studies have indicated that most are of varying value, with decreased density of the roots (1 above) being the most predictive.

Evidence based-studies and cost-saving measures may influence considerations of surgeons towards the early or late treatment of third molars. Third party payee or reimbursement for third molar removal and anesthesia may lead to a greater emphasis on clinical and/or radiographic monitoring for pathologic changes or symptoms. However, the absence of symptoms does not mean absence of pathology, and the need for vigilant documentation is key to the monitoring process. Accurate radiological interpretation and appropriate communication with the surgeon are key in distinguishing "close monitoring" from "supervised neglect."

29.4.1.2 Assessment of Third Molar Impactions

The plan for surgical removal of third molars varies greatly depending on the assessment of the degree of impaction present (Carvalho and Egito Vasconcelos 2011). Third molar impaction should be described in relation to angulation, impaction, application depth, and eruption.

Tooth Orientation and Depth of Impaction

Mandibular Third Molars

The traditional method of determining the position and depth of an impacted mandibular third molar was described by Winter (1926) and involves drawing three imaginary reference lines (Winter's Line) on periapical images. The imaginary lines are designated white, amber, and red (WAR). This technique can be applied to panoramic images reformatted from CBCT data (Fig. 29.23).

- **Occlusal reference (White line)**. Constructed along the occlusal surfaces of the erupted mandibular molars and extended posteriorly to intersect the ascending ramus. This line represents the difference in the occlusal height between the third molar and the first and second molars. A second line is drawn along the long axis of the crown and root of the 3rd molar to determine the axial inclination of the impacted tooth.
- **Projected external oblique (Amber line)**. A curved line drawn extended from the surface of the bone lying distally to the third molar to the crest of the interdental septum between the first and second mandibular molars. This line indicates the margin of the alveolar bone enclosing the tooth when the soft tissues are reflected.
- **Depth (Red line)**. A perpendicular constructed from the projected external oblique to an imaginary point of application for a tooth elevator. This is used to measure the depth of

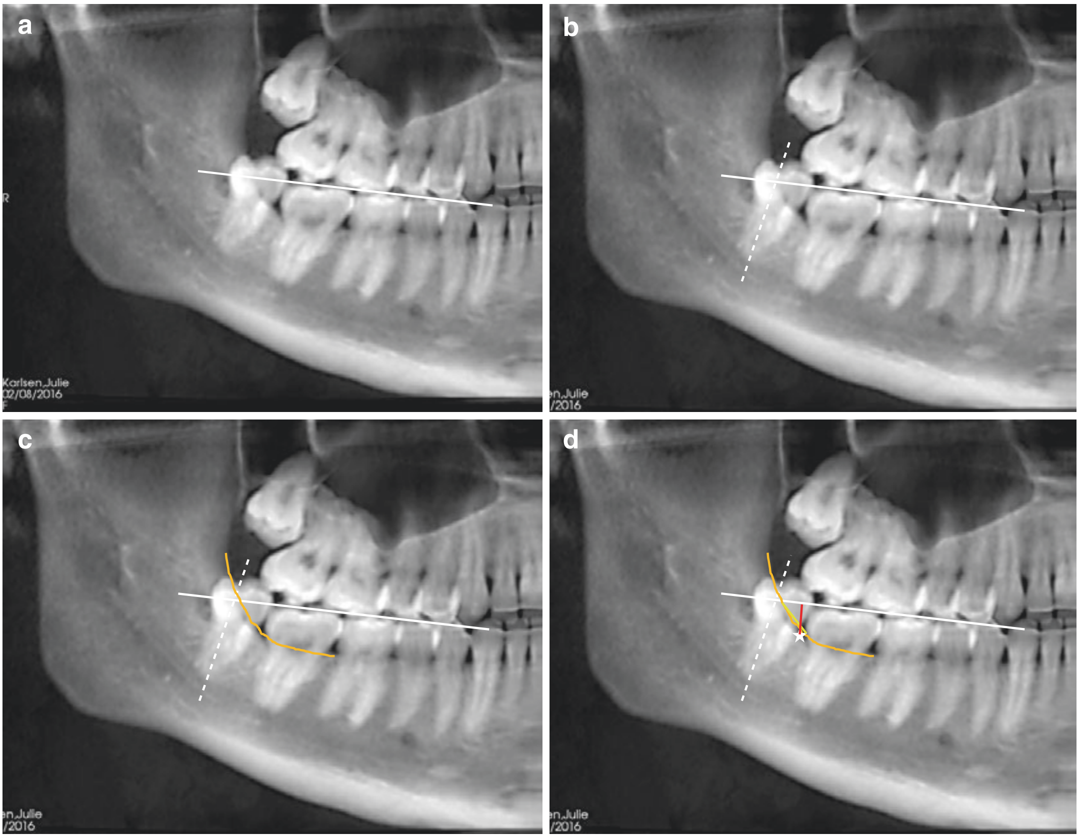

Fig. 29.23 Sequential construction of reference lines used to assess degree and depth of impaction. Initially an occlusal reference line (*white*) is constructed along the occlusal surfaces of the erupted mandibular molars (**a**). A second line (*dashed white*) is drawn along the long axis of the impacted third molar to determine the axial inclination of the impacted tooth (**b**). Then the projected location of the external oblique ridge (amber) is drawn (**c**). Finally, an imaginary point of application for a tooth elevator is identified (*white star*) and a perpendicular (*red*) constructed from the projected external oblique to this point (**d**)

the impacted tooth in the mandible. The longer this line, the more deeply embedded is the tooth, and the more difficult the extraction. As a rule of thumb, for each 1 mm in length, the extraction becomes about three times more difficult to complete. Using this as a basis, general anesthesia should be considered if the tooth is deep 5 mm or more.

The Pell–Gregory Scale (Pell and Gregory 1933) scale provides a difficulty index for the removal of impacted mandibular third molar based on tooth depth and ramus relationship. Nine categories of impaction are possible based on the amount of tooth covered by the anterior border of the ramus (Classes I, II and III) and the depth of the impaction relative to the adjacent tooth (Class A, B, and C) (Table 29.4).

Pederson (1988) proposed a modification of the Pell–Gregory scale including angulation that ascribed increasing difficulty values to categories of spatial relationship (Table 29.5), depth, and ramus relationship to provide an overall Difficulty Index.

Maxillary Third Molars

The removal of the maxillary third molar involves different clinical and surgical considerations than

Table 29.4 Classification of mandibular third molar impaction (after Pell and Gregory 1933)

Ramus relationship	Definition	Tooth depth	Definition
I	The distal aspect of the crown of the tooth is situated anterior to the ascending border of the ramus such that there is sufficient space available for the eruption	A	The occlusal plane of the impacted tooth is at the same level as the adjacent tooth
II	The distal aspect of the crown of the tooth lies posterior to the ascending border of the ramus	B	The occlusal plane of the impacted tooth is between the occlusal plane and the cervical line of the adjacent tooth.
III	The entire crown of the tooth lies posterior to the ascending border of the ramus. The tooth is totally embedded in bone	C	The occlusal plane of the impacted tooth is apical to the cervical line of the adjacent tooth.

Table 29.5 Categories of tooth angulation

Angulation	Definition	Significance	Difficulty[a]
Mesioangular	The long axis of the impacted tooth is angled towards the midline	The distal aspect of the 2nd molar should be evaluated for resorption and the crown of the impacted tooth for dental caries. The IAC may be in contact with more of the mesial aspect of the tooth root surface that other impactions	1
Horizontal	The long axis of the impacted tooth is parallel to the occlusal plane	The mesiodistally oriented tooth cause resorption on the distal aspect of the second molars. The faciolingually oriented tooth may protrude out of the facial or lingual cortices of the alveolar process	2
Vertical	The long axis of the impacted tooth is parallel the adjacent teeth but below the occlusal reference plane		3
Distoangular	The long axis of the impacted tooth is distally angled relative to the midline	This is generally a more difficult extraction with additional surgical considerations	4
Inverted	The crown is lower than the roots in reference to the occlusal plane	This is most commonly seen in supernumerary teeth, such as mesiodens, but can be seen in third molars as well	N/A

[a]After Pederson (1988): *N/A* not applicable, *IAC* inferior alveolar canal

those of the mandibular third molar due to this tooth's proximity to the maxillary sinus and possibility of oroantral perforation and sequelae of sinus infection, if not properly managed. Based on these concerns, alternate classifications more specific to maxillary third molars have been proposed.

Archer (1975) categorizes the anatomic position of the maxillary third molar according to the depth relative to the occlusal plane, orientation in relation to the adjacent second molar, and the position in relation to the maxillary sinus. Lim et al. (2012) provide a modified version of this classification (Table 29.6) and showed that while oroantral perforation associated with surgical removal of third molars is rare (2.43%), it occurs more frequently with Class D eruption status and transverse or buccopalatal angulation.

Table 29.6 Modified Archer (1975) classification of maxillary third molar impaction (Lim et al. 2012)

Relative depth of maxillary 3rd molar in bone	Relative angulation of long axis of maxillary 3rd molar to 2nd molar	Location of maxillary 3rd molar to maxillary sinus
Class A[a]	Vertical	Sinus approximation[e]
Class B[b]	Horizontal	No sinus approximation[f]
Class C[c]	Mesioangular	
Class D[d]	Distoangular	
	Inverse	
	Traverse or buccopalatal	

[a]Lowest portion of crown of impacted maxillary 3rd molar is on line with occlusal plane of 2nd molar
[b]Lowest portion of crown of impacted maxillary 3rd molar is between occlusal plane of 2nd molar and cervical line
[c]Lowest portion of crown of impacted maxillary 3rd molar is between cervical line and mid 1/3rd of the root of 2nd molar
[d]Lowest portion of crown of impacted maxillary 3rd molar is at or above apical 1/3rd of the root of 2nd molar
[e]No or thin partition of bone between impacted maxillary 3rd molar and maxillary
[f]$\geq$2 mm of bone between impacted maxillary 3rd molar and maxillary sinus

Relationship to the Adjacent Anatomical Structures

Maxillary Third Molars

- **Maxillary sinuses**. The maxillary molar roots are often intimately associated with the floor of the maxillary sinus, and may protrude slightly or fully into it. Therefore, maxillary third molar extraction may be associated with a risk of displacing the tooth or fractured fragments into the maxillary sinus. Apical inflammatory may result in odontogenic sinusitis while pericoronal pathology may displace the third molar into the maxillary sinus.
- **Pterygopalatine fissure/Infratemporal fossa**. This refers to the space immediately adjacent to the posterior wall of the maxillary sinus (Fig. 29.24). Disto-angularly or horizontally impacted third molars may protrude slightly into this fossa, or have a very thin bony separation between the tooth and the fossa. Attempts at extraction may result in displacement of the entire or components of the tooth into this fissure.

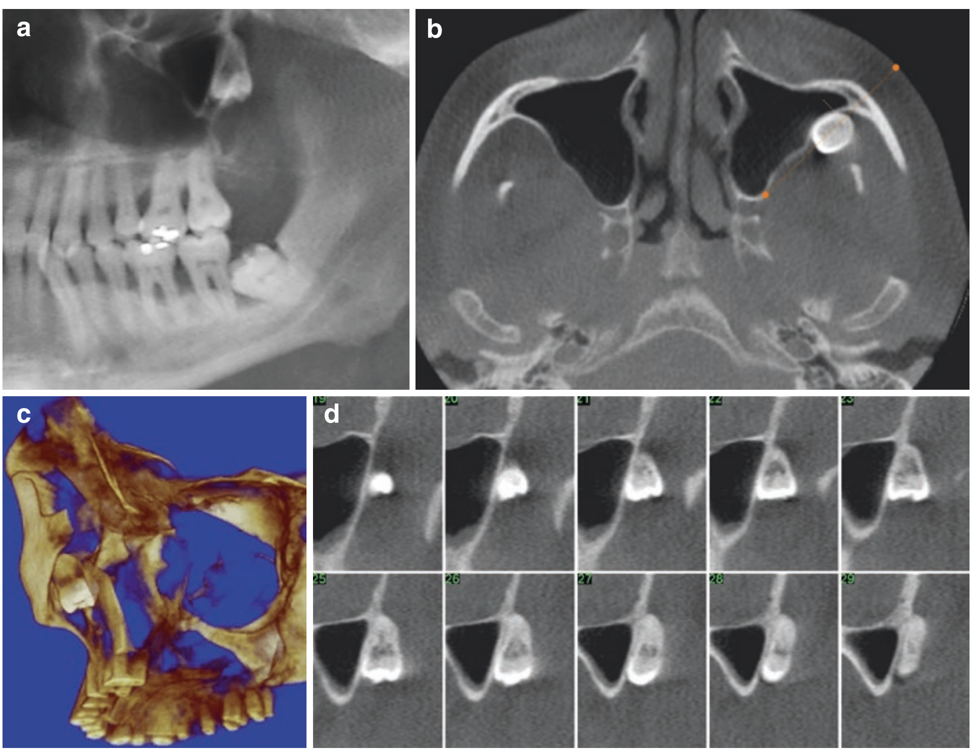

Fig. 29.24 Reformatted panoramic (**a**), axial reference, left posterior infero-oblique volumetric rendered (**c**) and serial 1 mm thick/1 mm interval cross-sectional (**d**) CBCT images demonstrate displacement of a left maxillary third molar into the pterygomaxillary fissure thought to have be previously extracted

- **Greater palatine foramen**. This structure is the exit for the greater palatine neurovasculature bundle as it traverses along the hard palate anteriorly and is located palatal to the third molar area. A bucco-palatally oriented, horizontally impacted third molar may lie adjacent to this foramen (Fig. 29.25).
- **Maxillary tuberosity**. The maxillary tuberosity is the posterior terminal maxillary alveolus and may be very thin due to the presence of an impacted third molar. Removal of the tuberosity leading to oroantral communication and loss of prosthetic support may occur with third molar removal fractured during extraction. The integrity of this structure should be noted when examining imaging data.
- **Adjacent tooth**. The status of the adjacent second molar tooth and its relationship with respect to the third molar should be assessed for impaction or resorption (Fig. 29.26).

Mandibular Third Molars

- **Inferior Alveolar Canal (IAC)/Mandibular Canal (MC)**. The IAC is a bilateral structure containing the inferior alveolar nerve and associated vasculature. It enters the mandibular ramus through the mandibular foramen and follows the curve of the mandibular anatomy in one of four patterns (Table 29.7, Fig. 29.27) (Nortjé et al. 1977) to the molar and premolar region, where it exits through the mental foramen. Anomalies include double canals (Fig. 29.28), retromolar canals and accessory foramina that exit in the third molar region. The IAC may be intimately related to an impacted third molar tooth and should be examined thoroughly in CBCT imaging prior to surgical removal to avoid injury to the inferior alveolar nerve (Auyong and Le 2011; Neves et al. 2012). The exact localization of the IAC greatly impacts the surgical extraction plan and method of removal of the tooth. Three principal relationships can exist between the third molar and the IAC (Table 29.8, Fig. 29.29) (Maegawa et al. 2003). Other relationships include partial or complete compression of the IAC by the roots (Fig. 29.30), indentation of the tooth by the IAC (Fig. 29.31), running through the furcation area of the tooth, particularly if the roots are separate (Fig. 29.32), or the tooth structure may develop around the IAC, enveloping it and giving the appearance

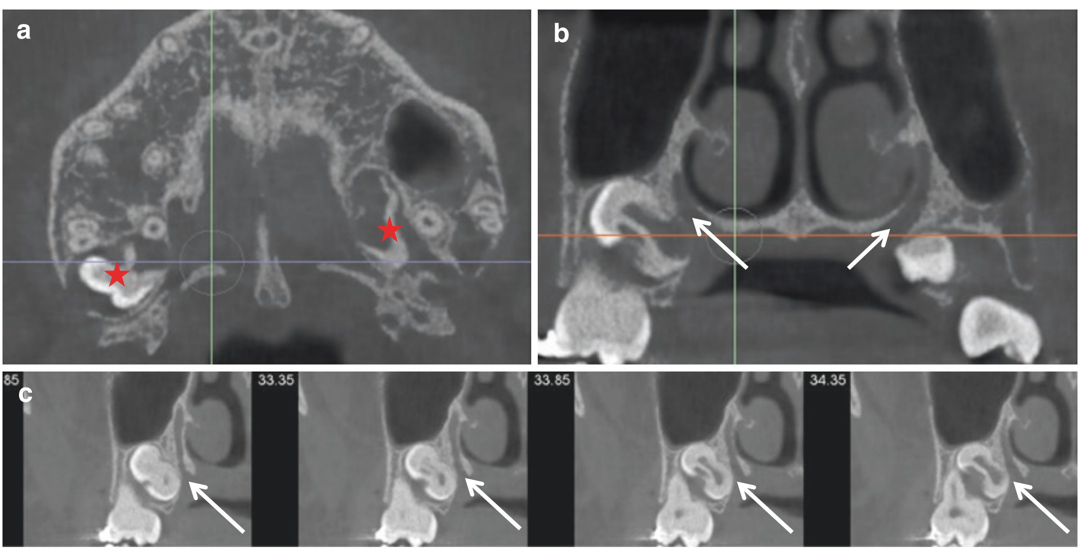

Fig. 29.25 Axial (**a**), coronal (**b**), and a series of cross-sectional images in the region of the maxillary right third molar (**c**), showing two unerupted and malformed maxillary third molars (*red stars*). The tooth bud of tooth the right maxillary third molar is displaced palatally and is in a close relationship with the root of the maxillary right second molar. Note the intimate relationship of both maxillary third molars to the respective greater palatine canals (*arrows*)

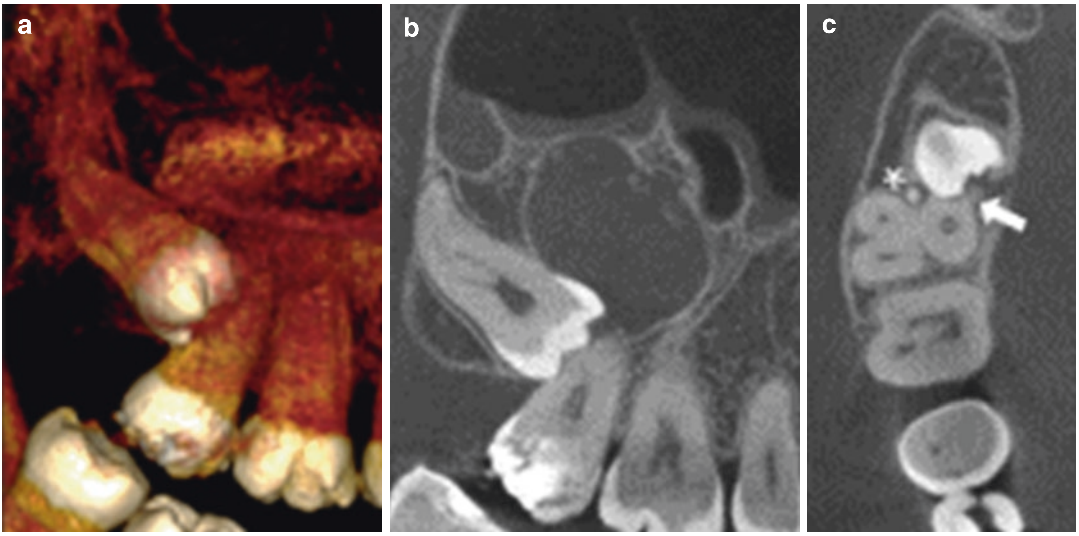

Fig. 29.26 Volumetric (**a**), sagittal (**b**), and axial (**c**) CBCT images of a completely bony impacted mesiopalatally impacted right maxillary third molar with a large pericoronal unilocular radiolucency causing external root resorption of the distal surface of the palatal root of the right second molar (*arrow*)

Table 29.7 Nortje classification (1977) of the pattern variants of the IAC as it traverses through the intramedullary space of the mandible

Type	Description
I	One mandibular foramen branches off two independent canals
II	A single main canal is present with a secondary smaller short branch extending superiorly at the level of the mandibular third or second molar (Fig. 29.27)
III	Two mandibular foramens are present with two canals (on superior and a second inferior) which join into one at the level of the molars
IV	A main canal branches off a smaller branching canal superiorly at the mandibular retromolar area, which curves back to join the main canal at the second/first molar area

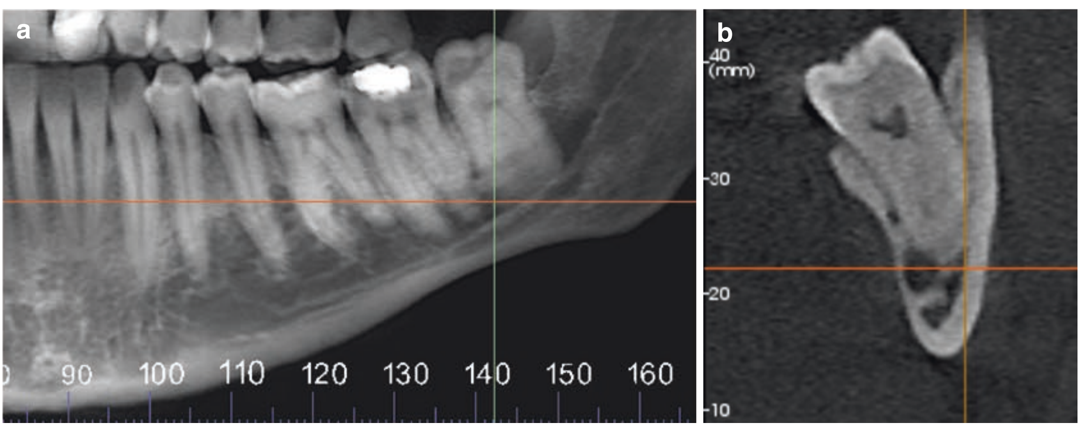

Fig. 29.27 Reformatted panoramic (**a**) with IAC tracing (**b**) and corresponding 1 mm thick cross-sectional image (**c**) with IAC tracing (**d**) demonstrating Type II IAC path pattern (Nortje et al. 1977) and Type B relationship (Maegawa et al. 2003)

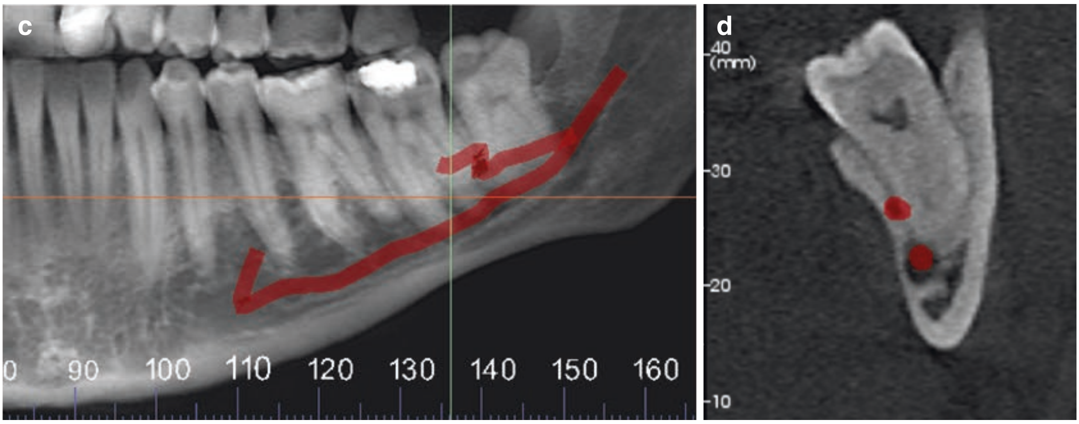

Fig. 29.27 (continued)

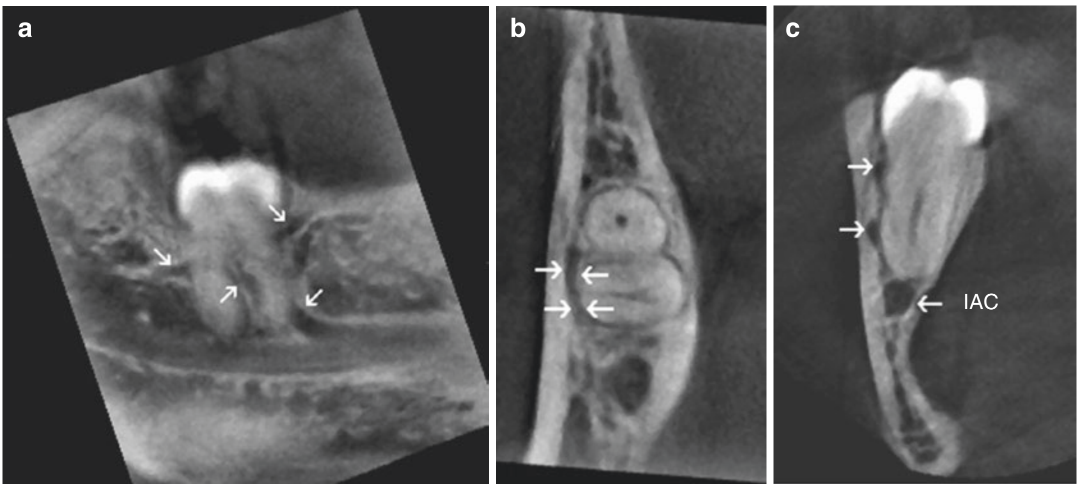

Fig. 29.28 Limited FOV sagittal (**a**), axial (**b**), and cross-sectional (**c**) CBCT images demonstrating multiple supplemental branches (*arrows*) of the inferior alveolar nerve canal (IAC) extending superior and buccal to an unerupted and bony disto-angularly impacted 3rd molar in a partially edentulous right mandibular arch

Table 29.8 Maegawa classification (2003) of the positional relationship of the third molar to the IAC

Type	Description
A	IAC located buccal to or contacts third molar
B	IAC located below third molar (Fig. 29.19)
C	IAC located lingual or contacts third molar

of the IAC penetrating the tooth structure (Fig. 29.33).

- **Adjacent teeth**. Evaluate for impingement on the adjacent tooth root or PDL, impaction of the adjacent tooth or pressure resorption of the distal aspect of the adjacent tooth.

29.4.2 Canines

29.4.2.1 Assessment of Canine Impaction

The primary assessment of an impacted canine is directed towards determining if the tooth is in a position within the dental arch where it can be successfully brought into occlusion. This analysis varies from that for third molars, which is essentially directed at surgical removal. The location of the crown is important in that surgical exposure must be performed to enable attachment of an orthodontic bracket (usually on the

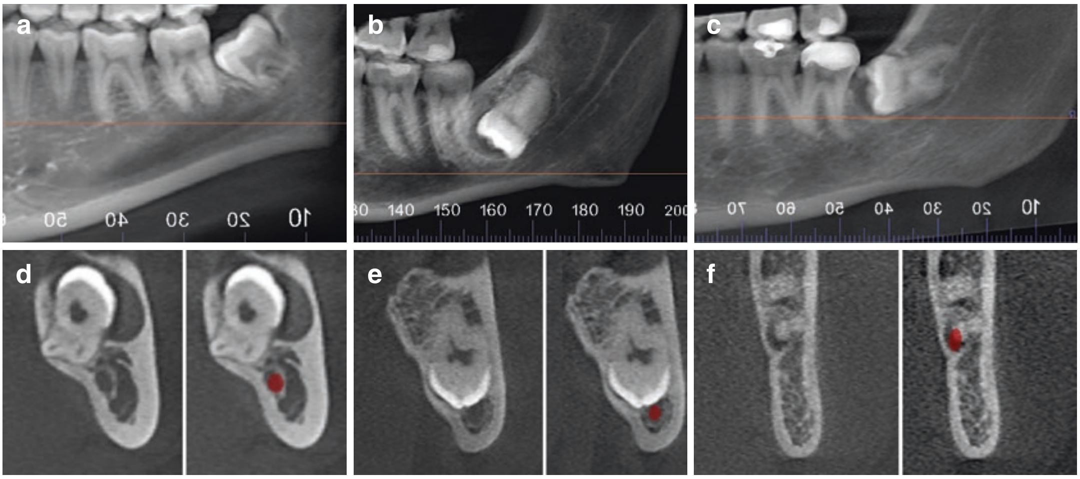

Fig. 29.29 Representative reformatted panoramic (**a**, **b**, and **c**) and cross-sectional CBCT images both with and without IAC tracing (**d**, **e,** and **f**) demonstrating the positional relationship of the third molar to the IAC according to Maegawa Classification (2003) Types A, B, and C, respectively

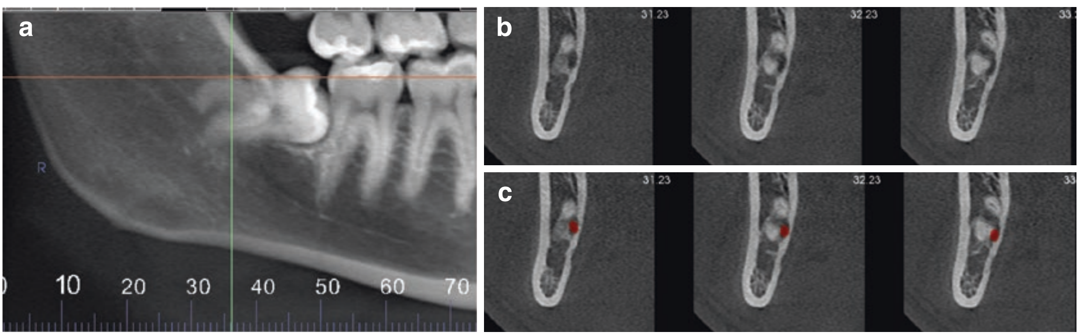

Fig. 29.30 Reformatted panoramic (**a**) and sequential 1 mm thick cross-sectional images (**b**) with IAC tracing (**c**) showing Type C Maegawa Classification (2003) with partial compression of the IAC by the roots of the impacted third molar and thinning of the internal margin of the lingual cortical plate

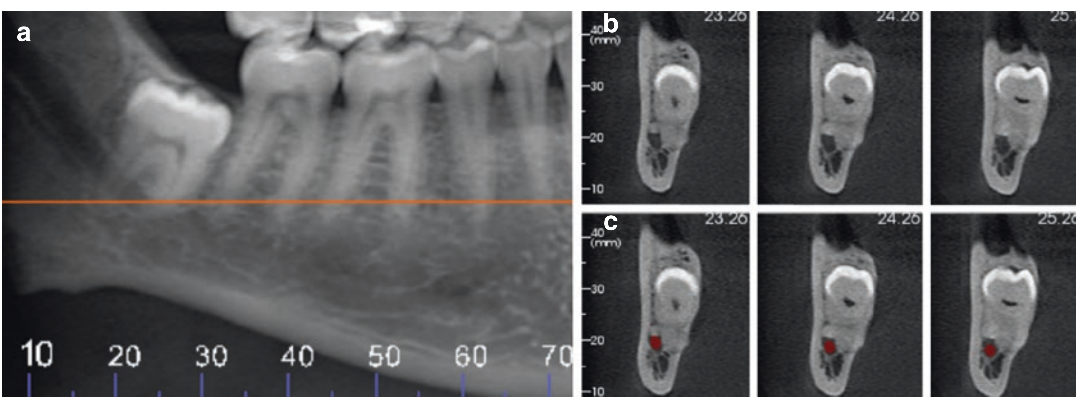

Fig. 29.31 Reformatted panoramic (**a**) and sequential 1 mm thick cross-sectional images (**b**) with IAC tracing (**c**) showing Type A Maegawa Classification (2003) showing indentation of apical portion of the mesial root of the right mandibular third molar by the IAC

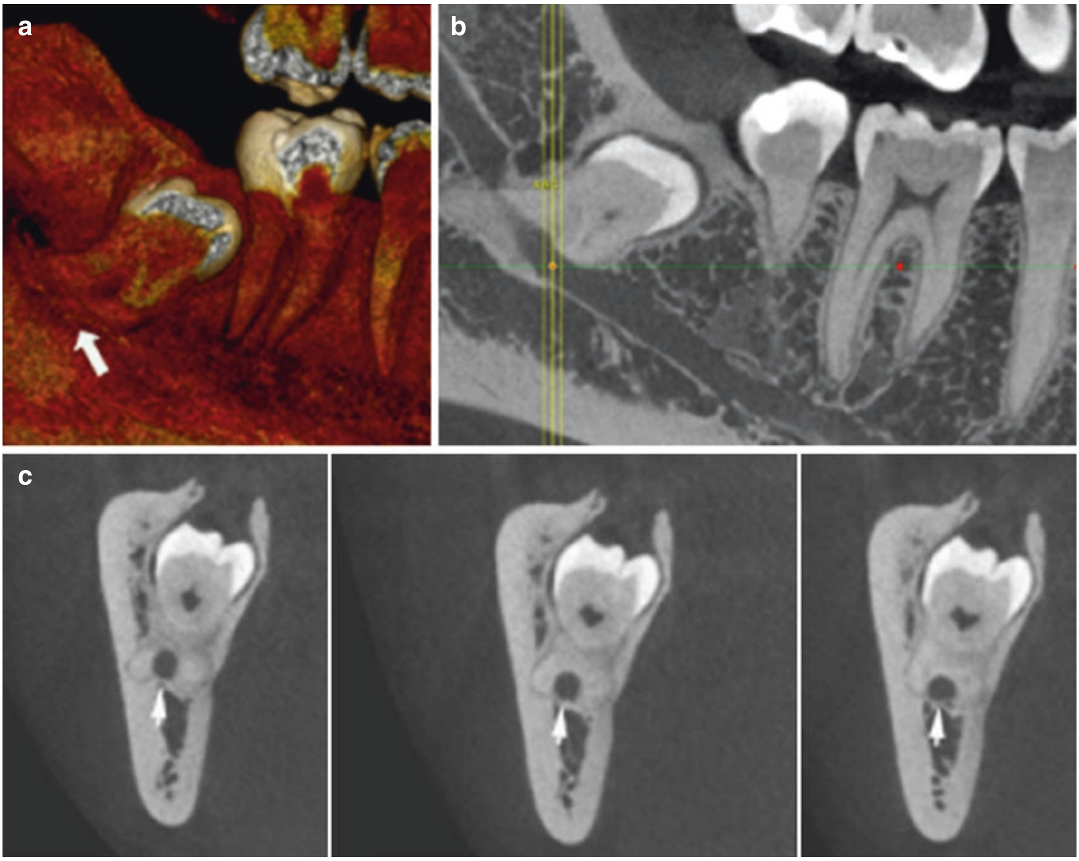

Fig. 29.32 Sections volumetric (**a**), parasagittal (**b**) and serial 1 mm thick/1 mm interval cross-sectional CBCT images showing the IAC running between the mesial roots of a completely bony impacted, mesioangular right mandibular third molar

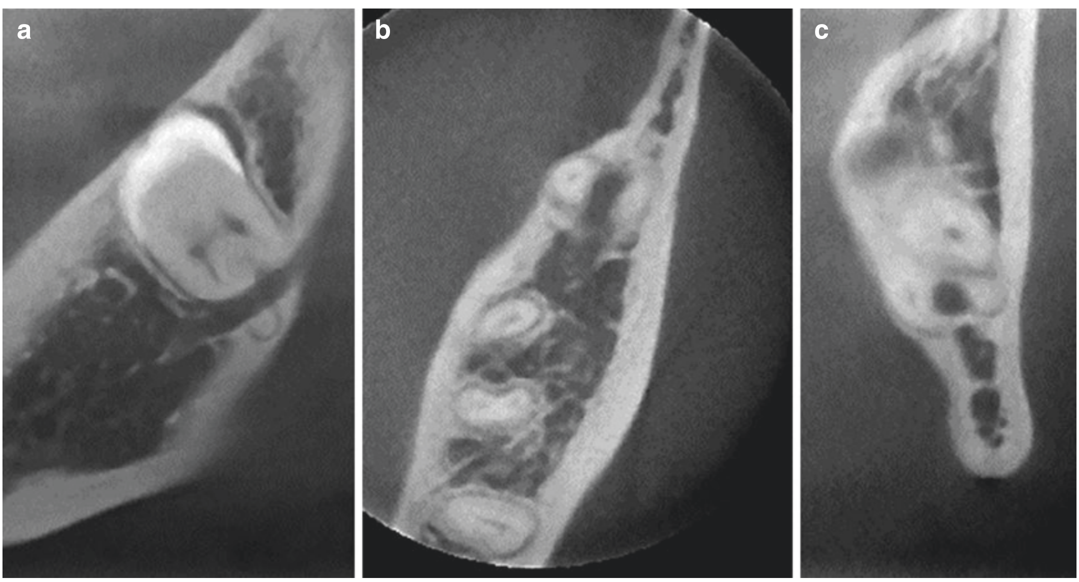

Fig. 29.33 Thin section sagittal (**a**), axial (**b**), and cross-sectional (**c**) limited FOV CBCT images the left mandibular posterior region showing a vertically oriented, completely bony impacted third molar with penetration of the IAC through the mesial root

facial aspect). Subsequently a ligature is attached and activated to produce an orthodontic force to move the canine into position (Becker 2012). Important radiographic factors that influence the orthodontists' decision whether to expose or remove an impacted permanent maxillary canine include mesial angulation relative to the midline (Table 29.9), vertical height, antero-posterior position of the root, overlap of the adjacent incisor (Table 29.10), and presence, location, and severity of root resorption of adjacent incisor(s) (Stivaros and Mandall 2000; Wriedt et al. 2012). Recently a CBCT enabled assessment, the KPG index, was proposed classifying treatment difficulty of impacted maxillary canines into four categories: easy, moderate, difficult, and very difficult (Kau et al. 2009). The index was named after Drs. Chung H. Kau, Philip Pan, and Ronald Gallerano of the University of Texas School of Dentistry at Houston. The KPG index is calculated adding together qualitative scores (range, 0 to 5) based on the deviation of the canine cusp and root apex cusp tip and root tip in *x*, *y*, and *z* planes. While intra- and interrater agreement are higher for KPG index, when compared to 2D indexes (Dalessandri et al. 2013, 2014), clinical implementation is time consuming.

Table 29.9 Classification of maxillary canine mesial angulation relative to the midline (after Stivaros and Mandall 2000)

Grade	Definition
1	0°–15°
2	16°–30°
3	≥31°

Table 29.10 Classification of overlap of the maxillary canine over the adjacent incisor root (after Power and Short (1993))

Grade	Definition
1	No horizontal overlap
2	Crown is horizontally overlapped less than half of the root width
3	Crown is horizontally overlapped more than half, but less than the whole root width
4	Crown is horizontally completely overlaps the root width or more

If a canine is unfavorably positioned, then the tooth may be left in situ particularly if surgical removal would potentially damage adjacent teeth. The rationale for canine assessment involves multiple considerations in two principle phases.

Tooth Location and Orientation

Maxillary Canines

- **Palatal impaction**. Palatal canine impactions occur approximately twice as often as facially impacted or erupted canines. Palatal impaction can be classified according to transverse relationship of the crown of the tooth to the line of the dental arch, so either close to the place of normal eruption of the canine or distant (closer to the midline), and according to the height of the crown of the tooth in relation to the occlusal place (high or low) (Fig. 29.34). The closer the canine is to its position of normal eruption and occlusal plane, the easier it is to treat. Typically, when the root is fully developed eruption potential has been lost (Figs. 29.35 and 29.36). Palatally positioned canines can tip the roots of the ipsilateral central and lateral incisors facially, and may cause pressure resorption of the roots. In severe cases, palatally impacted canines can become horizontal and may even encroach upon the incisive canal (Fig. 29.37). The relationship of the canine's root apex to the floor of the nasal cavity should be examined, as it may protrude into the nasal cavity. If the root tip is engaged between the cortices of the maxillary sinuses and nasal cavity, a mechanical impaction may occur, more frequently seen if the root tip is curved.
- **Facial impaction**. Facially erupted canines are the second most common presentation for maxillary canine impaction and are often a cause for patient concern because of esthetics. The developmental position of maxillary canine is slightly facial to the general line of the dental arch and since the two adjacent

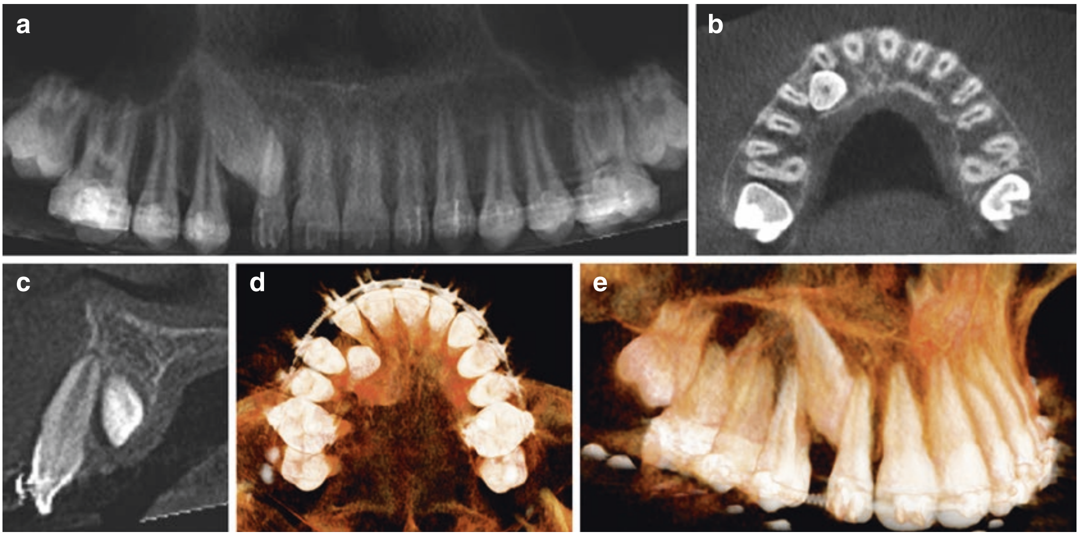

Fig. 29.34 Reformatted panoramic (**a**), axial (**b**), cross-section (**c**) and inferior (**d**) and right lateral superior oblique (**e**) volumetric renderings of a right impacted maxillary canine in a low relationship with a distant position relative to the occlusal plane and midline, respectively. The position of the tooth is further complicated in that it is rotated 90° which only allows bonding of an orthodontic bracket to the curved palatal surface

Fig. 29.35 Coronal CBCT shows a palatally impacted right maxillary canine with a fully developed root and an enlarged follicle. The right maxillary deciduous canine is present and displays normal physiologic resorption

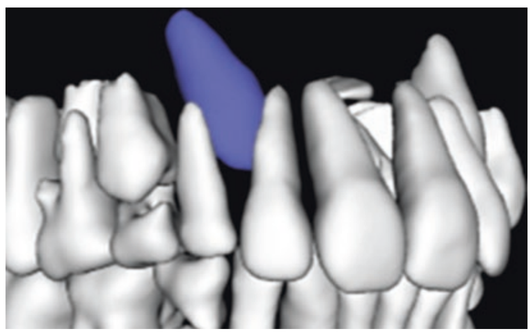

Fig. 29.36 Segmented dentition shows a palatally ectopically positioned and incompletely formed maxillary right canine with a potential for further eruption

teeth erupt before the canine, crowding with a high buccal eruption is common (Fig. 29.38). Complete transposition of the canine into the position of the lateral incisor may also occur (Fig. 29.39). Crowding is likely to exacerbate the facial position of a canine with an open root as the eruption progresses. Relative tooth size and arch length and shape play important roles in determining if impaction will be palatal or facial. Palatal impactions are associated with an excess of space in the dental arches whereas facial impactions often show marked crowding.

– *Mesially inclined facial impactions.* Most facially impacted canines have a slight mesial displacement, overlapping the disto-buccal aspect of the lateral incisor

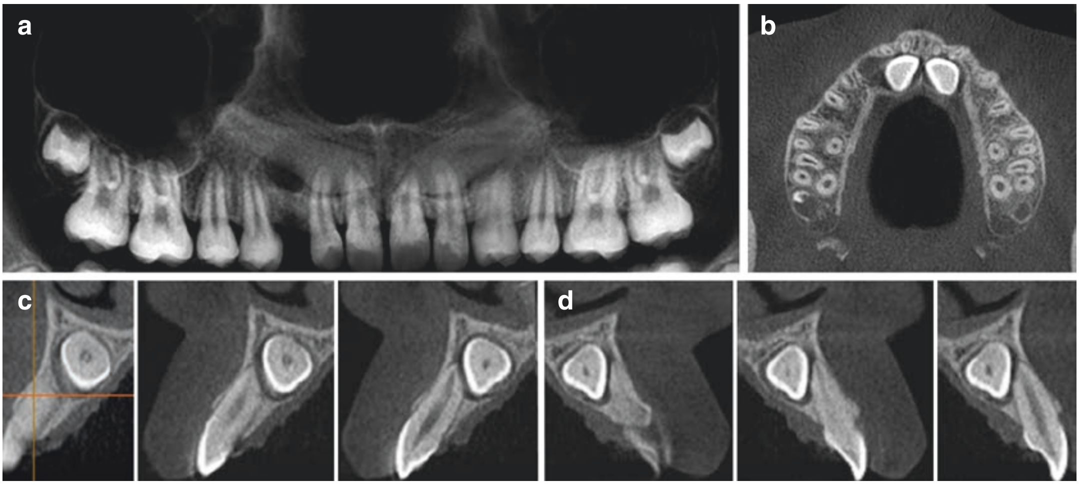

Fig. 29.37 Reformatted panoramic (**a**), axial (**b**) and left (**c**) and right (**d**) cross-sectional images showing fully formed, bilaterally palatally horizontally impacted maxillary canines encroaching on the midsagittal nasopalatine canal

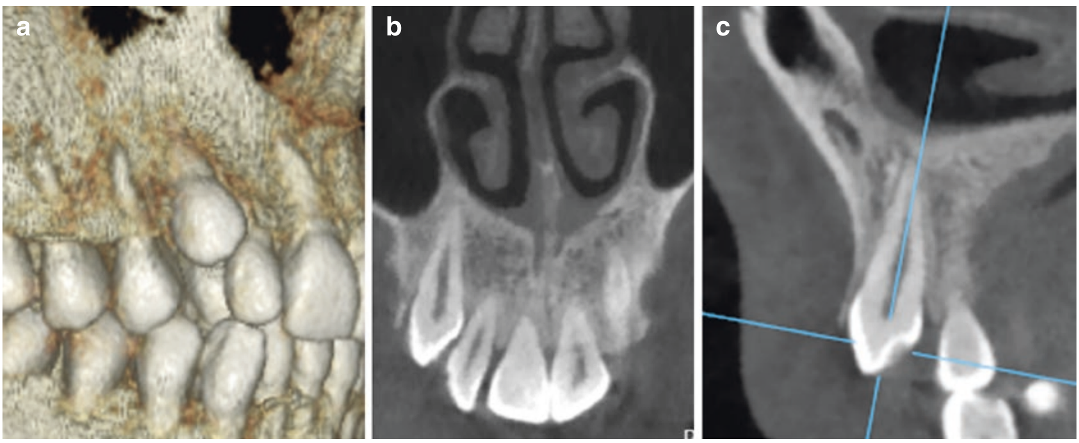

Fig. 29.38 3D surface shaded rendering (**a**), coronal (**b**) and parasagittal (**c**) CBCT images show a facially impacted right maxillary canine that is erupting ectopically due to crowding of the adjacent teeth. The apex of the canine is completely closed and therefore there is no eruption potential

(Fig. 29.39). Root resorption as well as mesial or distal tipping of the root of the lateral incisor may occur (Fig. 29.40). In cases of migration of the canine between the lateral and central incisors, the roots of the adjacent teeth may be splayed away from the canine (Fig. 29.41). Some more severely displaced teeth may extend to the mesial aspect of the lateral incisor root and even the distolingual aspect of the central incisor root (Fig. 29.41).

– *Distally inclined facial impactions.* This type of impaction is rare and is almost always associated with transposition with the first premolar. These may erupt fully, partially, or not at all. The roots of the transposed premolar are tipped mesially, but the crown is in its normal position. Evaluation of the first and second premolar roots for resorption is recommended, as well as the relationship of the canine root with the floor of the maxillary sinus.

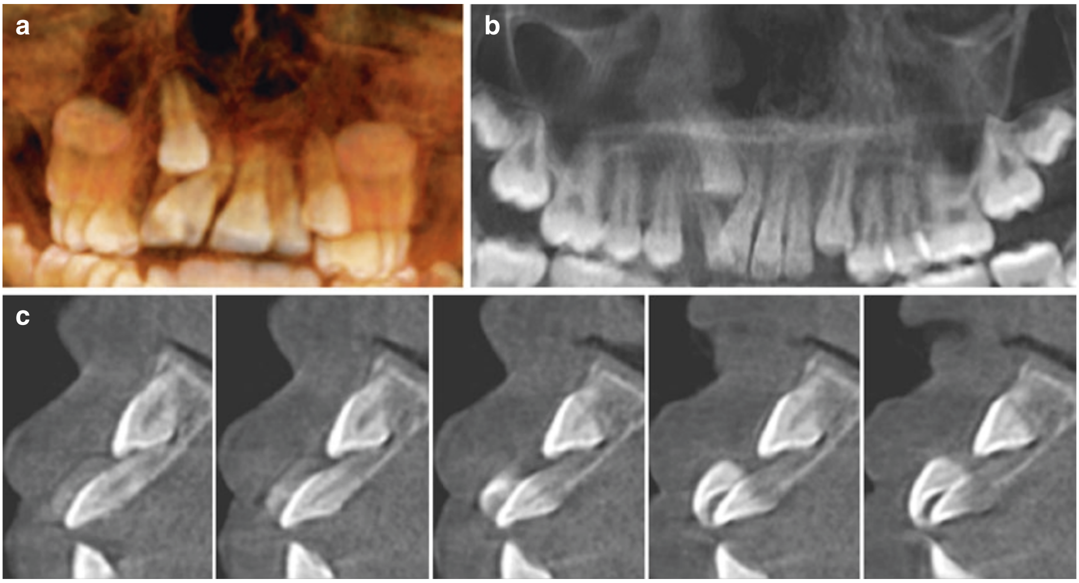

Fig. 29.39 Volumetric rendering (**a**), reformatted panoramic (**b**), and serial cross-sectional (**c**) CBCT images of a facially impacted right maxillary canine transposed inter-radicularly between the right central and lateral incisor causing buccal flaring of the crowns, distalization of the root apex of the lateral and distal tilting of the central. No root resorption is noted

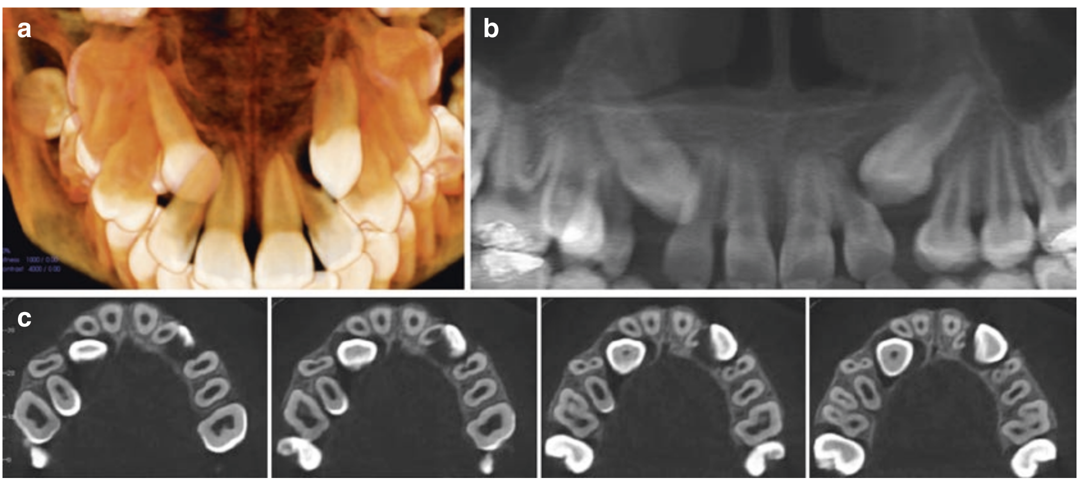

Fig. 29.40 Volumetric rendering (**a**), reformatted panoramic (**b**), and serial axial (**c**) CBCT images of a mesioangular palatally impacted right and mesioangular facially impacted left maxillary canine. Severe resorption involving the pulp canal of the disto-buccal aspect of the middle third of the root of the left canine is shown. Distal tipping and facial flaring of the lateral incisor is also observed

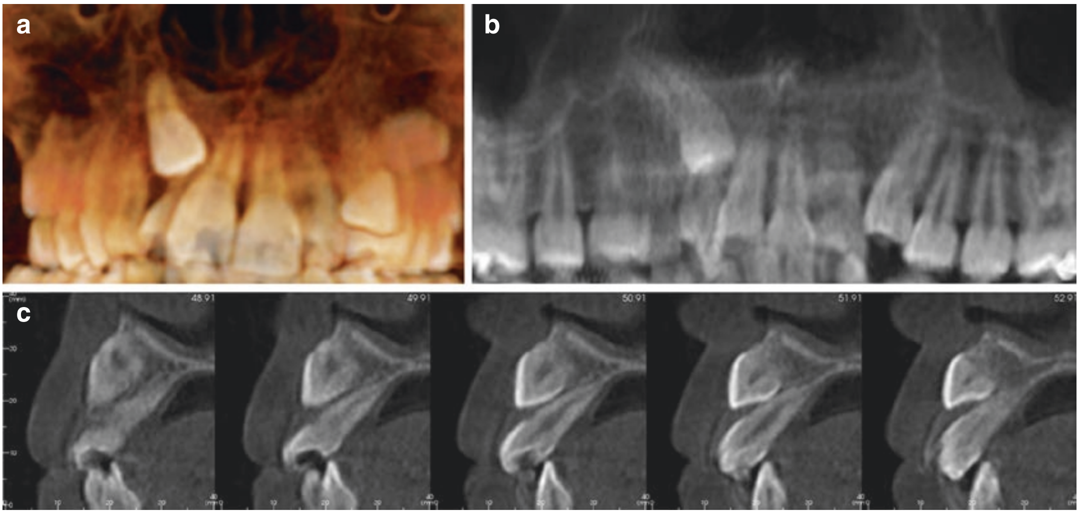

Fig. 29.41 Volumetric rendering (**a**), reformatted panoramic (**b**), and serial cross-sectional (**c**) CBCT images of a mesioangular, facially impacted right maxillary canine positioned buccal to the apical third of the right lateral incisor causing buccal flaring of the crown. No root resorption is noted

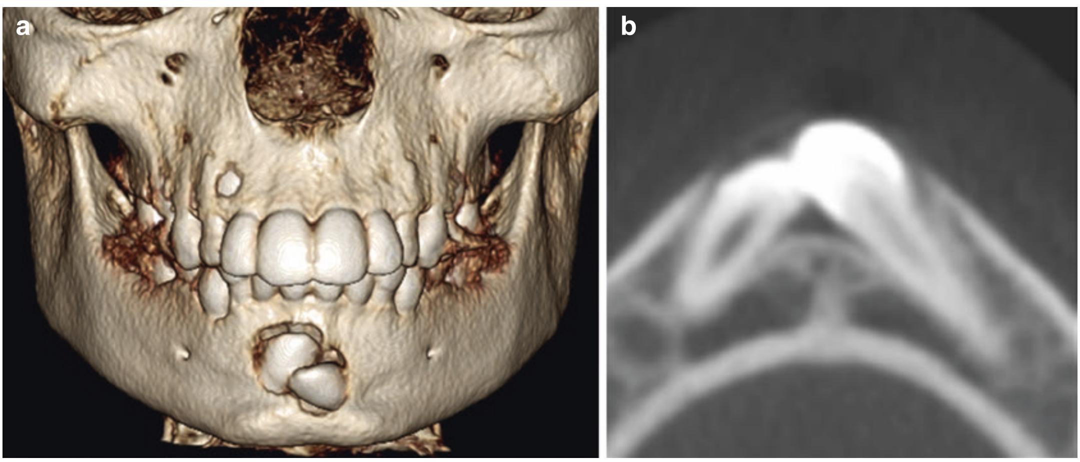

Fig. 29.42 Volumetric surface rendering and axial (**b**) CBCT images of bilateral mandibular impacted canines. The right canine is angled at approximately between 30° and 50° whereas the left canine is angled at almost 90°

Mandibular Canines

Impacted mandibular canines are uncommon, especially when compared to the maxillary canine (Fig. 29.42). This may be due to the difference in eruption pattern sequence and tooth size as the mandibular anterior teeth are smaller mesiodistally than the maxillary teeth. Impacted mandibular canines are often incidental findings as they do not usually cause malocclusion. Most cases are likely the result of the hereditary displacement of the primary predecessor tooth germ and developmental angulation of the developing canine follicle. This may cause abnormal angulation of the long axis of the tooth. Angulations between 30° and 50° are associated with good predictability that this tooth will migrate across the midline in a relatively short period of time. Angulations greater than 50° are an excellent predictor of this migration.

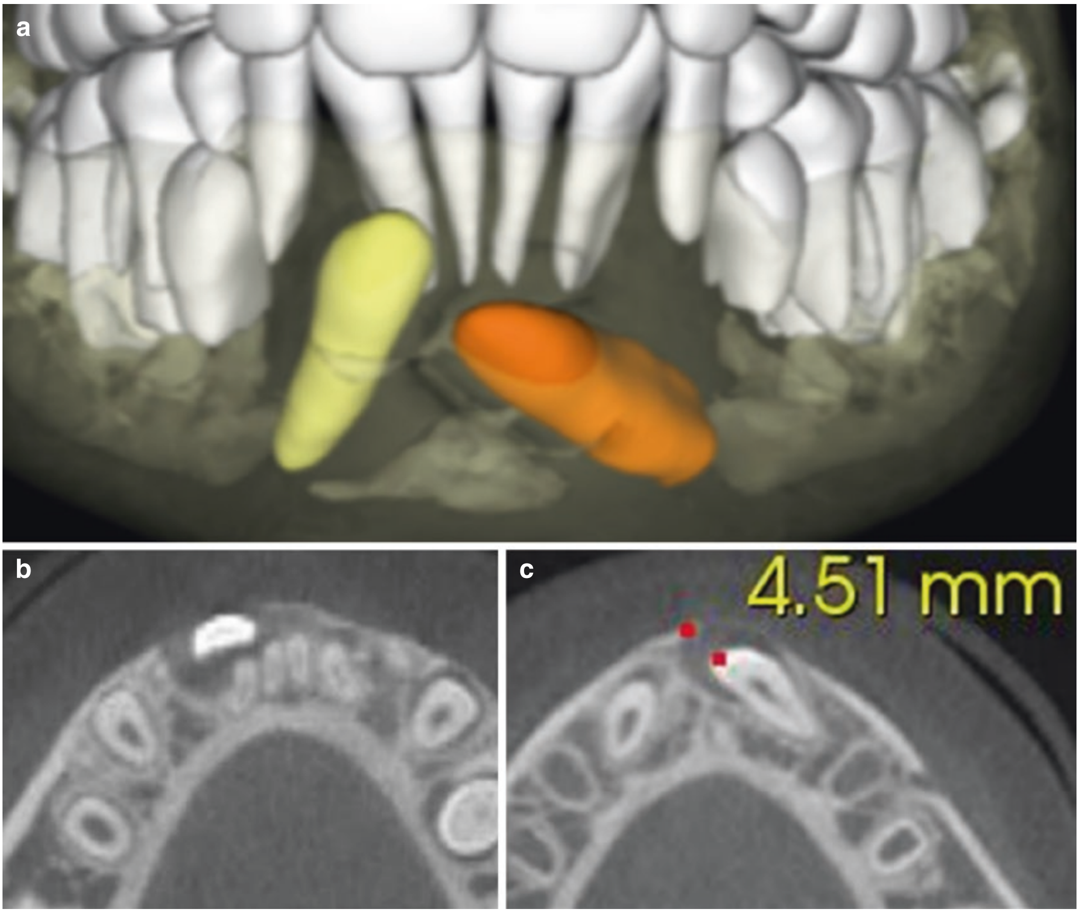

Fig. 29.43 Tooth segmented virtual model (**a**) and axial (**b**) and (**c**) CBCT images show a left mesioangular transmigrated mandibular canine (*orange*) and mesioangular facially ectopically positioned right mandibular canine (*yellow*). The cusp of the left canine is located facially to the apices of the incisor teeth yet still crosses the mandibular midline. The crown of this tooth is located within the facial cortex of the mandible

Unlike maxillary canines, mandibular canines may cross the midline or *transmigrate* even to the permanent molar on the contralateral side. These impacted canines are generally found facial to, or in line with, the dental arch. When the tooth is lingually positioned, the root apex will be invariably positioned in the normal position and the adjacent teeth roots will be tipped facially and their crowns lingually. Facially impacted canines that have crossed the midline can be classified into five types (Mupparapu 2002):

- **Mesioangular Impacted**. The mandibular canine lies mesioangularly inclined inferior to the anterior teeth with the crown crossing the midline. This is also called a *transmigrated* tooth (Fig. 29.43).
- **Horizontally Impacted, Ipsilateral**. The mandibular canine lies below the apices of the ipsilateral incisors (Fig. 29.44).
- **Erupted Mesially or Distally**. The mandibular canine lies mesially or distally oriented compared to the contralateral canine (Fig. 29.45).
- **Horizontally Impacted, Contralateral**. The mandibular canine lies below the apices of the contralateral canine and premolars.
- **Vertically Impacted**. The position of the mandibular canine coincides with the midline (true transposition). Relationship of this

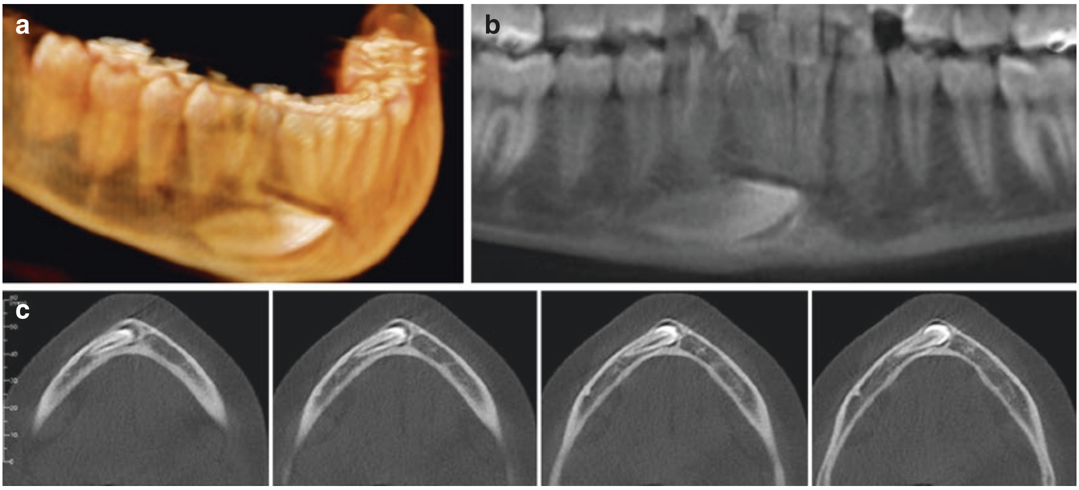

Fig. 29.44 Volumetric rendering (**a**), reformatted panoramic (**b**), and axial (**c**) CBCT images of a horizontally and facially impacted right mandibular canine below the apices of the ipsilateral incisors with part of the crown crossing the midline

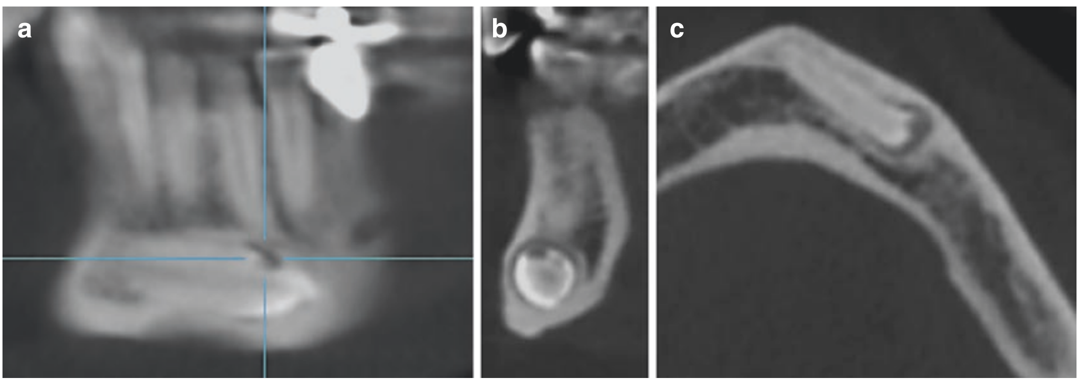

Fig. 29.45 Coronal (**a**), sagittal (**b**), and axial (**c**) CBCT images of a full bony horizontally impacted right mandibular canine that has completely crossed the midline, inferior to the apices of the incisors. The crown shows external resorption

migrated tooth to the adjacent structures, including the lingual canal and foramen, should be noted.

Relationship to the Adjacent Anatomic and Dental Structures

Maxillary Canines

- **Anterior superior alveolar canal**. This contains the terminal aspect of the maxillary branch of the trigeminal nerve prior to exiting the infraorbital canal. This nerve innervates the nasal cavity in the region of the inferior meatus and inferior adjacent region of the nasal septum and the maxillary sinus. The nerve descends through a sinuous canal to form the superior dental plexus, innervating part of the maxillary sinus, the maxillary incisors and canines, and the adjacent gingival and mucosa. A normally erupted maxillary canine is not usually in contact with the sinuous canal, however, when impacted, may approach or contact this canal. Identification of the position of the canal with coronal and cross-sectional reformations is recommended when evaluating maxillary canine impactions.

- **Nasal cavity**. Canines that are deeply impacted may have a portion of their root in close contact with or protrude slightly into the floor of the nasal fossa. This relationship is important to ascertain during surgical removal so as to avoid displacing the tooth into the nasal cavity. Also, there is a tendency for the root tip to dilacerate and lodge into the junction of the floors of the maxillary sinus and nasal cavity, causing mechanical ankylosis (Fig. 29.42).
- **Incisive canal:** When deeply impacted mesially angularly oriented and palatally positioned maxillary canines approach the midline, they may protrude into the incisive canal. Removal of these teeth, particularly those with pericoronal widening, may involve enucleation of the incisive canal contents and concomitant bone grafting.
- **Adjacent teeth:** The position of the canine crown in relation to the adjacent incisors is important for orthodontic treatment planning. If positioned in contact with the roots of adjacent teeth eruptive or external orthodontic forces may cause resorption. Surface resorption occurs most commonly on the distopalatal surface of the maxillary lateral incisor (64%), followed by the central incisors (23%) and first premolars (11.7%) (Doğramaci et al. 2015). The severity of root resorption can be graded according to degree of tooth structure loss relative to involvement of the dental pulp (Table 29.11) (Ericson and Kurol 2000; Ericson et al. 2002). The reported incidence and severity of root resorption associated with the root of the lateral incisor varies (Table 29.12) (Doğramaci et al. 2015; da Silva Santos et al. 2014; Lai et al. 2013; Algerban et al. 2011; Liu et al. 2008). Severe incisor root resorption occurs more frequently in females, and is associated with severely mesiodistally displaced and vertically positioned canines in the middle third of the adjacent incisor root, and with dental follicles wider than 2 mm (Chaushu et al. 2015). A greater degree of canine displacement might also be associated with severe incisal root

Table 29.11 Classification of degree of root resorption associated with maxillary canine impaction (after by Ericson and Kurol 2000; Ericson et al. 2002)

Grade	Description
1	None. intact root surfaces, except for loss of cementum
2	Slight. Resorptive loss of up to half of the dentine thickness to the pulp (Fig. 29.46)
3	Moderate. Resorptive loss half way to the pulp or more; the pulp is covered with dentine (Fig. 29.47)
4	Severe. Resorptive loss such that the pulp is exposed (Fig. 29.48)

Table 29.12 Comparison of selected studies reporting the incidence and degree of root resorption of the roots of maxillary lateral incisors by the crowns of maxillary canines on CBCT

		Sample (*n*)		Resorption				
Author (year)	Voxel size	Patients	Teeth	Patients	Lateral incisors	Mild	Moderate	Severe
Doğramaci et al. (2015)	0.125 mm	183	nr	85 (46%)	77/120 (65%)	42 (55%)	16 (21%)	19 (24%)
Da Silva Santos et al. (2014)	0.076 mm	66	79	nr	48/71 (67.6%)	33 (69%)	6 (13%)	9 (185)
Lai et al. (2013)	0.125 mm	113	134	nr	34/48 (70%)	12 (35%)	5 (15%)	17 (50%)
Algerban et al. (2011)	0.125 mm[a]	60	89	60	nr (53.9%)	nr (35.9%)	nr (9.9%)	nr (8.1%)
Liu et al. (2008)	nr	175	310	105 (60%)	56/105 (53%)	32 (52%)	13 (23%)	11 (21%)

nr not reported

[a]Accuitomo XYZ (J Morita, Kyoto, Japan) results only

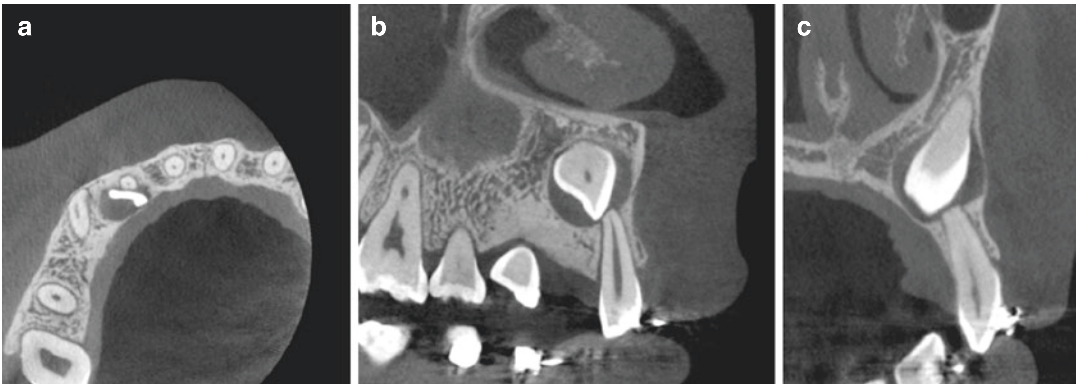

Fig. 29.46 Axial (**a**), sagittal (**b**), and cross-sectional (**c**) CBCT images of the maxillary right anterior region showing sight resorption of the apical portion of the lateral incisor by the crown of the impacted completely bony impacted canine

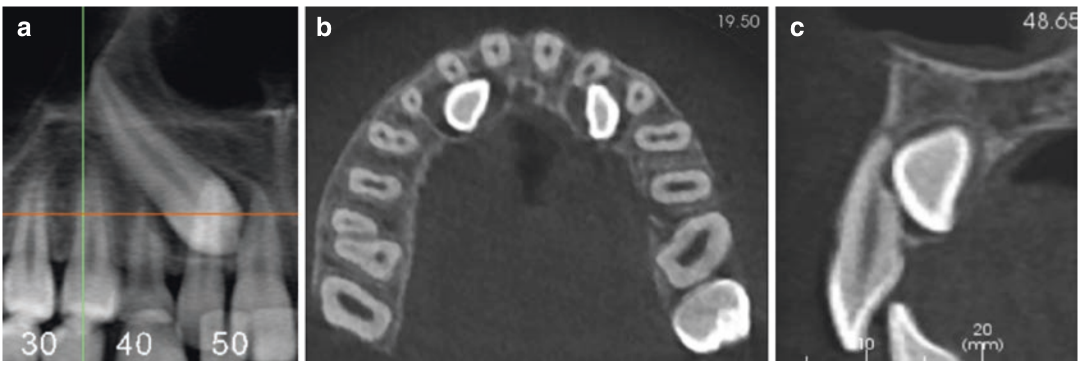

Fig. 29.47 Cropped reformatted panoramic (**a**), axial (**b**), and cross-sectional (**c**) CBCT images of the right anterior maxilla showing moderate resorption of the palatal surface of the mid- to apical third of the root of the lateral incisor by the crown of the mesioangularly ectopically palatally positioned and completely bony impacted canine

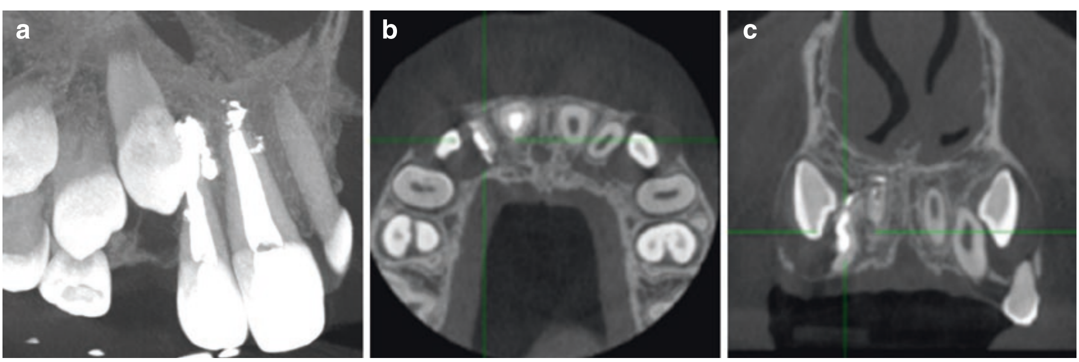

Fig. 29.48 Right lateral maximum intensity projection (**a**), axial (**b**), and coronal (**c**) CBCT image demonstrating severe resorption (involving the pulp canal) of the distal surface of the root of an endodontically right lateral incisor associated with the crown of a vertically completely bony impacted right maxillary canine

resorption. Similarly, the position of the root of the canine in relation to the premolars should be noted.

Mandibular Canines

- **Incisive canal**. The two terminal branches of the inferior alveolar nerve within the IAC are the mental nerve, exiting through the mental foramen, and the incisive nerve (also called the anterior branch of the IAN) which continues intramedullary to the mandibular midline. The relationship of an impacted mandibular canine to these structures is import to determine as incorrect surgical technique can lead to neurosensory morbidity.
- **Lingual canal and foramen**. Both structures are located on the lingual aspect in the mandibular midline and may be associated with impacted canines that cross the midline.

29.4.3 Premolars

29.4.3.1 Mandibular Second Premolar

Impaction of the mandibular second premolar may occur spontaneously (Fig. 29.49) although most commonly results from early loss of the deciduous mandibular second molar (Fig. 29.50). Loss of this primary tooth leads to mesial and lingual drift of the permanent mandibular first molar together with distal migration of the deciduous primary first molar. Consequently, the second premolar will either erupt lingually or remain impacted and submerged in the edentulous alveolar process. Alternately, the premolar tooth germ may develop ectopically and may drift distally resorbing the distal root of the deciduous second molar or the mesial root of the permanent first molar. This is often associated with retention of the deciduous second molar. As with all impacted mandibular teeth, the relationship with the IAC

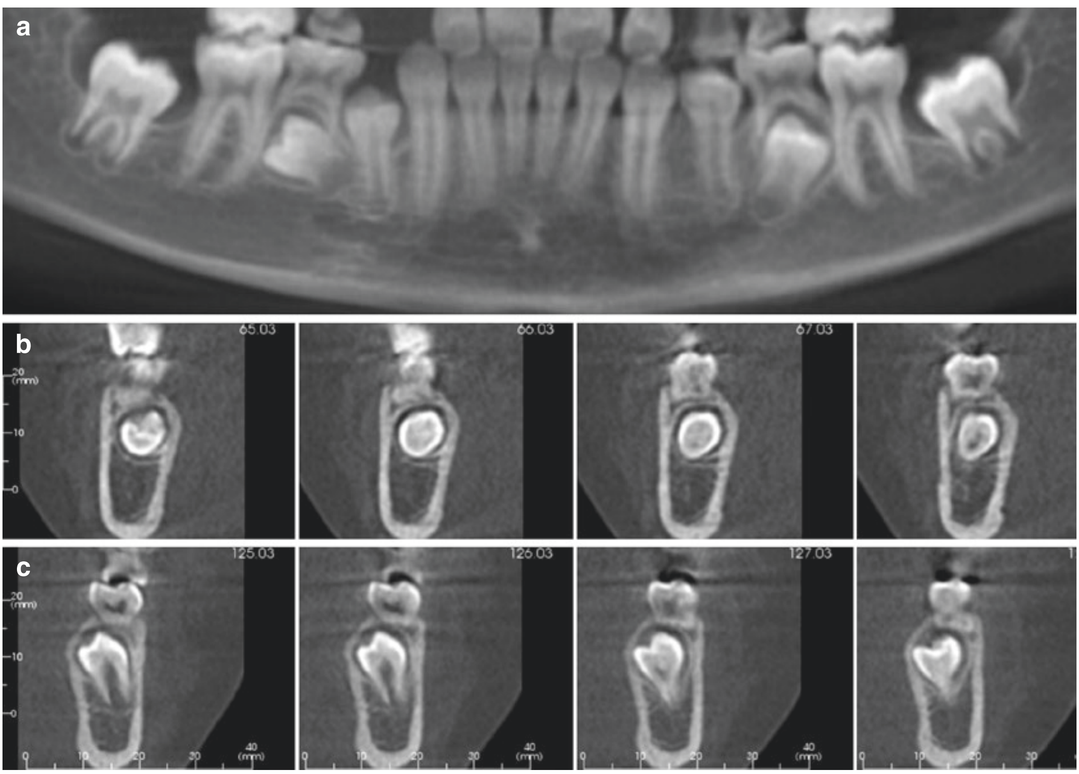

Fig. 29.49 Reformatted panoramic (**a**) and right (**b**) and left (**c**) sequential cross-sectional images demonstrating spontaneous complete distal horizontal and distoangular impaction of the right and left second premolars, respectively

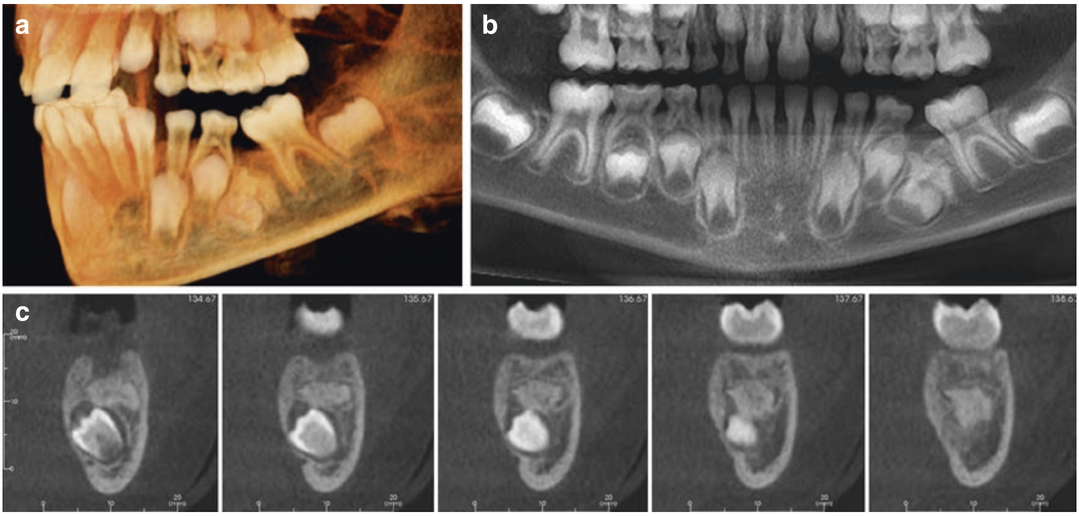

Fig. 29.50 Volumetric rendering (**a**), reformatted panoramic (**b**), and cross-sectional (**c**) CBCT images of a disto-angularly and lingually oriented unerupted and submerged left mandibular premolar tooth follicle impacted below the retained roots of a left deciduous second molar

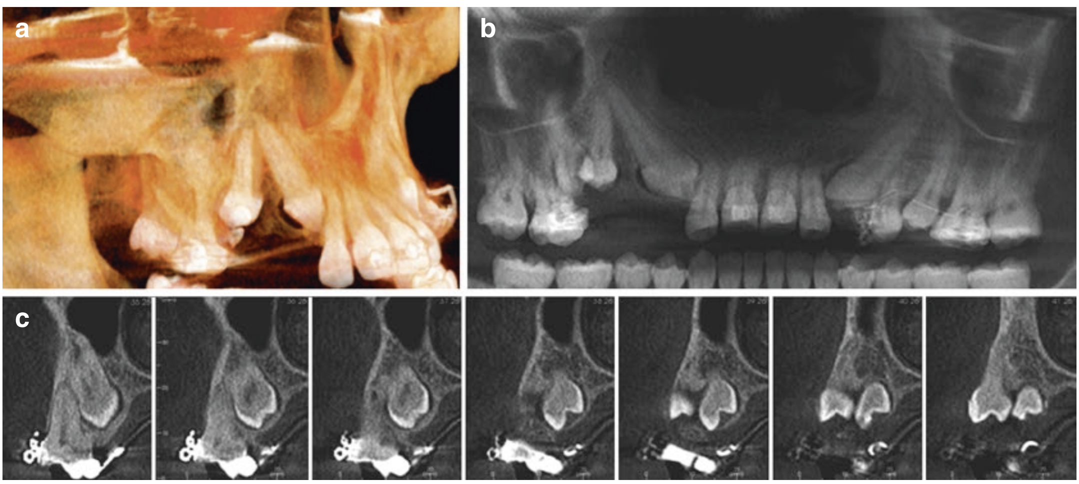

Fig. 29.51 Volumetric rendering (**a**), reformatted panoramic (**b**), and cross-sectional (**c**) CBCT images of a distally ectopically positioned, palatally oriented and submerged unerupted right maxillary second and first premolar associated with premature removal of the right deciduous molar teeth. Note that the right second premolar is impacted below the mesial coronal convexity of the right maxillary first molar

and particularly the mental foramen should be scrutinized.

29.4.3.2 Maxillary Second Premolar

Similarly, the most common cause for impaction of the maxillary second premolar is premature loss of the deciduous second molar leading to loss in dental arch length due to mesial drift of the permanent first molar and distal migration of the deciduous first molar (Fig. 29.51). As the line of eruption of the maxillary second premolars tends to be palatal, ectopic teeth often erupt or become impacted palatally. The relationship of the maxillary second premolar to the maxillary sinus and the posterior superior alveolar canal, if visible, should be examined.

29.4.4 Supernumerary Impacted Teeth

Supernumerary teeth are teeth that form in addition to the normal complement of teeth. They may occur in the permanent or the primary dentition and are often impacted. Prevalence ranges from 0.1% to 3.8% in the permanent dentition with much lower prevalence in the primary dentition (Rajab and Hamdan 2002). Supernumerary teeth are seen more often in the maxilla rather than mandible (Açikgöz et al. 2006) with the premaxilla being the most frequent location (Rajab and Hamdan 2002). They may resemble a regular tooth in size and morphology or may be irregular, malformed, or underdeveloped (Figs. 29.52

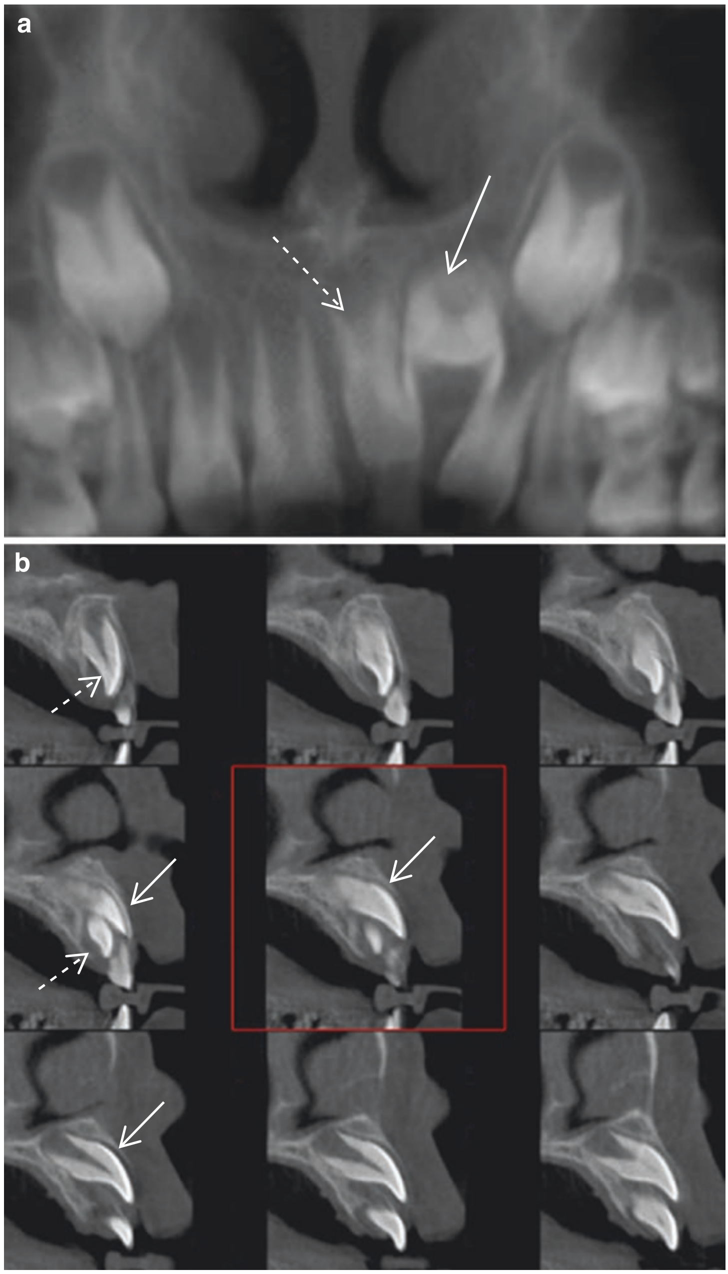

Fig. 29.52 Reformatted panoramic (**a**) and series of cross-sectional images in the region of the left central incisor region (**b**) showing two central incisors; one is partially erupted (*dashed arrow*) and the other (*solid arrow*) is impacted. One of the two teeth is supernumerary; however, it is impossible to say with certainty which one. Both show a similar development and crown shape and size. The presence of the supernumerary tooth has caused considerable crowding in the left anterior maxilla

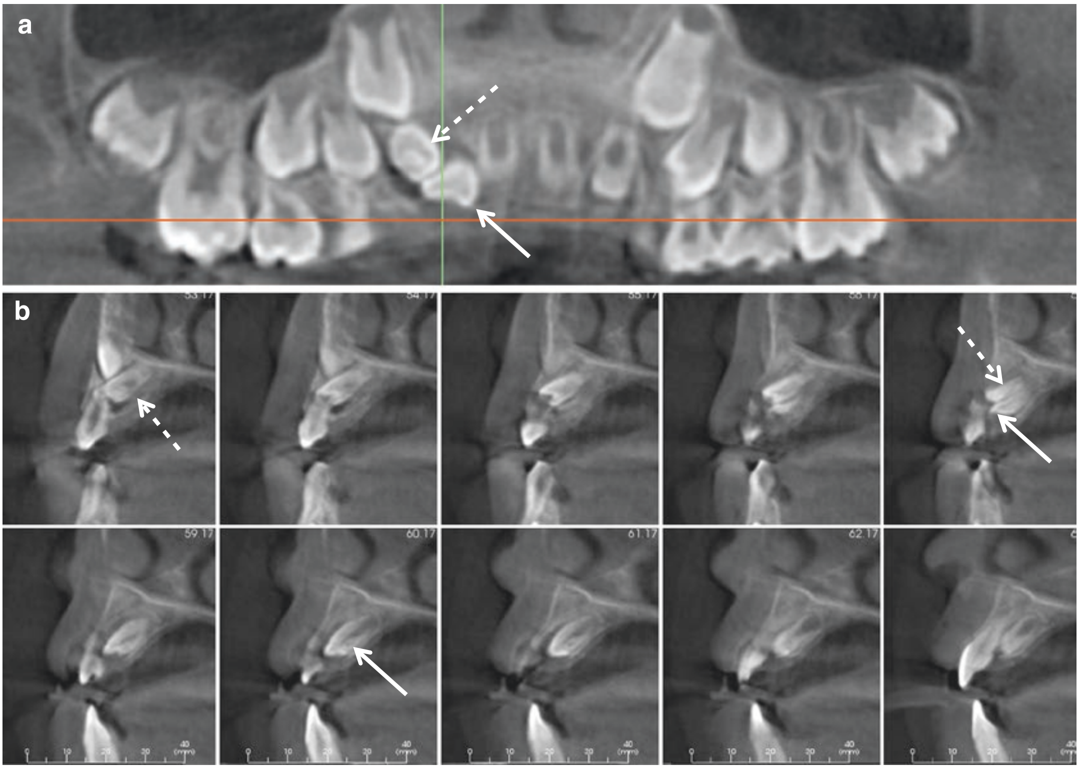

Fig. 29.53 Reformatted panoramic (**a**) of the maxilla and serial cross-sectional images (**b**) of the right maxillary canine and incisor region showing an impacted supernumerary tooth (*dashed arrow*) overlapping unerupted right maxillary lateral incisor (*solid arrow*); note the irregular shape of the crown of the supernumerary tooth

and 29.53). The most frequently seen impacted supernumerary is an irregular, microdontic, incisor-like tooth in or adjacent to the maxillary midline, often associated with the roots of the maxillary central incisors, known as mesiodens (Fig. 29.54). The next most common supernumerary teeth are maxillary premolars followed by molars. Premolars are the most frequently seen supernumerary teeth in mandible.

Supernumerary teeth occupy arch space and, thus, may displace teeth that are already erupted leading to occlusal changes, crowding, or spaces. Often, they may alter or prevent the eruption of regular teeth. Rarely, supernumeraries may be involved in pathological conditions associated with other impacted teeth such as root resorption or pericoronal disturbances including dentigerous cysts (Fig. 29.55).

Albeit the existence of an impacted supernumerary tooth is considered a pathological condition, the need for intervention (surgical removal, in most cases) is judged upon a variety of factors:

- The possible harm that the supernumerary tooth may impose to the surrounding teeth or other structures and the associated benefits from its extraction (Figs. 29.56, 29.57 and 29.58).
- The complexity of the surgical approach and possible risks to the neighboring anatomical structures associated with the procedure (Figs. 29.56 and 29.57).

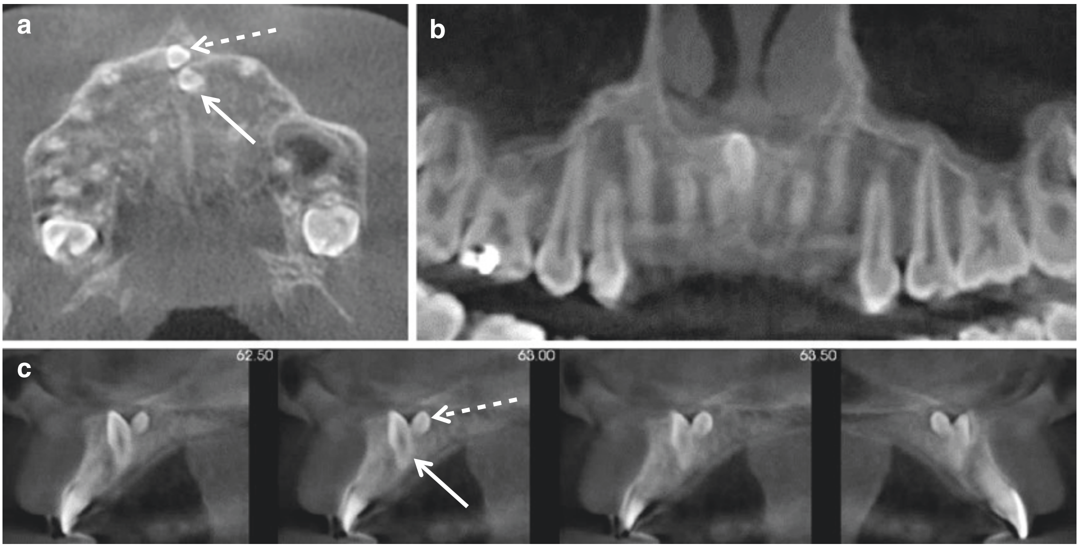

Fig. 29.54 Axial (**a**), reformatted panoramic (**b**) and series of cross-sectional images (**c**) of the maxillary midline showing two supernumerary impacted teeth (mesiodens) (*dashed* and *solid arrows*) causing some displacement of the roots of the maxillary incisor teeth. The mesiodens is the most frequently seen supernumerary tooth in the maxilla and most often located on the palatal aspect of the alveolar ridge (as shown here). Regularly the tooth is inverted with the crown directed towards the floor of the nasal cavity

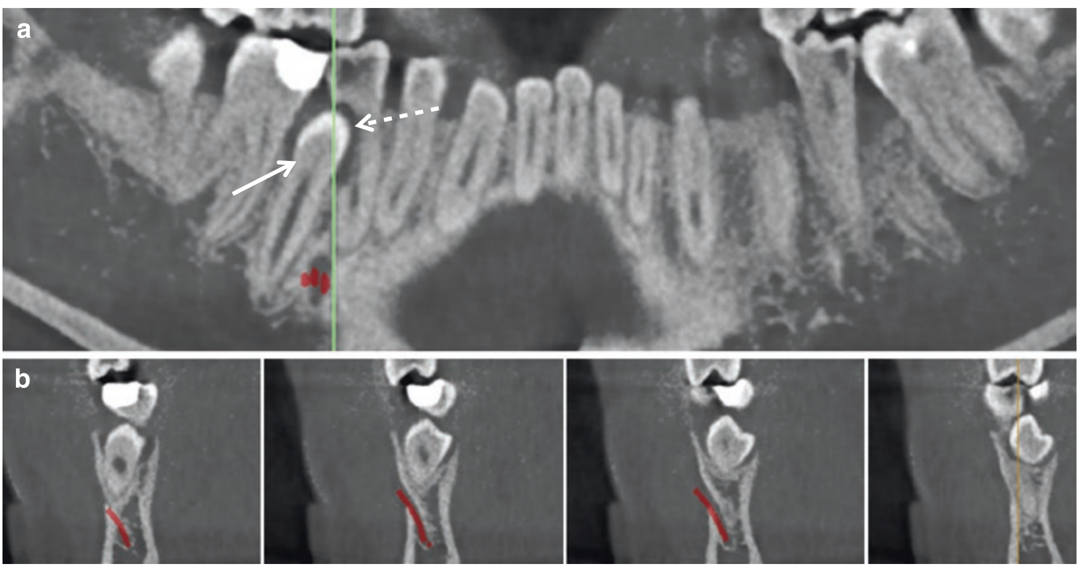

Fig. 29.55 Reformatted panoramic of the mandible (**a**) and serial cross-sectional images in the region of the left mandibular second premolar (**b**) showing an impacted fully developed supernumerary premolar tooth (*solid arrow*) impacted against the distal aspect of the root of the second premolar with severe external root resorption (*dashed arrow*). Note the intimate relationship of the root of the supernumrary tooth to the right mental foramen (*red line*)

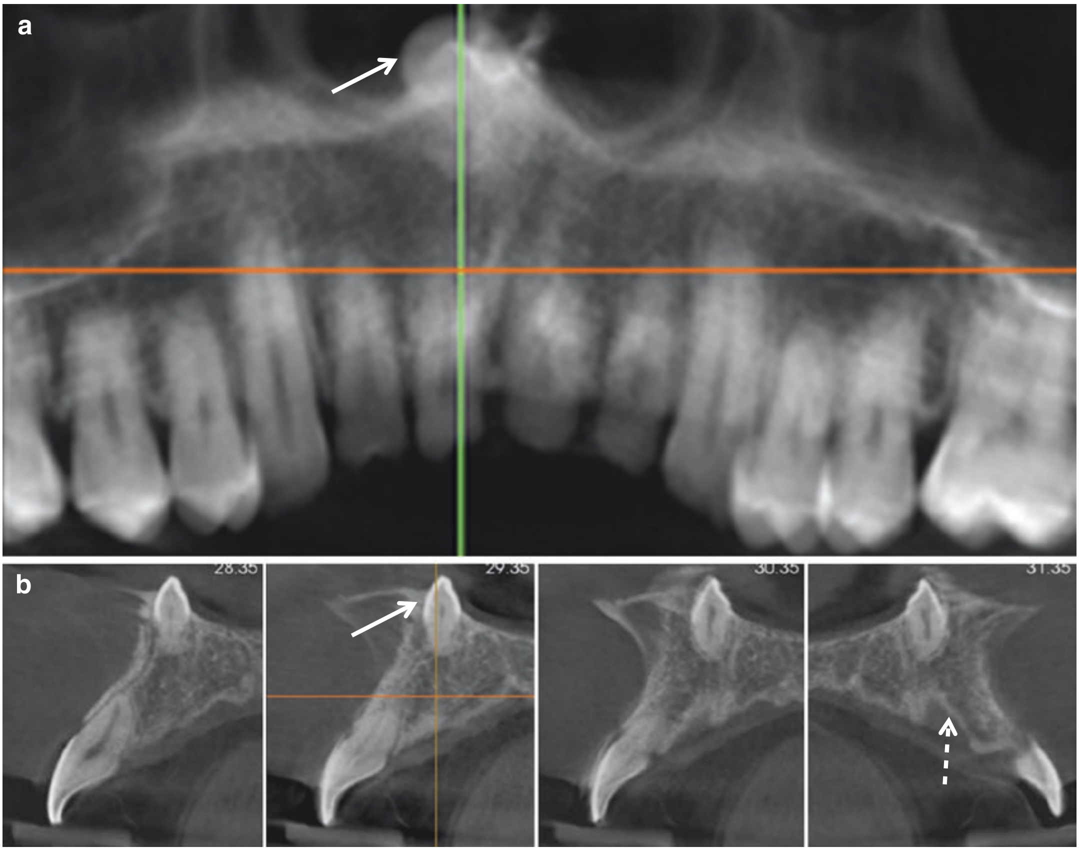

Fig. 29.56 Reformatted panoramic image of the maxilla (**a**) and serial cross-sectional images in the region of the maxillary central incisors showing an impacted inverted, microdontic supernumerary tooth (mesiodens) in the maxillary midline. The tooth has perforated the floor of the right nasal cavity and is projecting into the nasal cavity. The tooth is not involved with the anterior maxillary teeth or the nasopalatine canal (*dashed arrow*) and thus only periodic radiologic assessment was recommended

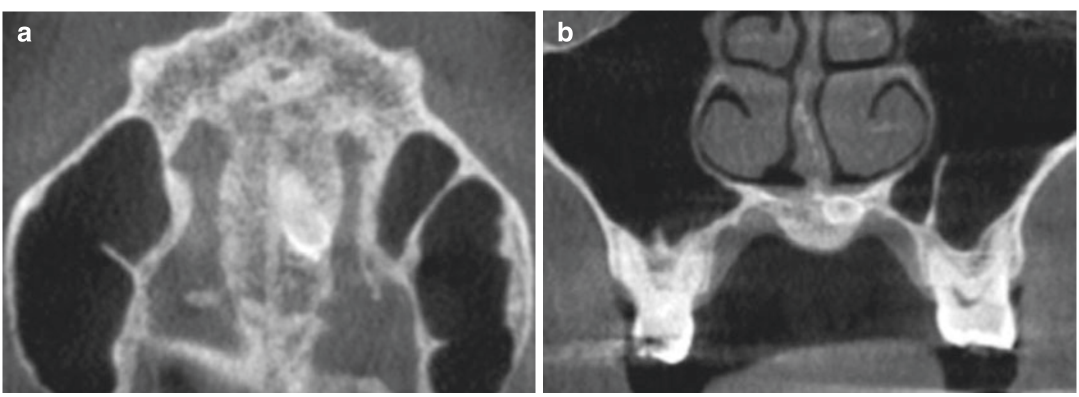

Fig. 29.57 Axial (**a**), coronal (**b**), and sagittal (**c**) orthogonal images showing an inverted supernumerary impacted tooth (mesiodens) along the palatal midline. As the tooth did not interfere with the dentition and was not associated with any pathology, periodic radiologic assessment was recommended

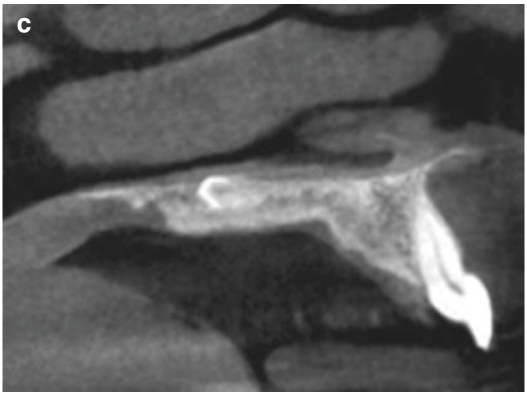

Fig. 29.57 (continued)

> **Conclusion**
> Any tooth in the jaws may become impacted with the most common being the third molars, canines, and premolars. Numerous planar reformatted images such as cross-sectional and axial images and volumetric renderings can be used to assess the depth of impaction, facio-lingual or lingual position relative to the dental arch, and location relative to adjacent teeth. For third molars, radiographic assessment is directed towards planning a surgical approach that negates or minimizes morbidity, principally damage to the inferior alveolar

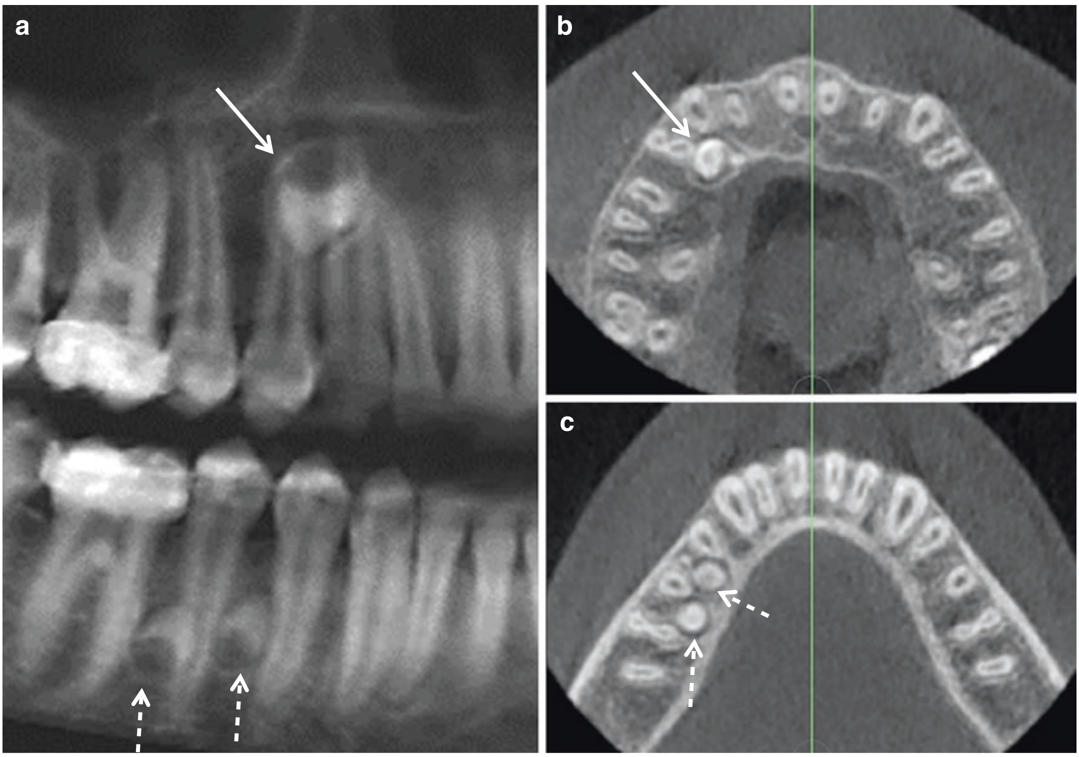

Fig. 29.58 Cropped reformatted panoramic image of the right maxilla and mandible (**a**) and corresponding maxillary (**b**) and mandibular axial sections (**c**) depicting multiple impacted, supernumerary, underdeveloped teeth; one in the maxilla (*solid arrow*) and two in the mandible (*dashed arrows*). There is no evidence of any effect on the neighboring teeth and thus periodic radiographic assessment was considered to be the most management

neurovascular bundle. CBCT imaging is therefore most often limited to patients where the relationship of the third molar to the IAC is difficult to determine. For impacted maxillary canines the use of CBCT may not provide significant treatment advantages in all cases compared to conventional radiography (Alqerban et al. 2014a); however, it enhances diagnostic assessment (Guerrero et al. 2011; Jung et al. 2012), increases planning confidence, and reduces treatment duration particularly for patients presenting with moderate to severe maxillary canine impaction (Algerban et al. 2011, 2014b; Haney et al. 2010).

References

Açikgöz A, Açikgöz G, Tunga U, Otan F (2006) Characteristics and prevalence of non syndrome multiple supernumerary teeth: a retrospective study. Dentomaxillofac Radiol 35:185–190

Algerban A, Jacobs R, Fieuws S, Willems G (2011) Comparison of two cone beam computed tomographic systems versus panoramic imaging for localization of impacted maxillary ca-nines and detection of root resorption. Eur J Orthod 33:93–102

Alqerban A, Jacobs R, van Keirsbilck PJ, Aly M, Swinnen S, Fieuws S, Willems G (2014a) The effect of using CBCT in the diagnosis of canine impaction and its impact on the ortho-dontic treatment outcome. J Orthod Sci 3:34–40

Alqerban A, Willems G, Bernaerts C, Vangastel J, Politis C, Jacobs R (2014b) Orthodontic treatment planning for impacted maxillary canines using conventional records versus 3D CBCT. Eur J Orthod 36:698–707

American Association of Oral and Maxillofacial Surgeons (2012) Parameters of care: clinical practice guidelines for oral and maxillofacial surgery (AAAOMS ParCar 2012). J Oral Maxillofac Surg 70:61–64

Archer WH (1975) Oral and maxillofacial surgery, 5th edn. Saunders, Philadelphia, p 311

Auyong GT, Le A (2011) Dentoalveolar nerve injury. Oral Maxillofac Clin North Am 23:395–400

Becker A (2012) Orthodontic treatment of impacted teeth, 3rd edn. Wiley-Blackwell, Singapore

Bianchi SD, Roccuzzo M (1991) Primary impaction of primary teeth: a review and report of three cases. J Clin Pediatr Dent 15:165–168

Carvalho RW, Egito Vasconcelos BC (2011) Assessment of factors associated with surgical difficulty during removal of impacted lower third molars. J Oral Maxillofac Surg 69:2714–2721

Chaushu S, Becker T, Becker A (2014) Impacted central incisors: factors affecting prognosis and treatment duration. Am J Orthod Dentofacial Orthop 147:355–362

Chaushu S, Kaczor-Urbanowicz K, Zadurska M, Becker A (2015) Predisposing factors for severe incisor root resorption associated with impacted maxillary canines. Am J Orthod Dentofacial Orthop 147:52–60

Curran AE, Damm DD, Drummond JF (2002) Pathologically significant pericoronal lesions in adults: histopathologic evaluation. J Oral Maxillofac Surg 60:613–617

Dalessandri D, Migliorati M, Rubiano R, Visconti L, Contardo L, Di Lenarda R, Martin C (2013) Reliability of a novel CBCT-based 3D classification system for maxillary canine impactions in orthodontics: the KPG index. Sci World J 2013:921234

Dalessandri D, Migliorati M, Visconti L, Contardo L, Kau CH, Martin C (2014) KPG index versus OPG measurements: a comparison between 3D and 2D methods in predicting treatment duration and difficulty level for patients with impacted maxillary canines. Biomed Res Int 2014:537620

Doğramaci EJ, Sherriff M, Rossi-Fedele G, McDonald F (2015) Location and severity of root resorption related to impacted maxillary canines: a cone beam computed tomography (CBCT) evaluation. Aust Orthod J 31:49–58

Ericson S, Kurol J (2000) Incisor resorptions due to ectopic maxillary canines imaged by computerized tomography: a comparative study in extracted teeth. Angle. Orthodontist 70:276–283

Ericson S, Bjerklin K, Falahat B (2002) Does the canine dental follicle cause resorption of permanent incisor roots? A computed tomographic study of erupting maxillary canines. Angle Orthod 72:95–104

Flygare L, Ohman A (2008) Preoperative imaging procedures for lower wisdom teeth removal. Clin Oral Investig 12:291–302

Ghaeminia H, Gerlach NL, Hoppenreijs TJ, Kicken M, Dings JP, Borstlap WA, de Haan T, Bergé SJ, Meijer GJ, Maal TJ (2015) Clinical relevance of cone beam computed tomography in mandibular third molar removal: a multicentre, randomised, controlled trial. J Craniomaxillofac Surg 43(10):2158–2167. pii: S1010-5182(15)00340-6

Guerrero ME, Shahbazian M, Elsiena Bekkering G, Nackaerts O, Jacobs R, Horner K (2011) The diagnostic efficacy of cone beam CT for impacted teeth and associated features: a systematic review. J Oral Rehabil 38:208–216

Guerrero ME, Botetano R, Beltran J, Horner K, Jacobs R (2014) Can preoperative imaging help to predict postoperative outcome after wisdom tooth removal? A randomized controlled trial using panoramic radiography versus cone-beam CT. Clin Oral Investig 18:335–342

Haney E, Gansky SA, Lee JS, Johnson E, Maki K, Miller AJ, Huang JC (2010) Comparative analysis of traditional radiographs and cone-beam computed tomography volumetric images in the diagnosis and treatment planning of maxillary impacted canines. Am J Orthod Dentofacial Orthop 137:590–597

Haug RH, Perrott DH, Gonzalez ML, Talwar RM (2005) The American Association of Oral and Maxillofacial Surgeons age-related third molar study. J Oral Maxillofac Surg 63:1106–1114

Huang GJ, Rue TC (2006) Third-molar extraction as a risk factor for temporomandibular disorder. J Am Dent Assoc 137:1547–1554

Huang GJ, Cunha-Cruz J, Rothen M, Spiekerman C, Drangsholt M, Anderson L, Roset GA (2014) A prospective study of clinical outcomes related to third molar removal or retention. Am J Public Health 104:728–234

Jung YH, Liang H, Benson BW, Flint DJ, Cho BH (2012) The assessment of impacted maxillary canine position with panoramic radiography and cone beam CT. Dentomaxillofac Radiol 41:356–360

Kau CH, Pan P, Gallerano RL, English JD (2009) A novel 3D classification system for canine impactions—the KPG index. Int J Med Robot 5:291–296

Komerik N, Muglali M, Tas B, Selcuk U (2014) Difficulty of impacted mandibular third molar tooth removal: predictive ability of senior surgeons and residents. J Oral Maxillofac Surg 72:1062.e1–1062.e6

Lai CS, Bornstein MM, Mock L, Heuberger BM, Dietrich T, Katsaros C (2013) Impacted maxillary canines and root resorptions of neighbouring teeth: a radiographic analysis using cone-beam computed tomography. Eur J Orthod 35:529–538

Lim AA, Wong CW, Allen JC Jr (2012) Maxillary third molar: patterns of impaction and their relation to oroantral perforation. J Oral Maxillofac Surg 70:1035–1039

Liu DG, Zhang WL, Zhang ZY, YT W, Ma XC (2008) Localization of impacted maxillary ca-nines and observation of adjacent incisor resorption with cone-beam computed tomography. Oral Surg Oral Med Oral Pathol Oral Radiol Endod 105:91–98

Maegawa H, Sano K, Kitagawa Y, Ogasawara T, Miyauchi K, Sekine J, Inokuchi T (2003) Pre-operative assessment of the relationship between the mandibular third molar and the mandibular canal by axial computed tomography with coronal and sagittal reconstruction. Oral Surg Oral Med Oral Pathol Oral Radiol Endod 96:639–646

Matzen LH, Wenzel A (2015) Efficacy of CBCT for assessment of impacted mandibular third molars: a review—based on a hierarchical model of evidence. Dentomaxillofac Radiol 44:20140189

McNamara JA, Brudon WL (2001) Dentitional development. In: Orthodontics and dentofacial orthopedics. Needham Press, Ann Arbor, pp 31–8

Mupparapu M (2002) Patterns of intraosseous transmigration and ectopic eruption of mandibular canines: review of literature and report of nine additional cases. Dentomaxillofac Radiol 31:355–360

Neves FS, Souza TC, Almeida SM, Haiter-Neto F, Freitas DQ, Bóscolo FN (2012) Correlation of panoramic radiography and cone beam CT findings in the assessment of the relationship between impacted mandibular third molars and the mandibular canal. Dentomaxillofac Radiol 41:553–557

Nishida I, Oda M, Tanaka T, Kito S, Seta Y, Yada N, Fujita Y, Saeki K, Morikawa K, Matsumoto-Takeda S, Wakasugi-Sato N, Habu M, Kodama M, Miyamoto I, Kokuryo S, Nishimura S, Matsuo K, Tominaga K, Yoshioka I, Maki K, Morimoto Y (2015) Detection and imaging characteristics of the gubernacular tract in children on cone beam and multidetector computed tomography. Oral Surg Oral Med Oral Pathol Oral Radiol 120:e109–e117

Nortjé CJ, Farman AG, Grotepass FW (1977) Variations in the normal anatomy of the inferior dental (mandibular) canal: a retrospective study of panoramic radiographs from 3612 routine dental patients. Br J Oral Surg 15:55–63

Oda M, Miyamoto I, Nishida I, Tanaka T, Kito S, Seta Y, Yada N, Saeki K, Matsumoto-Takeda S, Wakasugi-Sato N, Habu M, Kodama M, Kokuryo S, Nishimura S, Matsuo K, Tominaga K, Yoshioka I, Maki K, Morimoto Y (2016) A spatial association between odontomas and the gubernaculum tracts. Oral Surg Oral Med Oral Pathol Oral Radiol 121:91–95

Pederson GW (1988) Surgical removal of tooth. In: Pederson GW (ed) Oral surgery. WB Saunders, Philadelphia

Pell GJ, Gregory BT (1933) Impacted mandibular third molars: classification and modified techniques for removal. Dent Dig 39:330–338

Power M, Short BE (1993) An investigation into the response of palatally displaced canines to the removal of deciduous canines and an assessment of factors contributing to favourable eruption. Br J Orthod 20:215–223

Rajab LD, Hamdan MA (2002) Supernumerary teeth: review of the literature and a survey of 152 cases. Int J Paediatr Dent 12:244–254

Rood JP, Shehab BA (1990) The radiological prediction of inferior alveolar nerve injury during third molar surgery. Br J Oral Maxillofac Surg 28:20–25

da Silva Santos LM, Bastos LC, Oliveira-Santos C, da Silva SJ, Neves FS, Campos PS (2014) Cone-beam computed tomography findings of impacted upper canines. Imaging Sci Dent 44:287–292

Stivaros N, Mandall NA (2000) Radiographic factors affecting the management of impacted upper permanent canines. J Orthod 27:169–173

Ventä I (2012) How often do asymptomatic, disease-free third molars need to be removed? J Oral Maxillofac Surg 70:S41–S47

Winter GB (1926) Principles of exodontia as applied to the impacted third molar. American Medical Books, St Louis

Wriedt S, Jaklin J, Al-Nawas B, Wehrbein H (2012) Impacted upper canines: examination and treatment proposal based on 3D versus 2D diagnosis. J Orofac Orthop 73:28–40

CBCT Imaging of Sinonasal Disease

30

Kivanç Kamburoğlu, Dirk Schulze, Sema Murat, Saulo L. Sousa Melo, Zhimin Li, Michael M. Bornstein, Christos Angelopoulos, and William C. Scarfe

Contents

K. Kamburoğlu, D.D.S., M.Sc., Ph.D.
Faculty of Dentistry, Department of Oral and Maxillofacial Radiology, Ankara University, Ankara, Turkey
e-mail: dtkivo@yahoo.com

D. Schulze, Priv. Doz. Dr. Med. Dent.
Digitales Diagnostik Zentrum, Freiburg, Germany
e-mail: dirk.schulze@ghostdoc.de

S. Murat, D.D.S., M.S., Ph.D.
Faculty of Dentistry, Department of Prosthodontics, Ankara University, Ankara, Turkey
e-mail: semamurat47@yahoo.com.tr

S.L.S. Melo, M.Sc., Ph.D. (✉)
Department of Oral Pathology, Radiology and Medicine, University of Iowa College of Dentistry, Iowa City, IA, USA
e-mail: saulo-sousamelo@uiowa.edu

Z. Li, D.D.S., Ph.D.
Department of Oral Radiology, School and Hospital of Stomatology, Jilin University, Chang Chun, Jilin Province, China
e-mail: zhimin@jlu.edu.cn

M.M. Bornstein, Prof. Dr. Med. Dent.
Oral and Maxillofacial Radiology, Applied Oral Sciences, Faculty of Dentistry, The University of Hong Kong, Prince Philip Dental Hospital, Hong Kong SAR, China
e-mail: bornst@hku.hk

C. Angelopoulos, D.D.S., M.S.
Aristotle University of Thessaloniki, Thessaloniki, Greece

Columbia University, College of Dental Medicine, New York City, NY, USA
e-mail: angelopoulosc@gmail.com

W.C. Scarfe, B.D.S., F.R.AC.D.S., M.S.
Division of Radiology and Imaging Science, Department of Surgical/Hospital Dentistry, School of Dentistry, University of Louisville, Louisville, KY, USA
e-mail: William.scarfe@louisville.edu

W.C. Scarfe, C. Angelopoulos (eds.), *Maxillofacial Cone Beam Computed Tomography*,
https://doi.org/10.1007/978-3-319-62061-9_30

30.1 Introduction

In dental and maxillofacial CBCT imaging of the mid-facial region, it is highly likely that clinicians will observe various radiologic findings involving the paranasal sinuses. Dentists using CBCT are responsible for interpreting not only the radiologic findings needed for a specific dental task (e.g., implant treatment planning, detect periapical pathologies of posterior teeth in the maxilla) but also the structures, anatomic variability, and common diseases associated with the maxillary sinus (Carter et al. 2008; American Dental Association Council on Scientific Affairs 2012; Vogiatzi et al. 2014). Recognition of specific radiologic patterns indicative of sinonasal pathology is therefore important and certainly within the area of responsibility of dentists who use CBCT imaging.

CBCT has been proposed, by some, to replace multi-slice computerized tomography (MSCT) for routine, general diagnostic imaging of acute and chronic sinus inflammatory disease (Al Abduwani et al. 2016). CBCT image assessment of the nose and paranasal sinuses offers potential advantages over MSCT such as easier image acquisition, greater image accuracy facilitated by high quality bony definition, multiplanar reconstruction, lower effective radiation dose, faster scan time, and greater cost-effectiveness. However, CBCT has specific disadvantages in the detection of soft tissue features due to limited contrast resolution and the presence of beam-hardening artifacts caused by restorative materials and implants (Kamburoglu et al. 2017; Bornstein et al. 2012; Pazera et al. 2011). Despite these limitations, CBCT has been shown to be useful in the evaluation of inflammatory disease in the vast majority of patients without missing clinically relevant findings (Fakhran et al. 2012). However, CBCT imaging is inappropriate for imaging of soft tissue disease extension (e.g., immunocompromised patients, suspected invasive fungal rhinosinusitis, intracranial or periorbital complications of sinusitis) or for those with symptoms not directly attributable to the sinuses (Fakhran et al. 2012).

30.2 Overview of Sinus Disease

While CBCT studies investigating the frequency of healthy and diseased maxillary sinuses are limited, most report a similar disease prevalence (range, 46.8–56.3%). Higher prevalence rates (up to 82%) have been reported on specific cohorts whereas lower disease prevalence has been reported in edentulous (34.9%) and orthodontic patient samples (14.3%) (Vogiatzi et al. 2014). This may reflect the fact that there is currently no threshold value of mucosal thickness considered to be pathologic.

30.2.1 Inflammatory

30.2.1.1 Mucositis

Local or regional soft tissue thickening due to inflammation is the most commonly reported sinus pathology, usually with a higher prevalence in males. The normal respiratory lining of the paranasal sinuses is extremely thin and not discernible on CBCT images. The reported prevalence of mucositis is variable due mostly to differences in criteria defining a radiographic diagnostic threshold of the dimensions of the sinus mucosa indicative of pathologic changes (especially the maxillary sinus). Radiographically, mucositis presents as a uniformly thickened or slightly irregular soft tissue swelling adjacent the walls or floor of the sinus (Fig. 30.1). It may be present generalized throughout the sinus or localized to a particular wall. Mucositis is most often clinically asymptomatic unless it involves the ostia. Identification on CBCT images does not usually require further investigation.

Periapical Mucositis

Inflammation of the epithelium on the floor of the maxillary sinus adjacent and secondary to periapical inflammation may lead to localized mucosal thickening in the alveolar recess of the maxillary sinus due to collateral edema (Fig. 30.2). A recent study showed that the Schneiderian membrane in the vicinity of roots with apical lesions tends to be significantly thicker when compared with the roots of teeth without apical pathoses (Bornstein et al. 2012).

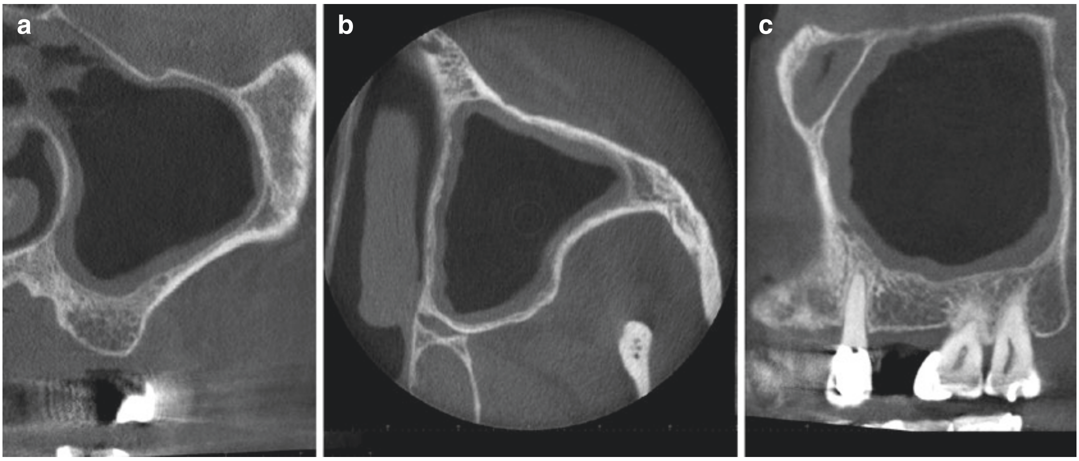

Fig. 30.1 Thin section coronal (**a**), axial (**b**), and sagittal (**c**) CBCT images showing generalized peripheral thickening of the mucosal lining in the left maxillary sinus (mucositis); such a finding is often found in allergic rhinosinusitis

This may present as variable localized mucosal thickening either in isolation or associated with a frank periapical osteolytic lesion (Fig. 30.3). Loss of continuity of the cortical bone adjacent to a periapical osteolytic process together with a thickened mucosa may be due to extension of apical disease or as a result of voxel averaging artifact. Nevertheless, the pulpal vitality status of the associated restored tooth should be investigated if localized mucosal thickening of the floor of the maxillary sinus is observed adjacent the periapical region of the posterior maxillary dentition. If the tooth is endodontically treated, then the appearance should be compared to previous radiographic presentations and, based on clinical presentation (i.e., patient signs and symptoms), retreatment considered (Fig. 30.3).

30.2.1.2 Rhinosinusitis

Various terms have been used to describe inflammation of the epithelium of the nasal and paranasal sinuses. Isolated inflammation of the paranasal sinuses and nasal mucosa have been referred to as *sinusitis* or *rhinitis* (Fig. 30.4), respectively. However, as both often occur concomitantly, *Rhinosinusitis* is now considered the correct terminology (Fokkens et al. 2012). Rhinosinusitis is classified according to the clinical length of presentation (acute or chronic) and not according to radiologic findings.

Rhinosinusitis (RS) is clinically defined by both clinical and either endoscopic and/or computed tomographic (CT) radiologic changes (Fokkens et al. 2012):

- **Clinical**. Inflammation of the nose and the paranasal sinuses characterized by two or more symptoms, one of which should be either nasal blockage/obstruction/congestion or nasal discharge (anterior/posterior nasal drip): ±facial pain/pressure, ±reduction or loss of smell
- **And either**
  - *Endoscopic*. Endoscopic signs of nasal polyps, and/or mucopurulent discharge primarily from middle meatus and/or edema/mucosal obstruction primarily in middle meatus, or
  - *CT*. CT observable mucosal changes within the ostiomeatal complex and/or sinuses.

Acute Rhinosinusitis

Acute rhinosinusitis (ARS) is an inflammatory condition that may be diagnosed clinically on the basis of acute symptoms of nasal blockage, obstruction, congestion with or without facial pain, or reduced smell. The etiologic agent is usually a bacterium and secondary to edematous mucosal changes as a result of a viral respiratory infection. Rhinitic swelling of the nasal mucosa can obstruct the different physiologic

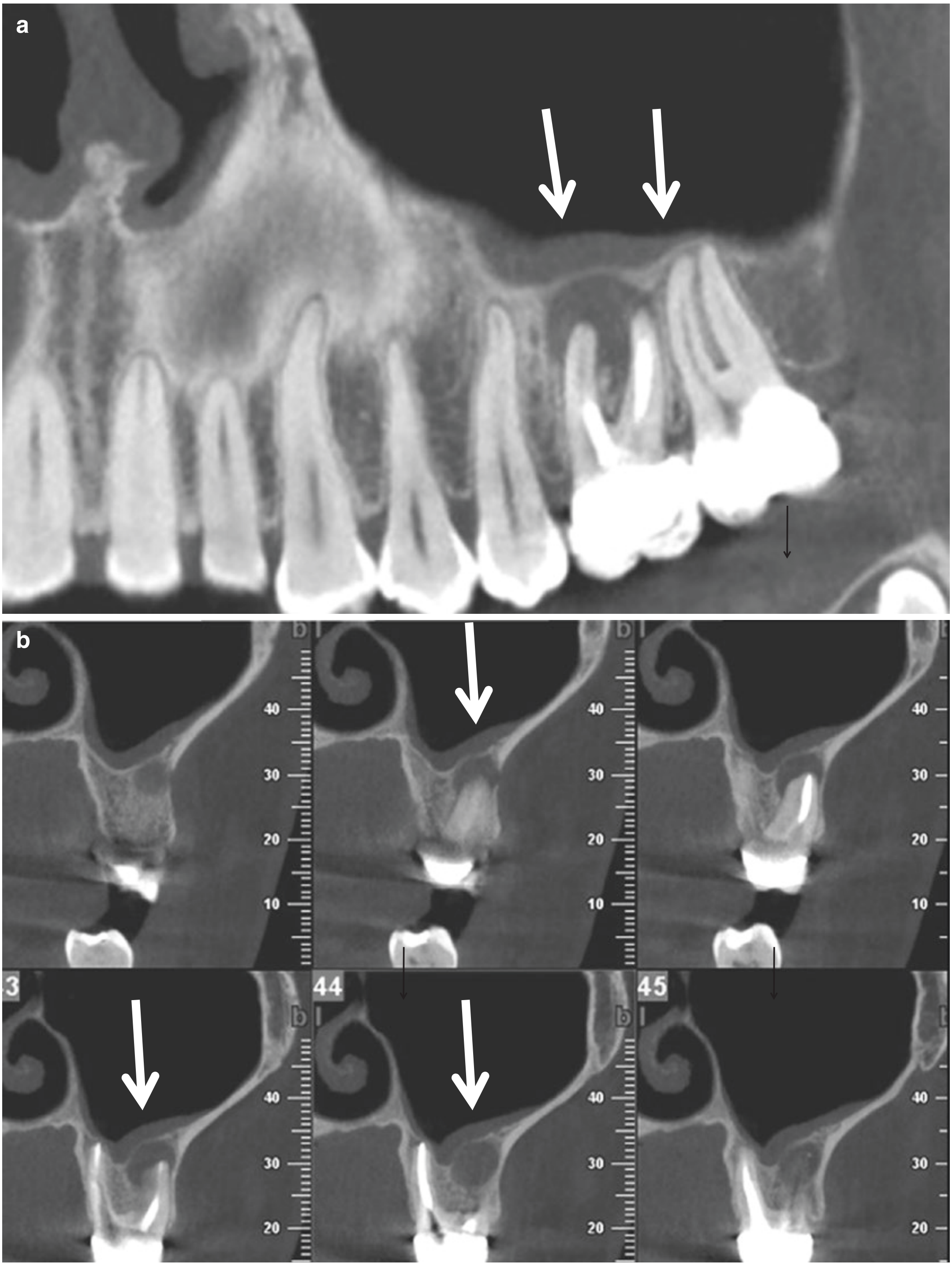

Fig. 30.2 Reformatted panoramic (**a**) and serial cross-sectional (**b**) CBCT images of the left maxillary posterior showing a root canal filled first molar. The cross-sectional images demonstrate a localized elevation of the mucosal floor of the maxillary sinus adjacent to the periapical hypodensity associated with the mesiobuccal root consistent with collateral edema

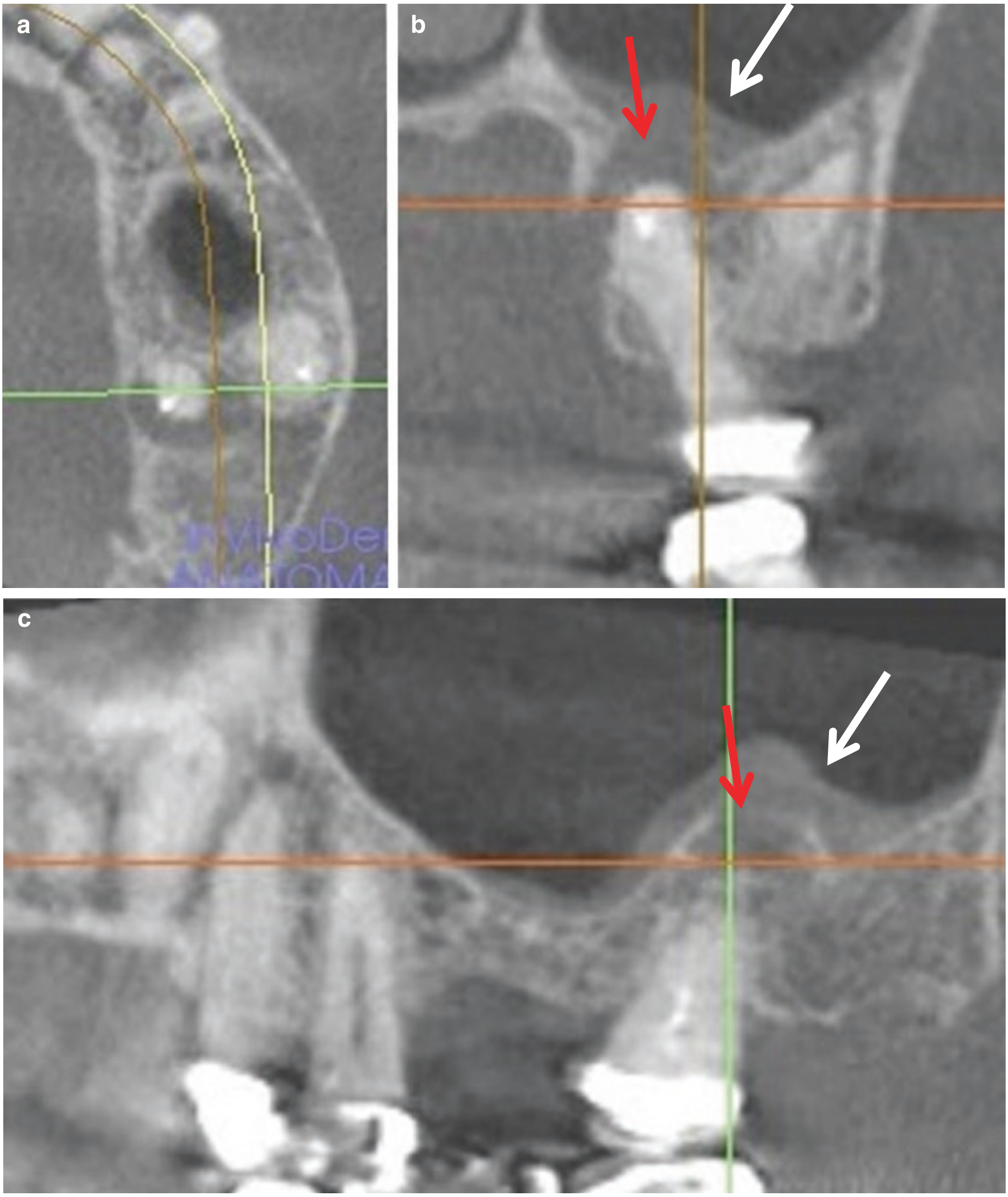

Fig. 30.3 Axial (**a**), cross-sectional (**b**), and sagittal (**c**) CBCT images of the left maxillary posterior showing a root canal filled first molar. Similar to Fig. 30.2. The images demonstrate a localized elevation of the mucosal floor of the maxillary sinus adjacent to the periapical hypodensity associated with the palatal root consistent with collateral edema. In this case there is loss of integrity of the cortical separation between the area of chronic apical periodontitis and collateral edema

apertures and occlude sinus drainage. This causes mucus retention and consecutively inhibits its ciliary function of the overlying respiratory mucosa.

The most common CBCT radiologic findings of ARS are related to the patterns of opacification demonstrated within the sinus or nasal lumen. In other words, the degree of “fullness” or the extent of presence of inflammatory tissue in the nasal cavity or paranasal sinuses; these may occur either separately or in combination.

- **Changes in the paranasal sinuses mucosa**. In the early stages of ARS, the only visible changes are thickening of the nasal and paranasal sinus mucosa. This may evolve into a nonuniform layer of soft in density tissue which is mainly inflammatory tissue often combined with inflammatory exudates, pus, etc. This may result in occupying the entire sinus cavity (Fig. 30.5d).

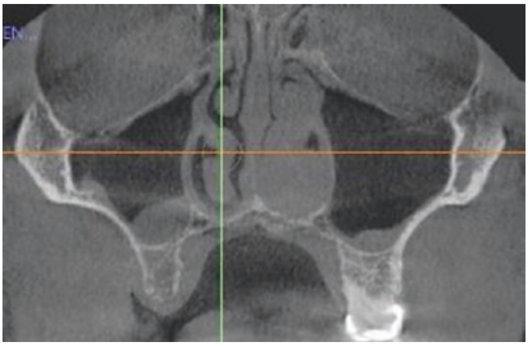

Fig. 30.4 CBCT coronal section of the nasal cavity and maxillary sinus showing marked thickening of the nasal mucosa in the left nasal cavity. This was accompanied with significant blockage of the respective nasal passage way and discharge. All findings were consistent with rhinosinusitis

There has been no consistent measurement defined to provide a distinction between normal and pathologic mucosa in CBCT studies reporting on the severity of mucosal thickening in the maxillary sinus. Smith et al. (2010) reported any mucosal thickening as pathologic, whereas others define disease as a thickening of greater than 1 mm (Gracco et al. 2012; Phothikhun et al. 2012). Most authors provide a value of 2 mm or greater (Janner et al. 2011; Lu et al. 2012; Maillet et al. 2011; Pazera et al. 2011; Bornstein et al. 2012; de Souza Nunes et al. 2013; Schneider et al. 2013; Yoo et al. 2011), and some a value of 3 mm or more (Brüllmann et al. 2012; Cha et al. 2007; Lana et al. 2012; Rege et al.

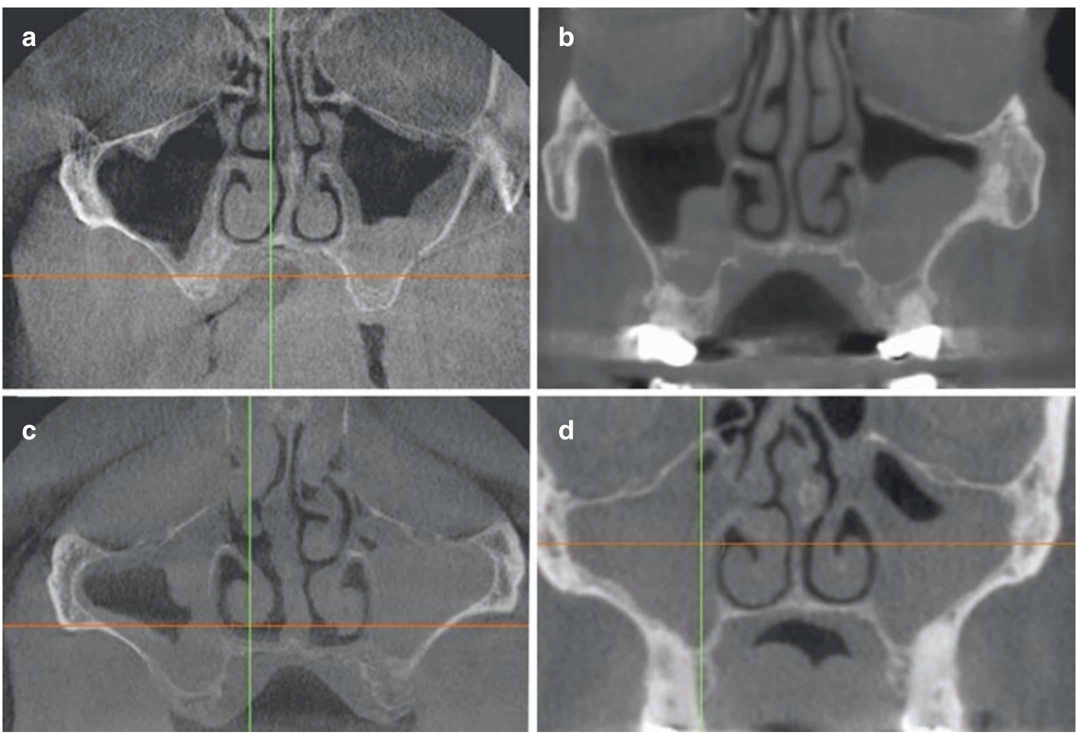

Fig. 30.5 Examples of mucosal thickening according to the criteria described by Soikkonen and Ainamo (1995). Flat (**a—**right); semispherical (**b**—right and left); mucocele-like (**c**—left, **d**—right); mixed flat and semispherical thickening (**a**—left, **c**—right); and other (**d**—left)

2012). In the medical literature, there is evidence that a mucosal thickness of up to 3 mm can be assessed as normal mucosa (Zinreich et al. 1988).

Assuming that a normal mucosal thickness varies in the range of 2–3 mm, mucosal thickening of the maxillary sinus greater than this can be described according to the following criteria (Soikkonen and Ainamo 1995) (Fig. 30.5):

– *Flat*: shallow thickening without well-defined outlines.
– *Semi-aspherical*: thickening with well-defined outlines rising in an angle of more than 30° from the floor or the walls of the sinus.
– *Mucocele-like*: complete opacification of the sinus.
– *Mixed flat and semi-aspherical thickenings*.
– *Other*. Addition mucosal thickening types or pathological findings not previous described.

- **Lumenal opacification presenting as an air-fluid level**. As long as the content of sinus is fluid, an air-fluid level can be observed. The position of the fluid depends on patient position at the time of the scan (e.g., supine vs. standing). In many cases a capillary effect can be seen peripherally adjacent the sinus walls resulting in a convex-shaped level (Fig. 30.6). If the fluid becomes thicker or denser, the detection of a fluid level gets difficult. Note that there is a high prevalence of paranasal sinus opacification in children (approximately 48%), particularly in the ethmoid (28.4%) and maxillary (27.8%) sinuses (Fig. 30.6) (Cho and Jung 2008). A fluid level may also be observed associated with traumatic injury or iatrogenic causes (Figs. 30.7 and 30.8).
- **Surface air loculation**. Multiple coalescing air bubbles associated with the superior surface of a soft tissue/fluid luminal opacification resembling "cappuccino foam" is highly

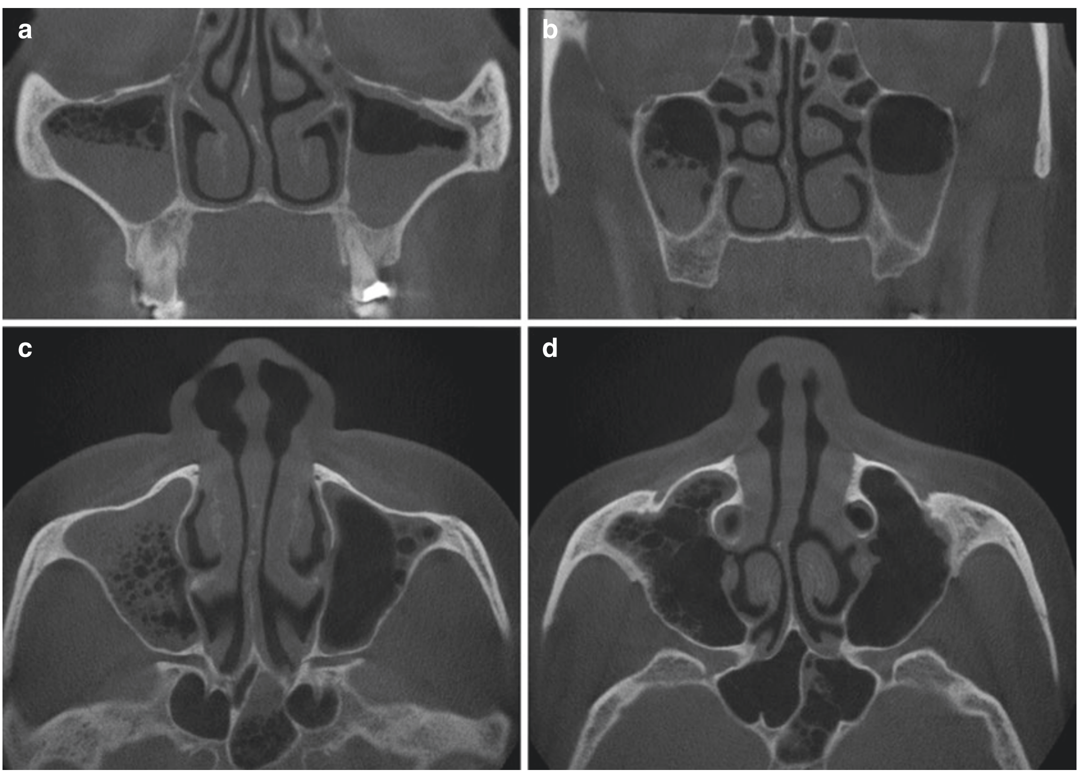

Fig. 30.6 Anterior (**a**) and posterior (**b**) coronal and inferior (**c**) and superior (**d**) axial CBCT images of a 27-year-old female showing bilateral maxillary sinus and right posterior sphenoid partial opacification consistent with ARS. The right sinus demonstrates extensive honeycomb-like surface loculation whereas the left shows a surface convexity consistent with an air-fluid level

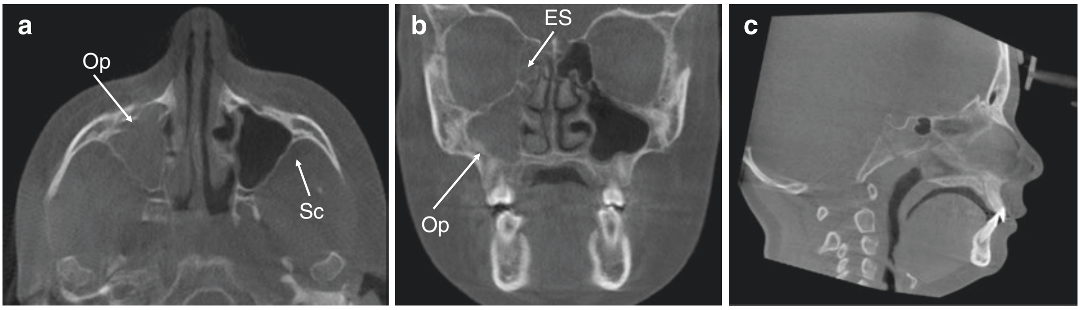

Fig. 30.7 Axial (**a**), coronal (**b**) CBCT images showing complete right unilateral opacification (Op) in the ethmoid sinus (ES) and maxillary sinus of a child (Images courtesy, Jack Fisher)

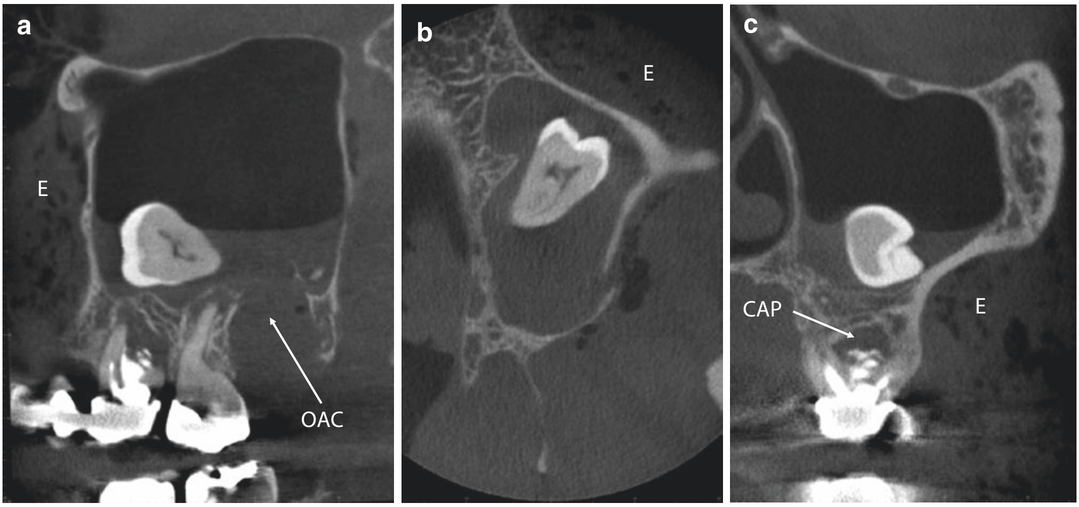

Fig. 30.8 Sagittal (**a**), axial (**b**), and coronal (**c**) CBCT images of a 64-year-old female with displacement of the upper left third molar into the left maxillary sinus with an air-fluid level. The images also show an oroantral communication (OAC) in the former third molar region, a chronic apical periodontitis (CAP) of the first molar and emphysema (E) in the surrounding soft tissues due to hemorrhage and saline rinse

suggestive of ARS (Figs. 30.6 and 30.9). The air results from the active anaerobic activity of associated bacteria.

- **Nasal mucosal changes**. ARS of nasal origin may be associated with concomitant changes of the nasal mucosa including mucosal thickening, obstruction of a nasal meatus or ostia, nasal septal deviation or nasal polyposis (Figs. 30.4 and 30.10).

Chronic Rhinosinusitis

The diagnosis of chronic rhinosinusitis (CRS) is also based on clinical criteria and occurs when symptoms have been present for more than 12 weeks. CRS can be subdivided into chronic rhinosinusitis with (CRSwNP) or without (CRSsNP) nasal polyps (Fokkens et al. 2012).

The overall prevalence of CRS is 10.9% with marked geographical variation (range, 6.9–27.1%) and is a significant healthcare problem. In the United States, up to 16% of the population is affected by CRS leading to a direct annual cost of 3.1 billion US$. Therefore, the recognition of sinusitis related changes on CBCT and appropriate referral for treatment can be an effective approach to prevent the development of a CRS (Rosenfeld 2007).

Inflammation is a result of either an allergic response or infection by bacteria, viruses, or

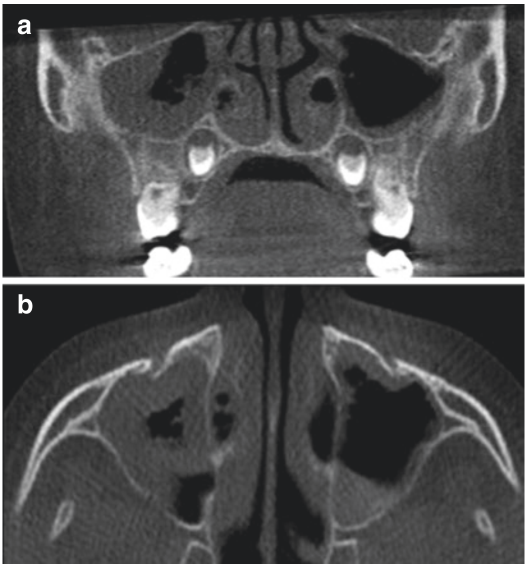

Fig. 30.9 Coronal (**a**) and axial (**b**) CBCT images of a child in the mixed dentition phase with acute bilateral sinusitis as evidenced by the honeycomb-like "cappuccino foam" appearance of air loculation on the surface of the maxillary sinus opacifications bilaterally. Note the concomitant bilateral mucosal hypertrophy of the inferior turbinates with meatal occlusion

fungi. Ciliary dysfunction, mucosal secretion retention, and mucosal thickening may lead to impeded drainage, particularly of the OMC. Other contributing factors include:

- **Smoking**. Smokers are more frequently affected by sinusitis than others. The noxes causes lesions comparable to the bacterial toxins thus inhibiting or decreasing the ciliary function. Moreover, there are more mucous glands in smokers than in the normal population (Lieu and Feinstein 2000; Saetta et al. 2000).
- **Drug sniffing**. Drug sniffing, especially the sniffing of cocaine, can easily lead to the destruction of large parts of the septal mucosal layer. Later on typical cartilage necrosis can be observed. Moreover, the sinus mucosa can be affected, mimicking a state of sinusitis caused by the astringent effect of the drug (Villa 1999).

Several CT staging systems have been developed for CRS in an attempt to score sinus disease with reproducibility and accuracy. These include

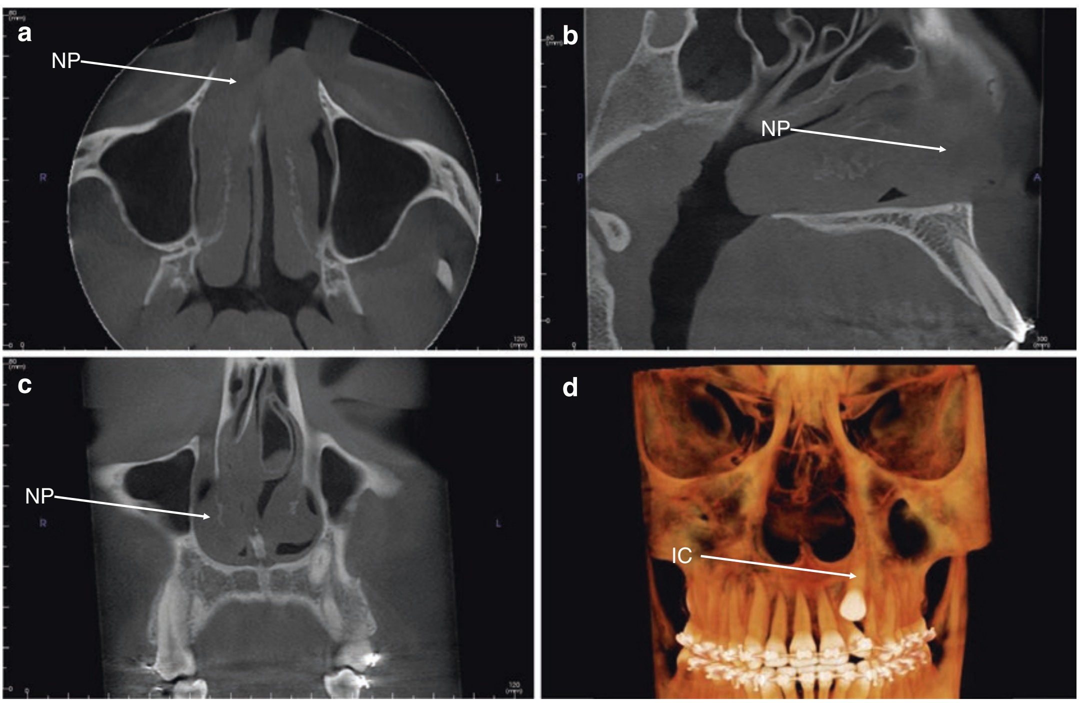

Fig. 30.10 Axial (**a**), right sagittal (**b**), coronal (**c**), and volumetric rendering (**d**) of a 16-year-old female who presented for assessment of an impacted left maxillary canine (IC). The images demonstrate localized enlargement of right inferior nasal concha that appears to be blocking the right nasal passage, suggestive of a nasal polyp (NP). The nasal septum is slightly deviated to the right and a large left concha bullosa is observed

the Harvard (Gliklich and Metson 1994), Newman (Newman et al. 1994), and Lund–Mackay (Lund and Mackay 1993) systems. However, outside of research purposes, these systems are not widely used because of difficulty in applying radiographic criteria and their lack of reproducibility.

The most common radiographic classification system is the Lund–Mackay System, recommended by the American Academy of Otolaryngology (Rhinosinusitis Task Force Committee 1997). Although imaging findings do not necessarily correlate with symptom severity (Smith and Smith 2001), this system offers an objective method for monitoring recurrent or chronic disease (Rosenfeld 2007). This scale grades the right and left sides independently, looking at the maxillary, anterior ethmoids, posterior ethmoids, sphenoid, and frontal sinuses and the OMC. Each sinus is scored a 0 (no abnormality), 1 (partial opacification), or 2 (total opacification), while the OMC is scored either a 0 or 2 (for presence or absence of disease). Scores range from 0 to 24.

The following radiographic features, which may occur separately or in combination, are associated with CRS:

- **Mucosal**
  - *Polypoidal mucoperiosteal thickenings.* The typical sign of a chronic sinusitis is "pillow-like" mucosal swellings (Fig. 30.11). These pillows are formed by a mucosal thickening which is bordered by scars. The scars are caused by earlier inflammations. The pillows can be detected in every sinus and attached to every wall. Depending on location, the pillows may appear "cyst-like" (Fig. 30.12). Differentiation between this entity and true cysts is not possible on CBCT images because of limited contrast resolution.

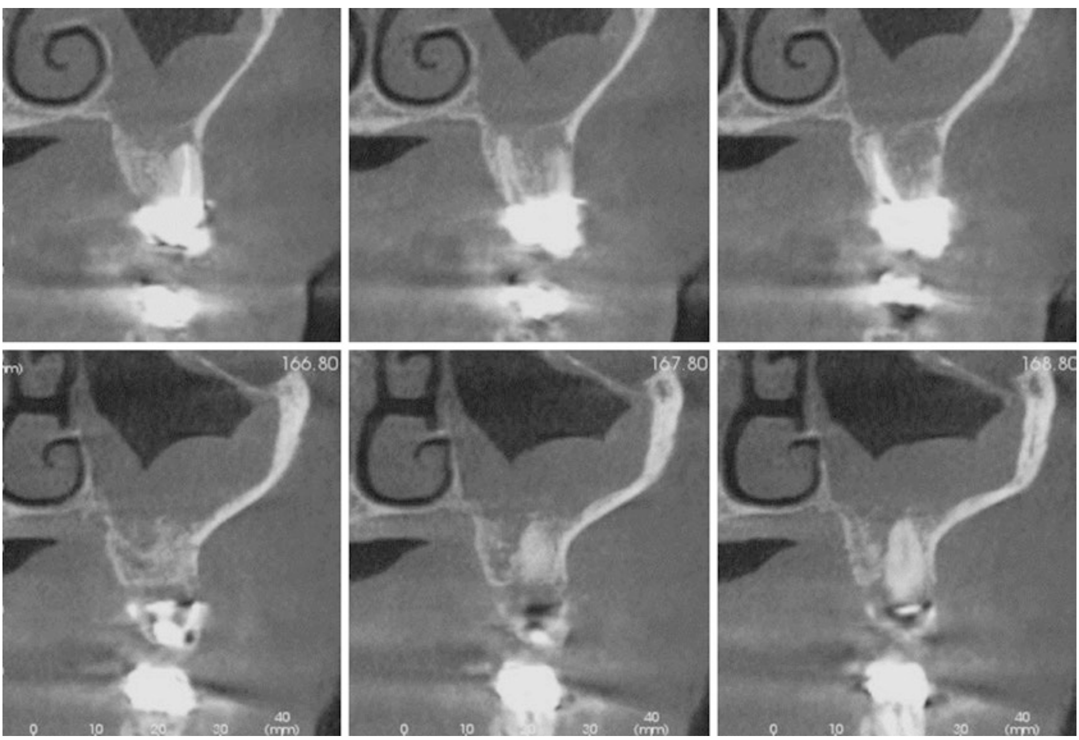

Fig. 30.11 Cross-sectional images of the left maxilla showing the characteristic "pillow"-like mucosal swellings on the floor and walls of the left maxillary sinus, indicating polypoidal mucosal thickening. This appearance is consistent with chronic rhinosinusitis

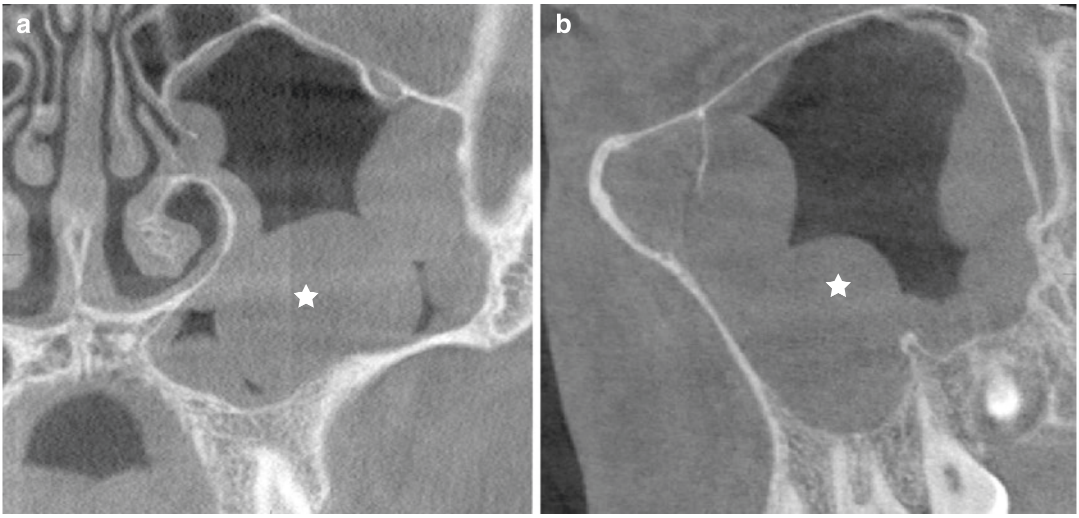

Fig. 30.12 Coronal (**a**) and sagittal (**b**) images of the left maxillary sinus showing polypoidal mucosal changes as a typical sign of chronic sinusitis with a concomitant large retention cyst arising from the floor (*filled star*)

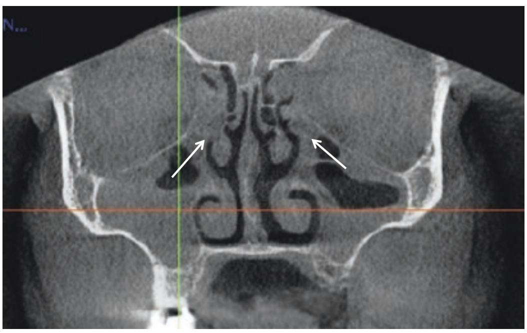

Fig. 30.13 CBCT coronal section showing partial opacification of the right and left maxillary sinuses and bilateral ostial obstruction of the maxillary sinuses (*white arrows*)

– *Sinus ostial obstruction.* Complete occlusion of the ostia by soft tissue/fluid opacification may be due to localized mucosal thickening or as a result of partial or complete luminal opacification (Fig. 30.13). Opacification on the afferent and efferent sides of the ostia is suggestive of previous or current CRS.
– *Partial or complete luminal opacification.* Filling of the lumen of a paranasal sinus presents a diagnostic dilemma because the nature of the contents is unable to be identified on CBCT images. While complete opacification is most likely due to chronic inflammatory changes such as mucosal thickening, edema, and fluid exudate, it is also possible that this represents obliteration of the lumen by neoplasia. Complete luminal opacification, particularly of the maxillary sinus, is frequently observed in children however is uncommon in adults. Therefore, in adults, this finding should be correlated with previous medical history and clinical findings (i.e., current signs and symptoms) (Schneider et al. 2013). Complete luminal opacification should be referred to an otolaryngologist for further assessment and management (Fig. 30.14).
– *Peripheral luminal soft tissue calcifications (Osteoblastic osteitis).* Calcifications associated with intra-luminal soft tissue of the paranasal sinuses are observed in a variety of diseases, including inflammatory conditions, especially fungal sinusitis, as well as benign or malignant tumors. Intra-sinus calcification is uncommon (approximately 3%) in non-fungal inflammatory sinonasal disease (Yoon et al. 1999). Two radiographic patterns are observed: central and peripheral. Central calcifications are associated with fungal sinusitis and papilloma (see later) whereas peripheral calcifications are only found in those with non-fungal sinusitis (Yoon et al. 1999). *Osteoblastic osteitis* is a rare kind of bone infection typified by a proliferative reaction of the periosteum and by exuberant bone formation as either round or "eggshell" type (Fig. 30.15) (Tovi et al. 1992).

Fig. 30.14 Coronal (**a**), sagittal (**b**), and axial (**c**) CBCT sections of the maxillary sinuses showing complete opacification of the left maxillary sinus and ostial blockage. This patient was symptomatic complaining mainly of fullness, pressure and pain

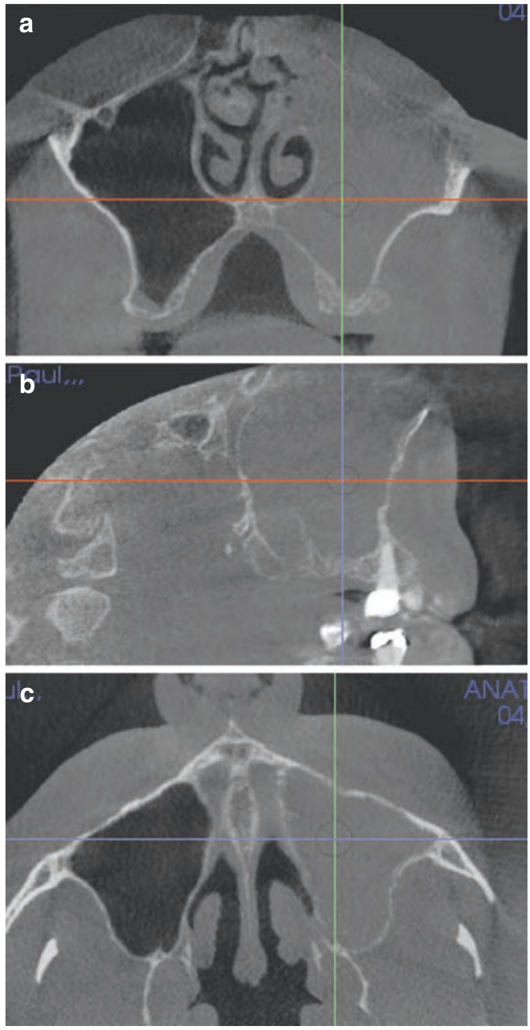

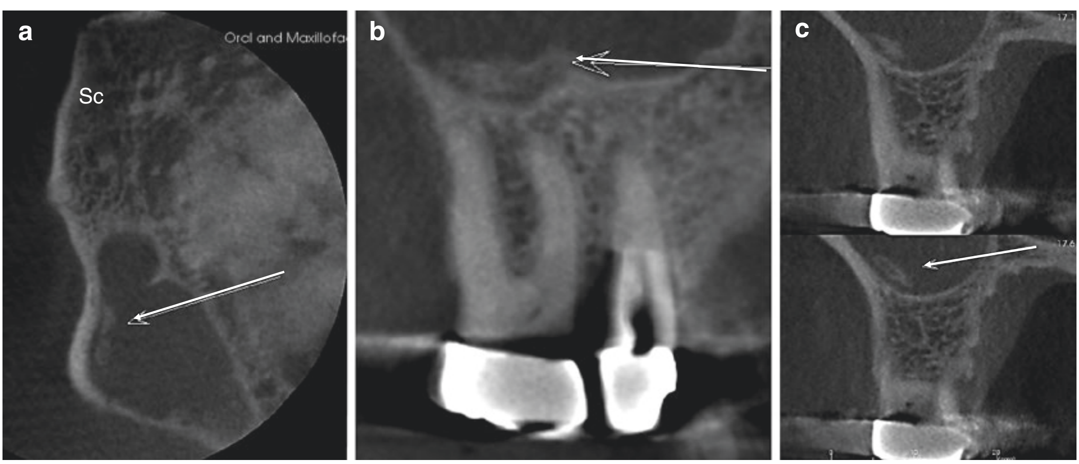

Fig. 30.15 Axial (**a**), para-sagittal (**b**), and (**c**) cross-sectional images in the region of the right maxillary first molar demonstrating “eggshell”-like calcifications typical of osteoblastic osteitis

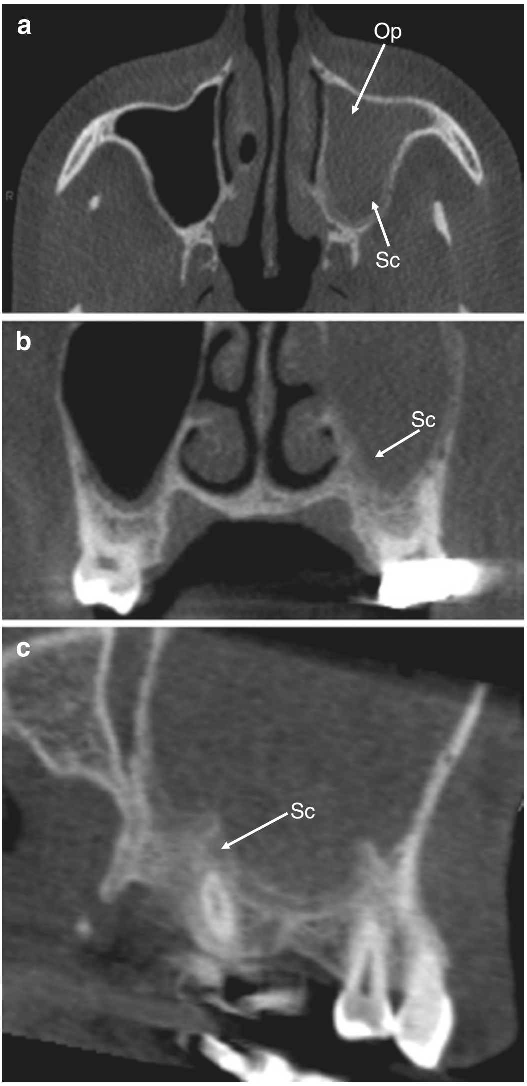

Fig. 30.16 Axial (**a**), coronal (**b**), and sagittal (**c**) CBCT images of the left maxillary sinus with complete opacification within the field of view (Op) and generalized sclerosis (Sc) of the wall and floor indicative of CRS

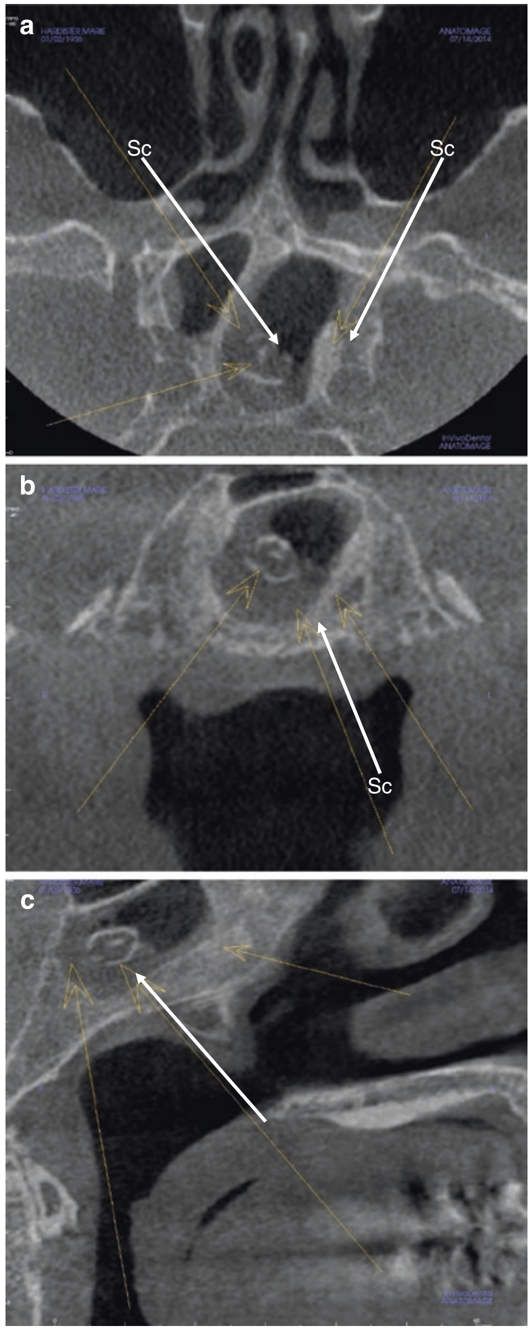

Fig. 30.17 Axial (**a**), coronal (**b**), and sagittal (**c**) CBCT images of the sphenoid sinus with partial opacification within the field of view, generalized sclerosis (Sc) and thickening of all walls and "eggshell"-like surface calcifications (osteoblastic osteolysis) consistent with chronic rhinosinusitis

- **Osseous**
  - *Sinus wall sclerosis.* CRS may illicit an osteoblastic response in the affected sinus walls and produces a typical sign: sinus wall cortical thickening. Generalized sinus wall cortical sclerosis is highly suggestive of a previous or current CRS (Figs. 30.16, 30.17, and 30.18). A similar finding has also been reported for chronic apical infections resulting in a localized thickening of the cortical bone separating the osteolytic lesion around the apex of the affected tooth from the maxillary sinus (Bornstein et al. 2012).

- *Generalized sinus wall expansion.* Long-term sinus occlusion associated with CRS may lead to remodeling of the walls of the sinus due to prolonged hydrostatic pressure.
- *Silent sinus syndrome.* Long-term, recurrent CRS can produce chronic scarification of the mucoperiosteum that can lead to an osseous retraction and a reduction in cavity size (Fig. 30.19). Deformity of the sinus walls result in changes of facial prominences, especially of the cheeks and secondary enlargement of the orbit with clinical ocular enophthalmos. CBCT radiographic features associated with this include: (1) an opacified maxillary sinus, (2) an uncinate process that abuts the infero-medial orbital wall resulting in infundibular occlusion, (3) enlargement of the middle meatus with lateral retraction of the middle turbinate, and (4) an inward retraction of sinus walls into the lumen with inferior collapse of the orbital floor and lateral wall (Illner et al. 2002; Whyte and Chapeikin 2005).

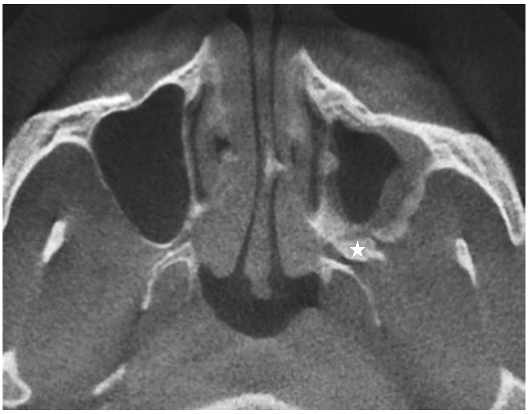

Fig. 30.18 Axial view of both maxillary sinuses showing typical signs of a long-term chronic sinusitis on the left including polypoidal mucosal thickening and sclerosis of bony walls (*filled star*)

Fungal Sinusitis

Fungal sinusitis (FS) is an uncommon but important infection of the paranasal sinuses which may demonstrate osteolytic features and rapid spread. Although FS often presents with similar imaging

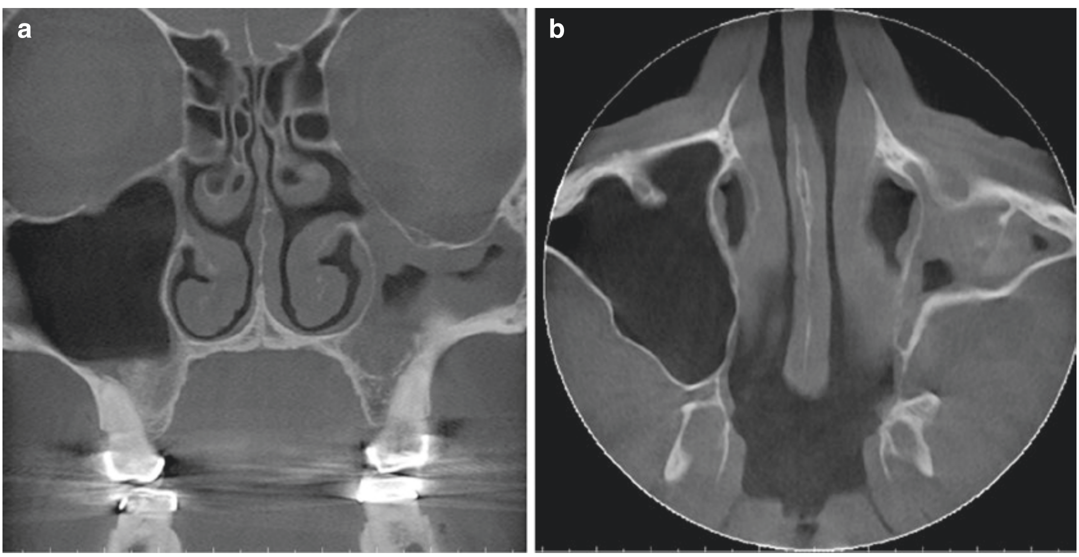

Fig. 30.19 Coronal (**a**) and axial (**b**) of a 70-year-old male with a left hypoplastic maxillary sinus with partial soft tissue opacification. Note that the floor of the left orbit appears inferior to its contralateral side and there is collapse of antero-lateral/postero-lateral walls of the left maxillary sinus inward, consistent with silent sinus syndrome

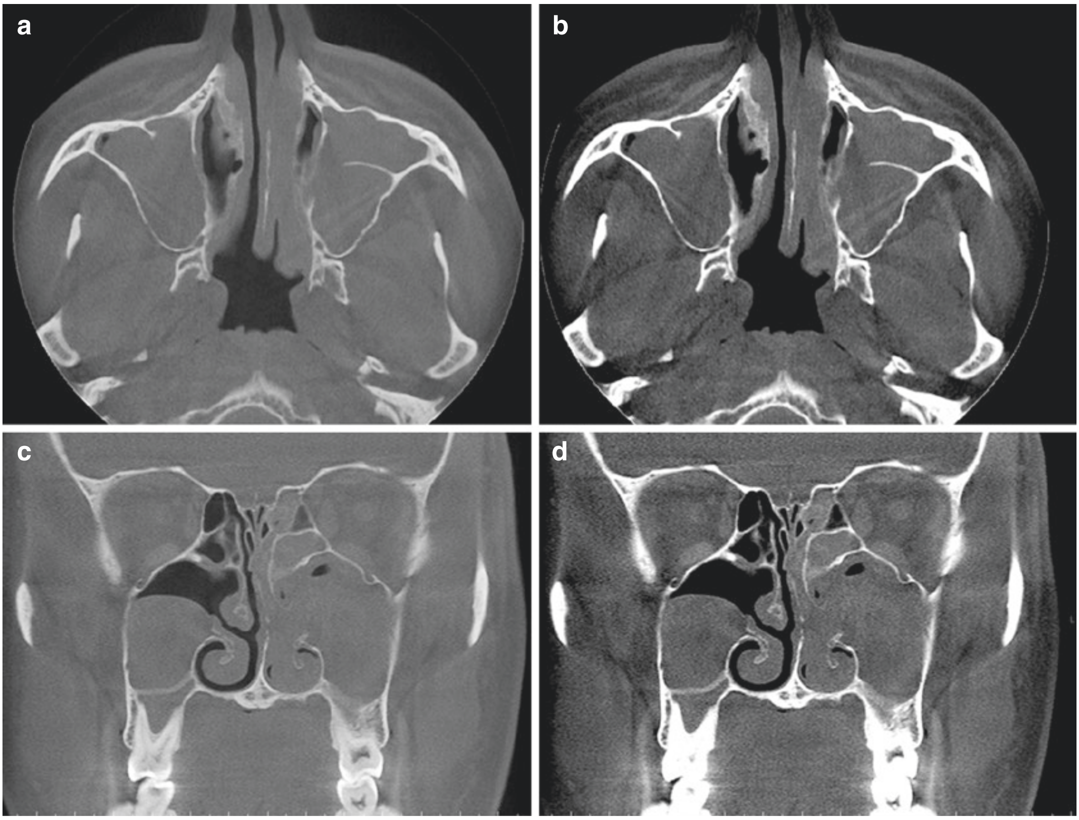

Fig. 30.20 Axial regular (**a**) and high contrast (**b**) and coronal regular (**c**) and high contrast (**d**) CBCT images of a patient with a history of long-term rhinosinusitis and nasal airway obstruction. Complete soft tissue opacification and loss of bony architecture of the medial wall of the left maxillary and ethmoid sinuses is noted. The opacification of the left maxillary sinus soft tissue on high contrast is heterogeneous

features to CRS such as mucosal thickening and partial or complete luminal soft tissue opacification, the following radiographic features, which may occur either separately or in combination, are particularly suggestive of FS (Figs. 30.20, 30.21, and 30.22):

- **Partial or complete luminal opacification**. A polypoidal mass which fills the sinus is a common finding. When complete opacification is present there may be associated disruption of the OMC and expansion into the nasal cavity.
- **Complete loss of bony architecture**. Destruction of the thinner cortical structures (e.g., medial wall of the maxillary sinus) and concomitant soft tissue opacification into an adjacent paranasal sinus is a sign of local aggression. Referral of patients to an otolaryngologist is highly recommended to differentiate determine if the imaging appearance is due to FS or neoplastic expansion (Frei et al. 2012).
- **Shape and distribution of intra-sinus calcifications**. Intra-sinus calcifications are common (range, 51–77%) in patients with FS, usually aspergillosis (Yoon et al. 1999). Although rare (approximately 3%) in non-fungal inflammatory diseases of the paranasal sinus (NFS) such as mucocele or bacterial sinusitis (Yoon et al. 1999), intra-sinus calcifications may also be present radiographically.

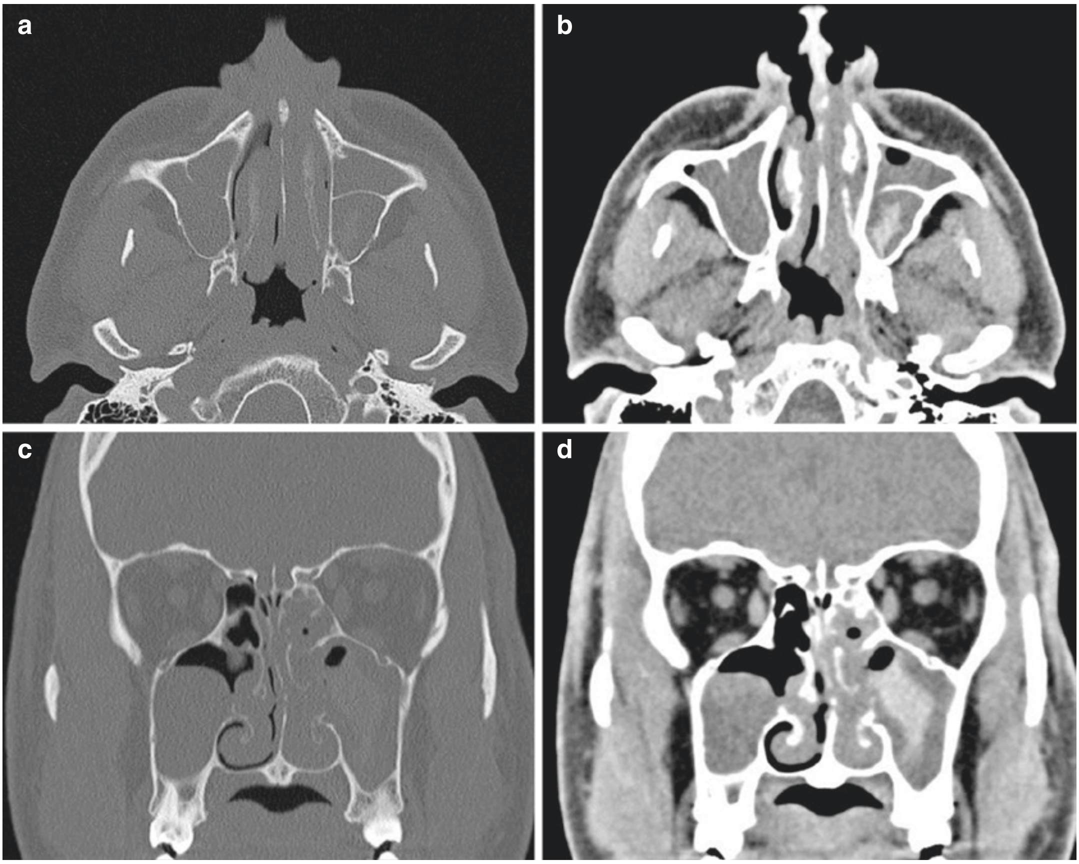

Fig. 30.21 Axial bone (**a**) and soft tissue (**b**) window and coronal bone (**c**) and soft tissue (**d**) window multidetector CT images of the same patient as in Fig. 30.20. Note the clearer depiction of the bone in the left maxillary sinus and the homogeneous stellate, central calcification within the soft tissue of the left maxillary sinus suggestive of fungal sinusitis. FESS and subsequent biopsy confirmed non aggressive fungal sinusitis

Differentiation between NFS and FS is important as the latter is an aggressive inflammatory response potentially resulting in bone destruction. In immunocompromised patients (e.g., transplant recipients, diabetics) FS can become invasive and lead to a significant morbidity and even death (Cho et al. 2015). The radiographic pattern of the calcification within soft tissue opacification on CBCT images for patients with FS differs from that observed in those with NFS and can be used as criteria for referral to an otolaryngologist for further evaluation and management (Figs. 30.20, 30.21 and 30.22). The principal radiographic features associated with FS include:

– *Centrally located calcifications.* In almost all FS patients (95%), calcifications are distributed centrally as compared to NFS patients who mostly (81%) demonstrate peripheral calcification distribution (Yoon et al. 1999). Microcalcifications or “metallic dense” spots are reported to occur in up to 1/3rd of cases (Fig. 30.20b) (Grosjean and Weber 2007).
– *Fine punctate, linear or nodular calcifications.* While nodular or linear-shaped calcifications occur both in FS and NFS, only fine punctate calcifications are seen in FS. Similarly, in NFS, only smooth-margined, round, or eggshell type calcification are found (Yoon et al. 1999).

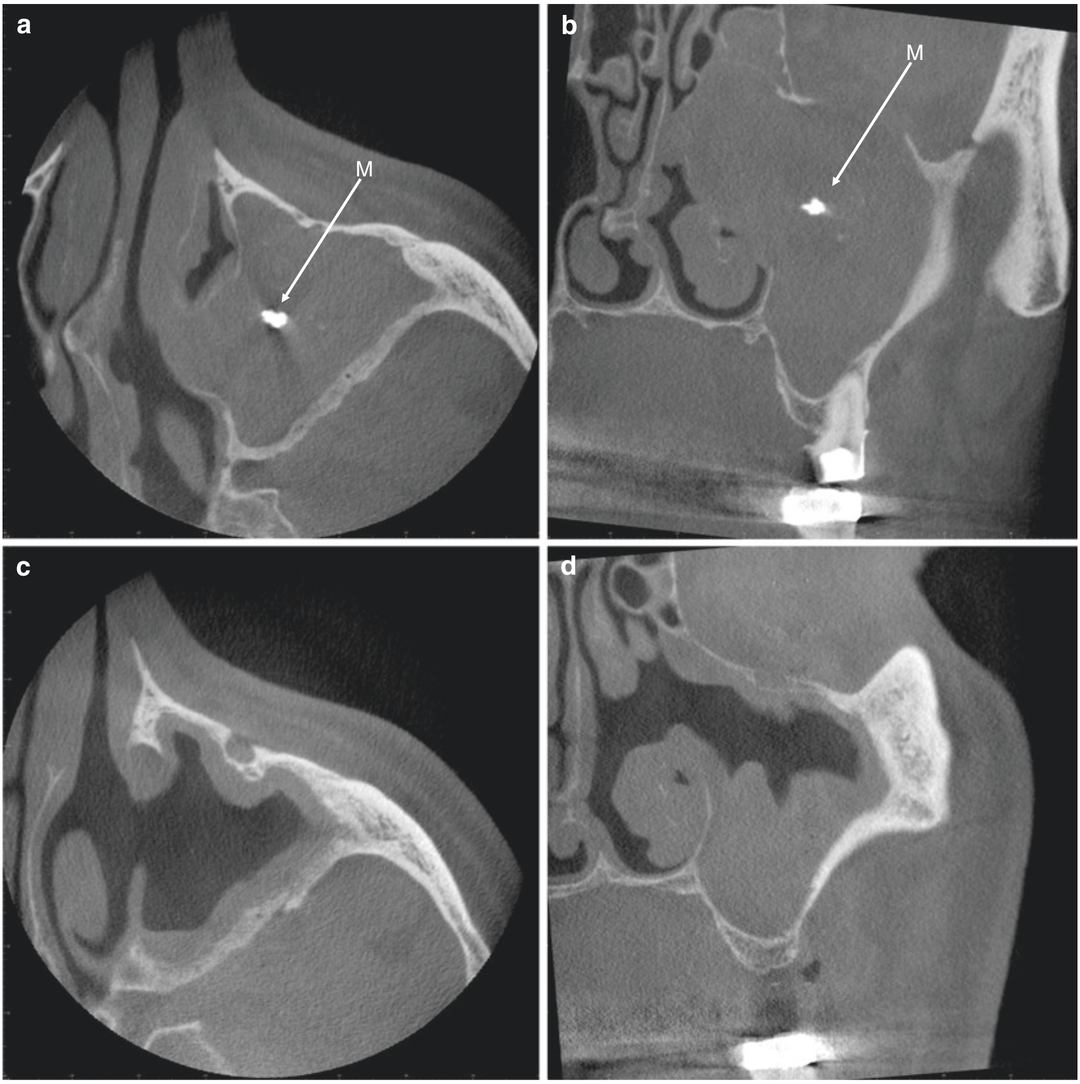

Fig. 30.22 Presurgical axial (**a**) and coronal (**b**) CBCT images of a 50-year-old male patient with complete maxillary sinus opacification, peripheral sclerosis and loss of medial wall architecture in the left maxillary sinus. Note the central singular hyper-attenuation with metallic density (M), found in about a third of all cases of aspergillosis, which was confirmed at biopsy. Postsurgical comparative axial (**c**) and coronal (**d**) CBCT images

Allergic Sinusitis

Allergic sinusitis is characterized by generalized nonspecific polypoidal mucosal thickening involving multiple paranasal sinuses as well as the mucosa of the turbinates of the nasal fossa. Luminal obstruction is common; however, the bony architecture is usually unaltered. Patient history usually indicates numerous previous bouts of seasonally related or allergen inducing symptoms. Mycoid infection (i.e., by Aspergillus, Candida, or Bipolaris species) is said to be a typical complication of allergic sinusitis—herein the term *allergic fungal sinusitis* is used (Matheny and Duncavage 2003; Mafee et al. 2006; Aribandi and Bazan 2007; Rosenfeld 2007).

Clinical Considerations of Rhinosinusitis on CBCT Images

Maxillary Sinusitis of Odontogenic Origin

Maxillary sinusitis of dental (MSDO) or odontogenic origin most likely accounts for between 10% and 12% of chronic rhinosinusitis (Brook 2006; Arias-Irimia et al. 2010) although rates as high as 25% (Melén et al. n.d.) up to 40% (Longhini et al. 2012) have been reported. However, MSDO is often overlooked by medical practitioners as a primary cause (Longhini et al. 2010) and only considered after failure of medical therapies or unsuccessful endoscopic sinus surgery (Longhini et al. 2010; Albu and Baciut 2010).

Clinically MSDO presents with unilateral dental pain and can be associated with foul smelling discharge. Radiographically, MSDO most often presents as unilateral sinus disease and demonstrates various degrees and patterns of relative soft tissue/fluid related opacification of the sinus lumen (Fig. 30.18). Bomeli et al. (2009) correlated the frequency of identifiable dental causes with degree of involvement and found that in sinuses with increasing fluid opacification an increasing proportion were attributable to dental origin. Specifically, they found that for less than 1/3rd, 1/3rd to 2/3rd, and >2/3rds sinus opacification, 17%, 53%, and 79%, respectively, had an identifiable dental source. Mucosal thickening demonstrated a similar relationship with dental sources, so that sinuses having both >2/3rd fluid opacification and moderate mucosal thickening were 86% likely to have an identifiable dental source.

While the most common cause of MSDO is periapical pathology associated with pulpal necrosis (Bomeli et al. 2009) (Figs. 30.23 and 30.24), periodontal conditions including

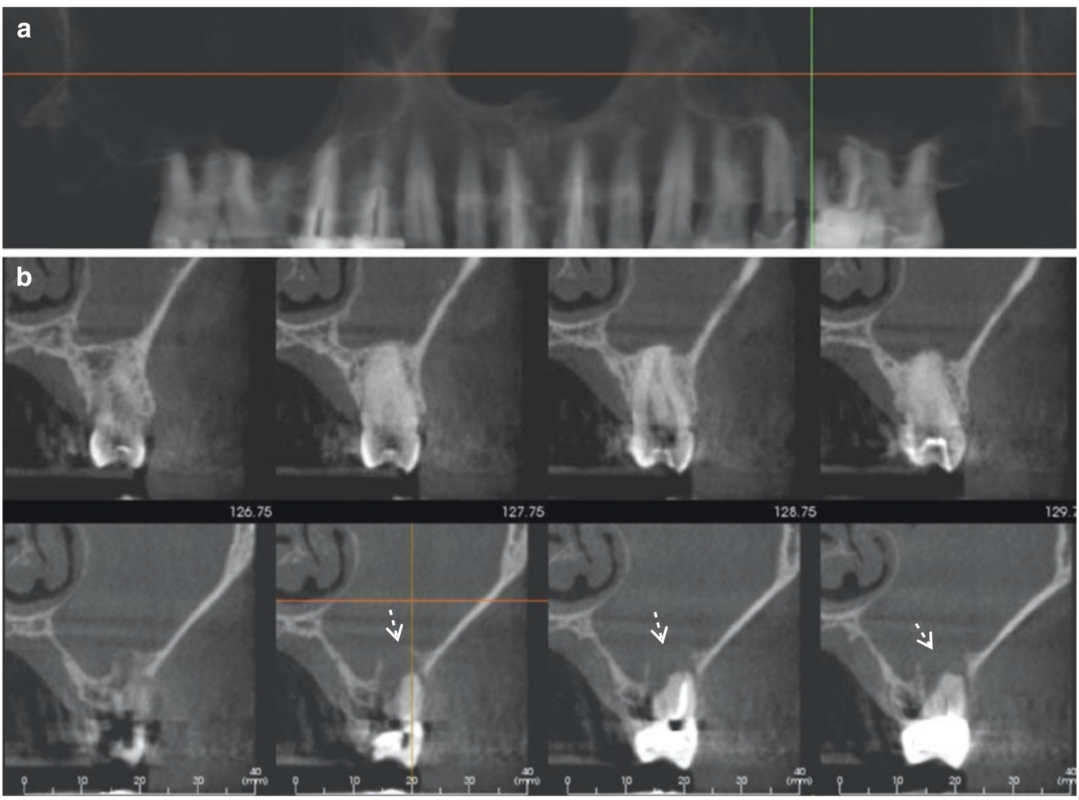

Fig. 30.23 Reformatted panoramic (**a**) and serial cross-sectional (**b**) images of the left maxillary sinus depicting a dome-shaped elevation of the sinus floor in the apical region of the root canal filled first molar associated with chronic apical periodontitis. Note the interrupted continuity of the sinus floor (*arrows*) caused by the apical inflammation. The left maxillary sinus within the FOV is fully opacified, consistent with MSDO

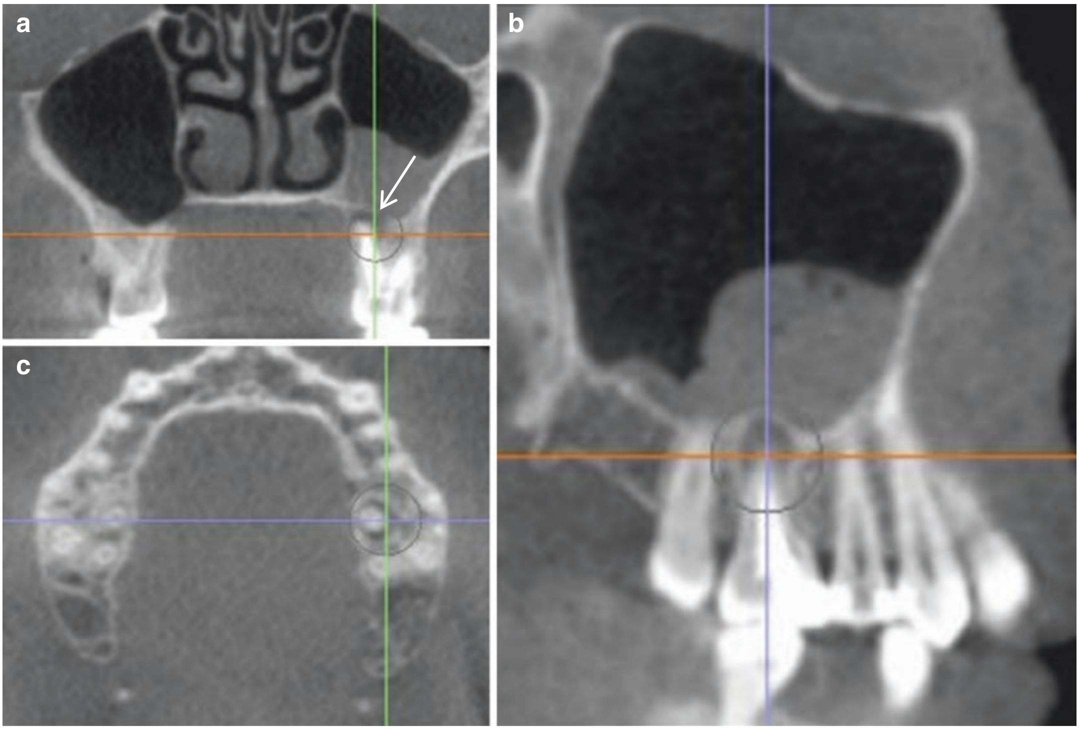

Fig. 30.24 Coronal (**a**), sagittal (**b**), and axial (**c**) CBCT images of the maxilla, showing a concentration of soft density tissue close to the apical region of tooth #14. There is a strong connection of the localized inflammation and the periapical inflammation evident on this tooth. The *arrow* in the coronal image (**a**) shows the destruction of the floor of the sinus caused by the periapical inflammation, hence that invasion point

periodontal abscesses and combined periodontic-endodontic lesions (Fig. 30.24) can contribute to up to 10% (Longhini and Ferguson 2011) to 13% (Pokorny and Tataryn 2013) of cases (Fig. 30.25).

Other less frequent dental sources of MSDO include:

- **Dental materials**. Many dental materials which can be dislocated into the maxillary sinus: root filling materials, filling materials, root canal preparation tools (drills, files), impression materials, and surgical instrument failures (Fig. 30.26). Dental implants may extend into the maxillary sinus without coverage of the apical area by the Schneiderian membrane result in an acute or chronic MS (Fig. 30.27). Furthermore, dental implants may be displaced into the sinus during surgery—mostly sinus grafting procedures—or during the healing period, so-called "migrating implants" (Fig. 30.28) (Chappuis et al. 2009). The reason for this is usually an insufficient vertical bone resulting in inadequate primary stability of the implant. In most cases, dislocation of material will cause sinusitis, the extent to which depends on the amount of dislocated material and local reaction.
- **Zinc oxide eugenol** (ZnOE). This material can cause a fungal infection especially with Aspergillus species—aspergillosis. This type of fungus can produce tumor-like soft tissue lesions called aspergilloma (*mycetoma*). They can collect calcium and sulfite thus leading to a central high-density structure. A mycetoma can easily be visualized by means of CBCT. Normally mycetoma appear radiographically as a convex-bordered mass within a sinus cavity with a central opaque structure (Fig. 30.29). Patient history should reveal dislocation of filling material; the only therapeutic approach is a complete surgical resection of the mycetoma (Odell and Pertl 1995;

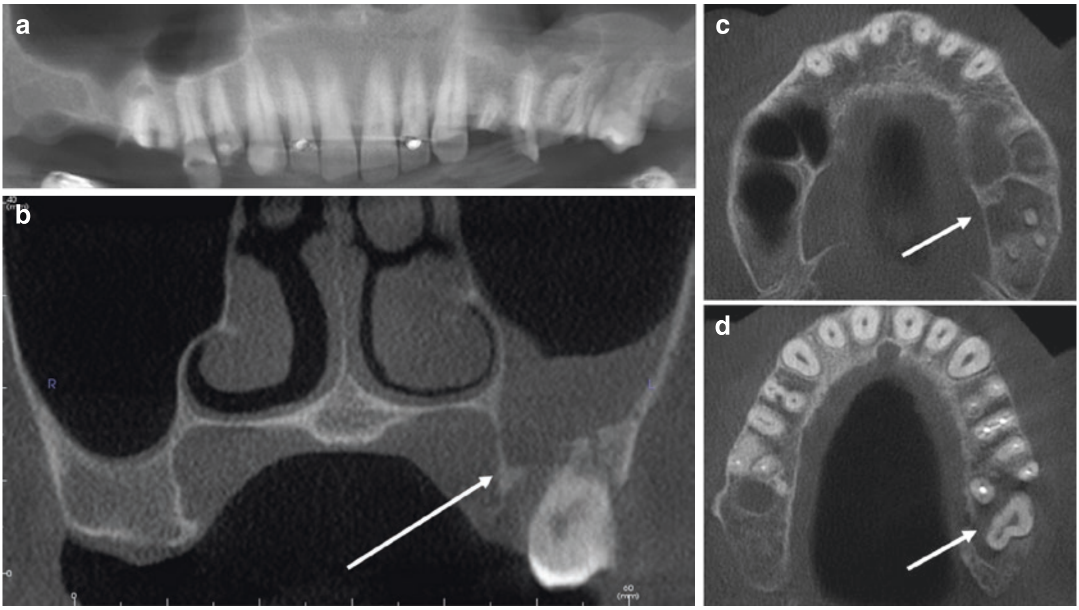

Fig. 30.25 CBCT reformatted panoramic image (**a**) of the maxilla showing generalized extensive coronal breakdown in the posterior segments with multiple root canal filled teeth. Polypoidal mucosal thickening attributable to maxillary sinusitis of odontogenic origin is seen on the floor of the left maxillary sinus associated with a periodontic-endodontic lesion on the left maxillary first molar. The periodontal involvement is extensive and penetrates the floor of the sinus as shown on the coronal (**b**) and axial (**c**) images and extends posteriorly to involve the second molar (**d**)

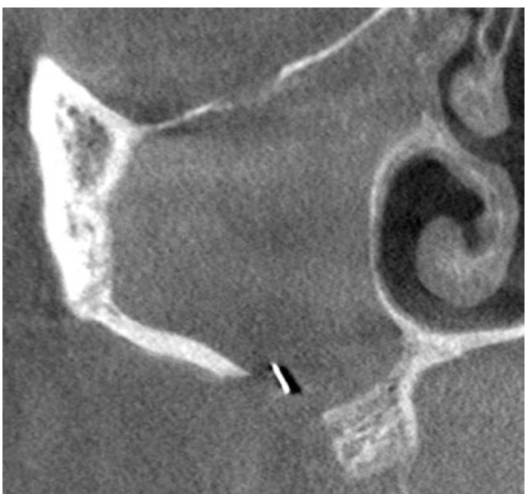

Fig. 30.26 Coronal MPR of the right maxillary sinus after antrostomy demonstrating a fractured instrument in a completely filled maxillary sinus suggestive of acute rhinosinusitis

Khongkhunthian and Reichart 2001; Mensi et al. 2004; Giardin et al. 2006; Aribandi and Bazan 2007).

Fig. 30.27 Sagittal MPR of the left maxillary sinus showing perforation of a dental implant through the sinus floor and concomitant acute sinusitis with retained air

- **Tooth fragments**. Restorative materials or tooth crown or root fragments (*radix relicta*) can be dislocated into the maxillary sinus and should be located in at least two planes (Figs. 30.30 and 30.31). In the case of a

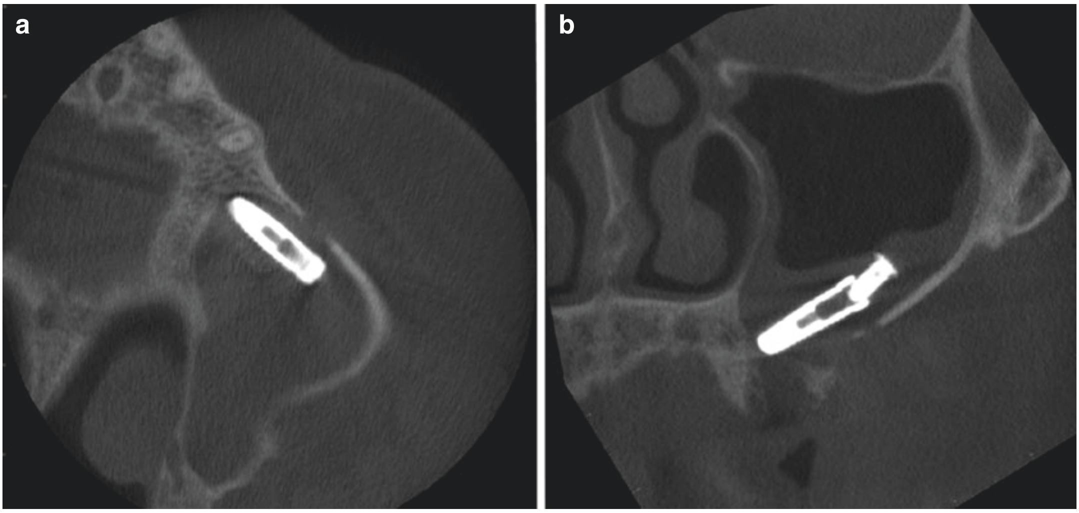

Fig. 30.28 Axial (**a**) and coronal (**b**) CBCT images of a 61-year-old female patient with partial opacification of the floor and lateral well of the left maxillary sinus associated with a displaced dental implant into the left maxillary sinus. The implant was displaced upon placement of the cover screw

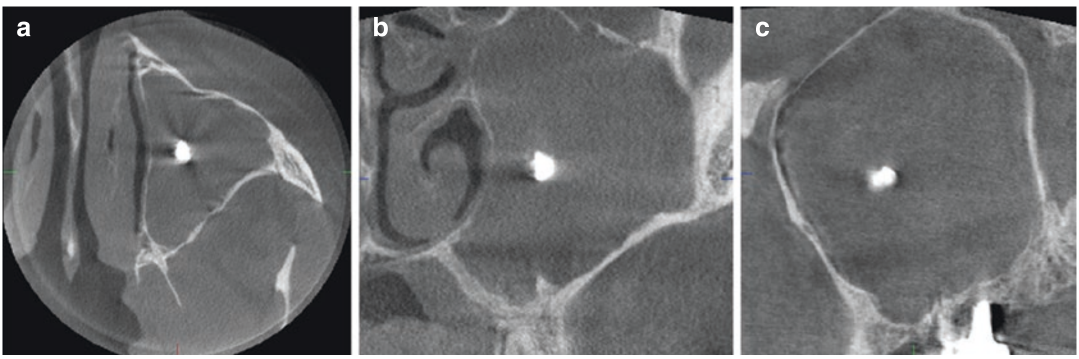

Fig. 30.29 Axial (**a**), coronal (**b**), and sagittal (**c**) MPR of the left maxillary sinus showing a completely filled left sinus with a small central hyperdense structure suggestive of a mycetoma with central metal-sulfite accumulation

recent intervention, the alveolar socket should be localized allowing a transalveolar approach for the removal of the dislocated item. Furthermore, all walls of the maxillary sinus should be examined because a sinusitis can be caused also by an obstruction of the ostium.

- **Odontogenic cysts**. Radicular cysts can extend into the maxillary sinus and mimic sinus cysts (Fig. 30.32). These entities are easily distinguished from CRS in that they have direct relationship with the apical portion of the root of a restored or carious tooth and have a well-defined corticated border. Pericoronal radiolucencies associated with impacted teeth can also result in reduction in luminal size and opacification of the maxillary sinus (Fig. 30.33). Cystic odontogenic lesions can also cause sinusitis. Often there is a small band of mucosal thickening adjacent on the evaginated wall of the cystic lesion.

Complications of Sinusitis

Although rare, numerous complications may arise from CRS including local osseous changes, orbital (e.g., cellulitis, subperiosteal abscess, cavernous venous thrombosis) or endocranial extensions of infection (e.g., meningitis, epidural or subdural abscesses).

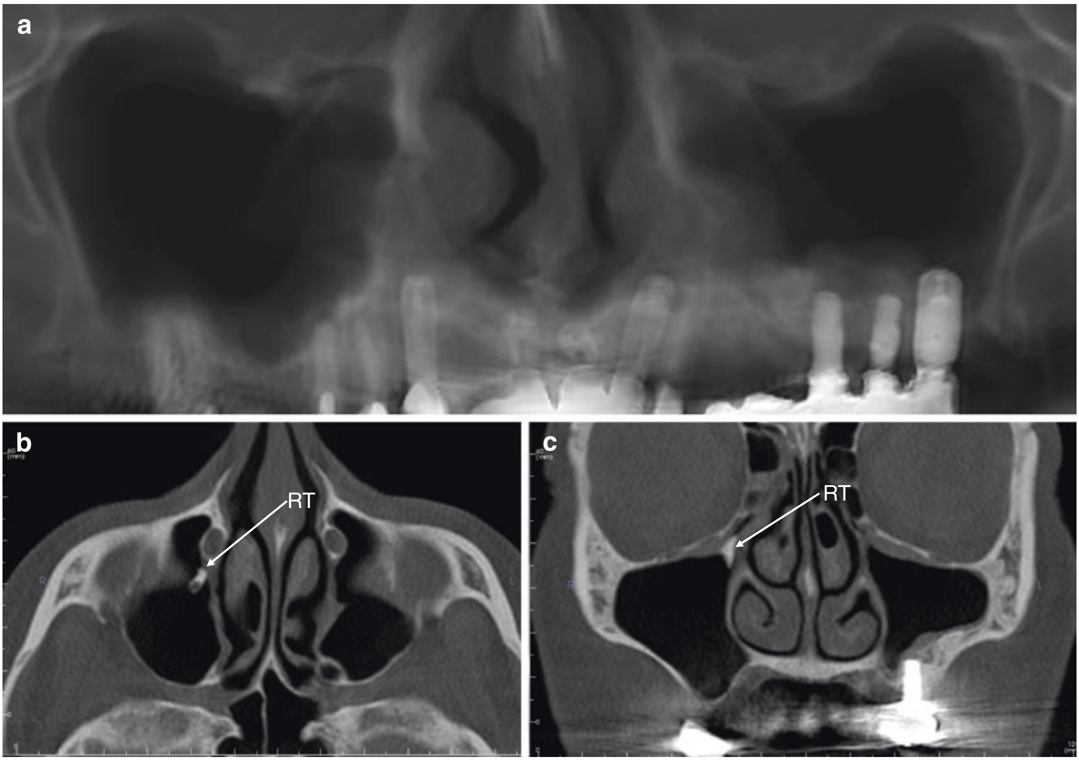

Fig. 30.30 Reformatted panoramic (**a**) and axial (**b**) and coronal (**c**) CBCT images of a 46-year-old asymptomatic female with a retained and displaced dental root tip at the level of the ostia of the right maxillary sinus. There is minimal local reaction however, monitoring should be considered due to the risk of blockage of the infundibulum

Whereas sphenoidal sinusitis in conjunction with inflammatory changes in other sinuses is relatively common, isolated sphenoidal sinusitis is unusual. The sphenoidal and posterior ethmoidal sinuses are usually affected together because they both drain into the sphenoethmoidal recess and subsequently into the superior meatus. Chronic inflammation of sphenoidal sinus mucosa may also affect adjacent thin-walled osseous structures and the cavernous sinus. Due to the intimate relationship between the sphenoidal sinus and the maxillary division of the trigeminal nerve, sinusitis may clinically present as trigeminal neuralgia. A diagnosis of trigeminal neuralgia can best be confirmed by a thickened maxillary nerve on MRI (Chong et al. 2000).

If multiple paranasal sinuses are opacified at one time, it is referred to as *pansinusitis* (Figs. 30.34 and 30.35). The sphenoid sinus often remains unaffected due to the relatively wide lumen of the sphenoethmoidal infundibulum.

Sinus Empyema

An empyema is defined as a bacterial abscess in an anatomic preformed space like a paranasal sinus. Superinfection of a sinusitis can cause an empyema. Although this is a rare condition, it will occur especially in immune incompetent patients like children, elderly and in case of diabetes, HIV and immuno-suppression (i.e., due to organ transplantation). Sinus empyema cannot be differentiated by means of CBCT from normal sinusitis though resulting in a typical odor from the patient. An empyema can be expansile like a mucocele. Therefore, it is important to consider in the differential diagnosis of any complete opacification of the sinuses (Gallagher et al. 1998; Reid 2004).

Antroliths

An antrolith is a generic term for a calcified mass within the maxillary sinus (or *antrum*) (Güneri et al. 2005). Antroliths form due to the

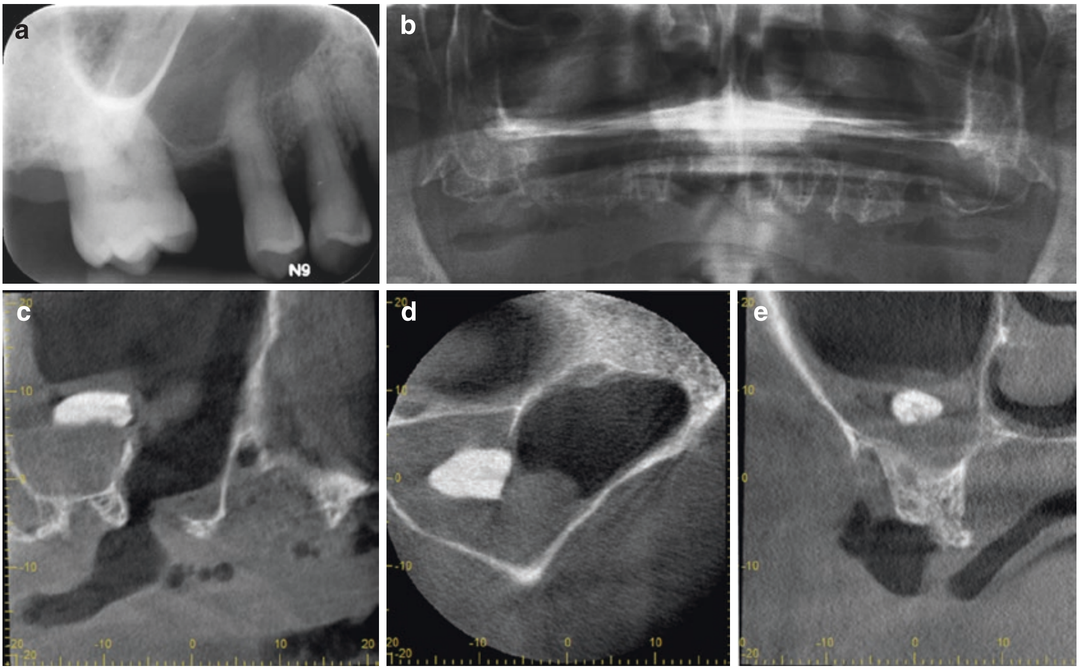

Fig. 30.31 Preoperative intraoral periapical (**a**) of the maxillary right posterior region and immediate postoperative panoramic image (**b**). A persistent oroantral communication clinically prompted localized CBCT imaging. Sagittal (**c**), axial (**d**), and cross-sectional (**e**) CBCT images demonstrate a palatal root tip displaced into the right maxillary sinus and embedded in the associated polypoidal mucosal thickening

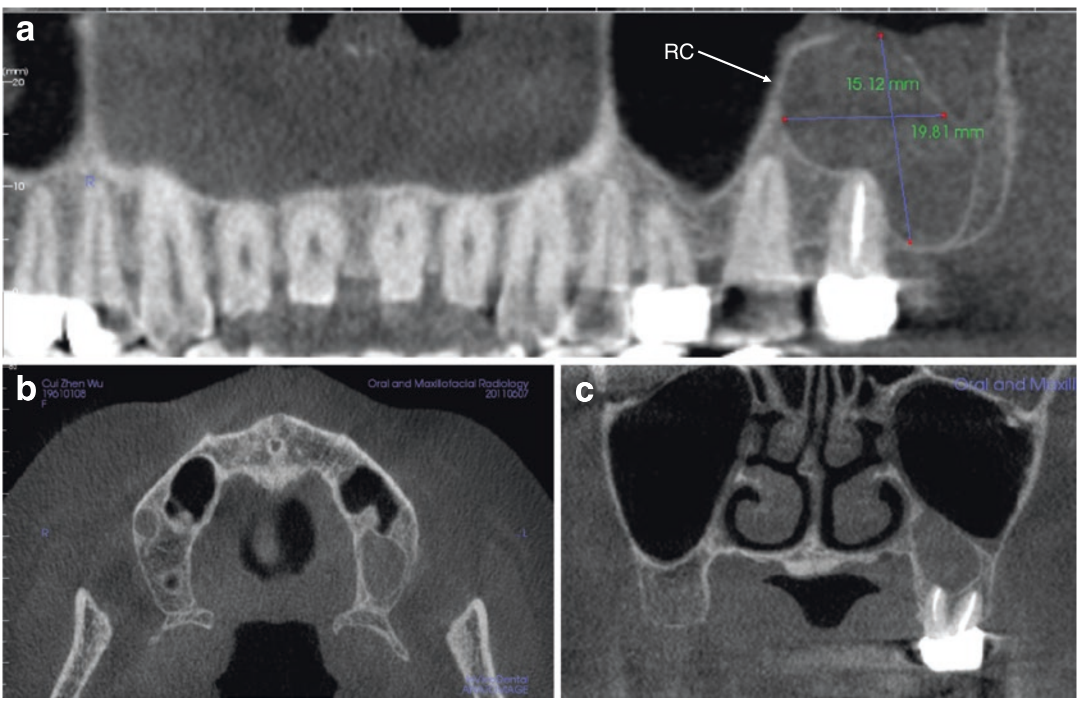

Fig. 30.32 Thin slice reformatted panoramic (**a**), axial (**b**), and coronal (**c**) CBCT images of a 50-year-old male demonstrating a large bi-lobular well defined corticated apical hypodensity associated with the palatal root of root canal filled left maxillary second molar consistent with a large radicular cyst with superior extension and elevation of the floor of the maxillary sinus

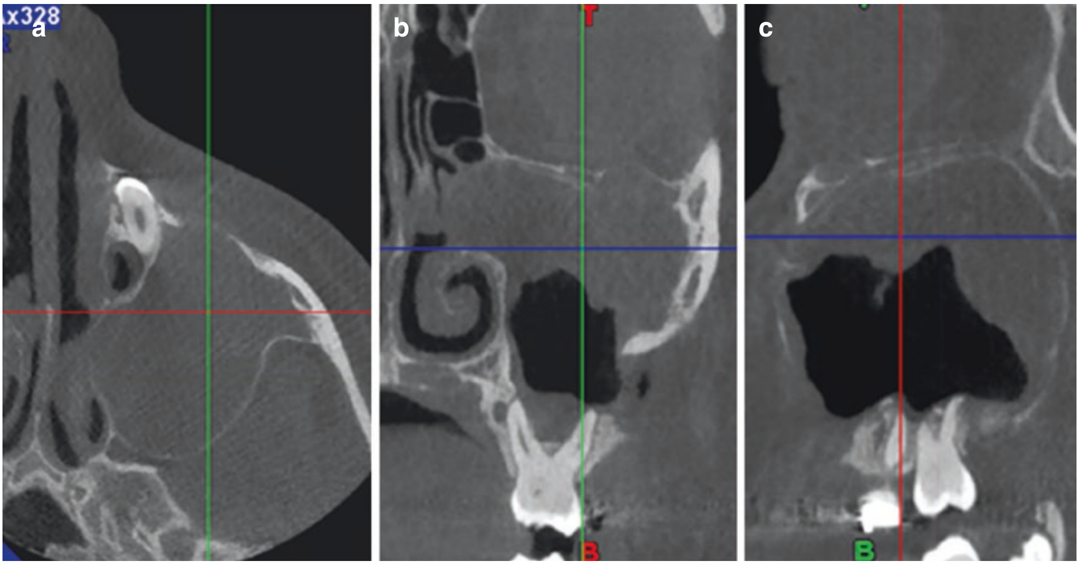

Fig. 30.33 Thin slice reformatted axial (**a**), coronal (**b**), and sagittal (**c**) CBCT images of an adolescent male demonstrating spherical expansion of the left maxillary sinus after removal of a maxillary impacted third molar and enucleation of the pericoronal dentigerous cyst. Note the residual irregular soft tissue density residual material and extension of the surgical access anteriorly above the apices of the first molar

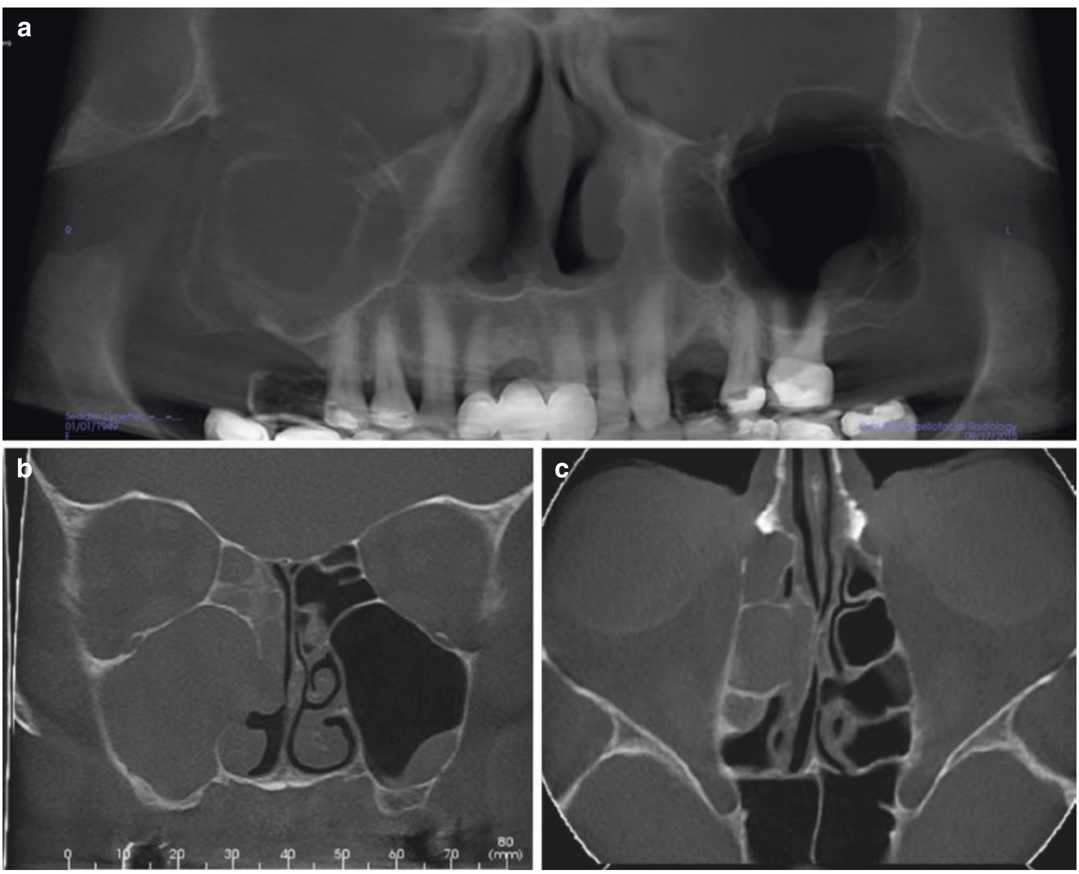

Fig. 30.34 Reformatted panoramic (**a**), coronal (**b**), and axial (**c**)image showing pansinusitis involving the right maxillary and anterior ethmoidal sinus

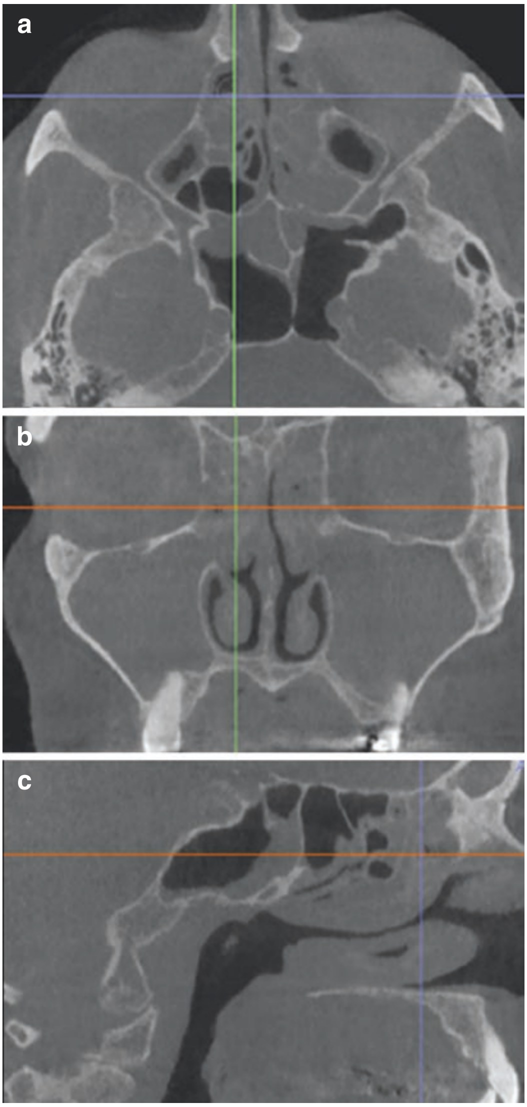

Fig. 30.35 Axial (**a**), coronal (**b**), and sagittal (**c**) sections of the paranasal sinuses showing inflammatory changes in multiple paranasal cavities (maxillary, ethmoid, sphenoid, frontal); the simultaneous inflammation of multiple sinuses is known as "pansinusitis"

accumulation of mineral salt deposition around a nidus within the maxillary sinus cavity (Fig. 30.36). Intrinsic or endogenous entities (referred to as true antroliths) may form around blood, mucus, pus, red blood cells, or white blood cells. Exogenous anthroliths (false antroliths) develop around a foreign body (e.g., tooth, tooth root, bead, button, paper, vegetable/bean pieces, snuff, and fruit seeds). Patients are usually asymptomatic and the discovery of the antrolith is usually an incidental radiographic finding. Most often antroliths are reported as nodular radiopaque masses with irregular borders associated with antral mucosal swelling, fluid, or polypoidal mucosal thickening.

Extrinsic Periapical Infection and the Maxillary Sinus

The apical sequelae of tooth pulpal necrosis can lead to the development of one of the three possible periapical pathologies: an abscess, granuloma, or cyst (radicular cyst). Radiographically these pathologies are indistinguishable and present as well-defined, smooth-surfaced, unilocular apical lesions. To establish a final diagnosis of an apical radiolucency, the tissue specimen should be evaluated histologically. Analysis of 2D and 3D radiographic images alike results only in a tentative diagnosis that should ideally be confirmed with a biopsy (Bornstein et al. 2015). In the maxillary sinus these entities often involve the floor of the maxillary sinus with various radiographic presentations.

- **Periapical Halo**. Initial periapical inflammatory exudate may slightly elevate the floor of the maxillary sinus adjacent the apex of the root of the non-vital tooth (Fig. 30.37) Expansion of this entity superiorly into the sinus is usually associated with a round intact and thinned cortical outline. This appearance is indicative of periapical pathology, and depending on the patient's signs symptoms, and radiographic size and progression, the involved tooth may require extraction or root canal treatment.
- **Radicular cyst**. A large periapical radicular cyst can occupy an extensive proportion of the floor of the maxillary sinus. While the contents may appear as a sinus loculation with complete opacification, these entities can be distinguished by a corticated border and loss of lamina dura or alveolar bone adjacent to the root apex (Fig. 30.38). Reactive mucosal thickening may be present adjacent to the cortical border of the lesion.
- **Collapsed/Collapsing Radicular Cyst**. Large periapical radicular cysts with extensive expansion into the lumen of the maxillary sinus resolve after surgical intervention such as removal of the tooth or successful root

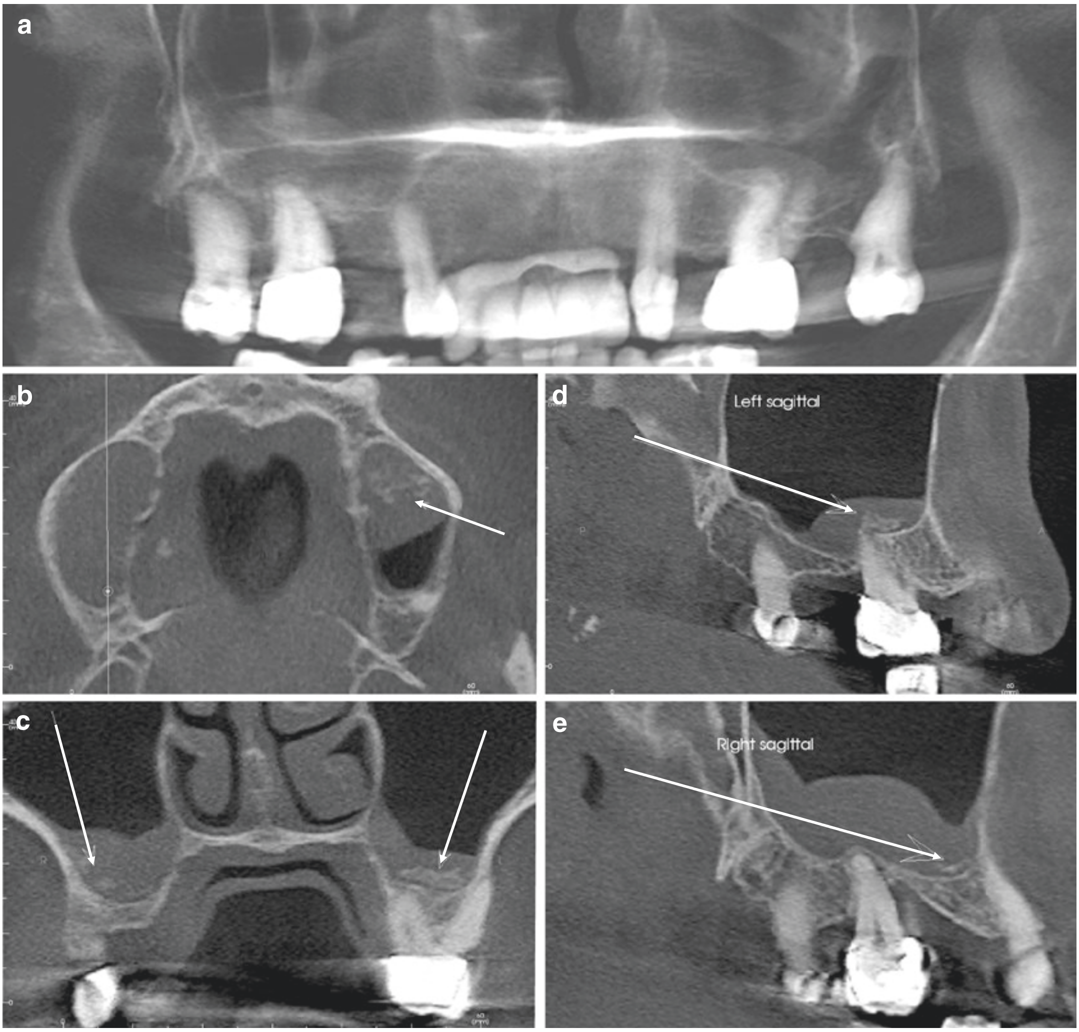

Fig. 30.36 Reconstructed panoramic (**a**), axial (**b**), coronal (**c**), left (**d**) and right (**e**) para-sagittal CBCT images demonstrating moderate generalized mucosal polypoidal thickening of the floor of the maxillary sinuses bilaterally with multiple antroliths. In the right sinus the antroliths appear as thin eggshell-like dystrophic calcifications within the soft tissue separated from the floor by a thin radiolucent line whereas in the left the antroliths are more modular

canal treatment. Because there is limited ability of the adjacent bone to remodel, the unilocular appearance of the cyst folds in onto itself and the cortical walls scleroses (Fig. 30.39). The appearance can be confused with a calcifying cyst. Differentiation requires careful analysis of the supplemental imaging findings (e.g., adjacent root canal filled teeth, apicoectomy), correlation with previous dental history, and comparison with earlier radiographic images.

30.2.2 Neoplasms

Neoplasms of the paranasal sinuses, both benign and malignant, all appear similarly, as opacifications within the lumen, contained by the bony walls. However, there are a number of radiographic features on CBCT that are useful in differentiating between benign and malignant entities (Table 30.1). In addition, neoplasm can arise from the osseous or mucosal components of the sinuses (intrinsic neoplasms) or, in the case of

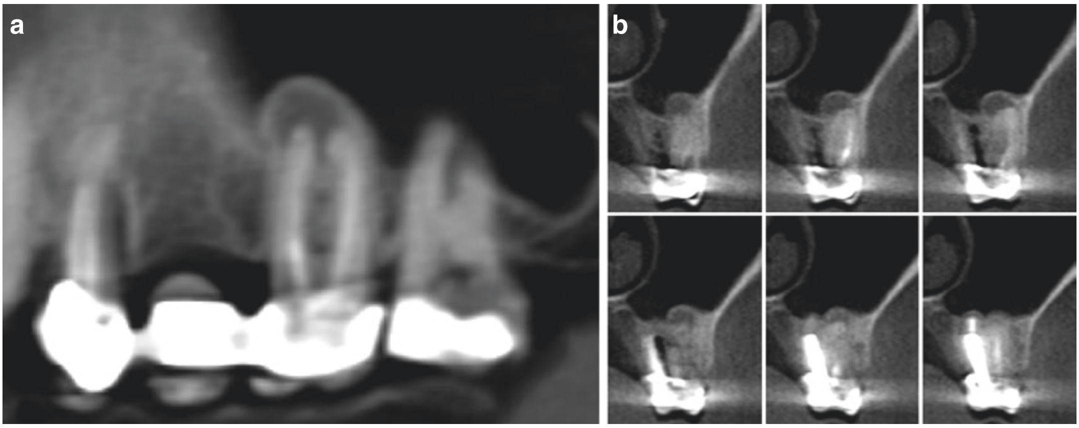

Fig. 30.37 Cropped left reformatted panoramic (**a**) and (**b**) serial 1 mm thick cross-sectional images of the left root canal filled maxillary first molar showing periapical “halo” associated with the mesial roots due to residual apical pathology

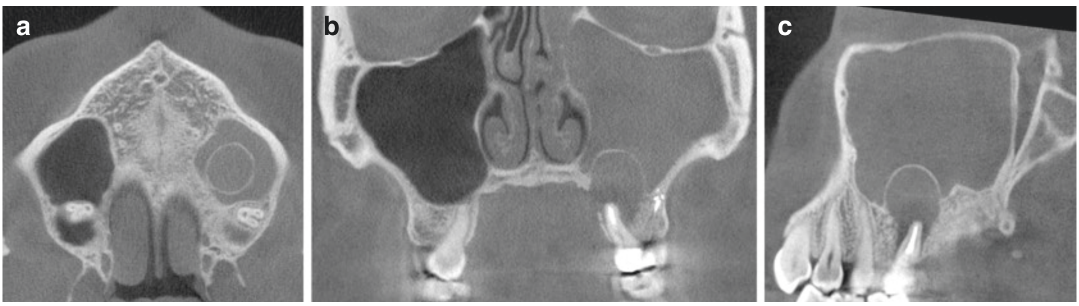

Fig. 30.38 Axial (**a**), coronal (**b**), and sagittal (**c**) CBCT images of the left maxillary posterior quadrant showing a moderately sized periapical corticated intact hypodensity associated with the palatal root of a root canal filled first molar with concomitant unilateral pansinusitis

the maxillary sinus, from odontogenic conditions arising from the alveolar process of the maxilla. In the latter case, these neoplasms involve the dentition (extrinsic neoplasms). In CBCT imaging involving the sinuses it is imperative that clinicians are skilled in identifying radiologic features associated with sinus conditions of extrinsic origin and recognizing changes suggestive of benign and malignant disease.

30.2.2.1 Benign Neoplasms

The most frequent benign neoplasms in the paranasal sinuses are cysts and polyps of mucosal origin. While their etiology varies, radiographic differentiation of these entities is difficult as they most often present as a single, smooth surface polypoidal mass arising from floor or wall of the involved sinuses.

Intrinsic Neoplasms

- **Retention Pseudocysts (mucous retention cysts)**. Gardner suggested the term *pseudocyst* for entities that mimic cysts radiologically (smooth, rounded, well defined) but histologically did not have an epithelial lining (1984) (Figs. 30.40 and 30.41). In the paranasal sinus several conditions appear as soft tissue pseudocysts without a cortical border. Therefore, depending on the tissue of origin, numerous terms have been proposed (Table 30.2). Despite terminology, primarily sinus pseudocysts are the result of obstructed seromucous secretory glands found in the mucoperiosteum lining the paranasal sinuses. They most commonly present as an asymptomatic well-defined, smooth surface, broad-based, dome-shaped single homogeneous soft tissue

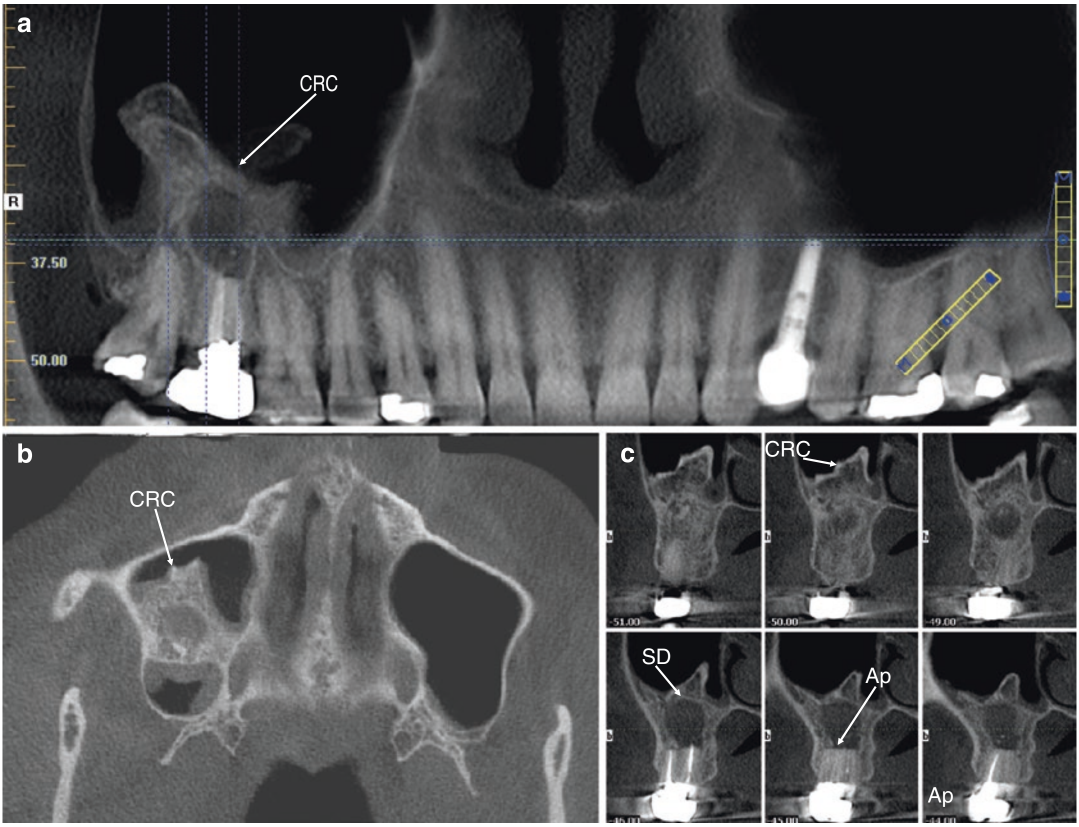

Fig. 30.39 Reformatted panoramic (**a**), axial (**b**), and (**c**) serial cross-sectional images demonstrating the appearance of a collapsing radicular cyst (CRC) associated with a root canal filled right maxillary second molar with evidence of a surgical defect (SD) and apicoectomy

Table 30.1 CBCT radiologic features that can be used to distinguish benign from malignant paranasal and nasal neoplasms

Radiographic characteristic	Benign	Malignant
Walls intact	✓	X
Regular mucosa border	✓	X
Air outside of the sinuses	X	✓
Free osseous bodies	X	✓

opaque mass arising from the floor or wall of a paranasal sinus. They are most commonly found associated with the floor of the maxillary sinus. Their growth is usually limited; however, season fluctuations in size have been reported. They may expand to fill the entire lumen of a maxillary sinus making differentiation from polyps difficult. Often adjacent mucosal thickening is absent.

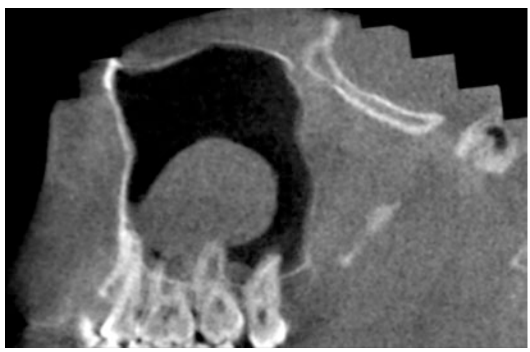

Fig. 30.40 Sagittal MPR CBCT image of the left maxillary sinus showing a well-defined, round hyperdense pedunculated structure arising from the floor of the left sinus in the absence of dental apical pathology consistent with a mucous retention cyst

- **Polyps**. Polyps present as irregular crenations or pedunculated soft tissue radiopaque

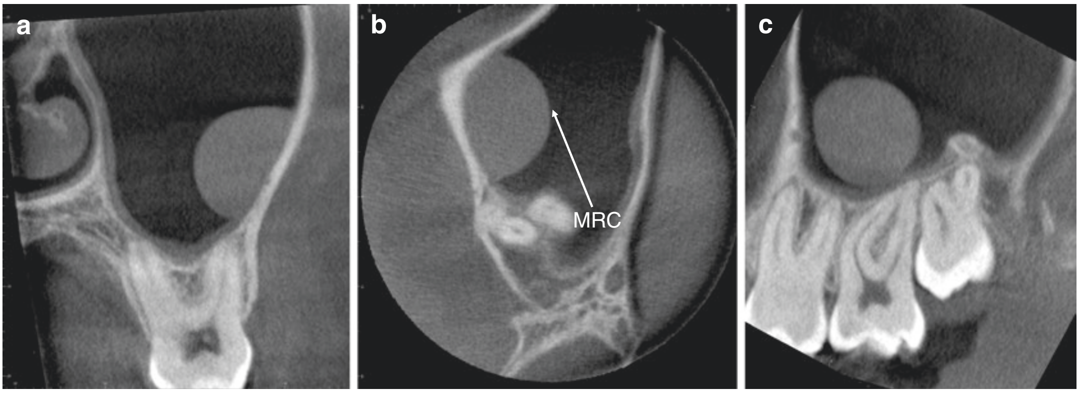

Fig. 30.41 Coronal (**a**), axial (**b**), and sagittal (**c**) CBCT images of an asymptomatic 22-year-old male referred for assessment of an impacted left maxillary third molar with a concomitant well-defined, smooth-surfaced, round soft tissue hyperdensity consistent with a mucous retention cyst (MRC)

Table 30.2 Synonyms for retention pseudocysts of the paranasal sinuses

Based on cell/tissue of origin		
Mucous	Other	Descriptive
• Mucous retention (pseudo) cyst	• Serous nonsecretory retention pseudocyst	• Benign cyst of the antrum
• Mucous retention phenomena	• Lymphangiectatic cyst	• Retention cyst of the maxillary sinus
• Antral mucosal pseudocyst	• Interstitial cyst	• False cyst
• Mucosal antral cyst	• Mesothelial cyst	• Antral pseudocyst
• Benign mucosal cyst of the sinus		
• Benign mucous cyst		

masses in association with thickened mucosal lining in response to allergic, reactive, or chronically inflamed changes of the Schneiderian membrane (Eggesbo 2006; Mafee 2007; Yasuda et al. 2007). Polyps can expand dramatically and protrude via the ostium into the nasal cavity. In case of maxillary sinus, polyps are then referred as *antro-choanal polyps* (Figs. 30.42 and 30.43). Polyps can be found on every wall of the paranasal sinuses. Polyps, particularly those of the ethmoid sinus, can expand or erode cortical bone and cause a mass effect on the contents of adjacent spaces.

- **Mucoceles**. Mucoceles form because of mucous retention secondarily to occlusion of an ostium and present as a completely opacified sinus. A mucocele moreover can thin, expand, and destroy sinus borders. Mucoceles can be accompanied with a bacterial inflammation of the sinus mucosa and are then referred to as *pyoceles*. Patients may complain of a fullness or swelling in the cheek. Expansile mucoceles are often with bone thickening and have to be differentiated from chronic sinusitis or osteomyelitic changes. Mucoceles are most often found in the frontal sinus, followed by the ethmoidal sinus and, rarely, the maxillary and sphenoidal sinuses. On CT, mucoceles typically produce smooth expansion of the involved sinus. Large mucoceles may breach bone and extend into the nasal cavity, orbit, or intracranial cavity. A delay in treatment often leads to orbital abscess, meningitis, subdural empyema, or cavernous sinus thrombosis (Lang 1989; Tan and Chong 2001). Any complete opacification of the sphenoid sinus, particularly with associated enlargement or erosion of the walls and particularly in the

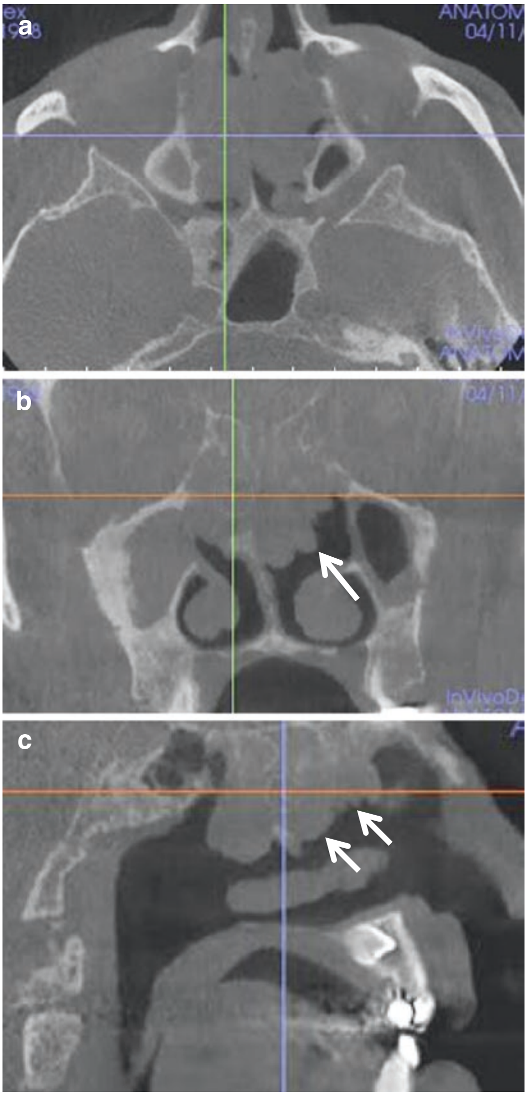

Fig. 30.42 Axial (**a**), coronal (**b**), and sagittal (**c**) CBCT sections of the ethmoid sinuses depicting extensive soft tissue masses in the ethmoid sinuses which are descending into the nasal chambers (*arrows*); consistent with antrochoanal polyps originating from the ethmoid sinuses

presence of a positive patient history of headache or pain, should be considered as a mucocele until proved otherwise. Referral to an otolaryngologist is highly recommended. In this situation, MRI should be considered the modality of choice, as it can identify early soft tissue thickening in the cavernous sinus and related abnormalities in the sphenoidal sinuses (Chong et al. 2000).

- **Papilloma**. Papillomas are the most common "solid" benign intrinsic tumor in the sinonasal tract. Three types of schneiderian papillomas occur:
  - *Fungiform or everted (50%).*This presents exclusively on the nasal septum and can cause obstruction and bleeding.
  - *Cylindric papilloma (3%).*This present on the lateral wall of the nose and also in the sinuses. They are composed of everted fronds with cystic mucus-containing spaces. These can recur; however, their malignant transformation is controversial.
  - *Inverting papilloma (47%).*The inverting papilloma is a polypoidal mass which typically occurs in males over 50 years of age and expands the middle meatus of the nasal wall resulting in unilateral, maxillary, anterior ethmoidal, and frontal sinusitis. It is the most common "solid" benign intrinsic tumor. There are often calcifications within the mass (approximately 40%); however, this is entrapped bone rather than dystrophic calcifications. This entity has a high recurrence rate and propensity for malignant transformation or coexistence with squamous cell carcinoma (10–27%). Therefore, inverting papilloma must be included in the differential diagnosis of conditions causing complete opacification, particularly in older patients presenting with unilateral sinusitis.

Extrinsic Neoplasms

- **Odontogenic Tumors**. Due to the proximity of the alveolar process to the maxillary sinus, odontogenic tumors, such as ameloblastoma,

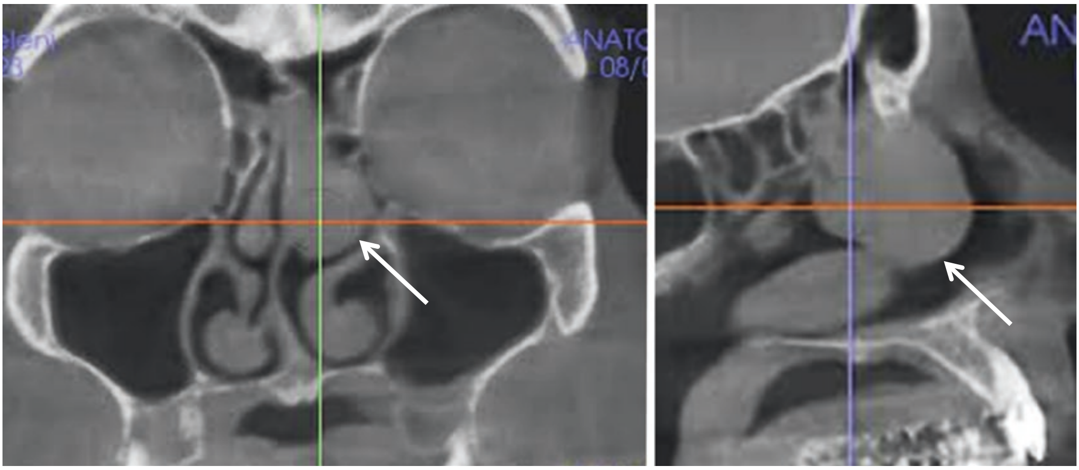

Fig. 30.43 Coronal (*left*) and sagittal (*right*) CBCT sections of the nasal cavities. The *arrow* shows a soft tissue mass descending from the anterior ethmoid air cells to the left nasal cavity, occluding the left middle nasal meatus, consistent with a nasal polyp

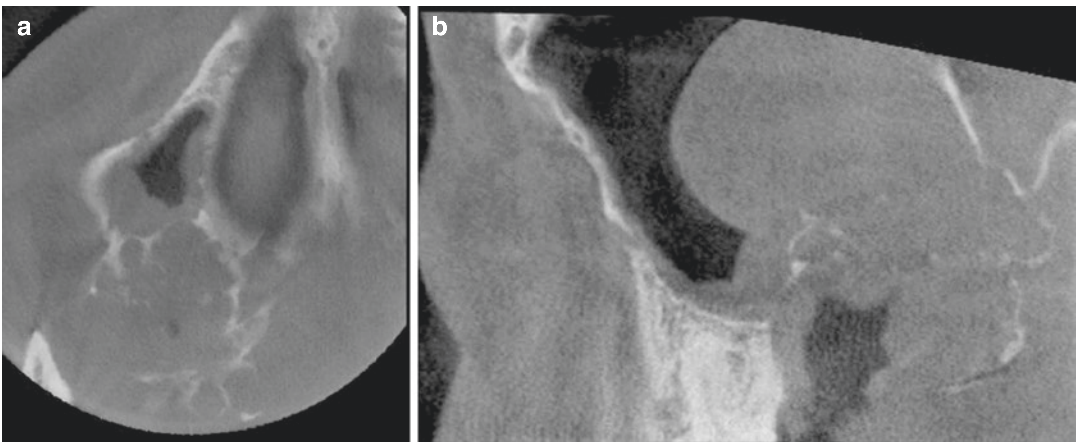

Fig. 30.44 Axial (**a**) and sagittal (**b**) view of the right maxillary sinus, note the honeycomb or bubble-like at the dorsal part of the sinus as a sign of a multicystic ameloblastoma. Note that on the sagittal image the soft tissue structure above the cystic tumor was a soft tissue extension of ameloblastoma

may present with extensions to the maxillary sinus (Fig. 30.44) (Gruica et al. 2003).

- **Bone tumors**. Fibrous dysplasia, although rare, may present as generalized osseous expansion of the walls of the paranasal sinuses with concomitant reduction in luminal size. More common however, are osteomas that appear as a dense, often pedunculated well-shaped mass adjacent to any wall of paranasal sinuses. They grow very slowly and become symptomatic at a very late stage. They are often misdiagnosed as complex or compound odontomas or even dislocated third molars (Mupparapu et al. 2004) (Figs. 30.45, 30.46, 30.47 and 30.48)

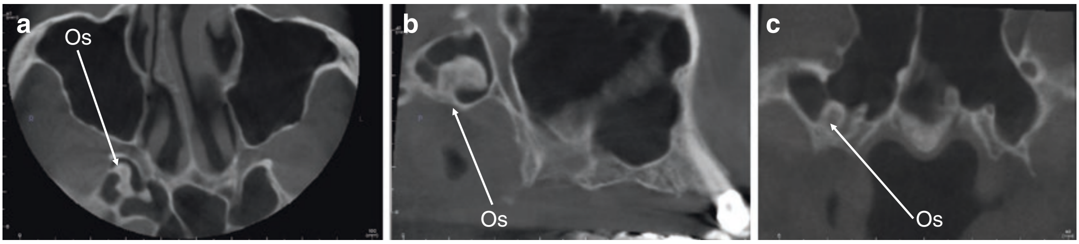

Fig. 30.45 Axial (**a**), para-sagittal (**b**), and coronal (**c**) CBCT images of the right sphenoid sinus of a 63-year-old female showing a single irregular small pedunculated osteoma (Os) arising from the floor

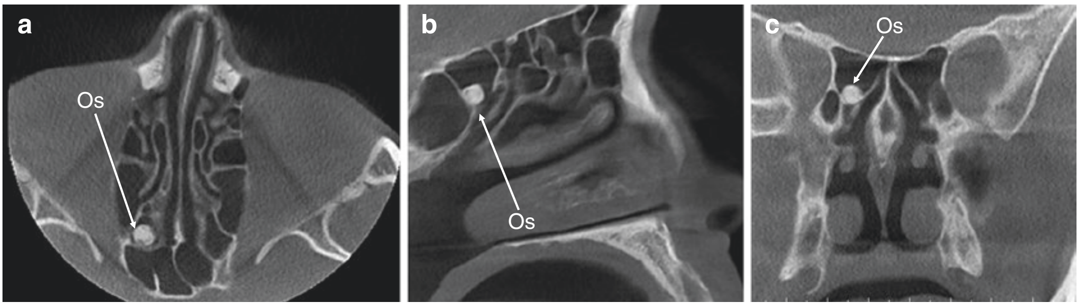

Fig. 30.46 Axial (**a**), sagittal (**b**), and coronal (**c**) images of the right sphenoid sinus showing a single regular "tooth-like" small osteoma (Os) arising from the floor of the and the anterior sphenoid

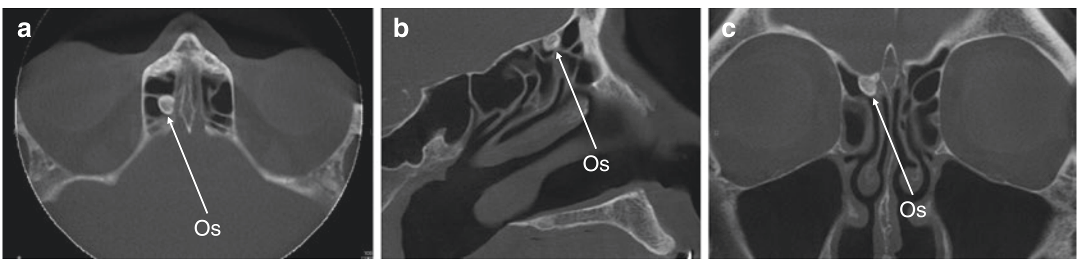

Fig. 30.47 Axial (**a**), sagittal (**b**), and coronal (**c**) images of the right ethmoid sinus showing a single irregular small osteoma (Os) arising from the roof and the anterior ethmoid, reducing the width of the fronto-ethmoidal recess

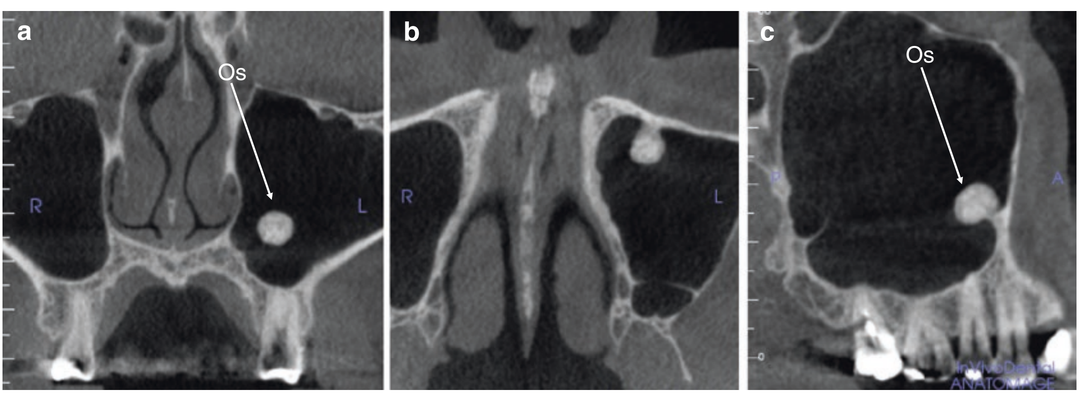

Fig. 30.48 Coronal (**a**), axial (**b**), and sagittal (**c**) CBCT images showing a single small pedunculated solid osteoma (Os) arising from the antero-medial wall of the left maxillary sinus

- **Soft Tissue Tumors**. Myxoma, lipoma, and even schwannomas may be present in the paranasal sinuses. Using CBCT images alone, neoplasia is not easily distinguishable from reactive soft tissue alterations in the sinus such as polyps or soft tissue cysts.

30.2.2.2 Malignant Tumors

Malignant paranasal sinus tumors are rare and often identified late because of (1) difficulty in differentiating benign from malignant lesions, and (2) lack of anatomic impediments to soft tissue spread and therefore delayed clinical presentation (Figs. 30.49 and 30.50). Squamous cell carcinoma is the most common accounting for approximately 85% of malignancies with adenocarcinomas, adenoid cystic and mucoepidermoid carcinomas comprising the remainder of epithelial-based malignancies in order of frequency. Other entities include osteogenic sarcoma and fibrosarcoma. In pediatric patients, rhabdomyosarcoma and lymphoma should be considered.

As nasal or sinus blockage associated with complete sinus opacification may be the first radiologic sign, differentiation between benign and malignancy is important (Table 30.3). The most important radiologic signs are complete sinus opacification, wall destruction and irregular degradation and deformation of the sinus mucosa. In rare cases, teeth in the posterior maxilla without any clear sign of decay such as caries or restorations may present with clinical symptoms such as loss of pulp sensitivity or root resorption as a first indicator of malignancy in the maxillary sinus (Bornstein et al. 2008a, b). Clinicians must maintain a high index of suspicion in patients whose conditions do not respond to medical treatment as demonstrated by the persistence of signs or symptoms or radiographic features.

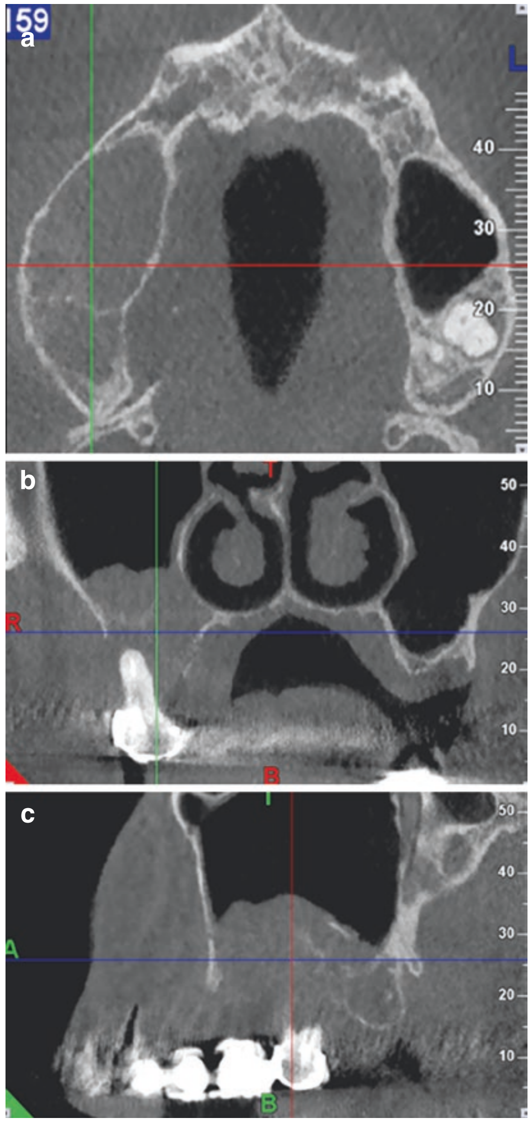

Fig. 30.49 Axial (**a**), coronal (**b**), and sagittal (**c**) CBCT sections of the right maxilla showing a soft tissue mass on the floor of the right sinus adjacent to an implant with substantial loss of alveolar bone. This was initially diagnosed as odontogenic sinusitis with concomitant peri-implantitis. However, after the implant was extracted, biopsy of the soft tissue on the sinus floor revealed this mass to be a lymphoma

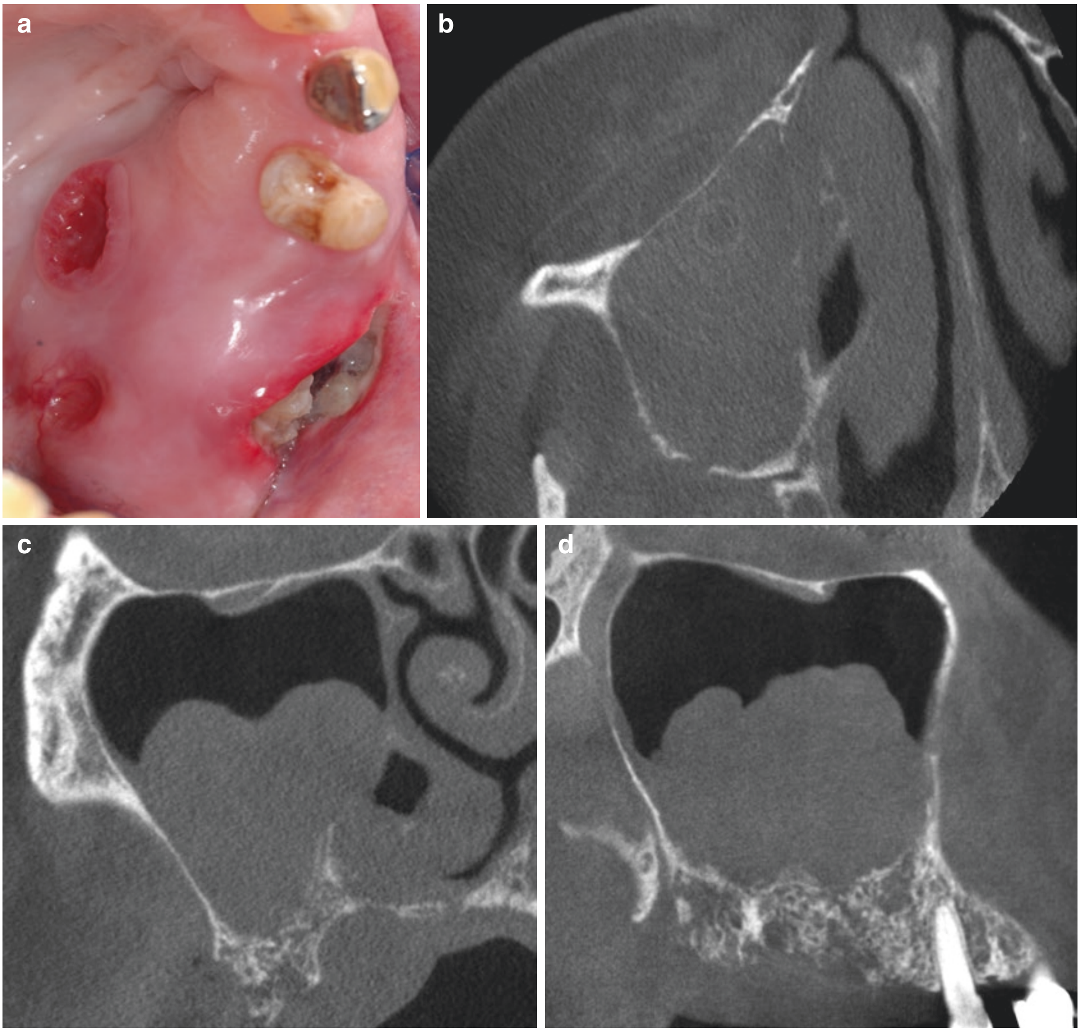

Fig. 30.50 Intraoral photograph (**a**) and axial (**b**), coronal (**c**), and sagittal (**d**) CBCT images of a 71-year-old female patient who presented with multiple intraoral ulcers of the left palate and edentulous maxillary alveolus. Imaging demonstrate partial polypoidal opacification of the right sinus with diffuse permeative osteolysis of the right alveolus and palate highly suggestive of malignant infiltration. Histopathologic biopsy confirmed adenocystic carcinoma

30.3 Disease in Other Paranasal Sinuses

In the preceding sections, a thorough review and description of sinus disease has been presented with an emphasis on the maxillary sinuses. For the dental practitioner, this is important as the maxillary sinuses comprise a significant proportion of the maxilla and posteriorly involve the dentition. Unlike other sinuses, maxillary sinus pathology often arises from conditions affecting the dentition. Furthermore, CBCT scans of the posterior maxilla almost always include some part of the maxillary sinus, even if the smallest FOV has been selected.

However, other paranasal sinuses such as the ethmoid air cells, frontal and sphenoid sinuses may be involved in disease processes similar to that involving the maxillary sinuses. These may range from localized mucositis (thickening of the mucosal lining) to more

Table 30.3 Checklist of radiographic features to be identified on CBCT images of the paranasal sinuses and their potential significance

Paranasal sinus	Feature	Significance
Frontal	Depth of the olfactory fossa (Keros 1962)	The deeper the fossa, the higher the chance for fracture or perforation with surgical intervention
Sphenoid	Degree of pneumatization of sphenoid sinus	The larger the pneumatization the greater the possibility of dehiscence in the bony covering of the carotid artery or optic nerve especially important in CRS
Ethmoid	Slope, thickness, and asymmetries in the height of the ethmoid roof	The prevalence of intracranial penetration during FESS is higher when this anatomic variation occurs
	Status of the lamina papyracea	Dehiscence in the lamina papyracea may indicate medial orbital "blow-out" fracture
	Presence of an Onodi cell	May contribute to ARS or CRS
Maxillary	Patency of the OMC	Blockage of the ostia may contribute to ARS or CRS
	Status of the middle turbinate	Attachment of the uncinate process and presence of conchae bullosa may contribute to ARS or CRS
	Width of the infundibulum	Narrow infundibulum may contribute to ARS or CRS
	Degree of pneumatization of the maxillary sinus	Important in MSEG procedures. Pneumatization directly correlates with the patient age
	Size and status of the maxillary sinuses	Hypoplastic or opacified sinus may affect proposed surgical procedures
Nasal Fossa	Alignment of the septum	Nasal septal deviation may contribute to ARS or CRS

ARS acute rhinosinusitis, *CRS* chronic rhinosinusitis, *FESS* Functional Endoscopic Sinus Surgery, *OMC* osteomeatal complex, *MSEG* Maxillary Sinus Elevation and Grafting

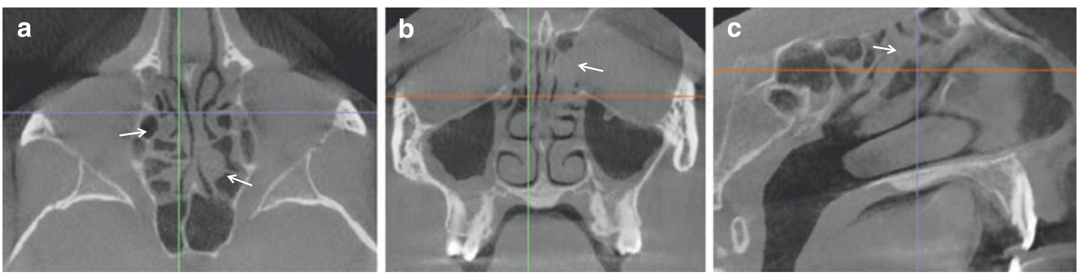

Fig. 30.51 Axial (**a**), coronal (**b**), and sagittal (**c**) CBCT sections of the ethmoid sinuses showing thickening of the mucosal lining (mucositis) in several ethmoid air cells (*arrows*). Note concomitant mucositis in the maxillary sinuses, bilaterally

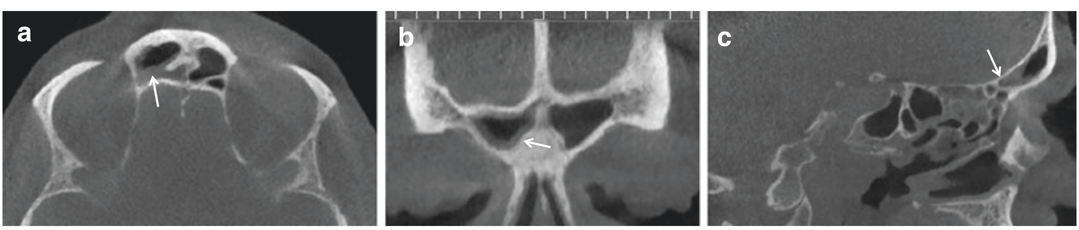

Fig. 30.52 Axial (**a**), coronal (**b**), and sagittal (**c**) sections of the frontal sinuses showing mucositis associated with the frontal sinus walls (*arrows*)

extensive inflammatory changes (chronic or acute) to neoplastic disease. Figures 30.51, 30.52, 30.53, 30.54, 30.55, 30.56, 30.57, 30.58, and 30.59 present examples of pathological entities of the paranasal sinuses other than the maxillary sinuses.

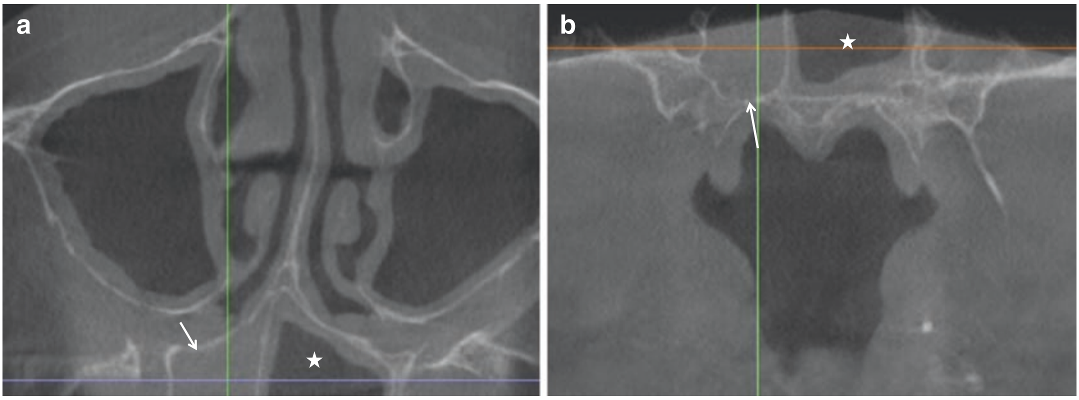

Fig. 30.53 Axial (**a**) and coronal (**b**) cropped sections of the sphenoid sinuses showing mucositis in the left sphenoid sinus (*arrows*) and concomitant inflammation (sphenoiditis) in the right sphenoid sinus (*star*)

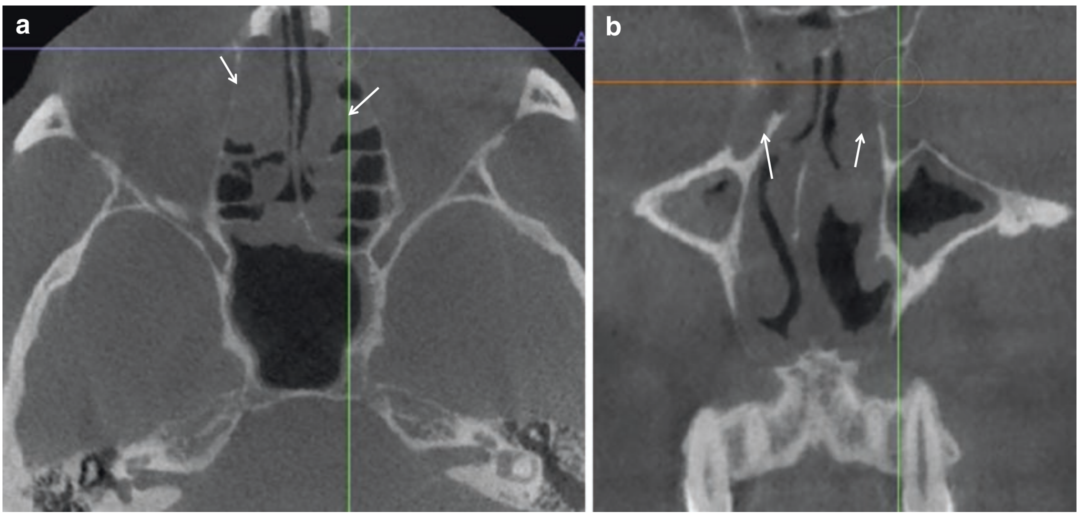

Fig. 30.54 Axial (**a**), coronal (**b**) CBCT sections of the ethmoid sinuses showing presence of soft tissue hypodensity in several air cells (*arrows*) consistent with ethmoid sinus inflammatory changes

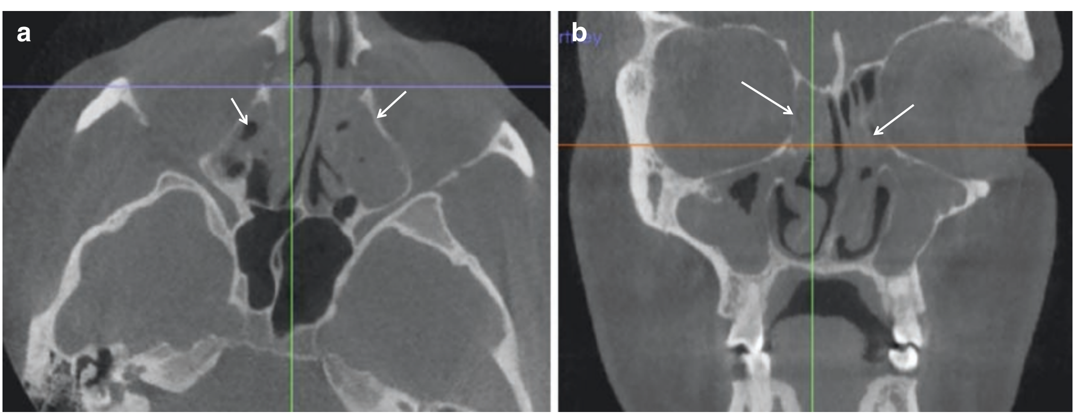

Fig. 30.55 Axial (**a**) and coronal (**b**) CBCT sections of the ethmoid sinuses showing extensive inflammatory changes in the ethmoid sinuses (*arrows*). Note concomitant inflammatory changes in the maxillary sinuses, bilaterally

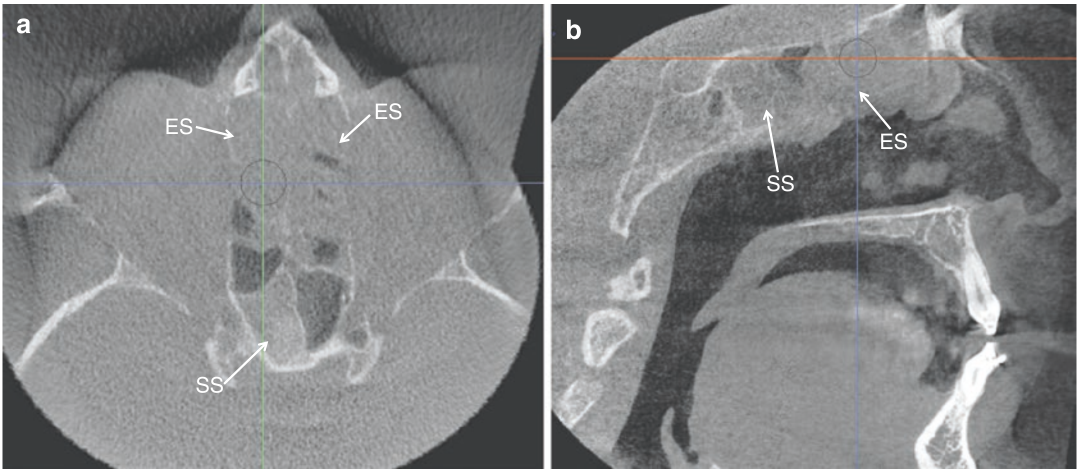

Fig. 30.56 Axial (**a**) and sagittal (**b**) CBCT sections of the ethmoid and sphenoid sinuses showing almost full opacification of the ethmoid sinuses by inflammatory tissues (ES) and concomitant complete opacification of the right sphenoid sinus which is fully occupied (SS) consistent with ethmoiditis and sphenoiditis

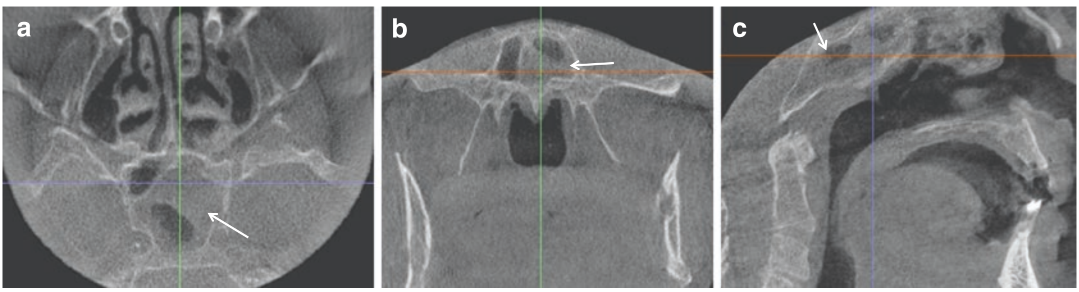

Fig. 30.57 Axial (**a**), coronal (**b**), and sagittal (**c**) CBCT sections of the sphenoid sinuses showing almost complete opacification in the left sphenoid (*arrows*); consistent with sphenoid sinus inflammation

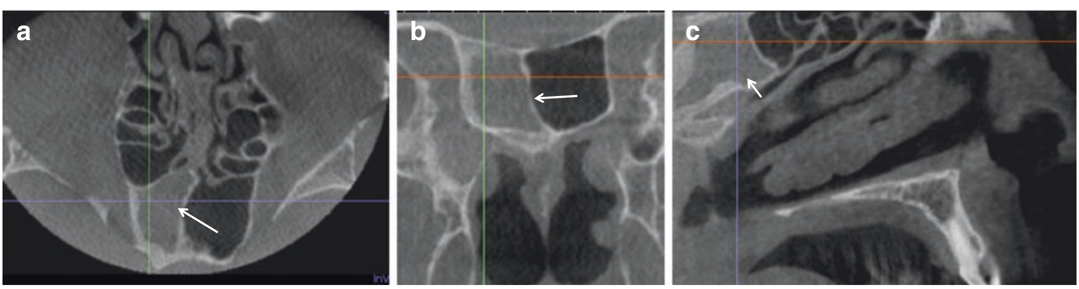

Fig. 30.58 Axial (**a**), coronal (**b**), and sagittal (**c**) sections of the sphenoid sinuses of a different patient showing right sphenoid sinus to be fully occupied by inflammatory tissue. Note, the thickened walls of the right sphenoid. This is consistent with chronic inflammatory changes (*white arrows*)

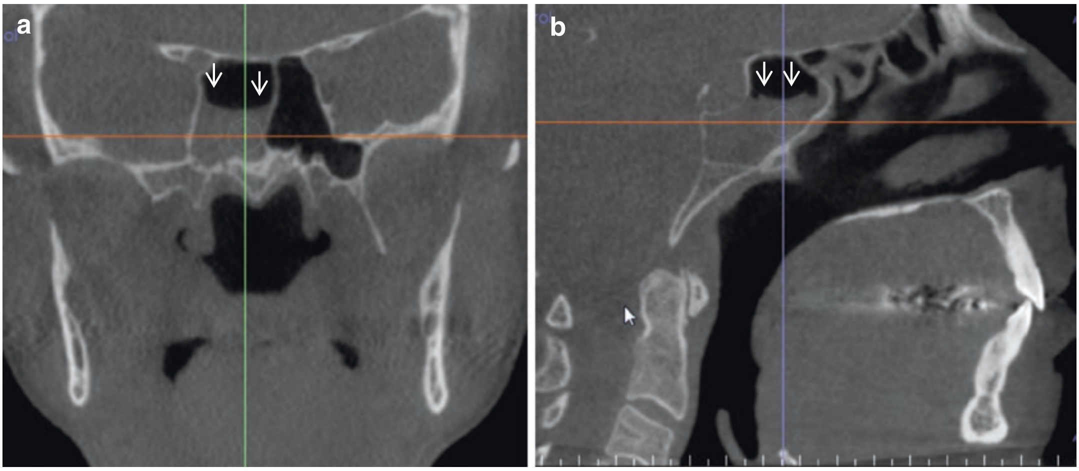

Fig. 30.59 Axial (**a**) and sagittal (**b**) CBCT images of the sphenoid sinuses showing soft density tissues in the right sphenoid; note the sharp, convex curved line depicting the superior border of the soft tissues (*arrows*). This is an indication of a fluid in the sphenoid sinus described above is known as "air/fluid" level and suggestive of acute sinusitis

30.4 Postoperative Maxillary Sinus Changes

Surgical interventions of the paranasal sinuses are performed frequently as treatment for CRS, to repair traumatically induced fractures, and for removal of neoplasms. In the maxillofacial region, the most frequent surgeries involve the maxillary sinus and adjacent nasal structures. Therefore, it is important for dental clinicians to be familiar with the radiographic postoperative changes of the maxillary sinuses associated with these procedures when interpreting CBCT datasets.

30.4.1 Sinus Postsurgical Changes

The paranasal sinuses can be approached either externally through the lateral walls or floor maxillary sinuses or internally through the nasal fossa.

30.4.1.1 External Approach Changes

While various surgical approaches to access the maxillary sinus are possible, the most well known is the Caldwell-Luc approach (Matheny and Duncavage 2003). In this technique, the facial wall of the maxillary sinus is opened in the canine fossa, the sinus mucosa, stripped out and finally an antrostomy to the inferior nasal duct or inferior turbinate is performed. Stripping of the mucosa or resecting a large part of the mucosa leads to scarification. These scars cannot be differentiated from mucosa in CBCT. The scars consist of collagen fibers which lose fluid over the years. The following radiographic findings are indicative of a Caldwell-Luc procedure.

- **Contraction of the maxillary sinus walls**. A concave and retracted facial wall can be seen in the axial plane. Consecutively the volume of the maxillary sinus is decreased. Sometimes no pneumatized volume is visible (Figs. 30.60 and 30.61). A persistent defect of the facial wall is caused by the anterior antrostomy and can be detected decades after the procedure was performed.
- **Wall thickening**. The bony walls of the maxillary sinus usually appeared sclerotic and thickened due to recurrent or chronic sinusitis after the intervention.
- **Soft tissue opacification**. Loss of the anterior wall of the maxillary sinus allows for soft tissue filling of the osseous defect and protrusion into the maxillary sinus (Fig. 30.62).

Fig. 30.60 Coronal CBCT image after a Caldwell-Luc procedure on the left maxillary sinus. Note the complete absence of the lateral wall of the left maxillary sinus and the soft tissue continuity, the paradox pneumatization of the inferior turbinates bilaterally (*filled star*), bilateral conchae bullosa, and the narrowing of the OMC on the right

Fig. 30.62 Axial CBCT image showing extensive opacification of the left sinus and cortical defect of the left anterior facial wall after antrostomy

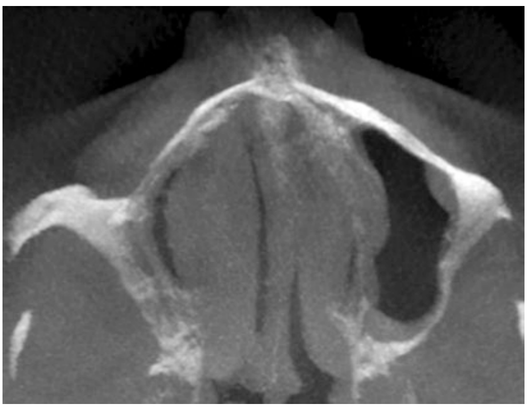

Fig. 30.61 Axial maximum intensity projection after a Caldwell-Luc procedure demonstrating substantial retraction of the facial wall of the right maxillary sinus and concomitant chronic maxillary sinusitis on left side (*thickened walls*)

- **Associated antrostomies**. Commonly a defect of the ipsilateral inferior meatus can be visualized. Moreover, there can be an additional middle meatus antrostomy to increase the physiologic sinus drainage.
- **Surgical Ciliated Cyst**. Also known as the *postoperative maxillary cyst*, forms after surgery when a portion of the sinus lining separated from the mucoperiosteum forms an epithelial lined cavity into which mucin accumulates. Surgical ciliated cyst is uncommon in Western countries but frequently reported in Asian populations, especially in Japan, as a frequent delayed complication of surgery (Kaneshiro et al. 1981). This entity presents as a mucocele in that it causes complete opacification of the operated maxillary sinus and may be associated with intranasal and intrasinus extension. Clinically the patient may present with rhinorrhea and nasal obstruction and demonstrate swelling of the cheek or tooth displacement.

30.4.1.2 Functional Endoscopic Sinus Surgery (FESS) Changes

The operative approach to the paranasal sinuses and especially to the maxillary sinus has changed dramatically in the last two decades. More and more FESS interventions are performed; the Caldwell-Luc approach is no longer a state-of-the-art technique (Fig. 30.63) (Al-Belasy 2004).

FESS can be performed for antrostomy, ethmoidectomy, uncinectomy, or turbinate removal (conchotomy). Typical postoperative radiographic changes comprise absence of the specific anatomical landmarks such as turbinates, ethmoid cells, or uncinate process (Busaba and Kieff 2002).

Two possible sequelae can occur due to scarification. The ciliary clearance function of the

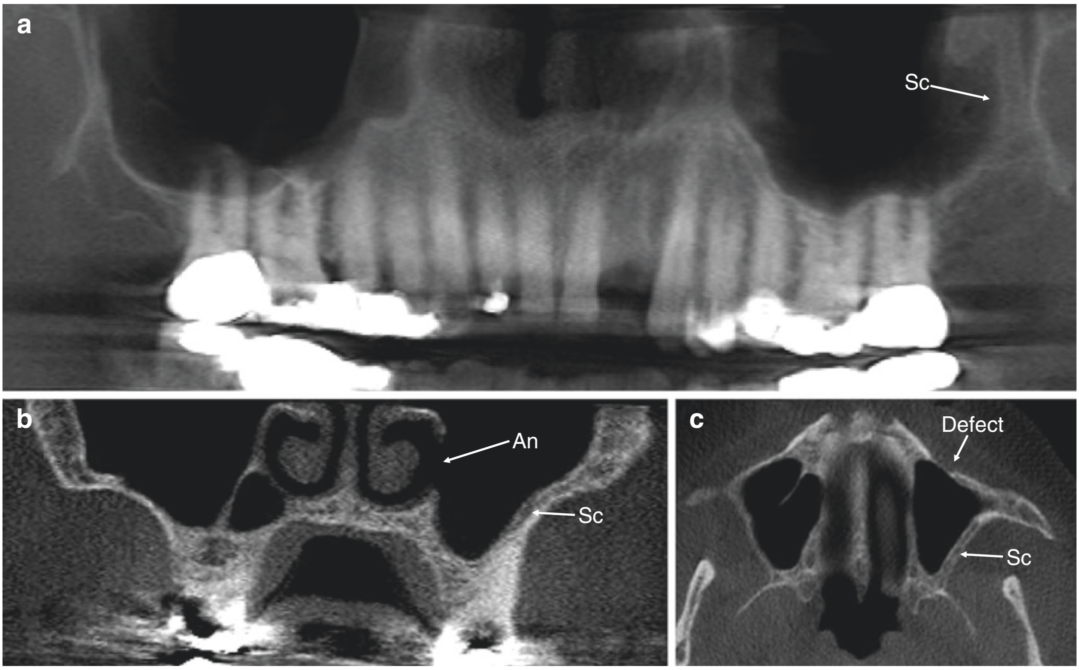

Fig. 30.63 Reformatted simulated panoramic (**a**), coronal (**b**), and axial (**c**) CBCT images demonstrating a defect in the anterior wall of the left maxillary sinus (Defect) and inferior turbinate antrostomy (An). While the maxillary sinuses are clear bilaterally, sclerosis of the lateral and anterior walls of the left maxillary sinus are indicative of previous chronic rhinosinusitis

sinus mucosa may be partially or totally disrupted and, as a result, mucus can accumulate producing a mucocele (DeFreitas and Lucente 1988; Cutler et al. 2003). In addition, a postoperative maxillary cyst can develop and occlude the drainage pathways (Basu et al. 1988). Another problem can occur if the patient underwent inferior antrostomy. Contrary to the belief that ciliary clearance evacuates mucus through the additional opening of the maxillary sinus, the mucus can recirculate through this artificial pathway. Ciliary movement is genetically defined and therefore clearance of the maxillary sinus uses a physical pathway. In case of an inferior antrostomy, a recirculation syndrome can develop which can be present as a CRS after FESS.

30.4.1.3 Surgical Changes Following Maxillary Sinus Elevation and Grafting (MSEG)

In the maxilla, the maxillary sinus elevation and bone grafting augmentation (MSEG) procedure has been the mainstay of implant-directed maxillary reconstruction in situations in the posterior maxilla with inadequate bone height (Tatum 1986). MSEG procedures, also known as the "sinus lift," involve access to and elevation of the maxillary sinus floor and the insertion of bone graft material. Two surgical approaches can be used either to simply raise the sinus lining or to additionally introduce bone regenerative material under the lining:

- **Lateral Window Approach (LWA)** (Tatum 1986). The technique is essentially a lateral antrostomy which involves the creation of a rectangular osseous window through the lateral wall of the maxillary sinus which is subsequently elevated as a hinge superiorly. Careful elevation of the mucoperiosteum (Schneiderian membrane) is performed creating a soft tissue pocket below which bone augmentation material is compacted. The amount of bone augmentation material placed depends on the amount of existing residual ridge resorption of the edentulous space and the length of the planned implant. This technique is usually performed for multiple implant sites. Various modifications of the technique have been reported without the creation of a bony hinge, and implants are either placed simultaneously or in a delayed procedure following bony remodeling of the augmentative material (Bornstein et al. 2008a, b)

- **Transalveolar Osteotomy (TAO)** (Summers 1994). A more conservative approach used is a transalveolar osteotomy which uses osteotomes through the crestal bone to raise the Schneiderian membrane and perform a ridge expansion osteotomy superiorly. This technique is usually performed for a single implant site.

Importance of Membrane Thickness on CBCT Images

In both techniques, a possible major complication is perforation of the Schneiderian membrane during the surgical procedure. Perforation increases the possible side effects of graft loss, infection that causes disruption of sinus function, and even implant survival (Viña-Almunia et al. 2009). Assessment of sinus membrane thickness prior to MSEG provides a potential index of perforation. For both the LWA (Lin et al. 2016) and TAO (Wen et al. 2014) techniques, lowest perforation rates occur when the membrane thickness as measured on CBCT images is 1–1.5 mm and higher when membranes are thicker (≥2 mm) or thinner (<1 mm).

Postoperative Radiographic Patterns

Without adequate dental history, the presence of graft material associated with MSEG procedures can be misinterpreted as a benign or malignant osteogenic neoplasia. Clinicians should be able to recognize the numerous CBCT radiographic appearances of the postsurgical MSEG maxillary sinus and their potential clinical significance. The most typical appearance associated with the sinus lift technique is a dome-shaped homogeneous dense radiodensity with or without flecks filling the floor of the maxillary sinus with an associated indentation, concavity, or defect on the adjacent lateral wall of the maxillary sinus (Fig. 30.64). If

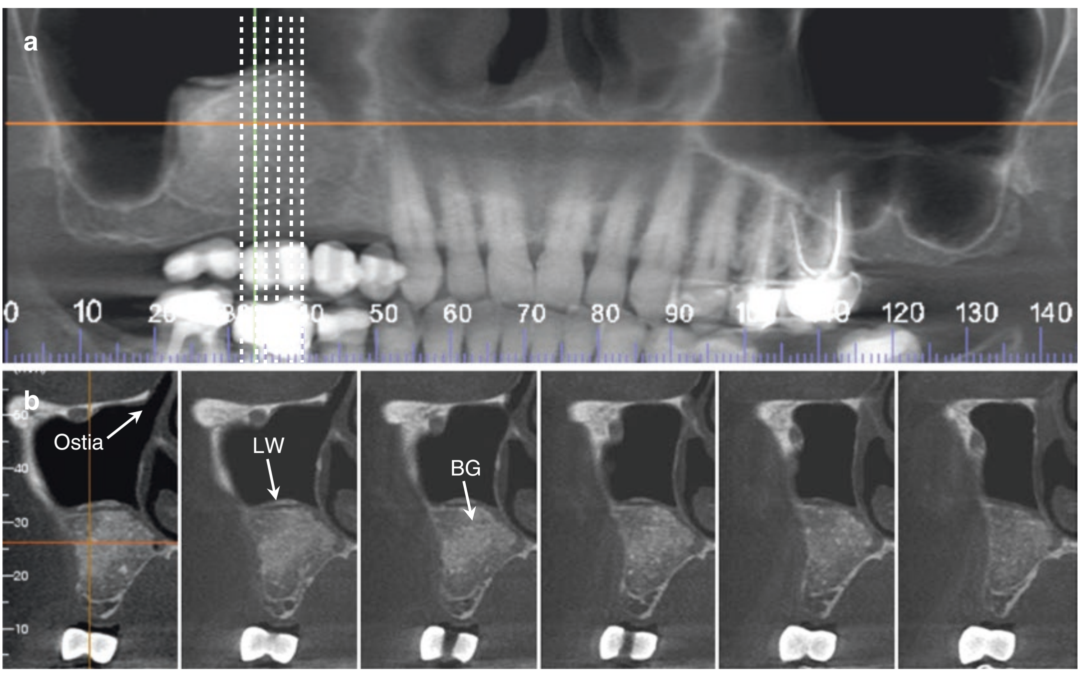

Fig. 30.64 Reformatted panoramic (**a**) with serial 1 mm thick cross-sectional CBCT images (**b**) showing homogeneous hyperdense bone graft (BG) material immediately below the cortical plate of the lateral window (LW) in the maxillary right molar region

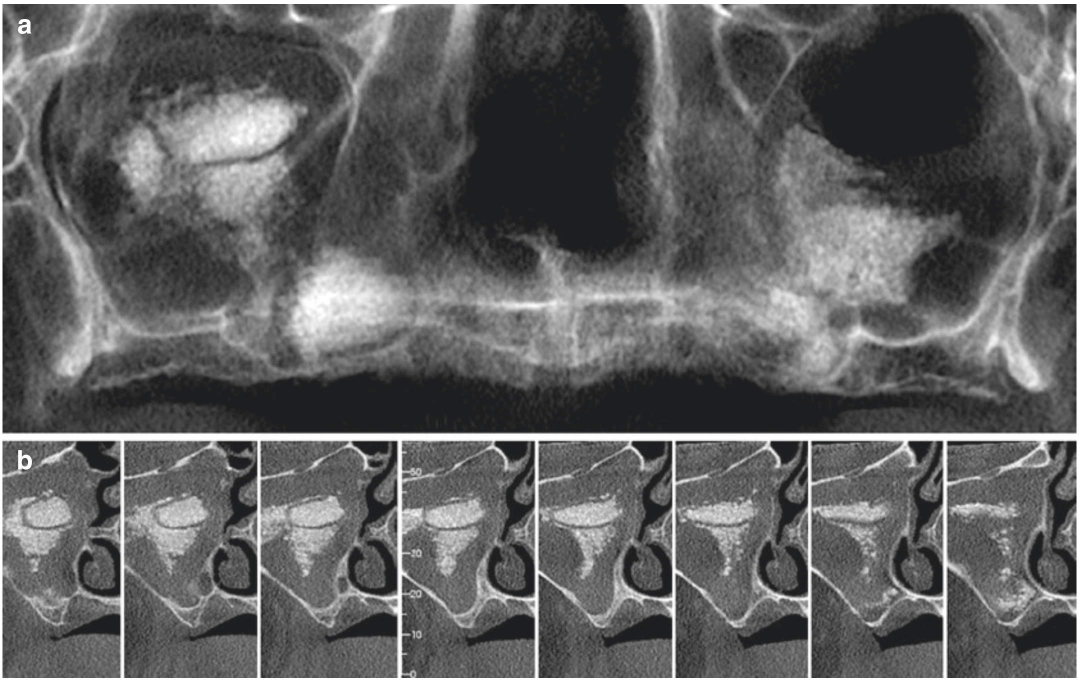

Fig. 30.65 Reformatted panoramic (**a**) and serial 1 mm thick cross-sectional CBCT images (**b**) of a completely edentulous maxilla showing complete right maxillary sinus postoperative infection with supero-lateral displacement and dispersion of hyperdense bone graft material in the maxillary right molar region associated with a sinus lift procedure

onlay grafting is performed, there will be no change in the sinus floor and the graft material will be observed superior or buccal to the alveolar bone. Imaging may also demonstrate postoperative sequelae such as acute sinusitis, graft infection, or formation of an oroantral communication (Fig. 30.65). Graft material scattered or displaced within the sinus can mean failure of incorporation of the graft material (Fig. 30.66). A full description of radiographic patterns of presentation are presented and illustrated in Chap. 22.

30.5 CBCT Imaging Considerations

30.5.1 Task Specific Imaging Protocols

30.5.1.1 Acquisition Recommendations

Guidelines for sinus imaging studies have been proposed by the American College of Radiology (ACR–ASNR–SPR 2014) for MSCT. Based on these recommendations, the following are suggested for CBCT imaging of the paranasal sinuses, particularly the maxillary sinuses:

- **Field of view (FOV)**: For the specific purposes of examining the paranasal sinuses, the inferior boundary of the FOV of the CBCT scan must be adequate to include the entire dentition, and extend superiorly to include at least the fronto-ethmoidal recess and inferior compartment of the frontal sinus. Posteriorly the FOV should extend to include the maximum range of the sphenoid sinuses. With attention to technique, collimation of the FOV for the maxillary sinuses, especially in children, can be performed at 8 cm (height) × 8 cm (diameter) rather than 12 cm (h) × 12 cm (d) FOV which results in a 70% dose reduction (Fig. 30.67) (Casselman et al. 2013).

  When CBCT imaging is performed for dental implant purposes and includes the maxilla, it is advisable that the FOV extends superiorly to the level of the maxillary ostia and include the OMC. Extension of the FOV superiorly to the level of the orbit for screen-

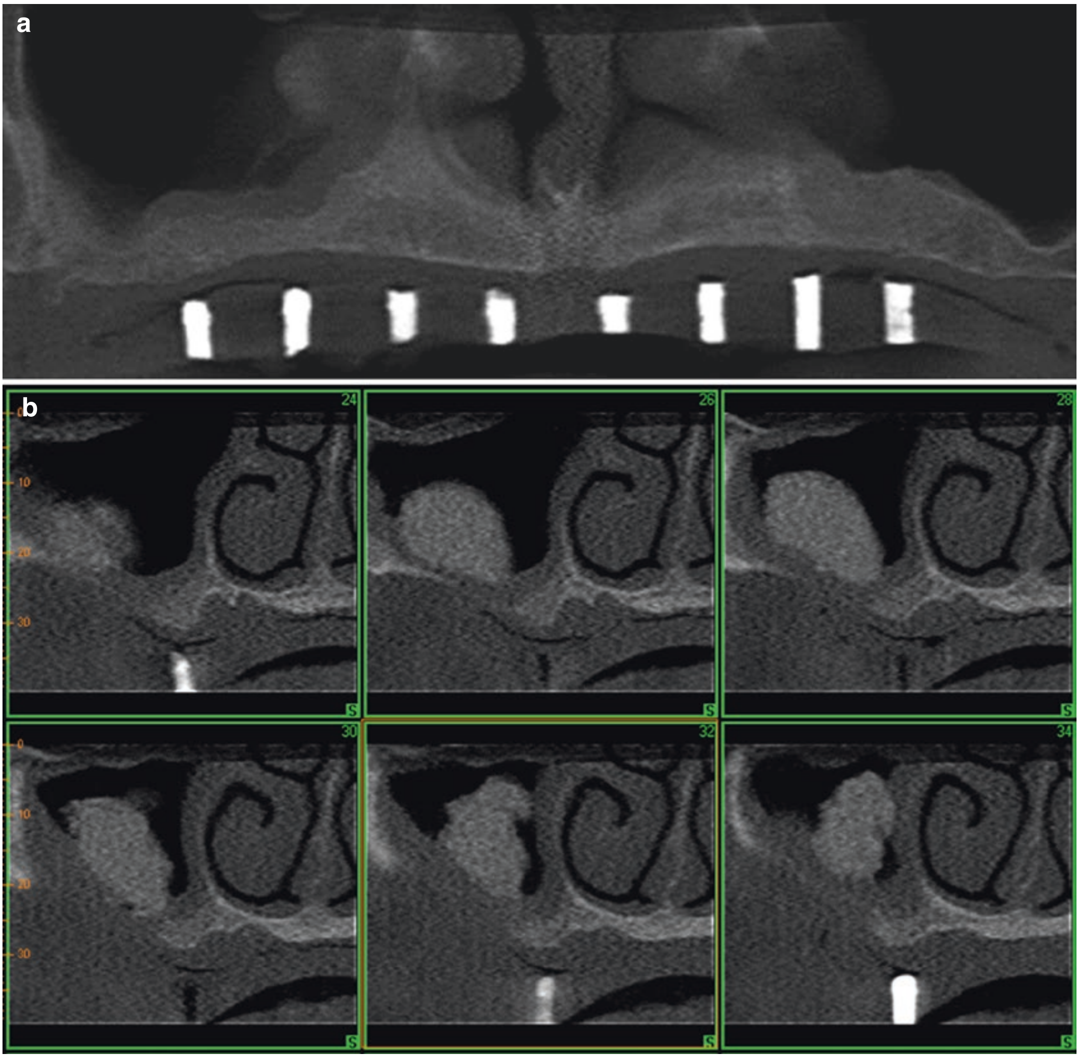

Fig. 30.66 Reformatted panoramic (**a**) and serial 1 mm thick coronal CBCT images (**b**) of a completely edentulous maxilla showing postoperative supero-lateral displacement of hyperdense bone graft material placed in the maxillary right premolar/molar region associated with a sinus lift procedure. The bone graft material is not visible on the panoramic image because of this displacement

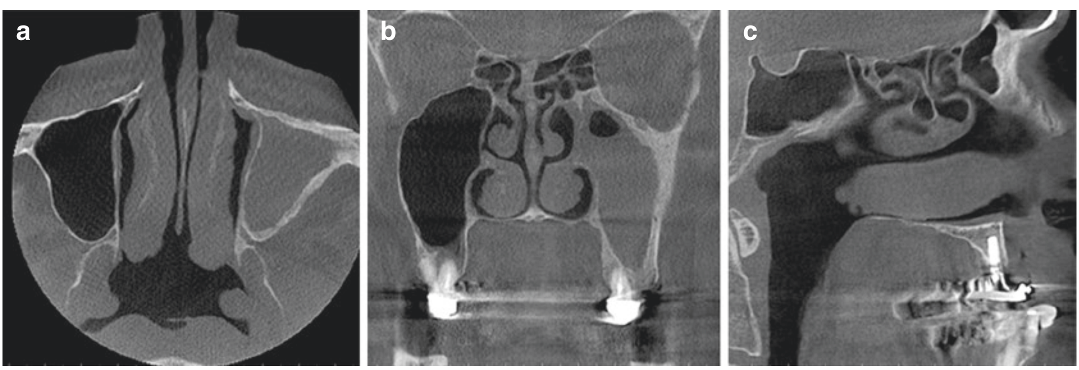

Fig. 30.67 Axial (**a**), coronal (**b**), and sagittal (**c**) CBCT images of the paranasal sinuses demonstrating CRS of the left maxillary sinus acquired at 8 cm (height) × 8 cm (diameter) FOV

ing the entire maxillary sinus for every dental implant patient is unwarranted, as the lenses are sensitive to radiation. If sinus opacification is present and extends beyond the FOV of a CBCT scan of the maxilla taken for any purpose (e.g., small FOV for endodontics, medium FOV of a maxillary edentulous quadrant for implant site assessment), it is highly recommended that: (1) the patient is re-scanned, extending the FOV to an area adequate to cover the entire opacification, or (2) the patient is referred for otolaryngologist assessment.

- **Basis images and reconstructed resolution:** Medical CT images (MCT) are acquired at between 0.6 and 1.0 mm slice thickness and pitches ranging from 0.8 to 5.0 mm resulting in minimally 20 images (1 mm thickness/5 mm gap). All CBCT devices acquire data at resolutions higher than MCT and provide a gapless dataset. While CBCT imaging for sinonasal disease produces noisier images (37.3% higher) and lower signal-to-noise ratios (75% lower), images produced are of comparable diagnostic quality to MCT (Leiva-Salinas et al. 2014).

Image Display Recommendations

- **Orientation**. Often CBCT imaging is performed with the patient head positioned without regard for task specific analysis. For assessment of the paranasal sinuses, the hard palate should be used as the reference plane (ACR–ASNR–SPR 2014). The volumetric dataset should be reoriented such that the sagittal plane is parallel to the antero-posterior hard palate, the coronal plane is parallel to the medio-lateral hard palate and, the axial plane rotated to equally bisect the maxilla in the midline.
- **Image Enhancement**. Bone algorithm or another edge-sharpening algorithm is recommended.
- **Image Reformats**
  - *Orthogonal images.* Dynamic screening of coronal and axial orthogonal images should be performed at 1.0–1.5 mm slice thickness and a comparable (1.0–1.5 mm) gapless slice interval. Lower slice thickness may be considered to identify surface characteristics of opacifications, especially when air surface loculations are suspected in ARS. Contiguous coronal images should be produced from the nasal vestibule to the sella turcica, axial images from the floor of the maxillary sinus (often lower than the palate) to the most superior extent of the FOV, and sagittal images from the midline to the most lateral extent of the maxillary sinuses bilaterally.

    Applying the image reformat parameters above for static display or dynamic assessment produces a series of up to 25 to 40 1.0 mm thick coronal and sagittal images, respectively—certainly too many to interpret or reproduce for most CBCT uses. As most radiologic findings in the paranasal sinuses involve rhinosinusitis, a modified image display has been proposed for MSCT displaying a limited number of representative coronal or axial images. Various names have been used for such protocols, including limited CT, limited axial CT, screening coronal CT, CT mini-series, and limited paranasal CT (Awaida et al. 2004; Cagici et al. 2005). Typically, the representative series includes coronal images at the midfrontal, anterior maxillary sinuses, posterior maxillary sinuses, and midsphenoidal levels. Although the relative accuracy of such protocols is approximately 80% compared to a complete series (Awaida et al. 2004; Cagici et al. 2005), for maxillofacial purposes this provides an adequate visualization of the status of the paranasal sinuses.

30.5.2 Systematic Interpretation of the Paranasal Sinuses

Systematic analysis of the paranasal sinuses should be part of a systematic method to CBCT interpretation. The approach should be directed towards identifying and differentiating anatomic features from radiologic patterns suggestive of disease and recording degrees of maxillary sinus opacification with a view towards appropriate referral to an otolaryngologist. For surgeons who are to encroach the maxillary sinus for MSEG procedures, relative and absolute radiographic contraindications should be acknowledged.

30.5.2.1 Identify Anatomic Features

Specific anatomic features should be identified as dynamic imaging is performed in the respective orthogonal planes (Table 30.3). Axial and then coronal images should be viewed initially.

CBCT imaging is being increasingly introduced as an ENT in-office imaging modality for the diagnosis of chronic rhinosinusitis. It provides excellent osseous anatomic detail, particularly prior to FESS. However, important information is inconsistently reported for sinus CT (Deutschmann et al. 2013). Radiologic reports for the paranasal sinuses should include clinically relevant content related to both critical and noncritical anatomic structures (Table 30.4).

Table 30.4 Critical and noncritical radiologic reporting items for a paranasal sinus scan in relation to FESS

Critical	Noncritical
• Lamina papyracea integrity	• Uncinate process insertion
• Cribriform plate anatomy	• Middle turbinate anatomy
• Ethmoid skull base integrity	• Maxillary/Frontal/ Sphenoid sinus size
• Anterior ethmoid artery	• Presence of infraorbital ethmoidal (Haller) cell
• Sphenoethmoidal (Onodi) cell	• Anterior clinoid process pneumatization
• Optic nerve anatomy	• Bony expansion/erosion
• ICA anatomy	• Degree of Opacification
	• Osteoneogenesis

ICA internal carotid artery

30.5.2.2 Recognize Radiologic Patterns

Few CBCT radiologic patterns are pathognomonic; however, others are suggestive of specific disease entities (Table 30.5).

30.5.2.3 Record Maxillary Sinus Opacification

Two approaches are available to evaluate the degree and pattern of opacity of the maxillary sinus on CBCT images.

- **Quantitative**. Min et al. (1994) described a method using the coronal view where an imaging line is drawn from the uppermost lateral wall to the lowest point of the maxillary sinus. A tangent is then constructed at the midpoint of this line and projected to the lateral wall and the thickness of the opacity measured in relation to this line (Fig. 30.68)
- **Qualitative**. van der Veken et al. (1992) proposed dividing the area of the lumen of the maxillary sinus as seen on the coronal view and subjectively quantifying degrees of soft tissue opacification:
  - Degree 1. 1% to 25% filled.
  - Degree 2. 25% to 50% of the sinus filled.
  - Degree 3.50% to 75% of the sinus filled.
  - Degree 4. 75% to 100% of the sinus filled.

Babbel et al. (1992) described five (5) recurring patterns of sinonasal disease, of which the first three are obstructive:

- *The infundibular pattern (I).* Isolated maxillary sinusitis due to ipsilateral obstruction of the infundibulum.
- *Ostiomeatal unit pattern (II).* Ipsilateral middle meatus is opacified resulting in sinusitis within some or all of the ipsilateral frontal, maxillary, and anterior and middle ethmoid sinuses.

Table 30.5 Principal CBCT radiologic features of the paranasal sinuses and their differential diagnosis

Radiologic feature	Pattern	Distribution	Possible entities	Involved sinuses
Extent and surface characteristics of soft tissue/fluid opacification	Local	Floor	Periapical mucosistis	Only MS
	Regional	Floor, walls	Mucositis, ARS, MSDO	All, especially ES and MS
	Polypoidal	Floor, walls	CRS, pseudocysts, polyps, FuS, herniated encephalocele (ES), antrochoanal polyp (MS), BN	All, especially MS
	Air locules	Floor, surface	ARS, MSDO	All, especially ES and MS
	Partial or complete	Floor	ARS, CRS, MSDO, B+MT	All, especially ES and MS
Variations of bony architecture	Localized, linear, thin	Floor, walls	Septae	All, especially SS and ES
	Localized. round or globular	Floor	Osteoma, periapical halo (MS), MSEG	All especially MS
	Unilocular, well defined	Floor, pericoronal	Odontogenic tumor (e.g., dentigerous cyst, radicular cyst, ameloblastoma, KCOT	Only MS
	Sclerosis	Floor, walls	CRS	All
	Expansion	Floor, walls	CRS, empyema, mucocele, BN	All
	Reduction	Walls	SSS	Only MS
	Erosion	Floor, walls	FuS, MN, PSC	All, especially MS
	Defect	Walls	PSC, MSEG	All, especially MS
Presence and distribution of calcifications within soft tissue	Local, hypodense, globular	Floor, walls	Collapsing radicular cyst (MS), osteoma, antrolith, MSEG	All, especially MS and ES
	Local, "eggshell" like	Peripheral, adjacent floor or lateral wall	CRS	All, especially MS
	Punctate, nodular	Central	FuS, mucocele, inverting papilloma (NF), MN	All, especially MS

MS maxillary sinus, *ES* ethmoid sinus, *FS* frontal sinus, *SS* sphenoid sinus, *ARS* acute rhinosinusitis, *CRS* chronic rhinosinusitis, *FuS* fungal sinusitis, *KCOT* keratocystic odontogenic tumor, *SSS* silent sinus syndrome, *MSDO* maxillary sinusitis of dental origin, *B+MT* benign and malignant tumor, *BN* benign neoplasm, *MN* malignant neoplasm, *NF* nasal fossa, *PSC* postsurgical change, *MSEG* maxillary sinus elevation and grafting

- *Sphenoethmoidal recess pattern (III).* Obstruction is present posteriorly within the region of the sphenoethmoidal recess, resulting in sphenoid and posterior ethmoid sinusitis.
- *Sinonasal polyposis pattern (IV).* Defined when a combination of polypoid soft tissue densities is present throughout the nasal cavity and paranasal sinuses in association with variable diffuse sinus opacification. This is associated with infundibular enlargement and attenuation of the nasal septum and ethmoid bony trabeculae.
- *Sporadic pattern (V).* Includes inflammatory sinus findings, such as retention cysts, mucoceles, and mild mucoperiosteal thickening without coexistent ostiomeatal unit or sphenoethmoidal recess obstruction.

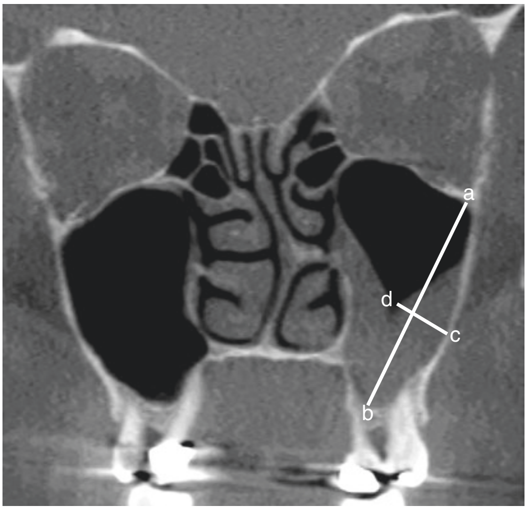

Fig. 30.68 Coronal CBCT imaging demonstrating application of the method proposed by Min et al. (1994) of measuring the thickness of opacity in the maxillary sinus. An imaging line (*a*, *b*) is drawn from the uppermost lateral wall (*a*) to the lowest point (*b*) of the sinus at the level of the maxillary ostium. A tangent is constructed at the midline of *ab* and projected towards the lateral wall and into the lumen. The thickness of the opacity (*cd*) is measured along this tangent

30.5.2.4 CBCT Radiologic Criteria for Specialist Referral

While the paranasal and nasal radiographic signs described above can be observed in the absence of a clinical diagnosis of sinonasal disease, the following CBCT imaging presentations may require, at a minimum, correlation with clinical and medical history or referral to an appropriate specialist (e.g., otolaryngologist) for consultation, further examination, or advanced imaging.

- Pansinusitis (Figs. 30.69 and 30.70).
- Complete sphenoidal soft tissue luminal opacification with or without cortical erosion.
- Extensive bilateral paranasal polypoidal mucoperiosteal thickening.
- Central calcifications within extensive luminal opacifications.
- Loss of osseous architecture, particularly in the region of the OMC.
- Nasal polyposis involving nasopharyngeal extension or loss of bony architecture.

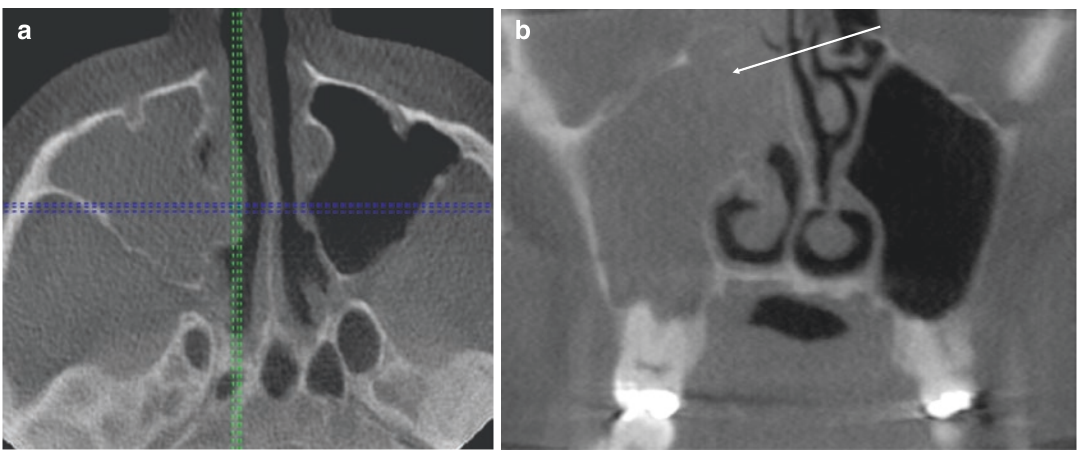

Fig. 30.69 Axial (**a**) and coronal (**b**) CBCT images of patient requiring immediate referral to otolaryngologist. There is complete unilateral opacification of the right sinus, mottling and thinning of the sinus walls, complete loss of osseous architecture involving the middle turbinate and osteomeatal complex and soft tissue expansion into the nasal fossa and ethmoid sinus

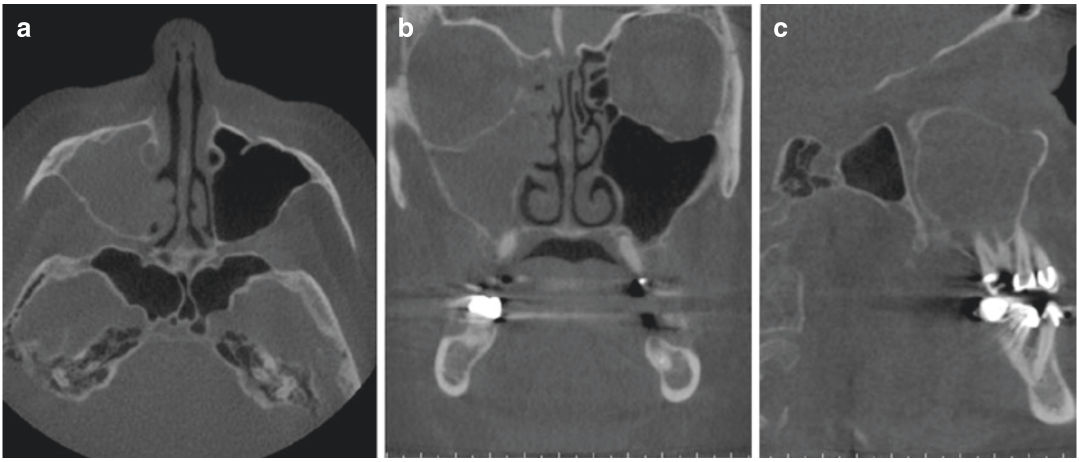

Fig. 30.70 Axial (**a**), coronal (**b**) and sagittal (**c**) CBCT images showing complete unilateral opacification of the right sinus, complete loss of osseous architecture of the medial wall, soft tissue expansion into the nasal fossa, thinning of the sinus walls and right ethmoid soft tissue opacification. Even though the patient is asymptomatic, immediate referral to otolaryngologist is recommended

References

ACR–ASNR–SPR (2014) ACR–ASNR–SPR practice parameter for the performance of computed tomography (CT) of the extracranial Head and Neck Res. 33—2011, Amended 2014 (Res. 39)

Al Abduwani J, ZilinSkiene L, Colley S, Ahmed S (2016) Cone beam CT paranasal sinuses versus standard multidetector and low dose multidetector CT studies. Am J Otolaryngol 37:59–64

Al-Belasy FA (2004) Inferior meatal antrostomy: is it necessary after radical sinus surgery through the Caldwell-Luc approach? J Oral Maxillofac Surg 62:559–562

Albu S, Baciut M (2010) Failures in endoscopic surgery of the maxillary sinus. Otolaryngol Head Neck Surg 142:196–201

American Academy of Otolaryngology Rhinosinusitis Task Force Committee (1997) Report of the Rhinosinusitis task Force Committee meeting. Alexandria, Virginia, august 17, 1996. Otolaryngol Head Neck Surg 117(3 Pt 2):S1–68

American Dental Association Council on Scientific Affairs (2012) The use of cone-beam computed tomography in dentistry: an advisory statement from the American Dental Association Council on Scientific Affairs. J Am Dent Assoc 143:899–902

Arias-Irimia O, Barona-Dorado C, Santos-Marino JA, Martinez-Rodriguez N, Martinez-Gonzalez JM (2010) Meta-analysis of the etiology of odontogenic maxillary sinusitis. Med Oral Patol Oral Cir Bucal 15:e70–e73

Aribandi M, Bazan C 3rd (2007) CT and MRI features in Bipolaris fungal sinusitis. Australas Radiol 51:127–132

Awaida JP, Woods SE, Doerzbacher M, Gonzales Y, Miller TJ (2004) Four-cut sinus computed tomographic scanning in screening for sinus disease. South Med J 97:18–20

Babbel RW, Harnsberger HR, Sonkens J, Hunt S (1992) Recurring patterns of inflammatory sinonasal disease demonstrated on screening sinus CT. AJNR Am J Neuroradiol 13:903–912

Basu MK, Rout PG, Rippin JW, Smith AJ (1988) The post-operative maxillary cyst. Experience with 23 cases. Int J Oral Maxillofac Surg 17:282–284

Bomeli SR, Branstetter BF, Ferguson BJ (2009) Frequency of a dental source for acute maxillary sinusitis. Laryngoscope 119:580–584

Bornstein MM, von Arx T, Altermatt HJ (2008a) Loss of pulp sensitivity and pain as the first symptoms of an Ewing's sarcoma in the right maxillary sinus and alveolar process: report of a case. J Endod 34:1549–1553

Bornstein MM, Chappuis V, von Arx T, Buser D (2008b) Performance of dental implants after staged sinus floor elevation (SFE) procedures. 5-year results of a prospective study in partially edentulous patients. Clin Oral Implants Res 19:1034–1043

Bornstein MM, Wasmer J, Sendi P, Janner SF, Buser D, von Arx T (2012) Characteristics and dimensions of the Schneiderian membrane and apical bone in maxillary molars referred for apical surgery: a comparative radiographic analysis using limited cone beam computed tomography. J Endod 38:51–57

Bornstein MM, Bingisser AC, Reichart PA, Sendi P, Bosshardt DD, von Arx T (2015) Comparison between radiographic (2D and 3D) and histologic findings of periapical lesions treated with apical surgery. J Endod 41:804–811

Brook I (2006) Sinusitis of odontogenic origin. Otolaryngol Head Neck Surg 135:349–355

Brüllmann DD, Schmidtmann I, Hornstein S, Schulze RK (2012) Correlation of cone beam computed tomography (CBCT) findings in the maxillary sinus with dental diagnoses: a retrospective cross-sectional study. Clin Oral Investig 16:1023–1029

Busaba NY, Kieff D (2002) Endoscopic sinus surgery for inflammatory maxillary sinus disease. Laryngoscope 112:1378–1383

Cagici CA, Cakmak O, Hurcan C, Tercan F (2005) Three-slice computerized tomography for the diagnosis and follow-up of rhinosinusitis. Eur Arch Otorhinolaryngol 262:744–750

Carter L, Farman AG, Geist J, Scarfe WC, Angelopoulos C, Nair MK, Hildebolt CF, Tyndall D, Shrout M (2008) American Academy of Oral and maxillofacial Radiology executive opinion statement on performing and interpreting diagnostic cone beam computed tomography. Oral Surg Oral Med Oral Pathol Oral Radiol Endod 106:561–562

Casselman JW, Gieraerts K, Volders D, Delanote J, Mermuys K, De Foer B, Swennen G (2013) Cone beam CT: non-dental applications. JBR-BTR 96:333–353

Cha JY, Mah J, Sinclair P (2007) Incidental findings in the maxillofacial area with 3-dimensional cone-beam imaging. Am J Orthod Dentofac Orthop 132:7–14

Chappuis V, Suter VGA, Bornstein MM (2009) Displacement of a dental implant into the maxillary sinus. Report of an unusual complication when performing staged sinus floor elevation (SFE) procedures. Int J Periodontics Restorative Dent 29:81–87

Cho B-H, Jung Y-H (2008) Prevalence of incidental paranasal sinus opacification in dental pediatric patients. Korean J Oral Maxillofac Radiol 38:219–223

Cho HJ, Jang MS, Hong SD, Chung SK, Kim HY, Dhong HJ (2015) Prognostic factors for survival in patients with acute invasive fungal rhinosinusitis. Am J Rhinol Allergy 29:48–53

Chong VF, Fan YF, Lau DP, Chee LW, Nguyen TM, Sethi DS (2000) Imaging the sphenoid sinus: pictorial essay. Australas Radiol 44:143–154

Cutler JL et al (2003) Results of Caldwell-Luc after failed endoscopic middle meatus antrostomy in patients with chronic sinusitis. Laryngoscope 113:2148–2150

DeFreitas J, Lucente FE (1988) The Caldwell-Luc procedure: institutional review of 670 cases: 1975–1985. Laryngoscope 98:1297–1300

Deutschmann MW, Yeung J, Bosch M, Lysack JT, Kingstone M, Kilty SJ, Rudmik LR (2013) Radiologic reporting for paranasal sinus computed tomography: a multi-institutional review of content and consistency. Laryngoscope 123:1100–1105

Eggesbo HB (2006) Radiological imaging of inflammatory lesions in the nasal cavity and paranasal sinuses. Eur Radiol 16:872–888

Fakhran S, Alhilali L, Sreedher G, Dohatcu AC, Lee S, Ferguson B, Branstetter BF 4th (2012) Comparison of simulated cone beam computed tomography to conventional helical computed tomography for imaging of rhinosinusitis. Laryngoscope 124:2002–2006

Fokkens WJ, Lund VJ, Mullol J, Bachert C, Alobid I, Baroody F, Cohen N, Cervin A, Douglas R, Gevaert P, Georgalas C, Goossens H, Harvey R, Hellings P, Hopkins C, Jones N, Joos G, Kalogjera L, Kern B, Kowalski M, Price D, Riechelmann H, Schlosser R, Senior B, Thomas M, Toskala E, Voegels R, Wang de Y, Wormald PJ (2012) European position paper on Rhinosinusitis and nasal polyps 2012. Rhinol Suppl 50(Suppl 23):1–299

Frei M, Dubach P, Reichart PA, Schmitt AM, Mueller-Garamvölgyi E, Bornstein MM (2012) Diffuse swelling of the buccal mucosa and palate as first and only manifestation of an extranodal non-Hodgkin “double-hit” lymphoma: report of a case. Oral Maxillofac Surg 16:69–74

Gallagher RM, Gross CW, Phillips CD (1998) Suppurative intracranial complications of sinusitis. Laryngoscope 108:1635–1642

Gardner DG (1984) Pseudocysts and retention cysts of the maxillary sinus. Oral Surg Oral Med Oral Pathol 58:561–567

Giardin L, Pontieri F, Savoldi E, Tallarigo F (2006) Aspergillus mycetoma of the maxillary sinus secondary to overfilling of a root canal. J Endod 32:692–694

Gliklich R, Metson R (1994) A comparison of sinus computed tomography (CT) staging systems for outcomes research. Am J Rhinol 8:291–297

Gracco A, Incerti Parenti S, Ioele C, Alessandri Bonetti G, Stellini E (2012) Prevalence of incidental maxillary sinus findings in Italian orthodontic patients: a retrospective cone-beam computed tomography study. Korean J Orthod 42:329–334

Grosjean P, Weber R (2007) Fungus balls of the paranasal sinuses: a review. Eur Arch Otorhinolaryngol 264:461–470

Gruica B, Stauffer E, Buser D, Bornstein MM (2003) Ameloblastoma of the follicular, plexiform, and acanthomatous type in the maxillary sinus: a case report. Quintessence Int 34:311–314

Güneri P, Kaya A, Calişkan MK (2005) Antroliths: survey of the literature and report of a case. Oral Surg Oral Med Oral Pathol Oral Radiol Endod 99:517–521

Illner A, Davidson HC, Harnsberger HR, Hoffman J (2002) The silent sinus syndrome: clinical and radiographic findings. AJR Am J Roentgenol 178:503–506

Janner SF, Caversaccio MD, Dubach P, Sendi P, Buser D, Bornstein MM (2011) Characteristics and dimensions of the Schneiderian membrane: a radiographic analysis using cone beam computed tomography in patients referred for dental implant surgery in the posterior maxilla. Clin Oral Implants Res 22:1446–1453

Kamburoğlu K, Yılmaz F, Gulsahi K, Gulen O, Gulsahi A (2017) Change in Periapical Lesion and Adjacent Mucosal Thickening Dimensions One Year after Endodontic Treatment: Volumetric Cone-beam Computed Tomography Assessment. J Endod 43(2):218–224

Kaneshiro S, Nakajima T, Yoshikawa Y, Iwasaki H, Tokiwa N (1981) The postoperative maxillary cyst: report of 71 cases. J Oral Surg 39:191–198

Keros P (1962) On the practical value of differences in the level of the lamina cribrosa of the ethmoidZ Laryngol Rhinol Otol 41:809–813 [German]

Khongkhunthian P, Reichart PA (2001) Aspergillosis of the maxillary sinus as a complication of overfilling root canal material into the sinus: report of two cases. J Endod 27:476–478

Lana JP, Carneiro PM, de Machado VC, de Souza PE, Manzi FR, Horta MC (2012) Anatomic variations and lesions of the maxillary sinus detected in cone beam computed tomography for dental implants. Clin Oral Implants Res 23:1398–1403

Lang J (1989) Clinical anatomy of the nose, nasal cavity and paranasal sinuses. Georg Thieme Verlag, Stuttgart, Germany

Leiva-Salinas C, Flors L, Gras P, Más-Estellés F, Lemercier P, Patrie JT, Wintermark M, Martí-Bonmatí L (2014) Dental flat panel conebeam CT in the evaluation of patients with inflammatory sinonasal disease: diagnostic efficacy and radiation dose savings. AJNR Am J Neuroradiol 35:2052–2057

Lieu JE, Feinstein AR (2000) Confirmations and surprises in the association of tobacco use with sinusitis. Arch Otolaryngol Head Neck Surg 126:940–946

Lin YH, Yang YC, Wen SC, Wang HL (2016) The influence of sinus membrane thickness upon membrane perforation during lateral window sinus augmentation. Clin Oral Implants Res 27(5):612–617. doi:10.1111/clr.12646

Longhini AB, Ferguson BJ (2011) Clinical aspects of odontogenic maxillary sinusitis: a case series. Int Forum Allergy Rhinol 1:409–415

Longhini AB, Branstetter BF, Ferguson BJ (2010) Unrecognized odontogenic maxillary sinusitis: a cause of endoscopic sinus surgery failure. Am J Rhinol Allergy 24:296–300

Longhini AB, Branstetter BF, Ferguson BJ (2012) Otolaryngologists' perceptions of odontogenic maxillary sinusitis. Laryngoscope 122:19

Lu Y, Liu Z, Zhang L et al (2012) Associations between maxillary sinus mucosal thickening and apical periodontitis using cone-beam computed tomography scanning: a retrospective study. J Endod 38:1069–1074

Lund V, Mackay I (1993) Staging in rhinosinusitis. Rhinology 31:183–184

Mafee MF (2007) Imaging of paranasal sinuses and rhinosinusitis. Clin Allergy Immunol 20:185–226

Mafee MF, Tran BH, Chapa AR (2006) Imaging of rhinosinusitis and its complications: plain film, CT, and MRI. Clin Rev Allergy Immunol 30:165–186

Maillet M, Bowles WR, McClanahan SL, John MT, Ahmad M (2011) Conebeam computed tomography evaluation of maxillary sinusitis. J Endod 37:753–757

Matheny KE, Duncavage JA (2003) Contemporary indications for the Caldwell-Luc procedure. Curr Opin Otolaryngol Head Neck Surg 11:23–26

Melén I, Lindahl L, Andréasson L, Rundcrantz H (1986) Chronic maxillary sinusitis. Definition, diagnosis and relation to dental infections and nasal polyposis. Acta Otolaryngol 101:320–327

Mensi M, Salgarello S, Pinsi G, Piccioni M (2004) Mycetoma of the maxillary sinus: endodontic and microbiological correlations. Oral Surg Oral Med Oral Pathol Oral Radiol Endod 98:119–123

Min YG, Lee JW, Shin JS (1994) Radiologic assessment of diseased mucosa of the maxillary sinus after functional endoscopic sinus surgery. Acta Otolaryngol (Stockh) 114:657–662

Mupparapu M, Singer SR, Rinaggio J (2004) Complex odontoma of unusual size involving the maxillary sinus: report of a case and review of CT and histopathologic features. Quintessence Int 35:641–645

Newman LJ, Platts-Mills TA, Phillips CD, Hazen KC, Gross CW (1994) Chronic sinusitis: relationship of computed tomographic findings to allergy, asthma, and eosinophilia. JAMA 271:363–367

Odel E, Pertl C (1995) Zinc as a growth factor for Aspergillus sp. and the antifungal effects of root canal sealants. Oral Surg Oral Med Oral Pathol Oral Radiol Endod 79:82–87

Pazera P, Bornstein MM, Pazera A, Sendi P, Katsaros C (2011) Incidental maxillary sinus findings in orthodontic patients: a radiographic analysis using cone-beam computed tomography (CBCT). Orthod Craniofac Res 14:17–24

Phothikhun S, Suphanantachat S, Chuenchompoonut V, Nisapakultorn K (2012) Cone-beam computed tomographic evidence of the association between periodontal bone loss and mucosal thickening of the maxillary sinus. J Periodontol 83:557–564

Pokorny A, Tataryn R (2013) Clinical and radiologic findings in a case series of maxillary sinusitis of dental origin. Int Forum Allergy Rhinol 3:973–979

Rege IC, Sousa TO, Leles CR, Mendonça EF (2012) Occurrence of maxillary sinus abnormalities detected by cone beam CT in asymptomatic patients. BMC Oral Health 12:30

Reid JR (2004) Complications of pediatric paranasal sinusitis. Pediatr Radiol 34:933–942

Rosenfeld RM (2007) Clinical practice guideline on adult sinusitis. Otolaryngol Head Neck Surg 137:365–377

Saetta M, Turato G, Baraldo S, Zanin A, Braccioni F, Mapp CE, Maestrelli P, Cavallesco G, Papi A, Fabbri LM (2000) Goblet cell hyperplasia and epithelial inflammation in peripheral airways of smokers with both symptoms of chronic bronchitis and chronic airflow limitation. Am J Respir Crit Care Med 161:1016–1021

Schneider AC, Bragger U, Sendi P, Caversaccio MD, Buser D, Bornstein MM (2013) Characteristics and dimensions of the sinus membrane in patients referred for single-implant treatment in the posterior maxilla: a cone beam computed tomographic analysis. Int J Oral Maxillofac Implants 28:587–596

Smith MM, Smith TL (2001) The role of CT imaging in rhinsinusitis and the need for a standardized CT reading system. Curr Opin Otolaryngol Head Neck Surg 9:17–22

Smith KD, Edwards PC, Saini TS, Norton NS (2010) The prevalence of concha bullosa and nasal septal deviation and their relationship to maxillary sinusitis by volumetric tomography. Int J Dent. doi:10.1155/2010/404982

Soikkonen K, Ainamo A (1995) Radiographic maxillary sinus findings in the elderly. Oral Surg Oral Med Oral Pathol Oral Radiol Endod 80:487–491 de Souza Nunes LS, Bornstein MM, Sendi P, Buser D (2013) Anatomical characteristics and dimensions of edentulous sites in the posterior maxillae of patients referred for implant therapy. Int J Period Rest Dent 33:337–345

Summers RB (1994) A new concept in maxillary implant surgery: the osteotome technique. Comp Cont Educ Dent 15:152–160

Tan HM, Chong VFH (2001) CT of the paranasal sinuses: normal anatomy, variants and pathology. CME Radiology 2:120–125

Tatum OH Jr (1986) Maxillary and sinus implant reconstructions. Dent Clin N Am 30:207–229

Tovi F, Benharroch D, Gatot A, Hertzanu Y (1992) Osteoblastic osteitis of the maxillary sinus. Laryngoscope 102:426–430

van der Veken PJ, Clement PA, Buisseret T, Desprechins B, Kaufman L, Derde MP (1992) Age related CT-scan study of the incidence of sinusitis in children. Am J Rhinol 6(2):45–48

Villa PD (1999) Midfacial complications of prolonged cocaine snorting. J Can Dent Assoc 65:218–223

Viña-Almunia J, Peñarrocha-Diago M, Peñarrocha-Diago M (2009) Influence of perforation of the sinus membrane on the survival rate of implants placed after direct sinus lift. Literature update. Med Oral Patol Oral Cir Bucal 14:E133–E136

Vogiatzi T, Kloukos D, Scarfe WC, Bornstein MM (2014) Incidence of anatomical variations and disease of the maxillary sinuses as identified by cone beam computed tomography: a systematic review. Int J Oral Maxillofac Implants 29:1301–1314

Wen SC, Lin YH, Yang YC, Wang HL (2014) The influence of sinus membrane thickness upon membrane perforation during transcrestal sinus lift procedure. Clin Oral Implants Res. doi:10.1111/clr.12429

Whyte A, Chapeikin G (2005) Opaque maxillary antrum: a pictorial review. Australas Radiol 49:203–213

Yasuda M et al (2007) Epithelial Na^+ channel and ion transport in human nasal polyp and paranasal sinus mucosa. Biochem Biophys Res Commun 362:753–758

Yoo JY, Pi SH, Kim YS, Jeong SN, You HK (2011) Healing pattern of the mucous membrane after tooth extraction in the maxillary sinus. J Periodontal Implant Sci 41:23–29

Yoon JH, Na DG, Byun HS, Koh YH, Chung SK, Dong HJ (1999) Calcification in chronic maxillary sinusitis: comparison of CT findings with histopathologic results. AJNR Am J Neuroradiol 20(4):571

Zinreich SJ, Kennedy DW, Kumar AJ, Rosenbaum AE, Arrington JA, Johns ME (1988) MR imaging of normal nasal cycle: comparison with sinus pathology. J Comput Assist Tomogr 12:1014–1019

CBCT and Additive Manufacturing Technology

31

Gerald T. Grant, Jayanthi Parthasarathy, Shivakumar Raman, Bruno Azevedo, and William C. Scarfe

Contents

G.T. Grant, D.M.D., M.S. (✉)
Department of Oral Health and Rehabilitation, University of Louisville School of Dentistry, Louisville, KY, USA
e-mail: gtgran01@louisville.edu

J. Parthasarathy, B.D.S., M.S., Ph.D.
Department of Engineering, Vanduzen Inc., MedCAD, Dallas, TX, USA
e-mail: jayanthi@medcad.net

S. Raman, Ph.D.
Center for Shape Engineering and Advanced Manufacturing, School of Industrial and Systems Engineering, University of Oklahoma, Norman, OK, USA
e-mail: raman@ou.edu

B. Azevedo, D.D.S., M.S. • W.C. Scarfe, B.D.S., M.S., F.R.A.C.D.S.
Division of Radiology and Imaging Science, Department of Surgical/Hospital Dentistry, University of Louisville School of Dentistry, Louisville, KY, USA
e-mail: Bruno.azevedo@louisville.edu; William.scarfe@louisville.edu

31.1 Introduction

Stereolithography (SLA), the foundational computer-assisted manufacturing (CAM) technology, was introduced by Charles Hull nearly three decades ago. Since then, numerous terms have been used to broadly describe the group of

W.C. Scarfe, C. Angelopoulos (eds.), *Maxillofacial Cone Beam Computed Tomography*,
https://doi.org/10.1007/978-3-319-62061-9_31

related processes and techniques used to fabricate physical scale models directly from three-dimensional (3D) computer-assisted design (CAD) data.

Initially the process was referred to as *rapid prototyping* (RP), being principally an engineering application in which "one off" prototype models were created on demand. Other terms include *solid free-form manufacturing*, *computer automated manufacturing,* and *layered manufacturing*. More recently the process has been called *3-D printing*; however, it is more correctly referred to as *additive manufacturing* (AM). This is as opposed to other principal manufacturing technologies including *subtractive manufacturing* (or, in the context of dentistry, *milling*) and *machining*. 3-D printing is but one of a range of AM processes in which material is extruded through fine nozzles or an energy source is applied to powders or polymers in layers to create an object—similar to inkjet printer print heads.

The original use of AM in medical imaging was to create a life size, dimensionally accurate model of an anatomic structure from computed tomographic (CT) or magnetic resonance imaging (MRI) data. Medical models are models that are sourced from individual patient data and used for patient specific medical applications. These models have been referred to as *stereomodels* (Cheung et al. 2002) or *biomodels* (D'Urso et al. 1999).

Until recently, anatomical models for dentistry have been provided exclusively by specific service providers including dental laboratories and the United States (US) military. Prior to 2005 only a few large-scale, commercial 3-D printers were available from companies like 3D Systems (Rockhill, SC, USA), Stratasys (Eden Prairie, MN, USA) and its subsidiaries Solidscape (formerly Sanders Prototype, Milton NH) and Objet Geometries (Rehovot, Israel), EOS GmbH (Munich, Germany), and Arcam (Mölndal, Sweden), to name a few, with most costing $150,000 USD or more. About 2008, the first commercially available smaller desktop printers (e.g., BfB RapMan 3D Bits from Bytes, Clevedon, UK) and Makerbot (MakerBot Industries LLC, Brooklyn, New York, USA) were introduced. Many more desktop 3-D printers, some of which use alternate printing processes to fabricate plastic objects, are now available in the $1000–$4000 USD range. There continues to be an explosion of systems available on the market (Table 31.1), and many are available in retail stores.

Table 31.1 Examples of commercially available desktop additive manufacturing 3D printers

Make	Manufacturer
Ultimaker 2	Ultimaker BV, Geldermalsen, Netherlands
UP! Box	Beijing TierTime Technology Co. Ltd., Beijing, China
MakerBot Replicator	MakerBot Industries, LLC, Brooklyn, New York, USA
da Vinci 2.0	XYZprinting, Inc., Taiwan, ROC
Threedy	PuzzleShed, Herts, UK
Robox	CEL, Portishead, UK
Cube 3	3D Systems, Rock Hill, South Carolina, USA
UP BOX	Beijing TierTime Technology Co. Ltd., Beijing, China
Form 2	FormLabs, Somerville, Massachusetts, USA

Given the commercial proliferation of this technology and reducing costs in recent years, it is not unreasonable to expect that dental AM will evolve to provide on-demand, on-site clinical manufacturing of surgical guides and anatomic models.

31.2 The AM Sequence

The AM printing process for medical models is simple and comprises the use of design software, a robotic mechanism, and an appropriate printing substrate. All current AM techniques include three consecutive stages (Fig. 31.1):

1. Data acquisition (CT/MRI) providing a 2D image dataset of the anatomic structure as digital imaging and communications in medicine (DICOM) files
2. Development of a virtual three-dimensional (3D) model using a computer graphics interface, referred to as *Computer-Aided Design* (CAD)

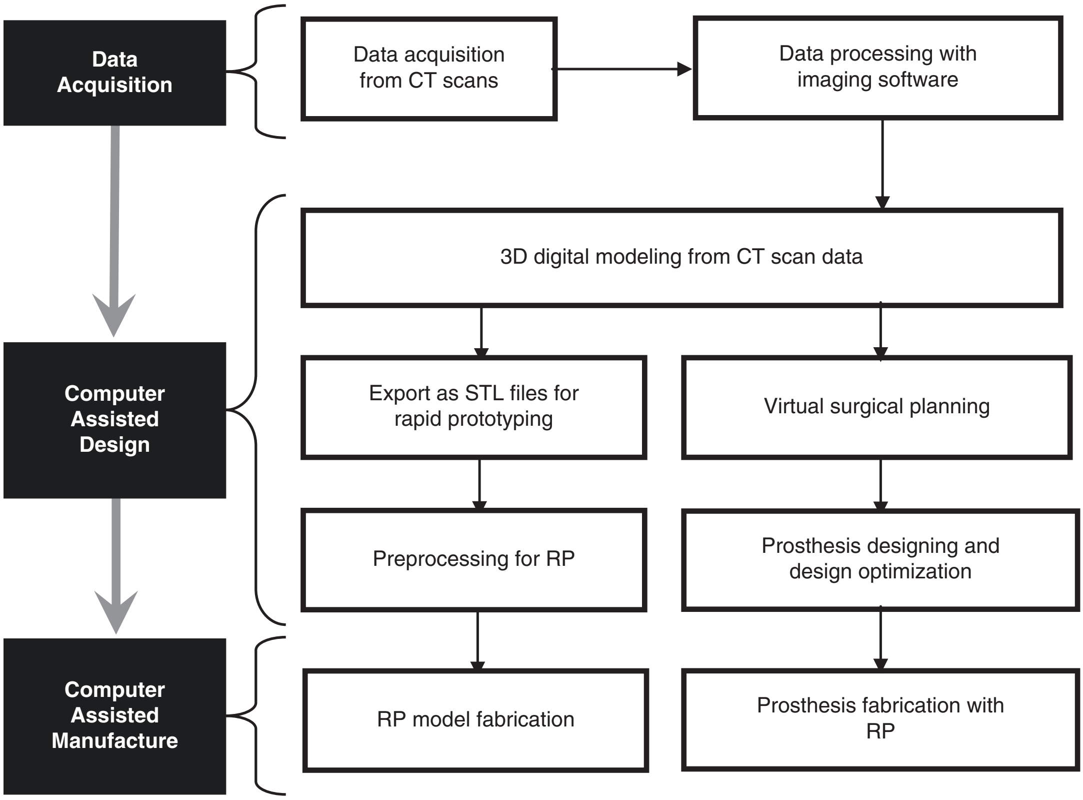

Fig. 31.1 The general scheme of the additive manufacturing process

3. Manufacture of the physical model using various technologies, a process known as *Computer-Aided Manufacturer* (CAM)

Communication between these elements is through CAD/CAM file formats encoded with all the necessary details describing the attributes and assembly instructions of any 3D model such as object shape, size, form, surface texture and color and internal structure and composition. This actually involves two virtual software-based interfaces: a CAD phase involving the use of 3-D modeling software and generation of 3-D model in one file format (e.g., *.skp, *.dae or, *.3ds) and a CAM phase with conversion of the CAD file to a CAM format to facilitate AM.

31.2.1 Data Acquisition

The CAD and CAM processes and subsequent accuracy of the biomodel depends on the quality of the image data. This quality is determined by the technical parameters under which the scan was performed, referred to as the *scan protocol*, and any subsequent alteration of the data prior to export.

31.2.1.1 Scan Protocol

The scan protocol is perhaps the most important stage in the AM process. For images generated using CBCT, many parameters contribute to image quality including section thickness, head orientation, tube current and voltage, patient movement, metallic artifact scatter effects associated with intraoral prostheses or metallic restorations, and image construction algorithm (Choi et al. 2002). For multi-detector CT (MDCT), additional parameters include *pitch*, which determines the interslice dimension, *gantry tilt* which determines head position in relation to axial slices and, *slice image construction algorithm*. For both modalities, section thickness is the major factor. Whether the data is obtained volumetrically (CBCT) or with a fan beam projection geometry (MDCT), the data is ultimately exported as axial slices in two dimensions; thus in order to reconstruct a 3D image, the third dimension is derived from the section thickness. In thick sections, the *interslice-averaging* or *volume-averaging* effect may reduce the precision of the model produced. However, imaging using higher resolution to provide very thin sections will inevitably increase the radiation exposure to the patient. Therefore, there should be a balance between the expected model accuracy and the radiation exposure.

During data acquisition, the patient must remain completely still during the scan. This is achieved by stabilizing the patient's head to prevent any movement during examination. The patient should not be dismissed until the axial data has been assessed for patient movement. Patient motion artifact appears as an unsharp or "double" corticated line and should be repeated if present. The region of interest should be oriented perpendicular to the secondary reconstructed axial slices or the data reoriented prior to data export. Collimation should be such that the image data is collected 2 cm above and below the region of interest. The scan should be performed at a voxel resolution of at least 1 mm or lower.

31.2.1.2 Image Preprocessing

The scan protocol not only includes physical considerations but should also provide guidance on software algorithms applied to optimize image quality. The image data histogram should be adjusted to feature bone—bone "window and leveling." In addition, and unlike MDCT data, CBCT allows reorientation of the volumetric data set prior to export. This should be performed prior to export to minimize "volume-averaging' effects.

31.2.1.3 Image Export

As data processing is performed using third party software, imaging data must be exported from the acquisition device in a format that is able to the read and imported. While cone beam data can be exported in common raster image formats such as TIFF, JPEG, PNG, GIF, and BMP, the most common radiological format is uncompressed DICOM (Digital Image Communications in Medicine) file format. Common to all exported formats is that the image data is provided as axial secondary reconstructions.

31.2.2 Computer-Aided Design

Before the production of the physical models, the data must be reassembled and processed to create a "virtual" model, a process consisting of using imaging processing software to create a model through dynamic and interactive simulation. This is referred to as computer-aided design (CAD). 3D design on a graphic computer interface requires that the original scan data is imported into a proprietary software package capable of generating virtual models, enabling visualization of the particular feature of individual cases. Numerous CAD software packages specific to the design of biomodels are currently commercially available (Table 31.2).

Software packages use anatomical data to create computer models of anatomical structures. There are three essential features of each software package:

- **Image Manipulation and Enhancement**. Use of these features optimize the image quality and orientation prior to 3D modeling and comprise bright contrast adjustment, rotation, scaling, reslicing, the ability to perform measurements, and image editing.
- **3D Modeling**. These features allow generation and manipulation for the digital reconstruction and comprise thresholding, segmentation and region growing functions, the ability to reorient and analyze three-dimensional volumetric data, allow for the assignment of different object names for various tissues and provide for the capability of visualizing the objects either individually or

Table 31.2 Examples of available CAD software

Product	Manufacturer	Web address
Analyze[C]	AnalyzeDirect, Lenexa, Kansas, USA	http://www.analyzedirect.com/
Velocity^{2TM} Plus[C]	Javelin 3D, LLC, Salt Lake City, Utah, USA	http://www.v2software.com/PlusPage.html
3D Doctor[C]	Able Software Corp. Lexington, Massachusetts, USA	http://www.ablesw.com/3d-doctor/index.html
Mimics[C]	Materialise HQ, Leuven, Belgium	http://www.materialise.com/materialise/view/en/86848-Prototyping+solutions.html
AnatomicsPro (formerly Biobuild) [C]	Anatomics Pty. Ltd., Melbourne, Victoria, Australia	http://www.anatomics.net/biobuild_software/index.html
T3D (formerly Slicer, formerly Dicer) [C]	Fortner Research, Sterling, Virginai, USA	
sliceOmatic[C]	TomoVision, Montreal, Quebec, Canada	http://www.tomovision.com/products/sliceomatic.htm
The Visualization Toolkit (VTK)[F]		http://www.vtk.org/
Slicer Dicer[F]	PIXOTEC, LLC, Renton, Washington, United States	http://www.slicerdicer.com/featur.html
3D Slicer[F]	Surgical Planning Laboratory, The Brigham and Women's Hospital, Inc., Massachusetts, USA	http://www.slicer.org/
VRMesh Studio[F]	VirtualGrid Company, Bellevue, Washington, USA	http://www.vrmesh.com/products/studio.asp

F free, *C* commercially available

collectively, visualizing internal structures by assigning transparency features to the external objects and maintaining all images within the same coordinate space.

- **Exporting**. Exporting the 3D data in a compatible format either to AM devices for model fabrication or into CAD software for further analysis such as Finite Element Analysis. This form of analysis allows specific material properties to be assigned to specific elements and provides for load bearing capabilities and other functionalities for the designed anatomical structure to be tested.

Some software packages have advanced features such as 3D image processing, the ability for image registration for multi-modality application, image fusion, image resizing and reslicing and allow for surgical planning.

Currently, generating a virtual model from imaging data can be a cumbersome and time-consuming task. The process to create a 3D digital reconstruction can be considered to involve four steps (Fig. 31.2).

- Image Dataset Creation
- Thresholding and Segmentation
- Modeling
- File Export

31.2.2.1 Creation of Image Datasets

From the DICOM directory of files, relevant axial images are selected within the region of interest is located. This involves selection and removal of axial image sections both above and below the ROI (Fig. 31.3). A 3D dataset is often very large in size and the image planes or slices are stored in separate files. Images can then be

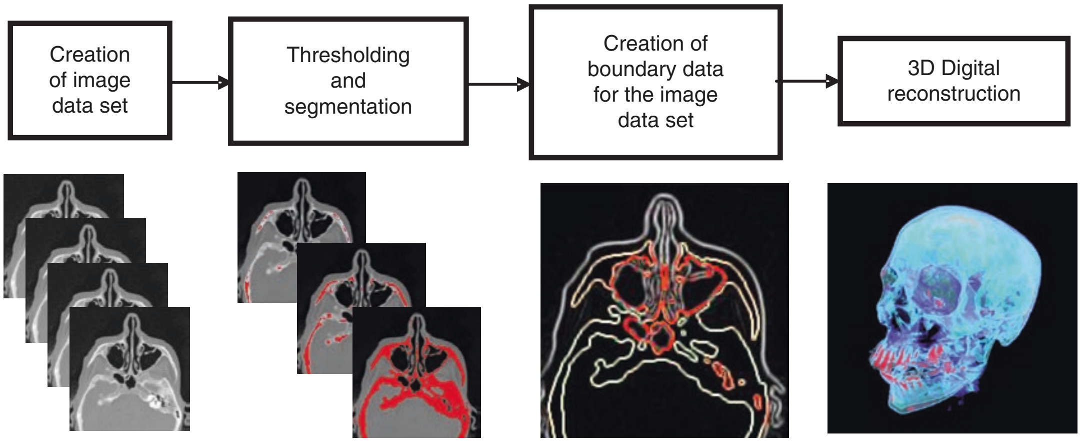

Fig. 31.2 The basic sequential stages in the development and design of 3D reconstruction digital construction creating a virtual computer-generated model

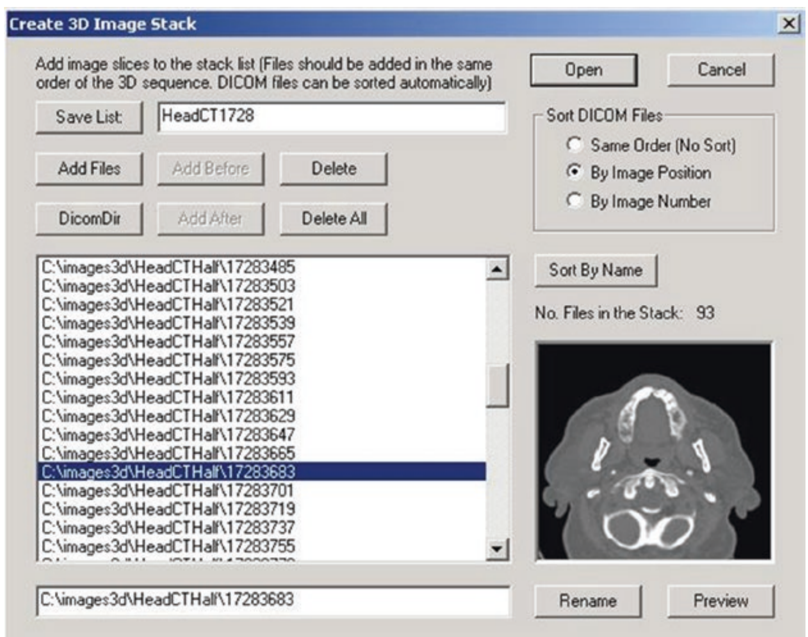

Fig. 31.3 Example of interface used to select and exclude axial images from consideration for inclusion in a 3D "stack"

rearranged and positioned in an image stack to be displayed for reconstruction via image position or image number.

31.2.2.2 Thresholding and Volume Segmentation

As the purpose of 3D modeling is to "extract" specific objects from the volumetric dataset so that they can be fabricated, the next stage involves a process to distinguish between the object(s) of interest and the remaining information, referred to as the "background." The techniques used to identify the objects of interest are denoted as *image segmentation*—they function by segmenting the foreground from the background. As this is applied to consecutive images, it is also called *volume segmentation*.

Segmentation techniques function to generate boundary (or contour) lines between the object of interest and the background. Boundary lines define the image regions to be used by both volume rendering and surface model creation. Segmentation is performed on representative 2D axial slice images by selecting specific image attenuation intensities within the region of interest. These image intensities provide an indication of the nature of the tissues being imaged. The segmentation process involves four steps:

- **Image calibration**. Prior to image segmentation the voxel size (image resolution) should be defined so that the digital reconstruction will have the correct scale in all three-dimensions and can be dimensionally accurate. This is performed by editing the image parameters within the software.
- **Selecting a region of interest**. Defining a region of interest before image segmentation will reduce the processing necessary to the defined region so that segmentation algorithms are only applied to relevant structures. This also reduces the amount of editing needed after image segmentation because object boundaries are only generated within the defined regions.
- **Thresholding**. Specific tissues, particularly bone, are identified visually by representation of their attenuation intensities within a grayscale. Thresholding is the process by which voxels are selected for inclusion and representation in the resultant 3D reconstruction based on their intensity value. This process is applied to all consecutive axial image planes where the specific object of interest is identified.

Thresholding when applied to craniofacial structures is not a trivial task. The size of the datasets and complexity and variability of the structures imaged together with the inherent shortcomings of CBI such as sampling artifacts, noise, patient motion, and low contrast may result in the boundaries of anatomical structures being indistinct and discontinuous. There is currently no threshold method that provides acceptable results for every application. Successful thresholding may therefore consist of the application of more than one algorithm sequentially. Selection of an appropriate algorithm or approach for segmentation can therefore be technically demanding. There are a number of thresholding methods strategies:

– *Interactive grayscale threshold based.* Pixel intensity thresholds are most commonly adjusted interactively and displayed in real time on screen. This technique uses two values to define the threshold range. The thresholds are adjusted interactively by showing all pixels within the range in one color and all pixels outside the range to a different color. Since the thresholds are displayed in real time on the image, the threshold range can be defined locally and varied from slice to slice (Fig. 31.4). When the values are defined properly, the boundaries are traced for all pixels within the range in the image. Grayscale thresholding is best applied when an image has uniform regions of intensity and a highly contrasting background.

– *Global Thresholding*. In this semi-automatic technique, a histogram of the 3-D image is calculated. Next an optimal threshold to divide the image into object and background is derived by determining visual graphical demarcation between pixel intensities representing the object and those of the remainder from the histogram.

– *Texture-based Thresholding*. Texture-based segmentation requires the user to define a specific region within which texture characteristics are calculated and then applied as a pixel classifier to other pixels in one cross-section image or the entire volume to separate them into groups.

– **Extraction of a contour from the serial slices**. The application of these techniques results in the identification of object boundaries within each slice. The resultant boundary data created for each image slice is used for 3D reconstruction (Fig. 31.5).

31.2.2.3 3D Digital Reconstruction

The process of design and construction of any object or entity with 3D space using software is referred to as *modeling*. In medical imaging, virtual models of tissues, usually bone and soft

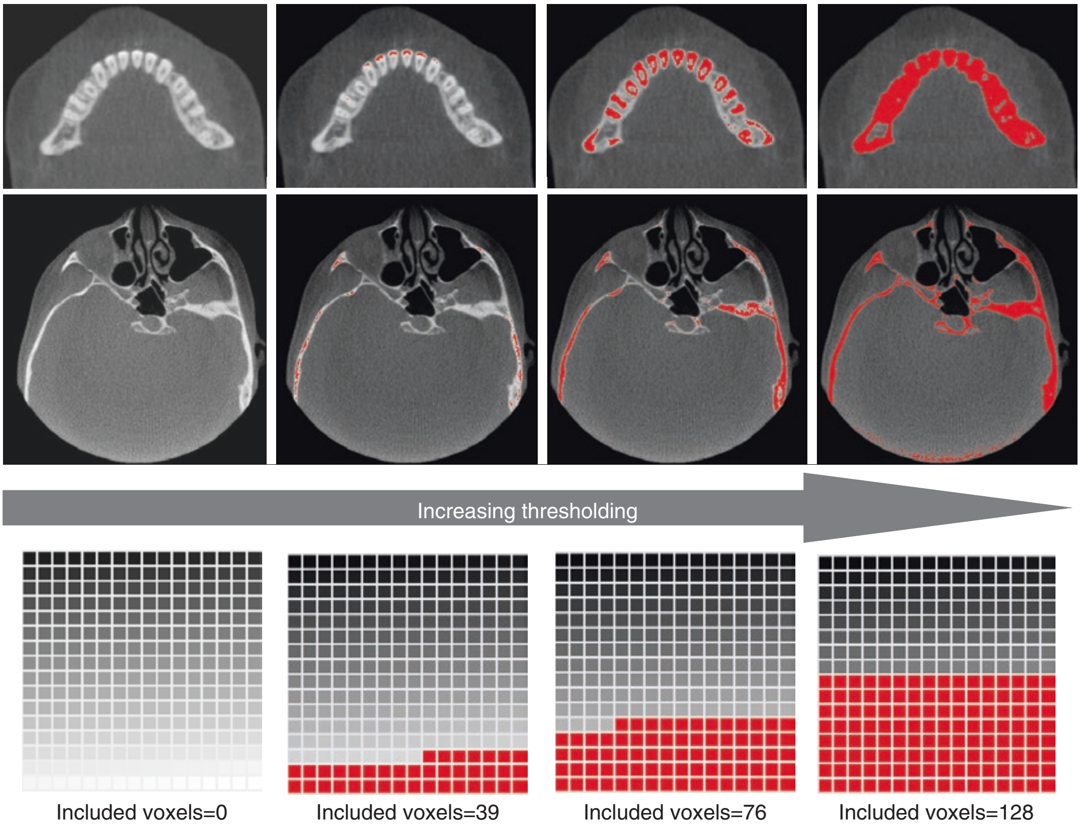

Fig. 31.4 Example of grayscale threshold-based thresholding to identify region of interest. Voxel intensities that are included for segmentation are colored red. As bone is the most highly attenuating structure it usually has the highest voxel value (*white*). As the number of included pixel intensities or grayscales increase and are designated a single color (*red*), the thresholds for inclusion are reduced accordingly (0 to 39 to 76 to 128). Note that threshold selection is structure specific. While the threshold value of 128 includes most of the structures of the mandible, many of the finer structures of the maxilla (e.g., posterior wall of the maxillary sinus) are not included. In addition, some of the image noise (e.g., posterior cranium) are included

tissues, are displayed as separate, surface-rendered objects.

The first phase is the creation of a 3D point cloud model by stacking the 2D axial image boundaries or contours. The previous thresholding and contour extraction processes applied to each image plane create boundary data within each slice which acts as cloud points and splines, relating each slice to the adjacent one. There are many different techniques that can be employed to create 3D "virtual" models including marching cubes algorithm and spline techniques.

After the creation of the model surface, image deconvolution is often used to remove or reduce degradations caused during the imaging process. Numerous 3D deconvolution methods are available to restore degraded 3D images; however, all are directed towards reducing the blurring introduced by image motion, as well as noise due to electronic sources.

The final result of these processes is a computer-generated surface-rendered 3D image of voxels that have been "extracted" from the volumetric dataset by the selection processes of thresholding and segmentation. These virtual models can be rotated, zoomed in and out, and quantitative assessments performed including area, volume, angles, distances, and image region histograms. In addition, other elements can be segmented and by Boolean operations, be displayed together or separately (Fig. 31.6).

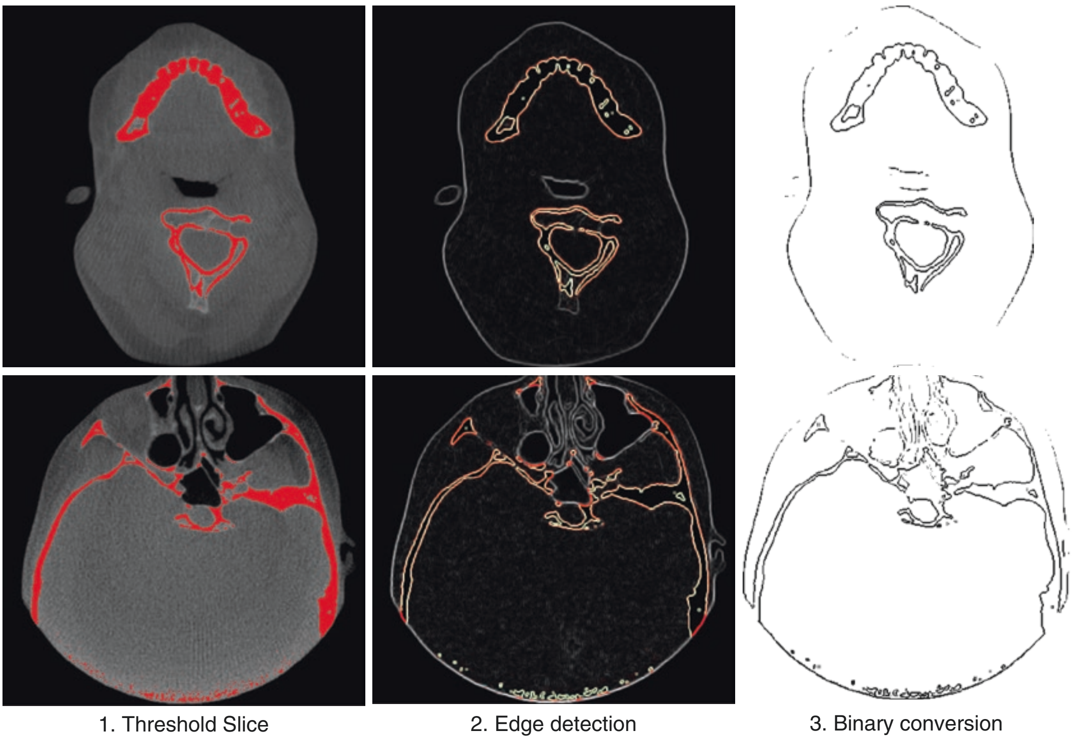

Fig. 31.5 Stage of extraction of contour from each 2D slice. Edge detection algorithms are applied to threshold slices to determine boundaries. Each boundary is reduced into a contour line by reduction into binary elements

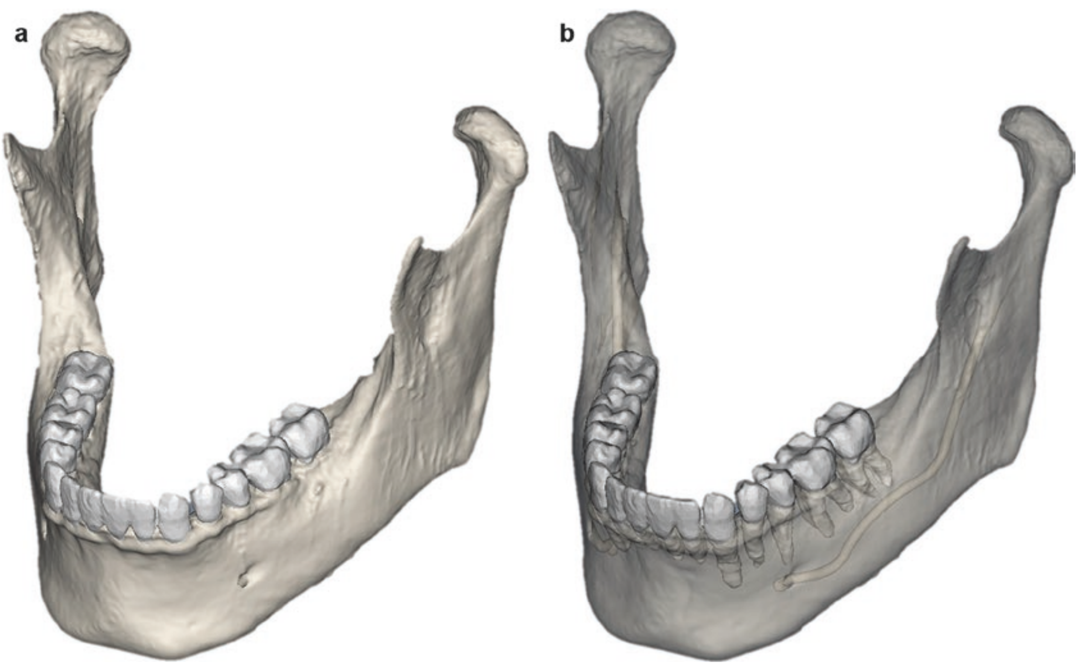

Fig. 31.6 Two virtual reconstructions, one is the surface (*left*) and the other is the body of the mandible with the teeth and the lingual nerve reconstructed as separate structures (*right*). Reconstruction of different anatomical landmarks allows for changes in color, texture, or density with some AM technologies

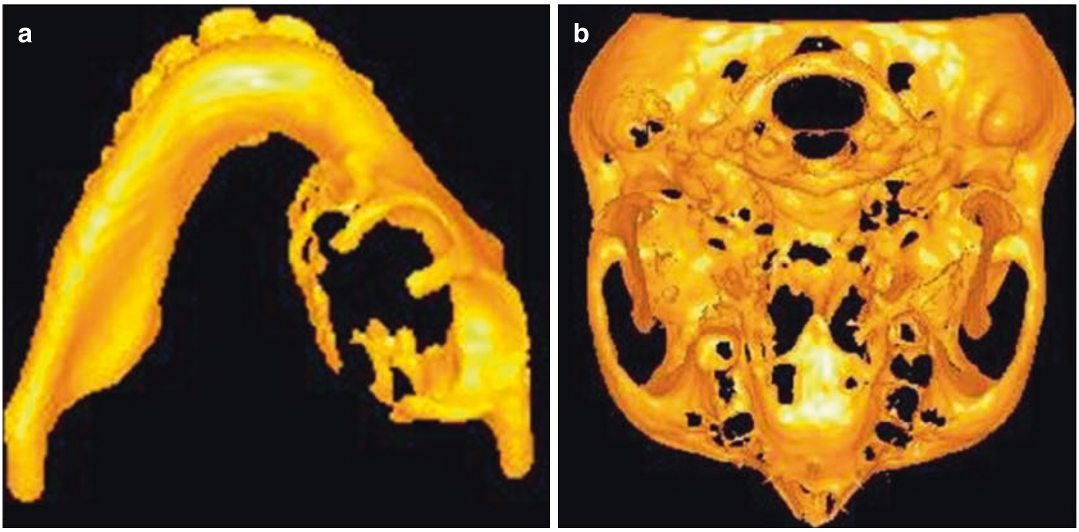

Fig. 31.7 Inferior view of computer-generated images of benign tumor in body of left mandible (**a**) and base of the skull (**b**)

The computer-generated models can be used to study the detailed anatomy of the internal anatomy and calculate measurements relevant to the clinical situation. The 3D model may also provide a discrete visualization of the extent of associated pathology and related anatomy (Fig. 31.7). The 3D reconstruction phase is subject to errors from the previous processes, namely the threshold value determination and volume-averaging effect. Errors can also be due to surface smoothing and interpolation methods for 3D image reconstruction.

31.2.2.4 Output Format for CAD and AM

Numerous file formats currently act as the basic digital output for CAD and AM. Printing files are a CAM format that converts CAD files into directions that printers read to produce 3-D objects. Standard tessellation language (STL) files (*.stl) was the first and remains *the* de-facto CAM file format. 3D Systems developed and published the STL (STL) format in 1987 for moving 3D CAD models to its Stereo-Lithography Apparatus (SLA).

Numerous other proprietary formats have emerged including Initial Graphic Exchange Specification (IGES), Autodesk (*.3ds), Polygon File Format (*.ply), Wavefront (*.obj), Standard for the Exchange of Product Model Data (STEP), Common Layer Interface (CLI), and Virtual Reality Modeling Language (VRML, *wrl). This complicates the process for 3D printing manufacturers in that their CAM software and devices need to support various file formats for 3D models in order to communicate with AM printers. This situation is similar to that encountered in medical and dental imaging almost 20 years ago and resulted in the development and acceptance of the DICOM standard. In addition, AM printers have evolved and innovated beyond the capabilities of current file formats and demand a more information-rich file format, including information on structure (mesh), textures, materials, colors, and print ticket specifically designed to support the needs of modern AM printing throughout the entire printing process.

There have been two approaches towards the development of CAM file formats facilitating interoperability.

- **Additive Manufacturing File Format (AMF)**. The International Standards Organization/American Society for Testing and Materials (ISO/ASTM) developed a non-proprietary format standard for characterizing

CAM objects for AM, the *Additive Manufacturing File* Format (AMF) (file suffix, *.3mf), released in May 2011. Similar to STL format in that it represents objects in a latticework of triangular mesh, it differs in that an AMF file can also specify the material, texture, and the color of each volume, as well as the color of each triangle in the mesh. In addition, to improve geometric accuracy and reduce the number of triangles representing a curved surface, the individual triangles within the object lattice can be curved.

- **3D Manufacturing Format (3MF)**. Since Windows is the main operating system on which CAD applications run, it was only to be expected that a commercial solution has been developed. The 3MF Consortium (http://www.3mf.io/), comprising seven leading companies in the global 3-D printing sector (Dassault Systèmes S.A., FIT AG/netfabb GmbH, Microsoft Corporation, Hewlett Packard, Shapeways, Inc., SLM Solutions Group AG, and Autodesk Inc.) announced the *3D Manufacturing Format* (3MF) (file suffix, *.3mf) specification at the *Build Conference 2015* in early May 2015. According to information provided by the Consortium, the 3MF specification eliminates the problems associated with currently available file formats, such as STL, and resolves interoperability and functionality issues by providing a 3D printing format with the complete model information contained within a single archive. 3MF is an XML-based data format—human-readable compressed XML—is available as open source and is able to read older codes such as STL and OBJ as well as write to 3MF.

31.3 AM Processes

While there are numerous manufacturing processes used to fabricate solid physical models from 3D CAD data, they can be essentially divided into two approaches: methods that create models through "additive" processes, and those that create models by the removal of materials (subtraction). Not only does each vary in the process involved, but also in a number of other aspects. Many of these processes are used in medical and dental application for models and devices (Mitsouras et al. 2015).

AM printing technologies have recently been categorized by the American Society for Testing and Materials Standards body (ASTM Active Standard F2792, June 2012) according to manufacturing process. Objects are now able to be manufactured not just as a solid plastic mass but with texture, in various colors, with internal structure, and using different materials. Several software packages are available; however, whichever method is employed to convert the 3D digital reconstruction into a physical biomodel, CAD data must be preprocessed.

All AM machines have proprietary software to slice the STL file into contiguous thin consecutive layers, one on top of the other. Apart from the layer thickness, other parameters which are determined during preprocessing are orientation of the object and nozzle diameter (for FDM which determines the thickness of the filament). Because the physical model may have separate components (e.g., maxilla and mandible), preprocessing also generates supports for overhanging structures which are also laid down during fabrication. The layer thickness ranges from 0.002 to 0.020 in. depending on the process and system. The layer thickness determines the final surface finish of the object. The less the layer thickness, the better is the surface finish. Decreasing layer thickness also increases the processing time and therefore the cost of production. Optimization of these parameters is therefore dependent on considerations of the trade-off of finish versus cost at this stage.

There are several commercial AM systems available. This review focuses on a current, commonly accepted classification of 3D printing technologies adopted as ASTM Standard F2792 (ASTM. F2792-12a 2014). There are seven groups of specific 3D printing technologies: vat photopolymerization, material jetting, binder jetting, material extrusion, powder bed fusion, sheet lamination, and directed energy deposition. The following describes the processes for the more popular systems used for fabricating dental and medical models and devices.

31.3.1 Vat Photopolymerization

This includes the original AM manufacturing process, stereolithography.

31.3.1.1 Stereolithography (SLA)

Stereolithography was the first and the most widely used commercial AM system. It was introduced in 1988 by 3D Systems Corporation (Valencia, California, USA). SLA uses an ultraviolet-based laser to selectively cure a cross-sectional computer-assisted design image of an object in a photopolymer layer of liquid to selectively solidify photocurable resins. Initial AM applications were used to manufacture parts and concept models for visualization, checking of form and fit. The earliest series reporting on the use of AM models in craniofacial surgery was reported by Fleiner et al. (1994).

There are four main parts of the stereolithography machine (Fig. 31.8):

- Vat of a photopolymer
- Light source, usually a laser
- Platform
- Elevators

Objects are built upon an elevator platform immersed in a vat containing photopolymer liquid. To build each layer, a laser beam is traced onto the surface (by servo-controlled galvanometer mirrors), drawing a cross-sectional pattern in the *x*–*y* plane to form a solid section. The platform is then lowered into the vat and the next layer is drawn and adhered to the previous layer. The steps are repeated, layer by layer, until the complete object is built.

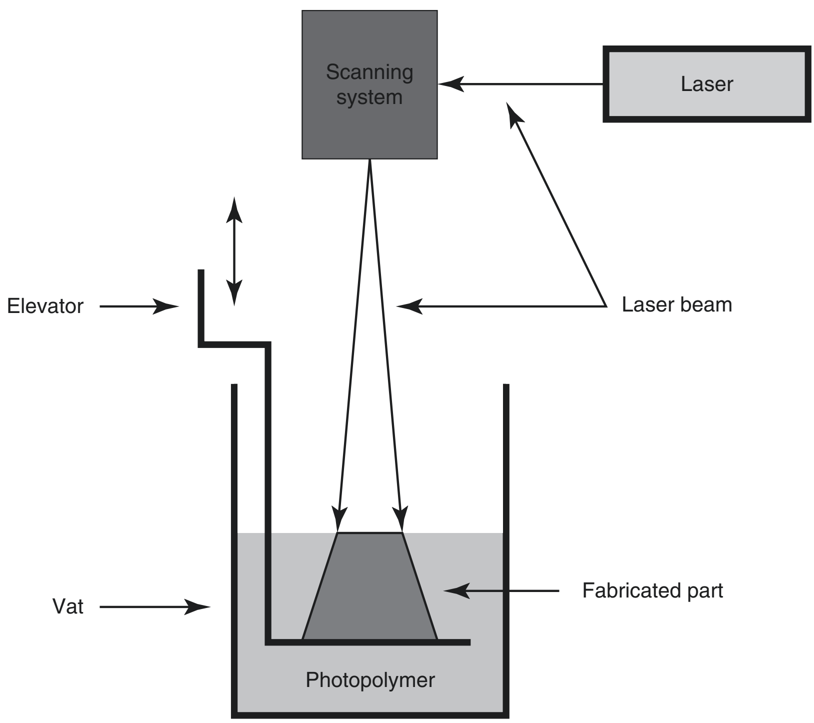

Fig. 31.8 Schematic demonstrating the four main components of SLA vat polymerization process including the liquid tank (vat) which holds several gallons of the clear, liquid plastic photopolymer (Photopolymer), a perforated platform which is immersed in the tank and can be moved up and down as the process is performed, an ultraviolet laser which transforms the liquid polymer into the 3D object (Laser), and a computer that controls the laser and movement of the platform (Elevator) during the printing process (image reproduced with permission, Liu et al. 2006)

Since photopolymers are relatively viscous lowering the elevator by a small distance of the layer thickness (i.e., −0.002 to −0.020 in.) down into the vat alone does not permit the liquid to uniformly recoat the upper surface of the part in a timely fashion. A recoating mechanism is therefore required to facilitate this process. Stereolithography uses a "deep dipping" recoating technique, whereby the elevator is first lowered several millimeters so that the liquid entirely flows over the current upper surface of the part. The elevator is then raised to the desired height and doctor-blade (wiper arm) traverses the surface to quickly level the excess viscous material. Features with gradually changing overhangs can be built up without support structures (Figs. 31.9 and 31.10).

Large overhanging features however require supports, since the initial layers that form them can warp or break off as the part moves down into liquid. The supports are typically built up as thin wall sections that can easily be broken away from the part upon completion. The design of the thickness, number, and width of the contact point with the model can influence the total amount of additional material used, orientation of the object, as well as the time required to fabricate the object (build time). In addition, these structures must be manually removed.

Because of the layered process, the biomodel may have a surface composed of stair steps. Sanding can remove the stair steps for a cosmetic finish. Model build orientation is important for stair stepping and build time. In general, orienting the long axis of the model vertically takes longer but has minimal stair steps. Orienting the long axis horizontally shortens build time but magnifies the stair steps. Models are transparent and have an advantage in medical applications as

Fig. 31.9 Example of desktop medium build (145 × 145 × 175 mm) desktop SLA 3D printer (From 2, FormLabs Inc., Somerville, Massachusetts, USA) with automated resin system and accessories required to post process model

Fig. 31.10 Example of professional large build (380 × 380 × 250 mm), ultrahigh resolution (0.001–0.002 in.) SLA 3D printer (ProJet 7000 3D Systems, Inc. Rock Hill, South Carolina) capable of custom medical product manufacturing using USP Class VI certified clear resin

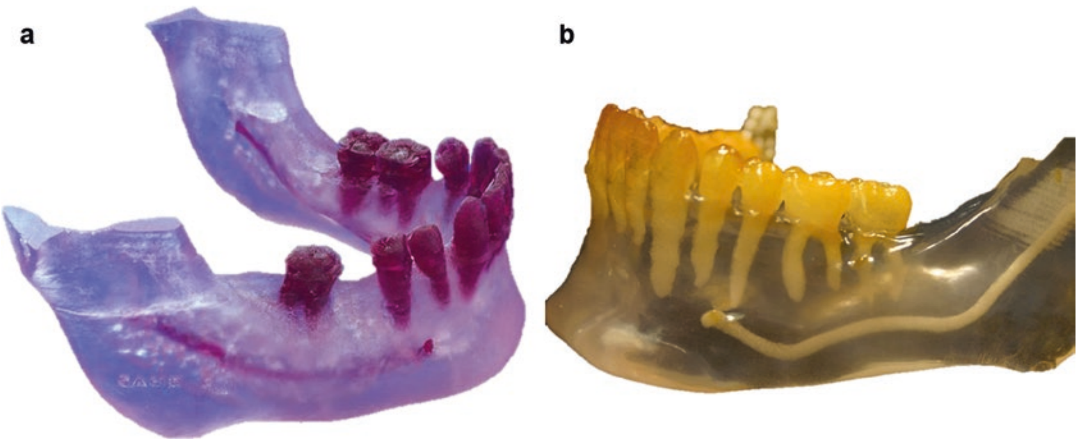

Fig. 31.11 SLA model with colored resin showing inferior alveolar nerve and teeth

the internal structures like teeth and the inferior alveolar canal can be built with colored resins (Fig. 31.11).

Because the laser used in the SLA process is not of high enough power to completely cure the model, there is a necessity for post-curing. In addition, long-term curing of the material used can lead to warping.

31.3.2 Material Jetting

31.3.2.1 Inkjet-Based Processes

The ink jet printing method is named after the process from the printer and plotter industry. This method utilizes ink jet technology to shoot droplets of liquid-to-solid compound and form a layer of an AM model. There are numerous ink jet printing techniques; however, while none have become as established as the SLA or SLS® systems, several show promise.

- **Thermal Phase Change Inkjet**. This technology, also referred to as ballistic particle manufacturing (BPM), uses a jet system to squirt a build material in a liquid or melted state, which cools or otherwise hardens to form a solid on impact (Fig. 31.12). Systems have multiple print heads arranged in a liner array which moves back and forth like a line printer, dropping the liquid on demand. Models are built on a platform which is lowered after each layer is deposited and another layer is deposited over the previous one until the object is completely built. Sanders Model Maker (Sanders Prototype, Inc., Wilton, New Hampshire, USA) and Multi-Jet Modeling (3D systems, Valencia, California, USA) are the popular systems.
- **UV Photopolymer Phase Change Systems**. First introduced in 2000 as PolyJet™ technology (Objet Geometries Ltd., Rehovot, Israel), this process is based on photopolymers, but uses a wide area inkjet head to layer wise deposit both build and support materials. It subsequently completely cures each layer after it is deposited with a UV flood lamp mounted on the print head. The support material, which is also a photopolymer, is removed by washing it away with pressurized water in a secondary operation. The layer thickness can be as thin as 16 µm. The surface and accuracy of these models are very good. Thin walled structures and complex anatomical details can be seen well on models built with this process (Fig. 31.13). An advantage to this technology is that soft and harder materials can be layered to a desired durometer, making it an excellent method to build complex polymer structures for dental and medical devices, recent advancements in this technology have provided limited ability to color the materials.

Another similar system (InVision™, 3D Systems, Rockhill, SC) uses wax as a support material that is melted away from the part, rather than washed away with water.

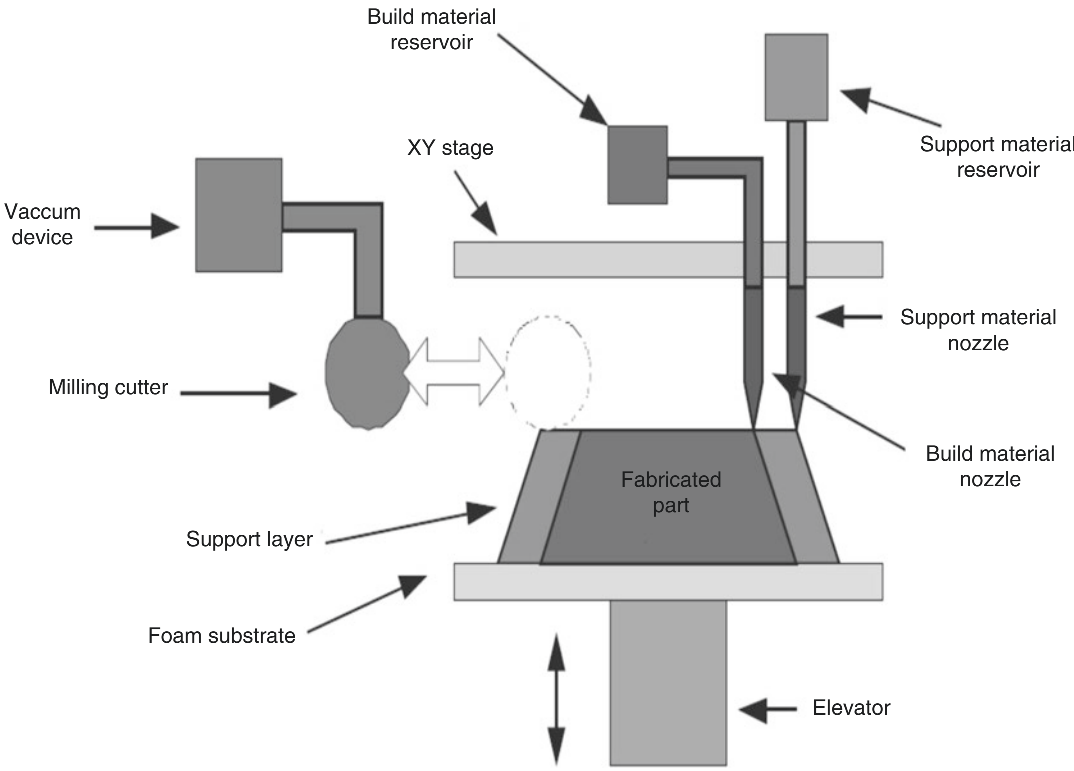

Fig. 31.12 Schematic of an inkjet-based AM system (image reproduced with permission, Liu et al. 2006)

Fig. 31.13 Materials jetting model with white and clear polymer (Connex 500, Stratasys Ltd., Eden Prairie, Minnesota, USA)

31.3.2.2 Binder Jetting

Process where a print head with a binder, selectively binds a powder, layer by layer. This process generally is supported by the powder. It allows for color models and recovery is by blowing away the unbound powder (Fig. 31.14).

- **3D Printing**. Three-Dimensional Printing (3DP), developed by MIT (Massachusetts Institute of Technology) and Soligen Inc., (Northridge, California, USA), uses powder that is spread on a platform and a binder is dropped to solidify the appropriate area (Fig. 31.14). A variety of materials ranging from starch to polymers can be used for fabrication and generally there is a need for post-processing of the product due the "green" stage of the materials. Wax, cyanoacrylate, and resins have been used to infuse the structures for a more durable product. The models can be sawed and realigned for proper anatomical fit of pre-contoured plates (Fig. 31.15). This technology is one of the few processes that allows for the printing of full color prototypes. It is also recognized as the fastest method. This technology is marketed commercially by 3D systems, Rock Hill, South Carolina, USA.

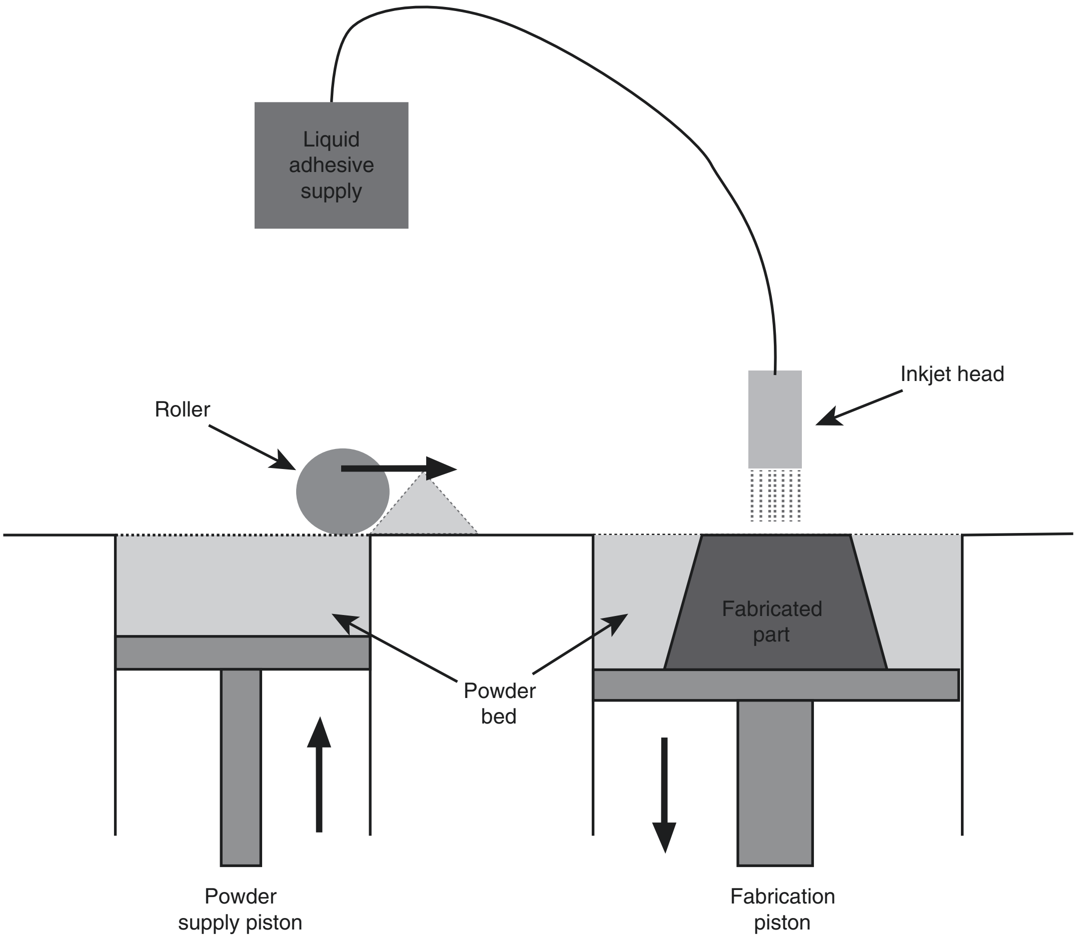

Fig. 31.14 Schematic of a binder jetting system (image reproduced with permission, Liu et al. 2006)

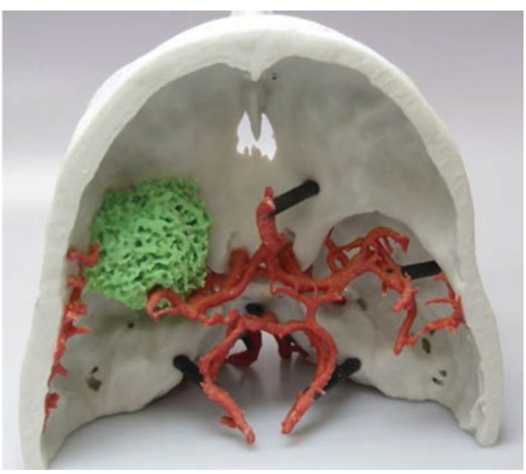

Fig. 31.15 Printed model cranial model to include tumor and vasculature. Binder jetting technologies allow for a variety of color choices to be used in the fabrication of medical models

31.3.3 Material Extrusion

This AM printing process involves the extrusion of thermoplastic material and is the most common process for desktop printing. Examples include the following:

31.3.3.1 Fused Deposit Modeling (FDM)

This trade named process, developed and commercialized by Stratasys (Eden Prairie, MN, USA), was the first to avoid the use of laser. A more fundamental form, *Freeform Fabrication*, is used by desktop 3D printers (Fig. 31.16). The fundamental process involves creation of a solid model by controlled deposition of a molten polymer monofilament. In contrast to SLA, which can only create models in resin, FDM can create biomodels fabricated from

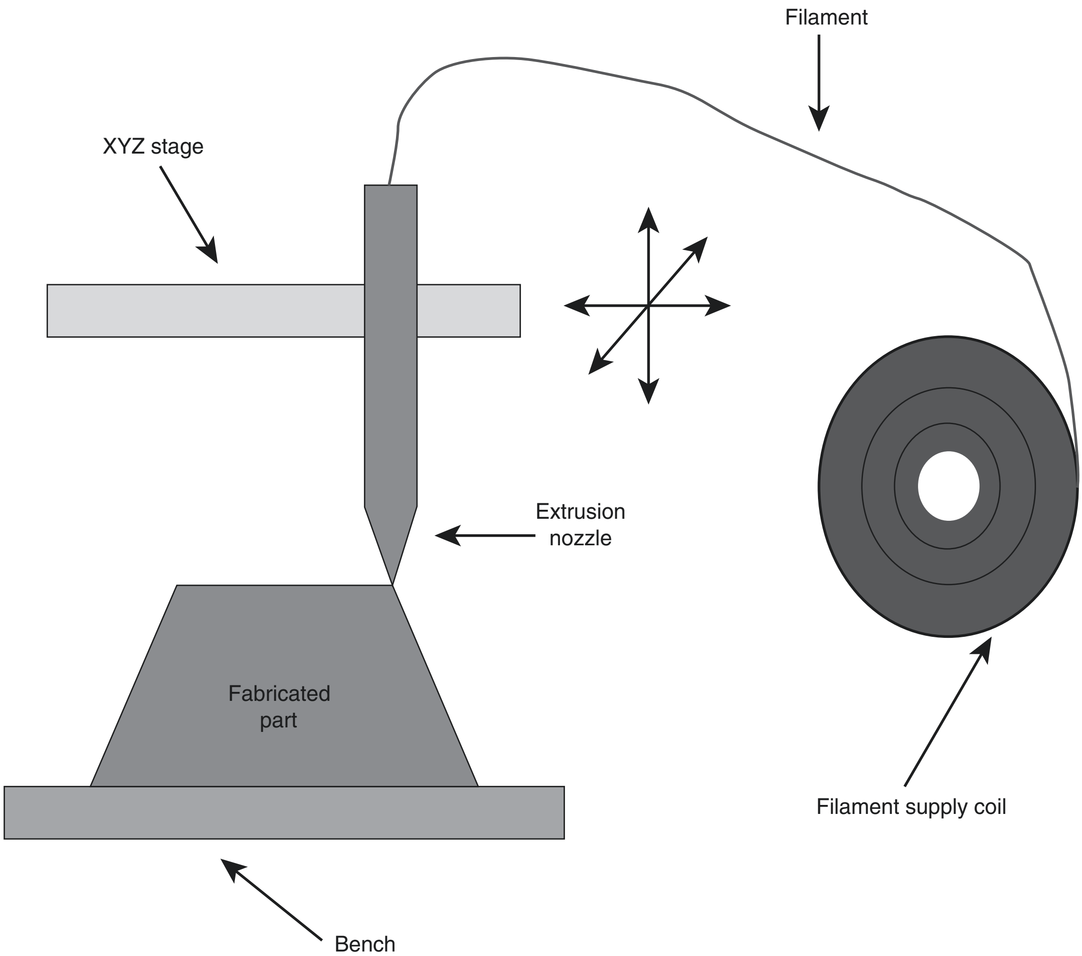

Fig. 31.16 Schematic of FDM process (image reproduced with permission, Liu et al. 2006)

materials such as polyester, Acrylonitrile Butadiene Styrene (ABS), elastomers, and investment casting wax. However, similar to SLA, object fabrication requires support structures.

The system has a platform which can go up and down by its movement in the *z* axis. The prototype is built on hard foam that is mounted on the platform. This expendable foam substrate is about 1-in. thick and can be fastened to the platform easily. More recently models have built over thin acrylic sheets instead of hard foam. This acrylic substrate is held onto the table firmly by vacuum clamping. The machine has a XY table at the top. The XY table carries a twin-extrusion head which can be moved in the XY plane along the desired path at the desired speed. One of these heads extrudes the model material and the other extrudes the support material. The XY table and the platform are inside an insulated cabin chamber. The raw material used in FDM is solid in the form of a wire/filiment roll placed in a cylindrical chamber whose inner diameter is the same as the wire/filiment diameter with the required allowance to permit smooth sliding. The chamber temperature depends primarily on the material being extruded and is maintained by the surrounding coils. The temperature of the chambers of modeling and supporting heads can be individually set by the user. At the entry to this chamber is a pair of pinch wheels through which the raw material wire passes through into the chamber. One of the pinch wheels is idler, the other is driven by a stepper motor at the desired speed. At the exit, a nozzle with different diameters can be fixed. The nozzle diameter ranges from 0.012 and 0.025. The wire/filiment passing through the pinch wheels absorbs heat along its path in the chamber, softening and finally becoming a semisolid. While the wire/filiment is in solid form it acts as a piston for the chamber and extrudes the semisolid material ahead of it. During the extrusion, a stream of thin filament of the semisolid material comes out of the nozzle with the diameter as that of the nozzle. A layer is formed by depositing the filament along its contours and filling the interiors of these contours by the filament in a zigzag fashion. A 3D feature is realized in the form of several 2D contours with the starting point for the deposition is the same in all the layers. The zigzag filling alone is used for the support material so that it will be easy to break.

Two types of support materials are used. One is a light gray colored plastic which is deposited sparsely. This material is light and can be easily broken off. The second is soluble supports, wherein the fabricated model is put in a tank of water with a solvent proprietary solution vibrated and maintaining the temperature of the tank. The supports dissolve leaving the model (Fig. 31.17).

One of the advantages of FDM over SLA is that the model is created in a single processing step and, unlike SLA, biomodels do not require additional cleaning and curing under ultraviolet light. This reduces the overall time to produce a model. This process has been successfully used by researchers for producing biodegradable scaffolds for cranioplasty using polycaprolactone (Zein et al. 2002). This is the type of printer that are available for home use due to the costs and availability of the materials and the simplicity of the technology.

Fig. 31.17 FDM Model of mandibular tumor

31.3.4 Powder Bed Fusion

This process involves a powder and power source. The powder is generally spread in a layer upon a platform and a power source such as a laser or an electron beam is used to fuse the powder in a given shape in a repeated manner until the structure is completed.

31.3.4.1 Selective Laser Sintering (SLS)

Selective laser sintering (SLS®, DTM™, Austin, TX, USA). A powder is spread over the build cylinder and CO_2 laser is traced with the help of a scanner system over fine powder (Fig. 31.18). The heat from the laser melts the powder particles just below the melting point and a solid layer is built. The next layer of powder is again spread and the process is repeated until the part is built. No supports are required for overhanging parts in process as the surrounding powder itself acts as a support. Metallic powders can be used in this process to build direct functional metallic components. The resultant object is usually stronger; however, the initial surface finish is powdery or rough, like the base material whose particles are fused together without complete melting; however, a varnish-like coating can be applied to SLS® parts to seal and strengthen them. While SLA is more accurate immediately after completion of object fabrication, SLS® is less prone to residual stresses that are caused by long-term curing and environmental stresses.

31.3.4.2 Direct Metal Laser Sintering (DMLS)

DMLS uses a high-powered 200 W Yb-fiber optic laser. Inside the build chamber area, there is a material dispensing platform and a build platform along with a recoater blade used to move new powder over the build platform. The technology fuses metal powder into a solid part by melting it locally using the focused laser beam. Parts are

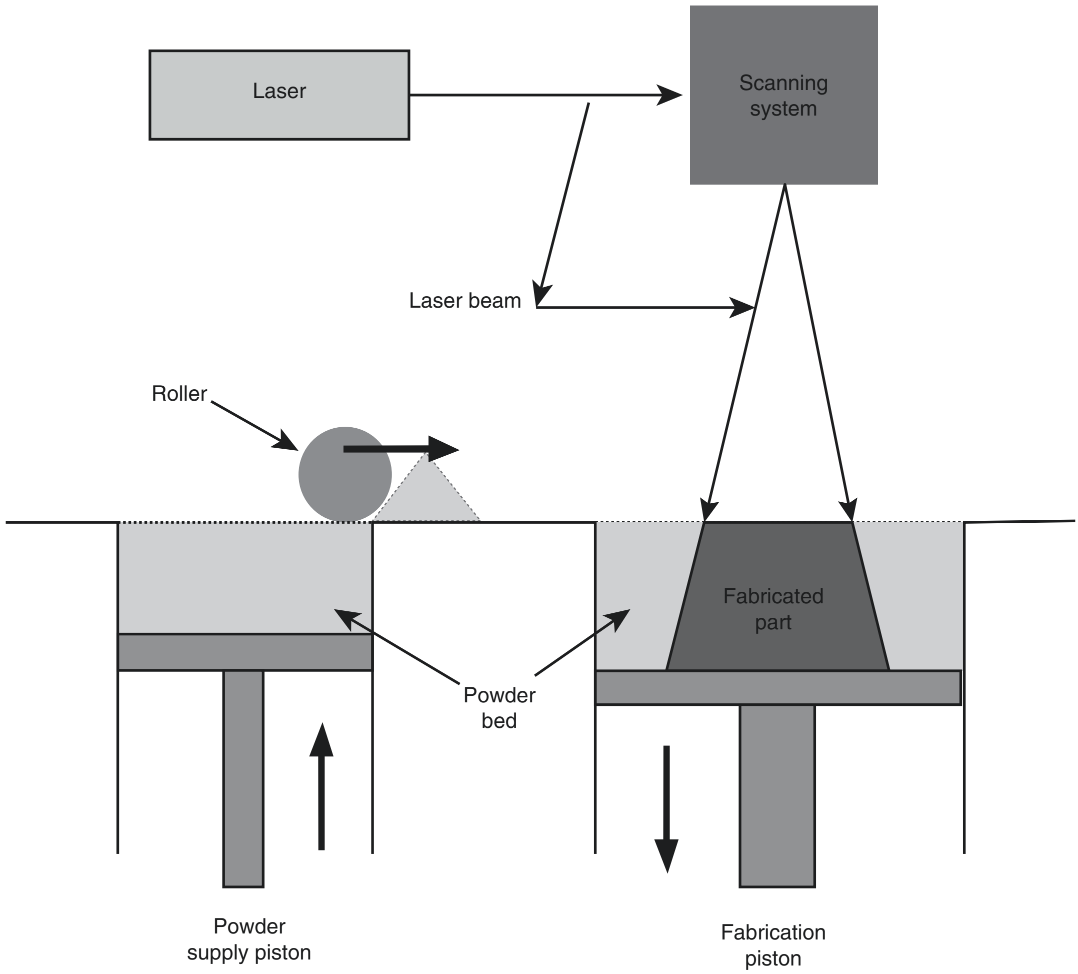

Fig. 31.18 Schematic of SLS process (image reproduced with permission, Liu et al. 2006)

built up additively layer by layer, typically using layers 20 µm thick. This process allows for highly complex geometries to be created directly from the 3D CAD data, fully automatically, in a relatively short time and without any tooling. DMLS is a net-shape process, producing parts with high accuracy and detail resolution, good surface quality and excellent mechanical properties. This technology is currently used in the fabrication of some dental restorations.

31.3.4.3 Electron Beam Melting (EBM)

This is a recently developed AM technology which makes the direct manufacture of custom metal implants possible. The system is manufactured by Arcam AB (Mölndal, Sweden) and marketed by Stratasys, Inc. (Eden Prairie, Minnesota, USA). The metals that can be used for this process include titanium alloys and cobalt-chromium. An electron beam melts the powder metal layer by layer to build parts. The process can be compared to laser-based systems but since an electron beam has much more energy than a laser beam and melts the material effectively, it is therefore more energy efficient. The electron beam is generated from a gun on the top of a vacuum chamber. The temperature of the electron beam is more than the melting or even vaporizing points of the metals and therefore melts the metal powder. The target area and point for melting are fixed by two magnetic fields: the first one for the diameter of the beam and the second for deflecting the beam to the precise point. The process has been successfully used to fabricate custom implants for craniofacial reconstruction (Fig. 31.19).

Fig. 31.19 Custom cranioplasty plate fabricated with EBM (Courtesy 3-D Medical Applications Center, Walter Reed National Military Medical Center Bethesda, Maryland, USA)

31.3.5 Sheet Lamination

This process, also known as laminated object manufacturing (LOM), stacks layers under pressure of thin sheets of paper or other material to fabricate an object. Each layer is cut using a laser to match a cross section of the model (Fig. 31.20). A binder such as glue is used to fuse the sheets of material together. A rather inexpensive process, the materials range from paper to metals. There is currently no medical or dental application.

31.3.6 Directed Energy Deposition

Directed Energy Deposition (DED) covers a range of terminology including laser engineered net shaping, directed light fabrication, direct metal deposition, and 3D laser cladding. It is a more complex printing process commonly used to repair or add additional material to existing components (Gibson et al. 2010).

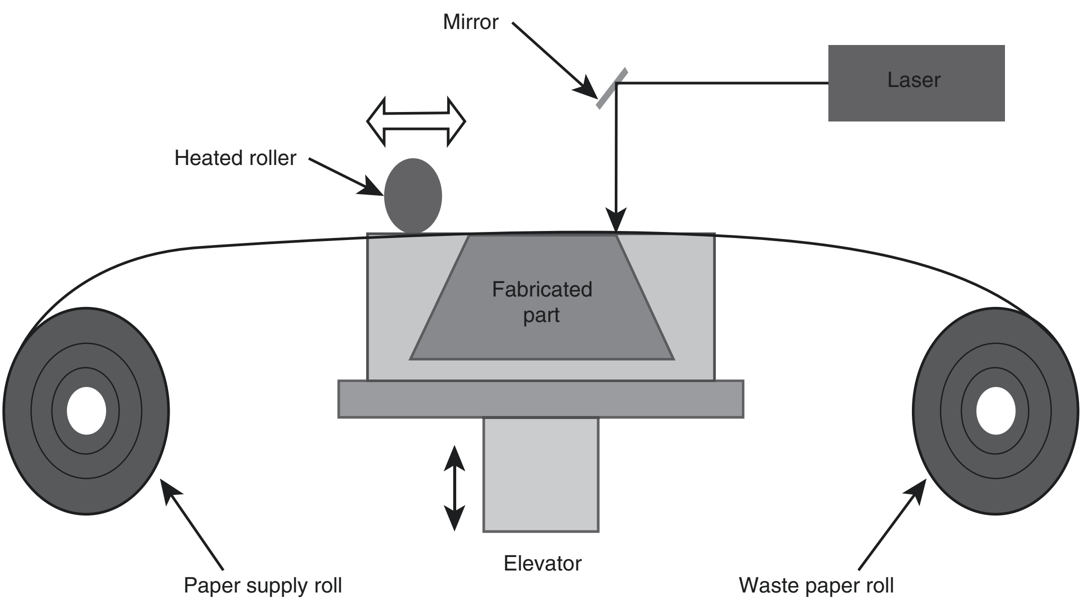

Fig. 31.20 Schematic of LOM process. Mechanically a ribbon of sheet material routed through several idler rollers which store and supply the material. Located above the platform is a heated roller capable of heating and compressing the ribbon between itself and the stack of laminations on the platform. The ribbon material is bonded to the top of the stack. An X–Y positioning table carries two mirrors, which reflect a beam from a CO_2 laser and a lens which focuses the beam on the upper surface of the laminated stack so as to cut the very top layer. After the cutting of one layer, excess paper is cut away to separate the layer from the web. Waste material is wound on a take-up roll. The laminated part is grown on a platform capable of a vertical incremental movement under the action of a stepper motor. (Image reproduced with permission, Liu et al. 2006)

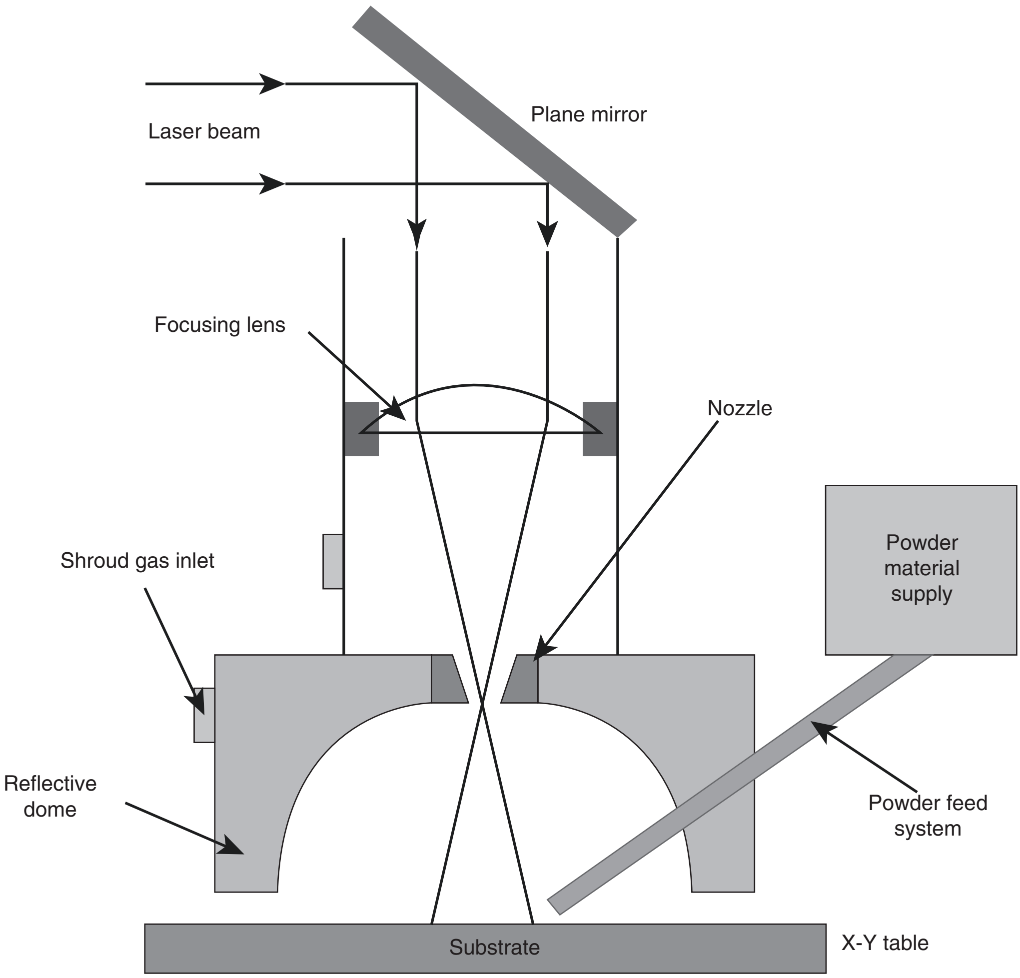

Fig. 31.21 Schematic showing the features of directed energy deposition. Metal is fabricated directly from CAD solid models using metal powders injected into a molten pool created by a focused, high-power laser beam. The laser beam is focused to a small spot by one or more lenses. The deposition head moves relative to the substrate to write lines of the metal with a finite width and thickness, forming layers to fabricate the final near net shape part. Metal powders are delivered and distributed either by gravity or by using a pressurized carrier gas (Image reproduced with permission, Liu et al. 2006)

A typical DED machine consists of a nozzle mounted on a multi axis arm, which deposits melted material onto the specified surface, where it solidifies. The process is similar in principle to material extrusion, but the nozzle can move in multiple directions and is not fixed to a specific axis. The material, which can be deposited from any angle due to 4 and 5 axis machines, is melted upon deposition with a laser or electron beam. The process can be used with polymers, ceramics but is typically used with metals, in the form of either powder or wire (Fig. 31.21). Currently there are no medical or dental applications associated with this technology.

31.4 Comparative Accuracy of AM in OMF Applications

The clinical success of AM technology for patient management and operative simulation is largely dependent on the dimensional accuracy of the biomodel (Lill et al. 1992; Barker et al. 1994;

Kragskov et al. 1996). While many factors interact to determine the dimensional accuracy of biomodels, the fundamental determinants are the nature of the anatomical structure of interest, the imaging technique, 3D modeling, the RP process itself, and measurement error (Choi et al. 2002; Taft et al. 2011).

- **Anatomic Structure of Interest**. Thin fine structures which may be unsupported are inherently more difficult to represent on RP models because of difficulties in thresholding and segmentation. They are more likely not to be reproduced than corticated regions. This is particularly evident in regions such as the maxillary tuberosity and walls of the maxillary antrum.
- **Imaging Technique**. The scanning stage is important as the quality of the original CT images is dependent on many common technical parameters associated with imaging (e.g., patient movement, metal artifact of intraoral prostheses, tube current and voltage, and the partial volume-averaging effect associated with the slice image construction algorithm itself), and technique specific parameters encountered in both conventional CT (section thickness, pitch, gantry tilt) and CB imaging (voxel dimensions).
- **Modeling**. The threshold value, a specified density on each image slice that separates the organ of interest and other regions, defines contour lines representing the boundary of the region of interest. The boundaries obtained from every slice form an isosurface with the same density. Choi et al. (2002) reported that the effect of threshold value on the dimensions of a craniofacial biomodel depended on whether it was an internal or external measurement. They found that for external measurements reducing threshold values compared to the optimal resulted in reducing the thickness by subtracting an additional layer from the original boundary and reducing the dimensional size whereas for internal measurements reducing the threshold increased dimensional size. They attributed this result to a phenomenon that they have referred to as the “dumb-bell effect.”

Additional sources of error in model reconstruction include topological defects, such as tessellation, triangle edge, and closure errors, decimation ratio for surface smoothing, and methods of interpolation. These produce areas of topological incompleteness and surface inhomogeneities which may contribute to reduced accuracy.

- **The AM Process**. Residual polymerization and transformation of the photosensitive resin, apart from laser diameter, laser path, layer thickness, timely creation and removal of support structures and finishing are among potential sources of error in the production of biomodels. While most dimensional inaccuracies introduced by the RP process can be considered to be within a clinically acceptable range (Choi et al. 2002; Taft et al. 2011), it is necessary to appreciate the potential errors that the technique can produce. Dimensional accuracy has also been reported to vary as much as 15% according to the technique used (Gibson et al. 2006). For example, FDM is unable to build fine bone features whereas 3D printing structures are brittle. In addition, the reduction in mechanical strength of up to 75% over 2 years exhibited by models created using SLA may result in inadvertent damage of the model

Many authors have reported an acceptable level of clinical accuracy for biomodels in maxillofacial applications (Table 31.3).

Despite the range of nominal differences between actual and RP model dimensions reported (Schicho et al. 2006; Lin et al. 2006; Bill and Reuther, 2004; Choi et al. 2002; Asaumi et al. 2001; Kragskov et al. 1996; Barker et al. 1994; Lill et al. 1992), this is approximately equivalent to the thickness of a dental or maxillofacial surgical saw and is much finer than the surgical bur. Thus, when surgeons plan osteotomy operations using the RP models, the amount of distortion within the model is actually well within the lost distance of the surgical osteotomy cuts.

Table 31.3 Selective summary of research reporting accuracy of biomodels in oral and maxillofacial applications

Study (year)	Comparison	Type	Difference: Mean absolute ± s.d. (mm)	Difference: Mean percentage ± s.d. (%)
Taft et al. (2011)	HS	RP	(Based on number of fiducial in *x*, *y*, *z*)	
Nazim et al. (2006)	HD	RP	0.23 (1.37)	0.08 (1.25)
Schicho et al. (2006)	HS	RP	2.5 (–)	2.2 (–)
Lin et al. (2006)	HS	RP	0.22 (1.04)	–
Bill and Reuther (2004)	PS	RP	0.88 (–)	2.7 (–)
Choi et al. (2002)	HS	RP	0.62 (0.53)	0.56 (0.39)
Asaumi et al.(2001)	HS	RP	–	0.63 (–)
Kragskov et al. (1996)	CT	RP	1.98 (1.20)	3.59 (2.67)
Barker et al. (1994)	HS	RP	1.90 (1.48)	2.54 (1.38)
Lill et al. (1992)	HS	MM	1.47 (0.94)	2.19 (1.37)

HS human skull, *PD* pig skull, *CT* #D computed tomography, *RP* rapid prototype model, *MM* milled model

31.5 Advantages and Limitations

31.5.1 Advantages

Biomodels provide a tactile, accurate representation of bony anatomical structures and, in some situations, of soft tissue. There are numerous advantages to the application of 3D modeling in cranio-maxillofacial surgery (Santler et al. 1998).

- **Diagnostic Information to Facilitate Operative Planning**. An important advantage of biomodels is that they may facilitate preoperative diagnosis. Because of the clinical accuracy, precise measurements defects can be assessed with clinical precision. For fractures, important information concerning the amount and orientation of dislocation is easily discerned. As some of this information may also be achieved by the use of 3D–CT visualization, the decision as to whether a 3D model is necessary, should be made after 3D CT assessment. In addition, dysmorphology resulting from asymmetry or craniofacial deformity can be quantitatively assessed and analyzed in three dimensions providing a basis for operative correction.
- **Surgical Simulations**. In complex deformity cases, surgery may be performed on the model prior to the definitive operation. While at this point it is not possible to routinely reproduce the facets of the dentition in enough accuracy to fabricate surgical stents, biomodels allow the performance of simulated surgery including osteotomies and prebending of osteosynthesis material and assessment of autogenous donor transplant size and shape.
- **Reconstruction of Defects**. Unilateral osseous defects requiring extensive reconstruction can be facilitated by using the contralateral unaffected side by fabricating a mirror version AM model as a template for reconstruction of the defect for the maxilla (Besimo et al 1995), mandible (Figs. 31.22 and 31.23), as well as the mandibular condyle (Lee et al. 2007). This technique has been successfully applied to the repair of craniofacial deficiencies (James et al. 1998), trauma to the midfacial skeleton (Gentile et al. 2013), in the fabrication of implants for cranioplasty (D'Urso et al. 1998, 1999; Eufinger and Wehmöller 1998; Gronet et al. 2003), construction of mandibular condylar implants (Worrell and Christensen 2006; Christensen

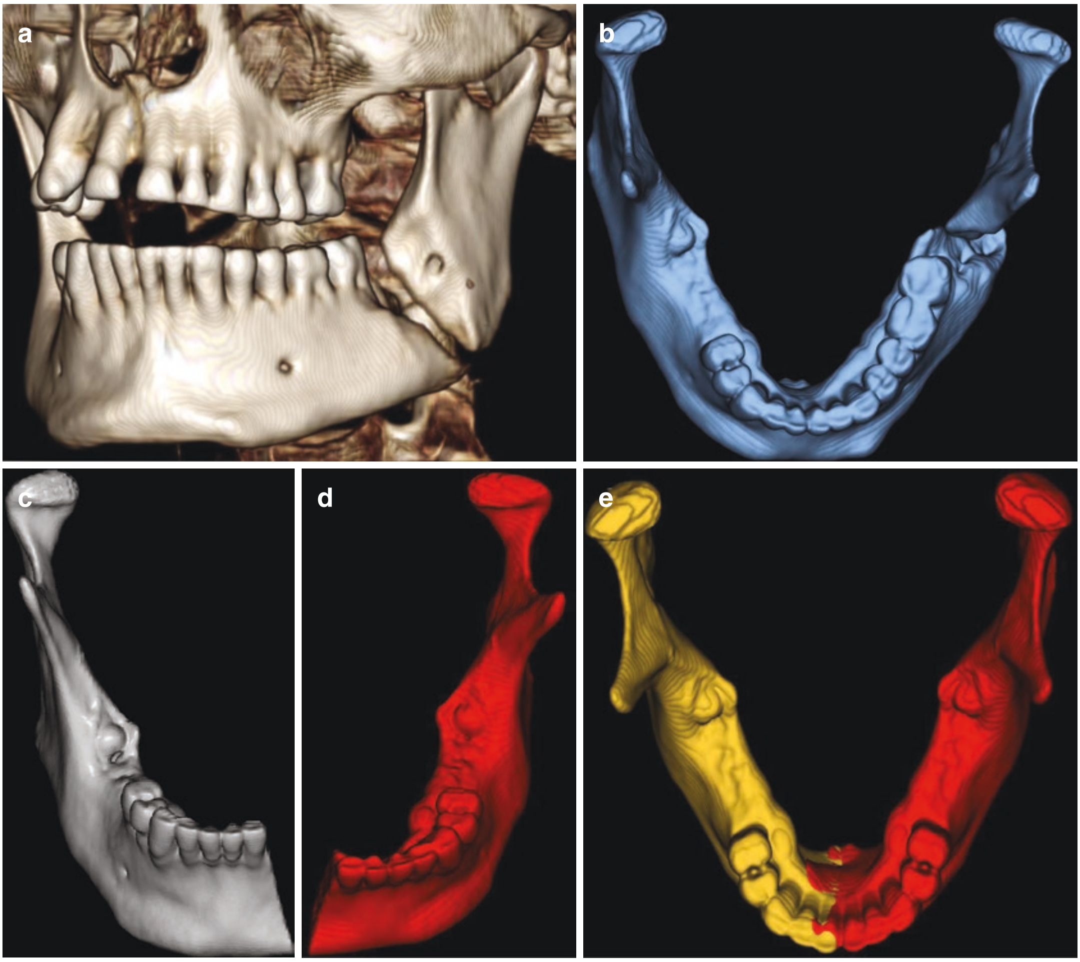

Fig. 31.22 CBCT volumetric rendering (**a**) and segmented model of the mandible (**b**) of a patient with a left mandibular pathologic fracture associated with osteomyelitis after removal of a large dentigerous cyst. The left side of the jaw was removed (**c**) and the right side mirrored (**d**) and virtually repositioned to create an STL model of a complete jaw (**e**)

et al. 2005), and in distraction osteogenesis (Poukens et al. 2003).

- **Clinical and Surgical Efficacy**. AM modeling has been shown to improve clinical and surgical efficacy of treatment. D'Urso et al. (1999) prospectively assessed the utility of 3D models on 45 patients with craniofacial, maxillofacial, skull base cervical spinal pathology. They found that biomodels significantly improved operative planning by 86%, diagnosis by 45%, reduced measurement error by 82%, reduced operating time by an estimated 18%, and improved informed consent procedures by 30%. Müller et al. (2003) also quantitatively measured the clinical efficacy of the use of biomodels for a group of patients requiring corrective cranioplasty, resection of osseous tumors and congenital and posttraumatic craniofacial deformities. They found that simulation of osteotomies reduced operating time and intraoperative errors. In addition, they reported that operative planning of approaches to uncommon and complex skull base tumors was significantly influenced by the stereolithographic models by a better understanding of the anatomy in specific cases reducing the morbidity associated with prolonged operation while at

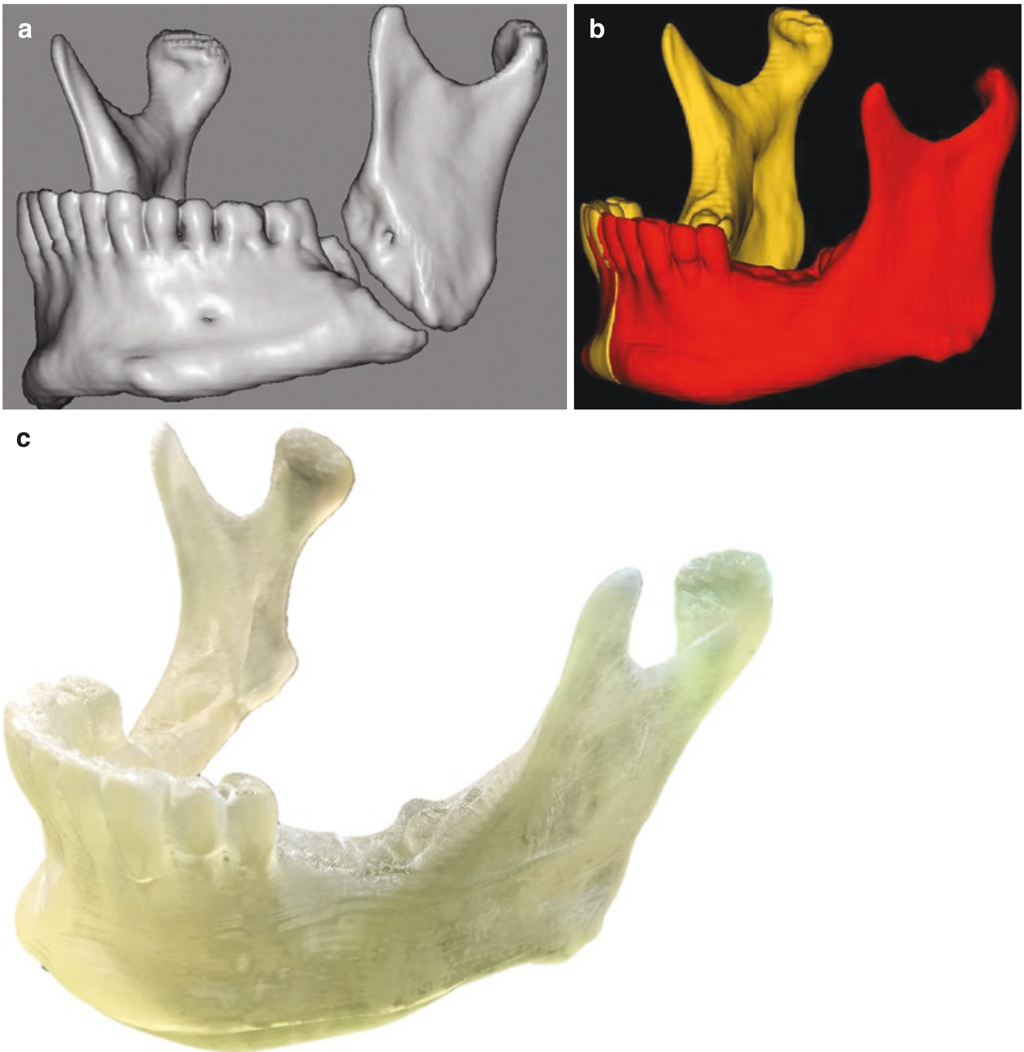

Fig. 31.23 Volumetric surface rendering (**a**), reconstructed mandible using the mirrored right side (**b**) and final SLA model (**c**) of the same patient as in Fig. 31.21. The model was used to preoperatively bend surgical plates used for the left mandibular reconstruction

the same time able to increase accuracy and minimized surgical complications (Bill et al. 1995).

31.5.2 Limitations

Medical models are useful visual aids in diagnosing and solving complex surgical problems; however, there are inherent limitations with existing RP technology restricting widespread application and clinical adoption.

- **Time**. The fabrication of biomodels can often take a day or even longer. Since medical data requires processing such as thresholding and segmentation, data preparation can take as long or even longer than the actual building time. Therefore, currently the construction of biomodels is usually limited for surgical procedures that require long-term planning, such as the reconstruction of development or congenital maxillofacial deformities. While AM has been reported for use in maxillofacial injury (Kremer et al. 1998; Wagner et al., 2004), the multistage nature and length of time required for the fabrication process usually preclude the use of RP as aids for emergency operations.

- **Cost**. Because commercial AM printers used to fabricate biomodels are expensive and the man-hours associated with each of the multiple phases in the manufacturing process can be of the order of 3–4 h, the physical cost of the biomodels models can be expensive, varying between $500 and $1000 USD each. As the purpose of medical models is to optimize surgeon's planning time and improve quality, effectiveness, and efficiency, these benefits, which are difficult to quantify in terms of cost, must be weighed against the expense of the model. Currently only the more complex cases can justify the expense of the models.
- **Materials**. Currently the AM process fabricates biomodels from a limited number of materials, only a few of which are suitable or safe for transport into the operating theatre and none are presently capable of being placed inside the body. Those machines that provide the most suitable material properties are generally the most expensive machines. This limits the range of applications for biomodels.
- **Convenience**. AM machines generally require a degree of technical expertise in order to achieve good quality models. This is particularly true of the larger, more complex, and more versatile machines, which are also not particularly well suited to medical laboratory environments. Coupled with the software skills required for data preparation, this implies a significant training investment for any medical establishment wishing to use the technology. While AM software packages provide visualization of "virtual" models, the depiction of a 3D volume on a 2D screen does not, as yet, substitute for the tactile relationship a surgeon develops with the patient's anatomy.

31.6 Clinical Indications

In maxillofacial imaging, the most obvious and widespread clinical application of the use of AM has been in the fabrication of surgical guides to assist in dental implant placement. However, for almost 20 years customized plastic anatomic models of the maxillofacial skeleton have been commercially available for patients with craniofacial deformities, traumatic injuries, prior to the removal of jaw pathology for visualization, and to assist in the subsequent reconstruction of surgical defects and deformities. In the latter instance, these anatomic models are used to identify vital structures such as the inferior alveolar canal, plan surgical approach such as the extent of surgical margins, custom modify prefabricated surgical templates or meshes to the defect, plan distraction osteogenesis, or even generate individualized replacement prostheses (e.g., TMJ implants). These plastic models are also referred to as an *anatomical model*, *Stereolithographic (SLA) model*, *biomodel,* or *CT-based anatomical model*. AM technologies currently do not have adequate precision to fabricate restorative components (e.g., custom implant abutments, intraoral crowns) or prostheses (e.g., Avadent Digital Dentures, Global Dental Science, Scottsdale AZ, USA), which are created using high precision milling technologies. A number of authors have described their experiences with AM (Santler et al. 1998; Gronet et al. 2003; Taft et al. 2011).

31.6.1 Cranio-Maxillofacial Surgery

For corrective surgery to the maxillofacial skeleton, the fabrication of biomodels via AM allows direct simulation of osteotomies and grafts, facilitates the measurements of segmental jaw movements, and allows for the preoperative construction of templates and surgical prostheses (Anderl et al. 1994; D'Urso et al. 1999; Kermer et al. 1998a, b).

- **Maxillofacial Pathology**. Benign tumors usually present with either localized expansile deformities of the jaw or regional osteolysis, resulting in unilateral dysmorphology which is difficult to correct intraoperatively and achieve a symmetrical outcome. Biomodels assist in these patients by provid-

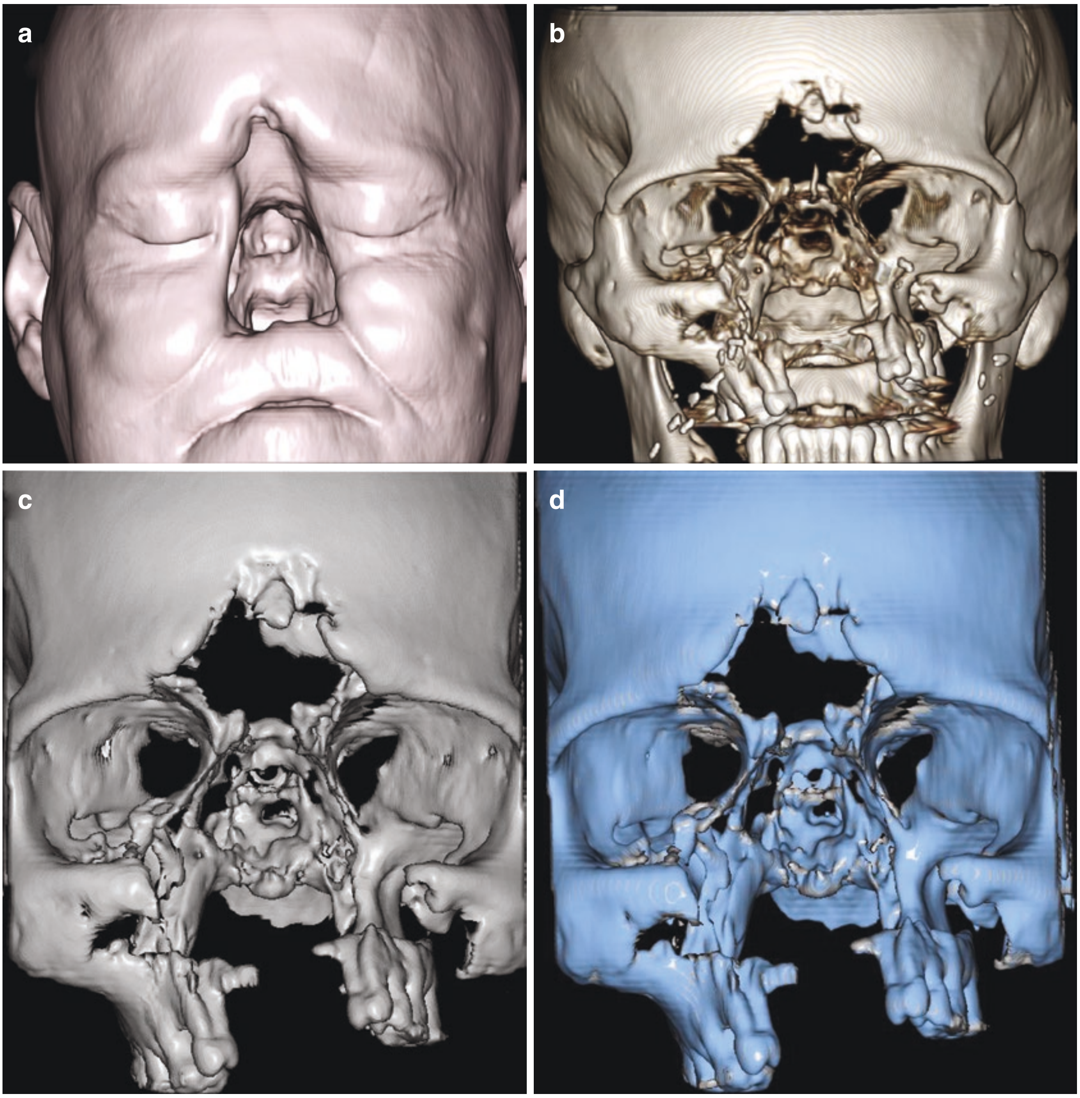

Fig. 31.24 Soft tissue surface (**a**) and volumetric CBCT rendering (**b**) of a patient with a large midline mid-facial defect involving the anterior maxilla and nasal fossa after removal of a nasal malignancy. CBCT surface rendering (**c**, **d**) and corresponding modeling of the midface prior to SLA biomodel fabrication

ing a surface from which a bridging plate can be prebent or, if the defect is large, to produce a side inverted model and use the mirrored, unaffected side for bending the bridging plate. Azuma et al. (2014) demonstrated the use of reconstruction plates that are prebent to fit AM models for mandibular reconstructive surgery provide superior mandibular symmetry and esthetic outcomes compared to the use of conventional reconstructive methods (Figs. 31.21 and 31.22).

For lesions producing defects larger than the plates where autogenous osseous transplants are required, a biomodel allows preoperative calculation of the quantity and shape of bone material needed from the donor sites (Figs. 31.24 and 31.25).

Santler et al. (1998) report that the assessment of tumor expansion can be facilitated by contouring artificial spikes on the bone model in the region of the radiological soft tissue border of the tumor. With a color-coding technique, specific

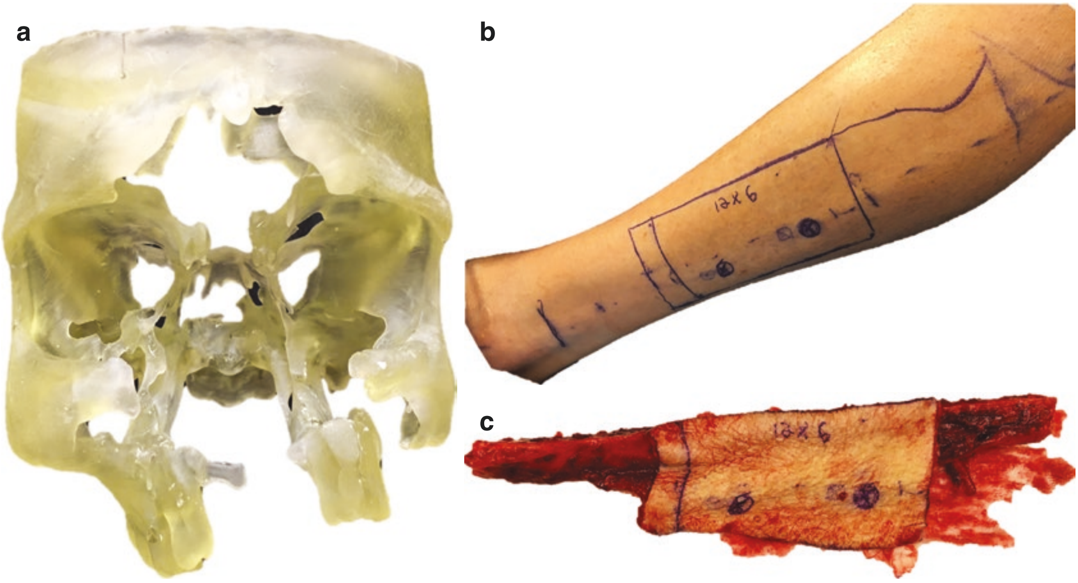

Fig. 31.25 SLA biomodel of the patient described in Fig. 31.24 (**a**) with presurgical measurements drawn on the patients left lower leg (**b**) and final autogenous host fibula graft (**c**). The dimensions of the graft necessary to reconstruct the recipient site at surgery was calculated using the model

structures such as teeth, nerves, and the extent of a tumor can be displayed, facilitating more detailed surgical planning on the model. More recently virtual surgical planning and AM fabrication of custom designed plates has been shown to provide significantly better adaptation of the virtual model compared with the physical model which favors manufacturing of patient specific prebent plates (Dérand and Hirsch 2009.)

- **Cranioplasty**. Cranial defects can be caused by trauma, tumor removal, or decompressive craniotomies. The process and material for repair of the defect should demonstrate adequate accuracy, be biocompatible, be radiolucent to facilitate postoperative imaging, be resistant to postoperative infection, biomechanically strong with a high strength-to-weight ratio, easy to shape, and inexpensive to fabricate. For many years, custom polymethylmethacrylate (PMMA) from silicone molds and titanium sheets and mesh implants have been created based on the use of anatomic plastic biomodel templates (Gronet et al. 2003). Recently EBM and DMLS fabricated cranial titanium prostheses as well as SLA porous bioceramic Hydroxy Apatite infused photopolymer implants have been used to fabricate prostheses directly without the need for an intermediary step. Polyetheretherketone (PEEK) implants milled from a block of extruded material have also been used.
- **Maxillofacial Deformity**. In congenital malformations, various advantages can be realized, depending on the specific condition. In adult cleft-lip-palate (CLP) patients demonstrating dysgnathia and, in severe cases, missing bone in the region of the premaxilla, osteotomies and transplants can be planned with a model operation. Other conditions producing asymmetry, such as hemifacial microsomia and maxillofacial malformations, model operations performed on the involved structures allow placement of the segments in a symmetrical, aesthetic position and facilitate operative decisions on whether transplants, osteotomies, or distraction osteogenesis treatments should be attempted. Micro vascular bone tissue grafting procedures for mid facial and mandible reconstruction based on precise harvesting of donor sites such as the fibula,

scapula, and iliac crest are now also possible based on the AM fabrication of resection and harvesting guides (Parthasarathy 2014).

- **Temporomandibular Joint**. In complex condylar fractures, biomodels may provide important diagnostic information on the necessity for surgical intervention and for choosing the most appropriate approach and osteosynthesis method (Santler et al. 1998). Several studies have used biomodeling from CBCT to evaluate follow-up on TMJ surgery, orthognathic and surgical resections on the TMJ complex (Goncalves et al. 2013). More recently, CBCT scanning and morphological reconstructions have been used to develop statistical models in hopes of developing more targeted classifications (Cevidanes et al. 2015).
- **Trauma**. In acute trauma cases, 3D models may help to recognize the position and the direction of fractures, the number of bone fragments and the degree of dislocation. For multifacial fractures with missing references, models can assist in reconstructing symmetrical proportions. However, specific restrictions do present in this application in that only dislocated fractures, with steps or bends in the outer contour, are usually demonstrated by 3D models. Other problems relate to surgical delay due to long model production (Powers et al. 1998; Holck et al. 1999; McAllister 1998).
- **Customized dental implants**. The fabrication of patient specific designed blade implants has demonstrated the future possibilities of custom designed implants using SLS technology (Mangano et al. 2013).
- **Tissue Scaffolds**. 3D printed model can be fabricated for specific defects that acts as a template for adapting the titanium mesh to an ideal arch form which is used as a bio-osseous or titanium graft space holder for bone grafts until integration with the host bone takes place (Hou et al. 2012). Many researchers are also currently investigating the creation of 3D tissue engineering scaffolds made of different materials such as biodegradable powders (Meininger et al. 2015) and polymers to hold bio-osseous cell cultures (Yang et al. 2002).
- **Maxillofacial Prosthodontics** Numerous applications have been reported for AM models in the construction of prostheses (Joshi (Bhuskute) et al. 2006; Sykes et al. 2004) and production of auricular and nasal prosthesis (Fig. 31.26) (Ciocca and Scotti 2004; Jiao et al. 2004). More recent articles describe direct design and AM fabrication of molds for silicone prosthesis (Sabol and Grant 2011; Liacouras et al. 2011; Grant et al. 2014, 2015).

31.6.2 Surgical Guide Fabrication

As summarized earlier, there are studies that validate the accuracy of 3D printed models from the conversion of medical images to printable file formats (Taft et al. 2011; Reyes et al. 2015). With the accessibility of 3D printers to dental and medical providers, the accepted use of medical models and virtual surgical software using medical imaging files for orthognathic reconstructions and implant placement (Geng et al. 2015) has given rise to digital manufacturing of surgical guides to transfer the virtual plan to a physical object. This has provided unprecedented opportunities for a team approach to dental, craniofacial, and orthopedic reconstructions (Van de Wiele et al. 2015) (Fig. 31.22).

Most additive manufacturing technologies can be used to fabricate the surgical guides; however, there are some concerns of irritation from residual surface chemicals of some polymers. USP (U.S. Pharmacopoeia) Class VI judges the suitability of plastic material intended for use as containers or accessories for parenteral preparations. Suitability under USP Class VI is typically a base requirement for medical device manufacturers. It is recommended that materials compliant with this test be used for all surgical guides as well as medical/dental models available in surgical settings. Most manufacturers of 3D printers will have a medical grade material that is Class VI compliant (USP) and recently an autoclavable photopolymer for SLS has been introduced to the dental market (Dental SG, Formlabs, Somerville, MA).

Fig. 31.26 Multiple guides fabricated for developing soft tissue changes to the nose

31.6.2.1 Surgical Template for Dental Implants

The American Academy of Prosthodontics defines a surgical template as a guide used to assist in proper surgical placement and angulations of dental implants (The glossary of prosthodontic terms 2005). The purpose of a surgical template is to assist the surgeon in the location and direction of the osteotomy prior to dental implant placement in accordance with a prosthetically driven, treatment plan. Based on the amount of the operative restriction of the drill, the design of the surgical template can be classified as non-restrictive, partially restrictive, or completely restrictive (Stumpel 2008; Misch and Dietsh-Misch 1999). Surgical guides for dental implants can also be categorized according to the tissue used to stabilize the guide as bone, mucosa or tooth supported. Surgical guides are fabricated conventionally on dental casts using a variety of

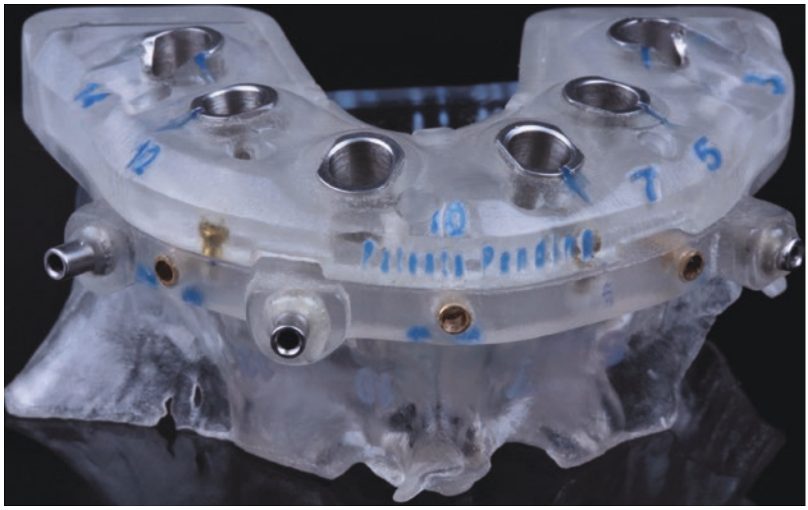

Fig. 31.27 Complex implant placement guide. This bone retained guide has indexes for bone reduction, implant placement and to "pick up" the provisional restoration at the appropriate occlusal relationship

techniques and materials including clear vacuum-formed matrix, free-form auto polymerizing acrylic resin and acrylic resin duplicates of the available prosthesis or diagnostic wax ups. These types of guides can be as simple as indicating an area of optimal implant placement, allowing the surgeon a lot of latitude, to a specific angulation for a single tooth implant placement (Fig. 31.27).

In many cases virtual implant placement can be a feature of many of the CBCT software viewers; however, since the developed plan is not exportable in most cases as a "printable file" (.stl, .amf, obj, or .3mf) they may be useful in determining the opportunity to place an implant, but are not useful in virtual planning that can be transferred to a treatment solution. Other forms of commercial software do allow for fabrication of guides and restoration, but there are different business models that can limit the freedom of use. Programs such as Simplant (Dentsply, York, Pennsylvania, USA), Nobelguide (Nobel Biocare, Yorba Linda, California, USA), and nSequence (Reno, Nevada, USA) offer complete planning services to include virtual planning, guide fabrication, and models only available through their services. Programs such as coDiagnostiX™ (Dental Wings, Germany) and Blue Sky Bio (USA) provide planning software compatible with a variety of restorative CAD/CAM solutions and allow for the export to your own printers or service provider.

Many provide the opportunity to virtually place implants based on a virtually developed restorative plan, using CBCT/CT images, intraoral images, or scanned casts of the patients. This workflow allows for "same day" implant retained restorations, even in more complicated cases requiring grafting (Cheng et al. 2008; Stapleton et al. 2014). Once the digital or virtual plans have been designed, the guides and the restorations can be produced with digital manufacturing—either additive or milled (Fig. 31.28).

31.6.2.2 Craniofacial Surgical Templates

The use of medical images in treatment planning gave rise to a number of software developments based on virtual surgical techniques. By segmenting different anatomical parts, they can be moved and manipulated to ideal positions for reconstruction. This can be augmented by designing cutting guides, positioning guides, bending guides, and in many cases custom reconstruction plates and bars (Steinbacher 2015; Mazzoni et al. 2015).

These techniques have been used for orthognathic surgical planning, surgical excision and reconstruction for cancer and other pathology, and in Trauma. The US military used this technology extensively in reconstruction of Wounded Warriors at the Walter Reed National Military Medical Center, formerly the Naval Medical

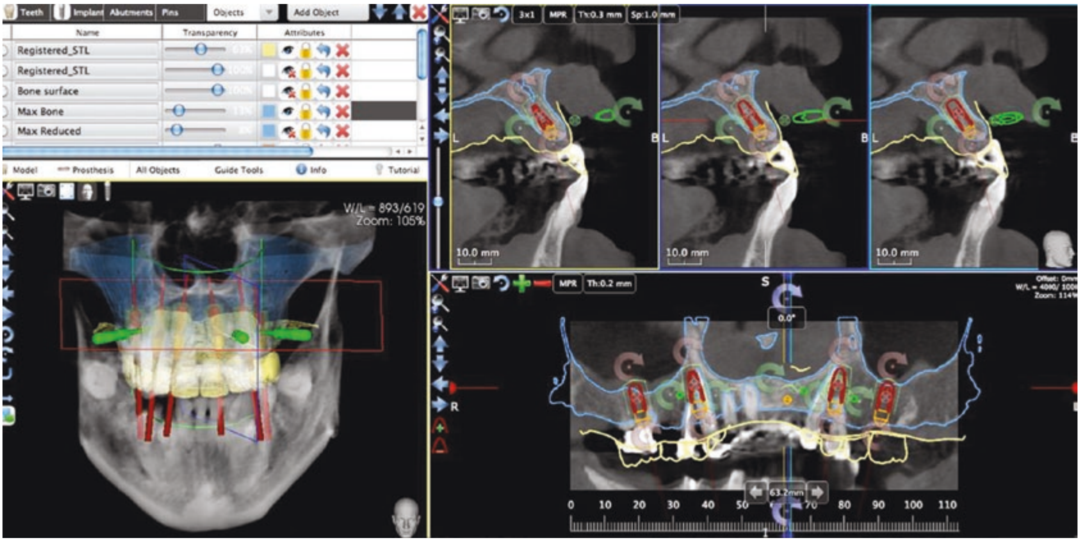

Fig. 31.28 Implant planning software using Cone Beam CT

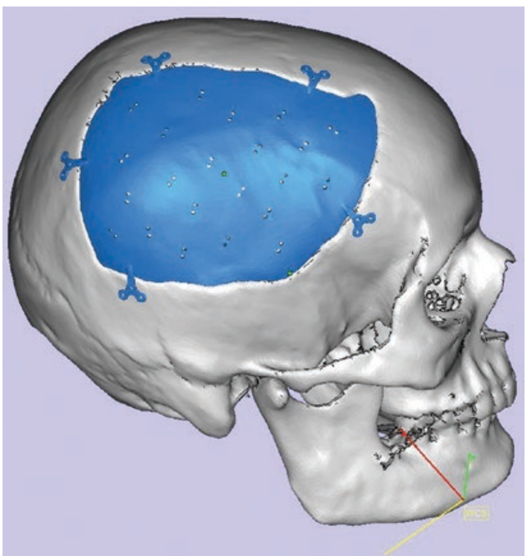

Fig. 31.29 Virtual design of a cranial implant

Fig. 31.30 Virtual plan for use of fibula graft to replace the left maxillary alveolus

Center Bethesda and Walter Reed Army Medical Center, for head and neck reconstruction since early 2000, citing speed of fabrication and reduction of operating times (Gronet et al. 2003; Tantawi et al. 2012) (Fig. 31.29).

Virtual surgical techniques allow for multiple planning such as orthognathic reconstruction and implant placement for which cutting and positioning guides can be developed and 3D printed (Scolozzi 2015). These techniques can be done either locally at an institution or through several commercial vendors which offer review of plans through on-line consultations giving the surgeon the opportunity to make changes to accommodate a variety of surgical challenges (Fig. 31.30).

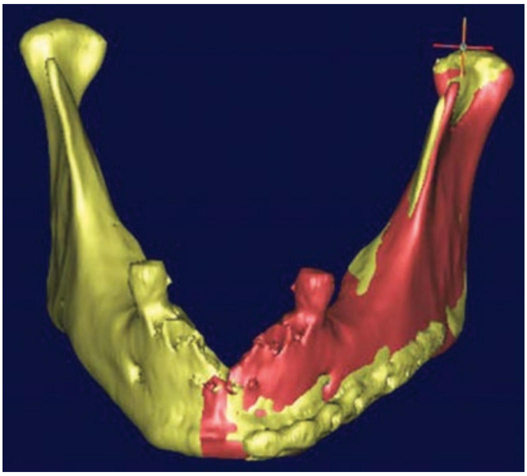

Fig. 31.31 Virtual reconstruction: missing mandibular section is replaced with the mirrored image of the opposite side to establish limits of contour

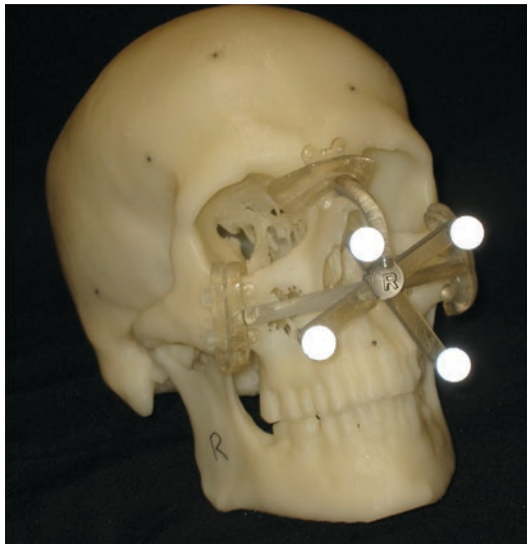

Fig. 31.32 Surgical guide for repositioning of the maxilla or for maxillary face transplant. Optical globes are used with a navigation system to ensure the correct angulation of placement for optimum occlusal schemes

Using virtual surgical techniques, the surgical guides assist the surgeon in osteotomy cuts, implant placement, positioning of boney and soft tissue for reconstruction, and assist in prebending of reconstruction plates. In other instances, anatomical support such as the sections of the mandible, zygoma, or orbit are fabricated of biocompatible materials. Virtual surgery uses the ability for different medical image modalities ability to be registered since they are in a common file format (Rengier et al. 2010) with the same patient, or an anatomical part from another patient (Fig. 31.31), mirror an image with design software, or directly design guides to the images (Hieu et al. 2005). Any and all of these files can be exported as a printable file for 3D printing.

Recent advances in transplant surgical technique has given rise to variations on total face transplants (Siemionow et al. 2010; Murphy et al. 2015a, b). As with the more complicated surgical demands, surgical guides become important in pretreatment planning to coordinate cuts on both the donor and the recipient of the allograph (Jacob et al. 2013). In an effort to allow more freedom, recent research has been focused on fabricating guides that have tracking ability that allow for “real-time” cephalometric calculations and simulated occlusion for modification of the donor graft to the recipient for optimal dental occlusion (Fig. 31.32) (Gordon et al. 2014; Murphy et al. 2015a, b). This technology has great potential in how guides are fabricated in not only craniofacial reconstructions, but in other orthopedic reconstructions as well.

References

American Society for Testing and Materials (ASTM) (2014) F2792-12a standard terminology for additive manufacturing technologies In: Electronics; declarable substances in materials; 3D imaging systems. ASTM, West Conshohocken, PA

Ander H, Zur Nedden D, Muhlbauer W (1994) CT-guided stereolithography as a new tool in craniofacial surgery. Br J Plast Surg 47:60–64

Asaumi J, Kawai N, Honda Y, Shigehara H, Wakasa T, Kishi K (2001) Comparison of three-dimensional computed tomography with rapid prototype models in the management of coronoid hyperplasia. Dentomaxillofac Radiol 30:330–335

Azuma M, Yanagawa T, Ishibashi-Kanno N, Uchida F, Ito T, Yamagata K, Hasegawa S, Sasaki K, Adachi K, Tabuchi K, Sekido M, Bukawa H (2014) Mandibular reconstruction using plates prebent to fit rapid prototyping 3-dimensional printing models ameliorates contour deformity. Head Face Med 10:45

Barker TM, Earwaker WJ, Lisle DA (1994) Accuracy of stereolithographic models of human anatomy. Australas Radiol 38:106–111

Besimo C, Lambrecht JT, Nidecker A (1995) Dental Implant Treatment Planning with reformatted computed tomography. Dentomaxillofac Radiol 24(4):264–267

Bill JS, Reuther JF (2004) Rapid prototyping in planning reconstructive surgery of the head and neck review and evaluation of indications in clinical use. Mund Kiefer Gesichtschir 8:135–53 (In German)

Bill JS, Reuther JF, Dittmann W, Kübler N, Meier JL, Pistner H, Wittenberg G (1995) Stereolithography in oral and maxillofacial operation planning. Int J Oral Maxillofac Surg 24:98–103

Cevidanes LH, Gomes LR, Jung BT, Gomes MR, Ruellas AC, Goncalves JR, Schilling J, Styner M, Nguyen T, Kapila S, Paniaqua B (2015) 3D superimposition and understanding of temporomandibular joint arthritis. Orthto Craniofac Res 18(Suppl 1):18–28

Cheng AC, Tee-Khin N, Siew-Luen C, Lee H, Wee AG (2008) The management of a severely resorbed edentulous maxilla using a bone graft and a CAD/CAM-guided immediately loaded definitive implant prosthesis: a clinical report. J Prosthet Dent 99:85–90

Cheung LK, Wong MCM, Wong LLS (2002) Refinement of facial reconstructive surgery by stereo-model planning. Ann R Australas Coll Dent Surg 16:129–132

Choi JH, Kim NK, Kim Y, Lee JK, Kim MK, Lee JH, Kim MJ (2002) Analysis of errors in medical rapid prototyping models. Int J Oral Maxillofac Surg 31:23–32

Christensen RW, Walker CR, Dollar JV (2005) New hope for Treacher-Collins syndrome: a surgical case report. Surg Technol Int 14:319–327

Ciocca L, Scotti R (2004) CAD-CAM generated ear cast by means of a laser scanner and rapid prototyping machine. J Prosthet Dent 92:591–595

Dean D, Min KJ, Bond A (2003) Computer aided design of large-format prefabricated cranial plates. J Craniofac Surg 14:819–832

Dérand P, Hirsch JM (2009) Virtual bending of mandibular reconstruction plates using a computer-aided design. J Oral Maxillofac Surg 67:1640–1643

D'Urso PS, Atkinson RL, Lanigan MW, Earwaker WJ, Bruce IJ, Holmes A, Barker TM, Effeney DJ, Thompson RG (1998) Stereolithographic (SL) biomodelling in craniofacial surgery. Br J Plast Surg 51:522–530

D'Urso PS, Barker TM, Earwaker WJ, Bruce LJ, Atkinson RL, Lanigan MW, Arvier JF, Effeney DJ (1999) Stereolithography biomodelling in cranio-maxillofacial surgery: a prospective trial. J Craniomaxillofac Surg 27:30–37

Eufinger H, Wehmöller M (1998) Individual prefabricated titanium implants in reconstructive craniofacial surgery: clinical and technical aspects of the first 22 cases. Plast Reconstr Surg 102:300–308

Fleiner B, Hoffmeister B, Kreusch T, Lambrecht T (1994) Three-dimensional surgical planning using a model—a critical overview of the current status. Fortschr Kiefer Gesichtschir 39:13–16 (German)

Geng W, Liu C, Su Y, Li J, Zhou Y (2015) Accuracy of different types of computer-aided design/computer-aided manufacturing surgical guides for dental implant placement. Int J Clin Exp Med 8:8442–8449

Gentile MA, Tellington AJ, Burke WJ, Jaskolka MS (2013) Management of midface maxillofacial trauma. Atlas of Oral Maxillofacial. Surg Clin North Am 21(1):69–95

Gibson I, Cheung LK, Chow SP, Cheung WL, Beh SL, Savalani M, Lee SH (2006) The use of rapid prototyping to assist medical applications. Rapid Prototyp J 12:53–58

Gibson I, Rosen D, Stucker B (2010) Additive manufacturing technologies. Springer, New York

Goncalves JR, Wolford LM, Cassano DS, da Prociuncula G, Pnaiqua B, Cevidanes LH (2013) Tempormandibular joint condylar changes following maxillomandibular advancement and articular disc repositioning. J Oral Maxillofac Surg 71:1759e1–175915

Gordon CR, Murphy RJ, Coon D, Basafa E, Otake Y, Al Rakan M, Rada E, Susarla S, Swanson E, Fishman E, Santiago G, Brandacher G, Liacouras P, Grant G, Armand M (2014) Preliminary development of a workstation for craniomaxillofacial surgical procedures: introducing a computer-assisted planning and execution system. J Craniofac Surg 25:273–283

Grant GT, Liacouras P, Santiago G, Garcia JR, Al Rakan M, Murphy R, Armand M, Gordon CR (2014) Restoration of the donor face after facial Allotransplantation: digital manufacturing techniques. Ann Plast Surg 72:720–724

Grant GT, Liacouras P, Aitaholmes C, Garnes J, Wilson WO (2015) Digital capture, design, and manufacturing of a facial prosthesis: clinical report of a pediatric patient. J Prosthet Dent 114:138–141

Gronet PM, Waskewicz GA, Richardson C (2003) Preformed acrylic cranial implants using fused deposition modeling: a clinical report. J Prosthet Dent 90:429–433

Hieu LC, Zlatov CN, Vander Sloten J, Bohez KL, Binh PH, Oris P, Toshev Y (2005) Medical rapid prototyping applications and methods. Assem Autom 25:284–292

Holck DEE, Boyd EM Jr, Ng J, Mauffray RO (1999) Benefits of stereolithography in orbital reconstruction. Ophthalmology 106:1214–1218

Hou JS, Chen M, Pan CB, Wang M, Wang JG, Zhang B et al (2012) Application of CAD/CAM-assisted technique with surgical treatment in reconstruction of the mandible. J Craniomaxillofac Surg 40:e432–e437

Jacobs JM, Dec W, Levine JP, McCarthy JG, Weimer K, Moore K, Ceradini DJ (2013) Best face forward: virtual modeling and custom device fabrication to optimize craniofacial vascularized composite Allotransplantation. Plast Reconstr Surg 131:64–70

James WJ, Slabbekoom MA, Edgin WA, Hardin C (1998) Correction of congenital malar hypoplasia using stereolithography for presurgical planning. J Oral Maxillofac Surg 56:512–517

Jiao T, Zhang F, Huang X, Wang C (2004) Design and fabrication of auricular prostheses by CAD/CAM system. Int J Prosthodont 17:460–463

Joshi (Bhuskute) MD, Dange SP, Khalikar AN (2006) Rapid prototyping technology in maxillofacial prosthodontics: basics and applications. J Indian Prosthodont Soc 6:175–178. http://wwwjprosthodontcom/textasp?2006/6/4/175/30691 (cited 2007 Jun 7)

Kermer C, Lindner A, Friede I, Wagner A, Millesi W (1998a) Preoperative stereolithographic model planning for primary reconstruction in craniomaxillofacial trauma surgery. Craniomaxillofac Surg 26:136–139

Kermer C, Rasse M, Lagogiannis G, Undt G, Wagner A, Millesi W (1998b) Colour stereolithography for planning complex maxillofacial tumor surgery. J Craniomaxillofac Surg 26:360–362

Kragskov J, Sindet-Pedersen S, Gyldensted C, Jensen KL (1996) A comparison of three-dimensional computed tomography scans ad stereolithographic models for evaluation of craniofacial anomalies. J Oral Maxillofac Surg 54:402–411

Lee JW, Fang JJ, Chang LR, CK Y (2007) Mandibular defect reconstruction with the help of mirror imaging coupled with laser stereolithographic modeling technique. J Formos Med Assoc 106:244–250

Liacouras P, Garnes J, Roman R, Grant GT (2011) Auricular prosthetic design and manufacturing using computed tomography, 3D photographic imaging and rapid prototyping. J Pros Dent 105:80–82

Lill W, Solar P, Ulm C, Watzek G, Blahout R, Matejka M (1992) Reproducibility of three dimensional CT-assisted model production in the maxillofacial area. Br J Oral Maxillofac Surg 30:233–236

Lin LS, Wang W, Wang ZH, Qi ZL, Mu XZ, Chen JJ (2006) Individual 3-D image prototyping models for orbital reconstruction. Zhonghua Zheng Xing Wai Ke Za Zhi 22:95–98. (In Chinese)

Liu Q, Leu MC, Schmitt SM (2006) Rapid prototyping in dentistry: technology and application. Int J Adv Manuf Technol 29:317–335

Mangano F, Bazzoli M, Tettamanti L, Farronato D, Maineri M, Macchi A et al (2013) Custom-made, selective laser sintering (SLS) blade implants as a non-conventional solution for the prosthetic rehabilitation of extremely atrophied posterior mandible. Lasers Med Sci 28:1241–1247

Mazzoni S, Bianchi A, Schiariti G, Badiali G, Marchetti C (2015) Computer-aided design and computer-aided manufacturing cutting guides and customized titanium plates are useful in upper maxilla waferless repositioning. J Oral Maxillofac Surg 73:701–707

McAllister ML (1998) Application of stereolithography to subperiosteal implants manufacture. J Oral Implantol 24:89–92

Meininger S, Mandal S, Kumar A, Groll J, Basu B, Gbureck U (2015) Strength reliability and in vitro degradation on three-dimensional powder printed strontium-substituted magnesium phosphate scaffolds. Acta Biomater 31:401–411

Misch CE, Dietsh-Misch F (1999) Diagnostic casts, preimplant prosthodontics, treatment prostheses, and surgical templates. In: Misch CE (ed) Contemporary implant dentistry, 2nd edn. Mosby, St Louis, pp 135–150

Mitsouras D, Liacouras P, Imanzadeh A, Giannopoulos AA, Cai T, Kumamaru KK, George E, Wake N, Caterson J, Pomahac B, Ho VB, Grant GT, Rybicki FJ (2015) Medical 3D printing for the radiologist. Radiographics 35:1965–1988

Müller A, Krishnan KG, Uhl E, Mast G (2003) The application of rapid prototyping techniques in cranial reconstruction and preoperative planning in neurosurgery. J Craniofac Surg 14:899–914

Murphy RJ, Basafa E, Hashemi S, Grant GT, Liacouras P, Susarla SM, Otake Y, Santiago G, Armand M, Gordon CR (2015a) Optimizing hybrid occlusion in face-jaw-teeth transplantation. A preliminary assessment of real-time cephalometery as part of the computer-assisted planning and execution workstation for crani-omaxillofacial surgery. Plast Reconstr Surg 136:350–362

Murphy RJ, Gordon CR, Basafa E, Liacouras P, Grant GT, Armand M (2015b) Computer-assisted, le fort-based, face-jaw-teeth transplantation: a pilot study on system feasibility and translational assessment. Int J Comput Assist Radiol Surg 10:1117–1126

Parthasarathy J (2014) 3D modeling, custom implants and its future perspectives in craniofacial surgery. Ann Maxillofac Surg 4:9–18

Poukens J, Haex J, Riediger D (2003) The use of rapid prototyping in the preoperative planning of distraction osteogenesis of the cranio-maxillofacial skeleton. Comput Aided Surg 8:146–154

Powers DB, Edgin WA, Tabatchnick L (1998) Stereolithography: a historical review and indications or use in the management of trauma. J Craniomaxillofac Trauma 4:16–23

PS D'U, Earwaker WJ, Barker TM, Redmond MJ, Thompson RG, Effeney DJ, Tomlinson FH (2000) Custom cranioplasty using stereolithography and acrylic. Br J Plast Surg 53:200–207

Rengier F, Mehndiratta A, von Tengg-Kobligk H, Zechmann CM, Unterhinninghofen R, Kauczor H, Giesel FL (2010) 3D printing based on imaging data: review of medical applications. Int J Comput Assist Radiol Surg 5:335–341

Reyes A, Turkyilmaz I, Prihoda TJ (2015) Accuracy of surgical guides made from conventional and a combination of digital scanning and rapid prototyping techniques. J Prosthet Dent 113:295–303

Sabol J, Grant GT (2011) Digital image capture and rapid prototyping of the maxillofacial defect. J Prosthodont 20:310–314

Santler G, Kärcher H, Ruda C (1998) Indications and limitations of three-dimensional models in cranio-maxillofacial surgery. J CranioMaxfac Surg 26:11–16

Schicho K, Figl M, Seemann R, Ewers R, Lambrecht JT, Wagner A, Watzinger F, Baumann A, Kainberger F, Fruehwald J, Klug C (2006) Accuracy of treatment planning based on stereolithography in computer assisted surgery. Med Phys 33:3408–3417

Scolozzi P (2015) Computer-aided design and computer-aided modeling (CAD/CAM) generated surgical splints, cutting guides and custom-made implants: which indications in orthognathic surgery? Rev Stomatol Chir Maxillofac Chir Orale 116(6):343–349

Siemionow MZ, Zor F, Gordon CR (2010) Face, upper extremity, and concomitant transplantation: potential concerns and challenges ahead. Plast Reconstr Surg 126:308–315

Stapleton BM, Lin WS, Ntounis A, Harris BT, Morton D (2014) Application of digital diagnostic impression, virtual planning, and computer-guided implant surgery for a CAD/CAM-fabricated, implant-supported fixed dental prosthesis: a clinical report. J Prosthet Dent 112:402–408

Steinbacher DM (2015) Three-dimensional analysis and surgical planning in Craniomaxillofacial surgery. J Oral Maxillofac Surg 73(12 Suppl):S40–S56

Stumpel LJ 3rd (2008) Cast-based guided implant placement: a novel technique J Prosthet Dent 100:61–69

Sykes LM, Parrott AM, Owen CP, Snaddon DR (2004) Applications of rapid prototyping technology in maxillofacial prosthetics. Int J Prosthodont 17: 454–459

Taft R, Kondor S, Grant G (2011) Accuracy of rapid prototype models for head and neck reconstruction. J Pros Dent 106:399–408

Tantawi D, Armonda R, Valerio I, Kumar AR (2012) Management of decompressive craniectomy defects: modern military treatment strategies. J Craniofac Surg 23(7 Suppl 1):2042–2045

The glossary of prosthodontic terms (2005) J Prosthet Dent 94:10–92

Van de Wiele G, Teughels W, Vercruyssen M, Coucke W, Temmerman A, Quirynen M (2015) The accuracy of guided surgery via mucosa-supported stereolithographic surgical templates in the hands of surgeons with little experience. Clin Oral Implants Res 26:1489–1494

Wagner JD, Baack B, Brown GA, Kelly J (2004) Rapid 3-dimensional prototyping for surgical repair of maxillofacial fractures: a technical note. J Oral Maxillofac Surg 62:898–901

Worrall SF, Christensen RW (2006) Alloplastic reconstruction of the temporomandibular joint in treatment of craniofacial developmental or congenital anomalies: a surgical case report. Surg Technol Int 15:291–301

Yang S, Leong KF, Du Z, Chua CK (2002) The Design of Scaffolds for use in tissue engineering part II rapid prototyping techniques tissue engineering. Tissue Eng 8:1–11

Zein I, Hutmacher DW, Tan KC, Teoh SH (2002) Fused deposition modeling of novel scaffold architecture for tissue engineering application. Biomaterials 23(4):1169–1185